Eighth Symposium

(International)

ON

DETONATION

Albuquerque, NM
July 15 - 19, 1985

NSWC M
Naval Surface
White Oak, Silver Spring

PROCEEDINGS
Eighth Symposium (International) on Detonation

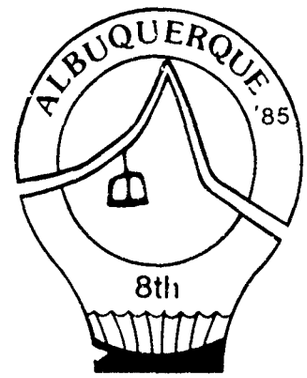

Sponsored Jointly By:
- Office of Naval Research
- Naval Sea Systems Command
- Naval Surface Weapons Center
- Army Ballistic Research Laboratory
- Army Armament Research and Development Center
- Air Force Armament Laboratory
- Lawrence Livermore National Laboratory
- Los Alamos National Laboratory
- Sandia National Laboratories

July 15 - 19, 1985

Albuquerque Convention Center
Albuquerque, New Mexico

PREFACE

The Eighth Symposium (International) on Detonation was held at the Albuquerque Convention Center in Albuquerque, New Mexico, from July 15 to 19, 1985.

This Symposium was one of a series started in 1951 as an Office of Naval Research (ONR) - sponsored "Conference on Detonation." Sponsorship has expanded over the years and now includes Army, Air Force, and Department of Energy, as well as Navy sponsors. The Symposia have had international attendance since the Fourth Symposium in 1965. The main purpose of these Symposia is to provide a forum for the discussion of the special problems of the field of energetic materials study, particularly those materials in condensed states. Problems in the field range from preparation of new and potentially useful energetic compounds to study of initiation, growth, detonation, and the ultimate energy release on detonation.

People came from 19 countries plus the United States to attend the Albuquerque Symposium. There were 488 registrants, 123 of whom came from outside the United States. Three papers were submitted by scientists from the USSR for presentation, and though they were unable to attend, their papers were presented by American scientists, and permission has been given to include the papers in these proceedings.

For the first time, in order to allow more papers to be presented in the five-day period, this Symposium had four parallel specialist sessions on one afternoon instead of the usual plenary ones. Thirty-one papers were presented in these specialist sessions. These proceedings may offer some of you the first opportunity to experience many of these papers.

Sixty papers were presented in the plenary sessions.

The Poster Session, certainly a highlight of the Symposium, consisted of 29 exhibits of research results specially suited to this format. The papers related to these displays, as well as copies of the display material, are included in this volume.

The Symposium also included displays by seventeen distributors of instrumentation and equipment, specialized to the needs of the detonation research community. These were presented in booth format on Tuesday and Wednesday with emphasis on attendance during plenary session breaks.

Professor Per-Anders Persson, late of Nitro-Nobel Detonics Laboratory in Sweden and now at the New Mexico Institute of Mining and Technology, Socorro, New Mexico, served as the Master of Ceremonies at the Symposium Banquet.

Mr. Dan Murphy, interpretative archaeologist with the regional office of the National Park Service in Santa Fe, New Mexico, addressed the Symposium Banquet on the "Indians of New Mexico," to add a bit of Southwest Americana to the Symposium.

This volume contains the complete text of papers of the plenary, specialist, and poster sessions as well as the poster presentations. An index of contributors and a list of Symposium attendees follow the text of the papers.

We feel the Eighth Symposium was an outstanding success in effecting discussions among participants and allowing a free flow of information in the field. The following people were responsible for the success we believe was achieved:

THE ORGANIZING COMMITTEE

James M. Short, Co-Chairman
Naval Surface Weapons Center
William E. Deal, Co-Chairman
Los Alamos National Laboratory
Raymond L. Beauregard
Naval Sea Systems Command
Milton Finger
Lawrence Livermore National Laboratory
Lee H. Hicks
Lawrence Livermore National Laboratory
Philip M. Howe
Ballistic Research Laboratory
Sigmund J. Jacobs
Naval Surface Weapons Center
James E. Kennedy
Sandia National Laboratories
Richard S. Miller
Office of Naval Research
Spero Nicolaides
Army Armament Research and Development Center
Alita M. Roach, Secretary-Treasurer
Los Alamos National Laboratory
Philip L. Stanton
Sandia National Laboratories
Martin F. Zimmer
Air Force Armament Laboratory

THE PREPRINTS

Lee H. Hicks
Lawrence Livermore National Laboratory

THE POSTER SESSION

James E. Kennedy
Sandia National Laboratories

AUDIOVISUAL

Ernest Inman
Naval Surface Weapons Center

THE PROCEEDINGS

James M. Short
Naval Surface Weapons Center
Patricia Leahy
Naval Surface Weapons Center

ALBUQUERQUE ARRANGEMENTS

William E. Deal
Los Alamos National Laboratory
James Kennedy
Sandia National Laboratories
Alita M. Roach
Los Alamos National Laboratory
Philip Stanton
Sandia National Laboratories

We wish to thank Barbara Glancy and Nancy Alessandrini of the Naval Surface Weapons Center for their participation in the assembly of the printed Proceedings.

We also wish to thank Mary Ann Lucero and Angie Martinez of Los Alamos National Laboratory, Karen Spurgeon and Jan McArthur of Lawrence Livermore National Laboratory, Carolyn Slagle of Sandia National Laboratories, and Patricia Leahy of Naval Surface Weapons Center for assistance they gave to help make the symposium one of the best ever.

ADVANCE NOTICE:

Preliminary plans for the next Symposium are already underway. The site selected is the Red Lion Inn/Columbia River in Portland Oregon. The NINTH SYMPOSIUM (INTERNATIONAL) ON DETONATION is planned for August 28, 1989.

James M. Short, Co-Chairman and Editor
Naval Surface Weapons Center,
White Oak, Silver Spring, Maryland

William E. Deal, Co-Chairman
Los Alamos National Laboratory
Los Alamos, New Mexico

CONTENTS

SESSION I. HOT SPOTS

SESSION II. REACTION ZONES I

SESSION III. REACTION ZONES II

SESSION IV. POSTER PAPERS

SESSION V. EQUATION OF STATE I

SESSION VI. EQUATION OF STATE II

SESSION VII. SDT/DDT

SESSION VIII. DETONATION SPECTROSCOPY

SESSION IX. SPECIALIST SESSIONS
EQUATION OF STATE

MOLECULAR DYNAMICS

SHOCK-TO-DETONATION TRANSITION/ DEFLAGRATION-TO-DETONATION TRANSITION

COMPOSITE AND NONIDEAL EXPLOSIVES

SESSION X. INITIATION AND SENSITIVITY I

SESSION XI. INITIATION AND SENSITIVITY II

Session I
HOT SPOTS

Chairman: John E. Field
Cavendish Laboratory
Cambridge University
Robert B. Frey
Ballistic Research Laboratory

THE RELATIONSHIP BETWEEN THE SHOCK SENSITIVITY AND THE SOLID PORE SIZES OF TATB POWDERS PRESSED TO VARIOUS DENSITIES

R. Lee*, G. Bloom, W. Von Holle, R. Weingart, L. Erickson, S. Sanders,
C. Slettevold and R. McGuire
Lawrence Livermore National Laboratory
Livermore, California, 94550

Mercury intrusion porosimetry measurements have been made on samples pressed from three different types of TATB powders having quite different particle size distributions. The samples had densities ranging from 74-99% of theoretical maximum density. Results of the porosimetry measurements are compared with shock initiation thresholds measured on the same materials. The growth of reaction in sustained pressure experiments is also compared for two of the TATB types.

INTRODUCTION

Shock initiation of pressed secondary high explosives is due to concentration of energy at inhomogeneities in the material, leading to localized "hot spots" and subsequent reaction. The level of stimulus required to initiate a detonation is a strong function of the density to which the explosive is pressed. Internal voids have been proposed as one of the means by which the shock wave energy may be concentrated (1,2). Some of the proposed mechanisms include viscoplastic flow (3), adiabatic heating of trapped gas (4) and shocks generated by void collapse (5). In addition, it is well known that the shock initiation threshold depends on the particle size distribution of the powder from which the explosive specimens are pressed (6,7). In an earlier study (8) we observed particle size effects on the initiability of pressed TATB specimens. One of the major objectives of the work reported here was to study further the effect of high explosive microstructure on initiability.

Mercury intrusion porosimetry provides a method for directly investigating the voids in a pressed sample. We have made mercury intrusion porosimetry measurements on pressed samples of the high explosive TATB (triaminotrinitrobenzene) for three quite different particle size distributions. The samples investigated were pressed to densities that ranged from 74-99% of theoretical maximum density. We compare the results of the mercury intrusion measurements with shock initiation thresholds measured on the same material.

TATB SAMPLES

TATB is an extremely insensitive high explosive that can be prepared in a number of ways leading to quite different particle size distributions. Our baseline TATB material, which we call production grade (PG TATB), is produced in a two-step dry amination process, which leads to a product with an arithmetic mean particle size of 60 micrometres, as determined by wet sieving (8). The specific surface area of this material, determined by the BET method, is about 0.5 m^2/g (8).

A finer material can be prepared from the production grade TATB by wet grinding in a fluid-energy mill. We designate TATB produced by this method as ultrafine TATB (UF TATB). UF TATB has an arithmetic mean particle size of

* Present address: Department of Physics, Cardwell Hall, Kansas State University, Manhattan, KS

about 10 micrometres and a specific surface area of about 4.5 m^2/g, determined by the same procedures as for the production grade material (8).

TATB with a much finer particle size distribution has recently been synthesized (9,10). This material is prepared by crash-precipitation and is designated as CP TATB. Particle size distributions have been determined using a Coulter N4 particle sizer. The mean particle size of a CP TATB sample, determined by weight, was 0.22 micrometres. Specific surface area was measured on the same sample by the BET method using a Digisorb 2600 system, and we obtained a specific surface area of 17.1 m^2/g, although values for individual lots range from 7 to 30 m^2/g. Particle size was calculated from the surface area data, assuming spherical particles and a density of 1.9 g/cm^3, yielding a mean particle size of 0.18 micrometres in good agreement with the data from the Coulter instrument.

MERCURY INTRUSION POROSIMETRY

Mercury intrusion porosimetry is based on the law which describes the penetration of a liquid into a small orifice. For a non-wetting liquid and cylindrical pores, the minimum pore diameter, D, through which the liquid will flow at a pressure, P, is given by

$$D = (4\gamma/P)\cos(\theta), \quad (1)$$

where γ is the surface tension of the liquid and θ is the contact angle between the liquid and the solid. Pore surface area is calculated from the PdV work required to force the mercury through the pores. The work dW that is needed to immerse an area dA of pore wall is given by

$$dW = \gamma\cos(\theta)dA = -PdV. \quad (2)$$

The experimental technique consists of evacuation of a sample tube which contains the specimen to a pressure of 10^{-2} Torr and backfilling with mercury to 10 kPa to fill the sample tube completely and those pores which exceed 117 micrometres in diameter. The bulk density is determined at this point from the mass of the sample and the volume. Pressure is then applied at logarithmic intervals to a maximum of 200 MPa. The pore volume distribution is determined from the incremental volume change at each pressure increase, assuming that the pores are cylindrical. A skeletal density is determined at 200 MPa and compared with the theoretical maximum density of 1.937 g/cm^3.

SHOCK INITIATION THRESHOLD MEASUREMENTS

The shock stimulus required to initiate a detonation in the TATB samples was produced by the impact of a thin plastic flyer plate. The Mylar flyer plates were 0.25 mm thick and had diameters ranging from 1.00 to 25.4 mm. The flyer plates were accelerated by electrically exploding 25.4 × 0.051 mm aluminum foils with a capacitor bank system. The flyer plate material was driven by the explosion down a barrel of the desired diameter to impact the TATB specimen. A calibration curve of flyer plate velocity versus bank charging voltage was obtained using a Fabry-Perot laser velocity interferometer. The system which accelerated the flyer plates is described at length elsewhere (11).

The threshold velocity for shock initiation was determined using a delayed Robbins-Monro (DRM) procedure for selecting the bank charging voltages. The DRM protocol optimizes the information that can be obtained from the limited number of samples (usually 6-8) available for each threshold determination. The DRM procedure is also described in detail elsewhere in the literature (12). The shock initiation threshold data are summarized in Table I.

INITIATION SPOT SIZE MEASUREMENTS

Figures 1 and 2 show the shock initiation threshold as a function of initiation spot size for four TATB forms. These are UF TATB; a UF TATB obtained from the AWRE, Aldermaston, England; CP TATB formulated at Livermore (designated CP-20), and CP TATB designated CCP that was formulated at Los Alamos National Laboratory by Howard Cady. The data for both 1.4 and 1.6 g/cm^3 density show a sharp rise in threshold for the UF materials as the flyer diameter approaches 1 mm, while the data for the CP materials do not exhibit such a trend. There is also a reversal in sensitiveness of the UF and CP materials. The UF material is easier to initiate with the larger flyers, while the CP material is easier to initiate at the smaller flyer diameters. We also performed initiation threshold experiments at reduced temperatures

(−54 °C) and again observed a significant difference in the behavior of the CP and UF materials. We could not initiate the UF TATB at the lower temperature with 1.59 and 1.00-mm-diameter flyers, but the CP samples were initiated with only a modest increase in threshold velocity.

COMPARISON OF THRESHOLD AND POROSIMETRY RESULTS

Figure 3 shows the results of mercury intrusion porosimetry measurements made on pressed cm samples of CP, UF, and PG TATB. The difference between the curves for the CP and UF samples reflects the difference in two materials with different particle size distributions but the same density. The curve for the PG sample shows the effect of a higher density, as well as a different particle size distribution. Total intrusion volume and average pore diameter are listed for all the materials in Table II.

The porosimetry data correlate fairly well with the threshold velocity that a 0.25-mm-thick, 3.18-mm-diameter Mylar flyer plate must have to initiate a detonation in TATB.

TABLE I

Shock Initiation Threshold Data (Cady CP refers to CP material produced at LANL, CP-20 refers to CP material produced at LLNL, UF-AWRE is UF material obtained from AWRE, Aldermaston. The threshold data designated as "cold" were obtained from shots fired at −54°C. The threshold velocities marked "N' were shots which did not detonate at that impact velocity, so the true threshold velocity is somewhat higher.)

EXPLOSIVE	THRESHOLD VELOCITY 25.4 MM FLYER (KM/S)	THRESHOLD VELOCITY 6.35 MM FLYER (KM/S)	THRESHOLD VELOCITY 3.18 MM FLYER (KM/S)	THRESHOLD VELOCITY 1.59 MM FLYER (KM/S)	THRESHOLD VELOCITY 1.0 MM FLYER (KM/S)
CADY CP (1.4 G/CC)	1.85	1.95	2.32	2.39	2.34
CADY CP (1.6 G/CC)	1.93	2.49	2.60	2.78	2.52
CADY CP (1.4 G/CC, COLD)	1.96			2.46	2.55
CADY CP (1.6 G/CC, COLD)				2.58	
CP-20 (1.4 G/CC)	1.99	2.12	2.18	2.36	2.37
CP-20 (1.4 G/CC)			2.18		
CP-20 (1.45 G/CC)			2.43		
CP-20 (1.50 G/CC)			2.52		
CP-20 (1.55 G/CC)			2.54		
CP-20 (1.6 G/CC)	2.29	2.63	2.84	2.72	3.20
CP-20 (1.60 G/CC)			2.79		
CP-20 (1.64 G/CC)			2.80		
CP-20 (1.70 G/CC)			2.99		
CP-20 (1.75 G/CC)			3.60 N		
CP-20 (1.80 G/CC)			3.60 N		
CP-20 (1.4 G/CC, COLD)	1.98			2.55	2.86
CP-20 (1.6 G/CC, COLD)	2.43			3.40	3.60 N
UF-AWRE (1.4 G/CC)	1.68	1.87	2.26	3.02	
UF-AWRE (1.6 G/CC)	2.01	2.07	2.35	3.07	
PRODUCTION (1.8 G/CC)	3.02				
ULTRAFINE (1.4 G/CC)	1.71	1.82	2.46	3.60 N	3.20 N
ULTRAFINE (1.6 G/CC)	1.91	1.95	2.35	3.60 N	3.60 N
ULTRAFINE (1.8 G/CC)	2.70				
ULTRAFINE (1.4 G/CC, COLD)	1.91			3.60 N	3.60 N
ULTRAFINE (1.6 G/CC, COLD)	2.07			3.60 N	3.60 N

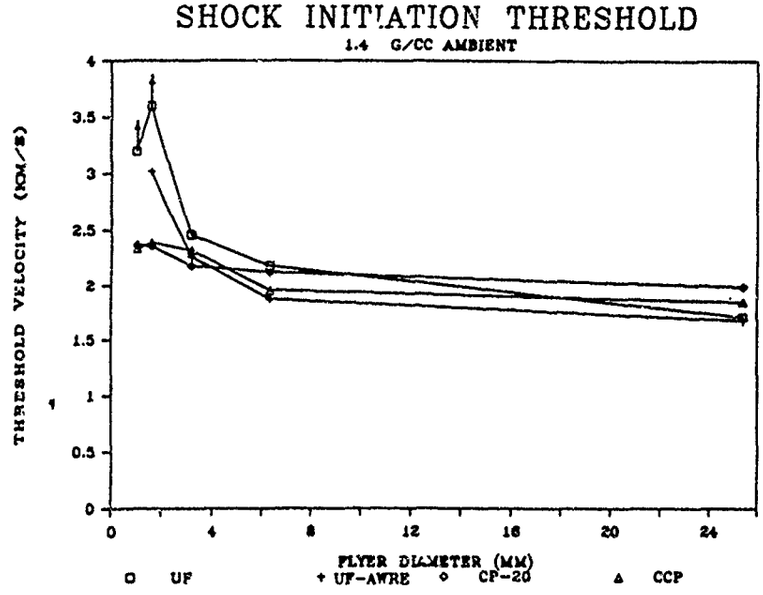

Fig. 1. Threshold velocity for shock initiation, measured at ambient temperature (In the legend, UF, UF-AWRE, CP-20 and CCP refer respectively to ultrafine, British ultrafine, LLNL crash-precipitated and LANL crash-precipitated TATB. The vertical arrows denote failure to detonate at that velocity. All of the samples had density 1.4 g/cc.)

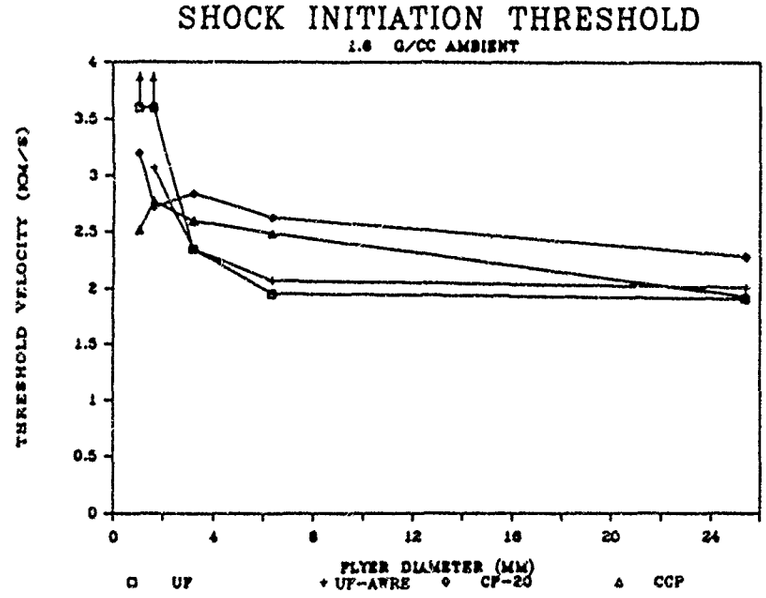

Fig. 2 Threshold velocity for shock initiation, measured at ambient temperature (In the legend, UF, UF-AWRE, CP-20 and CCP refer respectively to ultrafine, British ultrafine, LLNL crash-precipitated and LANL crash-precipitated TATB. Vertical arrows denote failure to detonate at that velocity. All of the samples had density 1.6 g/cc.)

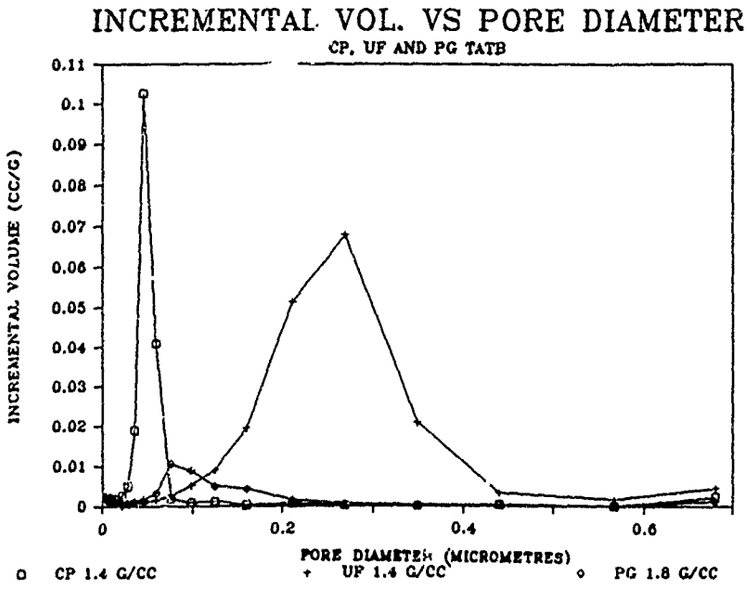

Fig. 3. Incremental volume vs pore diameter for three TATB samples with different densities and particle size distributions (CP, UF and PG refer respectively to crash-precipitated, ultrafine and production-grade TATB.)

TABLE II

Total pore volume and average pore diameter for some of the explosives tested

EXPLOSIVE	DENSITY G/CC	TOTAL PORE VOLUME CC/G	AVERAGE PORE DIAMETER μm
CADY CP	1.40	0.1854	0.0339
CADY CP	1.60	0.0982	0.0194
CP-20	1.40	0.1761	0.0284
CP-20	1.40	0.1879	0.0431
CP-20	1.45	0.1665	0.0234
CP-20	1.50	0.1299	0.0184
CP-20	1.55	0.1162	0.0161
CP-20	1.60	0.0950	0.0175
CP-20	1.60	0.0933	0.0153
CP-20	1.65	0.0658	0.0117
CP-20	1.70	0.0455	0.0110
CP-20	1.75	0.0306	0.0118
CP-20	1.80	0.0205	0.0112
UF-AWRE	1.40	0.1880	0.0965
PRODUCTION	1.80	0.0454	0.0446
ULTRAFINE	1.40	0.1966	0.1192
ULTRAFINE	1.60	0.1092	0.0743
ULTRAFINE	1.80	0.0322	0.0128

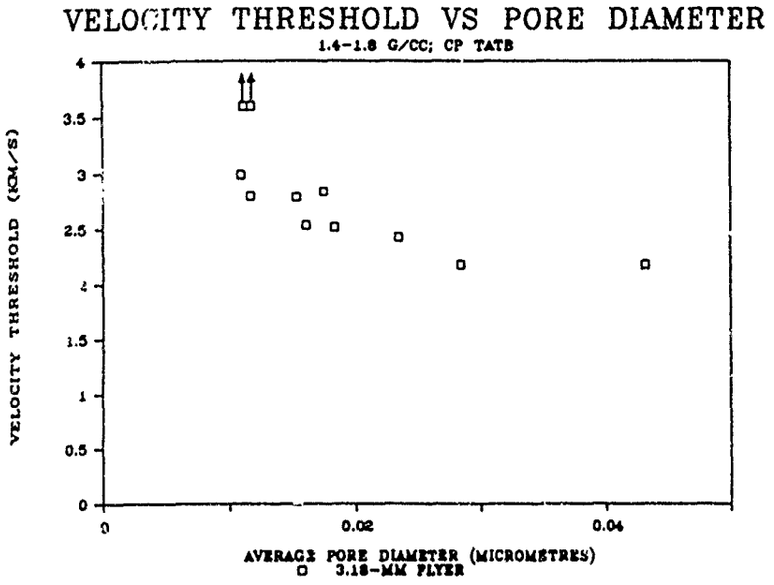

Fig. 4. Velocity threshold vs pore diameter for crash-precipitated TATB pressed to various densities, 1.4 - 1.8 g/cc (Vertical arrows denote failure to detonate at that velocity.)

In Fig. 4 we plot flyer velocity threshold for CP-20 versus average pore diameter as determined from 4V/A, where V is the total intrusion volume, A is the total void area and it is assumed that the voids are right circular cylinders.

In Fig. 5 we show the effect of pressing density on the void volume for samples of CP material. The figure clearly shows that pressing reduces the total pore volume and shifts the distribution of pore volumes toward smaller diameters. The effect of the change in density on velocity threshold is shown in Fig. 6. Density shows about the same degree of correlation with threshold velocity as does average pore diameter. In Fig. 7 we show the velocity threshold for 3.18-mm flyer impact as a function of average pore diameter for CP and UF TATB. At this flyer diameter, UF TATB has about the same threshold as CP, but has substantially greater average pore diameter. The dependence of the threshold on pore diameter is surprisingly weak, except for the smallest average pore diameters, where the curve rises steeply.

If a small-diameter flyer plate is used to initiate the TATB samples, we observe that pore diameter is not the only factor controlling the shock initiation threshold. Figure 8 shows the velocity threshold for 1.4- and 1.6-g/cc CP and UF TATB impacted by 1.0-, 6.35-, 3.18-, 1.59- and 1.00-mm-diameter flyers as a function of average pore diameter. The data points for pore diameters larger that 0.06 microns are for UF and UF-AWRE TATB and the data points for smaller pore diameters are for CP and CCP TATB. The velocity threshold for the CP material does not change much over the whole range of flyer diameters, while the threshold for the UF material increases drastically for flyer diameters less than 3 mm. This effect was also illustrated in Figs. 1 and 2. We attribute this difference in behavior between CP and UF material to the much-different particle size distributions. There are trivial chemical differences between the three types of TATB, especially between the CP and the two other materials, but the chemical differences do not lead to any marked thermochemical or performance differences. The remaining difference is in particle size and morphology. During shock compression, the intergranular forces will play a major role in determining the yield strength of the material and the way it fails when the yield strength is exceeded.

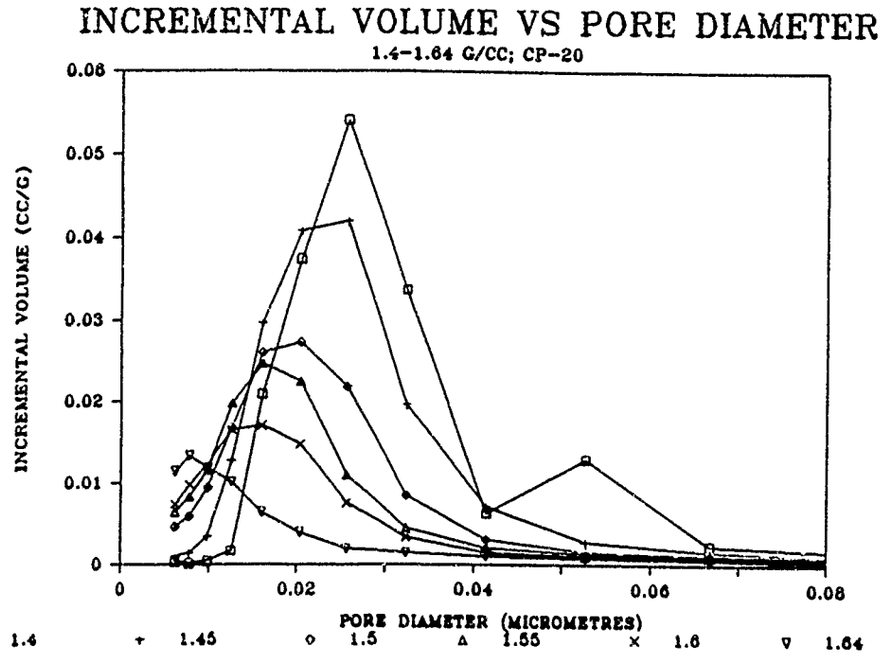

Fig. 5. Incremental volume vs pore diameter for crash-precipitated TATB pressed to various densities, 1.4 - 1.6 g/cc (The numbers in the legend are the density in g/cc.)

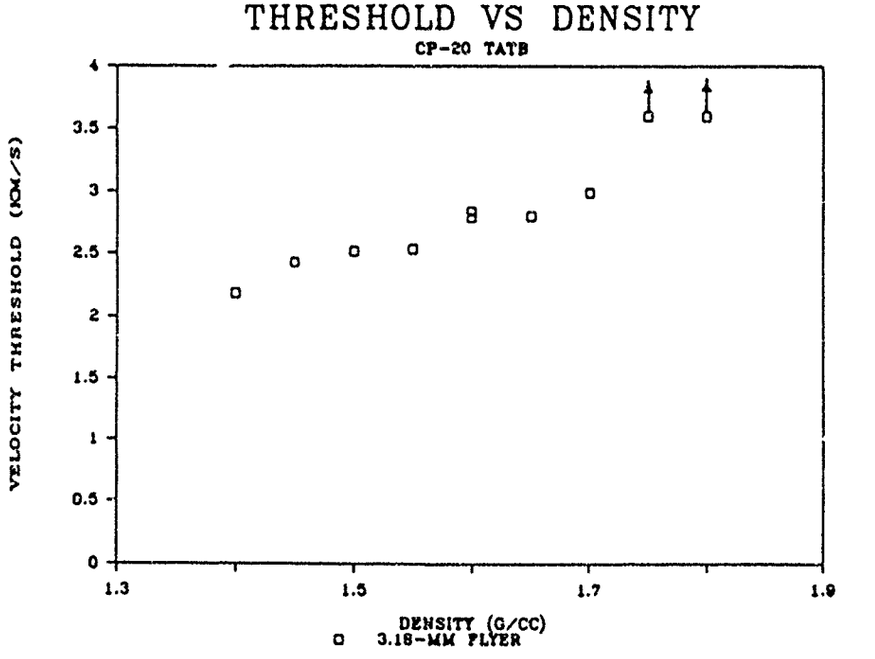

Fig. 6. Threshold velocity vs density for shock initiation of crash precipitated TATB, CP-20 (Vertical arrows denote failure to detonate at that velocity.)

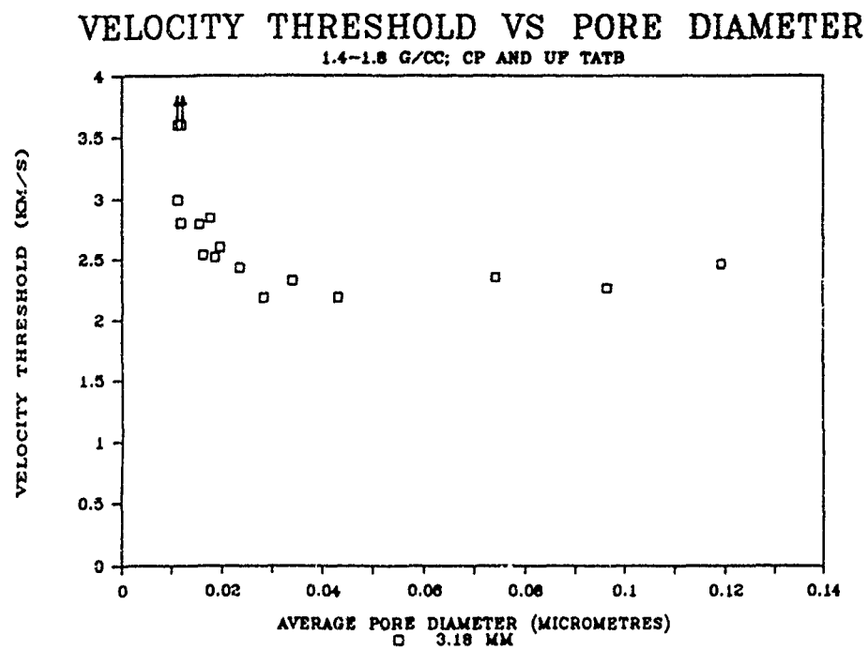

Fig. 7. Velocity threshold versus pore diameter for ultrafine and crash-precipitated TATB at various densities, 1.4 - 1.8 g/cc (Vertical arrows denote failure to detonate at that velocity.)

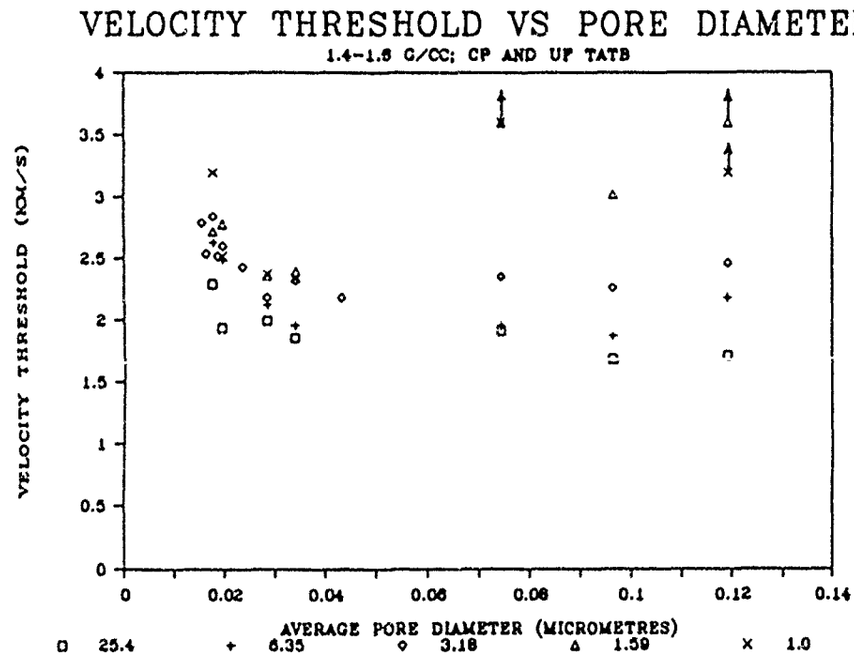

Fig. 8. Velocity threshold vs pore diameter for ultrafine and crash-precipitated TATB for various flyer plate diameters, and various densities (The numbers in the legend are the flyer plate diameter in mm. Vertical arrows denote failure to detonate at that velocity.)

It must be recognized that pore size distributions calculated from mercury intrusion porosimetry data depend on the assumption that the sample is incompressible. In reality, porous samples may be crushed by the pressures in the sample cell, and the material from which the porous sample is made may be incompressible. Figure 9 shows the total intrusion volume versus pressure for CP-20 TATB at 1.4 - 1.8 g/cc density. The solid line is the compression calculated for the bulk modulus of TATB. The bulk modulus was calculated from the sound speed measurements of Olinger and Hopson (13). At the higher pressures, the slope of the experimental curves approaches the slope of the calculated curve, suggesting that the apparent intrusion at these pressures is mostly due to compression of the TATB crystals. The curve for the 1.8 g/cc sample looks like virtually all of the apparent intrusion is due to compression of the sample. It is interesting to note the change in character of the curves between 1.6 and 1.7 g/cc density. This is the same density range where the initiation threshold increases sharply as shown in Fig. 6. Figure 10 shows the intrusion volume versus pressure for CP-20, PG and UF TATB at 1.8 g/cc density. At this density it appears that a good part of the intrusion is due to porosity for the UF and PG materials. One could correct for the sample compression by subtracting the calculated compressibility curve from the experimental curves and attributing the difference to intrusion of mercury into the pores.

102-MM-GUN EXPERIMENTS

The response of TATB to longer-duration pressure pulses has been studied using a 102-mm-gun facility that has been described elsewhere in the literature (14). Figure 11 shows stress gauge records for a PG TATB sample of density 1.80 g/cc that was impacted by a 12.5-mm-thick AD998 alumina flyer plate at 0.91 km/s, producing an 8 GPa pressure pulse. Figure 12 shows the stress-time records that were obtained when a UF TATB sample of 1.80 g/cc density was impacted by a 12.5 mm-thick AD998 alumina flyer plate at 1.36 km/s, producing a 10 GPa input pressure pulse. It is not possible to compare the run distances or times to detonation from these records, but it is clear from the record at the impact face that even at a higher input stress, the UF TATB reacts more slowly than the PG TATB. Also, the average shock velocity in the first 10 mm of run is considerably faster in the PG TATB. This behavior is consistent with earlier studies, where we observed that UF TATB is less sensitive than PG for sustained, lower pressure pulses, but for high pressures (>30 GPa) the UF material becomes more sensitive than the PG TATB.

SUMMARY AND CONCLUSIONS

We have measured shock initiation thresholds on TATB samples pressed from three different TATB powders which differ greatly in particle size distribution. The shock stimulus was produced by the impact of thin Mylar flyer plates accelerated by electrically-exploded metal foils. Flyer diameters ranged from 25.4 mm to 1.00 mm and flyer thickness was 0.25 mm.

The TATB powders were characterized by particle size determination and BET surface area measurements. The pressed samples were characterized by density measurements and mercury intrusion porosimetry.

The shock initiation threshold correlated well with total intrusion volume and average void diameter for measurements made on samples of the same material which differed only in density. There was more scatter in the correlations observed when type of material as well as the density was varied, indicating that other variables besides void size distribution are important in the shock initiation process. For small-diameter flyer plates the difference between materials was particularly evident. For decreased flyer diameter the thresholds for the UF TATB rose dramatically, but did not increase appreciably for the CP TATB. Our results suggest that pore collapse may not be the dominant mechanism for producing reaction sites during shock initiation for densities below 1.65 g/cc, because large changes in the average pore diameter produced only modest changes in the shock initiation threshold.

ACKNOWLEDGMENTS

We gratefully acknowledge the generosity of H. Cady of Los Alamos National Laboratory for providing samples of his crash-precipitated

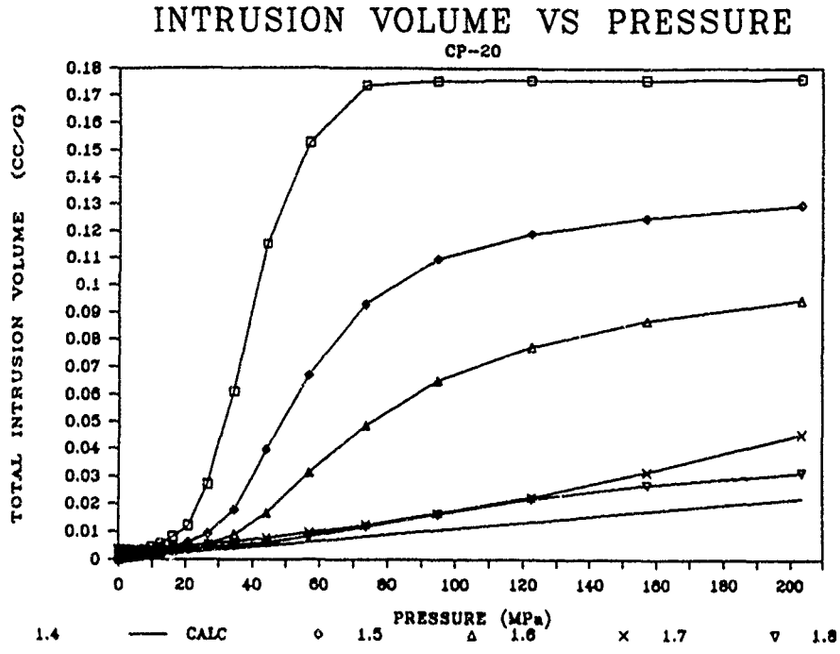

Fig. 9. Intrusion volume vs pressure for crash-precipitated TATB, CP-20 (The numbers in the legend are sample densities in g/cc. The solid line was calculated using a bulk modulus obtained from sound speed data.)

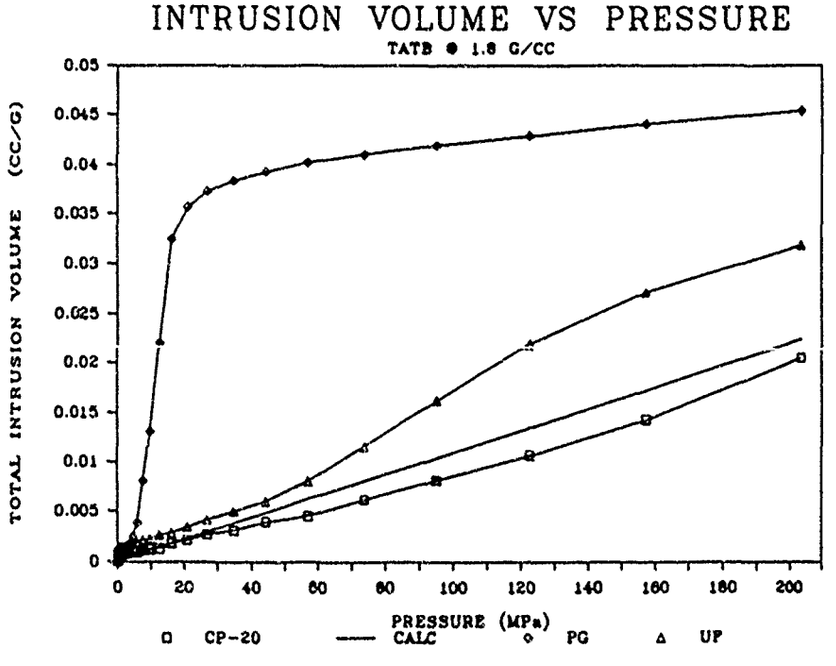

Fig. 10. Intrusion volume vs pressure for crash-precipitated, ultrafine and production-grade TATB pressed to 1.8 g/cc density (The solid line was calculated using a bulk modulus obtained from sound speed data.)

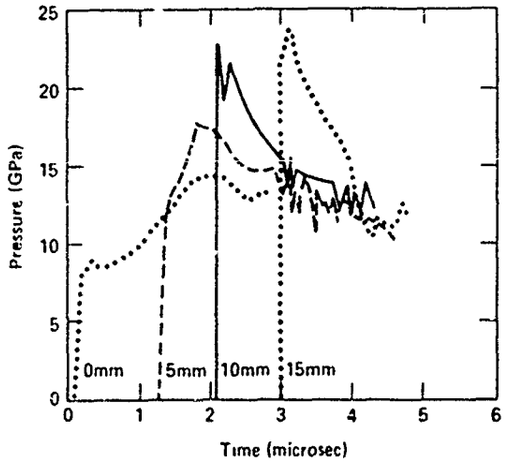

Fig. 11. Manganin gauge records of pressure vs time recorded at 0, 5, 10, and 15 mm from the front surface of a production grade TATB sample impacted in a gun experiment to a pressure of 8 GPa (Sample density was 1.80 g/cc.)

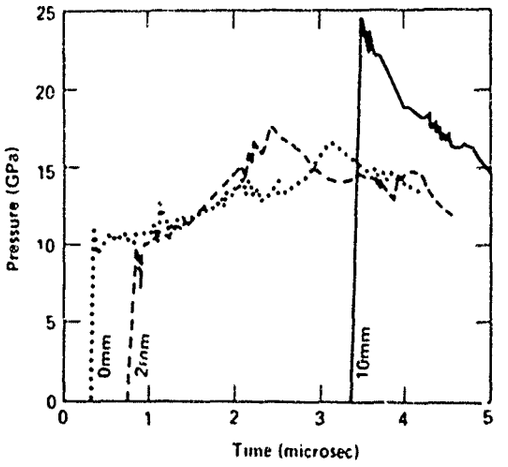

Fig. 12. Manganin gauge records of pressure vs time recorded at 0, 2, and 10 mm from the front surface of an ultrafine TATB sample impacted in a gun experiment to a pressure of 9.8 GPa (Sample density was 1.80 g/cc.)

material and to AWRE, Aldermaston, England, for sending us samples of ultrafine material, and thanks to Henry Chau for performing velocity calibration. Also, thanks to Robert Setchell of Sandia National Laboratory, Albuquerque for discussions on our use of mercury porosimetry.

*This work was performed under the auspices of the U.S. Department of Energy by Lawrence Livermore National Laboratory under contract No. W-7405-Eng-48.

DISCLAIMER

REFERENCES

1. A.W. Campbell, W.C. Davis, J.B. Ramsey, and J.R. Travis, Phys. Fluids *4*, 511 (1961).
2. M.J. Frankel and D.J. Pastine, *Proceedings of the Seventh Symposium (International) on Detonation*, Office of Naval Research, NSWC MP 82-334 (1981) p. 523.
3. B.A. Khsainov, A.A. Borisov, B.S. Ermolaev, and A.I. Korotkov, *Proceedings of the Seventh Symposium (International) on Detonation*, Office of Naval- Research, NSWC MP 82-334 (1981) p. 435.
4. Y. Partom, *Proceedings of the Seventh Symposium (International) on Detonation*, Office of Naval Research, NSWC MP 82-334 (1981) p. 506.
5. C. Mader, Phys, Fluids *8*, 1811 (1965).
6. C. Scott, *Proceedings of the Fifth Symposium (International) on Detonation*, Office of Naval Research, ACR-184 (1970) p. 259.

7. M.C. Chick, *Proceedings of the Fourth Symposium (International) on Detonation*, Office of Naval Research, ACR-126 (1965) p. 349.

8. C.A. Honodel, J.R. Humphrey, R.C. Weingart, R.S. Lee, and P. Kramer, *Proceedings of the Seventh Symposium (International) on Detonation*, Office of Naval Research, NSWC MP 82-334 (1981) p. 425.

9. R. McGuire, LLNL, private communication.

10. H. Cady, LANL, private communication.

11. R.C. Weingart, R.S. Lee, R.K. Jackson, and N.L. Parker, *Proceedings of the Sixth Symposium (International) on Detonation*, Office of Naval Research, ACR-221 (1976) p. 653.

12. G. Bloom, H. Chau, R. Glaser, C. Honodel, R.S. Lee, and R.C. Weingart, *Shock Waves in Condensed Matter-1983*, North Holland, New York (1984) p. 535.

13. B. Olinger and J.W. Hopson, *Actes du Symposium International sur le Comportement des Milieux denses sous Hautes Pressions Dynamiques*, Ed. Commissariat a l'Energie Atomique Centre d'Etudes Nucleaires de Saclay, Paris, France, 27-31 Aout 1978. p. 9.

14. L. Erickson, *Shock Waves in Condensed Matter-1981*, Am. Inst. of Physics, New York (1982) p. 605.

DISCUSSION

CHARLES DICKINSON, NSWC

Have you done any experiments to characterize the microstructural aspects, defects, grain size, etc., such as X-ray line broadening analysis?

REPLY BY R. LEE

No, we have not yet tried to use X rays to characterize the microstructure, but that might be a promising approach. There is a recent paper in Physical Review Letters (H.D. Bale and P.W. Schmidt, Phys. Rev. Lett., *53*, 596 (1984)), where small-angle X ray scattering was used to investigate the submicroscopic porosity of coal. The same technique should be applicable to a pressed high explosive sample.

EXPERIMENTAL STUDIES OF CHEMICAL REACTIVITY DURING SHOCK INITIATION OF HEXANITROSTILBENE

Robert E. Setchell
Shock Wave and Explosives Physics
Division 1131
Sandia National Laboratories
Albuquerque, New Mexico 87185

A new experimental approach has been used to examine the release of chemical energy during shock initiation of hexanitrostilbene (HNS). In this approach, the intensity of visible emission from an explosive/window interface, integrated over the spectral range 550-800 nm, was recorded in time as a measure of local chemical reactivity at this interface. Simultaneously, VISAR measurements were made of the particle velocity of the same interface in order to examine the relative effect of the energy release on the wave motion. Sustained and short-duration shocks, having pressures from 2.3 GPa to 4.0 GPa, were generated in two types of HNS materials that previously have shown significant differences in shock sensitivity. The emission intensity was found to be a very sensitive indicator of chemical reactivity. The combined measurements indicate that the temporal and spatial behavior of energy release during shock initiation is quite different in the two types of HNS.

INTRODUCTION

Shock wave growth towards detonation requires the progressive coupling of released chemical energy into the wave motion. When a plane shock wave of sufficient strength is generated in a granular, porous explosive, localized heating due to microstructural processes results in discrete ignition sites behind the shock. Chemical decomposition reactions subsequently spread from these sites through the shock-compressed material For a particular explosive composition, the spatial and temporal behavior of chemical energy release depends upon the shock amplitude, the heterogeneous microstructure within the unshocked material, and the mechanical and thermal material properties that govern the localized heating mechanisms. Direct experimental observations of the complex processes resulting in energy release and shock amplification are very difficult. Indirect measures of energy release obtained in previous studies have been in the form of optically measured free-surface velocities in excess of non-reactive values (1), increasing local stresses obtained with embedded manganin gauges (2), and increasing local particle velocities measured using embedded electromagnetic gauges (3) or laser velocity interferometry (VISAR) at an explosive/window interface (4). The information provided by these methods has been very useful, particularly when used to evaluate formulations for the local rate of energy release incorporated within numerical wave-propagation models (5-7). However, a more fundamental understanding of shock initiation processes requires different experimental techniques that can provide more direct information on chemical reactivity.

Optical emission has been examined in a number of studies of condensed explosives, although most of these studies have been investigations of propagating detonation waves. For transparent liquid explosives, the forward emission can be examined through the unreacted material. For solid explosives, emission can be examined from an explosive/window

interface or from a free surface under vacuum. One diagnostic technique has been to simply use photomultiplier tubes to record emission intensities integrated over one or more filter bandpasses (8,9). Other diagnostic techniques have involved focussing the emission into a spectrometer, then recording the spectrally resolved output using photomultiplier tubes behind slits (10,11), a framing camera (12), a streak camera (13), or a gated multi-channel vidicon detector (14). Extensive optical studies of shock-compressed explosives that have not yet reached detonation conditions have been made by Von Holle using two-channel infrared pyrometry (15-17). Emission intensities from an explosive/window interface have been measured within the spectral bands 2-5.5 μm and 4-5.5 μm using detectors with a 400 ns risetime, and more recently within the bands 2-5.5 μm and 5-11 μm using detectors with a 5 ns risetime. Granular explosives that have been examined include HMX, TATB, and PBX-9404. Brightness temperatures were determined from intensities integrated over each band, and color temperatures were determined from the ratios of the integrated band intensities. By assuming that the emittance within each band could be represented as the fractional coverage of preferentially heated material ("hot spots") times the emissivity of that material, Von Holle inferred the fractional area of hot-spots from differences between his brightness and color temperatures. He further assumed that this fractional area was essentially equal to the volume fraction of reacted material at the explosive/window interface, and inferred reaction rates at this position.

In the present study, several experimental techniques are combined into a new approach for examining chemical energy release during shock initiation experiments. In this approach, visible emission from an explosive/window interface is recorded simultaneously with VISAR measurements of the particle velocity history of the same interface. In preparing target assemblies for planar-impact experiments on a compressed-gas gun, the interface between an explosive sample and a fused silica window is left transparent except for a small area of vacuum-deposited aluminum centered on the sample. This small area provides the diffuse-reflecting surface required for velocity measurements. A turning mirror in a conventional VISAR optical system is replaced by a dichroic filter which reflects the 514.5 nm VISAR laser, but transmits light at longer wavelengths. A portion of the exposed rear surface of the explosive is imaged through the dichroic filter and onto both photomultiplier tubes and an image-converter streak camera. As a measure of chemical reactivity at the explosive surface, emission intensity integrated over the spectral range 550-800 nm is recorded as a function of time during the one-dimensional wave motion through the target assembly.

The present application of these combined techniques is an investigation of two explosive materials that have shown significant differences in shock sensitivity in previous studies. Both materials are hexanitrostilbene pressed without a binder to a common final density, but they differ in their characteristic grain sizes prior to pressing. A more detailed description of the experimental approach, together with additional information on hexanitrostilbene, can be found in the following section. Subsequent sections present and discuss the experimental results.

EXPERIMENTAL APPROACH

The experiments were conducted on a compressed-gas gun capable of producing repeatable, planar impacts of projectiles 6.3 cm in diameter at velocities up to 1.2 km/s. Both short-duration shocks and sustained shocks were generated in explosive samples during the present study. A sketch of the essential target and projectile components used for the short-duration shock experiments is shown in Fig. 1.

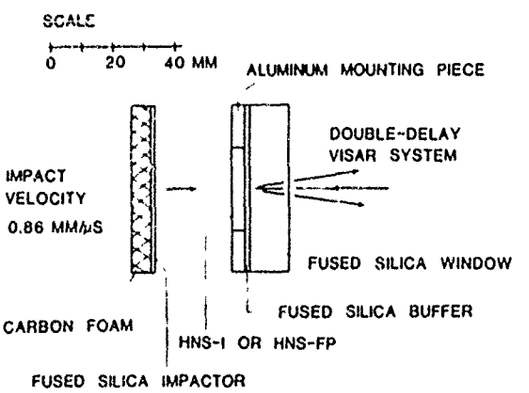

Fig. 1. Target and projectile components used for generating short-duration shock waves in samples of hexanitrostilbene

On the projectile a 1.0-mm thick fused silica impactor is backed with a 6.5-mm thick disc of low-density carbon foam. This combination is replaced by a 12.7-mm thick disc of fused silica in sustained-shock experiments. For the target assembly, 25.4-mm diameter discs of hexanitrostilbene are initially epoxied into an annular aluminum mounting piece so that both faces of the explosive sample can be carefully machined flat. The explosive is then attached to the window by applying thin-film epoxy to the annular aluminum piece. The window consists of two discs of fused silica 1.6 mm and 12.7 mm thick. The interface between these two pieces includes a diffuse-reflecting layer of vacuum-deposited aluminum confined to a centered 2-mm diameter area. The remainder of the explosive/window interface is transparent. A double-delay VISAR system was used to measure particle velocity histories at this reflective layer. The 1.6-mm thick "buffer" disc of fused silica was placed between the explosive and the VISAR measurement position in order to smooth spatial nonuniformities in the wave transmitted from the granular explosive. The elastic properties of fused silica were used in a method-of-characteristics calculation to find the corresponding one-dimensional waveform at the explosive/buffer interface. The measured velocities were also corrected for wave-generated, refractive-index changes in the 12.7-mm thick fused silica window. Further details on these procedures for VISAR measurements can be found in Ref. 4.

Combination VISAR/Emission Optics

A schematic drawing of the optica system used for measuring the intensity of visible emission from the explosive/window interface is shown in Fig. 2. A 75-mm diameter dichroic filter was used to reflect the 514.5 nm VISAR laser beam while transmitting light at wavelengths above 550 nm. The areas on the explosive surface that are imaged through this filter and onto the photomultiplier tubes and the streak camera are shown in Fig. 3. Emission from a thin, vertical slit 15.2 mm high was imaged onto the entrance slit of the streak camera using a magnification of 0.83, resulting in a streak record 12.7 mm high. For the last few experiments conducted during the present study, a proximity-focussed channel intensifier tube was added to the streak camera to greatly

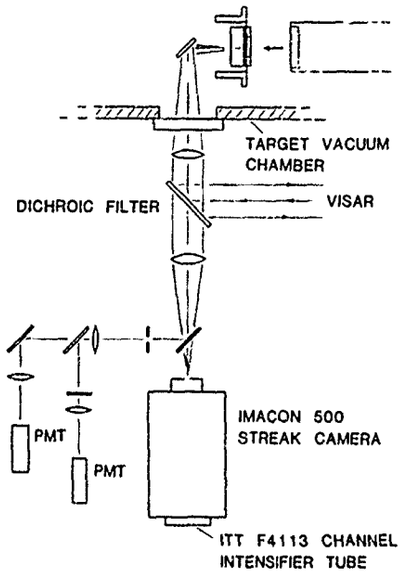

Fig. 2. Optical system for combination VISAR/emission measurements

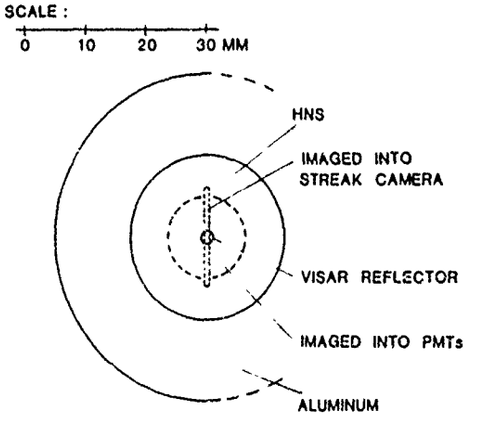

Fig. 3. Areas on the back surface of explosive samples that are used for VISAR measurements, imaged into photomultiplier tubes, and imaged into a streak camera

enhance its sensitivity. Emission from a circular area 12.7 mm in diameter centered on the explosive surface was imaged onto the 19-mm diameter photomultiplier tubes using lenses that produced a magnification of 1.5. To prevent

stray light detection an opaque mask with a 16-mm diameter hole was centered on the rear surface of the fused silica window, and the remainder of the target assembly exterior was painted flat black. In addition, the entire optical system outside the target vacuum chamber was enclosed.

The time response of the photomultiplier tubes and their recording oscilloscopes is less than 4 ns. The width of the entrance slit on the streak camera was varied from 0.4 to 1.0 mm during the course of the experiments, while the streak rate was varied from 50 to 100 ns/mm. The corresponding time resolution on the streak records varies from 20 to 100 ns. The length of the streak record is 40 mm, resulting in a total observation time of 2 to 4 μs. The relative spectral response of the optical detection system is shown in Fig. 4. This response was determined

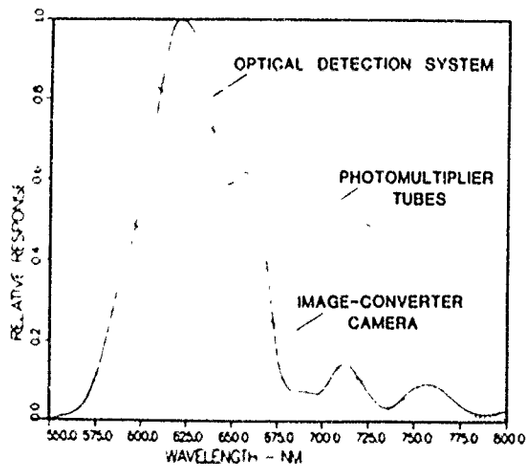

Fig. 4. Relative spectral response of the optical system (Also shown are the relative responses of the photomultiplier tubes and the image-converter streak camera.)

using a calibrated quartz-halogen lamp at the position of the explosive sample, together with a monochrometer and photomultiplier tube whose relative transmission and spectral response, respectively, were known. Also shown in Fig. 4 are the relative spectral responses for the streak camera and for the particular photomultiplier tubes used in the detection system.

Hexanitrostilbene

The combination VISAR/emission instrumentation was used to investigate two types of hexanitrostilbene (HNS) explosive. Both HNS types are pressed without a binder to a density of 1.60 $\pm$ 0.01 g/cc (92% of TMD), but they differ in their grain sizes prior to pressing. HNS-I samples were prepared from a powder having typical grain dimensions of 5-10 μm and a specific surface area of 2.1 m^2/g. HNS-FP samples were pressed from a powder having typical grain dimensions of 1-2 μm and a specific surface area of 8.2 m^2/g. These two materials have been examined previously in wave-evolution experiments using VISAR instrumentation (18,19). In these investigations both short-duration and sustained shocks were generated in HNS samples over the pressure range 2.5-4.0 GPa. For the conditions examined only the HNS-I samples showed evidence of chemical energy release and wave growth. Wedge tests to determine run distances to detonation have also been performed on these two materials for initial shock pressures from 3 to 7 GPa (20). These tests found that run distances are 2-3 times longer in HNS-FP than in HNS-I at any given pressure. Least-squares fits to these wedge test results were used to predict run distances for sustained-shock cases in the present study.

RESULTS

In the current experiments, sustained shocks having initial pressures from 2.3 to 4.0 GPa were generated in HNS samples either 2 or 3 mm thick. Initial shock pressures were chosen so that sample thicknesses corresponded to either $\sim$30% or $\sim$75% of predicted run distances to detonation. In addition, short-duration shocks having an initial pressure of 3.0 GPa sustained for 0.39 μs at the impact interface were generated in HNS samples from 2 to 6 mm thick. Because of the relatively small diameter of the explosive samples, the time period for observing one-dimensional wave motion was limited to $\sim$2 μs or less. Stronger shock waves were generated at impact within the annular aluminum piece surrounding the explosive, and eventually radial compressive waves converged on the region of the explosive/window interface under observation. This convergence of radial waves resulted in an abrupt termination of valid VISAR signals, but the emission instrumentation continued to respond. Figure 5 shows the VISAR-measured velocity histories obtained

for two cases of sustained shocks propagating in HNS-FP. The velocity profiles correspond to the transmitted waves in fused silica at the explosive/window interface. Zero time in this figure (and in all subsequent figures) corresponds to the time of shock arrival at this interface. Also shown are initial shock amplitudes calculated from the impact velocities and shock Hugoniot data. The lower waveform corresponds to conditions at 29% of the run distance to detonation for an initial shock pressure of 3.4 GPa, as predicted by a least-squares fit to available wedge-test data (20). The upper waveform corresponds to conditions at 76% of the run distance predicted in this fashion for a 4.0 GPa shock. Neither waveform shows any evidence of growth resulting from chemical energy release. The small rise observed ~0.7 μs after the wavefront in the lower curve is probably

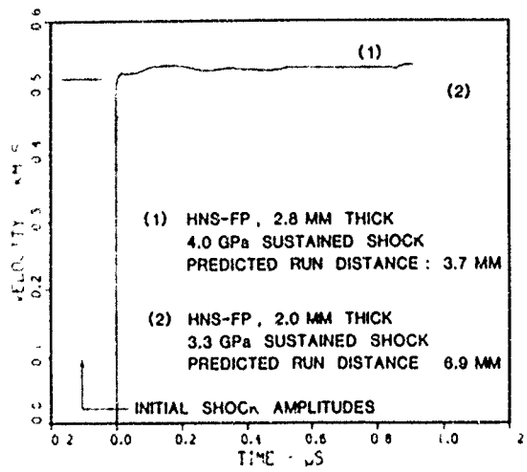

Fig. 5. VISAR-measured particle velocity histories obtained for two cases of sustained shocks propagating in HNS-FP (The profiles represent the waves in fused silica at the explosive/window interface, with zero time corresponding to the time of shock arrival at this interface.)

a weak re-reflected wave in the explosive due to a higher impedance material at both the window and impactor interfaces. Figure 6 shows VISAR-measured velocity histories obtained for two cases of sustained shocks propagating in the more sensitive explosive HNS-I. The lower and upper waveforms correspond to conditions at 31% and 71%, respectively, of run

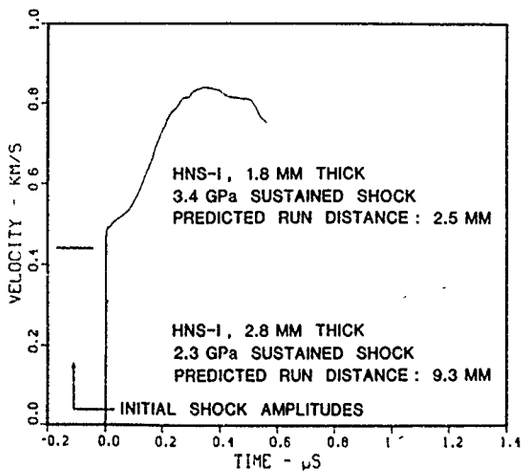

Fig. 6. Particle velocity histories obtained for two cases of sustained shocks propagating in HNS-I

distances predicted by a fit to wedge-test data for this material (20). The lower waveform shows no evidence of wave growth, but the upper waveform shows strong velocity increases associated with rapid release of chemical energy. The particle velocity may actually increase beyond the apparent maximum shown in Fig. 6, as the fused silica window is being compressed beyond a phase transformation at 9.4 GPa and VISAR data reduction becomes questionable (4).

Figures 7 and 8 show the photomultiplier tube signals recorded simultaneously with the VISAR data presented in the previous two figures. Zero time continues to correspond to shock arrival at the explosive/window interface, but establishing this reference time for the emission data introduces some additional uncertainties. In Fig. 7, a comparison is made between the signals observed from HNS-FP and from HNS-I for conditions corresponding to ~30% of expected run distances. The emission intensity from the HNS-I sample rises rapidly to a peak value approximately 1 μs following shock arrival, whereas the intensity from the HNS-FP sample shows a much smaller but steady increase for over 3 μs following shock arrival. Figure 8 shows a comparison between emission intensities for conditions corresponding to ~75% of the expected run distances. The scale

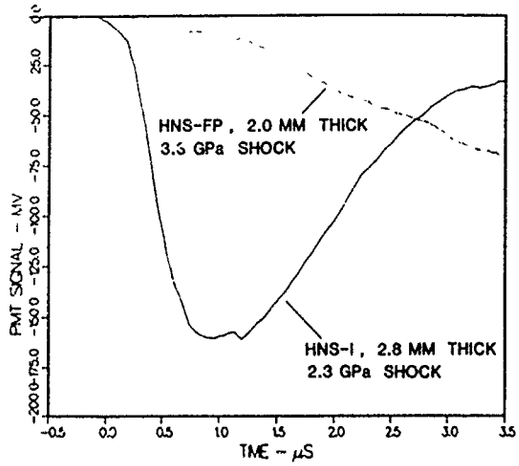

Fig. 7. Photomultiplier tube signals corresponding to emission intensity during sustained-shock experiments for conditions corresponding to ~30% of expected run distances (Zero time corresponds to the time of shock arrival at the explosive/window interface.)

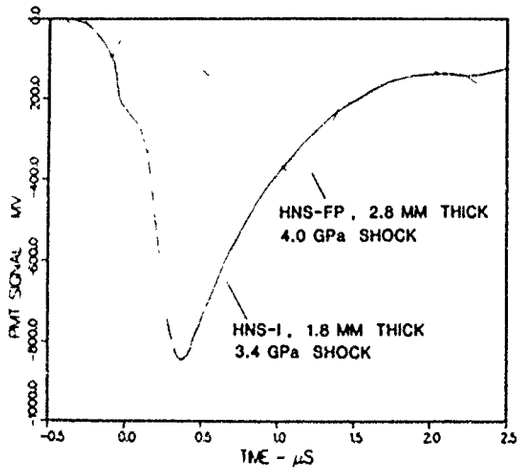

Fig. 8. Photomultiplier tube signals during sustained-shock experiments for conditions corresponding to~75% of expected run distances

for the photomultiplier tube signals has been changed to display much larger signals than shown in Fig. 7. The emission intensities from both materials show "precursors" detected prior to shock arrival at the explosive/window interface. As will be seen in a subsequent presentation of streak camera records, most of the emission intensity recorded from the HNS-FP sample is believed to be due to an "edge-ignition" phenomenon that is distinct from one-dimensional, shock-initiation processes. The streak record corresponding to the HNS-I signal in Fig. 8 does not show any unusual emission from the edge of the sample, and the precursor in the HNS-I signal probably indicates a slight transparency in this material.

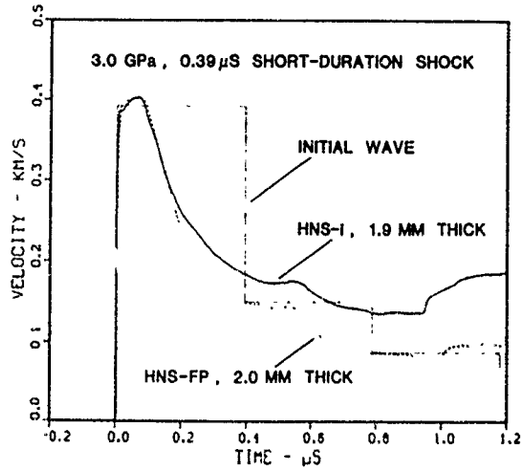

Fig. 9. Particle velocity histories obtained for the case of a 3.0 GPa shock, sustained for 0.39 μs at the impact interface, propagating through 2-mm thick samples of HNS-FP and HNS-I

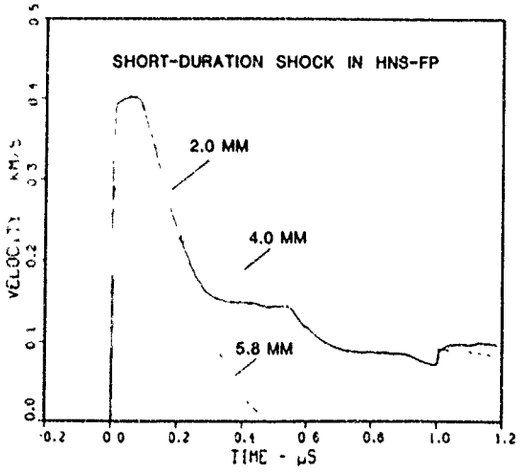

Fig. 10. Particle velocity histories obtained in short-duration shock experiments using HNS-FP samples having nominal thicknesses of 2, 4, and 6 mm

Figures 9-11 display the VISAR-measured velocity profiles obtained in the series of short-duration shock experiments on both HNS-FP and HNS-I. In Fig. 9, the observed waveforms

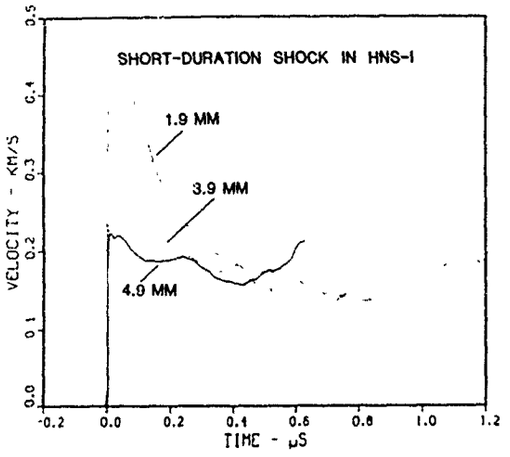

Fig. 11. Particle velocity histories obtained in short-duration shock experiments using HNS-I samples having nominal thicknesses of 2, 4, and 5 mm

after the initial wave had propagated through 2 mm of explosive are shown. Also shown in this figure is a calculated "initial wave" as would be observed if the waveform entering the explosive at the impact interface were to reach the explosive/window interface unaltered (21). The initial rarefaction due to the thin fused silica impactor has not reached the shock front in either of the measured waveforms, and the rarefaction velocity appears to be nearly equal in the two materials. The small velocity increases after ~0.9 μs are believed to be re-reflected compressive waves, as noted for a waveform shown in Fig. 5. The remainder of the velocity waveforms observed in HNS-FP for short-duration shock loading are shown in Fig. 10. A progressive decay of the shock amplitude occurs as multiple rarefactions overtake the wavefront. No evidence for chemical energy release is apparent, although the one-dimensional test time prior to the convergence of radial waves at the VISAR reflector is minimal for the case with a 6-mm thick explosive sample. In Fig. 11 the evolution of the same initial wave in HNS-I is displayed. After propagation through 4 mm of explosive the shock front is attenuated due to overtaking rarefactions, but a compressive wave late in time could indicate chemical reactivity. After a propagation distance of 5 mm the waveform shows compressive waves being generated by energy release both near the wavefront and at some distance behind the front in the shock-compressed material. A similar experiment using a 6-mm thick sample of HNS-I resulted in the complete loss of VISAR signals immediately after the wave arrival, indicating a much stronger wave as will develop near transition to detonation.

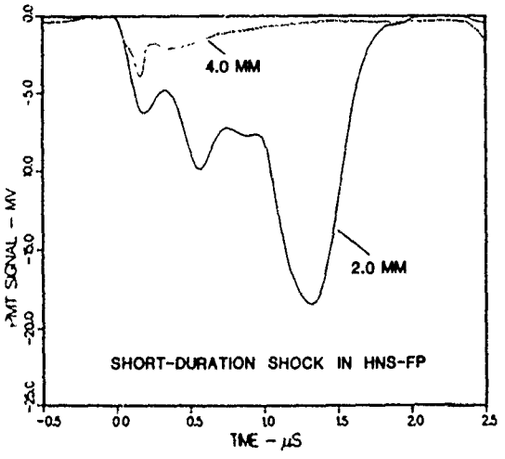

Fig. 12. Photomultiplier tube signals recorded during short-duration shock experiments using HNS-FP

Figures 12 and 13 show the photomultiplier tube signals recorded simultaneously with the VISAR data during the short-duration shock experiments. In the signals observed from HNS-FP shown in Fig. 12, the emission intensity is relatively weak after 2 mm of explosive

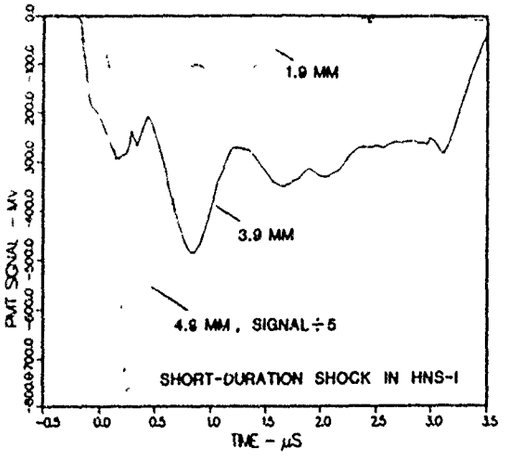

Fig. 13. Photomultiplier tube signals recorded during short-duration shock experiments using HNS-I

and barely detectable after 4 mm. In the experiment with a 6-mm thick sample, a very strong emission signal was recorded nearly a microsecond before the shock reached the explosive/window interface. A streak record for this case, to be discussed shortly, shows an early "edge-ignition" event as observed in one of the sustained-shock cases. The records shown in Fig. 13 for short-duration shocks in HNS-I display rapidly increasing emission intensities as the wave propagates. The intensity scale is 32 times larger than the scale in Fig. 12, and the signal from the 5-mm thick sample of HNS-I has also been reduced by a factor of five for plotting. The degree of precursor emission prior to shock arrival at the explosive/window interface also increases as the wave propagates. An experiment with a 6-mm thick sample of HNS-I resulted in off-scale photomultiplier signals.

Streak camera records of emission from the explosive samples (as shown in Figs. 2, 3) are displayed in Figs. 14 and 15. The 2-mm diameter aluminum coating used for VISAR measurements results in a clearly defined masking of emission from this centered area.

Figures 14a and 14b show sustained-shock cases where conditions corresponded to ~75% of the expected run distance to detonation. The main feature of the HNS-I record shown in Fig. 14a is a delay in the onset of observable emission over a fairly large region of the explosive surface. Figure 14b shows the HNS-FP sample experiencing "edge-ignition" at some position along the radial interface between the explosive and the surrounding aluminum mounting piece. This non-planar ignition probably resulted from a defect (small chip or crack) at the edge of the HNS-FP sample. A bright reactive front is observed propagating across the back surface of the explosive. Figure 14c was obtained with the channel tube intensifier on the camera, producing a luminous gain of approximately 600. This streak record was obtained for the sustained-shock case in HNS-FP in which conditions corresponded to 29% of the expected run distance. With the greatly enhanced sensitivity provided by the intensifier, local emission is clearly observed even though the recorded photomultiplier tube signals were very weak (Fig. 7). The onset and growth of local emission intensity is seen to be very non-uniform.

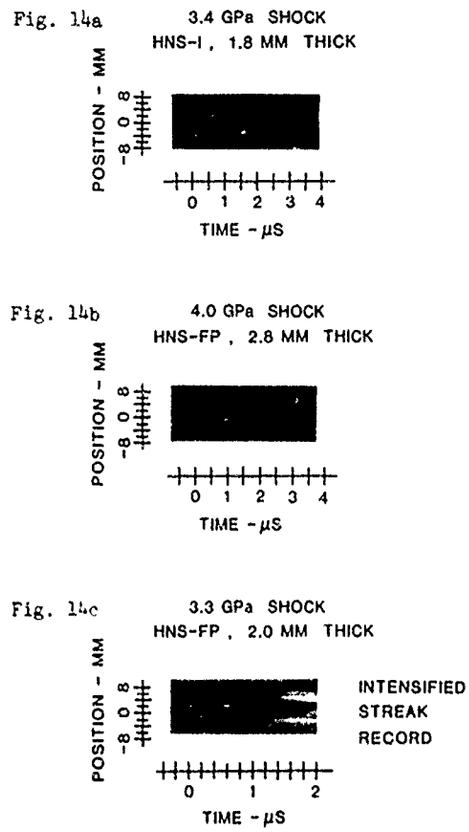

Fig. 14. Streak records of emission from the explosive/window interface obtained during sustained-shock experiments using HNS-I and HNS-FP (The third record was obtained using a channel tube intensifier on the camera.)

Figure 15a shows the streak record obtained for short-duration shock loading of a 6-mm thick sample of HNS-FP. A very early "edge-ignition" is observed, indicating that this ignition is a consequence of the much-faster shock wave propagating through the surrounding aluminum piece following impact. Figures 15b and 15c show the onset of relatively uniform emission from the explosive surface during short-duration shock experiments with HNS-I (a timing error resulted in a late start for the streak record in Fig. 15b). These records also show rather dramatic patterns of multi-dimensional wave motion coupled with released chemical energy occurring at later times. The corresponding particle velocity measurements (Fig. 11) show the VISAR data terminating before the apparent convergence of radial waves in the streak records.

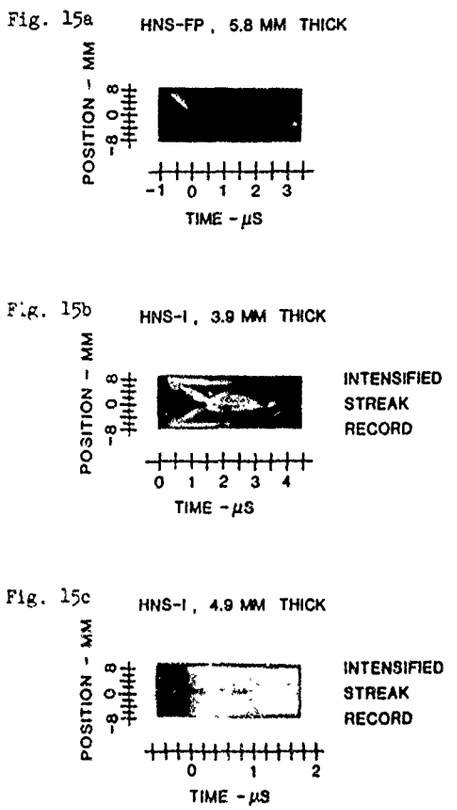

Fig. 15. Streak records of emission from the explosive/window interface obtained during short-duration shock experiments using HNS-FP and HNS-I

DISCUSSION

The purpose of the present investigation was to utilize a new experimental approach in order to examine the release of chemical energy during shock initiation of hexanitrostilbene. The two types of HNS studied, known previously to differ in their shock sensitivity, provided a good test of the experimental approach. Over the present range of initial conditions, with shock pressures varying from 2.3 to 4.0 GPa, the peak emission intensities varied from being barely detectable to driving the recording instrumentation off-scale. The particular spectral range of the detection system, therefore, was a useful choice. Comparisons between histories of emission intensity and VISAR-measured velocity histories show that the emission intensity is a far more sensitive indicator of chemical reactivity.

In the 3.0 GPa short-duration shock experiments, the velocity profiles recorded after wave propagation through 2 mm and 4 mm samples of both explosives showed only small differences. The emission intensities, however, differ by an order of magnitude after 2 mm and by two orders of magnitude after 4 mm. After a propagation distance of 6 mm the wave in HNS-I is near (or has reached) detonation conditions, whereas the wave in HNS-FP shows no evidence of one-dimensional growth towards detonation. In the sustained-shock experiments, the temporal features of the emission intensities suggest that the HNS-FP material has a fundamentally different initiation behavior than the HNS-I material. For experimental conditions corresponding to ~30% of expected run distances, the measured intensity from HNS-I (Fig. 7) rises smoothly to a peak approximately 1 μs after the shock arrival. This intensity history is consistent with a general description of energy release during relatively low-amplitude shock initiation of heterogeneous explosives (4). In this description, chemical energy released progressively throughout much of the shock-compressed material contributes to amplification of the shock wave. The corresponding emission history from the HNS-FP sample shows only a low level that increases slowly during the same time interval. For experimental conditions corresponding to 75% of expected run distances, the measured intensities (Fig. 8) show the same differences. The peak intensity from the HNS-I sample is much stronger than shown in the earlier HNS-I case, and the associated waveform (Fig. 6) now shows particle velocity increasing substantially behind the wave front. The much smaller rise in the corresponding emission history from the HNS-FP sample is largely due to the "edge-ignition" event that occurred in this experiment (Fig. 14b), leading to the conclusion that very little chemical energy is released throughout a comparable region behind the shock front in this case. For the shock in HNS-FP to achieve detonation within a small additional run distance, a very strong overtaking wave must be generated in the shock-compressed material late in time. This observation suggests that the very fine-grained HNS-FP material behaves more like a homogeneous explosive during shock initiation, with very little energy release within the shock-compressed material until a thermal

explosion occurs at the impact interface. The chemical reactivity that does occur in HNS-FP is depicted in the intensified streak record shown in Fig. 14c. This record indicates that the onset and growth of chemical reactivity is rather sporadic spatially. In contrast, the streak record in Fig. 15c shows that the onset and growth of chemical reactivity in HNS-I is far more uniform.

The present results are very encouraging in terms of the need to develop new experimental methods for direct, local measurements of chemical energy release in solid explosives. Future efforts to examine in greater detail the spatial, temporal, and spectral characteristics of visible emission should prove to be useful contributions to this goal.

ACKNOWLEDGEMENTS

The author would like to thank Ms. Merri Lewis for her very valuable assistance in preparing and conducting the experiments. The gas gun facility was skillfully operated by Mr. David Wackerbarth.

REFERENCES

1. For example, see Boyle, V.M., and Pilarski, D.L., "Shock Ignition Sensitivity of Multiply Shocked Pressed TNT," Proceedings of the Seventh Symposium (International) on Detonation, Naval Surface Weapons Center, White Oak, MD, NSWC MP 82-334, 1982, p. 906.

2. For example, see Weingart, R., Barlett, R., Cochran, S., Erickson, L., Chan, J., Janzen, J., Lee, R., Logan, D., and Rosenberg, J., "Manganin Stress Gauges in Reacting High Explosive Envionment," Symposium (International) on High Dynamic Pressures, Commissariat a l'Energie Atomique, Paris, 1978, p. 451.

3. For example, see Erickson, L., Johnson, C., Parker, N., Vantine, H., Weingart, R., and Lee, R., "The Electromagnetic Velocity Gauge: Use of Multiple Gauges, Time Response, and Flow Perturbations," Proceedings of the Seventh Symposium (International) on Detonation, Naval Surface Weapons Center, White Oak, MD, NSWC MP 82-334, 1982, p. 1062.

4. For example, see Setchell, R.E., "Ramp-Wave Initiation of Granular Explosives," Combust. Flame *43*, 255 (1981).

5. Lee, E.L., and Tarver, C.M., "Phenomenological Model of Shock Initiation in Heterogeneous Explosives," Phys. Fluids *23*, 2362 (1980).

6. Anderson, A.B., Ginsberg, M.J., Seitz, W.L., and Wackerle, J., "Shock Initiation of Porous TATB," Proceedings of the Seventh Symposium (International) on Detonation, Naval Surface Weapons Center, White Oak, MD, NSWC MP 82-334, 1982, p. 385.

7. Nunziato, J.W., Kipp, M.E., and Setchell, R.E., "Shock Initiation in Heterogeneous Explosives," Sandia National Laboratories Report SAND81-2173, September, 1982.

8. Persson, P-A., and Sjolin, T., "Light Emission During Initiation of Liquid Explosives," Proceedings of the Fifth Symposium (International) on Detonation, Office of Naval Research, ACR-184, Arlington, VA., 1970, p. 177.

9. Kato, Y., Bauer, P., Brochet, C., and Bouriannes, R., "Brightness Temperature of Detonation Wave in Nitromethane-Tetranitromethane Mixtures and in Gaseous Mixtures at a High Initial Pressure," Proceedings of the Seventh Symposium (International) on Detonation, Naval Surface Weapons Center, White Oak, MD, NSWC MP 82-334, 1982, p. 768.

10. Burton, J.T.A., Hawkins, S.J., and Hooper, G., "Detonation Temperature of Some Liquid Explosives," Proceedings of the Seventh Symposium (International) on Detonation, Naval Surface Weapons Center, White Oak, MD, NSWC MP 82-334, 1982, p. 759.

11. Malaval, C., and Conze, A.T., "Complementary Use of the Spectrograph and the Spectrophotometer in Detonation Temperture Measurements," in Proceedings of the Ninth International Congress on High-Speed Photography, W.G. Hyzer and W.G. Chace, Eds, (Society of Motion Picture and Television Engineers, New York, 1970), p. 427.

12. Hay, J.E., Peters, W.C., and Watson, R.W., "Observations of Detonation in a High Vacuum," Proceedings of the Fifth Symposium (International) on Detonation, Office of Naval Research, ACR-184, Arlington, VA, 1970, p. 559.

13. Schulz, C., Linares, B., Cherville, J., and Poulard, S., "Ultra-Fast Physico-Chemical Diagnoses of Detonation Initiation Mechanisms," Proceedings of the Eighth Symposium on Explosives and Pyrotechnics, The Franklin Institute, Philadelphia, PA, 1974, p. 49-1.

14. Renlund, A.M., and Trott, W.M., "Spectra of Visible Emission from Detonating PETN and PBX-9407," Sandia National Laboratories Report 83-2168, February, 1984.

15. Von Holle, W.G., "Temperature Measurements of Shocked Energetic Materials by Time-Resolved Infrared Radiometry," in *Fast Reactions in Energetic Systems*, C. Cappellos and R.F. Walker, Eds. (D. Reidel, Boston, 1980), p. 485.

16. Von Holle, W.G., and Tarver, C., "Temperature Measurement of Shocked Explosives by Time-Resolved Infrared Radiometry - A New Technique to Measure Shock-Induced Reaction," Proceedings of the Seventh Symposium (International) on Detonation, Naval Surface Weapons Center, White Oak, MD, NSWC MP 82-334, 1982, p. 993.

17. Von Holle, W.G., "Shock Wave Diagnostics by Time-Resolved Infrared Radiometry and Non-linear Raman Spectroscopy," in Shock Waves in Condensed Matter - 1983, J.R. Asay, R.A. Graham, and G.K. Straub, Eds. (North-Holland, New York, 1984), p. 283.

18. Setchell, R.E., "Grain-Size Effects on the Shock Sensitivity of Hexanitrostilbene (HNS) Explosive," Combust. Flame *56*, 343 (1984).

19. Setchell, R.E., and Taylor, P.A., "The Effects of Grain Size on Shock Initiation Mechanisms in Hexanitrostilbene (HNS) Explosive." in *Dynamics of Shock Waves, Explosions, and Detonations*, J.R. Bowen, N. Manson, A.K. Oppenheim, and R.I. Soloukin, Eds., Vol. 94 (AIAA, New York, 1984), p. 350.

20. Kramer, P.E., "HNS Wedge Tests," Mason & Hanger-Silas Mason Co., Pantex Plant, Report MHSMP-83-46, December, 1983.

21. Setchell, R.E., "Short-Pulse Shock Initiation of Granular Explosives," Proceedings of the Seventh Symposium (International) on Detonation, Naval Surface Weapons Center, White Oak, MD, NSWC MP 82-334, 1982, p. 857.

DISCUSSION

J.E. KENNEDY, Sandia National Laboratories

Have you made any direct observation of a strong overtaking wave, resembling superdetonation, in the fine HNS-FP explosive?

REPLY BY R.E. SETCHELL

To date we have not obtained a direct observation of a strong wave overtaking the initial shock in the HNS-FP material. However, in the wedge tests that were performed to determine run distances to detonation in this material (Ref. 20), large overshoots in detonation velocity were observed at transition. The detonation velocities then decayed to a value typical of stable detonation. These results, together with the observations in the present study, provide strong evidence that a superdetonation wave is generated in a manner similar to shock initiation in a homogeneous explosive. We plan to perform additional experiments on this very fine-grained material at conditions closer to transition in an effort to confirm this behavior.

THE EFFECTS OF MATERIAL MICROSTRUCTURE ON THE SHOCK SENSITIVITY OF POROUS GRANULAR EXPLOSIVES

Paul A. Taylor
Sandia National Laboratories
Albuquerque, NM 87185

The influence of material microstructure on the shock sensitivity of porous granular explosives is investigated. The analysis is based on the assumption that hot spot formation occurs exclusively by means of the mechanism of pore collapse due to shock loading. Defined within the analysis are the pore size and spacing parameters δ and λ associated with the initial grain size and density respectively and shown to be influential on the shock initiation characteristics of the explosive. Results show that hot spots formed in explosives with microstructures displaying a $\delta < 1$ exhibit reduced temperatures to the point where they may be sufficiently inadequate to ignite the grain burning process essential to the initiation process.

INTRODUCTION

The process of shock initiation in porous, granular explosives involves the nucleation of hot spots (i.e., localized regions of elevated thermal energy) behind the propagating shock front which act as ignition sites for a subsequent grain burning process that liberates energy by means of chemical reactions. For relatively low shock strengths, this chemical energy release occurs at some distance behind the shock front generating a pressure disturbance which overtakes and tends to enhance the shock front. As the shock strength increases, the chemical energy release occurs closer to the shock front thereby reducing the delay time associated with the coupling of energy to the front. If there is sufficient chemical energy release to overcome the dissipative mechanisms operating on the shock wave, then the wave will grow to detonation conditions given a sufficient run distance within the explosive. Thus, the initiation process is dependent upon the processes of hot spot formation and grain burning. Shock sensitivity studies are concerned with the influence of chemical composition, shock strength and duration, and material microstructure (i.e., porosity and/or granularity) on the rate at which the initiation process proceeds. To understand the influence of these parameters on the processes of hot spot formation and grain burning is to understand their influence on the shock sensitivity of the explosive in general.

The influence of material microstructure is manifested in the process of hot spot formation as well as that of grain burning (1). The interaction of a shock wave with a granular and/or porous microstructure naturally gives rise to such hot spot forming mechanisms as hydrodynamic pore collapse and associated microjetting (2,3), viscoplastic work associated with pore collapse (4,5), intergranular friction (6), and shear banding (7). Thus, the process of hot spot formation displays a dependence upon initial grain size and porosity. The grain burning process, however, is largely associated with a surface reaction mechanism, the rate of which, is dependent upon the specific surface area and hence, grain size (1). Previous experimental studies concerned with the influence of microstructure on the shock initiation characteristics of various explosives have provided an informative, if somewhat confusing, data base of information (8). Investigations by Campbell et al. (2) and Andreev et al. (9) involving the sustained shock loading of TNT and that of Hayes (10) with HNS observed that as the initial grain size was decreased with the initial density held fixed, the explosive displayed a higher chemical

reaction rate during the initiation process. In absence of any additional information, this behavior suggests that the chemical energy release is governed by a surface reaction alone, in view of which, one would expect an increase in shock sensitivity for a decrease in grain size. However, in addition to this result, the investigations by Howe et al. (11), Von Holle (12), deLongueville et al. (13), and Honodel et al. (14) on TNT, HMX, RDX, and TATB also reported that the coarser grained explosives exhibited lower reaction thresholds during low amplitude (~30 kbar) sustained shock loading. This behavior was also observed by Setchell (8) in his experiments on HNS where, in response to a 30 kbar sustained shock, a medium-grained material displayed progressive chemical decomposition whereas a finer-grained material pressed to the same initial density displayed no apparent chemical energy release whatever under identical conditions. These results suggest that a reversal in shock sensitivity might exist due to grain size effects alone. That is, for low amplitude sustained shock loading at fixed initial density, there exists a grain size, below which, the trend of increasing sensitivity for a decrease in grain size is reversed with the sensitivity now decreasing for a decrease in grain size. Indeed, Pop plot data (i.e., run distance to detonation as a function of initial plane shock amplitude) on HNS (15) substantiates this speculation on sensitivity reversal, where a medium-grained material (HNS-I) was reported to exhibit a shorter run distance to detonation than a finer-grained material (HNS-FP) for sustained shock loading with amplitudes under 60 kbar.

The reversal of shock sensitivity, as prompted by changes in grain size alone, suggests the existence of a regime of grain sizes where the mechanism of hot spot formation exerts a crucial influence on the sensitivity behavior of the explosive. The present study investigates the influence of material microstructure and specifically, the mechanism of hot spot formation on shock sensitivity. The analysis is based on the assumption that the primary mechanism of hot spot formation is that of pore collapse due to shock loading. In the next section, the influential parameters affecting shock sensitivity in general are identified and accompanied by a discussion of their significance. The following sections contain descriptions of the method ology and model used in the present analysis and a report of the results of the calculations. Finally, the paper closes with a discussion of the results along with concluding remarks.

ANALYSIS

It is generally agreed upon (see e.g., (3), (4), and (5)) that the the shock initiation behavior of porous granular explosives, when subjected to a plane shock wave of given amplitude and duration, is dependent upon the explosive's chemical composition, transport properties (associated with viscosity and heat conduction), compressibility, plastic yield strength, and material microstructure. In the following analysis, the run distance to detonation will suffice as a quantitative measure of shock sensitivity. The analysis is based on the assumption that hot spot formation occurs only at the original pore sites by means of the mechanism of pore collapse due to shock loading. Consequently, for a porous granular explosive of fixed chemical composition, the following relation is assumed to hold:

$$D = \phi(P, \tau, \varrho, \mu, \chi, Y, d, s) , \qquad (1)$$

where D is the run distance to detonation, P represents the increase in pressure across the shock front, τ is the shock duration, ϱ is the material density, and μ and $\chi(= \kappa/\varrho c_v)$ define the viscosity and thermal diffusivity, respectively, with κ and c_v the thermal conductivity and specific heat. In addition, Y is the plastic yield strength of the matrix material, and d and s characterize the material microstructure by denoting the initial average pore size and spacing, respectively. By means of the Pi-theorem of dimensional analysis, relation (1) assumes the form

$$D = \frac{\mu}{\sqrt{\varrho P}} \Psi \left(\frac{Y}{P}, \frac{\tau P}{\mu}, \frac{\mu}{\varrho\chi}, \frac{d\sqrt{\varrho P}}{\mu}, \frac{s}{d}\right), \qquad (2)$$

where the forms of the dimensionless parameters in (2) suggest the existence of the characteristic length and time scales defined by $x_c = \mu/\sqrt{\varrho P}$ and $t_c = \mu/P$, respectively. These scales are associated with the structure of the shock front where, in particular, x_c and t_c reflect the fact that the shock front width is determined by a viscosity associated with the conversion of

kinetic energy of directed motion into the kinetic energy of random (thermal) motion (16). Eq. (2) represents the dependence of shock sensitivity on the shock amplitude and duration, yield strength, transport properties, and microstructure in terms of a set of dimensionless parameters involving the relevant quantities. The first parameter Y/P ($=Yt_c/\mu$) determines the nature of the dissipative energy associated with shock compression. Here, dissipation is primarily due to viscous heating whenever Y/P<1 and plastic work whenever Y/P>1. This parameter is similar to the parameter N_3 introduced by Frey (5) to distinguish between the regime associated with viscous dissipation and that due to plastic work in his study of spherically symmetric pore collapse in an incompressible viscoplastic material. The parameter $\tau P/\mu$ ($=\tau/t_c$) determines the degree of influence of the shock duration τ on the run distance to detonation where, for $\tau P/\mu >> 1$, corresponding to sustained shock loading, there should be no influence. The parameter $\mu/\varrho\chi$ is the Prandtl number associated with transport properties at the shock front, where the structure of the front is primarily determined by viscous effects whenever $\mu/\varrho\chi>1$ and by heat conduction when $\mu/\varrho\chi<1$. The parameters $d\sqrt{\varrho P}/\mu$ ($=d/x_c$) and s/d represent the influence of the material microstructure on the shock sensitivity of the explosive where $d\sqrt{\varrho P}/\mu$ can be thought of as a Reynolds number associated with shock compression of the microstructure. The quantity $d\sqrt{\varrho P}/\mu$ is formally identical to the parameter Re identified by Khasainov et al. (4) in their model of spherically symmetric collapse of a pore in an incompressible viscoplastic material. There, they associate pore collapse in highly viscous fluids with Re<1 and low viscosity fluids whenever Re>1. In view of the significance of the parameters $d\sqrt{\varrho P}/\mu$ and s/d, the following pore size and spacing parameters δ and λ are defined:

$$\delta = \frac{d}{w_s} \left(\propto \frac{d\sqrt{\varrho P}}{\mu}\right) \text{ and } \lambda = \frac{s}{d}, \qquad (3)$$

where w_s denotes the shock front width which is proportional to the characteristic length scale $x_c = \mu/\sqrt{\varrho P}$. For a binderless pressed granular explosive, the pore size parameter δ represents the influence of either initial grain size or average pore size (these two are related in this instance), whereas the pore spacing parameter λ represents that of the initial porosity (or equivalently, the initial pressing density). Note that whenever $\delta \lesssim 1$, the average pore (of diameter d) will effectively experience collapse by a *structured* compressive wave, that is, one which displays a rise distance in bulk material at least as great as the pore diameter. However, for $\delta >> 1$, the average pore will experience collapse due to a sharp shock. In addition, whenever $\lambda \sim 1$, a high degree of interaction will exist between adjacent collapsing pores as well as that between the subsequently formed hot spots giving rise to shock diffraction and thermal energy transport between hot spots. For $\lambda >> 1$, this effect becomes negligible with adjacent pores and hot spots no longer interacting. As suggested by the forms for the dimensionless parameters $d\sqrt{\varrho P}/\mu$ and δ, a natural length scale associated with shock compression in general may be defined in terms of the shock front width w_s. This length scale, in turn, is determined by the material viscosity at the shock front and the shock strength. Within the context of the present analysis, the influence of the material microstructure on shock sensitivity may be examined through a study of the influence of the pore size and spacing parameters δ and λ on the sensitivity.

An appropriate candidate for the present study is the binderless granular explosive hexanitrostilbene (HNS) possessing a crystal density of 1.74 g/cc. This explosive displays a reversal in sensitivity as the initial grain size is decreased from coarse to fine, with all other factors held fixed. Specifically, Hayes (10) examined the coarse- and medium-grained materials HNS-II and HNS-I whereas Setchell (8) investigated the response of HNS-I and the fine-grained HNS-FP (see Table 1). Possessing identical compositions, the three HNS types HNS-II, I, and FP were each subjected to a sustained shock wave of approximately 30 kbar at a fixed initial density of 1.6 g/cc. In terms of an induction time after shock passage to completion of chemical energy release, Hayes found HNS-II to be less sensitive than HNS-I. Setchell, however, observed HNS-I displaying a significant amount of chemical energy release after shock passage whereas the fine-grained HNS-FP displayed no chemical reactivity whatever. This observation is verified by the Pop plot data of Kramer (15) showing HNS-I as more sensitive

TABLE 1
Microstructural dimensions of the three HNS types before and after pressing

	Pressing Powder Grain Dimensions (μm x μm)	Average Pore Size, d (μm)	Average Pore Spacing, s (μm)
HNS-II	167.0 × 51.0	5.30	42.80
HNS-I	8.8 × 4.0	0.61	4.86
HNS-FP	1.5 × 1.4	0.15	1.30

than HNS-FP for the conditions stated. The only parameter to vary in these experiments was the initial grain size, in view of which, it seems reasonable to attribute the observed reversal of shock sensitivity in HNS to the difference in initial grain size. SEM photographs of the three HNS types reveal porous microstructures without well defined grain boundaries which can be attibuted to the ductile behavior of the material during pressing. Thus, it seems reasonable to assume that the pore collapse mechanism is primarily responsible for hot spot formation in this explosive, thereby making it a perfect candidate for the present analysis.

Estimation of the values for the yield stress Y and shock front viscosity μ for HNS are based on observations of the mechanical response of the explosive and shock front thickness estimates (17), whereas $\varrho\chi$ is determined by means of the relation $\varrho\chi=\kappa/c_v$ along with the known values for κ and c_v (18,19). Consequently, Y=7 bar, μ is in the range from 10 to 100 poise, and $\varrho\chi$=5.6 g/cm-s. The shock front thickness w_s is estimated to be 0.4μm for a 30 kbar shock and the length scale x_c is assumed to lie in the range $w_s<x_c<10w_s$. As mentioned previously, the experimental conditions were such that P=30 kbar for a shock duration τ of $\sim$1μs thus, the first three dimensionless parameters in eq. (2), assume the following values:

$$\frac{Y}{P} = 2.3\times10^{-4}\,,\quad 300 < \frac{\tau P}{\mu} < 3000\,,$$
$$1.8 < \frac{\mu}{\varrho\chi} < 18. \qquad (4)$$

The values of these parameters suggest that 1) the energy dissipation associated with shock compression is due to viscous heating (rather than plastic work), 2) the experimental conditions are such that the shock duration is sufficiently long so as to have no affect on the initiation process, and 3) the shock front structure is primarily determined by viscous effects (instead of heat conduction). The values of the pore size and spacing parameters δ and λ are determined by means of the microstructure information in Table 1 and the estimated value of w_s. As seen from their values listed in Table 2, δ ranges over values greater than to less than 1, whereas λ is relatively constant for the three HNS types. That λ remains fixed is consistent with the fact that the three HNS types possess the same initial pressing density or equivalently, the same initial porosity. Thus, the only parameter to vary between the three types is the pore size parameter δ, which in view of its significance (i.e., representing initial grain size or pore size), the remainder of this work will be devoted to the study of the influence of initial grain size on the shock sensitivity of HNS.

TABLE 2
Measured values of the pore size and spacing parameters δ and λ for the three HNS types

	δ (=d/w_s)	λ (=s/d)
HNS-II	13.3	8.1
HNS-I	1.5	8.0
HNS-FP	0.4	8.7

METHODOLOGY

The methodology within the present analysis centers around the use of a microstructure model for HNS and observation of its response to shock loading for various values of the pore size parameter δ. The complexity of the model is substantially reduced by assuming the hot spots are noninteracting during their formation. This assumption appears justified for the HNS types considered herein due to the relatively

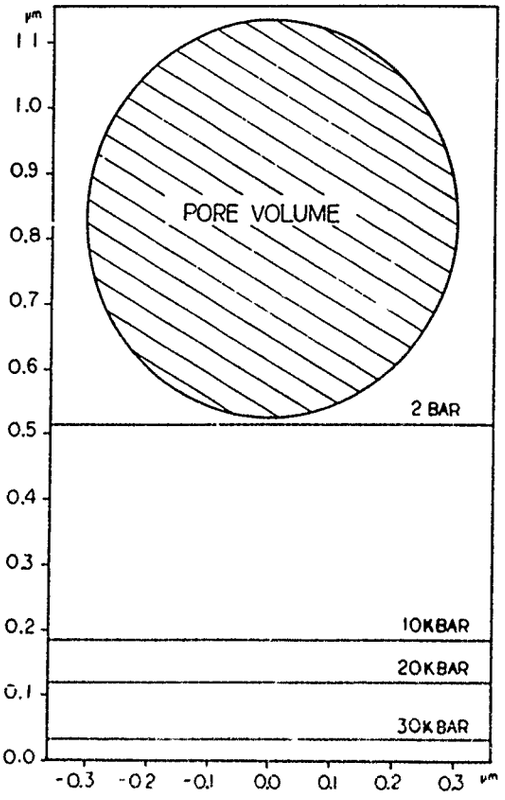

Fig. 1(a)

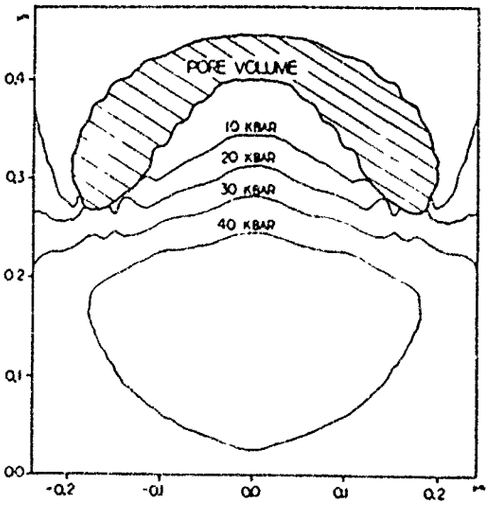

Fig. 1(b)

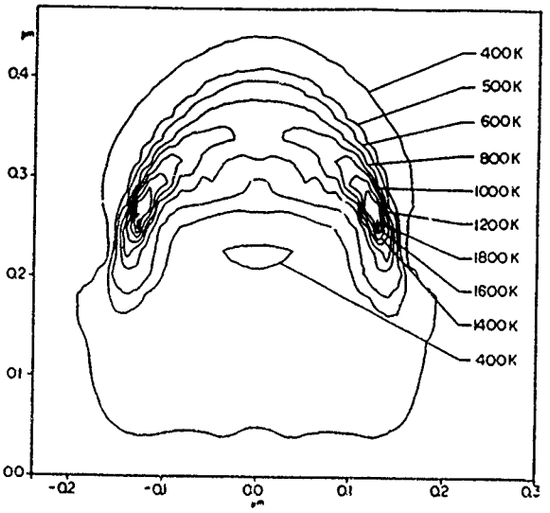

Fig.1(c)

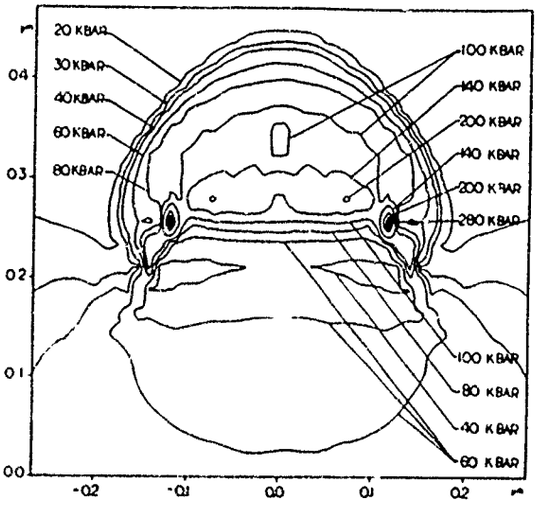

Fig. 1(d)

Fig. 1. Hot spot evolution by means of pore collapse ((a) A 30 kbar shock wave, propagating vertically upward, is located just below the pore. (b) Partial collapse of the pore. The lower portion of the pore surface is accelerating towards the upper portion. (c) and (d) Temperature and pressure contour plots of the hot spot at maturity, corresponding to $\delta = 1.36$.)

large values of the pore spacing parameter λ displayed by these types (see Table 2). Thus, the HNS microstructure may be represented by a self-consistent model that effectively models the

response of the complete network by considering only a small portion of it containing only the essential feature of the microstructure. Here, the model is comprised of a cylinder of unreactive HNS initially at the crystal density of 1.74 g/cc, within which, a single spherical pore of 0.6μm diameter is embedded. The dimensions of the cylinder are set such that the hydrodynamics of the pore collapse is unaffected by wave interactions with the lateral and downstream boundaries. The HNS material is modeled as an isotropic, elastic-perfectly plastic compressible material possessing a yield strength of 7 bar (20). Hugoniot information for the HNS material was obtained from the work of Sheffield et al. (21) and represented by the equation

$$U_s = (3.026 + 1.141 u_p) \frac{mm}{\mu s}. \qquad (5)$$

Plane shock waves of various rise-times were introduced at the lower boundary of the cylinder in order to observe hot spot formation by means of collapse of the embedded pore. The value of δ for any particular run was determined by dividing the fixed initial pore diameter by the corresponding shock front width.

RESULTS

Figure 1 illustrates the general features of hot spot evolution where in 1a, the wave is propagating vertically upward and located just below the pore. Figure 1b shows the pore partially collapsed with the lower portion of the pore's surface experiencing an acceleration towards the upper portion. Figures 1c and 1d display the temperature and pressure contour plots of the hot spot at maturity corresponding to the value of δ=1.36. The results of the calculations illustrate two important features of hot spot formation. The first being the impact of the lower portion of the pore surface with the upper portion, giving rise to temperatures that are dependent upon the corresponding value of the pore size parameter δ. This result is illustrated in Figure 2 showing impact temperature excursions for values of δ and between 0.39 and 1.57. The time origin of these plots corresponds to the moment of contact of the lower and upper surface portions, with the temperature excursions continuing to the onset of hot spot maturity. As seen in the figure, the maximum impact temperatures corresponding

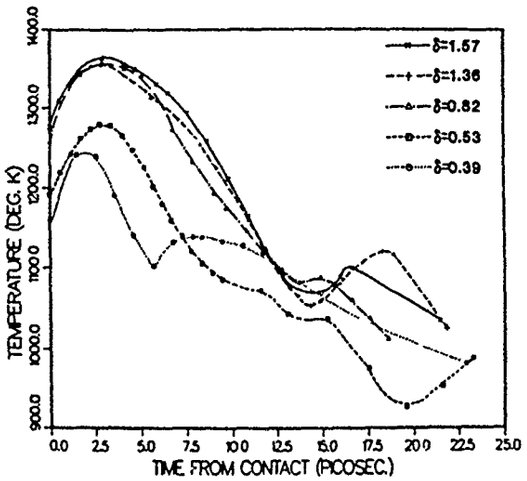

Fig. 2. Impact temperature excursions for various values of the pore size parameter δ

to values of δ greater than 0.8 exhibit no dependence on the pore size parameter. However, those temperatures corresponding to values of δ less than 0.8 do indeed display a dependence on δ, where the temperature now decreases for a decrease in δ. The second important feature of hot spot formation is associated with the irreversible work of closing the pore in an elastic-plastic material. This process leads to the deposition of thermal energy, denoted here by E_T, at the hot spot site. The calculated values of the hot spot thermal energy E_T appear in Table 3 for the various values of δ considered in the present analysis. These values of E_T represent the average thermal energy over the hot spot region at the onset of maturity, where the thermal energy at any point P in the hot spot region is caluclated according to the relation

$$E_T(P) = c_V \rho(P) T(P), \qquad (6)$$

TABLE 3

Calculated values of hot spot thermal energy E_T as a function of the pore size parameter δ

δ	E_T (J/cc)
1.57	1372
1.36	1403
0.82	1327
0.53	1352
0.39	1366

ave.=1364, max. dev.=3%

where ϱ and T denote the mass density and temperature and c_V(=1.5 J/g-K) the specific heat. As may be seen in Table 3, the hot spot thermal energy is independent of the pore size parameter δ for all values considered, where, the maximum deviation from the mean value of E_T is 3%. The temperature and pressure fields at hot spot maturity persist for approximately 0.5 ns after which, they begin to decay towards a thermomechanical equilibrium with the surrounding bulk-shocked material. Averaging the hot spot temperature field as generated by both the surface impact and plastic work mechanisms over the lifetime of the hot spot ($\sim$0.5$-$1.0 ns) yields the time-averaged temperature values listed in Table 4 as a function of the pore size parameter δ. Here, the temperatures exhibit no dependence on δ for values greater than 0.8, below which, the lifetime-averaged hot spot temperatures then decrease for a decrease in δ. In fact, the calculations predict a 9.3% reduction in this temperature for δ=0.39.

TABLE 4

Lifetime-averaged values of hot spot temperatures as a function of the pore size parameter δ

δ	T_{ave}(K)
1.57	1200
1.36	1192
0.82	1199
0.53	1099
0.39	1086

DISCUSSION

As mentioned in the previous section, the formation of a hot spot involves two essential features. The first being the impact of the upstream and downstream portions of the pore surface giving rise to temperatures that are dependent upon the parameter δ whenever δ<0.8. The second feature is associated with the collapse of the pore by means of irreversible work performed by the shock wave in an elastic-plastic material. The result of this second feature is the deposition of thermal energy, the amount of which, was found to be independent of the pore size parameter δ. As a result of these features, the lifetime-averaged hot spot temperatures decrease whenever δ is reduced to a value below 0.8. Assuming that hot spot chemical decomposition displays an induction time on the order of 1 ns, then as δ is decreased below 0.8, the results of the calculations suggest the formation of hot spots possessing temperatures that are insufficient to ignite the grain burning process. Indeed, this appears to be the case for HNS-FP, where the medium-grained HNS-I displays a shorter run distance to detonation than that of the fine-grained HNS-FP, corresponding to a reduction in δ from 1.5 to 0.4. The fact that the medium-grained HNS-I exhibits a shorter run distance to detonation than the coarse-grained HNS-II, and in view of the independence of hot spot temperatures on δ for δ>0.8, suggests that the dominant mechanism in the shock initiation process of both HNS-I and II is that of grain burning. However, as supported by experimental observation and the results of the present calculation, there is a critical average pore diameter (and hence grain size) below which, a sufficient portion of the hot spots formed are unable to ignite the grain burning process within the time required for an effective coupling of the energy release to the shock front. In the case of HNS, this critical average pore diameter lies somewhere in between those displayed by HNS-I and FP. The lack of dependence of E_T on δ in the present caluculation may be attributed to the absence of rate dependence in the constitutive model for the HNS material (recall the HNS was modeled as elastic-perfectly plastic). However, results of other investigations (4,5) incorporating rate dependent material response suggest that E_T would tend to decrease for a decrease in δ whenever $\delta\sim$1. This additional result would imply an even greater impotence of the hot spots than described above in their role of igniting the grain burning process.

Although the analysis described in this paper is specific to HNS, the underlying features of hot spot formation by means of pore collapse are universal and should be applicable to all heterogeneous explosives that depend upon the mechanism of pore collapse as a primary source of hot spot formation.

REFERENCES

1. Taylor, B.C. and Ervin, L.W., Proceedings of the Sixth Symposium (International) on Detonation, Office of Naval Research, ACR-221, Arlington, Va. 1976, p.3.

2. Campbell, A.W., Davis, W.C., Ramsay, J.B., and Travis, J.R., Phys. Fluids *4*, 511 (1961).

3. Mader, C.L., Phys. Fluids *8*, 1811 (1965).

4. Khasainov, B.A., Borisov, A.A., Ermolaev, B.S., and Korotkov, A.I., Proceedings of the Seventh Symposium (International) on Detonation, Naval Surface Weapons Center, White Oak, MD, NSWC MP 82-334, 1981, p.435.

5. Frey, R.B., Proceedings of the AGARD Meeting on Hazard Studies for Solid Propellant Rocket Motors, Lisse, Netherlands, May 1984.

6. Lee, E.L. and Tarver, C.M., Phys. Fluids *23*, 2362 (1980).

7. Winter, R.E. and Field, J.E., Proc. R. Soc. Lond. A*343*, 399 (1975).

8. Setchell, R.E. and Taylor P.A., Shock Waves, Explos., and Det., AIAA Progress in Astronautics and Aeronautics, (ed. by J.R. Bowen, N. Manson, A.K. Oppenheim, and R.I. Soloukhin) vol. 95, AIAA, New York, NY (1984).

9. Andreev, S.G., Boiko, M.M., and Solov'ev, V.S., Combust. Explos., and Shock Waves *12*, 102 (1976).

10. Hayes, D.B., Shock Waves, Explos., and Det., AIAA Progress in Astronautics and Aeronautics, (ed. by J.R. Bowen, N. Manson, A.K. Oppenheim, and R.I. Soloukhin) vol. 87, 445, AIAA, New York, NY (1983).

11. Howe, P., Frey,R., Taylor, B., and Boyle, V., Proceedings of the Sixth Symposium (International) on Detonation, Office of Naval Research, ACR-221, Arlington, Va. 1976, p.11.

12. Von Holle, W.G., Fast Reactions in Energetic Systems, (ed. by C. Capellos and R.F. Walker), 485, D. Reidel Publishing Co., Boston (1981).

13. deLongueville, Y., Fauquignon, C., And Moulard, H., Proceedings of the Sixth Symposium (International) on Detonation, Office of Naval Research, ACR-221, Arlington, Va. 1976, p.105.

14. Honodel, C.A., Humphrey, J.R., and Weingart, R.C., Proceedings of the Seventh Symposium (International) on Detonation, Naval Surface Weapons Center, White Oak, MD, NSWC MP 82-334, 1981, p.425.

15. Kramer, P.E., Pantex Plant Report No. MHSMP-83-46 (1983).

16. Zel'dovich Y.B. and Raizer, Y.P., *Physics of Shock Waves and High Temperature Hydrodynamic Phenomena*, vol. II, Academic Press, New York (1967).

17. Taylor P.A., Proceedings of the Topical Conference on Shock Waves in Condensed Matter held in Santa Fe., N.M., North-Holland, New York, NY. 1984, p.597.

18. Dobratz, B.M., *LLNL Explosives Handbook*, UCRL-52997, Univ. of California, Ca. (1981).

19. Hayes, D.B. and Mitchell, D.E., Proceedings of the Symposium HDP, Commissariat a L'Energie Atomique, Paris, France, 1978, p. 161.

20. The results here are invariant to changes up to at least an order of magnitude in the yield strength.

21. Sheffield, S.A., Mitchell, D.E., and Hayes, D.B., Proceedings of the Seventh Symposium (International) on Detonation, Office of Naval Research, ACR-221, Arlington, Va. 1976, p.748.

This work performed at Sandia National Laboratories supported by the U.S. DOE under contract # DE-AC04-76DP00789.

DISCUSSION

JULIUS ROTH, Portola Valley, California

It would appear that the coefficients in Eq. (5) of the paper may have been transposed. In the 5th Detonation Symposium p.222, we showed that $U_s = 1.00+3.18u_p$ for HNS-II, in good agreement with subsequent results by Sheffield et al. (6th Detonation Symposium p.752) for HNS-I and HNS-II. Both our work and that of Sheffield was for $\varrho = 1.58$ g/cm³ which is essentially the same as Taylor's initial density.

REPLY BY P.A. TAYLOR

My paper was based on simulating the details

of shock compression of the material microstructure which was modeled as a volume of HNS material at crystal density (ϱ = 1.74 g/cc) containing a spherical void. As such, the wave code that I used in the simulation required a Hugoniot for this HNS material at crystal density. Using the equation of state for HNS as determined by Sheffield et al. (6th Detonation Symposium, p. 748), I arrived at the U_s-U_ϱ Hugoniot for HNS at 1.74 g/cc that appears in Eq . (5). In response to your comment, I have checked this Hugoniot and find that it is indeed correct for HNS at crystal density.

DISCUSSION

EDWARD LEE, Lawrence Livermore National Laboratory

Does the HNS-FP show better divergence i.e., run distance shorter than HNS-I at higher pressure? If yes, how is this explained in your modeling analysis?

REPLY BY P.A. TAYLOR

Pop-plot data of P. Kramer (ref. 15 in paper) of Pantex suggests that for sustained shocks, HNS-FP will display shorter run distances than HNS-I at pressures above ~100 kbars. If, at these pressures, the hot spot model still holds as I have presented it in the paper, then it's quite possible that at these pressures, the pore size parameter $\acute{o}$ is now greater than 1 for HNS-FP since, by definition, $\acute{o}$ is proportional to the square root of the shock amplitude. Thus, adequate hot spot nucleation in HNS-FP is restored and its sensitivity will then be dominated by the availability of specific surface area. If so, then HNS-FP can then be expected to be more sensitive than HNS-I since it possesses a greater internal specific surface area. However, my personal view is that this process of ignition and growth that I have described is applicable only at lower shock amplitudes whereas, for the higher amplitudes, I suspect that the chemical energy release is occurring very close to the shock front and associated with various mechanisms among which, void collapse may not be the most important.

MODELING GRANULAR EXPLOSIVE DETONATIONS WITH SHEAR BAND CONCEPTS

M.E. Kipp
Sandia National Laboratories
Albuquerque, New Mexico 87185

In theories that are formulated to describe shock-induced reactions in granular explosives, it is necessary to identify and model mechanisms that contribute to the growth or decay of the reaction. The concept of hot spot formation and subsequent reaction is examined on the basis of recent work on shear-band nucleation. In this context, the energy dissipated by the shock preferentially heats a volume fraction of the material to a relatively high local temperature. Heat conduction takes place driving the temperatures toward equilibrium, in competition with the reaction of the heated material. As the amplitude of loading increases, the volume of nucleated hot material also increases, thus decreasing the volume of cold material remaining that must decompose by grain burning.

INTRODUCTION

As reactive flow models of porous granular explosives have developed, various physical concepts associated with mechanical loading and induced chemical reactions have been examined. In most formulations, concepts of nucleation and reaction of hot spots provide the initial step in the decomposition process (1, 2, 3, 4). In some cases, as in Nunziato, et al(5) and Hayes(6), the initial volume of available hot spot material was prescribed, and was generally associated with a volume of material equivalent to available pore volume. It was argued that the deformation during shock loading localizes around the pores, and as the pore collapses, this volume of highly deformed material is quite similar to that of the original pore volume (6). Numerical studies have shown that the pore collapse can involve jetting, and that the localized plastic deformation provides an energy dissipation mechanism (3, 6, 7). In addition, the studies by Taylor (7) indicate that this hot spot formation mechanism is related to grain size (and consequently pore size), and contributes to observed grain size sensitivity trends of pressed explosives.

At relatively low pressures, this equivalent pore volume concept is quite reasonable, but as the shock amplitude grows, the amount of energy required to be dissipated by crushing of the solid is too large to be confined to this fixed volume. In addition, as more porosity is introduced into the material, this prescribed volume of hot spots becomes large, and assumptions inherent in the application of the equivalent volume concept (e.g. widely-spaced voids) need to be reconsidered.

In the present paper, recent advances of shear-band concepts for shock-loaded metals are explored as a means to construct a mechanism that initiates the reaction in granular explosives due to shock loading. Although the study here deliberately excludes the porous collapse mechanisms mentioned above, it is to be expected that multiple types of localized deformation are responsible for the initiation of granular explosives and eventually must be included in a more complete model. As in previous models, reference is made to experimental evidence for the existence of localized heating, and the reported measurements of associated temperatures (8). The concepts are included in a thermomechanical continuum mixture model, in which

individual temperatures for the hot spots and parent grains are accommodated. An application to PBX-9404 is described.

FORMULATION

As a compressive shock wave passes through a material, dissipation of energy occurs at each material point as it is transformed from ambient conditions to the shocked state. One of the mechanisms proposed to account for this dissipated energy in metals is that of localized thermal trapping in the form of shear bands (9). The concept of shear bands and related reaction processes in explosives was discussed by Frey (10), and the general features of hot spot formation with subsequent thermal cooling has been treated by several authors, both in the application to metals (9, 11) and to explosives (3, 6, 8, 10).

A few key assumptions are required to permit a model to be constructed that has parallels in metal shear-band formation, and is consistent with observed explosive behavior. Although the fine structure of shear bands observed post-shock in metals cannot be readily seen in reacting materials, as noted in the introduction, there is evidence for the existence of hot spots in shocked explosive (e.g. (8)). The heterogeneous nature of granular explosives (and metals) contributes to the tendency to deform locally.

The energy available for dissipation during shock loading, ε_D, may be approximately represented by the area between the Hugoniot and the Rayleigh line (9), provided that the Hugoniot and release isentrope are nearly the same (Figure 1). (As the porosity increases, this assumption loses its validity, and more precise accounting must be made of the energy.) The dissipated energy is then

$$\varepsilon_D = -\int_{V_o}^{V} (P_R - P_H)dV, \qquad (1)$$

where P_R is the Rayleigh line upon which loading occurs, and P_H is the Hugoniot describing the shock end states. If we assume that this energy is dissipated in a relatively small volume fraction of the material, then large local temperature increases will occur. The magnitude of this volume fraction of hot material determines the relative temperature difference that will exist in the hot and cold solid. The total energy, ε_D, is a function of the shock amplitude and curvature of the Hugoniot, and given

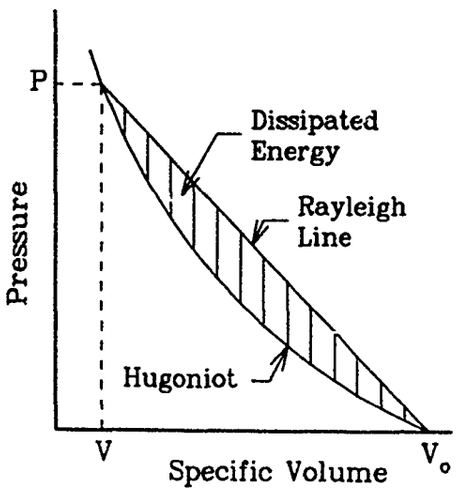

Fig. 1. Dissipated energy in shock loading

a partitioning of hot and cold volume fractions, governs the actual magnitude of the temperature increase.

The upper constraint imposed here on the formation of hot material is that in the steady detonation wave, all of the explosive will be transformed to hot material by the time the spike point is reached in the rise-time of the wave. At lower pressure shocks, during the growth to detonation, the nucleated volume fraction of hot material, ϕ_H, will be assumed to be proportional to ε_D of the local shock,

$$\phi_H = \varepsilon_D/\varepsilon_{DS}, \qquad (2)$$

where ε_{DS} is the calculated dissipated energy for a shock to the spike point. Since the temperature of the hot material is also proportional to the dissipated energy, ε_D, one immediate implication of this assumption is that the initial temperature of the hot material will be virtually independent of shock amplitude. The lack of perfect identity of the Hugoniot and the isentrope means that some temperature increase in the hot material will occur with increased shock amplitude for normal nonlinear material behavior. These minor variations in temperature are consistent with observations of von Holle (8), where over a range of shock amplitudes, relatively constant temperatures were achieved for an HMX-based explosive.

The distribution of the volume fraction of hot material must also be addressed, because characteristic lengths and available surface area will influence the heat conduction, as well as the

reaction kinetics. Guidance from shear-banding analysis is helpful here. Grady and Kipp (11) have determined that in materials with shear strength, the number, width, and spacing of the bands are influenced by concepts of momentum diffusion and heat conduction. The spacing is a function of wave communication times between bands, and the width is dependent on the heat transfer properties of the material. If we assume a band structure in the present case, then a characteristic configuration would appear as in Figure 2. As noted earlier, then, at an

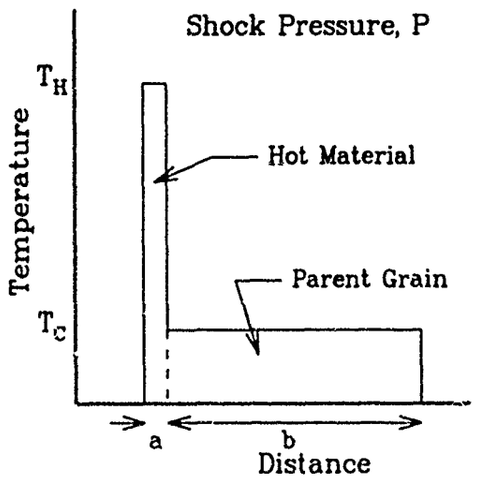

Fig. 2. Initial local temperature distributions resulting from shock to pressure P

increased shock amplitude, the temperature achieved in the hot material changes little, but an increased volume of hot material is formed. One possibility is for the band width to increase, retaining a constant spacing. It seems more likely, however, based on the work of Grady and Kipp (11), that the number of bands will increase with shock amplitude, thus decreasing the spacing between bands, and increasing the available surface area for grain burning. Usually an increased rate of loading and energy available for dissipation is associated with higher pressure amplitudes, with the result that more bands nucleate and grow before local relaxation effects or heat conduction can arrest their formation (11).

In Figure 2, the volume fraction of hot material, ϕ_H, is $a/(a+b)$. The shear band width, a, has been determined to be related to thermal conduction (11) by

$$a^2 = \frac{\kappa}{2\varrho C_v} t, \tag{3}$$

where t is the time available to grow during the rise time of the wave, κ is the thermal conductivity, ϱ is the density, and C_v is the specific heat. Approximate heat conduction under these circumstances has been related to the band width (11), and the amount of heat transferred to the cooler material will depend on the relative width of the hot bands. We assumed the form

$$\frac{dT_H}{dt} = \frac{\kappa}{\varrho C_v} \frac{T_C - T_H}{(1.4a)^2}, \tag{4}$$

where T_H is the temperature of the hot material, and T_C is the temperature of the cold material. (The factor 1.4 in the denominator provides a better approximation to the heat flow under the assumed initial circumstances of discontinuous temperatures in the hot and cold solid, Swegle (12).) At early times, the shear band width is very small, so that the heat conduction rates are large. When the loading rates and dissipated energy rates are large enough, the bands will grow to sufficient size that a discontinuous temperature distribution can be maintained.

Finally, reaction laws must be specified for the hot and cold material decomposition. As in past models, the reaction laws have tended to be tailored to the specific formulation (1, 2, 3, 4, 5), so parameters and forms have not been unique. Thermal explosion of the hot material is assumed here, and grain burning is treated by pressure dependent rules (2, 4, 5, 6).

REACTIVE MIXTURE MODEL

The thermomechanical structure into which the concepts of the previous section have been incorporated is a continuum theory of multiphase mixtures (5). This theory provides a consistent means whereby each constituent of the mixture can have its own equation of state with unique temperature, density, and pressure. The constituents interact with one another through mass and energy exchange terms that include the reaction kinetics, local heat transfer, and volume fraction changes. The latter two drive the mixture toward thermal and pressure equilibrium, respectively. (In this theory as applied to shock-wave problems, the characteristic times are sufficiently short that relative diffusion of the constituents has been neglected.)

The model has been incorporated into the WONDY finite difference wave propagation code (13) as an equation of state. The energy dissipation is calculated with the artificial viscosity in the code, Q, which is identified with the pressure difference between the Hugoniot and the Rayleigh line. The rate of dissipation is

$$\dot{\varepsilon}_D=\dot{\varrho}Q/\varrho^2, \tag{5}$$

where ϱ is the mixture density. This dissipated energy is then channelled into the heating of the hot bands of material via the constituent energy balance equations.

The nucleation of the hot bands out of the parent granular explosive is accomodated by the mass balance equations for the constituents (5). These balance laws also take into account the mass exchanges associated with the phase transformations due to chemical reaction.

The equation of state forms of the constituent materials are discussed in Numziato, et al (5), with the change that the solids are described more simply with the Helmholz free energy

$$F(T,V)=C_V\left[(T-T_0)(1-\frac{\Gamma}{V}(V_0-V))+T\ln(\frac{T_0}{T})\right]$$
$$+\frac{K_0V_0}{N(N-1)}\left[(\frac{V_0}{V})^{N-1}-(1-\frac{V}{V_0})(N-1)-1\right], \tag{6}$$

a form discussed by Hayes and Mitchell (14). As before, the pressure, p, and, internal energy, e, are defined by

$$p=\frac{-\partial F}{\partial V},\quad e=F-T\frac{\partial F}{\partial T}. \tag{7}$$

In the free energy function, Equation (6), Γ/V (assumed constant), the specific heat, C_V, reference volume, V_0, reference temperature, T_0, modulus, K_0, and power, N, form the equation of state parameters. The reaction products are described by an Abel equation of state (5).

APPLICATION TO PBX-9404

The equation of state parameters for PBX-9404, for use in Equation (6), are $C_V=1.5\times10^3$ J/kgK, $\Gamma/V=2.1$ Mg/m^3, $V_0=535\times10^{-6}$m^3/kg, $K_0=12.41$ GPa, $N=7.75$, and $T_0=298$K. This same equation of state holds for both the hot and cold solids. The specific energy released in the reaction of both the hot and cold material is assumed to be 5.73 MJ/kg.

Using the isentrope from Equations (6) and (7) to approximate the Hugoniot, calculation of the total available dissipated energy to an assumed spike point of 50 GPa for PBX-9404, results in a value for ε_{DS} of $\sim$2.5MJ/kg. From Equations (2) and (5), the volume fraction rate of formation of hot material, $\dot{\phi}_H$, is then

$$\dot{\phi}_H=\dot{\varrho}\frac{Q}{\varrho^2}/\varepsilon_{DS}. \tag{8}$$

The reaction rate of the hot material, $\dot{\phi}_{HR}$, is assumed to be exponential in the temperature of the hot material, taking the form

$$\dot{\phi}_{HR}=A\phi_H\phi_H^{max}\gamma_H e^{T_{H/B}}, \tag{9}$$

where γ_H is the density of the hot material, and the constants A and B are 100m^3/kgs and 298K respectively. ϕ_H^{max} is the maximum volume fraction of hot material that has existed locally, and supports increased rates of reaction for larger volumes of nucleated hot material. (Attempts to use thermal explosion data of Rogers (15) have been unsuccessful to date. The Arrhenius reaction rates cause the growth to be too rapid at the wave front in our calculations, and we were not able to obtain results that agree with available wave propagation data.) The responses of the HMX and binder have been combined for this application.

The rate of grain burning, $\dot{\phi}_{GB}$, has been assumed to take the form

$$\dot{\phi}_{GB}=C\gamma_C\phi_C^{1/9}\phi_R^{1/2}P_R e^{P_R/D}, \tag{10}$$

where P_R is the reaction products pressure, γ_C is the grain density, ϕ_C is the grain volume fraction, ϕ_R is the products volume fraction, and C and D are constants, 7×10^{-8} m^3/kgPa s and 10 GPa respectively.

The thermal conductivity, κ, required in Equation (4), was taken to be 0.29 J/msK.

RESULTS

When shocked to 3.8 GPa, the temperature in the hot material increases from ambient (298K) to about 1600K. This temperature is slightly higher than that reported by von Holle (8). The volume fraction of hot material at this pressure is about 1.6 percent, nearly the same as the assumed initial porosity of 1.5 percent. (If no heat conduction from the shear bands were permitted, the temperature reaches about 1900 K for this amplitude shock.) The calculated shear band temperature and volume fraction for a few initial pressures are illustrated in Figure 3. The temperature, as discussed above, indeed varies very little in the pressure regime of interest here. The volume fraction is increasing with pressure,

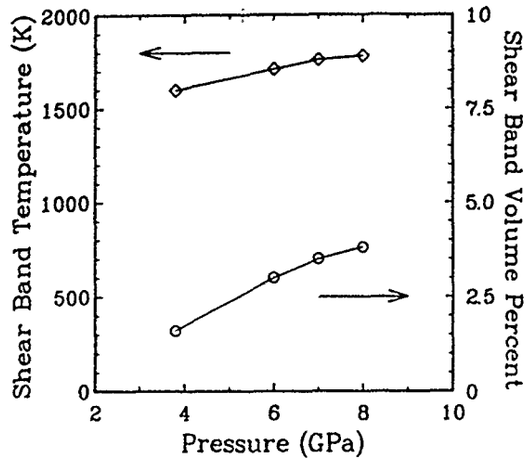

Fig. 3. Variation of temperature and volume fraction of shear bands with shock pressure

and when detonation conditions are reached (not shown in the figure), all of the material has been transformed to hot shear bands, and reacts according to Equation (9).

The calculated shear band width at 3.8 GPa is about 0.16μm, which is consistent with sizes in the analyses of Frey (10) and Grady and Kipp (11). As the amplitude of load increases, the band width decreases, until at detonation, the shear bands have time to grow only to 0.06μm in width.

The evolution of a 3.8 GPa supported shock at 1 mm intervals as reported by Kennedy and Nunziato (16) is shown in Figure 4. The agreement is very good through 5 mm, with some slight delay in final growth to detonation at 6 mm. However both the growth of the shock front and the increase in wave slope behind the shock are well represented.

The evolution of the same initial 3.8 GPa shock through detonation is presented in Figure 5. The development of the wave with the shock growing at the front and the pressure building behind the front to a steady detonation is characteristic of heterogeneous explosives, and is quite similar to that previously reported (e.g. 2, 4, 5). The detonation wave assumes the classic form of the von Neumann spike followed by unloading to Chapman-Jouguet conditions. The C-J pressure is about 37 GPa, and the detonation velocity has reached 8.8 km/s, both in agreement with tabulated values (17).

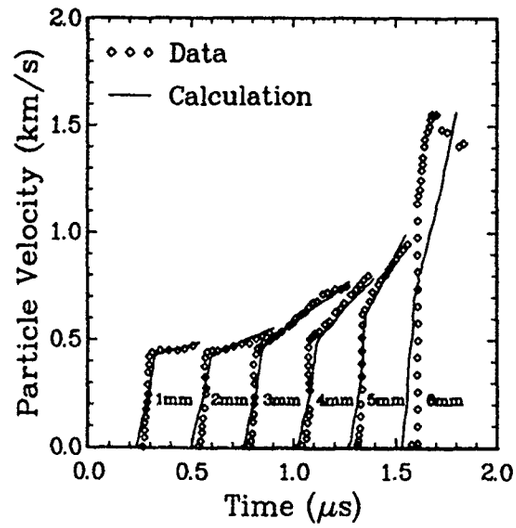

Fig. 4. Comparison of data from Kennedy and Nunziato (16) with calculations for a 3.8 GPa shock

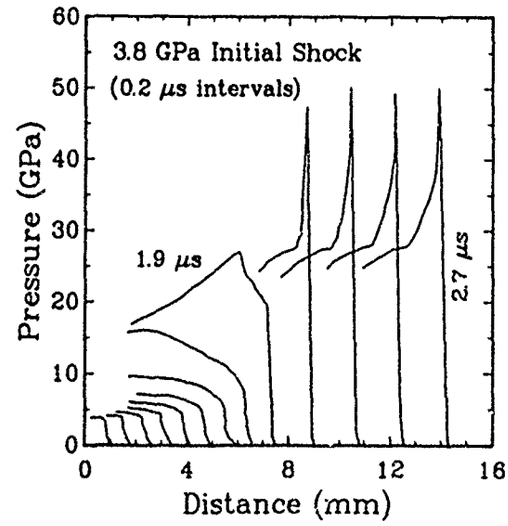

Fig. 5. Evolution of detonation in PBX-9404 from 3.8 GPa shock

Run distance to detonation calculations are compared with data (17) in Figure 6. Again, the results indicate that the reactions are evolving from the initial shock conditions in a satisfactory manner. We note that the low amplitude shock (2.5 GPa) has grown to detonation about 1-2 mm early.

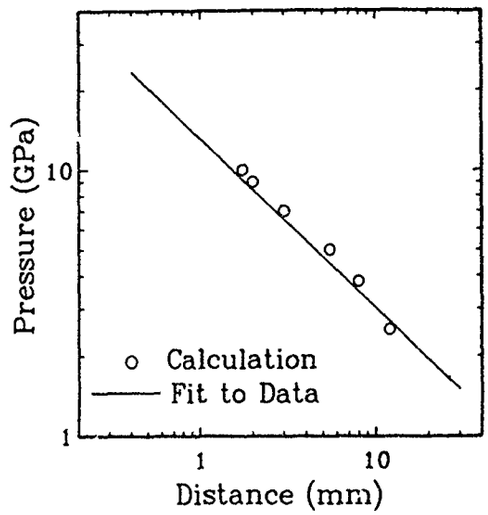

Fig. 6. Run distance to detonation in PBX-9404: Calculations and data (Reference 17)

Comparisons with a much wider body of data need to be made in order to conclude that the model has accounted for sufficient physical microstructural response. There are several issues that have been only briefly touched upon that need considerably more thought. These issues include the inital volume and distribution of porosity through the solid, effects of grain size, and explicit treatment of the binder. In addition, the temperature calculated in the hot bands of material is clearly well above the melting temperature of HMX. This phase change has not explicitly been incorporated, nor the possible consequences on reaction kinetics addressed. These concepts can, however, be accommodated in the present thermomechanical structure.

Finally, this study has shown that shear-band formation is a feasible mechanism for granular explosive initiation. It represents a satisfactory means for energy dissipation at all shock amplitudes, and results in temperatures that are within observed bounds. The length scale associated with the calculated shear band widths is also within realistic bounds. The provision for explicit and distinct temperatures and phases within the explosive continues to be viewed as an important model attribute.

ACKNOWLEDGMENTS

The author would like to acknowledge many helpful discussions with J.W. Swegle and D.E. Grady, and the continued support of J.E. Kennedy. This work performed at Sandia National Laboratories supported by the U.S. Department of Energy under contract number DE-AC04-76DP00789.

REFERENCES

1. P. Donguy and N. Legrand, "Numerical Simulations of Non-Ideal Detonations of a Heterogeneous Explosive with the Two Dimensional Eulerian Code C.E.E.," *Proc. Seventh Symp. (International) on Detonation*, Annapolis, MD, 695-702, 1981.

2. E.L. Lee and C.M. Tarver, "Phenomenological Model of Shock Initiation in Heterogeneous Explosives," *Phys. of Fluids*, 23, No. *12*, 2362-2372, 1980.

3. C.L. Mader, Numerical Modeling of Detonations, University of California Press, Berkeley, 1979.

4. J. Wackerle, R.L. Rabie, M.J. Ginsberg, and A.B. Anderson, "A Shock Initiation Study of PBX-9404," Symposium HDP (Behavior of Dense Media Under High Dynamic Pressure), Paris, August 1978.

5. J.W. Nunziato, M.E. Kipp, R.E. Setchell, and E.K. Walsh, "Shock Initiation in Heterogeneous Explosives," Sandia National Laboratories Report, SAND 81-2173, September 1982.

6. D.B. Hayes, "Shock Induced Hot-Spot Formation and Subsequent Decomposition in Granular, Porous HNS Explosive," Shock Waves, Explosions, and Detonations, J.R. Bowen, et al (eds.) Vol. 87 of Progress in Astronautics and Aeronautics, 1983.

7. P.A. Taylor, "The Effects of Material Microstructure on the Shock Sensitivity of Porous Granular Explosives," *Proc. Eighth Symp. (International) on Detonation*, Albuquerque, NM, 1985.

8. W.G. von Holle, "Temperature Measurements of Shocked Energetic Materials by Time-Resolved Infrared Radiometry," Fast

Reactions in Energetic Systems, ed. C. Capellos and R.F. Walker, 485-502, Reidel Publ., 1982.

9. D.E. Grady and J.R. Asay, "Calculation of Thermal Trapping in Shock Deformation of Aluminum," *J. of Appl. Phys., 53*, No. *11*, 7350-7354, 1982.

10. R.B. Frey, "The Initiation of Explosive Charges By Rapid Shear," *Proc. 7th Symp. (International) on Detonation*, Annapolis, MD, 36-42, 1981.

11. D.E. Grady and M.E. Kipp, "The Growth of Inhomogeneous Thermoplastic Shear," *Proc. Int. Conf. on Mechanical and Physical Behavior of Materials under Dynamic Loading*, Paris, September 2-5, 1985.

12. J.W. Swegle, Personal communication, 1985.

13. M.E. Kipp and R.J. Lawrence, "WONDY V - A One-Dimensional Finite-Difference Wave Propagation Code," Sandia National Laboratories Report SAND81-0930, 1982.

14. D.B. Hayes and D.E. Mitchell, "A Constitutive Equation for the Shock Response of Porous Hexanitrostilbene (HNS) Explosive," *Proc. of the Symp. HDP*, Commissariat a L'Energie Atomique, Paris, 1978.

15. R.N. Rogers, "Thermochemistry of Explosives," *Thermochimica Acta, 11*, 131-139, 1975.

16. J.E. Kennedy and J.W. Nunziato, "Shock-Wave Evolution in a Chemically Reacting Solid," *J. Mech Phys. Solids, 24*, 107-124, 1976.

17. B.M. Dobratz, "LLNL Explosives Handbook," Lawrence Livermore Laboratory Report, UCRL-52997, 1981.

DISCUSSION

B. MOROSIN, Sandia National Laboratories

How can 1500°K shear band temperatures be reasonable for weakly bonded, intermolecular forces in explosives? Would shearing of graphite-like materials be very different? Are there experimental values to indicate the 1500°K temperatures?

REPLY BY M.E. KIPP

The temperature rise in the shear bands that form during shock compression results from the dissipation of the shock energy in the volume of the shear bands. These calculated temperatures are 2-300°K higher than what was observed by W. von Holle (Reference 8 in the paper) for this explosive (PBX-9404). As noted in the paper, I assumed that all of the energy was dissipated in the shear bands, but that other dissipative mechanisms are likely at work, including pore collapse. This additional volume of material available for dissipation of energy will tend to lower the temperature of the hot regions.

THE THREE-DIMENSIONAL HYDRODYNAMIC HOT-SPOT MODEL

Charles L. Mader and James D. Kershner
Los Alamos National Laboratory
Los Alamos, New Mexico

The interaction of a shock wave with a single air hole and a matrix of air holes in PETN, HMX, and TATB has been numerically modeled. The hot-spot formation, interaction, and the resulting build up toward detonation were computed using three-dimensional numerical Eulerian hydrodynamics with Arrhenius chemical reaction and accurate equations of state according to the hydrodynamic hot-spot model. The basic differences between shock sensitive explosives (PETN, HMX) and shock insensitive explosives (TATB, NQ) may be described using the hydrodynamic hot-spot model. The reactive hydrodynamics of desensitization of heterogeneous explosives by a weak preshock has been numerically modeled. The preshock desensitizes the heterogeneous explosive by closing the air holes and making it more homogeneous. A higher pressure second shock has a lower temperature in the multiple shocked explosive than in single shocked explosive. The multiple shock temperature may be low enough to cause a detonation wave to fail to propagate through the preshocked explosive.

INTRODUCTION

A shocked homogeneous explosive such as nitromethane first completely decomposes at the piston-explosive interface and achieves a detonation with a peak pressure that builds up toward the C-J pressure of the high-density shocked nitromethane. The detonation wave overtakes the shock wave, and the pressure at the end of the reaction zone decays toward the piston pressure. (1)

If one introduces gas bubbles or grit into a homogeneous explosive such as a liquid or a single crystal, thereby producing a heterogeneous explosive, the minimum shock pressure necessary to initiate propagating detonation can be decreased by one order of magnitude.

Heterogeneous explosives, such as PBX-9404 or PBX-9502, show a different behavior than homogeneous explosives show when propagating along confining surfaces. A heterogeneous explosive can turn sharp corners and propagate outward, and depending upon its sensitivity, it may show either very little or much curvature when propagating along a metal surface. The mechanism of initiation for heterogeneous explosives is different from the simple Arrhenius kinetic model found adequate for homogeneous explosives. (1) Heterogeneous explosives are initiated and may propagate by the process of shock interaction with density discontinuities such as voids. These interactions result in hot regions that decompose and produce increasing pressures that cause more and hotter decomposing regions. The shock wave increases in strength, releasing more and more energy, until it becomes strong enough that all of the explosive reacts and detonation begins.

This process is described by the "hydrodynamic hot-spot" model, which models the hot-spot formation from the shock interactions that occur at density discontinuities and describes the decomposition using the Arrhenius rate law and the temperature from the HOM equation of state. (1)

The numerical modeling of the interaction of a shock wave with a single density discontinuity was reported in Ref. (1), where an 8.5-GPa shock interacting with a single spherical hole in nitromethane was studied. The study was extended to four rectangular holes. (1) It was determined that 0.0032-mm-radius cylindrical voids would build toward detonation and 0.001-mm-radius voids would form hot spots that failed to propagate because of rarefactions cooling the reactive wave.

The process of shock initiation of heterogeneous explosives has been investigated (2) numerically by studying the interaction of shock waves with a cube of nitromethane containing 91 holes. An 8.5-GPa shock interacting with a single 0.002-mm hole did not build toward detonation. When the shock wave interacted with a matrix of 0.002-mm holes, it became strong enough to build toward detonation. Reducing the size of the holes to 0.0004 mm resulted in a sufficient amount of the explosive decomposing to compensate for the loss in energy to the flow caused by the interaction of the shock wave with the holes. The shock wave slowly grew stronger, but it did not build to detonation in the time of the calculation.

A 5.5-GPa shock wave interacting with a matrix of 0.002-mm holes resulted in insufficient heating of the resulting hot spots to cause significant decomposition.

The process of desensitization by preshocking was found to be a result of the holes being closed by the low-pressure initial shock wave without resulting in appreciable explosive decomposition. The higher pressure shock that arrived later did not have holes with which to interact and behaved like a shock wave in a homogeneous explosive until it caught up with the lower pressure preshock wave.

The basic processes in the shock initiation of heterogeneous explosives have been numerically modeled in three dimensions. The interaction of a shock wave with density discontinuities, the resulting hot-spot formation, interaction, and the build up toward detonation or failure have been modeled. In this paper the hydrodynamic hot-spot model is used to investigate other explosives and other kinetics to study the basic differences between shock sensitive and shock insensitive explosives.

It has been observed that preshocking a heterogeneous explosive with a shock pressure too low to cause propagating detonation in the time of interest can cause a propagating detonation in unshocked explosive to fail to continue propagating when the detonation front arrives at the previously shocked explosive. The resulting explosive desensitization was modeled using a Forest Fire decomposition rate that was determined only by the initial shock pressure of the first shock wave passing through the explosive.(3) This model could reproduce the experimentally observed explosive desensitization of TATB (triaminotrinitrobenzene) explosives previously shocked by short duration 25 and 50-kilobar pulses. It could not reproduce the observed results for low or high preshock pressures that fail to quench a propagating detonation.

To determine the mechanism of the explosive desensitization by preshocking, we used a three-dimensional reactive hydrodynamic model of the process. With the mechanism determined, it was possible to modify the decomposition rate to include both the desensitization and failure to desensitize effects.

NUMERICAL MODELING OF SHOCK SENSITIVITY

The three-dimensional Eulerian reactive hydrodynamic code 3DE is described in Ref. (4). It uses techniques identical to those described in detail in Ref. (1) and used successfully for describing two-dimensional Eulerian flow with mixed cells and multicomponent equations of state and for modeling reactive flow. It has been used to study the interaction of multiple detonation waves, (5) the basic process in shock initiation of heterogeneous explosives, (2, 6) and the reactive hydrodynamics of a matrix of tungsten particles in HMX.(7)

The Arrhenius reactive rate law was used with the contants determined experimentally by Raymond N. Rogers and described in Ref. (1). The constants used are given in Table 1.

TABLE 1
Arrhenius Constants

Explosive	Activation Energy (kcal/mole)	Frequency Factor (μs^{-1})
Nitroguanidine	20.9	28.4
TATB	59.9	3.18×10^{13}
HMX	52.7	5.0×10^{13}
PETN	47.0	6.3×10^{13}

The HOM equation-of-state constants used for PETN are described in Ref. (1). The BKW detonation product and the solid equation-of-state constants used in the HOM equation of state are given in Ref. (6).

A constant velocity piston was applied to the bottom of the explosive cube, shocking the explosive initially to the desired pressure. When the shock wave interacts with a hole, a hot spot with temperatures several hundred degrees hotter than the surrounding explosive is formed in the region above the hole when it is collapsed by the shock wave. The hot region decomposes and contributes energy to the shock wave, which has been degraded by the hole interaction.

Whether this energy is sufficient to compensate for the loss from the hole interaction depends upon the magnitude of the initial shock wave, the hole size, and the interaction with the flow from nearest neighbor hot spots. The objective of the study was to investigate the nature of this complicated interaction and to determine if the hydrodynamic hot-spot model was adequate to describe the experimentally observed sensitivity to shock initiation of the heterogeneous explosives PETN, HMX, TATB, and Nitroguanidine with PETN being the most sensitive and Nitroguanidine the least sensitive.

For example, to initiate PBX-9404 (HMX-based explosive) or PBX-9502 (TATB-based explosive) at maximum pressed density within 4 mm of shock run requires a shock wave in PBX-9404 of 5 GPa and in PBX-9502 of 16 GPa as determined from the experimental Pop plots. (8)

To initiate PETN at 1.75 g/cm^3 (crystal density is 1.778) within 4 mm of shock run requires a pressure of only 2 GPa, while to initiate Nitroguanidine at 1.723 g/cm^3 (crystal density is 1.774) within 4 mm of shock run requires a pressure of 25 GPa (8).

The hole size present in such pressed explosives varies from holes of 20 to 300 A in the TATB crystals to holes as large as 0.5 mm in the explosive-binder matrix. Most of the holes vary in size from 0.05 to 0.005 mm in diameter so we examined holes in that range of diameters.

As shown in Ref. (1), the hot spot formed when a shock wave interacts with a spherical hole scales with the radius of the hole as long as no chemical reaction occurs. Using hot-spot temperatures in the calculated range of 700 to 1300 K and calculating the adiabatic explosion times, one observes the ordering according to sensitivity (time to explosion) shown in Table 2. The ordering is identical to that observed experimentally.

TABLE 2
Adiabatic Explosion Times

	Hot-Spot Temperature		
Explosive	700 K	1000 K	1300 K
Nitroguanidine	5504 μs	124 μs	18.47 μs
TATB	1290 μs	6×10^{-3} μs	1×10^{-5} μs
HMX	5.26 μs	1×10^{-4} μs	5×10^{-7} μs
PETN	0.08 μs	7×10^{-6} μs	5×10^{-8} μs

The interaction of shock waves of various pressures with single cubical air holes of various sizes in PETN, HMX, TATB, and NQ was investigated. The calculations model the hot-spot explosion and failure to propagate because of rarefactions cooling the reactive wave. If the reaction becomes too fast to numerically resolve the cooling by rarefactions, the flow builds toward a detonation too quickly.

A summary of the results of the study is shown in Table 3. The ordering of shock sensitivity of the explosives is again observed experimentally correlating well with the observed Pop plot data. (8)

To evaluate the sensitivity to shock more realistically, we studied the interaction of a 5-GPa shock wave in HMX with a matrix of spherical holes of 4×10^{-3}-mm diameter. The computational grid contained 24 $\times$ 22 by 36 cells, each 1×10^{-3} mm on a side. The 36 air holes were described by 4 cells per sphere diameter. Numerical tests with 2 to 6 cells per sphere diameter showed the results were independent of grid size for more than 3 cells per sphere diameter. The air holes were located on a hexagonal close-packed lattice (HCP). The closest distance for the HCP matrix between holes was 3.8×10^{-3} mm. The time step was 1.0×10^{-5} μs. The void fraction is 10%. While a single hole fails to build toward a detonation as shown in Fig. 1, the matrix of holes builds toward a detonation as shown in Fig. 2. The experimental run to detonation for a 5-GPa shock wave in 1.71 g/cm^3 HMX is 0.17 cm. While a propagating detonation would not be expected to occur experimentally in this geometry (the computed detonation is the result of insufficient numerical resolution to resolve the reaction at high pressures and temperature), the enhancement of the shock wave would occur.

TABLE 3
Single Cubical Air-Hole Study

Explosive	Air Cube Size (mm)	Pressure (GPa)	Result
HMX	5×10^{-3}	2.5	Fails to build toward a detonation
	5×10^{-3}	5.0	Fails to build toward a detonation
	5×10^{-3}	7.5	Builds toward a detonation
	5×10^{-2}	2.5	Fails to build toward a detonation
	5×10^{-2}	5.0	Marginal
	5×10^{-2}	7.5	Builds toward a detonation
TATB	5×10^{-3}	5.0	Fails
	5×10^{-3}	12.5	Fails
	5×10^{-3}	15.0	Builds toward a detonation
	5×10^{-2}	7.5	Fails
PETN	5×10^{-3}	2.5	Builds toward a detonation
	5×10^{-3}	7.5	Builds toward a detonation
Nitroguanidine	5×10^{-2}	25.0	Fails
	5.0	25.0	Builds toward a detonation

The interaction of a 12.5-GPa shock wave in TATB with a single spherical hole of 4×10^{-3}-mm diameter is shown in Fig. 3. It fails to build toward a detonation. The interaction of a 12.5 GPa shock wave in TATB with a matrix of spherical holes of 4×10^{-3}-mm diameter with a void fraction of 10% is shown in Fig. 4. The flow builds toward a detonation. The experimental run to detonation for a 12.5-GPa shock wave in 1.71 g/cm^3 TATB is 0.30 cm. The computed detonation occurs too quickly because of insufficient numerical resolution when the shock wave is enhanced to high enough pressures and temperatures by the interacting hot spots.

The interaction of a 2.0-GPa shock wave in PETN with a single spherical hole of 4×10^{-3}-mm diameter was calculated. Build up toward a detonation did not occur. The interaction of a 2.0-GPa shock wave in PETN with a matrix of spherical holes of 4×10^{-3}-mm diameter with a void fraction of 10% was calculated. The flow builds toward a detonation after the hot spots interact.

The experimental run toward detonation values are about the same for a 12.5-GPa shock wave interacting with TATB with 10% voids, for a 5.0-GPa shock wave interacting with HMX with 10% voids, and for a 2.0 GPa shock wave interacting with PETN with 10% voids.

The hydrodynamic hot-spot model describes the basic difference between shock sensitive and shock insensitive explosives. The interaction of a shock wave with air holes in PETN, HMX, TATB, and NQ, the resulting hot-spot formation, interaction, and the build up toward detonation or failure have been modeled. Increased hole size results in larger hot spots that decompose more of the explosive and add their energy to the shock wave and result in increased sensitivity of the explosive to shock. Increased number of holes also causes more hot spots that decompose more explosive and increase the sensitivity of the explosive to shock. The interaction between hole size and number of holes is complicated and requires numerical modeling for adequate evaluation of specific cases. The hole size can become sufficiently small (the critical hole size) that the hot spot is cooled by side rarefactions before appreciable decomposition can occur. Since increasing the number of holes while holding the percentage of voids present constant results in smaller holes, we have competing processes that may result in either a more or less shock sensitive explosive. If the hole size is below the critical hole size, then the explosive will become less sensitive with increasing number of holes of decreasing diameter.

To evaluate the potential shock sensitivity of an explosive for engineering purposes, one needs

to determine experimentally the Arrhenius constants. One then calculates the adiabatic explosion times for several assumed hot-spot temperatures to determine the relative sensitivity of the explosive compared with explosives of known sensitivity. A more detailed evaluation can be obtained from calculations using the hydrodynamic hot-spot model.

STUDIES OF DESENSITIZATION BY PRESHOCKING

Dick (9) performed a PHERMEX radiographic study of detonation waves in PBX-9502 (95/5 Triaminotrinitrobenzene/Kel-F binder at 1.894 g/cm^3) proceeding up a 6.5- by 15.0-cm block of explosive that was preshocked by a 0.635-cm steel plate moving at 0.08 (Shot 1698) or 0.046 cm/μs (Shot 1914). The static and dynamic radiograph for Shot 1698 are shown in Fig. 5. The preshocked PBX-9502 explosive quenches the detonation wave as it propagates into the block of explosive.

To investigate the mechanism of explosive desensitization by preshocking, we again used the reactive hydrodynamic code, 3DE.(4)

A constant velocity piston was applied to the bottom of TATB explosive cube shocking the explosive to the desired pressure. When a higher pressure second shock was to be introduced, the piston velocity was increased and other piston state values changed as appropriate for a multiple shock of the required pressure.

A single shock pressure of 290 kbars in TATB has a density of 2.8388 g/cm^3, particle velocity of 0.21798 cm/μs, energy of 0.02376 mb cc/g, and temperature of 1396°K. A second shock pressure of 290 kbars in TATB initially shocked to 40 kbars has a density of 2.878 g/cm^3, energy of 0.017759 mb-cc/g, particle velocity of 0.2040 cm/μs, and temperature of 804.2°K.

When a shock wave interacts with a hole, a hot spot with temperatures hotter than the surrounding explosive is formed in the region above the hole after it is collapsed by the shock wave. The hot region decomposes and contributes energy to the shock wave, which has been degraded by the hole interaction.

Whether this energy is sufficient to compensate for the loss from the hole interaction depends upon the magnitude of the initial shock wave, the hole size, and the interaction with the flow from nearest neighbor hot spots.

The interaction of a 40-kbar shock with a single 0.004-cm-diameter air hole in TATB was modeled. After 0.025 μs, the 40-kbar shock had collapsed the hole and a 290-kbar shock wave was introduced which passed through the 40-kbar preshocked region and overtook the 40-kbar shock wave.

The shock temperature in the bulk of the TATB and the adiabatic explosion times are given below:

First Shock (kbar)	40	290	40
Second Shock (kbar)			290
Temperature (°K)	362.5	1396	804.2
Explosion Time (μs)	10^{19}	10^{-6}	3.85

The density and burn faction surface contours are shown in Figs. 6 and 7 and the cross sections through the center of the hole are shown in Fig. 8.

The 40-kbar shock wave collapsed the hole and formed a small weak hot spot which was not hot enough to result in appreciable decomposition of the TATB.

The 290-kbar shock wave temperature was not hot enough to cause explosion during the time studied in the bulk of the explosive previously shocked to 40 kbars; however, the additional heat present in the hot spot formed by the 40-kbar shock wave after it interacted with the hole was sufficient to decompose some of the explosive after it was shocked by the 290-kbar wave.

Propagating detonation occurred immediately after the 290-kbar shock wave caught up with the 40-kbar preshock.

To investigate the effect of the interaction of a matrix of holes with a multiple shock profile, a matrix of 10% air holes located on a hexagonal close packed lattice in TATB was modeled. The spherical air holes had a diameter of 0.004 cm. The initial configuration is shown in Fig. 9. The three-dimensional computational grid contained 16 by 22 by 36 cells each 0.001 cm on a side. The time step was 0.0002 μs. Figure 10 shows the density and mass fraction cross sections for a 40-kbar shock wave followed after 0.045 μs by a 290-kbar shock wave interacting with a matrix of 10% air holes of 0.004-cm-diameter in TATB.

The preshock desensitized the explosive by closing the voids and made it more homogeneous.

The higher pressure second shock wave proceeded through the preshocked explosive until it caught up with the preshock.

The three-dimensional modeling study demonstrated that the desensitization occurs by the preshock interacting with the holes and eliminating the density discontinuities. The subsequent higher pressure shock waves interact with a more homogeneous explosive. The multiple shock temperature is lower than the single shock temperature at the same pressure, which is the cause of the observed failure of a detonation wave to propagate in preshocked explosives for some ranges of preshock pressure.

The modification indicated by the three-dimensional study to the Forest Fire decomposition rate being limited by the initial shock pressure was to add the Arrhenius rate law to the Forest Fire rate.

The Forest Fire rate for TATB is shown in Fig. 11 along with the Arrhenius rate calculated using the temperatures from the HOM equation of state for the partially burned TATB associated with the pressure as determined by Forest Fire. We will proceed using a burn rate determined by Forest Fire limited to the initial shock pressure and the Arrhenius rate using local partially burned explosive temperatures.

The experimental geometries studied using PHERMEX shown in Fig. 5 were numerically modeled using a reactive hydrodynamic computer code, 2DL, that solves the Navier-Stokes equation by the finite difference techniques described in Ref. (1). The users manual for the 2DL code is described in Ref. (10). For explosives that have been previously shocked, Craig (3) experimentally observed that the distance of run to detonation for several multiple shocked explosives was determined primarily by the distance after a second shock had overtaken the lower pressure shock wave (the preshock). To approximate this experimental observation, we programmed the calculation to use Forest Fire rates determined by the first shock wave or the rates determined by any subsequent release waves that result in lower pressures and lower decomposition rates. As suggested by the three-dimensional study, we added the Arrhenius rate using the local partially burned explosive temperatures. The HOM equation of state and Forest Fire constants used to describe PBX-9502 (X0290) are given in Ref. (1).

The calculated pressure and mass fraction contours for PHERMEX shot 1698 are shown in Fig. 12 along with the radiographic interfaces.

The 2DL calculation had 50 by 33 cells to describe the PBX-9502 and 50 by 5 cells to describe the steel plate. The mesh size was 0.2 cm and the time step was 0.04 μs.

The PHERMEX shot was numerically modeled using various velocity steel plates. The results are shown in Table 4. The results agree with the experimental evidence that detonation wave failure occurs in preshocked TATB shocked by steel plates with velocities of 0.046 and 0.08 cm/μs.

TABLE 4
9502 Desensitization Calculations

Steel Plate Velocity (cm/μs)	Preshock Pressure (kbar)	Result Upon Arrival of Detonation Wave
0.020	9	Detonates preshocked HE
0.030	14	Fails in preshocked HE
0.045	23	Fails in preshocked HE
0.080	50	Fails in preshocked HE
0.100	70	Fails in preshocked HE
0.120	90	Detonates preshocked HE and after 1.5 cm run
0.160	130	Detonates preshocked HE
0.200	180	Detonates preshocked HE

The desensitization of heterogeneous explosive by preshocking may be attributed to the preshock closing the voids, thus making the explosive more homogeneous. The failure of a detonation wave to propagate in the preshocked explosive may be attributed to the lower temperature that occurs in the multiple shocked explosive than the singly shocked explosive.

A rate law that combines the Forest Fire rate limited to the rate determined by the initial shock pressure and the Arrhenius rate law permits a description of multiple shocked explosive behavior for many engineering purposes.

REFERENCES

1. Charles L. Mader, *Numerical Modeling of Detonations*, University of California Press, Berkeley, 1979.
2. Charles L. Mader and James D. Kershner, "Three-Dimensional Modeling of Shock Initiation of Heterogeneous Explosives,"

2. Nineteenth Symposium (International) on Combustion, Williams and Wilkins, pp. 685-690, 1982

3. Charles L. Mader, Richard D. Dick, "Explosive Desensitization by Preshocking," Internationale Jahrestaging, 1979, Combustion and Detonation Processes, pp. 569-579, 1979.

4. Charles L. Mader and James D. Kershner, "Three-Dimensional Eulerian Calculations of Triple-Wave Initiated PBX-9404," Los Alamos Scientific Laboratory Report LA 8206, 1980.

5. Charles L. Mader, "Detonation Wave Interactions," Seventh Symposium (International) on Detonation, pp, 669-677, NSWC MP 82-334, 1981.

6. Charles L. Mader and James D. Kershner, "The Three-Dimensional Hydrodynamic Hot-Spot Model Applied to PETN, HMX, TATB, and NQ," Los Alamos National Report LA-10203-MS, 1984.

7. Charles L. Mader, James D. Kershner, and George H. Pimbley, "Three-Dimensional Modeling of Inert Metal-Loaded Explosives," Journal of Energetic Materials *1*, pp. 293-324, 1983.

8. Terry R. Gibbs and Alphonse Popolato, *LASL Explosive Property Data*, University of California Press, Berkeley, 1980.

9. Charles L. Mader, *LASL PHERMEX Data, Volume III*, University of California Press, Berkeley, 1980.

10. James N. Johnson, Charles L. Mader, and Milton S. Shaw, "2DL: A Lagrangian Two-Dimensional Finite-Difference Code for Reactive Media," Los Alamos National Laboratory Report LA-8922 M, 1981.

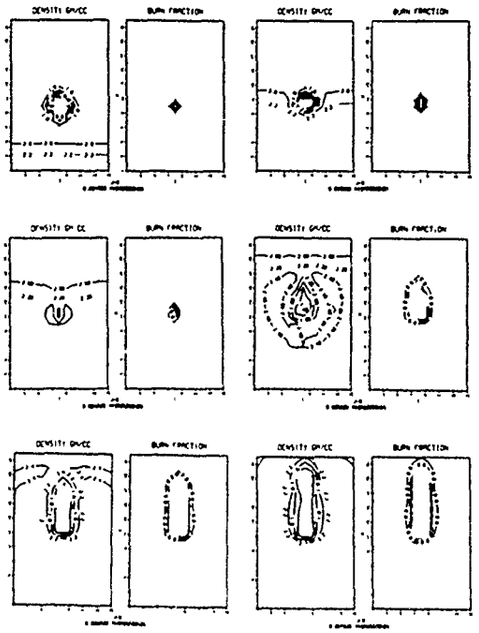

Fig. 1. A 4 × 10⁻³-mm diameter spherical air hole in HMX. The initial shock pressure is 5.0 GPa (The density and burn fraction cross sections through the center of the hole are shown at various times. It does not build toward detonation.)

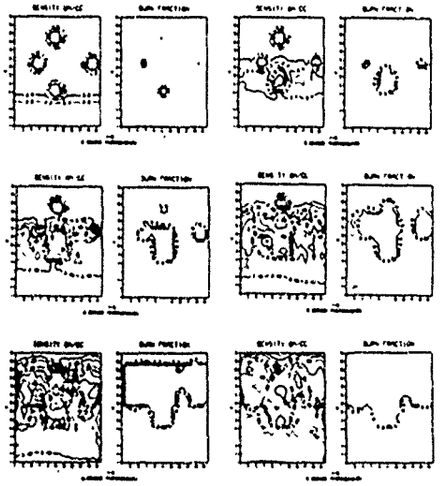

Fig. 2. A Matrix of 10% air holes in HMX. The spherical air holes have a diameter of 4 × 10⁻³ mm. The initial shock pressure is 5.0 GPa (The density and mass fraction contours are shown for a cross section through the center of the matrix. The flow builds toward a propagating detonation.)

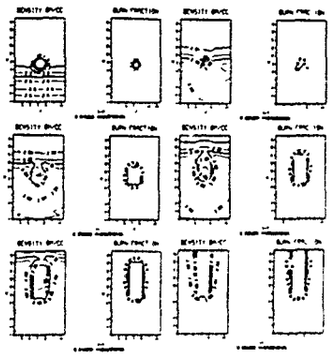

Fig. 3. A 4 × 10^{-3}-mm diameter spherical hole in TATB. The initial pressure is 12.5 GPa (The density and burn fraction cross sections through the center of the hole are shown at various times. The flow does not build toward a detonation.)

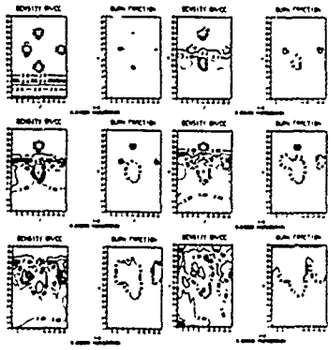

Fig. 4. A matrix of 10% air holes in TATB. The spherical air holes have a diameter of 4 × 10^{-3} mm (The initial shock pressure is 12.5 GPa. The density and mass fraction contours are shown for a cross section through the center of the matrix. The flow builds towards a detonation.)

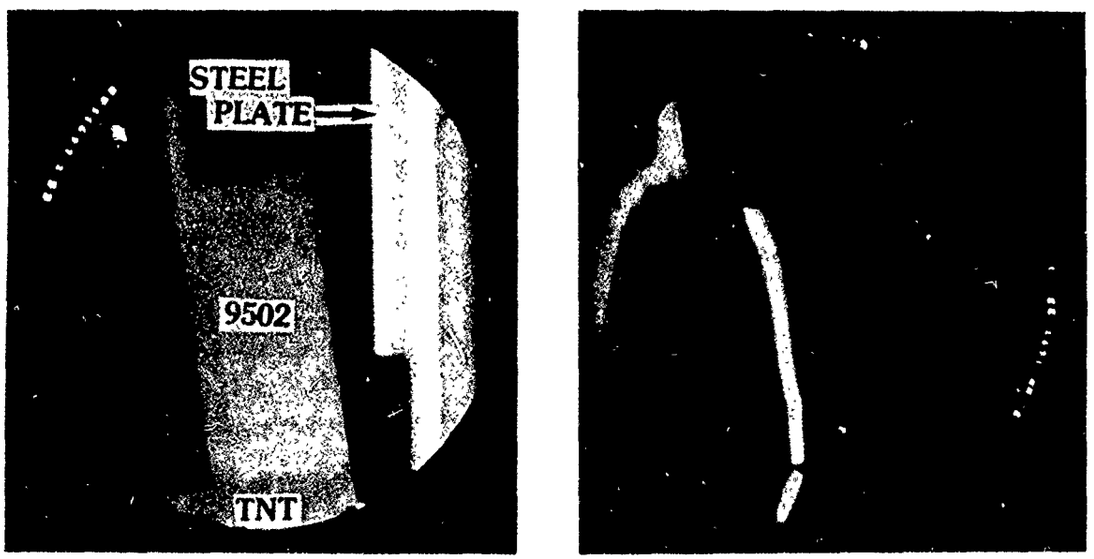

Fig 5. Static and dynamic radiograph 1698 of PBX-9502 shocked by a 0.635-cm-thick steel plate going 0.08 cm/μs and initiated by 2.54 cm of TNT and a P-40 lens

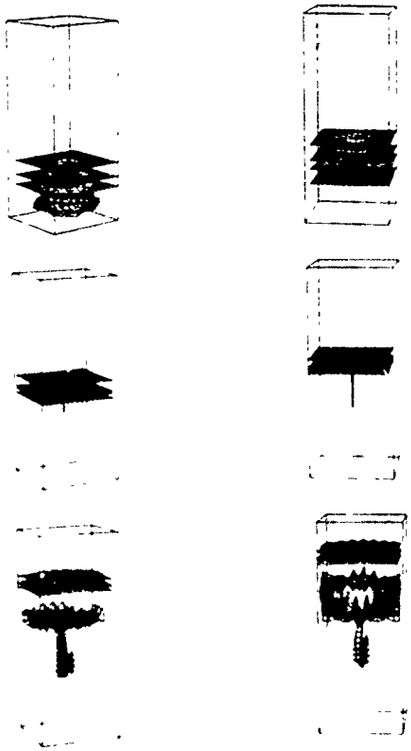

Fig. 6. The density surface contours for a 40-kbar shock interacting with a single 0.004-cm-diameter air hole in TATB followed after 0.025 μs by a 290-kbar shock wave

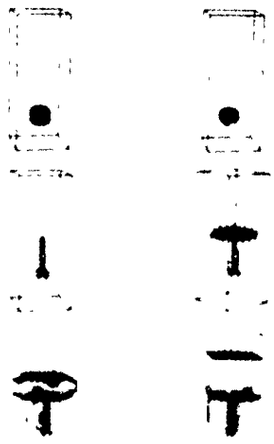

Fig 7 The burn fraction contours for the system shown in Fig 6

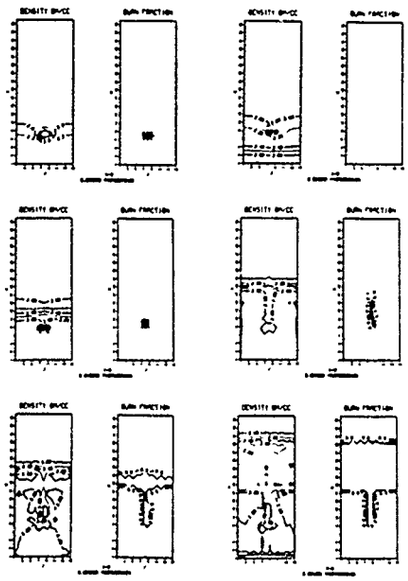

Fig. 8. The density and burn fraction cross sections through the center of the hole for the system shown in Fig. 6

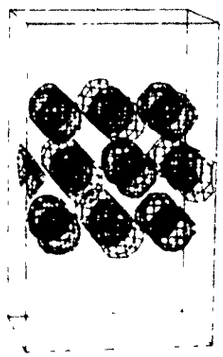

Fig. 9. The initial configuration of a matrix of 10% air holes in TATB

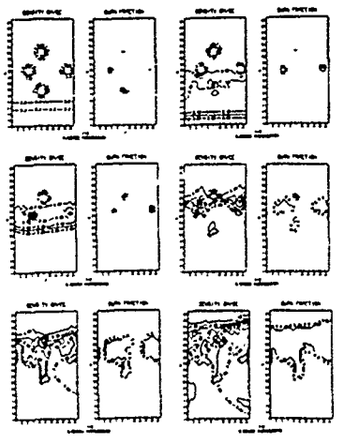

Fig. 10. The density and mass fractions cross sections are shown for a 40-kbar shock wave followed after 0.045 μs by a 290-kbar shock wave interacting with a matrix of 10% air holes of 0.004-cm-diameter in TATB

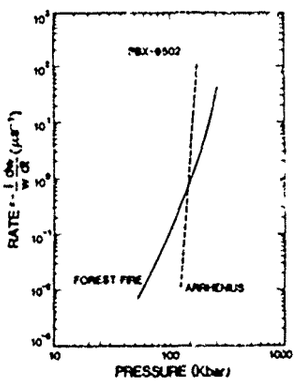

Fig. 11. The burn rate as a function of pressure for the Forest Fire burn model and the Arrhenius rate law using the HOM temperatures associated with the Forest Fire pressures

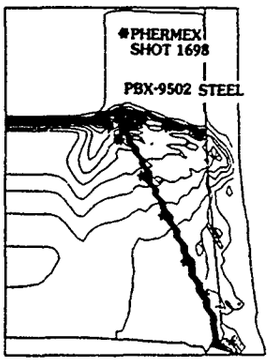

Fig. 12. The pressure and mass fraction contours for a detonation wave in PBX-9502 interacting with explosive that had been previously shocked to 50 kbars (The PHERMEX radiograph interfaces are shown by stars. The mass fraction contour interval is 0.1 and shown as a thick almost solid line. The pressure contour interval is 40 kbars

DISCUSSION

PER-ANDERS PERSSON, CETR/NM TECH

One has to admire the amount of patience shown by the programmer, and the amount of computer time that goes into producing this very illustrative film show.

One question: what are the boundary conditions on the faces of the box that contains the material/void lattice in these calculations?

REPLY BY CHARLES MADER

The boundary conditions are continuum boundaries.

MODELING HETEROGENEOUS HIGH EXPLOSIVE BURN WITH AN EXPLICIT HOT-SPOT PROCESS

P.K. Tang, J.N. Johnson, and C.A. Forest
Los Alamos National Laboratory
Los Alamos, New Mexico

We present a method of treating high explosive burn with a multi-step process which includes the hot-spot excitation, decomposition, and the propagation of reaction into the region outside the hot spots. The basic features of this model are the separation of the thermal-mechanical and chemical processes, and the partition of the explosive into hot spots and the region exclusive of the hot spots. The thermal-mechanical aspects are formulated in a way similar to the chemical process. The combined processes lead to a set of rate equations for the mass fractions of reactants, intermediate states, and final products. The rates are expressed initially in terms of general characteristic times, but with specific phenomenological correlations introduced in the final model. Computational examples are given of simulated flyer plate impacts, short-shock initiation, corner turning, and shock desensitization.

INTRODUCTION

The rapid burning of high explosives (HE) involves many complex thermal-mechanical and chemical processes. Here the term burn refers to the chemical energy release process associated with shock initiation; also, the thermal-mechanical process includes both hydrodynamics and transport. In the classical model of steady detonation, transport processes are not considered in detail since the shock thickness is quite small compared to any typical dimension; second, the chemical reaction rate is quite high and thus the reaction zone is thin, and the entire process is hydrodynamically controlled. Use of the Rankine-Hugoniot relations and the Chapman-Jouguet condition leads to a well-defined detonation velocity (1). This model ignores the chemical and transport aspects and thus simplifies the problem significantly. A large class of explosives follows this simplification with a constant detonation velocity under various conditions, provided the size of the explosive region is much greater than some characteristic dimension. The classical burn model, based on ideal steady detonation and known as programmed burn, has been used successfully in many engineering design applications.

With the advent of insensitive high explosives (IHE), the chemical reaction can no longer be assumed very fast compared to the hydrodynamic process, especially for initiation; in fact, the chemical process could be so sensitive to local instantaneous conditions that it may not start or reach completion within the time of interest, at least for a large portion of the HE. The above condition is called detonation failure. For the scenarios of shock-to-detonation transition, HE encountering a weak shock will undergo chemical reaction at some distance behind the shock front and the effect of reaction will propagate through the additional distance to reach the front, intensifiying and speeding it up until a final steady detonation is established. The total distance traversed by the shock to the point of detonation is known as the run. Obviously a weak initial shock requires a long run. The finite distance needed for the transition is nothing but an indication of the finite reaction rate involved. The unique experimental relationship between the initial shock pressure and the run distance is presented in the form of a Pop plot. This relationship is usually linear on a log-log scale (2)

and is used in the determination of the Forest-Fire reaction rate (3).

While many recognize that models of HE burn should be based on first principles, there are numerous difficulties with this approach. Even though the chemical composition of the HE is usually known for the major constituents, the chemical processes that lead to the final products are poorly understood and many intermediate species and some final products have not yet been identified. All of these make the description of the processes according to the principles of chemical kinetics almost impossible. The second difficulty in describing HE burn is that most solid HE's are not homogeneous; voids and cracks are present and distinct boundaries exist between various constituents. Physical heterogeneity requires mass and energy balance calculations among all components and phases if we are to describe the complete scenarios following the principles of continuum mechanics and chemical thermodynamics. The condition of extreme pressure during the burn adds more uncertainty in the determination of transport and thermal properties. In coupling with the detailed chemistry, the task of establishing a complete thermal-mechanical and chemical model appears impractical if not impossible. The motivation for the development of a new model is to avoid detailed calculations, but to include some essential physical concepts that a first-principles approach would contain. We consider this a compromise, but believe it offers many advantages and features frequently needed in computational models. The separation of thermal-mechanical and chemical processes, plus the partition of the HE into hot spots and the region other than hot spots are the main features of this model. The special attention paid to the treatment in the hot-spot region lends the name to the model, explicit hot-spot process. Details of the model have been presented elsewhere, along with a review of other HE burn models (4).

We begin our technical discussion with a review of some fundamental concepts related to combustion. This is not to suggest that shock initiation is physically the same as laminar combustion, but only that the two phenomena share similar general features, as we shall see. Following Zeldovich and Frank-Kamenetski thermal theory of pre-mixed laminar flame (5), the burning can be roughly divided into two phases: heat-up and chemical reaction. The heat-up phase involves the energy transfer from the already-burned hot region to the unburned cold region, bringing the cold region to the ignition condition. Only when the unburned region has reached high enough temperature will the chemical reaction take place at a sufficient rate and liberate energy. This concept leads to simplification of many combustion problems according to the dominance of either the transport-controlled (heat-up) or the chemical-controlled (reaction) process. To illustrate the relative importance of the two processes, we define the condition of a combustible material as a mixture of three distinct states; cold C, hot H, and burned B; each mass point contains some or all of the states. The processes of transformation from one state to the other are:

$$C \rightarrow H \quad \text{heat-up} , \tag{1}$$

$$H \rightarrow B \quad \text{chemical reaction} . \tag{2}$$

Following the chemical kinetics principle (6), with t being the time, the rates of the transformations can be written as:

$$\frac{dC}{dt} = -\frac{C}{\tau_h} , \tag{3}$$

$$\frac{dH}{dt} = \frac{C}{\tau_h} - \frac{H}{\tau_r} , \tag{4}$$

$$\frac{dB}{dt} = \frac{H}{\tau_r} , \tag{5}$$

where C and H represent the mass fractions of the material in cold and hot conditions and B is the burned portion with:

$$C + H + B = 1 . \tag{6}$$

Here τ_h and τ_r are the heat-up and chemical reaction characteristic times. The rate expression of Eq. (3) is based on the assumption that the energy transfer process is a volume rather than a surface effect. The chemical reaction given in Eq. (4) represents a first-order process; with constant τ_h and τ_r, the integration of Eqs. (3) through (5) with initial condition C=1, and H=B=0 yields

$$B = 1 + \left[\frac{\tau_h}{\tau_r} \exp(-\frac{t}{\tau_h}) - \exp(-\frac{t}{\tau_r}) \right] / (1 - \frac{\tau_h}{\tau_r}) . \tag{7}$$

If the heat-up process is much slower than the

chemical process, namely, $\tau_h >> \tau_r$, then we have the following extreme

$$B = 1 - \exp(-\frac{t}{\tau_h}) . \quad (8)$$

The other limiting case occurs when the chemical process is much slower than the heat-up process, $\tau_r >> \tau_h$, and

$$B = 1 - \exp(-\frac{t}{\tau_r}) . \quad (9)$$

Equations (8) and (9) each represents a single-rate controlled process, either thermal-mechanical or chemical. The single-step process is certainly simpler than the two-step case, and it is to our advantage to recognize when we have the former. When both characteristic times are comparable, the more general representation is the only acceptable one. In the following section, hot-spot formation, decomposition, energy transfer, etc., are considered from a general viewpoint, and then the relevant characteristic times are compared in order to reduce the entire system to a simpler, two-rate controlled process.

THE GENERAL MODEL

The heterogeneous nature of high explosives is widely recognized, as we have already discussed. The concepts of hot spots and the mechanisms leading to heterogeneous reaction are adiabatic gas compression (7), rapid shear (8), visco-plastic flow (9), void collapse (10), friction (11), and others. It is reasonable to anticipate that hot spots behave quite differently from the rest of the explosive, as far as responding to the shock action is concerned. Although adiabatic compression (pressure work) is a means of increasing the internal energy in general, dissipation associated with the irreversible stresses from the shock process is quite significant in the highly localized regions of heterogeneous material. The internal energy is increased even more and thus the temperature is much higher than the surroundings. The local high temperature starts the chemical process sooner than in the surrounding near-reversibly compressed portion. Accordingly, we divide the explosive into two major regions: the hot spots and the balance of explosive. Since we do not intend to include the details of the hot-spot formation here, we define the hot spots only in a very general way: there are sites within the HE that are potentially susceptible to mechanical stimulation (shock) and become energetic. These chemically unstable sites then proceed to decompose at a rate determined by a higher local temperature; we say that the hot spots have reached the ignition condition. Here the shock process is equivalent to the heat-up phase discussed earlier in relation to the pre-mixed flame. The balance of explosive responds to the shock in quite a different way. There are possibly some initial physical and/or chemical changes but no substantial exothermic chemical reaction. Only after a certain amount of hot-spot reaction can additional reaction propagate into the balance of the explosive. In summary, we propose the following major steps in shock-induced chemical reaction of heterogeneous explosives:

1. hot-spot creation, formation of ignition state

$$R_1 \rightarrow I_1 , \quad (10)$$

2. hot-spot decomposition, consumption of ignition state

$$I_1 \rightarrow P_1 , \quad (11)$$

3. heating of the balance of explosive by the hot-spot burned product, creation of the ignition state for that region

$$R_2 + P_1 \rightarrow I_2 + P_1^* , \quad (12)$$

4. decompostion of the balance of explosive

$$I_2 \rightarrow P_2 . \quad (13)$$

The symbols R, I, and P represent reactants, intermediates, and products; subscripts 1 and 2 are hot spots and balance of explosives, respectively. Here P_1^* represents P_1 at a cooler condition following energy transfer from the hot spots to the balance of explosive. The first two steps involve the hot spots only, but the last two control the burn in the balance of the explosive as a result of the hot-spot burn. We call this phase the burn propagation. The burn propagation plays an extremely important role, namely, the overall burning is determined by the ability of the hot spots to transfer energy to the balance of the explosive. It is further assumed that the hot-spot burn must exceed a certain threshold value to start the reaction in the balance of explosive. This leads to ignition delay in the burning of the explosive as a whole. Therefore, the critical pathway leading to the

complete burning of the HE is the propagation, step 3, without which burning will be confined to the hot spots. Since the hot-spot region is usually quite small, the HE as a whole can be considered unburned if there is no propagation at all or if it takes too long. The failure of burn propagation is basically the failure of transition from shock to detonation.

Let us define R_1, I_1, and P_1 to be the actual mass fractions of reactants, intermediates, and products in hot spots divided by μ, the fraction of material capable of being excited by the shock. We call these quantities normalized mass fractions and adopt similar definitions for R_2, I_2, and P_2 with $(1-\mu)$ replacing μ in the normalizing process for the balance of explosive. Using the conventional formulation in chemical kinetics (6), we obtain the time rates of change for the processes (10) through (13):

A. the consumption rate of the unactivated hot spots due to the shock action:

$$\frac{dR_1}{dt} = -\frac{R_1}{\tau_s} , \tag{14}$$

B. the creation and consumption of the ignition state of hot spots:

$$\frac{dI_1}{dt} = \frac{R_1}{\tau_s} - \frac{I_1}{\tau_c} , \tag{15}$$

C. the creation of the hot-spot burned product:

$$\frac{dP_1}{dt} = \frac{I_1}{\tau_c} , \tag{16}$$

D. the rate of consumption of the balance of explosive due to heating from the already burned hot spots:

$$\frac{dR_2}{dt} = -\mu \frac{R_2}{\tau_m} \left(\frac{P_1 - f_0}{1 - f_0} \right) , \tag{17}$$

E. the creation and consumption of the ignition state of the balance of explosive:

$$\frac{dI_2}{dt} = \mu \frac{R_2}{\tau_m} \left(\frac{P_1 - f_0}{1 - f_0} \right) - \frac{I_2}{\tau_c'} , \tag{18}$$

F the creation of the final product of the balance of explosive:

$$\frac{dP_2}{dt} = \frac{I_2}{\tau_c'} . \tag{19}$$

At any instant, the total unburned and burned fractions are

$$R = \mu R_1 + (1-\mu) R_2 , \tag{20}$$

$$P = \mu P_1 + (1-\mu) P_2 . \tag{21}$$

The mass fraction of hot spots μ is quite likely related to the microstructural properties such as the grain specific area and some characteristic thickness in the hot-spot region. The threshold f_0 is the normalized mass fraction of hot-spot reaction that must be reached before the burn can propagate into the balance of explosive. Equations (17) and (18) also contain the multiplication factor μ: this represents a condition that a vanishingly small mass fraction of hot spots would be incapable of inducing large scale reaction in the balance of explosive. We assume constant μ and f_0. For the normalized mass fractions,

$$R_1 + I_1 + P_1 = 1 , \tag{22}$$

$$R_2 + I_2 + P_2 = 1 . \tag{23}$$

In equations (14) and (15), τ_s represents the characteristic time for hot-spot excitation due to first-shock effect. If hot-spot temperature is chosen as the parameter representing the excited state, then τ_c is the characteristic time of the process leading to that temperature. It is quite likely a function of the shock strength and the material properties. The decomposition process in the ignition state is characterized by τ_c and is usually a function of the local temperature. The characteristic time τ_m controls the transport process for the energy transfer from the burned product of the hot spots to the cold balance of explosive. The mechanism of the energy transfer is possibly a turbulent mixing process at higher pressure range and simple heat conduction when the burning is less intense. It could be a function of pressure and temperature. The phenomenological correlations of these characteristic times will be described later.

Finally, τ_c' is the characteristic time for decomposition in the balance of explosive once the energy transfer from the hot spots has taken place.

Equation (17) deserves some additional explanation. Due to the normalized nature of the quantities R_1, R_2, I_1, I_2, P_1, and P_2, the presence of μ is required to give the absolute influence of the hot-spot mass fraction; $(1-f_0)$ is another normalizing factor so that when the hot spots have burned completely ($P_1=1$), the threshold effect vanishes and only the energy transfer mechanism through τ_m controls the rate.

THE SPECIFIC MODEL

We now use some physical arguments to simplify the above formulation. First, in the hot-spot region, we can expect the shock (thermal-mechanical) process to be much faster than the decomposition, ($\tau_c >> \tau_s$), and this should lead to an instantaneous change of R_1 from one to zero. Mathematically, Eqs. (14), (15), and (16) are replaced by a single rate equation:

$$\frac{dP_1}{dt} = \frac{1}{\tau_c}(1-P_1), \tag{24}$$

and from Eq. (22):

$$P_1 + I_1 = 1. \tag{25}$$

In the balance of explosive, the energy transfer (thermal-mechanical) process is expected to be much slower than the decomposition process that follows; i.e., $\tau_m >> \tau_c$, so we can make additional simplification that $I_2 = 0$, and from Eq. (23):

$$P_2 + R_2 = 1. \tag{26}$$

The consequence is again a single rate-controlled process:

$$\frac{dP_2}{dt} = \frac{\mu}{\tau_m}(1-P_2)\left(\frac{P_1-f_0}{1-f_0}\right). \tag{27}$$

The overall burned product rate equation is a summation of Eqs. (24) and (27) with the use of Eq. (21):

$$\frac{dP}{dt} = \frac{\mu}{\tau_c}(1-P_1) + \frac{\mu}{\tau_m}[(1-P)-\mu(1-P_1)]\left(\frac{P_1-f_0}{1-f_0}\right). \tag{28}$$

Equation (28) contains an unknown P_1 which is evaluated separately using Eq. (24). As we can see in Eqs. (24) and (28), if τ_c is much less than τ_m, (i.e., the reaction in the hot spots is much faster than the rest of the explosive, a condition that may be reached at high pressures), P_1 will reach unity much sooner than P; this will eventually lead to a single equation for the total burned mass fraction:

$$\frac{dP}{dt} = \frac{\mu}{\tau_m}(1-P). \tag{29}$$

This specific case is representative of reaction-rate models such as Forest Fire (3) in which μ/τ_m is specified as a function of pressure. The specific model described in the remainder of this paper is not of this form, but rather the explicit two-step process represented by Eqs. (24) and (28).

The relationship between the two characteristic times, τ_c and τ_m, and thermal-mechanical and chemical properties of the explosive are presented in detail elsewhere (4), of which we give here only a summary.

The passage of the initial shock wave of pressure amplitude p_s produces an average hot-spot temperature θ_s given by

$$\theta_s = \theta_0\left[1-m\frac{\theta_0}{\alpha}\ln\left(\frac{p_s}{p_0}\right)\right]^{-1}, \tag{30}$$

where m, θ_0 and p_0 are constant and α is the Arrhenius activation temperature. For hot-spot temperature θ_s there is an induction time for thermal explosion which we identify with the characteristic time τ_c:

$$\tau_c = \frac{\theta_s^2}{\alpha\beta Z}\exp\left(\frac{\alpha}{\theta_s}\right). \tag{31}$$

In Equation (31), β is the temperature coefficient due to chemical reaction and Z is the frequency factor for Arrhenius reaction. The quantity that is experimentally determined is the average delay for a given shock pressure. The justification for identification of τ_c in Eq. (24) with the induction time for thermal explosion is given in detail in ref. (4). Equations (30) and (31) are then used to obtain the average hot-spot temperature for assumed values of α, β and Z. The latter quantities are sometimes well-known from independent measurement, but are occasionally in doubt because of extreme thermodynamic conditions reached within the hot spots. Therefore, in this work as well as the earlier one (4), the hot-spot temperature means simply that particular temperature which gives the experimentally determined delay time for a given set of Arrhenius parameters. After the shock process, any further change of θ_s will be caused by isentropic compression or expansion (4):

$$\frac{d\theta_s}{dt} = \theta_s\Gamma_x\frac{dp}{dt}. \tag{32}$$

with Γ being the Grüneisen coefficient and κ the isentropic compressibility, both assumed constant. Here dp/dt is the time rate of change of pressure. Heat loss due to thermal conduction and radiation are assumed to be negligible for the application presented here.

As the hot spots burn, energy is transferred to the balance of explosive. The second phase of the burn, burn propagation, starts as soon as sufficient energy is received by the unburned explosive. We now discuss the correlation of τ_m with the thermodynamic state.

As we have mentioned earlier, τ_m represents the process of energy transfer. When the pressure is low, we expect the mechanism to be simple heat conduction, but at much higher pressure levels, convection and local mixing could be a major factor for the rapid increase of the effectiveness of energy transfer. The parameter τ_m in fact plays the role of both film coefficient and temperature difference between the hot and cold regions. Accordingly, we propose the following expression:

$$\tau_m = [G_0 p + G(p)]^{-1} . \qquad (33)$$

The linear term in p represents the weaker energy transfer mechanism, most likely thermal conduction, and G is a highly nonlinear function of the current pressure p; we speculate the effect is due to the more efficient energy transfer mechanism such as turbulence. For high pressures, G provides the dominant contribution; in fact, we can identify that term to the pressure dependence in the Forest-Fire rate (3), when we compare the Forest-Fire model with Eq. (29). The determination of G is therefore carried out through a procedure similar to the Forest Fire model using Pop plot information; G_0 is obtained from the embedded gauge data and the Pop plot in the low pressure range. Using the original Forest-Fire rate function form (3),

$$G(p) = \exp\left(\sum_{i=0}^{n} a_i p^i\right) . \qquad (34)$$

Since the current formulation has an explicit multiplier μ in the propagation term of Eq. (28), values of G_0 and a_0 differ from the original formulations (3,4).

The explicit hot-spot model of shock initiation represented by Eqs. (24), (28) and (30) through (32) also includes the physical effect of shock desensitization (12): A shock wave of insufficient amplitude to cause prompt initiation itself has the effect of desensitizing the explosive to additional compression. That this effect is indeed included in the model given here can be seen by starting with Eq. (30). Consider a first shock of pressure p_s that creates an average hot-spot temperature θ_s. If θ_s is small enough, the characteristic time τ_c due to the first shock is too long. Additional heating due to subsequent shocks takes place according to the adiabatic relationship, Eq. (32), which is much less efficient than Eq. (30) for producing high hot-spot temperatures. The physical explanation for this is that hot-spot creation is a highly irreversible and dissipative process, and can happen only once when the first shock arrives. Subsequent shocks can do only reversible mechanical work on relatively cool hot spots that have already been formed.

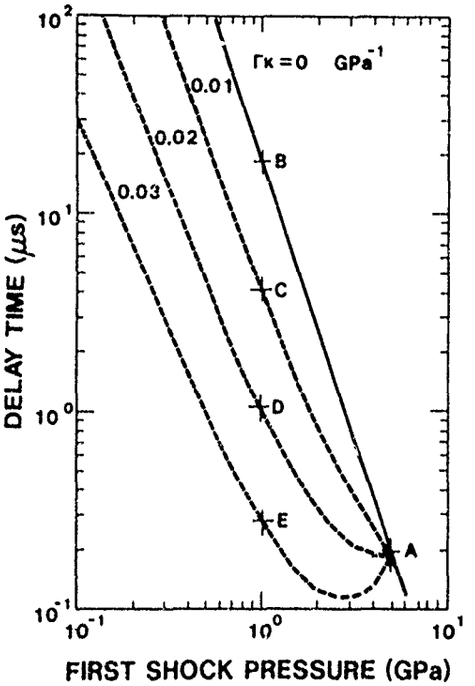

Fig. 1. Effect of the first shock on the delay time followed by a second 5-GPa shock

Figure 1 gives a quantitative description of this phenomenon for PBX-9404 (94% HMX/3% NC/3% CEF) with various values of $\Gamma\kappa$ in Eq. (32). The discussions are general and apply to explosives other than PBX-9404. Figure 1 gives the average induction time for hot-spot reaction

for a 5-GPa second shock preceeded by a first shock of amplitude p_s. For a single 5-GPa shock, the induction time is ~0.2 μs; point A on the solid line given by Eqs. (30) and (31) with p_s=5 GPa. If the 5-GPa shock is preceeded by a 1-GPa shock, the induction time for the first shock (1 GPa) is~11 μs, point B. If $\Gamma\chi$=0, there is no additional heating due to the second shock and the induction time remains at ~11 μs. If $\Gamma\chi$=0.01 GPa^{-1}, the induction time is reduced to 4 μs, point C; this is still quite long compared to ~0.2 μs for a single 5-GPa shock. As the compressibility is increased, the delay time behind the second shock gets closer to that for a single shock (points D and E in comparison with A). The dashed lines in Fig. 1 are the delay times behind a 5-GPa shock that follows a first shock of amplitude p_s. These delay times increase significantly as p_s is decreased until a threshold shock pressure is reached (below which hot spots cannot be created by the first shock). Below this threshold (not shown) the second shock travels into essentially virgin material and the delay time decreases rapidly to a value near that for a single shock (i.e., point A for a single 5-GPa shock).

COMPUTATIONAL RESULTS

Calibration of the explicit hot-spot model presented here is described in detail in (4) for sustained impact in PBX-9404. Computations were performed numerically by the method of characteristics tracking a single discontinous shock front. A thick lucalox impactor produced an initial particle velocity of 0.055 cm/μs in the PBX-9404 sample, experiment 547 (13). Comparison of the theoretical calculation with measured particle velocities at 0.5 mm, 2.5 mm, and 4.5 mm is shown in Fig. 2. The same model was used with identical rate parameters to compare with measured particle velocities for a finite-duration pulse. In experiment 532 (13), a 0.28-cm thick lucalox projectile produces a 0.51-μs pulse with initial particle velocity of 0.053 cm/μs in PBX-9404. Comparison of theory and experiment is shown in Fig. 3 for particle velocity gauges located at 0.2 mm, 1.2 mm, and 3.2 mm. The good agreement shown in Fig. 3 is very encouraging because calibration was performed for a sustained shock, Fig. 2. This result gives some confidence that the explicit hot-spot model represents reasonable departures from

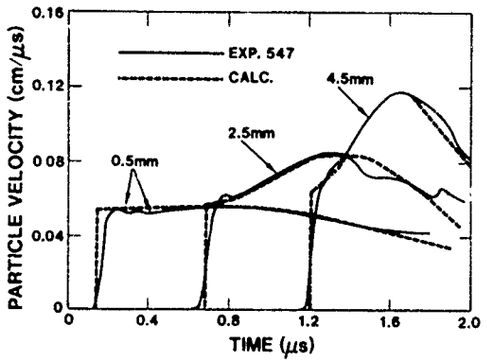

Fig. 2. Sustained impact results, experiment and calculation

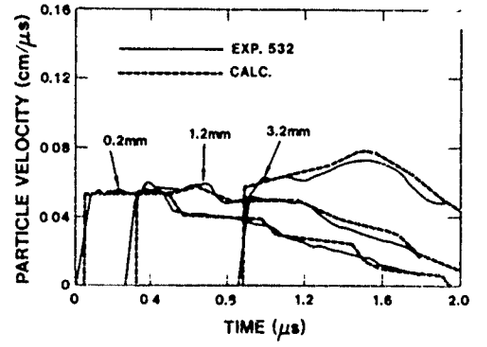

Fig. 3. Finite-duration pulse results, experiment and calculation

calibration situations. As obvious a requirement as this may be for shock initiation models, it has not always been demonstrated.

We have also included the explicit hot-spot model in the two-dimensional, hydrodynamic finite-element code DYNA2D (14). As one check of the explicit hot-spot model and the code, a number of distance-to-detonation calculations were performed and compared with the characteristic theory and the experimental data, the results are shown in Fig. 4. In addition to these comparisons, DYNA2D showed favorable comparison with the data and characteristic calculation given in Fig. 2.

In the remainder of the work described here, the DYNA2D code with the explicit hot-spot burn model was used to investigate two-dimensional effects of corner turning and shock desensitization in PBX-9502 (95% TATB/5% Kel-F). The model parameters for PBX-9502 were estimated from the Pop plot given in (15) and embedded gauge measurements for porous TATB (16), which give an approximate value of τ_c~1 μs for a shock pressure of ~8 GPa. The

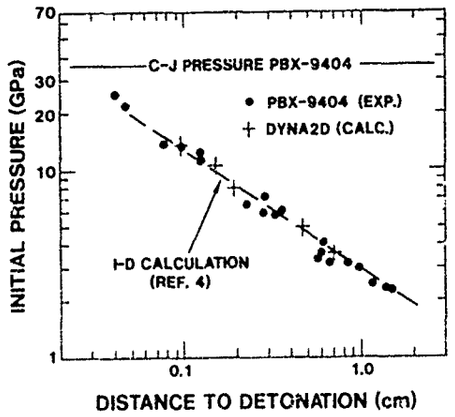

Fig. 4. Pop plot for PBX-9404, experiment, 1-D and 2-D calculations

Arrhenius constants for TATB are fiven in (17).

For the case of corner turning when the explosive changes size abruptly, we use a 2-cm long PBX-9404 booster to start the burn in PBX-9502. The explicit hot-spot burn model is used for PBX-9502 but programmed burn is imposed on PBX-9404. The problem configuration is given in Fig. 5 with the explosives bound by Plexiglas. With a radius of 1.3 cm in the first segment (4-cm long) and 6-cm radius in the second segment (3-cm long), the burned mass fraction contours are shown in Fig. 6 at 14 μs. A partially burned region is seen near the region where the explosive increases suddenly in size. The reason for this behavior is the rapid lowering of shock pressure when the detonation wave tries to expand suddenly, resulting in partial burn or even complete extinction, at least in some local region. However, the main burn front is still strong enough to maintain the burn so that an expanding detonation wave can be formed eventually, except the portion in the vicinity of the corner.

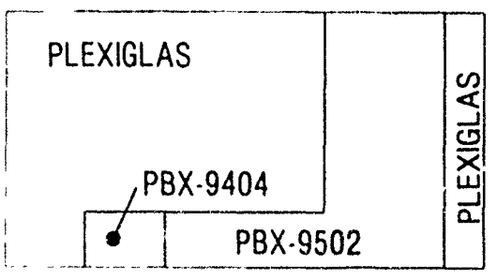

Fig 5 Configuration for corner turning simulation

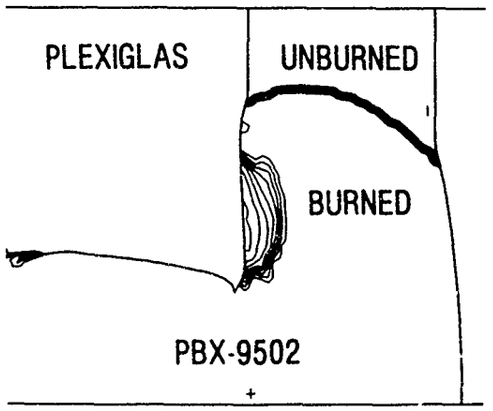

Fig.6. Burned mass fraction contours for a detonation wave turning a corner in PBX-9502

The final example is a study of shock desensitization, using the configuration of Fig. 5 but replacing the material bounded on the side with aluminum. A weak shock will travel through that medium and reach part of the explosive block sooner than the main detonation front because of the higher shock velocity for aluminum. Since the intensity of the shock is weak, the initial hot-spot temperature associated with the shock remains low and the ignition delay is very long. Even with subsequent compression of high intensity, the ignition delay is not reduced enough to cause significant burn in the hot-spot region as discussed earlier. The effect of the preshock on the burned mass fraction (P) at 14 μs is shown in Fig. 7; a well-defined unreacted region is seen between the aluminum and PBX-9502. Figure 8 shows the density contours exhibiting the sharp contrast of the density between the burned and unburned regions. A flash radiograph of shot no. 1746 (18) for PBX-9502 turning a 90- deg aluminum corner is reproduced in Fig. 9. Although the experiment was performed with a somewhat different geometry, the essential features are reproduced by the explicit hot-spot model.

CONCLUSION

We have presented a new HE burn model and demonstrated some of the experimentally observed features of the model in one and two dimensions. The results are quite encouraging and we shall continue the effort; in particular, we shall investigate further how those empirical parameters relate to the thermodynamic state

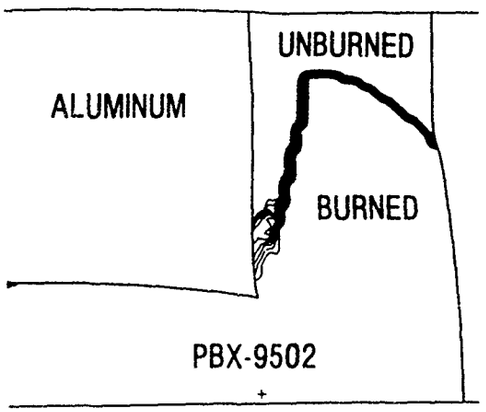

Fig. 7. Burned mass fraction contours for — BX-9502 with shock desensitization

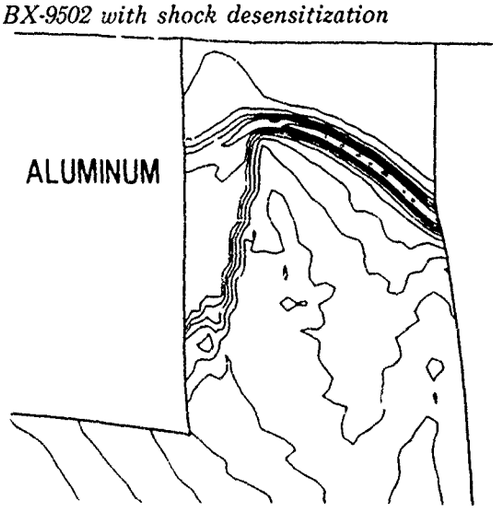

Fig. 8 Density contours showing the effect of shock desensitization

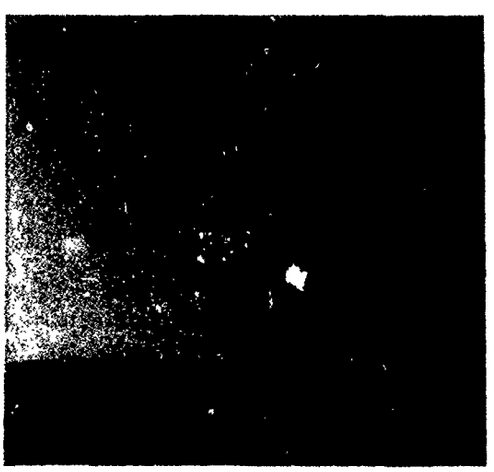

Fig. 9. Flash radiography

and material properties such as initial temperature and grain size. The energy transfer concept of this model prompts us to believe that those parameters θ_o, f_0, G_0, and a_i's must be related to the initial temperature. The hot-spot mass fraction, μ, must be linked to the grain size through the surface area and inter-granular inhomogeneity; a smaller grain size would result in a larger hot-spot mass fraction. Therefore it is possible that finer grain size may lead to shorter run distances as some experiments indicate (12). However, the grain size may also have some effect on the initial reference hot-spot temperature. As the grains become smaller, the material approaches a more homogeneous state which reduces the dissipation coming from the irreversible stress components. The net effect is a lower reference hot-spot temperature θ_0 which would decrease the hot-spot burn rate, resulting in longer run distance. Experimental evidence also supports this trend at low shock pressures (19). At the present time, the data needed for the model are limited and in some cases, preliminary. More experimental work is required to support the model improvement and actual application.

REFERENCES

1. W. Fickett and W. Davis, Detonation, pp. 16-20, University of California Press, Berkeley, 1979.

2. J.B. Ramsay and A. Popolato, "Analysis of Shock Wave and Initiation Data for Solid Explosives," pp. 233-238, Fourth Symposium on Detonation, ACR-126, 1965.

3. C. Mader and C. Forest, "Two-Dimensional Homogeneous and Heterogeneous Detonation Wave Phenomena," Los Alamos Scientific Laboratory Report, LA-6259, June 1976.

4. J. Johnson, P. Tang, and C. Forest, "Shock-Wave Initiation of Heterogeneous Reactive Solids," Journal of Applied Physics, Vol. 57, No. 9, pp. 4323-4334, May 1985.

5. A. Kanury, Introduction to Combustion Phenomena, pp. 297-300, Gordon and Beach, New York, 1975.

6. F. Williams, Combustion Theory, pp. 361, Addison-Wesley, Reading, 1965.

7. J. Starkenberg, "Ignition of Solid High Explosive by the Rapid Compression of an Adjacent Gas Layer," Seventh Symposium (International) on Detonation, NSWC MP 82-334, pp. 3-16, June 1981.

8. R. Frey, "The Initiation of Explosive Charges by Rapid Shear," Seventh Symposium (International) on Detonation, NSWC MP 82-334, pp. 36-42, June 1981.

9. R. Khasainov, A. Borisov, B. Ermolaev, and A. Korotkov, "Two-Phase Visco-Elastic Model of Shock Initiation in High Density Pressed Explosives," Seventh Symposium (International) on Detonation, NSWC MP 82-334, pp. 435-447, June 1981.

10. Y. Partom, "A Void Collapse Model for Shock Initiation," Seventh Symposium (International) on Detonation, NSWC MP 82-334, pp. 506-516, June 1981.

11. J. Dienes, "Frictional Hot-Spots and Statistical Crack Mechanics," 1983 Annual Meeting of Material Research Society, Nov. 1983.

12. A. Campbell, W. Davis, J. Ramsay, and J. Travis, "Shock Initiation of Solid Explosives," Physics of Fluids, Vol. 4, No. 4, pp. 511-521, April 1961.

13. J. Vorthman, personal communication.

14. J. Hallquist, "User's Manual for DYNA2D—An Explicit Two-Dimensional Hydrodynamic Finite Element Code with Interactive Rezoning," Lawrence Livermore National Laboratory, UCID-18756, Feb. 1982.

15. T. Gibbs and A. Popolato, LASL Explosive Data, pp. 397-399, University of California Press, Berkeley, 1980.

16. A. Anderson, M. Ginsberg, W. Seitz, and J. Wackerle, "Shock Initiation of TATB," Seventh Symposium (International) on Detonation, NSWC MP 82-334, pp. 385-393, June 1981.

17. R. Rogers, "Thermochemistry of Explosives," Thermocimica Acta, Vol. 11, pp. 131-139, 1975.

18. C. Mader, ed., LASL PHERMEX Data, Volume III, pp. 463, University of California Press, Berkeley, 1980.

19. R. Setchell, "Grain-Size Effects on the Shock Sensitivity of Hexanitrostilbene (HNS)," Combustion and Flame, Vol. 56, No. 3, pp. 343-345, June 1984.

DISCUSSION

M. SUMMERFIELD, Princeton Combustion Research Laboratory

This is a comment. It applies not simply to this paper but to several preceding papers as well.

When an author shows a graphical result that exhibits excellent agreement between his theoretical prediction and experimental data, it would be instructive to all of us if he would tell us at the same time the hypothetical relations or mechanisms that he had to insert in the theory to make the agreement so good and, above all, how many adjustable parameters he tried on the computer before the theoretical curve and the experimental data came into agreement.

REPLY BY P.K. TANG

The calibration procedure to obtain the input parameters is described in the paper and in the cited references. Some of them are related to the thermal-chemical properties of the explosive. The Forest Fire coefficients are determined in a relatively straightforward manner. Only the reference hot-spot temperature and the threshold require a few iterations to match the gauge data.

DISCUSSION

J.C. CUMMINGS, Sandia National Laboratory, Albuquerque

Why do your calculated values on the Pop plot appear to oscillate around a straight line fit?

REPLY BY P.K. TANG

The finite-difference code used does not have a good way to calculate the shock condition. The oscillatory behavior of the calculated points is the result of the numerical approximation using artificial viscosity.

HOT SPOT PRODUCTION BY MOVING DISLOCATIONS IN A RAPIDLY DEFORMING CRYSTALLINE EXPLOSIVE

C.S. Coffey
Naval Surface Weapons Center
White Oak
Silver Spring, Maryland 20910

The need to postulate the existence of localized hot spots to account for the ignition of explosives by impact or shock has long been recognized. In the past, attempts to understand hot spot formation during dynamic loading have used the classical continuum theory of deformation of a solid, and often relied on the presence of voids or pores to achieve energy localization. This continuum approach often fails to adequately treat the situation in which there are no voids or pores, nor can it adequately handle such things as particle size effects. Further, it ignores the large body of experimental evidence with shocks and impacts in inert solids which show the presence of an extensive microstructure in the form of shear bands and fracture sites. Here is outlined the progress to date of an attempt to provide a fundamental microscopic understanding of the energy localization proccess that occurs during shock or impact loading of crystalline solids. This approach invokes the fundamental mechanism of plastic deformation in a crystalline solid, the multiplication and motion of dislocations, and establishes energy localization and dislocation density distribution due to deformation by arbitrary shock or impact loading. Direct excitation of internal molecular vibrational modes is shown to occur for rapid, shock driven, deformation and this may have an important role in the detonation process.

INTRODUCTION

The need to postulate the existence of hot spots to account for the initiation of explosives during compressive wave or shock loading has been long and widely recognized. (1,2) There have been a number of attempts to describe the processes responsible for the formation of these hot spots. For the most part these efforts incorporated ideas from the classical continuum theory of the deformation of solids. Since this theory tends to distribute both energy and deformation over regions that approach the dimensions of the bulk of the solid, the need to achieve energy localization has often been satisfied by relying on macroscopic structural defects within the solid, such as voids or pores, to provide the focal points for concentrating energy.

While such theories may be adequate in some instances, they often fail to provide a satisfactory account of much of the experimental record, especially the more recent data. These experiments show, among other things, that in well prepared samples containing no detectable voids or pores, hot spots/ignition sites first occur in regions of high shear and shear rate. (3) Often these were regions of low to moderate pressure (<.1GPa), and yet were frequently close by regions of relatively high pressure, (>1 GPa), but of low shear where in well prepared, uniform samples first ignition has never been observed to happen. Other recent data from experiments in which infrared emissions were monitored show that heat is generated in impacted and apparently shocked crystals at the moment that deformation begins. (4,5) In these experiments

the apparent blackbody temperatures were in excess of 200 to 300 °C at the very beginning of the loading when the crystal deformation had only progessed about 10 microns or less. The classical continuum approach would predict temperature increases of only a few tenths of a degree centigrade for these circumstances. For some materials under high rate shock loading the apparent blackbody temperature was observed to be from 700 to 900 °C. This behavior was observed in both inert and energetic materials during impact or shock loading, and only when the heating was to a sufficient temperature did the energetic materials react chemically. Other recent experiments have shown a strong particle size effect on the impact sensitivity of RDX crystals when they were impacted between anvils faced with the relatively soft surfaces of heat sensitive film. (6) Identical imapct experiments, but with bare steel anvils, (R_C=64), show a much smaller particle size effect. (7) In the one case the crystals deform at a relatively slow rate due to the simultaneous deformation of the plastic film, while in the latter experiments crystal deformation and fracture occur more rapidly because of the unyielding anvils. In the case of slow deformation, it appears that the lattice dislocation velocities are small enough to permit dislocation pile-ups to develop before ignition occurs. This results in a typical Hall-Petch dependency with the drop height for ignition varying as the inverse square root of the particle size.(8) In the case of the rapid deformation, by the hard anvils, the dislocation velocities would be large enough to generate sufficient local heating for ignition to occur before the pile-ups can fully develop. These results are contained in equation (3) of this paper. Indications of a particle size effect have also been observed in shock expeiments with explosives but to date this evidence has not been as clearly demonstrated as with impact experiments.

Most if not all of the above observations indicate a discrete, sub particle size, process for concentrating the energy of deformation into small local regions or hot spots from which ignition can occur. For the impact experiments at least there appears no possibility that adiabatic compression of gas in voids has any significant role in the ignition process. The similarity of the shock and impact infrared experimental results and the fact that in our recent experiments the presence of voids was avoided mainly through the use of carefully grown cyrstals, suggests that adiabatic compression of gas in shocked explosive solids may not be the main contributor to ignition. Rather, when they occur the presence of pores and voids allows deformation to occur more readily and it is this deformation that generates the local energy concentrations which compete with adiabatic compression as the source of ignition sites.

ANALYSIS

With this background in mind, our efforts to understand and analyze the energy localization process due to impact or shock, have sought to examine the microscopic processes responsible for plastic deformation in crystalline solids. It is well established that this plastic deformation occurs by the generation and movement of dislocations. (9) It is also well established, by both shock and impact experiments in inert crystalline solids, that the deformation often occurs concentrated in narrow regions known as shear bands. (10) The regions on either side of the shear bands are usually relatively unaffected by the adjacent localized deformation. It is also known that shear bands within single crystals contain high concentrations of dislocations. (11) Since the plastic deformation is effectively localized within the narrow shear bands of a rapidly deforming crystal, these must be regions of localized plastic work and consequently regions of high temperature. These and similar observations by others (12) suggest that shear bands serve as a natural means of concentrating energy in rapidly deforming explosive crystals to produce hot spots which may eventually become ignition sites.

As part of this effort, we developed a quantum mechanical account of the rate of energy dissipation by a moving edge dislocation in a rapidly deforming crystalline solid. (13) Recently, this anlaysis was extended to include higher order processes which now enable it to treat the energy dissipation that occurs during the very rapid deformation and dislocation motion produced by high strength shock waves as well as the slower motion produced by less rapid compressive waves. (14) Equation (1), taken from this most recent work, describes the rate of energy dissipation by a collection of dislocations

moving with velocity v

$$\dot{E} = g\,\Gamma\,R^2 \int \sum_{k} (n_q+1)N_k\,(N_{k-q}+1)\,dq + \eta\omega \sum_{f,u} \left| \sum_{\iota} \frac{\langle f|H'|\iota\rangle\langle\iota|H/|u\rangle}{\omega_\iota - \omega u} \right|^2 dqdV$$

$$\text{where } \Gamma = \frac{1}{8(2\pi)^3 Nm} \left(\frac{Gb}{1-\nu}\right)^2 \frac{1}{d^2C} . \quad (1)$$

N_k is the number density of moving dislocations per cm of active slip plane, and N_{k-q} is the similar number density of dislocations after they have emitted a phonon of wave vector q. The quantity n_q is the phonon number density, G is the shear modulus, b is the Burgers displacement, Nm is the density, ν is the Poisson ratic, C is the shear wave sound speed, d is the intermolecular spacing, R is the dislocation radius, H′ symbolizes the second and higher order coupling between the moving dislocation and the phonon field, ω_ι is the internal vibrational frequency of the ιth vibrational level, ω_u is the phonon frequency generated by the moving dislocation and $|u\rangle$, $|\iota\rangle$, $|f\rangle$, are the initial, intermediate, and final molecular states respectively. The second term, containing the resonant denominators, describes the higher order processes accessible to excitation by shock driven dislocations. A complete derivation of this expression is given in reference 14. In reference 13 it was shown that the energy dissipated by the motion of edge dislocations was concentrated along the active slip planes mainly in front of the moving dislocations, so that the energy localization occurs naturally in the proper region indicated by experiment.

There are three limiting asymptotic regimes that are readily investigated. The first deals with a relatively dislocation free crystal for which $N_{k-q} \ll 1$ so that to a good approximation $N_{k-q} + 1 \approx 1$. The second asymptotic regime is the case of a heavily work hardened crystal for which $N_{k-q} \gg 1$, so that $N_{k-q} + 1 \approx N_{k-q}$. If the assumption is made that after emitting a phonon the motion of the dislocation stops or nearly stops so that $k-q=0$, then N_{k-q} can be written in terms of the known dislocation number density of a work hardened pile-up (15)

$$N_{k-q\approx 0} = \frac{2(1-\nu)\sigma}{Gb} \frac{x}{((\iota/2)^2 - x^2)^{1/2}} \quad (2)$$

where ι is the length of the pile-up, σ is the resolved applied shear stress, and x is the location of interest in the pile-up. If, as often occurs, ι can be made to approach the size of the crystal, D, then $N_{k-q\approx 0}$ has a $D^{-1/2}$ dependency and this accounts for a particle size effect. Since in neither of these two cases does $N_{k-q} + 1$ depend on k or q the expression can be taken outside of the summation and integral signs in equation (1). If the additional assumption is made that all the dislocations move with the same velocity v during the deformation, which is a standard simplifying assumption in dislocation theory, then the sum over N_k can be taken out from under the integral sign and the summation just reduces to the total number of moving dislocations, $N = \Sigma_k N_k$. Dividing equation (1) by N gives the energy density rate per moving dislocation as

$$\frac{\dot{E}}{N} = \frac{2\pi\Gamma}{dC} vR^2(N_{k-q}+1) + \frac{1}{N} \int \eta\omega \sum_{f,u} \left| \sum_{\iota} \frac{\langle f|H'|\iota\rangle\langle\iota H'|u\rangle|}{\omega_\iota - \omega_u} \right|^2 dq\, rdrd\theta \quad (3)$$

with units of ergs/cm-s, and where $q=2\pi$ v/dc. How this expression for q was obtained will be shown shortly.

Unfortunately, material properties data appropriate to explosive crystals are not presently available for substitution into equation (3). There does exist however an extensive data set on the response of lithium flouride during impact and shock. (16) The appropriate material properties data is given in Table 1. For illustrative purposes, Figure (1) shows a comparision of the predicted and experimental behavior of the energy dissipation rate per moving dislocation with the number of residual dislocations that remain in LiF crystals after they have been subjected to shock or impact. Since at this time it is not known how to calculate the number of dislocations that remain in a solid after the applied stress pulse is relieved, this number had to be obtained by scaling down the predicted total number density of dislocations due to the applied shear stress. (17) This scaling, by a factor of 1/30, just shifts the predicted curve along number density axis until it is in good agreement with the experimental data. However, the calculation of the rate of energy dissipation is exact and does not depend on the

TABLE 1
Pertinent Material Property Values for LiF

Poisson Ratio $\nu = .187$
Burgers vector $b = 2.84 \times 10^{-8}$cm
$Li^+ - Li^+$ separation distance $d = 4.01 \times 10^{-8}$cm
Approximate radius of interaction of dislocation potential $R = d/2 = 2.0 \times 10^{-8}$cm
Nominal Shear Modulus $G_o = .5 \times 10^{12}$ dynes/cm^2
Anisotrophy factor $A = 1.82$
Effective Shear Modulus $G = \frac{G_o}{A} = .27 \times 10^{12}$ dynes/cm^2
Shear wave speed $C_T = 3.6 \times 10^5$ cm/s
Approximate length of dislocation pile-up $\iota = 10^{-2}$cm
Approximate location of tail of pile-up $x = 10^{-7}$cm
Density $Nm = 2.6$ gm/cm^3

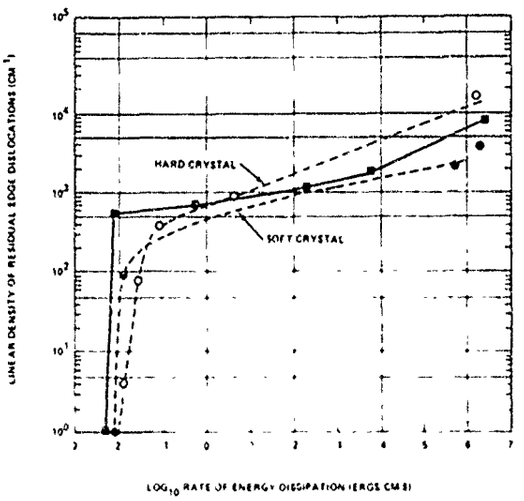

Fig. 1. Linear density of residual edge dislocations plotted against the rate of energy dissipation per cm of moving dislocation in LiF. The dashed curves are from experiment, the solid curve is the theorectical prediction. The experimental data is from Johnston and Gilman, reference (11).

number of dislocations after the stress is relieved, and therefore is not effected by the scaling. The point of major importance is that both experiment and theory give energy dissipation rates approaching 1 watt per cm of moving dislocation at mild shocks with .5 GPa shear stress. The potential exists for very high energy densities within an active shear band. It is reasonable to expect that in any shear band the number of moving dislocations will exceed 10^6. This energy is reduced considerably because the typical dislocation length does not approach 1 cm, and it is in motion for only a small fraction of a second. What is needed to determine this energy density is the number and velocity of the moving dislocations in the shear band, and this is the subject of much of our current research.

Finally, there exists an interesting asymptotic behavior when the dislocation velocity is very high as might occur in shock driven deformation. Consider the case of a dislocation moving with a velocity v in a crystal lattice with a simple Peierls-Nabarro sinesoidal intermolecular potential. (18) The time required to move the dislocation one intermolecular spacing, d, is just $t=d/v$, and the radial frequency of encounter is $\omega_u = 2\pi v/d$. For the Peierls-Nabarro potential this is the spectra of the emitted phonons, while for the more realistic intermolecular potentials, the phonon spectra will consist of bands centered about this frequency. For a modest dislocation velocity of 10^2m/s and an intermolecular separation of $d=10^{-9}$m, typical of RDX, the major component of the phonons generated by the moving dislocation is $\omega_u = .6 \times 10^{12}$ rad/s. The upper limit of possible dislocation velocities is nearly the shear wave sound speed of the material. (9) For the explosives of interest this velocity is of the order of 2×10^3 m/s, and is obtainable with dislocations driven by shock waves. Therefore, high velocity, shock driven dislocations will generate phonons with frequencies in excess of 10^{13} rad/s which is of the same order as the internal vibrational modes of most organic explosive molecules, $\omega_i \approx 10^{13}$ rad/s. It now follows that with increasing dislocation velocity, $\omega_u \rightarrow \omega_i$, so that the denominators of the higher order processes in equation (1) or (3) approach zero, and these terms will dominate the energy dissipation process. Thus, direct pumping of the internal molecular vibrational modes can occur which in turn can lead to rapid multiphonon induced molecular dissociation with the very short transition times required to support the detonation process. (19)

SUMMARY

The problem of hot spot formation in rapidly deforming explosive crystals has been treated

from a microscopic approach that builds on the fundamental role that the generation and motion of dislocations have in producing plastic deformation in crystalline solids. It is shown that energy localization occurs naturally in rapidly deforming crystalline solids and that high energy densities (temperatures) are possible. These occur simultaneously with the onset of deformation in keeping with recent experimental evidence that high temperatures appear essentially instantaneously with the start of deformation. At high rates of deformation, corresponding to high dislocation velocities, the energy dissipation rate can be very large as demonstrated by both experiment and theoretical prediction. At very large dislocation velocities, as would occur in shock induced deformation, the localized energy dissipated by the moving dislocations can directly excite the internal vibrational modes of many organic molecules. This process could be an effective way to obtian rapid molecular excitation and dissociation in a detonation wave.

Research is currently under way to further investigate the potential of this approach. One area in particular, is the need to more completely specify the shear band thickness and temperature distribution in terms of variables that can be related to the familar macroscopic quantities as pressure and shear stress for possible inclusion as a hot spot model in computer codes.

ACKNOWLEDGEMENTS

The author gratefully acknowledges the support of both the Office of Naval Research and the Naval Surface Weapons Center Independent Research funds.

REFERENCES

1. F.P. Bowden and A.D. Yoffe, "Fast Reactions in Solids," Butterworths, London (1958).
2. A.W. Campbell, W.C. Davis, J.B. Ramsay, and J.R. Travis, Phys. of Fluids, *4*, 511, (1961).
3. C.S. Coffey, M.J. Frankel, T.P. Liddiard and S.J. Jacobs, Proc. 7th Symp. on Detonations, Naval Surface Weapons Center, MP 82-334, P. 970, (1981).
4. P.J. Miller, C.S. Coffey and V.F. DeVost, A.P.S. Bulletin, Washington Mtg, April 23-26, (1984)
5. .J. Miller, C.S. Coffey, and V.F. DeVost, "Heating in Crystalline Solids Due to Rapid Deformation," Submitted to the J. of Appl. Physics.
6. C.S. Coffey and S.J. Jacobs, J. of Appl. Phys. *52* (11), 6991, 1981.
7. R.W. Armstrong, C.S. Coffey, V.F. DeVost and W.L. Elban "Crystal Size Dependence for Impact Initiation of RDX Explosive", submitted to Nature.
8. E.O. Hall, Proc. Phys. Soc., B64, 747, (1951) and N.J. Petch, J. Iron Steel Inst., *174*, 25 (1953).
9. J.P. Hirth and J. Lothe, "Theory of Dislocations," McGraw Hill Book Co., New York (1968).
10. There are many references available, see for example (a) "Shock Waves and High Strain Rate Phenomena in Metals" M.A. Meyers and L.E. Murr, eds., Plenum Press New York (1981), (b) C. Zener and J.H. Holloman, J. Appl. Phys. *15*, 22, (1944).
11. W.G. Johnston and J.J. Gilman, J. Appl. Phys., *30* (2), 129 (1959).
12. See for example D.E. Grady, J. Appl. Phys. *53* (1), 322, (1982).
13. C.S. Coffey, Phys. Rev. B *24* (12) 6984 (1981).
14. C.S. Coffey, "Energy Localization in Rapidly Deforming Crystalline Solids," accepted for publication in the Physical Review B.
15. J.P. Hirth and J. Lothe, "Theory of Dislocations," McGraw Hill Book Co., New York, p. 700 (1968).
16. J.J. Gilman and W.G. Johnston, "Solid State Physics," *13* 147-222 (1962).
17. J.P. Hirth and J. Lothe ibid p. 700.
18. W.T. Read, "Dislocations in Crystals," McGraw Hill Book Co., New York, pp. 24-25 (1953).
19. C.S. Coffey and E.T. Toton, J. Chem. Phys., *76* (2) 949, (1982).

DISCUSSION

Y.M. TIMNAT, Techninon, (Haifa, Israel)

Is there any evidence that shear bands are important in the initiation of explosives?

REPLY BY S. COFFEY

Yes. Perhaps the most direct evidence that shear bands are important in the initiation of explosive is to be found in the paper by Field, Swallowe, and Heavens. (1) They present data showing that on impact a pellet of PETN initiated on a macroscopic shear band and further that the chemical reaction initially propagated along that shear band. Frey has reported on experimental observations of shear banding in fragment impacted Composition B but without the direct correlation of the shear bands as the ignition sites. (2)

These are valid macroscopic manifestations of shear banding in pressed polycrystalline and composite materials. This paper however is more concerned with the microscopic processes of shear banding as they occur within a crystal. In this case establishing a direct correlation between shear banding and initaition is more difficult, and consequently at this time more reliance has to be placed on inferential arguments. Johnston and Gilman in their classic work on LiF crystals, which had been subjected to a wide range of deformation rates, measured very large dissipation rates for dislocations moving in the shear bands. (3) A large number of dislocations were observed in the shear bands, so the obvious inference is that the bands must have been hot. Similar inferences can be drawn from the great body of evidence on shear banding in metals. For example, in steels subjected to high rates of deformation there is evidence that suggests that temperatures in excess of 800 C were reached. (4) Of course if most of the plastic deformation is confined to the shear bands, as is generally the case, simple theoretical arguments require these regions to become hot.

To try to resolve this issue, a series of experiments are now beginning at the Naval Surface Weapons Center which use an array of infrared detectors to determine the spatial and spectral distributions of shear bands in single crystals during impact and shock loading.

REFERENCES

1. J.E. Field, G.M. Swallowe, and S.N. Heavens, "Ignition Mechanisms of Explosives During Mechanical Deformation", Proc. R. Soc. Lond. A *382*, 231-244, 1982.
2. R.B. Frey, "The Initiation of Explosive Charges by Rapid Shear", Proc. of the Seventh Symp. (Int.) on Detonations. NSWC MP 82-334, Naval Surface Weapons Center, White Oak, Silver Spring Md. 20910.
3. W.G. Johnston and J.J. Gilman, "Dislocation Velocities, Dislocation Densities, and Plastic Flow in Lithium Fluoride Crystals." J. of Appl. Phys. *30*, 2, 129, 1959.
4. H.C. Rogers and C.V. Shastry, "Material Factors in Adiabatic Shearing In Steels," in *Shock Waves and High-Strain-Rate Phenomena in Metals*, M.A. Meyers and L.E. Murr Eds., Plenum Press, 1981.

CAVITY COLLAPSE IN ENERGETIC MATERIALS

Robert B. Frey
Ballistic Research Laboratory
US Army Materiel Command
Aberdeen Proving Ground, Maryland 21005-5066

We have studied the mechanics of cavity collapse in an energetic material. During cavity collapse, several mechanisms can act individually or collectively to produce high temperature hot spots. Our goal is to understand how pressurization rate, cavity size, and material parameters affect hot spot formation. For this purpose we have considered the collapse of spherical cavities using a modified form of the model of Carroll and Holt. Using this analysis, we can consider hot spots produced by inviscid plastic work, viscoplastic work, gas phase heating, or solid phase compression (which occurs as the result of high pressures produced when material collides at the center of the cavity). Under the proper conditions, each of these mechanisms may be dominant, but viscous heating is the most efficient mechanism and is dominant when the rise time of the pressure is short, viscosity is high, and/or yield stress is low. The conditions under which the other mechanisms are dominant and the dependence of hot spot temperatures on the pressurization rate, cavity size, and material properties are discussed. Cavity size and melt point have an interesting effect on the computed temperatures. Melting is signficantly desensitizing when the cavities are small but can be sensitizing for larger cavaties.

INTRODUCTION

It is well known that cavities, or microporosity, can sensitize an energetic material to shock or compression waves. There are many reasons for this which have been discussed by many authors. Mader (1), in considering shock initiation, proposed a hydrodynamic mechanism in which the upstream surface of a cavity is accelerated by the shock and hits the downstream side of the cavity, producing a high impact pressure which is amplified by convergence effects during the collapse process. In this mechanism, the heating is produced by compression of the solid phase material and plastic or viscoplastic work is not required. Bowden and Yoffe (2) demonstrated that under some conditions gas compression in pores could cause ignition. Other experimental work (3,4) has demonstrated that this is not the controlling mechanism under the usual conditions of shock initiation, but Starkenberg (5) has demonstrated that it can be a dominant mechanism under conditions where the compression rate is relatively low (compared to shock waves) and the cavities are relatively large (a millimeter or more in diameter). Khasainov (6) and Carroll and Holt (7) have discussed heating due to plastic work in the vicinity of collapsing cavities. Carroll and Holt considered inviscid plastic work (in reference 8 they considered viscous effects but did not discuss thermal effects) and Khasainov considered purely viscous (stress varies linearly with strain rate) plastic work. In each case, significant temperature increases were predicted for a thin shell of material around the collapsing cavity. It is also possible that shear bands could form in the vicinity of collapsing cavities. Initiation as the result of shear banding was first discussed by Winter and Field (9), although not in the context of cavity collapse. The present author discussed shear

banding in reference 10, and it appears that shear banding is also a possible ignition mechanism.

A problem with all of the treatments mentioned above is that they do not relate the ignition thresholds to such obvious physical parameters as cavity size and pressurization rate or to such material properties as viscosity, yield strength, and melt point. Much experimental work (see reference 11, for instance) indicates that particle size (which affects cavity size) has a strong effect on ignition thresholds. Also, it is widely recognized that the pressurization rate must affect ignition thresholds, and this effect has been observed experimentally by Setchell (12). Of the theoretical treatments mentioned above, only Starkenberg's addresses these two questions, and Starkenberg discusses only the gas compression mechanism. None of the treatments mentioned above discusses the effect of melting.

Our goal in this paper is to combine the various heating mechanisms which can occur in the vicinity of a collapsing cavity into one model and to determine the conditions under which each is dominant. The model, which is described in the next section, is necessarily highly idealized, so we will be interested in general trends rather than specific ignition thresholds. We will consider the effects of pressurization rate, cavity size, viscosity, yield strength, and melt point. Unfortunately, it was not possible to include shear banding in the model, so this mechanism is ignored.

PRINCIPAL ASSUMPTIONS USED IN THE MODEL

We based our model on the work of Carroll and Holt (7) and Carroll, Holt, and Butcher (8). They considered the collapse of a spherical cavity at the center of a spherical shell of solid matrix material. The assumptions of the model are as follows:

1. The flow is spherically symmetric in the vicinity of the cavity, and the pressure in the vicinity of the cavity depends only on radius. These are severe restrictions, but there are two cases where they are reasonable assumptions. The first is the case where rate of pressure increase is sufficiently low that there is never any significant pressure gradient across the diameter of the cavity; i.e.,

$$\Delta P = \frac{dP}{dt}\frac{A}{C} << P_{max}, \qquad (1)$$

Where ΔP is the pressure gradient across the cavity, dp/dt is the rate of pressurization, A is the cavity radius, C is the sound speed, and P_{max} is the maximum applied pressure. For a 1000 micron cavity, assuming a sound speed of 2.5 km/sec, this relation is satisfied as long as the pressurization time (P_{max}/(dp/dt)) is greater than one microsecond. It will thus apply to all the situations of interest except those involving shocks with very short rise times. The second case is where the time required for the shock or compression wave to pass over the cavity is very short compared to the cavity collapse time; i.e.,

$$\frac{A}{C} << \tau, \qquad (2)$$

where τ is the cavity collapse time. Viscous effects, which will be discussed later, typically require that the cavity collapse time be of the order of a microsecond even for small cavities. Hence, this relation holds for cavities as big as 1000 microns.

2. The matrix material is incompressible. The use of this assumption has several ramifications. First, it limits us to cases where the collapse velocity is much less than the sound speed. By calculation, this was true for the results reported here. Second, it means that we cannot explicitly consider the hydrodynamic mechanism since the heating in this mechanism is due to compression of the solid. However, we will be able to determine when the collapse process leads to pressures where the hydrodynamic mechanism might apply. Finally, we are limited to relatively low applied pressures. Ben Reuven and Summerfield (13) analyzed the case of a collapsing cavity in an inviscid fluid without strength. Their results indicate that compressibility begins to affect computed pressure in the cavity when that pressure reaches about one gigapascal. When strength and viscosity are considered, the importance of compressibility may be less, but we will generally restrict ourselves to applied pressures of less than one gigapascal. The computed pressure in the vicinity of the collapsing cavity may exceed this limit, and when it does we must be aware of the possibility of error.

3. The following constitutive relations applies:

$$S_r = 2\mu\dot{e}_r + \frac{2}{3}Y$$
$$S_\theta = 2\mu\dot{e}_\theta - \frac{1}{3}Y, \tag{3}$$

where μ = viscosity, Y = yield strength, S_r and S_θ are the principle deviation stresses, and $\dot{e}_r$ and $\dot{e}_\theta$ are the principle deviator strain rates. This relation is appropriate for a rigid-plastic material, and it was our intention to limit ourselves to this case. However, in doing the calculations we found it necessary to relax this assumption as described below.

Computational Details

Carroll and Holt considered a hollow sphere with outer radius b, inner radius a, and porosity α, defined as the ratio of the actual volume to the fully compacted volume, where $\alpha = b^3/(b^3 - a^3)$. The equation of motion for this system is

$$\frac{\partial \sigma_r}{\partial r} + \frac{2}{r}(\sigma_r - \sigma_\theta) = \rho\ddot{r}, \tag{4}$$

where σ_r and σ_θ are the principle stresses, r is the radius, and dots imply differentiation with respect to time. Following Carroll and Holt, we note that

$$\sigma_r - \sigma_\theta = S_r - S_\theta = \mu\dot{e}_r + Y, \tag{5}$$

and apply the boundary conditions,

$$\sigma_r = P_g \text{ at } r = a$$
$$\sigma_r = -P \text{ at } r = b,$$

where P is the applied pressure and P_g is the pressure in the gas filled cavity.

We also note that

$$\dot{e}_r = +\frac{2}{3}\frac{\dot{B}}{r^3},$$

$$\text{where } B(t) = a_o^3 - a^3 = b_o^3 - b^3 \tag{6}$$
$$= a^3(\alpha_o - \alpha)/(\alpha_o - 1)$$

and a_o, b_o, and α_o are the initial values of a, b, and α. The equation of motion can then be integrated with respect to the radius and the result expressed as the following differential equation for α:

$$P - P_g - \int_a^b \frac{2y}{r}\,dr - \int_a^b \frac{4\mu}{3}\frac{\dot{B}}{r^4}\,dr = F(\ddot{\alpha}, \dot{\alpha}, \alpha) \tag{7}$$

$$F(\ddot{\alpha}, \dot{\alpha}, \alpha) = \frac{\rho a_o^2}{3(\alpha_o - 1)^{\frac{2}{3}}}\left[\frac{\dot{\alpha}^2}{6}\left[(\alpha-1)^{\frac{-4}{3}} - \alpha^{\frac{-4}{5}}\right] - \ddot{\alpha}\left[(\alpha-1)^{\frac{-1}{3}} - \alpha^{\frac{-1}{3}}\right]\right] \tag{7a}$$

For convenience, we will refer to the third term on the left side of Eq. (7) as the inviscid plastic yield stress, P_{eq}, and the fourth term as the viscous stress, P_v. The rate of plastic work per unit volume at any point in the flow may be computed from the following equation (14):

$$W = \sum_i \int_o^{e_i^f} S_i de_i, \tag{8}$$

where S_i is the principle deviatoric stress, e_i is the principle deviatoric strain, e_i^f is the final value of the deviatoric strain and p is the density. In our case, we divide the total work, W, into a plastic work term, W_p, and a viscoplastic work term, W_v. Using Eq. (5, 6, and 8) yields the results that

$$\dot{W}_p = \frac{2}{3}Y\frac{\dot{B}}{r^3} \tag{9}$$

$$\text{and } \dot{W}_v = \frac{2}{3}\frac{\dot{B}^2}{r^6} \tag{10}$$

Eq. (7) was integrated numerically to determine B, $\dot{B}$, r, and α. Simultaneously, we numerically integrated the heat equation for the material about the cavity to determine the local temperature T:

$$\frac{\partial T}{\partial t} = \frac{K}{\rho c}\left[\frac{\partial^2 T}{\partial r^2} + \frac{2}{r}\frac{\partial T}{\partial r}\right] + \frac{\dot{W}}{\rho c}, \tag{11}$$

where t is time K is heat conductivity, and C is heat capacity.

The gas in the cavity was treated using an Abel equation of state,

$$P_g(V - nV_c) = nRT \tag{12}$$

where V is the volume of the cavity, V_c is the

covolume of the gas, R is the gas constant, n is the number of moles of gas present, and T is temperature. The pressure was assumed to be uniform throughout the gas phase, but the temperature and density could vary as a function of radius. The temperature was obtained from the heat equation, which was simplified by assuming that the source term, the heat generated by pressure-volume work, was constant everywhere in the gas phase. When the temperature was known in each zone, the pressure could be determined from the following equation,

$$P_g = \frac{\sum_i (V_{oi} - n_i V_c) \frac{T_i}{T_o} P_{go}}{\frac{4}{3}\pi a^3 - \sum_i n_i V_c}, \qquad (13)$$

where V_{oi} is the initial volume of the ith element. n_i is the moles of gas in the ith element, T_i is the temperature of the ith element, T_o is the initial temperature, P_{go} is the initial pressure, and a is the cavity radius. Knowing P_g and T_i, Eq. (12) was used to compute the volume of each element of the gas phase.

At the gas-solid interface the inner most layer of solid and the outermost layer of gas were combined in a single zone. Heat inputs and outputs (by heat conduction, by gas phase pressure-volume work, and by solid phase plastic and viscoplastic work) were averaged over the entire zone. This procedure permitted a little heat to be transferred from the gas phase to the solid phase even when the gas phase heat conductivity was set equal to zero.

The computational mesh was set up so that the zones near the gas-solid boundary were always very small. The zone size gradually increased further from the boundary. The thickness of the innermost zone in the solid phase was initially 0.02 times the cavity radius and during the calculation it was never more than 0.25 times the instantaneous cavity radius. The calculation was rezoned to use a smaller zone size whenever this criterion was violated or when a large temperature difference was noted between the two innermost zones. Because of the small zone size, it was necessary to violate the VonNeumann stability condition in order to achieve reasonable computer times. However, the finite difference calculation was carried out using a predictor-corrector technique with several iterations at each time step and no problems with stability were observed.

The yield strength, Y, was varied in the calculations to observe its effect on the temperature achieved. When the temperature was more than 30°C below the melt point, Y was constant, and above the melt point it was zero. In the 30°C range of temperature just below the melt point, Y decreased linearly as a function of temperature. Two forms of the viscosity, μ, were used. In the constant viscosity model, the viscosity was independent of both temperature and pressure. This was convenient for studying the effect of viscosity but not very realistic. In the variable viscosity model, the viscosity varied according to the following equation:

$$\mu = \begin{cases} 1000 \text{ poise for } T < T_{melt} \\ \mu_o \exp\left(\frac{P}{P_s}\right) \exp\left(\frac{E}{T_s} - \frac{E}{T}\right) \text{ for } T > T_{melt}, \end{cases} \qquad (14)$$

where P_o, T_s, u_o, and E are constants. This type of relation has been discussed by Frankel (15) and Bridgeman (16). The value of 1000 poise for the viscosity below the melt point was chosen on the basis of Khasainov's (6) analysis of Wackerle's (17) data for the decay of pressure behind a shock wave in porous PETN. In another paper (18), Wackerle suggests a higher value of 10,000 poise, and at times we have used this value instead of 1000 poise in equation (14). For u_o, E, and T_s, we used values appropriate to TNT and determined by fit to very limited data in reference 19. For P_o we used a value appropriate to nitrobenzene and determined from data in the *International Critical Tables*. These values and values for some other parameters are shown in Table 1. In using these parameters, we are not attempting to model any particular material, but we are choosing parameters which we feel are representative of secondary explosives. The melt point was varied, but where it is not specified it is 353°K. Unless stated otherwise, we also assumed in all cases that the melt point increased by 200°/GPa. Gas phase heat conductivities increase greatly with pressure. Starkenberg (8) has shown that this effect must be included if one is to correctly model the ignition of explosives due to gas compression. In the calculations reported here, we restrict ourselves to a constant gas phase heat conductivity, but use a value ten times that of

air at atmospheric pressure and room temperature. We also discuss the effect of varying the gas phase heat conductivity.

For simplicity, we had hoped to use a rigid plastic model for determining the deviator stress, as depicted by equation (4). In some situations, however, the cavity "bounces" as it collapses. In these cases, $\dot{e}_r$ changes sign, and if the rigid plastic model is used the deviator

TABLE 1.
Material Properties Used

$u_o = 1.39 \times 10{-}2$ kg/m/s
$T_s = 358$°K
$E = 3{,}880$°K
$P_s = 0.165$ GPa
$\varrho = 1.6 \times 10^3$ kg/m^3
$C = 1.4 \times 10^3$ joule/(kg°C)
$K = 0.262$ joule/(m°C s)
$V_c = 28$ cm^3/mole
$K_g = .33$ joule/m°C s)
$C_g = 1 \times 10^3$ joule/(kg°C)
$\alpha_o = 1.05$

(K_g and C_g are the gas phase heat conductivity and heat capacity. They were assumed to be constant for simplicity, but see text.)

stresses all suddenly change sign. This causes convergence problems in the numerical integration of equation (6). In principle, this problem could be eliminated by using the full elastic-plastic form of the equations, as described in reference 10, but we wished to keep the problem as simple as possible. Consequently, we invented an artificial elastic behavior. During the first phase of the collapse, the matrix is treated as rigid-plastic as described above. If the cavity "bounces" and the radius begins to grow, the plastic yield stress, P_{eq}, is computed from the following equations:

$$P_{eq} = F(\alpha) \int \frac{2Y}{r}\, dr \tag{15}$$

$$F(\alpha) = 1 - \frac{\alpha - \alpha_{min}}{\alpha' - \alpha_{min}} \text{ for } \alpha < 2\alpha' + \alpha_{min} \tag{16}$$

$$F(\alpha) = -1 \text{ for } \alpha > 2\alpha' + \alpha_{min}$$

$$\alpha' = \alpha_{min} + \frac{Y}{2G}(\alpha_{min} - 1), \tag{17}$$

where α_{min} is the lowest porosity obtained on the preceding cycle of collapse and G is the shear modulus. If the cavity has been expanding and begins to contract, P_{eq} is given by equation (15) with $F(\alpha)$ defined as follows:

$$F(\alpha) = \frac{\alpha_{max} - \alpha}{\alpha_{max} - \alpha'} - 1 \quad \alpha > 2\alpha' - \alpha_{max} \tag{18}$$

$$F(\alpha) = 1 \qquad \alpha < 2\alpha' - \alpha_{max} \tag{19}$$

$$\alpha' = \frac{(2G\,\alpha_{max} + Y)}{2G + Y},$$

where α_{max} is the largest porosity obtained on the last cycle of expansion. P_{eq}, calculated for equation (15) to (17), replaces the third term on the left side of the equation (7).

PRESSURE AMPLIFICATION

During cavity collapse, the material in the vicinity of the cavity may be accelerated to relatively high velocity. In the final stage of cavity collapse this material must be abruptly decelerated, and the pressure may obtain very high values, many times that of the applied pressure. This is what we call pressure amplification or overshoot. In an inviscid, strengthless fluid overshoot always occurs (for instance, see reference 13). When overshoot occurs, the hydrodynamic ignition mechanism, which involves compression of matrix material, may be possible. When overshoot does not occur, the hydrodynamic mechanism will not be important (at least for the relatively low applied pressures which are considered here).

When the effects of viscosity and strength are considered, overshoot is not inevitable. It is important to understand when it does and does not occur. If the strength is sufficiently high and the pressurization rate is sufficiently low, the inviscid plastic yield stress (P_{eq}, the third term on the left side of equation 7) will increase (as the cavity collapses) fast enough to keep up with the applied pressure, and high collapse velocities do not occur. A dimensionless parameter, N_1, which describes this effect is the following:

$$N_1 = A \frac{dP}{dt} \sqrt{\frac{\rho}{Y}} \tag{20}$$

where A is initial cavity radius, P is pressure,

t is time, ϱ is density, and Y is the inviscid yield strength. Figure 1 shows the result of two calculations where the applied pressure was 0.4 GPa, the pressurization time was 10 microseconds, the viscosity was very low (1 poise), and the yield strength, Y, was 0.07 GPa. With a cavity size of 100 microns, the plastic yield stress keeps up with the imposed pressure and the cavity undergoes a "gentle" collapse. For larger cavities, with other parameters the same, P exceeds P_{eq} by a large amount early in the collapse process, and the radial velocity becomes large. When the cavity collapse is nearly complete, P_{eq} overshoots P, and the cavity "bounces." P_{eq} can become very large in this case, producing pressures which invalidate this model but make Mader's hydrodynamic model possible. Based on our calculations, the critical value of N_1 is about 1.0.

Viscous effects also prevent overshoot Khasainov, in dis ing purely viscous flow (Y=0) and infinitesimal pressure rise times, introduced another nondimensional parameter, which determines whether viscous damping can absorb the available energy fast enough to prevent the cavity from "bouncing." This parameter, N_2, is defined by the following expression:

$$N_2 = \frac{A\sqrt{\varrho P}}{\mu} . \qquad (21)$$

Figure 2 shows the results of two calculations which have a fast risetime (1 microsecond), yield strength of 0.035 GPa, initial cavity size of 100 microns, and viscosity of 200 and 1000 poise. N_1 is large (2.73) so the possibility of large collapse velocities and pressure overshoot exists in all cases. With the smaller viscosity, the cavity bounces and pressure overshoot occurs, but with higher viscosity, the cavity collapses "gently." Based on our calculations, the critical value of N_2 is about one.

If both N_1 and N_2 are greater than one, pressure overshoot can occur and hydrodynamic heating is possible. Figures 3 and 4 are intended to provide some perspective on the range of cavity sizes, pressures, and pressurization rates for which this can happen. In Figure 3, we have plotted the pressurization rate versus the cavity size on the curve $N_1=1$ for the case where $\varrho=1.6$ g/cm^3 and Y=0.035 GPa. In Figure 4, we have plotted the cavity radius as a function of pressure on the curve $N_2=1$. If either N_1 or N_2 is less than one, pressure overshoot does not occur and the hydrodynamic mechanism is not possible. If both are greater than one, hydrodynamic heating may occur as well as viscous and plastic work. Under shock wave conditions, where pressurization rates are very high, Figure 3 indicates that overshoot is possible, based on the N_1 criterion and the parameters mentioned above, for cavities larger than about one micron. However, if the pressurization rate was reduced to 0.052 GPa/microsecond, which is slow when compared to shock waves but still large when compared to many stimuli, a cavity as large as 1000 microns could collapse without overshoot. Figure 4 shows that for an applied pressure of 0.4 GPa, the N_2 criterion prevents overshoot for cavities as large as 40 micron. Figure 4 was computed with a viscosity of 1000 poise. If this value was raised to 10,000 poise, as suggested by Wackerle (18), the cavity size required for overshoot would increase by an order of magnitude.

VISCOPLASTIC HEATING

We will now consider the heating which occurs in the vicinity of the collapsing cavity due to viscoplastic work. The temperature which is produced is controlled by a number of factors, which are described as follows:

(1) The relation between the cavity collapse time and the pressurization time. The energy dissipated in the vicinity of the cavity is the integral of the pressure with respect to the change in volume. If the pressurization time is large compared to the collapse time, most of the volume change occurs while the pressure is low and the energy dissipated is relatively small (but not negligible). Two characteristic collapse times may be considered. One is an inertial collapse time, t_i, which applies to inviscid flows and is given by the following expression (13):

$$t_i = A\left(\frac{\varrho}{P}\right)^{1/2} \qquad (22)$$

For large cavities (greater than a millimeter) it is frequently the controlling parameter. The second is a viscous collapse time, t_v, which is independent of cavity size (a surprising fact in the opinion of this author). Khasainov (6) gave the following expression for t_v:

$$t_v = \frac{4\mu}{P} . \qquad (23)$$

For a viscosity of 1000 poise and an applied pressure of 0.4 GPa, t_v is about one microsecond. Since it is independent of cavity size, it is frequently the controlling parameter for small cavities (less than a millimeter). Figure 5 shows how the dissipated energy varies with the rise time, τ, of the pressure for a calculation with a cavity size of 40 micron, a pressure of 0.4 GPa, a yield strength of 0.07 GPa, and a viscosity of 1000 poise. The curve is "S" shaped with high dissipated energy for short rise times and low dissipated energy for long rise times. For the situation in Figure 5, the ratio of t_v/τ is the important parameter, and the dissipated energy changes as this parameter changes from more than one to less than one.

(2) The relation between inviscid plastic work and viscoplastic work. Depending upon circumstances, the plastic work may be predominantly of the inviscid type (controlled by the yield strength Y) or the viscous type (controlled by viscosity). From equations 9 and 10, we can see that viscoplastic work has a much stronger dependence on radius than does inviscid plastic work. Therefore, when viscoplastic work dominates, we expect the dissipation to be more localized and the temperature to be higher. Furthermore, the inviscid plastic yield stress goes to zero at the melt point, and this limits the heating which can be caused by inviscid plastic work. We find that there is a critical parameter, N_3, which determines whether viscous or inviscid effects dominant. It is the quotient of N_1 divided by N_2 and is expressed as follows:

$$N_3 = \frac{\mu\sqrt{\frac{P}{Y}}}{Y\tau} \qquad (24)$$

where μ is viscosity, P is the applied pressure, Y is the inviscid yield strength and τ is the rise time of the applied pressure. When N_3 is much greater than one (high viscosity, low yield strength, low rise time) viscous effects dominate Figure 6 illustrates the effect of N_3 It is a plot of the maximum temperature, T, obtained in the solid phase in the vicinity of a collapsing cavity, as a function of the rise time of the applied pressure for calculations where the viscosity was 1000 poise, the initial cavity radius was 40 microns, the applied pressure was 0.4 GPa, and the yield strength was 0.07 GPa. The curve has an "S" shape, and the transition from low to high temperature occurs when N_3 is about one. For the situation in Figure 6, the parameter t_v/τ changes from less than one to greater than one at about the same place, and this increases the effect of rise time on the temperature. As can be seen, the computed temperature is very strongly dependent on rise time, with the transition from low to high temperatures occurring for rise times in the one to ten microsecond range. Figure 7 shows the effect of viscosity on the maximum computed temperature (solid phase). The cavity size was 40 microns; the applied pressure was 0.4 GPa, and two curves are shown with different pressurization times. The temperatures increase with increasing viscosity, and the most rapid increase occurs as N_3 changes from less than one to more than one. Figure 8 shows how the rise time varies with the applied pressure P on the curve $N_3 = 1$ when μ=1000 poise and Y=0.035 GPa. For shock waves, where τ is very short, viscous heating will be dominant, and high temperatures are expected. With slower pressurization rates, plastic work may be dominant, and the temperature will be lower.

(3) Cavity size and level of applied pressure. The maximum energy available for dissipation at the cavity is the product of the cavity size and applied pressure. These parameters also influence the computed temperatures by their effect on the parameters N_1, N_2, and N_3 discussed above. It is interesting to note that in a purely hydrodynamic model, with plastic work and gas phase heating ignored, the temperature which can be achieved at a cavity is independent of cavity size if the rise time is infinitesimal (the size of the hot spot increases with cavity size, but its temperature does not). However, when plastic work is considered, cavity size has a strong effect on the results. This is shown in Figure 9. The upper curve in Figure 9 shows how the maximum computed temperature (in the solid phase) varies as a function of cavity size for a series of calculations with μ=1000 poise, τ=0.1 microseconds, and Y=0.07 GPa. For this series of calculations, N_3 is large, and

viscous heating dominates. Rather high temperatures are thus computed over the entire range of cavity sizes, but the temperature increases with cavity size. When the cavity size exceeds 100 microns, N_2 becomes larger than one, and pressure overshoot occurs. A sharp increase in the temperature occurs because the cavity radius is driven down to a very small value, and this causes greater localization of the energy (the high pressure may also cause hydrodynamic heating, but we do not consider that effect here). The lower curve in Figure 9 shows similar results for calculations with τ equal to ten microseconds. In this case, N_3 is less than one, and the temperatures are relatively low until the cavity size reaches 400 microns. At that point, both N_1 and N_2 become greater than one; overshoot occurs, and high temperatures are achieved.

(4) Heat conductivity. Khasainov (6) noted that heat conductivity did not significantly affect the temperature achieved unless the cavity size was less than one micron. He noted that the characteristic time for the cooling of the surface of a sphere is

$$t_c = A^2\varrho C/K, \tag{25}$$

where A is cavity radius, ϱ is density, C is heat capacity, and K is heat conductivity. For a one micron cavity, t_c is of the order of ten microseconds, and for bigger cavities it increases rapidly. We have already seen that t_v is of the order of one microsecond when the pressure is 0.4 GPa and the viscosity is 1000 poise. Thus cavity collapse should be complete before heat conduction can significantly affect the results. In the calculations which we have performed, with cavities in the range of 1 to 1000 microns, we have seen no effect due to heat conductivity unless gas compression was a major contributing mechanism (this will be discussed in the next section).

(5) The effect of yield strength and initial gas pressure. Yield strength (Y) and the initial gas pressure, P_{go}, in the cavity affect the results in a way that may seem surprising. Although there are exceptions, high strength generally reduces the temperature, sometimes markedly so. The results of some calculations demonstrating this are shown in Table II. The effect of high strength is to shift the dissipation from viscous to plastic forces and to increase the final radius of the cavity. Both of these effects are desensitizing. Higher values for the initial gas pressure are desensitizing for the same reason. The effect of initial gas pressure in two pairs of calcuations is shown in Table III. The calculations on the last two lines of Table III are cases where gas phase heating contributed significantly to the result, but even here a lower gas pressure produced a higher temperature.

(6) The effect of melt point and the temperature dependence of viscosity. The calculations shown so far all used the constant viscosity model and a melt point of 353 °K. Varying the melt point and using the variable viscosity model (equation 14) have some interesting effects on the results. When the constant viscosity model is used and $N_3 \ll 1$, inviscid plastic work dominates, and the temperature is limited to the melt point. With the constant velocity model and $N_3 \gg 1$, viscous effects dominate, and the temperature is not affected much by melt point. A better understanding of the real effect of melting is probably provided by the variable viscosity

TABLE II

Effect of Strength on Computed Temperature.
The applied pressure is 0.4 GPa and the viscosity is 1000 poise

Cavity Size (microns)	Rise Time (microseconds)	Yield Strength (GPa)	Gas Phase Heat Conductivity $\frac{\text{joule}}{\text{m °C}}$	Computed Temperature (°K)
400	10	0.07	0	749
400	10	0.007	0	976
1000	100	0.07	0	360
1000	100	0.007	0	687
1000	100	0.07	33×10^3	484
1000	100	0.007	33×10^3	898

TABLE III

Effect of Initial Gas Pressure

The applied pressure is 0.4 GPa, the viscosity is 1000 poise, and the yield strength is 0.07 GPa

Cavity Radius (microns)	Rise Time (microsec)	Gas Phase Heat Conductivity $\frac{\text{joule}}{\text{m °C sec}}$	Initial Gas Pressure (atm)	Maximum Temperature (°K)
400	10	0	0.0001	1773
400	10	0	1.0	749
1000	100	33×10^3	0.01	635
1000	100	33×10^3	1.0	484

TABLE IV

Calculations Where Gas Phase Heating Was Important

Cavity Radius (micron)	Rise Time (microsec)	Viscosity (Poise)	Yield Strength (GPa)	Pressure (GPa)	Gas Phase Heat Conductivity $\frac{10^3 \text{ joule}}{\text{m °C}}$	Max. Temp. (°K)
1000	100	1000	0.07	0.4	0	687
1000	100	1000	0.07	0.4	33	898*
1000	100	1000	0.7	0.4	0	463
1000	100	1000	0.7	0.4	33	635*
400	100	1000	0.7	0.4	0	361
400	100	1000	0.7	0.4	33	505*
400	100	**	0.7	0.8	0	375
400	100	**	0.7	0.8	33	656*

* Temperature was still rising when calculation was stopped.

** Calculations used the variable viscosity model described earlier

model which allows for a reduction of viscosity as well as yield strength upon melting. Figure 10 shows a comparison of the maximum temperature computed with the variable and constant viscosity models. The temperature is plotted as a function of cavity radius for a case where P=0.4 GPa, τ=0.1 microsecond, and Y=0.07 GPa. With the constant viscosity model, N_3>>1, viscous effects are dominant, and the temperature is relatively high for all radii. When the variable viscosity model is used, the computed temperatures are much lower (approaching the melt point) for small cavities, but they are quite large for big cavities and may even exceed those computed with the constant viscosity model. With the variable viscosity model, melting reduces the viscosity and reduces the heating as long as the pressure in the vicinity of the cavity (where the deformation is concentrated) is low. However, in the final stage of cavity collapse, the pressure may rise, and this will increase the viscosity and the rate of heating. For small cavities, where pressure amplification does not occur, melting tends to be strongly desensitizing when the variable viscosity model is used. With large cavities, melting may make overshoot more likely, by reducing viscosity (and thus increasing N_2). In this case the variable viscosity model may give higher temperatures than does the constant viscosity model. However, the most important observation is that melting can be strongly desensitizing for small cavities (of the order of 4 microns or less).

GAS PHASE HEATING

With the exception of the last two lines of Tables II and III, gas phase heating contributed a negligible amount to all of the calculations discussed so far. This was demonstrated

by running the calculations with the gas phase heat conductivity set equal to zero as well as to the value specified in Table I. However, in some cases, the gas phase heating can have a significant or dominant effect. The conditions under which gas phase heating is dominant are relatively large cavity size (so the gas will contain enough heat energy to affect the solid significantly), long rise time or low viscosity (otherwise viscous effects dominate), and a melt point below the ignition temperature (to suppress inviscid plastic work effects). When all of these conditions are met, gas phase heating can be dominant. Some cases where gas phase heating was important are shown in Table IV, and the importance of cavity radius in this mechanism is shown in Figure 11. However, in the context of this model it was difficult to find cases where gas phase heating was dominant, because the available energy was usually dissipated largely in the solid phase by viscous or plastic forces. In situations where cavity collapse can occur without deformation of the solid (for instance, gap at the base of an artillery shell), gas phase heating will be much more important. Starkenberg has shown that a pressure of 0.15 GPa applied to a planar gap of 0.5 mm can cause ignition in composition B

CONCLUSIONS

High temperatures may be produced in the vicinity of a collapsing cavity by viscoplastic work, plastic work, hydrodynamic compression, or gas phase heating. We have presented an analysis of the conditions where each mechanism will occur. Viscoplastic work is by far the most efficient mechanism for producing high temperatures, and it is favored by high viscosity, low yield strength. and short rise times. Using best guess estimates of viscosity (1000 poise) and yield strength (0.035 GPa), and considering pressures in the range of 0.1 to 2.0 GPa, viscoplastic work will dominate when the rise time is less than 5 to 20 microseconds. The hydrodynamic mechanism occurs when the parameters N_1 and N_2, discussed earlier, are both greater than one. This mechanism is probably never required, because other effects (viscoplastic heating) occur at the same time. For a 100 micron cavity, and using best guess estimates of yield strength and viscosity, the hydrodynamic mechanism will occur when the pressure is greater then 0.4 GPa and when the rise time (for a 0.4 GPa pulse) is less than about 8 microseconds. Smaller cavities require shorter rise times and higher pressure. Inviscid plastic work (as distinct from viscoplastic work) can cause ignition only if the melt point is higher than the ignition temperature. Gas phase heating is generally not a dominant effect in the context of this model, because the available energy is dissipated by viscous or plastic forces rather than in the gas phase. It can be important for large cavities and relatively long rise times (which suppresses other mechanisms). If cavity closure can occur without deformation of the solid (as in a planar gap), the gas phase mechanism will be more important.

In the context of this model, cavity size and pressurization rate both have a strong effect on the temperature which many be achieved.

The effect of some material properties on the temperature achieved is as follows. High strength is almost always desensitizing. High viscosity is sensitizing. A low melt point can be either sensitizing or desensitizing depending on conditions, but for small cavities (a few microns) it is significantly desensitizing. Heat conductivity is important only for very small cavities (less than a micron) or for situations where gas phase heating is important. These conclusions apply only for the cavity collapse mechanism and may not be extrapolated to other situations.

REFERENCES

1. C. Mader, "Initiation of Detonation by the Interaction of Shock with Density Discontinuities," The Physics of Fluids, Vol. 8, No. 10 (1965).
2. F.P. Bowden and A.D. Yoffe, *Initiation and Growth of Explosion in Liquids and Solids,* Cambridge University Press (1952).
3. M.C. Chick, "The Effect of Interstitial Gas on the Shock Sensitivity of How Density Explosive Compacts," Fourth Symposium on Detonation, Office of Naval Research, ACR-126, (1965).
4. G.E. Seay and L.B. Seely, Journal of Applied Physics 32, 1092, (1961).
5. J. Starkenberg, "Ignition of Solid High Explosive by the Rapid Compression of an Adjacent Gas Layer," Seventh Symposium

(International) on Detonation, Naval Surface Weapons Center, NSWC MP 82-334, White Oak, MD (1981).

6. B.A. Khasainov, A.A. Borisov, B.S. Ermolaev, and A.I. Korotkov; "Two Phase Visco-Plastic Model of Shock Initiation of Detonation on High Density Pressed Explosives;" Seventh Symposium (International) on Detonation; Naval Surface Weapons Center, NSWCP MP 82-334 (1981).
7. M.M. Carroll and A.C. Holt, "Static and Dynamic Pore-Collapse Relations for Ductile Porous Materials." Journal of Applied Physics, Vol 43, No. 4 (1972).
8. M M. Carroll, A.C. Holt, and B.M. Butcher; "Application of a New Theory for the Pressure Induced Collapse of Pores in Ductile Materials;" Proceedings of the International Symposium; *Pore Structure and Properties of Materials*, Praque (1973).
9. R. Winter and J. Field, "The Role of Localized Plastic Flow in the Impact Initiation of Explosives," Proceedings of the Royal Society of London A343 (1975).
10. R. Frey, "The Initiation of Explosives by Rapid Shear," Seventh Symposium (International) on Detonation, Naval Surface Weapons Center, NWSC MP 82-334 (1981).
11. P. Howe, R. Frey, B. Taylor, and V. Boyle; "Shock Initiation and the Critical Energy Concept," Sixth Symposium (International) on Detonation; Office of Naval Research, ACR-211, Arlington, VA (1970).
12. R Setchell, Combustion and flame 43, 255 (1981).11. B.A. Khasainov, A.A. Borisov, B.S. Ermolaev, and A.I. Korotkov; "Two Phase Visco-Plastic Model of Shock Initiation of Detonation in High Density Pressed Explosives;" Seventh Symposium (International) on Detonation; Naval Surface Weapons Center, NSWCP MP 82-334 (1981).
13. M Ben Reuven and M. Summerfield, "Theory of Bubble Dynamics in Condensed Explosives During Start-up Transient," 17th JANNAF Combustion Meeting, CPIA Publication 329, Volume II, (1980).
14. L.M Kachanov, *Foundations of the Theory of Plasticity*, North Holland Publishing Company, Amsterdam (1971).
15. J. Frenkel, *Kinetic Theory of Liquids*, Dover Publications, New York (1955).
16. P.W. Bridgeman, *The Physics of High Pressure*, G. Bell and Sons, London (1949).
17. J. Wackerle, J.O. Johnson, P.M. Halleck; "Shock Initiation of High Density PETN;" Sixth Symposium (International) on Detonation; Office of Naval Research, ACR-211, Arlington, VA (1970).
18. P.M. Halleck and J. Wackerle, "Dynamic Elastic-Plastic Properties of Single Crystal Pentaerythritol Tetranitrate," Journal of Applied Physics, Volume 47, No. 3 (1976).
19. *Engineering Design Handbook - Properties of Explosives of Military Interest*, U.S. Army Materiel Command, Arlington, VA, AMC Pamphlet No. 706-177.

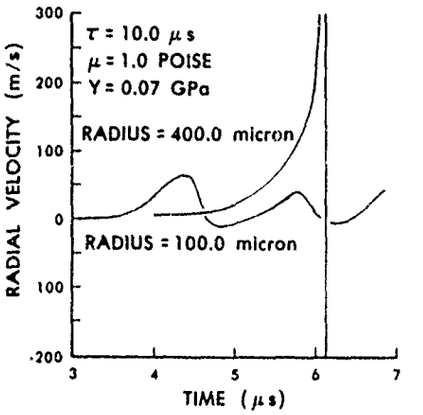

Fig 1a. The radial velocity of two collapsing cavities is shown as a function of time; τ=10 microseconds; Y=0.07 GPa, and μ=1.0 poise

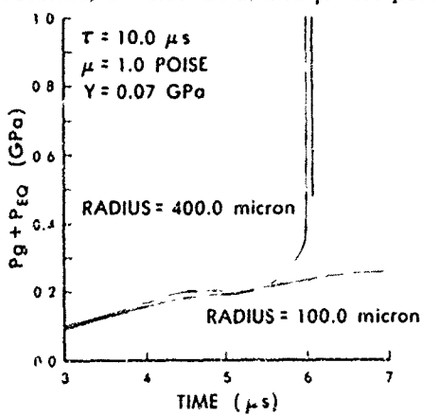

Fig. 1b. $P_g + P_{eq}$ is shown as a function of time for the same two calculations shown in Figure 1a

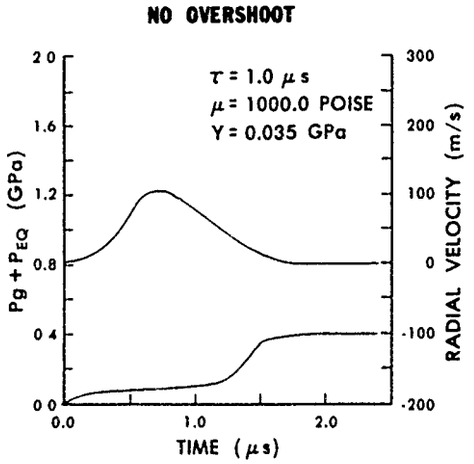

Fig. 2a. P_g+P_{eq} and radial velocity are shown as functions of time, for a calculation with A=100 micron, Y=0.035 GPa, τ=microsecond, and μ=1000 poise

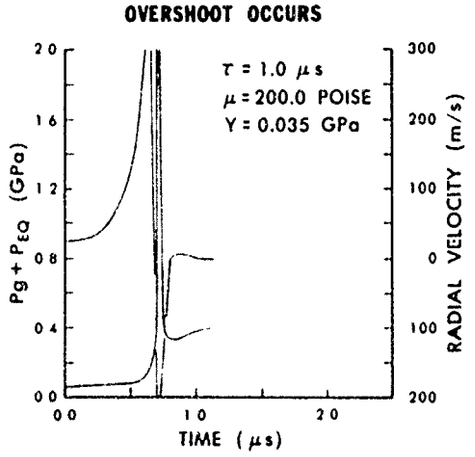

Fig 2b P_g+P_{eq} and radial velocity are shown as functions of time for a calculation identical to Figure 2a, except μ= 200 poise

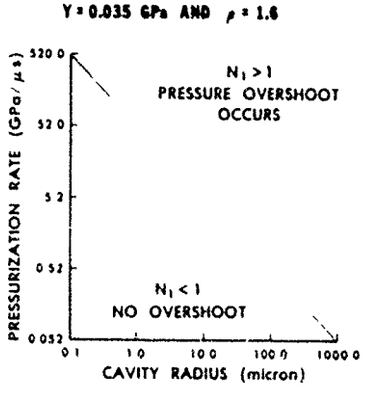

Fig 3 The N_1=1 is plotted for the case u here Y=0.035 GPa and ϱ= 1 6

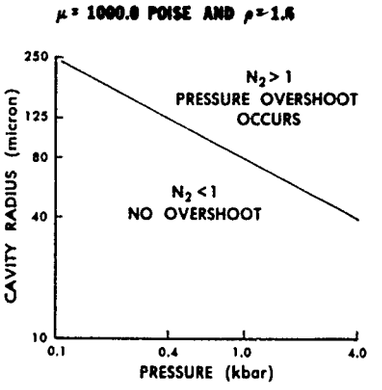

Fig. 4. The curve N_2=1 is plotted for the case where μ= 1000 poise and ϱ=1.6

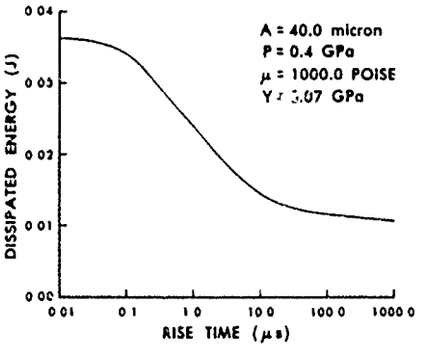

Fig. 5. Energy dissipated at a cavity is shown as a function of rise time for a calculation with P=0.4 GPa, A=40 micron, Y=0.07 GPa, and μ=1000 poise

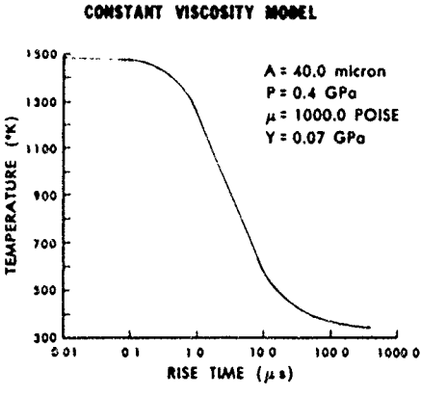

Fig. 6. The maximum temperature is plotted as a function of the rise time for a case where P=0.4 GPa, A=40 microns, Y=0.07 GPa, and μ= 1000 poise

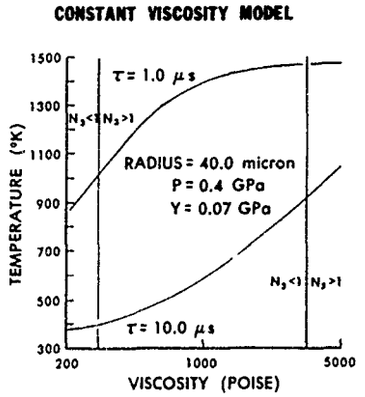

Fig. 7. Temperature as a function of viscosity for two calculations with A=40 micron, Y=0.07 GPa, and P=0.4 GPA. For dotted curve τ=1 microsecond; for the solid curve τ=10 microsecond

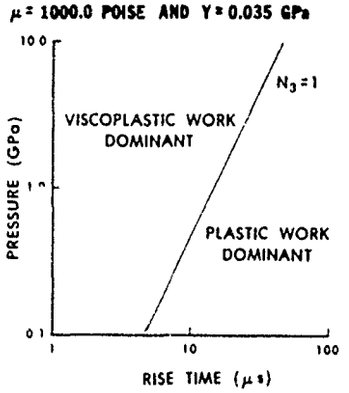

Fig. 8. The curve N_3=1 is plotted for the case where Y=0.035 GPa and μ=1000 poise

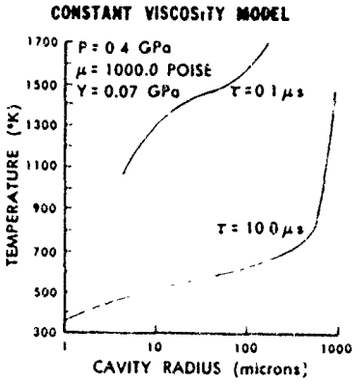

Fig. 9. The maximum temperature is plotted as a function of the cavity radius for two cases where P=0.4 GPa, μ=1000 poise, and Y=0.07 GPa. For the dotted curve τ=0.1 microsecond; for the solid curve τ=10 microsecond

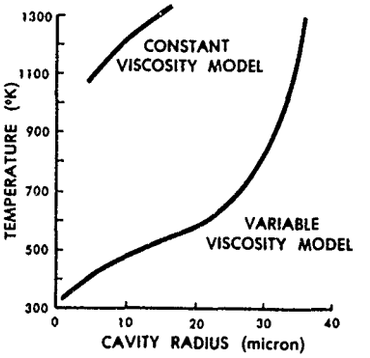

Fig. 10. Comparison of the maximum temperature, computed as a function of cavity radius, using the constant and variable viscosity models. P=0.4 GPa, τ=0.1 microsecond, and Y=0.07 GPa

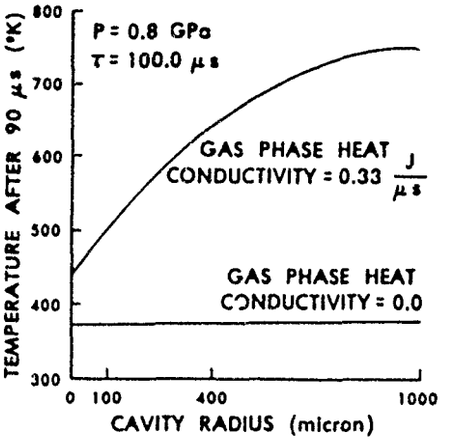

Fig. 11. The maximum temperature produced in the solid due to gas phase heating as a function of cavity radius

Session II
REACTION ZONES I

Chairmen: Roger Chéret
CEA Center D'Etudes de Vaujours
Michael Cowperthwaite
SRI International

HUGONIOTS AND REACTION RATES FROM EMV GAUGE MEASUREMENTS AND LAGRANGE ANALYSIS

Jiao Qinjie, Ding Jing, Liang Yunming,
Huang Zhengping and Zhao Hengyang
Beijing Institute of Technology
P.O. Box 327, Beijing, China

We formulate a reactive flow Lagrange analysis technique in which the only data required are that from the EMV gauge measurements instead of from both velocity and stress gauge. The one dimensional planar shock initiation of BH-1 explosive, a formulation containing mainly RDX, has been investigated. The particle velocity history is measured by EMV gauges. The Hugoniot of the explosive and its reaction rates are obtained.

INTRODUCTION

Fowles and Williams (1) introduced in 1970 the Lagrange analysis for analyzing data from a series of embedded gages in a material through which one-dimensional stress waves are passing. Cowperthwaite and Williams (2) provided a generalization of the Fowles-Williams method. Grady (3) used this method and introduced in 1973 the concept of the path line as an aid in computing derivatives needed for attenuating flow. Later a method has been developed by Seaman (4), which is applicable to arbitrarily complex materials undergoing multiple waves and attenuation using the path line technique.

Multiple Lagrange gage studies in reactive systems with direct analysis were done by Cowperthwaite (5,6), Wackerle (7), Dremin (8) and others. Vantine et al. (9) formulated a reactive-flow-Lagrange-analysis (RFLA) technique in which the derivatives needed are estimated by path line procedures. The accuracy of the RFLA using perfect gage records and its sensitivity to gage placement and to errors in the gage records were discussed. A set of particle velocity records and a pressure record are needed as input for the analysis of a reactive system of known constitutive relationship. Nutt and Erickson (10) obtained with RFLA the chemical reaction progress during the shock initiation of explosive RX-26-AF which is a plastic bonded explosive with 46.6% TATB and 49.3% HMX. The results show a two-stage reaction possibly associated with the different reaction rates of HMX and TATB. In a study of shock initiated pressed TNT with RFLA technique, Huan and Xue (11) found that there is an endothermic process after the leading shock and that the chemical behavior of pressed TNT is somewhat different from that of cast TNT (8).

In this paper the RFLA technique is used to study the initiation characteristic of a plastic bonded hexogen composition BH-1. We use only a set of particle velocity records as input for the analysis. The principal difficulty in the use of particle velocity histories alone arises in the computation of pressure. We use the method of inversion of the equation for particle velocity, which is developed by Seaman (4), with some modifications which will be discussed later. Hugoniots of BH-1 are also obtained with the EMV gages only.

MODEL FOR REACTION RATES

The shocked reacting explosive model developed by Cowperthwaite (12) is used here. Based on the idea that reaction starts in hot spots and then propagates into the bulk of the explosive, the explosive and its reaction products are treated as a mixture of phases that attains mechanical but not thermal equilibrium. It is assumed that only explosive molecules

surrounding the reaction sites receive the reaction heat and no appreciable amount of heat is transfered into the bulk of the explosive. The explosive is compressed or released isentropically as reaction proceeds. It is also assumed that the relative composition of the reaction products is constant along a particle path.

Here we use a simplified Gruneisen equation of state (13) to describe the explosive.

$$p_x = c_o^2(\varrho_x - \varrho_{xo}) + (\gamma-1)\varrho_x e_x \qquad (1)$$

The γ is related with the slopes in the Hugoniot equation

$$\gamma = 4s - 2\left(1 - \frac{\varrho_x}{\varrho_{xo}}\right)s^2 - 1 \qquad (2)$$

The detonation products are assumed polytropic with a constant k,

$$e_p = \frac{1}{k-1} p_p v_p \qquad (3)$$

In above equations, p-pressure, ϱ- density, v-specific volume, e-specific energy internal. The underscripts x and p stand for explosive and products respectively. c_o is the sound speed of explosive at normal condition with density ϱ_o.

It is assumed that the explosive and the products are in mechanical equilibrium, therefore

$$p_x = p_p = p \qquad (4)$$

Consistent with the picture given above, following relationships are obtained to calculate the reaction extent along a particle path.

$$\lambda = \left(\frac{pv}{k-1} - \frac{pv_x}{k-1} + \tilde{e}_x - e\right)\Big/\left(q + \tilde{e}_x - \frac{pv_x}{k-1}\right) \qquad (5)$$

$$\tilde{e}_x = \frac{pv_x}{\gamma-1} - \frac{c_o^2}{\gamma-1}\left(1 - \frac{v_x}{v_o}\right) \qquad (6)$$

$$v_x^{\gamma} = I(S_x)/\left(p + \frac{\varrho_o c_o^2}{\gamma}\right) \qquad (7)$$

The reaction rate along a particle path may be calculated with the following relationships.

$$\frac{\partial \lambda}{\partial t} = \left(B\frac{\partial p}{\partial t} - \frac{\partial v}{\partial t}\right)\Big/A \qquad (8)$$

$$\text{or } \left(\frac{\partial \lambda}{\partial t}\right)_i = \left(B_i \frac{p_{i+1}-p_i}{t_{i+1}-t_i} - \frac{v_{i+1}-v_i}{t_{i+1}-t_i}\right)\Big/A_i \qquad (9)$$

$$A = \frac{v_x}{k} - \frac{k-1}{kp}(q + \tilde{e}_x) \qquad (10)$$

$$B = [(1-\lambda)v_x - v]/kp - (1-\lambda)v_x^{\gamma+1}/\gamma I(S_x) \qquad (11)$$

Here, q is the heat of reaction. $I(S_x)$, the integration constant, is only related with the entropy of explosive S_x.

Lagrange Analysis of the Particle Velocity Histories

The basic equations upon which the Lagrange analysis rests are the conservation laws in Lagrangian coordinates.

$$\left(\frac{\partial v}{\partial t}\right)_h - \frac{1}{\varrho_o}\left(\frac{\partial u}{\partial h}\right)_t = 0 \qquad (12)$$

$$\left(\frac{\partial u}{\partial t}\right)_h + \frac{1}{\varrho_o}\left(\frac{\partial p}{\partial h}\right)_t = 0 \qquad (13)$$

$$\left(\frac{\partial e}{\partial t}\right)_h + \frac{p}{\varrho_o}\left(\frac{\partial u}{\partial h}\right)_t = 0 \qquad (14)$$

For known particle velocity data, Eq. (13) can be integrated to obtain an expression for the pressure:

$$p_2 = p_1 - \varrho_o \int_{h_1}^{h_2} \left(\frac{\partial u}{\partial t}\right)_h dh \qquad (15)$$

Here p_1 and p_2 are at the same time but at different Lagrange positions h_1 and h_2. From Eqs. (12) and (14), we get:

$$v_2 = v_1 + v_o \int_{t_1}^{t_2} \left(\frac{\partial u}{\partial h}\right)_t dt \qquad (16)$$

$$e_2 = e_1 - v_o \int_{t_1}^{t_2} \left(\frac{\partial u}{\partial h}\right)_t p\,dt \qquad (17)$$

The partial derivatives $(\frac{\partial u}{\partial h})_t$ and $(\frac{\partial u}{\partial t})_h$ needed to evaluate the integrals in above three equations are estimated from the particle velocity records by path line procedures where a new time coordinate j is introduced. Curves of constant j, called path lines, are generated from points on the gage histories. The partial derivatives $(\frac{\partial u}{\partial h})_t$ and $(\frac{\partial p}{\partial h})_t$ can now be obtained at any point on the path line if we expand it in terms of the total or directional derivative along the path line and a partial derivative along the gage line.

$$\left(\frac{\partial u}{\partial h}\right)_t = \frac{du}{dh} - \left(\frac{\partial u}{\partial t}\right)_h \frac{dt}{dh} \qquad (18)$$

$$\left(\frac{\partial p}{\partial h}\right)_t = \frac{dp}{dh} - \left(\frac{\partial p}{\partial t}\right)_h \frac{dt}{dh} \qquad (19)$$

The total derivatives, on the right, are obtained by fitting the velocity and time data to functions of h on each path line. Fitted functions

are used to obtain derivatives only and quantities other than derivatives (e.g., u, p, and t) are taken directly from the data, not from the fitted functions.

In the computation of pressure, we use the approach suggested by Seaman (4), with the inversion of equation for particle velocity and addition of a restraint. The differentiations are denoted by subscripts h and t, and h is a total derivative and t a partial derivative. It is assumed that we can always fit the pressure points along the path line with a cubic or lower order function, therefore p_{hhhh} vanishes.

From Eqs. (13) and (19), we get

$$p_t = (p_h + \varrho_o u_t)/t_h \tag{20}$$

By integration of Eq. (20) over a time step of $\Delta t = t_2 - t_1$, the pressure at the time t_2 is obtained:

$$p_2 = p_1 + \frac{\varrho_o \Delta u}{t_h} + \frac{1}{2}(p_{h2} + p_{h1})\frac{\Delta t}{t_h} \tag{21}$$

For the integration all terms have been treated as either constant or linearly varying over the time step. The Δ signifies a difference taken in the direction of increasing time, $\Delta u = u_2 - u_1$. Quantities that are not subscribed with a 1 or 2 should be taken as average over the time interval. At any step in the calculations, the pressure quantities with a subscript of 1 are known, so the only unknowns are p_2, p_{h2} etc.

The P_{h2} is obtained with the following equation:

$$p_{h2} = \Big[p_{h1}\Big(1 - \frac{\Delta t_h}{2t_h} + \frac{t_{hh}\Delta t}{2t_h^2} + \frac{\Delta t_{hh}\Delta t}{4t_h^2} - \frac{\Delta t_h^2}{2t_h^2} + \frac{t_{hh}\Delta t \Delta t_h}{2t_h^3}\Big) + p_{h1}\frac{\Delta t}{t_h} + \frac{\varrho_o \Delta u_{hh}}{2t_h^2} + \frac{\varrho_o}{t_h}\Big(\Delta u_h - \frac{t_{hh}}{t_h}\Delta u\Big)\Big(1 - \frac{\Delta t_h}{t_h}\Big) + 2p_{hhh1}\frac{(\Delta t)^2}{t_h^2}\Big] \times \Big[1 - \frac{3\Delta t_h}{2t_h} + \frac{3t_{hh}\Delta t}{2t_h^2} - \frac{\Delta t_{hh}\Delta t}{4t_h^2} + \frac{\Delta t_h^2}{2t_h^2} - \frac{t_{hh}\Delta t \Delta t_h}{2t_h^3}\Big]^{-1} \tag{22}$$

In deriving Eq. (22), it is assumed that all derivatives higher than third order equal to zero, whereas in the work of Seaman (4) p_{hhhh} is not reserved. This is a necessity in studying the initiation process of explosives, otherwise large errors will be resulted in neglecting the third order derivatives.

The starting step in our analysis is to fit a cubic spline to each measured particle velocity record. The purpose of this step is to eliminate the disturbance due to random factors. Care is taken in choosing knots at similar features like the peak or point of inflection. The u-h and p-h path lines are constructed through corresponding knots of each cubic spline and fitted with least square quadratic, whereas the p-h path lines are fitted with least square cubic. The first t-h path line is a quadratic approximation to the shock trajectory. A total of 100 pathlines has been constructed. The pressure is computed with Eqs. (21) and (22). Finally, the specific volume v_i and the specific energy e_i could be obtained along the i-th gage line.

EXPERIMENTAL PROCEDURE AND RESULTS

Hugoniot

The EMV gages are made from copper foils with an active element 10 mm long, 2.5 mm wide and 20 μm thick. The BH-1 explosive is pressed to a density of 1.70 $\pm$ 0.005 g/cm^3, in the shape of a slab with a length of 40 mm, a width of 10 mm and different thickness. The experimental assembly is shown in Fig. 1. The gage is orientated in the experiment so that the active element is perpendicular to the direction of the magnetic field.

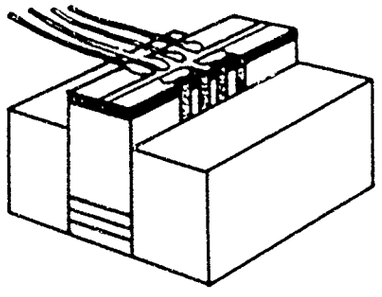

Fig. 1. Schematic of experimental assembly

We use the method developed by Liang and Zhao (14) to measure the particle velocity and the shock wave velocity with the same loop. At the position h_k, the particle velocity u_k can be calculated with the relationship $u_k = \varepsilon_k/BL$, where ε_k is the corresponding output voltage, B is the intensity of the magnetic field and L is the length of active element. With an initial

TABLE 1
Summary of Hugoniot Data for Explosive BH-1

h, mm	Shock Arriving Time		Shock Front Particle Velocity	
	μs	Std. dev., %	mm/μs	Std. dev., %
0		0	0.46	3.6
2	0.56	0.8	0.72	3.7
4	1.02	0.9	1.05	3.7
6	1.40	1.0	1.45	3.8
8	1.69	1.0	1.98	3.9

TABLE 2
Summary of RFLA Data and Results for Explosive BH-1.

h mm	Shock Arriving Time		Shock Front Parameters			
	μs	Std. dev.,%	Particle Velocity mm/μs	Pressure GPa	Specific Volume cm^3/g	Specific Energy KJ/g
0	0	0	0.40	2.125	0.513	0.0809
2	0.64	0.9	0.40	2.158	0.512	0.0822
4	1.27	1.0	0.41	2.190	0.511	0.0843
6	1.91	1.1	0.42	2.236	0.510	0.0875

shock of 2.6 GPa, the experimental data are shown in Table 1. From these data, a Hugoniot is obtained as follows:

$$D = 2.363 + 1.871u + 0.338u^2 + 0.07u^3 \quad (23)$$

It is a Hugoniot of partially reacting explosive. If plotted in the p-u plane as shown in Fig. 2, the shock increase curve passes the C-J point obtained by Zhao and Huang (15).

Reaction Rates

In the experiments for RFLA to obtain the reaction rates, separate loops are used at four Lagrangian positions, namely h=0, 2, 4, 6mm. The input shock wave characteristics are monitored by the EMV gage. The explosive BH-1 is initiated with an attenuating shock wave with an initial pressure about 2 GPa. Experimental data are shown in Table 2.

Results of the RFLA are shown in Figs. 3-8. In the calculation, the sound speed in the unreacted BH-1 is taken as 2.8 mm/μs and the γ in Eq. (1) has the value of 2.1.

DISCUSSION

The mechanism of initiation with a low pressure (2 GPa) attenuating shock wave is somewhat different to that with a typical square wave. The shock front particle velocities change very little and the peak value of particle velocity increases slowly in the interval of h=0 to h=6mm. In this case, there is only a small amount of explosive decomposed at the shock

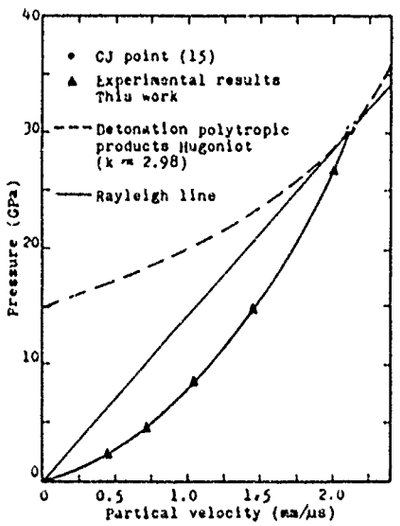

Fig. 2. Shock increase curve of pressed BH-1 explosive.

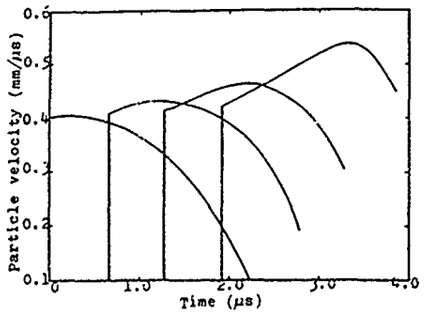

Fig. 3. Particle velocity histories of BH-1 at Lagrange positions of 0, 2, 4, and 6 mm.

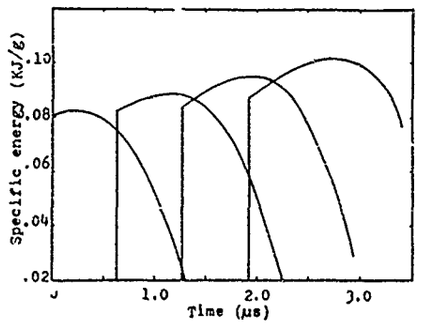

Fig. 6. Specific energy histories of BH-1 at Lagrange positions of 0, 2, 4, 6 mm.

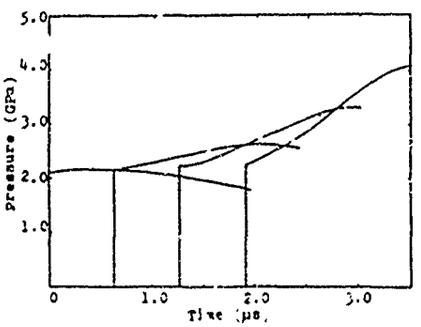

Fig. 4. Pressure histories of BH-1 at Lagrange positions of 0, 2, 4 and 6 mm.

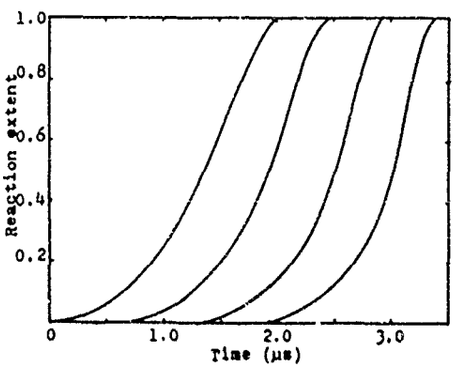

Fig. 7. Reaction extent histories of BH-1 at Lagrange positions of 0, 2, 4 and 6 mm.

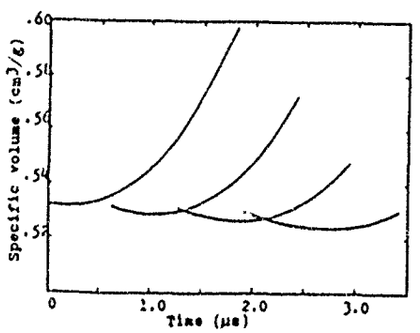

Fig. 5. Specific volume histories of BH-1 at Lagrange positions of 0, 2, 4 and 6 mm.

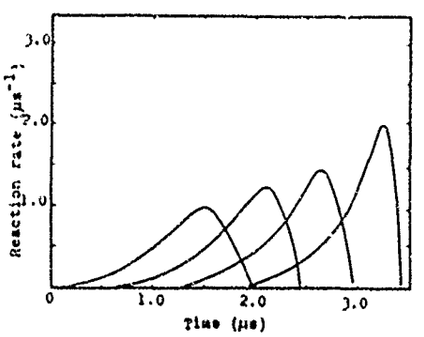

Fig. 8. Reaction rate histories of BH-1 at Lagrange positions of 0, 2, 4 and 6 mm.

front. The chemical reactions behind the shock front are responsible for the later growth of the shock wave.

It could be seen from the Fig. 8, that the reaction rate for any Lagrange position is relatively slow in the beginning, then the reaction speeds up and reaches a maximum. At the end of reaction, the rate drops rapidly to zero.

The RFLA technique outlined in this paper, using only particle velocity profiles in the study of shock initiation process of a real explosive, might have the advantages of being drift free and not requiring a pressure history anywhere in the flow. If it is standardized, this technique could be used as a safety test for new explosives or new compositions.

The accuracy of the RFLA method used here has been tested with similarity solution (9). At the Lagrange position h=2 mm, when there is 1% error in the particle velocity record, the errors in pressure and in reaction rate will be 2.7% and 15% respectively. In our experiments, the standard deviation of the measurement of particle velocity amounts 3%. Therefore, in this study the RFLA could only describe the global reaction rate qualitatively. For determining realistic rates in shocked explosive, the validity of RFLA to be regarded as a quantitative tool must be confirmed in advance.

REFERENCES

1. R. Fowles and R.F. Williams, "Plane Stress Wave Propagation in Solids," J. Appl. Phys., Vol. 41, p. 360, 1970.
2. M. Cowperthwaite and R.F. Williams, "Determination of Constitutive Relationships with Multiple Gauges in Nondivergent Waves," J. Appl. Phys., Vol. 42, p. 456, 1971.
3. D.E. Grady, "Experimental Analysis of Spherical Wave Propagation", J. Geophys. Res., Vol. 78, p. 1299, 1973.
4. L. Seaman, "Lagrangian Analysis for Multiple Stress or Velocity Gages in Attenuating Waves," J. Appl. Phys., Vol. 45, p. 4303, 1974.
5. M. Cowperthwaite, "Determination of Energy Release Rate with the Hydrodynamic Properties of Detonation Waves," Proceedings, Fourteenth Symposium (International) on Combustion, p. 1259, The Combustion Institute, Pittsburg, 1973.
6. M. Cowperthwaite and J.T. Rosenberg, "A Multiple Lagrange Gage Study of the Shock Initiation Process in Cast TNT," Proceedings, Sixth Symposium (International) on Detonation, p. 786, Office of Naval Research ACR-221, 1976.
7. J. Wackerle, J.O. Johnson and P.M. Halleck, "Shock Initiation of High Density PETN," ibid., p. 20, 1976.
8. G.I. Kanel and A.N. Dremin, "Decomposition of Cast Trotyl in Shock Waves," Combustion, Explosion and Shock Waves, Vol, 13, No. 1, p. 71, 1977.
9. H.C. Vantine, R.B. Rainsberger, W.D. Curtis, R.S. Lee, M. Cowperthwaite and J.J. Rosenberg, "The Accuracy of Reaction Rates Inferred from Lagrange Analysis and In-Situ Gauge Measurements," Proceedings, Seventh Symposium (International) on Detonation, p. 466, NSWC MP 82-334, 1981.
10. G.L. Nutt and I.M. Erickson, "Reactive Flow Lagrange Analysis in RX-26-AF," Shock Waves in Condensed Matter - 1983, p. 605, Elsevier Science Publishers B.V., 1984.
11. Huan Shi and Xue Hongloh, private communication, 1984.
12. M. Cowperthwaite, "Constitutive Model for Calculating Chemical Energy Release Rates from the Flow Fields in Shocked Explosives", Proceedings, Seventh Symposium (International) on Detonation, p. 498, NSWC MP 82-334, 1981.
13. Li Weixin, "A Simplified Equation of State in Condensed Medium," Explosion and Shock Waves (China), Vol. 3, No. 2, p. 30, 1983.
14. Liang Yunmin and Zhao Hengyang, "Two Methods for Measuring Shock Relations with Improved EMV Gauge," Shock Waves in Condensed Matter - 1983, p. 239, Elsevier Science Publishers B.V., 1984.
15. Zhao Hengyang and Huang Zhengping, unpublished data, 1983.

MEASUREMENT OF TWO-DIMENSIONAL SHOCK WAVE VELOCITIES AND A COMPOSITE PROBE

Fu Xinghai
Beijing Institute of Technology
Beijing, China

Difficulties on measuring two-dimensional shock wave velocity are discussed. A method of measuring shock wave form and velocity on a triple spherical target is described. According to the properties of oblique shock waves, a formula for experimental data treatment has been deduced by geometrical analysis. A new coaxial composite probe which can measure both optical and electrical signals has been developed. Experimental results show that this kind of probe is favorable.

INTRODUCTION

In most cases, the detonation and shock wave are not really one-dimensional, but generally two or three-dimensional. To measure the velocity of such shock waves is difficult. Although the shock pressure can be measured by different types of pressure sensors, and the particle velocity may be calculated from it, but these sensors can only be used in certain range of pressures. In many experiments, these sensors are not applicable, particularly for a spherical assembly. In this work we use the composite probes to measure a two-dimensional spherical wave. A series of probes are mounted at different depth and angles with respect to the axis of symmetry of a spherical target. When a shock wave reaches these probes, the time and consequently the shock velocities can be determined. According to the properties of the oblique shock wave, the method of data treatment of a two-dimensional shock wave is introduced and a formula is deduced.

In this work we also present a new type of coaxial composite-probe that can obtain both optical and electrical signal simultaneously. Experimental results show that this kind of probe is quite favorable.

PROBLEM ON MEASURING TWO-DIMENSIONAL SHOCK WAVE VELOCITIES

In the detonation experiments we usually study the detonation or shock waveforms, its develoment and propagation velocity. It is well-known that a waveform represents the arrival time of a shock or detonation wave at certain surface of the experimental assembly. These waves may be one-dimensional, two-dimensional or three-dimensional. Here only the two-dimensional shock waves are discussed. Fig. 1A shows a typical two-dimensional spherical waveform where t is the arrival time and θ is the angle with respect to the axis of symmetry Z of a spherical target, (Fig. 1B).

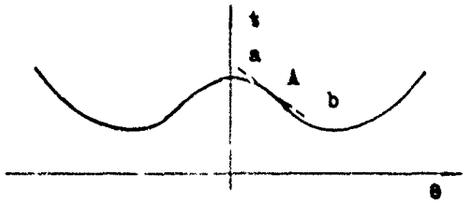

Fig. 1A. Two-dimensional waveform

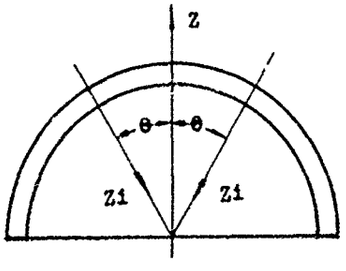

Fig. 1B. Spherical target

In order to study the wave propagation at any point on this wave, we may regard $\overline{ab}$ as an oblique incident plane shock wave at point A. Thus the wave propagation at the point A can be illustrated in Fig. 2 where Zi is the radial direction at that point and β represents the

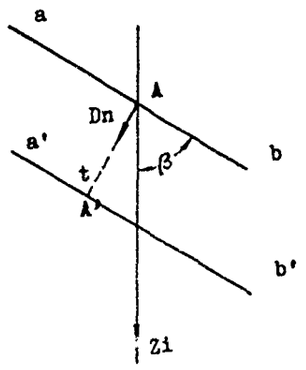

Fig. 2. Travelling front

angle between the oblique shock wave $\overline{ab}$ and Zi. Dn is the shock velocity at that point with the direction perpendicular to $\overline{ab}$. At instant t this shock wave reaches $\overline{a'b'}$ and the point A moves to A'. Because the angle β is unknown, Dn can't be measured directly. In a spherical experiment, one can only obtain an average velocity D by measuring the shock arrival time difference between two corresponding points with the same θ after the wave travels a certain distance h. Fig. 3 shows two waveforms at different depth of the target. At the wave peak G,E and the wave valley F, the measured D is equal to Dn, but at the rest portion of the wave, D and Dn are different. In order to determine the wave propogation direction β, a method of data treatment is introduced in this paper.

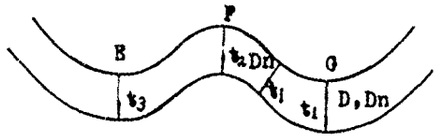

Fig. 3. Two waveforms at certain distance h

STRUCTURES OF THE SPHERICAL TARGET AND THE COMPOSITE PROBE

A triple target for measuring the waveforms and the velocities is shown in Fig. 4. It consists of three spherical shells: outer, intermediate and inner shell. There is a small air gap about 0.2mm between each two shells which emits strong light during shock wave arrival. The outer thin shell is used for protecting the probes on the intermediate shell from air shock wave. On the intermediate and inner shell two series of probes

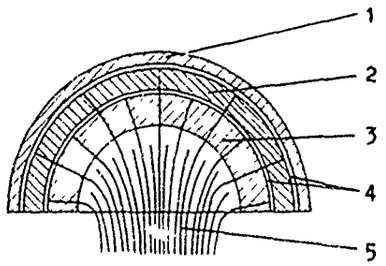

1. OUTER SHELL 2. INTERMEDIATE SHELL
3. INNER SHELL 4. AIR GAPS
5. PROBES

Fig. 4. Sketch diagram showing the spherical target

are distributed. The thickness of the intermediate shell is about 1mm. Dividing the thickness by the time difference of two corresponding probes with the same θ on two shells, one can obtain the average shock velocity D at that point. The probe may either be an electical pin or an optical fiber pin. The shock arrival time is detected by a high speed streak camera or an electrical oscilloscope. Fig. 5 is a typical waveform obtained by a series of optical fiber probes on two shells.

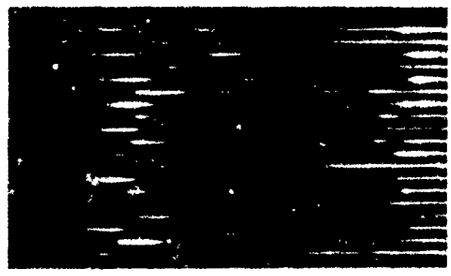

Fig. 5. Typical photograph of the optical fiber probes

Because the strength and direction of shock wave at different part vary widely, loss of some

optical or electrical signals in the experiment is usually occured. In order to overcome this demerit, a new coaxial composite probe is developed. Fig. 6 shows the construction of such a probe. It is made of optical glass fibers, copper pipe, plexiglas sheath and conducting wire.

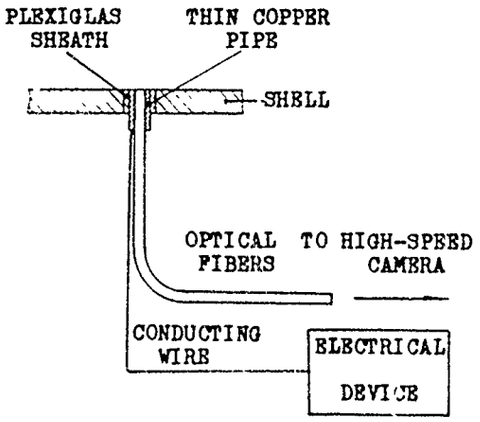

Fig. 6 Sketch diagram of a composite probe

The glass fiber is used as an optical signal transmitter. The copper pipe is an electrical probe which is used as an electrical signal transmitter. The Plexiglas sheath is used as an insulating sheath for the electrical probe. Using the composite probe, two signals, electrical and optical, can be detected simultaneously. Thus a whole shock waveform can be obtained completely and the measuring accuracy is better. We used such type of probes and got a good result. Every pair of electrical and optical data coincide each other very well within the accuracy of the measuring device about 20ns.

SHOCK VELOCITY TREATMENT

As mentioned above, in a two-dimensional spherical experiment, the experimental data must be treated in order to get the shock velocity Dn. Here a geometrical analysis will be introduced. Fig. 7 shows a part of the spherical target where A, A_1 are two neighboring measuring points on the outer surface of the intermediate shell and B, B_1 are the corresponding points on the inner shell. O is center of the spherical assembly. As an oblique incident plane shock wave $\overline{ab}$ with angle α reaches A, a signal is obtained at time t_A. This oblique shock wave will propagate into the intermediate shell with speed Dn in the direction perpendicular to its

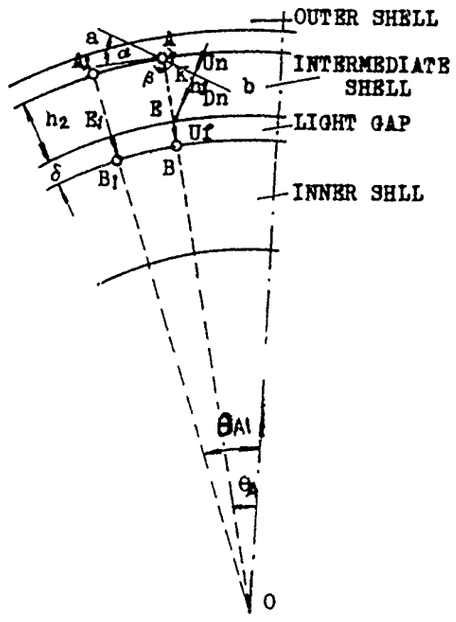

Fig. 7. Sketch diagram of the oblique incident shock front

shock wave front $\overline{AK}$. When it reaches probe B, a second time signal t_B is obtained. In the small air gap, the surface EE_1 moves in the direction EB perpendicular to it. Thus

$$t_{AB} = t_B - t_A = \frac{h_1}{Dn} + \frac{\delta}{Uf} \qquad (1)$$

where $Dn = Co + \lambda Un$ (2)

$$Uf = 2Un \qquad (3)$$

Co and λ are the experimental constants. From Fig. 7 we also have

$$\frac{h_1}{H_2} = \cos\alpha \qquad (4)$$

$$(t_{A1} - t_A)\, Dn - (\theta_{A1} - \theta_A)\, Ro \sin\alpha = 0 \qquad (5)$$

where $t_{A1} = t_A$ may be measured experimentally and Ro is the outer radius of the intermediate shell.

From the equations (1)-(5), we find

$$(\theta_{Ai+1} - \theta_{Ai})\,(B + \sqrt{B^2 - 4t_{ABi}\, w}) -$$

$$2t_{ABi}\, Ro\, (t_{Ai+1} - t_{Ai}) \sin\alpha = 0$$

where

$$B = t_{ABi}\, Co + h_2 \cos\alpha + \tfrac{1}{2}\lambda\delta$$

$$w = h_2 Co \cos\alpha$$

Using this equation, we calculated a series of Dn for a two-dimensional shock wave. The results differ from a 2D - theoretical value less than 5%.

RETONATION PHENOMENON IN SOLID EXPLOSIVES

Ding Jing, Bi Zhu, Hu Dong and Deng Quan-nong
Beijing Institute of Technology
P.O. Box 327, Beijing, China

The retonation phenomenon in solid explosives has been investigated both experimentally and theoretically. Different shock pressures are created on the surface of a plastic bonded HMX explosive BO-1 with metal flyers driven by a plane wave generator. The manganin stress gage is used to measure the change of the stress on the shocked surface. We found that the retonation may appear in the solid explosive when the initial shock is so weak that the explosive is only partially reacted.

INTRODUCTION

Retonation in gaseous explosives has been observed for a long time (1-3). For the solid explosive, Cook (4) found in the gap test that on the opposite side of the inert plate the detonation reformed in Comp. B at some distance beyond the plate and a hook appeared in the rotating mirror streak photograph. Johansson and Persson (5) conducted similar experiments and found a returning detonation in PETN and TNT. Campbell and others (6) did not find retonation happened in the wedge test experiments. Numerous gap experiments, as Dremin (7) wrote in his book, using the electromagnetic method clarified that along the axis of the charge no retonation wave was observed. It was argued that the presence of a retonation wave should have been manifested on the oscillograms of the mass velocity in the form of a sharp negative signal. However, Fauquignon (8) observed retonation phenomenon in the gap tests by the measurements of the electro-conductivity. In the initiation of covered Comp. B by a metal jet, a retonation moving back through the previously shocked explosive was clearly observed by Chick and Hatt (9) using flash radiography.

In this work the retonation phenomenon is investigated experimentally and also simulated numerically with a one dimensional model.

EXPERIMENTAL

A schematic drawing of the experiment is given in Fig. 1. The attenuator is made of PMMA 10 mm thick and H62 brass 15 mm thick. The flyer material is either Ly-12 duralumin or H62 brass. Explosive used in this study is a plastic-bonded HMX composition BO-1, which is similar to PBX 9404 in performance.

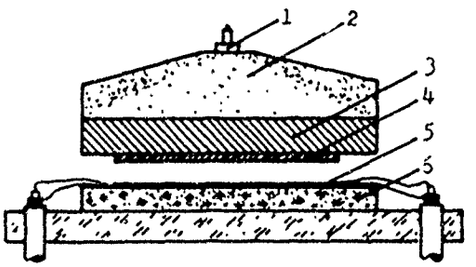

Fig. 1. Experimental arrangement of the shock initiation of BO-1 explosive: 1 - Detonator, 2 - Plane wave generator, 3 - Attenuator, 4 - Flyer, 5 - Manganin stress gage, 6 - Explosive sample.

The pressure profile is measured with an H type manganin stress gage which has a life time of 4-8 μs. The resistance of the manganin gage is 0.2 ohm. A teflon film 0.60 mm thick is used as an isolating cover. A constant current circuit is used for measurement with a current strength of about 6 A. A typical experimental record is shown in Fig. 2.

Fig. 2. Typical record of pressure profile
Attenuator - 10 mm PMMA and 15 mm H 62 brass
Flyer - Ly-12 duralumin, 1 mm thick
Explosive - Composition BO-1
V: 500 mV/Div. H: 2 μs/Div.

Wedge test is performed to obtain distance and time to detonation data.

Experiments similar to Cook's gap test are done with both donor and acceptor of Comp. B-3 and gap of steel plate. The donor has a diameter of 41.8 mm and the acceptor a diameter of 100 mm, all 20 mm thick. At the interface between the gap plate and acceptor, a manganin stress gage is placed to measure the pressure profile.

NUMERICAL SIMULATION

A one-dimensional Lagrange program CHD-3 is formulated for the study of the shock initiation mechanism of heterogeneous condensed explosive. (10-12)

Explosive initiation is described by a nucleation and growth rate law:

$$-r = Ap^m f + Bp^n(1-f)f \quad (1)$$

where r is the reaction rate, f the fraction of the explosive unreacted, p the pressure and A, B, m, n are constants.

The Gruneisen equation of state is used to describe the unreacted explosive.

$$P_s = P_H - \Gamma C v_s (T-T_H)/V_s \quad (2)$$

$$P_H = c^2(1-V_s)/v(1-s-sV_s)^2 \quad (3)$$

$$T_H = H_1 + H_2(H_3-V_s)/V_s H_4 \quad (4)$$

$$E_H = P_H(1-V_s)/2 \quad (5)$$

$$E_s = E_H + (P_s-P_H)V_s/\Gamma \quad (6)$$

The Jones - Wilkins - Lee equation of state is used to describe the pressure-volume-energy behavior of the detonation products. For the mixture of unreacted explosive and detonation product,

$$E = fE_s + (1-f)E_g \quad (7)$$

$$V = fV_s + (1-f)V_g \quad (8)$$

$$P = P_s = P_g \quad (9)$$

In the above equations, Γ - Gruneisen coefficient, V - relative specific volume, T - temperature, E - internal energy per unit volume, C_v - specific heat, c, s, - Hugoniot parameters, H_1, H_2, H_3, H_4 - constants. Subscripts s and g stand for solid explosive and gaseous products respectively. Subscript H stands for Hugoniot.

Constants for PBX-9404 used in computation are listed in Table 1.

TABLE 1
Value of Constants for PBX-9404

A	1.9×10^3 Ref. (1)	
B	24	
m	3.2	
n	1.0	
	$0.852 \leqslant V_s \leqslant 1$	$V_s < 0.852$
H_1	298	369
H_2	208.2	167.06
H_3	1.0	0.852
H_4	5.21	9.95

A method of perturbation acceleration has been developed. It takes one or two cycles only to get convergence, so a great deal of computer time is saved.

The program CHD-3 has been used to compute the distance to detonation vs the pressure for both energetic explosive like HMX and insensitive explosive like TATB. Results coincide with that obtained in wedge experiments.

RESULTS AND DISCUSSION

The behavior of PBX-9404 impacted with a 2.3 GPa shock is numerically simulated. Profiles p-R and f-R at different instants are shown in Fig. 3.

As shown in Fig. 3, from the instant of loading, the pressure profile rises gradually with time. At the instant of 3.28 μs, a detonation is initiated at R=0.5 cm. The explosive between

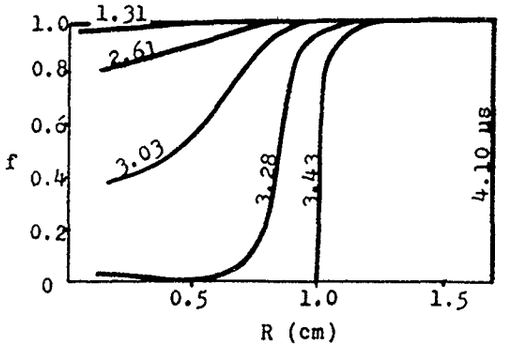

3a. Fraction of unreacted explosive f vs distance to loading surface R

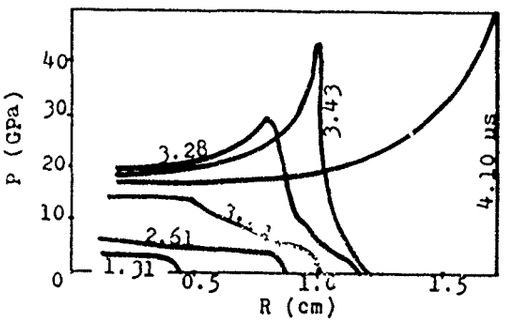

3b. Pressure P vs distance R.

Fig. 3. Numerical simulation of PBX-9404 impacted with a 2.3 GPa shock.

the loading surface and R=0.5 cm reacted only partially before. It decomposes then fastly to the end. This is a picture of the reaction taking place in the partially reacted explosive.

The initiation of PBX-9404 explosive by an impact of a low velocity thin flyer is numerically simulated with results shown in Fig. 4.

The curves in Fig. 4a indicate that although the detonation initiates at a certain time at different distances to the loading surface, the rest part of the explosive is only partially reacted. In these circumstances a retonation will eventually be formed as shown in Fig. 4b and Fig. 4c. A pessure hump and a negative particle velocity portion appear in respective figures.

The pressure profile record of the explosive BO-1 impacted with a flyer 1.02 mm thick is shown in Fig. 5a. In Fig. 5b the experimental record is compared with the result of numerical simulation.

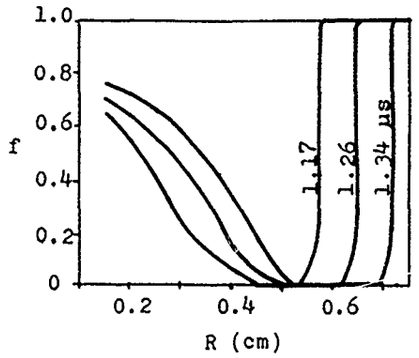

4a. Fraction of unreacted explosive f vs distance to loading surface R

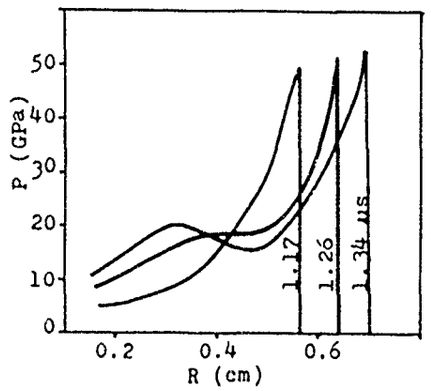

4b. Pressure P vs distance R

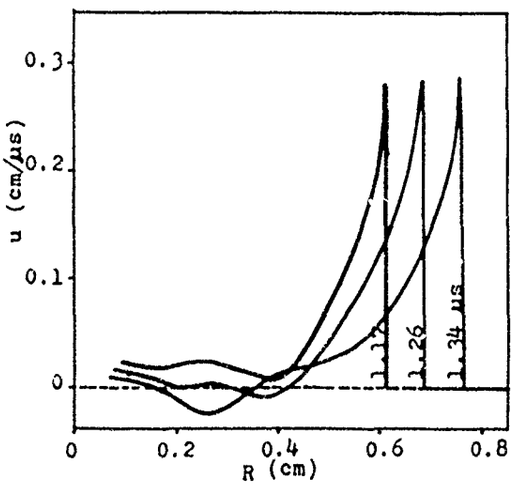

4c. Particle velocity u vs distance R

Fig. 4. Numerical simulation of the initiation of PBX-9404 explosive with impact of a copper flyer 1.1 mm thick with a velocity of 0.75 mm/μs.

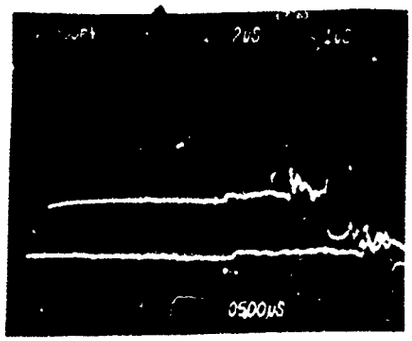

Fig. 5a. Record of pressure profile in explosive BO-1
V: 500 mV/div.
H: 2 μs/div.

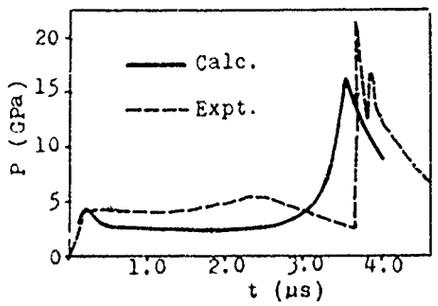

Fig 5b Result of numerical simulation
Explosive - PBX-9404
Flyer - copper, 1mm thick
Impact velocity - 0.79 mm/μs

Under the experimental condition of a sustained loading, there is no fore mentioned second pressure pulse on the loading surface detected by the manganin stress gage as shown in Fig. 6. In the numerical simulation of PBX-9404 impacted by a 15 mm thick copper flyer with an initial impact pressure of 3.44 GPa, there is also no indication of the presence of any retonation. However, we do find that the retonation appears in the numerical simulation of explosive PBX-9404 preshocked by a 1 mm plexiglas flyer and then weakly impacted by a 15 mm thick brass flyer.

In experiments similar to SPHF initiation method of Cook (4), no backward pressure jump in Comp. B-3 is registered by the manganin stress gage (Fig. 7). The same is the result of numerical simulation. The initiation takes place not at the surface of the gap plate but at certain depth in the acceptor. A divergent detonation with its center at the place of initiation arrives at the surface of the explosive cylinder and the detonation light will move both upward and downward along the lateral surface. The hook observed by Cook with streak camera is not a retonation.

Fig. 6. Record of pressure profile in BO-1 explosive impacted by a H62 brass flyer 15 mm thick
V: 500 mV/div.
H: 2μs/div.

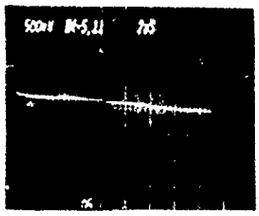

Fig. 7. Gap test record of Comp. B-3
Donor: Φ 41.8 ×20 mm
Acceptor: Φ 100×20 mm
Gap: Φ 50×18 mm steel plate

When the sample is impacted by a thin flyer, the explosive between the loading and the initiating surface is only partially reacted. The detonation initiated propagates forward into the unshocked explosive. At the same time, the detonation propagates backward in the shocked, partially reacted explosive. This is retonation.

Results obtained from experiments and numerical simulation are listed in Table 2. The experimental data are the average of 2 to 3 shots of explosive BO-1. The maximum deviations in measuring the distance and time to detonation are 0.5 mm and 0.3 μs respectively. In measuring pressure, the maximum deviation is 1 GPa. All the theoretical data are the result of numerical simulation of PBX-9404. The composition difference between BO-1 and PBX-9404 is responsible partly to the deviation between the

TABLE 2
Data of Initiation and Retonation

Flyer Material	Flyer Thickness mm	Impact Pressure GPa		Time to Detonation μs		Distance to Detonation mm		Retonation Time μs		Retonation Pressure GPa	
		Exp	Cal	Exp	Cal	Exp	Cal	Exp	Cal	Exp	Cal
Brass	1.02	3.92	3.40	2.36	2.99	9.35	10.80	3.56	3.61	23.5	15.5
Duralumin	1.00	4.89	4.48	2.69	2.94	9.95	12.00	3.78	4.40	21.0	23.3
Brass	15.00	3.44	3.44	1.69	1.35	7.80	6.44	No retonation			

experimental and calculated values. On the other hand, the stress gage used is thicker than normal for the purpose of keeping the gage in good condition when the retonation wave arrives. A peak pressure lower than normal is reasonable.

In their shock initiation experiments of pressed TNT, Huan and Xue (13) found that with an initial shock of about 5 GPa, a pressure hump was observed on the initiating surface at a time > 1.5 μs after the initial impact. It was also found in the Lagrange analysis that the reaction extent curves cross each other as shown in Fig. 8. A point of interest is that in the analysis the hump data is not included in the input pressure history.

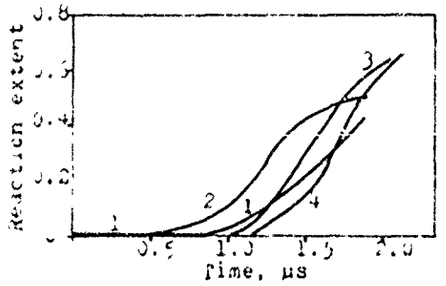

Fig 8 Reaction extent histories of pressed TNT (13)
1 - h=0.00 mm ; t=0.000 μs
2 - h=2.07 mm ; t=0.499 μs
3 - h=4.15 mm ; t= 0.979 μs
4 - h=4.72 mm ; t= 1.107 μs

As it could be seen in Fig. 8, at certain time later than 1.5 μs, the reaction extents of particles 3 and 4 are larger than that of particles 1 and 2, although later explosive particles have been shocked for a longer time. In this way a necessary condition for the appearance of retonation has been provided.

CONCLUSION

The retonation may be defined as a detonation wave which propagates backward through the partially reacted explosive.

Both the results of experiment and numerical calculation show that in explosive under impact of a thin flyer with a low impact velocity or in a preshocked explosive, the retonation may appear in general. While under sustained loading or impact with a thick flyer, the retonation might not appear.

The necessary and sufficient condition for the occurrence of retonation is not quite sure. The pressure hump and the negative particle velocity may be considered as two of the characteristics of a retonation process. The presence of a region of partially reacted or unreacted explosive in the back of a detonation front is one of the necessary premises for the happening of retonation.

ACKNOWLEGEMENT

The authors appreciate the expert technical assistance of Xiang Kaili and Gui Zhizhen, and valuable discussions with Su Linxiang, Ma Yuexian, Huang Zhengping and Huan Shi.

REFERENCES

1. H.B. Dixon, Phil Trans. Roy. Soc. London. A184, pp. 97-188, 1893.

2. H.W. Emmons, Editor, Fundamentals of Gas Dynamics, p. 645, Princeton University Press, 1958.

3. M.A. Cook, The Science of High Explosives, pp. 183-187, Reinhold Publishing Corporation, New York, 1958.

4. M.A. Cook, ibid, Fig. 8.11, p. 189.

5. C. H. Johansson and P. A. Persson, Detonics of High Explosives, pp. 105-107, Academic Press, London, 1970.

6. A. W. Campbell, W. C. Davis, J. R. Ramsay and J. R. Travis, "Shock Initiation of Solid Explosives", Phys. Fluids Vol. 4, p. 512, 1961.

7. A. N. Dremin, S. D. Savrov, V. S. Trofimov and K. K. Shvedov, Detonation Waves in Condensed Media, Nauka, Moscow, 1970.

8. C. Fauquignon, Contribution a l'etude de l'initiation de la detonation par choc dans les explosifs solides, CEA 206 3/2, 1961.

9. M. C. Chick and D. J. Hatt, "The Initiation of Covered Composition B by a Metal Jet", Propellants, Explosives, Pyrotechnics, Vol. 8, pp. 121-126, 1983.

10. Su Linxiang, Bi Zhu and Sun Yiting, "Numerical Simulation of Shock Initiation of Heterogeneous Condensed Explosives", Explosion and Shock Waves (China), Vol. 1, No. 2, pp. 12-22, 1981.

11. S. G. Cochran and J. Chan, "Shock Initiation and Detonation Models in One and Two Dimensions", Lawrence Livermore Laboratory Report UCID-18024, Jan. 20, 1979.

12. Charles L. Mader, Numerical Modeling of Detonations, University of California Press, Berkeley, 1979.

13. Huan Shi and Xue Hongloh, private communication, 1984.

REACTION RATES FROM ELECTROMAGNETIC GAUGE DATA

John Vorthman, George Andrews, and Jerry Wackerle
Los Alamos National Laboratory
Los Alamos, New Mexico, 87544

The determination of reaction rates in explosives from experimental data is a task that requires a great deal of care, patience, and curve fitting. We have found that by measuring more quantities than are mathematically necessary for a complete Lagrange analysis, curve fits to experimental data do not have to be as exacting as otherwise required. We present an experimental technique specifically designed for the determination of global reaction rates which uses both embedded electromagnetic impulse and particle velocity gauges. The methods used to efficiently analyze the data, and the results and conclusions reached from several such studies are also presented.

INTRODUCTION

The determination of global reaction rates from embedded-guage data has been a modest, but continuing effort at Los Alamos for nearly a decade (1-4). Other laboratories have had similar efforts (5-7). The usual procedure is to conduct one-dimensional experiments to measure, in a sufficiently reacting explosive, the pressure-field history, p(h,t). or particle-velocity-field history, u(h,t), or both, over as large a Lagrangian distance-time (h,t) region as practical. These data are then treated with a so-called Lagrange analysis, integrating the conservation relations for momentum, mass and energy:

$$\frac{\partial u}{\partial t} = - \frac{1}{\varrho_o} \frac{\partial p}{\partial h} \quad , \qquad (1)$$

$$\frac{\partial (1/\varrho)}{\partial t} = \frac{1}{\varrho_o} \frac{\partial u}{\partial h} \quad , \qquad (2)$$

and

$$\frac{\partial e}{\partial t} = - p \frac{\partial (1/\varrho)}{\partial t} = - \frac{p}{\varrho_o} \frac{\partial u}{\partial h} \quad , \qquad (3)$$

to determine the density- and energy-field histories, $\varrho(h,t)$ and e(h,t). With these fields known, an assumed reactant-product equation of state, $p(\varrho,e,\lambda)$ or $e(p,\varrho,\lambda)$ allows calculation of the global reaction progress field, here specified by the mass fraction of products, $\lambda(h,t)$. The time derivative of this variable determines a reaction rate, $r = \partial\lambda/\partial t$, which can be correlated to the other state variables to postulate, evaluate and calibrate "rate laws" for the explosive.

In this paper we describe electromagnetic (EM) gauging experiments specifically designed for the determination of reaction rates in shocked explosives. Projectiles from a light-gas gun are used to generate one-dimensional reactive flow in high-explosive targets, with impact velocities chosen so that the explosive is building up to, but does not attain, detonation in the distance-time region covered by the measurements. The explosive has a collection of electrical conductors (the EM gauge package) embedded in it and is surrounded by an external magnetic field. The motion of the conductors in the magnetic field generates a collection of voltages that are recorded and later used to determine the pressure- and velocity-field histories that characterize the shock-induced reactive flow in the explosive. The gauge package we presently use allows the measurement of particle velocity and impulse—the time integral of the pressure—at five locations in the explosive. This provides sufficient data to perform the Lagrange

analysis and rate determination.

The measurement of both velocity and impulse (with pressure available by time differentiation) histories and the sufficiency of data from a single experiment are two major advantages of our electromagnetic gauge system. The integration of Eqs. (1)-(3) requires the evaluation of spatial gradients through a few gauge locations. Consequently, Lagrange analysis becomes a considerable exercise in curve fitting. In the earlier work (1-3,5), only pressure measurements were acquired, so that the calculated density- and energy-field histories effectively depend on the curvatures of the functions fitted through the data. With the new system, single applications of first-order spatial derivatives suffice for all of the analysis. Investigations using only pressure data required combining results from several different shot experiments, and small shot-to-shot variations in loading conditions and reaction histories added difficulty to the analyses. The new system has some potential for further miniaturization and has less problems with electrical breakdown of gauge insulation than encountered with Manganin pressure gauges.

ANALYSIS OF THE GAUGE RESPONSE

The development of electromagnetic particle-velocity gauges for shock-dynamic measurements is over two decades old (8), and provided the first in-material gauging of any kind in reacting explosives (9). The usual design is sketched in Fig. 1-a. When a shock has traveled from the projectile-target interface past the line bc, the wire segment bc will be moving with the local particle velocity of the target material. Faraday's law gives

$$V = - \frac{d}{dt} \int \vec{B} \cdot d\vec{S}$$

for the voltage, V, produced in the wire, where B represents the magnetic field (taken to be uniform and constant in the laboratory, or Eulerian, reference frame), and the surface integral includes the changing area, S, inside the wire loop. Call x' the Eulerian coordinate of the wire segment bc and ℓ the constant length of the segment bc. Then, if B is perpendicular to the plane of the gauge,

$$V = - \ell B \frac{d}{dt} \int_{x'}^{a} dx = \ell B u , \qquad (4)$$

where u is the velocity of the wire segment bc. Thus a knowledge of the magnetic field, the length of the active element of the gauge ℓ, and the voltage produced allows one to determine the particle velocity of the target at a Lagrangian position inside the material.

Although the ability to use an EM gauge to find pressure was recognized some time ago (10), this method is neither widely known nor used.

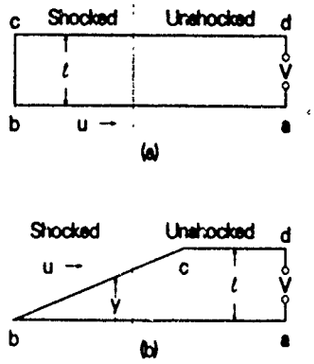

Fig. 1. Electromagnetic Gauges. (a) Velocity gauge, (b) Impulse gauge

Pressure can be found with the experimental configuration shown in Fig. 1-b and a slightly more complicated analysis than that used above. With the Eulerian-Lagrangian transformation $\varrho \, dx = \varrho_o \, dh$, Faraday's law gives

$$V = - B \frac{d}{dt} \int_b^c y(h) \frac{\varrho_o}{\varrho} \, dh$$

$$= - B \frac{d}{dt} \int_b^c \tan\theta \, (h\text{-}b) \frac{\varrho_o}{\varrho} \, dh$$

$$= - B \, \varrho_o \tan\theta \int_b^c (h\text{-}b) \frac{\partial (1/\varrho)}{\partial t} \, dh ,$$

where $\tan\theta$ is the initial slope of the wire and we restrict the analysis to times before the shock arrives at c. Substituting in the equation for mass conservation, Eq. (2), and integrating by parts, gives

$$V = - B \tan\theta \int_b^c (h\text{-}b) \frac{\partial u}{\partial h} \, dh$$

$$= - B \tan\theta \left((h\text{-}b) \, u \right]_b^c - \int_b^c u \, dh \right) .$$

Noting that u(c,t) = 0, one has

$$V = B \tan\theta \int_b^c u \, dh . \qquad (5)$$

In our usual situation, each mass point experiences a shock discontinuity followed by continuous motion. Consequently, the particle velocity in the field spanned by the gauge can be written:

$$u(h,t) = u_1 + \int_{t_1}^{t} \frac{\partial u}{\partial t}\, dt' ,$$

where $u_1(h)$ is the particle velocity behind the shock and $t_1(h)$ the shock arrival time, both depending on the distance coordinate alone. Use of momentum conservation, Eq. (1), and transfer of the spatial derivative to outside the integral give:

$$u(h,t) = u_1 - \frac{1}{\varrho_o} \int_{t_1}^{t} \frac{\partial p}{\partial h}\, dt'$$

$$= u_1 - \frac{1}{\varrho_o} \left(\frac{\partial}{\partial h} \int_{t_1}^{t} p\, dt' - p_1 \frac{dt_1}{dh} \right) .$$

Noting that dt_1/dh is just the reciprocal of the shock velocity, U_1, the first and third term of the last equation cancel from the Hugoniot relation, $p_1 = \varrho_o u_1 U_1$. Defining the impluse*, I(h,t), as the time integral of the pressure, there results:

$$\varrho_o u = -\frac{\partial I}{\partial h} = -\frac{\partial}{\partial h} \int_{t_1}^{t} p\, dt' . \qquad (6)$$

With this preparation, evaluating the response of the impulse gauge is simply a matter of substituting Eq. (6) for the particle velocity in Eq. (5). This gives

$$I(b,t) = -\int_{b}^{c} \frac{\partial I}{\partial h}\, dh = \frac{\varrho_o V}{B \tan\theta} \qquad (7)$$

for the impulse at the apex of the gauge element until the shock reaches point c.

The determination of pressure from the impulse measurement requires some differentiation of data. A simple, if not always best, method is to evaluate the time derivative:

$$p(b,t) = \frac{\partial I}{\partial t} = \frac{\varrho_o}{B \tan\theta} \frac{dV}{dt} . \qquad (8)$$

*Strictly speaking, I is the impulse per unit area; we will ignore this distinction.

If the data have any imperfections, these imperfections will be amplified when pressure is calculated in this manner. More serious, if the data have detailed structure, as in a short-shock experiment, this detail may be difficult to retain accurately through the time differentiation process. An effective alternative for calculating pressure-field histories under such circumstances will be discussed in the section on Lagrange analysis.

A PRACTICAL DESIGN

In practice, measuring particle velocity and impulse is not as simple as inserting wires into an explosive. As the explosive reacts, care must be taken to assure that the gauge elements move with and not through the gaseous products. In addition, the explosive products are electrically conductive so that gauge leads should be insulated (11). If , as some workers prefer, particle-velocity gauge leads are brought out of the explosive parallel to the shock front (unlike the gauge shown in Fig.1), care must be taken to assure that two-dimensional flow does not cause the leads to spread and generate extraneous voltages (12). The finite width of the gauge leads can also be a problem when trying to measure the distance ℓ (see Fig. 1-a).

The gauge package shown in Fig. 2 was designed to minimize the above problems. Leads are only 100-μm wide and 18-μm thick, and are sandwiched between two 25-μm-thick Teflon sheets. The Teflon coating acts as a mechanical substrate, a barrier to gas flow around the conductors, and as electrical insulation. Aluminum conductors are used because this metal is a relatively good shock impedance match to most explosives. This impedance match minimizes both perturbations to the flow and problems with gauge leads punching through the Teflon sheet.

The gauge package is inserted into the explosive at an angle, as shown in Fig. 3. This gauge insertion technique has the advantage that the explosive need be sliced only once, yet locates each pair of impulse and velocity gauges at different depths in the explosive. We commonly use a gauge package inclined twenty or thirty degrees to the impact face and 2-mm separation of gauge pairs in the package (see Fig. 2), giving 0.7- or 1-mm spacing of the gauge elements in the direction of particle motion.

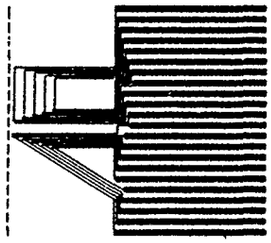

Fig. 2. The electromagnetic gauge package. The largest velocity gauge is 10-mm wide

Gauge leads are brought out through the rear edge of the target and the gauge-package dimensions are limited so that two-dimensional effects caused by edge rarefactions are avoided.

The gauge package and target are assembled by first bonding aluminum foil to a Teflon sheet that has been specially treated to accept the adhesive. The glue bond is kept as thin as possible, typically about 2-μm thick. Next, the conductor pattern shown in Fig. 2 is photo etched from the metal. Gauge construction is completed when the tops of the conductors are covered with another Teflon sheet, also bonded in place. Next, the explosive sample is sliced, the gauge package inserted, and the explosive pieces glued together. It is important to keep the gauge-glue combination as thin as possible. If the gauge or glue is too thick, the gauge will not record the bulk response of the explosive. The type of glue used to hold the gauge in the explosive can also affect the response of the gauge. Some glues approved for use with explosives contain solvents that can cause small voids in the explosive near the gauge package. Such glues are to be avoided if the bulk response of the explosive is to be measured.

The uniform magnetic field indicated in Fig. 3 is provided by a specially constructed electromagnet. The two pole pieces for the magnet are 0.28-m square and 0.25-m thick, and have a 0.28-m separation. These pole pieces are designed to be integrated into our gas-gun target chamber, which serves as the yoke and magnetic return path for the system. An aluminum alloy cylinder inside the magnet poles is used to protect it and the target chamber from shrapnel from the target assembly. The

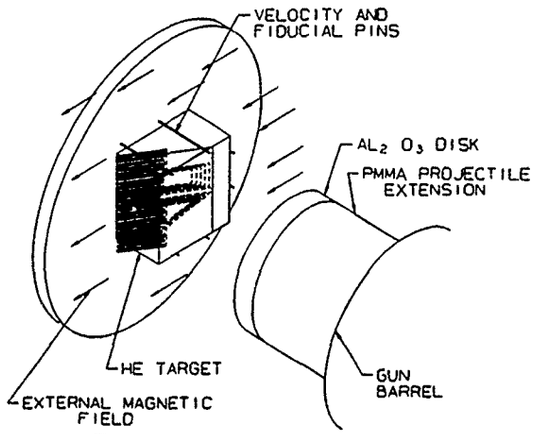

Fig. 3. Experimental Assembly

magnet pole pieces are each wound with three parallel coils on a 0.1-m iron core, powered by a 15-V, 300-A regulated DC supply. Magnetic field strengths are measured for each experiment, and are typically 825 gauss. A central, 25-mm cubic region between the poles has been shown to have ± 0.5-percent uniformity in magnetic field, and the gauge package is located within this region for all experiments. Disturbance of the magnetic field by an incoming, conducting projectile was avoided by using the plastic projectile extension and aluminum oxide (chosen for high shock impedance) flyer depicted in Fig. 3.

The magnetic-field strengths, gauge-element dimensions and particle velocities of our experiments combine to give typical signals of about a volt. These were recorded on Tektronix Model 7844 oscilloscopes or, more recently, Model 7612 transient digitizers. In both cases, the signals are recorded through Model 7A13 and 7A24 amplifiers used in the differential mode. Single ended measurements proved to be impractical because of grounding problems at the gauge.

In this paper, the experimental and analytic methods discussed above are illustrated with two results for PBX 9501, a plastic-bonded, 95 weight percent HMX similar to the PBX 9404 studied previously (2). Projectile velocities and ceramic flyer thicknesses were chosen to give a 3.5-GPa sustained-shock input for one experiment and a 3.9-GPa, 0.45-μs pulsed input for the other. In both cases, the first gauge-element pair was about 0.3 mm from the impact face; the fifth element was 3 mm from the impact face for the sustained-shock experiment and 4.3-mm

deep for the short-shock test. The deepest element pair was less than half of the run distance to detonation for both of the input shock conditions chosen. Impulse and particle-velocity data for the two experiments are shown as frames (a) and (b) in Figs. 4 and 5.

LAGRANGE ANALYSIS

Each of the experiments described above provides enough impluse- and velocity-field data to allow a Lagrange analysis of the reactive flow. As was the case for the analysis of pressure-gauge data only (3), we have found that the Lagrange analysis of these data is best accomplished using the so-called pathline method (13). In this analytic technique, the gauge data are fitted along arbitrary paths constructed through the entire h-t space of the observations. The spatial derivatives in Eqs. (1) to (3) are replaced with the directional derivatives, according to the transformation of any state variable, f, by

$$\frac{\partial f}{\partial h} = \frac{df}{dh} - \frac{1}{U}\frac{\partial f}{\partial t} , \qquad (9)$$

where df/dh denotes the derivative along the pathline and U = 1/(dt/dh) is termed the phase velocity. Although this transformation replaces an interpolation through a few gauge locations with the difference in two quantities, this does not lead to a less accurate analysis. The paths are chosen analytically, so no error occurs in U; the $\partial f/\partial t$ are fitted through dense data at each gauge station; finally, the paths can be chosen so that state variables do not change along them as much as at fixed time, so that the df/dh are smoother and more accurately evaluated than the $\partial f/\partial h$.

With the combined impulse and velocity data provided by the EM gauge package, an alternative to time differentiation of the impulse records is allowed by the pathline analysis method. Applying the transformation Eq. (9) to the impulse, and using Eqs. (6) and (8) for its spatial and time derivatives, we have:

$$p(h,t) = \left(\varrho_o u + \frac{dI}{dh} \right) U \cdot \qquad (8')$$

Note the resemblance of this expression of the pressure to the Hugoniot relations, with the phase velocity in the role of a shock velocity; it reduces to the Hugoniot relation on the first pathline, where $I_1 = 0$.

With the pressure-field history defined by Eq. (8) or Eq. (8'), the Lagrange analysis is completed by the integration of mass and energy conservation, Eqs. (2) and (3). Defining the compression, $\eta = 1 - \varrho_o/\varrho$, these are written:

$$\eta(h,t) = \eta_1(h) - \int_{t_1}^{t} \left(\frac{du}{dh} - \frac{1}{U}\frac{\partial u}{\partial t} \right) dt' \qquad (10)$$

and

$$e(h,t) = e_1(h) - \frac{1}{\varrho_o} \int_{t_1}^{t} p \left(\frac{du}{dh} - \frac{1}{U}\frac{\partial u}{\partial t} \right) dt' \cdot \qquad (11)$$

The Lagrange analyses of the two experiments described above had some common features and some important differences. In both cases, the analysis was done with a construction of 101 pathlines. Shock states on the first path line were specified by fitting the initial particle velocities and using the known unreacted Hugoniot for the explosive. Mathematical cubic spline fitting was used to construct smooth functions of the impulse- and velocity-gauge histories; these fitting functions are shown as solid curves in frames (a) and (b) of Figs. 4 and 5. The integration of Eqs. (10) and (11) was accomplished with a simple differencing scheme for both analyses. Our present analysis determines density and energy histories at the gauge locations only.

For the analysis of the sustained-shock data, simple time differentiation of the impulse data was found an adequate means of evaluating the pressure histories. Evaluating the derivatives of the spline fitting functions of Fig. 4-a gave the fairly pleasing result shown in Fig. 4-c. An uncomplicated, regular pathline construction was also found adequate; every tenth pathline of the construction used is shown in Fig. 4-d, with the symbols indicating the extent of the data. Pathline derivatives of the particle velocities, du/dh, were evaluated by cubic spline fitting of five velocity values on each pathline and calculating the derivative at each gauge location. These were combined with the time derivatives of the velocity and impulse fitting functions and the analytic formulations of the phase velocities to compute the density and energy histories according to Eqs. (10) and (11).

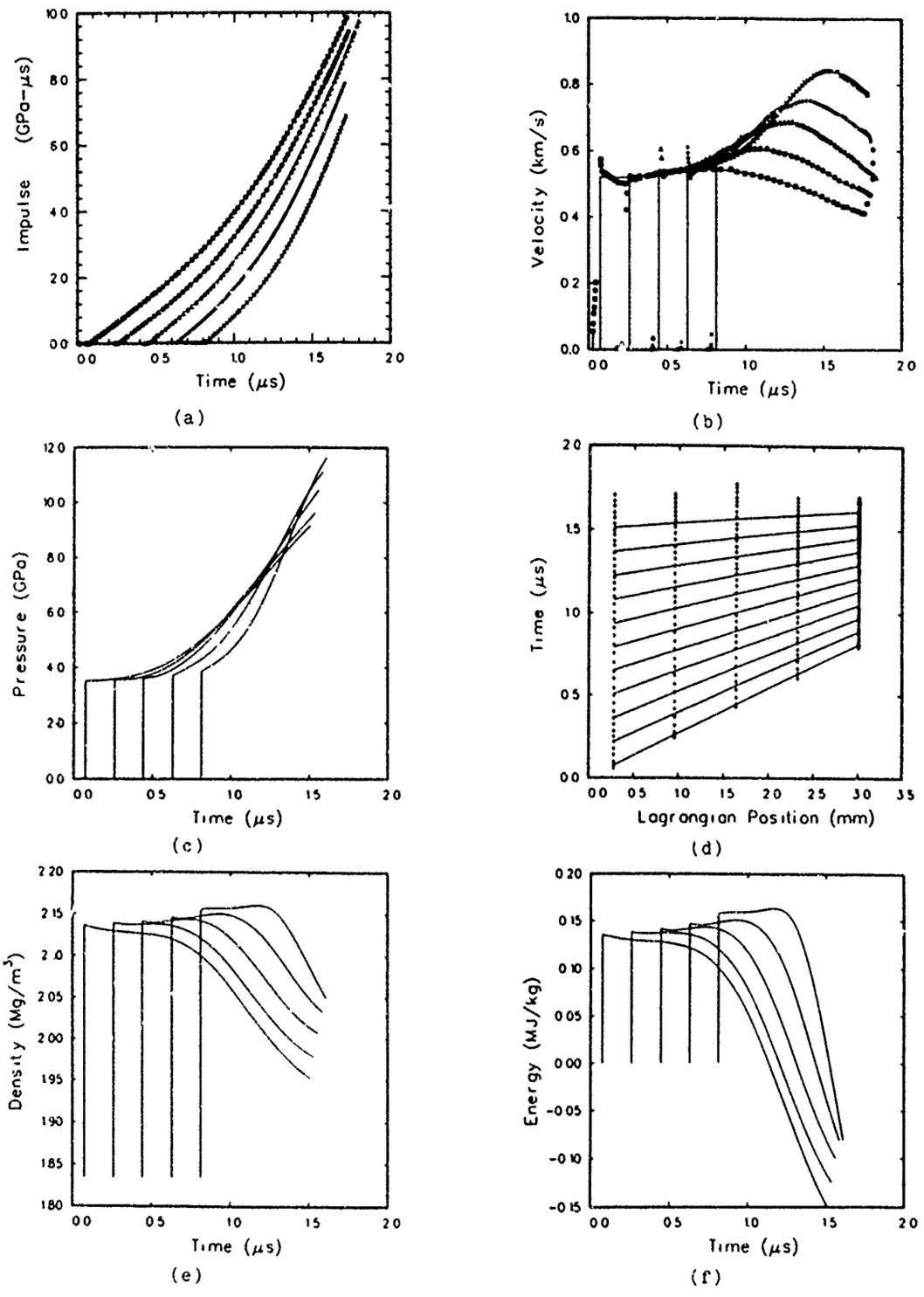

Fig. 4. State histories for a sustained-shock experiment on PBX 9501 (Gauge elements are located 0.27, 0.96, 1.64, 2.32 and 3.01 mm from the impact face.)

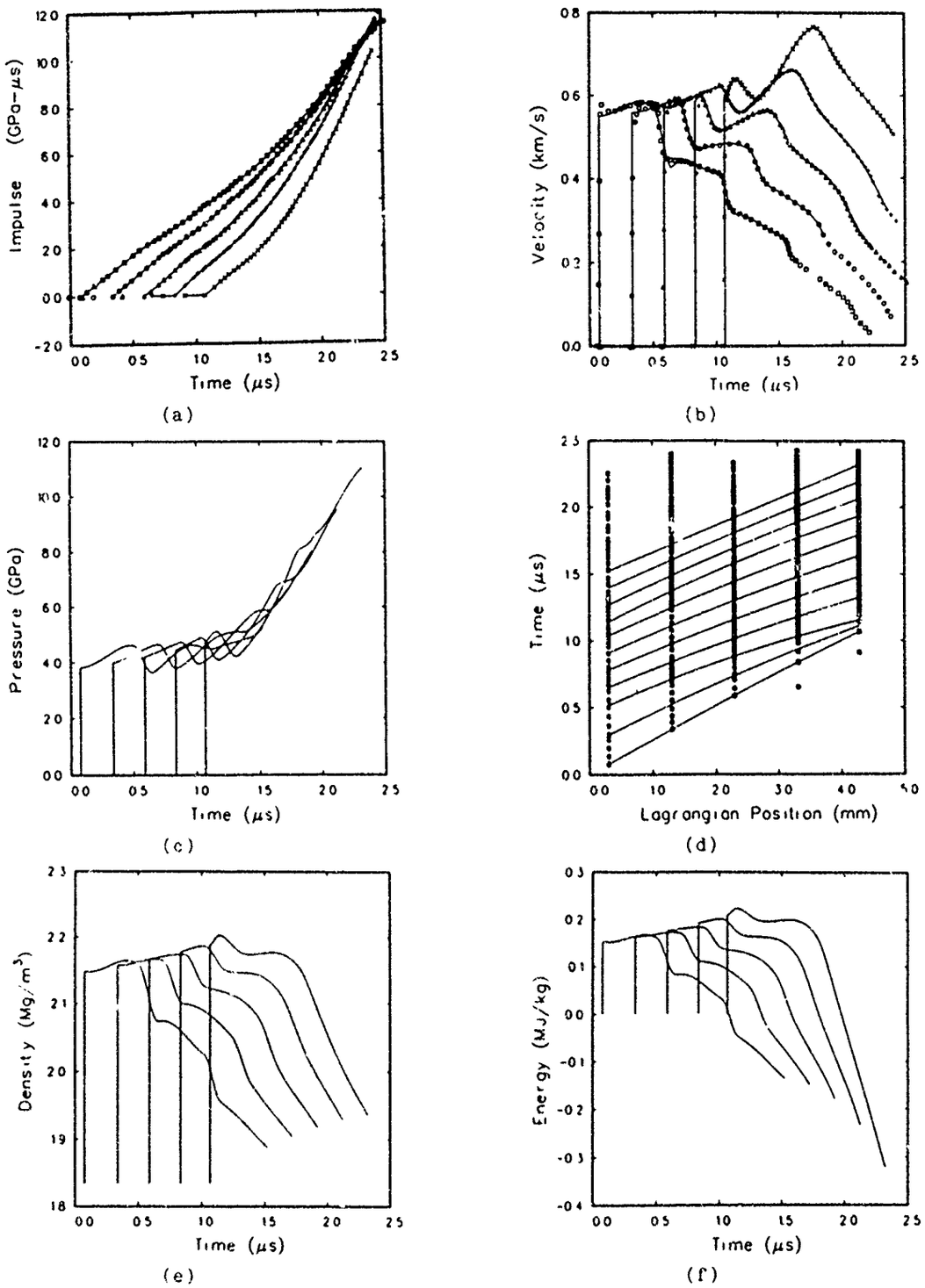

Fig. 5. State histories for a short-shock experiment on PBX 9501 (Gauge elements are located 0.30, 1.30, 2.29, 3.31 and 4.29 mm from the impact face.)

The results are shown in Fig. 4-e and 4-f and are similar in form and reasonably regular.

Some modification of the analysis is needed to treat short-shock data such as shown in Fig. 5. Although the impulse data of Fig. 5-a show some breaks and kinks associated with the successive rarefactions evident in the velocity data, reasonable pressure histories could not be obtained by simple time differentiation of spline functions fitted to the impulse histories. Consequently, the alternative analysis of pressure histories, Eq. (8'), was used. In order to avoid pathline to pathline irregularity in the U, du/dh and dI/dh factors in Eqs. (8'), (10) and (11), it was necessary to use very low-order, smooth functions for fitting velocity and impulse along the pathlines, and for the pathline functions as well. This was accomplished by fitting certain key pathlines through the flow features of heads and tails of the rarefaction waves, and spacing the intermediate path lines evenly; the resulting construction is shown in Fig. 5-d. We were able to use single quadratic segments for all fitting functions. The calculated pressures shown in Fig. 5-c have a generally increasing character, with superimposed reverberating rarefaction features synchronized with similar features in the velocity records. The detailed structure of the pressure histories is primarily due to the $\varrho_o u$ term in Eq. (8'), and the dI/dh term provides the increasing character. Similarly, in the calculation of density and energy histories, it is the du/dh term in Eqs. (10) and (11) that determines the general trends and the term with $\partial u/\partial t$ that superimposes the detailed structure. This ability of the experimental design and analysis to connect pressure, density and energy histories all to the particle-velocity histories permits the pleasing results in Fig. 5 and rate analyses for complex reactive flows.

EQUATION OF STATE AND REACTION RATES

Calculation of reaction and rate histories is effected by the assumption of a reactant-product equation of state. We consider the reacting explosive as a mixture of unreacted solid and fully reacted, mostly gaseous products and measure reaction progress in terms of the mass fraction of products, λ. As in most of our previous work, we have used the HOM equation

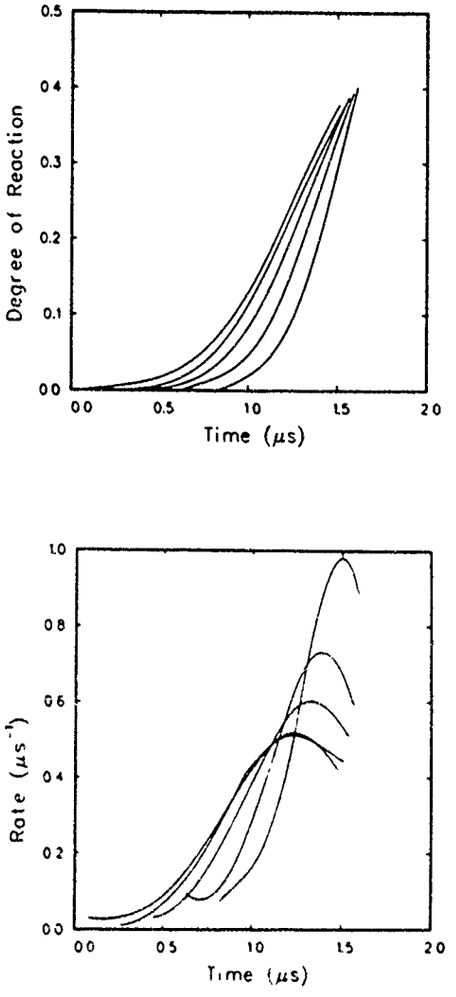

Fig. 6. Reaction and rate histories for sustained-shock experiments

of state (14). Mie-Gruneisen representations are used for both constitutents, with the measured Hugoniot serving as the reference curve for the solid and a well-calibrated BKW (14) calculation of the isentrope through the Chapman-Jouguet state references the products. Ideal mixing of specific volume and internal energy are assumed, along with pressure and temperature equilibrium. Our calculation of λ (ϱ,p,e) is done with a Newton's method iteration algorithm and computer subroutine devised by Charles Forest. The calculation also provides such thermodynamic derivatives as the sound speed, c, and the pressure derivative $p_\lambda = (\partial p/\partial \lambda)_{\varrho,e}$. A detailed description of a similar computation is in (15).

Reaction histories calculated with HOM for

the two experiments on PBX 9501 are shown in Figs. 6-a and 7-a. Both are quite regular. We exercise either of two options in calculating the rates. One is to evaluate time derivatives of pressure and density in the Lagrangian analysis and calculate

$$r = \frac{\partial \lambda}{\partial t} = \frac{(\partial p/\partial t) - c^2(\partial \rho/\partial t)}{p\lambda} . \quad (12)$$

This was done for the rate histories for the sustained-shock case shown in Fig. 6-b. The other alternative is spline-fitting of the reaction histories and differentiating. This was done for the three interior gauge locations for the short-shock case, Fig. 7-b. The results are more erratic than the sustained-shock case; we have not yet found a really effective fitting method. This was particularly the case for the first and fifth gauge stations, so only results at the central three locations are shown in Fig. 7.

EMPIRICAL REACTION-RATE CORRELATIONS

Since our group first attempted to obtain an empirical rate correlation for PBX 9404, we have recognized that a simple dependence on current pressure provided a reasonable correlation for rates analyzed from sustained-shock experiments (2). However, the same work showed that rates from short-shock experiments failed to correlate with current pressure, and that a larger range of initiation phenomena could be modeled with a reaction-rate dependence combining multiplicative factors in the depletion, shock strength and current state. Our empirical manifestation of the fact has been the Direct Analysis Generated Modified Arrhenius Rate, or DAGMAR. This form provided excellent correlations of rates from both sustained- and short-shock experiments on PBX 9404 (2), and subsequently a good rate calibration for 1.8-g/cm³ TATB(3). Both calibrations have been generally successful in hydrocode simulations of a variety of initiation phenomena, including those in state regions much different from those of the gauge experiments used to determine the rates. This success recently has been extended to detonation reaction zone observations on TATB(16).

The current-pressure correlations of the rates calculated for PBX 9501 are shown in Fig. 8, plotted in a coordinate system appropriate for

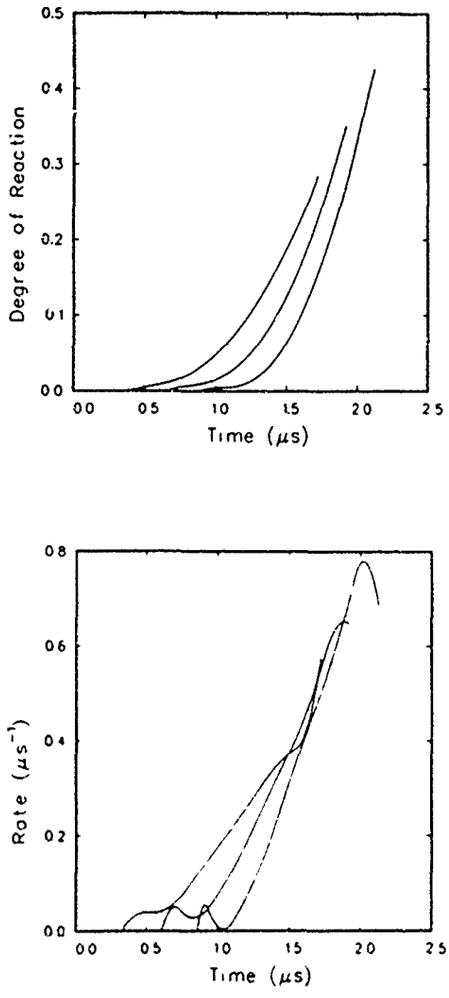

Fig. 7. Reaction and rate histories for short-shock experiments

the usual expression for the Forest Fire rate (14),

$$\ln\left(\frac{r}{1-\lambda}\right) = \sum_{j=0}^{n} a_j \, p^j \quad (13)$$

The rate histories for the sustained-shock experiment obviously admit to a current-pressure correlation over most of the $0 < \lambda < 0.4$ reaction range. Because the pressure histories in the short-shock case increase overall during the time covered by experiment (see Fig. 5-c), the correlation is reasonable overall. However, local portions with strongly increasing rates and constant or decreasing pressures are not consistent with Eq. (13). The dashed line is the Forest Fire rate calibrated in the usual manner, using

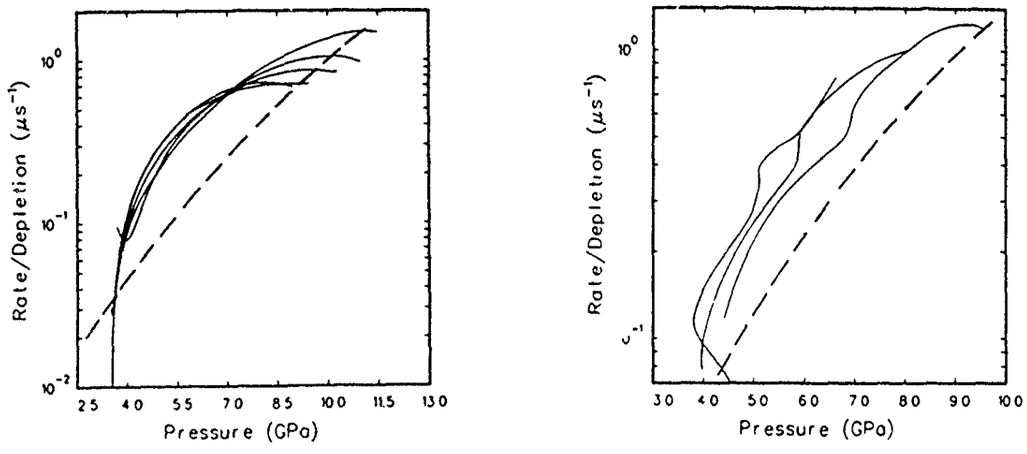

Fig. 8. Pressure correlation for (a) sustained- and (b) short-shock experiments

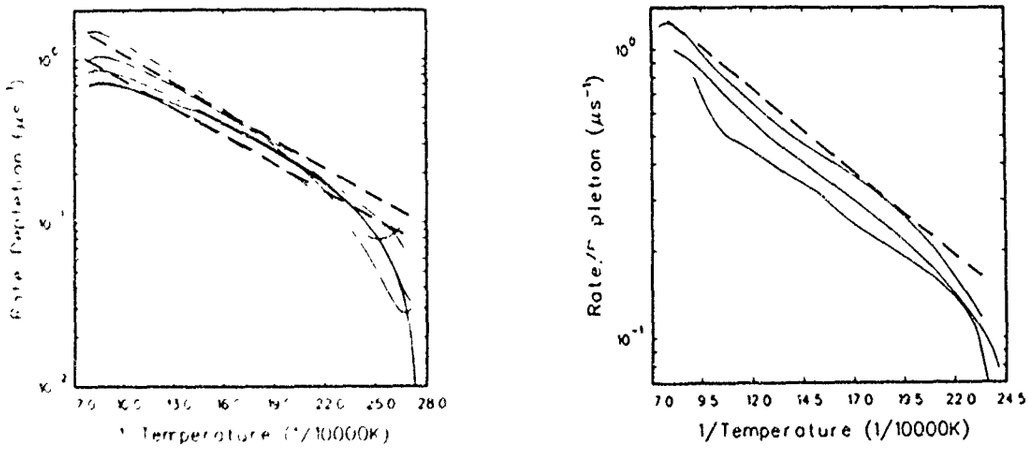

Fig 9 DAGMAR correlation for (a) sustained- and (b) short-shock experiments

explosive wedge data and a rather assumptive, shock-change analysis of the buildup of the shock front. Although the Forest Fire calibration is by no means a best fit to our rate histories, it is remarkable that it is in the general vicinity, considering the different types of data and analyses used.

The formulation of DAGMAR is:

$$\frac{r}{1-\lambda} = Z_0\, p_i^n\, G(p,t)\, e^{-(T^*/T)} \quad , \quad (14)$$

where p_i is shock-front pressure, T is the current temperature (a parameter of questionable physical significance calculated in HOM), and Z_0, n and T* are constants. G(p,t) is an induction-time factor that becomes unity in a few tenths of a microsecond; this was necessary for the PBX 9404 correlation, but not for the 1.8-g/cm³ TATB. On an Arrhenius plot, the function plots as a series of parallel straight lines except as modified by the G(p,t) factor at early times (lower temperatures).

Figure 9 shows that DAGMAR correlates well with our rate data for both sustained- and short-shock experiments on PBX 9501. In both cases, the curves lie at higher levels in sequence of increasing shock strength with deeper gauges. The range of shock pressures in these experiments is not enough to evaluate the

exponent n, so we presently use the n = 2 for PBX 9404 for this constant. The graphically matched dashed lines in Fig. 5-c correspond to the shock states at the first and last gauges, and represent $T^* = 1260$ K and $Z_O = 0.205$ -- slightly larger rate than for PBX 9404. The same constants are used to plot the rate for the center gauge for the short-shock data; it is a bit high. We have not yet attempted to calculate an induction-time factor, but the rates at early times indicate one is needed for PBX 9501.

Although the short-shock experiment on PBX 9404 made the point better, our intent in displaying the correlations above is to indicate that more can be learned about global reaction rates analyzing such experiments than with sustained-shock data. The Lagrange analyses of the pressure-gauge data for the short-shock experiments on PBX 9404 (2) are recalled by the responsible author (JW) as a process of lengthy labor and some rather shameful finagling. Anderson substantially improved the analysis of pressure-gauge data for the work on TATB (3), but was unable to accomplish a Lagrange analysis of the short-shock data at all. Although there are several improvements planned for the analysis reported here, it is already relatively little work, free of manipulation, and effective.

The electromagnetic combined impulse and particle-velocity system allows rate analyses of more complex one-dimensional reactive flow. In our group, the hope is to proceed from empirical correlations to more physical reaction-rate models for heterogeneous explosives, and our belief is that the proper way to test and calibrate these models is with global reaction-rate information. For those content with testing and calibrating their models with trial-and-error computer simulations of observations, we recommend embedded-gauge measurements that are less demanding experimentally than those we have described.

REFERENCES

1. Jerry Wackerle, J.O. Johnson, and P.M. Halleck, "Shock Initiation of High Density PETN," Sixth Symposium on Detonation, Office of Naval Research Report ACR-221, p. 20, 1976.
2. Jerry Wackerle, R.L. Rabie, M.J. Ginsberg, and A.B. Anderson, "A Shock Initiation Study of PBX 9404," Proceedings of the Symposium on High Dynamic Pressures, Paris, France, p. 127, 1978.
3. Allan B. Anderson, M.J. Ginsberg, W.L. Seitz, and Jerry Wackerle, "Shock Initiation of Porous TATB," Seventh Symposium on Detonation, Office of Naval Research Report MP 82-334, p. 385, 1981.
4. John Vorthman and Jerry Wackerle, "Multiple-Wave Effects on Explosives Decomposition Rates," Proceedings 1983 APS Topical Conference on Shock Waves, p. 613, North-Holland, Amsterdam, 1984.
5. G.I. Kanel and A.N. Dremin, "Decomposition of Cast TNT in Shock Waves," Fizika Goreniya i Vzryva, 13, No. 1, p. 85, 1977.
6. G.L. Nutt and L.M. Erickson, "Reactive Flow Lagrange Analysis in RX-26-AF", Proceedings 1983 APS Topical Conference on Shock Waves, p. 605, North-Holland, Amsterdam, 1984.
7. Jiao Quinjie, Ding Jing, Liang Yunming, Huang Zhengping and Zhao Hengyang, "Hugoniots and Reaction Rates from EMV Gauge Measurements and Lagrange Analysis," This symposium.
8. A.N. Dremin and G.A. Adadurov, "The Behavior of Glass Under Dynamic Loading," Soviet Physics-Solid State, 6, p. 1379, 1964.
9. A.N. Dremin, S.A. Koldunov, "Shock Initiation of Detonation in Cast and Pressed TNT," Vzrivnoe Delo, No. 63/20, p. 37, Moscow, Nedra, 1967.
10. C. Young, R. Fowles, and R.P. Swift, "Shock Waves and the Mechanical Properties of Solids," edited by J.J. Burke and V. Weiss, Syracuse University Press, 1971.
11. B. Hayes, "Electrical Measurements in Reaction Zones of High Explosives," 10th Symposium on Combustion, p. 869, The Combustion Inst., 1965.
12. L.M. Erickson, C.B. Johnson, N.L. Parker, H.C. Vantine, R.C. Weingart, and R.S. Lee, "The Electromagnetic Velocity Gauge: Use of Multiple Gauges, Time Response, and Flow Perturbations," Seventh Symposium on Detonation, Office of Naval Research Report MP 82-334, p. 1062, 1981.

13. Lynn Seaman, "Lagrangian Analysis for Multiple Stress or Velocity Gages in Attenuating Waves," J. Appl. Phys. 45, No. 10, p. 4303, 1974.

14. Charles L. Mader, "Numerical Modeling of Detonation," University of California Press, Berkeley, 1979.

15. J.N. Johnson, P.K. Tang, and C.A. Forest, "Shock-wave Initiation of Heterogeneous Reactive Solids," J. Appl. Phys. 57, No. 9, p. 4323, 1985.

16. W.L. Seitz, H.L. Stacy, and Jerry Wackerle, "Detonation Reaction Zone Studies on TATB Explosives," (this symposium.)

DISCUSSION

MICHAEL COWPERTHWAITE, SRI International

Does the reaction seem to be driven more by temperature than pressure because the HOM equation of state, based on the assumption of thermal equilibrium, was used to calculate the reaction coordinate from the gage data?

REPLY BY JERRY WACKERLE

In a sense, this is correct, although the result is not limited to the HOM equation of state. With thermal equilibrium assumed, the calculated temperature increase as reaction proceeds scales quite closely with the mass fraction reacted, or reaction coordinate, λ. Thus λ could be used as readily as temperature as the correlation variable for the current-state factor in a DAGMAR-like form; however, with an exponential, Arrhenius form, it seems more appropriate to use temperature parameterization. We have examined the DAGMAR correlation with the two-temperature, "isentropic solid" (ISE) alternative to thermal equilibrium you described in the Seventh Detonation Symposium (see p. 601 of Ref. 3 above); we find the evolution of the reaction coordinates in typical initiation configurations differ little between ISE and HOM. If a "bulk" mixture temperature history is calculated with ISE on a basis of ideal mixing of volume fractions, the evolution of this temperature function along a reactive state path is very similar to that of the equilibrium temperature evolution calculated with HOM. Thus, ISE also is found to admit to a good DAGMAR correlation in terms of current-state bulk temperature, again because it scales with the reaction extent. In any case, this work and that of Refs. 2 to 4 above all show that in short-shock experiments pressure is an inferior correlation variable for the current-state dependence of the rate, and that this purpose is served much better by some measure of the energy release, be it bulk temperature or reaction coordinate.

LAGRANGE GAGE STUDIES OF DETONATION IN SOME INTERMOLECULAR EA BASED EXPLOSIVES

M. Cowperthwaite and J.T. Rosenberg
SRI International
Menlo Park, CA 94025

Multiple Lagrange gages were used to record sets of particle velocity histories in detonation waves propagating in baseline EAK, prill-cast EAK and EAKL. Curves of constant particle velocity were constructed from these sets of histories to map the particle velocity fields in the regions spanned by the gages. The particle velocity fields were found to contain a steady-state zone and an unsteady zone exhibiting properties of nonideal detonation. Chapman-Jouguet (CJ) calculations, based on the premise that these steady-state zones represent the reaction zones in the explosives, led to the assignment of CJ parameters and reaction times to prill-cast EAK and EAKL but not to baseline EAK. Comparison of the structures of these reaction zones and the ensuing unsteady flows leads to the conclusion that aluminum (L) in this EAKL burns both in the reaction zone and in the release wave behind it.

INTRODUCTION

The demonstration by Hershkowitz and Akst (1) that the performance of nonideal intermolecular explosives containing ammonium nitrate (A) is improved by physical synthesis led to the development of explosives based on EA, the eutectic of ethylenediamine dinitrate (E) and A. This paper presents a study of detonation in some intermolecular explosives based on EA with the additives potassium nitrate (K) and aluminum (L). Multiple Lagrange particle velocity gage experiments were performed to characterize detonation in baseline EAK, prill-cast EAK, and EAKL.

Multiple Lagrange particle velocity histories were recorded in self-sustaining detonation waves propagating in baseline EAK, prill-cast EAK, and EAKL. These particle velocity histories were used to construct curves of constant particle velocity (2)-(4) in the time-Lagrange distance (t-h) plane and thereby map the particle velocity fields in the regions spanned by the gages. These curves of constant particle velocity were examined to determine steady-state and unsteady regions in the detonation waves in the explosives.

The particle velocity fields in the detonation waves were found to contain a steady-state zone and an unsteady zone. Calculations of Chapman-Jouguet (CJ) parameters were based on the assumption that the observed steady-state zones represent the reaction zones in the explosives. The results of these calculations led to the assignment of CJ parameters to prill-cast EAK and EAKL and also to the conclusion that the reaction zone in baseline EAK is not fully developed in the region spanned by the gages.

Atypical properties of the particle velocity contours in the unsteady regions demonstrate other nonideal features of the detonation process in these EA based explosives. The positive second derivatives exhibited by the particle velocity contours in prill-cast EAK indicate that its release wave is influenced by exothermic reactions; the remarkable differences exhibited by the contours in EAKL and prill-cast EAK are taken as evidence that the release wave in EAKL is strongly influenced by the burning of aluminum (l).

LAGRANGE TECHNIQUES

(1) Experimental Methods.

The SRI multiple Lagrange particle velocity gage technique used in the present work has been described previously (4,5) and is summarized here for the reader who may not be familiar with the technique. The objective of this technique is to measure histories along particle paths (Lagrange histories) of the particle velocity at several depths within an explosive undergoing planar reactive flow. The basic experiment configuration is shown in Figure 1.

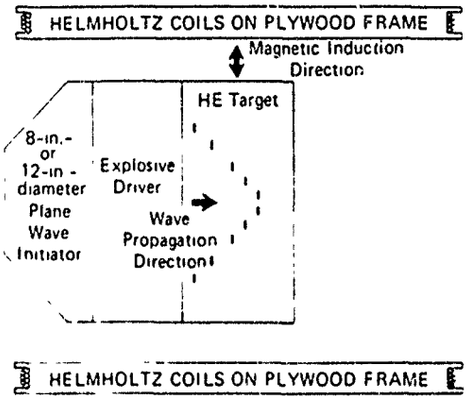

Fig. 1. Configuration of SRI intermediate-scale multiple Lagrange particle velocity gage experiments (Heavy dashes in the HE target indicate the active elements of the embedded particle velocity gages.)

The HE target is a right cylinder typically 0.2 to 0.3 m in diameter by about 0.1 m in height. A plane-wave lens (PWL) and appropriate HE driver are used to initiate reaction in the target HE. Electromagnetic particle velocity (EPV) gages, (6,7) described below, are embedded at various depths (Lagrange coordinates) in the target to record the particle velocities at these Lagrange coordinates. Expendable Helmholtz coils, wound on plywood frames and powered by a capacitive discharge system with a time constant of several milliseconds, provide a uniform uniaxial magnetic induction of 400 to 500 gauss in the region of the EPV gages. The magnetic induction is essentially constant during the measurement interval, about 10 μs.

The configuration in Figure 1 is large scale in comparison to Lagrange gage gas gun experiments performed in other laboratories, typically with 0.05-m-diameter targets, to study shock initiation of detonation for shorter times (8,9). However, here, in the context of nonideal HEs, it is termed intermediate scale.

The principle of the EPV gage is that an electrical conductor moving in a fixed magnetic field will generate a motional electromotive force (EMF) proportional to its velocity. If the conductor, motion, and magnetic induction are each uniaxial and mutually orthogonal, as in the present case, then by Faraday's law of induction for moving circuits

$$E(t) = B\ell u'(t) \qquad (1)$$

where E is the EMF, t is time, B is the magnitude of the magnetic induction, ℓ is the length of the conductor, and u' is its velocity.

The EPV gages used in this work were formed from aluminum strips nominally 0.15 mm thick by 3 mm wide. The strips are bent into rectilinear U-shapes, and ten are mounted on a standard linen-phenolic gage block for embedding in a target, as shown in Figure 2. The crossbar of the U is the active element of the gage and is 25.4 mm long. The sides of the U, electrical leads that carry the signal out the back of the target, do not contribute to the signal because they are strictly parallel to the direction of particle motion in the target. The gages are anodized and sealed to provide an electrical insulating layer 5 to 10 μ thick. Because the active elements of the EPV gages are only 0.15 mm thick in the wave propagation direction we estimate that the gages equilibrate with the flow in less than 0.1 μs. Therefore, u'(t) can be taken equal to the local velocity in the reactive flow, u(t), everywhere except at highly transient states such as those near the spike in a classic ideal HE.

A high-frequency recording circuit, consisting of RG 213 or RG 58 coaxial cables and a 51-Ω viewing-and-termination resistor in series with the EPV gage, monitors each gage. A Tektronix 7000 series analog oscilloscope, time-correlated to other analog oscilloscopes by a repetitive beam-blanking pulse simultaneously applied to each oscilloscope, and a Nicolet digital 2090III oscilloscope each records the potential drops across the viewing resistor for each gage. Typical peak potential drops are 2 V. E(t) is determined from the potential drop across the viewing resistor, and u'(t), interpreted as u(t), is then calculated from Eq. (1).

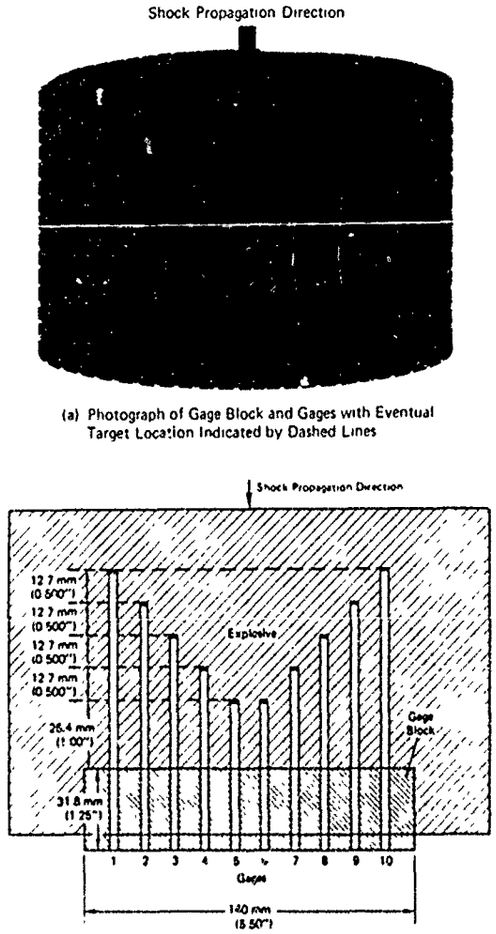

(a) Photograph of Gage Block and Gages with Eventual Target Location Indicated by Dashed Lines

(b) Schematic Side View Showing Gage Numbering System and Positions (These Dimensions used in Data Analysis)

Fig. 2. Configuration and numbering system of the ten particle velocity gages in each Lagrange experiment

Our standard ten-gage gage block was used in this work. The gage numbering system and dimensions in the wave propagation direction are shown in Figure 2. The gages are numbered sequentially from one end of the block to the other. The ten gages consist of two symmetrically placed 5-gage sets, 1 through 5 and 6 through 10. Thus there are two replicate gages, one from each 5-gage set in each of five planes (Lagrange positions) orthogonal to the detonation propagation direction. Adjacent gages are separated by 12.7 ± 0.1 mm in the propagation direction and by 12.0 ± 0.2 mm, center-to-center, in the lateral direction.

(2) Analytic Methods

A Lagrange analysis based on particle velocity (u) provides a quantitative description of the one-dimensional flow produced in a shock or detonation wave experiment from a set of particle velocity histories recorded along different particle paths. The pressure (p) and the specific volume (v) are generated by integrating the equations of motion with flow derivatives estimated from the gage records.

In an analysis based on curves of constant u it is convenient to write the momentum and continuity equations as

$$p(u,t) - p_f(t) = \varrho_o \int_{u_f}^{u} \left(\frac{\partial h}{\partial t}\right)_u du \qquad (2)$$

and

$$v(u,h) - v_f(h) = - v_o \int_{u_f}^{u} \left(\frac{\partial t}{\partial h}\right)_u du \qquad (3)$$

where t and h denote time and Lagrange distance, the subscript f denotes the wave front, the subscript o denoted the unshocked condition and $\varrho = v^{-1}$ denotes the density. The derivative $(\partial h/\partial t)_u$ represents the slope of the curves of constant u in the (h-t) plane, was introduced into Lagrange analysis by Fowles (2) as C_u, and satisfies the equation,

$$C_u \equiv \left(\frac{\partial h}{\partial t}\right)_u = - \frac{(\partial u/\partial t)_h}{(\partial u/\partial h)_t} \qquad (4)$$

The theoretical basis of our analysis based on curves of constant u in the (t-h) plane will now be presented. We first consider an expansive flow behind a shock propagating at constant velocity D consisting of a steady-state region followed by an unsteady region. It is convenient to use the subscript H to denote conditions at the shock front. Then, $u_f = u_H$, $p_f = p_H$, $v_f = v_H$ and the variables at the shock front are governed by the Rankine-Hugoniot jump conditions

$$v_H D = v_o (D - u_H) \qquad (5)$$

$$v_o p_H = D u_H = D^2 \left(1 - \frac{v_H}{v_o}\right) \qquad (6)$$

expressing the balance of mass and momentum across the shock front. Equations governing the steady-state region are readily derived using the steady-state condition expressed in Lagrange coordinates by the equation,

$$\left(\frac{\partial}{\partial t}\right)_h = -D\left(\frac{\partial}{\partial h}\right)_t \qquad (7)$$

The combination of Eqs. (7) and (4) gives the equation

$$C_u = D \qquad (8)$$

which shows that the curves of constant u in a steady-state region are parallel straight lines with a slope of $(\partial t/\partial h)_u = D^{-1}$ in the (t-h) plane. The integration of Eqs. (2) and (3) subject to Eq. (8) and the boundary conditions expressed by Eqs. (5) and (6) gives the equations

$$v\,D = v_o\,(D - u) \qquad (9)$$

$$v_o p = Du = D^2\left(1 - \frac{v}{v_o}\right) \qquad (10)$$

which show that the Rankine-Hugoniot jump conditions are satisfied everywhere in the steady-state region. We can now state an important flow property based on curves of constant u that is used in our analysis:

> In a region of the (t-h) plane where the curves of constant u are parallel straight lines the flow has attained a steady-state and satisfies the Rankine-Hugoniot jump conditions.

We now consider the flow in the unsteady region, use the subscript s to denote quantities at the end of the steady-state zone, and write Eqs. (2) and (3) respectively as,

$$p - p_s = \varrho_o \int_{u_s}^{u} C_u\,(u,t)\,du \qquad (11)$$

$$v - v_s = -v_o \int_{u_s}^{u} \left(\frac{\partial t(u,h)}{\partial h}\right)_u du \qquad (12)$$

Partially differentiating Eq. (11) with respect to t and Eq. (12) with respect to h gives the equations,

$$\left(\frac{\partial p}{\partial t}\right)_u = \varrho_o \int_{u_s}^{u} \left(\frac{\partial^2 h}{\partial t^2}\right)_u du \qquad (13)$$

$$\left(\frac{\partial v}{\partial h}\right)_u = -v_o \int_{u_s}^{u} \left(\frac{\partial^2 t}{\partial h^2}\right)_u du \qquad (14)$$

with

$$\left(\frac{\partial^2 t}{\partial h^2}\right)_u C_u^3 = -\left(\frac{\partial^2 h}{\partial t^2}\right)_u \qquad (15)$$

from the chain rule. We first consider the simplest case when the curves of constant u in the unsteady region are nonparallel straight lines. Then, $(\partial^2 t/\partial h^2)_u = (\partial^2 h/\partial t^2)_u = 0$, and it follows from Eqs. (13) and (14) that $(\partial p/\partial t)_u = (\partial v/\partial h)_u = 0$. We can now state another important flow property of release waves based on curves of constant u:

> In a region of the (t-h) plane where the curves of constant u are nonparallel straight lines the pressure and specific volume are only functions of u.

Moreover, because $p = \bar{p}(u)$, $v = \bar{v}(u)$, and $p = \bar{p}(v)$, the paths of all the particles in the release wave are represented in the (p-u), (v-u), and (p-v) planes by single curves that pass through the state at the end of the steady-state region.

In this paper, a detonation will be called ideal when the particle velocity contours in its release wave are straight lines, otherwise it will be called non-ideal.

We now consider nonideal detonation exhibiting particle velocity contours with a positive second derivative. In this case, $(\partial^2 t/\partial h^2)_u > 0$, and it follows from Eqs. (15) and (13) that $(\partial p/\partial t)_u > 0$. Thus the pressure is a function of u and h, $p = \bar{p}\,(u,h)$, and the particle paths in the release wave are represented in the (p-u) plane by a family of curves passing through (p_s, u_s). Because $(\partial p/\partial h)_u > 0$, the release curve for the particle with Lagrange coordinate $h + \delta h$ lies above the release curve for the particle with the Lagrange coordinate h. The corresponding representation in the (p-v) plane is obtained from the following equation

$$\left(\frac{\partial v}{\partial h}\right)_p = -v_o \int_{u_s}^{u} \left(\frac{\partial^2 t}{\partial h^2}\right)_u du + \frac{v_o}{C_u^2 C_p} \int_{u_s}^{u} \left(\frac{\partial^2 h}{\partial t^2}\right)_u du \qquad (16)$$

with $C_p = (\partial h/\partial t)_p$ which will not be derived here. Because $C_p > 0$, it follows from Eqs. (15) and (16) that $(\partial v/\partial h)_p > 0$ when $(\partial^2 t/\partial h^2)_u > 0$ and it follows from the identity,

$$\left(\frac{\partial v}{\partial h}\right)_p = -\left(\frac{\partial p}{\partial h}\right)_v \left(\frac{\partial v}{\partial p}\right)_h \tag{17}$$

that $(\partial p/\partial h)_v > 0$ in the release wave because $(\partial p/\partial v)_h < 0$. Thus $p = \bar{p}\,(v,h)$ and the particle paths in the release wave are represented in the (p-v) plane by a family of curves passing through (p_s, v_s). Because $(\partial p/\partial h)_v > 0$, the release curve for a particle with Lagrange coordinate $h + \delta h$ lies above the release curve for a particle with Lagrange coordinate h. We can now state another property of our nonideal detonation.

> When the curves of constant u are not straight lines in a region of the (t-h) plane adjacent to a constant state s, Lagrange paths in the (p-v) plane are represented by a family of release curves passing through (p_s, v_s).

Because such a family of curves in the (p-v) plane is associated with entropy changes in the flow, we intuitively assume that nonstraight curves of constant u arise because of reaction in the unsteady flow but this assumption is not verified here.

When the steady-state region in our shock-induced flow represents the reaction zone in a CJ detonation, we can replace the subscript s by the subscript CJ and write the sonic condition along the line of constant u at the end of the steady reagion as

$$D - u_{CJ} = c_{CJ} \tag{18}$$

where c denotes the sound speed. To describe the CJ state it is convenient to introduce the adiabatic exponent k and define the CJ sound speed by the equation

$$c^2_{CJ} = k(pv)_{CJ} \tag{19}$$

Then, the following equations relating CJ parameters at the end of the reaction zone,

$$D = (k+1)\,u_{CJ} = (k+1)\,\frac{c_{CJ}}{k}$$

$$v_{CJ} = \frac{k v_o}{(k+1)} \tag{20}$$

$$P_{CJ} = \frac{D^2}{(k+1)\,v_o}$$

are obtained by combining Eqs. (5), (6), (18), and (19).

We finally consider the case when the particle velocity histories exhibit extrema in the unsteady region behind the wave front. In the (t-h) plane, we denote the locus of the minima in the (u-t) profiles by VV', the locus of maxima by PP', and let $\check{S}_{\dot{u}}$ and $\hat{S}_{\dot{u}}$ denote their respective slopes. Then the equations for the directional derivatives of u and $\dot{u} = (\partial u/\partial t)_h$ along VV' and PP' give the equations,

$$\check{S}_{\dot{u}} = \hat{S}_{\dot{u}} = \frac{(\partial u/\partial h)_t}{(\partial u/\partial t)_{\dot{u}}} = v_o\,\frac{(\partial^2 p/\partial h^2)_t}{(\partial^2 u/\partial t^2)_h} \tag{21}$$

where it is understood that $\check{S}_{\dot{u}}$ and $\hat{S}_{\dot{u}}$ are associated respectively with positive and negative values of $(\partial^2 u/\partial t^2)_h$. When $(\partial u/\partial h)_t \neq 0$, Eq. (4) shows that $(\partial t/\partial h)_u$ becomes infinite when $(\partial u/\partial t)$ becomes zero. Thus when $\check{S}_{\dot{u}} > 0$, $\hat{S}_{\dot{u}} > 0$, and $(\partial u/\partial t)_{\dot{u}} \neq 0$, the curves of constant u in the (t-h) plane have a vertical slope where they intersect VV' and PP'. Furthermore, when $\check{S}_{\dot{u}} > 0$, and $\hat{S}_{\dot{u}} > 0$, $(\partial^2 p/\partial h^2)_t$ has the same sign as $(\partial^2 u/\partial t^2)_h$, and $(\partial u/\partial h)_t$ has the same sign as $(\partial u/\partial t)_{\dot{u}}$. Thus, the locus of minima and the locus of maxima in the pressure-Lagrange distance plane lie along VV' and $\check{S}_{\dot{u}}$ is greater than zero. It follows from Eq. (21) that $(\partial u/\partial h)_t = 0$ along VV' and the directional derivatives for $(\partial u/\partial t)_h$ and $(\partial u/\partial h)_t$ along VV' lead to the equation,

$$\check{S}_{\dot{u}} = \frac{(\partial^2 u/\partial t^2)_h}{(\partial^2 u/\partial h^2)_t} \tag{22}$$

which shows that $(\partial^2 u/\partial h^2)_t > 0$ along VV'. Thus the minima in the particle velocity-Lagrange distance profiles also lie on VV' when u is constant along VV' and the slope of VV' is positive.

DETONATION STUDIES OF BASELINE EAK, PRILL-CAST EAK, AND EAKL

Two experiments were performed with all three explosives to obtain the particle velocity data required to determine their detonation parameters in a Lagrange analysis. The baseline EAK experiments were labeled Shot 1 and Shot 2, the prill-cast EAK experiments were labeled Shot 5 and Shot 6, and the EAKL experiments were labeled Shot 7 and Shot 8. All the explosive targets were nominally 10 inches in diameter and were characterized by Los Alamos National Laboratory (LANL) under the direction of A.P. Torres and J.A. Sanchez. Additional control targets were cast from the same melts to provide specimens for the composition and density analysis.

The EAK in the baseline targets was creamed during the melt preparation operation and in the control target had an average composition 47.22/44.99/7.79 by weight, and an average density of 1.608 g/cm³. The prill-cast EAK control target had an average density of 1.563 g/cm³ and its composition was assumed to be the same as the baseline EAK control target. The EAKL control target had an average composition 38.60/38.13/7.69/15.57 by weight and an average density of 1.578 g/cm³. The EAKL targets were made with "Tritonal-grade" aluminum and the melt was creamed before the aluminum was added to prevent settling.

The driver system, consisting of a P-120 plane wave lens, a 2-inch-thick cylindrical pad of Composition B, and a 0.25-inch-thick cylindrical pad of PMMA, was designed in conjunction with Dr. B. G. Craig of Eglin Air Force Base.

Particle velocity was monitored by analog oscilloscopes in Shots 1 and 2, by analog and digital oscilloscopes in Shots 5 through 8, and was recorded at all five gage positions in all three explosives. The quality of the records is exemplified by the oscilloscope traces in baseline EAK from Shot 2 shown in Figure 3, and the composite plots shown in Figures 4, 6, and 8. As usual we observe perturbations on the record from a given gage when downstream gages enter the flow, but these perturbations are not large enough to interfere with data analysis and are useful for time correlation purposes. Particle velocity histories were constructed from the data recorded by the oscilloscopes in Shots 2 through 8 and used to construct curves of constant particle velocity for the explosives in the (t-h) plane but space limitations allow only a selection of these results to be presented here. These data will be introduced as required in the following discussion of the flows observed in each explosive.

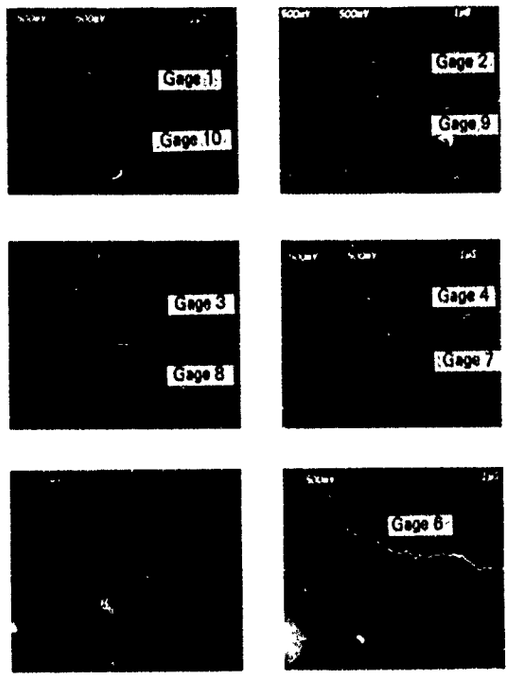

Fig. 3. EPV gage records from the analog oscilloscopes in shot 2 (detonation characterization experiment), baseline EAK

All oscilloscope settings are 0.5 V/division vertical and 1 μs/division horizontal

1. Self-Sustaining Detonation in Baseline EAK

Our discussion is based on the composite plot of (u-t) profiles from Shot 2 shown in Figure 4, and the curves of constant u constructed from them shown in Figure 5. Histories at the same gage position are superposed in the composite plot for comparative purposes. Comparison of the histories at a given gage plane shows that the histories recorded by gages in the same

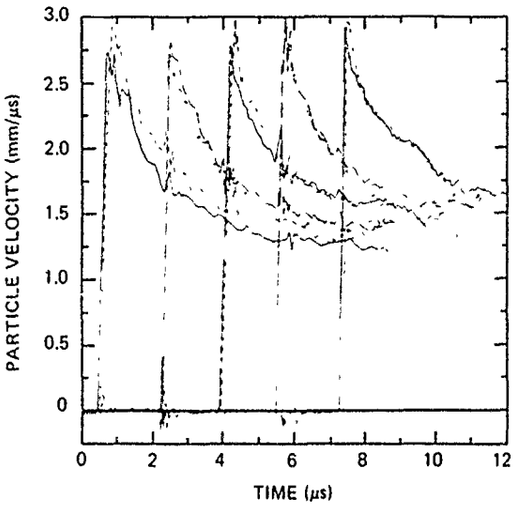

Fig. 4. Composite plot of Lagrange particle velocity histories from the analog oscilloscopes in Shot 2, baseline EAK

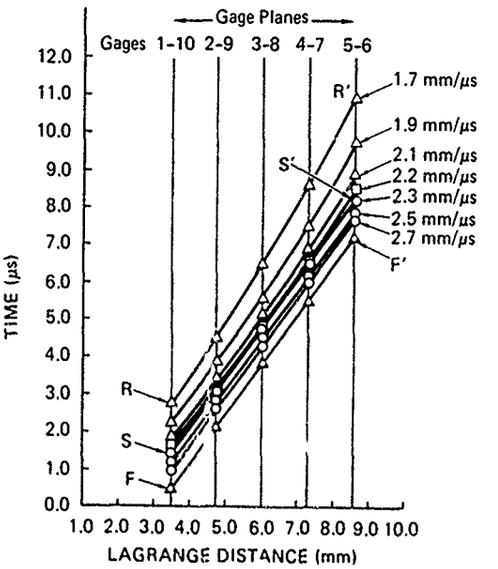

Fig. 5. Curves of constant particle velocity in the time-Lagrange distance plane constructed from the Lagrange particle velocity histories recorded by the analog oscilloscopes in Shot 2, baseline EAK

plane are in good agreement. Comparison of the histories at different gage planes indicates that the detonation velocity wave is in the final stages of the initiation process because the peak particle velocity increases from ≐ 2.75 mm/μs to 3.00 mm/μs and the detonation velocity attains a value of 7.57 mm/μs in the region spanned by the gages. The structure exhibited by the histories at the last three gage positions indicates that the wave is supported by different exothermic reactions propagating at markedly different rates (10) and also that the reaction zone may not have attained its final configuration in the region spanned by the gages.

Figure 5 shows the wave front as FF', and the curves of constant u plotted from u = 2.7 mm/μs to 1.7 mm/μs in intervals of 0.2 mm/μs with an additional curve at u = 2.1 mm/μs. Examination of these curves shows that the flow in FSS'F' between FF' and u = 2.3 mm/μs has attained a steady-state, that the flow in SRR'S' between u = 2.3 mm/μs and u = 1.7 mm/μs is unsteady, and also that the flow between u = 2.3 mm/μs and u= 2.1 mm/μs in the region spanned by the second and fourth gages has attained a psuedo-steady state. Moreover, the positive second derivatives exhibited by the curves in SRR'S show that the unsteady flow is not a Taylor wave. These atypical properties of the particle velocity field demonstrate either that the detonation wave is nonideal or that the initiation of the reaction zone is not complete.

Additional evidence that the formation of the reaction zone is incomplete however, was obtained by comparing CJ parameters based on the assumption that SS' represents the CJ state and the CJ parameters calculated by Kamlet's semi-empirical method (11) - (13). The assumption that SS' represents the CJ state gives the following set of CJ parameters: D = 7.57 mm/μs, u_{CJ} = 2.3 mm/μs, p_{CJ} = 280 kbar and k = 2.29. Kamlet's method, based on the assumption that EAK with a nominal composition 46/46/8 by weight reacts completely with K being converted into K_2CO_3, gives the following set of CJ parameters: D = 7.58 mm/μs, u_{CJ} = 1.94 mm/μs, p = 236 kbar, k = 2.91. This disagreement between the two sets of calculated CJ parameters led us to conclude that FSS'F' does not represent the fully developed reaction zone in baseline EAK, and consequently no CJ parameters were assigned to baseline EAK.

2. Self-Sustaining Detonation in Prill-Cast EAK

Our discussion is based on the (u-t) profiles recorded by the analog oscilloscopes in Shots 5 and 6 and the curves of constant u constructed from them. Histories from the analog oscilloscopes are presented because they are more easy to compare in a composite plot than those recorded by the digital oscilloscopes. A composite plot of the (u-t) profiles from Shot 6, and the curves of constant u constructed from the (u-t) profiles recorded in Shot 5 are shown respectively in Figures 6 and 7. Figure 6 shows that the histories recorded by the gages are in good agreement except at the first and last gage positions, and that the flow develops into a wave with an average peak particle velocity of ~2.6 mm/μs at the last four gage positions propagating with an average velocity D = 7.78 mm/μs. Examination of the curves of constant u constructed from Figure 6 shows that the flow develops at the second gage position into a wave with a steady-state region from u ~ 2.6 mm/μs to u = 1.9 mm/μs, and an unsteady state region with straight curves of constant u from u = 1.9 mm/μs to u = 1.5 mm/μs. The composite plot of the (u-t) histories from Shot 5 shows that the histories are in good agreement except at the first two gage positions, and that the flow develops into a wave with a peak particle velocity of ~ 2.6 mm/μs at the last three gage positions propagating with an average velocity D = 7.71 mm/μs. The corresponding curves of constant u, plotted from u = 2.3 mm/μs to 1.5 mm/μs in intervals of 0.2 mm/μs with an extra curve at u = 1.8 mm/μs, and the wave front FF'F", are shown in Figure 7. Examination of these curves shows that the flow is unsteady at the first two gage positions and develops at the third gage position into a wave with a steady-state region F'S'S"F" from u ~ 2.6 mm/μs to u= 1.9 mm/μs. and an unsteady state region S'R'R"F", from u = 1.9 mm/μs to u = 1.5 mm/μs, with curves of constant u exhibiting a positive second derivative. Furthermore, the shape of the curves in S'R'R"F" indicate that they will become straight lines as the flow develops. This was the observation that motivated the construction of a similarity solution for a reactive Taylor wave (14).

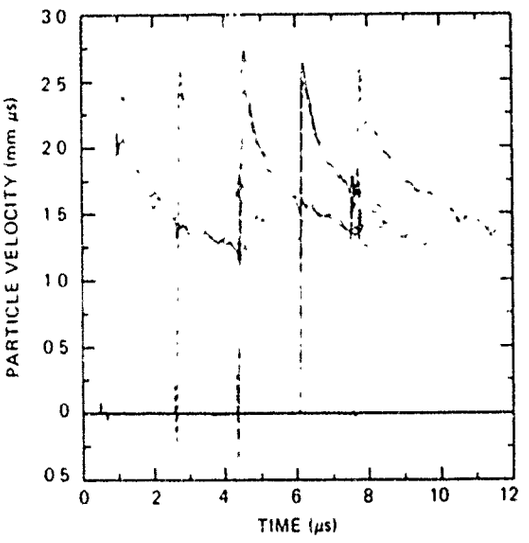

Fig. 6. Composite plot of Lagrange particle velocity histories from the analog oscilloscopes in Shot 6, prill-cast EAK

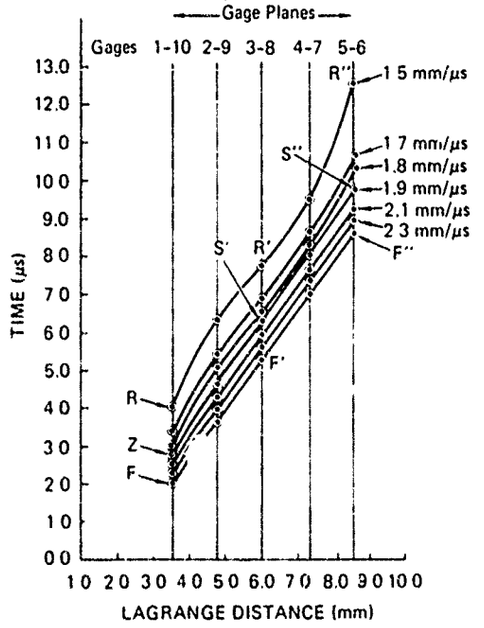

Fig. 7. Curves of constant particle velocity in the time-Lagrange distance plane constructed from the Lagrange particle velocity histories recorded by the analog oscilloscopes in Shot 5, prill-cast EAK

We are now in a position to discuss the detonation process in prill-cast EAK. We first remember the observation that the flow is unsteady in Shot 5 at the first two gage positions but is unsteady in Shot 6 at the first gage position. We then remember the observation that the curves of constant u indicate that the

unsteady flow behind the steady-state region observed in Shot 5 may develop into the type of unsteady flow behind the steady-state region observed in Shot 6. From these observations, we conclude that the flow observed in Shot 5 represents an earlier stage of the detonation process than the flow observed in Shot 6. Because the same steady-state region is observed in both shots, we assume that it represents the fully developed reaction zone in the explosive. The results of CJ calculations support this assumption and lead to the assignment of the following set of CJ parameters to prill-cast EAK: D = 7.78 mm/μs, u_{CJ} = 1.9 mm/μs, p_{CJ} = 231 kbars, v_{CJ} = 0.483 cm³/g, k=3.09. The reaction time is ∼1 μs, and the shape of the reaction zone indicates that the wave is supported by different exothermic reactions with different rates.

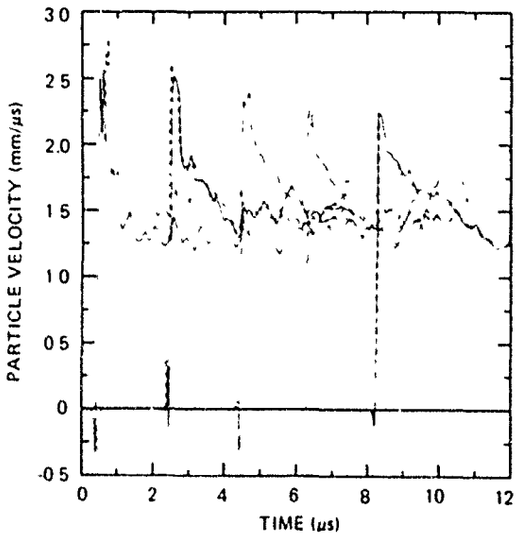

Fig. 8. Composite plot of Lagrange particle velocity histories from the analog oscilloscopes in Shot 7, EAKL

3. Self-Sustaining Detonation in EAKL

Our discussion is based on the (u-t) profiles shown in Figure 8 and the curves of constant u shown in Figure 9. Histories from the digital rather than the analog oscilloscopes were used to construct Figure 9 because they cover a larger time frame and consequently exhibit more features of the complicated flow observed in EAKL. Although the writing speed of the

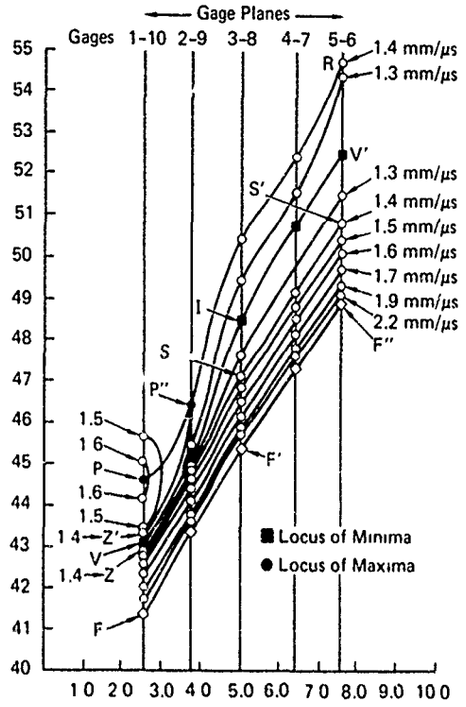

Fig. 9. Curves of constant particle velocity in the time-Lagrange distance plane constructed from the Lagrange particle velocity histories recorded by the digital oscilloscopes in Shot 8, EAKL

analog oscilloscopes is much higher than that of the digital oscilloscopes, we have demonstrated in other work with pulses with a similar frequency content that the histories recorded by both types of oscilloscopes agree to within 1-2 percent. Comparison of the histories at a given gage plane showed that the histories recorded by gages in the same plane are in relatively good agreement but, as expected, do not agree as well as those recorded in the other two explosives. Comparison of the histories at different gage planes shows that the wave was initially overdriven because the peak particle velocity recorded by the first two gages is ∼ 2.5 mm/μs while that recorded by the last three is ∼2.3 mm/μs. More detailed examination of the (u-t) histories recorded by the digital oscilloscopes in Shots 7 and 8 reveals that they exhibit more structure than the (u-t) histories recorded in baseline and prill-cast EAK and also exhibit minima and maxima.

A better understanding of the particle velocity field in EAKL is obtained from Figure 9 which shows the wave front as FF'F", the locus of maxima in the (u-t) profiles as PP", the locus of minima as VIV', and the curves of constant u with values from 2.2 mm/μs to 1.3 mm/μs. The contours with values of 1.6 mm/μs, 1.5 mm/μs, and 1.4 mm/μs have a verticle slope where they intersect PP" and the particle velocity gradient in that region of the flow is negative. VIV' lies between the u = 1.4 mm/μs contours, ZP"R and ZSS', and the value of u along IV' has a constant value of ≈1.25 mm/μs. Thus, IV' represents a locus of minima in the (u-h) and (p-h) profiles and the particle velocity gradient and the pressure gradient are negative in the region above IV'.

Our observation from the peak particle velocities that the wave is originally overdriven is supported by the shape of FF'F" which shows that the wave velocity decreases between the first two gages before it attains a constant value of 6.85 mm/μs. Examination of the contours between FF'F" and ZSS' shows that the flow attains a psuedo-steady state between the first two gages planes before it develops the steady-state region F'SS'F" between the third and fifth gage planes. Contours between the second and third gage planes bend away from the wave front, then back towards it, and become parallel again at the third gage plane as the steady-state is formed. Our characterization of detonation in EAKL is based on the assumption that the reaction zone is fully developed and represented by FSS'F". The results of CJ calculations support this assumption and lead to the assignment of the following CJ parameters to EAKL: D = 6.85 mm/μs, u_{CJ} = 1.4 mm/μs, p_{CJ} = 151 kbar, v_{CJ} = 0.504 cm^3/g, k = 3.89. The reaction time is ≈1.9 μs, and the shape of the reaction zone indicates that the wave is supported by different exothermic reactions with different rates.

The reaction zones in EAKL and prill-cast EAK thus have a similar structure but the reaction time in the former is approximately twice as long as the reaction time in the latter. We also conjecture that the reaction zones in baseline EAK and EAKL are formed in a similar manner, and conclude from the positive second derivatives exhibited by the particle velocity contours in Figure 5 that the first stages in the development of the reaction zone in baseline EAK are observed in Shot 2.

RESULTS AND CONCLUSIONS

Multiple Lagrange particle velocity gage experiments, designed to characterize detonation in baseline EAK, prill-cast EAK, and EAKL, were performed and sets of particle velocity histories were recorded in their self-sustaining detonation waves. Comparison of the peak particle velocities recorded by sets of gages showed that the constant velocity shock at the wave front of detonation in each explosive was formed in the region spanned by the gages. Curves of constant particle velocity in the time-Lagrange distance plane were constructed from the sets of particle velocity histories to map the corresponding particle velocity fields and determine their steady and unsteady zones. The particle velocity fields in all the explosives were found to exhibit a steady-state zone and an unsteady zone containing nonideal particle velocity contours with non-zero second derivatives.

Calculations of CJ parameters from the particle velocity gage data were based on the assumption that the observed steady-state zone in the particle velocity field represents the fully developed reaction zone in the explosive. In this case, the initiation of self-containing detonation is complete, the particle velocity at the end of the steady zone is the CJ particle velocity, and knowledge of the detonation velocity and the initial density is sufficient to calculate other CJ parameters in the explosive. CJ calculations with the particle velocity gage data led to the conclusion that the reaction zones in prill-cast EAK and EAKL are fully developed and resulted in the assignment of CJ parameters and reaction times to these explosives. CJ parameters were not assigned to baseline EAK however, because the calculated values were compared to those calculated from Kalmet's semi-empirical method and found to be theoretically unacceptable. We concluded from this comparison that the reaction zone in baseline EAK is not fully developed in the region spanned by the gages. Similarities between the particle velocity contours exhibited by EAKL in the region where the reaction zone is formed and those exhibited by baseline EAK in the region spanned by the gages also support this conclusion.

Properties of the reaction zones determined in our detonation study set the time scales for the exothermic reactions supporting self-sustaining detonation in EA based explosives and lead to a better understanding of the detonation process in nonideal explosives. Both reaction zones contain two regions with markedly different decelerations. The particle velocity drops rapidly from its peak value at the wave front in the first region, and then drops more gradually to the CJ point in the second. Because both reaction zones have a similar structure attributed to different exothermic reactions with different rates, we conclude that the exothermic reactions associated with ethylenediamine dinitrate (E) occur primarily in the first region and that the slower exothermic reactions associated with the other explosive components occur primarily in the second. The fact that the ratio of the reaction times in EAKL and prill-cast EAK is two to one is taken as direct evidence that aluminum (L) burns in the reaction zone and supports the propagation of detonation in EAKL.

Our conclusion that the reaction zone is formed in prill-cast EAK and EAKL but not in baseline EAK leads us to discuss the factors governing the initiation of the reaction zone in our EA based explosives. This discussion is based on the premise that the time scale for the initiation of the reaction zone in an explosive depends upon the time scales of the exothermic reactions supporting the flow. In this case, because the reaction times in our EA based explosives are an order of magnitude greater than those in ideal explosives, we expect this initiation process to take longer in EA based explosives than in ideal explosives and exhibit more features. Furthermore, because the faster exothermic reactions are assumed to equilibrate with the hydrodynamic flow before the slower ones, we expect the region of the reaction zone associated with the faster reactions to be formed before the region associated with the slower ones. Because the formation of the reaction zone in EAKL supports these expectations and the formation of the reaction zone is complete in prill-cast EAK but not in baseline EAK, we conclude first that the steady-state zone observed in baseline EAK is associated with the decomposition of ethylenediamine dinitrate (E), and second that the exothermic reactions associated with ammonium nitrate (A) proceed faster in prill-cast EAK than in baseline EAK.

Other unusual features of the detonation process in our EA based explosives are demonstrated by the atypical properties of the particle velocity contours in the unsteady flow regions. The non-zero second derivatives exhibited by these contours in prill-cast EAK and EAKL indicate that exothermic reactions continue behind the reaction zones in these explosives. The shape of these curves in prill-cast EAK suggests that the fully developed detonation wave in prill-cast EAK consists of a steady-state reaction zone followed by a reactive Taylor wave. The remarkable differences between the particle velocity fields in EAKL and prill-cast EAK, demonstrated by their particle velocity contours, are taken as evidence that aluminum (L) continues to burn behind the reaction zone in EAKL and strongly influences the ensuing hydrodynamic flows in the release wave.

We conclude that the multiple Lagrange gage techniques presented in this paper provide the means to characterize and develop a better understanding of the detonation process in nonideal explosives.

ACKNOWLEDGMENTS

Valuable contributions to this work were made by many people at SRI. We particularly acknowledge D.R. Henley for constructing the multiple Lagrange gage assemblies, D.F. Walter, K.E. Nelson, and H.E. Hanna for assistance with the detonation experiments, and B. Y. Lew and J. Zeiger for help with data reduction.

We are especially indebted to A.P. Torres and J.A. Sanchez of Los Alamos National Laboratory for their cooperation in fabricating the targets used in these detonation studies.

We also acknowledge G.H. Parsons and A.G. Taliancich of Eglin Air Force Base for useful discussions and thank B.G. Craig of Egiin Air Force Base for help in designing the driver systems for the detonation experiments.

This work was supported by Eglin Air Force Base under Contract F08635-83-K-0447.

REFERENCES

1. J. Hershkowitz and I. Akst, "Improvement of Performance of Composite Explosives Containing Ammonium Nitrate by Physical Synthesis," Sixth Symposium (International) on Detonation, ACR-221, 439-449 (1976).
2. G.R. Fowles and R.F. Williams, "Plane Stress Wave Propagation in Solids," J. Appl. Phys 41, 360-363 (1970).
3. M. Cowperthwaite and R.F. Williams, "Determination of Constitutive Relationships with Multiple Gages in Nondivergent Waves," J. Appl. Phys, 42, 456-462 (1971).
4. M. Cowperthwaite and J.T. Rosenberg, "A Multiple Lagrange Gage Study of the Shock Initiation Process in Cast TNT," Sixth Symposium (International) on Detonation, ACR-221, 786-793 (1976).
5. J.T. Rosenberg and M. Cowperthwaite, "Explosive Characterization by the Lagrange Gage and Analysis Technique," 1982 Conference on Instrumentation for Nuclear Weapons Effects. DNA-TR-82-17-VI, 287 299 (1982).
6. V.M. Zaitsev. P.F. Pokhil, and K.K. Shvedov, "The Electromagnetic Method for the Measurement of Velocities of Detonation Products," Doklady Akad. Sci. USSR 132 (6), 1339, (1960).
7. S.J. Jacobs and D.J. Edwards, "Experimental Study of the Electromagnetic Velocity Gage Technique," Fifth Symposium (International) on Detonation, ACR-184, 413-426 (1970).
8. A.B. Anderson, M.J. Ginsberg, W.L. Seitz, and J. Wackerle, "Shock Initiation of Porous TATB," Seventh Symposium (International) on Detonation, NSWC MP 82-334, 385-393 (1982).
9. H.C. Vantine, W.D. Curtis, L.M. Erickson, and R.S. Lee, "A Comparison of Stress and Velocity Measurements in PBX-9404," Eighteenth Symposium (International) on Combustion, The Combustion Institute (1981), 1631-1639.
10. M. Cowperthwaite, "Some Aspects of Nonideal Detonation in Composite Explosives," J. of Energetic Materials Vol. 1, p. 127, 1983.
11. M.J. Kamlet and S.J. Jacobs, "Chemistry of Detonations. I: A Simple Method for Calculation Detonation Properties of C-H-N) Explosives," J. Chem. Phys., 48, 23 (1968).
12. M.J. Kamlet and J.E. Ablard, "Chemistry of Detonations. II: Buffered Equilibria," J. Chem. Phys., 48, 36 (1968).
13. M.J. Kamlet and C. Dickinson, "Chemistry of Detonations. III: Evaluation of the Simplified Calculational Method for Chapman-Jouguet Detonation Pressures on the Basis of Available Experimental Information," J. Chem. Phys., 48, 43 (1968).
14. M. Cowperthwaite, "A Model Solution for Nonideal One-Dimensional Detonation Waves," (this symposium).

DISCUSSION

MARTIN SUMMERFIELD, Princton Combustion Research Laboratory, Inc.

How sensitive is the deduced chemical reaction rate in the detonation wave to the particular choice of the equation of state?

REPLY BY MICHAEL COWPERTHWAITE

As far as I know this question has not been addressed directly. Workers at Los Alamos have, however, addressed a related problem and have shown in machine calculations that Lagrange particle velocity histories are not significantly changed by changes in the equation of state when the energy release rate is kept constant.

DETONATION REACTION ZONE STUDIES ON TATB EXPLOSIVES

W. L. Seitz, H. L. Stacy, and Jerry Wackerle
Los Alamos National Laboratory
Los Alamos, NM 87545

Interface velocity histories between heterogeneous detonating explosives and transparent windows, separated by a thin (13 μm) aluminum shim, have been obtained with an image intensified rotating-mirror streak camera and a Fabry-Perot velocity interferometer system. Seven TATB-based explosives were studied with PMMA windows for typically three charge lengths. Two of the explosives were also studied with LiF windows. In each case a non-steady detonation was observed, with each increasing charge length showing a corresponding increase in the interface velocity histories. Time resolution and velocity error are estimated to be about 6 ns and 2% respectively. Numerical simulations for one of the explosives, for which a shock-strength modified Arrhenius rate law (DAGMAR) and an assumed equation of state (HOM) had been previously calibrated with shock initiation gauge data, gave good agreement with the experimental velocity histories.

INTRODUCTION

The detonation reaction zone in heterogeneous explosives has been the subject of many research studies. Numerous experimental techniques such as the plate-push (1), electromagnetic gauge (2), rate stick (3), Fabry-Perot interferometer (4), and ide-angle Michelson interferometer (5) have been used in an attempt to obtain CJ detonation pressures, detonation reaction zone thicknesses, spike pressures, and other details of the detonation process. In spite of the considerable research on the subject many unanswered questions concerning the flow in the reaction zone remain.

We describe in this paper an experimental study of the detonation reaction zones of seven TATB-based explosives by measuring the interface velocity histories between the detonating explosives and transparent windows, separated by a thin (13 μm) aluminum shim, with a Fabry-Perot velocimeter system. The seven explosives were a fine and coarse lot of PBX 9502 (95/5 weight percent TATB/Kel-F), PBX 9503 (80/15/5 weight percent TATB/HMX/Kel-F), X-0407 (70/25/5 weight percent TATB/PETN/Kel-F), and three particle-size distributions of 1.8-g/cm³ (7% porous) TATB (so called standard grind, superfine, and micronized).

Numerical simulations of the interface velocity histories for the 1.8-g/cm³ superfine TATB using a shock-strength modified Arrhenius reaction rate law (DAGMAR) and an assumed equation of state (HOM) that had been previously calibrated to Manganin-gauge data (6) are also presented and found to be in good agreement with experiment.

EXPERIMENTAL

An image-intensified rotating-mirror streak camera and a Fabry-Perot velocity interferometer system (7) were used to measure interface velocity hisotries between detonating explosive samples and transparent windows. A 13-μm aluminum shim was placed between the explosive and window to provide a reflective surface. Experiments were performed with PMMA windows for typically three charge lengths of 13, 25, and 50 mm for seven explosives. LiF windows were used for experiments on the fine lot of PBX 9502 and 1.8-g/cm³ superfine TATB

with charge length of 13 and 25 mm. All experiments were driven with a P-40 planewave lens, 25 mm of Composition B, and 10 mm of 6061 aluminum as shown in Fig. 1. This driving system was chosen to give a relatively prompt initiation of detonation (less than 2 mm of run) for each of the seven explosives, without having an overdriven detonation. Planarity of the initiating wave was about 40 ns. A diameter/

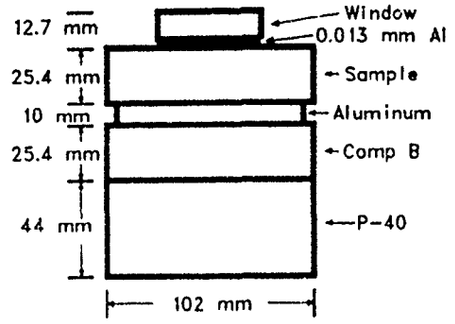

Fig. 1. Typical configuration for explosive driver and target system

length ratio of 2 or greater was used to avoid edge effects. Experiments were carefully constructed to hold necessary tolerances. Initial temperatures were controlled at 20 ± 1 °C. All PMMA windows were constructed from Rohm and Haas type II UVA Plexiglas with a density of 1.186 ± 0.001 g/cm³. The LiF windows were X-cut single crystals.

A schematic of the Fabry-Perot interferometer system (8,9) is shown in Fig. 2. The laser was a 12-watt (all lines) Spectra-Physics Model 171-07 argon-ion, which was operated single frequency at 514.5 nm with an output

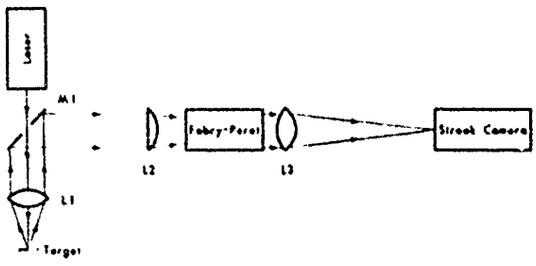

Fig 2 Schematic of the Fabry-Perot interferometer system

power of about 3 watts. The laser beam was sent to the target and the reflected light from the target (which had been carefully prepared to produce diffuse reflections) was collimated with lens L1 and directed to the Fabry-Perot interferometer. A cylindrical lens L2 positioned just before the interferometer converged the beam in one direction. Fringes produced by the Fabry-Perot were focused onto the camera slit with lens L3. By using a cylindrical lens to converge the beam in only one direction, constructive interference fringes appear as dot pairs at the camera slit, rather than the usual rings produced by a Fabry-Perot. Considerable intensity gain is attained by using the cylindrical lens. Typically the focal length of lens L2 was chosen to produce about 4 fringe pairs.

A Burleigh Model RC-110 Fabry-Perot interferometer with 50.8-mm-diameter mirrors was used. The mirrors were flat to within λ/200 with reflectivities of 93%.

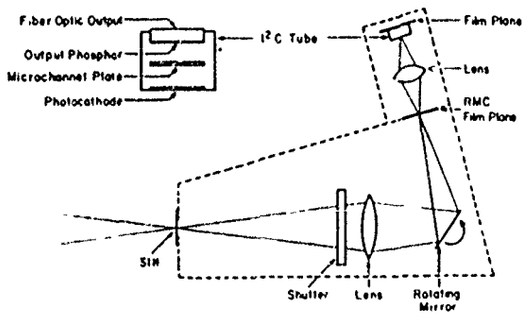

Fig. 3. Schematic of rotating mirror streak camera (I²RMC)

Figure 3 shows the image-intensified rotating-mirror streak camera (I²RMC). A 40-mm-diameter International Telephone and Telegraph image-intensifier tube (10) and a high aperture lens (f/2.5) were mounted such that the image formed at the streak-camera film plane was projected onto the image-intensifier tube. A magnification of 1.36 was used between the streak-camera film plane and the image-intensifier tube. The writing speed at the intensifier tube was about 21 mm/μs.

A Doppler shift in wavelength of the reflected laser light resulting from target motion, beginning at shock arrival time, produces a corresponding shift in fringe spacing. For our choice of window materials, target interface velocities are related to fringe spacing by (7)

$$V = \frac{c\lambda}{4L(1+k)} \cdot \left[\frac{d'^{2}_{n+m} - d^2_n}{d^2_{n+1} - d^2_n} + m\right], \qquad (1)$$

where c is the velocity of light in vacuum, λ is the initial wavelength of the laser, L is the Fabry-Perot mirror spacing, (1+k) is the correction factor for the change in index of refraction for the window material, d_n and d_{n+1} are the distances between dot pairs for the n and n+1 static fringes, and d'_{n+m} is the dynamic fringe spacing for the n+m fringe. The number of fringes shifted, m, at shock arrival time must be determined from some previous knowledge of the target velocity or nominally identical experiments must be performed with different fringe constants ($c\lambda/4L$). In the present work $c\lambda/4L$ was 3.8 mm/μs/fringe and the target velocities were known to within one fringe constant.

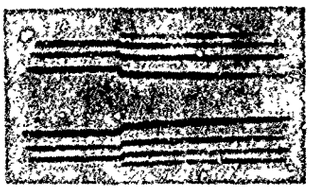

Fig. 4. Typical streak record with a total streak time of 1.9μs

A typical streak record of fringes is shown in Fig. 4. Streak records were digitized with an optical comparator, and position data were transformed into velocities and times with equation (1) and the known camera writing speed. Estimated time resolution and velocity errors were 6 ns and 2%, respectively. As would be expected, the reverberations in the 13-μm aluminum shim, estimated to be about 5 ns, were not resolved. All times are referenced to shock arrival at the window. Data points typically read such that velocities were obtained at 5-ns intervals for the first 50 ns and at 20-ns intervals for the remainder of the record.

RESULTS

Figure 5 shows typical scatter and a functional fit to the data for the fine PBX 9502. The purely empirical functional form,

$$V = ae^{-bt} - ct + d, \qquad (2)$$

was found to give a good fit to the velocity histories. Due to a strong correlation between constants and the different data ranges for each experiment, comparisons between specific constants for the various explosives are not meaningful. For times greater than the coverage of the data, the fit predicts arbitrarily large negative or positive velocities; therefore, extrapolations outside the data range should be avoided.

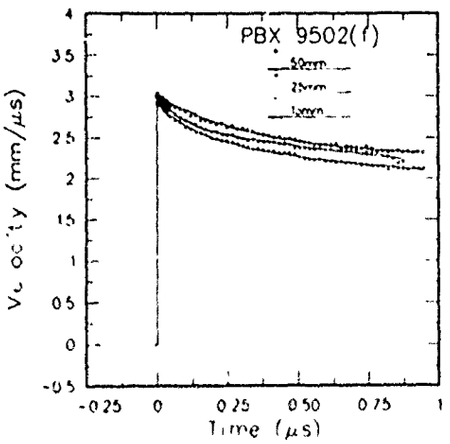

Fig. 5. Comparison of functional form with actual data for fine PBX 9502 with PMMA window

Functional fits to the experimental data points for the seven explosives studied are shown in Fig. 6. A tabulation of explosive densities and functional fit constants for PMMA and LiF windows are given in Tables 1 and 2, respectively. All of the interface velocity histories have the common feature that one cannot discern an outstanding demarcation that might be associated with attaining a Chapman-Jouguet state. This condition for TATB-based explosives and others, was also noted in Refs. (2) and (5). An additional common feature of the seven explosives studied is the increase in interface velocity histories with increasing run

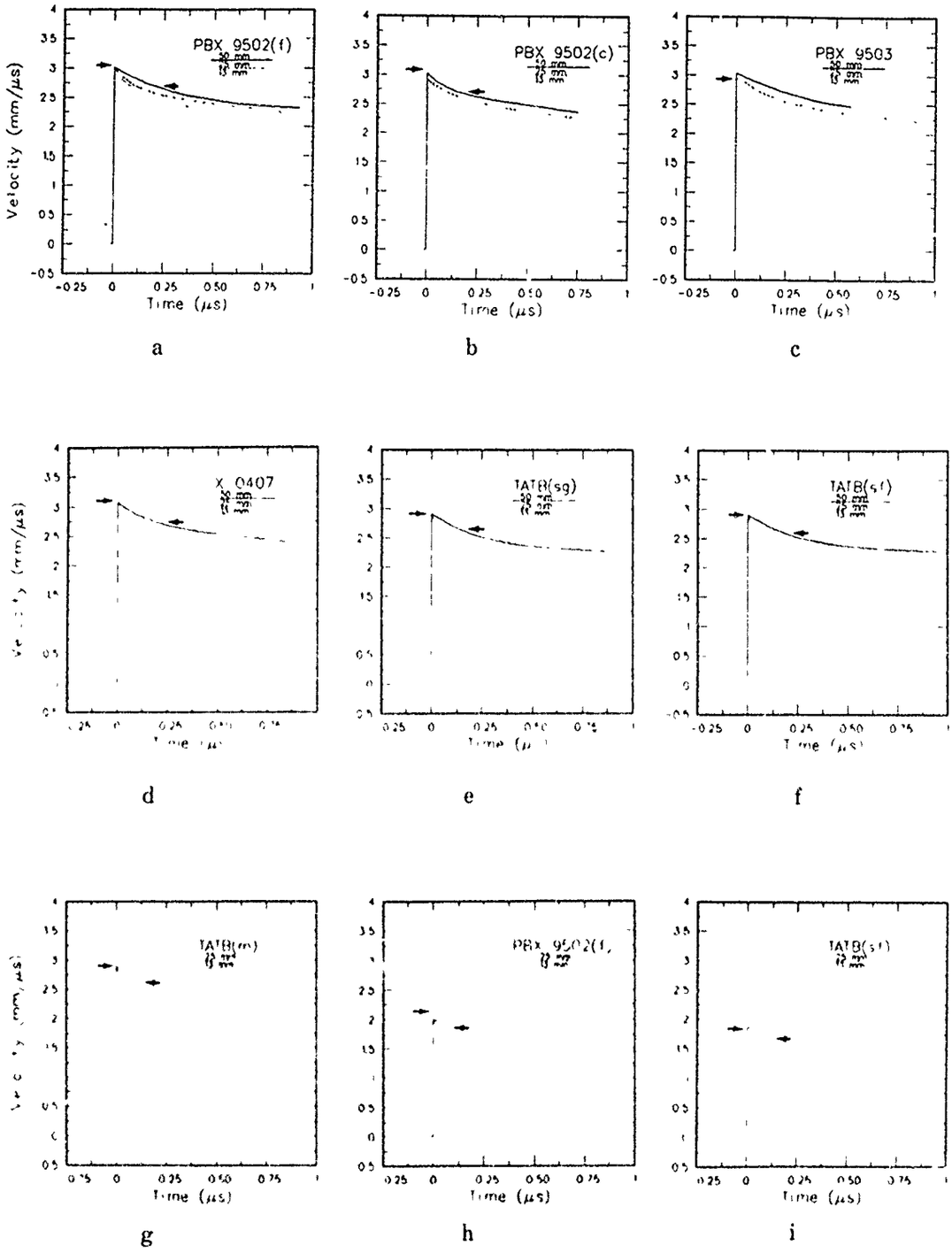

Fig. 6 Functional fit of $V = ae^{bt} - ct + d$ to measured interface velocity histories for fine PBX 9502(a), coarse PBX 9502(b), PBX 9503(c), X-0407(d), 1.8 g/cm³ standard grind TATB(e), 1.8 g/cm³ superfine TATB(f), and 1.8 g/cm³ micronized TATB(g) with PMMA windows, and for fine PBX 9502(h) and 1.8 g/cm³ superfine TATB(i) with LiF windows. Arrows show calculated VN spike and CJ interface velocities

TABLE 1

Initial density and constants for the empirical fit, $V = ae^{-bt} - ct + d$, for the explosive configurations with PMMA windows

Explosive Material	Charge Length (mm)	Initial Density (g/cm^3)	a ($mm/\mu s$)	b (μs^{-1})	c ($mm/\mu s^2$)	d ($mm/\mu s$)
PBX 9502(f)	13	1.893	0.51474	5.76843	0.31886	2.39794
"	25	1.893	0.39464	9.57291	0.41747	2.59944
"	50	1.891	0.76128	2.65347	−0.00616	2.24753
PBX 9502(c)	13	1.895	0.44476	9.85036	0.48507	2.50223
"	25	1.890	0.28930	9.87736	0.53415	2.67900
"	50	1.892	0.27690	12.69448	0.51769	2.74842
PBX 9503	13	1.876	0.48589	11.82438	0.42754	2.46726
"	25	1.872	0.47241	6.49196	0.33891	2.53148
"	50	1.878	2.49192	1.12038	−1.08401	0.54019
X-0407	13	1.859	0.50022	6.58338	0.32477	2.42810
"	25	1.858	0.36162	7.89929	0.39056	2.61543
"	50	1.855	0.39526	6.12678	0.33013	2.67922
Superfine	13	1.800	0.52690	6.00780	0.24853	2.29458
"	25	1.804	0.52713	6.23858	0.18610	2.34638
"	50	1.780	0.53345	4.64913	0.12170	2.38598
Std. Grind	13	1.805	0.57074	4.26505	0.17297	2.23027
"	25	1.807	0.54894	5.11110	0.17268	2.31207
"	50	1.799	0.56060	4.39603	0.11041	2.35296
Micronized	13	1.810	0.56821	6.02492	0.16353	2.26314
"	25	1.803	0.66430	4.49368	0.08306	2.23083

TABLE 2

Initial density and parameters for configurations with LiF windows

Explosive Material	Charge Length (mm)	Initial Density (g/cm^3)	a ($mm/\mu s$)	b (μs^{-1})	c ($mm/\mu s^2$)	d ($mm/\mu s$)
PBX 9502	13	1.893	1.16244	2.85397	−0.67360	0.79127
"	25	1.892	1.15112	2.79590	−0.67165	0.85717
Superfine	13	1.796	0.82673	2.38543	−0.21712	0.94906
"	25	1.801	0.65970	3.99618	−0.23873	1.21643

distances. As discussed in Ref. (2), this is indicative of a failure to attain a steady detonation in the run distances of the experiments.

SOME CALCULATIONAL RESULTS

As a first step in examining the data, we have calculated impedance-match solutions for the interface velocities using the classical Zeldovich-von Neumann-Doering (ZND) model of a steady detonation, and equation-of-state representations of the unreacted Hugoniot and fully reacted products in common use at Los Alamos. A typical result is displayed in pressure-particle velocity space in Fig. 7. Here the right-hand solid curve is the unreacted Hugoniot for the explosive, the left-hand solid curve is the products isentrope through the Chapman-Jouguet (CJ) state, and the dashed line connects this state with the von Neumann (VN) spike condition along the Rayleigh line of slope $\varrho_0 D$ (where ϱ_0 is the initial density and D is the detonation velocity). The unreacted Hugoniots are cast in the common linear shock velocity-particle velocity form $U=C+Su$. The constants C and S were obtained for all the explosives by least-square fitting to initial U-u data obtained from explosives wedge experiments; these data are obtained mostly at states well below the CJ condition, and typically have considerable scatter. The CJ isentrope is calculated with a Becker-Kistiakowsky-Wilson (BKW) equation of state (11). These calculations are generally well-calibrated to measured detonation velocities and Hugoniot data.

The upper, dotted curve of Fig. 7 is the calculation of the reflected-shock Hugoniot and rarefaction isentrope for the unreacted explosive, determined using a Mie-Gruneisen equation of state. The conditions of continuity of pressure and particle velocity at a contact surface provide a prediction of the initial interface particle velocities at the intercept of the dotted curve with the Hugoniot curves for LiF (chain dotted) and PMMA (chain dashed). In the context of the ZND model, the calculation is a legitimate test of the extrapolation of our unreacted Hugoniots.

The "extended impedance match solution" shown by the lower dotted curve is less legitimate. The locus is a reflection of the CJ isentrope, and may considerably oversimplify the match of the CJ state condition into a window.

The interface velocities calculated by impedance-match soluton are listed in Table 3, along with the more important characterization constants. Single listings are given for PBX 9502 and 1.8-g/cm^3 TATB because we have been unable to discriminate differences in Hugoniot data for different particle sizes of these two compositions. In Fig. 6 the calculated interface velocities are indicated by arrows for matching into the VN and CJ states. The VN points are reasonably consistent with observation.

We have conducted a few preliminary computational simulations of the observed reaction zones with our modification of the PAD 1D numerical hydrocode (12). Fickett has previously shown that such numerical calculations introduce spurious small amplitude oscillations in a nominally steady reaction zone profile (13). We eventually achieved reasonably smooth results using about 20 cells/mm, a linear combination of linear (Landshoff) and quadratic (Richtmeyer-von Neumann) artificial viscosity, and on the suggestion of Charles Forest, the imposition of 25% of the compressive artificial viscosity on rarefaction. Although these artifices were less than satisfying, they were found to give PAD calculations of steady detonation reaction zones in reasonable agreement with exact calculations of reaction-zone state histories as they evolve along the Rayleigh line. We found that we could simulate the standard driving system described earlier using 31 mm of Composition B with the "hot start" option of PAD, which constructs a CJ detonation at the explosive-alloy interface and imposes an analytic formulation of the Taylor wave. This configuration was used to drive the calculations of the experiments.

In this paper, we report only our most successful simulations, for 1.8-g/cm^3 superfine TATB, for which we had previously used embedded-gauge data to develop an empirical reaction-rate correlation (6). this correlation was developed using the HOM equation of state (11), which assumes the unreacted explosive and

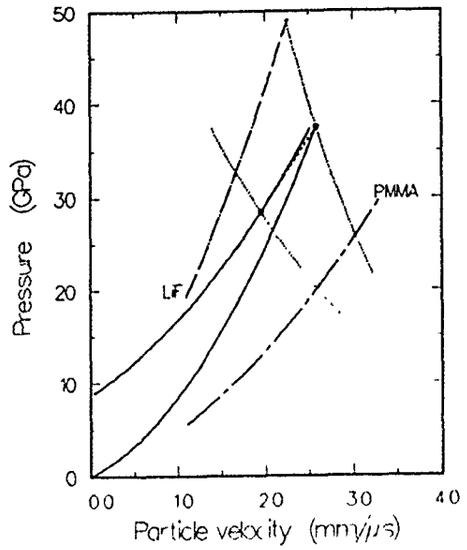

Fig. 7. Impedance-match solutions for interface velocities

products state equations described earlier, ideal mixing of specific volume and internal energy of the two constituents, and that the two phases are in pressure and temperature equilibrium. We used both a Newton's iteration algorithm (14) and a computer subroutine devised by Charles Forest for the numerical calculations.

The rate correlation calibrated in (6) was the "Direct Analysis Generated Modified Arrhenius Rate," or DAGMAR, first found useful for representing PBX 9404 (15). It is formulated,

$$r = \frac{\partial \lambda}{\partial t} = Z_0(1 - \lambda)\, p_s^n\, e^{-T^*/T}, \qquad (3)$$

where λ is the mass fraction reacted, p_s the pressure of the first shock at a given mass point, T the current temperature (calculated in the HOM equation of state) and Z_0, n and T* constants. The same HOM and DAGMAR constants (Z_0 = 0.0158, n = 2.61, T* = 1861 K, pressure in GPa) as employed in the previous work (6) were used in the simulations. Simulations with these constants indicated a 21-GPa input shock and approximately a 1-mm run distance to detonation, which is consistent with that observed for 1.8-g/cm^3 TATB (6). The detonation incident on the window was thus fully initiated and self-supporting for all thicknesses of TATB.

The numerical simulations of interface velocities were performed for 13- and 25-mm thicknesses of TATB, for both PMMA and LiF windows. The results are compared with data and the empirical fitting functions in Fig. 8. The numerical calculations neglected the aluminum foil, and the plotted values are from the first computational cell in the windows. Reaction histories calculated in the last cell of the explosive are shown as dashed lines in Fig. 8, and serve better to identify the calculated reaction zone durations. Agreement of computed and observed particle velocities during this reaction time is generally good; disagreement at later times could be the result of our failure to properly represent the driver system or the products equation of state, or both. Some test calculations showed that the velocity histories were not extremely sensitive to the choice of rate constants; however, calculations with Z_0 multiplied or divided by 3/2 were in discernibly poorer agreement than those shown.

DISCUSSION

The resolution of our Fabry-Perot laser velocimeter appears to be adequate to resolve the relatively wide reaction zone in TATB-based explosives. As was concluded in a previous study on one of these explosives (PBX 9502) with a better time resolution (5), detonation waves in all the explosives we studied appear to have a ZND character. Sharply rising, unreactive shocks are followed by decreasing particle velocities, pressures, densities, and internal energies through the reaction zones. This view is in good agreement in nearly every case with the impedance-match solutions for the VN spike state; where agreement is not as good, the imprecision of the existing Hugoniot data will admit to adjustment.

The experimental profiles for the seven explosives are rather similar in character, reflecting the fact that the interface velocity measurements are not highly sensitive to modest changes in reaction rates. This was also noted in the numerical simulations. Subtle, unknown differences in reaction rate magnitudes and form, generally associated with particle-size distributions, are much more manifest in high-pressure short-shock experiments (16) and detonation wave-spreading observations (17).

With sufficient modification of the PAD numerical hydrocode, we were able to simulate, reasonably well, the velocity histories for 1.8-

TABLE 3

Explosive Constants and Interface Velocities

Explosive	ϱ_o (g/cm^3)	C (mm/μs)	S	u_{CJ} (mm/μs)	D (mm/μs)	PMMA		LiF	
						VN (mm/μs)	CJ (mm/μs)	VN (mm/μs)	CJ (mm μs)
PBX 9502	1.890	2.400	2.050	1.953	7.695	3.1	2.6	2.2	1.7
PBX 9503	1.875	2.400	2.200	NA	7.840	2.9	NA	2.2	NA
X-0407	1.866	3.000	1.800	2.002	7.773	3.1	2.7	2.3	1.7
Pure TATB	1.800	2.054	2.357	1.984	7.552	2.9	2.6	1.8	1.6

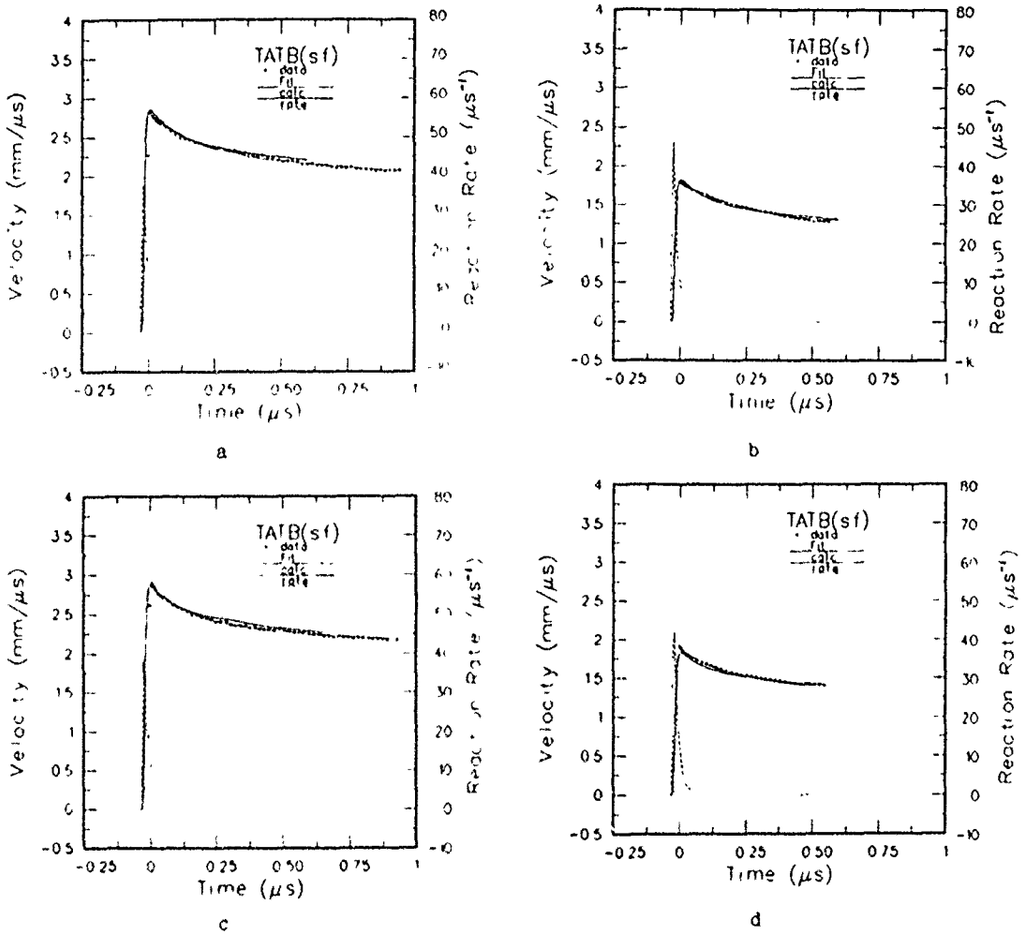

Fig 8 Comparison of numerical simulations (solid curve) with both data (symbols) and the empirical fitting function (chain dotted) for 13-mm run with PMMA (a), 13-mm run with LiF (b), 25-mm run with PMMA (c), and 25-mm run with L'F (d). (Calculated reaction-rate histories are also shown for each case with a dashed curve.)

g/cm^3 superfine TATB (the one TATB-based explosive for which we have a reaction rate calibration). The previous correlation was used without modification, despite being calibrated at pressures less than half those encountered with the detonation incident on a LiF window. In fitting the individual velocity histories at different run distances numerical calculations succeeded in simulating the non-steady character of the detonation.

In part, the successful simulation actually may result from the properties of the DAGMAR form. In particular, this rate correlation combines multiplicative factors in depletion, shock strength, and current state. Such a form has been repeatedly demonstrated to be effective in simulating a variety of shock initiation problems, and is beginning to be characteristic of more physically-based rate forms, such as Krakatoa (18) and the explicit hotspot model of Johnson, Tang, and Forest (14).

In simulating detonations colliding with inert windows, DAGMAR sets the p_s factor with the nearly constant VN spike pressure before the collision, and thus differs from a simple-depletion rate only in the modification due to the temperature dependence. With our HOM representation for 1.8-g/cm^3 TATB, the 2050 K VN spike temperature increases about 12% through a detonation reaction zone, increases 15% with the shock reflected from a LiF window, and decreases 10% with the rarefaction from PMMA. These conditions lead to little difference in the shape of the rate histories for PMMA and LiF windows seen in Fig. 8, with the higher initial rate value from the higher impedance-match temperature for the LiF windows being the most prominant feature. The reaction rate histories for each of the calculated cases have about the same 150-ns duration. With the impedance-match solutions indicating a 37-GPa initial pressure for the LiF window and a 22-GPa initial pressure for the PMMA window, one would not expect to obtain so small a difference in rates and in scaled interface velocity histories with a rate form strongly dependent on current pressure.

The DAGMAR and HOM representations also have properties leading to numerical simulations without a distinct CJ point in the velocity profile and an increasing interface velocity with run distance, as are consistently observed. Bdzil and Davis have made a detailed theoretical study of unsteady, underdriven detonation (19). They considered an explosive which is driven by a two-step heat-release rate. About 90% of the energy release is fast; the remainder is slow. Their analysis shows that the release of the last 10% of the energy is what controls the transients that precede the establishment of steady detonation. The physical basis for their results can be traced to a simple property of ZND detonation; the tangency of the Rayleigh line and totally reacted Hugoniot curve. Because of the tangency condition, the final 10% of the energy release controls about 50% of the pressure profile in the reaction zone. In addition, the flow is sonic at the point of tangency. As a consequence, the energy released near the end of the reaction zone is transported towards the shock very slowly. The result is an unsteady detonation wave for run distances of many tens of reaction zone thicknesses, with a building up of the velocity histories much as we observe and simulate numerically. In our case, the DAGMAR first-order depletion factor approaches full reaction asymptotically. In detonating 1.8-g/cm^3 TATB, HOM indicates that over 80% of the reaction occurs in less than 50% of the state change from the VN to the CJ state, characteristic of most solid explosives. Our numerical simulation of unsteady detonations is thus a natural consequence of the properties of our rate and equation-of-state form and the general characteristics of an almost ZND detonation.

The velocity profiles observed in the other six explosives are all similar to those for 1.8-g/cm^3 superfine TATB. They could probably be simulated with a rate form having a peak value of a few tens of reciprocal microseconds, a first-order depletion factor, and very little other dependence on current state. To extend the rate to treating initiation problems the rate should have, like DAGMAR, more current-state dependence as pressures are reduced.

ACKNOWLEDGEMENTS

We greatly appreciate the technical assistance of P.J. Ulibarri, O.D. Harkleroad, and S.E. Salazar. We also thank J.B. Bdzil and C.A. Forest for valuable discussions.

REFERENCES

1. Russell E. Duff and Edwin Houston, "Measurement of the Chapman-Jouguet Pressure and Reaction Zone Length in a Detonating High Explosive," J. Chem. Phys. 23, p. 1268, 1955.
2. W.C. Davis, "Magnetic Probe Measurement of Particle Velocity Profiles," Sixth Symposium on Detonation, Office of Naval Research Report ACR-221, p. 637, 1976.
3. A.W. Campbell and R. Engelke, "The Diameter Effect in High-Density Heterogeneous Explosives," Ibid., p. 642, 1976.
4. L.M. Erickson, H.G. Palmer, N.L. Parker, and H.C. Vantine, "Free-Surface Velocity Measurements of Plates Driven by Reacting and Detonating RX-03-BB and PBX-9404," Proceedings of the American Physical Society Topical Conference, Menlo Park, California, p. 553, 1981.
5. S.A. Sheffield, D.D. Bloomquist, and C.M. Tarver, "Subnanosecond Measurements of Detonation Fronts in Solid High Explosives," J. Chem. Phys. 80, p. 3831, 1984.
6. A. B. Anderson, M.J. Ginsberg, W.L. Seitz, and J. Wackerle, "Shock Initiation of Porous TATB," Seventh Symposium on Detonation, Office of Naval Research Report NSWC MP 82-334, p. 385, 1981.
7. W.L. Seitz and H.L. Stacy, "Fabry-Perot Interferometry Using An Image-Intensified Rotating-Mirror Streak Camera," Proc. SPIE on High Speed Photography, Videography and Photonics, 427, p. 186, 1983.
8. M. Durand, P. Leharrague, P. Lalle, A. Le Bihan, J. Morrian, and H. Pujols, "Interferometric Laser Technique for Accurate Velocity Measurement in Shock Wave Physics," Rev. Sci. Instru. 48, p. 275, 1977.
9. D.R. Goosman, "Measuring Velocities by Laser Doppler Interferometry," Energy and Technology Review, Lawrence Livermore National Laboratory Report UCRL-52000-79-3, 1979.
10. J.R. Parker, R. Engelke, W. Morton, and A.S. Lundy, "Resolution Loss in Microchannel Plate Image-Intensifier Tubes at high Gains," SPIE Semin. Proc., 190, LASL Optics Conf., 1979.
11. Charles L. Mader, "Numerical Modeling of Detonation," University of California Press, Berkeley, 1979.
12. W. Fickett, "PAD, A One-Dimensional Lagrangian Hydrocode," Los Alamos Scientific Laboratory Report LA-5910-MS, 1975.
13. W. Fickett, "Accuracy of the Conventional Lagrangian Scheme for One-Dimensional Hydrodynamics," Los Alamos Scientific Laboratory Report LA-6454, 1976.
14. J. Johnson, P. Tang, and C. Forest, "Shock-Wave Initiation of Heterogeneous Reactive Solids," J. Appl. Phys. 57, p. 4323, 1985.
15. J. Wackerle, R.L. Rabie, M.J. Ginsberg, and A.B. Anderson, "A Shock Initiation Study of PBX 9404," Proceedings of the Symposium on High Dynamic Pressures, Paris, France, p. 127, 1978.
16. W.L. Seitz, "Short-Duration Shock Initiation of Triaminotrinitrobenzene (TATB)," Proceedings of the American Physical Society Topical Conference, Santa Fe, New Mexico, p. 531, 1983.
17. C.A. Honodel, J.R. Humphrey, R.C. Weingart, R.S. Lee, and P. Kramer, "Shock Initiation of TATB Formulation," Seventh Symposium on Detonation, Office of Naval Research Report NSWC MP 82-334, p. 425, 1981.
18. J. Vanpoperynghe, J. Sorel, and H.C. Pujols, "Experiments and Numerical Simulation of High Explosives Delayed and Lowed Detonation," Eighth Symposium on Detonation, 1985.
19. J.B. Bzdil and W.C. Davis, "Time-Dependent Detonations," Los Alamos Scientific Laboratory Report LA-5926-MS, 1975.

DISCUSSION
A NEW APPROACH FOR STUDYING THE EXPANSION OF DETONATION PRODUCTS

Daniel Steinberg and Henry Chau
Lawrence Livermore National Laboratory

Single-crystal 100 LiF has well-known mechanical and optical properties. Consequently, it has been used for many years as a window when studying inert materials via the velocimeter technique. Because of its close impedance match to detonating HE, we have used this technique to probe the expansion of detonation products. Our data on LX14 clearly show the Von Neumann spike as well as many other structures not yet identified. The best estimate for the CJ pressure is 35.3 GPa.

INTRODUCTION

An ideal material to use in studying the equation of state of HE would be one that is optically transparent and has the same acoustic impedance as detonating HE. By measuring the HE/material interface velocity we would, in effect, be measuring the material velocity of the HE along the CJ adiabat. This kind of experiment has an advantage over the more common metal-plate acceleration tests because the former is directly related to the CJ adiabat itself, while the latter is only a consequence of the adiabatic expansion.

Single-crystal LiF is almost the ideal material; its acoustic impedance is about 10% higher than detonating LX14. Furthermore, LiF has been used in shockwave studies of inert materials for many years and its mechanical and optical properties are well known (1).

In this paper, we will show the results from two preliminary experiments using this technique.

PLAN OF THE EXPERIMENT

The basic experimental configuration is shown in Fig. 1. The HE charge for the first experiment (9523) had a machined surface. It was bonded to the aluminized LiF with ordinary vacuum grease using a lead brick to press the two together for about 4 hours. The mirror separation in the Fabry-Perot velocimeter was 7.01 mm, implying a time resolution of ~2.3 ns. The laser wave length was 5145 A and the Imacon camera was running at 20 ns/mm.

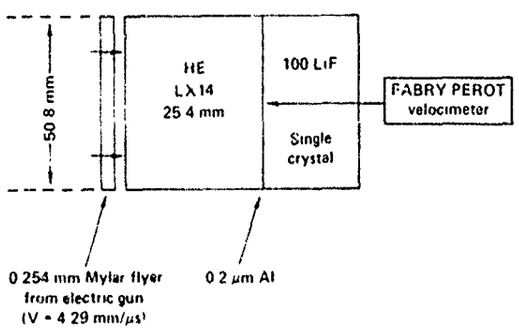

Fig. 1. Basic experimental configuration

The second experiment (9541) had a pressed surface and the bonding time was increased to about 12 hours. The mirror separation was 14.015 mm and the camera was again running at 20 ns/mm.

The total kinetic energy in the Mylar initiator was only about 1/3% of the total energy of the system Numerical simulations of the

experiment showed that the initiator had a negligible effect on the results.

DISCUSSION OF THE DATA

Fig. 2 shows the results of these two preliminary experiments. Note the surpassed zero. The reproducibility is good; the differences are only 1–2%. While there is a lot of structure, three points in particular seem to stand out. The first is a sharp spike, which presumably can be identified as the Von Neumann spike. Following this by about 10–20 ns is a small increase in velocity. Finally, there is a ~75-ns-long plateau that ends about 150 ns after the shock arrival.

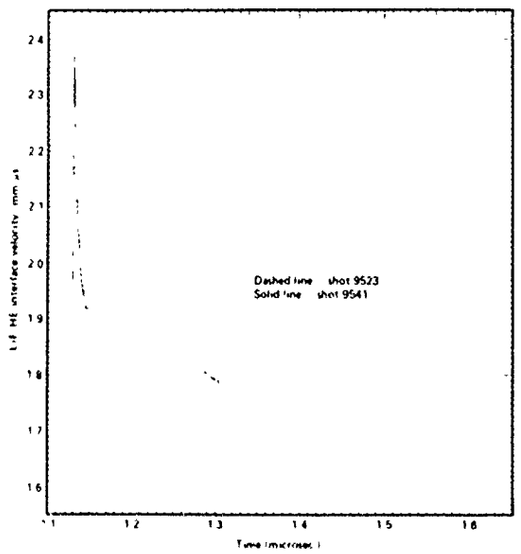

Fig. 2. LiF/HE interface velocity vs. time for two preliminary experiments

The small second bump could merely be a reflection of the complicated hydrodynamics of the Von Neumann spike interacting with the LiF, or it could be a sign of late-time chemical reactions. There is also a question about what point should be identified as the CJ point—is it at the base of the spike or perhaps at the end of the plateau? It depends on what size we expect the reaction zone to be. The best estimate of CJ pressure, using a JWL form to fit the data, is 35.3 GPa.

More work remains to be done. The LiF crystals were 5-mm thick, which permits only 500 ns of observation time. This is only enough time to drop the pressure from CJ to about 26 GPa. The 25-mm-thick crystals will let us go to about 10 GPa, which gives good overlap with cylinder expansion data. In the next experiments we will use highly polished HE surfaces and mineral oil to fill interface gaps. We will also study the effect of varying charge length as well as examining other HE such as PBX 9404 and TATB.

REFERENCE

1. J.L. Wise, to be published in the proceedings of the Fourth APS Topical Conference on Shock Waves in Condensed Matter (Spokane WA, July 22–25, 1985).

*Work performed under the auspices of the U.S. Department of Energy by the Lawrence Livermore National Laboratory under the contract no. W-7405-ENG-48.

EXPERIMENTS AND NUMERICAL SIMULATION OF HIGH EXPLOSIVE DELAYED AND LOWED DETONATION

J. Vanpoperynghe—J. Sorel—H.C. Pujols*
French Atomic Energy Commission
B.P. N° 7 77181 Courtry (France)
*French Atomic Energy Commission
B.P. N° 2 Le Barp 33830 Belin Beliet (France)

Using a Doppler Laser Interferometric technique, the reactions of shocked but not detonated HMX and TATB based explosive charges are studied. Hydrodynamic calculations using a shock initiation model are compared to the experimental results obtained in the TATB based explosive. The model is improved by stopping the reaction below 40 kbar. However further refinement of the model will be required to well describe delayed burning reactions.

INTRODUCTION

The majority of shock initiation experiments has concentrated on the trajectory of the shock front in the buildup region rather than reactions which improve behind the front. T.P. Liddiard (1) was first interested in the chemical reactions when PBX 9404 is initiated by low amplitude shock waves (5 to 15 kbar). Another kind of experiment was then conducted on shocked but not detonated PBX 9404 to evaluate the energy release rate. Using free surface velocity techniques, Craig and Marshall (2) and Kennedy et al. (3) reported significant decomposition for shock waves in the 25 to 60 kbar range. More recently the reaction buildup in PBX 9404 from low amplitude shock waves (4 to 14 kbar) has been studied by L. Green et al. (4) using Manganin pressure gauges impedded in 146 mm diameter by 114 mm thick PBX 9404 cylinders, which allow large record durations.

With the use of insensitive high explosive as TATB based explosive, the buildup region of shock initiation becomes larger and makes experiments easier to conduct. Most of them use Lagrange Analysis (5), (6). This type of experiment describes well the reactions happening behind the shock front and experimental results are very useful to better the numerical models of shock initiation (7), (8) but it doesn't describe the energy deposition from shocked explosive.

This paper first discusses the application of a Doppler Laser Interferometric technique to study the rate of energy liberated by shocked explosive charges. Two explosive compositions are of concern: the first one consists of 96 wt % HMX (Comp. X1)*, and the second one is an insensitive high explosive consisting of 97 wt% TATB (Comp. T2)*.

The obtained results for the Comp. T2 are compared with these obtained with a numerical model developed in our laboratory and called KRAKATOA (9).

EXPERIMENTAL SET UP

Doppler Laser Interferometric technique.

A method to accurately determine the free surface velocity of specimens consists in measuring by interferometer techniques the Döppler shift of a light beam reflected by the moving surface, and several apparatuses have been built according to this principle (10), (11). By means of this equipment the velocity can be derived by measuring with a photodiode or a photomultiplier the intensity of the light transmitted through the interferometer. The main characteristic of our apparatus (12) is the use of a Fabry-Perot interferometer together

* More information on Comp. X1 and T2 is given in ref. 13.

with a streak camera which photographs the variations in the diameters of the rings. We measure a ring diameter rather than a light intensity, which involves the following characteristic features.

First, of great importance in experiments with high explosives, the measurement is not very altered by the deterioration of the free surface optical properties as long as there is enough light from the interferometer for photographic recording, and no measurement of the interferometer output power is needed. Moreover, a single film recording enables us to distinguish acceleration from deceleration (two interferometer fringe signals in quadrature are needed when one records the intensity of tramsmitted light) and data reduction is easy.

The magnitude of error on the velocity according to experimental conditions is in order of 20 m/s.

EXPERIMENTAL CONFIGURATION AND RESULTS

Comp. X1:

This composition, as the other HMX based HE, is shock sensitive and so low amplitude shock waves are necessary to observe only a delayed detonation in a charge. In our experimental configuration plane shock waves were produced in 200 mm diameter and 25 mm or 50 mm thick explosive samples by the impact of a steel plate which was accelerated by a detonating charge (see Figure 1). The velocity of the impacting steel plate was always 1350 m/s. To reduce the shock intensity, the explosive charges were covered by multiple layers of metal and PMMA as shown in Figure 2. The corresponding input shock pressure histories have been computed before being verified. Figure 3 summarizes them.

Measured particle velocities histories from five experiments are shown in Figure 4. Each curve corresponds to an input shock pressure history and different geometrical conditions. The Table 1 summarizes the experimental conditions corresponding to each curve. To easily compare the reaction of an explosive charge in two different experiments we define a mean decomposition rate, which we calculate from the terminal velocity of the flying plate (appendix 1). By constructing a pressure-particle velocity plot an estimate of the shock pressure, P_I, at the explosive-flyer interface can be computed from the initial velocity, U_I, (see Figure 5).

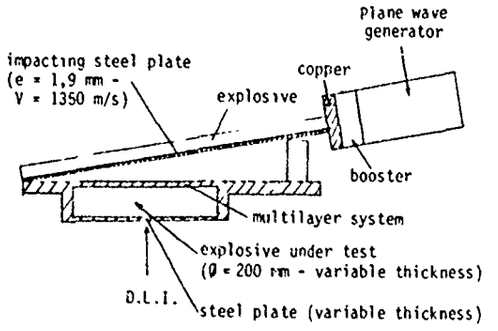

Fig. 1

Copper	e = 5 mm
PMMA	e = 10 mm
Steel	e = 5 mm

Steel	e = 6 mm
PMMA	e = 8 mm
Uranium	e = 5 mm

Steel	e = 6 mm
PMMA	e = 8 mm
Copper	e = 6 mm
PMMA	e = 8 mm
Copper	e = 6 mm

Fig. 2. Different multiple layers to reduce input shock intensity in the explosive samples. The impacting plate is in steel, 1.9 mm thick and its velocity 1350 m/s

The results which we obtain for the mean decomposition rate and the pressure P_I are summarized in Table 1.

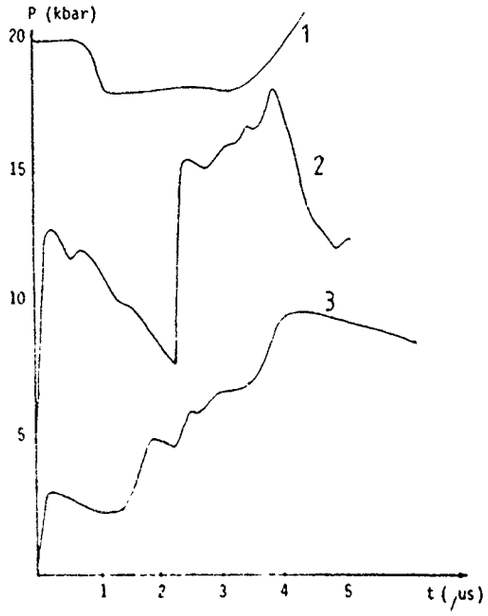

Fig. 3. Input pressure histories on the tested explosive samples (The curve numbers correspond to the scheme number of the Figure 2.)

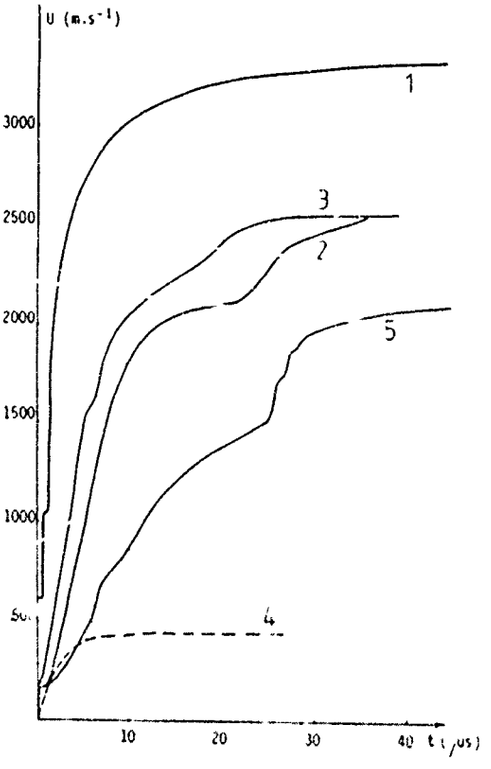

Fig. 4. Particle velocity histories (see Table 1 for corresponding experimental configurations)

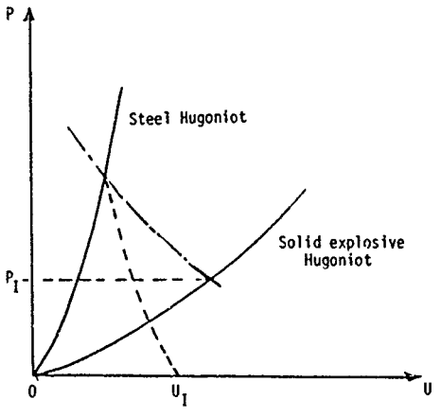

Fig. 5. Determination of the pressure at the interface explosive-driven plate (P_I) from the initial plate velocity (U_I)

For an input shock pressure of about 18 kbar (curve 1—Figure 4) the pressure grows up to 60 kbar in a 25 mm thick charge. This shows us a longer charge will detonate under the same initiation condition (the run distance corresponding to 18 kbar is about 50 mm for Comp. XI (13)). The explosive charge is completly decomposed and the final velocity of the flying plate is a little greater than the one we should observe in a 25 mm thick detonating charge, but it is reached later. The plate is so propelled more isentropically. In the other cases the charges don't completly decompose. The decomposition rate is however significant for an input shock pressure of about 12 kbar (curves 2 and 3—Figure 4), and it would be probably one if the diameter charge was greater. Indeed for a 200 mm diameter charge the flow is no more one dimensional on the axis for times greater than 30 μs. The chemical reactions are quenched by the lateral rarefaction waves. The acceleration of the plate observed at 26 μs is due to the shock wave which was reflected on the back of the charge. The curves 4 and 5 of the figure 4 correspond to more complicated input shock pressure histories (see curve 3—Figure 3). The first shock intensity is about 2,6 kbar and it is followed by 5 kbar and 9,5 kbar shock waves. We don't observe significant decomposition of the 25 mm thick charge (curve 4—Figure 4) but the mean decomposition rate of the 50 mm charge is about 50%. We explain the difference by constructing a time-distance diagram (see figure 6). The first shock is overtaken by the

TABLE 1

Curve Number (Fig. 4)	Input Pressure History Curve Number (Fig. 3)	Explosive thickness (mm)	Driven Plate thickness (mm)	P_I (kbar)	Global reaction rate (%)
1	1	25	1,77	60	77
2	2	25	2,5	16	60
3	2	50	5	20	64
4	3	25	2,5	—	2
5	3	50	5	15	50

following shock waves in a distance greater than 25 mm but smaller than 50 mm. In this last one the shock reflected on the steel plate is then greater and the decomposition is more important.

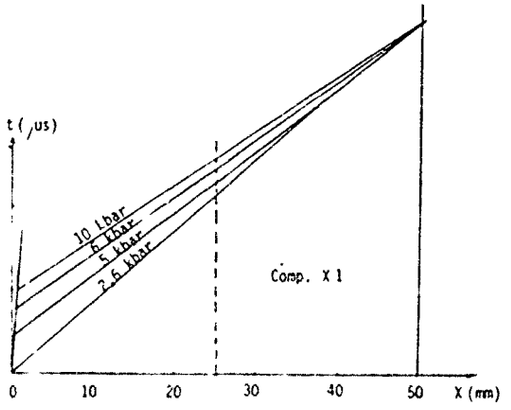

Fig 6. Time-distance diagram in Comp.X1 corresponding to the curve number 3 of the Figure 4

Comp. T2:

Experiments have been conducted on Comp. T2 to study how the reflected shock influences the explosive kinetics. Plane shock waves were produced in 70 mm diameter charges by the same generator as previously. We choose the thicknesses of the charges so that the rear rarefaction waves overtake the shock front at the explosive-flying plate interface. To use another charge thickness, we would have by the way to change the thicknesses of all the material to keep this property. The flying plate is in steel or in magnesium to have different reflected shock intensities: it is about the same as the incident shock with magnesium (96 kbar) and about 180 kbar with steel.

The Figure 7 shows the experimental set-up.

The corresponding time-distance diagram (Figure 8) has been constructed by assuming the explosive as an inert material. The shock pressure histories on the back of the charge are summarized in Figure 9.

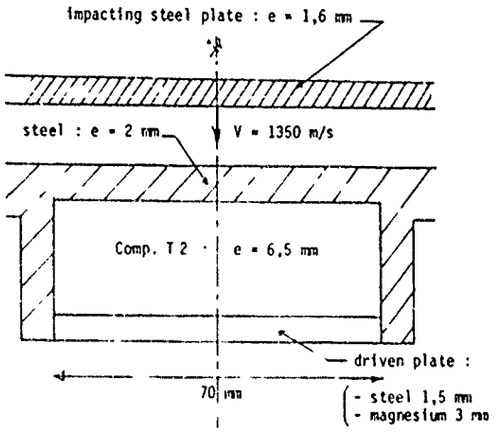

Fig. 7. Experimental set-up

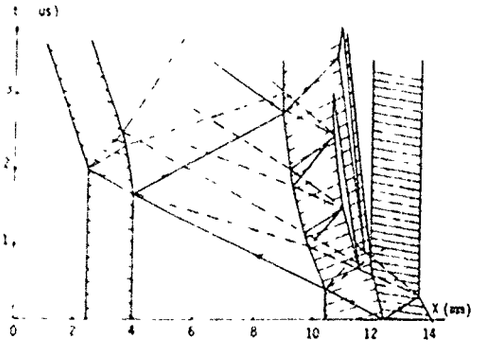

Fig. 8. Time distance diagram

Hydrodynamics calculations have been conducted with the KRAKATOA model of shock initiation. This model is able to deal with particular phenomena like, for instance, inhibition

(see appendix). It is necessary to model such experiments because of the reflected shock.This model is calibrated by computing the run distance to detonation as a function of shock pressure and has been successfully tested with short shock initiation experiments in the pressure range 100 kbar to 200 kbar (14). Earlier computations on the same kinds of experiments have shown we have to stop the decomposition whenever the pressure in the flow falls below 40 kbar. If we don't modify the rate form, the explosive charge burns completely and the terminal plate velocity is then much higher. This artifice doesn't violate the decomposition rate form which is calibrated above 75 kbar. The computations we present in this paper have been conducted with the same cut-off pressure. The same kind of experiments have been simulated by C.L. Mader with the multiple shock Forest Fire model (15) and by J. Wackerle with the "Direct Analysis Generated Modified Arrhenius Rate" (DAGMAR) form (16). This latter models likewise the terminal velocity by stopping the decomposition below 50 kbar.

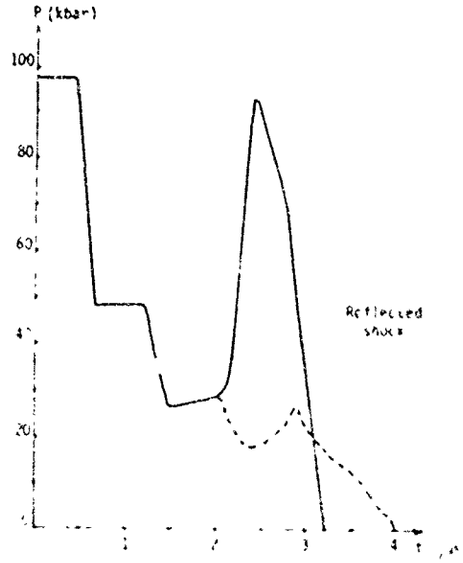

Fig. 9. Shock pressure histories on the rear of the explosive charge (1.5 mm thick driven plate in steel 3 mm thick driven plate in magnesium.)

Four experiments and four computations are presented here, two with a flying plate in steel and two with one in magnesium. As previously with Comp. X1, we calculate analytically a mean decomposition rate from the terminal velocity (appendix 1). The particle velocity histories are shown in Figures 10 and 11. The corresponding geometrical conditions and decomposition rates are summarized in Table 2.

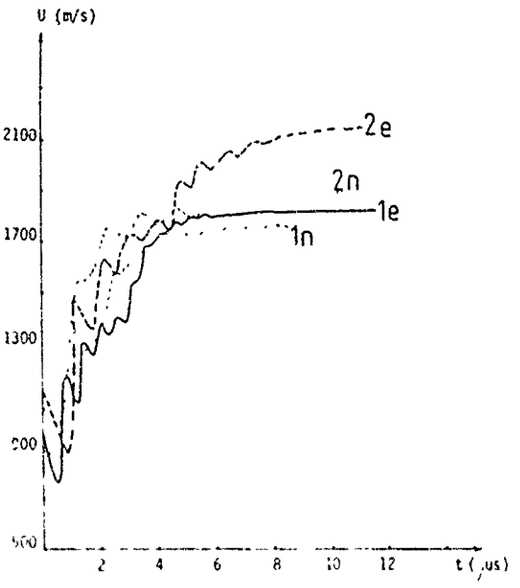

Fig. 10. Particle velocity histories obtained for steel driven plate (The corresponding geometrical dimensions are given in Table 2. The subscript e denotes experimental results and the subscript n denotes numerical results.)

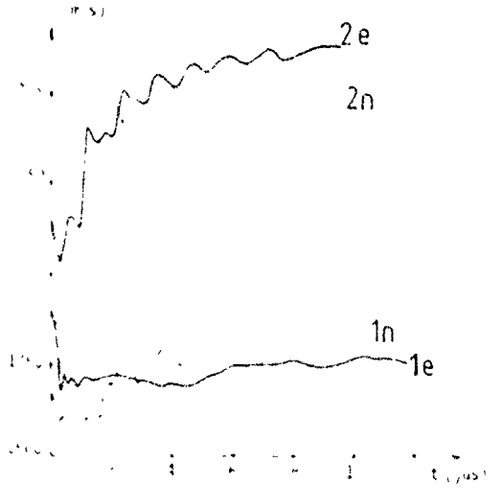

Fig. 11. Particle velocity histories obtained for a driven plate in magnesium (Geometrical dimensions are given in Table 2. The subscripts e and n denote experimental and numerical results.)

TABLE 2

	Geometrical dimensions	Driven Plate material	Decomposition Rate (%)
Figure 10, curve 1	See Figure 7	steel	56
Figure 10, curve 2	All demensions of Figure 7 multiplied by 1,5.	steel	100
Figure 11, curve 1	See Figure 7	magnesium	53
Figure 11, curve 2	All dimensions of Figure 7 multiplied by 1,5.	magnesium	76

In the two experiments with a 6,5 thick charge the measured initial velocity is equal to the one we obtain by considering the explosive as inert. It is greater with 9,75 mm thick charges, detonation would probably occur in a longer charge submitted to the same shock conditions. The rear rarefaction waves which overtake the shock front bring on a strong deceleration in the first microsecond. However it is less strong than the one we would observe if the explosive doesn't react. The interactions of these and the ones from the free surface reflected rarefaction waves involves fracture in the magnesium plates. The flyers are then accelerated by the process of compression and rarefaction throughout the flying of the plate. Spalls are closed and terminal velocities are attained in a few microseconds. In the experiments with steel flyers (curves 1e and 2e—Figure 10) we observe at 3 μs or at 4,5 μs the effect of the shock which is reflected from the rear steel cover-explosive interface.

The mean decomposition rate we calculate are about equal in the experiments with the thinner charges either with a steel plate or a magnesium one. The reflected shock seems to have no significant influence on the growth of chemical reactions just behind the shock front, and we observe a quenching of the rate when rarefaction is reflected into the reacting explosive. The 9,75 mm thick charge is completely decomposed when we have a steel flyer and only partially with magnesium one. This difference may be explained by being interested in the pressure histories at the flyer-explosive interface.

When we compare the experimental and the numerical results, which we obtain by stopping the decomposition below 40 kbar, we see the terminal plate velocity is well modeled in three experiments (see curve 1n—Figure 10 and curves 1n and 2n—Figure 11). In the fourth experiment (curve 2n—Figure 10), the computed final velocity is significantly lower. We conduct then a computation in the same geometrical conditions but without the 40 kbar cut-off pressure. We don't observe significant difference in the computed particle velocity history (but do with the other geometries). Indeed we have numerically a nearly total decomposition of the charge at pressure above 50 kbar. In the experiment the charge has decomposed more slowly and so the flyer has been pushed more isentropically. The measured final velocity is therefore greater than the computed one though the mean decomposition rate may be lower.

A more complete analysis of the results shows us our rate is too fast just behind the shock front and the growth of the chemical reactions doesn't depend on the local thermodynamical conditions. We may conclude that in the expression of our rate law: (see appendix 2) the number of hotspots we compute have too much authority though it provides computer simulations of many shock initiation data on Comp. T2. In future work we will try to take the temperature into account. Indeed we note that burning rates basically depend on an Arrhenius term in the solid-product interface temperature as in combustion theory (17). The difficulty remains the knowledge of such a temperature. It will be necessary to develop at first more physical

equations of state for the products and the solid explosive. Maybe we will also have to change some assumptions we made in the mixture.

ACKNOWLEDGEMENT

The authors thank G. Damamme and M. Missonnier for many informative discussions and E. Miette for his technical help.

REFERENCES

1. T.P. Liddiard, Fourth Symposium on Detonation.
2. B.G. Craig and E.F. Marshall, Fifth Symposium on Detonation.
3. J.E. Kennedy—J.W. Nunziato—D.R. Hardesty, Acta Astronautica Vol. 3 (1976).
4. L. Green—E. Niddick—E. Lee—C. Tarver, Symposium H.D.P. Paris (1978).
5. G.L. Nutt—L.M. Erickson, Shock Waves in Condensed Matter—Santa Fe (1983).
6. J Vorthman—J. Wackerle, Ibid.
7. S G. Cochran—C.M. Tarver, Ibid.
8. J. Wackerle—A.B. Anderson, Ibid.
9. G. Damamme—M. Missonnier, Seventh Symposium on Detonation.
10. L.M. Barker—R.E. Hollenbach, Rev. Sci. Instrum. 36, 1617 (1965).
11. D.D. Bloomquist—S.A. Sneffield, J. Appl. Phys. 54, 1717 (1983).
12. M. Durand—P. Laharrague—P. Lalle—A. Le Bihan—J. Morvan—H Pujols, Rev. Sci. Instrum. 48, 3 (1977)
13. J. Vanpoperynghe—J. Sorel—J. Aveillé-J. Adenis, this symposium.
14. J Adenis—H. Pujols—J. Sorel—J. Van poperynghe, Ninth International Pyrotechnics Seminar (1984).
15. C L. Mader—M.S. Shaw—J.B Ramsay Los Alamos report—LA 9053 MS (1981).
16. J Wackerle, private communication
17. F.H. Williams, Combustion Theory (Addition Wesley, Palo, Alto)
18. C Schwarz, Sandia Report, Sand 80-2372.
19. P L. Stanton, Explosive Driven Flying Plate Plane Wave Generator (University of Texas—1968).

APPENDIX 1

Mean decomposition rate of an explosive charge calculated from the terminal flyer velocity

A diagram of the experimental set-up is shown in the Figure 12.

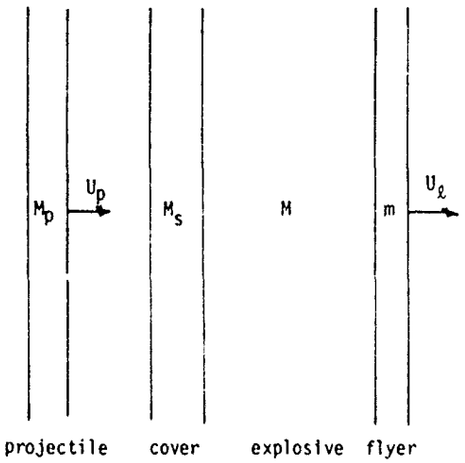

The final velocity of the flyer is calculated from the following identities (18)

$$U_\ell = U_\tau + V$$

$$V = \frac{2\,M_p}{M_p + M_s + m + M} \cdot U_p$$

(kinetic energy remains constant)

According to Stanton's formula (19), of the charge is completely decomposed ($\tau = 1$), we have:

$U = U(\tau = 1) = (2\,E_1)^{1/2}\, f(r, \lambda, A)$ with E_1 specific energy of the explosive

$$r = \frac{m}{M} \cdot \lambda = \frac{M_s}{M} \quad A = \frac{2r + 1}{2\lambda + 1}$$

$$f(V, \lambda, A) = \left[r + \lambda A^2 + \frac{1 - A + A^2}{3} \right]^{1/2}$$

If only a fraction is decomposed we write: $U = (2E_\tau)^{1/2}\, f(r,\lambda)$ with $E_\tau = \tau \cdot E_1$.

So the mean decomposition rate τ is obtain from U_ℓ with the following identity:

$$\tau = \frac{E_\tau}{E_1} = \left[\frac{U_\ell - V}{U_1} \right]^2$$

APPENDIX 2

KRAKATOA Model (9)

This model has been developed to predict the detonation and to describe the transient regime when an explosive charge is initiated by a shock wave.

According to the Z.N.D. scheme, we represent the detonation as a shock followed by chemical reactions which are expanding in a biphasic mixture (non reacted explosive and detonation products). The chemical reactions are represented by only one parameter which is the decomposition rate.

Physical Principles:

1) Rate law: the chemical reactions are initiated at certain detonation sites. It is assumed they are points and the reactions are propagation isotropically at a rate G. In this condition, analytical calculations give us for the rate law:

$$\frac{df}{dt} = N_o^{1/3} G (1-f) \left[-\ln(1-f)\right]^{2/3}$$

with - f decomposed explosive weight fraction

N_o detonation sites per volume unit, it is an increasing function of the shock intensity

G radial speed of growth.

For N_o and G we choose arbitrarily analytical expressions which are:

$-N_o^{1/3} = A \exp(I/Ia)$, I is a function which only depends on the first shock strength.

$G = p^b$

A, Ia and b are 3 coefficients which depend on the explosive composition. They are determined by computing the run detonation as a function of the input shock pressure (see ref. (13) for Comp. X1 and T2).

2) Biphasic zone: we assume the following identities: (subscript s is for solid explosive and subscript g is for the detonation gases)

- pressure: $P = Ps = Pg$
- specific volume: $V = (1 - f).Vs + f.Vg$
- total energy: $E = (1 - f).Es + f.Eg$

and $Es = es(Ps,Vs)$ where es(Ps,Vs) is a Mie Grüneisen E.O.S. calibrated on the Hugoniot.

$Eg = eg(Pg,Vs)$ where eg(Pg,Vg) is a J.W.L. E.O.S.

We assume we have an isentropic decomposition of the explosive and so es(Ps,Vs) = es(Vs).

3) Computations: in our computations, I is the work of the non reversing strengths after that the shock has passed. The 3 coefficients A, Ia and b are determined by computing the run to detonation and the excess transit time as a function of the shock pressure with a 1DL hydrodynamic code. the reactions start when the shock has passed in the cell. If we have more than one shock wave in an explosive charge, the second and the others interfere only on explosive decompositions in the radial speed of growth (G). So we deal with the inhibition.

PRESSURE VARIATION UPON INITIATION OF CAST RDX/TNT 50/50 CHARGE BY DIVERGING SHOCK WAVE

V.M. Titov, S.M. Karakhanov, S.A. Bordzilovsky
Lavrentyev Institute of Hydrodynamics
Siberian Division of the USSR Academy of Sciences
Novosibirsk 630090 USSR

Pressure evolution was investigated in a transient zone upon explosive initiation by a diverging shock wave. The detonation wave shape was controlled by streak-camera records. To measure profiles P(h,t) where h was the Lagrange distance, t time, strain compensated piezo-resistive gauges were used. The analysis of the form of profiles P(h,t) and pressure variation $P_s(R)$ along the shock trajectory R(t) showed that the flow parameters behind the hemi-shperical diverging detonation front monotonically changed, i.e. pressure decreased along the particle path and increased along the shock trajectory. To estimate the heat release rate along the shock trajectory, the generalized kinetic characteristic P was used related to flow derivatives. The estimates obtained from the experimental relations P(h,t) and $P_s(R)$ showed that the heat release rate along the shock trajectory $P_s(R)$ for 3.8 GPa to 21.5 GPa monotonically increased with increasing pressure for plane and diverging waves. Over the range P=(8÷17)GPa the relations $P_s(P)$ coincided for both cases. The peculiarities of $P_s(R)$ dependence for the direction at $\alpha=45^\circ$ to the initiating pulse and the maximum available on the failure curve were explained by the hydrodynamic loss related to the wave divergence

INTRODUCTION

An explosive initiation by shock waves in the regime close to a critical one is accompanied by a transient process which is characterized by a wide zone of a chemical reaction, much wider than that typical for a steady state detonation. Continuous measurements of flow parameters with the use of Lagrange gauges make it possible to obtain information on explosive decomposition kinetics (1-4). Variation of mass velocity and pressure derivatives in a reacting flow as well as the gradient sign of these values have been analyzed in (5).

The initiation dynamics is affected by the wave front curvature along with chemical kinetics (6). There are available the experimental works which suggest the results on continuous measurements of the shock front velocity upon initiation of a spherical diverging detonation, as well as the data on the particle velocity and pressure profiles in an asymtotical zone of the detonation development (7,8). In (4) the divergence effect was taken into account as a correction to the initiation in long cylindrical charges.

The present paper deals with the investigation of the pressure field in a transient zone when the cast RDX/TNT 50/50 charge is initiatied by diverging shock waves, with the wave front shape being close to a spherical one. To measure pressure, strain compensated manganin gauges were used (9). The goal of this paper is to compare the development of the RDX/TNT 50/50 initiation by diverging and plane detonation waves (10). To realize it, variation of gasdynamic parameters in the diverging shock waves was analyzed and the heat release rates in the zone adjacent to the front were estimated.

EXPERIMENT AND RESULTS

The experimental arrangement is shown in Fig. 1a. The cylindrical RDX/TNT donor charge whose length provides for the steady state detonation loads the RDX/TNT 50/50 test charge

through the PMMA gap 15 mm in dia. The amplitude of the pressure pulse induced into the test charge was varied by the gap length l. In the preliminary experiments the critical gap length l* was determined, at which the test charge 50 mm high, 90 mm in dia. could be initiated with 50% probability. Detonation or failure was defined with the use of the copper witness plate 5 mm thick. In these experiments l* =10.6 mm and ϱ=1.69 g/cm^3 (mean density of the test charge).

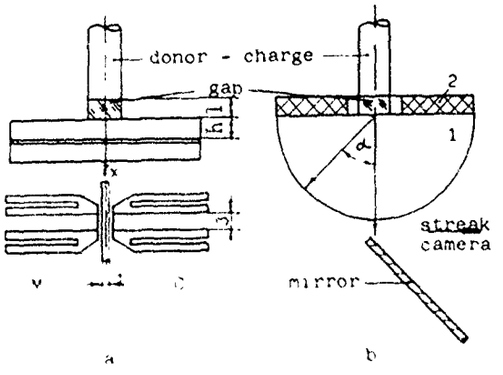

Fig. 1. Experimental arrangement a- measurements of P(h,t), b- measurements of the detonation wave shape. 1 - test charge, 2 - foam plastic ring, M - manganin, C - constantan elements.

The pressure profile measurements at the PMMA-test charge interface near the charge axis by the method described below give the peak pressure P_0=5.6 GPa with the exponential pressure decrease during τ=0.8 mcs at l=10.2 mm (Fig. 4, h=0). Over the range l=(8 - 10.6 mm) the experimental data for P_0 dependent on l were described by

$$P_0 = 22.09 \exp(-0.135\, l) \qquad (1)$$

with P_0 in GPa, l in mm. The detonation wave shape was determined by streak camera records as in (11). The test charge was of a hemispherical form (Fig. 1b). To eliminate the effect of the donor charge detonation products on a hemi-spherical detonation, a plane side of the hemisphere was protected by a foam plastic ring. The testing charge was placed inside the transparent vessel filled by argon. The obtained streak-camera records displayed detonation propagating along the donor-charge axis, the delay due to the passage of the diverging detonation through the test charge and the detonation wave at the emergence from the spherical surface. To increase resolution over the region close to the axis (α=0°), the mirror view was obtained. The streak camera records allowed in our experiment to control the detonation velocity in the test charge in the OX($\overline{D}_{ox}$) direction and time difference of the detonation wave emergence from the hemisphere surface dependent on α: $\Delta t(\alpha)=t(\alpha)-t(0)$. Besides, they enabled us to plot the shape of the detonation wave in the coordinates (r,α), where $R-r(\alpha)=\overline{D}_{ox}\Delta t(\alpha)$

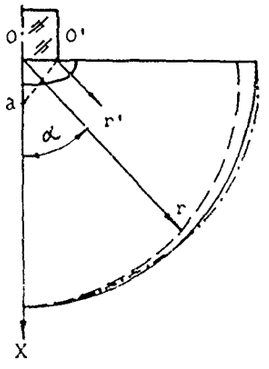

Fig. 2. Detonation wave shape
R = 50 mm - solid line,
P_0= 7.6 GPa - dashed line,
P_0= 7.5 GPa - dashed-dotted line

The results in Fig. 2 show that in the regime close to a critical one the detonation develops faster in the OX direction with $\overline{D}_{ox}$=6.6 km/s. In other directions the detonation delays, i.e. $\Delta t(45°)=-0.56$ mcs, $\Delta t(90°)=-1.18$ mcs. When the initiating pressure grows even insignificantly (up to P_0=7.5 GPa), the detonation wave shape becomes almost hemi-spherical with $\overline{D}_{ox}$ =7.3 km/s and a maximum $\Delta t(20°)$=0.18 mcs.

From here it follows that near the critical regime the wave shape is affected by the initiating pulse direction, and when the initiating pressure increases, the initiation phase configuration has an effect on the wave shape.

When the manganin gauges are used in a diverging flow, an additional change in resistance caused by stretching out the active element is observed. To distinguish the piezoresistive effect, it was suggested in (9) to make measurements under the same conditions by geometrically similar gauges comprising active

elements with different piezo-resistive coefficients. This principle has been used in the present paper. Manganin and constantan elements, 3×0.75 mm^2 in size, 20 mcm thick, lie in the same plane. Current leads were made of a copper foil, 20 mcm thick. The gauges were surrounded by a PTFE insulation (0.2÷0.3) mm thick. Their initial resistance was about 0.3 Ohm. The gauges were connected, according to a four-terminal scheme and were powered from the same current sources with I≈10A. Voltage output from each active element was subtracted at an output of a two-channel amplifier (Fig. 3).

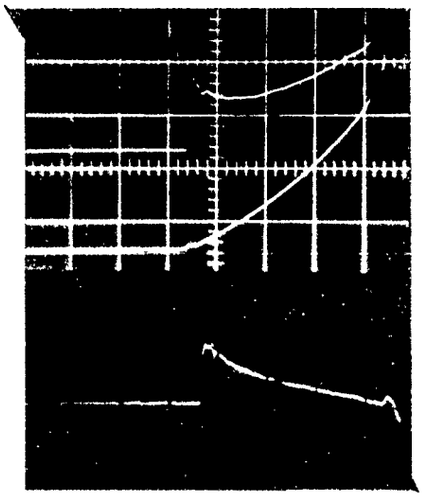

Fig 3 Voltage output from manganin and constantan elements. Lower trace-residual signal, 0.5μs div

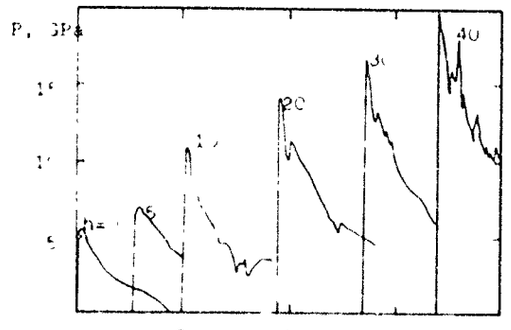

Fig 4 P(h,t) profiles for hemispherical diverging wave initiation in the OX direction

Signals were compensated at a zero pressure by the amplification of the constantan gauge channel

The relationship for the constantan piezo-resistance in plane shock waves can be described by (12):

$$k_c = d(\frac{\Delta R}{R_0})/dP = 1.43 \cdot 10^{-4}P(GPa^{-1}) \quad (2)$$

where $\frac{\Delta R}{R_0}$ is the fractional resistance change. Comparison with the piezo-resistivity coefficient for manganin, $k_m=2.94\times10^{-2}GPa^{-1}$, shows that at P≤10GPa the signal induced by the piezo-resistive constantan effect account for approximately 2.5% of the manganin signal. Thus the subtraction result (Fig. 3) can be regarded as a sufficiently exact pressure estimate. When the pressure range was 10 to 20 GPa, the measurement results were corrected taking into account the piezo-resistive effect of constantan $(\Delta R/R_0)_c\leq0.05(\Delta R/R_0)_m$. The oscilloscope records were satisfactory at P≤10 GPa. As is shown in Fig. 4, when P increases there is the depression on the signal fall which appears due to the detonatoin wave disturbance by an inert filler similar to the effect described in (10) for a steady-state detonation. When P≈10 GPa, a noise is observed on the signal fall (h=40), therefore the signals were smoothed before numerical processing. The pressure amplitude was measured by the manganin gauges with a relative error of 0.06 at P≤10 GPa and 0.1 at P=(10−20) GPa.

Three series of experiments with different initiating pressures were conducted. In the first series the profiles P(h,t) were recorded in different Lagrange coordinates h, in the regime close to a critical one with $P_0=5.6$ GPa. As may be seen from Fig. 4, pressure along the gauge trajectory, h=const, decreases throughout the region spanned by the gauges, $\partial P / \partial t<0$. Except for some increase in the pressure fall duration (from 0.8 mcs at h=0 to 2.5 mcs at h=40mm) the pulse profile is retained as h increases, and the pressure increases throughout the region behind the front, i.e $\partial P / \partial h>0$. The jump amplitude P_s along the shock trajectory R(t) increases too, $dP_s/dR>0$(Fig. 5.1). When the initiating pressure increases up to $P_0=7.5$ GPa, the features peculiar to the process do not change (Fig. 5.2). When the initiating pressure decreases below than a critical one, $P_0=5.4$ GPa, the dependence $P_s(R)$ becomes decaying (Fig 5.4) The maximum pressure available on this curve at R=5mm will be discussed below.

Curve 3 in Fig. 5 shows the $P_s(h)$ data in the direction $\alpha=45°$. In this case the gauge plane is perpendicular to the normal to the shock wave surface. The evolution of pressure P(h,t) along the axis $\alpha=45°$ is analogous to that along the axis OX when the pressure amplitude decreases by approximately 20% that testifies to the pressure distribution along the front with $dP_s/d\alpha<0$.

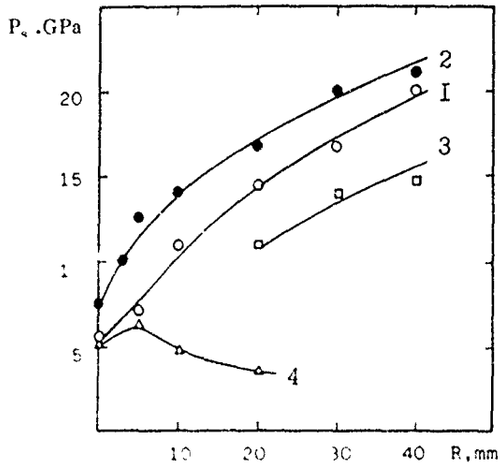

Fig. 5. The plot of shock amplitude vs shock trajectory. ▽ - 5.6 GPa, • - 7.5 GPa, Δ - 5.4 GPa, α=0, ○ - 5.6 GPa, α=45°

DISCUSSION

The streak camera records of the wave shape enable us to consider the flow near the shock surface to be a spherically symmetrical one to write the continuity and Euler equations as follows [13].

$$\frac{\partial V}{\partial t}=V_0\frac{1}{h^n}\frac{\partial}{\partial h}(r^n U) \tag{3}$$

$$\frac{\partial U}{\partial t}=-V_0\frac{r^n}{h^n}\frac{\partial P}{\partial h}, \tag{4}$$

where h is the Lagrange coordinate denoting the particle position before the front arrival, r=r(h,t) is the Euler coordinate connected with h by the condition $r^n dr\, V=h^n dh\, V_0$. U, P and V are the particle velocity, pressure and specific volume, respectively, the subscripts 0, s belong to the states before the shock and behind it, respectively. If the shock front trajectory is assumed to be dR=D(t)dt, where D is the shock wave velocity, the shock intensity variation (P_s or U_s) along the trajectory is connected with partial derivatives at the front

$$\frac{dP_s}{dR}=\frac{\partial P}{\partial h_s}+\frac{1}{D}\frac{\partial P}{\partial t_s} \tag{5}$$

$$\frac{dU_s}{dR}=\frac{\partial U}{\partial h_s}+\frac{1}{D}\frac{\partial U}{\partial t_s} \tag{6}$$

It follows from the experiment that $\partial P/\partial t<0$, $\partial P/\partial h>0$ throughout the region spanned by the gauges, and $dP_s/dR>0$ and $dU_s/dR>0$. Then it follows from (3), (4), (6) that in the flow behind the shock $\partial U/\partial h>0$ and $dV/dt>0$. In contrast to the case of initiation by a plane wave, where the flow derivatives behind the shock front change sign (5), in the given case all the flow parameters along the particle trajectory steadily change in time in the direction characteristic for the rarefaction wave. In the meantime, the shock wave intensity increases steadily along the shock trajectroy R(t). It can be concluded that the initiation ($dP_s/dR>0$) is governed by heat release in a narrow zone close to the shock or in the shock jump, according to the hypothesis suggested in (4). In the remaining flow the hydrodynamical losses associated with the expansion exceed the heat release rate. The structure and width (δ) of the heat release zone can not be resolved by gauges, however, for further estimates it can be assumed that $\delta<<\bar{D}\tau\approx5$ mm, where τ is the characteristic pressure pulse duration.

To estimate the heat release rate in the zone adjacent to the front, it is appropriate to use the approach [4, 14] at which the heat release rate is characterized by the generalized kinetic characteristic

$$P=\frac{\partial P}{\partial t}+c^2\frac{\partial V}{\partial t} \tag{7}$$

representing the pressure variation rate under adiabatic conditions at a constant volume. Equations (3), (4) (after transformation at $r^n\to R^n$, $h^n\to R^n$) and (5), (6) enable us to express $\partial V/\partial t_s$ through the values determined in the experiment, P_s, $\partial P/\partial t_s$, dP_s/dR. Conditionally, when transiting through the jump, $R>\bar{D}\tau>>\delta$ enables us to use the expression for a plane wave, $P_s=U_s D/V_0$. A final result, after substitution in (7), is

$$P_s=(n-1)\frac{\partial P}{\partial t_s}+\frac{nD}{U_s}\frac{d(P_s U_s)}{dR}+\lambda \tag{8}$$

where $n=\frac{c^2V_o^2}{D^2V^2}$, $\lambda=\frac{2nDP_s}{R}$,

c is the sound velocity. The first two terms in (8) describe the shock wave evolution, the third one λ takes into account the losses due to a spherical divergence of the wave. In an asymptotical zone if $R\to\infty$, $d(P_sU_s)/dR\to 0$) a main contribution to P_s is made by the first term containing the derivative $\partial P/\partial t_s$. In this flow the reaction zone width decreases, and because of an insufficient time resolution, it is possible to make estimation only for a stationary value of the heat release rate at the front (P_a).

Calculations for a plane initiation of RDX/TNT 50/50 are made using (6) and the oscillograms obtained in (10), and for a spherical case using the oscillograms presented in Fig. 4. This was done under the simplifying conditions with the Hugoniot $D=A+BU_s$, where A=0.249 cm/mcs, B=1.99, V_0=0.5882 (15). The sound velocity was estimated by the slope of the Hugoniot curve (16) with the Mie-Grüneizen equation of state:

$$\left(\frac{c}{V}\right)=-\left(\frac{dP}{dV}\right)_H+\frac{\Gamma}{2}\left[\left(\frac{P}{V}\right)_H+\left(\frac{V_o}{V}-1\right)\left(\frac{dP}{dV}\right)_H\right] \quad (9)$$

where $\left(\frac{dP}{dV}\right)_H$ is the slope of the Hugoniot curve. Γ is the Grüneizen parameter. To estimate Γ, the assumption $\Gamma V=\Gamma_o V_o$, Γ_o=0.947 was used (15).

The derivatives used in the calculations are listed in Tables 1,2. In the last line of Table 1 the values of $\partial P/\partial t_s$ are presented for the pressure profile in a steady-state regime with the maximum value of P_s from (10). Under the assumptions of the equation of state mentioned above the explosive behind the shock front is considered in the model of solid state as unreacted one. As a result, the maximum estimate for the sound velocity and P_a=335 GPa/mcs are obtained. If for estimating the sound velocity any of equations of state is used which describes the explosion products acceleration by the model of gaseous phase, we can obtain the lower estimate for the sound velocity and P_a=65 GPa/mcs. The sound velocity estimate in the model (17) taking into account a partial decomposition of the explosive behind the shock front gives P_a=75 GPa/mcs at P≈30 GPa. Due to a strong P_a dependence on the sound velocity, it is impossible to estimate an absolute value of the energy release rate without attracting additional experiments. However, it is appropriate to compare the $\dot{P}_s(P)$ dependences for the case of a plane and diverging wave with the estimation of the sound velocity by the simplified model. The $P_s(P)$ dependence for the plane case (Fig. 6.1) steadily increases up to 21.5 GPa and doesn't contain any peculiarities such as negative values of P_s in the region of low pressures for TNT (5). The profiles P(h,t) (10) do not allow to determine the $\dot{P}_s(P)$ dependences over the pressure range 21.5 to 30 GPa. The calculated data from (17) show, however, that this dependence passes through the maximum at pressures close to Chapman-Jouguet pressure.

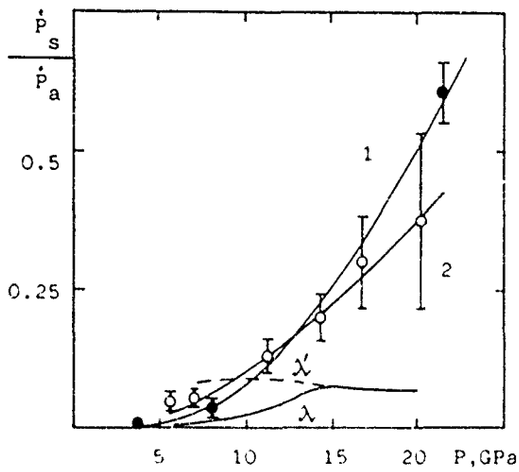

Fig. 6. Heat release rate at the shock front for plane (1) and hemi-spherical (2) wave. λ, λ' - spherical divergence losses

In the case of the geometry illustrated in Fig. 2 the diverging wave shape differs from a spherical one in the vicinity of an output side of the gap. The curvature radius of different wave parts depends on the wave propagation direction. The wave part propagating inside a cone where there is no effect of a lateral rarefaction has the same curvature radius $\bar{R}$ as the wave induced from the donor charge into the gap. Assume that $\bar{R}$=3.5d, where d is the donor charge diameter (18). The wave part in the vicinity of an angular point 0' propagating in the direction $\alpha=45^\circ$ can be characterized by the mean curvature radius equal to the coordinate R of the shock wave along OX. After passing the point a≈7.5 mm by the front, the curvature radius of the wave propagating along OX decreases

as approaching to R. The maximum on the failure curve (Fig. 5.4) can be associated with the increase in $\lambda(P)$. A top of this curve at R=5 mm testifies to the detonation decay after passing the point a. Beginning with R=20 mm, both directions are characterized by close mean curvature radii.

Under the assumption of a spherical shock of a uniform amplitude over the shock surface the dependences $\lambda(P)$ and $\lambda'(P)$ were estimated for the directions OX and O'r' respectively (Fig. 6.3). In calculations of $P_s(P)$ for a spherical wave (Fig. 6.2) the function $\lambda(P)$ was used. Curve 2 and curves $\lambda(P)$ and $\lambda'(P)$ show that at an initial stage the detonation is mainly developed in the direction OX, where the heat release rate is heat release rate does not exceed the divergence losses. This can take place due to a fast decrease in $\lambda'(P)$, decrease in P_s in the direction $\alpha=45°$ and re-distribution of energy over the shock wave surface, which is released in a central wave zone. Such an assumption is in qualitative agreement with the decrease in $P_s(R)$ along $\alpha=45°$ observed in the experiments (Fig. 5.3). The possibility of a partial decomposition of HE behind the shock with a small radius of curvature can be confirmed also by the experimental results (11).

Fig. 6 shows a correlation of the $P_s(P)$ dependences for plane and diverging hemispherical waves. The errors plotted in Fig. 6 take place when calculating by (6). When deter-

TABLE 1

Flow Derivatives and Heat Release Rate Along the Shock Path for Plane Wave

h, mm	P_s, GPa	$\frac{\partial P}{\partial t_s}$, $\frac{GPa}{mcs}$	$\frac{dP_s}{dh}$, $\frac{GPa}{mm}$	P_s/P_a
0	3.8	0	0.01	$(3\pm2)\times10^{-1}$
5	4.0	2.5	0.25	$(2.5\pm1.5)\times10^{-3}$
10	8.1	12.9	1.57	$(3.2\pm0.8)\times10^{-2}$
15	21.5	−19.4	4.03	0.61 ± 0.05
Stationary	31.4	−100	0	1

TABLE 2

Flow Derivatives and Heat Release Rate Along the Shock Path for a Hemi-Spherical Divergent Wave

R, mm	P_s, GPa	$\frac{\partial P}{\partial t_s}$, GPa/mcs	$\frac{dP_s}{dR}$, GPa/mm	$\bar{R}$, mm	λ, GPa/mcs	P_s/P_a
0	5.6	−8	0.3	50	2	$(4.6\pm0.8)\times10^{-2}$
5	7.0	−4.6	0.6	50	3	$(5.5\pm1.6)\times10^{-2}$
10	11.2	−10.4	0.5	30	11	$(1.3\pm0.3)\times10^{-1}$
20	14.4	−14.4	0.4	20	25	$(2\pm0.4)\times10^{-1}$
30	16.8	−30.5	0.26	30	21	0.3 ± 0.08
40	20.2	−37	0.13	40	23	0.37 ± 0.16

several times in excess of the divergence losses. In the direction $\alpha=45$ Curve 2 intersects the function $\lambda'(P)$ at $P\approx10$ GPa. Since the experiments were carried out under critical conditions with $P_0=5.6$ GPa, in the direction $\alpha=45$ there can arise the conditions $\lambda'(P)\geq P_s(P)$. When they are satisfied and $\partial P/\partial t_s$ is negative, it follows from (8) that $d(P_sU_s)/dR<0$, i.e. the wave in the direction $\alpha=45$ decays. The wave decays in a lateral direction as long as the mining $\partial P/\partial t_s$, values of 0.08 and 0.1−0.3 are assumed to be relative errors for a plane and hemi-spherical case respectively. Within these errors, curves 1 and 2 coincide over a pressure range of (8−17) GPa and diverge in the region of high and low pressures This can be caused by, first, the dependence of the reaction rate on the pressure profile following the shock (4). In the cases under consideration the wave profiles following the shock differ, for a plane initiation

this is a compression wave with the following change sign $\partial P/\partial t_s$, for a hemi-spherical case this is a rarefaction wave. The second possible cause is an error in determining P_s and $\partial P/\partial t_s$ due to amplitude distortions. The Hugoniots of TNT/RDX 50/50 and PTFE differ by ⩽4% in the pressure range ⩽20 GPa, so the main source of errors is a perturbation of the initial process by an inert layer, and peak pressure decay for profiles with a negative sign of $\frac{\partial P}{\partial t_s}$. Numerical estimates show that for $\partial P/\partial t_s = -80$ GPa/mcs the peak pressure P_s decreases by 10% at an insulation layer of 0.4 mm. In the case of a plane shock the value of $\partial P/\partial t_s$ is small in a transient zone, and the amplitude distortions can be neglected. However, in the diverging shock wave $\partial P/\partial t_s$ is high throughout the transient zone, that causes a systematic error. An accuracy of determing $\partial P/\partial t_s$ might be increased by means of numerical modelling of the pressure pulse transformation in the inert layer.

CONCLUSION

The results of this paper show that the flow parameters behind the hemi-spherical diverging detonation wave steadily change: the pressure decreases along the Lagrange particle path and increases along the shock front trajectory. The initiation process is governed by the heat release rate close to the shock front. The dependence of the generalized kinetic heat release characteristic, $P_s(P)$ steadily increases with pressure over the range up to 20 GPa for both plane and hemi-spherical waves. Over the range P=(8 – 17) GPa these dependences coincide. The peculiarities in the dependences $P_s(R)$ for the direction of 45° to the initiating pulse and the maximum available on the failure curve are explained by the effect of hydrodynamical losses due to wave divergence.

REFERENCES

1. G.I. Kanel, A.N. Dremin, "Decomposition of Cast TNT in the Shock Waves", Fizika Goreniia i Vzryva", Vol. 13, No. 1, pp. 85-91, 1977.
2. J. Wackerle, J.O. Johnson and P.M. Halleck, "Shock Initiation of High Density PETN", Sixth Symposium (International) on Detonation, pp. 20-28, ACR-221, Arlington, Virginia, 1976.
3. J. Wackerle, R. Rabie, M. Ginsberg, A. Anderson, "A Shock Initiation Study of PBX-9404", Symposium H.D.P., p. 127, Paris 1978.
4. V.S. Torfimov, G.P. Trofimova, "On a Possibility of Decomposition of Cast TNT in Shock Wave", Fizika Goreniia i Vzryva, Vol. 16, No. 2, pp. 92-99, 1980.
5. M. Cowperthwaite and J.T. Rosenberg, "A Multiple Lagrange Gage Study of the Shock Initiation Process in Cast TNT", Sixth Symposium (International) on Detonation, pp. 786-793, ACR-221, Arlington, Virginia, 1976.
6. P. Chen, J. Kennedy, "Chemical Kinetic and Curvature Effects on Shock Wave Evolution in Explosives", Sixth Symposium (International) on Detonation, pp. 379-388, ACR-221, Arlington, Virginia, 1976.
7. R. Chéret and G. Verdés, "Divergent Spherical Detonation Waves in a Solid Explosive", Fifth Symposium (International) on Detonation, pp. 31-40, ACR-184, Pasadena, California 1970.
8. A.A. Vorob'ev, "Spherical Detonation Development in Condensed Explosives", In: Khimicheskaya Fizika Processov Goreniia i Vzryva. Detonatsiya, Chernogolovka, 1980.
9. A.N. Dremin, G.I. Kanel, V.D. Gluzman, "Experimental Studies of Pressure Profiles in Regular Reflections of Cone Shock Waves in Plexiglass Cylinders", Fizika Goreniya i Vzryva, Vol. 8, No. 1, pp. 104-109, 1972.
10. S.A. Bordzilovsky, V.F. Lobanov, S.M. Karakhanov, "Transient Processes at Shock Initiation of Cast RDX/TNT Charges and HMX-RDX Ones", Fizika Goreniya i Vzryva, Vol. 19, No. 4, pp. 136-139, 1983.
11. F. Bonthoux, F. Deneuville, Y. de Longueville, "Diverging Detonations in RDX and PETN Based Cast-Cured PBX", pp. 408-415, Seventh Symposium (International) on Detonation, NSWC MP 82-334, White Oak, Silver Spring, Maryland, 1981.
12. G.I. Kanel, "Use of Manganin Gauges for Measuring Pressures in Shock Compressed

Condensed Media", VINITI, No. 477-74, 1974.

13. Ya.B.Zel'dovich, Yu.P.Reiser, "Physics of Shock Waves and High-Temperature Hydrodynamical Phenomena", Moscow, "Science", 1966.
14. T.J. Ahrens, G.E. Duvall, "Stress Relaxation behind Elastic Shock Waves in Rocks", J. Geophys, , Vol. 71, No. 18, pp. 4349-4360, Sep. 1966.
15. B.M. Dobratz, LLNL Explosives Handbook, "Properties of Chemical Explosives and Explosive Simulants", Lawrence Livermore Laboratory, California, 1981, UCRL-52997.
16. L.V. Al'tshuler, A.A. Bakanova, I.P. Duduladov, "Effect of Electron Structure on the Compressibility of Metals Subjected to High Pressures", J. Exp. and Theor. Phys., Vol. 53, No. 6, p. 1967, 1967.
17. V.M. Titov, V.F. Lobanov, S.A. Bordzilovsky, S.M. Karakhanov, "Determination of Transient and Kinetic Characteristic in Simulating RDX/TNT 50/50 Charge Initiation". This Symposium.
18. C.H. Yohansson and P.A. Persson, "Detonics of High Explosives", Academic Press. London and New York, 1970.

EXPERIMENTAL STUDY OF SPHERICALLY DIVERGING DETONATION WAVES

J. Aveillé, J. Baconin, N. Carion, J. Zoé
Commissariat à l'Energie Atomique
Centre d'Etudes de Vaujours
B.P. 7 - 77181 Courtry - France

We experimentally study spherical diverging detonation waves which are intrinsically unsteady. For this, we have designed a special explosive device called "LOGOSPHERE" which provides good measurements of diverging detonation celerity for detonation wave radii from 70 mm to 230 mm. Three different explosives HMX and TATB compositions were tested. We fit the data by means of a linear relationship between the detonation celerity and the curvature of the wave
The results compare favorably to those obtained in the axisymmetric case of explosives cylinders.

INTRODUCTION

The Chapman-Jouguet detonation D_* is a major physical constant of a given explosive and therefore deserves a large experimental effort. Theoretical studies show the actual importance of detonation celerity radius data on spherically diverging and converging detonation waves.

The most common part of this effort deals with the propagation along the axis of an explosive cylinder initiated at one end. It is experimentally proved that the ignition system no longer influences the propagation of the wave beyond some run and that the steady celerity D depends only on loading density, cylinder diameter ∅ and initial termperature. Moreover it is usually assumed that one gets an estimation of D_* by extrapolating D(1/∅) to infinite diameter This extrapolation procedure remains however questionable because of the unknown behavior of lateral boundary conditions at infinite diameter

On the contrary, it is well demonstrated by R Chéret in (1) that the spherically diverging detonation celerity asymptotically goes to D_* when the radius increases towards infinity.

Many years ago experiments on such propagations have been achieved in some RDX-TNT compositions (1) in nitromethane (2) by means of optical diagnostics, and recently in HMX, TATB and TATB/HMX compositions (3).

In this work we experimentally study the celerity-curvature relationship in solid explosives for spherically diverging detonation waves which are intrinsically unsteady. We have designed a special explosive device called "LOGOSPHERE" which provides a well defined spherically diverging detonation wave and allows the measurement of the detonation path by means of gauges without any perturbation to the spherical symmetry.

Our experimental celerity-curvature relationship obtained with this "LOGOSPHERE" method is favorably compared to the one obtained in the axisymmetric case of cylinders of the same heterogeneous solid high-explosives. We have performed a series of experiments to measure detonation celerity for spherically-diverging detonation waves in three solid explosives listed in the following table.

Explosive	% (weight)	Grain-size (μm)	Density (g.cm^{-3})
X1	96 HMX	<630	1,822
T1	95,5 TATB	40/60	1,880
T2	97 TATB	40/60	1,855

EXPERIMENTAL SET-UP

1. "LOGOSPHERE" explosive arrangement.

The explosive arrangement is axisymmetric, the explosives under investigation are machined in such way that the meridian of the outer boundary is a logarithmic spiral whose polar equation is:

$$R = R_a \cdot e^{\alpha \operatorname{tg}\Theta}$$

(α is the polar angle between $-\pi/2$ and $+\pi/2$, R is the polar radius, R_a is a constant, Θ is a constant angle made by spherical detonation wave with boundary). Figure 1.

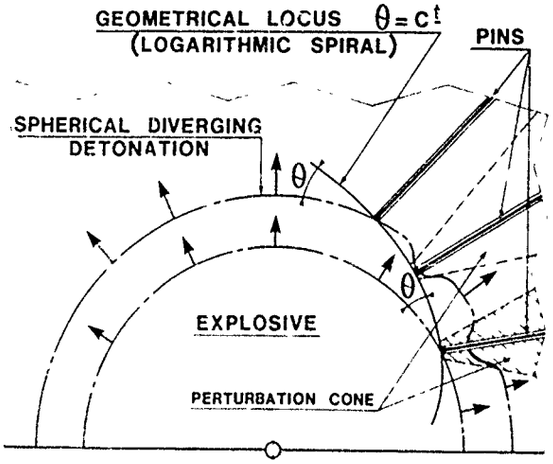

Fig. 1. Rule of Experimental Set-up

The angle Θ is the constant angle between the front of spherically diverging detonation and the explosive's meridian. It is small enough to avoid any perturbation on detonation propagation. In our experiments $\Theta = 20°$ and $R_a = 131.21$ mm

For obvious reasons we call such devices "LOGOSPHERES". The explosive is confined by an aluminum shell used as gauge support.

The detonation wave is initiated at point R= 0 by means of two E.B.W. detonators facing each other into two holes machines towards the center of explosive.

To initiate TATB explosives T1 and T2 it is necessary to use E.B.W. detonators associated with an HMX spherical booster. The experimental arrangement is shown in Figure 2.

Some complementary shots of small spheres initiated by means of such a system have been carried out to check the sphericity and to choose the observation loci. These shots show that the main problem is to avoid the different pieces (logosphere - pins support, booster and detonator) being out of true.

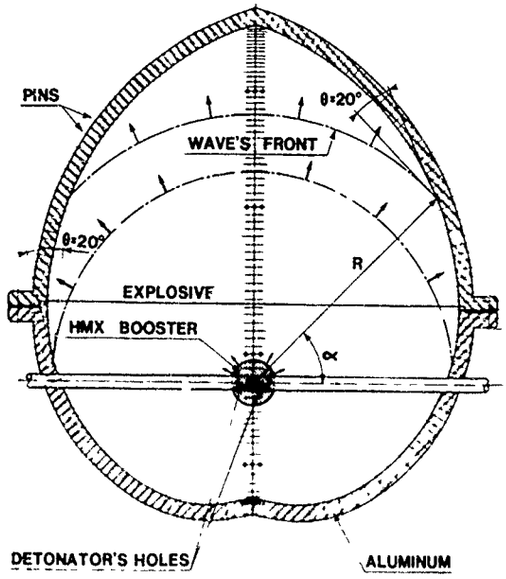

Fig.2. Logosphere Explosive Device

2. Measurements

Our experimental program aims at determining the (R,t) path of spherically diverging detonation initiated at the initial radius R = 0 of the explosive logosphere. The measurements consist in recording the time t_1 (within ± 2ns) at which the wave reaches predeterminated locations R_1 (within ± 0,01mm). The arrival times of detonation on the outer boundary are recorded by means of two pin methods.

One records the signal generated by short-cut of ionization gauges, for this we use three chronometers ± 1.10^{-9}s resolution (Thomson-CSF). The other technic records the light provided by optical fibers gauges on five electronic streak cameras – TSN 503 Thomson-CSF — with an appropriate nose.

Two series of gauges are used, for each shot, and located at up to 80 different values of the radius from R ≃ 70 mm to R ≃ 230 mm. An aluminum confinement is used as support for gauges which are located in a plane perpendicular to the axis of the detonator holes. Figure 2.

3. Reduction of the Data.

For spherical diverging detonations we assume the existence of a relation between curvature and celerity, as it was suggested for instance in (1) and (4):

$$D^S = \frac{dR}{dt} = D^s_* \left(1 - \frac{A}{R}\right) = D^S_* \ (1-AC) \quad (1)$$

t is the time, R is a wave radius, D^s is the detonation celerity at radius R. This relation (1), after integration gives a t (R) relation:

$$t\text{-}t_0 = \frac{1}{D^s_*} \left[R\text{-}R_0 + A \ \mathrm{Log} \frac{R\text{-}A}{P_0 - A} \right] \quad (2)$$

t_0 and R_0 are constant.

We fit experimental data (t_i, R_i) with Eq. 2. by use of a least squares method. This gives the D^s_*, R_0 and A values.

It could be possible to use the same method with a second order development:

$D^s = D^s_* \ (1 + A'C + A'' C^2)$ $C = \frac{1}{R}$ is a curvature of detonation wave - but the range of variation of the radius R_i is too small in our experiments ($70 < R_i < 230$mm) and celerity does not vary enough to need development beyond first order.

An example of experimental values (t_i, R_i) obtained with TATB composition T2 are plotted in Fig. 3.

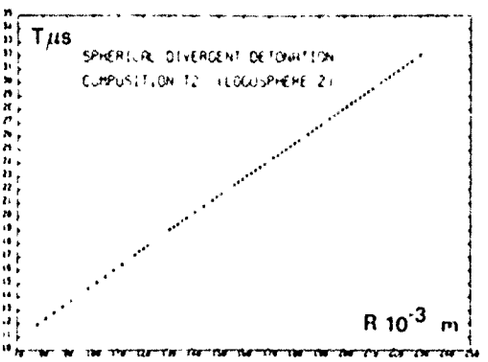

Fig 3. Time history T vs $(R\text{-}R_0)$ for Spherical Diverging Detonation Wave

The coefficients of the celerity curvature relationship (Eq. 1) are calculated for both series of measurements. For each shot we thus get two straight lines. They are averaged in order to take into account misalignment problems. The values D^s_* and A reported in table (2) are mean values obtained in two different shots.

TABLE 2.
Coefficients of celerity-curvature relationship
$D^s = D^s_* (1\text{-}AC)$ for 3 compositions

Explosive	D^s_* (m.s^{-1})	A (m)
X1 (HMX)	8802 ±20	$(0{,}877 \pm 0{,}46).10^{-3}$
T1 (TATB)	7737 ±15	$(2{,}891 \pm 0{,}03).10^{-3}$
T2 (TATB)	7680 ± 12	$(2{,}481 \pm 0{,}01).10^{-3}$

In Figure (4) we have plotted D^s/D^s_* versus reciprocal radius detonation wave ($\frac{1}{R} = C$).

It may be noticed that the reduction in spherically diverging detonation celerity at small radius ($R \simeq 70$ mm) is more pronounced for TATB compositions where it averages to a 3-4% decrement from D^s_*. In HMX composition X1 the decrement is only about 1,25%.

The spherical diverging detonation celerity D^s appears to approach smoothly the infinite-radius detonation celerity D^s_* in HMX composition while it is still rising sharply in TATB compositions.

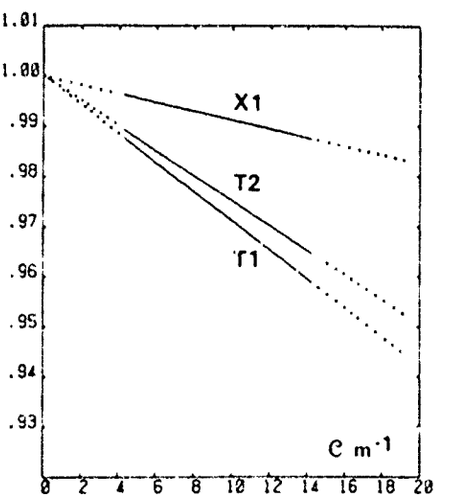

Fig 4. D^s/D^s_* vs $C = 1/R$

COMPARISON WITH AXISYMMETRIC MEASUREMENTS

We will compare spherical diverging detonation results with those obtained by means of axisymmetrical measurement of celerity in steady state detonation achieved with identical high explosives (5), (6). By means of electronic and optical methods we have performed experimental programs on right circular cylinders of H.E. (X1, T1, T2) in different diameters: between 3 to 200 mm for HMX composition X1 and 9 to 200 mm for TATB compositions T1, T2.

Measurements provide the detonation celerity D^p at each diamter (Ø) and the shape of detonation front is recorded by the streak camera. The curvature radius R_c on the axis of rods is obtained by fitting all points of record shape between (-Ø/4, +Ø/4) in best approximation by a circle.

When summarising the results of this axisymmetrical experiments we can observe that diameter effect curves obtained differ for HMX (X1) with concave downward in all diameter, and for TATB compositions T1 and T2 with concave upward with diameter up to near 15 mm. We have fitted results by a polynomial form in $(1/Ø)^3$ and $(1/R_c)^3$ for TATB compositions. For HMX composition the polynomial form is in $(1/Ø)^2$ and $(1/R_c)^2$.

Extrapolating to infinite diameter and infinite curvature radius we obtain the values of corresponding infinite celerity D^p_∞ and D^c_∞ reported in Table 3, where we write also the values of the infinite-spherical diverging celerity D^s_*.

Explosive	D^p_∞ m/s	D^c_∞ m/s	D^s_* m/s
X1	8789 ± 10	8783 ± 12	8802 ± 20
T1	7737 ± 15	7729 ± 20	7737 ± 20
T2	7732 ± 10	7735 ± 20	7680 ± 12

Table 3

We can see a very good agreement between this different values 0,2% for HMX and 0,6% for TATB

Results of measurements obtained in cylinder experiments are plotted in Fig. 5 $\frac{D^p}{D^p_\infty}$ versus reciprocal - diameter (1/Ø) and Fig. 6 $\frac{D^c}{D^c_\infty}$ versus reciprocal - curvature radius ($1/R_c$) of the detonation front.

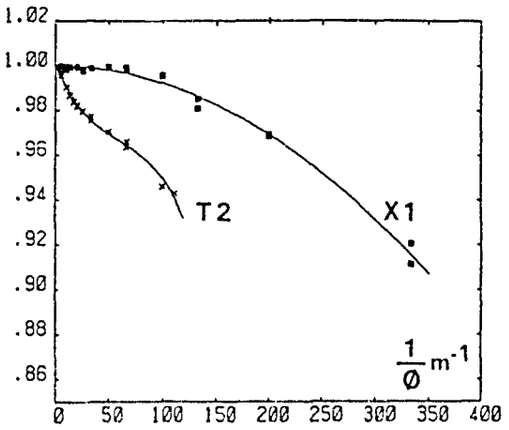

Fig. 5. D^p/D^p_∞ vs 1/Ø

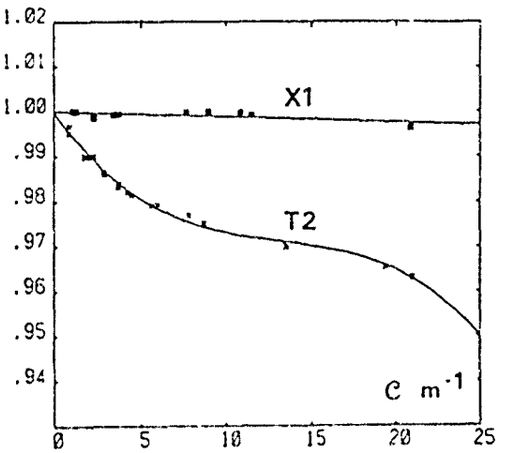

Fig 6. D^p/D^p_∞ vs C

For each composition we have drawn Fig. 7-8 and 9 the curvature effect curves obtained by plotting detonation celerity spherical D^s and axisymmetrical D^p versus the reciprocal radius of curvature of detonation wave.

It may be noticed that for smaller curvature (large curvature radius) spherical and cylinders experiments give practically the same values of celerity. But for larger curvatures (R_c small), the detonation celerity in the cylinder is significantly higher. These curves indicate different effects on the hydrodynamic behavior of detonation for a steady flow in a two-dimensional geometry and

for unsteady flow in a one-dimensional geometry; these two methods leading nevertheless to very consistent limiting values.

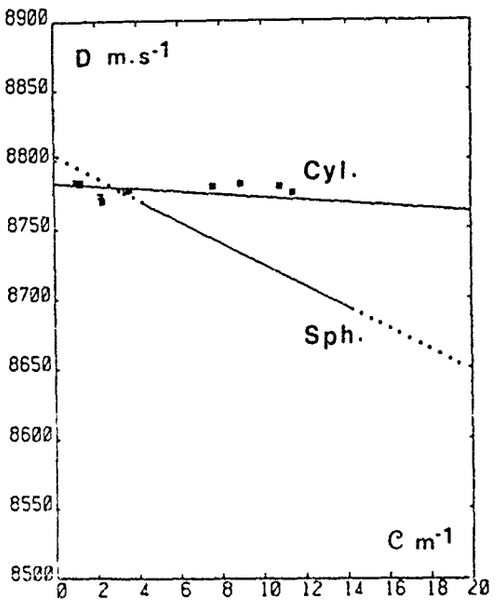

Fig 7 D vs C COMP.A1
Spherical & Cylindrical Results

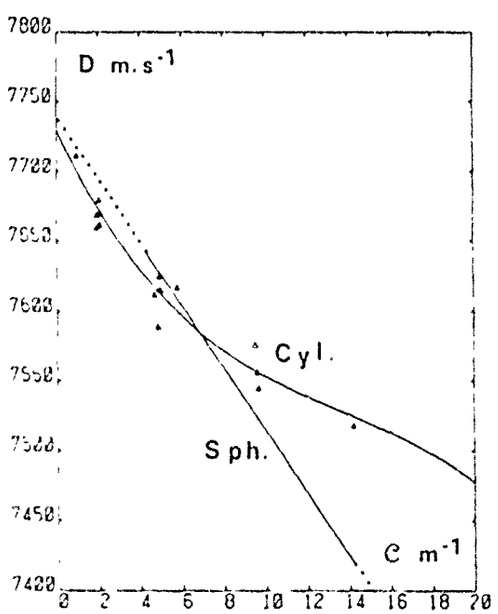

Fig 8 D vs C COMP.T1
Spherical & Cylindrical Results

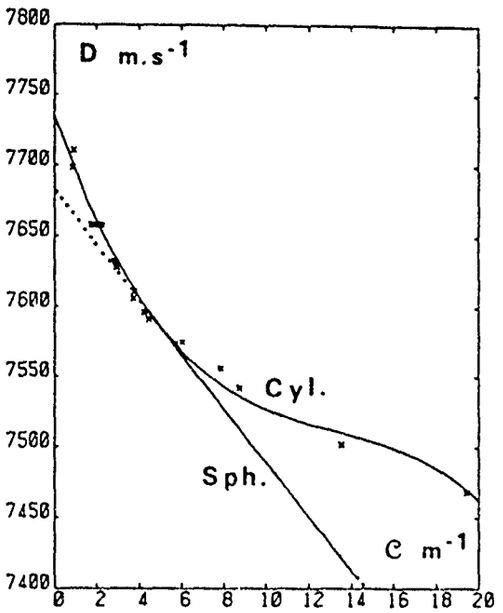

Fig 9. D vs C COMP.T2
Spherical & Cylindrical Results

CONCLUSION

We have described the "LOGOSPHERE" method which provides spherical diverging detonation wave velocity measurements with large variations of the wave radius - 70 - 230 mm. We have found a different behavior of spherical diverging detonation waves in TATB composition compared to those in HMX composition. In particular for small curvature radius of detonation wave, the decrement between infinite celerity D_*^* corresponding to infinite radius curvature is about 3-4 % for TATB and only 1,25 % for HMX composition.

A comparison made with axisymmetric detonation wave velocity measurements for the same compositions by means of curves D versus curvature shows a different behavior in the two geometries.

The axisymmetric wave gives a steady flow, the spherical diverging detonation gives an unsteady flow. We can notice the good agreement between the different velocities obtained by extrapolating to infinite values of curvature.

ACKNOWLEDGMENTS

Critical and helpful comments on this paper by R. Chéret are very gratefully acknowledged. Sincere thanks are also due to P. Veyrié for his strong encouragements.

REFERENCES

1. R. Chéret "Contribution à l'Etude des détonations Sphériques Divergentes dans les Expolosifs Solides". Thèse de Doctorat ès Sciences - Poitiers 1971.

2. R. Chéret and G. Verdes (1970) "Divergent Spherical Detonation Waves in a Solid Explosive" - Fifth Symposium (International) on Detonation. Office of Naval Research A.C.R. 184 - Pasadena, CA, 31-39.

3. K.L. Bahl. R.S. Lee and R.C. Weingart (1983) L.L.N.L. "Velocity of Spherically - Diverging Detonation Waves in RX-26-AF, LX-17 and LX-10," Shock Waves in Condensed Matter - Santa Fé (p.559-562) J.R. Asay, R.A. Graham, G.K. Straub, Editor 1984.

4. L. Brun, R. Chéret and J. Vacellier (1978) "Considération sur les détonations fortes". Symposium High Dynamic Pressure - Paris 1978 - p. 269.

5. J. Aveillé. J. Baconin, R. Chéret et al (1982). "Célérités de Détonation et Profondeurs d'Amorcage de deux Compositions Explosives à base d'Octogene et de TATB". Colloque International de Pyrotechnie Fondamentale et Appliquée - G.T.P.S. - Arcachon - Octobre 1982 - (396-411).

6. J. Aveillé, J. Baconin and J. Zoé (1984) "Experimental Study of the Spherical Diverging Detonation," 12th Symposium (International) on Explosives and Pyrotechnics - March 13-15 - 1984 San Diego, California.

Session III
REACTION ZONES II

Chairman: Ding Jing
Beijing Institute of Technology
Charles L. Mader
Los Alamos National Laboratory

A THEORETICAL ANALYSIS OF THE SHAPE OF A STEADY AXISYMMETRICAL REACTIVE SHOCK FRONT IN CYLINDRICAL CHARGES OF HIGH EXPLOSIVE, A CURVATURE–DIAMETER RELATIONSHIP.

F. Chaissé, J.M. Servas, J. Aveillé, J. Baconin, N. Carion, P. Bongrain
Commissariat á l'Energie Atomique–
Centre d'Etudes de Vaujours
B.P.n°7–77181 Courtry–France

We analyse the shape of an axisymmetric steady detonation front in high explosive using the natural coordinate system. Thus the flow equations associated with the jump relations allow to write two differential equations governing the shape of the front. The radius of curvature on the axis is an unknown parameter of their solution. Its value is determined by matching the calculated front with the experimental one within $2{,}10^{-1}$ mm. A comparison of the thicknesses of the reactive layers in TATB and HMX compositions is achieved through a relationship joining the radius of curvature on the axis, the layer thickness and the unconfined charge diameter.

INTRODUCTION

Studying the detonation wave in a right circular cylinder of high explosive, J.B. Bdzil (1-2) builds a mathematical statement of the reaction zone behind the shock whose solutions lead to a determination of the shock locus. Here we propound an other approach of the shape of the reactive shock front based on a transverse analysis of the physical variables in the infinitesimal neighborhood of the shock front. In the first part of the paper, a mathematical treatment of the flow equations, associated with the jumps relations, leads to write two differential equations governing the front shape. As is well explained, for instance by W. Fickett and W. Davis (7), the complete determination of the flow structure is extremely difficult. Here a special assumption allows the determination of front shape in term of the radius of curvature on axis. The second part shows how the proper radius yields a calculated front within 2.10^{-1} mm (inside 90% of the cartridge diameter) of the experimental one on TATB and HMX compositions. Finally, our analysis technique is used to derive a relationship between the "reaction zone" thickness, the radius of curvature on axis, and the diameter of the charge.

GENERAL NOTATIONS

Taking into account the axial symmetry, we work in a meridian plan and the following notations are used in this paper:

- M: point of the flow located just behind the shock Σ
- ox: axis of the flow
- or: axis of the radial coordinate
- ℓ: natural coordinate along the streamline
- n: natural coordinate along the normal to the streamline
- t: time
- u: magnitude of velocity
- D: celerity of detonation
- $u_\perp$: magnitude of velocity perpendicular to the shock surface
- $u_{//}$: magnitude of velocity parallel to the shock surface
- τ: coordinate along the shock
- χ: deviation's angle of the streamline through the shock $(\vec{ox}, \vec{u})$
- Ψ: normal inclination of the flow before the shock
- β: inclination's angle of the shock at point M $(\vec{ox}, \vec{\ell t})$; $(\Psi + \beta = \frac{\pi}{2})$

$\frac{I}{R} : \frac{d\chi}{dl}$: local curvature of the streamline

$\frac{1}{R_c} = \frac{d\beta}{d\tau}$: local curvature of the shock

P : :local pressure

v : specific volume

ϱ : denisty ($\varrho \cdot v = 1$)

ϱ_o : denisty of inert explosive

λ : explosive reaction progress variable ($o \leqslant \lambda \leqslant 1$)

$\frac{d\lambda}{dt}$: chemical rate

e : specific internal energy [$e = e(p,v,\lambda)$]

c : frozen sound speed

$H_{vp} = -\left(\frac{\partial e}{\partial \lambda}\right)_{v,p}$ Specific heat effect of the reaction at constant pressure and volume

$G_{\lambda o} = = v\left(\frac{\partial P}{\partial e}\right)_{v,\lambda = o}$: Grüneisen coefficient behind the shock

G_o : Grüneisen coefficient of the inert explosive

A;B : Classical, experimental coefficients of the linear relationship between shock and partical jump velocity

$Mo = \frac{D}{A}$: Initial Mach number

ϕ : diameter of the unconfined charge

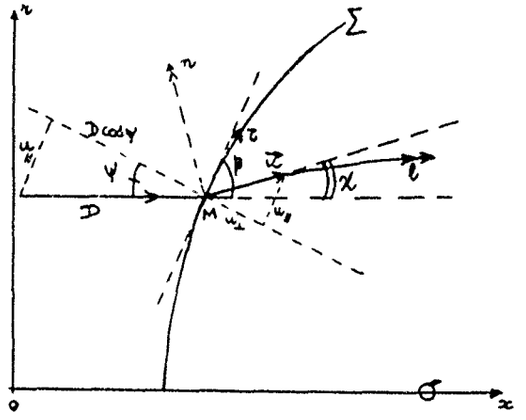

Fig. 1. Geometrical representation of some notations previously defined

Relationship Between the Streamline Curvature and the Shock Front Curvature

The flow equations, written for a cylindrically steady flow, in the natural coordinates fixed to a point M of the streamline are:

$$\text{(mass)}\quad \frac{\partial \pi u}{\partial t} + \pi u\left[\frac{\sin\chi}{r} + \frac{\partial \chi}{\partial n}\right] = 0 \qquad (1)$$

$$u \cdot \frac{\partial u}{\partial t} + \frac{1}{\varrho} \cdot \frac{\partial p}{\partial t} = 0 \qquad (2)$$

$$\text{(momentum)}\qquad \frac{u^2}{R} + \frac{1}{\varrho} \cdot \frac{\partial p}{\partial n} = 0 \qquad (3)$$

$$\text{(energy)}\qquad de + p \cdot dv = 0 \qquad (4)$$

The relation (4) may be written:

$$dp = c^2 dp + \left(\frac{\partial p}{\partial \lambda}\right)_{\varepsilon,\theta} \cdot d\lambda \qquad (5)$$

$$\text{with } c^2 = v^2\left(\left[\frac{\partial e}{\partial v}\right)_{p,\lambda} + p\right] / \left(\frac{\partial e}{\partial p}\right)_{v,\lambda}.$$

Now, using (2), we express the pressure along a streamline by:

$$(c^2 - u^2)\frac{\partial p}{\partial t} + u\left[c^2 \frac{\partial \varrho u}{\partial t} + p^*\right] = 0 \qquad (6)$$

where

$$p^* = u\left(\frac{\partial p}{\partial \lambda}\right)_{e,v} \cdot \frac{\partial \lambda}{\partial t} = p \cdot H_{vp} \cdot G_{\lambda o} \cdot \frac{d\lambda}{dt} \qquad (7)$$

characterizes the effect of chemical process conversion on the flow, and is proportional to the chemical rate law $d\lambda/dt$. We suppose that only one scalar variable λ drives the chemical reactions behind the shock ($\lambda = 0$ on Σ).

Between the operators $\frac{\partial}{\partial \tau}, \frac{\partial}{\partial t}$ and $\frac{\partial}{\partial n}$ we have the relations:

$$\frac{\partial}{\partial t} = \sin(\psi+\chi)\cdot\frac{\partial}{\partial \lambda} + \cos(\psi+\chi)\cdot\frac{\partial}{\partial n} = -\frac{1}{R_c}\frac{d}{d\psi} \qquad (8)$$

Equation (8) applied to χ and p with the use of (1), (2), (3), (6), gives finally the needed relation:

$$\frac{1}{R}\left[1 - \frac{u^2}{c^2}\cos^2(\psi-\chi)\right] = \frac{1}{R_c}\left[\frac{1}{\varrho}\left(\frac{1}{u^2} - \frac{1}{c^2}\right)\frac{dp}{d\psi}\cos(\psi+\chi) - \sin(\psi+\chi)\frac{d\chi}{d\psi}\right] + \cos(\psi+\chi)\sin(\psi+\chi)\cdot\left(\frac{\sin\chi}{r} - \frac{p^*}{\varrho u c^2}\right) \qquad (9)$$

The quantities introduced in relation (9) are known by mathematical analysis using the jump conditions.

The Shock Relationships

The equations for an oblique shock are:

$$\rho_o \cdot D \cdot \cos\psi = \rho \cdot u_\perp \quad (10)$$

$$p = \rho_o \cdot D \cdot \cos\psi (D\cos\psi - u_\perp) \quad (11)$$

$$u_{//} = D \cdot \sin\psi \quad (12)$$

We add to these relations, the classical expression between shock and particle jump velocity

$$D\cos\psi = A + B \cdot (D\cos\psi - u_\perp) \quad (13)$$

From equations (10), (13), we have:

$$u_\perp = A \cdot (B^{-1} + M_o \cdot \cos\psi \cdot (1 - B^{-1}))$$

$$tg(\psi + \chi) = M_o \cdot \sin\psi / (B^{-1} + M_o \cdot \cos\psi \cdot (1 - B^{-1}))$$

$$\rho = \rho_o \cdot M_o \cdot \cos\psi / (B^{-1} + M_o \cdot \cos\psi \cdot (1 - B^{-1}))$$

$$\rho = \rho_o \cdot \frac{A}{B} \cdot M_o \cdot \cos\psi (M_o \cdot \cos\psi - 1)$$

$$tg\chi = \frac{1}{2} \sin 2\psi \cdot (M_o - (\cos\psi)^{-1}) / (M_o \cdot B - M_o \cos^2\psi + \cos\psi)$$

$$\frac{dp}{d\psi} = \rho_o \cdot \frac{A}{B} \cdot M_o \cdot \sin\psi \cdot (1 - 2M_o \cos\psi)$$

and

$$\frac{d\chi}{d\psi} = \frac{y \cdot (2B-1) + y(2-B) - 1 - M_o^2 B}{(y-1)^2 + B[M_o^2 B - 2y(y-1)]}$$

$$(y = M_o \cdot \cos\psi)$$

Behind the shock, three angles are of fundamental interest for the study:

1) When M_o and B are fixed, the term $\chi(\psi)$ shows a maximum for $\psi = \psi_m$ solution of $\frac{d\chi}{d\psi} = 0$

This angle is given by:

$$\cos\psi_m = \frac{1}{M_o} \frac{2 - B - (B^2 + 4B - 4M_o^2 B + 8B^2 M_o^2)^{1/2}}{2 \cdot (1 - 2B)}$$

2) The point M_s on the shock front for which $\psi = \psi_s$ and where the flow is sonic ($u = c$)

Knowing that

$$c = v \cdot \left(\frac{dp}{dv}\right)_H + \frac{G_o \cdot v}{2} \left[(v_o - v)\left(\frac{dp}{dv}\right)_H + p\right],$$

where the derivative is taken along the inert shock adiabatic of the explosive, we obtain the angle ψ_s corresponding to the sonic point by $\psi_s = \cos^{-1}(\frac{y_s}{M_o})$ with y_s solution of the equation $(u + u_{//}) = c$

This equation may be written as:

$$\left[\frac{1}{B} + y\left(1 - \frac{1}{B}\right)\right]^2 \cdot \left[2(y-1) - G_o \frac{(y-1)^2}{By}\right] - M_o^2 + y^2 = 0,$$

where the Grüneisen coefficient $G_{\lambda o}$ is taken as:

$$\frac{G_o}{v_o} = \frac{G_{\lambda o}}{v}$$

3) There exists also a point located on the shock locus where an angle value ψ_k annuls the coefficient of R_c^{-1} in equation (9).

We call here this point "Crocco point" by analogy with a plane flow without chemical evolution.

We can show numerically that in most physical cases ($1 < M_o < 10$)

$$\psi_m < \psi_k < \psi_s.$$

For example, with $M_o = 3$ and $B = 2$, which are two values of consequence for our study, we get the following results:

$\psi_m = 32.98°$		$\chi_m = 9.9°$
$\psi_k = 36.49°$	and	$\chi_k = 9.79°$
$\psi_s = 40.61°$		$\chi_s = 9.39°$

With $\chi < \chi_m$, the initial deflection of the flow behind the shock is small compared to the associated incident angle ψ of the oncoming flow.

For angles determinations, the Grüneisen coefficient is chosen as:

$$G_o = 2B - 5/6$$

This is the average of the two values given by

$$G_o = 2B - 2/3 \text{ (Slater model)}$$

$$G_o = 2B - 1 \text{ (Dugdale Mac Donald model)}$$

Analytical Study of the Shape of the Reactive Shock Front

If x(r) is the equation of the shock locus (Σ) in a meridian plan, we can write (figure 1):

$$\frac{dx}{dr} = tg\psi \quad (14)$$

and the local curvature of the shock front at point M (x,r) is given by:

$$\frac{1}{Rc} = \pm \cos\psi \cdot \left(\frac{dr}{d\psi}\right)^{-1} \quad (15)$$

When the point M, on Σ, get out of place starting

from the axis, we have $\cos\psi > o$, and $\frac{dr}{d\psi} > o$, so we take minus sign in (15) to be consistent with the relation

$$\frac{1}{Rc} = \frac{d\beta}{d\tau} .$$

The substitution of (15) in (9) gives the equation

$$\frac{d\psi}{dr} = \frac{r \cdot Z_2 - \sin\chi}{r \cdot Z_1} \qquad (16)$$

where

$$Z_2 = \frac{p^*}{puc^2} + \frac{1}{R} \cdot \frac{1 - \frac{u^2}{c^2}\cos^2(\psi+\chi)}{\cos(\psi+\chi)\cdot\sin(\psi+\chi)} \qquad (17)$$

$$Z_1 = \frac{\cos\psi}{\cos(\psi+\chi)}\frac{d\chi}{d\psi} - \frac{1}{p}\left(\frac{1}{u^2} - \frac{1}{c^2}\right)\frac{\cos\psi}{\sin(\psi+\chi)} \cdot \frac{dp}{d\psi} \qquad (18)$$

Now it is possible to get, by a theoretical treatment of (14) and (16), a representation of the reactive shock front in cylindrical symmetry for given M_0 and B. Some remarks must be presented now. Equation (14) is a geometrical one, and equation (16) is set up by: the equations of the flow through the jump conditions, the initial chemical rate process through the p* term, and the curvature of streamline in the reaction zone behind the shock. We note that the streamline's curvature depends on the distribution of the flow variables in the entire reaction zone. Here, we do not look the problem of the internal structure of the detonation front, so we have to postulate some physical assumptions for the behavior of p* and R in the neighborhood of the shock locus. It may be noted that equation (16) was used in a similar form by the Russian scientists (3) in the analysis of a possible gas dynamic limit of propagation for a stationary detonation. As the problem we are looking, is only a local one, we restrict our study to the determination of the shock's curvature on the axis where we have, by symmetry, $R^{-1} = 0$. Before integration we study the behavior of equation (16).

This equation is not a linear one and we analyze the trajectories (r,ψ) in the Euclidean plane. Two singular points a and b appear in the first quadrant whose coordinates are solutions of

$$r \cdot Z_1 = 0$$

$$r \cdot Z_2 - \sin\chi = 0$$

$$a\begin{cases} r \doteq o \\ \psi = o \end{cases} \quad \text{and} \quad b\begin{cases} r = r_K = \sin\chi(\psi_K)/Z_2(\psi_K) \\ \psi = \psi_K = [Z_1(\psi_K) = 0] \end{cases}$$

We define also the fundamental curve F by

$$r = \sin\chi(\psi)/Z_2(\psi)$$

The trajectories, solutions of $\frac{dr}{d\psi}$, cross the two lines $r = o$ and $\psi = \psi_K$ horizontally and cross F vertically except the a and b points. As $\frac{dr}{d\psi}$ is positive everywhere on the shock locus, the associated trajectory T must be the one connecting a and b. In this case we sum up the mathematical properties of the two singular points on Table 1, using the classification of Poincaré (4). We have supposed that $Z_2(\psi) > o$ and that (rZ_1) and $(rZ_2 - \sin\chi)$ are analytic functions in the neighborhood of the singular points. In Table 1 we introduce the notations:

$$\Omega(\psi_K) = -\sin\chi(\psi_K)\cdot Z_1'(\psi_K) > 0$$

$$I(\psi_K) = \sin\chi(\psi_K)\cdot\frac{Z_2'(\psi_K)}{Z_2(\psi_K)} - \cos\chi(\psi_K)\cdot X'(\psi_K)$$

and "prime" is used as a derivative notation versus ψ.

In the first quadrant, the two regions, where $dr/d\psi > 0$, extend to infinity and the trajectory T exists only for an appropriate unknown law for $Z_2(\psi)$, associated to the flow properties in the reaction zone. So we propound an assumption for fundamental curve equation (F), taking the zero order approximation for the $Z_2(\psi)$ function:

$$Z_2(\psi) = Z_2(\psi = 0) = \text{constant} \qquad (19)$$

In this case, the b point is a focus, so that the approximation is not valid near the charge boundary where $\psi_K \sim \psi_s$. Anyway, a comparison between the numerical solution of (14), (16) with (19) and the experimental data about the shock locus will be of interest because it will give some insight into the validity of the approximation.

A Relationship between the Shock Front Curvature on the Axis (R_{co}^{-1}) and the Charge Diameter (ϕ)

Using formulation (15) and the result of table 1 concerning the saddle point we get:

$$\left|\frac{1}{R_{co}}\right| = \frac{Z_2(0)}{Z_1(0) + \chi'(0)} \qquad (20)$$

where Z_1, and Z_2 are calculated at $\psi=0$ using (17) and (18) for a given M_o and B.

We define now two physical quantities associated to $Z_2(o)$:

$$\frac{1}{\ell_{co}}=\left(\frac{p^*}{p\cdot u\cdot c^2}\right)_{\psi=0} \tag{21}$$

and

$$\frac{1}{\ell_{go}}\doteq \lim_{\psi\to 0}\left[\frac{1}{R}\cdot\frac{1-\frac{u^2}{c^2}\cos^2(\psi+\chi)}{\cos(\psi+\chi)\cdot\sin(\psi+\chi)}\right]. \tag{22}$$

ℓ_{co} and ℓ_{go} are two characteristic lengths associated respectively to the initial chemical conversion behind the shock and to the geometry of the flow in the reactive layer.

With these notation we get:

$$\left|\frac{1}{R_{co}}\right|=\left(\frac{1}{\ell_{co}}+\frac{1}{\ell_{go}}\right)\cdot\frac{1}{Z_1(0)+\chi'(0)} \tag{23}$$

Two other lengths characterize the flow in the reactive layer on the axis : e, the thickness of it and ϕ the diameter of the charge. When $\phi\to\infty$, we associate the following properties

$$M_o\to\bar{M}_{o(D=D_{CJ})}$$

$$e\to e\ ,\ \ell_{co}\to\ell_{go},\ell_{go}\to\ell_{go}$$

$$Z_1(o)+\chi'(o)\to Z_1(o)+\chi'(o)$$

When we consider the limit of the flow for $\phi\to\infty$, we introduce the perturbation parameter $\chi=e\ \phi$ and we express the physical properties of the reactive flow in an asymptotic expansion versus x. So we do that *for* the ratio $\ell_{co}/\ell_{go}=0(x)$ and we write (23) in the general form:

$$\left|\frac{1}{R_{co}}\right|=\frac{\alpha_o+\alpha_1\cdot\chi+\alpha_2\cdot\chi^2+o(\chi^2)}{\ell_{co}} \tag{24}$$

where the α_i are function of M_o and B

On the other hand, using the equation of the fundamental curve F we get:

$$Z_2(0)=\lim_{\psi\to 0}\frac{\sin\chi(\psi)}{r}$$

and also.

$$Z_2(\psi_K)=\frac{\sin\chi(\psi_K)}{r_K}\sim\frac{\sin\chi(\psi_s)}{r_s}$$

The sonic point of the trajectory is assumed to be at the charge boundary, so with (19) and (20) we get to first order:

$$\left|\frac{1}{R_{co}}\right|=\frac{2.\sin\chi(\Psi_s)}{z_1(o)+\chi'(o)}\cdot\frac{1}{\phi} \tag{25}$$

The coefficient of ϕ^{-1} in the right member of (25) depends of M_o, therefore of ϕ [(5) for instance] and we admit, as M_o, that it may be expressed by an asymptotic expansion versus $1/\phi$. In this case for large charge diameter we have:

$$\left|\frac{1}{R_{co}}\right|=\frac{\pi(\bar{M}_o,B)}{\phi}+0\ (\phi^{-2}) \tag{26}$$

A comparison of equations (24) and (26) indicates then:

$$\alpha_o = 0$$

and we have finally:

$$\frac{\phi}{|R_{co}|}=\frac{\bar{e}}{\ell_{co}}\cdot\left[\alpha_1+\alpha_2\cdot\frac{\bar{e}}{\phi}+0\left(\frac{\bar{e}}{\phi}\right)^2\right] \tag{27}$$

For large charge diameter, the approximations retained lead to the fact that the ratio between the diameter and the curvature radius of the reactive shock front on the axis tends to a finite value when the diameter of the charge tends to infinity. This limit is proportional to the total depth of the reactive layer, cross the initial chemical rate $d\lambda/dt\sim\dot{\ell}_{co}^{-1}$ on the axis divided by a characteristic celerity in the reactive flow.

AN APPLICATION OF THE MODEL FOR TWO EXPLOSIVES

We used shock shape measurements and detonation velocity as function of unconfined charge diameter achieved on two plastic bonded heterogeneous compositions: X and T involving respectively 96% T.A.T.B. (5). We summarize some important results on Table 2.

The emerging detonation wave is obtained either continuously by a streak camera or discretely by optic fibers and coaxial pins for a given diameter of the charge. We compare the whole experimental reactive shock shape we get to the theroetical one obtained by a numerical solving of (14), (16) with (19). In this case, $Z_2(o)$ is a parameter [M_o and B are given] we have to adjust by a least square method with the experiments. Using (20) our fitting gives a $|R_{co}|$ value and, in a first step, we retain this value as a first order approximation for the "true" value of the curvature radius of the reactive shock front on the axis.

TABLE 1

*Behavior of the Two Singular Points **a** and **b***

	ⓐ $\begin{cases} r = 0 \\ \psi = 0 \end{cases}$	ⓑ $\begin{cases} r = r_K = \dfrac{\sin \chi(\psi_K)}{Z_2(\psi_K)} \\ \psi = \psi_K \end{cases}$
properties of ⓐ and ⓑ	a saddle $[\chi(0) \cdot Z_1(0) > 0]$	a one tangent node if $0 < I^2(\psi_K) = 4\Omega(\psi_K)$ a two tangent node if $0 < 4\Omega(\psi_K) < I^2(\psi_K)$
Slope of the separatrice T connecting ⓐ and ⓑ	$\left(\frac{dr}{d\psi}\right)_{a_1} = [Z_1(0) + \chi'(0)] / Z_2(0) > 0$ $\left(\frac{dr}{d\psi}\right)_{a_2} = 0$ (the second separatrice of ⓐ point)	$\left(\frac{dr}{d\psi}\right)_{b\pm} = -I(\psi_K) \cdot Z_3(\psi_K) / 2 \cdot Z_2(\psi_K)$ with $Z_3(\psi_K) = 1 \pm \left[1 - 4\Omega(\psi_K)/I^2(\psi_K)\right]^{1/2}$
Slope of F	$\left(\frac{dr}{d\psi}\right)_{F\,ⓐ} = \chi'(0)/Z_2(0)$ $0 < \left(\frac{dr}{d\psi}\right)_{F\,ⓐ} < \left(\frac{dr}{d\psi}\right)_{a_1}$	$\left(\frac{dr}{d\psi}\right)_{F\,ⓑ} = -r_K \cdot \frac{I(\psi_K)}{\sin \chi(\psi_K)}$ $\left(\frac{dr}{d\psi}\right)_{F\,ⓑ} > \left(\frac{dr}{d\psi}\right)_{b\pm}$
Scheme of trajectories in the case of one tangent node for ⓑ	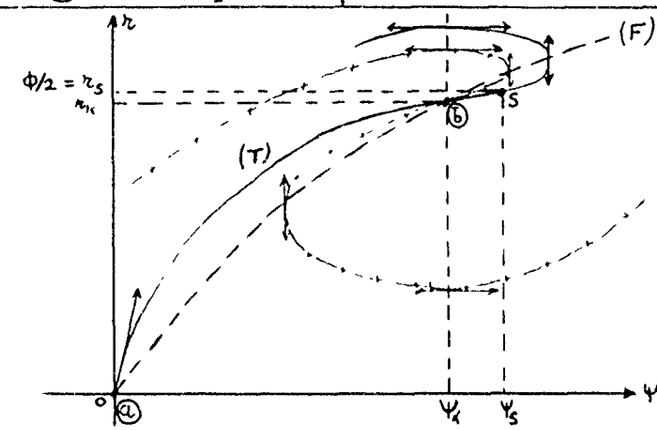	
	Calling Φ diameter of the unconfined charge, the point S which is on the boundary of the charge is a sonic one : $\psi = \psi_s$ (1,3) and we have also $\psi_s \sim \psi_K$	
Remark	$Z_2(\psi_K) > 0$ and $\left(\frac{dr}{d\psi}\right)_{F\,ⓑ} > 0 \longrightarrow I(\psi_K)$ and $Z'_2(\psi_K) < 0$ So, neglecting a ψ effect on the R^{-1} term in Z_2, we get $\frac{dp^*}{d\psi}(\psi_K) < 0$	

TABLE 2

Main Results about the Detonation and Shock Properties of the Two Explosives X and T

	ϱ_o ($g \cdot cm^{-3}$)	$D_\infty \sim D_{CJ}$ ($mm \cdot \mu s^{-1}$)	D^* ($mm \cdot \mu s^{-1}$)	Φ^* (mm)	A ($mm \cdot \mu s^{-1}$)	B
X	1.822	8.789	8.050	~3	2.890	1.996
T	1.800	7.715	7.350	~10	2.499	2.096

*indicate values near the critical diameter

The integration of

$$\frac{d\psi}{dr}=\frac{r\cdot Z_2{}^{(o)}-\sin\chi(\psi)}{r\cdot Z_1(\psi)}$$

$$\frac{dx}{dr}=tg\psi$$

(with $Z_2(o)=\frac{Z_1(o)+\chi'(o)}{|R_{co}|}$) by a fourth order Runge-Kutta method, is brought about using a starting point closed to a chosen as:

$$ro=5.10^{-3}mm$$

$$\psi o=\frac{ro}{|Rco|}$$ (|Rco| is the parameter adopted for integration)

$$xo=ro.tg\psi o$$

For this numerical trials, we separate the negative and positive values for r on the records to take into account the possible dissymmetrical effect due to experiments. By this way, we define the curvature radius on the axis by the average of the two values |Rco|± optimized after integration. On Figures 2, 3, 4, 5, we show some experimental (E) and theoretical reactive shock locus (M) obtained for X and T compositions. On Table 3 we have reported the final results we get for |Rco| at various ϕ, and on figures 6 and 7 the plot of $\phi/|Rco|$ versus $1/\phi$ compared to a linear regression.

Figures 2 to 5 show that the solution of our equations in the approximation retained fits the experimental front with a systematic error due to the difficulties in the adjustment of realistic boundary conditions taking account simultaneously of the specific properties of the singular points *a* and *b*. One of these point standing in the vicinity of the charge boundary ($\psi_K\sim\psi_s$). On the other hand, the determination of |Rco|, we got, agrees well with relation (27) to first order. Writing $\phi/|Rco|$ under the form

$$\frac{\phi}{Rco}=a+\frac{b}{\phi}\ ,$$

we get for the two explosives:

comp. X { a=0.0717, b=1.9539mm comp. T { a=0 1983, b=3.8394mm

Now using relation (27) and the data reported on Table 2, it is possible to estimate the ratio between the thickness of the reactive layer for the two chosen compositions. For that we take into account the analysis develped in (3) which shows that ϕ^* is determined only by the initial rate of the reaction behind the shock at the charge boundary. Assuming that $\frac{i}{\lambda c}$ given by (21) is of the same order of $\left(\frac{p^*}{\rho\cdot C^3}\right)^{o}_{\psi=\psi_s}$ at the critical diameter we can write: $ico\sim\phi^*$. Noting also that the quantity M_0 and B are of the same order for both compositions, we have:

$$\frac{[a]T}{[a]x}=\frac{[\dot{e}]T}{[\dot{e}]x}\cdot\frac{[\dot{\iota}co]x}{[\dot{\iota}co]T}\sim\frac{[\dot{e}]T}{[\dot{e}]x}\cdot\frac{[\dot{\phi}^*]x}{[\dot{\phi}^*]T}$$

A numerical trial gives:

$$\frac{[\dot{e}]T}{[\dot{e}]x}=9.2$$

With our assumptions, we show that the reaction layer is much larger in T composition than in X composition. This result agrees with the one obtained by ignition and detonation calculations on octogen and T.A.T.B. explosives (6). With an explosive such as T, the explosive energy is not released immediately on the shock front as assumed by the C.J. theory.

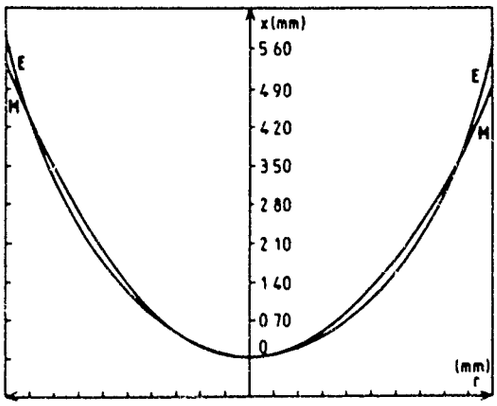

Fig. 2. Comp. T
ϕ=200 mm
D=7.726 mm.μs $^{-1}$

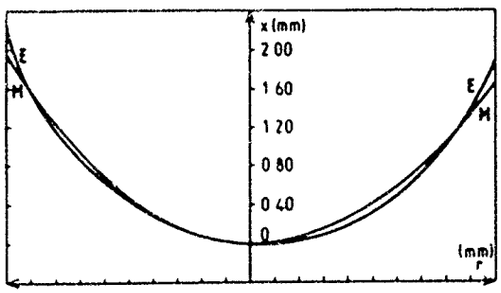

Fig. 3. Comp. T
ϕ=50 mm
D=7.621 mm.μs $^{-1}$

TABLE 3
Axial Curvature Effect on the Shock Front Versus Diameter of the Charge for X and T Compositions

Comp. X			Comp. T		
ϕ (mm)	D (mm.μs^{-1})	ϕ/|Rco|	ϕ (mm)	D (mm.μs^{-1})	ϕ/|Rco|
3	8.091	0.707	15	7.467	0.468
5	8.519	0.492	15	7.442	0.443
5	8.514	0.405	20	7.537	0.361
7.5	8.620	0.363	30	7.567	0.322
7.5	8.660	0.342	50	7.618	0.284
10	8.749	0.317	50	7.623	0.280
20	8.783	0.191	50	7.586	0.292
20	8.781	0.189	50	7.625	0.333
30	8.777	0.135	50	7.621	0.280
30	8.778	0.130	50	7.628	0.275
40	8.774	0.115	100	7.679	0.228
50	8.783	0.079	100	7.679	0.236
75	8.784	0.085	100	7.6876	0.229
7	8.784	0.090	100	7.696	0.231
75	8.784	0.089	200	7.726	0.194
75	8.784	0.084	200	7.726	0.201

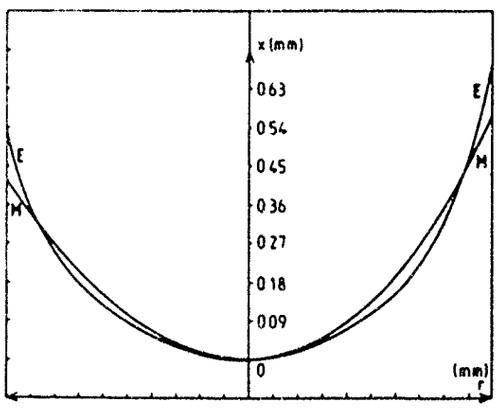

Fig. 4. Comp. X
ϕ=20 mm
D=8.781 mm.μs^{-1}

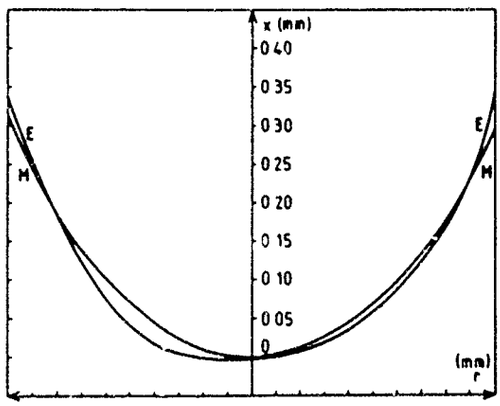

Fig. 5. Comp. X
ϕ=3 mm
D=8.091 mm.μs^{-1}

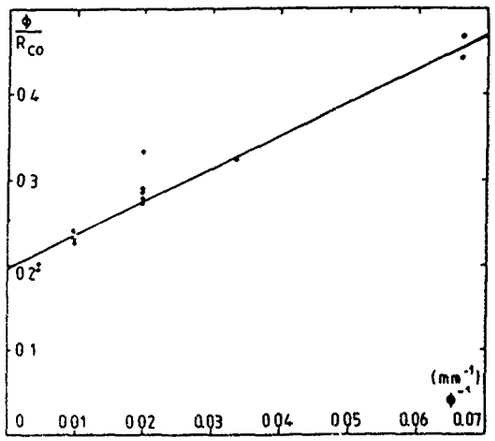

Fig 6 Comp. T
ϕ Rco (1/ϕ)

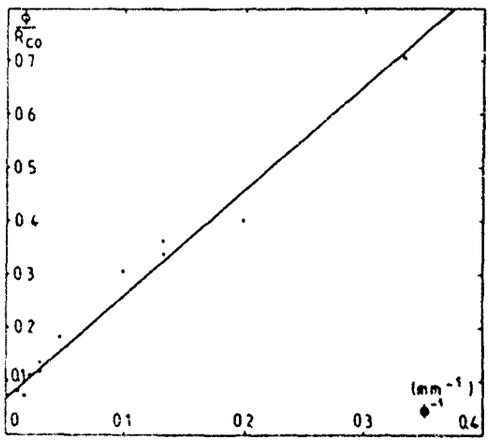

Fig. 7 Comp. X
ϕ Rco (1 ϕ)

CONCLUSIONS

The axisymmetrical reactive front has been analysed using flow equations and jumps conditions. As usual, the well known difficulties, to translate into tractable analytical expressions the boundary conditions, are encountered. They are resolved through a zero order analysis of differential equations leading to $Z'_2(\psi)=0$. Then the front shape is obtained as a function of curvature on the axis. Variations of this parameter can narrow the gap between the experimental and calculated fronts to less than 2.10 $^{-2}$mm inside 90% of the charge diameter. Outside, the rarefactions waves unvalid the adopted model. This hypothesis also permits us to derive a simple relation between the diameter of the charge, the curvature of the front on the axis and the so called "reaction zone" thickness. With this model, the ratio of the thickness of TATB composition to HMX one is of order of 10.

ACKNOWLEDGEMENTS

The authors gratefully acknowledge R. Cheret for his stimulating encouragements and helpful discussions we got with him on this study. The close support of the detonation physics group was greatly appreciated, in particular we wish to associate J. Appencourt, C. Mouchel and J. Montrosset for their scrupulous experimental works in the reduction of data.

REFERENCES

1. J.B. Bdzil, J. Fluid Mech. 108, 195 (1981)
2. R. Engelke, J.B. Bdzil, Phys. Fluid 26(5), 1210 (1983)
3. K.M. Mikhailyuk and V.S. Trofimov Fizika Goreniya i Vzryva, Vol. 13, No. 4, p. 606 (1977)
4. G. Sansone, R. Conti, Non-Linear differential equations, Chap. 2, Pergamon Press (1964)
5. J. Aveillé and all, Célérité de détonation et profondeur d'amorcage de deux compositions explosives a base d'octogene et de TATB. Tome 2. Colloque international de pyrotechnie fondamentale et appliquée, Substance et systeme, 5-7 Octobre 1982 - Arcachon, France.
6. S.G. Cochran and J. Chan, L.L.L. report, UCID 18024, 01/20 79
7. W. Fickett and W. Davis, Detonation University of California Press, (1979)

A GENERALIZED C-J CONDITION FOR SIMPLE AXIAL FLOW WITH A SPHERICAL SHOCK FRONT: ITS APPLICATION TO THE SLURRY EXPLOSIVES

H. Matsui, A. Moritani, K. Yoneda and T. Asaba
Department of Reaction Chemistry, The University of Tokyo
Tokyo, Japan

A simple theory with a generalized C-J condition is tested by solving the conservation equations for axial symmetric flow with an approximation of the loss term induced by the shock front curvature. The radius of it is estimated by simplifying the boundary condition at the interface of the unreacted explosive and the wall material. The realistic equations of state are used both for unreacted explosive and the reaction products. A confinement factor, Ψ, is introduced so that the effects of the radius of the explosive as well as the wall material can be discussed. Experimental results on the diameter effect of the slurry explosive are compared with the theory.

INTRODUCTION

There have been many theoretical studies on the diameter effect for steady propagation of detonation in condensed materials. The recent development of computers has made direct numerical calculations on the problems of multi-dimensional fluid dynamics possible, and many useful informations on this problem have been obtained by this technique (1). Such calculations, however, are usually time-consuming and inadequate to use for various parameters in order to discuss the general tendencies of steady detonation thus far.

There have been two types of models for obtaining analytical solutions. The first model is so-called "Nozzle Theory" which is based on the one dimensional conservation equations with variable cross section proposed by Jones (2). The similar model was employed in the works of Sommers and Morrison (3) and Jabora (4) et al.,.

These theories are semi-empirical since they employed additional assumption in order to obtain the steady condition. The rigorous steady condition for this model was obtained in the analysis of Tsuge et al., (5) who solved the eigen value problem by numerical integration of the one-dimensional conservation equations.

As the "Nozzle Theory" is based on the assumption that the leading shock wave is planar, it may be a good model for gaseous detonation with non-rigid boundary condition. The second type of the model is so-called "Curved Front Theory" which deals with the flow behind the non-planar shock wave. Eyring et al., (6) solved the problem based on the one dimensional conservation equations with spherical symmetry. The realistic treatment for the steady detonation in condensed explosives was done by Wood and Kirkwood (7), Fay (8), Sichel (9), Bdzil and co-workers (10-12), Thouvenin (13) and Chan (14).

Bdzil and co-workers solved two-dimensional, axial-symmetric flow problem by using small perturbation approximation originally proposed by Wood and Kirkwood. They calculated on various practical systems of detonation in condensed phase without employing any empirical assumption for obtaining the steady condition except for the shape of the shock wave.

The purpose of this study is to develop a simple theory without using a small-perturbation approximation so that the characteristics of condensed explosives which have relatively long reaction-zone length can be calculated.

The approximation of a spherical leading shock wave is used in this analysis.

In addition, only the central stream along the symmetric axis is taken into account for

simplicity. The effect of the shock front curvature on the axial flow is evaluated by the same method of Thouvenin (13), but the condition for steady propagation of detonation is evaluated non-empirical way, i.e., it is searched by solving eigen value problem numerically.

The effect of the wall material on the steady detonation is another important subject. Although only limited experimental informations about the relative efficiencies of the confinement of detonation by various wall materials have been obtained, prediction of it by using a simple theory may be useful. In the present study, experimental data on the detonation velocity of a slurry explosive are compared with the theoretical results. A parameter, Ψ, which is a measure of the efficiency of the confinement by the wall is tested by comparing the theory with the experimental data.

BASIC EQUATIONS

The model of the flow used in this study is schematically shown in Fig. 1. It is assumed that the flow is steady, inviscid and axially symmetric with a spherical leading shock (radius:Rc) which propagates in an explosive of radius Ro. Let the flow velocity incident to the shock be D, axial and radial coordinates be z and r, respectively, the velocity components for the shock-fixed coordinates be u and v, respectively. The conservation equations are expressed as follows.

conservation of mass:

$$u\,\partial\rho/\partial z + v\,\partial\rho/\partial r + \rho[\partial u/\partial z + v/r + \partial v/\partial r] = 0 \quad (1)$$

conservation of momentum:

$$u\partial u/\partial z + v\partial u/\partial r + (1/\rho)\partial p/\partial z = 0 \quad (2)$$

$$u\partial v/\partial z + v\partial v/\partial r + (1/\rho)\partial p/\partial r = 0 \quad (3)$$

conservation of energy:

$$u\partial e/\partial z + v\partial e/\partial r - (p/\rho^2)[u\partial\rho/\partial z + v\partial\rho/\partial r] = 0 \quad (4)$$

where, ρ is the total density of the flow, p is the pressure, and e is the total internal energy, respectively.

Now, if it is assumed that any central stream along the symmetric-axis is important in deciding the C-J condition, then the conservation equations at the center of the symmetry

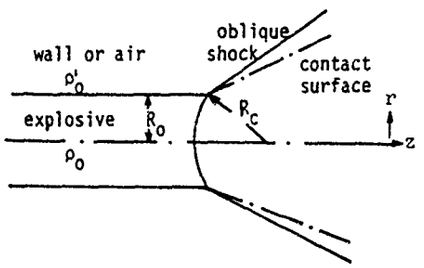

Fig. 1. The Model of The Flow Used in This Study

can be written as,

$$d(\rho u)/dz + 2\rho f(z) = 0 \quad (5)$$

$$du/dz + (1/\rho u)\,dp/dz = 0 \quad (6)$$

$$de/dz - p/\rho^2\, d\rho/dz = 0 \quad (7)$$

where, the loss term, f(z) can be expressed as follows (13).

$$f(z) = \partial v/\partial r|_{r=0} = \lim_{r\to 0}(v/r) = (D-u)/(Rc-z) \quad (8)$$

The expression in Eq. (8) is consistent with the results of small-perturbation theory for small z (14). The equation of state for the unreacted explosive is assumed to be expressed by Mie-Gruneisen equation, i.e.,

$$e_s - e_k = (p_s - p_k)/\Gamma \quad (9)$$

where Γ is Mie-Gruneisen parameter and subscripts s and k denote the conditions for the unreacted explosive and the reference state, respectively. The reaction products are treated as gas phase which obey the following equation of state,

$$p_g(V_g - b) = R\,T_g \quad (10)$$

where, b is a constant which is calculated so that Eq. (10) agrees with Kihara-Hikita equation (15) at the pressure and the temperature range of interest, R the gas constant and the subscript g denotes gas phase condition. The internal energy of the flow is written as,

$$e = w\,e_s + (1-w)\,e_g + w\,H_s + (1-w)\,H_g \quad (11)$$

where, H_s and H_g are the standard heat of formation summed over all the components of the unreacted explosive and the reaction products, respectively, and w is the weight fraction of the unreacted explosive. Also the total density can

be expressed by the combination of the composition of the reactive system as,

$$\varrho = [w/\varrho_s + (1-w)/\varrho_g]^{-1} \tag{12}$$

and the reaction rate law is assumed to have the form:

$$dw/dz = A_f w/u \; Exp(-Ea/RT) \tag{13}$$

where, A_f and Ea denote the Arrhenius' pre-exponential factor and the activation energy, respectively. Initial condition behind the shock front is calculated by using the simple relations,

$$D = c + s\,u_p \tag{14}$$

where, D is the detonation velocity, c and s are constants decided empirically for unreacted explosive and u_p is the flow velocity measured at laboratory coordinate. For the calculation of porous explosive, the simple relation proposed by Erkman and Edwards (16) is used, i.e.,

$$\begin{aligned} p_i = p^o\,(Voo - V_i - 2V_i/\Gamma) \\ /(Vo - V_i - 2V_i/\Gamma) \end{aligned} \tag{15}$$

where, $V = 1/\varrho$, subscript i denotes the condition behind the shock front, Vo is the specific volume of porous explosive in front of the shock wave, Voo is the specific volume of the same but non-porous explosive and p^o is the shock pressure for this non-porous explosive for the same V_i.

By using Eq. (14), (15) and the conservation equations, V_i, p_i, e_i and u_i are calculated successively. By assuming that heat capacities for the unreacted explosive Cv_s and the reaction products Cv_g are constant and that $T_s = T_g$ and $p_s = p_g$, then the other variables at the shock are all decided.

By introducing nondimensional variables, conservation equations are expressed as follows,

$$\begin{pmatrix} 1 & 0 & 0 & a_{14} \\ 0 & a_{22} & a_{23} & 1 \\ a_{31} & a_{32} & a_{33} & 0 \\ a_{41} & a_{42} & a_{43} & 0 \end{pmatrix} \begin{pmatrix} d\zeta/d\xi \\ d\psi_s/d\xi \\ d\psi_g/d\xi \\ d\phi/d\xi \end{pmatrix} = \begin{pmatrix} 0 \\ b_2 \\ b_3 \\ 0 \end{pmatrix} \tag{16}$$

where, $\xi = z/Ro$, $\zeta = p/\varrho_0 u_i D$, $\psi = \varrho/\varrho_0$, $\psi_s = \varrho_s/\varrho_0$, $\psi_g = \varrho_g/\varrho_0$, $\phi = u/u_i$, $C_g = Cv_g/R$, $Cs = Cv_s/R$, $\eta(\xi) = u_i\, f(z)/Ro$, $\lambda = u_i/D$, $\lambda' = u_k/D$, $b' = \varrho_0 b$, $e_g' = e_g/u_i D$, $H_s' = H_s/u_i D$, $H_g' = H_g/u_i D$ are the non-dimensional variables, and the matrix elements in Eq. (16) are defined as follows: $a_{14} = \lambda\psi\phi$, $a_{22} = w\psi\phi/\psi_s^2$, $a_{23} = (1-w)\psi\phi/\psi_g^2$, $a_{31} = w/(\Gamma\psi_s) + C_g(1-w)(1/\psi_g - b')$, $a_{32} = (w/\Gamma\psi_s^2)[(\lambda'/\lambda - \zeta)(\Gamma+1)/-\chi^2(\Gamma+2)\lambda\psi_s]$, $a_{33} = -\zeta/\psi_g(1-w)(1+C_g)$, $a_{41} = (1/\Gamma\psi_s) - C_s(1/\psi_g - b')$, $a_{42} = (1/\Gamma\psi_s)[\lambda^2/\lambda(\Gamma+1) - \lambda'^2/(\lambda\psi_s)(\Gamma+2) - \zeta]$, $a_{43} = C_s\zeta/\psi_g^2$, $b_2 = \psi\phi(1/\psi_s - 1/\psi_g)dw/d\xi - 2\eta)$, $b_3 = -[\zeta(1/\psi_s - 1/\psi_g) + (e_s' - e_g' + H_s' - H_g']$.

THE STEADY CONDITION (C-J CONDITION)

Eq. (16) can be written in the form of $dX_j/d\xi = F_j/G_j$, where X_j (j = 1,2,3,4) are ζ, ψ_s, ψ_g, and ϕ, respectively; i.e.,

nondimensional presure:

$$d\zeta/d\xi = F_1/G_1, \tag{17}$$

where,

$$F_1 = -a_{14}\,(c_1c_4 - c_2c_3)b_2 + (a_{23}c_3 - a_{22}c_4)d_1 - (a_{23}c_1 - a_{22}c_2)d_2$$

and

$$G_1 = (c_1c_4 - c_2c_3) \tag{18}$$

nondimensional density of the unreacted explosive:

$$\begin{aligned} d\psi_s/d\xi &= F_2/G_2 \\ &= (c_4d_1 - c_2d_2)/(c_1c_4 - c_2c_3) \end{aligned} \tag{19}$$

non-dimensional density of the reaction products:

$$\begin{aligned} d\psi_g/d\xi &= F_3/G_3 \\ &= (c_1d_2 - c_3d_1)/(c_1c_4 - c_2c_3) \end{aligned} \tag{20}$$

nondimensional flow velocity:

$$d\phi/d\xi = F_4/G_4 = -(d\zeta/d\xi)/a_{14} \tag{21}$$

where, $c_1 = a_{14}a_{22}a_{31} + a_{32}$,
$c_2 = a_{14}a_{23}a_{31} + a_{33}$,
$c_3 = a_{14}a_{22}a_{41} + a_{42}$,
$c_4 = a_{14}a_{22}a_{41} + a_{43}$,
$d_1 = a_{14}a_{31}b_2 + b_3$
and, $d_2 = a_{14}a_{41}b_2$.

Simultaneous equations of (17)-(21) can be integrated numerically if one assumes the velocity of the detonation D and the radius of the shock wave Rc. If the shock wave is sufficiently strong enough to induce the exothermic

reaction, flow is accelerated due to chemical heat release, then the denominators in these equations (G_1-G_4) approach to zero, i.e., the solution of the equations has a singular point at the condition,

$$c_1c_4 - c_2c_3 = 0 \qquad (22)$$

The fluid dynamical steady condition (C-J condition) is satisfied in the case that the numerators in the equations (F_1-F_4) also converge to zero at the singular point simultaneously. This can be easily proved by using Eq. (22). An example which shows the dependence of the asymptotic value of F_1 at $G_1 = 0$ on assumed D, is shown in Fig. 2. The condition that satisfies $F_1 = 0$ in the figure corresponds to the solution for the steady detonation.

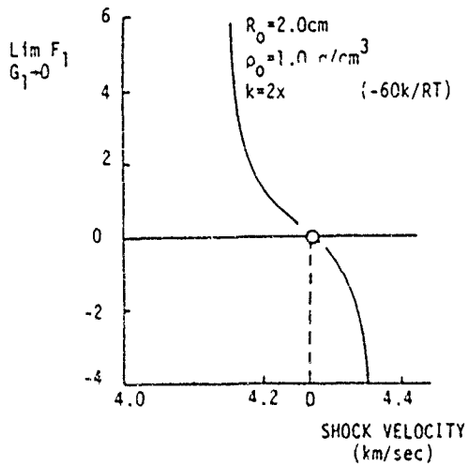

Fig. 2. An Example of The Calculation on The Asymptotic Value of F_1 at The Singular Point (G_1=0) for Obtaining The Eigen Value on The Detonation Velocity, D

RADIUS OF THE SPHERICAL SHOCK WAVE

In order to simplify the analyses, the shock front is assumed to have a constant radius Rc which can be calculated by giving a simplified boundary condition at the edge of the unreacted explosive For the oblique shock wave with an inclination angle α at the edge of the unreacted explosive, the empirical relation similar to Eq. (14),

$$D \sin\alpha = c + s\,u_p \qquad (23)$$

is assumed to hold where, u_p is the velocity component behind the shock front normal to it. For the spherical shock front, the curvature of the shock is calculated by the relation,

$$Rc/Ro = 1/\cos\alpha \qquad (24)$$

In the case that the explosive is unconfined, the boundary condition is written as follows,

$$\alpha = \sin^{-1}(c/D) \qquad (25)$$

then radius of the shock Rc is evaluated by Eq. (24).

In the case that the explosive is heavily confined, the flow in the wall material has to be considered. In the present study, the empirical shock relation for the oblique shock in the wall material,

$$D \sin\beta = c' + s'\,up' \qquad (26)$$

is again used where, the flow in the wall is also assumed to be supersonic, i.e., $D > c'$, β is the inclination angle of the shock wave in the wall at its inner boundary, c' and s' are the constants for the wall material and u'_p is the velocity component normal to the shock in the wall. It is assumed, in addition, that the reflected wave produced at the intersection of the two oblique shock wave at the interface of the explosive and the wall material is not so strong. In this case, the boundary condition is written in the following way,

* matching of the deflection angle of the stream:

$$\alpha - \tan^{-1}[(D \sin\alpha - u_p)/D \cos\alpha] = \beta - \tan^{-1}[(D \sin\beta - u_p')/D \cos\beta] \qquad (27)$$

* matching of the shock pressure:

$$\varrho_0 \sin\alpha(D \sin\alpha - c)/s = \varrho'_0 \sin\beta(D \sin\beta - c')/s' \qquad (28)$$

where, ϱ_0 and ϱ'_0 are the initial densities of the explosive and the wall material, respectively. By giving D, α and β can be calculated so that they can satisfy the conditions (27) and (28) simultaneously, then Rc is decided from Eq. (24).

It should be noted that the simplified boundary condition used in this analyses is not always valid, strong reflected shock wave or rarefaction wave produced at the interface can affect the flow condition behind the shock wave in some case, so the verification of the assumption has to be done.(17) In this study, measurement of the curvature of the shock front in a slurry-explosive has been performed via the multi-pin technique. The experimental results supported the above simplified model in this

case within the experimental accuracy, both for the unconfined case and for the heavily confined case in a thick steel-pipe.

According to the present simple theory, the loss term is governed by the magnitude of Rc, as can be seen in Eq. (8), i.e., as far as Rc is the same, the present theory yields the same steady condition even if the wall condition is different. The similar conclusion was derived in the perturbation theory by Wood and Kirkwood, and Bdzil and co-workers (7), (10)-(12).

The diameter effect of detonation velocity, D has been traditionally shown against reciprocal charge radius, 1/Ro.

It may be convenient to use a confinement parameter defined as,

$$\Psi = \text{Rc(confined)/Rc(unconfined)} \qquad (29)$$

since this parameter gives a rough measure on the efficiency of the confinement by the wall material. The correlation of D for different wall conditions may become clear if one plots D against $1/(\Psi \text{Ro})$ instead of 1/Ro.

EXPERIMENT ON SLURRY EXPLOSIVE

Experiment in a slurry explosive has been performed on the diameter effect and the effect of confinement in steel tubes. The composition of the explosive was; 31% ammonium nitrate + 56% monomethylamine nitrate + 13% water in weight fraction, respectively. The initial density of the explosive was adjusted by the fraction of added air-bubbles. The explosive was confined in steel tubes of 40 cm in length, 15, 27 and 40 mm i.d., with various wall thickness of 2 - 20 mm, each. For the experiments on the unconfined explosive, thin sheets of paper of the same diameter and the length were used. The initial density of the explosive was about 1 g/cm^3. The detonation velocity was monitored continuously by using the resistance wire method (18). Two examples of the measurements are shown in Fig. 3-(a) and (b). From the analyses of the slope of the oscillogram trace, velocity of the detonation can be evaluated. In Fig. 3-(a), the case for large charge-diameter with thick steel wall (Ro = 2 cm and wall-thickness, t = 5 mm) is shown.

In this case, detonation propagated stably. For the explosive with small charge-diameter and/or confined in thin wall tube, the propagation

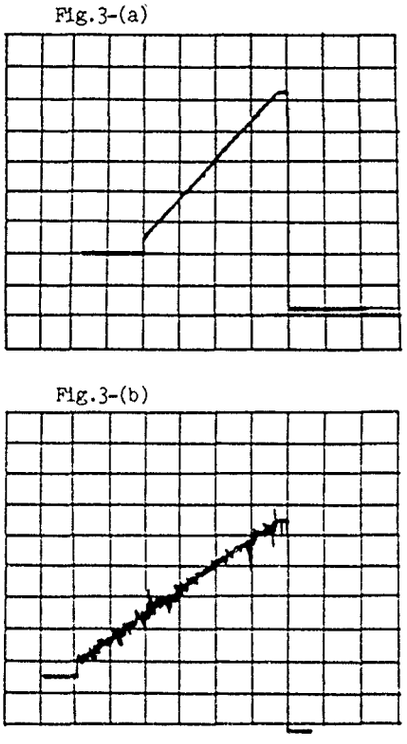

Fig. 3 Examples of Oscilloscope Traces for The Determination of The Detonation Velocity in The Slurry Explosive via The Resistance Wire Method

a) ϱ_0=0.96 g/cm^3, Ro=2.0 cm, wall thickness, t=0.5 cm.

b) ϱ_0=0.96 g/cm^3, Ro=0.75 cm, t=0.2 cm.

vertical scale indicates the distance of z-direction (8 cm/div.) and the abscissa the time (20 μ sec/div.)

became unstable as is shown in Fig.3-(b), (Ro = 0.75 cm, 6 = 2 mm), but still showed a steady propagation in average.

The experimental results of the dependence of D on the thickness of the wall, t and the charge-radius, Ro are summarized in Fig. 4. For the unconfined case, the explosive with Ro = 2 cm showed steady propagation of detonation, but for those with Ro = 1.35 and 0.75 cm no stable detonation was observed. It is also shown in the figure that the velocity of detonation increases as t increases but finally approaches to constant velocity for each charge-radius. This fact suggests that the perturbations induced at

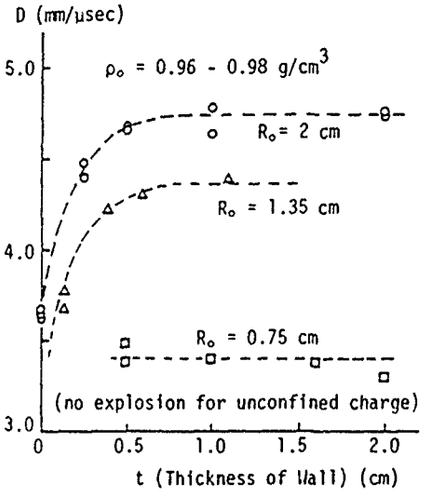

Fig. 4. Experimental Results on The Detonation Velocity in the Slurry Explosive Showing The Effects of The Charge Radius Ro and The Wall Thickness t Confined in Steel Tubes

the outer boundary of the steel tube cannot affect the effective reaction zone of the explosive, if the wall is sufficiently thick. The experimental data for sufficiently thick wall tube may correspond to the theoretical boundary condition of the present study because the effect of the outer boundary condition is ignored in the calculations.

COMPARISON OF THE THEORETICAL CALCULATION WITH THE EXPERIMENTAL RESULTS

In the practical calculation for the detonation in the slurry explosive, the following parameters are used:

Hs=-5.01×10^6 J/kg, Hg=-8.03×10^6 J/kg, $\varrho_0=10^3$ kg/m^3, c=2140 m/s, s=1.926, Γ=0.90, Cv_s=2100 J/kg K, Cv_g=600 J/kg K, ϱ_0'=7.84 kg/m^3, c'=3800 m/s and s'=1.58.

In the calculation, reaction is assumed to proceed via a single chemical process with first order reaction rate constant, $k = A_f \exp(-Ea/RT)$. The activation energy, Ea is assumed to be 40 kcal/mol or 60 kcal/mol. Integrations are performed by Gear method.

The result of the calculation for the unconfined case with Ro=0.5, 2.0 and 20.0 cm are summarized in Fig. 5, where the pre-exponential factor A_f is varied in a wide range. The detonation velocity in each diameter approaches to an ideal detonation velocity D_∞ for large A_f, while no steady solutions have been found for small A_f (limit for steady propagation).

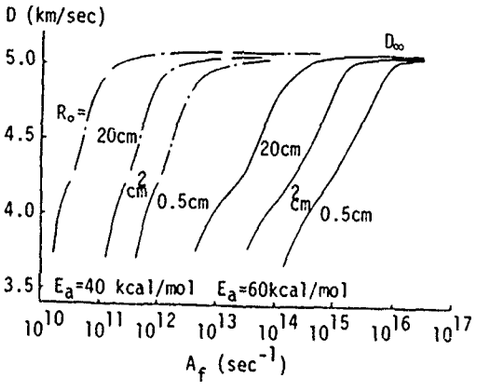

Fig. 5. Calculated Results of The Detonation Velocity in The Slurry Explosive against Arrhenius' Pre-exponential factor A_f: solid curves are the solution for Ea=60 kcal/mol and dash-dott curve for Ea=40 kcal/mol

The experimental results are compared with the theoretical ones in Fig. 6 with assumed Arrhenius' parameters. Both the experimental data on unconfined and experimental data on unconfined and heavily confined explosives are plotted in the same figures against $1/(\Psi Ro)$, where Ψ is estimated by using Eqs. (24), (25), (27) and (28). As is shown in the figure, the calculated detonation velocity depends nonlinearly on inverse of the charge radius. Also it is shown that the agreement of theory and experiment is excellent if the rate constant is properly chosen.

CONCLUSION

A simplified theory on the central stream of axial-symmetric flow behind a spherical shock has been tested for the slurry explosive. The dependence of the detonation velocity on reciprocal charge radius is shown to be nonlinear. Although the present theory is based on the approximations of simple axial flow with a spherical shock, it may be useful for the estimation of the general characters of the explosive. It is well known that the solutions for the

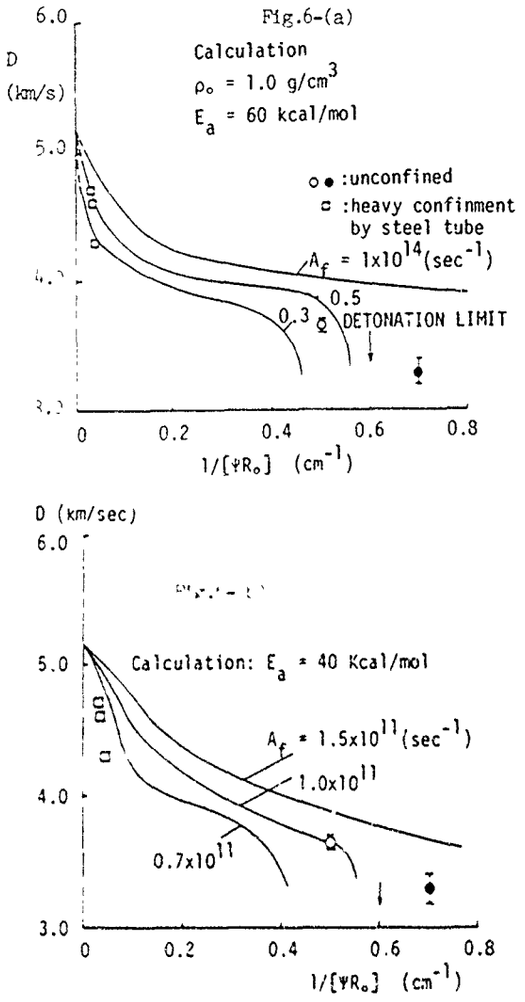

Fig 6 Comparison of The Experimental Data with Theory for Various Rate Constants on The Detonation Velocity of The Slurry Explosive: circle, experimental data for the unconfined charge, square, experimental data for confined charge in a steel tube (Open and shaded symbols denote the steady and unsteady propagation, respectively)
a) calculation for Ea=60 kcal/mol
b) calculation for Ea=40 kcal/mol

steady detonation by using the generalized C-J condition have two eigen values for a certain value of the charge diameter. In the present study the lower eigen value of the detonation velocity has not been searched because of the limit of the computation time.

Comparison of the experimental data with the theoretical ones may suggest that the theory can be applied to predict the diameter effect and the effect of the wall material, at least qualitatively, if a confinement factor is used in the analyses.

Although this factor seems very useful, many more works have to be done in order to test its validity.

REFERENCES

1. For example; C. L. Mader, Numerical Modeling of Detonations, Univ., Calif. Press, (1979).
2. H. Jones, Proc. Roy. Soc., A189, 145 (1947).
3. W. P. Sommers and R. B. Morrison. Phys. Fluids, 5, 241 (1962).
4. E. K. Dabora et al., Proceedings of Tenth Symp. (intern.) on Comb., p. 817, Comb. Inst., (1965).
5. S. Tsuge et al., Astro. Acta, 15, 377, (1970).
6. H. Eyring et al., Chem. Rev., 45, 69, (1949).
7. W W. Wood and J. G. Kirkwood, J. Chem. Phys., 1920, (1954).
8. J. A. Fay, Phys. Fluids, 2, 283 (1959).
9. M. Sichel, AIAA J., 4, 264 (1966).
10. J. B. Bdzil, J. Fluid Mech., 108, 195 (1981).
11. J. B. Bdzil et al., J. Chem. Phys., 74, 5694 (1981).
12. R. Engelke and J. B. Bdzil, Phys. Fluids, 26, 1210 (1983).
13. J. Thouvenin, Proc. Seventh Symp. (Intern.) on Detonation, p. 297 (1981).
14. S. K. Chan, Proc. Seventh Symp. (Intern.) on Detonation, p. 326 (1981).
15. K. Tanaka, J. Ind. Expl. Soc., Japan, 43, 239 (1982).
16. J. O. Erkman and D. J. Edwards, Proc. Fourth Symp. (Intern.) on Detonation, p. 266 (1966).
17. H. Matsui et al., to be submitted.
18. E. Kuroda and M. Kusakabe, J Ind. Expl. Soc., Japan, 37, 60 (1976).

DISCUSSION

C. G. BROCHET, Poitiers, France

Did you try to use intermediate confinements in your calculations or experiments, I mean light confinement whose impedance is between that of air and that of heavy confinement? In other words have you tried to check your confinement parameter Ψ?

REPLY BY H. MATSUI

The present theoretical analyses essentially requires that the flow inside the wall material should be supersonic as well, but this condition is not satisfied experimentally in our case for the light confined charges. This makes the situation too complex for usage of simple theories. Thus only what we could examine in our experiment were limited to the two extreme cases, i.e., unconfined and heavily confined charges, where we found that the measured curvature of the shock front was approximately the same with that predicted by the present simple theory for the unconfined case, while the experimental accuracy for the latter case was insufficient because the curvature was too large ($R_c \doteqdot 10\ R_0$).

A SMALL DIVERGENT DETONATION THEORY FOR INTERMOLECULAR EXPLOSIVES

I. J. Kirby & G. A. Leiper
Detonation Research Group
ICI PLC, Stevenston,
Ayrshire, Scotland

A specific application of the theory of small divergent detonation is presented which is particularly useful in describing the behaviour of intermolecular and commercial explosives. A new approach to the description of unconfined and confined hydrodynamics is used, and the explosive is characterized by a suitable equation of state and a new multiphase reaction rate function. The theory requires a numerical solution of the ordinary differential equations describing this behaviour.

This approach offers the commercial explosives manufacturer and user a convenient way of dealing with the non-ideal behaviour of explosives, and many of their characteristics in use can be predicted including energy delivered to the confinement, critical diameter, confined detonation velocity, and detonation run-up.

INTRODUCTION

A theory of small divergent detonation, based on that of Wood-Kirkwood (1) is described, which combines an equation of state for the partially reacted explosive, a multi-phase reaction rate function, and hydrodynamics for unconfined and confined cylindrical detonations. This represents a further development of the theory of Chan (2).

The theory requires the numerical solution of ordinary differential equations and corresponds to a boundary value problem involving the shock front and the CJ plane. The only empiricism is the assumed shape of the isobar surfaces within the reaction zone, and these have been chosen to agree with two dimensional models and published experimental data. Many problems related to the application of commercial explosives can be solved by this approach, while the numerical procedures are far simpler and more robust than those using Lagrangian or Eulerian techniques.

The steady state theory provides prediction of the change in detonation velocity and minimum initiator with diameter. Using reaction rate data on the behaviour of porous emulsion explosives obtained from electromagnetic particle velocity gauge experiments (3), these predictions are shown to be in good agreement with data from detonation velocity and card gap experiments.

It is shown how the theory is extended to predict detonation acceleration rates by using the full time dependent hydrodynamics. This demonstrates the stability of the solutions, and allows a prediction of the run-up to steady detonation behaviour.

The theory includes a treatment of the effect of confinement on the shape of the isobar surfaces. Application of this offers the commercial explosives manufacturer and user a practical method of predicting the behaviour of explosives in the field from a few simple experiments. In particular this should provide more realistic energy ratings than those obtained by the current practice of considering only ideal detonation, or performing experiments with empirical interpretation.

SMALL DIVERGENT DETONATION THEORY

The theory of flow in chemically reacting media, the associated ideal detonation, and small divergent detonation, have been described in some detail in recent years (4). Below is a summary of the theory in a form that allows the particular additions of this paper to be easily described.

The Euler equations of motion and chemical reaction are written in vector form as:

$$\dot{\rho} + \rho \operatorname{div} \underline{u} = 0 \qquad 1.1$$

$$\rho \dot{\underline{u}} + \operatorname{grad} p = 0 \qquad 1.2$$

$$E + pV = 0 \qquad 1.3$$

$$\dot{\underline{\lambda}} = \underline{r} \qquad 1.4$$

where the time derivative operator is defined by:

$$\cdot \equiv \partial/\partial t + (\underline{u} \cdot \operatorname{grad})$$

and ρ is density
$\underline{u}$ is particle velocity vector
p is pressure
V is specific volume
E is specific internal energy
$\underline{\lambda}$ is the chemical concentration vector
$\underline{r}$ is the chemical reaction rate vector

If the internal energy is assumed to be a function of the pressure, specific volume and chemical concentration vector, then the expansion of the internal energy time derivative can be combined with the enthalpy conservation equation (1.3) to yield an adiabatic relationship for the pressure time derivative.

$$\dot{p} = c^2\dot{\rho} + \rho c^2 \underline{\sigma} \cdot \dot{\underline{r}} \qquad 1.5$$

where c is the frozen reaction state sound speed
$\underline{\sigma}$ is the thermicity vector defined by

$$\underline{\sigma} = (\partial P/\partial \underline{\lambda})^{E,V}/\rho c^2 \qquad 1.6$$

It is useful to first consider the one dimensional steady detonation state. The essential feature of steady detonation is that in a reference frame attached to the shock front the flow of particles and other flow descriptors are independent of time. Transforming the equation of motion to one dimension and Lagrangian co-ordinates gives:

$$\rho u + u\rho = 0 \qquad 2.1$$

$$\rho uu + p = 0 \qquad 2.2$$

$$E + pV = 0 \qquad 2.3$$

The adiabatic relationship becomes:

$$\dot{p} = -\rho u^2 \underline{\sigma} \cdot \dot{\underline{\lambda}} /(1-u^2/c^2) \qquad 2.4$$

and the time derivative operator now refers to particle motion with respect to the shock

$$\cdot \equiv \partial/\partial t$$

These equations correspond to the ZND theory of detonation. The adiabatic relationship shows that the pressure falls in value behind the shock front as reaction occurs, and for there to be no discontinuity in the pressure as the reaction rate reaches zero, i.e. full reaction, the particle velocity, must equal the sound speed. This is the normal CJ condition.

The differential equations can be integrated, and combining these with a specific equation of state, the CJ condition, full chemical reaction condition, and an expression for the sound speed which is equation of state dependent, the ideal detonation state can be found by solving the set of non-linear simultaneous equations. Both the detonation velocity and the flow and thermodynamic state at all other points between the CJ plane and shock front can be determined.

For detonation along a cylinder in which a small radial expansion occurs the steady state equations of motion in Lagrangian co-ordinates become:

$$u\rho + \rho u = -2\rho u\omega r \qquad 3.1$$

$$\rho uu + p = 0 \qquad 3.2$$

$$E + pV = 0 \qquad 3.3$$

and the adiabatic relationship is:

$$p = -\rho u^2\{\underline{\sigma} \cdot \underline{\lambda} - 2\omega_r\}/\{1-u^2/c^2\} \qquad 3.4$$

in which ω_r is the divergence defined as the radial particle velocity at unit distance from the axis of the cylinder.

The adiabatic relationship shows that for there to be no discontinuity in the pressure at the CJ point ($u=c$) the reaction rate must be finite and given by:

$$\underline{\sigma} \cdot \underline{\lambda} - 2\omega_r = 0$$

which is sometimes called the second CJ condition

Finding the detonation state eigenvalues is less straightforward now because the mass and momentum conservation equations (3.1 and 3.2) can no longer be integrated analytically, and there is the additional divergence variable,

which as will be seen later is also usually related to other variables by a differential relationship. The problem is therefore an ordinary differential equation mixed boundary value problem, with the first and second CJ conditions providing boundary values at the CJ plane, and the unreacted shock state behind the curved shock front providing further conditions.

A bonus of moving to differential equations is that the reaction progress is best described in terms of reaction rate as a function of degree of reaction and pressure or temperature. This is now easily incorporated into the set of equations.

The complete general set of equations are:

$$A\rho u - \rho_0 D = 0 \qquad 4.1$$

$$\rho uu + p = 0 \qquad 4.2$$

$$E + pV + u^2/2 = E_0 + p_0V_0 + D^2/2 \qquad 4.3$$

$$E = E(p,V,\underline{\lambda}) \qquad 4.4$$

$$\underline{\lambda} = \underline{\lambda}(\lambda,p) \qquad 4.5$$

$$A = 2A\omega_r \qquad 4.6$$

$$\dot{\omega}_r = \dot{\omega}_r(\underline{\lambda}, x, u, D \ldots) \qquad 4.7$$

where D is the detonation velocity

A is the stream tube area which is defined as the area of a stream of particles which have unity area at the shock front.

The shock front boundary conditions are:

$$A = 1 \qquad 4.8$$

$$\lambda = 0 \qquad 4.9$$

$$\omega_r = (D-u)/R_s \qquad 4.10$$

where R_s is the curvature of the shock front. The CJ boundary conditions are simply the two CJ conditions. This set is sufficient to determine the detonation velocity eigenvalues for a given shock front curvature, and all the other variables at different distances behind the shock front.

As stated above in general a numerical solution to these equations is needed, especially if realistic equations of state (4.4), reaction rate laws (4.5), and divergence relationships (4.7) are to be used. There are a few aspects of this worth mentioning.

The main difficulty is related to the approach to zero of the denominator in the adiabatic relationship, which is implicit in these equations. This requires that any solution strategy must always have the second CJ condition exactly satisfied at the same point (u=c).

In integrating between the two boundaries it has been noticed that the equations leave some variables undetermined. A numerical integrator which can handle this must therefore be used.

Finally there are in general no solutions below some critical detonation velocity. This is normally characterized by the particle velocity and sonic velocity becoming equal at a location between the CJ and shock fronts. This does not correspond to the critical diameter of the explosive.

EQUATION OF STATE

The choice of equation of state to use in the above model depends on the application. For commercial explosives there are three main needs. The expansion isentrope of the products should be accurate between about 0.1 GPA and 10 GPA. Both isentrope and off-isentrope behaviour should be accurate in the reaction zone which is from 2 GPA to 20 GPA. In explosives with a heterogeneity in excess of a few microns the ingredient phase should be treated as being thermally isolated from the reacted phase.

The JWL equation has been used by Lee and Tarver (5) to model similar problems and largely meets the above criteria. However a simpler equation of state has been adopted for the calculation in this paper, its main advantage being a smoother fit to the isentrope over the pressure range of interest, at the expense of a slightly worse fit to Gruneisen gamma in the reaction zone.

The equation of state of a single phase is given the form

$$E = pV/(g-1) \qquad 5.1$$

$$g = g_0 + g_1\rho + g_2\rho^2 \qquad 5.2$$

The value of the constants g_0, g_1, g_2, etc. for the explosive products are determined by fitting to isentrope data from an ideal thermodynamic code. There are three constraints on the fitting procedure. Firstly g_0 is set equal to the ideal gas value. Secondly the CJ values of gamma $((d(\ln p)/d(\ln \rho))_s)$ and detonation velocity given by this equation of state must equal the thermodynamic code value.

The constants for the unreacted phase are obtained by considering the shock state of the explosive and using known Hugoniot data of the ingredients. The calculations are however complicated because the explosive is in general a mixture of ingredients, and also includes voids.

The calculations are based on those of Afanasenkov (6). There is assumed to be pressure equilibrium between all phases, each phase being compressed to its respective shock Hugoniot volume. This assumption leads to the shock velocities and particle velocities of each component having different values, and viscous effects are needed to bring them to the average value.

The theory departs from Afanasenkov in its treatment of gas bubble collapse. Calculations indicate that the particle velocity of liquid and solid phases are an order of magnitude too small to shock the gas phase to the same pressure. It is therefore assumed that the gas phase is adiabatically collapsed. Applying mass and momentum conservation laws, first to the overall system, and then to the individual phases, reveals an energy miss-match which requires the postulation that energy is stored in the form of turbulence or secondary shocks immediately behind the shock front. There is not space for the detailed calculations here, but the magnitude of the turbulent stored energy is found to be given by:

$$E_t = \frac{pV_{go}}{2}\left[1-\left(\frac{\gamma_g+1}{\gamma_g-1}\right)\left(\frac{p_o}{p}\right)^{1/\gamma_g}\right] \qquad 6.1$$

where E_t is the specific turbulent energy

V_{go} is the initial volume of gas per unit mass of explosive
p is the shock pressure
γ_g is the average value of gamma for the gas

The parameters used in the unreacted equation of state are now obtained by simply fitting to calculated E-p-V data but with this turbulent energy omitted from the internal energy.

The reactive equation of state now becomes:

$$E = (1-\lambda)pV_u/(g_u-1)+E_t + \lambda pV_R/(g_R-1-q] \qquad 7.1$$

where λ is the fraction of reacted explosive.
subscript u refers to the unreacted or ingredient phase
subscript R refers to the reacted or reacted or product phase

The turbulent energy has been assumed to decay at the same rate as the reaction takes place, and the model needs a better description than this. To determine all the variables in the equation of state, expressions for the total specific volume and isentropic expansion of the unreacted phase must be included.

$$V = (1-\lambda)V_u + \lambda V_R \qquad 7.2$$

$$p = \text{const}_u(g_u-1)\varrho_u^{g_{uo}} \qquad 7.3$$
$$\text{x } \exp g_{u1}+g_{u2}\varrho^2/2+..$$

At the CJ point expressions for both the frozen reaction sound speed and thermicity are needed. To calculate the sound speed it is assumed that the sound fluctuations cause each phase to change adiabatically, but with pressure equilibrium between the two phases. Differentiating the volume equation (7.2) with respect to pressure, holding entropy constant, and remembering that the sound speed is defined by $(dp/d\varrho)_s$, gives:

$$\frac{V^2}{C^2} = (1-\lambda)\frac{V_u^2}{C_u^2} + \lambda\frac{V_R^2}{C_R^2} \qquad 8.1$$

$$C_u^2 = g_u pV_u + p/(g_u-1)\frac{\delta g_u}{\delta \varrho_u} \qquad 8.2$$

$$C_R^2 = g_R pV_R + [p/(g_R-1)]\frac{\delta g_R}{\delta \varrho_R} \qquad 8.3$$

The thermicity is defined by equation (1.6), but it is better to write this in terms of energy derivatives as:

$$\sigma = -\left(\frac{\delta E}{\delta \lambda}\right)_{p,V}\Big/\varrho c^2\left(\frac{\delta E}{\delta p}\right)_{\lambda,V}$$

its value then being determined by differentiating equations (7).

HOTSPOT AND BURN REACTION MODEL

Experimental measurements of the reaction behaviour of commercial explosives using the electromagnetic particle velocity gauge indicate that at least three sequential reaction processes are needed to explain the observations. These can be thought of as the hotspot, liquid and solid reactions.

Measurement of liquid and solid burn rates (7) show they have a linear pressure dependence, while a simple but effective way of describing the hotspot behaviour is to consider reaction starting above some critical pressure, and the rate then proportional to the pressure excess. The reaction rate in this multi-phase hotspot and burn model is written as:

$$\dot{\lambda} = (1-\lambda)a_h(p-p_h)/\tau_h + a_l p/\tau_l + a_s p/\tau_s \qquad 9.1$$

where p_h is the critical hotspot pressure

τ are characteristic reaction times at unit pressure

a are functions of λ which switch the reaction on and off as the phases are ignited and consumed

subscripts h,l,s refer to hotspot, liquid and solid phases.

The mass fraction of hotspot is determined by the explosive formulation, and for this model is assumed to be equal to the ratio of the voidage to non-voidage in liquid explosives, and half that in solid explosives.

The principle of the reaction switch is that as the liquid phase reaction starts the hotspot phase reactions begin to extinguish. A gaussian function is used to define this process, with the half width point of the gaussian being reached when the degree of reaction corresponds to the mass fraction of hotspots. The same process applies to the solids being ignited by the liquid phase.

The half width of the gaussian ignitions are assumed to depend on the weight fraction of hotspots, liquids, and solids (WT_h, WT_l, WT_s). The full definitions of the parameters are:

$$a_h = \exp-((\lambda - W_l)/C_l)^2 \qquad 9.2$$

$$a_l = \exp-((\lambda - W_s)/C_s)^2 - a_h \qquad 9.3$$

$$a_s = 1 - a_h - a_l \qquad 9.4$$

$$W_l = WT_l^2 \qquad 9.5$$

$$W_s = 1 - WT_s^2 \qquad 9.6$$

$$C_l = WT_h(1-WT_h) \qquad 9.7$$

$$C_s = WT_s(1-WT_s) \qquad 9.8$$

UNCONFINED DETONATION

Several models of the variation of the divergence behind the shock front is unconfined detonations have been examined. Two simple approaches are to assume the divergence is constant, or to assume the curvature of pressure isobars behind the shock front are constant. Neither give good agreement with electromagnetic particle velocity data over the whole range though the constant curvature does well close to the shock front, and the constant divergence does well far behind the shock front.

The chosen model combines these two observations, and changes the isobar curvature smoothly to qualitatively agree with published numerical calculations (8) and x-ray experiments (9). In the CJ region the isobars are assumed to be spherical and to meet at a diameter equal to the radius of curvature of the shock front, as shown in the diagram.

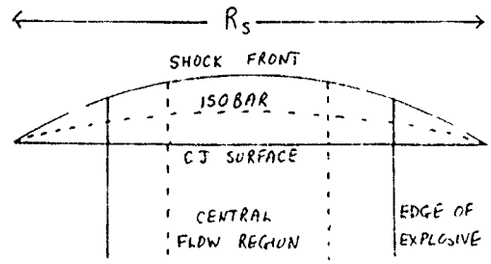

Fig. 1

It is assumed that the small divergent flow theory will only be obeyed in a central region with a diameter of about one third of the shock front curvature. This value is chosen because of much experimental data at diameters very large compared with the critical diameter.

The second concept, first proposed by Bdzil (10) is that in unconfined detonations there is an outer skin of the explosive which will not obey the small divergent flow theory, and which is about one CJ distance in thickness. The diameter of the explosive is therefore given by:

$$\text{dia} = \alpha R_s + \beta x_{CJ} \qquad 10.1$$

The values of α and β were determined by experimentally measuring both shock front curvature (streak photography) and CJ distance (electromagnetic gauge) of several commercial explosives at different diameters (3).

The equations defining the variation of divergence now become:

$$\omega = -u/R \qquad 10.2$$

$$R = R_s^2/(R_s - 8x_{CJ}) \qquad 10.3$$

$$x = u \qquad 10.4$$

where x_s is the distance behind the shock front

x_{CJ} is the CJ distance on the axis of the charge

These equations can be combined with the flow theory equations (4), equation of state (7), reaction rate (9), to predict the detonation behaviour at different diameters. Using parameter values typical of an air sensitized emulsion explosive, the four kinetics parameters being obtained from electromagnetic particle velocity data (3), a prediction of detonation velocity against diameter can be made, and is shown in Fig. 2.

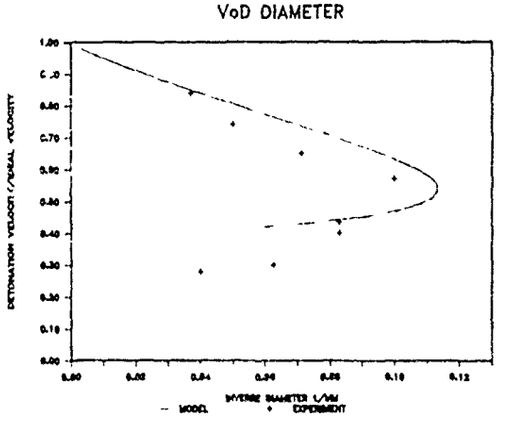

Fig. 2. VoD Diameter

This predicts a linear variation of detonation velocity with inverse diameter, in good agreement with experimental data shown as the crosses. The minimum diameter is also in good agreement with the measured critical diameter. The lower branch of the curve represents a minimum initiation condition. It corresponds to sets of conditions which can just maintain a steady detonation, but any fluctuation in velocity will be amplified leading either to failure or detonation at the higher value. The proof of this is briefly discussed later.

This lower branch can therefore be compared with initiation experimental data using PMMA card gaps (3). The agreement can only be expected to be approximate as each point on the lower curve has a particular pressure and divergence time profile and the output of the card gaps will not in general give the same time profile. In spite of this it provides a useful comparison.

CONFINED DETONATION

If the explosive is strongly confined the divergence is small over the whole area of the cylinder, the full cross-section of the explosive obeys the small divergent flow theory, and semi-empirical aspects are largely eliminated.

The concept used to determine the variation in divergence with distance behind the shock front is that explosive and confinement remain in contact at the borehole wall, that the explosive can slide over the confinement, and that there is pressure equilibrium at the borehole wall. It is then assumed that the confinement pressure can be represented by a second order differential equation in the stream tube area, which is related to divergence in the usual way.

$$p = k_1(A-1) + k_2 A \text{ dia} + k_3 \dot{A} \text{ dai}^2 \quad 11.1$$

$$\dot{A} = 2A\omega_r \quad 11.2$$

$$\dot{A} = 2\dot{A}\omega_r + 2A\omega_r \quad 11.3$$

The three terms in the pressure equation roughly correspond to the forces due to the steady strain in the expanded borehole, viscous and other inelastic processes due to the rate of expansion of the borehole, and inertia of the region of the confinement close to the borehole which undergoes acceleration during the expansion process.

If the sound velocity in the confinement exceeds the detonation velocity of the explosive then this provides an accurate description of the behaviour, and the shock front boundary conditions are $A=1$ and $\dot{A}=0$. Also values of the constants in equation 11.1 can be obtained for an elastic material in terms of density, Young's modulus and Poissons ratio by considering a conical shock in the material (11).

If however a shock is transmitted into the confinement then the divergence at the shock front is no longer zero, and the material close to the borehole wall undergoes plastic flow or failure and cannot be considered elastic.

The divergence at the shock front can be determined by using the theory of acute shocks (12) on both the confinement and unreacted explosive and choosing shock angles in each that match both pressure and divergence. In practice the maximum divergence in the rock may be insufficient to match the pressures, and in this case this maximum value is chosen, and the

pressure difference determines the acceleration of the borehole wall (equation 11.1) at the shock front.

The inelastic behaviour is less easily accommodated. In practice an annulus around the borehole will undergo plastic flow or will fail, and only beyond this region will the elastic behaviour of equation 11.1 be obeyed. To date this has been incorporated by simply choosing lower values of Young's modulus so that the equilibrium expansion of the borehole wall agrees with observed behaviour (12), though in the longer term a more detailed mathematical description is needed.

Fig. 3 compares the predicted and measured variation of detonation velocity with diameter of an emulsion explosive confined in steel. A value of Young's modulus equal to the static value was chosen and as can be seen the agreement between experiment and theory is satisfactory without introducing any empirical factors.

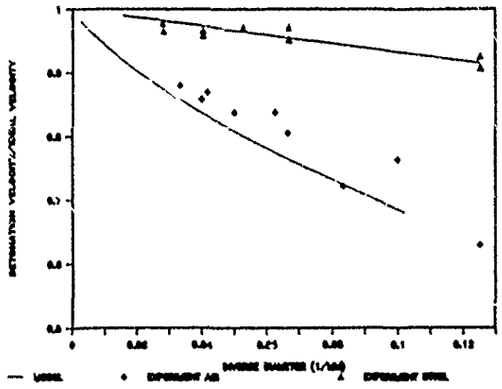

Fig. 3. Confined Behaviour

ENERGY DELIVERY TO CONFINEMENT

For many years it has been common practice to rate commercial explosives in terms of the energy they release as they expand isentropically from the ideal detonation or explosion state, to a lower pressure and density state. This non-ideal model provides a more realistic analysis and description of the energy delivery to the confinement.

The energy is partitioned into three types, the shock energy delivered to the rock, the equilibrium strain energy stored in the rock when the borehole has expanded, and the energy released by the explosive expanding adiabatically into a crack network in the rock until the whole rock mass is in equilibrium with explosive products. Typically this last state is at pressures around 0.1 GPA and densities 0.1 of the initial unreacted explosive density.

The shock energy delivered to the rock per unit mass of explosive is obtained by integrating the product of expansion, pressure and specific volume from the shock state to the steady state well behind the CJ plane:

$$E_{SHOCK} = \int_0^{\infty} (pV\dot{A})dt \qquad 12.1$$

The strain energy stored in the rock is proportional to the expansion of the borehole for small expansions, and per unit mass of explosive is given by:

$$E_{STRAIN} \approx \frac{1}{2}pV(A-1) \qquad 12.2$$

The shock energy is always greater than the strain energy, the difference corresponding to the energy lost by irreversible processes such as failing rock, plastic flow in the rock, and radiation of elastic waves from the borehole.

The delivery of shock energy is important in blasting operations, and the process is worth considering in greater detail. Fig. 4 shows the predicted variation of pressure with borehole area for an emulsion explosive confined in a medium strength rock at two different diameters.

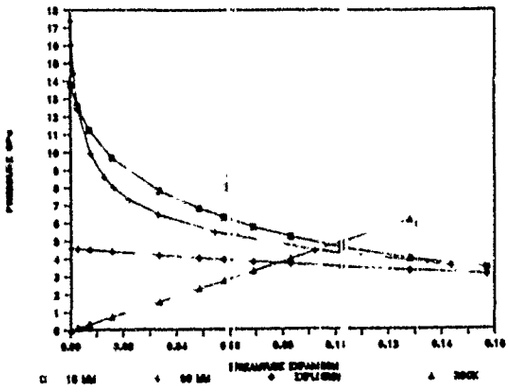

Fig. 4. Expansion Behaviour

The larger diameter explosive detonates at higher velocity with higher shock and CJ pressures, but the pressure falls more rapidly with radial expansion because the axial particle

velocity is reduced more rapidly than in the smaller diameter case. The total shock energy delivered may vary by as much as 40% above the explosion state values to as much below, and varies in a complex manner with the detonation velocity.

At distances within about ten borehole diameters of the initiation point the flow behind the CJ plane will include a Taylor rarefaction. This reduces the pressure more rapidly than in the above calculation, and therefore reduces the shock energy. It will be still further reduced if the initiation is sub-optimal and the explosive has to run up to steady detonation. The conclusion is that the current practice of using explosion state shock calculations must be treated only as a guide to the true behaviour.

The energy delivered during the later expansion of the explosive products into the crack network of the rock is essentially equal to the change in internal energy of the explosives. However the starting point for this expansion should correspond to zero axial velocity of the products. In an explosive of finite length the Taylor wave expansion to the rear of the detonation decelerates the forward particle motion without doing work on the surroundings. It is therefore reasonable to use as the initial state for the expansion a specific volume equal to the initial specific volume of the unreacted explosive corrected by the borehole expansion.

During the expansion process the explosive products and any unreacted ingredients are assumed to behave isentropically and to remain in pressure equilibrium. The pressure volume relationship is therefore determined by solving the three equations:

$$V = (1-\lambda)V_u + \lambda V_R \qquad 13.1$$

$$p = \text{const}_u(g_u-1)\varrho_u^{g_{uo}} \times \exp\{g_{u1}\varrho_u+g_{u2}\varrho_u^2/2+\ldots\} \qquad 13.2$$

$$p = \text{const}_R(g_R-1)\varrho_R^{g_{Ro}} \times \exp\{g_{R1}\varrho_R+g_{R2}\varrho_R^2/2+\ldots\} \qquad 13.3$$

The internal energy of the explosive is given by equation 7.1.

ACCELERATING DETONATIONS AND STABILITY CONDITIONS

The model can be used to estimate the detonation acceleration of an explosive by considering the time dependent slightly divergent equations. The result of this is the replacement of equations (4.1), (4.2) and (4.3) by:

$$A\varrho u - \varrho_o D = -\varrho_o D\int_0^t(\varrho'/\varrho)dt \qquad 14.1$$

$$\varrho u\dot{u} + \dot{\varrho} = -\varrho uu' \qquad 14.2$$

$$E + pV + u^2/2 - (E_o+p_oV_o+D^2/2) = \int_0^t(E'+pV'+uu')dt \qquad 14.3$$

and the second CJ condition becomes:

$$\underline{\sigma}\cdot\dot{\underline{\lambda}} - 2\omega_r = u'/u + \varrho'/\varrho \qquad 14.4$$

where $' \equiv (dD/dt)(\partial/\partial D)$

An estimate of the values of the right hand terms can be obtained by considering one dimensional flow. Differentiating the conservation equations with respect to time allows p, u, E to be expressed in terms of the normal variables, the detonation acceleration (dD/dt), and the rate of change of particle velocity with detonation velocity. The result is the ability to determine the right hand terms in the above equations at the shock front and the CJ plane as a function of detonation acceleration. The accuracy of determining acceleration rates by this process is unlikely to be better than 50%.

Fig. 5 shows the steady and decelerating detonation velocity against inverse diameter curves for the air sensitized emulsion. It is clear from this that the detonation accelerates at all points to the left of the steady curve, and decelerates at all points to the right. It demonstrates the unstable nature of the lower branch.

CONCLUSION

This paper has demonstrated a broad range of explosive characteristics that can be modelled using the small divergent flow theory. The current limitations of the theory have been discussed and further development is needed.

It does however already offer a method of characterizing the non-ideal behaviour of explosives by matching experimental detonation velocity - diameter and initiation - diameter data to the unconfined model. These characteristics

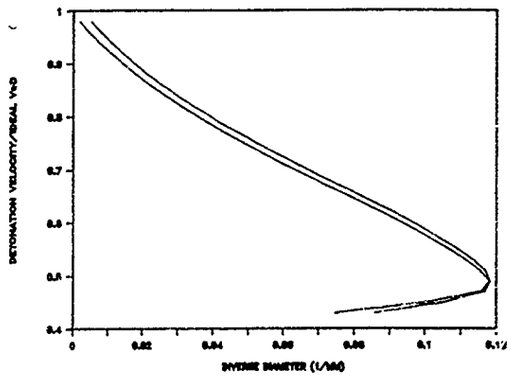

Fig. 5. Accelerating Detonation

can then be used to predict many confined detonation properties, and provide a far more realistic estimate of the useful energy available from the explosive under the particular conditions in which they are used.

REFERENCES

1. W. W. Wood & J. G. Kirkwood, "Diameter effect in condensed explosives. The relationship between velocity and radius of curvature of the detonation wave," J. Chem. Phys. Vol. 22, No. 11, pp. 1920-1924, 1954.
2. S. K. Chan, "A Theory to Predict the Velocity-Diameter relation of Explosives," Seventh Symp. (International) on Detonation, Annapolis, Maryland, June 1981.
3. G. A. Leiper, I. J. Kirby, A. Hackett, "Determination of Reaction Rates in Intermolecular Explosives using the Electromagnetic Particle Velocity Gauge," Eight Symp. (International) on Detonation. Albuquerque, July 1985.
4. W. Fickett & W. C. Davis, "Detonation" 1979, University of California press, Berkley.
5. Lee & Tarver, "Phenomenological Model of Shock Initiation of Heterogeneous Explosives," Phys. Fluids. Vol. 23, 12 1980, pp. 2362.
6. A. N. Afanasenkov, V. M. Bolomolar, I. M. Voskoboinikov, "Generalized shock hugoniot of condensed substance, "Zhur. Prok, Mekh. Tekh, Fig. Vol. 10, pp. 137-147, 1969.
7. C. M. Lowands. Internal ICI Report.
8. M. Yoskida, K. Tanaka, K. Yoneda, T. Hikita, "The Study of detonation on high explosives by flash x-ray," Journal of Explosives Soc. of Japan, 1982.
9. H. U. Freund & W. Geiger, "Velocity & density fields in reaction products of a detonating cylindrical charge," Acta Astro 1, pp. 405-16, 1974.
10. J. B. Bdzil, "Steady State Two-dimensional Detonation," J. Fluid Mech. 108, 195-226 (1981).
11. J. P. Tidman, Internal ICI Reports.
12. T. Neal, "Perpendicular Explosive Drive and Oblique Shocks," Sixth International Detonation Symp., p. 602, 1976.

ACKNOWLEDGEMENTS

The authors would like to acknowledge the very significant help from Dr. I. Parker, NSG, ICI, Runcorn in providing the strategy for the numerical solutions of the model. Also we would like to thank C. M. Lowands, AECI, Johannesburg for suggestions on energy delivery aspects, and J. P. Tidman, DRG, for calculations demonstrating the effects of confinement.

DISCUSSION

Y. TIMNAT, Isreal Inst. of Technion City, Haifa

I counted about 25 adjustable parameters - how do you determine them all?

REPLY BY I. J. KIRBY & G. A. LEIPER

The first point to make is that the theory contains only two truely adjustable parameters, namely the α & β in equation 10.1.

These are necessary because the theory is based on small divergent flow and the behaviour at large distances off axis has to be treated empirically. The second of our papers deals in some detail with the experimental method, using the electromagnetic gauge, that we adopted to determine these parameters.

The model certainly contains constants associated with the equation of state of the unreacted and reacted products. These constants are determined by the Hugoniot properties of

the ingredients of the explosive, with the Afanasenkov theory (see reference 6), and the thermochemical properties of the ingredients with any suitable ideal detonation code. There may be adjustable parameters in the ideal detonation code, though this is outside the scope of the paper.

Four parameters are used to describe the reaction behaviour of a gas - liquid - solid explosive system. It is these that characterize the non-ideal behaviour of the explosive, and they are determined, as described in the paper by measuring the variation of detonation velocity with diameter, determining the critical point, and measuring the initiation behaviour of the explosive.

The only remaining constants that were not fully defined in the paper are k_1, k_2 & k_3 in equation (11.1). These are determined as stated, by the elastic and Hugoniot properties of the confinement. The relationships used in the model are:

$$k = \tfrac{1}{2}E/(1+\gamma)$$
$$k_2 = 7\varrho c/4$$
$$k_3 = \varrho/8$$

where E is Young's modulus
γ is Poisson ratio
ϱ is density
c is sound speed

and are based on considering a conical shock in the confinement. The derivation of these simple relationships involves some approximations, but the resultant errors are believed to be trivial.

DISCUSSION

YUN K. HUANG, Latham, New York

It is not clear to me that your rate law is dimensionally consistent. Do you normalize all your pressure terms or introduce an inverse pressure factor to your Gaussian type a's in the viewgraph showing the rate law? If so, how?

REPLY BY I. J. KIRBY & G. A. LEIPER

The rate law in equation 9.1 contains non dimensional constants - "a_h, a_l, a_s - which are functions of the degree of reaction and the formulation of the explosion. Their values are defined in equation 9.2 to 9.8.

The characteristic rate parameters "τ", have the units of time x pressure. This is a result of the assumption in the model that the reaction rate of liquid and solid phases are proportional to pressure, while the reaction rate of the hotspots are proportional to the pressure in excess of a critical value.

Typical commercial explosives have values of τ in the range 1 μS x GPA to 50 μS x GPA.

DISCUSSION

W. C. DAVIS, Los Alamos National Laboratory

Would you contrast your work with that of Chaisse et al, and Matsui et al, presented just before your paper, and with the earlier work of Bdzil?

REPLY BY I. J. KIRBY & G. A. LEIPER

The paper by Matsui et al, is similar to an earlier model developed at our laboratory and presented by Chan at the Seventh Detonation Symposium.

There are however a number of important differences between Matsui and our current model.

The first is the use by Matsui of an Arrhenius rate law. We have found from gauge data that this poorly represents typical reaction behaviour of commercial explosives. The four parameters reaction rate law is much more suitable for this purpose.

The second is the empirical relationship used to relate the shock front curvature to the diameter of the charge, in unconfined explosive situations. As far as I can see Matsui points out the difficulties of doing this, but attempts no solutions. We have used the relationship in equation 10.1, and the experimental verification is covered in some detail in the second paper.

The third is the use by Matsui of a constant isobar curvature behind the shock front. For unconfined detonations our model varies this curvature using an empirical relationship that gives reasonable agreement with true two dimensional reactive flow modelling and with experimental x-ray work.

A fourth difference is in the treatment of confined detonations, Matsui matches pressure and divergence of explosive and confinement only at the shock front, while our model matches

these at all positions using the second order differential equation (11.1).

There are also differences in our choices of equations of state of explosive ingredients and products, and other less important aspects.

The paper by Chaisse et al, addresses the problem of the unconfined shock front curvature-diameter relationship, but does not attempt a complete solution of the two dimensional detonation. By considering the processes that occur at the shock front only they obtain the curvature relationship.

This theory can be used in our model to replace the empirical equation 10.1. It would clearly be superior for use in modelling fairly ideal high explosives in which the charge diameter is many times the reaction zone length. It would not be expected to work as well with the very non-ideal commercial explosives, but only comparison with experimental results on such explosives could determine the magnitude of the mismatch.

The principle advantage of Bdzil's theory over ours is that he solves the CJ condition both on and off the charge axis, and has therefore eliminated the main empirical aspect of our model, the curvature-diameter relationship. This is clearly a significant improvement.

The form of equation 10.1 was conceived as a result of reading Bdzil's paper, but that is as close as we have got to using his approach.

There is however a concern about applying the theory, which assumed diameters large compared to reaction zone length, to the non-ideal commercial explosives which often have reaction zone lengths similar to the charge diameter. As with the theory of Chaisse et al only experimental verification can determine the usefulness of the theory to such explosives.

DETERMINATION OF REACTION RATES IN INTERMOLECULAR EXPLOSIVES USING THE ELECTROMAGNETIC PARTICLE VELOCITY GAUGE

G. A. Leiper, I. J. Kirby, A. Hackett
Detonation Research Group, ICI PLC, Stevenston, UK.

The rate of reaction of a non-ideal air sensitised commercial explosive is reported as a function of initial voidage, bubble size and charge diameter. A suitable functional form for the reaction rate as a function of extent of reaction and of pressure is suggested. The proposed form is shown to have physical significance.

Experimental particle velocity time records of steady state detonation in cylindrical charges of various diameters were measured by the electromagnetic technique. This data was used to integrate flow equations to yield fraction reacted time profiles within the explosive. The reactive flow model was based on Wood-Kirkwood theory with a correction to flow divergence for experimentally observed shock front curvatures. A variable gamma law equation of state was used to describe both unreacted explosive and reaction products.

Limitations on the use of gauge data to calibrate phenomenological reaction rate models are discussed with specific relevance to the predictive capability of the slightly divergent flow approach. Reasons for breakdown of the model below certain voidages are given.

INTRODUCTION

Commercial air-sensitised explosives belong to the so-called non-ideal or Group II class of explosives as defined by Price (1). Such explosives are characterised by a strong dependence of detonation velocity on charge diameter, and an inverse relationship between critical diameter and voidage. The performance of these compositions is a function of both the environment in which they are used, the confinement, and the heterogeneous nature of the chemical reactions which occur during detonation. Prediction of the detonation performance of such compositions requires both a model of hydrodynamic flow and of chemical energy release rate, as proposed by Chan (2) or by Bdzil (3).

Kirby and Leiper (4), have developed such a model based on Wood-Kirkwood theory (5) and a phenomenological model of chemical reaction. In this paper experimental evidence based on electromagnetic particle velocity gauge (EPVG) records is presented which support the proposed reaction rate model. Further, data derived from EPVG traces are shown to be in agreement with the porous Hugoniot and flow models used in (4).

The EPVG technique has been well documented previously (6,7) and has been used to monitor both steady and non-steady flow. In non-steady state applications it has been the practice to use EPVG records to calibrate Ignition and Growth to detonation models (8) or to derive reaction rates by Lagrangian analysis (9); historically steady state measurements have only been used to measure CJ parameters, or flow in inert media (7). The method described in this work is based closely on that in (7) but with development in gauge protection, to facilitate use in reacting flows and small charge diameters. The single foil approach advocated in this paper offers a simpler experimental arrangement than multiple foil techniques yet provides similar data on the shocked state in the unreacted explosive and on the reaction rate behind the shock.

EXPERIMENTAL

A diagram of the experimental arrangement is shown below.

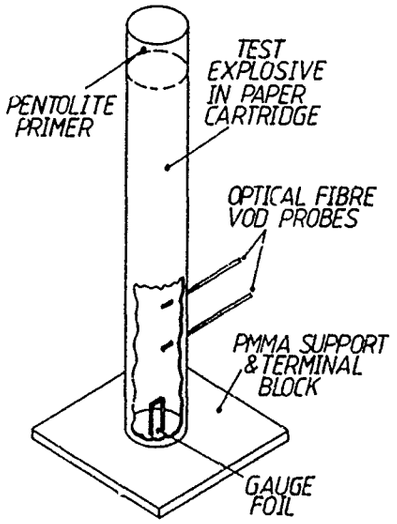

Fig. 1 Experimental Diagram

A standard stirrup shaped gauge foil was used, formed out of 99.9% pure Aluminium, into an open rectangle of leg length 15 mm and an active arm of 3 mm. The initial foil thickness was .05 mm which was anodised, after forming, to be a 12.5/25/12.5 micron thick composite of $Al_2O_3-Al-Al_2O_3$ (10). The oxide coating provided electrical insulation from the reacting explosive, and enhanced the structural rigidity of the assembly, facilitating handling and enplacement of the gauge. A pair of .5 m diameter helmholtz coils were used to form an air cored solenoid magnet. The coils, consisting of 210 turns of 4 mm^2 enamelled copper wire, potted into silicone rubber, gave a field of .05T when passing 100A at a separation of .25 m. The field was homogeneous to better than 1% over a central .1 m long, .1 m diameter right cylinder. Each coil assembly was protected from blast damage by a 10 mm thick non-magnetic stainless steel casing. The coils were energised by a high current contactor switching a pack of lead-acid cells. The current through the coils was slowly varying and could be considered constant in the timescale of the gauge measurement.

The explosive chosen for investigation was an ammonium nitrate, water, oil emulsion manufactured to have a viscosity such that it would flow round the gauge without distorting the foil or entrain any air. Sensitivity was obtained by the addition of glass walled microspheres to the desired voidage level. Control of void size was achieved by removing under vacuum, any air entrained during preparation of the explosives, and by seiving of the microspheres. Care was taken to ensure that the emulsion was reproducible from batch to batch. Emulsions were stored for no longer than four days; at that time NH_4NO_3 crystals could not be seen, and emulsion droplet size appeared unchanged.

The cartridge, a right cylinder of waxed paper, was long enough to give an explosive column length of at least six charge diameters between initiator and the first VOD probe. This was thought sufficient to ensure steady state detonation (11). The explosive was initiated with a pressed pentolite pellet, generating at least ten times the critical intiation pressure of the explosive in the gap test.

Measurements made for each shot were: magnetic field, monitored by the current through the coils; detonation velocity, calculated from the time of flight of the shock between two air gap fibre optic probes; and the gauge voltage time trace, captured digitally sampling at between 8 and 20 nS per point with 8 bit resolution.

Conditioning of the gauge records was confined to elimination of risetime effects. Signals were discarded, if the risetime was greater than 150 nS, equivalent to four shock reverberations in the foil plus the shock transit time across two sensitising voids: the shock was said to require a run of two void diameters to regenerate itself after interaction with a void. Risetimes greater than 150 nS are associated with non centrosymmetric shocks caused by gross inhomogeneity in the explosive. Risetimes on acceptable records were extrapolated back to zero time.

Gauge records were obtained for three voidage levels 10, 17 and 25%, each at a minimum of three charge diameters ranging from close to the critical to five times the critical. Two types of void were used; unclassified with a size range of 20-170 micron; and classified +75-90 micron.

ANALYSIS

The gauge signal was analysed in terms of a slightly divergent flow theory developed from the work of Wood and Kirkwood (5) with a correction to flow divergence for observed shock front curvature. It was an extension of the work of Chan (2). The gauge record was integrated in discrete time steps, to yield the state variables, particle velocity and fraction reacted as a function of time, from the shock front till the gauge was judged to have broken up. This was usually signified by a marked increase in noise on the trace followed by rapid excursions from a slowly varying state. Depending on the integrity of the gauge, it was possible to follow reaction from the shock to well beyond the CJ plane. The integration procedure was based on the following equations:

$$A = A_{n-1} + 2w_r dt \quad 1.1$$

$$u = (D \cdot G)\ /B/\sqrt{A} \quad 1.2$$

$$\dot{F} = F_{n-1} + [\dot{u}/u(1-u^2/c^2) + 2w_r]/S\ dt \quad 1.3$$

$$x = x_{n-1} + u dt \quad 1.4$$

$$R = R(R_s, x, x_{C,J}) \quad 1.5$$

$$p = p_{n-1} - \dot{u}u/v\ dt \quad 1.6$$

$$v = Auv_0/D \quad 1.7$$

$$g = g(g_u(p), g_r(p), F) \quad 1.8$$

$$c^2 = c^2(p, v, g, F) \quad 1.9$$

$$S = S(g, p, Q, E_T, v) \quad 1.10$$

$$w_r = w_r - \dot{u}/r\ dt \quad 1.11$$

where A is the streamtube area; w_r the divergence; u the shock fixed frame particle velocity; F the fraction reacted, c the sonic velocity, x the distance from the shock; R the isobar radius of curvature; R_s the shock front curvature; p the pressure; v the specific volume; D the detonation velocity; B the gauge factor; G the gauge signal; v_0 the initial volume; g the adiabatic exponent in the equation of state; S the reaction thermicity; Q the chemical energy; E_T the turbulent energy; subscripts u and r refer to the unreacted and reacted state respectively; dt is the time step; and • signifies the time derivative. These equations are further described in (4).

The integration scheme required as initial values the shock front particle velocity, the shock front curvature, and gamma for the unreacted and reacted explosive. The variation of the reacted gamma with pressure was also required.

The shock front particle velocity was obtained from the gauge record extrapolation to zero risetime, as stated previously. Justification of this procedure was obtained by comparison of the observed shock velocity - particle velocity hugoniot with that predicted on theoretical grounds.

The BKW equation of state, reparameterised to best fit the N_2 and O_2 hugoniots, was used to calculate the Hugoniot of the unreacted mixture (12), giving a condensed phase Hugoniot of U = 2400 + 1.71u, for the emulsion. The effect of aeration was included by a development of the theory of Vostoboinikov et al (13) as described in (4). The good agreement between experiment and theory (Figure 2 below) vindicated the extrapolation procedure used. Further, as the gauge data was well-represented both at 10 and 25% voidage, the theory proposed for calculating the effect of voidage was validated, and could be used to calculate the energy absorbed by void collapse and viscous effects in mixtures.

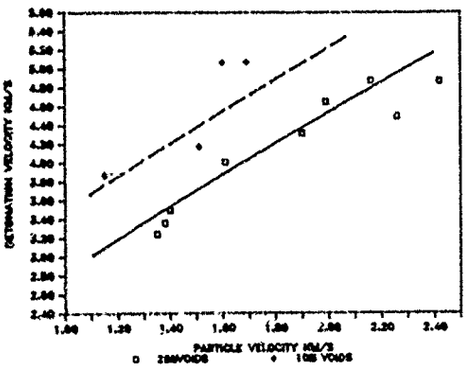

Fig. 2. Porous Hugoniot

The scatter on the plot is representative of the behaviour of commercial explosives, where heterogeneity both affects the local environment of the gauge and precludes accurate determination of VOD to better than 2%.

Shock front radius of curvature was measured for two of the voidage levels used in these experiments. A typical Imacon streak record of the air shock from the end of steady state

detonation in a right-cylinder of emulsion, is shown below with the digitised shock position in terms of the shock lag distance versus axial position. The charge was freely suspended in air and a black PVC end plate with PMMA air gap was used to brighten up the air shock and hold back the reaction products.

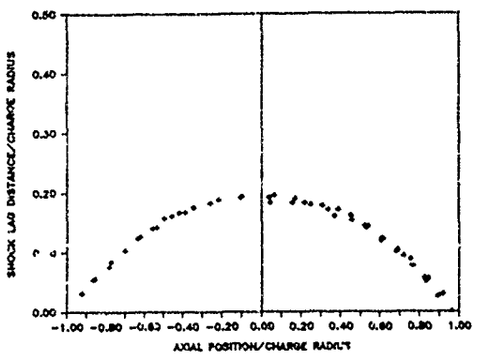

Fig. 3. Shock Curvature

The variation of shock curvature with diameter was found to differ substantially for the two different voidages used, 10 and 25%, either as a function of the diameter or the diameter normalised by the critical diameter. This will be discussed later.

Typical Shock Curvature Streak Record

Calculation of gamma for the unreacted and reacted states followed the method of (4).

A typical particle velocity profile is shown in Fig. 4, the CJ point is marked *. At early time the profile is a smoothly varying function. After approximately 500 nS the noise level on the trace increases, at this point we believe the foil is attacked by the reactive atmosphere surrounding it. At 2 μ S the signal is lost due to complete break-up of the foil in the flow. The useful life of the gauge is between 500 nS and 3 μS depending upon the hostility of the environment, higher shock pressures and higher voidages cause earlier foil breakup. In separate experiments, aluminum particles of similar dimensions have been observed to ignite at 2.5 μ S, close to the maximum foil survival time.

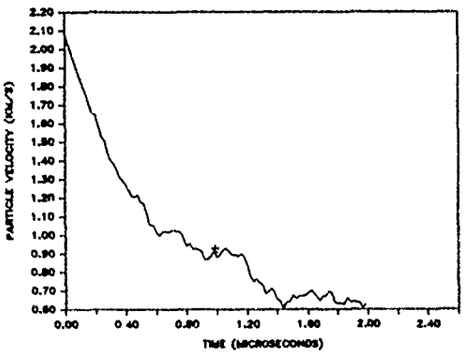

Fig. 4. Particle Velocity Profile

DISCUSSIONS OF RESULTS

Fraction reacted-time profiles, F(t), are illustrated in Figures 5-10 for the two void sizes and three voidage levels used. At each voidage combination, gauge experiments were performed at different charge diameters and thus at different effective shock pressures, and pressure time profiles. The reaction rate $\dot{F}$ for any voidage combination is therefore mapped as a function of both pressure and reaction coordinate. The F(t) profiles are reconstructed from least squares cubic B-spline representations of the original experimental data.

Trends associated with the data illustrate the kinetic behaviour of air-sensitised explosives. At low voidage, the reaction rate close to the shock front is governed by reactions in the hotspot formed by void collapse (14, 15). The hot-spots are well defined and not interacting. The mass of material in the hot spot is consumed by thermal explosion and by a competing outward burning front, initiated from the hot gas interface. The reaction rate is accelerated by either process, till all hotspot material is consumed. A flame front then propagates into the cooler non hotspot regions. The mass reaction

rate will accelerate as the surface area of the burning front increases until the outward moving fronts from the hotspot sites interact and a grain erosion process developes. Now the reaction rate decelerates as the surface area available for reaction is reduced (16). Superimposed on this geometric factor are the pressure and temperature effects. As reaction proceeds the pressure and temperature in the unreacted medium fall, imposing an overall envelope on the reaction rate.

The implicit assumption in the hypothesis, that thermal explosion in the bulk phase is insignificant, is justified by estimating the explosion times of the composition from experimentally measured kinetics (17) at the calculated

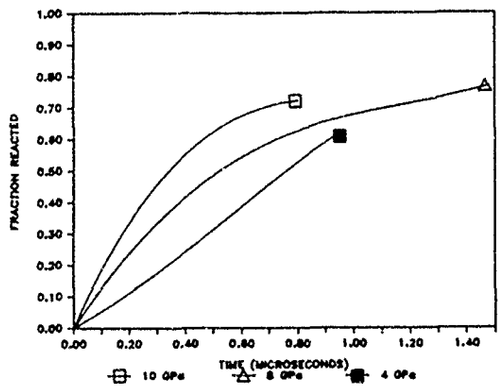

Fig. 5. F(t) 25% Voids (Unsieved)

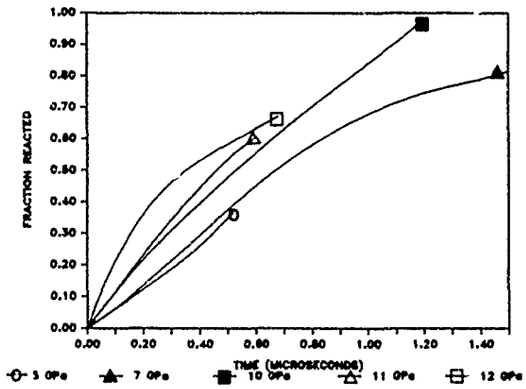

Fig. 6. F(t) 25% Voids (75-90 Micron)

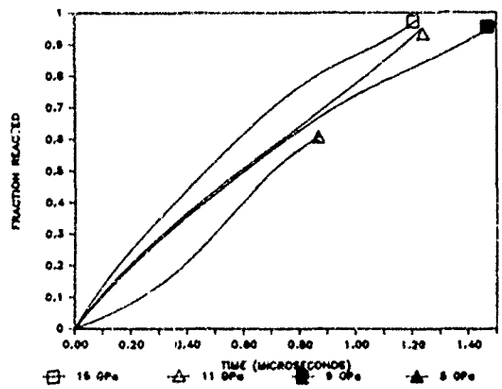

Fig. 7. F(t) 17% Voids (Unsieved)

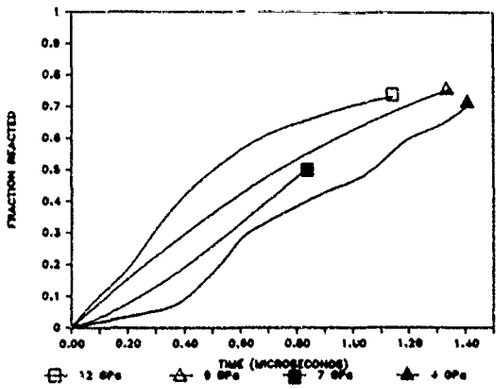

Fig. 8. F(t) 17% Voids (75-90 Micron)

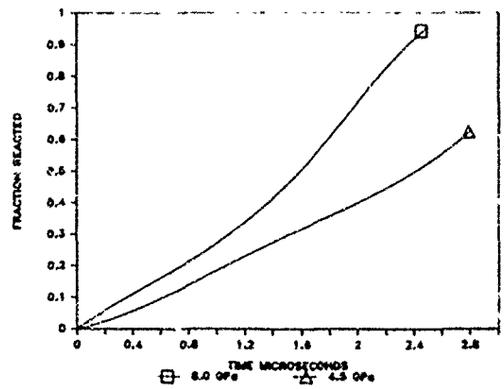

Fig. 9. F(t) 10% Voids (Unsieved)

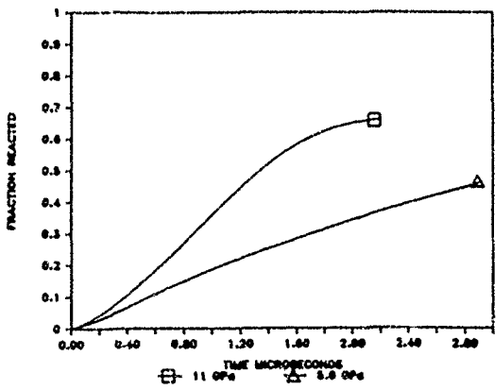

Fig. 10. F(t) 10% Voids (75-90 Micron)

shock temperature (18). The explosion time by this method is 15 μS, much longer than the gauge reaction times.

As voidage is increased two factors become important: more material is engulfed in the hotspot; and void collapse is no longer a well defined process but a complex interaction which may depend on the jetting and reverberation of upstream neighbours. Previously formed reacting hot spot sites may be skewed by the collapse of downstream voids. It is likely that second shock and turbulent motion play an important role in the reaction process. Energy considerations on the porous Hugoniot can be used to estimate the magnitude of such effects: at high voidage and low shock velocity, the turbulent energy can be 50% of the total energy in the shock. Chaotic motion of this magnitude is an important means of enhancing mass and thermal diffusivity in the system thus accelerating chemical reaction.

On moving to higher voidages, the reaction rate should therefore increase and the profile of the reaction will be less significant as turbulent effects destroy geometric effects. Addition of more voids will lead to a proportionally smaller increase in reaction rate, as proportionately less chaotic motion can be induced. If any geometric effects remain they will only be obvious at very low shock pressures where chaotic effects will be minimised.

These arguments are substantiated by the details of the gauge records. At early time, reaction rates are increased both by increasing pressure and by increasing voidage. As voidage is increased, any detail apparent in the reaction profile is lost as chaotic effects cause mixing and void-void interactions. At low voidage the reaction rate is low, even at high pressure, as the number of hotspot sites, and initial surface area for burning is much reduced.

Inspection of the results for the two voidage types, unsieved and $-75+90$ micron, show the latter to have a more characteristic profile, the hot spot reaction being time-correlated and uniform. The overall reaction rate of the material sensitised with sieved voids is lower, the number density of initiation sites being less than in the unsieved case. At high voidage this fall in rate is less obvious due to chaotic effects.

CALIBRATION OF THE FLOW EQUATIONS

The variation of shock front curvature, charge diameter and CJ distance from the gauge can be used to parameterise equation 10.1 of (4) based on the concept that the shock is spherically symmetric over the region close to the charge axis but suffers distortion when it approaches the charge axis boundary (3). i.e. in any charge of diameter d,

$$d = 2.0\ (\alpha R_s - \beta x_{CJ}) \qquad 2.1$$

where α is the sin of the angle subtended by the charge axis and a line connecting the origin of the shock radius of curvature and the point at which the first edge distortions is seen; and β is the fraction of CJ distances over which the edge effect extends. Equation 2.1 should yield a universal relationship for any family of explosives which can be described by a slightly divergent flow model. For the emulsion used in this work the observed shock front curvature data for both 25% and 17% voidage was found to lie on one line as illustrated.

Although a linear relationship as postulated in 2.1 is supported by the data, the assymptotic behaviour at large diameter gives shocks substantially more curved than have been reported in the literature (13). We are uncertain of the significance of this, other than that 2.1 must be replaced with a higher order function.

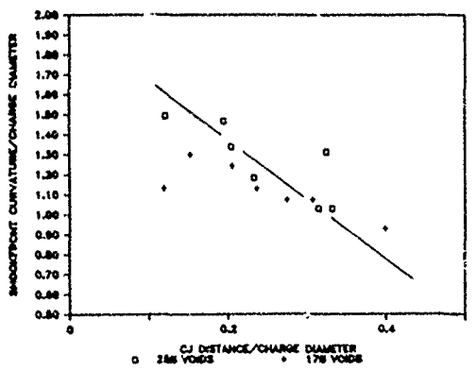

Fig. 11. Shock Curvature Function

PHENOMENOLOGICAL MODEL OF THE REACTION RATE

In (4) a functional form of the reaction rate is suggested based on decoupling the geometric

and pressure terms in the rate law. The geometric term is based on summation of Gaussian envelopes, one for each phase present. Each Gaussian may be delayed in F to simulate ignition and phase interdependent reactions. The width of each Gaussian represents the geometry of the phase reaction. A pressure dependency for each phase of the form ap^b is added (19). For a two phase system, hot spot and bulk liquid, this reduces to a type of Ignition and Growth model (2).

Assuming only two phases are present the model is defined by:

$$F = \{[(p-p_c)^{a_1}/R_1]G_1 + (p^{a_2}/R_2)\,G_2\}\,(1-F) \quad 3.1$$

$$G_1 = \exp[-(F-F_H]^2/M_H : G_2=0 : F>F_H \quad 3.2$$

$$G_1 = \exp[-(F_H-F)^2/M_H] : G_2=1-G_1 : F>F_H \quad 3.3$$

$$F_H = R_3(v_{TMD}/v_0-1) \quad 3.4$$

where F_H is the fraction of material said to be in the hotspot, p_c is the critical initiation pressure; M_H the geometry factor for the Gaussian; R_1 and R_2 are pressure time coefficients for the hot spot and liquid; and a_1, a_2 are pressure indices.

Of the variables, R_1, R_2 and R_3 are used as fitting parameters, and p_cM_H, a_1, a_2 are derived from experiment or are arbitrary functions of the formulation variables.

The critical pressure is taken to be the initiation pressure in a 25 mm diameter cartridge in a PMMA gap test.

The pressure index of the hotspot phase was found by plotting the absolute reaction rate at the shock front against shock pressure.

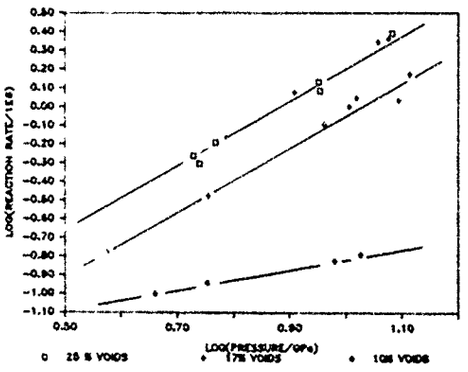

Fig. 12. Absolute Rate Plot

As no data was available on the a_2 index it was set equal to the a_1 index.

Parameter M_H was chosen to control the Gaussian half height width to simulate the acceleration and deceleration of reaction rate with the fraction reacted.

At least square procedure was used to fit R_1, R_2 and R_3 based on minimising the relative error in F(t) for any set of gauge traces. F(t) and p(t) data used in fitting was generated from a cubic spline fit to the gauge records. A Monte-Carlo splatter technique was used to avoid local minima in the error function.

TABLE 1
Gaussian Kinetic Parameters

Voids	Voidage %	R_1	R_2	R_3	a_1	pc/GPa
Unsieved	10	13.6	8.7	1.0	0.5	1.20
75-90	10	15.8	9.5	1.0	0.5	1.20
Unsieved	17	5.1	4.8	1.0	1.5	0.95
75-90	17	4.4	4.9	1.0	1.5	0.95
Unsieved	25	2.8	2.9	1.5	1.5	0.85
75-90	25	5.0	3.0	1.5	1.5	0.85

The behaviour of R_1 and R_2 shows the expected trend of increasing time constant with decreasing voidage. Variations in R_3 are interpreted as an increase in material in the hotspot at high voidage, in accordance with the view of increased chaotic motion.

Detonation measurements on high voidage emulsion, have shown that further increases in voidage do not substantially decrease the critical diameter, but do increase the fraction of the ideal velocity at which detonation fails, as expected if hotspot mass were greatly increased.

PREDICTION OF DETONATION & VELOCITY - DIAMETER RELATIONSHIPS

The parameterised Gaussian rate law was used in conjunction with (4) to predict the variation of detonation velocity with charge diameter. This was a stringent test of both the Gaussian rate model and the hydrodynamic theory, as there were no freely adjustable parameters in the system. Predictions were made from the six families of gauge traces illustrated previously. Those for which reliable velocity diameter data was available are shown to illustrate the trend.

At high and medium voidage, the predictions of critical point and slope of the velocity-diameter relationship were well reproduced. Error in absolute position was partly due to inadequacies in the code used to calculate the ideal detonation state, BKWR (28), which is known to be inaccurate at low densities. At low voidage the model breaks down catastrophically, failing to predict either the slope or the critical point correctly. The kinetic model does not treat the low voidage regime of well defined hotspots and bulk burning accurately. Failure to model the outward burning of the hotspots into the bulk reactant makes it impossible to return a sensible reaction rate at low degrees of reaction. This forces the second CJ condition to be satisfied at higher reaction, lengthening the CJ distance, and thus by 2.1 decreasing the diameter for any given shock front curvature.

A more realistic numerical model which accounts explicitly for geometry and for hotspot interactions, (21) or a Eulerian hydrocode approach (19) is required to cope with such effects.

CONCLUSION

A method has been proposed for the analysis of electromagnetic particle velocity gauge data. The analysis provides measurement of the hugoniot of the unreacted explosive and of the reaction profile behind the shocks. A hotspot ignition and bulk liquid burn model is found to reproduce the gauge data. Second shock and chaotic processes are postulated to be important in determining the reaction profile at higher voidages.

The kinetic model used to represent the gauge results has been used with a slightly divergent

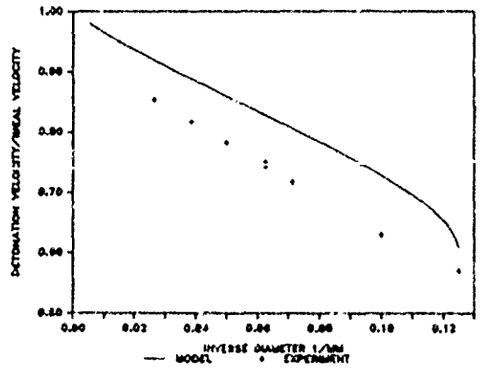

Fig. 13. D(d) 25% Voids (Unsieved)

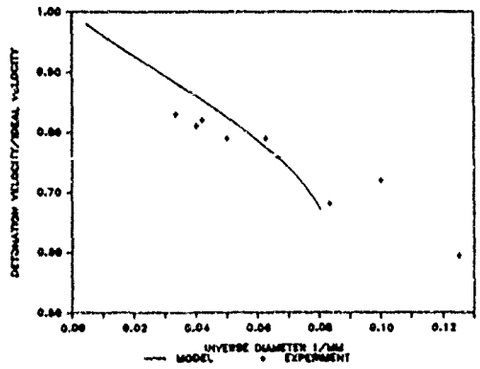

Fig. 14. D(d) 25% Voids (75-90 Micron)

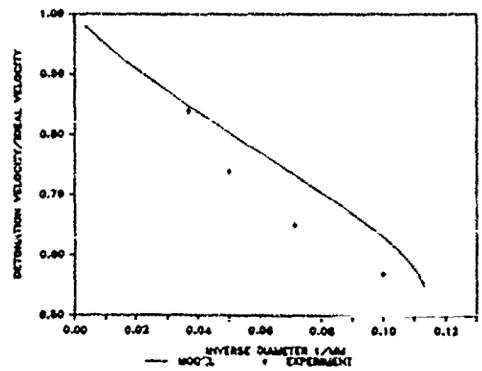

Fig. 15. D(d) 17% Voids (Unsieved)

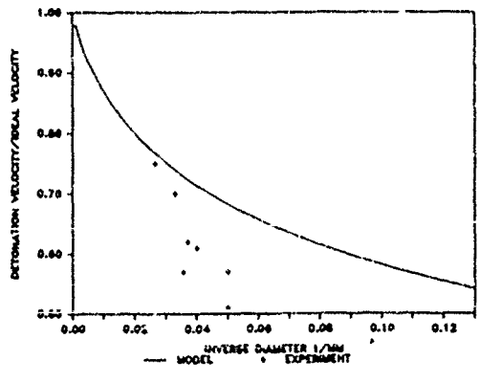

Fig. 16. D(d) 10% Voids (Unsieved)

hydrodynamic code to predict the velocity-diameter relationship of the explosive. Good agreement has been found with experimental observations at 17 and 25% voidage. At 10% voidage the prediction of critical velocity is correct but the critical diameter is a factor of five to small. Failure of the model at low voidage implies the form of the kinetic model is incorrect in the voidage region where hotspots are well defined and the reaction process can be thought of as energetic hot spot reaction igniting an outward propagating flame front. The model is unable to reproduce the correct geometry of the reaction and thus accelerates the reaction rate too slowly.

The failure of the simple model illustrates the need to adequately model the complex geometrical factors which control the reaction profile in heterogeneous bubble sensitised explosives. Until this is attempted, phenomenological models should not be expected to reproduce accurately detonation measurements made over a wide variety of densities and compositions.

REFERENCES

1. Price, Eleventh Symp. on Comb., p693-702
2. Chan, 7th Symp. on Detn, p589-601.
3. Bdzil, J. Fluid Mech., 108, p195-226.
4. Kirby & Leiper, ibid.
5. Wood & Kirkwood, J. Chem. Phys., 22, p1920-24
6. Zaitsev et al, Dokl. Acad. Nauk. SSSR, 132 p1339-40
7. Jacobs & Edwards, Fifth Symp on Detn, p413-426
8. Tarver et al, LLNL Report UCRL 89164.
9. Cowperthwaite and Rosenberg, SRI Report ADA 132760.
10. Anodised in 15% H_2SO_4 and sealed in boiling water. Oxide thickness checked by electron microscopy.
11. Cook, "The Science of High Explosives," Reinhold, 1958.
12. Lownds, "The State of Shocked Fluids," ICI Report CL-R82-1786/A.
13. Vostoboinikov et al, Comb. Expl. Sh. Wave, 3,(4), p359-64.
14. Mader, LASL report LA3235.
15. Mader and Kershner, Nineteenth Symp. on Comb., p685-90.
16. Chan and Lownds, Prop. Expl. Pyro., 8, p184-92.
17. Lownds, private communication.
18. Walsh and Christian, Phys. Rev., 97, p1544-56.
19. Andreyev, "Thermal Decomposition and Combustion of Explosive Substances," Izd-Vo, Moscow, 1966.
20. Lee and Tarver, Phys. Fluids, 23, p2362-72.
21. Finger et al, Sixth Symp. on Det. p710-22.

DETERMINATION OF TRANSIENT AND KINETIC CHARACTERISTICS IN SIMULATING RDX/TNT 50/50 CHARGE INITIATION

V.M. Titov, V.F. Lobanov. S.A. Bordzilovsky, S.M. Karakhanov
Lavrentyev Institute of Hydrodynamics
Siberian Division of the USSR Academy of Sciences
Novosibirsk 630090 USSR

This paper deals with a numerical simulation of the RDX/TNT 50/50 initiation by shock waves within the framework of a gasdynamical model. To describe detonation waves, the explosive decomposition in the reaction zone was defined by the "macrokinetics" equation. The basic parameters of the equation were improved by comparing the computer and experimental pressure profiles. The features of the initiating shock wave velocity variation under the impact of the aluminum plate of finite thickness upon a test charge were found. The computer results allow to determine the distance of run to detonation in dependence on initial shock pressure. The dynamics of pressure and specific volume variation at different stages of the initiating wave transition to the stationary detonation regime was considered. It has been established that the volumetric energy-release rate $\dot{p} = dp/dt + (C/V)^2\, dV/dt$ achieves maximum values throughout the transient zone, when pressure behind the initiating wave front becomes equal to Chapman-Jouguet pressure at a steady-state detonation.

INTRODUCTION

Shock initiation of heterogeneous condensed explosives is characterized by a reaction developing in hot points. This phenomenon is responsible for the reaction zone structure consisting of the mixture of shock-compressed unreacted explosive and reaction products, i.e. the matters with different physical-chemical properties. A numerical simulation makes it possible to obtain a detailed picture of the gasdynamical process in the reaction zone and adds the experimental data.

In (1,2) a numerical simulation of the TNT initiation was considered. In this present paper this method is used to describe transient processes in RDX/TNT 50/50 consisting of the components with different sensitivity to shock effects.

The basic assumptions of the mathematical model are the following:

1. Behind the shock front the explosive is represented as individual spherical particles of radius r_o. The number of particles per unit mass is constant and equal to N_o.

2. The explosive is converted to the detonation products in the decomposition wave. The wave front propagation velocity is proportional to pressure.

3. The components of the mixture of explosive and the detonation products with mass concentration of (1-q) and q, respectively, are subjected to the same pressures and different temperatures in the reaction zone.

Under the above assumptions the decomposition velocity is described by the "macrokinetics" equations:

$$\dot{q}_I = A\left(\frac{1-q}{1-\sigma}\right)\left(\frac{\varrho}{\varrho_o}\right)^{1/3} \cdot p \cdot \exp\left(-E^*/3E_T\right)\sigma^{2/3}$$

$$0 < q < q^*$$

$$\dot{q}_{II} = A\left(\frac{\varrho_1}{\varrho_o}\right)^{1/3} p \quad \exp\left(-\frac{E^*}{E_T}\right)(1-q^*)^{1/3}(1-\sigma)^{2/3},$$

$$q^* \leqslant q \leqslant 1\ ;$$

$$q^* = \exp\left(-\frac{E^*}{E_T}\right),$$

where ϱ_1, ϱ_2 are the densities of explosive and detonation products, respectively, ϱ_0 is the initial density of explosive, $\sigma = q \cdot \varrho / \varrho_2$ is the bulk concentration of detonation products in the mixture with density ϱ, E_T is the thermal component of the specific internal energy of explosive, E* and A are constants.

The equations of state have been chosen in the form of Mie-Grüneisen equation. The equations have been solved by the numerical method developed by Godunov. The constants in the "macrokinetic" equation were selected by comparing the computational and experimental pressure profiles $p(h_1, t)$ over different cross-sections of the charge, where h_1 is the Lagrange coordinate (the distance to the initiating plane), t-time.

INITIATING SHOCK WAVE PROPAGATION IN THE CHARGE EQUIPPED BY GAUGES

The RDX/TNT 50/50 specimens were loaded by a pad of HE with a plane wave lens through an attenuator being the impedance mismatch combination (3). When an initial pressure in the specimen is $p_0 \approx 3.8$ GPa, the gauges are uniformly distributed over the region, where the initiating shock wave is transformed into the detonation one at h = 0, 5, 10, 15.1 mm. In the pressure region behind the shock wave under 5 ÷ 10GPa the PTFE insulation 0.1 mm thick from each side of the gauge provides for recording of the signal for a few microseconds. Under pressures close to detonation ones the insulation thickness is increased up to 0.3 mm.

The inert layers between explosive plates can effect on the initiation process, therefore computations were made with allowance for the inert layers.

The pressure profile on the initiation surface p(o,t) was used in computations as boundary conditions.

When determining the parameters in the equations of state, the initial data are: the Hugoniot D =2.49 +1.99u (4) for the explosive, the Chapman-Jouguet state of the steady state detonation, D = 7.65 km/s, $P_{CH\text{-}J}$ = 24.8 GPa, $u_{CH\text{-}J}$ = 1.93 km/s for detonation products (5), the Hugoniot D = 1.865 + 1.712 u for PTFE with ϱ_0 = 2.193 g/cm³.

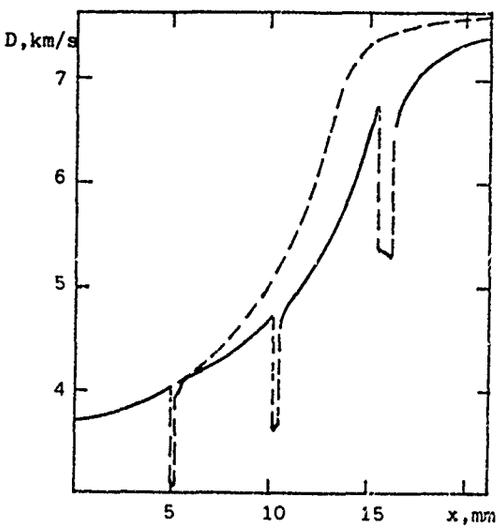

Fig. 1. Initiating wave velocity in the charges (——— with gauges, — — — without gauges) x is the distance to the initiating surface

Solid lines in Fig. 1 denote the values of the initiating shock wave velocity, D(x), between the gauges. The wave velocity within the measuring station is significantly less than D. At the exit of the wave from the gauge, the transient processes are observed, but as a whole the D(x) dependence is monotonic (x is the distance from the initiation plane).

Calculations made with the same boundary conditions, without taking into account the inert layers, show (the dashed line in Fig. 1). that the process is more intensive in the charge without gauges. A main difference becomes evident after the wave has passed through the gauge at h = 5 mm. This is due to the fact that when the shock wave passes through the inert layer, the energy inflow in the reaction zone decreases, and under moderate pressures the energy losses are significant. When the explosive temperature decreases, the decomposition velocity sharply decreases too. As follows from the plot of mass concentration q vs time presented in Fig. 2, after the wave has passed through the charge at h=5 and 10 mm, the decomposition rate almost halves.

The inert layers effect on the shock wave

velocity takes place as far as the value of (u + c) (u is the particle velocity, c the sound velocity) at the PTFE/ explosive interface is more than D(x). In the case under consideration the parameter distribution behind the shock front is such that the gauge makes effect for a longer time at h = 5 mm than at h =10 mm.

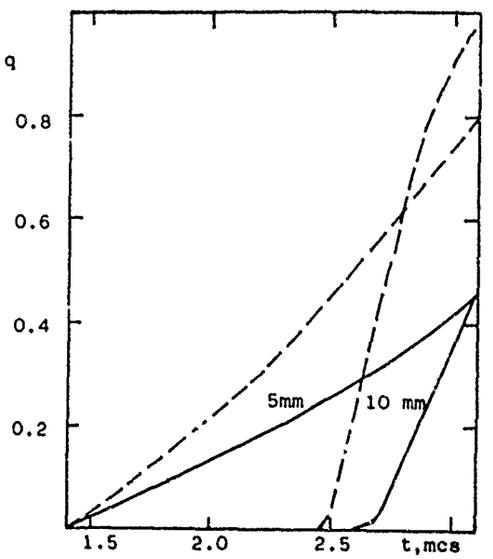

Fig. 2. The plot of concentration of detonation products vs time at h = 5 and 10 mm (— — — without gauges, ——— with gauges)

The q(x) dependences in both charges at the moment of the shock wave arrival to the gauges are presented in Fig. 3.

Under moderate pressures and a relatively thin PTFE insulation layer the pressure variation on the boundaries of the measuring station and in its center repeat one another and are in satisfactory agreement with the experimental dependences. At h = 15.1 mm p(t) varies in a different manner on the left and right boundaries (lines 1 and 3 in Fig. 4). After the shock has passed through the measuring station both the amplitude and phase signal deviations are observed. The pressure evolution character on the boundaries effects on the pressure profile at the gauge center (Fig. 4). Non-monotonic dependences of pressure vs time are recorded, as a rule, in the experiments (Curve 4 in Fig. 4).

PLATE IMPACT INITIATION

The "macrokinetics" parameters determined above were used in solving the following problem. The explosive charge positioned at $x \geqslant 0$ at $t = 0$ is impacted by the aluminum plate, 1 in thickness, with the velocity W. The resulting

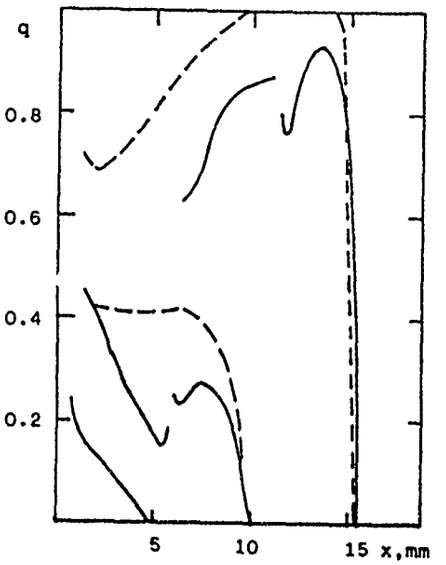

Fig. 3. Distribution of mass concentration of detonation products behind the front of the initiating wave (— — — without gauges, ——— with gauges), x is the distance to the initiation surface

transient processes in the driver and explosive were calculated in a gasdynamical approximation. The shock wave propagating in the explosive, the driver- explosive interface and the free surface of the driver were assumed to be the boundaries of the computational region.

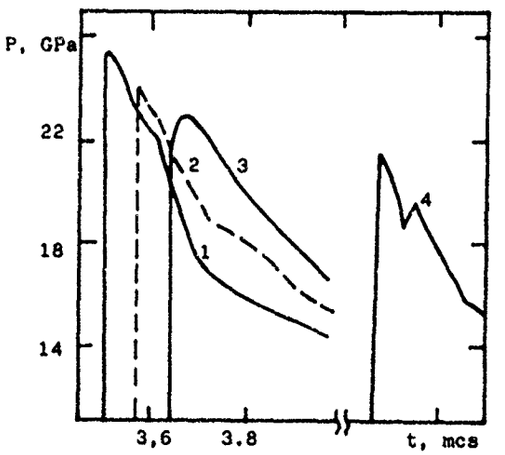

Fig. 4. Pressure profiles at h = 15.1 mm (1÷ 3 calculation, 4 - experiment)

The Hugoniot condition at the shock front, continuity of pressure and mass velocity at the interface and zero pressure on the free surface of the driver are assumed to be the boundary conditions.

The driver velocity W ranged between 0.9 and 2.4 km/s, and the initial amplitude (p_0) of the shock wave in the explosive varied from 5.5 to 14 GPa.

As is well-known, the detonation initiation is affected by amplitude as well as by the duration of the pressure pulse. To investigate the initiation pulse amplitude only, the driver thickness was selected so that to eliminate the rarefaction wave effect from the free surface of the driver. The value 1 = 3 mm satisfied this condition throughout the range W.

For all values of the driver velocity a qualitative character of the D(x) dependences has a form of Curve 1 presented in Fig. 5. (W = 1.2 km/s).

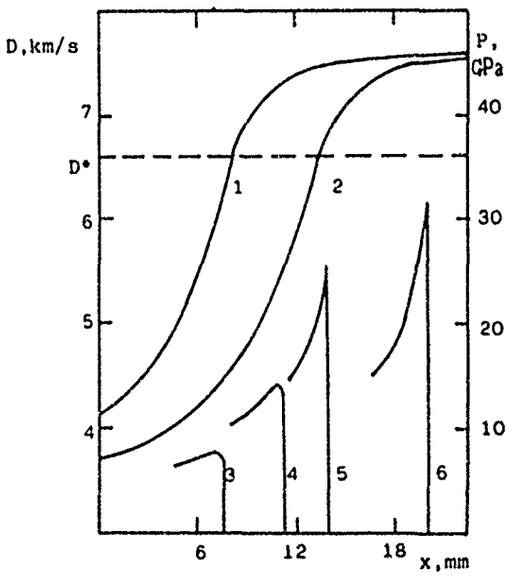

Fig. 5. The initiating wave velocity (Curves 1,2) and pressure distribution behind its front (Curves 3-6) at different distances to the initiation surface

The behaviour of D(x) is characterized by the fact that at all p_0 the maximum wave acceleration is realized for one and the same value of D* being some 15% below the ideal detonation velocity. Further asymptotical approximation of D to an ideal detonation value is independent of the initiating pulse parameters. Curve 2 shows the D(x) dependence obtained from the above-mentioned calculations under explosive loading of the specimen through the attenuator. Thus the differences in the lengths of the transient regions at different p_0 are fully conditioned by the distance from the initiation surface to the coordinate of maximum wave acceleration, $x^*(p_0)$.

The loading of explosive charges by the plate impact was researched in 6. Experiments show a sharp initiation wave acceleration in the vicinity of steady state values. The distance from the initiation surface to the plane of maximum gradients was defined in (6) as "the distance to detonation", X. The same work suggests an approximate relation, p_0X^b=const. The dependence approximating our calculated data,

$$\lg x^* = -1.27 \lg p_0 + 1.87$$

was obtained by the method of least squares (Fig. 6). This is in agreement with the

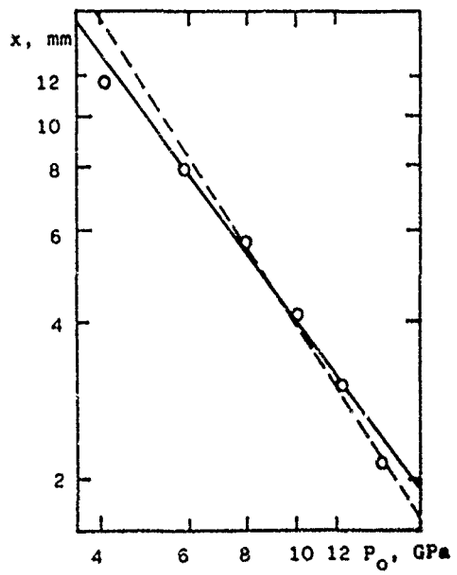

Fig. 6 Distance of run to detonation vs initial shock pressure (—TNT/RDX 50/50, — · Comp B (7)

experimentally determined dependence for the Comp B (7) close by its composition to RDX/TNT 50/50.

According to the above mentioned peculiarities of D(x) evolution, the transient region can be divided into two zones: the first, within the initial surface and the maximum wave acceleration coordinate, and the second, quasistationary

zone which bounds the transient region.

The values of D(x) in the first zone can be found by the formula

$$\frac{D(x)-D_0}{D^*-D_0} = \frac{(x)^\beta}{x^*},$$

where D_0 is the initial velocity of the initiating wave, $\beta = 1.65$.

In analyzing the driver thickness effect on the initiation process, evolution of the value $M = \frac{(u+c)}{D(x)}$ in the region between the driver and the shock front in the explosive is considered. For some time after impacting M>1 throughout the region. Then at $t=t_m$ the region is formed near the interface, where M<1. If the rarefaction wave transition time from the free surface of the driver is $t_2 \simeq 2l/c_0 > t_m$, (c_0 is the initial sound velocity in the driver), the rarefaction wave does not effect on the initiation process. Therefore for the drivers with the thickness $l \geqslant c_0 t_m/2$, the dependences D(x) are the same. The rarefaction wave does not effect on the process also in the case when $t_r < t_m$, but the following inequality is fulfilled:

$$\int_{t_r}^{t^*} (u+c)dt \leqslant \int_0^{t^*} D(t)dt$$

Here t^* is time of the shock wave arrival in point x^*, u and c are taken on the first rarefaction wave characteristic. When initiation is realized by the way considered, throughout the region between the driver and the shock wave the estimate $M \leqslant K \cdot M_s$ is valid for M ($K \simeq 1.1$, and M_s is determined for the explosive by the parameters at the shock front). In this case the inequality can be written as follows:

$$K \cdot M_s \cdot D_c t_r \geqslant (K \cdot M_s - 1)x^*$$

From here we can obtain the estimate for t_r

$$t_r \geqslant \frac{x^*}{D_0}\left(1-\frac{1}{K \cdot M_s}\right)$$

and an appropriate estimate for the driver thickness

$$l_0(W) \geqslant x^* \frac{c_0}{2D_0}\left(1-\frac{1}{K \cdot M_s}\right).$$

For the explosive with the Hugonoit taking the form $D=a+bu$, u and c in proximity to the front are equal (8)

$u=(D-a)/b$, $c=\varrho_0/\varrho \cdot (2D-a)$,

therefore

$$M_s = \frac{2b-1}{b} + \frac{a(b-2)}{bD} - \frac{a^2}{bD^2}$$

The rarefaction wave effect on the behaviour of D is illustrated in Fig. 7, where for the driver velocity W=0.9km/s, the initiation process was calculated at different $l \leqslant l_0(0.9) \simeq 3$mm. The plot of D(t) at $l=l_0$mm shows the effect of the first and second stages of the driver unloading. The pulse duration decrease (l=0.3mm) results in a strong delay of the process at the initial stage. Nevertheless, for the charge of an infinite length after passing a local minimum process transforms to a steady state detonation. When l=0.1mm, the initiating wave decays.

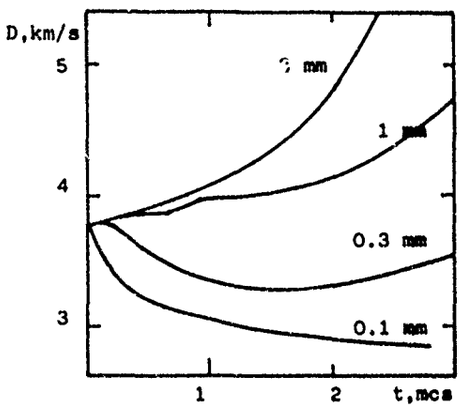

Fig. 7. Initiating wave velocity vs time at different driver thicknesses (W=0.9km/s)

THE BEHAVIOUR OF BASIC PARAMETERS OF THE INITIATING WAVE

Determination of pressure (p), specific volume (V) and energy release rate along with the analysis of the connection between these parameters plays an important role in the study of the reaction zone. With taking into account the laws of energy conservation and on the general assumptions upon the equations of state, the connection between the volumetric energy release rate $\dot{p}$ (9) and other flow parameters behind the shock wave is established by the equation

$$\dot{p} = \frac{dp}{dt} + \left(\frac{c}{V}\right)^2 \frac{dV}{dt}, \qquad (1)$$

where the derivatives in time t belong to Lagrange particles. According to definition in

(10), is the generalized kinetic characteristic which establishes the connection between pressure evolution and energy release in the medium at V=const.

A differential character of (1) is suitable for a qualitative analysis of the relationship between the basic parameters.

A modern state of experimental methods in principle enables determination of all the parameters in (1), and, consequently, $\dot{p}$ as a function of those parameters and specific energy (E). The value of $\dot{p}$ for TNT at the initiating wave front was determined in (9, 10), where a nonmonotonous character of $\dot{p}(p_s)$ dependence was emphasized (p_s is the pressure at the shock front). There are no available data on $\dot{p}$, therefore it is of great interest to study how this characteristic behaves throughout the reaction zone.

In the present paper $\dot{p}$ was determined on the basis of the above-mentioned results on numerical simulation of the RDX/TNT 50/50 initiation.

A qualitative character of the pressure field inside the charge behind the shock wave (Fig. 5) varies as the wave propagates through the specimen. In the initial zone behind the shock front there arises the compression wave, therefore the maximum value of p is at a certain distance from the wave front. A similar pressure distribution is maintained up to x*, where the compression wave is shocked up accompanied by a maximum shock wave acceleration. In a quasistationary zone the pressure steadily decreases as the distance to the front increases that is characteristic also for distribution in a stationary wave.

For all particles, an initial state after passing of the shock wave is the Hugoniot state corresponding to the velocity D(x). Phase trajectories in p−V plane for the particles positioned in different cross-sections of the charge are presented in Fig. 8. There are three regimes of p and V variation: (i) pressure increases when the specific volume decreases (dp/dt>0, dV/dt<0). (ii) pressure increases when the specific volume decreases (dp/dt>0, dV/dt>0), and (iii) pressure decreases when the specific volume increases (dp/dt<0, dV/dt>0).

For the particles in the initial zone, as they receed from the wave front, the three regimes are realized, from the first to the third. this state

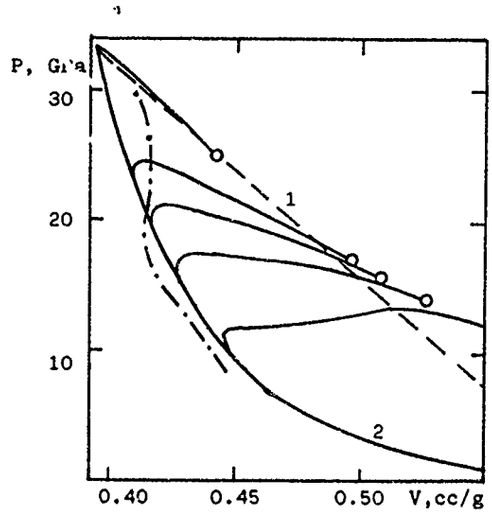

Fig. 8. Phase trajectories of Lagrange particles (0 - the end of reaction, 1 - Rayleigh-Mikhel'son line, 2 - Hugoniot D = 2.49+ 1.99u (4) . - . - . - denotes the Hugonoit calculated for a finite time of signal front resolution u(t)

evolution character is due to the presence of the compression wave behind the shock front.

In the quasistationary zone the particle states change, according to the second regime, and then, according to the third one. At the steady state detonation only the third regime is realized, and p and V vary along the Rayleigh-Mikhel'son line.

The characteristic $\dot{p}$ is determined by the sum of derivatives dp/dt and dV/dt, their absolute values being changed over a wide range. The signs of the terms are changed at different instants of time, therefore the $\dot{p}(p)$ dependences (p is the pressure) are of qualitatively different form.

Solid lines in Fig. 9 show the $\dot{p}(p)$ dependence for the particle situated at different points of the transient zone. They connect the values of $\dot{p}$ determined from the mean parameters during Δt=20 ns (that is why the curves are broken). The dashed line goes through the values of $\dot{p}$ obtained for different particles for the first 20 ns after the shock wave has passed through them. For each particle from the transient region as it recedes from the wave front, $\dot{p}$ increases up to its maximum values with a subsequent decrease to zero. This is actual for a steady-state detonation only. The values of $\dot{p}$

being 1.5 times as large as ones at the stationary wave front, are maximum throughout the region for the particles from the region close to x*, 30–50 ns after the action of the shock waves.

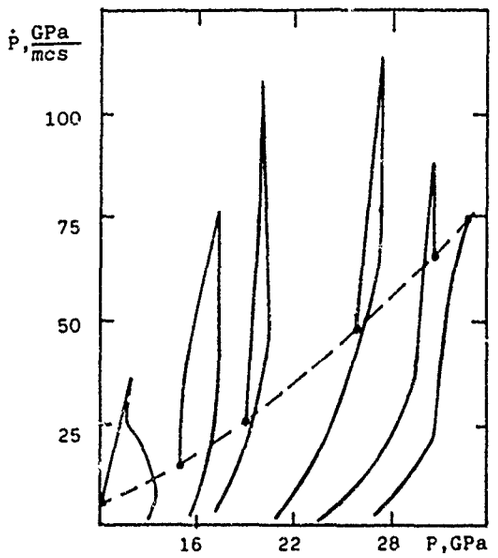

Fig. 9. The plot of ṗ vs pressure for different Lagrange particles

According to the assumptions made in the mathematical model, the medium in the reaction zone is a mixture of two components, such as an unreacted explosive and detonation products, and ṗ is expressed as follows (11):

$$\dot{p} = \left(\frac{c}{V}\right)^2 \left[\frac{\partial V_2}{\partial h_2} (h_1 - h_2) - (V_1 - V_2) \right] \frac{\partial q}{\partial t} \quad (2)$$

where h is the enthalpy, indices 1 and 2 are relating to the explosive and detonation products respectively. As follows from (2), ṗ is a complex function of states of individual components and explosive decomposition rate, therefore constructing a unitary analytical dependence ṗ(p, v) throughout the region of parameter variation is a hard-to-solve problem.

In analyzing the behavior of ṗ in a close vicinity to the shock front, it is appropriate to use the expression suggested in (10) for determining the characteristic from the experimentally recorded mass velocity profiles u(t):

$$\dot{p} = \varrho_0 DU \frac{dD}{dx} + \varrho_0 (D^2 + c^2) \frac{du}{dx} - \varrho_0 D \left(\frac{c^2}{D^2} - 1\right) \frac{\partial u}{\partial t} \quad (3)$$

where the derivatives in x are taken along the trajectories of the shock wave, and the time derivatives are relating to the u(t) dependence for the Lagrange particle.

For the first two terms in (3) the signs are not changes throughout the transient region. In the initial zone their monotonous growth is observed which abruptly decreases after x*, where the derivatives dD/dx and du/dx take their maximum values. In the quasistationary zone a contribution of the first two terms into (3) steadily decreases to zero at a stationary detonation (dD/dx=du/dx=0). The third term changes its sign, except for the absolute value variation as the shock wave propagates through the charge. In the initial zone $\partial u/\partial t > 0$, and in the quasistationary zone $\partial u/\partial t < 0$, as in the case of a steady-state detonation. The calculated value of the sound velocity c is always more than D. Taking into account the sign of the last term, we obtain that the contribution of the term with du/dt in the initial zone is negative, and in the quasistationary one it is positive. The last term achieves its maximum value in the case of the steady-state detonation.

Although the terms in (3) behave in a different manner, their sum in a close vicinity to the shock (the dashed line in Fig. 9.) steadily depends on pressure at the shock front. In order to show the difference between the rates of the term variation, it is expedient to determine ṗ from the parameters recorded at t_1 and $t_1 + \Delta t (t_1 \neq 0)$ after the shock wave has passed through the particles. In so doing the region of a close vicintiy to the front somewhat increases, meanwhile the values of ṗ, which are integral during t_1, are obtained. the ṗ(p) dependences in Fig. 10 have been determined at $\Delta t = 20$ ns, Curve 1 is relating to $t_1 = 0$, Curves 2 and 3 are relating to $t_1 = 20$ and 40 ns respectively, $(\tau = \frac{t_1 + \Delta t}{2})$.

In difference to the steady dependence at $\tau = 10$ ns, Curves 2 and 3 have maxima which decrease in their absolute value with increasing τ and shift to the region of less pressures.

When ṗ is determined experimentally, due to a finite time resolution (30 ÷ 50 ns) there can arise the conditions similar to those under which Curves 2 and 3 were constructed.

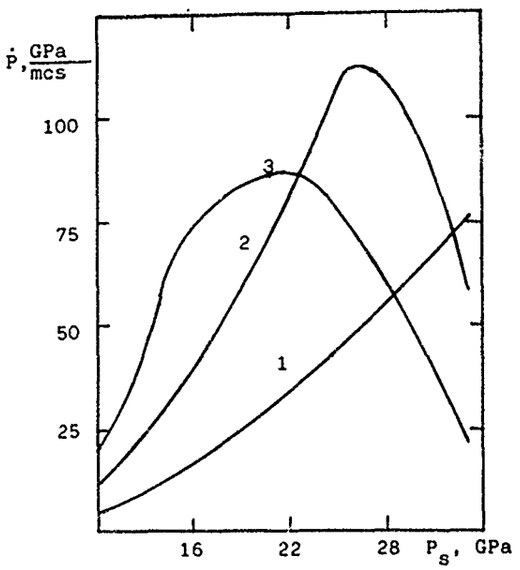

Fig. 10. The plot of $\dot{p}$ vs pressure at the front determined within different intervals of time (1−0÷20 ns, 2−20÷40 ns, 3−40÷60 ns)

Analogous dependences were observed in (10). It has been proposed that the explosive decomposition mainly takes place directly at the shock front. As follows from the above, the behaviour of $\dot{p}$ can be explained by a finite time resolution, without any supplements to the Zel'dovich - Neumann theory.

It is worthy to note one more possible manifestation of a finite time resolution. By the experiments similar to the above-mentioned ones, it is possible to determine the D(x) dependence exactly enough. Using the signals of the mass velocity gauges places in different cross-sections of the charge, by the initial evolution profiles u(x,T) it is possible to determine $p=\varrho_0 \cdot D(x) \cdot u(x,T)$ and $V=V_0\frac{D(x)-u(x,T)}{D(x)}$ (T is the front time resolution). The Hugoniot calculated in a similar way at T=50 ns has a form of an ambiguous dependence plotted in Fig. 8 by the dashed-dotted line.

In attempts to extrapolate the value u(x,T) to u(x,O), considerable difficulty has been experienced in the case of the particles from the vicinity of x*. Indefiniteness of the sign of derivative $\partial u/\partial t$ or its value in an initial phase of the particle motion behind the shock front ($t \leqslant T$) can lead to appreciable errors.

The experimental pressure or mass velocity can be determined by the gauges being inert inclusion into the explosive. The energy release interruption, when the detonation wave propagates over the charge, effects on the evolution of parameter variation in the reaction zone. The gauge effect is most considerable in the case of processes in the quasistationary zone. For this reason, taking into account that when determining $\dot{p}$ it is appropriate to differentiate the experimental data, analysis of the errors introduced by the gauges is a very complicated problem.

Calculations show that the initiating wave parameters vary with a maximum rate at D*, the pressure behind the shock wave front being equal to the Chapman-Jouguet pressure at the steady-state detonation. The parameters behind the shock front at $D \geqslant D^*$ are such that a homogeneous explosive decompsition becomes possible. To investigate the character of interaction between "hot-spot" and homogeneous mechanisms, it is expedient to investigate experimentally the quasistationary zone. However, in the case of using manganin and electromagnetic gauges, this investigation is hindered by a finite time resolution as well as by a possible effect of a gauge itself on the process under consideration.

REFERENCES

1. V.F. Lobanov, "Modelling of Detonation Waves in Heterogeneous Explosives", Fizika Goreniia i Vzryva," Vol. 16, No. 6, pp. 113-116, 1980.
2. V.F. Lobanov, S.M. Karakhanov, S.A. Bordzilovsky, "Study of Transient Processes at Shock Initiation of TNT," Fizika Goreniia i Vzryva, Vol. 18, No. 3, pp. 90-97, 1982.
3. S.A. Bordzilovsky, V.F. Lobanov, S.M. Karakhanov, "Transient Processes at Shock Initiation of Cast RDX/TNT Charges and HMX/TNT Ones", Fizika Goreniia i Vzryva", Vol. 19, No. 4, pp. 136-139, 1983.
4. M. Van Thiel, Compendium of Shock Wave Data, Lawrence Livermore National Laboratory, Livermore, UCRL - 50108, Vol. 3, 1977.
5. A.N. Dremin, S.D. Savrov, V.S. Trofimov, K.K. Shvedov, "Detonation Waves in Condensed Explosives," Nauka, Moscow, 1970.
6. J.B. Ramsay, A. Popolato, "Analysis of Shock Wave and Initiation Data for Solid

Explosives," Fourth Symposium (International) on Detonation, pp. 233-238, White Oak, Maryland, ACR-126,1965.

7. C.L. Mader, "Numerical Modelling of Detonations," University of California Press, Berkeley, p.277, 1979.
8. V.S. Trofimov, "Elementary Method of the Estimation of the Explosive Charge Parameters for the Flat Metallic Plat Throwing," Fizika Goreniia i Vzryva, Vol.12, No.1, pp. 96-104, 1976.
9. M. Cowperthwaite, J. Rosenberg, "A Multiple Lagrange Gage Study of the Shock Initiation Processes in Cast TNT," Sixth Symposium (International) on Detonation, pp. 786-793, Office of Naval Research, 1976.
10. V.S. Trofimov, "On Possible Acceleration of Reaction and Diffusion in Shock Detonation Front," Kriticheskie Yavleniya, Fiziko-Khimicheskie Prevrashcheniya v Udarnykh Volnakh, Detonatsiya, Chernogolovka, pp. 11-16, 1978.
11. M. Cowperthwaite, "A Constitutive Model for Calculating Chemical Energy Release Rates from the Flow Fields in Shocked Explosives," Seventh Symposium (International) on Detonation, pp. 498-505, NSWC MP 82-334, Dahlgren, Virginia, White Oak, Maryland, 1981.

Session IV
POSTER PAPERS

Chairman: James E. Kennedy
Sandia National Laboratories

THE INFLUENCE OF REACTIVE CASES ON AIRBLAST FROM HIGH EXPLOSIVES

William S. Filler
White Oak Laboratory
Naval Surface Weapons Center
Silver Spring, MD 20903-5000

Airblast results were obtained from high explosive charges surrounded by casings that are potentially reactive in air. Data was derived from two different test efforts: 5 kg and 750 kg cylindrical charges with l/d ≅ 1 fired to obtain shock wave pressure time histories in the 200 to 2 psi peak shock overpressure range. The data strongly supports a mechanism proposed earlier to explain anomalous shockwave attenuation with distance for inert friable casings.

In a prior paper (1) experimental data was presented showing that the typical shock wave attenuation with distance for a bare high explosive charge in air was affected only to a limited extent by the presence initially of inert friable casings about the charge. This was so even for a case mass several times that of the high explosive. This was contrary to results expected from energy partition considerations alone. Photographic and piezoelectric pressure gauge evidence clearly indicated that soon after detonation of the high explosive the solid casing material outdistanced the gaseous blast wave. The consequent loss by the fine casing fragments of kinetic energy due to drag in stationary air was apparent from the relative position on photographic and pressure records of precursor disturbances and the shock front. Such drag losses in air must be manifest in heating and accelerating the air as a body. Therefore, it was proposed that the main shock wave in its subsequent passage through this "fragment conditioned" air would attenuate more slowly — and thus exhibit a smaller loss of shock pressure with distance — than otherwise expected.

With reactive casings, however, the energy produced by reaction of the dispersed casing material — in this instance a fine molten spray — with ambient oxygen augments the heating due to drag in advance of the arrival of the blast wave. As a result, measurements show higher shock pressure levels than would be expected from high explosive alone — rather than merely the less than expected loss observed with the inert casings. At the same time it is apparent that geometric features of the cased charge play an important role in the shock wave pressure decay with distance and direction.

REFERENCES

1. W.S. Filler "The Influence of Inert Cases on Airblast: An Experimental Study," Proceedings of the Sixth Symposium (International) on Detonation, ACR-221, p. 777 (1976).

DISCUSSION

How is airblast pressure from a high explosive charge affected by an inert or reactive case?

REPLY

1. Before Negative-Phase-Onset (NPO) the peak pressure of the main shockwave is reduced due to early partition of energy between the explosion products and the case mass.
2. After NPO the main shockwave moves through gas previously heated by kinetic (drag) and reaction energy left by precursor case particles.
3. Main shockwave attenuation with distance is slowed resulting in higher peak overpressure at greater distance than otherwise expected.

EXPERIMENTAL BASIS FOR MODEL*

FIELD LAYOUT FOR PRESSURE MEASUREMENTS AND PHOTOGRAPHY

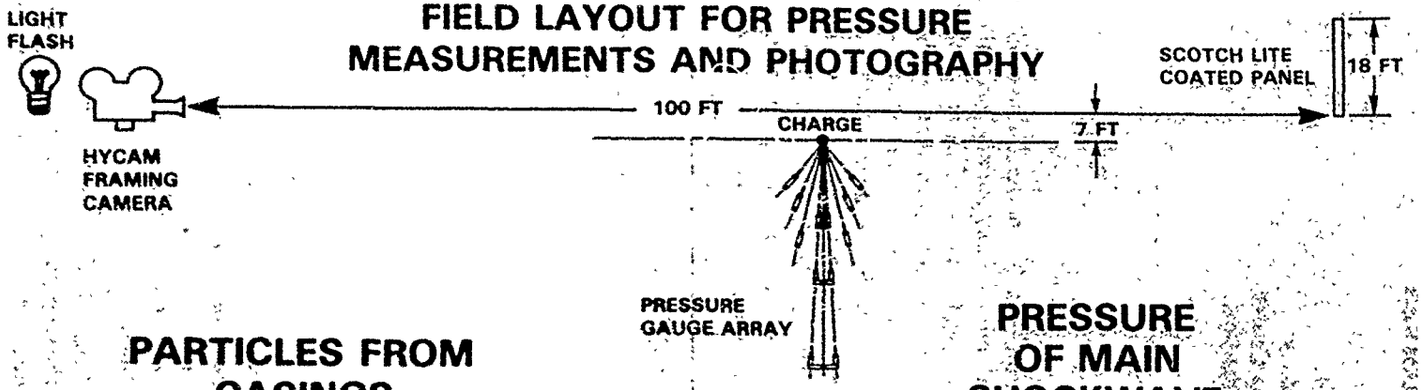

PARTICLES FROM CASINGS

CASING TYPES

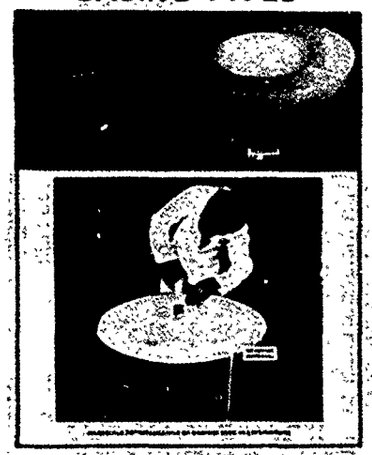

BOW SHOCK PHOTOGRAPHY

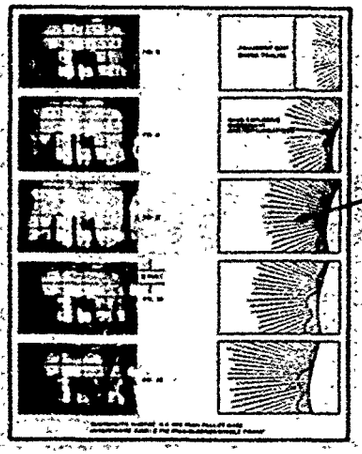

PRESSURE OF MAIN SHOCKWAVE

PEAK OVERPRESSURE TRENDS

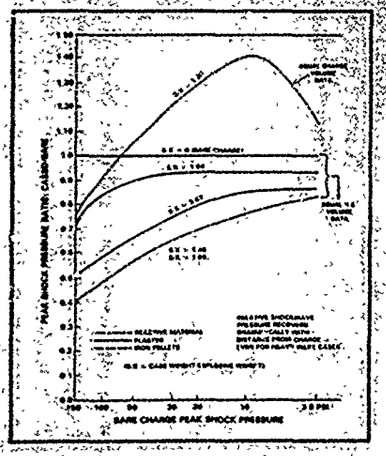

*INCLUDES ILLUSTRATIVE MATERIAL FROM REFERENCE 1

REACTIVE EXPLOSION MODEL

(A CASE FOR HOT PURSUIT)

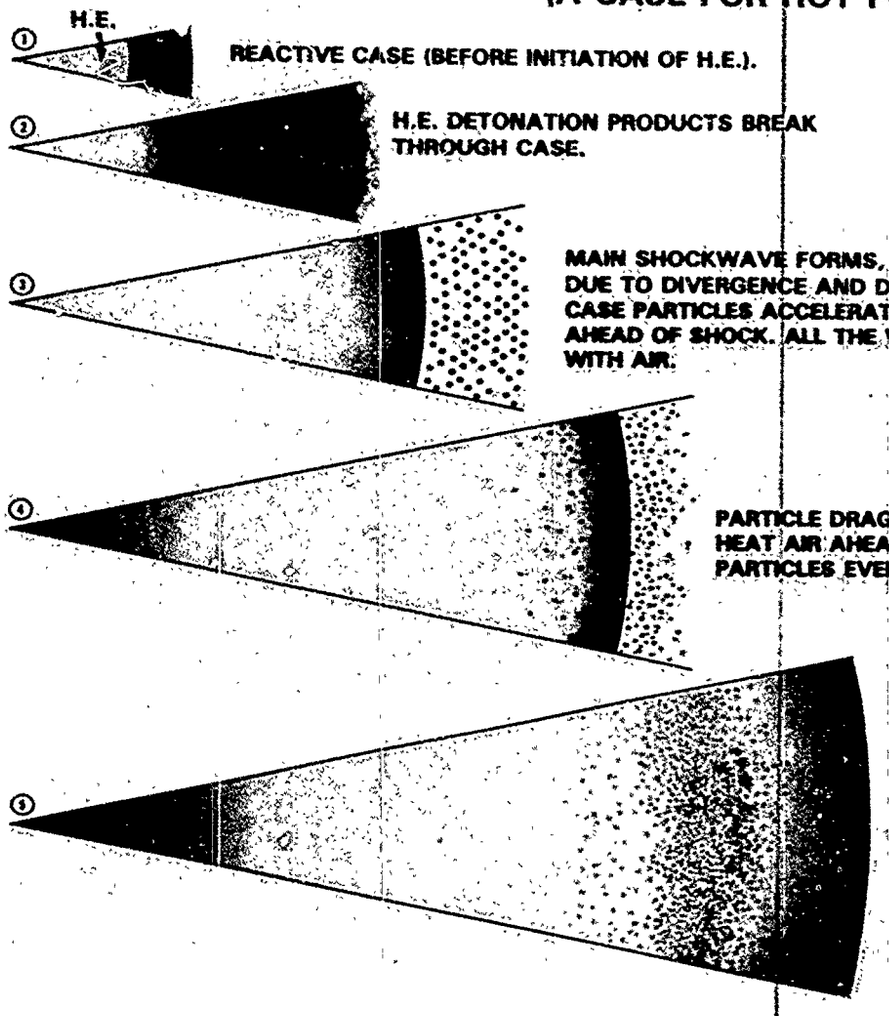

REACTIVE CASE (BEFORE INITIATION OF H.E.).

H.E. DETONATION PRODUCTS BREAK THROUGH CASE.

MAIN SHOCKWAVE FORMS, THEN SLOWS DUE TO DIVERGENCE AND DISSIPATION. CASE PARTICLES ACCELERATE AND MOVE AHEAD OF SHOCK, ALL THE WHILE REACTING WITH AIR.

PARTICLE DRAG AND CHEMICAL ENERGY HEAT AIR AHEAD OF MAIN SHOCKWAVE. PARTICLES EVENTUALLY STAGNATE.

SHOCKWAVE CATCHES UP AND MOVES THROUGH DUSTY HOT AIR WITH WAVE PRESSURE SUSTAINED TO GREATER DISTANCE THAN OTHERWISE.

A SPHERICAL OR CYLINDRICAL SECTOR VIEW.

RESUME

All cased charges undergo an intricate contrapuntal blast-fragment interaction sequence. Driven by a condensed detonation, case particles and the main shockwave — as they move through the ambient — are involved in an alternating energy exchange sequence that produces a blastwave that ultimately is stronger than is otherwise expected.

When the case particles are capable of reacting with ambient air along the way this process is reinforced leading to a still stronger blastwave.

THE GROWTH AND DECAY OF EXPLOSIVE DEFLAGRATIONS IN MUNITIONS IN SIMULATED FACTORY ACCIDENT SCENARIOS

A. S. Dyer, P. J. Haskins, P. J. Hubbard and C. D. Hutchinson

Royal Armament Research and Development Establishment
Fort Halstead, Sevenoaks, United Kingdom

Accident investigations into explosive events in Ordnance Factories in recent years have increasingly pointed to ignition and deflagration phenomena in the munitions involved. Experiments have been conducted to investigate the behaviour of RDX/TNT 60/40 and CW3 filled 155mm shell subjected to accidental stimuli such as pallet fires and torching from adjacent munitions. Other experiments have then examined the potential for these initial deflagration events to lead to mass detonation of adjacent shell or to produce merely a localised explosion of a single munition. Pallet fires have been demonstrated as a potential cause of mass detonation, localised explosion and, in the particular case of lightly plugged shell, a burning reaction without explosion. Torching experiments lead only to explosions. Other experiments have reproduced accidental ignitions in these munition fillings at ambient. The resulting deflagrations have produced one apparent deflagration/detonation transition but more routinely produced explosions which did not communicate to adjacent stores. There is some indication that detonation can be induced in adjacent shell by the impact of fragments from violently deflagrating donor shell. The introduction of explosives exhibiting lower levels of explosiveness could potentially improve safety in two ways. Explosive effects in munitions in which accidental deflagration events originated would produce fewer and slower fragments and the acceptor munitions would be more resistant to fragment attack. The RARDE Burning Tube test and the RARDE Small-Scale Fuel-Fire test have identified several explosives which exhibit low explosiveness in these accident scenarios.

1. INTRODUCTION

The RARDE paper presented at the 7th Detonation Symposium (1) described studies on the explosiveness of explosives commonly used as munition fillings. The paper proposed that the hazard associated with a munition involved in an accident should be assessed both on the likelihood of an initiation occurring, (the sensitiveness of an explosive) and on the nature or violence of any event initiated (the explosiveness of the material in that system). RARDE investigations of many different types of munition accidents have demonstrated that most events not directly attributable to fuze failure were caused by ignition of the main secondary high explosive filling. The violence of the event that ensued is a function of the explosiveness of the material in that system, which is itself dependent on the deflagrative properties of the explosive and the level of confinement it experiences. The work reported here is concerned with whether or not an initial deflagrative event induced in one munition is capable of inducing similar or more violent events in adjacent explosive filled stores. The possible extremes of consequence are failure of the event to propagate or transfer of the deflagrative event to

potential mass detonation.

1.1 Accidents involving munitions in filling factories.

In recent years, RARDE investigations into accidents involving munitions, particularly high explosive filled shell, have demonstrated that they have been caused by ignitions and deflagrations rather than by shock initiation/detonation processes. Typical examples occurred at the Royal Ordnance Factory Glascoed in 1972 and at the Royal Ordnance Factory Chorley in 1981. In the Glascoed incident a process worker was reworking some RDX/TNT filled 5.5" shell, part of the reworking involving the removal of a red phosphorus smokebox. The smokebox was positioned at the base of the exploder cavity at the nose-end of the shell. An explosion occurred which killed the worker involved but did not propagate into 15 adjacent shell awaiting attention. These shell were thrown around the workshop but showed no sign of having had any form of reaction induced in them. The workshop building was extensively damaged structurally.

The RARDE investigation demonstrated that mixtures of RDX/TNT and red phosphorus, with or without tetryl, were sensitive to impact and frictional forces in the order of those experienced in the top of the shell during the removal of a stubborn smokebox. It also showed that it was possible to induce an explosive deflagration in a 5.5" shell by dropping a 12kg weight from 2.7m onto a drift set on top of 50/50 mixture of red phosphorus and RDX/TNT. The resulting fragments were larger than those observed when the shell was deliberately detonated through its fuze train but were still indicative of a highly energetic deflagrative event having occurred in the item of ordnance.

The second incident at ROF Chorley occurred during routine sectioning of a 155mm shell also filled with RDX/TNT mixture. The explosive event did not damage the band saw irreparably but did cause damage to the building and to two adjacent 155mm shell by burning. Inspection of the shell involved in the original incident suggested that the ignition had occurred just as the saw blade had entered the explosive. Metallurgical examination of the fragments of the shell suggested that the explosive event was a deflagration. These recent events, where an original deflagrative event was caused by some form of ignition, both led to a decaying reaction. In other words, the event produced in adjacent shell was of a lower order than the original reaction.

An examination of the records of events concerning munitions in other incidents does not always show the same trend. An incident at the Morgan filling plant in New Jersey, USA in October 1918 is an example (2). The Morgan plant was the largest munition filling plant in the world at the time. An initial explosion in an Amatol kettle produced a fire. After approximately 15 minutes a number of 155mm and/or 8" shell in an adjacent shipping and painting room were described as exploding with their boosters 'popping'. Very soon afterwards there was a heavy explosion involving the apparent detonation of 200 to 475 shell stored in the shell 'hospital'. The roof of the shell hospital had been demolished by the first explosion and was on fire. The explosion made a crater 5' deep and 35' in diameter. Approximately 25 minutes later there was a third explosion of approximately 800 shell which were in a rail-car near the shipping room. Other explosions occurred at intervals which propelled burning shell and fragments into adjacent structures. At about 2 a.m. a fire which had apparently gone dormant in an adjacent magazine suddenly broke out again and resulted in the mass detonation of all the shell stored in the unit. Various rail-car loads then started to detonate at regular intervals. Events propagated through adjacent magazines containing bulk explosive and into storage areas containing shell. There is evidence that 66,000 155mm shell detonated en masse making a crater 25' deep and 100' wide, 600' long. When the final reckoning was made, it was estimated that the original event had led to the detonation or destruction of some 308,239 shell out of a total of 1,013,458 loaded shell at the plant at the time. In this event, or rather series of events, a variety of stimuli likely to promote ignitions led to many cases of mass detonation.

2. EXPERIMENTAL PROPAGATION TRIALS

Trials have been conducted to establish the degree of violence generated by various forms of deflagrative stimulus possible in an accident.

Other trials were then conducted to establish whether the events would propagate to adjacent stores and whether the propagation could lead to mass detonation.

2.1 Shell subjected to wooden pallet fires.

The first series of trials was concerned with events caused by munitions being subjected to a fire. The introduction of unit loads of ammunition and the consequent palletisation of munitions has introduced the possible hazard of a fire involving the wooden pallet on which shell are stored. At least one accident has been ascribed to this cause recently.

Experiments were first conducted with individual shell positioned on typical wooden pallets. The shell was either held vertically in a light steel framework or laid horizontally on the pallet. Fires were promoted using a small thermite charge and a minimal quantity of petrol or kerosene. Sufficient flammable fluid was used to ensure that the wooden pallet caught fire but not so much that the shell was subjected to a fuel-fire. The trials were conducted with 155mm shell containing either CW3, an RDX/TNT 60/40 modified with a nucleating agent (HNS) and containing small quantities of plasticiser or with normal UK RDX/TNT 60/40. The shell contained approximately 11.5kg of explosive. The trials were conducted at 3 separate locations designated A, B and C. Small variations in the experimental methods may have thus been introduced. Instrumentation for the measurements of air blast using piezo-gauges to an accuracy of $\pm$ 5% was only available at C. Approximate values of air blast were obtained for some events at locations A and B using foil gauges which are accurate to $\pm$ 25%. All events were recorded on CCTV video. Shell at location C were monitored with thermocouples. Vertically positioned shell were monitored at base, centre and nose. Horizontally positioned shell were monitored at three positions around their centres. The results are presented in Table 1.

Further experiments were then conducted with batches of three 155mm shell subjected to similar pallet fires. Again the shell were positioned either vertically in a light steel framework or were laid horizontally. They were placed at either 95mm, 135mm or 350mm apart. Most experiments were conducted with steel transit plug firmly screwed into the nose of the projectiles. In tests so designated either no transit plug or a light plastic plug was used. The results are presented in Table 2.

2.2 Shell subjected to 'torching' from adjacent shell.

An alternative mechanism for accidental ignition was explored by arranging for the ignition of the main secondary explosive in the top of an unplugged shell then directing the burning gases produced onto an adjacent shell or number of shell. The intense localised heating effect was similar to the action of a blow-torch. It was considered that this mechanism could apply in accidents similar to both the Chorley incident and the Morgan plant scenario described in 1.1 Standard 155mm CW3 filled shell were used in these experiments. The ignition of the donor was achieved using a small electrically ignited thermite charge. The events were monitored as before and the results are presented in Table 3.

2.3 Shell subjected to fragments from deflagrating donors at ambient temperature.

The final mechanism explored was the simulation of an ignition in a shell at ambient temperature. Impact, friction and fragment attack have all been demonstrated as possible sources of ignition and all could occur as either the primary source of the event or as a secondary effect from an explosive event in an adjacent store. Although all of these stimuli would be manifested by some thermo-mechanical process, the events in the donor shell were incited by solely thermal stimuli using a match-head igniter and 1.5g propellant charge. This was used for experimental simplification and to assist with the synchronisation of the event with high-speed cameras. The role of confinement on the explosiveness of the system has already been demonstrated (1). Therefore the two extremes of confinement afforded by nose and base ignition were used. High-speed cameras operating at 6-7000 fps were employed in addition to the normal CCTV video and blast assessment. Several detonating donors were added to the experimental series to provide a comparison for both blast measurement and high-speed cine record. The results are presented in Table 4 for those events originating from ignitions and

TABLE 1
Single Shell on Pallet Fire

Serial	Filling	Horizontal/ Vertical	Location	Time (mins)	Result	Remarks
(1)	Chorley CW3 unplugged	Vertical	A	17.5	Explosion	Large pieces of HE found. Large shell fragments.
(2)	Chorley CW3 plugged	Vertical	C	16.9	Explosion	Small pieces HE found. Large shell fragments.
(3)	Woolwich R/T	Vertical	C	5.6	Violent expolsion/ detonation	No explosive found. Blast pressure similar to detonated shell.
(4)	Chorley CW3 plastic cap	Vertical	C	11.2	Explosion	No explosive found. Large fragments of shell.
(5)	Chorley CW3 steel plug	Vertical	C	7.8	Explosion	No explosive found. Large fragments of shell.
(6)	Chorley CW3	Horizontal	C	2.75	Violent explosion/ detonation	No explosive found. Small blued fragments recovered. High blast pressure.
(7)	Chorley CW3	Horizontal	A	4.3	Explosion	Large pieces of HE found. Large fragments of shell.
(8)	Woolwich R/T plastic plug	Horizontal	C	Started burning at 3 mins. Extinguished at 14.Omins.	Steady Burn	All HE burnt out. Shell case intact.
(9)	Chorley CW3 steel plug	Horizontal	C	3.35	Violent explosion/ detonation	No explosive found. Small blued fragments of shell.

TABLE 2
Multiple Shells on Pallet Fire

Serial	Filling	Horizontal/ Vertical	Location	Time(mins)	Result	Remarks
(10)	3 x Chorley CW3 steel transit plugs	Vertical	C	4.3	Detonation	No shell or explosive fragments recovered. Blast pressure equivalent to detonation of all 3 shells.
(11)	3 x Woolwich R/T plastic plugs	Vertical	C	Plug blew out at 9.0. 2nd plug blew out at 9.5. Detonation at 15.8.	Initial venting on 2 shells. 3rd shell detonated, initiating remainder.	No explosive recovered. Blast pressure equivalent to detonation of several shells.
(12)	3 x Chorley CW3	Horizontal	C	1st explosion at 1.75. 2nd explosion 2.2.	1st event explosion 1 shell thrown clear. 2nd event detonation.	Blast pressure similar to one shell detonating. One shell left intact after being thrown clear.
(13)	3 x Woolwich R/T steel transit plugs	Horizontal	C	1st event explosion at 2.5. 2nd explosion at 4.2.	1st event explosion. 2nd event explosion 1 shell thrown clear.	One shell intact. Large shell fragments recovered. Low blast pressure.

TABLE 3
Torching Experiments

Serial	Filling	Location	Position on the acceptor (thickness of shell wall)	Time to event (mins)	Result	Remarks
(14)-(21)	Chorley CW3 single 155mm shells	B	—	—	Slow burn	All shells burnt out without explosion leaving the shell case empty and intact.
(22)	Chorley CW3 One donor. One acceptor without transit plug.	A	Driving band (21mm).	5.5	Acceptor exploded. Donor burnt for 70 mins.	The acceptor shell split into large fragments. Explosive recovered from acceptor. Donor completely burnt out after 70 mins.
(23)	Chorley CW3 One donor. One acceptor without transit plug.	A	Ogive, 280mm from nose (6mm)	0.8	Acceptor exploded extinguishing and fragmenting donor.	Acceptor and donor split open and large quantities of explosive recovered.
(24)	Chorley CW3 One donor. One acceptor with steel transit plug.	A	Ogive, 280mm from nose (6mm)	0.6	Acceptor exploded extinguishing donor	Large fragments of acceptor shell recovered together with explosive. Donor recovered nearly intact.
(25)	Chorley CW3 One donor. Two acceptor shell, one with steel transit plug, one without.	A	Three shells in line with the donor central and drawn back 350mm. Shells in contact at driving band.	HE Melted from unplugged shell. Explosion from plugged shell at 8.25.	Explosion of plugged acceptor. Steady burn of donor and unplugged acceptor.	Unconsumed explosive recovered from the plugged acceptor. Donor and unplugged acceptor burned out without explosion.
(26)	Chorley CW3 One donor. One acceptor plugged.	A	Donor torching directly into the base of the acceptor (30mm).	10.5	Explosion of acceptor. Steady burn of donor.	Shell case of acceptor split into one major and one minor fragment. Case went 100m in one direction, explosive in the other.
(27)	Chorley CW3 One donor. One acceptor plugged.	A	As (26)	9.9	Explosion of acceptor. Steady burn of donor.	Acceptor shell split open. Unconsumed HE recovered.

TABLE 4
Deflagrations Induced at Ambient

Serial	Filling	Location	Position of Ignition	Result	Blast Over-pressure (bars)	Remarks
(28)	CW3 without transit plug	A	Base	Violent Explosion	—	Small fragments of shell recovered. Small quantity of explosive recovered.
(29)	CW3 without transit plug	A	Base	Violent Explosion	<0.14 at 9.0m	Small fragments of shell base recovered.
(30)	CW3	A	Base	Explosion	<0.69 at 4.5m	Large fragments of nose and base recovered.
(31)	RDX/TNT 60/40	C	Base	Violent Explosion Possible Detonation	0.74 at 9.0m	No fragments of shell or residual explosive recovered.
(32)	RDX/TNT 60/40	C	Base	Violent Explosion	0.32 at 9.0m	No fragments of shell recovered but slight residue of explosive.
(33)	CW3 with steel transit plug	A	Nose	Mild Explosion	None-Recorded	Nose of shell blown open majority of explosive consumed.
(34)	CW3	C	Nose	Mild Explosion	None recorded	Nose of shell blown open, majority of explosive unconsumed.
(35)	CW3	C	Nose	Mild Explosion	0.11 at 9.0m	Nose of shell blown open, majority of shell intact containing HE.
(36)	Donor: CW3 without transit plug. Acceptors: CW3 one with and one without plugs. 95mm from donor.	A	Base of central shell.	Apparent Detonation of all three shells	0.4 at 9.0m	Small fragments of donor base recovered. No other fragments found. Crater produced.
(37)	Donor: CW3 without transit plug. Acceptors: CW3 one with and one without plugs. 135mm from donor.	A	Base of central shell	Apparent Detonation of all three shells	Not recorded	Small fragments of donor base found but none other.
(38)	Donor: CW3 Acceptors: CW3 on either side of donor at 135mm	A	Base of central shell	Explosion of donor. Acceptors little damaged.	Not recorded	Large fragments of donor base recovered and traces of explosive found. Acceptor shells thrown 7.5m and 10.0m with slight damage.
(39)	Donor: CW3 Acceptors: CW3 on either side of donor at 95mm	C	Base of central shell	Explosion of donor. Acceptors little damaged.	0.09 at 9.0m	Large fragments of donor base recovered and traces of explosive. Acceptor shells thrown about 8m with slight damage.
(40)	Donor: RDX/TNT 60/40 Acceptors: CW3 on either side of donor at 95mm	C	Base of central shell	Violent explosion of donor. Acceptors complete with heavy indentations.	0.31 at 9.0m	Fragments of base of donor recovered. No traces of explosive. Acceptor shells intact but heavily indented.

TABLE 4 (continued)
Deflagration Induced at Ambient

Serial	Filling	Location	Position of Ignition	Result	Blast over-pressure (bars)	Remarks
(41)	Donor: CW3 Acceptors: CW3 at 95mm on either side	C	Base of central shell	Explosion of donor. Acceptors intact	0.09 at 9.0m	Large fragments of base recovered and traces of explosive. Acceptor shells recovered intact with minor indentations.
(42)	Donor : CW3 Acceptors: CW3 at 95mm on either side.	C	Base of central shell	Violent Explosion of donor. One acceptor broken into two pieces; second acceptor punctured but no reaction.	0.23 at 9.0m	Fragments recovered from base of donor. One acceptor broken into two and thrown 35m with no sign of reaction. Second acceptor punctured and thrown 15m.
(43)	Donor: CW3 Acceptors: CW3 at 95mm on either side	C	Base of central shell	Moderately violent explosion of donor. One acceptor intact but cracked. Second acceptor intact but with moderate indentations.	0.13 at 9.0m	Fragments of donor and some residual HE from donor recovered. Both acceptors with slight to moderate damage.
(44)	Donor: CW3 Acceptors: CW3 at 95mm on either side	C	Base of central shell	Moderately violent explosion of donor. Both acceptors with slight indentations	0.18 at 9.0m	Fragments of donor recovered. Both acceptors recovered intact with slight indentations.
(45)	Donor: RDX/TNT 60/40 Acceptor: CW3 at 85mm	A	Base of central shell	Violent explosion of donor. Explosion of acceptor.	Not recorded	Small fragments of donor and large fragments of acceptor recovered. Small quantities of both RDX/TNT and CW3 recovered.
(46)	Donor: RDX/TNT 60/40 Acceptors: CW3 at 105mm and 350mm	A	Base of central shell	Violent explosion of donor. Explosion of closest acceptor.	Not recorded	Small fragments of donor and large fragments of closest acceptor recovered. Other acceptor intact. Small quantities of both RDX/TNT and CW3 recovered.
(47)	Donor: CW3 Acceptors: CW3	A	Nose of central shell	Mild explosion donor shell. Acceptors little damaged.	Not recorded	Damage to donor limited to nose area. Most of shell and explosive recovered. Acceptors practically undamaged.
(48)	Donor: CW3 Acceptors: CW3 at 95mm distant	C	Nose of central shell	Mild explosion donor shell. One acceptor with superficial damage. Other unmarked.	0.11 at 9.0m	Damage to donor limited to nose area. Left hand shell blown 8m left with damage to nose. Right hand shell blown 5m right.

Table 5 for the comparative detonations.

3. DISCUSSION

3.1 Shell subjected to pallet fires.

Examination of the results in Table 1 shows that three types of event can occur from a single unfuzed 155mm shell filled with RDX/TNT or CW3 being exposed to a pallet fire. The shell may detonate, it may explode or, in the special case of a shell with only a light plastic nose-cap, it may burn steadily without explosion.

RDX/TNT 60/40 and its variant, CW3, have been shown to exhibit high levels of explosiveness when measured in the RARDE Burning Tube test even with the explosive at ambient termperature (1). Indeed, deflagration velocities of the order of 1,400m s^{-1} have been measured for 500mm long charges of RDX/TNT 60/40. It has also been demonstrated that the explosiveness of RDX/TNT 60/40 can be enhanced and that it may detonate when subjected to a fuel fire under the conditions of total metal confinement afforded by the burning tube (1). It is not surprising therefore that deflagrations in RDX/TNT and its variant, CW3, did, on occasions, transit to detonation when subjected to these pallet fires. Even assuming that it was only the skin of the explosive that had time to have been conditioned to the several hundred degrees measured in these experiments, the rate of deflagration is likely to be more rapid than at ambient temperature.

The short times for the events to occur indicate that the reactions are probably promoted by ignitions at the metal/explosive interface rather than from some self-heating effect occurring internally. Assuming a doubling of the reaction rate for every 10K soon makes the attainment of deflagration velocities of sufficient magnitude that DDT becomes a possibility at the temperatures experienced in these tests. In fact it is remarkable that detonations are in a minority in these experiments presumably because of the overriding effects of confinement loss on deflagration reactions. A sudden reduction in confinement caused by the failure of the shell casing removes the pressurisation on the burning reaction which can fade rapidly. The many occasions that unreacted explosive was recovered was evidence for the role of confinement release in inhibiting the transition from deflagration to detonation.

From Table 1 there is an obvious correlation between the time to event and whether or not the shell was originally positioned vertically or horizontally. Vertically positioned shell seem to survive considerably longer before reacting, an average of 11.8 minutes compared with 3.5 minutes for horizontal shell. It would seem that the explosive contents of the shell in a horizontal position were subjected to a more uniform and possibly more intense heat than the contents of the vertical shell. The thermocouple results in general support this view but also show considerable variation from experiment to experiment. Comparison of thermocouple records from Serial (5) and (9) shows that the outer skin of the vertical shell in (5) reached a peak of 470 ° in 3.3 minutes but returned to less than 370 °C until explosion at 7.8 minutes. The skin temperature in (9) for the horizontal shell peaks at 500 °C after 2.5 minutes and remains in excess of 460 °C until detonation occurred at 3.35 minutes. However, in several other experiments thermocouple records of 600 °C were recorded. At the moment there does not seem to be a direct correlation between the temperature and whether or not a detonation occurred.

From Table 2, increasing the number of shell on the pallet fire does seem to increase the chance of mass detonation. Serial (10) presumably occurred as an apparent simultaneous detonation of all three shell through the initial deflagration/detonation transition of one of the projectiles which then detonated the two adjacent shell. An initial explosion on two occasions, Serials (12) and (13), did not transmit into adjacent shell and, in fact, served in both cases to throw a shell clear of the fire.

Most of the shell in these experiments were fitted with heavy steel transit plugs. These allowed any pressurisation in the shell caused by preconditioning in the fire and consequent ignition/deflagration to accelerate rapidly to a violent explosion or potential deflagration/detonation transition. As has been mentioned, early loss of confinement has been demonstrated as a means of reducing the explosiveness of a system. It has been anticipated that shell fitted with plastic caps should have produced less violent events as the caps would have encouraged early confinement loss. Evidence for

TABLE 5
Deliberate Detonations

Serial	Filling	Location	Position of detonation	Blast-over-pressure (bars)	Result	Remarks
49)	Chorley CW3	C	Base	Complete detonation	0.53 at 9.0m	Plastic explosive used to boost
50)	Chorley CW3	C	Nose	Complete detonation	0.49 at 9.0m	Single base fragment recovered
51)	Chorley CW3	C	Nose	Complete detonation	0.62 at 9.0m	— —
52)	Chorley CW3	C	Noes	Complete detonation	0.39 at 9.0	— —
53)	Chorley CW3 Donor: 2x Chorley CW3 acceptors at 95mm spacing on either side	C	Nose of central shell	Complete detonation of all 3 shells	No record	Base fragments recovered

this effect is provided by Serial (8) where the horizontal shell ignited and burned steadily without explosion. Even Serial (4) resulted in an explosion when the shell was positioned vertically with a plastic transit plug. However, Serial (11), while demonstrating uniquely that two of the three shell ejected their transit plugs at 9.0 minutes and 9.5 minutes, produced a detonation indistinguishable from the simultaneous detonation of all three shell at 15.8 minutes. It is presumed that the initial ignition occurred near the base as the shell were held vertically. Perhaps the particular configuration of these shell provided confinement by the wedge of explosive in the nose locking into the ogive during an ignition/deflagration originating at the base. This holds on the pressure generated by the deflagration for sufficient time to produce a transfer to detonation even when the transit cap is plastic.

3.2 Shell subjected to torching from adjacent shell.

Although relatively few torching experiments have been conducted, it is clear from Table 3 that torching produces low levels of deflagrative event in the acceptor munitions. None of the events produced were approaching the degree of violence observed in the pallet fire experiments. Serials (14) - (21) are further evidence of the vital role of confinement on the explosiveness of the system. All of the shell burned out completely taking between half to one hour. The deflagration, while non-explosive, was a vigorous reaction with flame jetting from the nose for up to a metre.

The experiments conducted with acceptor munitions show a close correlation between the thickness of the casing on which the torching was applied and the time for an event to occur. The thinner the casing, the more rapid was the onset of deflagration. The ignition times of less than a minute for the torching experiments on the ogive are also an indication of the intensity of the flame. Thermocouple readings were not made during these experiments but the record from Serial (8) from the previous experiments showed temperatures between 500-600 °C for the skin temperature of a shell that burned out steadily without explosion. Although all of the explosive events generated by torching were relatively mild explosive deflagrations, there is still a trend demonstrating that the confinement at the ignition point controls the violence of the event and hence the explosiveness of the system. Ignition at the ogive, with 5mm thick walls, resulted in recovery of most of the rear of the shell intact, complete with explosive. Ignition directly into the base, where the wall thickness is 30mm, resulted in a disruptive event.

The role of the transit plug in maintaining or releasing the confinement on the burning reaction is again shown in Serial (25), where the plugged acceptor exploded while the unplugged shell burned steadily without explosion. However, Serials (23) and (24), where identical shell were torched on the thin wall of the ogive, produced similar results in very similar timescales despite the fact that one was plugged and the other was not. For the unplugged shell to have produced an explosive deflagration at all reinforces further the theory postulated in 3.2 that the geometry of the ogive provides confinement. The wedge of explosive in the nose would seem to lock against the shell wall forming a gas-tight seal following the ignition/deflagration at the explosive/shell wall interface.

3.3 Deflagrations induced in 155m shell at ambient

The results of deflagrations induced with shell at ambient temperatures, Table 4, show a whole range of events from mild explosive deflagrations to apparent detonations. Experiments with single shell again show a strong correlation between the violence of the event and the position that the ignition originated. Base ignitions produced the most violent events as the base is surrounded by the greatest thickness of metal and hence has the highest level of confinement. The deflagration reaction therefore has the maximum opportunity to accelerate. Ignitions at the nose of the projectile have thinner walls to confine the resulting deflagration. The reaction is also in close proximity to the transit plug which soon releases from the threads of the shell further removing confinement. The rapid reduction in the confinement causes consequent collapse of the acceleration of the burning reaction. The blast overpressure measurements provide some indication of the violence of the event originating from an ignition but it is perhaps an oversimplification to equate the measurement of high overpressure alone as proof of detonation.

As has been mentioned in section 3.1, RDX/TNT 60/40 has been measured as deflagrating at a rate in the order of 1,400m s^{-1} over a 500mm confined run. These 155mm projectiles have an explosive length of 640mm. Therefore it would seem possible that deflagration reactions alone could produce substantial overpressure readings from the explosive in these projectiles. An event has only been termed a detonation when there was confirmatory evidence, e.g. there was no residue of explosive, a crater was produced and any fragments were small, jagged and blued.

Previous RARDE experiments to examine the deflagration characteristics of explosives have used a variety of explosive loadings and geometries. The largest Burning Tube used routinely was a cylindrical charge 750mm long with internal diameter 100mm with mild steel walls of 12.7mm thickness (1). This contained about 10kg of RDX/TNT 60/40 and proportionate weights of other explosives dependent upon their densities. The results with RDX/TNT 60/40 showed it to be high in the explosiveness ranking order producing an average of 20 fragments and 5% of unconsumed explosive. CW3 appeared in the next highest category with 15 fragments on average and 25% unconsumed explosive. In neither series was an observed explosive reaction positively identifiable as a detonation. Explosive residue was found after each experiment and the tube fragments were unthinned and showed burst fractures. However, there was no attempt made to monitor blast overpressure neither was there any means available for the assessment of fragment velocities.

The shell used in the present experiments were made of higher grade steel than the mild steel used in the RARDE Burning Tube tests. They would have therefore provided confinement to the burning reaction for a longer period before case rupture and loss in confinement. The geometry of the shell may have also afforded additional confinement (qv para. 3.1) although some parts of the shell walls were thinner than the 12.7mm thick walls of the burning tube. For whatever reason, Serial (31) seems to have produced a deflagration/detonation transition based upon the blast overpressure, the lack of explosive residue and the extensive fragmentation. However, none of the other 4 base ignited single shell seem to have done so.

It is reasonable to assume from Serial (53) and other work on vulnerability, that the detonation of one 155mm shell causes the detonation of other shell which are directly adjacent and hence could lead to a potential mass detonation in an area where shell are stored or worked upon in close proximity to one another. Serials (36) and (37), where two CW3 acceptor shell apparently detonated from the reaction induced in a base-ignited CW3 projectile are more difficult to explain. CW3 has been shown to exhibit a slightly lower level of explosiveness than RDX/TNT 60/40 in the large-scale RARDE Burning Tube. Since there is also no evidence of deflagration/detonation transition in any of the base-ignited single shell filled CW3, it is postulated that some other mechanism was operating. Many of the acceptor shell from the other base-ignition trials showed fragment damage as a result of a violent deflagration of the donor. It may have been possible for a violent deflagration from a CW3 or RDX/TNT 60/40 loaded projectile to produce fragments with sufficient kinetic energy to cause detonations in adjacent acceptors. Fragment attack data from other experiments (3) have shown that confined Composition B can be shock-initiated by fragments travelling at a velocity of 1,930m s^{-1}. Experiments in the RARDE Fragment Attack test (4) show velocities of 1,250m s^{-1} for the onset of detonation in UK RDX/TNT 60/40 Type A. Other workers have placed the velocity for a projectile attacking confined RDX/TNT to produce detonation as low as 1,000m s^{-1} (5). Whatever the true value, these velocities are not impossible values for fragments from a violently deflagrating munition. Perhaps the mechanism operating in Serials (36) and (37) is shock-initiation of the acceptors from projectiles propelled by the explosive deflagration of the donor. Any evidence of the initial deflagrative reaction could well be obscured by the fragments and explosive effects from the detonating acceptors initiating any unconsumed explosive remaining in the donor. The onset of such a 'knock-on' effect from an initial base-originating deflagration is obviously far from a foregone conclusion. The majority of the tests carried out showed that an initial deflagrative reaction produced a lower level of event in adjacent munitions. The trend was

therefore towards explosive events that would fade out rather than precipitate a mass detonation.

4. THE USE OF LOWER EXPLOSIVENESS MATERIALS TO IMPROVE SAFETY

The experiments described in the foregoing sections have demonstrated that both types of accidental event — mass detonation and localised explosion — can originate from an initial ignition. In the past, the emphasis on preventing such events has centered on the maintenance of safe practices and ensuring that the explosives being used are insensitive to the stimuli encountered during manufacture. These experiments suggest that this may not always be enough.

Safe practices must always be the keystone of safety. They ensure that the risks of explosive stores being subjected to hazard-creating stimuli are minimised. The use of insensitive explosives is also essential to ensure that the inception of an accidental event is unlikely unless considerable amounts of energy are applied to the store. However, it is only recently that attention has been focused on mitigating the effects of an event from the point of view of the explosiveness of the explosive formulation. Concern with the consequences of an accidental ignition can mean the difference between localised minor events and mass detonation.

The RARDE Burning Tube test (1) has demonstrated that it is possible to select explosives which exhibit low explosiveness in a wide variety of accident scenarios with no loss of detonative performance. These explosives show a marked reluctance to deflagrate violently from an ignition and yet will detonate successfully from an adequate shock input. Low explosiveness materials are characterised by minimal fragmentation in the Burning Tube test and large quantities of explosive residue remaining after the test. Such behaviour in the accident scenarios investigated in these experiments can only lead to minor explosive events and interruption of the explosive train leading to mass detonation. In experiments with the large-scale RARDE Burning Tubes, it was often possible to use fragile photo-flood light bulbs placed in close proximity to events induced with 10kg confined charges of materials exhibiting low explosiveness. If these bulbs could survive less than 0.5m from such explosive events, then certainly so could other munitions.

Experiments have been conducted to demonstrate that low explosiveness munition fillings will produce low levels of explosive event in adjacent stores. 155mm shell were filled with Plastic Explosive PE4 and base ignitions were induced. The resulting events produced little fragmentation of the donor and had no effect on adjacent acceptors placed 90mm away.

Additional experimental data have shown that test vehicles filled with low explosiveness formulations are more resistant to fragment attack than materials exhibiting high explosiveness (4). In consequence, munitions filled with low explosiveness materials subjected to the 'knock-on' stimulus postulated in this paper, would be more resistant to the production of violent events than the compositions in common use at the moment. Previous work has shown that fewer explosive formulations are immune to a fuel or pallet fire. The initial conditioning afforded by heating the explosive seems to increase the explosiveness of many systems over that observed at ambient (1). However, there are considerable data to suggest that most aluminised compositions and certain plastic-bonded explosives can survive the rigours of a fuel fire and not be brought to detonation. The designed-in reduction in the explosiveness of a munition filling provides bonuses in areas of the munition's life other than its manufacture. Low explosiveness stores will produce less damaging accidental events in service use. The consequences of premature explosions in gun-launched projectiles, the cook-off of munitions in hot guns and fuel fires, and even vulnerability of munitions to fragment attack are all related to the explosiveness of the store. Low explosiveness fillings for munitions provide an added safeguard to the use of insensitive explosive materials.

5. CONCLUSIONS

Experiments have been conducted to investigate the behaviour of munitions subjected to accidental stimuli such as pallet fires and torching from adjacent munitions. Particular attention was paid to the potential for initial deflagrative

events in RDX/TNT 60/40 or or CW3-filled shell to lead to mass detonation of adjacent shell or to produce merely a localised explosion of a single munition. Pallet fires have been demonstrated as a potential cause of mass detonation, localised explosion and, in the particular case of a lightly plugged shell, a burning reaction without explosion. Torching experiments lead only to explosions. The violence of the event induced by torching is closely allied to the position the donor torches onto the acceptor. Torching towards the nose produces a mild explosion; towards the base a more violent explosion.

Other experiments have reproduced accidental ignitions in these muniton fillings at ambient temperatures. The resulting deflagrations have produced an apparent deflagration/detonation transition in one case but more routinely produced explosions which did not communicate detonation to adjacent stores. There is some indication that detonation can be induced in adjacent shell from fragment impact from a violently deflagrating donor shell. The introduction of explosives exhibiting lower levels of explosiveness could potentially improve safety in two ways. Explosive effects in munitions in which accidental deflagrative events originated would produce fewer and slower fragments and the acceptor munitions would be more resistant to fragment attack. The RARDE Burning Tube test and RARDE Small-Scale Fuel Fire test have identified several explosives which exhibit low explosiveness in these accident scenarios.

REFERENCES

1. A. S. Dyer, P. J. Hubbard, P. R. Lee, D. G. Tisley, "Factors affecting the explosivenes of munition fillings", 7th Symposium (International) on Detonation, Annapolis, (1981), p1040-1047.
2. R. Assheton, "History of Explosions", Charles L. Story Company, 1930.
3. R. Frey, J. Trimble, P. Howe, G. Melani, J. Waddel, "Further studies of the initiation of explosive reactions in confined charges by projectile impact", 4th International Symposium on Ballistics, Monterey, (1978).
4. M.A. Barker, J.F. Bassett, J. Connor, P.J. Hubbard, "Response of confined explosive charges to projectile impact", 8th Symposium (International) on Detonation, Albuquerque, (1985).
5. R. Merrifield, "Shock-induced reactions in explosives and propellants", ERDE Report TR-103, Waltham Abbey, 1972.

ROYAL ARMAMENT RESEARCH AND DEVELOPMENT ESTABLISHMENT

FORT HALSTEAD UNITED KINGDOM

GROWTH AND DECAY OF EXPLOSIVE DEFLAGRATIONS IN MUNITIONS IN SIMULATED FACTORY ACCIDENT SCENARIOS

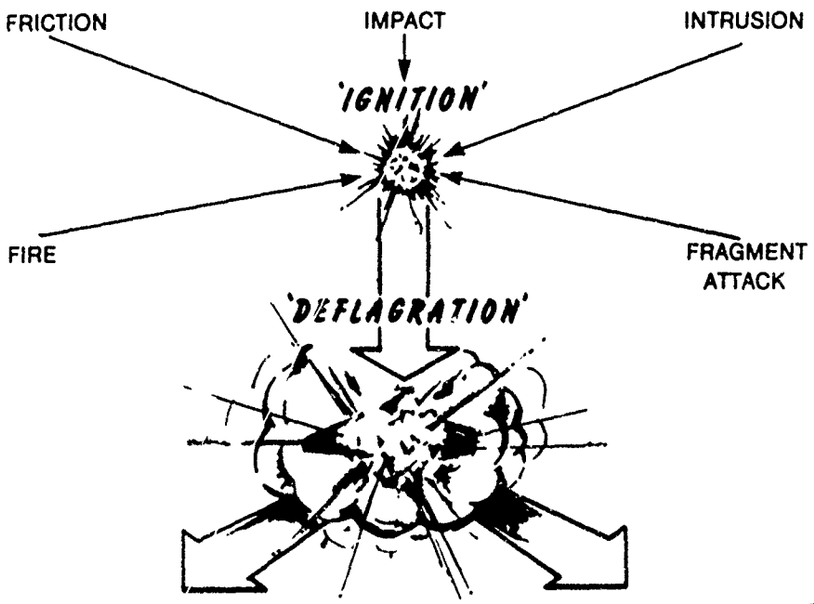

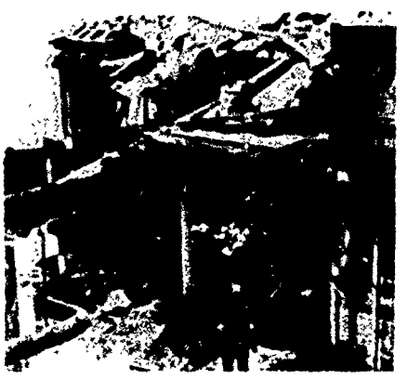

EXPLOSIVES IN MUNITIONS IGNITED AT AMBIENT

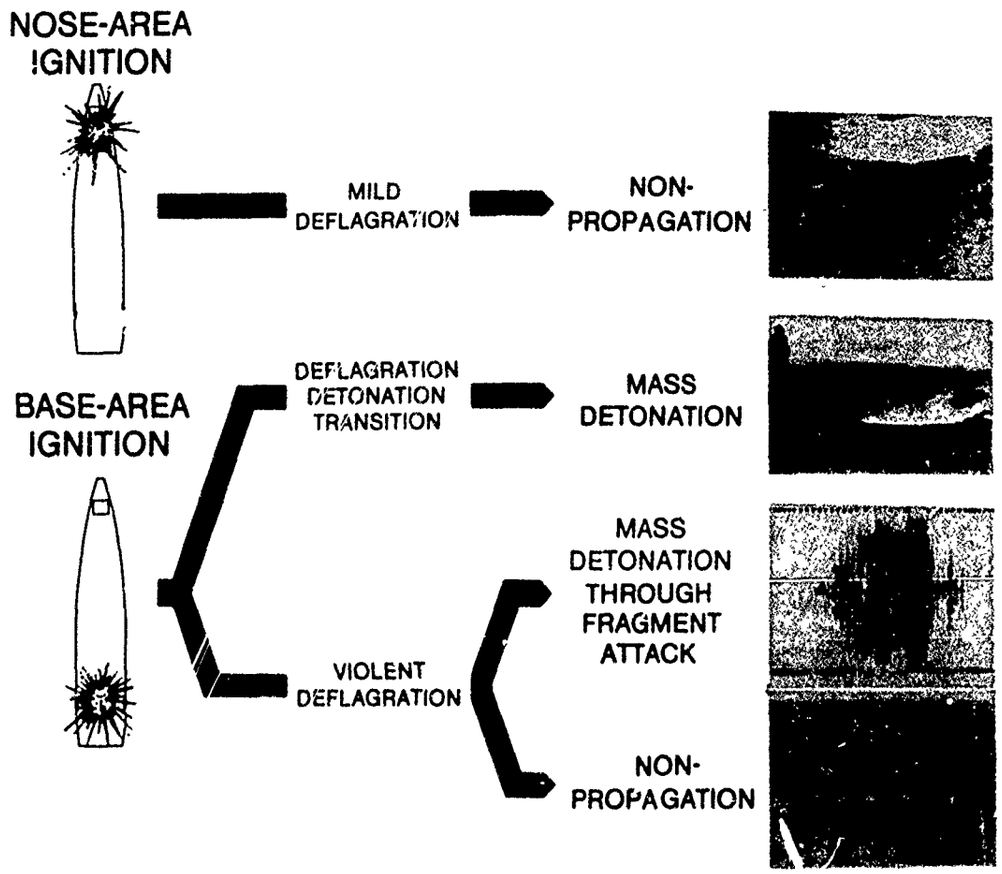

BURNING TUBE FILLED RDX/TNT 60/40 TYPE A

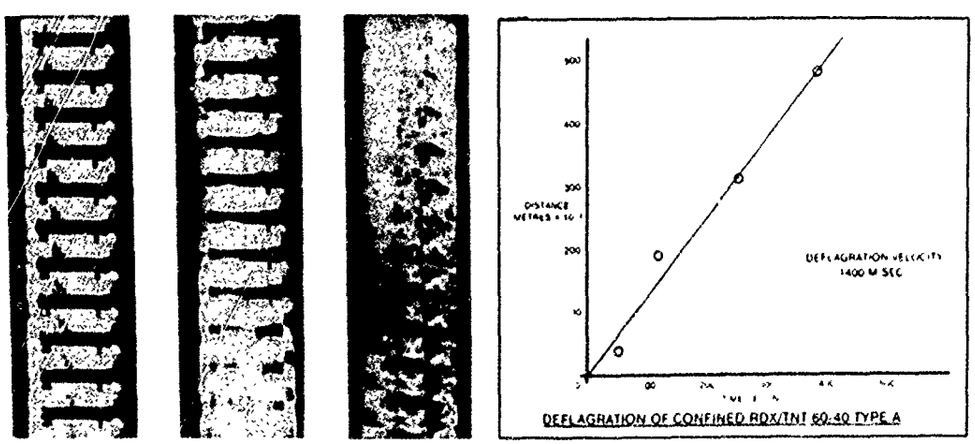

EXPLOSIVES IN MUNITIONS SUBJECTED TO FLAME

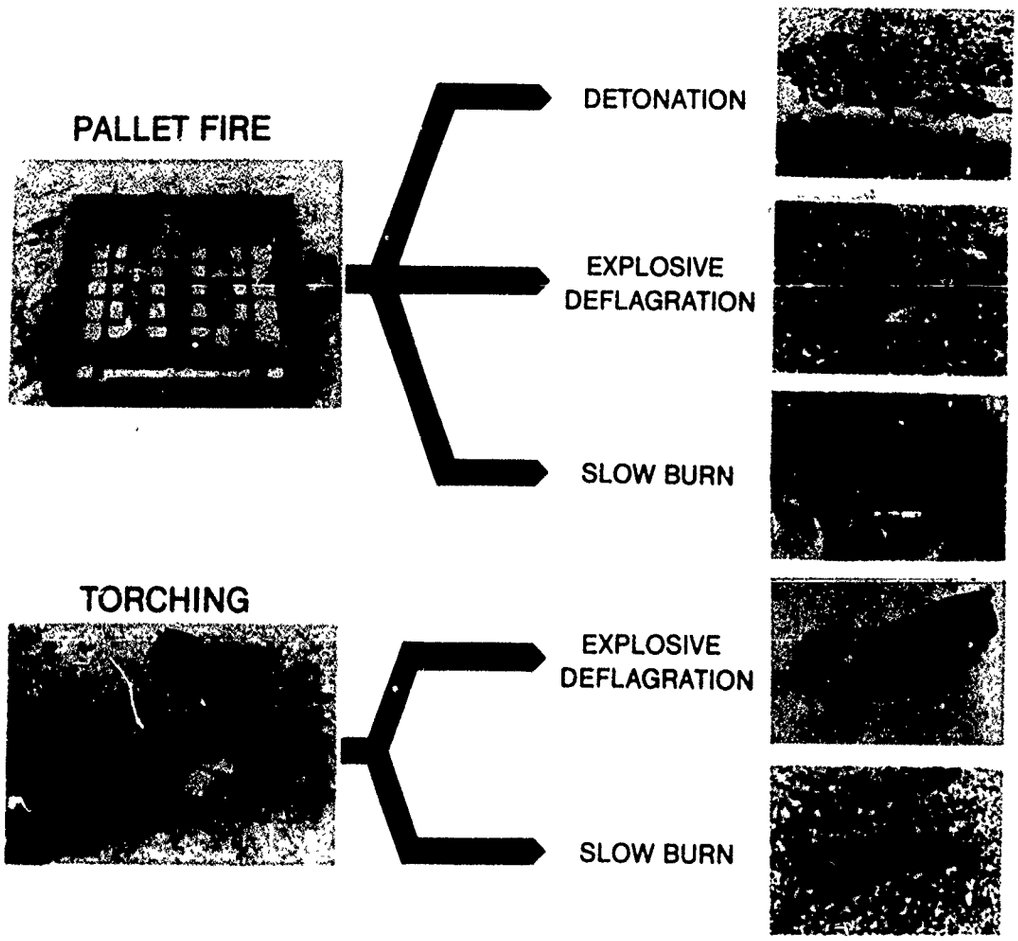

RARDE SMALL-SCALE FUEL-FIRE TEST

EXPLOSIVE	RESULT
RDX/TNT 60/40	11222
TNT	2222
RDX/WAX 88/12	12111

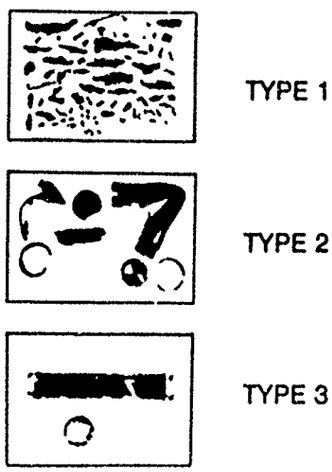

IMPROVEMENTS TO SAFETY THROUGH THE USE OF MUNITION FILLINGS EXHIBITING LOW EXPLOSIVENESS

BURNING TUBE FILLED PE6/Aℓ

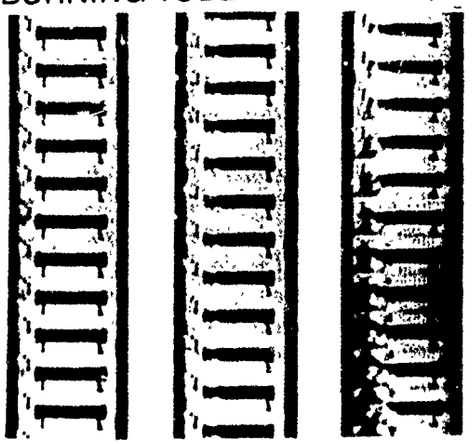

RARDE SMALL-SCALE FUEL - FIRE TEST

EXPLOSIVE	RESULT
PE6/Aℓ	233333
RDX/PU88/12	33333
RDX/WAX/Aℓ	33333

TYPE 1

TYPE 2

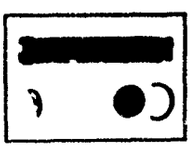

TYPE 3

DONOR SHELL FILLED PE4
ACCEPTOR SHELL FILLED CW3

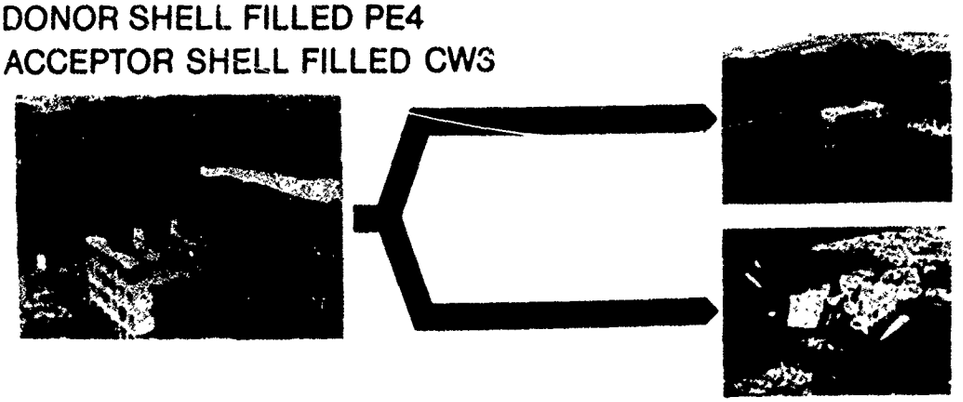

AN EIGHT-INCH DIAMETER, HEAVILY CONFINED CARD GAP TEST

Joseph C. Foster, Jr., Keith R. Forbes, Lt. USAF
Michael E. Gunger, and E G. Craig

Air Force Armament Laboratory
Eglin AFB, FL 32542

An instrumented card gap test which is useful for investigating the response of explosives to low pressure, long duration shock stimuli has been developed. The test was designed to screen for an explosive's (or propellant's) propensity to detonate or react violently as result of shock induced sympathetic detonation of large ordnance such as general purpose bombs. Both donor and acceptor are encased in an 8 in. outside diameter by 0.35-in wall steel pipe. The donor is Composition B, one-diameter long, and point-initiated on axis. Acceptors are two diameters long. Typically, both donor and acceptor tubes are closed with 0.50-in. thick steel end plates. Plexiglass, of varying thickness, and steel end plates are used to control the shock amplitude transmitted into the acceptor. The acceptor is instrumented with piezoelectric time of arrival pins. The assembly rests on a vee-groove wood block which rests on a 1-in. thick armor plate; the armor plate serves as a fragment witness. Hydrocode calculations were performed to describe input pressure profile as a function of gap thickness and configuration. The calculations show that the end plates result in significantly longer pressure durations and lower peak pressures than other gap tests, and in a more realistic mock of the shock loading experienced in large ordnance sympathetic detonation experiments. Results presented includes data for tritonal, Composition B, TNT/WAX, and TNT/NQ/WAX. The range of pressures resulting in transition to detonation for different explosives is narrower for this test than that measured in experiments such as the NOL LSGT. The instrumentation used permits a determination of detonation velocity as well as distance required to run up to detonation as a function of input shock strength.

INTRODUCTION

The storage of large quantities of high explosives presents a unique engineering problem from the point of view of the safety engineer (3). One aspect of understanding the potential hazard associated with explosive storage is the characterization of the shock sensitivity of the material of interest. In situations where large charges (100-1000 kg) are stored in near proximity, the conditions under which adjacent charges undergo sympathetic detonation might be significantly different than those determined from small scale experiments. The experimental techniques in this paper address this problem.

The scale of the experiment provides for characterization of explosive response to large amplitude long duration pressure pulses. A number of similar experimental techniques are used to measure the response of explosives and propellants to pressure pulses (1). The technique presented in this paper is distinguished from previous techniques by the long duration pulse which is the result of the relatively large scale of the experiment.

Several investigators have addressed the relationship between amplitude and duration of the applied shock as it applies to determining shock sensitivity of explosives (2, 3). The present

technique, however, provides loads of duration 10-40 microseconds as opposed to 1-10 microseconds usually discussed.

In addition to the long duration nature of the shock structure used in the experiment, the wave structure is modified by impedance discontinuities between the donor charge and the acceptor charge. There has been no attempt to specifically tailor the wave shape using this approach but rather to simply model in the experiment the wave structure representative of the problem posed by two adjacent steel encased charges. This problem provides data which applies directly to the storage of large unitary weapons such as the Mark 80 series of conventional general purpose bombs.

An investigation of shock sensitivity seeks to determine the minimum input (a limiting shock strength) that will produce steady-state detonation in an explosive. Steady-state detonation can occur only when chemical energy released in reaction continually restores energy loss by the shock wave through dissipation into internal and kinetic energy loss to the media. If an initial shock strength is greater than the steady-state detonation strength, the energy supplied through chemical reaction is insufficient to maintain such strength and the wave decelerates to the steady-state or Chapman-Jouguet (CJ) detonation. On the other hand if the initial shock strength is less than that of the CJ wave, the chemical energy supplied may not be sufficient to accelerate the shock wave to steady-state detonation. A limiting initial shock strength does exist that although weaker than the CJ wave is still strong enough to be boosted into detonation by the energy of chemical reaction. This limiting shock strength is an important experimental point in the definition of an explosive's shock sensivity.

A simple method for determining the shock sensitivity of an explosive is the Naval Ordnance Laboratory's (NOL) gap test. The NOL gap test consists of a 2-in. by 2-in. cylinder of pressed tetryl to supply an initial shock through a variable Lucite gap to a moderately confined acceptor charge (1.437-in. diameter by 5.5-in. length). "Go, no-go" is determined by a hole punched through a 3/8-in thick mild steel witness plate on the end of the acceptor. By adding thickness to the Lucite cards, the shock can be attenuated and thus a limiting shock for detonation can be determined.

The shock sensitivity of an explosive relates directly to questions of safety in the handling, transporting and storing of munitions. The scale of munitions, however, is much greater than the scale of the NOL large scale gap test. A MK-82 bomb, for example, has a diameter of 10.75-in. and contains about 200 lbs of explosive. The NOL gap test with a scale of 1.4-in diameter and less than ½ lb of explosive is inappropriate to study shock sensitivity in large munitions. A major difference is the time dependent signature of the pressure pulse transmitted in these two environments. In order to measure shock sensitivity as it applies to the safety of large munitions, an eight-inch diameter, super large scale gap test was devised which models the pressure-time pulse transmission of a detonating MK-82 to its nearest neighbor in a storage configuration.

The set-up of the super gap test is shown in Figs. 1 and 2. The donor charge in this test is a 7.15-in. diameter by 8-in. long Composition-B cylinder confined by a 0.35-in. thick steel case around the charge and 0.5-in. steel plates on both ends. The donor charge is initiated with an RP-2 EBW detonator boosted with a 1-in. by 1-in Composition A-5 pellet (Fig.3). Polymethylmethacrylate (PMMA) cards are used to attenuate the input shock. These cards are disks 8-in. in diameter and either one or two inches thick and are stacked to various thicknesses behind the donor charge. The acceptor charge is 7.15-in. in diameter and 16-in. long and confined by a 0.35-in. thick steel case and two 0.5-in. steel end plates.

The 6-ft by 3-ft by 1-in. rolled homogeneous armor (RHA) witness plate is not placed on the end of the acceptor as in the NOL gap test but is placed parallel to the length of the charges at a 6.75-in. stand-off from the centerline. This stand-off is maintained by a slotted "two-by-four" assembly which holds the charges and PMMA cards in place on top of the witness plate. The wood also supplies protection to the witness plate to prevent casing fragments from penetrating the plate. Sand bags positioned around the test set-up further protects the witness plate and more importantly protects the surrounding area. Fragments, however, do mark the plate on angles not covered by the wood and sand bags. The position of the fragment mark-

ings can be used to determine a distance of run for the test as well as "go, no-go". Figures 4 and 5 show the typical fragment markings found on a witness plate.

During reaction, a portion of the acceptor casing along the length of the charge is accelerated into the two by four stand resulting in a soft catch of a large fragment — in reality a strip off the acceptor can (Fig. 6). This fragment also maps the history of detonation in the charge. Adiabatic shear in the casing is witnessed on the strip when detonation is reached. The markings on this fragment corresponds well with markings on the witness plate.

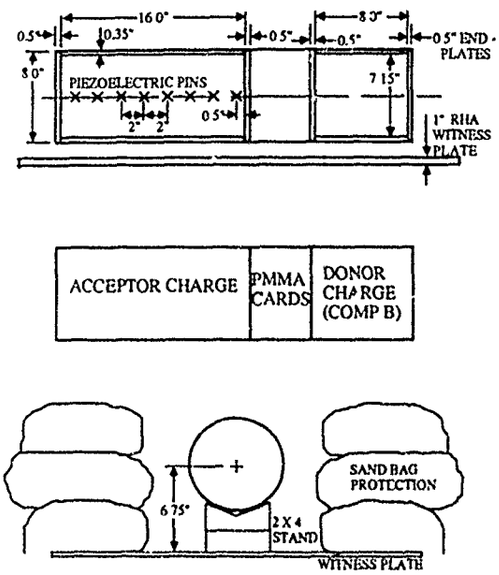

Fig. 1. Set-up of the super gap test

In order to further define the detonation velocity and run distance to detonation, piezoelectric pins (Dynasen Inc., CA-1136) are inserted through the acceptor casing into the explosive. These pins, 3/32-in. in diameter and 3-in long, are inserted nominally 2-in. into the acceptor explosive with approximately ½-in. remaining outside the casing to which cables (Dynasen Inc., C-1146-2) are attached to carry the signals to recording instruments. The cables are multiplexed into a single cable by means of a circuit shown in Fig. 7 and this cable is attached to a HP5180 transient digital recorder. The response of the recorder being 20 MHz, signals can be resolved within 50 nanoseconds. As a piezoelectric pin is stressed, it produces an

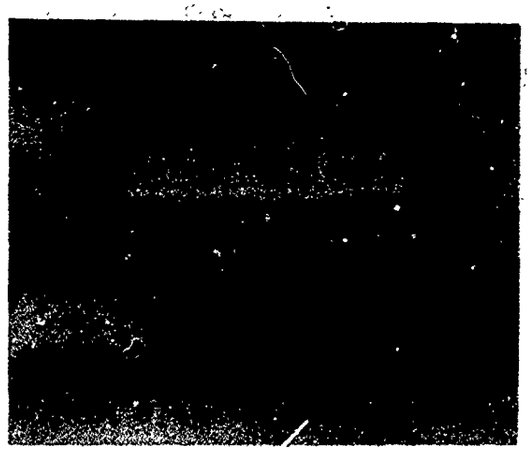

Fig. 2. Set-up of the super gap test (2-inch PMMA gap)

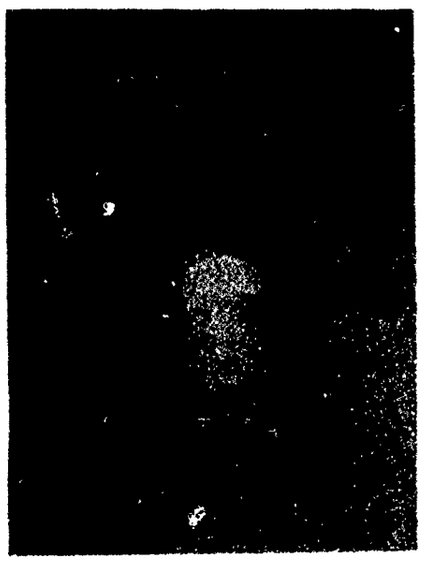

Fig. 3. Set-up of the super gap test with booster

electrical charge. Thus a shock wave passing across a pin would produce a sharp peak (typically 150 ns rise time) from which time of arrival can be measured. The multiplexing puts all of the pin signals on one channel. Thus the time between signals is simply the time it takes for the shock wave to travel between pins. In the test set-up, the pins are spaced every 2-in. along the acceptor charge with the first pin being ½-in. from the forward explosive metal interface. Knowing distance and time of arrival for each

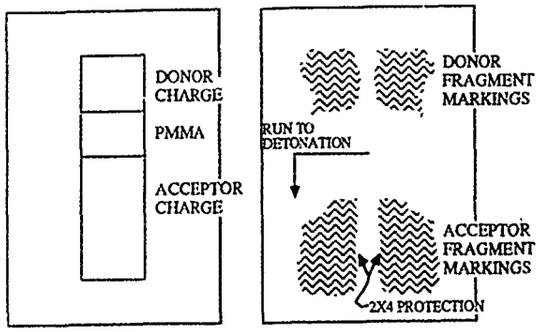

Fig. 4. Description of witness plate results

pin, the average wave velocity across the 2-in. intervals can be monitored along the length of the acceptor. Figure 8 shows the output of a typical channel of eight piezoelectric pins. The time of arrival of the shock wave along the acceptor is determined from this data.

Fig. 5. Typical witness plat data

The data from the pins can most effectively be plotted as velocity versus distance along the acceptor. In a detonating charge, sufficient data points may be obtained to calculate an accurate detonation velocity. Increasing thickness of PMMA corresponding to weaker input shock strength can be shown to result in increased run to detonation. Data from the witness plates and fragment strips confirm such measurements.

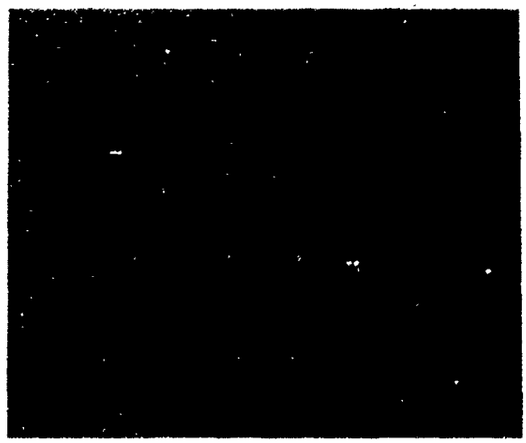

Fig. 6. Acceptor case fragment

The advantage of the super gap test is its ability to characterize run distance to detonation and shock velocity along the acceptor length which can better define the phenomenon of "go, no-go" in the study of shock sensitivity and the correlation of the test to full scale munitions which can prove more applicable to current military utilization and the study of safe handling, transportation and storage of weapons.

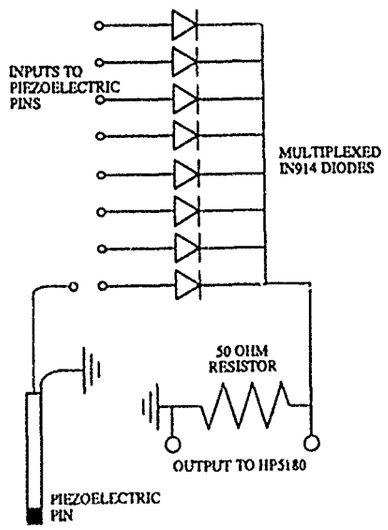

Fig. 7. Circuit for multiplexing piezoelectric pin response

Data is presented for a selection of well-known explosives (Composition-B,Tritonal). Another area of interest is the formulation techniques which can be used to desensitize the response. Data is presented on formulations which were

modified in an attempt to desensitize.

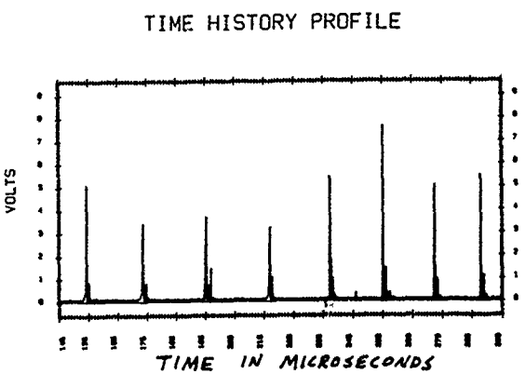

Fig. 8. Typical output of piezoelectric pins

CALCULATIONS

The Hull hydrocode was employed to assist in analyzing the results of the super gap test. Hull is an Eulerian hydrocode which solves the conservation equations of mass, momentum, and energy. Hull has an extensive material library which allowed for easy modification of existing material properties to model explosives and PMMA. The JWL (Jones-Wilkens-Lee) equation of state was used for the detonation products and the Mie-Gruneisen equation of state for the steel, PMMA and unreacted explosive. Hull does not currently have the capability to shock initiate explosives so the objectives of the computer analysis were to determine peak pressure, positive pulse duration, and time of arrival of the peak pulse in the acceptor charge.

The following is a list of some of the important properties used in the Hull Material Model code for PMMA and one developmental explosive used in the study, ethylene diamine dinitrate, ammonium nitrate, and potassium nitrate (EAK):

MATERIAL	SOUND SPEED (cm/sec)	DENSITY (gm/cm^3)	SLOPE (U_s/U_p)
EAK	2.657E5	1.61	1.796
PMMA	2.71E5	1.17	1.48

The data for EAK was taken from a report published by Los Almos. Due to a lack of time, no in-house experiments were specifically performed to check the above properties, however, since the peak arrival time calculated by Hull agreed fairly well (within 5% of the recorded data for undetonated EAK), the material properties were not changed throughout the calculational series.

A representative calculational model is shown in Fig. 9. The calculation was performed in 2D with cylindrical coordinates. The cell size was .2x.2 cm^2. Constant rezoning was employed to help track the wave front and ensure material interfaces were well preserved. Due to the simple model under consideration, a programmed burn with point initiation was used. Data collection stations were placed in the donor to ensure wave velocity and pressure were at the CJ point.

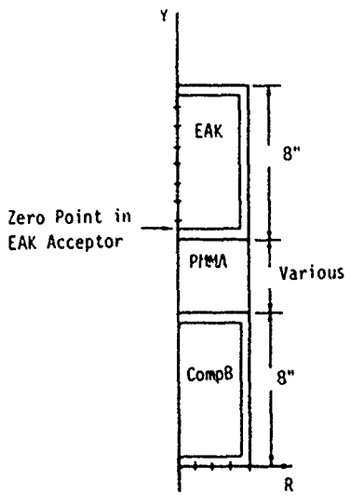

Fig. 9. Computational model of super gap test with EAK acceptor

The results of the calculations are shown in Fig. 10. The graph depicts the pressure calculated one-half inch into the EAK acceptor on the centerline. A simple P=K/R equation was used to curve fit the points. (P=pressure, K=constant, R=thickness of PMMA). Naturally, due to the reflections at the interfaces, this model only grossly approximates the curve and is at best only valid for the range under consideration.

Figure 11 is a model of the NOL card gap test (a pentolite donor models the tetryl donor) which was calculated to check the veracity of the Hull results. Figure 12 is a curve taken from

AMCP 706-180 which plots shock pressure as a function of gap thickness recorded from various NOL gap tests. The circles on the curve are the results of the HULL calculation of the same event. Some deviation occurs as the thickness of the lucite increases beyond 40mm but overall the comparison is very good.

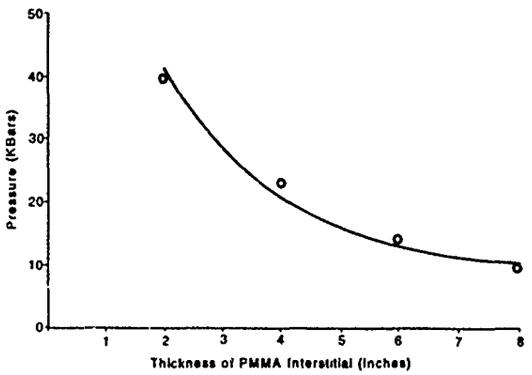

Fig. 10. Centerline pressure pulse of EAK acceptor (½" into EAK)

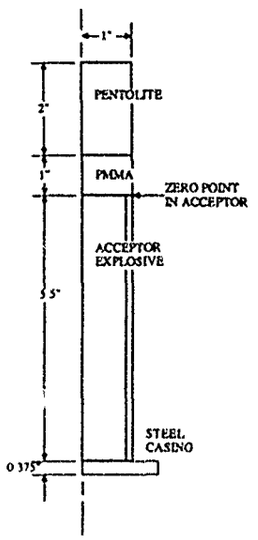

Fig. 11. Computational model of NOL gap test

Calculations were performed to describe input pressure to the acceptor as a function of gap thickness (Fig. 13). These calculations were performed to enable clarification of the function of the endplates of the charges in the role as shock attenuators. As can be seen, without endplates the pressure pulse decays rapidly until approximately 4 inches of PMMA have been traversed, at which time an inflection point is reached and the decay is moderated. However, with endplates, the pressure decays much slower and if an inflection point exists, it occurs between zero and one inch. Also the positive pulse duration of the transmitted pulse is longer with endplates than without.

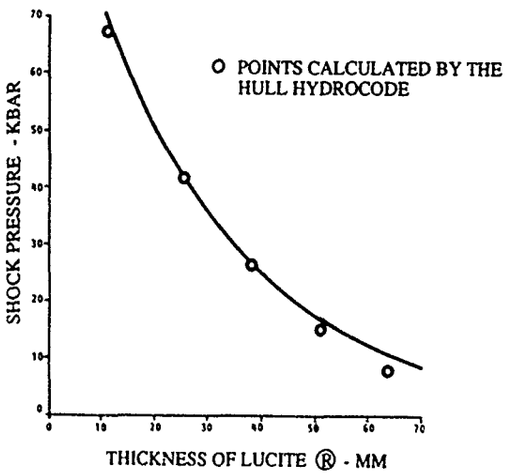

Fig. 12. Shock wave pressure at the end of the lucite gap in the NOL gap test

Calculations of transmitted impulse were also performed with and without endplates and the results plotted in Fig. 14. The graph depicts specific impulse plotted as a function of pressure. Note that the same impulse may be arrived at with two different peak pressures. This results from the attenuation ability of the endplates. Since,

$$I = \int Pdt$$

the conclusion to be drawn is that the positive pulse duration of the pressure spike is greater with endplates than without. This supports the P^2-t function which has been used for some time to approximate shock initiation criterion.

TEST RESULTS

To verify the utility of the super gap test, a series of baseline shots was accomplished with Composition-B acceptors. Figure 15 plots the time of arrival (TOA) of the shock wave pressure peak at various locations along the acceptor where piezoelectric pins are positioned. The first shot was set-up with a gap of 6-in.

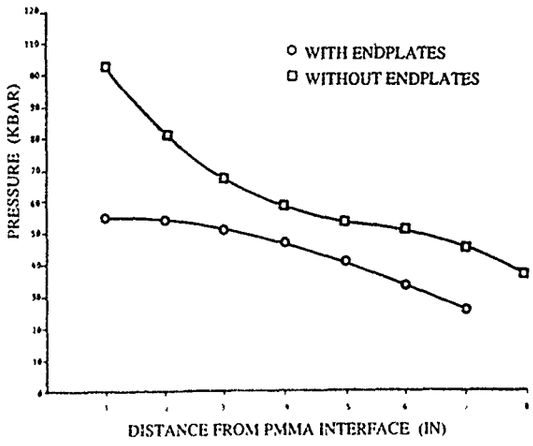

Fig. 13. Shock wave pressure at the end of the PMMA gap in the super gap test

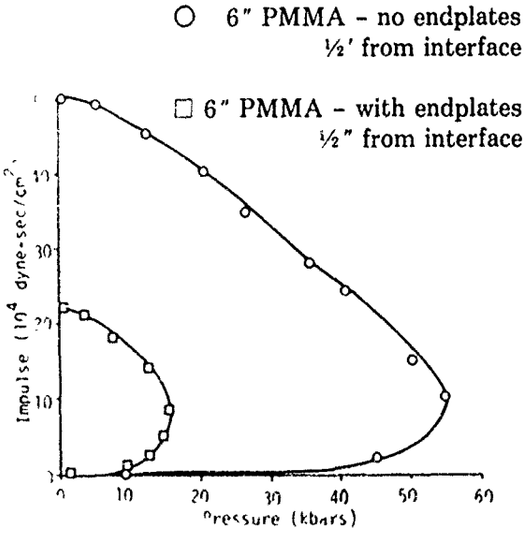

Fig. 14. Pressure vs. impulse for acceptor charges with and without endplates

PMMA between the donor and acceptor charges, corresponding to a 14 kbar input shock to the acceptor charge from calculations. The linear slope of the TOA vs distance curve reveals that a stable detonation velocity is reached early in the charge. A plot of the slope of the curves ($\Delta x/\Delta t$) shown in Fig. 16 further defines the shock wave velocity in the acceptor. In the 6-in. PMMA gap test, the shock wave reaches detonation velocity within four inches of run. The witness plate for this shot confirmed the four inch run to detonation. An 8-in. PMMA gap is then shot to define a "no-go" point. The slower response time and the velocity decay of this shot defines no detonation of the acceptor which is again confirmed with data from the witness plate and fragments. A 7-in. PMMA gap also produces a "go" with a run of five inches to detonation. A 9-in. PMMA gap with the endplates of the charges removed gives a peak pressure comparable to the 7-in. gap but with a differing impulse according to calculations. The pin data reveals a rise to detonation of 2.5 inches and gives good data points to determine a value for detonation velocity. Eighteen points from the tests for detonating Comp-B are available to calculate a detonation velocity of 7.91 mm/μs with a standard deviation of 0.17 mm/μs.

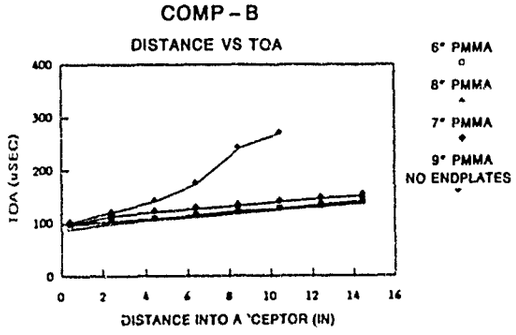

Fig. 15. Time of arrival vs. distancee along acceptor for Composition-B

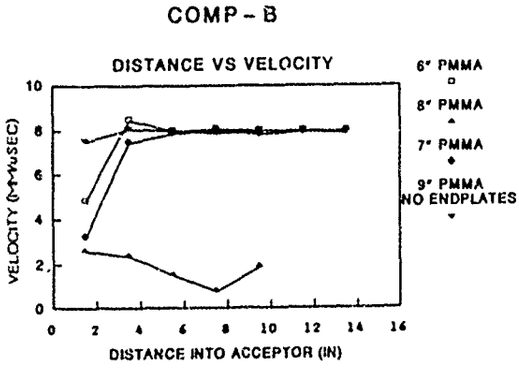

Fig. 16. Velocity vs. distance along acceptor for Composition-B

Baseline tritonal acceptors were also shot in the super gap test configuration (Fig. 17). Because of hardware constraints, half-length (8-inch) acceptors were used in tests with 4-in.

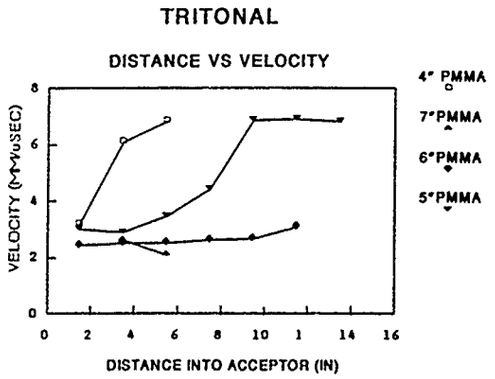

Fig. 17. Velocity vs. distance along acceptor for tritonal

PMMA and 7-in. PMMA gaps. The 4-in. PMMA gap produced a "go" rising to 6.9 mm/us in 5.5 inches and the 7-in. PMMA gap resulted in a "no-go". A shot with a 5-in. gap reached detonation with a 9.5 inch run. An additional shot was accomplished at a 6-in. PMMA gap which although tending to rise to detonation still resulted in a "no-go". The detonation velocity for tritonal was measured at 6.85 ± 0.04 mm/μs in these tests.

A series of shots of the super gap test with a TNT/5%-wax acceptor also illustrates the characteristics of the results of the piezoelectric pin data. Figure 18 shows the plot of velocity versus distance along the acceptor for this series of shots. The first shot was set-up with a gap of 6-in. PMMA between the donor and acceptor charges corresponding to 14 kbar input shock from calculations. The shock enters the acceptor at 2.5 mm/μs but quickly decelerates producing a "no-go". A 5-in. PMMA gap (18 kbar) is a "go" for the acceptor though detonation does not occur until after a run of 11.1-in. The shock velocity remains under 3 mm/μs for 8-in. before beginning to rise to the detonation velocity. A 4-in. PMMA gap (24 kbar) results in an even shorter run to detonation (6.3-in.) and a 2-in. PMMA gap (42 kbar) produces an almost immediate rise to detonation in only 3.5-in. for TNT/35%-NQ/5% wax. Witness plate markings for all of these shots confirm measurements of distance of run to detonation. The pin data also infers a constant detonation velocity for the acceptor. An analysis of thirteen data points from all shots where the acceptor is detonating reveals a mean detonation velocity of 6.75 mm/us with a standard deviation of 0.09 mm/us.

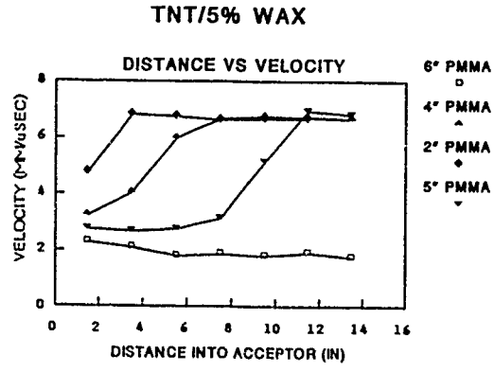

Fig. 18. Velocity vs distance along acceptor for TNT/5% wax

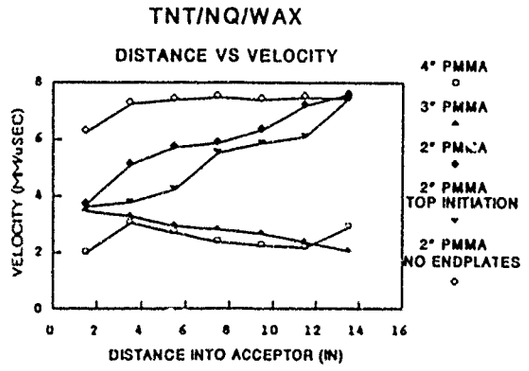

Fig. 19. Velocity vs. distance along acceptor for TNT/35%-NQ/5% wax

A series of shots with TNT/35%-NQ/5% was acceptors reveal additional utility of the super gap test. As shown in Fig. 19, two shots with a 4-in. PMMA gap and a 3-in. PMMA gap both resulted in a "no-go". A shot with 2-in. PMMA and no endplates (80 kbar) defined a detonation velocity at 7.42 mm/μs with a standard deviation of 0.05 mm/μs. A 2-in. PMMA shot (with endplates — 42 kbar) revealed an interesting result. The velocity along the length of the acceptor plateaus at 5.9 mm/μs before continuing to 7.42 mm/μs. The charges were case in acceptor casings in a vertical position and shots were conducted by shocking the bottom end of the charge. For the TNT/NQ/wax charges, however, questions were raised concerning the uniformity

of the mixing of TNT and NQ in the charge. A top initiated shot was also completed with 2-in. PMMA. This shot revealed a similar plateau in velocity but 2-in. later in the acceptor. The plateau effect was concluded to be caused by the initiation of TNT (detonation velocity of 6.9 mm/μs) before the NQ (detonation velocity of 8.0 mm/μs). Since heavier NQ (density, 1.69 gm/cm^3) settled in the TNT (density, 1.62 gm/cm^3) in the casting, the top of the charges contained less concentration of NQ and thus the lower plateau of the shock velocity must occur further along the acceptor in a top initiated charge. The super gap test results support these conclusions. However, no chemical analysis of this series of charges is available which would provide conclusive evidence.

RESULTS AND CONCLUSIONS

The results of the super gap test can be compared to published NOL large scale gap test data (4). Such a comparison concludes that detonation occurs at lower pressures in the super gap test than in the NOL test. Tritonal detonates in the NOL test at 25 kbar and in the super gap test at 15 kbar. Composition-B detonates in the NOL test at 18-20 kbar and in the super gap test at 12 kbar. The difference in pressure again relates to the relative size of these tests and the resulting difference in pressure-time response. The super gap test produces long duration pressure pulses such as occur in large munitions. The longer pressure pulse duration in the super gap test results in lower "go, no-go" pressures than those determined in the NOL gap test.

The super gap test can provide a more comparative study of the sensitivity of high explosives in large unitary weapons. The relatively small scale of the NOL gap test results in an unclear correlation to large scale events. The questions surrounding the sympathetic detonation of large munitions can only be answered with a properly scaled test. The super gap test provides such a scale for proper pressure-time correlation to large weapons.

Baseline tests of the super gap test were accomplished on tritonal and composition-B acceptors. The test was extensively used in the evaluation of EAK mixtures for use as an insensitive high explosive. The super gap test is currently being utilized in investigations of insensitive high explosive mixtures of TNT and wax. The super gap test promises to provide a comparative investigation of high explosive as it relates to utilization in large unitary weapons (5).

ACKNOWLEDGMENTS

The authors wish to express their appreciation to the personnel of the Air Force Armament Laboratory's High Explosive Research and Development group who formulated and fabricated all of the energetic materials used in these experiments. Special thanks is extended to Mr. B. G. Craig who has since retired. His participation in the design phase of the super gap test was invaluable.

REFERENCES

1. G. C. W. Foan and G. D. Coley, "Shock Initiation in Gap Test Configurations," *Proceedings of the Seventh Symposium on Detonation*, June 16-19, 1981.
2. E. F. Gittings, "Initiation of a Solid Explosive by a Short Duration Shock," *Proceedings of the Fourth International Detonation Symposium*, Naval Ordnance Laboratory, White Oak, MD, October 12-15, 1965. p. 373.
3. B. D. Trott and R. G. Jung, "Effect of Pulse Duration on the Impact Sensitivity of Solid Explosives," *Proceedings of the Fifth Symposium on Detonation*, Pasadena, CA, August 18-21, 1970, pp. 191-205.
4. Donna Price, A. R. Clairmont, Jr. and J. O Erkman, *The NOL Large Scale Gap Test III*, NOLTR-74-40, Naval Ordnance Laboratory, White Oak, MD, 8 March 1974.
5. Foster, Craig, Parsons and Gunger, "Suppression of Sympathetic Detonation," *Proceedings of the 22nd Explosive Safety Seminar*, Houston, TX, August 1983 (held under the sponsorship of the Department of Defense Explosive Safety Panel).

THE PROBLEM

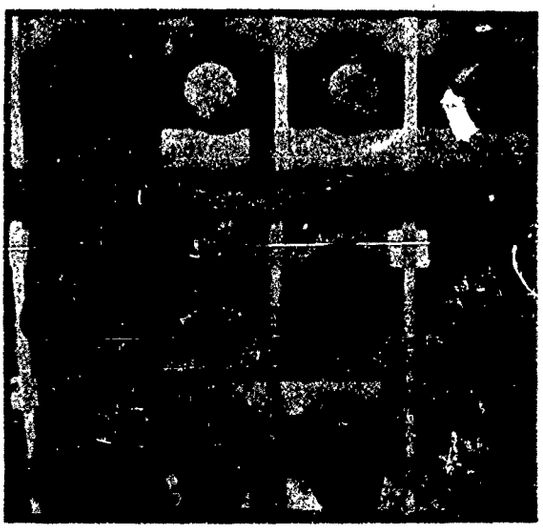

SHOCK SENSITIVITY IN LARGE SCALE EVENTS

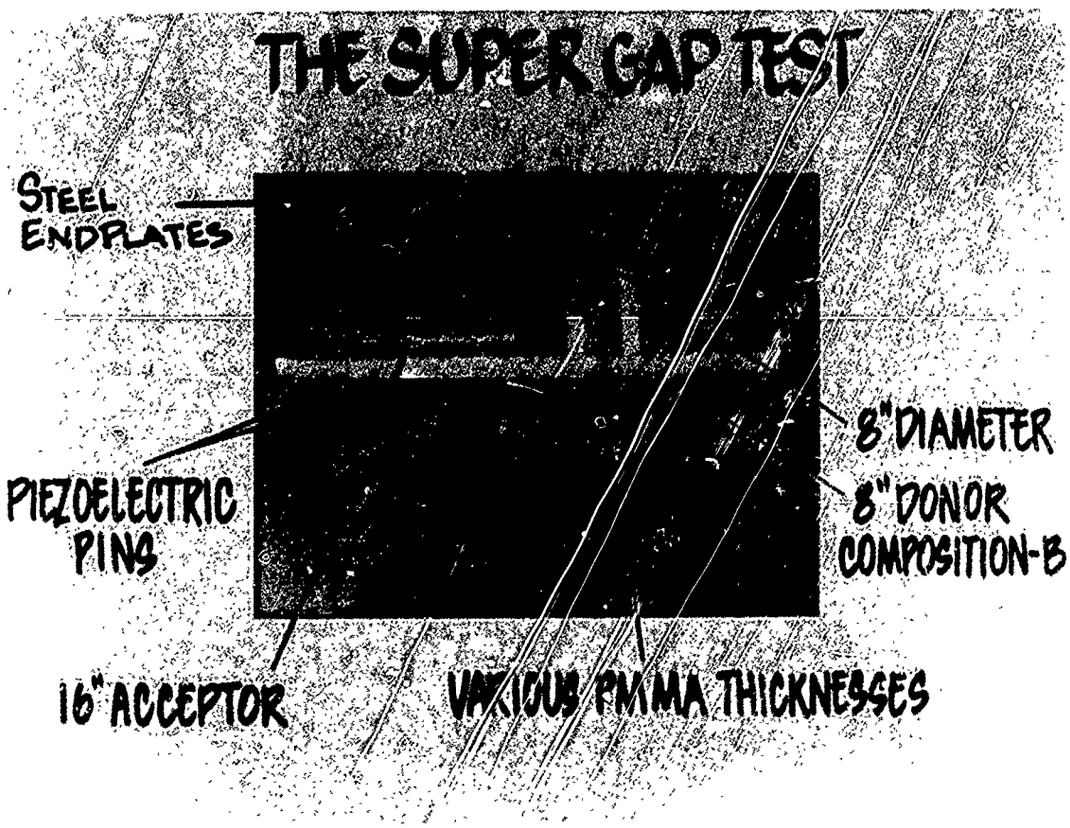
THE SUPER GAP TEST
STEEL ENDPLATES
PIEZOELECTRIC PINS
8" DIAMETER
8" DONOR COMPOSITION-B
16" ACCEPTOR
VARIOUS PMMA THICKNESSES

SUPER GAP VS NOL

	DENSITY gm/cm³	DET. VEL. mm/μs		
COMP-B	1.69	7.9	12	
TRITONAL	1.73	8.0	15	
TNT/WX	1.69	6.75	16	
TNT/NQ/WX	1.61	7.4	40	

COMPARISON OF "GO-NO GO" PRESSURE

TEST ANALYSIS

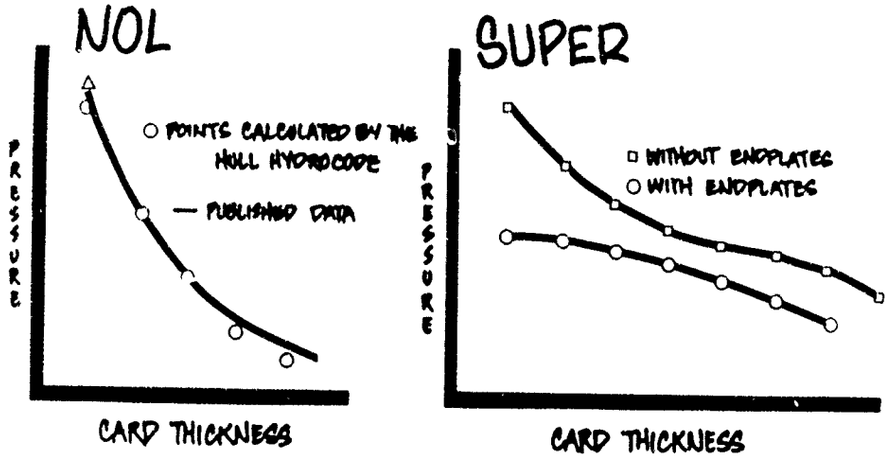

HULL CODE CALCULATIONS

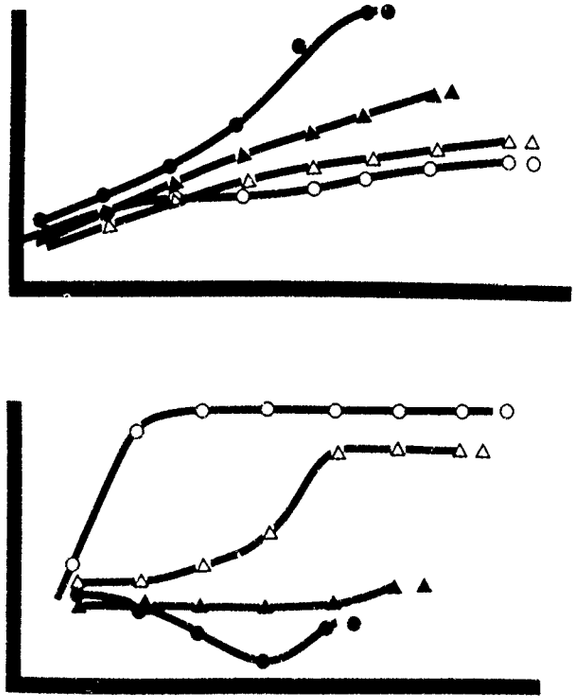

PIN DATA

○ COMPOSITION-B 7" GAP
● COMPOSITION-B 8" GAP
△ TRITONAL 5" GAP
▲ TRITONAL 6" GAP

POST TEST DATA

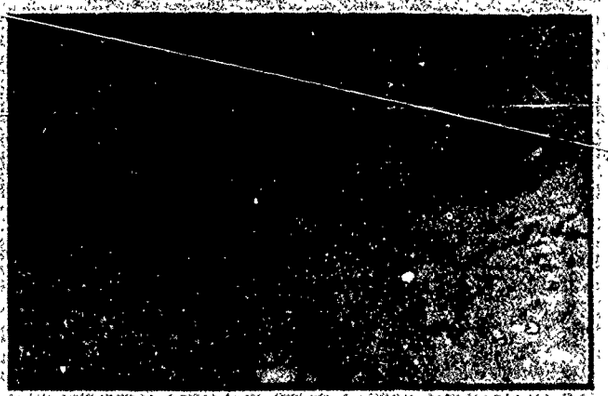

WITNESS PLATE
AND FRAGMENTS

CHEMICAL REACTION OF EXPLOSIVES AND GUN PROPELLANT DURING HIGH ACCELERATION

M. Y. D. Lanzerotti and J. Pinto
Energetic Materials Division
Large Caliber Weapon Systems Laboratory
U.S. Army Armament Research and Development Center
Dover, New Jersey 07801-5001

The fracture phenomena of energetic materials during high acceleration have been studied in an ultracentrifuge. The recovered samples have been studied by x-ray photoelectron spectroscopy (XPS) and electron paramagnetic resonance (EPR). The results of these measurements indicate that chemical reaction has occurred in TNT, TNT-1% HNS, and M30 propellant as a result of fracture and impact during high acceleration.

INTRODUCTION

Knowledge of the fracture phenomena of energetic materials subjected to high acceleration is important in such fields as ordnance, industry, and space applications where energetic materials are often subjected to high, fluctuating, and/or sustained accelerations. In particular, if energetic materials react during high acceleration, understanding this phenomena may be important for solving the problems of abnormal propellant burning and undesirable ignition or initiation of explosives.

Experiments using an ultracentrifuge have been initiated in order to investigate the behavior of energetic materials during high acceleration. Experimental results on the fracture behavior of explosives during high acceleration have previously been published (1, 2) as have results on the deformation and failure of M30 propellant (3). Chemical reactions have been discovered to occur in TNT, TNT-1% HNS, and M30 propellant as a result of fracture and impact during high acceleration in the ultracentrifuge (2). This discovery is discussed further herein with additional diagnostic measurements of the reacted materials. The reacted samples have been studied with electron paramagnetic resonance (EPR) and x-ray photoelectron spectroscopy (XPS) to verify that reaction has occurred and to investigate properties of the reaction products.

EXPERIMENT

A Beckman preparative ultracentrifuge (Model L8-80) with a swinging bucket rotor (Model SW 60 Ti) is used to rotate the sample under study up to 60,000 rpm. The distance of the specimen from the axis of rotation can be chosen as a variable between 6 and 12 cm.

Samples are prepared in two ways. Cylindrical polycrystalline plugs of explosive are prepared by pouring about one-half gram of molten material into 9 mm i.d. polycarbonate tubes and allowing it to crystallize. The open-ended sample tube is then joined to a short closed-end polycarbonate centrifuge tube as shown in Fig. 1. The as-cast surface of the explosive faces away from the axis of rotation. In a second experimental method, small pieces (0.05 g) of propellant are glued to individual aluminum disks. An individual disk with the sample facing away from the axis of rotation is joined to a short, closed-end polycarbonate tube, which supports the disk at a fixed distance from the axis of rotation.

The sample experiences a time rate of change of the acceleration up to a maximum acceleration. The sample then remains at this maximum acceleration for a time such that for each run there is a combined total elapsed time of 5 minutes. The sample then decelerates smoothly to zero acceleration. The initial maximum acceleration is less than the fracture acceleration for

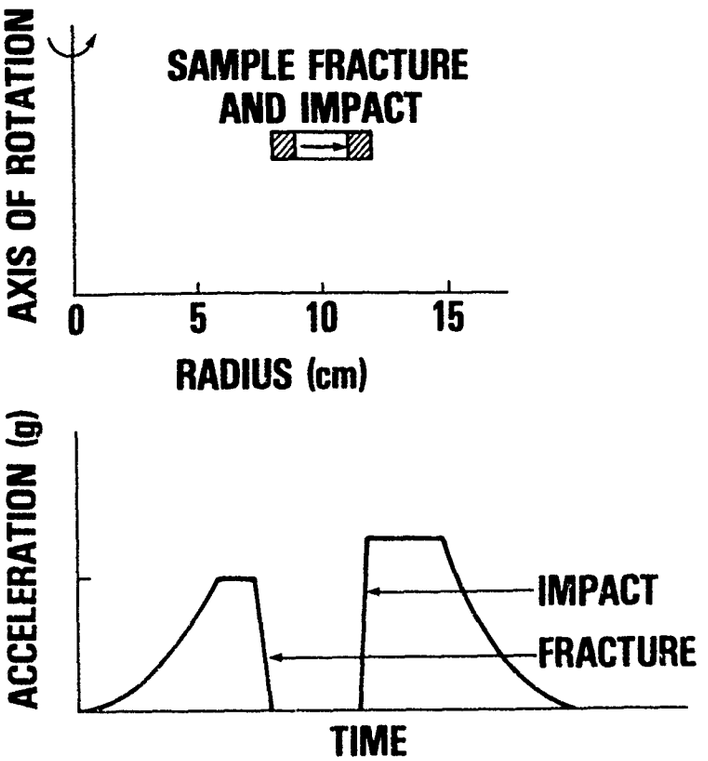

Fig. 1. Fracture and Impact of Melt-cast TNT During High Acceleration

the material. The maximum acceleration for the sample is then increased systematically in each successive 5-minute run until the sample fractures. In these experiments essentially all the sample mass fractures and transfers to the closed-end tube during one run as shown in Fig. 1. When the sample fractures its acceleration decreases to zero in a very short time (the travel time of the speed of sound through the sample); when the sample impacts the end of the tube its acceleration increases to the maximum acceleration in a very short time (the travel time of the stress wave through the sample) (4, 5).

RESULTS

Chemical reaction has been discovered to occur in TNT and TNT-1% HNS as a result of the fracture and the impact of the material at the end of the tube. Extensive black (to the eye) discoloration is observed in the recovered material. The pressure produced by the reaction is sufficient to cause a 2-cm long crack perpendicular to the axis of rotation in the polycarbonate collector tube.

The range of conditions for which chemical reaction has been observed has been estimated from the following equations. The acceleration at fracture or impact is the radial acceleration

$$a = \omega^2 r,$$

where ω is the angular velocity and r is the radius of the sample with respect to the axis of rotation. The velocity at fracture is the tangential velocity

$$v = \omega r.$$

The maximum velocity at impact and the minimum time between fracture and impact are calculated by solving Newton's law of motion using Coriolis' theorem (6). The minimum time between fracture and impact, t_{min}, is given by the expression

$$t_{min} = \frac{1}{\omega} \ln \left(\frac{r_f}{r_i} \pm \left(\frac{r_f^2}{r_i^2} - 1 \right)^{1/2} \right),$$

where r_i and r_f are the initial and final radius of the sample, respectively. The maximum velocity at impact, v_{max}, is given by the expression

$$v_{max} = \frac{r_i}{2} \omega \, (e^{\omega t_{min}} - e^{-\omega t_{min}}).$$

The estimated conditions at fracture are: acceleration 20,000-59,000 g; velocity 140-230 m/s; time 2.0 μs; load rate 1.0-2.9 x 10^{10} g/s. The estimated conditions at the moment of impact at the end of the polycarbonate tube are: acceleration 26,000-77,000 g; velocity 110-190 m/s; time 2.3 μs; load rate 1.2-3.4 x 10^{10} g/s. The estimated time between fracture and impact is 300-510 μs. These experiments have been performed at 0, 25 and 50°C; chemical reaction has occurred at all three temperatures.

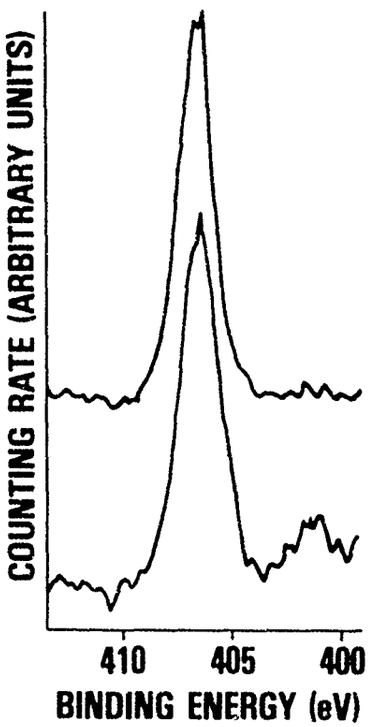

Fig. 2. XPS N 1s Spectra of Melt-cast TNT Before (Upper Spectrum) and After (Lower Spectrum) Acceleration and Impact

The XPS N 1s spectra of melt-cast TNT before (7-9) and after acceleration and impact is displayed in Fig. 2. A new line centered at about 401 eV is observed in the spectrum of the reacted TNT. This line has also been reported from experiments when TNT is subjected to heat (8-10), uv photolysis (7-9), and x-rays (10). There is also evidence of the 401 eV line in the XPS N 1s spectrum of reacted TNT-1% HNS from the acceleration experiment (not shown here).

The EPR spectrum of the TNT after acceleration and impact is displayed in Fig. 3. This is the EPR spectrum of the reacted TNT. A similar spectrum has also been observed when TNT is uv (11) and thermally (11,12) decomposed. The radical associated with the EPR spectrum has not as yet been identified.

Chemical reaction has also been discovered to occur in M30 propellant as a result of the fracture and the impact of the material at the end of the tube during high acceleration. Yellow (to the eye) discoloration is observed in the recovered material. The estimated conditions at fracture are: acceleration 130,000-240,000 g; velocity 340-460 m/s; time 1.0 μs; load rate 1.3-2.4 x 10^{11} g/s. The estimated conditions at the moment of impact at the end of the polycarbonate tube are: acceleration 170,000-310,000 g; velocity 290-390 m/s; time 1.0 μs; load rate 1.7-3.1 x 10^{11} g/s. The estimated time between fracture and impact is 150-200 μs. These experiments have been performed at 25°C.

The XPS N 1s spectra of M30 propellant before (13) and after acceleration and impact is displayed in Fig. 4. The intensities of the ONO_2 and NO_2 lines decrease relative to the intensity of the amine/imine line in the reacted M30 propellant. Nitrocellulose and nitroglycerin contain ONO_2 groups and nitroguanidine contains NO_2 groups. Thus, reaction may have occurred in these three components of M30 propellant (14).

DISCUSSION

The fracture phenomena of TNT, TNT-1% HNS, and M30 propellant during high acceleration have been studied in an ultracentrifuge. The recovered samples have been studied by XPS and EPR. The results of these measurements indicate that chemical reaction has occurred in these materials as a result of fracture and impact.

There are several mechanisms discussed in the literature which can be considered for producing the reaction. One mechanism is shock initiation. For example, the pressure at impact can

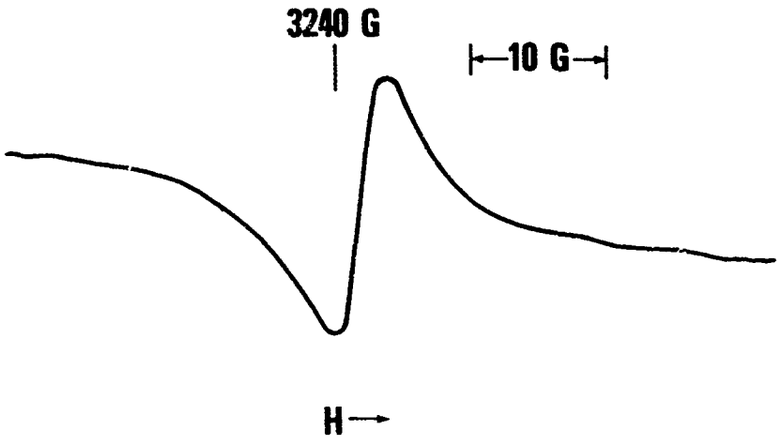

Fig. 3. EPR Spectrum of Melt-cast TNT After Acceleration and Impact

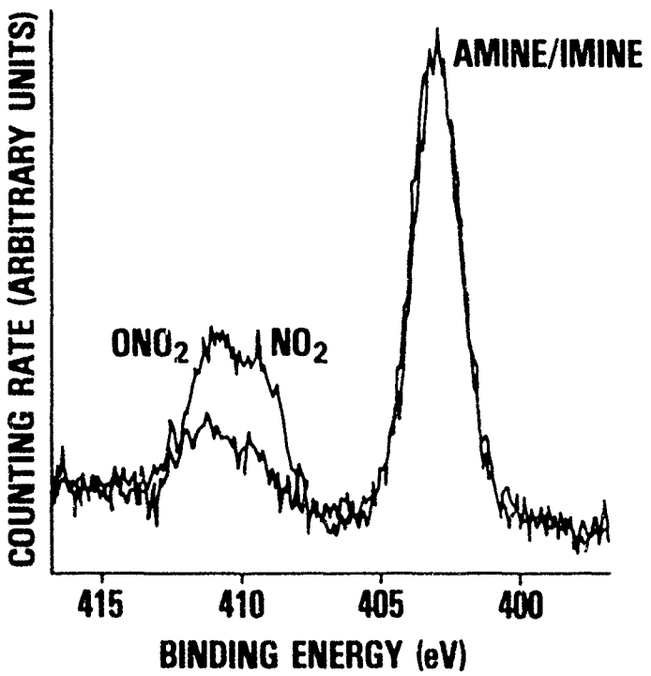

Fig. 4. XPS N 1s Spectra of M30 Propellant Before (Upper Spectrum) and After (Lower Spectrum) Acceleration and Impact

be estimated by matching the hugoniots of polycarbonate and TNT (5). From this, the temperature rise due to the pressure at impact, 0.3 GPa, is seen to be insufficient to ignite TNT (15). Therefore, it is unlikely that the reaction occurs during the time of impact.

Another mechanism is rapid shear. According to Frey (16), the impact pressure and a shear velocity produce a maximum temperature in the absence of reaction. If the shear velocity is the same order of magnitude as the impact velocity (110-190 m/s) a maximum temperature of the order of 250-350°C would be produced in the absence of reaction. For a temperature range of 250-350°C, the e-folding time of the reaction which produces the free radical (shown in the

EPR spectrum) would range between 21 minutes and 12 seconds, respectively (12). If the impact velocity is amplified by a factor of three (17), the maximum temperature would be 700°C and the e-folding time of the reaction would be about a millisecond. Even one millisecond is too long by almost two orders of magnitude for Frey's mechanism to cause the reaction during the time of impact.

Another mechanism is frictional heating. A normal force is produced by the Coriolis acceleration as the sample slides along the collector tube after fracture to impact. The resulting pressure of the sample against the polycarbonate tube is < 0.01 GPa. According to Frey (16), this pressure and a shear velocity of the order of the impact velocity would produce a negligible temperature rise. If the time between fracture and impact is assumed to be the e-folding time of the reaction, a TNT temperature of about 800°C would be expected (12).

In some other types of experiments (e.g., impact, compaction) Sandusky, Coffey, and Liddiard (18) have reported reaction thresholds in energetic materials at lower pressures than obtained here (< 0.1 GPa versus the ~0.3 GPa here) and at rates of bulk deformation (~ 80-200 m/s) which are similar to the impact velocity of the present experiment. The reaction-producing mechanisms involved in the Sandusky et al. process may be similar to that for the present experiment and need to be further studied. In the propelled impingement test, chemical reaction of TNT has been reported at an impingement velocity (19) which is within the range of impact velocities found to cause chemical reaction here. It is also interesting to note that a reaction in propellants has been reported at impact velocities similar to those of this experiment (19, 20).

ACKNOWLEDGEMENTS

The authors are indebted to F. J. Owens for the EPR spectrum of reacted TNT, to W. L. Garrett for the XPS N 1s spectra of M30 propellant before and after acceleration, and to J. Sharma, B. Fishburn, and D. Wiegand for helpful discussions.

REFERENCES

1. M. Y. D. Lanzerotti and J. Sharma, "Brittle Behavior of Explosives During High Acceleration," Applied Physics Letters, *39*, 455 (1981).

2. M. Y. D. Lanzerotti, "Fracture Phenomena of Energetic Materials During High Acceleration," Symposium on Thermomechanical Properties of Energetic Materials and Their Effects on Munitions Survivability, TTCP W-1/W-4 Joint Meeting, Naval Weapons Center, China Lake, CA, 18-20 September 1984, Vol. II, pp. 1-43, March 1985.

3. M. Y. D. Lanzerotti, "Mechanical Behavior of Gun Propellant During High Acceleration," 21st JANNAF Combustion Meeting, Johns Hopkins University, Applied Physics Laboratory, Laurel, MD, 1-4 October 1984, Volume I, pp. 275-280.

4. A. S. Argon, "Brittle Fracture," in *Mechanical Behavior of Materials*, ed. F. A. McClintock and A. S. Argon, Addison-Wesley Publishing Company Inc., Reading, MA, 489, 1966.

5. S. P. Marsh, Editor, *LASL Shock Hugoniot Data*, University of California Press, Berkeley, CA, pp. 483, 648, 1980.

6. K. R. Symon, *Mechanics*, Addison Wesley Publishing Company Inc., Reading, MA, 238, 1953.

7. J. Sharma, T. Gora, S. Bulusu, and D. A. Wiegand, "X-ray Photoelectron Spectroscopy of Explosive Solids," Proceedings U.S. Army Science Conference, West Point, NY, 1974.

8. F. J. Owens and J. Sharma, "X-ray Photoelectron Spectroscopy and Paramagnetic Resonance Evidence for Shock-Induced Intramolecular Bond Breaking in Some Energetic Solids," Journal of Applied Physics, *51*, 1494 (1980).

9. J. Sharma, "X-ray Photoelectron Spectroscopic (XPS) Detection and Identification of Explosives Residues," Proceedings of the International Symposium on Analysis and Detection of Explosives, FBI Academy, Quantico, VA, 29-31 March 1983, p. 181.

10. J. Pinto (unpublished).

11. F. J. Owens, "Paramagnetic Resonance Studies of uv and Thermally Induced Radicals in Trinitrotoluene and Dinitrotoluene," Mol. Cryst. Liq. Cryst., *101,* 235 (1983).

12. R. Guidry and L. P. Davis, "Thermochemical Decomposition of Explosives. I. TNT Kinetic Parameters Determined from ESR Investigations," ochimica Acta, *32,* 1 (1979).

13. P. P. Ostrowski, J. F. Grant, J. Sharma, W. L. Garrett, D. S. Downs, and S. Krasner, "Laser Ignition of Double and Triple Based Gun Propellants," 17th JANNAF Combustion Meeting, NASA Langley Research Center, Hampton, VA, 22-26 September 1980, Volume II, p. 175.

14. B. T. Fedoroff and O. E. Sheffield, "Cannon Propellant," in: Encyclopedia of Explosives and Related Items, PATR 2700, Volume 2, Picatinny Arsenal, Dover, NJ, USA, C34, 1962.

15. C. L. Mader, *Numerical Modeling of Detonations,* University of California Press, Berkeley, CA, 153, 1979.

16. R. B. Frey, The Initiation of Explosive Charges by Rapid Shear," Proceedings Seventh Symposium (International) on Detonation, Annapolis, 36, 1981.

17. M. Rosenblatt, L. A. DeAngelo, G. E. Eggum, and K. N. Kregenhagen, "Numerical Investigation of Water Drop Erosion Mechanisms in Infrared-Transparent Materials," California Research and Technology, Inc., Technical Report AFML-TR-76-193, 38, December 1976.

18. H. W. Sandusky, C. S. Coffey, and T. P. Liddiard, "Rate of Deformation as a Measure of Reaction Threshold in Energetic Materials," in *Mechanical Properties of Materials at High Rates of Strain,* 1984, ed. J. Harding, Adam Hilger, London, 373, 1984.

19. T. W. Ewing and W. A. Cabbage, "A Compilation of Hazards Test Data for Propellants and Related Materials," Final Engineering Report on Production Engineering Project PE-489, Radford Army Ammunition Plant, Hercules, Inc., Radford, VA, pp 69, 73, September 1976.

20. R. C. Jensen, E. J. Blommer, and B. Brown, "An Instrumented Shotgun Facility to Study Impact Initiated Explosive Reactions," Proceedings Seventh Symposium (International) on Detonation, Annapolis, 299, 1981.

CHEMICAL REACTION OF EXPLOSIVES AND GUN PROPELLANT DURING HIGH ACCELERATION

M.Y.D. LANZEROTTI AND J. PINTO

ENERGETIC MATERIALS DIVISION, LCWSL

US ARMY ARMAMENT RESEARCH AND DEVELOPMENT CENTER
DOVER NJ, 07801 5001

OBJECTIVES

- INVESTIGATE BEHAVIOR OF ENERGETIC MATERIALS DURING HIGH ACCELERATION
- IMPROVE ENERGETIC MATERIAL BEHAVIOR AND REDUCE HAZARD

0.4 gm TNT MELT-CAST IN POLYCARBONATE SLEEVE AS-CAST SURFACE

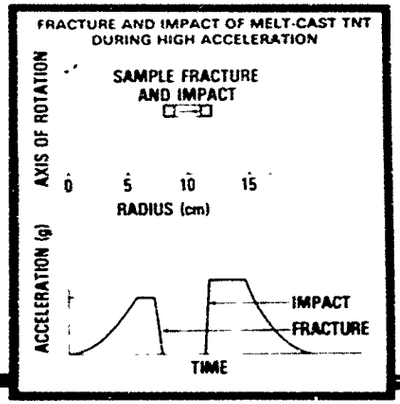

CHEMICAL REACTION OF EXPLOSIVES INDUCED DURING HIGH ACCELERATION

TNT

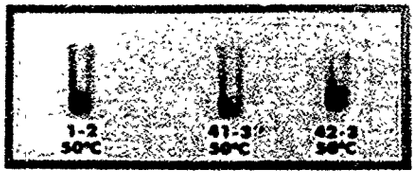

TNT-1% HNS

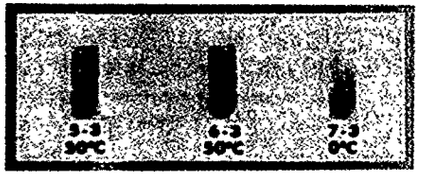

TNT-1% HNS

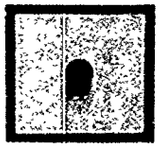

6-3
50°C

TNT

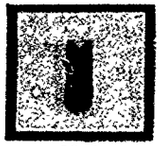

42-3
50°C

CRACK IN POLYCARBONATE TUBE

	FRACTURE	IMPACT
ACCELERATION (g)	20 000 59,000	26,000 77,000
VELOCITY (m/s)	140 230	110-190
TIME (μs)	2.0	2.3
LOAD RATE (g/s)	1.0 2.9 x 10^{10}	1.2-3.4 x 10^{10}
TIME BETWEEN FRACTURE & IMPACT (μs)	300 510	

XPS N1s SPECTRA OF MELT-CAST TNT BEFORE (UPPER SPECTRUM) AND AFTER (LOWER SPECTRUM) ACCELERATION AND IMPACT

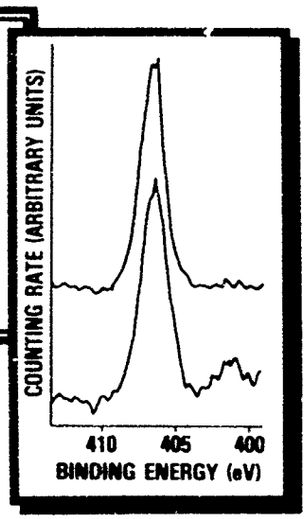

- A NEW LINE OBSERVED IN REACTED TNT

EPR SPECTRUM OF MELT-CAST TNT AFTER ACCELERATION AND IMPACT

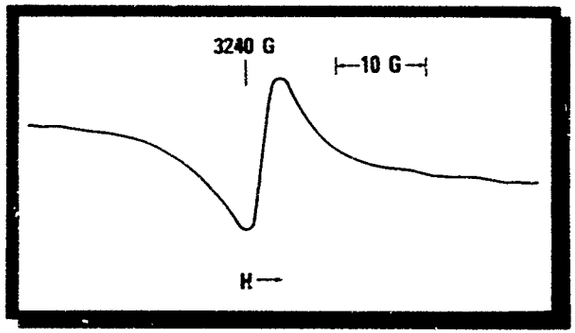

CHEMICAL REACTION OF M30 PROPELLANT INDUCED DURING HIGH ACCELERATION

XPS N 1s SPECTRA OF M30 PROPELLANT BEFORE (UPPER SPECTRUM) AND AFTER (LOWER SPECTRUM) ACCELERATION AND IMPACT

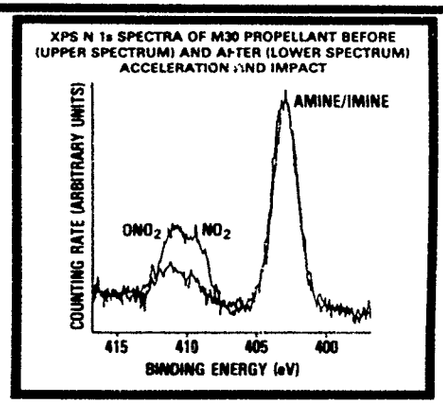

- ONO_2 AND NO_2 INTENSITIES DECREASE RELATIVE TO AMINE/IMINE INTENSITY IN REACTED M30 PROPELLANT

	FRACTURE	IMPACT
ACCELERATION (g)	130,000 240 000	170,000 310 000
VELOCITY (m/s)	340 460	290 390
TIME (μs)	1 0	1 0
LOAD RATE (g/s)	1.3 2 4 x 10^{11}	1 7 3.1 x 10^{11}
TIME BETWEEN FRACTURE & IMPACT (μs)	150 200	

CONCLUSIONS

- TNT, TNT-1% HNS & M30 PROPELLANT REACT DURING HIGH ACCELERATION
- CHEMICAL REACTION VERIFIED BY XPS AND EPR
- EXPERIMENT COMPARED WITH THEORIES

THE EFFECT OF SOME ADDITIVES ON THE CLOSED BOMB BURNING AND IGNITABILITY OF RDX/TNT (60/40)

R.W. Velicky, H.W. Voigt, and W.E. Voreck
United States Army Research and Development Center
Dover, New Jersey

The burning and ignition properties of Composition (Comp) B are studied so that formulation modification could be made that would reduce gun projectile in-bore thermal explosions. Comp B first burns on its surface like a gun propellant; then, at a pressure near 100 MPa, a sudden breakup burning phase develops. New surface area is created at a phenomenal rate, and this is the cuase of the catastropic reaction rates that it can experience. Coating its RDX constituent with a protectant significantly slows this reaction rate. It appears to do this by inhibiting the rate at which the RDX is released from the TNT matrix for burning, probably by infinitesimally delaying the ignition of the RDX in the particle ignition sequence. A new test that evaluates explosive ignitability as a function of pressure and energy indicates that an RDX protective coating may also increase the level of thermal ignition and delay the onset of a thermal explosion. Collectively, these three desirable properties, caused by a single modification, may significantly reduce the incidence of in-bore explosions where casting flaws would have precipitated this event.

INTRODUCTION

Composition (Comp) B is a powerful explosive; however, it cannot be used in the projectiles of new high performance guns because of its susceptibility to in-bore thermal explosions. The cause is attributed to the presence of an occasional casting flaw which under the stress of launch induced set-back forces causes the explosive to break up. Then in crushed, broken, or moving material, adiabatic compression and/or friction would stimulate a thermal ignition; and, because Comp B burns so rapidly, the projectile violently ruptures before it can exit the gun barrel. This premature problem, although occurring at an unacceptable level, is a rare event. This suggests that this hazard is a borderline result that is started when the right condition or combination of conditions are present. Techniques that would minimize the creation of casting flaws are being investigated. This study, however, is concerned with modifying the properties of Comp B to reduce further the likelihood of an in-bore explosion from Comp B castings that might escape the gauntlet of improved manufacturing procedures.

A threefold approach is being pursued. The explosive's mechanical properties should be improved. Even a modest improvement would favorably shift the relationship between casting flaws and launch induced set-back forces. When breakup still occurs, the minimum amount of heat energy needed to cause thermal initiation should also be increased. Then, in situations where a thermal reaction might still be initiated, the speed of burning should be slowed so that a safe out-of-bore explosion would result from the in-bore thermal initiation. Simultaneously, improving each of the contributory factors (castability, strength, ignitability, and burning speed), may reduce the incidence of in-bore explosions sufficiently to permit the use of a modified Comp B in the advanced weapons systems. The results of previously reported work suggest that some of these goals are attainable.

A study of the burning properties of Comp B and TNT (1) indicated that these materials break up during the combustion process and burn on the surface of their fragmented parts. The breakup of TNT, a major constituent of Comp B, takes place along cleavage paths at the boundary of neighboring crystals (2). The size, shape, and number of the fragments is determined by the casting procedure. The wax additive, which is used in standard Comp B does not interact with its TNT component to modify or change its burning behavior. Unlike TNT, Comp B initially burns on its surface like a gun propellant (3); then, at a pressure near 100 MPa, a sudden transition to a breakup burning phase takes place. New surface area is created at a phenomenal rate, and this is the cause of the catastrophic reaction rates that Comp B can experience. This transition appears to be too sharp and sudden to be explained only by breakup or melting of the TNT binder. The heat-of-reaction of HMX (an explosive similar in structure to RDX) increases, sharply, 102 calories/g at 30 MPa static pressure (4). A similar response for RDX could contribute toward Comp B's sharp transition to the breakup burning phase. The presence of the standard wax additive (1% added to the melt) in the 60/40 mixture of RDX/TNT significantly slows the burning of the reactive constituents during breakup. It appears that it does this because some of the wax (insoluble in TNT) migrates to the surface of the RDX particles where it inhibits the reaction rate. Coating the RDX particles with various protectants is, therefore, the approach being taken here to slow the reaction rate of Comp B.

It is believed that in-bore explosions begin with a finite heat source (hot-spot), in powdered or broken material that is being subjected to pressure. A test developed to simulate these conditions (5) shows that Comp B is more sensitive to thermal ignition in a projectile launch environment than, individually, are its constituents (RDX/TNT). Heat transfer in relation to physical properties cause this, suggesting the possibility that an RDX protectant may serve the double purpose of increasing the minimum energy of ignition in addition to slowing the deflagration rate of Comp B.

PROCEDURE

This work is concerned primarily with protective coatings for RDX that would reduce the deflagation hazard of Comp B, but, since this hazard is primarily related to casting flaws the burning behavior of Comp B with TNT modifiers, which may reduce their creation is also examined. Small quantities of hexanitrostilbene (HNS), a mild explosive or polysulfone can provide a fine random crystal structure to the TNT matrix that can improve cast quality (6). The polysulfone also has the potential for functioning as a protective coating for the RDX. In addition, under field conditions, Comp B can exhibit exudation problems that can be controlled by an anti-exudate, a 50/50 mixture of cellulose propionate and plasticizers (7, 8). Its effect on Comp B burning is also examined. The explosive portion of all the formulations tested is a 60/40 mixture of class 1 RDX (177 μm) and TNT except for one formulation where an RDX with a smaller particle size (105 μm) was used. The additives are added as a percentage of the original RDX/TNT mix. Single effects were first obtained, and then increasingly interactive multiple effects, by introducing additives to the TNT melt and/or as protective coatings of the suspended RDX. The general formulations are listed in Table 1.

Specimens were prepared for closed bomb testing in the form of cast solid cylinders and crushed powder. The cylinders were 2.54 cm in diameter and the lengths were adjusted to produce a constant 32.00 gram mass. Crushed samples (27.00 grams each) were obtained from cast specimens which had been broken into a fine powder with gentle impact blows. Three g and one g, respectively, of class 7 black powder were used to initiate the solid and crushed samples. The black powder was ignited with an M-100 electric match. Each specimen was burned in a 178 cc closed bomb producing pressure-vs-time data in response to the output of a piezo pressure transducer. The data was recorded with a Nicolet Explorer III Digital oscilloscope and stored on magnetic discs.

The results of these tests are presented in the form of dp/dt vs. pressure. A graphical example of the data is shown in Figures 1 and 2. Both compare the burning of standard Comp B with a polysulfone-coated RDX formulation for the solid and crushed versions, respectively. In Table 2, an attempt is made to reduce all the test data to a few pertinent values for com-

TABLE 1
Additive in 60/40 Mixtures of RDX/TNT

Sample no.	Additive in TNT	Additive on RDX
84-018	None	None
84-023	1% Petrolite Wax	None
84-066	1% Petrolite Wax, 0.12% HNS	None
84-080	1% Petrolite Wax, 0.12% HNS, 0.5% Anti-Exude	None
84-072	1% Petrolite Wax, 0.12% Polysulfone	None
84-082	0.12% HNS, 0.5% Anti-Exudate	1% Petrolite Wax
84-083A	0.12% HNS	1% Polycarbonate, 0.5 Anti-Exudate
84-025	0.5% Anti-Exudate	1% Polysulfone
84-026	0.5% Anti-Exudate	0.5% Polysulfone
84-038	None	1% Cellulose Propionate, plasticized
84-039	None	1% Polysulfone
84-083B*	None	1% Polysulfone*

*Fine particle RDX.

TABLE 2
Closed Bomb Results

Sample no.	Max Pressure, MPa		Max dp/dt MPa/ms		Pressure at max dp/dt, MPa		Area MPa^2/ms	
	Solid	Crushed	Solid	Crushed	Solid	Crushed	Solid	Crushed
84-018	234	210	153	255	186	93	15056	34320
84-023	234	209	106	217	188	92	9991	28016
	235	211	106	227	187	96	10398	32441
84-066	250	210	161	290	177	88	17513	37515
	225	209	162	241	162	89	16947	32718
84-080	213	210	119	240	174	90	10112	31854
	212	210	125	258	168	90	10479	33265
84-072	218	213	118	244	168	106	10592	34853
	221	212	113	170	174	118	10804	24490
84-082	212	209	60	230	168	85	4954	31849
	197	212	47	247	160	88	3613	31925
84-083A	214	210	58	244	168	87	5051	31746
	215		62		185		5244	
84-025	219	212	41	249	187	83	3106	33933
	224	204	41	230	196	79	3384	28812
84-026	222	209	83	252	187	80	7034	34122
	219		84		178		7107	
84-038	255	204	49	272	186	90	3780	34143
	226	207	49	239	185	91	3652	31551
84-039	230	204	53	292	189	92	4818	35924
	231	211	54	220	119	114	4408	31763
84-083B	232	200	40	250	177	74	3960	33161
	226	207	34	219	191	93	3113	29436

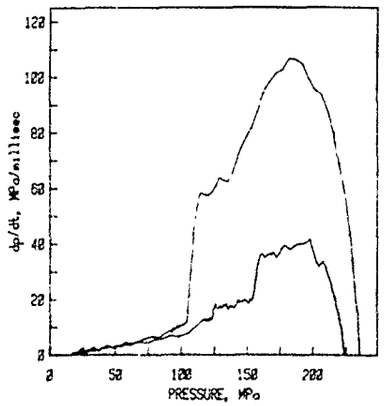

Fig. 1. Comp B vs. polysulfone coated RDX/TNT (solid)

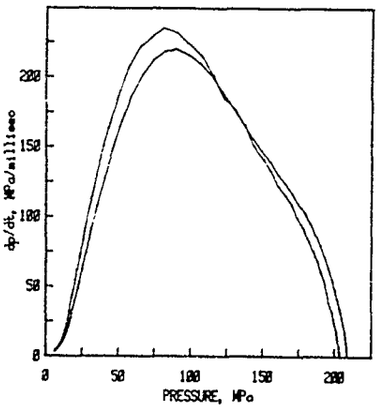

Fig. 2. Comp B vs. polysulfone coated RDX/TNT (crush)

parison. These include the maximum pressure (an indication of the energy provided by the reaction), the maximum dp/dt (representing the greatest surface area exposed for burning), and the pressure at the maximum dp/dt (related to the fraction of material consumed). However, the most important value listed in the table is the measurement of the area under the entire curve. When all things are equal such as mass, composition, and vessel volume, each dp/dt value represents the surface area taking part in the reaction in relation to the volume fraction of sample burned. A measurement of the area under the curve provides a number that can be used to evaluate the effect of an additive on the reaction rate of the composition's reactive constituent (RDX/TNT). This value, however, applies to a specimen of a particular mass and configuration burned in a particular vessel. The ratios developed cannot be extrapolated to any other conditions. This is because the dp/dt vs pressure curve (for materials which fragment on burning) combines the effect of several fundamental properties. Principally, these include the rate of surface area creation with the intrinsic burning rate of the fragmented parts. Presently these values are unknowns. Therefore, the quickness curve (dp/dt vs pressure) is limited to use as a comparator. This comparison, however, is useful to evaluate the degree of effectiveness various additives contribute toward the attempt to slow the burning of RDX/TNT (60/40). In Table 3, the area under the quickness curve for standard Comp B is assigned a value of 100% for each of the two geometrical configurations and a relative comparison based on this value is made for each appropriate experimental formulation.

The ignition test is performed on powdered explosive samples and provides a relative ignitability data as a function of pressure and energy. A 1-gram sample is compressed between 1.27 cm punches within a floating sleeve. At a desired pressure level (monitored with a piezo force gage) an 80 μsec, one half sine wave, energy pulse is dumped into a platinum heater

TABLE 3
Relative Reaction Rate with Respect to Regular Comp B

Sample no.	Solid (%)	Crushed (%)
84-018	148	114
84-023*	100*	100*
84-066	169	116
84-088	101	108
84-072	105	98
84-082	42	105
84-083A	50	105
84-025	32	104
84-026	69	113
84-038	36	109
84-045	45	112
84-083B	35	104

* Regular Comp B.

that is located in the center of the specimen. It has been found that explosives could be initiated at very modest energy levels as long as the test specimen was at a high enough pressure. In this test, the 50% threshold pressure of initiation, at a fixed level of energy deposition, is determined by varying the pressure according to a 25 shot Bruceton stair-step procedure (9). This is done at several energy levels for each explosive. A plot of the reciprocal of the threshold pressure versus the input energy should generate a reasonably straight line that can be used to evaluate the ability of an additive to change the ignitability of the RDX/TNT mixture. The sensitivity hazard increases in proportion to the reciprocal of the threshold pressure of initiation.

The ignitability test was performed on three psuedo Comp B variations. These specimens were not melt-cast. A fixed quantity of RDX (coated or uncoated) was blended with an appropriate amount of finely ground TNT. This was done in order to test the protective coating concept without risking (at this time) exposing bare RDX, a possible result of the crushing process, to the test. The control for the series was a 60/40 blend of RDX/TNT with uncoated RDX. Its ignitability was compared against that of pseudo Comp B's with an insulator (polysulfone) and a conductor (aluminum) coated on the RDX. The pressure at which 50% of the trials (threshold pressure) would be initiated by a specific energy input is listed in Table 4. A plot of the reciprocal of the pressure with respect to the input energy is shown in Fig. 3. In every series, approximately one-half of the tests result in a violent thermal explosion. The force gage, mounted with the test fixture, provides a signal which responds to this event in relation to the onset of the energy pulse. This measures the time to violent reaction and is also listed in Table 4. These data are plotted with respect to the threshold pressure of initiation and shown in Fig. 4.

CLOSED BOMB RESULTS

All the protectants, which were coated on the RDX, significantly slowed the burning of cast RDX/TNT (60/40). Even the wax, which is normally mixed into the TNT melt, slowed burning more effectively as an RDX protectant. It is difficult to rank the effectiveness of the several coatings tested because identical experiments were not conducted with all the additives. The tests were performed with all, part, or none, of the TNT modifiers, and because the reactions taking place are not understood completely, it would not be valid to extrapolate a ranking. It is premature, however, to select the ideal coating for RDX only on the basis of closed bomb results. None of the coatings tested failed to slow the burning of the explosive. This indicates that there is a wide choice of materials available. The final selection should be based also on the coating's ability to provide additional desirable properties to the explosive.

TABLE 4
Ignition Test Results

Energy (Joules)	Threshold Pressure (MPa)	Explosion Time (ms)
Polysulfone Coated RDX		
0.0951±0.0011	94.8± 6.0	4.7± 3.2
0.0771±0.0011	97.2± 8.5	4.3± 2.6
0.0610±0.0009	110.0±13.3	2.5± 0.9
0.0418±0.0012	131.6± 6.3	0.9± 0.2
Uncoated RDX		
0.0922±0.0010	81.6± 1.8	4.8±2.7
0.0761±0.0011	93.1± 5.4	4.1±1.0
0.0603±0.0010	100.0± 6.2	1.6±0.4
0.0438±0.0006	128.2±10.0	0.6±0.3
Aluminum Coated RDX		
0.0915±0.0020	77.8±10.6	5.6±2.8
0.0726±0.0021	89.5± 2.8	3.9±2.8
0.0582±0.0014	103.3±15.2	2.0±0.8
0.0423±0.0071	129.3±13.7	0.5±0.2

Crushed specimens of the explosives were tested because of work of Collett (10). He launched and recovered four M549 shells that had 100 mil cavities machined in the base of the explosive (cast Comp B). These shells were launched at 5000 g, 8000 g, and 10,000 g acceleration. The base of the shells launched at 8000 g and 10,000 g were completely filled with rubble from the breakup of the explosive. It was also suspected that there might have been significant quantities of powdered explosive associated with the rubble. If an in-bore explosion is initiated in powdered and broken

material, the burning properties of this type of explosive must also be examined. The data shows that, in the powdered form, the additives whether in the TNT or coated on the RDX do not modify the burning of RDX/TNT. This indicates that the protective coatings, all of which slow the burning of the cast material do so because they inhibit the rate at which RDX particles are released from the TNT matrix for burning. It probably does this by infinitesimally delaying the ignition of the RDX in the particle to particle ignition sequence.

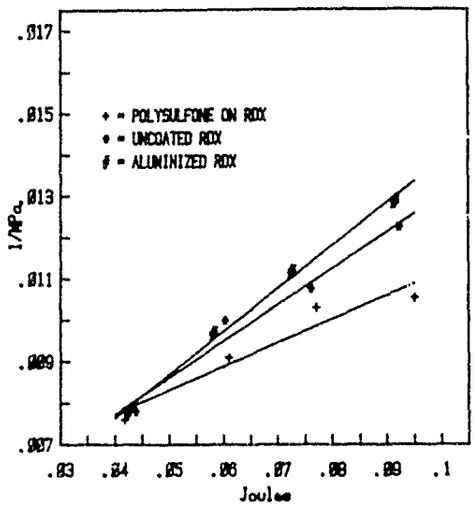

Fig. 3. Reciprocal of pressure vs. energy

Particle size of HMX has a significant effect on the burning of propellant containing 58% HMX (11). This material, like Comp B, broke up on burning for formulations with an HMX particle size of 45 and 92 microns. However, when the micron size was reduced to 4.1 typical gun propellant surface burning was approached. In order to test whether a similar trend occurred with Comp B, a formulation with a smaller RDX particle size was made. The results show that reducing the particle size from 177 μm to 105μm does not significantly slow its burning. It appears that a much smaller RDX particle size would be needed to slow Comp B's burning, and it would be difficult, if not impossible, to melt-pour this RDX/TNT mixture.

Of the TNT modifiers, only HNS appears to have a detrimental effect on the burning of Comp B. It appears to negate the beneficial effect provided by wax in standard Comp B. However, this speedup in burning is cancelled when the anti-exudate is added to the mixture. Whenever the anti-exudate is used, a significant reduction in the maximum pressure (energy) is observed. In some cases, the slowness of burning, caused by RDX protectants, contributes to this by increasing heat-leak through the walls of the closed bomb, but the predominant cause is attributed to side reactions which absorb energy from the reactive RDX/TNT mixture. This is desirable for slow cook-off reactions, and

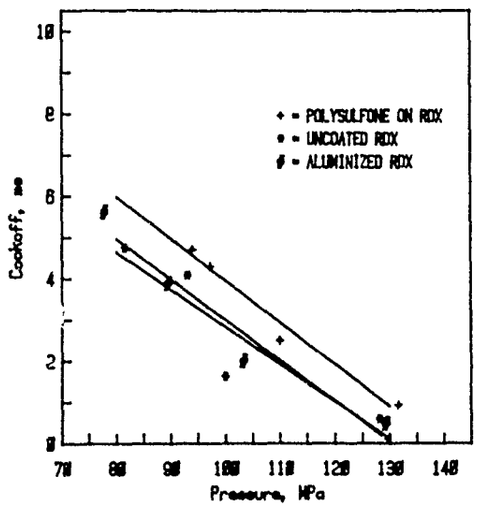

Fig. 4. Cookoff vs. pressure

it is unlikely that at detonation velocities (the working region of Comp B) there would be sufficient time for these side reactions to take place. This is supported by the burning of the crushed specimens. These samples burn at a much faster rate than the solid castings and several orders of magnitude slower than they would if stimulated to detonation velocities. The crushed specimens do not exhibit the energy-absorbing side reactions, thus suggesting that the exudation controlling additive can also decrease the severity of some cookoff hazards without seriously affecting performance. Although it is not established with absolute certainty, it appears that the anti-exudate and polysulfone (as a TNT modifier) do not interfere with the ability of protectant coatings from slowing the burning of cast RDX/TNT. From the perspective of burning properties, these additives can be included in the TNT matrix if

warranted by the cast quality and exudation control they provide.

IGNITION TEST RESULTS

The ignition tests were performed on pseudo Comp B in order to evaluate the feasibility of utilizing RDX protectants to reduce the sensitivity of RDX/TNT to in-bore type thermal initiation. The results are quite encouraging. Polysulfone, a candidate for use as an RDX protectant, as well as a TNT modifier, does reduce the sensitivity to thermal initiation in relation to the same formulation with uncoated RDX. The sensitivity of the formulation with aluminized RDX increases slightly, and this would appear to make this explosive more hazardous. The sensitivity of the three formulations converge as the pressure is increased to 130 MPa, indicating that the physical properties of the coating limit its effective working range.

A pleasant surprise was provided by the time-to-explosion results. The polysulfone coating increased the time to violent reaction by almost a millisecond across the entire threshold pressure range. It appears to do this in conjunction with its ability to slow burning and decrease the thermal sensitivity. If this is indeed a valid result, it means that the chance of a safer out-of-bore explosion is increased even if all the prospective improvements fail to prevent an in-bore initiation.

The encouraging results of the ignition test must be confirmed with Comp B formulations made in the traditional manner. In addition, the comparisons of RDX/TNT ignition properties caused by candidate RDX coatings should be made with respect to that of regular Comp B. In regard to the ignition test, the results are not as precise as is desired. The correlation of determination coefficients (r^2) for the reciprocal of pressure vs. energy curves is 0.93, 0.97, and 0.99, respectively, for formulations with polysulfone coated, uncoated, and aluminized RDX. These correlation coefficients are much poorer for the time to reaction vs. pressure curves; r^2 is 0.97, 0.83, and 0.95. for the same respective order. The ignitability test is a new test and as such it evolves as understanding grows with use. It is expected that experimental reproducibility will improve as experience develops the needed refinements.

CONCLUSIONS

This work established that a protectant coated on the RDX in a cast of 60/40 RDX/TNT will significantly slow the burning of these reactive constituents. All the coatings tested successfully performed this function; however, when these formulations were burned in their crushed form, the protectants did not slow the burning. This indicates that, in a cast, an additive on the surface of the RDX inhibits the rate at which the RDX is released from the TNT matrix for burning. It probably does this by sequentially delaying the ignition of the RDX particles. Preliminary results also indicate that additives which can slow the burning of RDX/TNT may also increase its minimum energy of ignition and delay the onset of a thermal explosion. These results must be confirmed and a search made for the ideal coating that will best perform all three desirable properties; which collectively should significantly reduce the incidence of in-bore explosions where casting flaws would have precipitated the event. The presence of TNT modifiers, which are intended to control cast quality and exudation, do not appear to interfer with the ability of RDX protectants to slow burning.

REFERENCES

1. R. W. Velicky and J. Hershkowitz, "Anomalous Burning Rate Characteristics of Composition B and TNT," Seventh Symposium (International) on Detonation, 1981.

2. R. W. Velicky, "The Burning Behavior of TNT in the Closed Bomb," Technical Report ARLCD-TR-83015, ARRADCOM, Dover, NJ, March 1983.

3. R.W. Velicky, "A Method to Evaluate the Burning Behavior of Secondary Explosives — Composition B," Technical Report ARLCD-TR-83030, ARRADCOM, Dover, NJ, June 1983.

4. R. W. Velicky, "A Calorimeter Designed to Determine the Heat-of-Reaction of Beta-HMX as a Function of Pressure," Technical Report ARLCD-TR-78039, ARDC, Dover, NJ, 1978.

5. R. W. Velicky and W. Voreck, "Thermal Initiation of Explosives as a Function of Pressure and Energy," Proceedings of the JANNAF Propulsion System Hazard Meeting, BRL, Aberdeen, MD, June 1984.

6. J. S. Back, J. Soderberg, and C. Hakanson, "Explosive," British Patent Specification 1249038, 6 October 1971 (and U.S. Patent 3,620,857).

7. H. W. Voigt, "Use of Thermoplastic Additives to Control Cracking and Exudation of Cast Explosives Containing TNT," Technical Report 3829, Picatinny Arsenal, Dover, NJ, February 1970.

8. H. W. Voigt, "Exudation Test for TNT Explosives Under Confinement: Exudation Control and Proposed Standards," Technical Report ARLCD-TR-83004, ARDC, Dover, NJ, February 1970.

9. "Statistical Analysis for a New Procedure in Sensitivity Experiments," AMP Report No. 101.R, SRG-P No. 40, Explosives Research Laboratory, Bruceton, PA, 1944.

10. B. D. Fishburn, "Ignition of Explosive Fills by Setback Acceleration Forces During Launch," ARDC, Dover, NJ, Technical Report being prepared for publication.

11. R. W. Velicky, "A Preliminary Analysis of Nitramine Propellant Burning Rate Anomalies," Technical Report ARLCD-TR 78048, ARDC, Dover, NJ, 1978.

UNITED STATES ARMY ARMAMENT RESEARCH AND DEVELOPMENT CENTER
DOVER, NEW JERSEY

THE EFFECT OF SOME ADDITIVES ON THE CLOSED BOMB BURNING AND IGNITABILITY OF RDX/TNT (60/40)

IN-BORE THERMAL EXPLOSIONS WITH COMPOSITION B

CAUSES:

- CASTING FLAW SET-BACK INDUCED HOT-SPOT
- SENSITIVITY TO THERMAL IGNITION
- CATASTROPHIC REACTION RATE

CURES:

- IMPROVE MANUFACTURING PROCEDURES TO MINIMIZE CREATION OF CASTING FLAWS
- UNDERSTAND BURNING MECHANISM IN ORDER TO INTRODUCE CHANGES THAT WOULD FURTHER REDUCE FREQUENCY OF THE HAZARD

COMP B BURNING MECHANISM AS SHOWN BY CLOSED BOMB TECHNIQUE

- INITIAL SURFACE BURNING REACTION RATE
- AT 100 MPa PHYSICAL STRUCTURE BREAKS UP, NEW SURFACE AREA IS CREATED AT A PHENOMENAL RATE
- COMP B's WAX ADDITIVE DOES NOT CHANGE BURNING BEHAVIOR OF ITS TNT CONSTITUENT
- SOME WAX MIGRATES TO RDX SURFACE TO SLOW REACTION RATE SLIGHTLY

CATASTROPHIC REACTION RATE OF COMP B CAN BE MODERATED

- PROTECTIVE COATING ON RDX SLOWS REACTION RATE
- ALL COATINGS TESTED SLOWED THE REACTION RATE

RELATIVE REACTION RATES

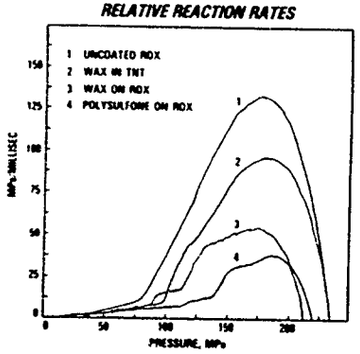

ADDITIVE EFFECT ON THE BURNING OF CAST RDX/TNT

ADDITIVES IN THE TNT BINDER CAN IMPROVE CAST QUALITY

- IMPROVE CASTABILITY
- IMPROVE MECHANICAL PROPERTIES

MOST TNT MODIFIERS DO NOT PREVENT RDX PROTECTIVE COATINGS FROM SLOWING THE OVERALL REACTION RATE

RDX PROTECTIVE COATINGS CAN ALSO REDUCE SENSITIVITY TO THERMAL INITIATION AND INCREASE THE TIME TO EXPLOSION

EXPLOSIVE IGNITION IS A FUNCTION OF PRESSURE AND ENERGY

- *IN EACH SERIES A FIXED, 80 μSEC, HEAT PULSE IS DISCHARGED INTO A PLATINUM HEATER CENTERED IN AN EXPLOSIVE SPECIMEN*
- *THE PRESSURE, MONITORED WITH A PIEZO FORCE GAGE, IS VARIED FOR EACH SHOT BY THE BRUCETON STAIR-STEP PROCEDURE*
- *THE 50% THRESHOLD PRESSURE OF INITIATION IS DETERMINED AT SEVERAL ENERGY LEVELS*
- *FORCE GAGE SENSES VIOLENT REACTIONS*

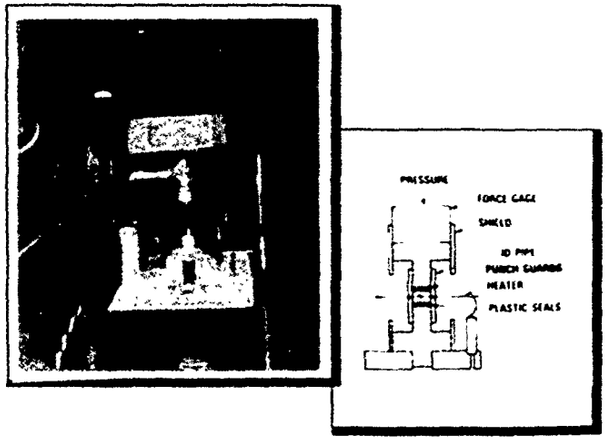

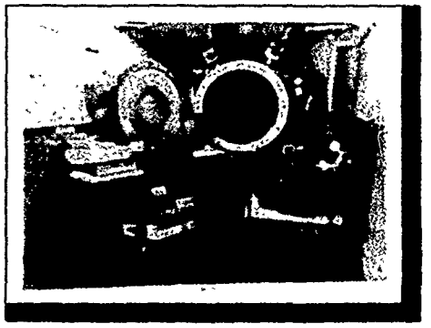

IGNITABILITY OF UNCOATED RDX IN RDX/TNT (60/40) COMPARED WITH MIXTURES WITH CONDUCTIVE AND INSULATING RDX COATINGS

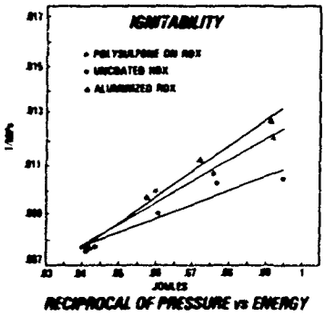

RECIPROCAL OF PRESSURE vs ENERGY

A PROTECTIVE COATING ON THE RDX CAN CHANGE THE IGNITABILITY OF THE RDX/TNT MIXTURE

- *A CONDUCTOR MAKES THE BASE MATERIAL MORE HAZARDOUS*
- *AN INSULATOR MAKES THE BASE MATERIAL LESS HAZARDOUS*
- *IGNITABILITY OF BASE MATERIAL CONVERGES AT 130 MPa*

REACTION TIME OF UNCOATED RDX IN RDX/TNT (60/40) COMPARED WITH MIXTURES WITH CONDUCTIVE AND INSULATING RDX COATINGS

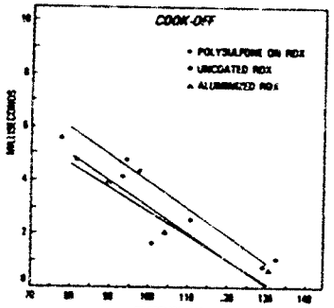

TIME TO EXPLOSION vs PRESSURE

RDX PROTECTIVE COATINGS CAN ALSO DELAY THE ONSET OF A VIOLENT REACTION

- *AN INSULATOR (1%) COATED, ON THE RDX DELAYS THE ONSET OF A THERMAL EXPLOSION BY APPROXIMATELY 1 MILLISEC*
- *NO SIGNIFICANT CHANGE OBSERVED WITH A CONDUCTOR COATED ON THE RDX*

SUMMARY

THREE DESIRABLE PROPERTIES CAN BE OBTAINED BY PRE-COATING THE RDX CONSTITUENT IN RDX/TNT WITH A PROTECTANT

- *THE THERMAL REACTION RATE CAN BE SIGNIFICANTLY SLOWED*
- *THE MINIMUM ENERGY OF INITIATION CAN BE INCREASED*
- *THE TIME REQUIRED TO REACH VIOLENT REACTION CAN BE INCREASED*

IN-BORE EXPLOSIONS WITH COMP B ARE A RARE EVENT, MODEST IMPROVEMENTS MADE AT EACH STEP IN THE SEQUENCE OF EVENTS COULD POSSIBLY REDUCE THIS FREQUENCY TO AN ACCEPTABLE LEVEL

MINIMIZE THE CAUSATIVE CASTING FLAW

- *REDUCE FLAWS BY IMPROVING CASTABILITY WITH TNT MODIFIERS*
- *IMPROVE PHYSICAL PROPERTIES WITH MODIFIERS, A MODEST IMPROVEMENT WOULD FAVORABLY SHIFT STRUCTURAL FAILURE RELATIONSHIP BETWEEN FLAW SIZE AND SET-BACK FORCES*
- *IMPROVE MANUFACTURING TECHNIQUES AND QUALITY CONTROL*

IF OR WHEN FLAW CREATION ESCAPES PREVENTATIVE MEASURES

- *RDX PROTECTIVE COATINGS WOULD INCREASE THE MINIMUM ENERGY OF INITIATION THEREBY REDUCING THE INCIDENCE OF IN-BORE INITIATIONS*
- *FOR THOSE INITIATIONS THAT MIGHT STILL TAKE PLACE THE EXPLOSIVE WOULD BURN AT A SLOWER REACTION RATE*
- *THE TIME TO REACH THE PROJECTILE RUPTURE PRESSURE COULD POSSIBLY BE INCREASED SUFFICIENTLY TO CAUSE A SAFE OUT-OF BORE EXPLOSION*

RESPONSE OF CONFINED EXPLOSIVE CHARGES TO FRAGMENT IMPACT

M. A. Barker, J. F. Bassett, J. Connor and P. J. Hubbard
Royal Armament Research and Development Establishment
Fort Halstead, Sevenoaks, Kent TN14 7BP, UK

A simple test of the response of cased explosive charges to high velocity fragment impact is described and results are presented for a range of explosives. It is shown that the minimum velocity of impact producing the most violent type of response in each explosive does not correlate well with the shock sensitivity of the explosive. However, a good correlation with explosiveness as measured in the RARDE Small-Scale Burning Tube Test is observed. The significance of this observation is discussed in the context of attempts to model fragment impact and proposals for more quantitative studies are made.

INTRODUCTION

The problem of predicting the response of cased HE charges to high velocity fragment impact is of considerable practical and academic interest. The processes which control this response are complex and their understanding requires detailed knowledge of the physics and chemistry of the systems involved. In the absence of this detailed knowledge the practical requirement for low vulnerability weapon systems has been addressed through a variety of ad hoc tests.

The RARDE Fragment Attack Test is one such test. It is intended to be used in the relatively early stages of the development of a new explosive formulation to give a measure of the violence of its response to fragment impact. Because of the difficulty in extrapolating results of this and similar small-scale tests to more realistic scenarios, a range of larger-scale tests culminating in complete weapon tests is applied before any explosive filled store is accepted as safe for service.

The long term goal of the work reported here is to reduce the requirement for ad hoc testing and to provide designers with more quantitative tools with which to assess the vulnerability of munitions to projectile impact. This goal can only be met through the development of detailed and soundly based models of the generation of shock waves by impact and their interaction with heterogeneous materials, the failure of metals and of explosives under impact loading and the ignition and growth of reaction in explosives.

This paper describes the RARDE Fragment Attack Test and reports results obtained with a variety of types of explosive. Some preliminary hydrocode studies of the test are presented and the test is discussed in the light of developing understanding of the response of explosives to ignition stimuli in order to point the direction for future, more quantitative studies.

THE RARDE FRAGMENT ATTACK TEST

The test employs a cylindrical steel projectile, 12.7mm diameter x 12.7mm long, which may be fired at a velocity in the range 400-2000 m s^{-1} to impact on a confined explosive charge using modified smooth bore Browning or RARDEN guns. The explosive charge is contained in a mild steel vehicle, 114mm long x 57mm internal diameter, with a wall thickness of 9.5mm. After filling with explosive in the form and to the density employed in normal service use, the vehicle is closed with a mild steel or aluminum end cap which provides a front septum with a thickness of 3.2mm.

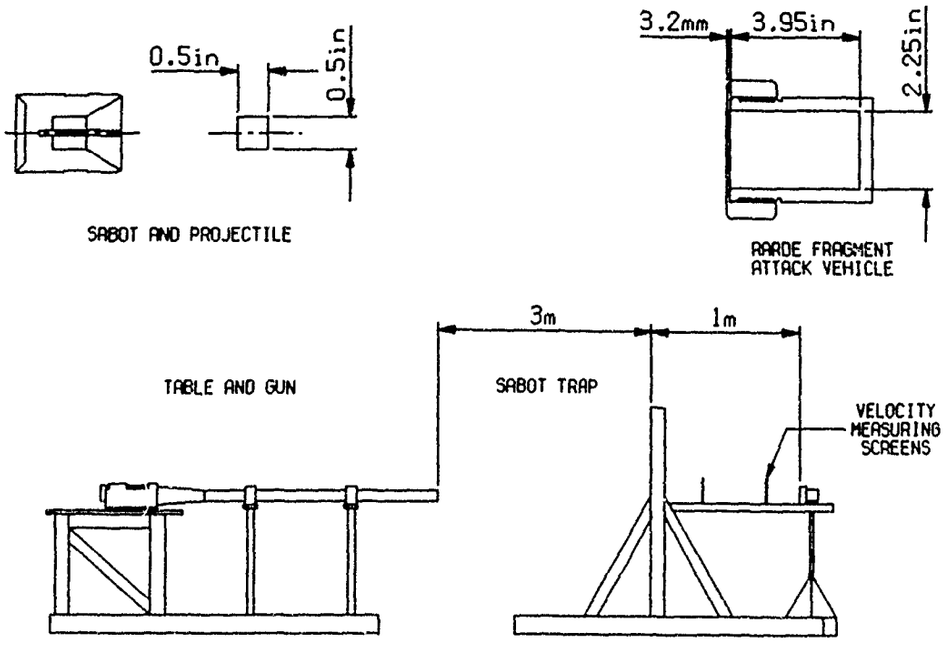

Fig. 1. Arrangement of fragment attack equipment

Projectile velocities are varied by changing the propellant charge weight and measured using foil screens connected to microsecond counters. Each firing is monitored using a ¼ height Fastax high speed framing camera at a framing rate of 28000fps to give a confirmation of projectile velocity and an indication of the response of the explosive charge. The test layout and details of the test vehicle are shown in Figure 1.

The response of the charge to the impact is assessed in terms of the damage to the test vehicle according to the following categories:

Degree 0 : No visible sign of reaction after penetration of the septum by the projectile

Degree 1 : Hint of a burning reaction which has faded rapidly, no obvious consumption of explosive

Degree 2 . Detachment of the septum, up to 20% of explosive consumed

Degree 3 : Septum detached, vehicle intact or broken into large fragments, more than 20% of explosive consumed

Degree 4 :100% of explosive consumed in a very violent reaction characterised by breaking up of vehicle into very many small fragments showing evidence of shear failure

These categories are rather crude but, in very general terms, responses of Degrees 0, 1 and 2 are rather mild whereas a response of Degree 4 would, if observed in a real weapon, be regarded as unacceptable.

Results are generally reported in the form of bar graphs showing degree of response against the range of velocities over which that response was observed.

RESULTS

Results are presented in Figure 2 for a series of UK secondary and booster explosive compositions. Details of the compositions employed, their mode of filling and density are given in Table 1 together with NOL Large-Scale Gap Test shock sensitivity and RARDE Small-Scale Burning Tube Test results.

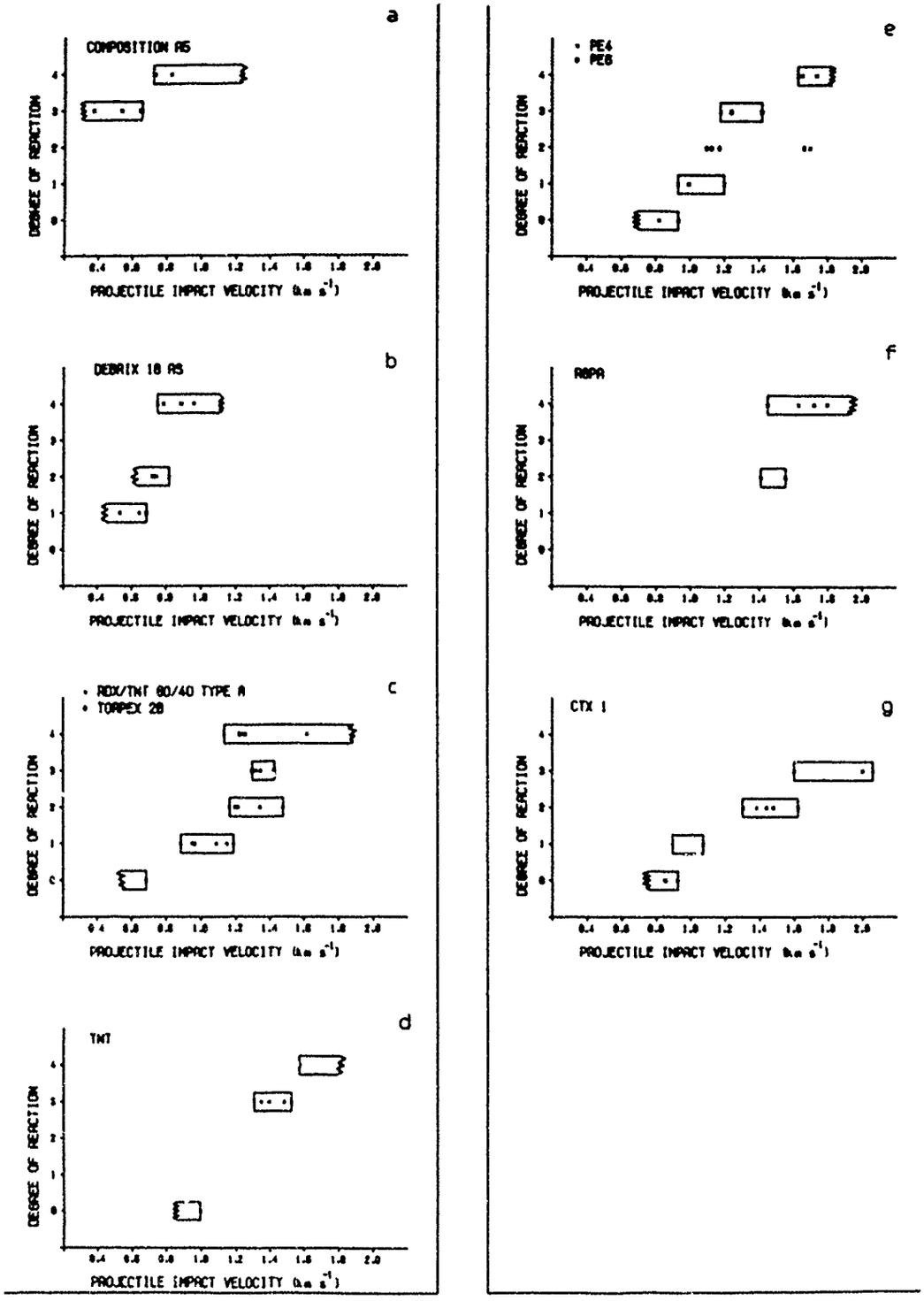

Fig. 2. Results for a range of explosive compositions

TABLE 1
Details of Compositions Tested and Sensitivity and Explosiveness of Data

	Composition	Filling method	Typical charge density (Mg m^{-3})	NOL Large-Scale Gap Test, Shock Sensitivity (GPa)	RARDE Small-Scale Burning Tube Test, Explosiveness (Fragments)
Composition A5	RDX/stearic acid 98.5/1.5	Pressed	1.68	—	100
Debrix 18AS	RDX/Wax/Flow additives 95.5/2.5/2	Pressed	1.64	—	30
RDX/TNT 60/40 Type A	RDX/TNT/Wax 59.5/39.5/1	Melt Cast	1.62	3.0	20
Torpex 2B	RDX/TNT/Al/ Desensitiser 42/40/18/5	Melt Cast	1.70	3.9	20
TNT		Melt Cast	1.59	6.3	7
PE4	RDX/Plasticiser 88/12	Extruded	1.60	2.4	2
RGPA	RDX/Plasticiser/ Polyurethane 70/19/5.5/5.5	Extruded	1.74	3.7	4
CTX-1	RDX/AP/Al/TNT + additives 15/40/23/22	Vacuum cast	1.84	4.8	4

Although the degree of reaction is a qualitative and, to some extent, subjective rating of response, the data of Figure 2 can nevertheless be used to obtain a better understanding of the key processes involved in the ignition and growth of reaction following fragment impact on cased explosive charges.

One important parameter, particularly from the viewpoint of defining Insensitive High Explosives (IHE), is the minimum velocity for the onset of violent, Degree 4 reactions. This velocity is shown in Figure 3 plotted against Large-Scale Gap Test shock sensitivity. There is some apparent correlation between these parameters but the wide disparity between the data points for PE4 and TNT indicates that this correlation can only be part of the total picture.

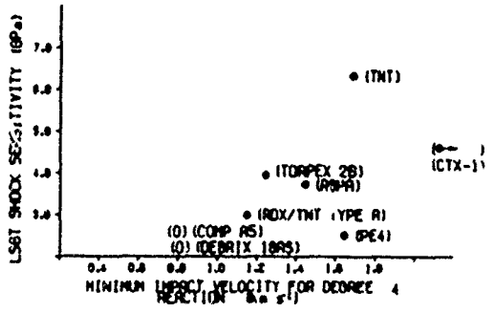

Fig. 3. Correlation between shock sensitivity and onset of Degree 4 reaction

An important distinction between TNT and PE4 is that the latter explosive exhibits lower explosiveness. This means that, when ignited under confinement, PE4 gives a less violent response than does TNT. At RARDE the Small-Scale Burning Tube Test (1) has been extensively used to provide an indication of the explosiveness of cased explosive charges. The explosive is filled in cast, pressed, extruded or other

form as employed in service into a mild steel tube 254mm long with internal diameter 31.4mm and wall thickness 6mm sealed by mild steel end caps and ignited at one end of the tube by a small ballistite charge. Explosiveness is estimated in terms of the number of fragments produced, usually as the mean of ten determinations.

Figure 4 shows plots of the minimum velocities at which reactions of Degree 1 to 4 are observed against the number of fragments produced by the same explosive in the Small-Scale Burning Tube Test. For Degree 4 reactions, which are of course the most violent, the correlation between minimum velocity and explosiveness is good but correlations for lower degrees of reaction are less convincing.

DISCUSSION

Quantitative experimental and theoretical studies of the response of explosives to fragment impact have tended to focus on direct initiation of detonation by shock. Tests to evaluate the well known Walker and Wasley (2) critical energy fluence criterion,

$$E_c = \frac{P^2 T}{\varrho_0 u}$$

where P is shock pressure, T shock duration, ϱ_0 initial density and u shock velocity are typical. In this type of experiment explosives are subjected to impact from flat plates or from cylindrical projectiles onto the bare explosive surface or onto metal cover plates in contact with the surface. Apart from this cover plate, the explosives are unconfined or very lightly confined. Reaction either transits rapidly to detonation or is quenched when it propagates to the charge boundaries, allowing a very clear distinction to be made in most cases between detonation and non-dentonation regimes. Thus, for example, Bahl, Vantine and Weingart (3) were able to produce shock initiation threshold curves plotting projectile diameter against impact velocity for bare and covered PBX 9404 and RX-26-AF. Green (4) has given a simple method for calculating these thresholds based on one dimensional sustained pressure run distance to detonation.

In order to further explore possible correlations of the RARDE Fragment Attack Test data with shock sensitivity and to facilitate

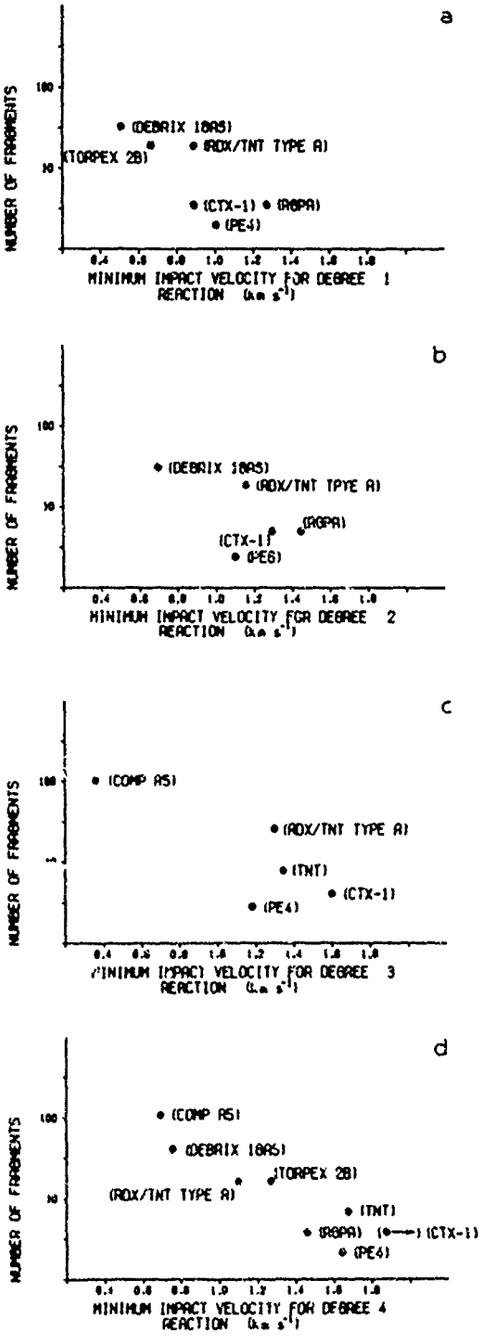

Fig. 4. Correlation between RARDE Small-Scale Burning Tube explosiveness and onset of Degree 1, 2, 3 and 4 reactions

comparison with other experimental and theoretical studies, we have estimated the shock pressures experienced by an explosive charge, Composition B for modelling purposes, in the test for various impact velocities. Simple 1-D impedance matching calculations for the impact of a steel projectile on a steel septum contacting Composition B gave a pressure in the explosive of ~7GPa for an impact velocity of 1.0km s^{-1}. Compared to the LSGT figure of 1.8GPa for 50% probability of initiation of Composition B (5), this figure suggests that prompt shock initiation of Compositon B might be possible for impact velocities rather less than 1.0km s^{-1}.

However, several workers, notably Gittings (6), Trott and Jung (7) and de Longueville (8), have shown that threshold conditions for shock initiation are determined not only by the amplitude of the pressure pulse, but also by its duration and it is just such considerations which led to the Walker and Wasley criterion (2). Foan and Coley (9) applied these ideas to a gap test using a strain-compensated pressure transducer to measure the critical pressure-time profile required by an acceptor charge to give a 50% probability of initiation for a variety of donors and acceptors. Clearly any attempt to compare results from fragment impact tests with gap test data must incorporate consideration of pulse duration. For this reason Hull hydrocode simulations of the impact event were computed.

Hydrocode calculations were carried out for steel projectile impact velocities of 0.5, 1.0 and 1.5km s^{-1} onto steel or aluminum septa covering a material represented by the thermomechanical properties of Composition B. No attempt was made to model chemical reactions. Calculated peak pressures, peak pressures corrected for numerical overshoot and particle velocities in the explosive are given in Table 3 with, for comparison, results of simple 1-D calculations.

When allowance is made for the numerical overshoot in peak pressure as calculated by the hydrocode, agreement with 1-D theory is good. However, the HULL calculations also allow the variation in pressure and particle velocity with time to be monitored and these calculations show that 1-D values are maintained for only very short times. Thus for a 1.5km s^{-1} impact of a steel projectile onto a steel septum, shock is transmitted into the explosive some 0.9μs after initial impact on the septum and, at the same time, a pressure release wave moves back into the septum. After 1.4μs this release wave reaches the septum projectile interface and this interface begins to separate so that, after 1.6μs, the initial shock in the explosive is separated from the septum. From this point the initial shock is no longer being driven by the projectile impact and it is rapidly dissipated by 2-D decay effects. The calculated pressure-time profile with correction for overshoot is shown in Figure 5 for a point just below the explosive surface.

TABLE 3

Calculated Pressures and Particle Velocities Produced by Fragment Impact

a .Steel projectile/Steel septum/Composition B

Impact Velocicy (km s^{-1})	1-D		Hydrocode		
	P (GPa)	U (km s^{-1})	Ppeak (GPa)	Pcorr (GPa)	U (km s^{-1})
1.5	10.9	1.24	15.0	11.0	1.20
1.0	6.4	0.84	7.6	6.6	0.86
0.5	2.7	0.43	2.5	1.5	0.45

b.Steel projectile/Aluminum septum/Composition B

Impact Velocicy (km s^{-1})	1-D		Hydrocode		
	P (GPa)	U (km s^{-1})	Ppeak (GPa)	Pcorr (GPa)	U (km s^{-1})
1.5	12.5	1.40	16.0	11.5	1.30
1.0	7.3	0.95	8.8	7.1	0.93
0.5	3.4	0.52	3.4	1.9	0.54

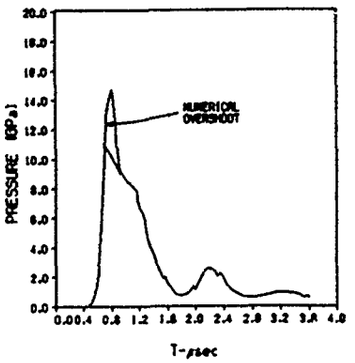

Fig. 5. Hydrocode generated pressure-time profile in Composition B for 1.5km s impact of steel projectile on steel septum in contact with the explosive

Because of the highly divergent geometry, plots of this ty[illegible] not be used in any very simple way to ca[illegible] energy fluence for comparison with Walker and Wasley criteria (2), nor can they be compared directly with the critical pressure-time profiles obtained by Foan and Coley (9) in a rather different geometry. However, it is clear that the prompt shock initiation of PE4, a relatively shock sensitive high explosive, must require an impact vlelocity in this test configuration in excess of 1.6km s^{-1}, the minimum velocity at which Degree 4 events are observed in PE4. Similarly, prompt shock initiation of relatively shock insensitive CTX-1 requires an impact velocity in excess of 2.0km s^{-1}. Torpex 2B, RGPA and RDX/TNT Type A are all less sensitive to shock than PE4 but all give Degree 4 events at lower impact velocities. Similarly, TNT is less sensitive to shock than CTX-1 but gives Degree 4 events at lower impact velocities. These events cannot be produced as a result of prompt shock initiation.

This conclusion is supported by Figure 4 which shows a good correlation between explosiveness and the minimum impact velocity for a Degree 4 event. The implication is that the violence of the observed event is a function of competition between the rate of acceleration of reaction in the explosive and the rate of failure of the confinement. Degree 4 events are observed when these rates allow the development of a very rapid reaction—perhaps involving deflagration to detonation transition (DDT)—before confinement is breached. Relatively frangible explosives such as RDX/TNT Type A tend to facilitate propagation of such rapidly accelerating reactions and hence give Degree 4 responses at velocities substantially below the threshold for prompt shock initiation. On the other hand, propagation of deflagrative reactions in PE4, a dough-like plastic explosive, is slow. Many experiments in a variety of test vehicles have shown that it is difficult, if not impossible, to induce violent reactions in PE4 by any other mechanism than prompt shock initiation. It is likely therefore that the minimum impact velocity for a Degree 4 event does in this case represent the critical velocity for prompt shock initiation.

The behaviour of CTX-1 in the Fragment Attack Test is also consistent with the view that for most materials violent reactions occur under conditions below the prompt initiation threshold. Although CTX-1 is relatively frangible and the ammonium perchlorate component in CTX-1 is sensitive to ignition by impact, reaction in CTX-1 proceeds by an inter- rather than intra-molecular mechanism and is thus intrinsically slower than reactions in more conventional explosives. For this reason, although reaction can be induced at relatively low impact velocities, Degree 1 events being observed at ~900m s^{-1}, these reactions never accelerate sufficiently to give a Degree 4 event. Presumably Degree 4 events will only be observed in CTX-1 at impact velocities sufficient to give prompt initiation. These velocities are outside the range of the present test with steel end caps.

Clearly it is not desirable that munitions should give violent responses to projectile impacts at velocities substantially below the threshold prompt shock initiation condition. This confined fragment impact test demonstrates that the tendency of explosives to give such a response is a function not of the sensitivity or sensitiveness of the explosives but of their explosiveness. More work needs to be done to identify the prompt shock initiation threshold for a range of explosives and to compare this threshold with the minimum impact velocity for Degree 4 reactions. Both experimental and hydrocode studies to this end are now underway.

A consequence of the significance of explosiveness in determining the responses of cased explosive charges to fragment impact is that

for violent, Degree 4 type, events the exact mode of ignition is unimportrant. This conclusion is implicit in Figure 4d, which shows a correlation between data obtained with very different initial stimuli and it also follows from consideration of the explosive reaction in terms of a simple qualitative ignition and growth model. For violent reactions the extent of reaction at the initially produced hot-spots will represent only a tiny fraction of the whole; response is dominated by growth rather than by ignition. Thus it should prove possible to model violent responses to fragment impact without detailed knowledge of the ignition process. This is not true for responses of a lesser degree of violence. As Figure 4 shows, responses of Degrees 3 to 1 are much less well correlated with explosiveness. In these cases sensitiveness, and hence the method by which hot-spots are actually formed, becomes of much more significance.

FUTURE WORK

Improved understanding of the response of cased explosives to fragment impact depends on the develpment of quantitative descriptions of this phenomenon. One of the greatest weaknesses of the RARDE Fragment Attack Test as it is currently conducted is the qualitative and subjective nature of the measure of response in terms of Degrees 1-4. In particular, it would be major advance to be able to distinguish between Degree 4 responses which involve prompt shock initiation and those which involve ignition and subsequent growth of reaction. As a first step to meeting this requirement, fragment attack test vehicles are being instrumented with strain gauges. This work is being supported by further hydrocode calculations and by attempts to utilize hydrocode generated pressure-time and pressure-space profiles to generate critical enegy fluence criterion data.

In addition to better experimental and theoretical tools to identify prompt shock initiation thresholds for impact on cased charges, a description of the ignition and growth process at lower velocities is also required. The data presented in this paper indicate that for violent responses this description can be based on models of the RARDE Small-Scale Burning Tube measure of explosiveness. It is intended that the Burning Tube ignition system should be modified to provide a more nearly planar reaction front and to allow a more accurate assessment of the onset of the reaction. The experiment will then be instrumented using externally mounted gauges and internal pressure gauges to give a measure of reaction growth which can be used to assess numerical models.

CONCLUSION

The threshold velocity for the onset of violent reactions in the RARDE Fragment Attack Test is a function not of the shock sensitivity of the explosives charge but of its explosiveness. Numerical modelling of this response should therefore be possible without detailed knowledge of the physics and chemistry of the ignition process. Instrumented RARDE Burning Tube Tests should provide a useful test vehicle for such models. Improved experimental and theoretical techniques are required to define the impact conditions under which prompt shock initiation does become a significant reaction mechanism.

ACKNOWLEDGEMENT

Hydrocode calculations were carried out on our behalf by Dr. I. Cullis. Only a minor part of these calculations is reported here. Full details will be published elsewhere at a later date.

REFERENCES

1. A.S. Dyer, P.J. Hubbard, P.R. Lee, D.G. Tisley, "Factors Affecting the Explosiveness of Muniton Fillings, Seventh Symposium (International) on Detonation, 1040, 1981.
2. F.E. Walker, R.G. Wasley, Explosivstoffe, *17* (1) (1969).
3. K.L. Bahl, H.C. Vantine, R.C. Weingart, Seventh Symposium (International) on Detonation, 325 (1981).
4. L. Green, Seventh Symposium (International) on Detonation, 273 (1981).
5. D. Price, A.R. Clairmont, J.O. Erkman, NOLTR 74-40 (1974).
6. E.F. Gittings, Fourth Symposium (International) on Detonation, 373 (1965).
7. B.D. Trott and R.C. Jung, Fifth Symposium (International) on Detonation, 191 (1970).

8. Y. de Longueville, Fifth International Colloquium on Gas Dynamics of Explosions and Reactive Systems, Bourges (1975).
9. G.C.W. Foan and G.D. Coley, Seventh Symposium (International) on Detonation, 278, (1981).

RESPONSE OF CONFINED EXPLOSIVE CHARGES TO FRAGMENT IMPACT

MR J. F. BASSETT
MR J. CONNOR
MR P. J. HUBBARD
MR M. A. BARKER

ROYAL ARMAMENTS RESEARCH AND DEVELOPMENT ESTABLISHMENT, FORT HALSTEAD, SEVENOAKS, KENT, UNITED KINGDOM

ARRANGEMENT OF FRAGMENT ATTACK EQUIPMENT.

RESPONSE OF THE CHARGE TO THE IMPACT IS ASSESSED IN TERMS OF THE DAMAGE TO THE VEHICLE ACCORDING TO THE FOLLOWING CATEGORIES:-

Degree 0 — No visible sign of reaction after penetration of the septum by the projectile

Degree 1 — Hint of a burning reaction which has faded rapidly no obvious consumption of explosive

Degree 2 — Detachment of the septum, up to 20% of explosive consumed

Degree 3 — Septum detached, vehicle intact or broken into large fragments, more than 20% of explosive consumed

Degree 4 — 100% of explosive consumed in a very violent reaction characterised by breaking up of vehicle into very many small fragments showing evidence of shear failure

BURNING REACTION

VIOLENT REACTION

CORRELATION BETWEEN SHOCK SENSITIVITY AND ONSET OF DEGREE 4 REACTION

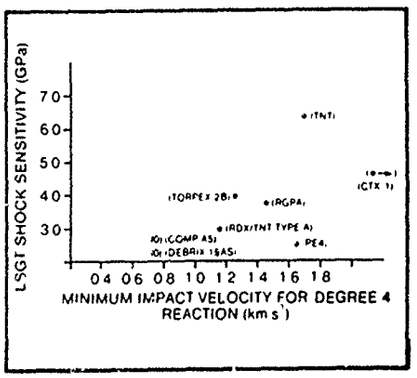

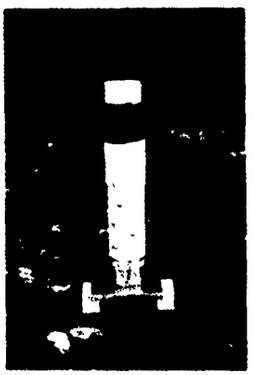

CORRELATION BETWEEN RARDE SMALL SCALE BURNING TUBE EXPLOSIVENESS AND ONSET OF DEGREES 1, 2, 3, AND 4 REACTIONS

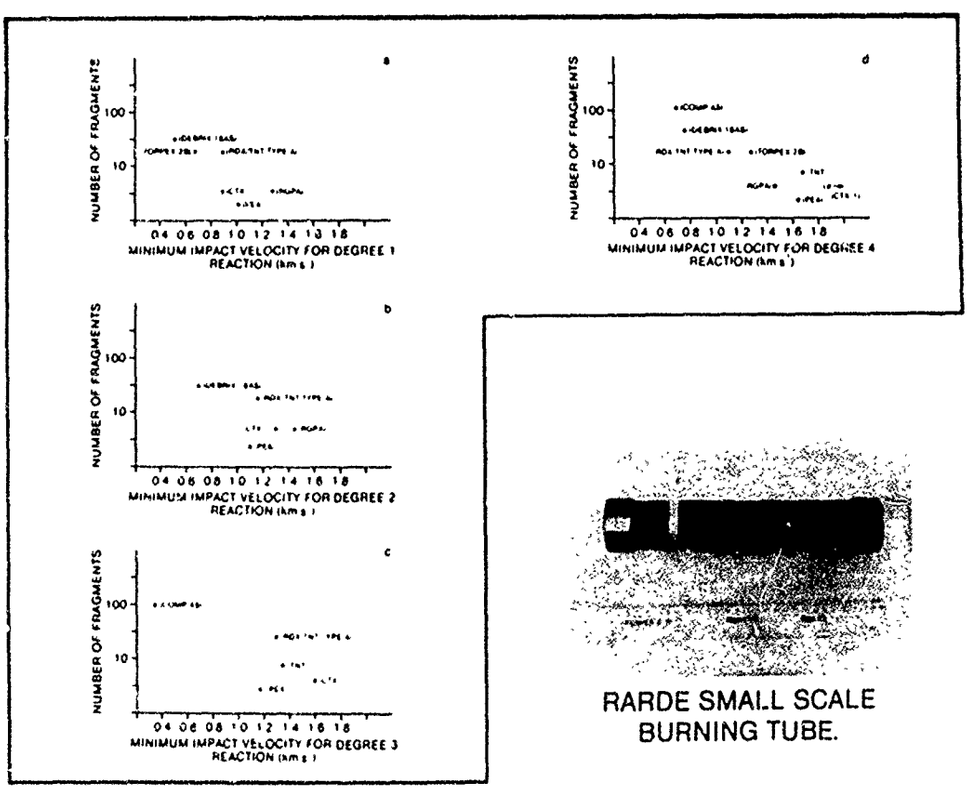

RARDE SMALL SCALE BURNING TUBE.

FUTURE WORK

EXPERIMENTAL

DISTINGUISH BETWEEN PROMPT SHOCK INITIATION AND IGNITION FOLLOWED BY DDT

PHOTOGRAPHY

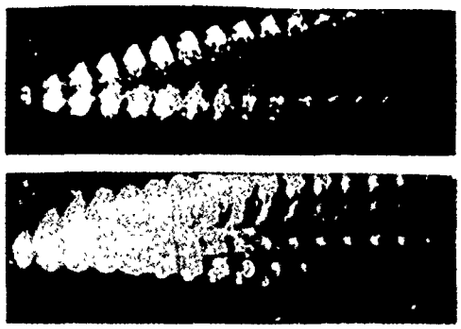

STRAIN GAUGES

INSTRUMENT BURNING TUBE - STRAIN GAUGES, PRESSURE PROBES

THEORETICAL

HYDROCODE CALCULATIONS OF CRITICAL ENERGY FLUENCE CRITERION

NUMERICAL MODELLING OF SMALL SCALE BURNING TUBE TEST

AIM

TO DEVELOP A PREDICTIVE CAPABILITY FOR THE RESPONSE OF CASED EXPLOSIVES TO FRAGMENT IMPACT

CONCLUSIONS

THE THRESHOLD VELOCITY FOR THE ONSET OF VIOLENT REACTIONS IN THE RARDE FRAGMENT ATTACK TEST IS A FUNCTION NOT OF THE SHOCK SENSITIVITY OF THE EXPLOSIVE CHARGE BUT OF ITS EXPLOSIVENESS

NUMERICAL MODELLING OF THIS RESPONSE SHOULD BE POSSIBLE WITHOUT DETAILED KNOWLEDGE OF THE PHYSICS AND CHEMISTRY OF THE IGNITION PROCESS

INSTRUMENTED RARDE BURNING TUBE TEST SHOULD PROVIDE A USEFUL TEST VEHICLE FOR SUCH MODELS

IMPROVED EXPERIMENTAL AND THEORETICAL TECHNIQUES ARE REQUIRED TO DEFINE THE IMPACT CONDITIONS UNDER WHICH PROMPT INITIATION DOES BECOME A SIGNIFICANT REACTION MECHANISM

PRESSURE-SHEAR LOADING OF PBX-9404

L. C. Chhabildas, M. E. Kipp
Sandia National Laboratories
Albuquerque, New Mexico 87185

One dimensional pressure-shear loading techniques have been used to obtain estimates of dynamic shear strength of PBX 9404 over the stress range of 0.3 to 1.0 GPa. A single-stage compressed gas gun was used to obtain normal impact of a projectile on a Y-cut quartz crystal with an explosive sample bonded to its rear surface. The anisotropic nature of the Y-cut quartz results in a two-wave structure having particle velocities in both the longitudinal and transverse directions. Results of these experiments indicate that a maximum shear stress of 0.04 GPa is obtained. The pulse amplitude and the sample thickness in the present experiments are not optimal to investigate the reaction sensitivity to shear loading. Numerical simulations of these experiments based on a thermomechanical, and an elastic, perfectly plastic model, are reported.

INTRODUCTION

As part of a program to develop material models for use in two- and three-dimensional computer codes, various experimental techniques (1) have been developed to obtain the uniaxial-strain loading response of many solid materials, including explosives. With these recent advances in experimental capabilities, the data base for many explosives has been augmented with detailed time-resolved measurements of stress or particle velocity (2,3) of shocked explosives. This data base is critical to the development of various thermomechanical material models (4-6) which include physical models of the shock-initiation process and which can be used to describe the response of explosive components subjected to a variety of loading and confinement conditions. Although considerable progress has been achieved based on hydrodynamic assumptions, a need exists to extend these dynamic studies to more generalized loading conditions. The dynamic pressure-shear loading technique (7,8) is one experimental method that can be used to determine directly the dynamic shear strength of the explosive, and would substantially aid in the development of more generalized mechanical material models. Including the strength of the explosive may be important at lower stress levels of loading where shear stresses may influence the extent or rate of reaction.

The purpose of this paper is to report the first measurements of pressure-shear loading of the explosive PBX-9404 at sub-detonation stress levels. PBX-9404 is an explosive which has been investigated thoroughly; uniaxial-strain data (9) exist from a few-tenths of a GPa to tens of GPa; the material has been studied under various loading conditions, i.e., shock (10), reshock (11), and ramp (12) loading conditions; and material models have also been developed (4-6) which can numerically simulate most of these experiments satisfactorily. Pressure-shear experiments on PBX-9404 are expected to complement these previous studies. They will allow the evaluation and development of material models under more general loading conditions for use in three-dimensional computer codes.

The pressure-shear experiments reported in this paper have been performed over the stress range of 0.3 to 1.0 GPa. These experiments have been specifically limited to sub-detonation stress levels, to obtain estimates of dynamic shear strength of the explosive. Information regarding its dynamic material strength at sub-

detonation stress levels cannot be obtained from uniaxial-strain experiments, since the measured particle velocity or stress profiles tend to be dispersive. The present experiments indicate that a maximum of 0.04 GPa shear stress is sustained in the material over the stress range of 0.3 to 1.0 GPa, but do not determine the reaction sensitivity of PBX-9404 to shear loading, since only thin samples were investigated.

In the following section the experimental technique is described in detail. The experimental results and numerical simulations are discussed in subsequent sections.

EXPERIMENTAL TECHNIQUE

Pressure–Shear Loading Technique

The technique used to generate one-dimensional pressure-shear waves (7) in the explosive specimens is depicted in Figure 1. As indicated in the diagram, a projectile impacts a Y-cut quartz crystal that has a sample bonded to its rear surface. The projectile is accelerated

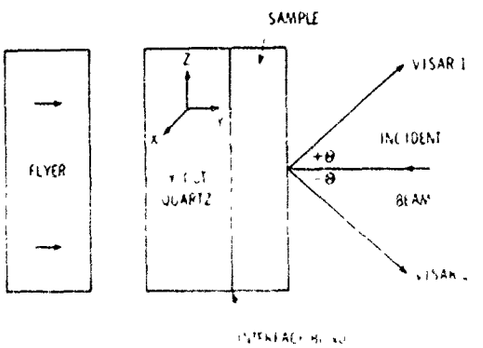

Fig. 1. Experimental impact configuration to produce pressure-shear loading in the sample

to the desired impact velocity using a single-stage compressed gas gun (13). Owing to the anisotropic structure of crystalline quartz, a pure longitudinal wave cannot propagate along its Y-axis (14). Upon normal impact of Y-cut quartz, a two-wave structure is generated with both waves having particle-velocity changes in both the longitudinal and transverse directions, i.e., the crystallographic Y and Z axes of the crystal. The fast wave, denoted as a quasilongitudinal (QL) wave, has particle-velocity changes primarily in the longitudinal (Y) direction, while the slow wave, denoted as a quasitransverse (QT) wave, has particle-velocity changes primarily in the transverse (Z) direction. These waves are shown as QL and QT in Figure 2(a). The particle velocity input at the bonded interface is indicated in Figure 2(b).

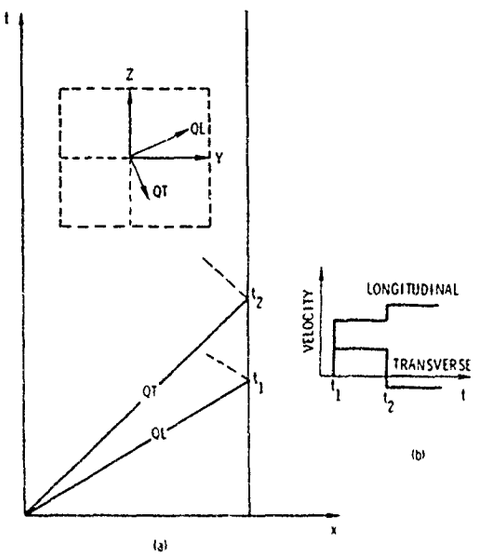

Fig. 2. Response of Y-cut quartz to normal impact loading. The stress pulse input at the bonded interface is indicated in (b).

Upon arrival of the QL wave at the interface, the sample is simultaneously loaded in compression and shear. The magnitudes of the particle-velocity changes associated with the arrival of the compression wave and shear wave at the free surface are determined using two velocity interferometers, VISARs, as indicated in Figure 1. By using one incident beam and monitoring two reflected beams at angles $+\theta_1$ and $-\theta_2$, the longitudinal velocity U(t) and the transverse velocity V(t) can be determined simultaneously (15). The two velocities measured by the interferometers are related to U(t) and V(t) by

$$u(+\theta_1,t)=\frac{1}{2}U(t)(1+\cos\theta_1)+\frac{1}{2}V(t)\sin\theta_1, \qquad (1)$$

and

$$u(-\theta_2,t)=\frac{1}{2}U(t)(1+\cos\theta_2)-\frac{1}{2}V(t)\sin\theta_2. \qquad (2)$$

The velocity $u(\theta,t)$ measured by each interferometer is related to the number of observed fringe shifts F(t) by the relation

$$u(t-\frac{1}{2}\tau)=\frac{\lambda}{2\tau}\frac{F(t)}{(1+\delta)} \quad (3)$$

where λ is the wavelength of the light used (514.5 nm). Fringes are produced in the interferometer by superimposing the light reflected from the target at any time with the light that was reflectd earlier in time by the delay time, τ, in the interferometer. The delay time, τ, was introduced by using either glass etalons (16) or a lens combination (17) in the delay leg of the interferometer. δ is a correction term due to the wavelength dependence of the refractive index of the etalon material (18). $\delta=0.034$ when etalons are used, otherwise $\delta=0$.

Reflected beams at θ_1 and $-\theta_2$ from the incident beam can be obtained by preferentially scratching the reflecting mirror on the free surface of the explosive specimen. Care was taken, however, to ensure that these marks were perpendicular to the plane of transverse wave propagation.

The projectile velocity was determined to an accuracy of 0.2% by measuring the transit time of the projectile between two precisely spaced charged pins located on the target plate. Impact tilt was determined by measuring the simultaneity of the projectile surface arrival at an array of co-planar charged pins located on the target plate. The average tilt for this series of shots was determined to be less than 0.5 mrad. These pins also provide fiducial signals used to determine transit times to the rear surface of the specimen.

Sample Preparation

The PBX-9404 samples studied in this investigation are from the same batch of material used in previous uniaxial-strain experiments (Ref. 6, 10-12). As indicated above, the samples were bonded to Y-cut quartz crystals. To minimize any slippage at the sample-crystal interface an alumina-filled epoxy bond was utilized. Alumina particles were mixed with an epoxy resin Hysol RE2038 and hardener Hysol HD3404 (9), having characteristic dimensions of 5-15 microns in the ratio 300/80/20 by weight. This epoxy and hardener does not react with the explosive. This bond has been previously demonstrated (21) to support a shear stress of at least 0.6 GPa.

Since interferometric techniques were used to measure pressure-shear waves, reflective coatings were necessary at the free surface of the explosive sample. Attempts at vapor depositing aluminum coatings were not successful, since the nitrocellulose in the PBX-9404 melted as the temperature of the explosive rose to approximately 150 °C, leaving a blistered surface after the process. An aluminum foil 25 μm thick was therefore bonded to the free surface using the above mentioned epoxy and hardener. It was found necessary to degrease and deionize the foil so that it would adhere to the explosive sample.

RESULTS AND DISCUSSION

The summary of impact conditions for the series of experiments performed on the explosive PBX-9404 is tabulated in Table I. Y-cut quartz crystals 12.7 mm thick were used to generate pressure-shear waves in the 2.996-mm thick explosive sample. Impactor materials (12.7-mm thick) used were PMMA (polymethyl methacrylate) in experiments EXP1 and EXP2, and 6061-T6 aluminum in experiment EXP3. An example of the longitudinal and transverse free-surface velocity profiles obtained in the pressure-shear experiments is indicated in Figure 3, for experiment EXP2.

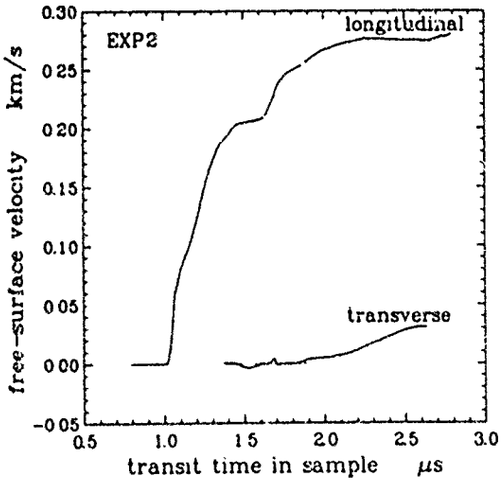

Fig. 3. Measured longitudinal and transverse free-surface velocity profiles for experiment EXP2

Wave Velocities

The arrival time of the longitudinal wave at the

TABLE 1
Results of Impact Experiments

Shot No.	Impact Vel. (km/s)	Shock Vel. (km/s)	Shear Vel. (km/s)	Particle[a] Vel. (km/s)	Shock[a] Stress (GPa)	Strain[a]	Rel.[b] Vel. (km/s)
EXP1	0.323	2.54	1.55	0.063/0.086	0.31/0.41	0.025/0.034	3.04
EXP2	0.495	2.45	1.65	0.104/0.140	0.48/0.66	0.041/0.055	3.32
EXP3	0.319	2.54	1.73	0.176/0.228	0.84/1.11	0.068/0.088	3.78
Ref. 20		2.34[c]	1.57				2.96

[a]The two different values reported represent longitudinal values and result from the two-wave structure generated by the Y-cut quartz crystal.

[b]The release wave velocity is assumed to be the elastic wave speed.

[c]Calculated bulk velocity based on ultrasonic measurements.

free surface of the explosive is determined to within 0.040 μs. The uncertainty in estimating the wave arrival time is primarily due to (i) impact misalignment between the projectile and the target, (ii) uncertainty in the thickness of the glue bond between the sample and the Y-cut quartz crystal, and (iii) the uncertainty in estimating the reflective foil/bond thickness.

The measured wave velocity for the toe of the longitudinal wave in the explosive sample agreed to within a few percent of the ultrasonic wave velocity of 2.96 km/s (20). This value was therefore used as a fiducial in determining the shock velocity, the release wave velocity, and the shear-wave velocity for the explosive.

These values are listed in Table 1. Due to the granular structure of the explosive, finite rise times are obtained for the longitudinal velocity profile, and the shock velocity has been determined at the midpoint of the first wave. As indicated in Figure 4, the shock velocity decreases as particle velocity increases to 0.1 km/s, and then increases again, a trend that has been observed previously (12, 22) for the explosive. This behavior is usually observed for porous materials and for composites where the constituents are materials that differ significantly in shock impedance. It is conceivable that the differences in the shock impedance of HMX grains and the nitrocellulose binder coupled with slight ($\sim$ 1.5%) porosity give rise to this behavior.

The anisotropic nature of the Y-cut quartz crystal introduces a two-step longitudinal loading in the explosive (see Figure 2). The arrival time of the leading edge of the second wave in the longitudinal profile yields estimates of

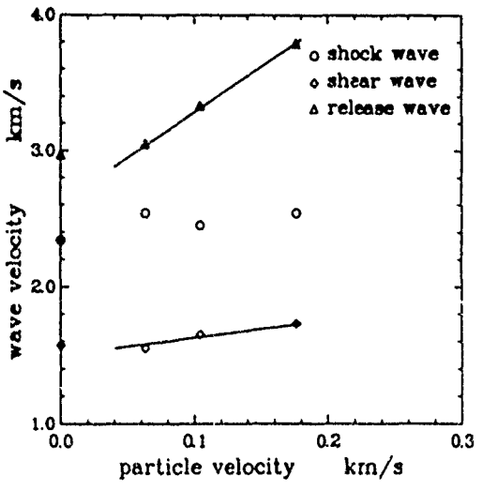

Fig. 4. Measured shock velocity, release-wave velocity, and shear-wave velocity vs particle velocity in PBX-9404. The values indicated at zero particle velocity are based on ultrasonic measurements.

acoustic sound speed in the shocked state, i.e., the release wave velocity. These values are plotted in Figure 4 as a function of particle velocity. The Lagrangian release wave velocity shows a systematic increase with increasing particle velocity over the same particle velocity range. The leading edge of the shear-wave velocity profile is used to determine the shear-wave velocity. The shear-wave velocity is also noted to increase with increasing particle velocity, although the percentage increase in the shear-wave velocity is less than that observed for the release wave velocity. If the release wave velocity is assumed to be the elastic wave speed

for the material as observed for other materials, then the Poisson ratio for the explosive is noted to increase from a value of 0.30 to 0.37 over the particle velocity range of 0.0 to 0.2 km/s.

Shock Stress And Shear Stress States

An incremental centered wave analysis has been used to estimate the shock stress and the shear stress sustained in the explosive. In the absence of significant chemical reaction behind the shock front, this analysis should be valid for the explosive as it is for other materials. The first and second longitudinal stress states in each experiment have been tabulated in Table 1.

These experiments suggest that a shear stress of approximately 0.04 GPa is sustained in the material. When compared to values measured in previous pressure-shear studies for other materials, this level is unusually low. Any systematic trend in the amplitude of the shear stress with increasing shock stress is masked due to experimental uncertainties. The experimental error in the estimates for the shear stress in this series of experiments is approximately 25%. The large uncertainty in these experiments is a direct consequence of the low amplitude for the measurements of the shear-wave particle velocity. Nevertheless, the present investigation indicates that shear stresses of magnitude 0.04 GPa can be sustained in the explosive over the stress range studied. The present results for shock stress are shown in Figure 5 as a function of strain. Due to low amplitude of the stress waves, the second shock states have been treated as Hugoniot states. A cubic fit to the data shown in Figure 5 yields $\sigma = 12.41\eta - 18.19\eta^2 + 247.7\eta^3$ where σ is the shock stress in GPa and η is the shock strain.

Numerical Simulation of Experiments

Most reactive models that have been used to simulate shock loading of explosives have been assumed to be hydrodynamic primarily because interest focused on higher pressures than are being considered here. At higher pressures, hydrodynamic behavior clearly dominates the reactive flow process. At the lower pressure amplitudes obtained in the present experiments, the shear response can be modeled by superposing deviatoric behavior on the hydrodynamic

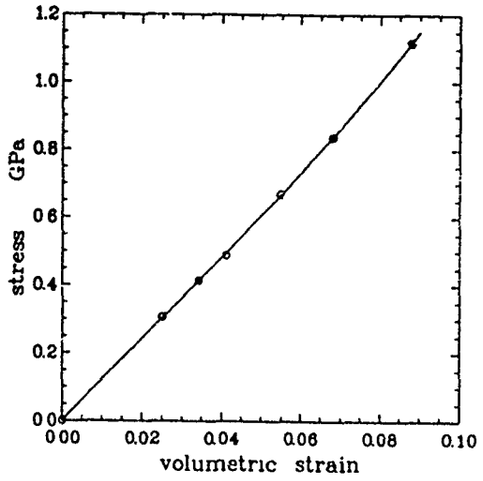

Fig. 5. Shock stress vs shock strain

response (23). The hydrodynamic model discussed by Nunziato, et al., (6) was supplemented by deviatoric response using the parameters for yield and Poisson ratio obtained in this study. For reference, a standard elastic-perfectly plastic model in TOODY (23) was also used to calculate these experiments. The anisotropic model for the Y-cut quartz is described by Chhabildas and Swegle (7).

Figure 6 summarizes the calculations of the three experiments for the longitudinal response. We note that the elastic-perfectly plastic model tends to preserve the elastic precursor, whereas

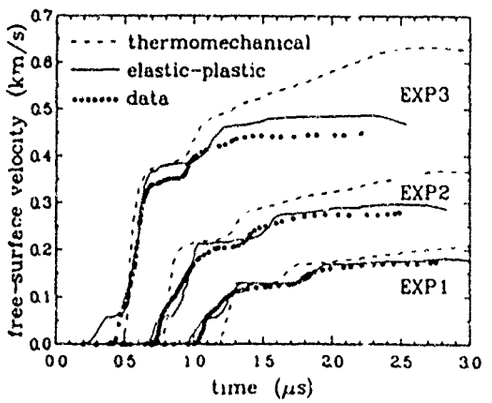

Fig. 6. Calculated and measured free-surface velocity profiles for the longitudinal wave in all experiments based on two different equations of state

the reactive model tends to completely lose the structure of the observed waves. The presence of porosity which is included in the reactive model but not in the elastic-perfectly plastic model causes the wave to shock up at low amplitudes, so that the structure of the wave due to strength characteristics is lost. There is clearly some additional modeling to be done if the structure of the wave is to be properly characterized. In addition, if a reaction takes place, one expects the strength to be degraded, and hydrodynamic behavior to again dominate.

The calculational simulations indicated in Figure 6 seem to suggest that minimizing rate effects in the hydrodynamic model (6) at low stresses could be adequate in representing the present experiments. In Figure 7 the experimental pressure-shear results are compared to the calculations for experiment EXP1.

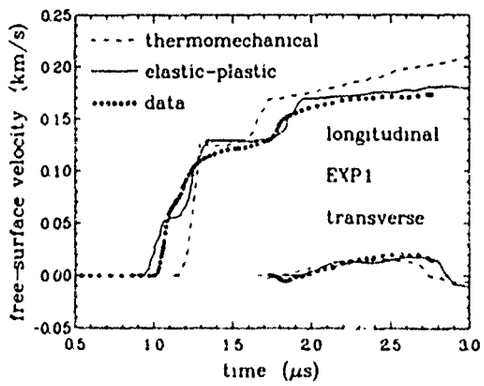

Fig 7 Calculated and measured free-surface velocity profiles for the longitudinal and transverse waves in experiment EXP1, based on two different equations of state

The agreement for the shear behavior is deemed satisfactory, considering that additional modeling is still necessary to reproduce the longitudinal profiles.

Shear Initiation Of Explosive

Most well controlled and instrumented studies on stress initiation of explosives have been performed under uniaxial strain states of compression. However, there is evidence from other experiments such as ballistic impact, skid tests, or penetration experiments, that the presence of shear may sensitize or even initiate the explosive. Unlike other studies in the past, the well controlled pressure-shear loading techniques present a unique opportunity to perform instrumented studies to investigate the shear initiation of explosive. The present experiments do not, however, allow a definitive evaluation on the sensitivity of PBX-9404 to shear for at least two reasons: (i) sample thickness used in this investigation being small, the stress pulse duration is not sufficient for the reaction, if any, to grow, and (ii) any initiation due to shear would tend to diminish due to stress relief from the free surface. The stress relief from the free surface has the effect of lowering the stress state in the explosive during shear wave propagation. This can be alleviated experimentally either by performing tests on thick specimens or by using an appropriate window to maintain the longitudinal stress states for a longer duration.

The oblique plate-impact experiment (8) would be an alternate choice for pursuing pressure-shear studies on explosives, since the technique would allow a convenient method to investigate thick specimens and at the same time maintain one-dimensionality for longer propagation times. The anisotropic crystal technique employed in these studies, although adequate for determining the shear-stress states in the explosive, limits the pulse duration available in the explosive sample if one-dimensionality is to be maintained.

ACKNOWLEDGEMENTS

The authors would like to acknowledge J. E. Kennedy, P. L. Stanton and R. E. Setchell for their continued support and valuable discussions during the course of this work. Many special thanks to B. H. VanDomelen for allowing the use of their explosive facility during sample fabrication. This work performed at Sandia National Laboratories was supported by the U.S. Department of Energy under contract number DE-AC04-76DP00789.

REFERENCES

1. R. A. Graham and J. R. Asay, "Measurement of Wave Profiles in Shock Loaded Solids," High Temp. Pressures, 10, p. 355, 1978.

2. L. Green, E. Nidick, E. Lee, and C. Tarver, "Reactions in PBX-9404 from Low Amplitude Shock Waves," Lawrence Livermore National Laboratory Report No. UCRL 80486, 1978.

3. J. E. Kennedy, J. W. Nunziato, and D. R. Hardesty, "Initiation and Detonation Studies of Condensed Explosives Using Interferometric Techniques," Acta Astronautica, Vol. 3, p. 811, 1976.

4. E. L. Lee and C. M. Tarver, "Phenomenological Model of Shock Initiation in Heterogeneous Explosives," Phys. Fluids, 23, p. 2362, 1980.

5. J. Wackerle, R. L. Rabie, M. J. Ginsberg, and A. B. Anderson, International Symposium on High Dynamic Pressures, Commissariat a l'Energie Atomique, Paris, p. 127, 1978.

6. J. W. Nunziato, M. E. Kipp, R. E. Setchell and E. K. Walsh, "Shock Initiation in Heterogeneous Explosives," Sandia National Laboratories Report No. SAND81-2173, 1982.

7. L. C. Chhabildas and J. W. Swegle, "Dynamic Pressure-Shear Loading of Materials Using Anisotropic Crystals," J. Appl. Phys. 45, p. 4799, 1980.

8. A. S. Abou-Sayed, R. J. Clifton and L. Hermann, "The Oblique Plate-Impact Experiment," Exper. Mech. 16, p. 127, 1976.

9. B. M. Dobratz, Lawrence Livermore National Laboratory Explosive handbook, UCRL-52997, 1981.

10. R. E. Setchell, "Short-Pulse Shock Initiation of Granular Explosives," Proceedings of the VII Symposium on Detonation, p. 781, 1981.

11. R. E. Setchell, "Effects of Precursor Waves in Shock Initiation of Granular Explosives," Combustion and Flame, 54, 171, 1983.

12. R. E. Setchell, "Ramp Wave Initiation of Granular Explosives," Combustion and Flame, 43, p. 255, 1981.

13. L. M. Barker and R. E. Hollenbach, "System for Measuring the Dynamic Properties of Materials," Rev. Sci. Instrum. 35, p. 742, 1964.

14. J. N. Johnson, "Shock Propagation Produced by Planar Impact in Linearly Elastic Anisotropic Media," J. Appl. Phys. 42, p. 5522, 1971.

15. L. C. Chhabildas, H. J. Sutherland and J. R. Asay, " A Velocity Interferometer Technique to Determine Shear-Wave Particle Velocity in Shock Loaded Solids," J. Appl. Phys. 50, p. 5196, 1979.

16. L. M. Barker and R. E. Hollenbach, "Laser Interferometer for Measuring High Velocities of any Reflecting Surface," J. Appl. Phys. 43, p. 4669, 1972.

17. B. T. Amery, "Wide-Range Velocity Interferometer," 6th Symposium on Detonation AC-R-221, Office of Naval Research-Department of the Navy, Arlington, VA, p. 681, 1976.

18. K. W. Schuler and L. M. Barker, "Correction to the Velocity per Fringe Relationship for the VISAR Interferometer," J. Appl. Phys., 45, p. 3692, 1974.

19. The Epoxy Resin and Hardener used to bond the foils to the sample are identified as Hysol 2038 Resin and Hysol 3490 Hardener respectively, and are products of the Dexter Corporation, Olean, NY.

20. H. J. Sutherland and J. E. Kennedy, "Acoustic Characterization of Two Unreacted Explosives," J. Appl. Physics, 46, p. 2439, 1975.

21. L. C. Chhabildas, "Dynamic Transverse Particle Velocity Measurements Using Interferometric Techniques," High Speed Photography, Videography and Photonics, Dennis L. Paisley, Editor, Proc. SPIE, 427, p. 136.

22. J. E. Kennedy, private communication, Sandia National Laboratories, Albuquerque, New Mexico 87185.

23. J. W. Swegle, "TOODY IV — A Computer Program for Two-Dimensional Wave Propagation," Sandia National Laboratories Report SAND78-0552, 1978.

PRESSURE-SHEAR LOADING OF PBX-9404

Lalit C. Chhabildas and Marlin E. Kipp

Sandia National Laboratories
Albuquerque, New Mexico 87185

MOTIVATION

- Strength of Explosive
- Modeling Explosives
- Shear Initiation
- Complement Previous Uniaxial Strain Experiments

EVIDENCE FOR SHEAR-INITIATION

- Drop Test
- Ballistic Impact
- Accidents

EXPERIMENTAL TECHNIQUE

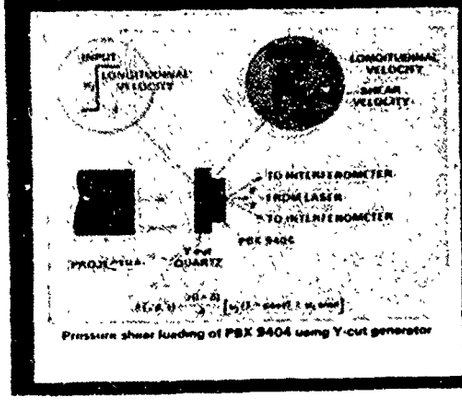

Pressure shear loading of PBX 9404 using Y-cut generator

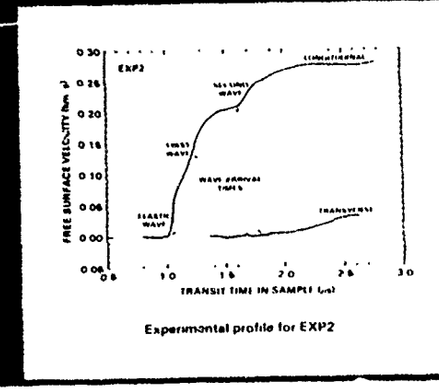

Experimental profile for EXP2

EXPERIMENTAL RESULTS

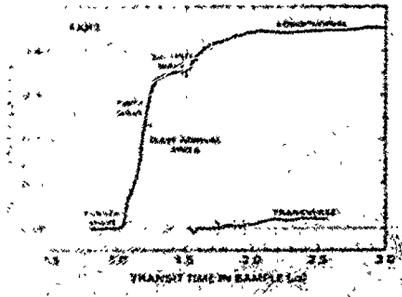

Measured longitudinal and transverse wave profiles in PBX-9404 from experiment EXP3

SUMMARY OF EXPERIMENTS

SHOT NO.	IMPACT MATERIAL	IMPACT VELOCITY (km/s)	PEAK STRESS (GPa)
EXP1	PMMA	0.223	0.41
EXP2	PMMA	0.486	0.86
EXP3	Aluminum	0.319	1.11

In all experiments,
(1) 12.7 mm thick y-cut quartz crystal was used as a pressure-shear wave generator.
(2) 2.0 mm thick PBX-9404 was used.

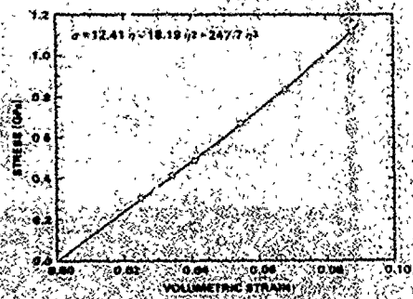

Stress vs strain behavior in PBX-9404

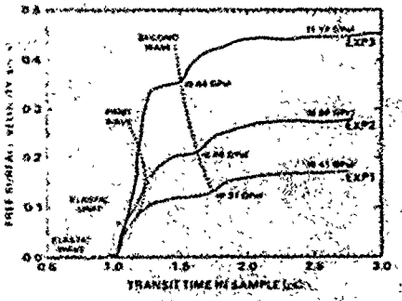

Measured longitudinal profiles depicting the dependence of the first (shock) wave and the second wave on the particle velocity

SUMMARY

Experiments performed over the stress range 0.3 GPa to 1.1 GPa.

0.04 GPa shear stress sensitivity was in PBX-9404 over this stress range.

The use of the longitudinal wave travel of an elastic wave velocity.

Shock wave, release wave, and shear wave speeds determined.

Shock velocity decreases as particle velocity increases to 0.1 km/s.

The shock stress vs strain relation is determined to be $\sigma = 12.41\ \eta - 18.19\ \eta^2 + 247.7\ \eta^3$.

The sensitivity of PBX-9404 to shear loading is not determined since
(a) the sample thickness is too small,
(b) the stress amplitude is too low, and
(c) the pulse duration is not sufficient.

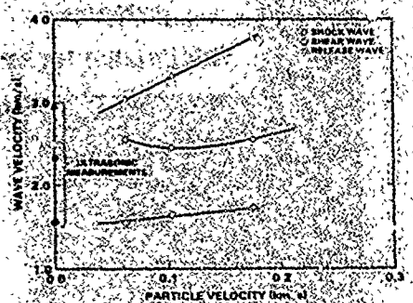

Variation of shock wave, release wave, and shear wave speeds with particle velocity

NUMERICAL SIMULATION

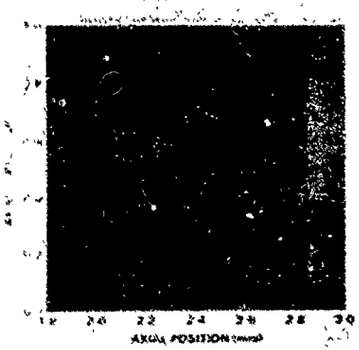

Axial stress evolution - Experiment EXP1

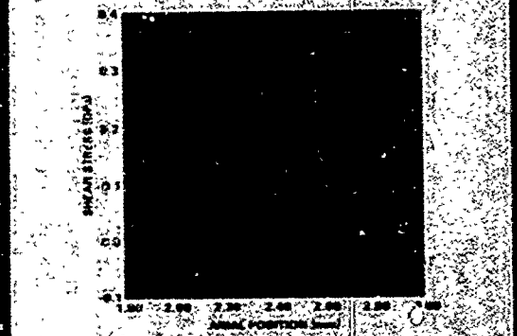

Shear stress evolution - Experiment EXP1

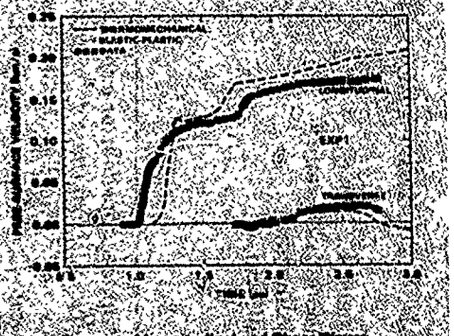

Computed Longitudinal and Shear Waves Experiment EXP1

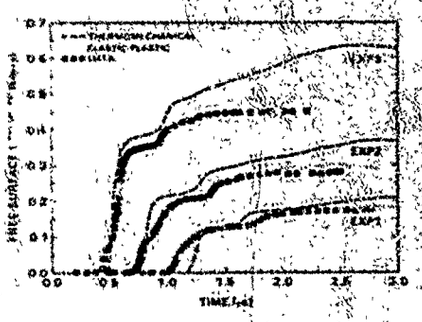

Computed Longitudinal Waves for Experiments EXP1, EXP2, and EXP3

COMPUTER CODE

- TOODY - Two Dimensional Finite Difference Wave Propagation Code

MATERIAL MODELS

- Y-cut Quartz - An Anisotropic Constitutive Equation of State
- PBX 9404 - (I) Elastic Perfectly Plastic Model
  (II) Thermomechanical Porous Reactive Model

SUMMARY OF RESULTS

- Elastic Perfectly Plastic Model Preserves Precursor
- Porous Part of Thermomechanical Model Overly Dissipative
- Shear Wave Response is Satisfactory Using Both Models

ENERGETIC RESPONSE OF PROPELLANTS TO HIGH VELOCITY IMPACT

L. Green, E. James and E. Lee
Lawrence Livermore National Laboratory
University of California
Livermore, California

An impact impulse on a full density intact propellant or explosive must be of high intensity (several gigapascals) to initiate detonation. Accident situation impact impulses are typically an order of magnitude less intense. The fact that detonation can arise from such lower level impulses is almost always the result of secondary compression of damaged (i.e. lower density) material. We have investigated a spectrum of possible conditions in order to evaluate threshold impact values which will cause detonation in damaged propellants. The results of new experiments involving in situ damage and impact of two propellants are reported.

INTRODUCTION

The direct initiation of shock sensitive propellants and explosives requires an intense shock wave with a magnitude of several gigapascals and a duration of tens of nanoseconds. However, under special conditions detonations can also be initiated from impulses an order of magnitude smaller. Typically, accidental explosions are the result these relatively low level impulses. Their understanding and explanation has been the object of an ongoing experimental and modeling program here at the Lawrence Livermore Laboratory as well as many other major laboratories and defense installations for a number of years.

We have studied a number of different experimental configurations in which we initiate violent reactions with comparatively low level impulses or shocks in order to study the accident type situation. These experiments have one thing in common. They involve a secondary compression of previously damaged or low density material.

In our earlier work (1,2) on various configurations we reported the following experimental observations:

1. For a cylinder of propellant subjected to an air shock from an adjacent explosion immediately after it had been impacted and damaged by a flying projectile, the "throw distance" for sympathetic initiation is dramatically increased over the distance required to initiate undamaged or unpreshocked acceptor propellant. The orientation of the target propellant cylinder at impact has little or no effect on the sympathetic detonation "throw distance."

2. For simple impact of the plane face of a right cylindrical projectile on the plane face of a cylindrical acceptor propellant in the impact velocity range less than required for direct shock initiation, delayed detonations occur in certain propellants following rarefaction and recompaction. We usually call this type reaction an XDT.

3. For an impact of the plane face of a cylindrical projectile on the curved surface of a cylindrical propellant target, the propellant undergoes deformation and fracture but in our experiments no delayed detonations have been observed. Flash radiography shows a flow pattern such that the recompressed region must be very much smaller than observed in planar impact so that there

*Work performed under the auspices of the U.S. Department of Energy by the Lawrence Livermore National Laboratory under contract No. W-7405-ENG-48.

may not be sufficient recompaction to cause delayed detonation. It is worth noting that in both observations "2" and "3" there is considerable smoke and fire evident at the impact surface.

4. For a somewhat related but quite different series of experiments, a granulated propellant confined in a plastic tube and compressed by a moving piston was observed to undergo a transition to detonation. These particular experiments were evidence that compaction of fractured porous propellant was an exceedingly easy route to detonation. For the particular propellants reported, the compaction pressure required to achieve detonation was only seventy or eighty megapascals. This is about the same magnitude as the stagnation pressure required to achieve detonation in the sympathetic detonation experiments mentioned under 1.

In this paper we report two new configuration experiments on one new propellant (E) as well as additional experiments with one of the same ones (D) reported earlier.

EXPERIMENTAL

Two propellants containing about 40% HMX were evaluated in the present series of experiments. Their mechanical properties are given in Table 1. Their shock sensitivity as measured by the Minimum Priming Charge test is also given. Propellant D and E can both be considered quite shock sensitive with E being the more sensitive. It is in fact only slightly less shock sensitive than PBX-9404 at 8.3 gigapascals initiation pressure using run distance to detonation as the measure of shock sensitivity. The mechanical properties of propellant E as measured both by low and high strain rate methods are noteable. In spite of the high σ solids content of propellant E, its large elongation would class it as very tough propellant and one that would not be expected to produce a large surface area under impact fracture.

First, 76-mm long by 76-mm diameter cylinders of propellant E were subjected to axisymmetrical impacts in the standard configuration (1) to establish the threshold velocity for delayed detonation or XDT. The results are summarized in Table 2. Values previously reported for propellant D (1) are summarized in Table 3 and compared to propellant E in Fig. 1. The results suggest that propellant E is less susceptible to delayed detonation than propellant D. An explanation that has been suggested involves the higher shock sensitivity of E. When E is recovered from an impact it is always much more shattered than D at the same velocity, in spite of its seemingly greater toughness. One would normally think that this shattering would make it more vulnerable to detonation because of the greater surface. Calculations (3) indicate that the gas produced from a reactive

TABLE 1
Properties of Propellants "D" and "E"

	Propellant D	Propellant E
Mechanical Properties		
Strain rate <1 per sec		
Max stress (psi)	100	110
Max strain (%)	200	400
Strain Rate Ca. 5000 per sec		
Peak stress (psi)	450-500	600-700
Plateau stress (psi)	300-250	400-350
Max Strain (%)	27-32	25-32
Minimum Priming Charge Test		
Mass of XTX (mg)	43.1	27.8
95% conf. limit (log)	0.05	0.05
XTX radius (mm)	2.37	2.05

shock wave works against recompression and would tend to make a delayed detonation more difficult to achieve. In fact, the minimum priming charge results indicate a substantially greater shock sensitivity than for propellant D. Therefore, it seems likely that both the highly shattered samples and the high threshold velocity value observed for delayed detonation are both due to gas from the reactive shock. If this hypothesis is true, a larger test sample of propellant E would have a lower threshold velocity, not only because the greater inertia would confine the reaction for a longer period of time, but also because much less gas would be produced by the lower impact pressure, allowing more efficient recompression of the propellant.

Most delayed detonation thresholds, when observed for large samples, are at a pressure of about one half that required for a direct shock initiation of the test sample. This same argument can also be applied to the failure of the 18-mm shotgun test to detonate a highly reactive propellant ("A") which had a threshold velocity of only 150 m/s in a 152-mm diameter axisymmetrical impact.

Next, we subjected solid cylinders of propellant to tandem side-on impact of the curved surfaces and, finally we subjected perforated cylinders to both axisymmetrical and side-on impact. These impact configurations are considered applicable to realistic scenarios that could occur in an accident situation. We were particularly interested to see if these tests could lead to detonation of propellants at velocities comparable to or less than those measured for delayed detonation from axisymmetrical impact of solid cylinders of the same propellant. The arrangement of the tandem side-on impact experiments is shown in Fig. 2. The experiments with the perforated cylinders are illustrated in Figs. 3a and b. The experimental results are tabulated in Tables 4 and 5 and graphically displayed in Fig. 4.

Propellant E, when these experiments were done, was expected to be rather insensitive based on what we knew of its mechanical properties. Instead, the side-on tandem impact proved to be an easy path to produce detonation and we ran out of test samples before we had established a threshold velocity. Furthermore, these reactions were observed in smaller cylinders than we normally test, i.e. 51-mm size. It is significant that test samples of a size smaller than used in the axisymmetrical impact experiments were observed to detonate at such low impact velocities. This means that in a real life situation fairly small chunks could very well detonate from tandem impact at easily attainable velocities. The size limits have not been explored. In the case of propellant D, size did not seem to play an important role in the two sizes tested.

Impact experiments on the perforated cylinders of propellant D did not show that the perforation increased sensitivity, Table 5. In fact, no side-on impacts resulted in detonations. In the axisymmetrical case the central hole actually desensitized propellant D. Once again the results were not as expected.

SUMMARY

The initiation and growth of delayed detonations from comparatively low-level shocks is a result of the interaction of mechanical properties of the propellant with a changing shock sensitivity due to the impact generated porosity. It has been known for many years that porosity enhanced the shock sensitivity of explosives. It is now clear that most, if not all, delayed detonations are related to damage induced porosity or from substantial initial porosity. Mechanical constitutive properties control the extent and timing of fracture and creation of new surface area through strain rate dependence. Delayed detonation is seen as a special case of shock initiation that operates under conditions where the shock sensitivity of a propellant increases substantially between the time of an initial impact process leading to fracture and rarefaction and the time of some recompaction process, which generates sufficient shock to drive the now porous propellant to detonation. The extent of coupling of the mechanical and kinetic response is determined by sample geometry and the chemical nature of the propellant.

Consider the side-on impact of a propellant cylinder vs. the axisymmetrical impact. At the same velocities the apparent damage appears to be similar. However, delayed detonation has not been observed in our side-on impact experiments. There is considerable fire and smoke in each case, but only the axisymmetrical impact leads to delayed detonation. The difference is believed to be due to a timely recompaction mechanism present in the axisymmetric case which is largely

TABLE 2
Results of Single Axisymmetric Impact of 76-mm Dia. × 76-mm Long Propellant E Cylinders

Impact Vel.	Results of Impact
292	No reaction
327	Mild reaction
339	Propellant well shattered
341	No impactor damage
359	Moderate reaction Propellant consumed No impactor damage
390	Detonation 108 μs after impact Impactor shattered

TABLE 3
Results of Single Axisymmetric Impact of 76-mm Dia. × 76-mm Long Propellant D Cylinders

Impact Velocity (m/s)	
Mild Reaction	Delayed Detonation
266	308
274	313
274	318
282	324
310	337
	347
321	401
341	408
406	410

absent in the side-on case. Flash x-ray images of impact experiments (4,5), manganin gauge pressure measurements (2), piston compaction experiments (1,2), delayed shock sympathetic detonation experiments (2), as well as calculational models by Tarver (1,2) and others support the recompaction mechanism.

The present tandem side-on impact experiments are yet another example of how impact damage can sensitize propellant to shock. The damaged region of the first cylinder is subject to recompression as it impacts the second cylinder and detonates from much lower amplitude shock than would be the case for undamaged propellant. The impact velocities are below those required for delayed detonation from axisymmetrical impact. This is additional evidence that it is not the damage level from single impact side-on impact experiments which prevents the development of delayed detonation in those experiments. Rather, it is the absence of a viable recompaction mechanism.

TABLE 4A
Tandem Impact of 51-mm Dia. × 51-mm Long Propellant E Cylinders

Impact Vel. (m/s)	Results of Impact
248	Detonation 45 μs after impact of 2nd target
263	Detonation 14 μs after impact of 2nd target
268	Detonation 33 μs after impact of 2nd target
297	Detonation 21 μs after impact of 2nd target

TABLE 4B
Tandem Impact of 51-mm Dia. × 51-mm Long Propellant D Cylinders

Impact Vel. (m/s)	Results of Impact
248	Mild Reaction
262	Detonation 87 μs after impact of 2nd target
297	Detonation 68 μs after impact of 2nd target

TABLE 4C
Tandem Impact of 76-mm Dia. × 76-mm Long Propellant D Cylinders

Impact Vel. (m/s)	Results of Impact
254	Mild Reaction
272	Mild Reaction
291	Detonation 27 μs after impact of 2nd target

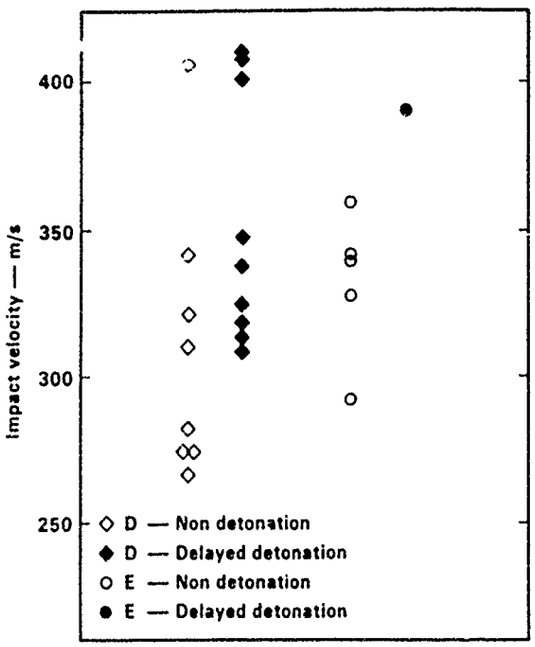

Fig. 1. Results of axisymmetrical impact test on 76-mm dia. x 76-mm long cylinder of propellants "D" and "E"

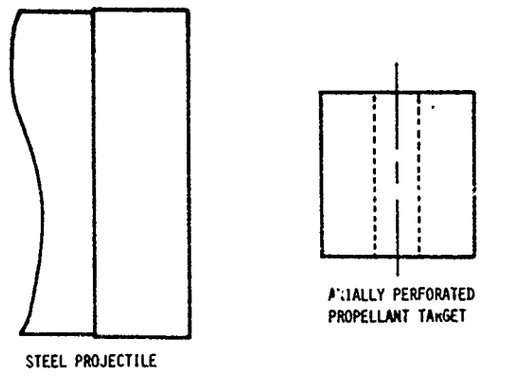

Fig. 3a. Test configuration for side-on impact experiments on propellant cylinders with axial holes

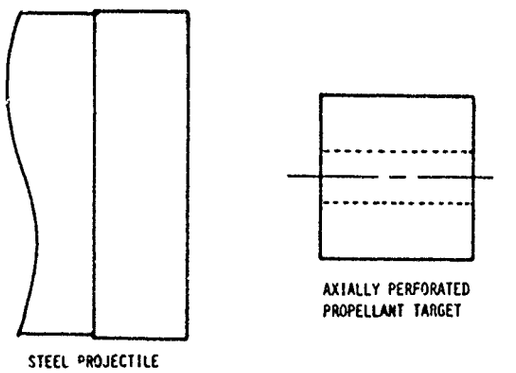

Fig. 3b. Test configuration for axisymmetrical impact experiments on propellant cylinders with axial holes

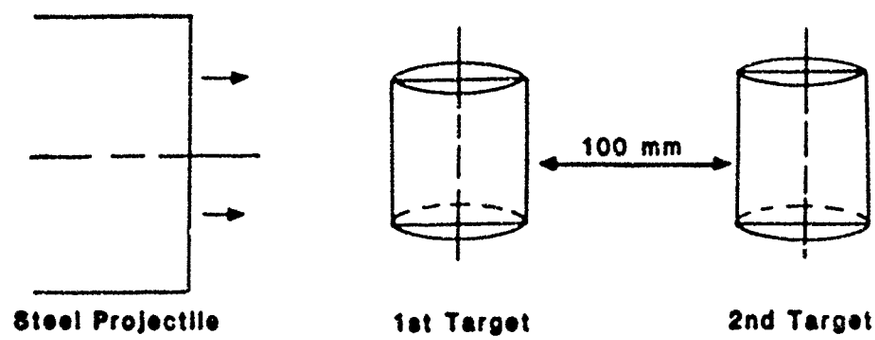

Fig. 2. Test configuration for tandem side-on impact experiment

TABLE 5
Results of Impact Tests on Propellant D Cylinders With Axial Holes

Target Size (mm)	Axial Hole Size (mm)	Orientation*	Impact Velocity	Results of Impact
76 dia. × 76 long	13	0°	320	Mild Reaction
		90°	430	Mild Reaction
76 dia. × 76 long	25	0°	269	Mild Reaction
		0°	308	Mild Reaction
		0°	325	Mild Reaction
		0°	379	Mild Reaction
		0°	387	Mild Reaction
		90°	282	Mild Reaction
		90°	347	Mild Reaction
		90°	394	Mild Reaction
76 dia. × 76 long	38	0°	331	Mild Reaction
		90°	391	Mild Reaction

* 0° = axisymmetrical impact
90° = side-on impact

REFERENCES

1. L. G. Green, E. James, E. L. Lee, E. S. Chambers, C. M. Tarver, C. Westmoreland, A. M. Weston, and B. Brown, "Delayed Detonation in Propellants from Low Velocity Impact," Seventh Symposium (International) on Detonation, Naval Surface Weapons Center, MP 82-334, Annapolis, MD, June 1981, p. 256.

2. E. L. Lee, E. James, L. Green, W. Von Holle, C. Tarver, D. Curran, W. Murri and D. Seaman, "Response of Propellants to High Dynamic Stresses," Hazard Studies for Solid Propellant Rocket Motors, Advisory Group for Aerospace Research & Development (AGARD), AGARD-CP-367, Lisse, Netherlands, May 28-30, 1984, p. 10-1—10-32.

3. C. M. Tarver, 1979, private communications.

4. R. C. Jensen, "Propellant Explosive Reactions in the Instrumented Shotgun Test," 16th JANNAF Combustion Meeting, Naval Postgraduate School, Monterey, CA, Sept. 10-14, 1979, p. 27, 35.

5. L. Green, 1979 unpublished data.

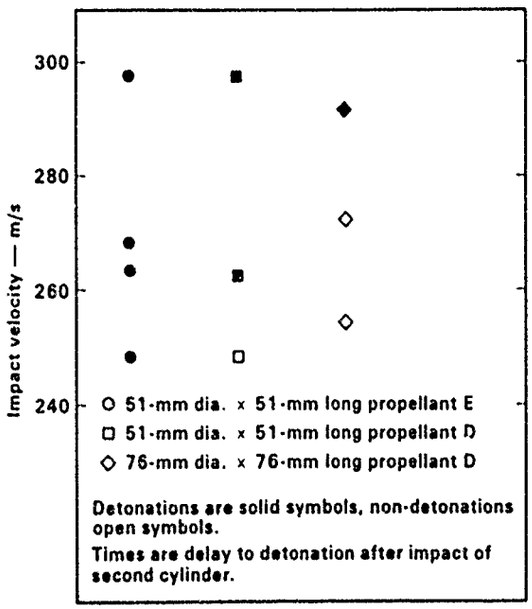

Fig. 4. Results of tandem side-on impact tests on propellants "D" and "E"

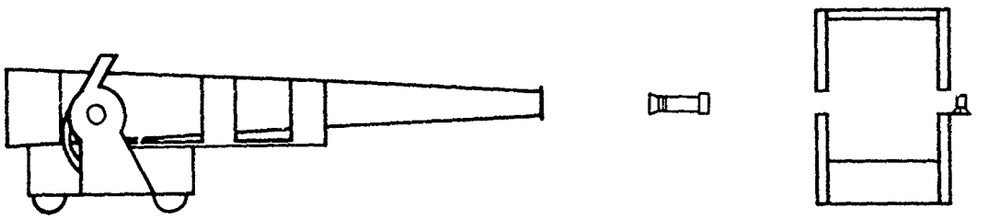

A 155-mm smooth-bore gun has been used to further explore the detonation threshold of impact-damaged and porous propellant.

Previous work showed that:

- The axisymmetrical impact of a propellant cylinder often resulted in a delayed detonation ("XDT") at half the pressure required for direct shock initiation of the size tested.

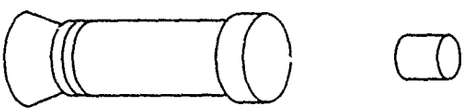

- The side-on impact of a propellant cylinder does not result in a delayed detonation.

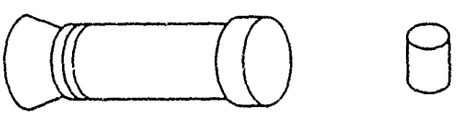

- There is a dramatic increase in the sympathetic detonation throw distance for impact damaged propellant compared to undamaged. Maximum stagnation shock pressures from air shock were about 60 or 70 megapascals at the threshold distance for detonation.

- The piston compaction of ambient temperature non-burning porous (70% TMD) propellant in a plastic pipe is a very easy route to detonation, piston velocities of 150 m/s and resultant compaction pressures of 70 or 80 megapascals being sufficient to cause the detonation of the propellants tested.

The present work explored three new test geometries. they were:

1) The tandem side-on impact of two solid cylinders of propellant.

2) The axisymmetrical (0°) impact of a perforated cylinder of propellant.

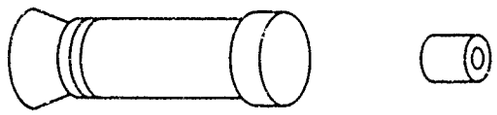

3) The side-on (90°) impact of a perforated cylinder of propellant.

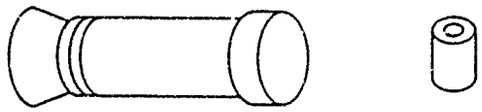

Results of these tests are summarized in the figures on the next panel. In addition, the axisymmetrical impact threshold for solid cylinders of propellant "E" is compared with that of propellant "D".

EXPERIMENTAL RESULTS

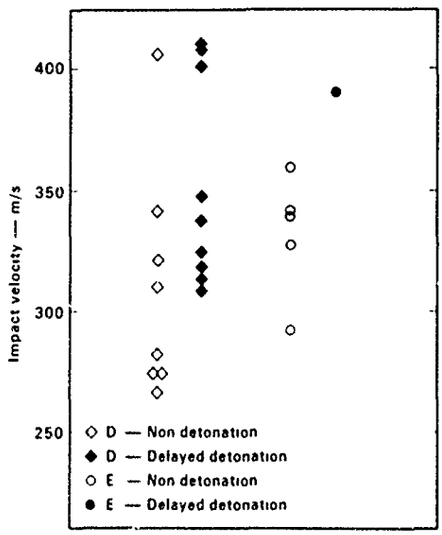

Results of axisymmetrical impact experiments on 76-mm dia. x 76-mm long cylinders of propellants "D" and "E".

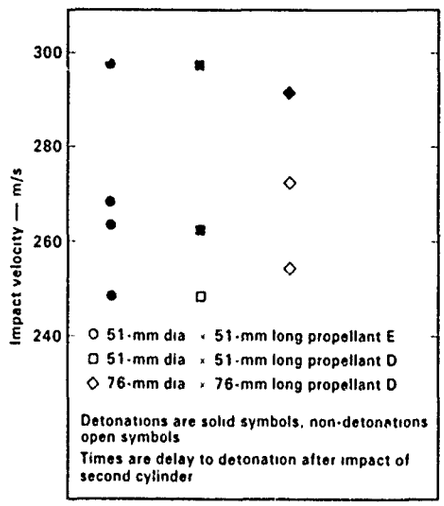

Results of tandem side-on impact experiments on cylinders of propellants "O" and "E". All cylinder separation distances were 100 mm.

Target Size (mm)	Axial Hole Size (mm)	Orientation*	Impact Velocity (m/s)	Results of Impact
76 dia x 76 long	13	0°	320	Mild Reaction
		90°	430	Mild Reaction
76 dia x 76 long	25	0°	269	Mild Reaction
		0°	308	Mild Reaction
		0°	325	Mild Reaction
		0°	379	Mild Reaction
		0°	387	Mild Reaction
		90°	282	Mild Reaction
		90°	347	Mild Reaction
		90°	394	Mild Reaction
76 dia x 76 long	38	0°	331	Mild Reaction
		90°	391	Mild Reaction

* 0° - axisymmetrical impact
90° - side-on impact

Results of axisymmetrical and side-on impact experiments on perforated cylinders of propellant "D".

SUMMARY OF RESULTS

- Tandem impact experiments are another example of how impact damage and the resultant porosity can greatly enhance sensitivity to detonation from impact.

- Perforated propellant cylinders did not show an enhanced tendency to detonate either from axisymmetrical impact or from side-on impact in the size tested. Larger scale tests might yield different results.

- The initiation of detonation in porous propellant by low amplitude stimuli seems to require a mechanical compaction process which may be driven either by direct mechanical means or by gas generated from the combustion of propellant.

AN EXPERIMENTAL INVESTIGATION OF THE ROLE OF SHEAR IN INITITATION OF DETONATION BY IMPACT

Philip M. Howe, Gould Gibbons, Jr., Patricia E. Webber
U.S. Army Ballistic Research Laboratory
U.S. Army Materiel Command
Aberdeen Proving Ground, Maryland

Heavily confined explosive targets were subjected to impacts by explosively launched plates and by penetrating fragments. In each experiment, the damaged explosive was collected, sectioned, and examined by optical and scanning electron microscopy. A number of different types of damage was observed, each of which is expected to contribute to the initiation process. The response of the explosive to impacts is more complicated than originally thought. Since the explosive is mechanically weak, the conditions for shear damage are almost entirely controlled by casing response to the impact, and the domain over which severe damage occurs is controlled by case deformation. We are as yet unable to rank these various explosive damage mechanisms with respect to their importance to the initation process.

INTRODUCTION

In recent years, numerous investigators have proposed different hot spot initiation models for the impact initiation of detonation. Field, et al (1) have shown that catastrophic shear failures can cause ignition, even if the catastrophic shear failures occur in inert plastics rather than in the explosive. They have also shown that crack propagation, by itself, is insufficient for ignition, but have speculated that the crack generation is sensitizing. Coffey (2) has proposed that dislocation pile up within crystals can cause shear banding, which in turn can lead to ignition. Mader (3) has used a hydrodynamic hot spot model to describe initiation and has stated that the hydrodynamic hot spot model is all that is required to model ignition and buildup to detonation for higher pressure (kbar) shock initiation of heterogeneous explosives (4). Cavity collapse processes have been modelled by Frey (5), using an extension of the model of Carroll and Holt (6). In the range of pressures of interest to Frey, the hydrodynamic heating processes treated by Mader were less important than plastic work and shear processes.

Most of these models were developed without access to experimental results under conditions of interest. In particular, very little experimental work has been published describing the various damage forms arising from impacts upon explosives under heavily confined conditions. Furthermore, given that a multiplicity of phenomena could contribute to the initiation process, it becomes important to identify which ones provide the most significant contributions. The experimental work described herein represents a first attempt at characterizing the material response processes which occur within heavily confined explosive charges subjected to impact.

EXPERIMENTAL

Samples of heavily confined explosive charges were impacted by flying steel plates. Two types of TNT loaded projectiles were impacted, creamed and not creamed. The term "creamed", refers to a process whereby TNT powder is added to the molten batch of TNT during the hot melt casting procedure. The addition of the powder provides a large number of nucleation sites, and induces small crystal growth.

The 76 mm x 152 mm x 6 mm mild steel plates were explosively driven by Dupont Deta Sheet, and were thrown at 340 and 440 m/sec. The

impacted rounds were prevented from hitting the wall of the firing site barbette by the use of sand bags. The different plate velocities provided different initial shocks, and different rates of projectile deformation. There were two variables functioning in the test configuration, plate velocity and TNT grain size. Fig. 1 is typical of the test setup in this firing program.

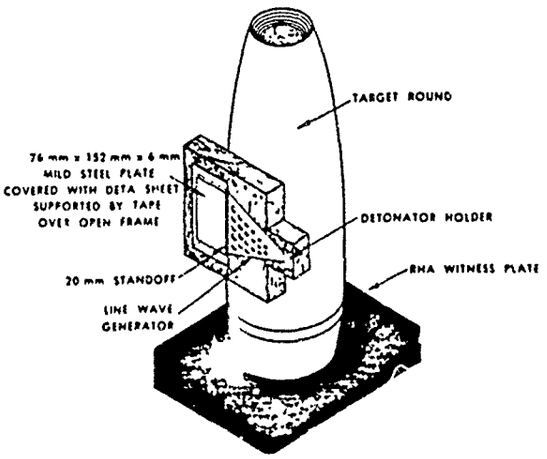

Fig. 1. Schematic of test setup for plate impact experiments

Control samples (not impacted) were kept from each lot, to be used as undamaged standards in the microstructural study of the impacted explosives.

Both the control and impacted projectiles were remotely cut, and cylindrical sections were removed for microscopic investigation. No fluids were used in the cutting process so as to minimize the probability of contamination. The sections taken were approximately 50 mm thick. Fig. 2 represents a typical cut projectile, and Fig. 3 shows a cylindrical section.

Sample corings were removed from various locations within the sections taken from the cut rounds. The corings were removed by hand, using a standard hole saw; no power equipment was used at this point in the sample preparation. The samples were sanded flat on one side, so that the flat was parallel to the plate impact; this flat provides an orientation landmark for the direction of the impact. The original cut surface (made when the round was sectioned), and a plane parallel to the cut surface, were coarse sanded using 150 grit sandpaper followed by 320 grit sandpaper. The flat opposite the cut surface was glued to an aluminum SEM sample stud using a silver base acrylic paint.

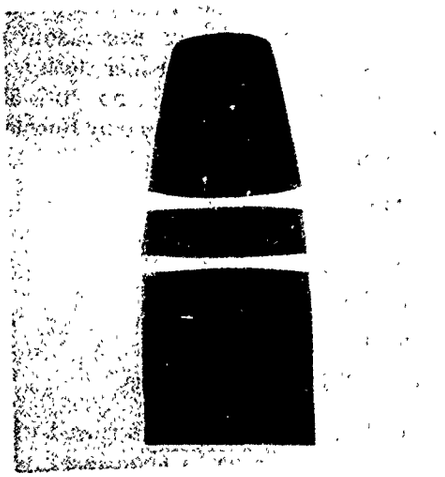

Fig. 2. Test projectile, sectioned after impact. Section was obtained from the center of the impacted region

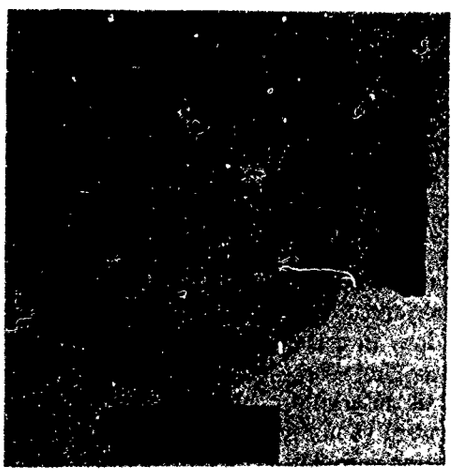

Fig. 3. Cylindrical cross section of impacted target. Corings were removed for microscopic examination. Top view.

The surface to be investigated was again sanded in final preparation for polishing using 150 and 320 grit sandpaper, and then fine sanded using 400 and 600 grit sandpaper. All sanding was done by hand, without water. An effort was made to keep the prepared surface

perpendicular to the axis of the mounting stud, and obtain a smooth 600 grit finish.

After sanding, the sample was hand polished using a wool polishing cloth saturated with distilled water. The wool cloth was manufactured by Buehler, Ltd. The Buehler cloth was cataloged as, "AB Kitten Ear", no. 40-7556. This material has been discontinued by Buehler, but can be purchased from:

J. I. Morris Company
394 Elm Street
P.O. Box 70
Southbridge, Mass. 01550

Phone: (617) 764-4394

Item: U-18 Pressed Wool Pad

The sample being polished was rinsed with distilled water, and dried with compressed Freon. Polishing was done with a light pressure, while moving the sample in a figure eight motion.

Optical microscopic examinations were done using an Optiphot Microscope by Nikon. Two types of surface lighting were used; polarized light, and normal or scattered light. Normal lighting provides the best delineation of the TNT grains; but both types of light have their advantages, each providing different data. A partially polarized light source also proved useful.

Samples for scanning electron microscopic examination were prepared by sputtering a conductive coating of gold, or gold/palladium onto the surface. The sputter coating for this work was done in a Denton Vacuum, Inc.; Desk 1; Sputter Unit. A gold/palladium coating was applied at an argon pressure of 75 mtorr, and a current of 15 mA for 2 minutes. These sputter conditions provide a conductive film thickness of about 500 angstroms. A film of this thickness has been found to be the minimum thickness suitable for SEM work on an explosive sample.

The sample can be chemically etched after polishing to enhance the TNT grain boundaries. It was found that 1,2-dichloroethane is an excellent solvent for etching TNT. This chemical is toxic and was not allowed to come in contact with skin, nor were the vapors inhaled. Etching was completed by dipping the sample in fresh stirring solvent, for 3 seconds. Dissolution was quenched after 3 seconds by immediate immersion in distilled water. The samples were rinsed with distilled water, and dried with compressed Freon. Pure solvent was used for each sample so that the rate of dissolution was constant from sample to sample. Mild stirring was effected by using a magnetic stirrer.

RESULTS AND DISCUSSION

Examination of sections of artillery shell subjected to impacts by explosively launched plates revealed several phenomena which appear to be important to the initiation process. The intensity with which these phenomena occur is an increasing function of severity of impact.

Shown in Fig. 3 and 4 is a cross sectional view of a target round, which had been impacted at 440 m/s by a 0.64 cm steel plate. Near the point of impact is a kidney bean shaped area which has been severely damaged. Grains have been comminuted, and intergranular separation has occurred. The blackened regions are localized areas of decomposition. Chemical analysis indicates that the decomposition is rather complete; the main product identified as being present was carbon.* Microscopic examination of these blackened regions revealed two morphologies, as shown schematically in Fig. 5 and in the microphotos of Fig. 6 and 7. One family of blackened regions appears as relatively long, narrow region oriented parallel to lines of principal shear, and is probably an example of shear-induced hot spot formation. Note that these regions occur at grain boundaries and as shear

*In the region of severe blackening, directly behind the impact point, decomposition of TNT was confirmed by chemical analysis The black material was found to be carbon. Surface analysis, via X-Ray Photoelectron Spectroscopy (XPS), indicated the possible presence of oxidation products of TNT. Peak broadening in the XPS spectra indicated the presence of the acid or aldehyde derivative, and also the possibility of a nitrile derivative. TLC was used to further evaluate the sample, and four compounds were identified. TLC comparison with reference compounds, and mass spectra confirmed the four compounds as TNT, 2, 4, 6 trinitrobenzaldehyde; 2, 4, 6 trinitrobenzonitrile; and 2, 4, 6 trinitrobenzaldoxime. The oxime is a second step decomposition product, in that it probably results from the reaction of trinitrobenzyl anion with nitrous acid. The nitrile is then formed by dehydration of the oxime. These results are consistent with a rather complete, localized decomposition of the TNT. (Private communication with J. Sharma; NSWC; White Oak; Silver Spring, Maryland 20910).

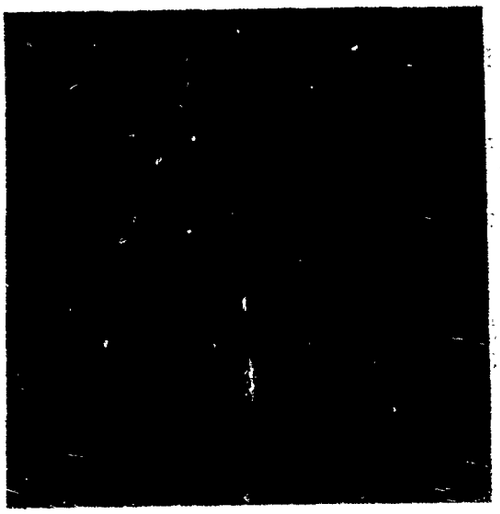

Fig. 4. Bottom view of cross section of impacted sample. Compare with Fig. 3; note difference in deformation and blackened region.

Fig. 6. Close up view of blackened region. Blackening is a result of chemical decomposition.

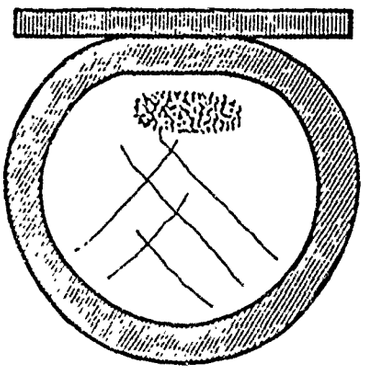

Fig. 5. Schematic of cross section of round, showing major shear cracks and regions of high damage

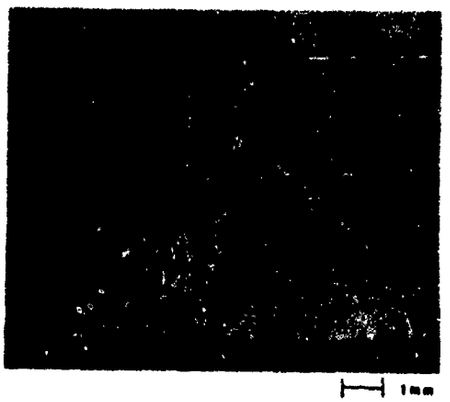

Fig. 7. Blackened region at higher magnification. Note boundary between case and blackened region.

failures within individual grains. The second family of blackened regions is more spherical in nature, has no preferred orientation, and quite probably is a result of cavity collapse processes. Note that, in this particular sample, the number density of shear-induced hot spots is greater than that of cavity collapse-induced hotspots, although both are present. The proportion will be a function of sample porosity and deviations from planar, uniaxial flow.

Between the bean-shaped region of high damage and the warhead casing is a narrow band showing little damage (see Fig. 3). This band is reproducible from shot to shot. Apparently, it was caused by heat conduction to the steel casing. If this is true, it indicates that the decomposition within the region of high damage was a relatively slow process.

The volume of the bean-shaped region of high damage correlates with case deformation. For similar impact geometries, higher impact velocities produced larger damaged volumes, and greater density of decomposed regions within these volumes. Where case thickness variations cause different deformations, the damaged volume appears to scale with total deformation,

and the density of hot spots within the damaged volume correlates with impact velocity. The fact that impacts in thinner cases yielded larger regions of high damage indicates that the damage was caused primarily by case deformation, not shock loading, as small changes in wall thickness would not cause appreciable differences in shock loading. To check this, computer calculations were conducted replicating the impact conditions. Results showed that the shock loading conditions are essentially the same for the two impact conditions.

Each of the impacted samples exhibited a field of major shear cracks, external to the regions of high damage, as shown in Fig. 3 and 4 and as shown schematically in Fig. 5. The width of individual shear cracks was found to vary significantly and randomly across a sample. Cracks as wide as 0.1 mm and as narrow as 0.01 mm were observed. Microscopic examination of these cracks revealed several interesting features. In the wider regions, the explosive was severely shattered within the crack, to the point where integrity of the sample was lost, and polishing was difficult or impossible (see Fig. 8). In the narrower regions, cracking and comminution of the grains occurred, and melting and fusing occurred as well. In these regions, sample integrity was reestablished, and polishing was possible. One such area is shown in Fig. 9a through 9c. In Fig. 9a, partial melting is clearly apparent. Some fractures are apparent

Fig. 8. Microphoto of major shear crack in TNT. Darkened region at end of crack is a result of powdered explosive removed from sample during polishing.

Fig. 9a. Optical micrograph of major crack, showing fracture damage and some internal healing (plane polarized light)

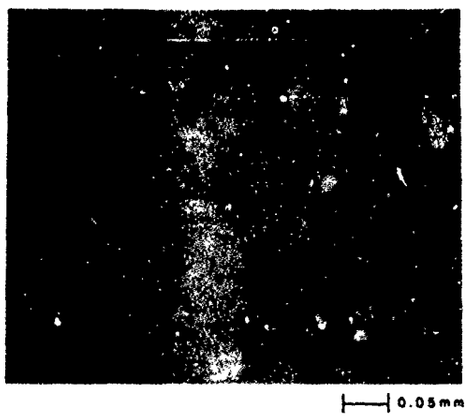

Fig. 9b. Same region of crack as in 9a, viewed with partially polarized light. Note outline of grain boundaries.

within the crack, but most have been healed. At the edges of the crack, many small fractures are apparent. These may have occurred after crack formation and healing, or they may have occurred during crack formation but, because they were at the edges of the crack, did not reach a high enough temperature to heal. Fig. 9a through 9c are photomicrographs of the same region, but with different lighting, to highlight different crack features. Figure 9a discussed above, was obtained with plane polarized light, to reduce surface reflections. Figure 9c was obtained with unpolarized light, to emphasize

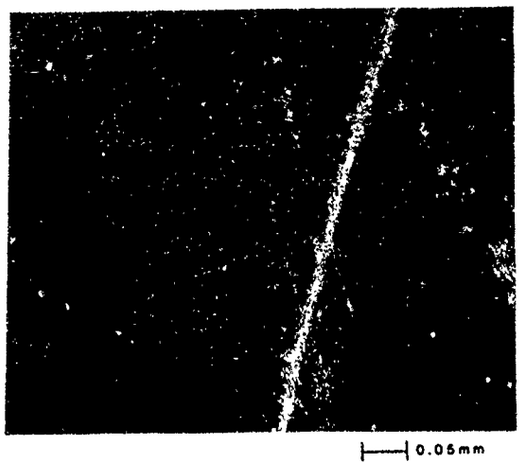

Fig. 9c. Crack region of 9a viewed with reflected light. Note high degree of flow, grain damage in crack region.

surface characteristics. Here, one can discuss the intersection of grain boundaries with the highly polished specimen surface. Note the large amount of flow which has occurred within the region. Healing of internal fractures has occurred, and partial melting has also occurred. Some discoloration within the crack was noted, indicating that partial decomposition may have occurred. Figure 9b was obtained with partially polarized light and permits comparison of 9a and 9c, having some features of each.

The majority of macroscopic shear cracks exhibit the features described above. Evidently, formation of these cracks involves local shear failures over a wide region, with shattering and grinding of the explosive occuring within the crack. If the motions and pressures are adequate, healing, melting, and decompositon can occur. Occasionally, macroscopic shear cracks can propagate with relatively little damage to the grain structure, and with little indication of decomposition or local heating. Such a crack is shown in Fig. 10. Note that, in one region, the crack width has narrowed to a dimension of the order of a grain boundary. Significant slip has occurred; Fig. 11 shows a collage made by cutting along the crack and matching grain boundaries. In this instance the total slip was $\sim$ 0.04mm.

Between major shear cracks, damage is considerably less. Impact damage shows up in the form of internal fractures, separation at grain boundaries, and slip. Slip induced by impact is relatively easy to distinguish from slip bands formed during crystallization due to the former displaying crushed regions where slip bands meet grain boundaries. An example of incipient grain boundary separation and impact-induced slip is shown in Fig. 12. For comparison, an unimpacted sample is shown in Fig. 13. In regions distant from the point of impact, none of these damage forms showed any indication of melting or significant decomposition, as indicated by discoloration of the sample, and such mild damage probably does not contribute to ignition. However, it is quite likely that there would be a significant contribution to processes, such as grain burning, which are involved in the post-ignition buildup to detonation.

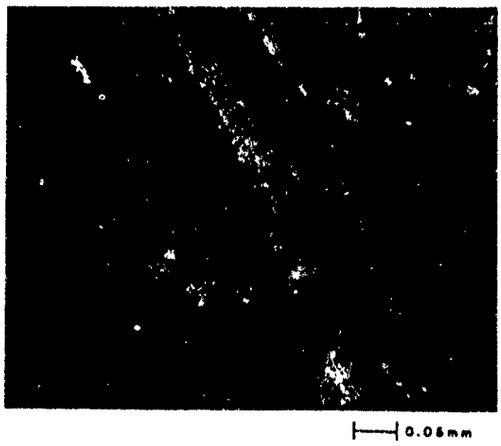

Fig. 10. Major shear crack showing region of very narrow crack width

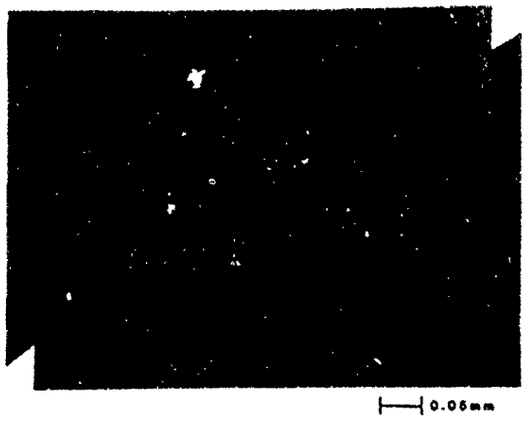

Fig. 11. Collage made from Fig. 10 showing extent of slip along crack

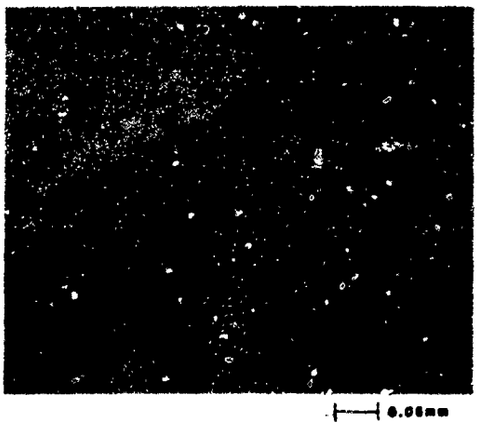

Fig. 12. Micrograph showing impact-induced slip and grain boundary damage

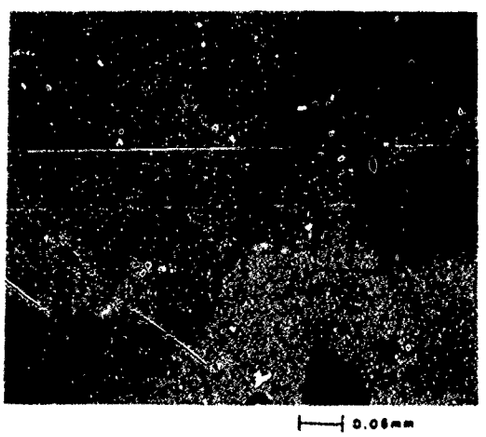

Fig. 13. Unimpacted sample showing slip

At a given impact velocity, damage was found to be more severe in the large grain size (uncreamed) TNT than in the fine grain size (creamed) samples. This difference is manifested most strongly in the region of high damage, near the point of impact, with the decomposition being much more extensive within the damaged volume, and the damaged volume much larger for the large grain sample.

Increases in impact velocity led to increased damaged, as expected. Fracture damage throughout the impacted sample is more severe at the higher impact velocity, with much more extensive grain separation, internal fracture damage, slip, and macroscopic shear crack formation. At the higher impact velocity, the number of macroscopic shear cracks is greater, and the extent of melting is greater. Discoloration due to decomposition is much more extensive in these cracks. A more quantitative description must await examination of samples impacted at more than two velocities.

A few experiments were conducted using gun launched cylindricl projectiles which led to perforating impacts. The region of high damage observed in the plate impact experiments is replaced by cratering. Away from the crater, damage to the sample was very similar to that for the plate impact experiments. However, almost all the deformation occurred within the TNT phase, with the RDX relatively untouched. This is shown in Fig. 14, where the explosive was composition B (60% RDX, 40% TNT). Chemical analysis identified the presence of partial decomposition products of TNT, but not of RDX.

In addition to the internal damage, there is clear evidence of significant melting and flow away from the point of impact, between the explosive and the casing. How important this is to initiation is unknown.

Fig. 14. Micrograph of major shear crack region in impacted composition B. Most of shear occurs in TNT phase.

SUMMARY

Heavily confined explosive targets were subjected to impacts by explosively launched plates and by penetrating fragments. In each experiment, the damaged explosive was collected, sectioned, and examined by optical and scanning electron microscopy. A number of different types of damage was observed, each of which

is expected to contribute to the initiation process. Near the point of impact, for non-perforating impacts, a severly damaged region was observed. This region showed evidence of decomposition of the explosive. The decomposition within this region was localized, and nearly complete; i.e., carbon was identified, but few intermediate decomposition products. Separating this region of high damage and decompositon from the casing was a thin layer of explosive, exhibiting no significant decomposition. This is probably a result of heat transfer to the casing, and indicates that the decomposition in this region at the impact conditions studied was rather slow.

Outside the region of high damage, the explosive exhibited families of major catastrophic shear cracks. The width of these cracks varied from ~0.01 mm to ~0.1 mm. Evidence of melting and decomposition was observed in the thinner regions of the cracks.

Results of impacts with perforating fragments were similar to those for plate impacts, except that cratering replaced the region of high damage. All the other phenomena were quite similar.

The response of the explosive to impacts is more complicated than originally thought. Since the explosive is mechanically weak, the conditions for shear damage are almost entirely controlled by casing response to the impact, and the domain over which severe damage occurs is controlled by case deformation. We are as yet unable to rank these various explosive damage mechanisms with respect to their importance to the initiation process.

ACKNOWLEDGEMENT

The authors are grateful to Mr. Jerry Watson for many helpful discussions.

REFERENCES

1. J. E. Field, G. M. Swallowe, S. N. Heavens, "Ignition Mechanisms of Explosives during Mechanical Deformation," Proc. R. Soc Lond. *A382* 231 (1982).
2. C. S. Coffey, M. J. Frankel, T. P. Liddiard, S. J. Jacobs, "Experimental Investigation of Hotspots Produced by High Rate Deformation and Shocks," Proc Seventh Symp (Int) on Detonation, pp. 970 (1981).
3. C. Mader, "Numerical Modeling of Detonation," Los Alamos Series in Basic and Applied Sciences, U of C. Press, Berkeley, (1979).
4. C. Mader, "Invited Discussions of Shock Initiation Mechanism," Proc. Sixth Symp (Int) on Detonation, pp. 89 (1976).
5. R. B. Frey, "Cavity Collapse in Energetic Materials," Proceedings, this symposium.
6. M. M. Carroll, A. C. Holt, "Static and Dynamic Pore Collapse Relations for Ductile Porous Materials," J Applied Phys. *43*, No. 4 (1972).

EXPERIMENTAL PROCEDURE

US ARMY MATERIEL COMMAND
BALLISTIC RESEARCH LABORATORY

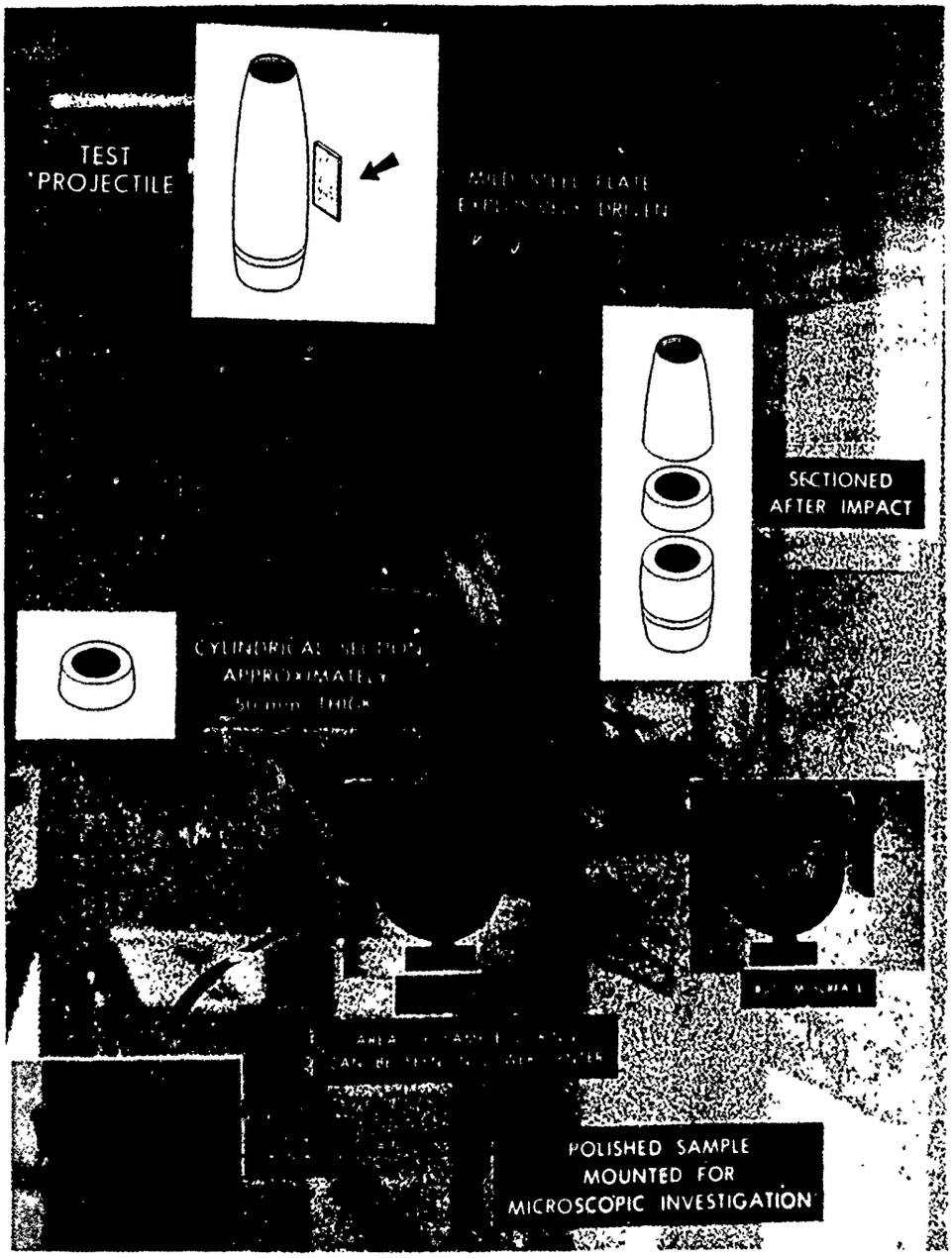

FEATURES OF IMPACT PROCESS

US ARMY MATERIEL COMMAND
BALLISTIC RESEARCH LABORATORY

I FLOW ALONG INTERFACE

- FLOW OF EXPLOSIVE OCCURS AT INTERFACE BETWEEN CASE AND EXPLOSIVE IN BOTH PROJECTILE AND PLATE IMPACTS
- RADIAL FLOW FROM PROJECTILE IMPACT IS MORE SEVERE THAN FROM A CRUSHING IMPACT
- DISCOLORATION AND FLOW INDICATES PARTIAL DECOMPOSITION AND MELTING

II DEFORMATION & SHOCK INDUCED DECOMPOSITION

- IN CRUSHING IMPACTS, A LOCALIZED REGION OF SEVERE DAMAGE OCCURS
- VOLUME OF SEVERELY DAMAGED REGION CORRELATES WITH CASE DEFORMATION
- WITHIN A DAMAGED REGION, LOCAL DECOMPOSITION OCCURS, DECOMPOSITION PRODUCT IS PRIMARILY CARBON
- GEOMETRY OF CARBONIZED REGIONS INDICATES PRIMARY CAUSE IS SHEAR CRACKING, ALTHOUGH SOME CAVITY COLLAPSE MAY HAVE OCCURRED

III DECOMPOSITION OCCURS IN MAJOR SHEAR CRACKS

- CATASTROPHIC SHEAR CRACKS ARE FOUND AWAY FROM REGION OF SEVERE DAMAGE
- WIDTH OF CRACKS VARIES, IN NARROW REGIONS, EVIDENCE OF MELTING AND DECOMPOSITION IS FOUND, DECOMPOSITION IS LESS COMPLETE THAN IN REGIONS OF SEVERE DAMAGE
- WITHIN MAJOR SHEAR CRACKS, FRACTURING AND COMMINUTION OF CRYSTAL GRAINS OCCURS

IV SHOCK & SHEAR DAMAGE IN BULK SAMPLES

- AWAY FROM SHEAR CRACKS, DAMAGE IS FOUND ALONG GRAIN BOUNDARIES WHERE GRAIN SURFACES ARE SLIPPING WITH RESPECT TO ONE ANOTHER
- SLIP INDUCED BY IMPACT CAN BE DISTINGUISHED FROM SLIP BANDS FORMED DURING CRYSTALLIZATION
- REGIONS OF MILD DAMAGE, AWAY FROM IMPACT POINT, SHOW INCOMPLETE MELTING

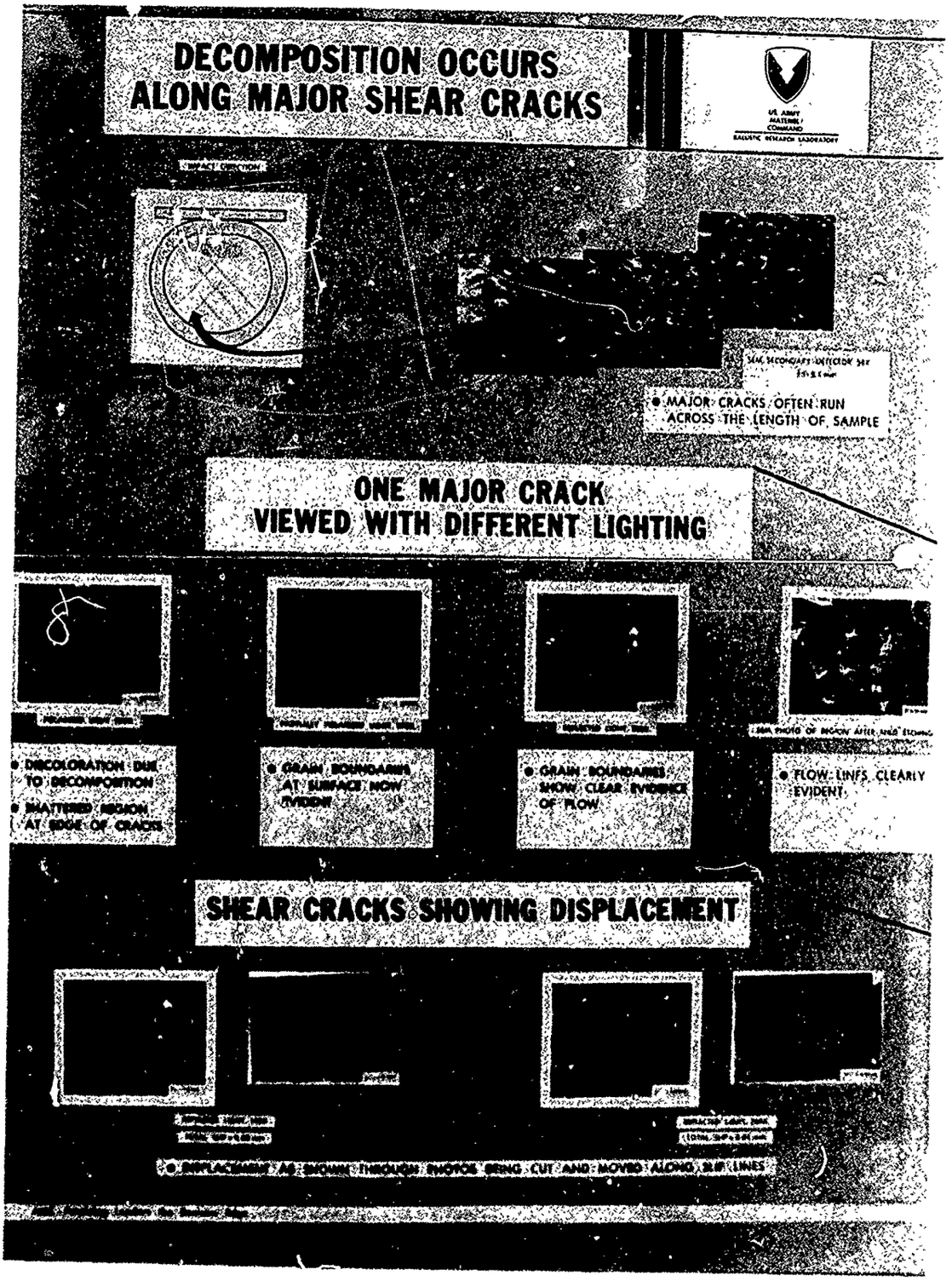
DECOMPOSITION OCCURS ALONG MAJOR SHEAR CRACKS
US ARMY MATERIEL COMMAND BALLISTIC RESEARCH LABORATORY
• MAJOR CRACKS OFTEN RUN ACROSS THE LENGTH OF SAMPLE
ONE MAJOR CRACK VIEWED WITH DIFFERENT LIGHTING
• DISCOLORATION DUE TO DECOMPOSITION
• SHATTERED REGION AT EDGE OF CRACK
• GRAIN BOUNDARIES AT SURFACE NOW EVIDENT
• GRAIN BOUNDARIES SHOW CLEAR EVIDENCE OF FLOW
• FLOW LINES CLEARLY EVIDENT
SHEAR CRACKS SHOWING DISPLACEMENT

SHOCK AND SHEAR DAMAGE IN BULK SAMPLES

US ARMY MATERIEL COMMAND
BALLISTIC RESEARCH LABORATORY

UNIMPACTED SAMPLE

- DARK REGIONS ARE HOLES OUT OF FOCUS, WHERE GRAINS WERE REMOVED DURING CUTTING AND POLISHING

IMPACTED SAMPLE

- DAMAGE AT GRAIN BOUNDARIES
- INTERSECTION OF SLIP SURFACE WITH GRAIN BOUNDARIES

UNIMPACTED SAMPLE

- SLIP BANDS FORMED DURING CRYSTALLIZATION LYING ALONG GRAINS

IMPACTED SAMPLE

- SLIP INDUCED BY IMPACT RUNS ACROSS GRAIN
- SLIP ORIENTED DOWNWARD IN DIRECTION OF IMPACT

IMPACTED SAMPLE

- DAMAGE IN CRACK SHOWING FLOW

IMPACTED SAMPLE

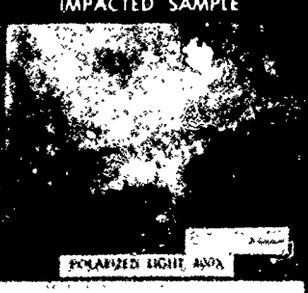

- SEVERE IMPACT CAUSING SHATTERING OF SAMPLE

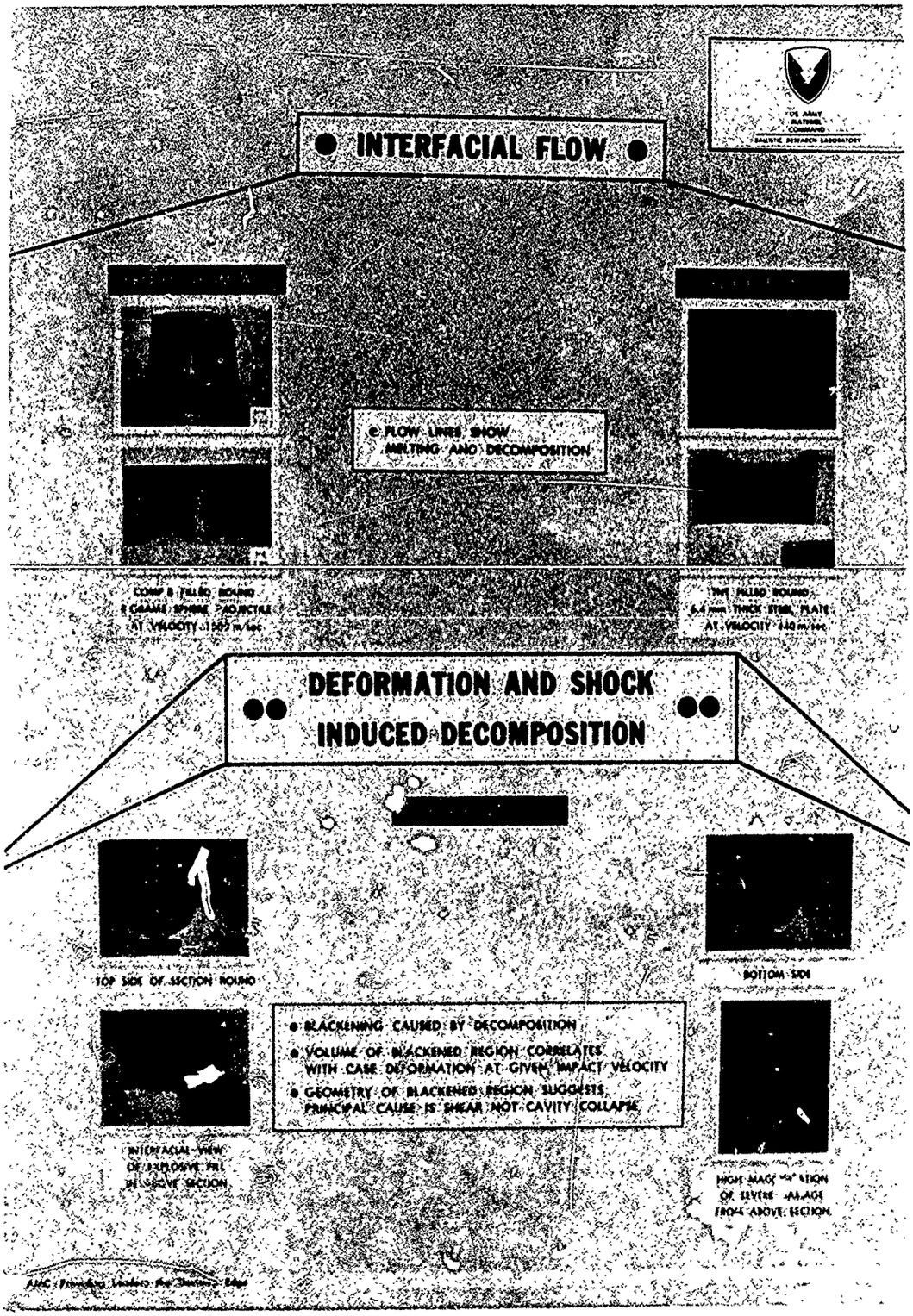
INTERFACIAL FLOW
FLOW LINES SHOW MELTING AND DECOMPOSITION
COMP B FILLED ROUND
8 CALIBER 30MM PROJECTILE
AT VELOCITY 1500 m/sec
TNT FILLED ROUND
6.4 mm THICK STEEL PLATE
AT VELOCITY 440 m/sec
DEFORMATION AND SHOCK
INDUCED DECOMPOSITION
TOP SIDE OF SECTION ROUND
BOTTOM SIDE
BLACKENING CAUSED BY DECOMPOSITION
VOLUME OF BLACKENED REGION CORRELATES WITH CASE DEFORMATION AT GIVEN IMPACT VELOCITY
GEOMETRY OF BLACKENED REGION SUGGESTS PRINCIPAL CAUSE IS SHEAR NOT CAVITY COLLAPSE
INTERFACIAL VIEW OF EXPLOSIVE FILL IN ABOVE SECTION
HIGH MAGNIFICATION OF SEVERAL AREAS FROM ABOVE SECTION

SOME NEW COMPUTED RESULTS FOR PROJECTILE-IMPACT SHOCK INITIATION OF SOLID EXPLOSIVES

Y.K. Huang, J.J. Starkenberg, and A.L. Arbuckle
U.S. Army Ballistic Research Laboratory
Aberdeen Proving Ground, Maryland 21005-5066

This paper offers some new results for the shock-to-detonation transition of bare explosive charges due to impact in one and two dimensions. These results exhibit a number of general trends and distinctive patterns which are represented by simple linear equations. Their physical basis and implications are discussed in this paper, and favorable evidence for their applicability has been sought. Thus, this work is intended to contribute not only to further understanding of projectile-impact shock initiation but also to the scaling of pertinent parameters within a range of practical interest.

INTRODUCTION

Substantial experimental (1-3) and computational (4, 5) results for the shock initiation of solid explosives by projectile-impact have been reported in the literature. Yet these have all gone little beyond the scaling law:

$$V = a + b/\sqrt{\varnothing} \qquad (1)$$

where V is the critical impact velocity, $\varnothing$ is the projectile diameter, and a and b are empirical constants (1). In two recent numerical studies (6,7), we have treated this problem using the reactive hydrodynamic computer codes (8), SIN (one-dimensional) and 2DE (two-dimensional), for the respective simulation of steel plates and steel cylinders impacting bare as well as covered composition-B charges. Our numerical results describe projectile-impact shock initiation in more detail and provide further correlations analogous to Equation (1) involving buildup parameters.

Because the shock response of a covered explosive charge is rather complicated, we only re-examine solutions to the bare charge problem in this paper. Our numerical results for both one- and two-dimensional impact (6) are presented in such a manner that general trends and distinctive patterns can be readily seen. Such trends and patterns are the bases of Equation (1) and further correlations developed in this work. The physical basis and applicability of these relations are discussed and it is concluded that the critical energy criterion is applicable to shock initiation by both one- and two-dimensional impact. However, dimensionality affects the shock buildup due to the absence or presence of lateral rarefaction waves.

NUMERICAL RESULTS

In Table 1 we list some of the 75 material constants (9). A and B are the empirical constants of the Pop plot (8), ($\ln\lambda = A + B\ln P_i$), in consistent units. Using these data, both the SIN and 2DE codes yield numerical results which describe the shock initiation of detonation by impact in considerable detail (6,7). It is worthwhile to re-examine some of these results as presented in Tables 2 and 3 with additional parameters denoted and defined as follows: θ=time to detonation, λ=distance to detonation, $\ell = U'_i\theta$ (distance traveled by the initial shock in the explosive disregarding its buildup), $X = (P_j - P_i)/\lambda$ (shock buildup gradient), and $Y = (P_j - P_i)/\theta$ (shock buildup rate). These parameters are tabulated for slightly supercritical cases in Table 2 (for the one-dimensional problem) and in Table 3 (for projectile-impact).

It is of particular interest to note the patterns of V/P_i, $V^2\varnothing$, $V^2\theta$, $\theta/\varnothing$, and X/P_i in Table 2. They appear to be all nearly constant. In Table 3 a similar trend is observed for V/P_i, $V^2\varnothing$, $V^2\lambda$,

TABLE 1
Material Constants (9)

Material	Initial Density ϱ_o, ϱ'_o (g/cm³)	Hugoniot Constants c,c′ (mm/μs)	s,s′	Detonation Velocity D (mm/μs)	CJ Pressure Pj (GPa)	Pop Plot Constants A	B
Steel	7.917	4.58	1.51	—	—	—	—
Comp.-B	1.715	2.47	1.88	8.08	28.4	4.095	−1.134

TABLE 2
Results from SIN Computation (6)

Ø*	(mm)	5	8	10	12	15	18
V	(mm/μs)	1.3	0.9	0.8	0.75	0.65	0.6
P_i	(GPa)	8.4	5.2	4.5	4.1	3.4	3.0
u	(mm/μs)	0.22	0.14	0.12	0.11	0.09	0.08
t**	(μs)	2.07	3.41	4.22	5.09	6.29	7.59
θ	(μs)	0.79	1.63	2.12	2.38	3.13	3.62
λ	(mm)	5.4	9.3	11.3	12.5	15.3	17.3
ℓ	(mm)	3.6	6.5	8.2	8.9	11.1	12.2
V/P_i	(mm/μs-GPa)	0.15	0.17	0.18	0.18	0.19	0.20
P_iut	(GPa-mm)	3.83	2.48	2.29	2.29	1.92	1.82
P_i^2t	(GPa^2-μs)	146	92.2	85.4	85.6	72.7	68.3
$V^2Ø$	($mm^3/\mu s^2$)	8.45	6.48	6.40	6.75	6.34	6.48
$V^2\theta$	($mm^2/\mu s$)	1.34	1.32	1.36	1.34	1.32	1.30
$\theta/Ø$	(μs/mm)	0.16	0.20	0.21	0.20	0.21	0.20
X/P_i	(mm^{-1})	0.44	0.48	0.47	0.48	0.48	0.49
X/V	(GPa-μs/mm^2)	2.85	2.77	2.65	2.60	2.50	2.45
Y/P_i	(μs^{-1})	3.01	2.73	2.51	2.49	2.35	2.33
Y/V	(GPa/mm)	19.5	15.8	14.1	13.6	12.3	11.4
λ/θ	(mm/μs)	6.8	5.7	5.3	5.3	4.9	4.8

*Ø denotes the plate thickness, **$t=2Ø\varrho_o u/P_i$=shock duration.

X/V^2, and Y/V^2, except those marked with * and # because of anomaly. In addition, parameter groups such as X/V, Y/P_i, Y/V, and λ/θ of Table 2 and also $\theta/Ø$, XØ, YØ, and λ/θ of Table 3 are roughly invariant. In view of the published criteria (10,12), we have also included P_iut and P_i^2t in Table 2.

From these trends or patterns we have determined the best data fit as shown in Figures 1-7. Clearly all the fits associated with these data are linear. The equations are summarized in Table 4.

These equations and figures constitute our assessment of projectile-impact shock initiation, describing not only the threshold but also the buildup to detonation.

DISCUSSION

The five P_iut values from Table 2 may be averaged to give a critical initiation energy of 2.16 GPa-mm as compared with its published value of 1.50 GPa-mm (11), The difference may be due to shock smearing by artificial viscosity. In view of the impedance mismatch, the critical energy concept is only an approximate rule. Note that $V^2Ø$ takes on values around 6.5. This appears to be a better representation of the energy dependence for projectile-impact

TABLE 3
Results from 2DE Computation (6)

$\varnothing$	(mm)	5*	8	10	12	15	18
V	(mm/μs)	1.4	1.0	0.9	0.8	0.7	0.6
P_i	(GPa)	11.5	6.4	5.8	4.8	3.8	2.8
u	mm/μs)	0.29	0.17	0.15	0.13	0.10	0.07
θ	(μs)	0.3	0.9	3.0	1.7	2.3	3.2
λ	(mm)	2.5	3.8	12.5	6.8	9.0	13.0
ℓ	(mm)	1.5	3.7	12.2	6.6	8.4	10.8
V/P_i	(mm/s-GPa)	0.12	0.16	0.15	0.17	0.18	0.21
$V^2\varnothing$	($mm^3/\mu s^2$)	.8	8.0	8.1	7.7	7.4	6.5
$V^2\lambda$	($mm^3/\mu s^2$)	.9	.8	0.1	4.4	4.4	4.7
$\theta/\varnothing$	(μs/mm)	.06	0.11	0.30	0.14	0.15	0.18
X/V^2	(GPa-$\mu s^2/mm^3$)	3.5	5.8	2.2	5.4	5.6	5.4
$X\varnothing$	(GPa)	33.8	46.3	18.1	41.6	40.9	34.7
Y/V^2	(GPa-$\mu s/mm^2$)	28.7	24.4	9.3	21.7	21.8	22.2
$Y\varnothing$	(GPa-mm/μs)	282	195	75	167	161	144
λ/θ	(mm/μs)	8.3	4.2	4.2	4.0	3.9	4.1

* Overdriven detonation λ/θ >D.

Delayed detonation with θ and λ exceeding Pop plot or wedge test data θ=1.4 μs, λ=8.2 mm at P_i=5.8 GPa.

TABLE 4
Equations for Scaling Projectile-Impact Shock Initiation

One-Dimensional	Two-Dimensional
(A1) $P_i = -1.67 + 7.74\ V$	(A2) $P_i = -2.341 + 8.823\ V$
(B1) $V = 0.02 + 2.50/\sqrt{\varnothing}$	(B2) $V = -0.14 + 3.26/\sqrt{\varnothing}$
(C1) $V = 0.013 + 1.167/\sqrt{\theta}$	(C2) $V = 0.14 + 1.70\sqrt{\lambda}$
(D1) $\theta = 0.110 + 0.195\varnothing$	(D2) $\theta = -0.7 + 0.2\varnothing$
(E1) $\lambda = 2.78 + 4.0\theta$	(E2) $\lambda = -0.099 + 4.058\theta$
(F1) $X = -0.314 + 0.430\ P_i$	(F2) $X = -0.24 + 6.03\ V^2$
(G1) $Y = -9.33 + 26.19\ V$	(G2) $Y = -2.26 + 26.86\ V^2$
(B1') $P_i = -1.043 + 11.304/\sqrt{t}$, for P_i^2t-scaling.	
(B2') $V = 0.0 + 3.13/\sqrt{\varnothing}$ ≡ NOL experimental data fit.	
(E1') $\lambda = 6.478\theta^{3.4}$, wedge test data fit.	
(F1') $X = -0.53 + 3.33\ V$, for X/V to complement X/P_i.	
(F2') $X = -0.686 + 51.428/\varnothing$, for $X\varnothing$ to complement X/V^2.	
(G2') $Y = -4.831 + 233.3/\varnothing$, for $Y\varnothing$ to complement Y/V^2.	

shock initiation, as given in Figure 1 and by (B1) of Table 4. Indeed, (B1) is a numerical confirmation of Equation (1). A complementary representation is given by (B1') since P_i^2t is considered to be a preferable criterion (12). Although the physical basis of $V^2\theta$ is not so apparent as that of $V^2\varnothing$, (C1) and its graph in Figure 1 provide a link between impact velocity and time to detonation. The higher the impact energy, the faster the initiation. Similarly $V^2\lambda$ is correlated in (C2). For convenience in graphic display, we have plotted Equations (A1), (G1) and (F1') in Figure 2. Figures 3 and 4 show results of two categories. Figures 5-7 are the two-dimensional

counterparts of Figures 1 and 2. Note the common features and dissimilarities of the respective equations, which may also reflect their numerical and physical bases.

Since the boundary conditions of impact implies

$$\frac{V}{P_i}=\frac{1}{\varrho_i U_i}+\frac{1}{\varrho_o' U_i'} \qquad (2)$$

both (A1) and (A2) turn out to be a good correlation for the impact parameters which determine the shock stimulus. It is worthwhile to compare (B2) with (B2') of Table 4; the two coefficients 3.26 and 3.13 are reasonably close; and this can serve as a favorable evidence of experimental support to our numerical investigation. Physically (F2) and (G2) mean that the buildup of shock to detonation increases with the impact energy. The correspondence of (F2') to (F2) is visible through the relation $X\varnothing=(X/V^2)\,V^2\varnothing$; so is (G2') to (G2). Let us now compare (F1) and (G1) with (F2') and (G2') respectively. Thus the one-dimensional shock buildup is directly proportional to the stimulus amplitude, and the two-dimensional shock buildup varies inversely with the lateral extent subject to rarefactions.

Again, it is a matter of convenience to display the equations (D1), (E1), (D2), and (E2) together in Figure 3. In one dimension it seems reasonable to form the link $\theta/\varnothing=V^2\theta/V^2\varnothing$, which underlies (D1). On the other hand, (D2) may be attributed to $\theta/\varnothing=(V^2\lambda/V^2\varnothing)\,(\lambda/\theta)^{-1}$ of Table 3. It is worth noting that (D1) and (D2) have almost equal slope in Figure 3. Since the one-dimensional (SIN) Forest Fire Burn results reproduce wedge test results faithfully (8), (E1) and (E1') coincide with each other within the computing range of this investigation. Moreover, the almost equal slopes of (E2) and (E1) indicates that the two-dimensional (2DE Forest Fire Burn) results are also compatible with the shock sensitivity data. Returning to Tables 2 and 3, let us compare the two distances ℓ and λ. From these we can recognize two different modes of shock buildup: detonation occurs earlier with the plane shock than with the cylindrical shock.

Thus far we have examined the physical basis and implications of Tables 2-4. Favorable evidence has been sought as a viable test of our equations of Table 4. These equations are applicable to problems with $\varnothing$ or V falling in the

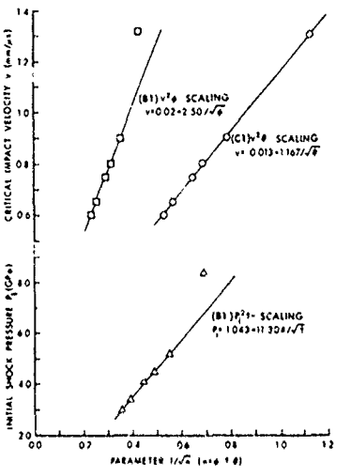

Fig. 1. Numerical Scaling of One-Dimensional Impact Shock Initiation

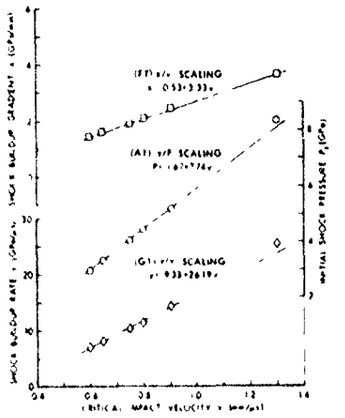

Fig. 2. Linear Fits of One-Dimensional Shock Buildup Data

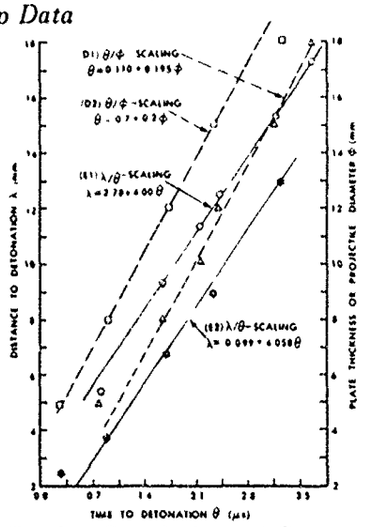

Fig. 3. Further Correlations of One- and Two-Dimensional Impact Shock Initiation

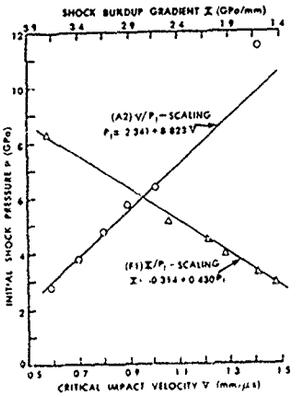

Fig. 4. Linear Fits of One- and Two-Dimensional Impact Shock Initiation Data

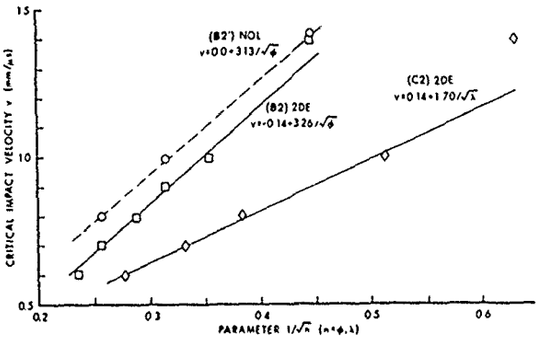

Fig. 5. Numerical Scaling of Two-Dimensional Shock Buildup Data

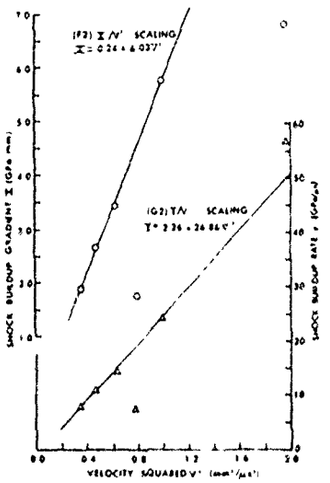

Fig. 6. Linear Fits of Two-Dimensional Shock Buildup Data

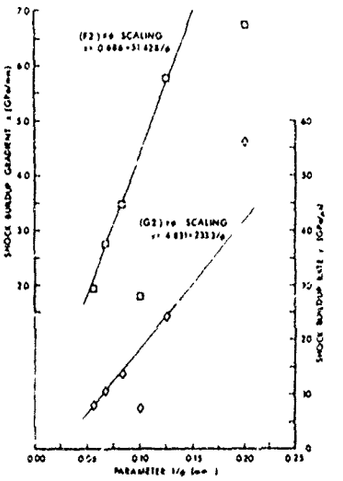

Fig. 7. Complementary Relations of Two-Dimensional Shock Buildup

computing range of this investigation. No extrapolation is recommended because the upper bound has P_i near the fifty percent point of the large scale gap test for composition-B. A number of issues arise if we are going to generalize our results to wider ranges. The linear data fit may fail. We may also have computational difficulty. Each computer code has its limitations such as differencing scheme, grid coarseness, time step, artificial viscosity, and modeling capacity.

CONCLUSION

Our results, summarized in Table 4, show some common features which can be described essentially as follows: An experimentally verifiable threshold velocity is determined by the critical energy for shock initiation. The initial shock pressure varies linearly with this critical velocity. The shock buildup is calculable from the initial pressure, the critical velocity, or one principal dimension of the projectile. Such a calculation reproduces the Pop plot. The higher the impact energy, the faster the shock initiation and buildup. While the shock buildup in one dimension is directly proportional to the stimulus amplitude, the two-dimensional shock buildup varies inversely with the extent to which lateral rarefaction wave may develop. Detonation occurs earlier with the one-dimensional

shock than with the two-dimensional shock.

This paper is intended to contribute not only to further understanding of projectile-impact shock initiation but also to the scaling of pertinent parameters within a range of practical interest.

REFERENCES

1. D.C. Slade and J. Dewey, "High-Order Initiation of Two Military Explosives by Projectile Impact," Ballistic Research Laboratory Report 1021, (July 1957), AD-145868).
2. S.M. Brown and E.G. Whitbread, "The Initiation of Detonation by Shock Waves of Known Duration and Intensity," Les Ondes de Detonation, C.N.R.S. No. 109, (Paris, 1962), pp. 69-80.
3. L.A. Roslund, J.W. Watt, and N.L. Coleburn, "Initiation of Warhead Explosives by the Impact of Controlled Fragments I. Normal Impact," Naval Ordnance Laboratory Technical Report NOLTR-73-124, (August 1974).
4. L. Green, "Shock Initiation of Explosives by the Impact of Small Diameter Cylindrical Projectiles," Seventh Symposium (International) on Detonation, NSWC MP 82-334, (June 1981), pp. 273-277.
5. K.L. Bahl, H.C. Vantine, and R.C. Weingart, "The Shock Initiation of Bare and Covered Explosives by Projectile Impact," Ibid., pp. 325-335.
6. Y.K. Huang, J.J. Starkenberg, and A.L. Arbuckle, "A Numerical Study of Shock Initiation of Composition-B by High-Speed Impact of Small Steel Projectiles," Ballistic Research Laboratory Technical Report, ARBRL-TR-02548, (February 1984), AD-A139629).
7. J. Starkenberg, Y. Huang, and A. Arbuckle, "Numerical Modeling of Porjectile Impact Shock Initiation of Bare and Covered Composition-B," Ballistic Research Laboratory Technical Report ARBRL-TR-02576, (August 1984).
8. C.L. Mader, "Numerical Modeling of Detonations," (University of California Press, Berkeley, 1979).
9. A.L. Bowman, J.D. Kershner, and C.L. Mader, "A Numerical Model of the Gap Test," Los Alamos Scientific Laboratory Report LA-8408, (October 1980).
10. F.E. Walker and R.J. Wasley, "Critical Energy for Shock Initiation of Heterogeneous Explosives," Explosivstoffe 17, 9 (1969).
11. F.E. Walker and R.J. Wasley, "A General Model for the Shock Initiation of Explosives," Propellants Expl. 1, 73 (1976).
12. P. Howe, R. Frey, B. Taylor, and V. Boyle, "Shock Initiation and the Critical Energy Concept," Sixth Symposium (International) on Detonation, ACR-221, (August 1976), pp. 11-19.

US ARMY
MATERIEL
COMMAND
BALLISTIC RESEARCH LABORATORY

SOME NEW COMPUTED RESULTS FOR PROJECTILE IMPACT SHOCK INITIATION OF SOLID EXPLOSIVES

Y. K HUANG, J. STARKENBERG, A. L. ARBUCKLE

US ARMY BALLISTIC RESEARCH LABORATORY
ABERDEEN PROVING GROUND MD

THE ONLY ESTABLISHED RELATION FOR A BARE EXPLOSIVE CHARGE INITIATED BY PROJECTILE IMPACT IS

$$V = a + b/\sqrt{\phi}$$

COMPUTER SIMULATION PROVIDES MORE DETAILED RESULTS INCLUDING SIMILAR RELATIONS FOR SHOCK BUILDUP PARAMETERS. USING THE REACTIVE HYDRODYNAMIC CODES, SIN AND 2DE, WE HAVE OBTAINED SUCH RESULTS FOR BOTH ONE AND TWO-DIMENSIONAL SHOCK INITIATION OF COMPOSITION B IMPACTED BY STEEL PLATES AND CYLINDERS

SIMULATED CONFIGURATIONS

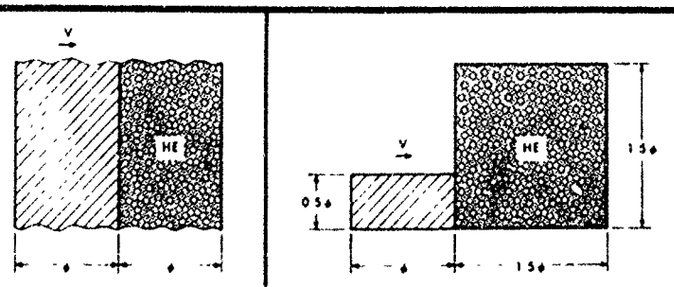

COMPUTATIONAL GRIDS

SIN

ϕ (mm)	STEEL ZONE ΔR (mm)	STEEL ZONE NR (cells)	STEEL ZONE ΔT (μs)	COMP B ZONE ΔR (mm)	COMP B ZONE NR (cells)	COMP B ZONE ΔT (μs)	NT (cycles)
5	0 072	70	0 0015	0 08	70	0 0015	500
8	0 080	100	0 0015	0 10	100	0 0015	800
10	0 100	100	0 0020	0 15	70	0 0020	1000
12	0 100	120	0 0020	0 15	80	0 0020	1000
15	0 100	150	0 0020	0 15	100	0 0020	1000
18	0 090	200	0 0015	0 18	100	0 0030	1500

2DE

ϕ (mm)	ΔR, ΔZ (mm)	NR (cells)	NZ (cells)	ΔT (μs)	NT (cycles)
5	0 25	45	68	0 005	400
8	0 40	45	68	0 010	350
10	0 50	45	68	0 010	400
12	0 40	65	98	0 010	530
15	0 50	65	98	0 010	530
18	0 60	65	98	0 015	400

SEQUENCE OF MASS FRACTION CONTOURS FROM 2DE COMPUTATION

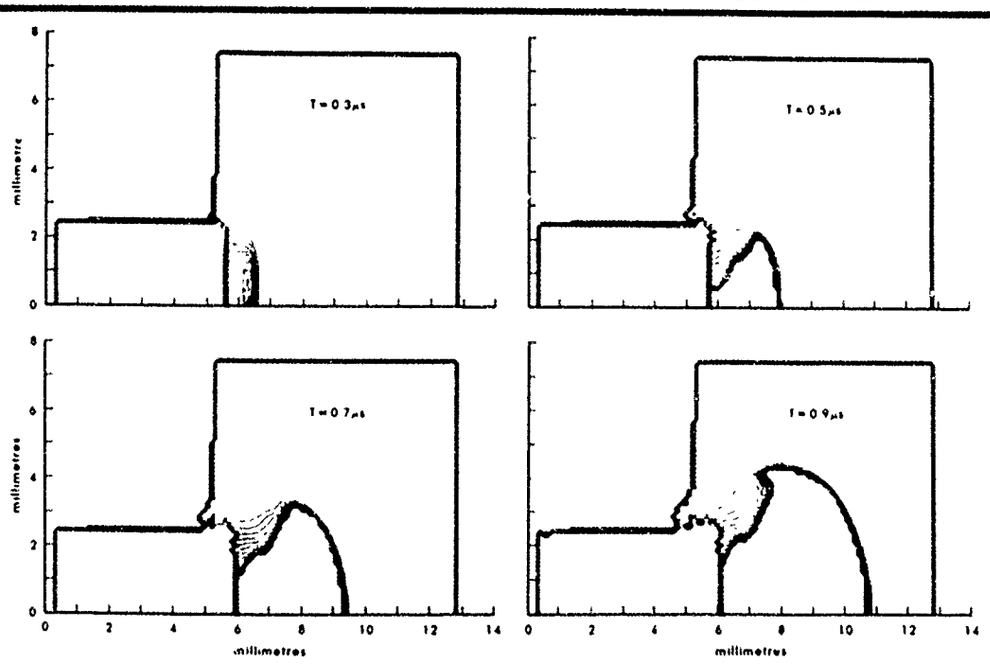

ϕ = 5mm, V = 1 4km/s, GO. MF INTERVALL = 0.05

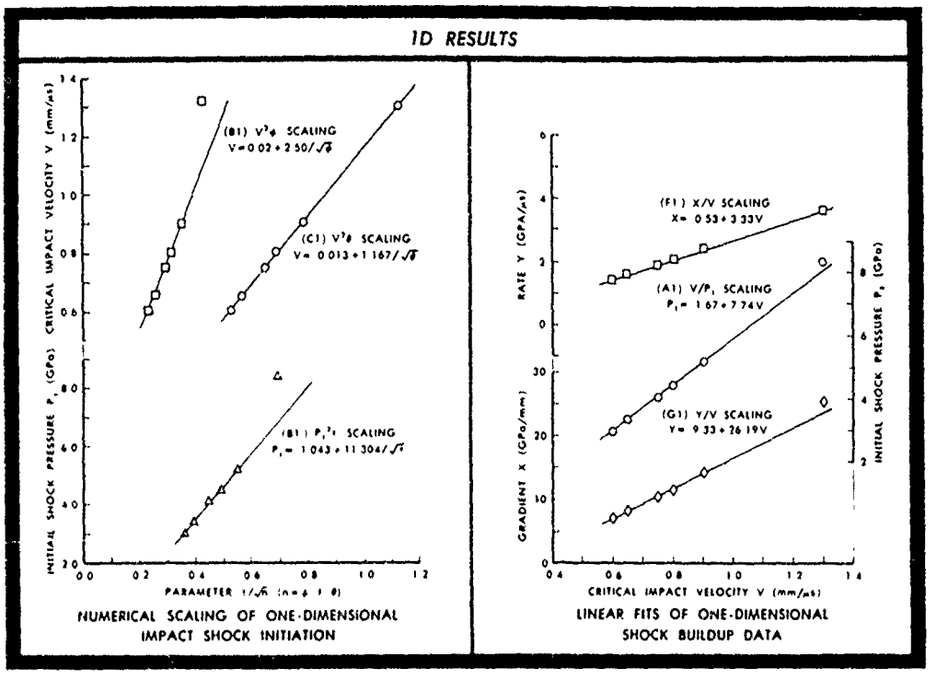

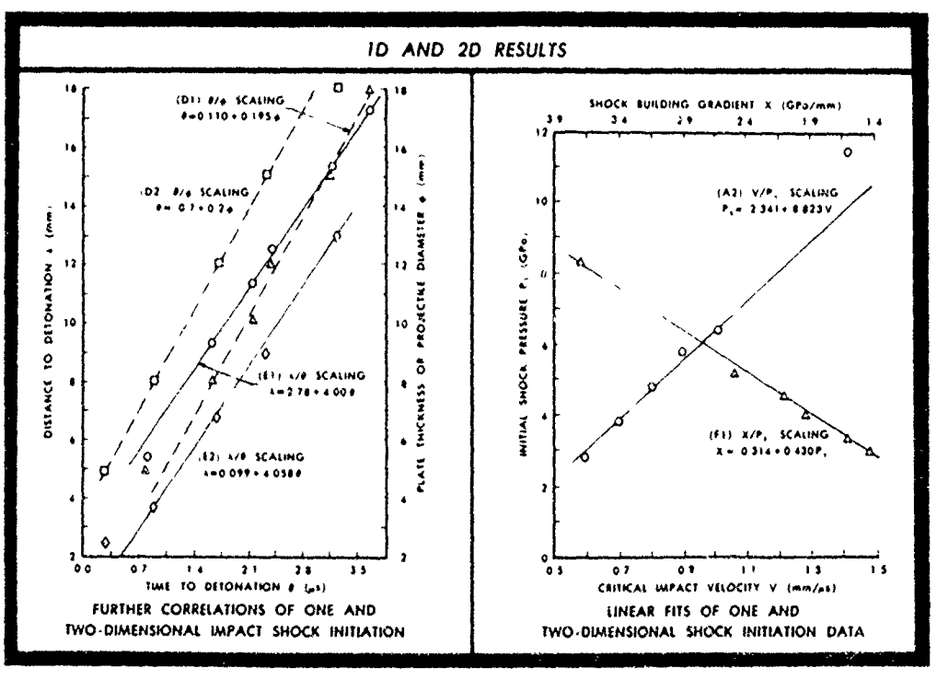

AMC Provid... ... Decisive Edge

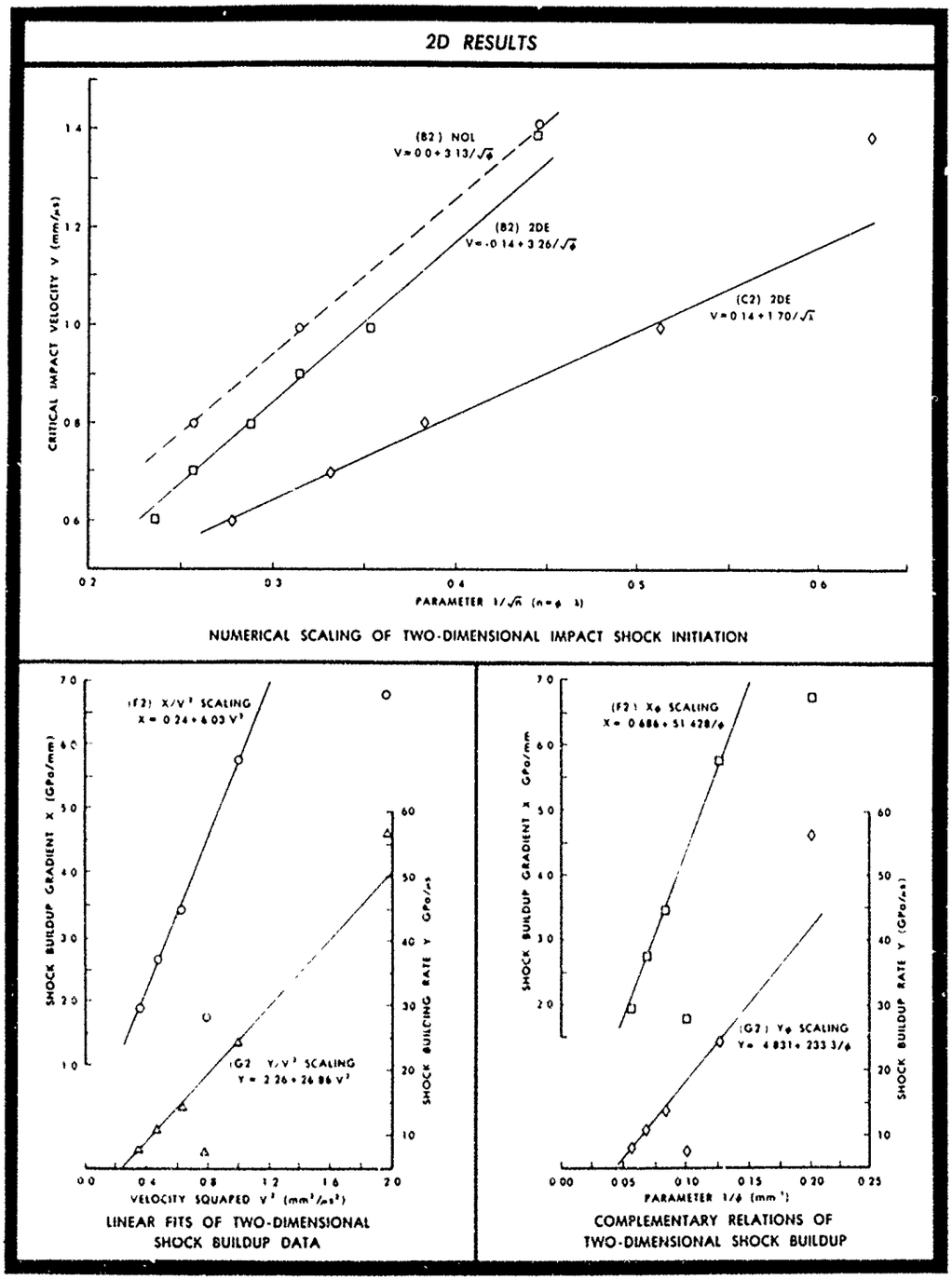
2D RESULTS
(82) NOL
V=0.0+3.13/√φ
(82) 2DE
V=-0.14+3.26/√φ
(C2) 2DE
V=0.14+1.70/√λ
CRITICAL IMPACT VELOCITY V (mm/μs)
PARAMETER 1/√λ (n=φ λ)
NUMERICAL SCALING OF TWO-DIMENSIONAL IMPACT SHOCK INITIATION
(F2) X/V² SCALING
X = 0.24+6.03 V²
(G2 Y/V² SCALING
Y = 2.26+26.86 V²
SHOCK BUILDUP GRADIENT X (GPa/mm)
SHOCK BUILDING RATE Y GPa/μs
VELOCITY SQUARED V² (mm²/μs²)
LINEAR FITS OF TWO-DIMENSIONAL SHOCK BUILDUP DATA
(F2) Xφ SCALING
X = 0.686+51.428/φ
(G2) Yφ SCALING
Y = 4.831+233.3/φ
SHOCK BUNDUP GRADIENT X GPa/mm
SHOCK BUILDUP RATE Y (GPa/μs)
PARAMETER 1/φ (mm⁻¹)
COMPLEMENTARY RELATIONS OF TWO-DIMENSIONAL SHOCK BUILDUP

SUMMARY OF SCALING EQUATIONS

ONE-DIMENSIONAL	TWO-DIMENSIONAL
(A1) $P_i = -1.670 + 7.740V$	(A2) $P_i = -2.341 + 8.823V$
(B1) $V = 0.020 + 2.500/\sqrt{\phi}$	(B2) $V = -0.140 + 3.260/\sqrt{\phi}$
(C1) $V = -0.013 + 1.167/\sqrt{\theta}$	(C2) $V = 0.140 + 1.700/\sqrt{\lambda}$
(D1) $\theta = 0.110 + 0.195\phi$	(D2) $\theta = -0.700 + 0.200\phi$
(E1) $\lambda = 2.780 + 4.000\theta$	(E2) $\lambda = -0.099 + 4.058\theta$
(F1) $X = -0.314 + 0.430P_i$	(F2) $X = -0.240 + 6.030V^2$
(G1) $Y = -9.330 + 26.19V$	(G2) $Y = -2.260 + 26.86V^2$

(B1') $Pi = -1.043 + 11.304/\sqrt{t}$, FOR $P_i^2 t$ SCALING

(B2') $V = 0.000 + 3.1300/\sqrt{\phi}$, NOL EXPERIMENTAL DATA FIT

(E1') $\lambda = 6.478\theta^{3/4}$, WEDGE TEST DATA FIT

(F1') $X = -0.530 + 3.3300V$, FOR X/V TO COMPLEMENT X/P_i

(F2') $X = -0.686 + 51.428/\phi$, FOR $X\phi$ TO COMPLEMENT X/V^2

(G2') $Y = -4.831 + 233.30/\phi$, FOR $Y\phi$ TO COMPLEMENT Y/V^2

CONCLUSIONS

- A THRESHOLD VELOCITY IS DETERMINED BY THE CRITICAL ENERGY FOR THE SHOCK INITIATION AND BUILDUP
- THE INITIAL SHOCK PRESSURE VARIES LINEARLY WITH THE CRITICAL VELOCITY
- SHOCK BUILDUP IS CALCULABLE GIVEN THE INITIAL PRESSURE, THE CRITICAL VELOCITY OR ONE PRINCIPAL DIMENSION OF THE PROJECTILE
- WHILE SHOCK BUILDUP IN ONE DIMENSION IS DIRECTLY PROPORTIONAL TO THE STIMULUS AMPLITUDE, TWO-DIMENSIONAL SHOCK BUILDUP VARIES INVERSELY WITH THE EXTENT TO WHICH LATERAL RAREFACTION WAVES MAY DEVELOP
- HIGH-ORDER DETONATION OCCURS EARLIER WITH THE PLANE SHOCK THAN THE AXISYMMETRIC SHOCK WAVE

THE JET INITIATION OF SOLID EXPLOSIVES

M. C. Chick and I. B. Macintyre
Materials Research Laboratories
Melbourne, Australia

and

R. B. Frey
Ballistic Research Laboratory
USA AMCCP
Aberdeen Proving Ground, MD, USA

Flash x-ray has been used to study the jet initiation of covered and bare Composition B and pressed TNT. Emphasis is placed on the covered configuration since this is the state more closely aligned to that found in munition systems. We have shown that the initiation of covered explosive is controlled by the bow wave shock associated with the jet penetration of the explosive. This mechanism is shown to have different characteristics from that for the jet initiation of bare explosive. Important parameters are discussed.

We have demonstrated that the bow wave can have a significant desensitising effect on both a cast and pressed explosive. A novel technique using a shaped charge jet to disrupt the explosive or cause prompt detonation at a predetermined position within the charge is described and demonstrated.

INTRODUCTION

High velocity metal jets generated by shaped charges are used for the destruction of explosive filled ordnance. This requires an understanding of the initiation process and development of appropriate models. Such models should, for example, be capable of predicting the conditions of the detonation/failure threshold which can exist for the jet attack of covered explosives (1).

This paper summarises the results of an ongoing investigation aimed at identifying the mechanisms and controlling parameters in the jet initiation of explosive fillings. Although we report on both covered and bare explosives, the emphasis is on the former since this is the state more closely aligned to that found in munition systems. This approach is supported by recent information that suggests that the initiation of bare and covered explosives can exhibit different characteristics (1, 2, 3, 4, 5).

EXPERIMENTAL CONFIGURATIONS AND TREATMENT OF DATA

The experimental layout has been described previously (2) and is shown in Figure 1. The copper jet was fired from a Composition B filled 38 mm diameter shaped charge from two charge diameters standoff (76 mm) at explosive receptors covered by various materials. Flash x-ray synchronisation was achieved by means of a flat electric sensor placed between the cover and receptor charge. Two orthogonal radiographs were taken for each firing. Delayed timing between the x-ray flashes was based on the calculated position of the jet, shock or phenomenon under study and was obtained by means of digital delay pulse generators. Times were recorded to $\pm$ 0.1 μs and distances on the flash radiographs were measured to $\pm$ 0.2 mm.

For each cover/explosive combination studied the (critical) cover thickness that produced detonations in 50% of a series of firings was determined. The Bruceton procedure was used

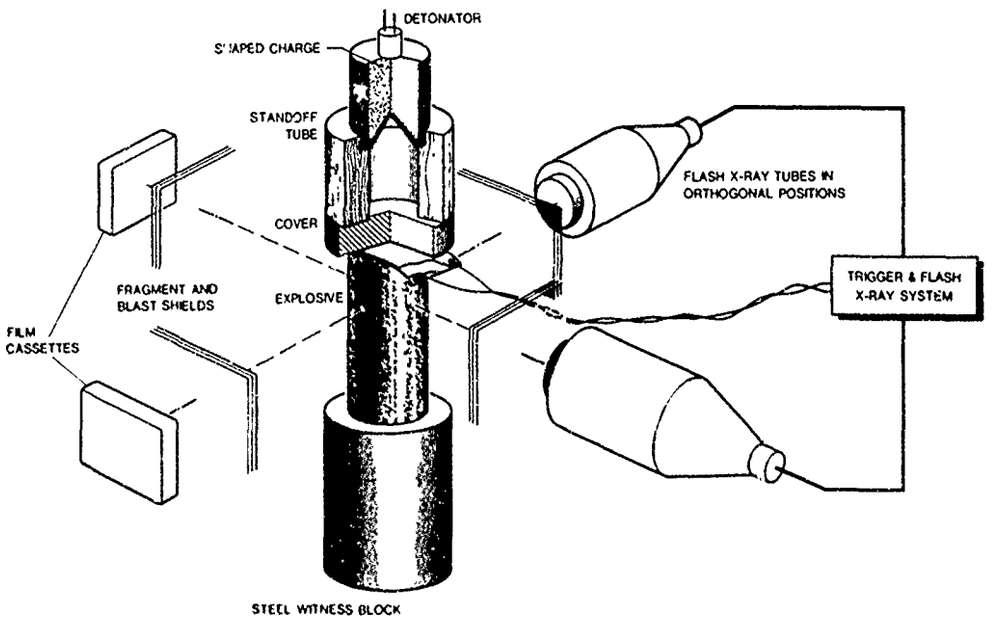

Fig. 1. Schematic Diagram of the Experimental Set-up for Investigating the Jet Initiation of Explosives

to vary the thickness of the cover in a prescribed manner depending on whether the previous event was a detonation or failure. There were between 10 and 20 firings per critical cover thickness determination. Where appropriate the results were analysed statistically by the Dixon and Mood method (6) to give a mean and standard deviation.

Measurements on bare explosives were made using a similar set-up to that shown in Figure 1 except that a 15 mm air gap was introduced between the cover and explosive. This arrangement was designed to remove any effects of the bow wave shock from the jet penetrating the cover thus enabling the jet to strike unstressed explosive while allowing the jet characteristics to be altered by varying the cover thickness.

The system was calibrated using flash x-ray to measure the jet velocity and diameter in air about 15 to 30 mm from the exit surface of the cover. For steel these measurements were made for 12 different thicknesses between 6 and 166 mm; this allowed the preparation of a calibration curve for estimating the jet velocity and diameter for any steel cover thickness. The measured jet penetration velocity at the exit surface of the cover was determined from (7):

$$U_p = \frac{V_j}{1+\gamma} \qquad (1)$$

where U_p the jet penetration velocity, V_j the jet velocity and γ the square root of the ratio of target density to jet density. Jet penetration velocities in the explosive and Plexiglas were measured directly using flash x-ray.

In all cases examined with the exception of the measurement of the critical conditions for the jet initiation of bare explosives, flash x-ray showed the jet to be continuous.

Jet penetration calculations used incompressible theory for a stretching jet (8) except

for the Plexiglas cover where the results of a recent study of compressibility effects were used (9). The essential equation for calculating the velocity of a stretching jet for a given depth of penetration in an incompressible target is given by (8):

$$V_j = V_{tip} \left[\frac{\tau+S}{S} \right]^{-\gamma} \qquad (2)$$

where V_{tip} the initial jet tip velocity, τ the depth of penetration from the cover surface and s the standoff from the virtual origin position of jet formation to the surface of the cover. U_p is then obtained from equation (1). The position of the virtual origin has not been determined for the 38 mm diameter shaped charge and was therefore scaled from the BRL 81 mm charge (9).

The various cover/explosive target systems were examined to assess the relative importance of the following jet/shock combinations on the threshold conditions to initiate or disrupt the explosive:

1. the decaying transient shock from the jet impact on the cover,
2. the bow wave shock from jet penetration of the cover,
3. the bow wave shock from jet penetration of the explosive.

The investigation used cover materials of steel, aluminum, Plexiglas and a steel/Plexiglas combination Receptor explosives used were cast Composition B (RDX/TNT/WAX, 55/45/1) and pressed TNT. The steel cover/Composition B target combination was also studied for cover thicknesses in the range 6 to 166 mm. The jet tip velocity was determined using flash x-ray to be 7.3 ± 0.1 mm/μs.

JET INITIATION OF COVERED EXPLOSIVES

The initiation of covered explosives has been shown to occur from shocks travelling ahead of the jet (1, 2). As explained in the previous section we have examined the system to assess the relative importance of the various jet/shock combinations. Our approach was to determine the critical conditions for the jet initiating Composition B covered by several different materials. It was then assumed that similar threshold shock conditions would exist for each cover material. Further, the critical jet penetration velocities in the cover and Composition B were directly related to the associated bow wave shock velocity and hence to their relative importance in the initiation process.

Table 1 lists results for the 38 mm diameter shaped charge jet attack of Composition B covered by various materials.

The first major column of Table 1 lists the measured critical cover thicknesses for steel, aluminum, Plexiglas and a steel/12.8 mm thick Plexiglas composite. The latter cover was selected on the basis of the results of the single material covers and as a simulant of a munition casing where the Plexiglas substitutes for low density liners such as asphalt. Plexiglas was selected as a simulant since it has well characterised physical and shock properties.

The second major column gives the predicted critical cover thickness assuming that the initiation is caused by the large transient shock from the jet impact on the cover surface decaying to produce a pressure in Composition B of about 2.5 GPa (1). The semi-empirical model used was developed by Green (10) for small diameter projectile impact.

Major columns 3 and 4 in Table 1 list the calculated and measured jet and penetration velocities at the interface of the cover and Composition B for the measured critical cover thicknesses. The differences between the two sets of values may be attributed to measurement error, variability in the shaped charge jets and/or the use of the virtual origin assumption in the analysis. The latter has been discussed in the detailed study of the jet penetration of Plexiglas (9).

Table 1 shows that the predicted cover thicknesses using the semi-empirical impact shock model do not correlate with the measured values, thus this mechanism is not supported for these conditions. However, previous results using a range of steel cover thicknesses (1, 11) indicated that in these tests thin covered Composition B detonates prior to the arrival of the jet and correlated with the impact shock from the jet striking the cover. This mode of initiation would be expected to be similar to that modelled by Starkenberg et al for the projectile impact of Composition B (12) and presumably

TABLE 1
Threshold Conditions For The Initiation Of Covered Composition B By a 38 mm Diameter Shaped Charge Jet

COVER CHARACTERISTICS			PREDICTED CRITICAL COVER THICKNESS FOR DECAYING JET IMPACT SHOCK USING GREEN'S APPROXIMATION	CALCULATED JET CHARACTERISTICS FOR CRITICAL COVER THICKNESS			MEASURED JET CHARACTERISTICS FOR CRITICAL COVER THICKNESS		
MATERIAL	DENSITY $Mg\,m^{-3}$	CRITICAL COVER THICKNESS $m_{50\%}$ ($\sigma m_{50\%}$) mm	mm	PENETRATION VELOCITY IN COVER mm/μs	FREE FLIGHT JET VELOCITY mm/μs	PENETRATION VELOCITY IN COMP B mm/μs	PENETRATION VELOCITY IN COVER mm/μs	FREE FLIGHT JET VELOCITY mm/μs	PENETRATION VELOCITY IN COMP. B mm/μs
STEEL	7 85	59 8(1 0)	60	2 40	4.66	3 26	2.7	5.2	3 8
ALUMINIUM	2 70	126 8(1 6)	57 5	2 98	4.61	3 22	3.2	5 0	3.6
PLEXIGLAS	1 18	200 8(3 6)	62	3 60	4 91	3.43	3.6	4 8	3.5
STEEL 12 8 mm PLEXI GLAS (STEEL THICK NESS VARIED)	7 850 1 18	61 7(1 6)	40	3 28	4 48	3 13	3.5	4.8	3.4

would be influenced by similar factors.

Reference to Table 1 shows that for the measured critical cover thicknesses there is reasonable agreement with both the jet free flight velocities and jet penetration velocities in Composition B. However, the correlation is not so good for the jet penetration velocities in the cover material. This suggests that the important factors in the initiation process are the characteristics of the bow wave associated with the jet penetration of the explosive. The data show a slight decrease in the measured critical jet penetration velocities in Composition B with decreasing density of the cover material. This may be a real effect and related to the consequent increase in cover penetration velocity with decreasing density and the production of a relatively higher transient shock across the cover/Composition B interface into the explosive. Thus the critical jet penetration velocity (with its associated bow wave) required to initiate detonation is lowered. The difference between the values for the steel and steel/Plexiglas combination may relate to the cover density effect since the Plexiglas was adjacent to the Composition B. Thus the shape of the critical bow wave shock that initiates the Composition B may be complicated from the influence of secondary effects.

A flash radiograph showing the initiation of steel covered Composition B at the critical condition is shown in Figure 2 and a radiograph of the jet and bow wave prior to detonation of the explosive is shown in Figure 3.

The importance of the bow wave in initiation suggests that jet velocity and diameter are the major parameters in controlling the process. Jet density would only appear to have an effect in that it controls the rate of penetration. Larger jet diameters would produce flatter topped bow wave shocks which would be less affected by rarefactions and therefore more effective at initiation. This conclusion regarding jet diameter is supported by the results of a study using jets from 3 different diameter shaped charges fired at steel cased Composition B. The threshold jet velocity was found to increase as the jet diameter decreased (13). The diameter of the bow wave is considerably greater than that of the jet and this may have important implications on the effect of explosive critical diameter on jet initiation. For example bare explosive

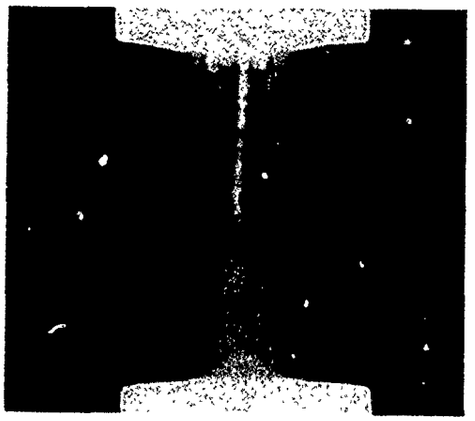

Fig. 2. Flash radiograph of covered Composition B detonating at the critical condition

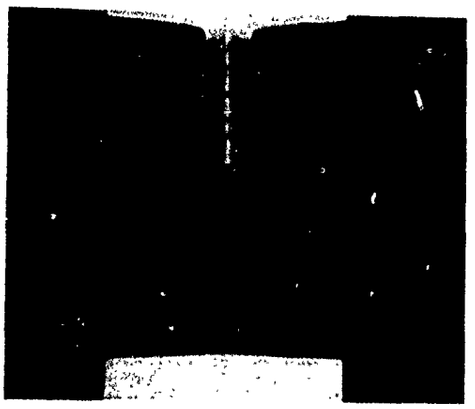

Fig. 3. Flash radiograph of the bow wave shock in covered Composition B prior to detonation

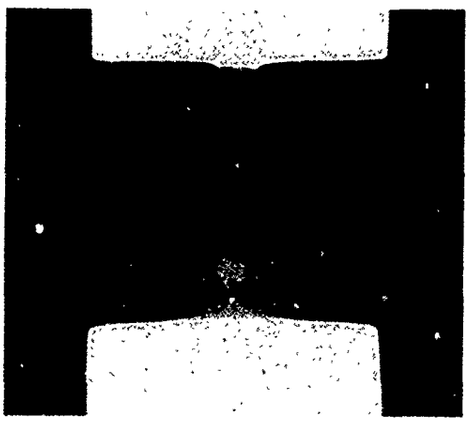

Fig. 4. Flash radiograph of bare Composition B detonating at the critical condition

which may fail to initiate from the jet impact process due to critical diameter effects (5) may subsequently detonate if the jet penetration mechanism produces a bow wave that builds up to a diameter greater than the critical size. Our current investigation includes an examination of jet density and diameter and the importance of explosive critical diameter.

JET INITIATION OF BARE EXPLOSIVE

A critical condition for the jet initiation of bare explosive was first reported by Held (3); more recently Mader and Pimbley have carried out extensive modelling of the process (4,5). Some differences between the jet initiation of covered and bare explosives were reported previously (1).

Table 2 shows measured threshold conditions for the jet initiation of a pressed (TNT) and cast explosive (Composition B). The V^2d value (where V the critical jet velocity and d the jet diameter) of 15 $mm^3/\mu s^2$ for Composition B falls between the values of 5.8 and 29 $mm^3/\mu s^2$ reported by Held (3) and Mader and Pimbley (5) respectively.

The V^2d value for pressed TNT represents the first reported measurement on this explosive and its relationship to that for Composition B is similar to that reported for other shock sensitivity type tests (14).

NATURE OF THE BOW WAVE AND EXPLOSIVE DENSITISATION

Reference to Tables 1 and 2 shows that the critical steel thicknesses for the initiation of covered and bare Composition B are 59.8 and 138 mm respectively. Corresponding values for pressed TNT are 104 and 166 mm. Another measure of the effect is obtained by comparing the critical free flight jet velocities. For Composition B the values are 5.2 and 3.2 mm/μs for the steel covered and bare configurations respectively (see Tables 1 and 2). For pressed TNT the corresponding values are 4.1 and 2.9 mm/μs.

These differences in the sensitivities of the bare and covered configurations are attributed to the bow wave in the latter case affecting the explosive so that it is not initiated by the action of the following jet. The similar pattern of results shown by Composition B and pressed TNT indicates that bow wave desensitisation is a significant effect that can occur in both cast and pressed explosives. Further the test arrangements shown in Figure 1 and described herein allow a convenient way of measuring and examining the effect.

TABLE 2
Jet Initiation Characteristics of Bare Explosives

Explosive	Critical Steel Cover Thickness mm	Critical Jet Characteristics		
		Velocity mm/μs	Diameter mm	V^2d $mm^3/\mu s^2$
COMPOSITION B (ϱ = 1.65 Mg/m^3)	138	3.2	1.5	15
PRESSED TNT (ϱ = 1.52 Mg/m^3)	166	2.9	1.5	13

Flash radiographs show that for bare Composition B initation at the critical condition occurs promptly within about 1 μs and a few millimeters of the jet striking the explosive surface. This is shown in Figure 4 and confirms the modelling results of Mader and Pimbley (5). These values are in contrast to the long runs (about 40 mm) and times (about 11 μs) to detonation for the critical initiation of covered Composition B (1), (illustrated by the radiograph in Figure 2).

The critical jet penetration velocities in Composition B have been measured and are given in the last column of Table 1. Also, by substituting the measured values for the critical free

flight jet velocities (given in Table 1), the following values are obtained for the jet penetration rate in Composition B; steel cover system 3.62 mm/μsec, aluminum cover system 3.48 mm/μsec, Plexiglas cover system 3.38 mm/μsec, and steel/Plexiglas cover system 3.38 mm/μsec. These values are slightly lower than the measured values and agree with the trend previously reported. Flash radiographs indicated a low density zone in the bow wave in Composition B immediately forward of the jet tip (see Figure 2). This zone is more evident close to the onset of detonation. These observations may be reconciled by assuming the explosive has reacted (not detonated) within the bow wave prior to the arrival of the jet tip and that product movement has commenced away from the low density zone. Thus the penetration velocity is higher than for an equivalent inert material. Furthermore, the intense shear occurring in the explosive between the front of the bow wave and the jet tip may be the cause of reaction but not detonation. Measurements from the radiographs suggest the bow wave to be up to about 10 mm thick with a duration of up to about 3 μs. We have not observed the low density zone in flash radiographs of the jet penetration of Plexiglas.

It has been suggested that the mechanism of shock desensitisation results from the initial low pressure part of a multiple shock compressing and removing the reaction sites from the following larger shock (15). However, as discussed above there is evidence that during the jet penetration of Composition B substantial reaction occurs within the bow wave and that this alters the shock profile by decreasing the pressure in the zone adjacent to the jet tip. Thus there may be more than one explanation for the observed shock desensitisation of explosives.

DEMONSTRATION OF BOW WAVE DESENSITISATION

Bow wave desensitisation is demonstrated by the sequence of flash radiographs shown in Figure 5(a), (b) and (c). The experimental set-up is similar to that shown in Figure 1. The Composition B receptor was composed of two 52 mm long cylinders separated by a 15 mm wide air gap. The steel cover thickness of 64 mm was selected to be greater than the critical value for the initiation of covered Composition B (59.8mm).

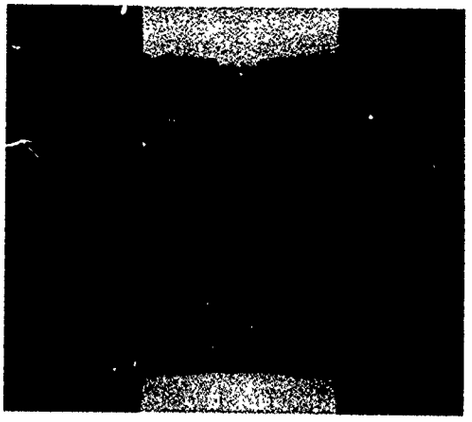

Fig. 5(a). Flash radiograph of a jet penetrating the top covered cylinder of two Composition B cylinders in series separated by an air gap. The top charge is not detonating

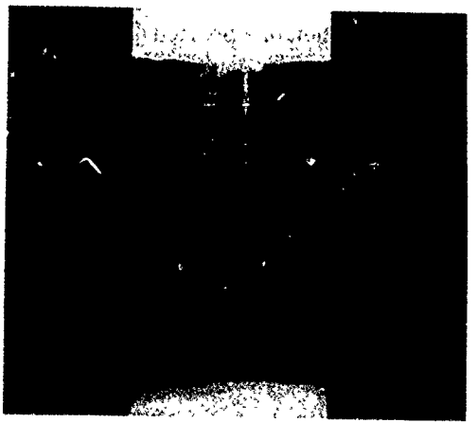

Fig. 5(b). Flash radiograph 3.5 μs later from 5(a) with jet in air gap. The top charge has failed to detonate

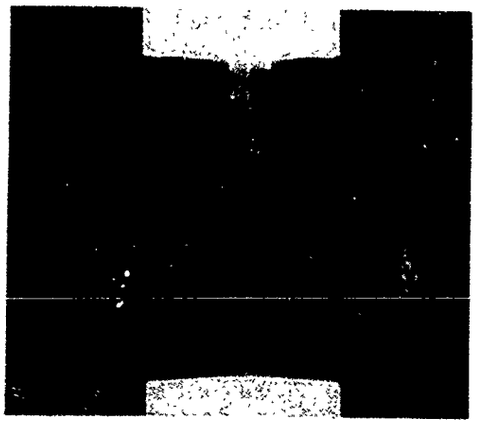

Fig. 5(c). Flash radiograph 7.0 μs later from 5(b) showing bottom charge detonating but top charge failing

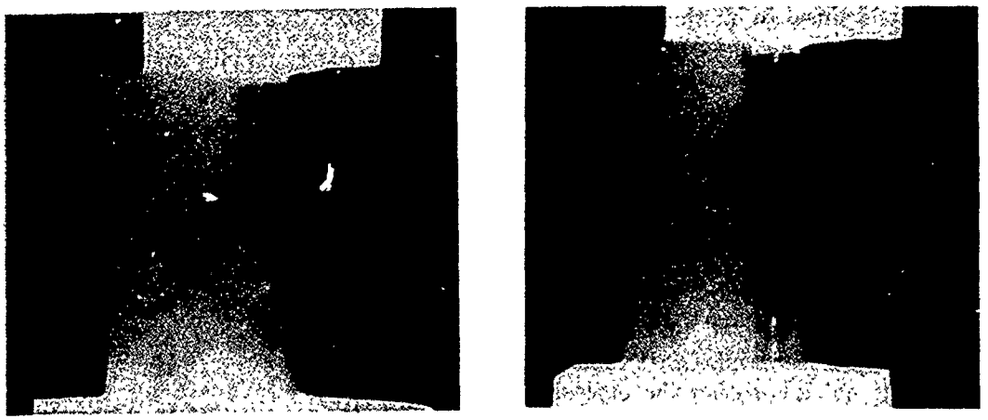

Fig. 6(a). Flash radiographs of a jet missing a void located at a predetermined position within a covered Composition B charge. The round failed to detonate

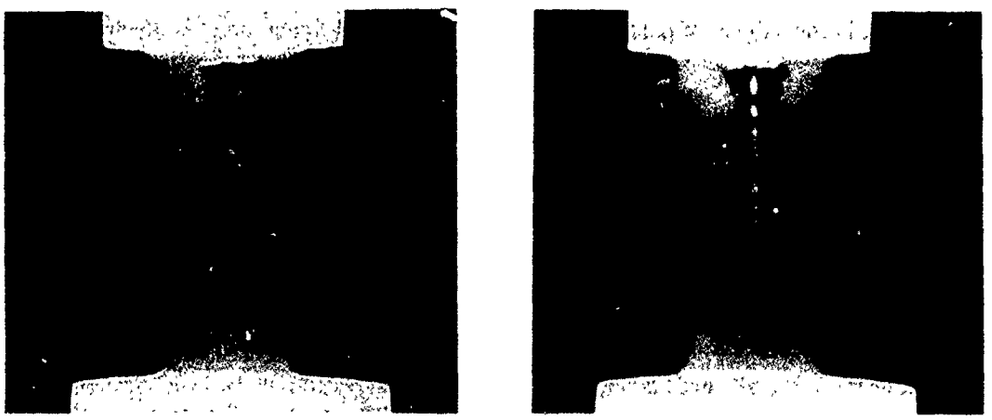

Fig. 6(b). Flash radiographs as per 6(a) but showing prompt detonation from the jet striking the far side of the void

Ten control shots fired using the 64 mm thick cover and a single Composition B cylinder of 102 mm long all failed to record a detonation. The function of the air gap was to dissipate the bow-wave shock and allow the jet to strike bare Composition B. Independent measurements gave the velocity of the jet exiting the steel plate as 5.1 mm/μsec (measured in air). The measured jet velocity in the air gap between the explosive cylinders was 4.6 mm/μsec.

Figure 5(a) shows that, as expected, the jet has penetrated the top cylinder of Composition B causing disruption but not detonation. Free surface movement of the Composition B into the air gap from the action of the bow wave is just visible. In Figure 5(b), 3.5 μs later, the jet is in the air gap. Figure 5(c) taken a further 7 μs later shows that the bottom cylinder has detonated promptly while the top cylinder has failed and is in a state of disruption.

NOVEL TECHNIQUE FOR THE CONTROLLED INITIATION OF EXPLOSIVES

The discoveries in the preceding sections have been used to devise a novel technique for the controlled initiation of explosives. The method consists of firing a high velocity jet at an appropriately covered explosive charge containing a void at a predetermined position. The void is located where the onset of prompt detonation is required and may be on the surface or within the bulk of the charge. The function of the void is to dissipate the desensitising bow wave shock.

When the jet is aimed to hit the void prompt detonation occurs on the far surface of the void and spreads consuming the explosive in all directions. However, when the jet is aimed to miss the void the explosive is disrupted and fails. The technique is demonstrated by the flash radiographs shown in Figures 6(a) and (b). The set-up consisted of a Composition B charge containing a spherical void 19 mm diameter along the axis and 60 mm from the top surface. The charge was covered by a 76 mm thick steel cover.

Figure 6(a) shows the jet missing the void and disrupting but not detonating the explosive. Figure 6(b) shows the jet hitting the void and prompt detonation occurring. Several shots have been fired for both conditions without a contradiction.

The technique is the subject of patent action.

SUMMARY

We have shown that the initiation of covered Composition B results from the bow wave associated with the jet penetration of the explosive. This mechanism has been shown to have different initiation characteristics to that for the jet initiation of bare Composition B. We have demonstrated that the bow wave can have a significant desensitising effect on both a cast explosive (Composition B) and a pressed explosive (TNT). These effects can be measured using the test arrangement described.

A novel technique is described and demonstrated that uses a shaped charge jet to either disrupt an explosive or cause prompt detonation at a predetermined position within the charge.

ACKNOWLEDGEMENTS

At MRL the authors wish to thank Dr. G. Jenks and Mr. F. May for helpful discussions and Messrs. L. Learmonth and T. Bussell for assistance with the experiments. At BRL the authors wish to thank Mr. G. Boyce for helpful discussions and assistance with the experiments.

REFERENCES

1. M. C. Chick and D. J. Hatt, "The Mechanism of Initiation of Composition B by a Metal Jet", Seventh Symposium (International) on Detonation, NSWC MP 82-334, pp 352-361, June 1981.
2. M. C. Chick and D. J. Hatt, "The Initiation of Covered Composition B by a Metal Jet", Propellants, Explosives, Pyrotechnics, 8, pp 121-126, 1983.
3. M. Held, "Initiating of Explosives, a Multiple Problem of the Physics of Detonation", Explosivstoffe, 5, pp 98-113, 1968.
4. C. L. Mader and G. H. Pimbley, "Jet Initiation of Explosives", L.A. Report 8647, Feb. 1981.
5. C. L. Mader and G. H. Pimbley, "Jet Initiation and Penetration of Explosives", J. Energetic Materials, 1, pp 3-44, 1983.
6. W. J. Dixon and M. A. Mood, "A Method for Obtaining and Analysing Sensitivity Data", American Statistical Ass., Vol. 43, pp 109-126, 1948.
7. G. Birkoff, D. MacDougall, E. M. Pugh and G. Taylor, "Explosives with Lined Cavities", J. Appl. Phys., Vol. 9, pp 563-582, 1948.
8. R. Di Persio and J. Simon, "The Penetration Standoff Relationship for Idealised Shaped Charge Jets", BRL Report MR 1542, 1964.
9. M. C. Chick, R. B. Frey, J. J. Trimble and A. Bines, "Jet Penetration in Plexiglas', Eighth International Symposium on Ballistics, Orlando, USA, pp V1121-V1126, Oct 1984.
10. L. Green, "Shock Initiation of Explosives by the Impact of Small Diameter Cylindrical Projectiles", Seventh Symposium (International) on Detonation, NSWC MP 82-334, pp 273-277, June 1981.
11. M. Chick Report in preparation.
12. J. Starkenberg, Y. Huang and A. Arbuckle, "Numerical Modelling of Projectile Impact Shock Initiation of Bare and Covered Composition B", J. Energetic Materials, Vol 2, pp 1-41, 1984.
13. R. Frey, G. Melani and S. M. Carter, "Determination of the Residual Jet Parameters Required to Initiate Cased Explosive Charges", BRL Report ARBRL-MR-2753, May 1977.

14. A. M. Weston, J. R. Walton, E. James, E. L. Lee and L. G. Green, "Correlation of Shock Initiation Tests for Explosives and Propellants", UCRL-85614, July 1981.

15. A. W. Campbell, W. C. Davis, J. B. Ramsay and J. R. Travis, "Shock Initiation of Solid Explosives", Phy. Fluids, 4, pp 511-521, 1961.


Jet Initiation of Solid Explosives
REMOVING DANGER
STUDY OUTLINE

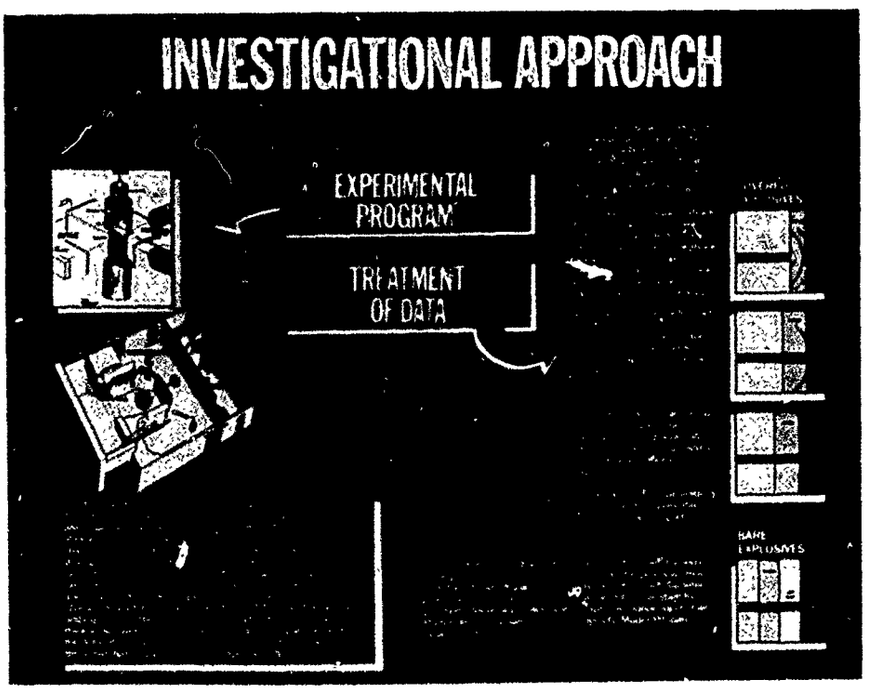
INVESTIGATIONAL APPROACH
EXPERIMENTAL PROGRAM
TREATMENT OF DATA
BARE EXPLOSIVES

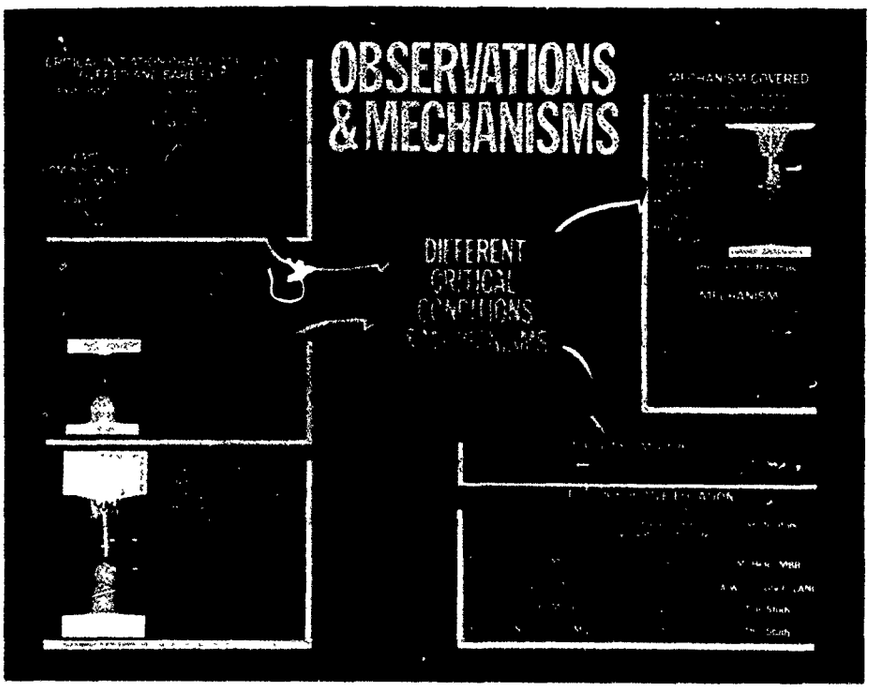
OBSERVATIONS
& MECHANISMS
DIFFERENT
CRITICAL

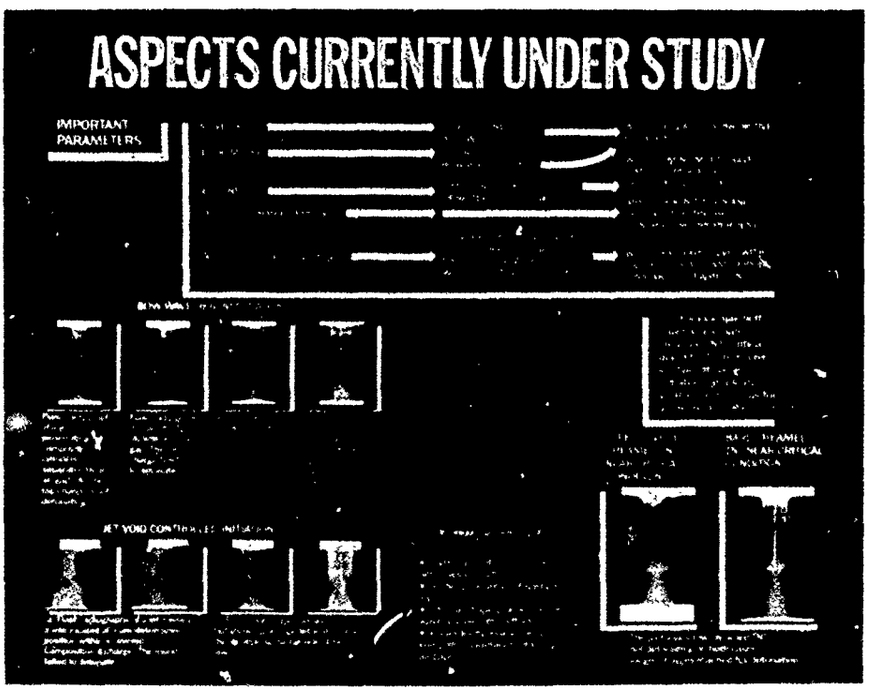
ASPECTS CURRENTLY UNDER STUDY
IMPORTANT
PARAMETERS

SUPERPOSITION OF SHOCK WAVES AND REACTION WAVES FOR THE INITIATION OF HIGH EXPLOSIVE CHARGES

Manfred Held
Messerschmitt-Bölkow-Blohm GmbH
D-8898 Schrobenhausen/W. Germany

For the investigation of detonative centering devices a so called biplanar observation method is well suited. With this method the wave front of donor charge and the symmetry of the wave at the output side of the acceptor charge are measured with high resolution. With channel plates made of 6 mm thick brass a superposition of the shock that had passed across the carrier plate and of the reaction wave emanating from the transfer charge was found. Surprisingly, for a critical transfer charge diameter the off-center distance of the detonation wave at the output of the acceptor charge is larger than that of the wave at the input. In this case also the time delay is relatively large. If the diameter of the transfer charge is increased by a factor of two compared to the critical diameter a symmetric detonation wave is produced with no additional time delay.

INTRODUCTION

In some shaped charge warheads "channel plates" are used as detonative centering devices. Therefore test arrangements were developed for such channel plate detonative centering devices using the experience gained from the testing devices initialiy developed for the point initiation coupler (1). These new test devices turned out to be even simpler than the previous ones.

TEST SET-UP

For the observation of the arriving detonation wave and of the detonation front behind a detonative centering device, it is required to observe the event in two different planes. The technique, which was developed for this purpose is therefore called "Biplanar Observation Technique" (2).

The so called "Profile Streak Technique" is used to determine the profiles of the detonation wave or shock wave, respectively. For this purpose a glass sheet of .1 mm thickness or a plexiglas foil of .5 mm thickness is arranged immediately in front of the centering device. The glass foil is back illuminated. The light source frequently consists of an exploding wire arranged in a small diameter plastic tube. The arriving detonation wave or shock wave destroys the glass or plexiglass layer in a pattern which corresponds to the profile of the arriving wave. It is therefore possible to determine exactly the amount of eccentricity as well as the time delay with respect to the axis of the centering device by the evaluation of this streak record. The phase velocities of the arriving detonation or shock waves are considerably higher than the velocity of sound in the transparent media.

The so called "Multi Streak Technique" (3) is used to determine the detonation front at the rear face of the acceptor charge along a set of spaced lines. A single line perpendicular to these and passing through the axis, serves as a reference mark on the multi-streak record.

A test arrangement was developed which uses precisely manufactured and tightly fitting components in order to make sure that the device is always assembled with a precision better than $\pm .1$ mm and to provide for the ruggedness in a rough test-site environment.

For this kind of tests, holes of different diameters were drilled in a brass disk (material

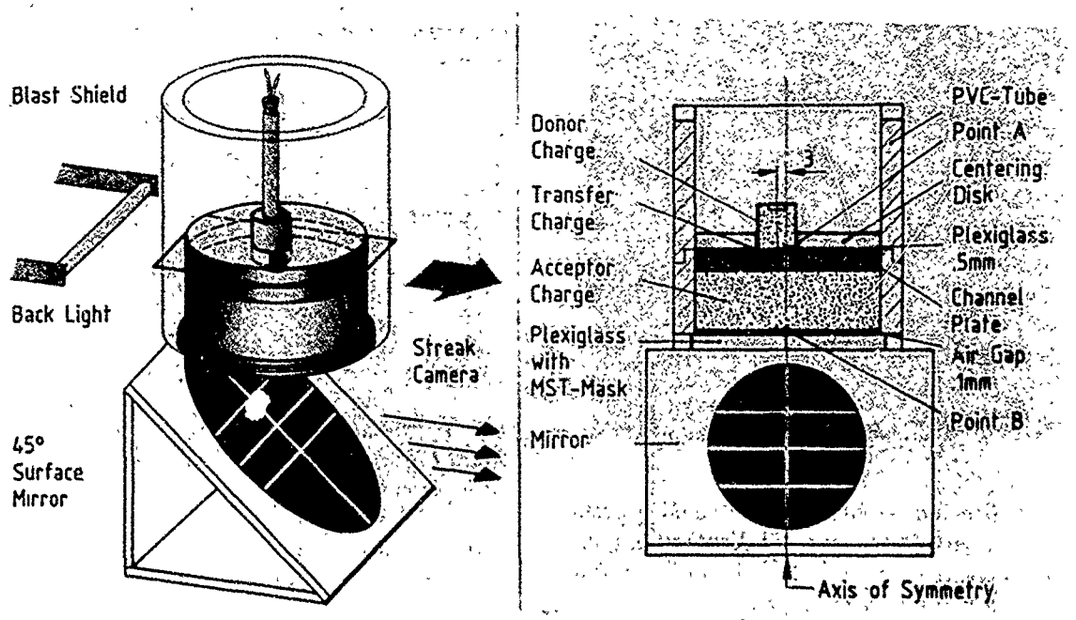

Fig. 1. Test set up to the Biplanar Observation Technique for measuring the output of the donor charge and the symmetry of the detonation wave at the output side of the acceptor charge

MS 58) and the holes were filled with RDX/Wax/Graphite 94/5/1 or Tetryl and pressed at pressures of 1000 bar. These charges are used as "transfer charges". A pressed explosive charge of RDX/Wax, 95/5 of 15 mm length and 14 mm diameter, was used as a donor charge in this example and a centering annular disk was used for aligning and retaining. An electric detonator $KX_1/20$ was used to initiate the donor charge with small time jitter and triggered from the streak camera. A plexiglass foil, .5 mm thick was arranged for monitoring the initiating detonation wave profile. As an acceptor, a cast explosive charge of the composition, TNT/RDX 25/75 ws used. The dimensions were 64 mm diameter and 20 mm length. The component parts were kept in place by a tube of PVC with an outer diameter 80 mm and a wall thickness of 8 mm. This tube acts also as a light shield against the luminous output from the donor charge. The plexiglass disk with the multistreak mask was centrally aligned with a precision of $\pm .1$ mm by this tube as well. Three streak lines were used at distances of 10 mm each, together with a perpendicular symmetry line. The arrival of the detonation wave at the rear end of the detonative centering device is imaged on the CORDIN streak camera model 200 with the aid of a 45° surface mirror. The streak-slit which is normally used in the streak camera is removed for applying this multistreak technique. The donor charge was always arranged 3 mm off-axis, such that the detonation wave had a delay of approximately .2 μs in the symmetry axis (Fig. 1).

This arrangement makes it possible to maintain the desired precision of the measuring device also under the adverse environments and rough treatment which normally occur in a test site.

TEST RESULTS

The following two figures show the streak records gained with this arrangement for RDX/Wax/Graphite 94/5/1 (Fig. 2) and Tetryl (Fig. 3) as transfer charges.

Fig. 4 gives the evaluation of the streak records made with the explosive charge of RDX/Wax/Graphite 94/5/1 used as a transfer charge. An almost symmetrical breakthrough is achieved at the donor charge of TNT/RDX

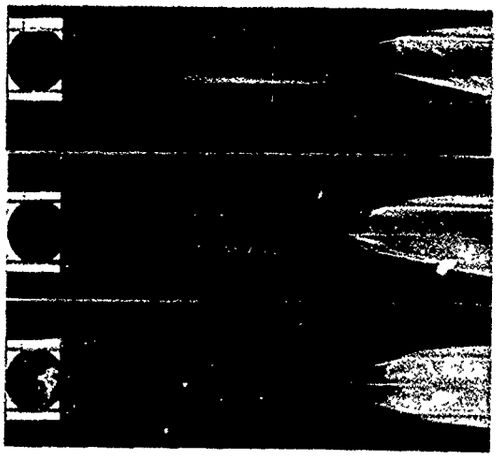

Fig. 2. Biplanar streak records of a detonating centering device using RDX/Wax/Graphite 94/5/1 as transfer charges in a 6 mm brass disk with 4, 5 and 6 mm diameter

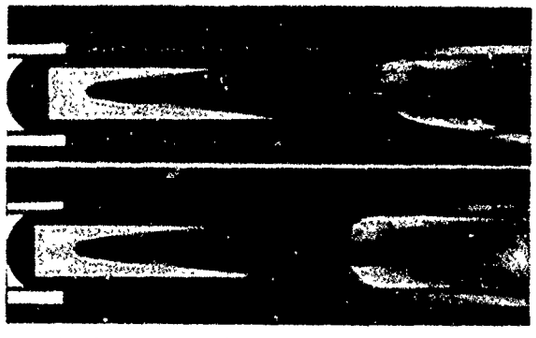

Fig. 3. Streak records of a detonating centering device using Tetryl as transfer charges in a 6 mm brass disk with 5 and 6 mm diameter

25/75 if a 6 mm diameter of the transfer charge is used. Only a very slight bulge can be observed on the initiation side. Using a 5 mm diameter transfer charge, the bulge on the branch of the streak line which faces the initiation side is much more distinct. In the test with a 4 mm diameter transfer charge, only an eccentric detonation wave appears. Surprisingly this detonation wave has an eccentricity of 6 mm while the eccentricity at the input is only 3 mm. In the experiments with 4 and 5 mm diameters of the transfer charge the acceptor does not fully detonate up to the outer periphery at 32 mm on the side opposite to the initiation. Obviously, the detonation is initiated only after a certain run-up distance and run-up time, respectively, due to an interaction between the shock wave behind the brass disk and the reaction wave (partial detonation) emerging form the transfer charge.

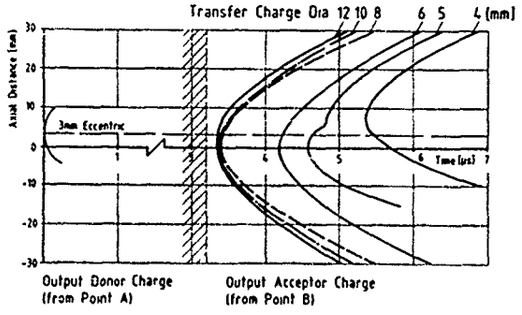

Fig. 4. Evaluation of the streak records of Fig. 2 and Fig. 7 with RDX/Wax/Graphite 94/5/1 as transfer charges

It must also be mentioned that initiation does no longer occur, when the RDX/Wax/Graphite 94/5/1 transfer charge is 3 mm in diameter or less. This means that the 6 mm brass disk attenuates the detonation wave from the donor charge so much that a direct initiation of the acceptor charge without any support from the transfer charge in the channel plate is not directly possible.

If Tetryl is used in the channel plate rather than RDX/Wax/Graphite the results are very similar. There is a difference, though, because transfer charge diameters in the Tetryl experiments 6 mm, 5 mm and 4 mm correspond to transfer charge diameters of 5 mm, 4 mm and 3mm in the RDX/Wax/Graphite experiments, respectively. A 4 mm diameter Tetryl transfer charge fails initiation of the acceptor charge just like a 3 mm diameter transfer charge of RDX/Wax/Graphite. In the test with a Tetryl transfer charge diameter of 5 mm an eccentric detonation wave occurs which does not completely propagate through to the periphery of the acceptor charge on the face opposite the initiation side. In the test with the 6 mm diameter of the transfer charge a marked bulge on the initiation side can be observed which is an interaction of the shock wave going through the brass and the reaction wave going through the transfer charge (Fig. 5).

In Fig. 6 the time differences between the output of the detonation wave of the donor charge (point A) and the first breakthrough of the detonation front on the face opposite the initiation

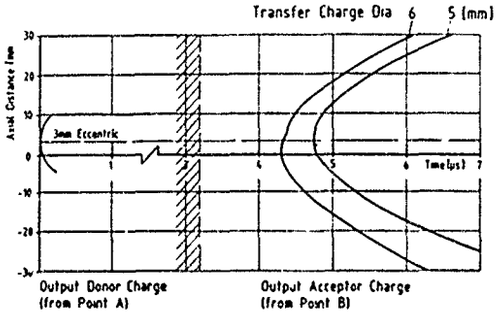

Fig. 5. Evaluation of the streak records of Fig. 3 with Tetryl as transfer charges of 5 and 6 mm diameter

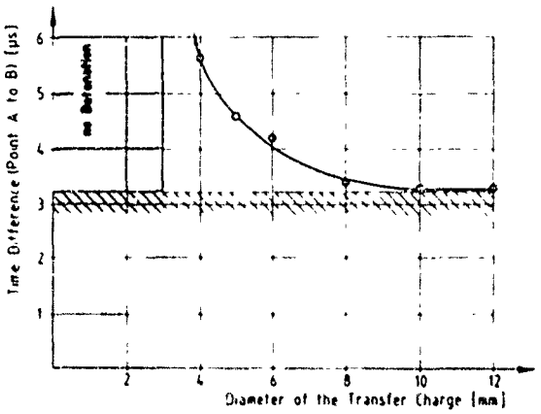

Fig 6 Time difference (points A to B) between the output of the detonation wave of the donor charge and the first breakthrough of the detonation front on the face opposite the initiation side of the acceptor charge

side of the acceptor charge (point B) are shown as a function of the diameter with RDX Wax. Graphite as a transfer charge. The time difference calculated from the theoretical detonation velocities and distances should be approximately 3.2 µs

With a transfer charge of 8 mm diameter and larger the measured time delay corresponds to the theoretical value of 3.2 µs within the accuracy of measurement

The streak records of the tests made using channel plates with transfer charges of 8, 10 and 12 mm diameter are shown on Fig. 7. Surprisingly the evaluations of the detonation breakthrough of the diaphragms with transfer charges of 8, 10 and 12 mm diameters show rather symmetric detonation waves for the diameters of 8 and 10 mm while the test with the transfer charges of 12 mm diameter already shows slight deviations from the symmetry (Fig. 4.).

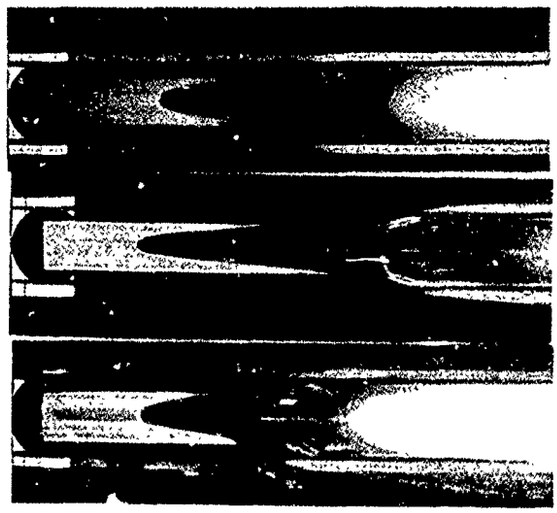

Fig. 7. Streak records of a detonating centering device using 8, 10 and 12 mm diameter RDX/ Wax/Graphite transfer charges in 6 mm brass (10 mm Dia was observed with a different streak velocity)

The influence of the plate thickness was tested with constant diameters of 5 mm for the transfer charges and eccentric initiation by an off-center distance of 3 mm. Tetryl was used for the transfer charges. The streak records of these experiments are shown in Fig. 8 for brass disks of 5 mm to 7 mm thickness. The corresponding evaluations of the breakthrough in the symmetry lines are plotted in Fig. 9. In the test with the 5 mm thick plate, the detonation breakthrough occurs eccentrically 6 mm out of the symmetry axis. In the test with the 6 mm plate, the off-set from the symmetry axis is 4 mm. With the 7 mm plate an almost symmetric breakthrough of the detonation front occurs with a distinct bulge on the initiation side. An increase of the delay time corresponding to the slightly increased detonation distance with the thicker disks is easily understandable. It is in the order of .13 µs per mm of thickness.

SUMMARY

For the investigation of detonation centering devices a so called biplanar observation method is well suited. In this method the arriving detonation wave or shock wave is measured

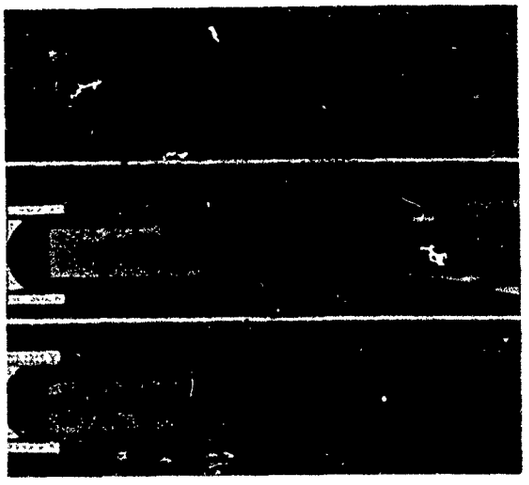

Fig. 8. Biplanar streak records of a detonation centering device with 4, 6 and 7 mm thick brass disks and with 5 mm diameter Tetryl transfer charges

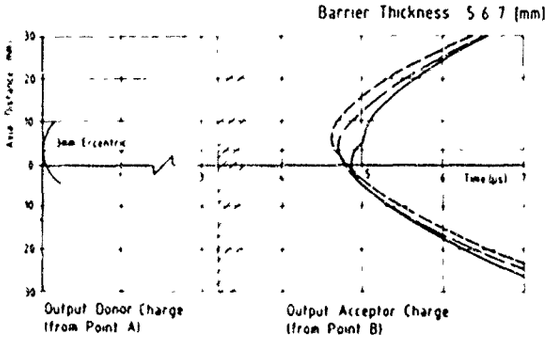

Fig 9. Evaluation of the streak records of Fig. 8 with different barrier thicknesses of 5, 6 and 7 mm

with respect to its eccentric position as well as with respect to the time delay in the symmetry axis. The symmetry of the detonation wave at the output side of the acceptor charge is also measured by this method.

With channel plates made of 6 mm thick brass disks, superpositions of the shock wave passing through the carrier plate and the reaction wave going through the transfer charge were found. Using the brass disk fo 6 mm thickness in the selected combination of donor and acceptor a detonation wave could no longer be observed, as long as the diameter of the transfer charge was kept small.

Surprisingly for a critical transfer charge diameter the off-set of the detonation wave at the output of the acceptor charge is larger than that determined by the wave at the input. In these cases also no complete detonation occurs at the face opposite to the initiation side of the acceptor charge. If the transfer charge diameter is increased by 1 mm compared to the critical transfer charge diameter a symmetric detonation wave with an eccentric bulge on the end facing the initiation side is the general result. If the transfer charge diameter is increased by 2 mm compared to the critical diameter an almost symmetric detonation wave is produced. If the transfer charge diameter is gradually increased beginning with the critical diameter, the time delay decreases with respect to the values expected from theory. With a diameter which exceeds the critical diameter by 4 mm or more, a more or less symmetric detonation wave with no significant time delay results.

A change of the plate thickness—increasing or decreasing - by 1 mm (to 5 and 7 mm respectively) from an initial value of 6 mm also shows that a thinner plate results in a higher influence of the shock wave with a more eccentric and less corrected output detonation wave. Conversely a thicker plate causes the shock wave to have less influence and thus the reaction wave through the channel is dominating. Therefore, in this case, a better corrected detonation wave at the output can be observed.

CONCLUSION

These series of experiments demonstrate the effect of two mechanisms. The first is the reaction wave through the transfer charge and the second is the shock wave through the barrier. With increased transfer charge diameter the reaction wave is dominant, resulting in an improved symmetry on the output of the acceptor charge (point B in Fig. 1). With increased barrier thickness the influence of the shock wave is diminished and so the symmetry of the detonation wave in the acceptor charge is also improved.

REFERENCES

1. M. Held, "Streak Technique as a Diagnosis Method in Detonics," I. Int. Symposium on Ballistics; IV; 177-210, 1974.

2. M. Held, "Method of Observing Processes in the Interior of Explosive," X. Int. Congress on High-Speed-Photography; 286-291, 1972.

3. M. Held, "Orthogonal Multi-Streak Recording Technique," IX. Int. Congress on High-Speed-Photograph; 126-129, 1970.

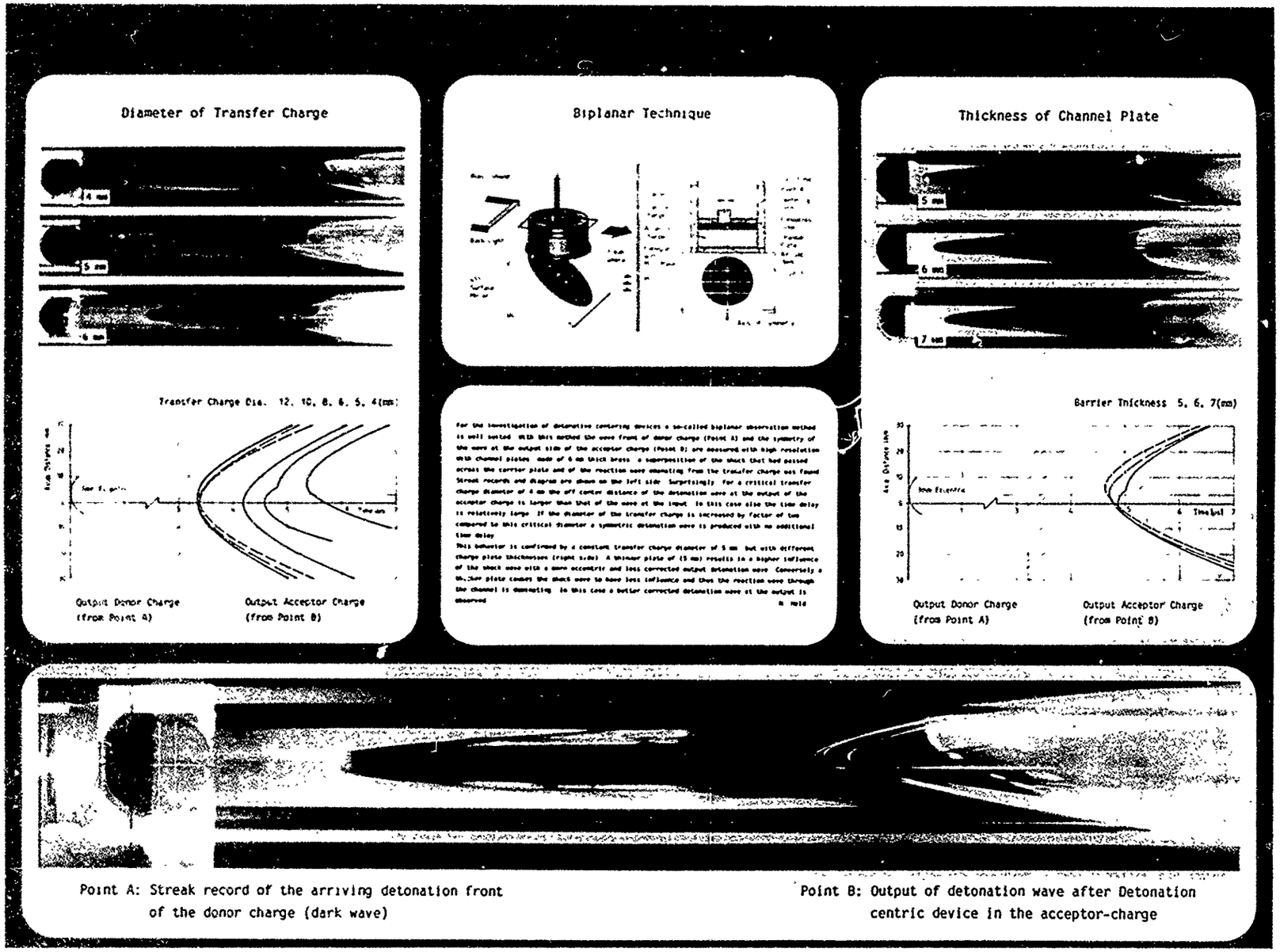
Diameter of Transfer Charge
4 mm
5 mm
6 mm
Transfer Charge Dia. 12, 10, 8, 6, 5, 4(mm)
Output Donor Charge
(from Point A)
Output Acceptor Charge
(from Point B)
Biplanar Technique
Thickness of Channel Plate
5 mm
6 mm
7 mm
Barrier Thickness 5, 6, 7(mm)
Output Donor Charge
(from Point A)
Output Acceptor Charge
(from Point B)
Point A: Streak record of the arriving detonation front
of the donor charge (dark wave)
Point B: Output of detonation wave after Detonation
centric device in the acceptor-charge

NUMERICAL SIMULATION OF JET PENETRATION OF HMX AND TATB EXPLOSIVES

D. Pirotais, J. P. Plotard, J. C. Braconnier
Commissariat á l'Energie Atomique
B.P. n° 27 — (94190) Villeneuve-St. Georges (France)

The initiation of aluminum coated X2 and T2 (HMX and TATB explosives) by the impact of shaped charge jets has been studied both experimentally and numerically. Our numerical calculations agree well with all the experimental data, and show the mechanism of initation for these explosives. X2 is initiated by the precursor shock travelling through aluminum. For T2, the reactive wave produced by this precursor shock must be sustained by the following compression wave in order to build up to detonation.

I — INTRODUCTION

The study of the initiation of explosives by projectiles is necessary in the assessment of the hazard and vulnerability of munitions.

A great number of publications has been devoted to the problem, but generally the diameters of the projectiles are relatively large ($\phi \geq 5$ mm) and their velocities are lower than 2.000 mm/μs. Some results and discussions about the initiation by this kind of projectiles can be found for example in (1) to (5).

It would be interesting to see how explosives react when impacted by smaller and faster projectiles like shaped charge jets. Some experimental results (6) lead us to question our understanding of the mechanism of initiation by these projectiles.

A numerical study of this kind of experiment is presented in (7); in (8), computations with high velocity and relatively large diameter (10 mm) projectiles are used to build a model for the penetration of inert and reactive materials.

Our goal in this paper is the knowledge of the critical conditions of initiation, but also of the build-up to detonation mechanism inside HMX and TATB explosives.

Therefore, we have impacted X2 (a HMX based explosive) and T2 (a TATB based explosive), with shaped charge jets. We have observed the targets optically and with flash X-ray tubes. Then, the numerical simulation of these experiments has been performed.

The numerical results are first compared with the experimental observations; then we give a description of the phenomena arising in the targets as they are computed by the code.

II — EXPERIMENTAL SET-UP

A shaped charge jet is fired into explosive targets at a 500 mm distance (Figure 1).

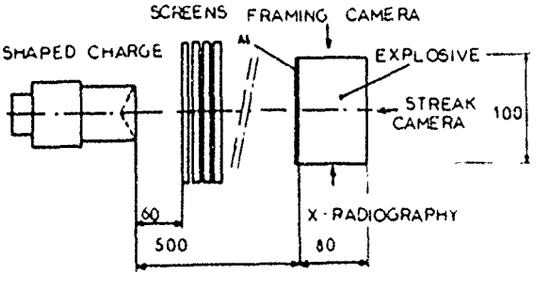

Fig. 1. Experimental set-up

The liner of the shaped charge is made of copper, its diameter is 60 mm. The jet diameter is 1.6 mm, and the maximum velocity at the jet tip is 7.8 mm/μs.

Steel barriers placed between the charge and the target absorb the first parts of the jet (those of maximum velocity) and thus allow to adjust the velocity of impact by varying the barriers thickness.

The targets are cylinders of explosives, 80 mm high and 50 mm in radius, coated on the impact face by a sheet of aluminum (2 mm of coating for T2 and 4 mm for X2).

Three experimental observations are made simultaneously:

- a general survey of the experiment is made through the means of a framing camera
- streak camera records are made on the rear face of the target to observe detonation.
- a visualization of the phenomena arising in the target itself is obtained by X-ray radiography.

Experimental results are presented together with numerical modeling in the course of the paper.

III – COMPUTATIONAL METHOD

Since the projectile is subject to large deformations before the detonation occurs, we have to use an eulerian code. The following computations have been performed with the hydrodynamic code CEE (9) including the TCD model for explosive decomposition (10).

The main features of this code have already been described in (9) and (10): a first order scheme is used to compute non-stationary flows of compressible fluids in either plane or cylindrical coordinates. The TCD model. which is described in more detail in (10), is based on the same principles as the Forest-Fire model (11).

We will now focus on the numerical and physical hypothesis of our computations.

III.1 – Jet representation

Shaped charge jets have an extremely complicated structure. They may be discontinuous, made of numerous fragments which in addition have different velocities, decreasing from high values (over 7 mm/μs) at the jet tip, to medium values at the rear of the jet (∼ 3 mm/μs). Moreover, measurements performed at the ISL (12) indicate that the jet is hot (600 K to 1200 K), generally in solid phase, and may exhibit a non negligable level of porosity which can reduce the metal density to 90% of its normal density.

In our computation we have modeled the jet by an infinite cylindrical projectile with flat end. We have also assumed a uniform velocity throughout the jet, a normal temperature and density (300 K, 8.90 g/cm³) and a fluid phase. Despite the evident approximations with regard to the preceeding description, we were able to verify, by computations of impact on inert targets, that the numerical results (penetration velocity and pressure at jet/target interface) were in good agreement with the experiments.

III.2 – Numerical grid

Two main conditions must be satisfied:

First, a good discretization of the projectiles which, according to their small diameters (1.6 mm), necessitates the use of mesh cells of about 0.1 mm to 0.2 mm.

Second, an accurate computation of the explosive reaction zone, which is of highest importance for the efficiency of the combustion model used. In the conclusion of (10), a minimum of 4 to 6 cells in the reaction zone was recommended in order to obtain reliable results. Since the width of the X2 reaction zone is about 0.3 – 0.4 mm, and that of T2 1.5 mm, we must at least use 0.1 mm cells for the first explosive and 0.3 mm for the second.

According to these remarks, we used mesh cells, whose sizes in the most refined regions (jet/target interface) were 0.1 mm for X2 and 0.125 mm for T2.

An other problem arises for T2: because of its low sensitivity, the projectile must reach a great depth in the explosive (3 to 4 cm) before the first zones of fully reacted explosive appear, when the size of the cells used permit to described only a square of about 2 cm, due to the memory limitations of the computer (CDC 7600). This difficulty is alleviated with the inclusion of an automatic tracking of the jet tip in the program, which matches the grid to the position of the jet

at each time of its progression in the explosive. We could then bring to the end our computation with T2.

III.3 — Reaction rate

Chemical reactions are expressed in terms of variations of the mass concentration of solid explosive

$$w = \frac{ms}{ms + mg}$$

$$\ln\left(-\frac{1}{w}\frac{dw}{dt}\cdot\Delta to\right) = \sum_{i=o}^{4} a_i \left(\frac{P}{Pcj}\right)^i \quad (P \leqslant P_1)$$

$$\ln\left(-\frac{1}{w}\frac{dw}{dt}\cdot\Delta to\right) = \sum_{i=o}^{4} a_i \left(\frac{P_1}{Pcj}\right)^i \quad (P \geqslant P_1)$$

The contents of the burn rate are listed in Table I.

TABLE I

	X2	T2
a_o	− 4.95	− 10.37
a_1	14.57	31.71
a_2	12.22	− 37.46
a_3	−44.9	23.25
a_4	32.11	− 4.00
P_1 (kb)	279	290
P_{cj} (kb)	354	300
Δto (s)	10^{-6}	10^{-6}

III.4 — Equations of state

For the solid phase of X2 and T2, we used the same equations and the same constants as in (10) for X2 and T. So did we for the detonation products and the mixture of gas-solid phases, except for the formula of T2 detonation isentrope. Instead of the usual formulation, $Pis = \sum_{i=o}^{4} a^i (\ln v)^i$, which in the case of T2 led to unacceptable difficulties, we chose a modified Wilkins formulation:

$$Pis = A\, v^{-\delta} + w\, G1\, v^{-(1+w)} \quad (v \leqslant v_c)$$

$$Pis = B\, e^{-kv} + w\, G2\, v^{-(1+w)} \quad (v \geqslant v_c)$$

with

$A = 2.555\ 10^{10}$ $\quad \delta = 2.8$ $\quad w = 0.35$
$B = 5.05\ 10^{12}$ $\quad k = 7.34$
$G_1 = 1.699\ 10^{8}$ $\quad G_2 = 2.095$ $\quad 10^{10}$
$v_c = 0.4$

(all constants in CGS units).

For copper (shaped charge liner) and aluminum (protection of the explosive against undesirable fragments) we used the so-called "multiphase" equation of state, a detailed description of which can be found in (13).

IV — EXPERIMENTAL AND NUMERICAL RESULTS

IV.1 — Explosive X2

The experimental result is the determination of the critical jet velocity. Three computations

TABLE II

JET TIP VELOCITY mm/μs	JET DIAMETER mm	RESULT	V^2d $mm^3/\mu s^{-2}$
X2 (experiments)			
		Critical	32 ± 4
6.5	0.5	Fail	21
6.3	1	Detonation	40.2
5.3	1	Fail	28.1
4.9	1.6	Detonation	38.4
3.6	2	Fail	25.9
X2 (computations)			
4.1	1.6	Fail	26.9
4.9	1.6	almost tail	38.4
5.2	1.6	Detonation	46.6

have been performed, with jet velocity close to the experimental critical velocity. The results are reported in Table II.

There is a good agreement between experimental and numerical results.

IV. 2 — Explosive T2

The critical velocity of the jet can be deduced from the results in Table III. But, of more interest than this velocity, are the informations given by the experimental data, especially by the X-ray radiographs. Therefore, we have simulated an experiment with a jet of 7.8 mm/μs of velocity and 1.6 mm in diameter.

a — General aspect of the flow

On Figure 2.a. to 2.c are presented the X-ray radiography and the numerical pressure field 3.8 μs after the impact of the shaped charge jet against the target.

In both cases we see:

— A reactive shock wave which is to become a detonation wave

— A compression wave, attached to the jet, travelling in the partially decomposed explosive

b — Penetration velocity of the jet

We have plotted the (x,t) diagram of the jet on Figure 3.

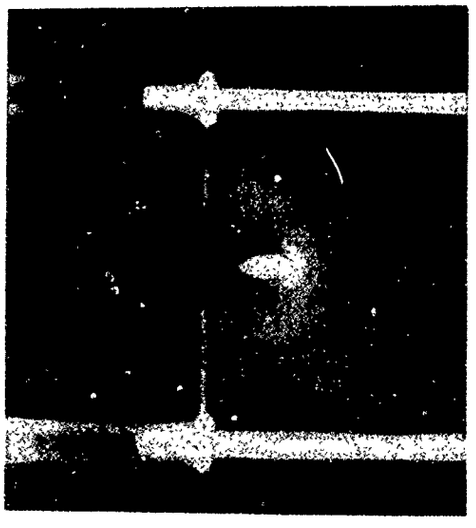

Figure 2.a. X-ray radiograph of the target, 3.8 ± 0.250 μs after jet impact
Copper jet $\phi = 1.6$ *mm*
$v = 7800$ *m/s*

The numerical points are affected by the error on the determination of the instant when the jet impacts the target (± 250 ns).

The computation gives a constant penetration velocity of the jet (5.13 mm/μs), according to the constant velocity simulation of the jet before the impact. This penetration velocity agrees with the measured velocity (5.3 mm at the beginning of the penetration and then 5.1 mm/μs).

TABLE III

JET TIP VELOCITY mm/μs	JET DIAMETER mm	RESULT	V^2d $mm^3/\mu s^{-2}$
T2 (experiment)		Critical	62 ± 3
7.8	1.6	Critical	97.3
6.8	1.8	Detonation	83.2
6.1	1.8	Detonation	66.9
5.8	1.8	Fail	60.5

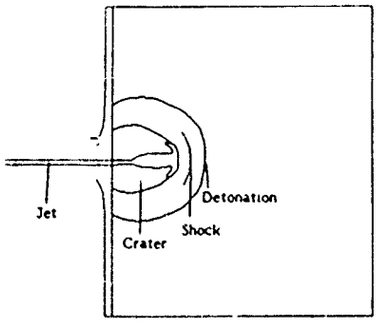

Fig. 2.b. Sketch of the radiograph showing the pressure waves

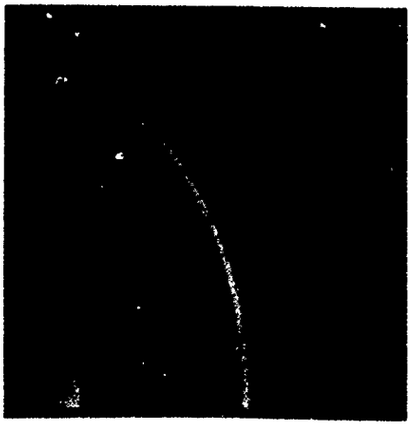

Figure 2.c. Computed pressure field in the target at the same instant (upper half of Figure 2.a) Target: T2 covered with 2mm of aluminum

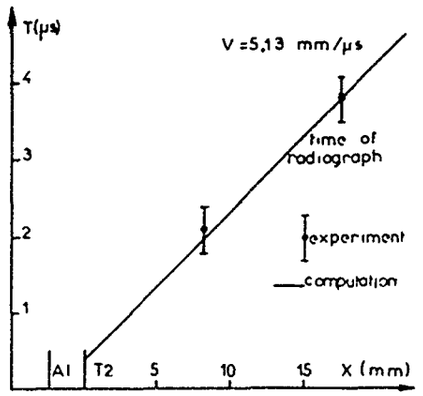

Fig. 3. Time vs position of jet-tip

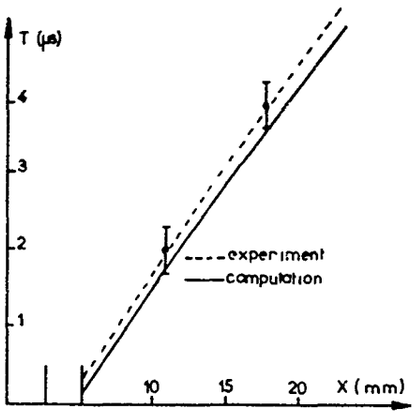

Fig. 4. Time vs position of the reactive wave

c — The reactive wave

On Figure 4 we can see the (x,t) diagram of the reactive wave along the axis of symmetry of the flow.

The detonation velocity is well computed. The numerical transition to detonation is shorter than the experimental transition; however, it is still within the experimental indeterminacy. An error of less than 10% on the intensity of the precursor shock in the aluminum, which initiates the reactive wave, can explain this difference. It can be due to:

- the poor thermodynamic simulation of the jet
- the equation of state of the aluminum and the copper at relatively high pressure (P≥100 GPa).
- the numerical calculation of the impact.

This point is not studied further in the present work, for the difference is rather small (Δt≤300 ns)

d — The compression wave

As we can see on Figure 2, a compression wave attached to the jet, travels through the partially decomposed explosive.

On Figure 5 we have plotted the computed pressure and density of the explosive along the axis of symetry of the flow, at the instant of the X-ray photography. The experimental positions of the reactive wave and of the compression wave are reported on the same figure.

As already explained, the numerical reactive wave is slightly ahead of the experimental wave, but the position of the compression wave is well calculated with regard to the position of the jet.

There is no discrepancy between these results. The reactive wave is created by the precursor shock, when it arrives in the explosive. On the

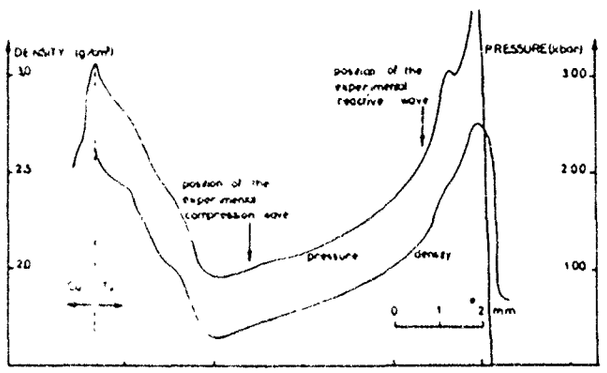

Fig 5 Pressure and density along the axis of symetry at t = 3.8 μs

contrary, the building up of the compression wave is a continuous process: it is not defined by the impact conditions and is not dependent on the time scale.

It depends on:

- the penetration velocity of the jet,
- the thermodynamical state of the explosive decomposition products through which it travels.

The good restitution of the position of the compression wave tends to show that the state of the partially decomposed explosive is well calculated, although there is no other experimental data to ascertain this.

e – Conclusion of these comparisons

The good agreement between experimental and computational results, on explosives X2 and T2, shows the correctness of our numerical simulation. Now, we look at the mechanism of the initiation of X2 and T2 by shaped charge jets as given by the numerical simulations.

V – MECHANISM OF INITIATION OF THE EXPLOSIVE BY JETS

V.1 – Explosive X2

Three geometries computed during the impact of X2 target covered by 4 mm of aluminum are shown on Figure 6. It is easy to see that the initiation is produced by the precursor shock, created at the impact, which travels throughout the aluminum. The detonation occurs when the jet itself has not yet impacted the explosive.

In this case, the precursor shock is strong enough to provide the initiation conditions. It is therefore reasonable to think that if its intensity was not sufficient to initiate the explosive, it could nevertheless be strong enough to alter the structure of the explosive so that the subsequent penetration of the jet had no effect. This remark agrees with the experimental observations of CHICK and HATT (6).

V.2 – Explosive T2

T2 is less sensitive than X2. Even with a higher jet velocity, the precursor wave alone (about 20 GPa, but in a small area) is not sufficient to provide the initiation conditions.

On Figure 7, we can see the difference in structure between the reactive waves induced

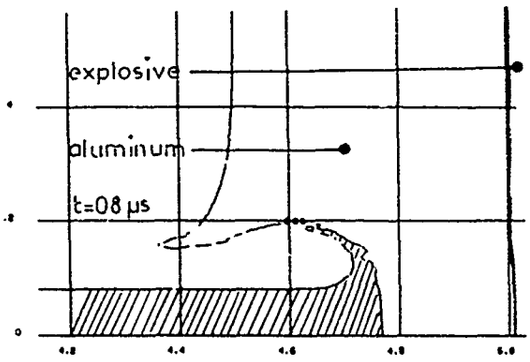

Fig. 6.a. The precursor shock arrives at the interface between A1 and X2

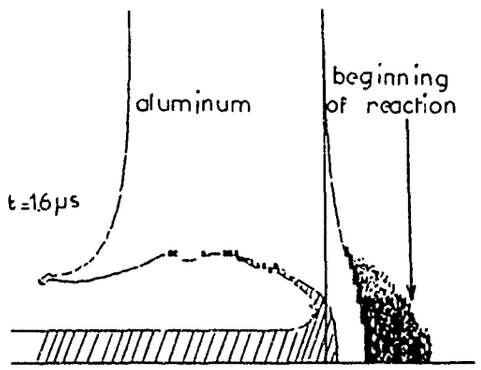

6.b. A reactive wave is created by the precursor shock

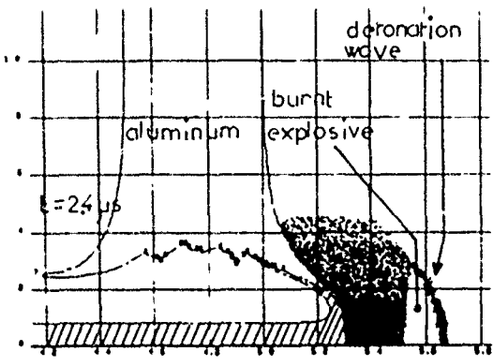

Fig. 6.c. The detonation occurs. At this instant the jet just begins to interact with the explosive

Fig. 6. Initiation of X2 by a jet
Velocity of the jet : 5.2 mm/µs

a — diameter of the jet: 1.6 mm
velocity of the jet: 7.8 mm/μs
target: T2 covered with 2 mm of aluminum

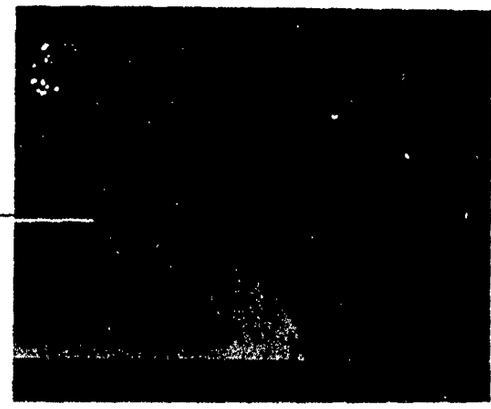

b — velocity of the jet: 5.2 mm/μs
target: X2 covered with 4 mm of aluminum

Figure 7 Interaction between a copper jet and explosives pressures and mass ratios of burnt explosive

in X2 and T2. In X2 the reaction wave diverges, and in T2 it burns out.

But, when the copper-jet impacts the explosive itself, a compression wave appears behind the reaction wave. As can be seen on Figure 8, this compression wave becomes larger and larger, its diameter becomes of the order of 6 or 10 jet diameters, and the decomposition products cannot expand.

If we remember the 1-D studies about the initiation of explosives by short duration shocks, and if we look at the phenomena which arise in this initiation process, we can explain the initiation of T2 by a jet, by the fact that the pressure is sustained on a great area and during a long time at the rear of the weak reaction wave created by the impact.

VI — CONCLUSION

Impacts of shaped charge jets against explosive targets coated with aluminum have shown differences between the mechanism of initiation of X2 (HMX explosive) and T2 (TATB explosive).

Numerical computations have been performed in order to explain these differences.

Fig. 8.a. $t = 1.0\ \mu s$ (see Fig. 7.a)

Fig. 8.c. $t = 3.8\ \mu s$

Fig 8 b $t = 2.6\ \mu s$

Fig 8 Evolution of the pressures and mass ratios of burnt explosive. Copper jet: $\varnothing = 1.6$ mm $V = 7.8$ mm/μs target: T2 coated with 2 mm of aluminum.

X2 seems to be initiated by the precursor shock created at the time of impact.

With T2, the detonation occurs with a longer delay after the impact, during which the jet reaches a great depth in the explosive. The jet creates a compression wave in the partially reacted explosive, which appears on the experimental X-ray photographs, as well as in our calculations. Therefore, the pressure is maintained behind the reactive front on a great surface and the detonation conditions are obtained.

REFERENCES

1. M. H. Rice "Penetration of High Explosives by Inert Projectiles", System-Science-Software Report SSS-R.78-3512, Novembre 1977.
2. H. Moulard, "Critical Conditions for Shock Initiation of Detonation by Small Projectile Impact", 7th Symposium (International) on Detonation, Annapolis, 1981.
3. L. Green, "Shock Initiation of Explosives by the Impact of Small Diameter Cylindrical Projectiles", 7th Symposium (Interna-

tional) on Detonation, Annapolis, 1981.

4. K. L. Ball, H. C. Vantine, R. C. Weingart, "The Shock Initiation of Bare and Covered Explosives by Projectile Impact", 7th Symposium (International) on Detonation, Annapolis, 1981

5. J. P. Plotard, D. Pirotais, G. Morin, "A Numerical Simulation of the Impact of Calibrated Explosives", Private communication.

6. M. C. Chick, D. J. Hatt, "The Mechanism of Initiation of Composition B by a Metal Jet", 7th Symposium (International) on Detonation, Annapolis, 1981.

7. C. L. Mader, G. H. Pimbley, "Jet Initiation of Explosives", LA-8647 UC-45, February 1981.

8. C. L. Mader, G. H. Pimbley, A. L. Bowman, "Jet Penetration of Inerts and Explosives", LA-9527-MS U S-45, November 1982.

9. N. Legrand, J. Ovadia, "Calcul d'écoulement engendrés par Explosif dans les Milieux Inertes Au Moyen du Code CEE", Symposium H D P., CEA, PARIS, 27-31/08/78

10. P. Donguy, N. Legrand, "Numerical Simulations of Non-ideal Detonations of a Heterogeneous Explosives with the Two Dimensional Eulerian Code CEE", 7th Symposium (International) on Detonation, Annapolis, 1981.

11. C. L. Mader, C. A. Forest, "2 Dimensional Homogeneous and Heterogeneous Detonation Wave Propagation", LA 6259 (1976)

12. E. Jamet, "Methodes d'analyse de L'état Physique d'un Jet de Charge Creuse", Institut Franco-Allemand de Recherche de St. Louis (FRANCE) Rapport CO 227/82.

13. C. Boissiere, G. Fiorese, "Equation d'état des Métaux Prenant en Compte les Changements d'état Entre 300K et 200000K pour Toute Compression. Application au Cas du Cuivre et de l'aluminium", Revue de Physique Appliquée (12), Mai 1977, pages 857-872.

NUMERICAL SIMULATION OF JET PENETRATION OF HMX AND TATB EXPLOSIVES

D. PIROTAIS, J.P. PLOTARD, J.C. BRACONNIER

commissariat a l'Energie Atomique

B.P.n°27-(94190) villeneuve-st-georges (France)

-GOALS-

- Determination of the critical conditions of initiation of HMX and TATB explosives by shaped-charge jets.

- Knowledge of the build-up to detonation mechanism inside HMX and TATB explosives when they are impacted by shaped-charge jets.

EXPERIMENTAL DEVICE

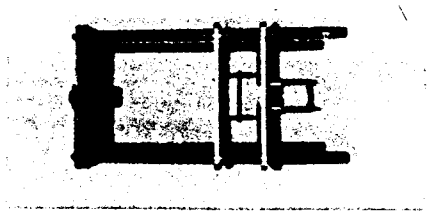

SHAPED CHARGE: -liner in copper
-maximum jet velocity: 7.8 mm/µs

SCREENS : Steel barriers placed between the charge and the target allow to adjust the velocity of impact.

TARGETS : Cylinders of explosive,coated on the impact face with a sheet of aluminum.(1mm of coating for X2 and 2mm for T2).

OBSERVATIONS: -Framing camera
-Streak camera on the rear face of the targets
-X-Ray radiography.

COMPUTATIONAL METHOD

-THE COMPUTATIONS ARE PERFORMED WITH THE 2D HYDRA-CODE "C.E.E"

-Finite difference,first order scheme
-Compressible flow
-Average number of cells : 30 000
-Minimum size of cells used :
-(0,1x0,1)mm (HMX)
-(0,125x0,125)mm (TATB)
-Computer :CDC 7600

-NUMERICAL GEOMETRY

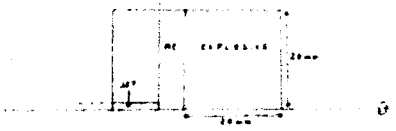

-JET REPRESENTATION

-Infinite cylindrical rod of copper
-Normal pressure and temperature (1 ata,300K)
-Uniform velocity

-EQUATIONS OF STATE

-Unburnt explosive

$$P_1(v) = P_0(v) + \frac{\Gamma_0}{v}\,(E_{1(v)} - E_{0(v)})$$

$$T_1(v) = T_0(v) + \frac{\Gamma_0}{C_v}\,(E_{1(v)} - E_{0(v)})$$

$$P_0(v) = a + b\left[\exp\beta(c - v^{-\frac{2}{3}}) + \exp\beta(c - v^{-\frac{2}{3}})\right] \quad \ldots (1)$$

$$E_0(v) = \int_v^{\infty} P_0\, dv \qquad \text{with } E_0(v) = 0$$

$$\Gamma(v) = -\frac{1}{v} - \frac{1}{2}\left[\frac{d^2P_0}{dv^2} \Big/ \frac{dP_0}{dv}\right] \quad \ldots (2)$$

$$\Gamma(v) = \alpha\left(\frac{v}{v_0}\right)^4 + \beta\left(\frac{v}{v_0}\right)^2 + \frac{1}{2} \quad \ldots (3)$$

-Detonation products

$$P_2 = P_H + \frac{\Gamma_H}{V_H}\,(E_2 - E_H)$$

$$T_2 = T_H + \frac{\Gamma_H}{C_v}\,(E_2 - E_H)$$

$$P_{2,0} = A\,v^{-4} + \omega\,\zeta_0\,e^{-(\lambda-\omega)\zeta_0} \quad \ldots (4)$$

$$P_{2,1} = B\,v^{-\beta_2} + \omega\,\zeta_1\,e^{-(\lambda-\omega)\zeta_1} \quad \ldots (5)$$

-Mixture

$$T = T_1 = T_2$$
$$P = P_1 = P_2$$
$$E = \omega E_1 + (1-\omega) E_2$$
$$v = \omega V_1 + (1-\omega) V_2 \qquad \text{with } \omega = \frac{\alpha_1}{\alpha_1 + \alpha_2}$$

-REACTION RATE (T.C.D)

-Defined like "FOREST-FIRE" rate

$$I_1\left(-\frac{dF}{dt}\,dt\right) = \frac{\dot{E}}{E_{ch}} = \left(\frac{P}{P_0}\right)^{\alpha} \qquad P \le P_0$$

$$I_2\left(-\frac{dF}{dt}\,dt\right) = \frac{\dot{E}}{E_{ch}} = \left(\frac{P}{P_0}\right)^{\beta} \qquad P > P_0$$

RESULTS WITH HMX (X 2)

EXAMPLE OF EXPERIMENTAL RECORDS WITH TWO JET VELOCITIES

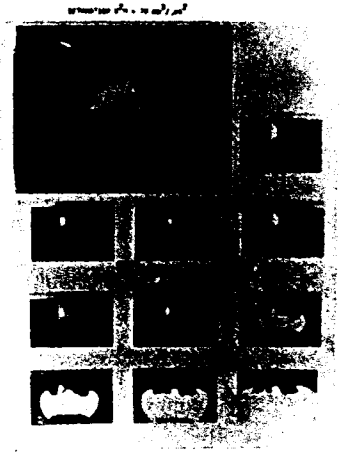

HMX (continued)

B - COMPARAISON BETWEEN NUMERICAL AND EXPERIMENTAL RESULTS

JET TIP VELOCITY mm/µs	JET DIAMETER mm	RESULT	V^2/d $mm^3/\mu s^2$
X2 (experiments)			
6.6	1.6	Critical	52 ± 4
6.4	"	Fail	"
6.3	"	Detonation	47.2
5.9	"	Fail	43.1
6.4	1.8	Detonation	50.4
5.6	"	Fail	43.7
X2 (computational)			
6.1	1.6	Fail	56.7
6.2	1.6	almost fail	57.4
6.2	1.8	Detonation	45.6

C - MECHANISM OF INITIATION OF EXPLOSIVE X2 BY A JET (VELOCITY OF THE JET : 6.2 mm/µs)

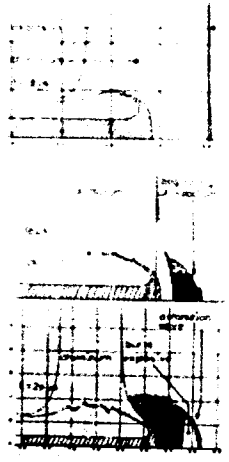

The precursor shock arrives at the Al-X2 interface ,

a reaction area is created by the precursor shock ,

and the detonation occurs, just before the jet interacts with the explosive.

In this case, the precursor shock is strong enough to provide the initiation conditions.

It is therefore reasonable to think that if the intensity was not sufficient to initiate the explosive, it could nevertheless be strong enough to alter the structure of the explosive so that the subsequent penetration of the jet had no effect.

RESULTS WITH TATB (T2)

A - EXAMPLE OF EXPERIMENTAL RECORD WITH TWO JET VELOCITIES

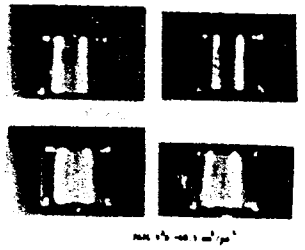

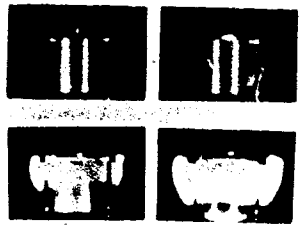

B - FIRST RESULTS

JET TIP VELOCITY mm/µs	JET DIAMETER mm	RESULT	V^2/d $mm^3/\mu s^2$
T2 (experiment)			
7.8	1.6	Critical Detonation	62 ± 3
6.8	1.8	" "	97.3
6.1	1.8	" "	83.2
5.8	1.8	Fail	66.9
			60.5

C - NUMERICAL STUDY

Because of the low sensitivity of the explosive T2, the projectile must reach a great depth in the explosive (3 to 4 cm) before the first zones of fully reacted explosive appear, when the size of the cells used permit to describe only a square of about 2 cm, due to the memory limitations of the computer (CDC 7600).

This difficulty is alleviated with the inclusion of an automatic tracking of the jet tip in the program, which matches the grid to the position of the jet at each time of its progression in the explosive.

We could then bring to the end our computation with T2.

With TATB we have not performed computations in order to determine the numerical criterion of initiation of the explosive. We have tried to reproduce the informations given by the experimental data, especially by the X-Ray radiographs, then we can look at the mechanism of the initiation of T2 by a shaped charge jet as given by the numerical simulation.

The numerical and experimental results presented on the next panel show the interaction of a (ϕ=1.6 mm, v=7.8 mm/µs) jet with a T2 target coated with 2mm of aluminum.

TATB (continued)

CONCLUSION

- The experimental data give a criterion for the initiation of the explosives by a shaped-charge jet.

- The good agreement between experimental and computational results on explosives x2 and t2, shows the correctness of our numerical simulation.

- We have shown the differences between the mechanism of initiation of HMX and of TATB by jets.

SENSITIVITY AND PERFORMANCE CHARACTERIZATION OF DINGU

M. M. Stinecipher, L. A. Stretz
Los Alamos National Laboratory
Los Alamos, New Mexico

DINGU, as a relatively insensitive HE, may have interesting applications. We have been working on better methods for preparation and characterization. We have achieved a particle size suitable for formulating this compound into a PBX and have tested DINGU/binder by plate dent. We have compared the sensitivity of DINGU with that of TATB in small-scale tests.

INTRODUCTION

At the Seventh Symposium on Detonation, evidence was presented in a French paper for low shock sensitivity of 1,4-dinitroglycoluril (DINGU) (1). We have decided to synthesize enough DINGU for our characterization tests to compare it with our data on TATB. Another reason for our interest was to gain a better understanding of the properties that affect the sensitiveness of explosives. DINGU has chemical and crystal structures that are different from those of TATB. By making a wide variety of less-sensitive explosives, we can examine their crystal, chemical, and thermal properties to gain understanding of which properties make explosives unexpectedly insensitive. This understanding will help us in our synthesis effort. The goal of our synthesis effort is to synthesize safe, powerful explosives that can be developed for use.

Often, sensitivity is affected by impurities and by crystal size or shape. To understand the role of small amounts of impurities, we characterized the by-products of the synthesis reaction (Fig. 1). The impurities formed in the reaction are 1,6-dinitroglycoluril (5 to 8% of the total product) and 1-nitroglycoluril (1 to 30% of the total product), the latter by incomplete nitration. In addition to these impurities, the French have identified 1,3-dinitroglycoluril in their synthesis reaction, but they used different synthesis procedures (2). Structure determination of the isomers was by proton and carbon-13 nuclear magnetic resonance (nmr) spectroscopy. We have not isolated enough 1,6-dinitroglycoluril to determine its sensitivity, but the 1-nitroglycoluril is too insensitive to "go" on our impact machine.

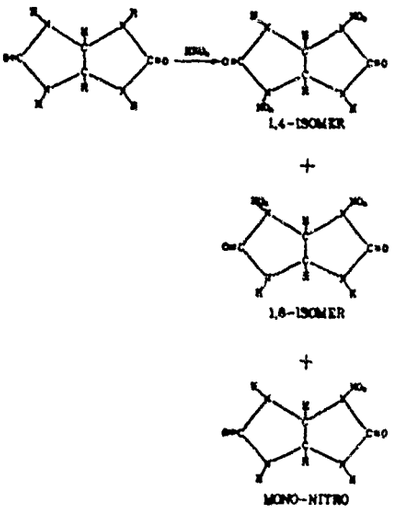

Fig. 1. Products of the DINGU synthesis reaction

We have overcome the two major experimental problems, particle size and brittleness of the pressed charge. The first problem was solved by using 85% instead of 98% nitric acid to avoid formation of a solvate between DINGU and nitric acid. If a solvate is present when the crystals are washed with water, the solvate breaks and

very fine crystals are formed. The second problem was solved by using a plastic binder to form a plastic-bonded explosive (PBX) formulation.

There is a major detonation problem that has not been solved. The French reported that DINGU is a Class 2 explosive, much like nitroguanidine, in that the detonation velocity stops increasing linearly with density at high densities (1). They found that formulating DINGU with more sensitive explosives solved the problem for them, but we have decided to characterize the properties of DINGU in as pure a state as possible.

MATERIAL PREPARATION AND ANALYSIS

Synthesis of DINGU - Batch Method

Glycoluril (4 kg) is dissolved in 85 wt% nitric acid (50*l*) and heated at 65 °C for one hour. The reaction mixture is slowly diluted with water (50*l*) and then heated to 90 °C for one hour during which time the sensitive isomers decompose. The mixture is cooled below 30 °C, filtered, washed with cold water, and dried in a forced-draft oven. The yield is 5.4 to 5.7 kg (90-95% theoretical yield). The rod-shaped crystals are 10 to 100 μm long and are stable during the washing. The material obtained is 99% 1,4-dinitroglycoluril suitable for formulating into a PBX.

Recrystallization of DINGU - Small Scale

DINGU (5 g) was dissolved in hot 90% nitric acid (120 m*l*) and added carefully to water (300 m*l*) at 70 °C. After a few seconds, the crystals began to appear. The mixture was cooled to 5 °C, filtered, and washed with cold water. We recovered 3.1 g (62%) of 40- to 60-μm diamond-shaped crystals, with a bulk density of 0.8 g/cm^3. They are the same polymorph as the rod-shaped crystals that were produced in the preceding synthesis.

Slurry Method for the Preparation of a DINGU PBX

PBXs have been formulated using Estane, Viton-A, Kel-F 800, Exon 461, and nitrocellulose binder systems. At present, we are evaluating a 95/5 wt% DINGU/Exon 461 (vinylidene chloride-chlorotrifluoroethylene copolymer) PBX formulation. We prepare the binder lacquer by dissolving 100 g Exon 461 in 800 m*l* of ethyl acetate. When the lacquer is ready for use, the slurry is prepared in a well-agitated, 19-*l* vessel. The slurry carrier consists of 10*l* H_2O, 2 g of a fluorocarbon surfactant, 130 m*l* of 70% HNO_3 (lowers pH to 1.5), and 800 m*l* ethyl acetate. With mild agitation at 50 °C, we add 1900 g of dry DINGU. Agitation is increased as the lacquer is added slowly. Additional solvent is added as necessary to aid agglomeration. As the solvent is removed by vacuum distillation, the agitation is gradually reduced to avoid excessive breakage of agglomerates. After most of the solvent has been removed, the material is filtered, rinsed well with water, and dried. Typical bulk density is 0.8 g/cm^3.

Deuterium-Labeled DINGU

DINGU (5 g) was dissolved in dimethyl sulfoxide (DMSO) (10 m*l*) with a drop of D_2SO_4 to prevent hydrolysis, and reprecipitated by D_2O (5 m*l*). The process was repeated twice giving a 92% exchange. A final recrystallization from deutero-nitric acid removed the solvate of DMSO, which could affect the thermal properties. Only the labile hydrogens on the nitrogens were replaced. Analysis of deuteration was done by proton nmr, which compared the integration of the peak from the N-hydrogens with that from the nondeuterated C-hydrogens.

Thin-Layer Chromatography

The DINGU reaction mixture dissolved in acetonitrile was spotted multiple times on 20-cm Whatman K1F silica gel plates prewashed with the eluting solvent, 1/19 volume ratio water/acetonitrile. After eluting in a closed chamber, the spots of the separated isomers were located by quench fluorescence (3). Column chromatography separated enough of each isomer to identify it by nmr.

TEST AND CALCULATION METHODS

Physical Properties

Heat of Formation. The heat of formation was determined from the heat of combustion measured in a Parr bomb where the sample was burned under 20 atmospheres of oxygen gas. The bomb was calibrated with standard benzoic acid and the calculation of the heat of formation from heat of combustion was by the method of Rouse (4).

The heat of formation was calculated by Ritchie using MINDO/3 and *ab initio* methods of group substituents (5).

Density. Gilardi did an x-ray crystal study at the Naval Research Laboratory (6).

Cady determined a density by gas pycnometry (7).

Sensitivity Tests

Impact Sensitivity. Impact sensitivity tests were determined by the method developed at Bruceton (8). Two tests are performed. In the first, conical piles of 40-mg samples are placed on garnet paper (Type 12 test); and in the second, the sample is placed on the bare anvil (Type 12B test). A striker is rested on the sample and struck by a free-falling, 2.5-kg weight. A "go" is determined by the sound produced. Using the Bruceton method, the drop height is varied to determine the height at which a "go" is obtained 50% of the time. Typical values are 22 cm for RDX and 150 cm for TNT.

Thermal Sensitivity. The thermal sensitivity was measured by the modified Henkin-critical-temperature method. A 40-mg sample of explosive is pressed into a cartridge and confined lightly by a metal cup. The cartridge is placed on a temperature-controlled bath of Wood's metal and timed until explosion. The lowest temperature that causes the sample to explode is the critical temperature (9).

A 0.5-g sample was tested in a standard accelerating-rate-calorimeter (ARC) sample bomb and analyzed in 5-degree steps from 50 to 350°C until it began to self-heat.

A standard vacuum stability test was run on a 0.2-g sample at 120°C for 48 h.

A large, confined thermal test was run by placing a 4-cm-diam by 15-cm-cylindrical pressed charge (1.75 g/cm³ density) into a stainless-steel pipe nipple with inside and outside thermocouples. The charge was heated at a rate of one degree per minute until it exploded.

Spark Sensitivity Test. In the spark sensitivity test a 30-mg sample of explosive is confined in a plastic holder between a steel dowel pin and a lead foil. Energy from a capacitor bank charged to known voltage is discharged through the sample via a needle, which penetrates the lead foil. Two thicknesses of foil, 0.076 and 0.254 mm, are used for two different tests. A "go" is indicated by a ruptured foil, while a foil with only the needle puncture indicates a "no go". Using the Bruceton method (8), the input energy is varied to determine the 50% point (10).

Small-Scale Gap Test. The small-scale gap test is a useful test for shock sensitivity if the amount of explosive is limited and the explosive detonates at a diameter less than 12.7 mm at the test density. In this test, the donor (PBX 9407, 94/6-RDX/Exon) provides a pressure pulse that decays through brass spacers onto an acceptor explosive, 12.7-mm diam by 38-mm long. If the pressure is sufficient for detonation, a dent is observed in the witness plate. The assembly is held together by Lucite. Fifteen to twenty shots are done to determine a statistical 50% gap height (G_{50}) (11).

Performance Calculations

The detonation pressure and velocity were calculated by computer code using the BKW equation of state (12).

Performance Tests

Plate-Dent Tests. Unconfined plate-dent tests have been correlated to detonation pressure. Samples, pressed to 1.27-, 2.54-, or 3.16-cm diam, were placed on a 5.1-cm-thick, 15 x 15-cm-square, cold-rolled steel plate. The resultant dent was compared with the dents of standard explosives, which had been correlated to their detonation pressures (13).

Burn Tests. DINGU was burned along a spatula as a powder, in a 95/5 wt% DINGU/Kraton-Oil PBX pressed to 1.8 g/cm³, and as a rocket-propellant formulation of 50/50 wt% DINGU/Energetic Binder.* The rocket formulations were prepared at NWC by May Chan and burned in a strand burner at 6.89 MPa (14).

RESULTS AND DISCUSSION

Chemical and Physical Properties

Heat of Formation. The heat of formation was measured to be -42.3 ± 0.1 kcal/mol, which agrees with the value reported by the French (-46 kcal/mol) (1).

*The energetic binders used were: PEG - polyethylene glycol; TMETN - trimethylolethane-trinitrate; GAP - glycidyl azide polymer; BTTN - butanetrioltrinitrate.

Ritchie calculated ΔH_f by the MINDO/3 and *ab initio* group replacement methods. The first method required shorter computer time, but results were 50 kcal too negative. The result from the second method was -45 to -55 kcal/mol.

Density. Gilardi found that the density of DINGU, 1.98 g/cm^3, was higher than that previously reported, 1.94 g/cm^3 (1). This was confirmed by Cady's gas pycnometer measurement of 1.96 g/cm^3.

Sensitivity Tests

Impact Sensitivity Test. The impact tests showed that DINGU is moderately sensitive, and that the Type 12 test does not depend significantly on the particle size or habit. However, the impact test without the garnet paper showed less sensitivity with increasing particle size (Table 1).

TABLE 1
Impact Sensitivity of DINGU

Particle Size (μm)	<5	1-30	20-40	30-60	30-100
Crystal Habit			Diamond		Rod
Impact Sensitivity					
Type 12 (cm)	88	100	108	103	125
Type 12B (cm)	78	153	175	204	212

TATB does not "go" on our impact machine so we cannot compare its behavior with particle size.

Thermal Sensitivity Tests. For small samples the thermal sensitivity of DINGU is also greater than that of TATB, but, rather than detonate like RDX, DINGU has a violent gas explosion above 180 °C, which is the temperature where it begins to self-heat in 0.5-g samples in the ARC bomb. With very small samples, such as the Henkin test, the critical temperature is 204 °C. In a larger, confined pipe test, it blew the pipe into 10-cm fragments at 190 °C

At lower temperatures, DINGU gave a vacuum stability measurement of 0.5 ml/g gas at 120 °C in 48 h

The labile hydrogens on the nitrogens were exchanged with deuterium. The Henkin critical temperature was higher, 210 °C for the deuterated DINGU. This indicates that the first decomposition step involves those hydrogens. TATB also shows a positive isotope effect.

Spark Sensitivity Test. The spark sensitivity of DINGU is quite low; it takes 1.27 J to cause a 50% reaction confined with a 0.076-mm foil and 3.99 J with a 0.254-mm foil. In the same tests, RDX only requires 0.22 J and 0.55 J, respectively, to react 50% of the time. Again, TATB does not react in this test.

Small Scale Gap Test. The shock sensitivity of both DINGU and TATB have been measured in the small-scale gap test. However, the diameter of the charge may be too close to their failure diameters to give more than a preliminary indication of their shock sensitivity (Table 2). We plan to do other shock sensitivity tests, but they will be done on a DINGU PBX because the pure material is difficult to press and machine at greater than 12.7-mm diameters.

TABLE 2
Small-Scale Gap Test of DINGU and TATB

	Density (g/cm^3)	Voids (%)	G_{50} (mm)
DINGU	1.76	11	0.18
TATB	1.7	12	0.51

Performance Calculations

BKW calculations of the performance of DINGU at different densities are shown in Table 3.

TABLE 3
Calculations of the Performance of DINGU

Density (g/cm^3)	1.75	1.85	1.94	1.98
CJ Pressure (GPa)	26.5	30.6	34.7	36.7
Det. Vel. (m/s)	7890	8300	8680	8870

Performance Tests

Plate-Dent Tests. Plate-dent tests were done on the pure material and on the various PBXs. The pressure derived from the dent is lower than calculated and the deviation becomes more pronounced as the density increases. The PBX

using Estane as a binder gave the weakest dents and failed to propagate at 25.4 mm at 89% TMD. Table 4 gives the compositions and pressures derived from some of the plate-dent tests.

TABLE 4
Plate-Dent Results For Several DINGU PBXs

Formulation	Test Diameter (mm)	Density (g/cm³)	%TMD	Indicated Pressure (GPa)
Estane 1[a]	25.4	1.715	90.3	18.8
		1.795	94.5	21.6
		1.825	96.0	18.4
		1.849	97.3	10.4
		1.867	98.3	failed
Estane 1[a]	41.3	1.828	96.2	25.2
		1.848	97.3	25.2
Estane 2[b]	25.4	1.722	90.0	20.9
		1.798	94.0	22.9
		1.817	95.0	23.6
		1.833	96.0	23.8
		1.855	97.0	24.2
		1.879	98+	23.5
Estane 2[b]	41.3	1.722	90.0	24.4
		1.798	94.0	24.0
		1.836	96.0	24.6
		1.875	98.0	24.8
Exon 1[c]	25.4	1.857	96.0	25.5
		1.892	98.0	26.2
Exon 1[c]	41.3	1.856	96.0	27.0
		1.877	97.0	27.6

[a] Estane 1 - 95/4/1 wt% DINGU/Estane/KR138-S
[b] Estane 2 - 96/3/1 wt% DINGU/Estane/KR138-S
[c] Exon 1 - 94/5/1 wt% DINGU/Exon/461 KR138-S

Figure 2 shows the differences between the measured and calculated pressures as a function of density. This behavior is likely due to diameter effects, indicating a large failure diameter for high-density DINGU PBXs.

Burn Tests. DINGU appears to have a fast burning rate when burned in a trough (1) or along a spatula, but when pressed or formulated in a binder, the burning rate is comparable to that of HMX We plan a more extensive burning rate study (Table 5).

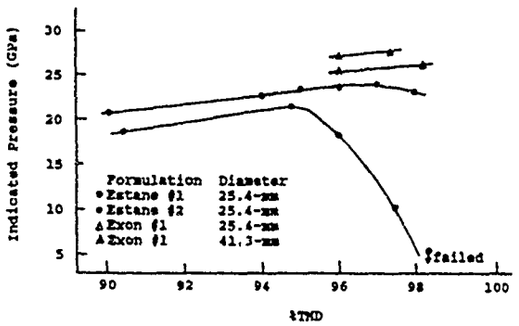

Fig. 2. Indicated Pressure Versus % TMD for DINGU PBXs

TABLE 5
Burning Rate Tests for DINGU and HMX

	DINGU	HMX
Burn rate (mm/s) 50/50 HE/binder 6.89 MPa (1000 psi)	5-6.6	10-12.7
Approx. burn rate (mm/s) 95/5 HE/binder ambient pressure	0.4	0.3

CONCLUSIONS

We found the sensitivity of DINGU to be between RDX and TATB. Much of the testing to date has been preliminary. We will have a sufficient amount of material for a more complete characterization of the material in the near future.

ACKNOWLEDGEMENTS

We greatly appreciate the help of M. J. Urizar, H. H. Cady, S. K. Yasuda, R. N. Rogers, J. L. Janney, H. L. Flaugh, T. E. Larson, C. L. Mader, J. P. Ritchie, M. A. Fletcher, B. M. Dobratz, M. L Clancy, C. E. Hannaford, C. C. Maxwell, and E. L. Roemer of our Laboratory. We also thank M. Chan of NWC for performing the strand-burning tests.

REFERENCES

1. P. Deneuville, C. Gaudin, Y. de Longueville, J. Mala, "Comparison of TATB and DINGU Explosive Properties," Proc. Seventh Symposium (Intl.) on Detonation, Annapolis, Maryland, pp. 540-547, June 1981.

2. J. Boileau, Private communication, October 1984.

3. S. K. Yasuda, Private communcation, September 1983.

4. P. E. Rouse, Jr., "Enthalpies of Formation and Calculated Detonation Properties of Some Thermally Stable Explosives," J. Chem. & Eng. Data, Vol. 21, No. 1, pp. 16-20, January 1976.

5. J. P. Ritchie, Private communication, January 1984.

6. R. Gilardi, Private communication, 1983.

7. H. H. Cady, Private communication, 1983.

8. L. C. Smith and E. H. Eyster, "Physical Testing of Explosives, Part III - Miscellaneous Sensitivity Tests," OSRD Report No. 5746, December 1945.

9. R. N. Rogers, "Thermochemistry of Explosives," Thermochim. Acta, Vol. 11, pp. 131-139, 1975.

10. T. R. Gibbs and A. Popolato, Ed., LASL Explosive Property Data, pp. 460-461, University of California Press, Berkeley, 1980.

11. M. J. Urizar, S. W. Peterson, L. C. Smith, "Detonation Sensitivity Tests," Los Alamos Scientific Laboratory report LA-7193-MS, April 1978.

12. C. L. Mader, "Fortran BKW: A Code for Computing the Detonation Properties of Explosives," Los Alamos Scientific Laboratory report LA-3704, July 1967.

13. L. C. Smith, "On Brisance and a Plate Denting Test for the Estimation of Detonation Pressure," Explosivstoffe, pp. 106-110, 130-134, 1967.

14. M. Chan, Private communication, 1983.

SENSITIVITY AND PERFORMANCE CHARACTERIZATION OF DINGU

by

M. M. STINECIPHER
L. A. STRETZ
LOS ALAMOS NATIONAL LABORATORY
LOS ALAMOS, NEW MEXICO

DINGU SYNTHESIS

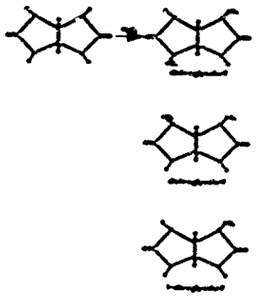

PRODUCTS OF THE DINGU SYNTHESIS REACTION

RECRYSTALLIZATION

DMSO - HIGHLY SOLUBLE BUT SOLVATE IS STABLE
HNO_3 - SOLUBLE AND SOLVATE REMOVED BY DILUTION

ANALYSIS METHODS

^1H AND ^{13}C NUCLEAR MAGNETIC RESONANCE
THIN LAYER CHROMATOGRAPHY
HIGH PRESSURE LIQUID CHROMATOGRAPHY

FORMULATIONS

DINGU (WT% RANGE)
93-98.5
BINDERS
ESTANE
EXON 461
VITON A
(WT% RANGE)
6.5-1
COUPLING AGENT
KR-138/S
(WT% RANGE)
1-0

SENSITIVITY

IMPACT SENSITIVITY OF DINGU

PARTICLE SIZE (μm)	5	1-30	30-40	30-60	30-100
CRYSTAL HABIT				DIAMOND	ROD
IMPACT SENSITIVITY					
TYPE 12 (cm)	88	101	108	108	125
TYPE 12B (cm)	76	153	175	204	212

DIAMOND CRYSTAL

ROD CRYSTAL

SMALL-SCALE GAP TEST OF DINGU AND TATB

	DENSITY (g/cm³)	VOIDS (%)	d_{50} (mm)
DINGU	1.76	11	0.18
TATB	1.7	12	0.51

TATB/HMX/DINGU COMPARISON

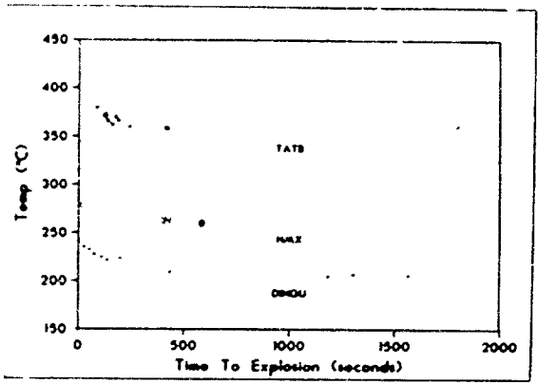

SPARK TEST

	d_{50} 0.076 mm FOIL	d_{50} 0.254 mm FOIL
DINGU	1.27	2.99
RDX	0.22	0.55
TATB	NO GO	NO GO

POSITIVE ISOTOPE EFFECT

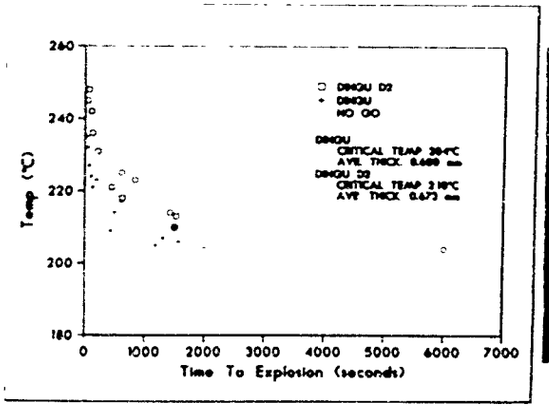

THERMAL EXPLOSION IN PIPE NIPPLE

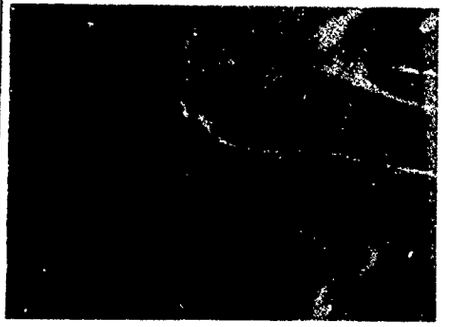

PERFORMANCE

CALCULATIONS

HEAT OF FORMATION

DENSITY

PERFORMANCE

PLATE DENTS

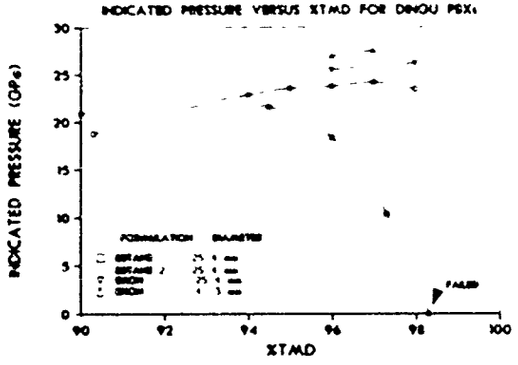

PLATE-DENT RESULTS FOR SEVERAL DINGU PBXs

FORMULATION	TEST DIAMETER (mm)	DENSITY (g/cc)	XTMD	INDICATED PRESSURE (GPa)
ESTANE 1*	25.4	1.715	98.2	18.8
		1.705	94.5	21.6
		1.685	98.8	18.4
		1.668	97.3	18.4
		1.667	83.3	FAILED
ESTANE 1*	41.3	1.688	96.2	23.2
		1.648	97.3	23.2
ESTANE 2*	25.4	1.722	98.8	28.9
		1.708	94.8	23.9
		1.617	92.8	23.4
		1.688	98.8	23.8
		1.685	97.8	24.2
		1.679	99*	23.5
ESTANE 2*	41.3	1.722	98.8	24.4
		1.708	94.8	24.9
		1.636	98.8	24.4
		1.675	98.8	24.8
EXON 1*	25.4	1.657	98.8	25.5
		1.692	98.8	26.2
EXON 1*	41.3	1.656	98.8	27.8
		1.677	97.8	27.4

ESTANE 1 - 95/4/1 WT% DINGU/ESTANE/KEL-F 800-5
ESTANE 2 - 94/3/1 WT% DINGU/ESTANE/KEL-F 800-5
EXON 1 - 94/3/1 WT% DINGU/EXON 461/KEL-F 800-5

BURN RATES

BURNING RATE TESTS FOR DINGU AND HMX

	DINGU	HMX
BURN RATE (mm/s)	5-6.6	10-12.7
90/10 HE/binder		
6.89 MPa (1000 psi)		
APPROX. BURN RATE (mm/s)	0.4	0.3
95/5 HE/binder		
AMBIENT PRESSURE		

CONCLUSIONS

- EASILY SYNTHESIZED AND INEXPENSIVE
- PARTICLE SIZE AFFECTED BY ACID CONCENTRATION
- PURITY DETERMINED BY NMR TLC, AND HPLC
- IMPACT SENSITIVITY LESS THAN RDX
- THERMAL SENSITIVITY ABOUT THE SAME AS RDX BUT EVENT LESS VIOLENT
- CALCULATED PERFORMANCE NOT VERIFIED IN SMALL-SCALE TEST
- SHOCK SENSITIVITY MUCH LESS THAN RDX
- SPARK SENSITIVITY MUCH LESS THAN RDX
- HIGH CRYSTAL DENSITY
- HIGHER CALCULATED PERFORMANCE THAN RDX
- HYDROLYTICALLY UNSTABLE IN BASE
- DINGU STILL UNDER INVESTIGATION

SHOCK SENSITIVITY STUDY OF THE CURABLE PLASTIC BONDED EXPLOSIVES

C. Bélanger, P. Pelletier and J. F. Drolet
Defence Research Establishment
Valcartier, Québec, Canada

The shock energy to initiate the castable plastic-bonded explosive CX-84A was measured. The evaluation was done by a flyer plate test designed in France and called the "Calibrated Shock Wave Test". The critical energy to initiate CX-84A varied significantly with shock duration. This explosive was initiated with a relatively low energy level of 132 J/cm² for a shock duration of 0.34 μs. For shock duration shorter than 0.25 μs and longer than 1.25 μs, the minimum initiation energies were evaluated at 175 and 275 J/cm², respectively.

A study for reducing the shock sensitivity of the curable plastic bonded explosive CX-84A has been started. The preliminary results obtained seem promising. The formulation of the CX-84A was modified and the new processed explosives were tested partially by the flyer plate test. For the shock duration of 0.34μs, the explosive CX-84B did not detonate when submitted to a shock energy of 194 J/cm², while CX-84A detonated with only 132 J cm².

INTRODUCTION

During the development of insensitive high explosives at DREV (Defence Research Establishment of Valcartier) a curable plastic bonded explosive called CX-84A was formulated to be less sensitive but as powerful as Composition B Grade A. Its performance was evaluated by measuring its detonation velocity and its energy by the cylinder test. Its energy, measured at 5 and 19-mm radial expansions was reported previously as 0.775 and 1.085 MJ kg or 87.8% and 86.3% respectively of those measured for Composition B. The detonation velocity was reported as 7.90 mm μs in comparison with 7.85 mm μs for Composition B. The shock sensitivity of this curable PBX was first evaluated by the DREV Gap Test (1). Surprisingly, it was found more sensitive than Composition B. The 50 percent barrier thickness was reported as 12.40 ± 0.18 mm compared to 11.48 ± 0.07 mm for Composition B. Consequently, a more precise evaluation of its shock sensitivity was desirable. Such a method, based on the energy transferred, was used in the present study.

A flyer plate test called the "Calibrated Shock Wave Test", designed at the French-German Research Institute of St-Louis (ISL), France (2, 3), was selected to carry on the shock sensitivity evaluation of these explosives. The flyer plate is accelerated laterally by a driver explosive. The ability of an explosive to drive a metal plate is characterized by the Richter formula

$$1\,\varnothing = b + c\mu, \qquad (1)$$

where $\varnothing$ is the flyer plate angle between its initial and its flying positions, μ is the mass ratio of the metal plate over that of the driver explosive, and b and c are the coefficients associated with the driver explosive selected.

At the impact with the receptor, the flyer plate generates an unidimensional shock wave well known in intensity and duration. Its intensity (pressure) is related to the flyer plate velocity normal to the top face of the explosive receptor, to the shock Hugoniot of the flyer plate and to that of the explosive receptor. The flyer plate velocity normal to the top of the receptor is

$$V_n = D \sin \varnothing , \qquad (2)$$

where D is the detonation velocity of the driver explosive. The duration of the shock wave is proportional to the thickness of the plate.

The energy E per unit area transferred to the explosive receptor is evaluated by the product of the impact pressure P, the shock duration t and the particle velocity u in the receptor:

$$E = P u_x t. \qquad (3)$$

The ISL flyer plate test was used to measure the shock sensitivity of the CX-84A, a curable plastic-bonded explosive. Also, this test was preliminarily used as an evaluation technique to improve the formulation of the CX-84A in order to reduce its shock sensitivity.

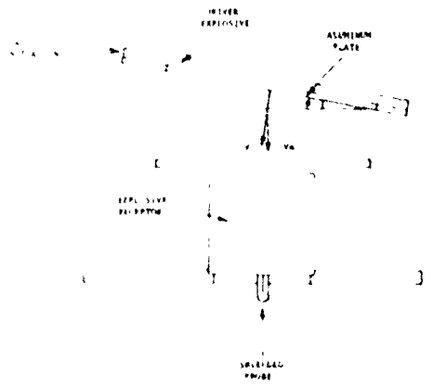

Fig 1 Schematic illustration of the flyer plate test

EXPERIMENTAL METHOD

The experimental method is similar to that described in Ref (2) with the added modifications described below. The experimental setup is illustrated schematically in Fig. 1 and photographed prior to firing in Fig. 2.

Simultaneous impact was achieved by setting accurately (+ 0.5 mrad) the angle ∅ between the initial position of the plate and the top face of the explosive receptor The coefficients of the Richter formula for the driver explosive have to be known

The pressure at impact was solved graphically on a large diagram of pressure vs particle velocity. The shock Hugoniot of the flyer plate and that of the explosive receptor were plotted The flyer plate velocity was used as the particle velocity of the 2024 aluminum alloy before impact (P = 0).

Fig. 2. Actual setup of a flyer plate test ready to be fired.

The duration of the shock wave produced at impact was evaluated by the time required for the shock wave to travel through the thickness of the metal plate e_m and come back:

$$t = 2e_m - U_m . \qquad (4)$$

The shock-to-detonation transition was deduced either by the time required for the shock wave to pass through the receptor or by the mounting base acting as a witness plate. Furthermore, this measured time, called here the initiation delay and to estimate the depth of initiation in the receptor.

Driver Explosive

The driver explosive used was the Detasheet C manufactured by Dupont. This sheet explosive was available in nine thicknesses up to about eight millimeters. The thickness, the density and the detonation velocity were measured experimentally on specimens from different sheet. The results are listed in Table 1. For the detonation velocity measurements, the explosive specimens were fired on a 9-mm thick styrofoam piece which kept the plastic explosive sheet in a plane without providing significant confinement. Ionization probes were used to monitor the detonation. In general, three charges were fired for each thickness.

The detonation velocity varied somewhat within the same thickness due to poor homogeneity as well as lack of thickness uniformity from one sheet to another. However, this deviation was taken into account in the evaluation of the

the flyer plate test conditions since the detonation velocity of the driver explosive was measured for each individual flyer plate test.

TABLE 1
Physical properties of Detasheet C

Sheet denomination	Thickness (mm)	Density (Mg/m^3)	Detonation Velocity (mm/μs) Recorded	mean
C 1	1.21	1 473	7 018 6 998 — — —	7 008
C 1 5	1 60	1 488	7 019 7 025 7 033	7 036
C 2	2 05	1 476	6 994 6 998 7 022	7 005
C 3	3 02	1 471	7 041 7 084 7 164	7 096
C 4	3 99	1 473	7 061 7 084 7 049	7 065
C 5	4 61	1 487	7 057 7 057 7 080	7 065
C 6	5 96	1 468	7 076 7 033 7 092	7 067
C 7	6 56	1 471	6 968 6 998 7 002	6 969
C 8	7 84	1 468	7 045 6 983 7 076	7 035

The coefficients b and c of the Richter formula for the Detasheet C were evaluated previously in Ref. (4) as 1.92 and 3.79 respectively.

For the flyer plate test, the driver explosive was initiated by a line wave generator accurate to within ± 50 ns and described in Ref. (5). This particular initiation permitted the flyer plate to remain in a plane after it had been accelerated.

The driver explosive was carefully stuck onto the flyer plate with a 0.012-mm thick transfer tape adhesive manufactured by 3M so as to avoid air gaps between the 2 components.

Flyer Plates

The flyer plate material was aluminum alloy 2024-T3. It was available in six readily usable thicknesses of 0.51, 0.98, 2.01, 3.23, 4.04 and 5.07 mm. The shock Hugoniot values used for this alloy, of density 2.785 Mg/m^3, were $U = 5.355 + 1.345\ u$ (6).

The planarity and the impact angle of the flyer plate with the top of the receptor were monitored just prior to impact for each test by flash X-ray. The radiograph was taken at the moment when the plate was flying between five to ten millimeters from the top of the receptor. The angle measured on the radiograph (Fig. 3) had to be within ±0.017 rad; otherwise the test was rejected.

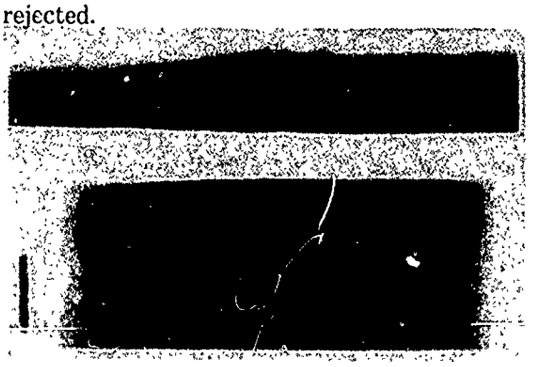

Fig. 3. Radiograph of the flyer plate (top) just prior impact

Explosive Receptors

The explosive receptors were cast in molds of 64-mm diameter and machined to a length of 60 mm. The CX-84A specimens were machined in lengths of 75 mm in order to record any possible initiation deeper than 60 mm, but none were observed.

The CX-84A contains 84 percent (weight) of RDX and 16 percent of a curable binder based on the hydroxyl-terminated polybutadiene prepolymer (R45-HT) with DOA (dioctyl adipate) and TDI (toluenediisocyanate). The complete formulation is given in a following section.

The shock Hugoniot values for all CX-84 explosives were estimated from a similar explosive in Ref. (3). For the French explosive (RDX/Polybutadiene binder – 86/14), the shock Hugoniot values were computed as $U = 2.3 + 1.8\ u$. Its density was reported at 1.60 Mg/m^3. The DREV explosive (RDX/Polybutadiene binder 84/16), with its lower density of 1.55 Mg/m^3, should have slightly lower shock Hugoniot values. The following values of $U = 2.3 + 1.6\ u$ were deemed to be representative, and will be eventually verified experimentally.

TABLE 2
Result of Flyer Plate Tests for the CX-84A

Test No.	Pressure (GPa)	Duration (μs)	Energy (J/cm²)	Results	Initiation Delay (μs)	Depth of Initation (mm)	Mean Shock Velocity (mm/μs)
1	9.27	0.167	212	Detonation	1.85	11.6	
2	7.83	0.170	159	No detonation			2.3
3	5.72	0.336	194	Detonation	2.77	17.5	
4	4.68	0.340	132	Detonation	2.83	17.9	
5	3.70	0.346	88	No detonation			2.3
6	4.52	0.700	256	Detonation	3.77	23.8	
7	3.00	0.716	129	No detonation			3.0
8	3.62	1.139	285	Detonation	4.43	28.0	
9	2.82	1.154	184	No detonation			2.7
10	3.40	1.432	320	Detonation	2.92	18.4	
11	3.5	1.442	272	No detonation			4.0
12	2.89	1.814	298	Detonation	4.44	28.0	
13	2.52	1.822	238	No detonation			3.1

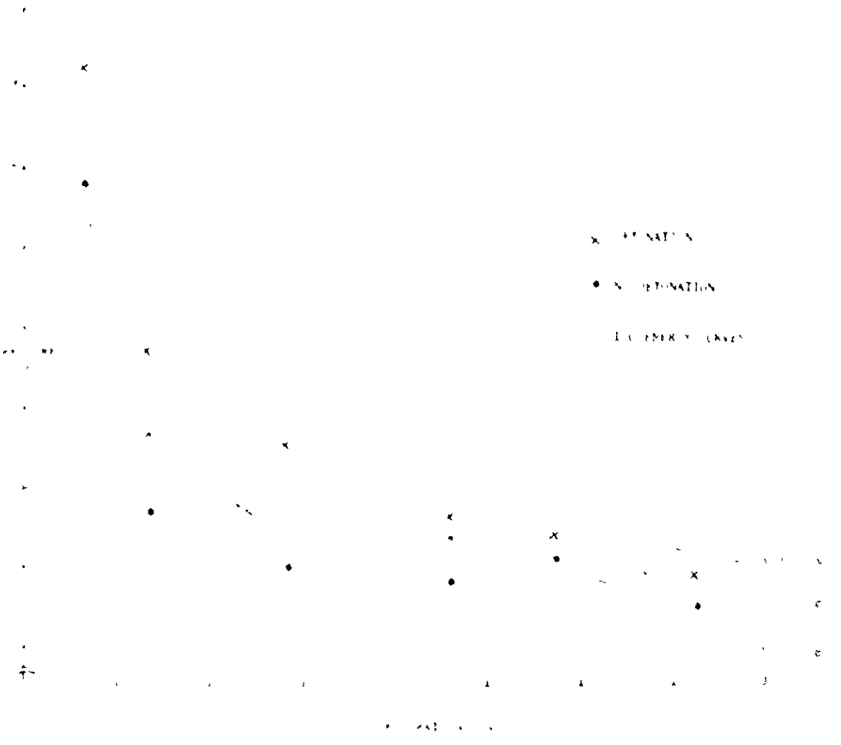

Fig. 4. Shock sensitivity of CX-84A to the flyer plate test

The impacted end of the explosive receptors was covered with a thin aluminum foil to prevent unwanted initiation by friction due to the slight lateral motion of the flyer plate. This foil, made of 1145 aluminum alloy, was 0.01 mm thick was considered thin enough to be ignored in investigating the energy transferred to the receptor at impact.

Shock-to-Detonation Transition

The shock-to-detonation transitions were derived either by the time required for the shock wave to pass through the receptor, called here the transfer time, or by the base plate of the setup acting as a witness plate. Furthermore, the the transfer time measured was compared to the theoretical detonation time (assumed to result from initiation at impact, i.e. $t = 0$) and the difference, if any, was considered to be the delay elapsed before the shock underwent transition to a detonation. This delay was used to evaluate the depth of initiation in the receptor from its impacted end. For non-detonation, the mean shock velocity in the receptor was calculated from the measured transfer time.

The above transfer time was derived from the total time monitored between the flash X-ray pulse and the moment at which the shock wave emerged at the terminal end of the receptor. The residual flying time of the plate before the impact, measured on the radiograph (Fig. 3), was subtracted. This residual flying time was obtained, knowing the velocity of the flyer plate, by the corrected distance between the plate and the receptor on the radiograph. That measured distance was corrected by the radiograph magnification factor evaluated from a tiny piece of lead 9.50 mm long stuck on the left side of the explosive receptor, and used as a reference.

A short-circuit type shielded probe monitored the time at which the shock wave surfaced at the terminal end of the receptor. This probe, shielded to prevent X-ray interference, was specially designed to pick-up both a weak shock wave as well as a detonation.

RESULTS AND DISCUSSION

CX-84A Explosive

The results of a series of thirteen flyer plate tests performed on the CX-84A are shown in Table 2. The critical initiation energy obtained varies appreciably with shock duration as illustrated by the dotted line in Fig. 4. An undesirable increase in shock sensitivity is shown for shock durations between 0.25 and 1.25 μs. The worst condition seems to be for the 0.34-μs duration test, where a detonation was obtained with only 132 J/cm^2. Furthermore, in this last condition, the relatively short delay of 2.83 μs measured before the detonation occurred, suggests that the energy level is not very close to the minimum required to get a detonation. Also, for the 0.34-μs shock duration, CX-84A was found more sensitive than Composition B which did not detonate under an energy of 141 J/cm^2 (7). However, for shock time durations shorter than 0.25 μs and longer than 1.25 μs, the minimum initiation energies for CX-84A were evaluated as 175 and 275 J/cm^2 respectively.

The complete formulation of the CX-84A is given in Table 3. Two different RDX particle sizes, a coarse (30-1250 μm) and a fine (0-44) μm), were used in the ratio of 70/30 (58.66% and 25.14% of the total weight respectively). The surface agents used were the Dantocol DHE (2-hydroxymethyl dimethylhydantoin) a commercial product of Glyco Chemical Inc. and the HDBA (4-hydroxy-N-N-dimethylbutyramide synthetized at DREV. A quantity of 0.075 percent of each surface agent was added. Also, a given reticulation rate of the binder was obtained with the NCO/OH ratio of 1.10.

The general shock initiation behavior of the CX-84A is rather different from that reported by de Longueville et al. in Ref. (3) for similar castable plastic-bonded explosive (RDX/Polybutadiene binder — 86 14). The same flyer plate test was used. A minimum initiation energy of 325 J/cm^2 was reported constant for shock durations ranging from 0.6 μs to 2.1 μs. For shock durations decreasing from 0.6μs, de Longueville et al. showed a progressive decrease in the required initiation energy down to 175 J/cm^2 for the shock duration of 0.16 μs.

New CX-84 Formulations

New CX-84 explosives were formulated in order to obtain a less shock sensitive explosive specially for the region of 0.34-μs duration. Starting with the original formulation, some modifications of the NCO/OH ratio of the binder, the surface active agents and the particle size of RDX were performed as indicated in Table 3. The two

Table 3
Formulation of New CX-84 Explosives

Explosive	RDX			Polybutadiene binder					NCO/OH ratio	HARDNESS Shore A
	Size	Lot	Percent Ratio	R-45HT (%)	DOA (%)	TDI (%)	Dan. ol (%)	HDBA (%)		
CX-84A	Coarse	7	58.666	9.711	5.588	0.667	0.075	0.075	1.10	57
	Fine	75	25.143							
CX-84B	Coarse	7	62.857	9.711	5.588	0.667	0.150	—	1.10	68
	Fine	78	20.952							
CX-84C	Coarse	7	58.666	9.681	5.571	0.665	—	0.200	1.05	17
	Fine	78	25.143							
CX-84D	Coarse	5A	62.857	9.711	5.588	0.667	0.150	—	1.10	68
	Fine	73	20.952							

surface agents, the Dantocol DHE and the HDBA were used either alone or combined. The different distributions of RDX particle size were obtained by varying the coarse/fine ratio and by using two different lots of coarse RDX (lot 5A and lot 7). The NCO/OH ratio was changed to modify the reticulation rate of the binder.

The formulation of CX-84B, in comparison to that of CX-84A, is characterized by the complete replacement of the surface active agent HDBA by the same quantity of Dantocol DHE (originally, the quantities of HDBA and DHE were equal). Also, the ratio of coarse/fine RDX particle size was changed from 70/30 to 75/25. In the CX-84C, the Dantocol DHE was eliminated and a total of 0.20% HDBA was used. The explosive names CX-84D is identical to CX84B, except that coarse RDX from lot 5A was used instead of from lot 7.

The particle size distributions of coarse RDX lot 5A and 7 are illustrated in Figures 5 and 6. An important difference in particle size was measured. Lot 5A contains, in one hand, more small particles between 100 and 200 μm and, in the other hand, less large ones between 500 and 750 μm than lot 7. The corrected retained fraction ε is expressed as :

$$\varepsilon = \text{Fraction Retained} \times 10^{\delta} \cdot \delta , \qquad (5)$$

where δ is the difference in microns between the sieve size considered and the preceding sieve size. For fine, RDX, the particle distributions for the lots 73, 75 and 78 (not shown here) were considered identical with an average size of 15 μm.

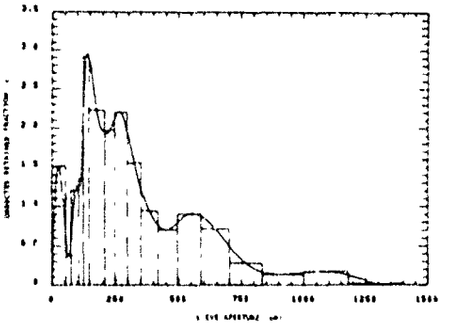

Fig. 5. Particle size distribution for coarse RDX lot 5A

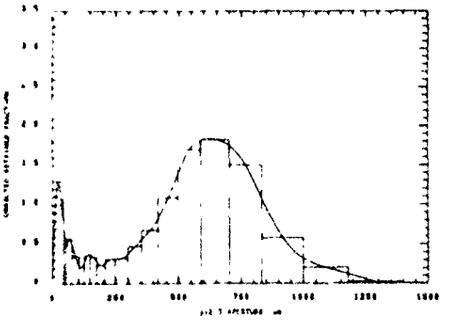

Fig 6. Particle size distribution for coarse RDX lot 7

TABLE 4
Results of Flyer Plate Test On New CX-84 Explosive

Explosive	Pressure (GPa)	Duration (μs)	Energy (J/cm^2)	Results	Initiation Delay (μs)	Depth of Initiation (mm)	Mean Shock Velocity (mm/μs)
CX-84B	4.68	0.340	132	No Detonation			2.56
CX-84B	5.72	0.336	194	No Detonation			2.88
CX-84B	5.72	0.336	194	No Detonation			2.54
CX-84C	4.68	0.340	132	No Detonation			2.40
CX-84C	5.72	0.336	194	Detonation	5.28	33.3	
CX-84D	5.72	0.336	194	Detonation	1.35	8.5	

The shock sensitivity of these new explosives was preliminarily evaluated by the Calibrated Shock Wave Test at the time duration of 0.34 μs, the duration at which the explosive CX-84A was the most shock sensitive. The less sensitive of these new formulations was the CX-84B. As indicated in Table 4, it did not detonate, when tested twice, for an energy of 194 J/cm^2 while the CX-84C and D detonated. CX-84A detonated at a shock energy of only 132 J/cm^2 for this time duration.

This preliminary study to optimize the formulation of curable plastic-bonded explosives with regard to their shock sensitivity, seems promising. The results obtained up to now suggest that the shock sensitivity of curable plastic-bonded explosives is reduced when the size of RDX particles is increased and when a unique surface active agent is used. The Dantocol or the HDBA used separately as surface agent seems more effective in covering RDX crystals than their combination. The effect of increasing particle size on shock sensitivity confirms the results obtained for previous studies on cast RDX/TNT mixtures (8). For the NCO/OH ratio, no effect on shock sensitivity has been pointed out yet.

This study has just been started and more work must be done to fully characterize the curable plastic-bonded explosive CX-84 with regard to shock sensitivity.

CONCLUSIONS

The minimum initiation energy of the curable plastic-bonded explosive CX-84A, varied significantly with shock duration. This explosive was found particularly shock sensitive for the duration of 0.34 μs, where it was initiated with only 132 J/cm^2. For shock durations shorter than 0.25 μs and longer than 1.25 μs, the minimum initiation energies were evaluated as 175 and 275 J/cm^2, respectively.

A preliminary study at 0.34 μs shock duration indicated that the shock sensitivity of CX-84A, evaluated by the flyer plate test, can be significantly reduced by using larger RDX particle size and using separately Dantocol or HDBA as surface active agent.

REFERENCES

1. Drolet, J. F., Lavertu, R. R., Bélanger, C. and Walker, G. R., "Castable Plastic Bonded Explosive CX-84A", Private Communication.

2. de Longueville, Y., "Description d'un mode opératoire standard pour l'étude de la sensibilité des explosifs condensés à l'onde de choc. Application à une composition coulée," Rapport ISL 19/74, mai 1974.

3. de Longueville, Y., Fauquignon, C. and Moulard, H., "Initiation of Several Condensed Explosives by a Given Duration

Shock Wave," Sixth Symposium (International) on Detonation, pp. 105-114, California, August 1976.

4. Constant, J., "Relevement latéral d'une plaque métallique par explosif et applications," DREV M-2472/79, avril 1979.

5. Bélanger, C., Walker, G. R. and Matte, Y., "Some Explosive Devices for Generating Plane Waves," DREV M-2572/82, January 1982.

6. Thiel, V., "Compendium of Shock Wave Data," Section A-1, A-2, UCRL-50108 (Vol. 1), June 1966.

7. Bélanger, C. and Matte, Y., "Shock Sensitivity of CX-84A and Composition B to Flyer Plate Test," Private Communication.

8. Wilson, W.S., The Use of Recrystallised RDX in Cast RDX/TNT Composition," MRL-R-805, March 1981.

SHOCK SENSITIVITY STUDY OF CURABLE PLASTIC BONDED EXPLOSIVES

By

C. Bélanger, P. Pelletier and J.F. Drolet

DEFENCE RESEARCH ESTABLISHMENT VALCARTIER

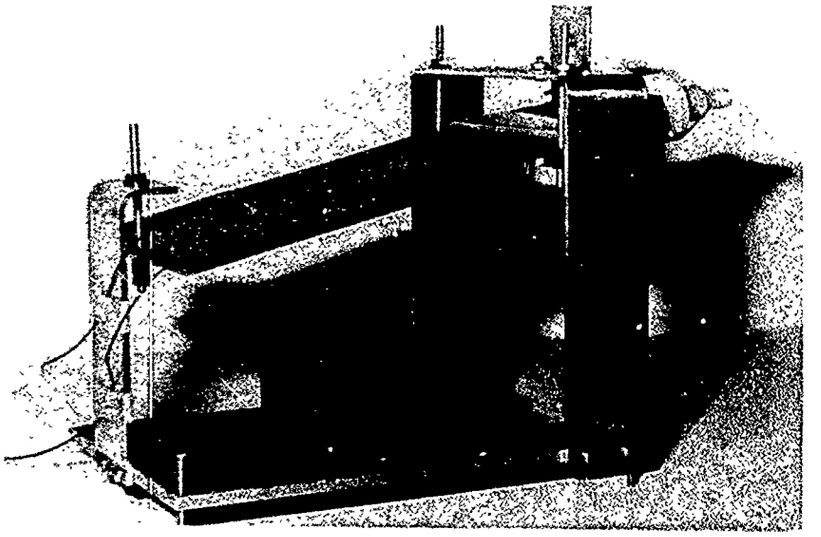

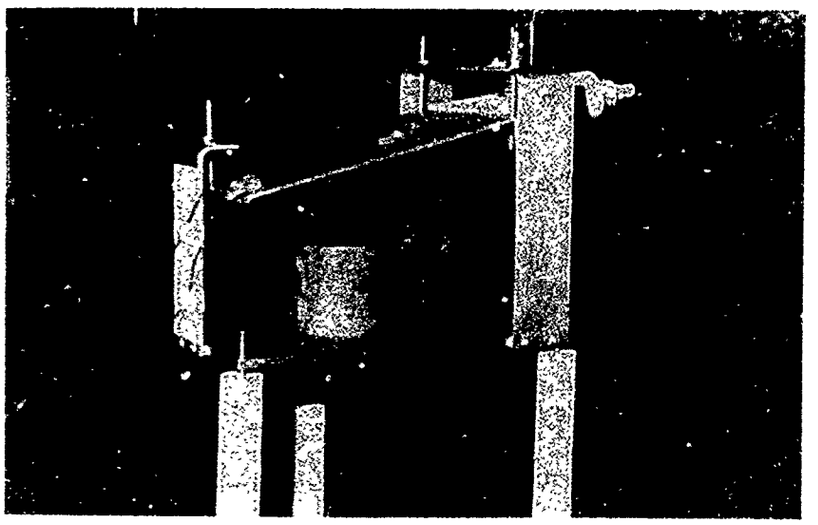

SHOCK SENSITIVITY OF CX-84A TO THE FLYER PLATE TEST

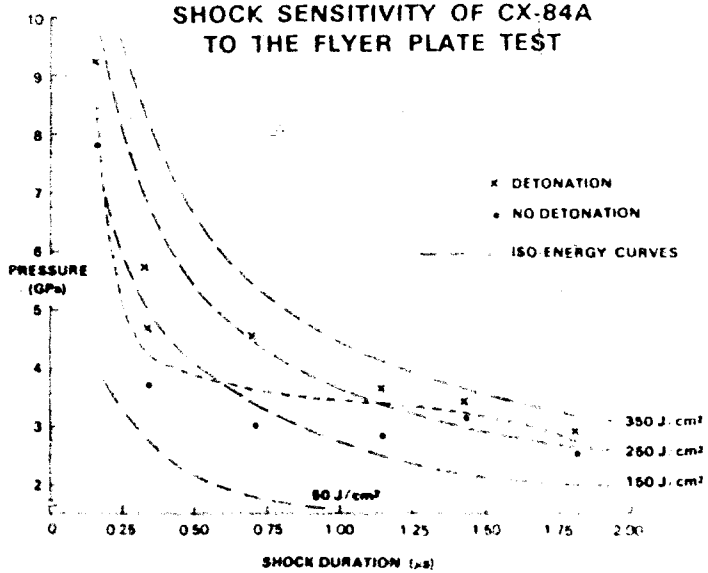

RESULTS OF FLYER PLATE TESTS ON THE CX-84A

Test No	Pressure (GPa)	Duration (μs)	Energy (J/cm²)	Results	Initiation Delay (μs)	Depth of Initiation (mm)	Mean Shock Velocity (mm/μs)
1	9.27	0.167	212	Detonation	1.85	11.6	
2	7.83	0.170	158	No detonation			2.3
3	5.72	0.338	194	Detonation	2.77	17.5	
4	4.88	0.340	132	Detonation	2.83	17.9	
5	3.70	0.346	88	No detonation			2.3
6	4.52	0.700	256	Detonation	3.77	23.8	
7	3.00	0.716	129	No detonation			3.0
8	3.62	1.139	285	Detonation	4.43	28.0	
9	2.82	1.154	184	No detonation			2.7
10	3.40	1.432	320	Detonation	2.92	18.4	
11	2.96	1.442	272	No detonation			4.0
12	2.89	1.814	298	Detonation	4.44	28.0	
13	2.62	1.822	238	No detonation			3.1

FORMULATIONS OF CX-84 EXPLOSIVES

Explosive	RDX Size	RDX Lot	RDX Percent Ratio	Polyisobutylene binder % WEIGHT (%)	DOA (%)	TOI (%)	Dantocol (%)	HCB-A (%)	NCO:OH ratio	HARDNESS Shore A
CX-84A	Coarse	7	60.67	0.71	0.50	0.67	0.075	0.075	1.15	57
	Fine	75	25.14							
CX-84B	Coarse	7	62.86	0.71	0.50	0.67	0.15		1.10	60
	Fine	75	25.95							
CX-84C	Coarse	7	60.67	0.86	0.57	0.67		0.20	1.05	57
	Fine	75	25.14							
CX-84D	Coarse	5A	62.86	0.71	0.50	0.67	0.15		1.10	60
	Fine	72	26.00							

PARTICLE SIZE DISTRIBUTION FOR COARSE RDX LOT 7

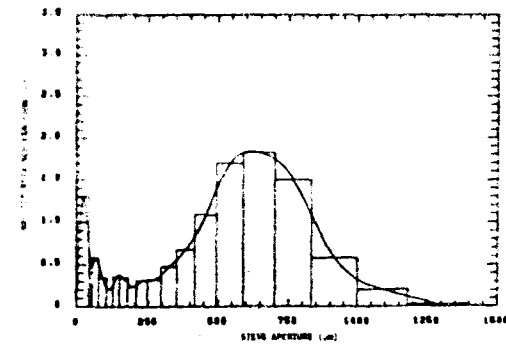

PARTICLE SIZE DISTRIBUTION FOR COARSE RDX LOT 5A

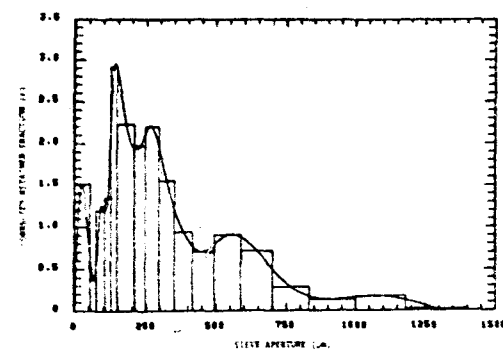

PARTIAL SHOCK SENSITIVITY OF NEW CX-84 EXPLOSIVES TO THE FLYER PLATE TEST

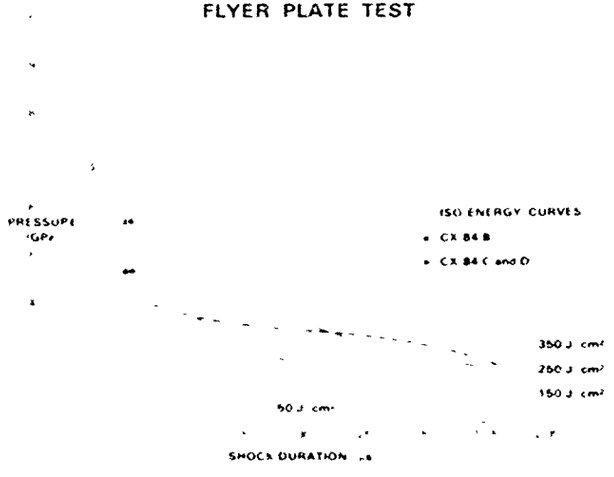

RESULTS OF FLYER PLATE TEST ON THE NEW CX-84 EXPLOSIVES

Explosive	Pressure (GPa)	Duration (μs)	Energy J/cm²	Results	Initiation Delay (μs)	Depth of Initiation (mm)	Mean Shock Velocity (mm/μs)
CX 84B	4 68	0 340	132	No Detonation			2 56
	5 72	0 336	194	No Detonation			2 88
	5 72	0 336	194	No Detonation			2 54
CX 84C	4 68	0 340	132	No Detonation			2 40
	5 72	0 336	194	Detonation	5 28	33 3	
CX 84D	5 72	0 336	194	Detonation	1 35	8 5	

SUMMARY OF RESULTS FOR CX-84 EXPLOSIVES

Explosive	RDX			Surface Agent		Results *	
	Fine	Coarse		Danto	HDBA	Energy	Initiation
	(%)	(%)	Lot	(%)	(%)	(J/cm²)	
CX 84A	25 1	58 7	Coarser #7	0 075	0 075	132	Detonation
CX 84B	20 9	62 8	Coarser #7	0 15	–	194 194	No detonation No detonation
CX 84C	25 1	58 7	Coarser #7	–	0 20	194 132	Detonation No detonation
CX 84D	20 9	62	Finer #5A	0 15	–	194	Detonation

* For 0 34 μs Shock Duration

SHOCK SENSITIVITY OF CURABLE PBX IS DECREASED BY USING:

- COARSER PARTICLE SIZE
- SINGLE SURFACE AGENT

EFFECT OF CONFINEMENT ON FAILURE IN 95 TATB/5 KEL-F

John B. Ramsay
Los Alamos National Laboratory
Los Alamos, New Mexico 87545

A modification of the usual wedge test for measuring the failure thickness has been developed that eliminates the effect of the confinement provided by the witness plate. The new test uses a prism of the explosive with a line initiator to start a detonation along the trapezoidal face of the prism. Experiments using PBX 9502 have shown that the failure thickness measured using the prism test is ½ the failure diameter measured in long cylindrical charges, provided the wave can propagate 15 to 25 times the failure width. No significant effect of confinement is observed for low impedance confinement, whereas high impedance materials reduce the failure thickness. Thin layers of confinement reduce the failure thickness significantly. Copper, 0.025 mm thick, and 0.25-mm aluminum each reduce the failure thickness of PBX 9502 by 35%.

INTRODUCTION

Confining an explosive charge in a high-density material reduces the lateral dimension at which a steady-state detonation will propagate. The earliest paper found with quantitative data on this topic was by Copp and Ubelohde (1) They published data on the effect of confinement on the detonation velocity of cast Amatol (60% TNT/40% NH_4NO_3) and showed an increase from 5100 m/s for an unconfined charge with a 1.74-cm radius to 5600 m/s confined in 1-mm steel with the same explosive radius. They assumed that inertia was the critical variable Campbell, Malin, and Holland (2) showed that thin layers of aluminum (0.025 mm) significantly reduced the failure diameter of nitromethane A theoretical analysis of two-dimensional detonation flow by Bdzil (3, 4) addresses the question of failure of unconfined (air) and effective infinte confined charges*. However, little or no experimental data appear to be available on the effect of confinement thickness on the failure diameter of polycrystalline explosives.

THE PRISM TEST

The precision measurement of the failure diameter of an unconfined explosive in cylindrical geometry requires the careful machining and firing of charges, sometimes at small diameters. The complication of casing these charges in a confinement material with a precise wall thickness requires considerable care and expense. In the usual wedge test (5) for estimating the failure thickness of an explosive, a wedge of explosive is initiated along the base with the detonation propagating into a uniformly decreasing thickness. The position of failure is determined from the depression created in a contacting witness plate. The witness plate provides support for one of the lateral edges of the detonation wave, and the test cannot be used to study the effect of confinement on the failure thickness. A modification of the test has been developed that eliminates the effect of the fixed confinement. The new test uses a prism of the explosive and, instead of initiating along the base of a wedge, a line initiator is used to start a detonation along the trapezoidal face of the prism.

*For the purposes of this paper the term "effective infinite confinement" refers to that thickness of confinement where an increase in thickness no longer causes a corresponding decrease in failure thickness

At any point along the length of the linear wave the detonation propagates in a constant thickness. Figure 1 is a line drawing of the test. The witness plate provides no confinement to the propagation. Confinement can be varied by placing material in contact with the rectangular faces parallel to the direction of propagation. For a detonation in a slab of finite thickness and infinite planar extent the failure thickness should be approximately one-half the failure diameter. This ratio will be discussed later in the paper.

The explosive studied was PBX 9502 (95 wt% TATB/5 wt% KEL-F 800). The wedge was 150 mm long, 50 mm wide, with a 2° taper. For most shots the base was 8 mm thick and the toe 2 mm thick. For special shots the thickness of the toe was reduced to 0.5 to 1.0 mm with a corresponding reduction in the thickness of the base. The detonation wave was initiated with a 150-mm long line-wave generator followed by a 12 by 12 by 150-mm booster of PBX 9501 (95 wt% HMX/5 wt% Estane) and then a 12 by 12 by 150-mm booster of PBX 9502. The thickness at failure is measured from the dent formed in a dural witness plate. Precision of the measurement is provided by measuring the length from the toe to the point of failure as indicated by the plate dent. A photograph of the resulting dent is shown in Fig. 2 with the point of failure marked for clarity.

In the current program no studies were made of the effect of wedge angle on the measured failure thickness. However, based on the data obtained, the argument is made that the values reported represent the magnitude and correct form of the functional relationship of the true slab-failure thickness with confinement material and thickness.

UNCONFINED FAILURE THICKNESS AND STABLE PROPAGATION

Shots were fired with the basic geometry described above at −55 °, 20 °, and 75 °C to compare the failure thickness measured using the prism technique with the failure diameter of PBX 9502 as reported by Campbell (6). The experimental results obtained are illustrated in Fig. 3. Also presented in the figure are Campbell's data multiplied by one-half to adjust the failure diameter to failure thickness. The prism data with a total travel of 50 mm in the PBX 9502 lie approximately parallel to and displaced by about 10% from the adjusted diameter data. At 20 °C the measured failure thickness is 3.5 mm, whereas one-half the failure diameter is 4.0 mm.

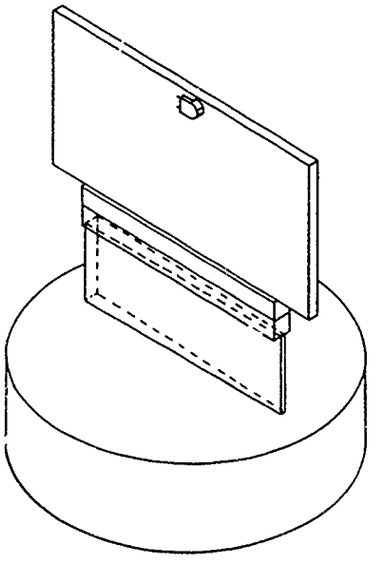

Fig. 1. Trapezoidal prism shot assembly. See the text for a description of the assembly (Note: Selected hidden lines have been added for clarity.)

One shot was fired at 20 °C in which two prisms were mounted edge-to-edge to provide a total run for the detonation wave of 100 mm. The measured failure thickness was 4.0 mm in agreement with ½ the failure diameter. With the 50-mm-wide prism the wave traveled 14 times the failure thickness, but the wave had not yet reached a stable configuration. Campbell showed that, in cylindrical geometry, a detonation wave can travel 25 times the diameter before failure occurs. The measured value with the longer distance of run does agree with the value of one-half the diameter, indicating that the factor of two between failure diameter and thickness is correct. This latter result, which was obtained late in the program, does raise the question of the validity of the remaining data. However, the parallel nature of the response with temperature compared with Campbell's data for long cylindrical charges over the failure thickness variation from 7 to 2 mm supports the contention that the magnitude and form of the effects reported are qualitatively correct. For precise, quantitative

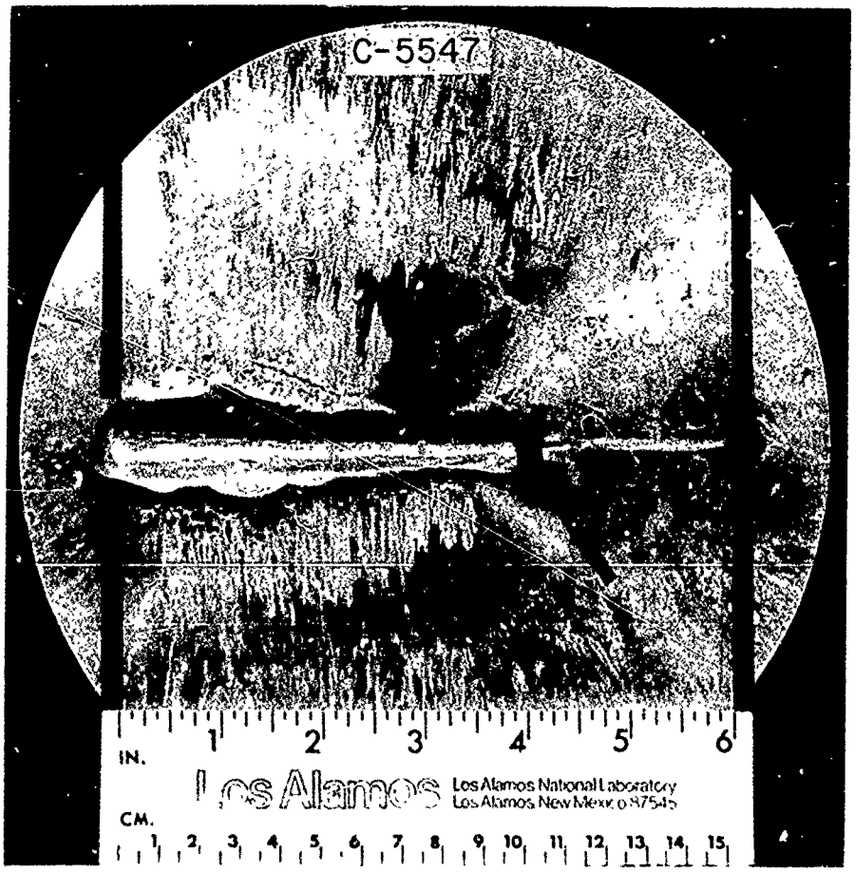

Fig. 2 Photograph of resulting dent in witness plate from a prism test. The black lines indicate the length of the prism and the arrow shows the point of failure.

data, experiments should be performed using slabs of fixed thickness, with the prism technique providing a preliminary estimate of the size range to be studied.

EFFECT OF CONFINEMENT MATERIAL

Experiments were performed with the prism confined in various materials ranging from air (no confinement), water, and polymethylmethacrylate (PMMA) to magnesium, aluminum, lead, and copper. K-Y Lubricating Jelly was used to insure a close fit between the confinement material and the explosive prism. For the thin layers of metal, 12.7-mm-thick PMMA was used as a backing, which did not affect the results. Experiments were performed to estimate the effect of aluminum and copper thickness on failure width. A failure width of 1.4 mm was obtained for aluminum thicknesses of 3.2 and 12.7 mm. The data obtained with aluminum, up to 3.2 mm, are plotted in Fig. 4. The most surprising result obtained was the magnitude of the effect of very thin layers of copper and aluminum. It was found that 0.025-mm copper reduced the failure width to 2.3 mm. The failure width was reduced to 2.6 mm with a 0.075-mm-thick aluminum confinement. Campbell, Malin, and Holland (2) showed that thin layers of aluminum drastically reduced the failure diameter of nitromethane. However, it was previously thought that this effect could be explained by the thin reaction zone of nitromethane. It was not expected for PBX 9502 with a relatively thick reaction zone.

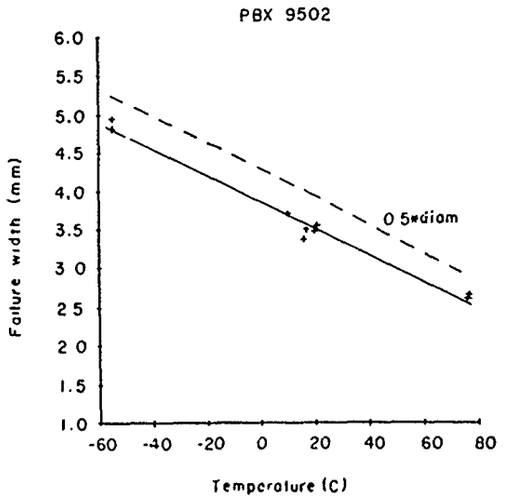

Fig. 3. Failure data obtained by the prism test compared with one-half the failure diameter measured in long cylindrical charges

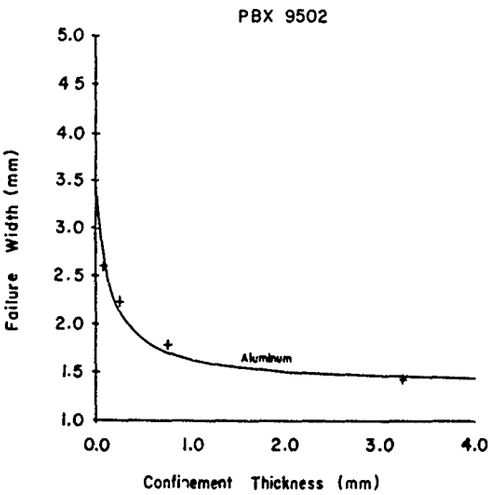

Fig. 4. Effect of aluminum thickness on the failure width of PBX 9502. An additional value of 1.39 mm for the failure width was obtained with 12.7-mm-thick aluminum confinement. This latter point was not plotted to allow enlargement of the abscissa.

Figure 5 shows the failure thickness for various confinement materials plotted as a function of the acoustic impedance (ρC_0). For air, water, and PMMA the confinement thickness probably represents the effective infinite thickness. Experiments showed that 3.2-mm-thick aluminum and 3.2-mm magnesium are effectively infinitely thick. Acoustic impedance has been used as an approximation for a more analytic and correct match between the explosive and the confinement. This approximation should not affect the general behavior reported. Straight lines have been used to illustrate the behavior. The horizontal line for materials of low impedance is supported by Bdzil's model. The straight line connecting the Mg and Al points has no theoretical basis. The intersection of the two lines is approximately equal to the acoustic impedance of unreacted PBX 9502.

The preceding data do not distinguish the impedance from density or total mass as an important variable. The acoustic impedance of copper is greater than for lead, whereas the density of lead is greater than copper. Figure 6 shows the results for 0.25-mm-thick aluminum, lead, and copper. Clearly, for this thickness of confinement, impedance is the critical variable. We do not have sufficient data to determine the effect of impedance greater than that of the explosive when it is confined at effectively infinite confinement.

DISCUSSION

The experimental results show that confinement affects the failure properties of explosives and that the important variable is the impedance of the confining material. Prior to and during the progress of the program various experienced workers in the field were questioned as to the predicted behavior. Most guessed correctly, but with a little encouragement could be persuaded to weaken their opinion. We have shown that confinement with a material of low impedance (less than the explosive) does not affect the failure behavior of PBX 9502, whereas with high impedance confinement, the failure thickness decreases with impedance.

However, the magnitude of the effect for thin confinement is surprising, particularly for a material with a thick reaction zone such as PBX 9502. A rational argument for the effect can be made from the two-dimensional model developed by Bdzil. Bdzil has shown that for an unconfined charge the sonic surface, which constitutes the boundary behind which energy production does not affect the shock wave, intersects the shock front at the free boundary. This is illustrated in a highly magnified sketch shown in Fig. 7a. When the explosive is confined in a material of high

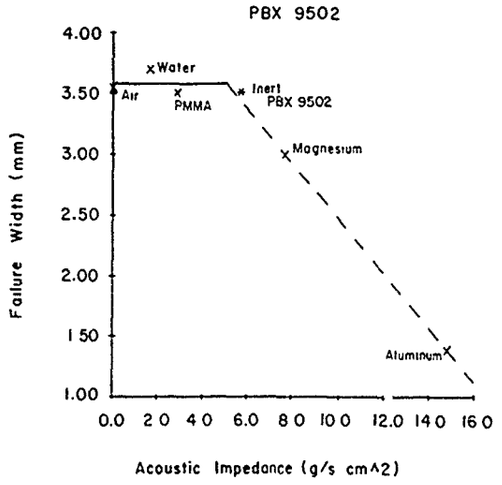

Fig. 5. Confinement effects for PBX 9502. The line between magnesium and aluminum was arbitrarily drawn to illustrate the data. The intersection of the two lines is approximately the acoustic impedance of ($\rho_o C_o$ = 5.65 g/cm²s) for inert PBX 9502, shown as the "".*

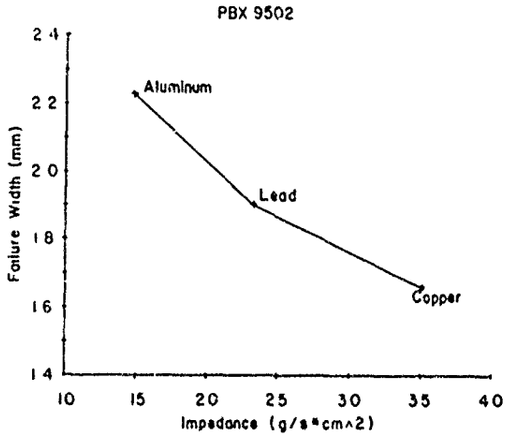

Fig 6. Effect of impedance on failure in PBX 9502. The acoustic impedance of copper is higher than lead, whereas the density of lead is higher. No data exist for effective infinite confinement for these metals.

shock impedance, the sonic surface separates from the shock front, providing an energy contribution to the shock front at the explosive/confinement boundary. Figure 7b shows the structure when the wave is confined in an effectively-infinite-thickness material of high impedance. Basically then, the effect of thin confinement is to drastically alter the reaction zone flow at the

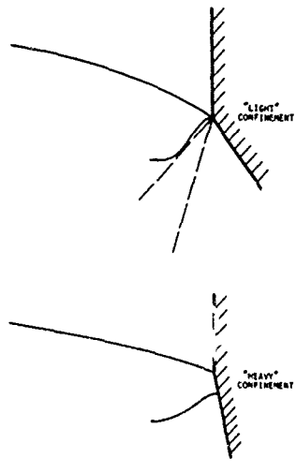

Fig. 7. a) The upper drawing shows the shock front (detonation front) and the sonic surface intersecting at the boundary. The left dashed line is the lead characteristic of the expansion fan. No energy generated behind the sonic plane can influence the reaction zone.

b) The lower drawing shows the shock wave and sonic surface for an effectively-infinitely-confined detonation in a high impedance material.

boundary of the explosive and greatly diminish the lateral dimension at which stable detonation will propagate.

The test that has been developed appears to be sensitive to production variables, including manufacturing lot and density. With minor modification the test could be easily used for production control.

REFERENCES

1. J. L. Copp and A. R. Ubelohde, "Physico-Chemical Processes Occurring at High Pressures and Temperatures. Part I. Interaction Between Trinitrotoluene and Ammonium Nitrate," Trans. Faraday Soc. XLIV, pp. 640-658, 1948.
2. A. W. Campbell, M. E. Malin, and T. E. Holland, "Detonation in Homogeneous Explosives," 2nd ONR Symposium on Detonation, Office of Naval Research, Department of the Navy, 1955.
3. J. B. Bdzil, "Perturbation Methods Applied to Problems of Detonation Physics," 6th

Symposium (International) on Detonation, Naval Surface Weapons Center, pp. 352-369, August 24-27, 1976.

4. J. B. Bdzil, "Steady State Two-Dimensional Detonation," J. Fluid Mech. 108, pp. 195-226, 1981.

5. M. J. Urizar, S. W. Peterson, and L. C. Smith, "Detonation Sensitivity Tests," LA-7193-MS, April 1978.

6. A. W. Campbell, "Diameter Effect and Failure Diameter of a TATB-Based Explosive," Propellant, Explosives, Pyrotechnics 9, pp. 183-187, 1984.

COMMENT

C. L. MADER, Los Alamos National Laboratory

Our modeling of the failure radius of PBX 9404 and PBX 9502 as a function of confinement was described in "Three-Dimensional Modeling of Inert Metal-Loaded Explosive," by Charles L. Mader, James D. Kershner, and George H. Pimbly, Journal of Energetic Materials, *1*, 293-294 (1983). We used 2DL and 2DE codes with Forest Fire as described in *Numerical Modeling of Detonations, University of California Press, 1979.* The 2 DE calculated results compared to your experimental results are shown in Table I. We also examined the effect of reducing the thickness of the copper aluminum confinement. These results are shown in Table II. The computational modeling demonstrate agreement with your results.

TABLE I
Half-Slab Failure Thickness for PBX 9502

Confinement (mm)	Calculated (mm)	Experimental (mm)
Air	2.5 - 2.0	1.75
Plexiglas	2.5 - 2.0	1.75
Aluminum	1.0 - 0.75	0.75
Copper	0.75 - 0.5	0.75
Tungsten	0.5 - 0.33	0.55

TABLE II
Effect of Confinement Thickness

	Goes (mm)	Fails (mm)	Experimental (mm)
Thick aluminum	1.0	0.75	0.75
0.25-mm aluminum	1.25	1.0	1.15
Thick copper	0.5	0.33	0.55
0.25 mm copper	1.0	0.72	0.85

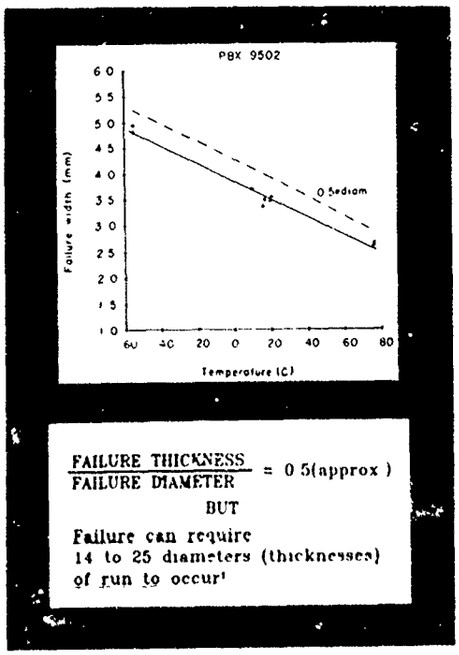
PBX 9502
Failure width (mm)
Temperature (C)
0 5diam
FAILURE THICKNESS / FAILURE DIAMETER = 0 5(approx)
BUT
Failure can require
14 to 25 diameters (thicknesses)
of run to occur

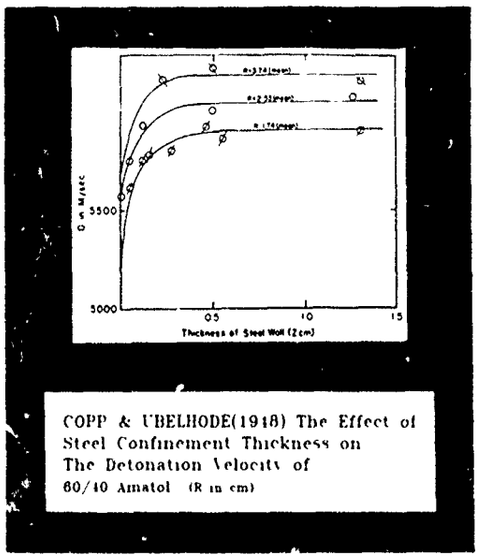
D m Msec
Thickness of Steel Wall (2cm)
COPP & UBELHODE(1918) The Effect of
Steel Confinement Thickness on
The Detonation Velocity of
60/40 Amatol (R in cm)

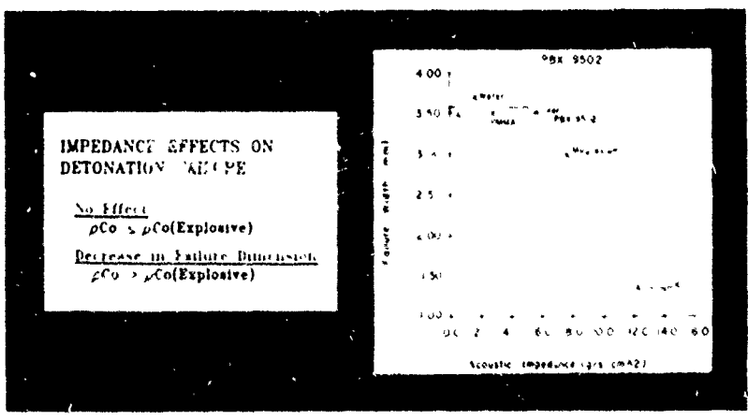
IMPEDANCE EFFECTS ON
DETONATION WAVE SHAPE
No Effect
ρCo > ρCo(Explosive)
Decrease in Failure Diameter
ρCo > ρCo(Explosive)
PBX 9502
Acoustic Impedance (gm/s cm^2)

THIN, HIGH-IMPEDANCE FOILS STRONGLY AFFECT FAILURE DIMENSION

PBX 9502

Air - Fails at 3.5 mm

0.025-mm Cu - Fails at 2.5 mm

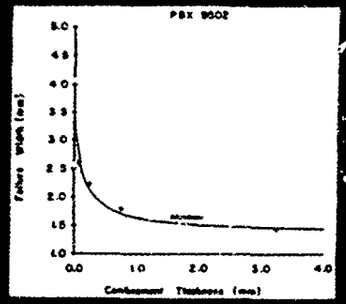

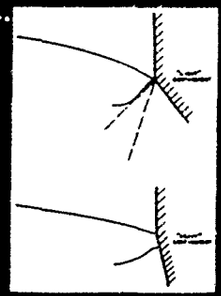

BDZIL'S MODEL -- Reaction zone Structure changes at boundary with The high impedance material.

MADER and PIMBLEY'S CALCULATED RESULTS ON CONFINEMENT THICKNESS.

	Goes	Fails	Exp.
Aluminum			
Thick	1.0	0.75	0.75
0.25-mm	1.25	1.0	1.15
Copper			
Thick	0.5	0.33	0.55
0.25-mm	1.0		0.85

MADER and PIMBLEY'S CALCULATED RESULTS (Half-Slab) COMPARED TO PRESENT EXPERIMENTAL RESULTS.

	Calculated	Experimental
Air	2.5-2.0	1.75
Plexiglas	2.5-2.0	1.75
Aluminum	1.0-0.75	0.73
Copper	0.75-0.5	0.55

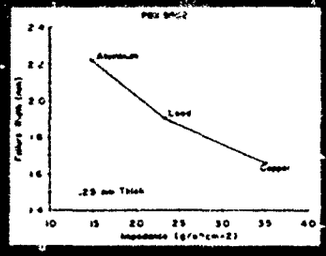

IMPEDANCE NOT DENSITY (or Mass) IS THE IMPORTANT PARAMETER.

RUN TO DETONATION IN TATB

D. Grief, S. H. Ward, G. D. Coley
Atomic Weapons Research Establishment
Aldermaston, Berkshire, UK

Run distance to detonation has been measured as a function of initial shock pressure in several TATB-based explosives. High amplitude, short duration shock stimuli generated by an electric gun were used to initiate small cylindrical wedges of explosive material. The transition from sub-detonative reaction to full detonation was monitored using a purpose-designed fibre-optic/streak camera diagnostic technique. This paper describes the experimental arrangement and presents the results in the form of Pop plots for four TATB compositions. The method has produced data which may help give some insight into the influence of particle size of the explosive and on the effect of pulse length on the initiation and growth to detonation characteristics in insensitive high explosives.

INTRODUCTION

Insensitive high explosives (IHE) such as TATB provide significant improvements in safety for the HE formulator when compared with HMX and RDX, and in order to exploit the increased safety it is necessary to characterise the response of IHE's to a variety of stimuli. An inevitable consequence of their enhanced safety properties is their insensitivity to shock. Several studies have shown that shock sensitivity can be tailored to some extent by adjusting void percentage and by modifying explosive particle size and shape (1,2).

An experimental method is described here in which the run distance to detonation as a function of shock pressure has been measured directly in several TATB-based IHE's. Two well-known techniques have been combined; the electric gun, which provides a high pressure, short shock pulse of known amplitude and duration, and the explosive wedge method, where the progress of a propagating reaction front can be followed as a function of distance through the explosive.

The work shows how particle size of the explosive can influence initiation characteristics, and by comparing the results with some recent work of Seitz (3) the effect of shock pulse duration can be seen.

EXPERIMENTAL

Since its introduction several years ago the electric gun has proved ideally suited to thin-pulse shock initiation studies. It produces a well-characterised, planar and reproducible shock stimulus that can be equalled in precision only by the much more costly and complicated explosive lens technique. It has been used to examine shock initiation in a number of explosives (4,5,6).

In essence, the technique involves the acceleration of a thin plastic disc (flyer) along a short barrel to impact an explosive sample. The drive for the flyer is provided by the expanding plasma of an electrically exploded metal foil confined behind the flyer. Flyer velocity is controlled by adjusting the energy discharged through the foil. A knowledge of the flyer velocity and of the Hugoniots of the flyer and explosive allows the input shock pressure to be calculated; in addition, values of flyer density and thickness permit calculations of the pulse duration. Table 1 gives details of the electric gun used in the

TABLE 1
The Electric Gun

Storage Capacitance	28.6 μF
Circuit Resistance	12 mΩ
Inductance	40 nH
Charging Voltage	10-25 kV
Stored Energy	1.4-8.9 kJ
Flyer - Mylar	12 mm Ø x 0.25 mm
Foil - Aluminum	12 mm x 12 mm x 0.025 mm
Barrel - PMMA	12 mm i.d. x 2.4 mm long
Flyer Velocity	~3-4.5 km s^{-1}
Flyer Simultaneity at Impact	$\lesssim$ 5 ns
Pulse Width in TATB	0.11-0.08μs
Input Pressure in TATB	11-26 GPa

TABLE 2
The Explosives

Explosive	Specific Surface Area m^2g^{-1}	Density (% TMD)[a] $Mg\ m^{-3}$	No. of Wedges
Ultrafine TATB	4.5	1.787 ± 0.003 (91.7)	5
Superfine TATB	0.7	1.783 ± 0.009 (92.0)	10
Standard TATB	0.5	1.779 ± 0.003 (92.2)	10
PBX 9502[b]	—	1.885 (97.1)	5
PBX 9503[c]	—	1.899 (97.6)	10

[a] percentage theoretical maximum density [b] 95/5 w/o TATB/Kel F
[c] 80/15/5 w/o TATB/HMX/Kel F

present study. The single most important attribute of the gun was its ability to provide flyers routinely which had a simultaneity of arrival over the central 6 mm of better than 5 ns on impact, ensuring the input of a precise square shock pulse.

The explosive samples, supplied by J. Wackerle and W. Seitz of LANL, were in the form of small cylindrical wedges, 6.3 mm diameter with toe thickness of $\lesssim$ 100 μm and accurately measured toe angles of ~30°. Five TATB explosives were tested, three of which were pure TATB compacts which used powder of different particle size, and two of which were LANL PBX compositions. Full details of composition and density are given in Table 2.

Following direct shock initiation over the base of the explosive wedge the angled face was interrogated optically using fibre-optic detectors and a streak camera to follow the progress of the reaction wave from the sub-detonative input shock to stable detonation. The run-distance-to-detonation was inferred from the streak records where by careful analysis the onset of stable detonation could be detected. Figures 1 and 2 show how 18 fibre-optic cables, 0.5 mm diameter, were accurately aligned in order to be placed across the angled face of the wedge with the help of a PMMA holder. A small air gap (a few microns) between the explosive and fibre ends acted as a "flash-gap" and improved the resolution of the streak records.

Two pairs of larger fibres were used as flyer velocity sensors. By recording the time taken for the flyer to travel the known distance between the ends of the fibres (stepped by ~1 mm)

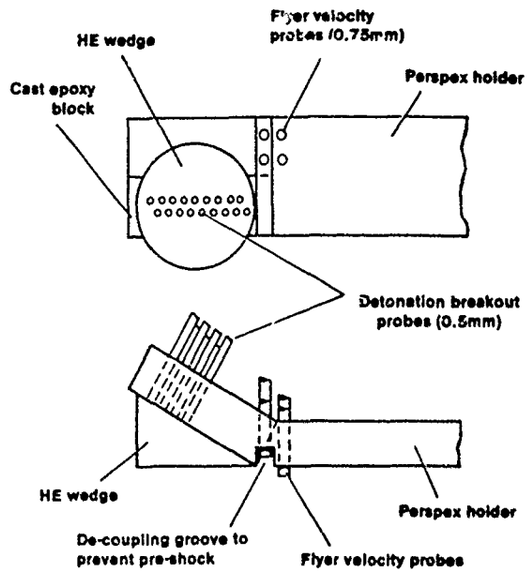

Fig. 1. Base and side views of the holder/ optical array/HE wedge in the experimental configuration

a velocity at impact was calculated. The groove in the holder was machined as a decoupling device to prevent preshocking of the explosive through the PMMA at impact.

The remote ends of the fibres were aligned horizontally to be focussed onto the film track of a rotating mirror streak camera.

RESULTS

Figure 3 shows a typical streak record (Standard TATB initiated by a 15 GPa, 0.1 μs pulse). The reaction wave shows an initial acceleration up to the point T where a constant velocity has been reached, and T therefore corresponds to the onset of stable detonation. Beyond T the wave velocity remains constant until rapid deceleration occurs somewhere towards the end of the wedge. In order to calculate shock input pressures the Hugoniots of the materials, together with the measured flyer velocities (from the streaks) were required.

Mylar

(ϱ = 1.4 Mg m^{-3}) $U_s = 2.54 + 1.49\ U_p$ (5)

TATB

(ϱ = 1.8 Mg m^{-3}) $U_s = 1.77 + 2.35\ U_p$ (2)

PBX9502

(ϱ = 1.9 Mg m^{-3}) $U_s = 3.26 + 1.68\ U_p$ (7)

Since no Hugoniot was found for PBX9503, that for PBX9502 was used. Very little error is incurred, since PBX9503 contains only 15% HMX, and the Hugoniots of HMX and TATB are similar over the limited pressure range studied.

Pop plots were constructed (log run distance vs log pressure) for each explosive, except PBX9502 which failed to detonate at all pressures. The plots are given in Figures 4-7. Errors are typically $\pm$ 0.15 mm in run distance and $\pm$ 3% in pressure. The high pressure point in Figure 4 (run distance $\sim$ 0.4 mm) is subject to a larger error, since it corresponds to a very short run to detonation. Stable detonation was achieved within the first or second light pipe, and the value shown is an upper limit on the run distance.

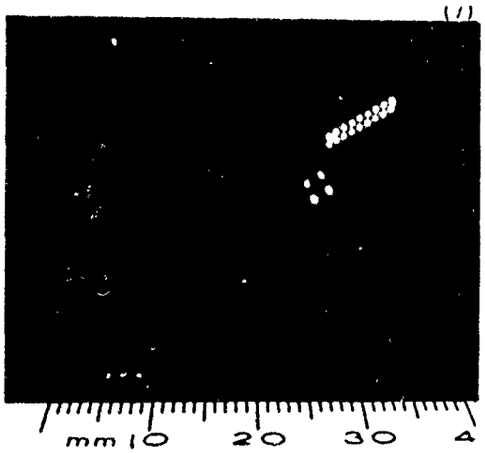

Fig. 2. The holder and fibre-optic array

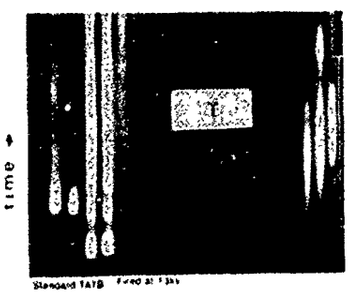

Fig. 3. Typical Streak Record. Standard TATB fired at 13 kV

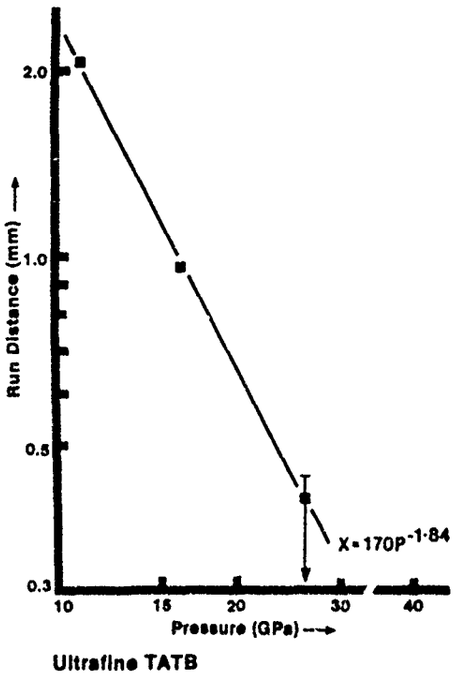

Figure 4

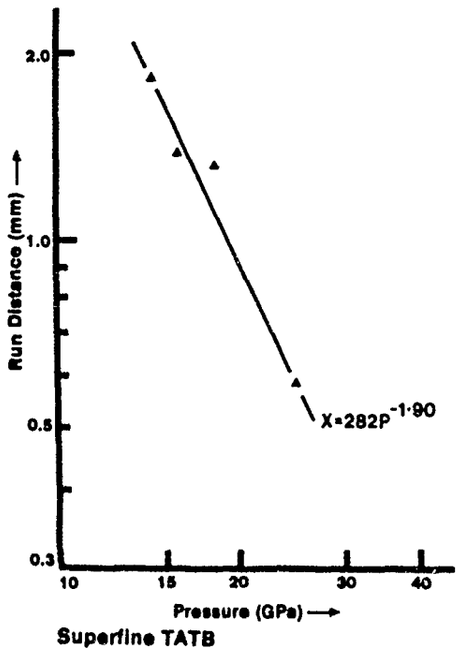

Figure 5

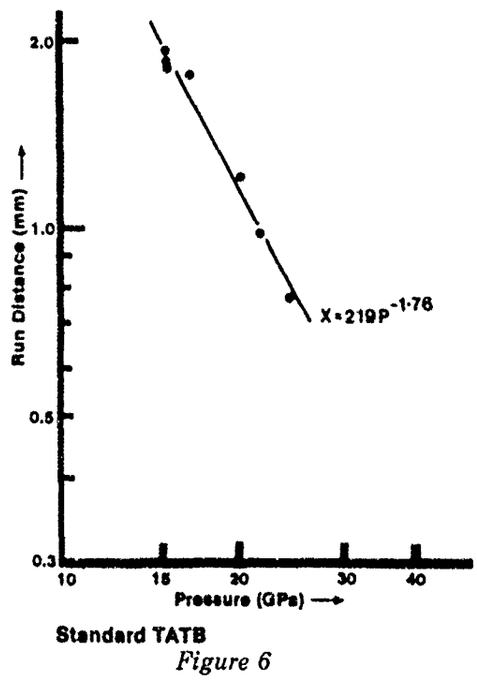

Figure 6

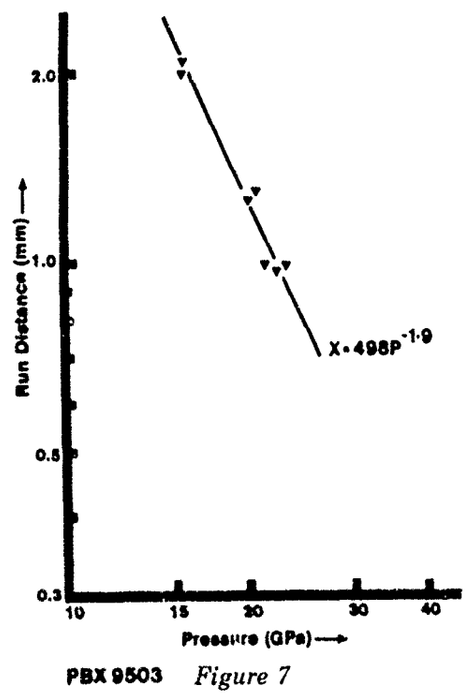

Figure 7

Figures 4-7. Pop plots for the pure TATB's and for PBX9503. Errors were typically ± 0.15 mm in distance and ± 3% in pressure (see text for a discussion of errors in Figure 4).

DISCUSSION

The data on the three pure TATB compacts (Figures 4, 5, 6) was obtained on material pressed to essentially the same density (and hence the same void percentage), but using explosives with different particle size distributions and specific surface areas. A comparison of the data is shown in Figure 8, where some recent results from Seitz [7] are also shown. Our data shows a trend of decreasing run distance with increasing powder surface area at any given input shock strength. The effect is most marked between ultrafine and superfine TATB. The correlation between distance to detonation and particle morphology has been observed previously. Howe et al (8) studying shock initiation of granular TNT and Lindstrom's (9) work on porous tetryl showed that decreased particle size resulted in significant reductions in run distance. Schwarz (10) has concluded that particle size was an important factor in influencing the promptness of detonation in HNS-based small slapper detonators.

A close comparison with Seitz's data, shown in Figure 8, gives some insight into the effect of pulse length. Generally, a pulse from an electric gun stimulus of ~0.1 μs is assumed to be a "short" pulse, but this can be somewhat misleading when looked at in terms of the explosive response.

Looking at Seitz's data, his Pop plots which were obtained in experiments using explosively driven, 12.5 mm thick flyers, provided sustained pulses of several micro-seconds duration. Within error, his data for both superfine and standard (sustained pulse) is indistinguishable from ours (0.1 μs). Run distance for these two materials therefore is independent of pulse width, at least down to pulses of 0.1 μs, and a 0.1 μs pulse in this instance is effectively a sustained pulse. Seitz has extended his data at a single pressure by measuring run distance in superfine and standard TATB from an initiation pulse of ~0.02 μs duration. In both cases a significant increase in the distance to detonation was observed. Taking the data together, a pulse width effect is seen between ~0.1 and ~0.02 μs.

The results on ultrafine TATB are not so easy to interpret, since, as stated earlier, our point at 25 GPa is subject to large error; it is plotted at 0.4 mm which represents an upper limit value. What is clear in Figure 8 is that for very short pulses (0.02 μs) Seitz has shown that distance to detonation increases over the value for a sustained pulse, but that the increase is very much less than for the coarser TATB's.

The lack of resolution in our 25 GPa measurement cannot however explain the apparent crossover in the 0.1 μs and sustained pulse Pop plots at around 14 GPa. It is very difficult to envisage a mechanism to account for the observation. It is possible that greater errors than are suspected may be attributed to the 11 GPa point since the ultrafine TATB is very close to its threshold initiation energy at this pressure (2). Around this region it may be expected that run distance will increase very steeply with reducing pressure - hence a small error in the flyer velocity measurement could lead to a disproportionately large error in run distance.

Also, if our Pop plot is as shown in Figure 8, Seitz's short pulse point falls on 0.1 μs curve. It is difficult to see why there should not be an extension in run distance as the pulse width reduces from 0.1 to 0.02 μs, since a reduction is seen in going from a sustained to a 0.1 μs pulse (at 17 GPa).

It seems most likely that our data has overestimated the 25 GPa run distance, and that the 0.1 μs Pop plot lies somewhere below where it is plotted in Figure 8.

Figure 7 shows the Pop plot obtained for PBX9503, which was pressed to a much higher density than the pure TATB's (see Table 2). The Pop plot is indistinguishable, within error, from that for standard TATB (Figure 6). It appears therefore that the factor which might be expected to have caused a reduction in run distance (introduction of 15% of the more shock sensitive HMX) has been cancelled out by the introduction of binder and by the reduction in void fraction from 8% to 2.4%.

PBX9502 failed to detonate at the highest available pressure, which on our gun was ~26 GPa (from a flyer travelling at ~4.5 km s^{-1}). The result was not unexpected since Jackson et al (6) have reported that for a 6.3 mm diameter flyer impacting a 25 mm diameter TATB charge, a velocity of 9.0 km s^{-1} just initiated detonation.

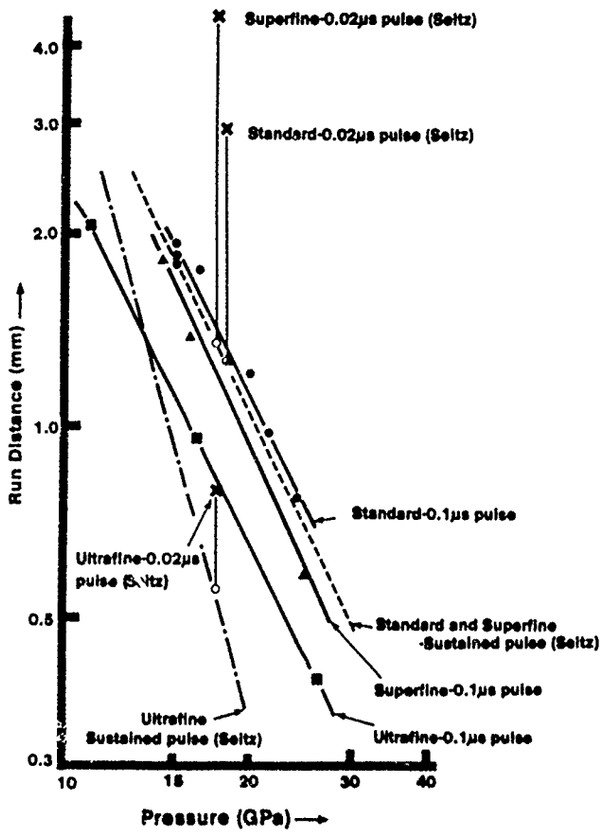

Fig. 8. Present data compared with that of Seitz (3) on the same explosives

The present experiments were not designed to yield accurate threshold data, but limits on the initiation energy fluences E_c (calculated from the Walker-Wasley $P^2\tau$ criterion (11)) could be inferred from the data. In those cases where at least one wedge failed to detonate, upper and lower bounds are quoted; for ultrafine TATB all wedges detonated and for PBX9503 all failed.

TABLE 3

Critical Energy Fluences

Explosive	E_c (MJ m^{-2})
Ultrafine TATB	$E_c < 1.9$
Superfine TATB	$2.3 < E_c < 2.6$
Standard TATB	$2.1 < E_c < 2.7$
PBX9503	$2.0 < E_c < 2.9$
PBX9502	$4.0 < E_c$

Where comparison is possible (for the pure TATB's) the results are in good agreement with those of Honodel (2).

CONCLUSIONS

1. By combining the electric gun and explosive wedge techniques run distance has been measured directly in various TATB-based explosives. Pop plots have been constructed by measuring the run distance as a function of input shock pressure.

2. Fine particle TATB (ultrafine) shows a significantly shorter run distance to detonation than do the coarser materials (superfine or standard) at any pressure over the range studied (11-26 GPa).

3. Comparison of the data with that of Seitz (3) on the same materials shows that for standard and superfine TATB the explosives do not distinguish between pressure pulses with durations

from several microseconds down to 0.1 microseconds but an extension in run distance occurs for pulses of ~0.02 μs duration.

ACKNOWLEDGEMENTS

The assistance of Jerry Wackerle and Wendell Seitz from LANL in supplying the explosive wedges is gratefully acknowledged. Some of the experimental work was done by P. Clucas.

REFERENCES

1. B. M. Dobratz et al, "The Sensitivity of TATB and TATB Formulations", UCID Rept. 17808, 1978.
2. C. A. Honodel, J. R. Humphrey, R. C. Weingart, R. S. Lee, P. Kramer, "Shock Initiation of TATB Formulations," Seventh Symposium on Detonation, p. 632, 1982.
3. W. Seitz, "Short Duration Shock Initiation of TATB", Proc. 3rd APS Topical Conference on Shock Waves in Condensed Matter," 1983.
4. R. C. Weingart et al, "The Electric Gun: A New Tool for Ultra High Pressure Research," UCRL-52752, 1979.
5. R. C. Weingart, R. S. Lee, R. K. Jackson, N. L. Parker, "Acceleration of Thin Flyers by Exploding Metal Foils: Application to Initiation Studies", Sixth Symposium on Detonation, p. 201, 1976.
6. R. K. Jackson et al., "Initiation and Detonation Characteristics of TATB," Sixth Symposium on Detonation, p. 257, 1976.
7. S. P. Marsh, ed. LASL Shock Hugoniot Data, University of California Press, Berkeley, p. 632, 1980.
8. P. Howe, R. Fry, B. Taylor, V. Boyle, "Shock Initiation and the Critical Energy Concept," Sixth Symposium on Detonation, p. 11, 1976.
9. Private Communication with J. Wackerle.
10. A. C. Schwarz, "Study of the Factors which Influence the Shock Initiation Sensitivity of HNS," Sandia Report, SAND 80-2372, 1981.
11. F. E. Walker, R. J. Wasley, "Critical Energy for Shock Initiation of Heterogeneous Explosives," Explosivestoffe, *17*(1), 9, 1969.

The Electric Gun & Explosives

Insensitive high explosives such as 1,3,5-triamino-2,4,6-trinitro- benzene(TATB) offer the designer insensitiveness and thermal stability in order to exploit their enhanced safety properties it is necessary to characterise their response to a variety of shock stimuli.Here we show how by applying the electric gun technique to small explosive wedges,we have constructed Pop-plots for four TATB-based IHEs

The method is capable of measuring very short run distances down to ~0 5mm, and it could if required be developed further to give increased resolution.

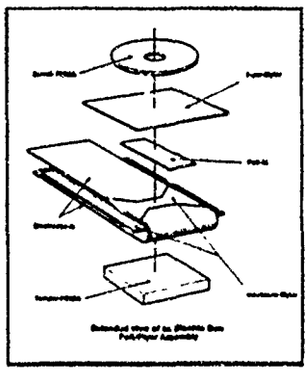

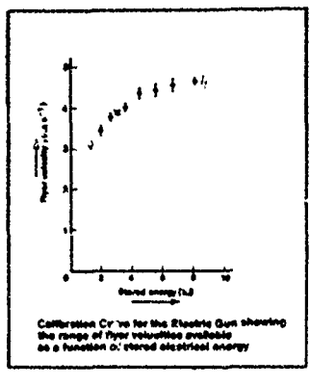

Calibration Curve for the Electric Gun showing the range of flyer velocities available as a function of stored electrical energy

The Electric Gun delivers a high velocity thin flying plate to provide a planar impact on a small HE sample.A high pressure(≥ 10GPa) short duration(~0.1μs shock pulse initiates the specimen ; flyer is driven along a short barrel by an electrically exploded metal foil.A knowledge of flyer velocity and material Hugoniots allows calculation of input shock pressure. Controlled variation in flyer velocity (and hence shock input pressure) is achieved by varying electrical energy to the bursting foil

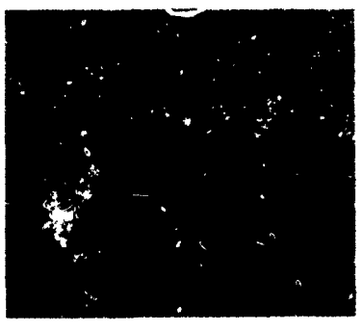

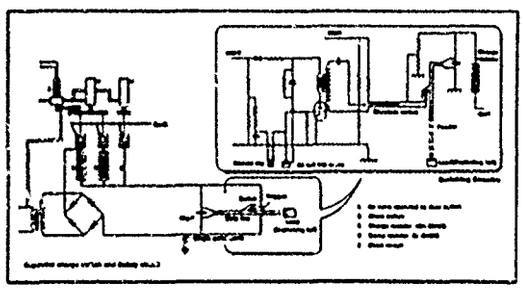

The Explosives were small cylindrical wedges of 5 compositions, supplied by J Wackerle of Los Alamos.

Dimensions 6.3mm diam., toe angle 30°, toe thickness ~100μm

HE	Surface Area cm^2	Density $kg\ m^{-3}$	% Theoretical max Density
Standard TATB	0 5	1 787±0 003	92 2
Superfine TATB	0 7	1 783±0 006	92 0
Ultrafine TATB	4 5	1 775±0 003	91 7
*PBX 9502	—	1 895	97 1
**PBX 9503	—	1 899	97 9

* 95/5 wt% TATB/Kel F

** 80/15/5 wt% TATB/HMX/Kel F

The Diagnostics

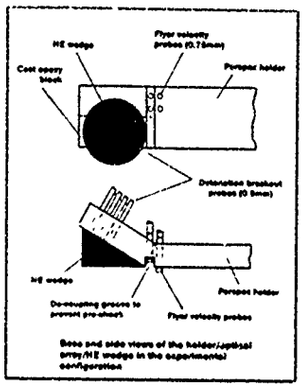

Base and side views of the holder/optical array/HE wedge in the experimental configuration

The angled face of the wedge was interrogated with an array of fine fibre-optic cables

The remote ends of the fibres were focussed onto the film track of a streak camera.
Four additional fibres monitored flyer velocity.
A PMMA fixture held the fibres and wedge over the end of the electric gun barrel
A de-coupling groove in the PMMA prevents pre-shocking of the HE by flyer impact on the wedge holder
A small(~10μm)av gap was found to be necessary between the explosives and the fibres to ensure reliable bright-up with shock arrival

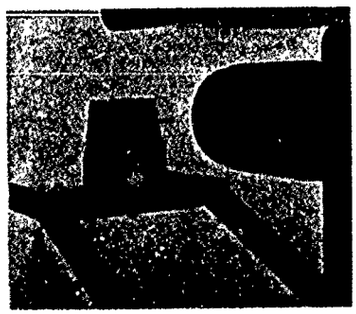

A completely assembled round ready for firing

Results - Typical Streak Photography

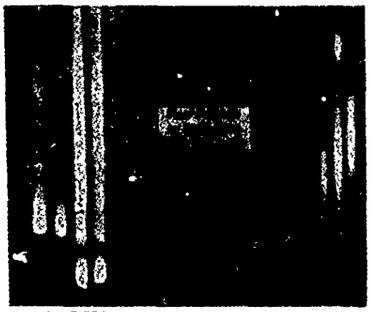

standard TATB fired at 13kv

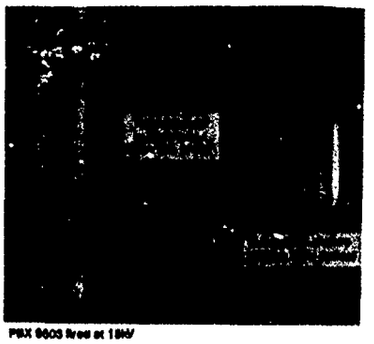

PBX 9503 fired at 18kV

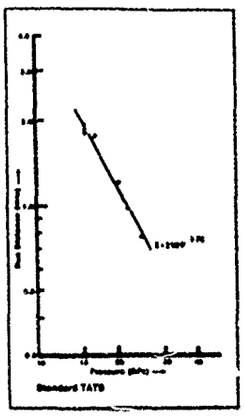

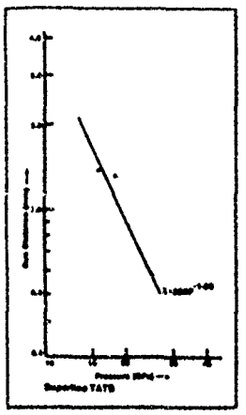

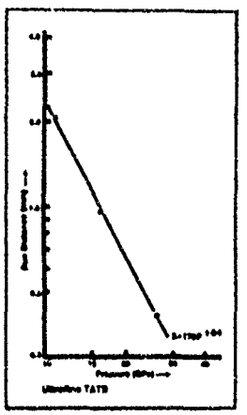

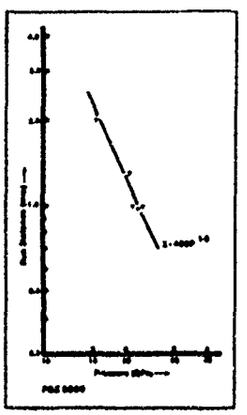

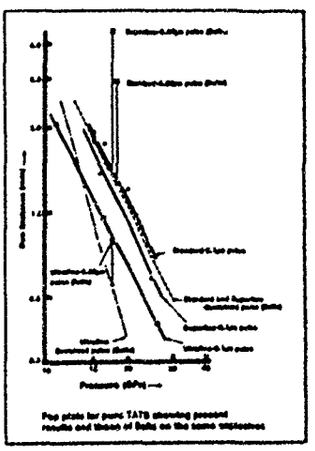

Pop plots for pure TATB showing present results and those of Seitz on the same explosive

Run distance to detonation as a function of initial shock pressure plotted on a log scale (Pop plots).
PBX 9502 failed to detonate at the highest pressure available

Pop plots for the pure TATBs plotted together. Also shown is the data of Seitz (Short Duration Shock Initiation of TATB,Proc 3rd APS. Topical Conference on Shock Waves in Condensed Matter,1983) for sustained pulse and very short pulse shock initiation of HE wedges showing how the run distance is independent of pulse length until initiated by very short pulses (~ 0.02μs)

THE USE OF THE DOUBLE PIPE TEST TO INVESTIGATE THE RUN-UP AND RUN-DOWN FROM INITIATION IN PNEUMATICALLY LOADED ANFO

M. P. du Plessis* and C. M. Lownds
AECI Explosives and Chemicals Limited
Research Department, PO North Rand 1645
South Africa

The Double Pipe Test (DPT) has been used to investigate run to detonation effects in pneumatically loaded ANFO in 40 and 50 mm diameter simulated boreholes. The results demonstrate that the DPT is a useful method of investigating transient detonation effects without sophisticated and costly instrumentation. The explosive is tested under conditions which are relevant to the conditions under which the explosive will be used in the field. Run-up distances of 5 charge diameters on either side of typical initiators of pneumatically loaded ANFO were observed.

INTRODUCTION

Pneumatically loaded ANFO is extensively used in South African mines in stoping, tunnelling and ring blasting with boreholes approximately 1.2 m, 2.0 m and up to 30 m long respectively.Boreholes vary from approximately 25 to 50 mm in diameter. A wide variety of initiators are used depending on conditions. In boreholes less than 3 m long detonators/primer cartridges are used as initiators. Regulations require that holes longer than 3 m be traced with detonating cord. Primer cartridges or pentolite boosters are used in combination with the detonating cord.

The wide variety of initiators used means that there is nearly always some mismatch between the detonation pressure and diameter of the initiatior and those of the ANFO in the borehole. The detonation therefore runs up or down to its steady state velocity (which depends on charge diameter). Unsteady detonation usually lasts from 3 to 6 charge diameters (1), but run-ups as long as 12 charge diameters have been observed (2).

*Present address:
Detonation Research Group, K. 29
ICI PLC, Stevenston
Ayrshire, KA20 3LN. Scotland.

Transient detonation effects are difficult to detect and relatively sophisticated instrumentation is required. A new test, the Double Pipe Test (DPT), has been devised (3) which permits the investigation of transient detonation effects. The test is simple to conduct and the explosive/initiator system is used in the same configuration as encountered in the borehole in rock. The DPT measures the peak pressure generated in the simulated borehole by the explosive.

It is not known what influence these transient detonation effects have on rock breaking. Recent tests on explosives in intermediate diameter boreholes (4) using the DPT suggest that considerable improvements in rock breaking performance are possible by controlling these transient detonation effects by choosing the appropriate initiating system. This paper describes the use of the DPT to investigate the run to detonation distances associated with the initiation of pneumatically loaded ANFO in simulated boreholes.

THE DOUBLE PIPE TEST (DPT)

The experiment consists of a thin walled steel tube filled with explosive (simulated borehole), this placed on top of a thick walled steel tube (witness pipe) which lies on a rigid steel anvil placed on the ground. After the explosive has

been detonated the witness pipe is recovered and its deformation measured. Computer analysis (5) shows that the dent made in the witness pipe correlates with the peak pressure generated in the top pipe by the explosive. The continuous dent depth record therefore reflects the continuous peak lateral pressure from the explosive along its length. The experimental set-up of the DPT is shown in Fig. 1.

The time-scale of the DPT is ca 40 μS for a 40 mm diameter charge. In essence the test provides information on the reaction of solid ingredients, and has been used particularly to investigate metal fuels (3). The DPT may therefore provide useful information on the reaction rates of solid ingredients during the run to a steady detonation.

EXPERIMENTAL

ANFO was pneumatically loaded into 40 mm and 50 mm diameter x 2 m long steel pipes. The pipes were closed at each end with cork stoppers. In the 40 mm pipes the initiators were placed half-way along the pipe (at 1000 mm) so as to investigate transient effects on both sides of the initiator. It was not always possible to fill the pipe completely. The detonating cord was centered in the 50 mm diameter pipes by passing the cord through the middle of cork stoppers. The cord was tensioned by knotting at the corks. Previous tests in open ended pipes indicated that these knots were initiating the ANFO. The corks were therefore introduced to reduce the shockwave due to the knot of detonating cord.

The witness pipe consisted of 50 mm o.d. x 36 mm i.d. steel hollow bar filled with water to prevent the top pipe smashing the bottom pipe. The response of the water filled witness pipe was thus non-linearly related to the peak pressure in the top pipe. ANFO (prill density ca 0.78 Mg m^{-3}) was pneumatically loaded to a density of ca 0.90 Mg m^{-3}.

The experiments are listed in Table 1.

RESULTS

The behaviour of pneumatically loaded ANFO in 40 mm diameter pipes is shown in Fig. 2.

Fig. 2 highlights cases of run-up and run-down to a steady state detonation. After the initial transient detonation the same steady state is established despite the different methods of initiation and applied to all the initiators tested in 40 mm diameter pipes. Differences in dent less than ca 2 mm are not significant. The witness pipe dents in the vicinity of all the

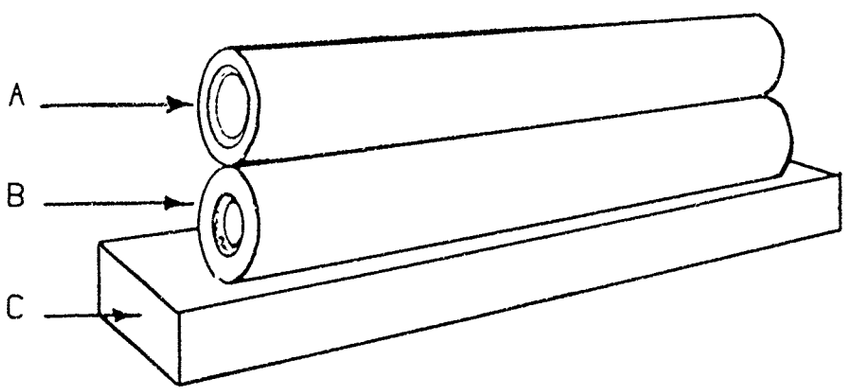

A -- Steel top pipe filled with explosive
B -- Steel witness pipe filled with water
C -- Steel anvil resting on firm ground

Fig. 1. The Double Pipe Test

TABLE 1
Initiators used in the Double Pipe Tests

Test No.	Top Pipe Diameter (mm)	Initiator	Position of Initiator Top Pipe (mm)
1	40	No. 4 Detonator (ca 0.09 g PETN)	1000
2	40	No. 8 Detonator (ca 0.78 g PETN)	1000
3	40	200 g Dynamite Primer (32x200 mm) + No. 6 Detonator (ca 0.36 g PETN)	1000
4	40	30 g Pentolite Booster + No. 6 Detonator	1000
5	50	30 g Pentolite Booster	0 (top of pipe)
6	50	10 gm^{-1} Detonating Cord	0 — 2000
7	50	4 gm^{-1} Detonating Cord	0 — 2000
8	50	10 gm^{-1}Detonating Cord + 30 g Pentolite Booster	Cord:0 — 2000 Booster:1000

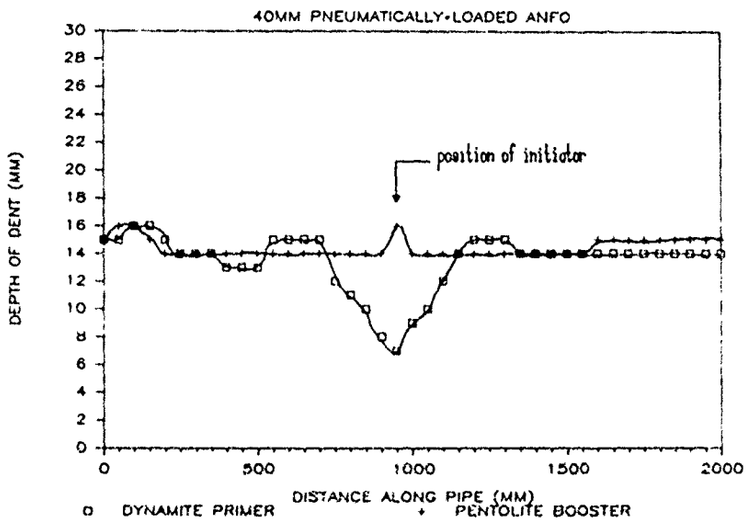

Fig. 2. Dents delivered to the witness pipes by different initiators

the initiators in 40 mm diameter pipes are shown in Fig. 3.

The dent profiles are symmetrical about the initiators and the detonation takes ca 200 mm (i.e. 5 charge diameters) to run up to a steady state on either side of the initiators. In the case of initiation with a pentolite booster there is over-boostering and the detonation runs down to a steady state within 60 mm (1.5 charge diameters)

In all cases initiation to the right (forward priming) and initiation to the left (reverse priming) appeared similar. The shapes of the "pressure wells" in the vicinity of the initiators differ. The trace of initiation with the dynamite primer includes the run-up to detonation within the primer as well as run-up in the ANFO The depths of the "pressure wells" and the slope of the dent vs distance curve is complicated by the different sizes and orientations of the initiators and possible shock reinforcement at the steel pipe walls.

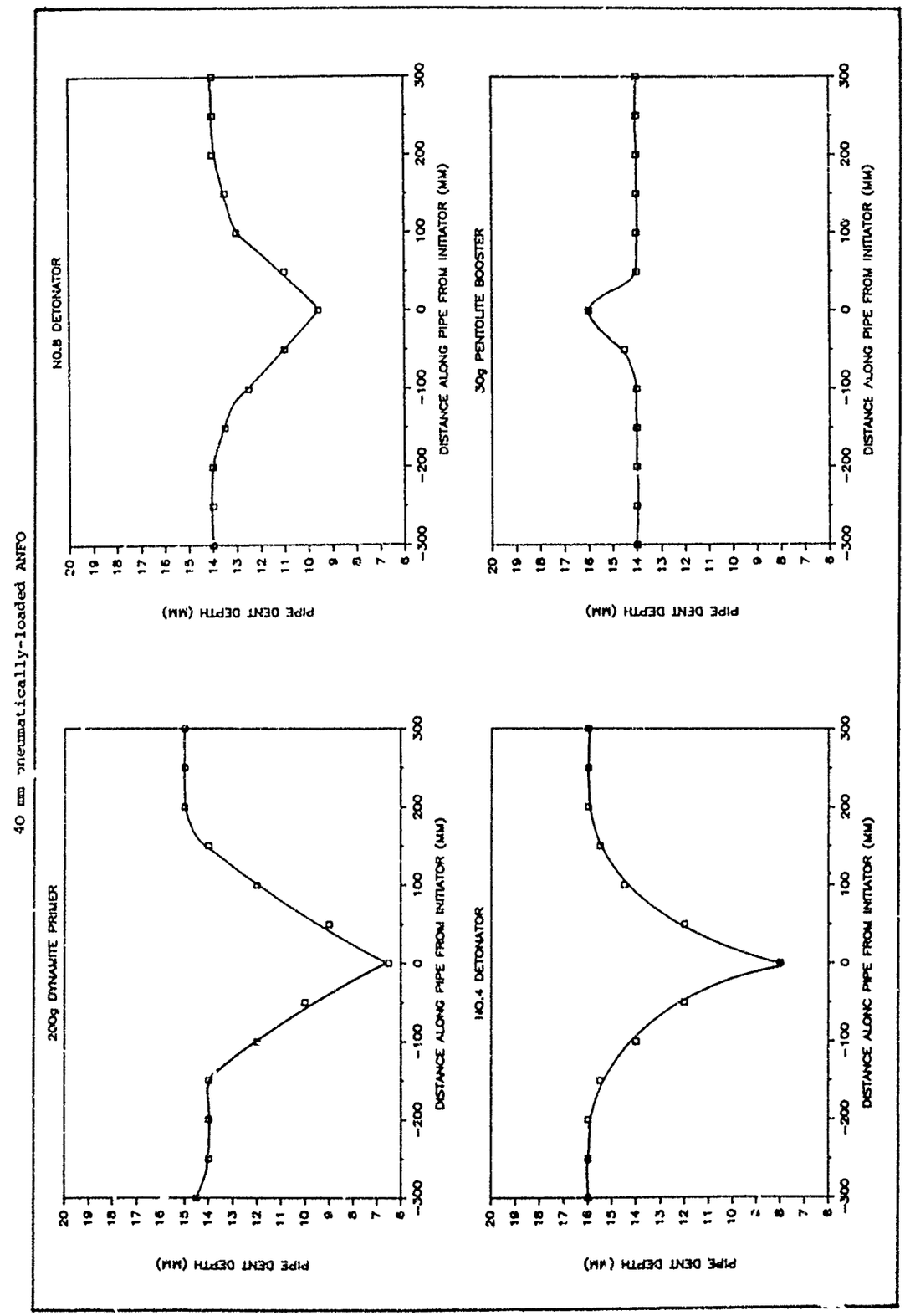

Fig 3. Expanded pipe dents on both sides of the initiator (smoothed curves)

The DPT results discussed above illustrate three important modes of ANFO initiation. These are discussed in terms of the variation of the steady detonation velocity with inverse diameter. Fig. 4. shows an idealised curve. This curve has three regions:

- the upper curve shows how stable detonation varies with diameter
- the turning point corresponds to the failure state (at the critical diameter)
- the lower curve shows how the minimum initiation impulse varies with the diameter of the initiator.

All the detonators used had diameters much less than critical diameter of the ANFO. After initiation the detonation velocity decreases and the diameter of the detonation increases with time, intersecting the minimum initiation conditions of the ANFO close to the critical point. From this point the detonation builds up to a steady state which is recorded in the appropriate DPT traces.

The pentolite booster had a diameter very close to the critical diameter of the ANFO. The rapid decay and expansion of the detonation velocity of the booster intersected the upper part of the curve, initiating a stable ANFO detonation very rapidly. The diameter and detonation velocity of the dynamite primer placed it in the acceleration region of the curve. Since the run-up distances from the primer and the detonators are very similar it is likely that the decaying impulse from the detonator intersected the curve close to the initiation point from the low detonation velocity primer (6).

Fig. 5 shows the initiation of pneumatically loaded ANFO in 50 mm diameter pipes. The depth of dent from point initiation by a pentolite booster yields a deeper dent than that obtained from axial initiation with detonating cord. The end effect between 0 and 250 mm along the pipe arises because of incomplete filling of the pipe. The detonating cord initiates a low-order, lateral detonation which steadily follows that in the cord. The effective diameter of the charge is halved because of the lateral initiation from the cord in the middle of the pipe. Previous results have shown that if the detonating cord is traced along the pipe inner wall deeper dents are obtained because of the larger effective charge diameter and the shock reinforcement at the pipe wall. In contrast the pentolite booster initiates a high-order detonation which propagates along the entire length of the charge.

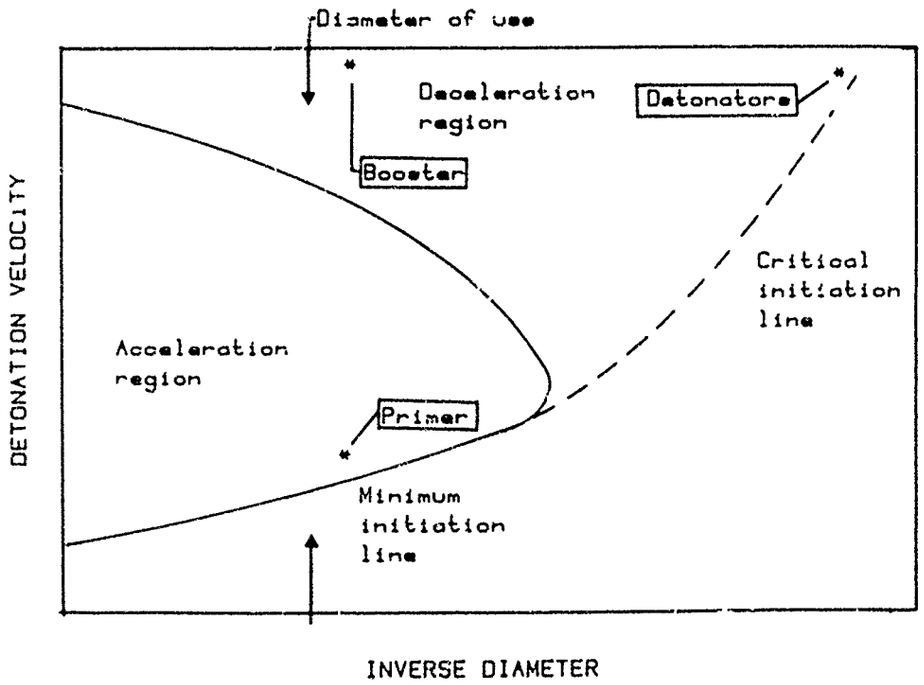

Fig. 4. Idealised inverse charge diameter vs detonation velocity curves for pneumatically-loaded ANFO

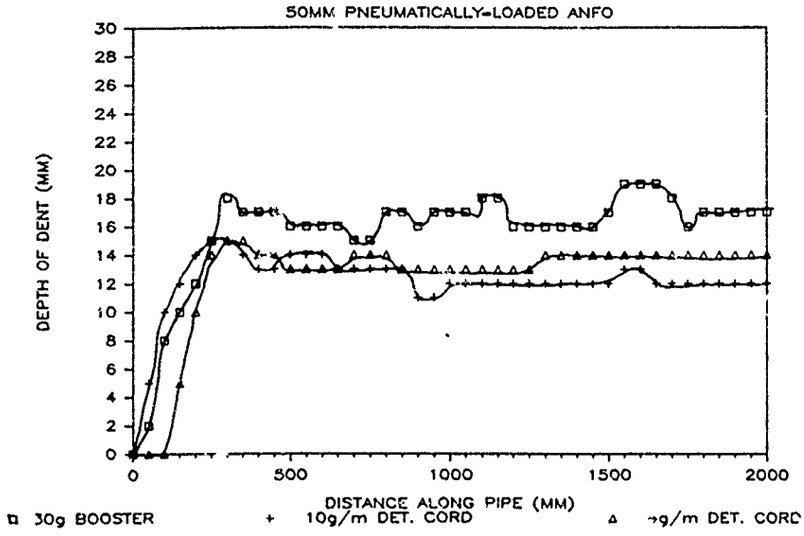

Fig. 5. Point and axial initiation

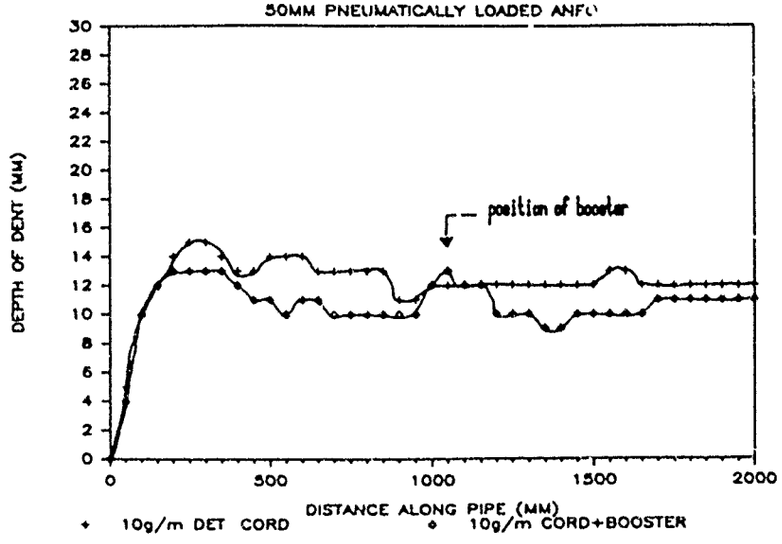

Fig. 6. The effect of a pentolite booster threaded along the detonating cord

The use of a pentolite booster threaded onto the detonating cord has a limited effect on the performance of the ANFO. The appropriate traces in Fig. 6 show that the effect of a 30 g pentolite booster (in a charge traced by cord) lasted about 400 mm or 8 charge diameters. Thereafter, the effect of the booster was soom "forgotten" by the detonation; the conical detonation of the low peak lateral pressure was soon re-established.

DISCUSSION

The results presented above indicate that a transient detonation exists for a distance of ca 200 mm on both sides of typical initiators of pneumatically loaded ANFO in 40 mm diameter steel pipes. If this situation occurs in boreholes in rock it means that the explosives will not perform optimally for ca 400 mm (10 charge diameters) along the explosive column. In short boreholes (ca 1-1.5 m long) this could constitute up to 30% of the column length. If the initiator is placed at some point in the bottom third of the borehole the run to detonation effects could have a significant influence on breaking in the end of

of borehole and on the formation of sockets.

Tests in 50 mm diameter pipes indicate that normal detonating cord will not initiate a high order detonation in pneumatically loaded ANFO. On the other hand, the use of detonating cord along the length of the borehole has the great advantage of exposing every section of the hole to the initiator. This is particularly important in long holes where gaps or obstructions in the column can cause propagation failures. It has also been demonstrated that boosters threaded along the detonating cord have little effect on the quality of the detonation in the borehole.

The results presented yield valuable information on the initiation and propagation of detonation in pneumatically loaded ANFO. This information is obtained without the use of costly and sophisticated instrumentation. In addition the explosive is tested in a manner which, as closely as possible, simulates its use in the field. The DPT is therefore a very useful method of investigating important aspects of the practical use of commercial explosive performance and can be conducted by a relatively unsophisticated user.

REFERENCES

1. C. H. Johansson and P. A. Persson, Detonics of High Explosives, pp. 89-108, Academic Press, London, 1970.
2. T. N. Hagen, "Optimum Priming Systems for Ammonium Nitrate/Fuel Oil — Type Explosives," Australian Institution of Mining and Metallurgy, Queensland (1974).
3. C. M. Lownds and M. P. du Plessis, "The Double Pipe Test for Commercial Explosives I. Description and Results," Propellants, Explosives, Pyrotechnics, Vol. 9, pp. 188-192, 1984.
4. C. M. Lownds and M. P. du Plessis, "The Behaviour of Explosives in Intermediate Diameter Boreholes," Quarry Management, December 1984, pp. 799-804.
5. C. M. Lownds and M. P. du Plessis, "The Double Pipe Test for Commercial Explosives II. Numerical Modelling and Interpretation," Propellants, Explosives, Pyrotechnics, in press.
6. I. J. Kirby and G. A. Leiper, "A Small Divergent Detonation Theory for Intermolecular Explosives", This symposium.

ACKNOWLEDGEMENT

The authors thank the Management of AECI Explosives and Chemicals Limited for permission to publish this work.

AECI EXPLOSIVES & CHEMICALS LTD SOUTH AFRICA

M P DU PLESSIS & C M LOWNDS

THE DOUBLE PIPE TEST – DPT

TEST

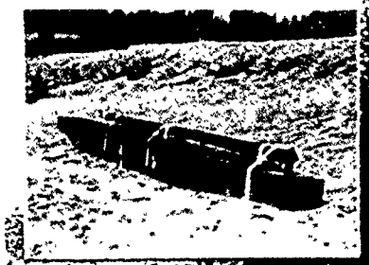

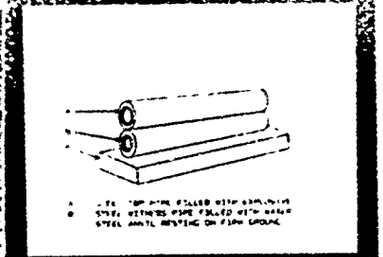

RESULT

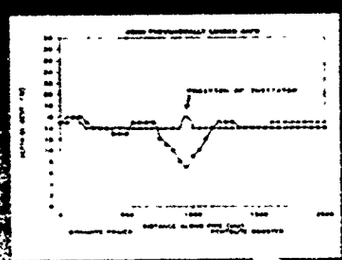

WITNESS PIPE

PIPE

DPT - MEASURES TRANSIENT DETONATION EFFECTS

- SIMULATES A BOREHOLE IN ROCK
- EASY TO CONDUCT
- NO SOPHISTICATED INSTRUMENTATION REQUIRED
- MEASURES EARLY WORK DONE BY EXPLOSIVES
- WITNESS PIPE DENT PROPORTIONAL TO PEAK PRESSURE IN TOP PIPE
- COMPUTER MODEL SHOWS TIME SCALE OF TEST APPROX 1 μS PER MM OF CHARGE DIAMETER

APPLICATIONS - INITIATION OF ANFO BY DETONATING CORD

- REACTION OF METAL FUELS IN EMULSIONS
- CHANNEL EFFECTS
- RUN TO DETONATION EFFECTS

RUN UP/DOWN FROM INITIATORS IN PNEUMATICALLY LOADED ANFO

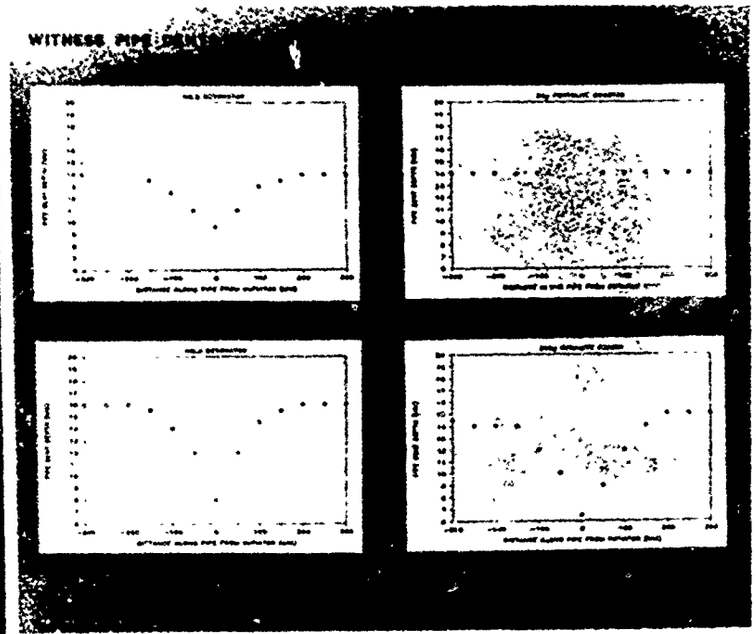

CONCLUSION - RUN UP AND DOWN TO STEADY DETONATION OBSERVED

- RUN UP DISTANCES OF 5 CHARGE DIAMETERS (200MM) ON BOTH SIDES OF INITIATORS OBSERVED IN 40MM PIPES
- IN SHORT BOREHOLES, 1M, THE TRANSIENT DETONATION EXISTS FOR UP TO 30% OF THE TOTAL BOREHOLE LENGTH
- RESULTS DEMONSTRATE THE USE OF THE DPT TO STUDY PRACTICAL APPLICATIONS OF COMMERCIAL EXPLOSIVES

SIMULATING THE INITIATION OF HIGH EXPLOSIVE BY EXPLOSIVE TRAINS

F. Leibundgut
Oerlikon-Buehrle AG. Zurich, Switzerland

The Initiation of the explosive charge of a 35mm air-defence shell by the booster charge was investigated by means of the 2-dimensional Lagrangian hydrodynamic code ALIEN. In the shell question, a portion of the booster projects into a cavity in the high explosive charge. The initiation of the high explosive depends on the geometry and relative positioning of booster and cavity. Experiments show that if the axial distance between these two elements is increased beyond a critical distance, then the initiation in the radial direction becomes impossible. The phenomena described were simulated for a cross-section of the shell and for various geometries; all components of the actual shell which might in reality affect the observed process were taken into consideration in the computations. The high explosive was assumed to be PBX-9404. The HE reaction was modelled according to the Forest-Fire Burn Model. Simulation results for a few geometrical arrangements are presented, showing the spacial and chronological development of pressure and reaction zone in the HE charge, as well as the location at which the initiation commences. Computed values for initiation delay times as a function of the booster/cavity design and for the corresponding critical distance for each design, are compared with experimental results.

INTRODUCTION

This paper deals with computational analysis of the initiation process of the HE in 35mm air-defence shell. All components around the booster have been taken into account in this analysis. The detonator as well as the initiation of the booster charge were not included in the simulation. In all the simulations carried out, it was assumed that the initiation of the booster charge by the detonator had already occurred, and that booster detonation at the booster/detonator interface had already commenced. The computations refer therefore to the interaction phenomena between the booster, the booster holder, the surrounding parts and the HE main charge.

The main charge is bounded on this fuze side by a supporting ring. This ring has the function of absorbing the setback forces during acceleration in the barrel on the main charge so as to prevent any break-up of the main charge in this critical region. This ring must have an opening through which the booster can project into the

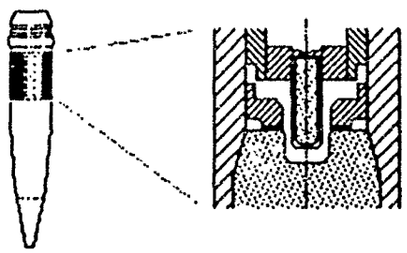

Fig. 1.

main charge. The variations within the manufacturing tolerances of all relevant parts mean that the axial gap (Fig. 2) between the booster end and the cavity bottom in the main charge can vary from shell to shell. A variation in the

relative booster position, however has a direct influence on the initiation behaviour of the main charge. When the above-mentioned axial gap is increased beyond a certain maximum gap distance the radial initiation of the main charge becomes impossible. Increasing the gap further eventually prevents the axial initiation of the main charge.

The aim of this paper is the analysis of the initiation capability of the booster as a function of the size of the axial gap. Calculations were also carried out without the presence of the supporting ring permitting the influence of that ring on the initiation capability of the main charge to be determined. Further investigations were made to determine the influence of the damping plastic ring placed between the supporting ring and the main charge.

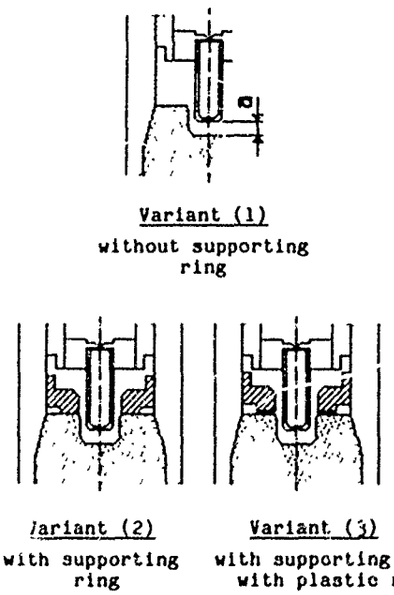

Fig. 2.

EXPERIMENTAL RESULTS

The following charts (Fig. 3) show the experimental results of initiation delay and fragment velocity measurements as a function of the axial gap between end of the booster and the bottom of the cavity in the main charge (Fig. 4). The initiation delay is defined as the time difference between booster initiation and the first emission of light by the exploding projectile. The measurements determined the critical axial gap value as being in the range of 7 to 12 mm.

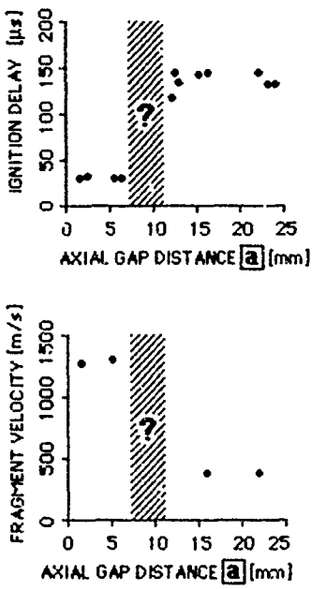

Fig. 3

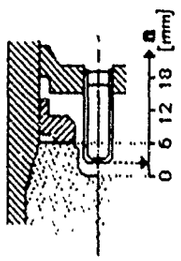

Fig. 4

NUMERICAL CALCULATIONS

The numerical calculations had been carried out with the computer program ALIEN. "ALIEN" is a two dimensional explicit Lagrangian finite difference code. The different components of a functional group can be defined independently, the computation takes automatically into account the interaction phenomena between those different parts. Individual parts may also be out of reactive materials.

MODELING

The booster holder is composed in reality of two parts (Figs. 1 & 2) but was taken as being one single part for the purpose of this analysis

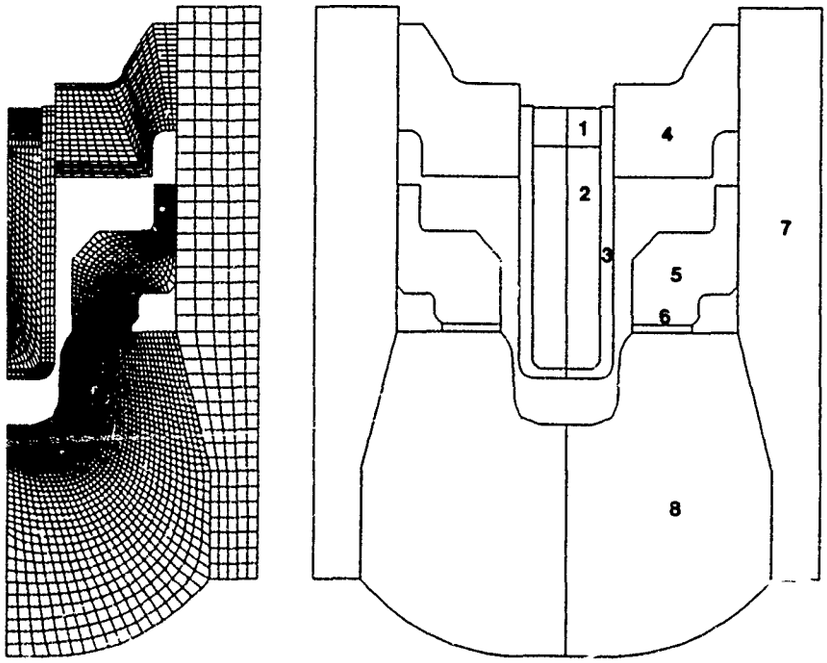

PROGRAM ALIEN

Part 1: Booster charge reacted; Part 2: Booster charge unreacted; Part 3: Booster housing (steel); Part 4: Booster holder (aluminum); Part 5: Supporting ring (aluminum); Part 6: Plastic ring; Part 7: Shell body (steel); Part 8: Main charge (PBX-9404).

Fig. 5.

(Fig. 5, Part 4). At the cavity surface, where the ignition of the main charge can be expected, a specially fine-meshed grid with a typical cell dimension of 0.1 mm was implemented. Part 1 (Fig. 5) represents the already ignited and completely reacted HE-mass of the booster charge at the start of the calculation. This reacted HE mass has an initial reaction velocity of -0.1 cm/μs and ignites with its piston-like-effect the still unreacted HE mass of part 2 (Fig. 5). We used the HOM equation of state for all parts except the plastic ring. The description of this equation as well as all material properties and parameters can be found in (1). A Polynominal of the type $P = a + b\mu + c\mu^2$ ($a = 0$), $b = 0.1$, $c = 0.2$; $\mu = \varrho/\varrho_0$) was used for the equation of state of the plastic ring. The HE-reaction was controlled by the Forest-Fire Burn Model. Table 1 displays a summary of the most important material properties.

RESULTS

The inside shape of the booster housing bottom determines the shaering of this section of the booster housing after the booster charge detonation into three parts: one is accelerated radially, one axially and one at 45° (Fig. 6).

The axially flying component which is a disk-shaped fragment, barely changes its shape over relatively large distances. This confers to the fragment the capability of transferring its kinetic energy to an HE-charge over a relatively large distance, much like the so-called "Flyers". The calculations have confirmed that the disk shaped fragment produces spontaneous initiation of the HE-main charge for all axial gaps and all 3 variants (Fig. 2). In reality however, a proper initiation of the HE main charge is no longer achievable for axial gaps larger than about 7 mm. This is probably due to the air mass enclosed in the cavity which produces an air drag or damping effect onto the disk in such a way that the resulting shock amplitude is not sufficient properly to initiate the HE main charge. This effect was not considered in our calculations since we assumed that the space between all the components were empty (vacuum).

TABLE 1

Material	EOS Model	Burn Model	Density (g/ccm)	Yield Strength (MBar)	Shear Modulus (MBar)
Aluminum	HOM	—	2.785	0.0055	0.23
Steel	HOM	—	7.917	0.0075	0.987
Plastic	POLYNOM	—	0.8	0	0
PBX-9404 Unreacted	HOM	Forest Fire	1.844	0	0
PBX-9404 Products	HOM	—	1.844	0	0

Whether the radial component of the booster housing is capable of initiating the main charge depends on the variant (Fig. 2). For Variant (1) without supporting ring the simulation shows only a partial reaction of the HE main charge which depends on the gap distance (Fig. 7). In Variant (2) and (3), on the other hand, spontaneous and radial initiation of the HE-charge takes place at the three-way boundary point (booster housing – supporting ring – HE main charge) for a gap distance less than 8 mm due to an "inclusion effect" (Fig. 8-10). The radially expanding booster housing first hits the supporting ring, producing a shock wave inside the ring which propagates towards the main charge. This shock wave is then superposed on a second wave, coming radially from the impact of the booster housing with the main charge at the above-mentioned three way boundary point. The superposition of these shock waves with a locally massive confinement cause a zone of increased pressure at the three way boundary point, which finally produces the reaction of the main charge. Variant (3) with the plastic ring shows no significant difference from Variant (2) concerning the initiation at the mentioned three way boundary point.

CONCLUSIONS

The simulation of the HE-initiation in a 35mm air-defence shell by means of a finite difference program allows a closer look into phenomena which, although observeable with experimental methods, are not open to experimental investigation and analysis with the same degree of thoroughness. The increasing demands for complex design analyses e.g. in relation with problems in detonics and more generally in ordnance technology will in the future increase the number of opportunities to use the powerful and efficient tool of numerical methods. The observed phenomena of shock wave superposition in a boundary zone will be object of further calculations. The control of shock wave propagation and of shock wave focusing in one determined point which at the same time could be a boundary point of different media could make feasible a proper initiation of HE charges with relative low energy levels.

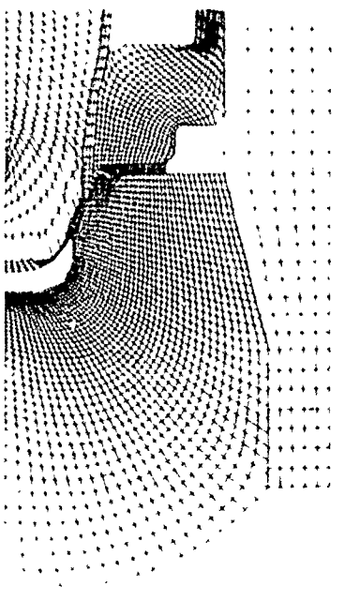

Fig. 6. Break-up booster housing

REFERENCES

1. Charles L. Mader, Numerical Modeling of Detonations, University of California Press/Berkeley
2. Charles L. Mader, "Detonation Wave Interactions", Seventh Symposium (International) on Detonation, U.S. Naval Academy Annapolis/Maryland (1981)
3. F. Leibundgut, "ALIEN"-User Manual, Oerlikon-Buehrle AG, Zürich/Switzerland (1984)

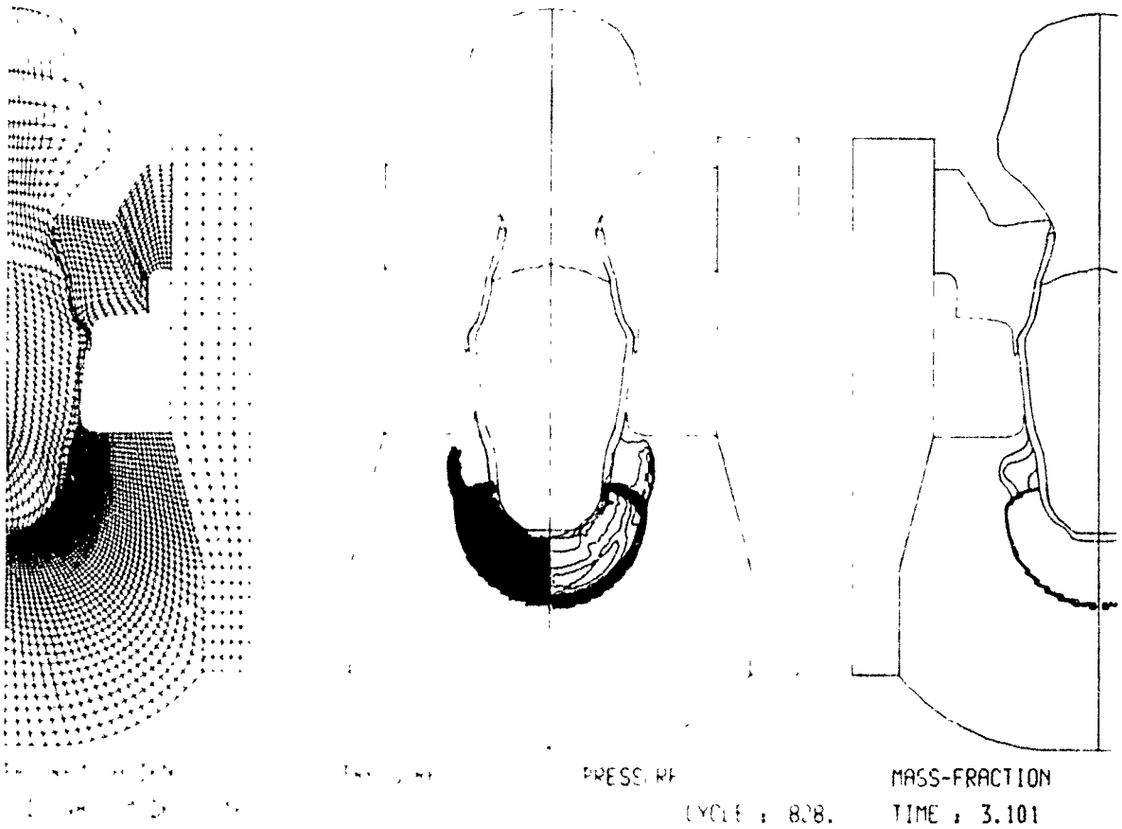

Fig 7 Variant (I), without supporting ring
Pressure contour-interval = 25 kBar
Mass-fraction contour-interval = 0.1

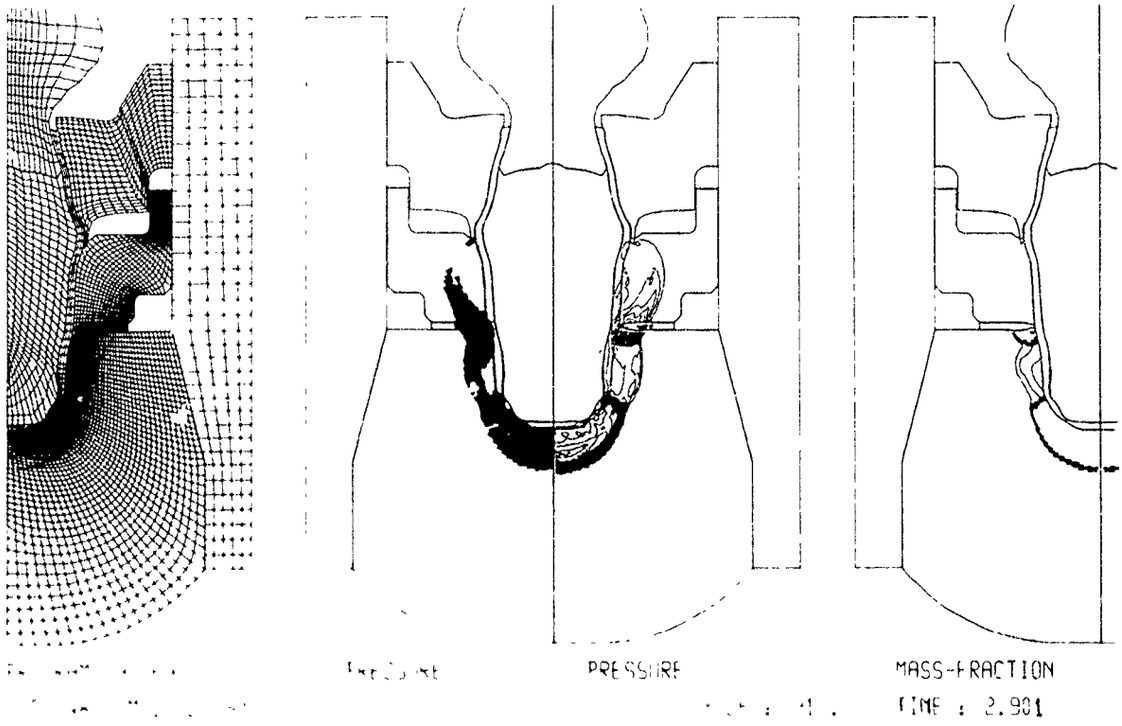

Fig. 8 Variant (3), with supporting ring and plastic ring.

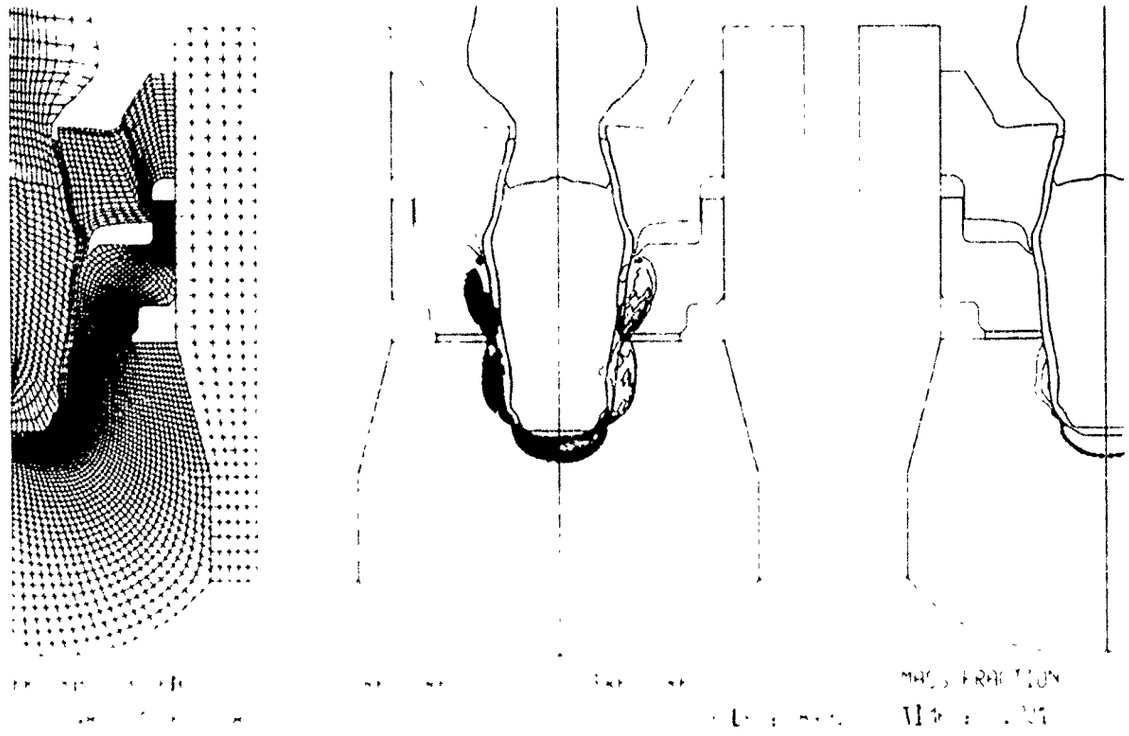

Fig. 9 Continuation of Fig. 8

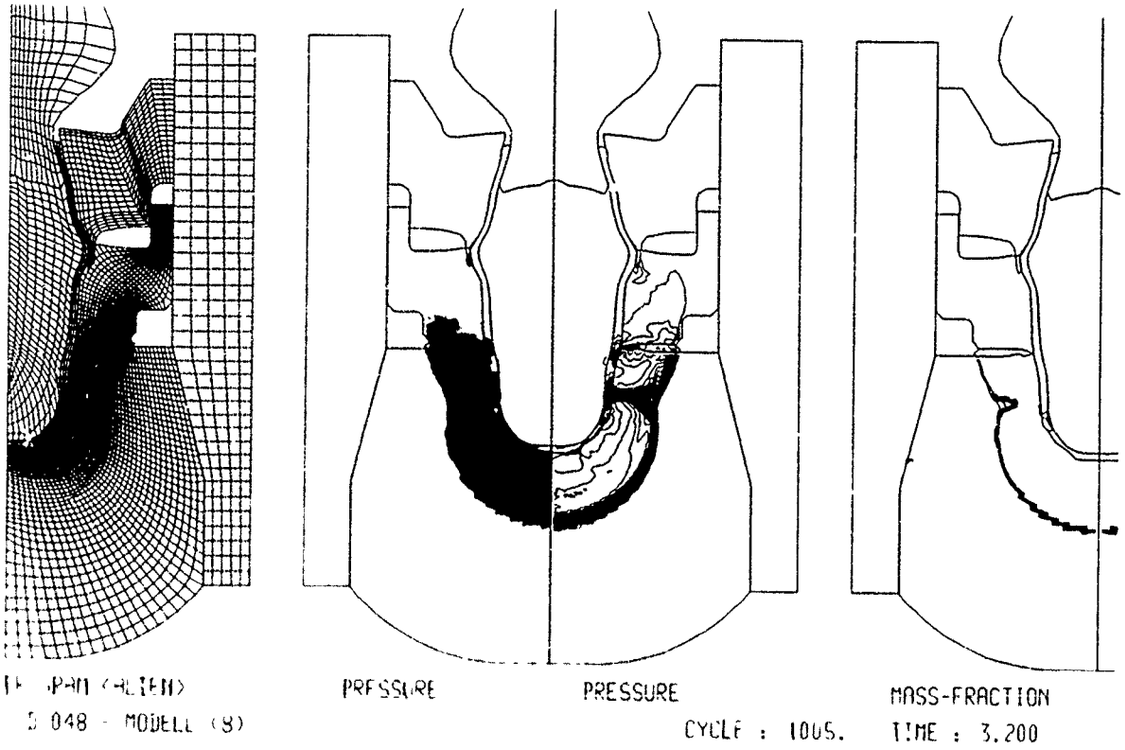

Fig. 10. Continuation of Fig. 9

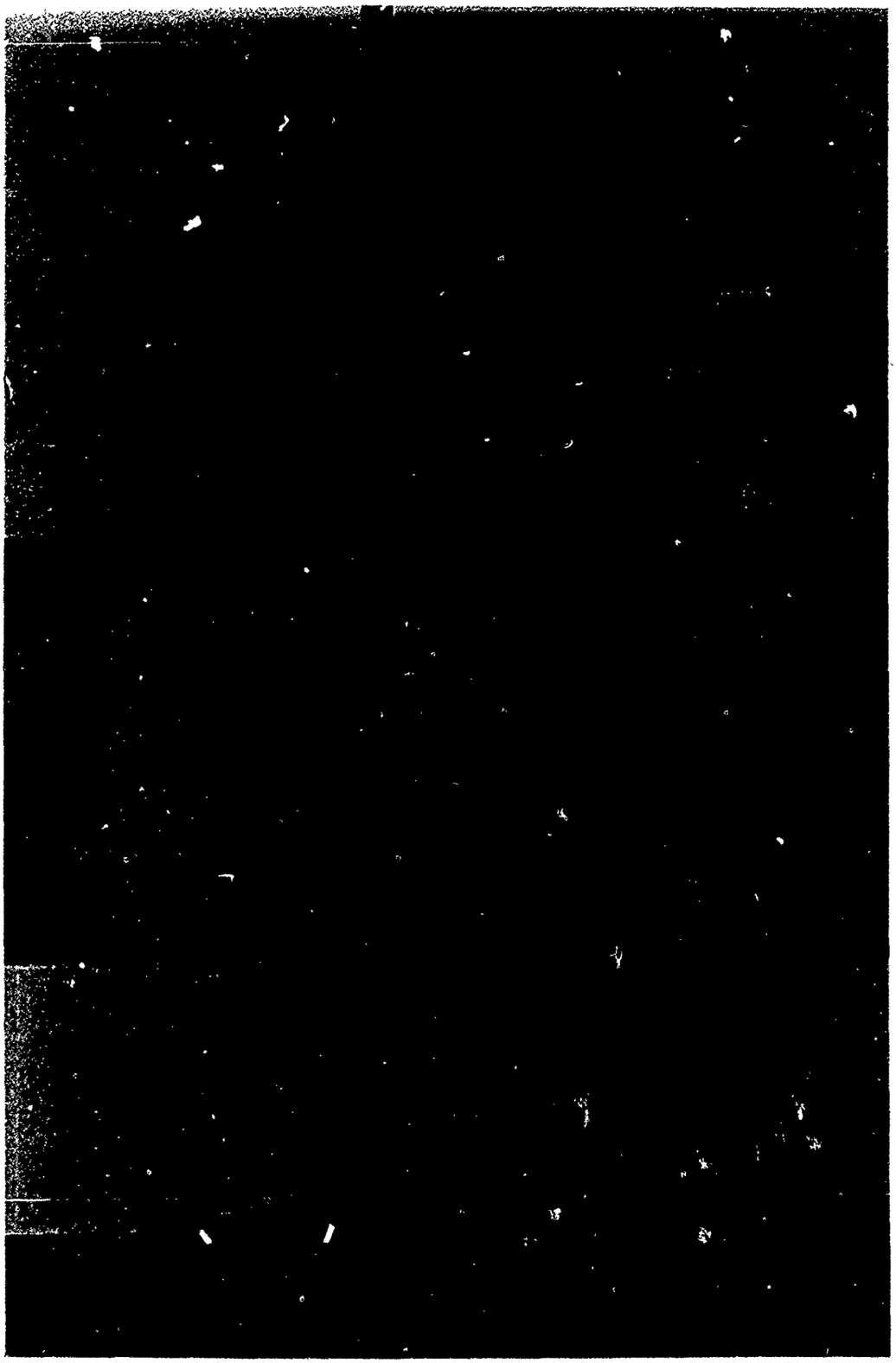

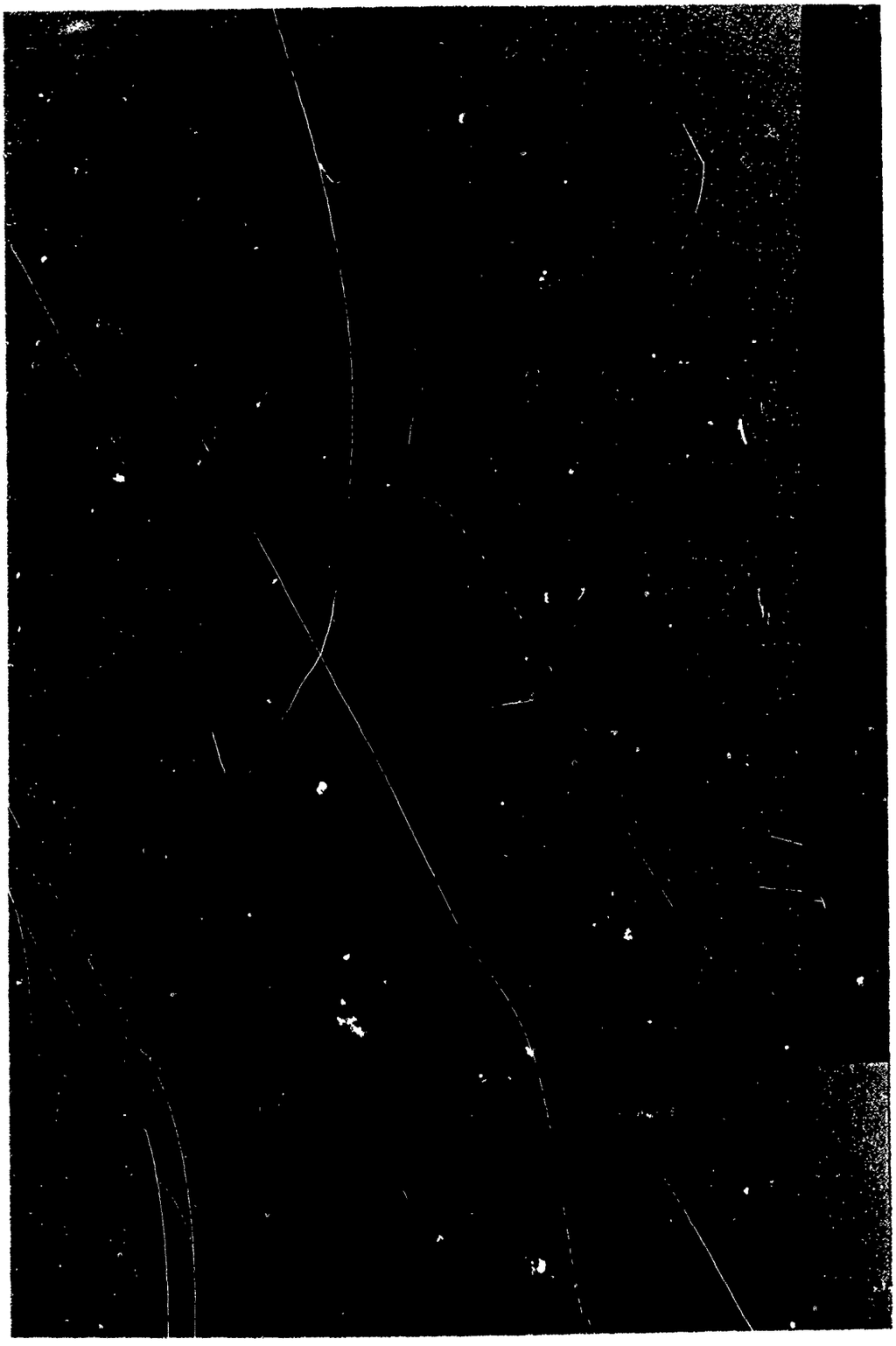

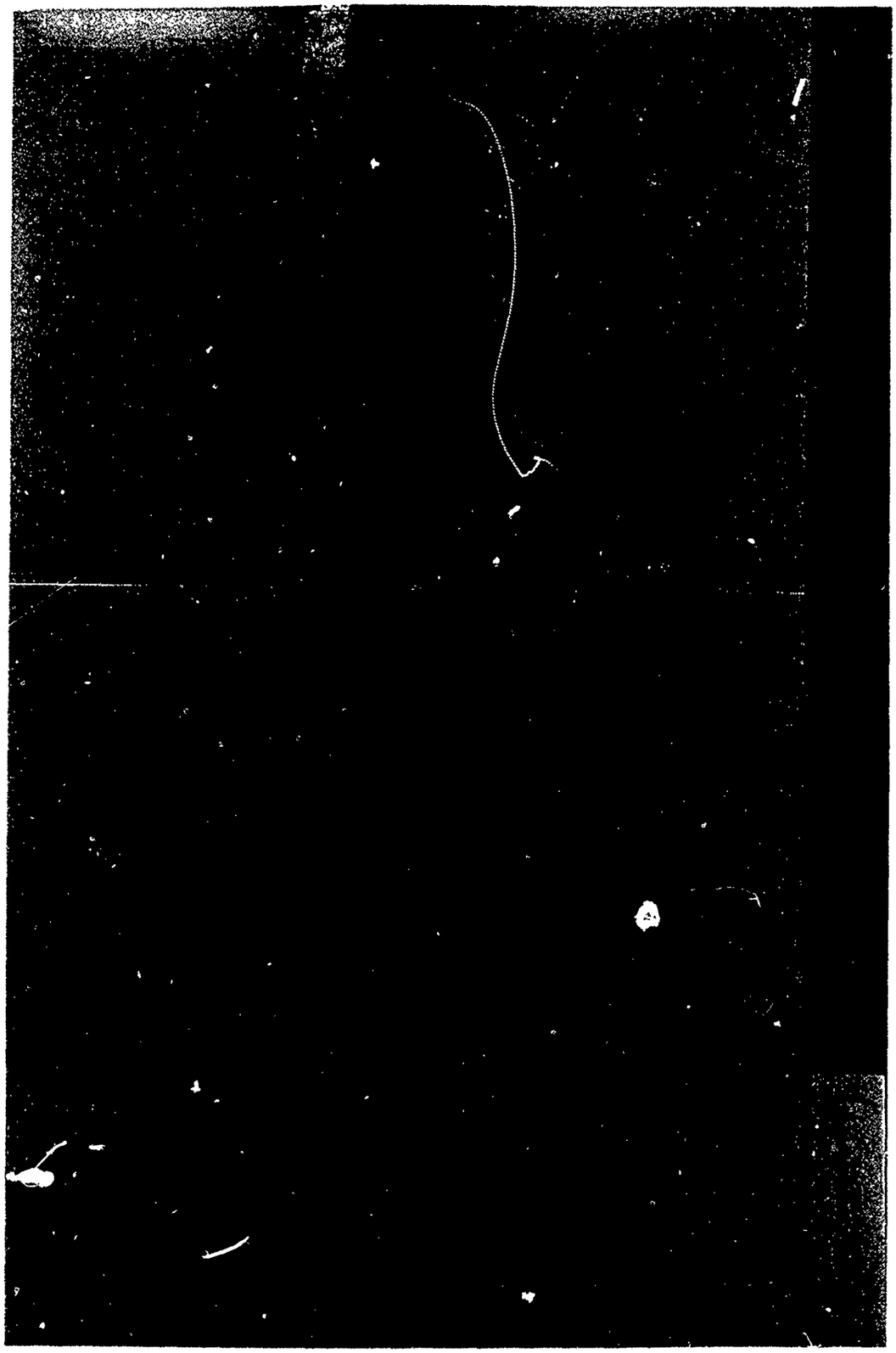

INFLUENCE OF AIR GAPS ON DETONATION PROPAGATION IN CHARGES CONSISTING OF STACKED BLOCKS OF CAST TNT

A. W. Gibb
Defence Research Establishment Suffield
Ralston, Alberta, Canada

A series of experiments was conducted to examine the influence on the uniformity of detonation propagation of air gaps between large blocks of slow-cooled cast TNT. Donor-receptor geometries examined were (i) two blocks with the detonation front parallel to the gap edge, and (ii) four blocks with one corner in common and the (planar) detonation front at an angle of 45° to the block edge. Air gaps from 3 mm to 25 mm were studied. The two-block configurations produced no distortion of the shape, but the measured detonation velocity in the donor blocks and the scatter in results in the receptor blocks were observed to be influenced by the orientation of the propagation velocity vector with respect to the long axis of the TNT crystals. The four-block configuration featured channelling of detonation gases ahead of the front in the air gaps, leading to an initially complex and distorted wave structure, as well as to a delay in reinitiation, in the vertically-opposite receptor block. The shape distortion and delay effects increased as the gap width was increased.

INTRODUCTION

From 1958-1970, a series of large-scale blast trials was conducted at Defence Research Establishment Suffield in Canada. The charges consisted of 450000 kilograms of TNT in the form of approximately 30000 rectangular TNT blocks stacked in a careful geometric arrangement (Figure 1) to produce the desired overall shape (sphere tangent to the ground surface or a hemisphere). Each charge was centrally initiated. On all of the shots in this series, anomalous behaviour of the fireball and shock wave were observed when the charge was detonated. An irregular fireball with large protuberances and jetlike fingers extending a great distance from ground-zero was documented by both ground level and aerial cameras. The anomalies in the shock wave and fireball produced air blast loadings which were unpredictable in both magnitude and direction. Several possible causes of these anomalies have been identified (1). These are:

(i) variable crystal structure within the blocks

(ii) inhomogeneities (air voids, cracks, density variations) within the blocks

(iii) physical or chemical impurities within the blocks

(iv) Taylor instabilities in the expanding fireball

(v) discontinuities (air gaps) between the blocks.

The purpose of the present work was to investigate whether the last factor listed, air gaps between blocks of TNT in the large block-built TNT charges, could be contributing to the observed anomalies. A full report on this work can be found in Reference (2).

EXPERIMENT GEOMETRIES

In Figure 2, typical cross-sections through one of the large charges are shown. It can be seen that the block geometry encountered by a radially-propagating detonation front changes constantly as one moves from a radius in the

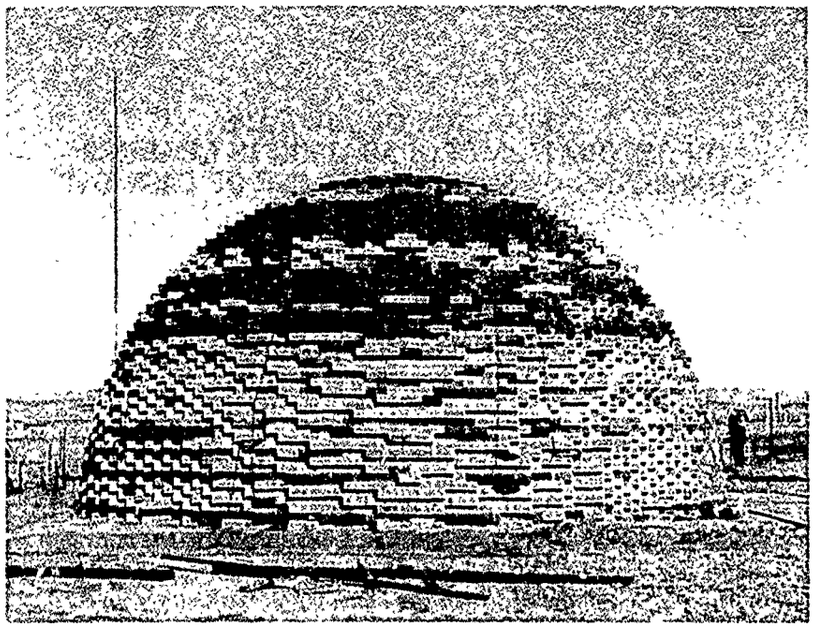

Fig. 1. Side view of stacked 500 ton TNT Hemisphere

equatorial plane to a radius along the vertical charge axis. Since it was not feasible to study all possible geometries, three distinct limiting cases were chosen for study. These are shown in Figure 3. Configuration 1 corresponds to a set of TNT blocks with the end surfaces touching and the detonation front proceeding normal to these surfaces. This configuration is encountered in the equatorial plane of the charge (directions 1 and 2 in Figure 2). Configuration 2 corresponds to a simple stack of TNT blocks with the large side surfaces in contact and the detonation front proceeding normal to these surfaces. This configuration is encountered along the vertical axis of the charge (direction 3 in Figure 2). Configuration 3 corresponds to a set of four TNT blocks with end surfaces touching, one corner in common, and the detonation front proceeding diagonally through the blocks. This configuration is encountered in the median plane of the charge (directions 4 and 5 in Figure 2).

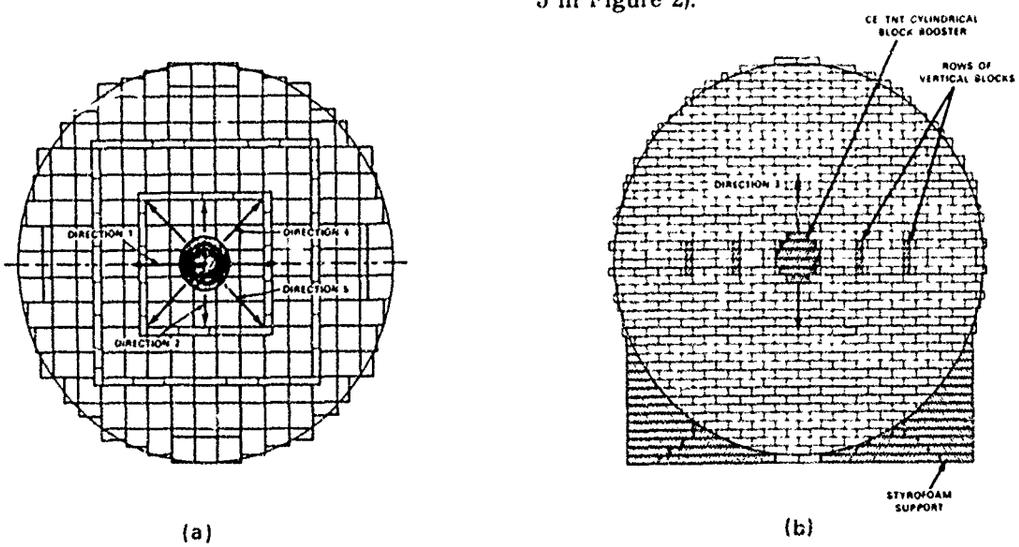

Fig. 2. Center sections through 100 ton spherical TNT charge, (a) top view, (b) side view

For ooth Configurations 1 and 2, the detonation front is parallel to the edge of the block as it crosses the interface between the blocks. In Configuration 1, the detonation front propagates across the long (30.5 cm) dimension of the block between discontinuities, whereas in Configuration 2 the discontinuities are separated by the short block dimension (10.5 cm). Configuration 3 is fundamentally different from Configurations 1 and 2 in that the detonation front, propagating diagonally across a block, intersects the interface between blocks at an angle. Since, for Configuration 3, a component of the velocities of the shock wave and following detonation products will lie parallel to the block edge, some motion of detonation products along the channel between blocks created by the air gap might reasonably be expected.

An inspection of photographs showing TNT blocks being laid in place in the large block-built charges reveals that gaps of up to 12 mm can occur between blocks; gaps of order 6 mm are more common; gaps of 25 mm represent an upper limit. In the present study, gap sizes up to 25 mm were investigated, except for Configuration 1 where gap sizes up to 75 mm were studied to provide a point of contact with previous DRES work.

On the interior of the large block-built TNT charges, detonation in a particular block is effectively confined by the surrounding TNT blocks. The experiments in the present work were set up to permit ultra-high speed photography of detonation propagation in two dimensions through the TNT blocks. This fact precluded the use of other TNT blocks as a confinement medium. In order to investigate whether confinement would alter the experimental results, some of the experiments employing unconfined TNT blocks were repeated with the blocks confined in transparent plexiglass boxes with 19 mm thick walls.

CHARGE PREPARATION

The method of preparation of the cast TNT blocks for the present experiments was identical to that employed for the large scale blast trials (3). They were formed by pouring molten TNT into rectangular molds made of 6 mm and 9 mm aluminum plate. Six molds were suspended in a cooling tank. A header of molten TNT was maintained above each mold to take up shrinkage as the TNT solidified. Once the TNT had been poured into the molds, the cooling tank was filled with water and water was allowed to circulate freely for 45 minutes. At the end of this period, the tank was drained and the blocks were allowed a natural cooling time of 4.5 hours. The final dimensions of the block were 30.5 cm x 30.5 cm x 10.5 cm. The block density was 1.59 g/cc.

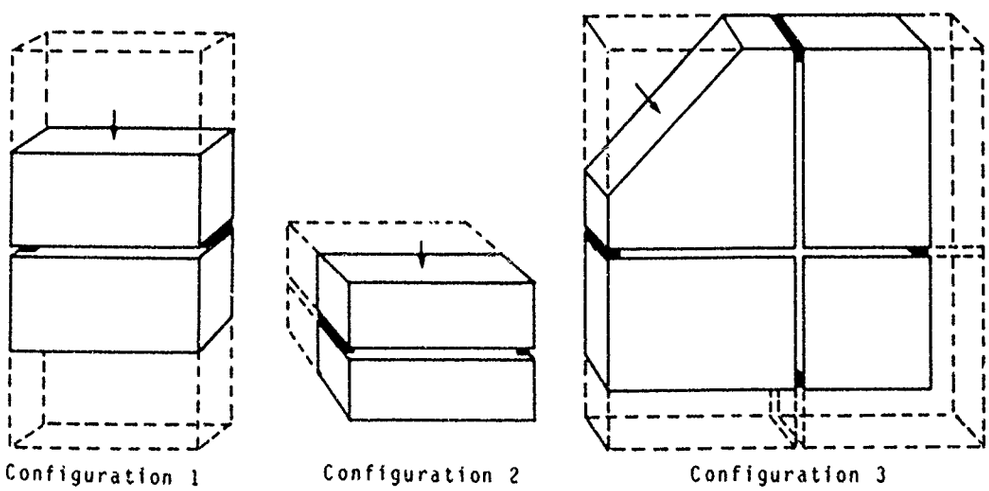

Fig. 3. Experimental Configurations Key: - - - outline of full blocks; ——— portion of full block used in experiments; → initiation plane

The cooling method resulted in large elongated crystals with the long axis growing perpendicular to the block surface. A cross-section through a block can be seen in Figure 4. For Configuration 1 experiments, the detonation front propagated across the long crystal axis, while for Configuration 2 experiments the detonation front propagated in the direction of the long crystal axis. This point will become important later in the discussion of experimental results.

To limit the total quantity of explosive used in each experiment, full TNT blocks were cast, but only a portion of each block was used in a given experiment. The solid lines in Figure 3 represent the portions of the full blocks which were actually used in the experiments. The blocks were cut using a steam knife. In the set up of the experiments, the blocks were arranged so that surfaces at the interfaces between blocks were never cut surfaces, but were always the original surfaces produced in the mold.

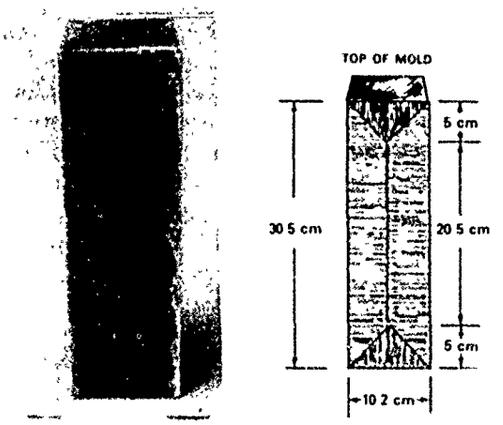

Fig. 4. Cross-section through center of TNT block revealing crystal structure

TECHNIQUE

Each experiment consisted of a single donor block and one to three receptor blocks. The donor blocks were initiated across a planar surface 105 mm in width by 305 mm in length using an explosive plane-wave generator of the 'mousetrap' variety with a tetrytol booster pad. The plane-wave generator produced a detonation wave with a variation in time of arrival on the initiation surface of less than one microsecond. This corresponds to a wave that is planar over the initiation surface to within 7 mm.

Simultaneous streak and framing photographs of the detonation front propagating across air gaps between the donor and receptor blocks were recorded for all experiments using a Cordin Model 330A ultra-high speed camera operated at framing rates in the vicinity of 10^6 frames/second (streak writing rate of 5.2 mm/μs. The front surfaces of the TNT blocks were covered with Scotchlite sheet and illuminated with a high intensity Xenon flashlamp to render the full block surfaces visible at all times during the detonation process. For Configuration 1 and 2 experiments, where the detonation front was expected to propagate parallel to the block edge, three resistive detonation velocity probes were cast into the midplane of each block normal to the expected direction of the detonation front. The positions of these probes within the blocks and the recording line for the streak measurement are indicated in Figure 5.

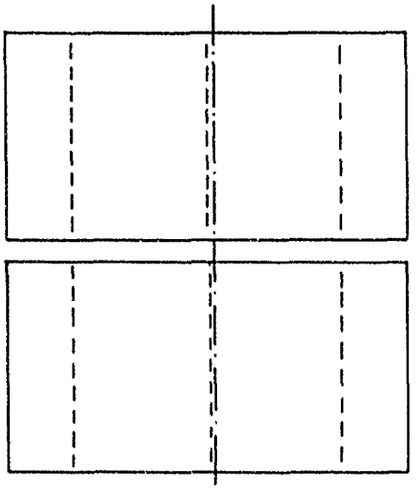

Fig. 5. Location of resistive probes in TNT blocks. Key: - - - resistive probes; —·— streak recording line

This arrangement permitted simultaneous detonation velocity measurements to be made on the surface and in the interior of the blocks. For Configuration 3 experiments, in which the propagation direction of the detonation front could not be predicted in advance, no detonation velocity probes were employed. For most Configuration 3 experiments, the streak recording line was aligned along the symmetry axis of the charge. Velocity measurements along lines other than the streak line were made by constructing a

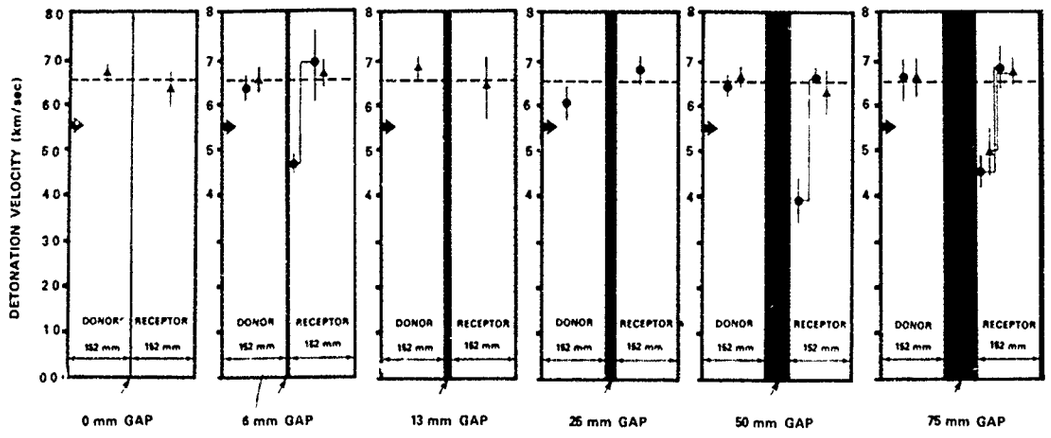

Fig. 6. Detonation velocity measurements from Configuration 1 experiments (unconfined TNT blocks) Key: ● streak; ▲ *resistive probe;* - - - *average detonation velocity in donor blocks;* ●—⌐● *denotes abrupt change in measured detonation velocity*

composite drawing from the framing records (using the outline of the TNT blocks in the photographs to register each frame), digitizing successive front positions on the drawing in the direction of interest, and fitting the resultant position-time curves with a polynomial.

RESULTS FOR CONFIGURATIONS 1 AND 2

Average detonation velocities recorded for unconfined TNT blocks in Configuration 1 are plotted in Figure 6.

To permit intercomparison of results, the results from individual experiments are plotted in sequence, in order of increasing air gap size. The horizontal dashed line in this figure represents a detonation velocity of 6.52 (0.08) km/sec. obtained by averaging measured detonation velocities in all donor blocks. The latter measured values all lie within one standard deviation of the average. The detonation velocities from the streak and probe records for each experiment agree within experimental error in those experiments where both types of records are available. In the receptor blocks, two distinct cases exist. In the first case (0 mm, 13 mm and 25 mm air gaps), detonation velocities recorded on the surface and interior of the receptor block are constant throughout the block. In the second case (6 mm, 50 mm and 75 mm air gaps), the probe records on the block interior indicate a constant velocity throughout the block, while the streak recordings on the block surface indicate two distinct velocities — a constant low-order velocity for the first 50 mm followed by an abrupt transition to a stable high order velocity in the remainder of the block. The high order velocity agrees within experimental error with the velocity measured on the block interior. If the high order velocities measured both on block surface and interior for all six experiments are averaged, the resultant value of 6.60 (0.11) km/sec. agrees with the corresponding value in the donor blocks within experimental error. The value 6.60 (0.11) km/sec. is in good agreement with the value of 6.55 km/sec. measured by Holsgrove (4) in previous DRES work on identical TNT blocks.

Average detonation velocities recorded for unconfined TNT blocks in Configuration 2 are plotted in Figure 7. The horizontal dashed line represents a detonation velocity of 6.22 (0.07) km/sec. obtained by averaging the results in identical unconfined donor blocks from five separate Configuration 2 experiments. This value is four standard deviations lower than the corresponding average value from six Configuration 1 experiments. The donor blocks for each set of experiments were identical and were initiated using identical plane-wave generator/boosters. The principal difference in the two configurations lies in the direction of the detonation front velocity vector with respect to the long axis of the TNT crystals — perpendicular for Configuration 1 and parallel for Configuration 2. The present results support the conclusion that the

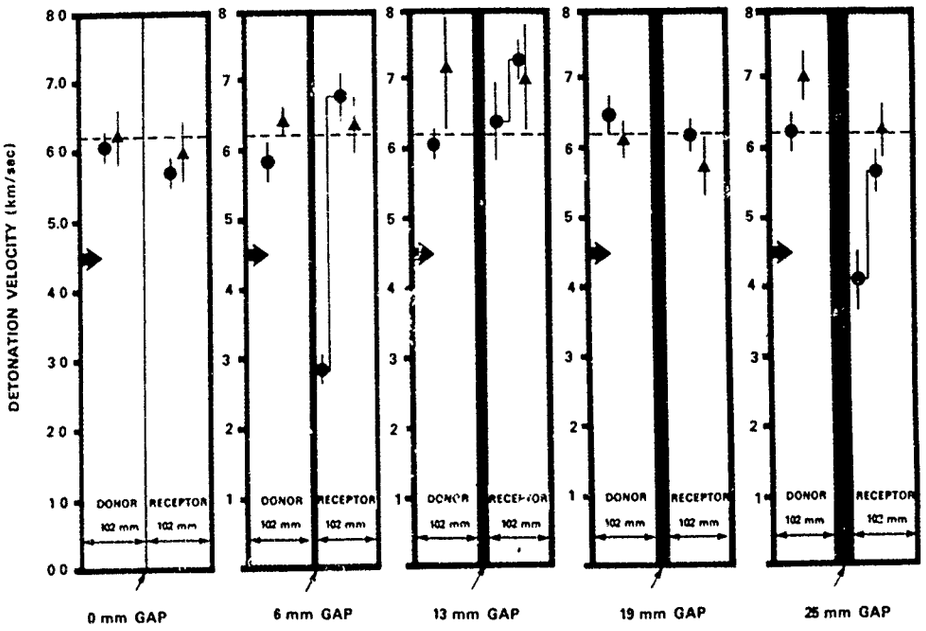

Fig. 7. Detonation velocity measurements from Configuration 2 experiments (unconfined TNT blocks) Key: streak; *resistive probe; - - - average detonation velocity in donor blocks;* *denotes abrupt change in measured detonation velocity*

high order detonation velocity in slow-cooled cast TNT blocks is approximately 5 percent lower when the detonation front is propagating parallel to, rather than across, the long axis of the TNT crystals. This effect, also reported by other workers (5, 6), could be contributing to the blast anomalies observed on large-scale TNT charges by making the detonation velocity a function of propagation direction within the charge.

Detonation propagated successfully into Configuration 2 receptor blocks for air gaps up to 25 mm. Results showed considerably more scatter than those from Configuration 1 blocks. This may be a further manifestation of the influence of crystal structure on detonation propagation. Results from donor and receptor blocks, taken together, suggest that detonation propagation in slow-cooled cast TNT blocks is more difficult when the propagation velocity vector is parallel to the long axis of the TNT crystals.

Three Configuration 1 experiments were repeated with the TNT blocks tightly confined in a plexiglass box with 19 mm thick walls. This confinement did not result in a statistically significant increase in detonation velocity in the donor-receptor system.

RESULTS FOR CONFIGURATION 3

Results from Configuration 3 experiments are summarized in Figures 8 and 9. Figure 8 shows composite drawings of the detonation process extracted from the framing records for experiments employing unconfined TNT blocks with 3 mm, 13 mm and 25 mm air gaps. For adjacent receptor blocks A and B, the initial direction in which the detonation front propagates in the blocks is a function of gap width. As shown in Figure 9, the angle between this direction and the propagation direction in the donor block increases from 16° to 20° to 23° as the air gap width increases from 3 mm to 13 mm to 25 mm respectively. In all cases, the propagation direction appears to change gradually back to a direction close to that in the donor block as the front advances into the receptor block. However, the receptor blocks were not large enough to establish if the original propagation direction would be completely restored.

In all Configuration 3 experiments, phenomena which appeared to be manifestations of

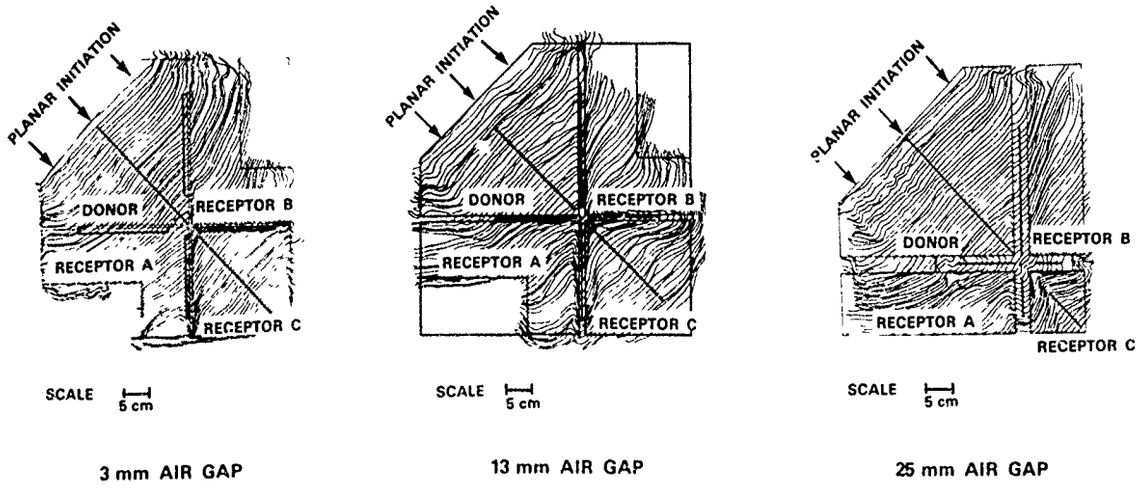

Fig. 8. Composite drawings of detonation front progress from framing camera for Configuration 3 experiments Key: ——— denotes region of constant measured propagation velocity

the internal channel effect (7, 8, 9) were observed. Luminous detonation product gases were observed to channel ahead of the detonation front. The hot channelled gases gave rise to reaction waves in vertically-opposite receptor block C, starting at the block surfaces bordering the gap. These slow-moving mutually perpendicular reaction waves intersected at an interior point. From the point of intersection, a detonation wave emerged moving more or less parallel to the original detonation front in the donor block. The structure is reminiscent of Mach stem formation resulting from the symmetric collision of two strong spherical shock waves.

In Figure 8, solid straight lines can be seen along the charge diagonal and in the air gaps. The position and length of each line indicate a region of constant propagation velocity. For each experiment, the stable detonation velocities in donor and receptor blocks are equal within experimental error. Measured gas velocities in the air gaps range from 8.4 to 10.1 km sec.

In Figure 9 can be seen a series of straight lines, superimposed on vertically-opposite receptor block C, and parallel to the detonation front in the donor block. These lines represent the predicted positions for the detonation front if the air gaps were not present. In formulating these predictions, the measured stable detonation velocity in the respective donor block was employed. The error bar on the predicted position reflects the uncertainty in the measured detonation velocity. Also shown in Figure 9 are the actual detonation front positions from the framing records at corresponding times. For the 3 mm air gap, the actual front position lags the 'predicted' position but lies one standard deviation from the predicted position. For 13 mm and 25 mm air gaps, the actual front position also lags the predicted position. The delay is well outside experimental error and is largest for the 25 mm air gap. Thus the air gap between blocks not only alters the initial shape of the detonation front in the vertically-opposite receptor block but also delays the front. The delay increases with air gap width (less than 2 microseconds for 3 mm gap, of order 9 microseconds for 25 mm air gap). When the blocks are confined by 19 mm of plexiglas, results are qualitatively the same as those obtained with unconfined blocks. Re-initiation occurs sooner in the vertically-opposite receptor block when confinement is present.

CONCLUSIONS

Air gaps of 6 to 25 mm between large cast TNT blocks can influence both the shape and rate of propagation of an initially-stable detonation front proceeding through the blocks. When the detonation front is parallel to the gap edge, no distortion of the wave shape occurs. The detonation velocity in the donor blocks and the

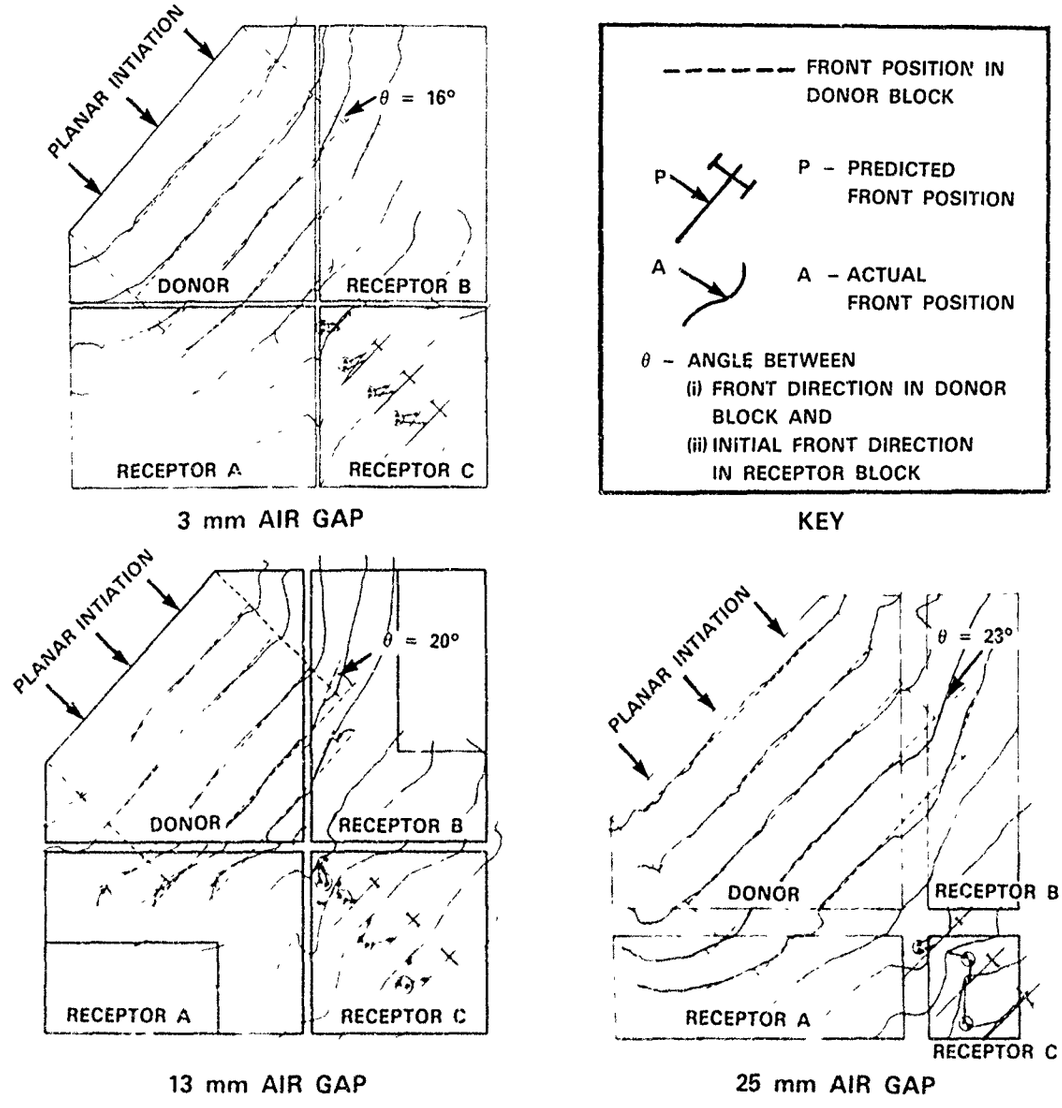

Fig 9. Changes in shape and position of detonation front in receptor blocks for Configuration 3 experiments

scatter in results in the receptor blocks are, however, influenced by the orientation of the propagation velocity vector with respect to the long axis of the TNT crystals. For a configuration featuring four blocks with one corner in common and the planar detonation front at an angle of 45° to the block edge, channelling of detonation gases ahead of the front in the air gaps occurs, leading to an initially complex and distorted wave structure, as well as to a delay in re-initiation, in the vertically-opposite receptor block. The shape distortion and delay effects increase as the gap width is increased. The delays in re-initiation are reduced if the blocks are confined by 19 mm of plexiglass.

REFERENCES

1. A. M. Patterson, C. N. Kingery, R. D. Rowe, J. Petes and J. M. Dewey, "Fireball and Shock Wave Anomalies", The Technical Cooperation Program Panel N-2 Technical Summary Report N2: TR 1-70, August 1970. UNCLASSIFIED.

2. A. W. Gibb, "The Effect of Air Gaps on the Propagation of Detonation in Charges Consisting of Stacked Blocks of Cast TNT (U)", Suffield Report No. 385, 1985. UNCLASSIFIED.

3. A. C. Phillips, W. J. Ditto and J. Holdsworth, "Building of Hemispheres of High Explosives from Cast TNT Blocks", Suffield Technical Paper No. 194, 1962. UNCLASSIFIED.

4. B. J. Holsgrove, "Detonation of Stacked TNT Blocks - A Review of the Attenuating Effects of Air Gaps", Suffield Memorandum No. 7/68, 1968. UNCLASSIFIED.

5. W. B. Cybulski, W. Payman and D. W. Woodhead, "Explosion Waves and Shock Waves, VII. The Velocity of Detonation in Cast TNT", Proc. Roy. Soc. (London) A197, p. 51, 1949.

6. W. Kegler, "Sensitization of Trinitrotoluene by Nitrocellulose and Other Additives", Explosivstoffe *11*, p. 209, 1963.

7. D. W. Woodhead and H. Titman, "Detonation Phenomena in a Tubular Charge of Explosive", Explosivstoffe *13*, pp. 115, 141, 1965.

8. H. Ahrens, "Über den Detonations-vorgang bei zylindrischen Sprengstofladungen mit Axialer Höhlung", Explosivstoffe *13*, pp. 124, 155, 180, 267, 295, 1965.

9. C. H. Johansson and P. A. Persson, "Detonics of High Explosives", pp. 68-74, Academic Press, London, 1970.

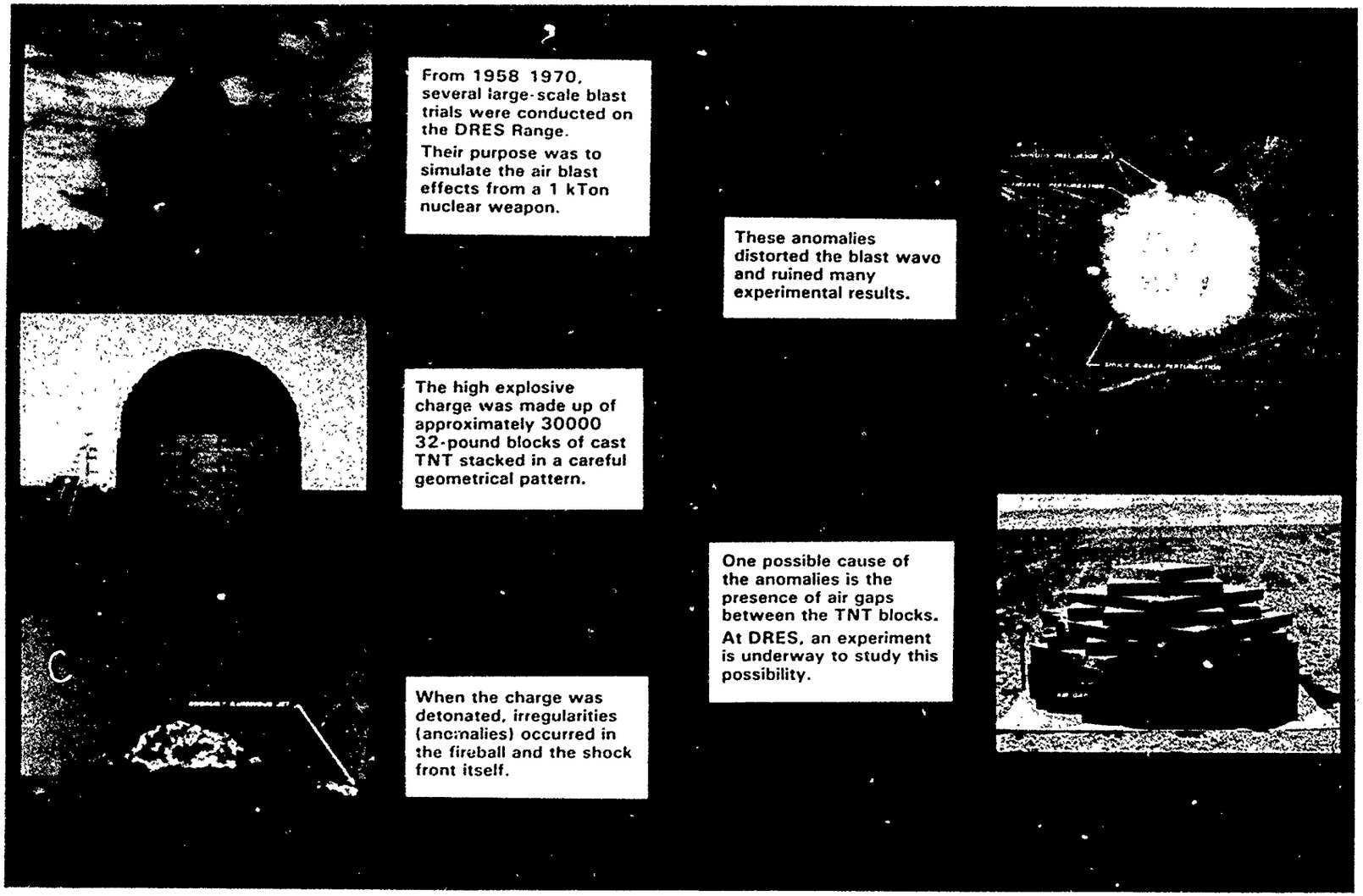

From 1958 1970, several large-scale blast trials were conducted on the DRES Range.

Their purpose was to simulate the air blast effects from a 1 kTon nuclear weapon.

The high explosive charge was made up of approximately 30000 32-pound blocks of cast TNT stacked in a careful geometrical pattern.

When the charge was detonated, irregularities (anomalies) occurred in the fireball and the shock front itself.

These anomalies distorted the blast wave and ruined many experimental results.

One possible cause of the anomalies is the presence of air gaps between the TNT blocks.

At DRES, an experiment is underway to study this possibility.

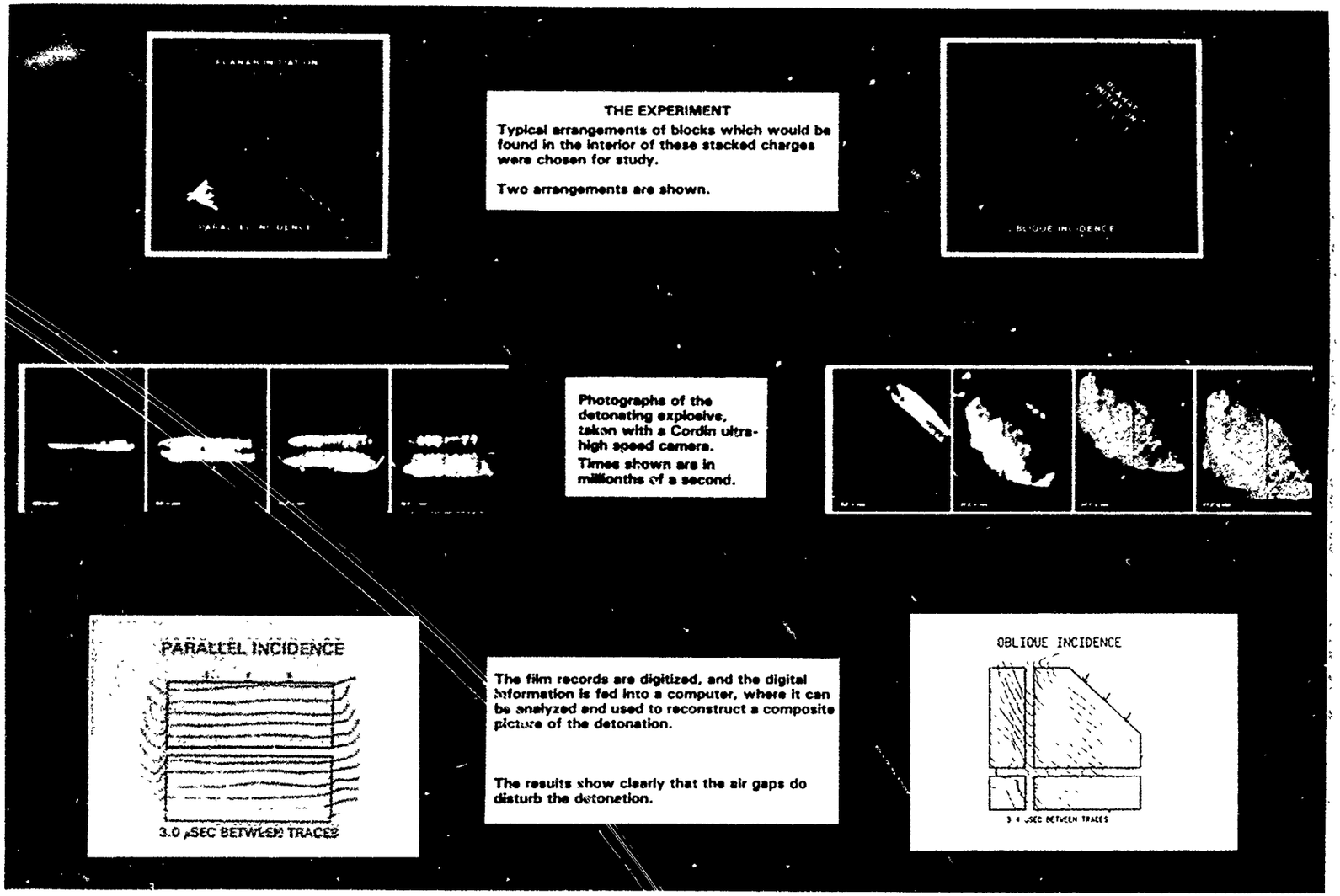
THE EXPERIMENT
Typical arrangements of blocks which would be found in the interior of these stacked charges were chosen for study.
Two arrangements are shown.
Photographs of the detonating explosive, taken with a Cordin ultra-high speed camera. Times shown are in millionths of a second.
PARALLEL INCIDENCE
3.0 μSEC BETWEEN TRACES
The film records are digitized, and the digital information is fed into a computer, where it can be analyzed and used to reconstruct a composite picture of the detonation.
The results show clearly that the air gaps do disturb the detonation.
OBLIQUE INCIDENCE

RESULTS—TWO-BLOCK EXPERIMENTS (PARALLEL INCIDENCE)

AIR GAPS EXAMINED:

CONFIGURATION 1 — 0, 6, 13, 25, 50, 75 mm
CONFIGURATION 2 — 0, 16, 13, 19, 25 mm

● DETONATION PROPAGATED SUCCESSFULLY IN UNCONFINED BLOCKS ACROSS AIR GAPS UP TO 75 mm.

2 ORDERED CRYSTAL STRUCTURE INFLUENCED DETONATION PROCESS. DETONATION VELOCITY WAS 6% HIGHER IN DONOR BLOCKS, AND RESULTS IN RECEPTOR BLOCKS LESS SCATTERED, WHEN DETONATION VELOCITY VECTOR WAS NORMAL TO (CONFIG. 1), RATHER THAN PARALLEL TO (CONFIG. 2), THE LONG CRYSTAL AXIS.

● CONFINEMENT OF CONFIGURATION 1 BLOCKS BY 19 mm PLEXIGLAS DID NOT RESULT IN A STATISTICALLY-SIGNIFICANT INCREASE IN DETONATION VELOCITY IN THE DONOR-RECEPTOR SYSTEM.

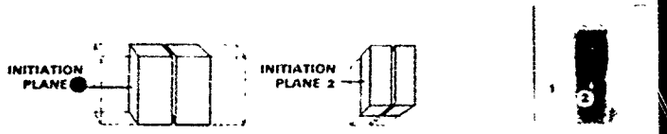

CONFIGURATION 1 CONFIGURATION 2 CRYSTAL STRUCTURE

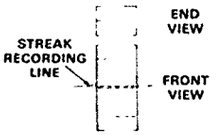

POSITION (- - - -) OF RESISTIVE VELOCITY PROBES CAST INTO CHARGES

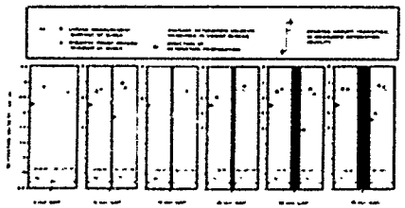

DETONATION VELOCITY MEASUREMENTS FROM CONFIGURATION 1 EXPERIMENTS (UNCONFINED BLOCKS)

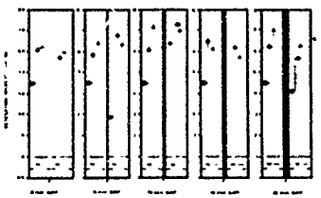

DETONATION VELOCITY MEASUREMENTS FROM CONFIGURATION 2 EXPERIMENTS (UNCONFINED BLOCKS)

RESULTS – FOUR-BLOCK EXPERIMENTS (OBLIQUE INCIDENCE)

AIR GAPS EXAMINED:

3 mm, 13 mm, 25 mm

- LUMINOUS GASES CHANNELLED AHEAD OF DETONATION FRONT AND INITIATED REACTION WAVES IN ADJACENT RECEPTOR BLOCKS (INITIAL PROPAGATION DIRECTION WAS FUNCTION OF AIR GAP WIDTH).

- 2 AT INTERSECTION OF FOUR BLOCKS, CHANNELLED GASES INITIATED LOW-VELOCITY REACTION WAVES ALONG TWO SURFACES OF BLOCK VERTICALLY-OPPOSITE DONOR BLOCK.

- FROM POINT OF INTERSECTION, PLANAR DETONATION FRONT EMERGED TRAVELLING PARALLEL TO FRONT IN DONOR BLOCK BUT DELAYED WITH RESPECT TO THAT FRONT.

- EFFECTS INCREASED AS AIR GAP INCREASED, AND WERE REDUCED, BUT NOT ELIMINATED, WHEN BLOCKS WERE CONFINED BY 19 mm PLEXIGLAS.

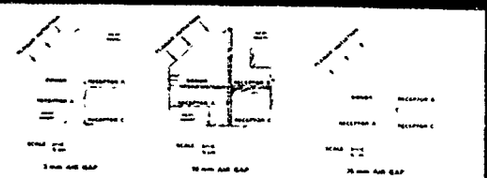

COMPOSITE TRACINGS FROM FRAMING CAMERA SHOWING PROGRESS OF DETONATION FRONT ACROSS AIR GAPS (UNCONFINED TNT BLOCKS)

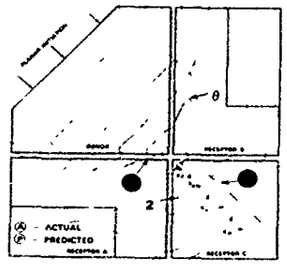

UNCONFINED TNT BLOCKS		
GAP WIDTH	θ	DELAY IN BLOCK C (MICROSECONDS)
3 mm	16°	< 2 μsec
13 mm	20°	~ 5 μsec
25 mm	23°	~ 9 μsec

DETONATION PROPERTIES OF LIQUID NITRIC OXIDE

W. C. Davis and W. C. Chiles
Los Alamos National Laboratory
Group M-3, MS J960
Los Alamos, New Mexico 87545

The detonation properties of liquid nitric oxide, chosen as a prototype explosive for extensive study under the Fundamental Research on Explosives program, are being measured. This paper concentrates on the details of the experiments, conducted at a temperature of −158 C. Detonation velocity as a function of diameter, detonation wave shape, and detonation pressure are the quantities being measured.

INTRODUCTION

The Fundamental Research on Explosives program is devoted to advancing explosive science by making a detailed study of a prototype explosive, chosen to be a simple molecule, nitric oxide (NO), for which many properties can be calculated. Detonation properties, equation of state, and chemistry are all under study.

Measurement and calculation of the products equation of state for liquid nitric oxide make it possible to test the Chapman-Jouguet theory by making a direct comparison of predicted and measured values for detonation properties. This paper describes how some of the measurements are made.

MEASUREMENTS

A test of detonation theory is provided by comparing the measured detonation pressure with that obtained from the calculated and measured equation of state of the detonation products. The measurements are made using the reflected wire technique described by Davis and Craig (1). The explosive is contained in a long tube, and the measurements are interpreted as described by Davis and Venable (2). The posters show diagrams and photographs of the experimental arrangements.

The global reaction rate, and its dependence on the local state, can be deduced from measurements of the detonation velocity and the wave shape for detonations in long tubes of several diameters. The analysis is described by Bdzil (3) and Engelke and Bdzil (4). The wave shape is measured using standard streak camera technique.

The experiments must be conducted using liquid nitric oxide, and it is a liquid (at atmospheric pressure) only at temperatures between -150 C and -162 C. The experimental difficulties of working at these temperatures are the usual problems with differential expansion of the materials used, of getting light signals out from a heavily insulated chamber, and of holding the temperature differences over the full dimensions of a large experiment within the necessary limits.

The experimental results are not yet extensive enough for a reasonable interpretation to be made. The purpose of this paper is to show in the posters how the experimental problems have been overcome.

REFERENCES

1. W. C. Davis and B. G. Craig, Rev. Sci. Inst. *32*, pp. 579-581, 1961.
2. W. C. Davis and D. Venable, Proceedings Fifth Symposium (International) on Detonation, ACR-184, Office of Naval Research, Figs. 6 and 7, pp. 13-21, 1970.
3. J. B. Bdzil, J. Fluid Mech. *108*, pp. 195-226, 1981.
4. R. Engelke and J. B. Bdzil, Phys. Fluids *26*, pp. 1210-21, 1983.

THIS WORK IS PART OF A PROGRAM CALLED FUNDAMENTAL RESEARCH ON EXPLOSIVES. NITRIC OXIDE WAS CHOSEN AS A PROTOTYPE EXPLOSIVE FOR STUDY BECAUSE IT IS A SIMPLE MOLECULE WITH SIMPLE DETONATION PRODUCTS. DESCRIBED HERE ARE SOME OF THE EXPERIMENTAL PROBLEMS OF USING A LIQUID WHICH MUST BE HANDLED REMOTELY CONDENSED FROM THE GAS AT -150 C AND HAVE THE TEMPERATURE CONTROLLED +or- 0.2 C OVER THE LENGTH OF A LONG TUBE. THE PROBLEMS OF DIFFERENTIAL THERMAL CONTRACTION ARE SEVERE.

THE DETONATION PROPERTIES TO BE MEASURED ARE THE DETONATION VELOCITY AT VARIOUS TUBE DIAMETERS, THE DETONATION PRESSURE, AND THE SHAPE OF THE WAVE FRONT IN TUBES OF VARIOUS DIAMETERS. WHEN THESE MEASUREMENTS ARE COMPLETED THEY WILL PROVIDE A TEST OF THE CHAPMAN-JOUGUET THEORY BECAUSE THE DETONATION HUGONIOT CURVE IS KNOWN FROM OTHER MEASUREMENTS AND CALCULATIONS AND THEY WILL PROVIDE A RATE LAW FOR THE CHEMICAL DECOMPOSITION WITH ITS DEPENDENCE ON PRESSURE AND TEMPERATURE.

GRAPHITE WAS CHOSEN AS THE MATERIAL FOR THE DETONATION TUBES BECAUSE

1) IT HAS A LOW SOUND SPEED COMPARED WITH THE DETONATION VELOCITY
2) ITS THERMAL EXPANSION COEFFICIENT IS ONLY 6 PPM/C
3) IT HAS HIGH THERMAL CONDUCTIVITY
4) IT IS AVAILABLE AND THE TECHNOLOGY FOR WORKING IT IS KNOWN
5) IT HAS A THERMAL EXPANSION NEAR THAT OF PYREX, SO THEY CAN BE CEMENTED TOGETHER

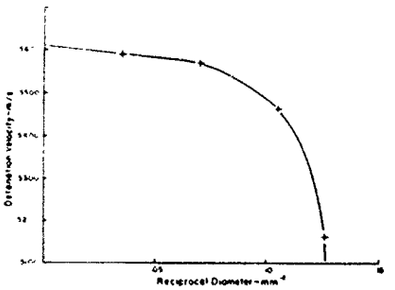

DETONATION VELOCITY vs THE RECIPROCAL OF THE TUBE DIAMETER

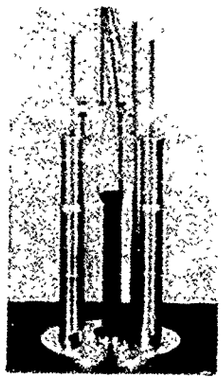

GRAPHITE TUBE AND ISO-PENTANE PUMPS ATTACHED TO BASE PLATE. VELOCITY AND THERMOCOUPLE WIRES CAN BE SEEN ON THE TUBE

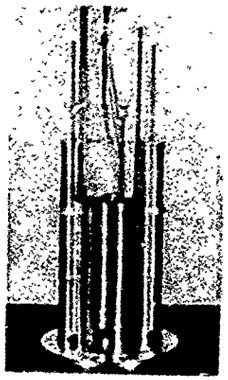

LIQUID NITROGEN COOLING COIL HAS BEEN ADDED

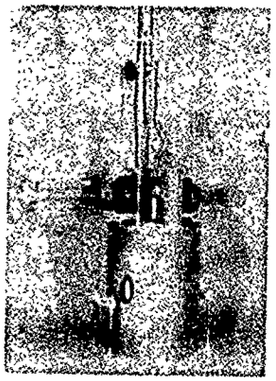

OPTICS SECTION FASTENED TO GRAPHITE TUBE AND LOWER HALF OF ISO-PENTANE VESSEL INSTALLED

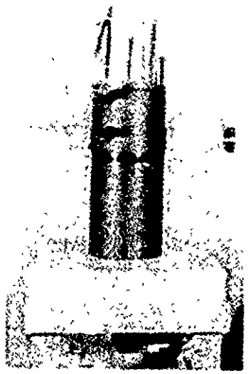

INSPECTION TUBES AND UPPER HALF OF INC PENTANE VESSEL IN PLACE

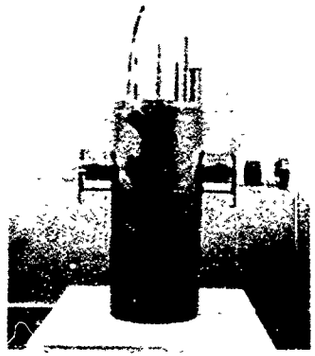

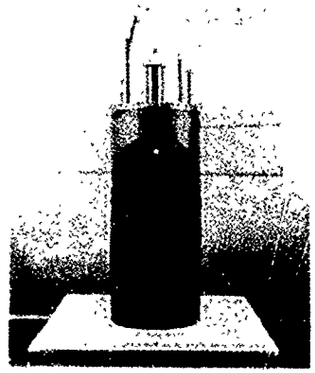

CONTRACTION BELLOWS INSTALLED SHOT ASSEMBLY READY TO BE PLACED ON THE INSULATED CONTAINER

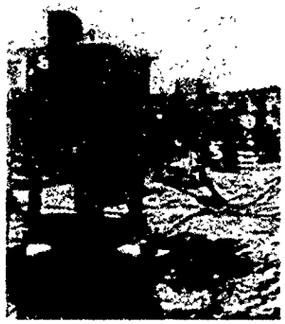

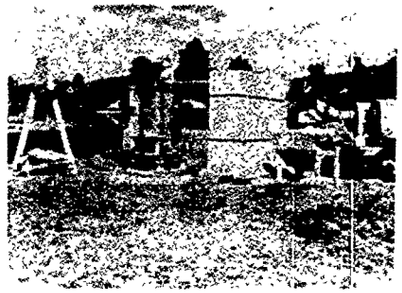

SHOT ASSEMBLY WITH ITS ASSOCIATED APPARATUS AND BLAST SHIELDING ON THE FIRING MOUND

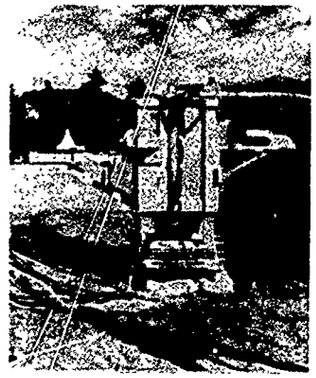

CHARACTERIZATION OF STRONG DETONATION WAVES IN NITROMETHANE

M. Sellam, H. N. Presles, C. Brochet
Laboratoire d'Energétique et de Détonique
Poitiers, France
and
R. Chéret
Commissariat a l'Energie Atomique
S ;ran, France

Six overdriven detonations were generated in nitromethane. Their velocity, pressure and brightness temperature were measured and compared with calculated data based on B.K.W. and K.H.T. equations of state. There is a quite good agreement between experimental and calculated data in the case of pressure. Brightness temperature measurements are not straight representative of detonation equilibrium temperature.

INTRODUCTION

Most of the experimental studies on detonation of condensed explosives have been conducted on the steady regime. So far, for most of explosives only one point of their detonation products Hugoniot has been checked. The upper part of the Hugoniot corresponds to overdriven detonations. Such detonations always exist during the initiation processes of liquid explosives but they are unsteady so their experimental study is difficult.

In order to check the calculations of the detonation products Hugoniot of nitromethane (N.M.) away from its C.J. state we produced six quasi-steady overdriven detonations in N.M. and measured their velocity, pressure and brightness temperature. The experimental data are compared with calculated values based on B.K.W. and K.H.T. equations of state.

EXPERIMENTAL DEVICE

Overdriven detonations were produced in a simple co-axial geometry (Fig 1). The outer chamber contains an explosive (astrolite - water mixture) whose detonation velocity is faster than that of N.M. which is contained in the internal cylindrical chamber.

The release of the detonation products of the outer explosive induce inside N.M. a complex

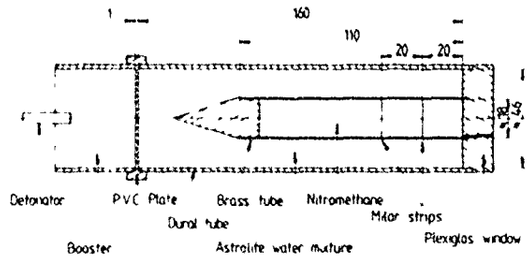

Fig. 1. Experimental setup

wave system (1) whose configuration and its development is determined by means of two transparent "mylar" strips (10 mm wide and 0.1 mm thick) placed perpendicularly to the axis of the cylinder. Indeed when the detonation waves interact with a "mylar" strip there is a fast decrease in the light emitted by the detonation fronts which produces a dark zone on a butt-end streak camera record (Fig. 2).

(There was no "mylar" strip inside the detonation tubes used to measure pressure and brightness temperature).

From such records it appears that the wave system is composed of a shock wave in a truncated cone shape, of an interacting C.J. detonation wave with the same shape and of an overdriven detonation.

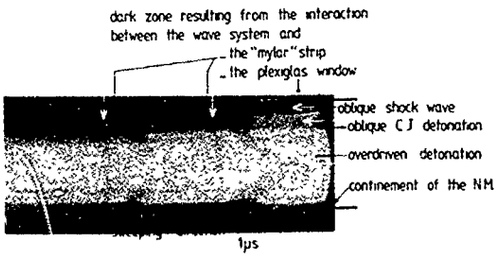

Fig. 2. Last part of a streak camera record.

Thin slits are made in the brass tube to stand up the 'mylar" strips. When the wave system crosses these slits, rarefaction waves are generated which propagate toward the axis of the tube. They lead to dark zone in "V" shape on the streak camera records.

Previous studies (2) have shown that an overdriven detonation wave becomes steady when the interacting waves are plane and steady. A similar result was obtained with an axisymmetric incident detonation wave (3 - 4).

Six different overdriven detonations with velocities ranging from 7000 to 8000 m/s were produced and the same result was obtained with each of them. The size of the overdriven detonation decreases with increasing the velocity. At 8000 m/s its diameter in the last part of the device is about 10 mm.

OVERDRIVEN DETONATION PRESSURE

We used the electromagnetic gage technique to measure the particle velocity of the overdriven detonation products and deduce their pressure. This method is based on the measurement of the voltage generated by a thin metallic foil moving with the flow of the detonation products through a magnetic field. The active part of the foil was 5 mm length and placed perpendicularly to the axis of the setup at 10 mm from the window. The experimental data (Table 1) are compared (Fig. 3) with calculated values based on B.K.W. (5) and K.H.T. (6) equations of state. The three sets of data (experimental and calculated) (Fig. 3) give the increase in pressure with the increase in velocity with respect to the C.J. corresponding values (Table 2).

TABLE 1

Overdriven Detonation Pressure

Overdriven detonation velocity (m/s)	Pressure (Kbar)
8000	350
7870	333
7730	321
7490	290
7320	271
7050	238

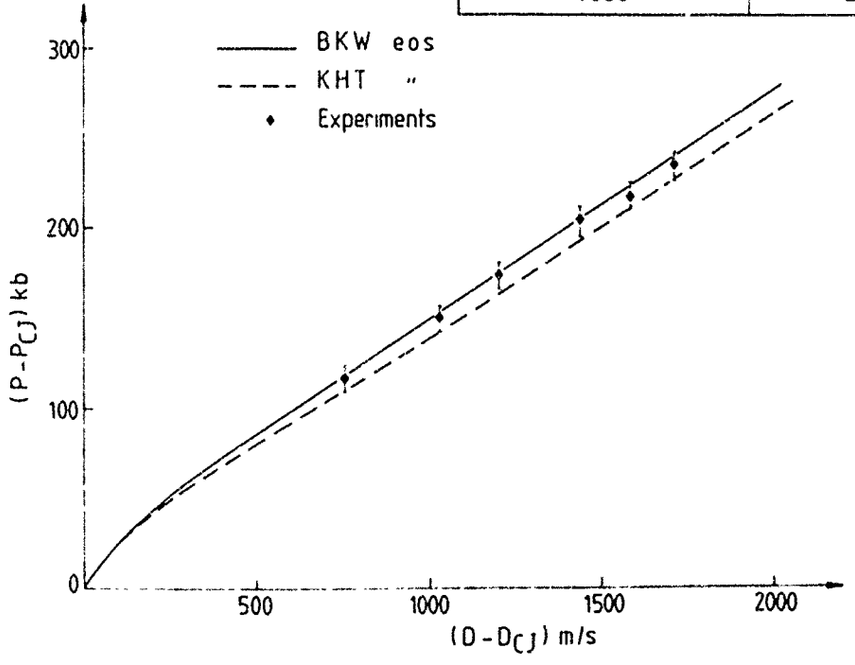

Fig 3. Pressure increase with detonation velocity increase with respect to C.J. values

TABLE 2
C.J. Detonation Characteristics of N.M.

	D(m/s)	P (Kbar)	T (K)
Experiment	6290	115	3400
B.K.W.	6290	124	3136
K.H.T.	6264	122	3300

The experimental data give a quite good confirmation of the calculated values.

BRIGHTNESS TEMPERATURE MEASUREMENTS

The brightness temperature of the detonation front in condensed explosives is investigated since about a decade. All the studies lead to the conclusion that the detonation front radiates like a blackbody in the visible and near infra-red range but none of them was able to tell whether the brightness temperature is representative of the thermodynamic equilibrium temperature.

So far, all the experiments were performed on C J. detonations and mainly in transparent liquid explosives such as N.M. In this work the brightness temperature of 5 overdriven detonation fronts was studied using a three color pyrometer (7) (λ = 0.657; 0.915; 1.008 μ).

The pyrometer was calibrated on the C.J. detonation front in N.M. considering that its brightness temperature is 3400 K (8).

The data obtained on each wavelength (Table 3) show that the overdriven detonation fronts radiate like a blackbody.

TABLE 3
Overdriven Detonation Brightness Temperature

Overdriven detonation velocity (m/s)	$T_{(\lambda=0.657\mu m)}$ (K)	$T_{(\lambda=0.915\mu m)}$ (K)	$T_{(\lambda=1.008\mu m)}$ (K)
8000	4450	4500	4476
7870	4337	4375	4342
7730	4177	4197	4179
7490	4032	4030	4006
7320	3954	3985	3892

As for pressure, we compare (Fig. 4) the increase in temperature (brightness and calculated ones) with increase in detonation velocity with respect to the corresponding C.J. values. This

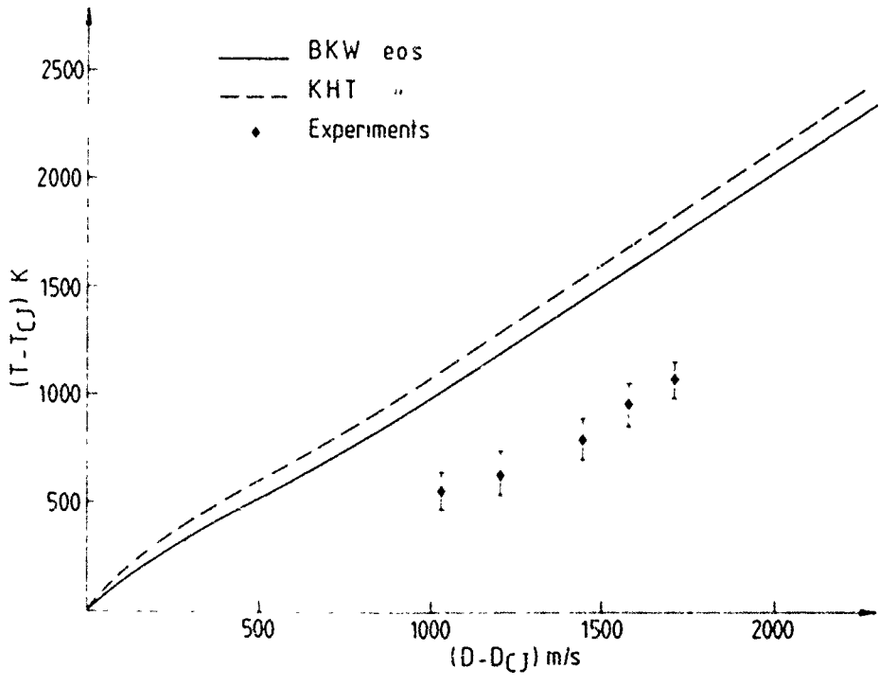

Fig 4 Temperature increase with detonation velocity increase with respect to C.J. values

shows that the increase in temperature given by the two equations of state is very similar and is faster than the increase in brightness temperature. For instance at a velocity of 8000 m/s the increase in equilibrium temperature is about 700 K higher than that of brightness temperature.

DISCUSSION

The study of the overdriven detonation characteristics was aimed to get data that could be compared with calculations based on equations of state.

We measured the velocity, pressure and brightness temperature of a few overdriven detonations in N.M.

About the pressure it appears that experimental data are in good agreement with the calculated ones based on B.K.W. and K.H.T. equations of state. The increase of pressure with velocity is very similar for the three sets of data and the discrepancy between these values is never more than 10 kbar.

Pressure is not very depending upon the equation of state and because of the uncertainty on the experimental values it is not possible to emphasize one equation of state.

The temperature is a more sensitive parameter to the equation of state and that's why a few people try to measure that detonation characteristic The increase in temperature with velocity from the C J. conditions is very similar with both equations of state used. The discrepancy on the range of velocity we are interested with never exceeds 100 K On the contrary there is a large discrepancy between the increases of the calculated temperature and brightness temperature

That seems to indicate that brightness temperature is not straight representative of the calculated equilibrium temperature at least in the case of overdriven detonations

In conclusion, the experimental study of overdriven detonations in N M. has shown that the pressure is well predicted either with B.K W. or K.H.T. equations of state. At the present time brightness temperature measurements do not permit to check the equations of state.

ACKNOWLEDGEMENT

This work was supported by the French Atomic Commission. The authors are very grateful to Y. Sarrazin for his experimental assistance and to MM. Raffougeot, Cobat and Lemoine from the Centre d'Etudes Du Ripault (C.E.A.) for the streak camera records.

REFERENCES

1. L. Hamada, H. N. Presles, C. Brochet, R. Bouriannes, C. Cheret, "Characterization of an Overdriven Detonation State in Nitromethane", Progress in Astronautics and Aeronautics, Vol. 94, pp. 343-349, 1985.
2. J. P. Argous, C. Peyre, J. Thouvenin, "Observations et études de conditons de formation d'une détonation de Mach", 4th Symposium (Int.) on Detonation, pp. 135-141, U.S. Government Printing Office, Washington D.C.. 1965.
3. L. Brun, R. Cheret, J. Vacellier, "Considérations sur les Détonations fortes", Actes du Symposium H.D.P., pp. 1-15, Paris, 1978.
4. S. Krishnan, C. Brochet, R. Cheret, "Mach reflection in condensed explosives", Propellants and Explosives, Vol. 6, pp. 170-172, 1981.
5. R. Cheret, "Contribution a l'étude numérique des produits de détonation d'une substance explosive ', Rapport C.E.A. 4122, 1971.
6. K. Tanaka, "Detonation Properties of Condensed Explosives Computed Using the Kihara-Hikita-Tanaka Equation of State", National Chemical Laboratory for Industry Report, Tsukuba, Japan, 1983.
7. R. Bouriannes, M. Moreau, J. Martinet, "Un pyrometre rapide a plusieurs couleurs", Rev. Phys., App., Vol. 12, pp. 893-899, 1977.
8. Y Kato, Private communication.

EXPERIMENTAL STUDY OF THE HUGONIOT CURVE OF NITROMETHANE DETONATION PRODUCTS BY :

- Producing overdriven detonation waves
- Measuring their detonation characteristics (D,P,T)

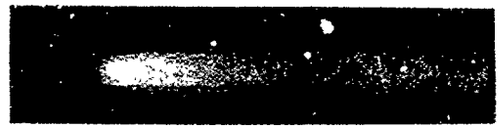

1. GENERATION OF OVERDRIVEN DETONATION WAVES

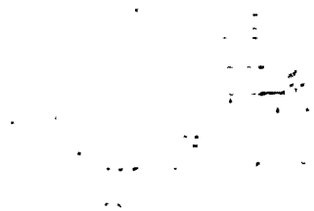

The detonation wave in the outer explosive drives an overdriven detonation wave in nitromethane

Six different astrolite-water mixtures were used
According to the mixture: $7000 \leq D \leq 8000$ m/s

The overdriven detonation velocity
- remains constant in the last part of the tube
- is equal to the detonation velocity of the outer explosive mixture

Six overdriven detonation states were studied

2. OVERDRIVEN DETONATIONS CHARACTERISTICS

PRESSURE

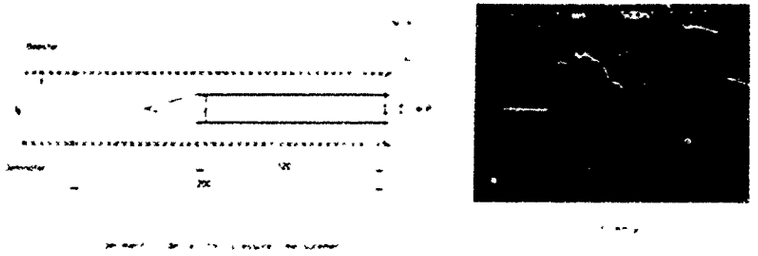

PRESSURE
The nitromethane detonation pressures are well predicted with BKW and KHT equations of state

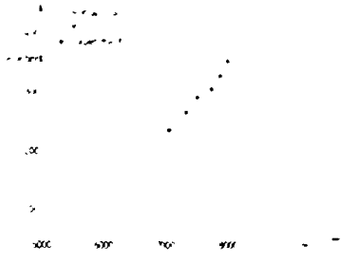

BRIGHTNESS TEMPERATURE

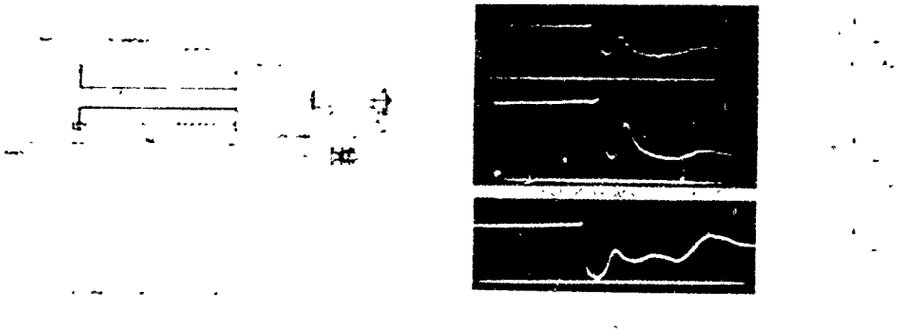

TEMPERATURE
Brightness temperature measurements of overdriven detonation waves do not permit to check the E.O.S.

CONTINUOUS OBSERVATION OF MACH BRIDGE AND MACH PHENOMENA

J. Souletis, J. Groux
Société Nationale des Poudres et Explosifs
Centre de Recherches du Bouchet
91710 Vert-Le-Petit - France

The Mach reflection is studied in two distinct cases: first, the intersection of two oblic plane waves and secondly, a conical wave with constant velocity. This study has been applied to various plastic bonded explosives. The first device makes it possible to observe the formation of the phenomenon and to differentiate among the various compositions on the basis of their reaction zone length. The second makes it possible to provide an accurate characterization of the state of the detonation that is reached in the center of the Mach wave and to compare measurements and equations of state.

INTRODUCTION

The Mach reflection of detonation waves has been examined in various theoretical and experimental studies (1-6). The results of these studies concern only a very small number of explosives. We have therefore developed two complementary types of Mach detonation wave generators in order to study the behaviour of cast-cured plastic bonded explosives. The first produces the intersection of two plane waves and allows continuous observation of the propagation of Mach's phenomenon. The second sample generates a driven conical wave that converges on the axis in a Mach disk. Because of its very simple shape, it makes it possible to conduct precise measurements of the velocity or pressure at the center of the overdriven detonation wave. Chapters 1 and 2, respectively, describe each of the generators and the results obtained with certain plastic bonded explosives. In both parts, results are connected to the nature of the tested explosive.

1 - INTERSECTION OF PLANE WAVES

The first generator allows the intersection of two steady plane detonation waves at a given angle of incidence α. The explosive sample to be tested is machined in such a way to get a truncated prism with a pentagonal cross-section and an angle 2α between the two initiation faces (Figure 1). The two P.W.G. produce two plane waves with a maximum distortion of 1 mm on a 320 x 60 mm² surface. They initiate two adaptive or booster sheets that are designed to absorb the transitory regime of the detonation. They have a thickness of .5 to 1 cm and are separated at the top by a very narrow lead confinement.

The prism is truncated by a plane that makes an angle $\beta = 14°$ with the edge of the dihedron that determines an angle 2α. This inclined plane represents the observation surface of the wave.

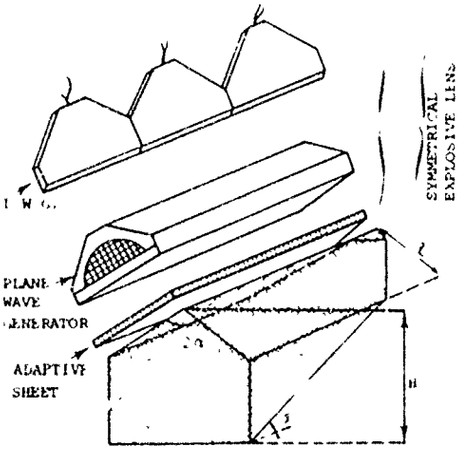

Fig 1

H = 82 mm − β = 14° − l = 60 mm

The emergence of the wave is observed in two different ways: either in a continuous way or at various moments during its propagation. In the first case, the streak camera is equipped with a diaphragm with three parallel slits, the middle slit coinciding with the plane of symmetry of the sample. In the second case, several optical fibres sheets, distributed over the output surface of the explosive, transmit the light signal up to a plane observed with the camera (Figure 2).

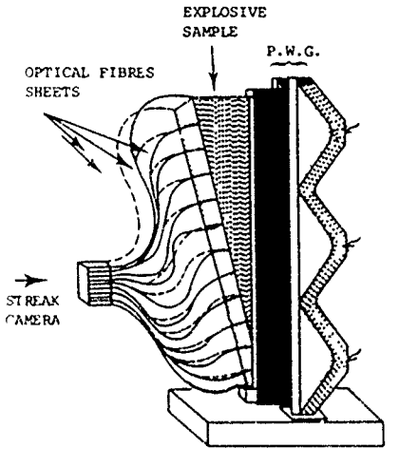

Fig 2 Experimental Device

The plastic bonded explosives B 2169, B 2174 and B 3003 were tested. Their composition is indicated in Table 5.

Two characteristic color recordings are represented in Figure 3. The one on the left is a continuous recording performed with the PBX-B2174 for $\alpha = 65°$. The one on the right represents all the space-time profiles of the detonation at different depths of propagation for the same composition and $\alpha = 55°$

All these tests have established that:

- The Mach front has the shape of a plateau but always has a slight curvature that depends on the composition.

- The critical angle for the appearance of the Mach wave (α_{cr}) is a function of the composition but lies most often between 40 and 60 degrees (see Table 1). This angle was measured by generating two divergent cylindrical detonation waves in the previously described sample and by applying to it the optical fibre observation technique described above (Figure 2).

TABLE 1

	MEASURED α_{cr}	POLYTROPIC α_{cr}
B 2169	55°.65 (±1°.45)	44.6
B 2174	43° (±2°.50)	45.4
B 3003	50° *	45.2

* extrapolated value (see Fig. 5)

In the second column of Table 1 we present the values of α_{cr} predicted by a polytropic equation of state and a triple plane waves configuration. There is an important difference between the calculated and measured values of α_{cr}, but it does not result from the lack of accuracy of the eos (the seond device shows (Fig. 11) that the Γ-eos gives results not very different from experimental points). The difference should result from the curvature of the real Mach wave in the neighbourhood of the triple point, which depends on the nature of the composition.

- After an initial phase of very rapid increase, the width l of the Mach plateau changes in linear fashion during propagation (Figure 4) as far as the maximal depth of the sample, i.e., 8 cm.

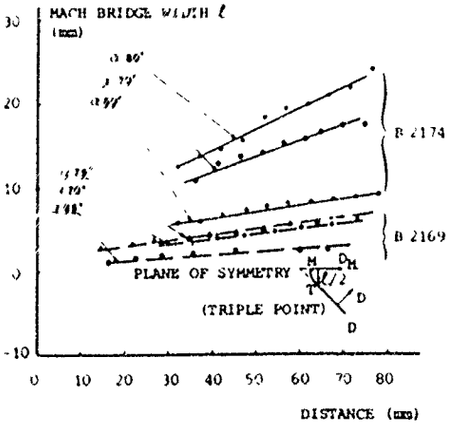

Fig. 4

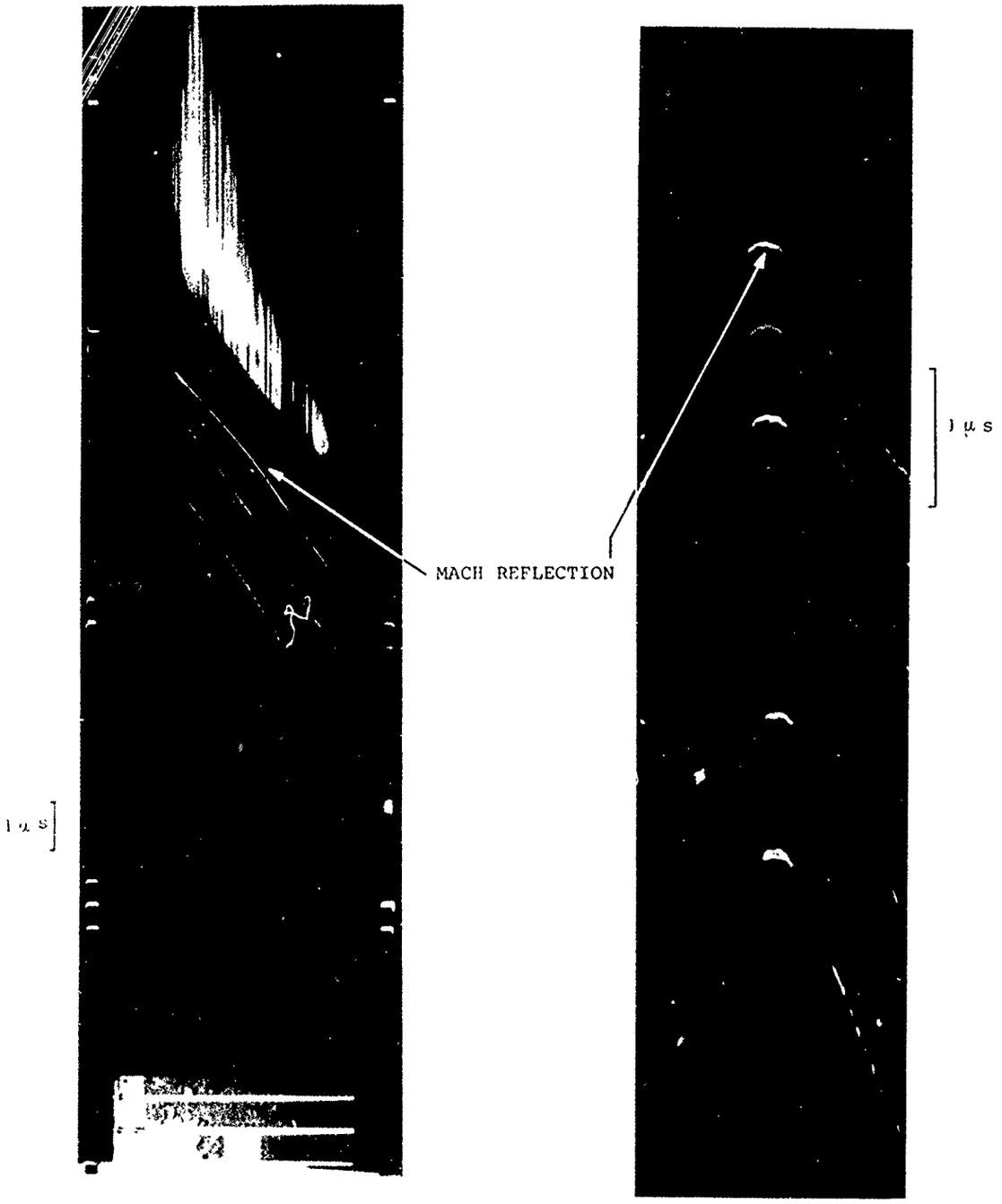

① : Continuous

② : At different depths of propagation

FIGURE 3

CHARACTERISTIC RECORDS OF THE PHENOMENON

- The angle X determined by the trajectory of the triple point and the plane of symmetry is a function of α and of the composition as is indicated by Figure 5.

- Finally, the velocity D_M of the Mach wave is a constant close to R, with $R = D \cos X / \sin(\alpha - X)$, the deviation between the values of R and D_M measured over ten tests not exceeding .10 mm/μs.

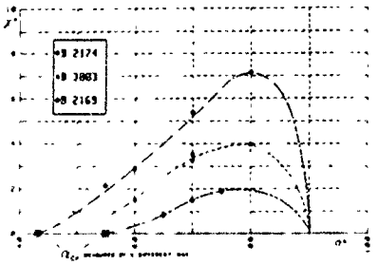

Fig. 5

Table 2 brings together two of the preceding properties and the reaction zone length "a" of the tested explosive. This reaction length is evaluated in this initial approach by the Eyring method (11). X max is the value of the maximum of the experimental curve $X = f(\alpha)$.

TABLE 2

COMPOSITION	$X_{max}(°)$	$\alpha_{cr}(°)$	a (mm)
B 2169	2.00	55.65	0.05
B 2174	7.25	43.00	2.8
B 3003	4.00	50.00	0.1
COMP. B	4.75*	44.00*	0.13*

* drawn from (2) (comp. B of unspecified density)
* drawn from (3) ($\varrho = 1.73$)
* drawn from (10) ($\varrho = 1.7$)

It is observed that α_{cr} varies inversely as the reaction zone length whereas X_{max} varies in the same way as that factor.

The curvature of the Mach wave is probably also a determining parameter. This parameter can give us information as to how to take into account flow in the neighbourhood of the triple point. However, it is more accurately measured in the case of the flow generated by the second device and is examined only at that time.

2 - DRIVEN CONICAL WAVE

The second generator is shown in Figure 6. A cylinder of explosive to be tested is surrounded with a concentric tube of rapid explosive, at the end of which is placed a capping cone. The detonation of the rapid explosive generates a conical wave in the slow explosive, that converges on the axes by giving rise to a Mach reflection.

The Mach wave is observed at the end of the sample by means of the streak camera. The velocity of the rapid explosive is measured during each firing. In addition, the sample was equipped during the tests either with manganin pressure gauges or with an axial electric probe, so as to allow continuous measurement of the velocity of the Mach wave.

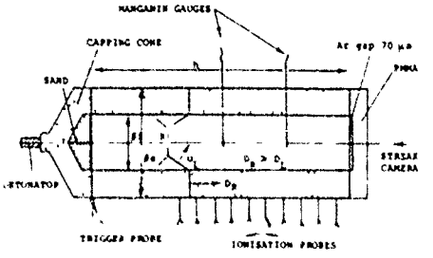

$\varnothing_i = 40$ mm $- \varnothing_e = 70$ mm

Fig 6. Sample Equipped With Manganin Gauges

Propagation of the phenomenon

The flow originated by this device is different from the one previously studied. The diameter of the Mach disk increases very markedly during the propagation of the wave up to a sample length of 2.5 to 3 $\varnothing_i$ (depending on the composition) and becomes quasi-stable beyond that length (Figure 7). Moreover, the stable value for the diameter $\varnothing$ of the Mach disk seems to depend on the central composition, as is shown in Figure 8, where the values $\varnothing / \varnothing_i$ are represented as a function of the ratio $1 / \sin\theta$ for 7 distinct compositions. The values θ measured are in each case equal to:

$$\text{Arc sin}\left(\frac{D_L\,(CJ)}{D_R\,(CJ)}\right)$$

i.e. the point representing the state CJ of the central explosive in a pressure-deviation diagram is adapted to the expansion curve of the rapid explosive so that there is never an overdriven detonation of the incident conical wave.

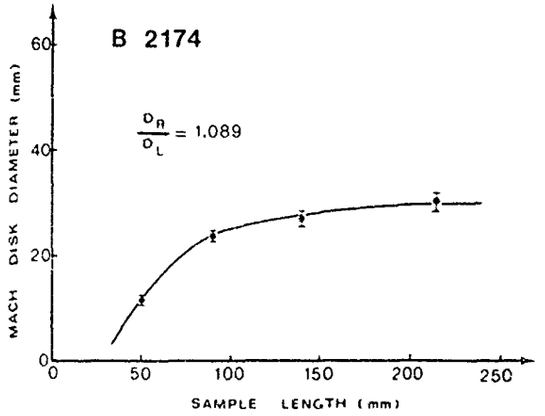

Fig. 7

Two types of behaviour appear (Figure 8): the upper curve connects all the results obtained with HMX/AP/Pb$(NO_3)_2$ compositions whereas the lower curve is obtained with PETN based compositions.

Fig 8. Ratio $\frac{\varnothing}{\varnothing_i}$ as a Function of 1/Sin θ, for Values Ø Established Beyond 4 $\varnothing_i$

For the shape of the Mach disk, a curvature is always observed, which is more or less great depending on the composition (Figure 9).

The curvature depends on the angle θ of the incident wave but also changes during the displacement of the Mach wave. The comparison of the Mach disk curvature radii of two distinct compositions cannot be performed unless the diameter of the disk is constant. Thus, in Table 3, we have compared, for three different values of θ, the ratios R/Ø obtained with distinct explosives.

TABLE 3

θ (°)	EXPLOSIVE	R (mm)	R / Ø
≅ 66.50	B 2174	15.60	0.769
	B 2169	10.48	0.953
≅ 61.70	B 2190	12.08	1.225
	B 2192	17.08	1.307
≅ 46.40	B 2191	15.43	0.986
	B 2161	18.98	1.321

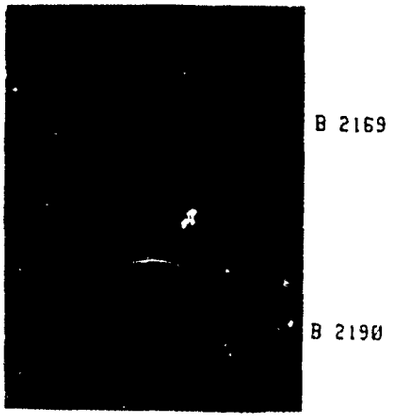

Fig. 9. Detonation wave at the end of the sample for 2 cast-cured PBX

Steadiness of the regime

The observation of the Mach disk at various propagation distances has shown that a quasi-steady regime was reached at the end of the sample. The continuous measurement of the velocity of propagation (Figure 10) shows that it is constant and equal to D_R beyond a zone of high acceleration that corresponds to the transitory regime previously observed. This measurement was performed with an axial electric probe with the same length as the sample, with a diameter of .3 mm, and a resistivity of 210 Ω/m. Figure 10 also shows a recording of pressure by a manganin piezoresistive gauge. It is placed in a plane perpendicular to the cylinder, on the axis of symmetry.

All measurements of pressure have been duplicated with an indirect measurement by means of a stack of PMMA at the end of the cylinder. There is a good agreement between the two types of measurements since the maximum deviation observed is less than 10%. Two tests with two distinct gauges placed on the same sample have made it possible to check the stability of the pressure beyond the transitory zone already observed. Table 4 shows this result:

TABLE 4

	D_R / D_L	$l / \varnothing_i$	P (megabars)
B 2174	1.068	3.75	0.410
		4.50	0.412
	1.084	2.50	0.449
		3.50	0.450

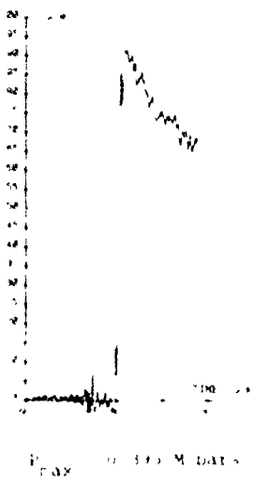

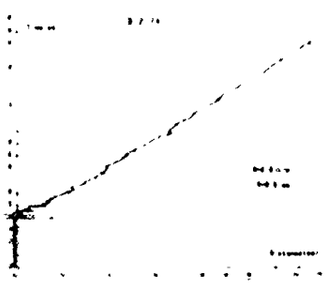

Fig 10. Characteristic signals delivered by a Manganin Gauge and by a Continuous Probe

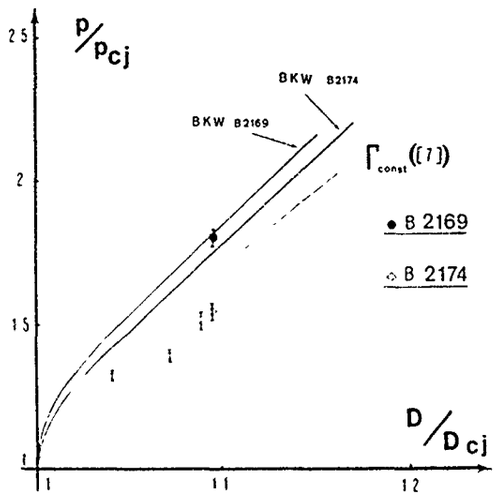

Fig. 11. Measurements of Overdriven Detonation States in B 2174 and B 2169 Compositions

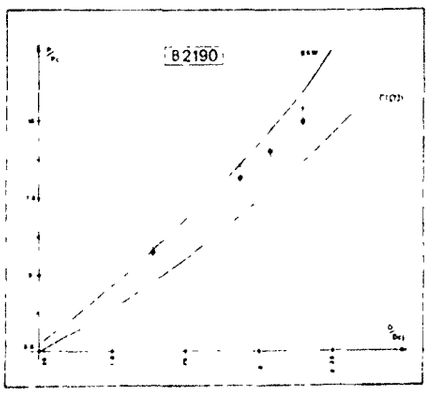

Fig. 12. Measurements of Detonation Pressure and Velocity in B 2190 Composition

Equation of state

The detonation regime of the Mach wave being steady at the end of the sample, it is interesting to characterize the overdriven detonation state attained with the tested composition.

Figures 11 and 12 show the comparison between the measurement points and the curves obtained from the BKW and polytropic equations of state.

Up to about 5*Pcj, a good agreement is noted between the measurements and the curves given by the BKW equation in the case of PBX B 2169 and B 2190. The polytropic equation

also gives an estimate of the pressure, even as far as about ten times the pressure P_{CJ}.

On the other hand, there is disagreement between the experimental points and the theoretical curves in the case of B 2174. This is essentially due to the fact that the BKW equation is established on the assumption of a complete reaction of the ammonium perchlorate at the level of the front of the detonation; and this assumption certainly does not holds (13). Moreover, as this explosive releases energy very gradually (9), it is possible that pressure is not recorded systematically at the same level in the decrease of the signal that follows the shock wave, the amplitude of the latter depending on.

CONCLUSION

The Mach wave generators we have defined make it possible to observe the formation of the Mach wave and to characterize the state of the overdriven detonation that is attained in it. They have provided us with interesting results for various plastic bonded explosives.

The first device produces the intersection of two unsustained plane waves and thus makes it possible to attain magnitudes such as X max, the maximum angle of increase of the Mach plateau or α_{cr}, the critical angle for the appearance of the phenomenon. These magnitudes change in the same direction as the length of the reaction zone in the first case and in the reverse direction in the second case. Granulometry (or, again, homogeneity) probably also has an effect on the characteristics of the Mach reflection. This initial test makes it possible to differentiate among the compositions with regard to this phenomenon and thus also must make it possible to obtain details on energy transfers within the reaction zone.

The second device, by creating a "sustained" Mach wave also makes it possible to link the curvature of the Mach disk to the nature of the composition and, in particular, must lead to a better definition of flow in the neighbourhood of the triple point. Finally, and above all, it makes it possible to acquire precise knowledge of states corresponding to the dynamic adiabatics of the detonation products of an explosive. In particular, this should allow a more accurate adjustment of the state equation of detonation products, as the comparison between calculated and measured values is no longer limited to the Chapman-Jouguet state.

TABLE 5
Composition of the Various Plastic Bonded Explosives Used in the Course of this Study

COMPOSITION	COMPONENTS	COMPOSITION (BY WEIGHT)	DENSITY (g/cm^3)
B 2161	HMX / AP / Al / PU	40/30/20/10	1 860
B 2169	PETN / PU	83/17	1 550
B 2174	HMX / AP / $Pb(NO_3)_2$ / PU	47/30/11/12	1 830
B 2190	PETN / HTPB	30/70	1 071
B 2191	HMX / AP / $Pb(NO_3)_2$ / PU	37/40/11/12	1 832
B 2192	HMX AP / $Pb(NO_3)_2$ / PU	27/50/11/12	1 836
B 3003	HMX / NC - NGL	80 20	1 810

PU = polyurethane binder
A P = ammonium perchlorate

ACKNOWLEDGEMENTS

The authors wish to thank F. Bonthoux for his measurements performed with manganin gauges and also B. Nouguez for his calculations of dynamic adiabatics by means of the BKW equation.

REFERENCES

1. J. P. Argous, C. Peyre and J. Thouvenin, "Observation et étude des conditions de formation d'une onde de détonation de Mach", 4th symposium (int.) on detonation, p. 135, ACR-126, 1965.

2. B. D. Lambourn and P. W. Wright, "Mach interaction of two plane detonation waves",4th symposium (int.) on detonation, p. 142, ACR-126, 1965.

3. S. D. Gardner and J. Wackerle, "Interactions of detonation waves in condensed explosives", 4th symposium (int.) on detonation, p. 154, ACR-126, 1965.

4. F. Müller, "Mach reflection of detonation waves in condensed high explosives", Propellants and Explosives 3, p. 115, 1978.

5. C. L. Mader, "Detonation wave interactions", 7th symposium (int.) on detonation, p. 669, NSWC MP 82-334, Silver Spring, Maryland, 1980.

6. S. Krishnan, C. Brochet, R. Cheret, "Mach reflection in condensed explosives", Propellants and explosives 6, p. 170, 1981.

7. I. C. Skidmore and S. Hart, "The equation of state of detonation products behind overdriven detonation waves in comp. B", 4th symposium (int.) on detonation, ACR-126, 1965.

8. J. Souletis. "Interaction d'ondes de détonation - Mise au point d'une épreuve pour l'étude des phénomenes de Mach, SNPE report 116/84/CRB/DR, France, 1984.

9. J. Souletis and J. Mala, "Influence of tests conditions on the ballistic classification of explosives", 8th symposium (int.) on detonation, 1985.

10. R. E. Duff and E. Houston, J. Chem. Phys. 23, 1268 - 1273, 1955.

11. H. Eyring, R. E. Powell. G. H. Duffey, and R. B. Prelin, Chem. rev. 45, 69-181, 1949.

12. M. Sellam, H. N. Presles, C. Brochet and R. Cheret, "Characterization of strong detonation waves in nitromethane", 8th symposium (int.) on detonation, 1985.

13. J. Groux, B. Nouguez and J. Souletis "Entrainement en détonation du perchlorate d'ammonium - Evaluation de sa vitesse de réaction". SNPE report CR 23/84/CRB/GTE/NP, France, 1984.

This work has been performed under the auspices of the French Ministry of Defense (DRET).

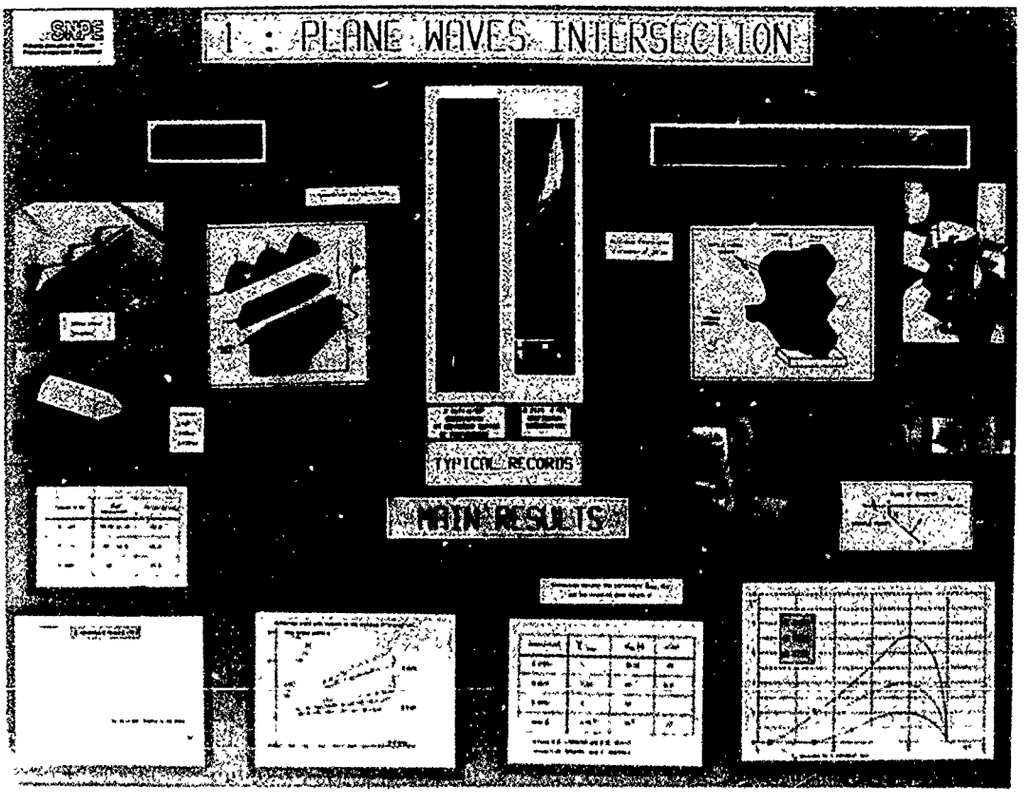
SNPE
1 : PLANE WAVES INTERSECTION
TYPICAL RECORDS
MAIN RESULTS

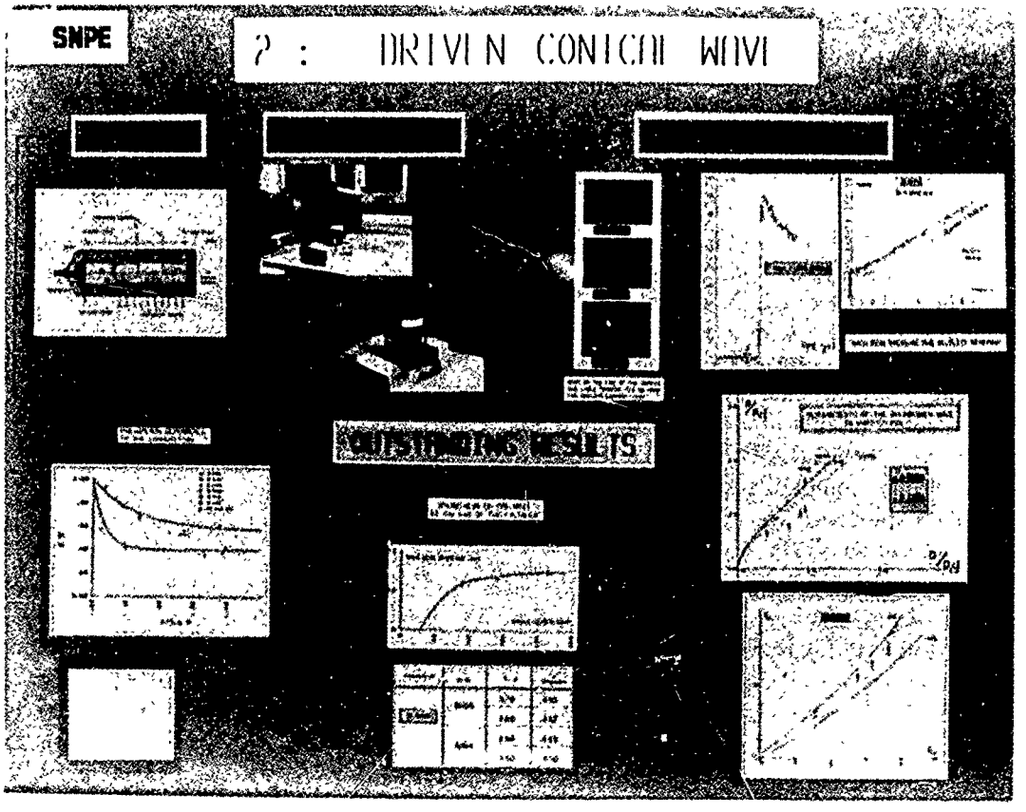
SNPE
2 : DRIVEN CONICAL WAVE

DISPLACEMENT GRADIENT METHOD FOR MEASURING DETONATION PARAMETERS USING FLASH X-RAY PHOTOGRAPHY

Li Huiling, Huang Zhengping and Ding Jing
Beijing Institute of Technology
P.O. Box 327, Beijing, China

Instead of several parallel foils, single metallic foil is embedded in explosive slantly at an angle to the plane of detonation wave front. A sequence of flash radiographs records the displacement of the foil at discrete times. This new technique, the displacement gradient method, is used for measuring detonation parameters of explosives. Detonation characteristics of two explosives - TNT and a plastic bonded RDX composition BH-1 are measured with this technique.

INTRODUCTION

Flash radiography today provides a diagnostic tool to make quantitative measurements for inert materials under high dynamic pressure and for explosives during the detonation process (1). Using the flash x-ray photography, Davis and Venable (2) trace the position of a rarefaction wave propagating into the explosive products. An upper limit of the detonation pressure is inferred from the rarefaction velocity. In the work of Rivard et al. (3), the flow behind a plane detonation wave front is examined radiographically by observing the motion of thin tantalum foils embedded in cubes of explosives. From data of the instant position of each foil and the time, together with the detonation front position, it is sufficient to determine the density particle velocity, pressure and internal energy throughout the flow with no a priori assumption of an equation of state. The shortcomings of this method is that the total weight of multiple parallel foils amounts to 2% of the weight of sample explosive. These foils will cause disturbances in the flow.

Instead of multiple parallel foils, we use a single metallic foil embedded in explosives slantly at an angle to the plane of detonation wave front. This new technique, the displacement gradient method, is described for measuring detonation parameters of explosives using flash x-ray photography.

THEORY

A schematic drawing of the explosive assembly is shown in Fig. 1. The sensing element of the displacement gauge is a thin copper foil in the shape of a span roof embedded in the explosive cube symmetrically.

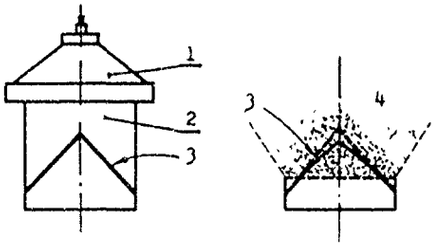

Fig 1 Schematic drawing of explosive assembly

1-Plane wave generator
2-Explosive sample
3-Copper foil
4-Detonation product

The diagram of the foil deformation is shown in Fig. 2. The original position of a segment of the embedded metal foil is CAB which is at an angle θ_0 with respect to the detonation front. When the detonation wave front arrives AE, the foil segment AB traversed by the detonation wave deforms to AB'. AB" is the tangent to AB' curve at the point A and at an angle θ to the

detonation front. R-X and R-x are the Lagrange coordinate and Euler coordinate respectively. The relation between x and X is:

$$x = X + w \tag{1}$$

where w is the particle displacement. The R axis is fixed on the initiation plane and the axis Ox is perpendicular to OR and passes A.

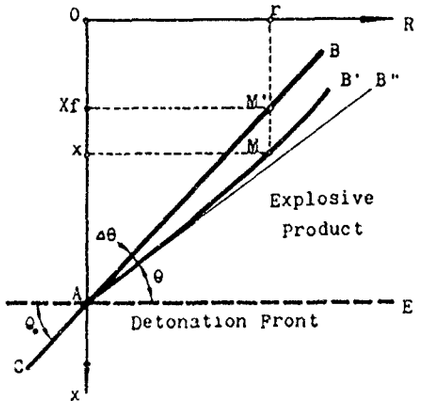

Fig 2 Diagram of the deformation of foil sensing element

From the conservation of mass and shock wave relations:

$$\rho_0 dX = \rho dx \tag{2}$$

$$\rho(D - u) = \rho_0 D \tag{3}$$

$$p = \rho_0 D u \tag{4}$$

and with Eq. (1), following relationships are derived.

$$\frac{\rho}{\rho_0} = \left(1 + \frac{dw}{dX}\right)^{-1} = \frac{t_g\theta_0}{t_g\theta} \tag{5}$$

$$\frac{p}{\rho_0 D^2} = \frac{u}{D} = -\frac{dw}{dX} = 1 - \frac{t_g\theta}{t_g\theta_0} \tag{6}$$

$$\gamma = \frac{1 - \frac{dw}{dX}}{\frac{dw}{dX}} = \frac{t_g\theta}{t_g\theta - t_g\theta} \tag{7}$$

Here ρ - density, p - pressure, u - particle velocity, and γ - polytropic constant of the detonation product. D is the detonation velocity and ρ_0 the density of the unreacted explosive.

All parameters of the flow are functions of the displacement gradient dw/dX, therefore this technique is called the displacement gradient method.

If we read directly the angle θ from the radiograph, the result obtained is usually not very accurate. A more reliable method is fitting the experimental record with a displacement function of the sensing element in a 1-D flow of detonation products.

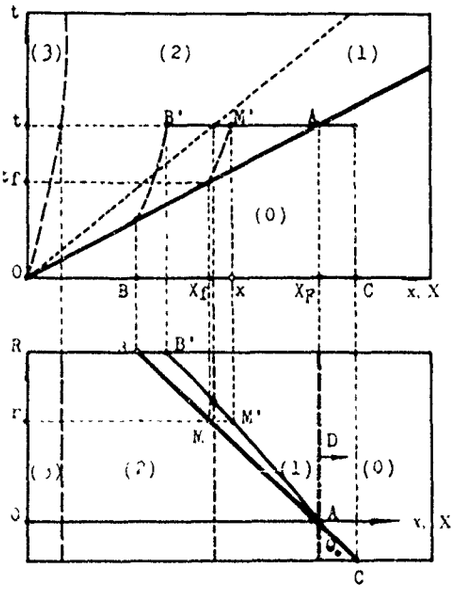

Fig 3 Flow diagram of 1-D detonation and the R x diagram

(0) - Unreacted explosive
(1) - Centered rarefaction wave region
(2) - Simple wave region
(3) - Simple wave region of the detonation product of initiator

As shown in Fig 3, the position of the detonation wave front is X_f at the time t_f and X_F at t. The particle in the flow moves from (X_f,t_f) to M'(x,t) in the x-t plane or from $M(X_f,r)$ to M'(x,r) in the R-x plane. The original foil segment AMB is compressed and deformed by the detonation wave to a curve AM'B' at time t.

In the centered rarefaction region (1), the flow line is expressed as:

$$x = -\frac{Dt}{\gamma-1} - \frac{\gamma}{\gamma-1}X_f\left(\frac{t}{t_f}\right)^{\frac{2}{\gamma+1}} \quad (8)$$

Substituting $D = X_f/t_f = X_F/t$ (9)
into Eq. (8), we get

$$x = -\frac{1}{\gamma-1}X_f + \frac{\gamma}{\gamma-1}X_f\left(\frac{X_F}{X_f}\right)^{\frac{2}{\gamma+1}} \quad (10)$$

or $$X_f = X_F\left(\frac{\gamma-1}{\gamma}\frac{x}{X_F} + \frac{1}{\gamma}\right)^{\frac{\gamma+1}{\gamma-1}} \quad (11)$$

Since $r = (X_F - X_f)/tg\ \theta o$, (12)

following expresssion is obtained:

$$r = \frac{X_F}{t_g\theta_o}\left[1-\left(\frac{\gamma-1}{\gamma}\frac{x}{X_F}+\frac{1}{\gamma}\right)^{\frac{\gamma+1}{\gamma-1}}\right] \quad (13)$$

(x,r) can be defined directly from the experimental record. γ and X_F are found by least square fitting in Eq. (13) a set of data (x_i, r_i).

On the question of lateral movement of the slant foil in the detonation flow, a 2-D numerical simulation has been worked out. As shown in Fig. 4, the central portion of the foil segment is nearly parallel to the theoretical position of the foil in 1-D calculation. This means that the lateral movement of the foil effected by the flow is negligible.

The deviations of Aa and Bb from a straight line parallel to 22' are due to the reflection at the 1a2 plane and the circumfluence around b respectively introduced in the numerical calculation. Actually, the length of the sensing element is more than fifty times of the length of the segment taken in numerical simulation. These effects, if there are any, would be insignificant.

The response time of the sensing element obtained in the 2-D calculation is about 0.05 μs

EXPERIMENTAL

The explosive sample is an assembly of several explosive pieces and the copper foil as shown in Fig 5. The output of the Ø50 mm wave shaper is a ca. 20 GPa plane wave. Thickness of the copper foil is 0.02 mm. The foil is embedded at an angle of 15 ± 2 degrees to the detonation front. One to three layers of copper foil have been used in experiments.

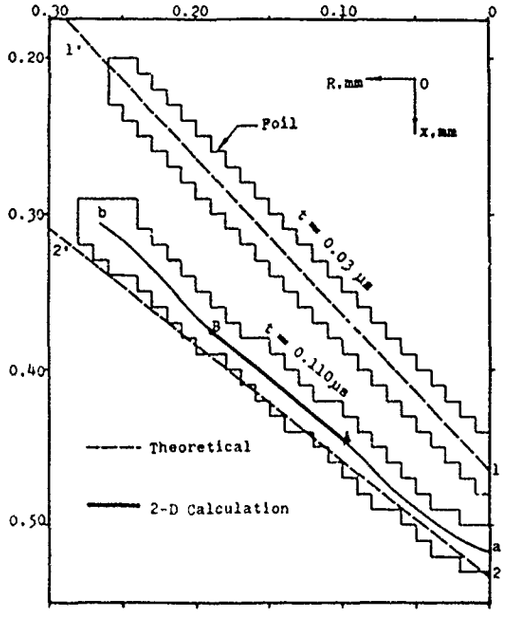

Fig. 4. Result of a 2-D calculation on the movement of a foil segment 11' — Center line of original foil, 22' — Theoretical position at time t, aABb — 2-D calculated position at t

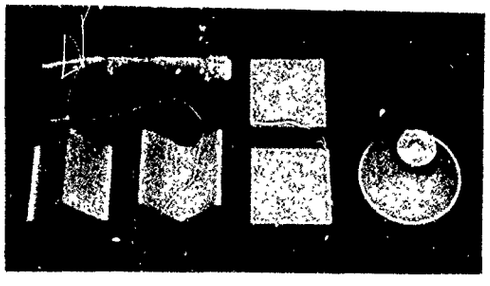

Fig. 5. Photograph of components of the explosive assembly

The radiographic experimental set-up is shown schematically in Fig. 6. The X-ray machine produces a pulsed beam of electrons of 300 KeV. A dimensional small source of X-rays of the order of 5 mm in diameter is used to cast a sharp shadow image of the object containing the embedded foil upon the photographic film. Radiation pulse of 0.03 μs with fluxes as low as 48 mR measured at 380 mm from the source is adequate to produce good contrasting images

with a = 220 mm and b = 1100 mm.

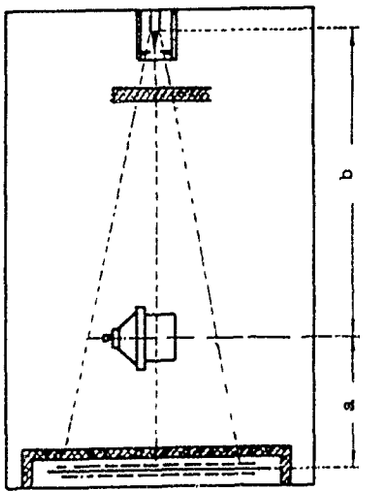

Fig. 6. Radiographic experimental setup

For two explosives, TNT and BH−1, a plastic bonded RDX composition, a total of 39 shots has been tested. Typical photographic records are shown in Fig. 7. Results obtained in these experiments are listed in Table 1.

to the detonation wave front is recorded continuously. In comparison with the method suggested by Rivard et al. (3), the displacement gradient method has the advantage of less disturbance due to the embedded foils and more information obtainable.

Expressions for calculating the detonation pressure, particle velocity and specific volume at the detonation wave front are derived from the equation of continuity and shock wave relations. The model of detonation is not concerned in the derivation.

If the flow behind the detonation is approximately a centered rarefaction wave, the detonation parameters can be obtained directly by fitting Eq. (13) with the experimental data.

There is no obvious lateral movement of the slantly placed metal foil in the flow of detonation products. It is proved by a 2-D calculation that the lateral displacement is insignificant in the life time of the sensing element.

The results published in this paper show that the relative error of the experiment is about 5%.

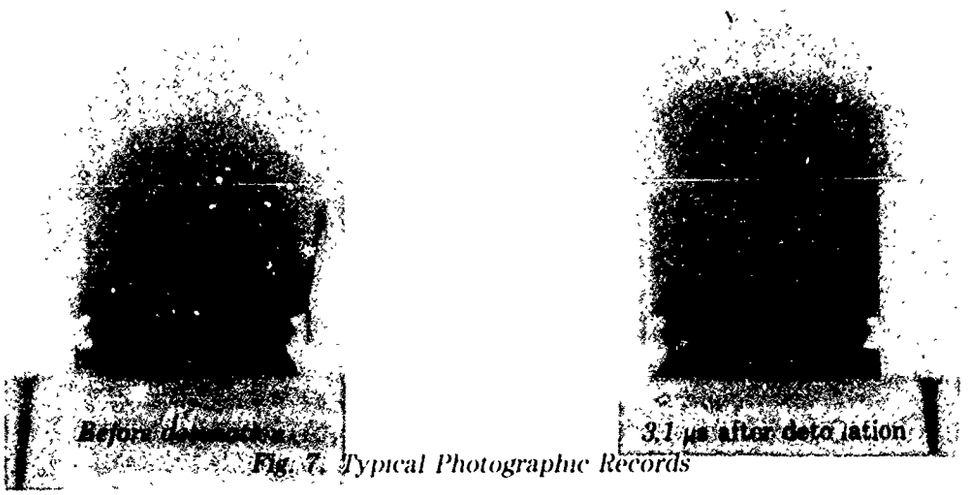

Fig. 7. Typical Photographic Records

CONCLUSIONS

A new technique for measuring the detonation parameters of solid explosive by flash X-ray photography is introduced. The displacement of the copper foil embedded in the explosive slantly

This is not the fault of the method itself. With a better radiographic equipment and a refined technique of the reading of the experimental record, a better precision could be obtained.

TABLE 1
Detonation Parameters Measured by Displacement Gradient Method

Expiosive	Density gm/cm³	Shots	C-J Detonation Parameters			
			Density gm/cm³	Pressure GPa	Particle Velocity mm/μs	Gamma
TNT	1.583	19	2.112±0.039	18.3±1.0	1.702±0.093	2.99±0.22
BH-1	1.673	20	2.236±0.030	28.7±1.2	2.076±0.084	2.97±0.16

ACKNOWLEDGEMENT

We would like to express our appreciation to Li Weixin for his advice in data processing and numerical simulation and to Wang Hongru for his assistance in performing the radiographic experiments.

REFERENCES

1. R. D. Dick, PHERMEX Applications to Study High Pressure Flow and Detonation Waves, LA UR-81-1270, Los Alamos Scientific Laboratory, 1981.
2. W. C. Davis and D. Venable, Pressure Measurements for Composition B-3, Preprints, The Fifth Symposium (International) on Detonation, pp. 9-16, ONR Report ACR-184, 1970.
3. W. C. Rivard, D. Venable, W. Fickett and W. C. Davis, Flash X-ray Observation of Marked Mass Points in Explosive Products, ibid., pp. 1-8, 1970.

Displacement Gradient Method

$$\frac{\rho}{\rho_0} = \left(1 + \frac{dW}{dX}\right)^{-1} = \frac{\operatorname{tg}\theta_0}{\operatorname{tg}\theta}$$

$$\frac{P}{\rho_0 D^2} = \frac{u}{D} = -\frac{dW}{dx} = 1 - \frac{\operatorname{tg}\theta_0}{\operatorname{tg}\theta}$$

$$\gamma = \left(\frac{dW}{dx}\right)^{-1} - 1 = \operatorname{tg}\theta\left(\operatorname{tg}\theta_0 - \operatorname{tg}\theta\right)^{-1}$$

$$r = \frac{X_F}{\operatorname{tg}\theta_0}\left[1 - \left(\frac{\gamma-1}{\gamma}\frac{x}{X_F} + \frac{1}{\gamma}\right)^{\frac{\gamma+1}{\gamma-1}}\right]$$

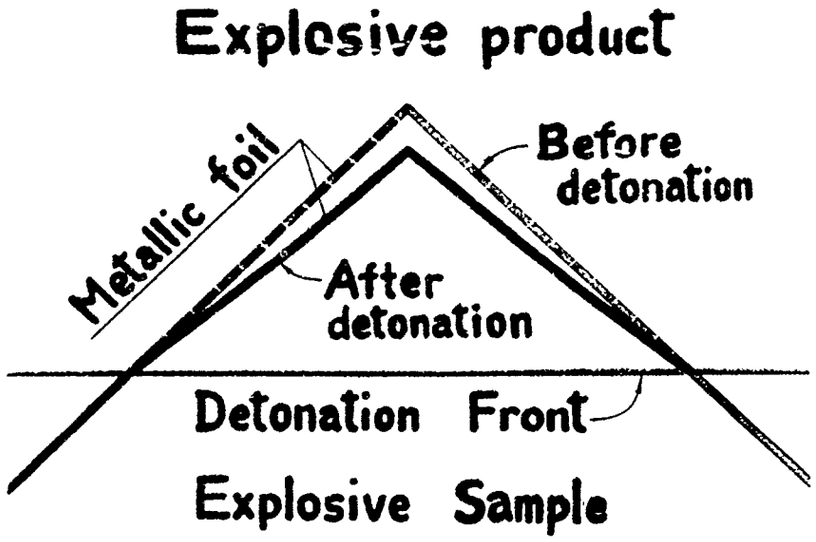

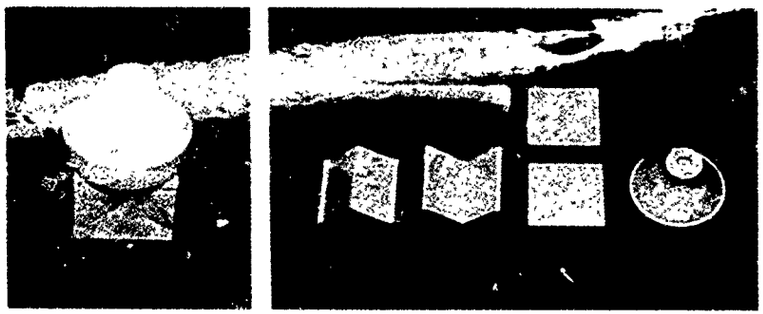

The Explosive Assembly

Typical Photographic Records

Flow diagram of a 1-D detonation

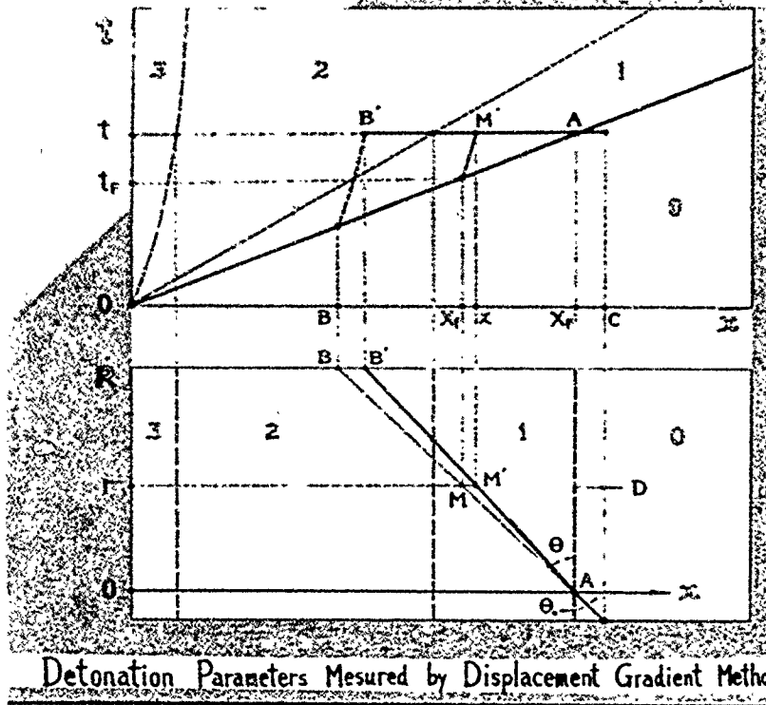

Detonation Parameters Mesured by Displacement Gradient Method

Explosive	Density	Shots	C-J Detonation Parameters		
			Density gm/cm³	Pressure GPa	Gamma γ
TNT	1.583	19	2.112 ± 0.039	18.3 ± 1.0	2.99 ± 0.22
BH-1	1.673	20	2.236 ± 0.030	28.7 ± 1.2	2.97 ± 0.16

Result of a 2-D calculation on the movement of a foil segment

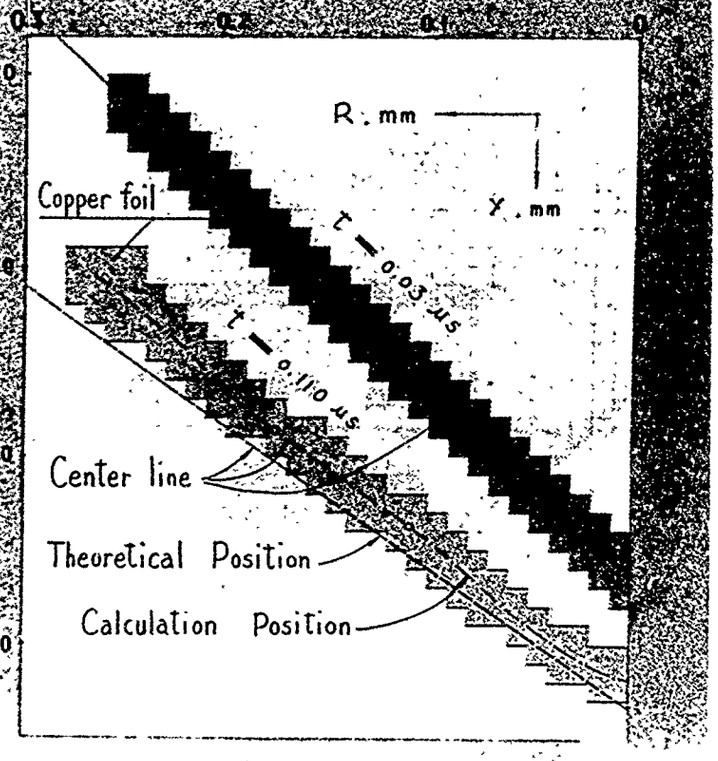

THE STUDY OF BOOSTER MATERIALS WITH ELECTROMAGNETIC PARTICLE VELOCITY GAUGES

Daniel A. Philippart
Royal Armament Research and Development Establishment
Fort Halstead, Sevenoaks, Kent TN14 7BP, England

A particle velocity gauge system incorporating a number of novel ideas has been designed and made and results obtained for the UK booster explosives, Tetryl and Debrix 2. Further a glass mousetrap has beer successfully developed and its performance measured. On the basis of the work done, more refined experiments are planned, in particular the use of perspex mousetraps for studying shock to detonation transitions.

1. INTRODUCTION

An important technique in detonation studies is the electromagnetic particle velocity gauge. A number of ways of instrumenting such a gauge have been reported in the literature (ref 1, 2, 3). Their full adoption at RARDE has been prevented by local experimental constraints. To overcome these difficulties, novel features have been introduced into the present design.

There is considerable interest in the UK in such subjects as the behaviour of improvised explosives and in finding new boosters to replace Tetryl. Present knowledge is based on many years of practical experience. In order to limit the extent of empirical testing, more quantitative descriptions of, for example, shock initiation characteristics are required. The particle velocity gauge is one tool for the production of such descriptions.

In this paper the gauge system which has been developed will be described and preliminary results obtained with Tetryl and Debrix 2 (nominally RDX 95%, Wax 5%), a replacement for Tetryl, will be presented. The design of a glass mousetrap device for the generation of planar shock waves will also be discussed.

To simplify the discussion, the experimental set-up will be shown immediately and then each part examined more closely.

2. EXPERIMENTAL

The gauge assembly is shown in Figure 1 and diagrammatically in Figure 2.

2.1 Principle of operation

As shown in the figures, a loop of foil is embedded in the explosive. The base of the loop of length, l, is the sensing element. When this strip is reached by the detonation front, it is moved forward at the surrounding particle velocity, "cutting" the magnetic flux, so having a voltage induced between its ends. If the magnetic field, motion and strip direction are mutually orthogonal, the induced voltage is given by

$$E = B\ l\ w \qquad (1)$$

where E is the potential, B the flux density, l the strip length and w the strip velocity or particle velocity. Hence the voltage is directly proportional to the forward velocity and the electromagnetic particle velocity gauge is, therefore, an absolute measuring transducer.

2.2 Minimum signal and field requirements

An initial estimate of expected noise levels in

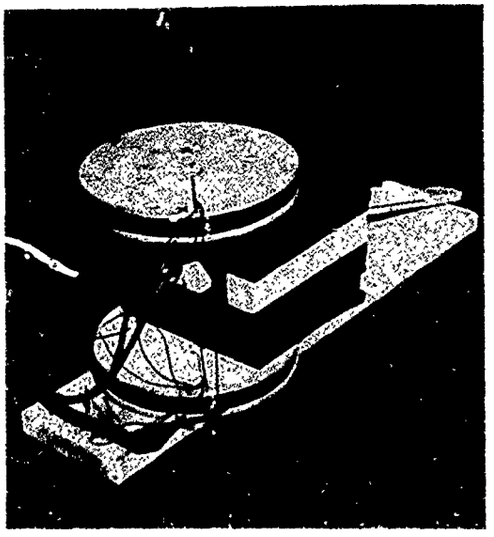

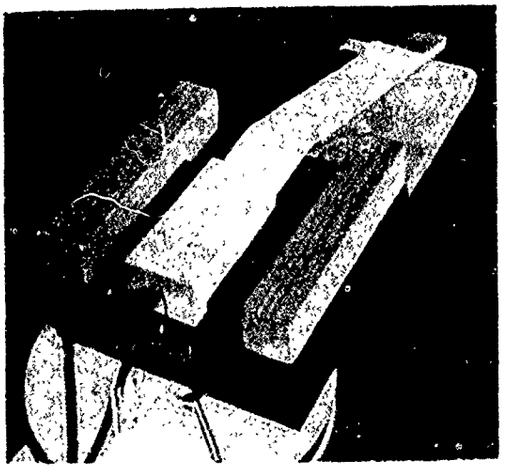

Fig. 1 Particle velocity gauge experiment - full view and with top section removed

the output signal led to a definition of a minimum peak signal of 100mV. The probe length was 6mm and a typical particle velocity is 1000m s $^{-1}$. Substitution in (1) gives a value of B of 20 mT (millitesla).

2.3 Design of explosive charge

When the leads are brought out of the back of the explosive charge, they are not subject to significant transverse flow during the period of experimental interest, so that only the element

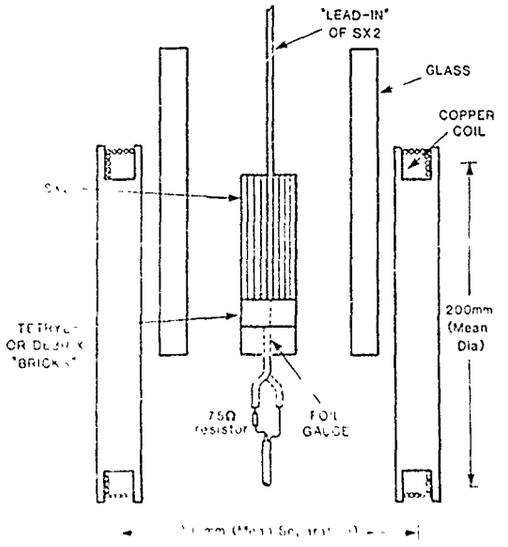

Fig. 2. Schematic side-view of particle velocity gauge experiment

of length l produces a signal. The method devised was to use small "bricks" of explosive, from which the final charge was assembled. They are double-end pressed in a specially designed mould and are of a uniform density, dimensionally accurate and with a good surface finish. Both Tetryl and Debrix 2 pressed very well without chipping at the corners. The bricks are of two sizes, 18 × 18 × 6mm and 18 × 18 × 18mm and are assembled as shown in the earlier figures.

For experimental convenience and because the quantities of booster materials available for evaluation may be limited, it is necessary to minimise the explosive charge weight. At the same time the charge size must be sufficient to allow proper measurements to be made. Two aspects need to be considered.

Firstly, there is the time for the release waves to travel inwards from the sides of the charge. They will travel at approximately 3·4mm μs^{-1} for the explosives being considered. The shortest distance from a side to the gauge is 13mm and hence there is a valid measuring time of about 3μs.

Secondly, there is curvature of the detonation front. This is affected by two factors, namely the critical diameter of the explosive and the geometric resolution. The critical diameters of Tetryl, Debrix and SX2 are small in relation

to the charge width of 36mm, and so do not contribute significantly to the curvature of the detonation front in the central measuring region. A point-initiated explosive charge produces an expanding spherical detonation front. The geometric resolution is the time taken for the curved front to sweep across the active region of the embedded gauge. By simple geometry it can be shown that if the centre of the curved detonation front strikes the gauge midway between the lead wires

$$t \approx \frac{h^2}{8\,Dr} \qquad \text{(for } r>h\text{)} \qquad (2)$$

where t is the time, h the probe length or width, D the detonation velocity and r the radius of curvature. It will be seen from Figures 1 and 2 that there are two radii of curvature, one vertical and one horizontal. The former is formed by the large "block" of SX2 of length 100mm, and the latter by the "lead-in" of SX2, which adds a further 300mm. The probe was 6mm long and 5mm wide. The effect due to the vertical radius is clearly dominant. Using equation (2) for SX2, $D = 8.2\text{mm}\,\mu\text{s}^{-1}$, r = 100mm, h =5mm, gives a value of t of approximately 4ns. This is less than the sampling interval of the transient recorder and may be ignored. The main purpose of the long lead-in of SX2 is to remove the detonator, a source of electrical noise from the measurement area. The flatness of the detonation front has been confirmed by the flash x-ray and is referred to in section 2.6.

The dimensions are evidently generous for materials such as Tetryl and Debrix, but improvised explosives, for example, have much larger critical radii. There is a clear requirement to replace the large block of SX2 with a plane-wave generator. Conical explosive plane-wave generators were not conveniently available at RARDE and instead a glass "mousetrap" plane-wave generator was developed which is described later.

2.1 The probe

The probe is inserted between the bricks of explosive as shown in Figs 1 and 2. It is made of annealed copper foil, 50μm thick and 5mm wide. Annealing of the copper made it easier to shape during assembly. The active probe length is the width of a brick, namely 6mm. The whole structure is bonded together with a very small quantity of Durofix adhesive. While the adhesive is setting, the assembly is positioned in a "V-block" for support.

Some authors have used aluminum instead of copper as the gauge material. In the choice of gauge material there are two main factors to consider, the need for electrical insulation and the thermal life of the gauge. The implications of these factors are discussed below.

The detonation front and to a lesser extent the detonation products are somewhat conductive, and there is a danger that this shunt resistance in conjunction with the series inductance may attenuate the output signal. In the experiments done, this shunt resistance was found to be sufficiently large not to cause problems, as additional insulating of the gauge leads with 50μm thick PTFE film made no difference to the recorded signal. If electrical insulation is required, an advantage of aluminum is that it may be anodised, a process which forms a mechanically tough, electrically insulating oxide film.

The thermal life of a gauge may be approximately estimated by calculating the time required for the middle of the gauge to melt. For a solid with two parallel bounding planes, that is, a slab, if the two faces are suddenly raised to a temperature θ_o and maintained there, the temperature rise from zero, θ, in the middle of the slab is given by (ref 4),

$$\theta = \theta_o \left\{1 - \frac{4}{\pi} \exp\left(-\frac{h^2\pi^2 t}{l^2}\right) + \frac{4}{3\pi} \exp\left(-\frac{9h^2\pi^2 t}{l^2}\right) - \ldots \right\} \qquad (3)$$

where h^2 is the diffusivity, t the time and l the thickness of the slab.

The diffusivities of the copper and aluminum and their melting points are 1.133, 0.826 cm^2s^{-1} and 1083, 660°C respectively. Using equation (3) and assuming an external temperature of 3000°C, the middle layer of both materials will melt after about 1.5μs. Although aluminum has a lower melting point, it has a smaller diffusivity which slows the rate of temperature rise. The gauges may be expected to fail after melting. This may partly explain why the particle velocity records given in Figures 5

and 6 show erratic deviations after 2μs and 1μs duration respectively.

An important point concerning equation (3) is that for a given temperature rise in the centre, the time will vary as the square of the thickness.

The diffusivities of PTFE and alumina are at least an order of magnitude less than those of copper and aluminum. Hence, even a thin layer of either material would extend the thermal life of a gauge. Of the two, alumina will be superior as it melts at 2050°C, as opposed to approximately 400°C at which PTFE decomposes.

A small practical advantage of copper over aluminum is that the electrical connections may be joined by soldering, a much more reliable and simpler procedure than the mechanical joints required with aluminum.

Finally, the thickness of a gauge affects the hydrodynamic rise-time, that is, the time for the shock wave to reverberate in the gauge until the gauge reaches the pressure and particle velocity of the explosive. From ref 3, for a 50μm thick copper gauge, the rise-time is estimated to be approximately 20ns.

2.5 The magnetic field

A uniform magnetic field is desirable if the results are to be easily interpretable. A suitable field might be provided by an iron-cored electromagnet or by Helmholtz coils. The gap, due to the presence of the explosive charge, will contribute greatly to the total magnetic reluctance of the circuit. This factor, and the problem of protection, particularly when dealing with military explosives, favoured expendable Helmholtz coils.

For a pair of coils the condition for the highest field uniformity in the central region is that their separation should equal their radius. This configuration, first proposed by Helmholtz, clearly raises a practical problem. The products from a detonating explosive column move sideways at a velocity similar to the detonation velocity, at least initially. The outermost part of the coil will always be damaged before the measurement can be made, unless some further steps are taken.

The proposed solution was to use a coil separation of twice the coil radius, and to use two glass plates to further delay the arrival of the shock wave at the coils. By minimising the needed increased separation of the coils, the flux-density in the measurement region is not reduced excessively, nor is its uniformity unduly compromised.

To simplify the experiment a continuous DC supply from lead-acid accumulators was chosen to drive the coils, rather than a pulsed system. The latter while allowing coils with fewer turns of small gauge wire, and so less costly, poses real problems of synchronization.

On this basis, a pair of coils was designed with a mean diameter of 200mm, each of 225 turns of 18 SWG enamelled copper wire, and which with a separation of 200mm and carrying 20A, produced a flux-density at the centre-point of 20mT. In constructing the coils, for greatest economy in wire, the current density must be as high as possible. The current density is limited either by the required voltage exceeding that available from the power supply or by the temperature rise occurring in the coils in the duration of an experiment.

The flux-density uniformity over the working volume (rather than a point) was then checked by calculation and measurement. The two-dimensional flux-density in the direction of the z-axis (Bz) for a circular loop at unit current is given by ref 5:

$$B_z = \frac{\mu_0}{2\pi}\left[(L+a)^2 + z^2\right]^{-1/2} \times \left[K(k) + \frac{a^2-L^2-Z^2}{(a-L)^2+Z^2}\,E(k)\right] \qquad (4)$$

where K(k) and E(k) are elliptic integrals of the first and second kinds respectively. Modulus k is the dimensionless ratio.

$$k^2 = \frac{4aL}{(L+a)^2 + Z^2} \qquad (5)$$

where L and Z are the cylindrical coordinates, a the radius of the current loop, μ_0 the permeability of free space. Equations (4) and (5) cannot be simplified except trivially and the only approach is to plot a matrix of values with a desktop computer. The results were in agreement with measurements made on a pair of coils with a Hall effect detector (RFL Teslameter 904T). The flux

density in the central measurement region varies very slightly with position. Errors in the flux density due to inaccurate positioning of the coils and probe, and the smaller effect due to the actual movement of the probe during an experiment, were estimated to be no greater than ±2%.

2.6 The role of the glass plates

The products from a detonating explosive column move sideways at a velocity similar to the detonation velocity, or at least initially. As may be appreciated from the geometry, increasing the separation of the coils to one diameter, as opposed to one radius will not completely overcome the difficulty of damage to the coils when measurements are being made in the central region between them. The explosive charge after all has a finite width, and additionally the coils will encroach slightly as their spacing is measured as a mean separation. Rather than trying to separate the coils even further, a more efficient solution was to insert two glass plates between the explosive and the coils so that the mass of glass delayed the expansion of the detonation products. For this role an electrical non-conductor is essential—a moving conductor would contain induced currents whose magnetic fields would both reduce and distort the field produced by the coils.

To calculate the required thickness of glass use was made of ref 6.

For a layer of explosive in contact with a plate, if

$$\alpha = \frac{\text{mass unit length of HE}}{\text{mass unit length of plate}} \qquad (6)$$

the normal component of the terminal plate velocity Vn is given by

$$Vn = 4.46 \frac{\alpha}{(\alpha + 2)} \qquad (7)$$

For tetryl (density 1.6Mg m^{-3} and thickness 36mm) and glass (density 2.5Mg m^{-3} and thickness 18mm) Vn is found to be 1.75mm μs^{-1}. The available air-gap between the tetryl and glass plate, and glass plate and coil, is 48mm. Hence, approximately 27μs will elapse before the coil is struck by the glass plate. If the glass were not present, the detonation products would strike the coils in about 8μs.

To appreciate the role of the glass plate, the time taken for the detonation front to travel from the position corresponding to the radius of the coils to the centre of the measurement region, some 100mm, is approximately 13μs, assuming a detonation velocity of 7.3mm μs^{-1} for Tetryl. In fact, the design allows the detonation front to reach the other side of the assembly before the coils are subject to damage—a generous margin against error.

Fig. 3. Flash radiography taken through side of assembly, showing relative movement of detonation front and glass plates. The inner faces of the coils are represented by brass discs.

For a given separation between explosive column and coils, it is possible to optimise the thickness of glass used, and also perhaps to use a lower density material. An important feature is that the glass is separated from the Tetryl column. This reduces the possibility of any scabbing of the glass plate, and also means that the tangential terminal plate velocity is less than that given by equation (7), giving a further margin of safety.

To test the design, an approximate half-scale assembly was built, but the coils were replaced by two brass discs and SX2 was used for the whole explosive column. A flash radiograph was taken (Fig. 3) after the detonation front had traversed most of the explosive column. To provide an accurate start time an exploding bridgewire detonator was used and the long tail of SX2 omitted. The result confirms the earlier approach and additionally provides a check on the planarity of the detonation front.

2.7 Method of recording signal

This is summarised in Figure 4. The use of a

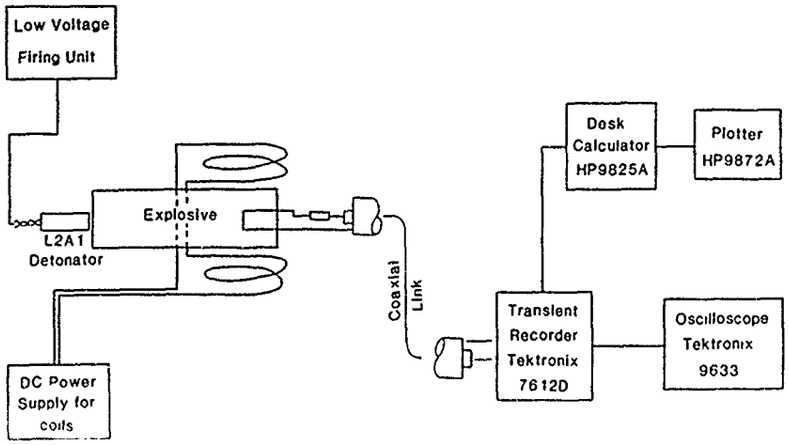

Fig. 4. Schematic of power supplies, and method of recording signals

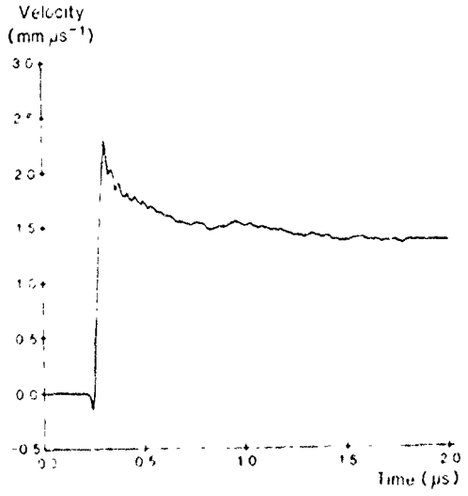

Fig 5 Particle velocity gauge record for Tetryl

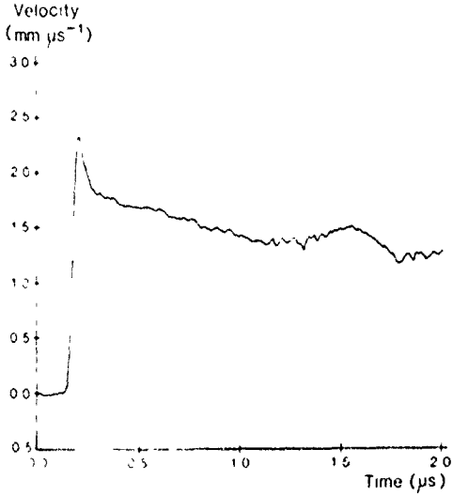

Fig 6 Particle velocity gauge record for Debrix 2

self-triggering transient digitiser neatly avoids the problem of synchronisation and the related need to use, for accurate timing, fast-acting exploding bridgewire detonators. These detonators are driven by high voltage pulses with sub-micro-second rise-times and so produce considerable electrical interference even with careful screening Instead, a low voltage, slow-acting fusehead type detonator is used. Additionally, the detonator is separated by the lead-in of SX2.

From the literature, the anticipated fastest rise-times which would be met are approximately 25ns. The instrument has a minimum sampling interval of 5ns at 6 bit resolution, which is adequate for such signals. However, allowance must be made for the inherent hydrodynamic rise time of the gauge. Two independent channels are available.

The oscilloscope provides an immediate visual presentation of the status and output of the transient recorder. To facilitate the setting of

trigger levels, etc., a hand-held, single-shot pulse generator was built, with an output similar to that expected from a gauge. The firing-cell and instrument room are linked by a 30m high-quality coaxial cable. To match the impedance of the cable, a 75Ω resistor is put in series with the probe.

3 RESULTS

Using equation (1) the particle velocity records can be derived from the voltage-time output. Results for Tetryl and Debrix 2 are shown in Figs 5 and 6 respectively. The C-J (Chapman-Jouguet) particle velocity is usually taken as the value at the beginning of the Taylor expansion as obtained by graphical extrapolation. From the record for tetryl and ignoring the slight "ringing" a value of 1.85mm μs^{-1} is obtained.

The recorded voltages are accurate to ± 2%. The flux-density depends on the current in the coils and the uniformity of the field in which the gauge operates. The former is about ± 1% and the latter will be no greater than ± 2%. The width of the pellet determines the gauge length and is better than ± 1%. From equation (1)

$$\frac{\delta_w}{w} = \frac{\delta_E}{E} - \frac{\delta_B}{B} - \frac{\delta_l}{l}$$

Hence it can be estimated that the total error in the particle velocity is no greater than ± 6%.

From the particle velocity the detonation pressure, P_{CJ}, can be calculated using the relation

$$P = \varrho c w \qquad (8)$$

where ϱ is the density, c the shock velocity and w the particle velocity For the Tetryl bricks, ϱ = 1.57Mg. m^{-3}, and using ref 7, c = 7.35mm us This gives a detonation pressure, using equation (8) of 21.3GPa, which is in good agreement with the value (ref 7) of 22.64GPa for a density of 1.614Mg. m^{-3}.

The Debrix 2 was pressed to a density of 1.65Mg. m^{-3}. The particle velocity as determined by extrapolating back the Taylor release wave is 1.8mm μs^{-1}. From ref 7, the particle velocity in detonating RDX is 2.21mm μs^{-1} at a density of 1.77Mg m^{-3}, suggesting the value obtained in this work is a little low The discrepancy may lie in the way the CJ point is determined and further firings are planned to investigate this aspect of the problem.

4 GLASS "MOUSETRAP"

4.1 Introduction

As mentioned earlier, conical explosive plane-wave generators were not conveniently available at RARDE and instead a glass mousetrap plane-wave generator was developed. Such a device has the additional advantage that by altering the ratio of explosive mass per unit length to driver plate mass per unit length, shock pulses of adjustable amplitude and duration are produced, without needing to use attenuators. Glass was chosen because

a) It is a non-conductor.

b) It will predictably deform at high pressures, as is evidenced by its ability to jet when used as a conical shaped-charge liner material.

c) Experience of its behaviour has been obtained and is described in section 2.6.

4.2 Design of mousetrap

It will be remembered that from equations (6) and (7), the tangential plate velocity, V_n, can be obtained. From simple geometry, it can be shown that for zero angle of tilt of the shock front in the receptor explosive, the included angle, θ, of the mousetrap is given by

$$\theta = \tan^{-1}\left(\frac{V_n}{V_D}\right) \qquad (9)$$

where V_D is the detonation velocity in the driver plate explosive.

A prototype mousetrap was built using float glass (thickness 1.98mm, ϱ 2.47 Mg.m^{-3}) and SX2 (thickness 6.3mm, ϱ 1.6 Mg.m^{-3}, V_D 8.2mm μs^{-1}). Using equations (6), (7) and (9), α, V_n and θ were found to be 2.08, 2.27mm μs^{-1} and 15.5° respectively. A side-on view is shown in Fig 7. The angle was set by the triangular end-pieces, and was accurate to ± 0.1°.

A little care is needed in the tolerancing of θ. It can be shown that the angle of tilt, γ, is given by

$$\tan\gamma = \frac{V_R}{V_D}\left[\cos\theta - \left(\frac{V_D}{V_n}\right)\sin\theta\right] \qquad (10)$$

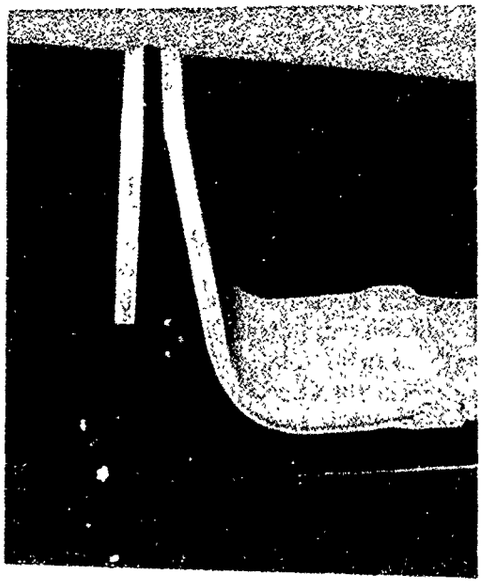

Fig. 7 Side-on view of glass mousetrap with a layer of SX2 as the receptor explosive.

where V_R is the shock velocity in the receptor explosive. For zero angle of tilt equation (10) reduces to (9). Differentiating (10) with respect to θ, and considering small values of γ,

$$\frac{\delta\gamma}{\delta\theta} = -\frac{V_R}{V_D}\left[\sin\theta + \left(\frac{V_D}{V_n}\right)\cos\theta\right]$$

In the present experiment the receptor explosive is SX2. V_R is approximately equal to V_D and substituting the values already given, yields

$$\delta\gamma = -4.08\ \delta\theta \qquad (11)$$

Hence, errors in θ are multiplied by a factor of 4 to give the error in γ, largely because V_n is less than V_D.

From the angle of tilt, the geometric resolution t, may be calculated. The geometric resolution is the time taken for the shock front to sweep across the active region of the embedded gauge, and is given by

$$t = \frac{h}{V_R}\tan\gamma \qquad (12)$$

where h is the probe height in this case. Differentiating with respect to γ, and considering small values of γ,

$$\delta t = \frac{h}{V_R}\delta\gamma \qquad (13)$$

Hence, for $\delta\theta = \pm 0.1°$, from (11), $\delta\gamma = \pm 0.4°$. For h = 5mm, and V_R = 8.2mm μs^{-1}, using (13), δt is approximately $\pm$ 5ns, which is the sample interval of the transient digitiser.

For clarity of explanation, and also because it can be easily measured the angle of tilt, γ, is used in the derivations. However, it does not fully define the behaviour of the mousetrap. Rather this is given by the geometric resolution for the following reason. The ratio $\tan\gamma/V_R$ is common to equations (10) and (12) which give the relation,

$$t = \frac{h}{V_D}\left[\cos\theta - \left(\frac{V_D}{V_n}\right)\sin\theta\right]$$

That is to say, the geometric resolution at the "output" of the mousetrap is determined solely by the mousetrap parameters and probe height, and is independent of the receptor explosive.

Apart from errors in θ, the other most likely source of variation lies in the bulk density and thickness of the driver explosive, SX2, as may occur between batches. The effect of these variables on γ, may be derived from equations (6), (7) and (10) to give,

$$\delta\gamma = \frac{2V_R\sin\theta}{V_n(\alpha+2)}\left\{\frac{\delta\varrho_D}{\varrho_D} + \frac{\delta t_D}{t_D} - \frac{\delta\varrho_G}{\varrho_G} - \frac{\delta t_G}{t_G}\right\}$$

where ϱ_D and t_D, ϱ_G and t_G, are the densities and thicknesses of explosive driver and glass respectively. Using the numerical values already given, it is found,

$$\delta\gamma \approx 0.5\left\{\frac{\delta\varrho_D}{\varrho_D} + \frac{\delta t_D}{t_D} - \frac{\delta\varrho_G}{\varrho_G} - \frac{\delta t_G}{t_G}\right\}$$

If $\delta\varrho_D/\varrho_D$ and $\delta t_D/t_D$ each vary from batch to batch by $\pm$ 5%, then $\delta\gamma = \pm 2.8°$. Substituting this in equation (13) gives $\delta t = \pm$ 30ns. This is excessive and to overcome the difficulty, in the experiments a batch of SX2 was set aside to be used only for mousetraps. Alternatively, an explosive with a more closely defined ϱ_D and t_D may be used and/or larger values of α.

Similarly, all the glass in the mousetraps was taken from one sheet.

To allow for edge effects, the face dimensions (80mm x 55mm) were larger than those of the rectangular receptor charges (54mm x 36mm). The whole glass assembly was bonded together with optical cement.

The function of the mousetrap was checked with a Beckman and Whitley Model 189 framing camera. The assembly was viewed side-on, with an angled mirror behind to show the output face of SX2. The results are shown in Fig 8. The mousetrap has closed correctly and the shock pressure was sufficient to initiate the SX2. It will be seen that the top is slightly ahead of the base and hence θ is slightly too large. From an enlarged photograph, the angle of tilt, γ, was measured to be 5.5°. Using equations (10) and (9), corrected values of V_n and θ were obtained, 2.075mm μs^{-1} and 14.2 respectively. More simply equation (11) could be used.

A mousetrap of angle 14.2° was then examined with a Cordin Model 132A streak camera. Along the horizontal direction, discounting edge effects, the detonation front showed the curvature of a circle whose centre was the point of initiation, as might be expected. In the vertical direction,

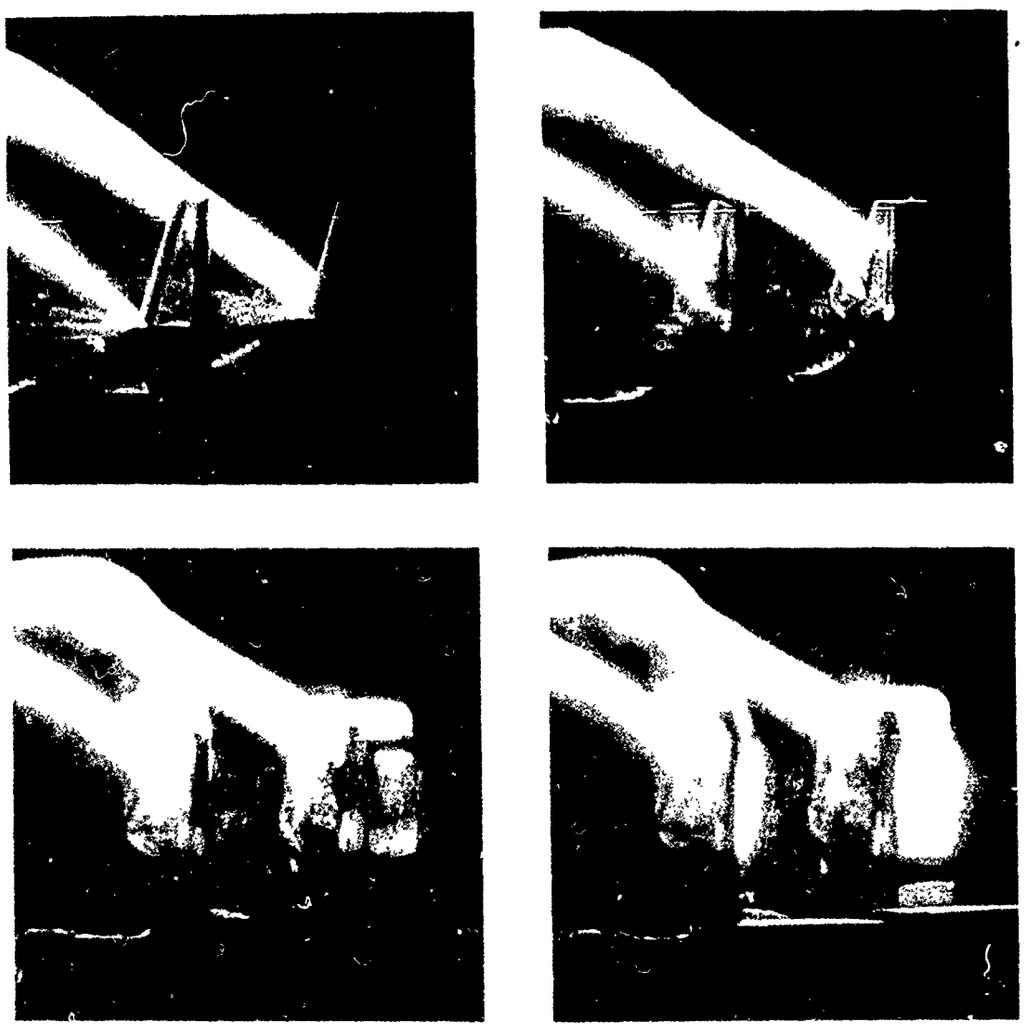

(3) (4)

Fig 8. Framing camera sequence. Mousetrap is viewed side-on. The right-hand image is formed by an angled mirror placed behind the mousetrap and shows the output face. Relative times are 0, 5, 8 and 9 μs.

however, the flatness of the shock front is critically affected by the uniform closing of the mousetrap.

The streak result is shown in Fig 9. The planarity is good except for the lowest 1/5 of the output from the mousetrap, which is slightly delayed. From the result, the angle of tilt, γ, of the planar part of the output, is found to be 0.9° - note, it is not to be confused with the angle of the front of the streak record.

From equation (12), the geometric resolution was found to be 10ns, which is acceptable.

4.3 Measurement of the shock pressure

For application to the study of shock to detonation transitions an important parameter in the present design is the shock pulse height and duration. This was obtained using the assembly shown in Fig 10. Float glass bonded together with optical cement was used throughout. Two probes were used, one set-back by a 1.3mm thick glass spacer. The particle velocity histories of both probes are shown in Fig 11. The first probe (solid line) shows the output from the mousetrap with a maximum particle velocity of 1.02mm μs^{-1}, which is half the value of V_n as expected. The dashed line is the output from the second probe slightly attenuated relative to that from the first probe, and delayed by 0.28μs. As the glass spacer thickness is known, this gives a shock velocity of 4.68mm μs^{-1}. The density of the glass is 2.47Mg m^{-3} and using equation (8),

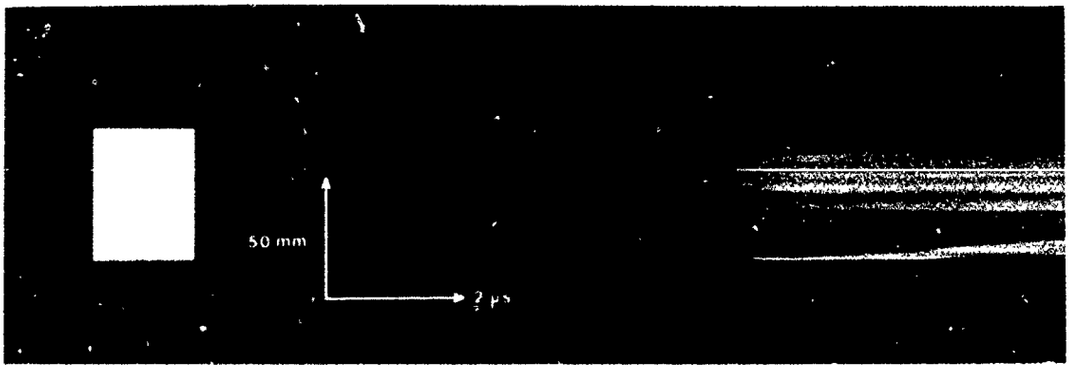

Fig. 9. Streak record of the centre vertical region of the mousetrap shown in Fig. 7

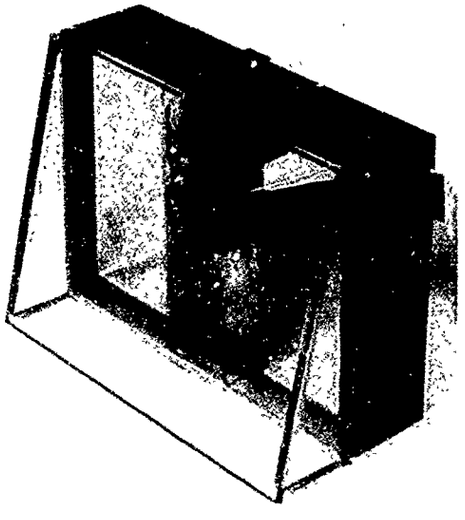

Fig 10. Assembly used for measuring shock pressure and duration produced by a glass mousetrap

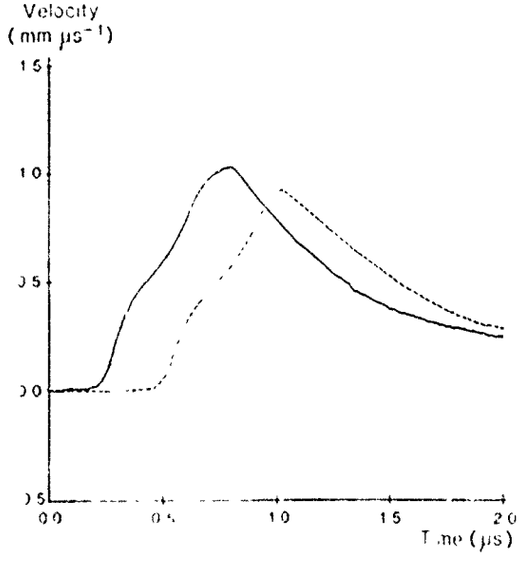

Fig 11 Particle velocity records produced from the experiment illustrated in Fig. 10

the maximum shock pressure is found to be 11.8GPa. This is in agreement with pressure versus particle velocity data given in ref 8.

An unexpected feature was the initial curvature of the particle velocity records. This can be attributed to an elastic precursor (ref 8).

It is partly due to the particularly high yield strength of glass, and is observed for pressures less than 22GPa. Above 22GPa the shock front only is observable. Aluminium and perspex also exhibit this behaviour, but at very much lower shock pressures, as they have much lower yield strengths.

4.1 Further work

For shock to detonation studies, shock pressures of 5-10GPa are required. From the experience obtained with glass mousetraps, such pressures can more easily be obtained using the less dense material, perspex. An additional advantage of perspex would be the absence of an elastic precursor. Such a device is being currently manufactured, and will be used to examine a range of explosives and boosters.

5 ACKNOWLEDGEMENTS

The author would like to thank Michael Jones for his assistance in executing all the experiments described.

REFERENCES

1. S. J. Jacobs, D. J. Edwards, "Experimental Study of Electromagnetic Velocity Gauge Technique," Proceedings of the Fifth Symposium (International) on Detonation (1970) p. 413-424.

2. M. Cowperthwaite, J. T. Rosenberg, "Lagrange Gauge Studies in Ideal and Non-Ideal Explosives," Proceedings of the Seventh Symposium (International) on Detonation (1981) p. 1072-1083.

3. B. Hayes, "Particle-Velocity Gauge System for Nanosecond Sampling Rate of Shock and Detonation Waves". Review of Scientific Instruments Vol. 52, No. 4, April 1981, p. 594-603.

4. L. Ingersoll, O. Zobel, A. Ingersoll, Heat Conduction, McGraw-Hill (1948) p. 125.

5. E. Weber, Electromagnetic Fields (Wiley, New York) Vol. 1, Chp. 4.

6. N. E. Hoskin, J. W. Allan, W. A. Bailey, J. W. Lethaby, I. C. Skidmore, "The Motion of Plates and Cylinders Driven by Detonation Waves at Tangential Incidence," Proceedings of the Fourth Symposium (International) on Detonation, p. 14-26.

7. T. R. Gibbs, A. Popolato, LASL-Explosive Property Data - University of California Press (1980).

8. P. J. Fuller, J. H. Price, AWRE Foulness, unpublished MOD Report.

ROYAL ARMAMENT RESEARCH AND DEVELOPMENT
ESTABLISHMENT, FORT HALSTEAD, UNITED KINGDOM

THE STUDY OF BOOSTER MATERIALS WITH ELECTROMAGNETIC PARTICLE VELOCITY GAUGES

(DANIEL A. PHILIPPART)

An electromagnetic particle velocity gauge system incorporating a number of novel ideas has been designed and used. Further, a glass mousetrap has been successfully developed and its performance measured.

PARTICLE VELOCITY GAUGE SYSTEM

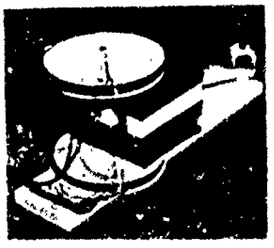

FULL VIEW

TOP SECTION REMOVED

SCHEMATIC OF POWER SUPPLIES, AND METHOD OF RECORDING SIGNAL

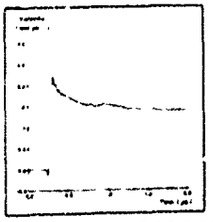

PARTICLE VELOCITY GAUGE RECORD FOR TETRYL

GLASS MOUSETRAP

A mousetrap is a convenient method for generating plane shock fronts of adjustable amplitude and duration. This makes the device valuable in shock to detonation studies. Glass will not interfere with the magnetic field of the particle velocity gauges.

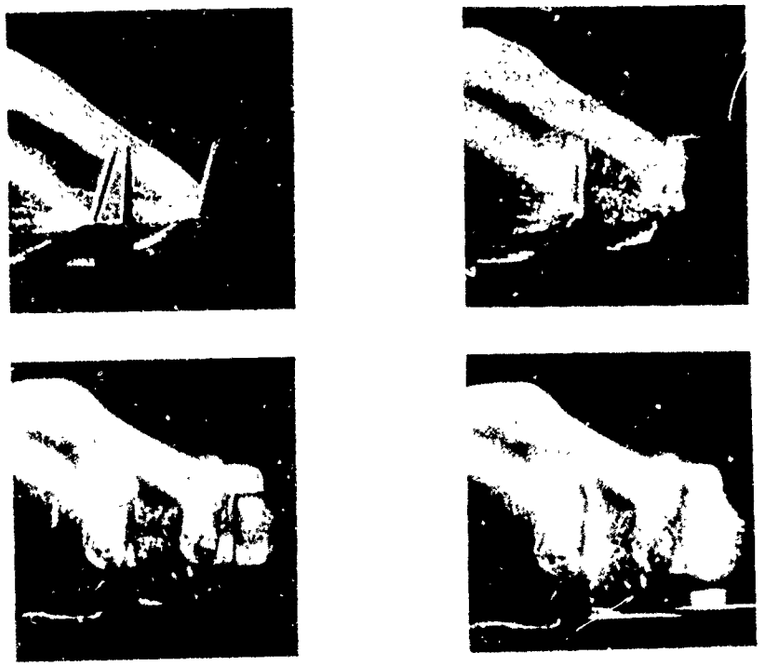

FRAMING CAMERA SEQUENCE OF CLOSING MOUSETRAP RELATIVE TIMES ARE 0, 5, 8 and 9 μs

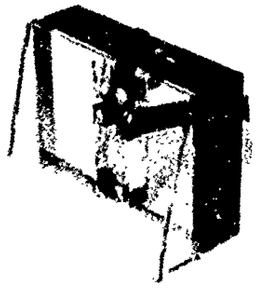

ASSEMBLY USED FOR MEASURING SHOCK PRESSURE AND DURATION

PARTICLE VELOCITY RECORDS

THE DESIGN ILLUSTRATED GIVES A MAXIMUM SHOCK PRESSURE OF 11 8GPa

APPLICATIONS OF FIBER OPTICS TO DETONATION EVENTS

P. Lu, E. Naiman and W.E. Voreck
U.S. Army Armament Research and Development Center
Dover, New Jersey

The fiber optics technique and choice of optical fiber are discussed. The application of the fiber optics technique in characterizing the detonation wave tilt in a cased shaped charge is also discussed. The wave tilt data is consistent with the caseless charge data taken via inverse multi-streak technique. Detonation velocity data of a multi-track plate recorded both by ionization probes and fiber optics are described.

INTRODUCTION

One of the m· ·ily measured properties in a detonation e .s the time of arrival of the shock detonation front. Typically, self-shorted electrical probes or ionization probes, incorporated with a fast raster oscilloscope or digitizer and storage memory are used in this kind of measurement. There are several shortcomings of the ionization probe technique. If more than one signal arrives at the same time, a separate recording channel must be provided for each When large numbers of signals are involved, this becomes very cumbersome and expensive. Complicated calibration and timing techniques are needed to assure accuracy and reliability Even when signals arrive sequentially, confusion can result from improper matching of signals to pins, that is, if signal arrives at a different time than anticipated, or if multiple closures occur due to motion of parts. If large, rugged pins are used, then accuracy of location is poor, on the other hand, small pins are delicate and easily damaged Conductive explosives require special insulated contacting switches, which introduce a delay in closure times Electronic circuits require low inductance, fast rise times, proper termination, and short pulses without ringing Finally, measurements cannot be made on experiments involving electromagnetic pulses

During the past ten years, there is an increasing usage of fiber optics, in place of ionization probes in measuring the time of arrival of shock/detonation front. Williams (1) applied the fiber optics to the measurements of the onset of detonation in an explosive, the velocity of a projectile and the shock front planarity. Held and Nikovitsch (2) used fiber optics to provide the precise time correlation information in their high resolution multi-streak technique. In all these works, the fiber optics were used without any modifications. Shaw et al. (3) developed the xenon gas-filled fiber optics probes to increase the light output.

We have used fiber optics quite routinely in our tests. Since most of our measurements involve multi-points, we found fiber optics greatly simplify the tracking and identifying each point. A few of the applications will be discussed here.

EXPERIMENTS

We chose to use opto-electronic grade single acrylic monofilament optical fiber manufactured by DuPont Company in all of our tests. This fiber optic is chosen — mainly for its relative low attenuation factor, about 700 db/km at 510 nanometer wavelength. Since it is desired to have a well defined light image of the fiber to minimize the onset reading error in data reduction, monofilament-type was preferred The diameter of the acrylic core is 1 millimeter, and the outside diameter of the black plastic jacket is 2.2 millimeters. We found that the protective jacket is a very useful feature, it protects against stray light and rough handling and hostile environments in a test range

We did not choose high light transmission (attenuation factor 40 db/Km) glass/quartz fiber optics for two reasons, the cost and the difficulty in preparing the ends. The plastic fiber can be cut easily with a heated knife blade which produces a reasonably smooth, flat surface, so there is no need to polish the cut end. This greatly simplifies and reduces the time and cost in the preparation of large quantity of fiber optics which must be replaced or the ends refinished after each test. The preparation of this kind of fiber is so simple that an unskilled worker can make smooth cuts after only a few trials. The other reason is that the cost of acrylic fiber is only 10% of the comparative quartz or glass fiber.

Since some of our tests were conducted in an open test range and require fairly long (16 meter) fiber which is much longer than the length (2-3 meters) used by earlier investigators, we performed tests to determine the maximum length of fibers which can produce good light transmission records. Held and Nikowitsch (4) have shown that luminosity of the shock front at the surface of a detonating explosive can be increased considerably by creating an air gap. After a few trials, we found that an air gap of 0.5 millimeters produced the best result. The typical installation of the fiber optics is shown in Fig. 1. The spatial resolution of the 1 millimeter optical fiber can be further improved by using an assembly arrangement shown in Fig. 2. However, the alternate method tends to be more susceptible to stray light problems. Using these arrangements, we have obtained good records transmitted through 25 meters long optic fibers without difficulty. The long fiber optics provide an advantage in testing relative large cased explosive devices which always pose problems in containing the fragmentation from damaging measuring instruments.

The camera end of the optical fibers were arranged in a straight array in a metal fixture as shown in Fig. 3 and viewed with a high speed streak camera. No slit was used in the camera. The writing speed of the image on the film typically was about 10 millimeters per microsecond to provide better time resolution. The photographic record is read off from a film reader with an accuracy of 2 nanoseconds. A typical photographic record is shown in Fig. 4. In spite of the presence of some precursor light

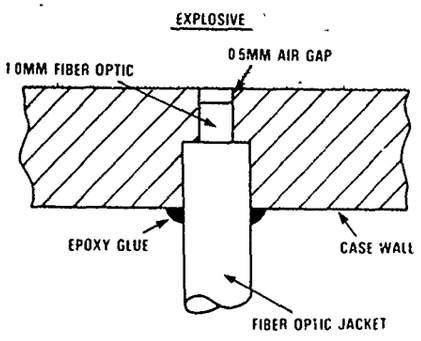

Fig. 1 Set up of fiber optics in a cased device

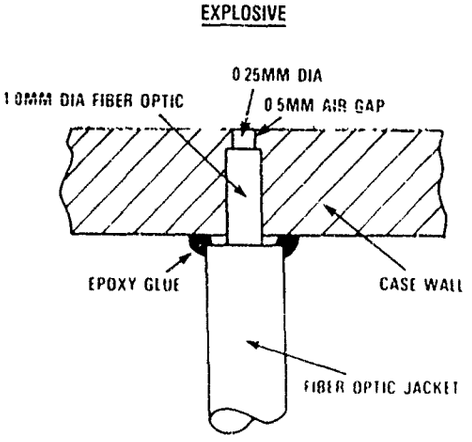

Fig 2. Alternate set up of fiber optics in a cased device

signals, the well-defined round leading edge of the main light signals is evident as shown in Fig. 4

SHAPED CHARGE EXPERIMENTS

It is generally desired to have a detonation wave, circumferentially symmetrical with respect to the axis in a shaped charge warhead. It is known that an unsymmetrical or tilted detonation wave, will generate a curved jet and affect penetration performance. Many investigators have looked into the effects of asymmetry in the detonation. Deas (4) applied ionization probes technique to a cased shaped charge device and found a correlation between the asymmetry of the detonation front and the direction of skew of the jet

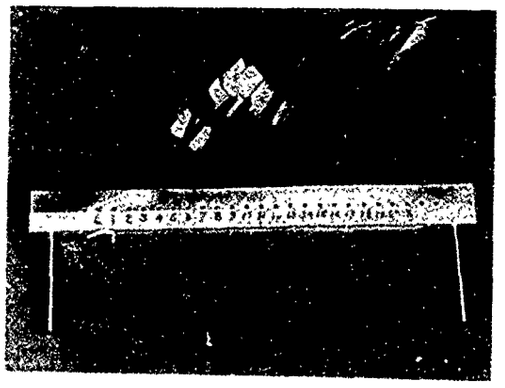

Fig. 3. Fiber optics arrangement facing to the recording streak camera

Fig. 4 Fiber optics record

More recently, Held and Nikowitsch (5) have developed a precision diagnostic technique, inverse-multi-streak photography to determine the detonation wave characteristics, such as the tilt or velocity in a caseless shaped charge device However, this technique requires that the surface of the explosive be exposed and be "seen" by a camera. As a result, (1) only caseless devices can be tested, and (2) the test device must be visible by the camera either in the line-of-sight or indirectly via mirrors. To avoid these difficulties, we have applied the fiber optic technique to diagnosing the detonation wave characteristics and performance of a cased shaped charge device (6). The test fixture and the fiber optics setup are shown in Fig. 5. There are eight measuring planes along the length of the device, and each plane is determined by three fiber optic points. Holes were drilled through the metal body to expose the explosive and to accommodate the fiber optics. The exact location of each hole was measured to facilitate accurate data reduction. The three external columns were used to support the soft fiber optics. We initiated the device both centrally as well as off center. Fig. 6 shows a test record from a shot initiated 3.1 millimeters off-center. The off-center initiation induces a tilted detonation wave front in the explosive charge, as portrayed by the various times of arrival of the light signals recorded at each measuring plane. Since the off-center initiation is directly opposite from Column B of fiber optics and was at an equal distance between the other two columns (A and C) of fiber optics, a detonation wave which tilted away from Column B, but more or less symmetrical to the bisector axis between Column A and C would be formed. Thus, at each measuring plane, the light signals from Column A and C are at the same time ordinate, while those from Column B are lagging behind.

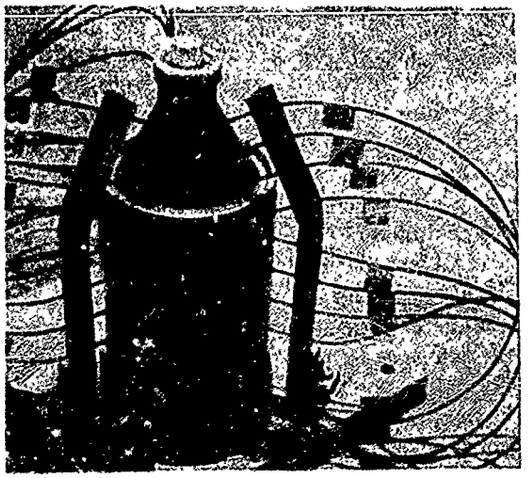

Fig.5. Fiber optics assembly and shaped charge test fixture

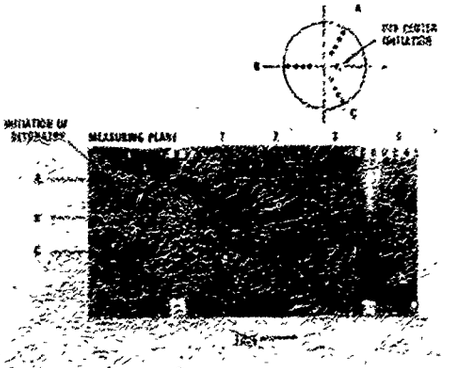

Fig. 6. Fiber optics multi-profile photographic record

With time of arrival information of the three light signal and their respective geometrical locations, it is possible to construct a wavefront plane to determine its perpendicularity with respect to the rotational axis of the charge. Certainly, the true shape of the whole detonation front is complicated and not in a flat plane.

Fig. 7 shows that a typical plot of the magnitude and the orientation of the detonation wave tilt at each measuring plane in a centrally initiated charge. The detonation tilt is defined as the angle between the normal of the detonation wave plane which is defined by the three light signals and the rotational axis of the charge. The angle of orientation is arbitrary and is used for reference only. It is interesting to note that the obliquity of the detonation wave is changing as the wave propagates from the top end to the bottom end of the device. It is not known the exact causes of this observation. However, certain local conditions, such as the explosive grain size, density, the confinement and the abrupt discontinuity of the geometrical configuration - may influence the local detonation velocities which in turn affect the local shaping of the detonation front.

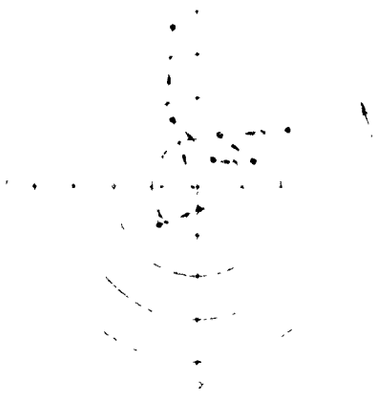

Fig. 7 Wave tilt orientation history (central initiation)

Fig. 8 shows the effect of an off-center initiation on the detonation wave front tilt in the charge. It is interesting to note that the off-center initiation effect dominates the detonation tilt characteristics in the whole charge. The magnitude of tilt is much larger and the orientation of the wave tilt is also confined within a very narrow angle. Although magnitude of detonation tilt decreases as the detonation propagates toward the bottom of the charge, it never reaches the level at which a central-initiation can be achieved.

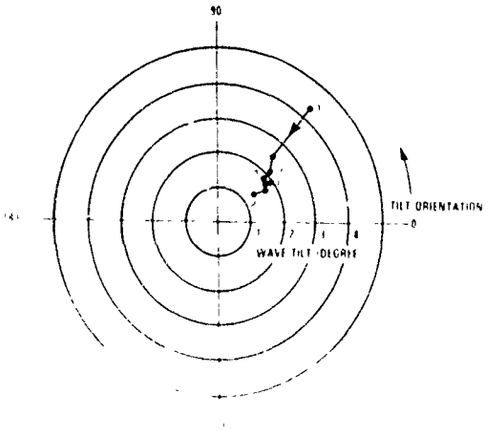

Fig. 8 Wave tilt orientation history (3.1 mm off center initiation)

For comparison purposes, we have measured the detonation wave characteristics near the tapered portion of the charge via inverse multi-streak techniques. The metal body of the device was removed so that a transparent mask could be used. Fig. 9 shows the photographic record of the detonation profile. The device was centrally initiated for this test. The average value of the detonation tilt at the measuring plane 1 (Fig. 5) of the four tests is 0.6°, while the average value of nine fiber optics measurement at corresponding location is 0.32°. The difference could be due to the change of confinement bare charge vs. cased charge, in the two sets of testing; however, it also may be due to the difference between the number of sampling points taken in these two techniques. In the fiber optic test, the detonation front plane is determined by only three data points. Any local disturbance in any one of the three points may provide a different wave plane. On the other hand, 32 sampling points were taken at each measuring plane in the multi-streak technique. Any local disturbance will not be as important in determining the wave plane.

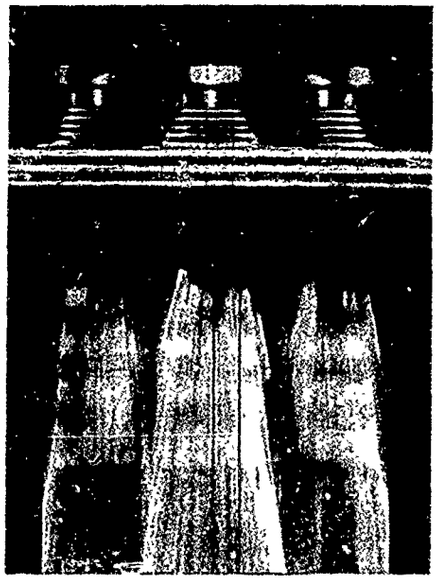

Fig. 9. Multi-streak photographic record of a centrally initiated caseless shaped charge

MULTI-TRACK EXPERIMENTS

For comparison purposes, we recorded the detonation velocity measurements via both ionization probes and fiber optics in a multi-track device. The photograph of the lucite multi-track plate is shown in Fig. 10. Holes which accommodate fiber optics are also visible in the picture. Six measuring tracks of three different sizes were machined into the lucite plate. The track width was 0.8, 1.2 and 1.6 millimeter and the depth of the tracks was 1.3, 1.7 and 2.1 millimeter, respectively. A PETN-plastic formulation, was loaded into the track manually. Slots were cut in between tracks to minimize "cross-talk". Fig 11 shows the photograph of the explosive loaded plate with fiber optics installed. The ionization probes were assembled in the top aluminum confinement plate as shown in Fig. 12. The signals of the ionization probes were recorded in a digital transient recorder which has a rise time of 10 nanosecond. The measured velocities are summarized in Table 1.

One of 0.8 mm track failed to detonate. This was caused by a defect in the explosive fill in the track

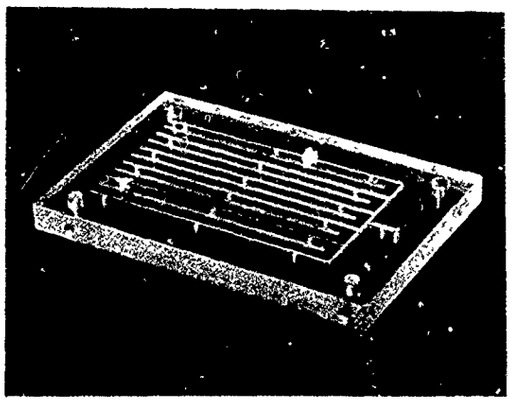

Fig. 10. Multi-track test plate

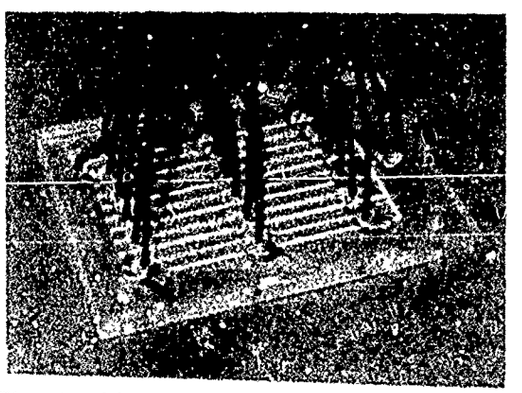

Fig. 11. Multi-track plate with fiber optics installed

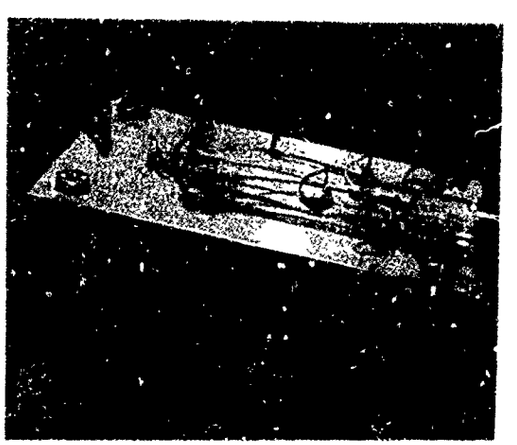

Fig 12. Confinement plate with ionization probes installed

In general, both ionization probe data and fiber optics data show the diameter effect on the detonation velocities. However, the fiber optics data has less spread and has more consistent trend.

TABLE 1

Detonation Velocity Measurements as a Function of Track Width

Track Width (mm)	DETONATION VELOCITY	
	Ionization Velocity (mm/μs)	Fiber Optics (mm/μs)
0.8	no data	no data
0.8	6.698	6.610
1.2	6.727	6.694
1.2	no data	6.731
1.6	6.533	6.899
1.6	6.799	6.899

SUMMARY

We have shown that the new opto-electronic grade plastic optic fiber is a reliable and more accurate alternative to ionization probes. With a 0.5 mm air gap, sufficient light signals can be transmitted by 25 meter long fiber optics without difficulty.

We compared the fiber optic technique with the inverse multi-streak technique in shaped charge investigation. The results taken by these two techniques are consistent. The fiber optic technique can be applied to shaped charges with metal bodies and has no restriction on the relative location of the test device and recording camera. We also compared the detonation velocity data recorded via ionization probes and fiber optics. The fiber optic data show a consistent increase in velocity, while the pin data was more erratic, but was in reasonable agreement.

ACKNOWLEDGEMENT

The authors would like to thank Messrs. E. Dalrymple and B. Fuchs, ARDC, for preparing and conducting the multi-track testing, Mr. J. Freiberg, Mason and Hanger-Silas Mason Company, for preparing and conducting the shaped charge tests, and Mr. D. Paisley, University of Dayton Research Institute, for operating the high speed camera in these tests. Mr Fuchs also worked with Mr. S. Kravitz, ARDC, editing and combining the film data.

REFERENCES

1. A.E. Williams, "Applications of Fiber Optics to Ultra High Speed Photography," Proceedings of the 13th International Congress in High Speed Photography and Photonics (1978).

2. M. Held and P. Nikowitsch, "Time Correlated Multi-Streak," Proceedings of the 13th International Congress on High Speed Photography and Photonics (1978).

3. L.L. Shaw, R.R. Donaldson, J.R. Murchie, and T.J. Ramos, "Nanosecond Hydrodynamic Diagnostics Using Fiber Optic Probes and a Streaking Camera," Proceedings of the 12th International Congress on High Speed Photography (1976).

4. P.J. Deas, "Factors Influencing the Performance of a Shaped Charge. The Symmetry of the Detonation. Wavefront," ARDE/MOS/UK, Unpublished paper, 1957.

5. M. Held and P. Nikowitsch, "Inverse Multi-Streak Technique," Proceedings of the 7th Symposium (International) on Detonation (1981).

6. P. Lu and E. Naiman, "Investigation of Shaped Charge Warhead Performance Characteristics via Fiber Optic Technique," Proceedings of the 8th Symposium (International) on Ballistics (1984).

APPLICATIONS OF FIBER OPTICS TO DETONATION EVENTS

U.S. ARMY
ARMAMENT RESEARCH
AND
DEVELOPMENT CENTER

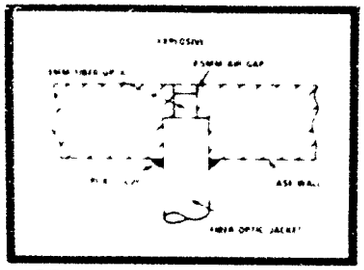

SET-UP OF FIBER OPTIC
IN A CASED DEVICE

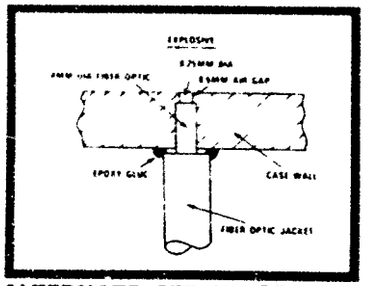

ALTERNATE SET-UP OF FIBER
OPTIC IN A CASED DEVICE

FIBER OPTICS ASSEMBLY
AND SHAPED CHARGE
TEST FIXTURE

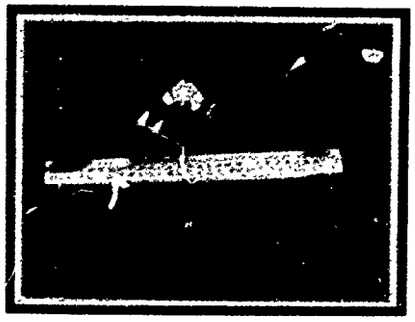

FIBER OPTICS ARRANGEMENT
FACING TO THE RECORDING
STREAK CAMERA

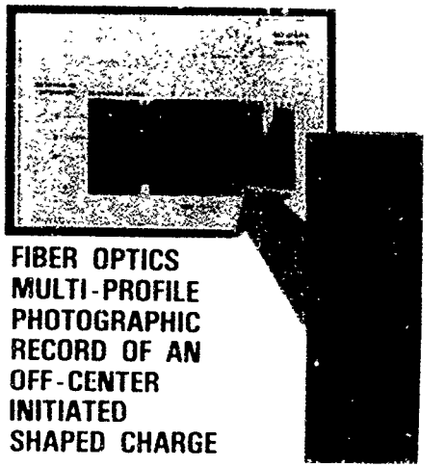

FIBER OPTICS
MULTI-PROFILE
PHOTOGRAPHIC
RECORD OF AN
OFF-CENTER
INITIATED
SHAPED CHARGE

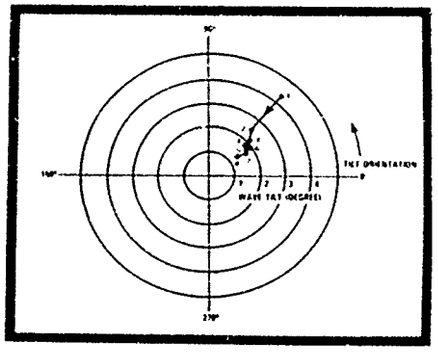

DETONATION WAVE TILT
(MAGNITUDE & POLAR
ORIENTATION)
OF A 3.1MM OFF-CENTER
INITIATED CHARGE

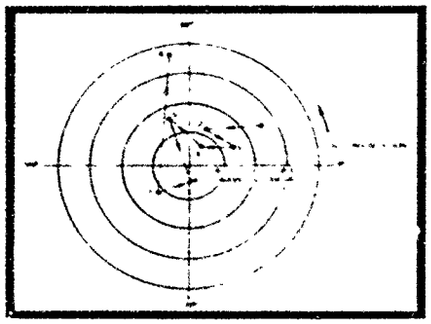

WAVE TILT (MAGNITUDE & POLAR ORIENTATION) OF A CENTRALLY INITIATED CHARGE

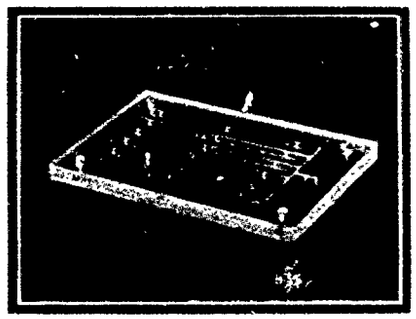

MULTI- TRACK TEST PLATE

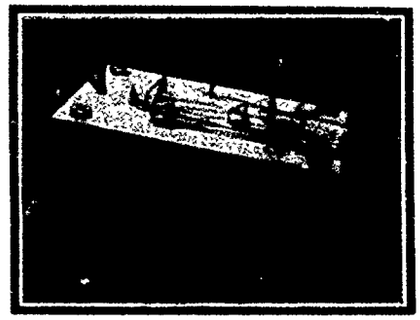

CONFINEMENT PLATE WITH IONIZATION PROBES INSTALLED

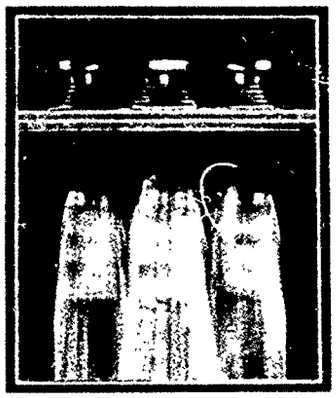

MULTI-STREAK PHOTOGRAPHIC RECORD OF A CENTRALLY INITIATED CASELESS SHAPED CHARGE

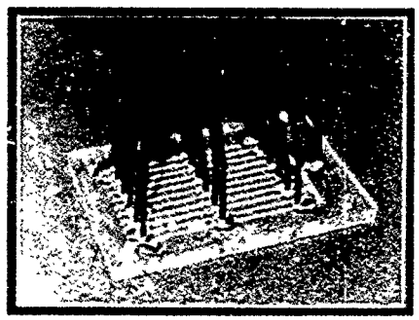

MULTI-TRACK PLATE WITH FIBER OPTICS INSTALLED

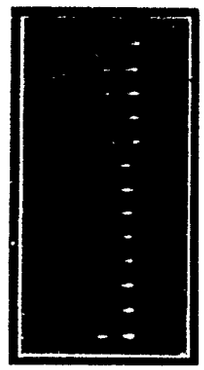

FIBER OPTICS RECORD

VISAR: INTERFEROMETER QUADRATURE SIGNAL RECORDING BY ELECTRONIC STREAK CAMERA

W. F. Hemsing
Los Alamos National Laboratory
Los Alamos, New Mexico

This short paper describes a demonstration to record the four quadrature signals from a push-pull VISAR velocity interferometer using an electronic streak camera. Optical fibers were used to transmit the interferometer outputs to the camera photocathode. Brightness variations of these signals were recorded on film during the experiment. Velocity information was later recovered from this record to give a continuous velocity history. Anticipated advantages over previous methods are increased time resolution, the ability to record multiple velocities simultaneously and greater dynamic range.

INTRODUCTION

Velocity interferometry using VISAR (1-5), Fabry-Perot (6-8), or other (9-11) systems to measure high velocities is being applied to an increasing number of experiments. Interferometers where output is proportional to velocity, rather than displacement, are employed to avoid the excessively high frequencies resulting from optical displacement interferometry.

DISCUSSION

The sensitivity to velocity of both VISAR and Fabry-Perot interferometers can be adjusted over a wide range. In most cases this useful feature allows a good match between the experiment and the velocity measurement system. Adjusting sensitivity to velocity, however, affects the response of each system differently.

The response time of a Fabry-Perot interferometer is proportional to its velocity sensitivity. This interferometer requires constructive interference between multiple beams that arrive to recombine over a finite interval of time. After a velocity change, at least a fraction of this photon fill-time (12) must pass before light output corresponding to the new velocity becomes visible. Velocity features that persist for less than this short time cannot be measured.

A VISAR uses a field-widened Michelson interferometer with a delay in one leg that is proportional to its velocity sensitivity. Because it depends on interference between only two beams, it produces continuous optical output. When an abrupt velocity change occurs, the output is somewhat like that obtained from a displacement interferometer over the interferom eter delay time. Although the output frequency over this short time may greatly exceed the response capability of available photodetectors, it still occurs. Thus, for VISAR, the response time is determined by its photodetector system rather than the interferometer itself.

At least three features of electronic streak cameras have motivated their use for velocity interferometry. They are fast response, great dynamic range, and the ability to record large amounts of information.

To date, most Fabry-Perot velocity measurements have made use of streak cameras. Furthermore, streak cameras have been applied to velocity measurements using wide-angle Michelson interferometers without quadrature coding.

Most VISAR systems presently use photomultipliers and oscilloscopes or digitizers to acquire signals and records. Several are microprocessor controlled and fast to operate.

In viewing this previous work, there appear to be four motivating reasons to apply an electronic-streak camera to record VISAR quadrature

signals. First, the streak camera provides fast speed that is compatible with the interferometer output. Second, the streak-camera dynamic range is much greater than that of the digitizer recorders. Third, by using optical fibers to transmit the optical signals to a very small area on a streak-camera photocathode, it should be possible to record other data or multiple velocities simultaneously. Last, the effect of speckle interference on data reduction is eliminated by the use of quadrature coding.

SUBSTITUTING A STREAK CAMERA FOR PHOTOMULTIPLIERS AND DIGITIZERS

Figure 1 shows a modified, push-pull VISAR (4) as used with oscilloscopes or digitizers. Differential amplifiers are used to subtract electrical signals detected at opposite sides of the interferometer for each polarization. This reduces the original four signals to two before recording. A digitizer record showing these two signals with time fiducials is included.

This system works well and will continue to be used. However, in experiments where the disadvantages of photomultipliers and electronic signal recorders are important, the system of Fig. 2 may be useful. Here the electronic streak camera is used to record the optical signals from the interferometer directly. An experimental record is shown.

RESULTS

Figure 3 is a more detailed analysis of the experimental record obtained by the system of Fig. 2. Several features are visible.

The enlargement shows considerable graininess. This is due to the microchannel-plate intensifier used to amplify the camera light output. Noise from this graininess is very evident in each scan of the microdensitometer isoplot. However, the plots showing each signal with several scans averaged together show much less noise. This noise reduction is very desirable but it requires greater photocathode space and, therefore, decreases the number of signals that can be recorded

No attempt has been made here to calibrate the response of the film, camera, and intensifier to light Further, the zero light level was assumed to be the film fog level before each trace. Conjugate signals were matched in amplitude using arbitrary constants and then subtracted for use in a simple data reduction program (13) using arctangent (3).

Results of subtraction, polar plotting, and reduction to velocity histories are shown in Fig. 4. Here the difference between each pair of conjugate signals is plotted in the upper left. These two traces are like the sine and cosine of an angle that is proportional to the surface velocity. They are similar to the digitizer record of Figure 1.

A polar (Lissajous) plot of these traces is at the upper right. Ideally this plot is a circle. Results of correcting for unequal amplitude and a phase difference other than 90° are shown to the far right. Velocity histories are shown at the bottom.

A variety of work remains to be done. Actual advantages and disadvantages of this technique will best be judged in the future.

CONCLUSION

Direct optical recording of the quadrature signals from a VISAR has been demonstrated. The quality of these records appears to be good. Data were read from the film by a microdensitometer and reduced to velocity plots using previously developed methods. This technique was simple to apply to an existing VISAR. It should give improved time resolution, the capability to simultaneously record multiple velocities on one camera, and greater dynamic range than previous systems.

ACKNOWLEDGEMENTS

Help was generously given by Mel Garcia who installed the optical system and assembled the experiments, by Clint Finley and Bob Benjamin who supplied and operated the Imacon 790 camera, and by Mary Luke and Robin Whitman who read the film. Encouragement and helpful suggestions from Norval Parker are greatly appreciated also. We thank each contributor for making this demonstration work.

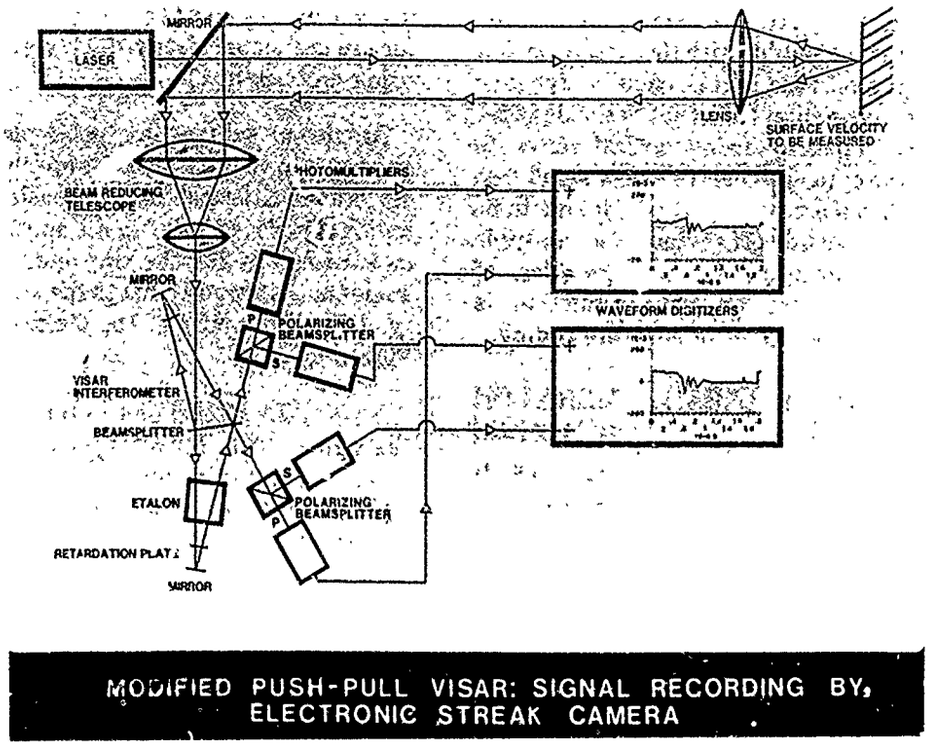

Fig 1 Diagram of push-pull VISAR with photomultipliers and digitizers. The four interferometer quadrature signals are reduced to two by differential amplifiers before recording.

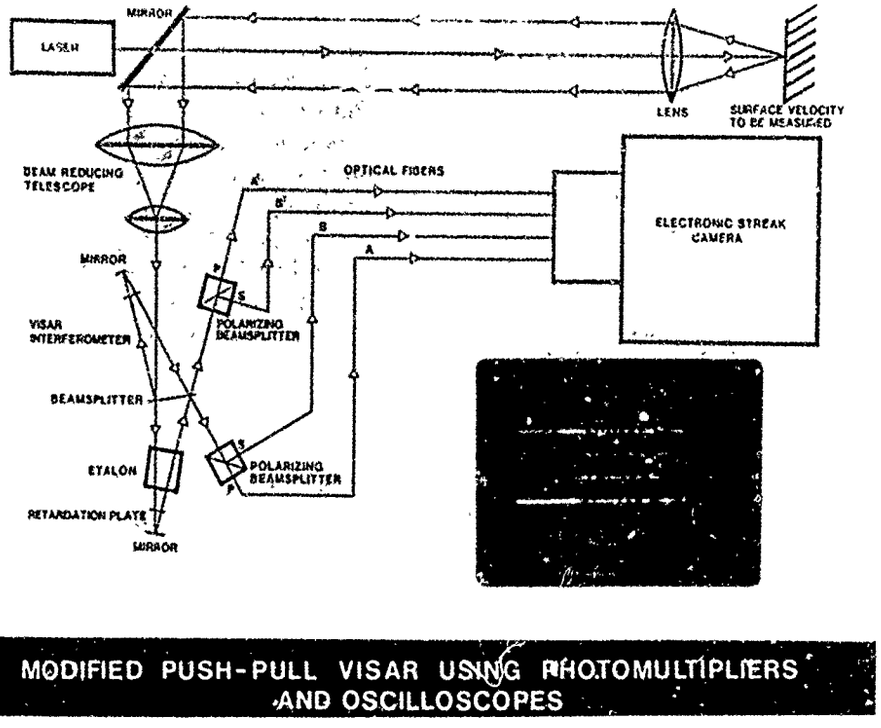

Fig 2 Push-pull VISAR directly coupled to electronic streak camera by optical fibers. All four quadrature signals are recorded.

VISAR: INTERFEROMETER QUADRATURE SIGNAL RECORDING BY ELECTRONIC STREAK CAMERA

W. F. Hemsing
Los Alamos National Laboratory
Los Alamos, New Mexico

This short paper describes a demonstration to record the four quadrature signals from a push-pull VISAR velocity interferometer using an electronic streak camera. Optical fibers were used to transmit the interferometer outputs to the camera photocathode. Brightness variations of these signals were recorded on film during the experiment. Velocity information was later recovered from this record to give a continuous velocity history. Anticipated advantages over previous methods are increased time resolution, the ability to record multiple velocities simultaneously and greater dynamic range.

INTRODUCTION

Velocity interferometry using VISAR (1-5), Fabry-Perot (6-8), or other (9-11) systems to measure high velocities is being applied to an increasing number of experiments. Interferometers where output is proportional to velocity, rather than displacement, are employed to avoid the excessively high frequencies resulting from optical displacement interferometry.

DISCUSSION

The sensitivity to velocity of both VISAR and Fabry-Perot interferometers can be adjusted over a wide range. In most cases this useful feature allows a good match between the experiment and the velocity measurement system. Adjusting sensitivity to velocity, however, affects the response of each system differently.

The response time of a Fabry-Perot interferometer is proportional to its velocity sensitivity. This interferometer requires constructive interference between multiple beams that arrive to recombine over a finite interval of time. After a velocity change, at least a fraction of this photon fill-time (12) must pass before light output corresponding to the new velocity becomes visible. Velocity features that persist for less than this short time cannot be measured.

A VISAR uses a field-widened Michelson interferometer with a delay in one leg that is proportional to its velocity sensitivity. Because it depends on interference between only two beams, it produces continuous optical output. When an abrupt velocity change occurs, the output is somewhat like that obtained from a displacement interferometer over the interferometer delay time. Although the output frequency over this short time may greatly exceed the response capability of available photodetectors, it still occurs. Thus, for VISAR, the response time is determined by its photodetector system rather than the interferometer itself.

At least three features of electronic streak cameras have motivated their use for velocity interferometry. They are fast response, great dynamic range, and the ability to record large amounts of information.

To date, most Fabry-Perot velocity measurements have made use of streak cameras. Furthermore, streak cameras have been applied to velocity measurements using wide-angle Michelson interferometers without quadrature coding.

Most VISAR systems presently use photomultipliers and oscilloscopes or digitizers to acquire signals and records. Several are microprocessor controlled and fast to operate.

In viewing this previous work, there appear to be four motivating reasons to apply an electronic-streak camera to record VISAR quadrature

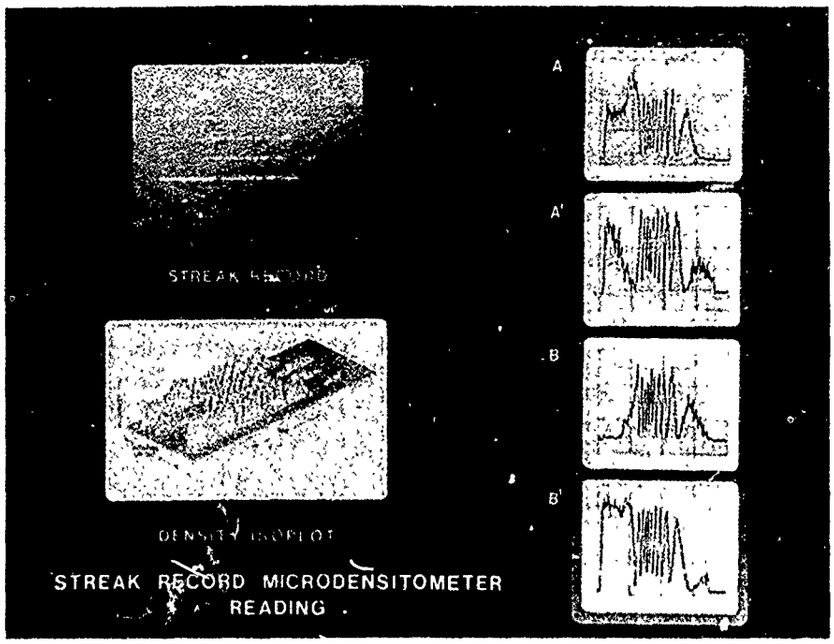

Fig. 3. Details of streak record obtained by system of Fig. 2. Graininess due to microchannel-plate intensifier is apparent in enlargement of film record and its density isoplot. The four traces at the right result from averaging several density scans from each signal to reduce noise.

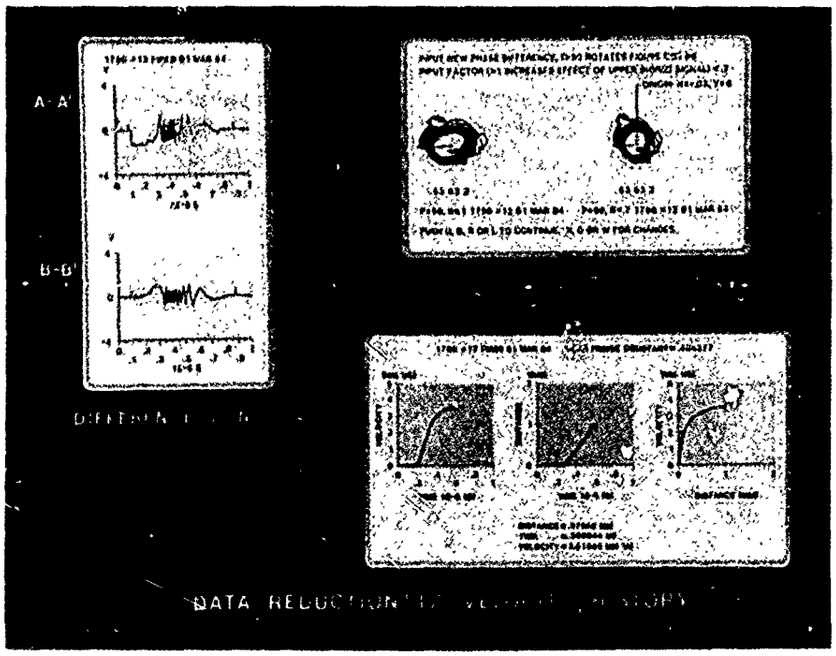

Fig 4. Difference signals at upper left are obtained from streak record of Fig. 3 by subtraction indicated. First Lissajous figure shows distortion due to unequal signal amplitudes and phase difference other than 90° Second Lissajous has operator input amplitude and phase corrections. Velocity plots are obtained by taking arctangent of the quotient of the difference signals using corrected phase difference and amplitudes. The resulting angle is related to the velocity by the VISAR fringe constant.

2. N. L. Parker, "Velocity Measurements of Mylar Flyers Using the VISAR," LLNL Rept. UCID-16846, July 25, 1975.

3. B. T. Amery, "Wide Range Velocity Interferometer," Sixth Symposium on Detonation (Office of Naval Research, Dept. of the Navy, Arlington, VA, 1976) p. 215, August 24-27, 1976.

4. W. F. Hemsing, "Velocity Sensing Interferometer (VISAR) Modification," Rev. Sci. Instrum. 50, No. 1, pp. 73-78, Jan. 1979.

5. W. F. Hemsing, "VISAR: Some Things You Should Know," High Speed Photography, Videography, and Photonics, Dennis L. Paisley, Editor, Proc. SPIE 427, pp. 119-202, August 23-25, 1983.

6. M. Durand, P. Laharrague, P. Lalle, A. LeBihan, J. Morvair, and H. Pujols, "Interferometric Laser Technique for Accurate Velocity Measurements in Shock Wave Physics," Rev. Sci, Instrum. 48, No. 3, pp. 275-278, March 1977.

7. D. R. Goosman, A. M. Frank, H. H. Chau, and N. L. Parker, "Fabry-Perot Velocimetry Techniques: Is Doppler Shift Affected By Surface Normal Direction?," High Speed Photography, Videography, and Photonics, Dennis L. Paisley, Editor, Proc. SPIE 427, pp. 127-135, August 23-25, 1983.

8. W. L. Seitz and H. L. Stacy, "Fabry-Perot Interferometry Using an Image Intensified Rotating-Mirror Streak Camera," High Speed Photography, Videography, and Photonics, Dennis L. Paisley, Editor, Proc. SPIE 427, pp. 186-192, August 23-25, 1983.

9. N. L. Parker and H. H. Chau, "Streak Camera Recording of Interferometer Fringes," LLNL Rept. UCID-17351, July 14, 1977.

10. G. Smeet, and H. George, "Instantaneous Laser Velocimeter Using a Fast Wavelength Tracking Michelson Interferometer," Rev. Sci. Instrum. 49, No. 11, pp. 1589-1596, Nov. 1978.

11. S. A. Sheffield and G. A. Fisk, "Particle Velocity Measurements of Laser-Induced Shock Waves Using ORVIS," High Speed Photography, Videography, and Photonics, Dennis L. Paisley, Editor, Proc. SPIE 427, pp. 193-198, August 23-25, 1983.

12. T. J. Burgess, "The Photon Fill-Time of a Fabry-Perot Spectrometer," LLNL Rept. UCID-15244, October 31, 1967.

13. W. F. Hemsing, "VISAR: 2½ Minutes for Data Reduction," High Speed Photography, Videography, and Photonics, Dennis L. Paisley, Editor, Proc. SPIE 427, pp. 199-101, August 23-25, 1983.

LASER AS A TOOL IN SENSITIVITY TESTING OF EXPLOSIVES

Henric Östmark
National Defence Research Institute
Stockholm, Sweden

A CO_2 laser was used to heat a pyrotechnic mixture of Mg and $NaNO_3$ at various power levels and various pulse widths. At short pulse widths the sensitivity could be characterized by a threshold ignition energy density. For long pulses the sensitivity is characterized by a threshold ignition energy power. For pulse widths between those extremes the ignition energy density is approximately proportional to the square-root of the pulse width. By measuring the critical ignition power at various beam radii, it was shown that the size of the irradiated area is an important parameter. The experimental results are validated by theoretically solving the heat-flow equation under certain conditions. This method also permits calculation of the ignition temperature, the optical absorption coefficient, the activation energy, and the frequency factor.

In order to test the general applicability of the method, some common high explosives (PETN, RDX, HMX, Tetryl, HNS and TNT) were tested superficially. The laser ignition technique is believed to be useful for calibration of conventional sensitivity tests as well as for risk analyses in practical situations.

INTRODUCTION

The thermal sensitivity of an explosive is essentially a heat balance problem. A certain amount of energy fed into an explosive sample will initiate a deflagration. The problem with conventional sensitivity tests is that the actual input of energy is difficult to control and measure, which makes it virtually impossible to understand the physical and chemical processes involved.

Electro Explosive Devices (EEDs) are ignited by sending an electric current through a wire which is in close contact with the priming charge of the EED. If the current pulse is short enough the ignition depends solely on the energy in the pulse. On the other hand if the current pulse is long enough, the ignition depends only on its power. Thus, an EED may be electrically characterized exclusively by its critical ignition energy, its critical power, and a characteristic time, its thermal time constant (1).

The same type of characterization should be possible for explosives initiated thermally. In order to control precisely the amount of energy and the duration of the pulse, it is convenient to use a laser to heat the explosive.

The relations between pulse width and ignition energy and between beam radius and ignition power, was determined for a number of pulse widths and beam radii. As those sensitivity curves are dependent upon the geometry of the sample as well as on the thermal and chemical behaviour of its constituents, it is difficult to compare different explosives, to tabulate results and to estimate sensitivities for other geometries. This means that in order to get some more information out of the test it

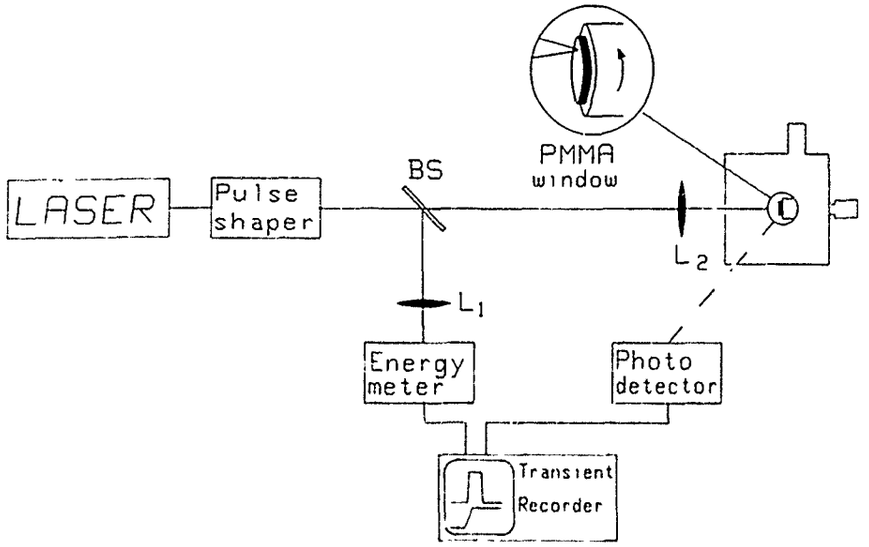

Fig. 1. Experimental set-up. The sample holder is shown in magnification

must be complemented with a mathematical model. The model chosen here is the thermal explosion theory (2,3), which makes it possible to determine "fundamental constants", with which it is fundamentally possible to calculate the sensitivity of an arbitrary geometry.

EXPERIMENTAL

Explosives

The samples used in the experiments were of two kinds; a pyrotechnic mixture (PM) and high explosives (HE) were compressed to 2 x 10 mm tablets. The HE, which was of technical grade, was compressed to 95% of theoretical maximum density (TMD). The PM was compressed to 85% of TMD. Further specification of the PM is shown in Table 1.

Experimental Set-up

The experiments were carried out with a 300 W CO_2-laser (λ = 10.6μm) with a mechanical shutter that gave pulse widths in the interval 1 ms - continuous. The set-up is shown in Fig. 1.

A beam splitter reflected 3% of the beam's power onto a power/energy detector while the main beam was focused to irradiate an area of about 3 mm of the sample surface. To protect the optics from sample debris, air was blown through a nozzle in front of the sample. A time record of the power incident upon the sample was obtained by reflecting the weaker beam against a diffuse reflector and measuring this power with a CMT detector. This set-up was calibrated with a calorimetric absolute value powermeter, which was inserted in the main beam in front of the lens.

TABLE 1

Composition	58% Mg+42% $NaNO_3$
Grain size	Mg: spec MIL-P-140C7B (95% <45μm) $NaNO_3$:< 75 μm, sieved
Compacting pressure	150-160 MPa
Density	1650 kg/m³
Reflection coefficient	0.71
Heat capacity	1.00 kJ/kg/K
Thermal conductivity	4.4 W/m/K

Reflection measurement

The reflection coefficient of the explosive sample was determined by irradiating it with a waveguide laser (λ = 10.6μm) and measuring the incident power as well as the scattered power (see Fig. 2). The incident power was measured by a powermeter, while the scattered power was measured as a function of the angle of reflection by an absolute value calibrated pyro-electric detector.

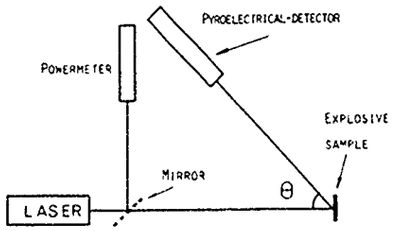

Fig. 2. Reflection measurements

The reflected power was then integrated over a semisphere, according to the formula:

$$P_{refl} = \int_0^{\pi/2} C\Delta P(\theta)\,\sin\theta d\theta = \sum_{\pi/2} C\Delta P(\theta)\sin\theta\Delta\theta \quad (1)$$

where C is an apparatus constant, ΔP is the detector signal and P_{refl} is the reflected power. The reflection coefficient is given by the ratio of the reflected power to the incident power.

Area measurements

The laser has a Gaussian intensity distribution given by

$$I(\varrho) = I_o\, e^{-\varrho^2/\omega^2} \quad (2)$$

This means that the irradiated area is not well defined. However, on condition that the radial losses are "small", an "effective" area may be determined. This area is defined as

$$A = \frac{E^G crit(\tau_p)}{\varepsilon\ crit\ (\tau_p)} \quad (3)$$

where $\varepsilon crit\ (\tau p)$ is an absolutely determined ignition energy density, and E^G_{crit} is the ignition energy at Gaussian intensity distribution at the same pulse width.

On condition that all measurements are made with a *fixed geometry,* the energy density

$$\varepsilon^G\ crit\ (\tau_p) = \frac{E^G_{crit}\ (\tau_p)}{A} \quad (4)$$

may be determined with a fair degree of accuracy for all values of τ_p.

The Gaussian intensity distribution was transformed by a beam integrator (4) to a rectangular transverse intensity, Fig. 3. This was imaged on the sample through a lens, and the irradiated area was measured by making an imprint in plexiglass. The critical ignition energy was measured as above.

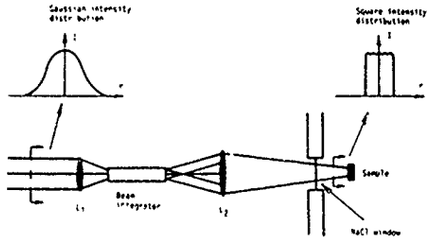

Fig. 3. Production of a flat top laser beam

RESULTS

Pyrotechnic mixture

The critical energy density (energy per unit area) necessary to ignite the sample was measured at various pre-set pulse widths by varying the energy incident upon the sample. At each pulse width the sample was first irradiated at a low power level. The sample was then rotated, so that a fresh surface was exposed next. The power was increased with each successive pulse until ignition occurred. On this occasion the energy content of the laser pulse as well as the time to ignition was recorded. The energy and power incident upon the sample was then converted to absorbed energy density and heat flux density by keeping the geometry fixed and using the quantities effective area and reflection coefficient.

The results of these experiments with pre-set pulse widths are given in Table. 2.

The critical power (total power) necessary to ignite the sample was measured at various pre-set beam radii. In these experiments, the pulse width was fixed (τ_p=500 ms) and the experiments were carried out as above.

The result of the experiment with pre-set beam radii are shown in Fig. 4.

High Explosives

In order to investigate the general applicability of the method, some common HEs (PETN, RDX, HMX, HNS, Tetryl and TNT) were tested superficially.

Complete sensitivity curves were not obtained. The sensitivity was measured for each HE at one pre-set pulse width only. Since the HEs proved difficult to ignite at atmospheric pressure, they

TABLE 2
Critical Ignition Data for the Pyrotechnic Mixture

Pulse width (s)	Heat flux (W)	Energy (J)	Time to ignition (s)	Heat flux density (W/cm²)	Energy density (J/cm²)
.00107	54.6	.058	——	1970	2.09
.00181	32.3	.058	——	1160	2.09
.00204	29.7	.061	——	1070	2.20
.00251	27.4	.068	——	987	2.45
.00311	23.9	.074	——	861	2.67
.00419	22.1	.093	——	796	3.35
.00553	18.2	.1	——	656	3.60
.0067	17.63	.118	.03	635	4.25
.00824	14.8	.122	——	533	4.39
.0098	13.8	.135	.031	497	4.86
.0101	13.56	.137	.03	488	4.94
.0154	10.1	.156	.04	364	5.62
.0154	11.36	.174	.032	409	6.27
.0193	7.32	.141	.045	264	5.08
.0276	6.24	.173	.05	225	6.23
.035	5.98	.209	.055	215	7.53
.051	5.41	.276	.066	195	9.94
.078	4.15	.324	.09	149	11.7
.103	3.77	.388	.114	136	14.0
.119	3.7	.438	.14	133	15.8
.143	3.55	.509	.165	128	18.3
.175	3.34	.584	.18	120	21.0
.201	3.08	.62	.225	111	22.3
.25	3.14	.79	.257	113	28.5
.293	3.16	.93	.258	114	33.5
.344	3.1	1.03	.261	112	37.1
.406	2.98	1.21	.39	107	43.6

were tested in air at a pressure of 3.1 MPa, using a bomb. The reflection was not measured. The reflection coefficient is estimated to be the same for all samples, about 0.7.

Table 3 shows the result of the experiments.

TABLE 3
Sensitivity of some common HEs

Explosive	Pulse width (ms)	Incident power (W)	Energy density (J/cm²)
RDX	5	11.2	2.8
HMX	5	11.2	2.8
PETN	5	12.3	3.1
Tetryl	5	16.9	4.2
HNS	5	29.0	7.2
TNT	94	22.2	103

Beam radius: 0.8 mm; Initial pressure: 3.1 MPa

THEORY AND CALCULATIONS

The temperature distribution, T(r.t) in a homogeneous solid can be described by the heat-flow equation:

$$\frac{1}{x}\frac{\partial T}{\partial t} - \Delta T = \frac{\varrho Q K_o}{\lambda} e^{-E_a/RT} + I_o(t)\frac{\alpha}{\lambda} e^{-r^2/\omega^2} e^{-\alpha Z} \quad (5)$$

The first term on the right hand side is the heat generation due to the exothermic reaction in the explosive; the second term is the volumetric heating caused by the laser.

We are not interested in the temperature distribution itself, but in expressing the critical ignition energy density. ε_{crit}, the time to ignition,

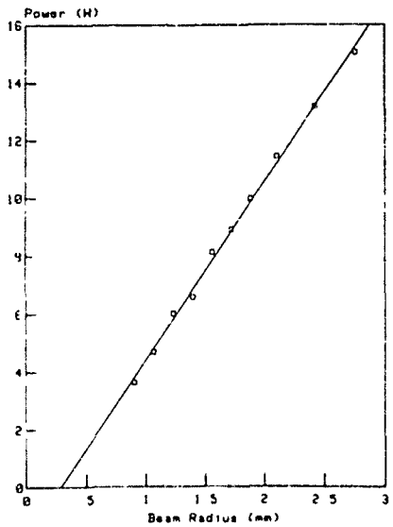

Fig. 4. Ignition power vs. laser beam radius for $Mg/NaNO_3$

T_i, and the critical ignition power, P_{crit}, in terms of $I_o(t)$, QK_o, E_a, α, λ, ω and T_o. To do this we need a physical condition which defines ignition.

Equation (5) cannot be solved analytically and since a numerical solution is difficult without approximately known initial values, only a few special cases will be treated here. However they should be useful for obtaining initial values for numerically fitting the experimental results to the general theory, as well as letting us get a feeling about the ignition process and what we are actually doing when we submit an explosive sample to a laser sensitivity test.

If we assume that ignition occurs at a constant temperature, T_i, and that the sample behaves like a chemically inert substance for temperatures less than the ignition temperature, we arrive at a simple model where ε_{crit} depends only on $I_o(t)$, T_i, α, λ and ω, given by the system:

$$\frac{1}{\kappa}\frac{\partial T}{\partial t} - \Delta T = \frac{I_o(t)}{\lambda} e^{-\alpha z} e^{-\frac{r^2}{\omega^2}} \tag{6a}$$

$$T(\bar{r},t) = T_o, t = 0 \tag{6b}$$

$$\frac{\partial T}{\partial z} \to 0,\ z \to \infty,\ t > 0 \tag{6c}$$

$$T_i = \text{const} \tag{6d}$$

When $\omega >> \sqrt{\kappa\tau_p}$, Eq. (6a) may be written

$$\frac{1}{\kappa}\frac{\partial T}{\partial t} - \frac{\partial^2 T}{\partial z^2} = \frac{I(t)}{\lambda} e^{-\alpha z} \tag{7}$$

We want to determine ε_{crit} as a function of $I_o(t)$ for this equation.

Two cases may be discerned:

1. The pulse width is so small that heat conduction may be ignored,

$$\alpha^{-1} >> \sqrt{\kappa\tau_p} \tag{8}$$

which gives the ignition energy as (5)

$$\varepsilon_{crit} = \varrho C_p \alpha^{-1} (T_i - T_o) \tag{9}$$

implying that

$$\varepsilon_{crit}(\tau) = \text{constant}. \tag{10}$$

2. The absorption depth is small in relation to the thermal diffusivity,

$$\alpha^{-1} << \sqrt{\kappa\tau_p}$$

i.e. the energy is absorbed in a thin surface layer. this gives the equation

$$\frac{\partial^2 T}{\partial z^2} - \frac{1}{\kappa}\frac{\partial T}{\partial t} = 0 \tag{11}$$

with the boundary condition

$$-\lambda \left.\frac{\partial T}{\partial z}\right|_{z=o} = I_o \tag{12}$$

The solution of which is (6)

$$T(z,t) = T_o + (2I_o/\lambda)\ (\kappa t)^{1/2} \cdot \text{ierfc}\ |(z/2(\kappa t)^{1/2})| \tag{13}$$

$$T_i = \text{Max}\ (T(z,t)\ ). \tag{14}$$

This leads to

$$T_i = T_o + (2I_o/\lambda)\ (\kappa t/\pi)^{1/2}. \tag{15}$$

The critical ignition energy is obtained as

$$\varepsilon_{crit}(\tau) = \frac{(T_i - T_o)\lambda}{2} \sqrt{\pi/\kappa} \sqrt{\tau} \quad (16)$$

The steady state solution of Eq. (6) is obtained as (7)

$$T = T_o + T_{max}\, N(R,Z,W) \quad (17)$$

$$T_{max} = \frac{P}{2\lambda\omega\pi^{1/2}} \quad (18a)$$

$$R = r/\omega,\ Z = z/\omega,\ W = \alpha\omega \quad (18b)$$

In [7], the function, N(R,Z,W) can be found plotted for various values of R,Z,W. For our purpose we need

$$\lim_{W \to \infty} N(O,O,W) = 1, \quad (19)$$

which leads to that the ignition temperature is given by

$$T_i = T_o + \frac{P}{2\lambda\omega\pi^{1/2}} \quad (20)$$

For wide pulse widths with a Gaussian intensity distribution, where the heat is absorbed in a narrow surface layer and then flows into the interior of the sample, this model predicts that the critical ignition power depends only on the beam radius and not on the pulse width:

$$P_{crit} = 2\lambda\omega \sqrt{\pi}\, (T_i - T_o) \quad (21)$$

Applying the relation to the experimental data in Fig. 4 enables the calculation of the ignition temperature;

$$T_i = 691K$$

This model also predicts that for narrow pulse widths, where heat conduction can be ignored, the critical ignition energy density is independent of the pulse width. The ignition energy density is then given by:

$$\varepsilon_{crit} = \alpha^{-1} C_\rho (T_i - T_o) \quad (22)$$

In Fig. 5, the energy density data from Table 2 is plotted as a function of the pulse width in a log-log diagram. For narrow pulse widths, the critical ignition energy density is constant, in accordance with the theory above, $\varepsilon_{crit} = 2.1$ J/cm. The optical absorption coefficient, α, can now be calculated using equation and the above values of T_i and ε_{crit}; $\alpha = 3.1 \cdot 10^4 m^{-1}$.

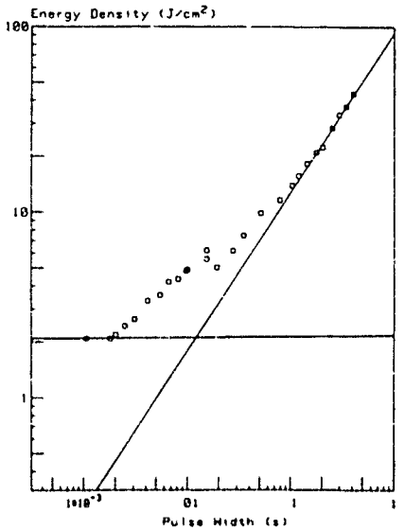

Fig. 5. Ignition energy density vs. pulse width for $Mg/NaNO_3$

The approximate solution to the theory outlined above is useful for getting the general behaviour of the sensitivity curve. In order to estimate the kinetic parameters, E_a and QK_o, another and more detailed approximation (5), in the interval $\alpha^{-1} << \sqrt{\chi\tau_p} << \omega$, is given by the system:

$$\frac{1}{\chi}\frac{\partial T}{\partial t} - \frac{\partial^2 T}{\partial z^2} = \frac{\varrho Q K_o}{\lambda} e - \frac{E_a}{R(T+T_o)} \quad (23)$$

$$-\left.\frac{\partial T}{\partial z}\right|_{z=0} = I_o$$

$$T(\vec{r},t) = T_o,\ t = 0$$

$$\frac{\partial T}{\partial z} \to 0,\ z \to \infty,\ t > 0$$

Introduce the ratio between absorbed laser energy and chemical energy generated by the sample as:

$$\Gamma = \left(\frac{\delta T(0,t)}{\delta t}\right)_{chem} \left(\frac{\delta T(0,t)}{\delta t}\right)^{-1}_{laser} \quad (24)$$

and define a characteristic time to ignition, τ^*, with $\Gamma = 1$ when $t = \tau^*$. The relation between τ^* and I_o may then be written as (8)

$$(\tau^*)^{1/2} \exp\left(-\frac{E_a/R}{(\varrho\tau^*)^{1/2} I_o + T_o}\right) = \frac{q^{1/2} C I_o}{2QK_o} \quad (25)$$

where

$$q \cong \frac{1.26}{\lambda \varrho C} \quad (26)$$

A numerical analysis (8) gives a good approximation of Eq. (25) to

$$\tau^* = \text{const } I_o^{-\mu} \quad (27)$$

or, rewritten,

$$\ln(I_o) = -\frac{1}{\mu}\ln(\tau^*) + A \quad (28)$$

In the experiments described in this paper the characteristic time to ignition, τ^*, corresponds to $\tau^* = \min(\tau p, \tau i)$ which is equal to τp in the given interval.

If the heat flux density, I_o, from Table 2 is plotted as a function of the time to ignition, in a log-log diagram, a high linearity is shown, in the interval $\alpha^{-1} << \sqrt{\kappa\tau} << \omega$. The data in Table 2 is plotted in Fig. 6.

A least square fit gives

$$\log(I_o) = A + B \log(\tau_p) \quad (29)$$

with A = 5.527 and B = −0.5730.

According to the theory outlined above it is possible to write the connection between I_o and τ_p as

$$\log(I_o) = A(E_a, QK_o) + B(E_a, QK_o) \cdot \log(\tau_p) \quad (30)$$

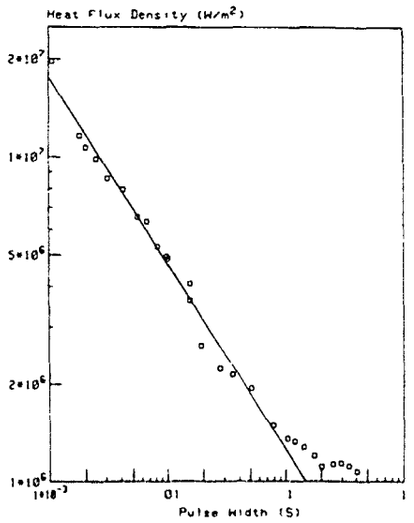

Fig. 6. Ignition heat flux density vs. pulse width for Mg/$NaNO_3$

Calculating A and B for different E_a and QK_o and comparing those values with the experimental values gives

E_a=148 kJ/mol
QK_o=6.0 10^{24} J/kg s
with Q=8.4 MJ/kg (9) we obtain K_o=7.1 10^{17} s^{-1}.

DISCUSSION

Fig. 7 shows schematically the "total" sensitivity of an explosive. ε_{crit} is the critical energy density for ignition, τ_p is the duration of the energy input

For short enough durations of energy input, the sensitivity is characterized by a threshold ignition energy density given by the internal properties of the explosive (e.g. thermal conductivity, heat capacity, and chemical properties), and independent of external parameters such as the shape of the sample and the structure of its immediate surroundings.

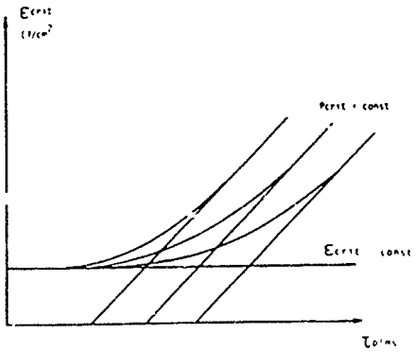

Fig. 7. Sensitivity curves. Each curve corresponds to a given radius on the laser beam

When the duration of energy input is long enough, the explosive is instead characterized by a threshold ignition power, P_{crit}=const, which is dependent on both the internal and the external parameters, as well as on the target size of the energy input.

This means that the total sensitivity is characterized by a series of curves, $\varepsilon_{crit} = \varepsilon_{crit}(\tau_p, \omega=\text{const})$ where each curve corresponds to a specific area of energy input, ω=const.

Conventional sensitivity tests (e.g. impact and friction tests) represent ony a specific duration and specific area of energy input and hence do not give as much information as a laser sensititivity test does.

CONCLUSIONS

The laser ignition technique is believed to be useful for calibration of conventional sensitivity tests as well as for risk analysis in practical situations. The described method has the advantage of making it possible to measure the sensitivity during the entire time span of energy input and of enabling the study of the geometry dependence of the ignition parameters, all this expressed in absolute physical units.

The method can also be seen as a first step towards relating the general sensitivity of an explosive to its chemical and physical parameters.

ACKNOWLEDGEMENTS

I would like to thank Mats Flaum, FOA, for letting me use his equipment, and Mats Flaum and Ola Listh, FOA, for many helpful discussions.

REFERENCES

1. N. Olohan, EMI Electronics, Feltham, (private communication).

2. D.A. Frank-Kamenetskii, Diffusion and Heat Transfer in Chemical Kinetics, Plenum Press, New York, 1969.

3. J. Zinn, R.N. Rogers, "Thermal Initiation of Explosives," J. Phys. Chem., Vol. 66. pp. 2646-2653, 1962.

4. R.E. Grojean, D. Feldman, J.F. Roach, "Production of flat top beam profiles for high energy lasers," Rev. Sci. Instr. 51, pp. 375, mars 1980.

5. H. Östmark, "Mätning av tändningsenergin för pyrotekniska satser," FOA Rapp D 20093-D1, April 1983.

6. H.S. Carlslaw and J.C. Jaeger, Conduction of Heat in Solids, 2nd ed. Oxford, 1959.

7. M. Lax, "Temperature rise induced by a laser beam," J. Appl. Phys., Vol. 48, No. 9, pp. 3919-3924, 1977.

8. R.J. Harrach, "Estimates on the ignition of high-explosives by laser pulses," J. Appl. Phys. Vol. 47, No. 6, pp. 2473-2483, 1976.

9. A.J. Beardell, D.A. Anderson, "Factors affecting the stoichiometry of the magnesium-sodiumnitrat combustion reaction," Proceedings Third International Pyrotechnics Seminar, 1972.

COMMENTS

MARTIN SUMMERFIELD, Princeton
Combustion Research Laboratory

Initiation by radiative energy has been tried and, I believe, is no longer used to characterize the ignitabilty of solid rocket propellants. The results obtained in this manner are generally quite different from the test results with hot gas ignition. For instance, at a typical energy flux of, say, 100 cal/cm^2, the time to ignition with a laser might be 10 to 100 times longer than for an equipment hot-gas convective flux. The latter represents more nearly the situation in a rocket and is therefore the preferred test method. A similar large discrepancy exists also for such quantities as minimum ignition energy. There are several physical and chemical processes that stretch out the radiative ignition process:

1. Due to finite absorptivity of the solid (even if it looks opaque to the eye) the radiative energy does not stop at the surface, as it does with hot gas flux.
2. Since the mechanism of ignition or initiation includes exothermic reaction at or near the gas-solid interface, the fact that the gas adjacent to the surface is cold in the radiative experiment, not hot as in the convective experiment, makes the exothermic process slower and weaker.
3. Part of the incident radiative flux is inevitably reflected and does not heat the solid. This could be measured, but in such tests, it usually is not.

Laser ignition test equipment

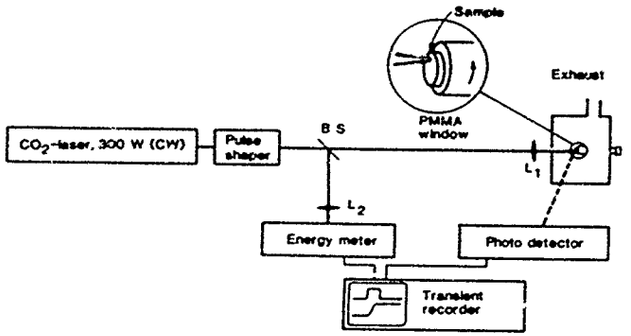

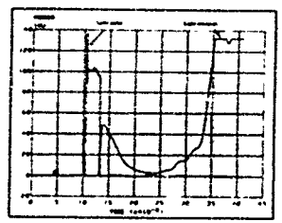

Experimental data: examples of registration

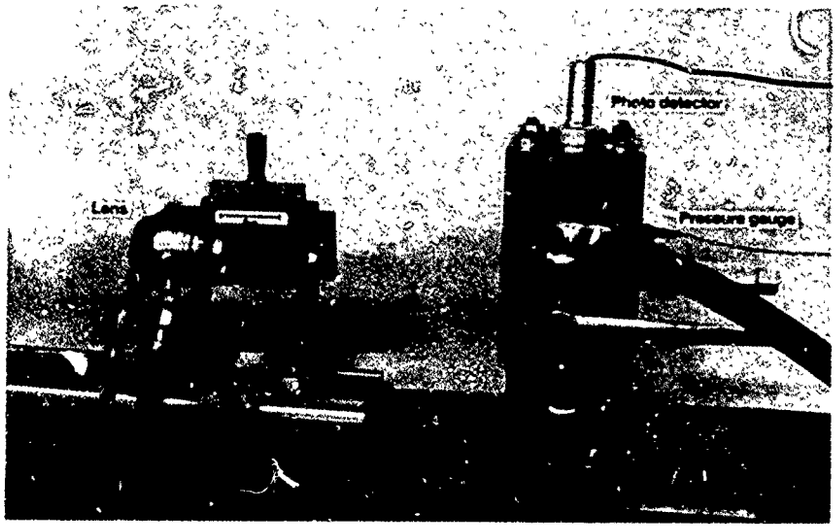

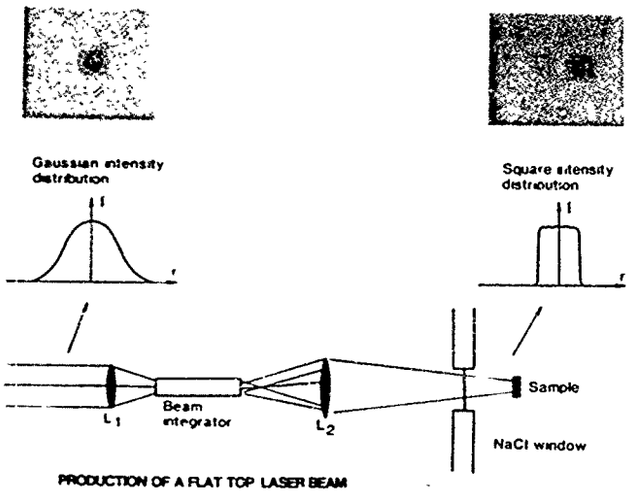

PRODUCTION OF A FLAT TOP LASER BEAM

Advantages of laser ignition technique

- Enables measurement of sensitivity (defined as least energy for ignition at given pulse width) in physical units (e.g. Wcm^{-2}, Jcm^{-2}).
- Duration of energy input (i.e. pulse width) can be varied.
- Area of energy input can be varied.
- Pressure dependence of ignition energy can be studied with use of a pressure vessel.
- Ignition process can be studied by measuring light emission from reaction.

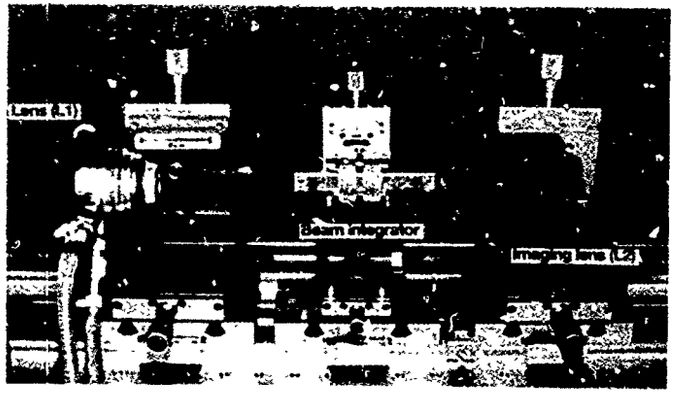

Results

Sensitivity of some common HEs.

Explosive	Pulse width (ms)	Incident power (W)	Energy density (J/cm^2)
RDX	5	11.1	2.8
HMX	5	11.2	2.8
PETN	5	12.3	3.1
Tetryl	5	16.9	4.2
HNS	5	29.3	7.3
TNT	94	82.2	103

Beam radius 0.5 mm
Initial pressure 5.1 MPa

Main results of total sensitivity measurements. Curves are characterized by

- a threshold ignition energy for short energy inputs, dependent only on internal sample properties
- a threshold ignition power for long energy inputs, dependent on both internal and external properties and on area of energy input.

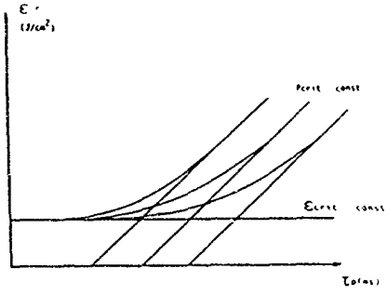

$$\frac{1}{\kappa}\frac{\partial T}{\partial t} - \Delta T = \frac{\rho Q K_o}{\lambda} e^{-E_a/RT} +$$

$$+ I_o(t)\frac{\alpha}{\lambda} e^{-r^2/\omega^2} e^{-\alpha Z}$$

Combination of the general theory of thermal explosions and the total sensitivity curves, yields three areas of interest characterized by the following formulas:

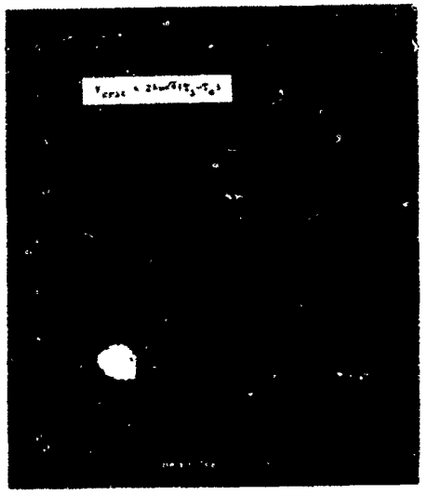

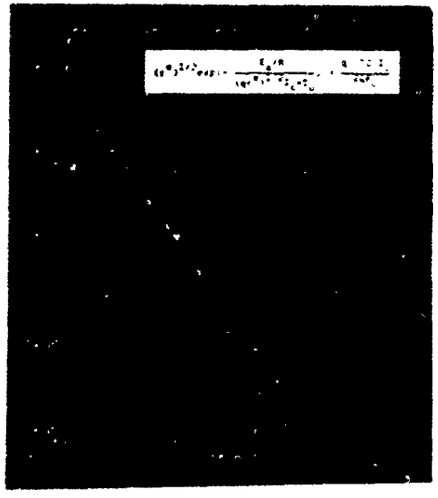

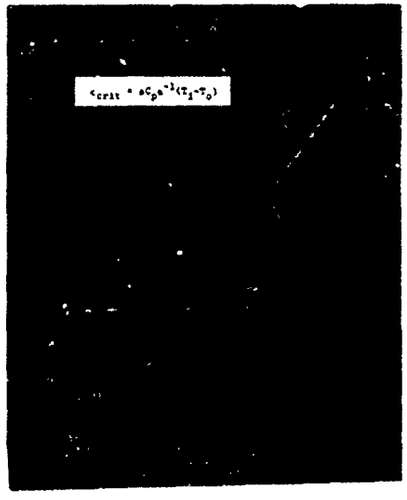

MICROWAVE INTERFEROMETER TECHNIQUES FOR DETONATION STUDY*

P. L. Stanton, E. L. Venturini, and R. W. Dietzel

Sandia National Laboratories*
Albuquerque, NM, USA

Techniques have been developed to improve resolution in microwave interferometry of detonating explosives. Unwanted reflections in the measurement arm of the interferometer result in phase distortion of the recorded signal. By using tuning techniques, unwanted reflections can be virtually eliminated, and phase distortion is minimized, for some experimental conditions. The use of a quadrature detector and an intensity monitor also improve the resolution of the interferometer. Data obtained in several detonation experiments are presented and interpreted.

INTRODUCTION

In the study of detonation waves, most experimental techniques involve an intrusive measurement which may disturb the progress of the reaction and introduce errors in the measurement itself. Microwave radiation is propagated readily through most explosive materials with almost no interaction. And, because microwaves reflect from a conductive region such as the reaction zone, they may be used in a simple interferometer to determine the instantaneous position of the detonation wave. In this paper we present a scheme for obtaining high resolution microwave interferometric data from a reacting explosive.

Previous investigators (1-8) have demonstrated the use of microwave interferometry in the study of propellant burn and of detonation of high explosives. In the case of burning propellants, the reaction rate is slow and variations in the rate are of greatest interest. Special techniques were developed by previous investigators to monitor the slow propellant burn rates. Prior work revealed that phase distortion is generally present in a detonating explosive experiment. Because the wavelength at microwave frequency is relatively long (1 to 30 mm), distortion of the recorded waveform introduces errors in the final answer which are often unacceptable for quantitative measurements. The distortion problem is even more exaggerated when the displacement-time history must be differentiated to obtain velocity information.

In this paper we present the results of an investigation of the problem of limited resolution. A solution is offered for simple detonation configurations. The solution involves 1) tuning methods to minimize phase distortion, 2) quadrature detection to improve resolution at all times in the fringe cycle, and 3) a method for cancellation of cross-talk from the reference leg to the data leg of the interferometer. We have developed three different microwave systems: X-band (10.6 GHz), K_a-band (35 GHz), and W-band (91 GHz). At the higher frequencies, the shorter wavelengths tend to permit higher resolution, However, because greater complexity is involved in the W-band system, tuning and quadrature detection are not yet commercially available. In this report experimental results are presented using the X-band interferometer for a variety of detonating systems and their interpretation is discussed.

BACKGROUND

The first study of microwave reflection from a detonation was by Koch in 1953 (1). He used a klystron microwave source operating at 2

GHz to observe a detonation in a 1:1 mixture of TNT and RDX, recording the difference frequency between the transmitted and reflected microwaves. His result was a detonation velocity of 7994 m/s which was 3.5% above the accepted value of 7700 m/s. In 1954 Cook, Doran and Morris (2) discussed microwave reflection from a detonation in four solid explosives, TNT, 50/50 Pentolite, 50/50 Amatol and 80/20 Tritonal. Their microwave interferometer employed a klystron at 9.415 GHz, a horn antenna to transmit and receive the reflected signal, and unconfined cast cylindrical bars of solid explosive. The detonation wave direction coincided with the incoming microwave beam. Their detonation velocity measurements differed from pin oscillograph results by between 0.3% for TNT to nearly 6% for Pentolite. The difference frequency waveforms are complex, and they attribute this to the excitation of multiple microwave propagation modes in the cylindrical explosive charge.

The results in the two papers above are criticized by Farrands and Cawsey (3) and Cawsey, Farrands and Thomas (4) who observe that microwave reflection from an unconfined explosive occurs partially from the detonation front and partially from the ionized detonation products expanding laterally from the sides of the charge, since part of the microwave energy propagates outside the unreacted explosive. This severly complicates the analysis of detonation velocities from the difference frequency. Farrands and Cawsey (3) use a klystron at 34.50 GHz, and their tetryl explosive charge fills a brass cylinder with a 15.2 mm outside diameter, 3.96 mm inside diameter, 50.8 mm long. The microwaves are guided over the entire forward and return path, and are coupled from the rectangular K_a-band waveguide into the tetryl-filled brass cylinder through a Teflon window. They suggest several experiments made possible by confining the explosive and the microwaves in a common guide, including the observation of variations in detonation velocity due to explosive density, diameter or confinement, the observation of contact transmission of a detonation, or the observation of instability in the detonation front.

These ideas are explored by Cawsey, Farrands and Thomas (4) who discuss the detonation velocity in tetryl as a function of density, and the observation of growth to detonation with microwaves. They point out that their 3.96 mm diameter cylindrical brass waveguide filled with tetryl propagates only the lowest microwave mode at 34.5 GHz for all densities of explosive used. This simplifies the analysis of the interferometer waveform considerably. A primary source of error in microwave interferometry is the presence of unwanted reflections at any point between the detector and the moving reflector (in this case the detonation wave). They show the dramatic improvement in the fringe pattern after using a stub tuner in the signal arm of the interferometer to minimize unwanted reflections. This permits much better spatial resolution of the detonation front position from the fringe pattern.

To convert the measured microwave fringe pattern to a displacement of the reflecting front versus time, the microwave wavelength in the explosive-filled guide must be accurately known. If the guide dimensions are determined, only the dielectric constant of the explosive at the measurement frequency is required. Cawsey, Farrands and Thomas (4) report the dielectric constant at 34.5 GHz for granulated tetryl, crystalline tetryl, ground TNT, crystalline TNT, crystalline PETN, 50/50 tetryl/PETN, and 90/10 RDX/paraffin for nine packing densities from 0.9 to 1.7 Mg/m^3. The dielectric constants range from a low of 1.891 to a high of 3.539.

With this information they measured detonation velocities in cylindrical columns of tetryl pressed to various densities between 1.3 and 1.6 Mg/m^3, and obtained a linear increase in velocity with increasing density. They also observed detonation transfer from a column partially filled with low density tetryl into the remainder filled with a higher density tetryl. Finally, they initiated a burn in six columns of tetryl pressed to different densities from 1.31 to 1.38 Mg/m^3. In each case they recorded a burn velocity near 2 km/s for the first 15 to 20 mm, followed by a transition to detonation velocity above 6 km/s. The transition typically occurred over a distance of 5 mm.

At the 4th International Symposium on Detonation in 1965 Johnson (5) discussed a microwave interferometer for studying explosives which employs an expendable dielectric rod as a waveguide to couple the microwave

signal into a cylindrical explosive charge. This technique was used to study growth to detonation in 25.4 mm diameter charges of Composition C-4, 50.8 mm diameter charges of ammonium perchlorate confined in glass, and 50.8 mm diameter charges of pentolite. The charges were divided into a short donor charge and a longer acceptor charge separated by a card gap which was a disk of Plexiglas of various thicknesses. Growth to detonation in the ammonium perchlorate was studied using a klystron at a frequency of 9.903 GHz.

The cylindrical explosive acted as a dielectric waveguide, and several modes could propagate, leading to a modulated fringe pattern. This pattern was obtained by mixing the signal reflected from the detonation front with other signals generated by fixed reflections in the transmission path. Hence the fringe pattern consisted of distorted waves. The microwave wavelength in the explosive was calculated by measuring the number of wavelengths in the fringe pattern produced by a detonation moving through a charge of known length. Growth to detonation was studied for an ammonium perchlorate charge with no card gap and three different Plexiglas gaps. A separate set of experiments used a microwave source at 24 GHz to observe growth to detonation in Composition C-4 pressed to 1.59 Mg/m^3 with several card gaps. Similar data were obtained at 20 GHz for (50/50) pentolite charges with various gaps.

Strand and coworkers (6,7) have developed a microwave interferometer to measure regression rates in solid propellants during rapid pressure transients. The klystron for these experiments operated near 10 GHz, and an E-H tuner was employed in the signal path to minimize unwanted reflections. Since the propellant burn rate is between 1 and 100 mm/s, a network analyzer can be used to compare reflected and transmitted signals, rather than the conventional mixer diode. The microwave system yielded high spatial and time resolution, but the results were hampered by inadequate knowledge of the free electron concentrations in the propellant flame zones which produce the reflected microwave signal. Russell (8) developed a similar system to study burning propellants with particular attention to the model of the burn region and the elimination of unwanted reflections in the microwave signal path.

THEORY OF OPERATION

In the classical model for a plane detonation wave in an explosive shown in Fig. 1, a shock wave precedes the reaction and compresses the material to the von Neumann spike pressure. The pressure decays during the reaction to the Chapman-Jouguet (C-J) pressure at the end of the reaction zone. The reaction zone thickness has been measured by other investigators and is found to vary between a few tenths of a millimeter for TNT and a few millimeters for TATB-based explosives (9). The reaction zone thickness has also been shown to decrease as the loading density of an explosive powder is increased (9,10). In the reaction zone the explosive is converted from its unreacted state to a hot plasma of gaseous reaction products. The plasma region is highly conductive (11) and is therefore a good reflector of microwaves.

A brief discussion of the reflection of the microwave signal by the detonation wave clarifies what is measured in these experiments. At the shock front shown in Fig. 1 the compression of the unreacted explosive by the von Neumann spike pressure produces a higher dielectric constant behind the shock. This propagating dielectric discontinuity results in a small reflection of the microwave signal, but most of the microwave energy continues into the reaction zone. The microwave electric field is transverse to the propagation direction in the waveguide, and the equations for transverse electromagnetic wave interactions with an isotropic plasma can be applied. The dielectric constant ϵ_p in the plasma is given by (12):

$$\epsilon_p = \epsilon_o \left[1 - \frac{\omega_e^2}{\omega^2 (1 - i/\omega\tau_e)} \right] \qquad (1)$$

where ϵ_o is the permittivity of free space, ω_e is the plasma resonance frequency for the electrons, ω is the frequency of the microwaves, and

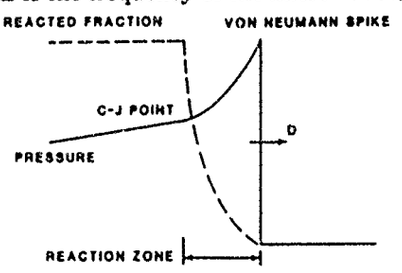

Fig. 1. Classical detonation wave model. The fraction of explosive reacted increases with distance through the reaction zone thickness.

τ_e is the electron collision time in the plasma. ω_e is determined by the electron density N_e, mass m_e and charge e:

$$\omega_e = e\,[N_e/\varepsilon_o m_e]^{1/2} \qquad (2)$$

When $\omega > \omega_e$, the real part of ε_p (Eq. (1)) is greater than zero, and microwave propagation is allowed. As ω_e approaches ω, the imaginary part of ε_p (representing microwave absorption) becomes significant. At the shock front shown in Fig. 1 the electron density is small and the plasma frequency ω_e in Eq. (2) is much less than the experimental frequency ω. Hence the microwaves propagate with negligible loss into the reaction zone. As the electron density N_e increases, ω_e approaches ω, and the microwave loss rises substantially. At the C-J point the electron density N_e is between 10^{21} and 10^{22} per cm^3 which gives a plasma frequency near 10^{15} Hz from Eq. (2). The microwaves are reflected at some point within the reaction zone when ω_e exceeds ω. Since the estimated ω_e at the C-J point is 4 orders of magnitude greater than ω, the reflection occurs very near the front of the reaction zone (within the first few microns (4)). Hence the microwave phase is not sensitive to temporal evolution of the reaction zone. The microwave loss near the reflection point depends on the gradient of the electron density at that point (related to the length of the reaction zone) and the electron collision time τ_e near the reflection point.

As the plasma propagates at the detonation velocity, the microwave path length changes. This results in a Doppler shift given by:

$$f_d = 2D^* / \lambda_g \qquad (3)$$

where D* is the wave velocity of the reflecting plasma front and λ_g is the microwave wavelength in the explosive-filled waveguide. Doppler frequencies on the order of 1 MHz are obtained in the present X-band experiments.

The guide wavelength λ_g for the transverse-electric-field propagating mode (TE_{mn}) is given by:

$$\lambda_g = \left[\frac{4}{4\varepsilon(\frac{f}{c})^2 - (\frac{m}{a})^2 - (\frac{n}{b})^2} \right]^{1/2} \qquad (4)$$

where ε is the relative dielectric constant of the unreacted explosive, f is the microwave frequency, c the velocity of light in vacuum, a the width of the waveguide, b the height, and m,n are integers. At 10.6 GHz the wavelength in air-filled, X-band waveguide (22.9x10.2mm) is about 3.6 cm for the TE_{10} mode, and no other modes will propagate because they are below their cut-off frequencies. When an explosive sample is inserted into the guide, the wavelength is decreased to about 2 cm. (for a typical explosive), and two of the higher-order modes will propagate. Significant microwave energy is not coupled to higher-order modes unless the reflecting plasma front is asymmetric with respect to the waveguide cross section. A transition to smaller size explosive-filled waveguide can be employed to eliminate higher order modes. The dielectric constant of the materials used including the explosives is measured to an accuracy of about one percent in a separate cavity resonance measurement.

MICROWAVE CIRCUIT

The interferometer circuit is shown schematically in Fig. 2. The microwave source is a Gunn diode operated at 10.6 GHz. The main beam is conducted to the explosive sample through a four-port circulator. The reflected energy is routed by the circulator to the quadrature intermediate frequency (QIF) detector. Part of the source signal is fed to the reference input of the QIF detector. The QIF has two output signals in quadrature, referred to as Data 1 and Data 2. Part of the reflected signal is fed to a simple diode detector which serves as an intensity monitor for the return signal. Isolators are used in the circuit to prevent unwanted internal reflections, and attenuators are used to reduce the signal to the proper operational level for the detectors. A phase shifter is used to set the initial phase.

The interferometer is designed to permit measurement of the instantaneous phase of the Doppler signal. Because the signal is sinusoidual in nature, sensitivity to changes in position varies cosinusoidually. The quadrature signals are used in a method analogous to the VISAR (13) laser interferometer system. Since the two detector signals are 90° out of phase, one signal is always in a relatively sensitive range. Furthermore, the quadrature signal removes the ambiguity of the interference signal at the maximum and minimum points, where reflection front reversals in direction of motion could occur without detection.

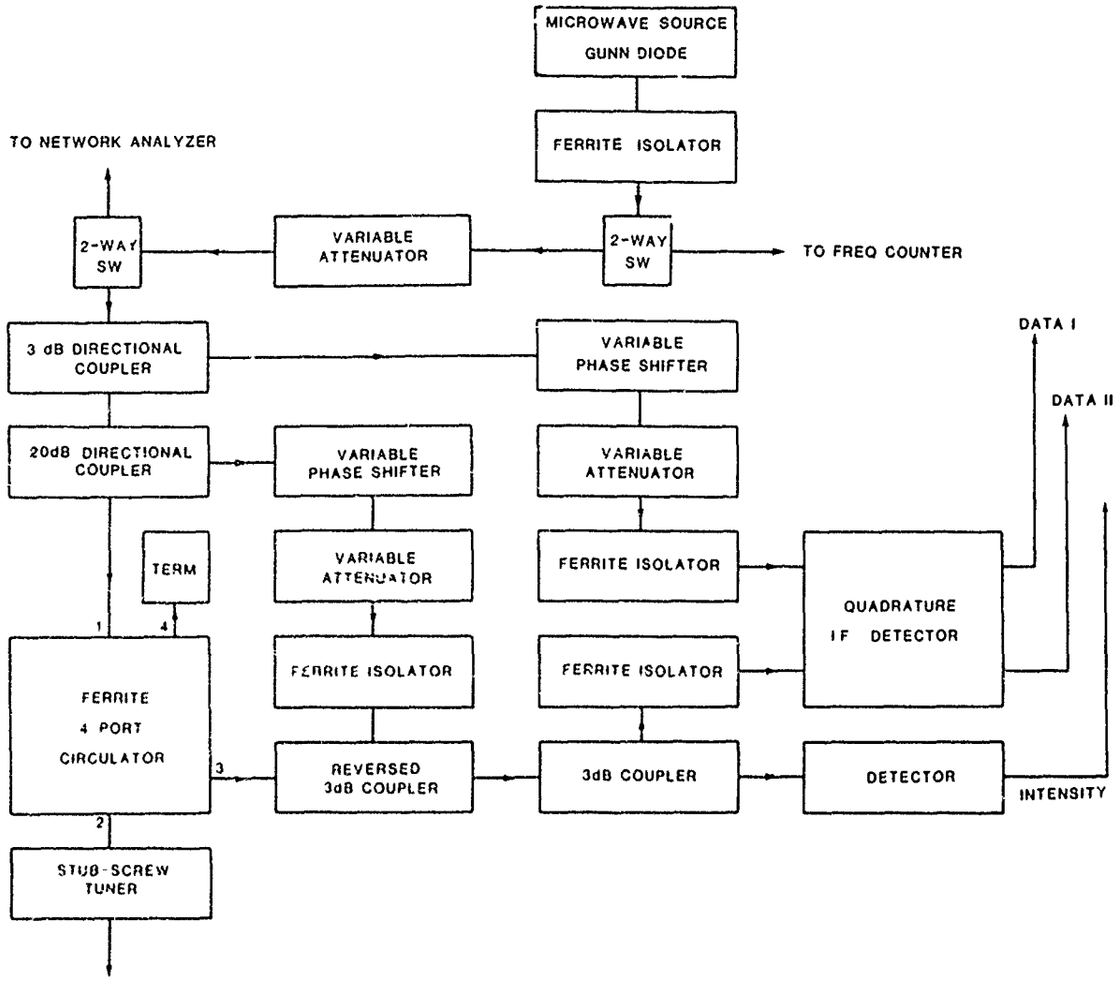

Fig. 2. 10-GHz microwave interferometer schematic

The four-port circulator routes the source signal to the device and routes the reflected signal to the intensity monitor and QIF. However, a certain amount of 'cross talk' reference signal is coupled from port 1 to port 3. This signal mixes with the Doppler-shifted signal and produces unwanted interference in the intensity monitor. To cancel the cross-talk signal, part of the source signal is taken from the source leg and, after attenuation and phase-shifting, is mixed with the signal coming out of port 3.

Unwanted reflections in the measurement leg of the interferometer can cause distortion of the data. Unwanted reflections can occur any place where a discontinuity exists in the dielectric properties of the waveguide. Changes in guide dimensions, flange couplings, and microwave components all represent sources for unwanted internal reflections. In a single frequency system, these reflections simply produce standing waves and reduce the efficiency of energy transmission. In the measurement leg of an interferometer, an unwanted partial reflection of the Doppler-shifted signal sends the higher frequency signal back to the moving reflector, where it is Doppler-shifted for a second time, and a third, and so on. The combination of the primary Doppler-shifted signal with second- and higher-order harmonics results in harmonic distortion in the detector output. A microwave tuner is used to cancel the effect of unwanted reflections in the measurement leg. The tuner

is adjusted to produce an additional reflection equal in amplitude and opposite in phase to the vector sum of all other unwanted reflections in the portion of the circuit being tuned. A network analyzer is used while adjusting the tuner to determine when the system is properly tuned. The analyzer is connected into the circuit in place of the explosive sample section of waveguide. Thus tuning is accomplished for the entire circuit except for the explosive sample section.

EXPERIMENTAL TECHNIQUE AND DATA ANALYSIS

The explosive is enclosed in waveguide (Fig. 3) in order to control the microwave propagation modes and the wavelength of the microwaves in the sample at the plane of reflection. This technique eliminates problems encountered when some microwave energy propagates outside the explosive. Rectangular waveguide is used to obtain the most clearly defined wavelength, although some experiments have been conducted with circular guide. To prevent damage to the sensitive microwave components during a detonation, a section of semi-rigid coaxial cable is used to connect the explosive sample section to the interferometer.

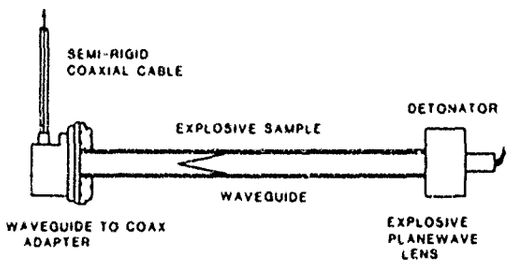

Fig. 3 Typical experimental device configuration

In most cases, a detonator and plane-wave lens are used to initiate a planar detonation in the sample. A thin aluminum foil is placed between the lens and the sample to serve as a reflector for the microwave signal prior to the arrival of the detonation front. A wedge at the other end of the explosive provides a gradual dielectric transition into the air-filled portion of the guide. This wedge is either made of Teflon or cut on the explosive itself and serves to minimize reflection of the microwaves due to the dielectric mismatch.

The interferometer produces two quadrature signals which indicate the phase of the reflected signal relative to the source reference. These two signals, called DI and DII, are used to compute the displacement of the reflector in the relationship

$$x(t) = \frac{\lambda_g}{4\pi}\left[\arctan\left\{\frac{DI\ (t)}{DII(t)}\right\} - \phi_o\right] \qquad (5)$$

where λ_g is the wavelength in the guide at the position of the reflector and ϕ_o is the initial phase.

EXPERIMENTAL RESULTS

A variety of successful experiments have been conducted using the improved microwave interferometric techniques. The results are in agreement with data obtained by conventional means. Some of the results provide new insight into the behavior of detonating explosives and are discussed as follows.

Simple Detonation – A planar detonation of a homogeneous explosive in a constant cross-section waveguide provides a simple check on the interferometric technique. Representative data obtained from a PBX-9404 experiment are shown in Fig. 4. The two quadrature signals are sinusoidual in shape, indicative of the extent to which the system has been tuned to eliminate unwanted microwave reflections. Using our measured value for ε of 3.315 for PBX-9404 at 10.6 GHz in Eq. (4) and (5) the quadrature signals yield the displacement time histories at the top of Fig. 4. The slope of the displacement curve indicates an average velocity of detonation of 8.98 km/s which is about two per cent above the published value of 8.80 km/s (9). This descrepancy is apparantly due to an error in the measurement of the dielectric constant of the unreacted PBX-9404. The resulting displacement history shown includes the air shock in the guide subsequent to the detonation.

The small ripple on the intensity monitor record during detonation indicates a slight mismatch at the explosive wedge interface. There is also a gradual increase in intensity with time during detonation. This intensity variation is attributed to the decrease with time of the length of unreacted material through which the microwave signal must propagate. Thus, the explosive material is somewhat lossy as a dielectric

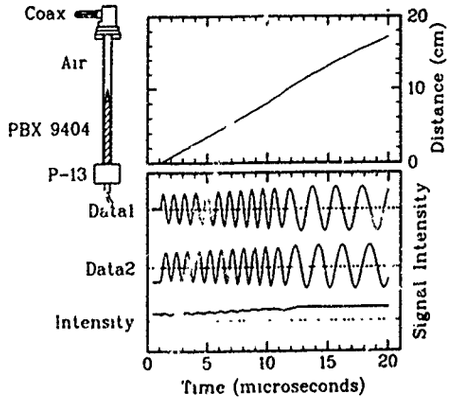

Fig. 4. Composite results from detonation of PBX-9404 explosive column. Data1, Data2, and Intensity are recorded waveforms. The displacement curve is computed using Eq. 5. P-13 is explosive plane wave generator, 1.3 inch diameter.

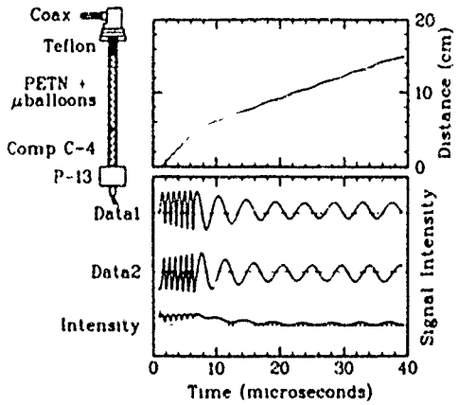

Fig. 5. Detonation transfer experiment. Composition C-4 overdrives low-density PETN/glass microballoon mixture.

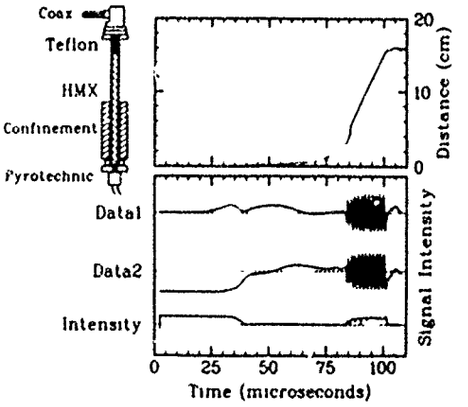

Fig 6. DDT experiment using HMX explosive at density 1.2

at microwave frequencies.

Detonation Transfer — Experiments have been conducted in which the explosive in Fig. 3 is replaced with two samples end-to-end having different detonation velocities. Interpretation of the results becomes more complicated in these cases, because the dielectric constant is different in each explosive and thus the wavelength is different. The parameters at the plane of reflection determine the wavelength for use in Eq. 5 for computation of displacement.

To produce an overdriven detonation, an experiment was conducted in which the first explosive was Composition C-4 and the second was a low-density mixture of PETN and glass microballoons. A PMMA wedge is inserted at the end of the explosive train to provide microwave impedance matching.

Results of this experiment are shown in Fig. 5. The first portion of this record shows that the Composition C-4 explosive with a dielectric constant of 3.59 detonated with a uniform velocity. When the detonation wave reached the interface with the PETN, a transition occcurred in the microwave interference signal. The low-density PETN/glass microballoon mixture has a dielectric constant of 1.41. Following the transition, the detonation velocity decreases indicating a period of over-driven detonation. The signal amplitude also decreases, indicating an increasing thickness of the reaction zone. The large dielectric mismatch at the C4-PETN interface produces the ripple in the intensity monitor and the distorted sine waves in the C4 portion of the fringe data.

DDT — A few experiments have been conducted to study the deflagration-to-detonation transition in porous granular explosives. The experimental configuration is similar to Fig. 3 except that a pyrotechnic ignitor is used, and the waveguide was bolstered by heavy steel plate on all sides to provide the necessary confinement for growth to detonation. A representative result obtained from HMX explosive at 1.2 density is shown in Fig. 6. The dielectric constant for this explosive is 2.21. The intensity of the return signal falls to a low level after about 40 microseconds, indicative of strong microwave absorption in the burning explosive. The interference fringes undergo several oscillations during this time, but interpretation of the

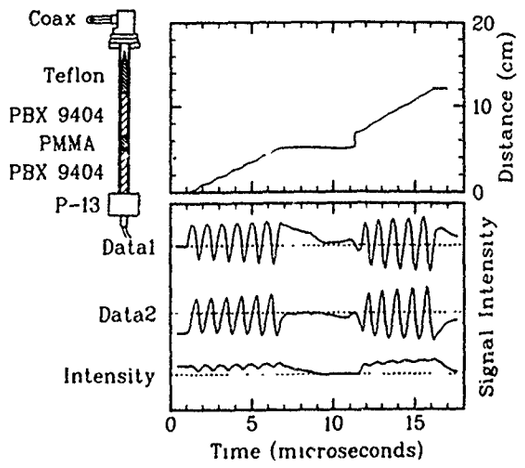

Fig. 7. PBX-9404 gap test experiment using 15 mm PMMA barrier

oscillations in terms of displacement is impossible. An abrupt transition to detonation occurs at about 85 microseconds. Even though displacement information is lost during the deflagration phase, the point of transition can be located by counting fringes back from the terminal end of the signal. In this experiment, the transition occurred after about 5 cm of deflagration.

Gap Test – Finally, a series of experiments was conducted to observe shock growth to detonation in a simulation of the traditional card gap test. The donor and acceptor are each 50.8 mm columns of PBX-9404. The gap is filled with PMMA of various thicknesses. It was found that a gap of about 15 mm produced a significant delay in initiation in the acceptor. The results from a 15 mm gap test are shown in Fig. 7. During the detonation of the donor column, a distorted but uniform fringe pattern is produced. The distortion is attributable to the internal reflection of the microwave signal at the PMMA/explosive interface, resulting in phase distortion. The intensity of the reflected microwave signal decreases as the shock traverses the gap and enters the acceptor column. Again, the low intensity is attributed to an extended reaction zone as the pre-detonation reaction proceeds in the acceptor column. Finally, the acceptor breaks into detonation which propagates to the end of the column. Lower ripple and less distortion are present in the acceptor column because fewer untuned mismatches are present in the remaining portion of the guide.

DISCUSSION

The various experiments discussed above are representative applications of microwave interferometry to the study of detonation. They illustrate that the interferometer can be used to evaluate the performance of detonating devices and to study basic detonation phenomena. The most intriguing aspect of microwave interferometry for detonation study is the fact that the microwaves propagate in the explosive and provide a continuous, non-intrusive, in situ probe of the reaction front.

The microwave interferometer described here has certain fundamental limitations which lie in the areas of resolution, size/wavelength considerations, and measurement accuracy. In this study we have attempted to maximize the resolution of the interferometer by tuning techniques. In a perfectly tuned system, the resolution should be limited only by the recording equipment. Practically speaking, resolution of the order of one per cent of the wavelength should be achievable in a well-tuned system. The experiments show, however, that tuning is not always possible, to the extent desired.

Microwave propagation characteristics must be considered when planning an experiment, and the frequency used must be sufficiently high to propagate in the device, but not so high that higher modes propagate in the region of interest. (Higher modes can propagate in the experiments described above and are a potential source of error in the resulting data.) Rectangular geometry is preferable in this regard, but circular geometry can be used. The higher modes generally will be present in circular guide geometries.

If independent measurements of displacement and velocity are to be made, the dielectric properties of the explosive material must be accurately measured at the specified frequency. Otherwise, the dielectric constant must be inferred from a known sample length and an observed fringe count.

CONCLUSIONS

Microwave interferometry offers a method of nonintrusively probing the reaction front in

an explosive material which is opaque to visible light. The limitations on microwave interferometry in explosives include the relatively long wavelengths at microwave frequencies and phase distortion due to unwanted reflections. These two factors have combined to limit the resolution of previous interferometer systems. By careful design of the interferometer circuit, using microwave components and instrumentation now available, it is possible to eliminate much of the unwanted reflections and obtain high resolution from relatively long wavelength systems.

The incorporation of an intensity monitor furnishes additional insight into the interferometer data. The intensity variations during deflagration and detonation have been related to propagation loss in the unreacted explosive and to the thickness and conductivity of the reaction zone and its evolution with time.

REFERENCES

*This work performed at Sandia National Laboratories supported by the U.S. Department of Energy under Contract No. DE-AC04-76DP00789.

1. B. Koch, "Reflexion de micro-ondes par des phenomenes de detonation", Compt. Rend. Acad. Sci., Paris, *236*, 661-663 (1953).
2. M. A. Cook, R. L. Doran and G. J. Morris, "Measurement of detonation velocity by Doppler effect at three-centimeter wavelength", J. Appl. Phys. *26*, 426-428 (1955).
3. J. L. Farrands and G. F. Cawsey, "Microwave observation of detonation", Nature *177*, 34-35 (1955).
4. G. F. Cawsey, J. L. Farrands and S. Thomas, "Observations of detonation in solid explosives by microwave interferometry", Proc. Royal Soc. A *248*, 499-521 (1958).
5. E. G. Johnson, "A Microwave technique for studying detonation phenomena", Proc. 4th Intern. Symp. on Detonation (Office of Naval Research – Department of the Navy, Washington, D.C. 1966), pp. 584-594; E. G. Johnson, Jr., "A microwave technique of determining growth to detonation", AIAA J. *3*, 2109-2111 (1965).
6. L. D. Strand, A. L. Schultz and G. K. Reedy, "Microwave Doppler shift technique for determining solid propellant transient regression rates", J. Spacecraft *11*, 75-83 (1974).
7. L. D. Strand, K. R. Magiawala and R. P. McNamara, "Microwave measurement of the solid-propellant pressure-coupled response function", J. Spacecraft *17*, 483-488 (1980).
8. L. H. Russell, "Burning velocities of a solid propellant via a microwave technique, at elevated pressures and pressurization rates", Naval Surface Weapons Center Report No. NSWC TR 79-378 (October, 1979) (Ph.D. thesis, Univ. of Pittsburgh, Pittsburgh, PA).
9. B. M. Dobratz, "LLNL Explosives Handbook, Properties of Chemical Explosives and Explosive Stimulants," UCRL-52997, Lawrence Livermore National Laboratories (1981), pp. 10-1/10-7.
10. M. J. Urizar, E. James, Jr., and L. C. Smith, Phys. Fluids *4*, 262-274 (1961).
11. A. M. Staver, A. P. Ershov and A. I. Lyamkin, "Study of detonations in condensed explosives by conduction methods", Fiz. Goreniya Vzryva *20*, 79-83 (1984).
12. H. G. Booker, "Cold Plasma Waves", (Martinus Nijhoff, Dordrecht, The Netherlands, 1984), pp. 23-38.
13. L. M. Barker and R. E. Hollenbach, "Laser interferometer for measuring high velocities of any reflecting surface," J. Appl. Phys. *43*, 4669-4675 (1972).

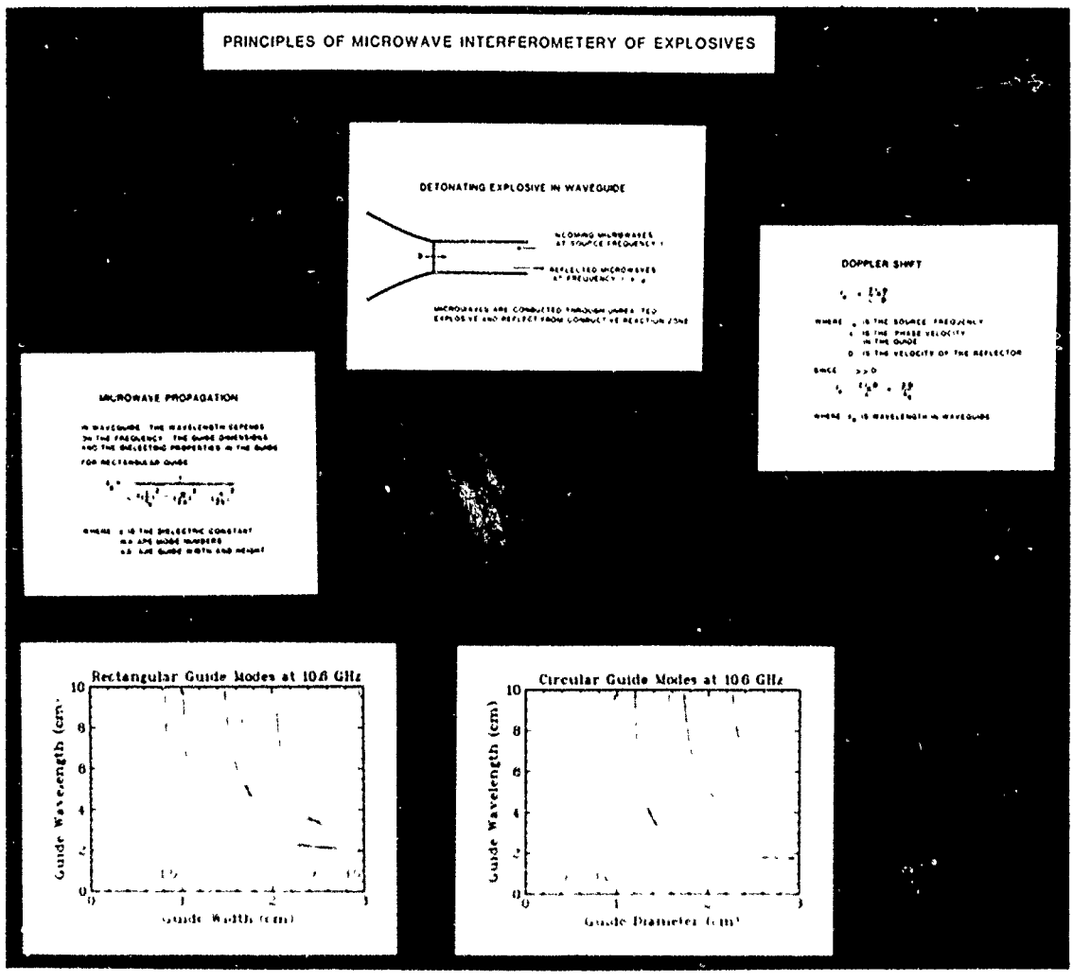
PRINCIPLES OF MICROWAVE INTERFEROMETERY OF EXPLOSIVES
DETONATING EXPLOSIVE IN WAVEGUIDE
DOPPLER SHIFT
MICROWAVE PROPAGATION
Rectangular Guide Modes at 10.6 GHz
Guide Wavelength (cm)
Guide Width (cm)
Circular Guide Modes at 10.6 GHz
Guide Wavelength (cm)
Guide Diameter (cm)

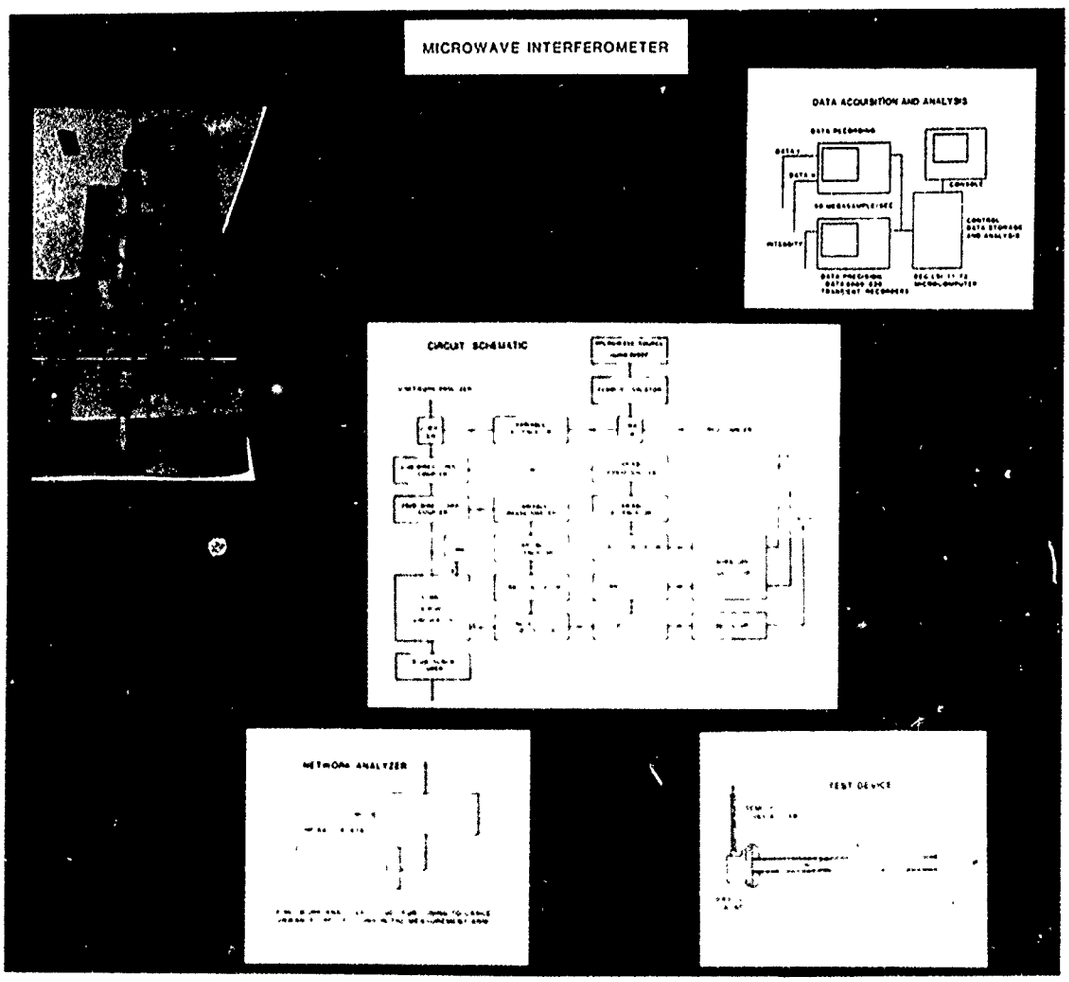
MICROWAVE INTERFEROMETER
DATA ACQUISITION AND ANALYSIS
CIRCUIT SCHEMATIC
NETWORK ANALYZER
TEST DEVICE

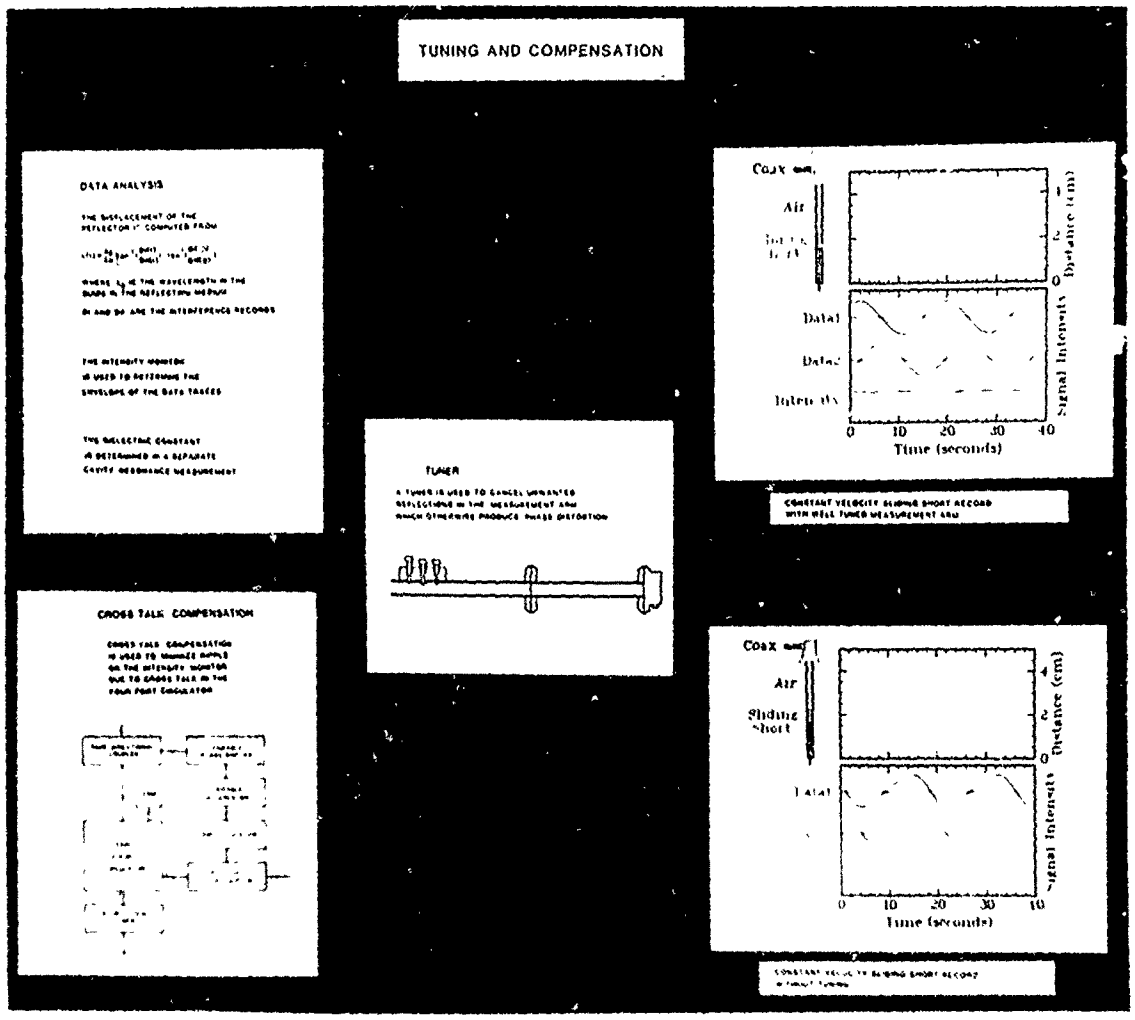
TUNING AND COMPENSATION
DATA ANALYSIS
TUNER
CROSS TALK COMPENSATION
Coax
Air
Sliding Short
Distance (cm)
Signal Intensity
Time (seconds)

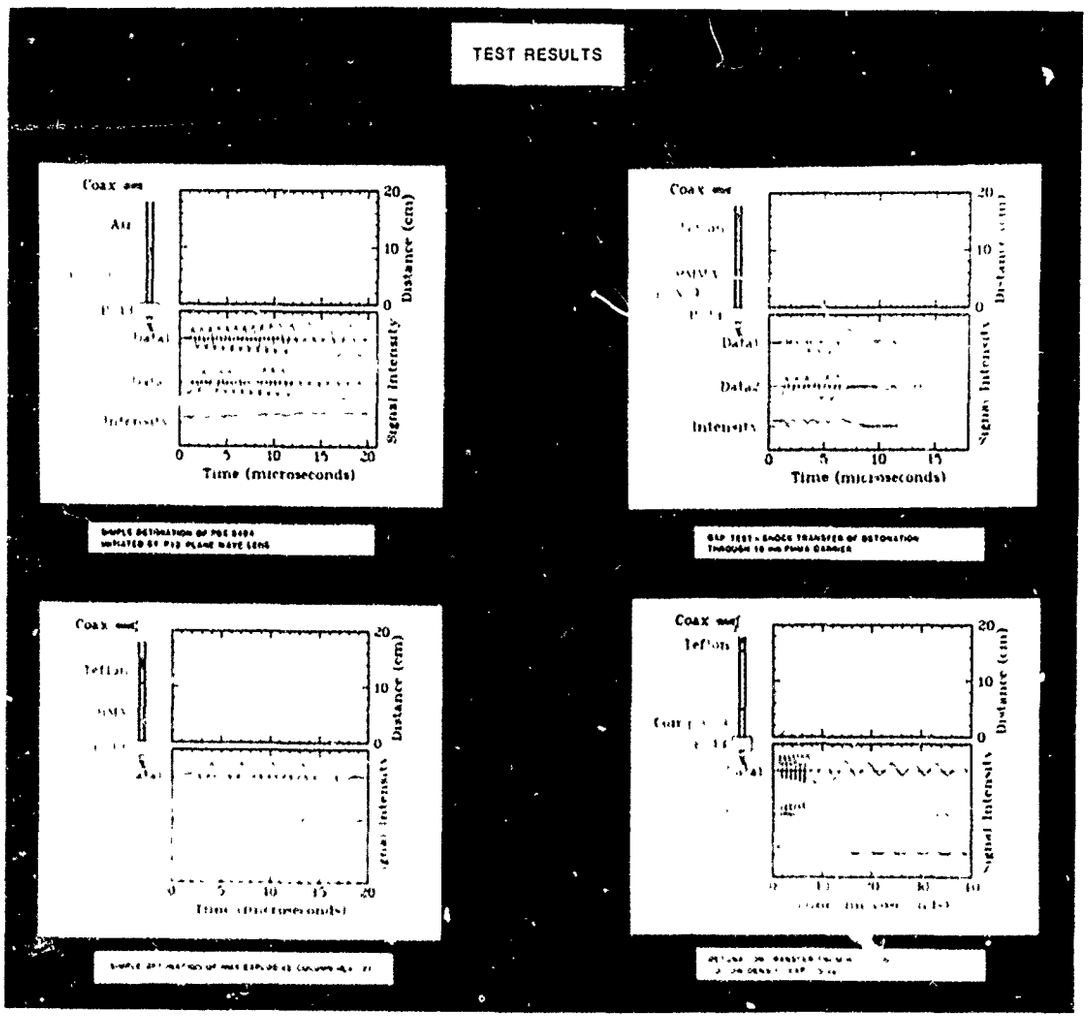
TEST RESULTS
Coax
Air
Time (microseconds)
Distance (cm)
Signal Intensity
Intensity

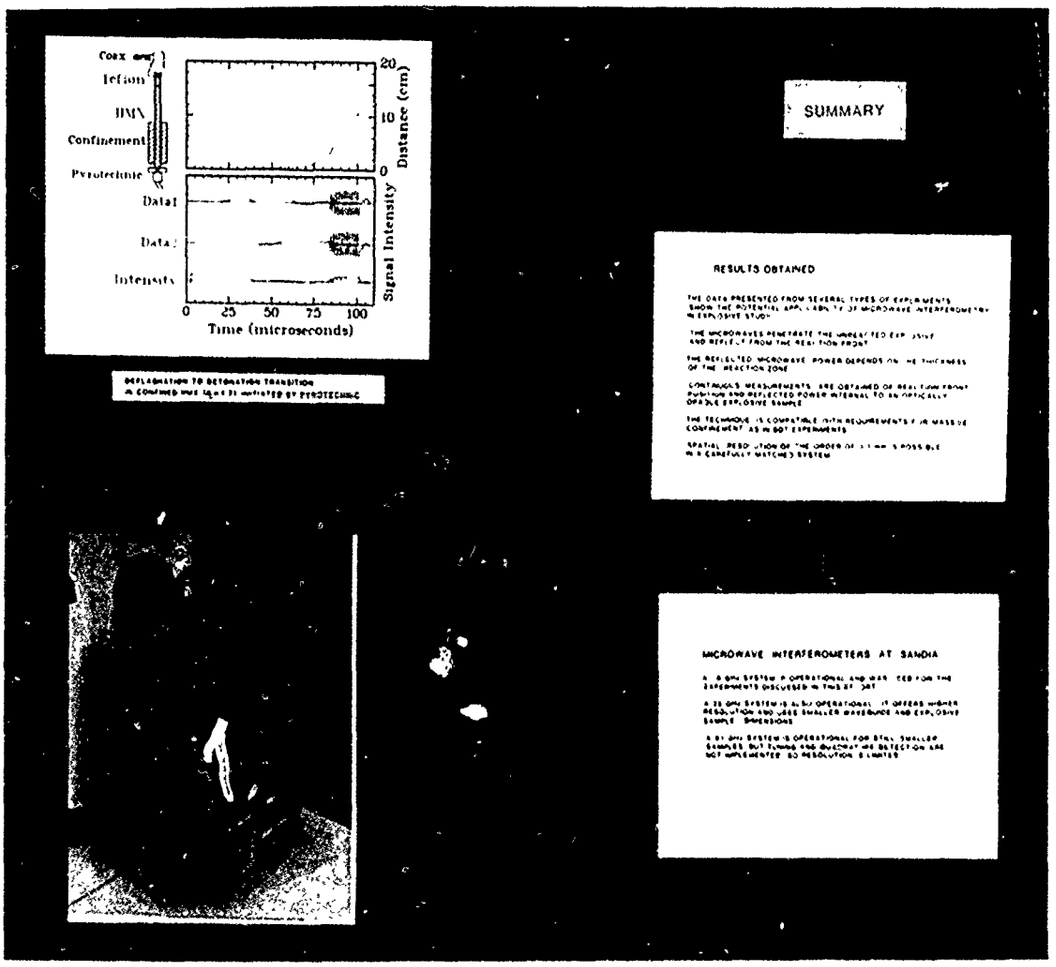
Coax
Teflon
HMX
Confinement
Pyrotechnic
Data1
Data2
Intensity
0
25
50
75
100
Time (microseconds)
20
10
0
Distance (cm)
Signal Intensity
SUMMARY
RESULTS OBTAINED
MICROWAVE INTERFEROMETERS AT SANDIA

Session V
EQUATION OF STATE I

Chairmen: Tsutomu Hikita
Fukui Institute of Technicology
Edward L. Lee
Lawrence Livermore National Laboratory

DETONATION BEHAVIOR OF LX-14 and PBX-9404: THEORETICAL ASPECT*

Francis H. Ree and Mat van Thiel
University of California
Lawrence Livermore National Laboratory
Livermore, California

We recently developed an a priori theory of statistical mechanics to describe post-detonation behavior of explosives. It is based on (1) reliable intermolecular potentials, (2) an accurate statistical mechanical theory of mixtures, and (3) an efficient technique to handle reactive multiphase mixtures. We have computed the detonation properties of LX-14 and PBX-9404. The Gibbs free energy of the mixture indicates that nitrogen will phase-separate from the rest of detonation products as do graphite or diamond. The theoretical Chapman-Jouguet (CJ) detonation velocities agree well with experiment, but the CJ pressures show a small discrepancy. We suggest that CJ experiments have been insensitive to slow carbon formation. Theoretical results of overdriven shocks, the CJ adiabat, and several useful fits to the theory will be discussed.

INTRODUCTION

At the 7th Symposium (International) on Detonation one of us reported calculations (1) of equations-of-state (EOS) of simple explosives (NO, HNB, and RX-23-AB), using a statistical mechanical theory and intermolecular potentials. These explosives were chosen for the study because concentrations of their major detonation products are largely unaffected by the changes in pressure (P) and temperature (T). The theoretical results were compared with Chapman-Jouguet (CJ) measurements and cylinder tests. The comparisons produced encouraging results, suggesting that post-detonation behavior of the simple explosives are, to a large extent, in equilibrium. This motivated us to extend the study to a more complex explosive. We expected that such a study would take about a year. This estimate (which was soon found to be too optimistic) seemed reasonable at the time of the symposium, because most calculational tools developed from the study of the simple explosives could be directly applied to more complex situations.

As it turned out, complex explosives require consideration of new physics inherent to themselves. They are: accurate parameterizations of complicated intermolecular potentials, a need to handle chemical reactions in an efficient manner, and a possibility that reacting mixtures may undergo a fluid-fluid phase separation. Except for the phase-separation problem, most calculational tools have been developed by now. Details of them have been published elsewhere (1,2). A fluid-fluid phase separation in multi-component systems is a complex statistical mechanical subject in its own light and is beyond the scope of the present paper. A separate paper (3) will address the issue in detail to show why and how a fluid-fluid phase separation in $N_2 + H_2O + CO_2$ mixtures is expected to affect the detonation behavior of explosives. In the present paper the allowance of the fluid-phase separation is assumed from the outset.

The main purpose of this paper is to discuss the results of our theoretical calculations on thermodynamic and hydrodynamic paths after detonation of PBX-9404 and LX-14 explosives from the calculations. We also precent several useful analytic representations of the theoretical EOS results. Prior to this, however, we want to give a brief outline of our theoretical model which is pertinent to the ensuing discussion.

*Work performed under the auspices of the U.S. Department of Energy by the Lawrence Livermore National Laboratory under contract number W-7405-ENG-48.

THEORETICAL MODEL

A successful theory of post-detonation behavior must contain several ingredients: (1) reliable intermolecular potentials; (2) reliable statistical mechanical theory of one- and multi-component systems; and (3) efficient techniques to handle reactive mixtures in multiphase equilibrium.

A. Intermolecular Potential and One-Component EOS Theory

An intermolecular potential which best describes experimental shock wave data is the exponential-6 (exp-6) potential:

$$\phi(r) = \varepsilon\left\{\left(\frac{6}{\alpha-6}\right)\exp[\alpha(1-r/r^*)] - \frac{\alpha}{\alpha-6}\left(\frac{r^*}{r}\right)^6\right\} \quad . \tag{1}$$

Note that the exp-6 potential has three parameters: ε = the depth of the attraction, r^* = the range of the repulsive core, and α = the slope of the repulsions. For most common detonation products, theoretical methods and shock wave data are available to fix these parameters. The original references for the shock wave data used to calibrate the parameters of our intermolecular potentials are given in Ref. 2. The calibration for chemical species (NH_3 and H_2O) with a strong electrostatic interaction requires a temperature-dependent ε, while a chemical species (H_2) with a strong many-body force is represented by a small (= 11.1) value of α. Table 2 in Ref. 2 lists the numerical values of ε, r^*, and α for all gaseous species considered in our work.

For the calibration of one-component equilibrium properties we used the free energy expression of Ross (4), which is an improved version of the variational theory of Mansoori and Canfield (5), and Rasiah and Stell (6). Monte Carlo and molecular dynamic calculations have shown that the soft-sphere variational theory of Ross and similar improved theories (7,8) which are developed more recently can reliably predict thermodynamic properties over the entire dense-fluid region relevant to detonation problems. It is important to mention that in our calculation the free energy was numerically evaluated, from the variational theory, *without* approximation.

B. Effective One-Component Potential for Reactive Mixtures

Post-detonation products generally exist as mixtures. To calculate thermodynamic properties of mixtures, we employ the improved van der Waals one-fluid (vdWlf) model (9), in which all molecules in the mixture are assumed to be identical and to interact with an "effective" one-component exp-6 potential. The ε, r^*, and α of the effective one-component potential are expressed in terms of the mole fractions (x_i) and the pair interaction constants (ε_{ij}, r^*_{ij}, α_{ij}) of the constituents of the mixture as follows:

$$(r^*)^3 = \sum_{i,j} x_i x_j \, (r^*_{ij})^3 \, . \tag{2}$$

$$\varepsilon = \sum_{i,j} x_i x_j \, \varepsilon_{ij} \, (r^*_{ij})^3/(r^*)^3 \, . \tag{3}$$

$$\alpha = \sum_{i,j} x_i x_j \, \alpha_{ij} \, \varepsilon_{ij}(r^*_{ij})^3/\varepsilon(r^*)^3 \, . \tag{4}$$

Since in our mixture model every molecule interacts with the same concentration-dependent potential as every other molecule, we can extend the one-component EOS theory discussed earlier to mixtures. The reliability of the improved vdWlf model has been verified by Monte Carlo simulations (9). As an example we chose an equimolar mixture of H_2 and He. Table 1 shows the pressures of a mixture computed from Monte Carlo simulation (216 particles) and our mixture model as decribed by Eqs. (1)-(4) and the soft-sphere variational theory. We note that the statistical mechanical results closely follow the Monte Carlo data.

C. Chemical Equilibrium Calculation by the CHEQ Code

Because the detonation products are chemically reactive, their concentrations change with T and P. This makes it necessary to determine the concentrations n_k (= $n\ x_k$; n = total number of moles in a given phase) of all constituents by minimizing the Gibbs free energy. Since ε, r^*, and α all depend on n_k through Eqs. (2)-(4), the minimization requires a frequent readjustment of the exp-6 parameters throughout the calculation. The chemical equilibrium code (CHEQ) was developed to make these adjustments.

The CHEQ code solves the chemical compositons of heterogenous mixtures, using the extent-of-reaction method. This portion of the

TABLE 1
Comparison of Pressure From the Two-Component Monte Carlo (MC) Calculation and the Theory of Mixtures[a]

T (°K)	V(cm³/mol)	Pressure (GPa)	
		2-Component MC	Theory
50	20	0.047 ± 0.001	0.05
100	14	0.338 ± 0.003	0.35
300	10	1.856 ± 0.008	1.91
4000	8	12.43 ± 0.02	12.6
7000	4.5	54 ± 1	55.3

[a] The exp-6 potential parameters used in the comparison are: (ϵ/k, r*, α) = (36.4 °K, 3.43 A, 11.1), (10.8 °K, 2.9673 A, 13.1), and (15.5 °K, 3.30 A, 13.0) for the H_2-H_2, He−He, and H_2−He interactions, respectively.

CHEQ code is the same as that of Levine's code (10). The CHEQ code is superior to other available computer codes in that it has some capability to handle several gas or liquid phases simultaneously. For a solid-phase of graphite or diamond, the CHEQ code employs the Murnaghan equation to represent P-V data. Note that no amorphous form of solid carbon is allowed in the present formulation, since the inclusion of such metastable (or possibly unstable) species directly contradicts the spirit of the calculation, namely an assumption of strict thermodynamic equilibrium. This is essential to determine the extent to which time-dependent factors influence experimentally measured detonation data.

APPLICATION TO PBX-9404 and LX-14

Chemical equilibrium calculations have been made on two HMX based explosives. PBX-9404 and LX-14 (11). The results are two theoretical data based of similar but not identical compositions as a function of T and P. They offer a good basis for comparing experimental and theoretical sensitivity to changes in composition and energy. LX-14 has the compositon C:H:N:O = 1.52:2.92:2.59:2.66 in moles per 100 g. For PBX-9404 this is C:H:N:O:Cl:P = 1.40:2.75:2.69:2.57:0.03:0.01. The detonation energies are the same to within 1%, yet, experimental differences are noticeable.

Figures 1 and 2 show comparison of the shock velocity vs P plots of PBX-9404 and LX-14 based on the present work (referred to as CHEQ), the Jones-Wilkins-Lee (JWL) EOS (12), the Becker-Kistiakowsky-Wilson (BKW) EOS (13) (the parameters of which are given by Finger *et al.* (14)), and the Jacobs-Cowperthwaite-Zwisler 3 (JCZ3) EOS (15). Figure 1 also includes the experimental data (16-18) of PBX-9404. Table 2 gives the comparison of the CJ data of the two explosives.

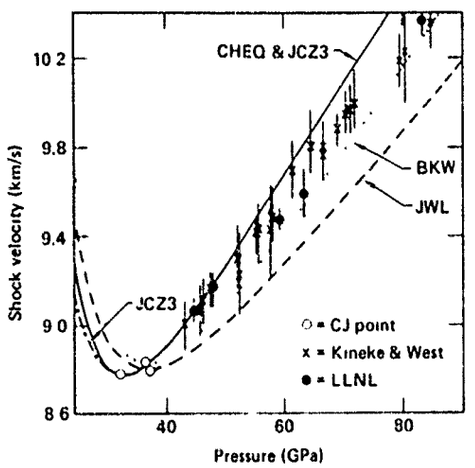

Fig. 1. The Hugoniots of PBX-9404 (ρ_o=1.84 g/cm³) (Calculated curves are: the present theory (CHEQ), the BKW EOS (13,14), the JCZ3 EOS (15), and the JWL EOS (12): Crosses are experimental data of Kineke and West (16) and solid circles are the Lawrence Livermore National Laboratory (LLNL) data by Lee et al., (17) and Green et al., (18).)

In the present work we allow detonation products to be in three different phases, i.e., a gaseous phase containing H_2, CH_4, O_2, CO_2, H_2O, N_2, CO, NO, NH_3, a second gaseous phase composed of only N_2 and H_2O, and a solid phase of carbon which may be either graphite or diamond. Note that the second fluid phase was *not* included in earlier calculations by other workers. The allowance of the second

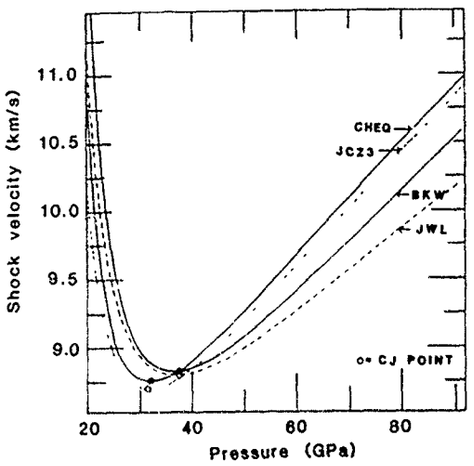

Fig. 2. The Hugoniots of LX-14 (ϱ_o=1.835 g/cm³) (Calculated curves are: the present work (CHEQ), the BKW EOS (13,14), the JCZ3 EOS (15), and the JWL EOS (11).)

phase does not necessarily mean that it should be physically present at all P and T. It is present only if its inclusion lowers the Gibbs free energy of the whole multiphase mixture system. This part of the computational chore is built into the CHEQ code.

Appearance of a second fluid phase depends sensitively on the values of the exp-6 parameters (r^*_{ij}, ε_{ij}, α_{ij}), where i=N_2 and j=H_2O. Our calculations employ $r^*_{ij} = k_{ij}(r^*_{ii} + r^*_{jj})/2$, $\varepsilon_{ij} = \sqrt{\varepsilon_{ii}\,\varepsilon_{jj}}$, and $\alpha_{ij} = \sqrt{\alpha_{ii}\,\alpha_{jj}}$ to compute the unlike-pair (i≠j) interaction parameters (19), where the k_{ij}'s are chosen to be unity for all species except $k_{H_2O\text{-}N_2} = 1.03$ and $k_{H_2O-CO_2} = 0.965$. These small changes ($\simeq$ 3%) from unity are within variations of experimentally determined r* values with different experimental techniques. The computed thermodynamic properties are largely unaffected by the changes, except in the neighborhood of the fluid-fluid phase separation boundary, which is sensitive to a small change in $k_{N_2-H_2O}$.

Our choice, $k_{N_2-H_2O} = 1.03$ and $k_{CO_2-H_2O} = 0.965$, was made to place the CJ point within the (P,T) region where three phases, i.e., N_2-rich and N_2-poor fluid phases plus a "diamond-like" solid phase of carbon, exist in thermodynamic equilibrium. Such a choice produces the CJ detonation velocity (D_{CJ} = 8.78 km/s for PBX-9404 and 8.74 km/s for LX-14. Both these values agree with the experimental values (12,20,21) in Table 2. Other theoretical justifications for the need of the fluid-fluid phase separation are given in Ref. 3. Further experimental work on

TABLE 2
Chapman-Jouguet (CJ) Data of PBX-9404 and LX-14

Explosives Variable[a]		Experiment[b]		Theory			
				CHEQ	BKW[c]	BKW[d]	JCZ3[c]
PBX-9404	D	8.80	8.78	8.81	8.83	8.88	8.78
ϱ_o=1.84	P	37.0	35.6	33.2	36.8	36.3	32.5
	ϱ	2.48	2.46	2.40	2.47	2.46	2.39
	T			4089	2280	2466	3678
	-	2.85	2.99	3.30	2.90	3.01	3.37
LX-14	D	8.79		8.78	8.83	8.75	8.70
ϱ_o=1.835	P			32.3	36.7	34.8	31.9
	ϱ			2.38	2.47	2.42	2.38
	T			4069	2248	2510	3612
	Γ			3.38	2.90	2.98	3.36

[a] D = detonation velocity in km/s; P = pressure in GPa, ϱ = density in g/cm³; T = Temperature in °K; Γ = adiabatic gamma [Eq. (5)].

[b] The first values of PBX-9404 are from Ref. 1 and the second values are from Ref 20. The value of ϱ_o quoted in Ref. 20 is 1.846 g/cm³. The value of LX-14 is from Ref. 21.

[c] These are computed using the same parameters in the TIGER code, as reported in Ref. 14.

[d] C. L. Mader, *Numerical Modeling of Detonations* (University of Calif. Press, Berkeley, CA, 1979), p. 57 and p. 65. The quoted values of ϱ_o are: 1.844 g/cm³ for PBX-9404 and 1.81 g/cm³ for LX-14.

LX-14 is in progress at the LLNL (21).

In contrast to the D_{CJ} value, the deviation between the theoretical (33.0 GPa) and the experimental (35-37 GPa) CJ pressures (P_{CJ}) is much larger. See Table 2. This is similar to the case of PETN (2), where the deviation probably occurred because of a slow kinetic effect present in the experimental P_{CJ} data. It is possible that the same kinetic effect is also responsible for the observed deviation in the present case. One candidate for the postulated slow reaction is a solidification process of carbon from the dissociation of chemical species (such as CO_2, CO, CH_4, etc.) (2). The experimental support for this view comes from the measurements of the luminosity and electrical conductivity of shock-compressed organic molecules (22,23). These data indicate that carbon condensation will occur not at the shock front but behind it with a finite induction time; e.g., 0.02 μs at 14.4 GPa for nitromethane (24).

Additional theoretical support is provided by the "experimental" behavior of the adiabatic gamma,

$$\Gamma_{JWL} = -\left[\partial \ln P / \partial \ln V\right]_S , \qquad (5)$$

obtained within the constraint of the CJ theory (25). Figure 3 shows the behavior of Γ along the CJ isentrope, in which the Γ values used are constrained to agree with: (I) the cylinder-test data at $\varrho<\varrho_{CJ}$ (12); (II) the Γ (=2.85) at $\varrho = \varrho_{CJ}$ [computed with the experimental P_{CJ} value of 37 GPa (12)]; and (III) the CJ isentrope inferred from the overdriven shock data at $\varrho>\varrho_{CJ}$ (16-18)

For an explosive with specified atomic compositions, its CJ point corresponds to a (P,V,T) state which should depend only on ϱ_o and the energy of formation of the explosive. Therefore, unless the CJ point accidentally coincides with a thermodynamic phase-transition point, a thermodynamic quantity (such as Γ) *should not* exhibit a near singularity at the CJ point as indicated in Fig. 3. It is worthwhile to mention that the observed anomaly will disappear if the experimental CJ point is replaced by the theoretical prediction. This modification would require a reduced P_{CJ} value (to 33GPa and 32Gpa for PBX-9404 and LX-14, respectively) and a similar reduction in ϱ_{CJ} (to 2.40 g/cm^3 and 2.38 g/cm^3 for PBX-9404 and LX-14, respectively). However, a more definitive conclusion must await further effort to reduce possible experimental and theoretical uncertainties in the P_{CJ} values.

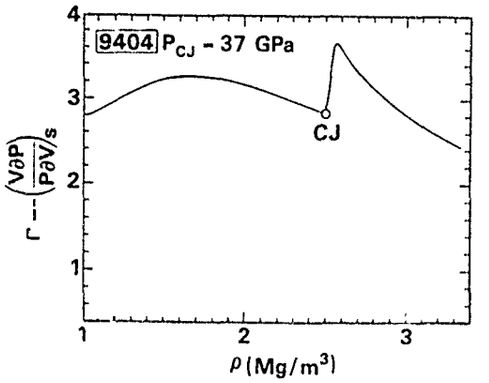

Fig. 3. The adiabatic gamma (Γ) [Eq. (5)] of PBX-9404 along the Chapman-Jouguet (CJ) adiabat (ϱ_o=1.84 g/cm^3), inferred all from the experimental data: cylinder test data (12); P_{CJ} and D_{CJ} (12), and the overdriven Hugoniot data (16-18)

Above 65 GPa, the CHEQ and the JCZ3 Hugoniots in Fig. 2 become slightly stiffer than the experimental data. This difference may be real and may bear a physical significance. A recent shock wave experiment of N_2 (26) which is a major detonation product of PBX-9404 and LX-14 shows that the Hugoniot pressures above 35 GPa become significantly lower than values extrapolated from the lower-P data. One possible explanation is that molecular nitrogen, when heated above 8000°K and pressurized above 35 GPa, may dissociate into a denser phase of monatomic nitrogen (27-29). In the case of mixtures the dissociation of N_2 could occur at lower temperatures but at higher pressures, relevant to overdriven states of PBX-9404 and LX-14 (27). Alternatively the observed deviations at P $\geq$ 65 GPa in Fig. 1 may be related to occurrence of multiple fluid phase separations. In this regard, it should be noted that the present study considers only two fluid phases. Our limited knowledge on multi-fluid phase separations in the (P,T)-range relevant to an explosive makes it impractical to extend our study to more than two fluid phases.

Figures 4 and 5 show comparison of the P-vs-v(=V/V_o) Chapman-Jouguet adiabatic paths (V_o= ϱ_o^{-1}) of PBX-9404 and LX-14 obtained

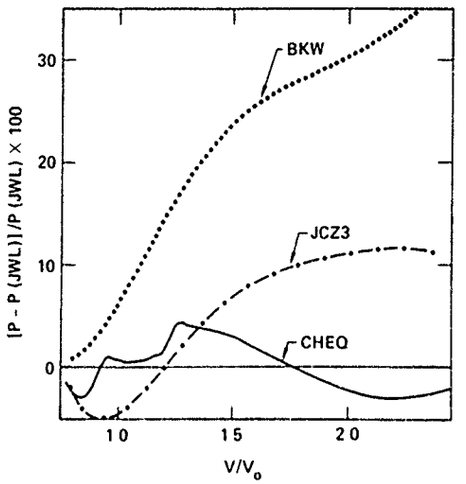

Fig. 4. The theoretical Chapman-Jouguet adiabats of PBX-9404 relative to that of the JWL EOS (ρ_0=1.84 g/cm³) (The theoretical results are based on this work (CHEQ), the BKW EOS, and the JCZ3 EOS.)

from the three theoretical models (CHEQ, BKW, and JCZ3) and the JWL adiabat, i.e.,

$$P_S = A_1 \exp(-R_1 v) + A_2 \exp(-R_2 v) + C v^{-(\omega+1)}, \quad (6)$$

where constants A_1, A_2, C, R_1, R_2, and ω for PBX-9404 (Fig. 4) are based on the cylinder-test data (12), while those for LX-14 (Fig. 5) are taken from Ref. 11. Since the CJ adiabat of PBX-9404 from the present theory is nearly indistinguishable from the JWL result, only deviations from the JWL result for the three theoretical models are shown in Fig. 4. Note that the deviations between the present work and JWL stay within 5% over the range of V/V_0 between 0.5 and 2. In comparison, the JCZ3 and the BKW models give larger deviations (i.e., up to 10% and 35%, respectively).

A much more sensitive test of the various EOS models is Γ [Eq. (5)], which is a second-order derivative of the free energy. Figures 6 and 7 show how Γ of PBX-9404 and LX-14 from the four EOS models behave as a function of density. The values of Γ(JWL) at the CJ points are seen to lie lower than the CHEQ and the JCZ3 predictions. We have already discussed this feature in conjunction with Fig. 3, where the experimentally measured high P_{CJ} value is seen to cause the observed low Γ(JWL) value. Another characteristic feature of the Γ(JWL) is double maxima, a feature common to many other explosives represented by the JWL EOS. This is due to the two exponential terms in Eq. (6) used to represent cylinder-test data and experimental CJ data (2).

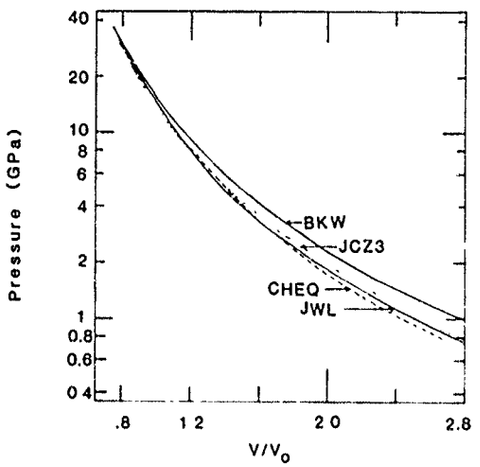

Fig. 5. The Chapman-Jouguet adiabats of LX-14 (ρ_0=1.835 g/cm³) predicted by the present theory (CHEQ), the BKW EOS, the JCZ3 EOS, and the JWL EOS

It is interesting to note that the present theory also produces Γ with double maxima. Occurrence of the maxima, however, is directly related to appearance of phase transition. These consist of the graphite-to-diamond transiton and separation of a N_2-rich and a N_2-poor phase. Both will significantly affect hydrodynamic calculations of experimental configurations, because similar fluctuations occur in sound speed as well. Such calculations would indeed require a very complex and accurate representation of the EOS data base near the transition regions.

ANALYTIC REPRESENTATIONS

For hydrodynamic applications it is convenient to represent the theoretical EOS data by an analytic form. For this purpose we have generated more than 2000 EOS data points from the present theory. The (ρ,T) range considered for PBX-9404 is shown in Fig. 7. The EOS data points are fitted by using a ratio-of-polynomials form with 28 coefficients; i.e.,

$$P(\mu,\varepsilon) = (1+\mu)\, X \frac{G_1(\mu) + G_2(\mu)\varepsilon + G_3(\mu)\varepsilon^2 + G_4(\mu)\varepsilon^3}{G_5(\mu) + G_6(\mu)\varepsilon + G_7(\mu)\varepsilon^2}, \quad (7)$$

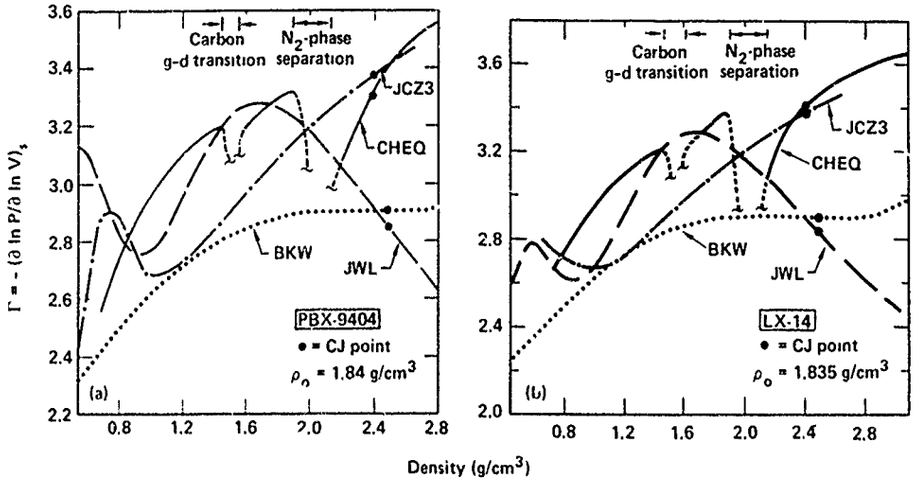

Fig. 6. Comparisons of the adiabatic gamma Γ [Eq. (5)] along the Chapman-Jouguet adiabats predicted by the present theory, the BKW EOS, the JCZ3 EOS, and the JWL EOS: (a) PBX-9404 (ϱ_o=1.84 g/cm³) and (b) LX-14 (ϱ_o= 1.835 g/cm³)

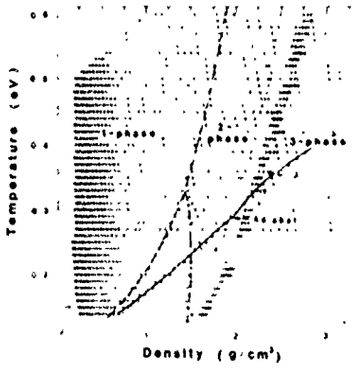

Fig. 7. The density-temperature grid points used to fit the theoretical (P,E) data of PBX-9404 by an analytic form [Eqs. (7) and (8)] (Within the 1-phase region, all detonation products occur as a single phase mixture. The 2-phase region consists of a fluid mixture phase plus condensed carbon which is in graphite or diamond-like (the boundary between the two is shown by dash-dotted line). The 3-phase region contains two fluid phases (i.e., N_2-rich and N_2-poor mixtures) and a solid diamond-like phase of carbon.)

where $\mu = \varrho/\varrho_0 - 1$, $\varepsilon = E\varrho_0$, and the $G_i(\mu)$'s are given by

$$G_i(\mu) = a_{i1} + a_{i2}\,\mu + a_{i3}\,\mu^2 + a_{i4}\,\mu^3, \ (i = 1,7) \ . \qquad (8)$$

Table 3 gives numerical values of constants a_{ij}'s for PBX-9404. A fit (30) for LX-14 is also given in Table 3. The rms deviation of the fit is 0.7% for PBX-9404 and 1.9% for LX-14. Except near the low-T end ($T \leqslant 0.17$eV and $\varrho \cong 1.5$ g/cm³) which is not important for a hydrodynamic study, the analytic fit for PBX-9404 agrees with CHEQ data within 3%. The largest errors occur near the N_2-phase separation boundary. The fitting errors for LX-14 lie mostly within 6%, except near the low-ϱ boundary ($\varrho \cong 0.09$ g/cm³). In Eq. (7) and Table 3 the zero-reference level for the energy corresponds to the state of the elements (composing PBX-9404 and LX-14) at 298.15 °K and 1 atm. The above definition gives the energies ε_o (= $E_o\varrho_o$) of formation of PBX-9404 and LX-14 to be $6.09.10^{-5}$ Mbar and $1.15\ 10^{-3}$ Mbar, respectively.

A simpler, but more approximate, way to represent the CHEQ EOS data base is to adopt the JWL form or its modification and to fit only the theoretical CJ adiabats (e.g., a solid line indicated in Fig. 7 for PBX-9404).

Tables 4 and 5 show fitting parameters and deviations between the JWL form and the EOS data base for PBX-9404 and LX-14 explosives. Two separate fits are given: the standard JWL EOS form with a constant ω and a form in which the principal isentrope is corrected with

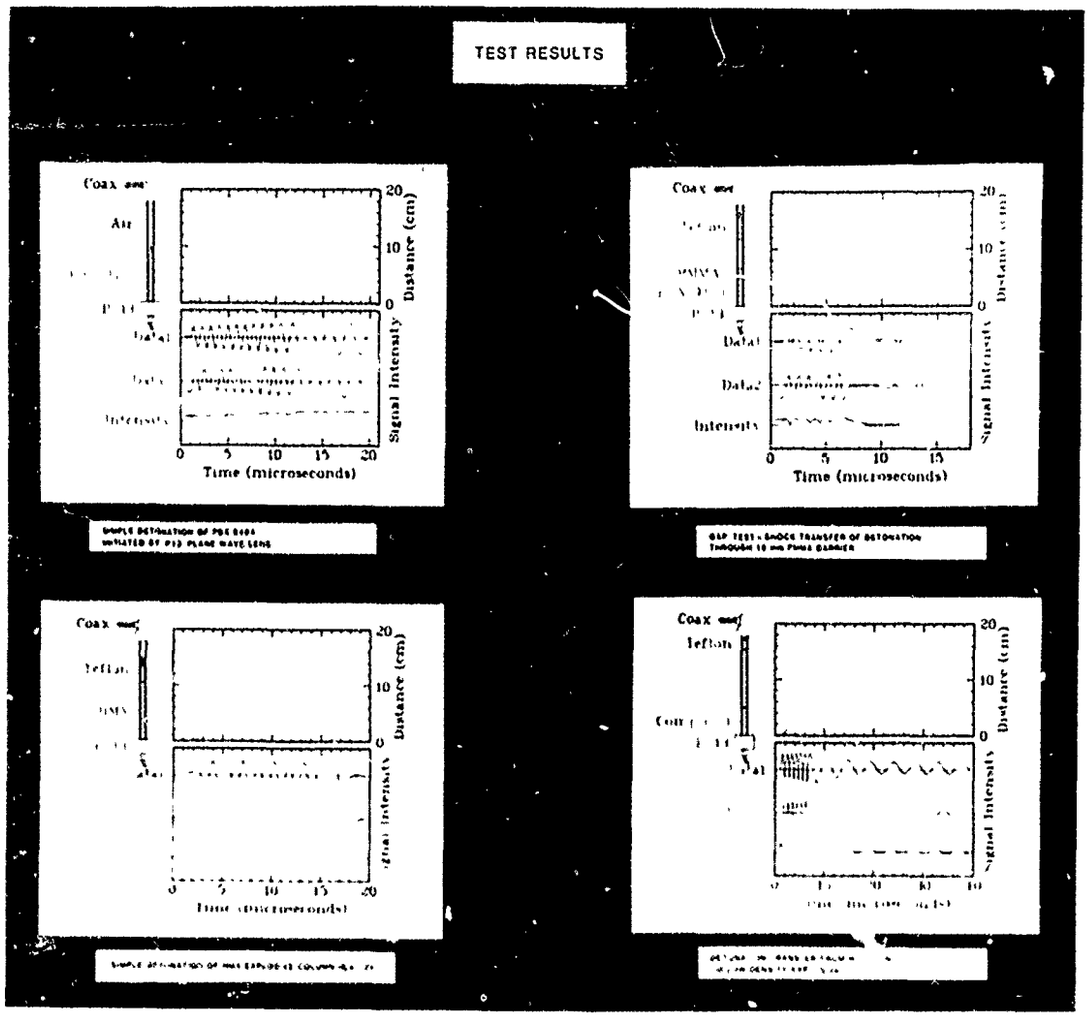
TEST RESULTS
Coax
Air
Teflon
Delay
Intensity
Signal Intensity
Distance (cm)
20
10
0
0
5
10
15
Time (microseconds)

TABLE 4
JWL fits to CHEQ PBS-9404 Data[a]
(P_{CJ} = 33 GPa; D_{CJ} = 8.78 km/s; ϱ_o = 1.84 g/cm³)

Fit	Coefficients A_1	A_2	C	R_1	R_2	ω	a	b
Eq. (9)	78.8552	1.3875	0.01531	8.700	2.470	0.380	0	0
Eq. (10)	77.6069	1.2390	0.01281	8.700	2.470	0.350	.74	6

			JWL Fit [Eq. (9)]			Modified JWL Fit [Eq. (10)]		
v	P(CHEQ)	ε(CHEQ)	1000 ΔP	1000 Δε	Γ	1000 ΔP	1000 Δε	Γ
2.6872	0.0078	0.0274	−2.0	+0.9	2.544	−1.8	+0.5	2.648
2.0706	0.0157	0.0342	−1.8	−0.4	3.885	−1.4	−0.6	3.772
1.4874	0.0425	0.0494	+1.8	−0.6	4.077	+2.0	−0.6	3.932
1.1752	0.0876	0.0688	+3.7	+0.2	3.894	+3.6	+0.3	3.770
0.9056	0.2003	0.1051	−4.6	+0.2	3.943	−4.7	+0.2	3.840
0.7949	0.2940	0.1318	+0.1	+0.0	4.055	+0.1	+0.0	3.960
0.7675[b]	0.3298	0.1403	+0.0	+0.0	4.081	+0.0	+0.0	3.988
0.7230	0.4044	0.1566	−1.6	−0.0	4.112	−1.6	−0.0	4.023
0.6228	0.6850	0.2095	−7.8	−0.5	4.083	−8.8	−0.5	4.005

[a] P and ε (= $E\varrho_0$) are in Mbars; v is V/V_0. The reference energy is chosen so that the CJ energy is E_0 + 0.5 P (V_0 − V) where ε_0 (= $E_0\varrho_0$) is given in Ref. 11. P(CHEQ) and ε(CHEQ) are calculated with the CHEQ code. ΔP and Δε are pressure and energy differences between the CHEQ data and the JWL or fits.

[b] CJ point.

TABLE 5
JWL Fits to CHEQ LX-14 Data[a]
(P_{CJ} = 34 GPa; D_{CJ} = 8.7883 km/s; ϱ_o = 1.833 g/cm³)

Fit	Coefficients A_1	A_2	C	R_1	R_2	ω	a	b
Eq. (9)	30.5948	1.2398	0.02995	7.3	2.58	0.60	.00	0
Eq. (10)	25.0145	0.8340	0.01212	6.8	2.24	0.33	.74	6

			JWL Fit [Eq. (9)]			Modified JWL Fit [Eq. (10)]		
v	P(CHEQ)	ε(CHEQ)	1000ΔP	1000Δε	Γ	1000ΔP	1000Δε	Γ
2.7283	0.0076	0.0274	− 0.5	+0.5	2.433	− 1.6	+1.2	3.058
2.1129	0.0150	0.0339	− 0.6	+0.1	3.031	− 1.2	+0.3	3.369
1.5177	0.0402	0.0486	+ 0.4	−0.0	3.121	+ 0.6	+0.2	3.102
1.1235	0.1006	0.0740	+ 1.0	+0.1	3.019	+ 0.5	+0.3	3.007
0.9011	0.2003	0.1062	− 1.2	−0.3	3.105	− 1.7	−0.2	3.128
0.7950	0.2922	0.1317	+ 2.8	−0.0	3.159	+ 2.7	0.0	3.170
0.7600[b]	0.3400	0.1428	0.0	0.0	3.168	0.0	0.0	3.168
0.7054	0.4408	0.1639	−10.0	−0.2	3.165	−10.3	−0.2	3.144
0.6076	0.7531	0.2205	−65.5	−3.3	3.083	−70.6	−3.5	3.016

[a] See footnote a in Table 4 for definition of various quantities in this Table.

[b] Note that the CJ pressure (34 GPa) used in the fit is raised from the value (32.3 GPa) in Table 2 to improve agreement with the data base.

consist mostly of C, H, N, and O, the fundamental approach developed here can provide quantitatively reliable EOS data for practical applications.

- Further "fine-tuning" of the EOS data is possible when and if we know more about

  a. the (P,T) boundaries where the N_2-rich fluid phase separates from the rest;

  b. the physical mechanism that gives rise to a significant lowering in pressure of the N_2 Hugoniot.

- Except near the CJ point, the rate effect appears to be insignificant. Initial efforts to understand the rate-dependent effects, as suggested by the present work and earlier work, should be directed to experimental and theoretical determination of the time constant characterizing the condensation of carbon under a strong shock environment.

ACKNOWLEDGEMENTS

We acknowledge the consultations with various members of the Lawrence Livermore National Laboratory. In particular, we would like to thank E.L. Lee, L. Green, C. Tarver of High Energy Technology Division and J. Slone, D. Steinberg, W. Quirk, L. Haselman, and R. Weingart of B Division for their pertinent experimental and theoretical suggestions related to the present work. J Sayer helped us at the initial stage of the analytic representation of the EOS of LX-14.

REFERENCES

1. F. H. Ree, "Postdetonation Behavior of Condensed High Explosives by Modern Methods of Statistical Mechanics," in *Proc. 7th Symposium on Detonation*, J. M. Short, Ed., Naval Surface Weapons Center, White Oak, MD, NSWC MP 82-334, (1981), pp. 646-660.
2. F. H. Ree, "A Statistical Mechanical Theory of Chemically Reacting Multiphase Mixture: Application to the Detonation Properties of PETN," J. Chem. Phys. *81*(3), 1251-1263 (1984).
3. F. H. Ree, "Supercritical fluid phase separations: Implications for detonation properties of condensed explosives," J. Chem. Phys. *84* (10), 5845-5856 (1986).
4. M. Ross, "A High-Density Fluid-Perturbation Theory Based on An Inverse 12th-Power Hard-Sphere Reference System," J. Chem. Phys. *71*(4), 1567-1571 (1979).
5. G.A. Mansoori and J.B. Canfield, "Variational Approach to the Equilibrium Thermodynamic Properties of Simple Liquids I," J. Chem. Phys. *51*(11), 4958-4967 (1969).
6. J.C. Rasiah and G. Stell, "Upper Bounds on Free Energies in Terms of Hard-Sphere Results," Mol. Phys. *18*(6), 249-260 (1970).
7. D. A. Young and F. J. Rogers, "Variational Fluid Theory with Inverse 12th Power Reference Potential," J. Chem. Phys. *81*(6), 2789-2793 (1984).
8. H. S. Kang, C. S. Lee, T. Ree, and F. H. Ree, "A Perturbation Theory of Classical Equilibrium Fluids," J. Chem. Phys. *82*(1), 414-423 (1985).
9. F. H. Ree, "Simple Mixing Rule for Mixture with Exp-6 Interactions," J. Chem. Phys. *78*(1), 409-415 (1983).
10. H. B. Levine, *Final Report on the Method of Univariant Descent for Solving Problems in Heterogeneous Chemical Equilibria*, Jaycor Report, J510-82-008154 (Jaycor, Del Mar, 1982). This work was undertaken under a contract with the Lawrence Livermore National Laboratory.
11. B. M. Dobratz, *LLNL Explosives Handbook — Properties of Chemical Explosives and Explosive Simulants*, Lawrence Livermore National Laboratory, Livermore, CA UCRL-52997 (1981).
12. E. L. Lee, H. C. Hornig, and J. W. Kury, *Adiabatic Expansion of High Explosive Detonation Products*, Lawrence Livermore National Laboratory, Livermore, CA UCRL-50422 (1968).
13. R. D. Cowan and W. Fickett, "Calculation of the Detonation Properties of Solid Explosives with the Kistiakowsky-Wilson Equation of State," J. Chem. Phys. *24*(5), 932-939 (1956).

14. M. Finger, E. Lee, F. H. Helm, B. Hayes, H. Hornig, R. McGuire, and M. Kahara, "The Effect of Elemental Composition on the Detonation Behavior of Explosives," in *Proc. 6th Symposium on Detonation*, D. J. Edwards, Ed. (Office of Naval Research, Department of the Navy, 1976), pp. 710-722.

15. M. Cowperthwaite and W. H. Zwisler, "The JCZ Equations of State for Detonation Products and Their Incorporation into the TIGER Code," in *Proc. 6th Symposium on Detonation*, D. J. Edwards, Ed. (Office of Naval Research, Department of the Navy, 1976), pp. 162-170.

16. J. H. Kineke, Jr. and C. E. West, Jr., "Shocked States of Four Overdriven Explosives," in *Proc. 5th Symposium on Detonation*, ACR-184, ONR 0851-0057, (U.S. Naval Ord. Lab., Silver Spring, MD 1970), pp. 533-543.

17. E. L. Lee, M. van Thiel, L. G. Green and A. Mitchell, "Detonation Product EOS: The Region above the Chapman-Jouguet Pressure," in *Shock Waves in Condensed Matter-1983*, J. R. Asay, R. A Graham, and G. K. Straub, Eds. (Elsevier Science Publishers B. V. 1984), pp. 617-620.

18. L. G. Green, E. L. Lee, A. Mitchell, and C. Tarver, "Supra-Compression of PBX-9404, LX-07, and RX-26-AF, and Equations of State of Detonation Products," in *Proc. 8th Symposium on Detonation* (this proceedings).

19. T. M. Reed and K. E. Gubbins, *Applied Statistical Mechanics*, (McGraw-Hill, New York, 1973). p. 132.

20. W. C. Davis and J. B. Ramsay, "Detonation Pressures of PBX-9404, Composition B, PBX-9502, and Nitromethane, " in *Proc. 6th Symposium on Detonation*, D. J. Edwards, Ed. (Office of Naval Research, Department of the Navy, 1976). pp. 531-539.

21. E. Lee, D. Breithaupt, C. McMillan, N. Parker, H. Chau, W. Quirk, P. Urtiew, and J. Walton, "The Motion of Thin Metal Walls and the Equation of State of Detonation Products," in *Proc. 8th Symposium on Detonation*, (this proceedings). The experimental D_{CJ} value (=8.79 km/s at $\varrho_0 = 1.83$ g/cm^3) for LX-14 is provided by D. Breithaupt (private communication, 1985).

22. W. J. Nellis, F. H. Ree, R. J. Trainor, A. C. Mitchell, and M. B. Boslough, "Equation of State and Optical Luminosity of Benzene, Polybutene, and Polyethlene Shocked to 210 GPa (2.1 Mbar)," J. Chem. Phys. *80*(60), 2789-2799 (1984).

23. O. B. Yakusheva, V. V. Yakushev, and A. N. Dremin, "The Opacity Mechanism of Shock-Compressed Organic Liquids," High Temp.—High Press. *3*, 261-266, (1971).

24. V. V. Yakushev, A. N. Dremin, S. S. Navatov, and Y. M. Shunin, "Physical Properties and Conversion of Nitrobenzene at Dynamic Pressures up to 30 GPa," Combust. Explos. Shock Waves (USSR) *15*(2), 226-233 (1979).

25. M. van Thiel, E. L. Lee, and S. Cochran, "Effect of Overdriven Shock States on the Equation of State of 9404 Explosives," J. App. Phys. *54*(11), 6760-6763 (1983).

26. W. J. Nellis, N. C. Holmes, A. C. Mitchell, and M. van Thiel, "Phase Transition in Fluid Nitrogen at High Densities and Temperatures," Phys. Rev. Letters *53*(17), 1661-1664 (1984).

27. R. Grover and F. H. Ree, "Evidences for Metallic Phases of Strong Covalent Materials in Shock Compression Data," in *High Pressure in Research and Industry*, C. M. Backman, T. Johannisson, and L. Tegner, Vol. 1 (Arkitektkopia, Sweden, 1982), pp. 217-222.

28. M. Ross, Lawrence Livermore National Laboratory, private communication, (1984).

29. A. K. McMahan and R. LeSar, *Pressure Dissociation of Solid Nitrogen Under 1 Mbar*, Phys. Rev. Letters, *54*(17), 1929 (1985).

30. J. Sayer, Lawrence Livermore National Laboratory, Livermore, private communication, (1985).

DISCUSSION

GERALD KERLEY, Sandia, Albuquerque

Are there any other explosves that should exhibit the nitrogen phase separation besides the two you have studied?

REPLY

BY F. H. REE AND MAT VAN THIEL

Our study of PETN also indicates such a phase change (3). In the case of PETN, however, the phase separation boundary crosses the Hugoniot above the CJ point at 48 GPa to 56 GPa. The agreement between the theoretical Hugoniot and the experimental data of Kineke [Ballistic Research Laboratories, Rept. DEA-G-1060MTG (1970)] is approximately similar to that of PBX-9404 in Fig. 1. A comparison of the PBX-9404 and PETN results shows that PBX-9404 has a lower CJ temperature (by about 600 K) but a higher CJ pressure (by 5 GPa). The higher temperature and lower pressure of PETN places its CJ point in the homogeneous fluid range.

The aforementioned fluid phase change is probably a general characteristic of explosives with a high-nitrogen content. This contention may be verified using RX-23-AB. It produces mostly H_2O and N_2 (14), both of which are chemically stable. Hugoniot experiments above 30 GPa should provide a simple test of the predicted fluid phase separation.

DISCUSSION

JAMES L. AUSTING, IIT Research Institute, Chicago, Illinois

Since your reported CJ temperatures for each explosive show a much broader range in comparison to the other CJ parameters, could you please comment on which values of temperature you consider to be the most valid. and most representative of what would be obtained experimentally?

REPLY

BY F. H. REE AND MAT VAN THIEL

The CHEQ and the JCZ3 temperatures in Table 2 should represent reasonable values for the equilibrium temperature. It is worth mentioning that the computed temperatures are very sensitive to the small changes in the parameters of the models in Table 2. Hence, the 10% difference between the CHEQ and the JCZ3 temperatures probably is within the uncertainties of these models. The BKW EOS tends to give a much lower temperature than the CHEQ and JCZ3 predictions. The BKW EOS predicts similar low temperatures for other explosives (14). It may be a basic shortcoming in the BKW EOS which ignores the static contributions to pressure and energy. Calculations by us as well as by others (see papers by Show and Johnson, Chirat and Baute, Byers Brown, and Kerley in this symposium) indicate that both the static and the thermal contributions to thermodynamic properties are about equally important in the pressure and temperature range of the CJ point.

It should be pointed out that the experimental shock temperature obtained from shock front luminosity may or may not represent a real equilibrium temperature at the CJ point, since the screening of the radiation by an optically thick reaction zone would prevent the radiation emitted from the equilibrated zone (i.e., CJ point) behind the reaction zone from reaching the measuring apparatus. The luminosity data (22) of benzene, for example, is consistent with this view.

COMPARISON OF EXPERIMENTAL DATA ON DETONATION VELOCITY AND CHAPMAN-JOUGUET PRESSURE VS INITIAL HE DENSITY WITH PREDICTIONS FROM REE'S MODEL EQUATION OF STATE*

D.J. Steinberg
Lawrence Livermore National Laboratory
Livermore, California

Data on the change of detonation velocity and Chapman-Jouguet pressure vs initial HE density for RDX and HMX have been compared with the theoretical predictions of Ree for PBX 9404. Ree's model predicts breaks or changes in the slope of these curves due to the solidification of carbon and the formation of a separate, nitrogen-rich phase. There is good evidence for the solidification of carbon at ϱ_0 about 1.15 g/cc, but the evidence for the nitrogen phase separation at ϱ_0 about 1.56 g/cc is conflicting.

INTRODUCTION

Data on the change of detonation velocity and Chapman-Jouguet pressure vs initial HE density ϱ_0 have been used to test the reliability of theoretical models of HE detonation products equation of state (EOS). Ree's theoretical model for 9404 predicts rather abrupt changes in these variables at approximately ϱ_0=1.15 and 1.56 g/cc. (14) The former change is due to the solidification of carbon; the latter to the formation of a separate, nitrogen-rich phase. This paper will compare Ree's prediction with these data for HMX and RDX explosives.**

DISCUSSION

In order to compare theoretical detonation velocities with experiments, it is necessary to convert all the experimental data D to the detonation velocity at infinite charge diameter D_i. This is not a straightforward procedure for a number of reasons. The first is simply that the charge diameter d is not always given; D was often measured as an adjunct to some other experiment, so little care was given to clearly reporting how the experiment was done. In addition, the obvious method of extrapolating D to infinite diameter is to plot D vs 1/d and let 1/d go to zero. However, this method is not universally accepted. (4)

Finally, it seems to be of dubious value to extrapolate D in a case where the incremental D is less than the uncertainty in the data. In Ref. 6, there are enough data to get good statistics at given values of ϱ_0 and d. (See, for example, the data at ϱ_0=1.2 g/cc and d=76.2 mm.) These data show an RMS uncertainty of 0.3%, which translates to 12 to 27 m/s for D between 4000 and 9000 m/s. (These same data also show an RMS uncertainty in ϱ_0 to be about 0.2%.)

Consequently, some judgment is required to determine D_i. Fortunately, the corrections were small, usually less than 20 m/s with the largest being 60 m/s.

---

*Work performed under the auspices of the U.S. Department of Energy by the Lawrence Livermore National Laboratory under the contract no. W-7405-ENG-48.

**RDX and HMX are homologous nitramines of the family $(CH_2N_2O_2)_n$ where n is 3 for RDX and 4 for HMX. Theoretical maximum density of RDX is 1.8 g/cc and 1.9 for HMX. The heat of formation is 14.7 Kcal/mole for RDX and 17.9 for HMX. Additionally, early U.S. produced RDX contained ~10% HMX, and HMX ~2-10% RDX. We can compare data for RDX and HMX with calculations for PBX 9404 because 9404 is ~94% HMX.

TABLE 1
HMX and RDX Detonation Velocity vs Density

HE	ϱ_o g/cc	D_i km/s	D km/s	Maximum Charge Diameter (mm)	Reference
RDX	0.53	4.06	4.00	30	8
HMX	0.533	—	3.92	76	10
RDX	0.56	4.07	4.05	40	1
HMX	0.561	—	3.98	76	10
RDX	0.61	4.43	4.390	30	8
RDX	0.70	4.82	4.780	30	8
RDX	0.70	4.67	4.65	40	1
HMX	0.750	—	4.88	76	10
RDX	0.80	5.27	5.240	30	8
RDX	0.899	5.603	—	78	6
RDX	0.90	5.81	5.750	20	8
RDX	0.95	5.82	5.80	40	1
RDX	0.986	5.925	—	76	6
RDX	0.999	5.935	—	76	6
HMX	1.00	—	5.80	(25)	10
RDX	1.00	6.10	6.040	20	8
RDX	1.0	6.05	6.03	40	12
RDX	1.013	6.100	—	76	6
RDX	1.03	6.0	6.0	60	11
RDX	1.048	6.188	—	78	6
RDX	1.070	6.28	6.26	40	1
RDX	1.10	6.45	6.45	19	4
HMX	1.10	—	6.21	(25)	10
RDX	1.10	6.20	6.18	40	1
HMX	1.148	—	6.42	(25)	10
HMX	1.189	6.713	6.674	25	5
RDX	1.199	6.723	—	102	6
HMX	1.20	—	6.58	(25)	10
HMX	1.20	—	6.51	(25)	10
RDX	1.20	6.77	6.75	(40)	3
RDX	1.29	7.02	7.00	40	1
HMX	1.30	—	6.93	(25)	10
HMX	1.30	—	6.99	(25)	10
HMX	1.388	—	7.21	(25)	10
HMX	1.40	—	7.20	(25)	10
HMX	1.40	—	7.30	(25)	10
RDX	1.40	7.46	7.44	(40)	3
RDX	1.401	7.426	—	146	6
RDX	1.44	7.53	7.53	60	11
RDX	1.46	7.62	7.60	40	1
HMX	1.50	—	7.53	(25)	10
RDX	1.501	7.692	—	25	6
HMX	1.529	—	7.68	(25)	10
HMX	1.59	—	7.85	(25)	10
RDX	1.59	8.12	8.10	(40)	3
RDX	1.60	8.15	8.13	40	1
HMX	1.60	—	7.91	(25)	10
RDX	1.60	8.099	—	150	2
HMX	1.602	—	8.01	(25)	10
HMX	1.613	—	8.02	(25)	10

TABLE 1
Continued

HE	ϱ_o g/cc	D_i km/s	D km/s	Maximum Charge Diameter (mm)	Reference
HMX	1.613	—	8.01	(25)	10
HMX	1.624	—	8.08	(25)	10
RDX	1.63	8.341	8.341	51	13
HMX	1.652	—	8.10	(25)	10
RDX	1.665	8.241	—	51	6
HMX	1.693	—	8.42	(25)	10
HMX	1.695	—	8.26	(25)	10
RDX	1.72	8.507	—	150	2
RDX	1.72	8.48	8.46	40	1
RDX	1.753	8.598	—	149	6
RDX	1.755	8.68	8.66	(40)	3
HMX	1.763	—	8.58	(25)	10
RDX	1.766	8.639	—	38	6
RDX	1.767	—	8.639	?	7
HMX	1.832	—	8.74	(25)	10
HMX	1.838	—	8.85	(25)	10
HMX	1.847	—	8.85	(25)	10
HMX	1.875	—	8.88	(25)	10
HMX	1.891	9.13	9.11	(25)	9

Table 1 gives the values for D at the maximum charge diameter and D_i. Values for d in parentheses are very uncertain. The data in Refs. 2 and 6 are so copious that statistical fluctuations can be clearly seen; i.e., even if $d_1<d_2$, D_1 might not be less than D_2. Therefore, no values for D are listed. The data of Kurrle (10) and the single points from Refs. 5 and 9 are the only results for HMX. The latter values of D agree with the RDX data while Kurrle's results are systematically low by ~150 m/s. No explanation of this has been found. Therefore, it seems meaningless to determine D_i from Kurrle's data. However, Kurrle's results have one distinct advantage; they cover a large density range, $0.533 < \varrho_o < 1.875$. Therefore, assuming these data to be internally consistent, the shape of the D vs ϱ_o curve for these data alone should prove a good test of Ree's theory.

Finally, the data of Setsik and Shvedova (8) are consistently high by about 150 m/s, yet the slope is the same as the other low-density data. (1, 6) Because of the wealth of data at $\varrho_o=1.00$ in Ref. 6, I have assumed that the value of D there is most likely correct in the absolute sense. Therefore, I have simply normalized the data of Stesik and Shvedova at this point.

COMPARISON OF THE DATA WITH REE'S THEORY

Figure 1 shows a comparison of the low-density data ($.5<\varrho_o<1.5$) with the prediction of Ree. All the data, except for Ref. 5, are for RDX, while the calculation is for PBX 9404. Ree's prediction appears to agree well with the data except at the lowest values of ϱ_o where it is slightly too high. The data point of Krivchenko et al. (11) at $\varrho_o=1.03$ is given with only two significant figures which may explain why it is low by ~1.5% when compared with Ree. More puzzling, however, is the data point of Kuznetsov and Shvedov (1) at $\varrho_o=1.1$. All their other data agree well with Ree's theory as well as with the other experimental data. This point is not

only ~3% low compared with Ree's theory, it is even lower than the data from the same source at ϱ_0=1.07. Figure 2 shows the same comparison for the HMX data of Kurrle. Again, the theory and experiment are in reasonable agreement.

While neither of these comparisons should be considered definitive, they do lend some credence to Ree's theory that carbon appears as a solid in the detonation products for an initial HE density less than 1.15 g/cc.

Figure 3 shows the same comparison for the high-density ($1.2<\varrho_0<1.9$) data. Again, all the data except for Refs. 5 and 9 are for RDX. The nitrogen-rich phase predicted by Ree to occur at ϱ_0=1.56 g/cc does not show in the experimental data. Indeed, Fig. 4 shows that these data can be represented very well by a linear fit. In addition, the HMX data of Kurrle can also be represented by a straight line with essentially the same slope (see Fig. 5).

Besides measuring D vs ϱ_c Kurrle also measured the Chapman-Jouguet pressure, P_{CJ}. These results are compared with Ree's prediction in Fig. 6. The experimental data are normalized to Ree's theory at ϱ_0=1.2 by subtracting 3 GPa from all the data. This is not unreasonable because pure HMX should have higher CJ pressures than PBX 9404.

Ree has difficulty in unambiguously determining P_{CJ} in the two-phase region, $1.56<\varrho_0<1.72$; the dashed line in the figure is a visual aid only. However, there is an indication in the data of a break in the P_{CJ} vs ϱ_0 curve at ϱ_0~1.51, not far from Ree's predicted value of 1.56.

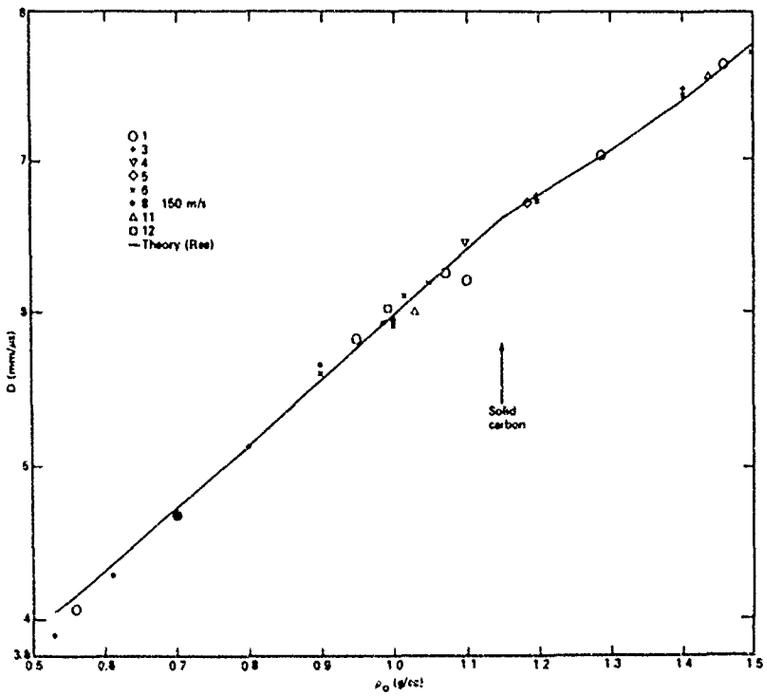

Fig. 1 Comparison of experimental data and theoretical prediction for detonation velocity vs initial HE density. All data for RDX except for Ref. 5

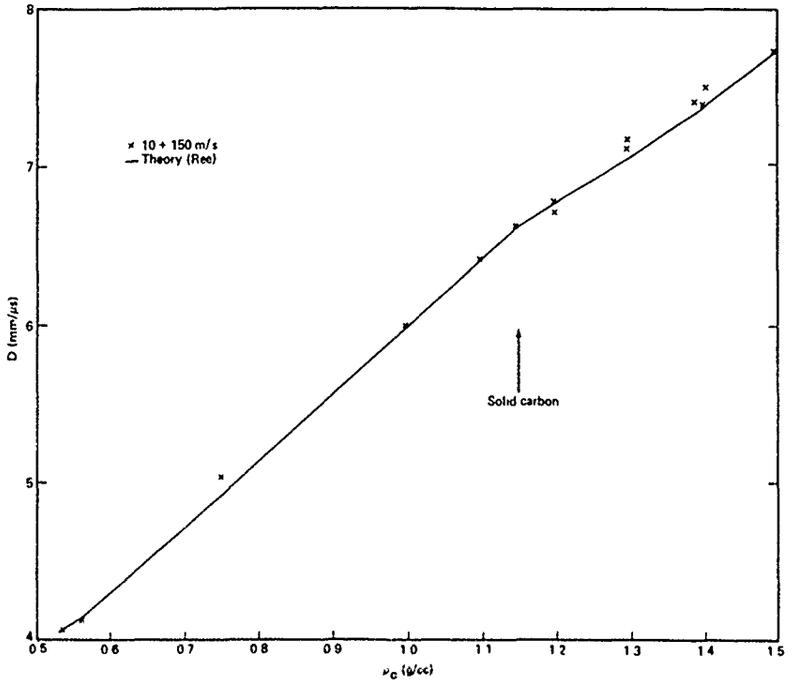

Fig. 2. Comparison of experimental data for HMX and theoretical prediction for detonation velocity vs initial HE density

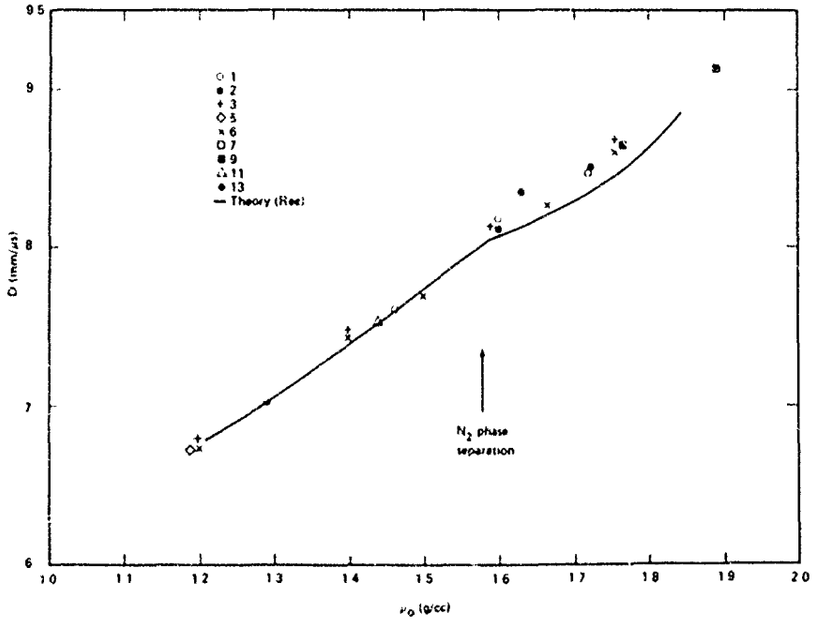

Fig 3. Comparison of experimental data and theoretical prediction for detonation velocity vs initial HE density. All data for RDX except for Refs. 5 and 9

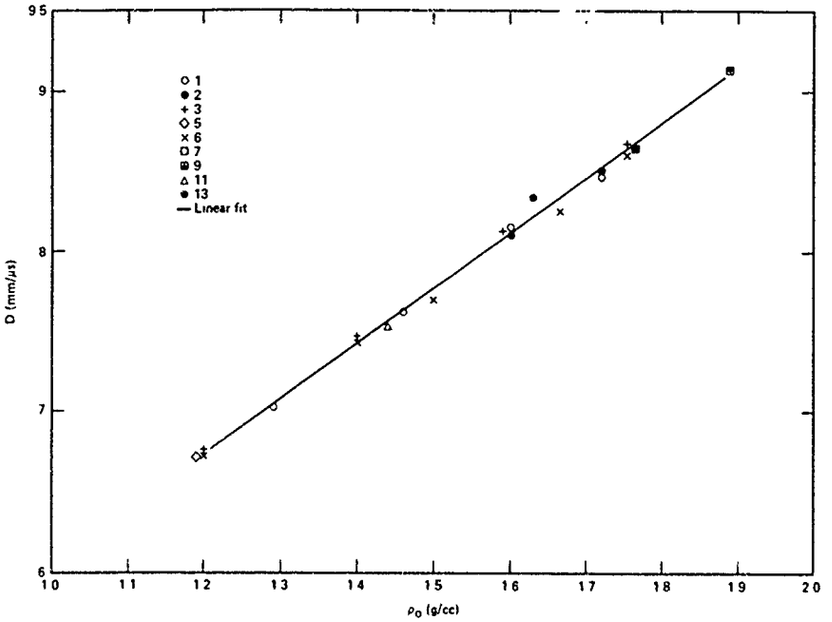

Fig. 4. Comparison of experimental data and a linear fit for detonation velocity vs initial HE density. All data for RDX except for Refs. 5 and 9

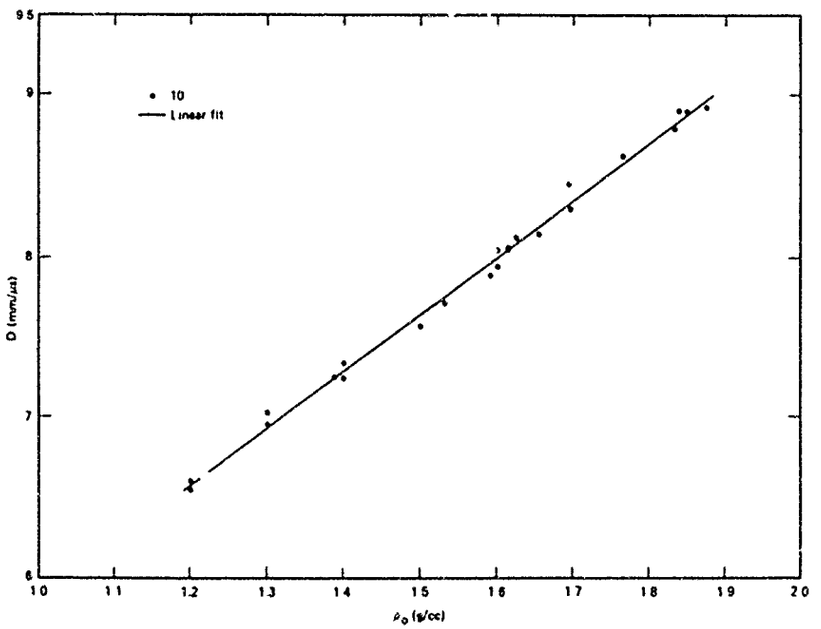

Fig 5. Comparison of experimental data for HMX and a linear fit for detonation velocity vs initial HE density

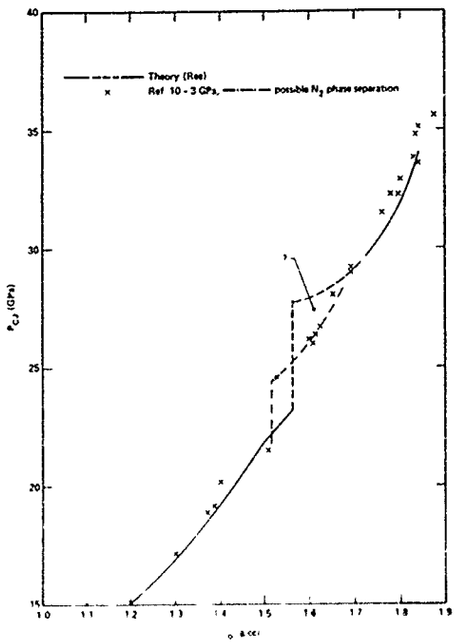

Fig. 6. Comparison of experimental data for HMX and theoretical prediction for Chapman-Jouguet pressure vs initial HE density

P_{CJ} is a more sensitive measure of the reliability of a theory than is D. Additional experiments should be undertaken to measure P_{CJ}, or some related quantity like particle velocity, to see if a break exists and if so at what value of ϱ_o.

For the sake of completeness, in Table 2, I have listed values of P_{CJ} vs ϱ_o for RDX. All but Ref. 7 are from the Russian literature. As with the data for D, there are many papers, but few authors. Consequently, it is hard to know whether a set of data is new or simply a reiteration of other work. For example, Dremin and Shevdov (15) give 3 data points at ϱ_o=1.0, 1.59 and 1.72 g/cc where the values of P_{CJ} are within 0.15 GPa of the data in Refs. 1 and 12.

TABLE 2
Chapman-Jouguet Pressure vs Initial Density for RDX

ϱ_o(g/cc)	P_{CJ}(GPa)	Ref.
0.56	3.16	1
0.70	4.72	1
0.95	9.46	1
1.0	8.85	12
1.03	9.50	11
1.07	11.60	1
1.10	12.00	1
1.20	15.2	3
1.29	16.40	1
1.40	21.3	3
1.44	19.52	11
1.46	20.80	1
1.59	28.70	3
1.60	26.00	1
1.63	28.3	13
1.72	30.85	1
1.755	36.6	3
1.767	33.79	7

REFERENCES*

1. N. M. Kuznetsov and K. K. Shvedov, Combustion. Explosion and Shock Waves *2* (4), 52 (1966).

2. Los Alamos National Laboratory, GMX-8 unpublished data, (July 1956).

3. A.N. Dremin, P.F. Pokhil, Acad. of Sciences, USSR, Proceedings, Phys. Chem. Section *128*, 839 (1959).

4. L.N. Stesik and L.N. Akimova, Russian Journal of Phys. Chem. *33* (8), 148 (1959).

5. Frank Helm, Lawrence Livermore National Laboratory unpublished data, (March 1979).

6. "Los Alamos Explosives Performance Data," C.L. Mader, J.N. Johnson and S.L. Crane eds. (University of California, Berkeley, 1982), pp. 348-435.

7. W.E Deal, J. Chem. Phys. *27*, 796 (1957).

8. L.N. Stesik and N.S. Shvedova, Zhurnal Prikladnoi Mekhaniki i Technicheskoi Fiziki (J. of Appl. Mech. and Tech. Phys.), No. 4, pp. 124-126, (1964) Russian only.

9. J.W. Kury, H.C. Hornig, E.L. Lee, J.L. McDonnel, D.L. Ornellas, M. Finger, F.M. Strange, and M.L. Wilkins, "Metal Acceleration by Chemical Explosives," in Proceedings - 4th Symposium (International) on Detonation, White Oak, Maryland, October 12-15, 1965 (Office of Naval Research, Department of the Navy, ACR-126, 1965), pp. 3-12.

10. J. Kurrle, 'HMX Detonation vs Density," Report OSAO No. 4148, SANL No. 901-003, (1971).

11. A.L. Krivchenko, K.K. Shvedov. A.N Dremin, and V.S. Kozlov, Combustion, Explosion and Shock Waves *8* (4), 377 (1972).

12. E.N. Aleksandrov, V.A. Veretennikov, A.N. Dremin, and K.K. Shvedov, Combustion, Explosion and Shock Waves *3* (4), 285 (1967).

13. N.L. Coleburn, "Chapman-Jouguet Pressures of Several Pure and Mixed Explosives," Naval Ordnance Lab., White Oak, Maryland, NOLTR 64-58 (1964).

14. Francis Ree, Lawrence Livermore National Laboratory, private communication, (October, 1984).

15. A.N. Dremin and K.K. Shedov, Zhurnal Prikladnoi Mekhaniki i Technicheskoi Fiziki (J. of Appl. Mech. and Tech. Phys.) No. 2, pp. 154-159 (1964) Russian Only.

*Except where noted, all references to Russian papers are for the English translations.

WHICH EQUATION OF STATE FOR CARBON IN DETONATION PRODUCTS?

J. Baute, R. Chirat
Commissariat à l'Energie Atomique
B.P. n° 27 - (94190) Villeneuve-St-Georges (France)
Now: B.P. n°7 - 77181 Courtry (France)

We present an improved self consistent version of our WCA4 equation of state for the fluid phase in detonation products. From the study of CO, CH_4 and aromatic hydrocarbons, a possible behaviour of the solid carbon phase appearing in their decomposition products is deduced. This interpretation applied to calculate Chapman-Jouguet properties of high carbon CHNO explosives allows to obtain excellent agreement between theoretical and experimental results. Carbon in detonation products can be diamond, as predicted by its phase diagram, or in some graphite-like phase even if its phase diagram would imply diamond formation.

I – INTRODUCTION

The most part of recent theoretical studies on high explosives detonation properties uses statistical mechanics equations of state (EOS) (1,2,3), in order to treat the chemical equilibrium existing behind the detonation front. In addition, for high carbon explosives, it is necessary to take account of a solid carbon phase. In previous papers (1,4), we present the various versions of the EOS we used for the fluid phase. Our walk in building our last version is based on three stages. First, we choose an EOS which gives good results compared with Monte Carlo (MC) runs for given potentials. Secondly, we use a fluid mixture treatment which agrees with MC results for binary mixtures. At last, we determine the potential parameters for each component existing in detonation products by fitting them on available experimental shock Hugoniot data.

As pointed out in ref. (1), WCA4 exhibits some weakness in the range of high density and temperature corresponding to shock experiments and detonation properties. So, in part II, we present new modifications of our fluid EOS in order to obtain a better agreement with MC results.

Up to now, we have treated the carbon solid phase as a graphite phase, with the Cowan-Fickett type EOS by Mader (5). In part III, after examining the various published phase diagrams for carbon, we build a new solid equation of state in order to introduce the diamond phase in our calculations.

In part IV, we review the influence of the nature of the carbon phase which can appear in the decomposition products of simple systems. We first examine the behaviour of two of the most important detonation products: carbon monoxide CO and methane CH_4. Moreover, we study some aromatic hydrocarbons which can reach under shock waves some states close to the Chapman-Jouguet points of high carbon explosives.

Finally, in part V, for several high carboned CHNO compositions, we compare calculated and experimental CJ properties with two different assumptions in the calculations: solid carbon exists in detonation products as graphite or as diamond. These calculated results are plotted on the temperature-pressure carbon phase diagram.

II – A NEW SELF-CONSISTENT WCA EQUATION OF STATE

As we remarked in ref. (1), our WCA4 EOS is less accurate, when we compare its results with MC simulations, in the range of high

density and temperature reached in detonation conditions for solid explosives. This drawback has led us to study an improved version which, from now on, we will call WCASC.

1) Fluid EOS principles

WCA4 and WCASC methods are statistical mechanical models based upon a simplification of the Weeks-Chandler-Andersen theory (6) proposed by Verlet and Weis (7) and extended to mixtures by Lee and Levesque (8). The interactions between molecules are represented by pairwise additive potentials of the exp-6 type:

$$v_{ij}(r)=\frac{\varepsilon_{ij}}{\alpha_{ij}-6}\left[6\exp(\alpha_{ij}(1-\frac{r}{\sigma_{ij}}))-\alpha_{ij}(\frac{\sigma_{ij}}{r})^6\right]$$

where (σ_{ij}, ε_{ij}, α_{ij}) are the parameters associated with the pair of chemical constituants i and j. In practice, we only need the potential parameters for the interaction between molecules of the same species (i=j), and we use the classical rules of mixtures:

$$\sigma_{ij}=\frac{\sigma_{ii}+\sigma_{jj}}{2},\quad \varepsilon_{ij}=(\varepsilon_{ii}\,\varepsilon_{jj})^{1/2},\ \alpha_{ij}=(\alpha_{ii}\,\alpha_{jj})^{1/2}\cdot \quad (1)$$

According to WCA's scheme, thermodynamical quantities are calculated by doing a double expansion of the free energy corresponding to a given potential $v_{ij}(r)$.

At first, the potential is divided into an attractive and a repulsive part

$$v_{ij}(r)=v^{o}_{ij}(r)+v^{p}_{ij}(r) \quad (2)$$

$$\text{with}\ \begin{cases} v^{o}_{ij}(r)=v_{ij}(r)+v^{m}_{ij} & \text{for } r\leqslant r^{m}_{ij} \\ v^{o}_{ij}(r)=0 & \text{for } r\geqslant r^{m}_{ij} \end{cases}$$

where r^{m}_{ij} and $-v^{m}_{ij}$ correspond to the minimum of potential. The configurational free energy can be written:

$$A=A^{0}+A^{p} \quad (3)$$

For both methods, we use the approximated expression of the first order perturbation term A^p, given and explained before (eq (17) in ref. (1)). In spite of Ree's remark (2), we have not yet revised this term because of the numerical speed of this approximation and the good agreement we obtained between our WCASC method and MC. For mixtures, it is necessary to notice that the mixture rules (1) only influence this perturbative term.

The second stage in the WCA method is the expansion of the reference repulsive term A^o in function of the difference between the Boltzmann factors of the repulsive fluid and an equivalent hard sphere fluid:

$$A^{o}=A^{HS}+\delta A+(\text{orders}\geqslant 2)$$

Our two methods WCA4 and WCASC differ by the criterion used to determine the hard sphere diameter. The former calculates a diameter which makes the term δA of the expansion to be zero. This is the original WCA criterion (6). The expression of this diameter d_{ii} is given and justified in previous works (4a, 4b). The we get:

$$A^{o}=A^{HS} \quad (4)$$

In the latter, we use the self consistent criterion proposed by Verlet and Weis (7). The diameter is calculated in order to obtain, for the reference fluid, the same value of the pressure either with the virial equation or the differentiation of the free energy A^o. We use in this case:

$$A^{o}=A^{HS}+kT\,\delta A \quad (5)$$

$$\delta A=-2\pi\rho\,(\sum_{i}x_i d_{ii}^{3} g_{ii}\delta_{ii})\varnothing \quad (6)$$

where T is the temperature, k the Boltzmann's constant, ρ the particle density, x_i the molar fraction, d_{ii} the equivalent hard sphere diameter given by eq. 25, 38 in ref. (7b), g_{ii} the contact value of the radial distribution function of hard spheres (eq. 9-14 in ref. (9)), δ_{ii} the integral given by eq. 14, 15 in ref. (7b).

Practically, instead of the expression of $\varnothing$ given in ref. (7b),

$$\varnothing = \psi-\sigma_1/2\sigma_0$$

we use a Taylor expansion up to the fifth order in the packing fraction η:

$$\varnothing = 0.5-0.75\eta-2.659\eta^2+1.679\eta^3+4.491\eta^4+5.427\eta^5 \quad (7)$$

This approximation is necessary because, for the highest values of η obtained in the perturbation method, the original term becomes insignificant and gives aberrant values of thermodynamic quantities.

In both WCA4 or WCASC cases, the hard sphere free energy is deduced from the MCSL theory (10) for the mixtures of hard spheres (cf. eq 13, 14 in ref. (1)).

2) Comparison with Monte-Carlo results.

For a pure fluid represented with an exp-6 potential (α=13.5), Fig. 1 shows the compres-

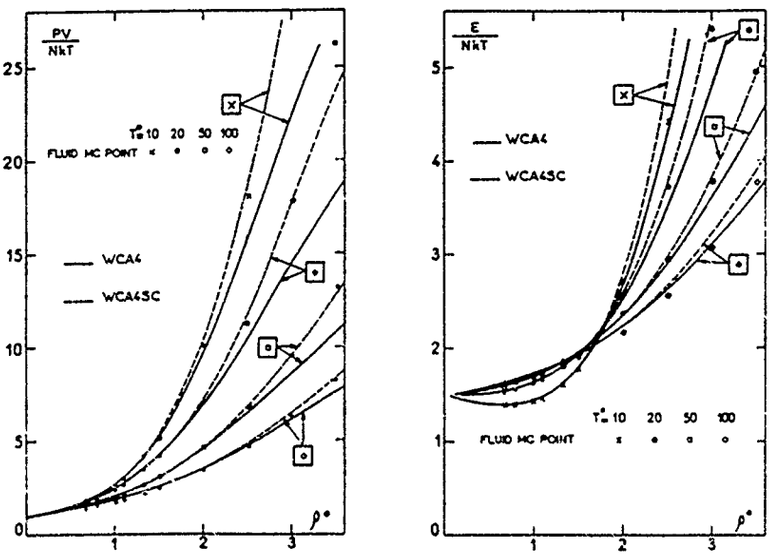

Fig. 1. Monte-Carlo and theoretical isotherms for expo-6 potential (α=13.5)

sibility factor ($\beta P/\rho$) and the reduced configurational energy ($\beta E/N$). Plots are MC results (11) while solid curves are from WCA4 and dotted curves from WCASC. We have to keep in mind that, for the majority of detonation products, the ranges of reduced temperature ($T^*=kT/\varepsilon_{ii}$) and reduced density ($\rho^*=N\sigma^3_{ii}/V$) concerned by the detonation properties of solid explosives or shock experiments are respectively:

$$10 \leqslant T^* \leqslant 100 \qquad 0 \leqslant \rho^* \leqslant 3.5$$

So we can see on Fig. 1 that the agreement between MC and WCASC results is excellent. This last version takes out WCA4's lacks in our region of interest.

3) Complete EOS

To the configurational free energy calculated as mentioned above, it is necessary to add the contribution of the various energetic levels of the free molecules. Assuming ideal mixture at P=1 atmosphere for a given T, we add the energetic quantities given by JANAF tables (12), by the mean of fits used by C. Mader (13).

III – CARBON SOLID PHASE EOS

1) *Phase diagram*

In spite of extensive studies, the phase diagram of carbon is not yet really well known. In fact, the equilibrium line between graphite and diamond is the only part established beyond any doubt. This line has been determined by calculations (14) and experimentally by Bundy (15). The other parts of the diagram are based on assumptions deduced from experiments or theoretical calculations (15).

The phase diagram, proposed by Bundy in 1964 (15d) exhibits in addition to the graphite-diamond equilibrium line, a graphite-liquid carbon equilibrium line, a diamond-liquid equilibrium line from the experiments made by Alder and Christian (16) and a triple point. On this diagram, Bundy added two lines, corresponding to the transition from metastable graphite to diamond, based on shock experiments and the transition from metastable diamond to graphite founded on graphitization of diamond experiments.

Afterwards, studies of the phase diagrams of Ge and Si led Bundy to propose the existence of a metallic phase (15). This hypothesis is confirmed by experimental results (17).

Grover proposed a phase diagram (18) using a semi-empirical model, which differs slightly from a diagram earlier given by Van Vechten (19). Grover's work has the advantage of agreeing well with carbon data and could be applied to other covalent materials (20). Even if this

model gives a good representation of the diagram, it is not possible to describe with thermodynamical equilibrium the multiple metastable phases of carbon. For example, what could be the treatment for vitreous carbon? It appears that hydrocarbon decomposition under static pressure gives an amorphous phase of carbon (21). So, it would be worthwhile to derive an equation of state for this kind of phase, to establish its zone of existence on the phase diagram and to determine the conditions which can produce it.

2) *Graphite equation of state*

Even if we admit that the phase of carbon occurring in detonation products is graphite, the determination of an EOS still remains arbitrary. Actually, many studies show the diversity of the behaviour of graphite during shock experiments. The results depend on the origin and porosity of the samples (22), (23).

For these reasons, we treat graphite in detonation products with the same equation as Mader (5). This EOS of the Cowan-Fickett type gives the pressure:

$$P = P_1(c) + a(c)T + b(c)T^2 \qquad (8)$$

where $c = \varrho_c/\varrho_c^o$

with ϱ_c: graphite density

ϱ^o_c: highest standard graphite density = 2.25 g/cm^3

The different terms of this equation are:

– $P_1(c)$, the cold curve or 0-Kelvin isotherm. If we compare the three cold curves given by the original Cowan-Fickett (24), Mader (6) or Kalitkin's (25) equations, we notice some discrepancies between the three curves, treating theoretically a graphite of density 2.25 g/cm^3. For pressures below 50 GPa, Mader's equation represents a graphite more compressible than others, behaving as if its density were about 2 g/cm^3. Over 50 GPa, Mader's 0-Kelvin isotherm exhibits some non physical behaviour. However, this range of pressure is far from the existence zone of graphite even if it is known that graphite remains stable during shock experiments far away from its transition line (23).

– a(c) is explained by Mader in (5).

$$a(c) = a_1 + a_2 c$$

with $$a_2 = \frac{3R\varrho_c^o}{2} \qquad (9)$$

and $$a_1 + a_2 = \frac{\partial P}{\partial T})v = v^0 \qquad (10)$$

neglecting the term $b(c)T^2$ (R is the constant of perfect gas).

– b(c) represents the electronic contribution. b(c) agrees, within a few percent with the results obtained by Kormer's formulae (26).

3) *Diamond equation of state*

For a diamond, we use an equation of the same type, for an initial density $\varrho_c^o = 3.512$ g/cm^3, which corresponds to homogeneous diamond.

The first term is an analytical fit of the 0-Kelvin isotherm in the M-Phase EOS (27).

$$P_1(c) = 3.203 - 12.741c + 11.722c^2 - 2.522c^3 + 0.336c^4 \qquad (11)$$

As Mader did for graphite, we obtain for diamond

$$a(c) = -0.19767 + 0.4232c \qquad (12)$$

For the electronic contribution, the term b(c) is the same for diamond as for graphite. Moreover, this contribution is not very large for temperatures corresponding to detonation properties.

For the graphite 1-atmosphere isobar, the contribution of temperature is calculated with Mader's fit (13) of JANAF tables. For diamond, in this work, we use the last fit given by Nellis et al. in ref. (28). This expression gives energetic values which diverge rapidly from those obtained by Barin and Knacke, and used in ref. (29) to interpret CO Hugoniot data. The divergence between the two fits for diamond explains the relative disagreement between this work and ref. (29) on CO Hugoniot.

IV – CO, CH AND HYDROCARBONS HUGONIOTS

We emphasize that, in our ETARC code (1), Hugoniots are calculated by solving the equation:

$$E - E_o = \tfrac{1}{2}(P + P_o)(V_o - V) \qquad (13)$$

for a given pressure, where

• E is the internal energy at given (P,V) conditions.

• E_o, P_o, V_o are the energy, pressure and volume for the initial state.

For the next results, where we assume (P,T) equilibrium between components, the composition of the solid-fluid mixture is obtained by minimizing the Gibbs free energy for given (P,T) conditions obtained by eq. (13). Chapman-Jouguet (CJ) points are calculated by locating the minimum of detonation velocity on the reactive Hugoniot. For fluid components, the potential parameters used are the same as in ref. (1).

As far as the detonation products are concerned, three very important components can be influenced by the possible existence of a carbon phase in the products of their decomposition under shock: carbon dioxyde CO_2, carbon monoxyde CO and methane CH_4. In the case of CO_2, there are still many outstanding questions on the interpretation of the experimental Hugoniot. So we do not think it could be worthwhile to discuss it since no more experimental results are available.

On the contrary, there are many experimental informations on hydrocarbons (31,32,28) which seem to reach along their Hugoniots some state neighbouring CJ points of solid explosives. Then, it is interesting to try to interpret their behaviour in connection with carbon in detonation products.

In this part, all our calculated results are made with the WCASC version of the fluid EOS while the potential parameters are those given in ref. (1). One could observe that the third stage of our walk in obtaining a good EOS (i.e. fitting potential parameters on experimental results with the considered EOS) is not respected. In fact, in this part of the paper, we include in our calculations only CO_2,CO, O_2, H_2 and CH_4, among the possible fluid detonation products; we have not fitted the potential of the two former components on Hugoniot curves. We use corresponding state laws as it is done in ref.(33). Oxygen only appears in negligible amount into CO decomposition products and its potential does not influence the results. Theoretical H_2 Hugoniot is not really changed by the choice of WCA4 or WCASC. So, from ref.(1), only CH_4 would need a revised potential. The coefficients were determined assuming inert CH_4. But we do not modify it, because with a new interpretation, experimental results and calculations agree within the experimental uncertainties.

1) Carbon monoxide Hugoniot

Nellis et al. (29) published experimental results on shock compression of liquid CO together with a theoretical intrepretation which assumed, for pressures higher than 10 GPa a decomposition giving CO, CO_2, O_2 and diamond. With our detonation products WCASC EOS, we calculate the Hugoniot for CO with the three different assumptions:

i) CO remains inert
ii) CO gives an equilibrium mixture of CO, CO_2, O_2 and graphite
iii) CO behaves as before but gives diamond instead of graphite

The initial conditions of the calculations are:
$E_0 = -4.199$ MJ/kg $\qquad V_0 = 1.239$ cm^3/g.

On Fig. 2, we compare the three calculations with the experimental results. Assumption i)

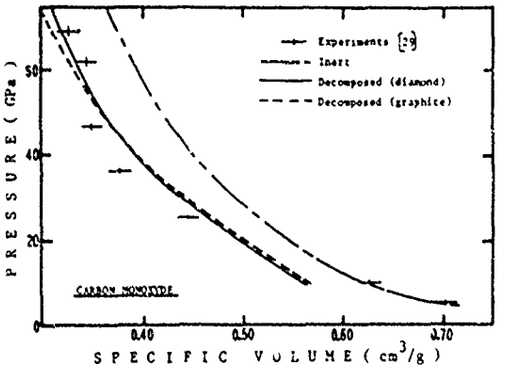

Fig. 2. Carbon monoxyde Hugoniot

gives an excellent agreement with experiment up to 10 GPa. The conclusion is that CO remains inert in this range of pressure.

Even if the two other hypotheses do not give very different curves, iii) is the best one for pressures over 20 GPa. But for pressures between 20 and 50 GPa, we remain out of error bars. So we can say that this hypothesis is not the right one. This conclusion is not in contradiction with the values of temperature calculated along the Hugoniot. From 20 to 50 GPa, we find temperatures from 5700 to 8000 K, which is far away the range of temperature where diamond exists, according to Bundy, Van Vechten or Grover's phase diagram. Carbon would have to be in the liquid metallic state. As it is shown by Grover on Fig. 3 of ref. (18), this phase is more compressible than

diamond. This behaviour would be the good one to improve our theoretical results. However, the validity of a statistical mechanics EOS with exp-6 potential would have to be revised. Actually, even if we could treat two separated phases, admitting demixtion between the liquid metallic phase and the molecular fluid, the range of temperature reached could introduce ionization phenomena, especially for the two upper points.

As a conclusion for CO, we will only say that this component seems to set some different problems than those which arise from solid explosives detonation.

2) Methane Hugoniot

Fig. 3 shows a similar work for methane. Experimental points come from ref. (29). Theoretical Hugoniots have been calculated with initial conditions:

$E_0 = -4.68$ MJ/kg $\qquad V_0 = 2.365$ cm^3/g.

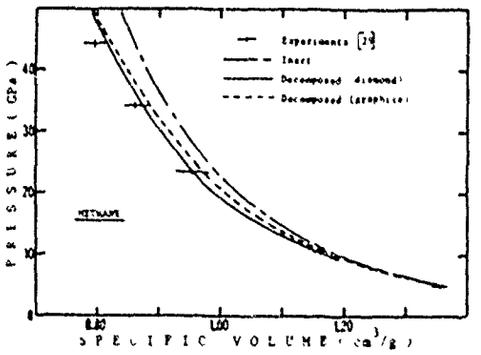

Fig. 3. Methane Hugoniot

The same three hypotheses as for CO have been used, H_2 and CH_4 replacing CO_2, O_2 and CO. The theoretical result is less influenced for CH_4 than for CO by the various assumptions. But in the same way, we have to admit dissociation to obtain the best agreement for pressures above 20 GPa. The diamond hypothesis allows the theoretical curve to lie within the experimental error. All along the Hugoniot curve, CH_4 is getting more dissociated when the pressure increases. At 20 GPa, only one third of CH_4 molecules are dissociated into H_2 et C diamond. Two thirds are dissociated near 50 GPa. The high temperature problem which arises for CO does not appear for CH_4, except for the highest experimental point on Fig. 3. From 20 to 40 GPa, temperature only increases from 2100 to 4000 K, what corresponds exactly to diamond existence zone.

3) Aromatic hydrocarbons Hugoniots

In this part, we present the theoretical Hugoniots, for different aromatic hydrocarbons, computed with our ETARC code, supposing complete dissociation in H_2, CH_4 and solid carbon (graphite or diamond). We do not take account of other hydrocarbons (28)(32) because we limit this study to explosive-close molecular structures. Indeed, the majority of CHNO explosives have aromatic ring structure. So, we can expect that a good interpretation of hydrocarbons Hugoniots data for the range of temperature and pressure obtained in detonation could give some information about explosive decomposition.

On the opposite of F.H. Ree in ref. (32) we include CH_4, in our calculated Hugoniots, in addition to solid carbon and H_2. For the highest pressures, only a little amount of methane is present among the products and there is no

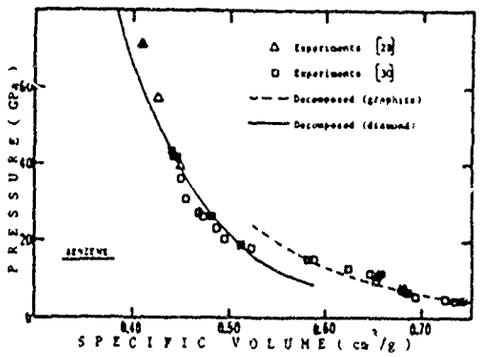

Fig. 4. Benzene Hugoniot

significant change if we omit or include CH_4. But, for lower pressures ($\leq$ 20 GPa) the percentage of CH_4 increases with decreasing pressure.

Fig. 4. shows the Hugoniot for benzene. Experimental results come from ref. (30) and (28). Between 17 and 45 GPa, the hypothesis assuming that benzene dissociates completely into diamond and a fluid mixture H_2-CH_4 gives an excellent agreement with experiments. At a pressure of 45 GPa, the calculated temperature reaches 5000K. So, it is not surprising that above 50 GPa, our theoretical curve leaves the experimental points because the diamond phase does not exist for such a temperature. Below 15 GPa, our calculations which assume decomposition giving graphite agree with experiments within the same order than calculations (28) for

a non reactive benzene. This could mean that when pressure increases, benzene could begin to decompose giving some graphite-like phase, without an evident phase transition on the Hugoniot curve.

For toluene, an intermediate zone seems to exist between 10 and 17 GPa.

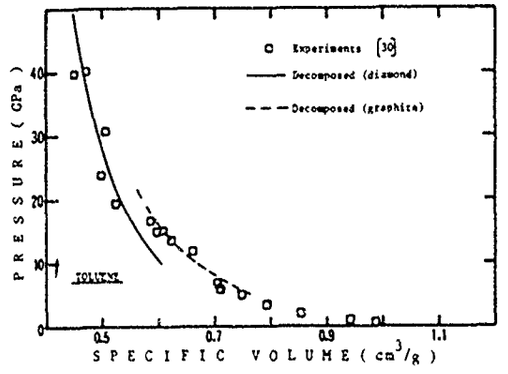

Fig. 5. Toluene Hugoniot

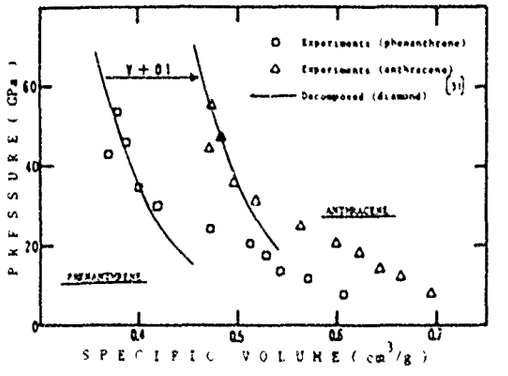

Fig 6 Anthracene and Phenanthene Hugoniots

Fig 6 shows that, for this range of pressure, the graphite assumption gives a good agreement theory-experiment (30), while, as for benzene, the diamond hypothesis is better over 17 GPa.

In the case of phenanthrene or anthracene (31), Fig. 6 exhibits a higher pressure for the transition into a mixture with diamond: 25 GPa. On the contrary, the range of temperature is the same for the four hydrocarbons. The diamond phase appears when the temperature exceeds 2500 K

We can conclude that the presence of diamond in decomposition products of hydrocarbons requires a sufficient pressure, higher than the one predicted by its phase diagram, and a minimum temperature is needed to allow the carbon atoms to move in order to build a new phase. When temperature is not sufficient, it seems that, even if some decomposition appears, the initial carbon structure can remain and behaves as if it were graphite.

For these hydrocarbons, CO and CH_4 (all of them decomposed giving diamond) and for graphite and diamond, Fig. 7 shows the calculated Hugoniots plotted on Grover's phase diagram. We can notice again the very high temperature for CO compared to the other studied products. On this diagram, the area where we find a great part of CJ points for solid explosives is indicated. We can see that including diamond in the treatment of the detonation could be worthwhile.

V. CHAPMAN-JOUGUET PROPERTIES FOR HIGH CARBON CHNO EXPLOSIVES

After using it to treat simple mixtures, we now use our equation of state for diamond in order to calculate CJ points for high carbon CHNO explosives. This is done with our WCA4

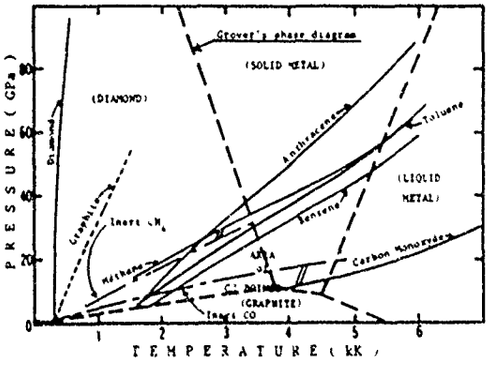

Fig. 7. Various Hugoniots on Grover's P–T carbon phase diagram (18)

equation of state for the fluid mixture, composed of H_2O, N_2, CO, CO_2, CH_4, NH_3, NO, O_2, H_2 (we could eventually include other substances but the calculations presented in this paper are limited to this list). We have performed these calculations without an equilibrium between the two possible carbon phases but supposing that carbon is either completely graphite or completely diamond.

Nine highly carboned explosives have been studied: TATB, DATB, ZTACOT, TNT, liquid TNT, HNS, Tetryl, Composition B and ABH. Table I gives for each explosive:

- detonation velocity D, pressure P and temperature T for the various experiments or

calculated with graphite or calculated with diamond at the CJ point.

- relative error between theoretical and experimental values.

- thermochemical data used in calculations for the different explosives (chemical formula, initial density ϱ_o, initial energy E_o of undetonated explosive.)

TABLE I

Name Eo (MJ/Kg) ϱo (g/cm^3)		D (m/s) , P (GPa) , T (K) Experiment	WCA4 + C graphite	WCA4 + C diamond
TNT sol $C_7H_5N_3O_6$ Eo = − 0 0265 ϱo = 1 64	D	6950	7110 (+ 2 3 %)	6809 (− 2 %)
	P	19 0 [5]	20 1 (+ 6 %)	18 3 (− 3 7 %)
	T		3618	3595
TNT Liq $C_7H_5N_3O_6$ Eo = 0 063 ϱo = 1 447	D	6580	6546 (− 0 5 %)	6250 (− 5 5 %)
	P	17 2 [5]	15 1 (− 12 %)	14 1 (− 18 %)
	T			3555
HNS $C_{14}H_6H_6O_{12}$ Eo = 0 129 ϱo = 1 74	D	7130 [5]	7400 (+ 3 8 %)	7144 (+ 0 2 %)
	P		23 5	21 7
	T		3977	3961
Tetryl $C_7H_5N_5O_8$ Eo = 0 117 ϱo = 1 7	D	7560 [5]	7727 (+ 2 2 %)	7510 (− 0 7 %)
	P		25 4	23 9
	T		4063	3991
Compo B $C_{685}H_{875}N_{765}O_{93}$ Eo = 0 4 ϱo = 1 714	D	8030 [5]	8179 (+ 1 9 %)	8013 (− 0 2 %)
	P	29 4	28 8 (− 2 %)	27 4 (− 6 8 %)
	T		4029	3981
ABH $C_{24}H_6N_{14}O_{24}$ Eo = 0 294 ϱo = 1 78	D	7600 [5]	7859 (+ 3 4 %)	7622 (+ 0 3 %)
	P		28 5	26 9
	T			4511
TATB $C_6H_6N_6O_6$ Eo = 0 2757 ϱo = 1 895	D	7860	8086 (+ 2 9 %)	7937 (+ 1 %)
	P	31 5 [5]	31 5	28 2 (− 10 %)
	T		2978	3004
TATB $C_6H_6N_6O_6$ Eo = 0 2757 ϱo = 1 847	D	7660	7946 (+ 3 7 %)	7772 (+ 1 46 %)
	P	25 9 [34]	29 3 (+ 13 1 %)	26 1 (+ 0 8 %)
	T		3050	3057
DATB $C_6H_5N_5O_6$ Eo = 0 207 ϱo = 1 79	D	7520	7883 (+ 4 6 %)	7667 (+ 2 0 %)
	P	25 9 [5]	27 6 (+ 6 6 %)	25 2 (− 2 7 %)
	T		3630	3595
ZTACOT $C_{12}H_4N_4O_8$ Eo = 1 44 ϱo = 1 85	D	7250 [*]	7490 (+ 3 3 %)	7503 (+ 3 5 %)
	P		28 1	24 8
	T			3866

From Table I, we can see that except for liquid TNT, all these explosives are better calculated with the diamond hypothesis than the graphite hypothesis Among them, only ZTACOT has not its calculated detonation velocity within 2% around the experimental velocity. The same agreement can be seen for CJ pressure when experimental results exist, even if the measure is far less precise for pressure than for velocity. This is the reason why we give two results for close initial densities of TATB, for which the two values of experimental pressure are in complete disagreement.

Fig. 8 shows the various calculated CJ points plotted on the different published phase diagrams. The given calculated CJ point for each explosive is the one which gives the best agreement between theory (graphite or diamond carbon phase) and experiment. We can see on Table I that the two hypotheses give almost the same temperature while pressure is some 10% higher with graphite instead of diamond. The three theoretical phase diagrams agree with our best assumption for TATB, DATB and solid TNT: thermochemical equilibrium gives carbon in a diamond phase. ZTACOT, HNS, Tetryl, Compo B and ABH might be in another phase, liquid or solid metal.

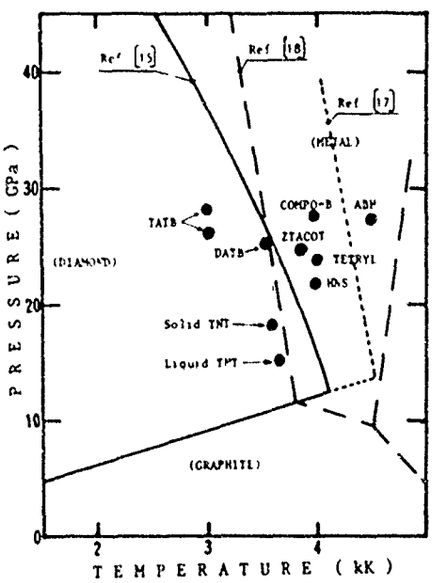

Fig. 8. Calculated CJ points on various P−T carbon phase diagrams

Finally, only liquid TNT is better handled with graphite assumption. This fact has to be connected with hydrocarbons behaviour. For this range of pressure, they seem to retain some graphite-close carbon. Even if decomposition exists, pressure is not sufficient to break the aromatic ring structures which can be transformed into hexagonal basal planes of graphite. On Fig. 9, we can see that for solid TNT at initial densities lower than 1.5 g/cm^3, the graphite assumption allows the theoretical results to be in agreement with experimental detonation velocities within 1%. For upper densities

($\rho_0 \geq 1.55$ g/cm^3), the equilibrium which gives diamond is more or less reached. The problem of this interpretation is: which conditions allow the equilibrium to be reached?

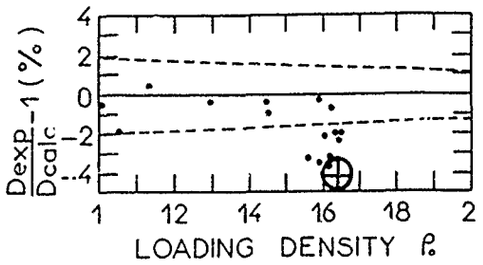

Fig. 9. CJ velocity error percent between experimental data and WCA4 with graphite for solid TNT. (⊕ calculated point with diamond)

CONCLUSION

We have developed a new WCASC EOS which allows us to obtain better agreement between theory and MC results with previous WCA4.

With this new EOS, the study of some detonation products (CO or CH_4) or aromatic hydrocarbons gives information on the possible behaviour of carbon during detonation of solid explosives. Except for decomposed CO which seems to give metallic liquid carbon phase, decompostion of these simple carbon substances can be interpreted with the formation of a diamond phase, on the condition that pressure but also temperature are sufficiently high, in order to break initial chemical bonds and allow a good rate of formation of this new phase. However, for low pressure, (10-20 GPa), the interpretation is not so clear because hydrocarbons give close theoretical Hugoniots if they are supposed inert or decomposed with a graphite phase.

If we consider now the Chapman-Jouguet temperature and pressure range for some CHNO explosive compositions, it appears that diamond is the most probable carbon phase which can exist in detonation products. Agreement between calculations and experiments confirms this hypothesis for TATB, DATB and solid TNT. We obtain also an excellent agreement for Compo B, Tetryl, ABH, ZTACOT and HNS even if carbon phase diagram would imply some other phase than diamond or graphite. For liquid TNT, as for low initial density solid TNT, the calculated CJ points are in agreement with experimental results if carbon is assumed to be graphite, even if P—T conditions are those of diamond stability.

This fact lets us think that, as for aromatic hydrocarbons, we do not reach a complete chemical equilibrium between all the existing atoms. So it seems that a better interpretation of detonation phenomenon would have to take into account chemical kinetics processes, at least to simulate the decomposition and formation of carbon structures.

ACKNOWLEDGEMENTS

We would like to thank G. Pittion-Rossillon with whom we began this work.

REFERENCES

1. R. Chirat, G. Pittion-Rossillon, Seventh Symposium on Detonation (Annapolis 1981) p. 703.
2. F.H. Ree, J. Chem. Phys. *81*, 3, p. 1251 (1984).
3. M.S. Shaw, J.D. Johnson, (this symposium)
4. R. Chirat, G. Pittion-Rossillon.
   a) J. Chem. Phys. *74*, p. 4634 (1981).
   b) Comb. and Flame *45*, p. 147 (1982).
5. C.L. Mader, Numerical Modeling of Detonations, Los Alamos Series, University of California Press (1979).
6. H.C. Anderson, et al., Phys. Rev. A*4*, 4, p. 1597 (1971).
7. L. Verlet, J.J. Weis.
   a) Phys. Rev. A *5*, p. 939 (1972).
   b) Mol. Phys. *24*, 5, 1013 (1972).
8. L.L. Lee, D. Levesque, Mol. Phys. *26*, p. 1351 (1973).
9. T.M. Reed, K.E. Gubbins, Applied Statistical Mechanics, McGraw-Hill (1973).
10. G.A. Mansoori, et al., J. Chem. Phys. *54*, p. 1523 (1971).
11. G. Fiorese, Thesis, Universite Pierre et Marie Curie Paris *VI* (1981).
12. D.R. Stull, et al. JANAF tables, NBS.
13. C.L. Madar, LANL, LA 3704 (1967).
14. R. Berman, F. Simon, Z. Electrochem *59*, p.. 333 (1955).

15. F.P. Bundy.
a) J. Chem. Phys. *35.* p. 383 (1961).
b) J. Chem. Phys. *38,* p. 618 (1963).
c) J. Chem. Phys. *38,* p. 631 (1963).
d) J. Chem. Phys. *41,* p. 3809 (1964).

16. B.J. Alder, R.H. Christian, Phys. Rev. Lett. *7,* p. 367 (1961).

17. L.F. Vereshchagin, et al., High Temp. High Pres. *6,* p. 505 (1974).

18. R. Grover, J. Chem. Phys. *71,* p. 3824 (1979).

19. J.A. Van Vechten, Phys. Rev. B, *7,* p. 1479 (1973).

20. R. Grover, F.H. Ree, Eighth AIRAPT Conference UPSALA (1981)

21. S. Block, et al. Science *169,* p. 586 (1970).

22. W.H. Gust, D.A. Young, High Press Science and Technology *1,* Timmerhaus and Barker, Plenum New York (1979).

23. R.G. MacQueen, S.P. Marsh, Proc. of Symp. on High Dyn. Press. (Paris) Gordon and Breach, New York (1968).

24. R.D. Cowan, W. Fickett, J. Chem. Phys. *24,* p 932 (1956).

25 N.N.Kalitkin, I.A. Govorukhina, Sov. Phys. Solid State *7,* p. 287 (1965).

26 S.B. Kormer, et al. Sov. Phys JETP *15,* p. 477 (1962).

27 C. Boissiere, G. Fiorese, Rev. Phys. Appl. *12,* p. 857 (1977).

28 W J. Nellis, et al. J. Chem. Phys. *80,* p. 2789 (1984)

29. W.J. Nellis, et al. J. Chem. Phys. *75,* p. 3055 (1981).

30. R.D. Dick.
a) J. Chem. Phys. *52,* p. 6021 (1970).
b) J. Chem. Phys. *71,* p. 3203 (1979).

31. M. Van Thiel, LLNL-UCRL 50108 (1977).

32. F.H. Ree, J. Chem. Phys. *70,* p 974 (1979).

33. M. Ross, F.H. Ree, J. Chem. Phys. *73,* p. 6146 (1980).

34. M.J. Kamlet, et al.
a) J. Chem. Phys. *48,* p. 3685 (1968).
b) J. Chem. Phys. *48,* p. 43 (1968).

DISCUSSION

M. VAN THIEL, Lawrence Livermore National Laboratory

At LLNL we have calculated the TNT CJ points for points for porous and normal density solid TNT. The deviations from experiment indicated a transformation from a graphite-like to a diamond-like phase near 20 GPa, (well above the standard diamond-graphite phase transition for pure carbon). I think this observation agrees with your calculations?

REPLY BY J. BAUTE

Our calculations show metastable graphite at the liquid (or low density solid) TNT CJ points and a diamond phase for solid TNT at high density.

THE THEORY OF DENSE MOLECULAR FLUID EQUATIONS OF STATE WITH APPLICATION TO DETONATION PRODUCTS

M. S. Shaw and J. D. Johnson
Los Alamos National Laboratory
Los Alamos, New Mexico 87545

A very accurate perturbation theory for the thermodynamics of dense molecular fluids is presented and compared with molecular dynamics (MD) simulations for N_2 and CO_2. Application of the theory is made to detonation products resulting in very good agreement with experiment.

INTRODUCTION

All current models (1) of the equation of state (EOS) of detonation products are based on spherical potentials. Given a thermodynamic theory, these potentials are usually fit to experimental data using that thermodynamic theory. When one looks at the degree of anisotropy of typical molecules in HE products (the N_2-N_2 potential varies by a factor of 20 with orientation for a fixed internuclear separation and the CO_2-CO_2 potential varies by 3 to 4 orders of magnitude), it is not at all obvious that spherical potentials are adequate. In fitting to Hugoniot data for the individual species, the pressure and energy on the Hugoniot will be correct, but the temperature may not be accurate. When one then calculates the EOS of a mixture, the temperature is important in determining the equilibrium composition. Also, in the mixture the state will not necessarily be near the conditions on the Hugoniots that were fit by the theory. Therefore, the question of how well the EOS extrapolates away from the Hugoniot is important.

PERTURBATION THEORY

Because of the uncertainty in using spherical potentials, we have made a series of benchmark calculations using molecular dynamics (MD) with realistic anisotropic potentials. An EOS calculation using MD involves solving Newton's equation ($F = ma$) for a collection of particles (usually a few hundred) with periodic boundary conditions and a realistic potential. Thermodynamic quantities are then obtained by time averages of appropriate functions. Further details, including tables of results, on the MD simulations can be found in Refs. (2) and (3).

These benchmark values of the EOS enabled us to find approximate methods that gave an accurate representation of that EOS with a very small cost in computer time. Using a perturbation expansion, a spherical reference system was determined that reproduces the thermodynamics of an anisotropic molecular potential with negligible contribution from higher order terms (4). For a given anisotropic potential, this effective spherical potential gives pressures and energies good to 1.5% for N_2 in the region of $1.3\ g/cm^3 \le \varrho \le 2.3\ g/cm^3$ and $500°K \le T \le 12000°K$ (results for CO_2 agree to about 3%). These results help justify the use of empirical spherical potentials for the equation of state of detonation products.

Thermodynamic perturbation series can be formulated in a fairly general form as shown by Smith (5). The configurational part of the Helmholtz free energy, A, for a given pair potential $u(r,\Omega)$ can be expanded in a Taylor series about a reference point A_0 given by a pair potential $u_0(r,\Omega)$. This is done by defining a potential $u_\gamma(r,\Omega)$ subject to the constraints $u_{\gamma=1}(r,\Omega) = u(r,\Omega)$ and $u_{\gamma=0}(r,\Omega) = u_0(r,\Omega)$. Then we can write

$$A = A_{\gamma=1} = A_{\gamma=0} + \frac{\partial A_\gamma}{\partial \gamma}\Big)_{\gamma=0} + \frac{1}{2}\frac{\partial^2 A_\gamma}{\partial \gamma^2}\Big)_{\gamma=0} + \cdots \quad (1)$$

the usual Taylor series in the variable γ. The values of the derivatives can be obtained from the definition of A.

$$A_\gamma = -\frac{1}{\beta} \ln Q_\gamma = -\frac{1}{\beta}\left[\ln \frac{1}{V^N} \int \exp(-\beta U_\gamma) d\vec{R}^N\right], \quad (2)$$

where Q_γ is the excess part of the partition function, $r_{ij} = |\vec{r}_i - \vec{r}_j|$, $u_\gamma = \frac{1}{2}\sum_{i=1}^{N}\sum_{j\neq i}^{N} u_\gamma(\vec{r}_{ij}, \Omega_{ij})$, and $\vec{R}$ includes both position and angular coordinates.

Evaluating the first two derivatives, we have

$$\frac{\partial A_\gamma}{\partial \gamma} = \frac{1}{Q_\gamma V^N} \int \frac{\partial U_\gamma}{\partial \gamma} \exp(-\beta U_\gamma) d\vec{R}^N \quad (3)$$

and

$$\frac{\partial^2 A_\gamma}{\partial \gamma^2} = \beta\left(\frac{\partial A_\gamma}{\partial \gamma}\right)^2 + \frac{1}{Q_\gamma V^N} \int \left[\frac{\partial^2 U_\gamma}{\partial \gamma^2} - \beta\left(\frac{\partial U_\gamma}{\partial \gamma}\right)^2\right] \exp(-\beta U_\gamma) d\vec{R}^N . \quad (4)$$

Now note that the radial distribution function, $g_\gamma(r_{12}, \Omega_{12})$, has the definition

$$g_{\gamma(r_{12},\Omega_{12})} = \frac{V^2}{Q_\gamma V^N} \int \exp(-\beta U_\gamma)\, d\vec{R}_3 \cdots d\vec{R}_N . \quad (5)$$

This is the probability that given a molecule at $\vec{r}_1$ with orientation ω_1, there is a molecule at $\vec{r}_2$ with orientation ω_2.

One can then easily show that

$$\frac{\partial A_\gamma}{\partial \gamma} = \frac{1}{2}\frac{N^2}{V^2} \iint g_\gamma(r_{12}, \Omega_{12}) \frac{\partial u_\gamma(r_{12}, \Omega_{12})}{\partial \gamma} d^3r_1 d^3r_2 d\Omega_{12} . \quad (6)$$

For the choice u_0 spherical, then g_0 is also spherical and we can write

$$\left(\frac{\partial A_\gamma}{\partial \gamma}\right)_{\gamma=0} = \frac{\rho^2}{2} \int g_0(r_{12}) d^3r_1 d^3r_2 \int \left(\frac{\partial u_\gamma(r_{12}, \Omega_{12})}{\partial \gamma}\right)_{\gamma=0} d\Omega_{12} . \quad (7)$$

The second derivative is more complicated because the $(\partial U_\gamma/\partial \gamma)^2$ term requires up to four particle distribution functions and care must be taken with certain limits. The full expression is given in Smith (5). For our purpose, it is sufficient to recognize that each term in the higher derivatives of A_γ has integrands proportional to products of derivatives of u_γ.

We have restricted the class of perturbation theories to those where $u_\gamma(r,\Omega)$ is given by

$$R(B(u_\gamma - u_0)) = \gamma R(B(u_1 - u_0)) \quad (8)$$

where R is an odd invertible function and B is a parameter. With the notation

$$u_0^{(n)} \equiv \left(\frac{\partial^n u_\gamma}{\partial \gamma^n}\right)_{\gamma=0}$$ we have

$$u_0^{(n)} = B^{-1} R_I^{(n)} [R(B(u_1 - u_0))]^n , \quad (9)$$

where $R_I^{(n)} \equiv d^n R^{-1}(x)/dx^n \big|_{x=0}$. Note that $u_0^{(2n)} = 0$ for all values of n because $R^{-1}(x)$ is also odd. This sets a large fraction of the terms in the perturbation series to zero. From Eq. (7) and (9), we see that a sufficient condition for $\left(\frac{\partial A_\gamma}{\partial \gamma}\right)_{\gamma=0} = 0$ is that

$$\int \int R(B(u_1 - u_0)) \, d\Omega = 0 . \quad (10)$$

We then choose $u_0(r)$ such that Eq. (10) is satisfied for all values of r.

We still have to choose a functional form for R. Note that if $R_I^{(n)}$ is bounded and R(x) behaves, at worst, like $(\ln x)^k$ as $x \to \infty$, then $u_0^{(n)}$ will be small for large values of B. We have used $R(x) = \sinh^{-1}(x)$. This leads to simple values for $R_I^{(n)}$; i.e.,

$$R_I^{(n)} = \begin{cases} 0 \text{ if n even} \\ 1 \text{ if n odd} \end{cases} . \quad (11)$$

As B increases, u_0 rapidly approaches a constant value. In the limit of $B \to \infty$ this is just the median of the potential. One does not expect the perturbation series to converge in the $B \to \infty$ limit, but for intermediate values of B, the series can converge and the u_0 obtained is almost identical to that for the $B \to \infty$ limit. Therefore, in practice we use the median as our choice of an effective spherical potential. One can show that $\left(\frac{\partial^2 A_\gamma}{\partial \gamma^2}\right)_{\gamma=0} \leq 0$ because $\left(\frac{\partial^2 U_\gamma}{\partial \gamma^2}\right)_{\gamma=0} = 0$ for our choice of perturbation theories. So to second order, the smallest choice of $u_0(r)$ allowed will be the best. This also leads to the choice of the median, except for parts of the attractive well which are not important at these densities and temperatures.

With a transformation of variables, one can obtain perturbation theories that give nearly the same results even in the small B limit where the convergence properties of the series are better. One special case we will call radial averaging. For a $u_1(r,\Omega)$ that is invertible, we can construct a radial function $r_1(u,\Omega)$, which is its inverse. The effective spherical potential is $r_0(u)$, which can be inverted to obtain $u_0(r)$. With the definition of r_γ given by

$$R(B(r_\gamma - r_0)) = \gamma R(B(r_1 - r_0)), \tag{12}$$

we can follow a similar derivation that leads to a choice for $r_0(u)$ of

$$\int\int R(B(r_1 - r_0))\, d\Omega = 0 . \tag{13}$$

Figure 1 compares the B dependence of this potential with the potential based perturbation theories. Note that even at $B \to 0$, the potential is within a few percent of the large B value. By changing variables, the anisotropy has been reduced from a factor of 20 to about 30%. Of course, the radius needs to be known more accurately to get the same accuracy in the potential, but the perturbation series converges faster because the anisotropy is smaller.

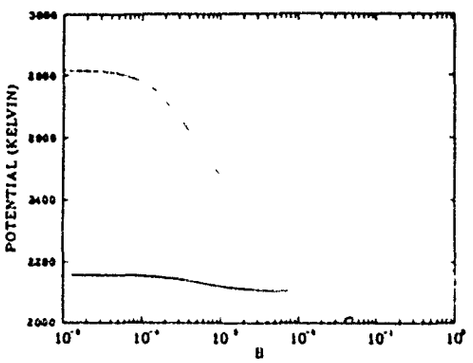

Fig. 1. N_2 at 3.0 Å ····· potential averaging, ——— radial averaging (plotted vs. 10^{-4} B)

We can write a general transformation of coordinates and choose a form that is similar to radial averaging, but preserves invertibility for the entire potential. Let F(u,r) be an invertible function of potential and radius. Also, let $u_\gamma(F,\Omega)$ depend on F(u,r) instead of r. One then has

$$\left.\frac{\partial u_\gamma^{(\gamma=0)}}{\partial \gamma}\right|_{F,\Omega} = \frac{1}{B}\, R_1^{-1}[R(B(u_1 - u_0))], \tag{14}$$

which differs from Eq. (9) in that the derivative is evaluated at constant F,Ω instead of r,Ω. We must then transform back to

$$\left.\frac{\partial u_\gamma^{(\gamma=0)}}{\partial \gamma}\right)_{r,\,\Omega} .$$

From the chain rule,

$$\left.\frac{\partial u}{\partial \gamma}\right)_{r,\Omega} = \left.\frac{\partial u}{\partial \gamma}\right)_{F,\Omega} + \left.\frac{\partial u}{\partial F}\right)_{\gamma,\Omega} \left.\frac{\partial F}{\partial \gamma}\right)_{r,\Omega}, \tag{15}$$

$$\left.\frac{\partial F}{\partial u}\right)_{\gamma,\Omega} = \left.\frac{\partial F}{\partial u}\right)_{r} + \left.\frac{\partial F}{\partial r}\right)_{u} \left.\frac{\partial r}{\partial u}\right)_{\gamma,\,\Omega}, \tag{16}$$

and

$$\left.\frac{\partial F}{\partial \gamma}\right)_{r,\Omega} = \left.\frac{\partial F}{\partial u}\right)_{r} \left.\frac{\partial u}{\partial \gamma}\right)_{r,\Omega} . \tag{17}$$

Note that for $\gamma = 0$, $\left.\frac{\partial u}{\partial r}\right)_{\gamma,\Omega} = \frac{du_0}{dr}$

Substituting Eqs. (16) and (17) in Eq. (15) and solving for $\left.\frac{\partial u}{\partial \gamma}\right)_{r,\Omega}$, we have

$$\left.\frac{\partial u}{\partial \gamma}\right)_{r,\Omega} = \left.\frac{\partial u}{\partial \gamma}\right)_{F,\Omega} \left(\frac{\left.\frac{\partial F}{\partial u}\right)_{r}}{\left.\frac{\partial F}{\partial r}\right)_{u} \frac{dr}{du_0}} + 1 \right) . \tag{18}$$

The term in parentheses is independent of Ω, so we have in analogy to Eq. (8),

$$\int\int R(B(u_1(F,\Omega) - u_0(F)))\, d\Omega = 0 , \tag{19}$$

for the determination of $u_0(F)$.

Another average besides the median sheds some light on the usefulness of spherical potentials to describe the thermodynamics of nonspherical potentials. One can find a spherical potential (denoted here the virial potential) that is exact (6) in the low density limit. For N_2 there is almost no difference between the median and the virial potentials. Figure 2 compares the virial potential, median, and potential average for CO_2.

The potential average would be correct for freely rotating molecules. There is some density dependence in the best effective spherical potential, but it is small enough, even for CO_2, to not significantly effect the results over the density range of interest.

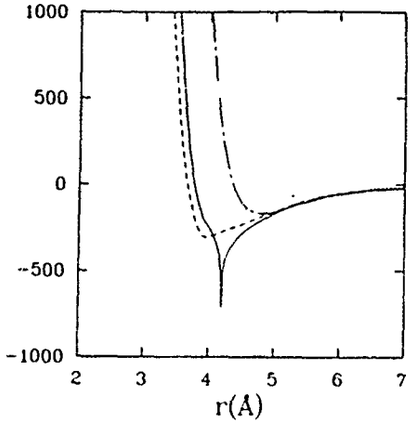

Fig. 2. Potentials for CO_2. ——— Virial potential, · · · · · Median, ——— — ——— Average, · · · · · Two orientations of the anisotropic potential

COMPARISON WITH MD

The effective spherical potentials give results for thermodynamics that are much more accurate than our knowledge of the anisotropic potentials themselves. Figure 3 compares the spherical theory with the anisotropic MD simulations (2) for N_2.

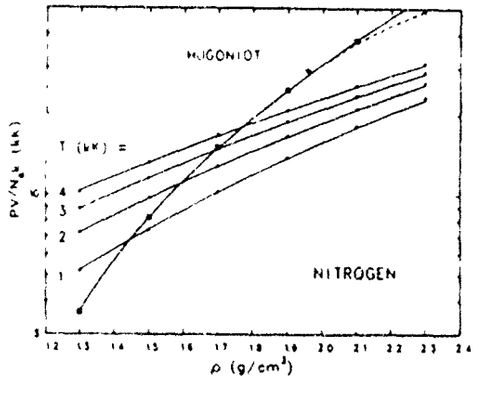

Fig. 3. Isotherms (+) and Hugoniot (¦) for N_2 from MD and from the median (———)

Figure 4 gives similar comparisons (3) for CO_2. Agreement is to about 1.5% for N_2 and about 3% for much of the CO_2. Where $35 \lesssim \varrho V/NkT \lesssim 20$, the accuracy is more like 5 to 10%. This is due to the formation of long lived dimer-like correlations (7) where lower energy relative orientations are preserved by a caging effect.

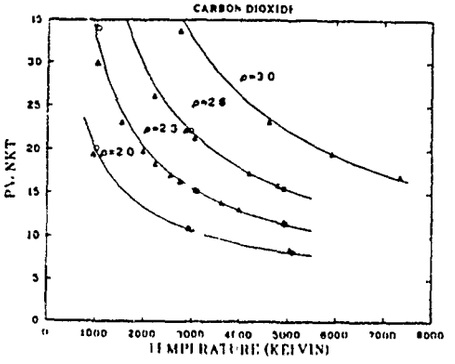

Fig. 4. Δ MD for anisotropic potential, 0 MD for median, ——— Ross for median

These results demonstrate that spherical potentials can be used for the thermodynamics of dense molecular fluids with anisotropies of the order of CO_2 or smaller. This includes N_2, O_2, CO, NO, CO_2 and H_2.

EOS FOR INDIVIDUAL SPECIES

Effective spherical potentials for N_2, O_2, NO, CO, and CO_2 are obtained by fitting to various experimental and calculated quantities.

We have chosen the Ross (8) procedure to evaluate the configurational free energy, A_c, for the spherical potential because it is both fast and accurate (2% or better in dense fluids). It is based on a variational principle (see, e.g., Mansoori and Canfield (9) and Rasaiah and Stell (10),

$$A_c \leq A_0 + \frac{N\varrho}{2} \int_0^\infty g_0(r)(u(r)-u_0(r)) \, d^3r \qquad (20)$$

That is, the true configurational free energy is bounded from above by the first two terms of the λ expansion perturbation theory of Zwanzig (11). The reference system configurational free energy, radial distribution function, and pair potential are denoted A_0, g_0 and u_0, respectively. The pair potential for the true system is u. For a hard-sphere reference system, convenient and accurate representations of $g_0(r)$ and A_0 are known. Ross found that if one added a function $F_{12}(\eta)NkT = -(\eta^4/2+\eta^2+\eta/2)NkT$ to Eq. (20), then the free energy for an r^{-12} potential could

be well reproduced by minimizing the right-hand side with respect to $\eta = \pi\varrho d^3/6$, where d is the hard-sphere radius. He then approximated the radial distribution function for the r^{-12} system by that for the hard-sphere system. This gave

$$A_c \leq A_0 + \frac{\varrho N}{2}\int_d^\infty g_0(r,\eta)u(r)d^3r + F_{12}(\eta)NkT, \quad (21)$$

which is then minimized with respect to η. In practice, the Laplace transform is used when a simple functional form of u(r) is chosen.

The other contributions to the Helmholtz free energy, A, for a single species are well approximated by several simple, separable contributions. [Note that the resulting procedure for obtaining A is essentially that of Ross (12) and Ree (13). However, the spherical potentials are obtained in a totally different manner.] The translational and rotational degrees of freedom can be separated exactly to give ideal contributions provided the bond lengths are kept constant. (Hindered rotation effects and "collisions" are incorporated in the configurational free energy.) The vibrational degrees of freedom are treated as isolated quantum vibrators. McQuarrie (14) is a convenient source for the form of these contributions. Electronic excitations are included using an isolated molecule Saha model (15). Electronic levels up to about 60,000 cm^{-1} are included. This cutoff will not cause significant truncation errors below around 10,000°K.

The effective spherical potentials used are given in Table 1. The parameters are for an exponential-six potential

$$u(r) = \frac{\varepsilon}{\alpha - 6}\left(6e^{\alpha(1-r/r^*)} - \alpha\left(\frac{r^*}{r}\right)^6\right) \quad (22)$$

TABLE 1
Exponential-Six Potential Parameters

	α	r*(Å)	ε/k (°K)
N_2	13.474	4.251	75.0
NO	12.08	3.995	117.1
O_2	13.117	4.110	75.0
CO	13.474	4.251	75.0
CO_2	13.781	4.096	335.0

The determination of the N_2 potential is well described elsewhere (2, 16). The O_2 potential was fit directly to the Hugoniot data rather than finding the effective spherical potential that reproduces the nonspherical thermodynamics that fits the Hugoniot. The NO potential was from a fit by Pack (17) to viscosity and virial data. We chose the potential that not only had a good fit to this data, but also was "parallel" to the N_2 and O_2 potentials in the repulsive region. Because there is considerable uncertainty in the NO potential, we decreased ε by 5% to get a slightly better fit to the liquid NO detonation velocity. However, the unadjusted potential gave results well within the experimental uncertainty. The CO potential was taken to be identical to that for N_2 since the two are isoelectronic. In addition, this potential gives a Hugoniot that agrees within experimental error with the data of Nellis, et al. (18) at 53.4 kbar and 99.6 kbar. Higher pressure data almost certainly includes some reaction to CO_2 + C and is, therefore, not useful for determining a CO potential. The CO_2 potential is a spherical potential fit to the thermodynamics of a very anisotropic potential. The anisotropic potential is an atom-atom potential with interaction sites only on the oxygens. The well depth, ε; well minimum position, r*; and O-O separation, ℓ, were taken from a normal density simulation of solid CO_2 by Gibbons and Klein (19). The steepness parameter α was fit to the cold curve of LeSar and Gordon (20) whose theory agrees extremely well with the 296°K isotherm measured by Olinger (21) up to 100 kbar. This potential then agrees reasonably well with the CO_2 Hugoniot of Zubarev and Telegin (22). However, an overall reduction by 10% gives the best fit to the data. The data is so sparse that there is a much greater uncertainty in the CO_2 potential than for N_2 and O_2. New CO_2 Hugoniot data would be very useful.

Results are given primarily in the form of figures comparing with data. First the fits to data are shown and then the comparison with data not used in fitting the potentials. Figure 5 shows our theory for N_2 compared with data (22, 23, 24, 25). Above 40 GPa new physics such as dissociation, significant excitation of electronic levels, etc., enter in the problem and we have not tried to fit that region. Figure 6 shows our best least squares fit to the O_2 data (25, 26) with a spherical exponential-six potential. Figure 7 compares with reflected shock data

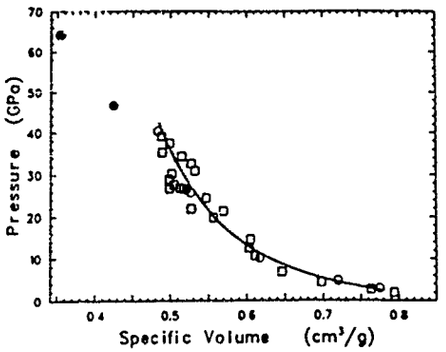

Fig. 5. Hugoniot results for nitrogen (Lines are present theory: solid, for ϱ_0=0.808 g/cm^3; dotted, for ϱ_0 = 0.820 g/cm^3. Data are: ⊕, from Ref. (23); O, from Ref. (22); □, from Ref. (24), as compiled in Ref. (25).)

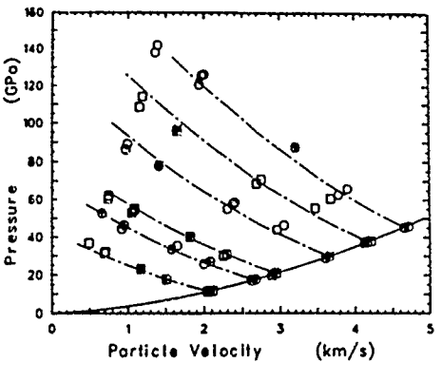

Fig. 7. Reflected-shock results for oxygen initially at ϱ_0 = 1.202 g/cm^3 (Lines are present theory: solid, principal Hugoniot; chain dashed, reflected Hugoniots. Data are from Ref. (26) [or Ref. (25)].)

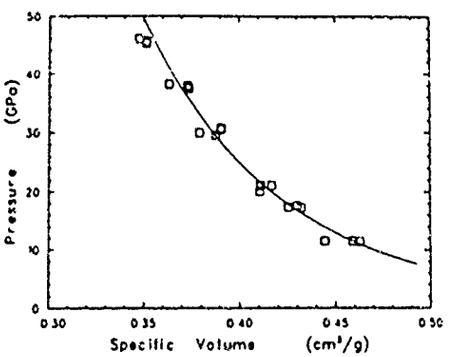

Fig. 6. Hugoniot results for oxygen at ϱ_0 = 1.202 g/cm^3. Line is present theory, and data are from Ref. (26), as compiled in Ref. (25).

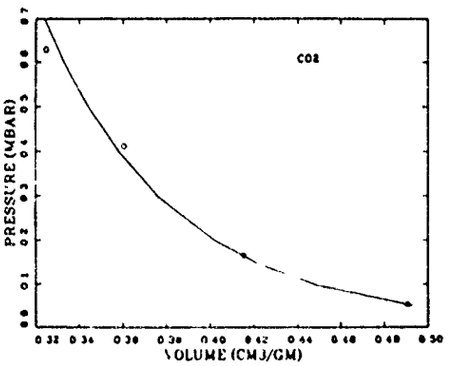

Fig. 8. Hugoniot for CO_2 ——— present theory O Data from Ref. (22)

and gives very good agreement. Figure 8 compares our theory with the CO_2 data (22). In Figure 9 we show the repulsive part of the potentials given in Table 1. Note that the parameters are not entirely independent. Therefore, a look at the table alone is not sufficient to order the potentials. Also, the attractive part of the potential makes a fairly small contribution to the thermodynamics in regions of interest to detonation products.

EOS FOR MIXTURES

We have used ideal mixing for our detonation products EOS. Ideal mixing takes into account

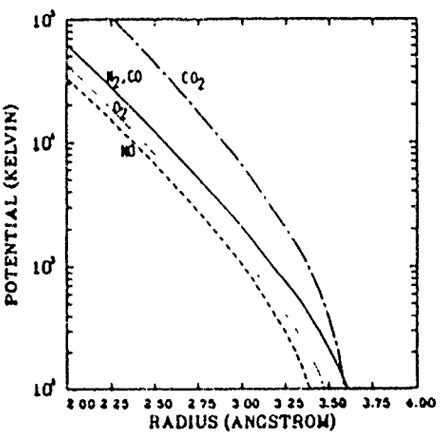

Fig. 9. Effective spherical potentials from Table 1

the distinguishability of different molecules, but assumes the total energy of a configuration of particles is independent of any interchange of particles. This is exact if all pair potentials are identical. For N_2, O_2, NO, and CO, this may be a very good approximation. For CO_2 mixed with any of the above, this may not be as good. However, more accurate mixing theories require cross potentials, i.e., not only u_{aa} and u_{bb}, but also u_{ab}. For ze[illegible]sure fluid mixtures, a few percent change in the cross potential may lead to a change in sign of excess properties (27). Ree (28) has found that a few percent change will significantly shift a fluid-fluid phase separation boundary in detonation products. Also, it is not certain that an accurate mixing theory for spherical potentials is still accurate for effective spherical potentials representing very anisotropic potentials. We intend to look at molecular mixtures with MD or Monte Carlo (MC), but we will continue with ideal mixing until it is clear what works better for molecular mixtures. Equilibrium composition of the detonation products is found by minimizing the Gibbs free energy of the mixture. A slightly modified form of the procedure of White et al. (29, 30) was used.

In Figures 10 and 11, we compare in P, V and P, E space the Hugoniot for overdriven NO detonations and an equimolar mixture of N_2 and O_2. There is excellent agreement with Schott's (31) data. Where the two Hugoniots cross, the thermodynamic states are identical. The uncertainty in the crossing point is smallest in P, E and the calculated crossing is also in excellent agreement with the data. In Figure 12 we have the detonation velocity (32) for O_3/O_2 mixtures. Considering the scatter in the data, the agreement is very good. Finally, the detonation velocities and pressures for NO, TNM, and HNB are compared with experiment in Table 2. Again, the agreement is very good.

CONCLUSION

We have an equation of state for detonation products that is in very good agreement with experiment for explosives containing some or all of C, N, O and for which there is no solid carbon in the products. We will investigate the EOS for solid carbon, H_2O, and other products in order to extend the capability to the more

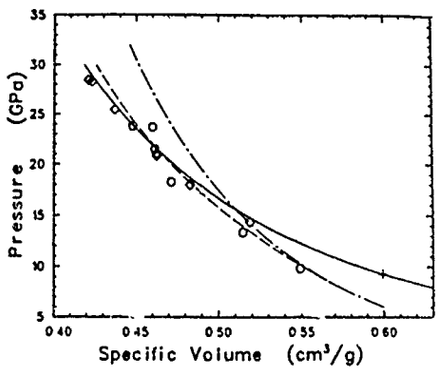

Fig. 10. Nitrogen-Oxygen systems [data from Ref. (31)] (Overdriven NO: ——— theory, data, + CJ state N_2+O_2 mixture: —— —— theory, O data, —— — —— theory without NO.)

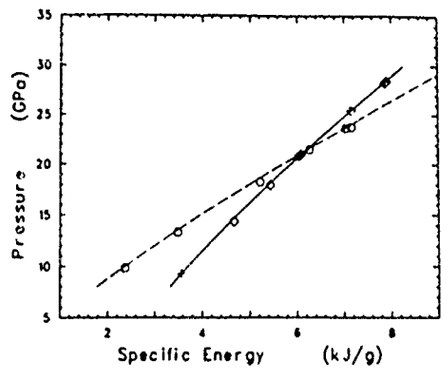

Fig. 11. Hugoniot pressure — energy results for dense nitrogen — oxygen system (Symbols and curves are as specified for Fig. 10)

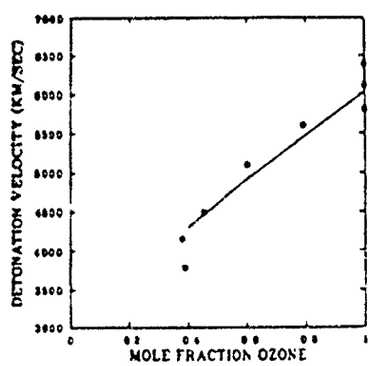

Fig. 12. Detonation velocity of O_3/O_2 mixtures ——— present theory, O data from Ref. (32)

TABLE 2
Detonation Velocities of NO (33), TNM (30), and HNB (34)

Explosive	Formula	ϱ_0 (g/cm^3)	D_{expt} (m/s)	P_{expt} (kbar)	D_{calc} (m/s)	P_{calc} (kbar)
Nitric Oxide	NO	1.294	5620±70	100±15	5621	98
TNM	C_4O_8	1.638	6360	159	6539	158
HNB	$C_6N_6O_{12}$	1.973	9335	400	9405	382

common CHNO explosives. Also, mixing questions will be addressed using MD or MC.

REFERENCES

1. e.g., R. Chirat and G. Pittion-Rossillon, J. Chem. Phys. *74,* 4634 (1981) and Proceedings of the Seventh Symposium (International) on Detonation, p.646 (1981); Francis H. Ree, Proceedings of the Seventh Symposium (International) on Detonation, p. 646 (1981); C. L. Mader, *Numerical Modeling of Detonations* (University of California, Los Angeles, 1979); W. Fickett, Los Alamos Scientific Laboratory Report LA-2712 (1962).
2. J D. Johnson, M. S. Shaw, and B. L. Holian, "The Thermodynamics of Dense Fluid Nitrogen by Molecular Dynamics," J. Chem Phys. *80,* 1279 (1984).
3. J. D. Johnson and M. S. Shaw, "Thermodynamics Using Effective Spherical Potentials for CO_2 Anisotropies," J. Chem. Phys. *83,* 1271 (1985).
4. M. S. Shaw, J. D. Johnson, and B. L. Holian, "Effective Spherical Potentials for Molecular Fluid Thermodynamics," Phys. Rev. Lett. *50,* 1141 (1983).
5. W. R. Smith, Can. J. Phys. *52,* 2022 (1974); see also W. R. Smith, I. Nezbeda, T. W. Melnyk, and D. D. Fitts, Faraday Discuss. Chem. Soc. *66,* 130 (1978).
6. M. S. Shaw and J. D. Johnson, "A Temperature and Independent Spherical Potential which Reproduces Exactly the Second Virial Coefficient of Nonpolar Molecules," J. Chem. Phys. *81,* 3360 (1984).
7. D. MacGowan, J. D. Johnson, and M. S. Shaw, "Angular Correlations in Dense Hot Diatomic Fluids," J. Chem. Phys. *82,* 3765 (1985).
8. Marvin Ross, J. Chem. Phys. *71,* 1567 (1979).
9. G. A. Mansoori and F. B. Canfield, J. Chem. Phys. *51,* 4958 (1969) and *53,* 1618 (1970).
10. J. C. Rasaiah and G. Stell, Mol. Phys. *18,* 249 (1970) and Chem. Phys. Lett. *4,* 651 (1970).
11. R. W. Zwanzig, J. Chem. Phys. *22,* 1420 (1954).
12. M. Ross and F. H. Ree, J. Chem. Phys. *73,* 6146 (1980).
13. Francis H. Ree, Proceedings of the Seventh Symposium (International) on Detonation (1981), p. 646.
14. Donald A. McQuarrie, *Statistical Mechanics* (Harper & Row, New York, 1976).
15. See, e.g., W. Ebeling, W. D. Kraeft, and D. Kremp, *Theory of Bound States and Ionization Equilibrium in Plasmas and Solids* (Akademie-Verlag, Berlin, 1976).
16. P. J. Hay, R. T. Pack, and R. L. Martin, "Electron Correlation Effects on the N_2-N_2 Interactions," J. Chem. Phys., *81,* 1360 (1984).
17. R. T. Pack, private communication.
18. W. J. Nellis, F. H. Ree, M. van Thiel, and A. C. Mitchell, J. Chem. Phys. *75,* 3055 (1981).
19. T. G. Gibbons and M. L. Klein, J. Chem. Phys. *60,* 112 (1974).
20. R. LeSar and R. G. Gordon, J. Chem. Phys. *78,* 4991 (1983).
21. B. Olinger, J. Chem. Phys. *77,* 6255 (1982).
22. V. N. Zubarev and G. S. Telegin, Soviet Physics — Doklady *7,* 34 (1962).

23. W. J. Nellis and A. C. Mitchell, J. Chem. Phys. *73,* 6137 (1980).

24. R. D. Dick, J. Chem. Phys. *52,* 6021 (1970).

25. S. P. Marsh, *LASL Shock Hugoniot Data* (University of California Press, Berkeley, 1980).

26. J. Wackerle, W. L. Seitz, and J. C. Jamieson, in *Behavior of Dense Media Under High Dynamic Pressure,* (Gordon and Breach, New York, 1968), pp. 85-93.

27. I. R. McDonald, in *Statistical Mechanics,* Vol. 1 (The Chemical Society, London, 1973), K. Singer (Ed.), Chapter 3.

28. Francis H. Ree, J. Chem. Phys. *81,* 1251 (1984).

29. W. B. White, S. M. Johnson, and G. B. Dantzig, J. Chem. Phys. *28,* 751 (1958).

30. Charles L. Mader, *Numerical Modeling of Detonations* (University of California Press, Berkeley, 1979).

31. G. L. Schott, M. S. Shaw, and J. D. Johnson, "Shocked States from Initially Liquid Oxygen-Nitrogen Systems," J. Chem. Phys. *82,* 4264 (1985).

32. R. O. Miller, J. Phys. Chem. *63,* 1054 (1959).

33. J. B. Ramsay and W. C. Chiles, Proceedings of the Sixth Symposium (International) on Detonation (1976), p. 723.

34. "Hexanitrobenzene: A New High-Energy Explosive," Energy and Technology Review, UCRL-52000-78-11 (Nov. 1978), p. ii.

THEORETICAL EQUATIONS OF STATE FOR THE DETONATION PRODUCTS OF EXPLOSIVES

Gerald I. Kerley
Sandia National Laboratories
Albuquerque, NM 87185

Equations of state (EOS) for the detonation products of explosives are calculated from EOS for the individual chemical species, using the approximation of ideal mixing. The theory is applied to 15 explosives of varying composition and loading density. To understand these explosives, it is necessary to identify the important reaction products and to determine their EOS parameters. For explosives that contain no carbon or are oxygen-rich, the principal species and their EOS are known reasonably well, and the theory gives good results. For carbon-rich explosives, it is found that formic acid competes with carbon as a reaction product. If formic acid is omitted from the equilibrium, the data for PETN and RDX cannot be fit with any reasonable modification to the carbon EOS. An EOS for formic acid is constructed, and the theory gives good results for all classes of CHNO explosives.

INTRODUCTION

In recent years there has been renewed interest in calculating the detonation properties of condensed explosives from basic principles of statistical mechanics (1-5). Assuming a steady-state detonation with chemical equilibrium behind the reaction zone, the EOS for the detonation products can be used to predict CJ velocities and pressures, release and reshock behavior, and the dependence of these properties on chemical composition and loading density. However, it has proven difficult to find an EOS model that is completely satisfactory for all classes of explosives. This fact has led to speculation that the steady state assumption may be a major source of error, particularly for high-density explosives that are rich in carbon (1,2). In this paper, we will show that the principal discrepancies observed in carbon-rich explosives are eliminated when formic acid is included as a reaction product.

The development of a theoretical model for detonation properties follows four basic steps.

1. Identify the important reaction products.
2. Determine EOS parameters for each component.
3. Construct a mixture EOS for an arbitrary composition.
4. Determine the equilibrium composition.

Despite recent advances in fluid theory, many approximations must be made in the first three steps. Only the last step can be carried out rigorously.

OVERVIEW OF OUR MODEL

In step 3, we make the simplifying assumption of ideal mixing, which may be described as follows (6). Starting with a heterogeneous mixture, allow the components to mix homogeneously at constant pressure and temperature. In an ideal mixture, there is no change in volume or internal energy, while the change in entropy is that for complete randomness. In this model, the mixture properties are completely determined from the EOS for the pure components. We will show that it gives good predictions for detonation properties when steps 1 and 2 can be carried out - when the

important chemical components have been identified and their EOS are known with reasonable accuracy.

For CHNO explosives, the chemical species that are normally included as detonation products are CO_2, N_2, H_2O, CO, NO, NH_3, CH_4, H_2, O_2, and elemental carbon (1). In this work, we also include formic acid (HCOOH) and atomic N, O, and H. HCOOH should be included because it is energetically favored over a mixture of H_2O and CO. This fact can be seen from the endothermic decomposition reaction,

$$HCOOH \rightarrow H_2O + CO, \quad \Delta H = -4.34 \text{ kcal/mole.} \qquad (1)$$

Early models for detonation properties included HCOOH (7), but it has been ignored in recent work. For explosives containing C, H, and O, we find HCOOH to be more important than CO. Methanol and formaldehyde were also considered but found to be unimportant.

The 15 explosives studied in this work are listed in Table 1, along with their formulas, oxygen balances (OB), and CJ properties (1-5, 8-12). Calculations were performed in the following way. First, the PANDA code (13) was used to construct EOS tables for the various species and add them to a data file that was used for explosives of all compositions. The tables were accessed by the POGO code (unpublished), which constructs thermodynamic quantities for a mixture of specified elemental composition and calculates the equilibrium molar concentrations by minimizing the Helmholtz function at constant density and temperature. The detonation properties were computed from the usual relations (1-4).

EOS FOR FLUID SPECIES

Our model for calculating the EOS of fluids is described elsewhere (14-16), and we discuss it only briefly in this paper. The Helmholtz free energy A was written as the sum of six contributions.

$$A = A_t + A_v + A_r + A_e + A_\phi + A_\theta \qquad (2)$$

The first four terms are independent of the intermolecular forces. A_t is the contribution from the translational degrees of freedom, given by the usual ideal gas expression. A_v, A_r, and A_e are contributions from vibrational, rotational, and electronic degrees of freedom and were calculated from spectroscopic data, using well-known expressions (1,13). The last two terms in Eq. (2) come from the interactions between the molecules. We define A_ϕ to be the contribution from the spherically symmetric part of the intermolecular forces - the average over all molecular orientations. A_θ is a correction for correlations between molecular orientations. For water and formic acid, which have large dipole moments, this term is important at low temperatures. Following the lead of Chirat and Pittion-Rossillon, we approximated A_θ by the expression for a hard-sphere fluid with embedded dipoles (3).

The term A_ϕ was calculated using the CRIS model, a perturbation theory of fluids (14). As in all fluid theories, the crucial problem in applying the model to a specific case is that of obtaining information about the intermolecular forces. For nearly spherical molecules, the CRIS model computes the energy of a molecule in the cage formed by its neighbors from the zero-Kelvin isotherm of the solid. For nonspherical molecules, the model uses an effective isotherm that corresponds to a fictitious solid in which the molecules rotate freely (15). In a few cases, this isotherm has been calculated theoretically, but in this work some of the EOS parameters were determined from experimental data, particularly the Hugoniot. Most of the species used in this work are discussed below. Parameters for CO were taken to be the same as for N_2. Our EOS for H_2 and CH_4 have been described elsewhere (14,16).

NITROGEN, OXYGEN, AND NITRIC OXIDE

We have previously reported EOS parameters for N_2 and O_2 (15) that match experiment except for the Hugoniot data above about 30 GPa, where dissociation must be taken into account. In this work we constructed EOS for atomic nitrogen and oxygen; we then used the POGO code to make the equilibrium calculation between the molecular and atomic species, as discussed above. EOS parameters for the atomic species are preliminary and were selected, from within reasonable bounds, to agree with Hugoniot data. Our calculated Hugoniots for nitrogen and oxygen, both with and without dissociation, are compared with the measurements (17) in Fig. 1.

Nitric oxide dissociates when shocked and is

itself an explosive, so analysis of shock wave data for NO requires a chemical equilibrium calculation. Reasonable EOS parameters for NO, intermediate between those for N_2 and O_2, were found to give satisfactory results. Our calculations are compared with the measured detonation properties (11) in Table 1; agreement is within experimental error. Our calculated Hugoniots for NO and N_2/O_2 mixtures are compared with experiment (5) in Fig. 2. The equilibrium molar concentration of the NO species was found to vary from about 9% at the CJ state to about 40% at the highest pressure studied. As seen in Fig. 2, the shock velocity for nitric oxide increases by about 4% when the NO species is eliminated from the equilibrium altogether. Atomic nitrogen and oxygen were also found to be important at high pressures.

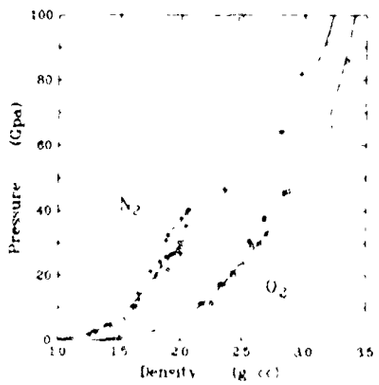

Fig 1 Hugoniots for liquid nitrogen and oxygen Calculated curves are dashed-no dissociation, solid-with dissociation

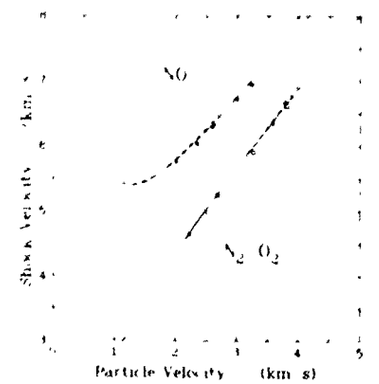

Fig 2 Hugoniots for nitric oxide and for an equimolar N_2/O_2 mixture Calculated curves are: dotted-allow only N_2 and O_2 species, dashed allow N_2, O_2, and NO, solid-allow N_2, O_2, NO, N, and O

WATER, AMMONIA, AND RX-23 EXPLOSIVES

Our calculated Hugoniots for water and ammonia are compared with experimental data (18) in Fig. 3. Chemical equilibrium calculations showed that dissociation is a small effect in both cases.

As a test of our EOS for these two species in calculating detonation properties, we considered three explosive mixtures containing only H, N, and O (8). The explosive RX-23-AB is a particularly interesting case because nitrogen and water are the only important chemical species formed in the detonation products. RX-23-AA and RX-23-AC also form ammonia. Our theoretical CJ properties are compared with experiment in Table 1. The agreement is good for all three compositions. The only significant discrepancy is the CJ temperature for RX-23-AB, and the experimental result may be in error for this case (8).

There are no measurements of the release isentropes for these explosives, but it is interesting to compare our theoretical predictions with isentropes calculated from the empirical JWL EOS. Because the JWL parameters were calibrated using cylinder tests, this comparison gives some indication of how well our model can predict expansion of the detonation products (4,8). The pressures on the isentropes are shown in Fig. 4. The agreement is good, and our model correctly predicts the differences between the three compositions.

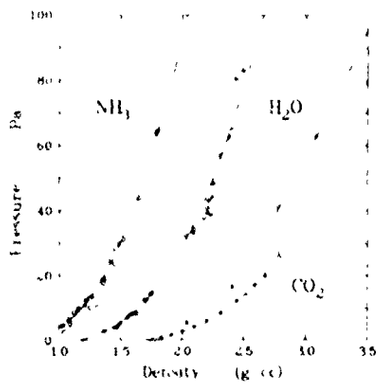

Fig. 3 Hugoniots for water, ammonia, and carbon dioxide. For CO_2, the dashed curve is our cold curve, and the points are from ref. 20.

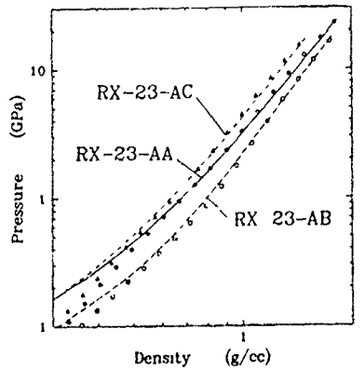

Fig. 4 Release isentropes for RX-23 explosives. Discrete points are from the JWL EOS and the curves are our calculations.

CARBON DIOXIDE AND HNB

CO_2 is one of the most important species in the detonation products of most explosives, and it is unfortunate that there is only one reported measurement of the Hugoniot for this substance (19). In addition to this data, we used the theoretical calculations of LeSar and Gordon (20) to construct the EOS. An equilibrium calculation was also performed, and dissociation was found to have a small effect at the highest pressures on the Hugoniot. The results are shown in Fig. 3. Because there are only four measured shock points, it is difficult to assess our EOS. However, we have found that our calculated detonation properties are fairly insensitive to variations in the EOS parameters over a reasonable range. Hence it appears that uncertainties in the CO_2 EOS are not a major source of error in our theory.

As a test of our CO_2 EOS in calculations of detonation properties, we consider the explosive HNB, because it decomposes primarily into CO_2 and N_2 (4). (However, our model predicts that small amounts of CO, NO, N, O_2, and O are also formed.) Our CJ properties, given in Table 1, are in good agreement with the experimental ones. Furthermore, our calculated release isentrope (not shown) agrees quite well with that from the JWL EOS derived to fit cylinder test data. (4).

OTHER LOW-CARBON EXPLOSIVES - NG and PETN

Because NG has a positive OB, it forms very little formic acid or elemental carbon in the detonation products and provides a test of the EOS of all the species considered thus far. As shown in Table 1, our theory gives good predictions for the CJ properties of this explosive.

The detonation velocity and pressure of PETN have been measured as functions of loading density (11) and are shown in Figs. 5 and 6, respectively. Because PETN has a small negative OB, it can form either elemental carbon or formic acid. The dotted lines show the results of our model when neither of these two species are allowed to form. These calculations agree well with the experimental data for loading densities below about 1.4 g/cc. As we will show below, the data for high densities are explained when formic acid is included as a reaction product. The good results for lower densities indicate that our EOS for the species considered above are satisfactory.

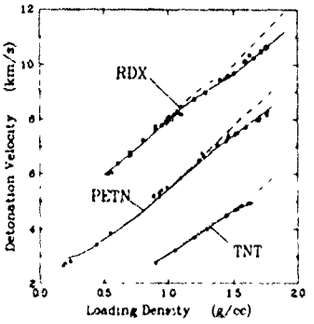

Fig. 5 Detonation velocity vs. loading density for 3 explosives. For clarity, the TNT and RDX velocities were shifted by −2 and +2 km/s, respectively. Calculated curves are discussed in the text.

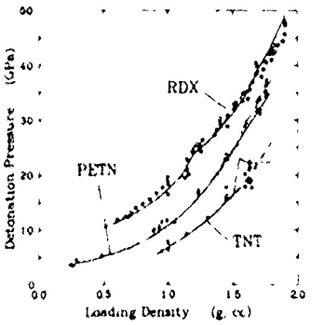

Fig. 6 Detonation pressure vs. loading density for 3 explosives. For clarity, the PETN and RDX pressures were shifted by +3 and +8 GPa, respectively. Calculated curves are the same as in Fig. 5.

FORMIC ACID - PETN, RDX AND HMX EXPLOSIVES

There are no shock wave data for formic acid, but it is possible to estimate EOS parameters for this species and to test the sensitivity of detonation properties to variations in these parameters. Our studies show that HCOOH is an important species in many explosives. We find that PETN and RDX form very little elemental carbon and that their properties are particularly sensitive to this EOS. (The CHO ratio for RDX is identical to that of HCOOH.) Because the properties of PETN and RDX are so sensitive to the parameters for formic acid, we refined our EOS by fitting the measured detonation velocity data for these explosives.

Three calculations of the detonation velocity for PETN are shown in Fig. 5. When elemental carbon and HCOOH are omitted from the detonation products (dotted line), the theory overestimates the velocity at high loading densities. When carbon is added to the equilibrium (dashed line), there is only slight improvement, and we could find no reasonable modification to the carbon EOS that would give satisfactory agreement with these data. Finally, when HCOOH is added to the equilibrium (solid line), the results show a dramatic change in slope at high densities and are in good agreement with the measurements. The calculated detonation pressures, shown if Fig. 6, are also in good agreement with experiment.

Two calculations of the detonation velocity and pressure for RDX are shown in Figs. 5 and 6. In the dashed curves, diamond and liquid carbon (see below) were included in the equilibrium, but formic acid was omitted. As in PETN, the theory overestimates the velocity, and no reasonable modification to the carbon EOS can be made to give agreement with the data. In contrast, very good results are obtained when HCOOH is added to the equilibrium (solid line). As shown in Table 1, our theory also gives good results for HMX, which has the same CHNO ratio as RDX.

CARBON EOS - BTF, NM, TNT, HNS, NQ, AND TATB

Three phases of elemental carbon were considered in our work - graphite, diamond, and liquid. Graphite and diamond can be regarded as idealizations of the solid phases that might be formed in a detonation. EOS for these two phases were constructed using standard solid models from the PANDA code (13). The results agree well with experimental data, and the two EOS match the graphite-diamond phase line quite well (21). An EOS for the liquid phase was constructed using the CRIS model. Very little data is available for liquid carbon; we adjusted the EOS parameters to match the melting curve in the vicinity of the graphite-diamond-liquid triple point. Our liquid EOS appears to be satisfactory for most explosive calculations, but it does not match the negative slope of the carbon melting curve and the low density of the liquid at low pressures. To account for those effects, we are working on an EOS that includes formation of molecules in the liquid phase. Such changes to the liquid EOS will affect some of our results, particularly for RDX at low loading densities.

The species of carbon that is formed depends markedly upon pressure and temperature. A study of the carbon phase diagram shows that liquid carbon should be formed in BTF, that graphite should be the principal species for NM and TNT, and that diamond should be the principal species for HNS. As seen in Table 1, our theory gives good results for the properties of these explosives.

BTF contains no hydrogen and cannot form HCOOH, but it has a negative OB and forms a large amount of elemental carbon in the detonation products. The good results obtained for BTF provide evidence that our carbon EOS is reasonable, and that a compound like HCOOH, containing both carbon and hydrogen, is needed to explain the data for the other explosives studied.

Three calculations of the detonation velocity and pressure for TNT are shown in Figs. 5 and 6. In the dotted curve, graphite was the only elemental form of carbon allowed in the equilibrium, and formic acid was omitted. The results are fair, but they have the wrong slope and consistently overestimate the velocity. When HCOOH is added to the equilibrium (dashed line), the calculations come into excellent agreement with experiment for densities below about 1.5 g/cc. When diamond is added to the equilibrium (solid line), the theory predicts a change in slope of the volocity curve

at high densities, as seen in the data.

The carbon phase diagram and shock data for graphite both suggest that the transition from graphite to diamond causes this observed change in slope, but the shock-induced transition occurs at about 10 times the equilibrium pressure (21). This fact can be explained by postulating imperfections in the diamond phase. Because the energy difference between graphite and diamond is small compared to the carbon bond energy, a small percentage of vacant sites in the diamond lattice can increase the transition pressure by an order of magnitude. In the calculations shown in Fig. 5 and 6, the binding energy of diamond was decreased by .9% in order to make the phase transition occur at about 20 GPa, as indicated by the measurements.

Finally, the calculated properties of NG and TATB are also compared with experiment in Table 1. The velocities for these two explosives are high by about 6% and are the only cases studied for which the agreement is not satisfactory. In both cases, diamond is the carbon species formed in the products, and no reasonable change in the diamond EOS substantially improves the results. Because both NQ and TATB have a high CJ pressure and low CJ temperature, it is possible that a more complex species, like acetic acid, is being formed in these explosives.

CONCLUSIONS

There are two main conclusions to be drawn from our work. First, the assumptions of ideal mixing and chemical equilibrium seem to be adequate for understanding detonation properties. Ideal mixing leads to great simplification of the problem. Second, discrepancies in theoretical predictions for explosives with negative OB, particularly for high loading densities, can be explained if formic acid is included in the equilibrium. Previously, these discrepancies have been attributed either to an inadequate carbon EOS or to nonequilibrium effects.

Certain problems may be singled out for further study. Shock wave data and other experiments on formic acid and carbon dioxide are needed to improve our EOS models for these species. Better data and modeling for liquid carbon are needed. Finally, the importance of other chemical species should be investigated.

ACKNOWLEDGEMENTS

This study began while I was at Los Alamos National Laboratory, and I am grateful to D.E. Carroll for his support at that time. The original version of the POGO code was written with the help of S.P. Lyon. I have learned much about explosives from my association with C.L. Mader over a period of many years. Finally, I am grateful to L.W. Davison and P. Yarrington for encouraging me to continue work on this problem at Sandia. This work performed at Sandia National Laboratories was supported by the U.S. Department of Energy under contract number DE-AC04-76DP00789.

REFERENCES

1. C.L. Mader, Numerical Modeling of Detonations (University of California, Berkeley, 1979).
2. W. Fickett and W.C. Davis, Detonation (University of California, Berkeley, 1979)
3. R. Chirat and G. Pitton-Rossillon, "Detonation Properties of Condensed Explosives Calculated with an Equation of State Based on Intermolecular Potentials," in *Proceedings of the Seventh Symposium (International) on Detonation*, J. M. Short, ed., NSWL MP 82-334 (Naval Surface Weapons Center, White Oak, MD. 1981), p. 695.
4. F.H. Ree, "Postdetonation Behavior of Condensed High Explosives by Modern Methods of Statistical Mechanics," in *Proceedings of the Seventh Symposium (International) on Detonation*, J.M. Short, ed., NSWC NIP 82-334 (Naval Surface Weapons Center, White Oak, MD, 1981), p. 646.
5. G.L. Schott, M.S. Shaw, and J.D. Johnson, "Shocked States from Initially Liquid Oxygen-Nitrogen Systems," *J. Chem. Phys.*, 85, 4263 (1985).
6. J.H. Hildebrand and R.L. Scott, The Solubility of Nonelectrolytes, (Dover, New York, 1964).
7. M.A. Cook, The Science of High Explosives (Reinhold, New York, 1958).
8. M. Finger, E. Lee, F.H. Helm, B. Hayes, H. Hornig, R. McGuire, M. Kahara, and

M. Guidry, "The Effect of Elemental Composition on the Detonation Behavior of Explosives", in *Proceedings of the Sixth Symposium (International) on Detonation*, D.J. Edwards, ed., ACR-221 (Office of Naval Research, Department of the Navy, 1976), p. 710.

9. T.R. Gibbs and A. Populato, LASL Explosive Property Data (University of California, Berkeley, 1980).

10. D.R. Hardesty and J.E. Kennedy, "Thermochemical Estimation of Explosive Energy Output," *Combust Flame*, 28, 45 (1977).

11. J.B. Ramsay and W.C. Chiles, "Detonation Characteristics of Liquid Nitric Oxide," in *Proceedings of the Sixth Symposium (International) on Detonation*, D.J. Edwards, ed., ACR-221 (Office of Naval Research, Department of the Navy, 1976), p. 723.

12. H.C. Hornig, E.L. Lee, M. Finger, and J.E. Kurrle, "Equation of State of Detonation Products," in *Proceedings of the Fifth Symposium (International) on Detonation*, D.J. Edwards, ed., ACR-184 (Office of Naval Research, Department of the Navy, 1970), p. 503.

13. G.I. Kerley, "User's Manual for PANDA: A Computer Code for Calculating Equations of State," Los Alamos National Laboratory, LA-8833-M, 1981.

14. G.I. Kerley, "A Model for the Calculation of Thermodynamic Properties of a Fluid," in Molecular-Based Study of Fluids, J.M. Haile and G.A. Mansoori, eds., (Am. Chem. Soc., Wash., D.C., 1983), pp. 107-138.

15. G.I. Kerley and J. Abdallah, Jr., "Theoretical Equations of State for Molecular Fluids: Nitrogen, Oxygen and Carbon Monoxide," *J. Chem. Phys.*, 73, 5337 (1980).

16. G.I. Kerley, "A Theoretical Equation of State for Methane," *J. Appl. Phys.*, 51, 5368 (1980).

17. W.J. Nellis and A.C. Mitchell, "Shock Compression of Liquid Argon, Nitrogen, and Oxygen to 90 GPa (900 kbar)," *J. Chem. Phys.*, 73, 6137 (1980).

18. A.C. Mitchell and W.J. Nellis, "Equation of State and Electrical Conductivity of Water and Ammonia Shocked to the 100 GPa (1 Mbar) Pressure Range," *J. Chem. Phys.*, 76, 6273 (1982).

19. V.N. Zubarev and G.S. Telegin, "The Impact Compressibility of Liquid Nitrogen and Solid Carbon Dioxide," *Sov. Phys. Dokl.*, 7, 34 (1962). The initial density of CO_2 is assumed to be 1.45, as implied by the data in Table 1, not 1.54 as stated in the text.

20. R. LeSar and R.G. Gordon "Density-Functional Theory for Solid Nitrogen and Carbon Monoxide at High Pressure," *J. Chem. Phys.*, 78, 4991 (1983).

21. F.P. Bundy, "The P,T Phase and Reaction Diagram for Elemental Carbon, 1979," *J. Geophys. Res.*, 85B, 6930 (1980).

DISCUSSION

Y. M. TIMNAT, Techninon, Haifa, Israel

Is there any experimental evidence for the presence of formic acid (i.e., spectroscopic)?

REPLY BY G. I. KERLEY

I do not know of any experiments that have shown formic acid to be present in the detonation products of explosives. Perhaps no one has ever looked for it. Furthermore, bomb calorimeter experiments might not be the best way to find it, because my calculations predict that there would be very little formic acid in the residual gases. For high loading densities, a substantial amount of it is formed near CJ conditions, but it decomposes to water and carbon monoxide as the gases expand. The mass spectrum of PETN detonation products, reported in the paper by Blais and Valentini at this conference, shows a peak at about 46 amu. They ascribe this peak to NO_2, but it could be due in part to HCOOH, which has the same molecular weight.

DISCUSSION

M. van Thiel, LLNL, Livermore, CA, USA

Is it possible that the small amount of graphite particles formed in the detonation product mixture are impure at least on their surface —

and that as a consequence the phase diagram of carbon shifts?

REPLY BY G. I. KERLEY

I have attributed the apparent shift in the pressure for the graphite-diamond transition to imperfections in the crystal lattices, causing changes in the free energy differences between the two phases. Dissolved or embedded impurities could have much the same effect. However, even pure carbon shows a shift in the transition pressure; in shocked graphite, the transformation to diamond occurs at about 200 kbar, much higher than the equilibrium pressure. If we could explain that effect, it might help us to understand what mechanisms are important in the detonation products.

DISCUSSION

F. VOLK, Fraunhofer Institut, Baden, Germany

In the species you mentioned, we missed *HCN* which we found in relatively large concentrations in the detonation gas of nitroguanadine. Because this molecule is highly metastable, you may explain the difference in D between experiment and calculation.

REPLY BY G. I. KERLEY

Your point is well taken. We have not given much attention to *HCN* as a possible detonation product because it has a rather high heat of formation when compared with other chemical species. Howe ·r, a sensitivity study should be made using a complete and realistic EOS.

TABLE 1

Explosives Studied in this Work

Explosive	Formula	OB	E_o^* (MJ/kg)	ϱ_o (g/cc)	D_{CJ} (km/s) calc.	D_{CJ} (km/s) expt.	P_{CJ} (GPa) calc.	P_{CJ} (GPa) expt.	T_{CJ} (K) calc.	T_{CJ} (K) expt.
NO	NO	+.53	+2.66	1.294	5.52	5.62	9.3	10.0	2693	—
RX-23-AA	$H_{6.78}N_{3.8}O_{2.49}$	−.14	−1.15	1.421	8.70	8.58	24.1	20.9	2954	2900
RX-23-AB	$H_{7.1}N_{2.58}O_{3.55}$	0.00	−5.29	1.384	7.70	7.48	17.4	18.6	2353	4000
RX-23-AC	$H_{10.31}N_{5.32}O_{.95}$	−.67	+0.93	1.135	7.86	7.87	15.4	16.9	2239	2180
HNB	$C_6H_6O_{12}$	0.00	+0.36	1.973	9.31	9.34	39.6	42.0	4935	—
NG	$C_3H_5N_3O_9$	+.35	−1.35	1.600	7.75	7.70	22.8	22.0	4504	—
PETN	$C_5H_8N_4O_{12}$	−.10	−1.36	1.770	8.36	8.27	31.2	32.0	4186	4200
				1.000	5.43	5.48	7.8	8.7	4724	—
HMX	$C_4H_8N_8O_8$	−.22	+0.62	1.890	9.15	9.11	40.3	39.0	3699	—
RDX	$C_3H_6N_6O_6$	−.22	+0.64	1.800	8.79	8.75	35.7	35.0	3869	—
				1.000	5.97	6.02	9.4	10.0	4355	—
BTF	$C_6N_6O_6$	−.38	+2.62	1.857	8.60	8.48	33.5	36.0	4742	—
NM	CH_3NO_2	−.39	−1 41	1.130	6.31	6.30	12.2	13.4	3652	3300
TNT	$C_7H_5N_3O_6$	−.74	+0.02	1.637	6.92	6.94	22.1	18.9	3832	—
				1.050	5.08	5.06	6.8	7.0	3559	—
HNS	$C_{14}H_6N_6O_{12}$	−.67	+0.39	1.690	7.07	7.08	20.3	20.5	4014	—
NQ	$CH_4N_4O_2$	−.3.	−0.46	1.629	8.43	7.98	25.1	—	2612	—
TATB	$C_6H_6N_6O_6$	−.56	−0.24	1.895	8.33	7.86	29.6	31.5	3005	—

* *Energy of unreacted explosive, relative to elements in standard states at 0 K*

DETONATION PROPERTIES OF HIGH EXPLOSIVES CALCULATED BY REVISED KIHARA-HIKITA EQUATION OF STATE

Katsumi Tanaka
National Chemical Laboratory for Industry
Tsukuba Research Center
Yatabe, Tsukuba, Ibaraki 305, Japan

The detonation properties have been calculated by using revised Kihara-Hikita equation of state (KHT). KHT parameters are determined from experimental Hugoniot of the detonation products, measured detonation velocities and pressures. The results show satisfactory agreement with experimental Chapman-Jouguet (CJ) data for general CHNO explosives by assuming the soft solid carbon. Non-ideal explosives which have large differences between calculated detonation properties and experimental results are (i) CNO explosives, (ii) explosives containing large amount of ammonium nitrate except the intermolecular explosives, (iii) aluminum and other metal loaded explosives and (iv) explosives containing large amount of non-reactive hydrocarbons.

INTRODUCTION

In 1952 Kihara and Hikita (1) (KH) described an equation of state (EOS) based on the Lennard-Jones (LJ) repulsive potential. In KH temperature is expressed as the form of explicit function of pressure and volume derived from the virial expansions. When Kihara and Hikita studied, there were very little information on the material state under high pressures and temperatures corresponding to the detonation conditions of high explosives. Although KH used a single potential and simple thermochemical data by assuming a fixed composition of detonation products, calculated results showed satisfactory agreement with experimental detonation velocities by adjusting the potential constants. In 1960, they calculated the detonation properties of TNT for the equilibrium composition of detonation products using Bridgman's equation of state for solid carbon which gave favorable agreement with experimental results.

After the study by Kihara and Hikita, in 1975 Tanaka and Hikita (2) calculated the detonation properties of high explosives assuming equilibrium C-J condition and C-J isentropes by using BKW thermodynamic data and EOS of the solid carbon (3). Results showed the satisfactory agreements with experimental detonation velocities for PETN but calculated detonation pressures were lower than those of experiments. The calculated results for TNT and other explosives with high content of carbon was not satisfactory.

Recently we have revised the KH (referred to as KHT) to improve the reproducibility of detonation properties. The EOS constants are adjusted to match the experimental compression data for various gaseous detonation products. KHT parameters are fully based on the experimental data. Our objective is to present the calculated results and limitations of KHT for various explosives.

2. EQUATION OF STATE

2.1 Gases

(i) Kihara-Hikita (KH)

The general expression for the relation of pressure P, volume V and temperature T for a gas is given by the virial expansion of the form,

$$PV/RT = 1 + \sum B_i(T)/V^i \quad , \quad (1)$$

where $B_i(T)$ is the virial coefficients and R is the gas constant.

Kihara and Hikita (1) derived the temperature as a function of pressure and volume , Eq. (10), using a repulsive intermolecular potential of the form

$$u(r) = \lambda / r^n \ , \qquad (2)$$

where λ and n are constant and r is equal to separation distance.

Assuming a repulsive potential, Eq. (2), virial coefficient B_i is given by

$$B_i = b_i \ (\lambda/RT)^{3i/n} \ , \ i = 1, 2, \ldots \ , \qquad (3)$$

where b_i is constant and depends on n. Substitution of eq. (3) in eq. (1) of virial expansion then gives

$$PV/RT = 1 + \Sigma b_i \ (\lambda/RT)^{3i/n} \ V^{-i} \ . \qquad (4)$$

Then the internal energy can be expressed as

$$E = E^*(T) + (3/n) \ \Sigma b_i \ (\lambda/RT)^{3i/n} \ V^{-i} \ . \qquad (5)$$

by introducing the classical thermodynamic relation, $\partial(E/T^2)/\partial V = \partial(P/T)/\partial T$, into Eq. (4). Substituting the second term in Eq. (4) into Eq. (5), the internal energy is represented by a formula:

$$E = E^*(T) + (3/n)(PV - RT) \ . \qquad (6)$$

Eq. (6) shows that the internal energy of gas is dependent only on n and independent of other parameters. In Eq. (4), pressure is expressed as a function of volume and temperature.

Temperature can also be expressed as a function of pressure and volume by introducing a parameter x defined by

$$x = (\lambda/PV)^{3/n} \ V^{-1} \ . \qquad (7)$$

Eq. (4) is rewritten as a series expansion of parameter x by the form:

$$PV/RT = 1 + b_1 x + (b_2 + (3/n) b_1^2) x^2 \ , \qquad (8)$$

neglecting higher order terms. Kihara and Koba (4) have theoretically calculated parameter b_i . The internal energy given by Eq. (6) at extremely higher pressure (PV >> RT) may be extrapolated to those expressed by the intermolecular potential model for closest packing state. Then Kihara and Hikita showed for extremely high pressure gas that

$$RT/PV = (2/(n+2))(1 - \alpha x) \sim 0$$
$$\text{with } \alpha = 2^{-1/2} (nC(n)/6)^{3/n} \ , \qquad (9)$$

where C(n) is approximately equal to the number of nearest neighbors (= 12) . Therefore a parameter x has a maximum equal to $1/\alpha$. PV/RT may be expressed as a function of x to satisfy both Eq. (8) for extremely lower density and Eq. (9) for extremely higher density, i.e.,

$$PV/RT = (1+ax+bx^2+cx^3)/(1-\alpha x) \ , \qquad (10)$$

where $0 < x < 1/\alpha$.

Eq. (10) is the Kihara-Hikita equation of state (KH).

(ii) Revised KH (KHT)

KH parameters given by the previous work was not satisfactory for the calculation of detonation properties of high explosives. KH parameters may be adjustable to match the experimental data of the detonation velocity (D), Chapman-Jouguet pressure (P_{C-J}) and Hugoniot data for the detonation products.

In this parameter study, an equation of state of the form

$$PV/RT = f(x)/(1 - \alpha x) \ ,$$
$$= F(x)$$
$$f(x) = 1+ax+bx^2+cx^3+dx^4+ex^5, \qquad (11)$$

is assumed, where f(x) is monotonically increasing function. From Eq. (11) expressions of thermodynamic function with imperfection term may be derived by the standard thermodynamic theory.

For the internal energy E, entropy S, and chemical potential μ_i can be expressed by,

$$E = E^*(T) + (3/n)(PV-RT) \ , \qquad (12)$$

$$S = S^*(T) - RT \int_{x'}^{x} F/x \ dx \ , \qquad (13)$$

$$\mu_i/RT = \mu_i^*(T)/RT + \ln X_i + (3/n + (\lambda_i/\lambda)^{3/n})(F-1) + \int_{x'}^{x} F/x \ dx \ , \qquad (14)$$

with $\lambda = \Sigma \lambda_i X_i / X$ and $X = \Sigma X_i$,

where superscript * and subscript i refer to the reference state (ideal gas at pressure P_0) and

component i respectively; X_i is the number of moles for gaseous components. In these expressions, the resulting form of the internal energy in Eq. (12) is same as Eq. (6).

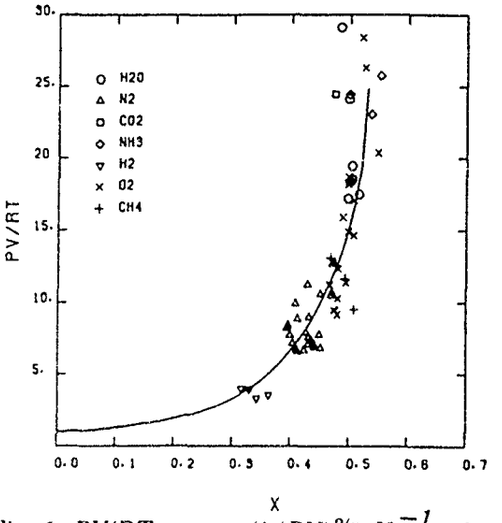

Fig. 1. PV/RT vs $x = (\lambda/PV)^{3/n}\ V^{-1}$ calculated by Eq. (12) and Eq. (17) for experimental (8) pressure-volume Hugoniot data assuming λ as shown in Table 1, where α=1.85 corresponding to n=9

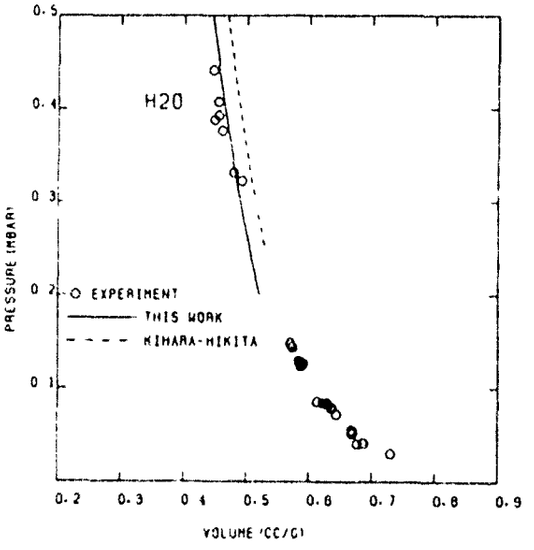

Fig. 2(a). Experimental (8) and calculated Hugoniot for water by KHT parameter shown in Table 1

Polynominal fittings of thermodynamic data as a function of temperature by Gordon et al (5) are used for the calculation of thermodynamic function to the reference state throughout this work.

TABLE 1

KH and KHT Parameters Derived from Experimental Hugoniots

	KH (1952) (*)	this work
α	1.878	1.85
n	9.0	9.0
a	0.958	−1.8523
b	1.635	40.245
c	−9.928	−235.06
d	–	661.49
e	–	−670.48
$\lambda^{3/9}$ $(cm^9\ 10^{12}\ erg/mole)^{3/9}$		
H_2O	6.665	6.1
H_2	3.154	2.9
O_2	8.153	9.2
CO_2	12.794	14.0
CO	9.283	9.8
N_2	9.283	9.8
NH_3	–	9.1
CH_4	11.604	11.0
NO	–	9.15(*)
OH	–	5.65(*)
H	–	1.25(*)

(*) Estimated from the molecular diameter or detonation velocity.

(iii) Evaluation of n and α for KHT

It is well known that C-J pressure is given by

$$P_{C-J} = \varrho_0 D^2/(\gamma+1)\ , \qquad (15)$$

for gases with the relation PV^γ = constant, where $\gamma \sim 3$ for the explosive with high loading density, i.e., high C-J pressure. From Eq. (9) it may easily be seen that P-V relation has the form

$$PV^{1+n/3} = \alpha^{n/3}\ \lambda = 2^{-n/6}\ nC(n)\lambda/6\ , \qquad (16)$$

at higher density where the effect of temperature is negligible. Since maximum γ is approximately equal to 3 from the empirical fact, n may be greater than 6. The detonation properties of the explosive with high loading density strongly depend on the parameter n.

As n is decreased, it may be expected from the Hugoniot relation that for the explosives with relatively higher density: (1) C-J temperature

(T_{C-J}) will decrease due to the contribution of imperfection term in the second term of Eq. (12) for the internal energy: (2) P_{C-J} will increase due to the decrease of γ in Eq. (15). In present work n=9 (α=1.85) is the best from results of the variation of detonation velocity with loading density ($D-\varrho_0$).

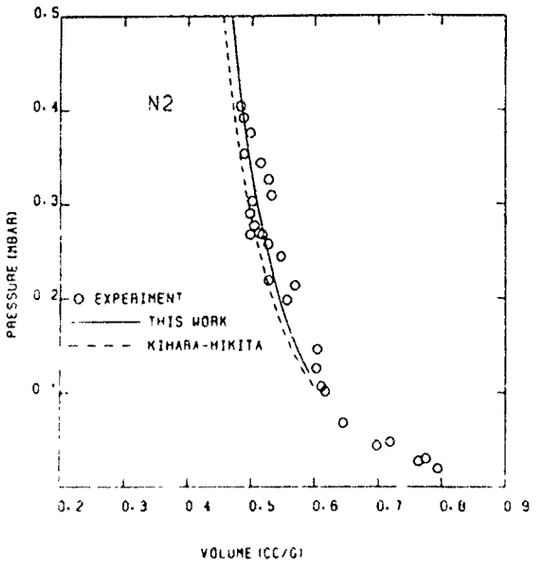

Fig. 2 (b) Experimental (8) and calculated Hugoniot for the liquid nitrogen using KHT parameter shown in Table 1

The λ is adjustable to match a detonation velocity data for a given value of n.

(iv) KHT parameters.

Experimental Hugoniot data for many species, H_2O, N_2, CO_2, O_2, CH_4, NH_3 are used to obtain the EOS constants in Eq. (11) and λ_1. Hugoniot temperatures are estimated by substituting experimental P-V Hugoniot data into Eq. (12) with the Rankine-Hugoniot relation,

$$E_H - E_0 = 1/2\,(P_H + P_0)(V_0 - V_H) \quad . \quad (17)$$

where subscripts 0 and H refers to the initial state of the explosive and Hugoniots respectively. Decomposition of these components is not considered.

The estimation of λ_1 also is required for the parameter study of f(x) in Eq. (11). Since the condition $x < 1/\alpha$ should be satisfied, λ_1 may be estimated from the experimental Hugoniot data of higher PV/RT with large variation. Experimental results of the liquid oxygen satisfies such a requirement. As shown in Fig. 1, most of experimental data we considered fall into the range of results of liquid oxygen except both the liquid hydrogen and the liquid nitrogen in which the variation of PV/RT is relatively small. The experimental result of the detonation property for liquid nitrogen monoxide by Ramsey (9) is useful to determine λ for nitrogen.

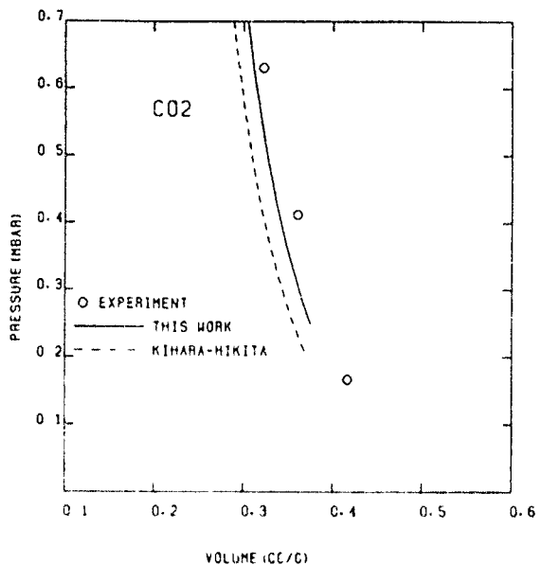

Fig. 2(c). Experimental and calculated Hugoniot for the solid carbon dioxide using KHT parameter shown in Table 1

In this way, a set of the relation for P-V-T and λ for each gaseous detonation products, i.e., f(x) vs x, are estimated. Then the constants in f(x) are determined by least squares fitting . λ for the hydrogen and other gases are estimated by considering molecular diameter. λ of carbon monooxide which decomposition is exothermic is expected to be same with the value for the nitrogen as studied by Nellis et al (6). KHT parameters are given in Table 1. Calculated Hugoniots for water, nitrogen and carbon dioxide are shown in Fig. 2 with experimental data.

2.2 Solids

For solid detonation products, EOS of Mie-Gruneisen of the form

$$P = P_c(V) + \Gamma(V)/V\,(E - E_c(V)) \quad , \quad (18)$$

$$E = E^*(T) + \int_{V_0}^{V} [C_V T - \int_0^T (\partial E/\partial T)_v dT]\, \Gamma(V)/V\, dv + E_c(V) \quad , \quad (19)$$

$$E_c(V) = -\int_{V^\circ}^{V} P_c \, dv \ , \qquad (20)$$

is used, where subscript c refers to the isotherm at 0 K and Γ is Gruneisen constant. Then chemical potential for solid components is given by

$$\mu_s = \mu_s^*(T) + PV_s - (PV_s)^* - \int_{V^\circ}^{V} (P_c(V) + E^*(T)\Gamma(V)/V)dv \ . \qquad (21)$$

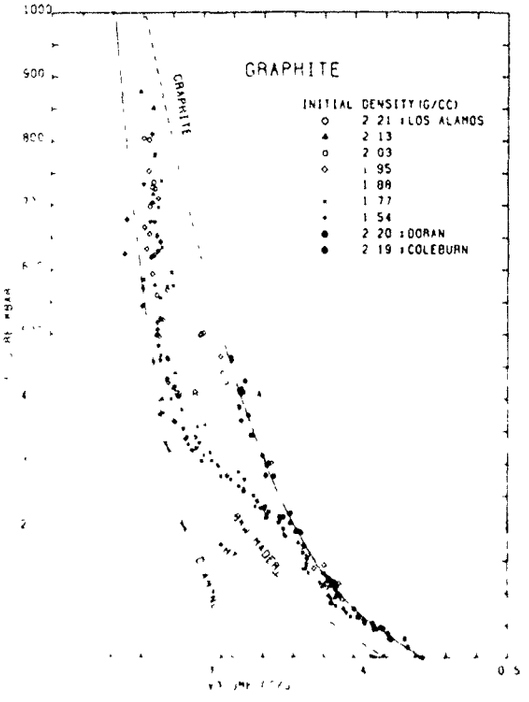

Fig. 3. Experimental Hugoniot data of graphite (8) and diamond (Curves for BKW and KHT show 0 K istotherm.)

The Mie-Gruneisen constant or the thermal expansion coefficient is a most effective parameter to calculated results of detonation properties when thermodynamic equilibrium state is assumed. Melting of the solid component is not included because the melting point under the high pressure is not reliable yet. However, calculated result of detonation properties of aluminum loaded explosives including melting is not so different.

Solid carbon is one of the most important detonation products. EOS of solid carbon, however, has several uncertainties due to the phase transformation under the high pressure as shown in Fig. 3. The Hugoniot of pyrolytic graphite for both the curve labeled A and B in Figure 3 gives higher detonation velocities for explosives with high carbon content, where JANAF thermochemical data is used for the solid carbon with $\Delta H_f = 0$.

It is found that considerably soft carbon

$$P_c(V) = 0.450653 + 4.17309\ V - 34.8893\ V^2 + 76.0323\ V^3 - 54.2024\ V^4 \ , \qquad (22)$$

where P(Mbar) and V(cm^3/g) with $\Gamma/V = 0.48$ (g/cm^3), reproduces the experimental results including the explosives with high content of carbon. Constant for the solid carbon is given in Table 2. A calculated equilibrium Hugoniot for liquid carbon monooxide with this soft carbon model reproduces the experimental shock Hugoniot of Nellis et al (6). It suggests the complicated mechanism of the formation of solid carbon such as coagulation (7) or diamond formation (6).

3. CHAPMAN-JOUGUET PROPERTIES

The detonation properties are calculated by modified BKW code (3). The modified code which defined C-J point as minimum shock velocity was checked by the comparison of calculated results of detonation properties of ideal gases calculated by using CEC (5) which defines C-J point that detonation velocity is equal to sum of the sound velocity and the mass velocity.

Calculated results of C-J detonation properties show that a soft equation of state of solid carbon gives better agreement for most of explosives as shown in Table 2, Figure 4 and Figure 5.

Solid carbon in the detonation products is disappeared as the loading density < 1.4 g/cm^3 for PETN and < 1.0 g/cm^3 for RDX as shown in Figure 4 and 5 by the change of the slope of detonation velocity to the density.

Calculated detonation pressure near the theoretical maximum density (TMD) is slightly lower than that of experiment.

Calculated C-J temperature for RDX is 3488 K while BKW[7] gives 2587 K. BKW using soft carbon and JANAF thermodata gives C-J temperature of 2701 K. C-J temperature is generally higher than several hundred Kelvins comparing with BKW results by Mader[7]. Calculated C-J temperature shows maximum to the

variation of initial density. Maximum temperatures are 4500 K for PETN at 0.6 g/cm^3, 4000 K for RDX of 1.1 g/cm^3 and 3500 K for TNT of 1.4 g/cm^3 to the variation of loading density.

For TNT in which the amount of solid carbon in detonation products is approximately 50 mole %, calculated detonation velocity and pressure for initial density at 1.64 g/cm^3 is 6950 m/s and 20.2 GPa respectively which shows satisfactory agreement with experimental detonation velocity of 6969 m/s and pressure of 19 GPa. A calculated result of TATB shows still higher detonation velocity than that measured.

Calculated results of KHT show significant disagreement for some explosives. These nonideal explosives are CNO explosives, mixtures with large amounts of ammonium nitrate or ammonium perchlorate or heavy metal loaded explosives as in BKW results by Mader (7) except the case of aluminum.

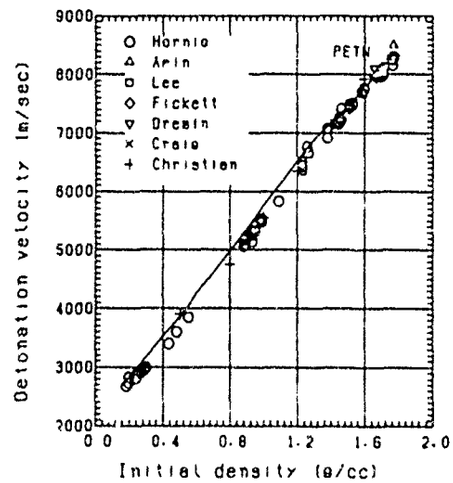

Fig. 4(a). Comparison of experimental[10] and calculated detonation velocity of PETN to the initial density

For CNO explosives near TMD, calculated results of detonation velocity are lower than experimental results which show significant increase of the detonation velocity to the variation of loading density near TMD. The higher repulsive constant λ of intermolecular potential for CO_2 reproduces the experimental results. (Table 3) For HNB, experimental detonation velocity is 9300 m/s while calculated velocity is 8626 m/s for the parameter shown in Table 1. The higher CO_2 KHT constant gives satisfactory result of 9129 m/s for HNB.

For explosives containing ammonium nitrate or perchlorates, calculated detonation velocities also are higher than experimental results. The difference for detonation velocities is generally 500 m/s or more. Numerical hydrodynamic calculations using the isentrope through C-J point, however, reproduce the result of underwater detonation tests. Recent intermolecular explosives containing large amounts of ammonium nitrate show the ideal detonation properties[12] as shown in Table 4. Extremely fine "particles" of ammonium nitrate may be ideal explosives.

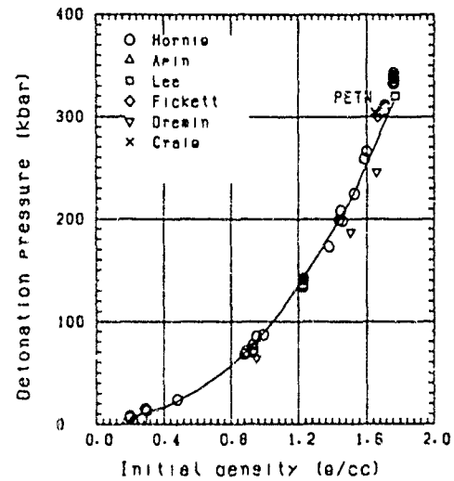

Fig. 4(b). Comparison of experimental[10] and calculated detonation pressure of PETN to the initial density

PETN with paraffin of 25 wt.% has detonation velocity of 7,200 m/s while calculated velocity is 6,000 m/s. Mixtures of explosives with large amours of hydrocarbons may also be nonideal.

For aluminum loaded explosives near the TMD, KHT results of detonation properties give satisfactory agreement with experimental results if aluminum is assumed to be an inert solid as shown in Table 5. However, numerical hydrodynamic solutions to reactive aluminum show the favorable agreement with results of energy measured by underwater detonation and cylinder test performed by Finger et al[13] and Bjarnholt[14].

TABLE 2

Summary of Calculated Results of Chapman-Jouguet Detonation Properties for CHNO Explosives

	HMX	RDX	TNT	PETN	TATB	NM	Comp.B
ϱ_0 (g/cm^3)	1.9	1.8	1.64	1.77	1.895	1.131	1.713
ΔH_f (kcal/mole)	17.89	16.9	−14.2	−127.	−33.4	−27.0	26.2(**)
D (m/s) calc.	9075	8743	6969	8289	8029	6272	7991
(*) expt'l	9100	8754	6950	8300	7860	6290	8030
P_{CJ} (kbar) calc.	394	336	202	303	302	122	277
(*) expt'l.	393	347	190	335	315	127	294
T_{CJ} (K)	3361	3488	3414	3657	2656	3296	3551
Γ (Gruneisen)	0.79	0.78	0.64	0.78	0.70	0.66	0.72
C-J equilibrium detonation composition (mole %) (***)							
H_2O	33.3	33.2	22.5	36.2	25.0	47.2	28.9
CO_2	16.5	16.3	14.9	35.4	12.5	7.22	15.8
CO	0.26	0.63	2.14	1.82	0.09	5.47	1.26
N_2	33.2	33.2	13.6	18.1	25.0	16.5	25.3
H_2	0.01	0.04	0.15	0.07	0.01	2.20	0.23
NH_3	0.02	0.04	0.06	0.04	0.01	0.60	0.06
OH	0.02	0.00	0.02	0.06	0.00	0.03	0.03
CH_4	0.00	0.00	0.00	0.00	0.00	0.04	0.00
NO	0.11	0.11	0.03	0.14	0.01	0.01	0.08
C(S)	16.6	16.4	46.6	8.20	37.5	20.8	28.5

(*) From Ref. (7) except for detonation pressure of NM. (**) Formula weight of 1kg.
(***) Calculated detonation products of O_2 and H were less than 0.01.

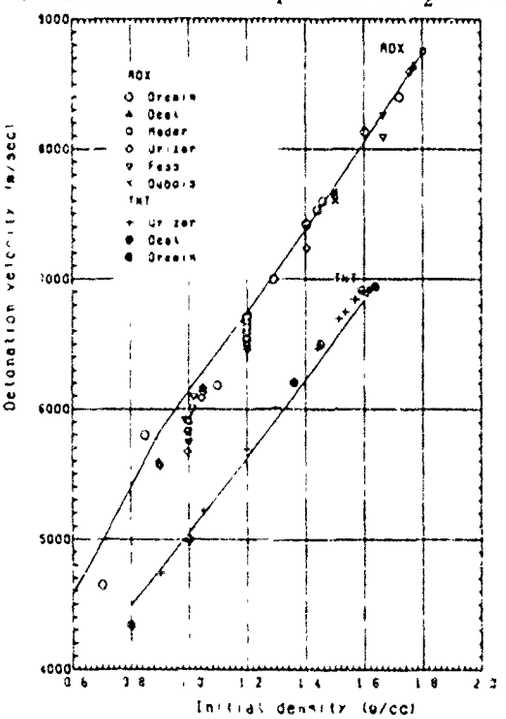

Fig 5 Comparison of experimental data[11] with calculated results of detonation velocity of RDX and TNT to the initial density

The calculation of C-J detonation properties of lead, copper or tungsten loaded explosives gives higher detonation pressure than those measured. For lead azide and silver azide, calculated results show the satisfactory agreement with experimental detonation velocity.

Details of calculated results are summarized in Ref. 16.

4. CHAPMAN-JOUGUET ISENTROPE

KHT isentrope through C-J point are calculated to study the energy measured by underwater detonation, cylinder test or blast wave properties or metal acceleration studies. The numerical hydrodynamic calculation using KHT isentrope gives several useful information for the research of industrial explosives.

KHT isentrope through C-J point for Composition B(RDX 64/TNT36) is compared with Jones-Wilkins-Lee (JWL) (13) as shown in Fig. 6. BKW isentrope for Composition B which is calculated by system presented here shows higher energy release than that of present work and JWL.

TABLE 3

Summary of Calculated Results of Chapman-Jouguet Detonation Properties for CNO Explosives

Explosive	C-J Parm.	Expt'l	KHT(*)	KHT(**)
TNM	D(m/s)	6360	6226	6342
ϱ_0 1.64 g/cm^3	P(kbar)	159	153	151
ΔH_f 8.8 kcal/mole	T(K)	2800	1645	1565
TNTAB	D(m/s	8576	8282	8506
ϱ_0 1.74 g/cm^3	P(kbar)		314	327
ΔH_f 270 kcal/mole	T(K)		4901	4680
HNB	D(m/s)	9300	8626	9129
ϱ_0 1.973 g/cm^3	P(kbar)		352	390
ΔH_f 10 kcal/mole	T(K)		4544	4216
BTF	D(m/s)	8485	8194	8504
ϱ_0 1.859 g/cm^3	P(kbar)	360	328	356
ΔH_f 144 kcal/mole	T(K)		4917	4709

(*) Result by KHT parameters shown in Table 1.

(**) Repulsive constant of λ for CO_2 (= 14.0) shown in Table 1 is changed to 15.5

TABLE 4

Summary of Calculated Results of Chapman-Jouguet Detonation Properties for Explosives with Ammonium Nitrate

Explosive	C-J Parm.	Expt'l	KHT
Amatex 20 (*)	D(m/s)	7009	7696
ϱ_0 1.61 g/cm^3	P(kbar)		235
ΔH_f −467 kcal/kg	T(K)		2849
Amatol (*)	D(m/s)	5760	7650
ϱ_0 1.60 g/cm^3	P(kbar)		224
ΔH_f −679 kcal/kg	T(K)		2519
W/O Emulsion (**)	D(m/s)	5800	5863
ϱ_0 1.1 g/cm^3	P(kbar)		95
ΔH_f −1337 kcal/kg	T(K)		2160
EAR (***)	D(m/s)	8170	8083
ϱ_0 1.63 g/cm^3	P(kbar)	250	249
ΔH_f −808 kcal/kg	T(K)		2157
EA (****)	D(m/s)	7870	7978
ϱ_0 1.61 g/cm^3	P(kbar)	230	237
ΔH_f −964 kcal/kg	T(K)		1938

(*) Amatex 20: RDX 20/TNT 38/AN 42, Amatol: TNT 40/AN 60 (Ref.7)

(**) AN 75/Water 10/Oil & Miscellaneous 15

(***) EDD (ethylenediamine dinitrate) 42.5/AN 42.5/RDX 15 (Ref.12)

(****) EDD 50/AN 50 (Ref.12)

TABLE 5

Summary of Calculated and Experimental Results [7] of Chapman-Jouguet Detonation Properties for Aluminum Loaded Explosives

Explosive	C-J Parm.	Expt'l	KHT (Al reactive)	KHT (Al inert)
Alex 20	D(m/s)	7530	7348	7523
ϱ_o 1.801 g/cm^3	P(kbar)	230	245	230
ΔH_f −6.6 kcal/kg	T(K)		5202	2869
Alex 32	D(m/s)	7300	6991	7398
ϱ_o 1.88 g/cm^3	P(kbar)	215	197	222
ΔH_f −8.7 kcal/kg	T(K)		5930	2615
HBX−1	D(m/s)	7224	7132	7234
ϱ_o 1.72 g/cm^3	P(kbar)		222	209
ΔH_f −18.3 kcal/kg	T(K)		4864	2916

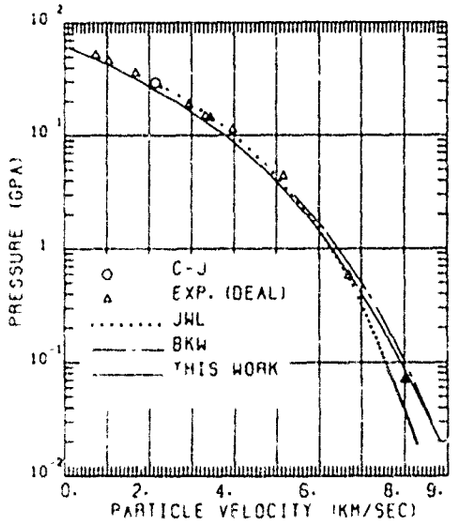

Fig 6. (a) Comp.B isentrope

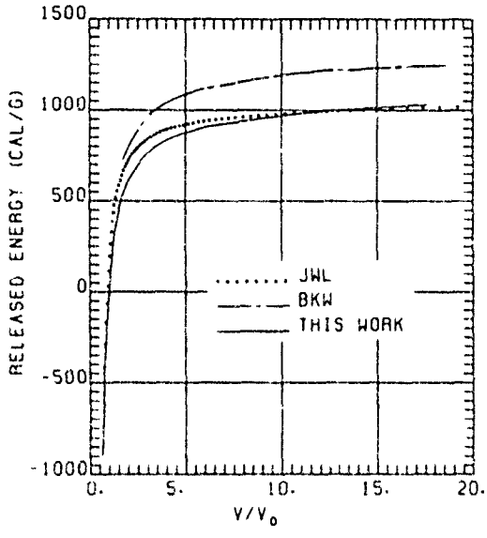

Fig. 6. (b) Comp. B isentrope

CONCLUSION

Modified Kihara-Hikita equation of state combined with soft carbon model and JANAF thermodata represents the detonation properties except the C-J properties of explosives with large amount of nitrate salts and inert additives and some other explosives. For practical application to blasting or mining, revised KH will be useful, but the adequate equation of state of solids under high temperature has to be investigated in detail for the calculation of the detonation properties.

REFERENCES

1. Kihara, T. and Hikita, T., Fourth Symp. on Comb., 458 (1953)
2. Tanaka, K. and Hikita, T., Kogyo Kayaku, 36, 210 (1975).
3. Mader, C. L., LA-3704 (1967).
4. Kihara, T. and Koba, S., J. Phys.Soc. (Japan) 7 (1952).

5. Gordon, S. and McBride B. J., NASA SP-273 (1971).
6. Nellis, W., J. et al, J. Chem. Phys., 75, 3055 (1981).
7. Mader, C. L., Numerical Modeling of Detonations, Univ. Calif. Press (1979).
8. Marsh, S.P., LANL Shock Hugoniot Data Univ. Calif. Press (1980).
9. Ramsey, J. B. and Chiles, W. C., Sixth Symp. on Detonation, 723 (1976).
10. Hornig, H. C., et al, Fifth Symp. on Detonation, 503 (1970).
11. Mader, C. L., et al, LASL Explosives Performance Data, Univ. Calif. Press (1982).
12. Akst, I. B., Seventh Symp. on Detonation, 548 (1981).
13. Fing et al, Fifth Symp. on Detonation, 137 (19 ..
14. Bjarnholt, G., Sixth Symp. on Detonation, 510 (1976).
15. Tanaka, K., Detonation Properties of Condensed Explosives, National Chemical Laboratory for Industry (1983).

DISCUSSION

P. A. BAUER, Lab. Energetique et de Detonique, Poiters, France

So far the KHT equation of state appeared to yield excellent agreement between the experimental and calculated CJ detonation characteristics in the case of most high explosives. Therefore, don't you think it would be worth, on a fundamental point of view, to look at the influence of the coefficient n that would likely increase the knowledge of the molecular interactions in the case of mixtures.

REPLY BY K. TANAKA

The change of both the detonation velocity and pressure of high explosives can be well reproduced for various initial densities by using the coefficient n equal to 9. However, some experimental results for the detonation temperature measurement suggests more higher coefficient n as shown in Table A. In our EOS, the contribution of imperfection term to the internal energy of the detonation products can be given by Eq. (12). Then higher n reduces the effect of imperfection term and leads to the increased C-J temperature.

TABLE A
Detonation Properties of Nitromethane (ρ = 1.131 g/cm^3) and Tetra Nitromethane Mixture, NM + x TNM

x (mole		0	0.071	0.12	0.25	0.5
n = 9	D (m/s)	6272	6669	6884	7018	6865
	P_{CJ} (kbar)	122	140	156	170	171
	T_{CJ} (K)	3296	3608	3832	4271	3687
n = 12	D	6281	6712	6946	7082	6946
	P_{CJ}	114	136	150	155	154
	T_{CJ}	3488	3910	4146	4587	4020
n = 18	D	6252	6719	6979	7057	6921
	P_{CJ}	111	134	147	151	143
	T_{CJ}	3682	4183	4459	4905	4367
experimental temperature (a)		3700	4130	4430	4910	4470

(a) Y. Kato, P. Bauer, C. Brochet and R. Bouriannes, Proc. Seventh Symp. (Intn'l) on Detonation, 768. NSWC MP 82-334 (1981)

DETONATION TEMPERATURE OF NITROMETHANE AND SOME SOLID HIGH EXPLOSIVES

Y. Kato, N. Mori, H. Sakai
Chemicals and Explosives Laboratory
Nippon Oil and Fats Co., Ltd.
Taketoyo, Aichi 470-23, Japan

K. Tanaka
National Chemical Laboratory for Industry
Yatabe, Ibaragi 305, Japan

T. Sakurai, T. Hikita
Fukui Institute of Technology
Gakuen, Fukui 910, Japan

Detonation temperature of nitromethane and some solid high explosives (TNT, tetryl, PETN, RDX, and HMX) was studied with a four colour pyrometer. It was measured not only the temperature of detonation front, but also the temperature of detonation products after the interaction between detonation front and transparent anvil. The measured temperature of detonation products was compared with the results of numerical simulation performed using two-dimensional Lagrangian hydrodynamic computer code. The good agreement was obtained between the measured and calculated temperature of detonation products. From these results, it was shown that the optical technique is capable of directly measuring the temperature of detonation products during isentropic expansion behind detonation front.

INTRODUCTION

It is important to know the detonation characteristics (velocity, pressure, temperature, etc.) of high explosives both from practical and theoretical point of view. Actually, detonation velocity and pressure can be measured with 1% and 5% respectively. Detonation temperature may be most important parameter to understand chemical kinetics in reaction zone and thermodynamic state of detonation products. Yet, detonation temperature remains a parameter which is difficult to be measured.

At present, for various applications, the detonation characteristics can be predicted using thermo-hydrodynamic computer codes with various types of equations of state for detonation products. It is well known that the detonation velocity and pressure are less dependent on the type of equation of state. Measurements of detonation temperatures are very important as criteria to check the validity of equation of state.

Recently, it has proved that the measurements of detonation temperature by optical technique are very useful tools in detonation study. Initial attempts to measure detonation temperature of high explosives were made by Gibson, et al. (1), followed by several investigators (2,3,4). The emission spectrum of detonation front was studied by Dremin and Savrov (5), and by Trofimov and Trojan (6) using photoelectric scanning spectrometer. More recently, significant contributions were made by Urtiew (7), Burton, et al. (8) and Kato, et al. (9,10) taking advantage of rapid advance of opto-electronics. However, in these studies,

the measurements were limited to transparent liquid explosives or explosive mixtures, and the measured detonation front temperature was referred to Chapman-Jouguet (CJ) temperature according to the physical considerations.

Measurements of detonation temperature of solid explosives, which are essentially opaque and granular, present serious experimental problems. Kato and Brochet (11) measured detonation temperature of opaque nitromethane-aluminum gels, and showed that the temperature of detonation products can be measured through shock loaded transparent anvil.

In this study, detonation temperature of nitromethane and some solid high explosives was investigated with optical technique. The measured detonation temperature was compared with the results of numerical simulation performed using two-dimensional Lagrangian hydrodynamic computer code. The good agreement was obtained between the measured and calculated detonation temperature. It was shown that the optical technique is capable of directly measuring the temperature of detonation products during isentropic expansion behind detonation front.

EXPERIMENT

Detonation temperature was measured with a four colour pyrometer which is similar to that described in the previous work (9). The four colour pyrometer is consisted of condensing optics, optical fibres, interferential filters (center wavelength λ=0.65, 0.75, 0.85, and 0.95 μm; band width at half peak transmission $\Delta\lambda$=0.01 μm), PIN photodiodes, and amplifier. Radiation, emitted from the area of 1 mm in diameter on the advancing detonation front or detonation products, was focused on one end of optical fibres by condensing lens. The output of amplifier was recorded by digital recorder (Sony-Tektronix 390 AD) via coaxial cables and 50 ohm load resistors. The rise time of overall system was measured to be less than 10 nsec. The calibration of the four colour pyrometer was performed with a tungsten ribbon lamp and a carbon arc. The calibration curve is different in the case of nitromethane and solid explosives because of the change of condensing optics.

The explosives studied were nitromethane and five pressed solid explosives (TNT, tetryl, PETN, RDX, and HMX). The properties of solid explosives are presented in Table 1. Nitromethane was contained in brass tube of 60 mm long, 18 mm in diameter and 1 mm thick. Solid explosives were contained in poly (vinyl chloride) (PVC) tube of 50 mm long, 20 mm in diameter and 2 mm thick. The detonation tubes have 10 mm thick transparent anvil (pyrex glass) at one end and booster explosive at the other end. The transparent anvil was pressed to the end surface of solid explosive to avoid voids at the interface between explosive and anvil. The detonation tube was placed in an explosion chamber whose internal pressure was reduced to 20-30 mmHg at each shot.

RESULTS AND DISCUSSION

Detonation Temperature of Nitromethane

Fig. 1 presents typical record of temperature measurements of nitromethane detonation. It was shown that detonation wave propagates at steady state after short overdriven state, and detonation front arrives at transparent anvil at about 9.5 μsec after initiation (part A in Fig.1). Five shots were performed, and one shot was effectuated with filter of center wavelength λ=0.55 μm. The measured detonation front

TABLE 1

Properties of Solid High Explosives Studied

Name	*Formula*	*Density (g/cm^3)*	*Composition*
TNT 2,4,6 Trinitrotoluene	$C_7H_5N_3O_6$	*1.51 ± 0.01*	
Tetryl N-Methyl-N,2,4,6 - tetranitroaniline	$C_7H_5N_5O_8$	1.61 ± 0.01	cont 1.0 wt. % graphite
PETN Pentaerythritol tetranitrate	$C_5H_8N_4O_{12}$	1.62 ± 0.01	cont 4.7 wt. % wax
RDX Cyclotrimethylene trinitramine	$C_3H_6N_6O_6$	1.66 ± 0.01	cont. 5.4 wt. % wax
HMX Cyclotetramethylene tetranitramine	$C_4H_8N_8O_8$	1.63 ± 0.01	cont 5.5 wt. % wax

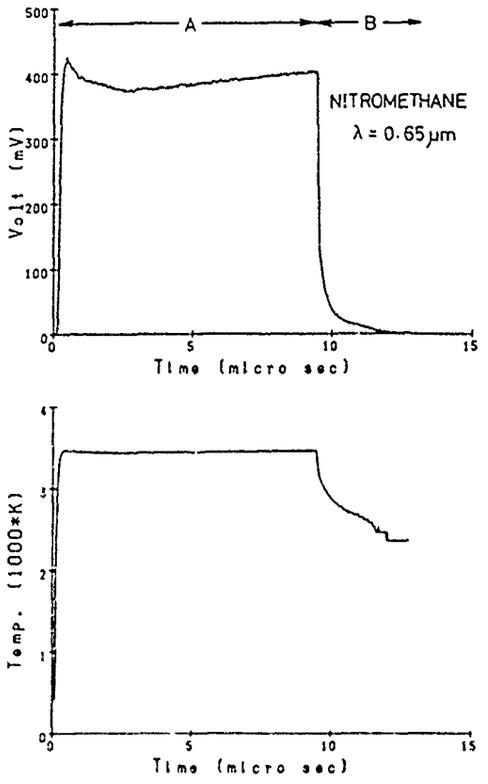

Fig. 1. Typical record of temperature measurements of nitromethane detonation

temperatures at each wavelength were presented in Table 2. Various experimetnal and theoretical values of detonation temperature of nitromethane were summarized in Table 3. The results of present work show good agreement with the experimental values obtained by Urtiew (7) and Burton, et al. (8), and with the CJ temperatures calculated with JCZ-3 (17,18), WCA-4 (19) and KHT (21) equations of state.

After detonation front arrives at transparent anvil, the four colour pyrometer measures the temperature of detonation products which were initially at the interface between explosive and anvil, because detonation products are optically thick (part B in Fig. 1). Fig. 2 shows the time history of measured temperature of detonation products front and anvil. Reflected shock propagates into detonation products, as shock impedance of pyrex glass is higher than that of

TABLE 2

Measured Detonation Front Temperature at Different Wavelength

Wavelength	*Measured Detonation Front Temperature*
λ = 0.55 μm	3390 ± 20 K
0.65	3440
0.75	3440
0.85	3370
0.95	3340

TABLE 3

Detonation Temperature of Nitromethane

Experimental			Theoretical			
Reference		Detonation Front Temperature	Reference		CJ Temperature	Equation of State
Gibson, et al.	(1)	3800K	Fickett	(14)	3808K	LJD
Voskobomikov and Apin	(2)	3700	Mader	(15)	3120	BKW
Davis and Mader	(3)	3380	Cheret	(16)	3136	BKW
Burton and Hicks	(4)	3380	Hardesty and Konnedy	(17)	3510	JCZ-3
Dremin and Savrov	(5)	3600	Finger, et al.	(18)	3467	JCZ-3
Trofimov and Trojan	(6)	3600	Pittion-Rossillon and Chirat	(19)	3380	WCA-4
Malaval and Conze	(12)	3513				
de Balzi, et al	(13)	3280	Tanaka	(21)	3300	KHT
Urtiew	(7)	3300				
Burton et al	(8)	3430				
present work		3400				

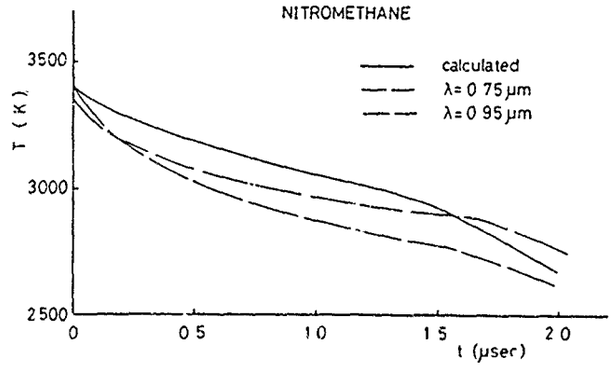

Fig. 2 Time History of Measured and Calculated Temperature of Detonation Products of Nitromethane

detonation products. But in most experiments, the slight temperature increase due to reflected shock is not observed. The temperature of detonation products is gradually decreased because of Taylor wave behind detonation front. An abrupt decrease of temperature, which is caused by side rarefaction waves, is observed at 1.5~1.7 μsec after the interaction.

Detonation propagation in nitro-methane contained in brass tube of the same configuration as experiments was simulated using two-deminsional Lagrangian hydrodynamic computer code 2DL, with CJ volume burn technique. KHT equation of state was applied to detonation products. Shock Hugoniot of pyrex glass was assumed to be equal to that of fused quartz (22). In the calculation, the Lagrangian hydrodynamic equation for cylindrical coordinate are transformed to the finite difference scheme which is consisted of 100 x 300 mesh points (ΔR, ΔZ = 0.2 mm) and time increment of 0.002 μsec. It is observed that side rarefaction waves arrive at charge axis at about 0.7 cm behind detonation front and decrease the temperature of detonation products, and that reflected shock propagates into detonation products after the interaction between detonation front and transparent anvil. The time history of calculated temperature of detonation products, which were initially at the interface and charge axis, is compared with that of experimental values in Fig. 2. The good agreement between the measured and calculated results was obtained, although during first 0.2-0.3 μsec, the rate of temperature decrease is greater in experimental results than in calculated results. From these results, it was shown that, with the optical technique, it is possible to measure the temperature of detonation products which were initially at the interface between explosive and transparent anvil. The optical technique was then applied to temperature measurements of sclid explosives which are essentially opaque and granular.

Detonation Temperature of Solid High Explosives

Fig. 3. presents typical record of temperature measurements of TNT. Because solid explosives are opaque, the four colour pyrometer begins to record the radiation emitted from detonation wave when detonation front approaches transparent anvil. During first 0.2-0.5 μsec, radiatio intensity increases exponentially as the decrease of radiation absorption by unreacted explosive, and it attains its maximum when detonation front interacts with transparent anvil.

The duration of this peak is less than 0.1 μsec.The measured temperature of this peak is strongly dependent on wavelength. It is erroneous to deduce detonation front temperature from this peak because of possible effects of voids contained in granular solid explosive.

As in the case of nitromethane detonation, the temperature of detonation products is measured after the interaction. In. Fig. 4, it is shown the time history of measured temperature of

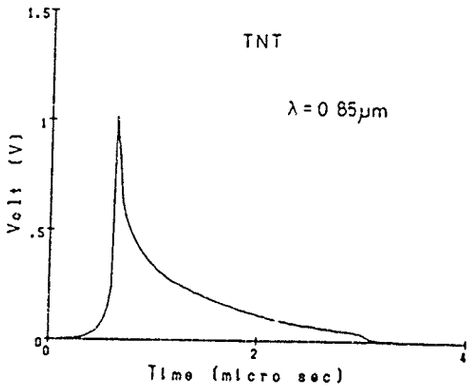

Fig. 3 Typical record of temperature measurements of TNT detonation

detonation products of TNT after interaction. From the physical considerations of the structure of detonation wave, it is considered that the four colour pyrometer measures the temperature of hot spots at the peak. It is estimated to be less than 0.1 μsec the duration of hot spots which are formed in the detonation front of pressed high density solid explosives. The temperature decrease due to side rarefaction waves is observed at about 1.0 μsec after the interaction.

Detonation propagation in solid high explosives contained in PVC tube was simulated using 2DL computer code with Forest Fire burn model. KHT equation of state was applied to detonation products. In the calculation, the charge length was reduced to 30 mm because no difference was observed in temperature and pressure profile of detonation wave, comparing with the case of charge length 50 mm. The mesh size and time increment were the same as in the case of nitromethane. The time history of calculated temperature of detonation products is compared with the measured values for TNT, in Fig. 4. The temperature of detonation products is slightly increased by reflected shock, as shock impedance of pyrex glass is slightly higher than that of detonation products of TNT. The effects of side rarefaction waves appear at about 1.0 μsec after the interaction. The good agreement was obtained between the measured and calculated results. From the time history of measured temperature of detonation products, detonation front temperature of TNT is determined to be 3600 ± 100 K, and it is compared with the CJ temperatures calculated with various types of equations of state in Fig. 5.

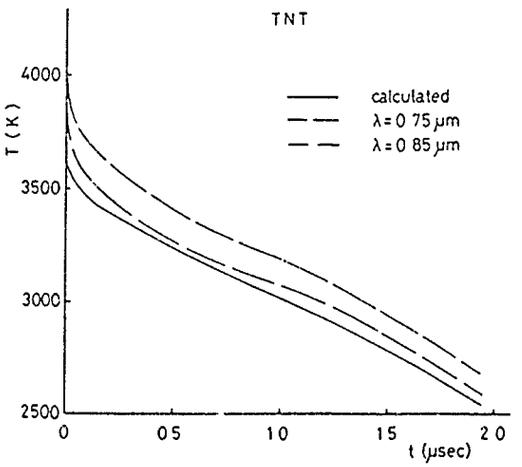

Fig. 4 Time history of measured and calculated temperature of detonation products of TNT

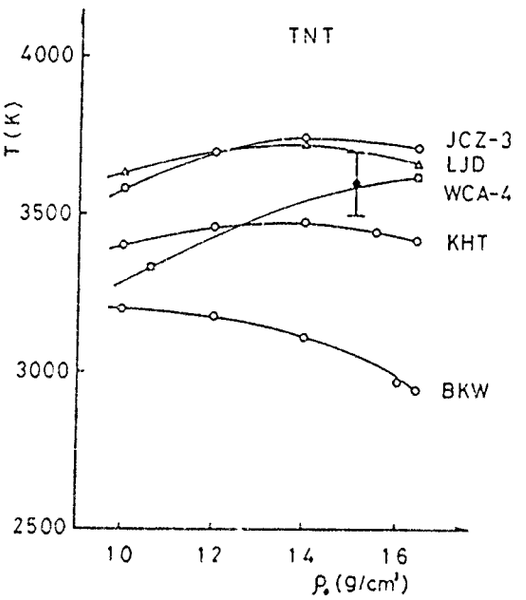

Fig. 5 Comparison of measured detonation front temperature and calculated CJ temperatures of TNT

The records of temperature measurements of tetryl, PETN, RDX, and HMX are similar to that of TNT. It is compared the time history of the measured and calculated temperature of detonation products for tetryl, PETN, RDX, and HMX in Fig. 6, 7, 8, and 9 respectively. The dispersion of measured temperature for these explosives is greater than that for TNT. In the calculation, after detonation front arrives at the

interface, rarefaction waves propagate into detonation products, as shock impedance of pyrex glass is slightly smaller than that of detonation products. The effects of side rarefaction waves appear at 0.8-1.0 μsec after the interaction in the experimental results, and at 0.6-0.8 μsec after the interaction in the calculated results. The good agreement was obtained between the measured and calculated results, although the measured temperatures are 500-800 K higher than calculated temperatures. From the time history of measured temperature of detonation products, detonation front temperatures of tetryl, PETN, RDX, and HMX are determined to be 4250±150, 4400±150, 4300±150, and 4300±150 K respectively. They are compared with the CJ temperatures calculated using various types of equations of state in Fig. 10, 11 and 13 respectively.

SUMMARY

The temperature of detonation products of nitromethane and five pressed solid explosives (TNT, tetryl, PETN, RDX, and HMX) was measured with a four colour pyrometer, as well as detonation front temperature. The measured temperature of detonation products is considered be very close to the temperature of detonation products in Taylor wave, because shock

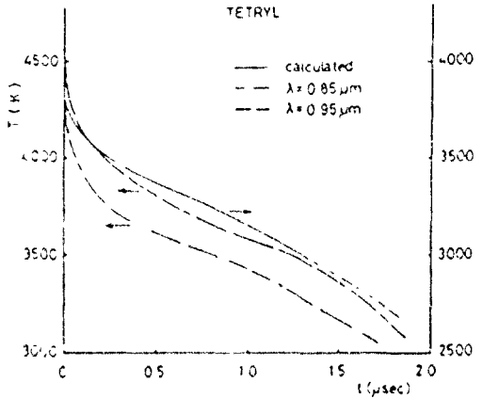

Fig 6. Time history of measured and calculated temperature of detonation products of tetryl

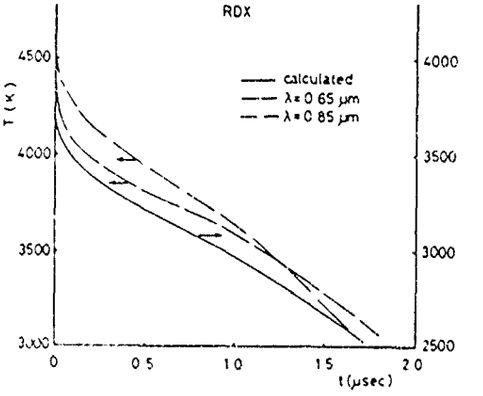

Fig. 8. Time history of measured and calculated temperature of detonation products of RDX

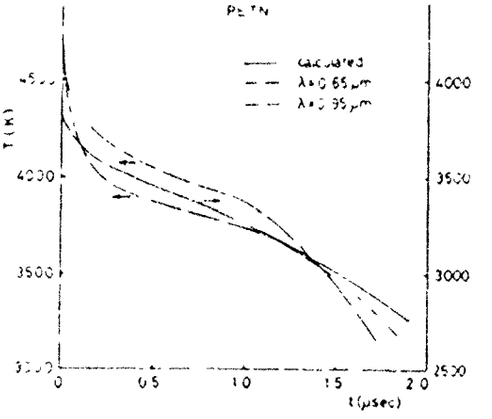

Fig 7 Time history of meaasured and calculated temperature of detonation products of PETN

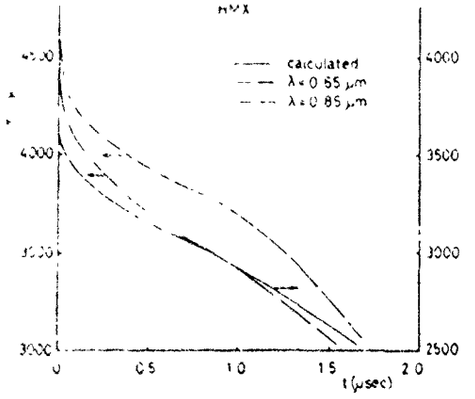

Fig. 9. Time history of measured and calculated temperature of detonation products of HMX

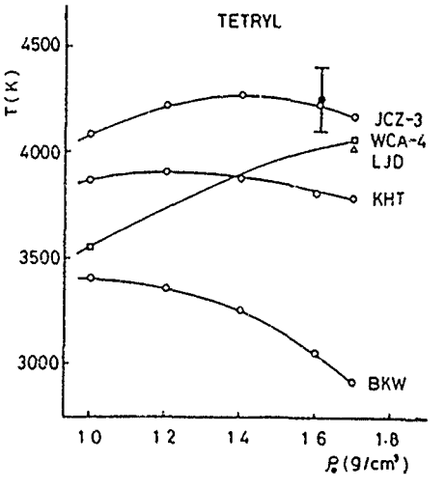

Fig. 10. Comparison of measured detonation front temperature and calculated CJ temperature of Tetryl

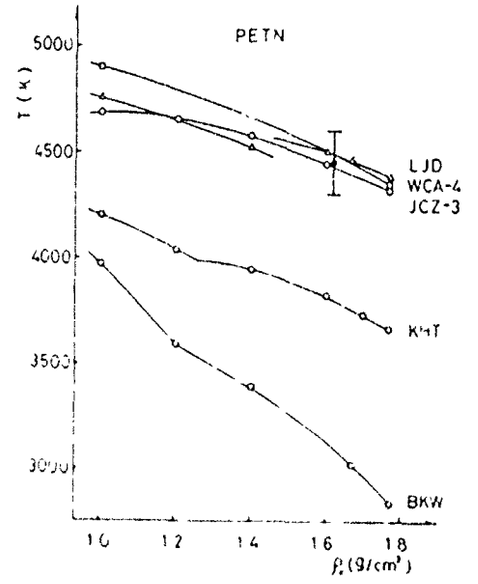

Fig 11 Comparison of measured detonation front temperature and calculated CJ temperature of PETN

impedance of transparent anvil is very close to that of detonation products of solid explosives studied. The P-T relation of detonation products in Taylor wave may be directly measured when co-operated with in-situ pressure gauge.

In the present study, small charge diameter was used by the limitation of experimental facility With larger charge diameter, the influences

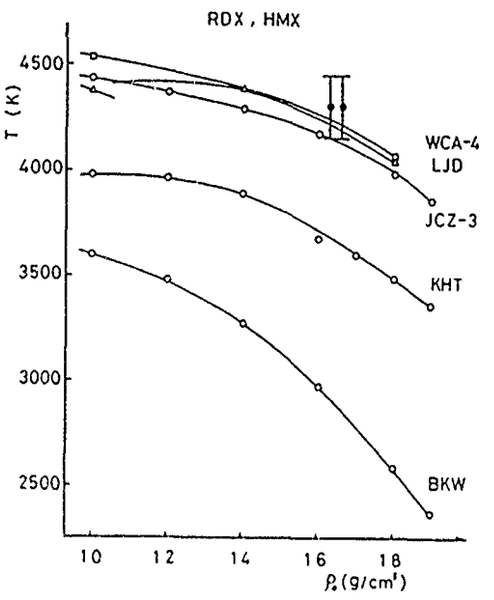

Fig. 12. Comparison of measures detonation front temperature and calculated CJ temperature of RDX and HMX

of side rarefaction waves can be retarded. No particular preparation was given to the surface of solid explosives which was pressed to transparent anvil. Radiation from hot spots formed at the interface between explosive and anvil can be eliminated by careful preparation of the surface of solid explosives.

The temperature of detonation products of low density solid explosives can be measured using the four colour pyrometer.

REFERENCES

1. F. C. Gibson, M. L. Bowser, C. R. Summers, F. H. Scott, and C. M. Mason, "Use of an Electro-Optical Method to Determine Detonation Temperatures in High Explosives", J. Appl. Phys., Vol. 29, No. 4, pp. 628-632, 1958.

2. I. M. Voskoboinikov and A. Ya. Apin, "Measurement of Detonation Front Temperature for Explosives", Dokl. Akad. Nauk SSSR, Vol. 130, No. 4, pp. 804-806, 1960.

3. W. C. Davis and C. L. Mader, cited in Los Alamos Sci. Lab. Report LA-2712, 1962.

4. J. T. A. Burton and J. A. Hicks, "Detonation Emissivity and Temperatures in Some Liquid Explosives", Nature, Vol. 202, pp. 758-759, 1964.

5. A. N. Dremin and S. D. Savrov, "Emission Spectrum of a Detonation Wave in Nitromethane", Z.P.M.T.F., No. 1, pp. 103-105, 1965.

6. V. S. Trofimov and A. V. Trojan, "Detonation Luminescence Spectrum of Nitromethane", Fiz. Gor. i Vzry., Vol. 5, No. 2, pp. 280-282, 1969.

7. P. A. Urtiew, "Brightness Temperature of Detonation Wave in Liquid Explosives", Acta Astronautica, Vol. 3, pp. 555-566, 1976.

8. J. T. A. Burton, S. J. Hawkins and G. Hooper, "Detonation Temperature of Some Liquid Explosives", Proc. of 7th Symp. (Int.) on Detonation, pp. 759-767, NSWC, White Oak, Md., 1983.

9. Y. Kato, R. Bouriannes et C. Brochet, "Mesure de température de luminance des détonations d'explosifs transparents et opaques", Proc. of H.D.P. Symp., pp. 439-449, CEA, Paris, 1979.

10. Y. Kato, P. Bauer, C. Brochet and R. Bouriannes, "Brightness Temperature of Detonation Wave in Nitromethane-Tetranitromethane Mixtures and in Gaseous Mixtures at High Initial Pressure", Proc. of 7th Symp. (Int.) on Detonation, pp. 768-774, NSWC, White Oak, Md., 1983.

11. Y. Kato and C. Brochet, "Detonation Temperatures of Nitromethane Aluminum Gels", pp. 416-426 in Dynamics of Shock Waves, Explosion and Detonations, Progress in Astronautics and Aeronautics, Vol. 94, AIAA, New York, 1984.

12. C. Malaval and A. T. Conze, Proc. of 9th Int. Congress on High Speed Photography, pp. 427-433, 1970.

13. P. Teychenne de Blazi, C. Malaval et J. M. Lombard, "Etude spectroscopique de la température de détonation d'un explosif contenant de l'aluminium", Rapport final S75-01, 1975.

14. W. Fickett, "Detonation Properties of Condensed Explosives Calculated with an Equation of State Based on Intermolecular Potentials", Los Alamos Sci. Lab. Report LA-2712, 1962.

15. C. L. Mader, "Detonation Properties of Condensed Explosives Computed Using the BKW Equation of State", Los Alamos Sci. Lab. Report LA-2900, 1963.

16. R. Chéret, "Contribution a l'étude numérique des produits de detonation d'une substance explosive", Rapport CEA R-4122, 1971.

17. D. R. Hardesty and J. E. Kennedy, "Thermochemical Estimation of Explosive Energy Output", Comb. & Flame, Vol. 28, pp. 45-59, 1977.

18. M. Finger, E. Lee, E. H. Helm, B. Hayes, H. Hornig, R. McGuire, M. Kahara and M. Guidry, "The Effect of Elemental Composition on the Detonation Behavior of Explosives", Proc. of 6th Symp. (Int.) on Detonation, pp. 710-722, ONR, Arlington, Vir., 1977.

19. G. Pittion-Rossillon and R. Chirat, CEA Centre d'Etudes de Limeil, private communication, 1982.

20. R. Chirat and G. Pittion-Rossillon, "Detonation Properties of Condensed Explosives Calculated with an Equation of State Based on Intermolecular Potentials", Proc. of 7th Symp. (Int.) on Detonation, pp. 703-715, NSWC, White Oak, Md., 1983.

21. K. Tanaka, "Detonation Properties of Condensed Explosives Computed Using Kihara-Hikita-Tanaka Equation of State" Nat. Chem. Lab. for Industry, 1983.

22. LASL Shock Hugoniot Data, Univ. of California Press, Calif., 1983.

DISCUSSION

M. HELD, Messerschmitt-Bolkow-Blohm GmbH

1. Have you used any glue between pyrex glass and HE?

2. Vacuum is not directly necessary for measurement, only for less blast effect. Is this correct?

REPLY BY Y. KATO

We used silicone oil between pyrex glass and HE to avoid voids. However, silicone oil lost its initial transparency immediately after shock attack, and the observed signal amplitude was reduced to less than 10% of that obtained without silicone oil.

Each shot was performed in vacuum only to reduce blast effects.

DISCUSSION

W. VON HOLLE, LLNL, Livermore, CA.

Why did you not fit the radiance data from your multi wavelength detection to black body curves with the emittance as an adjustable parameter; thus deriving a best fit emittance? Emittance values would be particularly interesting for the solids. Also, did you check to see if the pyrex anvil remained transparent after shocking?

REPLY BY Y. KATO

As you pointed out, it is very interesting to derive emittance values from black body curves fitting.

We did not check that the pyrex anvil remains transparent after shock attack. We consider that the good agreement between measurements and numerical simulation in the case of NM and the results obtained in Ref. 11 indicate the transparency of pyrex anvil shock attack.

DISCUSSION

JULIUS ROTH, Consultant, Portola Valley, CA

I understood you to say that you believed that NM and maybe the solid explosives behaved like black-body radiators. However, your Figs. 2, 4, 6, 7, 8, & 9 all show slightly different temperatures at different wave-lengths. Indeed in most instances the temperatures at the longer wave-lengths are somewhat greater than those at lower wave-lengths. Compacts of solid high explosives are generally excellent diffuse reflectors. Thus it is possible that the observed wave-length effect is a manifestation of light scattering? Of course, this would not explain this effect for NM.

REPLY BY Y. KATO

The precision of calibration of our pyrometer is ± 100 K at $\sim$ 3400 K. The measured temperatures do not present particular wavelength dependence. It is difficult to say that the slight temperature difference at different wavelength depend on the nature of detonation products. We performed many measurements with various liquid explosives, and we obtained the similar results. It is difficult to refer the observed wave-length effect to light scattering.

THE MEASUREMENT OF DETONATION TEMPERATURE OF CONDENSED EXPLOSIVES WITH TWO COLOUR-OPTICAL FIBER PYROMETER

He Xianchu, Han Chengbung and Kang Shufong
Xian No. 3 Chemical Industrial Institute
Xian, China

A transient optical-electrical two-colour pyrometer combined with optical-fiber have been developed for measuring detonation temperature of condensed explosives. The detonation temperature of NM and it's mixtures which consist of different ratios of nitroethane, acetone, chloroform or carbon tetrachloride, are measured. When the additives are increased to a certain content, an interruption-redetonation phenomenon happens, which is caused by the failure waves. Effects of treatment methods of charge of solid explosives on measurement of detonation temperature have been studied. Air or propane seriously affects the intensity of detonation light, but propane is more luminious than air. Treatment of charge with vacuum is better than others. The detonation temperature of TNT, Tetryl, HMX and PETN are measured.

INTRODUCTION

Being closely related with detonation kinetics and initiation mechanism, detonation temperature is very useful in the study of high explosives. So far as CJ temperature is concerned, it is extraordinarily important in the study of equation-of-state of detonation products. In practical applications the knowledge of detonation temperature is helpful for us to predict and control the performance of explosives.

The measurement of detonation temperature is more difficult than that of detonation velocity and detonation pressure, and the temperature profile of detonation wave in condensed explosives has not been measured experimentally yet, while good measurement has been carried out only on transparent liquid explosives. Because of some difficulties about equipment and technique, the experimental measurement of detonation temperature isn't enough, the reported values scatter in a very large range, thus it is exceptionally necessary to study a variety of measuring methods, so as to supplement and clarify the data of detonation temperatures.

The measurement of detonation temperature of condensed explosives was first performed by Gibson et al with photoelectric technique (1), and other investigators made a lot of contributions to this area thereafter (2-8). Before our measuring work, the measurement of detonation temperature was performed by determining thermal radiation of detonation front, then being derived with Wien's law, such a method either required high-quality optical system to enable light source produced through detonation to be imaged on spectrograph, or required to insert infrared detector into the charge assembly, so every shot costs a lot of time and money.

We now have developed a simple set-up for measurement of detonation temperature. Optical fiber, which is instead of the optical system, receives and transmits the detonation light. By directly inserting fiber into charge assembly and determining detonation temperature from paraxial zone of explosives, the set-up has increased spatial resolution and reliably prevents the measurement of detonation temperature from interfering of air-shock waves. Because of flexibility and nearly unconfined

DISCUSSION

GERALD KERLEY, Sandia, Albuquerque

Are there any other explosves that should exhibit the nitrogen phase separation besides the two you have studied?

REPLY

BY F. H. REE AND MAT VAN THIEL

Our study of PETN also indicates such a phase change (3). In the case of PETN, however, the phase separation boundary crosses the Hugoniot above the CJ point at 48 GPa to 56 GPa. The agreement between the theoretical Hugoniot and the experimental data of Kineke [Ballistic Research Laboratories, Rept. DEA-G-1060MTG (1970)] is approximately similar to that of PBX-9404 in Fig. 1. A comparison of the PBX-9404 and PETN results shows that PBX-9404 has a lower CJ temperature (by about 600 K) but a higher CJ pressure (by 5 GPa). The higher temperature and lower pressure of PETN places its CJ point in the homogeneous fluid range.

The aforementioned fluid phase change is probably a general characteristic of explosives with a high-nitrogen content. This contention may be verified using RX-23-AB. It produces mostly H_2O and N_2 (14), both of which are chemically stable. Hugoniot experiments above 30 GPa should provide a simple test of the predicted fluid phase separation.

DISCUSSION

JAMES L. AUSTING, IIT Research Institute, Chicago, Illinois

Since your reported CJ temperatures for each explosive show a much broader range in comparison to the other CJ parameters, could you please comment on which values of temperature you consider to be the most valid. and most representative of what would be obtained experimentally?

REPLY

BY F. H. REE AND MAT VAN THIEL

The CHEQ and the JCZ3 temperatures in Table 2 should represent reasonable values for the equilibrium temperature. It is worth mentioning that the computed temperatures are very sensitive to the small changes in the parameters of the models in Table 2. Hence, the 10% difference between the CHEQ and the JCZ3 temperatures probably is within the uncertainties of these models. The BKW EOS tends to give a much lower temperature than the CHEQ and JCZ3 predictions. The BKW EOS predicts similar low temperatures for other explosives (14). It may be a basic shortcoming in the BKW EOS which ignores the static contributions to pressure and energy. Calculations by us as well as by others (see papers by Show and Johnson, Chirat and Baute, Byers Brown, and Kerley in this symposium) indicate that both the static and the thermal contributions to thermodynamic properties are about equally important in the pressure and temperature range of the CJ point.

It should be pointed out that the experimental shock temperature obtained from shock front luminosity may or may not represent a real equilibrium temperature at the CJ point, since the screening of the radiation by an optically thick reaction zone would prevent the radiation emitted from the equilibrated zone (i.e., CJ point) behind the reaction zone from reaching the measuring apparatus. The luminosity data (22) of benzene, for example, is consistent with this view.

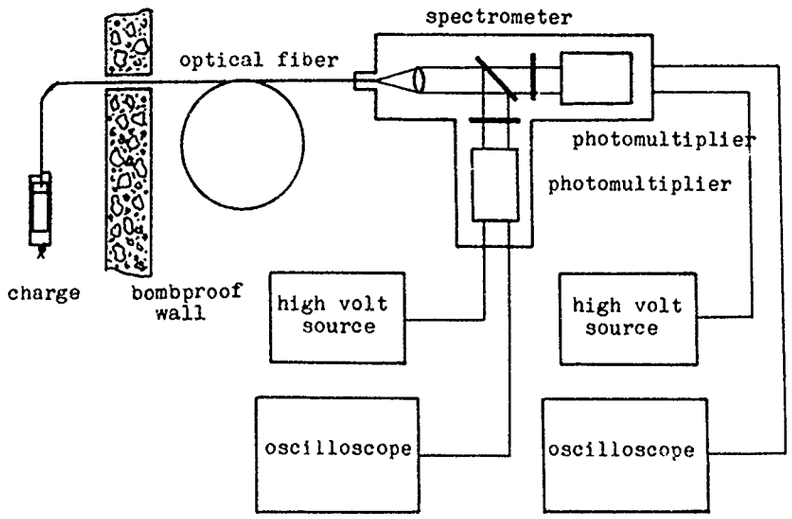

Fig. 1. Schematic diagram of the transient optical-electric two colour pyrometer

usable length of fiber, furthermore, the measurement is less limited by test site. In short, with our set-up we can not only save time and cost, but obtain more reliable data of detonation temperatures.

PRINCIPLE AND APPARATUS

The transient optical-electric two colour pyrometer combined with optical fiber is shown in Fig. 1. One of the ends of the fiber is assembled with the charge, and used for receiving and transmitting light signal of detonation. The light which goes into spectrometer from the other end of the fiber was split into two narrow-bands. The light signal was transformed into electrical signal with photomultiplier and recorded with wideband oscilloscope.

If $C_2/$ ` $T>2.5$, the intensity of spectral radiant can ᵓ expressed with Wien's law:

$$L^{\circ}(\lambda.T) = \varepsilon(\lambda.T)C_1\lambda^{-5}\exp(-C_2/\lambda T) \qquad (1)$$

where T-the temperature of radiant, λ-the wavelength of radiant light, $\varepsilon(\lambda.T)$—the emissivity of radiant, C_1, C_2—the first and second radiation constant respectively. When measurement is performed within a limit of definite spectral band, then

$$L(\lambda.T)=L^{\circ}(\lambda.T)\,(\Delta\lambda/1\mu) \qquad (11)$$

ψηερε Δλ-spectral-band width in μm. In this set-up, the radiant light radiates on photocathodes of photomultipliers through the optical system which was composed of fiber and a spectrometer, with effective power:

$$P = A \cdot \Omega \cdot \beta \cdot L(\lambda.T) \qquad (3)$$

where A,Ω-core area and light-receiving solid angle of fiber, β-effective transmissivity. The voltage recorded on the oscilloscope is:

$$V = P \cdot S \cdot G \qquad (4)$$

where S-spectral response sensitivity of photomultiplier, G-amplifier gain. The photoelectric colorimetric measurement of temperature determines the temperature of a radiator through measurement of voltage signal ratio of radiant lights which come from two spectral-bands. When we express two spectral-band channels by i and j, then:

$$\frac{V_i}{V_j} = \frac{\beta_i \cdot S_i \cdot G_i}{\beta_j \cdot S_j \cdot G_j} \cdot \frac{L(\lambda_i, \Delta\lambda_i, T)}{L(\lambda_j, \Delta\lambda_j, T)} \qquad (5)$$

If apparatus structure, element parameters and operation conditions are defined, then, β, G, S, λ and $\Delta\lambda$ are all determined, thus

$$\frac{V_i}{V_j} = K\frac{\varepsilon_i}{\varepsilon_j}\exp\left[-\frac{C_2}{T}\left(\frac{1}{\lambda_i}-\frac{1}{\lambda_j}\right)\right] \qquad (6)$$

where K is a constant. Being taken logarithmic transformation, the formula mentioned above becomes:

$$\mathrm{LnVi/Vj} - \mathrm{Ln}\varepsilon i/\varepsilon j = a + b\,(1/T) \qquad (7)$$

where a and b-instrumental constants under special operation conditions. For black body or grey body, the formula is converted to:

$$\mathrm{LnVi/Vj} = a + b\,(1/T) \qquad (8)$$

By formulas (7) and (8), this apparatus, once instrumental constants are calibrated, can immediately be used for measurement of temperature.

In the calibration, the luminous tungsten ribbon of a 2500 °C standard temperature lamp images on receiving end of the fiber through eliminable-color-difference lens. The radiant light of the radiator at known temperature is received and conducted with fiber, and radiates into temperature -measuring system. Corresponding to 6 temperature points of standard temperature lamp, we can obtain 6 sets of Vi and Vj. According to the 6 sets of T, Vi and Vj, and using least-square-method, we can derive instrumental constants a and b of formula (7). The test shows that the linear relation between LnVi/Vj and 1/T is rather good, and linear correlation coefficient can attain 0.999. After calibration, keeping operation conditions unchanged and transferring fiber into the charge assembly, we can perform the measurement of detonation temperature.

The fiber which we adopt has following specifications: core-diameter 0.06mm, outer-diameter 0.15mm, numerical aperture 0.18 and 1000 M length per disk. The fiber is damaged 1 M or so per shot and each disk can be used many times. Before test must cut fiber with diamond cutter, so as to obtain an end-face which approaches specular face in flatness.

Spectrometer is composed of field lens, spectral split mirror and filter. The half-width of the filter is less than 130 Å, the selection of colormetric wavelength depends on the range and the sensitivity requirement of temperature measurement by colormetry. Two central wavelengths which we chose are 4880 A and 6940 Å.

EXPERIMENTS AND RESULTS

1. The measurement of detonation temperature of NM. liquid explosive.

NM. is one of typical liquid explosives and its detonation temperature has been measured by some investigators. In order to examine our set-up and contrast with former data, we measured detonation temperature of NM. of first. The charge assembly which we adopted is shown in Fig. 2. Aluminized mylar film divides plastic tube of inner-diameter 32 mm into upper-chamber and lower-chamber and the fiber only receives NM. detonation radiant light from the upper-chamber. The typical oscilloscopic records are shown in Fig. 3 and Fig. 4.

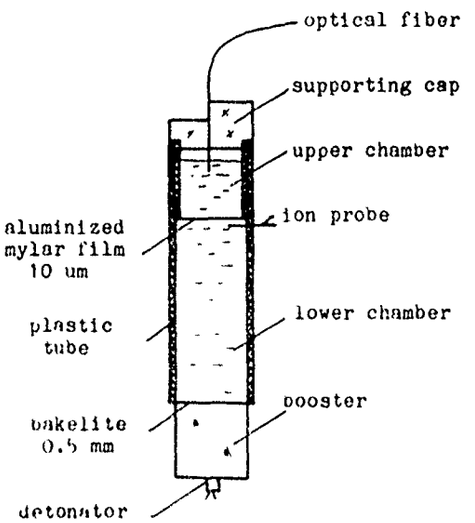

Fig. 2. Charge assembly for measurement of detonation temperature of NM

10mv/div 0.5μs/div. 10mn/div. 0.5μs/div
6940Å 4880Å

Fig. 3. The oscilloscopic records of the intensity of radiant light at two spectral bands in the detonation of NM. (fiber is immersed into NM.)

When the end-face of fiber was immersed into NM. and there was about 20 mm from the aluminized mylar, the results shown in Fig. 3 were obtained.

From Fig. 3, the sweep time base after oscilloscope being triggered by ion probe, and the plateau trace of detonation radiant light can be seen. If the liquid explosive is transparent and its detonation is steady, the light power received with fiber, which is proportional to core diameter and numerical aperture of fiber will be same during propagation of detonation wave, there upon oscillogram is presented as a plateau. (oscilloscopic trace reserve observation) When the end-face of fiber wasn't immersed into NM. and there was a short distance from liquid surface, the results shown in Fig. 4 were obtained.

10mv/div.1μs/div 6940Å

10mv/div.1μs/div. 4880Å

Fig 4 The oscilloscopic records of the intensity of radiant light at two spectral bands in the detonation of NM (fiber isn't immersed into NM)

It can be seen, when detonation wave arrives at the interface of liquid-air, that the intensity of the radiant light is first slightly weaker, then suddenly intensified. This extraordinary intense radiant light is attributed to strong compression of air by shock wave. We made detonation temperature measurement of NM. under 10°C-26°C surroundings. The average values of 52 tests is 3595K with standard error of 51K. For comparison some of measurement and calculation values are shown in Table 1.

2. Detonation temperatures of mixed liquid of NM. and inert additives.

We have determined detonation temperature of mixed liquid of NM with acetone, nitroethane, chloroform or carbon tetrachloride, and recorded change of radiant light in brightness during detonation. The charge assembly used for experiment is analogous with Fig. 2, but without mylar film, and inter-trigger means is adopted for oscilloscope.

TABLE 1
The Detonation Temperatures of NM

E/T	reference		temperature (K)
E	this paper		3595
E	Gibson	(1)	3800
E	Voskoboinikov	(2)	3700
E	Mader	(9)	3380
E	Burton	(3)	3380
E	Trofimov	(8)	3600
E	Malaval	(6)	3530
E	Persson	(5)	3120
E	Urbiew	(4)	3300
E	Burton	(10)	3430
T	Mader	(11)	3167(BKW)
T	Hardesty	(12)	3544. 3700
T	Finger	(13)	2600(BKW) 3467(JCZ3) 2954(BKWR)

E: Experimental value
T: Theoretical calculation value

Thus detonation light signal from the whole liquid explosive charge is received with fiber. The detonation temperature and behavior of these liquid explosives are shown in Table 2. The change of detonation temperature with contents of additives is shown in Fig. 5. It can be seen that a small quantity of acetone would cause a drastically decreasing of detonation temperature, while a great mass of CCl_4 still makes the detonation of the mixtures proceeding on, and the detonation temperature decreases slowly with the increasing of additive contents.

The "interruption" of detonation shown in Table 2 indicated: when the content of additives in NM increases to certain extent, liquid explosive mixtures can be still initiated by booster (diameter 30 mm, length 25 mm, TNT charge), however, the detonation wave can propagate no more after a definite duration. This phenomenon can be judged from the disappearance of brightness of radiant light and the fragments recaptured in cartridge case. The oscillogram of radiant light brightness of the mixed liquid of NM and CCl_4 during detonation is shown in

TABLE 2

The Detonation Temperature and Behavior of Mixed Liquid Explosives

Composition	V%	T(K)	Detonation Behavior
NM		3595	Complete Detonation
NM/Acet	95/5	3450	"
NM/Acet	90/10	3240	Interruption
NM/NE	90/10	3470	Complete Detonation
NM/NE	85/15	3400	Interruption Detonation
NM/NE	80/20	3220	Interruption
NM/$CHCL_3$	90/10	3530	Complete Detonation
NM/$CHCL_3$	80/20	3440	Interruption Redetonation
NM/$CHCL_3$	70/30	3340	Interruption
NM/CCL_4	90/10	3550	Complete Detonation
NM/CCL_4	80/20	3520	Complete Detonation
NM/CCL_4	70/30	3470	"
NM/CCL_4	60/40	3380	"
NM/CCL_4	50/50	3300	Interruption Redetonation
NM/CCL_4	45/55	2950	Interruption

NM-Nitromethane, Acet-Acetone,
NE-Nitroethane, $CHCL_3$-Chloroform,
CCL_4-Carbon tetrachloride

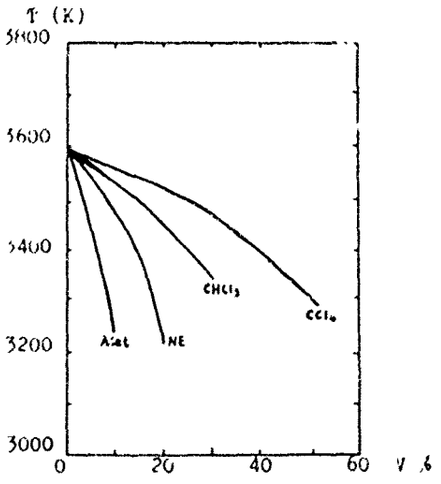

Fig. 5. The change of detonation temperature with contents of additives in liquid explosives

Fig. 6. When NM/CCL_4 is 45/55 (volume percentage) the propagation of detonation wave tends to break off after 4μs of propagation. However, when NM/CCL_4 is 50/50, the phenomenon of interruption-redetonation occurs, i.e, the detonation wave tending to break off repropagates again. When additive content increases, you know, reaction heat decreases, detonation temperature falls, reaction zone is widened, and the critical diameter of detonation increases, accordingly. When the diameter of tube approaches the critical value, detonation would be unsteady.

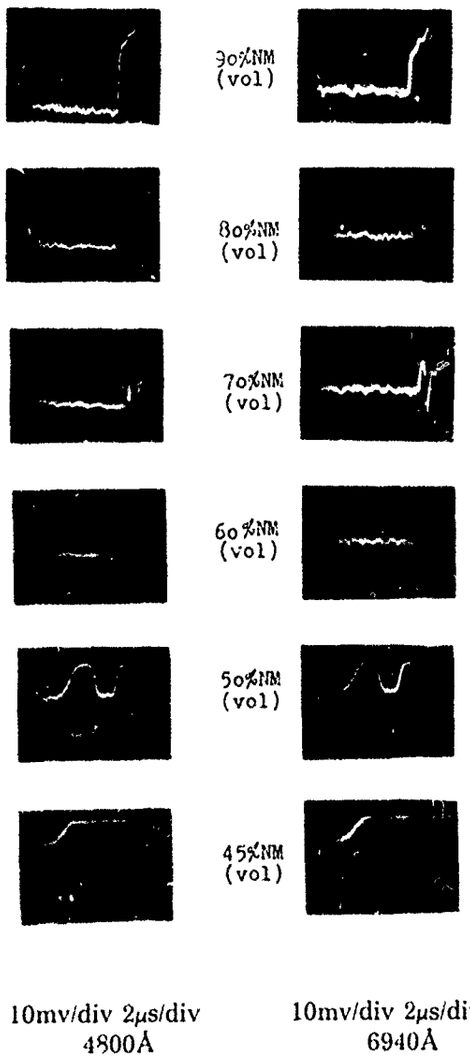

Fig. 6. The oscillogram of the brightness of radiant light at the two spectral bands in the detonation of NM/CCL_4

When failure wave eats up to central region of charge, the dark zone enters into visual field of fiber, so that light radiation power received by fiber reduces, and the oscillogram presents the state of trace of return-to-zero. As redetonation zone reenters into visual field of fiber, the radiant light power received with fiber increases to former value, thus presents the same trace of oscillogram as shown in Figure 6.

3. The measurement of detonation temperature of solid explosives.

The measurement of detonation temperature of solid explosives is more difficult than liquid explosives, because most solid explosives are not transparent, moreover, it is quite difficult to assemble the probe into charge. Even if the probe can be assembled into charge, there will be interface between the probe and explosive. As we determine temperature by radiametry, we can only determine the brightness of radiant light at the moment when it just radiates out from the end of the detonation charge. Thus the reflection of detonation wave at the interface will change the pressure of detonation products, and that would lead the temperature determined not corresponding to true detonation temperature. At present, we still can't evaluate how much effect there is. For this reason, we want to use a transparent material, which is of impedance-matching with the explosive, for covering over the end of charge, but it is difficult for us to get such matching really. The

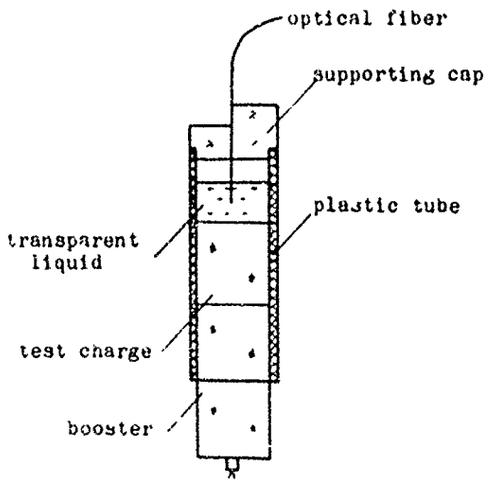

Fig 7 Charge assembly

charge assembly with which we determined detonation temperature is shown in Fig. 7. Covering over explosives with transparent liquid can not only eliminate the influence of luminescence of air-shock wave on the results, but improve the impedance matching. We have tested three transparent liquid, water, glycerin and bromoform, of different impedance. It is shown that if the voidage in charge is less, said three materials have no apparent effect on results of detonation temperature, and the data are within the experimental error. For convenience, from then on, we merely use water as closing medium of charge.

Supposing propane not luminous, Gibson et al has used propane to substitute air in charge (1) in order to eliminate the influence of air on the measurement of detonation temperature. It is considered that the intensity of detonation light doesn't depend on the properties of gases in the void of charge, and the brightness of detonation light (14) is unchanged by elimination of void gases. In order to determine temperature reliably, some experiments in regard to the effect of void gases on the measurement of detonation temperature have been done. Three treatment methods of charge have been used: the first method is an ordinary one, in which the charge is pressed in atmosphere and covered by water before measurement of detonation temperature; the second is that of filling charge with propane, i.e. the charge is pressed in propane atmosphere and covered by water before measurement of detonation temperature; the third is a vacuumization method, the charge is pressed in the vacuum condition, and covered by water under vacuum before measurement of detonation temperature.

The pressed charge were made into two sizes: one is 15 mm diameter by 15 mm length and the other 30 mm diameter by 30 mm length. Two or three pieces of charge were assembled in plastic tube shown as Fig. 7 for experiment. The result indicates that the data of detonation temperature determined with two sizes of charges are coincident. The oscillograms obtained in experiments are shown in Fig. 8. The detonation temperature of solid explosives was determined with peak values.

Detonation temperature of TNT and tetryl of different densities was determined with three

10 mv/div	10 mv/div
0.1 μs/div	0.1 μs/div
6940Å	4880Å

Fig. 8. The oscillograms of brightness of radiant light in detonation of Tetryl charge (=1.70) under vacuumization. (two spectral bands)

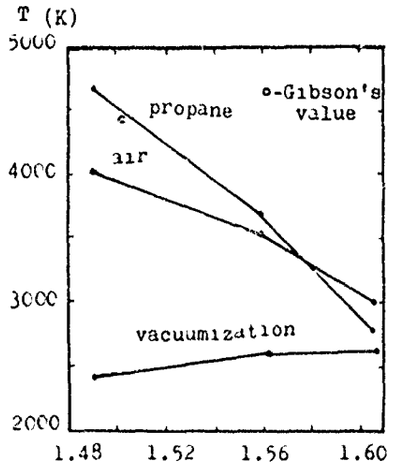

Fig. 9. The relation between detonation temperature and densities of TNT under different conditions

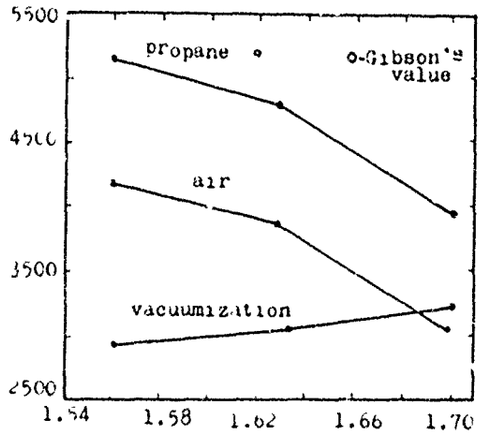

Fig 10. The relation between detonation temperature and densities of Tetryl under different conditions

different treatment methods of charge. The histories of detonation temperature variating with density of the two explosives are shown in Fig. 9 and Fig. 10. It can be seen from Fig. 9 and Fig. 10 that, although the luminescence caused by outer air shock wave is restrained with water, the air and propane in the charge will still increase the brightness of detonation light, as would effect the measurement results of detonation temperature. The lower the density of charge and the more the void gas, the more the effect would be and the more drastic, the rising of detonation temperature with decrease of density. But the detonation temperature of charges treated by vacuumization varies slightly with density, and would rise smoothly when density increases. This trend is distinct from that of air or propane. All these evidently show the influence of air and propane, the later being more than the former. Gibson's detonation temperature data are in agreement with outs in propane. Because of enlargement of the brightness of detonation light due to propane, it seems to be impossible that these data reflect detonation temperature of solid explosives truly.

In theoretical calculation of detonation temperature, there will be large differences between results obtained with different forms of EOS, and the variation trend be also different. Therefore, the experiment measurement of detonation temperature will be helpful for study of EOS of detonation products. Unfortunately, there are few measuring data on detonation temperature of solid explosives. We suppose that the values of detonation temperature of solid explosives treated by vacuumization are more reliable and comparable to many calculation values published recently. The results of detonation temperature determined by us for TNT Tetryl HMX and PETN are presented in Table 3 with standard error of about 100K, and other experimental and calculating values obtained by some investigators also presented for comparison.

At present the measurement of detonation temperature of solid explosives isn't very perfect yet, the following questions are worthy of consideration: first, does the method of end measurement reflects the detonation temperature of solid explosives truly? Second, when impedance mismatches, how much extent does

TABLE 3
The Detonation Temperature of Solid Explosives

E/T	D(g/cc)	T(k)	Reference
		TNT	
E	1.489	2514	This paper
	1.560	2587	
	1.607	2589	
	1.50	4417	Gibson (15)
T	1.60	4170	Cook (16)
	1.64	2937	Mader (11)
		2562(BKW)	
	1.63	3501(JCZ3)	Finger (13)
		2698(BKWR)	
		Tetryl	
E	1.559	2933	This paper
	1.631	3054	
	1.700	3248	
	1.62	5251	Gibson (1)
T	1.70	2751	Mader (11)
		HMX	
E	1.763	3038	This paper
T	1.89	2264(BKW)	Finger (13)
		3726(JCZ3)	
		3093(BKWR)	
		PETN	
E	1.709	3816	This paper
	1.56	5823	Gibson (1)
	1.77	4209	Voskoboinikov (2)
T	1.77	2631(BKW)	Finger (13)
		4237(JCZ3)	
		3445(BKWR)	

this method affect the measuring values? Third, when charges are covered with transparent materials, how long can the transparency last, and will the change of transparency fog the exact measurement of detonation temperature? And more, does the radiant nature of detonation front of solid explosives correspond to that of black body or grey body? All these questions mentioned above should be studied still further.

ACKNOWLEDGEMENTS

Guo zixi, Liu zhi jian and Liu Huilin took part in partial work. Huang Yimou and Chen Jizhi gave us much beneficial help. We are very grateful to them for their help.

REFERENCES

1. Gibson, F. C. et al, J. Apple. phys, 29, 628 (1958).
2. Voskoboinikov, I. M., et al, Dolk Akad Nauk SSSR. 130, 805 (1960).
3. Burton, J. T. A., et al, Nature, 202, 758 (1964).
4. Urtiew, P. A., UCRL-76516 (1975).
5. Persson, P. A., et al, Fifth Symp (Int) on Detonation, 153 (1972).
6. Malaval, C., et al, Ninth International Congress on High Speed Photography, 427 (1970).
7. Dremin, A. N., J. Photo. Sci., 17, 183 (1969).
8. Trofimov, V. S. et al, FiZika Goreniya I. Varyva, 5(2), 280 (1969).
9. Mader, C. L., La-2613 (1961).
10. Burton, J. T. A. et al, Seventh Symposium (int.) on Detonation, 700 (1981).
11. Mader. C. L., LA-2900 (1963).
12. Hardesty, D. R., et al, SLA 74-0165 (1974).
13. Figer, M., et al, Sixth Symp (Int.) on Detonation 710 (1976).
14. Blackburn, J. H., et al, Trans Farad Soc, 61, 507 537 (1965).
15. Gibson, F. C. et al US Bur. Mines Progress Rept. July 1, 1953 to June 30, 1955, Ordn Project TB-2-001, Army Project 599-01-004.
16. Cook, M. A., J. Chem. Phys, 15, 518 (1947).

Session VI
EQUATION OF STATE II

CoChairmen: Manfred Held
MBB Apparate
William C. Davis
Los Alamos National Laboratory

DETONATION PRODUCTS OF INSENSITIVE CAST HIGH EXPLOSIVES

F. Volk, H. Bathelt
F. Schedlbauer and J. Wagner
Fraunhofer Institut Fuer Treibund
Explosivstoffe; D-7507 PFINZTAL FRG

Cast high explosives based on TNT/nitroguanidine (Nigu) and TNT/ammoniumnitrate (AN) with and without different amounts of aluminium (Al) were initiated in a firing chamber in argon as the ambient gas.

As well the detonation gas mixture as the solid reaction products were analyzed with the aim to determine the energy output and the completeness of the detonation reaction. The experimental analysis was compared with values calculated by using TIGER BKW and TIGER JCZ3 Codes.

INTRODUCTION

Cast high explosives based on TNT and nitroguanidine (Nigu) or ammonium nitrate (AN) have become interesting over the last few years on account of their insensitivity to external influences, for cost reasons, and due to the easy accessibility of their components.

In particular, the possibilities of using spherical-grain nitroguanidine (1) and phase-stabilized ammonium nitrate (2), both manufactured at the Fraunhofer-Institut für Treib- and Explosivstoffe, have considerably improved the basic prerequisites for the preparation of these case explosives.

The components mentioned are especially suitable for preparing explosive charges for large calibers, as the problem otherwise encountered small-caliber quantities, i.e. the explosive behaviour of AN which deviates from the ideal, may be disregarded to the latter case.

At present, the behavior of detonation products in expansion is primarily determined in detonation calorimeters (3). On account of their limited volume, it is only possible to detonate charges in calorimetric bombs which have greatly limited charge diameters.

To study the behaviour of the castable high explosives quoted, charge diameters of at least 40 mm are required, as preliminary trials have shown, if no confinement is to be applied. From these masses of explosive charge amounting to more than 200 g come into consideration. If, as happened in the present case, charge diameters of 50 mm are used, explosive masses of approx. 300 g are obtained.

It is easy to understand that charges of this size can only be tested in detonation chambers (4).

OBJECTIVES

It is the aim of this study to test cast high explosives based on TNT and nitroguanidine or ammonium nitrate, with and without aluminium as additional component, in order to find out the degree of completeness with which their detonation reaction takes place. This should be performed in a manner which allows for a quantitative analysis of the reaction products in gaseous and condensed form produced during detonative reaction.

In doing so, the experimentally composition of the detonation products obtained is to be compared with results obtained with the aid of thermodynamic/hydrodynamic codes. In this case, the TIGER-BKW and the TIGER-JCZ3 Codes are concerned.

EXPERIMENTAL METHODS

1. Firing Chamber

In order to generate the detonation products required, explosives charges were used with diameters of 50mm and masses of over 300 g in a detonation chamber with a volume of 1.5 cubic meters. The chamber was designed for a static pressure of up to 40 bars. Gas changing was accomplished by evacuation.

In order to prevent a post detonation combustion with oxygen, the shots were fired in argon as the ambient gas or in vacuum.

2. Detonator and Booster

The detonator was a Dynamit Nobel blasting cap Nr. 8, commercially available. For all firings a cylindrical booster consisting of 10 g RDX was used. In some cases, an additional booster of 18 g of the same diameter as the test charge and 6 to 7 mm long was applied to improve the reproducibility of the shots. The heat of explosion was 5470 J/g.

3. High Explosives

For the preparation of the castable high explosives, we used 40-60% TNT and different amounts of spherical grain nitroguanidine (Nigu) with and without additional aluminium (Al). The same compositions were cast using 40-60% TNT and different portions of phase stabilized ammonium nitrate (AN) with and without additional Al. The bulk density of Nigu was 1,04 g/ccm and the average grain size 125μm. Aluminium exhibited a mean particle size of 15μm, and AN of 137μm.

The following compositions have been investigated:

- Composition B
- 50% TNT/50% NIGU
- 50% TNT/40% NIGU/10% Al
- 50% TNT/30% NIGU/20% Al
- 50% TNT/20% NIGU/30% Al
- 50% TNT/50% AN
- 50% TNT/40% AN/10% Al
- 50% TNT/30% AN/20% Al
- 50% TNT/20% AN/30% Al
- 50% TNT/50% NIGU (Vacuum)
- 50% TNT/50% AN (Vacuum)

4. Analysis of the gas mixture and the solid residue

When the shot was fired, the static pressure was measured and gas samples were taken for the mass spectrometric analysis of H_2, N_2, CO, CO_2, CH_4, NO, N_2O, HCN and the chemiluminescence analysis of NO/NO_x.

Samples of the solid residue were analyzed in order to determine the C, H, N content of carbon black and the content of NH_3. The amount of unreacted aluminium was analyzed according to the method of Schultze-Tiemann, which allows to determine the H_2-volume:

$$2\ Al + 6\ HCl \rightarrow 2\ AlCl_3 + 3\ H_2.$$

The amount of reaction water and ammonia was calculated via mass balance methods, this also including the proportion of solid carbon. For these calculations, a computer program was established. The same holds for the calculation of the heat of detonation ($-H_D$) as the enthalpy difference of the reaction products and the explosive. As a means of qualifying the energy output, additionally the freeze-out temperature (T_{WG}) of the water gas products was calculated via the equilibrium constant of the reaction $CO + H_2O \leftrightarrows CO_2 + H_2$; $\Delta H = -41{,}0$ kJ.

Finally, the result of the product composition was compared with values of a theoretical calculation using the TIGER-BKW-Code and TIGER-JCZ3-Code.

RESULTS

1. Composition B

In order to assess the analysis methods, Composition B was first of all examined, as analyses values on this explosive are already available to us in literature (3). In Table 1, the results obtained in the detonation chamber are compared with those measured in a detonation calorimeter by D.L. Ornellas (3). It must here be mentioned that the trials performed in the detonation chamber were set off without confinement of the explosive charge. The reaction products obtained in the detonation calorimeter were found to possess a higher CO_2 content and a low CO content. This is clearly due to the high confinement of the explosive material in a gold cylinder (3). The somewhat greater detonation heat can also be explained by the confinement. On the whole, the results agree quite good, if we take into account the different experimental preconditions.

In Table 2, the results obtained from detonation products in the firing chamber are compared with those obtained from theoretical calculations. Both computer codes show a different composition, as well compared with the result of Ornellas as with the result of ICT.

2. Explosive charges based on TNT and Nigu

2.1 50 TNT/50 Nigu (ZV)

The detonation products of an explosive charge consisting of 50% TNT and 50% Nigu are different to those found with Composition B, particularly due to the relatively high content of hydrogen cyanide (HCN) as well as the increased quantities of ammonia (NH_3), see Table 3. The increased formation of HCN is due to the presence of Nigu in the explosive charge. Because HCN is an endothermal compound, it is not possible to calculate it correctly using a thermodynamic code

2.2 TNT-Nigu charges containing Al

The presence of aluminium (Al) leads to an increase in detonation temperature, produced by the reaction of Al to form aluminium oxides. As the O_2-balance is greatly reduced with AT, H_2 increases and CO_2 decreases, see Tables 4, 5, 12. Table 4 and 5 show the product composition of the explosive charges with 10% and 20% Al. In addition, Table 12 gives the gas composition of different explosive mixtures with different contents of Al between 10% and 30%.

As seen from the formation of H_2, CO and CO_2, it is shown that an increase in the Al content to more than 20% produces no marked increase in the formation of H_2. This means that the reaction of Al with the water vapor in the detonation products is practically exhausted to its full extent at an Al content of 20% already. As, in the solid reaction products, a considerable amount of Al was found which had not participated in the reaction (Tables 4 and 5), the optimum in energy yields is thus already exceeded at a 20% Al content. It was also possible to see that an only incomplete reaction had been obtained in this case from the fact that detonation heat was lower than the value measured in the detonation charge containing 10% Al only (see Tables 4, 5 anad 13).

In this connection it may be of interest to compare the measured detonation velocities with the calculated values, see Table 13.

3. Detonation products of explosive charges based on TNT/AN

3.1 50 TNT/50 AN

Because of the higher oxygen content of ammonium nitrate (AN), compared with nitroguanidine, TNT/AN charges are supposed to produce a lower proportion of carbon in the solid residue. Whereas a carbon formation of 16.3 mol% was obtained on examination of the 50% TNT/50% Nigu charge (Table 3), it was possible to achieve a value as low as only 7.7 mol% carbon using an explosive charge containing 50% TNT/50% AN. A clear difference also manifested itself in the case of HCN, whose concentration was here much lower than in the charges containing NIGU, see Table 6.

3.3 TNT/AN charges containing Al

The relevant gas combinations determined with different Al contents can be seen in Table 12, whereas the complete product combinations are shown in Tables 7-9.

From Table 12, it is possible to deduce a clear dependency of the H_2 and CO_2 concentrations in conjunction with a rising Al content, starting from charges free of aluminium up to those containing 30% of the metal.

Whereas the charge containing 20% Al had a relatively complete reaction, recognizable from the high detonation heat (Tables 8 and 13), an increase in the Al content from 20 to 30% brought no further improvement of the energy output (see Tables 8 and 9).

Contrary to the explosives containing Nigu, which have a maximum detonation heat value at 10% aluminium content already, the maximum energy obtained in the explosives containing AN was not reached until a level of 20% Al was introduced, thanks to the improved O_2 balance of the charges containing AN[2].

4.Detonation in Vacuum

Additional tests have been accomplished to find out the difference of the product gas formation under the vacuum conditions compared with argon atmosphere.

For this, two different cast high explosives have been used: 50% TNT/50% NIGU and 50% TNT/50% AN.

4.1 50% TNT/50% NIGU

After placing the charge in its horizontal hanging position, the firing chamber was evacuated.

The results of the vacuum shot is compared with the shot in argon in Table 10.

We see very clear differences in the formation of H_2, CO, CO_2, H_2O and carbon. Because of the much lower content of CO_2 and carbon, the heat of detonation of the vacuum shot is by 20,7% lower than under argon as the ambient gas. It looks as if argon behaved as a confinement.

4.2 50% TNT/50% AN

It is not difficult to understand that an ammonium nitrate containing explosive charge reacts differently from a charge with nitroguanidine, if we compare the oxygen balances:

	O_2—balance
50% TNT/50% NIGU	−52,4%
50% TNT/50% AN	−27,0%

The higher the oxygen balance, the lower the carbon formation. This means that high explosives, which exhibit only a low oxygen deficiency, will produce nearly the same product gas, when initiated under the different conditions. Due to this circumstances, the heats of detonation are not very different, see Table 11.

5. Comparison of product composition with the results of the TIGER-BKW Code and TIGER-JCZ3 Code

In order to establish the relationship between the experimentally determined product compositions and the theoretically calculated results, comparitive calculations were performed using the TIGER-BKW and the TIGER-JCZ3 Codes. From Table 2, in which the results of the explosive charge containing Composition B were drawn up by comparison, it can be seen that, for example CO and CO_2 agree better with the experimental values if calculated with the JCZ3 Code than with the TIGER-BKW Code, although the proportions of H_2O and C(s) are greatly different from the result of analysis. Similiar conditions also apply to the explosive charges containing TNT/Nigu, TNT/AN and the charges with aluminum.

SUMMARY

This study deals with the determination of the detotation reaction of insensitive cast high explosives based on TNT/nitroguanidine (NIGU) and TNT/ammonium nitrate (AN), in each case with and without the addition of different quantities of Aluminium (Al), as tested in the detonation chamber.

It was found that nitroguanidine containing explosives give rise to a much higher concentration of hydrogen cyanide (HCN) than Composition B and ammonium nitrate containing charges.

The addition of 10% Al to a TNT/NIGU charge reacted in a more complete way, i.e. produced a higher energy output as compared to the degree of detonation heat, the explosive charges containing 20% and 30% Al.

In the last two cases, large amounts of unreacted Al could be analyzed in the solid residue.

Using TNT/AN charges, on the other hand, the maximum energy was not reached until 20% Al was added.

A comparison of the detonation products analyzed with values calculated using the TIGER Codes BKW and JCZ3 did not produce a satisfactory agreement, even when the experimentally determined freezing out temperatures of the detonation products were taken as a basis for the theoretical calculations.

This findings indicate the importance of experimental analysis of post detonation products in the detonation chamber.

REFERENCES

1. W. Engel, "Darstellung von kugeligem Nitroguanidin," Jahrestagung: Fraunhofer-Institut Für Treib- und Explosivstoffe 1981, pp. 21-29.
2. W. Engel, "Beitrag zur Phasenstabilisierung von Ammoniumnitrat," Explosivstoffe 21 (1973), pp. 9-13
3. D.L. Ornellas, "Calorimetric Determinations of the Heat and Products of Detonation for Explosives," October 1961 to April 1982, UCRL-52821, Lawrence Livermore National Laboratory, April 5, 1982.

TABLE 1
Detonation Products of Composition B: Comparison Between Firing Chamber and Detonation Calorimeter

	ICT	LNNL (D. Ornellas)
Charge weight, g	304,1	25,1
Charge Diameter	50 mm	12,7 mm
Booster	10 g RDX	0,25 g PETN
Products, mol%		
N_2	23,4	24,2
H_2	5,5	4,1
CO	20,4	14,9
CO_2	10,8	16,4
CH_4	0,2	0,7
HCN	0,6	0,4
NH_3	2,9	3,1
H_2O	19,6	20,2
C(s)	16,6	17,8
NO, ppm	25	
$-H_D$, J/g	4966	5299
T_{WG}, K	2760	2150

TABLE 2
Detonation Products of Composition B: Comparison of Experimental with Calculated Values

Charge weight:	304,1 g		
Charge diameter:	50 mm		
Products, mol%		TIGER BKW	TIGER JCZ3
N_2	23,4	24,2	26,3
H_2	5,5	0,6	11,0
CO	20,4	2,5	27,6
CO_2	10,8	15,5	12,6
CH_4	0,2	0,8	4,3
HCN	0,6	—	0.02
NH_3	2,9	0,4	0,3
H_2O	19,6	27,4	12,1
C(s)	16,6	28,3	5,8
NO, ppm	25		
$-H_D$, J/g	4966		
T_{WG}, K	2760		

TABLE 3
Detonation Products of 50% TNT/50% NIGU (ZV)

Charge weight:	305,1 g	
Charge diameter:	50mm	
Products, mol%		TIGER BKW
N_2	23,1	26,5
H_2	3,3	0,1
CO	14,9	0,6
CO_2	14,3	9,5
CH_4	0,2	0,3
HCN	2,9	—
NH_3	11,4	0,4
H_2O	13,7	30,7
C(s)	16,3	32,0
NO, ppm	66	
$-H_D$, J/g	3742	
T_{WG}, K	1935	

TABLE 4
Detonation Products of 50% TNT/40% NIGU/10% Al

Charge weight:	305,1 g	
Charge diameter:	50mm	
Products, mol%		TIGER BKW
N_2	21,8	26,2
H_2	5,7	4,3
CO	13,6	8,5
CO_2	7,3	5,2
CH_4	0,7	3,8
HCN	3,2	—
NH_3	8,9	0,7
H_2O	11,2	18,7
C(s)	23,2	28,2
Al_2O_3(s)	4,5	4,3
NO, ppm	136	
$-H_D$, J/g	5226	
T_{WG}, K	1770	
Solid residue: 8,6% Al		

TABLE 5
Detonation Products of
50% TNT/30% NIGU/20% Al

Charge weight: 308,4 g Charge diameter: 50 mm		
Products, mol%		TIGER BKW
N_2	17,9	23,0
H_2	14,5	20,6
CO	23,4	18,7
CO_2	3,5	0,4
CH_4	0,4	3,0
HCN	7,2	0,04
NH_3	3,5	0,14
H_2O	4,5	1,7
C(s)	11,4	23,4
Al(s)	9,1*	—
Al_2O_3(s)	4,5*	9,0
NO, ppm	1240	
$-H_D$, J/g	4226	
T_{WG}, K	1380	
Solid residue: 10-15% Al		

*For 50% conversion of Al

TABLE 6
Detonation Products of
50% TNT/50% AN

Charge weight: 301,6 g Charge diameter: 50mm			
Products, mol%		TIGER BKW	TIGER JCZ3
N_2	21,8	22,5	24,6
H_2	4,7	0,01	8,1
CO	14,8	0,2	14,7
CO_2	14,1	16,4	19,9
CH_4	0,1	0,1	4,8
HCN	0,35	—	0,02
NH_3	2,8	0,2	0,6
H_2O	33,7	41,3	27,2
C(s)	7,7	19,2	0,0
NO, ppm	10		
$-H_D$, J/g	4555		
T_{WG}, K	3140		

TABLE 7
Detonation Products of
50% TNT/40% AN/10% Al

Charge weight: 301 g Charge diameter: 50mm		
Products, mol%		TIGER BKW
N_2	17,4	22,6
H_2	12,2	4,4
CO	29,9	7,4
CO_2	9,1	13,8
CH_4	0,1	5,0
HCN	0,9	—
NH_3	10,2	0,4
H_2O	13,7	26,4
C(s)	1,6	15,2
Al_2O_3(s)	4,9	4,8
NO, ppm	3	
$-H_D$, J/g	5203	
T_{WG}, K	1770	
Solid residue: 2% Al		

TABLE 8
Detonation Products of
50% TNT/30% AN/20% Al

Charge weight: 302,3 g Charge diameter: 50mm		
Products, mol%		TIGER BKW
N_2	15,8	20,4
H_2	16,3	18,9
CO	29,0	25,4
CO_2	1,0	3,4
CH_4	0,1	5,4
HCN	0,5	0,01
NH_3	8,2	0,2
H_2O	7,2	6,9
C(s)	12,0	9,3
Al_2O_3(s)	9,9	10,-
NO, ppm	3	
$-H_D$, J/g	6549	
Solid residue: 1,8% Al		

TABLE 9
Detonation Products of 50% TNT/20% AN/30% AL

Charge weight:	299 g	
Charge diameter:	50 mm	
Products, mol%		
N_2	13,4	
H_2	12,6	
CO	24,6	
CO_2	0,4	
CH_4	0,05	
HCN	0,6	
NH_3	4,4	
H_2O	8,3	
C(s)	14,6	
Al(s)	14,1*	
Al_2O_3(s)	7,1*	
NO, ppm	22	
$-H_D$, J/g	5333	(incomplete reaction)

*Calculated for a 50% conversion of Al

TABLE 10
Comparison Between Argon as the Ambient Gas and Vacuum of the Charge 50% TNT/50% NIGU

Products, mol%	Argon	Vacuum
N_2	23,11	24,40
H_2	3,31	14,64
CO	14,88	38,29
CO_2	14,31	4,11
CH_4	0,19	0,03
HCN	2,89	0,85
NH_3	11,38	7,50
H_2O	13,67	7,96
C(s)	16,26	2,23
$-H_D$, J/g	3724	2968

TABLE 11
Comparison Between Argon as the Ambient Gas and Vacuum of the Charge 50% TNT/50% AN

Products, mol%	Argon	Vacuum
N_2	21,77	22,54
H_2	4,74	7,33
CO	14,77	19,82
CO_2	14,07	9,52
CH_4	0,12	0,01
HCN	0,35	—
NH_3	2,77	—
H_2O	33,72	35,53
C(s)	7,69	6,63
$-H_D$, J/g	4556	4500

DISCUSSION

Y.M. TIMNAT, Techninon, Haifa, Israel

What was the accuracy of your measurements?

REPLY BY F. VOLK

The accuracy of the main components, determined in volume percent by mass spectrometry, is better than ±0,5 percent.

The reproducibility of the shots is usually better than 1,5 Vol% for high concentrations.

DISCUSSION

JAMES RITCHIE, Los Alamos National Laboratory

What heat of formation, ΔH_f, of carbon did you use in your calculations.

It would be most interesting to measure this for each shot to see how the carbon varies from explosive to explosive. Additionally a C,H,N, analysis to determine elemental composition would be helpful. These experiments would serve to characterize what we, almost certainly incorrectly, call solid carbon. A further point is that, regardless of the problem with aftershocks ? being on the principal isentrope, it would be important to determine how the

TABLE 12
Detonation Gases of High Explosives Containing TNT-NIGU and TNT—AN

Trial No.	61/63	16	18	21	34/36	38	40	43/45
Composition wt.%	50 TNT 50 NIGU	50 TNT 40 NIGU 10 Al	50 TNT 30 NIGU 20 Al	50 TNT 20 NIGU 30 Al	50 TNT 50 AN	50 TNT 40 AN 10 Al	50 TNT 30 AN 20 Al	50 TNT 20 AN 30 Al
N_2	39,4	41,7	28,1	25,9	39,0	25,2	25,0	25,9
H_2	5,6	9,5	22,2	23,4	8,5	17,6	26,1	24,3
CO	25,4	26,4	34,4	41,7	26,5	42,6	46,4	47,7
CO_2	24,4	15,8	5,3	1,7	25,2	13,2	1,6	0,8
CH_4	0,3	1,0	0,5	0,4	0,2	0,2	0,1	0,1
HCN	4,9	5,6	9,4	7,5	0,6	1,2	0,8	1,2

TABLE 13
Experimental and Calculated Detonation Parameters

	O_2 balance %	Loading diameter mm	Heats of detonation J/g	Density g/cm³	D exper. m/s	D BKW m/s
Composition B with gold cylinder as confinement (3)		12,7	5229			
Composition B	-43,0	50	4966	1,73	7900	8190
60 TNT/40 NIGU	-56,7	50	3906	1,63	7106	7212
50 TNT/50 NIGU (ZV)	-52,4	50	3742	1,67	7239	7414
50 TNT/40 NIGU/10 Al	-58,2	50	5226	1,72	7109	7278
50 TNT/30 NIGU/20 Al	-64,0	50*	4226?	1,78	6841	7159
50 TNT/20 NIGU/30 Al	-67,2	50*	4968	1,80	?	(6274)
50 TNT/50 AN	-27,0	50	4555	1,61	6236	7296
50 TNT/40 AN/10 Al	-37,9	50	5203	1,68	6192	?
50 TNT/30 AN/20 Al	-48,8	50	6549	1,75	6246	7311
50 TNT/20 AN/30 Al	-57,0	50*	5333	1,82	?	(6732)
50 TNT/50 NIGU (Vacuum)	-52,4	50	2968			
50 TNT/50 AN (Vacuum)	-27,0	50	4500			

*incomplete reaction

forms under these conditions even if there are not the conditions of a full C-J- detonation.

REPLY BY F. VOLK

For calculating the reaction heat or detonation heat, we used a ΔH°_{f298} value of + 8,75 kcal/mol as published by D.L. Ornellas, LLNL, April 5, 1982. In most cases, we measured the C,H,N, content of the carbon residue. For example, an explosive charge consisting of 50% TNT and 50% NQ we found a carbon residue of 90,3% C; 0,7% H; 5,0% N; 4,0% O.

We didn't investigate the influence of possible after-shocks.

DISCUSSION

DON ORNELLAS, Lawrence Livermore National Laboratory.

1. Results reported show evidence of

reshocking of detonation products, resulting reequilibration of products.

I suggest conducting experiments under conditions to avoid reshocking. I would expect better agreement with theoretical calculations if these were done.

2. Determination of ΔH_f or carbon soot produced in a detonation chamber may not be very meaningful because such soot is contaminated with other solid materials from detonation or the contaminated vessel and contains substantial amounts of nitrogen and hydrogen.

REPLY BY F. VOLK

Reshocking cannot play a dominant role because of the relative good agreement we found between blasting chamber and detonation calorimeter results, see Table 1.

If we had severe reshocking, we would have found a much less amount of solid carbon.

May be argon as carrier gas can suppress reshocking. In vacuum (see Table 10) and in Helium as a carrier gas, we found much smaller amounts of solid carbon than under argon atmosphere.

DISCUSSION

CHRISTIAN BROCHET, Poitiers, France

It is known that generally the Al reacts in post reactions sometimes far from the main reaction zone or the CrJ state surface.

Your results show, especially for TNT/AN/Al mixtures containing up to 20% Al, a good agreement between measured $Al_2O_3(s)$ content and the TIGER BKW calculations which give, in principle the composition in the C-J state. Can you comment about this result?

REPLY BY F. VOLK

All calculations were done with regard to the freezing out temperature of the water gas equilibrium. Therefore we did not calculate C-J conditions, but the composition for the freeze-out temperature on the isentrope.

Because of the higher oxygen content of TNT/AN containing explosives, the amount of completely reacted Al is much higher in this case than in TNT/NQ containing explosive mixtures.

DISCUSSION

W.C. DAVIS, Los Alamos National Laboratory

Did you make my calculations of the chemical species expected on the isentrope for expansion from a divergent flow state, and did you compare the results with those for an expansion from a CJ state?

REPLY BY F. VOLK

Every gas composition was calculated with regard to an isentropic expansion from CJ state to the freezing out temperature (T_{wg}) of the water gas reaction, which is tabulated for most of the experiments:

T_{wg} = freezing out temperature of the water gas reaction, calculated from the isochore

$$K_p = \frac{p_{CO_2} \cdot p_{H_2O}}{p_{CO_2} \cdot p_{H_2}}$$

DISCUSSION

M. HELD. MBB Apparate, FRG

It may be useful to analyse reaction products of the high explosives with different initiators. With the small diameter of your RDX booster I expect in spite of the corner effect, especially with your insensitive high explosives, a large amount of incompletely reacted materials. This could be the explanation for the trace amounts of unreacted TNT.

REPLY BY F. VOLK

Additionally to the small diameter RDX booster, we were using a composite double base propellant sheet having the same diameter as the high explosive. Using those sheets we found a good reproducibility of the reaction products. Only in some cases we analysed larger amounts of unreacted explosive components, especially if no additional booster was used or if the initiation was not complete.

DISCUSSION

DR. OLDRICH, Machacek, Thermex Energy Corporation

The energy release of high aluminized formulation is surprisingly low. Is is possible that the confinement can significantly change the composition of detonation products? Our tests with formulations up to 40% aluminium indicate a high energy release.

REPLY BY F. VOLK

Not only the oxygen balance but also confinement plays a significant role with regard to the reaction of aluminium (Al). According to our experience is a content of 40% of Al to high to get a complete reaction.

DISCUSSION

HAROLD J. GRYTING, Southwest Research Institute

Have you calculated whether the loss in ΔH_D between 10 to 20% Al is due to the melting of the unreacted aluminum. How was composition of "soot" determined.

REPLY BY F. VOLK

The heat of melting of the unreacted aluminium (Al) is only 94 cal/g, but the heat of detonation of the explosives without and with 10% of the Al is 900 cal/g resp. 1248 cal/g for TNT/NQ/mixtures. Since the unreacted Al is only a small fraction of the total mass, we can neglect the heat of melting of Al.

The composition of the soot of 50% TNT/50% NQ is a follows:

Carbon	75,0 wt%
Hydrogen	1,4 "
Nitrogen	11,4 "

THE SUPRA-COMPRESSION OF LX-07, LX-17, PBX-9404, and RX-26-AF AND THE EQUATIONS OF STATE OF THE DETONATION PRODUCTS

L. Green, E. Lee, A. Mitchell and C. Tarver
Lawrence Livermore National Laboratory
University of California
Livermore, California, 94550

Shock velocity vs. input pressure in the range of 32 to 112 GPa has been measured for LX-07, LX-17, PBX-9404, and RX-26-AF. The average shock velocity for the first 2.8-mm of run was found to be within one percent of that for the run from 2.0 to 4.8-mm. Supra-compressive states of PBX-9404 were reflected to higher pressures by a copper barrier and the velocity in the copper measured. They were also rarefied by a magnesium barrier and the velocity in the magnesium measured. Equations of state derived for the reaction products of these explosives and normalized to accepted CJ pressures do not adequately predict measurements at pressures substantially greater than detonation pressure, normalization to lower than accepted CJ pressures is required to fit the data. The CJ state defined by the supra-compressive experiments appears to be different from the CJ state defined by the usual CJ pressure measurement.

INTRODUCTION

A principal purpose of our study was to determine the equation of state (EOS) of HMX and TATB based explosives at pressures well above the Chapman-Jouguet (CJ) pressure.

We have made measurements of the shock velocity for the explosives LX-07, LX-17, PBX-9404, and RX-26-AF, at input pressures of 30 to 110 GPa using our two-stage light gas gun facility. (1) Our data on PBX-9404 agrees with the previous work of Kineke and West (2) allowing for the larger uncertainty in their experimental measurements. In analyzing our results we have found that equations of state that have been derived for the reaction products of these explosives at pressures equal to and less than detonation pressure do not adequately predict measurements for pressures substantially greater than detonation pressure. At present, it appears that the CJ theory may have to be modified somewhat in order to fit all of the data, but this has not yet been proven. There is some indication from our work that the supra-compressive experiments define a different CJ state than that defined by ordinary self-supporting detonations.

EXPERIMENTAL

The supra-compression experiments that are being reported were conducted at LLNL on the two-stage light gas gun using ultrafast pin techniques (1) to monitor the progress of shock waves. Typical experiments consisted of an impactor of either 1100 aluminum or tantalum propelled by the two-stage gun, a buffer plate of either 1100 aluminum or explosive from which time zero is taken, and the specimen of explosive against the buffer plate through which the shock velocity is timed. See Fig. 1. Dimensions were chosen such that the measurements were unaffected by rarefactions. The nominal compositions of the test explosives are given in Table 1. Additional experiments were performed

* Work performed under the auspices of the U.S. Department of Energy by the Lawrence Livermore National Laboratory under contract No. W-7405-ENG-48.

with PBX-9404 where a supra-compressive state was reflected to a much higher pressure by a copper barrier and the shock velocity in the copper measured. In a similar way, a supra-compressive state of PBX-9404 was rarefied by unloading into a magnesium barrier and the shock velocity in the magnesium measured. See Fig. 2. For all experiments, the impactor velocity was determined to better than .1% using flash x-ray techniques. Densities of test explosive, buffer plates, and impactors were determined for the materials used in each experiment. All parts were lapped, polished, and carefully measured to minimize dimensional errors, which could amount to about 2 μm for most materials.

CALCULATIONS

The ignition and growth model (3, 4) of the reactive flows created during the shock initiation and detonation wave propagation of heterogeneous solid explosives has successfully calculated a great deal of one- and two- dimensional experimental data (4-10). In this paper the model is applied to the supra-compression data to determine if the effect of the reaction zone is truly negligible, for HMX-based explosive as had been assumed, and to model the LX-17 data, for which the reaction zone does have an effect. The parameters used for PBX-9404 and LX-17 are given in the recent paper of Tarver et al. (11). Very fine zoning (100 zones per millimeter) is required to accurately describe these small-scale, subnanosecond timing experiments. Reactive flow calculations for PBX-9404 do indeed show that the reaction zone effect is negligible in the single and reflected shock experiments shown in Fig. 8, because these calculations agreed very closely with C-J burn calculations. In the rarefaction experiments shown in Fig. 9, the reactive flow calculations indicated that the effect of the von Neumann spike decayed in the magnesium plate to a negligible level in just less than the one millimeter thickness, at which the magnesium shock velocity measurements were begun. However, the calculated pressures in the magnesium were always higher than measured, which suggests that the calculations may not have been completely free of reaction zone effects.

Previously reported ~C-J burn calculations (12) which showed that a P_{CJ}=34.0 GPa equation of state provides a better fit to the supra-compression data than the usual P_{CJ} 37.0 GPa for PBX-9404 have been verified by detailed reactive flow calculations. However, it has been demonstrated that reactive flow calculations using the P_{CJ} = 37.0 GPa reaction products equation of state for PBX-9404 accurately calculate embedded gauge and metal acceleration experiments on self-sustaining detonation waves (8,9). Similar calculations with a P_{CJ} = 34.0 GPa equation of state and the usual thin reaction zone for PBX-9404 greatly underestimate the resulting pressures, particle velocities, and metal acceleration properties. Tarver and Urtiew (8) demonstrated that the P_{CJ} = 37.0 GPa equation of state accurately calculates the self-sustaining, converging detonation velocity measurements of Cheret et al. (13). Since the P_{CJ} = 34.0 GPa equation of state yields higher shock velocities and pressures than the P_{CJ} = 37.0 GPa equation of state, a calculation of Cheret et al.'s data with the P_{CJ} = 34.0 GPa equation of state predicts converging detonation velocities that are much greater than the experimental measurements. Therefore, a dilemma exists in that the P_{CJ} = 37.0 GPa reaction product equation of state accurately describes experiments involving self-sustaining detonation waves which are followed by Taylor wave expansions, while the P_{CJ} = 34.0 GPa equation of state matches the supra-compression data and seems to agree more closely with thermodynamic chemical equilibrium code calculations (14).

The situation is even more complex for TATB-like explosives which produce relatively large amounts of carbon and whose reaction zone lengths are on the order of millimeters thick. Supra-compression experiments on such explosives must be calculated with reactive flow models. The LX-17 supra-compression experiments shown in Fig. 4 were calculated using the parameters given by Tarver et al. (11). In the lowest pressure experiment, the calculated higher average shock velocity in the 2-4 mm depth agreed very closely with the experimental observation. In the higher pressure experiments, the reactive flow calculations yield constant average shock velocities with run distance, although the shape of the reaction zone changes slightly during each calculation. Both the cited (15) P_{CJ} = 30.0 GPa and also a highly modified JWL reaction product equation of state with P_{CJ} = 27.5 GPa and D = 7.64 km/s yield calculated supra-compressive shock velocities that are lower than

the experimental values at the higher pressures. A lower P_{CJ} value (~25.GPa) allows a much better match between calculations and supra-compressive experiments (but not with P_{CJ} measurements).

EXPERIMENTAL RESULTS

The single-shock supra-compressive experiments on LX-07, LX-17, PBX-9404, and RX-26-AF are represented schematically in Fig. 1 and summarized in Table 2 and Figs. 3 through 7. Curves from the best JWL equations of state from cylinder test data (15) normalized to accepted C-J pressures are shown in the same figures. According to Chapman/Jouguet theory, the slope of the Hugoniot shock velocity vs. particle velocity detonation product curve should be zero at the C-J point, and the locus of pressure vs. relative volume states should be tangent to the Rayleigh line through the C-J point at the C-J point. An examination of Figs. 3 through 8 shows the difficulty. The supra-compressive data do not appear to be consistent with C-J theory in that the Hugoniot shock velocity vs. particle velocity curves do not appear to go to zero slope at the C-J points and the locus of pressure vs. relative volume states do not appear to become tangent to the Rayleigh lines at the accepted C-J points for the explosives tested. The data do not prove that C-J conditions cannot be met as one approaches the C-J state from the overdriven side but it strongly suggests that this is the case. If there were a significant change in slope of the shock velocity vs. particle velocity curve very near to the C-J state, it would not be detected by the present technique. The error limits are simply too large to permit resolution.

The reflected-shock supra-compressive experiments on PBX-9404 are summarized in Table 3 and in Fig. 8. A suitable choice of parameters would allow a reactive-flow hydrodynamic calculation of both the single-shock and reflected-shock experiments within experimental error. However, the same parameters do not accurately predict the initial motion of a thin metal plate being accelerated by a head on detonation of PBX-9404 in a metal acceleration experiment, the metal moving faster than predicted. The definition of CJ state appears to be different for the supra-compressive experiments.

The experiments on rarefaction of supra-compressive states of PBX-9404 are summarized in Table 3 and in Fig. 9. Differences between equation of state assumptions (i.e., P_{CJ} =34 GPa vs. P_{CJ} = 37 GPa) are too small to resolve the question of which describes the data better. The best value appears to lie between these two pressures. The experimental values of pressure are lower than calculated, probably due to reaction zone effects in the calculation. The error limits in both calculation and experiment are such that an accurate determination of the point of tangency to the Rayleigh line cannot be made within the accuracy required to determine the "CJ" pressure.

DISCUSSION

It can be reasonably postulated that the CJ detonation pressure of LX-07, LX-17, PBX-9404, and RX-26-AF as implied by supra-compression experiments really is lower than that measured in the usual detonation pressure measurements. The 34.0 GPa JWL calculation shown in Fig. 5 for PBX-9404 illustrates that a calculation based on a lower P_{CJ} can be fit to the supra-compressive data and have zero slope at the lower P_{CJ}. Such fits based on lower P_{CJ} can be made to the other data as well. (2) The question then becomes "why is there a difference between P_{CJ} as usually measured and P_{CJ} as defined in a supra-compressive experiment?" It is suggested that this lower P_{CJ} could occur if a relatively slow reaction (for example, carbon condensation or diffusion controlled equilibration of reaction products from different components of the explosive) followed a relatively fast reaction. With the usual measurement, any changes from a second, relatively slow reaction during expansion of products from the more rapid first reaction(s) would be extremely difficult to measure. Careful measurement can detect only the end of the relatively fast reaction(s), which is taken to be the CJ state. This state has most of the attributes of the CJ state and for many purposes may be assumed to be the CJ state. However, if the postulate just made is true, it is not an equilibrium state and hence, not a CJ state, and would be subject to scale effects to some degree.

Whether or not detonation velocity, for example, would be measurably affected by slow reactions in large charges is a matter of conjecture. Careful pressure or particle velocity vs. time measurements should be able to detect the effects of any slow reactions in large charges.

Supra-compressive experiments on LX-17 offer an interesting contrast with the other explosives tested. Because carbon is present in the detonation products of LX-17 to a much greater extent than in the products of PBX-9404, if carbon condensation were the "slow" reaction responsible for the differences in apparent P_{CJ}, then LX-17 might be expected to show an even larger difference between measured C-J detonation pressure and that inferred from supra-compression experiments. Such appears to be the case. It should be noted that this is true in spite of the fact that the reaction zone as usually measured is much longer for TATB-based explosives than for HMX-based explosives, so there is much more time for "slower" reactions to take place, which should tend to offset differences. A single equation of state of the detonation products of LX-17 is not adequate to describe expanded states, the C-J state, and supra compression states when incorporated into reactive flow hydrodynamic calculations. TATB and HMX-based systems appear similar in this respect.

An accurate description of both expansion and supra-compressive reaction product states with a single equation of state may not be possible if P_{CJ} as normally measured is in fact not an equillibrium state. A lack of equilibrium would imply chemical differences between the C-J states defined by the usual methods and that inferred from supra-compressive experiments. The discontinuities seen in derivative functions near the C-J point (12, 16, 17) as one moves from expansion states to supra-compressive states could be due to such chemical differences.

Experiments on PETN and other relatively oxygen rich explosives where there is very little carbon in the detonation products should help resolve these questions arising from the experiments on HMX and TATB-based explosives. A reactive flow model consisting of a fast exothermic reaction to one reaction product equation of state followed by a slower one to a lower C-J pressure reaction product equation of state had been proposed to explore the thermodynamic and reaction time parameters involved in this phenomenon. The current explanation centers on carbon condensation due to its thermodynamic properties and the chemical equilibrium calculations. (14)

TABLE I
Compositions of Test Explosives

Explosives	Wt.% Composition
LX-07	90/10 HMX/Viton A
LX-17	92.5/7.5 TATB/Kel-F 800
PBX-9404	94/3/3 HMX/NC/CEP
RX-26-AF	46.6/49.3/4.1

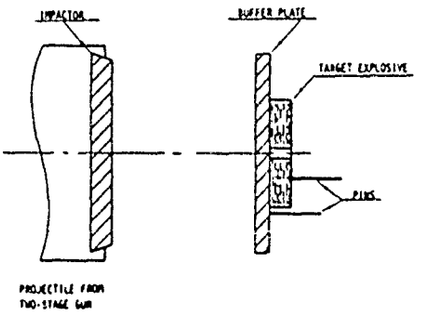

Fig. 1. Test configuration for single-shock supra-compression experiments on LX-07, LX-17, PBX-9404 and RX-26-AF. Some of the test samples of LX-17 were two-level and additional pins were used to enable accurate velocity stability determinations to be made.

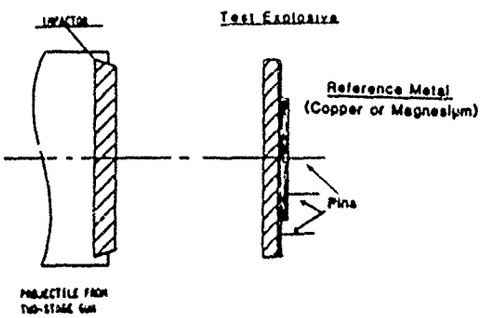

Fig. 2. Test configuration for reshock and rarefaction of supra-compressive states of PBX-9404

TABLE II

Conditions and Results of Single-Shock Supra-Compressive Experiments

Experiment	Impactor			Buffer Plate		Target						
	Velocity km/s	Material	Density g/cm^3	Material	Density g/cm^3	Material	Density	Shock Vel. km/s±2σ	Particle Vel. km/s±2σ	Pressure GPa	Rel. Vol. V/V_0	Run Measured mm
MG 8	4.796	1100 Al	2.712	1100 Al	2.716	LX-07	1.861	9.00±.06	2.730±.020	45.72	.6967	0 to 2.8
MG 24	4.892	1100 Al	2.707	LX-07	1.858	LX-07	1.860	8.94± 03	2.796±.007	46.49	.6872	2 to 4.8
MG 9	5.961	1100 Al	2.714	1100 Al	2.720	LX-07	1.863	9.57±.06	3.410±.029	60.80	.6437	0 to 2.8
MG 10	7.544	1100 Al	2.715	1100 Al	2.721	LX 07	1.864	10 33±.07	4.367±.030	93.90	.5771	0 to 2.8
MG 29	3.508	1100 Al	2.713	1100 Al	2.704	LX-17	1.907	7.44± 03				0 to 2.0
						LX-17	1.902	7.68±.06				2 to 4.0
MG 30	3 813	1100 Al	2 713	1100 Al	2.711	LX-17	1.906	7.70±.04	2.222±.015	32.16	.7114	0 to 2.0
						LX-17	1.903	7.70±.04	2.223±.015	32.57	.7113	2 to 4 0
MG 32	4 400	1100 Al	2.712	LX-17	1.899	LX-17	1.901	8.02±.04	2.563±.013	39.08	.6804	2 to 4.0
						LX-17	1 898	7.98±.04	2.569±.013	38.91	.6780	4 to 6.0
MG 36	4.436	1100 Al	2 712	LX-17	1.905	LX-17	1.905	8.00±.02	2.587±.007	39.42	.6766	2 to 4.8
MG 35	5.355	1100 Al	2 712	LX-17	1.903	LX-17	1.903	8.44±.04	3.134±.015	50.34	.6286	2 to 4.8
MG 31	5.612	1100 Al	2 713	1100 Al	2.705	LX-17	1 902	8.60±.03	3.284±.014	53.72	6181	0 to 4.0
MG 13	4 164	1100 Al	2.714	PBX-9404	1.844	PBX-9404	1.844	8.85±.04	2.353± 012	38.40	.7341	2 to 6.9
MG 4	4 779	1100 Al	2.714	1100 Al	2.719	PBX-9404	1.841	9.07±.06	2.723±.020	45.47	6998	0 to 2.8
MG 3	5.032	1100 Al	2 715	1100 Al	2.717	PBX-9404	1 841	9.17±.08	2.874±.024	48.52	.6866	0 to 2.8
MG 16	5 901	1100 Al	2 715	PBX-9404	1 845	PBX-9404	1.844	9 47± 05	3 399± 017	59 35	.6411	2 to 4.8
MG 15	6 218	1100 Al	2 715	PBX-9401	1 846	PBX-9404	1.844	9.59±.10	3.591±.036	63.50	6256	2 to 4.8
MG 1	7 533	1100 Al	2.715	1100 Al	2 718	PBX-9404	1 841	10.37± 07	4 343± 020	82.92	.5811	0 o 2 8
MG 14	6 402	Ta	16 675	PBX-9404	1 846	PBX-9404	1.841	11 03± 06	5.130±.021	105 14	5380	2 to 4.8
MG 12	6 760	Ta	16 681	PBX-9404	1.845	PBX-9404	1.843	11 23±.07	5.424± 036	112.27	5170	2 to 4.8
MG 20	4 547	1100 Al	2 715	1100 Al	2 711	RX-26-AF	1 835	8.50± 01	2 641± 013	41 20	6893	0 to 2.8
MG 5	4 710	1100 Al	2 712	1100 Al	2 713	RX-26-AF	1 837	8 62± 08	2 730± 026	43.24	6832	0 to 2 8
MG 19	5 028	1100 Al	2 716	1100 Al	2 716	RX-26-AF	1 832	8 72±.02	2 929± 012	46 79	6641	0 to 2 8
MG 25	5 416	1100 Al	2 715	RX-26-AF	1.835	RX-26-AF	1 836	8 82± 01	3 167±0 15	51 28	6110	2 to 4.8
MG 6	5 988	1100 Al	2 714	1100 Al	2 713	RX 26-AF	1 837	9 14± 08	3 500± 035	58 77	6171	0 to 2.8
MG 7	7 493	1100 Al	2 715	1100 Al	2 716	RX 26-AF	1 837	10 09± 07	4.361± 030	80 83	5678	0 to 2 8

TABLE III

Conditions and Results of Reflection and Rarefaction Experiments on Supra Compressive States of PBX-9404. See Fig. 2 for Experimental Configuration

Experiment	Impactor			PBX-9404	Impact Pressure*	Barrier			
	Velocity km/s	Material	Density g/cm^3	Density g/cm^3	PBX-9404 GPa	Material	Density g/cm^3	Shock Velocity km/s±2σ	Pressure GPA
MG 18	4.310	1100 Al	2 715	1.841	40.02	Cu	8.93	5.864±.026	67.41
MG 17	6.055	1100 Al	2.715	1 838	61.29	Cu	8.93	6.67±.10	108.68
MG 23	6.294	1000 Al	2.713	1.840	64.62	Cu	8.93	6.759±.022	113.71
MG 27	3.996	1100 Al	2.716	1.840	36.48	Mg	1.738	7.55±.06	32.22
MG 26	4.200	1100 Al	2.706	1.840	38.70	Mg	1.736	7.70±.07	34.50
MG 28	4.432	1100 Al	2.714	1.840	41.39	Mg	1.733	7.82±.06	36.45

* Calculated from best fit to single-shock supra-compressive data.

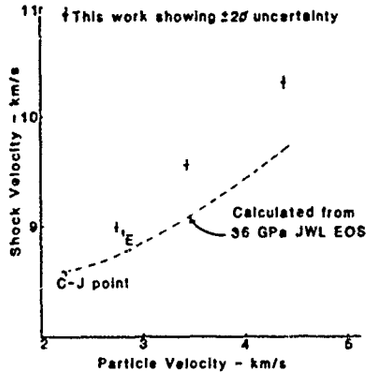

Fig. 3. Experimental LX-07 supra-compressive data. Measured shock velocity is vs. particle velocity derived from flyer velocity, density, and Hugoniot relationships. Data points marked "E" used an LX-07 buffer plate. All others used an 1100 A1 buffer plate. See Fig. 1.

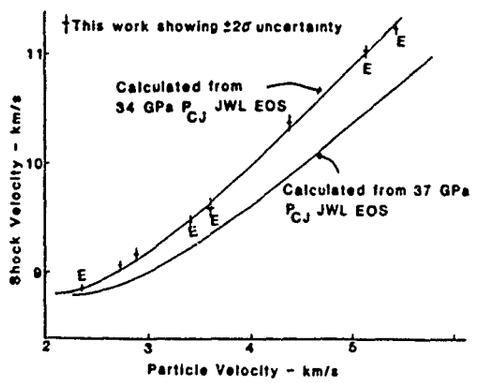

Fig. 5. Experimental PBX-9404 supra-compressive data. Measured shock velocity is vs. particle velocity derived from flyer velocity, density, and Hugoniot relationships. Data points marked "E" used a PBX-9404 buffer plate. All others used an 1100 A1 buffer plate. See Fig. 1.

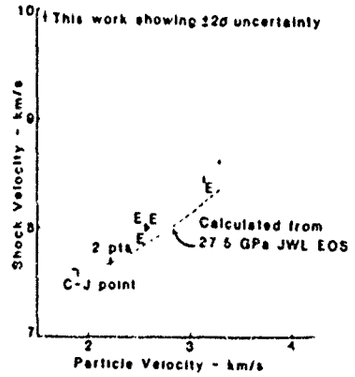

Fig 4. Experimental LX-17 supra-compressive data. Measured shock velocity is vs. particle velocity derived from flyer velocity, density, and Hugoniot relationships. Data points marked "E" used an LX-17 buffer plate. All others used an 1100 A1 buffer plate. See Fig. 1.

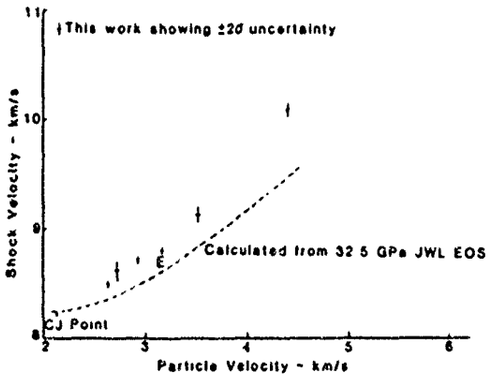

Fig. 6. Experimental RX-26-AF supra-compressive data. Measured shock velocity is vs. particle velocity derived from flyer velocity, density, and Hugoniot relationships. Data points marked "E" used an RX-26-AF buffer plate. All others used an 1100 A1 buffer plate. See Fig. 1.

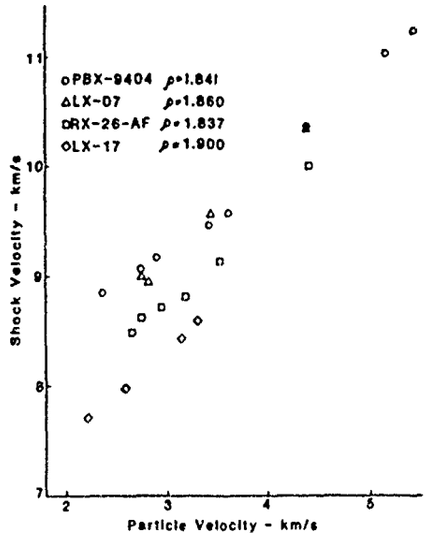

Fig. 7. Combined plot of shock velocity vs. particle velocity for all single-shock supra-compressive experiments to illustrate systematics of data.

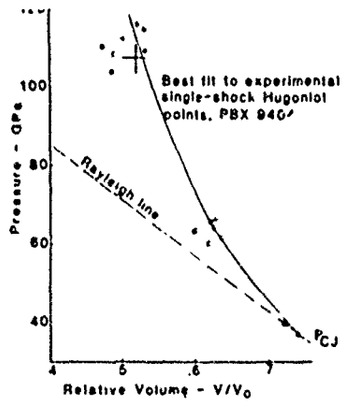

0 Calculated for single shock using 34.0 GPa P_{CJ} JWL EOS

• Calculated for reflected shock off of copper using 34.0 GPa P_{CJ} JWL EOS.
Calculated for single shock using published 37.0 GPa P_{CJ} JWL EOS.

■ Calculated for reflected shock off of copper using published 37.0 GPa P_{CJ} JWL EOS.

† Experimental reflected shock values off of copper, ± 2σ.

Fig. 8. Reflected and single-shock supra-compressive states of PBX-9404. Calculational results using two different equations of state are compared with experiment.

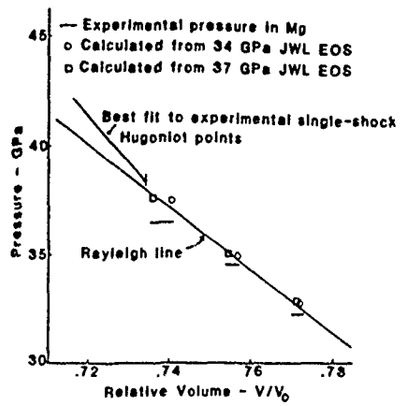

Fig. 9. Insentrope states from PBX-9404/Mg experiments near P_{CJ}. Calculations of pressure vs. relative volume for individual experiments using two different JWL equations of state are compared with experimental pressures calculated from shock velocity measured in magnesium using the same shock Hugoniot ($U_S = 4.52 + 1.233\ U_p$) for the calculations and the shock velocity to pressure conversions.

REFERENCES

1. A.C. Mitchell and W. J. Nellis, "Diagnostic System of the Lawrence Livermore National Laboratory Two-Stage Light-Gas Gun," Rev. Sci. Instrum. *52*, 3, Mar. 1981.
2. J. H. Kineke and C. E. West, Fifth Symposium (International) on Detonation, U.S. Naval Ord. Lab., Pasadena, CA., 1970, ACR-184, ONR 0851-0057.
3. E.L. Lee and C. M. Tarver, Phys. Fluids *23*, 2362 (1980).
4. C. M. Tarver and J. O. Hallquist, Seventh Symposium (International) on Detonation, Naval Surface Weapons Center, NSWC MP 82-334, Annapolis, MD, 1981, p. 488.
5. B. Hayes and C. Tarver, Seventh Symposium (International) on Detonation, Naval Surface Weapons Center, NSWC MP 82-334, Annapolis, MD, 1981, p. 1029.
6. W. G. Von Holle and C. M. Tarver, Seventh Symposium (International) on Detonation, Naval Surface Weapons Center, NSWC MP 82-334, Annapolis, MD, 1981, p. 993.

7. L. G. Green, W. James, E. L. Lee, C. S. Chambers, C. M. Tarver, C. Westmoreland, A. M. Weston, and B. Brown, Seventh Symposium (International) on Detonation, Naval Surface Weapons Center, NSWC MP 82-334, Annapolis, MD, 1981, p. 256.

8. C. M. Tarver and P. A. Urtiew, Progress in Astronautics and Aeronautics *94,* 369, (1983).

9. C. M. Tarver, N. L. Parker, H. G. Palmer, P. Hayes and L. M. Erickson, J. Energetic Materials *1,* 213 (1983).

10. C. M. Tarver, L. M. Erickson and N. L. Parker, *Shock Waves in Condensed Matter* (J. R. Asay, R. A. Graham, G. K. Straub (eds.)), 1983, p. 609.

11. C. M. Tarver, J. O. Hallquist, and L. M. Erickson, "Modeling Short Shock Pulse Duration Experiments on Solid Explosives," paper presented at this Symposium.

12. E. Lee, M. Van Thiel, L. Green and A. Mitchell, "Detonation Product EOS: The Region Above Chapman Jouguet Pressure," American Physical Society 1983 Topical Conference on Shock Waves, Santa Fe, NM July 18-21, 1983.

13. R. Cheret, F. Chaisse, and J. Zoe, Seventh Symposium (International) on Detonation, Naval Surface Weapons Center, NSWC MP 82-334, Annapolis, MD, 1981, p. 602.

14. F. H. Ree and M. Van Thiel, "Detonation Behavior of LX-14 and PBX-9404: Theoretical Aspect," paper presented at this Symposium.

15. B. M. Dobratz, "LLNL Explosives Handbook, Properties of Chemical Explosives and Explosive Simulants," UCID 52997, Lawrence Livermore National Laboratory, March 16, 1981.

16. L. Green, E. Lee, A. Mitchell, F. Ree, R. T. Tipton, and M. Van Thiel, "Detonation EOS Patterns for Several Explosive," UCRL-89006, submitted to Proc. IX AIRAPT Int. High Pressure Conference, July 24-29, 1983.

17. M. Van Thiel, E. L. Lee, and S. Cochran, "Effects of Overdriven Shock States on the Equation of State of 9404 Explosive," J. Appl. Phys, *54* (11), November 1983.

DISCUSSION

D. TASKER, NSWC, White Oak

We have observed small anomalies when coaxial ionization pins have been used to detect shock front arrival. The origin of these anomalies is as yet uncertain; they may be due to ejecta caused by pore collapse in porous explosives to electromagnetic effects. Is it possible that your measured shock velocities are too high because of these effects? If so then your data would agree more closely with published CJ pressures and JWL equations of state. I would like to add my appreciation for the high quality of the work presented in this paper.

REPLY BY L. GREEN

We have seen no significant difference (to ±0.5% precision) in shock velocity through the specimens when velocities measured from an aluminum buffer plate to the top surface of the test explosive are compared with those where a buffer plate of test explosive was used and systematic errors, if present, would cancel out. Any systematic errors due to the pins is lost in the .2 ns jitter in pin closure times and the overall uncertainty of about .5 ns in the individual measurements of pin time relative to the fiducial time.

DISCUSSION

DR. SYED ZULFIQAR HUSSAIN, ARDE A HQ Pakistan

What explosives were used to fly off the projector or impactor? And what was the free run distance between the impactor/projector and to the targets?

REPLY BY L. GREEN

When an explosive buffer was used it was the same as the test explosive. See Table 2. The free flight of the projectile is about 400 mm.

DISCUSSION

LOUIS ZERNOW, Zernow Tech. Services, San Dimas, CA

To what extent does wave tilt contribute as a source of error? To what extent does non-planarity of the shock wave, (e.g. due to grain size

of the explosive) contribute to the possible errors?

REPLY BY L. GREEN

Wave tilt is only a significant source of error if several pins on the same level fail. Otherwise, it is simply measured and accounted for when we reduce the data. The principal non-planarity of the shock wave is due to a parabolic distortion of the flyer from the launch conditions. Since this distortion (typically ~2 ns) is measured by the difference in time between the average of six pins on the buffer plate and a single center pin, the contribution to the overall experimental uncertainty is generally as great as all other sources. Unexpectedly, the effect of grain size appears to be small. The standard deviation from a plane fit to the reporting times of six pins on a PBX-9404 buffer plate is typically about .5 ns, not much different than when aluminum is used for the buffer plate.

DISCUSSION

GERALD KERLEY, Sandia, Albuquerque, NM

If there is nonequilibrium behavior in these explosives, it might be possible to see a dependence of the results on the distance of run. Please comment on what your measurements show and on the accuracy of these observations.

REPLY BY L. GREEN

The average supra-compression shock velocity in LX-17 at a given pressure appears to be the same (within .5%) for run distances of 0 to 2 mm, 2 to 4 mm, and 4 to 6 mm. For LX-07, PBX-9404 and RX-26-AF the average shock velocities for run distances of 2 to 4.8 mm are very slightly less than for run distances at corresponding pressures of 0 to 2.8 mm, but the differences (<1%) are not statistically significant. Even if the differences are real, they could be due to other causes such as uncertainties in the release adiabat of 1100 Al, for example. These measurements are consistent with the idea that conventional P_{CJ} experiments measures states further from equilibrium than the present measurements. Our failure to detect changes in shock velocity with run distance establishes that the wave is steady within rather narrow limits on the time scale of the experiment (600 to 800 ns total time). It does not prove that equilibrium conditions exist behind the shock front in supra-compressive experiments.

EOS OF DETONATION PRODUCTS OBTAINED FROM SYMMETRICAL DEFLECTION OF LINERS INVESTIGATED BY LASER INTERFEROMETRY TECHNIQUES

P. Gimenez, Y. de Longueville, C. Saint-Martin
Centre d'Etudes de Gramat 46500
Gramat, France

We present an experimental test to determine the coefficients of the J.W.L. equation of state of detonation products. The described configuration is symmetrical plane test monitored by an interferometric device. Hydrodynamic calculations and an experimental analysis allow to select the best material and set-up dimensions. The use of an interferometric device represents a major improvement. It appears to be possible to entirely characterize the detonation products by use of a single experiment. This experimental approach could be considered as a hopeful way to investigate the form of the E.O.S. for detonation products. The method has been applied to a cast PBX (octorane 86A).

BACKGROUND

Hydrodynamic calculations need an equation of state to describe the evolution of detonation products. The J.W.L. equation of state (1) is generally accepted as a good description of the pressure-volume-energy relationship for detonation products. Hydrodynamic experiments have been developed to determine the parameters of this equation. Usually cylinder test (see Figure 1a) is used to get experimental data for large expansion levels. This test can be precisely monitored by a streak camera which records the radial motion of a copper tube. Nevertheless, this experiment requires great care in the choice of the copper and in the machining. Symmetrical plane test (see Figure 1b) is easier to realize. However, this test is difficultly monitored by a streak camera and the expansion level which can be reached must be investigated, according to the chosen EOS. In the next section we show that symmetrical plane test can be precisely monitored by an interferometric device and that the use of low impedance materials for the liners fits the requirements involved in expansion levels.

The influence of experimental parameters is then studied and the coefficients of the J.W.L. equation of state are determined for the octorane 86A (cast PBX). Some general considerations are finally given on the comparison between the classical method (cylinder test) and the symmetrical plane tests.

FEASIBILITY OF THE METHOD

Use of Interferometric Devices

The free surface velocity of one of the liners has been monitored by interferometric devices.

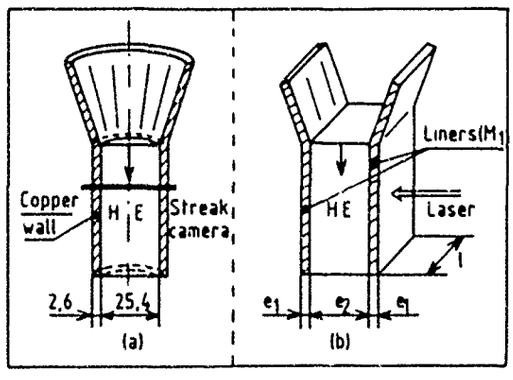

Fig. 1. Hydrodynamic experiments
(a) Cylinder test
(b) Symmetrical plane test

Two interferometers have been tested, a VISAR (2) and a Fabry-Perot (3), with very similar results. For the Fabry-Perot, the symmetrical plane test has been tilted before shot to compensate the rotation of the surface. This tilt explains the small gap between the two curves of the Figure 2. Nevertheless, the Fabry-Perot interferometer is less sensitive to extra lights so it has been selected for this study. The velocity is obtained with an accuracy of about ± 20m/s and the recording duration exceeds 10 μs.

Expansion Level

There is no limitation in the choice of the liner's material (M_1 on Table 1) of the symmetrical plane test. We have performed 2D-Hydrodynamic calculations (PISCES code (4)) to select the best material and set-up dimensions e_1 and e_2 (see Figure 1b). Some of the most significant configurations are defined on Table 1.

TABLE 1

Characteristics of the Calculated Configurations (the Configurations are Refered to Fig. 1b, except for Number 5 Which Represents Cylinder Test)

	e_1 (mm)	e_2 (mm)	M_1
1	4	20	Mg
2	6	20	Mg
3	6	20	A12024T4
4	2.5	25.4	Cu
5	2.5	25.4	Cu

The high explosive is always Comp B grade A, with J.W.L. parameters given in ref (1).

The results of the calculations are given on Figure 3 in a relative volume versus time diagram.

The geometrical effect is clearly seen between the configuration 5 (cylinder test) and the configuration 4 (symmetrical plane test with the same characteristics as cylinder test). But, by decreasing the mass of the liners, similar expansion level as cylinder test can be obtained during 10μs (configuration 2). Moreover, the configuration 1 (thicknesses are 4mm for magnesium and 20mm for H.E.) allows to reach a relative volume of about 6 after 10 μs.

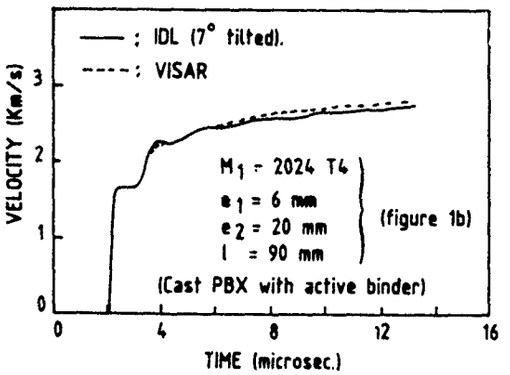

Fig. 2. Velocity of a liner obtained from two interferometric devices (symmetrical plane test)

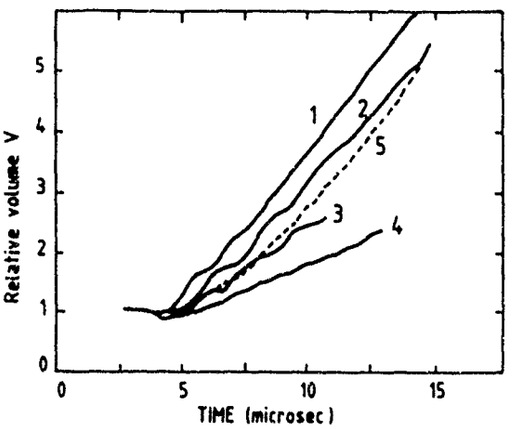

Fig. 3. Relative volume versus time (configurations described in Table 1)

The J.W.L. isentrope can be written (1):

$$P = P_1 + P_2 + P_3$$
$$P_1 = A\, e^{-R_1 V}$$
$$P_2 = B\, e^{-R_2 V} \qquad (1)$$
$$P_3 = C\, V^{-(\omega+1)}$$

with P = Pressure
V = Relative volume
A,B,C,R_1,R_2,ω=J.W.L. coefficients

Figure 4 shows that an expansion level of 6 is necessary to get a correct setting of the three pressure terms ($P_1P_2P_3$). So, the configuration 1 has been chosen as the standard configuration for the determination of the J.W.L. parameters.

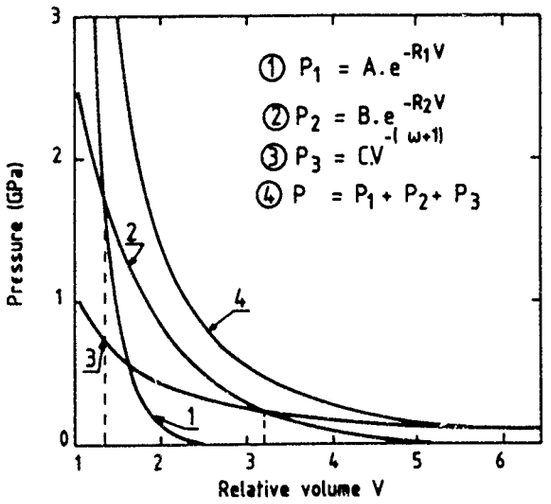

Fig. 4. Contribution of the three terms of the J.W.L. isentrope

EXPERIMENTAL ANALYSIS

For the experimental configuration, magnesium has been replaced by the alloy AZ31B (95.8% of Mg, ϱ_0=1770kg/m³). The liners are obtained from 4.15mm width laminated plates. A tilt of 17° with the incident laser beam is adjusted. So, light intensity remains nearly constant during 10μs. All the experimental results of this section have been obtained with a pressed PBX (94%HMX). Initiation of the device is made by a linear wave generator (LWG). The velocities obtained at 120, 130 and 140mm from the L.W.G. are given on the Figure 5. The differences between the three curves are within the experimental accuracy.

So, at 120mm from the LWG, the stationnarity is reached and the conditions of the initiation are forgotten.

The Figure 6 gives the results obtained with l=90 and 120mm (see Figure 1b). There is no significant differences between the two curves, supporting the fact that edge effects have no significant influence for l=90mm during more than 10μs of motion. In fact, due to the fast expansion, the sound velocity of the detonation products decreases very rapidly during the motion. An overestimated calculation, using the expansion ratio of the Figure 3 (curve 1), has been made. It shows that the rarefaction wave, issued from the edges and travelling inside the detonation products, doesn't reach the center of the liners before 11μs of motion. This is in agreement with the experimental results of Figure 6.

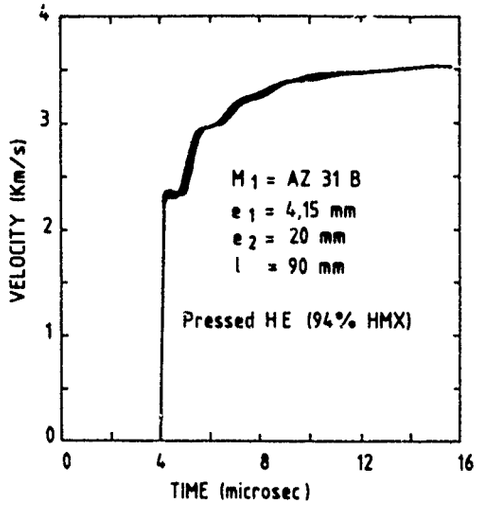

Fig. 5. Velocities obtained at 120, 130 and 140mm from the L.W.G. (e_1, e_2 and l are referred to Fig. 1b)

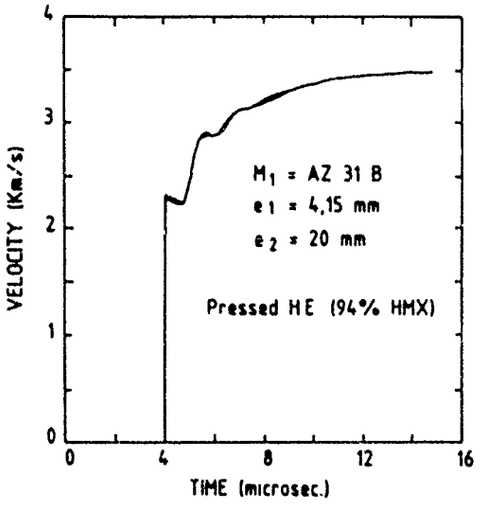

Fig. 6. Velocities obtained with l = 90 and l = 120mm

The thickness of the H.E sample (20mm) is generally sufficient to closely approximate infinite diameter behaviour. As in the case of cylinder test (1), this is not true for explosives with large reaction zones which are outside the field of this study.

The Figure 7 illustrates the effect of an important defect of the LWG (600ns of delay at the center). The significant increase in the velocity during the first microseconds ($\simeq$150m/s) can be related to the curvature of the detonation front. In fact, with this L.W.G. the stationnarity is not reached after 120mm of detonation.

After four microseconds of motion the velocities obtained with the two L.W.G. become comparable.

As a conclusion of this section, the specifications of the standard symmetrical plane test defined on Figure 1b are described as follows:

- M_1 = AZ31B
- e_1 = 4.15mm
- e_2 = 20mm
- l = 90mm
- instrumentation: Fabry-Perot interferometer
- velocity of one of the liners monitored at 120mm from the initiation
- initiator = LWG (imperfection less than 100ns)
- length of the device = 200mm

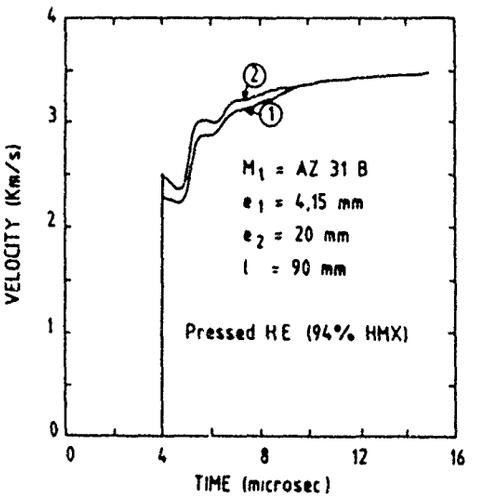

Fig. 7. Velocities obtained with two L.W.G.
1. Standard L.W.G. (imperfection less than 100ns)
2. L.W.G. with an important imperfection (600ns of delay at the center)

APPLICATIONS

EOS of a Cast PBX

The determination of the J.W.L. coefficients for the detonation products of a cast PBX (octorane 86A containing 86% HMX in a Pu binder) has been made. The experimental results obtained from the standard symmetrical plane test is given in Figure 8. Also shown in Figure 8 is our best calculation fit obtained with the following parameters:

P_{CJ} = CJ pressure = 30GPa

D = celerity of detonation = 8230m/s

ϱ_o = initial density = 1710kg/m^3

R_1 = 4.23 R_2 = 0.95

ω = 0.35

A = 601.64GPa

B = 4.398GPa

C = 1.092GPa

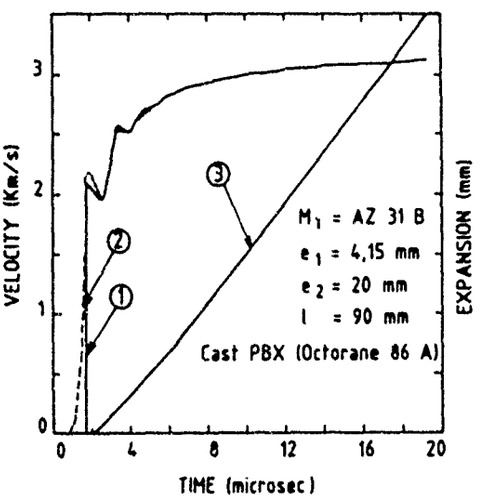

Fig. 8. 1. Experimental velocity curve
2. Calculated velocity curve
3. Motion of the liner obtained by integration of 1

Calculations have been made with the PISCES 2DELK code (4). The zoning is shown in Figure 9. The calculated velocity is directly compared with the experimental curve (inclination of the eulerian zoning). Due to the pseudo-viscosity of the code, the first step is not exactly fitted. After this first step, the fit becomes excellent.

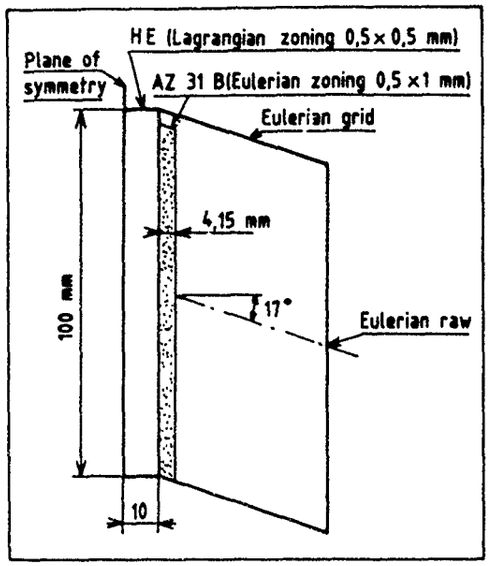

Fig. 9. Zoning for code calculation (the velocity is taken at 40mm from the lower end of the device)

Improvements Resulting of this Method.

The motion of a liner obtained by integrating the velocity curve is also shown in Figure 8. The fine structure observed on the velocity curve during the first four microsecondes almost does not affect the motion curve. This fine structure can give information on the CJ pressure (5) and on the parameter R_1 of the J.W.L. equation. So the direct monitoring of the velocity is much more fruitfull than an expansion curve obtained from a streak camera record.

The AZ31B alloy can be treated hydrodynamically or with an Hugoniot elastic limit of 0.11 GPa without significant influence on the calculated velocity. More generally, the calculated velocity doesn't depend strongly on the equation or state of the liner's material.

CONCLUSIONS

The symmetrical plane test can be used for the determination of the J.W.L. parameters of high explosives. The great simplicity of the set-up is the main advantage of this configuration.

The use of an interferometric device, which is also convenient for the monitoring of cylinder test, represents a major improvement. This experimental technique allows to finely detect the influence of all the expansion levels from the CJ point to an expansion ratio exceeding 6 in the case of the symmetrical plane test. Therefore it appears to be possible to entirely characterize the detonation products (CJ point and J.W.L. coefficients) by use of a single experiment.

Finally, this experimental approach could be considered as a hopeful way to eventually investigate a more appropriate form of an EOS for detonation products.

REFERENCES

1. E. L. Lee, H. C. Hornig, J. W. Kury, "Adiabatic expansion of high explosive detonation products". L.R.L. Rep. N°. UCRL-50422 (1968).

2. L. M. Barker, R. E. Hollenbach. "Laser interferometer for measuring high velocities of any reflecting surface". J. Appl. Phys., Vol. 43, n°11, November (1972).

3. M. Durand, P. Laharrague, P. Lalle, A. Le Bihan, J. Morvan and H. Pujols. "Interferometric laser technics for accurate velocity measurement in shock waves physics," Rev. Sci. Instrum., Vol. 48, n°3, March (1977).

4. Steven L. Hancok, "Finite difference equations for PISCES 2DELK. A coupled Euler Lagrange continum mechanics computer program," TCAM 76-2, April (1977). Physics International Company.

5. W. A. Barley, R. A. Belcher, D. K. Chilvers, G. Eden. "Explosive equation of state determination by AWRE method," Seventh Symposium on detonation, Annapolis, Maryland, June (1981).

DISCUSSION

MANFRED HELD. MBB Apparate, Germany

You have taken into account the release wave from the site. I expect an influence in your dimensions. Chanteret - I.S.L. - has made considerations to this point.

This work has been performed under the auspices of French Ministry of Defense (D.R.E.T. and S.T.P.E.)

REPLY BY P. GIMENEZ

Two approaches have been used to study the edge effects:

- experimentally, 90mm and 120mm width experimental devices were fired and no significant velocity differences were detected (Figure 6),

- analytically, expansion versus time curve obtained from numerical simulation (Figure 3, curve number 1) has been used to calculate the arrival time of the edge effects of the center of the plate.

Hypothesis were:

- stationnarity
- polytropic E.O.S. for the products

11μs was found to be { — a majorant of this arrival time / — an overvalue

MODELS OF EXPLOSIVELY DRIVEN METAL

J. T. Dehn
US Army Ballistic Research Laboratory
ATTN: AMXBR-TBD
Aberdeen Proving Ground, Maryland

Relations between the Taylor and Gurney Models of explosively-filled cylinders are discussed. A method is then introduced which simplifies Taylor's model, expressing his results in formulas not much more complicated than Gurney's for launch speeds. The time-and-angle-dependencies of Taylor's model are retained, making his model as easy to use as the time-dependent variations of Gurney's model. Finally, Taylor's model (both original and simplified) is extended to planar geometry, much as Gurney's formula was extended. These formula's should be useful in design work which requires space-time trajectories which are accurate enough to offer insight without the labor required for great precision.

INTRODUCTION

There is a continuing need for and interest in simple models of explosively driven metal. Military applications have received the most attention, beginning with the work of Taylor (1) and Gurney (2) on the launch speeds of fragments from explosively driven metal shells. Taylor also applied his ideas to the formation of shaped charge jets (3) and later published his results (4). Variations of these basic ideas are still being used today in design and analysis work. These ideas have also proven to be useful in the general field of shock physics (5), and several recent papers have appeared on applications of Gurney's analysis (6-9).

Here we will express Taylor's analysis (1) in simple formulas and extend it to cases of planar as well as cylindrical symmetry. Taylor's ... nerical analysis was presented in tabular form and has been virtually ignored. By contrast, Gurney's results were presented in simple formulas which have been widely used and extended. An exception is Taylor's simple formula for the projection angle. This small part of Taylor's model has also been widely used in a somewhat obscure combination with Gurney formulas to obtain a projection velocity (magnitude and direction).

In this paper we will establish the validity of using the exponent $\gamma = 3$ in the entropic equation of state. This is required for the simplification of Taylor's theory and its extension to planar geometry as will be discussed. A description and comparison of Taylor's and Gurney's models is given in this paper by way of preparation.

THE ADIABATIC EXPANSION OF DETONATION PRODUCT GASES

A key element in Taylor's analysis was provided by H. Jones who numerically evaluated one of Taylor's integrals. Jones worked with Taylor on the Research Committee of the Ministry of Home Security and wrote several papers with him (10-12). Jones gave an account of his methods in several Research Committee papers which are no longer available. Fortunately, his work was later published (13-14).

In reference (13), Jones gives his Equation (27)

$$p = B\rho^{\gamma} \qquad (1)$$

relating the pressure p and density ρ of the

product gas during its expansion. Here B and γ are constants. Equation (1) is called the entropic equation of state and applies to polytropic gases for which the internal energy depends only on the temperature (15). For ideal gases at moderate pressures and temperatures, γ is not much larger than unity. Jones estimates that γ should be close to three near the rear of the reaction zone of a typical solid explosive loading and remarks that such a high value occurs because the products initially form a very imperfect gas. He derives the value $\gamma = 3$ by assuming that the ratio of the densities at the front (ϱ_0) and rear (ϱ_1) of the reaction zone is $\varrho_0/\varrho_1 = 3/4$.

In reference (14) Jones and Miller used a virial equation of state to calculate pressure, volume, and product species for TNT and predicted an approximately linear dependence of both detonation velocity and detonation pressure on loading density. These results of Jones and Miller were again used by Taylor in a later paper (16) in which he demonstrated for the first time the possibility of a spherical detonation wave, contradicting an opinion previously expressed by Jouguet.

Many other authors have followed Jones by using $\gamma = 3$ to describe the high pressure gases which result from the detonation of condensed explosives near their maximum loading density. Jacobs (17) has pointed out that both the Kistiakowsky-Wilson equation of state and that used by Jones and Miller lead to calculated results which can be expressed by Equation (1) above with $\gamma = 3$ down to one per cent of the detonation pressure, with an accuracy acceptable for hydrodynamic usage.

In 1968, Jacobs, together with Kamlet, proposed a simple method of calculating detonation properties, that is, properties at the rear of the reaction zone (18). This was the first in a long series of papers which has not yet been completed. The sixth paper (19) in this series gives an empirical expression for γ in terms of the loading density with γ again approximately equal to three for military explosives at typical loading densities. In connection with this paper, we also note a recent paper by Andersen (20).

The fifth paper (21) in the above series provides us with a table of pressures and inverse densities (specific volumes) for various conditions during the expansion of the products from the detonation of twelve common explosive loadings, calculated by using a Kistiakowsky-Wilson equation of state.

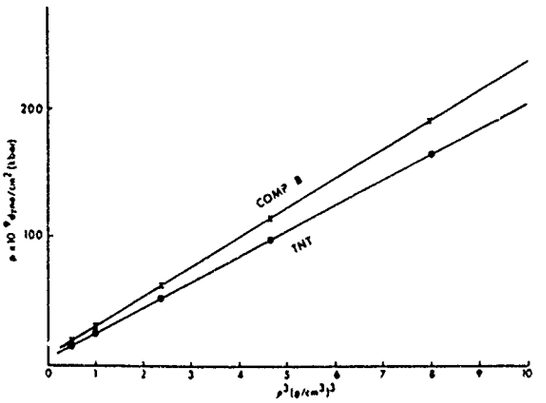

Fig.1. Linear relation between pressure and density cubed, illustrated by 64/36 RDX/TNT (ϱ_0 = 1.715 g/cm^3) and TNT (ϱ_0 = 1.55 g/cm^3)

If we use this table to plot p versus ϱ^3, we see that Equation (1) with $\gamma = 3$ can be fitted very closely to these calculated results, at least over the range of ϱ of interest to metal acceleration, confirming Jacobs' remark (17). Figure 1 illustrates this for two explosive loadings. The values marked X and O are from their table.

If we adjusted γ as well as B in Equation (1) we might obtain slightly better agreement. However, there is little justification for doing this since the values being fitted can be calculated from various equations of state chosen for convenience rather then theoretical reasons. Since almost any reasonable form will do, we should not place much weight on the fact that a particular form gives us reasonable results. As Jones and Miller remarked long ago (14), we have little information to guide us in choosing a correct form for the equation of state. There is no virture in using complicated empirical equations which are designed to cover critical phenomena controlled by weak molecular attractions. The best that can be done is to choose the simplest equation which is adequate for one's purpose, as they did and as we shall do.

If we let $\gamma = 3$ in Equation (1), analytical simplifications become possible, as we shall see

presently. One example of such simplification has already been given by Aziz and co-workers (22), who compared the results of an exact solution for rigid piston loading (possible if $\gamma = 3$) with numerical solutions in the parameter range $2.5 \leq \gamma \leq 3.5$. They concluded that only a one percent error would be made in calculating the energy transmitted to the piston, in spite of variations in the detonation pressure and velocity of about fifty per cent. Similar conclusions were reached earlier by Gurney in his discussion of gas leakage (23).

TAYLOR'S ANALYSIS OF A TUBULAR BOMB

Since the details of this model (1) are not widely known, we will summarize them here. Figure 2 shows a longitudinal cross section of an infinitely long tubular bomb in the neighborhood of a planar detonation front (solid vertical line) which is moving to the right at constant speed, D. To an observer in the laboratory, the process of gas expansion and metal acceleration appears to be complicated, since the gas first moves forward following the detonation wave front and later moves backward away from it so that it acts twice on the same element of the case, as we shall see. However, to an observer who travels with the detonation front and looks back at the expansion process, these complexities disappear, since the gas pressure and velocity at a given distance behind the front (dashed vertical line) do not change with time (steady state condition). Moreover, the velocity of a case element along its length ds is constant and equal to D, since there is no stretching along ds. The transformation between the laboratory coordinate X and the coordinate x used by the moving observer is

$$X = -(x - Dt) + X_o. \qquad (2)$$

as shown in Figure 2. Here t is the time, which is taken to be the same for both observers, since detonation wave speeds are negligible compared to the speed of light. The radial coordinates R = r are also the same for both observers as is the (ignorable) equatorial angle measured about the x-axis. The time derivative of Equation (2) gives us the relation between the speeds U = $\dot{X}$ and u = $\dot{x}$, using the dot convention for time derivative,

$$U = D - u. \qquad (3)$$

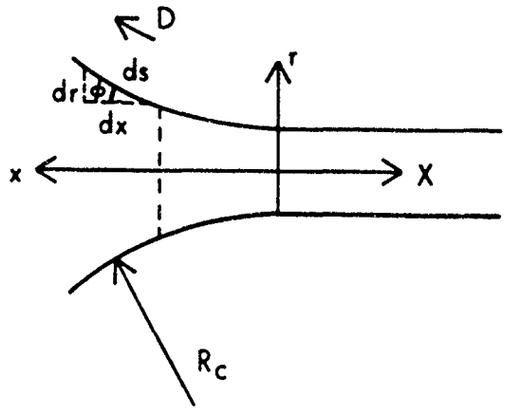

Fig. 2. Tubular case expansion geometry

Let M be the constant mass per unit length of the cylindrical shell casing and r be the radial position of the center of a ringlike element of the case wall, namely, the average of the inner and outer radii of the casing at any time t with r much larger than the wall thickness. If we take the ring to be of unit length, then the area acted on by the gas pressure is $2\pi r$ times unity and the mass per unit area is $M/(2\pi r)$. The pressure always acts normal to the metal surface and balances the centrifugal force $[M/(2\pi r)](D^2/R_c)$, where R_c is the radius of curvature (see Figure 2), the inverse of the curvature of the arc ds. Thus,

$$\frac{M}{2\pi r} D^2 \frac{\frac{d}{dx}\left(\frac{dr}{dx}\right)}{\left[1 + \left(\frac{dr}{dx}\right)^2\right]^{3/2}} = p \qquad (4)$$

where we have retained the exact expression for the curvature. For a sufficiently heavy case, $\tan^2\phi = \left(\frac{dr}{dx}\right)^2$ will be much less than unity (see Figure 2), approaching unity only as ϕ approaches 45°. Thus it is a good approximation to neglect it in the denominator of Equation (4) as Taylor implicitly did. However, there is no difficulty introduced by retaining it, at least for a while, so we will.

If we multiply both sides of Equation (4) by $(4\pi r dr)/MD^2 = (4\pi r \tan\phi\, dx)/(MD^2)$, we find

$$2 \frac{\tan\phi\, d(\tan\phi)}{\left[1 + \tan^2\phi\right]^{3/2}} = 2 \sin\phi\, d\phi = \frac{2\pi}{MD^2} p d(r^2) \qquad (5)$$

where we have used the identities $d(\tan\phi) = \sec^2\phi d\phi$, $1+\tan^2\phi = \sec^2\phi$ and $2\,rdr = d(r^2)$. The left side of Equation (5) is readily integrated from $\phi = 0$ to obtain (for any and small ϕ):

$$2(1-\cos\phi) = 4\sin^2(\phi/2) \approx \tan^2\phi \qquad (6)$$

We are interested in the square root of Equation (6). In moving coordinates, the components of the case velocity are $v_r = dr/dt = D\sin\phi$ and $v_x = dx/dt = D\cos\phi$ from Figure 2. In laboratory coordinates the components are $V_r = v_r$ and $V_x = D(1-\cos\phi)$, so that the magnitude of the case velocity in laboratory coordinates is

$$V = \sqrt{V_r^2 + V_x^2}$$

$$= D\sqrt{\sin^2\phi + (1-\cos\phi)^2} \qquad (7)$$

$$= D\sqrt{2(1-\cos\phi)} = 2D\sin(\phi/2),$$

where we have used the identity $\sin^2\phi + \cos^2\phi = 1$ and Equation (6). Equation (7) is the only formula in Taylor's analysis which has received wide use, clearly because of its simplicity. We also note by another identity that

$$\frac{V_x}{V_r} = \frac{1-\cos\phi}{\sin\phi} = \tan(\phi/2) \qquad (8)$$

so that the angle of projection in laboratory coordinates is $\phi/2$. Equations (7) and (8) are exact. If we follow Taylor and use $\tan\phi \approx 2\sin(\phi/2)$ for the integral of the left side of Equation (5), we make less than a 5% error for $\phi \leq 20°$. The exact expression in Equation (6) has already been used by others. In the journal literature it was used by Allison and co-workerss (24-25) who wrote $d\phi/ds = (dr/ds)(d\phi/dr) = \sin\phi\,(d\phi/dr)$ for the curvature in Equation (5). This is equivalent to retaining the exact curvature.

In order to integrate the right side of Equation (5) let us write down a few more useful relations. For an explosive gas mixture in a rigid cylinder, such as a hydrogen/oxygen mixture in a shock tube experiment, the equation of mass conservation in moving coordinates is

$$dm = \varrho_0 A_0 D dt = \varrho A u dt \qquad (9)$$

where Ddt and udt are the original and compressed length of a gas volume element of mass dm and constant cross sectional area $A = A_0$. Here ϱ_0 is the uncompressed gas density while ϱ is its compressed density. Since the tube is rigid, A is constant and $\varrho_0 D = \varrho u$. However, for the gaseous detonation products of a solid explosive high density loading expanding in a metal tube, A will not remain constant. For a tube with a circular cross section, the area before expansion is $A_0 = \pi r_0^2$, while after some expansion it becomes $A = \pi r^2 > A_0$. If we use these expressions in Equation (9) and cancel π, we find

$$\varrho_0 D r_0^2 = \varrho u r^2 \qquad (10)$$

for mass conservation. Now ϱ_0 is the loading density of the solid explosive before detonation. Since steady state flow conditions hold in moving coordinates, the equation of continuity is

$$\frac{1}{r}\frac{\partial}{\partial r}(r\varrho v) + \frac{\partial}{\partial x}(\varrho u) = 0 \qquad (11)$$

where v is the radial component of the gas velocity (as contrasted with v_r, the radial component of the metal velocity). It is interesting to conclude from Equation (10) that (ϱu) is independent of x, so that $(r\varrho v)$ in Equation (11) must be independent of r. Since ϱ is inversely proportional to r^2 from Equation (10) when $u \approx D$, then v must be proportional to r under these conditions. Thus we may write

$$v = r(v_B/r_B), \qquad (12)$$

where v_B and r_B are constants which we will define later. Equation (12) was introduced by Gurney (2) as a postulate, although it follows from the equation of continuity under the conditions mentioned. Gurney gave no indication that he ever noticed this fact. Instead, his assumption had quite a different motivation as we shall see.

In the Chapman-Jouguet model of detonation, the approximation is made that all chemical reaction is completed in such a short time that the width of the reaction zone is negligble. Thus we may approximate changes in variables like p, ϱ and u by discontinuous jumps instead of using derivatives with very large values. If we use the subscript unity to denote values just behind this very narrow reaction zone and the approximation $r_1 = r_0$ (no expansion in the reaction zone), then Equation (10) becomes

$$\varrho_0 D = \varrho_1 u_1 \qquad (13)$$

as in a rigid tube. Similarly, we can use Newton's second law in its impulse-momentum form to derive another jump condition. The impulse

delivered across the reaction zone is $(p_1-p_0)Adt$ which is equal to the change in momentum across this zone, namely, $dm(D-u_1)$ where dm is given by Equation (9). If we neglect the (ambient) pressure P_0 at the front of the reaction zone compared to the detonation pressure p_1 at its rear and cancel Adt, we obtain

$$p_1 = \varrho_0 D(D-u_1) \cdot \tag{14}$$

We need one other relation in order to integrate the right side of Equation (5). This is the strong form of Bernoulli's law for steady flow (26)

$$\int_{p_1}^{p} \frac{dp}{\varrho} = \tfrac{1}{2}u_1^2 - \tfrac{1}{2}(u^2 + v^2) \approx \tfrac{1}{2}(u_1^2 - u^2) \tag{15}$$

since $v^2 << u^2 \approx D^2$ as mentioned above. The approximate differential form of Equation (15) is then

$$dp = -\varrho u du. \tag{16}$$

The variable on the right side of Equation (5) was chosen to be r^2 so that we may use Equation (10) to introduce the new variable $1/(\varrho u)$. Then the integral of the right side of Equation (5) becomes

$$\begin{aligned}
&\frac{2\pi}{MD^2} \int_{r_o^2}^{r^2} p\,d(r^2) \\
&= \frac{2\pi\varrho_0 r_o^2}{MD} \int_1 p\,d\left(\frac{1}{\varrho u}\right) \\
&= \frac{2}{\alpha D}\left[\frac{p}{\varrho u} - \frac{p_1}{\varrho_1 u_1} - \int_1 \frac{dp}{\varrho u}\right] \qquad (17) \\
&= \frac{2}{\alpha D}\left[\frac{p}{\varrho u} + u - D\right] \\
&= 4\sin^2(\phi/2) \\
&= (V/D)^2 \approx \tan^2\phi
\end{aligned}$$

which is Taylor's (1) Equation (11) when $\tan^2\phi$ is used. In the third line of Equation (17), we have introduced Taylor's notation for the metal case to explosive charge mass ratio, $\alpha = M/C = M/(\varrho_0\pi r_0^2)$, where C is the explosive mass per unit length of cylinder. We have also integrated by parts from the highly compressed state 1 to an expanded state some distance x behind the detonation front (zero width reaction zone). In the third part of Equation (17), we have used Equation (16) to evaluate the remaining integral. In the fourth form, we have eliminated $\varrho_0 D$ in Equation (14) by using Equation (13) to obtain

$$\frac{p_1}{\varrho_0 D} + u_1 = \frac{p_1}{\varrho_1 u_1} + u_1 = D \tag{18}$$

then used Equation (18) in Equation (17). Finally, we have used Equations (6) and (7) to complete the derivation. Equation (17) gives V as a function of the variables p, ϱ and u and the parameters D and α. Taylor went on to find the shape of the case by numerically integrating the equation

$$x = \int_{r_o}^{r} dr/\tan\phi \tag{19}$$

which is derived from $\tan\phi = dr/dx$.

Equation (17) is rarely cited in the literature since p and u do not appear as simple functions of r, although (ϱu) has a simple form in Equation (10). Instead, u must be found from Equation (15) with u_1 given by Equation (13). As was mentioned above, H. Jones evaluated the integral in Equation (15) for Taylor. Once this was done, using $\varrho_0 = 1.51$ g/cm^3 and $D = 6.38 \times 10^5$ cm/s for TNT, Taylor presented his solution in tabular form. The first four columns in Table I here give some of his values for ϱ, p and u as a function of the expansion variable, $\iota = r/r_0$. The row of values in parenthesis has been added for u=D to bring out the point that u≈D, but (D−u) changes sign so that to a laboratory observer (Equation (3)) the gas at first appears to follow the detonation front, then recedes from it. The fifth column in Table I gives experimental values for the case velocity measured in a standard cylinder (27). V in column 6 was calculated from Equation (17). The values in column 5 were interpolated between Short's values for $\varrho_0 = 1.45$ and 1.63 g/cm^3. The values in column 6 lie a little below Short's values for $\varrho_0 = 1.45$ g/cm^3 and about 10% below the values in column 5. This is consistent with Taylor's neglect of the radial component of gas velocity. A variety of other reasons can also be used to explain this discrepancy. Here we only wish to note the rather good agreement, a trend we hope to emulate in a simplified version of Taylor's model to be explained below. Column 7 in Table I was calculated using this simplified version. Before doing this, however, let us examine Gurney's approach to the problem.

GURNEY'S MODEL AND THOMAS' SYNTHESIS

It is clear from Section 3 of his report (2) that Gurney wanted to explain an experimental observation; namely, the fact that the fragment launch speeds of very different size weapons containing the same explosive seemed to depend mainly on the ratio of the mass of the explosive to the mass of the metal; that is, $(C/M)^y$, where y is a power near 0.22 for large bombs, but closer to 0.50 for small projectiles. This led him to his basic assumption which he stated in his abstract and repeated in Section 4 of his report: namely, the contribution made to the total kinetic energy by the detonation of each unit mass of explosive is independent of the size of the projectile. He used the symbol E to denote this constant energy contribution per unit mass and $C = \varrho_o \pi r_o^2$ for the explosive mass per unit cylinder length. Thus, EC is the energy contribution per unit length. Initially, the energy released by the detonation appears entirely as the internal energy of the highly compressed detonation product gases. However, it is rapidly converted into kinetic energies of gas and metal as the case expands until, at the moment of bursting, most of it is in this form. Since Gurney knew from experiments that radial fragment motion completely dominates axial components, he partitioned EC into radial energies of metal and gas, integrating over $\frac{1}{2}\varrho v^2$ for the latter. He took Equation (12) above to be true, using the symbol v_o for v_B, the case velocity at the moment of bursting (equal to the gas velocity at the case), and the symbol a instead of r_B for the case radius at this time. He then wrote his Equation (1):

$$EC = \tfrac{1}{2}Mv_B^2 + \tfrac{1}{2}v_B^2 \int_o^{r_B} 2\pi r \varrho \frac{r^2}{r_B^2}\, dr \qquad (20)$$

Here we are using M for the case mass per unit length, a sum over mass elements which form a ring. Since his basic assumption required EC to be independent of r_B, the integral in Equation (20) must somehow be independent of r_B. Near the top of page 5 in his report, Gurney states that he assumed ϱ to be constant. Clearly he took $\varrho = C/(\pi r_B^2) = \varrho_o r_o^2/r_B^2$, a constant which can be taken outside the integral sign, putting r_B^4 in the denominator. Gurney's reason for assuming a linear dependence of v on r now becomes clear. Equation (12) puts r^2/r_B^2 in the integral. Since the integral of r^3 is $r^4/4$, r_B^4 appears in the numerator to cancel r_B^4 in the denominator and make EC independent of the projectile size. The integral becomes $CV_B^2/4$ and a solution for v_B gives us

$$v_B = \sqrt{2E/\,[(M/C) + \tfrac{1}{2}]} \qquad (21)$$

which is Gurney's widely used cylinder formula.

Gurney was also interested in small projectile warheads and grenades which more closely resemble spheres than long cylinders. His Equation (2) for a cased spherical charge is analogous to his Equation (1):

$$EC = \tfrac{1}{2}Mv_B^2 + \tfrac{1}{2}v_B^2 \int_o^{r_B} 4\pi r^2 \varrho \frac{r^2}{r_B^2}\, dr. \qquad (22)$$

where M is now the case mass and $C = \varrho_o (4/3\pi r_o^3)$ is the charge mass with r the spherical radial coordinate. Again he took $\varrho = 3C/(4\pi r_B^3)$ to be constant which put r_B^5 in the denominator. Of course the integral of r^4 is $r^5/5$ which puts r_B^5 in the numerator, making EC independent of projectile size in this geometry also. The integral becomes $3Cv_B^2/10$, and solution for v_B gives us

$$v_B = \sqrt{2E\,/\,[\,(M/C) + 3/5]} \qquad (23)$$

for a sphere. Gurney noted that Equations (21) and (23) make v_B vary as $(C/M)^{.5}$ for small C/M and as $(C/M)^{.25}$ for large C/M in agreement with the observations he set out to explain as simply as he could. Of course both equations tend to asymptotic values as $(C/M) \to \infty$ (bare charge). By using a value of E about 20% smaller than that estimated experimentally, he was able to obtain reasonable agreement with experiment. As we have seen in our discussion of Equations (11) and (12) above, Gurney was making an excellent approximation in Equation (12). In effect, he was letting u = D in Equation (10) when he let $\varrho = \varrho_B = C/(\pi r_B^2)$, which is very nearly true for bursts which occur for $r/r_o > 1.16$. As Taylor pointed out, the gas density is nearly a constant over an entire plane at any distance x from a moving observer, that is, for any given r/r_o. For a sphere in which only radial motion occurs, the analog of Equation (11) is

$$\frac{1}{r^2}\frac{d}{dr}(r^2 \varrho v) = 0 \qquad (24)$$

which can be considered together with mass conservation

$$C = \varrho_0 \frac{4}{3} \pi r_o^3 = \varrho \frac{4}{3} \pi r^3 \qquad (25)$$

to arrive at Equation (12) in this geometry also. If y is the cartesian coordinate normal to an initially planar explosive/metal interface and the detonation propagates along the x-axis, the analog of Equation (11) is

$$\frac{\partial}{\partial y} (\varrho v) + \frac{\partial}{\partial x} (\varrho u) = 0 \qquad (26)$$

where each term vanishes. Mass conservation requires $\varrho uy = \varrho_0 D y_0$ where y_0 is the initial explosive sheet thickness, so ϱu is not a function of x. For $u \approx D$, $\varrho \approx 1/y$ so $v \sim y$ to make ϱv independent of y.

Thomas (28) a co-worker of Gurney, compared Gurney's and Taylor's models. In his synthesis, Thomas began with a brief description of Gurney's model, generalizing Equations (21) and (23) to include the planar case

$$v = v_B = \sqrt{2E / [(M/C) + n/(n+2)]} \qquad (27)$$

where n=1, 2 and 3 for planar, cylindrical and spherical symmetries respectively. Following this, he gave a brief account of Taylor's model, but used the exact curvature $d\phi/ds = \sin\phi\ (d\phi/dr)$ as Allison and Shriempf (24) did sixteen years later. Thomas went on to solve the Lagrangian equations of motion by a series of successive approximations, using a parameter inverse to the detonation velocity. He obtained Gurney's result as the asymptotic limit of the zeroth order solution in which detonation is imagined to occur simultaneously everywhere in the explosive ($D=\infty$). Taylor's model emerged in higher order solutions. He concluded that Taylor's model should be an excellent approximation. Thomas also considered shocks and concluded that their effect on the energy is slight. After two or three brief reverberations, the motion settles down to an asymptotic form. For very thin shells stepwise shock acceleration at very early times has been observed by Allison and Shriempf (24). Eden and Wright (29) have observed a similar effect for thin plates. Theoretical studies of shock acceleration have also been carried out in recent years, using the method of characteristics (30, 31). Neither of these studies changes Thomas' conclusion that there is no need to consider shock effects when considering the motion of most practical devices.

Let us compare Gurney's model with Taylor's. Gurney's model is more elementary since it relies on an energy partition at a particular moment, while Taylor solves an equation of motion. With Gurney's model, we can only estimate a speed at a given time. With Taylor's model, we can calculate the position (case shape) and velocity (speed and direction) of each case element at any time. For many purposes, a Gurney speed with or without the addition of a Taylor angle is sufficient. If metal trajectories are required, Taylor's model might be preferred. Thomas' solution of the Lagrangian equations could be used, of course, but this is usually too complicated an approach for design work where the aim is insight with minimum effort rather than great precision.

TAYLOR'S MODEL SIMPLIFIED AND EXTENDED

Cylinder Struck Side-On

Since the publication of Taylor's papers by Batchelor in 1963 (1), his model has been more readily accessible to a wider audience than Gurney's report (2) which was, practically speaking, an internal laboratory memorandum which relatively few people have actually read. In spite of this, Gurney's model has been widely used and extended, while Taylor's model has been virtually ignored, except for one equation. Clearly, this is because of the relative simplicity of Gurney's model. In this section we will simplify Taylor's model in order to facilitate its use in problems for which it is appropriate.

As we mentioned after Equation (20) above, Gurney took ϱ to be uniform inside the case for any $\iota = r/r_o$ value. In effect, he took $\varrho = \varrho_o/\iota^2$ where $r = r_B$ (late in the expansion). Equation (10) can be written

$$\varrho = (\varrho_0 D)/(\iota^2 u) = \varrho_0/(\iota^2 f), \qquad (28)$$

where $f = u/D \approx 1$. If we put $\varrho = \varrho_o/\iota^2$ in Equation (1) with $\gamma=3$ and Equation (28) for (ϱu) in the first term of Equation (17), we find

$$\frac{p}{\varrho u} = \left[(B\varrho_0^2) / (Df^3)\right] / \iota^4 = U_B/\iota^4 \qquad (29)$$

which defines U_B. From Figure 1 for a TNT loading density near that discussed by Taylor, we see that $B \approx 2 \times 10^{10}$ (dyne/cm^2 / (g/cm^3)^3 = 2(mm/μs)^2 / (g/cm^3)^2. Consequently, for ϱ_0 = 1.51 g/cm^3 and D = 6.38 mm/μs, U_B = .7/f^3 = 1 mm/μs if f=0.89. This value of f can be taken as an effective value during the acceleration period and enables us to deal with U_B as a constant dependent only on explosive properties.

Next let us approximate u by the formula

$$u = U_\infty - U_B(1/t^2 + 1/t^4), \qquad (30)$$

where U_∞ = 6.914 mm/μs from Table I. If U_B = 1 mm/μs, Equation (30) can be used in Equation (28) to find

$$\varrho = 9.634/\left[6.914\ t^2 - (1 + 1/t^2)\right] \qquad (31)$$

where $\varrho_0 D$ = (1.51 g/cm^3) x (6.38 mm/μs) = 9.634 (g/cm^3) (mm/μs).

If we plot ϱ versus t from Table I and compare with Equation (31) we find them almost indistinguishable. A somewhat smaller U_B would improve the agreement except near t = 1.

We can do the same for u versus t from Table I and Equation (30). Now let us put Equation (29) and (30) in Equation (17) and require V = 0 for t = 1. We find

$$U_\infty = D + U_B, \qquad (32)$$

so that U_∞ can be estimated for any explosive loading from D, ϱ_0, B and f -- knowledge which is available for most cases of interest. We may assume f = 0.89 or use Taylor's f = u/D as a universal function. Equation (17) becomes

$$v = \varrho_0 f^{-3/2} \sqrt{(2B/a)(1 - 1/t^2)} \qquad (33)$$

which does not depend on D explicitly as in Taylor's model (only through ϱ_0 and B). The parameter a=M/C appears in the denominator under a square root sign as in Gurney's formula, although there is no constant added to a since Taylor neglects v compared to u. As

$t \to \infty$ and f $\approx$ 1, $V = \sqrt{(2B\varrho_0^2)/a}$

and $2B\varrho_0^2$ plays a similar role to 2E in Gurney's formula. Here, however, there is an explicit dependence on ϱ_0, as well as that implicit in B and a. It would be desirable to tabulate values of $2B\varrho_0^2$ for cases of practical interest. However, to do a proper job, we should make a critical comparison of p versus ϱ curves calculated by various methods. Alternatively, we can tabulate $2B\varrho_0^2$ from experimental information.

If we use Taylor's values of f in Equation (33) and with a = 2.67 for the standard cylinder, and B = 1.5 instead of 2, we find the values in column 7 of Table I which exhibit a root mean square error of 0.04 mm/μs relative to the six experimental values. Here we are lowering B by 25% much as Gurney lowered E from the value he expected.

Since $V \approx V_r = dr/dt = r_0 dt/dt$, we can integrate Equation (33) with f constant (U_B constant) to find

$$Dt \approx r_0 \sqrt{(aD)/(2U_B)(t^2 - 1)} \approx x \qquad (34)$$

since $v_x = dx/dt = D \cos\phi \approx D$ as was mentioned above in connection with Equation (7). If we put Equation (34) into Equation (2), it is clear that a case element which is seen by a laboratory observer to have very little axial motion ($X \approx X_0$) is said by the moving observer to recede axially at about the detonation speed. Of course, both observers see the same radial motion. We can rewrite Equation (34) as

$$r^2/r_0^2 - x^2/\left[r_0^2 aD/(2U_B)\right] = 1, \qquad (35)$$

which exhibits the approximately hyberbolic form of the case shape in moving coordinates.

Since $V_x/V_r = dX/dr = \tan(\phi/2)$ from Equation (8) and $\tan\phi \approx 2\sin(\phi/2) \approx 2\tan(\phi/2)$, we can integrate Equation (35) with U_B constant, using V = 2D sin (ϕ/2) from Equation (17) to find the X, r path of a case element in laboratory coordinates, namely

$$X - X_0 = r_0 \int_1^t \tan(\phi/2)\,dt \qquad (36)$$

$$= r_0 \sqrt{\frac{U_B}{2aD}}\left[\sqrt{t^2 - 1} - \cos^{-1}(1/t)\right]$$

which also gives us X(t) since t(t) is known from Equation (34). Accelerations as functions of time may also be found. High speed cinematography or a sequential series of still photographs as used by Taylor and Jones (12) could be used to check some of these relationships.

Column 8 of Table I gives experimental values (32) for 64/36 RDX/TNT with ϱ_0 = 1.717 g/cm^3

TABLE I
Numerical Examples

TNT							COMPOSITION B	
1	2	3	4	5	6	7	8	9
$\iota=r/r_o$	ϱ g/cm^3	px10^{-10} dyne/cm^2	u mm/μs	V_{exp} mm/μs	α=2.67 V mm/μs	V (B=1.5) mm/μs	V_{EXP} mm/μs	V (B=1.68) mm/μs
1.000	2.00	15.00	4.83		0	0		0
1.044	1.52	5.59	5.84		.66	.52		.68
1.074	1.39	3.75	6.04		.74	.63		.82
1.159	1.14	1.67	6.31		.88	.82		1.06
(1.217)	(1.02)	(1.15)	(6.38)		(.92)	.91		1.17
1.371	.78	.60	6.48	(1.13)	1.03	1.06	(1.43)	1.38
1.538	.62	.40	6.53	1.20	1.07	1.16	1.49	1.51
1.667	.53	.32	6.55	1.25	1.11	1.22	1.53	1.58
1.883	.41	.20	6.59	1.30	1.17	1.28	1.58	1.66
2.372	.26	.10	6.64	1.35	1.23	1.35	1.66	1.76
3.060	.15	.05	6.67	(1.37)	1.27	1.40	(1.68)	1.82
4.340	.08	.02	6.70		1.32	1.55		2.01
5.680	.04	.01	6.72		1.35	1.55		2.01
	0	0	6.914		34.74			

(α = 2.34) in the standard cylinder. Column 9 gives V calculated from Equation (33) for B = 1.68. This illustrates the fact that Equation (33) can be applied to other explosive loadings.

Plate Struck Side-On

Now let us apply Taylor's model to a planar rather than a cylindrical geometry. The situation is similar to that in Figure 2 except that we will use the Cartesian coordinate y instead of r, so tan ϕ = dy/dx. We will allow the metal plates to have different thicknesses h_i and h_o. We will let the thickness of the explosive sheet be $W_o = 2y_o$. The mass per unit area of each metal plate will be designated by $M_i = \varrho_{Mi}h_i$ with i = 0, 1 where we allow the plates to have different densities ϱ_{Mi} as well as different thicknesses. Equation (4) is now replaced by

$$M_iD^2 \frac{\frac{d}{dx}\left(\frac{dy}{dx}\right)}{\left[1+\left(\frac{dy}{dx}\right)^2\right]^{3/2}} = p \qquad (37)$$

We multiply each side of this equation by $2dy/(M_iD^2) = 2\tan\phi\, dx/(M_iD^2)$ and obtain

$$2\sin\phi\, d\phi = \frac{2}{M_iD^2}\, pdy\,, \qquad (38)$$

where the left side is readily integrated as in Equation (6). Equations (7) and (8) will have V_y instead of V_r but are otherwise unchanged. Equation (10) is replaced by $\varrho_oDy_o = \varrho uy$ and Equation (11) by Equation (26) which we have already discussed. Equations (13) through (16) are unchanged, so the analog of Equation (17) is

$$\frac{2}{M_iD^2}\int_{y_o}^{y} pdy = \frac{2\varrho_oDy_o}{M_iD^2}\int_1 pd\left(\frac{1}{pu}\right)$$

$$= \frac{1}{\alpha_iD}\left[\frac{p}{\varrho u} + u - D\right] \qquad (39)$$

$$= 4\sin^2(\phi/2) \approx \tan^2\phi = (V/D)^2$$

where $\alpha_i = M_i/(2y_o\varrho_o) = M_i/C$ and C is the explosive mass per unit area. We have not

repeated several steps here since they are the same as before. The analog of Equation (19) is

$$x = \int_{y_o}^{y} dy/\tan\phi \qquad (40)$$

Now let us simplify this model. Since $u=D(\varrho_o y_o)/(\varrho y)$ while in Equation (1) $\varrho=\varrho_o/(f\iota)$ where $\iota = y/y_o$ and $f=u/D$, we can write the analog of Equation (29)

$$\frac{p}{\varrho u} = \left[B\varrho_o{}^2/(Df^3) \right] / \iota^2 = U_B/\iota^2 , \qquad (41)$$

where U_B has the same form as in Equation (29).

Now let us approximate u by the formula

$$u = U_\infty - U_B \left(\frac{1}{\iota} + \frac{1}{\iota^2} \right) \qquad (42)$$

which is the analog of Equation (30). Here the inverse powers of ι are n and 2n with n=1, just as they were in Equation (30) with n=2. The spherical analog might consist of a disk-shaped detonation front rotating about a radius, a configuration very difficult to realize experimentally. If we use Equation (42) in $\varrho uy = \varrho_o D y_o$, we find

$$\varrho=\varrho_o D/\left[U_\infty \iota - U_B\left(1+\frac{1}{\iota}\right)\right] \qquad (43)$$

Next, let us put Equations (41) and (42) in Equation (39) and require $V \approx 0$ for $\iota = 1$, giving Equation (32) again. Equation (39) becomes

$$v= \varrho_o f^{-3/2} \sqrt{\left(\frac{B}{\alpha_i}\right)\left(1-\frac{1}{\iota}\right)} \qquad (44)$$

which is the analog of Equation (33) with n=1 replacing n=2 as the coefficient of B and the inverse power of ι.

Since $V \cong V_y = dy/dt = y_o d\iota/dt$, we can integrate Equation (44) with f constant to find the analog of Equation (34)

$$Dt \approx y_o \sqrt{\frac{\alpha_i D}{2U_B}} \left\{ \iota \sqrt{1-1/\iota} + \right.$$

$$\left. \tfrac{1}{2} \ln \left[\iota \sqrt{1-1/\iota} + \iota - \tfrac{1}{2}\right] - \tfrac{1}{2} \ln \tfrac{1}{2} \right\} \approx x \qquad (45)$$

Clearly the case shape (y versus x) is not approximately hyperbolic as it was for the cylinder. Of course we can also integrate Equation (40) with f constant to find the x, y path of a plate element in laboratory coordinates. Use of Equation (45) then gives X(t).

REFERENCES

1. G. I. Taylor, "Analysis of the Explosion of a Long Cylindrical Bomb Detonated at One End," paper written for the Civil Defense Research Committee, Ministry of Home Security in 1941, available in *The Scientific Papers of Sir Geoffrey Ingram Taylor,* Vol. III, G. K. Batchelor, ed., The University Press, Cambridge, 1963, p. 277.
2. R. W. Gurney, "The Initial Velocities of Fragments from Bombs, Shell, Grenades," Ballistic Research Laboratory R405, 1943. (AD ATI 36218)
3. G. I. Taylor, "A Formulation of Mr. Tuck's Conception of Munroe Jets," written in 1943 and available in *The Scientific Papers of Sir Geoffrey Ingram Taylor,* Vol. III, ed. by G. K. Batchelor, The University Press, Cambridge, 1963, p. 358.
4. G. Birkhoff, D. P. MacDougall, E. M. Pugh, and G. I. Taylor, "Explosives with Lined Cavities," *Journal of Applied Physics,* 19, 1948, p. 563.
5. M. A. Meyers and L. E. Murr, eds, Appendix E, "Nomograph for Determination of Flyer-Plate Velocity", *"Shock Waves and High-Strain Rate Phenomena in Metals,* proceedings of an International Conference on Metallurgical Effects of High-Strain-Rate Deformation and Fabrication, Plenum Press, NY and London, 1981, p. 1057.
6. G. E. Jones, J. E. Kennedy, and L. D. Bertholf, "Ballistic Calculations of R. W. Gurney," *American Journal of Physics,* 48, 1980, p. 264.
7. G. E. Jones, "The Gurney Equations for Multilayered Fragments," *Journal of Applied Physics,* 50, 1979, p. 3746.
8. M. J. Kamlet and M. Finger, "An Alternative Method for Calculating Gurney Velocities," *Combustion and Flame,* 34, 1979, p. 213.
9. D. R. Hardesty and J. E. Kennedy, "Thermochemical Estimation of Explosive Energy Output," *Combustion and Flame,* 28, 1977, p. 45.

10. G. I. Taylor and H. Jones, "Note on the Lateral Expansion behind a Detonation Wave," *The Scientific Papers of Sir Geoffrey Ingram Taylor,* Vol. III, G. K. Batchelor, ed., The University Press. Cambridge, 1963, p. 309.

11. G. I. Taylor and H. Jones, "Blast Impulse and Fragment Velocities from Cased Charges," *The Scientific Papers of Sir Geoffrey Ingram Taylor,* Vol. III, G. K. Batchelor, ed., The University Press, Cambridge, 1963, p. 363.

12. G. I. Taylor and H. Jones, "The Bursting of Cylindrical Cased Charges," *The Scientific Papers of Sir Geoffrey Ingram Taylor,* Vol. III, G. K. Batchelor, ed., The University Press, Cambridge, 1963, p. 379.

13. H. Jones, "A Theory of the Dependence of the Rate of Detonation of Solid Explosives on the Diameter of the Charge," *Proceedings of the Royal Society of London,* 189A, 1946, p. 415.

14. H. Jones and A. R. Miller, "The Detonation of Solid Explosives: the Equilibrium Conditions in the Detonation Wave-Front and the Adiabatic Expansion of the Products of Detonation," *Proceedings of the Royal Society of London,* 194A, 1948, p. 480.

15. R. Courant and K. O. Friedrichs, *Supersonic Flow and Shock Waves,* Interscience, NY, 1948, p. 6.

16. G. I. Taylor, "The Dynamics of the Combustion Products behind Plane and Spherical Detonation Fronts in Explosives," *Proceedings of the Royal Society of London,* 200A, 1950, p. 235.

17. S. J. Jacobs, "Recent Advances in Condensed Media Detonations," *American Rocket Society Journal,* 30, 1960, p. 151.

18. M. J. Kamlet and S. J. Jacobs, "Chemistry of Detonations, I: A Simple Method for Calculating Detonation Properties of C-H-N-O Explosives," *Journal of Chemical Physics,* 48, 1968, p. 23.

19. M. J. Kamlet and J. M. Short, "The Chemistry of Detonations, VI: A 'Rule for Gamma' as a Criterion for Choice among Conflicting Detonation Pressure Measurements," *Combustion and Flame,* 38, 1980, p. 221.

20. W. H. Anderson, "Comments on 'The Chemistry of Detonations'," *Combustion and Flame,* 45, 1982, p. 309.

21. M. J. Kamlet and H. Hurwitz, "The Chemistry of Detonations, V: Pressures of C-H-N-O Explosives at Various Stages of the Isentropic Expansion," NOLTR 68-44, 1968 or *Israel Journal of Technology,* 7, 1968, p. 431.

22. A. K. Aziz, H. Hurwitz, and H. M. Sternberg, "Energy Transfer to a Rigid Piston under Detonation Loading," *The Physics of Fluids,* 4, 1961, p. 380.

23. R. W. Gurney, "Fragmentation of Bombs, Shells and Grenades," Ballistic Research Laboratory Report 635, 1947.

24. F. E. Allison and J. T. Schriempf, "Explosively Loaded Metallic Cylinders, II," *Journal of Applied Physics,* 31, 1960, p. 846.

25. F. E. Allison and R. W. Watson, "Explosively Loaded Metallic Cylinders, I, "*Journal of Applied Physics,* 31, 1960, p. 842.

26. R. Courant and K. O. Friedrichs, *Supersonic Flow and Shock Waves,* Interscience, NY, 1948, p. 22.

27. J. M. Short, F. H. Helm, M. Finger and M. J. Kamlet, "The Chemistry of Detonations VII: A Simplified Method for Predicting Explosive Performance in the Cylinder Test," *Combustion and Flame,* 51, 1983, p. 325.

28. L. H. Thomas, "Theory of the Explosion of Cased Charges of Simple Shape," Ballistic Research Laboratory Report 475, 1944.

29. G. Eden and P. W. Wright, "A Technique for the Precise Measurement of the Motion of a Plane Free Surface" Fourth Symposium on Detonation, Naval Ordnance Laboratory ACR-126, 1965, p. 573.

30. B. D. Lambourn and J. E. Hartley, "The Calculation of the Hydrodynamic Behavior of Plane One Dimensional Explosive/Metal Systems," Fourth Symposium on Detonation, 1965, p. 538.

31. N. E. Hoskin and B. D. Lambourn, "The Acceleration of Two Metal Plates in an HE-Metal Sandwich," Seventh Symposium on Detonation, Naval Surface Weapons Center MP 82-334, 1981, p. 811.

32. E. L. Lee, H. C. Hornig, and J. W. Kury, "Adiabatic Expansion of High Explosive Detonation Products," UCRL-50422, Lawrence Radiation Laboratory, 1968.

THE MOTION OF THIN METAL WALLS AND THE EQUATION OF STATE OF DETONATION PRODUCTS*

E. Lee, D. Breithaupt, C. McMillan, N. Parker, J. Kury,
C. Tarver, W. Quirk, and J. Walton
Lawrence Livermore National Laboratory
Univeristy of California
Livermore, California, 94550

This paper reports dynamic high resolution measurements made using metal cylinders and flat plates accelerated by explosives to determine detonation product behavior. By using both thin walled cylinders and plates and by utilizing both streak camera and Fabry-Perot velocimeter techniques, resolution and accuracy greater than previously attained was achieved. As an example, results for LX-14, an explosive containing 95% HMX and 5 % polyurethane, are presented and compared to results of hydrodynamic calculations carried out with an accuracy equivalent to the experimental resolution. Calculations show that cylinder test measurements sample the detonation product equation of state (EOS) at expansion ratios $V/V_o > 1$. Thin flat plates aligned in the plane of the detonation front provide detailed information on the higher compression states ($V_{CJ} > V/V_o < 1.3$). The results of this study confirm earlier work with respect to the pressure derivatives. The results require that $(\partial \ln P/\partial \ln V)_S$ first increase as the products expand from the CJ state.

INTRODUCTION

Accurate experimental measurements of detonation product equations of state are needed both for precision applications and for basic studies of product behavior. The pressure range of interest is from 0.1 GPa to over 40 GPa and a temperature range form 1000°K and 4000°K. Because of the combination of high temperature and very high pressure, static pressure measurement techniques cannot be used to measure the equation of state for the mixture of gases and solids produced in a detonation. For this reason dynamic measurements have traditionally been used to evalaute detonation product equations of state.

Some of the earliest work (1) utilized the dependence of detonation velocity on loading density. A technique using witness materials (2,3) to determine pressure at the detonation front from shock impedance relationships is still used extensively. We have previously shown (4) that the velocity history of an explosively expanded copper cylinder can be used to develop a detonation product equation of state. The earlier work was limited by the geometry of the test and the resolution of our rotating mirror camera (RMC) measurement techniques. In particular, there were large uncertainties in the pressure regime above 10 GPa.

In order to obtain more precise data at high pressures, modifications have been made in the cylinder test and a flat plate test has been developed. Much greater accuracy and resolution can now be obtained by using Fabry-Perot velocimeters.(5) We have also made modifications to the RMC slit measurement technique and have compared the two techniques.

This paper describes the experimental techniques and presents results obtained for the plastic bonded explosive LX-14. The data are

*Work performed under the auspices of the U.S. Department of Energy by the Lawrence Livermore National Laboratory under contract No. W-7405-ENG-48.

used to refine the LX-14 detonation product equation of state previously determined from the cylinder test. Modern computer capacity and speed permits calculations with resolution comparable to the experimental measurements. Detailed material models can be implemented to study both the explosive and the witness materials. We will use hydrodynamic calculations to show the sensitivity of the results to changes in the equation of state.

EXPERIMENTAL

LX-14

The explosive used in this investigation was LX-14 containing 95.5% HMX and 4.5% estane 5702-F1. This plastic bonded explosive contains some HMX crystals that are 400 μ or larger in diameter. The cylinder experiments and most of the flat plate experiments were performed with this material pressed to 98.3 $\pm$ 0.3 percent of theoretical maximum density.

In order to explore particle size effects, a special fine grained version of LX-14 was prepared containing HMX crystals with diameters $< 40\ \mu$. This formulation was used in some of the flat plate experiments.

Cylinder Experiments

The configuration for the cylinder test has been modified for the work described here as shown in Fig. 1. Important features which differ from earlier work (4) are that a large plane wave booster is used to provide an initiation source which is as flat and as nearly normal to the tube axis as possible. The pin rings, one near each end of the cylinder, are used to determine detonation velocity but are also indexed so as to measure any tilt in the detonation wave.

Most of the previous cylinder tests were done with 1.00" inside diameter copper tubes having .100" thick walls. We now use 2.0011 inside diameter tubes with 0.100" thick walls. This geometry provides twice the time resolution in monitoring the pressure change in the detonation products.

In our earlier work two Model 75 streak cameras were used to measure the rate of cylinder expansion by observing the shadow of the back-lighted cylinder moving across the camera slit. A Model 132 streak camera is now also used to monitor cylinder expansion. This

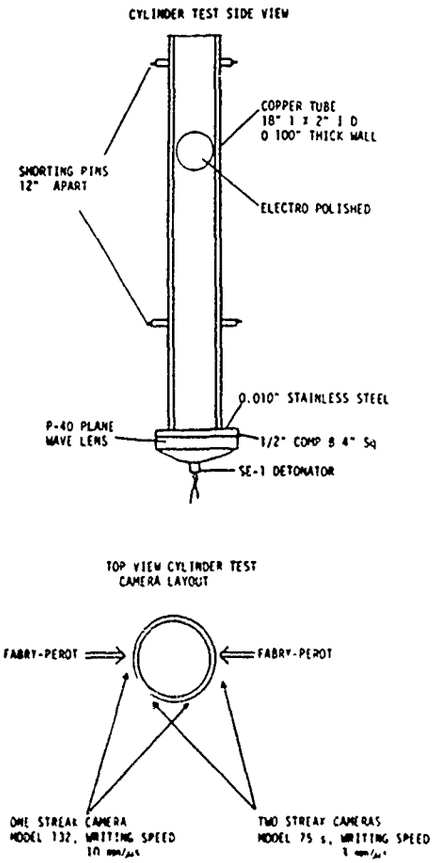

Fig. 1. Cylinder experiment

rotating mirror camera is run over three times as fast as the Model 75 cameras to better resolve the initial wall motion.

The principal modification is the addition of Fabry-Perot velocimeters to measure cylinder wall velocities directly. The two velocimeters are positioned to look at opposite sides of the cylinder at a position close to the same area monitored by the streak cameras. Comparison of results obtained by these independent techniques provide assurance of the precision and accuracy of the measurements.

Flat Plate Experiments

The geometries used in the flat plate experiments are shown in Figs. 2a and 2b. An electric gun (6) was used to initiate all except the 100-mm long LX-14 charges. These charges were initiated with a P-040 lens and 0.50" of Comp. B. Both initiation systems produce flat wave profiles and prompt initiation of LX-14.

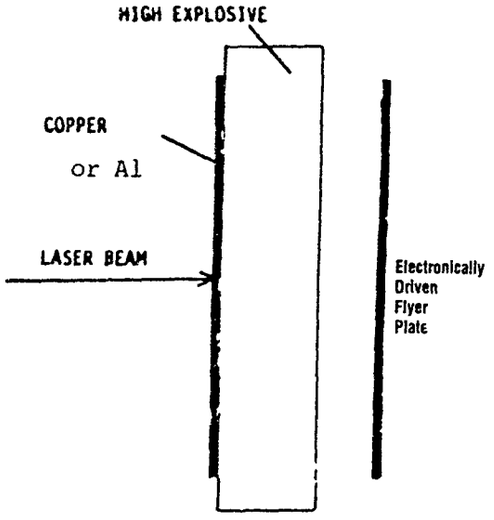

Fig. 2a. Flat plate experiment - electric gun initiation

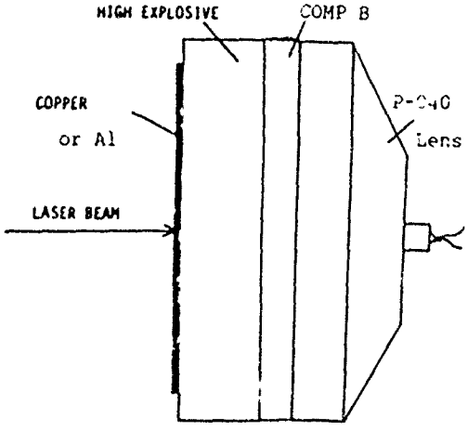

Fig. 2b. Flat plate experiment - plane wave lens initiation

CALCULATIONAL METHODS

The hydrodynamic analysis of the cylinder experiments was done using the 2D Lagrangian code HEMP (7) and the 1D Lagrangian code KOVEC (8) was used for the flat plate experiments. The speed and memory size of the Cray computers now allow fine enough zoning so that calculational resolution using these codes are comparable to the experimental resolution. A series of HEMP calculations were run to determine the effect of varying the zoning in cylinder test calculations. Resolution to that of the experiment was obtained with 0.02-cm axial and 0.011-cm radial zones in the copper and 0.04-cm axial and 0.053-cm radial zones in the explosive. This zoning was used for the cylinder test 2D calculations presented in this report.

The JWL equation of state (4) for the detonation products was used in the hydrodynamic calculations (Eq. 1).

$$P = A\left(1-\frac{\omega}{R_1V}\right)e^{-R_1V} + B\left(1-\frac{\omega}{R_2V}\right)e^{-R_2V} + \frac{\omega E}{V} \qquad (1)$$

where V = relative volume. This form is very flexible and permits analytic calculation of the pressure and energy. The important results are those derived from comparisons of experiments and calculations. These comparisons reveal the precision to which one can determine the equation of state of the detonation products. To this end the results are independent of the form of the EOS.

The Gruneisen equation of state was used for copper and aluminum. The coefficients used in Eqs. 2 and 3 are presented in Table 1.

$$U_s = C + S_1U_p + S_2U_p^2 + S_3U_p^3 \qquad (2)$$

$$P = \frac{P_oC^2\mu\left[1+\left(1-\frac{\gamma_o}{2}\right)\mu - \frac{a}{2}\mu^2\right]}{\left[1-(S_1-1)\mu-S_2\left(\frac{\mu^2}{\mu+1}\right)-S_3\left(\frac{\mu^2}{(\mu+1)^2}\right)\right]^2} + (\gamma_o+a\mu)e \qquad (3)$$

where $\mu = \frac{\varrho}{\varrho_o} - 1$.

TABLE 1

Gruneisen Equation of State Coefficients

	γ_o	C	S_1	S_2	S_3	γ_o	a
Copper	8.93	0.394	1.489	0.0	0.0	2.02	0.47
Aluminum	2.703	0.524	1.40	0.0	0.0	1.97	0.48

CYLINDER TESTS

Experimental Results

The streak camera records obtained from the cylinder test are read on a precision comparator. A computer program converts film coordinates into actual radius (R) at the slit and time, fits the data and calculates the wall arrival time at specified values of $R - R_o$. The results obtained for LX-14 at a density of 1.830 gm/cc are presented in Table 2.

TABLE 2
Radius-Time History of Copper Cylinder Expanded by LX-14

50.8-mm Diameter LX-14 2.725-mm Thick Copper Wall	
$R-R_o$ (mm)	t (μsec)
0	0
1.0	1.01
2.0	1.78
3.0	2.42
4.0	3.02
5.0	3.56
6.0	4.10
7.0	4.60
8.0	5.10
9.0	5.58
10.0	6.07
12.0	7.02
14.0	7.94
16.0	8.85
18.0	9.73
20.0	10.62
25.0	12.80
30.0	14.92
35.0	17.01

The Fabry-Perot velocimeter system consists of a cylindrical lens, a Fabry-Perot interferometer, a spherical lens, and an electronic streak camera. It works on the principle of recording the position vs. time of Fabry-Perot fringes produced by the Doppler-shifting of the reflected light from the cylinder wall. The fringes are produced by virture of the fact that the Fabry-Perot interferometer will pass light in only select discrete angles determined by the Fabry-Perot mirror spacing and the light wavelength. Light reflected from a target moving at constant velocity, though Doppler shifted, will give a static pattern. Accelerating the target will cause the reflected beam to be Doppler shifted to higher frequencies and result in an expanding pattern. The change in pattern is related to the change in velocity by the expression:

$$V(t) = \frac{\lambda c}{4L}\left[\frac{D_1^2(t)-D_{10}^2}{D_{20}^2-D_{10}^2}+m\right] \quad (4)$$

where λ = the initial beam wavelength, c = the velocity of light, L = the separation of the Fabry-Perot mirrors, D_{10} and D_{20} are the spacing of adjacent pairs of lines in the static pattern, and $D_1(t)$ is the spacing of the expanded pattern. Should the velocity excursion exceed the range between fringes, m is the number of fringes traversed.

In order to compare the cylinder test data from the Fabry-Perot velocimeter with the radius/time data taken from the rotating mirror streaking camera (RMC), it is necessary to make two adjustments, one in amplitude, the other in time. These adjustments are needed because the Fabry-Perot and the RMC are actually measuring two very different quantities. The RMC measures what might be called an "obscuration rate."

Referring to Fig. 3 for the geometry, the slit velocity can be written

$$V_S = V_d \tan\theta_S \quad (5)$$

where V_S is the velocity as measured along the slit of the RMC, V_d is the detonation velocity of the HE, and θ_S is the local angle of the cylinder surface relative to the unperturbed surface. The Fabry-Perot measures the particle velocity scaled by the dot product of the particle direction and the laser beam direction. This can be written

$$V_{fp} = V_p \cos(\theta_p - \theta_L) \quad (6)$$

where V_{fp} is the velocity as measured by the Fabry-Perot, V_p is the magnitude of the particle velocity, θ_p and θ_L are the angles formed by the particle trajectory and the laser with the original normal to the cylinder surface.

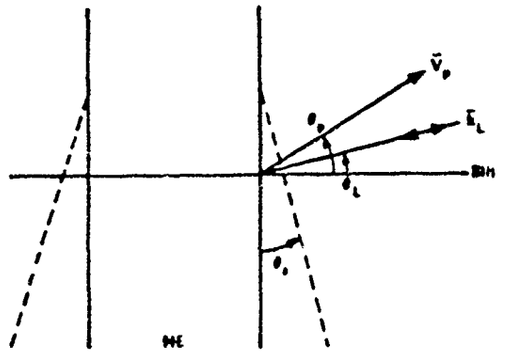

Fig. 3. Vector diagram of cylinder test wall motion

θ_S and $\vec{V}_P$ are related through the hydrodynamics of the cylinder shot. Two simplifying assumptions make it possible to generate an analytical relation between them. First, that the flow is self similar, second that the particle trajectories are adequately approximated by straight lines. The second, assumption is supported by hydrodynamic code calculations. From these assumptions, a relation between V_S and V_{fp} can be generated of the form:

$$V_S(t) = AV_{fp}(t+\Delta t) \qquad (7)$$

where:

$$A=\left[\frac{\cos(\theta_P-\theta_L)}{\cos\theta_P}-V_{fp}(t+\Delta t)\frac{\tan\theta_P}{V_d}\right]^{-1},$$

$$\Delta t = r(t)\tan\theta_L/V_d,$$

and

$$r(t) = \int_0^t V_S(\tau)\,d\tau$$

This relation has been tested by using the HEMP code to calculate both the Fabry-Perot record and the record that would be seen by the RMC. The transform was identical to the hydrodynamic code results.

The procedure described above for converting Fabry-Perot velocity measurements to velocities in the RMC slit plane was used on the LX-14 experiments in which the radius/time history (Table 2) was measured with streak cameras. The average for the two experiments is presented in Fig. 4 and compared to the streak camera results in the next section.

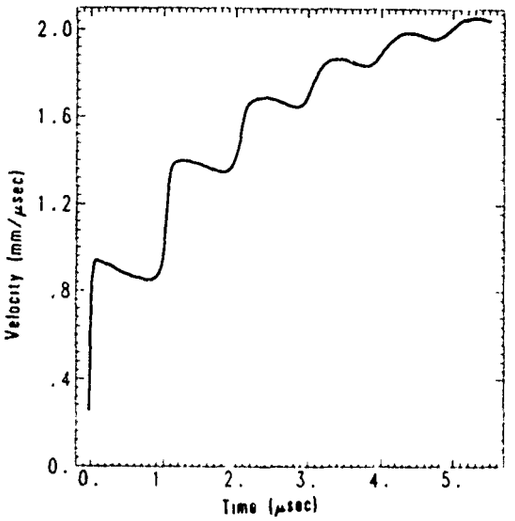

Fig. 4. Fabry-Perot determined average cylinder wall velocity from two LX-14 experiments

Comparison of Fabry-Perot and RMC Results

Results from the different diagnostic techniques were compared in two ways, to examine reproducibility from experiment to experiment, and to examine any systematic difference between the diagnostic techniques. Table 3 compares wall velocities at $R - R_o = 6.5$ mm.

TABLE 3

Cylinder Wall Velocity Comparison

Exp. No.	Density (gm/cc)	D (mm/μsec)	Average Velocity at $R-R_o = 6.5$ mm	
			RMX	F−P
K520	1.830	8.79	1.986	1.980
K521	1.830	8.80	1.976	2.000

Streak camera radius/time data has to be differentiated to make this comparison. Figure 5 presents the difference in expanded cylinder radius as a function of time. Fabry-Perot velocity/time data were integrated to make this comparison. The overall uncertainty in velocity is estimated as approximately 1/2% resulting in a 1% uncertainty in the cylinder wall energy.

Hydrodynamic Calculations

LX-14 cylinder test calculations have been done using four different equations of state (EOS) for the detonation products. The CJ parameters and EOS constants are presented in Table 4. The JWL EOS 370A is based on earlier cylinder test data and an estimated P_{CJ} of 370 kbars. The JWL EOS 336A and the

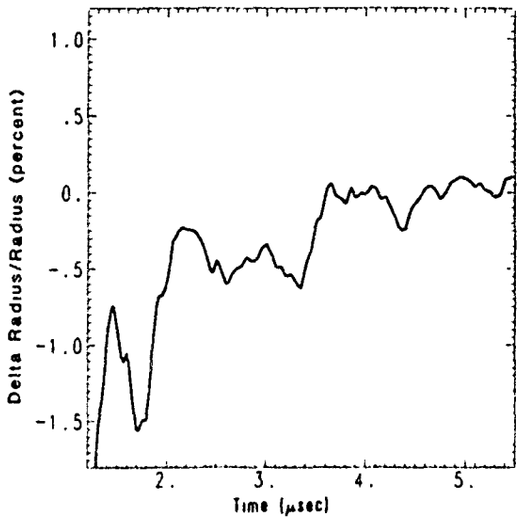

Fig. 5. Difference between streak cameras and Fabry-Perot velocimeters in cylinder radius/time history measurements for LX-14

gamma law EOS 370G were used to illustrate the sensitivity of the calculated results to changes in EOS. The JWL EOS 360A is the revised EOS for LX-14 based on the experimental results presented in this paper.

Figure 6 represents cylinder wall velocities at early expansions calculated with equations of state having P_{CJ} of 370 kbars and P_{CJ} of 336 kbars. The results are almost identical showing that P_{CJ} does not uniquely determine early wall motion. The cylinder results, however, are sensitive to pressure and energy changes in an EOS at relative volumes for the detonation products greater than ~1.1. The flat plate test described below is used to resolve changes in an EOS at lower relative volumes.

The fractional energy change in the detonation products during expansion corresponds closely to the change in cylin ler wall velocity squared. Figure 7 presents this detonation product energy change for various equations of state relative to that of JWL EOS 370A. Delta E is defined as:

$$\delta E = \frac{(\Delta E \text{ EOS(x)} - \Delta E \text{ EOS 370A})}{\Delta E \text{ EOS 370A}} \qquad (8)$$

TABLE 4
CJ Parameters and Equation of State Coefficients

Label	370A	360A	336A	370G
Parameters				
P	.370	.360	.336	.370 mb
ϱ_o	1.835	1.835	1.835	1.835 b/cm^{-3}
D	.880	.880	.883	.880 cm/sec
E_o	.102	.102	.088	.1005 mb
Γ	2.84	2.947	3.258	2.84
Coefficients				
A	8.261	11.65	129.46	-0-
B	.1724	.5572	1.693	-0-
C	.01296	.01844	.00183	.1303
R_1	4.55	5.4	9.6	4.
R_2	1.32	2.0	2.5	2.
ω	.38	.45	.1	1.84

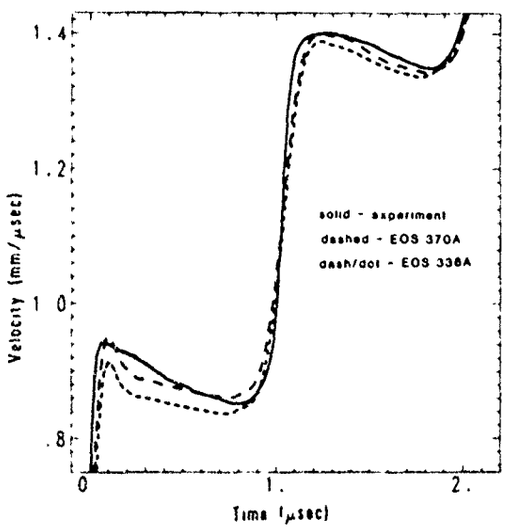

Fig. 6. Early cylinder motion calculated with P_{CJ} = 370 kbar and P_{CJ} = 336 kbar equations of state for LX-14

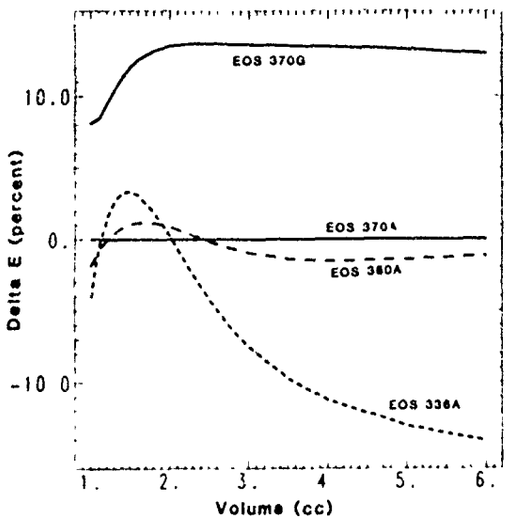

Fig. 7. The relative fractional energy change in the detonation products for the equations of state used in this study

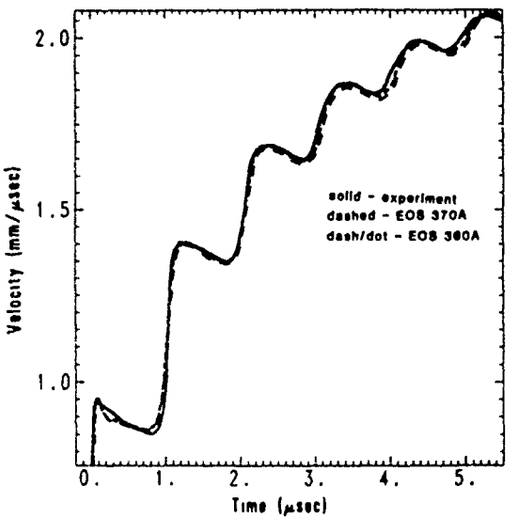

Fig. 8. Comparison of cylinder wall velocities predicted by the old and the revised equations of state with LX-14 experimental data

The revised LX-14 EOS 360A is very close to EOS 370A at all expansions and they both match the experimental cylinder data within experimental error as shown in Fig. 8. (EOS 360A was chosen over that previously used because it is more consistent with the flat plate data described below.) EOS 336A matches cylinder results reasonably well at early expansions but underestimates cylinder wall velocities at larger expansions. The gamma law EOS 370G calculates wall velocities higher than experiment over the entire range of expansion.

FLAT PLATE TESTS

Experimental Results

Nineteen flat plate experiments using LX-14 and copper were performed in the geometries depicted in Fig. 2. They were grouped into five categories characterized by the ratio of the copper plate thickness to LX-14 thickness. See Table 5. These categories tend to emphasize different high pressure EOS regimes.

TABLE 5
Metal to Explosive Ratios for Flat Plate Experiments

Length Cu/ Length LX-14	No. of Exps.	Plate Thickness (mm)	
		Minimum	Maximum
0.001	3	0.025	0.025
0.006	5	0.123	0.257
0.013	1	0.126	0.126
0.026	9	0.505	2.502
0.053	1	0.532	0.532

The Fabry-Perot records for these experiments were reduced to velocity/time histories in a manner similar to that used in the cylinder test. However, a particle velocity vector correction was not necessary since the plate motion is aligned with the impinging laser light.

Detailed velocity/time histories similar to that shown in Fig. 9 were obtained for each experiment and were used in comparisons with hydrodynamic calculations. In order to summarize the results for this report, average velocities for various stages of plate acceleration were defined as shown in Fig. 9 and are presented in Table 6. Results for two LX-14 experiments with aluminum plates are also presented in Table 6.

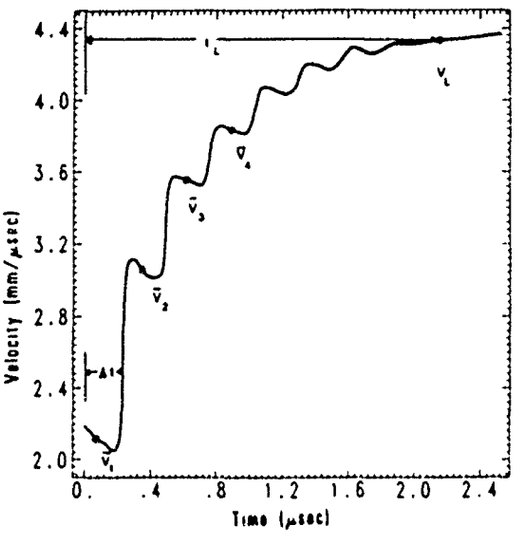

Fig. 9. Typical Fabry-Perot velocity results from the flate plate test (The average velocities and times depicted correspond to the values listed in Table 3.)

Examination of the data presented in Table 6 shows significant scatter in early time velocities. Explosive inhomogenities due to the presence of large HMX crystals were considered a possible cause. However, the four experiments done with all fine grained HMX do not support this conclusion. Further work is required to pinpoint the cause of this scatter that is well outside the precision of the Fabry-Perot measurements.

Hydrodynamic Calculations

The detonation product equations of state listed in Table 3 and others were used to calculate the flat plate experiments. Figures 10 and 11 present the results from such calculations for a typical experiment. In the flat plate test the initial plate velocity is directly related to the detonation front pressure. As can be seen in Fig. 10, a gamma law EOS and a JWL EOS with P_{CJ} of 370 kbars give the same initial velocities. Subsequent velocity increments are substantially different, however. The gamma law EOS predicts velocities higher than measured, whereas the JWL EOS is in close agreement with this experiment.

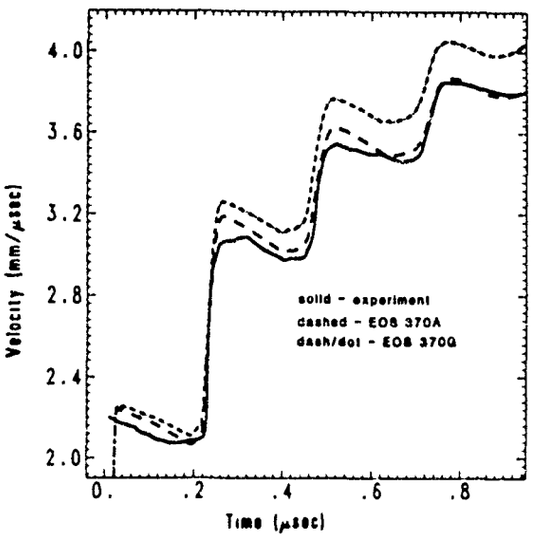

Fig. 10. Flat plate velocities predicted by two equations of state with P_{CJ} = 370 kbars

Figure 11 presents results for two JWL equations of state with different detonation pressures. Similar comparisons for all the experiments in Table 6 lead to the choice of 360 kbars for P_{CJ} and the use of EOS 360A for the comparisons between calculations and experiments presented in the Table.

The initial plate velocities measured for the very thin 0.025 mm copper plates are much higher than those measured for thicker plates. This clearly indicates that "von Neumann spike" effects are present. Figure 12 compares experiment to calculations done with and without a reactive flow model using the JWL 370A EOS for the products. The calculation using a reactive flow model proposed by Tarver (9) is in close agreement with the experiment.

TABLE 6

Flat Plate Experimental Results

SHOT	#9642	#9643	#9632	#9495	#9579	#9526	#9635	#9636	#9524
Copper Thickness (mm)	.0254			.123		.126	.257		.126
LX-14 Length (mm)	25.58			20.18		19.97	40.15[c]		10.00
$X_{Cu}/X_{LX\text{-}14}$	.0010			.0061		.0063	.0064		.0126
$\sim\Delta t$[a] (μsec)	.01			.05		.05	.10		.05
$\bar{V}_1$ (mm/μsec)	2.43[b] (+10.5%)	2.49 (+13.5%)	2.63 (+19.5%)	2.10 (−2.5%)	–	2.20 (+2%)	2.24 (+3.5%)	2.05 (−5%)	2.11 (−2%)
$\bar{V}_2$ (mm/μsec)	3.56 (+5%)	3.60 (+6%)	3.66 (+7.5%)	3.16 (−5%)	3.17 (−4.5%)	3.22 (−3%)	3.36 (+1.0%)	3.20 (−3.5%)	3.11 (−4.5%)
$\bar{V}_3$ (mm/μsec)	4.24 (+2.5%)	4.22 (+2.5%)	4.28 (+3.5%)	3.85 (−4%)	3.83 (−4.5%)	3.83 (−4.5%)	4.00 (0%)	3.88 (−3.5%)	3.72 (−3.5%)
$\bar{V}_4$ (mm/μsec)	4.68 (+1.5%)	4.64 (+.5%)							
$\bar{V}_L$ (mm/μsec)	5.60 (−1.5%)	5.48 (−.5%)				5.86 (0%)	5.50 (+2%)	5.37 (−.5%)	5.31 (−.5%)
t_L (μsec)	.08	.076				1.0	1.0	1.0	1.0

SHOT	#BP1	#BP2	#9578	#9577	#9634	#9633	#9527	#BP5	#BP6	#9528
Copper Thickness (mm)	2.502	2.520	.505		.526		.530	2.530	2.530	.532
LX-14 Length (mm)	101.61	101.60	20.15		19.95[(c)]		20.00	92.02	91.07	10.01
X_{Cu}/X_{LX-14}	.0246	.0248	.0251		.0265		.0265	.0265	.0275	0532
$\sim\Delta t$[(a)] (μsec)	1.00	1.00	.20		.20		.20	1.00	1.00	.20
$\bar{V}_1$ (mm/μsec)	2.14[(b)] (+1%)	2.17 (+2.5%)	2.02 (−4%)	2.22 (+6%)	2.12 (+1.5%)	2.12 (+1.5%)	2.11 (+1%)	2.11 (−.5%)	2.15 (+1.5%)	2.03 (+1%)
$\bar{V}_2$ (mm/μsec)	3.08 (+.5%)	3.16 (+3%)	3.04 (−1%)	3.09 (+1%)	3.07 (+1%)	3.03 (−.5%)	3.03 (−.5%)	3.06 (+.5%)	3.06 (+.5%)	2.79 (+1%)
$\bar{V}_3$ (mm/μsec)	3.60 (+1%)	3.67 (+3%)	3.62 (+2%)	3.60 (+1.5%)	3.55 (1%)	3.50 (−.5%)	3.57 (+1.5%)	3.55 (+.5%)	3.57 (+1%)	3.11 (+1.5%)
V_L (mm/μsec)			4.42 (+2%)	4.43 (+2%)	4.31 (+.5%)	4.35 (+1.5%)	4.35 (+2%)			3.42 (+1%)
t_L (μsec)			2.0	2.0	2.0	2.0	2.0			1.4

SHOT	#9586	#9587
Aluminum Thickness (mm)	.515	
LX-14 length (mm)	20.23	
$X_{AL}/X_{LX\text{-}14}$	.0255	
$\sim\Delta t$[(a)] (μsec)	.17	
$\bar{V}_2$ (mm/μsec)	4.79 (+1.5%)	4.65 (−1.5%)
$\bar{V}_3$ (mm/μsec)	5.22 (+1.5%)	5 10 (−1%)
V_L (mm/μsec)	5.87 (+1%)	5.82 (0%)
t_L (μsec)	1.5	1.5

[a] See Fig. 9 for definition of t and V

[b] Numbers in ( ) are differences of experimental velocities and those calculated with LX-14 EOS #360A.

[c] Special formulation with small particle size HMX.

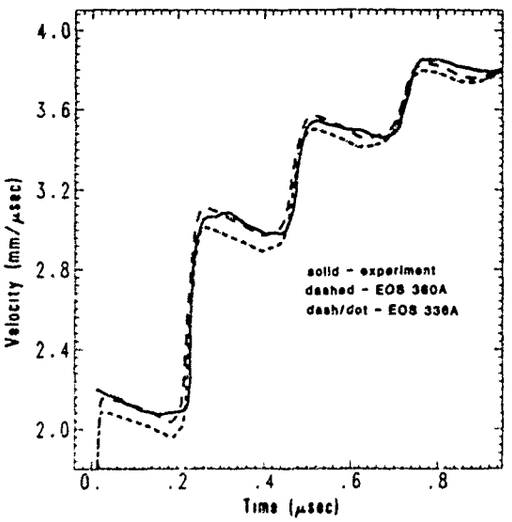

Fig. 11. Differences in flat plate velocities predicted by P_{CJ} = 360 kbar and P_{CJ} = 336 kbar equations of state

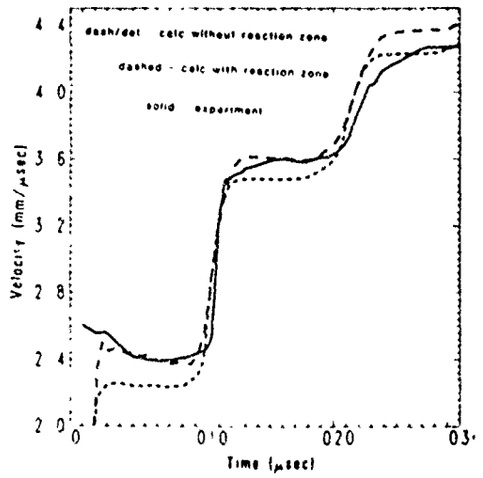

Fig. 12. Initial velocity of a very thin copper plate showed the effect of the reaction zone

The comparisons of experiment with calculation presented in Table 6 show three regimes. For very thin plates (0.025 mm) the effect of the reaction zone is apparent. The measured early velocities are higher than those calculated without a reactive model. Experiments with plates about 0.1 to 0.2-mm thick have early velocities considerably less than those calculated. If the plate is thicker than about 0.5-mm, the calculations agree fairly closely with experiment. No single EOS could be found (even using the reactive model) which would bring the results from all three regimes into perfect agreement. This is strongly indicative of time-dependent effects taking place later than those normally associated with the LX-14 reaction zone. Investigations in this area are continuing.

Several calculations were run to show the effect of different equations of state on plate velocity for both a thin and thick copper plate accelerated by 30-mm of LX-14. Figure 13 shows the pressure difference for the two equations of state, EOS 370A and EOS 336A, where:

$$\delta P = [P \text{ EOS } 336A] - [P \text{ EOS } 370A] \qquad (9)$$

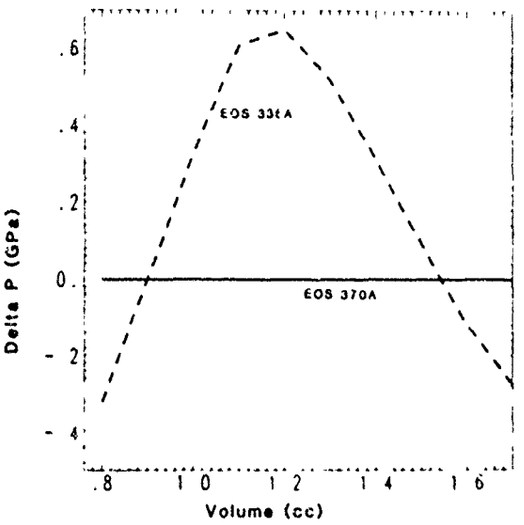

Fig. 13. Differences in pressure at small relative volumes for P_{CJ} = 370 kbar and P_{CJ} = 336 kbar equations of state

Figure 14 presents the results for the 0.127-mm copper plate. The initial velocity difference is due to the difference in P_{CJ}. The later velocities are primarily determined by the differences in pressure below a relative volume of 1.1.

Figure 15 presents the calculations for the 0.635-mm plate. This plate is five times as thick

as th thin" plate discussed above. The initial veloc .y difference is again determined by the differences in P_{CJ}. The velocity difference at later times however decreases because in this case the velocity history is determined by the pressure at relative volume up to about 1.5.

CONCLUSIONS

Improvements have been made both in experimental techniques and in our hydrodynamic calculational analysis which together permit a more precise determination of the equation of state of explosives. Experiments measuring the early expansion data of the products of LX-14 were reproducible to within 4% in energy while those emphasizing larger expansions were within 2% in energy. The empirical detonation product equation of state thus generated is useful both for designing metal/explosive assemblies and as a check on "first principle" equations of state.

The conventional definition of P_{CJ} was used throughout as a convenient initial condition at the shock front. We have considered "von Neumann spike" phenomena and accounted for the effects. We have not treated the problem of kinetic effects with longer time scales but have certainly not ruled out such effects. An "effective" shock front pressure and particle velocity corresponding to P_{CJ} = 360 kbars are consistent with the experimental results described here.

If the products are treated as an equilibrium mixture of gases and condensed phases, the expansion described here is the proper description. On this basis our results show that the isentrope index $\Gamma = (\partial \ln P/\partial \ln V)_S$ region of $V_{CJ} < V < 1.1$ in order to match the experimental data.

There is a small but clearly discernible discrepancy between the "thin" plate and "thick" plate results which has not been resolved by varying the EOS. Further experimental tests will be required to establish the exact nature of this discrepancy. Nevertheless kinetic effects beyond the "von Neumann spike" must be considered.

We believe that a consistent treatment of longer time scale (>0.1 μs) kinetic effects such as the form. ion of solid carbon following the detonation front may very well be required to explain the experimental results and would alter this equilibrium description.

ACKNOWLEDGMENT

We wish to acknowledge the considerable contributions of C. Pruneda, L. Meegan, and H. Chau to material preparation, test assembly and Fabry-Perot operation.

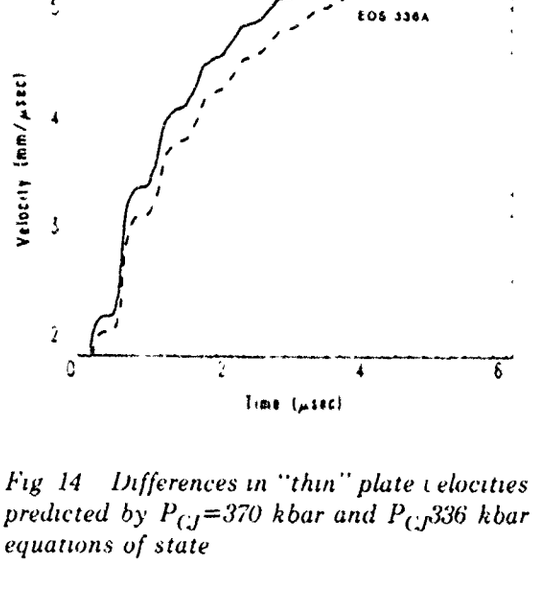

Fig 14 Differences in "thin" plate velocities predicted by P_{CJ}=370 kbar and P_{CJ}336 kbar equations of state

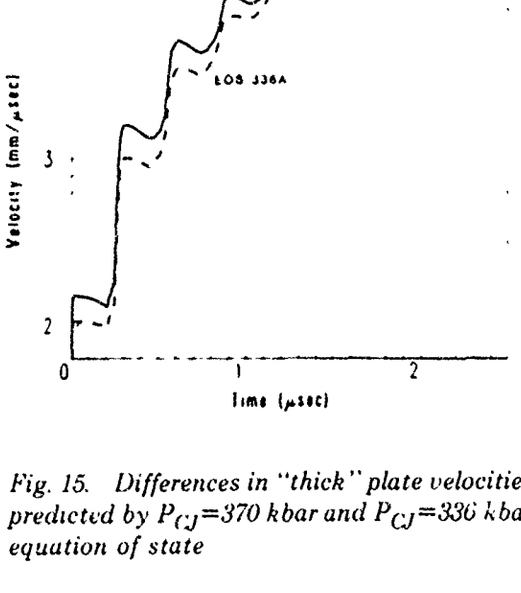

Fig. 15. Differences in "thick" plate velocities predicted by P_{CJ}=370 kbar and P_{CJ}=336 kbar equation of state

REFERENCES

1. H. Jones and A. R. Miller, "The Detonation of Solid Explosives," *Proc. Roy. Soc. London, A-194,* 480 (1948).
2. J. M. Walsh, M. H. Rice, R. G. McQueen, and F. L. Yarger, "Shock-Wave Compressions of Twenty-Seven Metals. Equations of State of Metals," *Phys. Rev. 108,* 196-216 (1957).
3. W. E. Deal, "Measurement of the Reflected Shock Hugoniot and Isentrope for Explosive Reaction Products," *J. Chem. Phys. 27,* 796 (1957).
4. E. L. Lee, H. C. Hornig, J. W. Kury, "Adiabatic Expansion of High Explosive Detonation Products," UCRL-50422, TID-4500, UC-4 Chemistry, Lawrence Radiation Laboratory, University of California, Livermore, CA, May 2, 1968.
5. H. Chau, D. Goosman, J. Lyle, and M. Summers, "A Simple Velocity Interferometer System," Conference on Laser and Electro-optical Systems, OSA/IEEE, Abstract TUHH4, p. 20 (1978).
6. M. L. Wilkins, "Methods in Computational Physics," Vol. 3 Academic Press Inc., N.Y., 1964, pp. 211-263.
7. R. C. Weingart, et. al., "Acceleration of Thin Flyers by Exploding Metal Foils: Application to Initiation Studies," Sixth Symposium (International) on Detonation, August 1976.
8. J. P. Woodruff, "KOVEC User's Manual," Lawrence Livermore National Laboratory Report, UCID-17306, September 1976.
9. C. M. Tarver, et. al., "Modeling Short Pulse Duration Shock Initiation of Solid Explosives," Eighth Symposium (International) on Detonation, July 1985.

DISCUSSION

M. HELD, MBB Apparate, Germany

How do you correct the shock wave in the air; in the streak record; and in front of the expanding copper?

REPLY BY E. LEE

The correction is very small, so that we normally ignore it. Tests in vacuum and comparisons with the Fabry-Perot measurements reveal that the magnitude of the error introduced is less than 1% for the initial velocity, and negligible for larger expansion.

DISCUSSION

DOUG LIND, Naval Weapons Center

What is the optimum metal to use for these experiments?

REPLY BY E. LEE

In earlier work, in addition to cooper, we performed tests using aluminum, tantalium, nickel and lead. Copper and aluminum tubes were the most fracture resistant, yielding reliable records at large expansion. Copper was chosen primarily to take advantage of its low sound speed and (for our purposes) higher density. Tantalum is more spall resistant than copper and thus makes a better choice for thick-walled tests. Of course tantalum is very expensive and more difficult to fabricate.

DISCUSSION

GERALD KERLEY, Sandia National Laboratory, Albuquerque

How much information do the cylinder tests provide for calibrating the linear terms in JWL? Francis Ree has predicted isentropes that agree with JWL for pressures above a few kbar but deviate at lower pressures. When his EOS is used in hydro simulations, do the predictions agree reasonably with the experiments?

REPLY BY E. LEE

I assume you are referring to the last term in the EOS, $\frac{\omega E}{V}$, or $\frac{C}{V^{\omega+1}}$ in the isentrope. The late expansion in the cylinder test contrains the behavior of ω if E_0 is fixed by thermo chemical information. The test will reveal pressure differences at pressures as low as .5kb.

For the special explosive, PETN, we have not run the cylinder test calculations for F. Ree's EOS, however, the pressure differences lead us to believe the results would be somewhat outside experimental error at large expansion.

We have examined F. Ree's EOS for LX-14 in cylinder test calculations. They are too low in energy to calculate the initial velocities.

INFLUENCE OF TEST CONDITIONS ON THE BALLISTIC CLASSIFICATION OF EXPLOSIVES*

J. Souletis - J. Mala

Société Nationale des Poudres et Explosifs

Centre de Recherches du Bouchet
91710 Vert-Le-Petit - France

The influence of the sample transverse dimensions on the results of a symetrical double lateral driving test is analysed. This test is applied to four cast-cured PBX. The results are compared as regards the various geometries and the subsequent ballistic classifications are related to the result obtained with a studied shaped charge.

INTRODUCTION

In many warheads, the energy that is released by the detonation of the explosive is used to propel a metal liner. The energy transfer occuring between the detonation products and the liner defines the ballistic performances of the explosive in the use configuration that is taken into consideration. Therefore, the research and the adjustment of explosive compositions having improved ballistic performances are based on the evaluation possibilities of such a transfer. Generally, this evaluation is carried out, at least as a first step, by means of simple tests which involve a tangential scanning of the metal liner by the detonation wave.

Among these tests, the so-called "ballistic capacity" tests are the most frequently used in France to characterize the new explosive compositions. They use the propulsion of plane metal plates by parallelopipedic explosive slab in order to determine the optimal energy transfer. These tests have some advantages associated to the use of a simple geometry for the samples. Moreover they do not require a precise knowledge of the mechanical behaviour of the plates. On the other hand, they have the disadvantage to be sensitive to rarefaction waves coming from the unconfined sides of the explosive, and particularly those coming from the edges of the sample.

*Work performed under the auspices of the French Ministry of Defense (STPE).

That means that the results should depend on the conditions of the experiment and on the dimensions taken for the set up as well. Moreover, for a given test configuration, the disturbance coming from the expansions may greatly vary according to the considered type of explosive. Indeed, for some compositions of thick reaction zone, the expansions when occuring too early or when being too strong may well lead to freeze late chemical reactions, and thus still more noticeably influence the ballistic performances.

The purpose of the present work is to study the influence of the testing conditions on the results obtained with ballistic capacity tests for various explosive compositions.

DESCRIPTION OF THE TESTS

The standard test to measure the ballistic performances was defined by M. Defourneaux and L. Jacques (1,2). It is a method of measuring by means of flash radiography the lateral driving angle of a metal plate that is placed on the largest side of a parallelopipedic explosive sample initiated on its smallest side.

Several experiments with plates of different thicknesses enable to determine the relationship between the lateral driving angle φ and the metal/explosive mass ratio μ. From the knowledge of this relationship and of the detonation velocities, the values of kinetic energy E transmitted to the liner may be approximated with the hypothesis of a two-dimensional and steady

flow in a system of axes associated to the detonation front. It is then shown that, for a certain value of μ, the transmitted energy goes through a maximum, the amplitude of which measures, by definition, the ballistic capacity (CBV_1) of the considered explosive.

In this study, the standard test was modified in order to limit the expansions coming from the unconfined side and at the opposite of the side where the lateral driving is observed. The modification consists in attaching on this side a metal plate that is similar to the existing one, thus leading to a symetrical sample in a sandwich form. In that last configuration, it is foreseen, in theory, that if the lateral driving is perfectly two-dimensional and steady, the E (μ) function has no maximum but that it is continually increasing and presenting an asymptote when $\mu \rightarrow \infty$. Indeed, in the case of the sandwich, the presence of a maximum is still experimentally noticed; its existence can only be due to the effects of the edges, that is to say to the finished size of the set up. Therefore, in order to quantify this influence, the dimensions of the sample were varied, and particularly the width (L) and the thickness (e) of the explosive slab.

As for the standard test, the sandwich is initiated at one of its ends by a liner wave generator. The studied explosive thicknesses are equal to 10, 20 or 30 mm. The linear plates are made of mild steel. Their thicknesses are between 1 and 8 mm. Their width is slightly less than that of the explosive slab ($L/L_p = 1.125$). During each firing, the detonation velocity D is measured as well as the angle φ of one of the two metal plates, from a RX negative taken at the end of the detonation propagating (see Fig. 1). The relationship $\varphi(\mu)$ is established with five to six experiments; from this relationship the transmitted energy is calculated with the following formula:

$$E = \mu \varrho_0 D^2 \left[1 - \cos\varphi \ (\mu) \right] \qquad (1)$$

The value of the energy maximum (CBV_2) is got from there; it is characteristic both of the composition and of the geometry of the test.

SELECTION OF COMPOSITIONS TO BE STUDIED

Four explosive compositions were selected for study; they were likely to behave differently in the considered test type. The selected substances are curable plastic bonded explosives; their compositions are shown in Table 1.

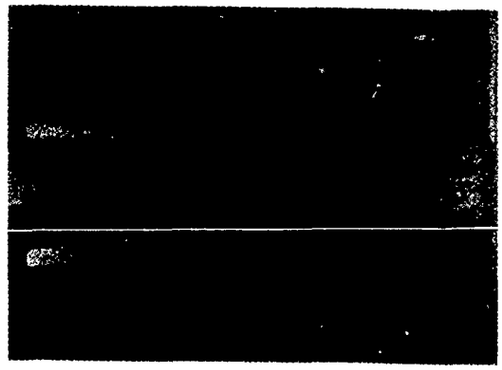

Fig. 1. Typical radiograph viewing the lateral driving of the two plates

TABLE 1

Explosive	Components	Composition (by weight)	Density (g/cm^3)
B 2142	PETN/PU	77/23	1.490
P 2100 B	HMX/HTPB	88/12	1 700
B 2174	HMX/AP/Pb $(NO_3)_2$/PU	47/30/11·12	1.830
B 2161	HMX/AP/Al/PU	40.30/20/10	1 860

AP: ammonium perchlorate,
PU: polyurethane binder.

TABLE 2
Detonation Characteristics

Compositions	D_{co} (m/s)	P (GPa)	Critical Thickness e_c (mm)	Critical Diameter θ_c (mm)	a (mm)
B 2142	7510	19 6	⩽1	⩽1	0 1
P 2100 B	8570	29 5	⩽1	⩽1	0 5
B 2174	7840	30 5	6	12	2 6
B 2161	7310	21 0	8	15	2 4

Table 2 presents the measured values of some of their detonation characteristics. The reaction zone lengths a were assessed with the Eyring method from detonation velocities measured in cylindrical cartridges (see Fig. 2) of various

diameters. It can be noted that the said values are consistent with the measured critical dimensions. The pressure P is measured, in an indirect way, by chronometry of the wave induced in a PMMA block. The value D ∞ of the ideal detonation velocity is extrapolated from the curves in Figure 2.

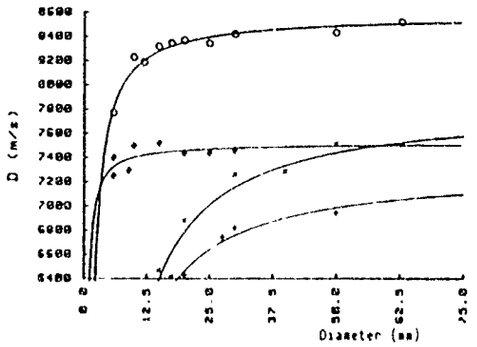

Fig. 2.

ANALYSIS OF SANDWICH TEST

Figure 3 shows the energy curves obtained for the composition B 2174 in the various geometries of the test. The expansions by the edges totally change the nature of the system as they lead to a maximum of the energy curve whereas the curve is increasing up to an asymptotic value in a two-dimensional system. Therefore the sample dimensions are playing an essential part as regards the energy transfer between the explosive and the plate.

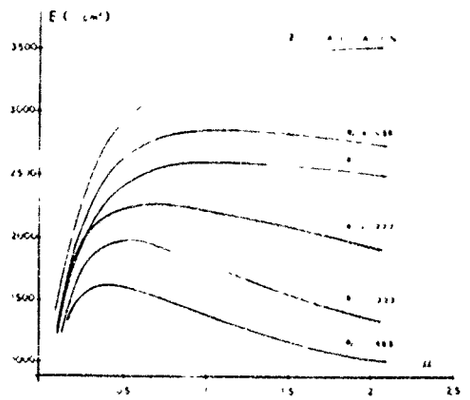

Fig. 3

When making the sample height vary, it is noted that the flow is steady rather soon, from the very fact of using a linear wave generator at the initiation end. However, the flow that is established is directly related to the sample geometry and particularly to the parameters e and 1 (thickness and width). An increase of width leads to a decrease of the detonation front curvature and, from this very fact, to an increase of the area that is not affected by the expansions behind the front. On the other hand an increase of thickness leads to an increase of the distance behind the front that is necessary to create an identical driving, for a given μ.

If indeed the width stays constant in this last case, the area that is not affected by the lateral expansions is about the same, and that leads to a much lower output in the energy transfer. Therefore the energy transmitted to a metal plate is a function of this ratio $(\frac{e}{L})$ although the thickness effect is probably slightly more important than the width effect, but in a way that is difficult to quantify.

ANALYTICAL MODEL

To get an asymptote for the function E (μ), in the case of a perfectly two-dimensional sandwich test, the relationship between $1/\varphi^2$ and μ must be linear when μ tends to infinity. 2D computations show that the function is always linear. We thus propose the following formula:

$$\frac{1}{\varphi^2} = b^2 + \frac{8}{3} bc\mu \qquad (2)$$

where b and c are the coefficients of the Richter relation, obtained from standard test. This formula takes the limiting conditions into account in the case of an unconfined explosive sample and it is consistant with the theoretical asymptotic value obtained for the transferred energy in a 2D sandwich test (3).

The positive curvature of the relation $\frac{1}{\varphi^2}$ vs μ, that is experimentally obtained, is therefore only due to an edge effect (see Fig. 4.).

In order to take this effect into account, we propose the following relation:

$$\frac{1}{\varphi^2} = b^2 + \frac{8bc}{3}\left(1+\lambda_1 \frac{e}{L}\right)\mu + \lambda_2^2\left(\frac{e}{L}\right)^2\mu^2 \qquad (3)$$

in which b, c, λ_1, λ_2 depend on the explosive.

The kinetic energy of a plate, referred to the explosive unit of volume can then be expressed by the relation E (μ), which gives a maximum value of energy CBV_2 such as:

$$\frac{\varrho_0 D^2}{(CBV_2)} \cong \frac{16}{3} bc + 4b \left[\frac{4}{3} c\lambda_1 + \lambda_2 \right] \left(\frac{e}{L} \right) \quad (4)$$

linear function of $\frac{e}{L}$, the coefficients of which depend on the explosive.

The parameters values λ_1 and λ_2 are inferred experimentally from the concavity of the parabola $\varphi^{-2}=f(\mu)$ and from the slope of the straight line mentioned above.

These datas are given for composition B 2174 on Fig. 4.

A comparison between $\frac{16}{3}$ bc and the asymptotic value of $\frac{E}{\varrho_0 D^2}$ in the two-dimensional case, inferred from experiments is made in the next paragraph for each composition.

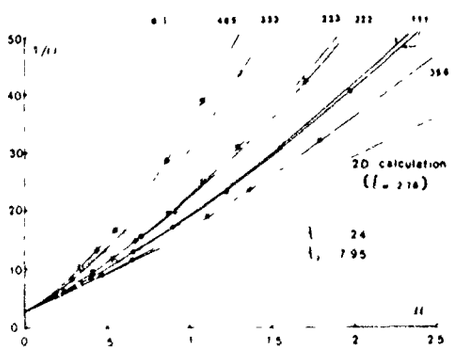

Fig. 4. Curves $1/\varphi^2$ vs μ for the composition B 2174 in different sandwich dimensions

RESULTS

Figure 5 represents the values of the volumic ballistic coefficients (CBV_2) of the tested compositions vs ratio $\frac{e}{L}$ relative to the geometry of each sandwich.

The experimental points obtained with the standard test (CBV_1) performed in its standard dimensions (i.e 90x20) have been added in figure 5 They allow to establish a comparison with the results supplied by the various sandwiches.

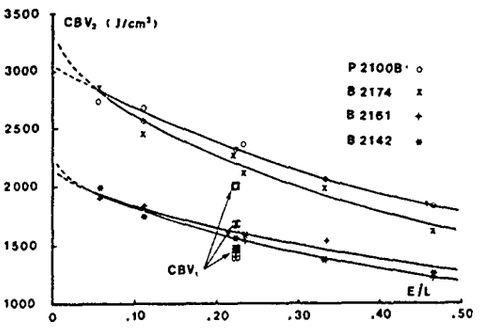

Fig. 5.

The evolution of CBV_2 vs $\frac{e}{L}$ is hyperbolic, as it can be expected from the model. Moreover, for a same composition, the test geometry has a noticeable influence on the result. Thus, for B 2174, the configurations going from $\frac{e}{L}$ = .47 to $\frac{e}{L}$ = .056 entails an increase of 70% of the transmitted energy. The difference of performances between two given compositions also very much depends on the test dimensions: for compositions P 2100 B and B 2174 it goes from +15% when

$$\frac{e}{L} = .47 \text{ to } -3,5\% \text{ when } \frac{e}{L} = .056,$$

which in this case corresponds to an inversion in the classification.

The form obtained for curves CBV_2 vs $\frac{e}{L}$ shows that such inversions are likely to occur for other geometries.

The value of CBV_2, which represents the rough results of the ballistic capacity test, very much depends, by definition, on the detonation velocity.

As a matter of fact, the critical dimensions of the compositions are not distant in the same way from the test dimensions, thus creating velocity variations that are very different as regards each explosive. Parameter $\frac{CBV_2}{\varrho_0 D^2}$ is then much more representative of the propelling character of these substances. Therefore figure 6 shows the curve $\varrho_0 D^2/CBV_2$ vs $\frac{e}{L}$ that presents the appearance of a straight line.

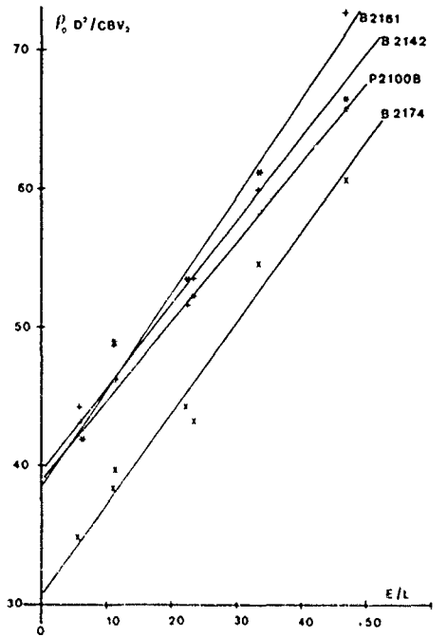

Fig. 6.

We note that:

- B 2174 gives values of $\frac{CBV}{\varrho_o D^2}$ that are much better than the values of the reference P 2100 B and this in every geometry.

- B 2161 has low performances compared to the three other ones; this comes partly from the fact that some test geometries are too near its critical dimensions.

- The gradients of the straight lines representing the behaviour of these last two compositions are higher than the two other ones; it expresses a higher sensitivity to edge effects. This result is in agreement with the evaluations that were previously made for the reaction zone lengths and it confirms, for these two compositions, the presence of chemical reactions behind the front that are likely to release energy in view of the propulsion.

The comparison between the compositions P 2100 B and B 2174 clearly indicates the propelling character due to Ammonium Perchlorate. Moreover, the fact that the composition B 2161 has a less markedly impulsive character comes from the granulometry of the used Ammonium Perchlorate which is lower on the average.

The various results are not exactly superimposing for a same ratio e/L. $\varrho_o D^2/CBV_2$ is not actually dependent at the same time on e and on L in a similar way: the double dots indicate that the thickness effect is higher than the wideness effect. The results being, however, not much different, the parameter e/L is sufficient, in the considered dimensions, to describe the edge effects. On the other hand, the extrapolation of the curves e/L = o only has a meaning for $e >> e_c$ and $L \to \infty$.

The ordinate at the origin of the straight lines in Figure 6 enables to determine the values of the ballistic coefficients without edge effect, that is to say the asymptotic values E^∞ of the curves $E(\mu)$ (see Figure 3). They are representing the maximum transferable energy in this test type and they are characteristic of the considered compositions. These values are given in Table 3 as well as the chemical energies that are inferred from them with the following relations:

$$\frac{1}{2}\left(\frac{W^\infty}{D}\right)^2 = \frac{E_c}{\varrho_o D^2} + \frac{1}{2} \qquad (5)$$

$$\frac{2E^\infty}{\varrho_o D^2} = \frac{W^\infty}{D} - 1 \qquad (6)$$

where W is the velocity of the particules flow at a given point.

These relations are the expression of the conservation of total enthalpy and of impulse when $\mu \to \infty$, between non-reacted state and particules flow to infinity.

TABLE 3

Compositions	$\frac{3\varrho_o D^2}{16bc}$ (J/cm³)	E^∞ (J/cm³)	$E_c/2$ (J/cm³)
B 2142	2 210	2 130	2 180
P 2100 B	3 165	3 195	3 280
B 2174	3 240	3 630	3 7··
B 2161	2 530	2 580	2 650

COMPARISON OF THE BALLISTIC CAPACITIES WITH PERFORMANCES IN SHAPED CHARGE

The four compositions were tested in a cylindrical and slightly confined shaped charge, with 90 mm caliber and a copper conical liner. For each composition, five shaped charges were fired on mild steel targets that were placed at a distance of two calibers. The obtained results (expressed in average perforation depths and hole volumes) are given in Table 4 where the four compositions are classified in order of decreasing performance.

TABLE 4

Compositions	Perforation Depth (mm)	Hole Volume (cm^3)
P 2100 B	455	142
B 2174	407	117
B 2142	403	94
B 2161	378	70

For the same compositions, Table 5 gives the values of the volumic ballistic coefficients that are obtained in three particular configurations of the lateral driving test: standard lateral driving (CBV_1) and sandwiches (CBV_2) corresponding to two values of the ratio e/L.

TABLE 5

Compositions	Volumic Ballistic Coefficient (J/cm^3)		
	Standard test (CBV_1) with e/L = 222	Sandwich (CBV_2) with e/L = 222	Sandwich (CBV_2) with e/L = 056
B 2142	1 435	1 554	1 983
B 2174	1 691	2 267	2 847
B 2161	1 432	1 720	1 897
P 2100 B	2 000	2 317	2 749

As previously indicated, some inversions in the classification of substances are noted, and particularly the configurations in which the expansions are less occurring are more favouring the long reaction zone compositions.

Finally Table 6 classifies the substances according to their performances, at the same time in the considered lateral driving tests and in shaped charge. The classifications obtained in shaped charge is identical to the one obtained in standard lateral driving, which is consistent with the low confinement of the utilized charge.

TABLE 6

Classification	Shaped Charge	Standard Test (CBV_1)	Sandwich (20x90)	Sandwich (10x180)
1	P 2100 B	P 2100 B	P 2100 B	B 2174
2	B 2174	B 2174	B 2174	P 2100 B
3	B 2142	B 2142	B 2161	B 2142
4	B 2161	B 2161	B 2142	B 2161

CONCLUSIONS

The plane lateral driving tests can differentiate the ballistic behaviours of the explosives. Particularly the sandwich type test can make obvious the propulsive character of some compositions having a relatively long reaction zone. Although the transferable maximum energy is very dependent on the adopted geometry, several tests performed in different dimensions supply a set of results that can be extrapolated up to e/L=0, thus leading to a characteristic value of the composition.

However, the classifications among substances, that can be inferred from these tests, remain very much related to the utilized configuration (importance of expansions and particularly of edge effects). To select a composition in order to use it in a weapon system would involve a geometry of the test that could be defined, such as the expansion rate would be near the one that occurs in the actual system. Generally this definition can only be qualitative. It leads to prefer standard lateral driving tests to take slightly confined systems into account and sandwich type configurations in all cases in which the system may favour a progressive release of energy.

REFERENCES

1. M. Defourneaux and L. Jacques, "Explosive deflection of a liner as a diagnostic of detonation flows," Proceedings - 5th Symposium on Detonation, 1970, p. 457.
2. M. Defourneaux, "The push-plate test for explosives," 1st International Symposium on Ballistics, 1974.
3. M. Defourneaux, "Transfert d'energie dans la propulsion par explosif," Sciences et Techniques de l'armement, 47, Vol. 3 et 4, 1973.

DISCUSSION

M. Held, M.B.B. Apparte, Germany

Have you measured in your shaped charge tests the jet tip velocities? This will give you direct information of the charge performance to the liner.

REPLY BY J. MALA

No; we have not measured the jet tip velocities; only the perforation depth and hole volume.

Session VII
SDT/DDT

Chairman: Philip M. Howe
Ballistic Research Laboratory
Martin Zimmer
Air Force Armament Laboratory

MECHANICAL PROPERTIES OF PBX'S AND THEIR BEHAVIOUR DURING DROP WEIGHT IMPACT

J. E. Field, S. J. P. Palmer, P. H. Pope,
R. Sundararajan and G. M. Swallowe
Cavendish Laboratory
Madingley Road
Cambridge CB3 OHE, U.K.

Experiments are described on the deformation and ignition behaviour of a range of explosives, including plastic bonded explosives (PBX's). An instrumented drop-weight apparatus was used to obtain stress-strain curves for strain rates in the range 10^2 to 10^3 s^{-1}. A novel drop-weight apparatus with transparent anvils allowed high-speed photographic recording of the impact and ignition processes. Laser speckle, used in conjunction with a specimen loaded in the Brazilian test geometry gave tensile strength and strain to failure data of PBX's. Finally, a modified Hopkinson bar apparatus gave data at strain rates up to 5 x $10^4 s^{-1}$

INTRODUCTION

It is generally accepted that explosive initiation is thermal in origin. In processes involving impact or shock, the mechanical energy is envisaged as being converted into heat in localized regions called "hot spots" (1, 2). The required "hot spot" radius for ignition is a function of the explosive, the temperature and its duration (3). For pentaerythritol tetranitrate (PETN), the calculated "hot spot" temperature for a time of 1 μs and radius 1μm is ca. 700 K. Experimental work by Bowden and Gurton (4, 5) largely confirmed these figures and showed that "hot spot" radii are typically 0.1 to 10 μm for initiation by friction or impact. In a recent paper (6) we have discussed the ignition mechanisms of explosives during mechanical deformation. Evidence was given for ignition by adiabatic heating of trapped gas, adiabatic shear of the explosive, friction, viscous flow, fracture or shear of added particles and triboluminescent discharge.

A feature of our work on the relation between mechanical properties and explosive behaviour has been the use of high-speed photography. The advantage of the photographic evidence is that it has allowed us to identify the conditions under which the various ignition mechanisms operate during deformation of an explosive.

In many modern applications, explosive crystals are bonded into a polymer matrix (so-called PBX explosives.) It is important with such systems to understand the factors which affect their mechanical and thermal properties, their sensitiveness (response to a prescribed stimulus) and their explosiveness (explosive response). There is usually a conflict between these various requirements and an optimum has to be sought. The present paper describes results on some PBX explosives based on cyclotetramethylene tetranitramine (HMX), and gives further evidence for the mechanisms of "hot spot" formation during mechanical deformation.

EXPERIMENTAL

Experiments have been carried out using the drop-weight machines illustrated in Fig. 1. The samples used are 5 to 7 mm in diameter and 1 mm high allowing strain rates of 10^2 to 10^3 s^{-1} to be obtained, depending on the drop-height of the weight. Fig. 1a illustrates the system which is used to obtain stress-strain curves. Strain gauges attached to R_1 allow the force-time history to be monitored. The area of deforming

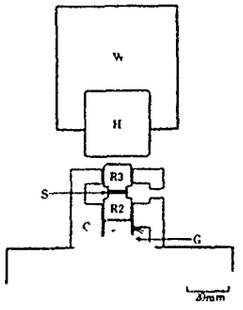

Fig. 1(a). Instrumented drop-weight: W, drop weight; H, R1, R2, R3, hardened steel rollers (The sample is between rollers R2 and R3.)

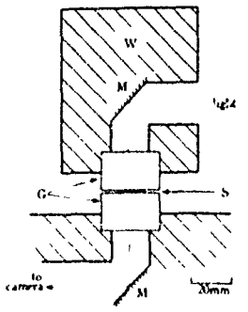

Fig. 1(b). Arrangement at instant of impact: W, drop-weight (5.5 kg) G, glass blocks; M, mirror; P, prism; S, sample

sample is determined by R_2 and R_3 and the sample size is chosen to be, initially, slightly greater than this area. The sample area under load is thus constant and the need for assumptions about volume conservation, which are not always valid for polymers or porous materials, is eliminated. Knowledge of the mass of the weight combined with a double integration of the force-time data produces force-displacement information which is then converted to a stress-strain curve. The system illustrated in Fig. 1b is unusual in that the anvils are made of toughened glass and a light path through the system allows the sample to be photographed by a high speed camera at framing rates up to 2×10^5 f.p.s. during the course of the impact. The sample strain-rates in both machines are the same so that direct comparisons between the photographic records and the stress-strain data can be carried out.

The third system used in this research was a miniaturised and modified Hopkinson bar apparatus (7). This enabled measurements to be made, and stress-strain curves determined, at strain rates up to $5 \times 10^4\ s^{-1}$. The samples used in these experiments are 4 mm diameter and 1 mm thick, and the pressure bar has a diameter of 3 mm.

Finally, the tensile strengths and rupture strains of a variety of PBX compositions were studied, at strain rates of ca. $10^{-4}\ s^{-1}$, using the "Brazilian" test geometry and laser speckle

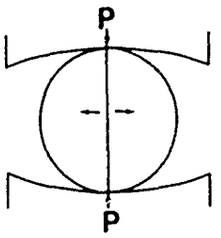

Fig. 2. Loading arrangement used in Brazilian test

photography. The Brazilian test is illustrated in Fig. 2. The compression induces tensile stresses normal to the loading axis which are sensibly constant over a region about the centre of a specimen. The tensile strength of the material is then calculated from

$$\sigma_t = 2P/\pi Dt \qquad (1)$$

in which P is the failure load, D and t the diameter and thickness of the specimen respectively. The validity of equation 1 is based on the assumptions that failure occurs at the point of maximum tensile stress (i.e. at the centre), and that the compressive stress has no influence on the failure. In practice, the use of plane anvils can produce very high contact stresses at the loading points, and lead to the collapse of the contact edge. Awaji and Sata (8) have shown that by using curved anvils, collapse of the edge can be avoided, and shear stresses under the points of loading may be substantially reduced. If the ratio of the contact half-width, b, to the disc radius, R, is larger than approximately 0.27, the maximum principle stresses near the contact area are compressive. Then the stresses near the centre of the disc control the fracture,

TABLE 1
Tensile Properties of PBX's

Code	Binder	% binder by weight	Explosive	% strain to failure	Failure stress/ MPa, b/R = 0.45
A	Polyurethane (PU)	2	M	0.95 ±0.06	1.38±0.21
B		2	A/M	0.50±0.10	1.20±0.09
C		5	M	0.98±0.05	3.20±0.06
D		5	A/M	1.24±0.02	1.06±0.08
E	Polyethylene (PE)	2	M	ca. 0.06	3.87±0.13
F		2	A/M	0.09±0.02	0.89±0.07
H		5	A/M	0.18±0.04	0.83±0.13
I	Viton	4	M	0.24±0.03	1.82±0.15
J		4	A/M	0.32±0.06	1.21±0.10
K		9	M	0.31±0.08	1.97±0.03
L		9	A/M	0.41±0.02	0.90±0.07
PBX 9502	KEL-F 800	5	TATB	0.23±0.01	4.13±0.20
X 0344	KEL-F 800	5	TATB/ HMX	0.13±0.01	1.97±0.10
G	(PE)	5	M		

A-L AWRE compositions; PBX 9502 and X 0344 Los Alamos.
M Micronised HMX (to pass 53 μm sieve).
A Size range 50-1000 μm, median diameter ca. 400 μm A/M ratio 63/35.
TATB/HMX for X 0344 in ratio 71.25/23.75

and cracking occurs at the centre, at a maximum tensile stress given by

$$\sigma_t^* = \{1 - (b/R)^2\}\, \sigma_t \qquad (2)$$

Other workers (9-11) using the Brazilian test geometry, have employed displacement transducers to measure the *average* tensile strain across a diameter. However the use of a relatively simple optical technique called "Speckle Photography," enables one to measure in-plane displacements to an accuracy of ca. 0.1 μm at different positions on the sample surface, and thereby determine the strain field at any point (12, 13). There is an added advantage that it is a remote sensing technique which does not involve adding gauges to the sample. For displacement and strain measurements, a double exposure is photographically recorded before and after deformation. The negative then consists of two identical speckle patterns that have been translated with respect to each other. Displacement information can be extracted in a pointwise manner, by allowing an unexpanded laser beam to pass through the negative. If at the point illuminated by the beam, the "speckles" have been displaced between exposures, the resulting displacement vector is manifested by a Young's fringe pattern observed on a screen placed at the far-field Fraunhofer diffraction plane. The displacement vector is perpendicular to the fringe orientation and the magnitude inversely proportional to the fringe spacing. However, complete analysis involved many measurements, and the procedure becomes tedious when performed manually. For this reason a fully automatic electro-optical system for measuring the displacement field from a double exposure speckle photograph has been constructed (14).

RESULTS AND DISCUSSION

Low Strain Rate Data.

Table 1 gives information on the PBX's studied. They were all based on HMX but with different binder polymers. The amount of binder

and the crystal size distributions of the HMX were varied. Included in Table 1 are the results on the strain to failure and the failure stress obtained using the speckle technique. Various general points can be made; (i) micronised samples are stronger, (ii) the more polymer the greater the strain to failure, (iii) PE gives the most brittle behaviour (lowest strain to failure) followed by Viton and PU, (iv) composition C had the highest combination of strength and strain to failure.

If the equivalent flaw size "2c" is calculated for β−HMX from the Griffiths fracture criterion, taking the results given in Table 1, it turns out the flaw size required for the fracture of crystals of micronised HMX is ca. 270 μm, and ca. 2.4 mm for the bi-model size distribution. This is assuming that for β-HMX the Young's Modulus, E, equals 3.10×10^{10} Nm^{-2} and the stress intensity factor, K_{Ic}, equals 6.2×10^{4} $Nm^{-3/2}$ (15). These flaw sizes are clearly much larger than the crystals! This strongly suggests that extensive crystal fracture in these composites at these stresses is unlikely, unless there are significant stress concentrating effects. However examination of the fracture surfaces of composition E containing micronised HMX, using scanning electron microsopy, has revealed clear examples of fractured crystals. An example is showns in Fig. 3, in which the mirror images of the fracture surfaces are clearly seen. The striations on the surface of the crystals are permanent twins. β-HMX, undergoes elastic twinning at low stresses, which convert to permanent twins at higher stresses (15). When a twin meets a surface it creates a small but sharp step, which acts as a site for stress concentrations (16). This could explain the low stresses at which the crystals fracture.

Fig. 3. Scanning electron micrographs of mirror failure surfaces of a composition E PBX (The β-HMX crystal which has cleaved shows extensive twinning.)

High Strain Rate Data

Fig. 4 and Table 2 summarise results on the PU compositions from the high rate of strain experiments (= 1.6×10^{4} s^{-1}). Note that the samples with micronised HMX exhibit the highest dynamic strengths, with C again proving the strongest. Table 2 also includes F of I and Labset figures. The micronized samples (A, C) had smaller Labset (explosiveness) values and this was also found with other binder materials.

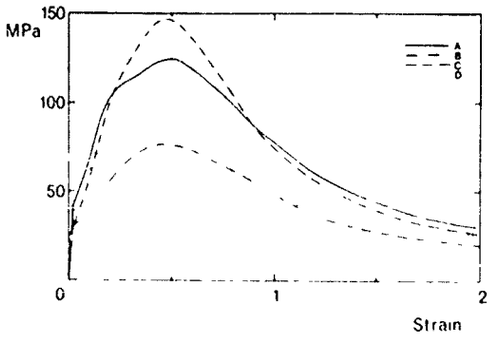

Fig. 4. Stress-strain curves for compositions A, B, C, D at a strain rate of 1.6 x 10^{4} s^{-1}

TABLE 2

Code	Dynamic strength (1.6×10^{4} s^{-1})/MPa	F of I[a]	Labset[b]
A	125	62	185
B	80	64	812
C	145	55	58
D	85	49	232

[a] Figure of Insensitiveness, based on a drop-height for RDX of 80. The greater the figure the less the sensitivness (AWRE data).

[b] Labset is the AWRE test for explosiveness. The greater the figure the greater the explosive response.

Drop-weight impact on PBX's.

The overall response of a PBX in drop-weight impact is illustrated by Fig. 5a which shows how stress varies with time for a mock PBX. The behaviour can be divided into three sections, the first peak corresponds to brittle failure of the sample into numerous fragments, this is followed

by a region of lower stress as the fragments are compacted and finally the thin layer of material is pinched between the anvils giving rise to the second stress peak. If a thinner sample is used, the compaction phase is shorter, or absent altogether, as in Fig. 5b where brittle failure is evident as a small inflexion of the leading edge of the pulse.

Knowledge of the stress and strain at brittle failure is useful in interpreting explosiveness data since reaction often propagates into undeformed material which is consequently disrupted. In our own work where sample sizes are small (ca. 25mg) initiation occurs during the pinch phase so that processes occuring during brittle failure are of indirect significance. It is important to realize that in the pinch geometry the sample strength is higher than the uniaxial yield stress of the material, σ_y. This is due to friction at the anvils which resists radial flow of the sample. Application of the von Mises yield criterion to a thin layer of thickness h and diameter d compressed between rigid plane anvils gives for the yield pressure

$$P_y = \sigma_y \{1 + (d/h3\sqrt{3})\} \qquad (3)$$

Note that the smaller the thickness or the greater the diameter, the higher the value for P_y. The existence of such high stresses, which may be 500-1000 MPa in our apparatus, is one of the factors which favours initiation in the pinch phase.

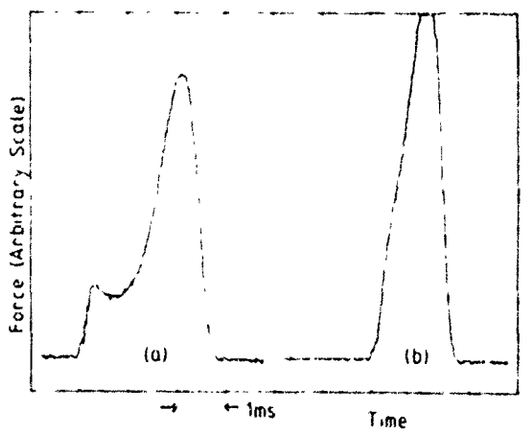

Fig. 5. Force time records for impact at 1 m s^{-1} on mock PBX samples for different aspect ratios. (a) sample diameter 6mm, height 2.5mm; (b) diameter 6mm, height 1.5mm

Another important factor can be seen in high speed photographs of the impact. Fig. 6 shows a typical case where the sample has been expanding quite slowly (radial velocity ca. 10 m s^{-1} over a period of 200 μs to reach the stage shown in frame 1. In frame 2 the radial velocity suddenly increased to the order of 100 m s^{-1} and this is quickly followed by ignition. Note that, though ignition occurs after rapid flow, rapid flow does not necessarily cause ignition. The observation that rapid deformation is a necessary prerequisite for ignition supports the many observations of Kholevo (17) and Afanas'ev and Bobolev (18) that

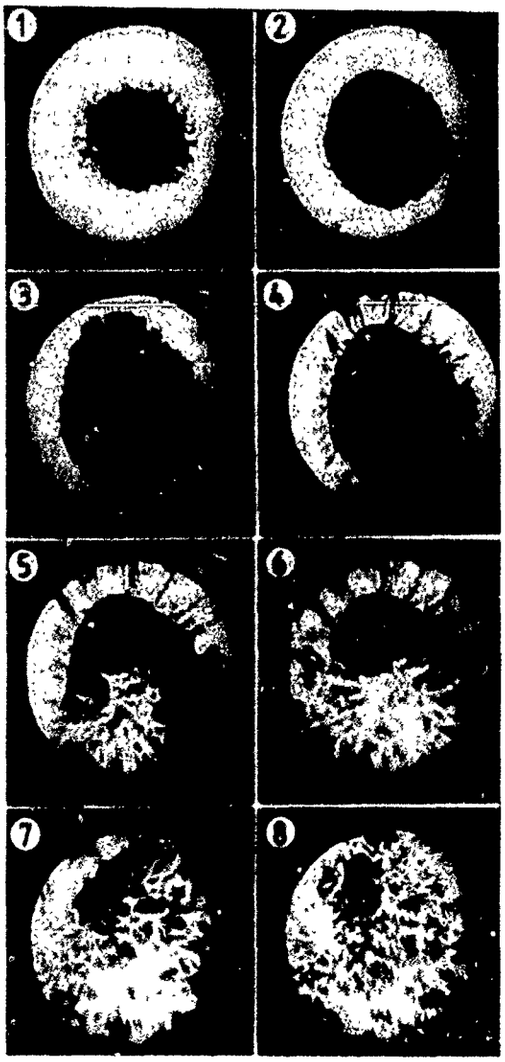

Fig. 6. Impact on a sample of composition B which undergoes rapid flow (2 and 3) and ignites (Extensive breakup with the production of internal surfaces aids reaction. Interframe times 2 to 8, 7μs. Field of view 20 mm.)

the prevention of flow in an explosive sample makes the sample less sensitive. Further support for this view is provided by the stress-time traces obtained with the instrumented drop-weight machine.

If the sample radius is plotted as a function of time (Fig. 7) the result is distinctive not only in showing rapid flow but also a period before this in which little or no flow occurs. This is at first sight surprising given the excess energy in the weight but can be explained by considering the elastic deformation of the glass anvils. An elastic analysis of the anvils considered as elastic half spaces shows that when the specimen thickness is reduced to 160 μm on the central axis sufficient deformation can occur at a mean pressure of 800 MPa to give contact at the rim which will account for the observations. The pinch geometry is therefore more complex with glass anvils since the sample is trapped in a shallow cavity, adding to the frictional restraint in preventing radial flow. This is one reason why initiation is more difficult in the glass apparatus than with steel anvils which have a higher modulus.

When ignition does occur, two distinctive forms of behaviour may be observed and these are illustrated in Figs. 6 and 8. Fig. 6 shows what we have called 'local' initiation and Fig. 8 shows 'widespread' initiation. Evidence from the time taken to reach initiation suggests that local initiation is the preferred mode in the early stages of impact while the sample is trapped in the shallow cavity. Since the confinement is

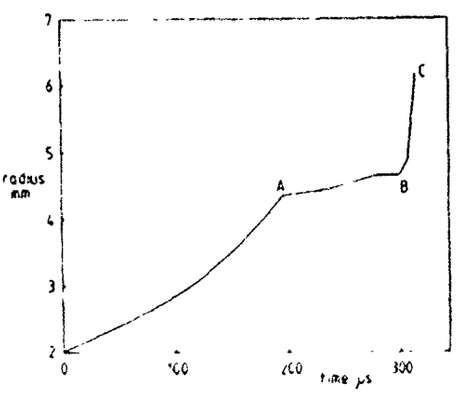

Fig 7 Radius time plot for composition C sample OA expansion; AB plateau region, BC rapid flow B corresponds to frame 1 in Fig. 8

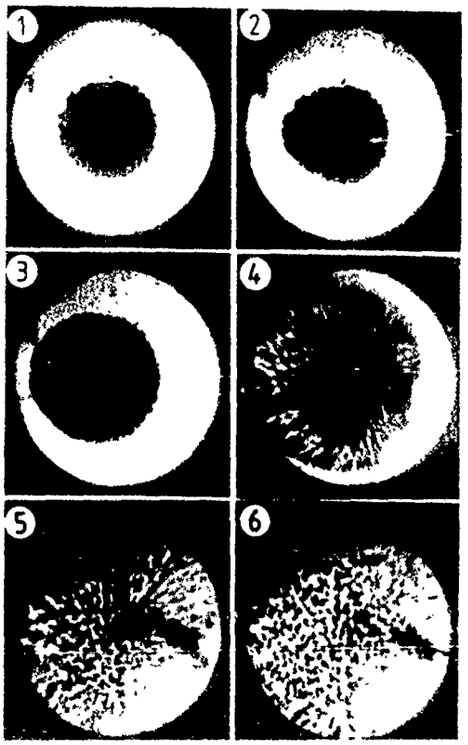

Fig. 8. Impact on a sample of composition C (The sample undergoes rapid flow (frames 2 and 3) and there are widespread ignition sites (see text). Inter-frame times 2 to 6, 7 μs. Field of view 20mm.)

good, reaction is violent and produces surface damage in the toughened glass. The high pressures generated in the bulk of the explosive are responsible for driving cracks through the sample, visible in frams 4 to 6 (Fig 6) and exposing surfaces for reaction.

If the sample survives the confined stage without ignition, then ignition can occur during rebound of the weight. A new condition is created which is very favourable for rapid flow since the constraint of the cavity is removed and simultaneously elastic energy stored in the anvils can be released, on a microsecond time scale, to drive the material outwards. Under these conditions, wide spread initiation is favoured and appears to take place at the interface between the explosive and glass (see frame 4, Fig. 8). The reaction products can easily escape along the interface leaving behind many

particles of unreacted explosive (frame 6) which then burn slowly over a period of ca. 100 μs. The reaction is less violent than in local initiation and leaves little or no damage on the glass.

There does not seem to be any correlation between the mode of initiation and the type of composition which is tested. A given PBX may exhibit local initiation in one experiment and widespread initiation in another which implies that the initiation mode is not a basic property of the material but depends critically on the mechanical interaction between the sample and the anvils. Factors which may affect this interaction are the coefficient of sliding friction, tilt of the anvils and the presence of flaws in the specimen.

The mechanisms of deformation may be inferred from Fig. 9 which shows a recovered sample from an experiment in which there was no event. Markings in the centre give evidence of localised shear. If conditions near the shear bands are adiabatic they could be responsible for ignition (19, 20).

The formation of shear bands is a discrete process in which strength is lost momentarily and this can be seen in the stress record obtained from the instrumented drop weight (Fig. 10). The numerous drops in stress are interpreted as shear band formation and it is often possible

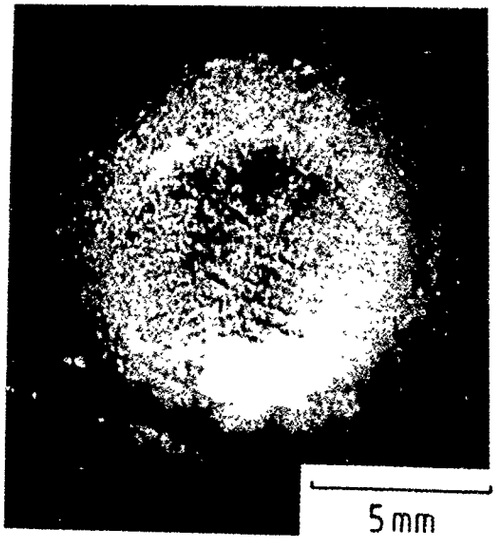

Fig. 9. A PBX (composition G) impacted from a sub-critical height (Note the shear band formation.)

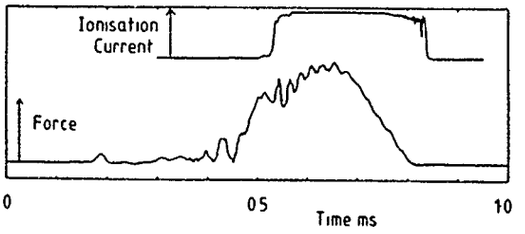

Fig. 10. Force time curve (lower trace) for impact on a composition B PBX (The pressure drops are caused by shear band formation.)

to detect ignition simultaneously through ionisation, as indicated by the upper trace in the figure. The mechanics of the apparatus dictate that each stress drop is associated with an increment of rapid flow, again confirming the link with initiation.

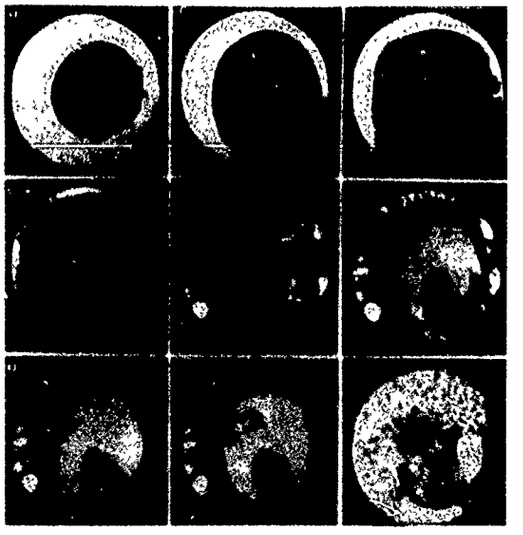

Fig. 11. Impact on a 25 mg PETN sample from a drop height of 1.3 (See text for details, but note in particular the shear band formation which causes ignition and the transparency which is due to sintering and fusion. Interframe times 0, 28, 49, 63, 77, 91, 105, 112, 133 μs. Field of view 20mm.)

Drop-weight impact on pure explosive.

Earlier work on pure explosives has been discussed in (6, 21). Further evidence that shear band formation occurs and can cause ignition is given in Figs. 11 and 12.

Fig. 11 is for a 25 mg sample of PETN impacted from 1.3m. At first the sample appears dark since it is viewed in silhouette. In frames

TABLE 3

Compound	Melting point/K	Yield stress/MPa	H_{50}/m	Rapid Flow	Ignition
TNT	351	34[a]	1.48[b]	No[c]	No
Picric acid	395	53	0.73	No	No
Tetryl	404	53	0.37	No	Yes[d]
Nitrocellulose	408	——	0.50	No	Yes[d]
PETN	414	60	0.13	Yes	Yes
RDX	474	82	0.28	Yes	Yes
AP	>493	——	——	Yes	Yes
HMX	553	125	0.32	Yes	Yes
HNS	588	140	0.54	Yes	Yes

a. All the yield stress values have been taken from (18) except for HNS (21).
b. Data from Lawrence Livermore Explosives Handbook, UCRL-52997 (1981)
c. The experimental observations for all compounds excluding tetryl and HNS.
d. Reaction fails to propagate.

1 to 3 the bulk flow is at a low velocity of ca. 10 m s^{-1} though in frame 3 a small amount of material is ejected as high speed jets. In frame 3 onwards families of shear bands become visible. The transparency is associated with sintering and fusion of the sample (6). Rapid bulk flow at ca. 125 m s^{-1} commences in frame 4 and ignition in frame 7. Note that the ignition and the initial directions of propagation are controlled by the shear bands. Fig. 12 is for a 25 mg sample of PETN impacted from 1.3 m. Shear bands are arrowed in frame 1 and are clearly associated with the ignition.

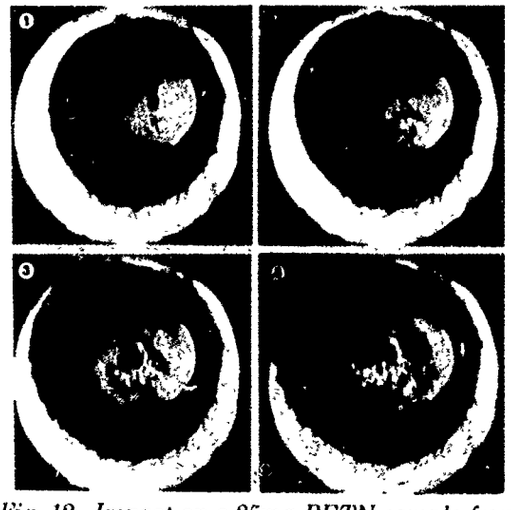

Fig. 12. Impact on a 25mg PETN sample from a drop height of 1.3m (Shear bands are arrowed in frame 1. Interframe times 0, 7. 14, 21 μs. Field of view 20mm.)

Shear band formation has now been observed by us in some primary explosives (19) PETN, RDX, HMX, and some PBX's. Other ignition mechanisms which can occur during mechanical deformation are discussed in reference (6).

Mechanical properties and behaviour during drop-weight impact.

Recently we have shown that the higher the yield stress of a pure explosive the higher its plastic flow velocity in the drop-weight test. Thus although with a strong sample the onset of irreversible deformation is delayed it eventually develops more rapidly when stored energy is released. This means that the likelihood of ignition during the conversion of mechanical energy is greater. Table 3 illustrates these results and explains why a relatively soft, low melting point explosive such as trinitrotoluene (TNT) does not ignite so readily in the drop-weight test. A fuller discussion can be found in Krishna Mohan and Field (21).

CONCLUSIONS

The combination of techniques used in this study has provided valuable information on the mechanical and ignition behaviour of explosives.

ACKNOWLEDGMENTS

This work was supported in part by the Ministry of Defence (Proc.Exec.) and Grants through the European Office of U.S. Research.

We thank A.W.R.E. Aldermaston U.K. and Los Alamos U.S.A. for samples.

REFERENCES

1. F. P. Bowden and A. D. Yoffe, Initiation and Growth of Explosions in Liquids and Solids, Cambridge University Press, 1952.
2. F. P. Bowden and A. D. Yoffe, Fast Reactions in Solids, Butterworths, London, 1958.
3. E. K. Rideal and A. J. B. Robertson "The Sensitiveness of Solid High Explosives to Impact," Proc. Roy. Soc. London, Vol. A195, pp. 135-150, 1949.
4. F. P. Bowden and O. A. Gurton, "Initiation of Solid Explosives by Impact and Friction: the influence of Grit," Proc. Roy. Soc. London, Vol. A198 pp. 337-349, 1949.
5. F. P. Bowden and O. A. Gurton, "Birth and Growth of Explosion in Liquids and Solids Initiated by Impact and Friction," Proc. Roy. Soc. London, Vol. A198, pp. 350-371, 1949.
6. J. E. Field, G. M. Swallowe and S. N. Heavens, "Ignition Mechanisms of Explosives during Mechanical Deformation," Proc., Roy. Soc. London, Vol. A382, pp. 231-242, 1982.
7. D. A Gorham, "Measurement of Stress-Strain Properties of Strong Metals at Very High Rates of Strain," Institute of Physics Conf. Series, Vol. 47, pp. 16-24, 1979.
8. H. Awaji and S. Sata, "Diametral Compressive Testing Method," J. Eng. Mater. and Tech., Vol. 101, pp. 140-147, 1979.
9. H. D. Johnson, "Mechanical Properties of LX-10-1 Evaluated with Diametric Disc Test," MHSMP-79-08, Jan. 1979.
10. H. D. Johnson, "An Investigation of the Effect of Granule Size on the Mechanical Properties of LX-14," MHSMP-79-26, April 1979.
11. H. D. Johnson, "Diametric Disc and Standard Tensile Test Correlation Study," MHSMP-81-22, April 1981.
12. F P Chiang, "Subjective Laser Speckle Method and its Application to Solid Mechanics Problems," Opt. Eng., Vol. 21, pp 379-390, 1982.
13. A. E. Ennos, "Speckle Interferometery," in Laser Speckle and Related Phenomena, Springer, pp. 203-253, Heidleberg, 1975.
14. J. M. Huntley, "An Image Processing System for Analysis of Speckle Photographs," J. Phys. E. Sci. Inst., Vol. 19, pp. 43-49, 1986.
15. S. J. P. Palmer and J. E. Field, "The Deformation and Fracture of β-HMX," Proc. Roy. Soc. London, Vol. A383, pp. 399-407, 1982.
16. D M. Marsh, "Stress Concentrations at Crystal Surfaces and the Embrittlement of Sodium Chloride," Phil. Mag., Vol. 5, pp. 1197-1199, 1960.
17. N. A. Kholevo, Trudy Kazan Khim. Tech. Inst.. Vol. 10, pp. 91, 1946.
18. G. T. Afanas'ev and V. K. Bobolev, Initiation of Solid Explosives by Impact, Israel Program for Scientific Publications, Jerusalem, 1971.
19. R. E. Winter and J. E. Field, "The Role of Localized Plastic Flow in the Impact Initiation of Explosives," Proc. Roy. Soc. London, Vol. A343, pp. 399-413, 1975.
20. R. B. Frey, "The Initiation of Explosive Charges by Rapid Shear," Proc. 7th Int. Symposium on Detonation, pp. 36-42, Annapolis, 1981.
21. V. Krishna Mohan and J. E. Field, "Impact Initiation of Hexanitrostilbene," Combust. Flame, Vol. 56, pp. 269-277, 1984.

DISCUSSION

SPERO NICOLAIDES, U.S. Army, ARDC, Dover, N.J.

I may have missed something, that is how are you defining yield strength in your correlation of it with initiation – are you using yield strength as being synonomous with elastic limit and considering the explosive resilience, or its ability to store elastic energy as the significant material property relating to the explosives initiation susceptibility, or are you identifying yield strength as a peak stress, which conceivably has work-hardening incorporated within it. Can you clarify this for me.

REPLY BY J. E. FIELD

Table 3 has yield stress, σ_y, values. These are usually measured by a hardness indentation method and would be the flow stress after work-hardening. We make the point in our discussion that the higher the yield stress the greater the release of stored energy when flow commences, and we believe this can affect the sensitiveness of the material. In the case of impact on a thin layer of explosive, the hydrostatic stress component affects the yield pressure (see our equation 3). Flow then takes place at a value P_y which is greater than σ_y and a correspondingly greater energy is released.

THE STRAIN RATE BEHAVIOR OF COARSE HMX POROUS BED COMPACTION

P.J. Coyne, Jr.*, W.L. Elban, and M.A. Chiarito**
Naval Surface Weapons Center
White Oak
Silver Spring, MD 20910

*Loyola College, Baltimore, MD 21210

**Current Address: General Electric Company, Space Systems Division, Springfield, VA 22153

The strain rate dependence of compaction of porous columns of coarse HMX has been assessed quantitatively from stress relaxation measurements on quasi-statically ($\dot{\varepsilon} \approx 10^{-1} s^{-1}$) compacted granular material. Building on the favorable results from a preliminary investigation of the strain rate sensitivity for powdered Teflon 7C compaction, logarithmic plots of intragranular stress versus plastic strain rate were obtained for coarse HMX. These graphical relationships were extrapolated to predict the intragranular stress levels which would exist in the porous beds at strain rates characteristic of dynamic ($\dot{\varepsilon} \approx 10^{5} s^{-1}$) compaction experiments. Estimates were compared with available dynamic measurements by another NSWC investigator. The variation of sound velocity with percent theoretical maximum density was computed from the elastic unloading moduli of the porous beds. The results connected favorably with available data obtained by other investigators. Ultrasonic sound velocity measurements were attempted on numerous recovered HMX compaction samples, and the difficulties encountered are discussed.

INTRODUCTION

It is now well known that considerable dynamic compaction occurs in the deflagration-to-detonation transition (DDT) process in high porosity beds of energetic materials confined in thick-walled tubes (e.g., Reference 1). Consequently, a compaction law (stress versus percent theoretical maximum density, %TMD), representative of dynamic conditions, is important to obtaining a quantitative understanding of DDT experiments and to the development of numerical models of DDT. Previously, quasi-static compaction measurements were performed because much useful information could be obtained quickly with a relatively simple experimental set-up (2-4). Such data helped develop a physical model of the early stages of DDT and provided a first formulation of a constitutive equation for compaction (5). Dynamic compaction studies (5-7) have also been performed to connect directly with the modeling effort and the quasi-static measurements. However, complications often arise due to material reaction during high strain rate compaction, thus precluding dynamic measurements in the high %TMD range, say above 90% (8)

To begin the determination of a strain rate dependent compaction law, the behavior of a material in a conventional engineering tensile test is considered. A general expression (9,10) of the form

$$\sigma_{\varepsilon,T} = C\varepsilon^{m} \qquad (1)$$

has been observed to be valid for a number of metallic systems relating flow stress, σ, at a constant strain, ε, and temperature, T, to strain rate, $\dot{\varepsilon}$, where the exponent m is called the strain rate sensitivity, and C is a constant. Lee and Hart (11) have successfully analyzed stress relaxation data on two metallic materials, tested in tension, to yield $\sigma-\dot{\varepsilon}$ relationships suitable for comparison with the behavior described by Equation (1).

A typical stress relaxation experiment (12) involves loading a sample in tension (or compression) to a given applied stress level using some type of a universal testing machine. The crosshead of the machine is then stopped allowing the applied stress to be measured as a function of time, t, at constant total strain. The stress is a maximum the moment the crosshead stops and then decreases with time because the plastic strain in the sample, ε_{pl}, increases with time due to creep, thus allowing a decrease in elastic strain, ε_{el}, since the total strain is constant. A decrease in elastic strain requires that the applied stress decrease also.

In the stress relaxation model proposed by Lee and Hart (11), a sample is loaded in tension by a force, F, to a constant strain. The sample length, L_1, is partitioned into an elastic length, F(t)/K, and a plastic length, L(t). The elastic spring constant of the sample, K, allows the elastic length to be specified using Hooke's Law. The plastic strain rate is given by

$$\dot{\varepsilon}_{pl}(t)=\frac{\dot{L}(t)}{L(t)}=\frac{-\dot{F}(t)/K}{L_1-F(t)/K}\,. \qquad (2)$$

Descriptions of this model have also been given by Hart (13) and by Lee and Woodford (14). Recently, it was determined that this analytic scheme could be applied to stress relaxation in quasi-statically compacted porous beds of Teflon 7C (model inert material) (15).

Following the development of Kuo, Moore, and Yang (16), the so-called intragranular stress or average axial compressive force per unit radial cross-sectional area of the solids in the porous bed, τ_i, (in contrast to the applied stress, σ_a) is representative of the stress level actually in the bed. It is defined as

$$\tau_i(t)=\frac{0.5(F_a(t)+F_t(t))}{A\,(1-\phi_{avg})}\,, \qquad (3)$$

where F_a is the applied force, F_t is the transmitted force, A is the cross-sectional area of the bed, and ϕ_{avg} is the average fractional porosity. The plastic strain rate defined in Equation (2) must be modified accordingly for stress relaxation in a compacted porous bed to give

$$\dot{\varepsilon}_{pl}(t)=\frac{\dfrac{-0.5\,(\dot{F}_a(t)+\dot{F}_t(t))}{K}}{L_1-\dfrac{0.5\,(F_a(t)+F_t(t))}{K}}\,. \qquad (4)$$

The analysis procedure has now been applied, with several important improvements in experimental technique, to a large number of quasi-static compaction experiments performed on coarse cyclotetramethylenetetranitramine (HMX). The HMX samples used were a so-called #20 sieve cut (+18, −20) and production-grade Class D HMX (NSWC designation X980) that was used in generating the sieve cut (4). These two materials have nearly the same average particle size (925 and 870 μm, respectively) but differ appreciably in their particle size distribution.

The purpose of the work was to assess quantitatively the strain rate behavior of porous bed compaction for the two types of coarse HMX over a broad %TMD range. Of particular interest was the effect of particle size distribution. It was also desired to compare the strain rate sensitivity of coarse HMX, a molecular crystalline solid, with that of Teflon 7C powder, a crystalline polymer. First, the stress relaxation experiments (15) on Teflon 7C will be reviewed. This will be followed by a more detailed description of current experiments on coarse HMX. Finally, the results of all of the experiments will be discussed.

EXPERIMENTAL PROCEDURE AND DATA ANALYSIS

Teflon 7C: A total of six stress relaxation experiments were performed (15) involving 15 g samples of Teflon 7C powder (average particle size, $\bar{\delta}$ = 30 μm) loaded at a constant crosshead speed of 2.54 mm/min using a Tinius Olsen Electomatic Universal Testing Machine (2-5, 15). A single-acting ram and mold (2.54 cm I.D.) assembly was used (2-5, 15) where the mold was rigidly held, allowing the vertical frictional force component between the porous bed and the mold wall to be determined. Duplicate experiments were performed at about 81.5, 85, and 92% TMD,

and a compilation of information on these experiments is given in Table 1. The compressibility of individual Teflon 7C powder particles in the compacted bed was not accounted for in the %TMD calculations. During each relaxation run, the applied and transmitted forces were each digitally recorded. The time derivatives of both forces were evaluated numerically to allow computation of $\dot{\varepsilon}_{pl}$ as given by Equation (4). The force recordings were digitally filtered to reduce noise prior to calculating the derivative (17). The stress relaxation of the compaction apparatus (without porous bed sample) was determined to be negligible.

The porous bed spring constant at each %TMD was evaluated (15) using a separate, presumably identical sample. This simply involved numerically determining the slope of the applied force curve during reloading of the sample at 2.54 mm/min which followed after having been successively compacted, briefly allowed to stress relax, and then quickly unloaded. A correction (18) was made to account for the displacement of the compaction apparatus (without sample). However, total displacement measurements were not made directly. Instead, a constant crosshead speed was assumed, and displacements were calculated on this basis.

Coarse HMX: Several refinements in the experimental procedure were made. These included (a) using a deflectometer to measure total displacement directly and (b) determining the compaction and stress relaxation behavior of the same sample, together with an evaluation of its spring constant by subsequently unloading the sample, once adequate stress relaxation had occurred. Some experiments also involved reloading the sample at constant crosshead speed to provide a check on the unloading data.

Simultaneous applied force, transmitted force, and porous bed displacement measurements were obtained digitally while each HMX sample was compacted remotely to stops using a Farquhar (2670 kN capacity) hydraulic press (4). The crosshead speed on loading was 18.8 cm/min. However, deceleration occurred as the top press platen encountered the stops. For each experiment, a 15 g sample of HMX was used. A compilation of information on the experiments appears in Tables 2 and 3 for #20 sieve cut and Class D HMX, respectively. The %TMD calculations are based on an ambient pressure crystal density of 1.903 g/cm^3 as determined by Olinger, Roof, and Cady (19). As such, the compressibility of individual HMX crystals in the compacted bed has been ignored. A few #20 sieve cut HMX samples were compacted non-remotely to low applied stress levels using the Tinius Olsen machine operating at the same crosshead speed. This series of experiments revealed (4) that widespread fracture of particles occurred at very low applied stress (at least as low as 1.1 MPa). The stress relaxation of the compaction apparatus (without sample) in the hydraulic press was determined to be quite small and was ignored.

Figure 1 is an analog plot of the applied force and porous bed displacement traces as a function of time for a typical experiment (HMX-23). The sample unloading was complicated by friction between the porous bed and the mold wall which caused the bed displacement to lag behind the force (i.e., had the appearance of an elastic aftereffect (20)). This required the use of the end points of the applied force and sample displacement traces to compute an effective unloading elastic spring constant. Determining the spring constant from the reloading traces was also complicated since there were very few (usually about 6) data points defining the linear portion of the curve. Thus, it was not clear that the linear region was well established in each case. Corrections were made to account for the spring constant of the compaction apparatus (without sample) and for the friction between the porous bed and the mold wall. The effect of friction was dealt with by using the slope of the highly linear F_t - F_a plot measured (4) on loading, where the very small intercept value was neglected. When appropriate, the radial expansion of the mold was calculated in the standard manner (21), assuming uniform internal radial pressure and externally balanced longitudinal pressure, and this was also included in the determination of the spring constant of the sample.

Sound Speed: Once corrected, the elastic spring constant, K, was converted to a modulus, M, using

$$M = \frac{Kl}{A}, \qquad (5)$$

TABLE 1
Teflon 7C Experiments

EXPERIMENT[15] #	INITIAL %TMD[a]	MAXIMUM %TMD[a]	MAX σ_a, MPa (psi)	C[b], MPa	m[b]	K_{RL}[c], kN/mm	M_{RL}, MPa	V_L(RL), m/s
TEF- 1	29.5	81.5	6.25 (906)	10.8	0.067	4.05	130	260
2	29.7	81.6	6.40 (928)	10.2	0.061			
3	28.8	84.8	8.39 (1220)	14.1	0.067	6.38	190	310
4	28.7	85.0	8.47 (1230)	13.8	0.065			
5	28.0	92.3	18.6 (2700)	27.2	0.055	18.2	500	490
6	28.1	91.6	18.5 (2690)	28.8	0.061			
AVG. = 28.8								

[a] %TMD CALCULATED USING AN AMBIENT PRESSURE CRYSTAL DENSITY OF 2.305 g/cm^3 (2).
[b] $\tau_1 = C\dot{\varepsilon}_{pl}^{m}$.
[c] SPRING CONSTANTS WERE MEASURED ON SEPARATE, ESSENTIALLY IDENTICAL SAMPLES.

TABLE 2
#20 Sieve Cut HMX Experiments

(a) First sampling[4]

EXPERIMENT #	INITIAL %TMD[a]	MAXIMUM %TMD[a]	MAX σ_a, MPa (psi)	C[b], MPa	m[b]	K_{UL}, kN/mm	M_{UL}, MPa	V_L(UL), m/s
HMX- 1	57.7	74.5	5.60 (813)	7.00	0.038	6.34	263	431
2	57.5	80.0	10.9 (1580)	13.0	0.042	13.7	529	590
3	56.5	85.1	24.7 (3590)	29.0	0.043	34.2	1240	876
4	56.3	85.1	24.4 (3530)	28.4	0.041	33.0	1200	860
5	56.4	90.3	62.9 (9130)	66.5	0.027	113	3880	1500
6	56.9	92.4	92.3 (13400)	93.9	0.023	154	5130	1710
7	57.0	94.6	143 (20800)	137	0.019	231	7510	2040
8	56.3	96.3	201 (29100)	189	0.019	316	10100	2350
9	55.9	95.3	235 (34000)	221	0.016	364	11700	2540
AVG = 56.7								

(b) Second sampling (low stress experiments)[4]

EXPERIMENT #	INITIAL %TMD[a]	MAXIMUM %TMD[a]	MAX σ_a, MPa (psi)	C[b], MPa	m[b]	K_{UL}, kN/mm	M_{UL}, MPa	V_L(UL), m/s
HMX- 1X	57.8	81.2	13.9 (2010)	14.9[c]	0.031[c]	17.7	675	661
2X	56.2	58.1	1.01 (146)	[c,d]	[c,d]	2.78	148	366
3X	56.0	57.9	.834 (121)	[c,d]	[c,d]	2.56	137	353
4X	55.7	58.5	1.07 (155)	[c,d]	[c,d]	1.94	102	304
5X	55.6	63.1	1.79 (259)	2.63[c]	0.054[c]	2.73	134	334
6X	56.8	70.4	3.69 (535)	[c,d]	[c,d]	5.16	227	412
AVG = 56.4								

[a] %TMD CALCULATED USING AN AMBIENT PRESSURE CRYSTAL DENSITY OF 1.903 g/cm^3 (19).
[b] $\tau_1 = C\dot{\varepsilon}_{pl}^{m}$.
[c] ONLY FIRST 24 POINTS WERE USED IN LEAST SQUARES FIT ANALYSIS.
[d] CORRELATION COEFFICIENT <0.90 FOR LEAST SQUARES FIT ANALYSIS

TABLE 3
Class D HMX Experiments

(a) First sampling[4]

EXPERIMENT #	INITIAL %TMD[a]	MAXIMUM %TMD[a]	MAX σ_a, MPa (psi)	C[b], MPa	m[b]	K_{UL}, kN/mm	M_{UL}, MPa	V_L(UL), m/s
HMX- 10	64.6	96.5	183 (26500)	___[c]	___[c]	308	9830	2310
11	64.6	97.3	227 (32900)	___[c]	___[c]	337	10600	2400
12	65.7	86.5	18.7 (2710)	___[c]	___[c]	22.6	809	701
13	64.6	93.3	64.5 (9350)	___[c]	___[c]	89.5	2960	1290
AVG. = 64.9								

(b) Second sampling[4]

EXPERIMENT #	INITIAL %TMD[a]	MAXIMUM %TMD[a]	MAX σ_a, MPa (psi)	C[b], MPa	m[b]	K_{UL}, kN/mm	M_{UL}, MPa	V_L(UL), m/s
HMX- 14	62.2	79.4	6.35 (920)	___[d]	___[d]	___[d]	___[d]	___[d]
15	64.1	92.7	75.4 (10900)	75.4	0.024	150	5000	1680
16	61.6	93.4	99.6 (14500)	96.6	0.021	207	6840	1960
17	60.5	96.7	232 (33700)	213	0.016	396	12600	2620
18	60.5	95.6	158 (22900)	149	0.017	339	10900	2450
AVG = 61.8								

(c) Third sampling

EXPERIMENT #	INITIAL %TMD[a]	MAXIMUM %TMD[a]	MAX σ_a, MPa (psi)	C[b], MPa	m[b]	K_{UL}, kN/mm	M_{UL}, MPa	V_L(UL), m/s
HMX- 19	66.0	83.0	9.47 (1370)	9.98	0.033	10.3	383	491
20	65.8	87.0	30.2 (4380)	31.4	0.029	30.9	1100	814
21	65.3	88.4	57.0 (8260)	57.8	0.024	50.8	1780	1030
22	63.9	88.9	91.8 (13300)	90.5	0.019	79.7	2770	1280
23	65.7	95.8	148 (21400)	136	0.017	177	5700	1770
24	66.9	100	221 (32100)	195	0.014	325	9950	2280
25	65.3	78.3	5.72 (830)	___[e]	___[e]	7.22	286	438
26	63.3	76.6	4.25 (617)	[e]	[e]	5.27	213	382
27	65.3	72.8	2.56 (371)	[e]	[e]	4.18	178	358
AVG = 65.3								

[a] %TMD CALCULATED USING AN AMBIENT PRESSURE CRYSTAL DENSITY OF 1.903 g/cm^3 (19).

[b] $\tau_i = C\dot{\varepsilon}_{pl}^{m}$

[c] ABNORMAL STRESS RELAXATION KINETICS WERE OBSERVED AND DISCOUNTED.

[d] TRANSMITTED FORCE TRACE WAS NOT PROPERLY RECORDED

[e] CORRELATION COEFFICIENT <0.90 FOR LEAST SQUARES FIT ANALYSIS

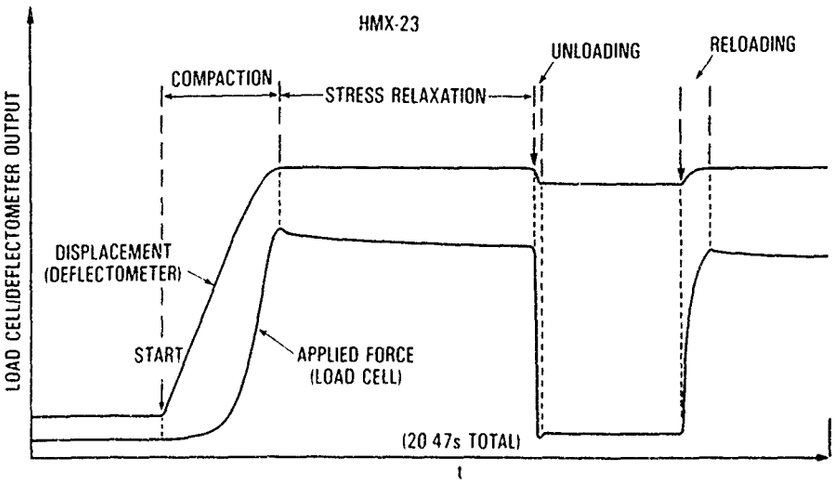

Fig. 1. Applied force and displacement versus time for a typical coarse HMX compaction/stress relaxation experiment

where l is the sample length on unloading or reloading. Then, sound speed, V, was calculated from

$$V = \sqrt{\frac{M}{\varrho}} \quad , \qquad (6)$$

where ϱ is the density of the sample.

Ultrasonic longitudinal velocity measurements were also attempted on a number of HMX samples using a radio frequency tone burst system (22) operating in through-transmission with a delay rod. The apparatus and experimental procedure have been described previously (23). The frequencies at which the measurements were made are given with the reporting of the velocities.

RESULTS AND DISCUSSION

$\tau_i(t)$ and $\dot{\varepsilon}_{pl}(t)$ were calculated at each instant of time for each stress relaxation experiment allowing these parameters to be graphically related by eliminating t as a variable. The first 48 points, corresponding to the highest plastic strain rate portion of the curve, were least squares fit to an equation having the functional form of Equation (1) yielding a determination of strain rate sensitivity. The resultant relationships were then extrapolated to a strain rate typical of actual dynamic experiments which provided an estimate of the intragranular stress necessary to obtain a given %TMD during dynamic compaction.

Teflon 7C: Figure 2 is a logarithmic plot (15) of τ_i versus $\dot{\varepsilon}_{pl}$ for all of the Teflon 7C experiments arranged such that a total strain rate typical of cold gas dynamic compaction experiments (7, 24), $\dot{\varepsilon}_{T_{dyn}}$, is included. Also shown is the maximum strain rate during quasi-static compaction, $\dot{\varepsilon}_{T_{Q\text{-}S}}$, which is greater than the maximum $\dot{\varepsilon}_{pl}$ calculated from stress relaxation. This serves as a check on the calculated $\dot{\varepsilon}_{pl}$ values since they cannot exceed $\dot{\varepsilon}_{T_{Q\text{-}S}}$. The τ_i values obtained from extrapolating to an order of magnitude strain rate of $10^3 s^{-1}$ are shown (15) in Figure 3. Available data from dynamic ($\dot{\varepsilon}_{T_{dyn}} \geq 10^3\ s^{-1}$) compaction experiments obtained by Sandusky and Liddiard (7, 24) are included along with a typical quasi-static compaction curve obtained (2) for a 15 g sample. The results show that reasonable estimates of the intragranular stress dependence on strain rate can be obtained for the compaction of Teflon 7C using this approach. Thus, it was shown (15) that a proper formulation of a compaction law for Teflon 7C would have to include the effect of strain rate.

Coarse HMX: Figure 4 is a logarithmic plot of τ_i versus $\dot{\varepsilon}_{pl}$ for two representative experiments on both #20 sieve cut HMX and Class D HMX. The extrapolation to a strain rate of $10^5\ s^{-1}$ provided an estimate of the intragranular stress necessary to obtain a given %TMD during dynamic compaction experiments (pulse rise

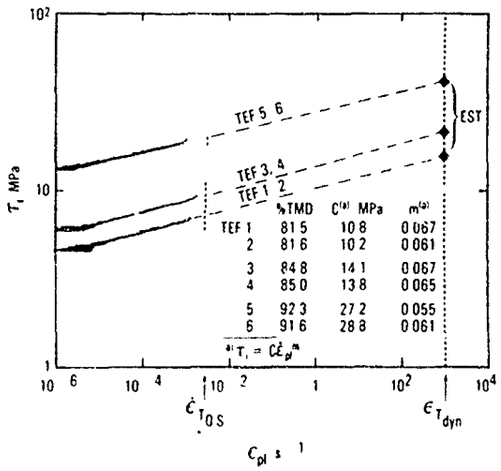

Fig. 2. Logarithmic variation of intragranular stress versus plastic strain rate for compacted Teflon 7C

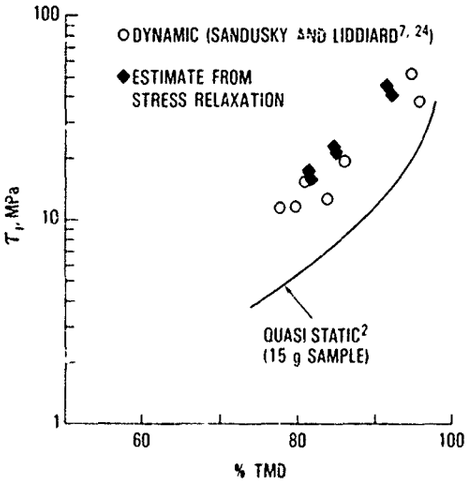

Fig. 3. Semilogarthmic variation of intragranular stress versus percent theoretical maximum density for compacted Teflon 7C

time ≈10 μs) performed by Sandusky (24). The extrapolated values (correlation coefficient ≥0.90) appear in Figures 5 and 6 for sieve cut and Class D HMX, respectively. Also appearing are representative quasi-static compaction results (4) and available dynamic measurements (24). The extrapolated values for sieve cut HMX follow a well-behaved functional form very similar to the quasi-static compaction curve shown for HMX-8. The estimates do tend toward the quasi-static curve at high %TMD, indicating a reduced strain rate effect with increasing %TMD.

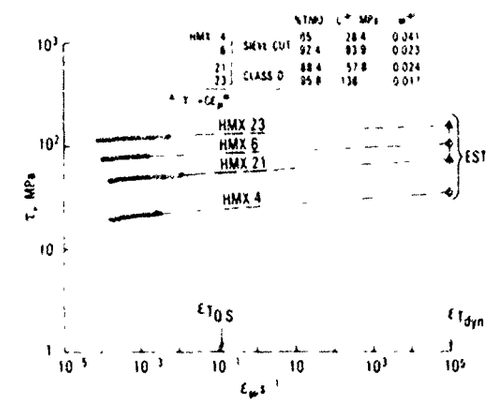

Fig 4. Logarithmic variation of intragranular stress versus plastic strain rate for selected compacted coarse HMX samples

An analogous trend occurs for Class D HMX. The significant scatter in extrapolated values is caused by the variation in quasi-static compaction results that is inherent for a material having a broad particle size distribution. The quasi-static curve shown is for HMX-11 which was previously considered (4) to be representative of Class D HMX quasi-static behavior. In the recently performed "third sampling' experiments, the curve for HMX-23 was virtually identical. However, significant variation in quasi-static compaction curves occurred. The maximum variation is depicted by the two solid lines which are portions of actual compaction curves for HMX-22 and 24. Note that a positive strain rate dependency is actually portrayed for HMX-24 when its quasi-static curve is compared to its extrapolated value. Thus, it is not possible to compare directly the extrapolated high strain rate τ_I values with the measured dynamic data because of the variation in quasi-static compaction data. Furthermore, the $(\%TMD)_0$ value for the dynamic Class D HMX compaction experiments was 7 or 8 percentage points (24) higher than for the quasi-static experiments. The actual quasi-static compaction curve for the sample undergoing dynamic compaction would be necessary for a proper assessment of strain rate dependency.

Although the stress relaxation data reveal that coarse HMX compaction has a small strain

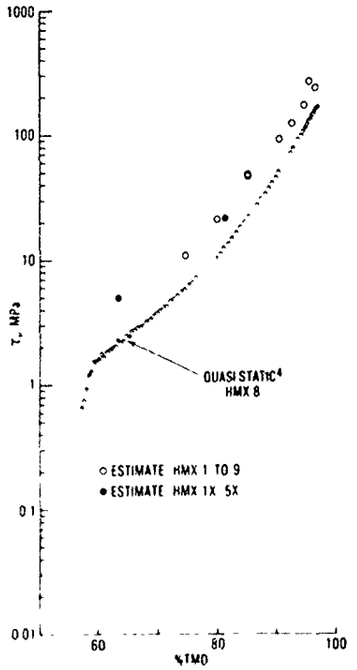

Fig. 5. Semilogarithmic variation of intragranular stress versus percent theoretical maximum density for compacted #20 sieve cut HMX

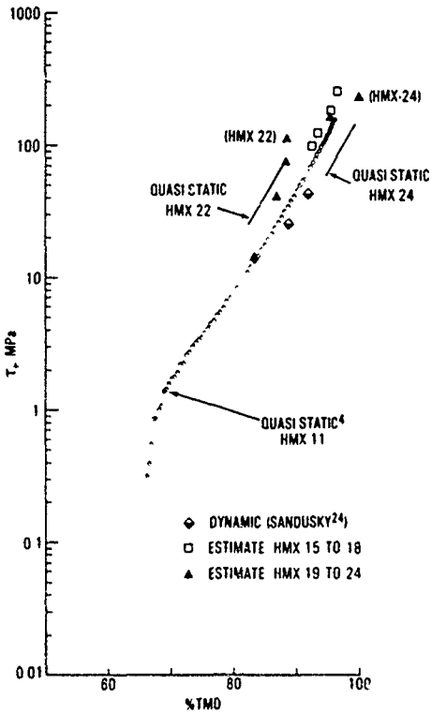

Fig. 6. Semilogarithmic variation of intragranular stress versus percent theoretical maximum density for compacted Class D HMX

rate sensitivity, the increase in stress in extrapolating over six decades is large, ranging from 28 to 130%. Furthermore, the statistical nature of the particle size distribution in Class D HMX is attributed to causing significant variations in the quasi-static compaction results. It is concluded that having samples with similar $(\%TMD)_0$ values does not insure similar quasi-static compaction behavior.

Figure 7 shows the overall trend of strain rate sensitivity (again correlation coefficient ≥0.90) versus %TMD for both Teflon 7C and coarse HMX. Teflon 7C does not show any definite variation of m with %TMD, although only a small %TMD range has been investigated. On the other hand, HMX shows an essentially linear reduction in strain rate sensitivity with increasing %TMD.

Sound Speeds: A by-product of the elastic spring constant determination was the ability to compute velocity as a function of %TMD. The results of the calculations for K, (subscripts RL and UL denote sample reloading and unloading, respectively), M, and V (V_L(RL) and V_L(UL) are the resultant longitudinal velocities for sample reloading and unloading, respectively) appear in Tables 1 to 3 for the appropriate materials. Only the results from unloading data for Class D HMX appear in Table 3 because less experimental uncertainty was associated with these values.

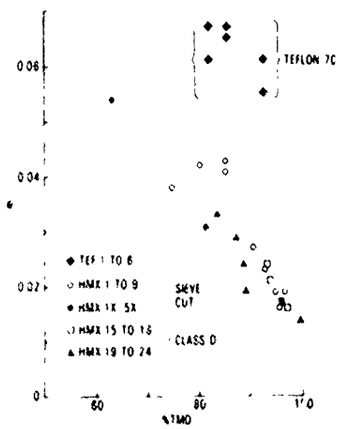

Fig. 7. Strain rate sensitivity versus percent theoretical maximum density for compacted Teflon 7C and coarse HMX

The sound speeds for compacted Teflon 7C determined from the elastic spring constants and longitudinal sound velocities, previously measured (2) ultrasonically, for compacted Teflon 7C and Teflon bar stock are shown as a function of %TMD in Figure 8. Also included is another ultrasonic measurement on Teflon bar stock (25). The sound speeds determined from the elastic spring constants measured on reloading compacted Teflon 7C in the mold at 2.54 mm/min are themselves longitudinal velocities, V_L, since the modulus obtained from loading (or unloading) a sample in uniaxial strain is $B+\frac{4}{3}G$, where B is the bulk modulus and G is the shear modulus (26). The testing machine-determined velocities are 550 to 820 m/s below the ultrasonically-determined velocities. This large difference is attributed primarily to viscoelastic dispersion (27) which gives an increase in velocity with increasing frequency. A second order effect (about 10% for polymers) is associated with the difference in adiabatic and isothermal bulk moduli determined ultrasonically and at very low frequency, respectively (28).

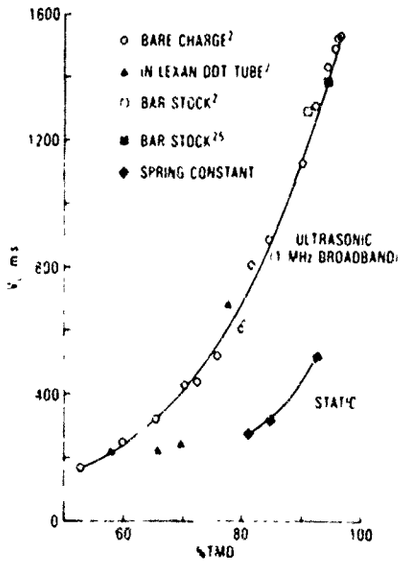

Fig. 8 Longitudinal sound velocity determined ultrasonically and from sample reloading versus percent theoretical maximum density for compacted Teflon 7C

A plot of longitudinal sound velocity versus %TMD obtained from unloading and corresponding reloading elastic spring constants is shown in Figure 9 for Class D experiments HMX 19 to 27 with one exception (HMX-27), the velocities calculated for sample unloading were always higher. Accounting for the noise on the reloading applied force and deflectometer traces and appropriately lowering the machine constant for the low %TMD experiments reduced but did not eliminate the difference in velocities. The reloading portion of the traces nad few data points, making it hard to guarantee a proper linear region for obtaining a slope. Thus, characteristically low velocities from reloading data could be explained by this uncertainty and, as such, provide a rough check on the unloading velocities.

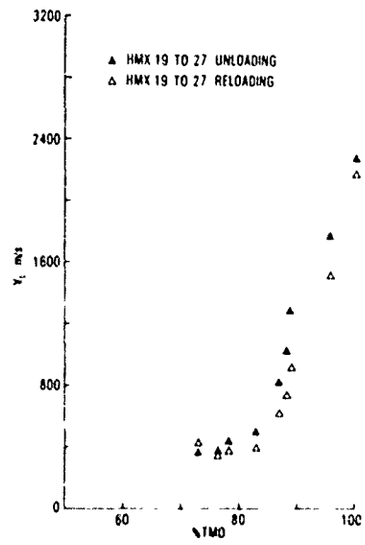

Fig. 9. Longitudinal sound velocity determined from sample unloading and reloading versus percent theoretical maximum density for compacted Class D HMX

The variation of longitudinal sound velocity (calculated from unloading elastic spring constants) with %TMD for all of the coarse HMX compaction experiments is shown in Figure 10. Extending the combined data set to 100% TMD yields, as expected, a value in excess of the bulk sound speed for compacted HMX reported by Olinger, Roof, and Cady (19). There is also good consistency with available experimental data for two pressed plastic bonded explosive (PBX) compositions (29-31) containing 94-95 weight % HMX.

Longitudinal sound velocities determined ultrasonically are shown as a function of %TMD in Figure 11 for various recovered coarse HMX

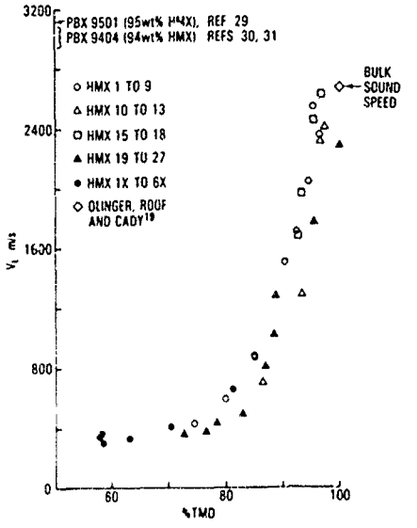

Fig. 10. Longitudinal sound velocity determined from sample unloading versus percent theoretical maximum density for compacted coarse HMX

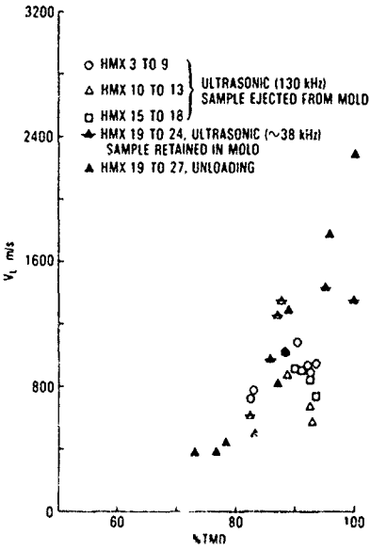

Fig. 11. Longitudinal sound velocity determined ultrasonically and from sample unloading versus percent theoretical maximum density for compacted coarse HMX

samples that had been compacted. Measurements on samples in and out of the mold are included along with values calculated from unloading elastic spring constants for HMX-19 to 27. Ultrasonic measurements performed outside the tube on HMX-3 to 18 revealed a disturbing decrease in velocity with increasing %TMD above 88 to 90% TMD. This decrease in velocity is attributed to the formation of numerous axial cracks during ejection of the samples from the mold that, in turn, cause a considerable increase in the transit time for wave propagation. These "cracks" were not visible per se but would be analogous to laminar cracking observed (32) in compacts that had been ejected from a mold. An improvement in experimental technique occurred by performing ultrasonic measurements on compacted samples retained in the mold after the top and bottom rams had been removed. Up to 90% TMD, the velocities determined in this manner were 4 to 21% higher than the velocities calculated from unloading data. Although there is considerable experimental uncertainty in the ultrasonic sound velocities measured on samples retained in the mold, it appears that wave propagation in coarse HMX porous beds is weakly and possibly mildly dispersive over the frequency and %TMD range studied. Additional work is needed to confirm this tentative conclusion. Above 90% TMD, the data sets intersected and then diverged with the ultrasonic velocities being much lower. At this degree of consolidation, some crack-like defect structure apparently forms on sample unloading, even in the tube, that gives the abnormally long transit times measured ultrasonically.

CONCLUSIONS

The strain rate sensitivity of porous bed compaction has been quantitatively assessed for two types of coarse HMX explosive, having about the same average particle size but widely differing particle size distribution. Over the same %TMD range, the strain rate sensitivity for porous bed compaction of coarse HMX was about 50% that of Teflon 7C powder (a model inert material) which had been studied previously. This does not seem to be inconsistent with actual dynamic measurements, obtained by other NSWC investigators, basically using two different driver systems, on these two materials when compared to separately determined quasi-static results. For the sieve cut HMX, intragranular stress values obtained (at various densities) by extrapolation to a strain rate typical of dynamic compaction experiments followed

a functional form very similar to the quasi-static compaction curve. The situation for Class D HMX was complicated because the quasi-static and dynamic compaction behaviors seem to be strongly dependent on both $(\%TMD)_0$ and initial particle size distribution.

Sound velocities determined from porous bed elastic unloading were an important by-product of this work. The values were found to be consistent with available experimental data. The indication from the present work is that ultrasonic velocity measurements should really be performed on the compacted sample while under stress in the mold. However, the unloading modulus approach appears to provide reasonable "ambient" pressure sound velocities over a large %TMD range for materials that are not strongly dispersive.

ACKNOWLEDGMENTS

The authors want to thank R. R. Bernecker for many valuable suggestions concerning the direction of the work. H. W. Sandusky and D. E. Kooker, U.S. Army Ballistic Research Laboratory, made a number of helpful comments. A. L. Gillis sieved the HMX, yielding a particle size analysis and the sieve cut material for the compaction/stress relaxation experiments. C. L. Groves provided a number of the HMX samples. M. E. Austin and R. W. Simkins helped perform a number of the experiments. T. A. Orlow and B. Glancy helped with the data analysis. Special thanks go to F. X. Spiegel, Loyola College, for his discussion about elastic aftereffect.

REFERENCES

1. R. R. Bernecker, H. W. Sandusky, and A. R. Clairmont, Jr., "Deflagration-to-Detonation Transition Studies of Porous Explosive Charges in Plastic Tubes," in Proceedings Seventh Symposium (International) on Detonation, NSWC MP 82-334, pp. 119-138, 1982.
2. W. L. Elban, S. B. Gross, K. Kim, and R. R. Bernecker, "Quasi-Static Compaction Studies for DDT Investigations: Inert Materials," NSWC TR 81-113, Dec 1982.
3. W. L. Elban, "Quasi-Static Compaction Studies for DDT Investigations: Ball Propellants," Propel., Explos., Pyrotech., Vol. 9, No. 4, pp. 119-129, 1984.
4. W. L. Elban and M. A. Chiarito, "Quasi-Static Compaction Study of Coarse HMX Explosive," Powder Technol., Vol. 46, No. 2-3, pp. 181-193, 1986.
5. H. W. Sandusky, W. L. Elban, K. Kim, R. R. Bernecker, S. B. Gross, and A. R. Clairmont, Jr., "Compaction of Porous Beds of Inert Materials," in Proceedings Seventh Sympcsium (International) on Detonation, NSWC MP 82-334, pp. 843-856, 1982.
6. H. W. Sandusky, R. R. Bernecker, and A. R. Clairmont, Jr., "Dynamic Compaction of Inert Porous Beds," NSWC TR 81-97, Oct 1983.
7. H. W. Sandusky, W. L. Elban, and T. P. Liddiard, "Compaction of Porous Beds," in Shock Waves in Condensed Matter — 1983, pp. 567-570, eds.: J. R. Asay, R. A. Graham, and G. K. Straub, North-Holland, Amsterdam, 1984.
8. H. W. Sandusky, "Compressive Ignition and Burning in Porous Beds of Energetic Materials," in Proceedings of the 1983 JANNAF Propulsion Systems Hazards Subcommittee Meeting, Vol. I, CPIA Publ. 381, pp. 249-257, 1983.
9. W. J. M. Tegart, Elements of Mechanical Metallurgy, pp. 36-37, Macmillian, New York, 1967.
10. G. E. Dieter, Mechanical Metallurgy, pp. 348-353, McGraw-Hill, New York, 2nd Edn., 1976.
11. D. Lee and E. W. Hart, "Stress Relaxation and Mechanical Behavior of Metals," Met. Trans., Vol. 2, No. 4, pp. 1245-1248, 1971.
12. J. Weertman and J. R. Weertman, "Mechanical Properties, Strongly Temperature Dependent," in Physical Metallurgy, p. 984, ed.: R. W. Cahn, North-Holland, Amsterdam-London, 2nd Rev. Edn., 1970.
13. E. W. Hart, "Theory of the Tensile Test," Acta Met., Vol. 15, No. 2, pp. 351-355, 1967.
14. D. Lee and D. A. Woodford, "Strain Rate Dependent Plastic Flow Behavior of Metals," in The Inhomogeneity of Plastic Deformation, pp. 113-134, American Society for Metals, Metals Park, OH, 1973.

15. P. J. Coyne, Jr. and W. L. Elban, "A Strain Rate Sensitivity Prediction for Porous Bed Compaction," in Shock Waves in Condensed Matter — 1983, pp. 147-150, eds.: J. R. Asay, R. A. Graham, and G. K. Straub, North-Holland, Amsterdam, 1984.

16. K. K. Kuo, B. B. Moore, and V. Yang, "Measurement and Correlation of Intragranular Stress and Particle-Wall Friction in Granular Propellant Beds," in Proceedings of the 16th JANNAF Combustion Meeting, Vol. I, CPIA Publ. 308, pp. 559-581, 1979; K. K. Kuo, V. Yang, and B. B. Moore, "Intragranular Stress, Particle-Wall Friction and Speed of Sound in Granular Propellant Beds," J. Ballistics, Vol. 4, No. 1, pp. 697-730, 1980.

17. A. Savitzky and M. J. E. Golay, "Smoothing and Differentiation of Data by Simplified Least Squares Procedures," Anal. Chem., Vol. 36, No. 8, pp. 1627-1639, 1964.

18. W. J. M. Tegart, *op. cit.*, pp. 25-29.

19. B. Olinger, B. Roof, and H. Cady, "The Linear and Volume Compression of β-HMX and RDX to 9 GPa (90 Kilobar)," in Actes du Symposium International sur le Comportement des Milieux Denses sous Hautes Pressions Dynamiques, Editions du Commissariat à l'Energie Atomique Centre d'Etudes Nucleaires de Saclay, pp. 3-8, 1978.

20. W. Hayden, W. G. Moffatt, and J. Wulff, The Structure and Properties of Materials — Volume III - Mechanical Behavior, pp. 51-52, John Wiley and Sons, New York, 1965.

21 R. J. Roark and W. C. Young, Formulas for Stress and Strain, p 504, McGraw-Hill, New York, 5th Edn., 1975.

22. E. P. Papadakis, "Ultrasonic Velocity and Attenuation: Measurement Methods with Scientific and Industrial Applications," in Physical Acoustics, Vol. XII, pp. 308-312, eds.: W. P. Mason and R. N. Thurston, Academic Press, New York, 1976.

23 J. W Forbes and W. L. Elban, "Comparison of Axial Longitudinal Velocity Measurements Determined Ultrasonically and by a Weak Shock Velocity Technique on an Aluminized Melt Cast Explosive," in Shock Waves in Condensed Matter — 1981, pp. 583-587, eds.: W. J. Nellis, L. Seaman, and R. A. Graham, American Institute of Physics, New York, 1982.

24. H. W. Sandusky and T. P. Liddiard, "Dynamic Compaction of Porous Beds," NSWC TR 83-246, 26 Dec 1985.

25. B. Hartmann and J. Jarzynski, "Immersion Apparatus for Ultrasonic Measurements in Polymers," J. Acoust. Soc. Am., Vol. 56, No. 5, pp. 1469-1477, 1974.

26. Ya. B. Zel'dovich and Yu. P. Raizer, Physics of Shock Waves and High-Temperature Hydrodynamic Phenomena, Vol. II, pp. 734 and 742-743, eds.: W. D. Hayes and R. F. Probstein, Academic Press, New York and London, 1967.

27. H. J. Sutherland, "Dispersion of Acoustic Waves by Fiber-Reinforced Viscoelastic Materials, " J. Acoust. Soc. Am., Vol. 57, No. 4, pp. 870-875, 1975.

28. B. Hartmann, "Ultrasonic Measurements," in Methods of Experimental Physics: Polymers — Physical Properties, Vol. 16c, pp. 59-90, ed.: R. A. Fava, Academic Press, New York, 1980.

29. B. Olinger and J. Hopson, "Dynamic Properties of Some Explosives and Explosives Simulants," in Actes du Symposium International sur le Comportement des Milieux Denses sous Hautes Pressions Dynamiques, Editions du Commissariat à l'Energie Atomique Centre d'Etudes Nucleaires de Saclay, pp. 9-19, 1978.

30. N. L. Coleburn and T. P. Liddiard, Jr., "Hugoniot Equations of State of Several Unreacted Explosives," J. Chem. Phys., Vol. 44, No. 5, pp. 1929-1936, 1966.

31. H. J. Sutherland and J. E. Kennedy, "Acoustic Characterization of Two Unreacted Explosives," J. Appl. Phys., Vol. 46, No. 6, pp. 2439-2444, 1975.

32. W. M. Long, "Radial Pressures in Powder Compaction," Powder Metall., No. 6, pp. 73-86, 1960.

DISCUSSION

J. DICK, Los Alamos National Laboratory

You stated that %TMD on your graphs means the bulk density at that stress level divided by the crystal density at ambient conditions. I have found that to be a misleading use of the term "percent theoretical maximum density" especially when one wishes to find a value for the residual porosity, since the compressibility of the solid phase is not accounted for. Perhaps the term "percent theoretical maximum initial density" (%TMID) would be less ambiguous.

REPLY BY P. J. COYNE, JR

The reason we report percent theoretical maximum density using the ambient pressure crystal density is primarily historical. Much of the existing literature on DDT has used this parameter. All previous plots of this nature, generated at the Naval Surface Weapons Center, have, as a result, followed this convention. We have been slow to change to what is a more appropriate parameter for two reasons. First, direct comparisons can be made with the existing body of information. Second, with the exception of HMX, there is little, if any, experimental data available to make this adjustment for other energetic materials of interest. In the future, we hope to generate a second version of the plots in question for HMX using data that is available (Ref. 19 of our paper) on the compressibility of solid HMX. Your suggestion of using %TMID is a good one, and merits future consideration.

DEFLAGRATION-TO-DETONATION TRANSITION (DDT) STUDIES OF A DOUBLE-BASE PROPELLANT

R. R. Bernecker, H. W. Sandusky, and A. R. Clairmont, Jr.
Naval Surface Weapons Center
White Oak, Silver Spring, Maryland

DDT experiments have been conducted with very porous columns of a double-base propellant confined in plastic and steel tubes. In addition to the regular ignition system, a special free volume ignition system has been used in the steel tubes to produce a slower pressurization of the columns during the pre-ignition stage. For both types of confinement it has proven very helpful to evaluate events relative to the location and time of the onset of detonation. Using this procedure, it was found that data from replicate experiments show a reasonably good degree of reproducibility. The use of the weaker ignition system increased the distance to detonation by about 10% in the steel tube arrangement. This increase in distance is attributed to a retardation of the compressive ("hot spot") reaction during the latter stages of the DDT process. Flash radiographic results from the plastic tube and pressure transducer measurements from the steel tube data are used to interpret predetonation events of the various stages of the DDT process.

INTRODUCTION

Research directed toward the elucidation of the stages of the deflagration-to-detonation transition (DDT) process in porous energetic materials has been carried out for decades. In more recent years attempts have been made to develop theoretical/numerical models of the total DDT process (1-3). However, these efforts have not been completely successful because of factors such as incomplete formulation of key constitutive relationships and quantitative descriptions of compressive reaction. Researchers at our Center have been working with a variety of simple energetic systems (ball powders and neat explosives) to quantify their compressibility relationships (4, 5), their shock reactivity (6), and their DDT behavior (7). These data provide useful experimental information for the development of more accurate numerical models. In this paper we wish to present DDT data for one of these ball powders, illustrating the effect of confinement and the type of ignition source on the DDT parameters. The experimental data are discussed in terms of each of the stages of the DDT process (see Table 1).

TABLE 1
Stages of DDT Mechanism for Porous Charges

1. Pre-ignition	
2. Ignition/Conductive Burning	
3. Convective Burning	
4. Compressive ("Hot Spot") Burning	
5. Shock Formation	SDT
6. Compressive Burning	SDT
7. Detonation	SDT

The material used in the study was a commercial reloading powder, WC 231; it has been very useful in the DDT studies since it undergoes a transition to detonation both in low confinement (plastic) tubes and in high confinement (steel) tubes (7). For the steel tube experiments, two different ignition sources were used: our regular ignitor and a free volume ignitor. The latter was designed to produce a lower pressurization rate (dP dt) during the pre-ignition stage

(see Table 1). Pre-ignition compaction and pyrolysis can pre-condition the porous column; it was of interest to contrast the pressure-time histories, along the predetonation columns, for the two ignition systems.

Replicate experiments were run to obtain a measure of the statistical variation in predetonation parameters. It has been very helpful in analyzing these data to evaluate the buildup process relative to the predetonation column length (l) and time to detonation, such that $x^* = x - l$ and $t^* = t - t_D$ (x is distance along the column, t is time relative to the response of an optical fiber/photodetector assembly terminated at the propellant interface and t_D is the corresponding time to detonation). Using this formalism, good agreement has been observed among predetonation observations for replicate experiments in both the plastic and steel tubes.

EXPERIMENTAL ARRANGEMENTS AND PROCEDURES

The plastic DDT tube and its experimental arrangement have been described and documented elsewhere (8, 9). The plastic tube is fabricated from polycarbonate rod (Lexan 101-111) and has an OD of 76.0 mm, an ID of 25.4 mm and a length of 305 mm. Associated instrumentation included externally mounted strain gages, conductivity and ionization probes, optical fiber/photodetector assemblies, high speed continuous-access streak and framing cameras and flash radiography units. The flash radiographic measurements of charge density are determined from x-ray tracers, usually tungsten wires, loaded between increments during charge fabrication.

In order to evaluate the susceptibility of all the various ball powders (4) to DDT, it was necessary to conduct experiments in steel tubes (7). For these experiments the plastic tube was simply replaced by a steel tube of nominally identical dimensions. In this manner, the lateral confinement was increased while retaining the same ignition arrangement and end clamping arrangement. This new steel tube system is called a "modified steel tube (MST) arrangement"; a schematic of this system (with our regular ignitor) is shown in Figure 1. Piezoelectric (PE) pressure transducers were located along the predetonation column length and mounted flush to the wall. For the PE transducer located next to the ignitor/propellant interface, a static gas calibration *in situ* was performed to ~30 MPa to confirm the manufacturer's calibration. The PE transducers used were manufactured by PCB (Model 109A02) and had a risetime of 1 μs and maximum pressure limit of 862 MPa. Their output was sent to both a high sensitivity recording channel (~30 MPa) and to a low sensitivity recording channel (>1000 MPa). The free volume (F.V.) ignition system differed from the regular system (9) by the presence of a 5.0 cc cavity (2.26 cm long) between the B/KNO_3 ignitor mixture and the free surface of the propellant column.

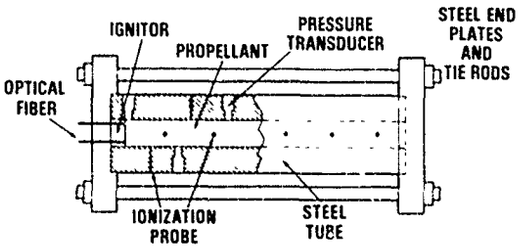

Fig. 1. Modified steel DDT tube arrangement

The propellant used in this study was an ammunition reloading powder manufactured by the Winchester Group of the Olin Corporation and was purchased locally; its designation is WC 231. This powder was undeterred but rolled; as a result of the rolling process some of the individual grains had notched regions (fracture points) (4). The particle size distribution of the powder was very broad, extending from 350 to 1000 μm. Theoretical maximum density (TMD) is taken to be 1.64 g/cc (4).

EXPERIMENTAL RESULTS

Plastic Tube Experiments

Two DDT experiments (Shots S74 and S82) were conducted, utilizing the regular ignition system. To document more completely the extent of compaction induced by the burning of the B/NKO_3, a dynamic compaction experiment (10) was also carried out, with the x-ray tracers spaced 6.4 mm apart.

A. Dynamic Compaction Experiment

A thin nickel disk (0.9 mm thick), slightly smaller than the ID of the tube, was placed between

the regular ignitor and the propellant in order to retard ignition of the propellant in this experiment (Shot A01). The main observations from this shot to be discussed here are the apparent density profiles (i.e., one-dimensional compaction) as determined from radiographs taken at 501 and 753 μs after the first detection of luminosity at the propellant interface. These data (see Figure 2) show that a low density wave front (called a weak compressive wave (WCW) (9)) had propagated to 104 mm at the x-ray time of 501 μs. This density profile is in accord with a low pressure loading from burning of the B/KNO_3 material. However, from ~32 mm back to the disk (at 16 mm) a negative density gradient illustrates a rarefaction of the previously compacted propellant. This rarified region is associated with the reaction (pyrolysis) of the propellant which ultimately led to convective combustion. In the convective combustion stage, a fluidized bed (with density lower than the original material) is located upstream of the compacted propellant. The presence of the fluidized bed can be seen upstream of 56 mm for the 753 μs data in Figure 2. At 753 μs the disk was no longer near the compacted column but had been "blown" back to the ignitor interface (x = 0). The front of the high density column at 86 mm represents the compressive (compaction) front (designated in Ref. 9 as the strong compressive (compaction) wave) and is driven by the convectively burning propellant. The density profile between 56 and 69 mm (as seen in Figure 2 for the 753 μs data) is only a semi-quantitative representation of the true profile since asymmetric burning of the propellant occurred and the tracers were badly and asymmetrically bent (a very rare happening).

It is experimentally difficult to define accurately the deformation of the inner wall of the plastic tube and the change in diameter of the propellant bed. Hence the data in Figure 2 (and later density profiles shown in this paper) are designated as "apparent" density profiles. However, using x-ray tracers placed along the inner wall, we occasionally measure the tube wall deformation. Using tracers placed along the wall between 25 and 30 mm, the tube expansion at 501 μs was minimal (an increase from 25.70 mm to 25.88 mm). Thus the 501 μs density profile is judged to be indicative of the actual densities, from the observed tube expansion at 753 μs this cannot be claimed for that density profile.

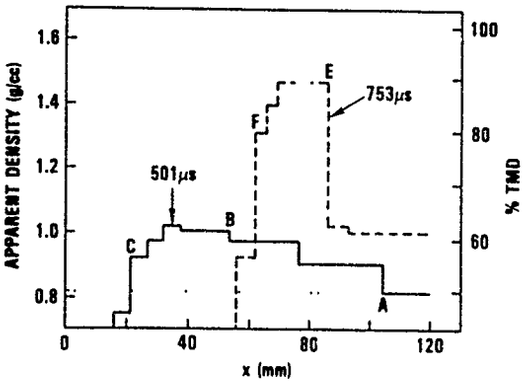

Fig. 2. Density profiles from Lexan tube (ignitor) compaction of WC 231, Shot A01

B. DDT Experiments

In the Lexan tube experiments (S74 and S82), a transition to detonation occurred at 222 and 235 mm, respectively. The times associated with the onset of detonation (t_D), the flash radiographs (t_{XR}) and the flash radiographs relative to the onset of detonation ($t_{XR}^* = t_{XR} - t_D$) are shown in Table 2. The density (apparent) profiles calculated from the x-rays are shown in Figures 3 and 4. Various letters have been used to designate the region associated with various fronts. The locations associated with the head of the WCW are designated by A and D. The strong compressive wave (SCW) region, driven primarily by the convective combustion of the propellant, is encompassed by the B-C and E-F designations.

In Table 3 are listed the regions, densities, shock (compaction front) velocities, particle velocities and pressures associated with the WCW and SCW. Most of these values were calculated directly from Figures 3 and 4. Others were calculated from the jump conditions. The data in Table 3 and Figure 2 show that the density associated with the WCW is fairly constant for the three plastic tube experiments. The data in Table 3 for the SCW show an apparent density increase between the two radiographs for each experiment. More interestingly, it appears that the % TMD at the front of the SCW increases with increasing t^*_{XR} values, indicating a certain reproducibility of events between S74 and S82. This reproducibility also appears to extend to the luminous events observed photographically.

TABLE 2
Lexan Tube DDT Experiments with WC 231 Propellant

SHOT NO.	DENSITY (g/cc)	DENSITY (% TMD)	l (mm)	t_D (μs)	t_{XR} (μs)	t^*_{XR} (μs)
S74	0.830	50.6	222	677	421	−256
					523	−154
S82	0.820	50.0	235	872	699	−173
					765	−107

TABLE 3
Lexan Tube DDT Data for WC 231 Propellant

		WCW					SCW				
SHOT	t^*_{XR} (μs)	x (mm)	% TMD[a]	U[b] (mm/μs)	u (mm/μs)	P[d] (MPa)	x (mm)	% TMD[a]	U[c] (mm/μs)	u[d] (mm/μs)	P[d] (MPa)
S74	−256	101.9	56.5	0.210	(0.021)	3.7	62.8	73.2	0.39[b]	0.09	29.0
									0.42	0.10	30.9
		87.7	61.3	0.224	0.037[d]	6.7	43.3	82.7	0.42	0.14	46.3
	−154	123.3	(56.5)	0.210	(0.021)	(3.7)	102.2	95.9	0.52	0.21	90.7
		110.5	(61.3)	0.224	(0.037)	(6.7)					
S82	−173	147.7	55.2	0.233	0.023[b]	4.4	104.6	94.3	0.52	0.21	87.5
		122.6	61.3	0.24	0.045[d]	8.7					
	−107	163.0	55.3	0.233	(0.023)	(4.4)	138.8	(100)	0.60	0.28	139

a. Apparent Density b: Average Value Between X-Ray Times c: Assumed from Luminosity d: Calculated

Shot S74 used a continuous-access streak camera while a continuous-access framing camera was used in S82. The photographic data for both experiments are shown in Figure 5 using x* and t* values; it can be seen that the predetonation luminosity is surprisingly reproducible. Moreover, when the flash radiographic data for the SCW (points B and E from Figures 3 and 4) are considered in Figure 5, there appears to be a fairly continuous propagation path for the SCW. It is also evident that the luminosity associated with the propagation of the SCW represents luminous gases in the annular region between the expanded tube and the compacted propellant (this feature was also illustrated for coarse HMX in Ref. 9). In the case of Shot S82, the non-luminous SCW appears to become luminous and increase in velocity just about the time it overtakes the WCW. On the other hand, in Shot S74 the SCW only became luminous 20 mm downstream of the intersection of the WCW and the SCW. Thus, there is no consistent interpretation from these data of what produces the accelerating shock wave.

STEEL TUBE EXPERIMENTS

The experimental parameters for the steel tube experiments are listed in Table 4. It appears that l is about 125 mm for the regular ignition system and 137 mm for the free volume (F.V.) ignition system. These data indicate that the "softer" F.V. ignition system yields a slightly longer predetonation column length. From Table 4 it is noted that t_D is much longer for the F.V. system, as expected. The locations of the pressure transducers used in these experiments are also listed in this table. In four of these experiments transducers were located in the ignition region such that the B/KNO_3 combustion process and initial reaction of the propellant could be monitored. In these same four experiments an additional transducer was located downstream to outline the propagation of the WCW, the SCW, and for Shot A97 the shock region.

The ionization probe data for two regular ignitor experiments (A142 and A143) are shown in Figure 6. Least square straight lines have been drawn through the two data sets. The data show

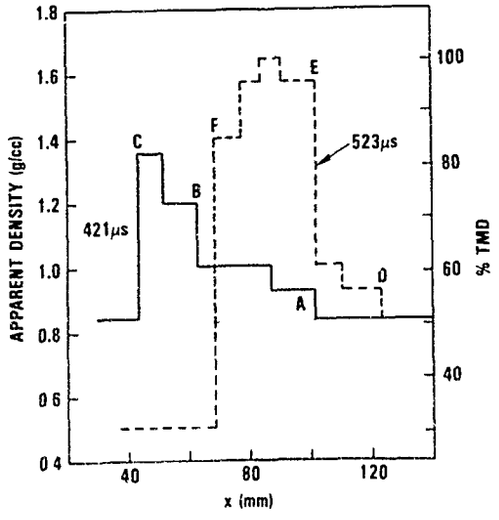

Fig. 3. Density profiles from Lexan tube DDT experiment with WC 231, Shot S74

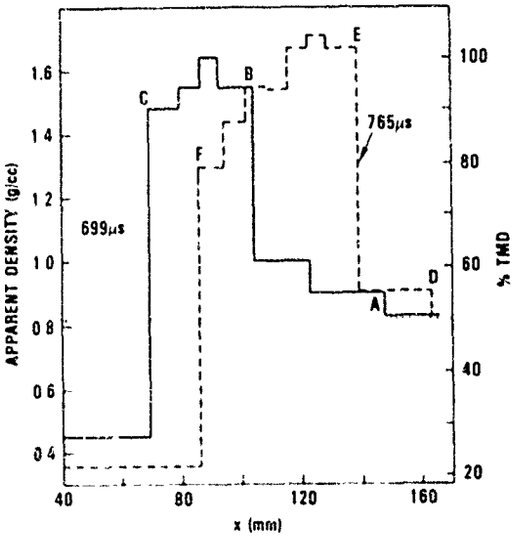

Fig. 4 Density profiles from Lexan tube DDT experiment with WC 231, Shot S82

a reproducible discharge rate of 0.67 and 0.66 mm/μs, respectively, except for the probes located less than 35 mm from the onset of detonation. The latter probe discharges indicate an accelerating process in accord with the luminous fronts shown in Figure 5. Similar reproducibility of the probe data for the F.V. ignitor experiments (A97 and A147) is seen in Figure 7. The two least squares straight lines would essentially overlay if the same l value of 137 mm (see Table 4) was selected for both experiments. The discharge rate is 0.57 mm/μs for both experiments. Not shown in Figures 6 and 7 (except for A97) are the response times of the first probe in these experiments.

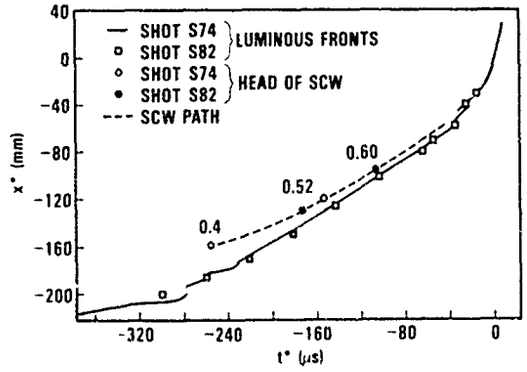

Fig. 5. Distance-time data from Lexan tube DDT experiments with WC 231 (Numerical value is velocity in mm/μs.)

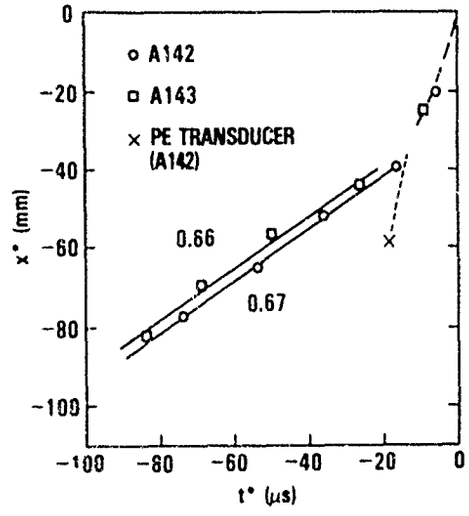

Fig. 6. Probe data from steel tube experiments (regular ignitor) with WC 231 (Key of Fig. 5)

The pressure-time (P-t) histories for these steel DDT experiments have provided considerable quantitative insight into predetonation events and their influence (or lack of such) on the location and time of the transition to detonation. To illustrate the reproducibility of events in the ignition region, the P-t data for the lower pressure range (<25 MPa) for experiments A97, A142, A143, and A147 are shown in Figure 8. In the time period of −500 to −200 μs, all four experiments have similar pressure levels and pressurization rates. For the regular ignitor shots (A142 and A143), the ignitor transducer at 3 mm detected the pressure

loading from the B/KNO_3 mixture at about -500 μs; this time is very close to the response time of an optical fiber/photodetector assembly at the ignitor interface (see t_D values in Table 4). When the F.V. ignitor experiments are considered, excellent reproducibility is evident for A97 and A147 data in the -600 to -200 μs period.

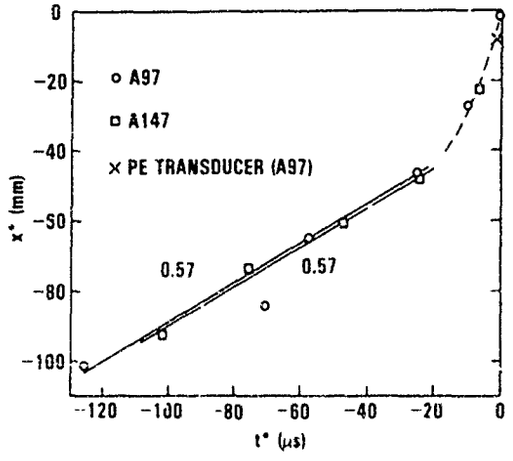

Fig. 7. Probe data from steel tube experiments (free volume ignitor) with WC 231 (Key of Fig. 5)

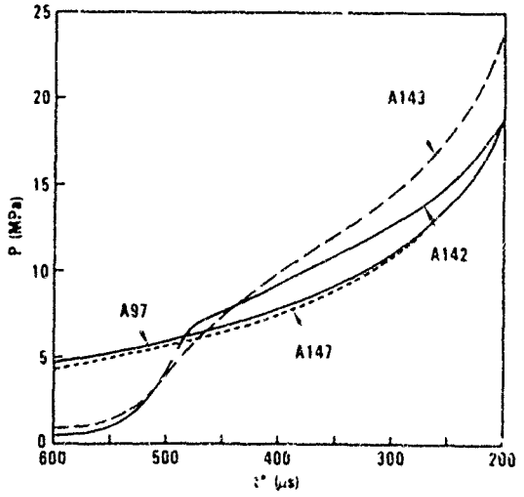

Fig. 8 Pressure-time data from ignition region in steel tube experiments with WC 231 (Regular ignitor: A142 and A143; free volume ignitor: A97 and A147)

While the pressure levels from the four experiments are similar in the -500 to -200 μs period, the agreement is very poor in the -100 to 0 μs time frame, even for replicate experiments with the same ignition system (see Figure 9).

At the time of detonation, the pressure levels in the ignition region are 283, 409, 333 and 342 MPa, respectively, for Shots A97, A142, A143 and A147. It is noted that the F.V. ignition system has the lower average pressure at the time of detonation and the larger average l value.

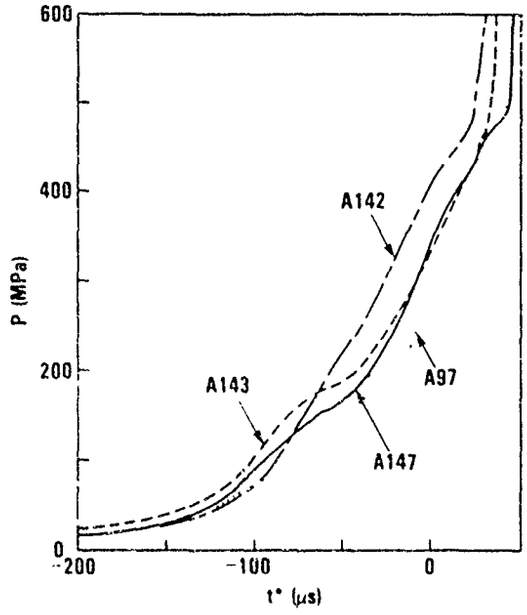

Fig. 9. Pressure-time data from ignition region in steel tube experiments with WC 231 (Key of Fig. 8)

The pressure-time histories of the downstream transducers (see locations in Table 4) showed a variety of pressurization rates and pressure plateaus. The simplest P-t data were seen in Shot A97 where the transducer was located 8.3 mm upstream of where detonation began. At that location an increase in pressure was not detected until ~2 μs before the onset of detonation. This datum is shown in Figure 7 and is consistent with the propagation of an accelerating shock wave. Because the time resolution of the transducer recorder was 2 μs per point, very little can be said about P or dP/dt associated with the shock wave. It should be noted, however, that at $t^* = -6$ μs, the pressure started to go negative, probably reflective of tube deformation ahead of the propagating shock wave. This negative excursion has been detected many times by externally mounted strain gages in our earlier work in steel tubes (11) and plastic tubes (8).

TABLE 4
Steel Tube DDT Data For 50.0% TMD WC 231 Propellant

SHOT	IGNITOR SYSTEM	TRANSDUCER LOCATION (mm) x	x*	l (mm)	t_D (μs)	DETONATION VELOCITY (mm/μs)
A27	REGULAR	—	—	121	595.5	4.66
A142	REGULAR	3.0	−122	125	510.4	4.63
		66.6	−58			
A143	REGULAR	3.3	−127	130	477.4	4.62
		50.4	−80			
A31	F.V.	—	—	140	181.3 + ?[a]	4.68
A97	F.V.	CAVITY	—	135	1588	4.61
		126.7	−8			
A147	F.V.	CAVITY	—	137	2235.0	4.63
		50.2	−87			

a: 181 3 + 2593 (most likely)

Low pressure data from downstream transducers in Shots A142 and A143 showed a slow, linear rise in pressure indicative of the WCW; its calculated velocity is 0.23 and 0.22 mm/μs, respectively. These velocities and the respective pressure levels (<5 MPa) are consistent with data for the WCW as seen in the plastic tube shots (see Table 3).

The low pressure data for the F.V. ignitor Shot A147 ($x^* = -87$ mm) had pressure levels and pressurization rates similar to the regular ignitor data of A143 ($x^* = -80$ mm) between −300 and −150 μs. However, it appears that with the F.V. ignitor system a gradual compaction of the propellant bed occurred over a long time period. At the −87 mm location pressure was first detected at about −1000 μs; the extent to which this pressurization is associated with gas flow or solid stress waves cannot be ascertained from our data. However, because of the low pressure levels (<4 MPa at −200 μs) very little compaction of the bed occurred from the first pressure rise (−1000 μs) to ∼−200 μs. The similarity in low pressure data for Shots A143 and A147 suggests that compaction of the propellant bed took place in a similar manner, irrespective of the ignition system.

The high pressure data from the downstream transducers are shown in Figure 10. A comparison of these data and the IP data of Figures 6 and 7 reveals that the discharge of the probes is associated with the propagation of the SCW (the IPs discharged at pressures of 40-50 MPa). Moreover, the magnitude and constant rate of discharge of the IPs from −90 to −40 μs in Figures 6 and 7 are in accord with the SCW data from the plastic tube experiment S82 (see value from $t^*_{XR} = -107$ μs in Table 3).

The higher pressure data in Figure 10 for the downstream transducer locations of Shots A147 and A143 show a plateau at 183 and 263 MPa, respectively. This plateau is interpreted as the end of the SCW; increasing pressure at later times is associated with the convective combustion front and its fluidized bed. With this interpretation, the breadth of the SCW is calculated to be roughly 42 mm for A143 and 35 mm for A147. These values are consistent with the length of the SCW from both radiographs of S82 (see Figure 4) and the second radiograph of S74 (see Figure 3).

The higher pressure data for the downstream transducer for Shot A142 show a distinctly different response than the downstream transducer from Shot A143 (Figure 10). Since the A142 transducer is closer to the location where detonation began, its output is representative of the pressure growth *within* the SCW until the onset of detonation. Thus, the increase in pressure at −18 μs is interpreted as pressure build-up from compressive reaction (stage 4 of Table 1) originating within the compacted bed.

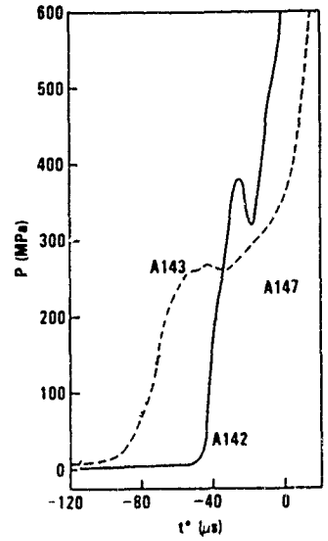

Fig. 10. Pressure-time data from downstream locations in steel tube experiments with WC 231. (Shot A142: $x^* = -58$ mm; Shot A143: $x^* = -80$ mm; Shot A147: $x^* = -87$ mm)

DISCUSSION

The experimental data from the plastic tube and steel tube experiments have provided quantitative insight concerning the parameters and processes associated with the predetonation period. These data will be discussed with reference to the stages of the DDT mechanism outlined in Table 1.

Pre-ignition Stage

Both flash radiographic data (plastic tube) and pressure transducer data (steel tube) have identified the pressure levels associated with pre-ignition gas loading of the propellant column. Elban has reported for WC 231 the stress – % TMD relationship (to 90% TMD) for quasi-static loading conditions (4). The % TMD and pressure of the WCW in the plastic tube are consistent with Elban's quasi-static data. However, data from the earlier radiograph of Shot S74 suggest a significant strain rate effect (similar to that reported for WC 231 in Ref. 5) during compaction associated with the growth of the SCW. Finally, a correlation of Elban's data and data from the plastic and steel tube experiments suggests that in the steel tubes a reduction in % TMD associated with the WCW may occur because of a greater wall frictional component.

The pressure-time data from the steel tube experiments indicate that the type of ignitor did not affect appreciably the densification of WC 231 in the pre-ignition period. However, the data confirm the possibility that under mild ignitor pressurization gas can flow downstream during the pre-ignition stage. Our data indicate that at 50 mm from the propellant interface the maximum gas pressure would be about 2 MPa before significant compaction of the bed occurred and choked off further gas flow.

Ignition/Conductive Burning Stage

With the current diagnostic instrumentation, the only useful information defining a time of ignition comes from the pressure-time data from the ignition region. With the regular ignition system, the data in Figure 8 can be used to estimate a value with an uncertainty of 50 μs. It would appear that a larger uncertainty would be associated with any value from the F.V. ignition system data in Figure 8.

Convective Burning Stage

Flash radiographic data have outlined the growth of the zone burning convectively and also provided some rough estimate of the amount of the original column involved in convective burning at various times. The onset of convective combustion produces extensive compaction and the propagation of a SCW which grows in strength (pressure level) with time. The radiographic data summarized in Table 3 illustrate this evolving process. Knowledge of the extent of compaction and pressure levels in this table have aided in the interpretation of the pressure-time records in the steel tube experiments. Thus, the maximum pressure associated with the SCW was estimated to be 183 and 262 MPa, respectively, for locations of 87 and 80 mm before the onset of detonation (Figure 10). Both are in fair agreement with an estimated pressure of 139 MPa at a x^* value of −96 mm for Shot S82 (Table 3). Also, the response of the ionization probes have outlined the propagation path of the SCW and its velocity. From these measurements and the data in Figure 5, it appears that the early portion of the buildup, just before and after the onset of convective combustion, occurs in a much smaller region of the column for the steel tube experiments (relative to the plastic tube). This is responsible, in large part, for the smaller

l values in steel tubes.

Compressive (Hot Spot) Burning Stage

Compressive burning (or reaction) occurs within the SCW region in this stage. While there was not direct evidence of this stage in the plastic tube data there was evidence of this reaction in the pressure-time records from the steel tube experiments. In the data of Figure 10, the pressure of the SCW has increased from x* locations of −80 to −58 mm (regular ignition system) as has also dP/dt at the front of the SCW. Moreover, the later time data at −58 mm indicate compressive reaction which occurred after −18 μs. Sandusky (6) has found a relationship between the time necessary for the onset of compressive reaction and the shock (compaction) pressure (an extension of that work is reported in these proceedings (12)). For an essentially square pulse pressure loading of 200 MPa, WC 231 should show compressive reaction after ∼17 μs (6). Since the pressure loading from convective burning can be considered a ramp loading (13), the time to reaction at 200 MPa within the SCW should be greater than 17 μs. A reaction delay time of 20 to 25 μs is consistent with the late response of the downstream transducer of Shot A142 in Figure 10 and the accelerating response times of ionization probes at less than −15 μs (see Figures 6 and 7). Moreover, it is believed that it is this compressive (reaction) burning which is responsible for changing the SCW into a propagating shock wave which ultimately drives the WC 231 propellant to detonation. In Figure 6 a hypothetical path has been drawn to show this late time compressive reaction within the SCW region. Evidence of extensive compressive reaction within the SCW can be found in the photographic recording of a 90/10 HMX/Al DDT experiment (9), inferred from the manganin pressure records of DDT experiments with 95/5 RDX/wax (see Figure 3C in Ref. 14), and seen in the strain gage data of earlier steel tube DDT experiments (see, for example, Ref. 11).

Shock Wave Through Detonation Stages

The later stages of the DDT process are essentially those associated with the shock initiation (or SDT) process. The ionization probe data in Figures 6 and 7 and the photographic data in Figure 5 outline the accelerating shock wave and the SDT process. A comparison of these data suggests (based upon reaction front velocities) that the buildup is relatively slower in the plastic tube. This is expected because of the effect of confinement on compressive reaction and the attainment of a transition to detonation (12). However, when comparing the ionization response times of the steel tube experiments for the two ignition systems, the data in Figures 6 and 7 seem to indicate that the buildup beyond the linear regions occurs more quickly for the regular ignition system. This feature may result from a retardation of compressive reaction (in stages 4 *and* 6 of Table 1) due to the presence of significant amounts of combustion gases in the pores of the WC 231 columns in the F.V. experiments. Data supporting this hypothesis can be found in the SDT study of Chick (15). He found that the shock pressure needed to initiate 60% TMD columns of HMX (in a two dimensional gap experiment) was dramatically increased as the initial interstitial gas presure was raised from 0.1 MPa to 7 MPa; the particle size of the HMX and composition of the gas influenced the degree of desensitization. Thus, the longer pre-ignition period for the F.V. experiments may help to retard the compressive reaction of the DDT process.

CONCLUSIONS

The WC 231 reloading propellant follows a MODE I DDT process (9), exhibiting extensive convective combustion during the buildup process. The use of a weaker (low dP/dt) ignition system led to a slightly longer distance to detonation in steel tubes. The longer pre-ignition time period with this weaker ignitor can lead to more gas flow into the granular bed. It is postulated that this gas pressure (less than 2 MPa at 50 mm into the bed) produces a retardation of compressive (hot spot) reaction during the later stages of the DDT process.

A consistent and reproducible set of predetonation parameters has been generated, from both the plastic and steel tube results, using the time and location of the onset of detonation as a common reference point. For WC 231 the extent of pre-ignition compaction appears to be small (increase in % TMD from 50% to about 60%) and of similar magnitude for both ignition systems. Flash radiographic data from the plastic

tube experiments have outlined the growth of the strong compressive wave (SCW). Pressure data from the steel tube experiments have indicated the pressure levels associated with the propagating SCW. The pressure data have also been interpreted as showing the presence of compressive reaction occurring within the SCW. This compressive reaction appears to be responsible for the formation of the accelerating shock wave which has been detected just prior to the onset of detonation.

The large difference in l values between the steel and plastic tubes indicates the important influence of confinement for the convective burning stage. Thus, the plastic tube data appear inappropriate for comparisons with predictions from one-dimensional modeling codes of DDT or the convective burning stage.

ACKNOWLEDGEMENTS

We would like to express our gratitude to Mr. Carl Groves for his very conscientious efforts in assembling and instrumenting the charges, and conducting, in large part, the experiments. In addition, we are grateful to Mr. Brian Glancy for support work in the calibration of the pressure transducers and their data reduction as well as in the firing of the experiments. Mr. William Freeman played a major role in the production of quality hardware for the execution of these experiments.

NOMENCLATURE

F.V. Free volume (ignitor)
l Predetonation column length, mm
PE Piezoelectric (transducer)
SCW Strong compressive (compaction) wave
x Distance along original porous column relative to propellant interface, mm
x^* $x - l$, mm
t Time relative to response of optical fiber/photodetector at propellant interface, μs
t_D Time of onset of detonation relative to response of optical fiber/photodetector, μs
t^* $t - t_D$, μs
t_{XR} Time of flash radiograph relative to response of optical fiber/photodetector, μs
TMD Theoretical maximum density, g/cc
u Particle velocity, mm/μs
U Shock (compaction) front velocity, mm/μs
WCW Weak compressive (compaction) wave

REFERENCES

1. M. W. Beckstead, N. L. Peterson, D. T. Pilcher, B. D. Hopkins and H. Krier, "Convective Combustion Modeling Applied to Deflagration-to-Detonation Transition of HMX," Combust. Flame, *30*, 231-241 (1977).
2. P. B. Butler, M. F. Lembeck, and H. Krier, "Modeling of Shock Development and Transition to Detonation Initiated by Burning in Porous Propellant Beds," Combust. Flame, *46*, 75-93 (1982).
3. M. R. Baer and J. W. Nunziato, "A Theory for Deflagration-to-Detonation Transition (DDT) in Granular Explosives," Sandia National Laboratories, SAND 82-0293 (December 1983).
4. W. L. Elban, "Quasi-static Compaction Studies for DDT Investigations: Ball Propellants," Propellant, Explosives and Pyrotechnics, *9*, 119-129 (1984).
5. H. W. Sandusky, W. E. Elban, and T. P. Liddiard, "Compaction of Porous Beds," Shock Waves in Condensed Matter - 1983, pp. 567-570, North Holland, Amsterdam, 1984.
6. H. W. Sandusky, "Compressive Ignition and Burning in Porous Beds of Energetic Materials," 1983 JANNAF Propulsion Systems Hazards Subcommittee Meeting, Vol. I, pp. 249-257, CPIA Publication 381, Sep 1983.
7. R. R. Bernecker, "The DDT Process for High Energy Propellants," Conference on Hazard Studies for Solid Propellant Rocket Motors, pp. 14:1-16; AGARD Conference Proceedings No. 367, Sep 1984.
8. H. W. Sandusky and R. R. Bernecker, "Transparent Tube Studies of Burning to Detonation Transition in Granular Explosives. I. Preliminary Framing Camera Results," NSWC TR 79-79, 27 Oct 1980.
9. R. R. Bernecker, H. W. Sandusky, and A. R. Clairmont, Jr., "Deflagration-to-Detonation Transition Studies of Porous Charges in Plastic Tubes," Seventh Symposium (International) on Detonation, pp. 119-138, NSWC MP 82-334, 1982.

10. H. W. Sandusky, W. L. Elban, K. Kim, R. R. Bernecker, S. B. Gross, and A. R. Clairmont, Jr., "Compaction of Porous Beds of Inert Materials," Seventh Symposium (International) on Detonation, pp. 843-856, NSWC MP 82-334, 1982.

11. R. R. Bernecker, D. Price, J. O. Erkman, and A. R. Clairmont, Jr., "Deflagration-to-Detonation Transition Behavior of Tetryl," Sixth Symposium (International) on Detonation, pp. 426-435, ACR-221, U. S. Gov. Print. Office, Washington, DC, 1976.

12. H. W. Sandusky and R. R. Bernecker, "Compressive Reaction in Porous Beds of Energetic Materials," (this symposium.)

13. R. R. Bernecker, "Experimental Techniques and Results for Propellants and Explosives," ONR/AFOSR Workshop on Deflagration-to-Detonation Transition, pp. 187-216, CPIA Publication 299, Sep 1978.

14. M. Samirant, "Deflagration Detonation Transition in Waxed RDX," Seventh Symposium (International) on Detonation, pp. 139-142, NSWC MP 82-334, 1982.

15. M. C. Chick, "The Effect of Interstitial Gas on the Shock Sensitivity of Low Density Explosive Compacts," Fourth Symposium (International) on Detonation, pp. 349-358, ACR-126, U. S. Gov. Print. Office, Washington, DC, 1965.

DISCUSSION

HERMAN KRIER, Univeristy of Illinois

I wonder whether your granular material (WC 231) was so porous (i.e., has % TMD ranging from 50-60%) that the insensitivity to the ignition process (dp/dt at early time) would not be observed for a less porous material "of the same type." Based on your earlier published paper, with other granular explosives, have you not shown that the shock-like initiation can change the DDT runup length?

REPLY BY R. BERNECKER

The pressurization rate in the earlier stages of the DDT process will definitely depend upon the % TMD of the charge (as reflected through changes in permeability and compressibility of the porous column). The "insensitivity of the ignition process" for 50% TMD WC 231 makes these data more useful for numerical modeling comparisons since one important experimental variable (gas loading by the ignition system) can essentially be neglected. For the second question, the answer is yes. The predetonation column length is affected both by convective combustion and compressive (hot spot) combustion. In earlier detailed studies, the comparisons were between different materials (i.e., HMX vs. tetryl). Here, we are concerned with changes (although they are small) in compressive reaction characteristics for the same material.

MODELLING OF DDT IN GRANULAR EXPLOSIVES

H. J. Verbeek
Prins Maurits Laboratory TNO
P.O. Box 45, 2280 AA Rijswijk
The Netherlands

A description is given of the set up of the DDT model that is being developed at PML. The results of two types of simulation are presented and the merits and shortcomings of the model are discussed. Finally it is indicated where the code needs improvement and in what direction the model will be further developed.

INTRODUCTION

During the last two decades the interest in DDT (deflagration to detonation transition) has steadily grown. The reasons for this are on the one hand the higher demands on the performance and reliability of explosive materials including a lower vulnerability of ammunition and on the other hand the development of new types of highly energetic materials with a higher tendency to DDT. At first the greater part of the research on DDT concentrated on the experimental investigation of the phenomenon (see e.g. refs. (1), (2), (3)), but in recent years also more and more work is being done in the field of computer simulation of the process (see e.g. ref. (6)). This development is strongly stimulated by the ever increasing performance/cost ratio of modern computer systems. The advantage of using a computer code is that many more parameters can be observed in a simulation than in an experiment while they also can be monitored continuously, both in time and in space. Simulations can be carried out in a much shorter time and at much lower cost than experiments while the ease of parameter variation is infinitely larger. On the other hand the time and cost needed for the development of a reliable code can be considerable, while it will still remain necessary to perform a limited number of experiments parallel to the simulation to compare the results with the predictions of the code. Besides, as input for the code the values of a number of parameters are needed that are often unknown and have to be measured in separate experiments. This problem tends to become more severe for more detailed simulations.

In view of the above at PML a combined DDT program has been set up, consisting of an experimental part in which a standard DDT test is being developed and a simulation part comprising the development of a computer code. After completion of the development stage both parts will be closely linked In this presentation a description will be given of the set-up of the simulation together with its first results.

THEORETICAL BASIS

The modelling of a DDT process is in fact a very complex matter. For the solid component(s) in principle a description has to be given of heat conduction processes, of the propagation of shock waves with the corresponding elastic and plastic deformation, of the phase transitions and chemical reactions that occur, while also the geometrical shape and the movement of the grains have to be specified. Most of the processes given above also have to be modelled for the various gaseous components. This has to be supplemented by a description of the mutual friction and the exchange of heat between the components. Also the interaction with the inert material that is present (e.g. the wall of a tube) has to be modelled. In the DDT process the relevant time intervals can diverge from 50 ns till several milliseconds, the typical distances vary from 10 μm till hundreds of mms, the speeds of the various processes can diverge

TABLE 1
Equations Used in the Simulation

$$\frac{\partial}{\partial t}(\phi\rho_g) = -\frac{\partial}{\partial z}(\phi\rho_g v_g)+\Gamma_{pg} \quad (1)$$

$$\frac{\partial}{\partial t}((1-\phi)\rho_p) = -\frac{\partial}{\partial z}((1-\phi)\rho_p v_p)-\Gamma_{pg} \quad (2)$$

$$\frac{\partial}{\partial t}(\phi\rho_g v_g) = -\frac{\partial}{\partial z}(\phi\rho_g v_g^2)-\frac{\partial P_g}{\partial z}+v_p\Gamma_{pg}-F_{gp} \quad (3)$$

$$\frac{\partial}{\partial t}((1-\phi)\rho_p v_p = -\frac{\partial}{\partial z}((1-\phi)\rho_p v_p^2)-(1-\phi)\frac{\partial P_p}{\partial z}-v_p\Gamma_{pg}+F_{gp} \quad (4)$$

$$\frac{\partial}{\partial t}(\phi\rho_g c_{vg}T_g) = -\frac{\partial}{\partial z}(\phi\rho_g c_{vg}T_g v_g)-P_g\frac{\partial}{\partial z}(\phi v_g)+\Gamma_{pg}(c_{vg}T_g+\tfrac{1}{2}(v_g-v_p)^2+E_{comb.}) +F_{gp}(v_g-v_p)-Q_{gp} \quad (5)$$

$$\frac{\partial}{\partial t}((1-\phi)\rho_p c_{vp}T_p) = -\frac{\partial}{\partial z}((1-\phi)\rho_p c_{vp}T_p v_p)-P_p\frac{\partial}{\partial z}((1-\phi)v_p)-\Gamma_{pg}c_{vp}T_p+Q_{gp} \quad (6)$$

$$\frac{\partial}{\partial t}(\rho_p d_p^3) = -v_p\frac{\partial}{\partial z}(\rho_p d_p^3)-\frac{d_p^3}{1-\phi}\Gamma_{pg} \quad (7)$$

$$P_g = \rho_g RT_g(1+\alpha\rho_g) \quad (8)$$

$$\rho_p = \rho_{po}\left(\frac{nP_p}{k_p}+1\right)^{1/n} \quad (9)$$

$$P_p = P_g + \tau_p \quad (10)$$

$$\tau_p = \begin{cases} 0 & : \phi > 0{,}26 \\ f(\phi,\frac{d\phi}{dt}) & : \phi \le 0{,}26 \end{cases} \quad (11)$$

$$\Gamma_{pg} = \begin{cases} 0 & : T_p < T_{ign} \\ \rho_p(1-\phi)\frac{6}{d_p}aP_g^{0,9} & : T_p > T_{ign} \end{cases} \quad (12)$$

$$F_{gp} = f(\phi,\rho_g,(v_g-v_p),d_p) \quad (13)$$

$$Q_{gp} = f(\phi,\rho_g,(T_g-T_p),(v_g-v_p),d_p) \quad (14)$$

from 0,01 mm/μs till 10 mm/μs while typical pressures range from 0,1 MPa till 50 GPa.

From the above it follows that for a precise modelling of the DDT process the use of tens of thousands of time levels and of at least an equal number of mesh-points in the calculations would be needed, requirements far beyond the reach of even the most powerful super-computer. To create a workable code therefore a lot of simplifications and approximations have to be applied.

The usual way to tackle this problem is by treating the system as a fluid mixture of two separate components, being the solid (unreacted) explosive and the gaseous reaction products. This treatment, originating from the multi-phase fluid flow community, has been pioneered for explosive materials especially by Kuo (4), Gough (5) and Krier (6), of which the first two specialize in the convective burning regime while the latter also takes into account the transition to the detonation stage. The method consists of composing a system of differential

TABLE 2
Values of Some Input Parameters Used in the Code

Symbol	Description	Value
ϕ_0	initial porosity	0,3
d_{p0}	initial particle diameter	0,4 mm
ϱ_{p0}	initial particle density	1900 kg/m^3
ϱ_{g0}	initial gas density	1 kg/m^3
T_{g0}	initial gas temperature	294 K
T_{p0}	initial particle temperature	294 K
c_{vg}	specific heat of gas phase	1570 J/kg/K
c_{vp}	specific heat of solid phase	1000 J/kg/K
E_{comb}	combustion energy	6,2 MJ/kg
α	covolume	4.10^{-3} m^3/kg
k_p	solid bulk modulus	14,3 GPa
n	exponent	

equations which is solved by a finite-difference procedure. The set of equations consists of the conservation laws of mass, momentum and energy for each phase. To this set are added a number of constitutive equations among which are the equations of state for each phase and some equations describing the interaction terms. By this method a large number of details in the process are discarded. It is hoped that by using a careful averaging method in the derivation of the equations the influence of the microprocesses is correctly accounted for. The models reported at present in the literature mainly differ in the way the averaging methods are carried out and the value the various authors attach to the influence of specific details.

The model that is under development at PML is based on the separated-flow approach used e.g. by Krier (6). The equations used are given in Table 1. In these equations the basic independent variables are the density, temperature and velocity of the gas and the particle phase represented by the symbols ϱ_g, T_g and v_g for the gas phase and ϱ_p, T_p and v_p for the solid phase, supplemented by the porosity ϕ (volume fraction of the gas) and the particle diameter d_p. The other variables used are derived quantities which are coupled to the other ones via the equations of state (for the pressures P_g and P_p of the two phases) or the other constitutive equations (as the exchange terms of mass, momentum and heat Γ_{pg}, F_{gp} and Q_{gp} resp.). Equations (1) and (2) represent the conservation laws of mass for each component, eqs. (3) and (4) the conservation laws of momentum and eqs. (5) and (6) stand for the conservation laws of energy. Equation (7) describes the variation of the particle diameter. The equations of state for both phases appear next, eq. (8) being a Nobel-Abel type of equation for the gas, eq. (9) a Tait type of equation for the solid. The total stress in the solid is considered to be the sum of the gas pressure and an extra term τ_p which represents the stress in the solid due to static and dynamic compression of the particle matrix (eqs. (10) and (11).) This last equation, not explicitly given here, is based on the pore-collapse model of Carroll and Holt (7), recently further elaborated by Frey (8). The system of equations is completed by expression (12) for the burning-rate law, by the Ergun relation (eq. 13) describing the interphase drag and by the Denton relation (eq. 14) which gives the interphase heat exchange (the last two not explicitly given here).

NUMERICAL SOLUTION

This system of equations is solved numerically by means of a finite difference procedure. To overcome the instability problems encountered usually when treating steep shock fronts the so called F(lux) C(orrected) T(ransport) method of Boris and Book (9) was adopted. In this method the instabilities are smeared out by means of an (explicit or implicit) artificial

viscosity term, which is only active in the neighbourhood of a sharp transition and not outside that region. This method gives an excellent shock description for many systems of equations, but is in itself not appropriate to account for the influence of the large source terms occurring in our case. Such systems of so called "stiff" equations should in fact be handled either by making the time step very small or by using an implicit solution method, in both cases requiring an unacceptable amount of computer time. In our code this problem is solved by using a semi-implicit method in which in one or two iterations a reasonable estimate of the correct solution is given with an acceptable increase in computer time.

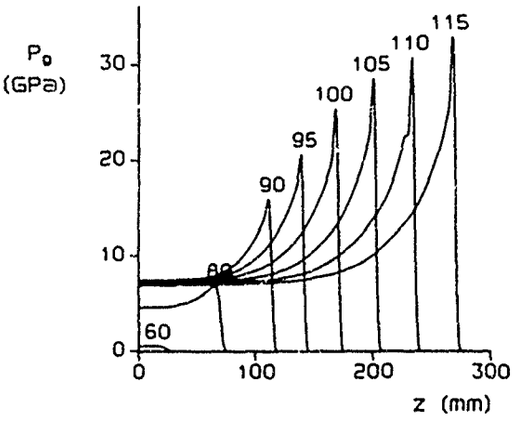

Fig. 1. Pressure profiles in the tube after thermal initiation at different points of time (times in microseconds)

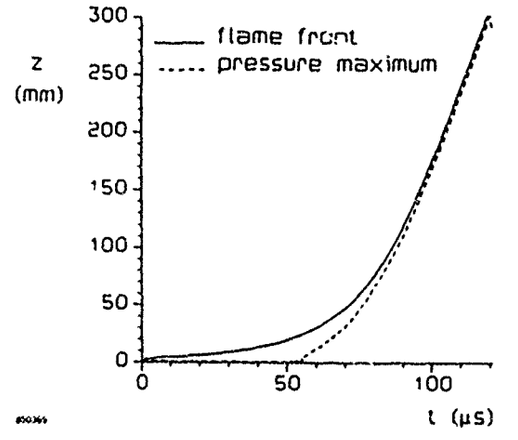

Fig. 2. Distance-time plots for the flame front and the location in the tube where the pressure is at its maximum

RESULTS

Up to the present two kinds of simulation experiments have been performed with the code. In these calculations a closed (1-dimensional) tube filled with the explosive HMX at 70% TMD is simulated. The values of most constants used in the program are given in Table 2. In the first type of simulation a purely thermal initiation is applied by suddenly heating the first two cells with an external source to a gas temperature of 3300 K, thereby igniting the particles in these cells. Next an initially quiet, slowly accelerating convective combustion is generated, until after some 50 μs a pressure peak arises well behind the flame front and near the front of the tube (see Fig. 1). This pressure peak steepens and approaches the flame front, causing a sharp acceleration of the front until a detonation-like velocity of 69 mm/μs is reached (see Fig. 2). This value is close to the estimated value of 72 mm/μs obtained from calculations with the TIGER code. Also the values of 14 GPa for the pressure and 3200 K for the temperature reached at the end of the reaction zone (corresponding to the point where the porosity attains the value 1, see Fig. 3) approach the TIGER values of 18 GPa for the CJ detonation pressure and 3000 K for the CJ temperature. Besides, at the end of the tube the process is not yet in a steady state; the velocity is still slowly increasing as well as the pressure, so it is expected that simulations for a longer tube would result in values closer yet to the CJ ones.

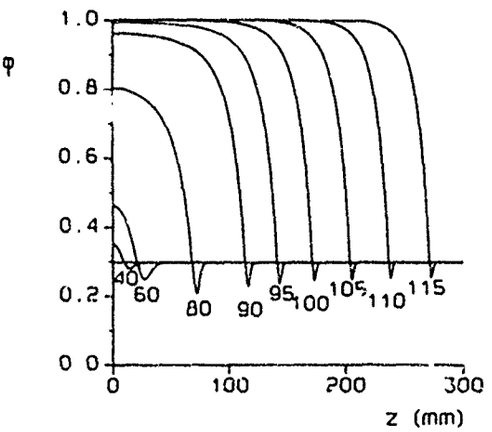

Fig. 3. Porosity profiles

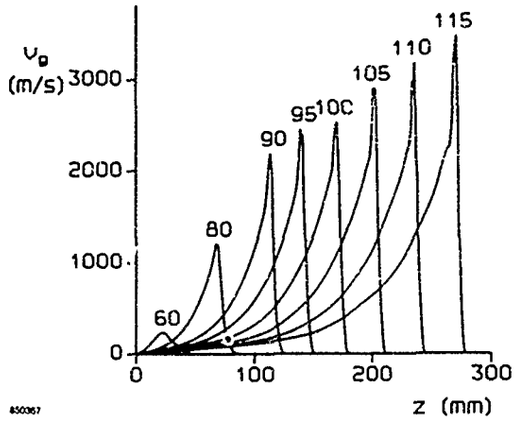

Fig. 4. Gas velocity profiles

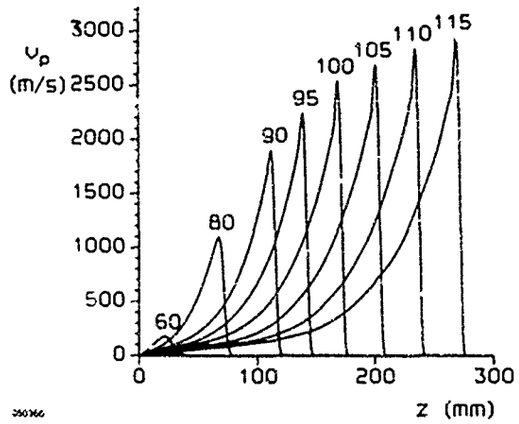

Fig. 5. Particle velocity profiles

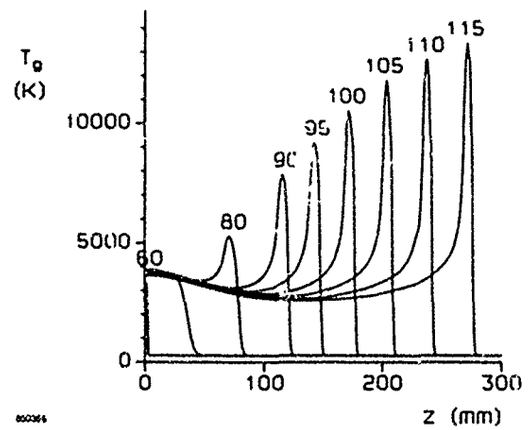

Fig. 6. Gas temperature profiles

In the second type of simulation experiment the striking of the tube by a shock is simulated by strongly raising the pressure of the first two cells during a time interval of 10 μs. The result is that below a shock strength of approximately 0,1 GPa no initiation occurs and the shock gradually decays, while above that value the shock passes into the "detonation" stage described above (see Figs. 7 and 8). The value of 0.3 GPa, however, is much lower than expected.

DISCUSSION OF THE RESULTS

Although the overall development of the process shows a reasonable conformity with the experimental results, a closer look at the results reveals the existence of a number of serious shortcomings. In the first place the final state reached is still not a correct description of a detonation, for one thing because the width of the reaction zone (± 50 mm) is two orders of magnitude larger than for a real detonation. Moreover, the temperatures reached in the reaction zone are unrealistically high (see Fig. 6). A further drawback is that the transition to the "detonation" stage is insufficiently sharp, in contrast to the discontinuous acceleration usually observed in experiments.

The main reason for the insufficiencies of the code appears to be the mechanism of initiation of the reaction. While in the initial stage the particles are ignited by means of convective heat transport, in the next stage the ignition is dominated by the mechanism of compressive heating of the gas phase and subsequent heat

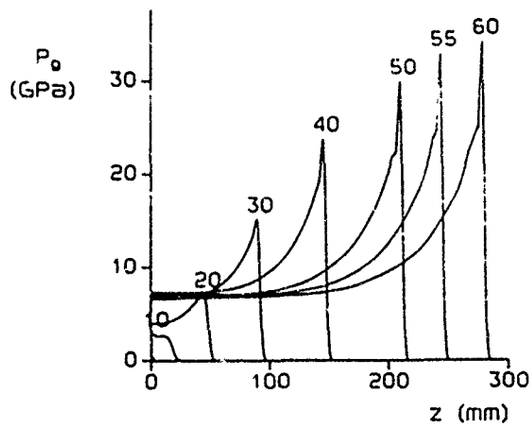

Fig. 7. Pressure profiles after initiation by a shock of 0,36 GPa

transfer from gas to solid phase. Although this process is faster than the convective heating mechanism it is still an indirect ignition process and as such much slower than direct processes as compressive heating and shear heating of the particles which are believed to dominate the shock-initiation process (see e.g. ref. (8)). Apparently the code is not yet capable to give a fair description of these direct processes, thereby explaining the excessive length of the reaction zone (the fact that the model cannot account for the process of shear heating is not surprising because such a model was not built into the code; it should, however, be capable of describing the compressive heating of the particles). Also the unduly high sensitivity to initiation by shock shows that the handling of shock processes is still incorrect.

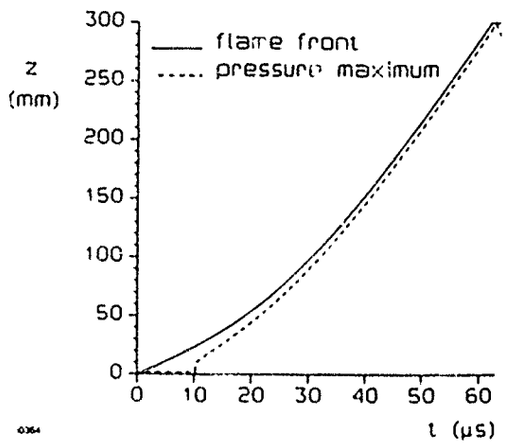

Fig. 8. Distance-time plots for flame front and pressure maximum after shock initiation

FURTHER DEVELOPMENT OF THE CODE

From the above analysis it can be concluded that the most important object for improvement of the code is the shock initiation stage. It has to be emphasized here that the aim of the code is not a detailed description of the detonation stage. For this purpose a number of other codes are available. The main goal of a DDT program, however, is to correctly predict under what circumstances and in which time interval the point of no return is reached, i.e., the point where the final acceleration to detonation sets in. To be able to give such a description, however, it is of crucial importance that a correct account of the shock initiation process is given, which should also result in at least a reasonable description of the detonation stage.

Another important factor in DDT modelling is to give a good description of the interaction with the surroundings. The tendency to DDT is not merely a property of the explosive itself but is a property of the whole explosive system; the strength and possible failure of the confinement of the explosive are extremely important. It is in fact only possible to give a reasonable account of the influence of the surroundings by using a two- or three-dimensional code. In the end a DDT code will have to be at least a two-dimensional one in order to be able to give reliable results.

In view of the above the work on the development of the code at PML is concentrated on refining the description of the shock-initiation process. In this respect an improvement of the equations of state is considered while also a reconsidering of certain terms in the conservation equations should be worthwhile, but in our view the most important point is to reach a better description of the heat transport and chemical processes in and around the solid particles as well as an improvement of the pore collapse model. In the present situation, where the processes are described by only the particle temperature parameter and a single reaction rate it is not possible to correctly account for the effects of the various ignition processes. In fact a good description of the temperature profile in the particles and a more complex model for the chemical reactions is needed. Since the strong decrease in mesh-size in the code needed to take actual account of the temperature profile exceeds the available computer power, at present at PML work is going on to give a simplified description of the temperature profile by the mere introduction of one or two extra parameters. Another addition to the code will probably be the introduction of an extra pyrolysis reaction, which will considerably increase the degree of acceleration from the convective burning stage to the detonation stage as was demonstrated by Boggs et al. (10). Further, in due time the code will be converted into a two-dimensional one, which probably will not cause large problems since during the set-up of the original code a later extension to two dimensions was anticipated.

CONCLUSIONS

In some qualitative and quantitative aspects the results of the present model are in reasonable agreement with the outcome of DDT experiments. In other aspects, the most important of which is the description of the shock-initiation stage, however, considerable improvement of the code is needed. The present work on the further development of the model at PML therefore concentrates on attaining a better description of the thermal and chemical processes in the solid phase which are the dominating factors in the shock-initiation process.

REFERENCES

1. N. Griffiths, J. M. Groocock, J. Chem. Soc., 1960, 4154

2. A. F. Belyaev, V. K. Bobolev, A. J. Korotkov, A. A. Sulimov, S. V. Chuiko, "Transition from Deflagration to Detonation in Condensed Phases", Moscow, 1973; Israel Program for Scientific Translations, Jerusalem, 1975.

3. R. W. Gipson, A. Macek, 8th Int. Symp. on Comb., 1962; R. R. Bernecker, D. Price, Comb. and Flame 22, 1974, 111;22, 1974, 119; 22, 1974, 161.

4. K. K. Kuo, J. H. Koo, T. R. Davis, G. R. Coates, Acta Astr. 3, 1976, 573.

5. P. S. Gough, F. J. Zwarts, AIAA J. 17, 1979, 17.

6. P. B. Butler, M. F. Lembeck, H. Krier, Comb. and Flame 46, 1982, 75 P. B. Butler, H. Krier, Proc. AGARD Conf. No. 367, May 1984, Lisse, The Netherlands.

7. M. M. Carroll, A. C. Holt, J. of Appl. Phys. 43, 1972, 1626.

8. R. B. Frey, Proc. AGARD Conf. No. 367, May 1984, Lisse, The Netherlands.

9. J. P. Boris, D. L. Book, J. of Comp. Phys. 20, 1976, 397.

10. T. L. Boggs, C. F. Price, R. L. Derr, Proc. AGARD Conf. No. 367, May 1984, Lisse, The Netherlands.

DISCUSSION

M. R. BAER and J. W. NUNZIATO,
Sandia National Labs

At Sandia National Labs., we have been studying DDT in granular explosives (ref 1-4) using an approach quite similar to the one presented in this paper. We, too use a model that is based on a multiphase flow theory that is generalized to allow complete nonequilibrium descriptions of the mixture phases. In our work, we include the compressibility of each phase, the effect of pressure nonequilibrium, and use a rate-dependent model of compaction.

Our early predictions for the explosives HMX and CP are similar to those seen in this current work, which is perhaps due to similar choices of the constitutive models. However, we have modified many of these models as influenced by experimental observations (see ref. 3). For example, we use experimentally-determined, porous bed permeabilities that are considerably different from those predicted by many of the packed-bed correlations. We have also found that it is very important to use appropriate equations of state for the gas (*i.e.* JWL) and solid phases as constructed using experimental Hugoniot and thermochemical data. Many more aspects of the combustion physics warrant continued study as guided by experimental observations.

It was gratifying to see additional numerical work which uses the FCT finite difference method with an appropriate numerical scheme which can cope with the inherent stiffness of the model descriptions. We use the FCT method to resolve the multiphase transport processes and employ a stiff ODE method to resolve phase interaction. These separate methods are unified using a fractional step approach. In our latest work, we have expanded our DDT model to two-dimensions using the forementioned methods. We have seen that this approach is robust, is free from unphysical numerical artifacts and is computationally efficient which allows us to continue to expand the combustion physics (*e.g.* pyrolysis). As an example, we have included a calculation which shows the temporal variations of total pressure and solid volume fraction as the two-phase combustion wave attempts to turn a corner in a bed of granular CP. As seen in these calculations, a release wave

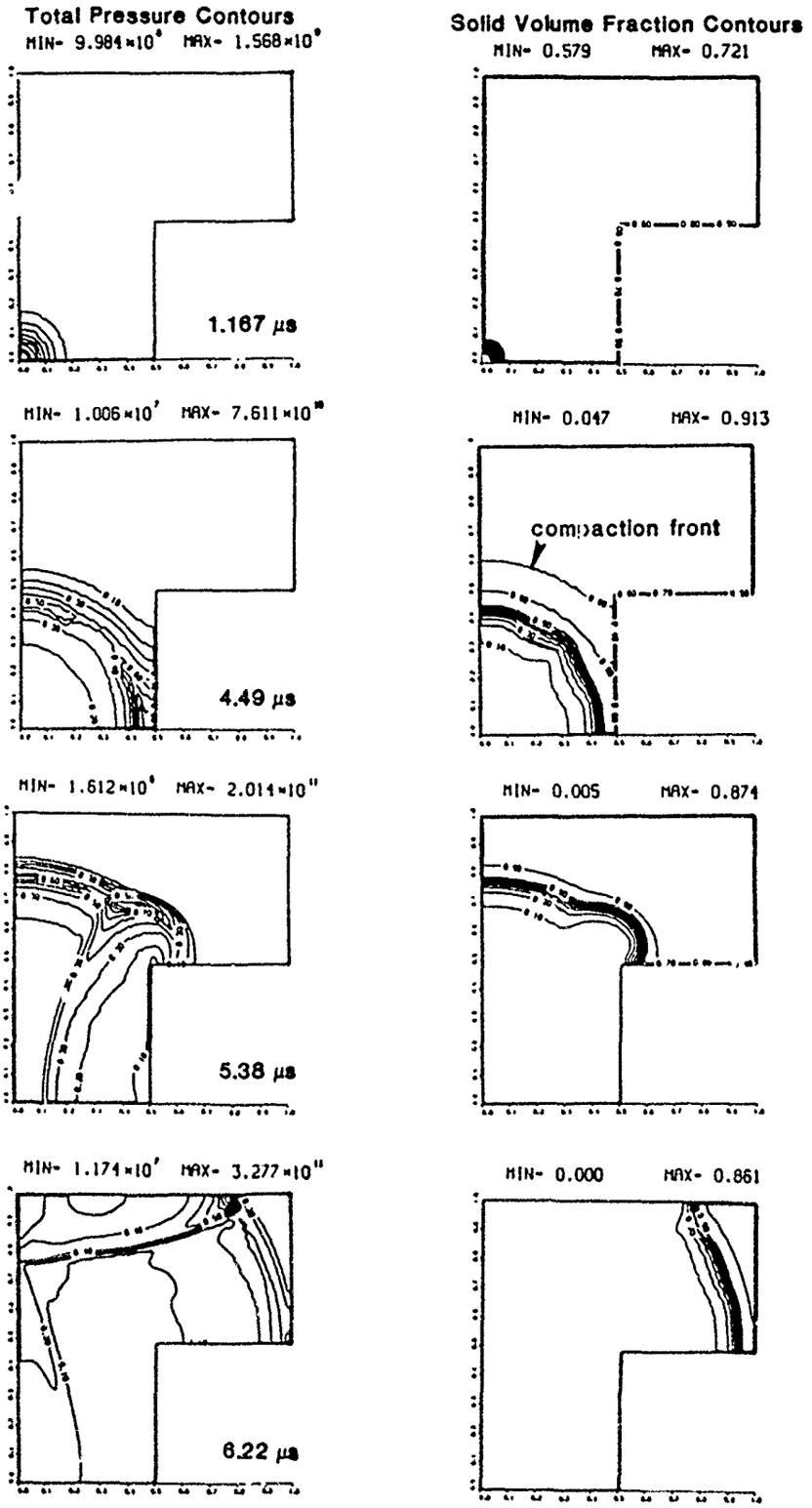

A DDT calculation of flame spread in the granular explosive, CP, which shows the evolution of the combustion wave as it turns a rigid corner

originates at the corner and resulting rarefaction impedes the flame spread around the corner. Details of the numerical method and additional multidimensional calculations were recently reported in reference 4.

1. Baer, M. R. and Nunziato, J. W., "A Theory of Deflagration-to-Detonation Transition in Granular Explosives", Sandia National Labs, SAND82-0293, 1982.
2. Baer, M. R., Igel, E. A., Gross, R. J. and Nunziato, J. W., "A Study of Deflagration-to-Detonation Transition (DDT) in the Granular Explosive, CP", Sandia National Labs, SAND83-1929, 1984.
3. Baer, M. R., Nunziato, J. W., and Gross, R. J. "A Thermal-Mechanical Model of DDT in Granular Energetic Materials", Proc. 1984 JANNAF Prop Sys. Hazards Mtg., Aberdeen Prov. Grnd., Md. 1984.
4. Baer, M. R., Benner, R. E., Gross, R. R., and Nunziato, J. W. "Modeling and Computation of Deflagration-to-Detonation DDT) in Reactive Granular Materials", Proc. 1985 AMS-SIAM Summer Seminar on Reacting Flows: Combustion and Chemical Reactions, American Mathematical Society, Prov., RI, appear.

REPLY BY J. VERBEEK

I am aware of the work that is being done at Sandia National Labs on the subject of DDT modelling and I am pleased to see the progress in the work.

It is unfortunate that the latest results could not be presented at this symposium.

ON THE MECHANISM OF THE REACTION "HOT SPOTS" ORIGIN AT LIQUID EXPLOSIVES DETONATION

A. N. Dremin, V. Yu. Klimenko
and I. Yu. Kosireva

Institute of Chemical Physics (Branch)
USSR Academy of Sciences 142432
Chernogolovka, Moscow Region
USSR

The three-stage model of the reaction spots origin at liquid explosives detonation has been developed. The interaction of the shock wave front with the density non-homogeneities in liquid has been investigated by the non-equilibrium molecular dynamic method. It has been revealed that the passing shock front changes small density negative fluctuations into large temperature fluctuations (overheated micro-regions). The regions turn into the decomposition reaction spots as the reaction rate inside the overheated micro-regions is 5-10 orders of magnitude faster than that in the surrounding substance. During the next stage the further increase of the reaction spots takes place due to the decomposition reaction chain nature. In case the decomposition is exothermic and if the spots reach some proper size, the spots further development will correspond to the thermal explosion regularities. The interpretation of the reaction spots origin at nitromethane detonation has been proposed in terms of this three-stage model.

INTRODUCTION

The attention lately has been increasingly given to the detailed mechanism of detonation. The development of new techniques for explosive decomposition kinetics investigation (1-3) has given rise to many experimental studies on the problem (see, for example, 7th Symposium (Int) on Detonation, 1981). The studies in their turn have provided a lot of data and promoted development of theoretical considerations on condensed explosives detonation mechanism. However, so far the problem has not been solved yet. In particular, the question of nature of the reaction "hot spots" origin at liquid explosives detonation is still open (4,5).

As early as in the sixties it was revealed that the condensed explosives detonation reaction time depends very little on the detonation pressure (6-8). For example, the TNT detonation reaction varied from 1.3×10^{-6}s to 0.2×10^{-6}s in the detonation pressure interval 2.5−20.0 Gpa. ZND classical detonation theory (9-11) fails to interpret the data. Early in the seventies a certain concept was introduced by one of the authors (12). The concept allowed to get over the data interpretation difficulties. The essence of the concept is the following. The shock wave front causes explosives specific decomposition, the decomposition being non-thermal nature and proceeds with a very fast rate. Some experimental data supporting the concept have been obtained later (13,14). In particular, it has been found out that under the shock effect liquid benzene decomposes easier than liquid hexane in spite of the fact that the former is thermally more stable than the latter. At the time, however, it was unknown what occured with the substance inside the shock front and therefore, the substance specific decomposition nature was not clear.

At the end of the seventies the nonequilibrium molecular dynamic method was intensively used for investigation the shock wave

front structure and the mechanism of the substance shock compression (15-19). The results obtained allowed one to elaborate the "accumulation" mechanism of the substance decomposition at the shock compression (20).

By the accumulation mechanism one has managed to interpret the benzene easier decomposition in comparison with that of hexane (21). Later the current interpretation of the condensed explosives detonation mechanism has been proposed (22) on the background of the accumulation mechanism.

The gist of the accumulation decomposition mechanism consists in the following. It is obvious that the shock wave front kinetic part of the shock compression energy is distributed behind the front equally among all translational, rotational and vibrational degrees of freedom of multiatomic molecules. However, inside the front, at first the energy is expanded only on the translation degrees of freedom, the latter being considerably overheated in comparison with those of the equilibrium state behind the front. Due to the translational-vibrational relaxation process the energy of the translational degrees of freedom is redistributed to the vibrational degrees of freedom, at first the energy flow, in general, being directed towards the vibrational degrees of freedom most rapidly excited. If the rate of the energy flow towards these degrees of freedom exceeds the flow rate of these degrees energy lose owing to the vibrational-vibrational relaxation process, they will accumulate superfluid energy. In other words, the energy provided for all the inner degrees of freedom for some time will be concentrated only on a certain fraction of these degrees of freedom, the latter being overexcited and decomposing faster in the shock front than behind the front at the equilibrium state.

The following necessary and sufficient conditions underlie the accumulation mechanism.

1. The molecules must be large enough so that the translational degrees of freedom overheating was substantial.
2. The excitation rates of the molecules, having various vibrational degrees of freedom, must differ considerably in order the main energy flow from the overheated tranlational degrees of freedom be directed only to a part of these degrees of freedom and as a result to cause their energy oversaturation.
3. The rate of the vibrational-vibrational energy exhange must be less than the excitation rate of degrees of freedom most rapidly excited. If even one of these conditions are not met, the accumulative mechanism is not operative. The mechanism does not come into action, for example, if the molecules are small like nitromethane molecules. But does this fact imply that in this very case the shock compression specific action manifests itself? In other words, if we assume that nitromethane is compressed and heated statically and dynamically (by the shock wave action) up to the same condition, does nitromethane decomposition proceed equally in both cases? It is not so easy to answer the question although nitromethane was indeed a subject of many investigations at static and dynamic conditions.

It has been experimentally shown (4) that nitromethane detonation proceeds at the shock wave initiation through formation of the reaction spots, the size of which is at certain conditions as large as 10 mm. Light scattering technique has been used (5), (23) to observe the spots at the initial state of their forming. These spots sizes are comparable with the wave length of the visible light, that is, the hotspots sizes are equal to some thousand Angstroms. It has been assumed (23,24) that the chain nature of nitromethane molecules decomposition reaction is responsible for the spots character of this shock wave decomposition.

The hotspots have been also observed by light scattering techniques under the shock effect in inert liquids (dichlorethane, acetone, benzene) (23). The appearance of the hotspots in chemically different liquids allows one to assume that there exists some common physical mechanism of their origin. It is obvious that the mechanism is conditioned by the peculiarities of the shock effect. In making efforts to elucidate the mechanism it has been shown that the cause of the spots origin might be some overheated micro-regions which are generated at the process of the shock front interaction with the medium density non-homogeneities. The paper deals with the detailed investigation of this mechanism.

CALCULATION METHOD

The investigation has been performed by the nonequilibrium molecular dynamic method developed in (15-17). Research of the shock wave front interaction with the density fluctuations has been carried out for liquid argon. Argon has a good approbated potential and has been intensively investigated in many works on the molecular dynamic modelling. The additive reciprocal potential (25) has been used in the paper

$$\psi(r)=\varepsilon\left[\frac{6}{\alpha-6}\,e^{\alpha(1-\frac{r}{\delta})}-\frac{\alpha}{\alpha-6}\left(\frac{\delta}{r}\right)^6\right]$$

where $\varepsilon/k=122°K$, $\delta=3.85A$ and $\alpha=13.0$. The potential describes well argon equation of state up to 10 Gpa. Differential equations of particles (argon atoms) motion have been solved numerically by well known difference scheme proposed by Verlet (26). An integration step was equal to 5×10^{-15}s. Some more details of the nonequilibrium molecular dynamic calculation method are in (15-17).

The shock wave (the front velocity D = 2920 ±50 m/s, the particle velocity U = 1200 m/s, the pressure P = 43.8±0.8 kbar) has been investigated in liquid argon of the initial density $\varrho_0=1.25$ g/cm^3, and the initial temperature $T_0=110°K$. The modelling shock wave spreads along the counting cell axis x (Fig. 1).

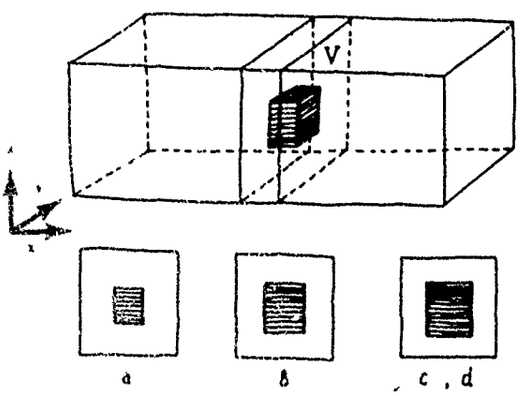

Fig. 1. The density fluctuation construction scheme

Some region of decreased density - negative fluctuation of density - is disposed on the shock path. The fluctuation has been arranged in the following way. A certain number of atoms have been removed from V region which was located inside the counting cell, and which initially contained approximately 300 argon atoms. For example, 36 atoms have been removed in 1a; 72 atoms in 1b; 144 atoms in 1c and 1d. Then during 50-100 steps V region has been relaxed due to the atoms motion. By time of the shock front arrival a fluctuation of density has formed rather stable in time (in the scale of the process under investigation). Various fluctuations have different density profiles (Fig. 2.). The travelling shock wave interacts with the fluctuation and spreads farther along the counting cell.

RESULTS AND DISCUSSIONS

The calculations have shown that the shock wave front passing through the fluctuation of negative density causes the appearance of some positive temperature fluctuation. The final temperature profiles are presented in Fig. 3. The a-d cases of both Fig. 2 and Fig. 3 correspond. One can see that the temperature fluctuation magnitude (its size and overheating extent) is determined by the density fluctuation size, namely, the greater are the density fluctuations, the larger is the temperature fluctuation. The comparison of the c and d cases shows that the heating extent is determined mainly by the integral value of decreasing the particles number in V region and practically does not depend on the particles density distribution in V region. The successive stages of the process of the shock front interaction with the density fluctuation for the case d are presented in Figs. 4, 5, 6.

From the calculation results it follows that the overheating region size exceeds tens times (in volume) the size of the initial region of the decreased density. The shock front is a kind of an amplifier. It converts very small density fluctuations in size into rather big space fluctuations of temperature. The evaluation made on the basis of the well known statistical formulas (29) shows that the probability of existence of the latter is at least 10 orders less than that of the former. Thus, the density fluctuations treated here (−36, −72 and −144 for 300 particles) exist with the probability equal to unit in volume of $\sim10^{10}$ particles. It is interesting to point out that the shock front produces the temperature fluctuation in volume of 10^{10} particles but in natural conditions the fluctuation exists in the number of $10^{(20\text{-}30)}$ particles. The initial density fluctuation under the shock effect as if accumulated some energy

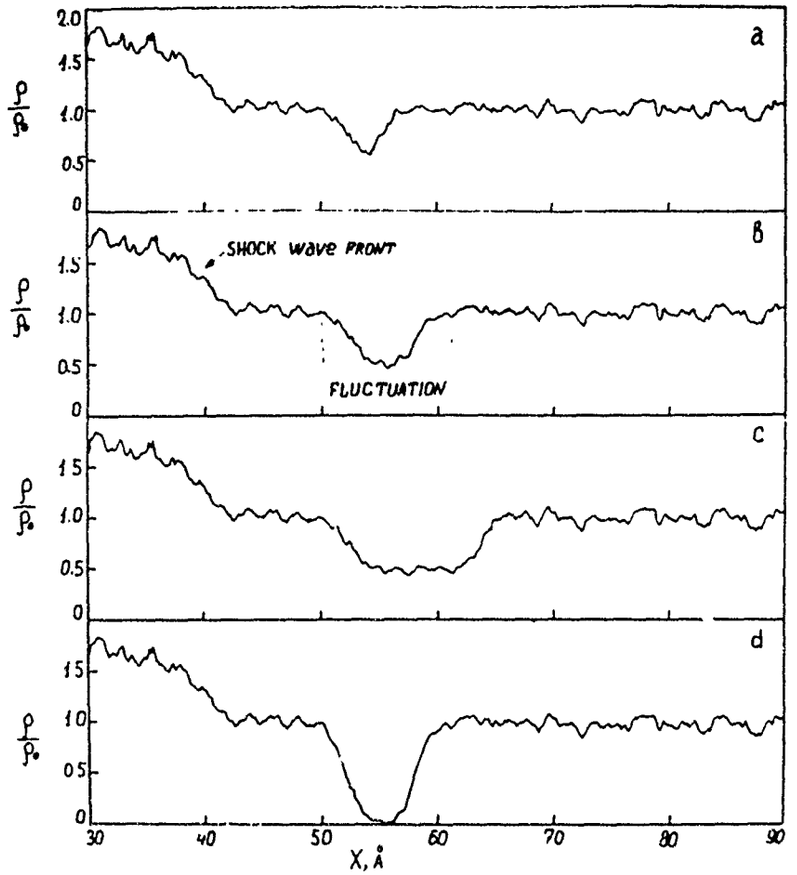

Fig. 2. The density initial fluctuations (before the shock front arrival)

from the surrounding volume, and, therefore, as a result, the heat fluctuation appears of surprisingly great size. Perhaps, it would be more correct to name it "overheated microregion".

This non-trivial fact enables us to assume it is the shock front that is responsible for the hot spots origin inside the substance under the shock effect. It also permits one to revise, in general, the shock front acceleration role among all the activation process involved in the shock compression effect. The evaluation shows that the acceleration scale may amount to 5-10 orders of magnitude. The acceleration depends on the value of the process activation energy and on the value of the medium equilibrium temperature behind the front.

So, the substance just behind the front is heated non-homogeneously. The overheated micro-regions of tens Angstroms size are inside the medium. The regions contain some thousand molecules. Because of thermoconductivity the region temperature relaxes to the temperature of the surrounding substance. If the characteristic time of the activation process (for example, the substance molecule decomposition) is comparable with the overheated micro-regions life time, the decomposition process inside the regions will have time to take place profoundly and for this reason, some decomposition micro-regions are formed inside the substance. It is obvious that if the decomposition reaction is of chain or autocatalytic type (that is, apparantly, valid for many explosives (27)), the micro-regions generate still larger regions. The subsequent development and growth of the regions can also proceed due to the chain mechanism. However, in case, the decomposition is the exothermal nature and the heat is generated and accumulated during

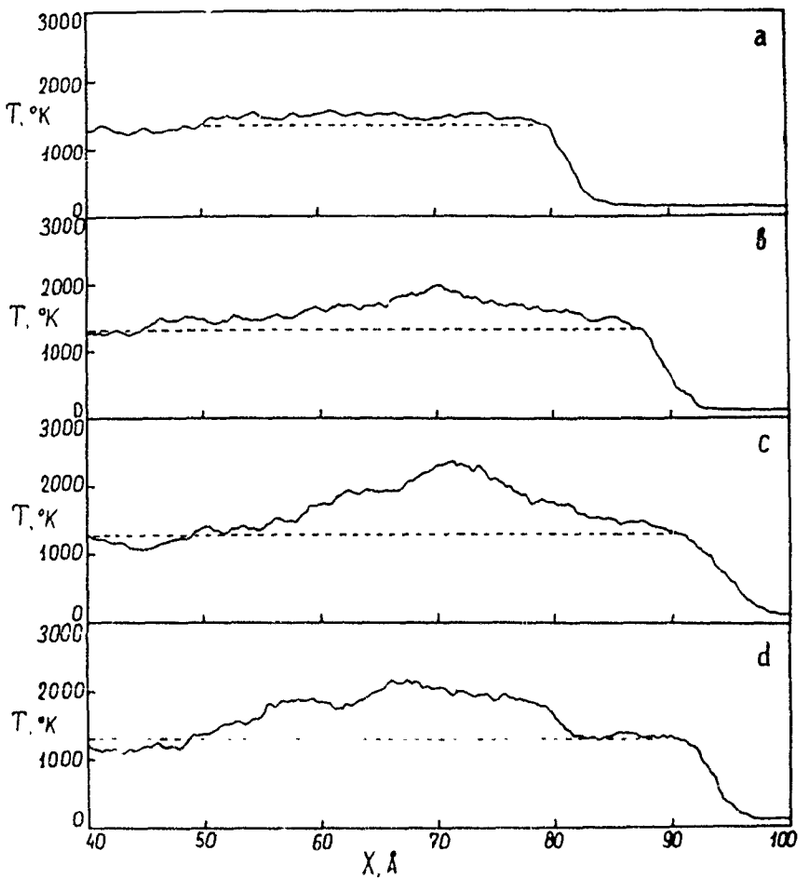

Fig. 3. The temperature final profiles (after the shock wave front passing)

the process then further development after some time will correspond to the thermal explosion regularities (23). It will take place when the regions size and temperature are equal to the critical values (28).

So, the macro-regions development occurs in three stages. During the first stage the shock front forms the overheated micro-regions. The nuclei of the decomposition regions are formed inside the micro-regions. During the second stage the larger micro-regions grow from the nuclei due to the decomposition reaction chain nature. During the third stage the further increase of the regions takes place by the mechanism of the thermal explosion and is in progress up to their confluence.

One can interpret in terms of the three-stage model the formation in nitromethane at first the micro-hot-spots (registered by the light scattering techniques (5)) and their subsequent transformation into the macro-hot-spots. As it has been mentioned above, the micro-hot-spots in the inert liquids are also formed at the expense of generating overheated micro-regions under the shock front effect. However, in this case the decomposition is non-exothermal and, therefore, the macro-hot-spots are not formed.

In conclusion one can say that whole activation process will accelerate at the shock compression due to the overheated micro-regions origin, if the characteristic time of their development is comparable or smaller than the characteristic life time of the overheated micro-regions.

REFERENCES

1. G.A. Adadurov, V.S. Trofimov, and V.A. Yakovleva, "Determination of Parameters of Unstable Shock Waves," Fizika Gorenija i Vzriva, Vol. 4, No. 3, pp. 397-399, 1968.

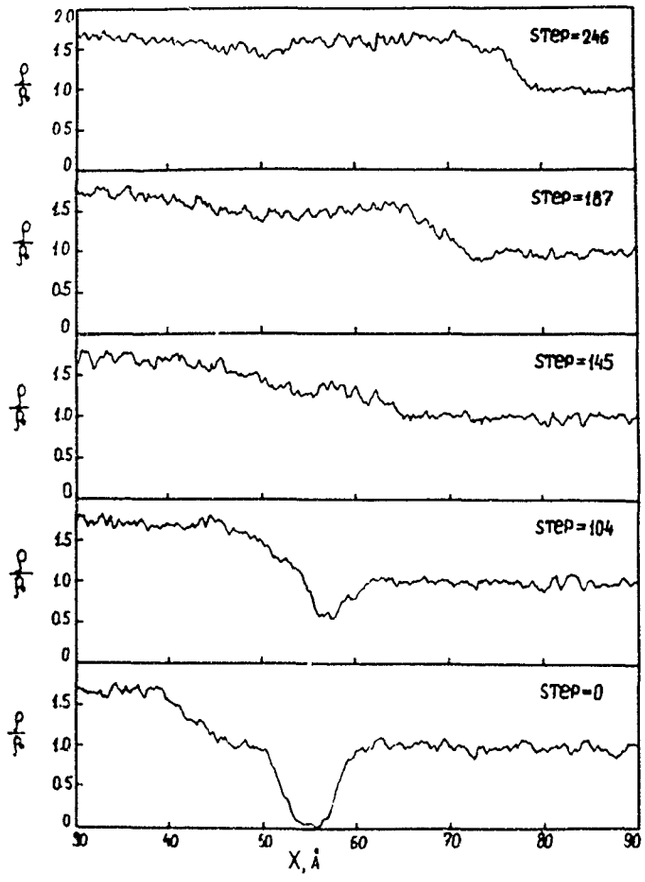

Fig. 4. The density profiles of various moments of time

2. M. Cowperthwaite, and J.T. Rosenberg, "A Multiple Lagrange Gauge Study of the Shock Initiation Process in Cast TNT," Sixth Symposium (International) on Detonation, Coronado, California, 1976, pp. 786-793, ACR-221 Office of Naval Research, Arlington, Virginia, 1976.

3. V.S. Trofimov, G.P. Trofimova, "Probability of Decomposition of Cast TNT in the Shock Wave," Fizika Gorenia i Vzriva, Vol. 16, No. 2, pp. 92-99, 1980.

4. F.E. Walker, and R.S. Wasley, "Initiation Patterns Produced in Explosives by Low-Pressure, Long Duration Shock Waves," Combust. and Flame, Vol. 22, pp. 53-68, 1974.

5. A.A. Vorobjev, and V.S. Trofimov, "Study on Dissipation of Light in Shock Compressed Nitromethane," Fizika Gorenia i Vzriva, Vol. 14, No. 3, pp. 152-153, 1978.

6. A.N. Dremin, and P.F. Pokhil, "Investigation of the Chemical Reaction Zone in Trotyl," Zh. Fiz. Khimija, Vol. 34, No. 11, pp. 2561-2570, 1960.

7. A.N. Dremin, and K.K. Schvedov, "Obtaining Ch.-J. Pressure and Time of Reaction for Detonation Waves in High Energy Explosives," Zh. Prikl. Mekh. Tekhn. Fiz., No. 2, pp. 154-159, 1964.

8. K.K. Schvedov, and S.A. Koldunov, "Dependence of the Decomposition Time of TNT and Detonation Waves on Its Physical State and Structure," Combustion and Explosion, pp. 439-443, Nauka, Moscow, 1972, (USSR).

9. Ya.B. Zeldovitch, "To the Theory of Detonation in Gases," Zh. Experim. Teor. Fiz., Vol. 10, pp. 542-568, 1940.

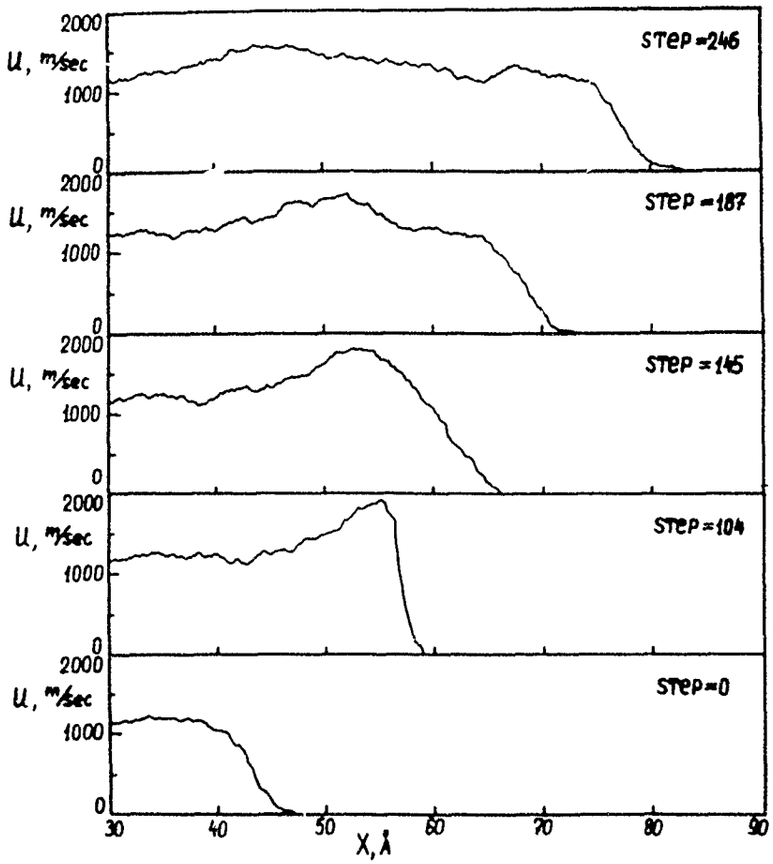

Fig. 5. The particles velocity profiles at various moments of time

10. J. Von Neuman, "Theory of Detonation Waves," OSRD Rept. 549, 1942.

11. W. Doring, "Uber den Detonationsvorgang in Gasen," Ann. Phys., Vol. 43, pp. 421-436, 1943.

12. A.N. Dremin, "The Current Problems of Study of Detonation Waves in Condensed Media," Transactions of the Mechanics Institute of Moscow State University, Vol. 21, No. 2, pp. 150-157, 1973 (USSR).

13. L.V. Babare, A.N. Dremin, and V.Yu. Klimenko, "Study of the Specific Mechanism of Organic Substances Destruction at Shock Wave Compression," Theses of the 5th All-Union Symposium on Mechanochemistry and Mechanoemission of Solids, p. 74, Tallin, 1975 (USSR).

14. V.Yu. Klimenko, A.N. Dremin, and L.V. Babare, "Effect of Substitutes on Aromatic Ring Destruction under Shock Compression," Theses of the 5th All-Union Symposium on Mechanochemistry and Mechanoemission of Solids, p. 76, Tallin, 1975 (USSR).

15. V.Yu. Klimenko, and A.N. Dremin, "The Structure of the Shock Waves Front in Liquids," Detonation, Critical Phenomena. Physico-Chemical Transformation in Shock Waves, pp. 79-84, Chernogolovka, 1978 (USSR).

16. V.Yu. Klimenko, and A.N. Dremin, "The Structure of the Shock Wave Front in Liquids," Soviets Physics, Doklady, Vol. 24, p. 984, 1979 (Russian original, Dokl. Akad. Nauk SSSR, Vol. 249, No. 4, pp. 840-843, 1979).

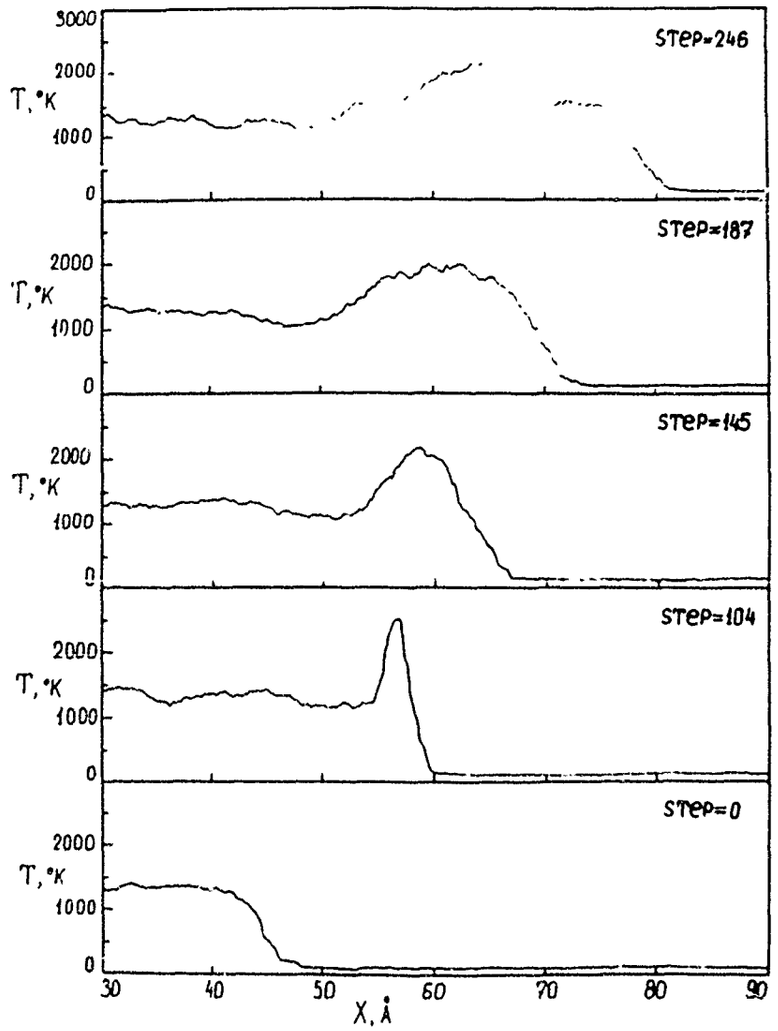

Fig. 6. The temperature profiles at various moments of time

17. A.N. Dremin, and V. Yu. Klimenko, "On the Effect of Shock Wave Front on the Reaction Origin," Progress in Astronautics and Aeronautics, Vol. 75, pp. 253-268, 1981.

18. B.L. Holian, W.G. Hoover, B. Moran, and G.K. Straub, "Shock Wave Structure Via Non-equilibrium Molecular Dynamics and Navier-Stokes Continuum Mechanics," Phys. Rev. A, Vol. 22, pp. 2798-2808, 1980.

19. D.H. Tsai, and S.F. Trevino, "Thermal Relaxation in a Dense Liquid under Shock Compression," Phys. Rev. A, Vol. 24, pp. 2743-2757, 1981.

20. V.Yu. Klimenko, and A.N. Dremin, "On the Decomposition Reaction Kinetics in the Shock Wave Front," Detonation, Chemical Physics of Combustion and Explosion Processes, pp. 69-73, Chernogolovka, 1980 (USSR) (English Translation in Sandia National Laboratories Report RS 3140/81/38, February 1981).

21. A.N. Dremin, V.Yu. Klimenko, "Shock Wave Front Role in Decomposition of Organic Substances," Theses of the Internat. Colloquium on Gasdynamics of Explosions and Reactive Systems, p. 60, Minsk, USSR, 1981.

22. A.N. Dremin, V.Yu. Klimenko, K.M. Mikhailjuk, and V.S. Trofimov, Seventh Symposium (Int) on Detonation, p. 789, U.S. Naval Academy, Annapolis, Maryland, 1981.

23. A.A. Vorobjev, and V.S. Trofimov, "Non-Homogeneous Decomposition Reaction Development of Shock-Compressed Homogeneous Explosives," Fizika Gorenija i Vzriva, Vol. 18, No. 6, pp. 74-81, 1982.

24. F.E. Walker, and R.J. Wasley, "A General Model for the Shock Initiation of Explosives," Propellant and Explosives, Vol. 1, pp. 73-80, 1976.

25. M. Ross, "The Repulsive Forces in Dense Argon," J. Chem. Phys., Vol. 73, p. 4445, 1980.

26. L. Verlet, Phys, Rev., Vol. 159, p. 98, 1967.

27. A.V. Starshinov, B.N. Kondrikov, G.D. Kosak, and V.M. Rajkova, "Homogeneous Catalysis at Nitromethane Detonation," Detonation Chemical Physics of Combustion and Explosion Processes, pp. 73-76, Chernogolovka, 1977, (USSR).

28. A.G. Merzhanov "On Critical Conditions for Thermal Explosion of a Hot Spot," Comb. Flame, Vol. 10, No. 4, pp. 341-348, 1966.

29. L.D. Landau, and E.M. Lifshits, Statistical Physics, Chap. 12, Nauka, Moscow, 1976.

DISCUSSION

MARTIN SUMMERFIELD, PCRL, Inc.

It seems that the theory postulates either a very high exothermic reactivity or a very low thermal conductivity of the liquid explosive or both in order to show detonability due to the very tiny inhomogeneities statistically present in a pure liquid explosive. Can the authors give the values postulated or derived in the theory and compare them with those of typical liquid explosives, for example, nitromethane?

REPLY BY A. N. DREMIN

In accordance to the three-stage model the hot-spot formation process can be presented as follows:

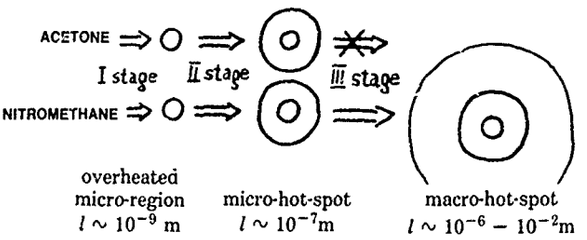

1) The micro-hot-spots have been experimentally observed at shock loading both acetone and nitromethane, and macro-hot spots have been observed only in nitromethane. Why? Why is the II-d stage realized? The point is that the decomposition of nitromethane is exothermal, the decomposition being sufficiently exothermal that the critical conditions of micro-hot-spot ignition be fulfilled. Therefore, the evaluation of the thermal explosion conditions must be carried out for the micro-hot-spot (the size $\sim 10^{-7}$m) rather than for the overheated micro-region (the size $\sim 10^{-9}$m).

2) The author of the question is interested, why the overheated micro-region generates the micro-hot-spot, i.e. the II-d stage is realized. It should be noted here, that the very stage is realized for various substances (nitromethane, acetone, benzene) with different activation energy and different (positive and negative) heats of reaction, that is, the reaction heat is not needed to interpret the II-d stage formation.

The level of the substance temperature around the overheated micro-region is rather high ($\sim$1000 °K). At this temperature the substance decomposition occurs even if there were no overheated micro-region. As the temperature of the overheated micro-regions is by 300-500 °K higher, the decomposition proceeds inside the regions 5-10 orders of magnitude faster. Owing to the chain reaction nature the decomposition spreads out of the micro-region, creating the micro-hot-spot. As a rule, at high temperatures condensed substance decomposition splinters (radicals, ions) of one molecule activate decomposition of neighbour molecules. If the

process is endothermal (e.g., acetone), the temperature in the hot-spot is falling down and, at last, enlarging the spot is stopped, but if the process is exothermal (e.g., nitromethane) the temperature increases and the moment comes when the size of the spot and temperature achieve the critical values (see reference 28) and the mechanism of the thermal explosion is ingaged.

3) Finally, the question about the heat conductivity. It can be transformed to the following — how long the overheated micro-region exists and may the region give the significant effect for this period? In our molecular dynamic simulation we observe existence of the overheated micro-region for 10^{-11}s. It is difficult to predict its further evolution. Nevertheless, even for this period the primary acts of the decomposition have time to be accomplished at these high temperatures and to engage the chain mechanism of the substance decomposition.

Session VIII
DETONATION SPECTROSCOPY

Co-Chairmen: Claude M. V. Fauquignon
Institute Saint-Louis
Frank J. Owens
Army Research and Development Command

TIME-RESOLVED SPECTROSCOPIC STUDIES OF DETONATING HETEROGENEOUS EXPLOSIVES*

Wayne M. Trott and Anita M. Renlund
Sandia National Laboratories
Albuquerque, New Mexico 87185

Emission spectroscopy and pulsed-laser-excited Raman scattering methods have been applied to the study of detonating heterogeneous explosives, including PETN, HMX and HNS. Time-resolved spectra of emission from detonating HNS show the evolution of features due to electronically-excited radical species. For HNS, the CN(B-X) system near 388 nm has been studied at a wavelength resolution of 0.5 Å. Boltzmann vibrational temperatures have been calculated by comparing the experimental data with computer-simulated spectra. These temperatures are consistent with the expected trend of detonation temperature as a function of charge density. Using 532-nm laser excitation, single-pulse Raman scattering measurements have been made at the free surface of detonating HMX and PETN samples. Monotonic attenuation of Raman scattering intensity over a 100-ns interval is observed after detonation front arrival at the free surface. Depletion of the Raman signal occurs prior to significant loss of the scattered laser light. The significance of the Raman measurements as a possible probe of reaction zone length in detonating explosives is discussed.

I. INTRODUCTION

A predictive understanding of the initiation and sustained detonation of heterogeneous (i.e., porous, granular) explosives requires characterization of both the mechanical response of the material and the chemical reaction mechanisms that control the rate at which the explosive is consumed. Real-time spectroscopic techniques offer considerable potential for providing much needed information on the important microscopic physical and chemical processes in such systems via *in situ* measurements of reaction intermediates, rates and temperatures. In this paper, we discuss the application of emission spectroscopy and pulsed-laser-excited Raman scattering methods to the study of detonating high explosives (HEs) including pentaerythritol tetranitrate (PETN), 1,3,5,7-tetranitro-1,3,5,7-tetraazacyclooctane (HMX) and 2,4,6,2',4',6'-hexanitrostilbene (HNS). Both techniques provide good temporal and spatial resolution and are applicable to pressed polycrystalline samples of many widely used HEs. In time-resolved emission studies, we have observed several electronically-excited transient species including CN*, CH*, C_2* and probably NO_2*. Results of high-resolution studies of CN (B-X) emission in detonating HNS have been used to calculate vibrational temperatures as a function of initial charge density. We have shown that single-pulse Raman scattering measurements can be made in the severe environment of a detonation and have monitored the attenuation of the Raman signal from PETN as a function of time after detonation-wave arrival at the free surface. These results are compared to previous estimates of reaction time in an unperturbed, steady-state detonation.

II. EXPERIMENTAL

The explosive device used for all emission and Raman measurements consisted of a pressed pellet of pure HE initiated by an exploding bridgewire detonator (Reynolds Industries,

*This work was performed at Sandia National Laboratories, Albuquerque, NM, supported by the U.S. Department of Energy under contract number DE-AC04-76DP00789.

RP-2). The pellet was affixed to the detonator output face using a thin layer of fast setting epoxy. The explosive assembly was mechanically held in a fixture providing for linear and angular alignment and all measurements were performed with the assembly confined in an evacuated chamber to avoid complications due to air. The detonator was connected to a 2.5-kV fireset using high-voltage vacuum feedthroughs. The specified detonator function time at this operating voltage is 1.8 μs with a standard deviation of less than 25 ns. The diameter of the HE pellet (6.4 mm) was roughly twice that of the detonator output face. The relatively small size of this configuration permitted reasonably frequent measurements with modest material consumption and minimal damage to the optical components mounted on the test chamber; however, the non-planar output of the device introduced some difficulty in data interpretation as discussed below. Samples of the various HEs were prepared by pressing approximately 100 mg of the loose powder. Densities of the pressed HMX and PETN were 1.87 and 1.69 g cm^{-3}, respectively. For HNS, material pressed to four different densities were used: ϱ_0 = 1.70, 1.65, 1.56 and 1.50 g cm^{-3}.

Temporal and spatial characteristics of the detonation light were examined using fast-framing photography. An Imacon 675 camera (Hadland Photonics, Ltd., S-20 response) was used to obtain images of the detonating pellets at a framing rate of 7.5 x 10^7 s^{-1}. The camera monitor pulse (nearly coincident with the first frame) was recorded on each shot for comparison with the temporal profile of emission intensity as determined by either a photomultiplier or biplanar phototube. The framing records were obtained on Polaroid Type 47 film. The images were then digitized and contrast enhanced using a COMTAL "Vision One/20" image processing system.

In studies of spectrally resolved emission, light from the front face of the exploding pellet was imaged onto the slit of a spectrometer (Jarrell-Ash 1/3 m or Spex 0.85 m). The dispersed spectrum of near-uv and visible emission was viewed by a gatable intensified diode array coupled to an optical multichannel analyzer (Tracor Northern) allowing temporal resolution of <20 ns. Timing of the detector gate pulse relative to the firing pulse was varied with digital delay generators. For studies of temporally resolved spectra, signals from the detector gate and from a photomultiplier tube viewing the total emitted light were displayed together on an oscilloscope to establish the exact time interval over which the spectrum was obtained.

Detailed discussions of the experimental design for the single-pulse Raman scattering studies have been presented elsewhere (1,2). A schematic of the experimental arrangement is given in Fig. 1. Briefly, the 532-nm output of a

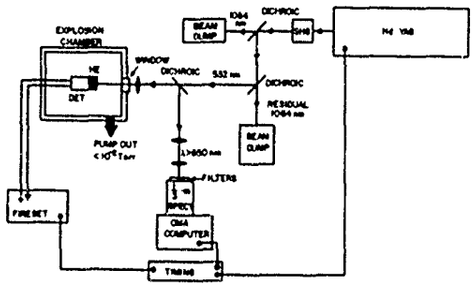

Fig. 1. Schematic drawing of experimental arrangement for single-pulse Raman measurements

frequency-doubled, pulsed Nd:YAG laser (~10 ns FWHM) was mildly focused to a 1-mm-diameter circular spot at the center of the free surface of the explosive pellet. Laser energy reaching the sample was controlled by varying the time delay to the Q-switch. The frequency-shifted radiation scattered from the sample was imaged onto a spectrometer and viewed with the intensified diode array and optical multichannel analyzer. A <100-ns-wide gate to the detector avoided signal loss due to timing jitter and provided some discrimination against the detonation emission. Digital delay generators were used to set the probe laser and detection system gate in relation to the fireset trigger pulse.

III. RESULTS AND DISCUSSION

A. Fast-Framing Photography

The emission phenomena observed in fast-framing photographic records of detonating HMX and HNS are generally consistent with the results of previous studies of detonation light (3,4). Most of these phenomena are illustrated by the sequential images of a detonating HNS pellet displayed in Fig. 2. The first frame

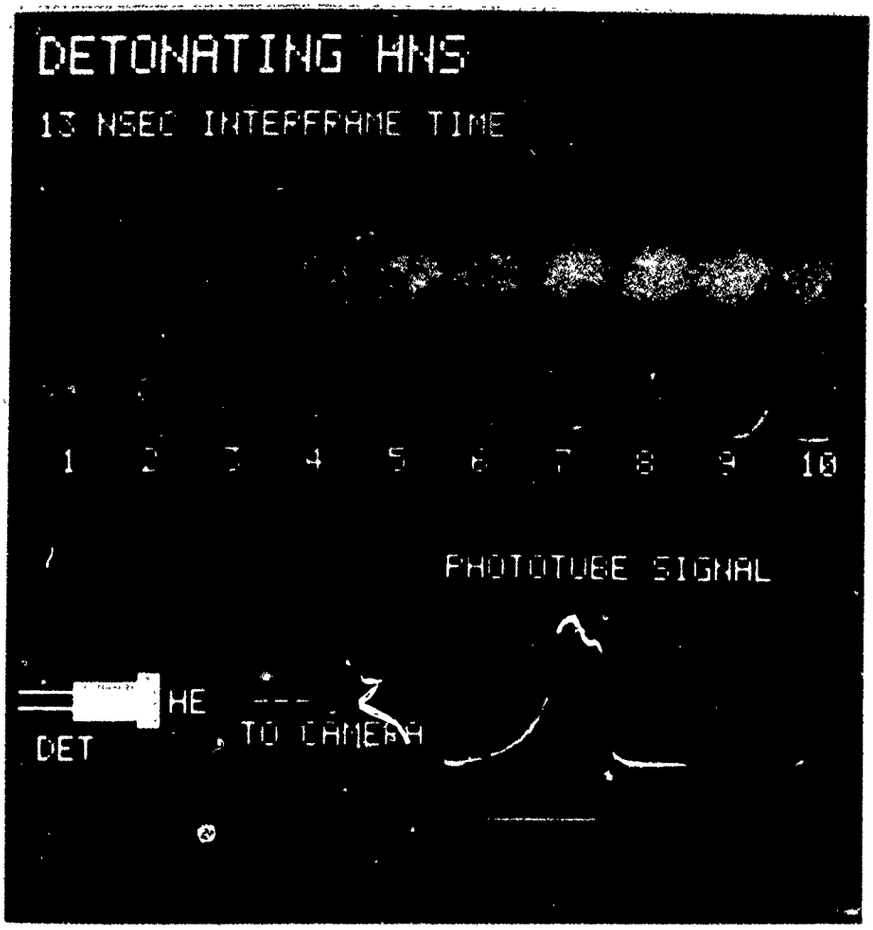

Fig. 2. Fast-framing photograph of detonating HNS. To illustrate the size of the image, the top trace is a record of the strobe-flash illuminated pellet

in this sequence shows a small bright spot of light corresponding to the emergence of the detonation wave at the center of the pellet surface. The rapidly expanding "ring" of bright emission seen in the next eight frames reveals the two-dimensional character of the detonation wave front in this device. This "ring" actually contains fine, granular structure which can be clearly seen in the images near the end of the sequence. The rapid quenching of the bright emission is especially evident in Frame 2 where the region surrounding the center of the pellet surface is relatively dark compared to the same region in Frame 1. From the width of the emission ring, we estimate the duration of emission at any point on the surface to be on the order of the single frame exposure time; i.e., 3 ns or less.

A weaker, diffuse glow precedes the emergence of the detonation wave at the surface. This phenomenon is barely discernible at the outer edges of the bright emission in Frames 1-3 of Fig. 2 and was much more obvious in the case of detonating HMX. We attribute the diffuse glow to so-called "shine through"; i.e., light scattered from inside the pressed sample. The intensity of neither the bright ring nor the diffuse glow is much affected by pressure of surrounding atmosphere over the range 0.01 - 1 Torr. In contrast, after the detonation wave reaches the outer rim of the pellet surface, we observe emission (primarily in the form of a rapidly expanding ring of light) whose intensity is markedly dependent on the chamber pressure. The function of the surrounding atmosphere in production of this effect

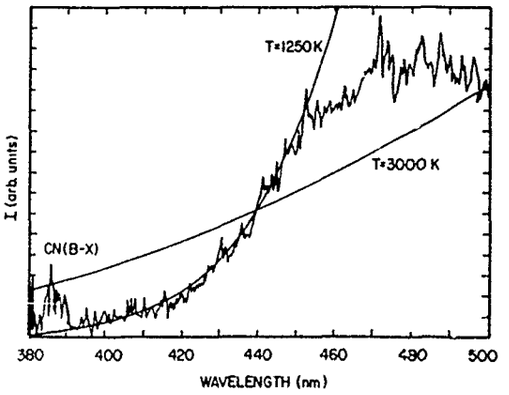

Fig. 3 Spectrum of emission from detonating HNS (ϱ_0=1.7 g cm^{-3}) acquired over a 30-ns interval just prior to the break-out of the detonation front onto the face of the pellet (see text) (The lines represent graybody curves at the temperatures shown, normalized to the observed emission intensity at 440 nm.)

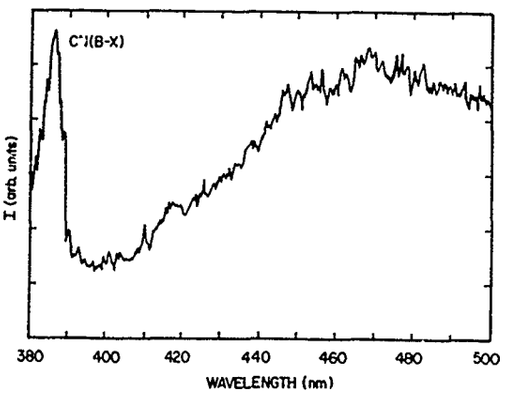

Fig. 4. Spectrum of emission from detonating HNS (ϱ_0=1.7 g cm^{-3}) acquired over a 30-ns interval during the peak of the emission intensity (see text)

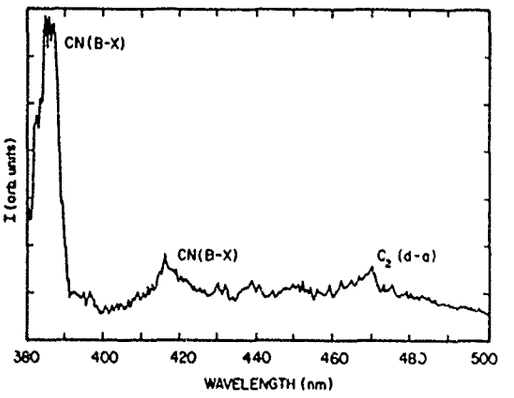

Fig. 5. Spectrum of emission from detonating HNS (ϱ_0 = 1.7 cm^{-3}) acquired over a 30-ns interval during the fall-off of the emission

has been discussed previously (4). At pressures below 50 mTorr, the observed "afterglow" intensity is approximately two orders of magnitude less than that of the bright emission coinciding with detonation front arrival at the surface of the sample. Accordingly, this phenomenon is not apparent in the late frames of Fig. 2 due to limited film contrast.

The various effects seen with fast-framing photography contribute to the observed temporal profile of emission intensity. In general, photomultiplier traces of the emission display (in order): (1) a slow-rising leading edge corresponding to increasing "shine through" as the detonation front approaches the free surface, (2) a rapid rise in signal intensity as the detonation wave front emerges from the end of the sample, (3) a plateau of high intensity due to the two-dimensional nature of the detonation front and (4) a rapid fall-off in signal as the detonation front reaches the outer rim of the material (see Section IIIC.) The photographic records are also very useful in the interpretation of our time-resolved emission spectra and provide an important measure of the non-planarity of the detonation front and its effect on our Raman scattering data.

B. Emission Spectroscopy

Figures 3-5 show spectra of emission from detonating HNS obtained at three different times relative to the arrival of the detonation wave at the free surface of the pellet. The spectra are corrected for the wavelength-dependent response of the spectrometer and detection system. In each case, emission was collected for a 30-ns interval to acquire sufficient signal. At the earliest time, which corresponds to primarily the "shine through" region and also to the initial break-out of the detonation (cf Frame 1 in Fig. 2) the main feature of the emission is a broad unstructured band with an apparent cutoff near 400 nm. We show calculated, relative optical emission profiles for graybody sources at two temperatures together with the spectrum in Fig. 3. While there may be an underlying component of the emission due to graybody emission, it is

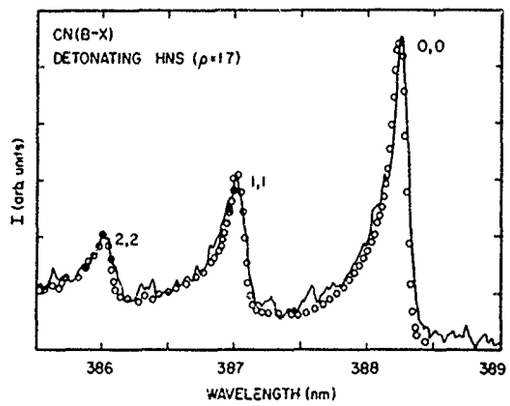

Fig. 6. Time-integrated spectrum of CN(B-X) emission observed from detonating HNS (ρ=1.70 g cm^{-3}) (The spectrum is corrected for the wavelength-dependent response of the spectrometer and detection system. The open circles are results from a computer-simulated spectrum with CN(B) rotational and vibrational temperatures of 5000 K.)

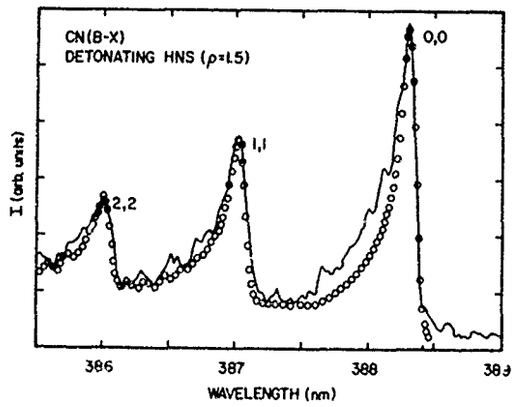

Fig. 7. Time-integrated spectrum of CN(B-X) emission observed from detonating HNS (ρ=1.50 g cm^{-3}) (The spectrum is corrected for the wavelength-dependent response of the spectrometer and detection system. The open circles are results from a computer-simulated spectrum with CN(B) rotational and vibrational temperatures of 6500 K.)

clear that the shape of this broad band is not that of graybody radiation.

Instead, this emission is consistent with NO_2(A-X) emission which is known to cut off at 398 nm due to predissociation of the NO_2 (5). A much smaller band in the 380-390 nm region is due to CN(B-X) emission. Figure 4 shows the spectrum obtained during the high-intensity emission corresponding to Frames 4-6 of Fig. 2. The most prominent feature is due to CN(B-X) emission. Approximately 100 ns later, we obtained the spectrum shown in Fig. 5 where products such as C_2(d) are also observed in emission. The presence of C_2(d-a) emission in the earlier spectra is not observed because of the intense broadband emission in the same spectral region. We have performed similar experiments with HMX. Again, the early emission appears to be primarily NO_2(A-X). Late-time emission, however, shows only weak discrete features of the electronically excited radical species and the spectrum is dominated by a broadband continuum different from the early emission. In general, the intensity of discrete emission appears to correlate in a reciprocal fashion with the degree to which the explosive is oxygen balanced, i.e., HNS > HMX > PETN.

In previous experiments, we have noted that the vibronic structure of the CN(B-X) and C_2 (d-a) bands observed from detonating HEs can be used to infer Boltzmann vibrational temperatures (6). We have now extended these studies to higher spectral resolution to observe the effect of the initial charge density on the temperature of the CN(B). To obtain higher resolution, we sacrifice the temporal resolution of the previous spectra. Instead, we integrate the emission over 300 ns which includes all the emission except some of the weak "afterglow." Figures 6 and 7 show spectra in the CN(B-X) spectral region from detonating samples of HNS pressed to initial densities of 1.70 and 1.50 g cm^{-3}, respectively. These are typical of the resolution (~0.5Å) and signal-to-noise ratio we are now able to achieve on a single shot. The most apparent difference between the two spectra is the smaller ratio of intensity in the (1,1) and (2,2) bands relative to the (0,0) band in the emission from detonating HNS pressed to the higher density (Fig. 6). To establish the vibrational temperature of the CN(B) in these two experiments, several CN(B-X) spectra were generated by computer simulation at temperatures between 3500 and 7500 K. To calculate these spectra, we assume equilibration of the vibrational and rotational degrees of freedom which allows relative populations in the rovibrational states of CN(B) to be described by a Boltzmann distribution at a single temperature. Published values of spectroscopic

constants (7) and Franck-Condon factors (8) were used to calculate individual transition intensities as a function of the Boltzmann population distributions (6). The spectra were then simulated using a Gaussian slit function appropriate for the resolution of the present experiments. The simulated spectra were compared to the data to obtain a best fit, and are shown by the open circles in Figs. 6 and 7. These fits establish the temperatures of the emitting CN(B) at 5000±200 K and 6500±400K from detonating HNS at the high and low densities, respectively. Data from HNS pressed to two intermediate densities gave temperatures between these two values, following a trend of increasing temperature with decreasing initial charge density. While the agreement between the simulated spectra and the data is generally good, the simulated spectra fail to reproducethe width on the short-wavelength side of the bandheads for emission from the detonating low-density HNS (cf. Fig. 7). This may indicate incomplete equilibration of the rotational and vibrational modes of the emitting CN.

Our results show that emission spectroscopy at sufficiently high resolution provides a spectroscopic "thermometer" which may correlate with detonation temperature. The trend of detonation temperature, as calculated by equation-of-state models, with initial charge density is the same as we observe in our CN(B-X) measurements (9). We note, however, that our measured temperatures are generally ~1000 K higher than results of most modelling calculations (9).

C. Single-pulse Raman Scattering

Recently, there has been considerable interest in spontaneous and coherent Raman scattering techniques as diagnostic probes for determining the microscopic phenomenology of shock-induced chemical reactions (10). Spontaneous Raman spectroscopy has been used in several studies of detonating liquid and monocrystalline explosives (11-14). We have shown (1, 2) that excellent single-pulse spontaneous Raman spectra can be obtained from many unshocked heterogeneous explosive samples and that Raman scattering measurements can be made in the severe environment of detonating PETN. Here, we utilize recent Raman scattering

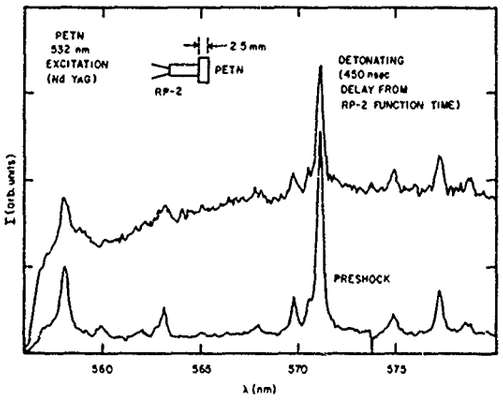

Fig. 8. Single-pulse Raman spectra from unshocked PETN and a detonating sample as recorded by the optical multichannel analyzer (100-ns gate width) (Broadband emission from the detonation is evident on the top trace.)

measurements from detonating HMX as well as the fast-framing photography data described in Section IIIA to expand our previous discussion (1) of Raman scattering from detonating heterogeneous explosives.

Our PETN results are reproduced in Figs. 8 and 9. Figure 8 compares the single-pulse Raman spectrum (800-1500 cm^{-1} range) of unshocked PETN with that obtained from a detonating sample at a time delay of 450 ns from the nominal RP-2 detonator function time, t_0. We observe remarkably similar positions of the Raman lines in the unshocked and detonating material; however, the significant attenuation of the Raman lines and simultaneous appearance of strong background emission are evidence that the detonation front has reached the free surface of the pellet. Under sustained compression at detonation pressures, substantial shifts in the molecular vibrational frequencies might be expected, but the complex interaction of the detonation wave front with the PETN/vacuum interface may preclude observation of such shifts. We also note that previously observed shock-induced frequency shifts in PETN single crystals have been much smaller than those seen in static compression studies (14, 15). In Fig. 9, the measured attenuation of the strongest Raman line (the 1296 cm^{-1} line associated with the summetric NO_2 stretching mode (16, 17)) is shown as a function of time

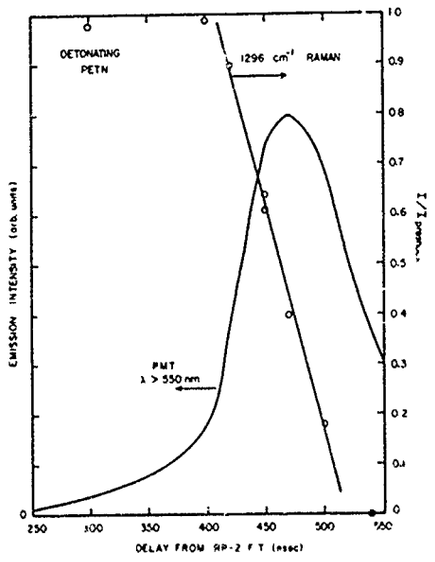

Fig. 9. Temporal profiles of Raman signal intensity and emission intensity from detonating PETN (Each open circle represents a single-shot measurement of the 1296 cm^{-1} Raman signal intensity at the indicated time delay divided by the signal intensity from the unshocked material. Raman signal intensities from the unshocked material were reproducible to within a few percent.)

delay from t_0. The same figure also displays a trace of the observed emission intensity versus time delay from t_0. Depletion of the parent molecule Raman signal occurs over a 100-ns interval.

The observed interval for attenuation of the PETN Raman scattering intensity may reflect the chemical reaction rate for the parent species in this system. Alternative interpretations of this phenomenon include the following: (1) the Raman signal attenuation arises from a fairly large probe depth, (2) the two-dimensional nature of the detonation front is responsible for the observed interval, and (3) the Raman signal loss simply reflects a reduced surface area for scattering or increased optical absorption at the pellet surface. The nonzero probe depth and nonideal detonation front certainly contribute to the apparent depletion time by permitting the simultaneous observation of unshocked and shocked material as the detonation wave front nears the free surface; however, the available data suggest that these are of only minor importance. Figure 9 shows that the onset of the Raman signal depletion coincides with a sharp rise in the emission intensity. As mentioned in Section IIIA, the rapid rise in the emission signal also coincides with the emergence of the detonation wave from the end of the pellet. Very little attenuation of the Raman scattering intensity occurs prior to this event (cf. Fig. 9). Hence, we infer that the probe depth is actually quite small. Direct evidence concerning the possible effect of the non-planar detonation front is provided by the first two frames in Fig. 2. At Frame 2, we see that the detonation front has already emerged from the pellet over a surface area larger than the 1-mm-diameter probe laser spot. Frame 1, on the other hand, shows emission corresponding to the initial arrival of the detonation front at the center of the free surface. From these images, we estimate that the resulting temporal contribution to the observed interval for Raman signal depletion can be no more than the fast-framing camera interframe time; i. e., 15 ns or less.

To address the third alternative interpretation mentioned above, we have examined the Raman signal loss in relation to the intensity of scattered 532-nm light for unshocked and detonating samples. Typical results for HMX are given in Figs. 10 and 11. The data in each figure were obtained using a single 532-nm laser pulse. The scattered laser light was attenuated by appropriate cutoff filters in order to view and display its intensity on scale with the Raman scattering intensity. The observed band positions in the Raman spectrum of the unshocked HMX (cf. Fig. 10) are in excellent agreement with cw laser Raman measurements on the beta-polymorph of this compound (18). As in the case of PETN, Fig. 11 shows a fairly uniform attenuation of the Raman spectrum during detonation but little or no shift in the band positions. It is interesting that we do not observe a comparable loss of scattered 532- nm light intensity at this point in the detonation. Additional measurements have shown that significant depletion of the scattered laser light does not occur until ~50 ns after the parent molecule Raman spectrum becomes so weak that is can no longer be distinguished from the background emission. Hence, the observed interval for Raman signal attenuation cannot be attributed

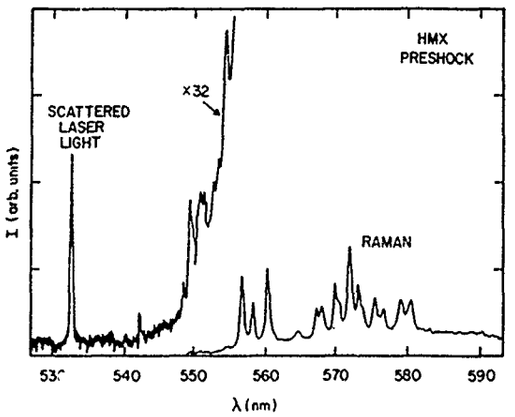

Fig. 10. Single-pulse Raman spectrum from unshocked HMX (The scattered 532-nm laser light is also displayed.)

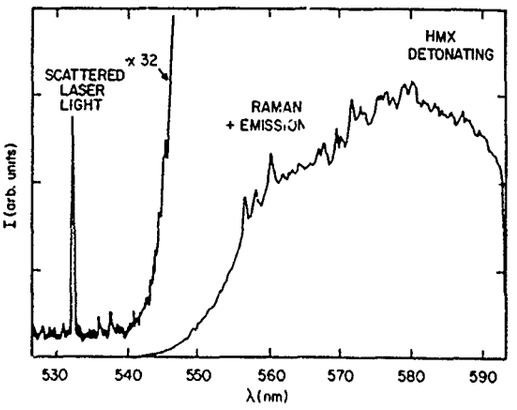

Fig. 11. Single-pulse Raman spectrum from detonating HMX acquired ~50 ns after arrival of the detonation front to the front surface of the pellet (Broad-band emission from the detonation contributes to the high background level. The Raman signal intensities are considerably reduced from the previous figure, but the scattered 532-nm laser light remains unaffected at this delay time.)

to a greatly reduced sufrace area for scattering and is not likely due to transient absorption.

We note that the reproducible, monotonic attenuation of PETN Raman scattering intensity over a 100 ns interval is consistent with previously obtained experimental and theoretical global reaction times for high-density PETN as well as recent velocity-interferometric measurements of reaction duration in other explosives (19-21). Reaction times inferred from these preliminary free-surface studies are clearly not directly applicable to an unperturbed detonation reaction zone since, in this configuration, a rarefaction is reflected back into the explosive when the detonation front reaches the HE/ vacuum interface. We anticipate less ambiguous results with optimal impedance-matching at the interface, and experiments utilizing appropriate window materials are planned. As yet, we have not observed Raman signals from transient or product species. Such observations may require a substantially improved signal-to-noise ratio, and we are currently implementing several modifications to the experimental arrangement which promise to greatly enhance the sensitivity and discrimination against background emission.

IV. SUMMARY

We have described the application of fast-framing photography and two real-time spectroscopic techniques to the study of microscopic chemical and physical changes in detonating HEs. Time-resolved emission spectroscopic results are consistent with early formation of $NO_2(A)$ followed by formation of other electronically excited radical products. High-resolution spectroscopy may be used to determine temperatures in the region of the detonation front. We have shown that quantitative single-pulse Raman scattering measurements can be made at the free surface of a detonating heterogeneous explosive and may provide a direct measure of reaction times in a detonation front. Refinement and further application of these techniques to experiments with well-characterized detonation fronts should provide valuable input for reactive flow models of detonation waves in heterogeneous explosives and lead to an improved predictive modelling capability of explosive initiation and performance.

ACKNOWLEDGMENTS

We wish to acknowledge the excellent technical assistance of H. C. Richardson and J. C. Pabst. We also thank S. A. Sheffield and M. E. Riley for helpful discussions.

REFERENCES

1. W. M. Trott and A. M. Renlund, "Single-pulse Raman Scattering Studies of Heterogeneous Explosive Materials," Applied Optics, in press.
2. W. M. Trott, A. M. Renlund and R. G. Jungst, "Single-pulse Raman and Photoacoustic Spectroscopy Studies of Triaminotrinitrobenzene (TATB) and Related Compounds," Proceedings, 1985 Southwest Conference on Optics, SPIE, in press.
3. J. H. Blackburn and L. B. Seely, Trans. Faraday Soc. *61*, 537 (1965).
4. N. Lundborg, Ark. Fys. *25*, 541 (1964).
5. G. Herzberg, Molecular Spectra and Molecular Structure III. Electronic Spectra and Electronic Structure of Polyatomic Molecules (Van Nostrand, New York, 1966).
6. A. M. Renlund and W. M. Trott, "Spectra of Visible Emission from Detonating PETN and PBX 9407," Sandia Report, SAND83-2168.
7. K. P. Huber and G. Herzberg, Molecular Spectra and Molecular Structure IV. Constants of Diatomic Molecules (Van Nostrand, New York, 1979).
8. S. N. Suchard, Spectroscopic Data Vol. 1 (IFI/Plenum, New York, 1975).
9. C. L. Mader, Numerical Modeling of Detonation (University of California Press, Berkeley, 1979).
10. S. C. Schmidt, D. S. Moore and J. W. Shaner, in Proceedings of the American Physical Society Topical Conference on Shock Waves in Condensed Matter (Santa Fe, NM, 1983) p. 293.
11. A. Delpuech and A. Menil, in Proceedings of the American Physical Society Topical Conference on Shock Waves in Condensed Matter (Santa Fe, NM, 1983) p. 309.
12. C. Schulz, B. Linares, J. Cherville and S. Poulard, in Proc. Symp. on Explosives and Pyrotechnics, 8th (Los Angeles, CA, 1974) AD-789, p. 49.
13. A. Delpuech, J. Cherville and C. Michaud, in Proceedings of the 7th Symposium on Detonation (Annapolis, MD, 1981) p. 65.
14. M. H. Tailleur and J. Cherville, Propellants, Expl. and Pyrotech. *7*, 22 (1982).
15. W. G. Von Holle, in Proceedings of the American Physical Society Topical Conference on Shock Waves in Condensed Matter (Santa Fe, NM, 1983) p. 283.
16. M. W. Jenner, T. J. Sinclair and D. P. Wyndham, in Raman Spectroscopy, Linear and Nonlinear, J. Lascombe and P. V. Huong, eds. (Wiley, New York, 1982) p. 243.
17. F. R. Dollish, W. G. Fateley and F. F. Bentley, Characteristic Raman Frequencies of Organic Compounds (Wiley, New York, 1974) p. 43.
18. Z. Iqbal, S. Bulusu and J. R. Autera, J. Chem. Phys. *60*, 221 (1974).
19. A. N. Dremin, S. D. Savrov, V. S. Trofimov and K. K. Shvedov, Detonation Waves in Condensed Media, edited translation, AD-751 417, Wright-Patterson Air Force Base, Ohio, August 1972, p. 133.
20. E. L. Lee and C. M. Tarver, Phys. Fluids *23*, 2362 (1980).
21. S. A. Sheffield, D D. Bloomquist and C. M. Tarver, J. Chem. Phys. *80*, 3831 (1984).

DISCUSSION

KERRY L. BAHL, Lawrence Livermore National Laboratory

Were the HE pellets pressed mechanically or isostatically pressed and machined? Was there any pellet surface preparation?

REPLY BY W. M. TROTT

The pellets were prepared by linear mechanical pressing (10000-25000 PSI) in a die and the surfaces were used as pressed.

DISCUSSION

JULIUS ROTH, Consultant

Your statement that emission spectroscopy provides a spectroscopic "thermometer" of detonation temperature may be overly optimistic. You yourself recognize that present results lead to temperatures that are about 1000 to 2000K too high (if one assumes HNS to behave like TNT

and makes the comparison with a BKW calculation). Furthermore, as shown by Kato *et al.* in this Symposium, other EOS lead to the reverse density effect for highly oxygen-poor materials (TNT, Tetryl) than you observed. Even the BKW method indicated a much smaller density effect than the 1500K difference between your Figs. 6 and 7.

REPLY BY W. M. TROTT

We do not feel that the statement "emission spectroscopy at sufficiently high resolution provides a spectroscopic 'thermometer' which may correlate with detonation temperature" is overly optimistic. We have reported direct measurements of CN(B-X) band intensities which, upon comparison with computer-simulated spectra derived from known properties of the CN(B-X) system, establish a definite trend of decreasing Boltzmann vibrational temperature as a function of increasing initial charge density. These measurements were made on HNS samples pressed to >85% of the crystal density. The calculations of Kato *et al.* indicate that most EOS lead to a similar temperature trend over the density range of 85-100%, even for oxygen-poor materials such as TNT and Tetryl. The temperatures reported here are for the CN(B-X) system and there is certainly no assurance at present that they are identical to "C-J temperatures" or even that they are in local equilibrium with the rest of the reacting system; however, the observed trend with material density provides encouragement that further application of these and similar methods will lead to a more complete and accurate description of temperatures in detonating explosives.

REAL TIME ANALYSIS OF PETN DETONATION PRODUCTS

N.C. Blais and J.J. Valentini
Los Alamos National Laboratory
Chemistry Division, MS G738
Los Alamos, NM 87545

The freely expanding gases from the detonation of pentaerythritol tetranitrate (PETN) pellets were analyzed as rapidly as the molecules arrived at the mass spectrometer detector. It was found that all of the products arriving at the detector earliest, irrespective of mass, had the same velocity, 11 km s^{-1} and peaked at 5 km s^{-1}. The width of the time distributions varied from one species to another. Mass and velocity spectra of the important products were obtained and the most intense signals were found to be H_2O, CO, and CO_2, but H_2O, was by far the largest. Smaller signals arising from O, HCN, HCO and NO_2 were also found. Comparisons of the spectrum with other experiments are discussed.

INTRODUCTION

We present the results of some recent experiments which were designed to measure some of the characteristics of the immediate detonation products of explosive substances. The characteristics we report here are the mass spectrum of the gaseous products of PETN detonation and their velocity distributions. Ideally we would like to report these properties as a function of time starting with the passage of the detonation front through a particular volume of the explosive. The best that we could do here is to examine the detonation products after they had expanded to a sufficient degree that no further changes of state could occur. Our experimental conditions are such that intermolecular collisions occur only between detonation products as they expand, and this expansion occurs freely, being unimpeded by any ambient gases or surfaces before the molecular products are detected. Therefore, we cannot claim that our observed distributions are characteristic of the detonation products immediately after detonation occurs, or before expansion occurs. On the other hand our measurements are much closer to achieving that claim than the usual mass spectrometric measurements.

Several mass spectrometric measurements of detonation products and decomposition products have been reported (1-7), including those from PETN (1,4,5,7). Most of these were made on time scales long compared to ours and with expansion constraints sufficiently restrictive that no time history of product formation could be deduced. Relatively fast measurements of decomposition products have been reported (4), but even these millisecond time scales are long compared to ours, which have resolutions in the microsecond range. Only two other groups have reported measurements on a time scale similar to ours: those of Schilf (6) and of Höh (7). Höh has examined PETN detonation. However, no subsequent work has appeared since these reports.

As we will discuss below, our distributions in time are not characteristic of products emanating from a gaseous volume at a thermodynamically prescribed temperature. There are significant differences between our results and those of Höh. Our mass spectra are different than those reported from usual mass spectrometric measurements.

EXPERIMENTAL

The essential features of our apparatus are represented schematically in Fig. 1. Explosive pellets, in this case PETN, of from 22 to 100 mg

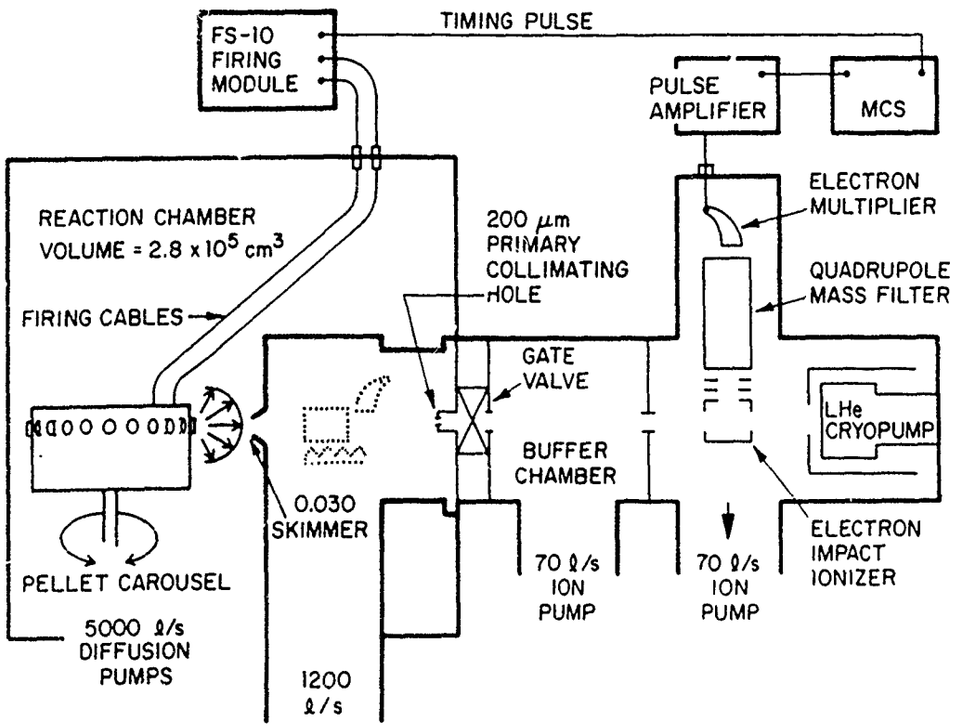

Fig. 1. Schematic of apparatus for detonation products studies. Dimensions are not to scale (Dotted section is an alternative detector placement sometimes used to check time scale of experiments.)

weight were detonated in a large vacuum vessel (119 cm long×48 cm wide×48 cm high). The gaseous products expanded adiabatically until they arrived at the first collimating aperture, a skimmer with a 0.076 cm hole. By the time the products reached this aperture, a distance of 43 cm, the number density had decreased sufficiently that very few collisions were occurring, so that the molecular state distributions were "frozen." Almost all of the molecules that passed through this aperture reached the electron impact ionizer and 1/1000 were ionized to be mass analyzed by the quadrupole mass filter.

Before firing the pellet, the pressure in the reaction vessel was 10^{-6} Torr, which subsequently rose to a maximum of 10^{-3} Torr before diminishing. However, this pressure rise occured only after the products had collided at least once, but probably several times, with the reaction vessel wall. By that time our measurements were completed. The three apertures through which the molecules passed to reach the detector served mostly to prevent the slow pressure rise in the reaction chamber from affecting the detector chamber. The solid angle subtended by the detector was determined by the entrance aperture of the ionizer, but all of the intervening apertures were only slightly larger than necessary to satisfy this condition. Typically, the detector chamber operated at 4 to 5×10^{-9} Torr and no pressure rise was observed after firing a pellet.

Several data acquisition schemes were used to accept the output signals of the Channeltron electron multiplier. Most of the data was processed by using a fast pulse preamplifier-amplifier/discriminator and a multichannel scaler (MCS) combination. Count rates of up to 5 MHz were observed, but some as high as 30 MHz were encountered, and special precautions were needed to prevent saturating the Channeltron. For accurate time-of-flight measurements the MCS was set at 10 μs/channel, but for quantitative pulse summation, a setting of 50 μs/channel was preferable. The flight distance from pellet to

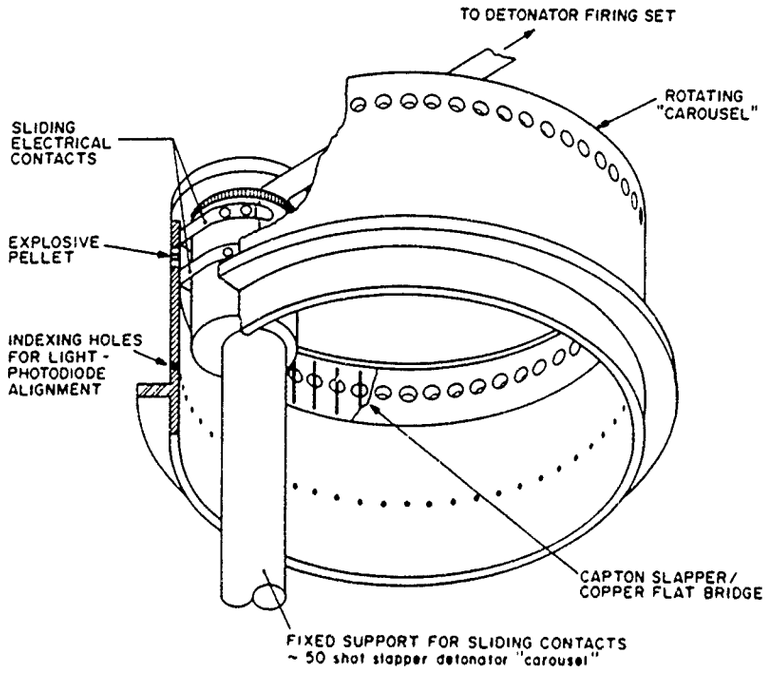

Fig. 2. Carousel on which pellets are mounted so that several detonation measurements can be made without breaking vacuum

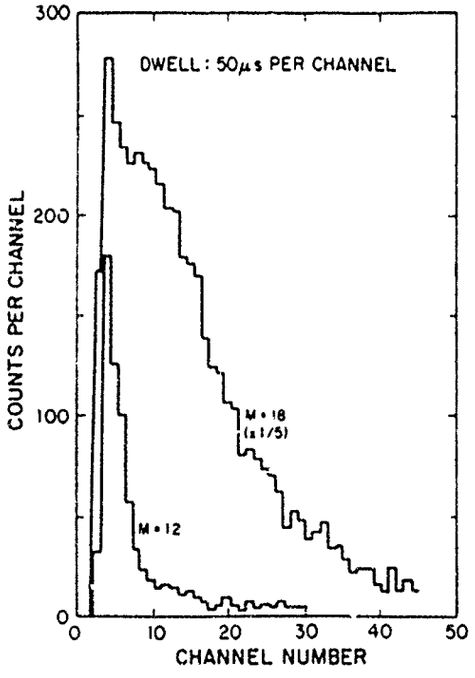

Fig. 3. A plot of raw data taken from the multichannel scaler (MCS) for two mass peaks, M=12 and M=18

ionizer was 110 cm. At masses higher than 44 it was necessary to use an alternative data acquisition method because of radio frequency interference from the quadrupole. A storage oscilloscope with an input impedance of 100 KΩ shunted by 20 pf converted the Channeltron output to an analog signal that was photographed. Signals ranging from 2 mV to 2.0 V were obtained. Both the MCS and the oscilloscope were triggered by a voltage pulse across a 50Ω load generated by the current induced in a one turn loop around one terminal of the firing module.

PETN pellets having a density of 1.5 to 1.6 were mounted on Kapton slapper assemblies driven by flat copper bridges and detonated electrically with a 5 J pulse from an FS-10 firing module (Reynolds Industries, EBW System). Up to 30 of these were mounted on a carousel that was rotated externally to the reaction vessel. Alignment of the pellet with the detector axis was done with a grain-of-wheat light bulb-photodiode arrangement through indexing holes in the carousel. Fig. 2 is a sketch of the carousel pellet holder.

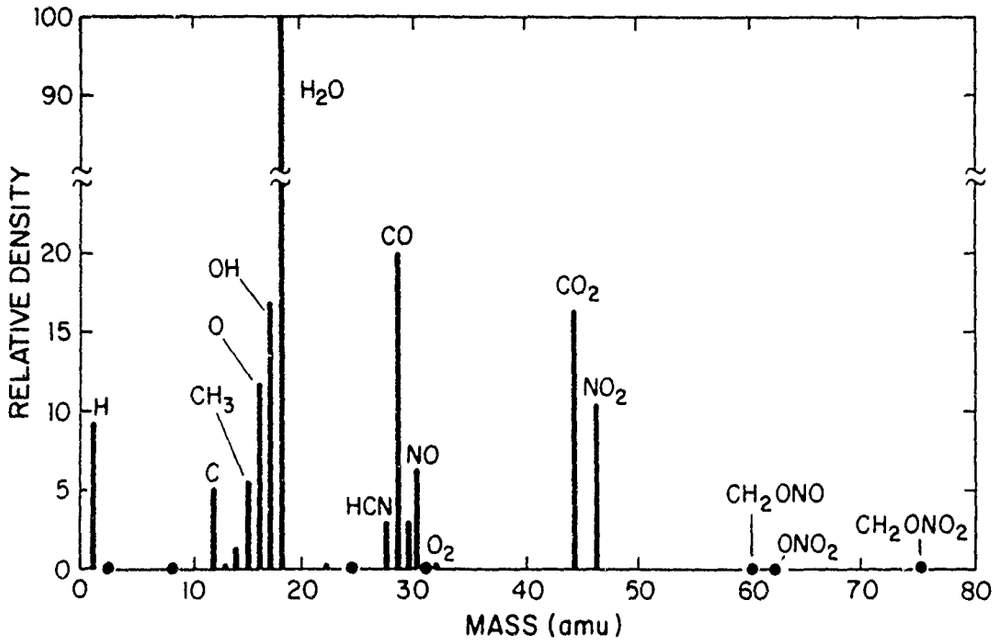

Fig. 4. Mass spectrum of PETN detonations. Intensities were obtained by summing all recorded counts of data such as in Fig. 3 and correcting for ionization efficiencies (Circles are masses for which no measureable signals were observed.)

RESULTS AND DATA ANALYSIS

Figure 3 is a plot of the number of counts stored in each channel of the MCS as a function of time for two mass peaks, M=12 and M=18. The dwell time was 50μs per channel. For the M=18 distribution it was necessary to reduce the electron ionizing current by a factor of 5 to eliminate saturating the Channeltron. Figure 4 is a plot of the mass spectrum for PETN. Each mass required detonating a pellet, and the quantity plotted for each mass is directly proportional to the sum of all the counts above background from distributions of the kind shown in Fig. 3. For the more important masses, M=1, 18, 28, 30, 44, from 2 to 6 shots were averaged. The results were normalized to make the counts recorded at M=18 have a value of 100 and corrected for ionization efficiency as discussed later.

Figure 5 shows flux distributions for M=18, 28, and 44 as a function of time, velocity, and energy. These were obtained from distributions of the kind shown if Fig. 3 by fitting the MCS data with cubic splines and then using the appropriate Jacobian to transform these analytical number densities to a flux distribution. The time at each channel was taken to be that at the center of the channel $t=(n-1/2)\Delta t$. Here n is the channel number and Δt is the dwell time of the MCS in acquiring the data. To convert to velocity, the Jacobian is proportional to the time t at each point and to convert to energy it is t^2.

DISCUSSION

The most prominent feature of the mass spectrum in Fig. 4 is that at mass 18, H_2O^+. Our best estimate is that it is about a factor of 5 larger than that at M=28, the next largest unrelated feature. Mass 17 is consistent with the dissociative ionization of H_2O to OH^+, and therefore there is very little NH_3^+ in the spectrum. The peak at M=15 is probably CH_3^+, so that at most only 3% of the M=16 can arise from CH_4^+. M=16 is then O^+, but it must be noticed that O_2^+ is very small. Mass 44 is clearly CO_2^+ since the expected peak at M=22, CO_2^{++} has the correct magnitude. Most likely mass 28 is predominantly CO^+. We cannot determine if the mass peaks at m=1, 12, 14 are fragmentation ions from larger parent molecules. We observe evidence for the presence of HCN, HCO, but the mass 30 peak is probably fragmen-

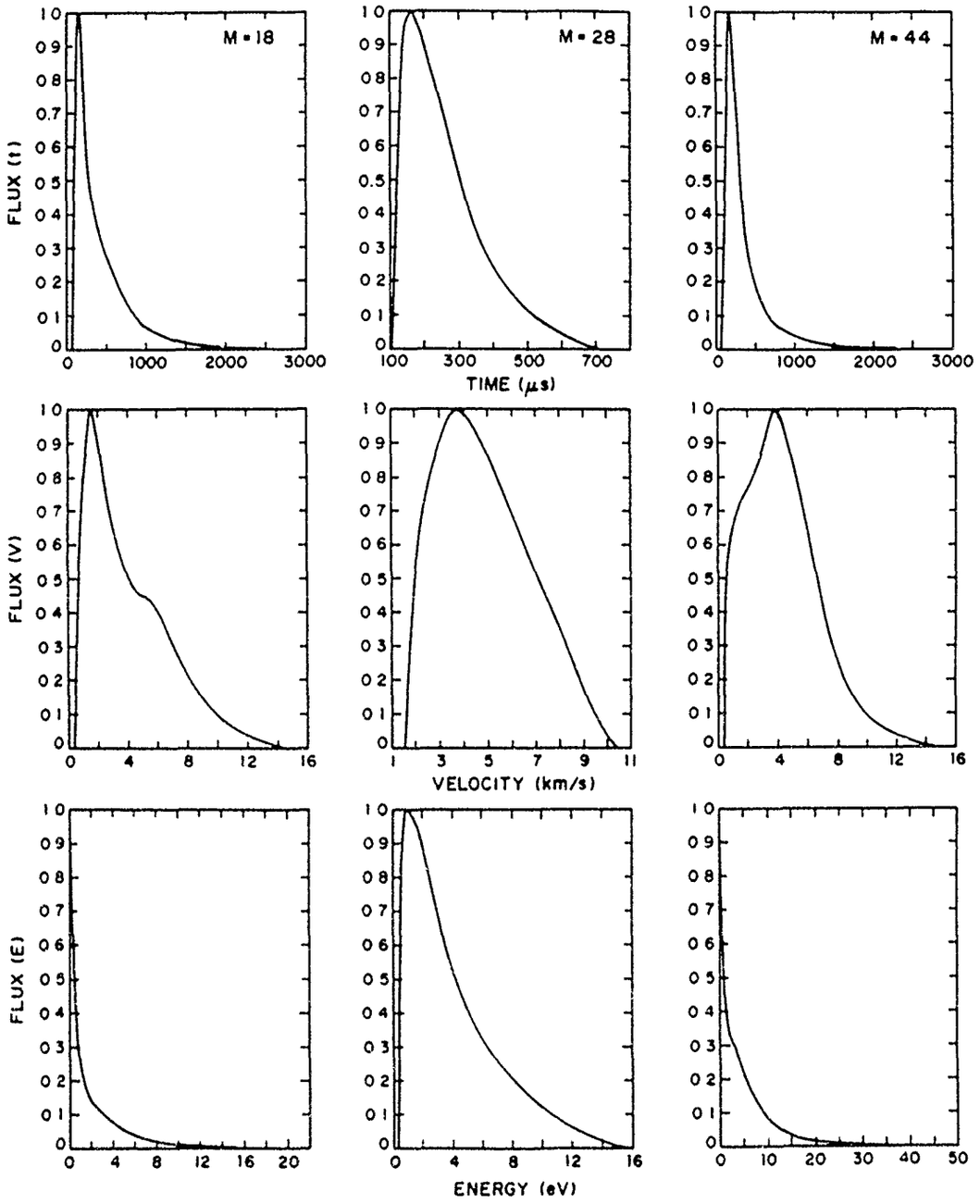

Fig. 5. Flux distributions for masses 18, 28, and 44 plotted as a function of time, velocity, and energy

tation from NO_2, the parent being clearly evident at mass 46. There are no signals at masses 2, 8, 24 (C_2^+) with significant intensity above the background or electrical noise.

The intensities in Fig. 4 have been corrected approximately for the ionization efficiency of the species. The stable molecules, H_2O, CO, and CO_2, NO_2, were corrected by using published tables of relative sensitivities (8) at electron impact energies of 70 eV. Our electon energy was actually 100 eV., but the relative intensities should be about the same. We corrected the ion signals at M=1, 12, 15 as though they were fragments from CH_4. For other masses, such as M=16 or 29, for which the species is too uncertain or for which no sensitivities were available, we left uncorrected.

This spectrum is in sharp contrast to the mass spectrum of confined or unconfined detonations of PETN (1) using steady state analysis methods. To the level of accuracy appropriate to these experiments, both the confined and unconfined detonations have similar product spectra, with most of the products appearing at M=18, 28 and 44. Each of these has about the same fractional molecular yield, 3.4 to 3.7 molecules per molecule of PETN. The strength of our mass 18 product is not consistent with this pattern of yield. The faster time resolved mass spectra obtained from fracturing studies (4) reveal the presence of radicals, such as CH_3 at mass 15, that are present in our spectrum but which are understandably absent in the equilibrium analysis. But for the fracturing experiments also, the peak at M=18 (H_2O) has a conspicuously lower relative intensity than our results indicate. Fracturing PETN also produces some high mass products, namely M=60 and 76, attributed to CH_2ONO and CH_2ONO_2. As the fracturing becomes more energetic, only the M=60 persists. Our experiments indicated the trace presence of M=60, M=62 (ONO_2) and M=76 but in such small amounts that a quantitative estimate is impractical to make. Höh (7), on the other hand, reports a spectrum with many features in common with ours, but the most prominent feature is mass 28. In contrast to our results, mass 28 is larger than the mass 18 by a factor of 3 and larger than mass 44 by a factor of 7. So while the presence of radicals is corroborated in both free expansion experiments, the quantitative details of the spectrum differ considerably.

Clearly the mass balance of all of these spectra must add up to that of the explosive, and the steady state mass spectra have been shown to do that. Our measurements are too quantitatively uncertain to allow such an analysis, especially since the time dependence must also be included in such an analysis.

Examinations of the plots of the kind shown in Fig. 3 or those of Fig. 5 show that the initial arrival time of all the masses has close to a common value, and that the most probable arrival time for all the distributions also show that same trend. Typically, the initial time is about 100 μs and the most probable 215 μs. These correspond to velocities of 11 km/s and 5 km/s (no corrections have been made for the uncertain ion flight time, but this correction is small). Of course, after transforming to velocity coordinates, the most probable flux velocity is not the same as the velocity corresponding to the peak of the arrival time. The most probable velocity becomes 4 km/s.

The uniformity of the early arrival times, or alternatively of the higher velocities irrespective of mass, clearly indicates that these molecules did not originate from a gas that could be characterized by a temperature distribution. This feature is reminiscent of a hydrodynamic expansion of a gas at very high Mach numbers with very little viscous slippage between the constituent masses. Using mass 28 as an example, the peak velocity would be appropriate to a temperature of 15000K, while the spread in velocity for our observed distribution is 4000K. However, as we see in Fig. 3, the width of the distribution depends on the mass of the ion observed. If the mass 12 signal is C^+ from the dissociative ionization of the heavier parent mass, such CH_3, one would not expect the widths to differ significantly from other masses. Perhaps mass 12 comes from unreacted C as a product.

Transforming to energy coordinates is easily done, as we show in Fig. 5, but the shape of the curves is more questionable. This is because of the broad time distributions and the large effect of the t^2 Jacobian. Even small waviness in the time distribution arising from the spline fitting procedure produces spurious bumps in the distribution. Where the energy distribution peaks is also very difficult to determine. Nonetheless, we see that there are a considerable

number of products with energies in the electron volt region.

The velocities we obtain are about half of those obtained by Höh, et al. (7) and our early arrival times are more uniform than theirs. Nonetheless, it is clear that for both experiments the distributions have a considerable mass flow velocity superimposed on the thermal kinetic energy distributions. It is tempting to speculate that our early arriving molecules are products that emanate from a thin layer near the closest surface of the PETN pellet. These are moving the fastest after the pellet detonates and are moving in the direction of the detector. Since most of our products have about the same mass and not very different collision cross sections, they become uniformly accelerated from behind by the remainder of the expanding products.

We speculate a bit further and suggest that for a particular species being detected, the time during which a molecule arrives at the detector is determined by the depth in the pellet from which it originated. The later a molecule arrives, the deeper in the pellet the product was formed. Those molecules arriving early should have experienced the fewest number of collisions, before the collisions ceased, and the late arrivals the most. Evidence supporting this picture arises from examining the time dependent data of the kind shown in Fig. 3. We observe that mass peaks that we have assigned to radicals have a shorter distribution of arrival times than the stable species, such as H_2O, CO, and CO_2. For example, from Fig. 3 we see that at arrival times longer than 1 ms (20 channels) there are effectively only background counts for M=12, while at 1 ms,the M=18 counts are only reduced to 35% of the peak value. Short time distributions are a characteristic of most of the mass peaks not associated with the stable molecules. The exceptions, such as H and O atoms and OH, indicate that some of these species are produced in the detector ionizer by electron impact with the stable species such as H_2O. The late arriving molecules have had a sufficient number of strong collisions to have approached equilibrium conditions so that radicals are missing. They have been consumed into the near-equilibrium population of product states. Apparently the fastest molecules have had fewer collisions so that radical products are "frozen" into the product distribution. Analyzing only products detected after 1 ms indicates that the stable product intensities, M=18, 28 and 44 are still considerably different than those obtained from steady-state conditions, (1) although the difference is not as dramatic as obtained from Fig. 4.

ACKNOWLEDGMENTS

We wish to thank F. Archuleta and A. Garcia for their enthusiasm and diligence in assembling the apparatus.

REFERENCES

1. D.L. Ornellas, "Calorimetric determinations of the heat and products of detonation for explosives: October 1961 to April 1982," UCRL-52821 (1982).

2. V. Krishna Mohan and Tong B. Tang, "Flow and explosive decomposition of thermally unstable solids: A study with time-resolved mass spectrometry," J. Chem. Phys. *79*,4271 (1983).

3. N.C. Paul, "Mass spectrometric analysis of complex gas mixtures," U.S. Nat. Tech. Inform. Serv., AD Rep. No. 737402. Available from Govt. Rep. Announce. (U.S.) 1972, *72*, 71-2.

4. H.M. Hauser, J.E. Field and V. Krishna Mohan, "Fracture induced decomposition of a brittle high explosive: pentaerythritol tetranitrate," Chem. Phys. Lett. *99*, 66 (1983).

5. G.D. Miller, L.D. Laws and R.H. Dinegar, "Kinetics of the thermal decomposition of solid PETN," Nineteenth Symposium (Int.) on Combustion, p. 701 (1982).

6. N. Schilf and H. Trinks, "Four-channel magnetic mass spectrometer for dynamic measurements of fast reactions," Int. J. Mass Spectrum. Ion Phys. *37*, 123 (1981).

7. A. Höh and F. Aulinger, "Mass spectrometric and time-of-flight analysis of gaseous detonation products in high vacuum," Dyn. Mass Spectrum. *5*, 165 (1977).

8. A. Cornu and R. Massot, "Compilation of Mass Spectral Data," 2nd edition, VI (Heyden & Son, 1975).

DISCUSSION

DR. RAYMOND F. WALKER, Walker Associates

Is it possible that the high intensity of H_2O seen in spectra derives from water vapor retained on the surface of the samples and components of your system? Normally many hours of high temp. baking are necessary to drive off such retained water. I presume you could not do this without decomposing the PETN. The detonation of the PETN would be expected to give a burst of released vapor at least from components in line wtih the detonation wave.

REPLY BY N.C. BLAIS

Your question is a very provocative one and I wish that I could give you a good answer one way or the other, but I can offer only some relevant comments. First, I will admit that the possibility of absorbed water had not occurred to me so your question takes me a little by surprise. I suppose that water retained near the surface of the pellet could be at least partly responsible and I certainly intend to investigate this as a possibility.

There are two observations that lead me to believe that absorbed surface water cannot be of great importance. Neither of these observations are discussed in the presented paper, but are the consequences of work done subsequently to these experiments.

We've done some experiments in which nonreactive constituents, such as Ar, have been deposited on the surface of detonating material, such as nitric oxide shocked by a PETN booster. These deposits were thin compared to the amount of nitric oxide being shocked. The time history of Ar detection was found to be what one would expect from a thin film, i.e., we observed a short pulse of mass 40 products. In other words, the time duration of Ar arrival at the detector was short compared to that of the detonation products, such as N_2. The comparison is similar to what is shown between M=12 and M=18 in Fig. 3. It would seem reasonable to me that any absorbed water would contribute signal primarily at the very early arrival times of M=18. Clearly there cannot be much contribution from water absorbed in the PETN pellet volume since this much water would have affected the measured density of the pellet.

Another observation that is relevant to your question is that HNS products do not exhibit an unexpectedly large water peak. On the basis of steady-state measurements, one expects M=28 to dominate the spectrum, which is what we observe, and M=18 is actually a little less than expected on this basis. Of course, each substance absorbs water differently than others, but I don't expect polycrystalline pellets to be remarkably different.

Any water absorbed on apparatus components has to be insignificant, since the molecular beam detector "sees" only the center of the pellet and one stainless steel defining aperture.

DISCUSSION

DR. CHARLES DICKINSON, Naval Surface Weapons Center

Do the elemental ratios of the products correspond, roughly, to those of PETN?

REPLY BY N.C. BLAIS

We haven't really worked at examining the mass or elemental balance of our results, and we so state in our presentation. Because of the present apparatus limitations, the uncertainties in the spectrum of Fig. 4 are large, amounting to at least 20% for the intense peaks and perhaps 40% for the weaker signals. Both the intensity and time dependence must be considered, and these vary from shot to shot, during which only one mass can be examined.

Also, we cannot distinguish between N_2 and CO at M=28. Without an independent experiment to differentiate between the two we would, in effect, be using mass balance to decide what fraction was N_2 and what was CO.

DISCUSSION

DR. FRED VOLK, Fraunhofer Institute, Baden, FRG

Was it possible to analyze HCN quantitatively?

REPLY BY N.C. BLAIS

Our results can be made quantitative in the following sense: we made the important corrections for apparatus discrimination arising from ionization efficiency, collection efficiency, etc.

so that our plot of Fig. 4 is what we feel is our best guess as to relative densities. Therefore, if we believe that our system satisfies mass balance, then about 0.5 mg of HCN was produced from each 22-mg pellet.

Several cautions are required in considering my reply. First, our experiments are not done under equilibrium conditions nor even at steady state. Therefore, it is quite possible that different size pellets or slightly different densities of pellet would change the relative yield of species such as HCN. This molecule is not an important stable detonation product of PETN. Our experiments were not intended to compete with equilibrium measurements, so the need to be quantitative is not urgent. Second, as I stated in a response to a question of C. Dickinson, our uncertainties are large, so that we made no effort to convert all of our time-number density distributions to flux distributions. It is the time integration of these fluxes that we should have plotted in Fig. 4, but the error in integrating the number densities instead was negligible compared to our uncertainties.

DISCUSSION

JOHN A. SANCHEZ, Los Alamos National Laboratory

I noticed a lack of N in your analysis of gaseous products. Do you believe it all has gone to NO, or NO_2, or can you not see it at the 28 peak?

REPLY BY N.C. BLAIS

I presume that you intended to address your question to the lack of nitrogen molecules rather than to nitrogen atoms. In truth, I cannot really distinguish between N_2 and CO which both have mass 28. My labeling of the mass peak at M=28 as CO is a resumption on my part based on two observations. One is that there is a considerable amount of nitrogen atoms bound into NO and NO_2. The other is that if M=28 was largely N_2, then the mass peak at M=14 should have had the same time dependence as M=28 because of electron impact fragmentation of N_2. But M=14 had a much narrower time distribution than did M=28. Incidently, neither NO nor NO_2 are significant steady-state products of PETN detonation, so that if a high temperature, high pressure is maintained, all of the nitrogen atoms in NO and NO_2 would appear eventually in N_2.

DISCUSSION

INDU B. MISHRA, Kanan Associates

I find it difficult to understand how you got H atom and no H_2 molecule, especially using a low resolution quadrupole MS. If it is indeed true, it can happen *only* if H atoms are formed in the decomp and are removed very fast in forming species other than H_2. Any thoughts on what the other fast recombination steps may be?

REPLY BY N.C. BLAIS

We checked carefully the point that it was indeed M=1 we were observing and not M=2. Since H_2O is our most prominent peak, it seems resonable that this is a likely place to find the H atoms from the initial PETN, and a smaller amount is also in CH_3. At least some of the H atom signal seems to arise from electron impact fragmentation in the detector of the products H_2O and CH_n. I must point out that H_2 is a minor constituent of steady-state products of PETN detonation.

FAST SPECTROGRAPHIC ANALYSIS OF LASER INITIATED DECOMPOSITION REACTIONS IN EXPLOSIVES

M. W. Leeuw, A. J. Th. Rooijers and
A. C. van der Steen

Prins Maurits Laboratorium TNO
P.O. Box 45, 2280 AA Rijswijk
The Netherlands

Lead styphnate and mercury fulminate are initiated with the ultraviolet pulse of an excimer laser. Emission spectra are recorded of the decomposition products formed during and immediately after initiation. In the spectra of lead styphnate the emission of atomic lead can be recognized. Transitions of the CN radical are found in the emission spectra of mercury fulminate. It is shown that the relative concentrations of the emitting particles depend very strongly upon the density of the primary explosive.

INTRODUCTION

For a better understanding of the sensitivity phenomenon of explosives it is of the utmost importance to know the kinetics of the decomposition reactions during and immediately after the initiation pulse.

The disadvantage of most detection techniques which try to follow these decomposition reactions is that they are rather slow as compared to the rate at which explosives decompose in detonation- and deflagration-like reactions. It is exactly this reaction rate regime which determines the explosive properties during initiation.

One of the examples of a technique which uses relatively high temperatures is the Thermal Step Test (1) in which the explosive is heated to temperatures up to 1400 K in a very short time interval. Subsequently the induction time, which can be as short as 50μs, is measured. From these experiments it has become evident that the decomposition of explosives at higher temperatures is not as straightforward as could be expected from extrapolation of the results at lower temperatures. This test also offers the possibility to distinguish between primary and secondary explosives and to correlate the induction times to the impact sensitivities of the explosives.

The laser is also an energy source which can add a large amount of energy to an explosive in a very short time interval. However, the literature on the use of a laser as an initiating source is scarce. Brish was the first to report on the initiation of lead azide with a Nd glass laser in 1966 (2). Later, other research groups in the USSR (3), UK (4) and USA (5, 6) used a laser to initiate high explosives.

The use of a laser in intiation experiments has two major advantages:

- firstly, a well-defined amount of energy is added to the explosive, contrary to other initiation mechanisms as impact or friction where the energy transfer to the explosive is not clear at all, and
- secondly, the wavelength of the laser can be made to coincide with an absorption band of the explosive to have an even more effective energy transfer to the explosive; hitherto this has not been the case in most experiments since ruby or Nd-YAG lasers are used which emit in the red or infrared part of the spectrum, whereas

most explosives absorb in the blue or ultraviolet part.

Recently, we published the first results on the initiation of primary explosives by an excimer laser emitting in the ultraviolet part of the spectrum (7). An unconfined pellet of explosive was irradiated by a laser pulse (1 kJ/m^2) and the light emitted by the explosive and/or its decomposition products was measured. It was found that the induction times, the time lapse between the laser pulse and the moment the light intensity is at maximum, increase in the order lead azide ≅ silver azide < diazodinitrophenol < lead styphnate < mercury fulminate, which is not the same order as found for the heat or impact sensitivities of these explosives. This might be an indication that the initiation of explosives by a laser is not purely thermal in origin.

In the experiments described above the light is not resolved spectroscopically and therefore no information is obtained about the reaction products formed during the initiation. In this paper the emission spectra of lead styphnate (LS, Pb ($C_6O_9N_3H_3$)) and mercury fulminate (MF, $Hg(ONC)_2$) which have been recorded immediately after initiation with an excimer laser are presented. As far as we are aware this is the first time that emission spectra due to atomic and molecular species formed within a few milliseconds after initiation are presented.

EXPERIMENTAL

A schematic representation of the experimental set-up is given in Fig. 1.

Fig. 1. Schematic representation of the experimental set-up (see also text)

About 20 mg of the explosive (MF or LS with a purity better than 99%) is pressed to a pellet of 5 mm diameter and about 0,5 mm thickness. The density of the explosive can be varied by varying the pressing force up to 0,15 MN. The pellet is placed on a hardened steel pin in a sample holder and the laser beam is focused directly on the sample.

The laser pulse is delivered by an excimer laser (Lambda Physik EMG 200) using the KrF line at 248 nm and a pulse duration of 15 ns. The beam is focused onto the sample by means of a lens so that a spot of about 1 x 2 mm^2 is irradiated with an energy density of 100 kJ/m^2.

The light emitted by the decomposition products is detected by a photodiode which is situated close to the sample holder, and whose signal is fed into a 100 MHz transient recorder (LeCroy, TR8818).

Simultaneously, the light emitted by the products just in front of the sample holder is focused via two lenses onto the entrance slit of a 60-cm spectrograph (Jobin Yvon, HRS-2, 1200 lines/mm). The resolved light is detected by an intensified optical multichannel analyser (Spectroscopy Instruments, IRY1024). With this combination the spectral resolution is better than 0,1 nm. The optical multichannel analyser is controlled by a control unit and a gate pulser triggered by a trigger pulse from the laser. With the gate pulser an initial delay (100 ns - 5 ms) and a gate (100 ns-5 ms) can be programmed to set the time interval in which the multichannel plate of the optical multichannel analyser is activated. A personal computer takes care of the control of all apparatus and of data handling.

RESULTS AND DISCUSSION

When a pellet of LS or MF is irradiated with a focused laser beam both ignite but the effects and the induction times differ considerably. In the case of LS a loud report is heard indicating a detonating type of reaction and the induction time varies between 170 and 240μs. Under comparable experimental conditions the sample of MF deflagrates with an induction time between 6 and 11 ms. Also the intensity of the light emitted is much more intense for LS than for MF (Fig. 2). The pellets of the explosives are hardly pressed, about 1 kN for LS and even less for MF. A higher loading force increases the induction time of LS up to about 700μs for pressing forces above 10 kN. Samples of MF cannot

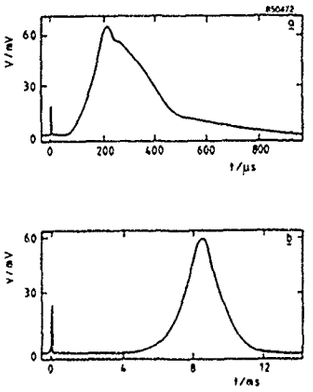

Fig. 2. The output of the photodiode for LS and MF (note the difference in time scale)

initiated any more when the density of the pellet is increased strongly (dead press effect) (7).

The emission spectra for these two explosives are quire different. The spectra have been obtained by focusing the light emitted about 1 cm in front of the sample onto the entrance slit of the spectrograph, so that the light emitted by species which are formed in an early stage of the decomposition process are monitored. The gate pulser is set at a time window between 0,1 ms and 2 ms after the laser pulse for LS and between 2 ms and 7 ms for MF.

The emission of LS consists of both narrow lines and broad bands. The most intense lines are observed at wavelengths between 360 and 410 nm (see Fig. 3). Weaker lines are found at 261, 266, 280, 283 and 287 nm. The broader bands are found for wavelengths longer than 410 nm and extend to over 700 nm (see Fig. 4).

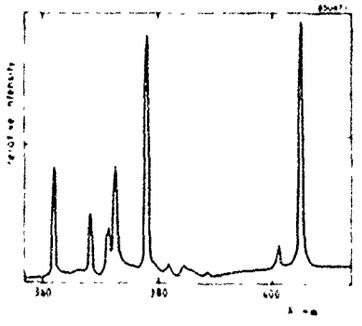

Fig. 3. Emission spectrum of decomposition products of LS between 350 nm and 410 nm

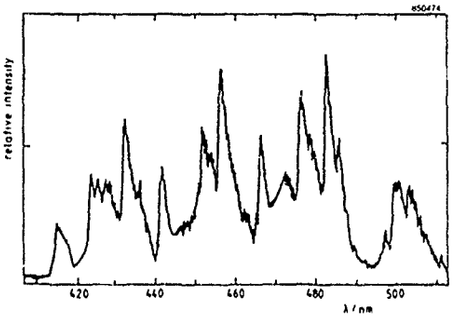

Fig. 4. Emission spectrum of decomposition products of LS between 410 nm and 520 nm

The positions of the lines correspond with electronic transitions of the lead atom, indicating that atomic lead is already formed in an early stage of the initiation (8).

Contrary to the atomic lines the bands at longer wavelengths have to be ascribed to the emission of molecular species. The broad features are characterized by a regular pattern with a progression of about 500 cm^{-1}.

The spectrum of MF looks completely different and more complicated. As is the case for LS atomic lines of mercury are also found, but much less intense than for lead (313 and 365 nm). Besides, a much larger number of lines is found, see for example Figs. 5, 6, and 7.

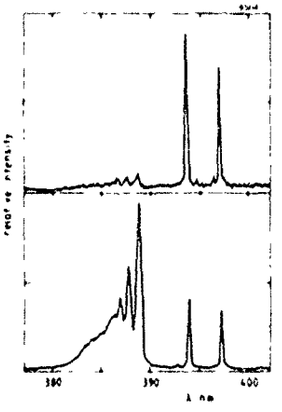

Fig. 5. Emission spectrum of decomposition products of MF showing the emission due to the CN radical; for a) the pressing force on the sample has been increased slightly compared to b)

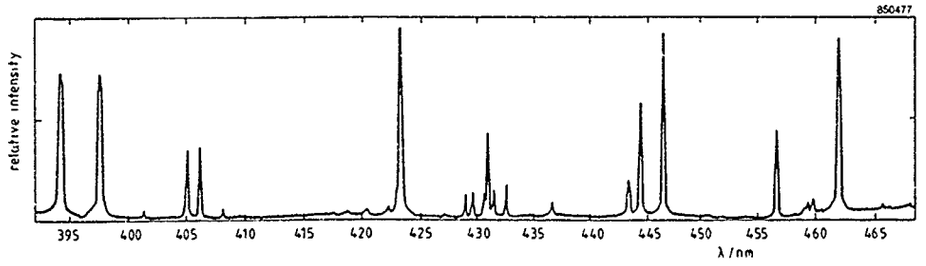

Fig. 6. Emission spectrum of decomposition products of MF between 395 nm and 465 nm

The line at 389.1 nm in fig. 5b can be ascribed to the vibrationless transition $B^2\Sigma \rightarrow A^2\pi$ of the CN radical (9). The lines at 387.9 and 385.0 nm belong to transitions from higher vibrational levels while the vibrational quantum number does not change. The transitions at which the vibrational quantum number does change are found around 359 nm ($\Delta v = -1$) and between 415 and 422.5 nm ($\Delta v = +1$), see Fig. 6. The occurrence of these bands indicates that CN radicals are formed during the initiation of the fulminate. However, the amount of CN radicals is strongly dependent on the experimental conditions. As has already been mentioned a very small increase in the pressing force drastically reduces the light output after initiation of MF. This reduction is accompanied by a change in the relative intensities of the peaks in the spectra, see Fig. 5a. An increase in the sample density decreases the CN emission.

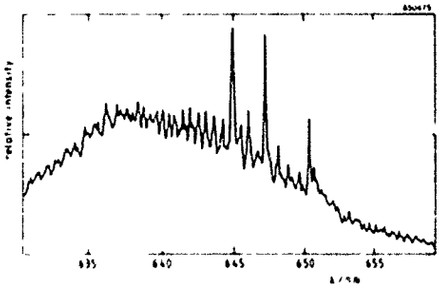

Fig. 7. Emission band with rotational structure of a decomposition product of MF

The emission band at about 645 nm shows a distinctly rotational structure, see Fig. 7. Unfortunately, we did not yet succeed in ascribing this band or one of the others to one of the small particles formed during the initiation of the fulminate. They do not originate from the ONC radical, so it appears that bond breaking between the mercury and the fulminate group is not the first step in the initiation of MF (10).

It is the purpose of this paper to show that it is feasible to follow decomposition kinetics during the initiation of explosives. It is not our objective to give a full description of all the phenomena observed. The results shown here indicate that a large amount of information can be obtained by this detection technique and that the influence of numerous parameters has to be further investigated such as for instance: confinement, laser energy, laser wavelength, position etc. Also the laser initiation of secondary explosives will be reported in the near future.

REFERENCES

1. M. A. Schrader, M. W. Leeuw and A. C. van der Steen, The Thermal Step Test: A Key to High Temperature Behaviour of Explosives, Proceedings of the Ninth International Pyrotechnic Seminar, Colorado Springs (1984)

2. A. A. Brish, I. A. Galeev, B. N. Zaitsev, E. A. Sbitnev and L. V. Tatarintsev, Laser-excited Detonation of Condensed Explosives, Comb. Expl. Shock Waves *2*, 81 (1966).

3. E. I. Aleksandrov and A. G. Voznyuk, Initiation of Lead Azide with Laser Radiation, Comb. Expl. Shock Waves *14*, 480 (1978).

4. J. T. Hagan and M. M., Chaudhri, Low Energy Laser Initiation of Single Crystals of β-lead Azide, J. Mat. Science *16*, 2457 (1981).

5. L. C. Yang and V. J. Menichelli, Laser Initiation of Insensitive High Explosives, Proc. 6th Symp. Detonation, Coronado, 612 (1976).

6. J. J. Dick, "Attempts at Ultraviolet Laser Initiation of Nitrometane and PETN" LA-9489-MS, August 1982.

7. A. J. Th. Rooijers, W. C. Prinse, M. W. Leeuw and A. C. van der Steen, Ultraviolet Laser Initiation of Primary Explosives, Proceedings of the Ninth International Pyrotechnic Seminar, Colorado Springs (1984).

8. P. W. J. M. Boumans, Coincidence Tables for Inductively Coupled Plasma Atomic Emission Spectrometry, Pergamon Press (1980).

9. W. M. Jackson and J. B. Halpern, Multiphoton Ultraviolet Photodissociation of C_2N_2, J. Chem. Phys. *70,* 2373 (1979).

10. R. N. Dixon, The Absorption Spectrum of the Free NCO Radical, Phil. Trans. Roy. Soc. 252 A, *165* (1960).

STATIC HIGH PRESSURE STUDY OF NITRIC OXIDE CHEMISTRY: PROPOSED MECHANISM FOR NITRIC OXIDE DETONATION

Basil I. Swanson, Stephen F. Agnew and N. Roy Greiner
Los Alamos National Laboratory
Los Alamos, New Mexico

The chemistry of nitric oxide under static high pressure conditions has been studied using diamond anvil cells and spectroscopic methods. Pressurized samples warmed rapidly to room temperature undergo facile disproportionation to first form an intermediate which further reacts to form N_2O, N_2O_3, N_2O_4 and $NO^+NO_3^-$. Crystalline nitric oxide maintained at 80K is observed to react at ca. 2.5 GPa to form, dominantly, N_2, C_2 and $NO^+NO_3^-$. The complex chemistry of nitric oxide is best explained in terms of two competing primary reaction mechanisms involving the direct formation of N_2 and O_2, and disproportionation to form N_2O and $NO^+NO_3^-$. The disproportionation reaction, which is favored under higher temperature conditions, releases two-thirds of the total energy content, and is believed to be important in the early chemistry accompanying shock-initiation of nitric oxide. Laboratory scale detonation studies, where the gaseous products are anlyzed spectroscopically, show evidence for, dominantly, disproportionation and a small amount of N_2/O_2 production. This study points to the importance of condensed phase concerted reactions as well as ions and ionic reaction mechanisms in the shock-initiated detonation of HE's.

INTRODUCTION

The macroscopic properties of a large variety of high explosives have been studied extensively in the past. However, it is still not possible to describe and verify the microscopic phenomena leading to shock-initiated detonation. Shock propagation in condensed-phase materials is expected to induce the transfer and localization of energy leading to chemical transformations on an extremely short time scale. Our intent in this work is to clarify those early chemical transformations that are important in the energy release accompanying shock-initiated detonation of nitric oxide. In large measure, the problem of developing a microscopic understanding of shock-initiated detonation results from the difficulty in detecting transient chemical intermediates within the shock front. While there has been considerable effort and success in developing time-resolved optical probes of chemical species behind shock fronts (1-4), these methods have not yet been successfully applied to real explosives. The experimental difficulties are compounded by the absence of information on what intermediates are likely to be important and the paucity of data on the behavior of such transients under extreme pressure and temperature. We report here static high pressure studies which provide direct insight into the early chemical transformations associated with detonation of nitric oxide.

Nitric oxide, although stable in the gas phase, is a high explosive in the condensed phase with an enthalpy (5) of 0.72 kcal/g relative to O_2 and N_2 at 298 K. It is one of the simplest known high explosives and is, therefore, an attractive model explosive for detailed theoretical and

experimental studies. The molecular form of NO and the expected detonation products, N_2 and O_2, are tractable to both ab initio electronic structure calculation and hydrodynamic modeling. In order to study nitric oxide detonation, a multi-disciplinary study entitled the Fundamental Research on Explosives (FRE) program has been established at Los Alamos National Laboratory. Our part in this program has been to provide a data base to guide theory, planning, and interpretation of time-resolved spectroscopic studies of shock-initiated detonation of NO by means of static high pressure studies of the various oxides of nitrogen. The focus of this report is the chemistry of NO and its reaction products under high pressure conditions.

Previous studies (6) on gas-phase nitric oxide have shown evidence for slow disproportionation, which is third order in [NO]. Other investigators (7,8) have also noted problems in obtaining thermodynamic information on pure NO at high pressure. We will show that NO undergoes facile and complex pressure-induced chemistry at low temperature. The disproportionation of nitric oxide at 176 K and 1.5 GPa to form N_2O, N_2O_4, and N_2O_3 has already been reported (9). The unusual behavior of pure N_2O_4 at elevated pressures, including formation of $NO^+NO_3^-$, has also been reported (10). This autoionization of N_2O_4 has been implicated (11) in the solution chemistry of N_2O_4 and observed for the nitrite isomer in low temperature N_2O_4 films as well (12,13). In this work, we report new observations of pressure-induced chemistry of crystalline NO to form N_2, and O_2 as well as the above disproportionation products at 80 K as well as identification of the products resulting from laboratory scale samples of solid NO shocked at 15 K.

EXPERIMENTAL

A. High Pressure Spectroscopic Studies:

Merrill-Bassett diamond-anvil cells with either hardened beryllium or beryllium-copper backings and type IIa diamonds were loaded with the indium-dam technique previously described (9). Two different types of experiments have been performed. First, high-purity nitric oxide was condensed into the diamond-anvil cells at 115 K (which is within the liquid range of N_2O_2), pressurized to form a clear solid, and then warmed to room temperature at high pressure. The contents of the cells were then interrogated using vibrational (IR and Raman) and UV-visible absorption spectroscopies. In the second type of experiment, the NO was loaded into a cell mounted to the cold finger of an Air Products Displex cryostat equipped with a tailpiece that allowed access to adjust pressure. This permitted the measurement of the pressure dependence of the Raman features at 80 K. The low temperature studies were performed using two different approaches; in procedure I, liquid N_2O_2 was first frozen to form a single crystal, lowered to 80K, and then pressurized; in procedure II the liquid was pressurized at 115 K. The results obtained for these two procedures are distinctly different as will be discussed below.

Raman spectra were obtained on a SPEX Model 1403 double monochromator by use of a back-scattering technique. The resolution was 3 cm^{-1} and, typically, ten or more spectra were signal-averaged using a Nicolet 1180E Raman data system. Spectra-Physics Model 171 Ar^+ and Kr^+ ion lasers were employed with incident power of 30 mW or less at the sample. Infrared spectra were obtained with a Nicolet 7000-series Fourier-transform spectrometer using a liquid nitrogen cooled mercury-cadmium-telluride detector. Typically, 8000 scans with a 2 cm^{-1} resolution were signal averaged. Absorption of the diamonds obscured the IR spectra over the approximate ranges 1300-1350 and 1800-2500 cm^{-1}. Visible absorption spectra were obtained with a Perkin Elmer 330 spectrometer equipped with a beam condenser and the Model 2600 data station. Pressures were measured by the ruby flourescence method, assuming the R_1 line shift to be 0.1322 GPa/cm^{-1}. The known temperature shift of the R_1 ruby flourescence was used to correct the R_1 line shift for the low temperature studies.

B. Laboratory Scale Studies of Shocked NO:

The experiments were carried out in an evacuable firing chamber containing a detonating device mounted behind a thin foil. Solid NO was deposited from a stream of gaseous NO directed to the surface of the foil, which was maintained at 15 K by a Air Products Displex cryostat. The detonating device consists of an electrically energized device that propels a 1.3 mm diameter × 0.05 mm long cylinder piece of plastic through a ruby barrel at a velocity of several km/s (a slapper), which impacts at

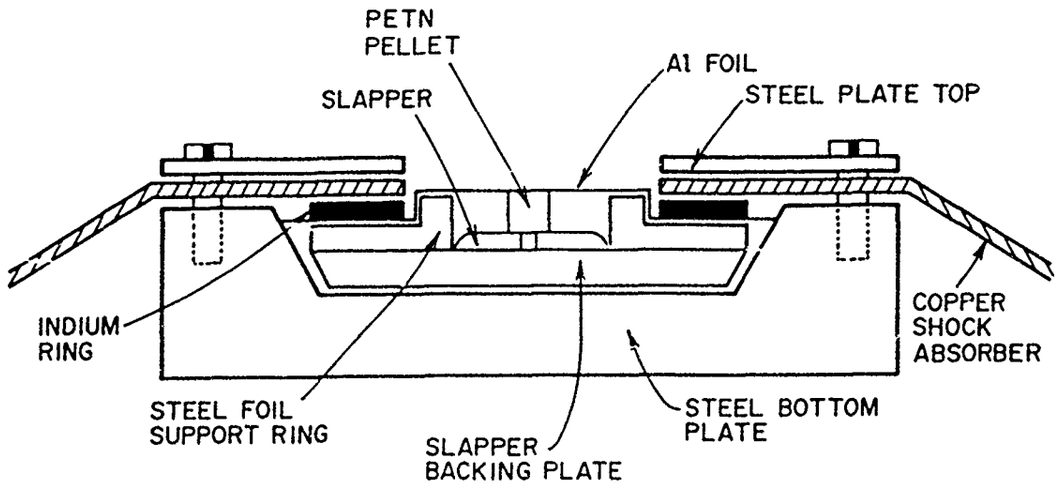

Fig. 1. Diagram of slapper and booster used in PETN-driven NO reaction

a 6 mg pellet of pentaerithratol tetranitrate (PETN) that is glued to the end of the ruby barrel (Fig. 1). Two isotopic compositions of NO were used to dis-distinguish N_2 originating from NO from either the PETN booster or inadvertent air leaks. The entire assembly was housed in a bell jar connected to two liquid nitrogen traps in series to capture the expected products, the first an empty common stainless steel U-trap, and the second packed with activated 5X molecular sieve. The products N_2O, NO_2, N_2O_3, N_2O_4, CO_2 (from PETN), and unreacted NO are found in the first trap and are determined by gas-phase IR spectrophotometry. The N_2 and CO (from PETN) are found in the second trap and measured by mass spectrometry.

RESULTS

A. High Pressure Studies: The results obtained from studies of nitric oxide at high pressure in diamond anvil cells which were warmed to room temperature have been described elsewhere (9) and will be summarized here. Upon warming, the sample remains clear and colorless until *ca.* 170 K where the reaction begins. The sample first turns deep red, then black, and finally becomes transparent, exhibiting either a straw-yellow fractured solid or a mixed straw-yellow or blue solid.

Detailed IR, Raman and UV-visible spectroscopic studies of the cell contents have revealed the presence of varying amounts of N_2O, N_2O_4, N_2O_3 molecular species as well as the ions NO^+, NO_2^+ and NO_3^-. The above species show complex equilibria as a function of pressure and temperature. At low pressure in the fluid phase (*ca.* 1.8 GPa) only molecular species are observed while the ions are more prevalent at higher pressures in the solid phase. Both molecular and ionic species are present in the original solid samples upon warming to room temperature. It is stressed that no N_2 or O_2 could be observed in any of the samples which had been allowed to react by warming to room temperature. Raman spectral analysis of the cell contents was made difficult by the photolysis of N_2O_4 and N_2O_3 which resulted in the formation of geometric isomers of each species, as well as the formation of $NO_2^+NO_3^-$ and N_2O_3 by photolysis of N_2O_4.

B. Pressure Dependence at Low Temperature: As noted above, the low temperature experiments were performed using two different procedures. For procedure I the cell was first filled with liquid N_2O_2 and the temperature lowered to form a crystalline solid. The pressure dependence of this crystalline material was then probed as is discussed below. In procedure II the liquid N_2O_2 was pressurized directly to form an intermediate and the pressure dependence of this intermediate was then probed.

Procedure I: Nitric oxide entrapped in a diamond-anvil cell and maintained at 80 K was found to be stable at pressures below *ca.* 2.5 GPa. The zero bar vibrational phonon features at 38.7 and 53.2 cm^{-1} are consistent with those

previously reported (14) in studies of solid N_2O_2 condensed on a cold surface. The internal modes appear at 93.4 cm^{-1} (ν_4, torsion), 185.2 cm^{-1} (ν_2, N-N stretch), 263.4 cm^{-1} (ν_3, symmetric bend), and 1865.1 cm^{-1} (ν_1, symmetric N-O stretch). Survey scans showed no evidence of any other features in the range 50-2450 cm^{-1}.

The spectrum in Fig. 2 was taken after a 2.43 GPa spectrum of normal N_2O_2 was recorded and indicated that a dramatic transformation had taken place with the NO sample. The phonon region changed and the internal modes for NO disappeared. We did observe very weak features indicating the presence of several particular species. They include $NO^+NO_3^-$ by 108.6 cm^{-1} (interionic), 722.7 cm^{-1} (ν_4, NO_3^- bend), 1062.7 cm^{-1} (ν_1, symmetric NO_3^- stretch), and 2246.7 cm^{-1} (NO^+ stretch), O_2 by the 1565.8 and 1572.9 cm^{-1} doublet, N_2 by the 2339.3 cm^{-1} N-N stretch, N_2O_4 by the 822.9 cm^{-1} (ν_2 scissor) and 286.7, 308.4 cm^{-1} doublet (ν_3 N-N stretch), and N_2O by 589.1 cm (ν_2 bend). The features at 2035.7 and 2206.9 cm^{-1} could be due to an as yet unknown complex of the NO^+ ion and the band at 1644.9 cm^{-1} could be the associated NO_2 symmetric stretch for such a species. The band at 500 cm^{-1} remains unexplained. The pressure increased dramatically for this sample from 2.3 to 4.1 GPa after this transformation occurred and the intensity of the N_2 and O_2 peaks indicate that a substantial amount of these species had formed. It should be noted that this is the first indication of either O_2 or N_2 in the NO reaction products for any cell that we observed that had been loaded by the previous technique, which always involved pressurizing liquid N_2O_2 followed by fairly rapid warming to room temperature before any analysis took place.

Following this transformation, the optical quality of the cell did not change noticeably as viewed through a microscope, although the cell contents had become pale yellow with increasing pressure. Not until the cell had been warmed to 200 K and the pressure released to under 0.5 GPa did a noticeable transformation occur. A clear to pale yellow solution finally resulted which, when cooled to 180 K produced the spectrum in Fig. 3 Very prominent features are now evident for N_2O_4, N_2O, N_2, and O_2, with no evidence for any remaining unreacted nitric oxide. Also present in this spectrum are features due to NO_3^- and NO_2^+, and NO^+, although they are much weaker than before.

Procedure II: For these experiments liquid N_2O_2 was solidified by increasing the pressure to *ca.* 0.5 GPa while maintaining the temperature at 115K. The sample was then cooled to 100K and the pressure dependence followed using Raman scattering. The Raman spectrum of this material is distinctly different than that obtained for the crystalline material discussed above. In particular, there was no evidence for phonon features which could be attributed to crystalline N_2O_2 and the internal mode features were quite broad. In addition, the frequency positions of the internal modes were quite different than that observed for N_2O_2 in either the liquid or crystalline phases. For example, in the N-O stretch region, three bands were observed at 1543, 1631, and 1844 cm^{-1}. While the identity of the material formed in this manner is not well understood, it is clear that it represents a chemically distinct intermediate. On the basis of the observed frequencies, we propose that this intermediate is an amorphous aggregate of nitric oxide, $(N_2O_2)_x$. The frequencies of the internal modes are consistent with a cyclical trimer or dimer with functional units much like that of N_2O_3.

The intermediate was found to be stable to 3.5 GPa at 100 K. Increasing the temperature while maintaining the pressure at *ca.* 3.5 GPa led to reaction at 190-200 K. The sample first turned red and then, upon warming to room temperature, straw yellow or blue. The behavior of samples formed in this manner was essentially identical to that observed by loading the DAC and warming to room temperature after first increasing the pressure (Results section A). Raman spectra of the reaction products showed evidence for N_2O, N_2O_3, N_2O_4, NO^+, and NO_3^-; in contrast to the results obtained for crystalline samples, there was no evidence for N_2 or O_2.

C. Laboratory Scale Studies of Shocked NO:

Initially, it was thought that a slapper alone would detonate solid NO and several attempts were made to achieve this. However, less than 1% decomposition of the deposited NO (*ca.* 100 mg), was observed, and indeed, under the same conditions the slapper could not even detonate a 6 mg pellet of PETN. With the pellet of PETN glued directly to the slapper, however, the PETN did detonate and the solid NO deposited on the opposite side of the foil that covered the

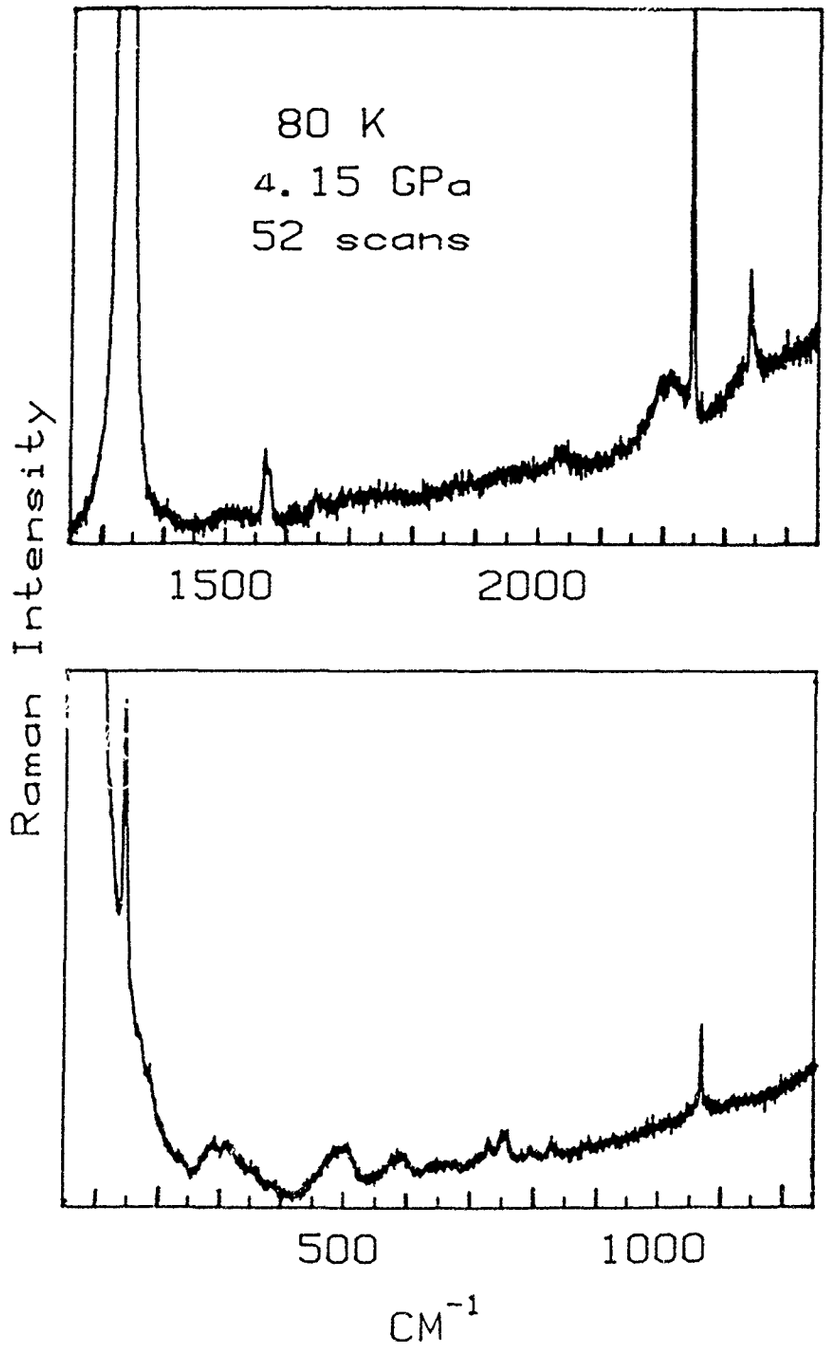

Fig. 2. Raman spectrum of solid NO reaction product at 80 K and 4.15 GPa

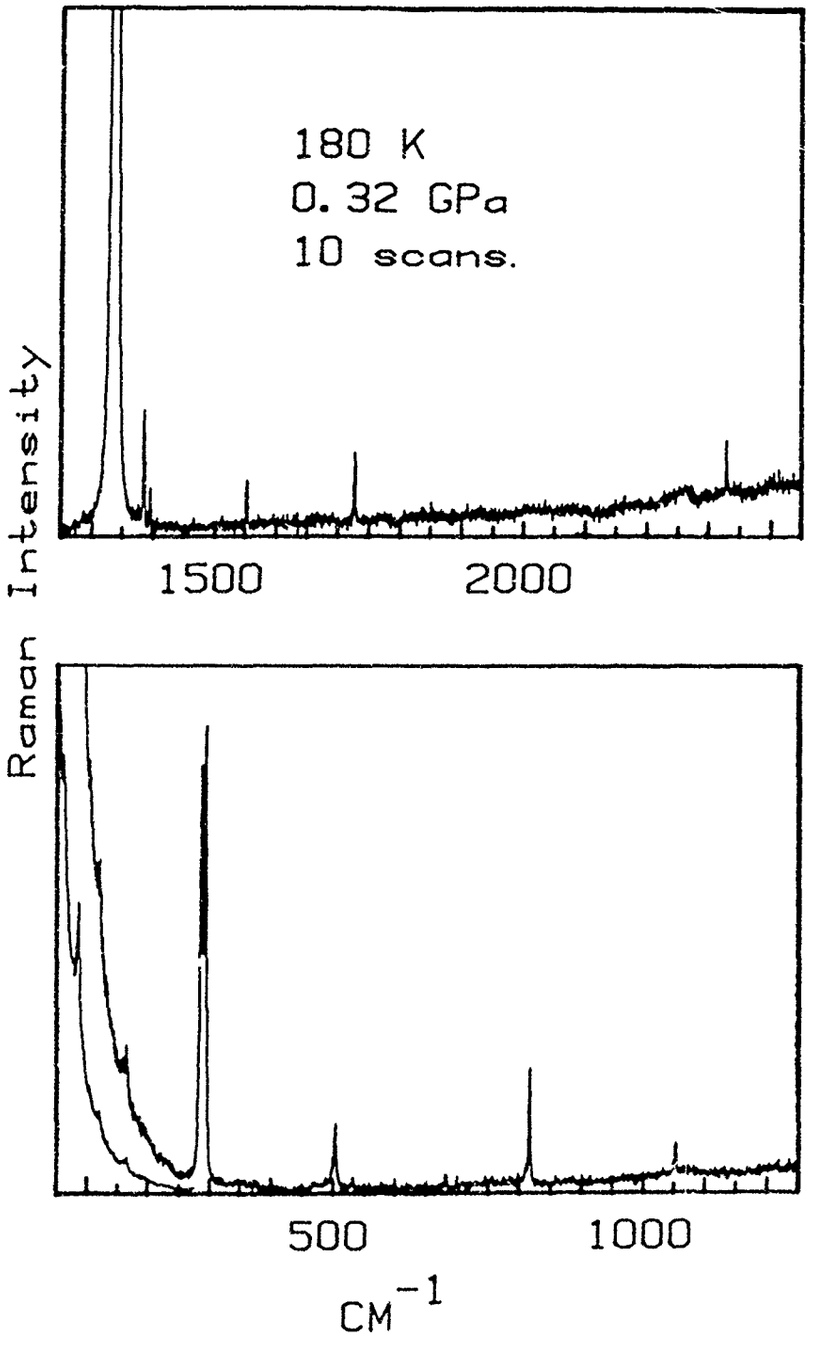

Fig 3. Raman spectrum of NO reaction products at 180 K after annealing at 220 K and lowering pressure to 0.32 GPa

PETN decomposed into a variety of products. Five experiments have been done in this configuration. Molecular nitrogen is the only expected detonation product common to both PETN and solid NO. However, both the small amount of N_2 that results from the PETN (0.04 mmol) as well as the fact that ^{15}NO was used to label the nitrogen source, allowed unambiguous determination of the nitrogen yield from the nitric oxide.

The products collected from the PETN-driven nitric oxide reaction were N_2O, N_2, NO_2, N_2O_3, N_2O_4 and unreacted NO. Presumably any O_2, which is formed due to the NO decomposition, would subsequently react with NO in the gas phase to form additional NO_2. Thus, oxygen may or may not have formed originally from the shock-induced reaction. In addition, the various gas-phase equilibria involving NO_2, as well as its substantial loss by reaction with CO, metal surfaces, O-rings, etc., complicate the determination of the NO_2 in the original products. The product yields measured from five separate experiments are presented in Table 1. In all cases a substantial portion (29-53%) of the nitric oxide reacted and, of that amount, most ended up as N_2O with a smaller amount ending up as N_2+NO_2. The N_2 result was corrected for the N_2 produced by PETN, which was determined by means of isotopically labeled NO.

All the experiments in Table 1 except Experiment 3 were done with the bell jar evacuated. Experiment 3 was done with 1 torr of He in the chamber to prevent reshock of the products at the wall. Reshock may have caused the product N_2O and NO_2 to further react, thereby producing N_2. The amount of N_2 produced was indeed the smallest of all the experiments, suggesting that some of the N_2 observed in the other experiments was produced by reshock at the walls of the apparatus.

DISCUSSION

Prior to our work on the chemistry of nitric oxide under static high pressure conditions, it was suspected that shock-initiated detonation of N_2O_2 proceeds through a single chemical reaction to produce N_2 and O_2. We have shown, on the other hand, that the reaction chemistry under both static high pressure and shock conditions is much more complex involving, most likely, several distinct mechanisms and at least one chemical intermediate. The static high pressure studies demonstrate that nitric oxide reacts rapidly under even modest pressure and temperature conditions to produce a multitude of molecular and ionic species. The fact that this pressure-induced chemistry is quite facile and releases significant amounts of energy strongly suggests that similar reactions dominate the chemistry of shock-initiated detonation of nitric oxide.

The chemistry of samples warmed rapidly to room temperature or pressurized to *ca.* 3.5 GPa at 100 K and then warmed to room temperature can be explained to arise from the initial formation of an intermediate, $(N_2O_2)_x$. The final products can be attributed to three possible reactions

$$(N_2O_2)_x \rightarrow N_2O + N_2O_3 \quad (1)$$

$$(N_2O_2)_x \rightarrow 2N_2O + N_2O_4 \quad (2)$$

$$(N_2O_2)_x \rightarrow 2N_2O + NO^+NO_3^- \quad (3)$$

The chemistry of crystalline NO samples as well as the PETN driven NO decomposition show evidence for another reaction pathway,

$$N_2O_2(\text{crystalline}) \rightarrow N_2 + O_2 \quad (4)$$

The presence of N_2O_3 in the reaction products could arise from its direct production via equation (1) or from reaction of N_2O_4 with excess NO. Equations (2) and (3) differ only in that (2) involves a molecular reaction mechanism while (3) involves the direct production of ionic species. The ions NO^+, and NO_3^- could result from their direct production via equation (3) or through the autoionization of N_2O_4 at high pressures. We have previously shown (10) that molecular N_2O_4 does autoionize at elevated pressures. However, on the basis of the ubiquitous presence of ions in all of the samples reacted under high static pressures and the observation of deep red color (indicative of NO^+ in N_2O_2) in the initial reaction, we presently favor the ionic mechanism (Eq. 3).

The pressure-induced chemistry observed for crystalline nitric oxide at low temperatures further complicates the situation. Whereas N_2 or O_2 could never by detected for samples warmed to room temperature following pressurization of liquid NO, the pressure-induced reaction of crystalline NO at low temperature produces significant and equal amounts of N_2 and O_2. Despite the rather weak relative intensities of the O_2 and N_2 features in the Raman spectra

TABLE 1

Products from solid NO shocked with 6 mg of PETN

	Experiment Number				
	1	2	3	4	5
NO gas used,[a] mmol	3.4	4.6	6.3	10.0	11.2
NO accounted for,[b] mmol	3.3	3.4	4.2	7.5	8.8
NO unreacted, mmol (%)	2.3 (70)	1.6 (47)	3.0 (71)	4.8 (64)	4.4 (50)
N_2O found, mmol	0.33	0.43	0.37	0.60	1.17
N_2 found, mmol	_[c]	0.13	0.03	0.23	0.23

[a]Some NO excapes while forming the solid.

[b]Assuming the overall reaction stoichiometries,

$3\ NO \rightarrow N_2O + NO_2$ (i)

$4\ NO \rightarrow N_2 + 2\ NO_2$ (ii)

to account for the N_2O and N_2 observed. The small amount of NO tied up as N_2O_3 is ignored.

[c]N_2 not measured and not accounted for in collected material.

(Figs. 2 and 3) these species are in significant concentration as their Raman cross sections are known to be substantially less that that of the other species present. While it has not been possible to quantify the amounts of N_2 and O_2 production relative to the production of disproportionation products (dominantly $NO^+ NO_3^-$) it is clear that N_2 and O_2 are produced in nearly equal concentrations. The PETN-driven NO decomposition suggests that the predominant reaction of shocked NO is (3) with reaction (4) present as a minor pathway. This is certainly consistent with the results of static high-pressure measurements upon rapid warming. The implication of the low-temperature high-pressure work (i.e., the importance of reaction (4)) is not yet completely clear, but the PETN-driven NO reaction does show evidence for reaction (4) as well.

The overall reactions depicted above do not necessarily represent the primary reactions, and one could imagine many different possible schemes. One possibility, which we believe can be eliminated, is that the primary reaction involves direct production of N_2 and O_2. The ubiquitous formation of disproportionation products (N_2O, N_2O_4, $NO^+NO_3^-$) would then result from subsequent reactions of N_2, O_2 and excess NO. The formation of N_2O_4 and $NO^+NO_3^-$ is easily explained to arise from

$$O_2 + N_2O_2 \rightarrow N_2O_4 \rightleftarrows NO^+NO_3^- \quad (5)$$

However, the formation of N_2O is more difficult to explain. While gas phase radical reactions are known to result in the formation of N_2O, these are unlikely to occur under low-temperature high-density conditions. In addition, several observations mitigate against this single primary reaction mechanism. First, the nearly equal concentration of N_2 and O_2 in the low temperature crystal experiment is difficult to rationalize because the facile reaction of O_2 and excess N_2O_2 would be expected to deplete the O_2 concentration to a much greater extent than that of N_2. Furthermore, no N_2 or O_2 could be detected in the samples warmed to room temperature: it is extremely unlikely that all of the N_2 could be converted to N_2O under these modest high density conditions. Finally, the observation that the thermodynamically more stable products, N_2/O_2, are formed under low temperature conditions and *not* formed under higher temperature conditions is counter-intuitive. If a single primary reaction to produce N_2 and O_2 is operative, one should certainly observe these species in cells which were allowed to warm to room temperature.

At present, the results presented here are best explained in terms of two, and possibly more, primary reaction mechanisms. In effect, one mechanism leads to the production of N_2 and O_2 while the other proceeds to form the disproportionation products.

$$N_2O_2 \text{ (liq)} \rightarrow \text{(intermediate)} \rightarrow 2N_2O + NO^+ NO_3^- \quad (6)$$

$$N_2O_2 \text{ (crystalline)} \rightarrow N_2 + O_2 \quad (7)$$

The branching between these two primary reaction paths is then quite sensitive to the initial form of the nitric oxide and, therefore, the temperature and pressure conditions employed. It is likely that the relative rates of these two global reactions diverge significantly depending on whether solid or liquid NO is shocked and the temperature and pressure profiles corresponding to the shock conditions employed. Additional work is needed to fully understand the complex reaction chemistry of nitric oxide under high density conditions, and work is underway to follow the static high pressure chemistry by careful control of both temperature and pressure.

Implication Regarding Shock-Initiated Detonation of Nitric Oxide: While a detailed chemical mechanism is not yet available for the pressure-induced chemistry of nitric oxide, several conclusions can, nonetheless, be inferred. First, condensed-phase concerted reactions appear to dominate the chemistry of nitric oxide under static and dynamic high density conditions. By analogy, gas phase radical type mechanisms known from studies of gaseous NO at low density are not important in the early chemistry of shock initiation of nitric oxide. Second, the present results strongly suggest that disproportionation to form N_2O and $NO^+NO_3^-$ dominates the early chemistry under shock conditions. This reaction would account for 2/3 of the total enthalpy content of nitric oxide and the accompanying energy release could, in turn, drive subsequent reactions to form N_2 and O_2. The ubiquitous presence of ions such as NO^+ and NO_3^- at high densities points to the importance of ions and ionic reaction mechanisms in shock-initiated detonation. The thermodynamic driving force for the formation of ions at high density presumably derives from the strong inter-ionic interactions and the attendant volume reduction relative to molecular species.

Finally, given the strong dependence of the static high pressure chemistry of nitric oxide on the phase of the material studied, it is likely that shock initiated detonation of NO also exhibits phase dependence.

REFERENCES

1. G.E. Duvall, K.M. Ogilvie, R. Wilson, P.M. Bellamy, and P.S.P. Wei, "Optical Spectroscopy in a Shocked Liquid," Nature, Vol. 296, p. 946, 1982; K.M. Ogilvie, G.E. Duvall, "Shock-Induced Changes in the Electronic Spectra of Liquid CS_2," J. Chem. Phys., Vol. 78, p. 1007, 1983.
2. S.C. Schmidt, D.S. Moore, D. Schiferl, and J.W. Shaner, "Backward Stimulated Raman Scattering in a Shock-Compressed Benzene," Phys. Rev. Lett., Vol. 50, pp. 661-664, 1983.
3. N.C. Holmes, A.C. Mitchell, W.J. Nellis, and W.B. Graham, "Raman Spectroscopy of Shocked Water," in J.R. Asay (ed.), Proceedings of the Topical Conference on Shock Waves in Condensed Matter, Santa Fe, NM, July 18-21, pp. 307-308, 1983.
4. Alain Delpuech and Albert Menil, "Raman Scattering Temperature Measurement behind a Shock Wave," ibid, pp. 309-312.
5. J. Ribovich, J. Murphy, and R.J. Watson, "Detonation Studies with Nitrous Oxide, Nitric Oxide, Carbon Monoxide, and Ethylene," J. Hazardous Mater., Vol. 1, pp. 275-287, 1975-1977.
6. T.P. Melia, "Decomposition of Nitric Oxide at Elevated Pressures," J. Inorg. Nucl. Chem., Vol. 27, pp. 95-98, 1965.
7. B.H. Golding and B.H. Sage, "Volumetric Behavior of Nitric Oxide," Ind. Eng. Chem., Vol. 43, pp. 160-161, 1951.
8. E.C. Kerr, "I. The Second Virial Coefficient of Argon at Low Temperatures. II. The Heat Capacity of Liquid Nitric Oxide above its Normal Boiling Point," Ph.D. Thesis, Ohio State University, 1957.
9. S.F Agnew, B.I. Swanson, L.H. Jones, and R.L. Mills, "Disproportionation of Nitric Oxide at High Pressure," J. Phys. Chem., Vol. 89, pp. 1678-1682, 1985.

REFERENCES (continued)

10. S.F. Agnew, B.I. Swanson, L.H. Jones, R.L. Mills, and D. Schiferl, "Chemistry of N_2O_4 at High Pressure: Observation of a Reversible Transformational Between Molecular and Ionic Crystalline Forms," J. Phys. Chem., Vol. 87, pp. 5065-5068, 1983.
11. Peter Gray, "The Chemistry of Dinitrogen Tetroxide," Royal Inst. Chem., No. 4, 30 Russell Square, London, 1958.
12. F. Bolduan and H.J. Jodl, "Raman Study of Solid N_2O_4: Temperature-Induced Autoionization," J. Chem. Phys. Lett., Vol. 85, pp. 283-286, 1982.
13. L.H. Jones, B.I. Swanson, and S.F. Agnew, "Infrared Studies of Autoionization of Thin Films of Dinitrogen Tetroxide," J. Chem. Phys., Vol. 82, pp. 4389-4390, 1985.
14. A. Anderson and B. Lassier-Govers, "Infrared and Raman Spectra of Crystalline Nitric Oxide," Chem. Phys. Lett., Vol. 50, pp. 124-128, 1977.

DISCUSSION

JAMES P. RITCHIE, Los Alamos National Laboratory

At your lowest temperatures N_2, O_2 and NO+ were observed; as temperature is raised, other reaction products are observed. Isn't it probable then, that N_2 and O_2 are your fastest formal products and that subsequent reactions of these species at higher temperatures leads to the other reaction products.

REPLY BY BASIL SWANSON

As noted in the manuscript, the two different reaction paths result naturally from the substantial differences in the initial phase of the nitric oxide studied. That is, pressure-induced reactions of crystalline NO results in the formation of N_2 and O_2 while that of liquid NO results first in the formation of and intermediate and the subsequent formation of the disproportionation products N_2O, N_2O_4, N_2O_3, NO^+, and NO_3^-. The formation of disproportionation products cannot be explained to arise from the reaction of N_2 and O_2 with excess nitric oxide as the temperature increases. While it is easy to explain the formation of N_2O_4 and the ions by reaction of O_2 and excess NO, the formation of N_2O and the disappearance of N_2 cannot be explained. Also, the absence of *any* N_2 and O_2 in the products of the pressure induced chemistry of liquid NO mitigates against this explanation.

SUB-IGNITION REACTIONS AT MOLECULAR LEVELS IN EXPLOSIVES SUBJECTED TO IMPACT AND UNDERWATER SHOCK

J. Sharma, J. C. Hoffsommer, D. J. Glover, C. S. Coffey,
J. W. Forbes, T. P. Liddiard, W. L. Elban and F. Santiago
Naval Surface Weapons Center, White Oak Laboratory
Silver Spring, MD, 20910

To determine the scarce reaction products of explosives in the sub-ignition regime, a combination of sensitive analytical techniques, such as X-ray Photoelectron Spectroscopy (XPS), Thin Layer Chromatography (TLC), and Chemical Ionization Mass Spectrometry (CIMS) has been applied. RDX, TNT, AP, and TATB have been subjected to drop-weight impact or to an underwater shock at a level very close to ignition and the solid residues have been investigated. Impacted RDX showed transformation into nitroso compounds as well as compounds having the functionality of melamine. The impacted trinitroso derivative of RDX showed loss of nitroso groups, together with the formation of further reduced nitrogen products. Impacted TNT yielded anthranil, nitrile, and aldehyde-oxime as decomposition products. Similarly, TATB evidenced furoxan and furazan products. All of these reaction products are similar to those of thermal decomposition. In the case of TATB and TNT, creation of water molecule during the formation of furazan and anthranil indicates an important exothermic step. The present work shows that "hot spot" formation involves thermally decomposed intermediate products, some of which may be less stable than the original explosives.

INTRODUCTION

Explosives, when subjected to mechanical forces, have the characteristic that in the sub-ignition regime, very little reaction occurs prior to the onset of the catastrophic processes. Based on earlier work (1, 2), it is estimated that even when the explosive is on the verge of violent reaction only 10^{-2} to 10^{-10}% of the molecules show any evidence of alteration. This explains why very little is known about the molecular changes that take place in the sub-ignition regime, and only fragmentary information is available about the molecular processes that cause the explosives to react. Of course, free radicals (3) play very important roles, and their creation could be the rate determining step. However, concrete step-by-step understanding of the ignition process is lacking. The idea of "hot spots" is invoked in order to explain inadvertent explosions and sensitization of explosives by rough handling. However, the chemical and physical nature of "hot spots" is a mystery. Study of "hot spots" can provide valuable information which can elucidate the ignition mechanism. It is also necessary to identify the early stage endothermic and exothermic reactions caused by various stimuli, such as impact, shock, heat, and irradiations. A number of studies on slow decomposition have been reported (4, 5, 6) which have brought a measure of understanding but the exact relationship between slow thermal decomposition and fast reactions is not well-established. Information on slow decomposition should be pertinent to the case of ignition, but the extent of this generalization has not been established. Also, there is the question whether the different ways in which the explosives can be ignited have the same basic mechanism or

different ones in different cases. This question has become more important because of the possibility of igniting explosives using electron, particle, and x-ray beams. Since explosives have indefinite shelf life and need an activation energy, the ignition process has to start in all cases with endothermic steps. For the development of the self-sustaining stage, however, exothermic reactions have to take over. The identification of these steps has been a challenging problem, and it is being addressed in this paper.

In order to determine the scarce reaction products generated in the pre-ignition regime, we have used a combination of sensitive analytical techniques, such as x-ray photoelectron spectroscopy, thin layer chromatography, and chemical ionization mass spectrometry. Common explosives like RDX, TNT and TATB, and the inorganic oxidizer, ammonium perchlorate (AP), have been taken to the threshold of ignition by impact or shock and then investigated for reaction products. In this effort, XPS has been found to be especially useful. Firstly, the chemical shift exhibited by the XPS spectra helps to detect and identify the reaction products on the sample in situ. Secondly, being a surface sensitive technique, XPS can magnify the changes taking place in the "hot spots". When explosives are exposed to impact or shock, the points on the surface of the particles where one particle is in touch with the other can become the nuclei of the "hot spots" due to concentration of mechanical forces. Therefore, in the XPS analysis, which probes only a few molecular layers, the ratio of the affected and non-affected molecules increases and becomes more favorable for detection. For example, according to Hoffsommer, Glover, and Elban, (7) impacted RDX showed a maximum production of about 600x10 $^{-6}$% of trinitroso derivative by weight as a reaction product, but XPS spectra of the same samples showed as high as 10% concentration of the nitroso derivative. In the XPS studies, if the impacted samples are ground up in a mortar and scrambled, then the apparent magnifying effect is lost. Thus, on account of its high surface sensitivity, XPS facilitates detection and identification of the early stage reaction products in the sub-ignition regime, which could not be done previously.

The XPS spectra, through changes of electronic levels, display the oxidation states of the atoms in the molecules and thereby can follow alterations. The results are interpreted from consideration of the oxidation states and by matching spectra of known molecules. However, XPS spectra do not provide unique identification of the products like giving mass numbers. In this respect, simultaneous study with chemical ionization mass spectrometry is a great advantage, because it unequivocally identifies the product molecules and, of course, is a very sensitive analytical technique. TLC has provided guidance on the number of products encountered. In the present work, we have found that the combination of the analytical techniques applied is far more effective for the study of the pre-ignition reactions than any single method. Therefore, depending upon the situation, we have used XPS, TLC, gas and liquid chromatography, and chemical ionization mass spectrometry to detect and identify the products of interest. However, it is possible that some reaction products are escaping our notice by being insoluble or volatile.

EXPERIMENTAL

In order to study the effect of impact on the explosives, either powder (10 to 40 mg) or pellet (30 mg: 1 mm thick, 5 mm diameter) samples were used. The sample was placed between two layers of heat sensitive viewgraph films as described by Coffey and Jacobs (8) such that the active surfaces of the film were in contact with the powder. The sandwich of films and explosive was placed on the anvil of a drop-weight impact machine, and a 10 kg weight was dropped from a predetermined height. The effective drop height could be adjusted up to four meters. The duration of the impact was 300-350 μs, and the loading was closely approximated to a half-sinewave. The samples, for maximum effect, were impacted very close to the level of ignition. The impacted sample was investigated if a residue remained. For XPS studies 1 mg of the sample was selected and examined. For TLC and mass spectrometric studies, the whole of the sample could be used.

For studying the pre-ignition reactions caused by underwater shock, a modified NSWC aquarium test (9) was developed. Pressed, 30 mg samples of TATB were mounted in Teflon plugs to achieve good impedance matching between the sample and the surrounding medium. In

some cases silicone grease was applied to the pellets to provide good contact with the Teflon plugs and to eliminate air pockets. However, silicone posed contamination problems in the XPS analysis and its use was discontinued. Four plugs of Teflon, containing the explosive samples, were mounted in thin-walled tubes of steel and placed around a spherical pentolite charge as shown in Fig. 1. The samples were placed at different distances to obtain various pressures. The system had been carefully calibrated previously. A shock wave of 10-18 kbar pressure and a few microseconds duration was imparted to the samples by detonating the donor charge. The Teflon plugs were recovered from the water after detonation and carefully cut open to obtain the TATB samples.

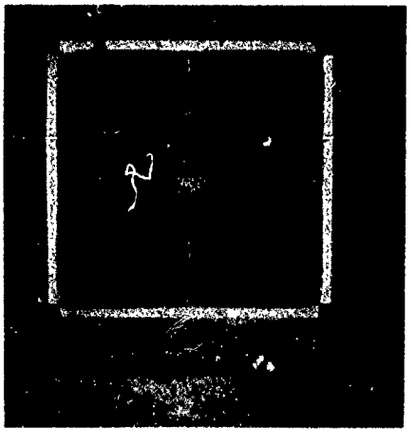

Fig. 1. Aquarium arrangement for underwater shocking explosives using a donor charge suspended at the center (after Liddiard)

During XPS studies, special attention was given to protecting the sample from undue long exposures in the XPS instrument. This was done to avoid decomposition of the material caused by exposure to x-rays of the XPS instrument. A five minute exposure was considered proper, because it gave an x-ray dose of less than 10^5 rads and showed no effect in the control experiments. A noisy spectrum was accepted rather than to adversely affect the sample in the analysis process. In the present work, XPS studies were carried out with a Kratos ES 300 instrument without an x-ray monochromator. The spectra were calibrated with the $4f_{7/2}$ line of gold, assumed to be 84.1 eV.

A Finnigan 4000 GC/MS EI-CI mass spectrometer was used with methane plasma in the chemical ionization mode for mass spectrometric studies. TLC studies were carried out by using Silica Gel HF_{254} plates.

RESULTS

For all of the impacted samples, it was found that the central area, where maximum pressure was reached, showed little or minimum reaction. Maximum reaction was detected in the peripheral region, where a pattern of streaking (discoloration) occurred on the heat sensitive film. This is understandable because the streaked area corresponds to the region of intense shear. According to Coffey (10), and Hauser, Field, and Mohan (11), reaction sites are generated by dislocation movement and fracture respectively and would be most favored in the area where the flow of material between the two sheets of film is a maximum. Since the streaking and flow does not take place uniformly in all azimuthal directions, samples selected at various sites yielded different degrees of decomposition.

RDX

Fig. 2 shows the nitrogen 1s spectra of impacted (14 cm drop height) and control RDX from which three conclusions can be made. The nitro peak at 406 eV has decreased by 20%. A new peak, about 10% of the amine peak has developed at 402 eV. Probably two peaks in the 399-397 eV region have developed by 20%. The peak at 402 eV corresponds to the nitroso nitrogen (Fig. 4a) while that of 399-397 eV is assignable to some more reduced nitrogen products. Melamine gave a peak in this region. The first result is in agreement with the finding of Hoffsommer, Glover, and Elban (7), who observed, by gas chromatography the trinitroso and dinitroso derivatives of RDX in the impacted sample. They measured only about 10×10^{-5}% of dinitroso and $1.3\text{-}557 \times 10^{-5}$% of trinitroso, whereas XPS shows as high as 10% nitroso conversion. XPS magnifies the concentration of the product by more than three orders of magnitude. It indicates the global concentration of the nitroso functional groups and does not discriminate between dinitroso and trinitroso derivatives as separate molecules. The present results show that at least 10% of the nitro nitrogen is lost and some of it is shifted to the position of the nitroso groups.

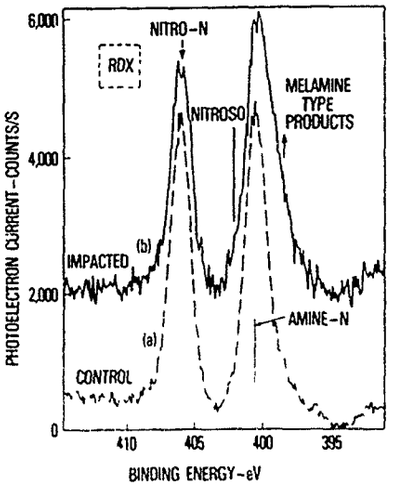

Fig. 2. XPS spectra of N 1s level in (a) control and (b) impacted RDX, showing decrease of the nitro at 406 eV accompanied by the creation of nitroso at 402 eV and other reduced products in 399-397 eV range

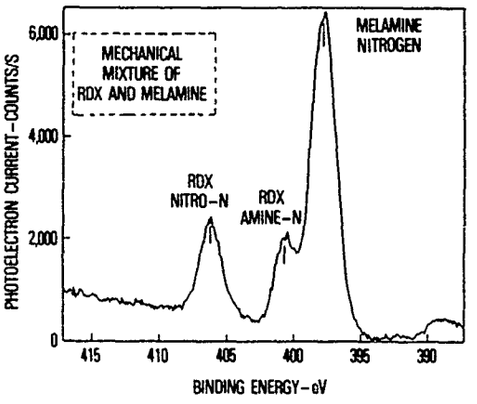

Fig. 3. XPS spectrum of N 1s level in a mechanical mixture of RDX and melamine, showing coincidence of melamine peak at 398 eV with the new peaks seen in impacted RDX in the 399-397 eV region

It is also evident that the decrease of the nitro nitrogen is not fully compensated by the increase of the nitroso. Probably some of the nitro groups are converted into other unknown functional groups. Fig. 3 shows the spectrum of a mechanical mixture of RDX and melamine. The position of the nitrogen peak in the melamine agrees with the 399-397 eV product from RDX. This implies that impact produces melamine-type products from RDX besides converting some of the nitro groups into nitroso groups. In fact, the former effect is more pronounced than the loss of the nitro groups.

In order to further understand the decomposition behavior of impacted RDX, a sample of the trinitroso derivative of RDX was impacted from a drop height of 125 cm to determine what decomposition occurs. The results are shown in Fig. 4 and are similar to those of RDX. In this case, the nitroso groups decrease instead of the nitros, while the formation of melamine-like products is even more pronounced.

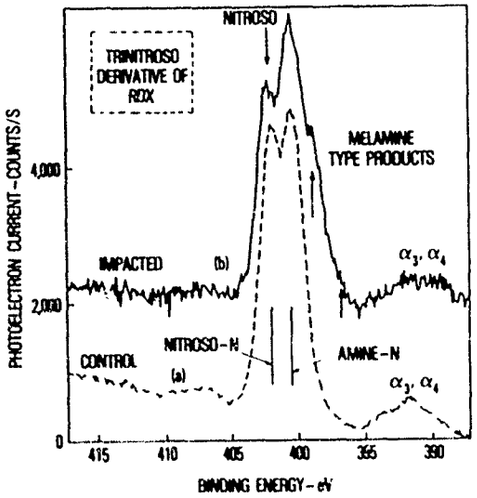

Fig. 4. XPS spectra of N 1s level in (a) control and (b) impacted trinitroso derivative of RDX, showing decrease in the nitroso at 402 eV and creation of other reduced products in the 399-397 eV region

TNT

Fig. 5 shows the effect of 150 cm impact on TNT. Additional peaks situated 5-7 eV on the lower binding energy side of the nitro peak are evident. The concentration of the products caused by impact is about 30% of the parent molecule, as detected by XPS. In order to determine the chemical nature of these products, the spectrum was compared with those of known thermal decomposition products of TNT (4, 5, 12). The following compounds were considered: 4,6-dinitroanthranil; 2,4 6-trinitrobenzyl alcohol;

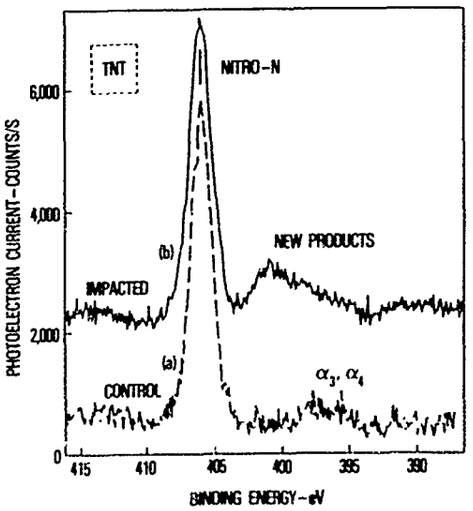

Fig. 5. XPS spectra of N 1s level in (a) control and (b) impacted TNT, showing creation of a new peak 5-7 eV away from the nitro peak towards lower binding energy side, assigned to anthranil, nitrile, and aldehydeoxime formation (The α_3, α_4 peaks arise from the spurious non-diagram line excitation from the x-ray anode and should be ignored.)

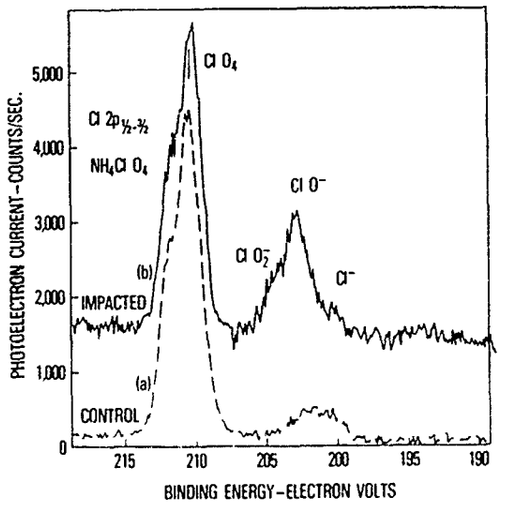

Fig. 6. XPS spectra of Cl $2_{P1/2,3/2}$ level in (a) control and (b) impacted ammonium perchlorate, showing ClO_2^-, ClO^-, and Cl^- products of lower oxidation state than the perchlorate chlorine

2,4,6-trinitrobenzaldehyde; 2,4,6-trinitrobenzoic acid; trinitrobenzene; tetranitroazoxytoluene; 2,4,6-trinitrobenzonitrile; picric acid; 5-nitroso-2-nitrotoluene; 3,5-dinitro-4-amino toluene and 2,4,6-trinitrobenzaldehyde oxime. From this comparison the peaks can be interpreted in terms of anthranil, nitrile, and aldehyde-oxime of TNT. Trinitrobenzaldehyde, trinitrobenzoic acid, and trinitrobenzyl alcohol, did not show separate XPS peaks other than that of the nitro group. Only some broadening of the nitro peaks was observed in these compounds. Broadening was also observed in the impacted samples of TNT. Thus, there is possibility that these compounds were formed. TLC studies evidenced the formation of aldehyde, nitrile, and oxime. None of the nitroso derivatives of TNT were observed. The production of 2,4,6-trinitrobenzonitrile and 2,4,6-trinitrobenzaldehyde oxime suggests that intermolecular reactions are also taking place.

AMMONIUM PERCHLORATE

The results of impacting AP from a height of 150 cm are shown in Fig. 6. Very large decomposition of AP is observed, so that the area of the products is as large as 55%. From the shifts of the Cl 2p levels, by comparing them with the spectra of different halogen oxyacids, it is concluded that ClO_2^-, ClO^-, and Cl^- products are produced. In other words, the highly oxidized ClO_4^- gets reduced. No evidence of ClO_3^- was noticed, however; similar products are yielded when AP is heated to 300-400°C. (13).

Some of the results on TATB were reported earlier (14). Fig. 7 shows the spectra of impacted and control TATB, from which it is clear that impact causes the nitro groups to be drastically lost. The main nitro peak and its shakep-up peak (Fig. 7) on the left are decreased by as much as 30%. Some broadening of the amine peak at 401.5 eV has taken place, indicating that a new functional group involving nitrogen is being produced, although the loss of the nitro groups is not fully compensated. As discussed previously (14), this corresponds to the formation of the furazan derivative of TATB by the loss of eighteen units of mass. Formation of some furoxan at 403 eV was also observed, but this is not clear in this particular figure. In the samples which were over-driven to ignition during impact, the amout of furazan and furoxan production decreased. This implies that these products are transients and not final products

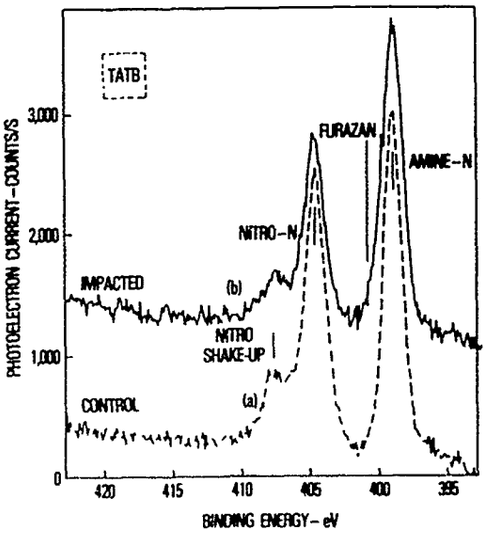

Fig. 7 XPS spectra of N 1s level of (a) control and (b) impacted TATB, showing decrease of the nitro peak and creation of a new peak at 402 eV due to furazan formation (The nitro peak in TATB shows structure due to shake-up satellite.)

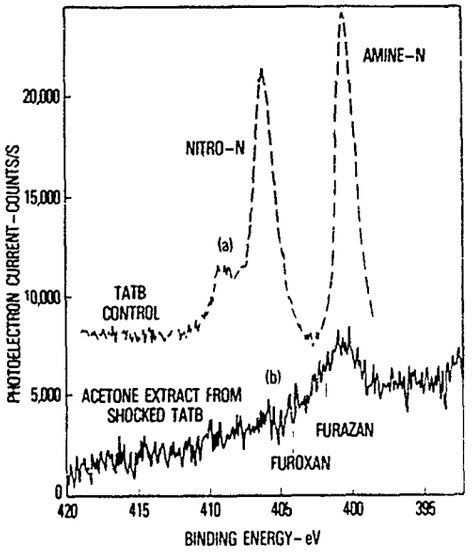

Fig. 8. XPS spectra of N ls level of shocked TATB after extracting the residue with acetone, showing evidence of furoxan and furazan formation

from the reaction. Samples of TATB subjected to an underwater shock showed only 4-6% loss of the nitro groups. The XPS spectrum of the acetone extract of shocked TATB is shown in Fig. 8 and gives evidence of furazan formation with some production of furoxan. TLC and CI/mass spectrometry confirmed the production of only furoxan in samples of TATB exposed to underwater shock. In summary, the impacted and shocked samples of TATB showed varying amounts of furazan and furoxan derivatives in different experiments. No broadening of the amine peak on the low energy side was noticeable in the impacted or shocked TATB, although it was prominent in the case of thermally decomposed samples (15).

DISCUSSION

The results on RDX tend to show that the nitroso conversion is an intermediate step and is smaller in magnitude than the more reduced spectra similar to melamine. The nitrogen in the new products is in a more reduced state than even the amine nitrogen of RDX. In the production of the more reduced products, the nitro as well as the ring nitrogen are involved because even in a case when the nitro peak has not decreased, the products containing reduced nitrogen appear. From the present work, it is not possible to determine the nature of the reduced products. The surprising feature is that the reduced products are greater in concentration than the nitroso derivatives. The formation of nitroso derivatives suggests that impact causes reactions similar to those occurring in thermal decomposition, as reported by Hoffsommer and Glover (16).

Observation of anthranil, benzaldehyde, nitrile, and oxime products in the impacted samples of TNT indicates an essential similarity of the fast reactions during impact to those of thermal decomposition as reported by earlier workers (4, 5, 12, 16).

TATB provides the best case for discussion. Monofuroxan and monofurazan derivatives are the products formed during impact and underwater shock. As reported earlier (14), four products were observed in TATB exposed to an electron beam or to heat, as given below:

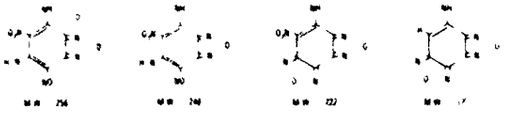

The mono derivatives alone are seen in the shocked and impacted samples. The production of monofurazan provides distinct insight in to the ignition process. Its formation by the development of the side ring destroys the aromaticity of the TATB and causes a decrease in the inter- and intra-molecular hydrogen bonding. This would weaken the molecule. The dehydration of TATB by the creation of one molecule of water yields 58 kcal/mole of energy, which compares well with the activation energy of TATB (60 kcal/mole). Thus, the formation of furazan may be the first exothermic step needed by the molecule for ignition. In general furazans are thermally not very stable (17). The present result would support the suggestion made by Loughran, Wewerka, Rogers, and Berlin (18) that C_2N_2O breaks off from the monofurazan derivative causing full disruption of the TATB. The present results also agree with the findings of Britt, Moniz, Chingas, Moore, Heller, and Ko (19) and of Taylor and Andrews (20) who have detected water as the first decomposition product during the thermal decomposition of TATB. Thus the creation of the monofurazan product agrees well with the expected pattern for the ignition process. The endothermic processes modify the structure of the molecule so that a succeeding violent reaction step can occur. This argument is also valid for TNT, in which anthranil formation was observed. Anthranil molecule possesses decreased aromaticity and is produced from TNT by the formation and loss of water.

The spectra of impacted AP also show that the decomposition is very much like thermal decomposition as reported by Solymosi (21) and by Sharma and Santiago (13). The highly oxidized chlorine in the perchlorate goes into less oxidized states, so that Cl_2O^-, ClO^- and Cl^- are observed.

The present work shows that by combining sensitive analytical techniques, such as XPS, TLC, C.I./mass spectrometry, and gas chromatography, it is possible to detect and identify chemical changes in explosives in the subignition region. In the XPS studies, the chemical shift of nitrogen is fundamental to such an investigation. The present work opens up the possibility of examining explosives which have been exposed to critical stimuli such as inadvertent shocks or particle beams, in order to understand sensitization and vulnerability.

The present study shows that (at least in the cases of explosives investigated) the pre-ignition reactions during impact are similar to those for thermal decomposition. Both inter- and intramolecular reactions occur. The involvement of the C-H and N-H bonds in the early part of the reaction, as observed in the present work, is also supported by the results on kinetic isotope effects observed by Shackelford, Beckman, and Wilkes (12), Rogers, Janney, and Ebinger (22) and by Bulusu and Autera (23). The present study also shows that the "hot spot" formation involves thermally decomposed intermediate products, some of which can be less stable than the original explosives.

ACKNOWLEDGMENTS

The authors are thankful to E. G. Kayser for supplying some of the rare derivatives of TNT which facilitated the identification of the decomposition products. They are thankful to M. J. Kamlet for many helpful discussions and valuable remarks. The authors are also thankful to R. N. Rogers, Los Alamos Scientific Laboratory, Los Alamos, NM, for his suggestion that the spectrum of impacted RDX should be compared with melamine to elucidate the growth of peak associated with the highly reduced state of nitrogen.

REFERENCES

1. F. P. Bowden, P. G. Fox, and J. Soria-Ruiz, "Direct Observation of Thermal Decomposition Produced by Fracture in Brittle Crystalline Solids," Nature, Vol. 220, No. 5169, pp. 778-779, 1968.
2. P. G. Fox and J. Soria-Ruiz, "Fracture-Induced Thermal Decomposition in Brittle Crystalline Solids," Proc. Roy. Soc. Lond. Vol. A 317, pp. 79-90, 1970.
3. F. E. Walker, "Quantum Mechanics and Molecular Dynamics Calculations Provide New Evidence for a Free-Radical Shock Initiation Model," Propellants Explos. Pyrotechnics, Vol. 7, No. 1, pp. 2-7, 1982.
4. R. N. Rogers, "Combined Pyrolysis and Thin Layer Chromatography — A Method for the Study of Decomposition Mechanisms," Anal. Chem., Vol. 39, No. 7, pp. 730-733, 1967.

5. J. C. Dacons, H. G. Adolph, and M. J. Kamlet, "Some Novel Observations Concerning the Thermal Decomposition of 2, 4, 6-Trinitrotoluene," J. Phys. Chemistry, Vol. 74, No. 10, pp . 3035-3040, 1970.

6. M. A. Schroeder, "Critical Analysis of Nitramine Decomposition Data, Product Distribution From HMX and RDX Decomposition," Proc. 18th JANNAF Combustion Meeting, Pasadena, Cal., CPIA Publication No. 347, pp. 395-413, 1981.

7. J. C. Hoffsommer, D. J. Glover, and W. L. Elban, "Evidence for Nitroso Compound Formation in Impacted RDX Crystals," J. of Energetic Materials, (in publication).

8. C. S. Coffey and S. J. Jacobs, "Determination of Local Heating in Impact or Shock Experiments with Thermally Sensitive Films," J. Appl. Phys., Vol. 52, No. 11, pp. 6991-6993, 1981.

9. T. P. Liddiard, Jr., "Initiation of Burning in High Explosives by Shock Waves," Fourth (International) Symposium on Detonation, U.S. Naval Ordnance Laboratory, White Oak, MD, Oct. 12-15, pp. 487-495, 1965.

10. C. S. Coffey, "Phonon Generation and Energy Localization by Moving Edge Dislocations," Phys. Rev., Vol. B, 24, No. 12, pp. 6984-6990, 1981.

11. H. M. Hauser, J. E. Field, and V. K. Mohan, "Fracture-Induced Decomposition of a Brittle High Explosive: Pentaerythritol Tetranitrate," Chem. Phys. Lett., Vol. 99, No 1, pp. 66-70, 1983.

12. S. A. Shackelford, J. W. Beckman, and J. S. Wilkes, "Deuterium Isotope Effects and the Thermochemical Decomposition of Liquid 2, 4, 6-Trinitrotoluene: Application to Mechanistic Studies Using Isothermal Differential Scanning Calorimetric Analysis," J. Org. Chem, Vol. 42, No. 26, pp. 4201-4206, 1977.

13. J. Sharma and F. Santiago, "XPS Study of the Surface Activity of Ammonium Perchlorate," Bull. Am. Physical Soc., Vol. 28, p. 553, March 1983.

14. J. Sharma, J. C. Hofsommer, D. J. Glover, C. S. Coffey, F. Santiago, A. Stolovy, and S. Yasuda, "Comparative Study of Molecular Fragmentation in Sub-Initiated TATB Caused by Impact, UV, Heat and Electron Beams," Shock Waves in Condensed Matter, J. R. Assay, R. A. Graham, and G. K. Straub (editors), Elseveir Science Publishers B. V., pp. 543-546, 1984.

15. J. Sharma, W. L. Garrett, F. J. Owens, and V. L. Vogel, "X-ray Photoelectron Study of the Electronic Structure and Ultraviolet and Isothermal Decomposition of 1,3,5-Triamino-2,4,6-trinitrobenzene," J. Phys. Chem, 86, pp. 1657-1661, 1982.

16. J. C. Hoffsommer and D. J. Glover, "Thermal Decomposition of 1,3,5-Trinitro-1,3,5-Triazacyclohexane (RDX): Kinetics of Nitroso Intermediates Formation," Combustion and Flame, Vol. 59, pp. 303-310, 1985.

17. R. J. Gaughran, J. P. Picard, and J. V. R. Kaufman," Contribution to the Chemistry of Benzfuroxan and Benzfurazan Derivatives," J. Amer. Chem. Soc. Vol. 76, pp. 2233-2236, 1954.

18. E. D. Loughran, E. M. Wewerka, R. N. Rogers, and J. K. Berlin, "The Influence of Metals on the Thermal Decomposition of s-TATB," Los Alamos Scientific Laboratory Informal Report, LA-6873-MS, pp. 1-7, 1977.

19. A. D. Britt, W. B. Moniz, G. C. Chingas, D. W. Moore, C. A. Heller, and C. L. Ko, "Free Radicals of TATB," Propell. Explos., Vol. 6, No. 3, pp. 94-95, 1981.

20. G. W. Taylor and G. H. Andrews, Jr., "Flowing Afterglow Spectroscopy: An Ultrasensitive Probe into Solid Phase Decomposition Kinetics," Proc. of Fifth Symposium on Chemical Problems Connected with Stability of Explosives, Sandbyberg, Sweden, pp. 297-327, 1979.

21. F. Solymosi, Structure and Stability of Salts of Halogen Oxyacids in the Solid Phase, John Wiley & Sons, N.Y., p. 213, 1971.

22. R. N. Rogers, J. L. Janney, and M. H. Ebinger, "Kinetic-Isotope Effects in Thermal Explosions," Thermochimica Acta, Vol. 59, pp. 287-298, 1982.

23. S. Bulusu and J. R. Autera, "Initiation Mechanism of TNT: Deuterium Isotope Effect as an Experimental Probe," J. of Energetic Materials, Vol. 1, No. 2, pp. 133-140, 1983.

DISCUSSION

GEORGE ANDREAS, Los Alamos National Lab

Did you eliminate the possibility that the species observed by XPS were produced by x-ray damage?

REPLY BY J. SHARMA

Yes. As mentioned in the written paper, stringent precautions were taken so that x-ray damage in the XPS could not foul up the results. The exposure on sample was kept below 10^5 Rads. A typical run changed specimen by about 1% whereas the observational changes reported were twenty to fifty times larger.

DISCUSSION

DR. F. VOLK, Fraunhofer Institute, Bader, F.R.G.

We analyzed the reaction products of nitroguanidine (NQ) using HPLC method. We could analyze not only melamine, but also ammeline, melam, and other products could be found..

REPLY BY J. SHARMA

I am not surprised. Impact does seem to cause polymerization in general, besides causing other reactions

PARAMAGNETIC DECOMPOSITION PRODUCTS FROM ENERGETIC MATERIALS

M.D. Pace, A.D. Britt*, W.B. Moniz and D. Stec III
Chemistry Division
Naval Research Laboratory
Washington, D.C. 20375-5000

During thermal or photochemical decomposition certain energetic materials including cyclotrimethylenetrinitramine (RDX) and cyclotetramethylenetetranitramine (HMX) evolve molecular products which are paramagnetic. These products (more commonly called free radicals) are detected by using electron paramagnetic resonance (epr) spectroscopy. Epr spectra of nitroxyl radicals are observed from both photochemical and thermal decomposition of these nitramines in the solution phase. An unsolved epr spectrum of RDX in solution at 170°C matches that observed during liquefaction of RDX at 200°C. Recent work includes nmr and epr results from spin trapping to detect transient radicals in solution phase RDX in the temperature range 130°-150°C (ca. 50°-70°C below the decomposition temperature of this material). The identification of the spin trapped products has been hampered by broad linewidths and weak hyperfine couplings. Research in progress includes the application of specialized traps and isotopically labeled energetic materials to enhance spectral analysis and to provide structural information about the adduct radicals.

INTRODUCTION

Several energetic materials including RDX and HMX produce free radicals during their decompositions which are detected by using electron paramagnetic resonance (epr) spectroscopy (1). This is true for both photochemically and thermally initiated decompositions. Photochemical decompositions of solution phase and solid phase energetic materials involve mechanisms such as addition of hydrogen to the parent compound forming an adduct radical, one electron reduction of the parent molecules to form anion radicals and homolytic bond cleavage to form radical fragments (2-4). In this review we focus on thermal decomposition processes.

The lifetime of an individual solution phase free radical is usually very short (ca. milliseconds or less) since the unpaired electron seeks to lower its electronic energy state. Reduction of the electronic energy state can occur by reaction of the free radical with another molecule to form a diamagnetic product (not detectable with epr) having its molecular orbitals occupied by electron pairs. The formation of many free radicals ($>10^{12}$ radicals per cm length of cavity) must be achieved to enable detection by continuous wave (cw) epr. Thermal decomposition of solutions of RDX or HMX dissolved in dimethylsulfoxide or sulfolane produces a dectectable number of free radicals as evidenced by the epr spectra in Fig. 1a-c (5,6). We have found it experimentally beneficial to dissolve the energetic material into a chemically inert solvent. This enhances the signal-to-noise ratio of the spectral lines without introducing spectral artifacts. Typical solvents used for solution phase photochemical experiments include dioxane, acetonitrile, or water. In thermal experiments the solvent must have a high boiling point (>170 °C). For most experiments we have chosen sulfolane (b.p. 285°C) or

*recently deceased

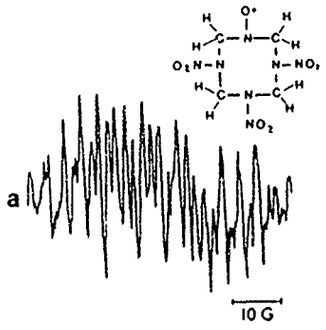

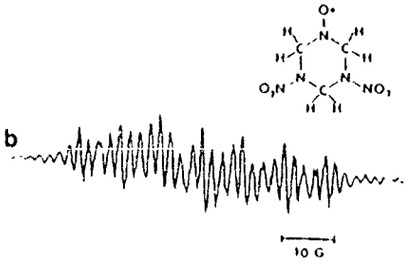

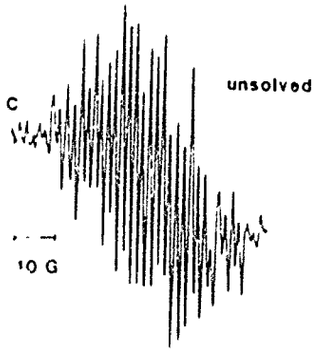

Fig. 1a. First-derivative epr spectrum of solution phase HMX (in sulfolane) at 200°C

Fig. 1b. Epr spectrum of solution phase RDX (in solfolane) at 170° C

Fig. 1c. Epr spectrum of solution phase RDX (in sulfolane) at 170°C after a time-lapse of 10 minutes

dimethylsulfoxide (b.p. 189°C). No signals are detected from either solvent when heated to their respective boiling points. Epr spectra were recorded using an IBM-Bruker ER200 spectrometer. During heating of the HMX sample the spectrum in Fig. 1a does not change, but with the RDX sample a gradual spectral change is observed (from the spectrum in Fig. 1b into the spectrum in Fig. 1c) within 30 minutes from the start of heating. Epr signals (Fig. 1a and 1c) are detected for up to 8 hours indicating that a steady-state concentration of free radicals is produced by slow decomposition of these nitramines in solution when the temperature is maintained at 170°C.

The structural assignments are shown above each spectrum in Fig. 1a-b. These structures represent a nitroxyl type of free radical having most of the unpaired electron spin population localized in the nitrogen-oxygen bond. These assignments are consistent with the patterns and intensities of the spectral lines, the ^{14}N hyperfine couplings, the beta proton hyperfine couplings, and spectral g-values (see EPR Theory Section). The formation of these free radicals occurs by a net loss of •NO from each of their respective parent molecules. Experiments using anaerobic samples indicate that dissolved O_2 is not a requirement for this free radical formation.

Establishing an assignment of the free radical structure is not easy if more than one type of free radical contributes to the epr spectrum or if many spectral lines from a single free radical overlap to create unrecognizable patterns. The spectrum produced by prolonged thermal decomposition of RDX in sulfolane at 170°C has 36 resolved spectral lines (Fig. 1c). An identical spectrum has been recorded during liquefaction of RDX at 200°C (7). The structure of the free radical which produces this spectrum is unsolved. The complex spectral pattern indicates that the unpaired electron spin population of this free radical is more delocalized than that of the simple nitroxyl radical. Some possible structures for this free radical include a nitronyl nitroxyl radical or dimer type of structure such as the radical anion produced by electron transfer between azobenzene and hydrazobenzene (8). Understanding this spectrum is a major goal.

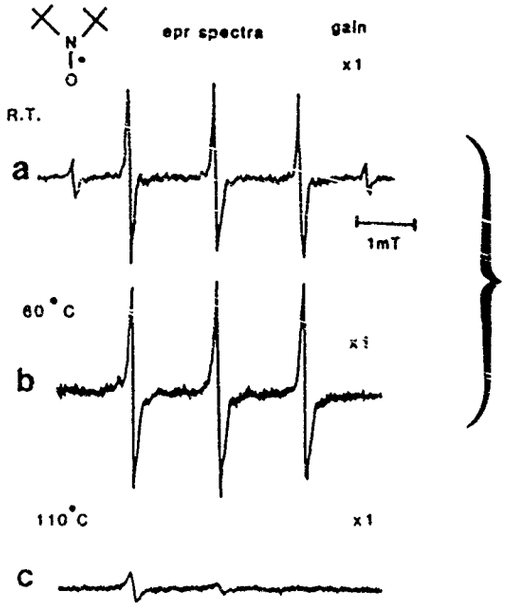

Fig. 2a-b. First-derivative epr of di-tert-butylnitroxyl radical (produced by MNP trap) in a solution composed of RDX, MNP, and Me_2SO-d_6 at room temperature and at 60°C

Fig. 2c. Decay of the di-tert-butylnitroxyl radical occurs at 110°C as shown by a disappearance of epr signals

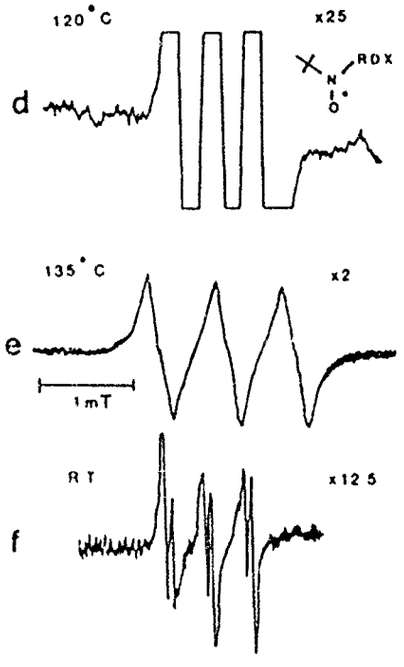

Fig. 2d. Adduct radical spectrum produced from MNP spin trap and an RDX reactant at 120°C (No spectrum is detected when RDX is excluded from the solution.)

Fig. 2e. Epr spectrum of the RDX-MNP adduct persists at 135°C (The three lines are attributed to an ^{14}N hyperfine coupling. The linewidth is unusually broad (ca. 0.3mT).)

Fig. 2f. Epr spectrum of the RDX-MNP adduct at room temperature. A decrease in linewidth (from the spectrum in 2e) reveals a second hyperfine coupling

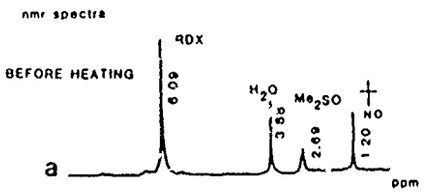

Fig. 3a. Proton nmr spectrum of a solution composed of RDX, MMP, and Me_2SO-d_6 before a single heat-cycle

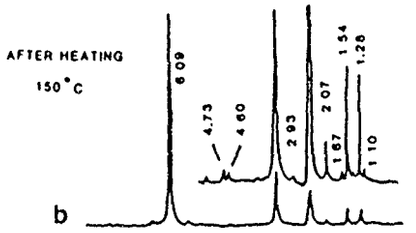

Fig. 3b. Proton nmr spectrum of the RDX-MNP solution after a heat-cool cycle shows several new peaks arising from decomposition of RDX and MNP

When a free radical is hard to identify or rapidly decays (resulting in loss of epr signal) a technique called "spin trapping" can often provide epr information which would otherwise be lost. Spin trapping experiments were performed during thermal decomposition of solution phase RDX.

SPIN TRAPPING

The technique of spin trapping is firmly established as an analytical tool in many areas of research. Several reviews of this technique have been published (9). The general reaction follows equation 1 below.

$$\underset{\text{reactant}}{\cdot R} + \underset{\text{trap}}{T} \dashrightarrow \underset{\text{spin adduct}}{\cdot RT} \qquad (1)$$

A reactant free radical (in this case formed by decomposition of either RDX or HMX) encounters a molecular "trap" and undergoes an addition reaction to produce a spin adduct free radical. The main objectives are to record an epr spectrum of the spin adduct and to deduce from this spectrum the structures of the adduct and the reactant. We used the following spin traps in these experiments: 2-methyl-2-nitrosopropane (MNP); N-tert-butyl-α-phenylnitrone (PBN); α-(4-pyridyl-1-oxide)-N-tert-butyl-nitrone (4-PCBN), 3,3,5,5-tetramethylpyrroline N-oxide (TMPO); and 2,4,6-tritert-butylnitrosobenzene (TBN). Table 1 gives structures and melting points of these traps. The reactant free radical can add to a trap in two positions. Where it adds depends upon the location of the double bond in the trap as indicated by PBN and TBN in equations (2) and (3).

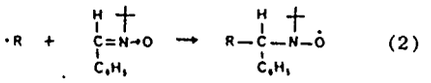

(2)

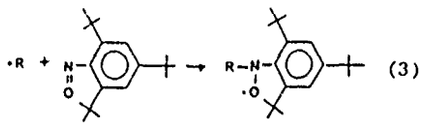

(3)

The photochemical decomposition of these spin traps has been studied, but their thermal decomposition in solution required experimental investigation. Our approach was to record a proton nmr spectrum and an epr spectrum from solutions of spin trap plus perdeuterodimethylsulfoxide (Me_2SO-d_6) before and after a heat-cool cycle. (The heat-cool cycle consisted of heating the sample to 150°C within one minute, maintaining the temperataure at 150°C for one minute, and then cooling the solution to room temperature over several minutes). No new products were detected by the nmr or epr spectra for any of the spin traps in Table 1 after a single heat-cool cycle. (At 200°C PBN and TBN in Me_2SO-d_6 show epr signals attributed to decomposition of the spin trap. Room light initiates a photochemical decomposition of MNP and Me_2SO-d_6 at room temperature to produce an epr spectrum attributed to the di-tert-butylnitroxyl radical. At 110°C the di-tert-butylnitroxyl radical decays and does not interfere with measurements at 150°C).

With this background information in hand thermal experiments were repeated with solutions having a weight composition of 0.5% spin trap, 9.5% RDX, and ca. 90% perdeuterodimethylsulfoxide (water and ca. 0.5% Me_2SO were present). The epr spectra recorded from a solution containing RDX and MNP during a heat-cool cycle is shown in Fig. 2a-f. The spectra in Fig. 2a-c are attributed to di-tert-butylnitroxyl radicals as mentioned above. At 110°C this radical decays. At 120°C (Fig. 2d) a spin adduct spectrum of MNP and a reactant free radical from the decomposition of RDX is observed. The spin adduct spectrum at 135°C

TABLE 1

Structures and Formulas of Spin Traps

Spin Trap	Structure	Molecular Formula	Formula Weight	Melting Point (°C)
MNP	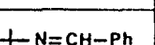	C_4H_9NO	87.0	83°
PBN	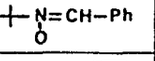	$C_{11}H_{15}NO$	177.1	74°
4-POBN	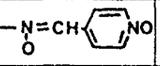	$C_{10}H_{14}N_2O_2$	194.1	185°
TMPO	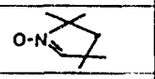	$C_8H_{15}NO$	141.2	61°
TBN	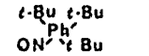	$C_{18}H_{29}NO$	275.2	173°

TABLE 2

Spin Trapping Spectral Data

Solution Phase Components in Me_2SO-d_6[a]		epr				nmr
Spin Trap	Nitramine	Ratio of line intensities[b]	HFS[c] (mT)	Line-width (mT)	Temp.[d] (°C)	Spectral line positions (ppm)[e]
MNP	RDX	1:1:1 1:1:1:1:1:1	a^N=.738 a^N=.158 a^H=.042	316 042	130 25	6.09 (RDX), 4.73, 4.60, 3.38, (H_2O), 2.93, 2.49, (Me_2SO-d_6), 2.07, 1.54, 1.19 (MNP)
PBN	RDX	1:1:1:1:1:1	a^N= 738 a^H= 211	.105	150	g
4-POBN	RDX	1:1:1	a^N= 737	158	150	g
TMPO	RDX	1:1:1	a^N= 756	184	110	g
TBN	RDX	f				4.73, 4.60, 2.07 (new products)

a typical weight % composition: 90% Me_2SO-d_6, 9.5% RDX, 0.5% spin trap.
b. ^{14}N and proton hyperfine couplings produced spectra with either 3 or 6 lines.
c electron-nuclear hyperfine splitting (or coupling) in millitesla (10 gauss = 1 mT).
d. Temperature at which the epr spectrum has constant spectral line intensities.
e nmr line positions relative to tetramethylsilane (an internal standard).
f epr data unavailable.
g no new products were detected after a single heat-cool cycle.

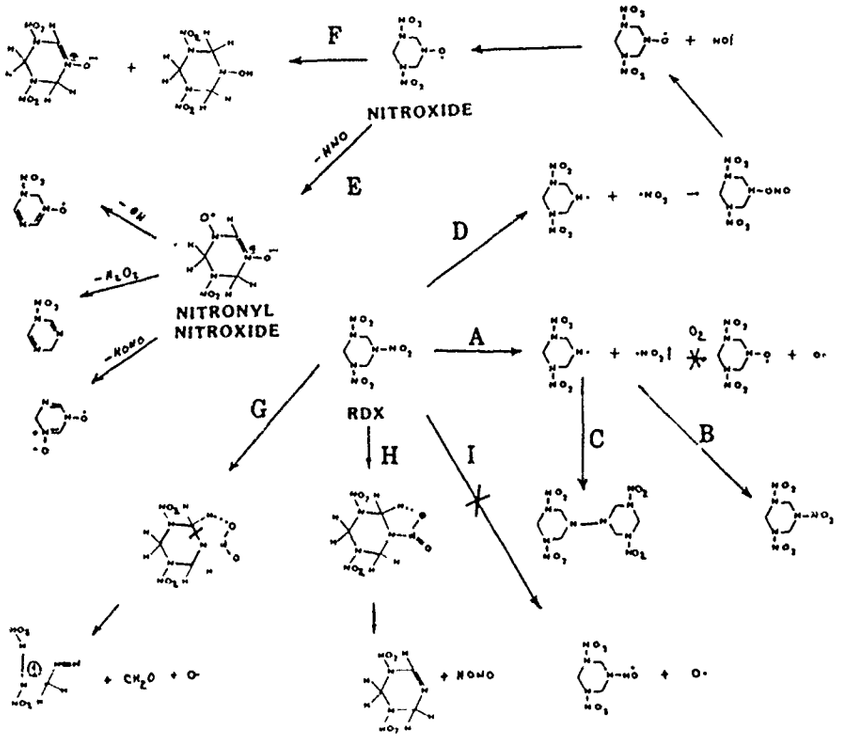

Fig. 4. Suggested pathways for slow thermal decomposition of solution phase RDX

(Fig. 2e) persisted during a time lapse of 30 minutes. After recooling the sample to room temperature the spectrum remained stable and showed a reduction in linewidth and resolution of a second hyperfine coupling (Fig. 2f). This room temperature spectrum persisted for 2 hours before completely decaying. The 6 line spectrum in Fig. 2f is attributed to an ^{14}N hyperfine coupling of 7.38 gauss (0.738 millitesla) and a proton hyperfine coupling of 1.58 gauss (0.158 millitesla).

The proton nmr spectra of the RDX-MNP-Me_2SO-d_6 solution are shown in Fig. 3a-b. The top spectrum indicates that the components of the solution before heating are RDX, Me_2SO (Me_2SO-d_6 contains ca. 0.5% Me_2SO), H_2O (Me_2SO-d_6 is hydroscopic) and MNP. After a single heat-cool cycle new proton nmr peaks appear as shown in spectrum 3b. The most prominent new peaks are at 2.07 ppm, and 1.54 ppm (possibly t-butylnitrosohydroxylamine). Weaker new peaks occur at 4.73, 4.60, 2.93, 1.67, 1.41, 1.30, and 1.53 ppm. Possible assignments to these peaks include t-butanol (1.23 ppm) and isobutene (4.6 and 1.7 ppm).

Similar experiments using the other spin traps in solutions with RDX and Me_2SO-d_6 are summarized in Table 2. A spin adduct attributed to addition of an RDX decomposition reactant with the trap was detected in each case. Our motive for pursuing these experiments was to trap the free radical responsible for Fig. 1c. Unfortunately the broad linewidths have impeded the extraction of useful structural information from these spin trapping spectra. It was surprising to find that spin adducts formed at such low temperatures (110°C-150°C).

DISCUSSION

There are many possible pathways through which RDX or HMX might thermally decompose. Several of these possibilities for RDX are depicted in Fig. 4. The formation of a nitroxyl (sometimes called nitroxide) radical (Fig. 1b) indicates that an NO_2 group is displaced from the RDX molecule by an oxygen atom. This requires cleavage of the N-NO_2 bond. A homolytic bond cleavage forms paramagnetic NO_2 and a highly reactive nitrogen-centered radical

as shown in path A. These free radicals can recombine to form the RDX molecule (path B) or perhaps dimerize with other free radicals (path C). The formation of a nitroxyl radical by reaction with dissolved oxygen molecules is likely, but experiments with anaerobic solutions show that O_2 is not required. This leads us to consider other paths.

A nitroxyl radical may result from a recombination of the nitrogen centered radical and ONO following cleavage of the RDX N-NO_2 bond. This possibility is indicated in path D. Recombination can occur via the cage-effect (the rate of recombination of two radicals is assumed much faster than their diffusion rates) and a subsequent loss of NO produces a nitroxyl radical which is observed in Fig. 1b. The nitroxyl radical can decay by a disproportionation reaction (path F) to form a nitrone and hydroxylamine or can form a second radical by net loss of HNO. (The loss of HNO yields a nitronyl nitroxyl structure. This is the structure which is suggested by the spectrum in Fig. 1c. Experiments are underway to confirm this). The spectrum in Fig. 1c strongly suggests that the free radical is a closed ring structure. Thesimplest computer match to the spectrum in Fig. 1c requires five inequivalent hyperfine couplings (10). Such a large number of couplings indicates that the electron spin population is distributed over several bonds. This is more likely for a ring type structure than for a chain structure. As decomposition progresses the presumed nitronyl nitroxyl radical can form other radical or non-radical products such as those indicated in Fig. 4.

This scheme is not the only pathway through which RDX may undergo slow thermal decomposition. Other paths such as G and H can lead to non-radical products, or can be clearly ruled out. For example, path I is rejected because the indicated nitroxyl radical's structure does not agree with the spectrum in Fig. 1b.

In summary, path D is the most logical scheme which fits our experimental observations. A nitronyl nitroxyl radical is the suggested candidate for Fig. 1c based upon the data available at this time. The spin trapping experiments did not produce information sufficient to identify the free radical in Fig. 1c, but indicated that free radicals occur in solution phase RDX at temperatures much lower than its decomposition temperature.

EPR THEORY

The unpaired electron is a distinctive property which separates free-radicals from diamagnetic molecules having molecular orbitals occupied by paired electrons. In the presence of a magnetic field the unpaired electron spin is space-quantized. This means that the z component of the electron's spin angular momentum (L_{sz}) with respect to the direction of an applied magnetic field has a specific value equal to $| m_s h |$. From quantum mechanics the values of the electron spin magnetic quantum number are $m_s=+½$ and $m_s=-½$ (h is Boltzmann's constant divided by 2π). This restricts the orientation of the electon spin vector L_{sz} to $+½h$ and $-½h$ (alignment with or against the magnetic field, respectively). The energy of these two orientations of L_{sz} is $E_1 = + ½g\beta H$ for $m_s = + ½$ and $E_2 = -½g\beta H$ for $m_s = -½$ (β is a constant equal to eh/2mc where e is the value of electron charge, m is the electron's mass, c is the velocity of light. The g value is considered a constant here, but actually varies slightly in organic systems. H is the value of the applied magnetic field). The difference in energy between these levels is $\Delta E = E_1 - E_2 = g\beta H$. ΔE increases linearly with magnetic field.

The epr experiment detects a change in the populations of E_1 and E_2 when energy equal to ΔE is applied from an external source. The quantized energy for a particular frequency (ν) is $h\nu$, so the value of the frequency which must be chosen to match a particular magnetic field value is determined by the equation $h\nu = g\beta H$. This describes the condition of "resonance". Experimentally it is easier to select a constant frequency and vary the magnetic field to achieve resonance. The most common type of spectrometer (as used in our experiments) operates at a microwave frequency of $\nu = 9.5$ GHz (x-band) and the magnetic field varies from 3300 to 3500 gauss in order to record an entire spectrum. The spectral lines are displayed as the first-derivative of the microwave power absorption curve.

This description is simplified and in most experiments the resonance equation must have other terms to account for all observed spectral lines. To express the dipolar interaction of the

electron magnetic moment with the nuclear magnetic moments of nearby atomic nuclei in the free-radical, a second term (aI · S) is added. This gives n energy levels having $E_n = \pm$ ½ gβH + aI · S. . S is the electron spin magnetic quantum number having values $m_s = \pm$½ and I is the nuclear spin magnetic quantum number which usually has ₹ different value for each atomic nucleus. The factor, α, gives the magnitude of interaction. For protons I has values of $m_I = \pm$½; for ^{14}N nuclei $m_I = \pm 1,0$). In solutions and melt phase spectra the isotropic coupling is usually adequate to account for all allowed transitions. In the solid state the second term generally has an anisotropic part and is written S · A · I where A is the anisotropic hyperfine coupling tensor. Other terms are often added to the resonance equation including the nuclear Zeeman interaction and the nuclear quadrupole interaction.

A good overview of nmr and epr theory can be found in reference 11.

REFERENCES

1. H.L. Pugh, L.P. Davis, J.S. Wilkes, W.R. Carper and R.C. Dorey, Proceedings - Seventh Symposium (International) on Detonation, U.S. Naval Academy, Annapolis, MD, pp. 75-83, 1981.

2. A.D. Britt, W.B. Moniz, G.C. Chingas, D.W. Moore, C A. Heller, and C.L. Ko, Propellants and Explosives, Vol. 6, p. 94, 1981.

3. H.H. Miles, K.L. DeVries, A.D. Britt, and W.B. Moniz, Propellants Explosives Pyrotech., Vol. 7, p. 100, 1982.

4. M.D. Pace and W.B. Moniz, J. Magn. Reson., Vol. 47, p. 510, 1982.

5. M.D. Pace, A.D. Britt, and W.B. Moniz, J. Energetic Materials, Vol. 1, p. 127, 1983.

6. A.D. Britt, M.D. Pace, and W.B. Moniz, J. Energetic Materials, Vol. 1, p. 367, 1983.

7. C. Dorey, J.S. Wilkes, L.P. Davis, H.L. Pugh, W.R. Carper, A.G. Turner, and K.E. Siegenthaler, Frank J. Seiler Research Laboratory, Report FISRL-TR-80-0026, 1980.

8. G.A. Russell, E.G. Janzen, and E.T. Strom, J. Am. Chem. Soc., Vol. 84, p. 4153, 1962.

9. E.G. Janzen, Acc. Chem. Res. Vol. 4, p. 31, 1971;
   C. Lagercrantz, J. Phys. Chem., Vol. 75, p. 3466, 1971;
   C.A. Evans, Aldrichimica Acta, Vol. 12, p. 23, 1979.

10. M.D. Pace, D.R. Farrar, A.D. Britt, and W.B. Moniz, NRL Memorandum Report 5212, 1983.

11. A. Carrington and A.D. McLachlan, Introduction to Magnetic Resonance, Harper and Row, New York, 1967.

PARAMAGNETIC RESONANCE OF RADICALS IN DECOMPOSED TRINITROAROMATICS

F.J. Owens
U.S. Army Armament Research and Development Center
Dover, New Jersey 07801-5001

Electron paramagnetic resonance (EPR) has been used to identify radicals produced in the uv and thermal decomposition of tetryl, 2,4,6 TNT, 3,4,5 TNT, 3,5 DNT, 3,5 Dichloro-TNT, Picramide and DATB.

INTRODUCTION

Despite the long history of the use of the phenomena of the initiation of detonation in such molecules as trinitrotoluene, there remains little knowledge of the initial chemical steps of the process. Global reaction rates obtained from differential scanning calorimetry (DSC) experiments are able to predict explosive behavior, such as the critical temperature for thermal explosion when used to solve the Frank-Kamenetzky thermal explosion equation (1). However, the detailed chemical steps that constitute this global rate are unknown. One possibility is that there is a rate controlling step, perhaps the initial step, which dominates and controls the process. The verification of this possibility and the identification of the rate controlling step would be a significant advance in the understanding of the initial process. It is generally agreed that the initial step is an endothermic scission of the internal molecular bonds of the molecules that make up the explosive followed by an exothermic reaction between the fragments which are quite likely radicals. In fact, electron paramagnetic resonance studies of energetic organic materials thermally decomposed in the molten phase indicate the role of radicals in the early stages of the chemistry of initiation (2,3).

Although detailed studies of the kinetics of the formation of these spectra were made, no identification of the radicals giving rise to the spectrum was reported

As well as thermally produced radicals, species produced by uv light and gamma radiation are studied. An impetus for studying radiation induced radicals comes from possible future directed energy weapons. A particularly vulnerable component of a nuclear weapon is the chemical explosive. The production of a high concentration of radicals, highly reactive species, could drastically alter the explosive parameters, such as sensitivity. For example, it has been shown that HMX subjected to 10^9 R of gamma rays has its five second temperature reduced by 99 °C (4). Similarly, impact sensitivity of HMX was strongly affected by gamma irradiation which has been shown to produce radicals (5).

EXPERIMENTAL APPROACH

To date most of the past work which attempts to identify radicals in decomposed secondary explosives has been performed in the liquid phase either in the molten phase or with the decomposed material dissolved in solution. Because the radical is rotating rapidly, only the isotropic hyperfine parameter is obtained. The intensity dependence of the lines also gives information about number and kind of nuclei in the radical. Unfortunately, assignments based solely on liquid phase data are not unambiguous. This is because different radicals with the same nuclei can have the same isotropic hyperfine splitting. Further, isotropic hyperfine splittings can depend of the dielectric constant of the solution. Much more information about the electronic structure and valence molecular orbital of the unpaired electron which can assist in identification can be obtained if a fixed radical trapped in a solid or matrix can be studied.

In principle, it is possible to obtain the anisotropic hyperfine interaction tensor and, thus, with the isotropic interaction, construct the complete molecular orbital of the unpaired electron. Also, the principle components of the g tensor can give information about energy levels of the molecule. Thus, the emphasis of this work is to attempt to study radicals fixed in the solid in order to maximize information obtained providing a positive identification. The general procedure used here has been to study the spectrum in the solid phase, dissolved in appropriate solutions, and in the molten phase of the explosive.

RESULT AND ANALYSIS

Tetryl

Because work has been done on a number of explosives, it will not be possible here to present detailed analysis for each explosive. Rather, this will be done for one case (that of tetryl) to illustrate the approach and the results will be presented for the others. In this work the EPR spectrum is studied both in the liquid phase and trapped in the solid state in order that all the parameters of the spin Hamiltonian be obtained. It is possible to construct the molecular orbital of the unpaired electron from the components of the hyperfine tensor. Such information assists in assigning the radicals

Powders of tetryl were irradiated at room temperature and dissolved in benzene and the EPR spectrum recorded. The spectrum obtained in benzene at room temperature is shown in Figure 1(a). It consists of 6 lines, each separated from each other by 10.0 Gauss. The g value at the center of the spectrum is 2.0058. The relative intensity of the six lines is 19, 67,1,.67,.19. When the modulation and the power were reduced, no further structure could be observed on the individual resonance. It was possible to simulate this spectrum on a computer by assuming a radical having one unpaired electron interacting with one nitrogen nucleus (I=1) and three hydrogen nuclei and assuming that the isotropic hyperfine interaction with the nitrogen and hydrogen nuclei were both 10.9 G. Figure 1(b) shows the computer generated spectrum assuming a Gaussian line shape of 4.9 Gauss width. The simulated spectrum is in excellent agreement with the experimental spectrum

In order to obtain further information about the spectrum, the EPR of fixed, but randomly oriented, radicals was measured by recording the spectrum in frozen benzene. When a molecule or radical is fixed with respect to the direction of the dc magnetic field, the anisotropic dipolar hyperfine interactions are no longer averaged to zero as in the liquid phase and the separation of the resonances from each other are dependent on the orientation of the symmetry axis of the molecule with respect to the direction of the dc magnetic field. The spectrum recorded in frozen benzene therefore consists of a superposition of spectra (weighted by the function governing the angular dependence of the splittings) arising from all possible orientations of the axis of the radical with respect to the dc magnetic field. Figure 2(a) shows the spectrum recorded on the frozen benzene. This spectrum is then the powder spectrum of the 6 line spectrum. This powder spectrum is consistent with an unpaired electron on a radical having an isotropic hyperfine interaction with 3 hydrogen nuclei and an axially symmetric anisotropic hyperfine interaction with one nitrogen nuclei. The outer lines of the spectrum in Figure 3 are separated from each other by 10.0 G and are due to the hydrogen splittings. The parallel component of the hyperfine tensor can be obtained directly from the powder spectrum shown in Figure 2. The perpendicular component cannot. As 10 G is the nitrogen isotropic hyperfine splitting determined from the liquid spectrum, for axial symmetry $A_\perp$ can be calculated from the measured A_{11} and the trace of the hyperfine tensor given by

$$A_{iso}=\frac{A_{11}+2A_\perp}{3} \qquad (1)$$

Assuming the signs of all components are the same $A_\perp$ as 1.5.

Figure 2(b) shows the spectrum obtained directly from the irradiated powders of tetryl is the same as that obtained in the frozen benzene indicating that the radical trapped in the lattice is the same as that observed in the benzene solution.

The EPR spectrum of uv-irradiated solid tetryl which was dissolved in liquid benzene is consistent with an unpaired electron having an equal hyperfine interaction with 3 hydrogen nuclei of 10.0 G and an istropic interaction with

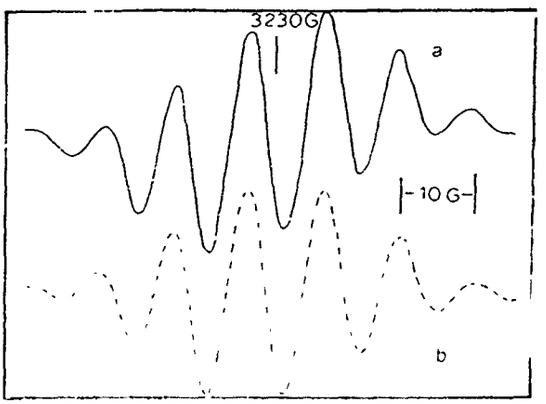

Fig. 1. (a) EPR spectrum of irradiated powders of tetryl dissolved in benzene and recorded at room temperature; (b) Computer simulated spectrum assuming the signs of all the tensor components are the same

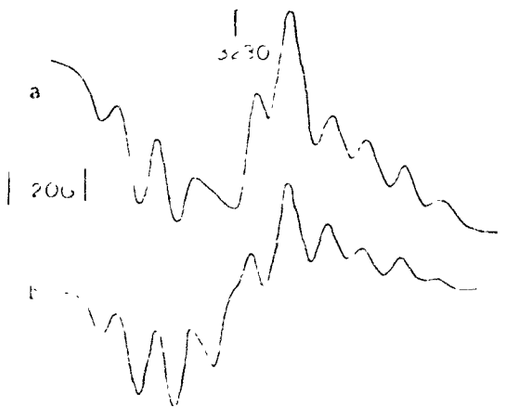

Fig 2 (a) EPR of irradiated tetryl in frozen benzene; (b) Directly from irradiated fine powders of tetryl

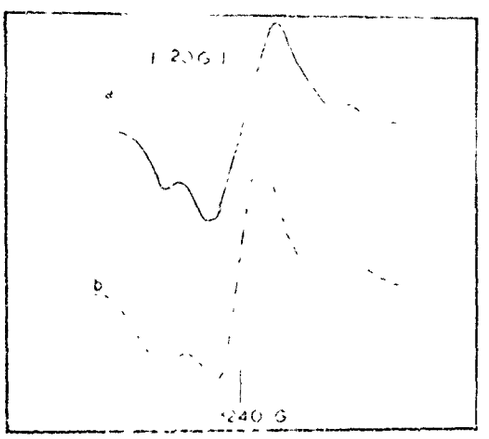

Fig 3 (a) EPR spectrum of fine powders of unirradiated TNT; (b) Computer simulation of the powder spectrum

one nitrogen nuclei also of 10.0 G. The principal components of the nitrogen hyperfine tensor are obtained from the powder pattern of the fixed radicals in the frozen benzene and are A_{11}=27.0G and $A_{\perp}$ =1.5 G. In the frozen spectrum the hydrogen splitting is 10.0 G as in the liquid phase. Similar g and A tensor components are obtained from the spectrum obtained directly from the irradiated powders.

The principal components of the nitrogen tensor are in accord with those expected for an unpaired electron localized on an NO group. For example, the nitrogen hyperfine tensor components of di-t-butyl nitroxide are $A_{\perp}$ =6.3 G and A_{11}=32.0 G quite close to those observed here (6). Generally, for an unpaired electron localized on an NO group, the nitrogen hyperfine tensor is axial and $A_{\perp}$ is small because the unpaired electron is localized mostly in a P type orbital made up of oxygen p and nitrogen p atomic orbitals oriented perpendicular to the N-O axis. Since there are nodes in the plane of the N-O axis, the components of the hyperfine tensor parallel to the molecular axis will be small, in this case, the perpendicular to the p orbitals. The isotropic splitting of 10.0 g is also consistent with that for an NO group on a benzene ring. For example, the average nitrogen isotropic hyperfine splitting in different solutions is 9.1 G for the C_6H_5NO. The observation of the equal interactions with the three hydrogen nuclei indicates that the NO is formed on the CH_3NNO_2 group of the tetryl molecule. In other words, the radical is assigned to $C_6(NO_2)_3H_2(CH_3)NO$.

Further support for this assignment comes from similarity of the measured EPR parameters to those measured in such radicals as 2,4,6 tri-t-butyl nitrosobenzene and 2,3,5,6 tetra methylphenylmethylnitroxide also observed by EPR dissolved in benzene which have analogous structures as the radical proposed here (8).

Nitrotoluenes

The same experimental approach has been used to identify radicals in 4,6 DNT, 2,4,6 TNT, and 3,4,5 TNT. Figure 3a shows the spectrum obtained in powders of 2,4,6 TNT. In Figure 3b is a computer-generated spectrum assuming a Gaussian line of width 7.0 G and spin Hamiltonian parameters $A_{\perp}$ = 4.0G, A_{11}=27.0G, g_{11}=2.0023, and $g_{\perp}$=.2007.

When the decomposed TNT is dissolved in benzene, a spectrum with the same spin Hamiltonian parameters is obtained, but a further hyperfine interaction with five equivalent hydrogen nuclei is observed. Spectra having the same parameters were also observed when 3,4,5 TNT and 3,5 DNT were dissolved in benzene after decomposition. The spectra are assigned to a radical having an unpaired electron localized on an NO group formed by the removal of an 0^+ from the NO_2 group of TNT. An irreversible decrease of the isotropic hyperfine splitting with the nitrogen nucleus was observed with increasing temperature in the molten phase of TNT.

The radicals in TNT are assigned to $C_6H_2(CH_3)(NO_2)_2NOX$, where X is unknown but could be an H atom or electron. Table 1 summarizes the results for the various nitrotoluenes studied.

TABLE 1

Spin Hamiltonian Parameters of Nitroso Radicals in Nitrotoluenes Obtained from Frozen Benzene Solutions of the Irradiated Material

	Hydrogen		Nitrogen				
	A_h	A_n (Gauss)	A_{11}	$A_{\perp}$	g_{11}	$g_{\perp}$	Radical
4,6 DNT	2.5	10.0	25.0	2.5	2.002	2.006	$C_6H_3(CH_3)(NO_2)NOX$
2,4,6 TNT	2.5	10.0	25.5	2.25	2.003	2.007	$C_6H_3(CH_3)(NO_2)_2NOX$
3,4,5 TNT	2.5	10.0	24.0	3.0	2.002	2.006	$C_6H_1(CH_3)(NO_2)_2NOX$
Dichloro TNT		10.0					$C_6Cl_2(CH_3)(NO_2)NOX$

X -> Electron, H Atom

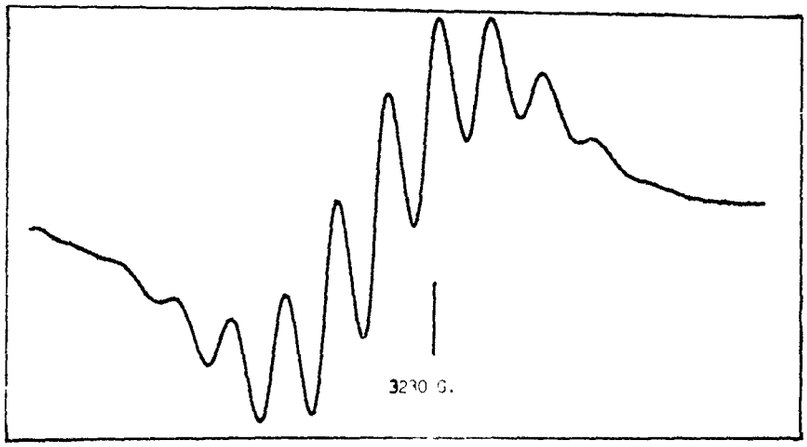

Fig. 4. EPR Spectrim of UV-Irradiated DATB and TNA Dissolved in Benzene

Trinitroanilines

Powders of uv-irradiated trinitroaniline (TNA, picramide), diaminotrinitrobenzene (DATB) and triaminotrinitrobenzene (TATB) show a broad singlet at g_e, having little structure to assist in identification. When irradiated TNA and DATB are dissolved in benzene, the spectrum shown if Figure 4 is obtained. A reasonable computer simulation of this spectrum can be made assuming an unpaired electron interacting equally with 3 nitrogen nuclei having A_n=3.0 G and 3 hydrogen nuclei with A_H=6.0 G. When account is taken of solution dielectric constant, these values are consistent with EPR observations of the RH-anion, R being $C_6H_2(NO_2)_3$. Since this assignment is based only on a computer simulation (which is not unique) of a solution spectrum, the assignment is only suggestive at most, and further work is needed.

REFERENCES

1. R.N. Rogers, Thermochimica Acta *11*, 131 (1975).
2. E.G. Janzen, J. Am. Chem. Soc. *87*, 1356 (1965).
3. R.M. Guidry and L.P. Davis, Thermochimica Acta *32*,1 (1979).
4. L. Avremi, H.J. Jackson, and M.S. Kirshenbaum, Picatinny Arsenal Technical Report 4602 (1973).
5. M.H. Miles, K.L. DeVries, A.D. Britt, and W.B. Moniz, Propellants, Explosives and Pyrotechnics *8*, 49 (1983).
6. L.J. Libertini and O.H. Griffith, J. Chem. Phys. *53*, 1359 (1970).
7. G.A. Russell, E.J. Geels, F.J. Semetowski, K.Y. Chang, J. Reynolds, and G. Knapp, J. Am. Chem. Soc. *89*, 3821 (1967).
8. S. Terable and R. Konaka, J. Chem. Soc. (Perkings II) 270 (1973).

Session IX
Specialist Sessions

EQUATION OF STATE

MOLECULAR DYNAMICS

SHOCK-TO-DETONATION TRANSITION/ DEFLAGRATION-TO-DETONATION TRANSITION

COMPOSITE AND NONIDEAL EXPLOSIVES

Session IX
Specialist Session
EQUATION OF STATE

Co-chairmen: Sigmund J. Jacobs
Naval Surface Weapons Center
Wildon Fickett
Los Alamos National Laboratory

AN EXTENSIVE APPLICATION OF WCA4 EQUATION OF STATE FOR EXPLOSIVES

R. Chirat and J. Baute
Commissariat à l'Energie Atomique
B. P. No. 17 – 77181 Courtry (France)

We present an extensive application of our WCA4 equation of state based on the WCA mixture theory of dense fluid to evaluate the explosive performances. A large set of partially or entirely CHON explosives (22 compositions) are studied at Chapman-Jouguet (CJ) conditions and are in good agreement with experiment. For CJ isentropes of two compositions X2 (made of HMX) and T2 (highly carboned with TATB), we compare WCA4 results with experimental data obtained by two different methods. To explore the vicinity of the CJ isentrope, several WCA4 second shock Hugoniots are calculated from initial states (0.5 GPa to 50 GPa). At last, we calculate thermodynamical WCA4 values which can simulate the reaction zone.

INTRODUCTION

After the first Fickett's attempt (1962) to determine an equation of state (EOS) for detonation products by statistical mechanics (LJD (1)), it is only recently that many other EOS appeared, they are based on superposition of solid and fluid theory (JCZ (2)) or fluid theory (WCA (3, 4, 7), Ross' variational (5, 6)). In this paper, we use extensively the WCA4 version of our EOS (4). We recall in part I the way of building this EOS. In part II, a lot of WCA4 Chapman-Jouguet (CJ) results are compared with experiments, some typical values are summed up. Part III treats of CJ isentrope. The two measurement methods used in our laboratory are compared for two compositions: X2 (made of HMX) and T2 (highly carboned explosive with TATB). A critical analysis of experiments is reviewed before a comparison with our calculations. T2 is dealt with graphite or diamond assumptions for the solid phase. In part IV, from several points on the CJ isentrope of T2 explosive, the second shock Hugoniots are evaluated to know the vicinity of the CJ isentrope. Part V consists in an approach of the reaction zone.

I. STRUCTURE OF THE WCA4 EOS

With a statistical mechanics EOS (1-7) it is logical that theoretical results verify:

—results of numerical experiments (Monte-Carlo (MC) or molecular dynamics) for pure fluid and binary mixture.

—the behaviour of each component alone (its Hugoniot for example).

—CJ results of explosives of various compositions and loading densities; the EOS must agree with experiments outside the CJ zone (CJ isentrope,).

We recall rapidly the WCA4 structure (4). The detonation products of CHNO explosive include two phases (solid for carbon and fluid for other species mixture) assumed at P-T equilibrium. The total energy is the sum of an perfect gas energy and a configurational energy. The former is calculated with Mader's fits (8) of the 1 atm. isobar, in complement with Nellis's (9) for diamond. The carbon EOS is of Cowan-Fickett type for graphite or diamond (10). The configurational energy of the fluid phase is deduced from the Weeks-Chandler-Andersen (WCA) theory (11), expressed with Verlet-Weis formulae (12) and extended to mixture by Lee-Levesque (13). Each component is described with an EXP-6 potential. The mixing rules are classical (4). There is no change for every parameter of potentials (H_2O,N_2,CH_4,O_2,H_2, NH_3,NO,CO,CO_2) with those of Table 1 in (4).

We can obtain good agreement with the recent experimental CO Hugoniot (9). With a thermochemical code (14), the complete equilibrium is achieved when the Gibbs enthalpy is minimum at fixed P-T. We have no other parameters to evaluate explosive performances.

II. CJ RESULTS FOR VARIOUS COMPOSITIONS

The CJ point of an explosive is reached at the minimum of detonation velocity along the reactive Hugoniot. The studied explosive is characterized by its chemical formula, formation energy E_o, loading density ϱ_o; most values are taken from (15). We choose a great deal of compositions.

Table 1 collects all CJ results on partially or entirely CHNO explosives. At normal ϱ_o of solid TNT, HNS, TATB, DATB, TETRYL, COMP B, the values can be found in (10) with graphite or diamond assumptions (in (10), the fit of the 1 atm. isobar for diamond is made as in (5b), different from (9)). In Table 1, graphite solid carbon is admitted to exist in detonation products if C element is present in the chemical formula.

A previous WCA version was verified (3b) to agree with the nearly linear Kamlet's curves D_{CJ} (ϱ_o) and P_{CJ} (ϱ_o^2). To be able to interpolate D_{CJ} and P_{CJ} with these laws, we give two ϱ_o values in Table 1. If several measurements of detonation velocities are considered from various laboratories and different methods, there is a data scattering of 1% (even 2%). The scattering for pressure reaches 10%.

The BKW EOS is an almost empirical EOS to evaluate CJ performances, only the RDX values of (β, x) (15) are coherent to agree with the most numerous (CO_2, H_2O, N_2) components of detonation products; so, only the BKW previsions with RDX-(β, x) values are discussed here. In opposite of BKW giving too low temperatures, the EOS based on statistical mechanics show a rather good agreement with experiment. In a general way, WCA4 CJ pressures are always higher than those given by LJD or JCZ; WCA4 is generally closer to experiment. An exception must be noticed for HNB which is a very high explosive. WCA4 finds only CO_2 and N_2 in its detonation products, in fact, the only experimental CO_2 points were obtained in 1962 (16) and re-analysed in 1980 (17) So, there is a lack of a recent experimental Hugoniot to fit the CO_2 EXP-6 potential parameters. Ree (5a) obtains a rather good agreement for HNB but he changes lightly his CO_2 parameters. This modification varies much the CJ result with WCA4. Then, we will await new CO_2 experiments to consider again the HNB problem.

Now we sum up typical values of CJ point quantities for a large range of ϱ_o (1 to 1.9 g/cm^3). We refer to appendix 1 to define Γ_{CJ}, γ_{CJ}, Z_F, ϱ^*, T^*, η, C_v.

The Γ_{CJ} value varies from 2.5 to 3.4. For this same ϱ_o zone, γ_{CJ} remains approximately constant (1.1 to 1.2). C_v varies between 1.5 and 2.5 kJ/kg. Considering the total number of molecules (with solid carbon when it is present), the molar heat capacity at constant volume ranges from 37.5 to 70 J/mol (i.e. 4.5 R to 8.5 R where R is the perfect gas constant).

First, we study the higher ϱ_o area (1.7 to 1.9 g/cm^3); Z_F lies between 12 and 13 for low carbon content explosives (such as HMX, RDX) and between 14 and 15 for high carbon content explosives (such as TATB).

The packing fraction at the CJ point η_{CJ} is approximately 0.55 for low carboned explosives and 0.60 for the others. A hard sphere fluid becomes solid when η exceeds 0.49; a real fluid treated with WCA theory changes into a solid phase when η is over 0.56 to 0.63 according to some authors (18).

Then, for the lower ϱ_o area (about 1.0 g/cm^3), we find Z_F between 4.0 and 4.5 and η_{CJ} between 0.35 and 0.4.

III. CJ ISENTROPES

In order to build the EOS of an explosive, we must calculate values far from CJ point conditions. Moreover, in hydrodynamic codes, the EOS of an explosive is often approximated by a Taylor expansion to a first order about the CJ isentrope; this EOS is Mie- Grüneisen type (e.g. modified Wilkins EOS (19)), JWL EOS (20, 21).

Because of a lack of detailed published experiments on CJ isentrope, we study two compositions of our laboratory, described in appendix 1.

Two measurement methods are used for the isentropic curve near the CJ point; we discuss their respective advantages and drawbacks.

TABLE 1

CJ results (D in m/s, P in GPa, T in K, E_o in kcal/mol)

CJ STATE OF CN, CNO, HNO, HN EXPLOSIVES				
Explosive Chemical formula Loading density Energy of formation		Experiment (15)	WCA4	Elements
2, 4, 6 - Triazido -s-triazine	D	5600	6131	
C_3N_{12}	P		10.4	CN
ϱ_o = 1.15				
E_o = 234.6	T		4345	
TNM	D	6360	6263	
CN_4O_4	P	15.9	15.3	CNO
ϱ_o = 1.64	T	2800	2409	
E_o = 21.6				
TNTAB	D	8576	8541	
$C_6N_{12}O_6$	P		35.6	CNO
ϱ_o = 1.74	T		5620	
E_o = 290.6				
HNB	D	≃ 9300	8340	
$C_6N_6O_{12}$	P		35.8	CNO
ϱ_o = 1.973	T		5389	
E_o = −2.54				
BTF	D	8485	8442	
$C_6N_6O_6$	P		37.4	CNO
ϱ_o = 1.859	T		5600	
E_o = 157.8				
Hydrazine azide	D	≃ 6000	6529	
H_5N_5	P		10.1	HN
ϱ_o = 1.0	T		2307	
E_o = 55				
Hydrazine nitrate	D	8691	8190	
$H_5N_3O_3$	P		27.8	HNO
ϱ_o = 1.626	T		2442	
E_o = −47.7				
Hydrazine /21 azide /79 nitrate	D	8600	8390	
$H_{8.154}N_{4.577}O_3$	P		24.9	HNO
ϱ_o = 1.4418				
E_o = −33.37	T	2900	2720	
Hydrazine /70 azide /30 nitrate	D	8025	7760	
$H_{32.685}N_{16.8430}O_3$	P		15.8	HNO
ϱ_o = 1.14				
E_o = 78.06	T	2180	2128	
Ammonium nitrate	D	4500	4746	
$H_4N_2O_3$	P		5.42	HNO
ϱ_o = 1.05	T		1745	
E_o = −78.1				

CJ STATE OF CHNO EXPLOSIVES				
Explosive Chemical formula Formation Energy E_o	ϱ_o (g/cm^3)	D P T	Experiment (15)	WCA4
TNT $C_7H_5N_3O_6$ E_o = −1.44	1.061	D P T	5254 11.0	5312 7.7 ≃3333
HNS $C_{14}H_6N_6O_{12}$ E_o = 44.22	1	D P T		5188 6.75 3604
TATB $C_6H_6N_6O_6$	1.895	D P T	7860 31.5	8085 31.4 2979
E_o = −17	1	D P T		5114 6.8 3078
DATB $C_6H_5N_5O_6$ E_o = 12	1	D P T		5386 7.3 3407
TETRYL $C_7H_5N_5O_8$ E_o = 8	1	D P T		5731 8.0 3552
NM CH_3NO_2	1.128	D P T	6290 14.1 3380	6660 12.5 3388
E_o = −14.92	0.9	D P T		5681 7.5 3464
NQ $CH_4N_4O_2$	1.629	D P T	7980	8013 24.8
E_o = −11.1	1	D P T	5460	5480 7.3 2672
RDX $C_3H_6N_6O_6$	1.80	D P T	8754 34.7	8835 35.6 4074
E_o = 33.97	1	D P T	5981	6064 9.5 4529
HMX $C_4H_8N_8O_8$	1.90	D P T	9100 39.3	9070 41.0 ≃4150
E_o = 43.46	1	D P T		6056 9.5 4510
PETN $C_5H_8N_4O_{12}$	1.77	D P T	8300 33.5 3400	8416 31.5 4349
E_o = −95.5	1	D P T	5480 8.7	5494 8.0 4899
NG $C_3H_5N_3O_9$ E_o = −66.52	1.59	D P T	7580 3470 4000 (1a)	7447 22.2 ≃4870
	1	D P T		5184 7.23 4944

These methods are: the velocity of a thin flyer obtained with Laser Doppler Interferometry (LDI) and the impedance matching method.

1. Velocity of a Thin Flyer Obtained with LDI

This measurement method is a generalization of that of Boïko et al. (22), only explained for inert materials. A thick plate is projected onto the considered explosive, the detonation transferring velocity to the thin flyer. The LDI (23) measures the free surface velocity U_s of this flyer within 10 m/s. In Fig. 1, the set-up used is shown and the propagation of releases and shocks is indicated. Between the two characteristics MN and PQ (Fig. 1A), the LDI measured velocities of the flyer can be easily connected to points situated on the detonation products isentrope from P_D-U_D. The aim of the method is

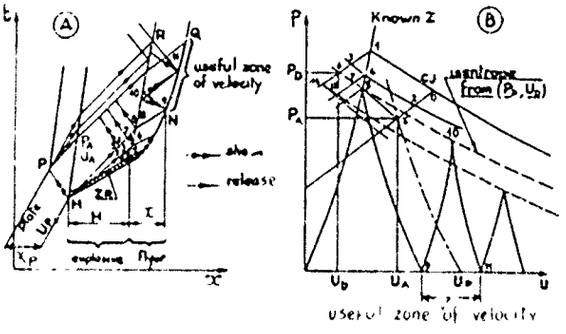

Fig. 1 Set-up and method of the velocity of a thin flyer obtained with LDI

to (Fig. 1b) obtain a maximum of to and-fros in the useful zone of velocity (Fig. 1B). So in the original Boïko's method, the flyer must be very thin and have a high impedance. Attention must be paid to ensure (Fig. 1A) that the release fan (PQ, PR) from the rear of the plate does not interfere with the useful zone; otherwise, the LDI measured velocities will correspond to other isentropes which are lower than the P_D-U_D isentrope. This last troublesome phenomenon can be delayed if we use a larger thickness X_p for the plate.

In this LDI method, values for P-u are calculated at the explosive-flyer interface with a code based on the characteristics going back in time t (23). Only the measured profile U_s (t) of the flyer free surface is used.

2. Impedance Matching Method (Fig. 2)

With the help of the shock velocity in several materials of known impedance, some points (pressure P - material velocity u) are deduced on the detonation products isentrope. With solid or liquid materials (uranium, iron, aluminum, magnesium, water), shock transition is observed before and after the considered material by the luminous track produced in plexiglas. Several thicknesses χ (Fig. 2B) were investigated; the shock velocity must be considered for χ near zero.

To obtain P-u points at low pressures ($P \leqslant 10$ GPa) on the isentrope, gaseous materials (such as argon) are used with different initial pressures (between 800 and 10^{-2} atm); the argon becomes luminous under shock and the tracks are photographed with a streak camera (24). A critical view of this analysis leads us to conclude that:

—if the influence of the explosive reaction zone is neglected, then the pressure profile versus distance in the explosive has a triangular form; the CJ pressure occurs just before the Taylor release. The shock transmitted to the adjacent material decreases continuously; so, the velocity D_0 of this shock must be considered when χ equals zero.

—in fact, the explosive reaction zone always exists (Fig. 3). Let a be the thickness of the reaction zone. The front of the pressure profile must be completed with a strong gradient (going from the Von Neuman peak to the CJ point). Thus the reaction zone perturbs the transmitted shock on a distance b.

With such hypotheses, result analysis of the free surface velocity U_s of flyer would lead to

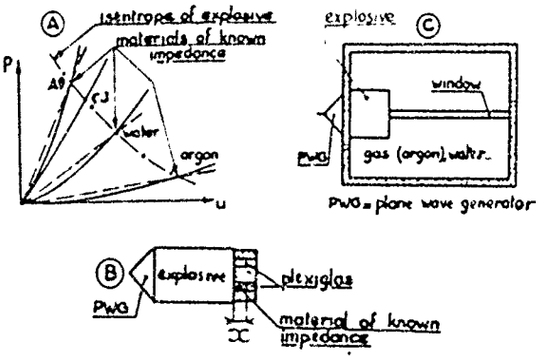

Fig. 2 Impedance matching method (set-up for solid (B) and gaseous (C) material)

choose U_{som} for the experimental value instead of U_{sot} (Fig. 3B). With a finer model (25) than Duff and Houston's one (26), the spread b of the reaction zone appears larger at low pressures.

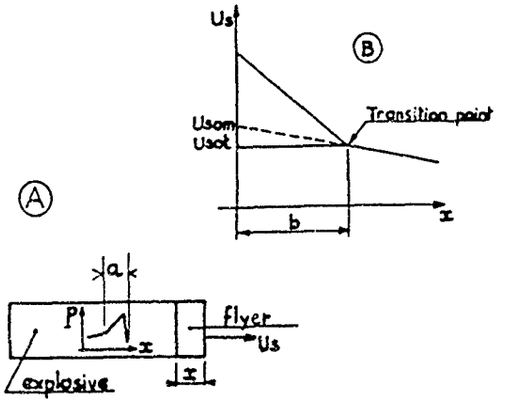

Fig. 3. Influence of the reaction zone in the impedance matching method

For measured points with solid or liquid reference materials, reaction zone influence can be neglected. The argon points are much more difficult to analyse. It is necessary to have a good EOS for argon and to consider the luminous track analysis.

Two models for argon EOS have been used. A first model, due to Pinegre, Aveille et al. (PA) (24) is build in three steps:

i) a perfect gas,

ii) a perfect gas with ionization (Saha EOS),

iii) a dense fluid EOS (fitting of MC results with Lennard-Jones potential (27)) and a simplified ionization

A second model, due to Zerah and Jevais (ZJ) (28) consists in an ionic thermal contribution based on the CRIS model (29) for the fluid phase and an electronic thermal contribution based on the self consistent field model ("INFERNO" by Liberman (30)). The CRIS model is taken from PANDA code (31).

Now we present two analysis methods of luminous track in argon. With X2 composition, the space-time track is fitted with a least squares parabola over 10 mm; to get some information about reaction zone influence, the velocity in argon is obtained by the tangent at 3 mm from explosive; another series of values considers the velocity as the slope at 0 mm. With T2 composition, a more accurate analysis (24) takes account of the Thouvenin's model (25).

3. Difficulties of Interpretation of Experimental Results

The experimental P-u results and analysis are due to (24) with PA model for argon, (32) with ZJ model, (23) with LDI method. The three steps of PA model lead to conclude that ionization contribution is more important than real gas contribution below 2 GPa; above it is the opposite conclusion.

Analysis at 0 mm gives a more "energetic" explosive than analysis at 3 mm; this is to be expected if the pressure gradient influence between the Von Neuman peak and the CJ point is taken into account. The thickness of the reaction zone is about 0.3 to 0.4 mm for X2 whereas the T2 reaction zone is about 1.5 mm thick. We verify a greater discrepancy between the 3 and 0 mm analysis for X2 when the pressure decreases.

A perfect continuity between results measured with argon or with solids and liquids is difficult to reach.

Below 0.1 GPa for CJ isentrope, WCA4 calculations can be less accurate because the parameters of intermolecular potentials become less valid: each component is fitted on Hugoniot results ($P \geq 0.1$ GPa). However, it does not seem necessary to consider a new phenomenon for detonation products such as ionization because of low temperatures ($T \leq 1800$ K at $P \leq 1$ GPa).

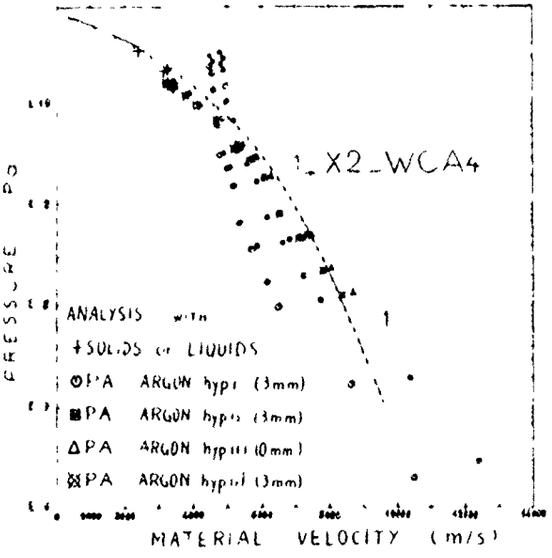

Fig 4 CJ isentrope for X2 composition

With the LDI method, it is difficult to be sure that the rear release fan (Fig. 1) does not invalidate the low pressure zones; however this method should be less perturbed by the reaction zone and can obtain several experimental points in one shot.

4. X2 Results

X2 is principally made of HMX. On Fig. 4, we plot all data obtained from impedance matching method when using solid or liquid material and PA argon. We can see the influence of the various improvements of PA EOS (i to iii) and of the position of luminous track at 0 or 3 mm. The P-u analysis appears more and more energetic when we consider the assumptions from i to iii.

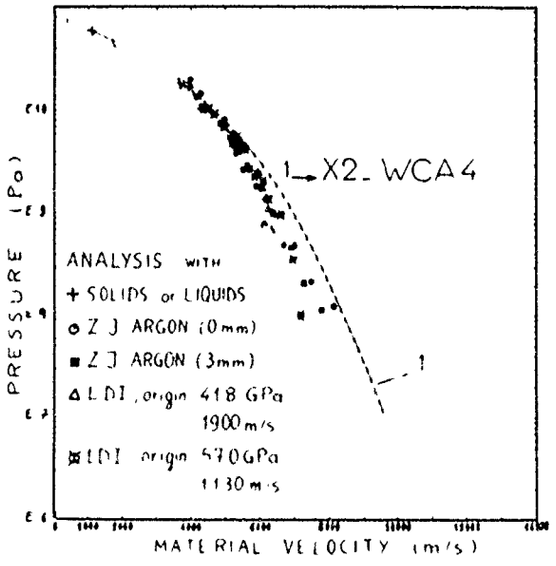

Fig. 5 CJ isentrope for X2 composition

Fig. 5 shows the data found from LDI method and from impedance matching method when using solids or liquids or ZJ argon. There is a good continuity between experimental data reached from solid and ZJ argon. The distance of points at 0 and 3 mm in using ZJ argon is similar with this one using PA argon. The LDI results are situated on two experimental isentropes respectively from points (P = 41.8 GPa, u = 1900 m/s) and (P =57.0 GPa, u= 1130 m/s) which are not very far from the CJ point. Above 2 GPa, LDI results agree with those of ZJ EOS. Below 0 5 GPa, LDI results would not be significant because of the release fan (Fig. 1).

5. T2 Results

The T2 explosive is a high carboned explosive. Two theoretical WCA4 CJ isentropes are drawn (Fig. 6) with assumptions of graphite or diamond solid. After a comparison with experimental D_{CJ} and P_{CJ}, these both WCA4 simulations are admitted as extreme hypotheses (10). The experimental curves issued from PA and ZJ EOS cross over about 2 GPa, ZJ being more energetic at high pressures. LDI results are slightly above the two previous series. A hump exists between solid and argon points. Below 2 GPa, diamond WCA4 agrees better with experience. The CJ isentrope drawn in the P-T Grover's diagram of carbon (33) goes from the metastable graphite zone (or diamond zone) to the metastable diamond phase (or graphite zone) when pressure decreases.

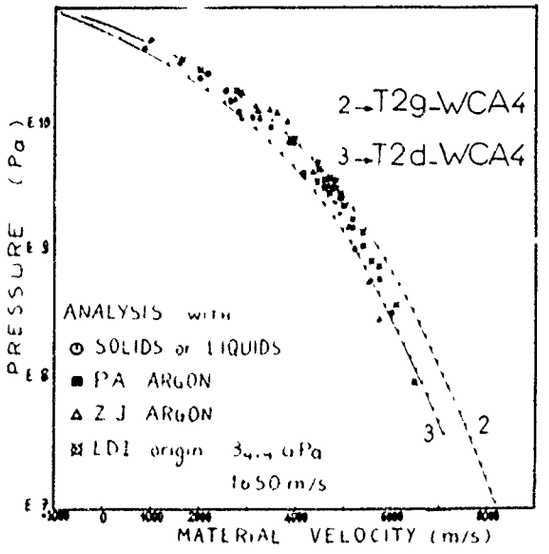

Fig. 6. CJ isentrope for T2 composition

6. Shape of Γ(P) and G(P) on CJ Isentrope

If we simulate locally the influence of detonation products with a perfect gas EOS, Γ(V) is very useful. Moreover, a Mie-Grüneisen EOS can be improved by including G(V) rather than G constant.

Γ(P) and G(P) are deduced with equations (A.2) and (A.3) from a fitting of the triplets P, V, T along CJ isentrope. For X2 T2g T2d, CJ points are situated beyond the maximum (Fig. 7) of Γ(P). For large volumes, WCA4 EOS

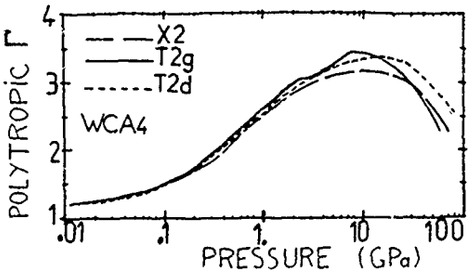

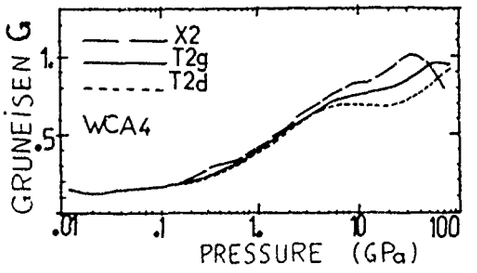

Fig. 7 and 8. Γ(P) and G(P) along CJ isentrope

approaches the perfect gas; so we find $\Gamma = \gamma$ and $\Gamma = G + 1$. The CJ point of X2 is not situated (Fig. 8) in the same place than T2g and T2d on the G(P).

Jacobs (34) indicates with another EOS (later JCZ EOS (2)) that in decreasing G can be associated with solidification tendancy of the fluid mixture. Our high η_{CJ} values near the CJ point (appendix 1) confirm this idea.

IV. T2 SECOND SHOCK HUGONIOTS

To explore the EOS surface, several second shock Hugoniots are calculated with WCA4 from points of the CJ isentrope. These evaluations are made with T2 composition in assumptions of graphite or diamond for carbon. The initial points are CJ point and points with pressures close to 50 for T2g (40 for T2d), 10, 5, 0.5 GPa. This study contributes to understand the supracompression of high explosive detonation products ((35) for example).

In Fig. 9, the higher part of P-V diagrams are shown for T2g. The WCA4 second shock Hugoniots are very close to WCA4 CJ isentrope when initial pressure is above 5 GPa; only the curve of 0.5 GPa origin diverges. Because of the definition equation (A.2) of Γ and the very narrow network of second shock Hugoniots, Γ have very similar values to those on Fig. 7. For the 0.5 GPa origin curve, Γ(P) is lower than Γ(P) calculated along CJ isentrope.

The same WCA4 results are shown (Fig. 10) in the (P-u) diagram. The set of curves is very tight, but the 0.5 GPa origin curve is very below the others.

The same WCA4 second shock Hugoniots are drawn (Fig. 11) in the T-P diagram. To reach a fixed pressure, we verify the temperature is all the higher as the origin is lower. We must be suspicious of the validity of WCA4 beyond 6000 K because of the fit of the 1 atm. isobar and beyond 60 GPa because of carbon EOS.

The shapes of G(P) along these second Hugoniots are grouped in Fig. 12. Because of the maximum of G, we can conclude that as pressure increases, the thermal contribution in WCA4 becomes less important than the potential contribution. The same remark can be made on CJ isentrope (Fig. 8).

The T2d results show similar shapes for all the preceeding curves.

V. EXPLORATION OF THE REACTION ZONE

To give orders of magnitude in the reaction zone, we calculate reactive Hugoniots with only a fraction τ of chemical energy laid in the Hugoniot equation. We call these curves: partially reactive Hugoniots. To be consistent with the origin on the energy of our equation, we define the chemical energy Ech as the difference between the formation energy E_o of initial explosive and the energy E_o^{DP} of detonation products at ($P = 1$ atm, $V = 1/\varrho_o$). With T2g, we find:

$$E_o = -0.22635 \text{ MJ/kg},$$

$$E_o^{DP} = -5.2742 \text{ MJ/kg},$$

$$\text{thus } Ech = +5.0479 \text{ MJ/kg}.$$

The T2g WCA4 partially reactive Hugoniots are plotted in Fig. 13 for the various chemical energy rates τ. A CJ point can be determined as in Part II on each curve. To have an idea in the initiation problems of detonation, we draw also in Fig. 13 the experimental results obtained for shocked "undetonated" solid explosive; in fact, the explosive probably partially reacts. On T2 composition, measurements give:

$D = 1857 + 3.1\,u$ (manganin gage) $\quad 0 \leqslant P \leqslant 5$ GPa

$D = 2118 + 2.305\,u$ (corner method (36)) $\quad 9 \leqslant P \leqslant 25$ GPa

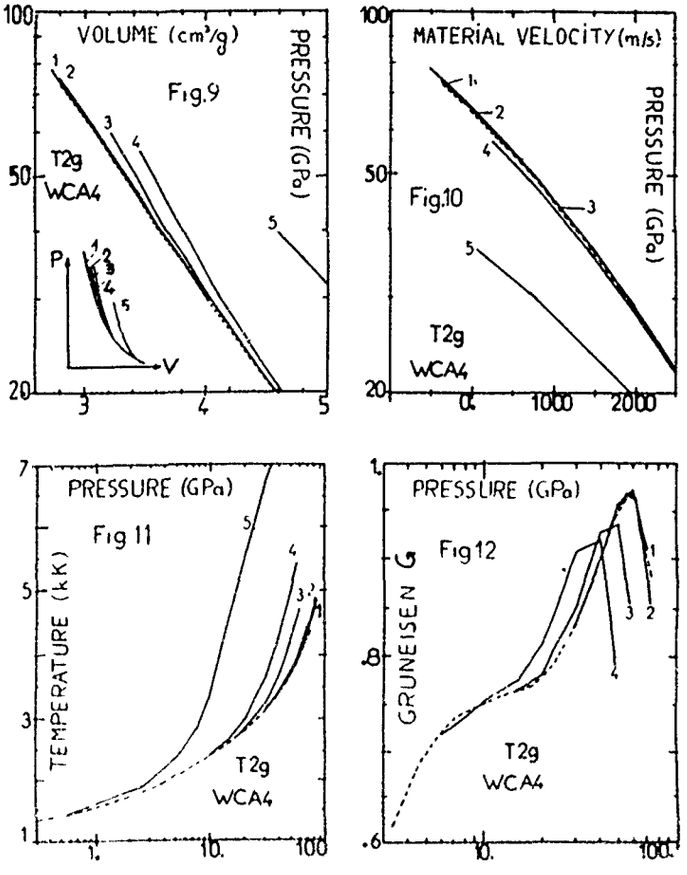

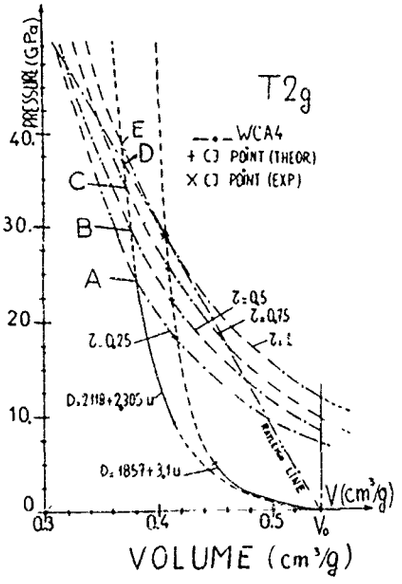

Fig. 13. Partially reactive and "inert" Hugoniots

Fig. 9, 10, 11, 12: - - - - - CJ isentrope; 2nd Hugoniot from ~50 GPa (1), CJ point (2), ~10 GPa (3), ~ 5 GPa (4), ~0.5 GPa (5)

We extrapolate these "inert" Hugoniots, which intersect the previous network of Hugoniots (Fig. 13) in labeled points (A to E). For each point, thermodynamical values are grouped in Table 2; the notations are explained in appendix 1.

CONCLUSION

The present paper uses very extensively our WCA4 EOS. At first, CJ points are evaluated for a large set of partially or entirely CHNO explosives. Except for HNB, we obtain a good agreement with experiment; HNB will be probably well evaluated when new experimental CO_2 Hugoniot data will be available. Then, we study CJ isentropes of two compositions of our laboratory X2 (near HMX) and T2 (near TATB). Two measurement methods (impedance matching velocity of a thin flyer obtained with LDI) give complementary results to know the CJ isentrope; there is a large sensibility of the points analysis with the choice of an argon EOS as reference material; WCA4 isentrope passes through experimental points. Theoretical WCA4 second shock Hugoniots from points on CJ isentrope stay in a close vicinity of this curve in (P-V) and (P-u) diagrams except if origin point is below 1 GPa. An evaluation of thermodynamical values is given in the reaction zone with our EOS.

ACKNOWLEDGMENTS

We shall thank G. Pittion-Rossillon with whom we began this work and found the CJ results of Table 1.

TABLE 2

Simulation of values in reaction zone with WCA4 EOS for T2 composition (T2g hypothesis)

Point (Fig. 13)	CJ τ=1	CJ τ=0.75	CJ τ=0.50	CJ τ=0.25	A τ=0.25	B τ=0.50	C τ=0.75	D	E τ=1
P (kbar)	290	257	222	179	245	300	345	370	390
D (m/s)	7935	7542	7103	6537	6688	7262	7703		8117
U (m/s)	1982	1844	1690	1485	1983	2236	2424		2600
Γ	3.007	3.085	3.194	3.381		2.894	2.807	2.775	2.775
ϱ (g/cm^3)	2.462	2.445	2.424	2.391	2.626	2.669	2.696	2.703	2.718
T (K)	3088	2421	1735	970	1137	1943	2669	31?4	3434
C_v (kJ/kg/K)	2.13	2.27	2.09	1.77			2.28	2.10	2.03
γ	1.149	1.114	1.104	1.113			1.129	1.151	1.169
N_F (moles/kg)	29.3	29.0	28.9	28.9	28.9	28.9	28.9	29.1	29.2
N_c (moles/kg)	18.4	18.9	19.1	19.2	19.2	19 1	18.9	18.6	18.4
Z_F	13.1	14.9	18.1	26.3	27.8	19.7	16.4	15.0	14.3
η	0.574	0.596	0.627	0.681	0.698	0.649	0.620	0.605	0.598
ϱ^*	2.965	2.930	2.909	2.882	3.183	3.215	3.237	3.247	3.270
C_s (m/s)	5956	5693	5405	5037		5703	5993	6164	6309
C_T (m/s)	5554	5397	5153	4787			5648	5771	5841
U + C_s (m/s)	7938	7537	7096	6522		7939	8417		8909
G	0.826.	0.765	0.846	..171		0.913	0.806	0.857	0.898

REFERENCES

1. W. Fickett, (a) LANL Report 2712, (1962) (b) Phys. Fluids *6*, 997, (1963).
2. M. Cowperthwaite, W. H. Zwisler, 6th Symp. on Detonation, 162, (1976).
3. R. Chirat, G. Pittion-Rossillon, (a) J. Chem. Phys. *74*, (8) 4634, (1981); (b) Comb. and Flame *45*, 147, (1982).
4. R. Chirat, G. Pittion-Rossillon, 7th Symp. on Detonation, 703 (1981).
5. F. H. Ree, (a) in ref. (4) p. 646; (b) J Chem. Phys. *81*, 1251 (1984).
6. M. Shaw-Johnson-Holian, private communication.
7. H. Jones in ref. (4) p. 716.
8. C. Mader LANL, LA 3704 (1967).
9. W. Nellis, et al., J. Chem Phys *75*, 3055 (1981).
10. J. Baute, R. Chirat, 8th Symp. on Detonation (1985).
11. J. P. Hansen, I. R. McDonald, Theory of simple liquids, Academic Press, 1976.
12. L. Verlet, J. J. Weis, Mol. Phys. *28*, 3, (1974).
13. L. L. Lee, D. Levesque, Mol. Phys. *26*, 1351, (1973).
14. R. Chirat, G. Pittion-Rossillon, G. Guri, ETARC Code (unpublished work).
15. C. L. Mader, (a) Numerical modeling of detonation (University of California, 1979); (b) LANL, LA 2900 (1963).
16. V. N. Zubarev, G. S. Telegin, Soviet Physics, 7, 34, (1962).
17. M. Ross, F. H. Ree, J. Chem. Phys. *73*, 12, 6146, (1980).
18. F. H. Ree, J. Chem. Phys. 64, 4601, (1976).
19. J. Allan, B. Lambourn, Fourth Symposium on Detonation, p. 52.
20. H. Hornig, R. McGuire, UCID 18534, (Jan. 1980).
21. E. Lee, M. Finger, W. Collins, UCID 16189, (Jan. 1973).
22. Boiko, Andreev, Letyagin, Solovev Comb. expl. and shock waves, 7, n°3.
23. H. C. Pujols (private communication).

24. M. Pinegre, J. Aveille et al., Conf. DEA 7304, Albuquerque, (1984).

25. J. Thouvenin (internal report).

26. R. E. Duff, E. Houston, J. Chem. Phys. *23*, 1268, (1955).

27. F. H. Ree, J. Chem. Phys. *73*, 5401, (1980).

28. G. Zerah, J. R. Jevais, (private communication)

29. G. Kerley, J. Chem. Phys. *73*, 469, (1980).

30. D. Liberman, Phys. Rev. B, *20*, 4981, (1979).

31. G. Kerley, LANL LA 88.33.M.

32. G. Zerah, C. Boissiere, G. Marzin, Internal results, (1984).

33. Grover, J. Chem. Phys. *71*, 3824 (1979).

34. S. J. Jacobs, Naval Ordnance Laboratory NOLTR 68-214, (1968).

35. E. Lee, L.G. Green, Energy and Technology Review (LLNL) p. 24, (1984).

36. R. Droux, C. Mouchel, Symposium HDP, (Paris Aug. 1978).

APPENDIX 1: X2 and T2 Compositions

Initial data introduced in ETARC code to realize calculations are given in Table A1.

X2 and T2 are respectively HMX/binder/94/6 and TATB/binder/97/3 compositions.

The WCA4 results at the CJ point are grouped in Tables A2. Only T2 is studied with graphite (T2g) or diamond (T2d) in the solid phase.

More explanations are given in (4) for notations. Let:

$(\sigma_{ii}\varepsilon_{ii}\alpha_{ii})$ be the EXP-6 potential parameters between two species i-i.

d_{ii}, the WCA diameter between two species i-i,

N_i, the number of moles of species i,

N_F, the number of moles for the fluid phase,

N_c, the number of moles of solid carbon

N_T, the total number of moles of all components

V_F, the volume of the fluid phase (i.e. $V_F = V_{total} - V_{solid\ carbon}$)

then:

$$\eta_{CJ} = \frac{\pi}{6V_F}\sum_i N_i d_{ii}^3 = \text{packing fraction}$$

$$\varrho^*_{CJ} = \frac{\sum_i N_i\,\sigma_{ii}^3}{V_F} = \text{reduced density}$$

T^*_{ii} = reduced temperature for species i

$$= \frac{kT}{\varepsilon_{ii}}$$

Z_F = compressibility factor of the fluid phase $= \dfrac{P \cdot V_F}{N_F\,kT}$

$$\gamma = \frac{C_P}{C_V} = \frac{(\partial \ell n P/\partial \ell n V)_s}{(\partial \ell n P/\partial \ell n V)_T} \qquad (A.1)$$

$$\Gamma = \text{polytropic gamma} = -\left.\frac{d\ell n\,P}{d\ell n V}\right)_s \qquad (A.2)$$

G = Grüneisen coefficient

$$= V\left.\frac{\partial P}{\partial E}\right)_V = -\left.\frac{\partial \ell n\,T}{\partial \ell n V}\right)_s \qquad (A.3)$$

$$C_V = \left.\frac{\partial E}{\partial T}\right)_V$$

$$C_S^2 = (\text{adiabatic sound velocity})^2 = V^2\left.\frac{\partial P}{\partial V}\right)_S$$

$$C_T^2 = (\text{isotherm sound velocity})^2 = V^2\left.\frac{\partial P}{\partial V}\right)_T$$

TABLE A1
Data for WCA4 Calculations

Explosive	X2	T2
Global formula	$C_{14.95}H_{27.92}N_{25.82}O_{26.84}$	$C_{24.46}H_{24.67}N_{22.56}O_{22.875}$
Initial density ϱ_0 (g/cm^3)	1.835	1.847
Combustion energy in oxygen (cal/g)	2420	~3000
Formation energy E_0 (J/kg)	+ 0.64619 10^6	−0.22635 10^6

TABLE A2
CJ WCA4 Results

Explosive (ϱ_o g/cm^3)	P_{CJ} (GPa)	D_{CJ} (m/s)	Γ_{CJ}	T_{CJ} (K)	Z_F	η_{CJ}	ϱ^*_{CJ}	$\left(\frac{N_c}{N_T}\right)_{CJ}$
X2 ≡ X2g (1.835)	37.29	8874	2.875	4105	12.05	0.563	3.140	0.159
T2g (1.847)	29.02	7935	3.008	3087	13.10	0.574	2.964	0.385
T2d (1.847)	24.91	7630	3.318	2945	12.36	0.561	2.820	0.390

TABLE A3
**measurement on a cylinder* Ø50 H200 mm

Experimental data	ϱ_o (g/cm^3)	D_{CJ} (m/s)	P_{CJ} (GPa)
X2	1.835	8778	$36.5 \leqslant P_{CJ} \leqslant 38.5$
T2	1.847	7583 *	$p \sim 28.8 \pm 10$

THE EQUATIONS OF STATE OF DETONATION PRODUCTS AND THEIR INCORPORATION INTO THE QUATUOR CODE

O. Heuzé, P. Bauer, H. N. Presles, C. Brochet
Laboratoire d'Energétique et de Détonique
Poitiers, France

A thermochemical code (QUATUOR) was built to predict the main detonation characteristics of a wide range of explosives. A general subroutine allows to insert any equation of state (E.o.S.). The detonation velocities computed on the basis of seven different E.o.S. were compared to experimental ones available in the field of gaseous explosive mixtures at a high initial pressure. The virial E.o.S. yields results in good agreement with experimental ones but are expected to lead to large deviations when increasing the pressure. Empirical E.o.S. used with condensed explosives lead to good agreement provided their coefficients are properly adjusted. The JCZ3 E.o.S. seems to be at now the sole able one to describe the properties of detonation products of various explosives such as gaseous mixtures or condensed ones.

INTRODUCTION

Among the classical equations which are used to describe the thermodynamic behavior of a detonation front, the only one which is, so far, most discussed is the equation of state (E.o.S.). In the lower field of pressures - i.e. from several tens of bars to a hundred bars - the problem seems to be solved and some thermochemical codes are available (1, 2) to calculate the Chapman - Jouguet (CJ) detonation characteristics of these "low explosives". In this particular case, the ideal gas E.o.S. can obviously be used.

In the range of high explosives yielding detonation products at a pressure higher than a hundred kilobars, the problem appears in a more complex form. Several thermochemical codes have been built, either based on empirical E.o.S. such as B.K.W. (3), (4), (5), Kamlet & Jacobs E.o.S. (6) or on more sophisticated E.o.S. based on intermolecular considerations (7, 8, 9, 10). Actually, it appears that in this particular field of explosives, KHT E.o.S. (11) as well as JCZ3 E.o.S. (12) lead to results that are in good agreement with the experimental detonation properties. In the medium range of detonation pressures - i.e. from several hundred bars to several kilobars - a lack of knowledge on the appropriate E.o.S. remains. Although several E.o.S. had been checked for calculation of detonation properties in gaseous C-H-O-N explosives at initial pressures up to 50 bars (13, 14, 15), it seemed necessary to point out which was the range of validity of the main E.o.S. used in the field of high explosives. Therefore a thermochemical code was built. It allows to insert any E.o.S. In the present study, the results obtained with this code named QUATUOR are proposed on the basis of seven different E.o.S. These results are compared with experimental ones concerning gaseous explosives at a high initial pressure. But, so far, the only experimental values that are available are those related to the detonation velocity. These data were obtained in previous studies (13, 14, 16).

THERMODYNAMIC BACKGROUND AND DESCRIPTION OF THE QUATUOR CODE

This code runs on a HP 45 microcomputer and solves the hydrodynamic equations of the detonation front at the CJ point. Let the E.o.S. be presented in the form of:

$$\frac{pV}{nRT} = \varphi(V, T, X_i) \qquad (1)$$

where p, V, T are respectively the pressure, volume, temperature of the products, X_i and n being the molar fraction of the specie i and the total number of moles of products respectively. The isentropic slope $(\partial p/\partial V)_S$ and the deviation from the ideal gas of the enthalpy ΔH and chemical potential $\Delta\mu_i$ of specie i can be expressed in terms of the partial derivatives of σ:

$$\sigma_T = \frac{\partial \sigma}{\partial \text{Ln } T}\Big)_{V,X_i} \tag{2}$$

$$\sigma_V = \frac{\partial \sigma}{\partial \text{Ln } V}\Big)_{T,X_i} \tag{3}$$

$$\sigma_i = \frac{\partial \sigma}{\partial X_i}\Big)_{V,T,X_j \neq X_i} \tag{4}$$

Thus:

$$\Delta H = \int_{\infty}^{V} RT\,(\sigma_T + \sigma_V)\,\frac{dV}{V} \tag{5}$$

$$\frac{\partial p}{\partial V}\Big)_S = -\frac{\gamma n RT}{V^2}\,(\sigma - \sigma_V) \tag{6}$$

$$\frac{\Delta\mu_i(P,T)}{RT} = \int_{V}^{\infty}(\sigma - 1 + \sigma_i)\frac{dV}{V} - \text{Ln } \sigma \tag{7}$$

Eq. (5) is derived from statistical thermodynamics (see Appendix I), whereas Eq. (6) (see Appendix II) and (7) (see Appendix III) are obtained from classical thermodynamic laws.

γ is the ratio C_p/C_v in equilibrium conditions while the thermodynamic functions of the ideal gas are calculated using the polynomial developments proposed by Gordon & McBride (2).

The values of σ, σ_T, σ_V and σ_i are calculated within a run of the code, using specific subroutines depending upon the E.o.S. that is involved.

The iterative process includes a chemical equilibrium calculation whose details are described elsewhere (17, 18). The following species are taken into account in the calculation: CO_2, CO, H_2O, N_2, H_2, O_2, NO, OH, H, O, N, CH_4, NH_3 and solid carbon C(S). However, any new specie may be added if it is in such amount that it cannot be neglected. The corresponding molecular parameters of the species are listed in Table I. Instead of minimizing the value of the detonation velocity D along the Hugoniot curve as it is mainly done in other code (3), the QUATUOR code runs until the following relation is achieved:

$$D - \frac{1}{\varrho_o}\sqrt{-\frac{\partial p}{\partial V}\Big)_S'} = 0 \tag{8}$$

ϱ_o being the initital density of the mixture. This yields the detonation characteristics at the CJ point and appears to converge faster.

TABLE I

	BKW	Boltzmann BKW	P-Y	C-S		KHT	JCZ3	
	(a) B_i (cm³/mole)	(b) B_i (cm³/mole)	(c) r_i^* (Å)	(d) ϵ_i/k (K)	(d) r_i^* (Å)	(e) $\lambda_i^{1/3}$	(f) ϵ_i/k (K)	(f) r_i^* (Å)
CO_2	600	58 7	4.076	205	3.81	14	200	4,20
CO	390	35 1	3,788	100	3.7	9,8	120	4,05
H_2O	250	8,9	3,258	500	2.9	6,1	138	3,35
N_2	380	33,2	3,715	91.5	3,66	9 8	120	4,05
H_2	80	14,8	2,87	33	2,95	2,9	37	3,34
O_2	350	30,4	3,5	113	3.5	9,2	132	3,73
NO	386	21,0	3,41	120	3,4	9	105	3,97
OH	413		4,214	175	3.8	5,65		
H	76	7	3.5	750	2,1	1 25		
N	148	26	3,5			9,8		
O	120	85	3.5			9		
CH_4	528		3.5			1,1	154	4,29
NH_3	476		3,52			9,1	138	3,55

a) Mader C L - *Numerical Modeling of detonations* (University of California, Los Angeles 1979)
b) Pujol, Y - Manson, N "Calcul,compte tenu du second coefficient de virel" C R Acad Sc. Paris, t 262, pp 582-585 (1966)
c) Ref .8 - (r_i^* is taken equal to 3,5 Å for components whose value does not appear in the reference)
d) ref 22
e) Ref 11 - (λ_i expressed in $[cm^3\ (10^5 J)^{1/3}]$)
f) Finger M - "The effect of elemental composition on the detonation behavior of explosives," 6th Symposium (International) on Detonation ACR-221 ONR (1976), pp 710-722

EQUATIONS OF STATE USED IN THE QUATUOR CODE

Ideal Gas E.o.S.

This E.o.S. obviously leads to very simple calculations as $\sigma = 1$ in that case. Although it can be considered as baseless in the field of pressures which are dealt within the present work, it has been kept as a reference to show the deviation with other E.o.S. and more particularly with experimental results.

B.K.W. E.o.S.

This well known E.o.S. has been largely used and described by Mader (3). The general expression is:

$$\sigma = 1 + X \exp(\beta X) \tag{9}$$

where

$$X = \kappa \frac{\Sigma x_i B_i}{V(T + \theta)^{\alpha}} \quad (10)$$

$\beta, \kappa, \theta, \alpha$ are semi-empirical constants to be adjusted whereas B_i is the covolume of specie i.

This E.o.S. gives useful results in the field of high explosives (3). Although the empirical parameters were thoroughly studied, the agreement with experimental results was not very satisfactory in this medium range of density (13), until the appropriate molecular parameters were chosen (15).

Boltzmann (B) E.o.S.

This E.o.S. is based on the virial development (19, 20):

$$o = 1 + x + 0.625\ x^2 + 0.287\ x^3 + 0.193\ x^4 \quad (11)$$

where x is calculated according to the Corner method (21):

$$x = \sum_i \frac{x_i B_i}{V} \quad (12)$$

B_i is the covolume of specie i.

In other words, the mixing rule is based on the assumption that only like molecules interact.

Carnahan and Starling (CS) E.o.S.

In that case:

$$o = \frac{1 + y + y^2 - y^3}{(1 - y)^3} \quad (13)$$

y is derived from the Rowlinson relation (22) as a function of the reduced temperature $T^* = kT/\varepsilon^*$

$$y = B(T^*)\ N\ n\ r^{*3}/V \quad (14)$$

where

$$B(T^*) = \frac{\Pi\sqrt{2}}{6} (T^*)^{-3/\alpha} \left(1 + \frac{A(T^*)}{\alpha}\right)^3 \quad (15)$$

k, N, n are respectively the Boltzmann constant, the Avogadro number, and the total number of moles in the mixture, α is the repulsive potential exponent which can be taken equal to 12 for example but can have another value as suggested by Parlin & Giddings (14). $A(T^*)$ is a polynomial development (14), r^* and ε^* are derived from the following interaction laws:

$$r^* = \lambda \left(\sum_i \sum_j X_i X_j r_{ij}^{*3}\right)^{1/3} \quad (16)$$

$$\varepsilon^* = \sum_i \sum_j X_i X_j \varepsilon_{ij}\ r_{ij}^{*3} / r^{*3} \quad (17)$$

λ is an adjustable constant, X_i, X_j being the molar fractions of species i and j. The combination rules for r_{ij}^* and ε_{ij} are expressed as:

$$r_{ij}^* = \frac{r_i^* + r_j^*}{2} \quad (18)$$

$$\varepsilon_{ij} = (\varepsilon_i\ \varepsilon_j)^{1/2} \quad (19)$$

These values are listed in Table I.

Percus Yevick (PY) E.o.S.

This E.o.S. has a quite similar form to the (CS) E.o.S.:

$$o = \frac{1 + z + z^2}{(1 - z)^3} \quad (20)$$

Since it can be considered as a summation of a virial development.

However, z is expressed as follows:

$$z = \frac{\pi}{6} r^{*3} \frac{N\ n}{V} \quad (21)$$

The interaction laws between the molecular diameters r_i^* are the same as in Eq. (16) and (18).

The main difference with the CS E.o.S. lies in the interaction energy, which does not appear in the virial development.

Kihara-Hikita-Tanaka (KHT) E.o.S.

This E.o.S. is described by the following expression (11, 23):

$$o = \frac{1 + ax + bx^2 + cx^3 + dx^4 + ex^5}{1 - f\,x} \quad (22)$$

with:

$$x = \sum_i \frac{x_i\ \lambda_i^{3/\alpha}}{(pV)^{3/\alpha}} \frac{1}{V} \quad (23)$$

where a, b, c, d, e, f are constants (see Table II), λ_i is a molecular constant for specie i (see Table I) and α is the exponent involved in the repulsive potential ($\alpha = 9$).

TABLE II

	BKW (RDX Parameters)	BKW (This work)
α	0,5	0,25
β	0,16	0,625
κ	10.909	7,91
θ	400	400

KHT

α	9
a	−1,8523
b	40,245
c	−235,06
d	661,49
e	−670,48
f	1,85
a_0	−0,165
a_1	−0,307
a_2	39,676
a_3	−161,66
a_4	362,42

	C.S.	P.Y.
λ	0,88	0,475
α	12	/

JCZ3 E.o.S.

The Jacobs E.o.S. (9) proposed for pure gases has been extended for mixtures by Cowperthwaite and Zwisler (24). It is expressed as a sum of two terms:

$$\sigma = G(V, T, x_i) + \frac{p_o(V)V}{nRT} \qquad (24)$$

which reduces to a virial expansion at low density and approaches, at high density, the value determined by the repulsive potential:

$$\varepsilon(r) = \frac{B_l}{l} \exp\,[l(1 - r/r^*)] \qquad (25)$$

For all the E.o.S. that have just been expressed, the corresponding analytical expressions of σ_T, σ_V and $\Delta\mu_i$ are presented in Table III. A more detailed explanation of JCZ3 E.o.S. should be obtained in ref. (24).

RESULTS AND DISCUSSION

The results of a calculation based on the preceding equations of state performed with the QUATUOR code is presented here for a slightly rich C_2H_4-air mixture at initial pressures ranging from 5 bars to 100 bars (see Fig. 1).

An obvious discrepancy may be observed between either the results based on the ideal gas E.o.S. or on the BKW E.o.S. with the parameters fitted for high explosives, and the experimental results. Of course, the comparison only holds for

TABLE III

E.o.S.		σ	σ_V	σ_T	$\frac{\Delta\mu_i}{RT}(V,T)$
Ideal Gas		1	0	0	0
BKW	$X = \frac{\kappa B}{V(T+\theta)^\alpha}$	$1 + X \exp(\beta X)$	$X(1+\beta X)\exp(\beta X)$	$\frac{\alpha}{T+\theta}\sigma_V$	$\frac{\exp(\beta X_i) - 1}{\beta} + \frac{B_i}{B}(\sigma - 1)$
Boltzmann	$x = \frac{B}{V}$	$1 + x + 0.625x^2 + 0.287x^3 + 0.193x^4$	$x\,\sigma(x)$	0	$x + 0.625\frac{x^2}{2} + 0.287\frac{x^3}{3} + 0.193\frac{x^4}{4} + \frac{B_i}{B}(\sigma - 1)$
Percus Yevick	$Z = \frac{2\pi}{3}\frac{nN}{V}r^{*3}$	$\frac{1+Z+Z^2}{(1-Z)^3}$	$\frac{Z(Z+2)^2}{(1-Z)^4}$	0	$-\mathrm{Ln}(1-Z) + \frac{3}{2}\frac{1}{(1-Z)^2} - \frac{3}{2} + (\sigma-1)\left(\frac{\partial r^{*3}}{r^{*3}\partial X_i} + 1\right)$
Carnahan Starling	$y = \frac{\pi}{6}\frac{N}{V}B(T)r^{*3}$	$\frac{1+y+y^2-y^3}{(1-y)^3}$	$\frac{2y(2+2y-y^2)}{(1-y)^4}$	$\frac{3\sigma_V}{\sigma}\left(1 - \frac{A'(T)}{1+A(T)\sigma}\right)$	$\frac{1}{(1-y)^3} + \frac{2}{1-y} - 3 + (\sigma-1)\left(\frac{3}{\sigma}\frac{1}{\varepsilon}\frac{\partial\varepsilon}{\partial X_i} + \frac{1}{r^{*3}}\frac{\partial r^{*3}}{\partial X_i} + 1\right)$
JCZ 3	$l = \mathrm{Ln}(f_g + f_s)$ (*)	$1 - V\frac{\partial l}{\partial V} - \frac{V}{nRT}\frac{\partial E_c}{\partial V}$	$1 - \sigma + \frac{V^2}{nRT}\frac{\partial^2 E_o}{\partial V^2} + V^2\frac{\partial^2 l}{\partial V^2}$	$\frac{V}{nRT}\frac{\partial E_o}{\partial V} - TV\frac{\partial^2 l}{\partial T\partial V}$	$\frac{1}{RT}\frac{\partial E_o}{\partial n_i} + 1 + n\frac{\partial l}{\partial n_i}$
KHT	$x = \left(\frac{\lambda}{PV}\right)^{3\alpha}\frac{1}{V}$	$\frac{1+ax+bx^2+cx^3+dx^4+ex^5}{1-fx}$	$\frac{\sigma\,x\,\sigma'(x)\,\sigma}{\sigma\sigma+3x\sigma'(x)}$	$\frac{3}{\alpha}(\sigma-1)$	$\frac{a_4x^4}{4} + \frac{a_3x^3}{3} + \frac{a_2x^2}{2} + a_1x + a_0\mathrm{Ln}(1-fx) + (\sigma-1)\left(\frac{\lambda}{x}\right)^{3\alpha}$

(*) see ref. (24)

initial pressures higher than 10 bars. Otherwise the low deviation between ideal behavior of the products and the real one doesn't allow to check the validity of any E.o.S.. Apart from these particular E.o.S. the other results are fairly close.

The JCZ3 E.o.S. leads to an excellent agreement with experimental values for initial pressures ranging from several bars to 50 bars. This agreement remains very good at higher initial pressures (less than 1% at 100 bars).

A good agreement has been obtained with the B.K.W. E.o.S. once the parameters were adjusted to fit the experimental results, but provided the covolumes were changed as well. It can be observed in Table I, that these covolumes are drastically different from those used in the case of high explosives.

The results obtained on the basis of the Boltzmann E.o.S. have already been presented elsewhere (26) and appear to be in a quite good agreement with experimental ones. This conclusion is quite satisfactory owing to the simplicity of the calculation.

In a previous work, the CS E.o.S. parameters had been chosen in order to lead to a good compatibility with experimental conditions (15). These parameters are recalled in Table I. Moreover, here, an adjustable parameter (λ) was inserted in the relation describing the mixing rule – i.e. Eq. (16). This parameter was adjusted as suggested by Edwards and Chaiken (8). Thus, calculated values are in good agreement with experimental ones. This parameter may be considered as a semi empirical mean for combining the molecular sizes in the case of mixtures, as long as the combining laws have never been confirmed accurately by experimental results. In other words the mixing rules are not, so far, unambiguously defined. The value $\lambda = 0.88$ appeared to fit quite well the experimental results. The same agreement has been obtained with PY E.o.S. but taking $\lambda = 0.475$. This latter value is not far from the one proposed by Edwards and Chaiken (8) in the case of high explosives. The present value is, however, a bit higher (roughly 10%) and this might be explained by the fact that this parameter has an increasing value as the density decreases, due to an increasing diameter of the rigid spheres.

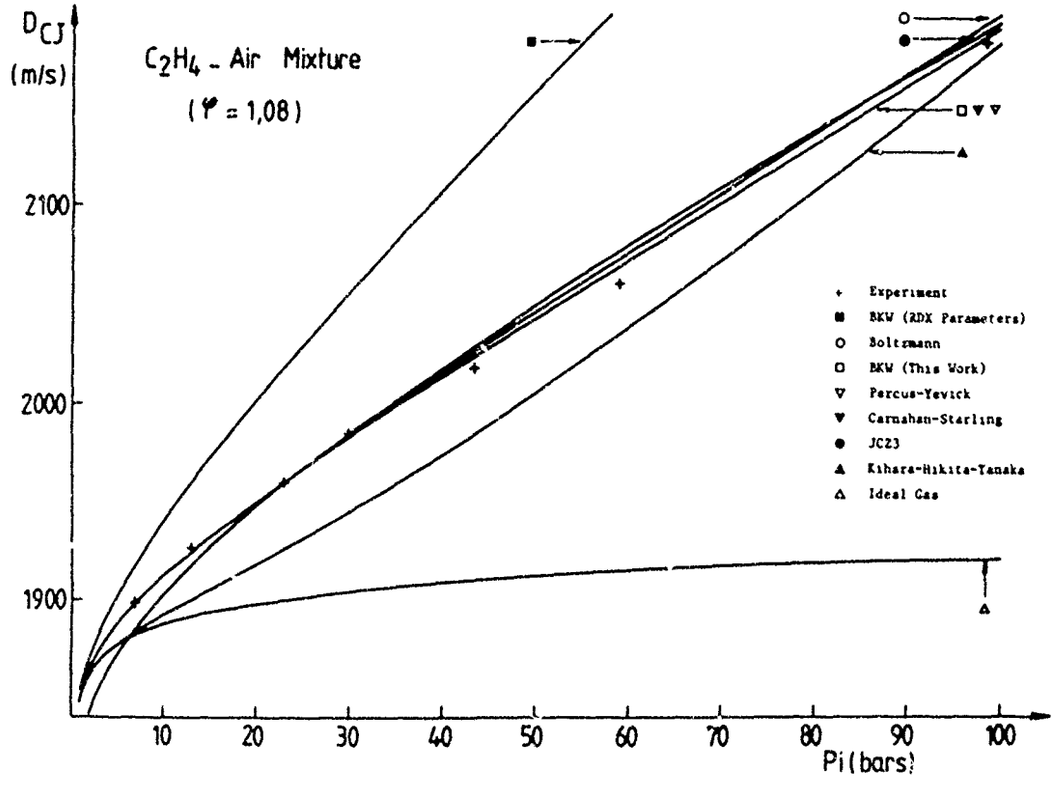

Fig 1 Detonation velocity vs. initial pressure

The results obtained with the K.H.T. E.o.S. calculation are close to the experimental ones as well. However, the profile of the curve is utterly different from the experimental one. This former profile is very similar to that obtained in the case of high explosives with various proportions of additives (25).

SUMMARY AND CONCLUSION

A new thermochemical code is presented in this work. Its main purpose is to provide data on the thermodynamic properties of the detonation products for gaseous explosives at a high initial pressure (up to 100 bars). The code is based on thermodynamic relations which allow the use of several E.o.S. The seven following ones were presented in this paper:

(i) the ideal gas E.o.S.

(ii) an empirical one (B.K.W.),

(iii) a simple one based on the assumption of simple molecular interactions (B),

(iv) two others (CS, PY) based on an improved model for rigid spheres and ponderated with an adjustable coefficient which is supposed to give a more suitable formulation of the interaction rules used to correlate the molecular diameters in the case of mixtures,

(v) two sophisticated ones based on complex considerations of molecular interactions (KHT, JCZ3).

The calculated values of detonation velocities were compared to available experimental data.

It appears that the empirical B.K.W. E.o.S. yields results that are in good agreement with experiments, provided its coefficients together with the covolumes were properly adjusted.

The (B) E.o.S. which, in some way, describes a behavior of ideal mixtures yields results with a deviation from the experimental values lesser than 3%, even at such high initial pressures as 100 bars. The other results are even closer from experiments, more particularly in the case of the CS and PY E.o.S. where an adjustable parameter was chosen in order to fit the experimental data. In the PY E.o.S., this parameter takes a value quite close to the one used in the case of high explosives at a low initial density.

The profile of the curve obtained with the KHT E.o.S. is different from the experimental one, although the values are in a quite good agreement (discrepancy lesser than 2%).

The main result of this work is that the JCZ3 E.o.S. is the only one capable of describing the properties of the detonation products of high explosives and gaseous explosive mixtures at a high pressure on the basis of the same assumptions.

APPENDIX I

Let's recall the main relations derived from the statistical thermodynamics which led to Eq. (5). From the Helmoltz free energy:

$$F = -nRT \operatorname{Ln} Z$$

where Z is the partition function. Pressure and enthalpy can be expressed straightforward through the following relations:

$$p = -\left.\frac{\partial F}{\partial V}\right)_T$$

$$H = RT\left[T\left.\frac{\partial \operatorname{Ln} Z}{\partial T}\right)_V + V\left.\frac{\partial \operatorname{Ln} Z}{\partial V}\right)_T\right]$$

Hence:

$$\sigma = \frac{pV}{nRT} = V\left.\frac{\partial \operatorname{Ln} Z}{\partial V}\right)_T = \left.\frac{\partial \operatorname{Ln} Z}{\partial \operatorname{Ln} V}\right)_T$$

and:

$$\left.\frac{\partial H}{\partial V}\right)_T = \frac{RT}{V}\left.\frac{\partial}{\partial \operatorname{Ln} V}\right)_T\left[\left.\frac{\partial \operatorname{Ln} Z}{\partial \operatorname{Ln} T}\right)_V + \left.\frac{\partial \operatorname{Ln} Z}{\partial \operatorname{Ln} V}\right)_T\right]$$

$$\left.\frac{\partial H}{\partial V}\right)_T = \frac{RT}{V}(\sigma_T + \sigma_V)$$

APPENDIX II

The well known Reech's formula:

$$\left.\frac{\partial p}{\partial V}\right)_S = \gamma\left.\frac{\partial p}{\partial V}\right)_T \qquad \text{(II.1)}$$

together with the following expressions for σ, σ_V:

$$\sigma = \frac{PV}{nRT}\ ;\quad \sigma_V = \left.\frac{\partial \sigma}{\partial \operatorname{Ln} V}\right)_{T,x_i} \qquad \text{(II.2)}$$

yield:

$$\left.\frac{\partial p}{\partial V}\right)_T = -\frac{nRT}{V^2}(\sigma - \sigma_V) \qquad \text{(II.3)}$$

Thus,

$$-\frac{\partial p}{\partial V}\Big)_S = \gamma\frac{nRT}{V^2}\left(\sigma - \sigma_V\right) \qquad \text{(II.4)}$$

APPENDIX III

$$S = S^o(T) + \int_{V^*}^{V}\frac{\partial S}{\partial V}\Big)_T dV \qquad \text{(III.1)}$$

Maxwell formulation yields

$$\frac{\partial S}{\partial V}\Big)_T = \frac{\partial P}{\partial T}\Big)_V \text{ , then}$$

$$S = S^o(T) + \int_{V^*}^{V}\frac{\partial P}{\partial T}\Big)_V dV \qquad \text{(III.2)}$$

$$U = U^o(T) + \int_{V^*}^{V}\frac{\partial U}{\partial V}\Big)_T dV \qquad \text{(III.3)}$$

$$\frac{\partial U}{\partial V}\Big)_T = -P + T\frac{\partial P}{\partial T}\Big)_V \qquad \text{(III.4)}$$

$$U = U^o(T) + \int_{V^*}^{V}\left(T\frac{\partial P}{\partial T} - P\right)dV \qquad \text{(III.5)}$$

$$F = U - TS = U^o(T) + \int_{V^*}^{V}\left(T\frac{\partial P}{\partial T} - P\right)dV -$$

$$TS^o(T) - \int_{V^*}^{V} T\frac{\partial P}{\partial T}\Big)_V dV \qquad \text{(III.6)}$$

$$= F^o(T) + \int_{V}^{V^*} PdV = F^o(T) + RT\int_{V}^{V^*}\sigma\frac{dV}{V} \qquad \text{(III.7)}$$

In the case of mixtures, the term: $RT\sum_i X_i \text{ Ln } X_i$ must be added. Thus:

$$F = F^o(T) - RT\text{ Ln }\left(\frac{V}{V^*}\right) + RT\sum_i X_i \text{ Ln } X_i$$

$$+ RT\int_{V}^{V^*}\frac{(\sigma - 1)\,dV}{V} \qquad \text{(III.8)}$$

The deviation from the ideal gas becomes:

$$\frac{\Delta F}{RT} = \int_{V}^{V^*}\frac{(\sigma - 1)dV}{V} \qquad \text{(III.9)}$$

Hence:

$$\frac{\Delta\mu_i(V,T)}{RT} = \frac{1}{RT}\frac{\partial(\Delta F)}{\partial X_i}\Big)_{V,T}$$

$$= \int_{V}^{V^*}\frac{(\sigma - 1)dV}{V} + \int_{V}^{V^*}\frac{\partial\sigma}{\partial X_i}\frac{dV}{V}$$

$$= \int_{V}^{V^*}(\sigma - 1 + \sigma_i)\frac{dV}{V} \qquad \text{(III.10)}$$

$$\frac{\Delta\mu_i(p,T)}{RT} = \frac{\Delta\mu_i(V,T)}{RT} - \text{Ln }\sigma$$

$$= \int_{V}^{V^*}(\sigma - 1 + \sigma_i)\frac{dV}{V} - \text{Ln }\sigma \qquad \text{(III.11)}$$

REFERENCES

1. C. Johnson, "Contribution à l'étude des détonations dans les Mélanges gazeux," Thèse de Doctorat d'Etat, Université de Poitiers, Poitiers, France (1968).
2. S. Gordon, B. J. McBride, "Computer program for calculation of complex chemical equilibrium compositions, rocket performance, incident and reflected shocks and Chapman-Jouguet detonations," Report NASA SP-273 (1971).
3. C. L. Mader, "Fortran B. K. W.: a code for computing the detonation properties of explosives," Los Alamos Scientific Laboratory, Report LA-3704 (1967).
4. R. Chéret, "Contribution à l'étude numérique des produits de détonation d'une substance explosive," Rapport CEA-R-4122 (1971).
5. H. B. Levine, R. E. Sharples, "Operators manual of RUBY," Lawrence Livermore Laboratory, Report UCRL, 6815 (1962).
6. M. J. Kamlet-S. J. Jacobs - I: J. Chem. Phys. 48, 23 (1968).
   M. J. Kamlet-J. E. Ablard - II: J. Chem. Phys. 48, 36 (1968).
   M. J. Kamlet-C. Dickinson - III: J. Chem. Phys. 48, 43 (1968).
   M. J. Kamlet-H. Hurwitz - IV: J. Chem. Phys. 48, 3685 (1968).
7. N. F. Carnahan, K. E. Starling, "Equation of state for non attracting rigid spheres," J. Chem. Phys. 31, 635 (1969).

8. J. C. Edwards, R. F. Chaiken, "Detonation calculations with a Percus-Yevick equation of state," Combustion and Flame 22, 269 (1974).

9. S. J. Jacobs, "On the equation of state for detonation products at high density," 12th Symposium (International) on Combustion, p. 501, The Combustion Institute, Pittsburgh, (1969).

10. W. Fickett, "Detonation properties of condensed explosives calculated with an equation of state based on intermolecular potentials," Los Alamos, Report LA-2712 (1962).

11. K. Tanaka, "Detonation properties of condensed explosives computed using the Kihara-Hikita-Tanaka equation of state," Report from National Chemical Laboratory for Industry, Ibaraki, Japan (1983).

12. Y. Kato, P. Bauer, C. Brochet, R. Bouriannes, "Brightness temperature of detonation wave in nitromethane - tetranitromethane mixtures and in gaseous mixtures at a high initial pressure," 7th Symposium on Detonation, Annapolis, pp. 403-408 (1981).

13. P. Bauer, S. Krishnan, C. Brochet, "Detonation characteristics of gaseous ethylene, oxygen and nitrogen mixtures at high initial pressures," AIAA, Progress in Astronautics and Aeronautics, 75, pp. 408-422 (1981).

14. P. Bauer, C. Brochet, "Properties of detonation waves in hydrocarbon - oxygen - nitrogen mixtures at high initial pressures," AIAA, Progress in Astronautics and Aeronautics, 87, p. 331 (1983).

15. P. Bauer, C. Brochet, O. Heuzé, H.N. Presles, "Equation of state for dense gases," Arch. Comb., 5, pp. 35-45 (1985).

16. P. Bauer, C. Brochet, H. N. Presles, "Detonation study of gaseous mixtures at initial pressures reaching 10 MPa," Arch. Comb, 4, pp. 191-195 (1984).

17. O. Heuzé, H. N. Presles, P. Bauer, "Computation of chemical equilibria," J. Chem. Phys. 83, 4734 (1985).

18. O. Heuze, P. Bauer, H. N. Presles, "Calculation of the composition of combustion products," 4th Int. Conf. on Numerical Methods in thermal problems, Swansea, U.K., 15th-18th July 1985, published in "Communications in Applied Numerical Methods".

19. J. Taylor, "Detonation in condensed explosives," Oxford Press, Oxford, England (1952).

20. S. Paterson, "The hydrodynamic theory of detonation, Part II, On absolute calculation for condensed explosives," Research Supplement, 5, 1, pp. 221-233 (1948).

21. P. Jacquemin, M. Nicolas, "Calcul des performances thermodynamiques des poudres aux hautes densités de chargement," 5th Symp. (Int.) de Balistique, Toulouse, France (1980).

22. M. Barrére, private communication (1976).

23. T. Kihara, T. Hikita, 4th Symposium (Int.) on Combustion, p. 458, Baltimore, The Williams & Wilkins Co., (1953).

24. H. Cowperthwaite, W. H. Zwisler, "The JCZ Equations of state for detonation products and their incorporation into the TIGER CODE," 6th Symposium on Detonation, ACR 221, San Diego, pp. 110-116 (1976).

25. H. N. Presles, C. Brochet, Y. Kato, K. Tanaka, "Influence of additives on Nitromethane detonation characteristics," 7th Symposium on Detonation, Annapolis, pp. 583-588 (1981).

26. H. N. Presles, P. Bauer, O. Heuzé, C. Brochet, "Investigation on Detonations of gaseous explosive mixtures at very high initial pressures," Comb. Sci. and Tech., 43, 315 (1985).

SENSITIVITY ANALYSIS OF THE IDEAL DETONATION STATE TO ERRORS IN MOLECULAR PROPERTIES AND INTERMOLECULAR FORCE PARAMETERS

W. Byers Brown
Department of Chemistry
University of Manchester
Manchester M13 9PL
UK

and

Detonation Research Group
Imperial Chemical Industries
Stevenston Works
Ayrshire KA20 3LN
UK

A sensitivity analysis of calculations of the ideal detonation state to errors in intramolecular and intermolecular parameters is presented, based on the Hellmann-Feynman formula of statistical mechanics. Equations are derived for discussing the accuracy of the calculation of the detonation velocity and the temperature, pressure and density of the Chapman-Jouguet point in the general case of mobile chemical equilibrium. In the special case of frozen chemical equilibrium comparatively simple equations are derived for overall fractional changes in molecular parameters, and in particular for intermolecular well-depths ε, collision diameters σ and repulsion indices α. Quantitative results are presented for a typical case, and are mainly in agreement with intuitive thinking, although some details are unexpected.

1. INTRODUCTION

Recent calculations of the ideal detonation state for explosive materials are all based on statistical mechanical theories of the thermodynamic equation of state, and require knowledge of the properties of the product molecules and the intermolecular forces between them. The accuracy of quantities calculated in this way, such as the detonation velocity or the temperature, pressure and density of the Chapman-Jouguet point, depend on (a) the fundamental assumptions underlying the statistical theory, (b) any further approximations made to simplify the calculations, and (c) the actual values, experimental or theoretical, of the various intramolecular and intermolecular parameters involved. The most important molecular parameters are the masses, moments of inertia, vibration frequencies and anharmonicities, electronic degeneracies and low-lying excitation energies, rotation-vibration coupling parameters, etc., for all the species present. The intermolecular force parameters are first of all the energy, size and repulsion indices occurring in the potential energy function for central interactions between molecules of different species. In addition, there may be parameters describing orientation-dependent interactions such as dipole and quadrupole moments.

The molecular properties are on the whole well-known, but this is far from the case with the intermolecular force parameters. It is therefore important to be able to estimate the effect of an uncertainty in a particular parameter,

or indeed a whole class of parameters (for example, intermolecular energy well-depths), on the calculation of a detonation quantity of interest.

The object of this paper is to present an analysis of the sensitivity of such calculations based on the Hellmann-Feynman formulae of statistical mechanics. It turns out that only very general and mainly acceptable assumptions need to be made, for example that classical statistics and mechanics suffice for treating molecular interactions and that these are additive. It is then possible to express the sensitivity coefficients, that is the fractional change in a quantity of interest, for example the detonation velocity, caused by a fractional change in an intermolecular parameter, for example the collision diameter, largely in terms of thermodynamic or easily calculated statistical quantities. It is not necessary to assume a particular statistical theory, such as the hard-sphere perturbation theory, although the equations can be particularized if desired.

2. STATISTICAL THERMODYNAMICS OF INTERNAL PARAMETER CHANGES

The first thing we need to know is the effect on the thermodynamic properties of a multicomponent system of changing an internal parameter, say ξ, which describes some molecular or intermolecular feature of importance, such as an intramolecular vibration frequency or an intermolecular well-depth. This problem is solved by the statistical Hellmann-Feynman formula (1), which in its application to the canonical ensemble describing the Helmholtz free energy $A(T,V,\underset{\sim}{n})$ takes the form

$$(\partial A/\partial \xi)_{T,V,\underset{\sim}{n}} = \langle \partial H/\partial \xi \rangle, \tag{2.1}$$

where H is the Hamiltonian operator for the system, and the angle brackets indicate the ensemble average. The derivation starts from the normalization condition for the density in the canonical ensemble, namely

$$\mathrm{Tr}\{\exp[(A - H)/k_B T]\} = 1 \tag{2.2}$$

where k_B is Boltzmann's constant. By differentiating equation (2.2) with respect to ξ we get

$$\mathrm{Tr}\{(\partial A/\partial \xi - \partial H/\partial \xi)\exp[(A - H)/k_B T]\} = 0$$

or

$$\partial A/\partial \xi = \mathrm{Tr}\{\partial H/\partial \xi \exp[(A-H)/k_B T]\},$$

$$= \langle \partial H/\partial \xi \rangle.$$

In what follows we shall assume (a) that quantal effects and statistics can be ignored in dealing with molecular rotations and intermolecular motions, (b) that the interaction of inter- and intra-molecular motions can be neglected, and (c) that the intermolecular potentials are additive and effectively central; this last assumption can be easily relaxed if desired. The Hamiltonian can then be written in the form

$$H = H_{intra} + H_{inter}, \tag{2.3}$$

where

H_{intra} and H_{inter} commute, and

$$H_{intra} = H_{vib} + K_{rot}, \tag{2.4}$$

$$H_{inter} = K_{trans} + U, \tag{2.5}$$

where H_{vib} is the Hamiltonian for all the internal vibrational motions, K_{rot} and K_{trans} are the kinetic energy operators for rotation and translation of the N molecules, and U is the total potential energy for their interaction given by

$$U = \sum_i \sum_j \sum_{s>t} \sum u_{ij}(r_{st}) \tag{2.6}$$

where $u_{ij}(r_{st})$ is the intermolecular potential for two molecules of species i and j with their centres of mass at positions $\underset{\sim}{r}_s$ and $\underset{\sim}{r}_t$, $r_{st} = |\underset{\sim}{r}_s - \underset{\sim}{r}_t|$, and the sum is over all pairs of molecules. The free energy A can be written as the sum of two parts,

$$A = A_{ideal} + A_{excess} \tag{2.7}$$

where A_{ideal} is the ideal free energy given by

$$\mathrm{Tr}\{\exp[(A_{ideal} - H_{intra} - K_{trans})/k_B T]\} = 1, \tag{2.8}$$

and the trace operation is defined so that it includes the ideal mixing term, and A_{excess} is the excess or residual free energy defined by

$$V^{-N} \int \ldots (N) \ldots \int \exp[(A_{excess} - U)/k_B T] d^3\underset{\sim}{r}_1 \ldots d^3\underset{\sim}{r}_N = 1. \tag{2.9}$$

The immediate point of this separation is that the molecular parameters occur only in A_{ideal} and the intermolecular parameters only in A_{excess}.

3. MOLECULAR PARAMETERS

We shall consider a few typical molecular parameters such as total masses m, moments of inertia I, and normal vibration frequencies ω_k, which will be treated as independent. Let

$$X_i^m = (\partial A/\partial m_i)_{T,V,\underset{\sim}{n}} = (\partial A_{ideal}/\partial m_i)_{T,V,\underset{\sim}{n}} \quad (3.1)$$

where m_i is the molecular mass of species i, and all other properties are considered to be held constant during differentiation. It follows from (2.1) and (2.3) that

$$X_i^m = <\partial K_{trans} / \partial m_i>, \quad (3.2)$$

and since

$$K_{trans} = \sum_i \sum_s \underset{\sim}{p}_s^2 / 2m_i,$$

we have

$$X_i^m = -<\sum_s \underset{\sim}{p}_s^2 /2m_i^2>.$$

But since translational motion is assumed to be classical we have

$$<\sum \underset{\sim}{p}_s^2/2m_i> = 3N_i k_B T/2,$$

and so

$$X_i^m = -3N_i k_B T/ 2m_i. \quad (3.3)$$

Similarly for $\xi = I_{i\gamma}$, the γ^{th} principal moment of inertia of the N_i molecules of the i^{th} species, we have

$$X_{i\gamma}^I = (\partial A/\partial I_{i\gamma})_{T,V,\underset{\sim}{n}} = <\partial K_{rot}/\partial I_{I_\gamma}>, \quad (3.4)$$

where

$$K_{rot} = \sum_i \sum_s \sum_\gamma L_{s\gamma}^2 /2I_{i\gamma}$$

where $L_{s\gamma}$ are the angular momenta about the principal (molecule-fixed) axes. Hence

$$X_{i\gamma}^I = -N_i k_B T/2I_{i\gamma} \quad (3.5)$$

Turning lastly to vibrational parameters, let ω_{ik} be the k^{th} normal (angular) vibration frequency of a molecule of species i, and define

$$X_{ik}^\omega = (\partial A/\partial \omega_{ik})_{T,V,\underset{\sim}{n}} = <\partial H_{vib}/\partial \omega_{ik}>. \quad (3.6)$$

Now, assuming the vibrations are harmonic, we have in an obvious notation

$$H_{vib} = \sum_i \sum_s \sum_k \tfrac{1}{2} (p_{sk}^2 + \omega_{ik}^2 q_{sk}^2), \quad (3.7)$$

so that

$$X_{ik}^\omega = <\sum_s \omega_{ik} q_{ik}^2>. \quad (3.8)$$

Since the average potential energy of a normal vibration is equal to the average kinetic energy, and using the well-known formula for the average energy of a normal mode, we can show that

$$X_{ik}^\omega = N_i h [\exp(h\omega_{ik}/k_B T) - 1]^{-1}. \quad (3.9)$$

4. INTERMOLECULAR PARAMETERS

We now consider a few typical intermolecular parameters, in particular the attractive well-depths ε_{ij}, the sizes σ_{ij} and the repulsion indices α_{ij} for the interaction of two molecules of species i and j. From the statistical Hellmann-Feynman formula (2.1) we have

$$X_{ij}^\varepsilon = (\partial A/\partial \varepsilon_{ij})_{T,V,\underset{\sim}{n}} = (\partial A_{excess})/\partial \varepsilon_{ij})_{T,V,\underset{\sim}{n}} = <\partial U/\partial \varepsilon_{ij}>. \quad (4.1)$$

By substituting from (2.6) we get

$$X_{ij}^\varepsilon = <\sum_{s>t} \sum \partial u_{ij}(r_{st})/\partial \varepsilon_{ij}>, \quad (4.2)$$

where we have supposed for convenience that ε_{ij} and ε_{ij} are independent. Let us further assume that u_{ij} has the form

$$u_{ij}(r) = \varepsilon_{ij} f(r/\sigma_{ij}; \alpha_{ij}), \quad (4.3)$$

so that

$$\partial u_{ij} / \partial \varepsilon_{ij} = u_{ij} / \varepsilon_{ij}. \quad (4.4)$$

Hence

$$X_{ij}^\varepsilon = <\sum_{s<t} \sum u_{ij}(r_{st})> /\varepsilon_{ij}, = (N_i N_j/2V\varepsilon_{ij}) \int u_{ij}(r) g_{ij}(r) d^3 \underset{\sim}{r} \quad (4.5)$$

where $g_{ij}(r;T,V,\underset{\sim}{n})$ is the radial distribution function (RDF) for molecules of species i and j a distance r apart.

Similarly

$$X_{ij}^\sigma = (\partial A/\partial \sigma_{ij})_{T,V,\underset{\sim}{n}} = <\partial U/\partial \sigma_{ij}> = -(N_i N_j/2V\sigma_{ij}) \int v_{ij}(r) g_{ij}(r) d^3 \underset{\sim}{r} \quad (4.6)$$

where $v_{ij}(r)$ is the intermolecular virial function defined by

$$v(r) = r du/dr. \tag{4.7}$$

The coefficient for the effect of a change in the repulsion index α_{ij} can likewise be reduced to

$$\begin{aligned} X^{\alpha}_{ij} &= (\partial A/\partial \alpha_{ij})_{T,V,\underset{\sim}{n}} \\ &= \langle \partial U/\partial \alpha_{ij} \rangle \\ &= (N_i N_j/2V) \int (\partial u_{ij}/\partial \alpha_{ij}) g_{ij} d^3\underset{\sim}{r}. \end{aligned} \tag{4.8}$$

However, the form of $\partial u/\partial \alpha$ depends on the precise form of the function f in the intermolecular potential (4.3). For example, if u(r) has the Buckingham α-exp-6 form

$$u(r) = \varepsilon\{6\exp[\alpha(1-r/r_m)] - \alpha(r_m/r)^6\}/(\alpha-6), \tag{4.9}$$

where r_m is the equilibrium distance, then it is easily shown that the corresponding derivative (holding ε and r_m constant) is given by

$$\alpha(\partial u/\partial \alpha) = \alpha((\alpha-7)/(\alpha-6))u(r) + v(r) - (\alpha-7)u_{disp}(r) \tag{4.10}$$

where

$$u_{disp}(r) = -(\varepsilon\alpha/(\alpha-6))(r_m/r)^6 \tag{4.11}$$

is the attractive (dispersion) energy term in (4.9), and v(r) is the intermolecular virial of (4.7). Hence

$$\begin{aligned} \alpha_{ij} X^{\alpha}_{ij} &= \alpha_{ij}((\alpha_{ij}-7)/(\alpha_{ij}-6))\varepsilon_{ij} X^{\varepsilon}_{ij} - \sigma_{ij} X^{\sigma}_{ij} \\ &- (\alpha_{ij}-7)(N_i N_j/2V) \times \int u^{disp}_{ij}(r) g_{ij}(r) d^3\underset{\sim}{r}. \end{aligned} \tag{4.12}$$

5. OVERALL PARAMETER CHANGES

The coefficients X^{ξ}_{ij} of the previous section can be calculated by substituting explicit forms for the RDF's $g_{ij}(r)$ into equations (4.5), (4.6) and (4.12) and integrating. However, the *overall* effect of fractional errors $\delta\varepsilon_{ij}/\varepsilon_{ij}$ in all the energy parameters can be related exactly to the excess energy in the following way. From (4.5) and (2.6)

$$\begin{aligned} \sum_i \sum_j \varepsilon_{ij} X^{\varepsilon}_{ij} &= \langle \sum_i \sum_j \sum_{s>t} \sum u_{ij}(r_{st}) \rangle, \\ &= \langle U \rangle \\ &= U_{excess}. \end{aligned} \tag{5.1}$$

Similarly the overall effect of fractional errors $\delta\sigma_{ij}/\sigma_{ij}$ in all the size parameters is given by the equation

$$\begin{aligned} \sum_i \sum_j \sigma_{ij} X^{\sigma}_{ij} &= -\langle \sum_i \sum_j \sum_{s>t} \sum v_{ij}(r_{st}) \rangle, \\ &= 3(PV - Nk_BT). \end{aligned} \tag{5.2}$$

The corresponding quantity for the repulsion indices α_{ij} cannot be written in terms of excess thermodynamic quantities in general, although it can be calculated using a statistical theory such as the perturbation theory based on the hard-sphere fluid. The quantity is much simplified by assuming that the α_{ij} are the same for all species, which is the condition that the intermolecular potentials u_{ij} are "conformal", when

$$\sum_i \sum_j \alpha_{ij} X^{\alpha}_{ij} = \alpha((\alpha-7)/(\alpha-6))U_{ex} - 3(PV - Nk_BT) - (\alpha-7)U_{disp} \tag{5 3}$$

where U_{disp} is the attractive (dispersion) contribution to the excess energy, and must be calculated specially.

Equations (5.1) and (5.2) are exact and general, and could equally well be derived directly by applying Euler's theorem for homogeneous functions to the excess free energy $A_{ex}(T,V,\underset{\sim}{N}; \underset{\approx}{\varepsilon}, \underset{\approx}{\sigma}, \underset{\approx}{\alpha})$ which is homogeneous of degree one in T and the set $\{\varepsilon_{ij}\}$, and homogeneous of degree zero in $V^{1/3}$ and the set $\{\sigma_{ij}\}$ or $\{r_{mij}\}$.

Similar quantities describing the overall change in thermodynamic properties for fractional changes $\delta\xi/\xi$ in the molecular parameters can be written down. Thus, for the change in the masses, it follows from (3.3) that

$$\sum_i m_i X^{m}_{i} = -\frac{3}{2} Nk_BT. \tag{5.4}$$

Similarly for changes in the moments of inertia

$$\sum_i \sum_\gamma I_{i\gamma} X^{m}_{i\gamma} = -\frac{\nu}{2} Nk_BT. \tag{5.5}$$

where ν is the average number of rotational degrees of freedom of molecules in the fluid (ν=2 for linear, and 3 for non-linear, molecules). For changes in vibrational frequencies

$$\begin{aligned} \sum_i \sum_k \omega_{ik} X^{\omega}_{ik} &= \sum N_i \sum_k h\omega_{ik} \\ &[\exp(h\omega_{ik}/k_BT) - 1]^{-1}, \\ &= E_{vib}, \end{aligned} \tag{5.6}$$

the total vibrational energy of the molecules, which approaches Nk_BT per normal mode at high temperatures.

6. IDEAL DETONATION STATE

The ideal detonation state (IDS) is determined by three sets of conditions (2):

(a) The Rankine-Hugoniot equation which describes the conservation of mass, momentum and energy across the detonation front, and can be written

$$E-E_o=\tfrac{1}{2}(P+P_o)(V_o-V), \tag{6.1}$$

where the extensive quantities are specific (i.e., per unit mass), the subscript zero indicates the initial state of the explosive material and the unsubscripted quantities are for the explosive products, and E is the internal energy.

(b) The Chapman-Jouguet condition

$$(P-P_o)/(V_o-V)=-(\partial P/\partial V)_S. \tag{6.2}$$

(c) The conditions of chemical equilibrium among the detonation products. These can be most succinctly expressed in terms of the chemical affinities $A_1, A_2, \ldots, A_r$ and extents of reaction $\lambda_1, \lambda_2, \ldots, \lambda_r$ for the r possible independent reactions among the c chemical species. The affinities are defined in terms of the chemical potentials μ_i by

$$A_j=-\sum_{i=1}^{c}\mu_i\nu_{ij}\ (j=1,2,\ldots,r) \tag{6.3}$$

where $\underset{\sim}{\nu}$ is the stoichiometric reaction matrix of order $\underset{\sim}{c}$ x r. The conditions for chemical equilibrium are then simply

$$A_j=0 \qquad (j=1,2,\ldots,r), \tag{6.4}$$

and will be denoted if necessary by "eq". The derivative on the left-hand side of equation (6.2) expressing the Chapman-Jouguet condition is incompletely specified. For frozen chemical equilibrium the molar masses $\underset{\sim}{n}$, and therefore the extents of reaction $\underset{\sim}{\lambda}$, would be held constant in addition to the entropy S, while for the actual state of chemical equilibrium (6.4) hold, and (6.2) should read

$$(P-P_o)/(V_o-V)=-(\partial P/\partial V)_{S,eq}. \tag{6.5}$$

The values of the pressure, volume, temperature, and extents of reaction of the ideal detonation state will be denoted by P_{CJ}, V_{CJ}, T_{CJ} and $\underset{\sim}{\lambda}_{CJ}$, which are the solution of (6.1), (6.4) and (6.5). The detonation velocity in the IDS will be detonated by D_{CJ} where

$$D_{CJ}^2=V_o^2(-\partial P/\partial V)_{S,eq}. \tag{6.6}$$

7. EFFECT OF PARAMETER CHANGES ON IDEAL DETONATION STATE

All the thermodynamic quantities for the detonation products will depend on the intra- and inter-molecular parameters ξ. In calculating the effect of a change $\delta\xi$ on the IDS the question arises as to which set of independent thermodynamic variables to use. These must be one of the "canonical" sets occurring in the fundamental statistical thermodynamic equations along with the parametric dependence on the ξ. The most natural choice is the set $S,V,\underset{\sim}{n},\underset{\sim}{\xi}$ which are the canonical variables for the internal energy function $E(S,V,\underset{\sim}{n};\underset{\sim}{\xi})$. This is because the extensive quantities E,V,S all occur in the Rankine-Hugoniot and Chapman-Jouguet equations, and

$$P=-(\partial E/\partial V)_{S,\underset{\sim}{n}}, \quad A_j=-(\partial E/\partial\lambda_j)_{S,\underset{\sim}{\lambda}}, \tag{7.1}$$

so that even chemical equilibrium can be discussed using these variables. Also it follows from the fundamental Pfaffian of thermodynamics, extended to include a change in a molecular parameter ξ, that

$$dE=TdS-PdV+\sum_i\mu_i du_i+Xd\xi, \tag{7.2}$$

$$=TdS-PdV-\sum_j A_j d\lambda_j+Xd\xi, \tag{7.3}$$

so that

$$X=(\partial A/\partial\xi)_{T,V,\underset{\sim}{n}}=(\partial E/\partial\xi)_{S,V,\underset{\sim}{n}}. \tag{7.4}$$

In terms of the chosen set, the IDS equations (6.1), (6.4) and (6.5) may be written

$$E-E_o=\tfrac{1}{2}(V_o-V)(P_o-\partial E/\partial V), \tag{7.5}$$

$$\partial E/\partial V+P_o+(V_o-V)(\partial^2E/\partial V^2+\tilde{E}_{VV})=0, \tag{7.6}$$

where $\tilde{E}_{VV}$ describes the contribution to the second derivative d^2E/dV^2 of the shift of the chemical equilibrium at constant entropy, and is given by

$$\tilde{E}_{VV}=-\sum_j\sum_k(\partial^2E/\partial\lambda_j\partial V)\,\tilde{A}_{jk}(\partial^2E/\partial\lambda_k\partial V) \tag{7.7}$$

where $\tilde{A}$ is inverse of the chemical stability matrix $\underset{\approx}{A}$ whose elements are

$$A_{jk}=-(\partial^2E/\partial\lambda_j\partial\lambda_k). \tag{7.8}$$

Consider now the effect of a change $\delta\xi$ in the value of the parameter ξ causing a general change δ in (7.5), (7.6) and (6.4):

$$\delta E=-\tfrac{1}{2}(P_o-\partial E/\partial V)\delta V-\tfrac{1}{2}(V_o -V)\delta(\partial E/\partial V), \tag{7.9}$$

$$\delta(\partial E/\partial V)-(\partial^2 E/\partial V^2+\hat{E}_{VV})\delta V +(V^o-V)[\delta(\partial^2 E/\partial V^2)+\delta\hat{E}_{VV}]=0, \tag{7.10}$$

$$\delta(\partial E/\partial \lambda_j)=O \qquad (j=1,2,..,n). \tag{7.11}$$

For any thermodynamic quantity Q we have

$$\delta Q=(\partial Q/\partial S)\delta S+(\partial Q/\partial V)\delta V +\sum_j(\partial Q/\partial \lambda_j)\delta\lambda_j+(\partial Q/\partial\xi)\delta\xi, \tag{7.12}$$

where the variables being held constant are obvious, and in particular the first-order form of (7.2) is

$$\delta E=T\delta S-P\delta V-\sum_j A_j\delta\lambda_j+X\delta\xi. \tag{7.13}$$

Now that we are sure of the independent variables we can return to using $P=-\partial E/\partial V$ etc. By substituting (7.13) into (7.9) and using (7.12) we get

$$[T-\tfrac{1}{2}(V_o-V)T_V]\delta S=\tfrac{1}{2}(V_o-V)\,\hat{E}_{VV}\delta V -[X-\tfrac{1}{2}(V_o-V)P_\xi]\delta\xi+\tfrac{1}{2}(V_o-V)\sum_i P_j\delta\lambda_j \tag{7.14}$$

where

$$T_V=\partial T/\partial V,\quad P_\xi=\partial P/\partial\xi \quad\text{and}\quad P_j=\partial P/\partial\lambda_j.$$

Similarly we get equations of this kind from (7.10) and (7.11). To solve them for the effect of $\delta\xi$ on S,V and the $\underset{\sim}{\lambda}$, we have to treat them as linear simultaneous equations.

We shall not proceed further with the full treatment allowing for mobile chemical equilibrium, since it clearly gives rise to extremely complicated equations. In any case, the effect of shifting the position of equilibrium depends on rather specific features of the chemistry of the detonation reactants and products. We are after a broad understanding of the phenomena, rather than a detailed one, and in the next section we shall abandon the chemical equilibrium conditions, and replace them by the constancy of the extents of reaction $\underset{\sim}{\lambda}$.

8. THE CASE OF FROZEN CHEMICAL EQUILIBRIUM

The equations simplify greatly if it is assumed that a change in the molecular parameter ξ does not affect the chemical equilibrium composition. Then (7.11) can be ignored, and (7.14) and (7.10) reduced to

$$[T+\tfrac{1}{2}(V_o-V)T_V]\delta S=-[X-\tfrac{1}{2}(V_o-V)P_\xi]\delta\xi \tag{8.1}$$

$$[T_V+(V_o-V)T_{VV}]\delta S=(V_o-V)P_{VV}\delta V +[P_\xi+(V_o-V)P_{\xi V}]\delta\xi, \tag{8.2}$$

where the quantities with subscripts are derivatives with respect to the subscripted variable holding the other members of the set S,V,$\underset{\sim}{n}$, ξ constant. Thus, for example,

$$\left.\begin{aligned} T_V&=(\partial T/\partial V)_{S,\xi}=\partial^2 E/\partial S\,\partial V,\\ P_\xi&=(\partial P/\partial\xi)_{S,V}=-\partial^2 E/\partial V\,\partial\xi. \end{aligned}\right\} \tag{8.3}$$

Equation (8.1) already gives the change in entropy with ξ for the CJ IDS, namely

$$(\partial S/\partial\xi)_{CJ}=-(X+\tfrac{1}{2}\Delta V.P_\xi)/(T-\tfrac{1}{2}\Delta V.T_V), \tag{8.4}$$

where $\Delta V=V-V_o$ is the total change in the specific volume (<0).

By substituting (8.1) into (8.2) we get for the volume derivative

$$\left[\frac{\partial V}{\partial \xi}\right]_{CJ}=\frac{XT_V+TP_\xi-\Delta V(XT_{VV}+TP_{\xi V})+\frac{1}{2}(\Delta V)^2(T_VP_{\xi V}-P_\xi T_{VV})}{P_{VV}\Delta V(T-\frac{1}{2}\Delta V.T_V)} \quad . \tag{8.5}$$

The pressure and temperature coefficients can now be obtained from the equations

$$(\partial P/\partial \xi)_{CJ}=P_\xi+P_S(\partial S/\partial \xi)_{CJ}+P_V(\partial V/\partial \xi)_{CJ} \tag{8.6}$$

$$(\partial T/\partial \xi)_{CJ}=T_\xi+T_S(\partial S/\partial \xi)_{CJ}+T_V(\partial V/\partial \xi)_{CJ}. \tag{8.7}$$

The change in the detonation velocity D is of special interest, and can be deduced from the equation

$$D^2=V_o^2\,(P-P_o)/(V_o-V) \tag{8.8}$$

which follows from (6.5) and (6.6). We have

$$\delta D^2=V_o^2\,[\delta P+(P-P_o)\delta V/(V_o-V)]/(V_o-V),$$

which can be reduced to

$$\delta D^2=V_o^2[P_S\delta S+P_\xi\delta\xi)]/(V_o-V). \tag{8.9}$$

For the fractional change in D for a fractional change in ξ under IDS conditions we get

$$\frac{\xi}{D}\left[\frac{\partial D}{\partial \xi}\right]_{CJ}=\left[\frac{\partial \log D}{\partial \log \xi}\right]_{CJ}=\frac{1}{\Delta P}\left[\frac{T_\xi P_\xi+T_V\xi X}{2T-\Delta V.T_V}\right] \tag{8.10}$$

The various thermodynamic derivatives of E with respect to S and V occurring in equations (4.4) to (8.10) are not convenient for calculations, and need to be related to derivatives of A with respect to T and V, which can be done by means of standard thermodynamics.

9. RESULTS ASSUMING FROZEN CHEMICAL EQUILIBRIUM

In this preliminary study the greatest practical interest lies in gaining an understanding of the effect of global errors in the intermolecular parameters affecting the IDS properties through the thermodynamic equation of state rather than through the possible idiosyncrasies of the chemical reactions. The calculations presented here are therefore for overall changes in the parameters ε,σ and α assuming frozen chemical equilibrium.

In Table 1 we present some typical sensitivity results for the ideal detonation state of an explosive like PETN. The assumed initial state has reduced density 1.35, and the final detonation state has reduced density $\varrho_{a\varphi}=1.8$ and reduced temperature $T_{CJ}=30$. The thermodynamic properties were calculated using the modified Weeks-Chandler-Anderson (WCA) hard-sphere perturbation theory recently proposed by Ree and co-workers (3), assuming the 13.5-exp-6 intermolecular potential and an ideal heat capacity $C_V/R=4.75$; the predicted reduced detonation pressure is $P_{CJ}=262$.

The results shown in Table 1 are broadly in keeping with intuition, but do hold a few surprises. The density and temperature are the least sensitive properties, which is perhaps unexpected, while the size parameter σ and the repulsion index α are the most important parameters, which is as expected. (Note that the actual size parameter σ used was the distance of the potential minimum r_m rather than the conventional collision diameter). The sensitivity of the detonation pressure P_{CJ} to errors in σ and α is surprising: a 1% error in all the molecular sizes will increase the pressure by 4%, and a similar error in α (e.g. from 13.50 to 13.64) will increase it by 6% (i.e. from 262 to 278 in reduced units). Another surprising feature of the results is the comparative importance of the intermolecular potential well-depth ε for the detonation velocity and pressure, even at a temperature some 30 times greater than ε/k_B. Thus a 2.5% error in the ε's is enough to alter the detonation velocity by 1%. However, this assumes that σ and α are constant, and therefore involves a shift in the whole potential wave. It is therefore not so suprising.

10. CONCLUSION

It has been shown that it is possible to set up a simple theory for the sensitivity analysis of calculations of the ideal detonation state to errors in intra-molecular and inter-molecular parameters. The analysis has only been developed explicitly for the case of frozen chemical equilibrium, and has only been applied to errors in inter-molecular force parameters, for which results have been calculated for overall changes in a typical case. The theory can clearly be extended to the actual case of mobile chemical equilibrium and applied to the probably less important errors in intra-molecular

TABLE 1

Overall fractional sensitivity coefficients ∂ Log (property)/∂ Log (parameter) for IDS properties to errors in inter-molecular force parameters

IMF Parameter	Ideal detonation state property			
	Velocity	Density	Pressure	Temperature
	D_{CJ}	ϱ_{CJ}	P_{CJ}	T_{CJ}
Energy well-depth ε	0.39	−0.02	0.72	0.04
Diameter at minimum σ	2.42	−0.27	4.03	−0.54
Repulsion index α	2.91	0.13	6.22	−0.40

properties. However, the results presented in Table 1 already sharpen one's perception both of the order of accuracy to be expected in an IDS calculation even with the best thermodynamic equation of state, and of the relative importance of the various inter-molecular parameters.

It is a pleasure to thank the members of the ICI Detonation Research Group at Ardeer for their interest and help in this work, and in particular Dr. C.M. Lownds and Mr. Gwyn Harries. I am also grateful to Dr. F. H. Ree for a comment made at the Symposium.

REFERENCES

1. L.D. Landau and E.M. Lifschitz, Statistical Physics (Part 1), 3rd edition, p. 49, Pergamon, Oxford, 1980.
2. W. Fickett and W. C. Davis, Detonation, University of California, Berkeley, 1978.
3. H.S. King, C.S. Lee, T. Ree and F.H. Ree "A perturbation theory of classical equilibrium fluids," J. Chem. Phys. Vol. 82, No. 1, pp. 414-423, Jan. 1985.

DERIVATIVES OF THE CHAPMAN-JOUGUET STATE

B.D. Lambourn
AWRE, Aldermaston
READING, England

In this paper the Jones-Stanyukovich-Manson relations for the partial derivative of detonation velocity with initial density and detonation energy are extended to give the partial derivatives of Chapman-Jouguet pressure, specific volume adiabatic exponent γ, using second order derivatives of the equation of state. As an example, the CJ derivatives are calculated for a JWL equation of state for a typical high explosive.

1. INTRODUCTION

Except for very simple cases, the Chapman-Jouguet (CJ) parameters for any equation of state for detonation products have to be determined by solving a set of non-linear equations. The non-linear equations would have to be solved repeatedly for the CJ parameters at any other initial density (ϱ_0) or detonation energy (E_0). However, this problem would be eased in local regions of the $\varrho_0 - E_0$ plane, if the partial derivatives of the CJ parameters could be evaluated.

The Jones-Stanyukovich-Manson (JSM) relation (1,2) gives the derivatives of detonation velocity (D) with ϱ_0 and E_0 in terms of first order differentials of the equation of state (EOS), by differentiating the Hugoniot curve and Rayleigh line relations. In this paper, the JSM relations are extended to the partial derivatives of the other CJ parameters in terms of both first and second order differentials of the EOS, by differentiating one of the CJ relations.

The CJ and JSM relations are derived in Section 2 following the method of Wood and Fickett (1). The extended derivatives are developed in Section 3 and applied to a typical equation of state in Section 4.

2. The Chapman-Jouguet and Jones-Stanyukovich-Manson Relations

For a steady state detonation wave the Rankine-Hugoniot relations hold. In particular the locus of states which could exist at the end of the reaction zone are given by the Hugoniot relation and Rayleigh line:

$$E = E_0 + \frac{1}{2} p(v_0 - v) \tag{1}$$

$$\frac{D^2}{v_0^2} = \frac{p}{v_0 - v} \tag{2}$$

where p is pressure, v is specific volume, v_0 is initial specific volume, E is specific internal energy, E_0 is detonation energy and D is detonation velocity.

E is related to p and v through the equation of state and the detonation products

$$E = E(p,v) \tag{3}$$

In general for any detonation velocity, the Rayleigh line intersects the Hugoniot 0, 1 or 2 times. The Chapman-Jouguet sonic condition requires that steady state plane detonation velocity is given by that Rayleigh line which is tangent to the Hugoniot, ie at the CJ state

$$\left(\frac{\partial p}{\partial v}\right)_H\Big|_{cj} = - \frac{p_{cj}}{v_0 - v_{cj}} \tag{4}$$

2.1 First Derivatives of the Equation of State

Before deriving the CJ conditions, it is necessary to define some parameters for a general form of equation of state for the detonation products. Letting subscripts p and v represent

partial derivations of internal energy so that

$$E_P = \left(\frac{\partial E}{\partial p}\right)_v ; E_v = \left(\frac{\partial E}{\partial v}\right)_p \tag{5}$$

then two non-dimensional parameters can be defined

$$\Gamma = v/E_p ; \alpha = p/E_v \tag{6}$$

where Γ is Gruneisen Gamma, and α is a corresponding parameter defined by Jones (3).

Differentiating the EOS (3) at constant entropy S, remembering that

$$\left(\frac{\partial E}{\partial v}\right)_S = - p$$

and using the definition of the adiabatic exponent γ as

$$\gamma = - \frac{v}{p}\left(\frac{\partial p}{\partial v}\right)_S = - \left(\frac{\partial \ln p}{\partial \ln v}\right)_S \tag{7}$$

gives the general thermodynamic relation

$$\gamma p E_p = v(E_v + p) \tag{8}$$

which from (6) may be written

$$\gamma = \Gamma(\alpha + 1)/\alpha ; \Gamma = \frac{\alpha\gamma}{\alpha + 1} \tag{9}$$

or $$\alpha = \frac{\Gamma}{\gamma - \Gamma}$$

2.2 The Chapman-Jouguet State

The locus of p-v states along with the Hugoniot curve is given by (1). Differentiating wrt v along the Hugoniot at constant E_o and v_o gives

$$E_p\left(\frac{dp}{dv}\right)_H + E_v = \frac{1}{2}(v_o - v)\left(\frac{dp}{dv}\right)_H - \frac{1}{2}p$$

But as the CJ state, $\left(\frac{dp}{dv}\right)_H$ is given by (4). Hence the Chapman-Jouguet state is, using (8),

$$\gamma_{cj} = \frac{v_{cj}}{v_o - v_{cj}} \text{ or } \frac{v_{cj}}{v_o} = \frac{\gamma_{cj}}{\gamma_{cj} + 1} \tag{10}$$

The CJ pressure is given by the Rayleigh line (2):

$$p_{cj} = \frac{\rho_o D^2}{\gamma_{cj} + 1} \tag{11}$$

For clarity in this paper, the subscript cj will henceforth be dropped, it being understood that all parameters are evaluated at the CJ state.

2.3 The Jones-Stanyukovich-Manson Relation

The Chapman-Jouguet relations (10), (11) hold for a given initial charge density and detonation energy. We now wish to find how conditions vary along the locus of CJ states as ρ_o and E_o vary. For each initial state, the CJ state satisfies the Rayleigh line and Hugoniot. We began by differentiating the Rayleigh line written in the form

$$p v_o^2 = D^2(v_o - v)$$

along the locus of CJ state giving

$$v_o^2 dp + 2pv_o dv_o = 2(v_o - v)DdD + D^2 dv_o - D^2 dv$$

Dividing by pv_o^2 and using (10) and (11) gives

$$\frac{dp}{p} + \gamma\frac{dv}{v} = (\gamma - 1)\frac{dv_o}{v_o} + 2\frac{dD}{D} \tag{12}$$

Now differentiating the Hugoniot (1), along the locus of CJ states allowing E_o and v_o to vary and substituting for E_p and E_v from (6), and using (10) gives

$$\frac{dp}{p} + \gamma\frac{dv}{v} = \frac{\alpha}{\alpha + 2}\left[(\gamma + 1)\frac{dv_o}{v_o} + \frac{2\gamma}{pv}dE_o\right] \tag{13}$$

Equating the right hand sides of (12) and (13) and using (10), (11) gives the Jones-Stanyukovich-Manson result

$$\frac{dD}{D} = \frac{\gamma - 1 - \alpha}{\alpha + 2}\frac{d\rho_o}{\rho_o} + \frac{\alpha(\gamma + 1)^2}{\alpha + 2}\frac{dE_o}{D^2} \tag{14}$$

The variations of detonation velocity with density and detonation energy are given by

$$\left(\frac{\partial \ln D}{\partial \ln \rho_o}\right)_{E_o} = \frac{\gamma + 1}{\alpha + 2} - 1 \tag{15}$$

$$\left(\frac{\partial D^2}{\partial E_o}\right)_{\rho_o} = \frac{2\alpha(\gamma + 1)^2}{\alpha + 2} \tag{16}$$

The LHS of (15) was written by Jones as b. Then from (15)

$$(\gamma + 1) = (\alpha + 2)(1 + b) \tag{17}$$

Hence detonation pressure p_{cj}

$$p_{cj} = \frac{\rho_o D^2}{\gamma + 1} = \frac{\rho_o D^2}{(\alpha + 2)(1 + b)}$$

Since for a typical explosive with $\varrho_o = 1.75$ g/cm^3 D $\sim$ 0.8 cm/μs.

$$\frac{dD}{d\varrho_o} \sim 0.31 \therefore b \sim \frac{1.75}{0.8}.0.31 \sim 0.68$$

If $\alpha \sim 0.25$ then $\gamma \sim 2.78$. Hence in principle good estimates of the Chapman-Jouguet conditions can be determined from the measured gradient of detonation velocity with density.

3. DERIVATIVES OF p_{cj} AND v_{cj}

Equations (12) and (13) cannot be solved to find the variation of CJ pressure and specific volume with density and detonation energy. The simplest way of deriving a third equation is to differentiate the CJ relation (10) regarding the thermodynamic parameter γ as a function of p and v. It is convenient to take logs first. Then

$$G\frac{dp}{p} + (\gamma + 1 + H)\frac{dv}{v} = (\gamma + 1)\frac{dv_o}{v_o} \qquad (18)$$

where

$$G = -\left(\frac{\partial \ell n\gamma}{\partial \ell np}\right)_v ; H = -\left(\frac{\partial \ell n\gamma}{\partial \ell nv}\right)_p \qquad (19)$$

are non-dimensional parameters which are clearly zero for a perfect gas.

To find the derivatives of p_{cj} and v_{cj} it is necessary to solve (18) with (12) or (13). Choosing the latter gives

$$\frac{dp}{p} = \Big[-\{\gamma - \frac{(\gamma + 1 + H)}{\alpha + 2}\alpha\}(\gamma + 1)\frac{dv_o}{v_o} + (\gamma + 1 + H)\frac{2\alpha}{\alpha + 2}\gamma\frac{dE_o}{pv}\Big] / \{\gamma(1 - G) + 1 + H\} \qquad (20)$$

$$\frac{dv}{v} = \Big[\{1 - \frac{\alpha G}{\alpha + 2}\}(\gamma + 1)\frac{dv_o}{v_o} - \frac{2\alpha}{\alpha + 2}G\frac{\gamma dE_o}{pv}\Big] / \{\gamma(1 - G) + 1 + H\} \qquad (21)$$

The variation of the adiabatic exponent γ along the locus of Chapman-Jouguet states can be found from (10) and (21)

$$\frac{d\gamma}{\gamma} = (\gamma + 1)\left(\frac{dv}{v} - \frac{dv_o}{v_o}\right)$$

or

$$\frac{d\gamma}{\gamma} = \Big[\{\gamma G - H - \frac{\alpha(\gamma + 1)G}{\alpha + 2}\}(\gamma + 1)\frac{dv_o}{v_o} - \frac{\alpha}{\alpha + 2}(\gamma + 1)G\frac{\gamma dE_o}{pv}\Big] / \{\gamma(1 - G) + 1 + H\} \qquad (22)$$

Equations (20), (21) and (22) are general relations applying to any EOS for detonation products. They give the variation of Chapman-Jouguet pressure, specific volume and γ with initial density and detonation energy. Some typical values of the coefficients will be given in Section 4 for a JWL equation of state.

G and H, the logarithmic derivatives of γ at constant v and constant p are unfamiliar parameters of the EOS. There are many other ways in which these second order derivatives could be expressed, but it seems reasonable to relate them to derivatives of α, Γ and γ along an adiabat. In the remainder of the section G and H and hence the derivatives of the CJ state will be expressed first in terms of first order derivatives of γ and Γ at constant entropy, and then in terms of derivatives of γ and α at constant entropy.

3.1 G and H in Terms of Second Derivatives of E

Taking logs and differentiating (8) wrt ℓnp at constant v and wrt ℓn v at constant p gives from (19)

$$G = 1 + \frac{\gamma pE_{pp} - v(E_{vp} + 1)}{\gamma E_p} \qquad (23)$$

$$H = \frac{v(\gamma pE_{pv} - vE_{vv})}{\gamma pE_p} - 1 \qquad (24)$$

3.2 G and H in Terms of Derivatives of γ and Γ

We begin by differentiating Γ from equation (6) logarithmically wrt ℓn p and then ℓn v

$$\left(\frac{\partial \ell n\Gamma}{\partial \ell np}\right)_v = -\frac{pE_{pp}}{E_p} \qquad (25)$$

$$\left(\frac{\partial \ell n\Gamma}{\partial \ell nv}\right)_p = 1 - \frac{vE_{pv}}{E_p} \qquad (26)$$

We also note that along an adiabatic, regarding Γ as a function of p and v

$$\frac{\partial \ell n \Gamma}{\partial \ell n v}\Big)_S = \frac{\partial \ell n \Gamma}{\partial \ell n v}\Big)_p - \gamma \frac{\partial \ell n \Gamma}{\partial \ell n p}\Big)_v \quad (27)$$

or

$$\frac{\partial \ell n \Gamma}{\partial \ell n v}\Big)_S = 1 + \frac{\gamma p E_{pp} - v E_{pv}}{E_p} \quad (28)$$

Hence combining with (23) and (6) to eliminate derivatives of E we find

$$G = 1 - \frac{\Delta}{\gamma} \quad (29)$$

where

$$\Delta = \Gamma + 1 - \frac{\partial \ell n \Gamma}{\partial \ell n v}\Big)_S \quad (30)$$

It can be shown that

$$\Delta = \frac{\partial K}{\partial p}\Big)_v$$

Where K is the bulk modulus, by using (23) and remembering that $K = \gamma p$.

It is not possible to express E_{vv} in terms of derivatives of Γ, but corresponding to (27)

$$\frac{\partial \ell n \gamma}{\partial \ell n v}\Big)_S = \frac{\partial \ell n \gamma}{\partial \ell n v}\Big)_p - \gamma \frac{\partial \ell n \gamma}{\partial \ell n p}\Big)_v$$

Hence from (19)

$$H = \gamma G - \frac{\partial \ell n \gamma}{\partial \ell n v}\Big)_S \quad (31)$$

Swan and Thornhill (4) defined δ the second adiabatic exponent in terms of second and third order derivatives of E wrt v at constant S. It is shown in the appendix that

$$\delta = \gamma + 1 - \frac{\partial \ell n \gamma}{\partial \ell n v}\Big)_S \quad (32)$$

Hence

$$H = \delta - \Delta - 1 \quad (33)$$

It is also interesting to note from (29) that the denominator in equations (20) to (22)

$$\gamma(1 - G) + 1 + H = \delta \quad (34)$$

Hence the derivatives of D, p, and v and γ along the trajectory of CJ states are given in non-dimensional form by

$$\frac{\partial \ell n D}{\partial \ell n \varrho_o} = \gamma \frac{(\gamma - 1 - \Gamma)}{2\gamma - \Gamma};$$

$$\frac{\partial D^2}{\partial E_o} = \frac{2\Gamma(\gamma + 1)^2}{2\gamma - \Gamma} \quad (35)$$

$$\frac{\partial \ell n p_{cj}}{\partial \ell n \varrho_o} = \left\{ \gamma - \left(\frac{\gamma + \delta - \Delta}{2\gamma - \Gamma}\right)\Gamma \right\} \frac{(\gamma + 1)}{\delta};$$

$$\frac{1}{\varrho_o}\frac{\partial p_{cj}}{\partial E_o} = \left(\frac{2\Gamma}{2\gamma - \Gamma}\right)\left(\frac{\gamma + \delta - \Delta}{\delta}\right)(\gamma + 1) \quad (36)$$

$$\frac{\partial \ell n v_{cj}}{\partial \ell n v_o} = \left\{ 1 - \left(\frac{\gamma - \Delta}{2\gamma - \Gamma}\right)\frac{\Gamma}{\gamma} \right\} \frac{(\gamma + 1)}{\delta};$$

$$p_{cj}\frac{\partial v_{cj}}{\partial E_o} = -\left(\frac{2\Gamma}{2\gamma - \Gamma}\right)\frac{(\gamma - \Delta)}{\delta} \quad (37)$$

$$\frac{\partial \ell n \gamma_{cj}}{\partial \ell n \varrho_o} = -\left\{\gamma + 1 - \delta - \frac{(\gamma+1)(\gamma-\Delta)}{(2\gamma-\Gamma)}\frac{\Gamma}{\gamma} \times \frac{(\gamma + 1)}{\delta}\right.;$$

$$D^2\frac{\partial \gamma_{cj}}{\partial E_o} = -\left(\frac{2\Gamma}{2\gamma - \Gamma}\right)\frac{(\gamma + 1)^3(\gamma - \Delta)}{\delta} \quad (38)$$

3.3 G and H in Terms of Derivatives of γ and α

Following the same path, but differentiating α logarithmically wrt p at constant entropy

$$\frac{\partial \ell n \alpha}{\partial \ell n p}\Big)_S = 1 - \frac{\gamma p E_{vp} - v E_{vv}}{\gamma^{\Gamma}_{v}} \quad (39)$$

Eliminating derivatives of E using (6), (8) and (24) gives an expression for H

$$H = \gamma\chi - 1 \quad (40)$$

where

$$\chi = \frac{1 - \frac{\partial \ell n \alpha}{\partial \ell n p}\Big)_S}{\alpha + 1} \quad (41)$$

and it can be shown that

$$\chi = \frac{\partial (v/\gamma)}{\partial v}\Big)_p \quad (42)$$

To find an expression for G it is necessary to use the adiabatic derivative of γ wrt p giving

$$G = \frac{H}{\gamma} - \frac{\partial \ell n \gamma}{\partial \ell n p}\Big)_S \quad (43)$$

It is shown in the appendix that corresponding to Thornhill's adiabatic exponent there is a pressure exponent ξ

$$\xi = \frac{1}{\gamma}\left[1 + \frac{\partial \ell n \gamma}{\partial \ell n p}\Big)_S\right] \quad (44)$$

Hence from (40), (43) and (44)

$$G = \chi - \xi \quad (45)$$

As before the denominator in equations (20) to (22) simplifies to

$$\gamma(1 - G) + 1 + H = \gamma(1 + \xi) \qquad (46)$$

Hence from (20) to (22) the differentials of the CJ conditions become in non-dimensionalised form

$$\frac{\partial \ln D}{\partial \ln \rho_o} = \frac{\gamma + 1}{\alpha + 2} - 1;$$

$$\frac{\partial D^2}{\partial E_o} = \frac{2\alpha(\gamma + 1)^2}{\alpha + 2} \qquad (47)$$

$$\frac{\partial \ln p_{cj}}{\partial \ln \rho_o} = (1 - \frac{\alpha(1 + \chi)}{\alpha + 2})(\frac{\gamma + 1}{1 + \xi});$$

$$\frac{1}{\rho_o}\frac{\partial p_{cj}}{\partial E_o} = (\frac{2\alpha}{\alpha + 2})(\frac{1 + \chi}{1 + \xi})(\gamma + 1) \qquad (48)$$

$$\frac{\partial \ln v_{cj}}{\partial \ln v_o} = \{1 - \frac{\alpha(\chi - \xi)}{\alpha + 2}\}\frac{(\gamma + 1)}{\gamma(1 + \xi)};$$

$$p_{cj}\frac{dv_{cj}}{dE_o} = -(\frac{2\alpha}{\alpha + 2})(\frac{\chi - \xi}{1 + \xi}) \qquad (49)$$

$$\frac{\partial \ln \gamma_{cj}}{\partial \ln \rho_o} = -\{1 - \gamma\xi - \frac{\alpha(\gamma + 1)}{\alpha + 2}(\chi - \xi)\}$$

$$\frac{(\gamma + 1)}{\gamma(1 + \xi)};$$

$$D^2\frac{d\gamma_{cj}}{dE_o} = -(\frac{2\alpha}{\alpha + 2})\frac{(\gamma + 1)^3(\chi - \xi)}{1 + \xi} \qquad (50)$$

4. EXAMPLE - THE JWL EQUATION OF STATE

As an example, we consider the JWL equation of state (5) for detonation products, which is of Gruneisen form with constant Gruneisen Gamma. It can be written

$$E = \frac{pv}{w} - (\frac{k_1 v - w}{k_1 w})A \exp(-k_1 v)$$

$$-(\frac{k_2 v - w}{k_2 w})B \exp(-k_2 v) \qquad (51)$$

where A, B, k_1, k_2 and w are constants for a given explosive.

Partially differentiating (51) wrt p and v gives

$$E_p = \frac{v}{w}$$

$$E_v = \Big[p + (k_1 v - 1 - w)A \exp(-k_1 v) + (k_2 v - 1 - w)B \exp(-k_2 v)\Big]/w \qquad (53)$$

Hence from (6)

$$\Gamma = v/E_p = w \qquad (54)$$

$$\alpha = p/E_v = w/\Big[1 + \frac{1}{p}\{(k_1 v - 1 - w)A \exp(-k_1 v) + (k_2 v - 1 - w)B \exp(-k_2 v)\}\Big] \qquad (55)$$

So that Γ is constant and α is a function of p and v, s.t $\alpha \to w$ as $v \to \infty$.

From (9) we can find γ

$$\gamma = \frac{v(E_v + p)}{pE_p} = 1 + w + \Big[(k_1 v - 1 - w)A \exp(-k_1 v) + (k_2 v - 1 - w)B \exp(-k_2 v)\Big]/p \qquad (56)$$

So that $\gamma \to (1 + w)$ as $v \to \infty$.

The second derivatives of E are

$$E_{pp} = 0 \qquad (57)$$

$$E_{pv} = \frac{1}{w} \qquad (58)$$

$$E_{vv} = -\frac{k_1}{w}(k_1 v - 2 - w)A \exp(-k_1 v) - \frac{k_2}{w}(k_2 v - 2 - w)B \exp(-k_2 v) \qquad (59)$$

From these equations we can find the non-dimensional parameters

$$G = \Big(\frac{\partial \ln \gamma}{\partial \ln p}\Big)_v = 1 + \frac{\gamma\rho E_{pp} - v(E_{vp} + 1)}{\gamma E_p}$$

$$= 1 - \frac{1 + w}{\gamma} \qquad (60)$$

$$H = -\left(\frac{\partial \ell n \gamma}{\partial \ell n v}\right)_p = \frac{v(\gamma p E_{pv} - v E_{vv})}{\gamma p E_p} - 1$$
$$= \left[k_1 v(k_1 v - 2 - w) A \exp(-k_1 v) + k_2 v(k_2 v - 2 - w) B \exp(-k_2 v) \right] / (\gamma p) \quad (61)$$

so that

$$\Delta = \Gamma + 1 - \left(\frac{\partial \ell n \Gamma}{\partial \ell n v}\right)_S = 1 + w \quad (62)$$

and δ, χ and ξ follow from (33), (40) and (45).

In particular

$$\delta = \gamma + 1 - \left(\frac{\partial \ell n \gamma}{\partial \ell n v}\right)_S = H + \Delta + 1$$
$$= 2 + w + \left[k_1 v(k_1 v - 2 - w) A \exp(-k_1 v) + k_2 v(k_2 v - 2 - w) B \exp(-k_2 v)\right] / (\gamma p) \quad (63)$$

4.1 Numerical Example

In reference (6), Bailey et al. gave the JWL parameters for an explosive with composition 95 w/o HMX, 5 w/o polyurethane as

$\rho_o = 1.787$ g/cc
$p_{cj} = 0.36$ Mbar
$A = 7.41073$ Mbar
$B = 0.0180222$ Mbar
$C = 0.0180019$ Mbar
$D = 0.8761$ cm/μs
$E_o = 0.0713979$ Mbar cc/g
$k_1 = 7.95215$ g/cc
$k_2 = 2.8592$ g/cc
$w = 0.25$

which has non-dimensional parameters

$\gamma_{cj} = 2.81004$

$\alpha = 0.0976548$	$\Gamma = 0.25$
$G = 0.555166$	$H = 0.862667$
$\delta = 3.11267$	$\Delta = 1.25$
$\xi = 0.107695$	$\chi = 0.662862$

and some non-dimensional derivatives of the CJ state are

$$\frac{\partial \ell n D}{\partial \ell n \rho_o} = 0.816 \qquad \frac{\partial D^2}{\partial E_o} = 1.352$$

$$\frac{\partial \ell n p_{cj}}{\partial \ell n \rho_o} = 3.17 \qquad \frac{1}{\rho_o}\frac{\partial p_{cj}}{\partial E_o} = 0.533$$

$$\frac{\partial \ell n v_{cj}}{\partial \ell n v_o} = 1.192 \qquad p_{cj}\frac{\partial v_{cj}}{\partial E_o} = -0.0467$$

$$\frac{\partial \ell n \gamma_{cj}}{\partial \ell n \rho_o} = -0.733 \qquad D^2\frac{\partial \gamma_{cj}}{\partial E_o} = -2.581$$

It is convenient to evaluate the changes in the CJ parameters for a change of 0.01 g/cc in density and 100 cal/g in E_o

	+ 0.01 g/cc	+ 100 cal/g
D	+ 0.04 mm/μs	+ 0.032 mm/μs
p_{cj}	+ 6.4 kbar	+ 4.0 kbar
v_{cj}	− 0.0028 cm^3/g	− 0.00054 cm^3/g
γ	− 0.012	− 0.014

Note that if a simple polytropic equation of state had been used the derivatives would have been totally different. For a perfect gas with $\gamma = \gamma_{cj} = 2.81004$

$$\frac{\partial \ell n D}{\partial \ell n \rho_o} = 0 \qquad \frac{\partial D^2}{\partial E_o} = 2(\gamma^2 - 1) = 13.79$$

$$\frac{\partial \ell n p_{cj}}{\partial \ell n \rho_o} = 1 \qquad \frac{1}{\rho_o}\frac{\partial p_{cj}}{\partial E_o} = 2(\gamma - 1) = 3.620$$

$$\frac{\partial \ell n v_{cj}}{\partial \ell n v_o} = 1 \qquad p_{cj}\frac{\partial v_{cj}}{\partial E_o} = 0$$

$$\frac{\partial \ell n \gamma_{cj}}{\partial \ell n \rho_o} = 0 \qquad D^2\frac{\partial \gamma_{cj}}{\partial E_o} = 0$$

SUMMARY

The Jones-Stanyukovich-Manson relations for the partial derivatives of detonation velocity with initial loading density ρ_o and detonation energy E_o, have been extended in this paper to give the derivatives of p_{cj}, v_{cj} and γ_{cj} with ρ_o and E_o in terms of second order derivatives of a general E(p,v) equation of state for the detonation products. Typical values of the derivatives have been calculated from the JWL parameters of an HE.

Given one evaluation of CJ conditions and an equation of state, the derivatives can be used, for example, to estimate the CJ pressure at a slightly different loading density or composition, or at a different initial temperature.

REFERENCES

1. W. W. Wood & W. Fickett: "Investigation of the Chapman-Jouguet Hypothesis by the 'Inverse Method' "; Phys-Fluids *6*, 648-652 (1963).
2. W. Fickett & W. C. Davis: "Detonation," (University of California Press, 1979).
3. H. Jones: "The Properties of Gases at High Pressure Which Can be Deduced from Explosion Experiments," 3rd Symposium on Combustion, Flame and Explosion Phenomena, 590-594 (Baltimore 1949).
4. G. W. Swan & C. K. Thornhill: "Thermodynamic Systems for Solids and Liquids," J. Mech. Phys. Solids, *22*, 349-370 (1974).
5. J. W. Kury, et al.: "Metal Acceleration by Chemical Explosives," 4th Symposium on Detonation, USNOL (October 1965), ACR-126.
6. W. Bailey, et al.: "Explosive EOS Determination by the AWRE Method," 7th Symposium on Detonation, NSWC MP 82-334 (June 1981).

APPENDIX

Summary of Parameters and Their Adiabatic Derivatives

In terms of first and second partial derivatives of specific internal energy, the thermodynamic parameters used in this paper are

$$\Gamma = v/E_p \tag{A1}$$

$$\Delta = \left(\frac{\partial K}{\partial p}\right)_v = \Gamma + 1 - \left(\frac{\partial \ell n \Gamma}{\partial \ell n v}\right)_S$$

$$= \frac{V}{E_p}\left\{1 + \frac{\gamma p v E_{vp} - \gamma^2 p^2 E_{pp}}{\gamma p v}\right\} \tag{A2}$$

$$\alpha = p/E_v \tag{A3}$$

$$\chi = \left(\frac{\partial v/\gamma}{\partial v}\right)_p = \frac{1 - \left(\frac{\partial \ell n \alpha}{\partial \ell n p}\right)_S}{1 + \alpha}$$

$$= \frac{\gamma p v E_{pv} - v^2 E_{vv}}{\gamma v (E_v + p)} \tag{A4}$$

$$\gamma = -\left(\frac{\partial \ell n p}{\partial \ell n v}\right)_S = \frac{v(E_v + p)}{p E_p} \tag{A5}$$

$$\delta = \gamma + 1 - \left(\frac{\partial \ell n \gamma}{\partial \ell n v}\right)_S$$

$$= \frac{v}{E_p}\left\{1 - \frac{\gamma^2 p^2 E_{pp} - 2\gamma p v E_{pv} + v^2 E_{vv}}{\gamma p v}\right\} \tag{A6}$$

$$\xi = \frac{1}{\gamma}\left[1 + \gamma\left(\frac{\partial \ell n \gamma}{\partial \ell n p}\right)_S\right]$$

$$= \frac{p}{(E_v + p)}\left\{1 - \left[\gamma^2 p^2 E_{pp} - 2\gamma p v E_{pv} + v^2 E_{vv}\right] / (\gamma p v)\right\} - 1 \tag{A7}$$

It follows that

$$\gamma = \Gamma(\alpha + 1)/\alpha \tag{A8}$$

$$\delta = \gamma(1 + \xi) = \gamma\chi + \Delta \tag{A9}$$

Swan and Thornhill (4) define the first and second Adiabatic Exponents as

$$\gamma = -v\left(\frac{\partial^2 E}{\partial v^2}\right)_S \Big/ \left(\frac{\partial E}{\partial v}\right)_S \tag{A10}$$

$$\delta = -v\left(\frac{\partial^3 E}{\partial v^3}\right)_S \Big/ \left(\frac{\partial^2 E}{\partial v^2}\right)_S \tag{A11}$$

Correspondingly ξ can be defined by

$$\xi = -p\left(\frac{\partial^2 E}{\partial p^2}\right)_S \Big/ \left(\frac{\partial E}{\partial p}\right)_S \tag{A12}$$

from which the first parts of equations (A6) and (A7) follow, by differentiating

$$p = -\left(\frac{\partial E}{\partial v}\right)_S$$

and using (A5).

EQUATION OF STATE FOR DETONATION PRODUCTS

W. C. Davis
Los Alamos National Laboratory
Los Alamos, N.M. 87545

The concepts of hydrodynamics and thermodynamics as they apply to equations of state for explosive products are collected and discussed. The physics behind the behavior of dense gases is considered. Some ideas about applications are presented. This paper is intended as an introduction to the subject of equation of state for detonation products.

I. INTRODUCTION

The concepts and formulas that are pertinent to the development and use of an equation of state for explosive products gases, taken from hydrodynamics, thermodynamics, and the physics of gases are collected and discussed in this paper. Perhaps having them collected in one place will help clarify the confusing subject usually called "equation of state" by those who work with explosives.

The second and third sections are devoted to the equations of hydrodynamics and their solutions. The fourth section presents thermodynamics for use with hydrodynamics, and the fifth a discussion of incomplete equations of state as they are used for explosives. The sixth section presents the simple physical principles that determine the general form for an equation of state. Sections seven, eight, and nine discuss engineering applications, the choice of a fitting form for an equation of state, and the calibration of the fitting form.

This paper is intended to be an introduction to the mysteries of the subject, and is certainly not the final description of all the intricacies.

II. EQUATIONS OF HYDRODYNAMICS

The equations for the conservation of mass, momentum, and energy, for flow in one dimension, can be written as

$$\dot{v} - v u_x = 0 \tag{2.1}$$

$$\dot{u} + v p_x + A = 0 \tag{2.2}$$

$$\dot{\left(E + \tfrac{1}{2}u^2 \right)} + v(pu)_x = B \tag{2.3}$$

where v is the specific volume, u is the particle velocity, p is the pressure, and E is the specific internal energy. The dot denotes the total time derivative such that $\dot{v} = \partial v/\partial t + u\, \partial v/\partial x$, and $u_x = \partial u/\partial x$ is a partial derivative. In Eq. (2.3) the term $E + \frac{1}{2}u^2$ is the sum of the internal and kinetic energies, and is the total specific energy of the fluid element. The term A in Eq. (2.2) represents nonequilibrium processes that transfer momentum, usually viscous effects. The term B in Eq. (2.3) represents nonequilibrium processes that transfer energy, usually viscous and thermal diffusion processes.

In addition to these equations, there is an equilibrium equation of state for the material

$$E = E(p,v) \tag{2.4}$$

that describes the equilibrium material properties. The equilibrium equation of state can be used to expand the term in $\dot{E}$ in Eq. (2.3) as

$$\dot{E} = E_p \dot{p} + E_v \dot{v} , \tag{2.5}$$

where

$$E_p = (\partial E/\partial p)_v \,, \; E_v = (\partial E/\partial v)_p \,. \tag{2.6}$$

Equation (2.3) can be written, after doing the indicated differentiation and substituting terms from Eqs. (2.1), (2.2), and (2.5), as

$$\dot{p} + \frac{(E_v + p)}{pE_p}(p/v)\,\dot{v} = (v/E_p)(uA + B)/v \,. \tag{2.7}$$

The coefficients that describe the material properties have their own special names. The coefficient (v/E_p) is called the Gruneisen gamma and is represented as

$$v/E_p = \Gamma \,. \tag{2.8}$$

The coefficient $v(E_v + p)/pE_p$ is called the adiabatic gamma and is written

$$v(E_v + p)/pE_p = \gamma \,. \tag{2.9}$$

With these definitions, Eq. (2.7) becomes

$$\dot{p}/p + \gamma\dot{v}/v = \Gamma(uA + B)/pv \,. \tag{2.10}$$

The conservation equations Eqs. (2.1), (2.2), and (2.3), can now be replaced by

$$\dot{v} - vu_x = 0 \tag{2.11}$$

$$\dot{u} + vp_x + A = 0 \tag{2.12}$$

$$\dot{p}/p + \gamma\dot{v}/v = \Gamma(uA + B)/pv \,. \tag{2.13}$$

All the description of the material is given in the two derivatives, γ and Γ. If the two derivatives are given as functions of p and v, the equations are a complete set of three equations with three dependent variables.

III. SOLUTIONS OF THE EQUATIONS

The equations of hydrodynamics have simple solutions for special cases, and these solutions allow some insights into the physical meaning of the various terms in the equations.

Let us first consider the important case of a steady shock wave propagating in the material. Steady means independent of time, and thus the partial derivatives with respect to time in Eqs. (2.1), (2.2), and (2.3) are all zero. The equations become

$$uv_x - vu_x = 0 \tag{3.1}$$

$$uu_x + vp_x + A = 0 \tag{3.2}$$

$$uE_x + u^2u_x + vup_x + vpu_x = B \,. \tag{3.3}$$

The first equation can be immediately integrated to give u/v = constant. If we require that the shock wave be localized near $x = 0$ with the material flowing in the positive direction from negative values of x at velocity u_o, and set the specific volume in the undisturbed material at v_o, then the solution is

$$u/v = u_o/v_o \,. \tag{3.4}$$

For the solution of the next two equations more information about A and B is needed. In the Navier-Stokes equations,

$$A/v = -\frac{\partial}{\partial x}\left[(4/3)\mu u_x\right] \tag{3.5}$$

$$B/u = (v_o/u_o)\frac{\partial}{\partial x}\left[(4/3)\mu u u_x + kT_x\right] \tag{3.6}$$

Equation (3.2) can be written, using Eq. (3.4) and (3.5), as

$$(u_o/v_o)u_x + p_x - \frac{\partial}{\partial x}\left[(4/3)\mu u_x\right] = 0 \tag{3.7}$$

and immediately integrated to give, with the boundary conditions imposed,

$$p - p_o = \varrho_o u_o(u_o - u) + (4/3)\mu u_x \,, \tag{3.8}$$

where $\varrho_o = 1/v_o$. After dividing by u, and using Eq. (3.1) to eliminate u_x/u, one can write Eq. (3.3) as

$$E_x + uu_x + vp_x + pv_x = (v_o/u_o)\frac{\partial}{\partial x}\left[(4/3)\mu u u_x + kT_x\right] \,, \tag{3.9}$$

and this can be integrated to give, with the boundary conditions imposed,

$$(E + pv) - (E_o + p_o v_o) = \tfrac{1}{2}\left(u_o^2 - u^2\right) + (v_o/u_o)\left[(4/3)\mu u u_x + kT_x\right) \,. \tag{3.10}$$

Far from the shock in the region of large positive x, the terms in Eqs. (3.8) and (3.10) containing derivatives have decreased to zero, and the Eqs. (3.4), (3.8), and (3.10) can be written as the usual jump conditions for a steady shock wave. These are

$$v/v_o = u/u_o \tag{3.11}$$

or

$$v/v_o = 1 - (u_o - u)/u_o \tag{3.12}$$

for the conservation of mass, from Eq. (3.4). Equation (3.12) is written to correspond to the more familiar form in laboratory coordinates, where the mass velocity is $(u_o - u)$. Equation (3.8) becomes

$$p - p_o = \varrho_o u_o (u_o - u) , \tag{3.13}$$

already in its familiar form. It can also be written, using Eq. (3.12) to eliminate $(u_o - v)$, in its Rayleigh line form as

$$p - p_o = \varrho_o^2 u_o^2 (v_o - v) . \tag{3.14}$$

Equation (3.10) can be written in its several familiar forms as

$$(E+pv) - (E_o + p_o v_o) = \tfrac{1}{2} u_o^2 - \tfrac{1}{2} u^2 \tag{3.15}$$

$$E - E_o = \tfrac{1}{2}(u_o - u)^2 + p_o(v_o - v) \tag{3.16}$$

$$E - E_o = \tfrac{1}{2}(p + p_o)(v_o - v) . \tag{3.17}$$

Equation (3.16) is obtained from (3.15) by substituting $p = p_o + (u/v)(u_o - u)$, which is obtained from Eqs. (3.13) and (3.11). Equation (3.17) is obtained from (3.16) by substituting for one of the terms $(u_o - u)$ from Eq. (3.13), and for the other one in the squared term from Eq. (3.12). These equations describe the conditions far from the shock wave, relating the properties on the two sides of the shock.

The details of the shock itself can be obtained by integrating Eqs. (3.8) and (3.10), considering them as the differential equations that describe the shock itself. Some additional assumptions about the equation of state and the values of the shear viscosity μ and thermal conductivity k are required. The problem is well treated by Hayes (1).

The jump in entropy is also interesting. The equations show that the entropy is increased by the dissipative processes in the shock. From the first law of thermodynamics

$$TdS = dE + pdv , \tag{3.18}$$

one can write

$$TS_x = E_x + pv_x . \tag{3.19}$$

Using Eqs. (3.7) and (3.9) to substitute for terms on the rhs, one finds

$$S_x = -(v/T)\frac{\partial}{\partial x}\left[(4/3)\mu u_x\right] + (v_o/u_o)(1/T)\frac{\partial}{\partial x}\left[(4/3)\mu u u_x + kT_x\right] \tag{3.20}$$

The equation can be simplified to

$$\varrho_o u_o S_x = (4/3)\mu (u_x)^2/T + (k/T)\frac{\partial}{\partial x}(T_x) . \tag{3.21}$$

Integration then gives

$$\varrho_o u_o (S - S_o) = \frac{k}{T}\left(\frac{\partial T}{\partial x}\right)\Bigg|_{x_o}^{x} + \int_{x_o}^{x} \frac{k}{T^2}\left(\frac{\partial T}{\partial x}\right)^2 dx + \int_{x_o}^{x} (4/3)\mu \frac{(u_x)^2}{T}\, dx . \tag{3.22}$$

While the first term on the rhs is zero far from the shock, the two integral terms are positive contributions to the entropy.

At this point, although it has nothing to do with finding special solutions to the equations, let us look briefly at the viscous terms in the equations, represented by A and part of B in Eqs. (2.2) and (2.3) or (3.2) and (3.3). Often writers use the term "viscous pressure," usually denoted by q, and it is identified with the terms in Eqs. (3.5) and (3.6) as

$$q = -(4/3)\mu u_x . \tag{3.23}$$

For numerical solution of the equations, artificial viscosity is used to make the solutions of the equations stable to perturbations by numerical noise. Many different forms have been used for q. We see that q has the dimensions of pressure, and that the coefficient of u_x in Eq. (3.23) must be a product of density, velocity, and distance. The important distance for numerical stability is the mesh spacing Δx for the calculation, and the density ϱ must be the local density, but the velocity term can be chosen to make the numerical oscillations damp in optimal fashion. Some popular choices are the Landshoff form

$$q \sim -\varrho c \Delta x u_x \tag{3.24}$$

using the sound velocity, the Richtmyer-von Neuman or quadratic form

$$q \sim -\varrho(\Delta x u_x)\Delta x u_x \tag{3.25}$$

using $\Delta x u_x$ as a velocity, and the Harlow or PIC form

$$q \sim -\varrho u \Delta x u_x \tag{3.26}$$

using the local particle velocity. In a numerical calculation all three forms may be used in linear combination, with dimensionless multipliers chosen for optimum damping.

Now let us turn away from the strong shock wave, and look for solutions corresponding to the propagation of an infinitesimal disturbance, a sound wave. We wish to consider a uniform medium with no strong gradients, so the viscous and heat conduction terms are negligible. We use Eqs. (2.11), (2.12), and (2.13), rewritten here as

$$\dot{v} - v u_x = 0 \tag{3.27}$$

$$\dot{u} + v p_x = 0 \tag{3.28}$$

$$\dot{p}/p + \gamma \dot{v}/v = 0 \,. \tag{3.29}$$

We look for solutions for infinitesimal waves moving at constant velocity c without change of shape, described by

$$v = v_o + v_1 f(x - ct) \tag{3.30}$$

$$u = 0 + u_1 f(x - ct) \tag{3.31}$$

$$p = p_o + p_1 f(x - ct) \,, \tag{3.32}$$

where v_1, u_1, and p_1 are very small. Differentiating, and neglecting terms higher than first order in the small perturbations, we find

$$\dot{v} = -c v_1 f' \tag{3.33}$$

$$u_x = u_1 f' \tag{3.34}$$

$$\dot{u} = -c u_1 f' \tag{3.35}$$

$$p_x = p_1 f' \tag{3.36}$$

$$\dot{p} = -c p_1 f' \,. \tag{3.37}$$

Substituting these values into the original differential equations gives

$$c v_1 + v_o v_1 = 0 \tag{3.38}$$

$$c u_1 - v_o p_1 = 0 \tag{3.39}$$

$$p_1 + (\gamma p_o / v_o) v_1 = 0 \,. \tag{3.40}$$

From Eqs. (3.38) and (3.39) we find

$$c^2 = -v_o^2 \, p_1 / v_1 \,, \tag{3.41}$$

corresponding to the usual definition

$$c^2 = -v^2 (\partial p / \partial v)_S \tag{3.42}$$

if p_1 and v_1 are infinitesimals. Using Eqs. (3.40) and (3.41) we find

$$\gamma = c^2 / p_o v_o \,, \tag{3.43}$$

corresponding to the usual definition, after we substitute from Eq. (3.42),

$$\gamma = -(v/p)(\partial p / \partial v)_S \,. \tag{3.44}$$

Thus we have shown that our equations describe a medium that transmits sound waves and the γ, defined by Eq. (2.9), is simply the square of the dimensionless sound speed.

In Eqs. (3.27) through (3.29) the dissipative terms A and B were neglected. Inclusion of these terms allows for dissipation of energy, and therefore attenuation of sound. For most cases of physical interest, the damping is small. The sound velocity remains that for the nondissipative case. Discussions of the damping are given by Bond, Watson, and Welch (2), and by Lighthill (3).

IV. THERMODYNAMICS FOR HYDRODYNAMICS

Compressible flows usually contain large regions where the flow is approximately isentropic separated from other isentropic regions by small regions where the flow is strongly nonequilibrium and nonisentropic. The natural thermodynamic potential to describe such flows is the specific internal energy E, written as

$$E = E(S, v) \tag{4.1}$$

where S is the specific entropy and v is the specific volume. For the regions of isentropic flow the potential E is a function only of volume.

The differential expansion of Eq. (4.1) is

$$dE = T \, dS - p \, dv \tag{4.2}$$

where

$$T = (\partial E / \partial S)_v \quad \text{and} \quad p = -(\partial E / \partial v)_S \tag{4.3}$$

The independent variables S and v, and the variables obtained from the first partial derivatives, are the variables of thermodynamics.

The derivatives of these variables can be expressed as second derivatives of the potential. There are three independent second derivatives, so all the derivatives can be expressed in terms of three independent second derivatives. In what follows, we use the subscript notation for differentiation, so that, for example,

$$E_{vv} = (\partial^2 E/\partial v^2)_S \tag{4.4}$$

and the independent variable held constant is obvious from the context. The definitions used here are

$$\gamma = vE_{vv}/p = -(v/p)(\partial p/\partial v)_S \tag{4.5}$$

$$\Gamma = -vE_{Sv}/T = -(v/T)(\partial T/\partial v)_S = (v/T)(\partial p/\partial S)_v \tag{4.6}$$

$$g = pvE_{SS}/T^2 = pv/C_vT\,. \tag{4.7}$$

These three partial derivatives form the standard set for hydrodynamics; all other thermodynamic first derivatives can be written in terms of them.

The meaning of these second derivatives that form the standard set for hydrodynamics may be made clearer by considering the following expressions:

$$\gamma = -(\partial \ln p/\partial \ln v)_S \tag{4.8}$$

$$\Gamma = -(\partial \ln T/\partial \ln v)_S\,. \tag{4.9}$$

Now suppose that γ and Γ are constants. Then one can integrate to find, on an isentrope, that

$$pv^\gamma = \text{constant} \tag{4.10}$$

$$Tv^\Gamma = \text{constant}\,. \tag{4.11}$$

Similarly, one can write

$$\Gamma(TS/pv) = (\partial \ln p/\partial \ln S)_v \tag{4.12}$$

$$g(TS/pv) = (\partial \ln T/\partial \ln S)_v \tag{4.13}$$

and integrate these to get expressions on the curves of constant volume. (The factor TS/pv enters because we did not use S when we made the second derivatives dimensionless.) Since we do not measure S, perhaps the ratio of the two,

$$T^\Gamma/p^g = \text{constant} \tag{4.14}$$

on a curve of constant volume, is more useful.

In the real physical case γ, Γ, and g are not constants, yet the expressions obtained this way are tangents to the real curves at points where the exponents have the chosen values.

Thermodynamics books usually use another standard set of derivatives, obtained from the Gibbs potential, G = G(T,p), defined as

$$C_p = -TG_{TT} \tag{4.15}$$

$$\beta = G_{Tp}/v \tag{4.16}$$

$$\kappa_T = -G_{pp}/v\,. \tag{4.17}$$

The reason for this choice is, of course, that many experiments are done with either T or p held constant, and G(T,p) is the natural potential. This usual standard set can be expressed in terms of the hydrodynamic standard set as follows:

$$C_p = (pv/gT)\gamma/(\gamma - \Gamma^2/g) \tag{4.18}$$

$$\beta = (\Gamma/gT)/(\gamma - \Gamma^2/g) \tag{4.19}$$

$$\kappa_T = p^{-1}/(\gamma - \Gamma^2/g)\,. \tag{4.20}$$

The denominator in each expression can be shown to be $-(v/p)(\partial p/\partial v)_T$, and it must be positive to ensure mechanical stability (4). For an ideal gas the denominator is one.

The choice of symbols is hopelessly confusing. Various authors use various symbols; worse still, they use the same symbols with different meanings. Until some standardization takes place, readers will just have to resign themselves to being very careful to check the definitions. Perhaps the most bothersome is our definition of the adiabatic gamma. The symbol γ has been widely used for many years to denote the ratio of specific heats; our definition, common in hydrodynamics, is given by Eq. (4.5). The adiabatic gamma and the ratio of specific heats are identical for an ideal gas, but not for real gases, as can be seen by combining Eqs. (4.7) and (4.18).

One higher derivative is important in the context of empirical equations of state. It is called the "fundamental derivative of gas dynamics" by Thompson (5), and is defined as

$$G = \tfrac{1}{2}\left[\gamma + 1 - (v/\gamma)(\partial\gamma/\partial v)_S\right]\,. \tag{4.21}$$

For ordinary materials, G is positive. Its importance is that when G is positive, compression shock waves form. If G is negative, rarefaction

shocks form. For the purposes of this paper, one must be careful not to choose forms for gamma that lead to G less than zero unless rarefaction shocks are desired. G can also be written, using the notation of Eqs. (4.5) through (4.7) as

$$G = - vE_{vvv}/2E_{vv} \cdot \tag{4.22}$$

It is often glibly said that the condition for compression shocks to form is that the sound speed must increase with pressure. Really the condition is that higher pressure waves from behind must overtake the front, and they travel at velocity u + c rather than c, and u also increases with pressure. The difference can be made especially clear by relating G to these derivatives. It can be shown that

$$\left(\frac{\partial c}{\partial p}\right)_S = (G - 1)/\varrho c \,, \tag{4.23}$$

so the sound velocity increases with pressure only if G is greater than 1. However,

$$\frac{d(u + c)}{dp} = G/\varrho c \tag{4.24}$$

on the characteristics behind the shock, so compression shocks will form as long as G is greater than zero.

V. INCOMPLETE EQUATION OF STATE

E = E(S,v) is a complete equation of state. All thermodynamic derivatives can be obtained from it. E = E(p,v) is not a complete equation of state, but is very useful for hydrodynamics.

The relationship between E(S,v) and E(p,v) is easy to see. If one has E(S,v), then $- E_v = p(S,v)$. In principle, at least, this expression for p can be inverted to give S(p,v), and then S can be eliminated in E(S,v) to give E(p,v). However, there is no way to go backward; that is, one cannot get back from E(p,v) to E(S,v). Therefore, E(p,v) is incomplete.

Most of the experiments in hydrodynamics are mechanical experiments. Their variables are p and v. Temperature and entropy are not measured quantities, and they cannot be inferred from E(p,v). On the other hand, the variables that cannot be measured must not be really needed, or they could be measured. For many purposes the incomplete equation of state E = E(p,v) is adequate.

The differential of this incomplete equation of state is

$$dE = E_p dp + E_v dv \cdot \tag{5.1}$$

If we use Eq. (5.1) to find the derivative with respect to v at constant S we get

$$(\partial E/\partial v)_S = E_p(\partial p/\partial v)_S + E_v \,; \tag{5.2}$$

but we know that

$$(\partial E/\partial v)_S = - p \tag{5.3}$$

and using this we can rearrange Eq. (5.2) to give

$$- (\partial p/\partial v)_S = (E_v + p)/E_p \cdot \tag{5.4}$$

Comparing this result with Eq. (4.5) we find

$$\gamma = v(E_v + p)/pE_p \cdot \tag{5.5}$$

Similarly, taking the derivative with respect to S at constant v one can show that

$$(\partial p/\partial S)_v = T/E_p \cdot \tag{5.6}$$

Using this result with Eq. (4.6) one finds that

$$\Gamma = v/E_p \cdot \tag{5.7}$$

The incomplete equation of state E(p,v) thus gives the adiabatic gamma and the Gruneisen gamma. As shown in Sec. II, it is adequate for simple hydrodynamics.

From the incomplete equation of state, g cannot be determined; however, a differential equation for g can be obtained, and g is thus determined, except for a constant, along an isentrope where γ and Γ are known. The differential equation is obtained by requiring that the partial derivatives of E(S,v) do not depend on the order of differentiation, so that $E_{SvS} = E_{SSv}$. E_{Sv} and E_{SS} are given by Eqs. (4.6) and (4.7). Some manipulation gives the differential equation

$$(v/g)(\partial g/\partial v)_S$$

$$= \Gamma + 1 - \gamma - (\Gamma p/g)(\partial \Gamma/\partial p)_v \cdot \tag{5.8}$$

A differential equation for the temperature is also available, so temperature can be determined, within a constant multiplier, along an isentrope. One form of Eq. (4.6) is

$$(v/T)(\partial T/\partial v)_S = - \Gamma \cdot \tag{5.9}$$

If Γ is known, this can be integrated immediately, except for the constant.

Expressions for T and g are especially useful for detecting flaws in the choice of a form for an empirical equation of state. One may not know exactly what to expect for T or g, but one can expect them to be smooth, positive, and monotone on the isentrope.

VI. PHYSICAL PRINCIPLES

It was shown in Section II that the adiabatic gamma and the Gruneisen gamma are the important features of the equation of state for hydrodynamics. In Section III it was shown that the adiabatic gamma is the square of the dimensionless sound speed, or

$$\gamma = c^2/pv \quad . \tag{6-1}$$

Here we ask what we know about the behavior of the adiabatic gamma and the Gruneisen gamma as functions of specific volume along an isentrope.

Molecules interact with each other when the distance between their centers is a few tenths of a nanometer. In a gas at room temperature and pressure the average distance between molecules is about 3 nm, so most of the time a molecule drifts at thermal velocity, unaffected by any other molecule. A disturbance, such as a sound wave, is transmitted through the gas by molecules traveling at thermal velocities, and the velocity of a sound wave is about two-thirds of the average thermal velocity. Collisions are rare events. The details of the molecular interaction have a trivial effect on the velocity of sound.

If the gas, originally at room temperature and pressure, is compressed a thousandfold, so the number of molecules in a cubic centimeter increases from 27×10^{18} to 27×10^{21}, the average intermolecular spacing decreases from 3.3 nm to 0.33 nm. The effect of a disturbance, a sound wave, is transmitted by molecules that drift a short distance and then collide with another molecule. The motion is then transmitted through the molecule by the electrical forces at nearly the velocity of light. Then there is another thermal drift, but only for a short distance. Thus when the intermolecular spacing is of the same order as the molecular size, the speed of sound increases above the low density value. The change takes place, for ordinary explosive products, at a density near one gram per cubic centimeter. The adiabatic gamma, the square of the dimensionless sound velocity, changes markedly with specific volume in this region.

As compression is continued up the isentrope, the sound velocity continues to increase. Its value depends in detail on the exact form of the molecular interaction. The adiabatic gamma, however, levels off at nearly a constant value. This happens because we have defined gamma by normalizing with respect to pv, as shown in Eq. (6-1). Because of the energy in the molecular interactions, pv/RT increases to large values. For most reasonable forms for the molecular repulsion, the adiabatic gamma seems to be nearly constant at small specific volume. It is easy to show that if the repulsive potential for the interaction energy of two molecules varies inversely as the nth power of the separation, there is an upper bound for the adiabatic gamma,

$$\gamma < 1 + n/3 \, . \tag{6-2}$$

A schematic plot of the variation of gamma with specific volume is shown in Fig. 1. It always has this general shape, but details of the potential, and effects from phase changes and phase separation can cause small perturbations in local regions.

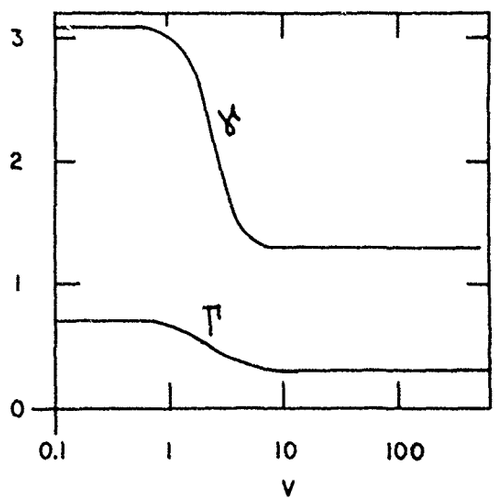

Fig. 1. The dependence of the adiabatic and Gruneisen gammas on specific volume

It should be mentioned that this discussion is to be applied to the temperatures and volumes of interest for explosives. That is, regions where the thermal energy of the molecule is much less than its ionization energy. When there is appreciable ionization and dissociation, new effects are important.

The Gruneisen gamma has behavior very similar to that of the adiabatic gamma. At very large specific volume,

$$\Gamma = \gamma - 1 \,, \tag{6.3}$$

so it has a value near 0.3. It increases as the volume decreases, and levels off at 0.6 or 0.7 at small volume. Figure 1 shows a schematic diagram of the usual behavior of the Gruneisen gamma.

VII. ENGINEERING APPLICATIONS

The preceding sections have been devoted to the properties of the thermodynamic equation of state of detonation product gases. The words "equation of state" are often used to denote something very different.

Explosive systems are usually designed with the help of computer programs that solve the hydrodynamic equations. Often the computed system differs markedly from the actual physical system. For example, the shape may be idealized by neglecting glue joints, small voids, or plastic potting compounds. The initiation is usually idealized in important ways and not computed in detail. The chemical reaction zone is not modeled properly. The properties of the material being driven, perhaps metal or rock, are simplified. And in the interest of getting things done, sometimes the mesh size is made large and the computer does not give an accurate solution of the equations. All these defects are accommodated by adjusting the "equation of state."

A system designer, then, cannot use a real, thermodynamic equation of state. What he needs is an approximate form that will allow him to design a first approximation to the required system using his computer, with all its defects. Then he must test his first design, and use the results to change the "equation of state." Then he must try again. If the requirements have tight tolerances, this iteration can be very expensive and time consuming.

One of the problems with the fitting forms in common use is that they have so many adjustable constants. There are too many ways to adjust the "equation of state" for a good fit to the experiment. An "equation of state" with just one adjustable parameter provides all the necessary adjustment, but still allows the user to make systematic changes: so much positive for this defect, so much the other sign for another, etc.

The one adjustable parameter for a fitting form will probably not be one of the constants in the form but some real physical parameter of importance for the system being designed. For example, for reproducing the results of a cylinder test, the important parameter is the cylinder wall energy at large expansion, and this is the one that must be adjusted. The constants in the fitting form must be varied so that the other calibration parameters are held fixed, and only this energy is changed. For a shock wave in air, the low pressure expansion is important, and for an overdriven or convergent detonation the high pressure region is the one to adjust. The vital thing is to adjust only that important region, and to use only one parameter. In this way, a systematic understanding of the adjustments that correct for various defects can be obtained.

VIII. DESIGNING A FITTING FORM

The usual approach, and the one discussed here, is to find a fitting form for the incomplete equation of state discussed in Section V,

$$E = E(p,v) \,. \tag{8.1}$$

It is convenient and customary to choose a particular isentrope, usually the principal isentrope that passes through the Chapman-Jouguet point, and find a fit for it. Because it is a particular isentrope, any function on the isentrope can be expressed as a function of volume only. Thus on the isentrope the specific internal energy is

$$E_S = E_S(v) \,, \tag{8.2}$$

where the subscript S is used to indicate that the subscripted variable is to be taken on the particular isentrope. The definition of the Gruneisen gamma, given in Eq. (2-8), is

$$\Gamma = v/E_p \,, \tag{8.3}$$

so in the immediate neighborhood of the isentrope the energy may be expanded as

$$E(p,v) = E_S(v) + (v/\Gamma)\,[p - p_S(v)] \quad . \tag{8.4}$$

To make a useful equation of state, it is assumed that Eq. (8.4) applies throughout the region of interest, and that the Gruneisen gamma is a function of volume only,

$$\Gamma = \Gamma(v) \quad . \tag{8.5}$$

These two assumptions are not as bad as they might seem, because the entropy produced in shock processes in explosive-driven systems is never large, and the region of interest is a narrow strip always close to the principal isentrope.

Perhaps physical intuition is best for the form of the adiabatic gamma on the principal isentrope, as was discussed in Section VI. If its form is chosen, one has

$$\gamma_S = \gamma_S(v) \quad . \tag{8.6}$$

The definition of the adiabatic gamma, Eq. (3-44), can then be written as

$$dp_S/p_S = -\gamma_S dv/v \quad , \tag{8.7}$$

and then integration gives

$$p_S = p_S(v) \quad . \tag{8.8}$$

The internal energy on the isentrope can be obtained from the first law of thermodynamics with the entropy held constant,

$$dE_S = -p_S dv \quad . \tag{8.9}$$

Each integration introduces a constant of integration; the one from the pressure equation, Eq. (8.7), allows one to choose the particular isentrope, making it pass through a chosen p,v point, and the one from the energy equation, Eq. (8.9), sets the zero of energy, usually taken so the energy is zero at infinite volume.

The program outlined here seems very simple, but when one attempts to carry it through, it quickly becomes apparent that the integrals cannot be expressed in closed form if $\gamma_s(v)$ is chosen with enough complexity to give a reasonable representation of its real form. One response to this difficulty is to let the integrals be expressed as interpolations in tables obtained from numerical integration, or as series expansions. Another possible response is to divide the volume into small intervals with simple fits in each interval. And a third response is to start with the energy represented by a sum of functions, so that

$$E_S(v) = \Sigma a_i \varnothing_i(v) \quad . \tag{8.10}$$

Then by differentiation one finds

$$p_S(v) = -\Sigma a_i \varnothing'_i(v) \quad , \tag{8.11}$$

and

$$\gamma_S(v) = V\Sigma\, a_i \varnothing''_i(v)/\Sigma\, a_i \varnothing'_i(v) \quad . \tag{8.12}$$

This form for γ_S can then be fit to the chosen form for $\gamma_S(v)$. The widely used JWL equation of state is of this type.

A form for the Gruneisen gamma must also be chosen. Many workers have chosen it to be constant. It seems that a better choice is to give it the same form as the adiabatic gamma, but with values near those discussed at the end of Section VI.

An expression for the adiabatic gamma off the principal isentrope is obtained by using the definition of gamma, Eq. (2.9), and substituting in the partial derivatives obtained from Eq. (8.4). After simplifying the result by substituting from Eqs. (8.7) and (8.9), the result is

$$\gamma(p,v) = (p_S/p)\gamma_S + (1 - p_S/p)(\Gamma + 1 - d\ln\Gamma/d\ln v). \tag{8.13}$$

This expression makes it clear that a discontinuity in the slope of the Gruneisen gamma will lead to a discontinuity in the adiabatic gamma itself. Similarly, Eq. (4.21) shows that a discontinuity in the slope of the adiabatic gamma will lead to a discontinuity in G. Such discontinuities are nonphysical, but it isn't clear what spurious effects might appear in a calculation where an equation of state with discontinuities in the slopes of either of the gammas on the isentrope was used.

Expressions for new isentropes, above or below the principal isentrope, are obtained by integrating Eq. (8.13). Hugoniot curves are obtained by using the equation of state, Eq. (8.4), and the Hugoniot relation

$$E - E_o = \tfrac{1}{2} p(v_o - v) \quad , \tag{8.14}$$

and eliminating E. Particle velocities on the isentrope are obtained by integrating

$$dp/du = \pm c/v = \pm (\gamma p/v)^{1/2} \quad . \tag{8.15}$$

Even for simple choices of functions for the adiabatic gamma, the integration almost always has to be done numerically.

IX. CALIBRATION

The calibration of a fitting form for an equation of state opens opportunity for prejudice and personal preference. There are no absolute rules. The importance of various measurements to the calibration depends on the application.

Calibration of an equation of state begins with the Chapman-Jouguet state. A subscript j denotes that state in what follows. First there is the requirement that the principal isentrope pass through the point p_j, v_j. Then there is the additional requirement that the Rayleigh line and the Hugoniot curve be tangent at that point (the Chapman-Jouguet condition); this requirement is met by requiring

$$p_j = \varrho_o D_j^2/(\gamma_j + 1) \qquad (9.1)$$

and

$$v_j/v_o = \gamma_j/(\gamma_j + 1) \quad . \qquad (9.2)$$

One might proceed, for example, by measuring the detonation velocity and the CJ pressure. Then γ_j can be obtained from Eq. (9.1), and v_j from Eq. (9.2).

The problem with this approach is that apparently no one knows how to measure CJ pressure. One need only thumb through the seven Detonation Symposium volumes to see that there was no more agreement in 1981 than there was in 1951, and that the discussions get more and more complex with time. For calibrating an equation of state, one need only realize that if it made a lot of difference, it would have been measured by now. For many purposes the exact value is not very important. This fact has led to the development of "rules for gamma", that give the value for the adiabatic gamma at the CJ point simply in terms of the initial density of the explosive. A simple rule that works satisfactorily is

$$\gamma_j = 1.6 + 0.8\,\varrho_o \quad . \qquad (9.3)$$

The initial density and the measured detonation velocity can then be used with Eqs. (9.1) and (9.2) to find p_j and v_j.

The second thing to get right in the calibration of an equation of state is the amount of energy available for the system under consideration. For almost any system there is a "cut-off pressure", where once the explosive products have expanded to the volume where the pressure reaches this value, little additional work is done on the system. Either the metal or rock breaks, allowing the gases to escape, or the time is too long and the additional acceleration too late, or some other external condition makes the energy remaining in the products useless. For metal systems driven by explosive, the cut-off pressure is about 0.1 GPa in many cases. It has become customary to fix the energy delivered for an expansion down to that pressure with a calibration experiment. Perhaps the best known experiment is the cylinder test (6). For high-density, high-energy explosives the cut-off pressure comes at an expansion of six or seven times the initial volume, and the cylinder test is designed to measure an appropriate value. For other explosives and other uses, alternative tests have been used.

The Jacobs engine and the Fickett-Jacobs cycle described by Fickett and Davis (7) make it easy to understand this calibration. Figure 2

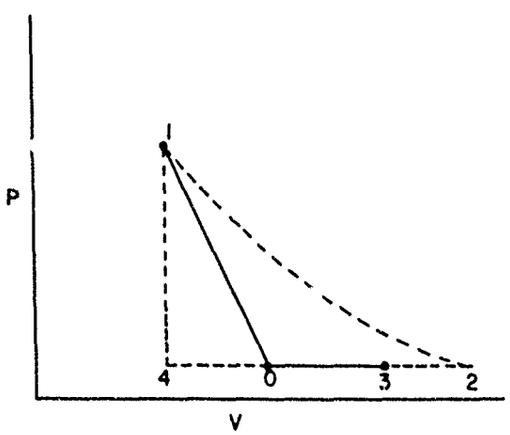

Fig. 2. The Fickett-Jacobs cycle. The initial state, unreacted explosive is at point 0. The CJ state is at point 1. The product gases expand against a piston from point 1 to point 2, doing useful work. The gases are cooled so they contract from 2 to 3, and this energy is lost to the system. The gases are reacted from 3 to 0, back into the original explosive. To get all the gas uniformly into the CJ state, work must be done on it, and this work is represented by the area 0-1-4. The maximum useful output work is the area 0-1-2

is a diagram of the cycle; it is described in the caption. The area between the base line, the Rayleigh line, and the principal isentrope is equal to the maximum useful work that could be obtained from the explosive. Some of that energy is not useful, because the pressure is too low for the application. Therefore, the diagram must be truncated, as shown in Fig. 3, at the limiting useful pressure. For the useful energy calibration, the area to the left of the truncation line must be made proportional to the energy obtained from the test. Several rules for an approximate calibration have been used. The total area is E_o, and the area to the right of the truncation line is E_5, so the rule is

$$E_{test} \sim E_o - E_5 \quad . \tag{9-4}$$

The equation of state parameters are adjusted to satisfy this relationship.

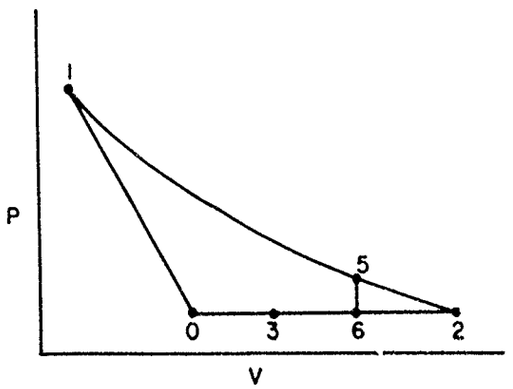

Fig. 3. In most applications of explosives, the product gases do useful work only when their pressure is above some cut-off pressure, shown here at point 5. The useful work is then represented by the area 0-1-5-6-0

A third calibration point is to set the total energy, E_o, equal to the calculated chemical energy of the explosive. Although it is esthetically satisfying to have the work available equal to the chemical energy, it is not an important calibration point. In the first place, there is no application of explosives where the energy at low pressure is important; if low pressure could do the work, one wouldn't use explosive. And in the second place, heat energy of the explosive is not used (see the segment 2.3 in Fig. 2), and is rejected to the surroundings. Therefore, E_o is not equal to the chemical energy. It is really more important to get the sound velocity about right at low pressure than to worry about adjusting for the total energy.

These calibrations determine the principal isentrope. The remaining calibration is for the Gruneisen gamma, that influences the values for states off the principal isentrope. Overdriven, colliding, and convergent detonations provide the data for determining Gruneisen gamma. So far, there have been no definitive calibrations. If overdriven detonations are important in the application of the equation of state, Gruneisen gamma should be adjusted to fit the data. Otherwise, the choice is not important, and a simple form or even a constant value can be used with little effect on the calculations.

ACKNOWLEDGMENTS

W. Fickett, M. Finger, B. D. Lambourn, E. L. Lee, C. L. Mader, M. S. Shaw, R. C. Weingart, and many others have helped me to understand some things about equations of state, and I wish to thank them all for their help.

REFERENCES

1. W. D. Hayes, "The Basic Theory of Gasdynamic Discontinuities," in Fundmentals of Gasdynamics, H. W. Emmons, Ed., Vol. III, High Speed Aerodynamics and Jet Propulsion, Princeton University Press, Princeton, N.J., pp. 416-481, 1958.
2. J. W. Bond, K. M. Watson, and J. A. Welch, *Atomic Theory of Gas Dynamics*, pp. 274-6, Addison-Wesley, Reading, Mass., 1965.
3. J. Lighthill, *Waves in Fluids, pp. 76-85, Cambridge University Press, Cambridge, Mass., 1979.*
4. H. B. Callen, *Thermodynamics*, p . 134, John Wiley and Sons, New York, 1960.
5. P. A. Thompson, *Compressible-Fluid Dynamics*, p. 252 and p. 577, McGraw-Hill, New York, 1972.
6. J. W. Kury et al., "Metal Acceleration by Chemical Explosives," Proceedings Fourth Symposium (International) on Detonation, ACR-126, Office of Naval Research, pp. 3-12, 1965.
7. W. Fickett and W. C. Davis, *Detonation*, Univ. of California Press, Berkeley, California, pp. 35-39, 1979.

DETONATION PROPERTIES OF CONDENSED EXPLOSIVES COMPUTED WITH THE VLW EQUATION OF STATE

Wu Xiong
Xian Modern Chemistry Research Institute
Xian, China

A simplified virial equation of state based on Lennard-Jones 6-12 potential called VLW EOS is proposed for detonation products. The detonation properties of explosives composed of CHNO, CNO, HNO, NO, HN, CHNOF, and CHNF have been calculated by this equation, and the results are compared with experimental data, and with the results computed by BKW EOS and LJD EOS. The principal feature of our approach is that the third and fourth virial coefficients can be conveniently obtained from the well known second one. It is shown that the agreement between the predicted detonation parameters and the experimental data is reasonably satisfactory.

INTRODUCTION

An equation of state of detonation products is required for predicting the detonation performance data so as to give guidance to the direction of explosives development.

The most widely used equation of state is the semi-empirical BKW equation of state. With it and its FORTRAN BKW code, the detonation properties of more than one hundred explosives have been calculated and most of the calculated results are in good agreement with the experimental data (9). It is evident that the BKW EOS and its FORTRAN BKW code have perfect functions. However, the detonation temperatures computed by BKW EOS are much lower than those of experiments. Furthermore, for a few special explosives whose reactive products at C-J state contain predominantly the chemical species NH3 or CO2, the errors in calculation are considerable. And it seems difficult to get essential improvement. For those explosives, which nowadays chemists are interested in, we attempt to find a way to simplify the theoretical virial equation of state based on Lennard-Jones 6-12 potential as an equation of state of detonation products called VLW EOS to predict the detonation properties of various explosives.

A FORTRAN VLW code has been set up. By using it, we have calculated the detonation properties of some commonly used explosives composed of CHNO, and various special explosives composed of CNO, HNO, NO, HN, CHNOF, and CHNF and the computed results have been compared with the experimental data.

The VLW equation of state has some distinct features. First, good agreement is obtained between measured and calculated detonation values. Second, the calculated detonation temperature increases with increasing loading density, which is different from that obtained by some equations of state, but is in agreement with the theoretical work of Bvacco (1) and that of Edwards and Chaiken (2). And third, our calculations show that the detonation products contain an amount of NO, the order of magnitude of which (PETN for example) is in agreement with the experimental data (7), and also with the calculations by P-Y theory (2).

It seems that the VLW EOS holds better promise for predicting detonation properties.

THE VLW EQUATION OF STATE OF DETONATION PRODUCTS

Theoretically speaking, the equation of state of any gases may be written in virial form, which was described in detail by Hirschfelder and Curtiss (11), and Qian Xuesen (10), that is

$$\frac{Pv}{RT}=1+\frac{B}{v}+\frac{C}{v^2}+\frac{D}{v^3}+\ldots. \qquad (2\text{-}1)$$

where

B is the second virial coefficient, C is the third virial coefficient, etc., v is the molar volume.

The virial equation of state has clear physical meaning. The first term corresponds to the behavior of ideal gases; the second term describes the action between two molecules, and the third one considers the interaction for three molecules and so on. At lower pressure, the opportunity of interaction for more than three molecules seldom occurs, so it is good enough to reflect the gaseous properties with former two terms, but at high pressure the interaction of several molecules cannot be neglected any longer. In this case, the higher virial coefficients have to be considered. Unfortunately, as the complexity increases rapidly for the higher virial coefficients, the calculations of them become more and more difficult, except the most simple hard spheres being used. This is why the perfect theoretical virial equation of state has seldom been put into practice. For this reason, with the aid of similarity theory (8), we suppose that the virial coefficients are similar to each other, so higher virial coefficients may be obtained from the second one, and then a facilitating approximation of the virial equation of state can be obtained.

According to the classicial mechanics we have (11)

$$B(T)=\frac{2\pi\tilde{N}}{3KT}\int_o^\infty r^3\frac{d\varphi}{dr}e^{-\varphi(r)/KT}dr \qquad (2\text{-}2)$$

Here we use the Lennard-Jones 6-12 potential for φ. Namely,

$$\varphi(r)=4\varepsilon[(\frac{\sigma}{r})^{12}-(\frac{\sigma}{r})^6] \qquad (2\text{-}3)$$

where

ε is the depth of potential well. σ is the value of r for which the potential $\varphi(r)=0$. And we define two reduced variables as follows

$$T^*=\frac{KT}{\varepsilon};r^*=\frac{r}{\sigma} \qquad (2\text{-}4)$$

In addition, it is necessary to define another dimensionless quantity

$$B^*=\frac{B}{b_o}$$

where

B is the second virial coefficient.

$$b_o=\tfrac{2}{3}\pi\tilde{N}\sigma^3$$

Thus

$$B(T)=(\frac{2}{3}\pi\tilde{N}r^3)[-\frac{4}{T^*}\int_0^\infty r^{*2}\ (-\frac{12}{r^{*12}}+\frac{6}{r^{*6}})\cdot$$

$$\exp[-\frac{4}{T^*}(\frac{1}{r^{*12}}-\frac{1}{r^{*6}})dr^*]=b_oB^*(T^*) \qquad (2\text{-}6)$$

here

$$B^*(T^*)=\sum_{j=o}^{\infty}[-\frac{2^{j+1/2}}{4j!}\Gamma(\frac{j}{2}-\frac{1}{4})T^{*-(2j+1)/4}]$$

Hirschfelder and Curtiss have shown that the third virial coefficient C(T), also has the similar form (11)

$$C(T)=b_o^2\,C^*(T^*)$$

The similarity leads us to suppose that the above expression may be extended, the fourth virial coefficient is

$$D(T)=b_o^3\,D^*(T^*)$$

Over the range of interested, for T^* is between 20 and 100 (in the case of detonation, T^* varies always from 25 to 40), we have found

$$C^*(T^*)=\frac{B^*}{T^{*1/4}}$$

is a good approximation (see Table 2 and Fig. 1). That is, the reduced third virial coefficient may be expressed by the agency of the reduced second one. Owing to the similarity among the reduced virial coefficients, we assume that the reduced higher virial coefficients may be described with

$$D_n^*(T^*)=\frac{B^*}{(n-2)^{n'}T^{*1/4}}\ (n=3,4,\ldots)$$

Here we take

$$\bar{T}^*=\sum_i\sum_j x_ix_j\cdot T_{ij}^*/\bar{x}^2$$

as an average characteristic parameter (4) and use the following mixing rules

$$T_{ij}^*=(T_i^*T_j^*)^{1/2};b_o=\sum_i\frac{x_i}{\bar{x}}(b_o)_i$$

where

$$\bar{X}=\sum_i x_i$$

In the case of detonation, it is good enough to get to the fourth virial coefficient, thus Eq.(2-1) becomes

$$\frac{Pv}{RT}=1+\frac{b_o}{v}B^*+\frac{B^*}{\bar{T}^{*1/4}}\sum_{n=3}^{4}\frac{(b_o/v)^{(n-1)}}{(n-2)^n} \quad (2\text{-}7)$$

Let

$$W=\frac{b_o}{v};q=B^*/\bar{T}^{*1/4}$$

then EQ.(2-7) becomes

$$\frac{Pv}{RT}=1+WB^*+W^2q+W^3q/16 \quad (2\text{-}8)$$

Eq.(2-8) is called the VLW equation of state of detonation products.

TABLE 1

The Potential Parameters of Products Species

	L-J 6-12(10)(11)			This paper		
	(Å)	ε/K(°K)	b_0(cc/mol)	(Å)	ε/K(°K)	b_0(cc/mol)
H_2O				2.889	180.0	30.42
H_2	2.87	29.20	29.76	2.868	29.20	29.76
C_2	3.58	117.5	57.75	3.575	117.5	57.75
CO_2	4.07	205.0	85.05	4.070	205.0	85.05
CO	3.763	100.2	67.22	3.763	100.2	67.22
NH_3				3.814	138.0	70.00
NO	3.17	131.0	40.00	3.165	131.0	40.00
N_2	3.698	95.05	63.78	3.698	95.05	63.78
CH_4	3.817	148.2	70.16	3.817	148.2	70.16
HF				2.843	100.0	29.00
CF_4	4.70	152.5	131.0	4.700	152.5	131.0

TABLE 2

Comparison of the Values of C^* Given by This Paper with Those Taken From (11). And the Relations B^* vs. T^*, C^* vs. T^*, and D^* vs. T^*

T^*	B^*	C^*		D^*(VLW)
		From (11)	C^*(VLW)	
10	0.4609	0.2861	0.2592	0.0162
20	0.5254	0.2464	0.2484	0.0155
30	0.5269	0.2195	0.2251	0.0141
40	0.5186	0.2001	0.2062	0.0129
50	0.5084	0.1853	0.1912	0.0119
60	0.4982	0.1735	0.1790	0.0112
70	0.4887	0.1638	0.1689	0.0105
80	0.4798	0.1556	0.1604	0.0100
90	0.4716	0.1486	0.1531	0.0096
100	0.4641	0.1425	0.1467	0.0092
200	0.4114	0.1068	0.1094	0.0068

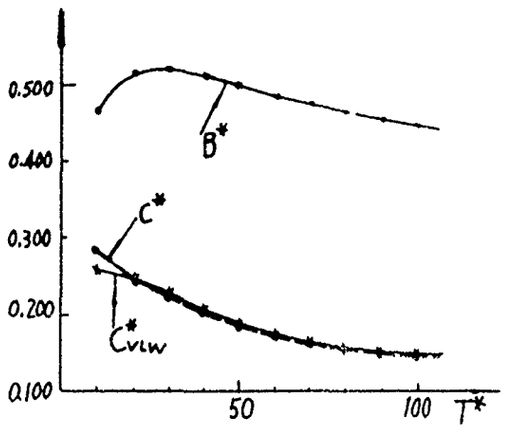

Fig. 1. Comparison of the solid curve C^* given by this paper with the broken curve C^* taken from (11). And the relations B^* vs. T^*, C^* vs. T^*

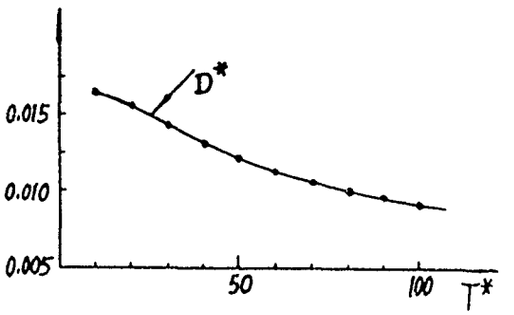

Fig. 2. The relation between D^* (given by this paper) and T^*

THERMODYNAMIC FUNCTIONS OF DETONATION PRODUCTS

In accordance with the theory of thermodynamics, if the temperature T, volume V, and the molar species X_i are chosen as the independent variables, all the thermodynamic functions can be derived from the free energy F. Immediately, we have:

Equation of state

$$P=-\left(\frac{\partial F}{\partial v}\right)_{T,x_i} \tag{3-1}$$

Internal energy

$$E=-T^2\frac{\partial}{\partial T}\left(\frac{F}{T}\right)_{v,x_i} \tag{3-2}$$

Entropy

$$S=-\left(\frac{\partial F}{\partial T}\right)_{v,x_i} \tag{3-3}$$

Chemical potential

$$\mu_i=\left(\frac{\partial F}{\partial x_i}\right)_{T,v} \tag{3-4}$$

Notice the Eq. (3-1) — Eq. (3-4) are derived without any restrictions, so they are valid for any thermodynamic systems. The point is how to determine the free energy F. First, consider the case of idea gases

$$F^i=\Sigma x_i RT\left(\varphi_i-1+\ln\frac{x_i RT}{v}\right) \tag{3-5}$$

where

$$\varphi_i=\frac{\mu_i^\circ}{RT}=\frac{1}{RT}[(F^\circ-H^\circ_{298})_i+(H^\circ_{298})_i]$$

Second, consider the case of detonation products. In order to show signs of the independent variables T, V, and X_i, we apply $V=\bar{X}v$, thus, the VLW EOS becomes

$$P=\frac{\bar{X}RT}{V}(1+WB^*+W^2q+W^3q/16) \tag{3-6}$$

From Eq. (3-1) and Eq.(3-6) we get

$$-\frac{\partial F}{\partial v}=\frac{\bar{X}RT}{v}(1+WB^*+W^2q+W^3q/16)$$

After solving this differential equation, we obtain,

$$F=\Sigma x_i RT(\varphi_i-1+\ln\frac{x_i RT}{v})$$
$$+\bar{X}RT(WB^*+\frac{qw^2}{2}+\frac{qw^3}{48}) \tag{3-7}$$

From Eq.(3-2) and Eq.(3-7), the internal energy for one mole gases is

$$\tilde{E}=\Sigma\frac{x_i}{\bar{X}}[(H^\circ-H^\circ_{298})-RT+(H^\circ_{298})]$$
$$-RTW(\bar{T}^*\frac{\partial B^*}{\partial\bar{T}^*}+\frac{Wg}{2}+\frac{W^2g}{48}) \tag{3-8}$$

where

$$\bar{T}^*\frac{\partial B^*}{\partial\bar{T}^*}=\sum_{j=0}^{\infty}\left(\frac{2j+1}{4}\cdot\frac{2^{j+1/2}}{4j!}\right)\Gamma\left(\frac{j}{2}-\frac{1}{4}\right)\bar{T}^{*-(2j+1)/4}$$

$$g=\bar{T}^{*-1/4}\left(\bar{T}^*\frac{\partial B^*}{\partial\bar{T}^*}-B^*/4\right)$$

the entropy for one mole gases,

$$\tilde{S}=\Sigma\frac{x_i}{\bar{X}}(s_i^\circ-R\ln\frac{x_i RT}{v}-RW[\bar{T}^*\frac{\partial B^*}{\partial\bar{T}^*}+B^*$$
$$+\frac{W}{2}(q+g)(1+\frac{W}{24})] \tag{3-9}$$

and the chemical potential for component i

$$\mu_i=[(F^\circ-H^\circ_{298})_i+(H^\circ_{298})_i+RT\lambda n\frac{X_i RT}{v}]$$
$$+RTB^*(W+\frac{(bo)_i}{v})+RTqW(\frac{W}{2}+\frac{(bo)_i}{v})+\frac{RTqW^2}{16}$$
$$(\frac{W}{3}+\frac{(bo)_i}{v})$$

THE CALCULATION FOR $H^o-H^o_{298}$, S^o, AND $F^o-H^o_{298}$

The thermodynamic functions of $H^o-H^o_{298}$, S^o, and $F^o-H^o_{298}$ based on a fit from $H^o-H^o_{298}$ which differ from those based on a fit from C_p^o or S^o, are proposed here.

Let

$$H^o-H^o_{298}=C_1+C_2T+C_3T^2+C_4T^3+C_5T^4$$

thus,

$$C_p^o=C_2+2C_3T+3C_4T^2+4C_5T^3$$

$$S^o=C_6+C_2\ln T+2C_3T+\frac{3}{2}C_4T^2+\frac{4}{3}C_5T^3$$

$$-(F^o-H^o_{298})=-C_1+C_6T+C_2T(\ln T-1)$$

$$+C_3T^2+\frac{C_4}{2}T^3+\frac{C_5}{3}T^4$$

where C_1, C_2, ...C_6 are the constants.

Calculated C-J Properties and Quantities of VLW Equation of State of Detonation Products

With the FORTRAN VLW code, the detonation properties of various explosives and the quantities of VLW EOS have been calculated and listed as follows:

TABLE 3

Comparison of Calculating Results with Experimental Data

Explosive			EXPT (9)	Calculations		
				BKW(9)	LJD (9)	VLW
	RDX	D	8754	8754	8778	8760
	$C_3H_6N_6O_6$	P	347	347	362	344
	ρ_o=1.80	T		2587	4027	4921
	ΔH=14.71					
	RDX	D	5981	6128	6118	6116
	$C_3H_6N_6O_6$	P		108	103	93.7
	ρ_o=1.00	T		3600	4[illegible]8	4574
	ΔH=14.71					
	HMX	D	9100	9159	9215	9043
	$C_4H_8N_8O_8$	P	393	395	375	392
	ρ_o=1.90	T		2364	3871	4866
	ΔH=11.3					
CHNO	PETN	D	8300	8421	8087	8453
	$C_5H_8N_4O_{12}$	P	335	318	287	322
	ρ_o=1.77	T	3400	2833	4378	5109
	ΔH=−128.7					
	PETN	D	5480	5947	5603	5645
	$C_5H_8N_4O_{12}$	P	87	101	90	87.1
	ρ_o=1.00	T		3970	4731	4888
	ΔH=−128.7					

(Continued)

	TNT	D	6950	7179, 6950*	6878	6934
	$C_7H_5N_3O_6$	P	190	213, 206*	183	193
	ϱ_o=1.64	T		2820, 2937*	3662	4133
	ΔH=−15					
	Tetryl	D	7560	7629	7421	7621
	$C_7H_5N_5O_8$	P		251	226	240
	ϱ_o=1.70	T		2917	4018	4591
	ΔH=−12					
	TATB	D	7860	8411, 7874*	8458	7931
	$C_6H_6N_6O_6$	P	315	326, 297*	304	271
	ϱ_o=1.895	T		1887, 2128*	3270	3799
	ΔH=−33.4					
	NM	D	6290	6463	6339	6139
	CH_3NO_2	P	141	130	124	116
	ϱ_o=1.128	T	3380, 3800(4)	3120	3790	3878
	ΔH=−27					
	HNB	D	9300	8466	8411	9115
	$C_6N_6O_{12}$	P		355	321	371
	ϱ_o=1.973	T		3269	4893	6135
	ΔH=35					
	BTF	D	8485	8156	8241	8610
	$C_6N_6O_6$	P		325	331	385
CNO	ϱ_o=1.859	T		4059	5228	6214
	ΔH=147					
	TNTAB	D	8576	8094	8357	8678
	$C_6N_{12}O_6$	P		300	317	359
	ϱ_o=1.74	T		4046	5282	6250
	ΔH=270					
	Ammonium					
	Nitrate	D	4500	5262	4578	4354
	$H_4N_2O_3$	P		73.2	52.3	50.3
	ϱ_o=1.05	T		1112	1642	2218
	ΔH=−79					
HNO						
	RXAC					
	$H_{32.69}$					
	$N_{16.84}$	D	8025	9393	9240	7813
	$O_{3.0}$	P	228	227	201	152
	ϱ_o=1.14	T	2180	1008	1816	250-
	ΔH=24					
	TFNA	D	7400	7569		7457
CHNOF	$C_5H_7N_4O_6F_3$	P	249	242		229
	ϱ_o=1.692	T		2204		4291
	ΔH=−180					
	1,2DP	D	5960(6)	6430(6), 6790 (JCZ3)(6)		6079
CHNF	$C_3H_6N_2F_4$	P	140(6)	175(6), 165 (JCZ3)(6)		110
	ϱ_o=1.26	T		3614(6), 4910 (JCZ3)(6)		5705
	ΔH=−39.3					
	Nitric Oxide	D	5620	5607	5145	5268
NO	NO	P	103	106	91	103
	ϱ_o=1.30	T		1854	2635	3467
	ΔH=21.1					

(Continued)

HN	Hydrazine Azide H_5N_5 ϱ_0=1.00 ΔH=44	D	6000	7390	6534
		P		135	98.3
		T		1400	2575

Units: ϱ_0=g/cc, ΔH=kcal/mole, D=M/sec, P=Kbar, T=°K
*notes Mader's TNT parameters.
RDX Cyclotrimethylene trinitramine
TNT Trinitrotoluene
HMX Cyclotetramethylene tetranitramine
PETN Pentaerythritol tetranitrate
Tetryl N-Methyl-N,2,4,6-tetranitroaniline
TATB 1,3,5-Triamino-2,4,6-trinitrobenzene
NM Nitromethane
HNB Hexanitrobenzene
BTF Benzotris (1,2,5-oxadiazole-oxide)
TNTAB 1,3,5-Triazido-2,4,6-trinitrobenzene
TFNA 1,1,1-Trifluoro-3,5,5-trinitro-3-azahexane
1,2-DP 1,2-bis(difluoramino) propane
RXAC 70/30 Hyrdrazine/Hydrazine nitrate

TABLE 4

RDX (ϱ_0=1.80) Detonation Products Computed in the Number of Moles per Mole of Explosive

species	BKW(9)	LJD(9)	this paper
H_2O	3.00	2.96	2.972
H_2		0.023	0.007
CO_2	1.49	1.45	1.238
CO	0.022	0.101	0.365
NH_3			0.008
NO		0.034	0.187
N_2	3.00	2.96	2.902
CH_4		0.008	0.004
C(solid)	1.49	1.44	1.392

TABLE 5

RDX (ϱ_0=1.00) Detonation Products Computed in the Number of Moles per Mole of Explosive

species	BKW(9)	LJD(9)	this paper
H_2O	2.80	2.20	2.433
H_2	0.111	0.512	0.380
CO_2	0.67	0.93	0.595
CO	1.855	1.925	2.359
NH_3	0.029		0.064
NO		0.012	0.016
N_2	2.98	2.99	2.960
CH_4	0.021	0.144	0.045
C(solid)	0.45	0.00	0.000

TABLE 6

RXAC (ϱ_0=1.14) Detonation Products Computed in the Number of Moles per Mole of Explosive

species	BKW(9)	LJD(9)	this paper
H_2O	3.00	3.00	3.00
H_2		0.616	0.853
NH_3	8.895	8.480	8.326
N_2	3.97	4.18	4.258

TABLE 7

PETN (ϱ_0=1.77) Detonation Products Computed in the Number of Moles per Mole of Explosive

species	BKW(9)	LJD(9)	this paper
H_2O	4.00	3.93	3.967
H_2			0.010
CO_2	3.89	3.78	3.422
CO	0.223	0.447	0.947
NH_3			0.007
NO		0.062	0.240
N_2	2.00	1.97	1.876
CH_4		0.012	0.005
C(solid)	0.89	0.76	0.625

TABLE 8

HNB (ϱ_0=1.973) Detonation Products Computed in the Number of Moles per Mole of Explosive

species	BKW(9)	LJD(9)	this paper
O_2			0.007
CO_2	5.98	5.51	4.993
CO	0.019	0.488	1.007
NO	0.009	0.843	0.992
N_2	2.99	2.76	2.504

TABLE 9
The Quantities of VLW EOS Itself of Typical Explosives

	RDX(ϱ_0=1.80)	TNT(ϱ_0=1.64)	PETN(ϱ_0=1.77)	TFNA(ϱ_0=1.692)
b_0	53.87	55.61	57.83	49.60
v	11.414	13.78	12.49	12.06
T*	36.40	29.11	33.28	34.817
B*	0.522	0.527	0.525	0.5241
C*	0.2125	0.227	0.2186	0.2160
D*	0.0133	0.0142	0.0137	0.0135
B	28.108	29.317	30.366	25.996
C	616.47	701.88	730.9	530.7
D	2075.6	2439.5	2641.0	1645.3
WB*	2.463	2.127	2.432	2.155
W^2q	4.732	3.696	4.687	3.649
$W^3q/16$	1.396	0.9323	1.356	0.938
Pv/RT	9.590	7.756	9.476	7.734

B*, C*, and D* are the reduced second, third and fourth virial coefficient. B,C, and D are the second, third and fourth virial coefficient. Units: B=cc/mole, C=(cc/mole)^2, D=(cc/mole)^3, b_0=cc/mole, v=cc/mole

CONCLUSION

From

$$Pv/RT=1+WB^*+W^2q+W^3q/16$$
$$=1+B/v+C/v^2+D/v^3$$
$$=1+2.463+4.732+1.396$$
$$=9.59 \text{ (RDX for example)}$$

it follows that

(A) The value of VLW EOS increases from the first term to the third which is the maximum, and then decreases rapidly.

(B)The second and the third terms, and the value of virial coefficients of them are fairly in agreement with those from numerical calculation by Hirchfelder and Curtiss (11) over the interest range of T*, exert the greatest influence on calculation of the VLW equation of state.

To summarize, it may be said that the VLW equation of state is probably more reliable for detonation products of explosives and perhaps as satisfactory as any which has yet been proposed, insofar an agreement between results and experimental data is concerned. However, the isentrope calculation still remains to be done in future.

ACKNOWLEDGEMENTS

The author wishes to thank Dr. C. L. Mader for his advice. In fact, the FORTRAN VLW code is based upon his FORTRAN BKW code. The author is indebted to Professor Yu Feng, Professor Li Fuping, Professor Zhang Mingnan, Professor Ding Jing, and Engineer Yang Zhengquan for their encouragement and support during the course of this work.

REFERENCES

1. F.V. Bvacco, Comments on the Equation of State of High Density Explosives, Combustion and Flame 22,9 (1974).
2. J.C. Edwards and R.F. Chaiken, Detonation with A percus-Yevik Equation of State, Combustion and Flame 22,296 (1974).
3. L.H. Nosanow, J. Chem. Phys. 30, 1596 (1959).
4. F.G. Gibson, etc., J. Applied Phys. 29, 628 (1958).

5. C.L. Mader, FORTRAN BKW: A Code for Computing the Detonation Properties of Explosives, LA-3704 (1967).
6. M. Finger, E. Lee, etc., The Effects of Elemental Composition on Detonation Behavior of Explosives, AD AO59120 (1978).
7. R.F. Chaiken, E. Cook and T. Ruke, Toxic Fumes from Explosives: Ammonium Nitrate-Fuel Oil Mixture, U.S. Bureau of Mines Report of Investigations, 7867 (1974).
8. Zhang Guangjian, On Similarity (Private Communication) (1982).
9. C.L. Mader, Numerical Modeling of Detonation (California 1979).
10. Qian Xuesen, Text Book of Physical Mechanic (Scientific Press, Beijing 1962)(In Chinese).
11. J.O. Hirschfelder and C.F. Cutiss, Molecular Theory of Gases and Liquids (New York 1954).

CALCULATION OF DETONATION PRODUCTS BY MEANS OF THE CS HARD-SPHERE EQUATION OF STATE

K. K. Feng
Canadian Explosives Research Laboratory
Ottawa, Canada

W. K. Chung and B. C.-Y. Lu
University of Ottawa
Ottawa, Canada

Detonation calculations at the Chapman-Jouguet (CJ) state were carried out by means of the Carnahan-Starling (CS) hard-sphere equation of state together with the TIGER code for eleven CHNO explosives, including TNT, TATB, NM, RDX, HMX and PETN. The calculated results are compared with those obtained from the equation proposed by Chirat and Pittion-Rossillon and from the JCZ 3 model. While the detonation velocity and pressure values obtained from the CS equation are less satisfactory than the other two methods, the CS equation is the only one that yields the variation of detonation temperature as a function of loading density with a trend following that indicated by the experimental values. The predicted presence of solid carbon at the CJ state is more consistent the results reported by Chirat and Pittion-Rossillon. The applicability of the CS equation to detonation calculations for slurry explosives has also been demonstrated.

INTRODUCTION

Various equations of state have been used to establish the performance of explosives. Among the frequently used equations are the Becker-Kistiakowsky-Wilson (BKW) (1), JCZ 2 (2), JCZ 3 (2), BRL-SRI (3) and the compressibility form of the Percus-Yevick (PYC) (4,5) equation. In a recent article (6), five hard-sphere equations of state (EOS) were used for calculating the Chapman-Jouguet (CJ) detonation velocity, pressure, and temperature for two explosives (PETN and ANFO). The analytical expressions of the compressibility factor for hard-sphere EOS included those proposed by Carnahan-Starling (CS) (7), Guggenheim (8), Thiele (4), Scott (9) and the PYC EOS. The calculated values obtained from these hard-sphere EOS as well as those obtained from the BKW, JCZ 2, JCZ 3 and BRL-SRI equations were compared with experimental values reported in the literature, and the relative performance of these equations was evaluated. The results indicate that, with the inclusion of an adjustable parameter, the hard-sphere EOS can yield approximately the same values for CJ detonation velocity, pressure, and temperature. The CS hard-sphere EOS was selected because it yields a virial expression very close to that of Rae and Hoover (10). The calculated CJ detonation temperatures for PETN from this equation are closer to the experimental values than the other EOS investigated (6).

Recently, Chirat and Pittion-Rossillon (CPR) (11,12) modified the Weeks-Chandler-Andensen (WCA) model for liquid and applied their EOS to a number of CHNO explosives. The major components of a CHNO explosive at the CJ state are CO_2, H_2O, CO, N_2 and sometimes solid carbon. In order to obtain good evaluation of explosive values from their EOS, it is necessary to know the value of three potential parameters for each major detonation product.

In their calculation, an unpublished chemical equilibrium code (ETARC code) was used.

It should be mentioned that in the application of the CS hard-sphere EOS, an existing chemical equilibrium detonation computer code (TIGER) was used to compute the detonation properties of the various explosives.

One of the objectives of this study is to apply the CS hard-sphere EOS to a number of CHNO explosives and to compare the results with those obtained from the more complex CPR EOS.

Another objective of this study is to extend the CS hard-sphere EOS to the calculation of detonations properties of slurry explosives and to compare the results with those obtained from the BKW EOS, using the modified parameter suggested by Mohan and Hay (13).

It is also intended to include the results obtained from the JCZ 3 model for comparison.

CARNAHAN-STARLING HARD-SPHERE EOS

The CS hard-sphere EOS used in the calculation is of the following form

$$P = RT\,(1+y+y^2-y^3)\,/\,V(1-y)^3 \qquad (1)$$

where P is the pressure; T, the absolute temperature; V, the molar volume; and R, the gas constant. The quantity y is a density variable and is defined by

$$y = \pi\, N_d \sigma^3/6 \qquad (2)$$

where N_d is the number density and σ, the molecular diameter. In the calculation, the expression for the quantity σ^3 for mixtures followed that adopted by Edwards and Chaiken (14),

$$\sigma^3 = \lambda \sum_{i=1}^{n} \sum_{j=1}^{n} x_i\, x_j\, \sigma_{ij}^3 \qquad (3)$$

where $\sigma_{ij} = (\sigma_i+\sigma_j)/2$; n is the number of species; x_i, the mole fraction of species i; and λ, the adjustable parameter. In this work, a λ value of 0.35 was used throughout the calculation.

CALCULATION RESULTS

CJ detonation calculations were carried out for eleven CHNO explosives and twelve slurry explosives. The standard heats of formation of the CHNO explosives and the components of slurry explosives are presented in Table 1. The values for the eleven CHNO explosives were taken from Hardesty and Kennedy (15); and for the slurry components, from Ref. 16-19.

CHNO Explosives

The results obtained from the CS hard-sphere EOS for the eleven selected CHNO explosives are presented in Tables 2-4. The possible presence of solid carbon at the CJ point for the eleven CHNO explosives investigated is presented in Table 2, and the calculated CJ detonation velocity (D_{CJ}), pressure (P_{CJ}) and temperature (T_{CJ}) for these explosives are presented in Table 3. The results reported by Chirat and Pittion-Rossillon (12), and the values obtained from the JCZ 3 model are also included in these two tables for comparison. In addition, the CJ temperatures obtained for TETRYL, RDX, PETN and NG are depicted in Figures 1 to 4, respectively. Experimental values reported by Gibson et al. (20), together with the calculated values obtained from the JCZ 3 model and the CPR equation for these four explosives are included in these figures for comparison. The CJ temperatures obtained for the other seven CHNO explosives are compared with those reported by Chirat and Pittion-Rossillon and those calculated from the JCZ 3 model in Figure 5. The concentration of the gas components in the detonation product at the CJ state were obtained for all eleven CHNO explosives. However, due to the lack of experimental and calculated values in the literature on the compositions produced at the CJ state, no meaningful comparison can be made for all the eleven explosives. For this reason, only the concentrations of the major gas components obtained for PETN at the CJ state are reported (Table 4).

Slurry Explosives

An attempt was made in this study to extend the application of the CS hard-sphere EOS to the calculation of detonation properties for slurry explosives. A total of twelve slurry explosives were arbitrarily selected. The elemental compositions of these explosives are pre-

TABLE 1
Standard Heats of Formation at 298.15 K

Explosive or Component of Slurry Explosive	Chemical Formula	ΔH_f° (Kcal/mole)	Ref.
TNT	$C_7H_5N_3O_6$	− 15.00	15
HNS	$C_{14}H_6N_6O_{12}$	13.88	15
TATB	$C_6H_6N_6O_6$	− 36.85	15
DATB	$C_6H_5N_5O_6$	− 29.2	15
TETRYL	$C_7H_5N_5O_8$	4.67	15
NM	CH_3NO_2	− 27.03	15
NQ	$CH_4N_4O_2$	− 23.60	15
RDX	$C_3H_6N_6O_6$	14.71	15
HMX	$C_4H_8N_8O_8$	17.93	15
PETN	$C_5H_8N_4O_{12}$	−128.70	15
NG	$C_3H_5N_3O_9$	− 90.80	15
AN	$H_4N_2O_3$	− 87.40	16
Sodium Nitrate	$NaNO_3$	−111.70	16
Water	H_2O	− 68.40	17
Man	$CH_3NH_3NO_3$	− 58.00	17
Guar	$C_6H_{12}O_6$	− 55.40	18
Silica	S_iO_2	−202.46	16
Aluminum	Al	0.0	16
Calcium Nitrate	CaN_2O_6	−224.05	16
Ethylene Glycol	$C_2H_6O_2$	−107.91	16
Fuel Oil	$C_{7.17}H_{14}$	− 45.00	19
Carbon	C	0.0	16

TABLE 2

Correlation Between Oxygen Balance, Solid Carbon Phase

Explosive	Oxygen Balance	Solid Carbon at the CJ Point		
		CS	JCZ3	CPR
TNT	− 0.74	Yes	Yes	Yes
HNS	− 0.667	Yes	Yes	Yes
TATB	− 0.560	Yes	Yes	Yes
DATB	− 0.559	Yes	Yes	Yes
TETRYL	− 0.474	Yes	Yes	Yes
NM	− 0.39	No	Yes	No
NQ	− 0.307	No	Yes	Yes
RDX	− 0.22	No	Yes	No
HMX	−0.216	No	Yes	No
PETN	− 0.100	No	No	No
NG	0.035	No	No	No

TABLE 3

Calculated CJ Detonation Properties for Eleven CHNO Explosives

Explosive	Loading density ϱ(g/cm^3)	CS			JCZ 3			CPR		
		D_{CJ} (m/s)	P_{CJ} (GPa)	T_{CJ} (K)	D_{CJ} (m/s)	P_{CJ} (GPa)	T_{CJ} (K)	D_{CJ} (m/s)	P_{CJ} (GPa)	T_{CJ} (K)
TNT	1.00	4024	4.36	3305	5101	7.34	3500	4910	6.34	3230
	1.64	6370	14.39	3904	6912	18.95	3647	7018	19.51	3330
HNS	1.00	4291	4.81	3635	5196	7.62	3774	4951	6.35	3467
	1.30	5736	9.53	3931	5797	11.94	3951	—	—	—
	1.50	6047	12.23	4128	6617	16.50	4004	—	—	—
TATB	1.25	5505	8.08	3178	5811	10.75	3222	4924	6.30	2911
	1.50	6098	11.51	3382	6581	15.48	3191	—	—	—
	1.75	8369	21.90	3661	7503	22.34	3053	—	—	—
	1.85	8617	24.56	3725	8053	26.68	2957	—	—	—
DATB	1.00	3964	4.17	3125	5100	7.22	3307	5147	6.94	3287
	1.79	8817	25.08	3946	7624	23.81	3269	7762	27.00	3278
TETRYL	1.00	4868	6.03	3984	5607	8.97	3957	5354	7.50	3587
	1.70	6925	18.02	4582	7607	23.95	4065	7621	24.44	3616
NM	0.90	4688	5.22	3489	5555	8.15	3394	5430	7.35	3508
	1.13	5285	7.82	3610	6245	12.06	3515	6175	11.44	3421
	1.30	5693	10.05	3695	6700	15.25	3514	—	—	—
NQ	1.25	4758	6.64	2824	6084	11.35	2657	6167	11.66	2512
	1.55	5561	10.24	2937	7453	19.06	2474	7282	20.55	2387
RDX	1.25	6290	11.18	4614	6907	15.97	4145	6867	15.10	4322
	1.77	8146	23.58	4849	8697	31.13	3887	8533	32.98	3788
HMX	1.25	6279	11.14	4599	6898	15.92	4133	6867	15.10	4322
	1.50	7213	16.57	4721	7594	21.81	4083	—	—	—
	1.65	7731	20.30	4788	8087	26.17	3993	—	—	—
PETN	1.00	4880	6.17	4760	5706	8.96	4545	—	—	—
	1.25	5850	9.82	4869	6500	14.18	4499	6504	13.48	4744
	1.77	8463	23.47	5126	8279	29.07	4232	8418	31.89	4314
NG	1.00	4745	5.87	4696	5420	8.07	4610	5287	7.50	4790
	1.60	7013	15.89	4985	7535	21.66	4445	7687	23.40	4582

TABLE 4

Calculated Gas Compositions at the CJ State for PETN (CS Hard-Sphere EOS)

Loading density ρ(g/cm^3)	Concentration (mole/kg)							
	CO_2	H_2O	CO	N_2	H_2	NO	NH_3	Total gas
1.0	9.49	11.65	6.33	6.00	0.89	0.62	0.02	35.31
1.25	9.71	11.69	6.11	6.02	0.85	0.56	0.045	35.14
1.77	10.44	11.32	5.29	5.94	0.69	0.44	0.34	34.55

TABLE 5

Elemental Compositions of Twelve Slurry Explosives

Explosive	Loading density (g/cm^3)	Experimental D_{CJ} (m/sec)	Composition (mole percent)							
			C	H	N	O	Na	Al	Ca	S_i
1	1.509	—	5.39	46.66	11.92	33.57	0.10	0.98	1.37	0.00
2	1.060	—	2.23	44.09	20.09	30.14	0.00	3.45	0.00	0.00
3	1.130	—	3.90	45.42	15.42	32.88	2.38	0.00	0.00	0.00
4	1.400	—	7.04	41.14	15.90	34.32	1.61	0.00	0.00	0.00
5	1.156	—	0.00	52.04	10.84	31.43	0.00	5.72	0.00	0.00
6	1.150	4000	3.14	43.22	12.65	35.60	0.67	3.37	1.34	0.00
7	1.120	4000	2.96	43.09	12.76	35.80	0.80	3.30	1.29	0.00
8	1.300	—	2.63	42.14	12.83	35.03	0.47	5.50	1.41	0.00
9	1.000	3490	2.15	47.26	10.28	36.04	0.65	2.39	1.22	0.00
10	1.180	4280	2.57	42.03	12.68	35.40	0.55	5.32	1.47	0.00
11	1.350	—	3.14	41.70	15.34	33.28	2.91	3.38	0.00	0.23
12	1.350	—	3.58	43.23	15.81	32.56	2.77	0.49	0.00	1.45

TABLE 6

Comparison of Calculated CJ Conditions for Twelve Slurry Explosives

Explosive	CS			JCZ 3			BKW		
	D_{CJ} (m/s)	P_{CJ} (GPa)	T_{CJ} (K)	D_{CJ} (m/s)	P_{CJ} (GPa)	T_{CJ} (K)	D_{CJ} (m/s)	P_{CJ} (GPa)	T_{CJ} (K)
1	4603	7.50	2467	—	—	—	5870	12.80	2283
2	4545	5.56	3777	5506	8.50	3589	4998	7.68	3383
3	4243	4.80	2605	5385	8.00	2391	4903	7.39	2298
4	5184	9.12	3031	6417	12.98	2497	5534	11.28	2355
5	4511	5.77	3473	5335	8.53	3335	6165	8.49	3129
6	3585	4.55	3043	5042	7.23	3191	—	—	—
7	3532	4.68	3020	4883	6.64	3074	—	—	—
8	4250	5.98	3685	5710	10.54	3672	5239	9.64	3474
9	3227	2.80	2387	4278	4.63	2353	—	—	—
10	3724	4.34	3593	4995	7.19	3630	4691	7.06	3470
11	4220	5.65	2703	—	—	—	—	—	—
12	3883	4.62	2040	5790	9.46	1959	—	—	—

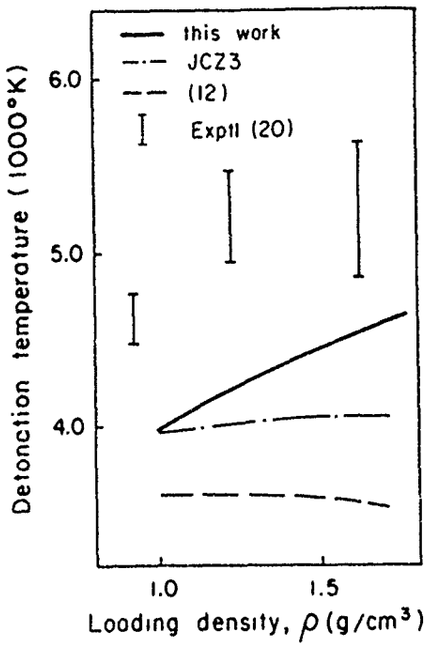

Fig. 1. TETRYL

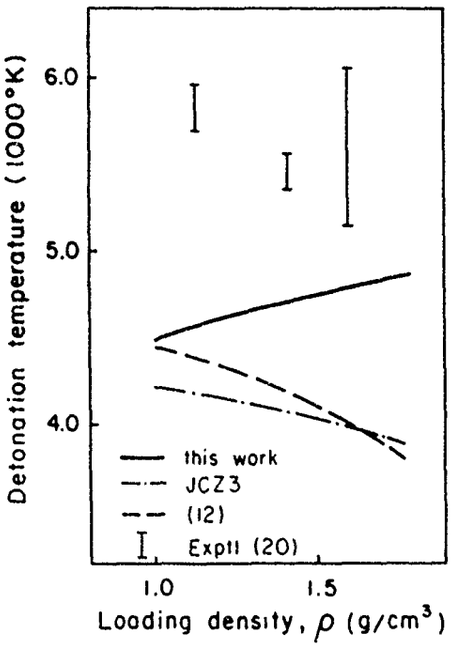

Fig. 2. RDX

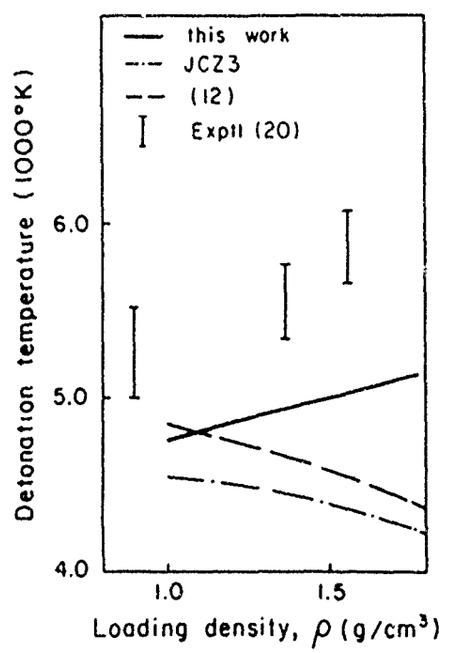

Fig. 3. PL 'N

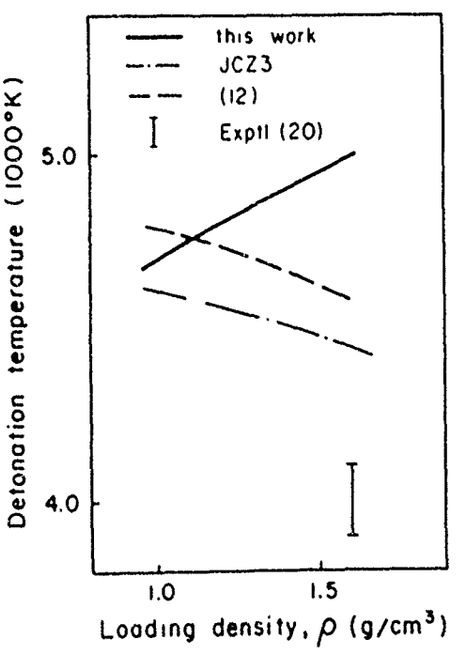

Fig. 4. NG

Figs. 1-4. Comparison of calculated and experimental CJ detonation temperatures

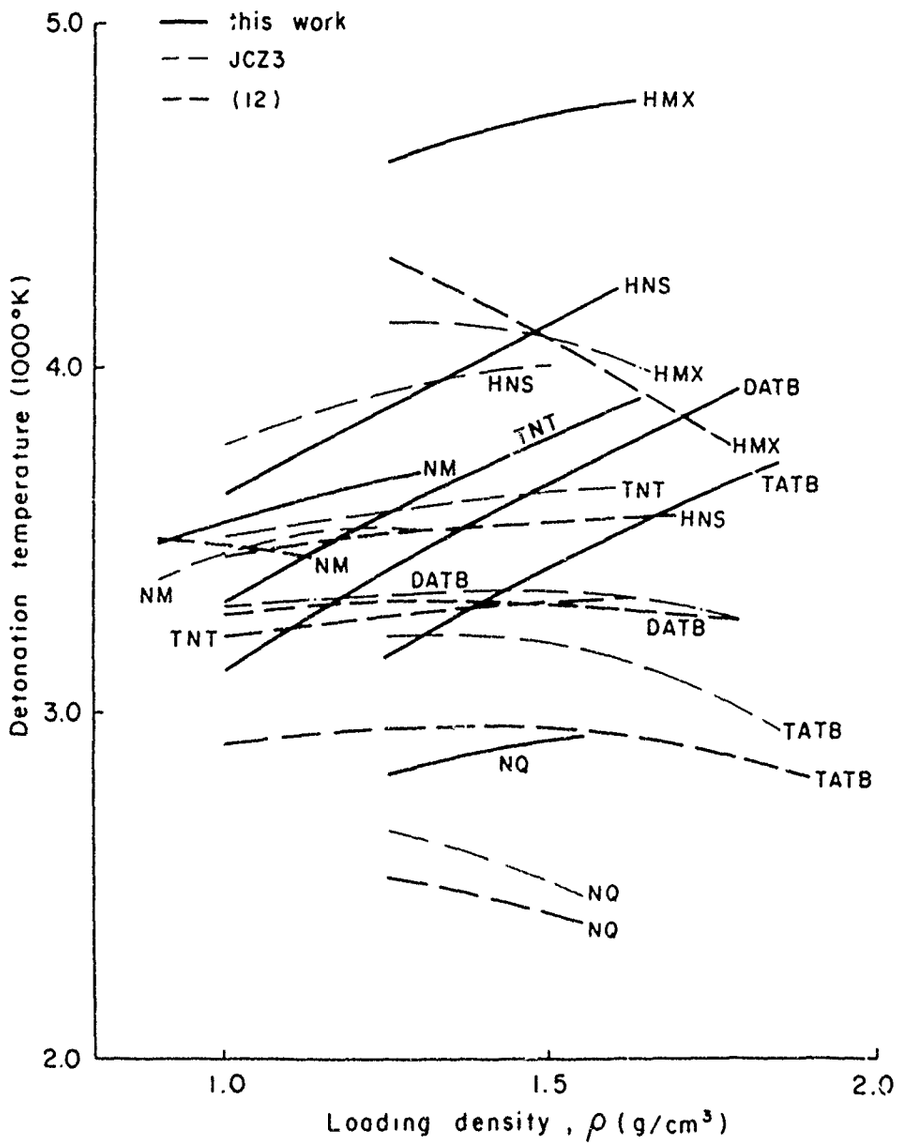

Fig. 5. Comparison of calculated and experimental CJ detonation temperatures for seven CHNO explosives

to use, it does not require any values of the force constant ε/k, and did not encounter any computational difficulties in the calculation.

REFERENCES

1. C. L. Mader, Numerical Modeling of Detonation, pp. 412-418, University of California Press, 1979.
2. M. Cowperthwaithe, W.H. Zwisler, "The JCZ Equation of State for Detonation Products and Their Incorporation into the TIGER CODE," Proceedings of the Sixth Symposium (International) on Detonation, Naval Weapons Center, pp. 162-172, 1976.
3. M. Cowperthwaite and W. H. Zwisler, "Theoretical and Mathematical Formulations for the TIGER Computer Program," Stanford Research Institute, California, 1973.
4. E. T. Thiele, "Equation of State for Hard Spheres," J. Chem. Phys. Vol. 39, pp. 474-479, 1963.
5. M. S. Wertheim, "Analytical Solution of the Percus-Yevick Equation" J. Math. Phys. Vol. 5 No. 5 pp. 643-651, May, 1964.
6. K. K. Feng, W. K. Chung and B. C.-Y. Lu, "Detonation Calculation with Hard-Sphere Equation of State," Proceedings of Twelfth Symposium on Explosives and Pyrotechnics, pp. 163-170, 1984.
7. N. F. Carnahan and K. E. Starling "Equation of State for Non-attracting Rigid Spheres", J. Chem. Phys. Vol. 46, pp. 635-636, 1969.
8. E. A. Guggenheim, "Variation on van der Waals' Equation of State for High Densities," Mol. Phys. Vol. 9. pp. 199-200, 1965.
9. R. L. Scott, "Physical Chemistry, an Advanced Treatise," D. Henderson Ed. Vol. 8A, Chapter 1, Academic Press, New York, 1971.
10. F. H. Rae and W. G. Hoover, "Seventh Virial Coefficients for Hard-Spheres and Hard Disks," J. Chem. Phys. Vol. 46, pp. 4181-4197, 1967.
11. R. Chirat and G. Pittion-Rossillon, "A New Equation of State for Detonation Products," J. Chem. Phys. Vol. 74, No. 8, pp. 4634-4642, April, 1981.
12. R. Chirat and G. Pittion-Rossillon, "A Theoretical Equation of State for Detonation Products: Application to Twelve CHNO Explosives," Combustion and Flame, Vol. 45, pp. 147-159, 1982.
13. V. K. Mohan and J. E. Hay, "Reparameterization of the Becker-Kistiakowsky-Wilson Equation of State for Water-Gel Explosives," Combustion and Flame, Vol. 50, pp. 207-218, 1983.
14. J. C. Edwards and R. F. Chaiken, "Detonation Calculations with a Percus-Yevick Equation of State," U.S. Bureau of Mines, RI 7905, 1974.
15. D. R. Hardesty and J. E. Kennedy, "Thermochemical Estimation of Explosive Energy Output," Combustion and Flame, Vol. 28, pp. 45-59 (1977).
16. R. H. Perry and D. W. Green, Ed. "Perry's Chemical Engineers' Handbook," 6th Ed. Table 3-206. McGraw-Hill, New York, 1984.
17. M. A. Cook, "The Science of High Explosives," p. 404, Reinhold Publishing Co., New York, 1958.
18. "Handbook of Chemistry and Physics" 48th Ed. p. D-189, The Chemical Rubber Co. 1967.
19. R. F. Chaiken, E. B. Cook and T. Rube, "Toxic Fumes From Explosives: Ammonium Nitrate-Fuel Oil Mixtures," p. 309, U.S. Bureau of Mines, RI 7867, 1974.
20. F. C. Gibson, M. L. Bowser, C. R. Summers, F. H. Scott and C. M. Mason, "Use of an Electro-Optical Method to Determine Detonation Temperatures in High Explosives," J. Applied Phys. Vol. 29 No. 4, 628-632, April, 1958.

CONCLUSIONS

1. The hard-sphere equations used in the calculation yield approximately the same values for C-J detonation velocity, pressure and temperature.
2. The hard-sphere compressibility factor is not sufficient enough to make the hard-sphere equation capable of fitting exactly the experimental data for PETN.
3. The calculated C-J detonation velocity and temperature for PETN from hard-sphere equations are closer to the experimental values than other equations of state investigated. However, the BKW equation yields better results for detonation pressure.
4. The calculated results of detonation products for ANFO indicate that the hard-sphere equations are more suitable than many other equations.

EXPANSION ISENTROPES OF TATB COMPOSITIONS RELEASED INTO ARGON

M. Pinègre, J. Aveillé, M. Leroy, J. C. Protat, R. Chéret, and N. Camarcat
Commissariat à l'Energie Atomique, Centre d'études de Vaujours, B.P 7, 77181, Courtry, France

The expansion isentropes of TATB compositions are determined using argon as the adjacent inert medium, the shock impedance of which is varied by adjusting the initial pressure in the experimental chamber. The technique requires a precise knowledge of the thermodynamic properties of argon in the region of parameter space of interest. The experimental results obtained are compared to isentrope data of other workers (1) using Doppler Laser Interferometry (DLI) measurements of thin flyer plates driven by the same explosives. Comparisons to calculations using various equations of state (2,3) are also reported. Possible improvements are examined, particularly in the choice of the argon equation of state.

I. INTRODUCTION

The method of impedance matching is widely used to determine experimentally the expansion isentrope of high explosives. This is equivalent to the knowledge of the equation of state of the detonation products in a limited region (i.e. a curve) in p,v space. Experimental points are obtained by measuring the velocity of the shock induced by the explosive in adjacent media of various impedances. Argon is well suited for this task since the shock impedance can be varied by adjusting the initial pressure in the experimental chamber. This paper reports on the use of such a method to measure the expansion isentrope of TATB compositions in the pressure range 0.1-17 GPa. It requires a precise knowledge of the thermodynamic properties of argon in the region of parameter space of interest. These features and the experimental conditions are examined in Section II. Section III deals with the experimental results obtained with the argon technique and compares them to isentrope data of other workers using Doppler Laser Interferometry (1) (DLI) measurements of thin flyer plates driven by the same composition. Comparisons to calculations (2) using various equations of state (EOS) are also reported. Section IV examines possible improvements, in the experimental determination of the argon equation of state.

II. THE SHOCK DRIVEN IN ARGON

A. Apparatus. The impedance matching technique with inert argon in contact with the detonating explosive, is recalled in Fig. 1. U is the shock velocity in argon, P_o and ϱ_o the initial argon pressure and density, p and u are the pressure and the particle velocity (lab. frame) behind the shock front. Subscript o refers to the region not reached by the shock. To each initial pressure in argon P_o corresponds an argon Hugoniot $H(P_o)$. In p,u space, and with the help of the familiar conservation equations, this curve is defined by

$$u = u(U,P_o) \tag{1}$$

$$p = P_o + \varrho_o U u \tag{2}$$

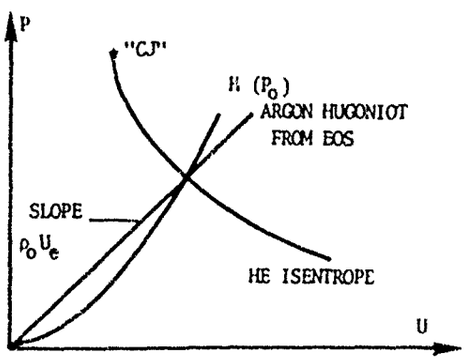

Fig. 1. The impedance matching technique

The intersection in (p,u) space of the $H(P_o)$ curve with the line of slope $\varrho_o U$ gives a point of the detonation product expansion isentrope provided that $H(P_o)$ is below the CJ point. Practically, an experimental shock velocity U_e is measured in argon, and the intersection of the corresponding straight line

$$p - P_o = \varrho_o U_e u \tag{3}$$

with $H(P_o)$ gives the point required on the HE isentrope. The experimental effort is therefore directed towards measuring U_e while the theoretical effort is devoted to obtaining a precise equation of state for argon since this is the critical factor affecting $u(U,P_o)$.

Figure 2 shows the experimental chamber containing the explosive cylinder and argon at initial pressure P_o. The explosive composition is initiated by an external plane wave generator outside the chamber flange. The pressure pulse is transmitted through the flange to an HMX booster inside the chamber which in turn initiates the TATB explosive tested. It consists of a straight cylinder with dimensions: O.D 50 mm, height 200 mm, initial density between 1.879 and 1.886 g/cm³. Corrections to the experimental measurements (Section III.A) are performed to compare the argon experiments to those with different adjacent media (water or solids) and different dimensions of the explosive cylinders (O.D 100mm, height 200 mm). The shock driven in argon by the detonation is recorded with a streak camera (CF6) and backlighted by a flash at high initial argon pressures. At low initial filling pressures, shocked argon emits enough light so that a backlighting source is no longer needed. Typical experimental records are shown in Fig. 3. At low initial pressures (P_o=1 MPa) argon is ionized, while at higher pressures (P_o=70.5 MPa) ionization is not seen.

B. Argon Equation of State. The conservation equations are written as (4)

$$p - P_o = \varrho_o U u \tag{4}$$

$$h - h_o = \frac{1}{2}(p - P_o)\left(\frac{1}{\varrho_o} + \frac{1}{\varrho}\right) \tag{5}$$

$$\varrho_o U = \varrho(U - u) \tag{6}$$

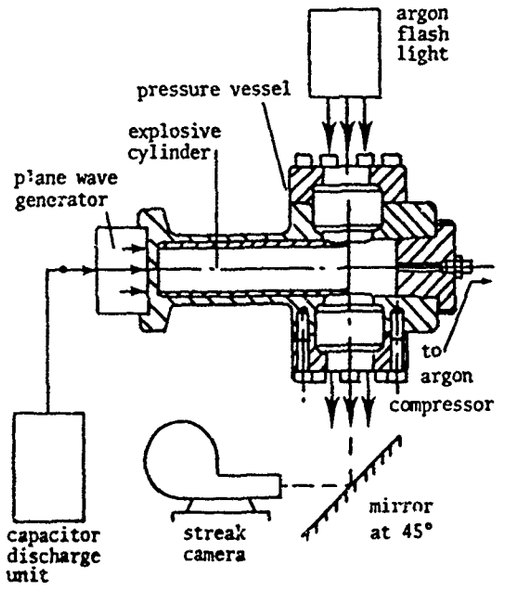

Fig. 2. Experimental Set-up

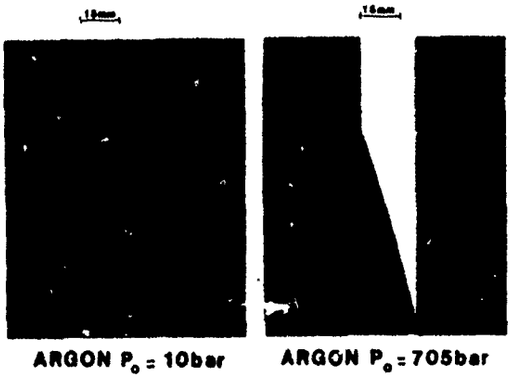

Fig. 3. Shock wave propagation in argon streak camera records composition T2

Standard texts (4) give U in terms of u when h is the enthalpy of an ideal gas with specific heat ratio γ

$$h(p,\varrho) = \frac{\gamma}{\gamma - 1}\frac{p}{\varrho} \tag{7}$$

For practical considerations, the temperature is introduced with the "engineering" form of the equation of state (4)

$$\begin{array}{ll} p = p(\varrho,T) & T = T(\varrho,p) \\ \text{or} & \\ h = h(\varrho,T) & h = h(\varrho,T) \end{array} \tag{8}$$

The use of an ideal gas equation of state in (5) leads to uncorrect curves $U(u,P_o)$ and therefore to HE expansion isentropes nearly an order of magnitude below the experimental ones in (p,u) space, for $p < 1$ GPa. Ionization has to be taken into account. Our approach follows the general procedure outlined by Zel'dovich-Raizer (4). The free energy $F(T,\varrho)$ is expressed in terms of partition functions $Z(T,\varrho)$. Equations (8) for $h(T,\varrho)$ and $p(T,\varrho)$ are obtained through thermodynamic derivatives of F. Ionization is introduced through the partition functions of the translational degrees of freedom and of the electrons. Then

$$Z(T,\varrho) = Z_{trans}(T,\varrho)\, Z_{el}(T,\varrho) \qquad (9)$$

When $Z_{eL} = 1$, i.e. ionization is absent, eq. (9) yields the standard ideal gas equation (7).

The free energy of the ionized mixture is obtained by minimizing F with respect to the numbers per unit mass of argon atoms N_{A^o}, argon ions N_{A^+} and electrons N_e under the constraints set by the ionization reaction

$$A \longrightarrow A^+ + e \qquad (10)$$

Introducing the degree of ionization

$\alpha = N_{A^+}/N_{A^o}$ one obtains a quadratic expression for α with density and temperature dependent coefficients

$$\frac{\alpha^2 - 1}{\alpha} = \frac{1}{\varrho N_{A,o}} K(T) \qquad (11)$$

$K(T)$ is the dissociative equilibrium constant of the ionization reaction (10). If I is the ionization potential, M the atomic mass of argon, m_e the electron mass, h_p the Planck constant, $Q_i(T)$ and $Q_o(T)$ the partition functions of the ion and neutral atom, K is given by

$$K = 2\,\frac{Q_i(T)}{Q_o(T)}\left[\frac{2\pi\, m_e\, kT}{h_p^2}\right]^{3/2} e^{-\frac{I}{kT}} \qquad (12)$$

We have modified the standard (4,5) notations u_i and u_o for the partition functions. Equations (8) become for the non ideal state

$$p = (1+\alpha)\varrho\, r\, T \qquad (13)$$

$$h = \frac{5}{2}(1+\alpha)\, r\, T + \frac{\alpha I}{M} \qquad (14)$$

this neglects the contribution of the excited states of A, A^+ to the specific enthalpy h.

Various approximations (4,5) are commonly used to compute Q_i, Q_o, I, since the sums contributing to the partition functions Q_i have to be truncated after a finite number of terms n* depending on α. A lowering correction Δ to the ionization potential is introduced, taking into account the effect of the free electrons, i.e., α. Then $n^* \sim (I_o/\Delta)^{1/2}$. We follow approximately the Unsold theory outlined in ref. (5). Assuming $T = 20000\,^\circ K$ and $\Delta = 0$, we look-up Q_i/Q_o in a table (5) and calculate α from (11). Next we compute Δ from a Debye-Hückel potential surrounding the argon ions.

$$\Delta = \frac{e^3}{3}\left[\frac{\pi\,\varrho}{M\,kT}\right]^{1/2}(2\alpha)^{1/2}\,\frac{6+4\alpha}{1+\alpha} \qquad (15)$$

The value $I = I_o - \Delta$ with $I_o = 15.85$ eV is then used in all the other α calculations at any ϱ,T.

In the medium argon pressure range $1 < P_o < 12$ MPa, the results obtained are reasonable. For lower initial pressures, and high U_e's the calculated values of α are large, above 0.1. One should therefore take into account multiple ionizations. However, comparison of our results to those of ref. (6) including multiple ionization shows only a 4% difference for u, our values being smaller, and an 8% difference for p, our values being greater. (For T and ϱ, which are less significant here, discrepancies can reach a factor 2.) At higher initial pressures $P_o > 12$ Mpa, the hypotheses of ideal gas translational partition function in eqn. (9) has to be altered. This applies both upstream and downstream of the shock. Equation (13) becomes

$$p(\varrho) = p^o(\varrho) + p^+(\varrho) \qquad (16)$$

p^o referring to the neutral atoms in the mixture and p^+ to the ions. For $p^o(\varrho)$ we follow F. H. Ree (7), and $p^+(\varrho)$ includes the Coulomb interactions between charged particles.

$$p^+(\varrho) = \alpha\,\varrho\, r\, T - \frac{1}{24\pi}\left[\frac{1}{kT}\right]^{1/2}\left[\frac{2\alpha\varrho e^2}{\varepsilon_o M}\right]^{3/2} \qquad (17)$$

e is the electron charge and ε_o the dielectric constant of vacuum. The specific enthalpy (7) becomes

$$h = \frac{3}{2}rT + \frac{p}{\varrho} + \int_0^{\varrho}\left[p - T\frac{\partial p}{\partial T}\right]\frac{d\varrho}{\varrho^2} + \frac{5}{2}\alpha rT + \alpha\frac{I}{M} - h^+ \quad (18)$$

$$h^+ = (e^3/6\pi)\,(\varrho/kT)^{1/2}\,(2\alpha/\varepsilon_0 M)^{3/2} \quad (19)$$

The degree of ionization is obtained from (11) and (12) as above, with the dissociative equilibrium constant K of the ideal gas.

In the expansion isentropes (composition T_i) obtained with these thermodynamic hypotheses, the influence of the non ideal gas translational partition function is seen for p>7 GPa, i.e., P_0>12 MPa. Starting with the same primary data the experimental U_s's, the different expansion isentropes in (p,u) space corresponding to the ideal and non ideal gas argon Hugoniot diverge above 7 GPa while agreement between the two curves is reasonable below this value.

III. EXPANSION ISENTROPES FOR TATB COMPOSITIONS

A. Data reduction techniques. The simple theory of impedance matching outlined in Section I is strictly valid for shock transmission between two inert media. Detonation waves consist (in the ZND model) of a shock front followed by a reaction zone, which is not taken into account in the derivation of eqns. (1)-(3). Experimentally, the influence of the reaction zone thickness is evidenced by the axial decrease of U_e along the z axis (Fig. 2) with different values at z=0 mm and z=3 mm noted U_0 and U_3. Beyond z=3 mm, the shock velocity remains more or less constant. This is evidenced in Fig. 4 where $U_0 - U_3$ is plotted against P_0 for composition T_1 and T_2.

J. Thouvenin (8) has proposed a model in which the position (at time t) of the shock front in argon x measured by the streak camera can be expressed by (λ<1)

$$x_s = \frac{Ut^4}{\lambda\tau_A{}^{41}} \qquad \text{for } t < \tau_A$$

$$x_s = U(t - \tau_A) + \frac{U\tau_A}{\lambda} \qquad \text{for } t > \tau_A \quad (20a)$$

τ_A depending on the shock impedance of the adjacent medium, and on the reaction zone

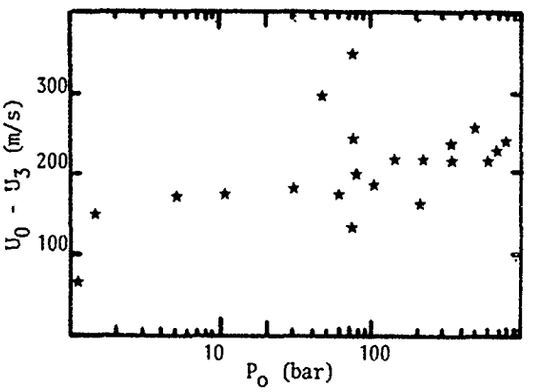

Fig. 4a. Influence of the reaction zone thickness on the argon shock velocity U_e for composition T_1

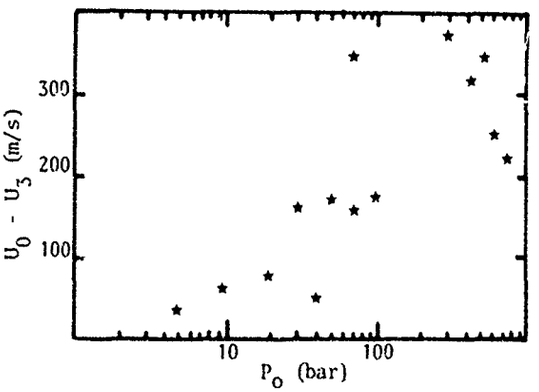

Fig. 4b. Influence of the reaction zone thickness on the argon shock velocity U_e for composition T_2

thickness z. The following empirical dependence of τ_A on the initial argon pressure P_0 has been found

$$\tau_A(0.5\text{ MPa}) > \tau_A(70.5\text{ MPa}) > z/D_* \quad (20b)$$

D_* being the extrapolated stick detonation velocity, z the values proposed by Pujols (1) (1.2 and 1.5 mm for TATB compositions T_1 and T_2). For composition T_2 we obtain from streak camera data

$$\tau_A(0.5\text{ MPa}) = 550\text{ ns} \quad x_A = 3.62\text{ mm}$$

$$\tau_A(70.5\text{ MPa}) = 380\text{ ns} \quad x_A = 2.33\text{ mm} \quad (21)$$

$$\tau_A(P_0) = \frac{\tau_A(70.5) - \tau_A(0.5)}{70}(P_0 - 0.5)$$

for $0.5 < P_0 < 70.5$ MPa

The experimental shock velocity U_e is measured on the film at position x_A corresponding to τ_A.

Density corrections are also taken into account for high initial argon pressures which modify the initial density and the detonation velocity in the explosive stick. At $P_o = 70$ MPa, the explosive density variation results in a variation of D of 90 m/s which is significant. For this reason, all the data are normalized to the detonation velocity in a reference stick with φ_n=100 mm, h_n=200 mm, $\varrho_{n,1}$=1.880 g/cm^3, $\varrho_{n,2}$=1.855 g/cm^3. For such sticks, $D_{n,1}$= 7715±10 m/s (composition T_1) and $D_{n,2}$=7685±10 m/s (composition T_2). If subscript e refers to experimental measurements, the following normalizing procedure is used:

$$U_n = U_e \frac{D_n}{D_{50} + A(\varrho_e - \varrho_n) + AK\varrho_e} \quad (22)$$

D_{50} = 7600±10 m/s for composition T_2 ,

A_2 = 2.900 m^4.s^{-1}.kg^{-1}

D_{50} = 7662±10 m/s for composition T_1 ,

A_1 = 2.787 m^4.s^{-1}.kg^{-1}

K being the (measured) relative volume variation $\Delta V/V$ at pressure P_o. This allows the comparison of the argon isentrope results to those where the adjacent medium is a solid, with different dimensions and initial density for the explosive cylinder.

B. RESULTS AND DISCUSSION

Figure 5 shows the expansion isentrope of composition T_2 in (p,u) space for 0.34 GPa < p < 24.9 GPa. The corresponding tabulated values are shown in Table 1, both for argon experiments and for water and solid adjacent media up to 48.8 GPa. In the low pressure part p < 3.3 Gpa including our argon data, Doppler Laser Interferometry (DLI) measurements on the same composition have been published independently by H. C. Pujols (1).

The good agreement between the DLI and argon experimental data supports the validity of our argon equation of state for P_o < 7 MPa (p < 3.42 GPa) as described in Section II. The

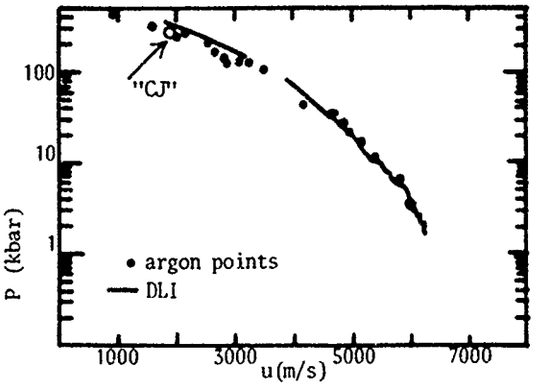

Fig. 5. Detonation product Hugoniot and expansion isentrope for composition T_2. The DLI points for this composition are due to the courtesy of H. C. Pujols.

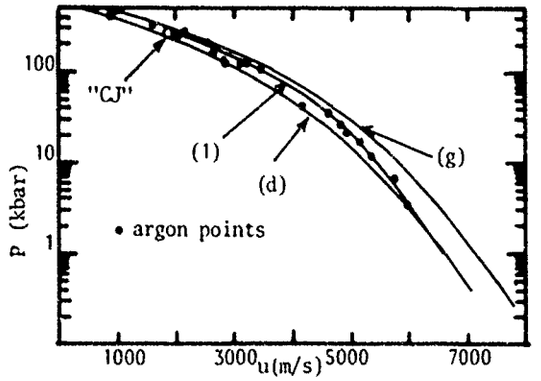

Fig. 6. Comparison of experimental results to calculations for composition T_2. The calculated curves are due to the courtesy of Mrs. Chirat-Baute (g, d) and Sorel-Vanpoperynghe (1). The g and d curves refer to carbon formed in the graphite or diamond phase.

last argon point in Table 1 comparable to the DLI measurement (shot # 17) gives (p,u) = (4.34 GPa, 4169 m/s) to be compared to the nearby point of Pujols (4.06 GPa, 4738 m/s). This could indicate that above 3.4 GPa the argon EOS described in Section II yields experimental isentrope points "too low" in (p,u) space.

Next we compare (for composition T_2) the isentrope experimental results to the theoretical calculations obtained with 2 equations of state coupled to thermochemical codes determining the molar composition of the detonation products.

TABLE 1

Experimental Isentrope Data for Composition T_2

shot #	dens. T_2 (g/cc)	geom. T_2 (mm)	adjacent medium	T_o (°K)	P_o (bar)	ϱ_o g/cc)	u_A (m/s)	u_n (m/s)	p (kbar)	u (m/s)
01	1.860	φ 100 h 200	Copper	T. Amb.	P. Atm.	8.93	5451	5443	488	1002
02	1.858	"	"	"	"	"	5281	5275	419	889
03	1.854	"	"	"	"	"	5424	5426	480	991
04	1.852	"	Aluminum	"	"	2.70	7574	7563	328	1605
05	1.860	"	Magnesium	"	"	1.74	7233	7219	271	2161
06	1.852	"	"	"	"	"	7048	7054	249	2029
07	1.854	"	"	"	"	"	7027	7030	246	2010
08	1.861	"	"	"	"	"	7220	7203	269	2148
09	1.855	"	Transarryl	"	"	1.18	6489	6485	196	2560
10	1.856	φ 50 h 200	Water	"	"	1	5990	6054	161	2656
11	1.856	"	"	"	"	1	6022	6087	163	2679
12	1.864	"	Argon	286	705	0.874	5383	5384	133.8	2828
13	1.852	"	"	289	588	0.799	5281	5309	122.4	2873
14	1.855	"	"	291	493	0.723	5488	5518	124.3	3102
15	1.864	"	"	289	415	0.658	5583	5599	120	3240
16	1.863	"	"	287	297	0.524	5627	5651	103.3	3480
17	1.864	"	"	285	100	0.184	5593	5631	43.4	4169
18	1.864	"	"	287	70	0.126	5848	5888	34.2	4607
19	1.855	"	"	286	50	0.089	5894	5958	25.5	4810
20	1.864	"	"	286	40	0.071	5941	5986	20.8	4908
21	1.850	"	"	290	30	0.052	6064	6144	16.4	5164
22	1.855	"	"	291	20	0.034	6199	6269	11.5	5384
23	1.850	"	"	290	10	0.017	6430	6513	6.4	5757
24	1.860	"	"	291	5	0.008	6607	6668	3.4	6000

The first one WCA4 (3) coupled to the ETARC thermochemical code relies on the Weeks-Chandler-Andersen theory for the fluid phase of the detonation products. For CHNO explosives, a solid carbon phase can also exist, in particular for T_1 and T_2 compositions. In these cases, a pressure and temperature equilibrium is realized between the two phases. For carbon, assumed to be formed in the graphite or diamond phase, an equation of state of the Cowan-Fickett type is used. For a simple liquid, WCA theory is in good agreement with Monte-Carlo or molecular dynamics results. Each component of detonation products is described with an exponential -6 intermolecular potential fitted to experimental data. Very classical mixture laws between potential coefficients of pure components are used; excess properties are in rather good agreement with Monte-Carlo simulations. The detonation performances of an explosive are deduced from such an EOS without any other parameter. Several results on various explosive compositions have been calculated with success. (14).

The second one WM coupled to the ARPEGE thermochemical code (9) relies on the classical

BKW equation of state with an empirical WM isentrope. The BKW κ and β coefficients leading to the "CJ" values are obtained from measured stick velocities. The adjustable WM isentrope coefficients are calibrated in a detonation experiment (2) with a fluid flow pattern different from the one described in Section II A.

Figure 6 (for composition T_2) shows that our experimental points up to 13.3 GPa lie on the WM/BKW isentrope. Agreement is good for p < 3.4 GPa (as for the case of the DLI measurements) while slight discrepancies start to appear around 10 GPa. Two WCA4 isentropes are also shown (3), the upper one corresponding to carbon formed in the graphite phase (notation g) and the lower one to carbon formed in the diamond phase (notation d).

The same comparisons are also performed for composition T_1, with the same argon EOS as above. For this composition, DLI measurements are not available so far. Figure 7 shows our experimental argon points.

Figure 8 compares them to the WM/BKW and WCA4 isentropes. Above 4.5 GPa, the argon points are below the low WM/BKW

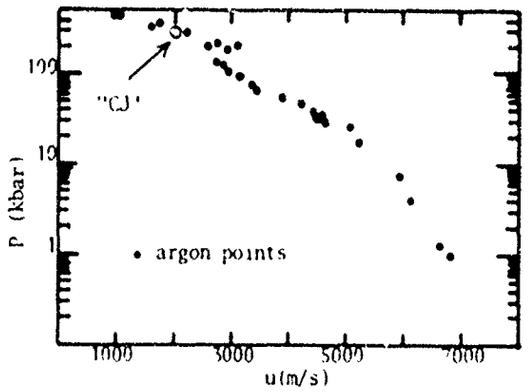

Fig. 7 Detonation product Hugoniot and expansion isentrope for composition T_1

isentrope, with a change of slope around 10 GPa at the crossing of the argon and water points. This change of slope is less sharp for composition T_2 and has been recently the object of careful analysis for composition T_1 around 10 GPa by Zerah-Boissiere (10), using an argon EOS differing from eqns. (16-19). These authors use the same experimental shock velocities U_e, either U_o, U_3 or U but modify the argon shock Hugoniot $H(P_o)$ with an argon EOS technique similar to the one proposed by Kerley (11). The ϱ,T space is divided into three regions bounded by the straight lines $\varrho=\varrho_L$, $T=_L$, ϱ_L and T_L being adjustable parameters. For $\varrho>\varrho_L$ and all T's the electronic part $Z_{eL}(\varrho,T)$ of the partition function is computed with the Liberman (12) self-consistent field model.

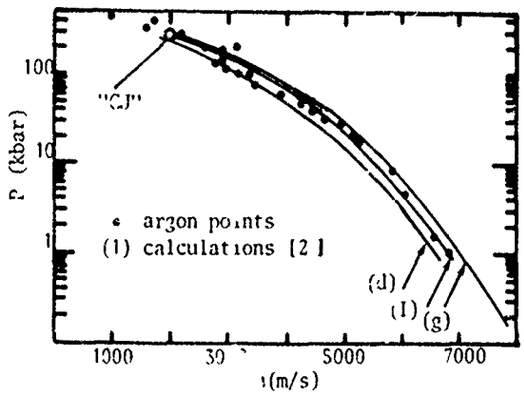

Fig. 8. Comparison of experimental results to calculations for composition T_1. The calculated points are due to the courtesy of Messrs. Chirat-Baute and Sorel-Vanpoperynghe. The g and d curves refer to carbon formed in the graphite and diamond phase.

Agreement of this model with liquid and solid argon shock data (13) is quite good. The value $\varrho_L=0.8$ g/cm^3 is chosen. For $\varrho<\varrho_L$, two analytic models are used depending on the temperature. For $T>T_L$, a linear dependence of (total) pressure on density is used:

$$p(\varrho,T) = (\varrho,\varrho_L)\, p(\varrho_L,T) \qquad (23)$$

For $T<T_L$, Z takes the form

$$Z(\varrho,T) = C_1(T/T_L)^2 + C_2(T,T_L)^3 \qquad (24)$$

which defines at any ϱ a value of $Z_{eL}(\varrho,T)$ and an electronic pressure $p_e(\varrho,T)$.

Empirical variations of T_L are performed until the Hugoniot $H'(P_o)$ in (p,ϱ) space corresponding to $\varrho_o=0.0013$ g/cm^3 goes through the Los Alamos experimental points of Christian-Yarger (15). This gives $T_L=2.5$ eV. Agreement with the more recent data of Gryaznov et al. (18) is satisfactory. These data also correspond to low values of ϱ_o's and ϱ's. Obviously, they are quite far away from our experimental regime at P_o ranging between 10 and 70 MPa or $0.524 < \varrho_o < 0.874$ g/cm^3.

The effect of this other argon EOS is to raise the experimental isentrope points in (p,u) space around 10 GPa and bring them along the WCA4 isentrope. Below 3 GPa, there is little change between the two EOS. This raises the question of the experimental verification of the argon equation of state. Preliminary experiments endeavouring to answer this question are presented in the next Section.

IV. Further Improvements

A closer look at Section II shows that in fact the argon equation of state is required so that the material velocity at the explosive-argon interface u be deduced from the shock velocity U. Reversing the argument, the simultaneous knowledge of U_e and u_e in the experiments described in Section II would eliminate the need for the argon EOS. Instead of obtaining a point on the HE expansion isentrope (Fig. 1) by the intersection of $H(P_o)$ and the straight line

$$p - P_o = \varrho_o U_e u \qquad (25)$$

this point would be the point of abscissa u_e on the straight line defined by (25). Such an experimental determination is not possible for high-explosive in direct contact with argon, so that a different one has to be performed. The shock velocity U_e and the material velocity u_e behind it are simultaneously measured not when the explosive is adjacent to argon in which case the interface velocity cannot be followed precisely, but when the explosive is replaced by an inert material such as aluminum (A9) or copper. This plate is driven by an external generator which has to deliver a sustained shock of constant amplitude during a time of the order of 1.5 μs compatible with the diagnostic techniques. The diagnostics have to be able to measure simultaneously both the shock velocity in argon U and the material velocity of u of the piston driving it. For this parameter, we have chosen Doppler Laser Interferometry and performed preliminary experiments to demonstrate the viability of the technique. Since argon is ionized by the shock, it was important to check experimentally that the electron density n_e would remain below the critical density $n_c = 4.2\ 10^{27}\ m^{-3}$ cutting off the laser radiation at $\lambda = 0.5145\ \mu m$. Even for $P_o = 1$ atm. (worst case) eqs. (11-19) show that n_e remains below n_c. The simple experimental set-up shown in Fig. 9 confirms the calculation since Doppler shifted fringes are registered for $\sim 1.3\mu s$. The Doppler shift is converted into velocities u(t) by standard formulae. The result shown in Figure 10 does not take into account any correction for the variation of the refraction index of argon between the piston and the shock front. This is equivalent to the assumption that the refraction index of argon varies according to the Gladstone-Dalle law. The first plateau in Fig. 10 at 3400 m/s is in agreement with $2u_1$, u_1 being at the intersection in (p,u) space of the release isentrope of the plane wave generator and the shock Hugoniot of the aluminum plate. In this approximation, argon at atmospheric pressure is identified to vacuum. Future improvements of these simple evaluations involve the precise calculation of the refraction index of argon at density ϱ and temperature T (17) and the simulation of the experiment with an hydrocode. A more powerful shock generator is being defined, capable of reaching dynamic pressures of $\sim$20 kb in an argon chamber designed for initial filling pressures of up to 10 MPa. The rotating camera techniques described above should be capable of measuring the shock velocity in argon, thus completing the experiment. Higher regions in (p,u) space will be studied by our colleagues (18) using a two stage light-gas gun to generate the shock.

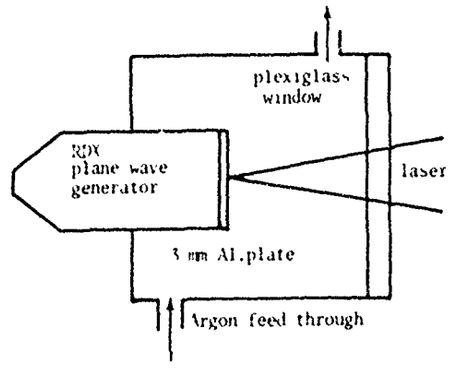

Fig. 9 Experimental set-up to measure the material velocity u in argon at atmospheric pressure by Doppler Laser Interferometry

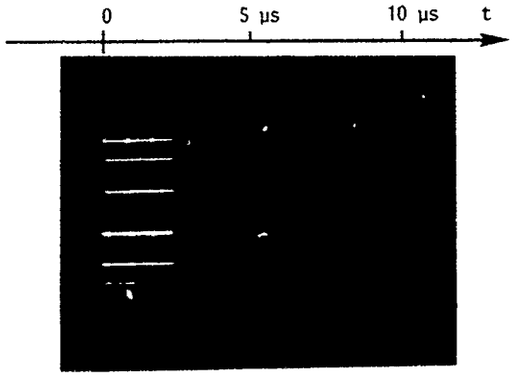

Fig. 10a. Doppler shifted fringes recorded on the streak camera for the experimental set-up of Figure 9

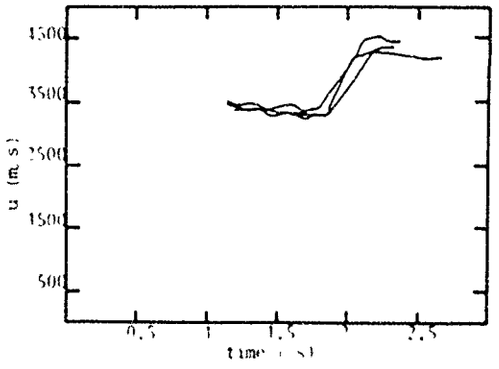

Fig 10b Material velocity u(t) in argon deduced from the Doppler shifted fringes without refractive index corrections

CONCLUSION

Experimental points have been obtained on the expansion isentropes of two TATB explosive compositions using the impedance matching technique with argon as the adjacent inert medium. Data analysis is performed so far with a simplified argon equation of state. The experimental results are compared to DLI measurements and to calculations using two explosive equations of state combining various hypotheses. In order to obtain better information about the equation of state of argon, experiments are in progress to measure simultaneously the shock and material velocities in gaseous argon. The practicability of Doppler-Laser Interferometry for the material velocity has been established

ACKNOWLEDGEMENTS

The isentrope experiments were fielded by R. Louboutin, and the preliminary ones of the argon equation of state by B. Udiment, G. Berthelon and A. Chicheportiche. The work of our colleagues is individually acknowledged both in the reference list and in the figure captions.

REFERENCES

1. H. C. Pujols, Internal Results, (1982).
2. J. Sorel and J. Vanpoperynghe, private communication, (1984).
3. R. Chirat and J. Baute, Internal Results (October 1983).
4. Ya. B. Zel'dovich and Yu. P. Raizer. "Physics of Shock Waves and High-Temperature Hydrodynamic Phenomena," Vol. I, Chap. III, Academic Press, New York, (1966).
5. H. W. Drawin and P. Felenbok. "Data for Plasmas in Local Thermodynamic Equilibrium," Gauthier-Villars, Paris, (1965).
6. C. G. Miller and S. E. Wilder. "Table and Charts of Equilibrium Normal Shock for Pure Argon," Internal Report, NASA, SP 3098, (1976).
7. F. H. Ree. J. Chem. Phys. *73*, 5401 (1980).
8. J Thouvenin "La zone de réaction d'un explosif et son action sur un milieu adjacent," Rapport Interne DARF/ASF/568 (1979).
9. R. Chéret. Acta Astronautica, *1*, 893 (1974).
10. G. Zerah, C. Boissiere, J R. Gevais. Internal Results (1984) and also "Equation D'Etat de l'Argon," International Report DO 84010, Centre d'Etudes de Limeil-Valenton (1984).
11. G I Kerley "User's Manual for PANDA," LASL Internal Report, LA 88.33.M, (unpublished).
12. D. A. Liberman. Phys. Rev. B, *20*, 4981 (1979).
13. W. J. Nellis and A. C. Mitchell. J. Chem Phys. *73*, 6137 (1980), and also M. Van Thiel and B. J. Alder. J. Chem. Phys. *44*, 1056 (1966).

14. R. Chirat and G. Pittion Rossillon. Proc. of the seventh symposium detonation, Annapolis, MD, (June 1981) and references therein.

15. R. H. Christian and F. L. Yarger. J. Chem. Phys. *23*, 2042 (1955).

16. V. K. Gryaznov, M. V. Zhernokletov, V. N. Zubarev, I. L. Iosilevskii, and V. E. Tortov. Sov. Phys. JETP, *51*, 288 (1980).

17. T. P. Hughes. "Plasmas and Laser Light," Adam Hilger, London, (1975).

18. J. Lezaud et al., private communication.

Session IX
Specialist Session
MOLECULAR DYNAMICS

Co-chairmen: Garry L. Schott
Los Alamos National Laboratory
Donald H. Tsai
National Bureau of Standards

QUANTUM CHEMICAL STUDIES OF ENERGETIC MATERIALS

P. J. Haskins, M. D. Cook
Royal Armament Research and Development Establishment, Fort Halstead, Sevenoaks, Kent TN14 7BP, England

The results of ab initio molecular orbital calculations are presented for the energetic molecules HN_3, CH_3NO_2, CH_3NHNO_2, TNT and RDX. These calculations have been geometry optimised, and where possible the results compared with experimental data. Computed potential energy surfaces for unimolecular bond scission reactions in HN_3 and CH_3NO_2 are also reported. The likely effects of high pressure on the decomposition of explosives are discussed, and it is suggested that the heavy metal azides may show a significant reduction in activation energy with increase in pressure.

1. INTRODUCTION

Most theoretical work on explosives has, until recently, concentrated on the hydrodynamic aspects. The hydrodynamic theory of detonation has been used with considerable success to predict detonation properties without the need for detailed chemical information. However, its very strength, in that it requires no knowledge of electronic structure and kinetics, is also its weakness, for it cannot be used to make predictions concerning the chemical reactions occurring or on the rates of energy release which are dependent on them. The understanding of time-dependent properties, such as shock initiation and deflagration to detonation transition (DDT), requires a more fundamental approach which considers the detailed chemical processes.

Recently there has been an increased awareness of the need to consider explosives at a molecular level. Because of the difficulties in obtaining experimental data to elucidate reaction mechanisms at the high pressures and temperatures occurring in explosions, theoretical studies are particularly valuable. Whilst theoretical studies still have a long way to go it is clear that a thorough knowledge of the electronic structure of explosives and the potential energy surfaces for the possible modes of reaction must form the basis of the way ahead.

In this paper ab initio RHF and UHF molecular orbital calculations are reported for a number of energetic species. All calculations have been carried out on a CRAY-1 computer using a vectorised form of the GAUSSIAN 76 code distributed by QCPE(1). The calculations are single configuration and employ a range of standard contracted gaussian basis sets (2, 3, 4, 5). The basis sets used have depended for practical reasons, on the molecule considered, and are listed below:

(i) STO-3G: A minimal basis set with degree of contraction = 3

(ii) STO-6G: A minimal basis set with degree of contraction = 6

(iii) 6-31G: A split valence basis set with degree of contraction =6

(iv) 6-31G**: As for 6-31G but augmented by a d-shell of 6 second-order gaussians on each first row atom, and an uncontracted p-shell on each hydrogen atom.

In Section 2 we present the results of calculations on the ground states of HN_3, CH_3NO_2, CH_3NHNO_2, TNT and RDX. Geometry optimisations have been carried out, and where possible the resulting geometries have been compared with experimental data. Section 3 describes the studies being undertaken to generate potential energy surfaces for decomposition reactions and details the surfaces computed for unimolecular bond scission in HN_3 and CH_3NO_2. In Section

4 we discuss the likely effects of high pressure on the decomposition of explosives, and in particular the inorganic azides. We conclude by outlining our future program and briefly describing some preliminary results.

2. GROUND STATE CALCULATIONS

2.1 Hydrazoic Acid (HN_3)

Hydrazoic acid is a low boiling point liquid with dangerously explosive properties. Whilst it is of no practical interest as an explosive it is of theoretical interest, being the simplest azide. Complete geometry optimisations of HN_3 have been carried out in two basis sets (6-31G** and STO-6G) and the optimum geometries found are given in Table 1 along with the experimental values for comparison. A diagram of the molecule with the labelling employed is shown in Fig. 1.

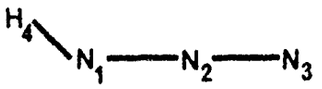

Fig. 1. Hydrazoic Acid

The general features of the orbitals and charge distribution were found to be in agreement with earlier ab initio M.O. studies (refs 6 and 7), which used a fixed (experimental) geometry. The total energy calculated using the 6-31G** basis is approximately 0.3 a.u. lower than the best previously reported value by Wyatt et al. (6). Both basis sets give bond lengths in excellent agreement with the experimental data, but the $N_2N_1H_4$ bond angle is too low by about 6° and 12° for the 6-31G** and STO-6G calculations respectively. The 6-31G** optimised geometry has been used as the starting point for a study of the uni-molecular decomposition of HN_3, the results of which are given in section 3.1.

2.2 Nitromethane (CH_3NO_2)

Nitromethane, like hydrazoic acid, is a liquid at room temperature. Our interest in nitromethane stems from the fact that it is probably the most simple explosive that carries the NO_2 functional group.

We have carried out isolated molecule calculations in three basis sets STO-3G, STO-6G and 6-31G**, using the geometry illustrated in Figure 2. The results of these calculations, which are full geometry optimisations, are summarised in Table 2. The bond lengths and angles are seen to be in excellent agreement with the experimentally determined values (10a). As expected, the extended 6-31G** basis set yields the lowest energy.

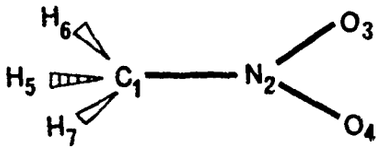

Fig. 2. Nitromethane

The calculated values given in Table 2 refer to the molecule in the lowest singlet state. We have also performed calculations on the lowest triplet state and for STO-6G the triplet state was found to lie 0.0347 a.u. below the singlet. A similar situation was found with the STO-3G minimal basis set. However, calculations employing the extended 6-31G** basis set gave values of −243.5944 a.u., and −243.6666 a.u. for the triplet and singlet states respectively. Thus, the minimal basis sets predict that the triplet is the ground state, whilst the extended 6-31G** basis set correctly predicts a singlet ground state. The inadequacy of minimal basis sets to correctly predict the ground state of nitrocompounds has been reported previously (11), and attributed to a significant singlet biradical character in the ground state.

The 6-31G** calculations presented here provide a starting point for the unimolecular decomposition reaction discussed in Section 3.2.

2.3 N-Methylnitramine (CH_3NHNO_2)

N-methylnitramine is of interest as a prototype molecule for the study of nitramine explosives. It appears to have been less extensively studied than nitramine (NH_2NO_2) and N,N-dimethylnitramine, both of which have been the subject of ab initio calculations (12). Some limited INDO calculations have been performed on N-methylnitramine (13) and the structure has been partially determined by electron diffraction (14). Unlike nitramine, which is known to be pyramidal and N,N-dimethylnitramine which is known to be planar, electron diffraction experiments were unable to reliably determine the configuration of the bonds formed by the amine nitrogen atom. Here

TABLE 1
Results of Hydrazoic Acid Calculations

PARAMETER \ BASIS SET	STO-6G	6-31G**	EXPERIMENTAL (8, 9)
ENERGY (a.u.)	−163.2398	−163.8420	—
DIPOLE MOMENT (D)	1.4747	1.7294	0.847
CHARGE ON N_1	− 0.2442	− 0.4975	—
CHARGE ON N_2	+ 0.0745	+ 0.3871	—
CHARGE ON N_3	− 0.0015	− 0.2074	—
CHARGE ON H_4	+ 0.1713	+ 0.3178	—
$N_1 - N_2$ (Å)	1.285	1.235	1.237
$N_2 - N_3$ (Å)	1.162	1.100	1.133
$N_1 - H_4$ (Å)	1.046	1.006	0.980
$N_2\hat{N}_1H_4$	102.0°	107.8°	114.1°

TABLE 2
Comparison of experimental and calculated parameters of nitromethane

Basis Set	6-31G**	STO-6G	STO-3G	EXPERIMENTAL (10a, b)
ENERGY (a.u.) \ PARAMETER	−243.6666	−242.7453	−240.4246	—
C-N (Å)	1.472	1.592	1.539	1.489
N-O (Å)	1.188	1.280	1.270	1.224
C-H (Å)	1.078	1.089	1.088	1.088
$H\hat{C}N$	107.6°	107.4°	107.9°	107.2°
$O\hat{N}C$	117.1°	117.6°	117.5°	117.3°
Dipole moment (D)	4.010	3.300	3.171	3.46

we report the results of complete geometry optimisations using STO-6G and 6-31G basis sets. The molecular geometry is illustrated in figure 3 and the results are summarised in Table 3.

The results reported in Table 3 refer to the lowest energy singlet state. However as was found for nitromethane, the STO-6G minimal basis set predicts a triplet ground state, the energy of the triplet being 0.0545 a.u. below the singlet. The 6-31G split valence basis set correctly predicts a singlet ground state, with the lowest triplet state being 0.383 a.u. higher in energy. It is also interesting to note that the optimum geometry predicted by the STO-6G calculation is pyramidal whilst the 6-31G basis gave the lowest energy in a planar conformation. However, in both basis sets the energy does not seem to be greatly altered by values of α between 0° (planar) and ≈56° (pyramidal). In particular the STO-6G calculation gives a barrier to inversion of only 0.0086 a.u. (5.4 kcal.mole^{-1}). On the basis of these results and the inconclusive experimental evidence it seems likely that the planar and pyramidal forms have very similar energies, and that at normal temperatures the molecules are inverting rapidly.

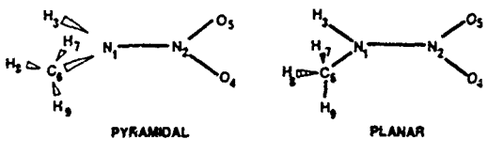

Fig. 3. Methyl Nitramine

TABLE 3
Results of N-Methylnitramine Calculations

PARAMETER \ BASIS SET	STO-6G	6-31G	EXPERIMENTAL (14, 15)
ENERGY (a.u.)	−297.5801	−298.5089	—
DIPOLE MOMENT (D)	3.443	5.772	4.40
$N_1 - N_2$ (A°)	1.472	1.327	1.381
$N_2 - O_{4,5}$ (A°)	1.284	1.244	1.228
$C_6 - N_1$ (A°)	1.497	1.460	1.452
$N_1 - H_3$ (A°)	1.042	1.003	1.021
$C_6 - H_{7,8,9}$ (A°)	1.093	1.088	1.133
$O_4\hat{N}_2O_5$	126.4°	124.5°	125.3°
$C_6\hat{N}_1N_2$	113.0°	121.3°	109.0°
$N_2\hat{N}_1H$	104.3°	114.6°	—
α*	56.1°	0.0°	—
β**	22.8°	0.0°	—

*α is defined as the angle the C_6N_1 bond makes with the $H_3N_1N_2$ plane.

**β is defined as the angle of rotation of the nitro group about the N_1N_2 bond relative to the plane $H_3N_1N_2$

2.4 2, 4, 6 — Trinitrotoluene (TNT)

2, 4, 6 — Trinitrotoluene (TNT) is still an important and widely used explosive. Its thermochemical decomposition, together with those of other nitroaromatics has been the centre of intense investigation for the past 50 years. Yet, despite this fact, the initial decomposition steps are still uncertain, either during slow decomposition at low temperatures, or at higher temperatures when the reaction is self-sustaining.

The starting point for elucidating the decomposition reaction mechanism must be an investigation of the structure of an isolated molecule. X-ray crystallography (16) shows that TNT occurs in the crystal in two forms, A and B, which differ in bond lengths and angles, but maintain the same general structure (see Figure 4). However, the TNT molecule is not as symmetrical as one might think, and the benzene ring is somewhat distorted, such that carbon atoms carrying nitro groups all have interior angles greater than 120°. There is also the added complication of steric crowding between the o-nitro-groups and the methyl group, which results in the nitro groups being twisted out-of-plane. Despite these distortions, the benzene ring itself is reasonably planar in both forms. The methyl

and nitro groups are displaced from the ring plane.

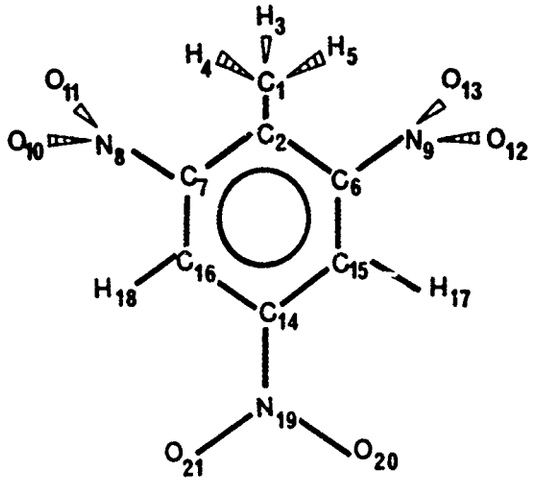

Fig. 4.—2, 4, 6 Trinitrotoluene

For our preliminary studies of TNT we decided to carry out an isolated molecule geometry optimisation. The symmetrical structure illustrated in figure 4 was chosen as the basis of these calculations as a geometry optimisation would necessarily lead to a symmetrical structure. We propose at a later date to carry out calculations using the experimental geometry. All our calculations were limited to the minimal basis set STO-3G, and the results are given in Table 4, together with the experimental values obtained by x-ray crystallography. The total energy of the optimum configuration was found to be −868.5775 a.u.. It can be seen that the calculated values of the bond lengths are in close agreement with the averaged experimental values. However, the calculated dihedral angles between the o-nitro groups and the ring plane are slightly smaller in magnitude than the averaged experimental results of forms A and B (49°). Our calculations do show however, that the lowest energy configuration is obtained when the o-nitro groups are rotated out of plane, such that O_{11} and O_{13} are pointing in the same direction, away from the plane of the ring (as illustrated in Figure 4). This is in agreement with the experimentally determined structure. The difference between the calculated and experimental dihedral angles is not unexpected as the angles in the crystal will be determined not only by the steric effects of the methyl group but also by the intermolecular packing. In the crystal the p-nitro group is also rotated out of the ring plane, but for reasons of symmetry such a rotation cannot be modelled in an isolated molecule calculation.

The results of our TNT calculations have not yet been fully analysed, and we intend in particular to look at bond overlap populations which can be used as indicators of bond strengths to help identify likely initiation mechanisms. The preliminary results that we have reported here will form the basis for a future investigation of possible decomposition reactions.

2.5 1, 3, 5-Trinitro-1, 3, 5-triazine (RDX)

The compound 1, 3, 5-trinitro-1, 3, 5-triazine, better known as RDX, is an important military explosive. Two polymeric forms of RDX are known, RDX(I) and RDX(II). The structure of RDX(I) has been studied by a number of workers in some detail (17, 18). However, RDX(II) is extremely unstable, hence its crystal structure has not been completely determined.

RDX(I) has C_s symmetry (see Figure 5) with two nitro groups in axial positions and the third placed equatorially with respect to the triazine ring. It is thought that this structure is more strained than one having equivalent NO_2 groups. RDX(II) though, is believed to possess higher symmetry than RDX(I). Two structures having C_{3v} symmetry have been proposed for RDX(II), one having axial NO_2 groups, and the other equatorial NO_2 groups. Simple considerations suggest, and CNDO calculations (19) confirm that a C_{3v} structure results in a less strained molecule. Infra-red spectral studies also show that whilst RDX(I) exists only in the solid phase and possesses a unique structure defined by C_s symmetry, RDX(II), the liquid and the gas phases of RDX, all have C_{3v} symmetry.

It seems that although RDX(I) is a strained molecule, crystal forces give it stability at room temperature. In fact, RDX(I), despite its strained molecular geometry, is much more stable than RDX(II). Moreover, the RDX(II) lattice readily converts to the RDX(I) lattice.

In our molecular orbital studies on RDX we have limited our attention so far to the RDX(I) C_s structure illustrated in Figure 5, although it is our intention to examine the C_{3v} structures in the near future. We have carried out partial geometry optimisations in the STO-3G minimal

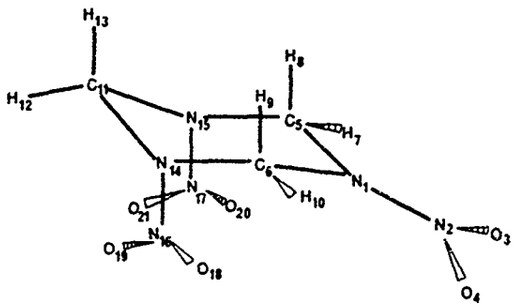

Fig. 5. RDX (1, 3, 5 - Trinitro - 1, 3, 5 - Triazine)

basis set and the results together with the experimental values are given in Table 5. The bond lengths and angles are in reasonable agreement with experiment. However, these calculations require further refinement because of the complex geometry of the RDX molecule, and are not yet fully analysed.

Further studies on RDX will include unimolecular bond scission processes such as cleavage of the nitramine N-N bond, as well as other intramolecular reactions. As has been pointed out by Hariharan et al. (20), it will probably be necessary to use configuration interaction to obtain a good representation of the bond breaking process. It is clear though, that intermolecular crystal forces play a crucial role in giving stability to RDX(I), and it is desirable, if at all possible, to study their effect. There is certainly some evidence that the crystal structure is somewhat distorted from that predicted by the geometry optimisation, lending further support to the assertion of a strained molecule whose geometry is strongly influenced by intermolecular forces.

3. POTENTIAL ENERGY SURFACES

3.1 Unimolecular Decomposition of Hydrazoic Acid

Whilst a number of mechanisms can be proposed for the decomposition of hydrazoic acid there is considerable evidence from matrix isolation studies (21), gas phase photolysis (22, 23) glow discharge (24) and pyrolysis (24) experiments that the primary and rate determining step for these decomposition regimes is scission of the $N_1 - N_2$ bond to form nitrogen and the imine radical (NH).

$$HN_3 \rightarrow NH + N_2$$

We therefore decided to begin our investigation of hydrazoic acid decomposition by computing the potential energy surface for this process. The results are given in Figure 6, which is a plot of energy against $N_1 - N_2$ separation, computed using a 6-31G** basis set. The plot was generated by stretching the $N_1 - N_2$ bond from its equilibrium value in increments of 0.1A° and fully optimising the geometry at each point.

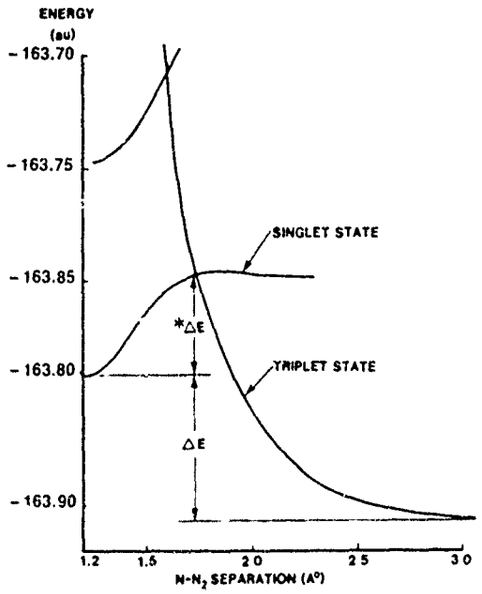

Fig. 6. Potential Energy Surface for the Unimolecular Decomposition of HN_3 ($HN—N_2$)

$\Delta E^* = 0.044$ a.u. (27.6 kcal mole $^{-1}$
$\Delta E = 0.648$ a.u. (40.7 kcal mole $^{-1}$

It can be seen that the singlet ground state rises in energy as the bond stretches, before passing over a very shallow maximum (1kcal mole^{-1}) at 1.9A° to form N_2 and singlet NH. Also plotted is the lowest energy triplet state, which at $N_1 - N_2$ separations below 1.6A° is a bound state, but at greater separations a dissociative triplet state is lower in energy. The dissociative triplet state, which yields the products N_2 and triplet NH (the $^3\Sigma^-$ ground state), crosses the singlet state curve near to its maximum energy and at an $N_1 - N_2$ separation of 1.74A°. The activation energy (ΔE^*) is determined by this crossing of the singlet and triplet curves and is found to be 0.044 a.u. (27.6 kcal mole^{-1}).

TABLE 4

Comparison of Experimental and Calculated Parameters of TNT

Bond lengths	Experimental Values (16) Molecular Form		Calculated Values
	A	B	STO-3G
$C_1 - C_2$		1.507	1.535
$C_2 - C_6$	1.390	1.395	1.407
$C_2 - C_7$	1.408	1.379	"
$C_6 - C_{15}$	1.364	1.383	1.385
$C_7 - C_{16}$	1.373	1.387	"
$C_{14} - C_{15}$	1.415	1.344	1.390
$C_{14} - C_{16}$	1.375	1.373	"
$C_6 - N_9$	1.496	1.469	1.509
$C_7 - N_8$	1.449	1.494	"
$C_{14} - N_{19}$	1.443	1.482	1.480
$C_{15} - N_{17}$	NOT REPORTED		1.509
$C_{16} - H_{18}$			"
$N_{19} - O_{20}$			1.287
$N_{19} - O_{21}$			"
$N_8 - O_{10}$			1.288
$N_8 - O_{11}$			"
$N_9 - O_{12}$			1.288
$N_9 - O_{13}$			"
$C_1 - H_{3,4,5}$			1.094

Dihedral Angles of NO_2 with plane of ring (Deg)					
			MINDO/3	MINDO	THIS WORK
Position	2	51	60	45	85	37
	4	24	30	0	90	-
	6	43	45	45	84	37

TABLE 5

Comparison of Experimental and Calculated Parameters of RDX

Bond lengths (A°)	Experimental values	Calculated values
$N_1 - N_2$	1.351(3)	1.451
$N_2 - O_3$	1.233(4)	1.284
$N_2 - O_4$	1.209(5)	1.284
$N_1 - C_5$	1.464(4)	1.505
$N_1 - C_6$	1.450(4)	1.505
$C_5 - H_7$	1.092(8)	1.098
$C_5 - H_8$	1.058(10)	1.102
$C_6 - H_9$	1.088(8)	1.102
$C_6 - H_{10}$	1.075(9)	1.098
$C_5 - N_{15}$	1.443(4)	1.504
$C_6 - N_{14}$	1.440(4)	1.504
$N_{14} - N_{16}$	1.398(3)	1.486
$N_{15} - N_{17}$	1.392(3)	1.486
$N_{16} - O_{18}$	1.205(2)	1.279
$N_{16} - O_{19}$	1.201(5)	1.290
$N_{17} - O_{20}$	1.207(5)	1.279
$N_{17} - O_{21}$	1.203(5)	1.292
$N_{14} - C_{11}$	1.458(4)	1.433
$N_{15} - C_{11}$	1.468(4)	1.433
$C_{11} - H_{12}$	1.085(8)	1.100
$C_{11} - H_{13}$	1.087(7)	1.106
Bond Angles (deg)		
$N_1 - N_2 - O_3$	117.2	116.3
$N_1 - N_2 - O_4$	117.8	116.3
$N_1 - N_2 - C_5$	119.7	121.5
$N_1 - N_2 - C_6$	120.9	121.5
$N_1 - C_5 - H_7$	110.0	110.7
$N_1 - C_5 - H_8$	109.9	110.5
$N_1 - C_6 - H_9$	109.6	112.1
$N_1 - C_6 - H_{10}$	111.3	108.1
$N_{14} - C_{11} - H_{12}$	110.7	111.8
$N_{15} - C_{11} - H_{12}$	110.1	111.8
$N_{16} - N_{14} - C_{11}$	117.5	115.1
$N_{17} - N_{15} - C_{11}$	116.6	115.1
$N_{14} - N_{16} - O_{18}$	117.0	117.1
$N_{14} - N_{16} - O_{19}$	117.3	117.1
$N_{15} - N_{17} - O_{20}$	116.8	117.4
$N_{15} - N_{17} - O_{21}$	117.2	117.4

There appears to have been no experimental determination of ΔE^*. The reaction is predicted to be exothermic by 0.064 a.u. (40.7 kcal mole^{-1}) which is in rather poor agreement with Gray and Waddington's (25) deduction from experimental data that the reaction is nearly thermoneutral ($\approx$ 5kcal mole^{-1} endothermic). The calculated heats of formation (ΔH_f) of HN_3 and NH ($^3\Sigma^-$) are 87.68kcal mole^{-1} and 47.08kcal mole^{-1} respectively, as against experimental values (25) of 71.66kcal mole^{-1} and 77kcal mole^{-1}. It can therefore be seen that the excessive exothermicity predicted for the reaction is largely the result of the low heat of formation calculated for NH. This is a common situation with SCF MO calculations as correlation energy plays a smaller part in determining the energy of triplet states, thus lowering the energy of triplet states relative to singlets.

The low heat of formation calculated for $\dot{N}H$ is unlikely to have a significant bearing on the calculated activation energy as the triplet curve crosses the singlet near to its shallow maximum and any correction would move the crossing to the right along the plateau region. Indeed the low activation energy calculated seems highly plausible in view of the known high sensitiveness of hydrazoic acid. As part of our future program we intend to refine these calculations and hopefully improve the estimate of ΔE by the use of configuration interaction.

3.2 Unimolecular Decomposition of Nitromethane

We have begun our investigations of nitromethane decomposition by looking at the CH_3—NO_2 unimolecular bond scission. The results, which are illustrated in Figure 7, were computed using a 6-31G** basis set. Like the calculations on hydrazoic acid, the curves were obtained by stretching the appropriate bond in increments of 0.1A° and fully optimising the geometry at each point.

It can be seen from Figure 7 that the energy of the lowest lying singlet state rises as the C-N separation increases from its equilibrium value, and is crossed by a dissociative triplet state

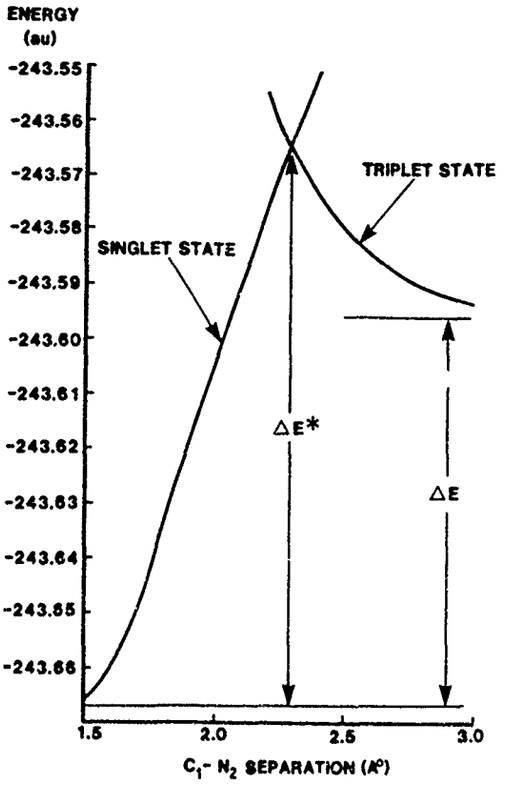

Fig. 7. Potential Energy Surface for the Unimolecular Decomposition of $MeNO_2$ ($Me—NO_2$)

$\Delta E^* = 0.1016$ a.u. (63.7kcal mole^{-1})
$\Delta E = 0.0725$ a.u. (45.5kcal mole^{-1})

at C-N = 2.3A°. The triplet state dissociates into CH_3 and NO_2 radicals, with an overall endothermicity, $\Delta E = 0.0725$ a.u. (45.5kcal mole^{-1}). This is somewhat lower than the experimental value of 60.3kcal mole^{-1} (26). The discrepancy between the experimental and calculated values probably arises for the same reasons as those given for hydrazoic acid. The activation energy (ΔE^*) is determined by the crossing of the singlet and triplet curves and is calculated to be 0.1016 a.u. (63.7kcal mole^{-1}). It is likely, for the reasons given above, that the calculated activation energy is also slightly low. As for hydrazoic acid it is intended to refine these calculations by the use of configuration interaction.

4. HIGH PRESSURE EFFECTS

Detonation pressures in solid explosives may be in excess of 30GPa, and at these pressures

compressions of about 30% are to be expected. Whilst shock initiation thresholds may be considerably lower than detonation pressures, for most explosives the threshold will still correspond to a considerable compression. It is quite probable that at such high pressures electronic effects may substantially alter activation energies and possibly lead to reactions proceeding by different mechanisms to those observed at ambient pressure.

High pressure can be regarded as having two fundamental effects on the electronic structure of a material (27). The first is to increase the overlap between adjacent molecular orbitals, leading to increased delocalisation of electrons and a consequent broadening of allowed energy bands. The second effect is to cause a relative displacement of one type of orbital with respect to another. Both of these effects may be of relevance to explosives.

It has often been assumed that the first and rate determining step in the decomposition of secondary explosives is an endothermic unimolecular bond scission process. However, in some cases a bimolecular process may well be faster at the high pressures produced by a shock wave since bimolecular reactions are pressure enhanced as a result of the compressed nature of the transition state. In addition to the enhancement of bimolecular processes Bardo (28) has pointed out that pressure could also lead to the lowering in energy of a dissociative excited state relative to the ground state. If this occurred to the extent that the potential energy curves intersect, then there is the possibility of a radiationless transition to the dissociative state and a new lower barrier for bond scission.

For insulators and semiconductors the most general effect of pressure is a reduction in the forbidden energy gap due to broadening of both the conduction and valence bands. However, this effect may be either complemented or opposed by relative shifts in the two bands. The optical absorption spectrum of many insulating or semiconducting solids shows an absorption edge, wavelengths below the edge being almost totally absorbed. The frequency of the absorption edge is a measure of the forbidden energy gap, and in general large red shifts of the absorption edge are observed with increase in pressure. Such shifts may be of significance for a number of explosives, but it is interesting to consider the inorganic azides in particular since their mode of decomposition is sufficiently well understood for a direct comparison to be made with the activation energy.

It is generally believed that the first step in the decomposition of the heavy metal azides (e.g., AgN_3, PbN_6) is the promotion of an electron from the valence to the conducting band. The reaction then proceeds by the single exothermic step:

$$2N_3 \rightarrow 3N_2 - \Delta H = 232 \text{ kcal mole}^{-1}$$

The band gap is therefore a direct measure of the activation energy for photo-chemical decomposition. The activation energy for thermal decomposition is lower but related by:

$$\frac{E_{optical}}{E_{thermal}} = \frac{K_l}{K_h}$$

where K_l and K_h are the low and high-frequency dielectric constants.

Whilst there do not appear to have been any results reported on shifts of absorption edge with pressure for the azides, there have been a number of experiments reported on metal halides (27). These compounds have similar bonding to the azides, the electron affinity of the azide radical being between that of bromine and iodine. Furthermore, since the conduction band is an excited state it can be argued that it will usually be more sensitive to compression than the valence band. Consequently it is often observed that changes in the absorption edge with pressure are relatively insensitive to the anion, whose wave functions mainly form the valence band. It is therefore tempting to use the results for the halides to suggest an approximate magnitude for shifts in the azides. By way of example lead chloride and bromide both show a red shift in the absorption edge of about 0.5eV at 10GPa. It is clear that, if the azides undergo shifts of similar magnitude the activation energies appropriate to detonations will be significantly lower than those at ambient pressure. It is intended that these effects will be investigated experimentally using diamond anvil cells.

In keeping with these observations on the likely effects of pressure on the decomposition of energetic species we will be extending our

MO studies in an attempt to simulate pressure effects. Work has recently commenced on the effect of pressure on the unimolecular decomposition of HN_3 and CH_3NO_2 which were discussed in Section 3. In these studies two molecules are being placed at various fixed separations and allowed to decompose. It will be particularly interesting to see how the proximity of a neighbouring molecule effects the singlet/triplet crossing and therefore the activation energy. It is also proposed to look at various other decomposition mechanisms, including bimolecular processes, for these and other energetic species. Figure 8 illustrates the results of a preliminary calculation on two nitromethane molecules interacting in a side-on orientation. In this computation all internal geometric variables have been kept fixed at the equilibrium values for the isolated molecules. The results show a shallow minimum at an O-H separation of 2.1Å as the result of hydrogen bonding. At closer separations the energy rises steeply.

Finally, it is hoped to correlate our future theoretical work on pressure effects with spectroscopic data from diamond anvil cell experiments on a range of energetic species.

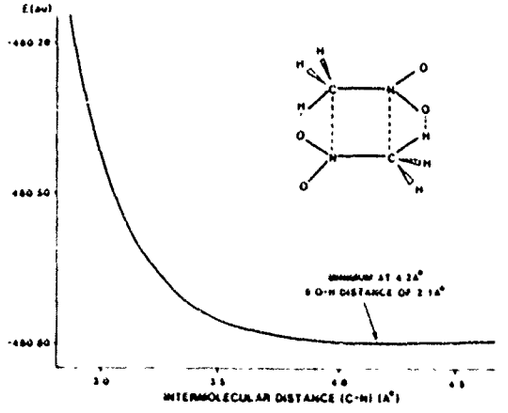

Fig. 8. 2 CH_3NO_2 Molecules Side-on (STO 3G)

REFERENCES

1. Pople, J A et al., QCPE *11*, 368, (1978).
2. Hehre, W J, Stewart, R F and Pople, J A, J.Chem.Phys. *51*, 2657, (1969).
3. Ditchfield, R, Hehre W J & Pople J A, J.Chem.Phys. *54*, 724, (1971).
4. Hariharan, P C and Pople, J A, Chem.Phys.Lett. *16*, 217, (1972).
5. Mulliken, R S, J.Chem.Phys. *23*, 1833, 1841, 2338, 2343, (1955).
6. Wyatt, J F, Hillier, I H, Saunders, V R, Connor, J A, J.Chem.Phys., *54*, 5311, (1971).
7. Bonnaccorsi, R, Petrongolo, C, Scrocco, E & Tomasi, J, J.Chem.Phys. *48*, 1500, (1968).
8. Amble, E & Dailey, B P, J.Chem.Phys. *18*, 1422, (1950).
9. Winnewisser, M & Cook, R L, J.Chem.Phys. *41*, 999, (1964).

10a Cox, A P & Waring, S, J.Chem.Soc., Farad.Trans.II, *68*, 1060, (1972).

10b CRC Handbook of Chemistry and Physics, 63rd Edn., Ed. R C Weast, E60

11. Kleiner, D A & Lipton, M A, J.Mol.Structure, *109*, 39, (1984).
12. Duke, B J, J.Mol.Struct., *50*, 109, (1978).
13. Farminer, A R and Webb, G A, J.Mol. Struct., *27*, 417, (1975).
14. Sadova, N I, Slepnev, G E, Tarasenko, N A, Zenkin, A A, Vilkov, L V, Shishkov, I F, & Pankrushev, Yu A, Zh.Strukt.Khin., *18*(5), 865, (1977).
15. Stals, J, Aust.J.Chem., *22*, 2505, (1969).
16. Carper, W R & Davis, L P, J.Phys.Chem., *86*, 459, (1982).
17. Choi, C S & Prince, E, Acta Cryst. *B28*, 2857, (1972).
18. Karpowicz, R S & Brill, T B, J.Phys.Chem., *88*, 348, (1984).
19. Orloff, M K, Mullen, P A, & Rauch, F C, J.Phys.Chem., *74*, 2189, (1970).
20. Hariharan, P C, Walter, S K, Kaufman, J J, Miller, R S and Lowrey, A H, Int.J.Quantum.Chem. Quantum Chem.Symp., *16*, 363, (1982).
21. Becker, E D, Pimentel, G C and Thiel, M V, J.Chem.Phys., *26*, 145, (1957).
22. Beckman, A O and Dickinson, R G, J.Amer. Chem.Soc., *50*, 1870, (1928) *52*, 124, (1930).
23. Thrush, B A, Proc.Roy.Soc., A235, 143, (1956).
24. Rice, R O & Freamo, M, J.Amer.Chem.Soc., *73*, 5529, (1951); *75*, 548, (1953).

25. Gray, P & Waddington, T C, Proc.Roy.Soc., *A235*, 106, 481 (1956).

26. Knobel, Yu K, Miroshichenko, E A, Lebedev, Yu A. Izv.Akad.Navk SSSR, Ser.Khim, (3), 485, (1971).

27. Drickamer, H G & Frank, C W, 'Electronic Transitions and the High Pressure Chemistry and Physics of Solids', Chapman and Hall (1973).

28. Bardo, R D, Proceedings of the Seventh Symposium (International) on Detonation, United States Naval Academy, Annapolis, Maryland (1981).

ELECTRON DENSITY DISTRIBUTION ANALYSIS FOR NITROGUANIDINE

James P. Ritchie, Don T. Cromer, Robert R. Ryan,
Robert F. Stewart,* and Harvey J. Wasserman
Los Alamos National Laboratory
Los Alamos, New Mexico

*Permanent address: Department of Chemistry; Carnegie-Mellon University;
Pittsburgh, PA 15213

The electron density distribution of nitroquanidine was analyzed with both experimental and theoretical techniques to determine how well these methods would work for an explosive molecule. Explosives present special problems with these methods because many atoms are usually involved, which can cause the calculations to become intractable, and because the molecules have many polar bonds. We found that, although the polar character of the space group made the experiment analysis difficult, the two techniques yielded results very much in harmony. Specifically, electrostatic potentials, which play a large role in determining crystal geometry, were in very good agreement. A discrepancy, however, was observed between the theoretically optimized geometry and the observed geometry. This discrepancy appears to be the result of crystal packing forces which are not present in the theoretical calculations. We also observed some similarities between the hydrogen-bond network in NQ and that in TATB.

INTRODUCTION

Nitroguanidine (NQ) is an explosive noted for its shock insensitivity. The large scale gap test yields G_{50} = 5.00 mm, for a sample at 1.609 g/cc, and both Type 12 and 12B drop tests give H_{50} > 320 cm (1). BKW calculations give P_{cj} = 318 kbar and D_{cj} = 8.7 mm/μs, using the observed room temperature crystal density of 1.77 g/cc, and P_{cj} = 287 kbar and D_{cj} = 8.4 mm/μs, using the observed pressed sample density of 1.70 g/cc. In comparison, TATB has G_{50} = 21.92 mm from the large-scale gap test, for a sample at 1.870 g/cc, and H_{50} > 320 cm by either drop test. At 1.895 g/cc, P_{cj} = 315 kbar and D_{cj} = 7.9 mm/μs are observed (1). Clearly then, NQ is an explosive of practical importance.

We have investigated the electron density distribution of NQ with both experimental and theoretical techniques in an attempt to identify any characteristics that may result in its shock insensitivity, such as the hydrogen-bond network in the crystal, and to determine what changes may accompany the incorporation of a single isolated molecule of NQ (for which the theoretical results are appropriate) into the crystal environment. NQ is amenable to study with ab initio molecular orbital calculations because of its relatively small size. From an experimental standpoint, the crystals are hard and have relatively small thermal motion for an organic molecule. Because x-ray diffraction data

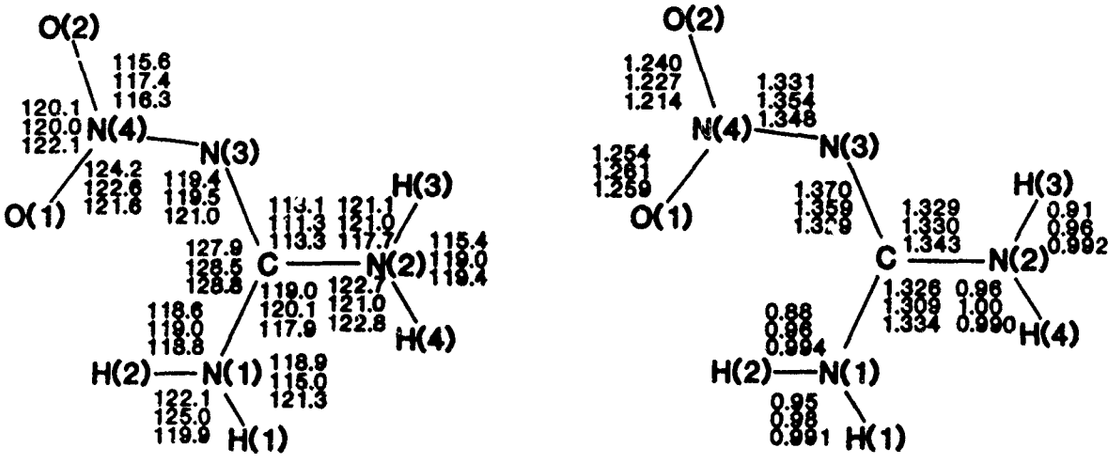

Fig. 1. Bond lengths (Å) and angles (°) in NQ. Upper figures are from the present work, middle figures are neutron diffraction results from Choi (7), and lower figures are from an optimized 6-31G planar molecule. Standard deviations for the present work are 0.0006-0.0009 Å for heavy atom distances, 0.03 Å for N-H distances, 0.1° for heavy atom angles, and 1-2° for angles involving hydrogen. Standard deviations for the neutron work are 0.006-0.009 Å for heavy atoms, 0.02 Å for N-H, 0.7° for heavy atom angles, and 0.1° for angles involving hydrogen.

can be obtained rather far in reciprocal space, it seemed like a good candidate for study. Difficulties do arise, however, because NQ crystallizes in the non-centrosymmetric space group Fdd2, which is polar in the z direction. This polar nature introduces large correlations between the z parameters and many of the multipole parameters. These correlations reduce the accuracy of the results.

METHODS

Experimental: X-ray diffraction data were collected on a CAD-4 diffractometer at c.a. −160 °C with graphite monochromated MoKα radiation to a maximum $\sin\theta/\lambda = 1.22$ Å^{-1}. Crystallographic data and details of the data collection are available from the authors upon written request. The data were processed as described previously (2).

Theoretical: Molecular orbital calculations were performed with the program HONDO5 (3), using a variety of basis sets. The results reported herein were obtained with the 6-31G basis set (4), which is of split-valence quality, but lacks polarization functions. Calculations were performed both at the theoretically optimized geometry, using the 6-31G basis set, and at the experimentally determined geometry.

The electron density distributions and atom-centered multipole expansions were obtained from the approximate wavefunctions as described previously (5). X-ray structure factors were calculated from the approximate wavefunctions using the program of Chandler and Spackman (6).

RESULTS

Initial Structure Refinements: The structure was refined with the program GENLES, from the Los Alamos Crystallographic System, using the neutron powder diffraction results of Choi (7) as a starting point. A high angle refinement ($\sin\theta/\lambda > 0.8$ Å^{-1}) yielded non-hydrogen positional and thermal parameters essentially identical to a refinement with all data and all multipoles up to and including octopoles (8). The positional and thermal parameters from the multipole refinement are given in Table 2. The derived bond lengths and angles are shown in Fig. 1. Subsequent refinements had little effect on these parameters, and the bond lengths and angles shown in Fig. 1 did not change. The quantity minimized in the initial calculations was $\Sigma w(F_o - F_c)^2$ and for the 2642 observed reflections $wR_f = 0.030$. The standard deviations of bond lengths in this work are a factor of ten less than in the work of Choi (7). Bond length dif-

TABLE 1

Crystallographic Data for Nitroguanidine

Space Group: Fdd2

Lattice Constants (λ = 0.70926 Å) (T~ −160 C)

a = 17.5671 (26) Å
b = 24.8511 (48) Å
c = 3.4880 (9) Å

2θ Range	Octants	Reflections	Unique Reflections
0 - 50°	4	1756	394
50 - 100°	2	3598	1799
100 - 120°	1	943	943
	Total	6297	3136
	Observed > 3σ (I)		2642

Comparison of Equivalent Reflections

R_f = 0.0175
R_f^2 = 0.0291
WR_f = 0.0190
WR_f^2 = 0.0483

TABLE 2

Positional and Thermal Parameters for NQ
The U's have been multiplied by 100

Atom	x	y	z
O(1)	0.17693(3)	0.00984(2)	0.20800*
O(2)	0.07292(3)	0.02430(2)	0.5226(3)
N(1)	0.25836(3)	0.09303(2)	0.0194(3)
N(2)	0.19567(4)	0.17127(2)	0.1604(4)
N(3)	0.13604(3)	0.09513(2)	0.3400(3)
N(4)	0.13000(2)	0.04180(2)	0.3549(3)
C	0.19833(3)	0.11783(2)	0.1676(3)
H(1)	0.297(1)	0.114(1)	−0.098(8)
H(2)	0.258(1)	0.058(1)	0.008(13)
H(3)	0.155(1)	0.190(1)	0.262(9)
H(4)	0.231(2)	0.193(1)	0.014(1)
	H Positions from Neutron Diffraction		
H(1)	0.2986	0.1166	−0.0794
H(2)	0.2605	0.0544	0.0266
H(3)	0 1535	0.1897	0.2741
H(4)	0.2361	0.1932	0.0313

Thermal Parameters

Atom	U_{11}	U_{22}	U_{33}	U_{12}	U_{13}	U_{23}
O(1)	1 02(1)	0.82(1)	1 82(2)	0.17(1)	0.28(2)	- 0.02(2)
O(2)	1 03(2)	0.99(1)	2 11(2)	−0.11(1)	0.52(2)	0.19(2)
N(1)	0.82(1)	1.07(1)	1.38(2)	−0.02(1)	0.25(1)	−0.03(1)
N(2)	1.38(2)	0.76(1)	1 20(2)	−0.01(1)	0.18(1)	0.04(1)
N(3)	0.77(1)	0 76(1)	1.20(2)	−0.01(1)	0.18(1)	0.04(1)
N(4)	0.72(1)	0 78(1)	1 15(2)	0.02(1)	0.07(1)	0.08(1)
C	0.80(1)	0 82(1)	1 04(2)	−0.04(1)	0.09(1)	−0 01(1)
H(1)	1 9 (7)					
H(2)	6.1 (10)					
H(3)	2.6 (7)					
H(4)	6 0 (9)					

*Fixed to define the origin

ferences are less than $2\sigma_{Choi}$.

Electron Density and Electrostatic Potential Calculations: For subsequent work, the hydrogen atoms from the x-ray structure were fixed relative to N(1) and N(2) according to the N-H vectors found in the neutron results of Choi (7). Multipole refinements were made using the VALRAY system of programs developed by Stewart and co-workers. Refinements minimized $\Sigma w(F_0^2 - F_c^2)^2$ and all 3136 data were used. For independent atom models (IAM) used in electrostatic potential calculation and in difference electron density calculations, Hartree-Fock scattering factors were used for heavy atoms. For hydrogen, the contracted scattering factor of Stewart et al. was used (9). Two models were refined. Model I refined positional parameters, anisotropic thermal parameters, monopoles, and κ for the heavy atoms. (κ is a parameter that accounts for the contraction or expansion of the valence shell as electrons are removed or added by charge transfer (10).) For hydrogens, the isotropic thermal parameters and monopoles were varied while keeping the positions fixed. Single exponential radial functions $r^n \exp(-\alpha r)$ were used for the valence electrons with standard molecular values of α (11). Hartree-Fock scattering factors were used for the core electrons. Model II introduced dipoles, quadrupoles, and octopoles for the heavy atoms. The weighted residual of 0.093 obtained with this model is higher than one would like, and is much higher than the refinement based on F with the GENLES program noted earlier. The weak or unobserved reflections, most of which are at high angles, are generally omitted in an F refinement. Many of the reflections over 100° 2θ were subject to a systematic error because the gonimeter head was sometimes in the cold stream. Model II gives the most accurate parameter set, however, and is used for subsequent calculations.

Figure 2 shows a model deformation density map. It shows the expected features; i.e., increased density in the bonding regions and in the lone-pair regions. The average variance of this function is about 0.06 $e\text{Å}^{-3}$

The electrostatic potential (EP) of the molecules as they occur in the crystal was calculated directly from the diffraction data (12). A plot of the EP is shown in Fig. 3. For this figure, the variance peaks at about 0.2 at the atom centers

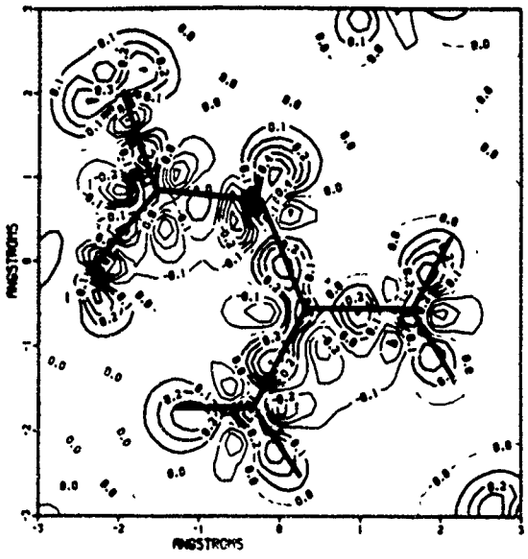

Fig. 2. Deformation electron density of NQ calculated as:

$$\Delta\varrho^5\varrho_{\text{Model}} - \varrho_{\text{IAM}}$$

The plane is that of C, N(2), N(3). The origin is at the midpoint of the C-N(3) bond and the x-direction is along the C-N(2) bond. Contours appear every 0.1 $e\text{Å}^{-3}$.

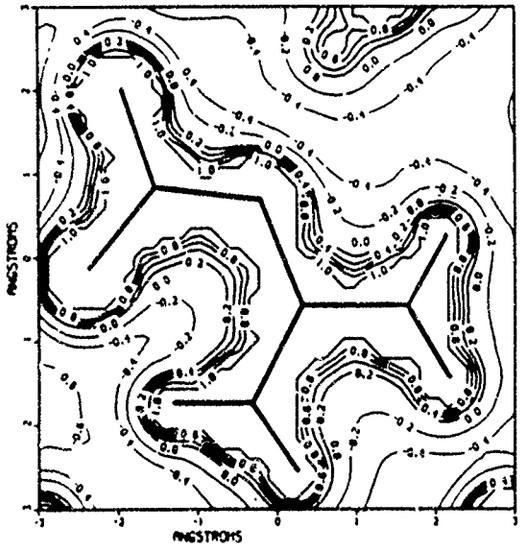

Fig. 3. Electrostatic potential of NQ in the unit cell. The plane and orientation of the molecule are the same as shown in Fig. 2. Contours are at 0.2 e Å^{-1}. (1 e Å^{-1} = 332.1 kcal/mole.).

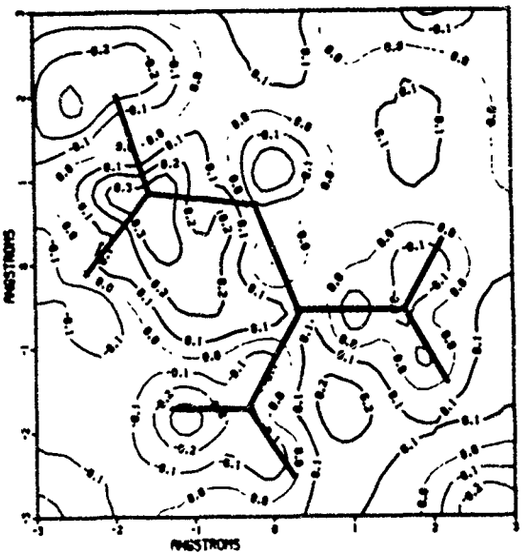

Fig. 4. Electrostatic potential difference between Model II and IAM model. Contours occur every 0.1 e Å $^{-1}$

and is about 0.12 to 0.08 e Å^{-1} at the −0.2 to −0.4 contours.

Figure 4 illustrates the difference between the electrostatic potential obtained from Model II and that obtained from the IAM. This is a measure of the potential differences that occur upon formation of a molecule from independent atoms. The variance in this map is the same as in Fig. 3.

Theoretical Calculations: The energy optimized geometry obtained for NQ with the 6-31G basis set is indicated in Fig. 1, along with the experimental results. These calculations were performed assuming a planar structure, but optimizing all other geometrical variables.

X-ray structure factors were calculated using the 6-31G basis set and the experimental geometry (H atom positions were obtained from Choi). These calculations take account of thermal motion through the observed thermal parameters, except for those of hydrogen, which were taken at 1.1 times the equivalent isotropic parameters of the attached nitrogen atom. These structure factors were then subjected to the same model refinements as were the observed data and used to construct deformation maps, electrostatic potential maps, and the difference electrostatic potential maps. The quantities obtained in this fashion are illustrated in Figs. 5, 6, and 7. These quantities are to be compared with the experimental quantities illustrated in Figs. 2, 3, and 4, respectively.

The density deformation map at the theoretically optimized geometry, which shows how the electron density distribution of the molecule differs from that of a superposition of spherically-

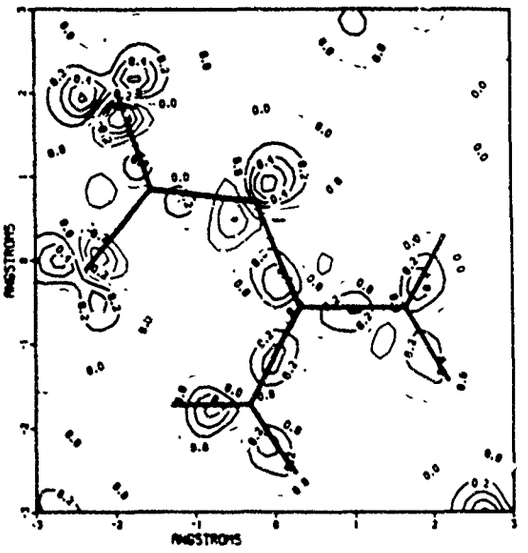

Fig. 5. As Fig. 2, but calculated from the theoretical structure factors. Contours are at 0.2 e Å^{-3}

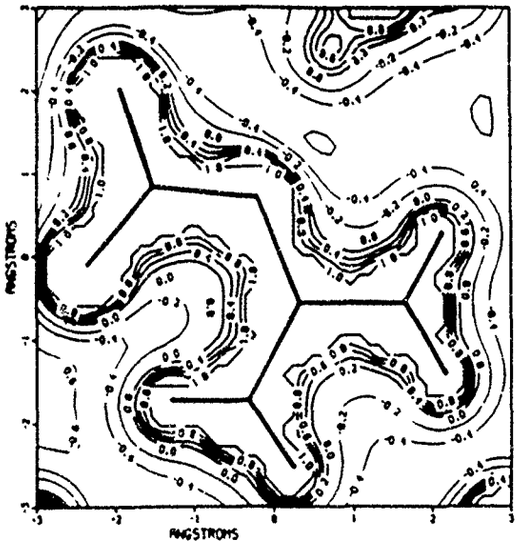

Fig. 6. As Fig. 3, but calculated from the theoretical structure factors

averaged atoms, is shown in Fig. 8. This theoretical map is obtained in a manner roughly analogous to that used to determine the maps illustrated in Figs. 2 and 5, but does not include vibrational or thermal motion in the molecule. Partly because of this, its features are more pronounced than those in Figs. 2 and 5.

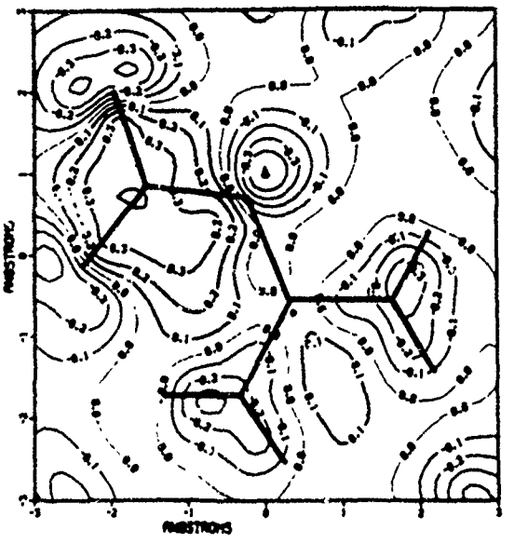

Fig. 7. As Fig. 4, but calculated from the theoretical structure factors

Atom-centered multipole expansions were also obtained at the theoretically obtained geometry. These expansions were then used to determine the electrostatic potential of an isolated molecule of NQ at rest, which is illustrated in Fig. 9.

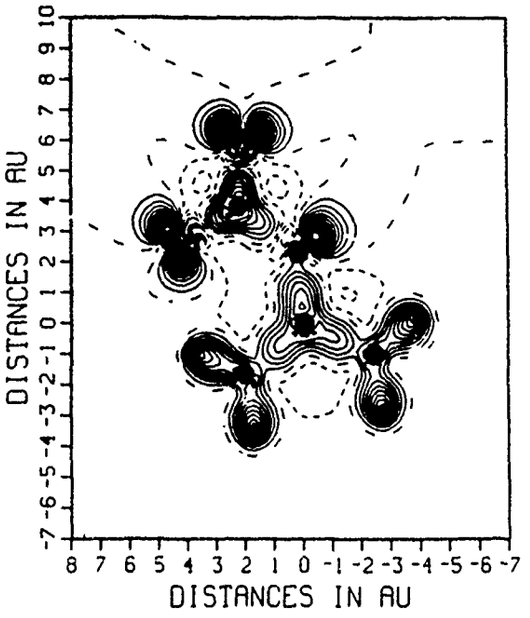

Fig. 8. Density deformation map as obtained from the single-molecule theoretical calculation without consideration of thermal or vibrational motion. The illustrated plane contains all the atoms, the positions of which are indicated by heavy circles. The nitro group is in the upper left-hand quadrant. Solid lines indicate positive values, dashed lines indicate negative values, and the combination dashed and dotted lines indicate zero as a value. Contours occur 0.2 e Å^{-3}.

DISCUSSION

Molecular Geometry: The structure has been previously discussed by Choi (7) and by Bryden et al. (13). Nitroguanidine is a nearly planar molecule. O(1) deviates the most, and is about 0.08 Å from the least-squares plane. The nitro group is twisted about 3° from the plane of the carbon and nitrogen. These results suggest that the assumption of a planar molecule in the theoretical geometry optimization calculations is reasonable.

Hydrogen Bonding: There are ribbons of molecules connected by the shorter hydrogen bonds N(1)-H(1)---N(3), which have H(1)---N(3) distances of 2.16 Å and N(1)---N(3) distances of 3.10 Å, and N(2)-H(4)---O(2), which have H(4)---O(2) distances of 2.00 Å and N(2)---O(2) distances of 2.91 Å. These ribbons are alternately on the 301 and 30$\bar{1}$ planes, the adjacent ribbons being joined by the longer hydrogen bonds N(2)-H(3)---O(1), which have H(3)---O(1) distances of 2.37 Å and N(2)---O(1) distances of 3.25 Å, andN(1)-H(2)---O(1), which have H(2)---O(1) distances of 2.28 Å and N(1)---O(1) distances of 3.00 Å. Of note is an apparent intra-molecular hydrogen bond, N(1)-H(2)---O(1).

Some authors have suggested that a hydrogen-bond network in a crystal acts as an energy sink by providing many weak bonds that can be broken with little effect on the explosive single molecule (14). This implies that the hydrogen-bond network results in a decreased sensitivity of the crystal relative to a hypothetical crystal without hydrogen-bonds. The insensitive explosives TATB and NQ are somewhat similar in that both are approximately planar, both have

intramolecular hydrogen bonds, and both have many inter-molecular hydrogen bonds. It is known that TATB is layered in an almost graphitic fashion. In contrast, the ribbons of NQ joined by strong hydrogen bonds are nearly planar, but adjacent ribbons joined by weak hydrogen bonds are canted by about 22°.

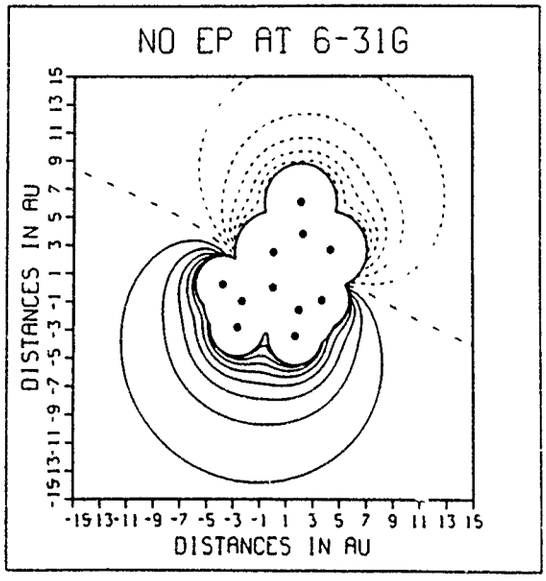

Fig. 9. Electrostatic potential map as obtained from atom-centered multipole expansions for a single molecule without consideration of thermal or vibrational motion. The illustrated plane and contour line types are the same as in Fig. 8. Contours occur every 10 kcal.

The intra-molecular hydrogen bond found in NQ suggests the possibility of an energetically accessible aci-form that arises from actually transferring H(2) to O(1). Preliminary theoretical calculations indicate that the aci-form of NQ lies within 40 kcal of NQ itself.

Effects of Crystal Environment: A comparison of the calculated and observed geometrical parameters (Fig. 1) reveals some serious discrepancies. In particular, the theoretical predictions of R(C-N) and R(N-N) are unusually poor for this level of theory. Despite the large differences in the geometrical parameters, the energy difference between the theoretically energy-optimized structure and that observed is only 4.5 kcal. Nevertheless, the bond length discrepancies are abnormally large and require an explanation.

One explanation is that, because of the large and polar character of NQ, the current level theory is still inadequate to give a proper description of the molecule. Calculations including polarization functions were carried out, but indicate no improvement in the geometry compared with the x-ray structure.

Another explanation is that the crystal environment induces a change in geometry from that of an isolated molecule in field-free space, for which the calculations are most appropriate. This explanation is supported by the existence of a charge-separated resonance structure for NQ that would be stabilized in the crystal environment and that would explain the observed pattern of discrepancies between the calculated and observed structures. So, in the resonance structure illustrated below, formal double bonds occur where the calculations predict a bond too long and formal single bonds appear where the calculations predict a bond too short.

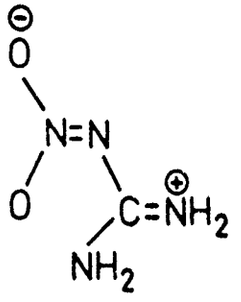

Thus, an increased contribution of this resonance structure in the crystal would shorten the formally single bonds, which acquire some double bond character, and lengthen the formally double bonds, which acquire some single bond character, relative to those expected for an isolated molecule in field-free space. The calculated multipole expansions at the theoretical and observed geometries indicate changes in the charge distribution expected from the greater contribution of the above resonance structure in the crystal.

We are pursuing higher levels of theory and an investigation of the crystal environment to resolve this question.

CONCLUSION

This is the first attempt at a detailed experiment electron density of an organic explosive compound. We have obtained results from both theoretical and experimental techniques that are in reasonable agreement.

Nitroguanidine proved to be a difficult molecule to analyze because of the polar space group. Unfortunately, our experimental data are not adequate to distinguish with any certainty between the electron distributions of theoretical calculations with different basis sets.

Further calculations are being performed to determine if the difference between calculated and observed geometrical parameters is a result of crystal packing forces.

REFERENCES

1. Terry R. Gibbs and Alphonse Popolato, Eds., "LASL Explosive Property Data," University of California Press, Berkeley, 1980.
2. D. T. Cromer and A. C. Larson, "The Crystal Structure of $Pu_{31}Pt_{20}$ and $Pu_{31}Rh_{20}$," Acta Cryst. *B33*, 2620 (1977).
3. M. Dupuis, J. Rys, and H. King, Quantum Chemistry Program Exchange, Indiana University, Bloomington, Ind., No. 401.
4. W. J. Hehre, R. Ditchfield, and J. Pople, J. Chem. Phys. *56*, 2257 (1972).
5. J. Ritchie, "Electron Density Distribution Analysis for Nitromethane, Nitromethide, and Nitramide," J. Am. Chem. Soc. *107*, 1829 (1985).
6. G. S. Chandler and M. A. Spackman, "Fourier Transforms of Gaussian Orbital Products." Acta Cryst. *A34*, 341 (1978).
7. C. S. Choi, "Refinement of 2-Nitroguanidine by Neutron Powder Diffraction," Acta Cryst. *B37*, 1955 (1981).
8. a) D. T. Cromer, A. C. Larson, and R. F. Stewart, "Crystal Structure Refinements with Generalized Scattering Factors. III. Refinement of 1,1'-Azobiscarbamide and Melamine, 2, 4, 6-Triamino-s-triazine, at the Octopole Level," J. Chem. Phys. *65*, 336 (1976). (b) R. F. Stewart, "Generalized X-ray Scattering Factors," J. Chem. Phys. *51*, 4569 (1969).
9. R. F. Stewart, E. R. Davidson, and W. T. Simpson, "Coherent X-ray Scattering for the Hydrogen Atom in the Hydrogen Molecule," J. Chem. Phys. *42*, 3175 (1965).
10. P. Coppens, T. N. Guru Row, P. Leung, E. D. Stevens, P. J. Becker, and Y. W. Yang, "Net Atomic Charges and Molecular Dipole Moments from Spherical Atom X-ray Refinements, and the Relation between Atomic Charge and Shape," Acta Cryst. *A35*, 63 (1979).
11. W. H. Hehre, R. F. Stewart, and J. A. Pople, "Self-Consistent Gaussian Molecular Orbital Methods. I. Use of Gaussian Expansions of Slater-Type Atomic Orbitals," J. Chem. Phys. *51*, 2657 (1969).
12. R. F. Stewart, "On the Mapping of Electrostatic Properties from Bragg Diffraction Data," Chem. Phys. Letters *65*, 335 (1979).
13. J. H. Bryden, L. A. Burkardt, and E. W. Hughes, "The Crystal Structure of Nitroguanidine," Acta Cryst. *9*, 573 (1956).
14. J. W. Rogers, Jr., H. C. Peebles, R. R. Rye, J. E. Houston, J. S. Binkley, "A Carbon Auger Line Shape Study of Nitroaromatic Explosives," J. Chem. Phys., *80*, 4513 (1984).

A MOLECULAR MECHANISM FOR THE INITIATION OF SECONDARY EXPLOSIVES. INFLUENCE OF A SHOCK LIGHT-COUPLING

S. Dufort
Commissariat à l'Energie Atomique — Centre d'Etudes de Vaujours
Boîte postale n° 7 - 77181 Courtry - France

and

A. Delpuech
Commissariat a l'Energie Atomique
Centre d'Etudes Scientifiques et Techniques d'Aquitaine
Boîte postale n°2 - 33820 Belin Beliet - France

This paper describes the theoretical and experimental investigations carried out in order to study the structural modifications of the explosive molecule just behind a shock front. These works led to consider the population of non dissociative electronic excited states as predominant for the establishment of a given decomposition rate. The experiments presented here show that the velocity of decomposition increases as the concentration of non dissociative excited states is artificially enlarged by an excimer laser. This effect is all the more sensible as the decomposition mode departs from detonation.

INTRODUCTION

A twofold approach, theoretical (quantum chemistry) and experimental (ultra fast Raman spectrometry), of the structural modifications of the explosive molecule right behind the shock front and before explosive decomposition, has led to consider that the molecular population in this zone is the sum of three populations:

$P(M^0)$: population of molecules in ground state,

$P(M_D^*)$: population of molecules in an excited state leading to molecular decomposition,

$P(M_{ND}^*)$: population of molecules in the various non dissociative excited states.

It follows from this result that the first step of the initiation phase may be thought of as the existence, in certain locations of the explosive, of zones in which, due to the electronic modifications of the molecules:

- energy transfer properties among molecules are strongly altered. This follows from the existence of population $P(M_{ND}^*)$.
- simultaneously some molecules are brought to a dissociative state and decompose [$P(M_D^*)$].

We have shown that the molecular characteristic parameters of this population $P(M_D^*)$ perfectly correlate with the shock sensitivity of the substance. This agrees with the fact that in any case, this type of sensitivity only reflects the decomposition of the explosive without referring to the nature of the mode: detonation, deflagration, combustion ..

In order to build up a model representative of this second phase of the explosive phenomenon, it is necessary to bear one's attention on the population $P(M_{ND}^*)$ of the excited but non decomposed molecules. Indeed, it is within such a population that exchange and energy transfer phenomena may develop, thus leading to a cooperative process of decomposition. Quite obviously such a process depends on the concentration $\partial P(M_{ND}^*)/\partial V$ of these molecules and on their lifetime in the considered excited state.

In order to study such a hypothesis experimentally, we have realized a set-up which allows to create artificially, by means of a light pulse, a population $P(M_{ND}^*)$ in the shock front. The increase of this population in these conditions must,

if our hypothesis are correct, modify the decomposition parameters of the explosive. We analyse in this paper the first results obtained in the case of HMX.

I. ELECTRONIC STRUCTURE AND SHOCK SENSITIVITY

In order to account for the experimentally observed correlation, in the case of nitrated secondary explosives, between shock sensitivity and selective absorption of the incident energy by a particular molecular bond, we have studied by quantum chemistry methods the electronic structure of these compounds.

This study allowed us to conclude that the shock sensitivity of an explosive may be considered as a molecular property. This proposition results from a good correlation established between the electronic structure of the molecule and the behavior under shock of the concerned explosive.

The validity of this correlation leads to propose that the same process of variable intensity precedes the decomposition of any explosive.

From this mechanism, the study of 40 molecules belonging to the five following families of organic explosives: nitroaromatics, nitramines, nitric esters, picrylazoles and tetrazoles, has led us to state four essential conclusions (1):

1. During the initiation phase, the explosive molecule reaches an excited state.

2. There exists in each explosive molecule a privileged bond whose electronic structure determines the shock sensitivity. The nature of this bond is characteristic of the concerned family. In the case of nitroaromatics, nitramines and nitric esters, it is respectively one of the C-NO_2, N-NO_2 or O-NO_2 bond of the molecule. In the case of picrylazoles, it is one of the C-NO_2 bonds of the picryl ring in ortho position of the azole ring. In the case of tetrazoles, the bonds to consider are the nitrogen-nitrogen bonds of the ring in β of the carbon.

3. The relative variation of polarity (δ) of this bond during excitation enables to classify explosives in large families differing greatly in their sensitivity.

- In the case of nitroaromatics:
  $15\% < \delta < 30\%$
- In the case of nitramines:
  $25\% < \delta < 55\%$
- In the case of nitric esters:
  $40\% < \delta < 50\%$
- In the case of picrylazoles:
  $10\% < \delta < 65\%$
- In the case of tetrazoles:
  $75\% < \delta < 95\%$

On the other hand, if we note that, in the case of primary explosives, the first step of the decomposition consists in the extraction of one valence electron, amounting to $\delta = 100\%$, it appears that this parameter, characteristic of the tendancy of an explosive to decompose under shock, allows a continuous ordering of explosive families from the least sensitive secondary ones to the primary ones.

4. Within these families, the minimum polarity ΔC^* of the explosophorous bond after excitation enables to classify explosives according to the scale of shock sensitivity commonly admitted - Table 1.

II. ELECTRONIC STRUCTURE AND INITIATION

The discovery of this good correlation between the shock sensitivity of the substance and the molecular electronic structure leads to think that the explosive decomposition finds its origin in a rapid modification of the latter. In order to relate this modification to the molecular decomposition parameters, we have determined the dissociative character of the various electronic states of the molecule. This determination has required to evaluate by CNDO-S/CI method the variations of the electronic transition energies in terms of length of the various bonds in the molecule. Because of the complexity of such determination, our study is limited to the case of RDX, HMX and PETN. It allowed to conclude (2):

a) The excited electronic state characterized by a minimal R-NO_2 bond polarity is a dissociative state for this bond, thus freeing NO_2.

b) Excited electronic states, whose energy is less than that of these dissociative states, are non-dissociative states of the molecule.

This important result leads, if we propose as first explosive decomposition step the filling up of the excited electronic states in the molecule, to consider the shock front as the sum of three populations:

TABLE 1

Explosive	ΔC^*	$\frac{\Delta C^*}{\Delta C^*_{NG}}$	$\frac{\Delta C^*}{\Delta C^*_{RDX}}$	$\frac{\Delta C^*}{\Delta C^*_{TNB}}$
Nitroglycerine (NG)	0,625	1,00		
Dinitroglycerine	0,651	1,04		
Dinitroglycerine	0,648	1,04		
Nitroglycide	0,659	1,05		
PETN	0,670	1,07		
Nitrometriol	0,691 to	1,11 to		
Dimethylolnitroethane dinitrate	0,730	1,17		
Nitroglycol	0,753	1,20		
	0,753	1,20		
RDX	0,511		1,00	
HMX δ	0,602		1,18	
HMX β	0,727		1,42	
HMX α	0,735		1,44	
Tetryl	0,786		1,54	
Haleite	0,846		1,66	
Nitroguanidine	0,962		1,88	
Tetranitroaniline	0,518			0,85
TNX	0,526			0,86
Trinitrophenetole	0,565			0,93
s.trinitrobenzene	0,609			1,00
m.dinitrobenzene	0,612			1,01
TATB	0,620			1,02

$P(M^0)$: population of molecules in ground state,

$P(M_D^*)$: population of molecules in an excited electronic state leading to molecular decomposition. If we distinguish excited states directly correlated to shock sensitivity scale (emission of NO_2 in the case of nitrated secondary explosive M^*_{NO2}) and other dissociative states i:

$$P(M_D^*) = P(M^*_{NO2}) + \sum_i P(M_D^{*i})$$

$P(M^*_{ND})$: population of molecules in the various non dissociative excited electronic states j:

$$P(M^*_{ND}) = \sum_j P(M^{*j}_{ND})$$

Wherefrom

$$P(M) = P(M^0) + P(M^*_{NO_2}) + \sum_i P(M_D^{*i}) + \sum_j P(M^{*j}_{ND})$$

2) Experimental Study of the Structural Modification of the Molecule Behind the Shock Front.

In order to confirm these hypotheses experimentally, we have studied the structural modifications of an explosive molecule, right behind shock front and before decomposition.

The technique used to this effect is the ultra fast Raman spectrometry (3). Indeed, this technique is the only experimental method providing information about molecular structure in a specified point and within a short enough time.

The principle of this experiment consists in comparing Raman spectrum sent out by an explosive crystal with the spectrum given by the same zone of the same crystal but immediately behind the shock front.

Explosives (RDX and PETN) are studied under the form of single crystals. The shock is generated by a pyrotechnical device which delivers a pressure at the entrance of crystal of about 100 kbar. The studied zone is located 1 mm from the face of admission, and the phenomenon is observed during 10 ns in a time interval of several tens of nanoseconds after that shock wave has passed through the observed area.

The first conclusion resulting from the analysis of the results obtained is that the decomposition of the totality of molecule is not immediate behind the shock front. Indeed, we observe (4),(5) that during several tens of nanoseconds behind shock front, the spectrum

is characteristic of the molecule and presents the same lines as those registered at rest.

The second conclusion is that all observations agree with the hypothesis of existence behind this front, and before explosive decomposition, of a population of molecules for which the only structural modifications would consist in a reorganization of the electronic structure. Indeed we observe that the spectra obtained are characterized, by comparison with the spectrum at rest, by very important fluctuations in intensity of most spectral bands (Figure 1) while line frequencies are unchanged (shift $< 5\ cm^{-1}$). In these conditions, these fluctuations can be explained only by modifications in the number and in the characteristics of the occupied excited levels (electronic and vibrational). They particularly depend on pressure and temperature conditions, and the lifetime of the concerned levels.

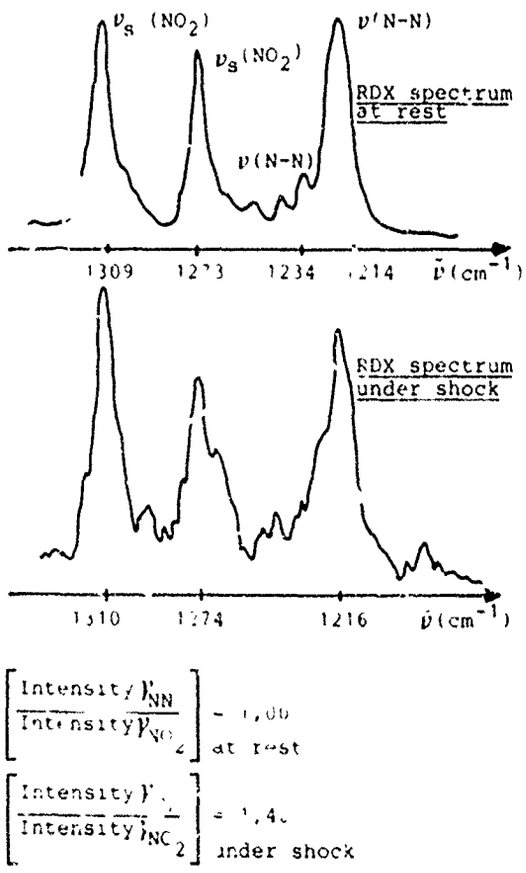

Fig 1 Study by ultra fast Raman spectrometry of structural modifications of RDX under shock. Examination of vibrational frequencies of N-NO_2 group.

On the other hand, it has not been possible to show the existence during this period of the population $P(M^*_D)$, e.g. decomposing molecules.

However, one may think that reasons why no spectrum corresponding to NO_2 or (M-NO_2) has been obtained are these:

— On one hand, population $P(M^*_{NO_2})$ is weak compared to the total molecular population.

— On the other hand, the species formed are not stable enough to be observed by this method (6).

3) Electronic Structure and Initiation

It follows from these results that the first step of the initiation phase may be looked at as the existence, in certain locations of the crystal, of areas in which, due to the electronic changes in molecules:

a) energy transfer properties are strongly altered. This follows from population $P(M^*_{ND})$. As a matter of fact, the energy transfer among molecules is directly related to bond polarity (7), and in excited electronic states this polarity is quite different from that of ground state.

b) simultaneously some molecules are brought in a dissociative state and decompose: $P(M^*_{NO_2})$. This population has not yet been proven experimentally by ultra fast Raman spectrometry. Let us note, however, that the hypothesis of its existence is not based only on the results of our theoretical computations. Indeed, J. Sharma et al. have shown by X-ray photoelectron spectroscopy, in the case of nitrated explosives (RDX, TATB), the preferred breaking under shock of one of the R-NO_2 bonds of the molecule. On the other hand, they conclude in their study (8) that the mechanism of the molecular break-up is similar by photolysis or impact; this may indicate that during initiation, electronic and vibrational excitations are exhangeable.

Note at least the molecular characteristic parameters of population $P(M^*_{NO_2})$ correlate with the shock sensitivity of the material. This perfectly agrees with the fact that, in any case, this type of sensitivity only reflects the decomposition of the explosive without referring to the nature of the mode: detonation, deflagration, combustion .

On the other hand, one may suppose that

these conditions for initiation of detonation, related to conditions to obtain a cooperative mode, depend on population $P(M^*_{ND})$. Indeed the mechanism of bond rupture being instantaneous, we understand that parameters of states characterized by an important lifetime (which is the case for the first excited state, if non dissociative) allow to satisfy these conditions.

In other words, growth of detonation would imply, in a restricted area, the existence of zones where the electronic structure of most molecules is modified during a sufficiently long time and within which decomposition of the molecule takes place simultaneously.

III. INFLUENCE OF A SHOCK-LIGHT COUPLING ON THE DECOMPOSITION MODE

The foregoing propositions show that in order to build up a model representative of the detonation mode, it is necessary to bear one's attention on the population $P(M^*_{ND})$ of excited but non decomposed molecules. It is indeed within such a population that exchange and energy transfer phenomena may develop, thus leading to a cooperative process of decomposition. Quite obviously such a process depends on the concentration $\partial P(M^*_{ND})/\partial V$ of these molecules and on their lifetime in the considered excited state.

In order to verify experimentally this proposition, we have considered to artificially create, behind the shock front, a population of excited and non decomposed molecules. If the hypothesis that we have formulated are correct, this modification of $\partial P(M^*_{ND})/\partial V$ should entail a modification of the decomposition parameters.

1) Experimental Set-up

a) Choice of the studied explosive.

This choice obeys two imperatives:
possibility to create non dissociative electronic excited states by light radiation,

initiation threshold compatible with the use of a laboratory priming system.

The explosive retained is HMX. It presents some non dissociative states which may be populated by an excimer laser emitting at 249 nm (which corresponds to an energy of about 5 ev/photon). Moreover a pyrotechnic device of modest dimensions is able to generate the detonation of a single crystal.

b) Shock generation.

The device generating the shock should allow to modulate the energy transmitted to the HMX single crystal. The pyrotechnic arrangement is adapted from "gap test" experiments; the various constitutive elements are given in the following diagram (Figure 2).

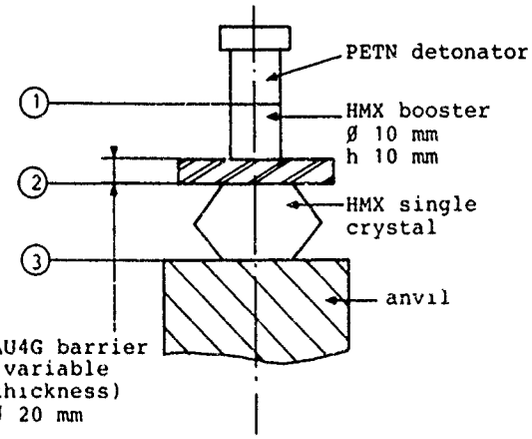

Fig. 2. Shock wave generator

①, ② and ③ represent ionization gauges inserted in the pyrotechnic line to verify the chronometry of the shot. The shock front geometry obtained by this priming system being divergent, the active part of the gauges are placed on its revolution axis.

The pressure induced in the crystal as a function of the thickness of the AU 4G barrier has been determined by DOPPLER-laser interferometry measurements. Pressures at the entrance of the single crystal range from 80 to 330 kbar.

c) Light source.

The light source is an excimer laser. The flash emitted at 249 nanometers (in the U.V. field) is associated to the dissociation of Kr F molecule, and corresponds to 1 joule of energy with a duration of 20 nanoseconds.

The rectangular beam (35 mm x 15 mm), which comes out the laser head, is focused by a complex optical device. The dimensions of the focal spot obtained are then: 6 mm x 6 mm.

Taking into account absorption due to the lenses and to the path of the beam in air, the energy deposited by the laser pulse is 300 mJ.

In order to make sure that the laser has been correctly operated, two types of detectors are used:

— a vacuum photodiode allows to record on an oscilloscope the evolution of the laser beam intensity as a function of time,

— a joulemeter measures the pulse energy.

— Two beam splitters with small reflection coefficient (0,04) insure sampling of part of the incident beam energy, and its dispatching between the vacuum photodiode and the joulemeter.

A continuous helium-neon laser is used to carry out the alignment of the whole optical device.

d) Shock-light synchronization.

The single crystal is irradiated at right angle with the direction of the shock front propagation. The synchronization in the single crystal and its excitation by the laser has been so defined that it is not influenced by the lifetime of the created excited states. To this end, irradiation is turned on only when the shock wave has covered through the crystal a distance of about 0,6 mm.

2) Results

In order to study the influence of a shock-light coupling, we compared the decomposition velocity of the explosive, measured for various thicknesses of the AU 4G barrier, in the case of:

- the shock alone (velocity V_1),
- the shock coupled to the irradiation of the explosive by the laser beam (velocity V_2).

Figure 3 shows the evolution and the dispersion of the decomposition velocity measured for these two types of solicitations (pure shock, shock + light), for 3 values of shock pressure. The average values obtained from 8 shots for each pressure are summarized in Table 2. The lower value of 160 kbar is dictated by the answer of the gauges which do not allow a correct measurement for lower pressures.

Examination of this set of results leads to the following conclusions:

1. For pressures of 160 and 210 kbar, the velocity dispersion in the case of shock-light coupling is quite clearly smaller than in the case of the shock alone. Moreover, the V_2 values

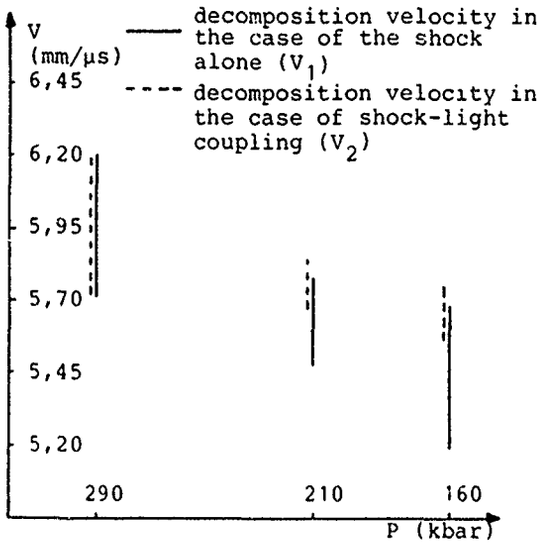

Fig. 3. Decomposition velocity of HMX single crystal as a function of the applied pressure

range among the higher values of V_1,

2. For the pressure of 290 kbar, the two previous effects are no longer observed and the dispersion bars of V_1 and V_2 coincide.

3. The mean decomposition velocity for the shock-light coupling at 160 kbar equals the one at 210 kbar in the case of the shock alone. In other words, the pressure difference (50 kbar) generated in the crystal is compensated by the laser effect.

3) Comments

The first conclusion of these experiments is that the results relative to these first series of tests are in agreement with the theoretical previsions.

Indeed, it appears that the creation of excited states behind the shock front by U.V. radiation entails a change in the decomposition velocity of the HMX single crystal. Moreover, the influence of this shock-light coupling is all the more so effective as the decomposition mode departs from detonation.

However, it seems indispensable to better separate the decomposition velocity relative to the two modes of solicitations. In other words, the problem is to increase the concentration in excited species, relatively weak in these series of tests, due to the geometry of the device (U.V. beam at right angle with the direction of the

TABLE 2

P (kbar)	Decomposition velocity shock alone V_1 (mm/μs)	Decomposition velocity shock + light V_2 (mm/μs)	$\Delta V = V_2 - V_1$ (mm/μs)
290	5,92	5,92	0
210	5,60	5,73	0,13
160	5,42	5,61	0,16

shock front propagation); indeed in these conditions, the absorption coefficient of the explosive limits the excitation to the edges of the crystal. We thus intend in a next phase to create excited states on the face of admission of the shock, at the moment of the shock. In these conditions the use of flying plate priming system is required.

At least, the examination of a counter-example (explosive not absorbent in this excitation range) is necessary to discriminate any macroscopic modification imputable to an other effect of the laser beam that molecular excitation. The explosive chosen to that effect is PETN ($\varepsilon_{249\ nm} \cong 0$).

CONCLUSION

The whole of the theoretical (quantum chemistry) and experimental (ultra fast Raman spectrometry) studies that we are carrying about the initiation of the explosives at the molecular level, had let us to propose that explosive decomposition finds its origin in a steep modification of the molecular electronic structure. The study of these modifications shows the major role played by the electronic characteristics of the molecular population behind the shock front. We can conclude in particular that if we take into account these characteristics we are able to:

1. determine the shock sensitivity of the substance. This result is even now used for the synthesis of new explosive molecules, the sensitivity of which are determined a priori, by computations and from the structure,

2. Analyse the conditions for the initiation of the detonation mode. In order to verify this proposition, we defined and carried out an original experiment allowing to artificially increase in the shock front, by a light pulse, the concentration in excited and non decomposed molecules. The influence of this increase on the decomposition parameters of the explosive has been studied at the level of the decomposition velocity. The first results obtained do show an influence of the molecular population so created on that velocity.

REFERENCES

1. A. Delpuech, THese Doctorat es-Sciences n°656 Université de Bordeaux I (1980).

   A. Delpuech, J. Cherville, Propellants and Explosives

   3 (6), 169 (1978)
   4 (2), 61 (1979)
   4 (6), 121 (1979)

   A. Delpuech, J. Cherville, Symposium International sur le comportement des milieux denses sous hautes pressions dynamiques - Paris, (1978).

   A. Delpuech, J. Cherville, Colloque International de Pyrotechnie fondamentale et appliquée. Arcachon - France, (1982).

2. A. Delpuech, J. Cherville, C. Michaud, "Molecular Electronic Structure and Initiation of Secondary Explosives," Seventh Symposium on Detonation - Annapolis, (1981).

3. F. Boisard, B. Linares, A. Delpuech, J. Cherville, Symposium International sur le comportement des milieux denses sous hautes pressions dynamiques - Paris, (1978).

   F. Boisard, C. Tombini, A. Menil, "Raman Scattering Temperature Measurement Behind a Shock Wave," Seventh Symposium on Detonation - Annapolis, (1981).

A. Delpuech, A. Menil, Shock Waves in Condensed Matter, Santa Fe, (1983).

4. M. H. Tailleur, Thése spécialité, Université de Bordeaux I, (1980).
5. M. H. Tailleur, J. Cherville, Propellants, Explosives, Pyrotechnics 7, 22 (1982).
6. C. Darnez, Int. J. Radiat. Phys. chem. 4,11, (1972).
7. J. Stals, Trans. Farad. Soc., 67, 1739 (51971), Australian J. Chem., 22, 2505 (1969).
8. F. J. Owens, J. Sharma, J. Appl. phys. 51 (3) 1494, (1980).

DISCUSSION

JAMES RITCHIE, Los Alamos National Laboratory

NQ is thermally unstable, but shock stable. To which region is your correlation applicable? How far does the laser penetrate into the crystal?

REPLY BY S. DUFORT

Our correlation was established between shock sensitivity and molecular parameters associated with electronic excited states. Thermal stability only affects the vibrational structure of the electronic ground state. So, the mechanisms are very different and our model only refers to the electronic excitation of the molecule.

The geometry of the experiment favours a non-homogeneous excitation of the crystal. But, the density of energy deposited on the crystal (>0,8 $J.cm^{-2}$) is sufficient to ensure a penetration of the laser beam larger than expectations of Beer's law. Recent experiments have shown that a weak quantity of energy was able to cross the whole crystal. So, molecular excitation occurs in the whole volume of the HMX single crystal.

CALCULATED REACTION PATHWAYS FOR NITROMETHANE AND THEIR ROLE IN THE SHOCK INITIATION PROCESS

Richard D. Bardo
White Oak Laboratory
Naval Surface Weapons Center
Silver Spring, Maryland 20910

A new reaction mechanism for nitromethane is introduced. The reaction pathways are calculated with semiempirical electronic structure methods. A minimum of 10 steps is needed to obtain the known detonation products. All steps are pressure-accelerated so that they have the high rates necessary to satisfy the temporal constraints imposed by strong initiating shocks. The short reaction times and exothermicities of the steps make them particularly well-suited for further study of the microscopic foundation of initiation and detonation of nitromethane.

I. INTRODUCTION

In the past, the study of shock initiation and detonation in condensed nitromethane has utilized chemical reaction kinetics which were extracted from low pressure data and from fittings of induction time data. The serious problems which arise when this rate information is applied to high pressure (P) and temperature (T) phenomena have been discussed previously (1). In view of the absence of empirical data from which reactions corresponding to the initiation and detonation of nitromethane may be unambiguously identified, electronic structure calculations of reaction pathways were undertaken. In Section II of this paper, a new reaction mechanism is introduced which involves the simultaneous breaking and formation of bonds. The final products formed are identical to those determined by experiment.

In Section III, it is shown that this mechanism, which excludes those reactions with rates strongly retarded at high P and T, is described by sufficiently fast Arrhenius kinetics such that ignition can occur close to the shock front. It is mentioned that the new mechanism may be included as part of a more complete microscopic description of the shock initiation of nitromethane which avoids some past pitfalls arising from the use of unrealistic chemical kinetics. Thermal explosion times are obtained from the new kinetics, and are shown to be incompatible with observed induction times. From these results, the implication is made that the induction time may be obtained from rate-determining steps corresponding to non-chemical processes.

II. CALCULATIONS OF REACTION PATHWAYS

A. Methods of Calculation

The mechanism presented here pertains to the evolution of the supermolecule $(CH_3NO_2)_2$. Since states at high compression are being studied, all results apply to complete clusters of 14 atoms which correspond to reactants, intermediates, and products. For example, the activation energy E_a for each step $A+B \rightarrow C^*$ includes the energy of the activated complex, $E(C^*)$, and the potential energy of $A+B$, $E(A+B)$, so that $E_a = E(C^*) - E(A+B)$. This procedure is necessary since the repulsive interaction energy of $A+B$ is not negligible at high pressure. Volumes and entropies of activation as well as reaction energies, which are designated as $V_a = V(C^*) - V(A+B)$, $S_a = S(C^*) - S(A+B)$, and ΔE = E (products) $- E(A+B)$, respectively, are also changed from their ambient pressure, gas-phase values.

All calculations were done with both MINDO/3 and MNDO semiempirical methods (2) in order to ascertain their relative capabilities for predicting new pathways. Both approaches were found to give the same types of transition states, each of which was identified by a negative eigenvalue of the force constant matrix. While both also gave the same metastable intermediates, products, and signs for the heats of reaction, MINDO/3 gave improved geometries, activation energies, and magnitudes of the reaction energies, in accordance with past studies on other nitro compounds (3).

A comparison of geometries and energies obtained with MINDO/3 and an ab initio self-consistent-field (SCF), linear-combination-of-atomic-orbitals (LCAO), molecular orbital (MO) method is currently underway. The results of this study thus far indicate that both methods give similar geometries for dimers of nitromethane, but widely different activation and reaction energies. Since MINDO/3 is already known to give much better energies for nitro compounds, and since more sophisticated ab initio techniques, which would be more accurate than the SCF-LCAO-MO method, still remain more costly to perform on reacting clusters of CH_3NO_2 molecules, it appears that semiempirical approaches will continue to be indispensible for some time to come in providing direction for investigations of microscopic processes at high pressure. A general discussion of the relative merits of MINDO/3 and MNDO in relation to ab initio methods has been made by Dewar (2).

B. RESULTS AND DISCUSSION

Since the thrust of this paper is concerned with the relevance of the new mechanism to shock initiation, the detailed geometries and nature of the bonding for the reactants, activated complexes, metastable intermediates, and products will be given elsewhere (4). Only general structures are given here. All activation parameters are presented in Table I.

The following mechanism is based on the formation of a rearranged dimer from the head-to-tail reaction of CH_3NO_2 monomers. While the selection of this first step is intuitively reasonable, its importance rests fundamentally on an alignment effect which occurs at high shock compression, and which makes the reaction rate-determining. It will be seen that this bimolecular reaction is strongly pressure-accelerated at the known initiation shock strengths. At these pressures, the rates of all unimolecular bond scissions are so greatly retarded that only those reactions are considered which involve the simultaneous rupture and formation of bonds.

TABLE I

Activation Parameters and Energies for Shocked Nitromethane[a]

Reaction[b]	E_a[c]	V_a[d]	S_a[e]	ΔE[c]
1	47.1	−14	−10	−47.7
	22.5	−12	−10	−47.7
2	46	>−1	>−1	−17.9
3	37	>−1	>−1	−7.2
4	40	>−1	>−1	+9.7
5	39	>−1	>−1	−25.3
6	59	>−3	>−2	−40

[a]Initiating shock pressure is P=80 kbar and T=850K.

[b]For Reaction (1), first and second sets of values pertain to constrained linear head-to-tail and minimum energy pathways, respectively.

[c]Energies of activation and energies of reaction given in the kcal/mol.

[d]Volume of activation given in cm^3/mol.

[e]Entropy of activation given in eu/mol, where 1 eu=1cal/K.

The first reaction step is

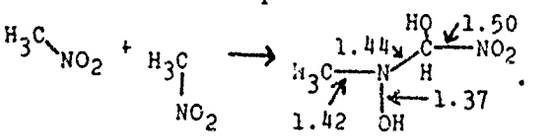

(1)

Calculation of the reaction pathway along the intermolecular reaction coordinate R_{CN} between adjacent NO_2 and CH_3 groups shows that two H atoms are transferred first from the C atom to the O atoms followed by the formation of new single C-O and C-N bonds. Some internuclear distances (in Å) are shown above for the product (hereafter referred to as P1). The structures of the CH_3 and NO_2 groups in P1 and CH_3NO_2 are negligibly different.

For Reaction (1), the activation energy E_a= 22.5 kcal/mol given in Table I was determined from the MINDO/3 heats of formation −10.5 kcal/mol and 11.5 kcal/mol for CH_3NO_2 and the

transition state, respectively, and the interaction energy U=10 kcal/mol at the center-of-mass separation R_{CM}=4.8Å. This latter energy was determined from previous calculations of the interaction potentials (5), which were used in a theoretical determination of the zero-degree Kelvin isotherm for shocked nitromethane (6). In Ref. (6), the volume (V) and Hugoniot pressure (P_H) corresponding to the above values of U and R_{CM} were estimated to be 32 cm^3/mol and 80 kbar, respectively. This pressure is near the known threshold value for shock initiation (7).

The larger value E_a=47.1 kcal/mol listed in Table I was calculated by constraining the monomers in a linear head-to-tail (LHT) collision with the C-N bonds on the same axis. A comparison of this result with the lower energy pathway shows the need to eliminate the artificial constraints of low dimensionality which are often imposed to simplify calculations and models of shock initiation.

For Reaction (1), the volume of activation V_a=−12 cm^3/mol given in Table I was determined from the reaction coordinates R_{CN}=2.1Å in the transition state, and R_{CN}=3.8Å for the reactants at P=80 kbar. The expression for V_a used here is

$$V_a=(\delta R_{CN}/L_O)(2V),$$

where δR_{CN}=−1.6Å and L_O=8.5Å are, respectively, the change of C-N distance and the initial "chain length," which includes covalent radii. A small error is introduced by assuming the constancy of the cross-sectional area during collision. The other value V_a=−14 cm^3/mol in Table I corresponds to the LHT collision discussed previously. It is important to note here that V_a is much larger than the value of about −30 cm^3/mol at ambient pressure for the same bimolecular reaction. High pressure experiments have also shown V_a to increase significantly with increasing P (8).

The entropy of activation S_a is a very sensitive function of the temperature and, as a result, is more difficult to evaluate than V_a or E_a. The value of S_a=−10 eu/mol (1 eu=1 cal/K) listed in Table I for Reaction (1) is obtained in the way described in the Appendix. It is important to note that S_a for Reaction (1) at high pressure is much larger than the usual values for bimolecular reactions at much lower pressures. In the gas and liquid phases, the compression causes a significant loss of rotational and translational entropy of the monomers. In the solid phase, there is a loss of translational and librational entropy. Hamann (9) has discussed the effects of hydrostatic pressure on dimerization reactions. As shown in the Appendix, these effects are also incorporated into the values of S_a in Table I by using known shock compression data (10).

The reaction energy ΔE=−47.7 kcal/mol given in Table I was obtained from the calculated heats of formation −58.7 kcal/mol and −10.5 kcal/mol for P1 and CH_3NO_2, respectively, as well as the interaction energy of the monomers given previously. The exothermicity of Reaction (1) makes it an important source of energy for subsequent reaction. New reactions which may utilize this energy are now introduced.

A possible next step is the transformation of P1,

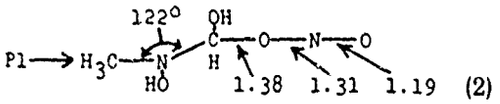

(2)

This reaction proceeds by the increase of the NO_2 bond angle so that the O atom forms a new bond with C. This rearrangement is also known to lead to other nitrite compounds. In fact, E_a=46 kcal/mol in Table I is close to the value calculated for the formation of methyl nitrite (11). Values for V_a and S_a are slightly negative, as indicated in Table I. Reaction (2) is exothermic with ΔE=−17.9 kcal/mol. The changed bondlengths in the new product (hereafter referred to as P2) are shown above.

It should be mentioned at this point that the formation of methyl nitrite may compete with Reaction (1) or actually precede it. It is readily shown, however, that its rate of production at high P is slower than that for Reaction (1), since $|V_a|$ is much smaller (see Eq. (11) in the sequel). Reaction (1) will dominate when the two reactions are considered in parallel.

Another step, which may occur simultaneously with Reaction (2), involves the bending of the O-C-H bond angle to form a new O-H bond with the ejection of H_2O, as well as formation of a new intermediate (hereafter referred to as P3),

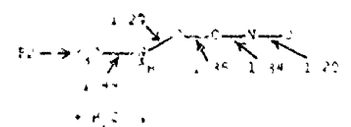
(3)

This is the lowest energy pathway with E_a=37 kcal/mol. Again, as for Reaction (2), V_a and S_a are slightly negative.

Reaction (4), which yields another new intermediate (hereafter referred to as P4) and CH_4, is

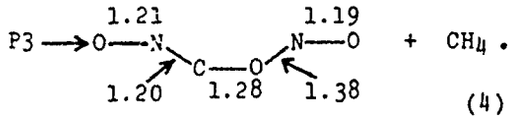

(4)

This reaction actually consists of several steps, itself. The first one involves formation of CH_3OH from the bending of the C-N-O bond angle, where H remains bonded to O. The values for E_a, V_a, and S_a listed in Table I pertain to this process. The precise pathways for the remaining steps are somewhat uncertain at this time. However, preliminary calculations do indicate that reaction between CH_3OH and NCONO can occur to form P4 and CH_4. Overall, Reaction (4) is slightly endothermic at 9.7 kcal/mol. The complete set of reactions will be made available elsewhere (4).

The next reaction leads to CO and the dimer intermediate trans-ONNO,

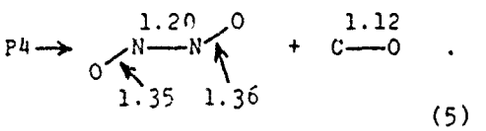

(5)

Here, the lowest energy pathway requires the bending of N-C-O and C-O-N bond angles in P4. A four-centered transition state involving two N atoms, and C and O is formed, corresponding to an activation energy of E_a=37 kcal/mol and the slightly negative values of V_a and S_a indicated in Table I. It is interesting to note that the bond lengths of N_2O_2 of Reaction (5) are closer to those of the cyclic dimer II described in Ref. (12) than to those of the known cis-ONNO dimer existing in the liquid state at low pressure.

The next reaction likely involves the transformation

$$N_2O_2 \rightarrow N_2+O_2, \qquad (6)$$

which was discussed previously in connection with possible reaction pathways for initiating and detonating nitric oxide (12). In that work, it was suggested that a two-step mechanism occurs with the generation of an intermediate dimer (denoted as dimer II) followed by a radiationless transition to form N_2 and O_2. In the first step, an activation energy E_a= 59 kcal/mol was calculated. With the UMINDO/3 method, Ritchie (13) estimated E_a=22.1 kcal/mol for the second step. Since the first step is rate-determining for Reaction (6), its activation energy is given in Table I. At high pressure, the heat of reaction may be nearly −40 kcal/mol.

Reactions (1)-(6) may be summarized as

$$2\ CH_3NO_2 \rightarrow H_2O+CO+N_2+O_2+CH_4.$$

Here, only O_2 is not one of the products of detonation which have been determined by Ornellas (14) to be H_2O, CO, N_2, H_2, CO_2, NH_3, C(s), and CH_4. It is possible to eliminate O_2 and generate the rest of the products by augmenting Reactions (1)-(6) with the well-known reactions,

$$H_2O+CO \rightarrow H_2+CO_2, \qquad (7)$$

$$CH_4 \rightarrow C(s)+2H_2, \qquad (8)$$

$$2H_2+O_2 \rightarrow 2H_2O \qquad (9)$$

and

$$3H_2+N_2 \rightarrow 2NH_3. \qquad (10)$$

Activation parameters for these processes were not calculated, and so are not included in Table I.

While the reversibility of Reactions (1)-(10) must be considered at high P and T, this mechanism is still much shorter than the set of more than 60 steps proposed for detonations on the basis of experiments performed at much lower pressure in shock tubes, where the rate-determining step is taken to be the breaking of the C-N bond (15). On the basis of diffusion rates which may be estimated at high pressure, it is doubtful that such large mechanisms could be completed within the short reaction zones of detonating condensed nitromethane where t(rxn) can be as small as 10^{-11} sec. Since the new mechanism leads directly to the known detonation products in a relatively small number of steps, a framework based on chemical kinetics is established which permits a fundamental analysis of the known initiation schemes for nitromethane. It is now shown how the new kinetics may be applied to initiation.

III. APPLICATION TO INITIATION

In order to correctly describe initiating and detonating nitromethane, the appropriate reaction

pathways must be chosen on the basis of spatial and temporal constraints imposed on the system by the shock. In contrast to reactions occurring at high temperatures in gas, liquid, and solid phases at ambient pressure, high compression greatly accelerates some reactions and greatly reduces the probability of others. In this connection, two types of spatial constraints which strongly influence the kinds of reactions which can occur are: (1) the quenching of molecular rotation which increases the chance of reaction between appropriately aligned molecules, and (2) the inhibition of molecular expansion such as unimolecular bond scission. The temporal constraints depend on the shape of the initiating shock pulse and length of the reaction zone.

Pertinent pressures and duration times for nitromethane are known to be P>60 kbar and $t<10^{-5}$ sec. Here, t may be the induction time t(ind) or the time available for reaction t(rxn) within the reaction zone. Experiment has shown, for example, that at the sustained pressure P=75.3 kbar, $t(ind)=2\times10^{-6}$ sec (16). From an estimate of the reaction zone length of 1000Å (17), which appears to be the smallest value estimated so far for nitromethane, and from the approximate detonation velocity of 7000 m/sec, it is found that $t(rxn)\simeq10^{-11}$ sec.

The rates of Reactions (1)-(6) at known shock initiation pressures and temperatures are obtained by substituting the activation parameters of Table I into the following expression for the rate coefficient (18),

$$\ln k=\ln v+\frac{S_a}{R}-\frac{PV_a}{RT}-\frac{E_a}{RT}. \qquad (11)$$

In Eq. (11), v=RT/Nh, where R is the gas constant and N is the Avogadro number. The third term in Eq. (11) is the very important pressure contribution to the rate, which is accelerated when $V_a<0$ and decelerated when $V_a>0$. At a sustained pressure P=80 kbar and the calculated temperature T=850 K (10), the rate coefficient of Reaction (1) is $k=1.1\times10^{6}$ sec^{-1} when $E_a=47.1$ kcal/mol. The corresponding reaction half-life is $t(\frac{1}{2})=k^{-1}=9.1\times10^{-7}$ sec for 1 mole of nitromethane. For the minimum value of $E_a=22.5$ kcal/mol corresponding to the minimum energy pathway $k=2\times10^{11}$ and $t(\frac{1}{2})=5\times10^{-12}$ sec at the P and T given above.

Reaction (1) easily satisfies the constraint that $t(\frac{1}{2})<t(ind)$, where the induction time t(ind) is known to be about 1.4×10^{-6} sec at P=7.94 GPa (16). However, this is not the case for Reactions (2)-(6) at P=80 kbar and T=850 K, since the shortest half-life is 10^{-4} sec. Thus, if these reactions are to occur during initiation, the local T must be higher, T>1200 K. By Le Chatelier's principle, higher T will also tend to increasingly favor the reverse of those reactions which are exothermic.

Much higher local temperatures will arise as a consequence of the exothermicity of Reaction (1). However, Reaction (1) does not release energy which is immediately made available for other reactions. Instead, other processes, such as, for example, vibrational-to-translational energy transfer, may dominate before significant further reaction occurs. In this sense, then, Reaction (1) behaves like a slow step.

The Arrhenius activation energy $E_a(Arr)$ and pre-exponential factor for Reaction (1) are determined from the data of Table I. From Ref. (1),

$$E_a(Arr)=E_a'+V_a(P-T\frac{dP}{dT}), \qquad (12)$$

where $E_a=E_a'-RT$ and V_a are the fundamental parameters given in Table I. From $k=A\exp(-E_a(Arr)/RT)$ and Eqs. (11) and (12), the natural logarithm of A is

$$\ln A=1+\ln v+\frac{S_a}{R}-(T\frac{dP}{dT},\frac{V_a}{RT}. \qquad (13)$$

At P=80 kbar and T=850 K, T(dP/dT)=85 kbar, where dP/dT is approximately 100 atm/K. Then, $E_a(Arr)=29.3$ kcal/mol and $A=5.5\times10^{18}$ sec^{-1} for $E_a=22.5$ kcal/mol in Table I. Also $E_a(Arr)=54.7$ kcal/mol and $A=2.8\times10^{20}$ sec^{-1} for $E_a=47.1$ kcal/mol. Since dP/dT, E_a, and S_a are relatively insensitive functions of P and T over the range $80\leq P\leq90$ kbar, $E_a(Arr)$ and A will differ little from the above values.

These very large values of A are essentially due to the large contribution of the last term in Eq. (13). As indicated previously (1), the magnitudes of such terms which include V_a are negligible at ambient pressure. In the past, the supposition has often been made that the initiation reaction is unimolecular, and involves the breaking of the C-N bond. However, as mentioned earlier, very high compression retards an expansion of the molecule during bond-scission. Indeed, at P=80 kbar and T=850K, for example, the ratio r=k (Reaction 1)/k(unimolec) lies

in the range $10^7 \leq r \leq 10^{11}$, when the activation parameters of Table I and the typical bond-scission values S_a=3 eu/mol, V_a=3 cm^3/mol, and E_a=54 kcal/mol are used. For the same P and T, the half-life for bond-scission is 25 sec, which is much too long to satisfy the known temporal constraints given previously. Even if it is assumed that a much higher local T exists, such as, for example, T=2000K, r is still large at P=80kbar. Thus, Reaction (1) will be dominant over the simple bond-scission process in the ignition of nitromethane.

When the large Arrhenius factors A given above are used to calculate thermal explosion times, the resulting values are seen to be much smaller than those determined in the past from assumed kinetics which have no pressure dependence. Here, the explosion time t(exp) is obtained from the expression derived in Ref. (19),

$$\ln \frac{t(exp)}{T^2} = \ln \frac{c_v R}{Q E_a(Arr)} - \ln k. \qquad (14)$$

From the heat capacity c_v=0.46 cal/g-K, the heat of reaction Q=782 cal/g, T=850K, E_a(Arr)=54.7 kcal/mol, and $A=2.8\times10^{20}$ sec^{-1}, it is found that $t(exp)=5.2\times10^{-9}$ sec. Campbell, et al. (20) obtained a larger value $t(exp)=6\times10^{-7}$ sec at T=1140K by assuming typical Arrhenius parameters of $A=10^{14.6}$ and E_a=53.6 kcal/mol. While this value of t(exp) appears to be a better approximation of t(ind), the ratio r given above is still very large, making Reaction (1) the better choice.

The fact that t(exp) for Reaction (1) is so small compared to the experimental induction time $t(ind)\cong10^{-6}$ sec at P=80 kbar suggests that, in contrast to previous interpretations of initiation, it may not be possible to invoke simple thermal explosion theory alone. Utilization of this theory has led to the thermal ignition theory (20). Hardesty's experimental inductive time data for liquid nitromethane appear to have provided additional support for this model by indicating that thermal explosion occurs far behind the shock front and near the driver-plate/nitromethane interface where the explosive has had the longest time to react (16). From his induction time data, he used Eq. (14) to obtain E_a(Arr)=23 kcal/mol and $A=2.6\times10^9$ sec^{-1} for $75\leq P\leq92$ kbar and $934\leq T\leq1087$ K. These parameters are seen to be much smaller than those calculated previously for Reaction (1).

In view of these results, Reaction (1) appears to be more appropriate for an analysis of initiation in terms of another model, which has evolved from the observations of Walker and Wasley (21), and which as the central feature that initiation occurs close to the shock front after a delay time. After consideration of chemical reaction times, they suggested that high, transient, nonequilibrium temperatures would have to exist at sufficiently high P in order to achieve runaway reaction soon after shock wave growth and acceleration.

In this model, the need for high, nonequilibrium temperatures and, therefore, non-Arrhenius kinetics is avoided if Reaction (1) is utilized. It was shown earlier that t(½) is as small as 5×10^{-12} sec along the minimum energy pathway at P=80 kbar and T=850K. Thus, Reaction (1) could occur during the short times available in a non-square wave profile corresponding to rapidly decreasing pressure and temperature behind the shock front.

Nunziato, et al. (22) have examined the results of the experiments leading to the two models, and have suggested that the differences are due to the use of a square pressure pulse or supported wave by Campbell, et al. (20) and Hardesty (16), and a "triangular" pressure pulse or unsupported wave by Walker and Wasley (21). Here, then, it is reasonable to expect that the same kinetics would apply to both types of phenomena. If, for example, Reaction (1) is to be employed in both cases, it would be necessary to modify or give up altogether the thermal explosion interpretation based on Eq. (14). A broader picture which includes additional microscopic processes would, then, have to be considered. Substantial support for such an alternative approach is given in Ref. (23), where the transfer of energy into the molecules prior to Reaction (1) is shown to be the slow step. Confirmation is given there of earlier calculations which indicate that the time for energy transfer from acoustic to molecular modes is of the order of the induction time t(ind) (24).

It should be mentioned that, when energy relaxation processes are sufficiently slow so that nonequilibrium temperatures exist, the use of Eqs. (11)-(14) for calculation of very short reaction times must be exercised with care. Herein lies an essential reason for utilizing quantum mechanical methods to describe the relative

rates of energy transfer steps and chemical reactions when the latter become as rapid as Reaction (1) (23).

Currently, these results are serving as input into research now underway in this laboratory where the very fast Reaction (1) is being treated as a kind of microscopic "hot spot." It now appears that a critical distribution of these "hot spots" permits the creation of a kind of structure similar to that described in connection with Mach stem theory.

IV. CONCLUSIONS

A new reaction mechanism for nitromethane was introduced. All of the calculated steps are pressure accelerated since they have negative volumes of activation. As a consequence, the reactions have sufficiently high rates which satisfy the temporal constraints imposed at the threshold shock pressures and temperatures for initiation. The total mechanism, which leads to the known detonation products, is much shorter than those proposed in the past. The mechanism is, therefore, well-suited to studies of very short reaction zones. Six reactions are found to be exothermic, so that they are important sources of energy for detonation.

The first step, which is a bimolecular reaction, was shown to exothermically form a stable dimer intermediate. This reaction, the rate of which is enhanced as a result of spatial constraints in shocks, may play an especially important role in initiation caused by both supported and unsupported pressure pulses. This reaction was used in a brief, comparative study of the two best-known initiation models for nitromethane to show that thermal explosion times are much shorter than those calculated in the past. On the basis of these results, the suggestion was made that energy transfer processes may be more important than previously realized.

APPENDIX

For Reaction (1), an ab initio calculation of the entropy of activation S_a at high pressure requires the intramolecular and intermolecular vibrational and librational frequencies of the monomers and activated complex. Although these frequencies are known for gaseous and crystalline nitromethane at ambient pressure, they are unknown at shock initiation pressures. A semiempirical estimation of S_a may be made, however, by utilizing values of the total entropy S_T obtained by Hardesty and Lysne (10) for shocked, unreacted nitromethane.

Estimates of the intermolecular contribution S_i for the monomers may be obtained by making the reasonable assumption that, with the exception of the torsional motion of the CH_3 group, the variation of frequency with compression is much smaller for intramolecular vibrations than for intermolecular modes. Here, then, the frequencies for gas phase nitromethane (25) may be substituted into the well-known harmonic oscillator expression (26) for the intramolecular vibrational contribution S_v to the entropy. At T=850K, $S_v \cong 3$ eu/mol. At P=80 kbar and T= 850 K, $S_T = 15$ eu/mol so that $S_i = S_T - S_v \cong 12$ eu/mol. This latter value includes the largest contribution from translational motion as well as a smaller effect from librational motion, but excludes gross monomer rotations, which are quenched at high pressure. This value of S_i is also taken to include the torsion, which is expected to be strongly affected by pressure.

The entropy S_T^* of the activated complex also consists of intermolecular S_i^* and intramolecular S_v^* components. Values for S_i^* may be estimated by assuming that its largest contribution is due to "translational" motion. Since the molecular mass M will enter the "translational" entropy as approximately (3/2)R ln M, $S_i^* - S_i \cong 2$ so that $S_i^* \cong 14$ eu/mol at P=80 kbar and T=850K. The component S_v^* may also be obtained from S_v for the monomer. Since the ratio of the number of real normal modes in the activated complex to that of the monomer is about 2.3, and S_v^* and S_v are sums over modes (26), $S_v^* \cong 2S_v = 6$ eu/mol at P=80 kbar and T=850K. Thus, in first approximation, $S_T^* \cong 20$ eu/mol.

From these results, $S_a \cong S_T^* - 2S_T = -10$ eu/mol at P=80 kbar and T=850K. This value is a reasonable lower bound so that, for Reaction (1), $-10 \leqslant S_a < 0$ eu/mol at this P and T. This estimate may be compared with the empirical results given by Hamann (9), who shows that S_a increases from -31 eu/mol to -18 eu/mol in the range $1 \leqslant P \leqslant 4000$ atm for the dimerization of cyclopentadiene at T=293 K. It is expected that S_a for this reaction will increase further with P.

ACKNOWLEDGMENTS

This work was supported by the NSWC Independent Research Program. Special thanks are extended to M. J. Kamlet, D. G. Tasker, and C. Dickinson for helpful discussions.

REFERENCES

1. R.D. Bardo, T.N. Hall, and M.J. Kamlet, "Energies and Volumes of Activation for Condensed Detonating Explosives," J. Chem. Phys. *77*, 5858(1982).
2. M.J.S. Dewar, "Development and Status of MINDO/3 and MNDO," J. Molec. Structure *100*, 41 (1983).
3. L.P. Davis, A.G. Turner, R.M. Guidry, and T.B. Menard, "Theoretical Chemical Calculations on Molecules of Air Force Interest," Rept. FJSRL-TR-83-0014, Nov. 1983.
4. R.D. Bardo, paper to be published in J. Am. Chem. Soc.
5. The potential energy calculations were done on the supermolecule $(CH_3NO_2)_2$ so that the energy quoted here includes both repulsion and attraction contributions.
6. R.D. Bardo and W.H. Jones, "A Theoretical Calculation of the 0 K Isotherm for Shocked Nitromethane," in Shock Waves in Condensed Matter-1983, J.R. Asay, et al., Eds., Elsevier, Chapter XIII:4.
7. Y. deLongueville, C. Fauguignon, and H. Moulard, "Initiation of Several Condensed Explosives by a Given Duration Shock Wave," Proceedings Sixth Symposium (Int.) on Detonation, Office of Naval Research, ARC-221, p. 105, 1976.
8. S.D. Hamann, "Chemical Kinetics," in High Pressure Physics and Chemistry, Vol. 2, R.S. Bradley, Ed., pp. 176-182, Academic Press, 1963.
9. S.D. Hamann, "Physico-Chemical Effects of Pressure" pp. 189-192, Academic Press, New York, 1957.
10. D.R. Hardesty and P.C. Lysne, "Shock Initiation and Detonation Properties of Homogeneous Explosives," Sandia Report SLA 74-0165, May 1974.
11. J.P. Ritchie, "A Molecular Orbital Study of the Ozonolysis of Ethylene and of the Mechanisms of Decomposition and Properties of Nitrated Hydrocarbons," Ph.D. Thesis, University of Texas, Dec. 1981.
12. R.D. Bardo, "A Theoretical Prediction of the Structure and Energy of the Metastable Symmetric cis-Nitric Oxide Dimer," J. Phys. Chem. *86*, 4658 (1982).
13. J.P. Ritchie, "Comments on the Cis, Trans, and Cyclic Dimers of NO," J. Phys. Chem. *87*, 2466 (1983).
14. D.L. Ornellas, "Calorimetric Determinations of the Heat and Products of Detonation for Explosives: October 1961 to April 1982," LLNL Rept. UCRL-52821, April 5, 1982, pp. 55.
15. R.H. Guirguis, "Investigation of the Thermal Initiation of Detonation in Nitromethane," NRL Rept. J206-83-011/-6223, October 21, 1983.
16. D.R. Hardesty, "An Investigation of Shock Initiation of Liquid Nitromethane, " Comb. and Flame *27*, 229 (1976).
17. B.G. Craig, Tenth Symposium (Int.) on Combustion, p. 863, The Combustion Institute (1965).
18. K.J. Laidler, Chemical Kinetics, 2nd Ed., p. 89, McGraw-Hill, New York, 1965.
19. U.S. Army Materiel Command, Principles of Explosive Behavior, Engineering Design Handbook, AMCP-706-180, April 1972, pp. 10-3 to 10-7.
20. A.W. Campbell, W.C. Davis, and J.R. Travis, "Shock Initiation of Detonation in Liquid Explosives," Phys. Fluids *4*, 498 (1961).
21. F.E. Walker and R.J. Wasley, "Initiation of Nitromethane with Relatively Long-Duration, Low-Amplitude Shock Waves," Comb. and Flame *15*, 233 (1970).
22. J.W. Nunziato, J.E. Kennedy, and D.R. Hardesty, "Modes of Shock Wave Growth in the Initiation of Explosives," Proceedings Sixth Symposium (Int.) on Detonation, Office of Naval Research, ACR-221, p. 47, 1976.
23. R.D. Bardo, "Rate-Determining Steps for Ignition of Shocked Nitromethane," Y.M. Gupta, Ed., pp. 843-856, Plenum Press, New York, 1986.

24. F.J. Zerilli and E.T. Toton, "Shock-induced Molecular Excitation in Solids," Phys. Rev. B *29*, 5891 (1984).

25. A.J. Wells and E.B. Wilson, Jr., "Infrared and Raman Spectra of Polyatomic Molecules XIII. Nitromethane," J. Chem. Phys. *9*, 314 (1941).

26. G. Herzberg, Molecular Spectra and Molecular Structure II. Infrared and Raman Spectra of Polyatomic Molecules, pp. 519-526, D. Van Nostrand Co., Inc., Princeton, 1945.

DISCUSSION

JAMES RITCHIE, Los Alamos National Laboratory

Might not trimolecular, tetramolecular, pentamolecular reactions, etc., be possible? Not only for the first reaction, but for subsequent reactions? How does one know when to stop?

REPLY BY RICHARD BARDO

On a statistical basis, reactions of molecularity $m>2$ are always possible, as is the pressure-retarded unimolecular bond-scission process ($m=1$). At any pressure, a reactive collision between, say, three molecules will take place much less frequently than a reaction with $m=2$. This fact is conveniently expressed through the entropy of activation S_a in the absolute reaction rate theory, where the rate coefficient k is expressed as $\ln k=\ln (k_BT/h)+S_a/R-PV_a/RT-E_a/RT$. Here, $S_a<0$ for all m, and decreases with increasing m. This rule applies at elevated pressures and temperatures. On this basis alone, the bimolecular reaction is the most probable or rate-determining one. For the trimolecular reaction ($m = 3$), $V_a \cong -12$ cm^3/mol and the calculated value of E_a is 28.8 kcal/mol at $P=80$ kbar, so that k for $m=3$ is smaller. Since S_a increases with P for all m, the rates of the higher order reactions increase and compete more effectively with the bimolecular reaction, thereby increasing the yield of higher polymers. Once S_a, V_a, and E_a are known for the various reactions, the reaction half-lives $t_m(½)$ may be calculated from the rate coefficients k_m. The maximum value of m for shock initiation and detonation is then determined from the requirement that $t_m(½)\lesssim 10^{-6}$ sec. It should be emphasized that not only is the bimolecular reaction a sufficiently fast initial reaction, it is also exothermic and, as such, is an important source of energy for initiation. It is in this context that the terminology of microscopic "hot spot" is used in the paper.

THE DYNAMICS OF SHOCK-INDUCED ENERGY FLUX IN MOLECULAR BONDS*

Arnold M. Karo and Marc H. Mehlman
Lawrence Livermore National Laboratory
Livermore, California, 94550
and
John R . Hardy
Behlen Laboratory of Physics, University of Nebraska
Lincoln, Nebraska 68588

Over the past ten years we have made many computer studies of shock propagation in condensed media. These studies employed the techniques of computer molecular dynamics (CMD), based on computer solutions of the classical equations of motion for the individual atoms in the condensed media. Recently, we have begun to re-evaluate the information obtained in order to achieve a flexible compromise between "brute force" averaging and continual monitoring of the detailed motion of the individual atoms. The method we have chosen is Fourier analysis in the temporal domain of the motions of groups of atoms which can be preselected.

Here, we present an analysis of our early canonical studies and of new data on disordered systems. The present work also utilizes our current codes which contain "neighborhood look-up" procedures designed to examine the system at regular intervals and to determine which bonds should be retained, removed, or added as the system rearranges under shock loading.

INTRODUCTION

It is now well-established that computer molecular dynamics (CMD) can provide a unique insight into the behavior of shocked systems which, at present, is inaccessible to direct experimental investigation (1, 2). The basic reason is that CMD studies show that shock fronts are characterized by violent local structure at the atomic and molecular levels, which varies drastically over time scales of picosecond to femtosecond duration. Since present experimental studies typically examine a system over nanosecond or greater time intervals and in micrometer dimensions, it follows that they will monitor spatial and temporal average behavior rather than the true local behavior. While it is true that experiments have been done with considerably shorter scales of time or distance, none has yet been done where *both* scales have been shortened simultaneously. However, recent studies on shocks in water (3) represent major steps towards this goal.

Since presenting our first work (1) on CMD at the Sixth International Colloquium on Gasdynamics of Explosions and Reactive Systems, we have carried out many studies with the aim of achieving an increasingly accurate description of reality (2, 4). Most recently we have concentrated on developing techniques for post-processing of the raw CMD data, with the principal aim of achieving some optimum capability, which will combine reasonable compactness with the retention of the maximum amount of information about the CMD history of each shock study. From the outset we have stressed the importance of avoiding the wholesale destruction of information (obtained at a non-trivial expense in computer time) that is inherent in the formation of broad averages over many atoms and/or long time intervals. Moreover, this destruction is no longer necessary with contemporary computer facilities; since it is now possible to carry out a

*Work performed under the auspices of the U.S. Department of Energy by the Lawrence Livermore National Laboratory under contract number W-7405-ENG-48, and under the auspices of the Office of Naval Research.

virtually unlimited number of post processing operations at a fixed cost by the use of a dedicated microcomputer, it is no longer necessary to use mainframe computer time to perform such studies.

Given these facts, it seemed logical to begin by monitoring *local* variables, such as energy, as a function of time for a selected unit. In this manner we could observe the manner in which energy flowed into and out of this unit and, in the case of a polyatomic unit, the energy flux between different degrees of freedom. Then, by enlarging our unit, we could progressively monitor increasingly less local conditions if this appeared desirable. We have recently reported the earliest of our findings (5, 6) employing this approach and demonstrated its potential usefulness. However, it was also evident that further compacting of the data was desirable, and the most promising approach was to compute their temporal Fourier transforms. This can be done for varying time intervals, provided they are not too short (a circumstance that we wish to avoid in any event if we are to achieve any useful compacting of the data), and the whole history thus reduced to a manageable number of figures.

This additional capability, together with the greatly increased sophistication of our CMD codes, has made it desirable that we repeat a selected set of our earlier calculations, which we regard as canonical; in addition, we have added some completely novel investigations which address new areas not previously explored.

Thus, in the present paper, we focus on studies of diatomic systems (which have earlier only been reported in summary form), which are important in their own right as the first step to the truly polyatomic systems represented by organic explosives and binders and which also lead naturally to the introduction of the simplest possible type of disorder in a controlled fashion. This comes about because if one introduces only mass disorder by inserting in a random fashion "wrong" masses in a monatomic host, then one is introducing both position and mass disorder simultaneously. However, if one begins from a regular diatomic host and replaces atoms of *one* sub-lattice by atoms of the other sub-lattice species, but retains an ordered array for the other sub-lattice, one is introducing only mass disorder.

SPECIFIC STUDIES

The techniques of CMD are now well documented by both others and ourselves (2, 7). The only novel features are the use of "look-up" procedures to keep track of the interatomic bonding and the various post processing options referred to in the Introduction. In the present rather preliminary account, our basic objective is to "revisit" some of our earlier studies with the aid of these new techniques. As before, for reasons of computational economy, these studies have been primarily restricted to two-dimensional systems.

DIATOMIC STUDIES

We begin by reporting the results of two runs on regular diatomic lattices, subject to loading by impact of a plate composed entirely of heavy atoms (= 10 amu). They differ only in the nature of the column of atoms which the plate initially strikes: in the first case, it is composed of heavy atoms (= 10 amu), in the second case, it is composed of light atoms (= 1 amu).

In Figures 1 and 2, we show a sequence of stills from the movie history of the first case (heavy on heavy) designed to reveal the overall history of this system. Evidently there is considerable lattice disruption which is both coherent and athermal. The behavior of the last spalled fragment on the right is particularly interesting, since it appears to evolve in a manner revealing considerable shock-induced (athermal) chemistry, involving rupture and subsequent "healing" of a number of bonds.

In Figures 3 and 4, we show a similar sequence of stills from the history of the lattice with light atoms forming the initial column on the left. (Since the choice of such stills is determined by the history itself, the selected times are not necessarily the same for every run.) It can be seen that the "rupture pattern" is very different from that of the previous run. Apparently the somewhat less "impulsive" shock loading due to the "indirect" (light-atom-mediated) impact, rather than the direct impact of heavy plate atoms on heavy lattice atoms, has favored the spall of larger more coherent lattice fragments; additionally, the high degree of local activity at the pointed end is no longer present.

In order to exploit our new post processing

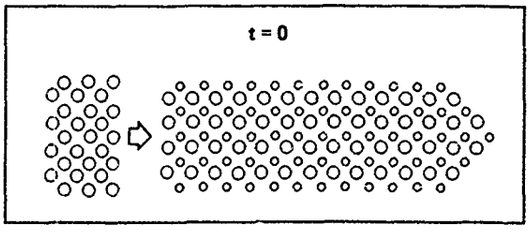

Figure 1. Initial configuration for a diatomic lattice (masses = 1 and 10 amu) shock loaded by impact by a monatomic (mass 10) plate: plate striking column of mass 10 atoms. Smaller and larger circles designate mass 1 and mass 10 atoms, respectively.

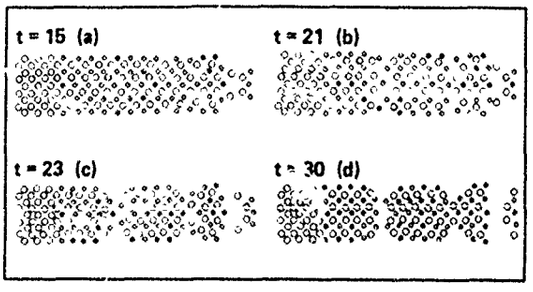

Figure 2 Configurations of the diatomic system of Fig. 1 at various times (in units of 10^{-14} s). Smaller and larger circles designate mass 1 and mass 10 atoms, respectively. a) t=15. b) t=20. c) t=23. d) t=30.

techniques, we Fourier transformed the energy of a pair of near-identically situated light and heavy atoms for both histories. We did this by dividing the thirty-time unit history into three blocks of ten units (one time unit $=10^{-14}$ s). The resultant transforms are shown in Figures 5 and 6. Probably since the atom pairs are located within the coherent lattice fragments, the transforms show no very dramatic features, but the data reduction is very promising, and further study is indicated.

DISORDERED SYSTEMS

In order to characterize the effects of disorder, we set up three diatomic systems identical to the first set of studies described above (Figures 1 and 2), except that the lattices have been disordered on the "light atom" sublattices by random replacement of ∿45%, 67%, and 84%,

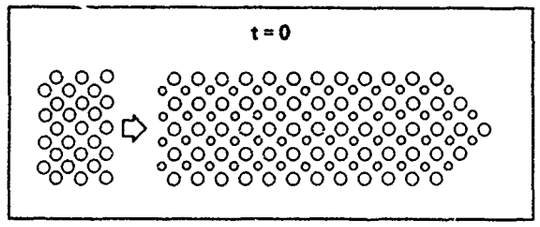

Figure 3. Initial configuration for a diatomic lattice (masses = 1 and 10 amu) shock loaded by impact by a monatomic (mass 10) plate: plate striking column of mass 1 atoms. Smaller and larger circles designate mass 1 and mass 10 atoms, respectively.

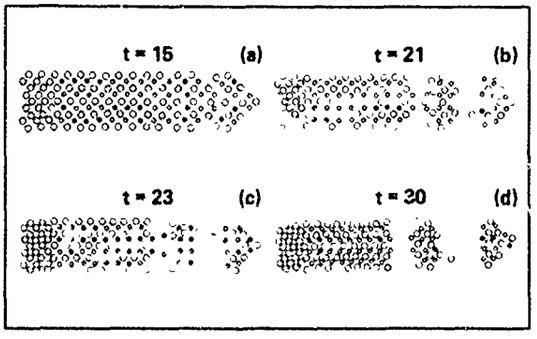

Figure 4. Configurations for the diatomic system of Fig. 3 at later times (in units of 10^{-14} s). a) t=15. b) t=21. c) t=23. d) t=30. Smaller and larger circles designate mass 1 and mass 10 atoms, respectively.

respectively, of the light masses by heavy atoms. Selected stills from the history of the 67% case are shown in Figure 7.

The most striking effect is the almost complete suppression of the atomically sharp shock front found in the ordered systems. This is most clearly manifested by the disappearance of spall and a general tendency for the coherent shock energy to degrade into quasi-random atomic motion leading to "quasi-melting" (semi-random emission of fragments).

In order to quantify this behavior, we again performed Fourier transform post processing for a pair of atoms situated in near proximity to the position of the pair selected in the first study (a heavy plate impacting a diatomic lattice in which the first column is composed of heavy atoms).

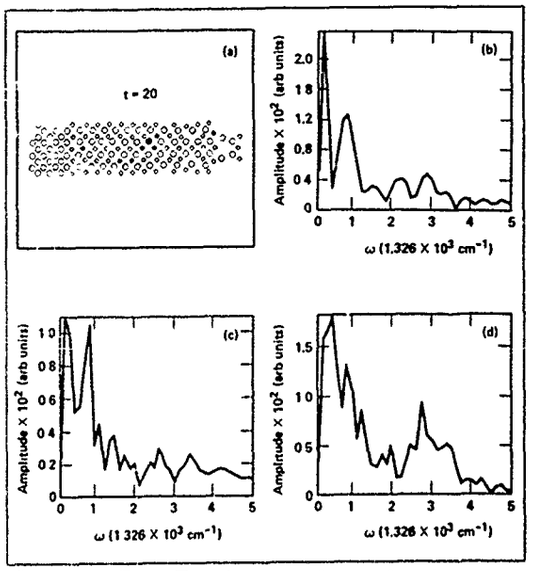

Figure 5. Fast Fourier transforms for the vibrational energy of a single diatom (masses 10 and 1) in a diatomic lattice shock loaded by a heavy plate (mass 10 atoms) initially striking column of mass 10 atoms (units of time in 10^{-14} s). a) Configuration at t = 20 showing tagged diatom, indicated by filled circles. Light masses shown as smaller circles. b) FFT, t = 0-10. c) FFT, t = 10 - 20. d) FFT, t = 20 - 30.

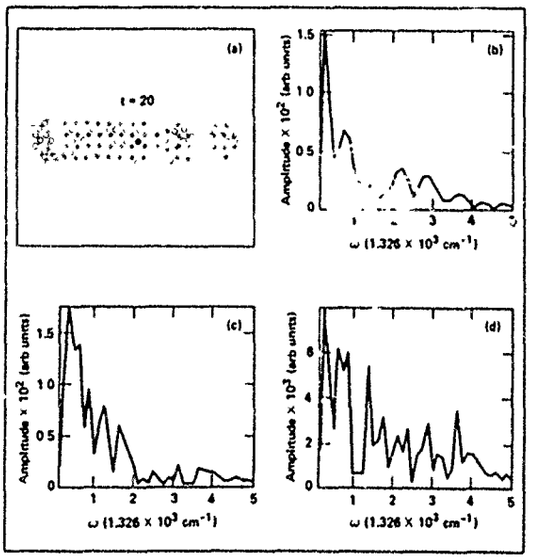

Figure 6. The same sequence as Fig. 5 except that the plate strikes a light column and the tagged diatom is somewhat differently situated (units of time in 10^{-14} s). a) Configuration at t = 20 showing tagged diatom indicated by filled circles. Light masses shown as smaller circles. b) FFT, t = 0 - 10. c) FFT, t = 10 - 20. d) FFT, t = 20 - 30.

The results are shown in Figure 8.

In all cases it is of interest to observe the amount of energy delivered to the diatomic unit whose history is being studied, and to compare this with the bond rupture energy, in order to determine whether bond rupture would be possible at some local surface (bond rupture in the bulk of the lattice is precluded by the caging effect of the neighboring atoms). In all three studies it appears that surface bond breaking is indeed the case even though (except in the disordered systems) the actual lattice "temperature" is quite low—the principal reason for this apparent paradox is that bond rupture at a surface is an irreversible process which is likely to occur whenever the *instantaneous* bond energy exceeds the bond rupture energy. Thus, while in the bulk, energy flows coherently into and out of bonds as the shock transits the lattice and, after the passage of the front, the average bond energy reverts essentially to its value prior to the shock incidence, at the surface/void the instantaneous bond extension can exceed the bond energy and readily produce rupture, or monomolecular decomposition. Hence, by this means are formed atomic (ionic/radical) fragments of high reactivity which can initiate a propagating chemical reaction when produced in sufficiently large concentrations. In Figure 9, we show a comparison of the vibrational energies of the diatoms chosen for the ordered diatomic lattice and the disordered diatomic lattice (Figures 5 and 8).

One additional feature is that examination of energy propagation through the light and heavy sub-lattices reveals that propagation occurs primarily through the heavy sub-lattice. This is consistent with the partition of energy between the center-of-mass (CM) and internal motion of each diatomic unit. The internal (within the CM system) motion, by definition, has no net momentum, thus momentum propagation is confined entirely to the overall CM motion and, for widely disparate masses, is primarily carried by the heavier atom.

This is a somewhat simplified picture since, at first sight, it would seem to imply that energy never reaches the internal motion, at least not beyond the first pair of columns. However, a little closer examination of the problem reveals that this is incorrect. The impact of a neighboring pair of shocked columns on their

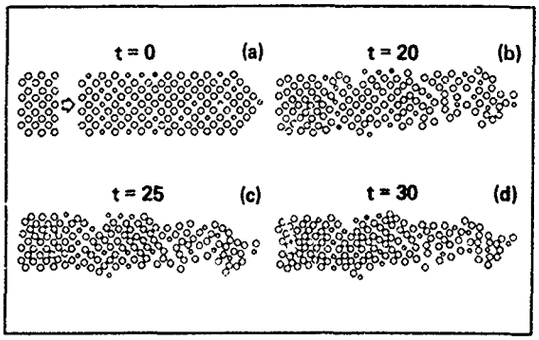

Figure 7. a) Initial configuration for a diatomic (masses = 1 and 10 amu) lattice disordered on the light sublattice by random replacement of ∼67% of the light masses by mass 10 atoms. Smaller circles designate mass 1 atoms. History of the disordered lattice at later times (in units of 10^{-14} s). b) t = 20. c) t = 25. d) t = 30.

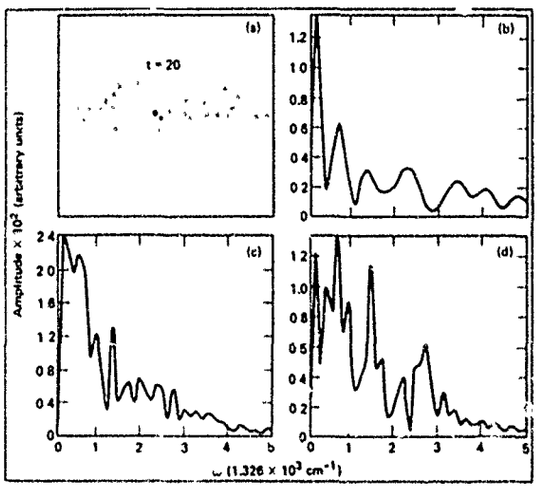

Figure 8. Fast Fourier transforms of the vibrational energy of a diatom in the disordered lattice during the simulation shown in Fig. 7. a) Configuration at t = 20 showing the tagged diatom indicated by filled circles. Light masses shown as smaller circles. b) FFT, t = 0 - 10. c) FFT, t = 10 - 20. d) FFT, t = 20 - 30. The additional "spike" in the t = 20 - 30 transform at a frequency ∼1.5 (∼1990 cm^{-1}) is probably the "pumping" of energy into the tagged pair by the motion of the heavy atom first neighbor of the tagged heavy atom.

unshocked forward neighbors is a more complex process because the pairs do not strike

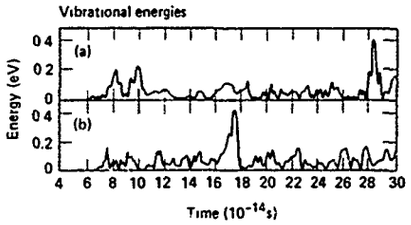

Figure 9. Comparison of the vibrational energie of the corresponding diatoms in (a) the ordered diatomic lattice, Fig. 5, and (b) the disordered diatomic lattice, Fig. 8.

one another as hard rods; rather, the heavy members of the moving pair push directly only against the light column of the unshocked pair. Thus, initially they effectively push the light column before them without resistance. However, as this process compresses the initially unshocked columns, the bonds between them become more and more rigid, until the heavy column has assumed the bulk of the CM motion of the impacting pair of columns. At this point the shock front has effectively jumped one pair of columns and the transfer of energy is complete, *including the transfer of energy to the internal motion (light atom beating against heavy atom) within the CM system.* This is an important point, possibly crucial, because it implies that the internal motion will be drastically athermal due both to the coherent and rapid nature of the energy transfer during a time ∼10-100 femtosecs. Hence, arise the bond ruptures at surfaces and other imperfections that we observe in our simulations (1, 2).

CONCLUSIONS

We have presented results demonstrating the potential usefulness of post-processing Fourier transforms as a means of "fingerprinting" the nature of shock loading in a variety of situations. The one single common feature is that these transforms again show that shock loading can excite high frequency intramolecular motions over picosecond time intervals in a strongly athermal manner. The transforms, themselves, although not particularly dramatic for these selected studies, do reveal a high degree of promise as a data reduction scheme which drastically reduces the amount of output while retaining all, or almost all, of the important microscopic information.

REFERENCES

1. A. M. Karo, J. R. Hardy, and F. E. Walker, "Theoretical Studies of Shock-Initiated Detonations," Acta Astronautica, Vol. 5, pp. 1041-1050, 1978.
2. A. M. Karo and J. R. Hardy, "The Study of Fast Shock-Induced Dissociation by Computer Molecular Dynamics," Proceedings of the NATO Advanced Study Institute on Fast Reactions in Energetic Systems, edited by C. Capellos and R. F. Walker (D. Reidel Publishing Co., Dordrecht-Holland, Boston, USA, 1981), pp. 611-643.
3. P. Harris and H. N. Presles, "Comparison of the Optical Reflectivity of a Shock Front in Liquid Water and in Liquid Nitromethane," J. Chem. Phys. Vol. 77 (10), pp. 5157-5164," 1982.
4. J. R. Hardy, A. M. Karo, and F. E. Walker, "The Molecular Dynamics of Shock and Detonation Phenomena in Condensed Matter," Progress in Aeronautics and Astronautics," Vol. 75, edited by J. R. Bowen et al. (American Institute of Aeronautics and Astronautics, 1981), pp. 209-225.
5. A. M. Karo, F. E. Walker, T. M. Deboni and J. R. Hardy, "The Simulation of Shock-Induced Energy Flux in Molecular Solids," Progress in Aeronautics and Astronautics, Vol. 94, edited by J. R. Bowen et al. (American Institute of Aeronautics and Astronautics, 1984), pp. 405-415.
6. F. E. Walker, A. M. Karo and J. R. Hardy, "Non-Equilibrium Effects Seen in Molecular Dynamics Calculations of Shock Waves in Solids," Proceedings of the NATO Advanced Study Institute on Nonequilibrium Cooperative Phenomena in Physics and Related Fields, edited by M. S. Velarde (Plenum Press, New York, London, 1984), pp. 363-370.
7. R. A. MacDonald and D. H. Tsai, Phys. Reports, Vol. 46, pp. 1-41, 1978.

DISCUSSION

DR. J. RITCHIE, Los Alamos National Laboratory

1. How do you obtain your potentials and how realistic are they?

2. How do changes in the potentials affect the results?

REPLY BY ARNOLD M. KARO

Two specific studies are presented in this contribution: shock loading and propagation in diatomic lattices and in disordered systems. The potentials used in the simulations are of the analytic form proposed by Morse with parameters chosen to correspond to the realistic frequencies and binding energies that would occur in condensed molecular systems. The effects we have discussed in the paper of course will depend quantitatively on the mass ratios chosen and on the binding forces. However, over large variations of the parameters describing the potentials the significant qualitative features will remain: for the diatomic lattice coherent and athermal lattice disruption with flux propagation mainly through the heavier sublattice; for the disordered system the disappearance of the sharp shock front found in ordered systems; and for all cases excitation of high-frequency intramolecular motions in sub-picosecond time intervals.

SIMULATION OF THE INITIATION OF DETONATION IN AN ENERGETIC MOLECULAR CRYSTAL: THE OVERDRIVEN CASE

S. F. Trevino
Energetic Materials Division, LCWSL, Armament Research and Development Center
Dover, New Jersey 07801

and

Reactor Radiation Division National Bureau of Standards
Gaithersburg, Maryland 20899

and

D. H. Tsai
Thermophysics Division, National Bureau of Standards
Gaithersburg, Maryland 20899

We have employed the method of molecular dynamics in a study of the detonation process in a model of a molecular crystal capable of undergoing exothermic reactions by dissociation. The model was initially heated at the boundary. Simultaneously it was subjected to shock compression by mechanical impact. Our results showed both thermally initiated and shock initiated reactions which combined to form a propagating reaction front, driving a shock wave ahead of it. The velocity of the reaction front depended strongly on the rate of energy transfer from the shock compresion to internal modes of the molecules. Under strong compression, the shock initiation time was short, and we obtained a steady detonation wave profile which corresponded to an overdriven case below the Chapman-Jouguet condition.

INTRODUCTION

Detonation in a chemically reactive system has been extensively studied from the viewpoint of continuum mechanics under the assumption of local equilibrium in all thermodynamic parameters except chemical compositon (1, 2). In a steady detonation wave, this means that various energy relaxation processes are assumed to occur at a rate at least equal to the local sound velocity. Pastine et al. (3), however, have pointed out that the average frequency of the intramolecular vibrations in a dense system may be expected to be much higher than that of the intermolecular vibrations, and consequently the relaxation processes for energy transfer between V-R, V-T and R-T (V = vibrational, R = rotational, T = translational) degrees of freedom should be rather slow. Assuming a constant relaxation time τ_R, Pastine et al. constructed a simple model of shock initiation of deontation which predicted an initiation time controlled by τ_R, in good agreement with the experiment for one material. But for a different material they obtained poor agreement.

The problems of energy relaxation are of very general interest in physics and chemistry. With the development of lasers, computers and chemical studies in the picosecond regime, studies of these problems have become active and interesting because it is now possible to investigate the energy transfer processes on the time scale of real chemical reactions. The initiation of detonation is of special interest because it is a limiting case of an extremely fast reaction, its

time scale (10^{-13} to 10^{-10} s) matches well the time scale of molecular dynamical (MD) computations. For these reasons, and in an attempt to develop further understanding of the problems of energy transport and energy sharing on a molecular scale, we have initiated an MD study of the initiation and propagation of detonation in a model of an energetic molecular crystal. In our first paper (4) we briefly reported on some MD results of thermally initiated reactions which produced an unsteady detonation wave. These results showed that for the case under consideration, the energy transfer processes were slower than shock propagation, in qualitative agreement with Pastine et al. The results also contained many details of the molecular motion and of the mechanisms of thermal as well as shock initiation. Moreover, the energy relaxation processes in our simplified model appeared to be consistent with those discussed by, for example, Nesbitt and Hynes (5), who studied the theory of vibrational relaxation of I_2 in liquid CCl_4. Thus we have been encouraged to extend the calculations to the case of an "overdriven" detonation wave at different piston velocities. In this report, we limit the discussion to the combined effects of heating and mechanical compression on the initiation process in our model.

MODEL

The chemical model used here was the same as that described in Refs. (6, 7):

$$A_2 \underset{k_2}{\overset{k_1}{\rightleftharpoons}} A + A + \text{energy}.$$

This model was chosen mainly for its simplicity, but as we showed in Refs. (6, 7), the dynamical characteristics of the model were well-behaved, whether the dissociation was exothermic or endothermic. The A atoms were considered to be independent particles interacting with one another through a compound Morse potential $V_1 - V_2$:

$$V_1 = \varepsilon \{\exp[-2a_1(R-R_1)] - 2\exp[-a_1(R-R_1)]\},$$

$$\text{for } R \geqslant R_{dis};$$

$$V_2 = b_2\, \varepsilon\{\exp[-2a_2(R-0.15R_1)]$$

$$-2\exp[-a_2(R-0.15R_1)]\} + Q\varepsilon, \text{ for } R<R_{dis}.$$

Here $R=R_{ij}$ is the separation distance between atoms i and j, ε is the unit of energy, $R_1 = 1.0$ is the unit of length, $a_1 = \ln 2/0.255$, $a_2 = \ln 2/0.05$, $b_2 = 0.4$, and Q, the exothermicity parameter, is 32. With these values, $V_1 = V_2$ at $R_{dis} = 0.2983$. When $R_{ij} < R_{dis}$, atom i forms a molecule with atom j and interacts with j through V_2. Once formed, bond ij is saturated, such that other neighbors k of atom i interact with i through V_1. When $R_{ij} \geqslant R_{dis}$, molecule ij is dissociated, i and j now interact also through V_1. The atomic mass, M, was taken to be unity and the unit of time τ to be $R_1(M/\varepsilon)^{1/2}$. The range of interaction (cutoff) for V_1 was set at $R = 1.2R_1$. At the cutoff, $V_1 = 0.8241\varepsilon$. The potential energy axis for both V_1 and V_2 was then shifted by this amount so that at $R \geqslant 1.2R_1$, $V_1 = 0$ and $\partial V_1/\partial R = 0$. We chose the parameters a_1, a_2, and b_2 so as to make the vibrational frequency of A_2 only slightly higher (by a factor of three or four) than the intermolecular frequency. This was done in order to increase the coupling of energy to the internal mode. This should make it easier for the reaction to occur and hence should shorten our model calculation.

As in Refs. (4) and (8), the system we studied here was a filament of bcc crystal of molecular A_2. The filament was made up with blocks of crystallites each with 4 X 4 X 4 unit cells, containing 128 molecules (256 atoms), and having periodic boundary conditions on opposite faces (see below). The crystalline axes were aligned in the Cartesian coordinates, and the filament was formed by joining the crystallites in the Z direction, the direction of propagation of detonation. The boundary condition at Z = 0 was that of a stationary mirror plane, the boundary conditions in the transverse X and Y directions were periodic. The crystallites in the filament were initially in thermal equilibrium. As the detonation moved into the filament from the mirror plane, the periodic boundary condition in the Z direction was not imposed on the various blocks between the mirror plane and the shock front. But beyond the shock front, the filament was not yet disturbed, so that it could be joined smoothly to a single block of crystallite still at equilibrium, through the periodic boundary in the Z direction. This block thus served to terminate the computation at each time step. As the shock front advanced, we would move this

block keeping it just ahead of the shock front. The decision as to when the block must be moved was dictated by the condition upstream (toward the mirror plane) of the terminating block. In order that the terminating block be a valid "periodic block" in the Z direction, the motion of the upstream particles within the cutoff distance from the terminating block must be identical to the motion of their respective periodic images inside the terminating block. As the shock front advanced, it would progressively disturb these particles, and the disturbance averaged over lattice planes would generally advance one plane at a time. Our criterion, therefore, was that if the average motion in the Z direction of the particles in the two farthest lattice planes (one unit cell) upstream has been disturbed beyond some small preassigned limit, but that the disturbance has not travelled farther downstream, we would move the *periodic boundary* downstream by one unit cell. In this way we were able to preserve the periodic condition of the terminating block, while at the same time ensure a smooth junction between the shock front and the terminating block. We were also able to effect considerable saving in computation which in turn allowed us to follow the detonation process for a longer time.

Prior to starting, the system was prepared in its meta-stable molecular form at a low temperature, with an average kinetic energy of around 0.25 ε per atom which was below the threshold of spontaneous dissociation. At starting time $\tau = 0$, the first six crystalline planes of the filament were rapidly heated to initiate dissociation reactions in these planes. This followed the same procedure as in Ref. (4), i.e., the heating was applied by scaling the velocities of the particles in these planes by a factor of 1.03526 per time step (at $\Delta\tau = 0.01$) for 80 steps. In addition to the initial heating at $\tau = 0$, we also imposed a mass average velocity of U_p on the whole filament toward the stationary mirror plane to simulate mechanical impact of the filament with its mirror image at $Z = 0$. Our problem was to follow the motion of all the molecules and atoms affected by these disturbances and thus obtain a detailed description of the initiation and the dynamics of the detonation process on a molecular scale. Our calculations were limited by the availability of computing facilities. The most extensive profile we have obtained thus far reached 360 planes into the filament and at that point the system contained approximately 14400 atoms.

RESULTS

Figs. 1a to 1c show the profiles of the average of the normal stress components along the filament at different times for three representative cases: In Fig. 1a the filament was stationary ($U_p = 0$) ahead of the shock front, in Fig. 1b U_p was -1.6 (in units of R_1/τ, the negative sign indicating that U_p was toward the mirror plane), and in Fig. 1c U_p was -2.4. The distance along the horizontal axis is expressed in number of lattice planes, N_a, from the mirror planes of the undisturbed filament. For the three cases here the interplanar distance was 0.5455 R_1. In effect, in these figures and in Figs. 2 and 3, we used the unit cell structure in the filament at $\tau = 0$ as a stationary reference coordinate system for monitoring the stress, density, and energy profiles, etc., as these evolved in time. The profiles at different times have been displaced in the vertical direction to show the details and the wave patterns in these profiles. We shall discuss these presently.

Figs. 2a to 2c are similar plots of the relative number density ϱ/ϱ_0 of the dissociated free atoms corresponding to Figs. 1a to 1c. ϱ_0 was taken to be the number density of the filament ahead of the shock front. These show the extent of the chemical reactions, averaged over lattice planes, as functions of distance and time.

Figs. 3a to 3c show further details in the profiles of the kinetic energies of the system at an arbitrarily selected time ($\tau = 21$ in these figures) for the three cases a, b, and c. The solid curves are the kinetic energy per degree of freedom averaged over all particles at each position, i.e., over all molecules and free atoms. The symbols show the partition into the T,R,V degrees of freedom of the average kinetic energy of the molecules. These figures correspond to the combined Figs. 1c and 1e* of Ref. (4). The stress and density profiles (Figs. 1a to 1c, 2a to 2c) correspond to Figs. 1a and 1b of Ref. (4).

*The vertical axes of Figs. 1c - 1e of Ref. (4) were incorrectly labeled: the scale was too large by a factor of 2. We regret this error.

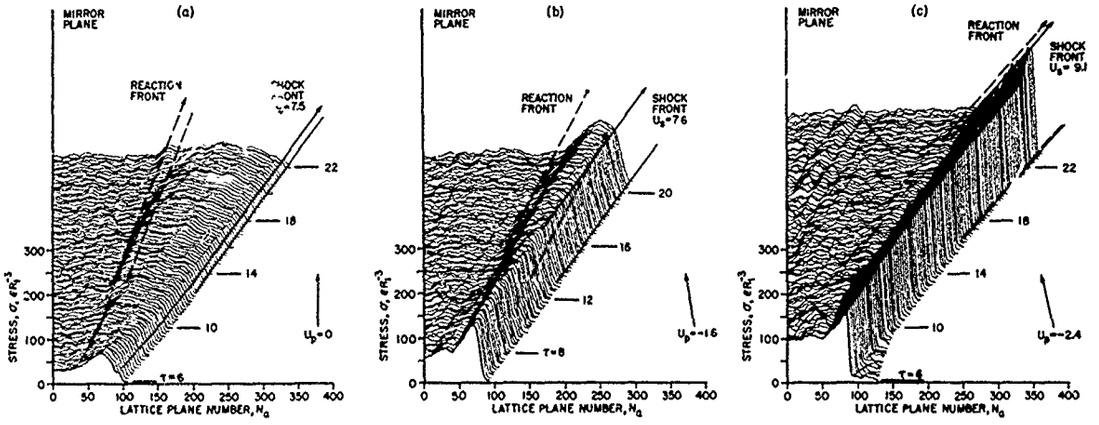

Fig. 1. Profiles of the average normal stress σ vs. distance form the mirror plane at different times τ resulting from the initiation of detonation under three different conditions. Distance is expressed in lattice plane number N_a of the undistrubed filament spaced at $0.5455R_1$ between lattice planes. The system was subjected simultaneously to initial heating (see text) and to mechanical compression from U_p. In (a), $U_p = 0$ and there was no mechanical compression; in (b), $U_p = -1.6\, R_1/\tau$; in (c), $U_p = -2.4\, R_1/\tau$. The data have been smoothed by averaging over neighboring plane: ± 3 planes in the shock front region and ± 6 planes behind the shock front; and over ± 15 time steps. Solid lines are the steady-state trajectories of the crest and the foot, respectively, of the shock front. Dashed lines are the corresponding trajectories of the reaction front obtained from Fig. 2. Velocities refer to the stationary mirror plane.

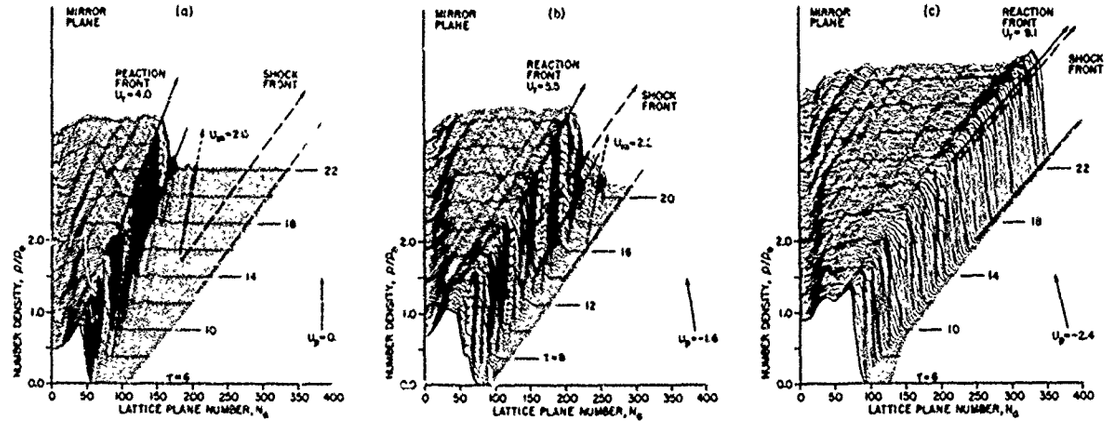

Fig. 2. Profiles of the density ϱ/ϱ_0 of the dissociated free atoms vs. distance in the three cases of Fig. 1. The data have been similarly smoothed by averaging over neighboring planes ± 2 planes ahead of the reaction front and ± 6 planes behind the reaction front, and overtime as in Fig. 1. Solid lines are the steady-state trajectories of the head and the foot of the reaction front. Dashed lines are the corresponding trajectories of the shock front obtained from Fig. 1. Dotted lines in (a) and (b) mark the trajectories of some local reaction sites initiated by shock compression. Velocities refer to the stationary mirror plane.

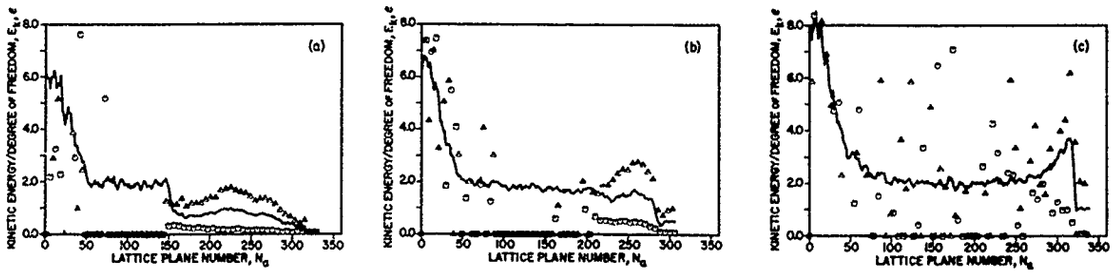

Fig. 3. Profiles of the average kinetic energy per degree of freedom E_k of the molecules and dissociated free atoms (heavy curve) in the three cases of Figs. 1 and 2, at $\tau = 21$. Local kinetic energies of the molecules in the T, R, V degrees of freedom are shown as individual points: $T = \Delta$, $R = \square$, $V = O$. The data have been smoothed by averaging over $\pm$ 2 neighboring planes. Some points have been omitted to reduce clutter.

In Figs. 1a to 1c (here) we have drawn straight lines through the first crest as well as the foot of the shock wave profiles after their propagation velocity had become steady. In Figs. 2a and 2c we have similarly traced out the propagation of the main reaction front. From these constructions, the velocities U_s of the shock front and U_r of the reaction front may be determined. The velocities shown in these figures, including U_p, were measured with respect to the stationary mirror plane. A simple coordinate transformation would refer these velocities to the filament ahead of the shock front. Note that although U_s and U_r appeared to be steady in these figures, we really do not have enough information at this time to determine their long-time behavior. For example, in Fig. 1a the amplitude of the stress at the shock front showed a steady decrease by about 16 percent with increasing time in the interval τ = 14-22. But beginning at τ = 21.2 some dissociaton occurred near the shock front (Fig. 2a), and how this should affect the steadiness of the shock front can only be determined with further calculation.

We now discuss the details of these figures. As mechanical compression (U_p) was changed, our results (Figs. 1a to 2c) showed that the stress level and the velocities of the shock front and those of the reaction front all increased with increasing mechanical compression. In the first two cases of lower U_p, U_r was slower than U_s so that these detonation profiles were not steady. But in the case of $U_p = -2.4$, U_r was the same as U_s, to within the accuracy of our data, and the detonation profile was steady. In this case the wavelets (sound waves) behind the reaction front appeared to travel at a lower velocity than the reaction front (i.e., the reaction front was supersonic with respect to the reaction products). Thus this case corresponded to an overdriven case below the Chapman-Jouguet point for this particular model (2). Between the mirror boundary and the reaction front the stress levels as well as the stress components (not shown here, but cf. Figure 1a, Ref. (4)) were well equilibrated except for the small wavelets already mentioned. Between the reaction front and the shock front the stress level was generally higher and the stress components were not equilibrated. Here the Z-component of the normal stress was higher than the X- and Y-components, showing the effect of shock compression. We shall return to this point later.

In Figures 2a to 2c we have practically only dissociated free atoms in the region between the mirror plane and the main reaction front. A few of these did occasionally recombine into short-lived molecules and their kinetic energies showed a wide scatter, Figs. 3a to 3c. The density immediately adjacent to the mirror boundary was low because of the initial heating. The thermal expansion of the suddenly heated region drove a shock wave into the filament. The heating also caused the affected molecules to undergo exothermic dissociation which in turn caused further heating and expansion of the reacted region as well as further dissociation of adjacent molecules. In this way the reacted region moved forward by *thermally initiated reactions*. The kinetic energy in the reacted region was well thermalized and the temperature was much higher than that ahead of the

shock front (e.g., Figure 3a). Between the reaction front and the shock front the density of free atoms dropped rather precipitously through the reaction front in Figure 2a, but the total density in this region (i.e., total number of particles of the undissociated molecules and free atoms, not shown here, but cf. Figure 1b, Ref. (4)) was considerably higher than the density in the region between the mirror boundary and the reaction front. This indicated that the hot, expanding region of reaction ws continuously compressing the unreacted region, rather similar to the compression from a moving piston. We see this clearly from the motion of the scattered reaction sites (see below) ahead of the reaction front in Figure 2a. A typical local mass average velocity U_m, of these reaction sites was about 2.0 R_1/τ, which was quite large. Note that in general this local mass average velocity was not uniform in this region. In Figure 2b a typical U_m was approximately 2.2 R_1/τ, larger in magnitude than the -1.6 from U_p. In Figure 2c U_m could not be measured, because the reaction front and the shock front were too close together, but compression from the reacted region was definitely taking place, as evidenced by the stress increase ahead of the reaction front. Thus, in all three cases we see that the expansion of the reacted region generated strong shock compression in the system, over and above the mechanical compression from U_p. The strength of this compression may be expected to depend on the exothermicity of the reaction, the velocity U_r of the reaction front, i.e., on the dynamics of the detonation process and the thermophysical propeties, e.g., thermal expansion, of the system. We hope to study these problems in the future.

The energy of compression from the reacted region on one side and from the mechanical compression of $-U_p$ on the other side did not immediately heat up the unreacted material. This may be seen especially clearly from Figure 3a which shows that the kinetic energies in the V and R degrees of freedom of the molecules were much lower than in the T degrees of freedom, the latter being mostly associated with the local mass average velocity U_m. This inefficient energy transfer was principally responsible for the delay in the initiation of dissociation reactions in this region. But in time some reactions did occur at a few scattered sites and these increased in size and moved with the local mass average velocity, as discussed above. These are the *shock initiated reactions*. Since U_m (in Figures 2a and 2b) was smaller tha U_r, these reaction sites were soon overtaken by the thermally initiated reaction front, and the interaction between the scattered reaction sites and the advancing main reaction front caused the structure of the latter to become somewhat irregular, and generated additional stress and density waves running toward the shock front and toward the mirror plane, in opposite directions, as seen in Figures 1a and 2a. The merging of the shock initiated reaction sites and the thermally initiated reaction front was equivalent to increasing locally the velocity U_r of the reaction front and hence the compression of the material ahead of the reaction front. With higher energy of compression, the induction time became shorter so that the shock initiated reaction now started sooner and grew more rapidly. This would also increase the velocity U_s of the shock front. In Figures 1a, 1b, 2a, 2b, $U_p = 0$ and -1.6, the system appeared to reach steady-state conditions, with U_r trailing U_s. But in Figures 1c and 2c, $U_p = -2.4$, U_r and U_s were the same. Note that in this case the structure of the reaction front (Figure 2c) had become relatively smooth, in contrast to the jagged structures in Figures 2a and 2b.

In Table I we summarize the characteristics of the three detonation wave profiles discussed above. The velocities M_p, M_s, and M_r refer respectively to the Mach numbers of the particle velocity of the reacted region, the velocity of the shock front and the velocity of the reaction front, relative to the unreacted material ahead of the shock front. M_m is the Mach number of some representative local mass average velocity of the material ahead of the reaction front. The longitudinal sound velocity ahead of the shock front was 9.4 lattice spacings per unit τ or 5.13 R_1/τ. The intervals of averaging refer to the distance in Figures 3a to 3c (at $\tau = 21$) over which the averages of density, stress and kinetic energy were taken, the second number in this range corresponds to the end position of the reaction front. The region near the mirror boundary affected by the initial heating was not included in this range. Within this range the normal stress components and the kinetic energies associated with the velocity components had equilibrated in all three cases. Both the number

TABLE I

Summary of the Characteristics of the Detonation Wave Profiles at τ = (Figs. 3a to 3c)

	Mach Number				Average values in the Reacted Region			
	M_p	M_s	M_r	M_m	Interval of Averaging	Density of Free Atom*	Stress (Pressure)* ε/R_1^3	Kinetic Energy* ε
Case a	0	1.47	0.78	0.39	60-145	0.72(.08)	28.5(8.)	5.81(.8)
Case b	0.31	1.79	1.38	0.74	60-190	1.10(.07)	73.5(10.)	5.44(.6)
Case c	0.47	2.24	2.24	- -	100-250	1.27(.08)	107.4(14.)	6.16(.7)

*The numbers in parentheses correspond to one standard deviation of the averages.

density and the pressure increased monotonically with higher compression (increasing M_p), but the kinetic energy actually suffered a small drop in case b. However, the difference was well within one standard deviation of the scatter of the data, and thus not considered to be significant. But further investigation, particularly of the exothermicity of the reaction under the dynamical condition of detonation, will be needed to determine how the temperature in this region changes with compression.

DISCUSSION AND CONCLUSIONS

In the foregoing discussions we have shown that the method of molecular dynamics provided a valid method for studying the detonation process and the details of the mechanism of initiation on a molecular scale. In our simplified model, the reactions were initiated by thermal conduction from the reacted region, by thermal expansion of the reacted region driving additional compression (shock) waves into the unreacted region and causing further reactions by shock heating, and by shock compression from mechanical impact (the piston problem). The transfer of energy between the translational and the internal degrees of freedom of the molecules was not efficient. In the case(s) of low compression, the induction time for dissociation was long, so that the reaction front propagated behind the shock front at a lower velocity and the detonation wave profile was not steady. In the case of high compression, the induction time was much shorter, the reaction front propagated closely behind the shock front at very nearly the same velocity, and the detonation wave profile appeared steady. Thus, the effect of shock compression, both from the expansion of the reacted region and from the mechanical impact, on the induction time plays a crucial role in the dynamics of the detonation wave. We shall need further investigations to determine whether or not these results also apply to other models and other systems.

To make these results more quantitative, we would have to have more detailed information on the rate of energy transfer and energy sharing between the T-V, T-R, and R-V degrees of freedom for the molecules as they undergo this kind of shock compression. This would presumably enable us to calculate the absolute reaction rate and hence determine the entire detonation wave profile under different conditions. This problem is difficult because we have a dense system here, and the non-linear, many-body interactions must be fully considered. Moreover, the large departure from local equilibrium resulting from shock compression, as shown in Figs. 3a to 3c, presents additional difficulties. To our knowledge, analytical solutions to these problems are not available at this time. But model study of the kind shown here and in Refs. (6, 7) appear to be capable of providing some information, especially on the problems of energy transfer. This kind of information from modeling should be useful for further development of theories. For example, since the equilibrium properties of our simple model are known or may be determined, as in Ref. (6), it should be instructive to compare the detonation profiles obtained from the equilibrium properties of the model with those obtained here under

non-equilibrium conditions. In addition, the details of the molecular motion and of the stress and energy profiles should be useful for studying such problems as the sensitivity of an explosive to external disturbances, the induction time, the effect of reaction volume, the net energy release from the reaction in dense sytems, etc.

On the minus side, there are, of course, also rather serious difficulties with modeling. For example, it would have been useful to extend our calculations to much longer times, by a factor of 10 or more, in order to investigate how the detonation process develops into a steady profile (Fig. 1c). But, we were not able to do this owing to inadequate computing facilities. More serious is the question that our present model was perhaps too simplistic and unreal. The $P\Delta V$ term was positive and rather too large, so that the reaction rate must have been greatly reduced by increasing pressure. A more realistic model would be

$$2AB = 2A + 2B - \text{energy}$$

$$A+A = A_2 + \text{energy}$$

$$B+B = B_2 + \text{energy}$$

---

giving $2AB = A_2 + B_2 + \text{energy}.$

In these reactions, the dissociation of AB into A + B would be endothermic, but the combining of the "free radicals" A and B to form A_2 and B_2 would be highly exothermic. In addition to being more realistic as a model for an energetic chemical reaction, the sign and the magnitude of the $P\Delta V$ term could be adjusted by suitable adjustment of the potential so that the effect of pressure on the reaction rate could be investigated. We plan to study some of these problems in the future.

REFERENCES

1. W. Fickett and W. C. Davis, "Detonation," (University of California, Berkeley, 1979), and references therein; S. A. Sheffield, D. D. Bloomquist, and C. M. Tarver, J. Chem. Phys. *80*, 3831 (1984), and references therein.
2. J. O. Hirschfelder, C. F. Curtiss, and R. B. Bird, "Molecular Theory of Gases and Liquids," (Wiley, New York, 1954), Chapt. 11.
3. D. J. Pastine, D. J. Edwards, H. D. Jones, C. T Richmond, and K. Kim, in 'High Pressure Science and Technology," edited by K. D. Timmerhaus and M. S. Barber (Plenum, New York, 1979), Vol. 2.
4. D. H. Tsai and S. F. Trevino, J. Chem. Phys. *81*, 5636 (1984).
5. D. J. Nesbitt and J. T. Hynes, J. Chem. Phys. *77*, 2130 (1982).
6. D. H. Tsai and S. F. Trevino, J. Chem. Phys. *79*, 1684 (1983).
7. S. F. Trevino and D. H. Tsai, J. Chem. Phys. *81*, 248 (1984).
8. D. H. Tsai and R. A. MacDonald, Phys. Rev. *B14*, 4714 (1976); High Temp. High Pressures, *8*, 403 (1976); D. H. Tsai and S. F. Trevino, Phys. Rev. *A24*, 2743 (1981).

DISCUSSION

JAMES P. RITCHIE, Los Alamos National Laboratory

1. What are your comments regarding the hydrodynamic prediction of periodic data waves rather than stable waves?
2. What are your boundary conditions? Please bear in mind that explosives show a finite failure diameter.

RELY BY T. TREVINO AND D. TSAI

1. Although the model used in the present work should be capable of addressing this question, the time scale of the calculation (due to limited computer resources) is too short to allow the detection of this phenomena.
2. The boundary condition in the direction perpendicular to the propagation of the disturbance (shock and reaction) are periodic thus simulating a semi-infinite state of material. The question of failure diameter is thus not addressed.

Session IX
Specialist Session

SHOCK-TO-DETONATION TRANSITION/ DEFLAGRATION-TO-DETONATION TRANSITION

Co-chairmen: Peter R. Lee
Royal Ordnance Ammunition
Milton Finger
Lawrence Livermore National Laboratory

COMPRESSIVE REACTION IN POROUS BEDS OF ENERGETIC MATERIALS

H. W. Sandusky and R. R. Bernecker
Naval Surface Weapons Center
White Oak
Silver Spring, Maryland 20903-5000

The rapid growth of reaction that occurs in the final stages of deflagration-to-detonation (DDT) transition in porous materials is initiated by high strain rate deformation within a strong compressive wave. To study the compressive reaction mechanism, porous beds of various energetic materials were radially confined and subjected to a long duration (>200 μs), low-level shock loading (<180 MPa). For loadings which exceeded the reaction threshold (13-76 MPa), the time delay for detecting reaction appeared to be inversely proportional to the square of the average material stress. Somewhat higher loadings (35-108 MPa) resulted in rapid growth of reaction for those materials without an inert binder. In high confinement tubes the rapid growth of reaction would build to detonation. Higher loadings were required for a transition in low confinement tubes. Relatively long run distances to detonation (36-140 mm) reasonably agree with extrapolation of higher pressure data found in the literature for several porous materials.

INTRODUCTION

Compressive reaction, as used here, refers to the onset and subsequent growth of reaction caused by high strain rate deformation of the energetic material. Such a reaction mechanism occurs in drop-weight impact, projectile impact, and dynamic compaction of porous beds. In these experiments, the threshold of reaction occurs for similar bulk rates of deformation (80-200 m/s) for a variety of materials (1). When a pressure gradient exists, such as the radial pressure during drop-weight impact, threshold reaction occurs in the low pressure zone where the deformation is the greatest; therefore, it appears that the primary role of pressure is to drive the deformation. Of interest to this paper is the reaction that occurs from dynamic compaction of porous beds and how that relates to the rapid pressure buildup in the final stages of DDT.

During the DDT process for porous columns, the accelerating conductive/convective burning at the ignited end leads to the propagation of compressive (compaction) waves into the unreacted material. Near the zone of burning, the increasing pressure gradually compacts the bed; however, further down the porous column the compressive waves are coalescing, resulting in a much more rapid rate of compaction. The high rate of bulk deformation will generate hot spots from friction between particles, plastic deformation of and shear banding within particles, cracking of brittle particles, and possibly gas compression. If the temperature and size of the hot spots are sufficient, ignition will occur after some delay. The continued growth of reaction will itself drive compressive waves into the bed which strengthen the compaction front, resulting in a reduced ignition delay and more vigorous ignition at points further downstream.

Within the limitations of confinement, the compaction front can develop into a shock of sufficient intensity for shock-to-detonation transition (SDT), the final stage of DDT. In DDT studies at this Center (2), for example, very porous beds of a number of energetic materials transited to detonation within the relatively low confinement of plastic tubes. This indicates for these materials both their sensitivity to the onset of compressive reaction and the subsequent rapid growth of reaction that must occur in order to avoid failure from loss of confinement.

The objectives of this experimental study of compressive reaction are to determine for various energetic materials 1) the reaction threshold, 2) the growth of reaction, and 3) the propensity to detonate as a function of initial compaction parameters, bed properties, and confinement. In earlier work, Leroy Green presented (3) compressive reaction data for a granulated propellant that was ramp loaded, similar to the pressure loading that occurs during DDT. In order to avoid the uncertainty of what pressures during ramp loading are associated with the reaction, the approach of the present study has been to drive relatively constant pressure waves into confined porous materials by impacting them with a long projectile. As compared to typical SDT studies, the driving pressures are low (<180 MPa) and maintained for a relatively long duration (<200 μs).

DESCRIPTION OF THE EXPERIMENTS

The experimental arrangement uses a powder gun to propel a 25.4 mm diameter by 305 mm long piston into the tube that contains the porous bed. The schematic of the apparatus shown in Figure 1 is a recent version used in most of the reported experiments. The muzzle end of the barrel has a replaceable extension that is damaged by violent bed reactions; one end of the extension screws into the barrel while the other end is clamped to the confining tube. Slots in the barrel extender serve several purposes, one of which is to vent the air between the piston and the porous bed. Air injection into the bed is further prevented by a disk (usually a 0.8 mm thickness of plastic) which covers the end of the bed; that disk also keeps the bed from spilling or springing out of the tube during setup. Another purpose of the slots in the barrel

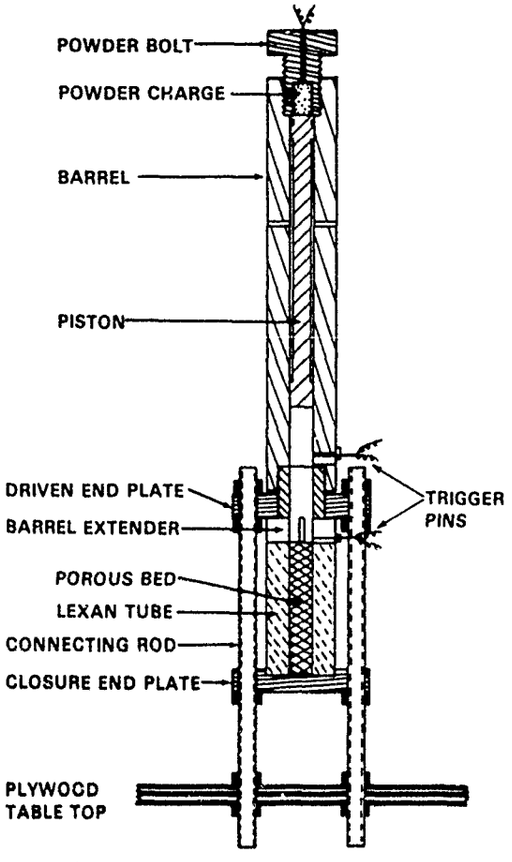

Fig. 1. Schematic apparatus for piston impact of porous energetic materials

extender is to permit photographic measurements of the piston velocity before and after bed impact. This is accomplished by backlighting the slotted region and using a transparent piston (Lexan 101-111) which is circumferentially scribed at several positions. In some experiments, the piston velocity prior to bed impact, v_p, was determined from the elapsed time between the responses of an optical switch about 18 mm from the end of the bed and a shorting switch on the disk that covers the end of the bed; the piston velocity after bed impact was determined from flash radiographs in this situation.

Four different confining tubes were used; all had an inner diameter only slightly larger (generally <0.1 mm) than the piston to avoid extrusion of bed material between the piston and the tube. A thick (~25 mm) wall Lexan tube, as shown in Figure 1, was used for low confinement

TABLE 1
Description of Porous Bed Materials

Material	Ingredients[a]	TMD[b] (g/cm^3)	Average Particle Size (mm)
Tetryl		1.73	0.470
HMX, Class D		1.903	0.870
HMX, Class E		1.903	0.015
PBXW-108(E)	RDX/Inert binder	1.555	2.17 (cubes)
PBXW-109(E)	RDX/Al/Inert binder	1.655	2.17 (cubes)
WC 231[c]	NC/NG (~75/25)	1.64	0.79 dia. x 0.23 thick (disks)
HEP "X"[d]		1.88	0.5 x 1.6 x 25 (rough shreds)
HEP "Y"	Al/AP/Energetic	1.895	1.3 dia. x 1.3 long casting powder
HEP "Z"	binder/HMX/NG	1.84	0.8 x 2.5 x 1.6 (short shreds) 6.4 (long shreds)

[a] Al = aluminum; AP = ammonium perchlorate
NC = nitrocellulose; HMX = cyclotetramethylenetetranitramine
NG = nitroglycerin; RDX = cyclotrimethylenetrinitramine
[b] Theoretical maximum density
[c] Commercial reloading powder
[d] HEP = high energy propellant

experiments involving high speed photography of luminous reaction and, sometimes, flash radiography of bed compaction. Early in the study, bed compaction was measured by backlighting the tube and photographing the motion of transparent disks within the bed; however, this was abandoned because the disks perturbed the growth of compressive reaction. Some observations of compressive reaction were made with an intermediate confinement apparatus designed for one-dimensional compaction measurements. In this apparatus, there is a thin (~3.2 mm) wall aluminum tube with lengthwise steel supports over half of the outer wall; the primary instrumentation is radiography of the core of the porous bed (4). When high confinement was required, a thick (~25 mm) wall steel tube was used with ionization and self-shorting probes for recording progress of the compaction/reaction front. If detonaton occurred in these tubes, the appearance of the inner wall of the tube fragments was often used in locating the onset of detonation. One tube of a high strength steel (HSS, hardened 4340) was used because of the suspicion that even a regular steel tube provided marginal confinement in some experiments.

The porous bed materials are described in Table 1. Those materials were weighed out for increment heights of 6.4 or 12.7 mm, poured into the confining tube, and then hand pressed to stops. This provided relatively uniform density for the entire bed length, generally ~140 mm. In preparation for flash radiography measurements, small metallic tracers were placed between the bed increments.

PRESENTATION OF DATA

A summary of the initial conditions and results for each experiment appears in Table 2. The compaction parameters (u, U, %TMD, and τ_i) are based on measurements near the impacted end of the bed in an effort to avoid the influence of reaction. The particle velocity, u, was the most readily measured parameter, often being equated with the piston velocity immediately following impact. The compaction front velocity, U, and the extent of compaction, %TMD, were often measured; the measurements of %TMD consistently agreed (±2%) with the jump condition calculation

$$\%\text{TMD} = \frac{\%\text{TMD}_o\, U}{U - u} \quad .$$

When measurements of U and %TMD were not obtained or reaction had obviously influenced the measurements, the %TMD was assumed and U was calculated from from the above equation. When %TMD was not assumed, the calculated %TMD is tabulated since compaction

TABLE 2

Summary of Compressive Reaction Experiments

Initial Conditions					Results							
Shot PDC-	Mat'l	%TMD$_o$	Tube*	v_p (m/s)	u (m/s)	U (m/s)	%TMD	P (MPa)	τ_i (MPa)	Δt (μs)	Reaction Growth+	x_D (mm)
13	Tetryl	57.8	L	190	149	380	95.1	56.7	59.6	163	None	f
57				~290	-	-	-	-	-	-	Vig.	36
21			L	74	55	300	89.4	23.0	25.7	f[b]	f[b]	f[b]
25			L	102	76	359	92.6	37.9	41.0	394	Weak	f
54	HMX	73.0	Al	116	80	393	91.8	43.7	47.7	f	f	f
22	Class D		L	125	102	438	95.2	62.1	65.2	117	Weak	f
59			S	223	144	540	99.5	108.0	108.5	<42	Vig.	39
27			L	267	161	775	92.1	173.2	187.9	~21	Vig.	50
39			S	200	160	360	79.4	48.5	61.0	<215	Sudden	81
58	HMX	44.1	Al	202	180	387	82.5	58.6	71.0	f	f	f
46	Class E		L	216	170	362	83.1	51.8	62.3	215	None	f
50			L	308	252	494	90[a]	105	116	52	Sudden	40
29	PBXW-	75.0	L	134	112	375	101.1	47.7	47.7	f	f	f
30	108(E)			260	151	457	100.8	76.3	76.3	167	None	f
20			L	75	61	276	94.3	20.8	22.0	f	f	f
23			L	128	102	364	98.3	44.8	45.6	<361	None	f
26	PBXW-	75.0	L	178	117	404	96.2	56.0	58.3	<258	None	f
31	109(E)		L	280	175	477	103.8	96.9	96.9	-	None	f
42			Al	~270	159	602	101.9	118.9	118.9	<156	Mod.	f
12		49.4		120	104	313	74.0	26.5	35.8	511	Weak	f
4	WC 231	50.0	L	~190	-	-	-	-	-	-	Vig.	f
60		49.4		380	310	669	92.1	168	182	31	Vig.	84
18		58.5		165	150	360	100[a]	59	59	20	Vig.	50
14	HEP "X"	58.5	L	200	180	430	100[a]	89	89	5	Vig.	55
15		74.5		~190	~180	710	100[a]	178	178	-	Vig.	39
52		64.4	Al	76	59	364	76.8	26.3	34.2	<262	Weak	f
55		64.4	Al	137	118	448	87.4	64.6	73.9	<121	Mod.	f
40	HEP "Y"	64.9	L	192	131	460	90[a]	74	82	18	Mod.	f
43		64.9	S	219	160	497	95[a]	98	103	<64	Vig.	140
47		64.9	S	284	194	545	100[a]	130	130	<20	Vig.	132
34			L	75	68	167	100.9	12.6	12.6	579	Weak	f
36			L	103	86	213	100.3	20.3	20.3	320	Weak	f
35			L	129	113	280	100[a]	34.9	34.9	36	Vig.	f
38	Short Shreds		S	130	113	280	100[a]	34.9	34.9	<81	Vig.	127
37			L	~270	-	-	-	~120	-	-	Vig.	f
44	HEP "Z"	59.8	S	~270	-	-	-	~120	-	<15	Vig.	76
48			HSS	294	-	-	-	~130	-	<20	Vig.	73
32	Long Shreds		L	270	210	520	100[a]	120	120	~9	Vig.	f
33			L	270	200	500	100[a]	110	110	~9	Vig.	f

See Nomenclature for parameter definitions

* Thick wall tubes: L = Lexan, S = Steel, HSS = High strength steel; Al = Thin wall aluminum tube with steel supports

\+ Vig. = Vigorous, Mod. = Moderate

[a] Assumed %TMD used in calculations for U, p, & τ_i

[b] f = Failure

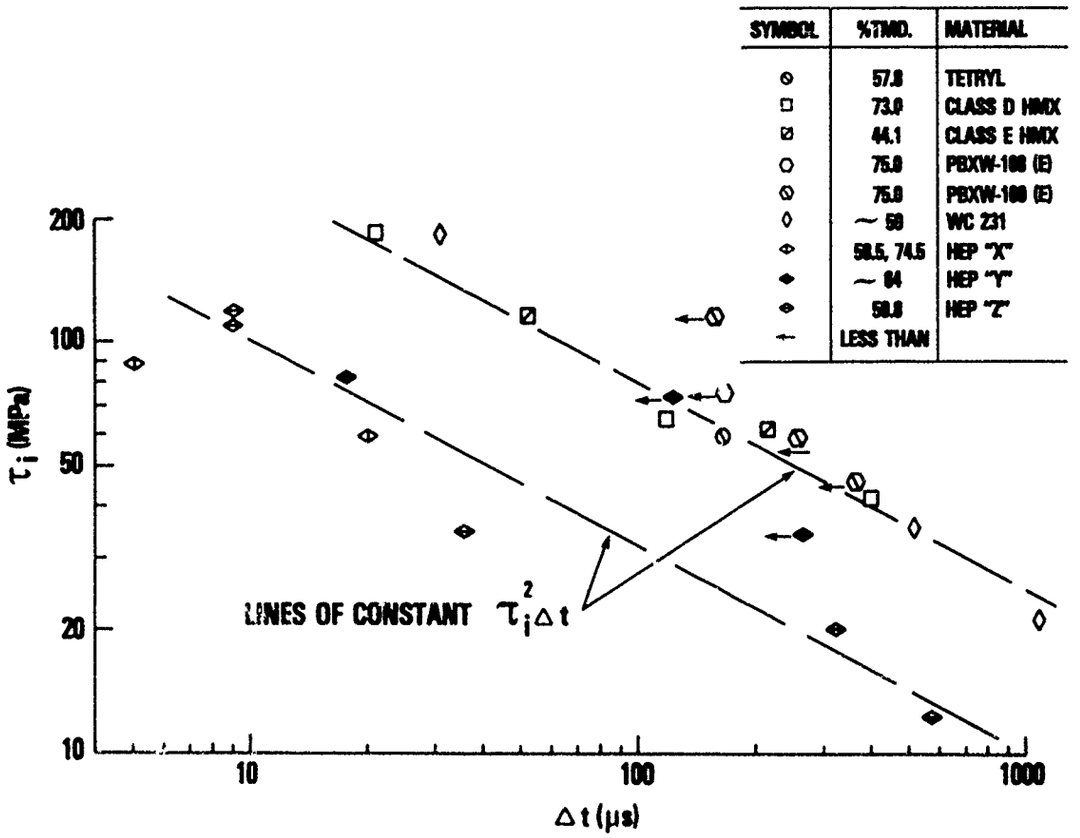

Fig. 2. Average solid stress versus time for detection of reaction

pressure, p, was obtained solely from the jump condition calculation

$$p(\text{MPa}) = p_0 + 10^{-5}\text{TMD}\ \%\text{TMD}_0\ Uu$$

where $p_0 = 0.1$ MPa and both velocities are in units of m/s. The compaction parameter correlated with the threshold of reaction is the average solid stress:

$$\tau_i = \begin{cases} 100\ p/\%\text{TMD}, & \%\text{TMD} < 100 \\ p, & \%\text{TMD} > 100. \end{cases}$$

For the Lexan tube experiments with PBXs, corrections to %TMD, p and τ_i for tube expansion were based on strain gage measurements (4). The same reference contains more detailed data for dynamic compaction of all materials, except for the HEPs.

Reaction commences with the generation of hot spots by the compaction process, but there is a time delay, Δt, between bed impact and the detection of that reaction. "Ignition" will not be associated with the detection of reaction (as done in Ref. 5) since it does not necessarily spread to the material surrounding the hot spots, as will be discussed later. The values for Δt in Table 2 are based usually on first reaction light on a camera film in low confinement experiments, changes in bed density in intermediate confinement experiments, and probe responses and changes in piston velocity in high confinement experiments. In low confinement experiments with continuous camera coverage, reaction was usually detected first at the driven end of the bed. However, this was often not the case for beds of fine particles or beds that were highly compacted, probably because the pores were too small for the hot luminous gases to expose the camera film.

In order to establish the threshold for reaction, data is tabulated also for experiments in which no reaction was detected within the time frame of the experiment. For the various

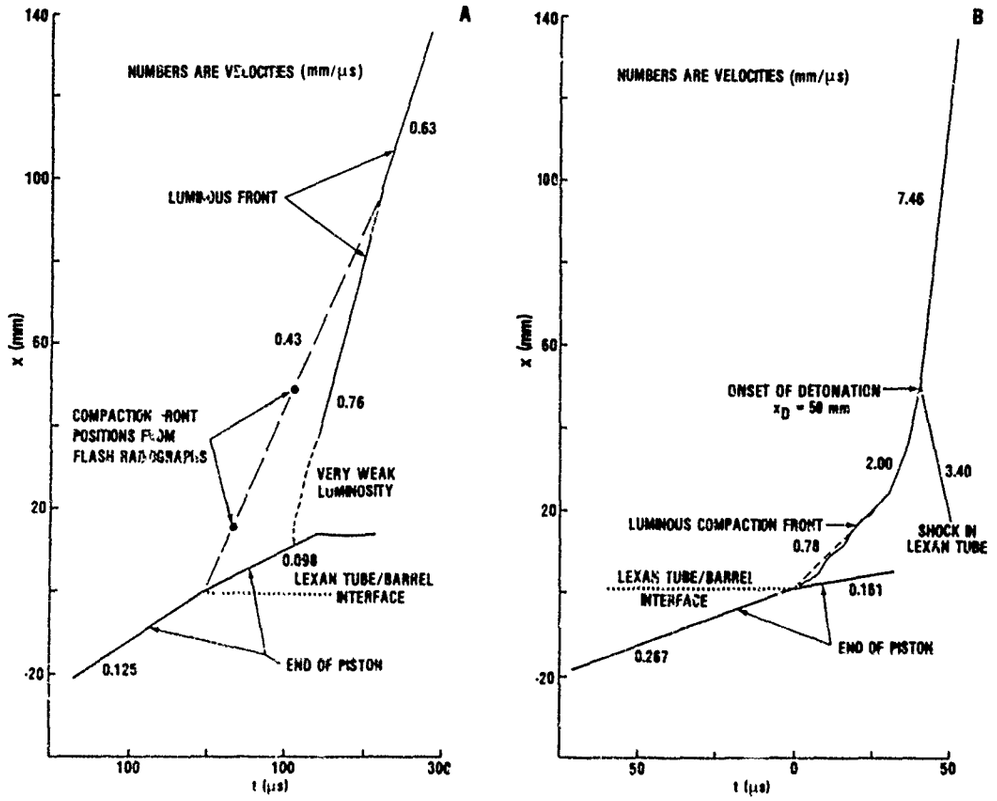

Fig. 3. Distance-time data for piston impact of 73 %TMD Class D HMX. a. Shot PDC-22, b. Shot PDC-27

materials examined, the threshold ranges from bed pressures of 12.6 to 76.3 MPa and particle velocities of 59 to 151 m/s. Because of the relatively low pressures, confinement should not appreciably affect the threshold; however, for mild impacts of Class D and Class E HMX, reaction seemed less likely to occur in intermediate confinement as compared to low and high confinement. This may be due to a carbon gage package on the end of those beds.

For conditions which exceed the threshold of reaction, it is of interest to correlate Δt with a compaction parameter in order to evaluate the time frame for participation of compressive reaction in DDT. One such correlation which is somewhat material independent is made with τ_i in Figure 2. The plot does not contain high confinement data because of the uncertainty in Δt; low confinement data for the PBXs and intermediate confinement data are plotted with left going arrows to indicate that Δt is less than that shown. In addition to the data in Table 2, there is a WC 231 datum (τ_i = 21.5 MPa, Δt = 1090 μs) from a gas driven compaction experiment, Shot CGC-23 (5). Two lines corresponding to constant $\tau_i^2 \Delta t$ are drawn on the plot; one line is characteristic of the explosives and WC 231, while the other line is characteristic of the HEPs. The relationship between Δt and τ_i is somewhat subjective in view of the difficulties of detecting reaction

After the detection of reaction, its growth varied considerably as described in Table 2. Near the reaction threshold there was sometimes no evidence of reaction growth ("none") or no significant acceleration of the reaction front ("weak"). The data in Figure 3a for Shot PDC-22 is an example of "weak" reaction growth. In that experiment, a weakly luminous, 760 m/s reaction front overtook the initial

438 m/s compaction front and produced a steady 630 m/s reaction front which propagated through the remaining 27 mm of the bed. In contrast to this, the data in Figure 3b for a higher velocity piston impact on the same material illustrates "vigorous" growth of reaction. The luminous, 2000 m/s reaction front, which breaks away from the compaction front, is accelerating; it is postulated that a "nonluminous" reaction front originated at the driven end and overtook the compaction front when the 2000 m/s front first appears. Vigorous reaction does not always transit to detonation because of bed length and confinement limitations. When loss of confinement appears to limit reaction buildup, those experiments are listed in Table 2 as having "moderate" growth of reaction. In two fine (Class E) HMX experiments, the reaction growth is listed as "sudden" because the onset of detonation was nearly coincident with the first detection of reaction.

Both "vigorous" and "sudden" growth of compressive reaction will transit to detonation in <100 μs given adequate confinement; therefore, the thresholds for these categories of reaction rate correspond to the onset of the final stages of DDT. Within the limitations of these experiments, each material exhibited rapid growth of compressive reaction except for the PBXs (probably because they contain an inert binder). The threshold for rapid growth of compressive reaction in the non-PBXs ranged from compaction pressures of 35 to 108 MPa and particle velocities of 113 to 160 m/s. Low confinement did not appear to raise the threshold for rapid growth of compressive reaction, anymore than the threshold for reaction, except for the materials which are relatively insensitive to compressive reaction (the PBXs) or resistant to compaction (HEP "Y"). For these materials, the compaction pressures for the threshold of rapid reaction are high enough (≥100 MPa) to cause substantial yielding of a Lexan tube.

For those experiments in which detonation occurred, the total buildup distance, x_D, is listed in Table 2. The smaller x_D measurements in steel (versus Lexan) tubes for coarse HMX and HEP "Z" demonstrate that low confinement delayed the onset of detonation in these materials. Although even steel tube confinement was suspected of delaying detonation in HEP "Z" (Shot PDC-44), the use of a higher strength steel tube in Shot PDC-48 resulted in no discernible reduction in x_D. The plots of x_D versus p and u in Figure 4 include data from Table 2 as well as from the literature for 75.1% TMD tetryl (6), 65.2 %TMD Class A HMX (7), and a HEP designated as Propellant B (8). For comparison, data are plotted also for essentially TMD samples of tetryl (6), HMX (9), and a typical HEP (9). In plotting x_D versus p, there is a band of data characteristic of the porous materials that is considerably different from the essentially TMD materials. Although the data in Table 2 for x_D are relatively accurate, ±3 mm, the pressures are less certain since the values of U used in calculating p in detonating experiments often had to be estimated because of the rapid onset of reaction. Partly because of this uncertainty in p, a logarithmic plot of x_D versus the most directly measured compaction parameter, u, is shown in Figure 4b. In this plot, the data for both the porous and essentially TMD materials fall within a band of constant slope.

DISCUSSION

The experimental observations are consistent with a model for shock initiation of porous explosives (10) that basically involves creation of hot spots by the compaction process, decomposition of the material in the hot spots, and then grain burning of the remaining material. For those experiments described as having "none" or "weak" reaction growth, there was probably a low concentration of spots with temperatures barely sufficient for reaction, and even then, the chemical heat release at those spots was strongly competing with heat conduction to the surrounding, cooler material. For the other categories of compressive reaction, there apparently was significant reaction within the hot spots near the impacted end of the bed, but that reaction did not quickly involve the surrounding material. Instead, compressive waves driven by that reaction coalesced with the compaction front, which now created "hotter" spots with higher reaction rates, as indicated in Figure 2 by the reduction in Δt for an increase in τ_i. It appears that these "hotter" spots ignite the grain burning of the surrounding material, which causes the pressure buildup to accelerate rapidly For those experiments described as having "moderate" reaction growth, the onset

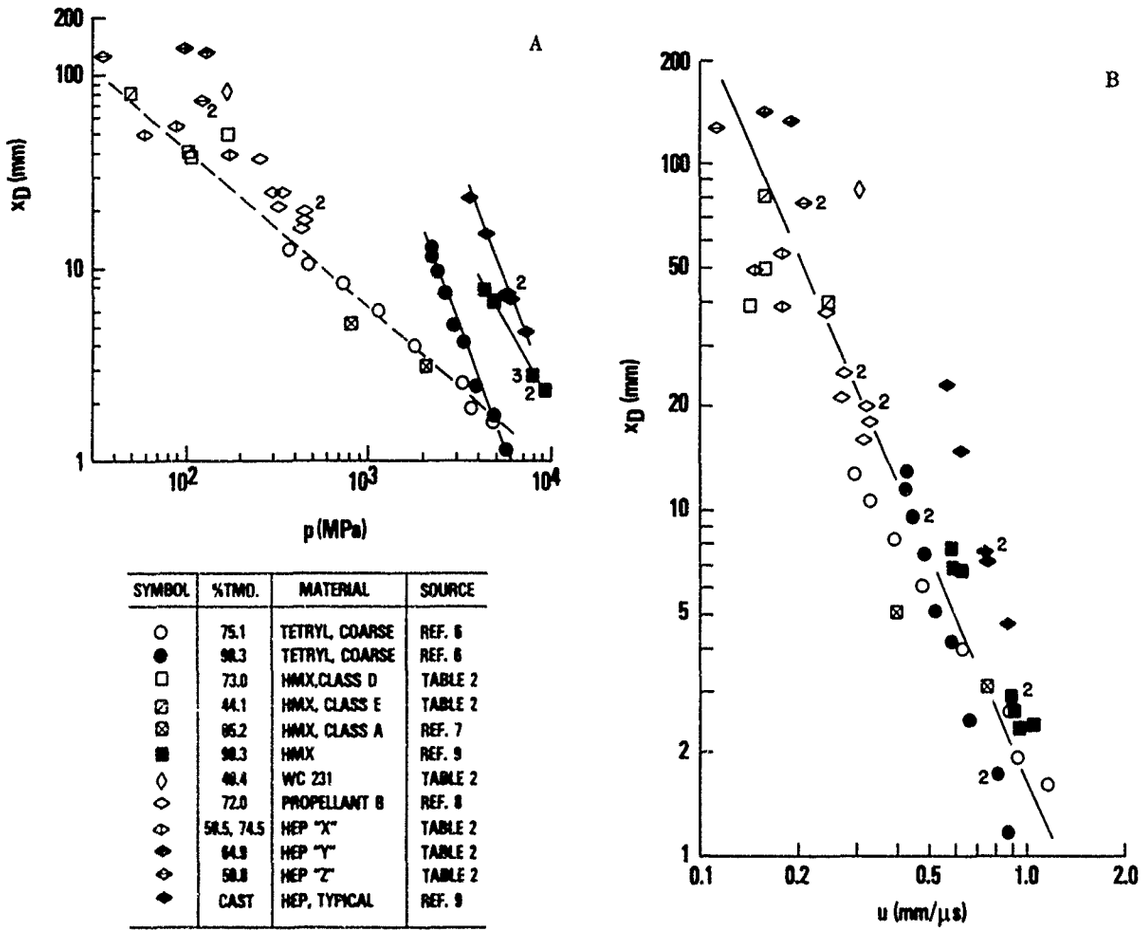

SYMBOL	%TMD.	MATERIAL	SOURCE
○	75.1	TETRYL, COARSE	REF. 6
●	98.3	TETRYL, COARSE	REF. 6
□	73.0	HMX,CLASS D	TABLE 2
▨	44.1	HMX, CLASS E	TABLE 2
⊠	95.2	HMX, CLASS A	REF. 7
■	98.3	HMX	REF. 9
◊	48.4	WC 231	TABLE 2
◇	72.0	PROPELLANT B	REF. 8
◈	58.5, 74.5	HEP "X"	TABLE 2
◆	64.9	HEP "Y"	TABLE 2
◈	58.8	HEP "Z"	TABLE 2
◆	CAST	HEP, TYPICAL	REF. 9

Fig. 4. Distance to detonation data. a. Pressure dependence, b. Particle velocity dependence

of grain burning perhaps occurred, but the pressure buildup from reaction was negated by the loss of confinement. Both "vigorous" and "sudden" growth of reaction should involve extensive grain burning, the difference being the higher concentration of "hotter" spots and the greater surface area available for grain burning in the "sudden" reaction growth of fine HMX. Also, a difference in the mechanism for hot spot generation may be occurring (e.g., friction versus shear banding).

Those materials which transited to detonation in low confinement — HMX, tetryl, WC 231 and HEP "X" — also detonated in low confinement DDT experiments at this Center (2, 11, 12). Whereas tube expansion in low confinement experiments resulted in a two-dimensional buildup process, the high confinement experiments may be viewed as a technique for studying one-dimensional buildup of weak shocks to detonation. The critical condition for initiation of detonation in high confinement is equivalent to the threshold of rapid growth of reaction. For the various materials without an inert binder, that threshold occurred for a narrow range of particle velocities (113-160 m/s) relative to the corresponding range of compaction pressures (35-108 MPa). Roth (13) suggested that a relatively narrow range of particle velocities defined the critical conditions for SDT in gap and wedge tests on various densities of RDX, PETN, HNS and tetryl. Whereas the critical pressures ranged by a factor of ten (0.25-2.5 GPa), the critical particle velocities ranged by a factor of two (260-560 m/s). The higher particle velocities and pressures required for typical SDT studies versus the experiments reported here are due to the shorter run distances to

detonation and the narrow pulse width of the initiating shocks.

The logarithmic plot of x_D versus p in Figure 4a is a typical method of presenting shock initiation data (14), in which straight line representations of the data are used. The straight line through the porous data is based on the data of Lindstrom for 75 %TMD tetryl (6). A frequently considered question is whether a straight line representation is valid at large x_D values (i.e., lower pressures), or whether the data will show a concave upward curvature as a failure threshold is approached. The new data reported here suggests such a curavture; however, experimental uncertainty in pressure or inadequate confinement may be responsible for this trend. Hence, future work will be directed toward removing these uncertainties and addressing the adequacy of a straight line representation out to very long distances to detonation.

SUMMARY AND CONCLUSIONS

The threshold for compressive reaction for various porous materials ranged from 12.6 to 76.3 MPa, pressures which could be easily attained in a mishap. Beyond threshold conditions, the time for detection of reaction was inversely proportional to the square of the average solid stress. A somewhat higher range of pressures, 35 to 108 MPa, initiated rapid growth of reaction in all of the materials tested except the two with inert binders. With high confinement, the rapid growth of reaction would build to detonation in less than 100 μs. With low confinement, higher compaction pressures were required to achieve detonation; even then, some materials failed to transit. Those materials which detonated in low confinement, also experienced DDT in low confinement experiments at this Center. The threshold for rapid growth of reaction occurred over a narrow range of particle velocities (113-160 m/s); a relatively narrow, but higher, range of critical particle velocities (260-560 m/s) was reported for SDT in gap and wedge tests (13). The run distances to detonation measured in this study are long (36 to 140 mm) relative to those in typical SDT studies, but there is fair agreement with a linear extrapolation of data in the literature for SDT in porous materials. The experimental data support a model in which hot spots are generated by the compaction process, the reaction is at first isolated to the hot spots, and then spreads to the surrounding material.

ACKNOWLEDGMENTS

The efforts of A. R. Clairmont, Jr., Carl Groves and Brian Glancy in assisting with or conducting various aspects of the experiments are greatly appreciated. The machining of hardware by Bill Freeman and the electronics support by Nick Vogle are equally appreciated.

NOMENCLATURE

%TMD	volume percentage of a porous bed occupied by the energetic material
p	pressure
u	particle velocity
U	compaction front velocity
v_p	piston velocity just prior to bed impact
x_D	distance to detonation
Δt	time between bed impact and detection of reaction
τ_i	average solid stress
subscript "o"	initial conditions

REFERENCES

1. H. W. Sandusky, C. S. Coffey and T. P. Liddiard, "Rate of Deformation as a Measure of Reaction Threshold in Energetic Materials," Mechanical Properties at High Rates of Strain, pp. 373-380, The Institute of Physics, Bristol, 1984.
2. R. R. Bernecker, H. W. Sandusky and A. R. Clairmont, Jr., Deflagration-to-Detonation Transition Studies of Porous Explosive Charges in Plastic Tubes," Seventh Symposium (International) on Detonation, pp. 119-138, NSWC MP 82-334, 1982.
3. L. G. Green, E. James, E. L. Lee, E. S. Chambers, C. M. Tarver, C. Westmoreland, A. M. Weston and B. Brown, "Delayed Detonation in Propellants from Low Velocity Impact," Seventh Symposium (International) on Detonation, pp. 256-264, NSWC MP 82-334, 1982.

4. H. W. Sandusky and T. P. Liddiard, "Dynamic Compaction of Porous Beds," NSWC TR 83-246, 26 Dec 1985.

5. H. W. Sandusky, "Compressive Ignition and Burning in Porous Beds of Energetic Materials," Proceedings of the 3rd JANNAF Propulsion Systems Hazards Meeting, pp. 249-257, CPIA Publ. 381, Vol. 1, 1983.

6. I. E. Lindstrom, "Plane Shock Initiation of an RDX Plastic-Bonded Explosive," J. Applied Physics, Vol. 37, No. 13, pp. 4873-4880, Dec. 1966.

7. J. J. Dick, "Measurement of the Shock Initiation Sensitivity of Low Density HMX," Combustion and Flame, Vol. 54, pp. 121-129, 1983.

8. E. L. Lee, E. James, L. Green, W. VanHolle, C. Tarver, D. Curran, W. Murri, and D. Seaman, "Responses of Propellants to High Dynamic Stresses," Hazard Studies for Solid Propellant Rocket Motors, p. 10-25, AGARD-CP-367, 1984.

9. T. R. Gibbs and A. Popolato, LASL Explosive Property Data, Univ. California Press, Berkeley, 1980.

10. P. Howe, R. Frey, B. Taylor and V. Boyle, "Shock Initiation and the Critical Energy Concept," Sixth Symposium (International) on Detonation, pp. 11-19, ACR-221, U.S. Government Printing Office, Washington, D.C. 1977.

11. R. R. Bernecker, "The DDT Process for High Energy Propellants," Hazard Studies for Solid Propellant Rocket Motors, p. 14-9, AGARD-CP-367, 1984.

12. R. R. Bernecker, D. Price and H. W. Sandusky, "Burning to Detonation Transition in Porous Beds of a High-Energy Propellant," Proceedings of the 16th JANNAF Combustion Meeting, pp. 51-78, CPIA Publ. 308, Vol. 1, 1980.

13. J. Roth, "Shock Sensitivity and Shock Hugoniots of High Density Granular Explosives, "Fifth Symposium (International) on Detonation, pp. 219-230, ACR-184, U.S. Government Printing Office, Washington, D.C., 1971.

14. J. B. Ramsay and A. Popolato, "Analysis of Shock Wave and Initiation Data for Solid Explosives," Fourth Symposium (International) on Detonation, pp. 233-238, ACR-126, U.S. Government Printing Office, Washington, D.C 1965.

DISCUSSION

JOHN B. RAMSAY, Los Alamos National Laboratory

Considering your log-log plot of x_D (distance to detonation) vs u (particle velocity), does not the correlation simply define the experimentally accessible range? That is, materials which might fall on the lower left are too sensitive and those that might lie in the upper right are too insensitive. The particle velocity axis must compress the data clustering relative to plotting against pressure giving an apparent improvement in correlation.

REPLY BY H. W. SANDUSKY

There was a wide range of relevant materials investigated that included explosives as well as materials intended only to burn (double-base and high-energy propellants). The x_D data obtained in this study for relatively weak shocks do not appear to correlate any better with u than with p. However, the x_D data in the literature for strong shocks correlates well with u for various porosities, whereas the correlation of x_D versus p is distinctly different for near TMD and porous samples of even the same material. J. Roth (13) reported similar findings at the Fifth Detonation Symposium (see the Discussion within the paper and the following comment by J. Roth). Whether this correlation will be valid as more energetic materials are investigated remains a point for future consideration.

REPLY BY JULIUS ROTH
Consultant

Run-up distance to detonation in a number of explosives correlates quite well with threshold particle velocity and is essentially independent of porosity over a wide range of %TMD, except in experiments near 100 %TMD. This has been reported in the Proceedings of the Fifth Detonation Symposium.

DISCUSSION (Cont.)

JOHN C. CUMMINGS, Sandia National Laboratory

Have you developed a physical or mathematical model to explain your correlation for run distance to detonation with particle velocity?

REPLY BY H. W. SANDUSKY

We plan to model the experiments, but some processes are not understood well enough to proceed directly. The first process which occurs, compaction of the very porous bed, is not physically described by existing models; to overcome this, Sigmund Jacobs and Harold Sandusky are developing a model that views the porous bed as a collection of spheres with deforming contact surfaces. The next step is to describe the heating that occurs within those locally deforming regions.

DICK STRESAU, Consultant

From initial bulk density and compression wave propagation and particle velocity it should be possible to calculate bulk density at onset of detonation. Have results of such calculations been compared with other data?

REPLY BY H. W. SANDUSKY

In these experiments, there is no evidence that the onset and propagation of detonation occurred in a region previously affected by compression waves.

SHOCK INITIATION OF TATB AND HMX EXPLOSIVE COMPOSITIONS

J. Vanpoperynghe, J. Sorel, J. Aveillé, J.C. Adenis
Commissariat á l'Energie Atomique
Centre d'Etudes de Vaujours
B.P. 7 — 77181 Courtry — FRANCE

We have experimentally studied the initiation of detonation in TATB and HMX explosive compositions by shock waves of different amplitude and duration using a double wedge test, an electrical gun and a gap test. The achieved experimental program provides us characteristic parameters: run-to-detonation, excess transit time, and initiation thresholds for short shock pulse. These allow to compare the shock sensitivity of TATB and HMX compositions. Numerical computations have been then conducted with the shock initiation model we call "KRAKATOA" for 1-D and 2-D geometries.

INTRODUCTION

We are focusing on the behavior of heterogeneous solid explosives when undergoing plane shock wave. The dynamic characterization of explosive needs two kinds of shock-to-detonation experiments.

In the first kind of experiments, the shock is produced by a plane projectile thick enough which induces a shock with a square pulse a long time - the shock is said to be sustained. In particular we determine characteristic values: the run to detonation (h) and the excess transit time (T_t) which are function of the initial intensity of shock.

When we initiate the detonation with a pyrotechnical device we produce a short duration pulse "unsustained". The study of the sensitivity and the initiation must be achieved by the second kind of experiments where the duration time of shock is a main parameter. The intensity of the induced shock in the explosive is defined by the velocity of projectile, its nature and the explosive sample target characteristics. The limited shock duration is produced by impact of a sufficiently thin projectile. The shock duration depends on the conditions of the shock and on the thickness: the thinner the projectile, the shorter the duration.

Gap-Tests measure the shock sensitivity of an explosive as the thickness of inert spacer material which is located between the HE sample and a standard detonating charge, and that will allow 50% probability. Therefore, gap-tests give only approximate indications of the relative shock sensitivity. The sample may fail to detonate for different reasons: first of all, an insufficient pressure, a too short pressure duration, or a too small size of the acceptor explosive.

The experimental studies are compared to numerical simulations. To our computations we use the KRAKATOA rate model of shock initiation with a 1-D or a 2-D Lagrangian hydrodynamic code. The rate law is calibrated using the results of long duration shock initiation experiments and is used to model other types of experiments. Numerical computations have been so conducted to predict detonation in an explosive charge which is impacted by a long cylindrical projectile.

We have conducted the experimental and the numerical studies on 2 explosive compositions, some properties of which are presented in the following table.

TABLE I

Explosive	% weight	Density g/cm^3
X1	96 HMX	1,822
T2	97 TATB	1,856

LONG DURATION SHOCK INITIATION

Experimental Method - Double-Wedge Method. To study the behavior of unreacted high explosive and the shock-to-detonation transition we use the double-wedge method as it has been described many times. The experimental device, the recording apparatus and the reduction of the data have been reported in detail in (1), (2). Figures 1 and 2 give the schematic description and the scheme of a typical record. Let us recall below the main features of the experiments.

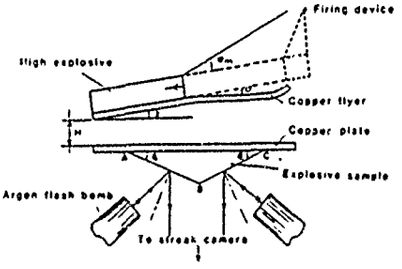

Fig. 1.

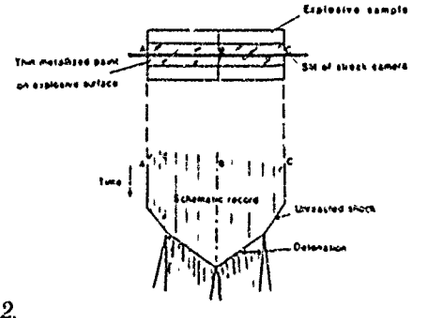

Fig. 2.

The shock is generated by the impact of a thick flat projectile with velocity V_p on a transmitter on the top of which lies the high-explosive sample under study. The projectile is a copper plate launched by a special explosive device. The transmitter is also made of copper. The high-explosive sample is shaped a β-wedge out of one piece of homogeneous explosive; the angle β is small enough to ensure a 1-D flow in the direction of impact. The side faces of the wedge are lit by an argon flash and looked at by means of a streak camera. The pressure and velocity at the interface transmitter-sample are lying at the intersection of the release isentrope of the transmitter and the ϱ_{02}. U_2 - slope straight line (ϱ_{02} is the initial density of the sample - U_2 is the shock velocity in inert explosive). In other terms, each experiment leads to a point of the Hugoniot curve of the unreacted

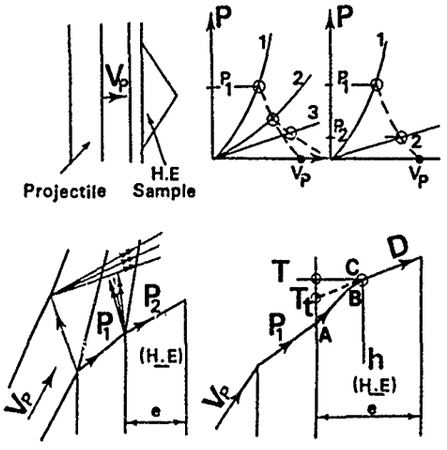

Fig. 3.

explosive, provided the projectile and transmitter are known as to their shock (release) behavior from (to) ambiant conditions. Moreover, in the case of low intensity shock, the propagation of the shock wave may be schemed as shown in Figure 3 - drawn in x-t plane. The streak camera records shock trajectory which may roughly be divided in three typical zones.

- a nearly unreacted zone AB
- a transition zone BC
- a detonation - type propagation zone CD.

When the sample is thick enough, the value of inert shock velocity U_2 is identified to the initial slope of the trajectory - while the run to detonation (h) and excess transit time T_t are estimated from the whole trajectory - The intensity and duration are varied by changing the thickness of the plate (1,6 to 5 mm) and the impact velocity V_p (800 to 2800 m/s), which lead to a duration τ of shock in the sample (0,5 to 2 μs).

Results — Hugoniot Curves The data on Hugoniot curve of high-explosive when remaining unreacted have been reduced through a linear relationship $U=A+Bu$ between the shock velocity and the material velocity u. The Table II summarizes the reduced results obtained on X1 composition and T2 composition which are plotted - Figure 4 - Detonation build-up.

TABLE II

Explosive	ϱ_0 g/cm^3	A m/s	B	Pressure Range (kbar)
X1	1,822	2890	1,996	50–152
T2	1,855	2118	2,305	90–250

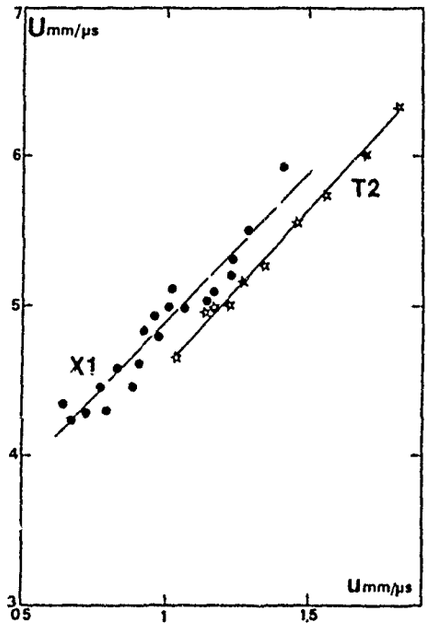

Fig. 4. Unreacted explosive U vs u

The run-to-detonation, h, is strongly dependent of the pressure P of the shock induced in the explosive sample. Therefore these datas have been reduced by means of linear relationship log h and log P (Pop-plot curve) Table III gives the coefficients A1 and B1 of this linear fit. For each experiment the excess transit time T_t follows from h ($T_t = T_h - \frac{h}{D_{CJ}}$). It appears that the values of T_t are also nicely fitted by a linear relationship between log T_t and log P - corresponding coefficients A2 and B2 are in Table III.

TABLE III

Explosive	log h=A1+B log P (mm) (kbar)		log T_t=A2+B2 log P (μs) (kbar)	
	A1	B1	A2	B2
X1	3,331	−1,368	4,053	−2,349
T2	7,545	−3,111	9,491	−4,697

Figure 5 and 6 illustrate these results.

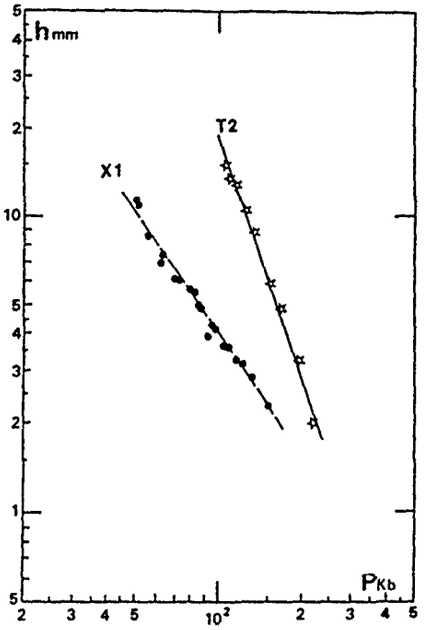

Fig. 5. Run-to-detonation h vs P

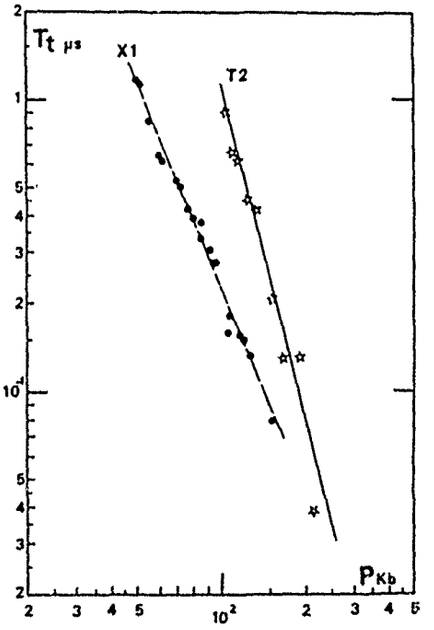

Figure 6. Excess transit time T_t vs P

SHORT DURATION SHOCK INITIATION

The limited short duration is produced by impact of a sufficiently thin projectile on explosive sample. The thinner the projectile, the shorter the duration.

For this we use an electrical launcher with exploded foil (electric gun). The electrical set up that we achieved is an extension of one which has been built in 1970 (3) upgrading the results of Keller-Penning and Guenther (4), (5). The principle of this electric device has been described many times in earlier papers, i.e., in (6).

We store an electrical energy E_o in a condenser bank. The fast discharge of the condensers in the resistance made of a thin aluminum foil (25 to 50 μm thick) induced the melting and vaporization of the metal. (The foil is said to explode). A thin Kapton plate (polyimide) or mylar (polyester) lying on the aluminum foil - Figure 7 - is thrown by the explosion with velocities as high as several km/s. We confine the projection in a hollow cylinder made of isolant material on the top of which we set explosive sample.

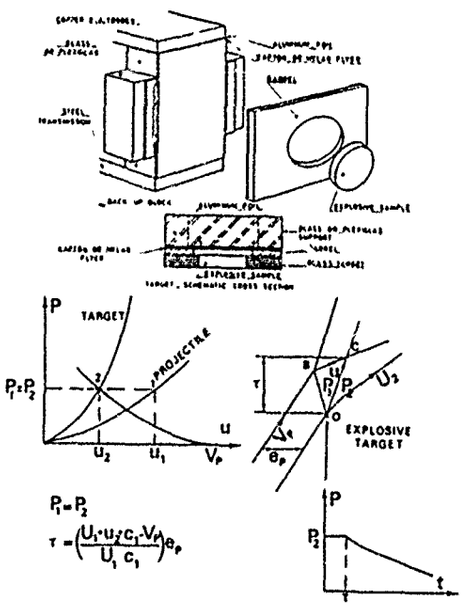

Fig. 7b.

The storage of energy (E_o=53 kJ) is produced by a battery of 10 condensers set in parallel ($C_o \cong 42{,}4\ \mu F$), the voltage may be about 50 kV. To ensure a perfectly synchroneous discharge, we use a switch obtained by two "spark-gaps". Large range of velocity impact is obtained (1000 to 10000 m/s) by changing electrical conditions, geometry of flyer and launcher tube. Aluminum foil thickness ε ranging from 10 to 50 μm, flyer thickness e_p ranging from (55 to 1050 μm). The diameter of launcher tube confinement is 7 to 30 mm and a variable height x(2 to 8 mm).

The impact of flyer is characterized by means of streak camera and checked recently by an interferometric method (VISAR). The flatness of the impact is low as 50 ns for a diameter Ø 20 mm.

The conditions of shock during the impact of the projectile on explosive sample target are provided by the impedance mismatch method as shown on the schematic drawing in the diagram P vs material velocity u. Figure 7b.

We can determine all the parameters connected to an impact at velocity V_p. Parameters with number (1) are those in projectile with number (2) are in target sample - ϱ_{oi} the initial density - u_i the material velocity, U_i the shock velocity, P_i the pressure, c_i is the sound speed, ϱ_i is the shocked density.

At the back face of sample the pressure P2=P1 is constant between O and C during the time τ. P2 and τ define the short pulse shock. τ depends on the impact conditions and the thickness projectile.

For each values V_p we can define the impact conditions and write:

$$\tau = \left(\frac{U1+u2+c1-V_p}{U1.c1} \right). e_p$$

The Hugoniot data on Kapton are taken from (7), τ takes values between 10 ns and 800 ns. The provided pressures are between 20 to 800 kbar with impact velocities varying from 1mm/μs to 10mm/μs.

Sensitivity Study of HMX Composition: X1

The explosive targets are right circular cylinders (20 mm in diameter, h in height (6 to 10 mm), are located in a glass confinement. With the help of a streak frame camera we can measure the mean velocity of flying foil at location x in the barrel, and check the flatness of the impact on the target. The processing of the light records at explosive free surface gives informations about detonation or no-detonation state in the samples. With the same kind of sample we achieve a set of experiments varying V_p and τ. Each detonation threshold experiment consists of test firing using "up-down" method in which P and τ are adjusted upwards after a no detonation and downwards after detonation. On Figure 8, we give the values V_p.

versus thickness e_p and Figure 9, we show the results obtained P versus τ.

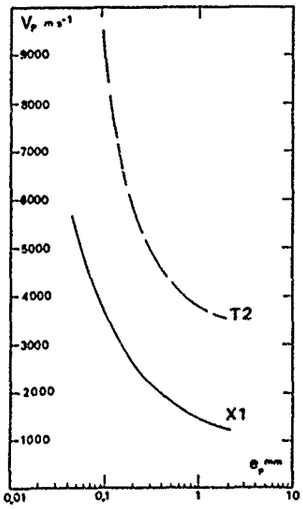

Fig. 8. Threshold velocity V_p vs. e_p

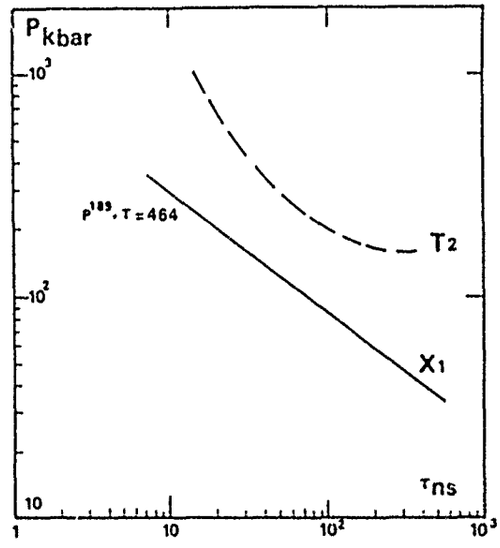

Fig. 9. Threshold Pressure P vs. τ

We find out that the critical kinetic energy (E_c) of flying plate increases for the points at the threshold detonation/non detonation. (The pressure P_2 decreases and τ increases). E_c takes values from 95 J/cm^2 for P_2 near 300 kbar to 145 J/cm^2 for P_2 near 30 kbar. These results show that for low amplitude sustained shocks, the critical kinetic energy is larger than for large amplitude short sustained shocks. Between both curves $E_c = c^{te}$ (95 J/cm^2 and 145 J/cm^2) the limit curve threshold, for X1 composition can be written in the form $P^n\tau = 464$ (kbar)^n.μs with n=1,89.

Sensitivity Study of TATB Composition T2.

The diameter sample is 20 mm and height h=15 mm. To obtain the wanted velocities the diameter of flyer varies from 30 to 9 mm. In comparison Fig. 8 and Fig. 9 with the results on X1 the minimum projectile impact velocities needed to detonate T2 are very large (between 4 and 10 mm/μs).

We find out that the detonation threshold is not obtained with large velocities near 7,5 mm/μs to 9,8 mm/μs. This corresponds with shorter pulse duration near 20 ns. These data are obtained with a small projectile Ø 9 mm which is an order of magnitude of failure diameter $Ø_{cr}$ (under $Ø_{cr}$ the detonation does not propagate) of T2 ($Ø_{cr} \cong 10$ mm). So, the greatest velocities were obtained with a large length barrel and for some of the experiments the flyer impact on explosive sample is rather curved (defect flatness>100 ns). Some no detonation results can be explained by the fact that a diverging shock cannot initiate a detonation in TATB composition T2 near failure diameter.

The experimental values E_c increase when P decreases and τ increases. These values are between 700 and 1500 J/cm^2. T2 composition seems to deviate from the relation E_c = constant in the region of the lower pressures P and of the larger pulses duration shocks.

TABLE IV

	DONOR		ACCEPTOR	SPACER	
	composition	Size (mm)	Size (mm)	mat'l	dia (mm)
MHSMP	LX 04	025,4H38,1	025,4H,25,4	Cu	25,4
NSWC SSGT	RDX	025,4H,38,1	025,4H,38,1	Lucite	25,4
LANL SSGT	PBX 9407	07,62Hd5,26	012,7H38,1	Cu	20
LANL SSGT	PBX 9205	041,3H 102	041,3H102	Al	41,3
AWRE 2	HMX/P	012,7H25,4	012,7H75	Alg	25,4

GAP TEST

Many laboratories use the Gap test in order to evaluate the sensibility of explosive compositions to shock waves. There are a great number of Gap tests (8) through (13), the main dimensions of which are summarized in Table IV.

Experimental Set-Up

The experimental set-up (Figure 10) is made of:

- a Comp. X1 donor explosive initiated by a EBW PETN detonator.
- a brass or copper spacer of various thickness.
- an acceptor explosive closed to steel witness plate.
- a 10 mm thick PMMA cylinder as confinement.

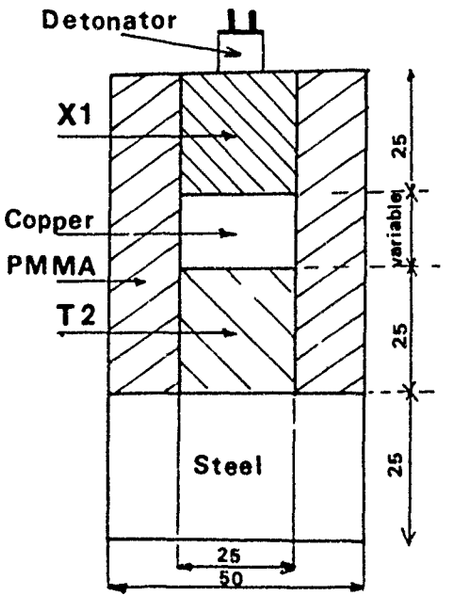

Fig. 10. Gap test set-up

Results

We first examine with a streak camera the emergence of the detonation wave from the donor. We notice that there is a 250 nanoseconds delay between the axis emergence and the side one. That corresponds to a 35 mm wave curvature radius. We secondly verify that a Ø 25 H 25 Comp. X1 detonation broke the steel witness plate.

Two series of experiments were made with Comp. X1 and Comp. T2 as acceptors. The results are summarized in the following Table V.

NUMERICAL MODELING

The KRAKATOA model (appendix 1) of shock initiation of heterogeneous solid explosives is used to study the above described experiments.

At first we calibrate our model for each explosive composition by determining the three coefficients of the rate law so that we obtain numerically the "Pop Plot". The results which we obtain for the Comp. X1 and the Comp. T2 are presented on the Figure 11. The following figure represents pressure histories in cells of the buildup region for a sustained shock of 100 kbar in the Comp. T2.

TABLE V

explosive acceptor Comp. T2			explosive acceptor Comp. X1		
e(mm)	h(mm)		e(mm)	h(mm)	
15	0	ND	22	0	ND
8	0	ND	20	0	ND
4	0	ND	19	0	ND
3	0	ND	18	2,1	D
2,5	0	ND	18	2,1	D
2	1,5	ND	18	2,1	D
2	0.85	ND	17,5	2,8	D
1	broken	D	17.5	2,2	D
1	broken	D	15	broken	D

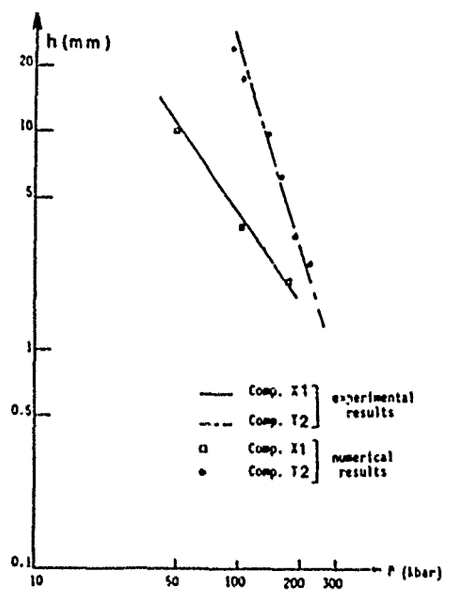

Fig. 11. Run-to-detonation

Short Shock Initiation

The sensitivity of the Comp. T2 to short pulse with shock pressure ranging from 100 to 200 kbar has been then studied numerically. Results are presented in a LnP-LnT diagram (Figure 13).

The 2-D geometry and the test sizes of the gap test are thought to be easy modelized. The obtained results are only useful to validate the

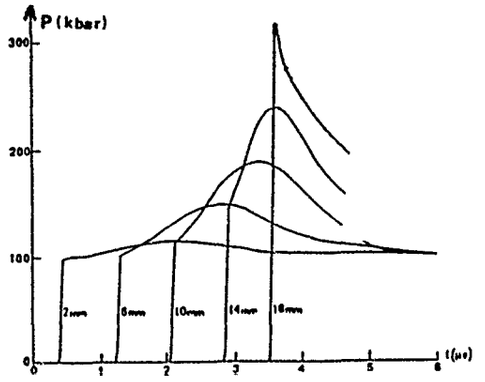

Fig. 12. Pressure history

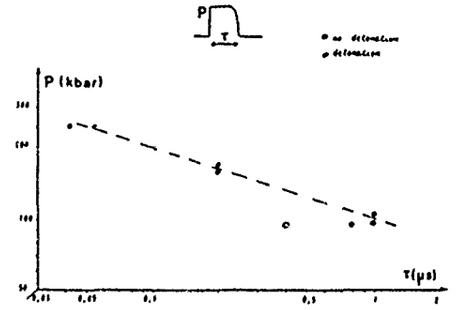

Fig. 13. Numerical P vs. τ

investigated explosive (acceptor) kinetics in a 2-D geometry, after that it has been developed in a 1-D geometry. Similar testings have been performed at NOL and at LANL. They were simulated with the Forest fire model on different explosive compositions (14).

For the computations we used a 2 dimensional lagrangian hydrodynamic code. Solid materials (brass for the spacer and steel for the witness plate) are treated with the Steinberg-Cochran and Guinan's model (15).

The detonation wave propagation in the donor (Comp. X1) is calculated geometrically. We initiate the explosive on a zone in contact with the detonator. This zone has been determined to give a good agreement with the experimental wave curvature measured at the interface between the donor and the spacer (R=35 mm).

Detonation initiation of the acceptor is dealed with the Krakatoa model. The zoning on the Figure 14 corresponds to a 2 mm thick spacer.

Meshes dimensions are resumed on the next table for each material:

material	r(mm)	z(mm)
Comp. X1	0.96	1
Comp. T2	0.96	1
Brass	0.96	0.5
Steel	1.02	1
PMMA	1.67	1

The obtained mesh does not lead to long duration computations.

The detonation wave front in the Comp. X1 is shown at different times in the Figure 15. The pressure profile at the interface Comp. X1 brass can be observed on the Figure 16. We have plotted the pressure history in an axis zone on the Figure 16. We notice that the maximum pressure is less than the C.J. pressure (340 kbar). This is due to the numerical scheme, which limits the high gradients. The pressure profile must be compared with this which we obtain for a steady detonation wave in a long 25 mm diameter cylinder in Comp. X1.

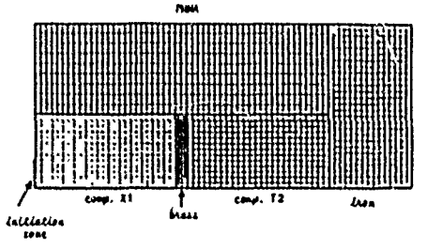

Fig. 14.

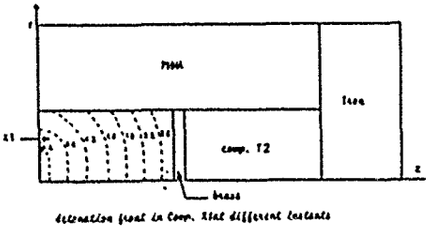

Fig. 15.

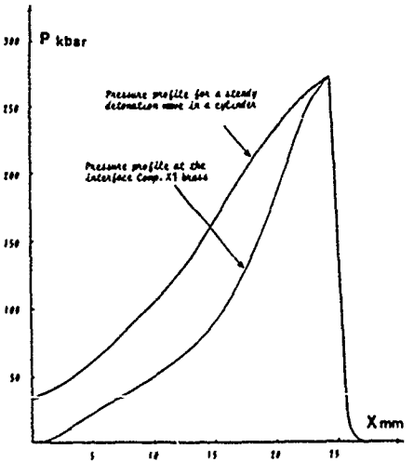

Fig. 16.

The detonation regime in the Comp. T2 is obtained for a 1mm thick spacer and for a 2mm thick spacer we don't observe detonation. However, in this last case the results presented on the Figure 17 show that great part of the explosive has fully reacted and the pressure stays at a high level during a long time.

Impact of Cylindrical Projectile

When the projectile is long enough, the pressure field in the target is controlled by lateral release waves starting at impact time from impact surface periphery. Consequently when the length of the projectile is greater than the radius only the diameter, or the radius of the projectile is important. The velocity and the nature of the projectile determine impact shock pressure.

Experimentally for a cylindrical with a diameter D, the detonation regime is obtained for velocities greater than a critical velocity. So we can express initiation threshold curve with the projectile velocities plotted versus projectile diameter.

Here are presented numerical results obtained for a Comp. X1 charge impacted by a cylindrical projectile.

We compute the thresholds corresponding to the detonation regime for a bare or a covered charge. This numerical results are obtained before the experiments, which could not still be performed. Despite they were very useful for the choice of sizes and the volocities of the projectile and the target.

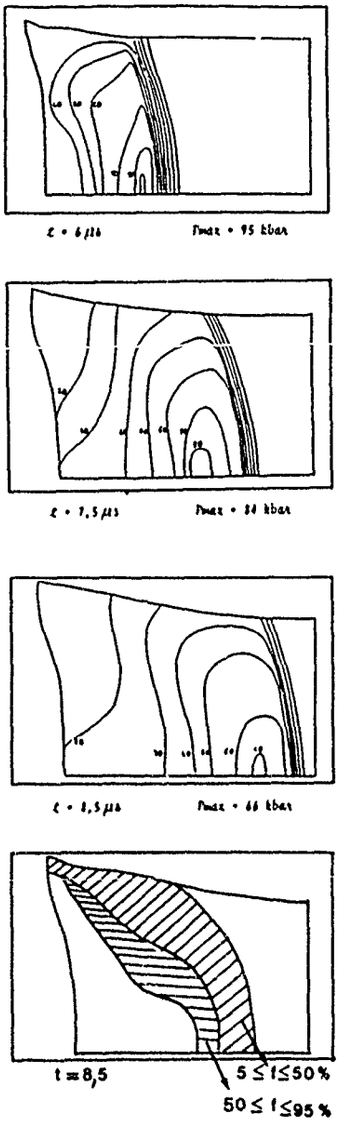

Fig. 17.

The Figure 18 shows a typical computer model which we used.

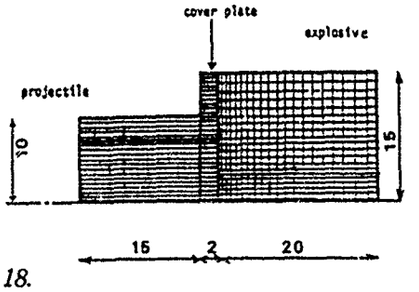

Fig. 18.

The thresholds corresponding to a bare explosive charge and a 2 mm or 6 mm cover plate in tantalum are shown in Figure 19.

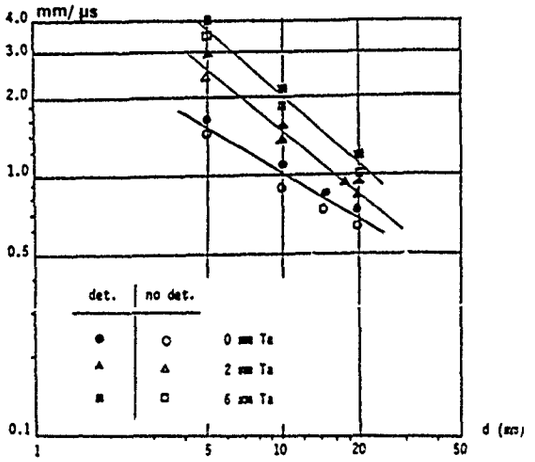

Fig. 19.

APPENDIX 1

Krakatoa Model (16). This model has been developed to predict the detonation and to describe the transient regime when an explosive charge is initiated by a shock wave.

According to the Z.N.D. scheme we represent the detonation as a shock followed by chemical reactions which are expanding in a biphasic mixture (non reacted explosive and detonation products). The chemical reactions are represented by only one parameter which is the decomposition rate.

Physical Princips

1) Rate law: the chemical reactions are initiated at certain detonation sites. It is assumed they are points and the reactions are propagating isotropically at a rate G. In this conditions analytical calculations give us for the rate law:

$$\frac{df}{dt} = N_0^{1/3} \cdot G \cdot (1-f) \cdot \left| \mathrm{Ln}(1-f) \right|^{2/3}$$

with:- f decomposed explosive weight fraction

- N_0 detonation sites per volume unit, it is an increasing function of the shock intensity.

- G radial speed of growth. For N_0 and G we choose arbitrarily analytical expressions which are:

$-N_0^{1/3} = A.\exp(I/Ia)$, I is a function which depends on the shock strength.

- $G = p^b$

A, Ia and b are 3 coefficients which depend on the explosive composition.

2)Biphasic zone: we assume the following identities: (subscript s is for solid explosive and subscript g is for the detonation gases)

- pressure: $P = Ps = Pg$
- specific volume: $V = (1-f).Vs + f.Vg$
- internal energy $e = (1-f).es + f.eg$

es (Ps,Vs) is a Mie Gruneisen E.O.S. calibrated on the Hugoniot

eg (Pg,Vg) is a J.W.L. E.O.S.

We assume we have an isentropic decomposition of the explosive and so es (Ps,Vs)=es (Vs).

3) Computations: in our computations I is the work of the non reversing strengths after that the shock has passed. The 3 coefficients A, Ia and b are determined by computing the run to detonation and the excess transit time as a function of the shock pressure with a 1DL hydrodynamic code. The reactions start when the shock has passed in the cell, as it is shown in the Figure 20.

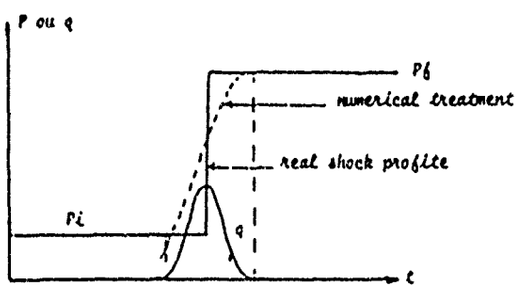

Fig. 20.

ACKNOWLEDGEMENTS

Valuable contributions to this work were made by many people at C.E. Vaujours. We particularly acknowledge J. Appencourt, G. Sancan, C. Mouchel, J. Montrosset, M. Charaix for their technical assistance. We greatly appreciate the many helpful suggestions and discussions concerning this work made by J. Baconin.

REFERENCES

1. A.W. Campbell, W.C. Davis, J.B. Ramsay, J.R. Travis. Shock Initiation of solid explosives. Phys. Fluids, 1961,4,4,511-521.
2. R. Droux, C. Mouchel. Etude du comportement sous choc et de la generation de la detonation d'explosifs heterogenes par la methode du double coin. Symposium HDP-27-31 août 1978-CEA-Paris p. 103.
3. J. Baconin, Ch. Fouquoire. Unpublished report CEA 19/05/1971.
4. D.V. Keller and J.R. Penning. Exploding Wires-Vol. 2. W.G. Chase and H.D. Moore, Editors. 1962 p. 26.
5. A.H. Guenther, D.C. Wunsch and J.D. Scapes. Exploding Wires-Vol.2. 1962-p. 279.
6. R.K. Jackson, L.G. Green, R.G. Barlett, W.W. Hofer, P.E. Kramer, R.S. Lee, E.J. Nidick, L.L. Shaw and R.C. Weingart. Sixth Symposium (Int) on detonation. Office of Naval Research, ACR-22A (1976) p. 653.
7. S.P. Marsh. ED. LASL Shock Hugoniot Data. University of California Press, Berkeley, (1980), pp. 436, 444.
8. J.N. Ayres. Standardization of the Small Scale Gap Test. Navweps report 7342-16 janvier 1961.
9. M.J. Urizar, S.W. Peterson, L.C. Smith. Detonation Sensitivity Tests. LA 7193-MS (1978).
10. P.E. Kramer, TATB Sensitivity Testing. MHS MP 74-35 T (1974).
11. H. Bartels, Gap Testing Explosive Device for Better Judging of Detonation Safety. 8th International Seminar on Pyrotechnics.
12. R.L. Grant, N.E. Marma, R.W. Van Dolah. New Gap Sensitivity Methods for Explosives. Bureau of Mines BM-RI 6947 (1966).
13. D.M. Dobratz, M. Finger. L.G. Green and Col. Selected Sensitivity Tests of TATB and TATB Formulations and their Evaluation. UCID 18026 (23 mars 1979).
14. A.L. Bowman, J.D. Kershner, C.L. Mader. A Numerical Model of the Gap Test. LA 84 08.
15. Steinberg, Cochran, Quinan. A constitutive Model for Metal Applicable at High Strain Rate. J.A.P.-mars 1980-pp. 1498-1509.
16. G. Damamme, M. Missonnier, "Modeling of Reaction Zone of Detonation," 7th Symposium on Detonation 1981-Annapolis.

DISCUSSION

J. E. KENNEDY, Sandia National Laboratories

The shock amplitude and waveform which you compute to be transmitted through the brass gap material may be quite sensitive to your assumptions concerning the strength of the brass. Did you find it in your calculations?

REPLY BY J. VANPOPERYNGHE

In previous one dimensional computations with the same elastic-plastic model we find the shock transmitted through a material is little dependent on the shock strength. In the computations which have been presented in this symposium we don't study the influence of the materials constants (yield strength, shear modulus . . .).

DISCUSSION

J. E. KENNEDY, Sandia National Laboratories

Have you experimentally confirmed the shape of the shock waveform history predicted in your calculations.

REPLY BY J. VANPOPERYNGHE

No, we haven't confirmed experimentally the pressure history at the interface donor-gap. Such confirmation has only been made with manganin gauges in your laboratory for a 100 mm diameter charge of comp. X1 with PMMA brass.

DISCUSSION

MANFRED HELD, MBB

Have you calculated the energy density $\int pu\,dt$ in your gap test and how these values fit your experimental values of energy density with your flying plate in fail tests?

REPLY BY J. VANPOPERYNGHE

We don't compute the energy density which you define. We will do it in further computations.

THE EFFECT OF RDX PARTICLE SIZE ON THE SHOCK SENSITIVITY OF CAST PBX FORMULATIONS

H. Moulard
Franco-German Research Institute
P.O. Box 301 – 68301 Saint-Louis, France (ISL)

and

J. W. Kury*
Lawrence Livermore National Laboratory
P.O. Box 808, Livermore, CA 94550

and

A. Delclos
Societe Nationale des Poudres et Explosifs
C. R. du Bouchet – 91710 Vert-le-Petit, France

Two special monomodal RDX/polyurethane cast PBX formulations have been used in a series of experiments designed to provide information on the effect of explosive particle size on shock sensitivity. The formulations contained 70% by weight RDX (either 6 μm or 134 μm median particle size) and 30% by weight polyurethane. The shock-to-detonation behavior of these formulations was measured in thin plate impact, projectile impact and wedge tests. The formulation containing the fine RDX was significantly less sensitive than that with the coarse RDX. In contrast, the detonation failure diameter of the coarse RDX formulation was much larger than that for the fine. The experiments were modeled with a three-term ignition and growth model. The results indicate that at the same shock input pressure (in the range of 4 GPa to 6 GPa) there are at least an order of magnitude more ignition sites in the formulation containing the coarse RDX, but that the growth rates are about the same for the two formulations.

INTRODUCTION

High energy explosives such as RDX and HMX are too sensitive to accidental ignition to be used in the pure form in ammunition. These materials have been desensitized over the years by a variety of additives. The safety and vulnerability of the resultant formulation is influenced not only by the additive but also by the particle size of the crystalline explosive. Since particle size is an important variable used by formulators to maximize energy and ease of processing it is important to know how this parameter effects sensitivity. Thus, a major program has been undertaken to elucidate the role particle size plays in determining shock sensitivity.

To minimize the effect of other factors that contribute to shock sensitivity, two special RDX/polyurethane formulations were prepared. Both contained 70% by weight RDX (one with $\bar{6}$ μm RDX, the other with $\bar{134}$ μm RDX). These PBX formulations were carefully prepared and cast to >99.9% theoretical maximum density to insure essentially no voids. This hopefully eliminates void collapse as an initiation mechanism.

To date, the shock-to-detonation (SDT) behavior of these formulations has been measured

* Work performed under the auspices of the U.S. Department of Energy by the Lawrence Livermore National Laboratory under contract No. W-7405-ENG-48.

TABLE 1
Monomodal Cast PBX Formulations

		WEIGHT PERCENT	VOLUME PERCENT	LOADING DENSITY (g/cm^3)	MEDIAN RDX PARTICLE SIZE (μm)	BET SPECIFIC SURFACE AREA (m^2/g)
FINE RDX FORMULATION	RDX	70.00	55.80	1.44	6	1.53
	Polyurethane	29.30	43.80			
	Graphite	0.70	0.40			
COARSE RDX FORMULATION	RDX	70.00	55.60	1.44	134	0.08
	Polyurethane	29.65	44.20			
	Graphite	0.35	0.20			

in thin plate impact, projectile impact and wedge tests. The detonation velocity as a function of charge diameter has also been investigated. The experiments have been computer simulated using ignition and growth models (1, 2). This paper describes the formulations and presents the experimental results and interpretation.

CAST PBX FORMULATIONS

The cast PBX formulations contained crystalline RDX, polyurethane as a binder and a small amount of graphite coating on the RDX to facilitate safe handling of the dry RDX prior to mixing. Composition, density and average particle characteristics are presented in Table 1. The size distribution for fine RDX (batch #48/52) and coarse RDX (batch #303/81) are given in Table 2. Photomicrographs of both the fine and coarse RDX are presented in Figs. 1 and 2.

The formulations are made by mixing the graphite coated RDX with pre-polymer in a horizontal two blade mixer. The spacing between the blades and the mixer surface is about one mm. After mixing under vacuum the paste is cast into a metal mold at atmospheric pressure. The viscosity of the formulation with fine RDX is 80,000 poises (@80 °C) while that with the coarse is only 6,000 poises (@40 °C). Because of this the plastic binder for the coarse formulation is partially cross-linked prior to mixing in order to prevent segregation during the curing process. After casting, the mold is vibrated under vacuum to deareate the paste.

Parts are cured for seven days at temperatures of 80 °C for the fine formulation and 40 °C for the coarse. Radiographs are taken of the cured parts and their densities are determined by the immersion method. The above procedure produces high quality parts with minimum

TABLE 2
RDX Particle Size Distribution

PARTICLE DIAMETER (μm)	FINE (%)	COARSE (%)
<1.5	1.2	
1.5 - 2.4	1.4	
2.4 - 3.0	2.6	
3.0 - 3.8	6.9	
3.8 - 4.8	12.5	
4.8 - 6.0	18.8	
6.0 - 7.5	22.6	
7.5 - 9.5	18.8	
9.5 - 12.0	8.4	
12.0 - 19.0	4.2	
◊19.0	2.6	
⊕26		2.4
26 - 41		2.3
41 - 65		2.6
65 - 103		8.2
103 - 130		30.3
130 - 164		43.0
164 - 206		10.5
◊206		

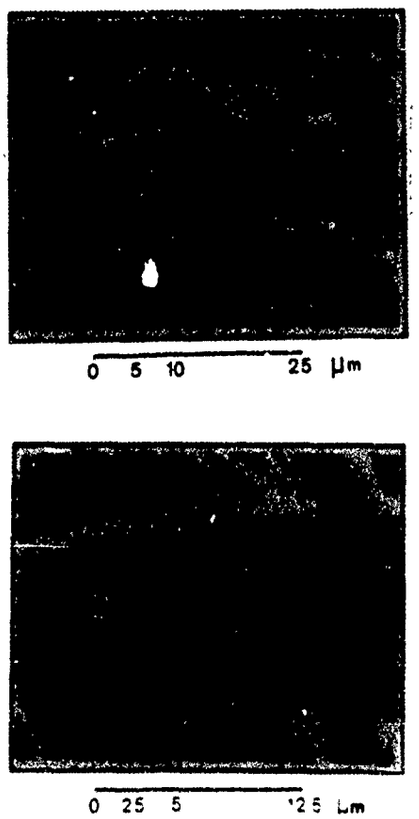

Fig. 1. Fine RDX Crystals

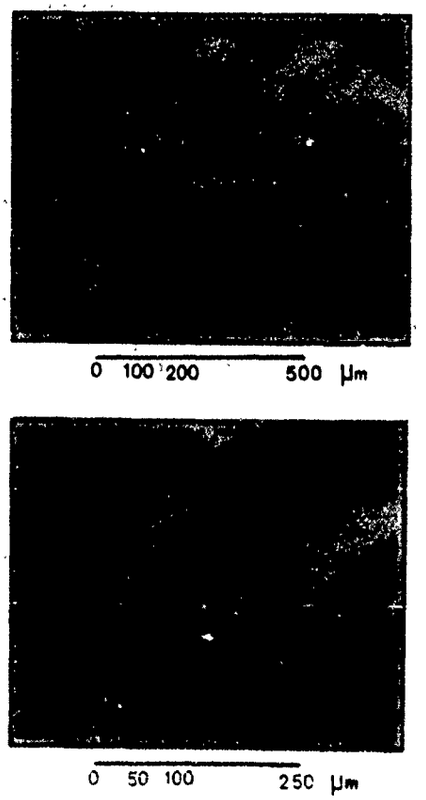

Fig. 2. Coarse RDX Crystals

void content. It has also been shown in previous work with both the fine and coarse RDX that the RDX particle size and shape are not changed during processing.

EXPERIMENTAL RESULTS

Short Duration Plane Shock Wave Experiments

The response of both the fine and coarse RDX formulations to short duration shocks was measured using explosively propelled thin plates (3). The plate, varying in thickness from 1 mm to 5 mm, impacted explosive samples 63 mm in diameter and 60 mm long. Flyer plate velocity and planarity at impact were measured using flash x-ray double exposures. Ionization probes on the explosive sample measured the shock transit time. This time was used to determine if SDT had occurred. Results are summarized in Table 3, Table 4 and Fig. 3. The fine RDX formulation is considerably less sensitive than the coarse. At a pressure pulse duration of 1.5 µsec its critical energy fluence is twice that of the coarse (1000 J/cm^2 vs. 500 J/cm^2).

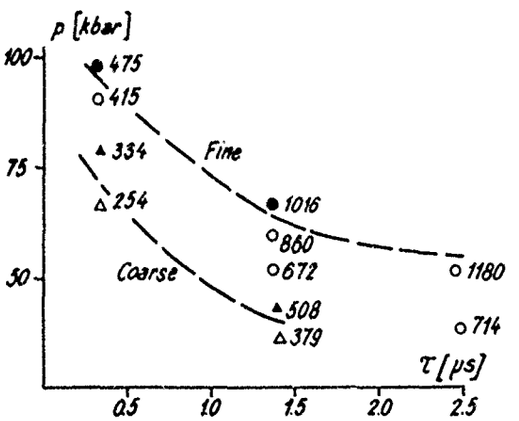

Fig. 3. Input pressure vs. pulse duration for fine and coarse RDX formulations. Solid points indicate detonation. Numbers next to the points are critical energy fluence (p•u•t).

TABLE 3
Thin Plate Experiments with Fine RDX Formulation

PLATE	PLATE VELOCITY (mm / μsec)	
	2.280	Detonation
	2.025	Detonation
1 mm Al		
	1.910	No Detonation
	1.560	No Detonation
	1.490	No Detonation
	1.525	Detonation
4 mm Al		
	1.400	No Detonation
	1.250	No Detonation
	1.075	No Detonation
4 mm Steel	0.086	No Detonation

TABLE 4
Thin Plate Experiments with Coarse RDX Formation

PLATE	PLATE VELOCITY (mm/μsec)	
	1.910	Detonation
	1.750	Detonation
1 mm Al	1.725	Detonation
	1.530	No Detonation
	1.110	Detonation
4 mm Al		
	0.960	No Detonation

Wedge Test Experiments

The experimental set-up for the wedge tests is shown in Fig. 4 The explosive sample with a 20° wedge angle is bonded to a 6 mm thick aluminum plate. A sustained pressure pulse is obtained by explosively propelling an 8 mm thick aluminum plate against the aluminum/explosive target. Light from argon flash bombs is reflected from the explosive surface into a streak camera. The light intensity decreases markedly when the shock reaches the surface of the explosive wedge.

Figure 5 shows side-by-side the streak records obtained from experiments when fine and coarse RDX formulations were impacted at the same flyer velocity (1.50 mm/μsec). By taking into account camera writing speed and magnification and correcting for any residual flyer plate obliquity at impact one can reconstruct the space-time diagram for shock wave propagation in the explosive sample (4). See Fig. 6. The fine RDX formulation both takes longer and has a sharper transition to detonation.

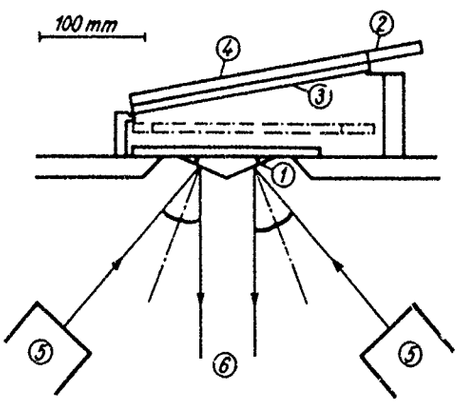

Fig. 4. Wedge test configuration (1) explosive wedge; (2) line wave generator; (3) flyer plate; (4) propelling explosive; (5) argon light bombs; (6) direction of streak cameras

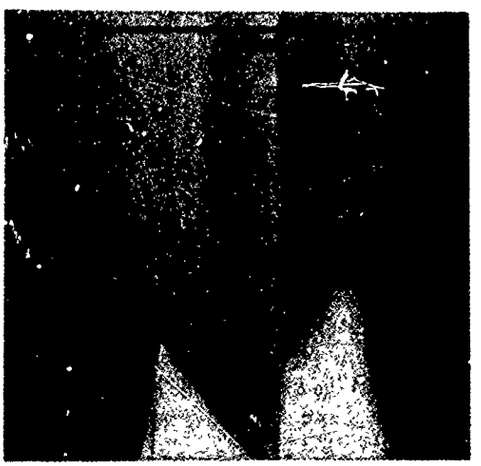

Fig. 5. Wedge test streak camera records for fine (left) and coarse (right) RDX explosives. Aluminum flyer velocities were both 1.50 mm/μsec.

TABLE 5
Detonation Velocity vs. Charge Diameter

CHARGE DIMENSIONS DIAM. (mm)	LENG. (mm)	DETONATION VELOCITY (mm/μsec)* FINE RDX FORMULATION (ρ_0 = 1.45 g/cm^3)	COARSE RDX FORMULATION (ρ_0 = 1.45 g/cm^3)
50	325	7.44	7.39
30	250	7.42	7.22
20	200	7.41	6.84
15	200	7.38	Failed
10	200	7.37	— —

* Measured over the last 50% in length of the charge.

as a function of 1/R in Fig. 9. The behavior of the fine RDX formulation is similar to that observed for liquids. The coarse, however, resembles that of a pressed PBX.

Small Cylindrical Projectile Impact Experiments

A series of experiments were carried out in which small cylindrical steel projectiles were impacted onto 50 mm diameter — 40 mm thick explosive samples. The results are presented in Fig. 10 and Table 6.

In these experiments steel flat-nosed projectiles were launched from a small powder gun (20 mm diameter) into a detonation chamber through an orifice. The explosive samples in the chamber were 2 meters from the muzzle, thus eliminating the effect of muzzle blast on the samples during the experiment. A Cranz-Schardin camera was used to verify this. Double exposure flash radiography was used to measure projectile velocity and monitor projectile orientation. Shock transit times were measured using ionization probes to determine if SDT had occurred.

The fine RDX formulation is significantly less sensitive than the coarse.

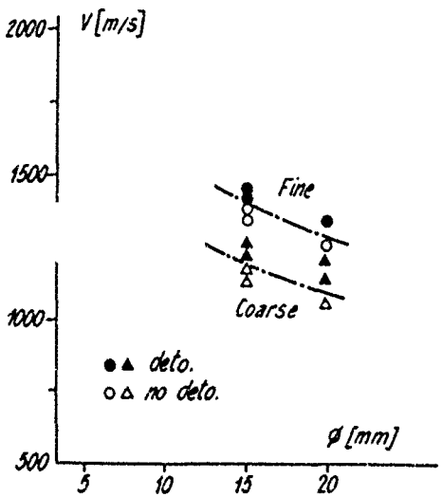

Fig 10. Critical SDT impact velocities for blunt-nosed steel cylinders

TABLE 6
Steel Projectile Impact Experiments

	PROJECTILE DIMENSIONS	PROJECTILE VELOCITY (mm/μsec)	
COARSE RDX FORMULATION	D= 15 mm L = 20 mm	1.261	Detonation
		1.228	Detonation
		1.188	No Detonation
		1.130	No Detonation
	D = 20 mm L = 27 mm	1.316	Detonation
		1.205	Detonation
		1.133	Detonation
		1.052	No Detonation
FINE RDX FORMULATION	D = 15 mm L = 20 mm	1.440	Detonation
		1.408	Detonation
		1.378	No Detonation
		1.350	No Detonation
	D = 20 mm L = 27 mm	1.350	Detonation
		1.240	No Detonation

Hugoniot Experiments

The small powder gun was also used to check the non-reactive Hugoniot used in computer simulations of the SDT experiments. The experimental geometry is shown in Fig. 11. A 20 mm diameter aluminum projectile is used to impact the target assembly. The target is placed at the gun muzzle and the surrounding volume is evacuated. PVF_2 gauges (5) are used to measure the shock transit time across a known thickness of explosive. The results are presented in Table 7. The experimental transit times agree very well with those calculated using the JWL non-reactive equation of state presented in the next section.

TABLE 5
Detonation Velocity vs. Charge Diameter

CHARGE DIMENSIONS DIAM. (mm)	LENG. (mm)	DETONATION VELOCITY (mm/μsec)* FINE RDX FORMULATION (ρ_0 = 1.45 g/cm^3)	COARSE RDX FORMULATION (ρ_0 = 1.45 g/cm^3)
50	325	7.44	7.39
30	250	7.42	7.22
20	200	7.41	6.84
15	200	7.38	Failed
10	200	7.37	—

* Measured over the last 50% in length of the charge.

as a function of 1/R in Fig. 9. The behavior of the fine RDX formulation is similar to that observed for liquids. The coarse, however, resembles that of a pressed PBX.

Small Cylindrical Projectile Impact Experiments

A series of experiments were carried out in which small cylindrical steel projectiles were impacted onto 50 mm diameter – 40 mm thick explosive samples. The results are presented in Fig. 10 and Table 6.

In these experiments steel flat-nosed projectiles were launched from a small powder gun (20 mm diameter) into a detonation chamber through an orifice. The explosive samples in the chamber were 2 meters from the muzzle, thus eliminating the effect of muzzle blast on the samples during the experiment. A Cranz-Schardin camera was used to verify this. Double exposure flash radiography was used to measure projectile velocity and monitor projectile orientation. Shock transit times were measured using ionization probes to determine if SDT had occurred.

The fine RDX formulation is significantly less sensitive than the coarse.

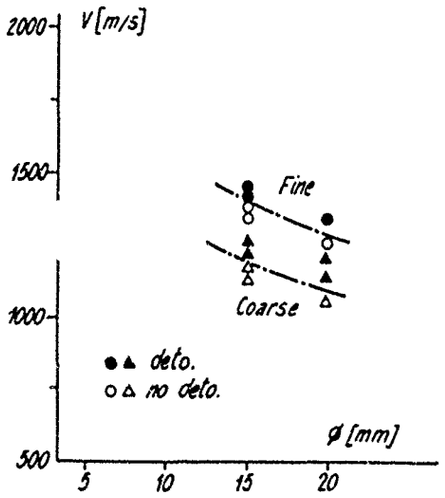

Fig 10. Critical SDT impact velocities for blunt-nosed steel cylinders

TABLE 6
Steel Projectile Impact Experiments

	PROJECTILE DIMENSIONS	PROJECTILE VELOCITY (mm/μsec)	
COARSE RDX FORMULATION	D= 15 mm L = 20 mm	1.261	Detonation
		1.228	Detonation
		1 188	No Detonation
		1.130	No Detonation
	D = 20 mm L = 27 mm	1.316	Detonation
		1.205	Detonation
		1.133	Detonation
		1.052	No Detonation
FINE RDX FORMULATION	D = 15 mm L = 20 mm	1.440	Detonation
		1 408	Detonation
		1.378	No Detonation
		1.350	No Detonation
	D = 20 mm L = 27 mm	1.350	Detonation
		1.240	No Detonation

Hugoniot Experiments

The small powder gun was also used to check the non-reactive Hugoniot used in computer simulations of the SDT experiments. The experimental geometry is shown in Fig. 11. A 20 mm diameter aluminum projectile is used to impact the target assembly. The target is placed at the gun muzzle and the surrounding volume is evacuated. PVF_2 gauges (5) are used to measure the shock transit time across a known thickness of explosive. The results are presented in Table 7. The experimental transit times agree very well with those calculated using the JWL non-reactive equation of state presented in the next section.

TABLE 7
Non-Reactive Hugoniot Experiments

	ALUMINUM PROJECTILE VELOCITY (mm/μsec)	EXPERIMENTAL EXPLOSIVE THICKNESS (mm)	EXPERIMENTAL TRANSIT TIME (μsec)	CALCULATED*		
				TRANSIT TIME (μsec)	PRESSURE (GPa)	PARTICLE VELOCITY (mm/μsec)
FINE RDX FORMULATION	1.010	4.080	1.105	1.100	4.05	0.77
	1.312	3.980	0.965	0.970	5.85	0.98
	1.505	4.020	0.925	0.924	7.15	1.13
	1.518	4.100	0.940	0.940	7.20	1.14
COARSE RDX FORMULATION	1.032	4.040	1.080	1.080	4.20	0.78
	1.290	4.010	0.990	0.984	5.70	0.97

* Calculated using the JWL non-reactive Hugoniot constants presented in this paper.

INTERPRETATION

The experimental results presented in this paper have been interpreted using a three term ignition and growth model that has accurately reproduced the large body of experimental results available for PBX-9404 and LX-17 (HMX and TATB containing explosives respectively (2). The general form of the reaction rate used in this model is given by Eq. 1.

$$\frac{dF}{dt} = I\,(1-f)^a\left(\frac{\varrho}{\varrho_o}-1-b\right)^x + G_1(1-F)^c F^d P^y + G_2\,(1-F)^e F^f P^e \qquad (1)$$

F is the fraction of explosive reacted. P is pressure. ϱ is explosive density. For a detailed discussion of the form and the effect of the other constants see Ref. 2. The JWL equation of state is used for both unreacted explosive and explosive products in this model (6).

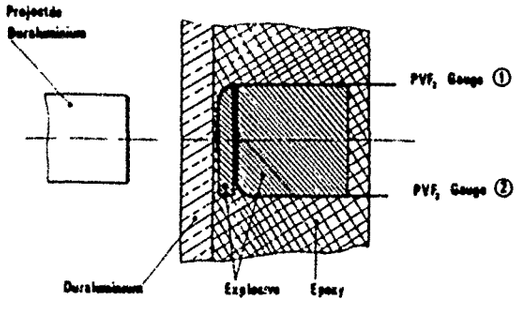

Fig.11. Experimental geometry to determine the non-reactive Hugoniot

The procedure followed for computer simulation of the experiments was to first estimate coefficients for the two JWL equations of state. Using these, the coefficients in the reaction rate equation were varied until the computer simulation and experimental wedge test results agreed. The model was then used to calculate the results for the thin plate, projectile impact and detonation velocity vs. diameter experiments. The variation in ignition and growth parameters obtained for the fine and coarse RDX formulations was examined to gain insight into the cause of the different SDT behavior of these two explosives.

Equations of State

Shock velocity-particle velocity data exist for mock explosives 905-03 and 900-10 and Melmac (7). One can also use the method of Torvik (8) to estimate at low pressures the Hugoniot of a mixture of RDX and Adiprene rubber with the same composition as the RDX formulations of interest. The JWL constants for the unreacted explosive presented in Table 8 are consistent with these data and produce a von Neumann spike pressure of 1.5 times the Chapman-Jouguet pressure.

The product JWL equation of state was estimated as follows. The measured explosive density and detonation velocity were combined with an estimated gamma of 2.8 to fix the Chapman-Jouguet pressure at 21 GPa. The E_o was estimated assuming that for each one volume percent polyurethane added to pure RDX its energy is reduced 1.1 percent (9). The values of R_1, R_2, and ω were chosen to be

similar to those previously determined for a variety of explosives (10). This resulted in the constants listed in Table 8 for the JWL products equation of state.

Since the formulations differ only in RDX particle size the same constants were used for both.

TABLE 8
JWL Equation of State Parameters

JWL PARAMETER	RDX-POLYURETHANE EXPLOSIVE	
	UNREACTED	PRODUCTS
A (Mbars)	83.21	4.512
B (Mbars)	−0.03624	0.09769
R_1	9.6	4.5
R_2	0.96	1.15
ω	1.041	0.30
C_V (Mbars/°K)	2.657×10^{-5}	10^{-5}
E (Mbars-cc/cc)	7.92×10^{-3}	0.05

Reaction Rate Equation

The specific three term reaction rate equation used for the computer simulations is Eq. 2.

$$\frac{dF}{dt} = 100(1\text{-}F)^{0.1}\left(\frac{\rho}{1.45} - 1\right)^4 + G_1(1\text{-}F)^{0.667}F^{0.083}P + 2250\,(1\text{-}F)^{0.222}F^{0.667}P^3 \qquad (2)$$

The first term is an ignition term and the model permits one to force this term to zero after a specified amount of material has reacted ($F_{max\ I}$). The constants and values of $F_{max\ I}$ were so chosen that it contributed only in the immediate region of the shock front. The last two terms govern the growth of the reaction. The first with a pressure exponent of 1 maximizes at about ten percent reaction while the second with a pressure exponent of 3 maximizes at about seventy percent reaction. The model also permits forcing the first growth term to zero after a specified amount of reaction ($F_{max\ G_1}$).

Wedge Test Calculations

The computer simulations of the wedge test were done using a 1D hydrodynamic code. Comparison of calculated vs. experimental shock distance-time data was used to assess how well the calculation reproduced the experimental results. This procedure is a more stringent test than merely comparing distances or times to detonation (Pop plots).

Initial screening calculations using only an ignition term and one growth term showed that the fine and coarse RDX formulations differed most in their early time reaction behavior. Because of this the constant G_2 in Eq. 1 was fixed at 2250 and only G_1, $F_{max\ I}$ and $F_{max\ G_1}$ were varied to fit the experimental data.

The data from four wedge tests with input pressures in the 5 GPa to 9 GPa range were used to determine the rate parameters for the fine RDX formulation. It was hoped that a unique set of G_1, $F_{max\ I}$ and $F_{max\ G_1}$ could be found that would reproduce the data for all the experiments. Approximate agreement was found with $G_1 = 0.4$, $F_{max\ I} = 0.002$ and $F_{max\ G_1} = 0.20$. However, in order to obtain the agreement between calculations and experiments shown in Fig. 12, it was necessary to slightly increase the contribution of the first growth term with input pressure. The values used are presented in Table 9.

The data from three wedge tests were used to determine the rate parameters for the coarse RDX formulation. Again an attempt was made to find a unique set of values for G_1, and $F_{max\ I}$ and $F_{max\ G_1}$ that would reproduce the experimental data. This was not possible. In fact,

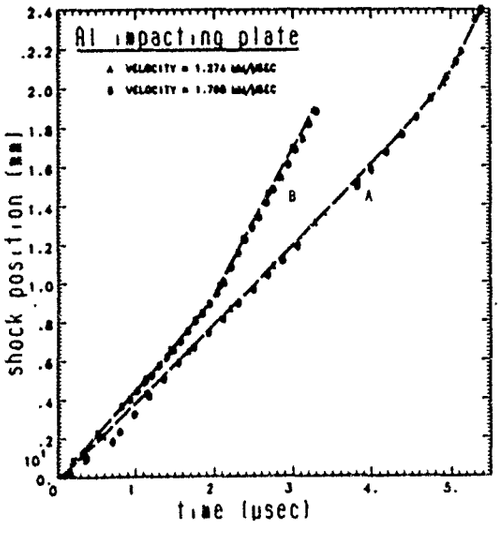

Fig. 12. Comparison of experimental and calculated wedge test data for fine RDX formulation. Solid points are experimental results.

TABLE 9
Rate Parameters for RDX Formulations from Wedge Test Data

	ALUMINUM IMPACT VELOCITY (mm/μsec)	$F_{max\ I}$	G_1	$F_{max}\ G_1$
FINE RDX FORMULATION	1.274	.002	0.3	0.2
	1.498	.002	0.4	0.2
	1.700	.002	0.5	0.2
	1.926	.002	0.6	0.2
COARSE RDX FORMULATION	1.338	.05	0.5	0.5
	1.510	.09	1.5	0.5
	1.810	.13	13.0	0.5

it was necessary to vary both G_1 and $F_{max\ I}$ to obtain the agreement shown in Fig. 13. The values used are presented in Table 9.

The major difference in the two formulations is that only about .2 percent of the fine RDX is reacted near the shock front whereas 5 percent or more of the coarse is reacted. Also, for the coarse formulation the amount reacted near the shock front and the growth rate increase significantly as the input pressure is increased above 6 GPa.

Calculations for the Other Experiments

The reaction rate parameters obtained from the wedge test calculations were used in computer

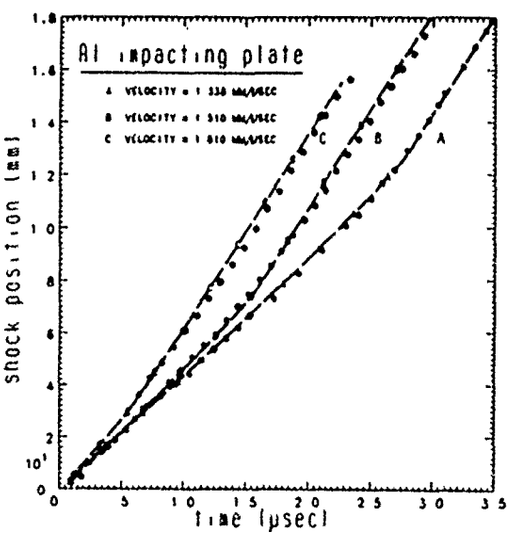

Fig. 13. Comparison of experimental and calculated wedge test data for coarse RDX formulation. Solid points are experimental results

simulations of the other experiments reported above. Good agreement was obtained for all the thin plate experiments except the 1 mm plate impacting the fine RDX formulation. See Table 10. In order to obtain agreement with experiment the amount of RDX ignited in the calculation had to be increased from 0.2 percent to 6 percent. Tarver (2) has observed similar behavior when simulating thin pulse initiation of pressed PBX.

The 4 mm experiments were calculated using a 2D hydrodynamic finite element code. When failure of detonation occurred it was due to the errosion of the pressure on the charge axis by sideways rarefaction. Figure 14 presents pressure contours for the coarse RDX formulation 7 μsecs after being impacted by a 4 mm aluminum plate with velocity of .96 mm/μsec. As in the experiment SDT does not occur.

TABLE 10
Calculated Results for Thin Plate Experiments

		PLATE VELOCITY	CALCULATED RESULTS
1 mm thick Al plate	FINE RDX FORMULATION	2.025	No detonation*
		1.910	No detonation
	COARSE RDX FORMULATION	1.725	Detonation ~8mm into explosive
		1.530	No detonation
4 mm thick Al plate	FINE RDX FORMULATION	1.525	Detonation ~14 mm into explosive
		1.400	No detonation
	COARSE RDX FORMULATION	1.110	Detonation ~24 mm into explosive
		0.960	No detonation

* All but this calculation agreed with the experimental results.

2D calculations were done for both a 15-mm and 20-mm diameter steel projectile impacting the coarse RDX formulation at a velocity of 1.13 mm/μsec. Results are presented in Table 11. Comparing the results in Fig. 15 and Fig. 16 shows that the smaller diameter projectile allows rarefactions to reduce the pressure sufficiently to prevent transition to detonation.

The 2D code was used to investigate the detonation failure diameter of both the fine and

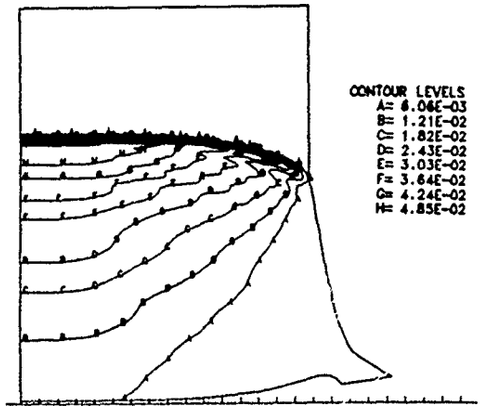

Fig. 14. Pressure contours in coarse RDX explosive 7 μsec after impact by 4-mm thick Al plate with velocity of 0.96 mm/μsecs. Pressures are in megabars. SDT does not occur.

coarse RDX formulations. The ignition and growth parameters obtained from the initiation experiments do not predict that the fine RDX formulation has a smaller failure diameter than the coarse. A much larger fraction of the fine RDX must be ignited at high pressure for this to occur.

TABLE 11
Calculated Results for Steel Projectile Impact Experiments

	PROJECTILE VELOCITY (mm/μsec)	PROJECTILE DIMENSIONS	CALCULATED RESULT*
COARSE RDX FORMULATION	1.133	D=20 mm L=27 mm	Detonation ~30 mm into explosive
	1.130	D=15 mm L=20 mm	No detonation

* Both agreed with experiment.

CONCLUSIONS

An ignition and growth model has been used to simulate the SDT experiments involving fine and coarse RDX formulations. The values of the parameters required in the model to fit the experimental data provide insight into the different response of these two explosives.

Table 12 summarizes the ignitior and growth characteristics as a function of input pressure in the range 4 GPa to 9 GPa. About 0.2 percent of the RDX in the fine formulation is ignited by the shock. At low pressure 5 percent of the coarse RDX is ignited. The ratio of these amounts is approximately that of the ratio of the particle sizes of the RDX.

TABLE 12
Calculated Ignition and Growth Behavior

INPUT PRESSURE	APPROXIMATE AMOUNT IGNITED		AVERAGE RELATIVE GROWTH RATE TO 50% REACTED	
	FINE RDX	COARSE RDX	FINE RDX	COARSE RDX
4 GPA	0.2%	5%	1.0	1.1
6 GPa	0.2%	5%	1*	1.1
7 Gpa	0.2%	7%	1.0	1.3
9 GPa	0.2%	13%	1.0	2.5

* Reference average growth rate. This growth rate varies from ~0.1 μsec^{-1} at 10% reacted to ~0.7 μsec^{-1} at 50% reacted.

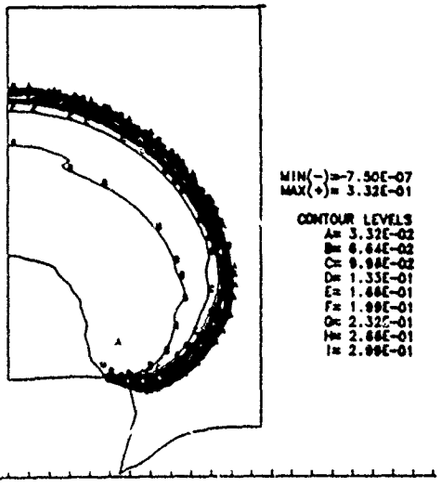

Fig. 15. Pressure contours in megabars for 20-mm steel projectile impacting the coarse RDX formulation. SDT has occurred

The reaction growth rates for the fine RDX formulation at input pressures up to 9 GPa and the coarse RDX formulation at input pressures up to 6 GPa are very similar. These average relative growth rates were calculated using the parameters

listed in Table 9 for the first fifty percent of reaction and pressures ranging from input pressure to input pressure plus 2 GPa.

Above 6 GPa input pressure both the amount ignited and the growth rate increased for the coarse RDX formulation. Fracturing of the coarse RDX crystals could be a possible reason for this, but additional experiments would be required to elucidate any such postulated mechanism.

Simulation of the thinnest pressure pulse experiments and detonation velocity vs. diameter behavior indicate a crossover in sensitivity of the fine and coarse RDX formulations at high pressure. Additional experiments are required before one can pin point the reason for this.

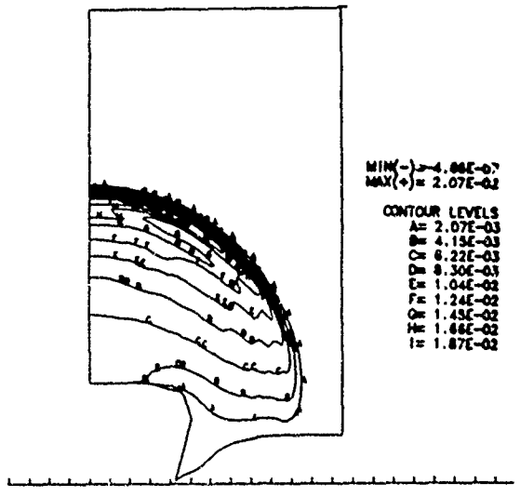

Fig. 16. Pressure contours in megabars for a 15-mm steel projectile impacting coarse RDX explosive. Projectile velocity and time after impact is the same as in Fig. 15. SDT does not occur.

ACKNOWLEDGEMENTS

The work at the Franco-German Research Institute was carried out under contract from the Societe Nationale des Poudres et Explosifs. The authors wish to acknowledge the help of Dr. F. Bauer with the PVF_2 non-reactive Hugoniot experiments and Mr. Matt Wraith for the large number of 1D and 2D computer simulations he provided. The authors also wish to acknowledge many helpful discussions with Drs. C. Fauquignon, E. Lee and C. Tarver.

REFERENCES

1. E. L. Lee and C. M. Tarver, Phys. Fluids *23*, 2362 (1980).

2. C. M. Tarver, J. O. Hallquist and L. M. Erickson, "Modeling Short Duration Shock Initiation of Heterogeneous Explosives," presented at this Symposium.

3. Y. de Longueville, C. Fauquignon and H. Moulard, "Initiation of Several Condensed Explosives by a Given Duration Shock Wave," Sixth Symposium (International) on Detonation, ACR-221, Coronado, CA, August 1976, p. 105.

4. R. Droux and C. Mouchel, "Etude du Comportement Sous Choc et de la Generation de la Detonation d'explosifs Heterogenes par la Methode du Double Coin," Symposium on High Dynamic Pressures, Paris, France, August 1978, p. 103.

5. F. Bauer, "PVF2 Polymers: Ferroelectric Polarization and Piezoelectric Properties Under Dynamic Pressure and Shock Wave Action," Ferroelectrics, *49*, 231 (1983).

6. C. M. Tarver amd J. O. Hallquist, "Modeling Shock Initiation and Detonation Wave Phenomena in PBX-9404 and LX-17," Seventh Symposium (International) on Detonation, NSWC MP 82-334, Annapolis, MD, June 1981, p. 488.

7. LASL Shock Hugoniot Data, Stanley P. Marsh, ed., University of California Press, Berkeley, CA (1980).

8. P. J. Torvik, "Hugoniot for a Mixture," Air Force Technical Institute Report, AFIT TR 70-3, May 1970.

9. J. W. Kury, et al., "Metal Acceleration by Chemical Explosives," Fourth Symposium (International) on Detonation, ACR-126, Silver Spring, MD, October 1965, p. 3.

10. B. M. Dobratz, ed., "LLNL Explosives Handbook — Properties of Chemical Explosives and Explosives Simulants," Lawrence Livermore National Laboratory Report, UCRL-52997, pp. 8-22, March 1981.

DISCUSSION

HOWARD CADY, Los Alamos

Is the fine RDX used in this study manufactured by grinding the coarse RDX?

REPLY BY H. MOULARD

No. The fine RDX is made by a separate recrystallisation process.

DISCUSSION

DR. P. R. LEE, Royal Ordnance, U.K.

Would you come to comment on the apparent opposite conclusions you reach in connection with the relative shock sensitivity of the fine and coarse RDX-based PBXs?

REPLY BY H. MOULARD

A discrepancy appears actually between our results and the DREV WORK (BELLANGER et al.) presented at this symposium: formulation differences should be the explanation. It is certainly important to note in our work that a very high level of shock insensitivity has been obtained with ultrafine RDX particles and no voids formulation (>99.9% T.M.D.)

DISCUSSION

LOUIS ZERNOW, Zernow Tech. Services, Inc., San Dimas, CA

My question concerns your assumption that porosity was eliminated as a variable by preparing your samples with identical compositions and identical densities.

My concern involves the question about the nature of the residual porosity, even though the average (small) porosity is identical in both the fine grained and coarse grained samples, as indicated by their identical average densities.

I would expect the pore size distribution to be substantially different in the fine grained and coarse grained samples, and not necessarily uniformly distributed within the sample.

Have you made photomicrographic observations of the actual pore sizes and their size distribution within the two types of samples?

Is it possible that such differences in the pore size distribution (even for identical average porosities) could affect the observed results?

REPLY BY H. MOULARD

We eliminate porosity as a variable because we use a casting technique giving essentially no voids formulations (>99.9%T.M.D.). In this case, ignition can be controlled concurrently by other mechanisms (density discontinuity, shear banding.)

MODELING 1-D DEFLAGRATION TO DETONATION TRANSITION (DDT) IN POROUS EXPLOSIVE

A. M. Weston
Brobeck Corp.
Berkeley, California

and

E. L. Lee*
Lawrence Livermore National Laboratory
University of California
Livermore, California

A one dimensional Lagrange hydrodynamic computer model is presented that describes gas flow, compaction, ignition, and deflagration processes in deformable porous beds. The model makes use of a consumable finite element cell that allows gas to flow through a compacting matrix. The model can be regarded as structural in the sense that the initial cell dimension is directly related to mean particle size. Experimental investigation of the DDT phenomenon are typically carried out using long thick-walled tubes filled with a granular porous bed of reactive material. In this configuration, much of the process can be described by flow in one dimension. We will present calculations that simulate both squib initiated and piston initiated experiments on porous HMX to point our various observed features. Our purpose is to establish a basis for setting bounds on the physical parameters that describe such transient reaction processes.

INTRODUCTION

We will present hydrodynamic calculations which simulate deflagration and compaction plug formation in three experiments that produced a detonation transition in porous HMX. The three experiments involve (1) squib ignited 61% Theoretical Maximum Density (TMD) coarse HMX with an average particle size of 1.08 mm inside a thick walled Lexan tube,(1) (2) an impact driven piston acting on 62% TMD LX-04-1 Grade HMX inside a thick walled plexiglas tube, (2,3), and (3) a gas driven piston acting on 64% TMD class C HMX inside a high strength steel tube.(4)

Additional calculations are presented that simulate shock initiation run distance to detonation (RDD) experiments (5) performed on 65% TMD class A HMX.

Deflagration and gas flow are incorporated into a one dimensional, planar, Lagrange, elastic-plastic, computer model. A finite differenced thermal calculation is included within each hydrodynamic cell to treat heat transfer between the gas and solid phase HMX and heat flow in plastically deformed HMX.

Detailed temperature calculations allow explosion time data obtained on solid HMX to be used as a criterion to trigger the onset of deflagration.

We will show that the calculations are quite sensitive to variations for many of the parameters used in the model.

*Work performed under the auspices of the U.S. Department of Energy by the Lawrence Livermore National Laboratory under contract No. W-7405-ENG-48.

CALCULATION PROCEDURE

The three geometric models illustrated in Figure 1 are helpful in visualizing the compaction and gas flow computation algorithms. The constant frontal area model (Figure 1a) represents the hydrodynamic relations. The spherical pore model (Figure 1b) represents the compaction equation of state (EOS), and the intersecting tube model (Figure 1c) represents the gas flow equations, the gas to matrix heat transfer area piror to ignition, and burn area after ignition.

Most hydrodynamic calculations proceed on the basis of pressure, relative volume, mass, and energy. Explicit determinations of material temperatures are not necessary. Here our objective is to apply thermal criteria to the onset of rapid deflagration and to be able to regulate the rate of growth of reaction as a compaction plug is formed.

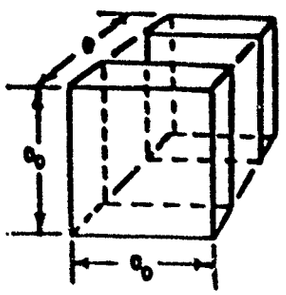

Fig. 1a. Constant frontal area cell for 1D hydrodynamics

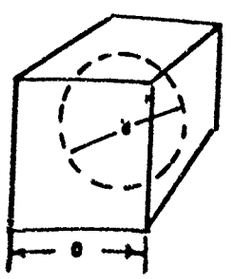

Fig. 1b. Spherical pore compaction cell for pressure vs. volume

DEFLAGRATION CRITERIA

There are 40 thermal zones in the unburned material surface of each cell for the heat conduction calculation. This calculation includes both heat transfer from the flowing gas and

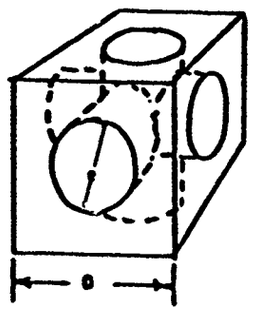

Fig. 1c. Cylindrical tube cell for gas flow

distributed plastic work. A theoretical convective surface heat transfer coefficient is calculated that is consistent with pebble bed data, (6) where porosity is high, and with the flow of air in ducts, where porosity is low.(7) Calculated Reynold's numbers and Mach numbers exhibit trubulent choking flow characteristics where compaction is occurring.

The One-Dimensional Time To Explosion Experiment (8) (ODTX) measures the induction time to thermal runaway when the surface of a sphere of full density reactive material is suddenly enclosed by anvils preheated to a given temperature. For explosion times that range between 1 and 1000 seconds, the results can be described as

$$\ln t_E = \ln D + \frac{K}{\theta_S(t)} \qquad (1)$$

where t_E is the explosion time and θ_S is the surface temperature. This data is then extropolated several decades to the microsecond time range of our interest.

A trigger parameter (R) was set to an initial value of one. Thereafter,

$$R = 1. - \int \frac{dt}{D\exp[K/\theta_S(t)]} \qquad (2)$$

where dt is a time increment. Deflagration is assumed to begin when R = 0. Following this, the advance of the burning process along the tube, that leads to compaction plug formation prior to detonation, in controlled by the solid matrix surface temperature (θ_S) achieved in the first cell for which R became equal to zero. Also, cells are ignited when gas pressure exceeds 0.1 GPa (1.0 kb) to compute turnover to detonation using a conventional hydrodynamic calculation procedure, after a plug has been formed.

It was necessary to adjust the rising surface temperature so that it would trigger deflagration at a time consisent with the experimental data. To do this for the squib ignited experiment, the convective heat transfer coefficient was divided by a constant ($C_H = 5.16$). For the piston impact experiment the distributed plastic compaction work was mulitiplied by a contant ($C_C = 21.3$).

GAS LAW

We use the JWL(9) EOS to produce realistic detonation performance

$$P_G = Ae^{-R_1V} + Be^{-R_2V} + \frac{\omega C_V T}{V} \qquad (3)$$

where V is the relative volume (1.0 at 100% TMD); C_V is the specific heat energy per unit volume of 100% TMD HMX; and A, B, R_1, R_2, ω are JWL EOS constants for 100% TMD HMX.

It can be shown that the 3rd term of the JWL EOS (Eq. 3) is equivalent to the ideal gas EOS.

BULK MODULUS

The calculation procedure for composite gas phase plus solid phase bulk modulus assumes that the solid phase bulk compaction is in "parallel" with the gas phase bulk compression so that the resisting component bulk moduli are additive,

$$K = \frac{K_S}{\alpha} + \frac{K_G}{\alpha}(\alpha - 1) \; ; \; K_G = -V\frac{dP_S}{dV} \qquad (4)$$

$$P_S = Ae^{-R_1V} + Be^{-R_2V} + CV^{-(\omega+1)}$$

$$\alpha = \frac{\text{Total Volume}}{\text{Solid Volume}}$$

where α is the porosity; P_S is the pressure from the JWL CJ isentrope; K is the composite bulk modulus; K_G is the bulk modulus for the gas; K_S is the bulk modulus for the solid; and C is another JWL EOS constant. For an expanding cell, in which gas pressure is the controlling factor, a second form is used,

$$K = \frac{K_G K_S \alpha}{[K_G + K_S(\alpha - 1)]} \qquad (5)$$

In Eq. (5), a "series" arrangement is assumed (for which solid and gaseous compressions are additive) so that the composite bulk modulus is less than either of the component bulk moduli. While Eqs. (4) and (5) meet the same limits when $\alpha \rightarrow \infty$ and $\alpha \rightarrow 1.0$, values in-between will greatly differ.

BURNING SURFACE AREA

A cell's burn area (A_B) is equal to its geometric (Figure 1c) internal surface area (A_G), multiplied by a function of the incrementally accumulated plastic compaction work (P_W). Let P_{W1} equal a critical value for P_W. P_{W1} occurs when the compaction pressure reaches a critical value ($H_C = 0.035$ GPa). Then,

$$A_B = A_G \times N_1, \text{ for } P_W < P_{W1} \text{ and} \qquad (6)$$

$$A_B = A_G \times [N_1 + N_2 \times \frac{(P_W - P_{W1})}{P_{W1}}], \text{ for } P_W > P_{W1}$$

When deflagration has proceeded to a point where the hole dimension equals the cell dimension, the burn area (A_B) is geometrically related to the corner shape and the unburned fraction.

The incremental decrease in the solid material volume (δV) is the product of the time increment (δT), the burn area (A_B), and the experimentally determined gas pressure dependent regression rate for solid HMX(10) (R_B).

$$\delta V = R_B \times A_B \times \delta T \qquad (7)$$

where

$$R_B = \text{Const} \times (P_G)^{0.83}$$

GAS TRANSPORT

Cell to cell gas transfer is controlled by a set of three difference expressions based upon the differentail equations(11) for adiabatic, one dimensional, steady, compressible flow with friction in a constant area circular duct, (Figure 1c). The difference equations are written for Mach No. (M), gas pressure (P_G), and gas temperature (T_G). The friction factor (f), depends upon the Reynolds No. (Re) and the duct "roughness".

$$\frac{\delta M}{M} = \frac{f}{2}\left(\frac{\delta X}{e}\right)\frac{\gamma M^2}{(1-M^2)}\left[1 + \left(\frac{\gamma - 1}{2}\right)M^2\right] \qquad (8)$$

$$\frac{\delta P_G}{P_G} = -\frac{f}{2}\left(\frac{\delta X}{e}\right)\frac{\gamma M^2}{(1-M^2)}\left[1+(\gamma-1)M^2\right]$$

$$\frac{\delta T_G}{T_G} = \frac{-(\gamma-1)M^2}{\left[1+\left(\frac{\gamma-1}{2}\right)M^2\right]}\left(\frac{\delta M}{M}\right)$$

As a consequence of the denominator expression $(1 - M^2)$, when gas flow begins subsonically, the flow rate can never exceed a value corresponding to $M = 1$.

Cell to cell pressure drop is increased by a "flow rate squared" term that accounts for assumed duct entering, exiting, and turning effects. Also, the duct length connecting adjacent cells, (δX), is increased by a multiplier (current value = 1.5) to account for a tortuous flow path. While transient gas flow inertia is not considered in the formulation of equations (8), the mass of the transferred gas is included in the hydrodynamic equation for conservation of mass

$$\frac{\dot{\varrho}}{\varrho} = \frac{\dot{m}}{m} - \frac{\partial U}{\partial r} \qquad (9)$$

where ϱ is the cell density; m is the cell mass; U is the velocity; r is the position; and $\dot{m}$ is the cell to cell gas transfer rate.

COMPACTION BEHAVIOR

The Lagrange hydrodynamic conservation equations for momentum and energy are formulated in the conventional way.(12) The yielding behavior of the compacting porous bed is controlled by a Von Mises yield condition where 1D planar stress deviators are included.

The constitutive equation for compacting porous materials has been fitted to experimental quasi-static data.(13,14) The isotropic mechanical flow pressure (P_M) is given by

$$P_M = P_G + H(\alpha) \times \Phi(\alpha) \qquad (10)$$

where α is the porosity; P_G is the pore gas pressure; H is the operating flow (yield) stress as the cell is compacting; and Φ is a non-dimensional cell geometry parameter. Φ is described by an equation for the closing of a spherical pore, somewhat similar to (but simpler than) the relationships derived by Carroll and Holt.(15)

While the three different kinds of tube experiment, and the run distance experiment each used a different grade of HMX, it can be inferred from coarse HMX quasi-static compaction data that when density exceeds 80% TMD the effect of grade difference is not large.

The yield condition, bulk modulus, shear modulus, and stress deviators are all functions of porosity and gas pressure. The effective hydrodynamic response at any position and time can be elastic, plastic or gas driven as determined by the unburned matrix fraction and by other local loading details. An option is included so that steady gas flow through a "rigid" porous matrix can be calculated and calibrated to experimental permeability data.

Our calculational results are quite sensitive to parameters that directly effect heat transfer coefficient, deflagration temperature (energy), distribution of compaction work, material thermal properties as a function of temperature, and burn rate.

COMPARISON OF EXPERIMENTAL AND CALCULATIONAL RESULTS

Squib Ignited Experiment(1)

This experiment was first modeled by Kim(16) using the DETOVA program. We used results from his calculation to create our squib burn model. The squib drives an 80% TMD compaction wave through the porous bed.

Figure 2 is a plot of calculated displacment profiles at 300 μs and 400 μs. The experiment included an axial array of tungsten pins. The plotted data points show pin displacement from radiographs taken at 303 μs and 403μs. Figure 3 is a plot of the tube position where calculated artificial viscosity is maximum versus time. The experimental streak record features have been superposed. Figure 2 and 3 illustrate the correspondence between the experimental data and the simulation.

Figure 4 is a sequence of compaction profiles between 340 μs and 410 μs showing the process of plug formation. Figure 5 is a similar sequence between 420 μs and 438 μs illustrating the turnover to detonation. Figures 3, 5, and 6 clearly show retonation as well as detonation as the high density compaction plug is reduced to product gas. Figures 7 and 8 show both gas and hydrodynamic pressure profiles at 400 μs before turnover to detonation and at 428 μs after detonation is

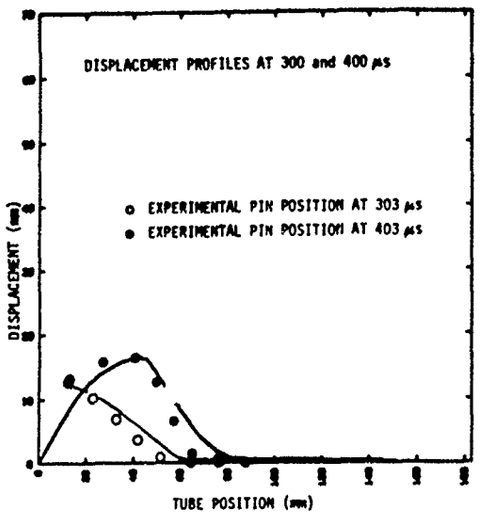

Fig. 2. Squib ignited experiment experiments vs. calculated pin displacement

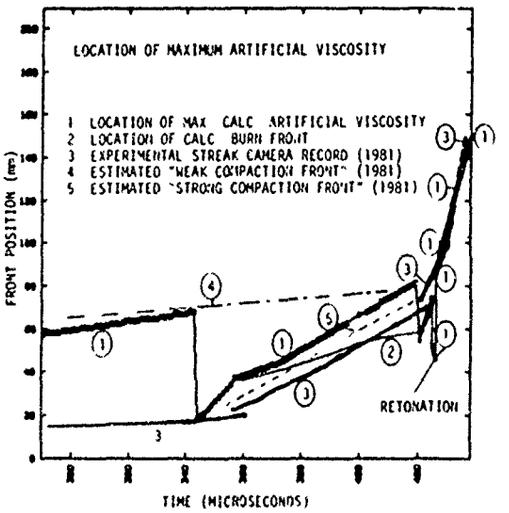

Fig. 3. Calculated front location versus time and experimental streak record for squib ignited experiment

well developed. Figures 9 and 10 show the corresponding velocity profiles. The theoretical detonation velocity for 61% TMD HMX is 6.28 mm/μs. The illustrated maximum calculated detonation velocity is 5.3 mm/μs. The experimental streak record maximum velocity was 5.9 mm/μs. These lower than theoretical detonation velocities illustrate that the turnover process was not quite complete before the end of the experiment. In calculations performed with a larger assumed burn rate, the calculated detonation velocity approaches but does not exceed the theoretical value. The theoretical Chapman-Jouguet (CJ) pressure is 14.4 GPa (144 kb). The calculated CJ pressure at 428 μs plotted on Figure 8 is of that order of magnitude.

Figure 11 shows profiles of the ODTX trigger parameter (R) at 280 μs, and 290 μs. Ignition occurred at 286 μs. Figure 12 shows matrix surface temperature profiles for surface zones at different depths at 280 μs, about the time of ignition. The thermal zone thickness is about 4 x 10^{-7} mm.

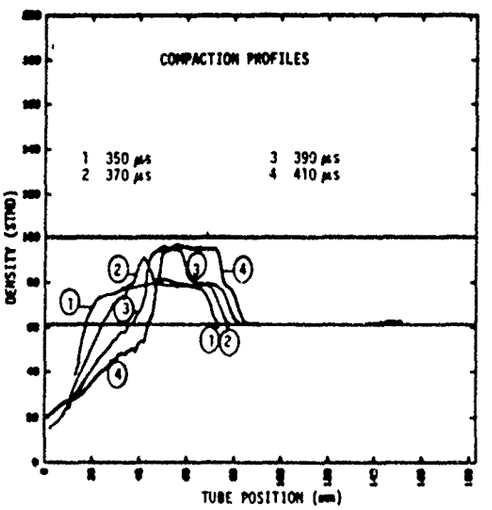

Fig. 4. Squib ignited experiment and formation of a compaction plug

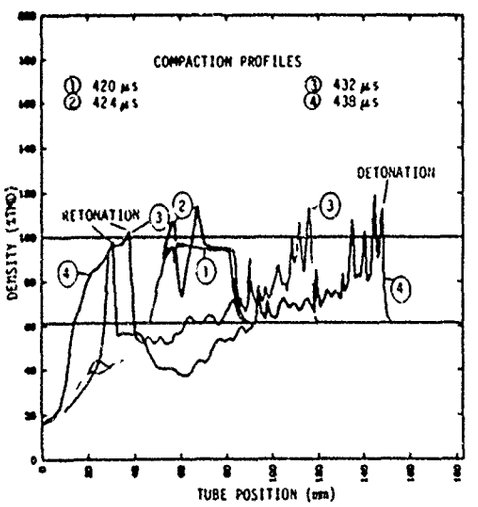

Fig. 5. Squib ignited experiment and transition to detonation.

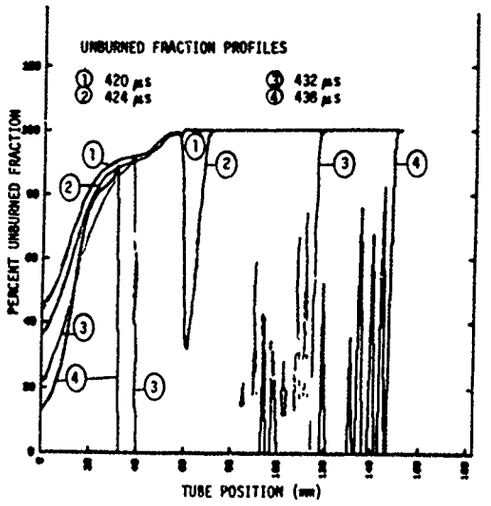

Fig. 6. Squib ignited experiment and transition to detonation

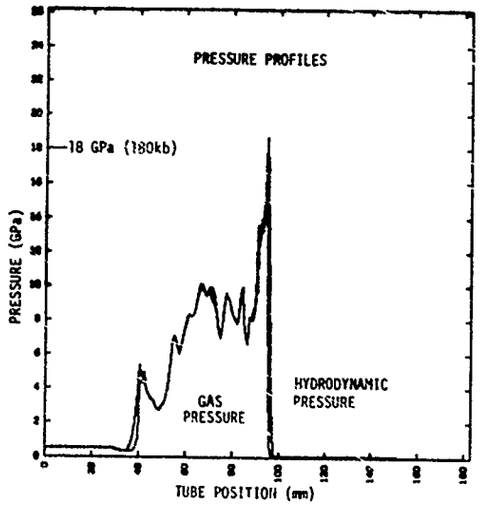

Fig. 8. Squib ignited experiment pressure at 428 μs

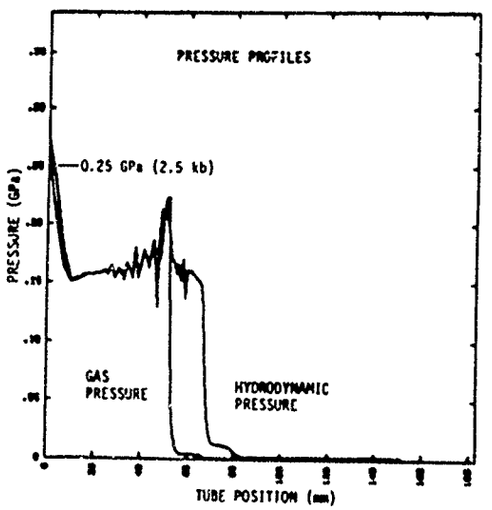

Fig. 7. Squib ignited experiment pressure at 400 μs

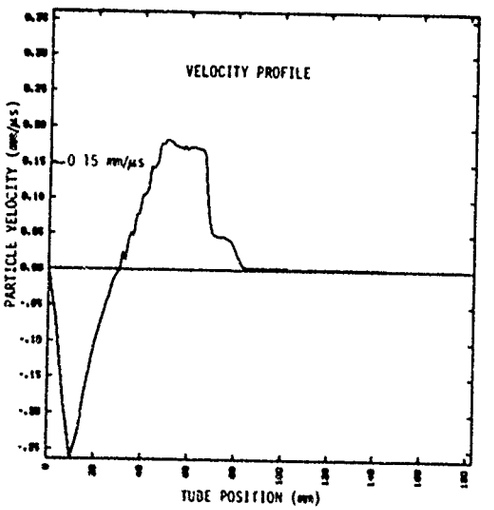

Fig. 9. Squib ignited experiment velocity at 400 μs

The sensitivity to change of input parameter is given in Table 1. Column 1 lists input parameters and calculated timing for the reference simulation, Figure 2 to 12. Column 2 is for a calculation where the squib burn rate is reduced by 10%. Column 3 is for a calculation where the assumed granulation has been reduced by a factor of 2, i.e., an initial porous material cell dimension of 0.54 mm rather than 1.08 mm. Also, Figure 13 illustrates the superposed plots for front velocity versus time. A 10% reduction in squib burn rate increased the time to detonation from 420 μs to 457 μs. A 2 to 1 reduction in cell dimension (granulation) decreases the time to detonation from 420 μs to 331 μs.

IMPACT PISTON EXPERIMENT (2,3)

The record for this experiment is a set of framing camera photographs. A steel cylinder in an aluminum sabot assembly that weighted 24.5 kg, with a pre-impact velocity of 324 m/s, struck an aluminum attenuator 50 mm in diameter and 25.3 mm long, adjacent to a steel piston 50 mm in diameter and 190.4 mm long.

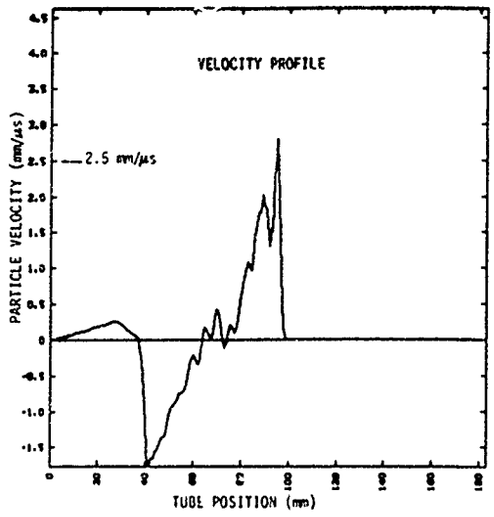

Fig. 10. Squib ignited experiment velocity at 428 μs

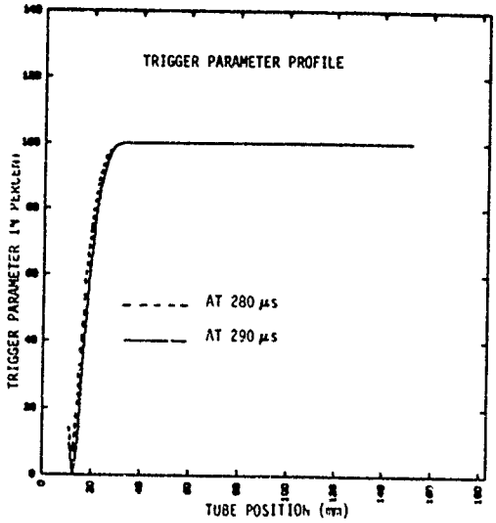

Fig. 11. Squib ignited experiment ODTX ignition trigger parameter

TABLE 1

Input Parameter Variations for Squib Ignited DDT Tube

Column	1 Reference	2 0.9 x Squib burn Rate	3 ½ Zone Size
Initial Matrix Density	61% TMD	61% TMD	61% TMD
Initial Cell Width	1.08 mm	1.08 mm	0.54 mm
Convection Divisor, C_H	5.16	5.16	5.16
Compaction Multiplier, C_P	21.3	21.3	21.3
Matrix Burn Rate Exponent	0.83	0.83	0.83
Burn Area Multiplier, N_1	0.95	0.95	0.95
Burn Area Multiplier, N_2	45.0	45.0	45.0
Crit. Comp. Press., H_C	0.085 GPa	0.085 Gpa	0.085 GPa
Time to Ignition	286 μs	302 μs	246 μs
Time to Start of Plug Formation	343 μs	366 μs	290 μs
Time to Start of Detonation Turnover	420 μs	457 μs	331 μs

The piston extended inside a thick wall plexiglas tube containing a porous bed of HMX that was 294 mm in length. From the photographs, fourteen data points provided compaction front location versus time and detonation front location versus time. Also, seven data points provided piston front location versus time.

The piston displacement history was used to produce the velocity versus time plot illustrated on Figure 14 (used as input to the hydrodynamic calculation). The final velocity (conserving momentum) for the impactor-target piston assembly was 288 m/s. After detonation began, the pre-programmed velocity was bypassed and the piston-attenuator system was allowed to slow down in response to the large hydrodynamic pressure. The calculation was terminated shortly after the detonation process began and the iteration cycle time became very short.

Figure 15 illustrates the calculated X-t net for compaction front, detonation front, and other piston front positions versus time. Just as in the squib initiated experiment, the compaction and detonation front locations are identified

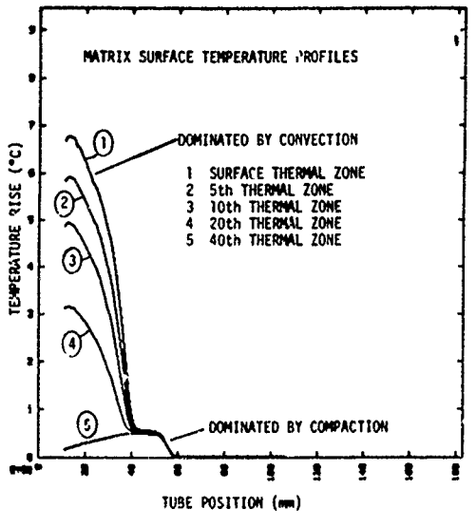

Fig. 12. Squib ignited experiment matrix surface temperature at 280 μs just prior to ignition

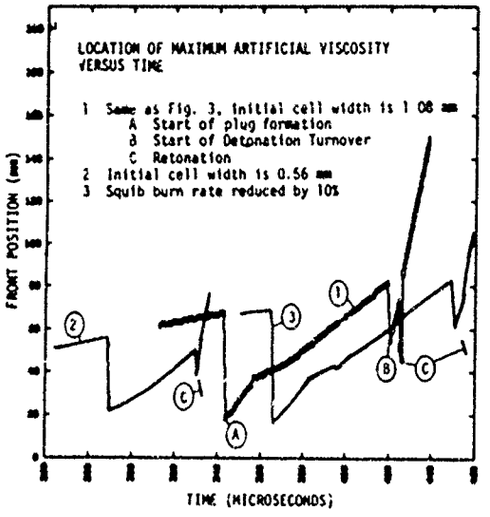

Fig. 13. Calculation sensitivity to change of input parameters. Compare to Fig. 3

by the position of maximum artificial viscosity. Note that the plotted experimental front positions agree well with the calculated front positions to a time of 250 μs. After this time the experimental data lags the calculated result. The pressure on the right hand side of the second compaction front is 0.32 GPa (3.2 kb) which is substantially larger than the pressure on the left of 0.064 GPa (0.64 kb). The framing camera photographs clearly show radial tube expansion after 264 μs. Also, a very bright line at 448 μs seems to indicate detonation at the compaction front rather

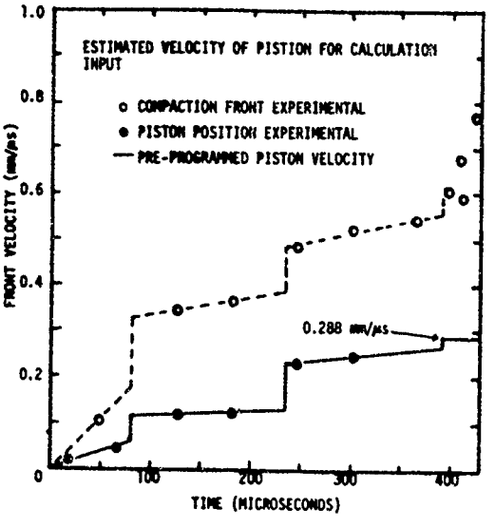

Fig. 14. Impact piston experiment central differenced experimental velocities and preprogrammed piston velocity vs. time from Fig. 15 X-T plot

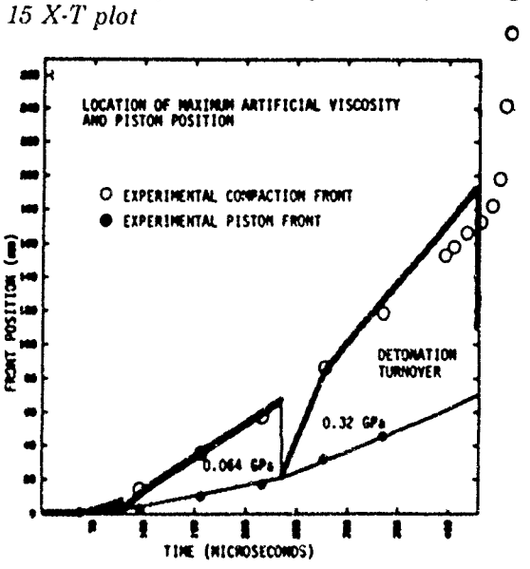

Fig. 15. Impact piston experiment calculated and experimental X-T plot

than between the piston and compaction front as calculated.

Figure 16 is a sequence of compaction profiles after 416 μs during turnover to detonation. Figure 17 is a corresponding series of unburned fraction profiles. Note that while burning starts at the piston, it creates a more heavily compacted region in front of the piston which is where the 1D detonation process begins.

It would be desirable if the same set of porous material behavior assumptions could be used to simulate both the squib initiated experiment and the impact piston experiment. This is almost the case. Equation 6 describes the burn area relationship. It was necessary to nearly double the material pressure (H_C = 0.166 GPa) when the critical value for plastic work (P_{W1}) occurred in the impact piston simulation. Possible reasons for this discrepancy are (1) HMX particle size, (2) sudden plexiglas tube expansion during the impact piston experiment, and (3) lack of an adequate description of strain rate effects in the expressions for compaction, heating, and burn rate surface.

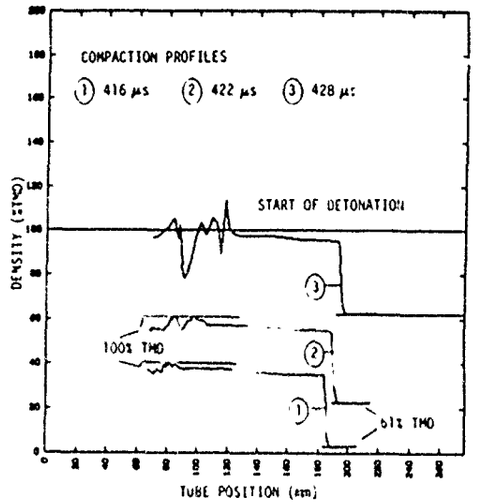

Fig 16 Impact piston experiment turnover to detonation

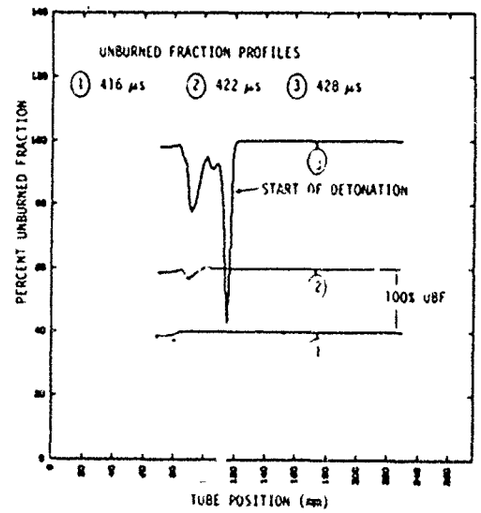

Fig 17 Impact piston experiment turnover to detonation

Gas Driven Piston Experiment (4)

In Campbell's experiment, a piston was accelerated into porous 64% TMD HMX by gas pressure produced in a gas volume in back of the piston filled with very low density HMX that was initiated by an SE-1 ignitor. The experiment was contained inside a 13.4 mm bore diameter strong maraging steel tube 305 mm in length. The piston initially was partially sealed with epoxy resin to the tube* and did not release until significant gas pressure (0.05 GPa) had been created in front of the piston.

The driving pressure was monitored; an array of thin (0.13 mm) lead foils was spaced through the porous HMX; and there were arrays of capped pins and ionization pins. Detonation was produced 780 μs after the initiation and 500 μs after piston motion began. Radiographs showing lead foil position were taken at 180 μs and 204 μs after piston motion began.

We performed a non-rective hydrodynamic calculation on this system that reproduced the experimental foil displacements at the times of the radiographs. The pistion and leakage gas was pushing an 88% TMD plug at .11mm/μs. This velocity is only 44% of the velocity observed by Green (3) at ignition time. From this we infer that Campbell's experiment would not have ignited from compaction alone and that hot gas blowing past the piston was involved. Campbell has improved his test setup to eliminate gas blow-by and plans to repeat the experiment.

Campbell's ionization pins monitored shock front velocity versus time during turnover to detonation. The highest velocity (10.3 mm/μs) occurred soon after turnover. It then slowed to a stable velocity of 6.36 mm/μs, a value near expected steady value of 6.65 mm/μs The sequence of higher velocity to be followed by final stable lower velocity is consistent with the 1D performance we calculated for Green's impact piston experiment.

We feel that Campbell's experimental setup and instrumentation provides a good 1D test. The high strength steel tube maintains high confinement for a significant portion of the DDT process so that a 1D hydrodynamic calculation remains relevant for much of its duration.

*It was estimated that about ½ the piston clearance volume was filled with epoxy cement.

TABLE 2
Calculational vs. Experimental Results for Run Distance Experiments on Class A HMX

		J. Dick	Calc.
Particle Velocity	mm/μs	0.3923	0.3923
Estimated Pressure	Kb	7.929	7.96
Shocked Density	% TMD	85.81	86.0
Shock Velocity	mm/μs	1.63	1.60
Transit Time	μs	3.01	--
Est. Matrix Flow Stress	Kb	--	7.3
Quasi-Static Data Fit Multiple	---	---	37X
Particle Velocity	mm/μs	0.7438	0.7438
Estimated Pressure	Kb	20.66	20.6
Shocked Density	% TMD	97.55	98.0
Shock Velocity	mm/μs	2.24	2.25
Transit Time	μs	1.41	---
Est. Matrix Flow Stress	Kb	---	9.477
Quasi-Static Data Fit Multiple	---	---	15 X

Also, the response of the gas driven piston is relatively free of strong reverberations.

Shock Initiation Experiment (5)

These interesting experiments represent a 1-D shock impact giving rise to an incremental change of particle velocity. In the other three DDT tube experiments, pressure and velocity build over a comparatively long time.

The pre-detonation particle velocity in the HMX was calculated using the standard shock matching procedure for J. Dick's experimental setup. This particle velocity was then treated as a constant piston velocity driving the porous matrix. Table 2 tabulates both experimental and calculated parameters. It was necessary to multiply our fit to Elban's quasi-static HMX compaction pressure (14) by factors of 37 for the 8 Kb test series and 15 for the 20 Kb test series, in order for our code to simulate the experimental data. The low level of pre-detonation compaction (86% and 98%) in these test series was unexpected. The HMX in the run distance experiments may be reacting at a high rate during the run up period.

We intend to perform reactive calculations on J Dick's experiments to ascertain whether we can simulate his results with reduced plastic yield and greater gas production. At this time we do not explicitly include the effect of the rate of compaction (rate of change of porosity) in our constitutive model. It is probable that such a strain rate variable will be necessary to compute this kind of data.

CONCLUSIONS

We have developed a Lagrange calculation procedure that is well suited to the study of reactive porous material where it is necessary to follow mechanical and thermo chemical processes in detail.

Calculations were performed on four distinctly different types of low density porous HMX experiments. With the exception of the high pressure shock initiation experiment, the results reveal that a compaction plug is formed before detonation transition and that the location of the turnover is forward of the burn front that drives the process of compaction plug formation in the squib ignited experiment. The pressure histories and shock trajectories preceeding transition are strikingly similar whether piston or initially squib driven.

The results show that the ignition criteria strongly effects the results. We also found that the burn area had to be at least an order of magnitude greater than that based on the surface

area of the compacted pore. This is a clear indication that the compaction and subsequent burning of the porous material cannot be described simply as plastic work developed in closing a spherical void.

Nevertheless, the calculations lead us to believe that the principal features of DDT can be described and predicted and that a framework has been developed here to investigate details of the process.

REFERENCES

1. R. R. Bernecker, H. W. Sandusky, and A. R. Clairmont, "Deflagration-to-Detonation Transition Studies of Porous Explosive Charges in Plastic Tubes," Seventh Symposium (International) on Detonation, 119 (1981).
2. L. G. Green, E. James, E. L. Lee, E. S. Chambers, C. M. Tarver, C. Westmoreland, A. M. Weston, B. Brown, "Delayed Detonation in Propellants from Low Velocity Impact," Seventh Symposium (International) on Detonation, 256 (1981).
3. L. G. Green, private communication, December 1984, Lawrence Livermore National Laboratory.
4. W. Campbell and J. McAfee, private communication, December 1984, Los Alamos National Laboratory.
5. J. J. Dick, "Measurement of the Shock Initiation Sensitivity of Low Density HMX," Combustion and Flame 54: 121-129 (1983), Elsevier Science Publishing Co., 1983.
6. M. Jakob, "*Heat Transfer, Volume II*," John Wiley and Sons, 19, Section 42-4, p. 550.
7. F. Kreith, "*Principles of Heat Transfer*," International Textbook Company, Scranton, PA, 2nd Printing, 1959, Chapter 8, Fig. 8-2.
8. C. M. Tarver, R. R. McGuire, E. L. Lee, E. W. Wrenn, and K. R. Brein, "The Thermal Decomposition of Explosives with Full Containment in One-Dimensional Geometries," Seventh Combustion Symposium, August 1978, Leeds, U.K., Combustion Institute.
9. H. E. Hornig, E. L. Lee, M. Finger, and J. E. Kurrie, "Equation of State of Detonation Products," Fifth International Symposium on Detonation, Pasadena, CA, August 18-21, 1970.
10. T. L. Boggs, "The Thermal Behavior of Cyclotrimethylenetrinitramine (RDX) and Cyclotetramethylenetetranitramine (HMX)," Fundamentals of Solid Propellant Combustion, edited by K. K. Kuo and M. Sommerfield, Volume 90 of Progress in Astronautics and Aeronautics, Chap. 3, p. 163, 1984.
11. A. H. Shapiro and W. R. Hawthorne, "The Mechanics and Thermodynamics of Steady One-Dimensional Gas Flow," Journal of Applied Mechanics, Dec. 1947.
12. M. L. Wilkins, "Calculation of Elastic-Plastic Flow," UCRL-7322 Rev. 1, January 1969, Lawrence Livermore National Laboratory.
13. H. W. Sandusky, W. L. Elban, K. Kim, R. R. Bernecker, S. B. Gross, A. R. Clairmont, "Compaction of Porous Beds of Inert Materials," Seventh Detonation Symposium, June 16-19, 1981, pp. 44 and 456, Figs. 8 and 9.
14. W. L. Elban and M. A. Chiarito, "Quasi-Static Compaction Study of Coarse HMX Explosive," to be submitted to Powder Technology.
15. M. M. Carroll and A. Holt, "Static and Dynamic Pore-Collapse Relations for Ductile Porous Materials," J. Appl. Phys. *43*, 1626 (1972).
16. K. Kim, "Theoretical Study of Convective Combustion of Coarse HMX Particles," 1983, JANNAF Propulsion Systems Hazards Subcommittee Meeting, CPIA Publication 381, Vol. 1, September 1983, pp. 155-161.

DISCUSSION

HERMAN KRIER, Universtiy of Illinois

Your model apparently treats unsteady flow through a hard sponge-like matrix. What advantage do you get, compared to the previously published two-phase flow models (1,2) which have nicely predicted DDT in porous explosives?

Clearly I can think of many disadvantages in going ahead with your methodology, since it can be calculated (and has been observed) that the solid is often free to move, to change permeability, and to compact to shock initiation. The

1 Butler, Lembeck, Krier, "*Combustion & Flame*," Vol. 46, pp. 75-93 (1982).

2 Baer and Nunziato, SANL Report #SAND 82-0293 (1983).

deflagration in granular beds is, in my opinion, porperly modeled by solving the coupled conservation equations for mass, momentum and energy, for each (solid, gas) phase.

REPLY BY A. M. WESTON

We agree with Prof. Krier that the previously published two phase flow models (1,2) are mathematically well stated solutions to the coupled conservation equations.

However, Prof. Krier appears to be unaware that our structural model includes detailed treatment of compaction and the associated change in gas permeability. We thought this was clear from our paper. An important difference in our treatment is that we did not use an Ergun type quasi-static drag correlation for the calculation of gas permeation. While such a correlation is well suited to packed beds of very low solid fraction at low gas pressure, crucial stages in the DDT process occur after compaction to solid fractions well in excess of 80% TMD.

We see several advantages to the approach we have followed. These include the capability to follow details of gas flow through pores and passages, and to compute details of heat conduction, all within a standard procedure for shock front propagation in Lagrange coordinates. Our research model allows us to examine the physical assumptions associated with gas flow, heat transfer, compaction, ignition, and shock propagation.

DISCUSSION

BARRY BUTLER, Universtiy of Iowa

Would you please comment on the oscillations which appear in your Mach No. profiles?

REPLY BY A. M. WESTON

In the presentation we exhibited a supplementary viewgraph that illustrated both Mach number (M) profiles and Reynold's No. (Re) profiles for the squib ignited HMX experiment, in a description of early time squib gas permeation. The forward region of these profiles showed negligible values for Reynolds No. but significant values (.15-.3) for Mach Number. We assume professor Butler's question relates to this.

The ratio, Mach Number divided by Reynold's Number (M/Re), is independent of gas flow mole rate but is inversely proportional to gas pressure. Therefore, very small values for Re can be associated with appreciable values for M when gas pressure is small, i.e., at 1 atm. The computer code calculates gas flow in relation to cell to cell pressure drop to an error limit of 0.01 atm. All cells are calculated, even those well forward of the early time compaction and gas fronts. In these forward cells, insignificant numerical changes in cell dimensions and pressures give rise to very low mass but high velocity forward and aft gas flows. Absolute values are used for M and Re. This numerical process is the source of the Mach. No. oscillations observed on the viewgraph in question.

DISCUSSION

DICK STRESAU, Spooner, Wisconsin

Has a model considered deformation and failure of the porous structure?

REPLY BY A. M. WESTON

Our model does consider deformation and collapse of the porous structure. We match experimental porous HMX constitutive data.

MODELING OF REACTION BUILDUP PROCESSES IN SHOCKED POROUS EXPLOSIVES

Kibong Kim, Chang-Hyun Sohn
Korea Advanced Institute of Science and Technology
Seoul, Korea

Various mechanical deformation mechanisms such as shock interaction with discontinuities, friction, particle rearrangement, and shear banding in local areas of shocked porous explosives are examined as primary sources of thermal energy generation. These local areas of elevated temperature (hot spots) then lead chemical reaction in the explosives. The above two processes — hot spot generation and subsequent chemcial reaction — are numerically modeled. Results of the model is compared against existing experimental data on shock sensitivity of PBX-9404.

INTRODUCTION

Walker and Wasley (1) examined data of thin flyer plate experiments of Gittings (2) and proposed the concept of critical energy for shock intiaition of heterogeneous explosives. When they divided data of the test results into two groups; one group which does not show detonation after the flyer plate impact, and the other group which does, they found that there is a constant associated with energy delivered to explosive samples by the flyer plates which marks the boundary between the two groups. This energy, proportional to $p^2\tau$, where p is the strength and τ is the duration of the shock delivered to the explosive samples by the flyer plates, was called the critical energy.

de Longueville, et al. (3), among others, found that this critical energy is smaller than necessary to heat the bulk of the explosive uniformly for initiation of sustained chemical reaction. They explained that the observed chemical reaction is due to a non-uniform spatial temperature distribution within which regions of high temperature (hot spots) were sufficiently dense to initiate the chemical reaction leading to detonation.

Various physical mechanisms have been examined as sources of the hot spot generation in shocked porous explosives. They include adiabatic gas compression (4), microjetting (5,6), plastic flow (7), shock interaction with discontinuities (8), shear zones and dislocation pileup (9). With an exception of adiabatic gas compression, all the above mechanisms represent one or other forms of mechanical deformation of the solid explosives. For example, friction is none other than mechanical deformation of asperities near the surface. The shock interaction with discontinuities of three-dimensional geometries (inclusions, bubbles) also represent mechanical deformation around these discontinuities. It is likely that a real explosive undergoing shock induced localized heating may see a number of the above mechanisms *simultaneously*.

In one form or another, many people-Kim (10), Wackerle and others (11), Kooker and Anderson (12), and Khasainov and others (13)-chose to represent the above complex mechanisms with a mathematically simple form and adapted a hollow sphere geometry which Carroll and Holt (14) originally used in the study of compaction of inert porous materials. They used the geometry to simulate the deformation behavior around a pore and assumed that the explosive undergoes one type of deformation-bulk viscoplastic deformation.

Other theoretical studies include calculations of hot spot temperatures by Kipp and others (15) based on a continuum mixture theory, and Hayes (16) and Pastine and Frankel (17) based on the assumption that plastic work generated

around a pore of explosive is converted into heat into a volume equal to the original pore volume. Still other theoretical studies (18, 19) avoided direct calculation of the hot spot temperature in representation of the overall chemical reaction rate in porous explosives under shocks.

This paper is an extension of the paper by Kim (10). First, it reexamines material behavior in the compaction process, especially the role of particle rearrangements in generation of heat in hot spots. Using the hollow sphere geometry, the temperature distribution in the explosive can be calculated as a function of time and location (radius). Then, an Arrhenius type chemical kinetics is assumed to start. This reaction eventually leads to a quasi-static chemical reaction (surface regression) balanced on one hand by heat transfer, and on the other hand by the chemical kinetics.

Hot Spot Formation

One can assume that in the process of compaction of shocked explosives all of the deformation mechanisms (particle rearrangement, shear banding, and bulk plastic deformation and others) occur as follows:

As an external stress is applied, particles immediately go through elastic and plastic deformation. Soon slip planes and shear bands form and generate small particles. Some of these particles may move from their original position with or without much resistance settling into different locations before further compaction of the bulk material starts. Some particles may impact on other particles. The particles may or may not break into still smaller particles while going through subsequent compaction. Dynamic friction, shear banding and viscoplastic deformation all become a factor here. Eventually the deformation approaches an asymptotic state which is independent of dynamic (rate-dependent) parameters. the final porosity may be defined by the applied stress and the non-dynamic parameters of the material.

The study of each of the isolated phenomena such as shear bands, impacts, local plastic deformation, frictional surfaces between particles and relative motion among particles is not possible. Here, we attempt to predict a global behavior of the deforming region, using a continuum approach with an assumption of statistical randomness of the structural irregularities in a given control volume small enough to be a part of a single original crystal but large enough to contain many of the above phenomena in it.

The material behavior of compaction of shocked explosives under the global description can be termed elastic-viscoplastic, in the sense that there are mechanisms which are strain-rate dependent (viscous) and other which are strain dependent (elastic-plastic). The strain-rate dependent mechanisms may include shear banding, dynamic friction and bulk viscoplastic deformation. The strain dependent terms may include the particle rearrangement mechanism as well as the bulk elastic-plastic deformation of the particles.

Exact mathematical functional form of the elasto-viscoplasticity is difficult to obtain for these materials. Therefore, an a priori quantitative analysis is not available. However, some important features dominating the compaction process of shocked explosives and the resulting sensitivity may be qualitatively obtainable by assuming a simple mathematical form. The following linear relationship for the elastic viscoplastic material has been adopted as the simple form:

$$\frac{d\varepsilon}{dt} = \dot{\varepsilon} = \gamma_1(\sigma - \sigma_0) + \frac{1}{E}\frac{d\sigma}{dt} \qquad (1)$$

where ε is the strain, $\dot{\varepsilon}$ is the strain rate, σ is the stress, t is the time, γ_1 and E are constants and σ_0 is the static yield strength of the material. The exact values of γ_1 and E are unknown a priori, but may be estimated with appropriate experimental data.

One still needs further simplification to study the three-dimensional compaction process. Carroll and Holt (14) showed that a simple hollow sphere model approximates dynamic compaction process of powdered materials reasonably well. The model, shown in Fig. 1, assumes that pores in the explosive are uniform in size and distribution, that the size of the void sphere in Fig. 1 equals the average pore size, with the ratio of volumes of spheres with inner and outer radii r_i and r_o equal to the porosity of the explosive, and that the compaction of this hollow sphere represents the overall compaction behavior of the explosive. This model was chosen in this paper.

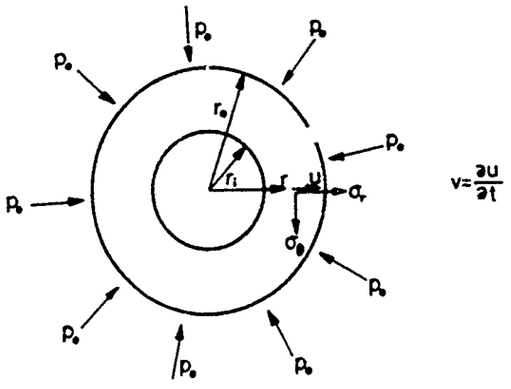

Fig. 1. Hollow sphere model: r_i is the pore radius, r_o is the solid radius, r is the space coordinate

For the problem under consideration, the set of equations describing the material behavior and the force balance for the given system, neglecting inertial effects and bulk compressibility, is (20]):

$$\frac{\partial \sigma_r}{\partial r} + 2\frac{(\sigma_r - \sigma_\theta)}{r} = 0 \tag{2}$$

$$\frac{\partial v}{\partial r} - \frac{v}{r} = \sqrt{3}\,\gamma\left(\frac{(\sigma_r - \sigma_\theta)}{\sqrt{3}\,k} - 1\right) + \frac{1}{2G}\frac{\partial}{\partial t}(\sigma_r - \sigma_\theta) \tag{3}$$

$$\frac{\partial v}{\partial r} + 2\frac{v}{r} = 0 \tag{4}$$

where σ_r is the radial stress, σ_θ is the tangential stress, r is the space coordinate, v is the radial displacement rate,

$$\gamma = \gamma_1 \sigma_0,\ k = \sigma_0/\sqrt{3},\ \text{and}\ G = E/3.$$

G is the shear modulus of the material going through the complex deformation process described above, but not that of the matrix material in the conventional sense. Eq. (2) describes the force balance of the system, Eq. (3) is a rewritten form of Eq. (1) for spherical symmetry and Eq. (4) shows the volume conservation of the solid mational.

The boundary and initial conditions are:

$$\sigma_r(r_i,t) = -p_g$$

$$\sigma_r(r_o,t) = -p_o$$

$$\sigma_r(r,\,0) = 0$$

$$\sigma_\theta(r,\,0) = 0$$

where p_o is the applied stress at r_o and p_g is the gas pressure in the void. The negative signs in the first and second equations indicate that p_o and p_g are compressive stresses.

The solution of v for the above set of partial differential equations can be obtained in an analytical form by use of Laplace transformation:

$$v(r,t) = \left[\frac{p_o - p_g}{4G(r_o^{-3} - r_i^{-3})r^2}\right]\delta(t) + \frac{\gamma}{2(r_o^{-3} - r_i^{-3})r^2 k}\left\{p_o - p_g - 2\sqrt{3}\,k\,\ln\frac{r_o}{r_i}\right\} \tag{6}$$

where $\delta(t)$ means a Delta function at t=0. Details of the solution procedure are not given here.

The first term represents an instantaneous (since the inertial effect is neglected) elastic shear deformation caused by the stress difference between the applied stress p_o and the gas pressure in the void, and the second term represents viscous shear deformation by an overstress, $p_o - p_g - 2\sqrt{3}\,k\,\ln\frac{r_o}{r_i}$.

The term overstress is used for the following reason. The term,

$$p_s = 2\sqrt{3}\,k\,\ln\frac{r_o}{r_i} = \frac{2}{\sqrt{3}}k\,\ln\frac{1}{\phi} \tag{7}$$

where ϕ is the porosity of the material, is the current static compaction stress which is a stress required to compact the material eventually to the current porosity (refer to Eq. (8)). Therefore the term $(p_o - p_g) - p_s$ represents the difference betweeen the driving stress $(p_o - p_g)$ and the current static compaction stress as ϕ changes with time. When the current compaction stress becomes equal to the driving stress, the deformation stops. The porosity at this stage is calculated from Eq. (6) as:

$$\phi_f = \exp\left\{-\frac{\sqrt{3}(p_o - p_g)}{2k}\right\} \tag{8}$$

This result compares favorably with existing experimental data (21).

A typical compaction process for a set of selected parameters is shown in Figure 2. In the figure, ϕ_1 is the porosity reached after the instantaneous elastic deformation. The viscous deformation gradually progresses until the final porosity ϕ_f is reached.

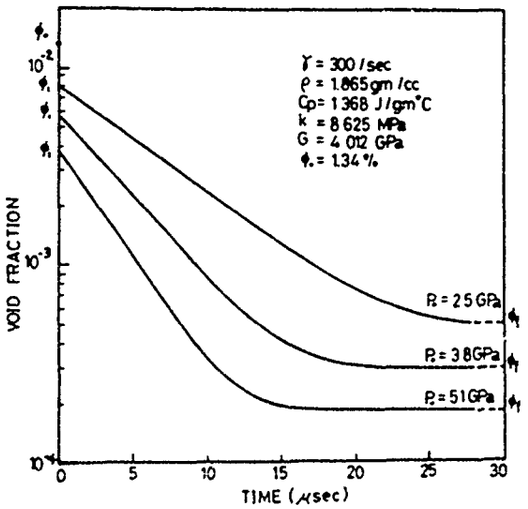

Fig. 2. Dynamic compaction process of a void

The temperature increase due to the elastic-viscoplastic deformation can be computed as follows. The work done dW by the deformation is given by:

$$dW = (\sigma_r - \sigma_\theta)d\varepsilon_r \tag{9}$$

where $\varepsilon_r = \frac{du}{dr}$.

If the temperature increase due to the elastic deformation is assumed negligible, assuming that this deformation represents most of the deformation by particle rearrangements which involves little heating, then the stress is related to the strain as:

$$(\sigma_r - \sigma_\theta) = \sqrt{3}\ k\left[\frac{1}{\sqrt{3}\ \gamma}\left(\frac{\partial v}{\partial r} - \frac{v}{r}\right) - 1\right] \tag{10}$$

Since

$$d\varepsilon_r = \frac{\partial v}{\partial r}\,dt, \tag{11}$$

the mechanical work dW can be obtained by substituting Eq. (6) into Eqs. (10) and (11) and then into (9). Then with an approximation that $p_o >> k$, dW becomes

$$dW = \frac{9}{4}\frac{(p_o - p_g - 2\sqrt{3}\ k \ln\frac{r_o}{r_i})^2}{(r_i^{-3} - r_o^{-3})^2 r^6}\frac{\gamma}{k}\,dt \tag{12}$$

The temperature rise dT due to the mechanical work done is given by

$$\varrho C_p dT = dW,$$

here ϱ is the solid density and C_p is its heat capacity. Therefore

$$\left(\frac{dT}{dt}\right)_{M.D.} = \left(\frac{9}{4\varrho C_p}\right)\frac{(p_o - p_g - 2\sqrt{3}\ k\ln\frac{r_o}{r_i})^2}{(r_i^{-3} - r_o^{-3})^2 r^6}\cdot\frac{\gamma}{k} \tag{13}$$

where the subscript M.D. denotes mechanical deformation.

The temperature rise shown above is a monotonically increasing function of time and a monotonically decreasing function of space (radius). Therefore, the extent of the hot spot region is readily known by observing the temperature profile. This elimintes the necessity of determining the size of the hot spot region a priori as an independent parameter. Also, it eliminate requirement (15,16,17) that the temperature is constant in the hot spot region. The inner radius, $r=r_i$, is the hottest location, and therefore it is of interest to follow the temperature here.

Figure 3 shows the temperature rise at the inner radius in PBX-9404 under 2.5 GPa as a function of tempeature. It shows the temperature increase to more than 3,000°K by mechanical deformation based on the same conditions given in the legends of Figure 2.

Heat Conduction and Chemical Reaction

The temperature rise due to the mechanical deformation is followed by two other processes in the explosives; heat conduction and chemical reaction. Both of these processes are dependent on and, at the same time, modify the temperature distribution in the explosives. Therefore, the overall temperature change can be expressed as follows.

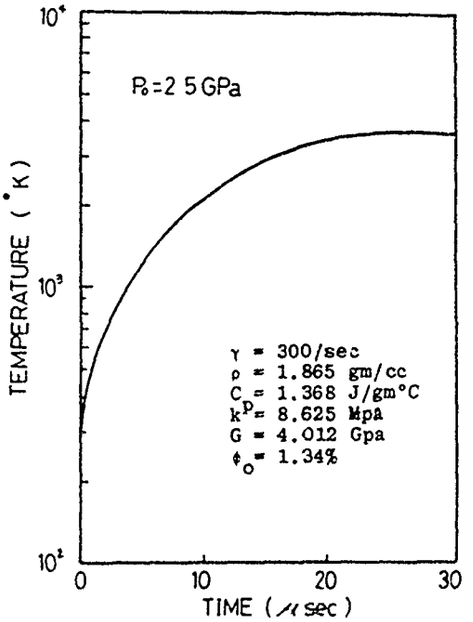

Fig. 3. Temperature profile at the inner radius

$$\varrho C_p \frac{\partial T(r,t)}{\partial t} = \varrho C_p \left(\frac{\partial T}{\partial t}\right)_{M.D.} + \frac{1}{r^2}\frac{\partial}{\partial r}\left(r^2 k^* \frac{\partial T}{\partial r}\right) + Q\frac{\partial \lambda(r,t)}{\partial t} \quad (14)$$

Here, k* is the thermal conductivity, Q is the heat of reaction of the explosive and λ is the degree of reaction of the explosive. $\lambda=1$ when the explosive is fully reacted. The last term is, according to Arrhenius reaction law,

$$\dot{\lambda}(r,t)=(1-\lambda)A\exp\left\{-\frac{T^*}{T(r,t)}\right\} \quad (15)$$

Here, A is a frequency factor and T* is an activation temperature.

As mentioned above, $\dot{\lambda}(r,t)$ represents the local chemical reaction rate in the hollow sphere, showing the maximum at the inner radius, the minimum at the outer radius, and a monotonic decrease between them. Since one is interested in the total averaged chemical reaction rate in the hollow sphere, the local chemical reaction rate is integrated over the whole volume of the hollow sphere.

$$\dot{\lambda}(t)_{ign}=\int_{r_i}^{r_o}\dot{\lambda}(r,t)4\pi r^2 dr \Big/ \frac{4}{3}\pi(r_o^3-r_i^3) \quad (16)$$

The subscript 'ign' is added to emphasize that the above chemical reaction rate is calculated based on the temperature rise from the mechanical deformation of the explosives in hot spots, and therefore, is an ignition term.

Once the explosive is ignited in such a fashion the chemical reaction products will accumulate in the void. The pressure and the temperature of the product gas in the void will steadily increase and at some point in time the heat transfer from the hot gas onto the unreacted solid becomes important. In the end, a quasi-steady process will develop where the speed of heat penetration into the solid surface dictated by the interphase heat transfer and the heat conduction in the solid is balanced by the speed of surface regression due to chemical reaction. This is the surface burning. It is hard to express the combined effects of the above phenomena exactly. Therefore, in place of the exact description of the above phenomenon, an approximate representation was used after Lee and Tarver (18). That is, the total reaction rate at any time can be expressed as a sum of two terms; chemical reaction rate during the ignition process (described above) and a chemical reaction rate due to surface burning,

$$\dot{\lambda}(t)=\dot{\lambda}(t)_{ign}+\dot{\lambda}(t)_{surface\ burn} \quad (17)$$

$$\dot{\lambda}(t)_{surface\ burn}=B(1-\lambda)^{2/9}\lambda^{2/3}p_g^z \quad (18)$$

Eq. (18) is identical to Lee and Tarver's growth term. At the beginning, both the ignition term and the growth term is zero. Once the mechanical deformation starts, the temperature rises causing both the ignition term and the growth term to become different from zero. At this stage, the ignition term is larger than the growth term. At some point in time, the gas generated by chemical reaction increases the gas pressure in the void and the mechanical deformation is slowed down due to increasingly smaller pressure difference between the outside and the inside of the hollow sphere. At the same time, the growth term becomes stronger and eventually the second term dominates the first term.

Ideally, the surface burn term should not exist at the beginning and the ignition term should be dropped when the surface burn term becomes important. However, since the time

when the transition occurs is unclear, both terms are retained throughout. Its shortcoming is somewhat lessened by the fact that most of the time one term or the other dominates the counterpart term, and introduces small error in the modelling. Furthermore, as will be seen later it is further compromised when some of the constants in either terms will be adjusted to curvefit experimental data. The gas pressure in the void $p_g(t)$ was calcu' ted using the HOM (22) equation of state . ype

$$p_g = p_g(v_g) \tag{19}$$

where the specific volume v_g was calculated from the void volume divided by the amount of explosive reacted in the void

$$v_g = \frac{r_i(t)^3}{r_o(o)^3 - r_i(o)^3 - r_o(t)^3 + r_i(t)^3} \cdot v_s \tag{20}$$

Here v_s is the original specific volume of the unreacted explosive.

Numerical Simulation

The above model (Eqs. (6·20)) contains five constants, G, γ, k*, B and z to be determined from comparisons with experimental data. All the other constants in the model are assumed to be known. They are ρ, Cp, k, A, T*, and Q. Actually, if one were to deal with a perfectly symmetric hollow sphere model with known mechanical deformation behavior, the five constants mentioned above would also be known. However, since we are not dealing with a perfectly symmetric hollow sphere, some uncertainties are introduced in them. The five constants mentioned are the ones easily affected by the change of geometry.

The values of G, γ, k*, B and z for PBX-9404 were selected to yield calculational results in good agreement with the experimental manganin gage pressure histories PBX-9404 at several gage locations for a sustained shock pulse of 2.5 GPa (18), these are G=4.912 GPa, $\gamma = 3.0\times10^{-4}/\mu$sec, $k^* = 5.0\times10^{-3}$cal/cmsec°C, B=45.0 $\mu sec^{-1}Mbar^{-z}$, and z=1.2. In the calculation, a one-dimensional hydrodynamic code called STEALTH was used.

Figure 4 shows the comparison between the calculated and experimental results using the above five constants. The time of arrival of the shock and subsequent reaction growth give good comparisons.

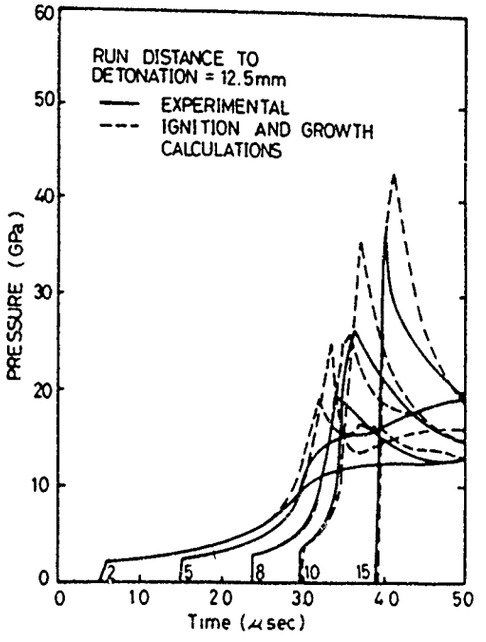

Fig. 4. Calculated and experimental pressure histories for a sustained shock pulse of 2.5 GPa in PBX-9404

Test of the Model

The above model with the five constants determined by the Fig. (4) is tested now against other existing experimental data on PBX-9404. These are particle velocity histories at the back side of PBX-9404 slabs of various thicknesses under 3.7 GPa strength, 1.1 μsec duration shocks impacting on the front side of the slabs, and those under 5.1 GPa peak-pressure, 0.3 μsec rise-time ramp waves, and those under 5.1 GPa peak-pressure, 0.8 μsec rise-time ramp waves and also a Pop-plot.

Fig. (5) shows the calculated and experimental particle velocity histories recorded at the opposite side of PBX-9404 slabs when a 3.7 GPa, 1.1 μsec shock is applied on one side (15). The model calculation is slightly lower than the experimental data.

Fig. (6) shows the measured wave forms, the model prediction and the results of the Sandia model compared together for 0.3 μsec rise-time, 5.1 GPa peak-pressure initial ramp waves in PBX-9404. Again, the current model shows slightly lower results than the measured ones. Fig. (7) shows the similar comparisons under

0.8μsec rise-time, 5.1 GPa ramp waves (15). Once again, the current model slightly underpredicts the measured results, but seems to follow the general trend favorably. Overall, the agreement between the prediction and the experimental data are good at the early stages of pressure developn ents.

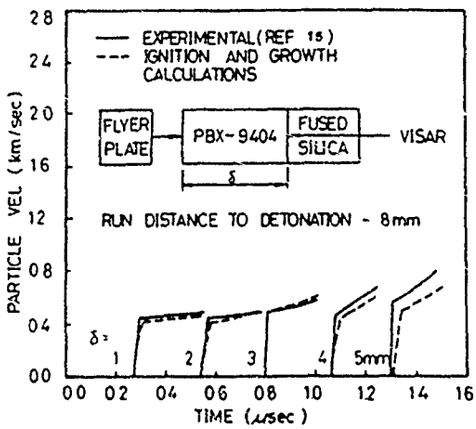

Fig. 5. Calculated and experimental particle velocity histories for 3.7 GPa, 1.1 μsec shocks in PBX-9404

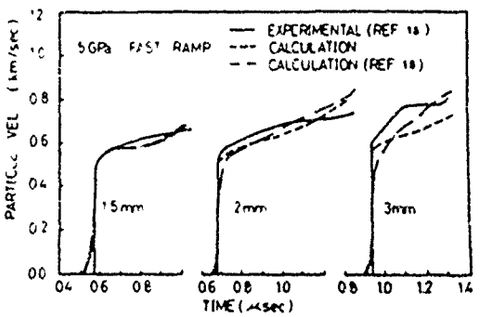

Fig. 6 Measured waveforms and model predictions for a 0.3μsec rise-time, 5.1 GPa peak-pressure initial ramp wave in PBX-9404

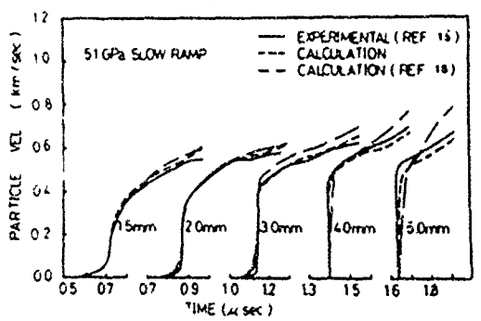

Fig. 7. Measured waveforms and model predictions for a 0.8μsec rise-time, 5.1 GPa peak-pressure initial ramp wave in PBX-9404

Finally, a Pop-plot data is compared in Fig. (8). The solid line represents the experimental data while results of three model predictions are shown together; Lee and Tarver's, Sandia's, and the current. They all show more or less similar deviations from the experimental curve. This discrepancy between the experimental curve and the three models seems to come from the surface burn term, which is included in all the above models in slightly different forms, and it requires a further study.

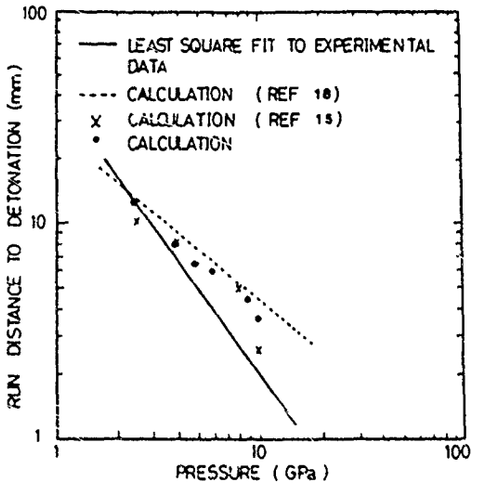

Fig. 8. Calculated and experimental run distance to detonation versus shock pressure data for sustained pulses

CONCLUSION

A new model was developed to describe the chemical reaction process induced by loading of pressure waves in heterogeneous explosives based on a phenomenologically developed hot spot model and subsequent chemical kinetics considerations. Comparisons with experiments show good agreements at early stages of pressure buildup but shows some discrepancies later. This probably means that the description of the ignition term is satisfactory and that of the reaction growth term needs a further study.

Acknowledgment

The work was funded by Naval Surface Weapons Center, and Korea Advanced Institute of Science and Technology.

REFERENCES

1. F.E. Walker and R.J. Wasley, "Critical Energy for Shock Initiation of Heterogeneous Explosives," Explosivstoffe, Nr. 1, pp. 9-13, 1969.
2. E.F. Gittings, "Initiation of a Solid Explosive by a Short-Duration Shock," Proc. Fourth Symp. on Detonation, pp. 373-380, 1965.
3. Y. de Longueville, C. Fauquignon and H. Moulard, "Initiation of Several Condensed Explosives by a Given Duration Shock Wave," Proc. Sixth Symp. on Detonation, pp. 105-114, 1976.
4. M. Chaudhri and J.E. Field, "The Role of Rapidly compressed Gas Pockets in the Initiation of Condensed Explosives," Proc. Roy. Soc. London, A. 340, pp. 113-128, 1974.
5. F.P. Bowden and M.P. McOnie, "Formation of Cavities and Microjets in Liquids and Their Role in Initiation and Growth of Explosion," Proc. Roy. Soc. London, A. 298, pp. 38-50, 1967.
6. C.L. Mader, Numerical Modeling of Detonations, Los Alamos Series in Basic and Applied Sciences, Univ. of Calif. Press, P171, 1979.
7. R.E. Winter and J.E. Field, "The Role of Localized Plastic Flow in the Impact Initiation of Explosives," Proc. Roy. Soc., pp. 399-413, 1975.
8. J.R. Travis, "Experimental Observations of Initiation of Nitro-methane by Shock Interactions at Discontinuities," Proc. Fourth Symp. on Detonation, pp. 386-393, 1965.
9. C.S. Coffey and R. Armstrong, Shock Waves and High Strain Rate phenomena in Metals, Plenum, 1981.
10. K. Kim, "Shock Sensitivity of Energetic Materials," Proc. 1980 JANNAF Prop. Syst. Hazards Mtg., Vol. 1, pp. 277-288, 1980.
11. J. Wackerle, J.O. Johnson and P.M. Halleck, "Reactive Shock-Wave Buildup in Porous PETN," LA-UR-75-1912, Los Alamos National Lab., 1975.
12. D.E. Kooker and R.D. Anderson, "A Mechanism for the Burning Rate of High Density, Porous, Energetic Materials," Proc. of Seventh Symp. on Detonation, pp. 198-215, 1981.
13. B.A. Khasainov, A.A. Borisov, B.S. Ermolaev, and A.I. Kotrov, "Two-Phase Visco-Plastic Model of Shock Initiation of Detonation in High Density Pressed Explosives," Proc. Seventh Symp. on Detonation, pp. 435-447, 1981.
14. M.M. Carroll and A.C. Holt, "Static and Dynamic Pore-Collapse Relations for Ductile Porous Materials," J. Appl. Phys., Vol. 43, No. 4, 1972.
15. M.E. Kipp, J.W. Nunziato and R.E. Setchell, "Hot Spot Initiation of Heterogeneous Explosives," Proc. Seventh Symp. on Detonation, pp. 394-407, 1981.
16. D.B. Hayes, "Shock Induced Hot Spot Formation and Subsequent Decomposition in Granular, Porous, Hexanitrostilbene Explosive," Proc. Eigth Int'l. Collo. on Gasdynamics of Explosions and Reactive Systems, 1981.
17. M.J. Frankel and D.J. Pastine, "Hot Spot and Bulk Temperature Induction in Shock Compressed Explosives," Proc. Seventh Symp. on Detonation, pp. 523-528, 1981.
18. E.L. Lee and C.M. Tarver, "Phenomenological Model of Shock Initiation in Heterogeneous Explosives," Phys. Fluids, Vol. 23, No. 12, pp. 2362-2372, 1980.
19. C.L. Mader and C.A. Forest, "Two-Dimensional Homogeneous and Heterogeneous Detonation Wave Propagation," Los Alamos Scientific Laboratory Report LA-6259, 1976.
20. P. Perzyna, Fundamental Problems in Viscoplasticity, Advances in Applied Mechanics, Vol. 9, pp. 350, 1966.
21. R.W. Heckel, "An Analysis of Powder Compaction Phenomena," Trans. Met. Soc. of AIME, Vol. 221, 1961.
22. C.L. Mader, Numerical Modeling of Detonations, Los Alamos Series in Basic and Applied Sciences, Univeristy of California, Press, pp. 325-328, 1979.

MODELING THE DEFLAGRATION TO DETONATION TRANSITION IN POROUS BEDS OF PROPELLANT

Channon F. Price, Thomas L. Boggs
Naval Weapons Center
China Lake, California

INTRODUCTION

Modeling the complete deflagration-to-detonation process in porous beds of propellant from igniter initiation to fully developed steady-state detonation is a difficult task. Selected portions of the process, such as wave-steepening and detonation have been successfully modeled, and compaction phenomena have been simulated. However, there has been little success in modeling the total process with consistent and realistic parameters; a model that may describe one part of the process may require totally unrealistic parameters to match another part (e.g. exceedingly high surface temperatures of the solid phase, or exceedingly large values of the burn rate exponent). Often these problems can be traced to an overly simplified description of the combustion events which preceded and in turn set up the other events in the overall process.

A previous paper, "Role of Gas Phase Reactions in Deflagration-to-Detonation Transition," Seventh Symposium (International) on Detonation (1), discusses much of the experimental evidence and rationale leading to the analytical treatment of the combustion process utilized in the model to be described. The reader is urged to refer to this paper, as in the interests of brevity that discussion is not repeated in this paper.

DESCRIPTION OF MODEL

Before beginning a discussion of the analytical model, it is useful to discuss those experimental observations such a model should describe if it is to be considered truly relevant. Among these are (1) incorporation of the results of transient combustion research as reported in Reference 1 and its citations, (2) application to the entire DDT event, which may last several hundred to several thousand microseconds, (3) evidence of hydrodynamic propriety by the ability to predict shock tube behavior, (4) incorporation of realistic compaction behavior as determined by experiment, (5) ability to generate accelerating compaction profiles (both weak compaction waves and strong compaction waves) and steepening pressure fronts, (6) generation of pressure-time histories at discrete locations having the typical "cross-over" pattern, and (7) the ability to predict the effects due to a change in igniter strength.

The model we used was a modification of that used by Pilcher, Beckstead, et al, (2-6). Their model, based partially on the earlier work of Krier (7-9), included the effects of confinement as well as the gas flow, ignition, flame spread, and pressure build-up due to burning within the porous material. Our model is a composite of several conservation equations, auxiliary relationships, and submodels. The basic elements and methods are:

1. Gas-phase conservation equations, one-dimensional, similar to those proposed by Culick (10).

2. Condensed-phase (particle) conservation equations, quasi-one-dimensional involving the center of mass and motion relative to it.

3. Porous-bed drag (permeability) relations of Ergun (11) or Jones and Krier (12), optional choice, with provision for defining increased drag due to irregular particles.

4. Heat transfer to the bed, Denton's correlation (13).

5. Intergranular stress (compaction), relationship of Carroll-Holt (14), as modified by Kooker-Anderson (15). Experimental data of Elban

(16-17) used for evaluation of compaction parameters.

6. Thermal response of particle, finite-difference solution for external heat source, ablating surface, cast in spherical coordinates, and with the provision for condensed-phase reaction kinetics.

7. Igniter source optionally described as mass rate, distance versus time, or as a weight of material, with pressure-dependent burn rate, paticle size, and energy release.

8. Tube wall confinement, described by coupling to a finite-element stress code, HONDO (18).

9. Gas-Phase Reactions. This area encompases the major differences between our model and those of others. Based on the phenomena and rationale presented in Reference 1, it seemed mandatory to separate the rate of energy release from the rate of solid gasification. Most other models utilize a single reaction step of solid going to final products with concomitant equilibrium energy release at a rate given by a burn rate (usually $r=Cp^n$). All the experimental and analytical data pointed to the need for at least a two-step energy release during the transient period, with only a portion of the energy, that associated with the pyrolysis, being directly related to the condensed phase-conversion (pyrolysis) rate. The rate of release of the remaining energy, due to the conversion of reactive intermediate gaseous products to products of final molecular weight is assumed to be controlled by second-order, reaction kinetics (Arrhenius form) in each control volume.

To accomplish this, three additional conservation equations had to be added to track individually the mass of reactive intermediate (pyrolysis) gas and totally reacted gas, as well as the molar density of the gas. The auxiliary relations employed include the mass rate of gas due to surface pyrolysis and a second-order, Arrhenius kinetic reaction, for transfer from the pyrolysis products to the final-products state. The energy conservation equation was modified to reflect the partial-energy release associated with the pyrolysis, and the independently controlled release of the remainder, associated with the gas phase reaction.

These equations are solved by forward-differencing methods, with very close control of the calculational time increment with relationship to the most critical variable. It utilizes an artificial viscosity for stability, which is cast in the modified Rusinov form employed by Baer and Nunziato (19).

The failure to reference the many other researchers involved in this field should not be construed as ignorance of or lack of appreciation of their efforts. We have simply limited our references to those with direct bearing to our model and this paper.

The situation modeled is depicted in Figure 1 showing the igniter A, the sample B, and the tube, or confinement, C. The sample is described in terms of initial loading density (% TMD), compaction properties, material decomposition/pyrolysis kinetics and energetics, gas-phase reaction kinetics and energetics, thermal properties of the particle, particle diameter, and the obvious initial conditions of pressure and temperature. The confinement is described in terms of dilations of the tube is stress analysis described as for a normal (although to date, all runs have treated the tube as infinitely strong — no dilation). The required input parameters are listed below.

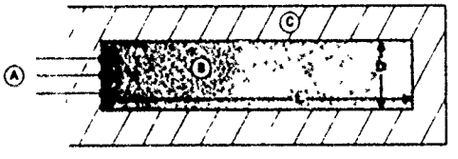

A IGNITER STRENGTH

B SAMPLE
- LOADING DENSITY
- COMPACTION PROPERTIES
- INTERGRANULAR STRESS
- MATERIAL DECOMPOSITION/PYROLYSIS
- SURFACE HEAT RELEASE
- GAS PHASE REACTIONS
- THERMAL CONDUCTIVITY OF SOLID
- PARTICLE DIAMETER
- IGNITION CRITERIA - SPECIAL CASE
- PRE-PRESSURIZATION

C CONFINEMENT

Fig. 1. Situation Modeled

INPUT PARAMETERS REQUIRED

TUBE
- Diameter
- Length
- Thickness
- Material Properties

IGNITER
- Weight
- Particle Diameter
- Burn Rate (C,n)
- Energy Release
- Molecular Weight of Products
- Percent Condensible in Products

CHARGE
- % TMD
- Ullage (Void Region)
- Particle "Roughness," if nonspherical
- Burn Rate (C,n) [Note: This is an option for comparison.]
- Pyrolysis Rate (As, Es)
- Pyrolysis → Final Products Rate (Ag,Eg)
- Molecular Weights (Pyrolysis, Final Products)
- Properties of Solid (thermal conductivity diffusivity, specific heat, density)
- Mechanical Properties, Compaction Model (Stress Free Porosity, Shear Modulus, Yield Stress)
- Initial Temperature and Pressure
- Gas Viscosity
- Gas V-Colume (as a function of gas-density)

For each calculation, gas pressure, gas temperature, particle surface temperature, compaction (%TMD), intergranular stress, 'flame" development, and the fraction of pyrolyzed and totally-reacted gases as a function of time and distance are among the variables which are recorded and may be plotted.

SOME RESULTS OF CALCULATIONS

As a check of the validity of the hydrodynamic equations, a case was calculated in which an igniter, localized at one end, was fired into an empty tube. (Actually a tube with 4.5 % TMD of particles.) No heat transfer, drag, or reactions were present. The resulting pressure-time behavior, shown in Figure 2, predicts a typical shock-tube type behavior with pressure oscillations, out of phase at the opposite ends of the tube, with the mean value growing until the igniter burns out. A second similar case was run, in which the tube was loaded to 60.4% TMD with spherical particles. Heat transfer to the particles was considered, but neither particle drag nor chemical reaction was allowed. The results in Figure 3 indicate a

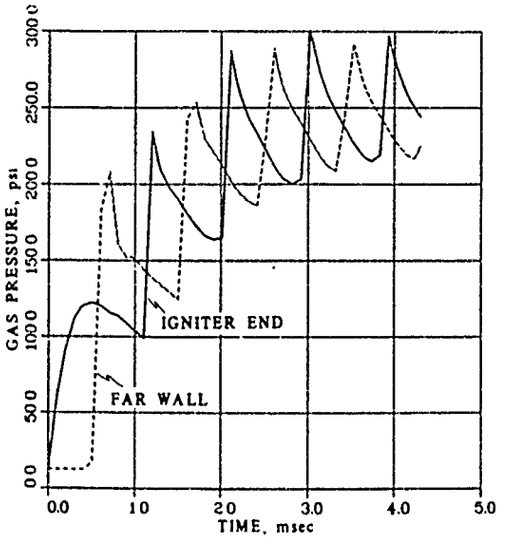

Fig. 2. Pressure-time behavior of tube with 4.5% TMD particle loading, no heat transfer drag or reaction of particles

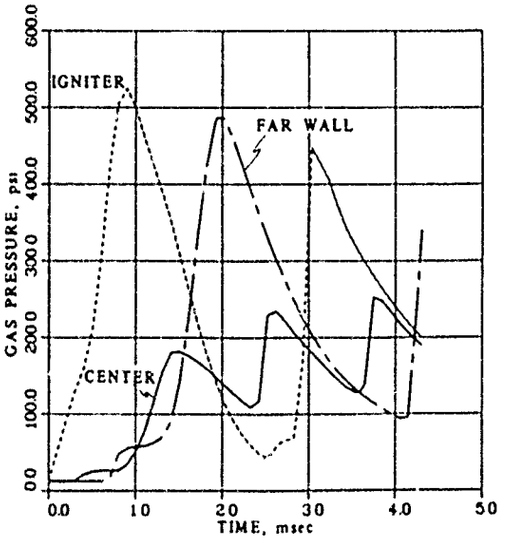

Fig. 3. Pressure-time behavior, 60.4% TMD particle loading, heat transfer from gas to particles, no drag, no reaction of particles

similar behavior. The initial igniter-end pressure is higher, due to the higher igniter loading density, but the heat transferred to the particles rapidly leads to lower mean pressures, and an expectedly lower frequency of oscillation due to lower sonic velocities. A third case was investigated, similar to the second, adding the

effect of particle drag. The results in Figure 4 show rapid pressurization of the igniter-end, while the combination of drag-induced compaction and convection heat loss from the gas serve to limit severely the pressure response at either center or far-wall positions.

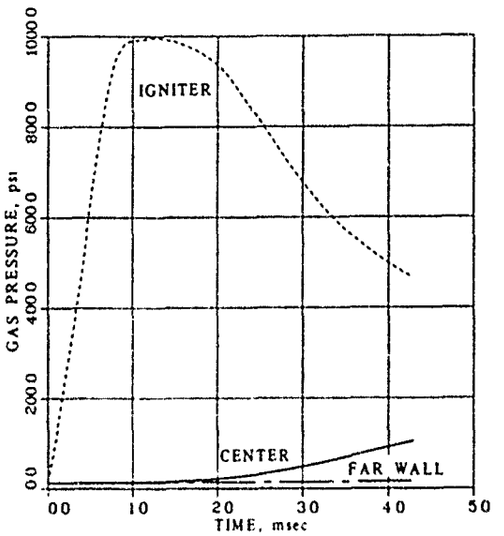

Fig. 4. Pressure-time behavior, 60.4% TMD particle loading, heat transfer from gas to particles, drag, no reaction of particles

The next step was to consider igniter firing into live, relatively incompressible propellant, such as ball powders. Several investigators have studied this situation in a manner different from the more familiar DDT tube type of experiments. These experiments were concerned with the early portion of the event and utilized pressure transducers down the tube. Their results show crossing of the individual transducer traces. The typical "cross-over" of pressure time histories at discrete gauge locations is well demonstrated in the work of Gerri et al (20), and that of Alkidas et al (21). A calculation was made, attempting to utilize parameters consistent with an experiment in the former reference, and the resulting calculated pressure-time histories at the four actual pressure guage locations are shown in Figure 5. Although not an exact match for the experimental data, the agreement in shape, timing, and relative magnitude appear to be quite excellent. The corresponding pressure-distance profiles at five different times are shown in Figure 6. The steepening (and acceleration) of the pressure front with time is quite evident. In Gerri's experiments, a rupture disc limited pressures at the end wall opposite the igniter. In our analysis, the calculations were simply halted at that time. The factors leading to the "peaking" and acceleration of the pressure front are direct causes of the pressure-time "cross-over" phenomena, and the often-referenced "negative pressure gradient."

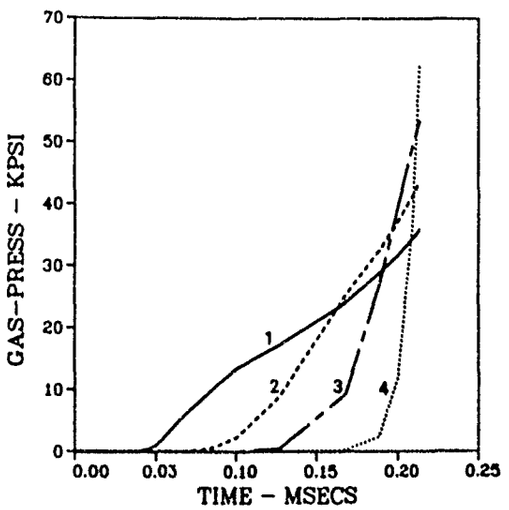

Fig. 5. Pressure vs. time at 4 locations, showing crossing of the curves as in Gerri's experiments

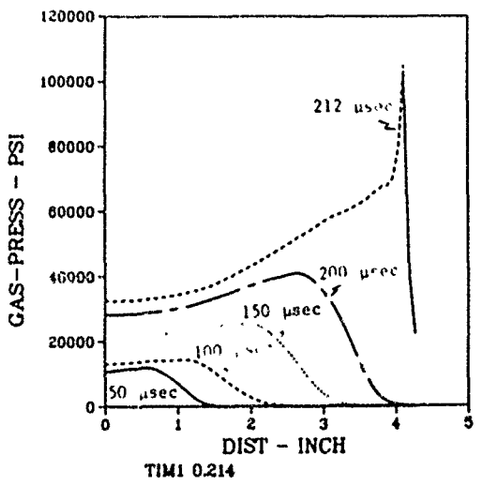

Fig. 6. Pressure vs distance at 5 times

Gerri's experiment utilized a rather short duration (or hard) igniter system, being conducted as part of an artillery research program. Most investigations of porous bed transition pehnomena utilize a longer duration (or soft) ignition system, to better separate combustion and mechanical effects. The results of calculations made with such an igniter system, in a

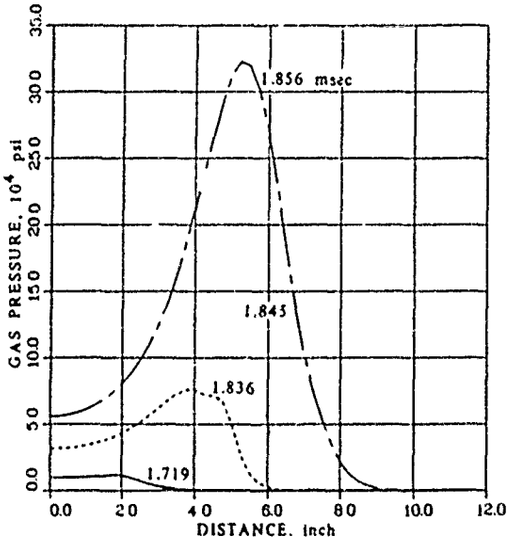

Fig. 7. Typical gas pressure-distance-time results of analytical modeling of DDT tube experiments using ball powder

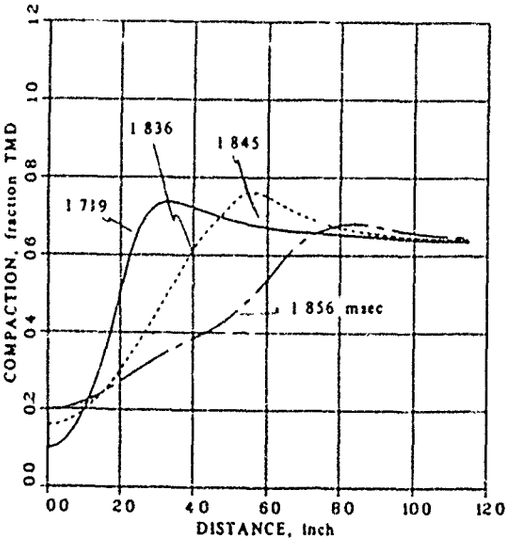

Fig 8 Compaction (• TMD) vs distance plots The bed was at 60 4% TMD at time zero

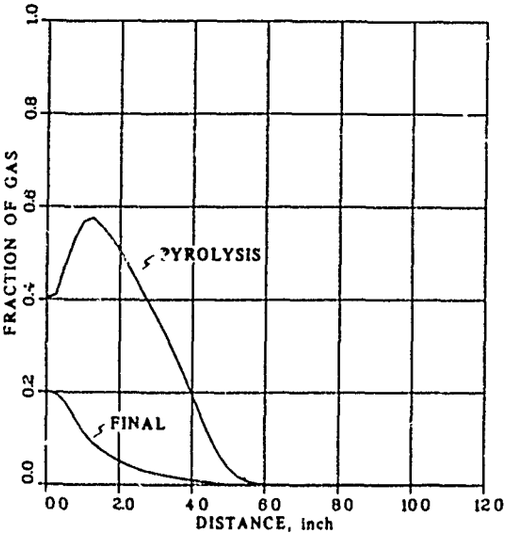

(a) 1.216 msec, 0.4% of solid has gasified

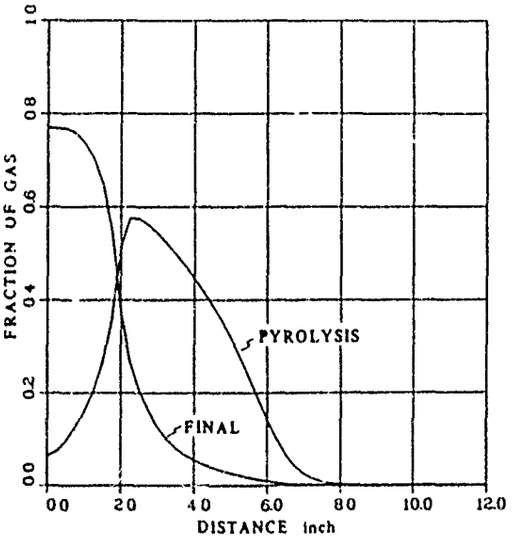

(b) 1.719 msed, 1.6% of solid has gasified

Fig 9. Fraction of gases due to pyrolysis and fraction of final gases

geometry typical of the DDT tube or "pipe" test, are shown in Figures 7-9. A spherical propellant (undeterred ball powder) was the bed material, loaded to 60.4% TMD, in a tube 12 inches long, with a ½-inch igniter-end ullage.

The computations were made for 424 μn diameter ball powder. The reasons for the choice of the material were that the sample geometry, compaction parameters, and transient combustion parameters were known, for these materials. The igniter action time was several milliseconds, rather that the microseconds modeled in the previous case.

Figure 7 presents the gas pressure-distance plots for various times. The solid curve shows the pressure at 1.719 msec after igniter initiation. Note the low value of pressure, only approximately 12,000 psi. This pressure is due to the igniter and a small amount of pyrolysis gases (less than 1.6% of the solid has reacted to gas). At 1.835 msec, the pressure has reached 76,000 psi, 6.9% of the solid has gasified and reaction of pyrolysis gases to final products has started (as will be shown in Figure 9). At 10 μsec later, the maximum pressure has increased from 76 to 146 kpsi and moved from about 4 to 4.6 inches down the tube and the amount of solid gasified from 6.9 to 10.4%. At 11 μsec later, the maximum pressure has gone from 150 to 350 kpsi and from 4.6 inches to over 5.2 inches down the tube, the amount of solid gasified has gone from 10.4 to 20.6%, and the dp/dt at P_{max} has reached approximately 10^{10} psi/sec. This case most likely would have resulted in a detonation.

The compaction profiles for this case which started with the tube being uniformly full to 60.4% TMD at time zero are shown in Figure 8. Even for hard spheres, such as ball powder, significant compaction is seen. At 1.719 msec the material that had been at the head end of the tube has been displaced down the tube. Since only 1.6% of the solid has gasified at this time, the low values of the TMD at the igniter end is due almost entirely to displacement of material caused by the igniter rather than by ignition and reaction of the powder. [Remember that the tube was originally filled to 60.4% TMD.] At 1.836 msec the compacted region has moved down the tube. The third time, 1.845 msec, shows a decrease in the amplitude of the compaction. This is primarily due to reaction consuming the solid (as will be seen in Figure 9). The last curve corresponding to end of run, 1.856 msec, shows little compaction with the backside of the compacted region (≈ 4- to 8-inch region) having been consumed by gasification.

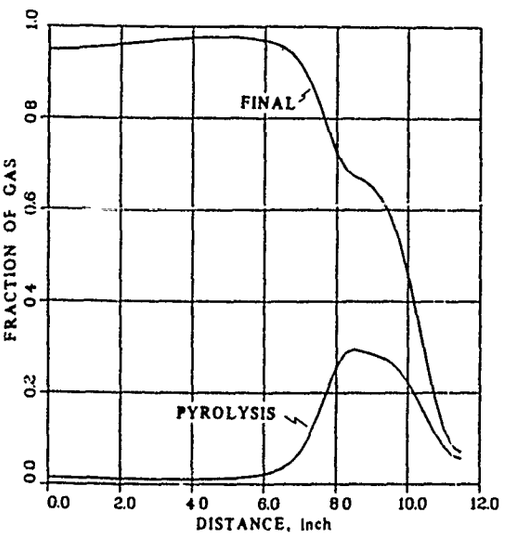

(c) 1.856 msec, 20.6• of solid has gasified

Fig. 9. Fraction of gases due to pyrolysis and fraction of final gases

Figures 9a-9c show the change in fraction of gases that are pyrolysis products and fraction of gases that are final product gases. The difference between 100% and the sum of the two curves is due to igniter gases and the gases that were originally in the tube. (Note: The curves only give the portion of the gas as pyrolysis products and final products. It does not indicate how much solid has gasified. The amount of solid that has gasified is calculated and will be presented in discussion of the figures.] In Figure 9a while only 0.4% of the solid has been converted to gas, the pyrolysis products are a significant portion of the gas in the tube and there has not been much reaction of the pyrolysis gases to final products. In Figure 9b 1.6% of the solid has gasified with pyrolysis products being formed downstream and conversion of pyrolysis products to final products near the head end. Figure 9c (20.6% of the solid has gasified) shows that pyrolysis reactions have reached the end of the tube and reaction has reached almost 10 inches down the tube. The P_{max} of 350,000 psi occurs at approximately 5.3 inches and the dp/dt at this point is greater than 10^{10} psi/sec.

The above calculations are presented as examples. Many other calculations have been

performed with several presented in Reference 22. Most of the calculations were for single parameter variations, that is, only on input parameter at a time was varied. The variations included change in gas phase kinetic parameters up to the infinitely fast reactions assumed by others, particle size, material properties, igniter strength, loading density (initial % TMD), material roughness, initial sample temperature, tube diameter and wall friction, and prepressurization with nitrogen gas.

Additional studies of such systems, both analytical and experimental, are underway, as well as development of techniques for determining the proper description of a given material in terms of the model parameters. These include the kinetics, energetics, and thermal and mechanical response of the chosen test material.

CONCLUSIONS

We have constructed a model which includes a mathematical description of the transient combustion processes. This inclusion of the transient combustion processes differentiates our work from the work of others who largely use ignition criteria and steady state burning relationships. We have demonstrated the validity (and stability) of the code by treating cases of increasing complexity, and have shown an agreement with experimental observations in each case. The model as now constructed utilizes the best constitutive (or auxiliary) relations available to us, but its structure is such that incorporation of a better representation of any of the phenomena is an easy task, should such description(s) become available.

Our inclusion of gas-phase reactions, and the consequent separation of gas- and energy-generation rates, enables us to more realistically describe the deflagration portion of the deflagration to detonation transition. This is in marked contrast to the models of others who must use artificially high "ignition" temperatures in order to delay pressurization and use unrealistic "burn-rate-exponents" or burn area to achieve the accelerating, steepening pressure profile. In our work we have attempted to model the transition process as a continuous, albeit rapidly changing, process without recourse to criteria or switches to proceed from one combustion "phase" to another

REFERENCES

1. T. L. Boggs, C. F. Price, A. I. Atwood, D. E. Zurn, and R. L. Derr. "Role of Gas Phase Reactions in Deflagration to Detonation Transition," Seventh Symposium (International) on Detonation, Naval Surface Weapons Center, White Oak, MD, MP 82-334, 1981, pp. 216-224.
2. B. D. Hopkins, A. G. Butcher, D. T. Pilcher, and M. W. Beckstead. "A Comparison of DDT Calculations and Experiments for Granulated Rocket Propellant," 16th JANNAF Combustion Meeting, Vol. 3, pp. 33-41, September 1974.
3. M. W. Beckstead, N. L. Peterson, D. T. Pilcher, B. D. Hopkins, and H. Krier. Convective Combustion Modeling Applied to Deflagration-to-Detonation Transition of HMX," Comb. and Flame, Vol. 30, pp. 231-241, 1977.
4. D. T. Pilcher, M. W. Beckstead, L. W. Christensen, and A. J. King. "A Comparison of Model Predictions and Experimental Results of DDT Tests," Sixth Symposium (International) on Detonation, pp. 258-266, 1976.
5. D. T. Pilcher, M. W. Beckstead, L. W. Christensen, and A. J. King. "A Comparison of Model Predictions and Experimental Results of Deflagration-to-Detonation Tests," AIAA/SAE 13th Joint Propulsion Conference, AIAA Paper 77-858.
6. D. T. Pilcher. "Modeling the DDT Process," ONR/AFOSR Workshop on DDT, CPIA Pub. 299, pp. 142-160, September 1978.
7. H. Krier, S. Ragan, and W. F. Van Tassell. "Flame Spreading and Combustion in Packed Beds of Propellant Grains," AIAA Journal, Vol 3, pp. 301-309, 1976.
8. H. Krier and S. S. Gokhale. "Modeling of Convective Mode Combustion Through Granulated Propellant to Predict Detonation Transition," AIAA Journal, Vol. 16, pp. 177-183, February 1978.
9. H. Krier and J. A. Kezerle. "Modeling of Convective Mode Combustion Through Granulated Propellant to Predict Transition to Detonation," University of Illinois,

Urbana, IL, Final Report, October 1976-September 1977, AFOSR-TR-78-0007, October 1977.

10. F. E. C. Culick. "Conservation Equations for a Reacting Two-Phase Flow Based on Continuum Theory," 12th JANNAF Combustion Meeting, summary notes for workshop, Newport, RI, August 1975.

11. S. Ergun. "Fluid Flow Through Packed Columns," Chemical Engineering Progress, Vol. 48, pp. 89-94, February 1952.

12. D. P. Jones and H. Krier. "Gas Flow Resistance Measurements Through Packed Beds at High Reynolds Numbers, "Journal of Fluids Engineering, Vol. 105, pp. 168-173, June 1983.

13. W. H. Denton. "The Heat Transfer and Flow Resistance for Fluid Flow Through Randomly Packed Spheres," General Discussion on Heat Transfer, Institute of Mechanical Engineering and ASME, London, pp. 370-373, 1951.

14. M. M. Carroll and A. C. Holt. "Static and Dynamic Pore-Collapse Relations for Ductile Porous Materials," Journal of Applied Physics., Vol. 43, pp. 1626-1636, April 1972.

15. D. E. Kooker and R. D. Anderson. "A Mechanism for the Burning Rate of High Density, Porous, Energetic Materials," 7th Symposium (International) on Detonation, pp. 198-215, 1977.

16. Naval Surface Weapons Center. "Quasi-Static Compaction of Porous Columns of Inert Materials," by W. L. Elban, S. B. Gross, and R. R. Bernecker, NSWC TR-81-113.

17. W. L. Elban. Private communication.

18. Sandia Laboratories. "HONDO - A Finite Element Computer Program for the Large Deformation Response of Axisymetric Solids," by S. W. Key, Albuquerque, NM, Sandia Laboratories (SL-A-74-0039), April 1974.

19. M. R Baer and J. W. Nunziato. "A Theory for Deflagration-to-Detonation Transition (DDT) in Granular Explosives," Sandia National Laboratories, (SAND82-0293), December 1983.

20. N. J. Gerri, S. P. Pfaff, and A. E.an Ortega. "Gas Flow and Flame Spreading in Porous Beds of Ball Propellant," 11th JANNAF Combustion Meeting, CPIA Pub. 261, Vol. 1, pp. 177-198, December 1974. Also see BRL-IMR-159, 1973.

21. A. S. Alkidas, S. O. Morris, L. H. Caveny, and M. Summerfield. "An Experimental Study of Pressure Wave Propagation in Granular Propellant Beds," AIAA Journal, Vol. 14, No. 6, pp. 789-792, 1976. Also see AIAA Paper 75-242.

22. T. L. Boggs, C. F. Price, and R. L. Derr. "Transient Combustion: An Important Consideration in Deflagration-to-Detonation Transition," AGARD Conference on Hazard Studies for Solid Propellant Rocket Motors, AGARD Conference Preprint No. 367, May 1984, pp. 12-1 to 12-21.

DISCUSSION

MARTIN SUMMERFIELD, Princeton Comb. Research Laboratory, New Jersey

I believe the general theoretical approach described in this progress report is sound. We should all await with optimism further results of the work.

What is the physical meaning of the statement in the conclusion that the model requires no further "switching"? I interpret this to mean that, for example, no additional chemical reactions need be introduced in the model. But, are the authors sure that, at high pressure developed in the advancing, growing pressure wave, no condensed-phase exothermic chemical reactions occur? Their model has no condensed phase chemical reactions, but there are many experiments with shocks weaker than the threshold required to cause detonation in high explosives that indicates that chemical reaction can be caused by high pressure. Why not include a term for such condensed phase reaction in the model?

REPLY BY C. PRICE

Thank you for the compliment.

When we say that we have modeled the process without recourse to criteria or switches to proceed from one combustion "phase" to

another, we are really trying to highlight how our work differs from others. Almost all other DDT models treat the behavior of a particle as either inert heating (off) or fully developed combustion (on) with equilibrium energy release and a pressure dependent rate, usually given by $r = C\varrho^n$. The switch from off to on occurs as a step function and at a point referred to as the "ignition criteria." This ignition criteria is usually cast in terms of a critical surface temperature or when the sample has received some critical energy input.

In contrast, we do not use off-on switches nor ignition criteria. Instead we model the process:

solid $\xrightarrow{1}$ reactive intermediate

gaseous products $\xrightarrow{2}$ final products

with individual rates and energy releases for reaction 1 and 2. The description is continuous rather than discontinuous.

The point about condensed phase reactions is well taken. At the time the paper was written, we had included such reactions in the model but we had not had sufficient time to run example cases. Thus the paper presented an earlier version of the model and its example cases.

A SEMI-ANALYTICAL APPROACH TO SHOCK INITIATION IN HETEROGENEOUS EXPLOSIVES

Y. K. Huang, A L. Arbuckle
US Army Ballistic Research Laboratory
US Army Material Command
Aberdeen Proving Ground, MD 21005-5066

We have described a partially reacted explosive as a two-phase, multicomponent mixture with Hugoniot states determined by the component Hugoniots or equations of state and the mass fraction decomposed. Shock-to-detonation transition is then represented by an appropriate succession of such states. This leads to a semi-analytical model of explosive burn.

INTRODUCTION

When a heterogeneous solid explosive is subjected to shock compression, it is liable to decompose, liberating energy which in turn accelerates the initial shock into a detonation. This shock-to-detonation problem is quite a challenge, calling for considerable effort to reach a solution as exemplified by the work of Mader (1) and Lee and Tarver (2). These investigators modeled shock initiation of explosives numerically. Their methodology is very specialized and some aspects of their characterization of the explosive behavior and properties are not definitive. In this investigation we have taken a simpler approach, and our results should be of interest to the reader who seeks some insight into the problem.

The essense of our treatment is outlined as follows. We begin with a basic treatment of the equations for reactive shock waves in which the partially reacted explosive is regarded as a two-phase, multicomponent mixture. Equations of state or Hugoniots for each phase are assumed to be known. Using these we construct the two-phase Hugoniot for a given decomposition fraction. The shock buildup to detonation may then be considered as a succession of shocked states with decomposition fraction increasing from 0 to 1. From these we derive a new model of explosive burn. The time dependence of this model is then given with the rate of shock buildup characterized essentially by the Pop plot. Finally, we give computed results using both analytical and experimental constants as input data.

REACTIVE SHOCK WAVES

Interaction between a shock wave and an explosive poses a complicated problem. Chemical reaction generates both energy and product gases in the presence of unreacted solid. The shock wave may be accelerated and may eventually become a steady detonation. Let ξ $(0 \leq \xi \leq 1)$ represent the mass fraction of solid that has been decomposed into gases. The enthalpy of the two-phase mixture is given by $H = \xi H_g + (1-\xi) H_s$ where the subscripts g and s refer to the gas and solid phases respectively We assume that the two phases are in thermodynamic equilibrium, with $P_g = P_s = P$ and $\phi_g = \phi_s = \phi$. From thermodynamics we have $H = H(P, \phi)$ and $dH = d(E + PV) = Td\phi + VdP$, where P, V, T, E, and ϕ denote pressure, volume, temperature, internal energy, and entropy respectively. Thus,

$$V = (\partial H/\partial P)_\phi = \xi(\partial H_g/\partial P)_\phi + (1-\xi)(\partial H_s/\partial P)_\phi = \xi V_g + (1-\xi)V_s \quad (1)$$

$$T = \left(\frac{\partial H}{\partial \phi}\right)_p = \xi\left(\frac{\partial H_g}{\partial \phi_g}\right)_p + (1-\xi)\left(\frac{\partial H_s}{\partial \phi_s}\right)_p = \xi T_g + (1-g)T_s \quad (2)$$

$$E = \xi H_g + (1-\xi)H_s - P\,[\xi V_g + (1-\xi)V_s] = \xi E_g + (1-\xi)E_s \qquad (3)$$

Schematically we have established five simple relations which determine the frozen state (P,V,T,E, ϕ, $0<\xi<1$) in terms of the phase states (P_g, V_g, T_g, E_g, ϕ_g, $\xi=1$) and (P_s, V_s, T_s, E_s, ϕ_s, $\xi=0$). For heuristic purposes, we first use the γ-law gas equation of state and the linear solid Hugoniot to derive the two-phase relation for the mixture. Later we will also use the JWL equation for both phases to increase accuracy.

Thus, the γ-law gas ($\xi=1$) is simply characterized as follows:

$$V_g = V_o \left[\frac{(\gamma-1)\,P_g + (\gamma+1)P_o}{(\gamma+1)\,P_g + (\gamma-1)P_o} \right] \qquad (4)$$

$$E_g = E_o + \tfrac{1}{2}\,(V_o-V_g)\,(P_g + P_o) \qquad (5)$$

$$T_g = T_g(V_g) \rightarrow \frac{dT_g}{dV_g} + \frac{\Gamma_g}{V_g} T_g = \frac{1}{2C_{vg}} \left[(V_o-V_g) \frac{dP_g}{dV_g} + (P_g-P_o) \right] \qquad (6)$$

$$\phi_g = C_{vg} ln \left[\frac{T_g}{T_o} \left(\frac{V_g}{V_o} \right)^{\Gamma_g} \right] \qquad (7)$$

Here the parameters γ, V_o, P_o, E_o and T_o denote properties of the detonation products. They are given by $\gamma=\rho_o D^2 / P_j - 1$, $V_o = 1/\rho_o$, $P_o = \frac{\gamma}{\gamma+1} P_j$, $E_o = P_o V_o/(\gamma-1)$, and $T_o \approx T_j (V_1/V_o)^{\Gamma_g}$, where ρ_o, D, P_j, V_1 and T_1 are, respectively, the initial density, detonation velocity, CJ pressure, CJ volume, and CJ temperature of the explosive. Note that the Grüneisen constant Γ_g and specific heat C_{vg} are to be determined by Equations (A5) and (A6) of Appendix A.

Collaterally, the unreacted explosives ($\xi=0$) is described as a Grüneisen solid with linear shock Hugoniot $U_s = C + S\,U_p$ where U_s and U_p denote shock and particle velocities, C and S being empirical contants. The following algorithm is meant to be tractably concise:

$$P_H = C^2 (V_o-V_H) \quad [V_o - S(V_o-V_H)]^2 \qquad (8)$$

$$E_H = \tfrac{1}{2}\,(V_o-V_H)\,P_H \qquad (9)$$

$$T_H = T_H(V_H) \rightarrow \frac{dT_H}{dV_H} + \frac{\Gamma_s}{V_H} T_H = \frac{1}{2C_{vs}} \left[(V_o-V_H) \frac{dP_H}{dV_H} + P_H \right] \qquad (10)$$

$$\phi_s = C_{vs}\, ln \left[\frac{T_H}{T_1} \left(\frac{V_H}{V_o} \right)^{\Gamma_s} \right] \text{ with } T_1 = 298^\circ K$$

It is now essential to locate the state point (P_a, V_a, T_a, E_a, ϕ_s, $\xi=0$) by solving for V_a with $\phi_s(V_a)=\phi_g$ and $T_a=T_H(V_a)$. We also have $P_a=P_H(V_a)$ and $E_a=E_H(V_a)$. Starting from this state point we construct an isentrope:

$$P_s=P_s(V_s) \rightarrow \frac{dP_s}{dV_s} + \frac{\Gamma_s}{V_s} P_s = \frac{d}{dV_s} \left[1 - \frac{\Gamma_s}{2V_s} (V_o-V_s)\,P_H \right] \qquad (12)$$

$$E_s = \tfrac{1}{2}\,(V_o-V_s)\,P_H + \frac{V_s}{\Gamma_s} (P_s-P_H) \quad \text{with } P_H=P_H(V_s) \qquad (13)$$

$$T_s = T_H + \frac{V_s}{\Gamma_s C_{vs}} (P_s-P_H) \text{ with } T_H=T_H(V_s) \qquad (14)$$

Note that numerical integration of Equation (12) needs to be done from V_a to V_s until $P_s(V_s) = P_g$. Thus, our algorithm involves two iteration procedures which compute the phase states using Equations (4)–(14). The mixture state follows from $P=P_g=P_s$, $\phi=\phi_g=\phi_s$, and Equations (1)–(3). A more crude description is given in Appendix B.

EXPLOSIVE BURN MODELS

Let us rewrite Equation (1) to give

$$\xi = (V-V_s) / (V_g-V_s) \qquad (15)$$

If we adopt the linear reactive shock (buildup) Hugoniot (1, 3) which implies

$$P = c_o^2\,(V_o-V) / [V_o - S_j(V_o-V)]^2 \qquad (16)$$

where c_o is the bulk sound velocity in the explosive and $S_j = (\gamma+1)\,(1-c_o/D)$, then we can compute V, V_s, and V_g using Equations (16), (12) and (4) in order to determine ξ for a given P. Equation (15) gives a more realistic model

than the CJ volume burn (1), $\xi=(V_o-V)/(V_o-V_j)$.

So far we have been concerned with a two-phase equation and its implications in shock initiation, regardless of rate effect or time dependence. In what follows we will look for some missing links to complete the framework of this investigation.

The Pop plot [1, 3, 4] is a valuable descriptor of shock initiation behavior. Let us denote this by $P_i^m\theta = k$ where P_i is the initial shock pressure, θ the time of shock buildup to detonation, and m and k are two experimental constants. We shall see that the following rate process, which is consistent with the Pop Plot, can be incorporated into our two-phase burn model nicely:

$$dP/dt = AP^n \qquad (17)$$

Here P is the shock pressure at time t and A and n are two adjustable constants. Integrating Equation (17) from $P = P_i$ at $t = 0$ gives

$$P=P_i\left[1-A(n-1)P_i^{n-1}t\right]^{1/(1-n)} \qquad (18)$$

Using $P=P_i$ and $t=\theta$ in Equation (18) and comparing with the Pop plot, we deduce $n=1+m$, and $A=(mk)^{-1}[1-(P_i/P_j)^m]$. Thus, the two-parameter model of Equation (17) is justifiable. Since ξ is an implicit function of P, Equations (15) and (18) can be used to compute the rate of burning for the entire shock-to-detonation process. Our two-phase relation can be used to complete the description of the buildup of the reactive shock waves in a succession of states.

COMPUTED RESULTS

In order to derive meaningful results, special attention should be paid to the choice of reliable data as input. We need well calibrated shock property and detonation constants for explosives which have been tested sufficiently. Tables 1 and 2 give such data from references (2, 4, 5, and 6). Note that our γ-law calculation requires less input data than a similar version using the JWL equations, which are

$$P_g=A_g(1-W_gR_gV_g)\exp(-R_gV_g)+B_g(1-W_gS_gV_g)\exp(-S_gV_g)+W_gE_g/V_g \qquad (19)$$

$$P_s=A_s(1-W_s/R_sV_s)\exp(-R_sV_s)+B_s(1-W_s/S_sV_s)\exp(-S_sV_s)+W_sE_s/V_s \qquad (20)$$

with all the V's and E's already divided by V_o.

On the other hand, the JWL equations are more accurate because they are based on cylinder test data (2, 5). In Tables 1 and 2, LX-17 is the same plastic-bonded explosive as RX-03-BB (92.5% TATB, 7.5% Kel-F800), but its experimental data are considered to be more refined (6). Likewise, PBX-9404R is updated (6) as shown in Table 2. Since parameter A of Equations (17) and (18) has to be determined with a given initial shock P_i, it is not listed side by side with n in Table 1.

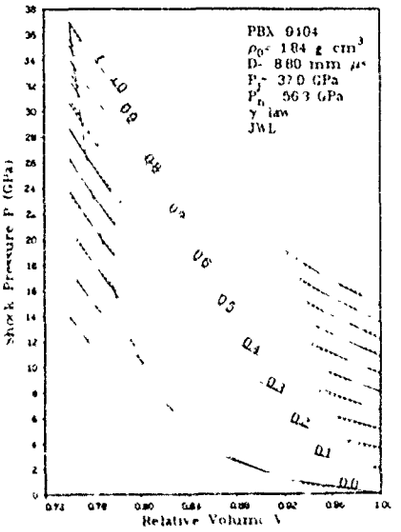

Fig 1 Partially reacted and reactive Hugoniots for PBX-9404 in the P-V plane

Using the data from Tables 1 and 2 in Equations (1) through (20), we have carried out detailed computations. In this paper we present only the results for PBX-9404 as plotted in Figures 1 through 6. Similar features are shared by the computed results for the other explosives (7). In Figure 1, the solid lines describe the JWL version of the two-phase equation $F(P, V, E, \xi) = 0$ based on Equations (1), (2), (16), (19), and (20), and the dotted lines are corresponding γ-law results from Equations (1) through (14). These results are also mapped in the U_s-U_p plane (Figure 2) as partially reacted shock Hugoniots bounded by the unreacted ($\xi=0$) and

TABLE 1
Parameters for γ-Law Calculation

	Cast TNT [2]	PETN [2]	RX-03-BB [2]	PBX-9404 [2]	LX-17[6]	PBX-9404R[6]
ϱ_o (g/cm^3)	1.61	1.75	1.90	1.842	1.895	1.84
D (mm/μs)	6.845	8.21	7.596	8.80	7.596	8.80
P_j (GPa)	21.0	33.5	27.5	37.0	27.5	37.0
V_j (cm^3/g)	0.4545	0.4544	0.3843	0.4019	0.3953	0.4022
T_j (°K)	2937	3400	2063	2466	2063	2466
γ	2.727	2.640	2.987	2.851	2.987	2.846
u_n* (mm/μs)	2.547	3.19	2.46	3.47	2.336	2.455
P_n* (GPa)	28.1	45.2	35.5	56.3	33.7	39.8
C (mm/μs)	2.57	2.30	2.33	2.30	2.33	2.26
S	1.678	1.847	2.141	1.873	2.254	2.664
c_o (mm /μs)	2.57	2.30	2.33	2.30	2.33	2.26
s_j	2.328	2.621	2.764	2.844	2.764	2.858
m	3.226	4.545	3.636	1.852	3.636	1.852
$k_{(GPa^m\ \mu s)}$	$5.52X10^3$	31.62	$1.79701X10^4$	18.96	$1.79701X10^4$	18.96
n	4.226	5.545	4.636	2.852	4.636	2.852
a (mm/μs)	1.785	2.887	2.48	2.176	2.48	2.176
b $\left(\frac{mm}{\mu s}\ \frac{cm^3}{g}\right)$	3.225	3.05	2.852	3.60	2.852	3.60

* von Neumann spike parameters. All m, k, n, data are taken from Reference (4).

detonation ($\xi=1$) Hugonicts. In Figure 3 we compare Equation (15) (using both γ-law and JWL equations), with the CJ volume burn. Combined with the two-phase Hugoniot, this yields the single buildup curve of Figure 4. Figure 5 shows the transient shock buildup of Equation (18) from three initial pressures, P_j, which fall within the range of validity of the Pop plot (4). Figure 6 is a consequence of Figures 4 and 5.

DISCUSSION AND CONCLUSION

Our two-phase equation of state evaluation offers a short cut for characterizing the states and changes involved in a shock-to-detonation transition process. As shown in Figures 1 and 2, the partially reacted Hugoniot curves describe the two-phase shocked states with chemical reaction frozen at levels between $\xi=0$ and $\xi=1$ in increments of 0.1. Thus we have simplified our treatment considerably without calling for thermal and chemical equilibria. Our analysis has been further enhanced by the use of the linear reactive shock Hugoniot (1, 3) describing single curve buildup (the curve intersecting all others in Figures 1 and 2). Our γ-law results differ from the JWL results for two reasons. While the

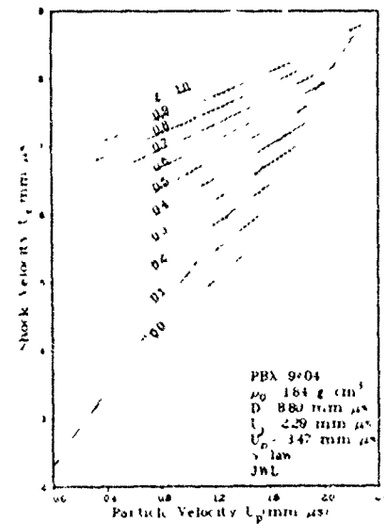

Fig. 2. Partially reacted and reactive Hugoniots for PBX-9404 in the $U_s - U_p$ plane

TABLE 2
Parameters for JWL Calculation

	Cast TNT [2]	PETN [2]	RX-03-BB [2]	PBX-9404 [2]	LX-17 [6]	PBX-9404R [6]
ϱ_o (g/cm^3)	1.61	1.75	1.90	1.842	1.895	1.84
D (mm / μs)	6.845	8.21	7.596	8.80	7.596	8.80
P_j (GPa)	21.0	33.5	27.5	37.0	27.5	37.0
V_j	0.7317	0.7953	0.7492	0.7403	0.7492	0.740
T_j (°K)	2937	3400	2063	2466	2063	2466
γ	2.727	2.640	2.987	2.851	2.987	2.846
u_n (mm/μs)	2.547	3.19	2.46	3.47	2.336	2.455
P_n (GPa)	28.1	45.2	35.5	56.3	33.7	39.8
C (mm/μs)	2.57	2.30	2.33	2.30	2.33	2.26
S	1.678	1.847	2.141	1.873	2.254	2.664
c_o (mm/μs)	2.57	2.30	2.33	2.30	2.33	2.26
s_j	2.328	2.621	2.764	2.844	2.764	2.858
$Q_{(GPa\text{-}cm^3/cm^3)}$	7.0	10.1	6.9	10.2	6.9	10.2
A_g (GPa)	371.2	617.0	654.67	852.4	654.67	852.4
B_g (GPa)	3.231	16.926	7.1236	18.02	7.1236	18.02
C_g* (GPa)	1.045	0.699	0.80	1.207	0.80	1.207
R_g	4.15	4.40	4.45	4.55	4.45	4.60
S_g	0.95	1.20	1.20	1.30	1.20	1.30
W_g	0.30	0.25	0.35	0.38	0.35	0.38
A_s (GPa)	$1.798X10^3$	$3.746X10^3$	$1.082X10^4$	$6.969X10^3$	$7.781X10^4$	$9.522X10^5$
B_s (GPa)	−93.1	−131.3	−240.6	−172.7	−5.031	−5.944
R_s	6.2	7.2	8.2	7.8	11.3	14.1
S_s	3.1	3.6	4.1	3.9	1.13	1.41
W_s	0.8926	1.173	1.251	0.8578	0.8939	0.8867

* JWL isentrope (release adiabat) parameter

unreacted shock Hugoniot ($\xi=0$) tends to lower the γ-law results (dotted lines), the release adiabat ($\xi=1.0$) raises them as clearly shown in Figures 1 and 2. In this connection the JWL results are more accurate.

In Figure 1, there are nine intersection points between the reactive shock Hugoniot and the partially reacted Hugoniots ($\xi=0.1$ to 0.9). These represent some of the successive states which describe the single curve shock buildup. Figure 3 is generated by use of Equation (15). This offers a more realistic burn model than the CJ volume burn because the latter makes no attempt to describe partially reacted states. Note that even the trend of CJ volume burn is misleading as compared with our two-phase prediction in Figure 4.

It is convenient to consider a two-parameter expression like Equation (17) as a time-rate description of the two-phase buildup. Since the Pop plot is a two-parameter representation of shock-initiation test results, we find it is most desirable to fit Equation (17) with these parameters for this investigation. So we have used

and also observed in Lagrange analysis of embedded gauge records (15). Mechanical dissipation processes or endothermic chemical reactions can be added to the model when they are identified and measured quantitatively.

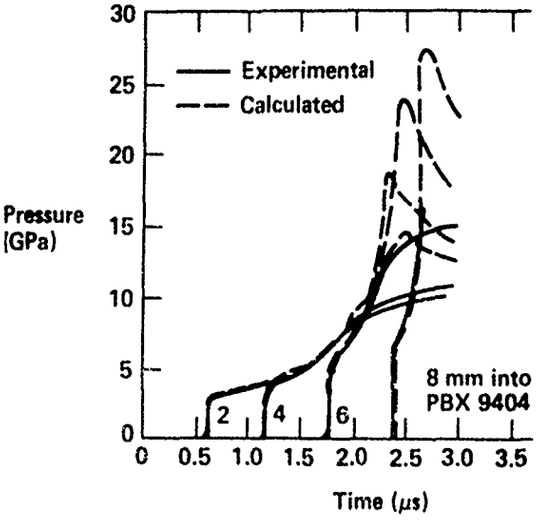

Fig 3. Pressure Histories for a 3 GPa sustained shock wave in PBX 9404

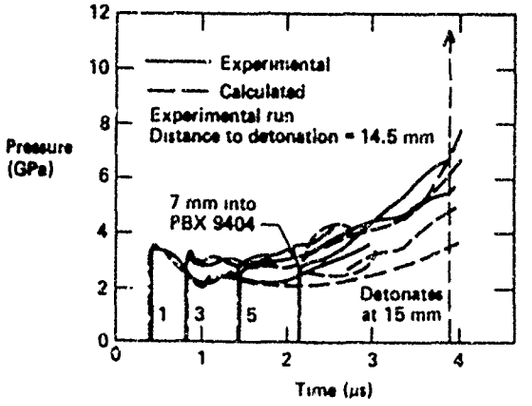

Fig 4 Pressure histories for a 3 GPa, 0.33 μs shock pulse into PBX 9404

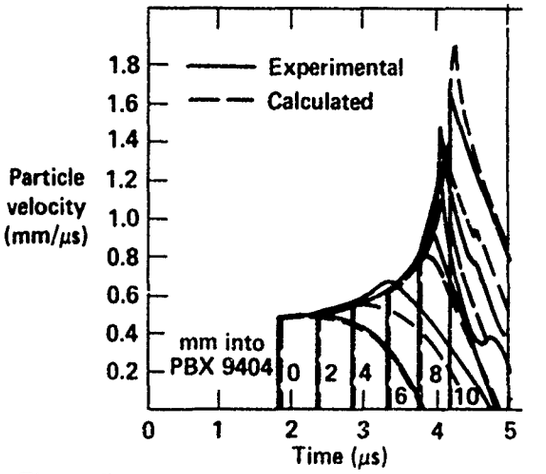

Fig. 5. Particle velocity histories of a sustained 3.5 GPa shock wave into PBX 9404

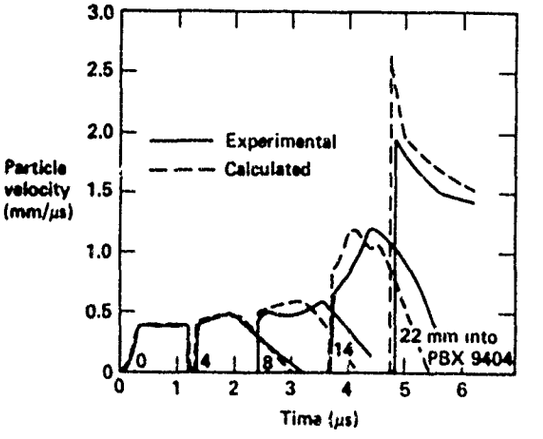

Fig. 6. Particle velocity histories for a dynasil flyer plate short duration shock pulse in PBX 9404

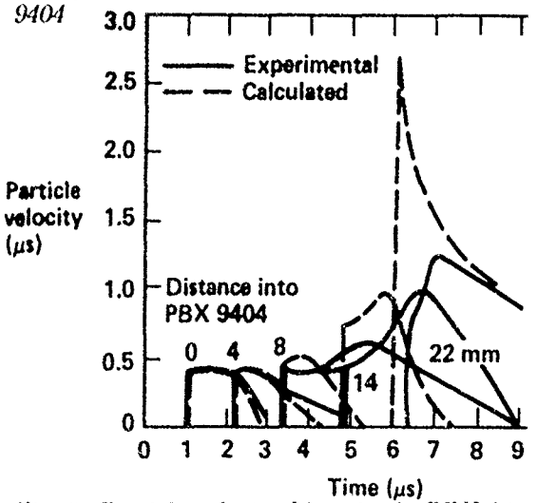

Fig 7 Particle velocity histories in PBX 9404 for a Kel-F flyer plate short duration shock pulse

Equation (18) to generate the shock pressure histories of Figure 5 for three initial shocks which are typical of the Pop plot range. To go a step further, we derived the reaction histories of Figure 6 as a consequence of Figures 4 and 5. Yet it is especially useful to relate successive two-phase states to time-dependent processes. This has become possible in this work by incorporating the Pop plot in a semi-analytical model of shock buildup.

In conclusion, this investigation is concerned with the successive states of a solid explosive undergoing shock initiation and buildup to detonation. We compute these states analytically by means of a two-phase Hugoniot which is in turn determined by the component equations of state or Hugoniots and a decomposition parameter. Any desirable equations of state can be chosen for the characterization of unreacted explosive and reaction products. For simplicity as well as accuracy, we have used the linear solid Hugoniot and γ-law gas equations of state as well as JWL equations of state. To model the change of states by a rate process, we have introduced an equation for the time rate of shock buildup to be based on Pop plot data. Out two-phase states and two-parameter time rate for the change of states provide a detailed assessment of shock initiation in solid explosives. Our methods and results are meant to be practical rather than sophisticated.

Our approach has been developed with an eye toward numerical modeling of reactive shock waves. Since partially reacted states are described in a physically consistent manner, it can be used in a fashion analogous to the CJ volume burn model. Then an independent burn model can be used to describe reaction in the region downstream of the shock.

APPENDIX A

Gaseous detonation products may be characterized adiabatically by

$$PV^{\gamma} = P_j V_j^{\gamma}, \quad \gamma = -(\partial ln\, P / \partial\, ln\, V)\phi \qquad (A1)$$

$$TV^{\Gamma g} = T_j V_j^{\Gamma g}, \quad \Gamma g = -(\partial ln\, T / \partial\, ln\, V)\,\phi \qquad (A2)$$

From these follows

$$\frac{\gamma}{\Gamma g} = \left(\frac{\partial ln P}{\partial ln T}\right)_{\phi} = \frac{T}{P}\left(\frac{\partial P}{\partial T}\right)_{\phi} = \frac{T}{P}\left(\frac{\partial \phi}{\partial V}\right)_{p} = \left(\frac{\partial H}{\partial PV}\right)_{p} = 1 + \frac{1}{\alpha} \qquad (A3)$$

if we define $\alpha = (\partial PV/\partial E)_p$ and $\Gamma_g = (\partial PV/\partial E)_v = 1/\beta$ as in Reference (8). In fact Equation (A3) is the relation $1+\alpha = \alpha\beta\gamma$ as derived from a different approach (8). It is also shown (8) that

$$\frac{\partial\, ln\, D}{\partial\, ln\, \varrho_o} = \frac{\gamma-\alpha-1}{\alpha+2} \qquad (A4)$$

Since experimental results have established the linear relation $D = a + b\,\varrho_o$ with a and b denoting the appropriate constants, Equations (A3), (A4) and this can be combined to give

$$\Gamma g = \gamma\left[\frac{(\gamma-3)\,D + 2a}{(\gamma-1)\,D + a}\right] \qquad (A5)$$

Note that Equation (A5) gives the Grüneisen constant Γ_g of dense gases, which is not the same as that of the unreacted explosive, Γ_s.

Yet another important parameter is the specific heat C_{vg}. This can be computed as follows. Let us consider

$$dE_g = \left(\frac{\partial E_g}{\partial T_g}\right)_{,} dT_g + \left(\frac{\partial E_g}{\partial V_g}\right)_T dV_g$$

$$= C_{vg}\, dT_g + \left[T_g\left(\frac{\partial P_g}{\partial T_g}\right)_{,} - P_g\right] dV_g$$

$$= C_{vg}\, dT_g + (\Gamma_g C_{vg} T_g/V_g - P_g)\, dV_g \approx C_{vg}\, dT_g + (\Gamma_g E_g/V_g - P_g)\, dV_g = C_{vg}\, dT_g + \{P_o\left(1+\frac{\Gamma_g}{\gamma-1}\frac{V_o}{V_g}\right) - \left[1-\frac{\Gamma_g}{2V_g}(V_o-V_g)\right](P_g+P_o)\}dV_g$$

Assuming C_{vg} to be constant, we deduce

$$C_{vg} = (E_j - E_o - E_x)/(T_j - T_o) \qquad (A6)$$

with

$$E_j - E_o = \tfrac{1}{2}(V_o - V_j)(P_j + P_o) = \frac{P_j V_j}{\gamma(\gamma+1)}\left(\frac{2\gamma+1}{3\gamma+1}\right)$$

$$Ex = \int_{V_o}^{V_j} \{ (1 + \frac{\Gamma g}{\gamma - 1} \frac{Vo}{Vg}) P_o -$$

$$[1 - \frac{\Gamma g}{2Vg} (Vo - Vg)] (P_g + P_o) \} dV_g$$

$$T_o \approx T_j (Vj/Vo)^{\Gamma g}$$

If we assume $C_{vg} = C_4 + C_1 T_g + C_2 T_g^2 + C_3 T_g^3$, then the four coefficients (C_1, C_2, C_3, C_4) may be determined by integrations based on four data points (P_g, V_g, T_g, E_g) with $T_g \cong T_j (V_j/V_g)^{\Gamma g}$. That is all we can do analytically.

APPENDIX B

An analytically simplified version of the two-phase Hugoniot can be established by ignoring the entropy change along the component Hugoniots. Thus, we have

$E_g = \frac{PVg}{\gamma - 1}$ and $E_s = \frac{1}{2} (V_o - V_s) P$ in view of

$P_g = P_s = P$.

Substituting these and Equation (1) into Equation (2), we obtain

$$Vs = \frac{2V}{(1-\xi)(\gamma+1)} + \frac{\gamma-1}{\gamma+1} \left[Vo - \frac{2E}{(1-\xi)P} \right] \qquad (B1)$$

Since the linear solid Hugoniot implies

$$P = C^2 (V_o - V_s) / [V_o - S(V_o - V_s)]^2, \qquad (B2)$$

we can combine Equations (B1) and (B2) to give

$$P \left\{ V_o - \frac{2S}{\gamma+1} \left[V_o + \frac{1}{1-\xi} \left(\frac{E}{P} (\gamma - 1) - V \right) \right] \right\}^2$$

$$= \frac{2C^2}{\gamma+1} \left[V_o + \frac{1}{1-\xi} \left(\frac{E}{P} (\gamma - 1) - V \right) \right] \qquad (B3)$$

This is the two-phase Hugoniot for a partially reacted explosive in the form $F(P,V,E,\xi)=0$. Such a crude model may not be numerically realistic.

REFERENCES

1. C. L. Mader, "Numerical Modeling of Detonations," University of California Press, Berkeley, 1979.
2. E. L. Lee and C. M. Tarver, "Phenomenological Model of Shock Initiation in Hetergeneous Explosives," Phys. Fluids Vol 23, No. 12, December 1980, pp. 2362-2372.
3. J. B. Ramsey and A. Popolato, "Analysis of Shock Waves and Initiation Data for Solid Explosives," Proc. 4th Symposium (International) on Detonation, ACR-126, Office of Naval Research, Washington, D.C. 1965, pp. 233-238.
4. T. R. Gibbs and A. Popolato, "LASL Explosive Property Data," University of California Press, Berkeley, 1980.
5. B. M. Dobratz, "LLNL Explosive Handbook," UCRL-52997, Lawrence Livermore Laboratory, 1981.
6. C. M. Tarver and J.O. Hallquist, "Modeling Two-Dimensional Shock Initiation and Detonation Wave Phenomena in PBX-9404 and LX-17," Proc. 7th Symposium (International) on Detonation, NSWC MP 82-334, Naval Surface Weapons Center, White Oak, MD, 1981, pp. 448-497. Ibid, p. 1034.
7. Y. K. Huang, J. J. Starkenberg, and A. L. Arbuckle, "Calculations of Reactive Shock Waves in Several Solid Explosives," BRL Technical Report to be published.
8. W. Fickett and W. C. Davis, "Detonation," University of California Press, Berkeley, 1979.

DISCUSSION

MARTIN SUMMERFIELD, Princeton Combustion Research Laboratory

I believe the equation at the beginning, that says that the entropy of the unreacted solid and the entropy of the hot product gas are equal, is wrong. They are very unequal. Further, inserting this equality as one of the initial equations forces a distortion of the resulting two-phase Rankine-Hugoniot relations. I believe the theory is incorrect.

REPLY BY Y. K. HUANG

To clarify the above criticism, I have undertaken considerable revision of this paper herein. Apparently, it is not the validity but the readability of the Preprint that invites such a criticism. I hope that our paper will be judged finally by a wider audience of this Symposium when its Proceedings appear in the open literature.

MODELING SHORT PULSE DURATION SHOCK INITIATION OF SOLID EXPLOSIVES

C.M. Tarver, J.O. Hallquist and L.M. Erickson
Lawrence Livermore National Laboratory
University of California
Livermore, California 94550

The chemical reaction rate law in the ignition and growth model of shock initiation and detonation of solid explosives is modified so that the model can accurately simulate short pulse duration shock initiation. The reaction rate law contains three terms to model the ignition of hot spots by shock compression, the slow growth of reaction from these isolated hot spots, and the rapid completion of reaction as the hot spots coalesce. Comparisons for PBX 9404 between calculated and experimental records are presented for the electric gun mylar flyer plate system, the minimum priming charge test, embedded manganin pressure and particle velocity gauges, and VISAR particle velocity measurements for a wide variety of input pressures, rise times and pulse durations. The ignition and growth model is now a fully developed phenomenological tool that can be applied with confidence to almost any hazard, vulnerability or explosive performance problem.

INTRODUCTION

As an integral part of our High Explosives Research Program, the phenomenological ignition and growth computer model of shock initiation and detonation wave propagation has been developed to simulate the available experimental data and then to predict the hazard, vulnerability, and performance of solid explosives to various stimuli in complex geometries. The original one-dimensional ignition and growth model (1) successfully calculated a great deal of experimental data on several explosives including: embedded manganin pressure gauge and particle velocity gauge data, VISAR data, run distance to detonation versus initial shock pressure data, and quantitative failure versus initiation data. After more experimental data was obtained and the model implemented in the two- and three-dimensional versions of the Lagrangian DYNA code (2), the ignition and growth model was modified and successfully applied to many one-, two-, and three-dimensional initiation and detonation wave propagation problems in explosives and propellants (3-10). In general, this concept of dividing the chemical reaction rate into two terms to describe the ignition of reaction by shock compression in localized hot spots and the subsequent growth of these hot spots to consume the explosive charge has proved sufficient for modeling sustained pulse shock initiation and detonation wave reaction zones. However, as noted in the original paper (1), detailed quantitative modeling of embedded gauge or VISAR data from short pulse duration shock initiation experiments was not possible unless the coefficient for the growth of reaction was increased by a factor of two or three. Although such a relatively simple phenomenological model cannot be expected to perfectly simulate every shock initiation and detonation experiment, it is essential that the ignition

*Work performed under the auspices of the U.S. Department of Energy by the Lawrence Livermore National Laboratory under contract No. W-7405-ENG-48.

and growth model accurately model initiation caused by a wide variety of input pressures, rise times and pulse durations. This paper describes the modifications to the chemical reaction rate law that were made to meet this requirement and the parameters generated for the solid explosives PBX 9404 (HMX-based) and LX-17 (TATB-based). This paper also contains several examples of the agreement between the calculations and recent experimental data from several laboratories on PBX 9404. Examples of modeling short pulse duration shock initiation of LX-17, shock initiation of a cast explosive, detonation wave propagation and metal acceleration, and supra-compression experiments with the current ignition and growth model are contained in four other papers presented at this Symposium (11-14).

THREE TERM REACTION RATE MODEL

During a review of embedded gauge data, of Lagrange Analysis of such data (15), and of very high shock pressure, very short shock pulse duration initiation data, it became apparent that shock initiation of heterogeneous solid explosives must be modeled as at least a three step process. The first step is obviously the formation of hot spots created by various mechanisms (void closure, viscous heating, shear banding, etc.) during shock compression and the subsequent ignition (or failure to ignite due to heat conduction losses) of these heated regions. At relatively low input shock pressures, the ignition of a fraction of the explosive on the order of the original void fraction of the charge is sufficient to calculate initiation/failure data and the increase in shock front pressure at increasing depths in embedded gauge experiments (1). However, when modeling high input pressure, short pulse duration experiments, such as the minimum priming charge test (16) and initiation by thin mylar flyer plates in the electric gun (17), a larger fraction of the explosive must be rapidly ignited, especially with pressure dependent reaction growth rates. Therefore, the main change in the ignition term of the reaction rate law was to increase the dependence of the amount of explosive ignited on the degree of shock compression, thereby igniting much more explosive at high pressures approaching detonation pressures and much less explosive at low input pressures of a few kilobars.

The second step in the process is assumed to be a relatively slow growth of reaction in inward and/or outward "burning" of the isolated hot spots. Although this analogy with deflagration processes may not be strictly appropriate under all shock initiation conditions, embedded gauge and VISAR experiments definitely show regions of relatively slow pressure and particle velocity increases behind the shock front. Modeling this portion of the reactive flow as a pressure dependent burn with an exponent near unity, as measured in deflagration experiments (18), readily matches sustained and short duration shock pulse data. In their Lagrange gauge and modeling work, Wackerle and Anderson (19) found that a simple spherical inward grain burning model yielded a better correlation with experimental data than a simple spherical outward hole burning model. Obviously the real situation of reacting hot spots is a much more complex geometry, but in this paper a spherical inward grain burning form is used along with a pressure exponent of one in the second or slow growth term of the reaction rate law.

The third step in the shock initiation process is a rapid completion of the reaction as the reacting hot spots begin to coalesce. Fast decomposition of the remaining pockets of unreacted explosive causes the rapid transition to detonation observed in wedge test run distance to detonation experiments (20). If each hot spot is taken to be a sphere at the center of a cube, then, when the diameter of the sphere equals the length of a side of cube, the ratio of volume of the sphere to the volume of the cube is $\pi/6$ or 0.52. Therefore, these idealized "spherical hot spots in a box" would begin to coalesce when the explosive is approximately half-reacted. Even for a relatively low input pressure of 2 GPa, the pressure exceeds 10 GPa when the explosive is half-reacted, and all conceivable reactive surface area generation mechanisms will be rapidly occurring. This rapid completion of reaction has been modeled in two ways: as an Arrhenius rate law with a realistic activation energy and realistic assumptions about the temperature of the unreacted explosive or as a pressure dependent growth rate with an exponent of two or three to match run distance to detonation data and to yield the correct reaction zone width for

self-sustaining detonation. In this phenomenological model, the pressure dependent form is used to represent the third part of the initiation model: the rapid completion of reaction as the turnover to detonation occurs.

Therefore, the form of the chemical reaction rate equation in the three term ignition and growth model is:

$$\partial F/\partial t = I(1-F)^b(\rho/\rho_o - 1 - a)^x + G_1(1-F)^c F^d p^y + G_2(1-F)^e F^g p^Z \quad (1)$$

where F is the fraction of the explosive that has reacted, t is time, ρ_o is the initial density of the explosive, p is pressure in megabars, and I, G_1, G_2, a, b, c, d, e, g, x, y, and Z are constants. The parameter a is a critical compression that is used to prohibit ignition until a certain degree of compression (or a certain input pressure) has been reached. In most cases, the parameter y in the first growth rate term is set equal to one to represent a deflagration process. The parameters b and c on the $(1-F)$ terms in the ignition and first growth terms are set equal to $^2/_3$ to represent inward spherical grain burning. The parameters I and x control the amount of ignition as a function of shock strength and duration, G_1 and d control the early growth of reaction following ignition, and G_2 and Z determine the high pressure reaction rates. Maximum and minimum values of F have been added to the reaction rate computations so that each of the three rates can be turned off (or turned on) at appropriate values. The ignition rate is set equal to zero when F exceeds the parameter Figmax. The first growth rate is set equal to zero when F exceeds the parameter F_{G1max}. The second growth rate is zero when F is less than F_{G2min}.

The values of all the parameters used for PBX 9404 and LX-17 are listed in Table 1. The unreacted and reaction product equations of state for PBX 9404 and LX-17 remain the same as those given by Tarver and Hallquist (3). The mixture rules and methods of calculation remain the same as in the original description (1). The results of using this three term rate law to simulate many experiments on PBX 9404 are described in the next section. Similar calculations of the available LX-17 experimental data are contained in a companion paper (11).

TABLE 1

Chemical Reaction Rate Parameters for PBX 9404 and LX-17

Parameter (EQ.(1))	PBX 9404	LX-17
I (μsec^{-1})	7.43×10^{11}	4.0×10^6
b	0.667	0.667
a	0.0	0.22
x	20.0	7.0
G_1 ($Mbars^{-\gamma}\mu sec^{-1}$)	3.1	0.6
c	0.667	0.667
d	0.111	0.111
y	1.0	1.0
G_2 ($Mbars^{-Z}\mu sec^{-1}$)	400.0	400.0
e	0.333	0.333
g	1.0	1.0
Z	2.0	3.0
Figmax	0.3	0.5
F_{G1max}	0.5	0.5
F_{G2min}	0.0	0.0

COMPARISON OF CALCULATIONS AND EXPERIMENTAL RESULTS FOR PBX 9404

1. High Pressure, Short Pulse Duration Tests

A good, overall quantitative test of a reactive flow model is the one-dimensional initiation/failure data generated by accelerating various thicknesses of mylar by electrically exploded aluminum foils, as described by Weingart et al. (17). The decay of the pressure behind the mylar foil depends on its acceleration history, the amount of electrical energy used, and the presence of remaining aluminum vapor. For conservative modeling, the mylar flying plates are assumed to be fully accelerated with no vaporized material still accelerating them. The experimental threshold velocities for six thicknesses of mylar ranging from 1.27-mm to 0.025-mm for shock initiation of 19-mm thick PBX 9404 charges are listed in Table 2, along with the calculated threshold velocities for comparison. The pressures produced by the thinnest flyers may approach the von Neumann spike pressure of the explosive and the shock pulse duration may be only a few nanoseconds, so very finely zoned calculations with 100 zones/mm in the explosive are necessary to accurately resolve these shock fronts. The agreement between the calculations and experiments is good at the higher pressures, where 20-30% of

the explosive is ignited by the shock front, and at the lower pressures where a few tenths of a percent of the explosive is promptly ignited. At the two intermediate pressures the calculations predict higher threshold velocities than measured. However, in these experiments, considerable aluminum vapor is still accelerating the plates, and the pressure decay behind the flyer is not as steep as assumed in the calculations and more reaction can occur behind the main front, thus lowering the initiation threshold. Care must also be taken in defining detonation, because, in these experiments, a flash from $Al_2(SiF_6)_3$ coated on the rear face of explosive charge detects a shock wave pressure of approximately 20 GPa. The calculations show that it is possible with a high initial shock pressure to obtain a 20 GPa shock front emerging from the explosive rear boundary that is actually slowly failing or slowly building toward detonation. Considering these experimental uncertainties, which must be considered when calculating any experiment, the three term reaction rate model does a reasonably good job on the electric gun data.

TABLE 2

Velocity Thresholds for Mylar Flyer Initiation of PBX 9404 in the Electric Gun

Mylar Flyer Thickness (mm)	Experimental Velocity Threshold (Km/s)	Calculated Velocity Threshold (Km/s)
1 27	1 1±0.2	0 95±0 05
0 508	1 4±0 2	1 30±0 10
0 254	1 9±0 2	2 55±0 05
0 127	2 6±0 2	2 95±0 05
0 051	3 3±0 3	3 55±0 05
0 025	4 2±0 3	3 95±0 05

2. Minimum Priming Charge Test

A tougher high pressure, short shock pulse duration test for this model is the one-dimensional, spherically divergent initiation of PBX 9404 by PETN-based EXTEX in the minimum priming charge test (16). Hemispheres of EXTEX of varying radii are centrally detonated and produce 20.5 GPa peak pressure pulses with different Taylor waves in the acceptor samples. The critical radius for initiation of detonation is then determined. For PBX 9404 the 50% point for shock initiation is 0.195 cm of EXTEX. In modeling this test, a spherically divergent Chapman Jouguet detonation wave in EXTEX (ρ_o=1.54g/cm^3, D=7.35 mm/μs, P_{CJ}=20.5 GPa, JWL coefficients: A=5.39165 Mbars, B=0.0334709 Mbars, R=4.6, R_2=1.1, ω=0.4, E_0=0.066 Mbars-cc/cc) is assumed to impact finely zoned (100 zones/mm) PBX 9404. Figure 1 shows calculated pressure profiles at various distances into PBX 9404 for a 0.19 cm radius EXTEX charge which illustrate the failure to shock initiate the PBX 9404. Figure 2 shows similar profiles for a 0.20 cm radius EXTEX charge which illustrate the successful initiation of spherically divergent detonation in the PBX 9404. The reactive flow model clearly has the correct pressure, time duration and geometric dependences for successful calculations of this test.

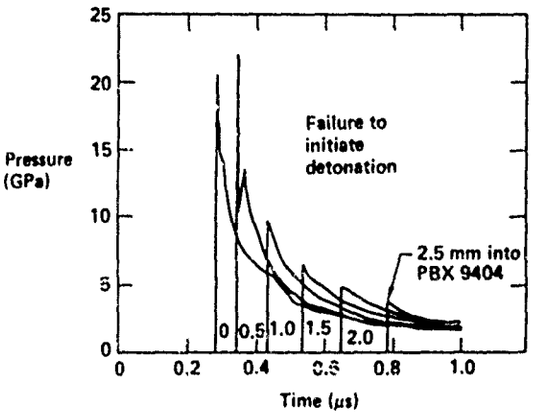

Fig. 1. Calculated pressure histories in PBX 9404 for a 0.19 cm radius minimum priming charge

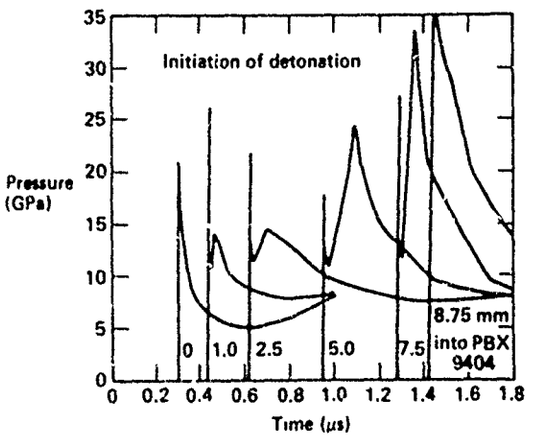

Fig. 2 Calculated pressure histories in PBX 9404 for a 0.2 cm radius minimum priming charge

3. Lower Pressure Sustained and Short Duration Embedded Gauge Experiments

Two classical sets of embedded gauge experiments of PBX 9404 have been done in the 2.5-3.5 GPa initial shock pressure range to demonstrate the differences in the growth to detonation for sustained and short duration shock pulses. Wackerle et al. (21) placed one manganin pressure gauge in each sample and fired several PBX 9404 samples with gauges placed at different depths. The experimental records from these experiments are superimposed in Figures 3 and 4 for a 3 GPa sustained shock and a 3 GPa, 0.33 μs shock pulse, respectively. The calculations must be done exactly as were the experiments, since the finite thickness of a manganin gauge (typically 1 mil of manganin foil sandwiched between two 5 to 10 mil thick layers of teflon, kapton, mylar or mica insulation) does perturb the reactive flow. This is even more important in multiple manganin gauge experiments (1,3,11) in which several gauges are placed in the same explosive sample. Figures 3 and 4 also contain the calculated pressure histories at the various gauge positions. The calculated pressures agree well with the gauge records up to the pressures at which these gauges failed. The calculated run distances to detonation of 9.5-mm and 15-mm for the sustained shock and the 0.33 μs pulse, respectively, agree with the experimental values of 9.5-mm and 14.5-mm. At the 1-mm and 3-mm gauge positions of Figure 4, the calculated shock front amplitude and initial rarefaction agree with the gauge records but subsequent pressures are lower than the gauge records indicate. It is difficult to determine whether this difference is totally due to the reaction rate law or whether part of the difference is due to the current lack of knowledge of the reaction products equation of state and of the accuracy of the mixture assumptions in this pressure and temperature regime. Since the ignition and growth model must also describe detonation and its metal acceleration ability correctly, it uses JWL equation of state for the reaction products measured by expansion in detonation experiments. There is no guarantee that this equation of state accurately predicts the states of products generated in low pressure shock initiation experiments, but this is the assumption that must be made in this general purpose model. It should be mentioned that manganin pressure gauges have undergone further development and currently can record the entire reactive flow process without failing in both shock initiation and full detonation (3,7,11).

In the other set of embedded gauge experiments, multiple particle velocity gauges measured the growth to detonation caused by a sustained 3 GPa shock pressure in Figure 5, a 2.5 GPa, 1 μs shock pulse from a dynasil flyer in Figure 6, and a 2.2 GPa, 1 μs shock pulse from a Kel-F flyer in Figure 7. These embedded particle velocity gauges have the advantage that they are much thinner than manganin gauges (typically 1 mil of aluminum with 1 mil of teflon on each side), but the disadvantage that non-metallic flyer plates must be used. Thus not all pressure regimes are easily accessible and the non-metallic materials have equations of state that are not as well understood as those of metals. These experimental details are modeled as completely as possible in Figures 5, 6, and 7. The agreement between the calculated and experimental shock front and subsequent growth in the sustained shock experiment in Figure 5 is quite close. In the dynasil flyer experiment shown in Figure 6, the calculated shock front particle velocity is high at the 14-mm gauge position and the calculated peak particle velocity occurs early, thus implying a slightly early transition to detonation. By the 22-mm gauge position, however, both the calculation and the gauge record indicate that detonation has occurred It should be mentioned that the particle gauges used in Figs. 5 and 6 recorded incorrect (low) velocities only at full detonation. This problem was solved by teflon insulation, as demonstrated by published gauge records in full detonation (7,9). In the Kel-F flyer experiment shown in Fig. 7, the reactive flow is building toward detonation but does not quite make the transition in 22-mm sample of PBX 9404. The calculations predict slightly high particle velocities, particularly at the 14-mm position, and a transition to detonation in less than 22-mm. Therefore, it appears that the model predicts slightly too much ignition and early growth at these low input shock pressures, perhaps due to the fact that the unreacted equation of state does not fully describe the dissipative processes first measured by Kennedy and Nunziato (22) in PBX 9404 below 3 GPa

and also observed in Lagrange analysis of embedded gauge records (15). Mechanical dissipation processes or endothermic chemical reactions can be added to the model when they are identified and measured quantitatively.

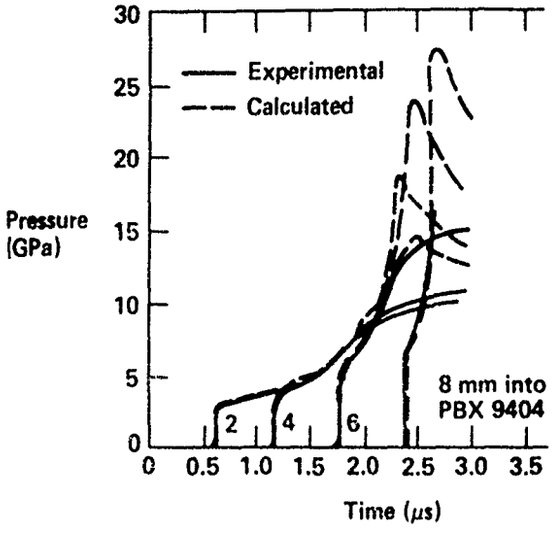

Fig 3 Pressure Histories for a 3 GPa sustained shock wave in PBX 9404

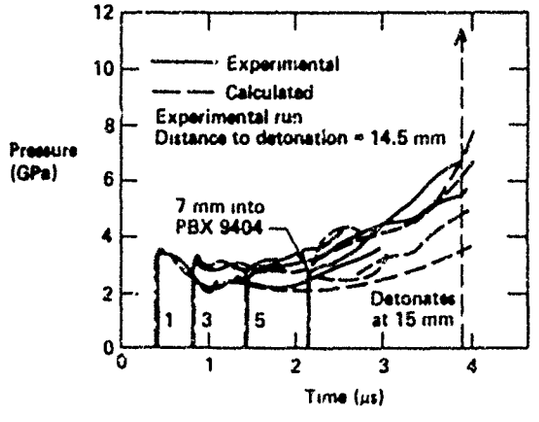

Fig 4 Pressure histories for a 3 GPa, 0.33 μs shock pulse into PBX 9404

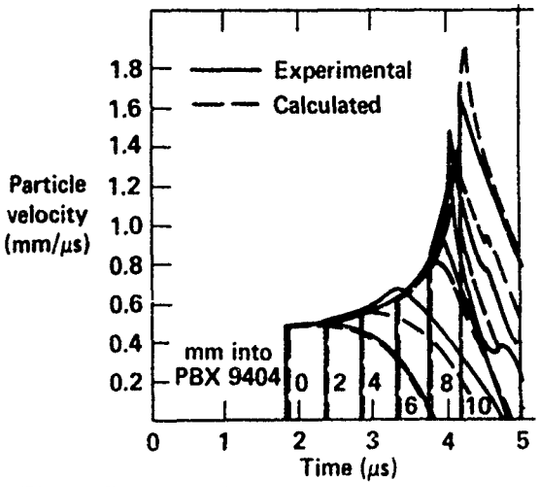

Fig. 5. Particle velocity histories of a sustained 3.5 GPa shock wave into PBX 9404

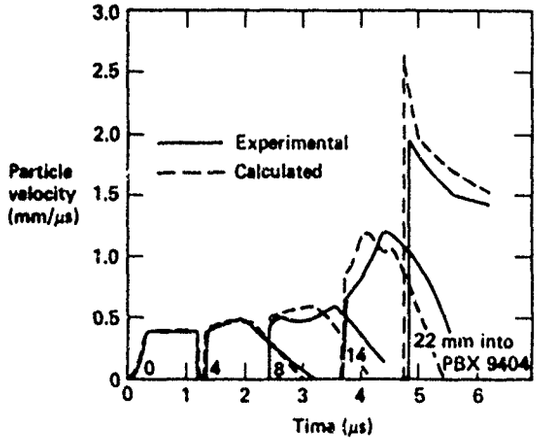

Fig. 6. Particle velocity histories for a dynasil flyer plate short duration shock pulse in PBX 9404

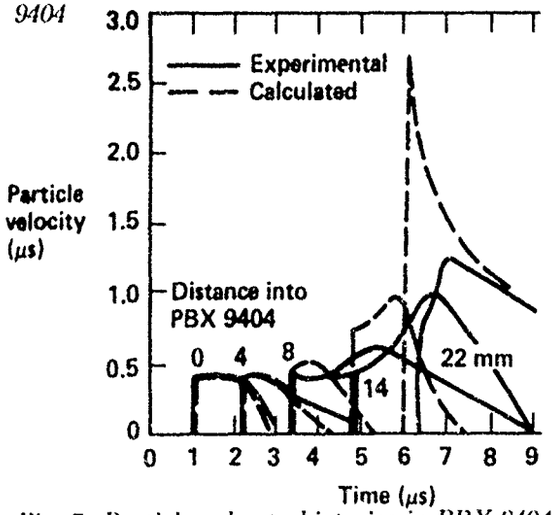

Fig. 7. Particle velocity histories in PBX 9404 for a Kel-F flyer plate short duration shock pulse

4. VISAR Records of Various Initiation Experiments on PBX 9404

In an imaginative series of experiments on PBX 9404, Setchell (23-25) measured the growth of reaction in PBX 9404 subjected to several types of input stresses using a VISAR particle velocity measurement technique. Setchell used various combinations of flyer plate and buffer materials in front of the explosive samples to produce short duration shock pulses with different unloading histories, ramp waves, two step shocks, ramp/shock loading, and low amplitude precursor/shock loading. These experiments produced sets of particle velocity histories for various thicknesses of PBX 9404 that represent excellent tests for computer modeling. Besides testing the reactive flow model, these experiments also test the complex material models for the flyer plate, buffer and window materials: fused silica, sapphire, copper, pyroceram, 6061-T6 aluminum, tungsten, and even the carbon foam backing on the impactors. The VISAR records are very accurate measurements of the ignition and early slow growth of reaction, but are limited to stresses below 7.5 GPa in PBX 9404 because of a phase transition at 9.4 GPa in the fused silica window behind the explosive sample. To test the effect of different unloading histories on the growth of reaction in a short duration shock pulse experiment, Setchell (23) impacted PBX 9404 with fused silica (fast unloading) and sapphire (slow unloading) to produce 3.2 GPa, 0.37 μs initial shock pressures. The resulting particle velocity histories are shown in Figure 8 for 2,4,6 and 10mm of PBX 9404 impacted by fused silica and in Figure 9 for 2,4,6 and 8mm samples impacted by sapphire. The slower unloading properties of sapphire obviously allowed more reaction to occur and thus higher particle velocities were recorded. Figures 8 and 9 also contain the calculated particle velocity histories for each of the eight experiments. In the case of fused silica impact in Fig. 8, the initial shock pulse and unloading are well modeled since the 2-mm records agree closely. At greater depths, the calculated initial particle velocities are higher than measured, due to slightly too much ignition or a lack of dissipation processes, and the later portions of the calculated records are generally slightly lower than the measurements. The late time agreement in the 10-mm experiment is very good. In the case of sapphire impact in Fig. 9, much less shock front decay is observed and the calculated initial particle velocities are in better agreement. Again the calculated particle velocities are generally slightly lower than the experimental records, but the overall more rapid growth for sapphire impact is reproduced by the calculations shown in Fig. 9.

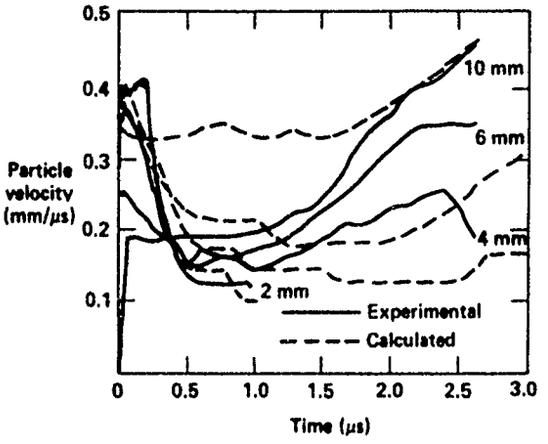

Fig. 8. Particle velocity histories in PBX 9404 for fused silica flyer plate experiments

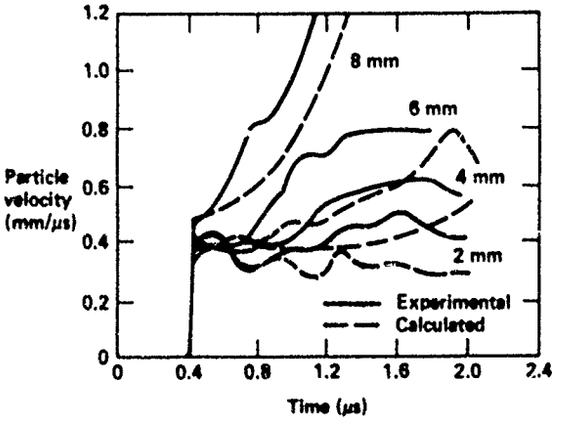

Fig. 9. Particle velocity histories in PBX 9404 for the sapphire flyer plate experiments

The same relationship between experimental and calculated particle velocity histories is observed for Setchell's experiments in which 6061-T6 aluminum is placed in front of PBX 9404 producing a low amplitude precursor which precedes a 3.5 GPa shock (25). The comparison for 1.5, 4 and 6mm of PBX 9404 are shown in Figure 10. However, this relationship does not always hold, as shown in Figure 11, which contains comparisons at 2,3 4 and 5mm

depths for the case of "ramp/shock" loading. A 2 GPa, 0.5 μs ramp preceding a 5 GPa shock is produced by using a 19mm thick fused silica buffer ahead of the PBX 9404. In Fig. 11, the calculations lie slightly above the experimental records at 2,3 and 4mm and slightly below at 5mm. For the case of a two step shock produced by a composite flyer plate of fused silica and tungsten (25), the calculations predict slightly higher particle velocities than measured at 2,3 and 4mm of PBX 9404, as shown in Fig. 12.

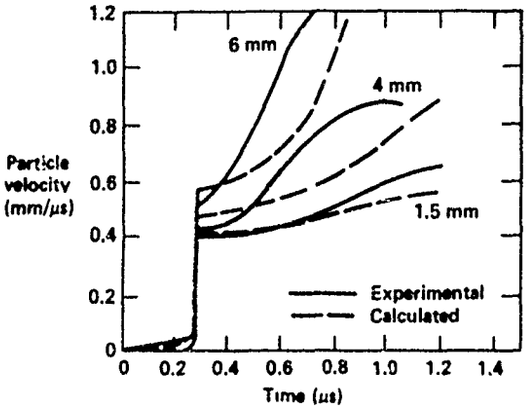

Fig 10 Particle velocity histories in PBX 9404 for GPa shocks preceded by low amplitude precursors

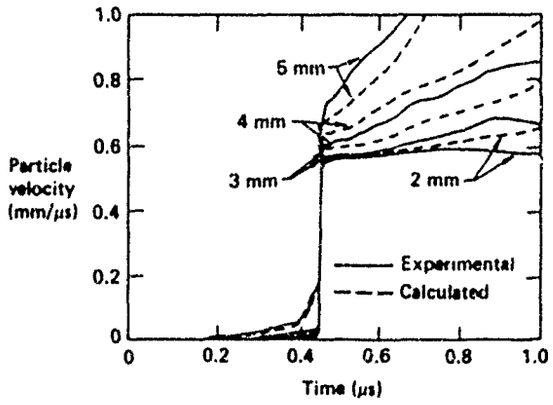

Fig 11 Particle velocity histories in PBX 9404 for the ramp shock experiments

The final three comparisons with Setchell's data are shown in Figs. 13, 14 and 15 for the cases of slow rising (0.8μs) ramp waves, faster rising (0.3 μs) ramp waves, and sharp shock loading to a final pressure of 5.1 GPa, respectively (24). The calculations accurately predict the initial ramp wave loadings in Figs. 13 and 14. In the slow ramp case in Fig. 13, the calculated particle velocities are low at 1.5 and 2-mm and then high at 3,4 and 5mm. In the fast ramp and shock cases of Figs. 14 and 15, respectively, the calculated particle velocity histories are all slightly lower than the VISAR records.

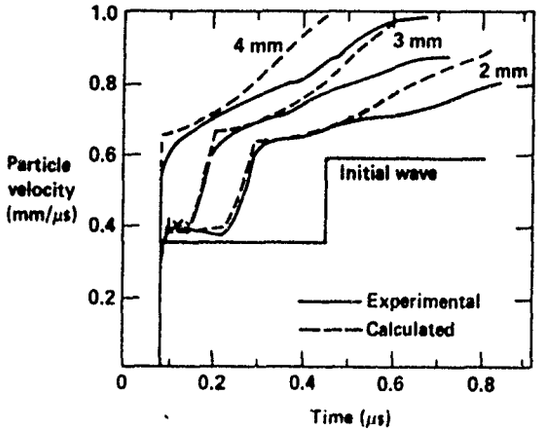

Fig. 12. Particle velocity histories in PBX 9404 for the two step shock loading experiments

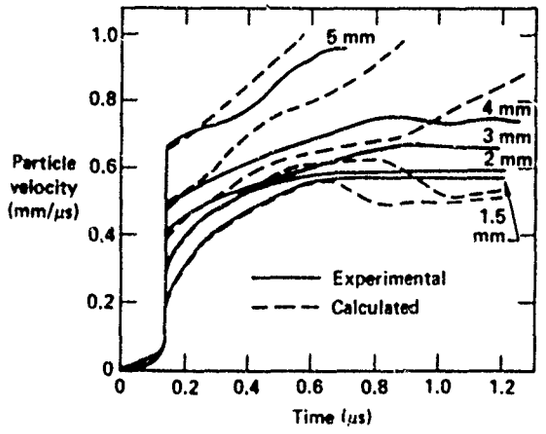

Fig. 13. Particle velocity histories in PBX 9404 for the slow ramp wave experiments

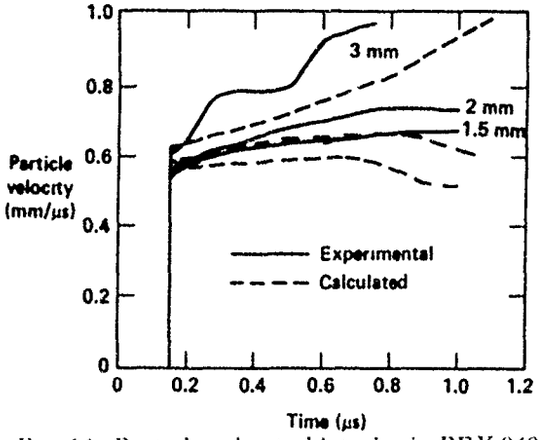

Fig. 14. Particle velocity histories in PBX 9404 for the fast ramp wave experiments

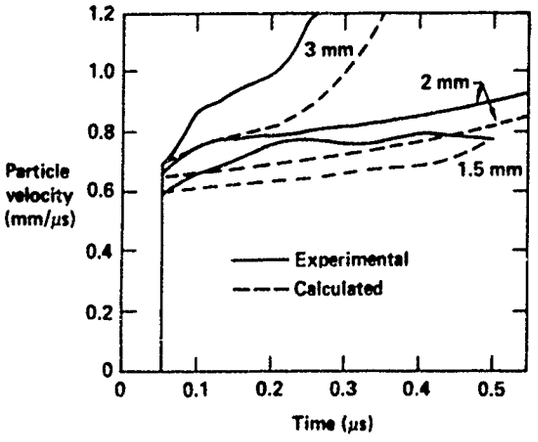

Fig. 15. Particle velocity histories in PBX 9404 for the 5.1 GPa sustained shock experiments

The main result of these comparisons is that the three reaction rate law for PBX 9404 does a good overall job of describing initiation under a wide range of loading and unloading conditions. Further small modifications in the ignition and early growth rates, plus the inclusion of energy dissipation terms in the unreacted equation of state, would result in slightly improved agreement in various pressure and time regimes. However, the current agreement certainly demonstrates the soundness of this modeling approach.

One other interesting comparison between a embedded gauge experiment and a PBX 9404 reactive flow calculation is currently available. Many hazard and vulnerability scenarios for explosives involve two or more shocks separated in time by various unloading processes. In the experiment shown in Fig. 16, embedded particle velocity gauges at 0,4,7,12 and 20mm depths measured the double shocks produced by the impact of a composite flyer consisting of two ceramic plates separated by low density carbon foam. The growth of reaction during the time between shocks and after the second shock produces a complex wave structure that is approaching the transition to detonation after 20mm of propagation. The calculated particle velocity histories are also shown in Fig. 16. The double shock structure is evident but the calculated particle velocities behind the first shock are low and the second shock arrivals are later in time than measured. This most likely results from an incomplete understanding of the equation of state of the ceramic flyer and buffer plate material and of the density and thickness of the compressible carbon foam when impact actually occurs. More experiments of this type should enable us to understand these materials and to "fine tune" the ignition and growth coefficients for reliable multiple shock scenario predictions.

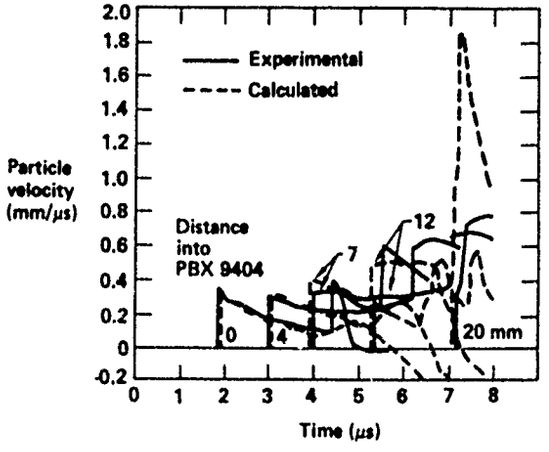

Fig. 16. Particle velocity histories in PBX 9404 for a double separated shock experiment

CONCLUSIONS

The results presented in this paper show that the use of a three term chemical reaction rate equation in the phenomenological ignition and growth model yields good overall agreement with a large collection of shock initiation data on PBX 9404 from three laboratories. Therefore, we now have a general purpose model that can be used with confidence to simulate most initiation scenarios. Obviously, the coefficients in the model can be further modified to improve the agreement with existing and future data. As a by-product of this work, the consistent agreement of the calculations with the various experimental techniques (embedded manganin pressure gauges, embedded particle velocity gauges and VISAR) implies that the three techniques are all accurately recording the effects of the shock initiation process.

With the completion of the phenomenological model of shock initiation, the direction for future work is the development of more fundamental, microscopic models that describe actual ignition and growth processes. These models are needed to predict the effects of particle size and initial temperature on shock

initiation. Our first step in this direction is the statistical hot spot model, which contains a critical hot spot size parameter and does accurately simulate particle size effects in TATB (26). This model has recently been made entirely temperature dependent (27) and represents the starting point for the next generation of shock initiation models for solid explosives.

ACKNOWLEDGMENTS

The authors would like to thank all of the scientists that have taught us so much about reactive flow over the years, especially: M. Cowperthwaite of SRI International; R. Setchell, J. Kennedy, J. Nunziato and P. Taylor of Sandia National Laboratory; J. Wackerle, M. Ginsberg, J. Vorthmann, W. Seitz, A. Anderson, P. Tang and C. Forest of Los Alamos National Laboratory; and all of our co-workers at Lawrence Livermore National Laboratory.

REFERENCES

1. E.L. Lee and C.M. Tarver, Phys. Fluids *23*, 2362 (1980).
2. J.O. Hallquist, "User's Manual for DYNA2D," Lawrence Livermore National Laboratory Report UCID-18756 Rev. 2, January 1984.
3. C.M. Tarver and J.O. Hallquist, Seventh Symposium (International) on Detonation, Naval Surface Weapons Center NSWC MP-82-334, Annapolis, MD, 1981, p. 488.
4. B. Hayes and C.M. Tarver, ibid., p. 1029.
5. W.G. VonHolle and C.M. Tarver, ibid., p. 993.
6. L.G. Green, E. James, E.L. Lee, E.S. Chambers, C.M. Tarver, C. Westmoreland, A.M. Weston and B. Brown, ibid., p. 256.
7. C.M. Tarver, N.L. Parker, H.G. Palmer, B. Hayes and L.M. Erickson, J. Energetic Materials *1*, 213 (1983).
8. C.M. Tarver and P.A. Urtiew, Progress in Astronautics and Aeronautics *94*, 369 (1984).
9. C.M. Tarver, L.M. Erickson and N.L. Parker, Shock Waves in Condensed Matter-1983 (J.R. Asay, R.A. Graham, G.K. Straub, eds.), North-Holland, Amsterdam, 1984, p. 609.
10. S.A. Sheffield, D.D. Bloomquist and C.M. Tarver, J. Chem. Phys. *80*, 3831 (1984).
11. K. Bahl, G. Bloom, L. Erickson, R. Lee, C. Tarver, W. Von Holle, and R. Weingart, "Initiation Studies on LX-17 Explosive," paper presented at this Symposium.
12. L.G. Green. E.L. Lee, A.C. Mitchell and C.M. Tarver, "The Supra-compression of LX-07, LX-17, PBX-9404, and RX-26-AF and the Equations of State of the Detonation Products," UCRL-91485, paper presented at this Symposium.
13. E. Lee, D. Breithaupt, C. McMillian, N. Parker, J. Kury, C. Tarver, W. Quirk, and J. Walton, "The Motion of Thin Metal Walls and the Equation of State of Detonation Products," UCRL-91490, paper presented at this Symposium.
14. H. Moulard, J.K. Kury, and A. Delclois, "The Effect of RDX Particle Size on the Shock Sensitivity of Cast PBX Formulations," UCRL-92473, paper presented at this Symposium.
15. G.L. Nutt and L.M. Erickson, J. Energetic Materials *2*, 263 (1984).
16. C.A. Forest, "Numerical Modeling of the Minimum Priming Charge Test," Los Alamos National Laboratory Report LA-8075, February 1980.
17. R.C. Weingart, R.K. Jackson, C.A. Honodel and R.S. Lee, Propellants and Explosives *5*, 158 (1980).
18. T.L. Boggs, C.F. Price, A.I. Atwood, D.E. Zurn, and R.L. Derr, Seventh Symposium (International) on Detonation, Naval Surface Weapons Center NSWC MP82-334, Annapolis, MD 1981, p. 216.
19 J. Wackerle and A.B. Anderson, Shock Waves in Condensed Matter - 1983 (J.R. Asay, R.A. Graham, G.K. Straub, eds.), North-Holland, Amsterdam, 1984, p. 601.
20. J.B. Ramsay and A. Popolato, Fourth Symposium (International) on Detonation, Office of Naval Research ACR-126, White Oak, MD, 1965,p. 233.
21. J. Wackerle, R.L. Rabie, M.J. Ginsberg, and A.B. Anderson, Symposium (International) on High Dynamic Pressures, Commissariat a l'Energie Atomique, Paris, 1978, p. 127.

22. J.E. Kennedy and J.W. Nunziato, J. Mech. Phys. Solids *24*, 107 (1976).

23. R.E. Setchell, Seventh Symposium (International) on Detonation, Naval Surface Weapons Center NSWC MP82-334, Annapolis, MD, 1981, p. 857.

24. R.E. Setchell, Comb. Flame *43*, 255 (1981).

25. R.E. Setchell, Comb. Flame *54*, 171 (1983).

26. S.G. Cochran and C.M. Tarver, Shock Waves in Condensed Matter - 1983 (J.R. Asay, R.A. Graham, G.K. Straub, eds.), North-Holland, Amsterdam, 1984, p. 593.

27. J.D. Immele, Private Communication, LLNL, 1985.

DISCUSSION

MARTIN SUMMERFIELD, Princeton Comb. Res. Laboratory

Has any effort been made to measure F, the fraction reacted, independently of tracking the pressure-time-distance trajectories, in order to validate the deduced reaction rate of equation? If not, it should be attempted, perhaps by measuring F chemically in shocked but not detonated specimens.

This kind of work is fundamental, it seems to me, to the modeling of DDT in granulated or cracked (damaged) propellant of the type envisioned in the theories of Boggs and Price, Krier, and Kuo. Why don't they use Tarver's equation, or something like it, in their models? It is my belief that inserting such condensed-phase exothermic reactions in their models, to explain the transition from their calculated pressure build-up over to detonation, would make the physical model more believable.

ALBERT WESTON, Brobeck Corporation

The ignition and growth model has been in the RDUCT model DDT calculations described in a paper presented at this Symposium (Weston & Lee). It does work well in creating a "clean" detonation turnover.

We do not use ignition and growth as a matter of course (yet) because in RDUCT there is a degree of arbitrariness in when to turn it on.

REPLY BY C. TARVER

It is obviously very difficult to independently measure the fraction reacted F (whatever F means in a complex decomposition process) as a function of time in a shock initiation experiment. The closest approach to such a measurement thus far is the time-resolved infrared radiometry experimental technique developed by William Von Holle at LLNL. This technique measures the amount of infrared radiation being produced at the interface between a shocked, reacting high explosive and an impedance matching infrared transparent window (salt crystal). After making some reasonable assumptions about the emittence of the shocked explosive, the fraction of the explosive emitting as a function of time and its average temperature can be calculated. Assuming that this fraction of omitting material is the fraction reacted, fraction reacted histories at various initial pressures and explosive thicknesses have been measured for many explosives. We have compared these measured fraction reacted histories to those calculated by the ignition and growth model, previously fit to pressure and particle velocity histories, for PBX-9404 in the Seventh Detonation Symposium (Von Holle and Tarver). Several other papers and reports by Bill Von Holle are available on his nanosecond time-resolved infrared radiometry technique.

TABLE 9
Rate Parameters for RDX Formulations from Wedge Test Data

	ALUMINUM IMPACT VELOCITY (mm/μsec)	$F_{max\ I}$	G_1	$F_{max\ G_1}$
FINE RDX FORMULATION	1.274	.002	0.3	0.2
	1.498	.002	0.4	0.2
	1.700	.002	0.5	0.2
	1.926	.002	0.6	0.2
COARSE RDX FORMULATION	1.338	.05	0.5	0.5
	1.510	.09	1.5	0.5
	1.810	.13	13.0	0.5

it was necessary to vary both G_1 and $F_{max\ I}$ to obtain the agreement shown in Fig. 13. The values used are presented in Table 9.

The major difference in the two formulations is that only about .2 percent of the fine RDX is reacted near the shock front whereas 5 percent or more of the coarse is reacted. Also, for the coarse formulation the amount reacted near the shock front and the growth rate increase significantly as the input pressure is increased above 6 GPa.

Calculations for the Other Experiments

The reaction rate parameters obtained from the wedge test calculations were used in computer simulations of the other experiments reported above. Good agreement was obtained for all the thin plate experiments except the 1 mm plate impacting the fine RDX formulation. See Table 10. In order to obtain agreement with experiment the amount of RDX ignited in the calculation had to be increased from 0.2 percent to 6 percent. Tarver (2) has observed similar behavior when simulating thin pulse initiation of pressed PBX.

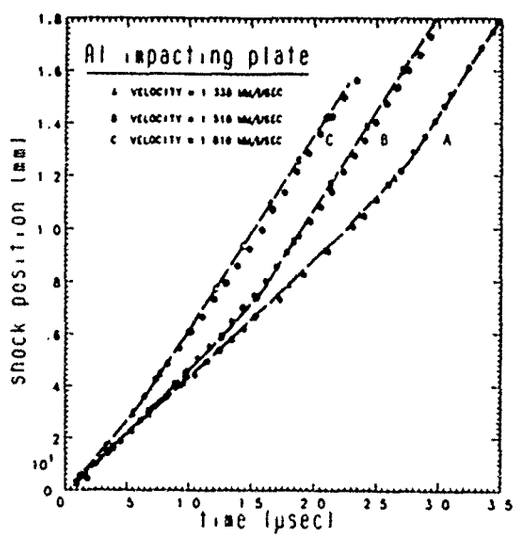

Fig. 13. Comparison of experimental and calculated wedge test data for coarse RDX formulation. Solid points are experimental results

The 4 mm experiments were calculated using a 2D hydrodynamic finite element code. When failure of detonation occurred it was due to the errosion of the pressure on the charge axis by sideways rarefaction. Figure 14 presents pressure contours for the coarse RDX formulation 7 μsecs after being impacted by a 4 mm aluminum plate with velocity of .96 mm/μsec. As in the experiment SDT does not occur.

TABLE 10
Calculated Results for Thin Plate Experiments

		PLATE VELOCITY	CALCULATED RESULTS
1 mm thick Al plate	FINE RDX FORMULATION	2.025	No detonation*
		1.910	No detonation
	COARSE RDX FORMULATION	1.725	Detonation ~8mm into explosive
		1.530	No detonation
4 mm thick Al plate	FINE RDX FORMULATION	1.525	Detonation ~14 mm into explosive
		1.400	No detonation
	COARSE RDX FORMULATION	1.110	Detonation ~24 mm into explosive
		0.960	No detonation

* All but this calculation agreed with the experimental results.

2D calculations were done for both a 15-mm and 20-mm diameter steel projectile impacting the coarse RDX formulation at a velocity of 1.13 mm/μsec. Results are presented in Table 11. Comparing the results in Fig. 15 and Fig. 16 shows that the smaller diameter projectile allows rarefactions to reduce the pressure sufficiently to prevent transition to detonation.

The 2D code was used to investigate the detonation failure diameter of both the fine and

A MODEL FOR SHOCK INITIATION OF POROUS PROPELLANTS BY RAMP-INDUCED COMPRESSION PROCESSES

H. Krier, C. A. Cudak, J. R. Stewart
The University of Illinois
Urbana, Illinois
and
P. B. Butler
The University of Iowa
Iowa City, Iowa

Increasing the nitramine content of solid rocket propellants increases the overall performance of the system as well as the sensitivity to detonation by shock initiation. In some instances a confined zone of granulated propellant adjacent to a zone of cast propellant can provide a rapid enough pressure-rise rate to shock initiate the cast material. If the cast propellant is porous, the detonation will initiate at some location ahead of the granulated bed/cast material interface. The work presented here is an effort to numerically model this Deflagration to Detonation Transition (DDT) event. Results will be presented showing the build up to detonation for propellant beds with various initial configurations and pressure-rise rates.

INTRODUCTION

Increasing the nitramine content of solid rocket propellants increases the overall performance of the system as well as the sensitivity to Shock to Detonation Transition (SDT) and Deflagration to Detonation Transition (DDT). This paper deals primarily with the analysis and numerical modeling of a combined SDT/DDT event. The results will show that in some instances a zone of burning granulated propellant, confined and adjacent to a zone of cast propellant, can provide a rapid enough pressure-rise rate to shock initiate the cast material. This type of detonation hazard scenario is a real possibility in any high-energy rocket motor environment.

In order for a DDT to occur in a full-scale motor, the grain must first be damaged. This has been demonstrated in the laboratory many times when small-scale (20-40 cm) packed beds of granulated propellant undergo the transition from deflagration to detonation. Combustion of the high surface-to-volume ratio micron-sized fragments provides the rapid pressurization rate necessary to shock initiate the remaining fragments. By increasing the nitramine content of the propellant mixture the propensity to detonate is increased in two ways: the decomposition rate of the propellant increases and the shock sensitivity increases. Although little has been done to experimentally verify it, one can also assume that the particle morphology (size, shape and surface roughness) greatly influences the decomposition rate and thus, the build-up to detonation.

We propose two possible methods where by DDT can occur in a solid rocket motor. In the first case a length, L, of the motor grain is completely fragmented. This case was the topic of several research papers (1-3) by our group and will be discussed here only to provide a comparison with the second case proposed. In Case 1, the bed is of sufficient length to allow the transition to detonation to occur within the *granulated* material. That is $L > \varphi_{CJ}$ where φ_{CJ} is the detonation run-up length measured from the ignition source. In case 2, $L < \varphi_{CJ}$ and the detonation occurs in the upstream *cast* material. However, in both cases, the confined burning

of the propellant fragments is what drives the deflagration wave to a high-order detonation. The reader should consult Ref. 4 for a general overview of DDT in different propellants and explosives and Ref. 5 for typical experimental results.

In Case 1, the length of the packed bed is longer than the critical length necessary for accelerated convective combustion to occur, and subsequent detonation is inevitable. Figure 1 illustrates the Case 1 bed configuration. The second DDT scenario involves a region of burning granulated propellant providing the impetus to shock initiate an adjacent region of cast propellant. This is illustrated in Fig. 2. The cast material (Zone 1) can contain 'blind' pores, and is assumed to be impermeable to the flow of hot gases from the zone of fragmented material (Zone 2). This implies that, unlike the first DDT scenario discussed, only stress waves can be transmitted across the Zone 1/Zone 2 interface. Figure 3 shows a schematic representation of the sequence of events leading to this type of DDT. Superimposed on each section of the figure is a solid line representing the local gas porosity (volume of gas/total volume) as a function of x, the bed location. A value of ϕ equal to unity represents a zone of all gas while ϕ equal to zero indicates a voidless solid.

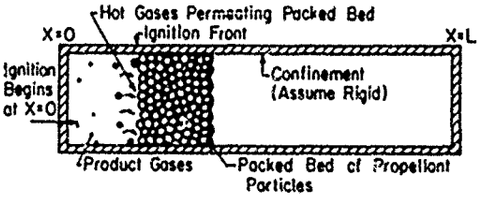

Fig. 1. Sketch of DDT-case 1 packed bed configuration

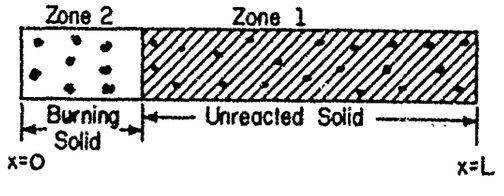

Fig. 2. Sketch of DDT-case 2 configuration. Zone 1 is cast propellant, Zone 2 is burning fragments

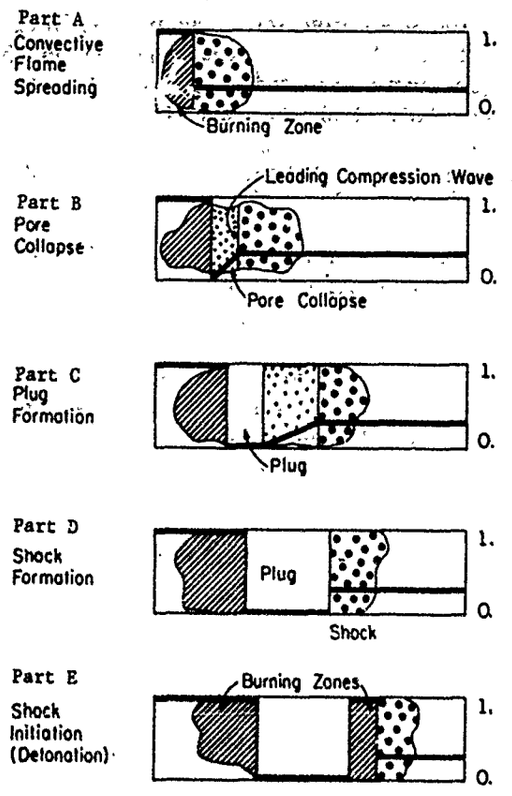

Fig. 3. Five-part sequence of events leading to DDT-case 2

Part A shows a zone of burning granular propellant adjacent to a zone of porous, cast propellant. Here, the heavy black dots are representative of microvoids in the cast material. Illustrated in Part B is the collapse of the pores, a result of the stress load transmitted across the granulated bed/cast propellant interface. Parts C and D show the length of the pore collapse zone to increase with time as the lead compression waves travel farther into the propellant bed. The finite compression waves coalesce into a shock front which subsequently shock initiates the cast propellant at a location φ_{CJ} ahead of the interface. From this location a detonation wave propagates through the porous material while a retonation wave propagates back through the compressed material (Part E).

In related research, Setchell (6) studied ramp-wave initiation mechanisms using waves with rise-times of 0.3 to 0.8 μs. In Ref. 6 the ramp-waves were developed by propagation of an impact-generated shock wave through a unique

material which has the property of spreading out the shock front into a ramp-wave. In the work presented here, the rise-times were much longer than those cited in (6), typically of the order of tens of microseconds. These slower rise-times are typical pressure-time histories generated within a deflagrating bed of granular HMX.

The purpose of this work is to model the key elements of the five part scenario shown in Fig. 3. A one-dimensional hydrodynamic Lagrangian finite difference technique is used to numerically solve the conservation equations. A static pore collapse model (7) which demarcates three regimes of deformation, elastic, elastic-plastic, and plastic, is utilized to determine the rate of compaction and the development of the solid plug. Furthermore, a hot spot model (8) is incorporated in the code to define the sensitivity to reaction. By introducing reactive chemistry to the code, a strong effort is made to model the detonation and retonation waves which are initiated by a shock wave generated from ramp-wave inputs with rise times on the order of tens of microseconds. It was shown in Ref. (9) that rise times, t*, of this order are typical for burning, granulated beds which have lengths *less* than their critical detonation run-up length.

THE MODEL

The scope of the work presented in this paper is to model DDT in the granulated bed/cast propellant configuration shown in Fig. 2. It is assumed that the granulated bed is not long enough ($L < \varphi_{CJ}$) to undergo DDT in the usual sense (Case 1), but by convective burning can provide the driving force necessary to shock initiate the upstream cast propellant. For this analysis the cast propellant is assumed to have 'blind' pores and to be impermeable to the flow of product gases generated in the granular bed. This implies that only stress waves can be transmitted across the granular bed/cast propellant interface. The rate at which the reacting granulated bed stresses the cast propellant is a function of many of the granular bed parameters including: particle size, loading density, solid density and reaction rate. In the analysis to follow, the boundary condition pressure-rise rate was determined by executing the DDT code discussed in Ref. 2 for granular beds with lengths, L, less than the detonation run-up length and recording the pressure-rise rate at the end opposite the igniter. The pressurization-rate in the granular bed, dP^*/dt^*, is strongly dependent on the size of the particles being consumed. The larger the particles being consumed, the slower the pressurization rate on the interface. Thus from this type of analysis we have been able to determine the P(t) boundary condition for the stress wave analysis of the upstream cast propellant.

The P(t) functions obtained from this modeling effort have been linearized for this work and are expressed as

$$P(t) = (P^* - P_o)\,(t/t^*) + P_o \quad t \leq t^* \tag{1a}$$

and

$$P(t) = P^* \qquad t > t^* \tag{1b}$$

where P^* is the maximum stress in the bed. The parameter t^* is a characteristic rise-time for the ramp-wave input function.

The Lagrangian or material form of the governing equations is incorporated in the hydrodynamic analysis of a continuous material with a moving boundary. In the problem addressed, the moving boundary is a result of the applied stress load from the burning granulated bed. The one-dimensional unsteady form of the conservation of mass, momentum, and energy equations are expressed for the two-phase mechanical mixture as

$$v_t = vu_x \tag{2}$$

$$u_t = -vP_x \tag{3}$$

and

$$e_t = -Pv_t + Q \tag{4}$$

In the above expressions v represents specific volume of the mixture, u, particle velocity, e, specific internal energy, P, total stress, and Q, heat added per unit mass per unit time. The subscripts x and t indicate partial derivatives with respect to the Lagrangian spatial coordinate and time, respectively. In addition to the conservation equations, a material equation of state, $P=P(v,e)$ and appropriate constitutive relations provide for mathematical closure.

For the solid material the equation of state $P_s(v_s,e_s)$ and the caloric equation $e_s(v_s,T_s)$ are expressed in terms of a Helmholtz free energy

function (10), $\psi(v_s,T_s)$ and its thermodynamic derivatives through the Second Law of Thermodynamics reciprocity relations

$$P_s = -\left(\frac{\partial \psi}{\partial v_s}\right)_T \tag{5}$$

$$e_s = \psi - T_s\left(\frac{\partial \psi}{\partial T_s}\right)_v \tag{6}$$

With the assumption that the Gruneisen coefficient is constant, the Helmholtz free energy function takes the form (10)

$$\psi = J(v_s) + \Gamma C_{vs}\ln(v_o/v_s)\,(T_s - T_o)$$

$$+ C_{vs}[T_s\ln(T_o/T_s) + T_s - T_o] \tag{7}$$

where Γ is the Gruneisen coefficient defined by the thermodynamic derivative

$$\Gamma(v) = -v\left(\frac{\partial P}{\partial e}\right)_v \tag{8}$$

and C_{vs} is the specific heat at constant volume of the solid phase

$$C_{vs} = \left(\frac{\partial e}{\partial T}\right)_v \tag{9}$$

The term $J(v_s)$ in Eq. (7) is a nonlinear volume-dependent function determined from shock Hugoniot experiments (10).

With the introduction of product gases into the system, a constitutive law for the gas phase must also be provided. A non-ideal covolume equation of state is utilized

$$P_g = \rho_g RT_g(1 + \beta\rho_g) \tag{10}$$

where R is the gas constant and β is a covolume correction term. The value of β is determined from the values for pressure, temperature and density at the CJ state predicted by the TIGER code (11). Table 1 gives a listing of those values for several loading densities of HMX. In accordance with the reciprocity relations defined earlier (Eqs. (5-6)) the caloric equation of state for the gas phase is

$$de_g = C_{vg}dT_g \tag{11}$$

where C_{vg} is the specific heat at constant volume of the product gases.

The governing equations (Eqs. (2-4)) are expressed in terms of the thermodynamic properties (P,v,e) and dynamic variable u of the two-phase mixture. The individual phase volumes sum to equal the total, $V_T = V_s + V_g$ where $V_i = v_i m_i (i = g,s)$. Likewise for the mixture total energy, $E_T = E_g + E_s$.

TABLE 1
CJ Parameters (P,T,v,D ,rom TIGER)

α_o	P_{CJ} (GPa)	T_{CJ}(K)	v_{CJ} (cc/g)	D (mm/μs)	β (cc/g)
1	36.57	3840	.4067	9.20	4.86
1.06	32.25	3973	.4260	8.77	4.50
1.12	28.50	4083	.4471	8.36	4.22
1.19	25.20	4171	.4707	7.98	4.00
1.27	22.22	4280	.5276	7.33	3.74
1.46	17.26	4304	.5629	7.05	3.68

We define the material porosity (α) as the ratio of total volume to volume occupied by the solid phase

$$\alpha = V_T/V_s \tag{13}$$

and incorporate a 3-step static material collapse model (7). Current work by our research group involves an investigation of the more realistic dynamic material response models.

A first order Arrhenius burn model is used to describe the chemical decomposition of the reactive material

$$\frac{dW}{dt} = -ZW\exp(-E^*/\bar{R}T^*) \tag{14}$$

In the above equation W is the mass fraction of unreacted explosive, $W = m_s/m_{so}$, Z is the frequency factor, E^* is the activation energy, $\bar{R}$, the universal gas constant and T^*, the characteristic burn temperature. During compression of the porous bed, T^* represents a "hot spot" temperature due to irreversible heating at pore sites. The localized hot spot temperature is different from the bulk shock temperature and is calculated from an energy partition model (8). The underlying assumption in this hot-spot model is that the shocked porous material is at one of two possible temperatures, a bulk shock temperature T, or a hot spot temperature T_H. The energy deposited by the shock wave is equated on a mass fraction basis to the sum of the reversible work done in isentropically

compressing the bulk of the material, plus the irreversible heating of localized hot spots. (8)

$$\frac{P+P_o}{2}(v_{to}-v) = W_H e(v,T_H) + (1-W_H)e_i(P). \quad (15)$$

In Eq. (15) the left-hand side represents the total energy deposited in the material by the shock of strength P. The term $e_i(P)$ represents the energy required to isentropically compress the bulk of the material to the final shock pressure and the remaining energy term, $e(v,T_H)$, is the energy available to irreversibly heat the hot spots. This model assumes the mass fraction of the hot spots, W_H, to be equal to the preshock volume fraction of pores.

$$W_H = (v_{to}/v_{so}-1) = \alpha_o - 1 \quad (16)$$

Here, the subscript "to" represents the initial porous state and the subscript "sc" refers to the homogeneous initial state. This particular macroscopic hot spot model was chosen since it is more applicable to the problem at hand. The reader should consult other papers in this volume for one of the more detailed microscopic approaches to the theory of hot spots.

Equations (2-16) define the fluid motion and thermodynamic state of continuous, reactive, porous media. The system of equations are solved by using a finite difference numerical technique. At t=0 the bed of porous propellant is discretized into J cells labeled from left to right as j=1,2, . . . , J. The thermodynamic properties pressure, temperature, internal energy and specific volume are assumed to be constant over the width of each cell. At the boundaries between the cells, values for particle velocity and spatial location are assumed known at t=0. The reader is referred to Ref. 12 for a listing of the finite difference approximations to the governing differential equations and constitutive relations.

RESULTS

As stated earlier, the purpose of this work is to predict the transient events leading to detonation in a bed of porous, cast propellant being stress loaded at one end by a burning, granulated bed of the same material. In our preliminary calculations we found that rise-times of 10 $\mu s < t^* < 30\ \mu s$ were typical of most

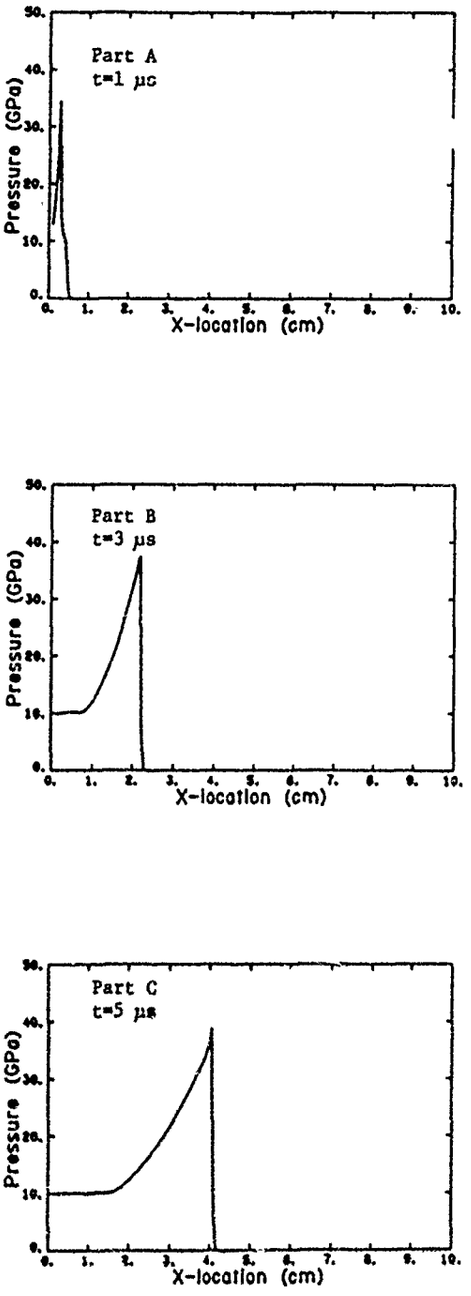

Fig. 4. Pressure-distance profiles for SDT test case. Part A, t=1μs; Part B, t=3μs; Part C, t=5μs. The material is HMX (ρ_o =1.9g/cc) D=9.3mm/μs. See Table 2 for other CJ-parameters.

of the granulated beds studied. Note that these are greater than those cited earlier (6).

As a test of the numerical solution technique, the first calculations considered a homogeneous bed of HMX. This case was selected since HMX represents one of the energetic constituents of modern day propellants. A shock strength ($t^* \rightarrow 0$) of 10 GPa was used to initiate a detonation in the bed. Figure 4 shows a sequence of P-x profiles prior to and after detonation. Listed in Table 2 are the CJ parameters predicted by the computer code along with the CJ parameters predicted by TIGER (11). As stated earlier, this exercise was only conducted in order to check the consistency of the computer code.

TABLE 2
CJ Parameters

	P_{CJ} (GPa)	T_{CJ} (K)	v_{CJ} (cc/g)	D (mm/μs)
Ref. 9	36.57	3840	0.4067	9.20
DDT Code	38.90	3953	0.4041	9.39

The next step in the research was to show that the code could reproduce experimental data for shock initiating *porous* materials. Several calculations were made using an initial porosity which matched the one used in experiments conducted by Dick (13). The results are shown in Fig. 5, a Pop-plot of φ_{CJ} vs. P*. As the figure indicates, the slopes agree for $P^* > 2.2$ GPa. For 1.5 GPa $< P^* \leq 2.2$ GPa, our calculations show little change in run-up distance as a function of P*.

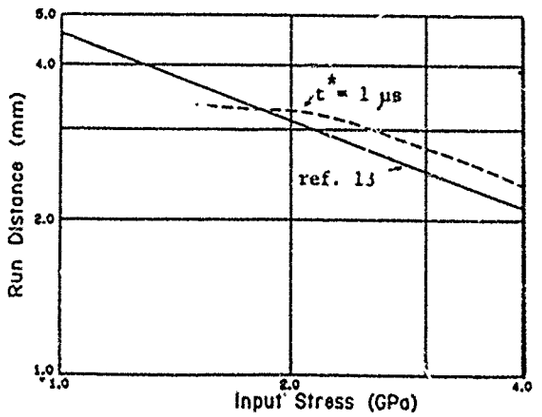

Fig. 5. Pop-plot data for porous HMX. Solid line represents data from Ref. 9, dashed line are data from DDT computer code

Several cases, with various maximum input stresses, characteristic rise times and initial porosities, were chosen to test the trends of the computer model. The first case considered has an initial porosity of $\alpha_0 = 1.1176$, and is initiatied by a "ramp" wave with a maximum input pressure of P*= 2 GPa and characteristic rise time of $t^* = 10$ μsec. Figures 6-8 illustrate the distribution history of three key parameters, namely P, α, and (1-W). For this particular case, three specific segments in time were chosen for illustration purposes. The first time shown in all the three separate figures is t=10 μsec. By viewing Fig. 6a, one can see that the compression wave has propagated into the bed to a distance of 1.5 cm. Notice even though the left boundary has reached the maximum input stress, shown approximately at a location of 2 mm into the bed, the shock front has not fully developed. Figure 7a illustrates the closure of the voids as a result of the compression wave. One can see from Fig. 8a (gas-phase mass fraction) that the reaction has yet to commence.

As time progresses to 12 μsec, Fig. 8b shows that the reaction has commenced. This occurrence can also be viewed by an increase in porosity (alpha), as displayed in Fig. 7b at that instant. Induced by the initiation of propellant decomposition, an increase in strength of the compression front occurs, as is evident in Fig. 6b. With the increase in the degree of reaction, the chemical energy further contributes to strengthen the compression front.

At t = 13 μsec, the decomposition of the propellant is complete in a small region of the bed near x = 2 cm, as pictured in Fig. 8c. The porosity distribution, displayed in Fig. 7c (at 13μsec), shows compression ahead of the decomposition region. The net effect of all of this is a right moving detonation wave and a left (or rearward) moving retonation wave, as illustrated in Fig. 6c. Note that the retonation wave has a higher peak pressure than the detonation wave, due to the higher density of the material the wave is propagating through. The steady detonation wave continues to propagate even further into the bed at a predicted CJ pressure of 25 GPa and a corresponding CJ temperature of 3923 K.

In addition to the figures just presented, the locus of the stress and reaction fronts are shown in Fig. 9. The dashed line depicts the stress wave as propagation into the bed, initiating the

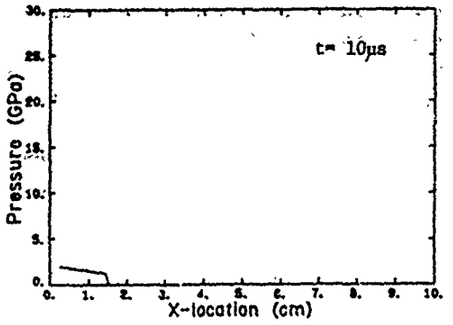

Fig. 6a. Pressure-distance profile at t=10μs for porous (α_0=1.1176) HMX. No reaction noticeable

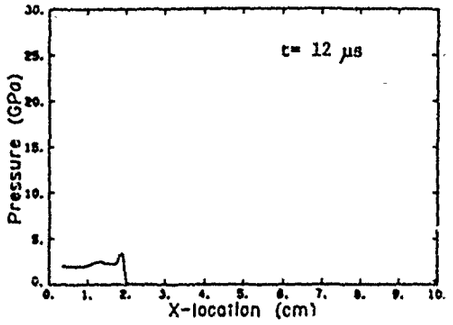

Fig. 6b. Pressure-distance profile at t=12μs. Reaction has commenced

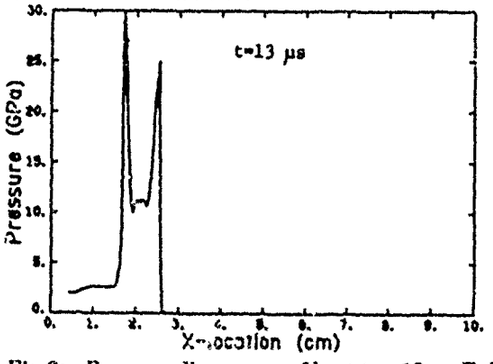

Fig 6c. Pressure-distance profile at t = 13μs. Full reaction with P_{CJ} = 25 GPa, D = 8.8 mm/μsec

detonation at t = 12.41 μsec, at x = 2.05 cm. The solid lines represent the locus of the right and left traveling detonation fronts. Figure 9 also shows the termination point of the retonation wave. A change in velocity is apparent in the left traveling wave at the termination point. The slopes of the solid lines correspond to a detonation and retonation velocity of D = 8.8 mm/μsec and R = 9.1 mm/μsec, respectively.

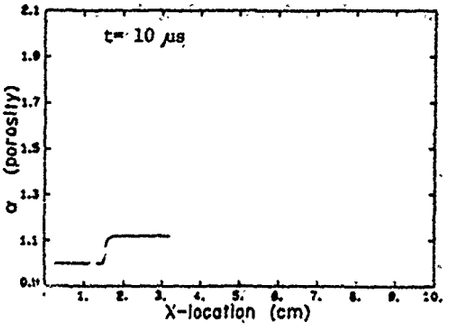

Fig. 7a. Porosity-distance profile prior to detonation (α_0 = 1.1176) at t = 10μs. α = 1.0 indicates complete compaction

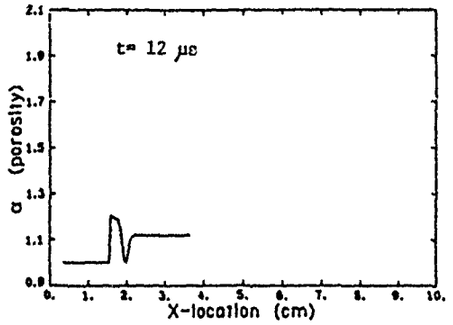

Fig. 7b. Porosity-distance profile at t = 12μs showing the reaction zone development

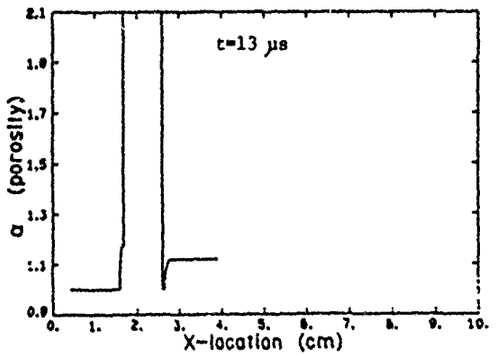

Fig. 7c. Porosity-distance profile at t = 13μs showing detonated zone (1.6 <x <2.6 cm)

As stated earlier in the text, the granular bed (Zone 2, Fig. 2) provides the driving force to shock initiate the cast material (Zone 1, Fig.2). In addition, the pressure-rise rate at the Zone 1/Zone 2 interface is a function of several key parameters in the granulated bed. Figure 10 illustrates the influence of pressure-rise rate on the run-up

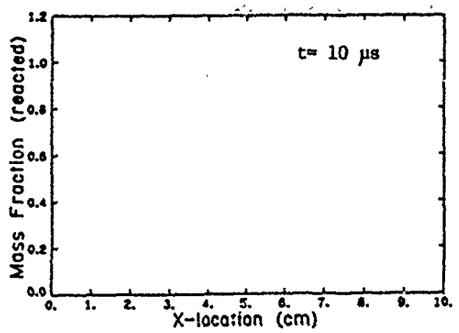

Fig. 8a. Reacted mass fraction-distance profile at t = 10μs showing no reaction.

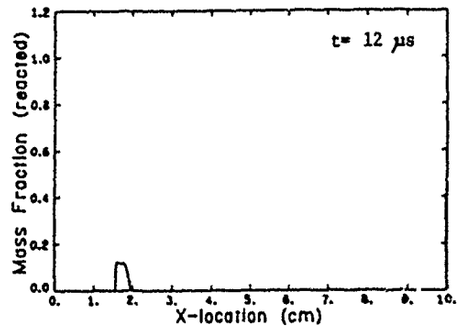

Fig. 8b. Reacted mass fraction-distance profile at t = 12μs showing initiation of reaction.

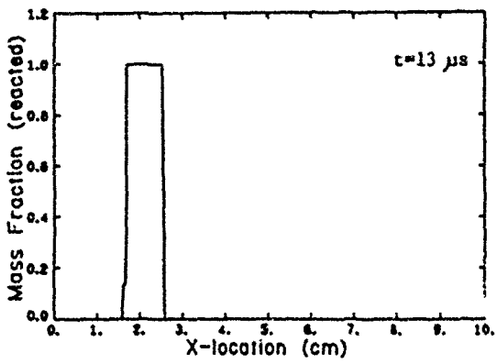

Fig. 8c. Reacted mass fraction profile at t = 13μs showing zone of complete decomposition (1.6 < x < 2.6 cm).

distance to detonation, φ_{CJ}. Data are presented for four different values of t* (1,3,5 and 10 μs, respectively). The slower rise rate, t* = 10 μs, corresponds to a granular bed with d_0 = 500 μm particles driving the shock build-up process. Previous calculations show that HMX particles of this size would require a rather long bed length in order to DDT in the Case 1 situation. In general, one would expect a greater run-up distance to correspond to a longer characteristic rise time for a specific input pressure, since the compression front will reach the critical pressure needed to initiate detonation later for the longer characteristic rise time. Indeed, Figure 10 demonstrates the occurrence of a longer run-up distance for a specific input pressure for a longer characteristic rise time. Therefore, for low input pressures and critically long characteristic rise times, detonation is not expected to occur in a ten centimeter bed, eliminating the hazard of DDT in the Case 2 configuration. In regards to the actual rocket motor configuration, this implies that the DDT Case 2 hazard does exist if the granular particles are sufficiently small and the Zone 1 bed length is greater than φ_{CJ} for the corresponding dP*/dt*.

Figure 11 shows the run-up distance to detonation φ_{CJ} as a function of t*, the compression wave rise time, for two values of initial porosity, φ_0. Here, the sample with the lower α_0 is observed to have a shorter run-up distance than the more porous sample. This is explained as follows. Although the higher porosity material has a larger hot spot volume (as predicted by Eq. (16)), the low porosity material has a much higher local density and thus contributes more energy to the shock front upon decomposition.

CONCLUSIONS

It has been shown by numerical simulation that under certain circumstances a porous, cast propellant will transition to a detonation when stress loaded in a ramp-wave fashion by an adjacent bed of granulated propellant. Rise-times for the waves studied ranged from 1 μs to 30 μs, much longer than previously studied. In most cases, the bed detonated at a location downstream of the stress-loaded boundary and exhibited detonation properties as predicted by an independent thermo-equilibrium calculation. In addition, an energy sustaining retonation wave was shown traveling rearward towards the driving wall. The values predicted for the detonation properties were in agreement with TIGER data.

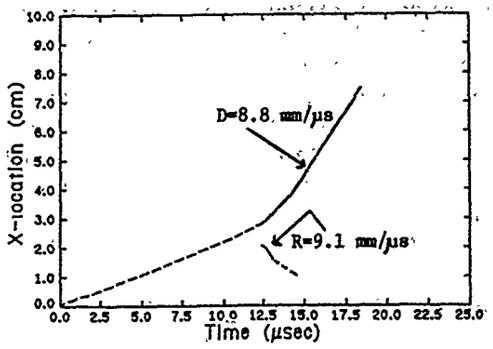

Fig. 9. Physical plane, showing compression, detonation and retonation fronts
(α = 1.1176, P = 2GPa, t* = 1μs)*

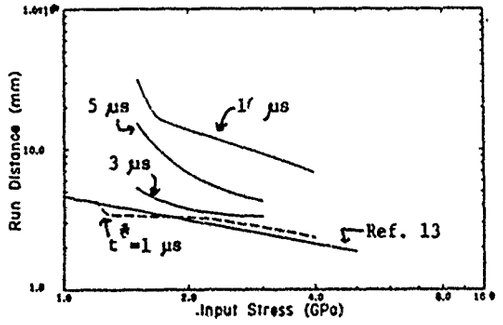

Fig. 10. Predicted effect of pressure-rise rate on detonation run up distance φ_{CJ}. Slower rise times result in longer run up distance φ_{CJ}.

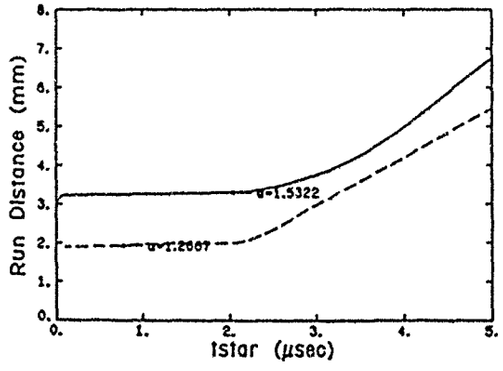

Fig. 11. Effect of ramp wave rise time on run-up distance to detonation for two different initial porosities α_o

LIST OF SYMBOLS

C_v	specific heat (erg/g/K)
d	particle diameter (cm)
e	specific internal energy (erg/g)
E	total energy (erg)
E*	activation energy (erg/mole)
L	bed length (cm)
m	mass (g)
φ_{CJ}	detonation run-up length (cm)
P	stress (dynes/cm^2)
P*	maximum axial stress (dynes/cm^2)
Q	chemical energy release rate (erg/g/s)
R	gas constant (erg/g/K)
$\overline{R}$	universal gas constant
t	time (s)
t*	characteristic rise time(s)
T	temperature (K)
T*	characteristic burn temperature (K)
u	particle velocity (cm/s)
v	specific volume (cm^3/g)
V	volume (cm^3)
W	unreacted mass fraction
x	spatial location (cm)
Z	frequency factor (1/s)

Greek

α	$V_T/V_s = 1/(1-\phi)$
β	covolume (cm^3/g)
Γ	Gruneisen coefficient
ϕ	porosity, V_g/V_T
ϱ	density (g/cm^3)
ψ	Helmholtz free energy (erg/g)

Subscripts

CJ	Chapman-Jouguet state
i	isentrope
g	gas
H	hot spot
o	initial state
x	$\partial(\,)/\partial x$
s	solid
t	$\partial(\,)/\partial t$

ACKNOWLEDGEMENTS

Work is supported by Air Force grant AFOSR-81-0145. Dr. Robert J. Barker is contract monitor.

REFERENCES

1. Butler, P.B., Lembeck, M.L. and Krier, H., "Modelling of Shock Development and Transition to Detonation Initiated by Burning Porous Propellant Reds," *Combustion and Flame*, 46, (1982), 75-93.

2. Butler, P.B. and Krier, H., "Analysis of Deflagration to Shock to Detonation Transition (DSDT) in Porous Energetic Solid Propellants," AGARD Conference Preprint No. 367, paper No. 5, Lisse, The Netherlands, (1984).

3. Butler, P.B. and Krier, H., "Analysis of Deflagration to Detonation Transition in High-Energy Solid Propellants," to appear, *Combustion and Flame*, vol. 63, pp. 31-48 (1986).

4. Bernecker, R.R., "The DDT Process for High Energy Propellants," AGARD Conference Preprint No. 367, paper No. 14, Lisse, The Netherlands, (1984).

5. Price, D. and Bernecker, R.R., "Sensitivity of Porous Explosives to Transition from Deflagration to Detonation," *Combustion and Flame*, 25, (1975), 91-100.

6. Setchell, R.E., "Effects of Precursor Waves in Shock Initiation of Granular Explosives," *Combustion and Flame*, 54, (1983), 171-182.

7. Carroll, M.M. and Holt, A.C., "Static and Dynamic Pore-Collapse Relations for Ductile Porous Materials," *J. Appl. Physics*, 43, No. 4, (1972), 1627-1636.

8. Hayes, D.B., "Shock Induced Hot-Spot Formation and Subsequent Decomposition in Granular, Porous, Hexanitrostilbene Explosive," Detonation Physics Symposium, Minsk, Russia, (1981).

9. Cudak, C.A., Krier, H., and Butler, P.B., "Transition to Detonation from Rapid-Compression (Ramp-Waves) Generated in a Burning Porous Bed," JANNAF Propulsion Hazards Subcommittee Meeting, June, 1984.

10. Baer, M.R. and Nunziato, J.W., "A Theory for Deflagration-to-Detonation Transition (DDT) in Granular Explosives," SAND Report, SAND82-0293, (1983).

11. Cowperthwaite, M. and Zwisler, W.H., "TIGER[1] Computer Code Documentation," Rept. PYV-1281, Stanford Research Institute, (1974).

12. Coyne, D.W., Butler, P.B. and Krier, H., "Shock Development From Compression Waves Due to Confined Burning in Porous Solid Propellants and Explosives," AIAA paper No. 83-0480, Reno, Nevada, (1983).

13. Dick, J.J., "Measurement of the Shock Initiation Sensitivity of Low Density HMX," *Combustion and Flame*, 54, (1983), 121-129.

DDT IN RDX AND BALL POWDER: BEHAVIOR OF THE POROUS BED

M. Samirant

Franco-German Research Institute
P.O. Box 301 — 68301 Saint-Louis, France (ISL)

In highly confined pulverulent RDX-wax the transition from deflagration to detonation is a rapid and well-localized phenomenon, resulting from a shock running downstream. In ball powder this transition is a progressive and continuous phenomenon. It is shown that the transition mode is not directly related to the chemical composition of the reactive bed, but that this difference of behavior is due to mechanical properties of the grains.

On the 7th Symposium on Detonation at Annapolis in 1981, we presented a series of results on the transition combustion-deflagration-detonation in pulverulent RDX-wax confined in a steel tube. This presentation concerns the continuation of this study. The same experimental set-up as before has been applied to a ball powder. The results lead us to a particular study of the behavior of the porous reactive bed during transition.

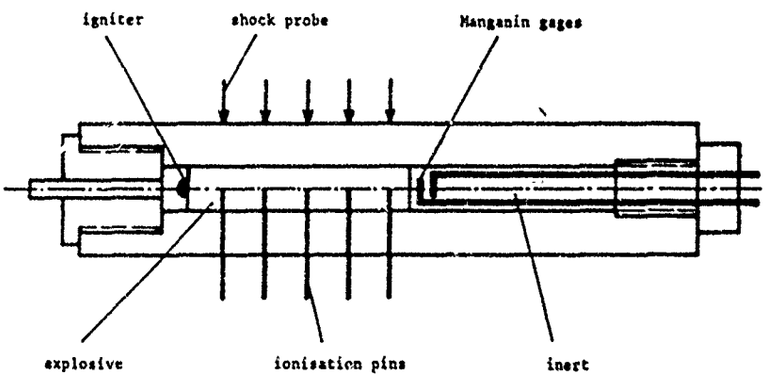

Fig. 1. DDT steel tube

1. EXPERIMENTAL SET-UP

We chose a classical experimental set-up in order to make use of the important number of data published on this topic (1,2,3). We were not interested in an exhaustive study of parameters which are involved in transition but we tried to understand some of the essential mechanisms.

Figure 1 shows a schematic presentation of the set-up. It is a thick steel tube (16mm ID, 50mm OD, 390mm length) with heavy end closures. Two kinds of gages are distributed along the tube. Ionisation pins which detect the passage of the combustion front and needle pins detecting the shock waves on the tube's outer surface. The results are registered on a multichronometer (resolution 1 ns) triggered by the first ionisation pin. Manganin gages are placed in an inert medium to allow larger measurements and register pressure profiles as a function of time in the porous bed. The igniter is a thick wire (0.3mm) heated by a 24V battery reinforced by 50mg of a mixture of potassium nitrate with zirconium and titanium. It generates neither gas nor shock.

II. RESULTS WITH RDX

We used as explosive RDX with 5% wax with a grain-size of 150-200 μm (95%), 80 μm (4%), <40 μm(1%). It was gently pressed at 8 MPa and the resulting density was 1.28 g/cm^{-3} (73% TMD). Figure 2 shows the results of the test. One recognizes:

I an accelerated combustion zone,
II a deflagration zone with constant velocity (450 ms^{-1}),
III a transition zone,
IV the full detonation.

It can be seen that transition is the result of the interaction of a shock running downstream (2000 ms^{-1}) with the combustion zone. The special study of this shock and the deflagration at constant velocity has already been presented (4).

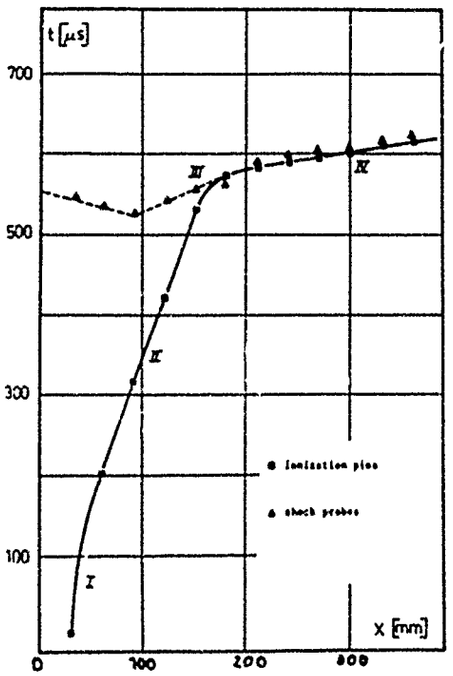

Fig. 2. Combustion and shock front path in waxed RDX

III. RESULTS IN BALL POWER

We used the same set-up and the same loading method to examine a double-base ball powder. The grain-diameter was 400 μm and the loading density was 1.07 g/cm^{-3}. The results can be seen on Figure 3. The trajectory of the combustion wave is continuous and the wave accelerates progressively until it reaches the detonation velocity D=5240 ms^{-1}. The transition itself cannot be precisely localized, there is no bend in the curve. The needle pins detect no shock at all, their responses are random in time and correspond to strong pressure waves.

IV. POSSIBLE PHENOMENOLOGICAL EXPLANATION OF THE TWO TRANSITION MODES

In the classical DDT scheme combustion gases are injected into the porous medium. The injection increases the volume of the reaction zone and the burning surface area and leads to an increase of the measured combustion velocity and of the pressure. This brings about a new gas injection and so on until transition takes place.

That scheme fully explains the continuous

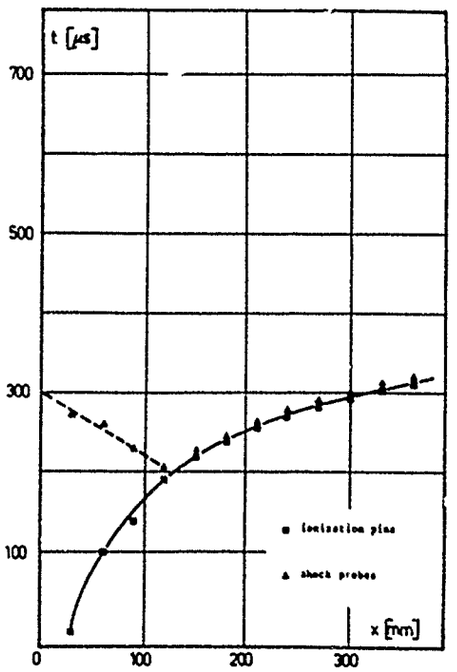

Fig. 3. Combustion front path in ball-powder

transition inside the powder. In case of the explosive the deflagration at constant velocity is regarded as a dynamic equilibrium between gas injection in the pores and their closure by the pressure waves resulting from the pressure increase. The flow is blocked and the combustion is quasi-stationary. Most often the brutal transition to detonation is explained by the formation of a compact non-permeable stopper which leads to a steep pressure rise and a SDT.

Another theory presented by AKHATOV and VAINSHTEIN (5,6) is based on the different behavior of the porous beds during the compression by the combustion gases. If the mechanical compacting energy of the solid particles propagates in an elastic way in the porous bed, the volume of the combustion zone reaches a limit value and provokes a rapid and stable deflagration. If the mechanical energy injected in the porous bed results in important plastic deformations and shears in the grains, the liberated energy can trigger the combustion and increase the reacting volume leading to a progressive transition. In a test series we tried to make a choice between these two models.

V. BEHAVIOR OF THE POROUS BED DURING COMBUSTION

In the RDX the registration of pressure profiles as a function of time with a Manganin gage shows a regular wave profile corresponding to the observed phenomena (Fig. 4.). If, however, the combustion of the reactive column is stopped before transition by a thick inert stopper in the bed, it can be seen on the recovered confinement tube that a large deformation near the downstream end closure has taken place (Fig. 5). This deformation shows the result of the reflexion of the compression waves. (Measurement of the density of the porous bed during the transition leads to the same observation (4).)

In the ball powder, and in the same conditions the Manganin gages data cannot be explained by pure compression wave.

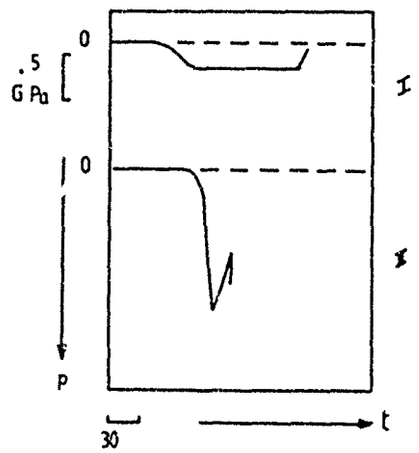

Fig. 4 Manganin gages pressure profiles in RDX
I deflagration zone
II transition zone

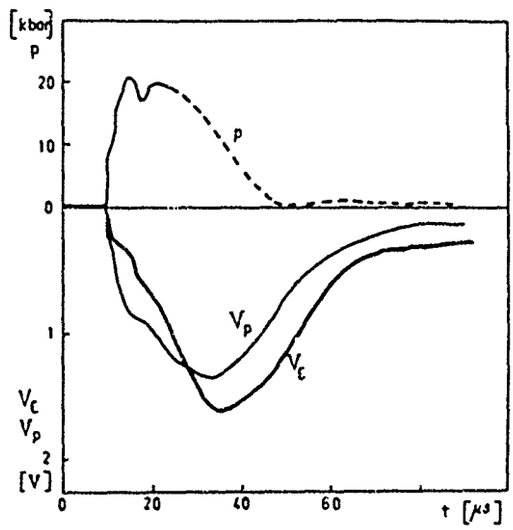

Fig. 6. Voltage delivered by a Manganin (V_p) and a constantan (V_c) gage in ball powder. Resulting pressure profile (p)

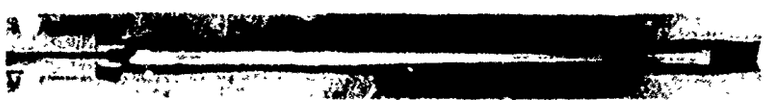

Fig. 5. Steel tube recovered after RDX combustion

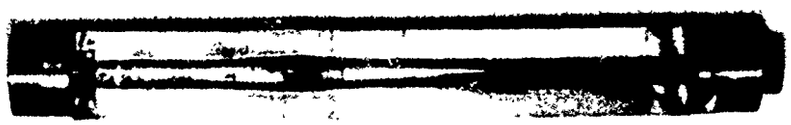

Fig. 7. Steel tube recovered after ball powder combustion

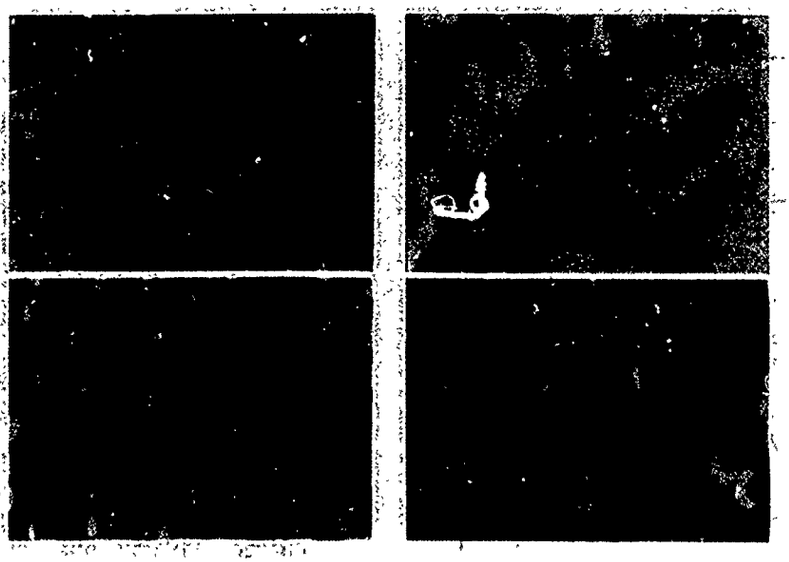

Fig. 8. Four types of reacting material

a) fine RDX
b) ball powder
c) coarse RDX
d) grounded ball powder

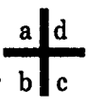

Simultaneous measurement with Manganin and constantan gages of the pressures and the strains in the porous bed shows important shears (Fig. 6). These results reveal the important mechanical work inside the porous bed. Finally, observations of the recovered confinement tube in the same conditions as before show that the compression waves only propagate near the combustion front and that their behavior is inelastic (Fig. 7).

VI. MODIFICATION OF THE STRUCTURES OF THE POROUS BED

In a test series we have compared the results obtained with four different kinds of reactive material.

a) RDX-wax (95-5), irregular crystals, grain-size 150-200 μm (95%), 80 μm (4%), <40 μm (1%);

b) double-base ball powder, grain-size 400 μm;

c) RDX-wax (95-5) quasi-spherical crystals, grain-size 350-400 μm;

d) double-base ball powder grounded and screened, grain-size 150-200 μm (95%), <150 μm (5%).

Figure 8 shows an enlarged view of these four materials. The results of the DDT test are given in Figures 9-10. If we take into account the total duration of the phenomenon which depends on the chemical reaction we find that a and d and b and c are comparable. If we take into account the shape of the trajectories of the combustion fronts which depends on the transition mode we find that a and d and b and c are comparable.

On the other hand the shock trajectories given by the needle pins show inside the fine RDX (a) a shock coming from behind, its origin is unexplained up to now. To verify the nature of the phenomenon we have introduced a stopper into the porous bed just before the transition zone. This stopper consists of the same explosive pressed up to theoretical density. In the test this stopper had no influence on the transition which occurred at its habitual position.

VII. CONCLUSION

It seems nowadays well established that the mechanical and thermical behavior of the porous bed under the influence of compression waves is the most important parameter which controls the mode of transition in the reactive media. We will continue our studies to determine the origin of the shock which is responsible for the transition in the medium with stationary deflagration.

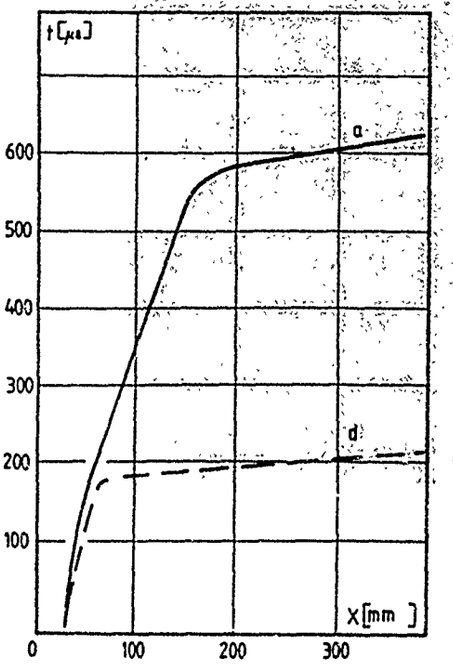

Fig. 9. Combustion front path in fine RDX (a) and grounded ball powder (d)

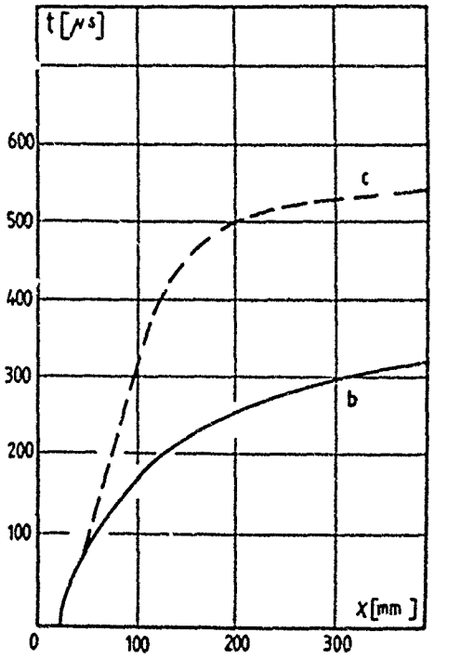

Fig. 10. Combustion front path in ball powder (b) and coarse RDX (c)

REFERENCES

1. Richard R. Bernecker and Donna Price Studies on the transition from deflagration to detonation in granular explosives, Combustion and Flame 22, 111-117 (1974), Combustion and Flame 22, 119-124 (1974), Combustion and Flame 22, 161-170 (1974).
2. M. Cowperthwaite and W.J. Murri, Deflagration-to-detonation in HMX-based propellants, AFOSR-TR-82-0673, ADA-A 118, 616/2 Bolling AFB, 1982.
3. R.R. Bernecker, H.W. Sandusky and A.R. Clarimont, Jr., Deflagration-to-detonation transition studies of porous explosive charges in plastic tubes. The Seventh Symposium on Detonation, Annapolis, Maryland, June 1981.
4. M. Samirant, Deflagration detonation transition in waxed RDX, The Seventh Symposium on Detonation, Annapolis, Maryland, June 1981.
5. I. Sh. Akhatov and P.B. Vainshtein, Nonstationary combustion regimes in porous powders, Combustion Explosion and Shock Waves, Vol. 19, No. 3, pp. 297-309, May-June 1983.
6. R.I. Nigmatulin, P.B. Vainshtein and I. Sh. Akhatov, Transition of powdered explosive connective combustion into detonation, Combustion Explosion and Shock Waves, Vol. 19, No. 5, pp. 618-621, September-October 1983.

Session IX
Specialist Session
COMPOSITE AND NONIDEAL EXPLOSIVES

Co-chairmen: Conrad Belanger
Defense Research Establishment
Valcartier
Joseph Hershkowitz
West Caldwell, NJ

DETONATION IN TUNGSTEN-LOADED HMX

Selma Goldstein and Charles L. Mader
Los Alamos National Laboratory
Los Alamos, New Mexico 87545

The detonation behavior of X-0233, a heavily tungsten-loaded HMX explosive, has been studied using failure diameter measurements, plate dents, and aquarium tests. A model with features resembling those of a weak detonation describe the experimental results.

I. INTRODUCTION

Heavy-metal-loaded explosives have been investigated at various times in the past for applications in achieving metal motion with minimal fragmentation (1). However, aside from empirical information on their special performance characteristics, their behavior has not been well understood.

Al'tschuler et al. have proposed a theoretical model which envisioned multiple detonation wavelets propagating in the high explosive in the interstices between metal particles and being observed macroscopically as a detonation with an average propagation velocity. This velocity would be lower than in pure explosive because of the path taken by the detonation front between the metal particles, resulting in a nonideal explosive. Calculated detonation pressures (2) are much greater than those observed for these systems when using computational methods that work well for ideal explosives.

We have made a thorough study of X-0233, a heavily tungsten-loaded HMX explosive fabricated at Los Alamos, using various experimental and theoretical techniques, and have developed an understanding of the operative mechanisms in the detonation of this material. The mechanisms explain and correlate seemingly contradictory data.

II. EXPERIMENTAL RESULTS

A. Failure Measurements. Several types of experiments have been performed to determine the detonation properties of X-0233. This material consists of 85.48 wt% W, 13.22 wt% HMX, 0.8 wt% polystyrene, and 0.5 w% DOP (55/34/11% by volume). The density of the pressed material is 7.47 g/cc.

Failure size of X-0233 was determined using two different plate-dent configurations, shown in Figs. 1 and 2. In the first geometry, a cone of the explosive was laid on a mild steel plate. The cone was 127 mm in altitude and had a half angle of 5.7° at the apex. It was initiated by a P16 planewave lens from the base, and the detonation was allowed to travel down the material axis until it failed. A measurement of the length of the plate dent and the smear camera record obtained indicated a failure diameter of 2.5 mm. Due to the convergent geometry, we interpret this failure size as a lower limit: even after failure, the shock front might have coasted for some time before it ceased to produce a dent in the metal, or light.

The second failure experiment consisted of a wedge instead of a cone, initiated with a line-wave generator. This system was recorded in the same manner as the conical one. However, while being overdriven in one dimension, it is divergent in the other, and so would be expected to give a larger failure thickness measurement than the diameter obtained above. In fact, this was observed, and we measured a failure thickness of 3.25 mm.

B. Aquarium Tests. Aquarium tests were performed to obtain detonation velocity, shock and particle velocities, detonation pressure, and temperature effects. These tests were also done in two distinct configurations using different optical diagnostics.

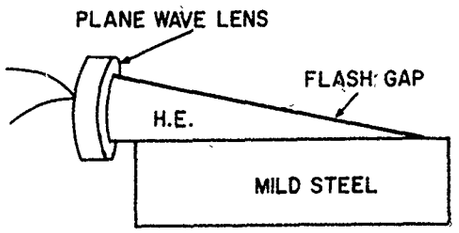

Fig. 1. Schematic setup of failure cone experiment. Smear camera image slit is aligned with flash gap on cone surface

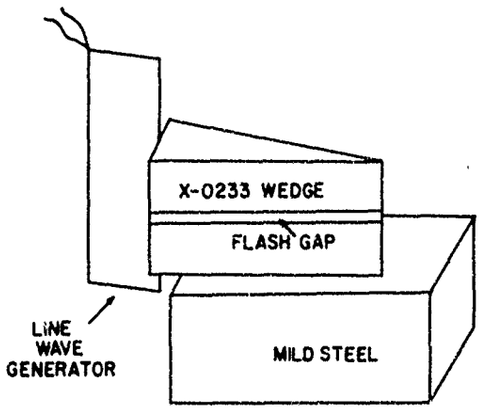

Fig. 2. Schematic setup of failure wedge. Smear camera slit observes flash gap on wedge face

One aquarium test for this type of explosive, which can be pressed and fired as a bare cylindrical charge, is a modification of the large scale test used to examine commercial blasting agents (3,4). The water tank volume is approximately 28 000 cc and the standard explosive diameter is 25mm. Multiple exposure image-intensifier camera pictures are taken of the detonating cylinder so that detonation velocity and wave structure may be observed and recorded.

Initially, two shots were fired, each yielding two doubly exposed frames of film. One shot was done at ambient temperature and the other at −54°C (using ethanol instead of water in the tank). Although the equation of state of ethanol was not known at −54°C, we only needed to correct for the density difference between it and water to empirically compare the shot data. We determined this to be sufficient by first testing PBX 9501, which should show no change with temperature. There was also no evidence of degradation of performance with lower temperature in X-0233 at the 25 mm diameter; however, we do not know if there might be some effect with smaller diameter charges, especially as the failure diameter is approached.

From the aquarium test we get pictures showing the positions in the x−t plane of the trajectory of the shock front in the fluid and of the material interface between shocked fluid and detonation product gases (the "bubble"). We also measure detonation velocity from the known times of the exposures and the measured distance between the detonation fronts along the charge axis.

Detonation velocity was measured to be between 4.50 and 4.64 mm/μs, averaging to 4.54 mm/μs. Bubble trajectories from the two exposures, representing the detonation at two different positions in the explosive cylinder, can be overlayed with no discernible differences. Since the two exposures are taken at approximately three and five charge diameters in distance down the charge from the detonator, we take their agreement to be an indication of the existence of a steady detonation in the material.

The basic aquarium test picture is shown in Fig. 3. We see the detonation front at both times and the bubble and shock front expanding into the water. In comparison with a similar photograph from PBX 9501 (Fig. 4), the interface in X-0233 shows a great deal of structure. We will return to this point later in our discussion.

We have fit the curves of these bubbles and shock fronts with power functions of the form

$$R - R_o = P_1 z^{P_2} + P_3$$

by nonlinear regression, where R is the radial position of the front measured from the axis of symmetry, R_o is the initial charge radius, z is the reduced time, and P_1, P_2, P_3 are coefficients determined by a least squares fit. These curves are shown in Figs. 5 and 6, while the actual coefficients are in Table I. While initially the X-0233 products are not expanding as fast as the PBX 9501 products, in time the X-0233 will overtake the PBX 9501 bubble. The shock expansion, however, remains behind that of PBX 9501.

Fig. 3. Image-intensifier camera photograph of detonating X-0233 in water aquarium. Shot C-5412

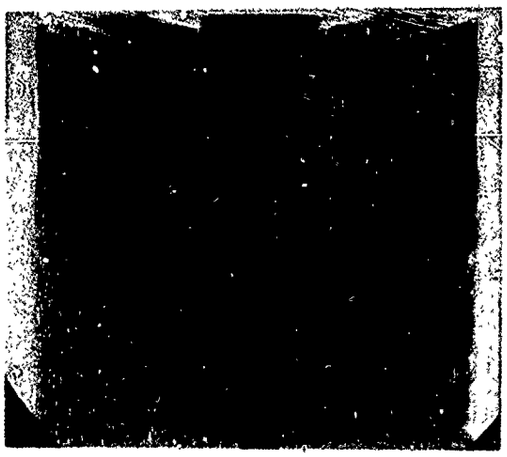

Fig. 4. Image-intensifier camera photograph of detonating PBX 9501 in water. Shot C-4972

By differentiating the fit to the bubble with respect to z, we get the velocity of expansion of the detonation product gases. These curves are shown in Fig. 7 for X-0233 and PBX 9501. These curves illustrate again that PBX 9501 has a very large expansion velocity initially, which then drops below that of X-0233 at later times.

A measure of the impulse carried by the detonation product is $I = \int v dt$, where v is the expansion velocity as a function of time. Since the densities of X-0233 and PBX 9501 are different, we know that a large part of the difference in energy transport will be determined by the mass term, but we can calculate the integrals by using the expansion velocities already obtained as functions of Z.

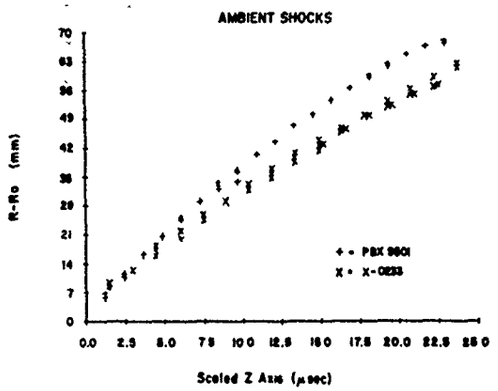

Fig. 5. Shock front profiles of PBX 9501 compared with X-0233 at ambient temperature. Shots C-5067 and C-5412

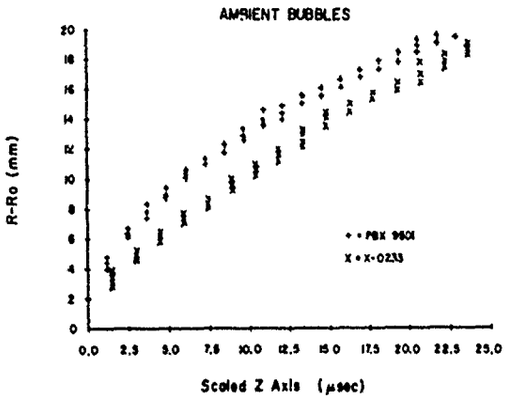

Fig. 6. Bubble interfaces of PBX 9501 and X-0233 at ambient temperature. Shots C-5067 and C-5412

Thus we have

$$I = \int m \frac{dx}{dz} \frac{dz}{dt} dt \cdot$$

After looking at the velocity curves (Fig. 7), we see that we can approximate the integrals by simply cutting off the curves at the point where the graph ends. The result of this calculation is 0.0206 for PBX 9501 and 0.0813 for X-0233.

This means that if available energy is measured by these integrals, then X-0233 has approximately four times as much as PBX 9501. Indeed, the ratio of the densities of the two explosives is 4.06, so we can assume that much of the difference is due to the presence of the tungsten.

TABLE I

	X-0233	PBX 9501
P_1	1.889	4.795
P_2	0.713	0.460
P_3	0.616	−0.548

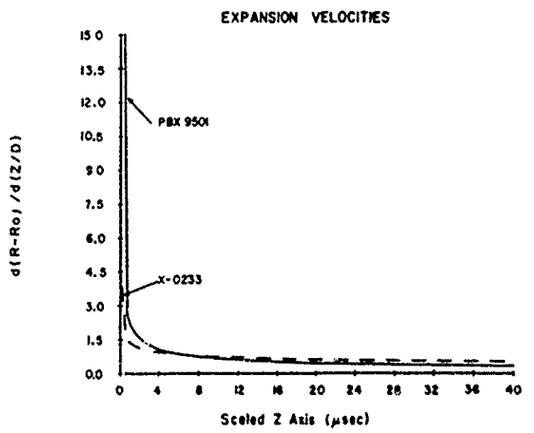

Fig. 7. Expansion velocities of the bubbles from PBX 9501 and X-0233 at ambient temperature

The partition of energy between the detonation products and shock wave is very different in the two materials. X-0223 has a larger amount in mass motion, because the tungsten particles provide a mechanism for momentum transfer.

Additional data can be obtained about X-0233 performance by varying the aquarium test and using it as Rigdon and Akst (5) did. This means changing the setup only slightly but using a smear camera to record the emerging waves from the end of the cylindrical charge. These results are shown in Fig. 8. They represent the shock and particle velocities in the water, immediately behind the detonation front. Following Rigdon and Akst, we analyze the initial 2 mm of motion to calculate the peak shock velocity and particle velocity, and use these values to calculate a detonation pressure by shock-matching into the water surrounding the explosive. The following equations apply, assuming of course C-J conditions:

$$P = \varrho_o u_s u_p$$

$$P_j = P \frac{\varrho_o u_s + \varrho_{HE} D}{2 \varrho_o u_s} .$$

Here u_s is the shock velocity and u_p the particle velocity of the water in the proper pressure range (6); p is transmitted pressure, or the pressure in the water just behind the detonation front. P_j is the C-J pressure and D the detonation velocity. ϱ_o is the initial denisty of the water and ϱ_{HE} the initial density of the explosive in question. u_s and u_p can be obtained from the data in Fig. 8, and also from the linear approximation to the Hugoniot for water, $u_s = 1.483 + 2.0\ u_p$.

Using this scheme, and our data extrapolated to the charge surface, we have $u_s = 4.5$ mm per μs, $u_p = 1.508$ mm per μs, p = 67.8 kb, P_j = 289 kb, and $\gamma = 4.3$. These results are in fairly good agreement to the plate dent test performed by M. Urizar at Los Alamos, which gives a pj of 297 kb from a dent of 8.53 mm, using a charge 41.275-mm diam. (7).

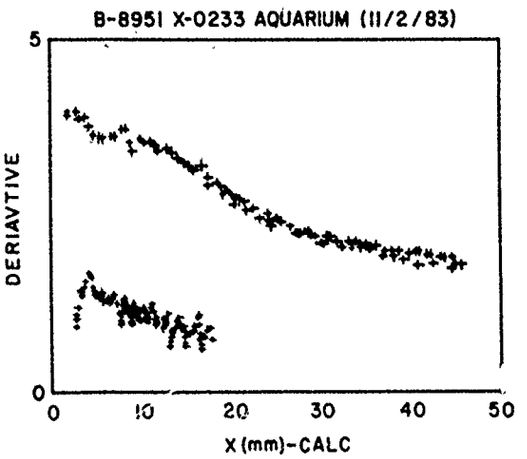

Fig. 8. Shock (above) and particle (below) velocity profiles from smear camera aquarium shot of X-0233, fit with 10-point running quadratic curves

Looking back at Fig. 8, we notice that there is a plateau in the velocity curves at between 5- and 10-mm expansion, especially in the shock velocity, which would not appear in an ideal explosive like PBX 9501. In the ideal case, we would have a monotonically decreasing curve representing the Taylor wave in the flow. In the case of X-0233, we obviously do not have that behavior, and in reality the C-J conditions are not a good model for this detonation.

A phenomenological explanation for two different sets of detonation parameters postulates

a two-phase flow behind the detonation front, where the plateau in the shock velocity curve represents a point at which the shock is supported by the material motion. Some evidence for this is the initial bubble motion in Fig. 8, at less than 5-mm expansion, which appears just before that time as a peak in bubble velocity.

If we take the velocity at the plateau, we calculate $u_s = 3.6$ mm/μs, $u_p = 1.058$ mm/μs, p = 38.1 kb, $P_j = 159$ kb, and $\gamma = 8.7$.

III. CALCULATION

The extrapolated "C-J parameters" from the acquarium test just discussed that agree with the plate dent result do not allow correct modeling of the image-intensifier photographs of the flow obtained from the aquarium test.

A hydrodynamic calculation to duplicate aquarium data gives a detonation pressure of 160 kb while reproducing the detonation velocity as described in Ref. 2.

The nonideal behavior of X-0233 is implicit in the fact that a low detonation pressure is needed to reproduce the aquarium test curves, while the plate dent result, in contrast, requires a very high C-J pressure. These apparently contradictory results are explained by a three-dimensional model (2) that allows for the propagation of individual detonation wavelets through a matrix of tungsten particles. Depending on the spacing of these particles, the wavelets may fail due to a very small effective explosive thickness, smaller than the failure diameter (PBX 9501 has an unconfined failure diameter of approximately 1.2 mm). The dense packing of tungsten in X-0233 makes this phenomenon possible. The shocked, partly burned explosive continues to release energy after the front has passed, contributing to the energy release at late times (2). The higher the metal concentration, the smaller the interstitial distances, and therefore the more failures and lower detonation pressure.

The expansion isentrope is less steep for X-0233 compared with an ideal explosive, due to the later time energy release from additional burning behind the detonation front. This isentrope used in a hydrodynamic calculation allows matching of both the plate dent depth and the aquarium test curves. A comparison with the γ-law isentrope (if C-J conditions were present and all energy were released at the front) is shown in Fig. 9.

The equation of state for X-0233 can be used to reproduce the aquarium test results from Fig. 8. The velocity profile resembles that produced by a weak detonation (Fig. 10).

Looking back at the aquarium test photograph in Fig. 3, we can now infer that part of the irregular interface at the bubble is evidence of the irregular burning, in agreement with the model of propagating and failing wavelets among the tungsten particles.

IV. CONCLUSION

The nonideal behavior of heavily tungsten-loaded HMX may be understood by modeling it as a matrix of detonation wavelets in the interstices between particles, which may fail and contribute to a late energy release. This model furnishes a self-consistent interpretation for all the data obtained on X-0233.

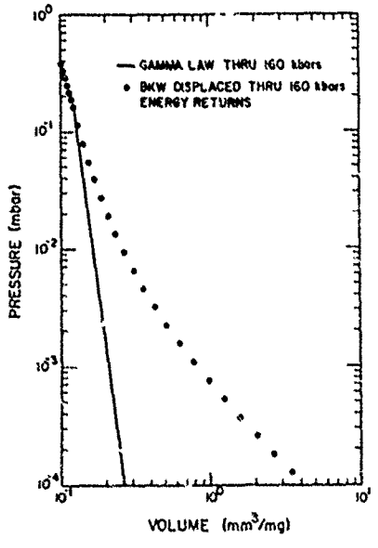

Fig. 9. The X-0233 gamma-law isentrope through the experimental detonation pressure and velocity and the BKW isentrope displaced through the same experimental state with the energy returned

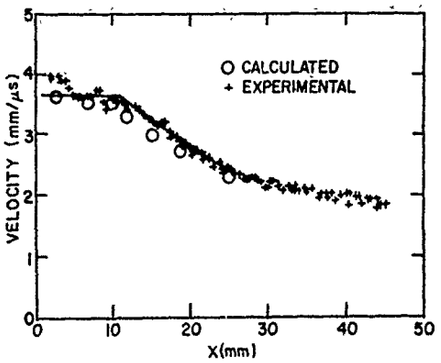

Fig. 10. The calculated and experimental water shock velocities from the end of the X-0233 cylinder. The calculation used the BKW isentrope displaced through the experimental detonation pressure and velocity with the energy returned.

REFERENCES

1. U.S. Patent Office No. 3528864, "High Impulse Explosive Containing Tungsten," C.W. Weiland, 1970.
2. Charles L. Mader, James D. Kershner, and George H. Pimbley, "Three-Dimensional Modeling of Inert Metal-Loaded Explosives," Journal of Energetic Materials *1* p. 293, 1983.
3. J.N. Johnson, C.L. Mader, and S. Goldstein, "Performance Properties of Commercial Explosives," Propellants, Explosives, Pyrotechnics *8*, p. 8, 1983.
4. S. Goldstein and J.N. Johnson, "Aquarium Tests on Aluminized ANFO," Seventh Symposium (International) on Detonation, Annapolis, MD, NSWC, MP82-334, p. 1016, 1981.
5. J.K. Rigdon and I.B. Akst, "An Analysis of the Aquarium Technique as a Precision Detonation Pressure Measurement and Gage," Fifth Symposium (International) on Detonation, Pasadena, CA, ONR report DR-163, p. 59. 1970.
6. M.H. Rice and J.M. Walsh, "Equation of State for Water to 250 kb," J. Chem. Phys, *26*, p. 824, 1957.
7. Louis C. Smith, "On Brisance, and a Plate-Denting Test for the Estimating of Detonation Pressure," Explosivstoffe No. 5, p. 106, 1967.

DISCUSSION

DR. ALLAN W. KING, Space Research Corp., Belgium

1. How practical are explosives such as tungsten—loaded HMX for purposes of accelerating metals such as uranium without causing spalling?

2. What metal was the impedance of this explosive designed to match?

3. How important is it in explosives such as this, for the metallic element to remain nonreactive with the detonation products?

REPLY BY S. GOLDSTEIN

1. The evidence is that this is what they are particularly good for, but they are expensive to manufacture.

2. Steel.

3. We don't really know; however, most heavy metals will react only after a much longer time than the time scale we are concerned about. I suspect that participation in the reaction will increase the energy of the HE also and not sharpen the impulse peak very much.

DISCUSSION

OM G. REDDY, IDL Chemicals LTD., India

Question: The tungston and HMX differ in their densities. How did you achieve homogeneous mixture for your study? What technique did you use for mixing.

REPLY BY S. GOLDSTEIN

The mixture was made uniform and the high density achieved by using a special mix of W particles that was a tri-modal size distribution. The actual formulation was prepared in Group M-1 of our Laboratory by Steven Harmony.

DISCUSSION

INDU B. MISHRA, Kanan Assoc., Northridge, CA

If I understand you correctly, heavy metal in HMX gives rise to non-ideal nature. How about DU (Depleted Uranium) and HMX?

REPLY BY S. GOLDSTEIN

We have never tried DU. It might be useful also.

CALCULATION OF THE BLASTING PERFORMANCE OF SOME COMMERICIAL EXPLOSIVES

Algot Persson
Nitro Nobel AB, Vinterviken, 117 48 Stockholm, Sweden
and
Per-Anders Persson
Center for Explosives Technology Research
New Mexico Institute of Mining and Technology
Socorro, New Mexico 87801, U.S.A.

The new generation of commercial explosives, the water-in-oil emulsions, show detonation velocities close to those calculated by equilibrium thermochemical calculations assuming complete reaction, even at small charge diameters. This is due to the very intimate contact between fuel and oxidizer obtained by the emulsion process. ANFO, in sufficiently large diameter drillholes in rock shows a similar behavior. ANFO and Dynamite at small charge diameters, and TNT-slurry even in 250 mm drillholes in rock have detonation velocities 24 and 22% below the calculated equilibrium complete reaction values.

To account for these strongly non-ideal detonations we have made calculations in which up to 86% of the oxidizer salt is assumed not to take part in the chemical reaction at the detonation front. The salt is then reacted in an additional burn that we have modelled by a stepwise release of ingredients to burn instantaneously at discrete points along the expansion line. These calculations reproduce the observed field performance characteristics of slurry and emulsion explosives. A simple model for the reaction rate controlling mechanisms is discussed.

INTRODUCTION

In the past, the total chemical energy released in the explosion reaction has been used as a measure of an explosive's rock blasting performance. The energy was obtained by simple equilibrium thermo-chemical calculations, and a reasonable agreement was obtained by comparison with experiment from the lead block test (1) and the ballistic mortar (2). The most reliable method of measuring total explosion energy is the underwater explosion test according to Cole (3). If this test is calibrated with TNT spheres as done by Bjarnholt (4), and the charge size is chosen with respect for the type of explosive, then its accuracy in predicting total energy is fairly good.

Particularly for explosives that have considerably more or less reaction product gas volume than the normal, the total chemical energy is insufficient in itself to predict blasting performance. Johansson and Langefors (5) introduced the concept of weight strength, in which a correction term was brought in to account for the observed increase in blasting performance with increasing gas volume at constant explosion energy.

Recent experience with the new generation of commercial explosives, the water-in-oil emulsions, have led us to re-evaluate the methods of predicting blasting performance used in the past for slurry and dynamite explosives. Because of the greatly increased intimacy of contact between oxidizer and fuel brought about by the emulsion process, the emulsion

explosives show a detonation velocity versus density relation approaching that of ideal explosives. We compared the blasting performance of emulsion and slurry explosives on the basis of the weight strength as defined by Johansson and Langefors. We found, by reference to actual field experience, that the weight strength generally over-estimates the performance of slurry and dynamite explosives. In spite of their relatively low explosion energy and low density, the emulsion explosives outperformed or equalled the performance of heavy TNT slurries or high density, high energy dynamites in blasts using the same diameter drillholes and the same hole patterns.

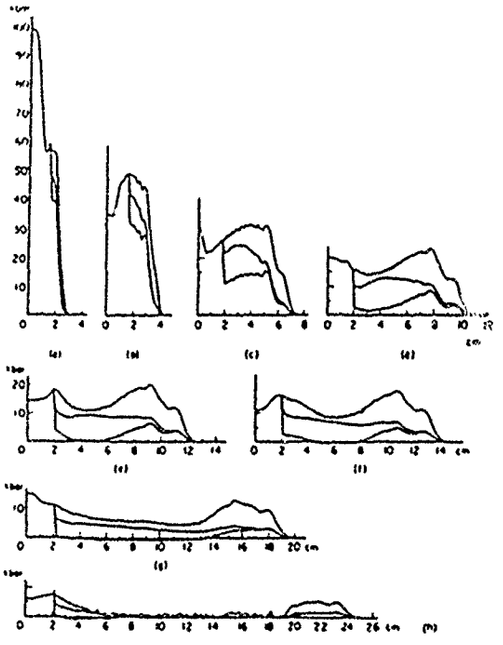

Fig. 1. Reaction product pressure in a 30 mm diameter drillhole and principal stresses in granite as a function of radius. Initial pressure in drillhole 100 kbar. Upper curves, radial, intermediate curves, axial, and lower curves, tangential stresses. a) 1 μsec, b) 2μsec, c) 7μsec, d) 13.9 μsec, e) 15.4 μsec, f) 20 μsec, g) 28 μsec, and h) 39 *μsec after start of motion, resulting from a constant volume explosion of nitroglycerine in the drillhole.*

The present study was made in an effort to see if a partial reaction, delayed burn mechanism could account for the observed discrepancies.

The Expansion Work Process in Rock Blasting

Our calculations technique is based on the calculations of Asklöf and Nylander (8) on the dynamic stress field around a 30 mm diameter drillhole in granite, suddenly loaded along its whole length by the 10 GPa (100 kbar) pressure of the constant volume explosion reaction products of nitroglycerine. Figure 1 shows the radial, tangential, and axial stresses and the reaction product pressure in the rock at different times during the subsequent process.

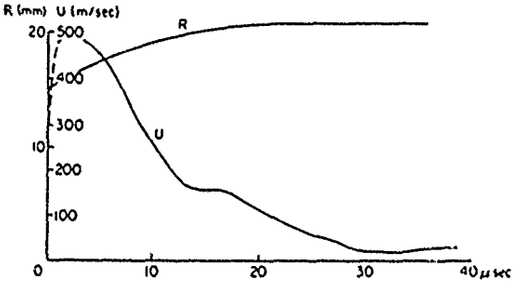

Fig. 2. Radial velocity U and position R of the drillhole wall, as a function of time

Figure 2 shows the drillhole radius as well as the velocity of the drillhole wall as functions of time. The hole expands to double its volume ($R = R_0 \times \sqrt{2}$) in about 30 μsec. The hole wall has almost come to rest in about the same time. From Figure 1 it is seen that at 39 μsec the tangential stress is negative close to the drillhole wall indicating that the material may start developing cracks. The gas pressure at that time is around 0.5 GPa. In our present calculations we assume that only parts of the ingredients of the explosive have reacted at the Chapman Jouguet plane close to the detonation front, and that the rest of the ingredients will burn during the subsequent expansion. We have allowed the initial reaction products and the unreacted rest of the explosive ingredients to expand from the compressed CJ-state to a volume equal to the initial. Half of the remaining unreacted ingredients are then released to react at the volume and allowed to expand, without further reaction, to double the initial volume. Finally, all the remaining unreacted ingredients are allowed to react at that volume and then expand isentropically to volume $V/V_0 = 1000$. The choice of the volume ratio $V/V_0 = 2$, at which the stepwise burning is completed, is

motivated by the observation that the drillhole will stay at that volume for a relatively long time (several microseconds for a 30 mm drillhole) before the radial cracks open. Cracks open mainly by the interaction between the stress field around the drillhole and the tensile wave formed by reflection of the outgoing stress wave at the free surface. Therefore, we may assume no ventilation of the drillhole until the reflected wave returns to the drillhole.

MEASURED DETONATION VELOCITIES

Table 1 and Figure 3 show experimental as well as calculated detonation velocities of five explosives, one TNT slurry, one dynamite, ANFO and two emulsion explosives. The velocities given for large diameters are measured in drillholes. Most of the smaller ones were measured in steel tubes or concrete confinement. The measurements were made with the well-known "pin technique" using switches made by either twisted copper wires or two parallel bare ends of ordinary lead wires for electrical detonators covered with an aluminum cap. The switches discharge a capacitor through a resistor. The discharge pulse was recorded on a transient recorder or a tape recorder, with an accuracy of ±50 m and ±300 m, respectively. All measurements were made by Nitro Nobel except the large diameter experiments with ANFO which were reported by Rylund (9). It will be noticed that even in 38 mm charges the detonation velocity of the emulsion explosive was fairly close to the ideal. TNT slurry and dynamite showed velocities which differed from those calculated with more than 20% even at large diameters. Crushed ANFO prills in 268 and 380 mm drillholes detonates with a velocity slightly lower than those calculated with the BKW equation of state using RDX parameters.

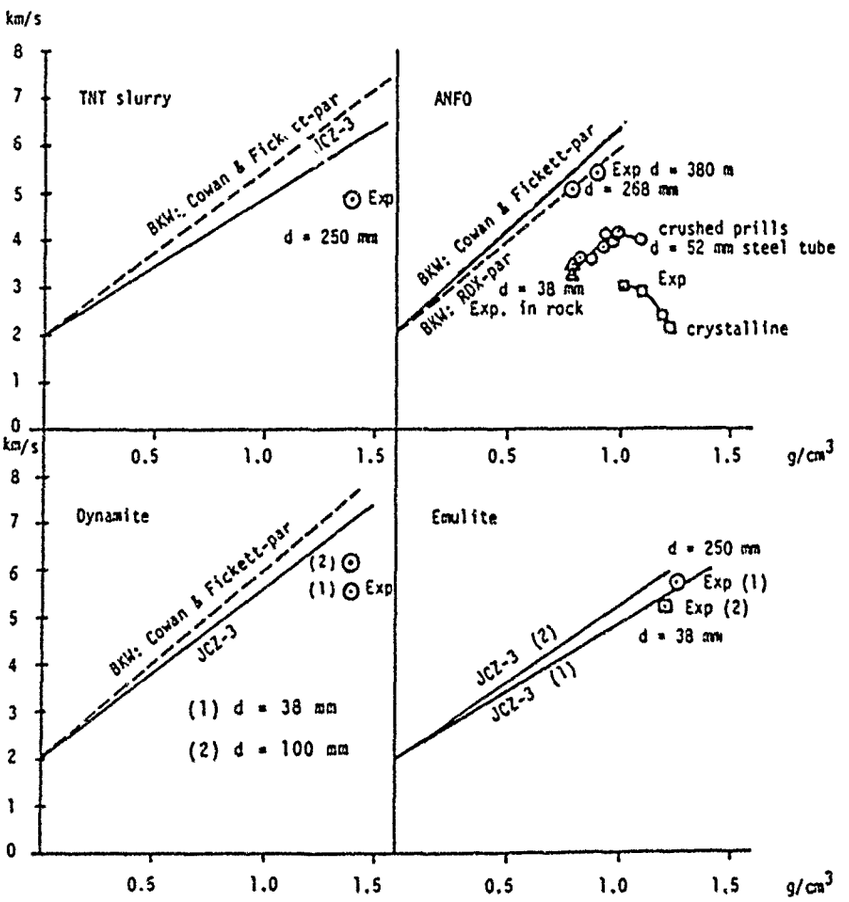

Fig. 3. Comparison between calculated and experimental detonation velocities for a TNT-slurry, ANFO, Dynamite, and two emulsion explosives. All large diameter detonation velocities are in drillholes in rock.

TABLE 1

Detonation velocities and expansion work for four commercial explosives. Comparison between calculated and experimental results.

Explosive	Density	Detonation velocty m/s			Expansion work MJ/kg				ΔH MJ/kg	Ao/A 100C
		Experiment m/s/Ø mm	Calculated BKW 3)	JCZ 3	Underwater detonation A_0	Tiger Calculation JCZ3 A_{10}	A_{100}	A_{1000}		
Emulsion bulk	1.27	5770/250 ±300	7000	5600		2.67	3.42	3.77	3.59	
Emulsion cartr.	1.20	5200/38	6630	5720	3.71	2.79	3.56	3.99	3.94	0.93
TNT slurry, ideal det	1.45	—	7200	6290	4.28	2.81	3.58	4.09	4.30	1.05
TNT slurry, non ideal d.[1]	1.45	4800/250	6575	4900	4.28	2.40	3.42	3.89	—	1.10
ANFO, ideal det.	0.9	5650/380	5920 5440 4)	5158	3.95	2.70		3.90	3.78	1.01
Dynamite, ideal det.	1.40	—	7589	7050	4.09	3.62	4.31	4.63	4.50	0.88
Dynamite non ideal d.[2]	1.40	5500/38		5530	4.09	3.00	3.96	4.46	—	0.92

1) Frozen components 62% AN, SN, A1
2) Frozen components 86% AN
3) Parameter values: $\alpha = 0.50$ $\beta=0.10$ $\theta=400$ $\kappa=11.85$
4) Parameter values: $\alpha=0.54$ $\beta=0.181$ $\theta=400$ $\kappa=14.15$

CALCULATION OF THE EXPANSION WORK

Ideal Detonation. There are several thermohydrodynamic codes for calculating the equilibrium, complete reaction, ideal detonation parameters at the Chapman-Jouguet plane and the expansion isentrope from that state. No such code is bettter than the input data used, the critical ones of which are the parameters and the general form of the equation of state for the reaction products. The BKW equation of state with parameters fitted to reproduce the detonation and expansion of RDX detonated at near crystal density reproduces well most military high explosives, Mader (7). As a group, these are characterized by a high density in the range 1.5 to 2 g/cm^3, a relatively high oxygen deficiency, and an excess of carbon. For the lower density, oxygen-balanced commercial explosives, we have found the JCZ-3 equation of state to give a better agreement with experimental data in the low pressure expansion region than the BKW-RDX, Bjarnholt (4).

For each explosive, we made a Tiger (6) calculation, with the JCZ-3 equation of state, for an ideal CJ-state detonation complete with an expansion isentrope to a volume ratio of $V/V_0=1000$. For some of the explosives, for comparison, we also made a Tiger calculation with the BKW equation of state, using parameters according to Cowan and Fickett (12), or a BKW calculation with the RDX-fitted parameters Mader, (13).

Non-ideal Detonations. Bjarnholt (10) showed that the experimentally determined work A_0 done by the reaction products in the underwater detonation of an explosive charge is comparable to the calculated isentropic expansion work of the reaction products to a volume 10^4 to 10^5 times the initial volume. For small deviations from ideal detonation velocity, Bjarnholt found the measured energy to be redistributed between shockwave and bubble energy, but the total remained essentially unchanged. This indicates there is time enough for a complete reaction when a one-kg charge expands to these very large volume expansion ratios. At larger deviations from ideal, such as for small diameter slurry explosives, a decrease in the total measured energy for the underwater test indicated incomplete reaction.

The expansion volume ratio at which the effective work in rock blasting is completed is in the range $V/V_0=3$ to 10, Bjarnholt (10). Therefore, even small deviations from ideal detonation may lead to considerable decreases in blasting efficiency.

To get a quantitative measure of how big this efficiency decrease can be for some real commercial explosives, we used the Tiger code with the JCZ-3 equation of state. After debugging the "Freeze" and "Freadj" routines, Srinivas (11), we were able to use these to make repeated calculations in which predetermined parts of some ingredients were first kept unreacted, then released to react stepwise at different points along the expansion isentrope.

For each of the two non-ideal explosives, the TNT slurry and the Dynamite, we made the following calculations:

A C-J state detonation with a percentage of some of the ingredients "frozen" (unreacted), (point 1 in Figure 4) followed by an expansion isentrope calculation from that C-J state to the volume ratio $V/V_0=1$. At that point (2), half of the "frozen" or unreacted ingredients are released to react, giving a new starting point (3), for a second expansion isentrope to the volume ratio $V/V_0=2$, point (4), where the rest of the unreacted ingredients are released to react. From the resulting final starting point (5), a final expansion isentrope is calculated out to point (6) at $V/V_0=1000$.

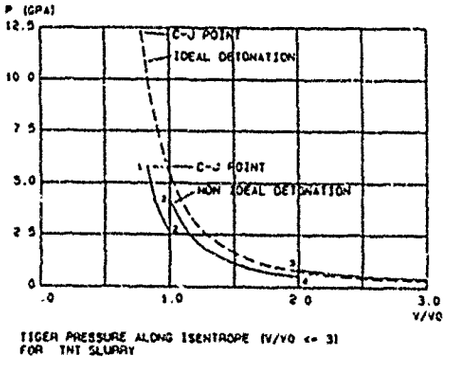

Fig. 4. The pressure along the isentrope for the reaction products of a TNT slurry. Dotted curve, ideal detonation calculation. Unbroken line, calculated with the described method for non-ideal detonation.

CALCULATION RESULT

Running the Tiger-JCZ-3 code with the TNT slurry ingredients and keeping 62% of ammonium nitrate, sodium nitrate and aluminum unreacted in the CJ state reduced the CJ detonation velocity from the ideal value 6290 m/s to 4900 m/s. Continuing with isentropic expansion and releasing the "frozen" ingredients in two steps as described earlier, this resulted in a P,V relation shown in Fig. 4 which can be compared with the gas expansion of the ideal detonation. The CJ pressure is considerably lower which will affect the expansion work also. In the diagram Figure 5, the isentropic expansion work is plotted against the volume ratio. Curve a) is the work performed by the expanding reaction products of an ideal detonation of the TNT slurry; curve b) shows the work done by expansion and step-wise burning for a non-ideal detonation obtained by the described technique. Curve c) shows the expansion work for an emulsion explosive (bulk type) with a density of 1.27 g/cm^3.

The expansion works A 10, A 100, and A 1000 at V/V_0 equal to 10, 100 and 1000 respectively, are gathered for all five explosives in Table 1. For dynamite, the work of A 10 (non-ideal) is about 17 % lower than A 10 (ideal). For the TNT slurry the same difference is 15%.

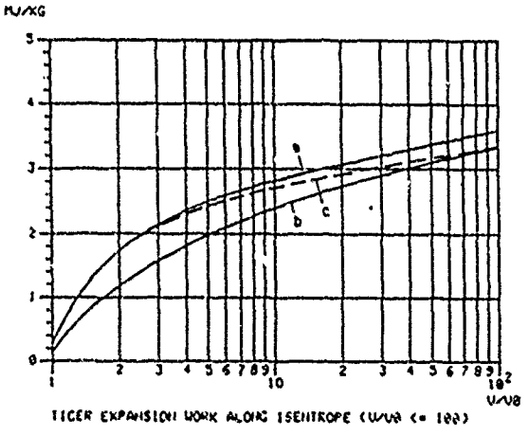

Fig. 5. Calculated expansio. work of reaction products. a) TNT-slurry (ideal det.), b) TNT-slurry (non-ideal det.), c) emulsion explosive (ideal det.).

A SIMPLE BURNING MODEL

We have made an attempt to calculate the total burning time of that part of the explosive which will react behind the CJ-plane. A simple model of a TNT slurry was chosen, as follows:

The slurry contains 18% by weight of TNT flakes 2-5 mm wide and about 1 mm thick. If we

assume the TNT flakes to be about 3×4 mm and 1 mm thick, then the weight of a flake is 0.018 g and the number of flakes in one cm^3 about 15. If the flakes are just a little shorter, there are 16 flakes per cm^3. We assume that they are stacked symmetrically as in Figure 6. The distances between the parallel surfaces are 1.5 mm and between the edges 1 and 2 mm, respectively.

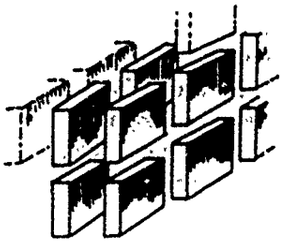

Fig. 6. Positions of the TNT flakes in the burning model

Let us further assume that all the flakes are initiated and decompose instantaneously when passed by the detonation shock front. Their reaction products, rich in carbon and hydrogen, then burn outwards by gradually consuming the intermediate oxidizer layers over their total area. The mechanism is thus similar to grain burning, although in this case the fuel is gaseous and the oxidizer in the condensed phase. At the CJ-state about ⅓ of the AN SN, Al solution has reacted. The thickness of the unreacted volume between the flakes is then 1.0 - 1.4 mm. As this volume can be looked upon as a slab burning on both faces, the depth of the solution that remains to react is 0.5 - 0.7 mm. Half of this volume is assumed to react during the expansion of the reaction products from the CJ volume to the initial volume, V_0, and the other half will react during the continued expansion to 2 V_0.

The linear burning velocity, r, depends on the pressure, p, as $r=ap^b$ where a and b are constants commonly determined by observing the burning velocity at pressures between 0.1 - 500 MPa. According to the Tiger code calculations, the CJ pressure is 5.7 GPa (57 kbar). The pressure after expansion to the initial volume and instant reaction of half of the remaining component is 1.2 GPa. To be able to calculate the time at which all of the explosive components are reacted behind the CJ plane we tried to determine a mean burning velocity during the two expansion steps. The mean burning pressure during the first expansion step was estimated to be 5 GPa (5 kbar). However, no values of the constants a and b for the linear burning rate of the slurry were available. Chan (14) reports some burning experiments on AN, SN, FO water gels. Using his values for a and b we got a burning velocity of 1.82 m/s during the first expansion and 0.29 m/s for the second part. The burning time between the CJ state and the initial volume state was then calculated to be 140 μs and the total time of after-burning about 1 ms. Even after this time the reaction products have probably not expanded to a volume much larger than 2 V_0 as the crack volume available for expansion is small until the cracks open up to the free surface of the rock. The crack growth to the surface is the result of interaction with the reflected stress wave and the arrival time of this is of the order of ms. The time for the drillhole to expand to a certain diameter scales lineary with the diameter. Thus, extrapolating from the data in Figure 1, for a 250 mm hole the time to double the hole volume (radial expansion ratio 1.4) is 250 μs. The assumption that all of the explosive has reacted after expansion to about double the drillhole volume seems reasonable.

DISCUSSION

As shown in Figure 1 there is still a pressure of 0.5 GPa when the drillhole has reached its maximum volume ($2V_0$), where it will stay for several microseconds. Even if the reaction products will expand into cracks arriving at the borehole wall, there will still be about 0.05 to 0.1 GPa pressure when the drillhole ventilates in a common bench blast. According to Figure 7, which shows the pressure along the isentrope, this corresponds to a volume expansion ratio of about 7 to 10. Therefore, it is more relevant to compare the energy released while expanding to $V/V_0=10$, A 10, when trying to decide which explosive will be the most efficient one for rock blasting.

Comparing, in Table 1, A 10 for the buld emulsion with that for the non-ideal detonating TNT slurry, the value for the emulsion is about 11% larger than for the TNT slurry. A 1000, however, is 7% lower. The expansion work performed in an underwater detonation A_0 differs remarkably

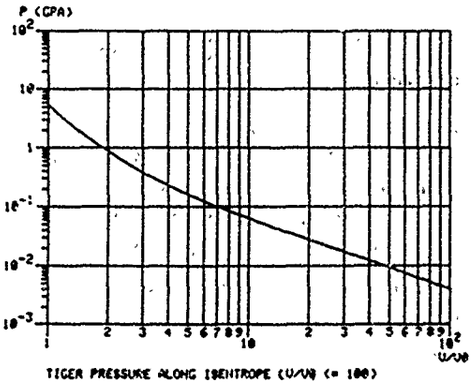

Fig. 7. The pressure along the isentrope for the reaction products of a TNT slurry

if we compare the values of the slurry and the emulsion.

The observations made in blasting practice, that an emulsion explosive can replace a TNT slurry in the same drill pattern, are verified by these calculations.

Comparing the values of A 10 for ANFO, Dynamite, and the emulsion explosives against the background of Figure 3, we can understand that the full potential of ANFO and Dynamite may only be realized in very large charge diameters, where they may approach ideal detonation. The emulsion explosives, even at diameters as small as 38 mm, still approach ideal detonation. As a consequence, they have a fairly large effective work A 10 approaching that of the greatly non-ideal A 10 of Dynamite and ANFO in small diameters. This makes the emulsion, in spite of their relatively low total energies A 1000 or ΔH, competitive with ANFO and Dynamite, on a weight-for-weight basis.

ACKNOWLEDGMENTS

This work has been carried out as an R&D investigation within Nitro Nobel AB and the authors are grateful to Nitro Nobel for the permission to publish it. The authors wish to acknowledge the assistance of Karl-Göran Norman in running the computer codes.

REFERENCES

1. W.E. Gordon, F.E. Reed, and B.A. Leper, "Lead Block Tes' 3 for Explosives" Ind. and Eng. Chem., Vol. 47, p. 1794, 1955.
2. C.H. Johansson and T. Sjolin, "Measurements of the 'Strength' of Explosives by the Ballistic Mortar," Review of Scientific Instruments, Vol. 39. p. 1173, 1968.
3. R.H. Cole, Underwater Explosions, Princeton University Press, Princeton, N.J., 1948.
4. G. Bjarnholt and R. Holmberg, "Explosive Expansion Works in Underwater Detonations." Proc. 6th Symposium (Int.) on Detonation. Aug. 24-27, 1976, Office of Naval Research, Dept. of the Navy, ACR-221.
5. C.H. Johansson and U. Langefors, "Methods of Physical Characterization of Explosives," Proc. 36th Int. Congr. of Ind. Chemistry, Brussels, Vol. III, 610, 1966.
6. M. Cowperthwaite and W.H. Zwisler, "Tiger Computer Program," Documentation, SRI, Pub. No. Z 106, 1973.
7. C.L. Mader, " A Code for Computing the Detonation Properties of Explosives," Los Alamos Scientific Lab. Report LA 3704, Los Alamos, N.M., 1967.
8. C.A. Asklof and A. Nylander, "Cylindrical and Spherical Wave Expansion Processes in Rock Materials," Swedish Research Institute of National Defense, Report FOA 2 C 2286-4, 1968.
9. P.H. Rylund, "Maximum Utilization of ANFO Energy by Proper Initiation," Proc. SME Fall Meeting & Exhibit, Birmingham, Al., Oct. 18-20, 1972.
10. G. Bjarnholt, "Suggestion on Standards for Measurement and Data Evaluation in the Underwater Explosion Test," Swedish Detonic Research Foundation Report DS 1978:13.
11. M.A. Srinivas, "Changes to Tiger," Private Comm., Swedish Detonic Research Foundation, Stockholm, Sweden.
12. R.D. Cowan and W. Ficket, "Calculation of the Detonation Products of Solid Explosives with the Kistiakowsky-Wilson equation of state," J. Chem. Physics, Vol. 24, p. 932, 1956.
13. C.L. Mader, Numerical Modeling of Detonations, University of California Press, Berkeley and Los Angeles, CA, 1979.

14. S.K. Chan, "Ignition and Combustion Characteristics of Water-Gel Explosives," Report, Canadian Industries, Ltd., McMasterville, Quebec, Canada.

DISCUSSION

OLDRICH MACHACEK, Thermex Energy Corporation

Two Comments: (1) The emulsion explosives referred to are w/o type. A simplified typical formulation contains, say, 18% water, 7% oil, 2% glass microspheres, 72% ammonium nitrate and 1% w/o emulsifier. However, we can make the same formulation as o/w emulsion (watergel type) in which the only difference will be the use of 1% modified guar gum instead of 1% w/o emulsifier. Density, formulation will be the same but the explosive characteristics strikingly different. The w/o emulsion will detonate at 2½" with a high detonation velocity, o/w at probably 5" with a minimum booster at least 5x bigger with characteristics more similar and ANFO. Differences between w/o and o/w will get smaller in larger diameters as 8" and up. If we suppose the same size droplets for both emulsions, then the only principal difference in these two types of explosives is the amount of droplets in the continuous phase. In simplified calculation, we have approximately 10x of the oxidizer than of the fuel phase and approximately a double in density of the oxidizer compared to the fuel. The amount of droplets for the w/o emulsion is then approximately 5x higher compared to the o/w emulsion. The contact area between the oil phase and the oxidizer phase is therefore also 5x higher for the w/o emulsion.

(2) Calculation of blasting performance of commerical explosives is a very difficult task and as to my understanding, each commercial explosives manufacturer in the U.S. uses his own program. These programs are difficult to compare. It would be useful to have some standardized method which would make a more objective comparison possible. The CETR could be of help in this matter.

DISCUSSION

MR. M. CHAUDHRI, Cavendish Lab, Cambridge, UK.

You stated that although the volume of the bore-hole becomes twice its original size, no cracking of the hard rock occurs before the stress' waves come back to the bore-hole after having been reflected at the free surfaces.

I am afraid, I disagree with the statement of yours because of a two-fold increase in the volume of the bore-hole will produce a strain of ~ 1.4 at the bore-hole surface. Hard rocks will not be able to sustain such high strains without cracking, as these materials are highly brittle, and the fact that the loading is at a very high rate will make them, in common with other brittle materials, even more brittle. Moreover, the cracks thus produced are likely to be along planes containing the bore-hole axis and can be of considerable size (i.e., the crack velocity and the duration in which the cracks formed). Would you please comment on these thoughts?

REPLY BY A. PERSSON

When the bore-hole is expanded to double its original volume the rock material around the hole is strongly compressed too. As the diagram in Fig. 1 shows, the principal stresses are all positive when the pressure has been applied in the bore-hole. Later when the pressure in the bore-hole is released the tangential stress first becomes negative in the rock material some distance away from the surface of the hole and the first cracks that will appear are shear cracks. These cracks form an angle against the radii and do not reach the wall of the hole. The radial cracks are formed much later and will grow out to a free surface under influence of the gas pressure. If the rock material is not homogeneous the stress relations can be very different of course.

DETONATION BEHAVIOR OF EMULSION EXPLOSIVES CONTAINING GLASS MICROBALLOONS

M. Yoshida, M. Iida, K. Tanaka, S. Fujiwara,
M. Kusakabe and K. Shiino
National Chemical Laboratory for Industry
Tsukuba Research Center
Yatabe, Tsukuba, Ibaraki 305, Japan

Detonation behavior of emulsion explosives containing glass microballoon (GMB) was studied. Detonation velocity of several emulsion explosives of the same matrix and with variable fraction of GMB was measured at several diameter values for each GMB fraction. Critical charge thickness for detonation propagation was also measured using explosive wedge samples. Diameter effect showed a remarkable difference from that of high explosives. Extrapolated detonation velocities to infinite diameter agreed fairly well with those of theoretical calculations especially at low fraction of GMB. Critical charge thickness for detonation propagation showed a strong dependence on the volume fraction of GMB. The relation between the critical thickness and the volume fraction of GMB exhibited two vertical asymptotes. The minimum critical thickness was approximately 0.5 mm. This value, comparable to those of high explosives, suggests a very small reaction zone length for ammonium nitrate based explosives.

INTRODUCTION

The steady detonation propagation and its failure in cylindrical geometry have been paid considerable attention by many workers not only for high explosives but also for industrial explosives. Price (1) classified explosives into two groups according to the dependence of detonation velocity and critical (or failure) diameter on the initial density of explosives. Most of the industrial explosives belong to group 2, which means that the detonation velocity at a fixed charge diameter has a maximum at a density less than its maximum loading density and that the critical diameter increases with increasing the initial density. These features are quite different compared to group 1 explosives which most high explosives belong to. Mader (2) proposed another classification comparing the measured detonation velocity with a theoretically calculated result. The explosives are "non-ideal" if their detonation velocity at infinite diameter is less than the calculated one by more than 0.5 mm/μs. Most explosives containing ammonium nitrate (AN), such as ANFO, slurry explosives, some dynamites, Amatols and so on, are believed to be non-ideal.

Two explosive formulations, eutectic explosives (3, 4) and emulsion explosives (5), have been studied of which detonation behavior are almost ideal (3-6) although they contain AN as a main composition. Emulsion explosives, which appeared in the patents (7, 8) about 20 years ago, have become rather important in industrial use because of its high detonation velocity and high measure of safety. The remarkable features of emulsion explosives are that AN and other salts exist in an aqueous solution state confined with a very thin layer of oil and that the particle size of emulsion is very small — an order of a micrometer or less (5).

In this paper the detonation behavior of emulsion explosives containing glass microballoons (GMB) was reported. The dependence of the

detonation velocity and critical thickness for detonation propagation on the fraction of GMB were studied in a wide range of volume fraction of GMB.

2. MATERIALS

Composition of emulsion matrix is shown in Table 1. Aqueous solution of AN and sodium nitrate was added to a mixture of paraffins and surface activation agent under proper agitation to form a water-in-oil type emulsion. Temperature was maintained at about 80 °C and agitation was continued about 30 minutes to form fine particles. Particle size of the emulsion was estimated to be about one micrometer or less because particles could not be observed with an optical microscope which has 0.42 μm resolution.

TABLE 1

Material composition of emulsion matrix

Material	wt. %
Ammonium nitrate	72
Sodium nitrate	10
Water	12
Liquid paraffin	2
Solid paraffin	2
Sorbitan monooleate (*)	2

(*) Surface activation agent

GMB (Glass Bubbles B15/250, 3M) was used to control the density of explosives. GMB was washed by water to remove crushed particles and only the floating part was dried and used for explosives. Fig. 1 shows a photograph of GMB after being dried. Explosives were prepared by mixing the emulsion matrix with variable contents of GMB. Mixing was done carefully by hand using a flexible plastic sheet until the distribution of GMB in the matrix became uniform. The initial loading density of emulsion explosives was calculated from their weight and volume in a PMMA tube. The measured density was fitted by,

$$\varrho_0 = (0.746 + 9.43\ x\ )^{-1}, \qquad (1)$$

where ϱ_0 is initial density in g/cm^3 and x is the weight fraction of GMB. From this fitting the density of emulsion matrix and GMB was estimated to be 1.34 and 0.0983 g/cm^3 respectively. The emulsion matrix has inclusions of air bubbles in the mixing process and the measured density is not the true matrix density but the apparent one.

The density of emulsion explosives ranged from 0.38 to 1.31 g/cm^3. Corresponding volume fraction of GMB, calculated using Eq. (1), was from 0.77 to 0.025 respectively.

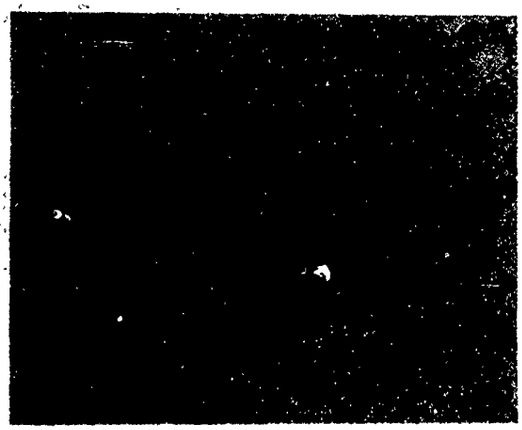

Fig. 1. Microscopic Photograph of Glass Microballoons

3. EXPERIMENTAL

3.1 Detonation Velocity. Diameter effect on the detonation velocity was investigated at five volume fractions of GMB; 0.12, 0.22, 0.30, 0.42 and 0.54. Explosives were confined in PMMA tubes. Inner diameter of the tubes were between 6 and 31 mm. Wall thickness of the tubes was about 20% of inner diameter. The ratio of length to diameter was about 20 for small diameters and about 10 for the largest diameter. These values were large enough for the measurement of steady state detonation velocity. Booster explosive (SEP, Ashai Chemical Industry) was used in the same diameter PMMA tube with 5 to 15 mm thickness.

Streak camera method was employed for the detonation velocity measurement. Rotating mirror streak camera (SP-1, Hitachi) recorded the self-luminous light of the detonation of emulsion explosives. Several markers on the PMMA tubes, streak speed and the slope of the recorded detonation light on the film determined the detonation velocity with about 0.2% accuracy.

3.2 Critical Thickness. Critical thickness for the detonation propagation was measured with an explosive wedge confined between two PMMA

plates. Volume fraction of explosive samples was from 0.025 to 0.77. The configuration is shown in Fig. 2. Booster explosive (SEP) of about 10 mm length was used. PMMA plates were 5 mm thick, 20 mm wide and about 200 mm long. Wedge angles were between 0.6 and 4.3 degrees. Critical thickness of detonation propagation was measured from the trace recorded on an aluminum alloy plate attached in contact with one PMMA plate.

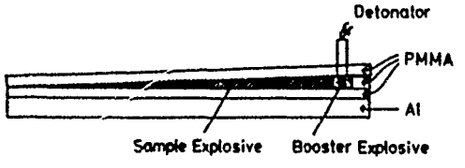

Fig. 2. Explosive wedge for critical thickness measurement

4. RESULTS AND DISCUSSION

4.1 Diameter Effect. Steady detonation propagation was observed for all charges except two failed charges of 6 and 8 mm inner diameter at 0.12 volume fraction of GMB. Measured detonation velocity (D) was plotted against the reciprocal charge radius (1/R) in Fig. 3.

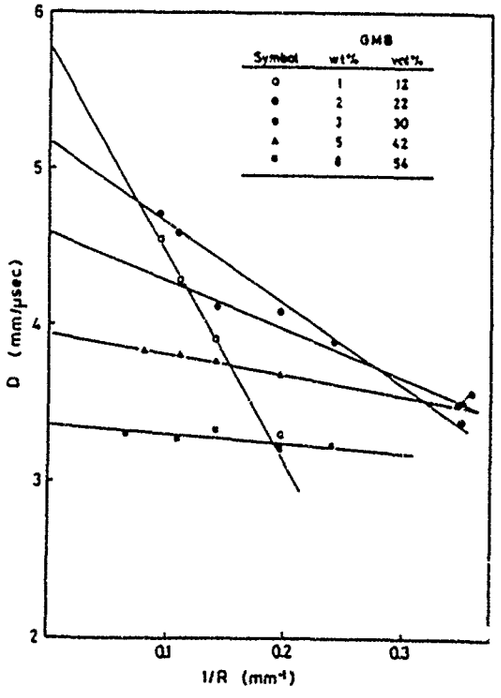

Fig. 3. Detonation velocity (D) of emulsion explosives vs. reciprocal charge radius (1/R).

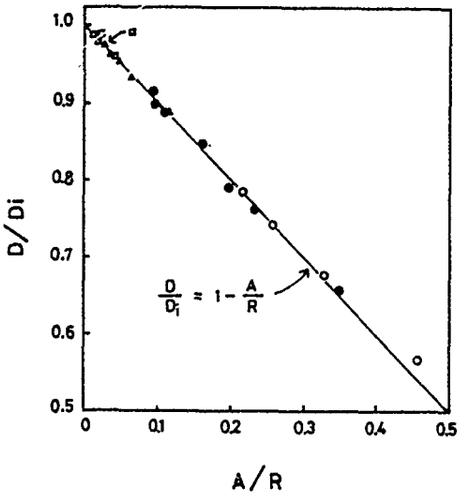

Fig. 4. D/D_i vs. A/R for all data. For symbols see Fig. 3

The experimental results for each fraction of GMB were fitted by linear relationships and represented by

$$D/D_i = 1 - A/R \,, \qquad (2)$$

where D_i is an extrapolated detonation velocity to infinite diameter and A is a constant. Campbell and Engelke (9) used $R - R_c$ instead of R in Eq. (2) for high explosives at high density, where R_c is a constant and was positive except a few cases. Our results did not need R_c and the data were well fitted by linear relationships. Fig. 4 shows the all data plotted in D/D_i versus A/R plane, which indicates that the fitting by Eq. (2) is quite satisfactory. The minimum value of observed D/D_i for emulsion explosives was about 0.57 at the lowest GMB fraction (89% of the maximum density), while the minimum value for high explosives at high density was about 0.85 (9).

Table 2 shows the summary of D_i and A for five explosives. Both D_i and A increased with increasing the initial density of explosives. The diameter effect relationships, Eq. (2), for different volume fraction of GMB cross together in D vs. 1/R plane (Fig. 3). If detonation velocity is plotted against initial density for each fraction of GMB, the curve is upward convex and has a maximum density less than the maximum density. Although the emulsion explosives investigated do not have the same composition due to the addition of GMB, the tendency is the same as that of group 2 explosives. A remarkable difference of diameter effect between

TABLE 2

Diameter effect parameters and calculated C-J properties using Kihara-Hikita-Tanaka equation of state

GMB		Density	Experimental		Calculated C-J Properties		
			A	D_i	D	P	T
wt. %	vol. %	g/cm^3	mm	mm/μs	mm/μs	GPa	K
0	0	1.34	——	6.41 (*)	6.42	13.6	1601
1	12	1.19	2.31	5.78	5.87	10.4	1749
2	22	1.07	1.01	5.17	5.41	8.0	1841
3	30	0.97	0.67	4.58	5.02	6.3	1904
5	42	0.82	0.33	3.94	4.39	4.2	1995
8	54	0.67	0.17	3.35	3.71	2.6	2065
10	60	0.59	——	——	3.38	2.1	2088(**)
20	77	0.38	——	——	2.40	0.7	2028

(*) Estimated by Eq. (3).

(**) Calculated maximum C-J temperature.

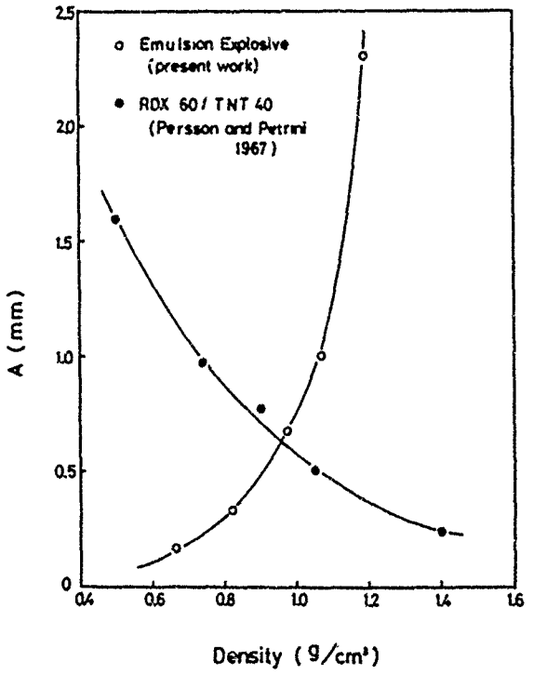

Fig. 5. Dependence of A (Eq. (2)) on the initial density

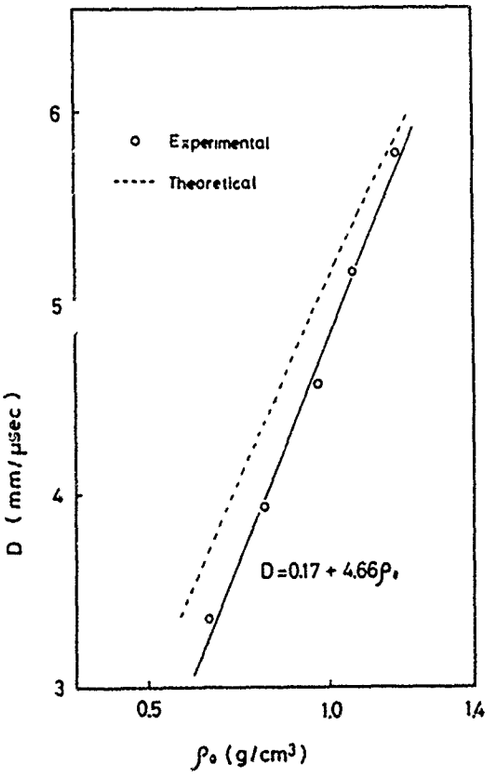

Fig. 6. Comparison of experimental and calculated detonation velocity

group 1 explosives and emulsion explosives is clearly seen in the behavior of A because the dependence of D_i on the initial density is the same for two groups. Fig. 5 shows the dependence of A on the initial density for emulsion explosives and a high explosive 60/40 RDX/TNT (10). The coefficient A of emulsion explosives increased with increasing the initial density, while that of 60/40 RDX/TNT decreased.

According to Eyring (11), A is proportional to the thickness of the reaction zone. If it can be applied to both emulsion explosives and 60/40 RDX/TNT, Fig. 5 directly indicates a contrast behavior of the dependence of the reaction zone length on the initial density between two explosive formulations.

4.2 Detonation Velocity at Infinite Diameter. Detonation velocities extrapolated to infinite diameter were compared with theoretical calculations. Kihara-Hikita-Tanaka (KHT) equation of state (6) was used for the calculations of equilibrium state at the Chapman-Jouguet condition. Table 2 and Fig. 6 show the results of calculations together with experimentally obtained detonation velocity at infinite diameter. The experimental results were fitted by

$$D = 0.17 + 4.66\,\varrho_o, \qquad (3)$$

where D in mm/μs and ϱ_o in g/cm^3. The agreement between experimental and theoretical values is very good, especially at high density or low fraction of GMB.

The agreement is generally rather poor for other AN based explosives, possibly due to the incomplete reaction at the detonation front (2, 12). Tanaka and Yoneda (12) compared the measured and calculated detonation velocity of slurry explosives containing AN and concluded that only 50-70% of AN decomposed at the front. Mader (2) showed that low fraction of decomposed AN at the front should be assumed for the agreement between measured and calculated detonation velocity of Amatols.

On the contrary, experimentally obtained detonation velocities of emulsion explosives agreed well with calculated detonation velocities with complete AN decomposition, which indicates that the detonation behavior of emulsion explosives is ideal unlike other non-ideal AN based explosives. Akst (3) and Stinecipher (4) also showed a good agreement between measured and calculated detonation velocities for eutectic explosives containing AN. It is interesting that the particle size of AN based eutectic explosives is about a few micrometer, which is close to the value of emulsion explosives. This suggests that particle size of an order of a micrometer is sufficiently small for the reaction completion at the front.

The difference between measured and calculated detonation velocity increased as the initial density decreased. The possible reasons for the disagreement at lower density would be as follows:

1) Equilibrium state is not attained.
2) Diameter effect is not represented by Eq. (2) at large charge diameters.
3) The input data of the calculation for solid component is not known exactly.
4) Reaction completion cannot be reached at lower density.
5) The parameters of KHT equation of state are not suitable for low density gas products.

The first one is considered to be the main reason because of a large fraction of void at lower density, leading to significant temperature distribution in the reaction zone. Experimental (13) and theoretical (14) investigations suggest that the second, non-linear diameter effect at large charge diameter, is also possible for emulsion explosives.

4.3 Critical Thickness. The results of critical thickness (T_{cr}) measurements by explosive wedge samples were plotted against the volume fraction (V) of GMB in Fig. 7. The relationship between T_{cr} and V exhibited two vertical asymptotes and the curve was U shaped. A low fraction of GMB, the dependence of T_{cr} on V had a feature of group 2 explosives — critical thickness increases as density increases, while at high fraction of GMB the feature was that of group 1 explosives. A similar curve was also reported in the detonation of gas mixtures with variable ratio of flammable gas to oxygen (15,16).

The solid line in Fig. 7 is a least square fitting by the following equation,

$$T_{cr} = 0.50\,(V+0.026)^{-1} + 0.15\,(V-0.81)^{-1} - 0.98 \quad (4)$$

where T_{cr} in mm. The obtained data scattered considerably and it was difficult to determine the constants in Eq. (4) accurately. Furthermore as the failure was observed on an aluminum-alloy plate through a 5 mm thick PMMA plate, the attenuation of shock wave in a PMMA plate possibly produced a systematic error in T_{cr}. Eq. (4) should be considered as representing a qualitative feature of T_{cr} vs. V relationship. One aymptote was at negative value of V. The U curve crossed the T_{cr} axis at about 18 mm. This value gives a rough estimation of critical diameter of matrix emulsion, which will be several times greater than the value measured by wedge samples (17).

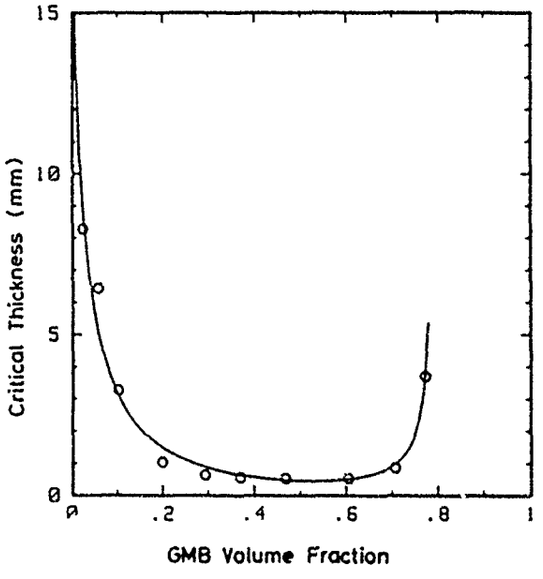

Fig. 7. Critical thickness for detonation propagation

One notable feature in T_{cr} is its very small value at from 0.2 to 0.7 volume fraction of GMB. The smallest critical thickness was about 0.5 mm and this value is about the same order to those of high explosives (17). This suggests that the reaction zone length of emulsion explosives is very small, because T_{cr} is considered to be approximately proportional to the reaction zone length.

An attempt to correlate A in Eq. (2) with critical radius was not successful for high explosives (9).

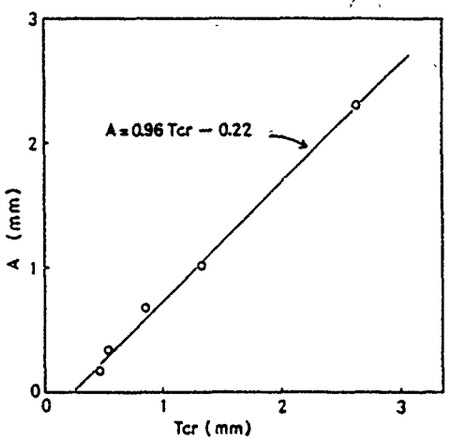

Fig. 8. Coefficient A in Eq. (2) vs. critical thickness (T_{cr})

Fig. 8 shows a plot of A against T_{cr} for emulsion explosives. The data were well fitted by a linear relation,

$$A = 0.96\,T_{cr} - 0.22. \quad (5)$$

It should be noted that the values of A were obtained from 0.12 to 0.54 volume fraction of GMB, which are in the left side of U shape curve in Fig. 7.

5. CONCLUSIONS

The detonation behavior of emulsion explosives containing GMB was studied in a wide range of GMB volume fraction. Diameter effect on the detonation velocity was satisfactorily expressed by Eq. (2) and the dependence of the coefficient A on initial density exhibited a remarkable difference compared to a high explosive 60/40 RDX/TNT (Fig. 5). The detonation velocities extrapolated to infinite diameter agreed well with theoretical calculations using KHT equation of state. The agreement was especially good at high density, which indicates a completion of AN decomposition at the detonation front. The critical thickness measured by explosive wedge samples showed a strong dependence on the volume fraction of GMB. The curve (Fig. 7) exhibited two vertical asymptotes. The minimum value of critical thickness was about 0.5 mm. The value is close to those of high explosives and suggests a small reaction zone length.

REFERENCES

1. D. Price, "Contrasting Patterns in the Behavior of High Explosives," Eleventh Symposium on Combustion, The Combustion Institute, Pittsburgh, p. 693, 1967.
2. C. L. Mader, "Numerical Modeling of Detonations," University of California Press, Berkeley, 1979.
3. I. B. Akst, "Detonation in Intermolecular Explosives: Characteristics of Some Eutectic Formulations," Seventh Symposium on Detonation. NSWC MP 82-334, p. 548, 1981.
4. M. M. Stinecipher, "Eutectic Composite Explosives Containing Ammonium Nitrate, ibid, p. 801, 1981.
5. F. Takeuchi, K. Yamamoto and H. Sakai, "Emulsion Type Explosives," Kogyo Kayaku 43, 285, 1982.
6. K. Tanaka, "Detonation Properties of High Explosives Calculated by Revised Kihara-Hikita Equation of State," This symposium.
7. R. S. Egly and A. E. Neckar, "Water-Resistant Sensitizers for Blasting Agents," United States Patent 3, 161, 551, 1964.
8. N. E. Gehrig, "Aqueous Emulsified Ammonium Nitrate Blasting Compositions Containing Nitric acid," United States Patent 3, 164, 503, 1965.
9. A. W. Campbell and R. Engelke, "The Diameter Effect in High-Density Heterogeneous Explosives," Sixth Symposium on Detonation, ACR 221, p. 642, 1976.
10. P. A. Persson and M. Petrini, "The Detonation Velocity of 60/40 RDX/TNT with Varying Density and Charge Diameter," Swedish Detonic Research Foundation Report DL 1967, 20, 1967.
11. H. Eyring, R. E. Powell, G. H. Duffy and R. B. Parlin, "The Stability of Detonation," Chem. Rev. 45, 69, 1949.
12. K. Tanaka and K. Yoneda, "Detonation Properties of Some Unconfined Water Gels (1)," Kogyo Kayaku 38, 185, 1977.
13. A. W. Campbell, "Diameter Effect and Failure Diameter of a TATB-Based Explosive," Prop. Exp. Pyrotechnics 9, 183, 1984.
14. H. Matsui, K. Yoneda, A. Moritani and T. Asaba, "A Generalized C-J Condition for A Simple Axial Flow with a Spherical Shock: Its Application to Slurry Explosives," This Symposium.
15. N. Manson, "La Theorie Hydrodynamique et le Diametre Limit de Propagation des Ondes Explosives," Z. Electrochemie 61, 586, 1957.
16. W. Pusch and H. Gg. Wagner, "Investigation of the Dependence of the Limits of Detonability on Tube Diameter," Comb. Flame 6, 157, 1962.
17. T. R. Gibbs and A. Popolato, eds., "LASL Explosive Property Data," University of California Press, Berkeley, 1980.

DISCUSSION

M. M. CHAUDHRI, Cavendish Laboratory, Cambridge, U.K.

In one of your viewgraphs you showed that the reaction zone length of a typical high explosive decreases with the increase in its density, whereas for the case of your microballoon sensitized emulsion explosive the reaction zone length increases with the increase in the explosives density. This fundamental difference is very significant. Would you please comment as to why this dramatic difference in behavior of the two types of explosive occurs?

REPLY BY M. YOSHIDA

One possible reason for the discrepancy found in Fig. 5 might be the completely different relationships of the CJ temperature and initial density between these two types of explosives. As many CJ calculations show (e.g. K. Tanaka 'Detonation Properties of Condensed Explosives' NCLI, 1983) the CJ temperature of high explosives, or group 1 explosives, decreases as the initial density decreases, whereas that of group 2 explosives increases (Table 2) at this density range.

Although we couldn't check whether A vs. density curve has its minimum or not, the critical thickness, which is also considered to be roughly proportional to reaction zone length, had a minimum value with its density value

roughly corresponding to the density of maximum CJ temperature. This will support the above explanation.

DISCUSSION

G. OM. REDDY. IDL Chemicals Ltd.

You mentioned that the air is trapped during water-in-oil emulsion explosive. Where do you observe air bubbles? Are they in oil phase or aqueous phase? What is the size of the bubbles and how are they determined?

REPLY BY M. YOSHIDA

The size of the largest air bubbles, which existed outside of emulsion cells, was about a few milimeters. As we could not observe a cell of emulsion matrix by our microscope of which resolution was 0.42 μm, we can say nothing about the possibility of existence of air in oil or aqueous phase.

DISCUSSION

S. GOLDSTEIN, Los Alamos National Laboratory

In your failure thickness experiments, did you worry about confinement effect of the PMMA plates around the explosive?

REPLY BY M. YOSHIDA

The confinement effect of PMMA will not be considered as negligible due to the low density of explosives. Fig. 7 should be considered to represent a qualitative feature of critical thickness.

DISCUSSION

OLDRICH MACHACEK, Thermex Energy Corporation

The w/o type explosive emulsions are made by emulsifying the oxidizer solution into the oil phase. The oxidizer is completely dissolved at f.e. 180 degrees F and introduced with a vigorous mixing into heated oil phase containing w/o emulsifier. If we suppose that the crystallization point of the oxidizer solution is around 140 degrees F, we could anticipate that at room temperature the individual oxidizer droplets contain a mixture of solid and liquid particles. However, if we cool the explosive emulsions to a low enough temperature (say — 40 degrees F) and then to expose them to a strong mechanical impulse, the temperature of the whole body of emulsion suddenly may rise by 30-50 degrees F, and the emulsion loses all excellent explosive characteristics irreversibly. This can be explained if we suppose that the oxidizer solution is in a supercooled state as liquid. This aspect should also be considered in evaluating explosive emulsions of the o/w type.

INTERMOLECULAR EXPLOSIVES

I. B. Akst
Los Alamos National Laboratory
Group M-8, MS J960
Los Alamos, New Mexico 87545

The steady-state detonation characteristics of a few intermolecular explosives are examined along with results of wedge experiments on initiation and reaction growth in one system (EAK), toward a better understanding of this class of explosives. The importance of factors such as products and their states, and temperature, to performance of these systems and explosives in general is discussed.

Hydrogen compounds may be superior enough to carbon and its compounds as fuels and products for quick metal-accelerating explosives that the effect of the generally lower density is offset. High temperatures and condensation of solid products are probably the main causes of late appearance of energy in metal motion.

The unusual shock sensitiveness and explosiveness of EAK are indicated by wedge results including pseudo-Pop-plots of overtaking waves, and by plots of shock velocity versus transit distance in the wedges.

INTRODUCTION

Intermolecular explosives are the most used class, but not the most researched nor the best understood. They can be defined as a class of composites in which a significant part of the performance comes from fast reactions between mixed substances. A principal criterion and aim is synergy, performance greater than that of the individual components. The research and applications studies have as a purpose the better understanding of these systems; this might result in the development of better explosives by transcending some of the present limits on stability, sensitivity, density, performance, ease of manufacture, availability, and cost of single compounds.

The combinatorial reactions of intermoleculars are in contrast to decomposition in monomolecular (an easier term than intramolecular) explosives and the intermediate performance in mixtures of essentially noninterreactive composites such as cyclotols and monomoleculars diluted with inerts. Average and maximum distances between reactants are orders of magnitude greater in intermoleculars than in monomoleculars, resulting in much more mass transport before reaction and a broader spectrum of reaction times. Reaction orders are at least superficially different also, the principal type being

$$A + B + \ldots \rightarrow C + \ldots ,$$

with reaction type

$$A \rightarrow B + C + \ldots$$

being dominant in monomoleculars but not as important in intermoleculars. However, the orders may not be very different if one of the reactants is itself an explosive, and/or the important energy-producing reactions between oxidizer and fuel moieties are preceded by intermediate decomposition routes into those moieties in particular monomoleculars.

In addition to these principal intrinsic differences, the materials used in many intermoleculars are chemically quite different from

the compounds of most common monomolecular explosives. This is no doubt a result of the former being so heavily used industrially, where cost and performance considerations are different from those of military explosives. Using the ideas of one world in the other, particularly to yield new explosives with special characteristics for military use, has resulted in some explorations which have produced practical formulations and which can be used to further the science of explosives in general.

There are still other differences, some of them, like microstructure or particle size, related to the intrinsic differences above. I would like to focus on the apparent effect of some chemical differences on steady-state detonation, and then describe some non-steady-state effects seen in one system, EAK, which is a eutectic composition (46/46/8 by weight, also with variations) of ethylenediamine dinitrate (EDD), ammonium nitrate (AN), and potassium nitrate (KN).

EXPERIMENTAL

The materials and acquisition of most of the data have been described previously (1, 2, 3, 4, 5). Material for the wedge tests was made by Group M-1 at Los Alamos. Most was made by synthesizing EDD as described in (5), melting it with AN and KN in a kettle, and then casting it into cylindrical molds from which wedges were machined in several orientations with respect to the casting geometry. Some EAK was made by synthesizing and melting under perchloroethylene, and one set of wedges was made by pressing after granulation in cold perchloroethylene.

The wedge test for quantitative determination of shock sensitivity has been described elsewhere (6) and was used with wedges not less than 76 mm in width and 150 mm long. The wedge angle was 30° for most tests with a maximum run of 55 mm; a few of the early tests used 25° and a maximum run of 30 mm. One test was carried out in double width (with a 300-mm-diameter plane-wave lens replacing the usual 200 mm one) to assure that erosion of shock strength from the sides did not occur during the free run.

STEADY-STATE DETONATION

Mass transport, longer reaction time, and different reaction orders notwithstanding, the reaction front velocity (detonation speed, D) may be faster and the performance higher, both calculationally and experimentally, in particular intermolecular systems than in some detonating monomoleculars of the same density and available thermochemical energy. This can be true even when one of the intermolecular partners is itself a high-performing ideal monomolecular. Note the EA systems in Table I, especially EAK (50/42.5/7.5 by weight): its D of 8.02 km/s in 102 mm diameter confined in 10 mm of copper is above those (7.86 and 7.73 km/s calculated by the Tiger code using the BKWR equation of state (7) or by the Kamlet-Jacobs short method (8), and above that of EDD. EDD is a powerful explosive, with both D — 7.7 km/s at high density — and pressure (about 23 GPa) higher than TNT. It is not necessary, although it may be advantageous, for the intermolecularly reacting partners to be themselves detonable, as has been demonstrated in an all-solids system (4) and various ones with a liquid component, such as ANFO.

In some cases the equation of state calculational differences are greater than the difference between experiment and ideal calculation.

High pressure and relatively fast reaction are suggested by high detonation speed. Performance synergism is verified by metal propulsion as in heavily confined plate-dent tests in small diameter (1, 2, 5) and cylinder tests (1, 2), Table I. But these tests integrate pressure-time variables, hence do not necessarily confirm high pressure or very fast reaction. In fact, very high pressures can hardly have occurred in the confined plate dent tests, which had maximum shock (detonation) velocities of 5 or 6 km/s (1, 2, 4, 5) because of the small diameter.

It may be noted that reaction rate or reaction zone effects may be reflected in the cylinder test by changes in D with diameter, while the cylinder wall energy may or may not be invariant over the same range of diameters: EAR (15 wt% RDX) increases greatly in D from 25.4 to 50.8 to 101.6 mm, while the cylinder energy (wall speed) changes very slightly, observable only by small changes in arrival times at particular expansion distances, which is an integration of the wall velocity. EA 50/50 increases in both D and energy with diameter, as did an aluminum/ perchlorate formulation reported by

Finger et al. (9).

Other systems may yield experimental speeds, pressures, and performance considerably lower than expected, ever though they are or appear to be similar to well-performing intermoleculars in stoichiometries (oxygen balance), potential chemical energies, density, and detonability. They may even have the same oxidizers and calculate as well. The TNT mixtures, Amatols, in Table I are of that nature; TATB in mixture with lithium nitrate appears to be of that kind also (10). On the other hand, hydrazine/hydrazine nitrate systems perform well (11), as does the eutectic of ADNT/AN (1, 12).

The differences in performance are hypothesized to be a result of different reactants — fuels, mostly, because there seems to be a better present chance to decode carbon-hydrogen differences than, for example, oxygen-fluorine differences, although there is progress there (13). Reactant differences lead to differences in products and their states, or detonation characteristics including the quantity of gas, the average molecular weight of the gases, and detonation temperature. Table II gives those parameters for some hydrogen and carbon fuel systems.

It is suggested that hydrogen is a better fuel than carbon for producing higher performance of some kinds, including metal acceleration, at least in moderate explosive mass to metal mass ratios. This thesis is supported by observations made previously (1): the speed with which energy delivery is effected is indicated by the ratios of energies at expansions of 7 and 2 times the original volume, that is $(v_7/v_2)^2$ where v is cylinder wall radial velocity. It is also supported by a paper on the chemistry of detonations (14) in which higher mole fractions of water are observed to correlate well with early cylinder energy, that is, by smaller ratios of $(v_7/v_2)^2$, wh... explosives having more carbon products have higher ratios; and by an observation in (15), in which it was noted that HNO explosives deviated positively from the performance predicted by an otherwise tight correlation and fitted equation (15), while CNOs deviated negatively.

Four hypotheses about hydrogen and its products being better than carbon in this performance connection are:

(1) More gas is produced. Assuming that an explosive charge is volume-limited and that the hydrogenous explosive has density comparable to carbonaceous explosive (although on the whole it is lower, in practice it need not be greatly so), then there are more moles of hydrogen than carbon, and there can be more moles of water than carbon oxides by 1.56-2.44 to 1 (H_2O/CO-H_2O/CO_2). On average, including lower density, the ratio of H/C oxide gases predicted by simple stoichiometry will be somewhere near 2. In thermohydrodynamic code calculations and experiment, the ratios of the total gases are nearer 4/3. See Table II for some numbers.

(2) The average molecular weight of the gases will be lower. If there are no solid products, of course the molecular weight is the reciprocal of the number of moles of gas produced, so the more gas, the lower the MW. In reaction motors, or in Defourneaux's thesis on propulsion by explosives (16), the velocity of the rocket or the metal, respectively, is inversely proportional to the molecular weight of the working fluid gas.

(3) The temperature of the fluid is lower. The various thermohydrodynamic codes calculate detonation temperatures of water-rich systems perhaps 500°K or more lower than CO_2-rich systems. The total thermochemical energies of the two kinds of systems can easily be about the same; EA systems heats of detonation are close to those of TNT and Amatols, both calculationally and by calorimetry (17, 1) on both weight and volume bases. If total energies are equal, then partition to lower rotational and vibrational energies means greater translational energy.

(4) Transitional states of carbon during explosive decomposition may produce thermic events of a nature not usually considered. It has been reported (18) that at CJ all molecular bonds are broken. If that occurs, or to the extent that occurs, carbon not yet reacted nor condensed to solids or quasi-solids is effectively a gas (if not ionized), which has the high positive heat of formation of +172 kcal/mol or over 14 kcal/gm. The heat sink of unreacted, uncondensed carbon would reduce the system's immediately available energy, while the carbon would not be a good low-molecular-weight gas because of its elevated thermal state and the

TABLE I
Performance in Cylinder Tests

Explosive	Diameter	Density	TMD	D	Wall Velocity km/s		
	mm	gm/cc	%	km/s	$V/V_0=2$	$V/V_0=7$	$V/V_0=11$
TNT	25.4	1.63	98.5	6.99	1.23	1.40	1.46
EDD	25.4	1.55	97.2	7.55	1.29	1.44	1.46
Comp B 64 RDX	25.4	1.72	98.5	7.99	1.44	1.63	1.68
EA 50/50	25.4	1.60	96.5	6+	1.06	1.24	1.33
	50.8	1.59	95.9	7.67	1.28	1.45	1.50
	101.6	1.61	97.1	7.87	1.34	1.49	1.53
EAK 50/42.5/7.5	101.6	1.64	98.5	8.02	1.33	1.47	1.52
EAR 42.5/42.5/15	25.4	1.62	96.6	6.93	1.35	1.52	1.57
	50.8	1.60	95.4	7.70	1.36	1.50	1.56
	101.6	1.63	97.2	8.17	1.36	1.50	1.56
EARL−1, 5.2 Al	50.8	1.65	96.4	7.46	1.34	1.51	1.52
	101.6	1.66	97.0	8.02	1.37	1.54	1.61
EARL−2, 14.8 Al	50.8	1.72	96.8	7.23	1.30	1.46	1.49
	101.6	1.71	96.2	7.70	1.39	1.61	1.69
Amatol 57AN 5μm	25.4	1.61	95.1	6.07	1.01	1.18	1.23
54AN 25μm	50.8	1.61	95.2	6.05	1.01	1.18	1.24

Compositions are weight percent. Cylinder wall thickness was 0.1 x I.D. (diameter shown). Amatol data courtesy F. Helm, D. Breithaupt, R. McGuire, Lawrence Livermore National Laboratory.

ensuing condensation.

Aluminum is a fuel of interest and pragmatic importance, differing from carbon in practice because it is usually in elemental particles in formulations. If small particles were converted to a gas by the detonation or by liberation from a compound, as suggested for carbon, the effects might be quite similar to those of carbon: Upon forming individual molecules of oxides, those too would be what is normally a solid in the gaseous state, with very high positive heat of formation and a hard-to-predict thermic situation dependent on condensation states and rates.

The effects of aluminum on performance in moderate time frames such as in the cylinder test or plate dent may change considerably with variations in the amount in the formulation: In relatively small quantities in fine particulate form it may help by both burning and condensing quickly enough to raise the ambient temperature of the fluid and thereby increase the overall reaction rate; the influence of temperature on the reaction rate is discussed by McGuire in this symposium (10). In larger amounts the times might be too long. The formulations EARL-1 and EARL-2 have approximately 5 and 15 percent by weight aluminum (5 to 20 micrometers diameter), and as may be seen from the cylinder data of Table I, the lesser amount of aluminum depressed the detonation velocity of the nonaluminized EAR only slightly in either 50 or 100 mm diameter, with D over 8 km/s in the larger size. At the same time it had little if any effect on the energy in 50 mm diameter but increased it in 100 mm diameter at expansions greater than V/Vo=2. The greater amount of aluminum reduced the detonation velocity in both sizes and reduced the cylinder energy in 50 mm diameter but increased it significantly at all expansions in 100 mm size. Such crossovers point toward nonlossy ways to tailor energetics effects.

WEDGE TESTS OF SHOCK INITIATION

One of the effects of plane shocks of moderate duration in EAK was a rather linear increase in shock speed through the wedge thickness (maximum 55 mm) over a wide range of input pressures. Slopes and intercepts are shown in Fig. 1, which illustrates the effects of input pressure and composition proportions. The eutectic EAK composition, 46/46/8 by weight,

TABLE II

Some Calculated Product and Detonation Parameters

Explosive	Fuel Ratios		KSM[a]			BKWR[b]				BKW			
	Atoms H/C	Wt% H/(H+C)	N mols/kg	MW gm/mol	C mols/kg	N mols/kg	T °K	D km/s	P GPa	N mols/kg	T °K	D km/s	P GPa
TNT	0.71	5.6	25.3	28.5	23.1	27.9	2711	7.18	20.4	28.5	2905	6.99	20.8
Amatol (60AN)	3.14	20.8	36.3	25.7	5.5	36.4	2421	8.37	28.0	36.3	1616	8.45	29.9
Amatol (79AN)	6.71	35.9	39.8	25.1	0	40.0	2265	8.68	29.5	40.0	1292	8.74	31.2
TATB	1.00	7.7	29.1	27.2	17.4	29.0	2177	8.39	31.3	29.1	2128	7.85	29.7
HMX	2.00	14.3	33.8	27.2	6.8	33.8	3093	9.38	40.2	33.8	2264	9.01	39.4
EDD	5.00	29.4	40.3	22.4	8.1	40.3	2140	7.78	24.1	40.3	1337	8.49	27.6
EA 44/56	11.00	47.8	42.2	23.7	0	42.2	2176	8.68	28.3	42.2	1196	8.85	30.5

[a] Kamlet-Jacobs H_2O-CO_2 "arbitrary" (8); MW is average of gases; C is carbon

[b] BKW with modified parameters (7)

Some calculations (a and b) at TMD, others at 95 to 98 TMD

is apparently more sensitive than 50/42/8, even though there is less of the detonable component, EDD. It is not unreasonable to expect the sensitivity to be near the maximum at eutectic proportions because the intimacy of mixing should be greatest and the effect of particle size smallest. Reducing the EDD to 42/50/8 depressed sensitivity and produced almost the only failing waves observed, in 4 out of 5 tests.

Some batches appeared to have a low maximum velocity. This could mask classical transitions to high detonation velocity, and can even give the impression of failing, if the input shock is very strong, overdriving the materials, as in Batch 334, Fig. 2. The low performance is probably a result of coarse microstructure, as seen along with considerable anisotropy, in Figs. 3 through 6. These scanning electron micrographs are from three mutually orthogonal cuts of the same sample, the fourth picture identifying the particles which are AN.

There were a few occurrences of the classical wedge-test result, rapid transition to high-speed detonation. One of these is seen in Fig. 7, where there is also evidence of overshoot to higher-than-normal D.

Figures 8 and 9 show two other responses often seen. One (Fig. 8) shows fairly steady shock velocity increases through the wedge after a period of 20 mm or so of no acceleration, implying slow or late growth in reaction behind the front. There is a suggestion of an overtaking wave at 35 mm, followed by further linear increase in velocity to near-normal D. In Fig. 9 there is evidence of instability, possibly reflecting irregularity and anisotropy in the microstructure; the structure of the shock progress is very complex, with, possibly, more than one transition.

Figure 10 shows shock velocity decreasing, taken to be incipient failure in EAK 42.

Because of the dearth of clear, quick transitions to known high detonation velocity, true Pop-plots could not be fitted; but nonlinear increases in velocity of the shock suggested overtaking waves often enough to try fitting distances to these "transitions" to input pressure in log-log space. In Fig. 11, which also includes Pop-plots of several standard materials for comparison, the right ends of these plots occupy positions near those of insensitive explosives, but with relatively long run even at high pressures. The slopes are much flatter, putting the left ends nearer the region of more sensitive explosives, with only moderately longer runs at lower pressures than at high pressures.

In the context of duality in the nature of sensitivity, these materials might be said to exhibit low explosiveness — likelihood of escalation to very violent reactions — but not low sensitiveness. The results of Foster and Craig (19) using a large scale (200 mm diameter confined,

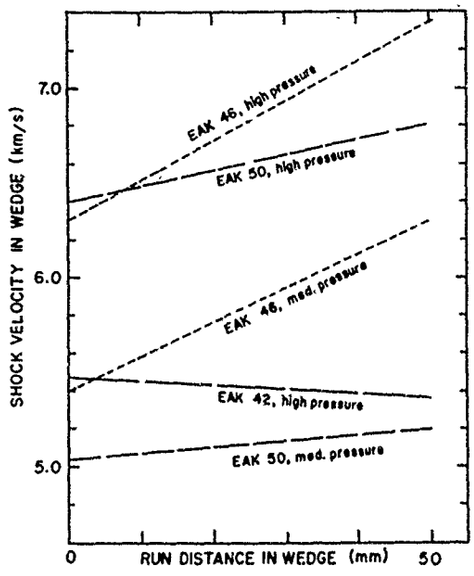

Fig. 1. Slopes and intercepts, or initial and final velocities. The eutectic composition (EAK 46) is apparently more reactive than one with more of the detonable component, EDD (EAK 50). EAK 42 displayed incipient failure.

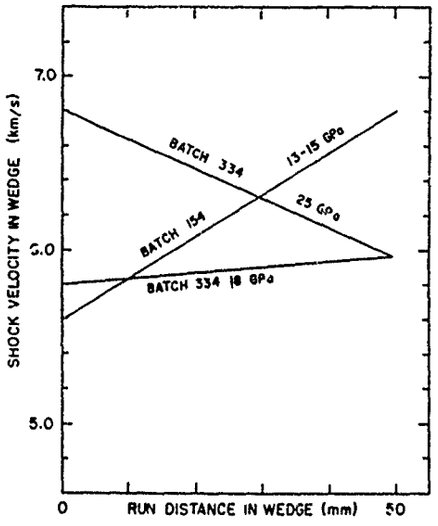

Fig. 2. Slopes and intercepts, or initial and final velocities. Batch 334 apparently has a maximum D of about 6 km/s, even when directly initiated by Comp. B (upper line) and not too high density, with 6% voids. Batch 154 shots had only 1% voids.

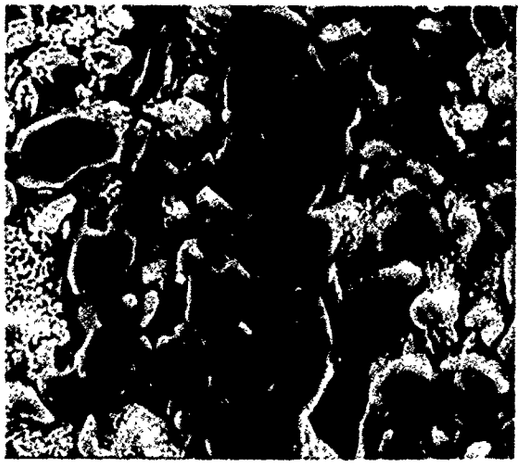

Fig. 3.

Fig.4

Figs. 3 — 6. Scanning electron micrographs of a sample of cast EAK 46 cut in three mutually orthogonal planes. Fig. 5 is along the cleavage plane. Fig. 6 is a potassium x-ray distribution map of the field in Fig. 5.

Fig. 5 *Fig. 6.*

Fig. 5 and 6. See caption on previous page

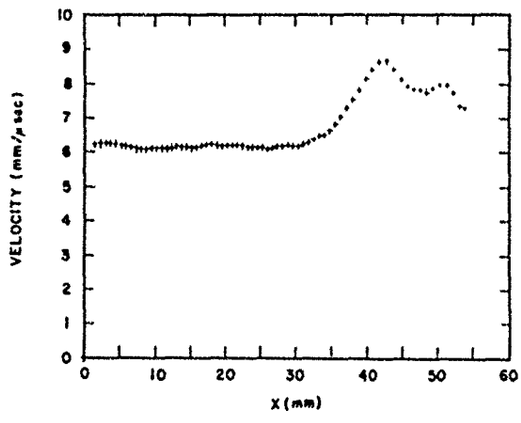

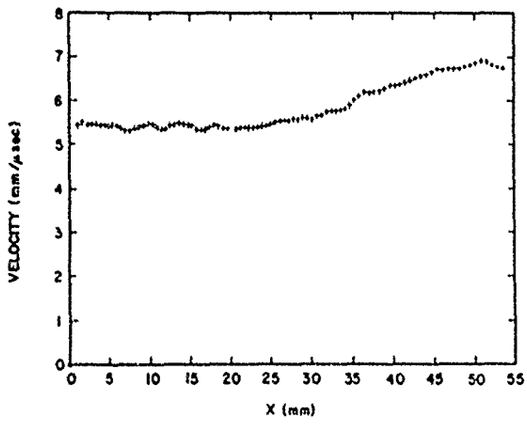

Fig. 7. Cast EAK-46 at 1.657 gm/cc, .992 of TMD, pressure of 21.4 GPa in the wedge. A true transition to detonation occurred about 35 mm free run.

Fig. 8. Cast EAK-46 at 1.65 gm/cc, .99 of TMD, pressure of 13.0 GPa in the wedge.

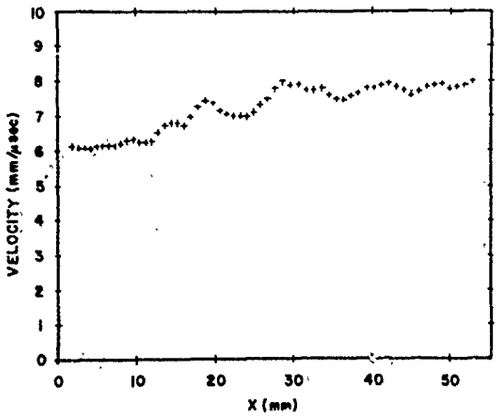

Fig. 9. Pressed EAK-46 at 1.664 m/oc, .995 of TMD, pressure of 20 GPa in the wedge. Transition at 14 mm is followed by instability, perhaps another transition or growth, finally reaching the known high D.

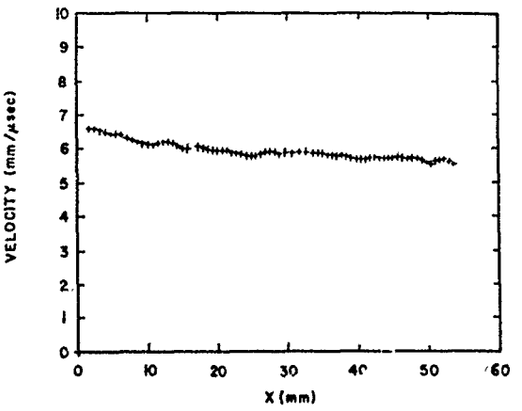

Fig. 10. Cast EAK-42 at 1.65 gm/cc, .984 of TMD, pressure in wedge directly from 12.7 mm thick Comp. B (no attenuator). The plot is interpreted as a failing wave.

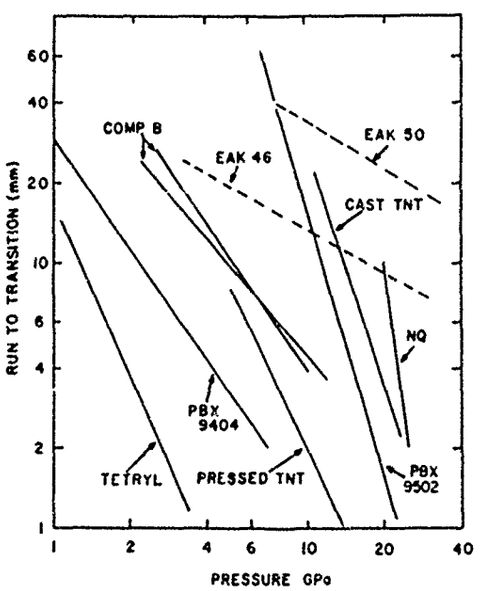

Fig. 11. Pop-plots (solid lines) of some well-known explosives, and runs to transitions versus pressure in EAKs.

200 mm long run) "gap test" are not antithetical to such a description.

The effect of void space or its lack was variable: densities were mostly quite high, and density was often overridden by other strong variables. For example, fast-frozen, fine-microstructure EAK pressed to high density was as insensitive as any of the other batches, yet one of the few fast transitions to high D occurred in this material at over .99 of theoretical maximum density.

High-energy composite propellants can sometimes exhibit reaction structure similar to EAK in wedge tests, as observed from the work of Dick (20). The slow growth of reaction in all these materials, with failure of EAK — most of the time — to transit in these experiments to known steady-state detonation velocities of 7.5 km/s and higher, is, we suppose, idiocratic to intermolecular systems. The events in the early states of initiation and growth of reaction are made clearer by the wedge method, while the test's constraints on run time and distance to maintain one-dimensionality and minimize confusion with diameter effects limit definition of the final stages before steady state.

CONCLUSIONS

Explosives physicists should find it worthwhile to study detonation products and their

states more comprehensively. Explosives chemists might look for intermolecular systems and monomolecular compounds with more hydrogen fuel and less carbon fuel even at some cost in density, a parameter skewing the search for new compounds toward carbon. Such new intermoleculars and compounds are reasonably sure to be good and useful explosives in some way, if only to advance detonation science.

The wedge test or some other non-invasive experiment with internal shock following, plus longer runs, could provide basic data on reaction buildup in intermoleculars and other composite systems. The data might also be useful in the safety contexts of sensitiveness versus explosiveness.

ACKNOWLEDGMENTS

The work discussed was supported by Eglin Air Force Base (Armament Laboratory), Air Force office of Scientific Research, Picatinny Arsenal, and the Army Research Office, over a period of time.

Many people have helped carry out the research and provided guidance and explication. While it is not possible to recognize everyone by name, I do thank you all, and to the lists of those previously mentioned, I would like to add, with special thanks, W. C. Davis, G. H. Parsons, A. P. Torres, and J. R. Travis.

REFERENCES

1. I. B. Akst, "Detonation in Intermolecular Explosives: Characteristics of Some Eutectic Formulations," Seventh Symposium (International) on Detonation, Annapolis, Maryland, pp. 548-559. NSWC MP 82-334, June 16-19, 1981.

2. I. B. Akst, "Nonideal Explosives Research: Intermoleculars, Eutectics, and EAK," AFATL-TR-82-79, Air Force Armament Laboratory, Eglin AFB, FL, 1982.

3. I. B. Akst, "Nonideal Explosives Research," AFATL-TR-79-95, Air Force Armament Laboratory, Eglin AFB, FL. 1979.

4. J. Hershkowitz, I. Akst, "A New Approach to Improving the Performance of Nonideal Explosives Containing Ammonium Nitrate," Picatinny Arsenal Technical Report 4789, March 1975.

5. I. Akst, J. Hershkowitz, "Explosive Performance Modification by Cosolidification of Ammonium Nitrate with Fuels," Picatinny Arsenal Technical Report 4987, October 1976.

6. A. W. Campbell, W. C. Davis, J. B. Ramsay, J. R. Travis, "Shock Initiation of Solid Explosives," Phys, Fluids, Vol. 4, No. 4, pp. 511-524, 1961.

7. M. Finger, E. Lee, F. H. Helm, B. Hayes, H. Hornig, R. McGuire, and M. Kahara, "The Effect of Elemental Composition on the Detonation Behavior of Explosives," Sixth Symposium (International) on Detonation, Coronado California, ACR 221, pp. 710-722, 1976.

8. M. J. Kamlet and S. J. Jacobs, "Chemistry of Detonations: I. A Simple Method of Calculating Detonation Properties of C-H-N-O Explosives," J. Chem. Phys. 48, 23 1968.

9. M. Finger, H. C. Hornig, E. L. Lee, J. W. Kury. "Metal Acceleration by Composite Explosives," Fifth Symposium (International) on Detonation, Pasadena, California, ACR-184 Office of Naval Research, pp. 137-151, 1970.

10. R. R. McGuire, "Composite Explosives for Metal Acceleration," this symposium.

11. M. Finger, E. Lee, F. H. Helm, B. Hayes, H. Hornig, R. McGuire, and M. Kahara, "The Effect of Elemental Composition on the Detonation Behavior of Explosives," Sixth Symposium (International) on Detonation, Coronado, California, ACR 221, p. 720, 1976.

12. M. M. Stinecipher, "Eutectic Explosives Containing Ammonium Nitrate," LA-9973-MS, Los Alamos April, 1984.

13. R. R. McGuire, D. L. Ornellas, F. H. Helm, C. L. Coon, and M. Finger, "Detonation Chemistry: An Investigation of Fluorine as an Oxidizing Moiety in Explosives," Seventh Symposium (International) on Detonation, Annapolis, Maryland, NSWC MP 82-334, pp. 940-951, June 16-19, 1981.

14. M. J. Kamlet, J. M. Short, M. Finger, F. Helm, R. R. McGuire, and I. B. Akst, Combustion and Flame 51: 325-333 (1983).

15. J. M. Short, F. Helm, M. Finger, and M. J. Kamlet, Combustion and Flame 43:99 (1981).

16. M. Defourneaux, "Explosive Deflection of a Liner as a Diagnostic of Detonation Flows," Fifth Symposium (International) on Detonation, Pasadena, California, ACR-184 Office of Naval Research, 1970, pp. 457-466, 1976.

17. D. L. Ornellas, "Calorimetric Determination of the Heat and Products of Detonation for Explosives: October 1961 to April 1982," UCRL 52821, April 1982.

18. R. R. McGuire, D. L. Ornellas, "An Investigation of Chapman-Jouguet Detonation Theory Using Isotopic Labeling," Frank J. Seiler Research Laboratory, Report SRL-TR-75-0004, April 1975.

19. J. E. Foster, B. G. Craig, and M. E. Gunger, "An Eight-Inch Diameter, Heavily Confined Card Gap Test," this symposium.

20. J. J. Dick, "Nonideal Detonation and Initiation Behavior of a Composite Solid Rocket Propellant," Seventh Symposium (International) on Detonation, Annapolis, Maryland, NSWC MP 82-334, June 16-19, pp. 620-623, 1981.

DISCUSSION

INDU B. MISRA, Kanam Associates, Northridge, CA.

If higher hydrogen content results in nonideality, perhaps we should revive pentaborane- or carborane-oxidizer work in intermolecular explosives. We should not be perturbed by the pentaborane-hydrazine failure experiment of the past. Comments?

REPLY BY IRVING AKST

The choice of substances for the intermolecular fuel, including hydrogen, need not *per se* affect nonideality, but rather the performance observed in various kinds of experiments, some of which are not entirely indicative of ideality. While the hydrides of boron might be interesting on a phenomenological basis, the chances for pragmatic explosives would likely be poor, because, for example, the densities are very low, less than one gram per cubic centimeter.

THE DETONATION REACTION OF HETEROGENEOUS COMPOSITE EXPLOSIVE

Guo Yuxian, Peng Guoshu, Song Jialiang and Xu Laibin

Xian Modern Chemistry Research Institute
Xian,China

and

Wang Aiqin and Zou Quanqing
Gansu Chemical Industrial Institute
Lanzhou, China

The present paper deals with the further study concerning the experimental results of heterogeneous composite explosives (H.C.X.). The mechanism of detonation reaction of H.C.X. is suggested, and some experiments are designed in order to confirm the mechanism. The percentage reacted between the components of H.C.X. in detonation region (R%) is calculated by using the Nitrogen Equivalent Equation which is corrected by the experimental detonation data of single explosives. The R% of H.C.X. composed of bis-(trinitroethyl) nitramine and TNT, TATB or HMX, in which the mean size is about 0.4 - 1.0 μM, is about 40-50%. The thickness of diffusion layer of the above systems is about 0.10-0.15 μM which is calculated from R% and particle size distribution.

INTRODUCTION

Some papers about H.C.X. have been published (1)-(8). In these papers, the nitrate, perchlorate or tetranitromethane was selected as oxidizer or positive oxygen balance explosive, the TNT, RDX, HMX or nitromethane as negative oxygen balance explosive, the graphite, aluminum, boron or some hydrocarbons as fuel. The most of particle diam of solid components was over 10μM. The purpose in studying these systems was to obtain higher detonation parameters or higher ability accelerated metal than single explosive. Experimental results indicated that neither the former nor the latter was higher, except the explosion energy of some systems.

Price (2), McGuire (7) and others have pointed out that the diffusion is the control process in detonation reaction of H.C.X., but did not mention it in detail.

Some systematic studies of H.C.X. have been made in our laboratory (9). The bis-(trinitroethyl)nitramine (I) was selected as a typical positive oxygen balance explosive, TNT, TATB, HMX, C, Al, or some hydrocarbons were used to mix with (I). These systems were prepared as superfine particle with mean size about 0.40-1.0μM. The experimental results indicated that the detonation velocity of superfine systems is about 300M/s higher than those of the same systems with coarse particles, and the detonation pressure is also higher.

The present paper is a further study concerning experimental results of H.C.X. composed of (I) and negative OB explosives. The mechanism of detonation reaction of H.C.X. is suggested, some experiments are designed in order to verify the mechanism, the percentage reacted between the components of H.C.X. and the thickness of diffusion layer in detonation region are calculated.

EXPERIMENTAL PROCEDURES AND RESULTS

Procedures. The mean size and particle size distribution are measured by Microscope with 10-20% deviation of reproductive tests and Disc Centrifuger with 5% deviation of reproductive tests, the detonation velocity by Probe-Frequency Meter with 0.3% standard error, the detonation pressure by Air Shock Wave method with 3% standard error, the explosion energy by Calorimeter bomb with 2% standard error.

Results. See Table 1 - Table 5.

Mean size - $\overline{d}$, μM

Particle size distribution - μM, -%

Detonation velocity - D, m/s

Detonation pressure - P, Mbar

Explosion energy - Q, cal/g

DETONATION REACTION OF H.C.X.

Due to the fact that the components of H.C.X are mixed with particles contained in a large number of molecules, i.e., one of 1μM diam particle of (I) contains about 1.6×10^{11} molecules, HMX about 2.0×10^{11} molecules, therefore, the detonation reaction of H.C.X. is more complex than that of single explosives or homogeneous composite explosives.

We suggest the process of detonation reaction of H.C.X. as follows.

a. At first, the components of H.C.X. detonate individually according to its self detonation process.

b. Then the detonation products mix with each other through diffusion. The diffusion starts as soon as the detonation starts, not at C-J plane.

c Mixed products undergo chemical reaction immediately. The velocity of chemical reaction is so fast in comparison with diffusion that it can be considered to complete instantaneously. All energy delivered before C-J plane contribute to the detonation parameters. The detonation reaction is controlled by diffusion.

d. The relationship of detonation characteristics of products (P, T, mass speed, etc.) with diffusion velocity is that the higher detonation characteristics the faster diffusion velocity. The quantity reacted in detonation region is decided by the component whose diffusion velocity of products is slowest or its detonation characteristics are lowest.

e. If the diffusion velocity is δv, the time of detonation reaction is δt, the thickness of diffusion layer $L=\delta v \times \delta t$. L is definite for an explosive, it is only defined by δv and δt in spite of the particle size.

CALCULATION OF R%

Detonation velocity is one of the most simple and the most precise parameters to be determined. Therefore, it is considered that R% is more reasonablely calculated from the effect of different reaction degree of H.C.X. on D. The standard error of D measured in our laboratory is about 30 m/s, the effect of which on R% is about 5%. The procedure selected for calculating R% must be controlled within the measurement error.

Through the comparison of several calculating methods of D, we selected the Nitrogen Equivalent Equation (10).

Nitrogen Equivalent Equation is an empirical formula given by Y. Guo in 1964 for calculating D. Later, Zhang Housheng (II) developed it for calculating P. In designing this equation, the effects of both energy and characteristics of products on D are considered. Because the effect of energy on D is not very sensitive, therefore the formation energy of explosive is neglected. This simplification is satisfactory for most explosives, but a large deviation appears when the formation energy is very high or very low.

The effect of neglecting formation energy on R% can be eliminated by using the Nitrogen Equivalent Equation corrected by measured D of single explosives which are the components of H.C.X. Calculated results are shown in Table 6.

The Nitrogen Equivalent Equation and calculating method of R% are described in the appendix of this paper.

CALCULATION OF THICKNESS OF DIFFUSION LAYER

The thickness of diffusion layer of H.C.X. (L) is calculated by the following equation. The results are listed in Table 6.

TABLE 1

Performances of (I)

Formula	M. P. °C	Sp.Gr. g/cm^3	D/ϱ_o	P/ϱ_o	Q
0_2N-N-$(CH_2C(NO_2)_3)_2$	95.0	1.97	8554/1.885	35.8/1.927	1303

TABLE 2

Detonation parameters of explosives

Explosive	D/ϱ_o	P/ϱ_o	Q
TNT	6880/1.590	19.0/1.64	987
TATB	7582/1.855	25.9/1.85	770
HMX	8868/1.829	37.3/1.847	1346

TABLE 3

Particle size of H.C.X.

Serial No.	Composition Wt.%	$\bar{d}$	Distribution			
			<0.5	0.5−1.0	1.0−1.5	>1.5
1	(I) 81.8/TNT 18.2	0.97	9	44	40	7
2	(I) 81.8/TNT 18.2	51×5	—	—	—	—

(by Microscope)

TABLE 4

Particle size of H.C.X.

Serial No.	Composition Wt. %	$\bar{d}$	Distribution						
			0.14 −0.19	0.19 −0.30	0.30 −0.50	0.50 −1.06	1.06 −1.43	1.43 −2.03	2.03 −2.73
3	(I) 77/TATB 23	0.44	18.2	29.0	28.3	19.8	2.8	1.5	0.4
4	(I) 57/HMX 43	0.73	0.33 −0.48	0.48 −0.75	0.75 −1.00	1.00 −1.41	1.41 −1.88	1.88 −3.26	
			33.7	34.6	15.0	10.8	4.3	1.6	

(by Disc Centrifuger)

TABLE 5

Performances of H.C.X.

Serial No.	Composition Wt.%	$\bar{d}$	D/ϱ_o	P/ϱ_o
1	(I) 81.8/TNT 18.2	0.97	8432/1.792	30.6/1.792
2	(I) 81.8/TNT 18.2	51×5	8098/1.792	28.6/1.735
3	(I) 77/TATB 23	0.44	8686/1.881	40.3/1.876
4	(I) 57/HMX 43	0.73	9046/1.883	39.6/1.878

TABLE 6
The R% and L

Serial No.	Composition Wt.%	d	D/ϱ_0	R%	L
1	(I) 81.8/TNT 18.2	0.97	8432/1.792	41.3	0.10
2	(I) 81.8/TNT 18.2	51×5	8098/1.792	0.0	—
3	(I) 77/TATB 23	0.44	8686/1.881	41.0	0.09
4	(I) 57/HMX 43	0.73	9046/1.883	50.8	0.15

$$R\% = \frac{100\varrho_X \cdot \frac{\pi}{6} \cdot \sum_{i=1}^{n} P_i[d_i^3-(d_i-2L)^3]}{\varrho_x \cdot \frac{\pi}{6} \cdot \sum_{i=1}^{n} P_i d_i^3}$$

$$= \frac{100 \sum_{i=1}^{n} P_i[d_i^3-(d_i-2L)^3]}{\sum_{i=1}^{n} P_i d_i^3} \quad (1)$$

where

ϱ_X= Specific Gravity of H.C.X.

P_i = The percentage of i particle

d_i = The diam of i particle, μM

L = μM

THE VERIFICATION OF DIFFUSION CONTROL

In terms of the mechanism of detonation reaction described above, diffusion is the control process, reacted quantity is decided by the component of the lowest diffusion velocity. Some experiments are designed for verifying the mechanism.

a. The systems listed in Table 6 are zero OB. In these cases, the R% is identical for (I) and negative OB explosive. As for a negative OB system composed of lower (I) and higher TNT content than that of zero OB. In detonation reaction of H.C.X., when the particle size of both systems is identical, the R% of (I) in both systems must be the same. If the detonation reaction of H.C.X. is controlled not only by diffusion but also by the chemical reaction of products, the R% of (I) in negative OB system would be higher than that of zero OB.

Another system is prepared, in which the higher (I) and lower content TNT are contained than that of zero OB. As the same reason, the R% of TNT in positive system ought to identify with that of zero OB.

b. The particle size of (I) and negative OB explosive is nearby, which are contained in same system listed in Table 6. When superfine (I) is mixed with coarse HMX, in terms of the detonation mechanism of H.C.X., the R% is decided by coarse HMX. It is because the quantity diffused of coarse particle is less than that of the fine one. In consequence, there is insufficient diffusion quantity of HMX products to react with that of (I).

The results listed in Table 7 show that the R% of (I) in negative OB and TNT in positive OB systems are identical with that of zero OB. The deviation of both is within the experimental error. But the R% of TNT in former case or (I) in latter case is much lower than that of zero OB. The R% of the system composed of superfine (I) and coarse HMX is close to the R% of that system with coarse of both (I) and HMX, and much lower than that of superfine one.

From these results it is shown that the detonation mechanism of H.C.X. described above is reasonable.

DISCUSSION

We assume L=0.10μM, from equation (1) the relationship of R% with particle size can be calculated. The results are shown in Table 8. It can be seen that the R% depend strongly on the particle size. If particle size is larger than 10μM, the R% will be smaller than the effect of experimental error on R%.

According to the detonation mechanism of H.C.X., the R% is controlled by the component with the lowest detonation characteristics. The detonation characteristics of nitrate and perchlorate are very low, when they are used as an oxidizer of H.C.X. must be prepared a system with very fine particles ($<<1\mu$M).

TABLE 7
Verification of Detonation Mechanism

Serial No.	Composition Wt.%	OB%	$\overline{d}$	D/ϱ_0	R%	
					(I)	−OBX
1	(I) 81.8/TNT 18.2	0	0.97	8432/1.792	41.3	41.3
5	(I) 60/TNT 40	−19.6	0.97	8150/1.763	43.8	14.6
6	(I) 94/TNT 6	+11.1	0.97	8470/1.846	10.4	36.2
7	(I) 57/HMX 43	0	*	8710/1.846	12.8	12.8

* $\overline{d}$ - (I), 1.21 μM, by Disc Centrifuger
- HMX, 10 μM, by Microscope
$\overline{d}$ - Serial No. 1,5 and 6 all by Microscope

TABLE 8
Relationship of R% with Particle Size
($L=0.10\mu M$)

d	0.2	0.3	0.5	1.0	3.0	5.0	10	30
R%	100	96.3	78.4	48.8	18.7	11.5	5.9	2.0

It is worth pointing out that some investigators only take notice of the particle size of positive OB explosive or oxidizer and neglect the particle size of other components. This is not suitable in studying H.C.X.

SUMMARY

The mechanism of detonation reaction in heterogeneous composite explosive is suggested and some experiments are designed in order to verify the mechanism. The reacted percentage and the thickness of diffusion layer in detonation region of some systems composed of bis(trinitroethyl)nitramine and TNT, TATB or HMX are calculated.

REFERENCES

1. A. Ya. Apin, I.M. Voskoboinikov, G.S. Sonova PMTF No. 5, 115 (1963).
2. D. Price, A.R. Clairmont, Jr., J.O. Erkman, and D.J. Edwards, "Ideal Detonation Velocity of Ammonium Perchlorate and Its Mixture with H.E.," NOLTR 68-182, AD 683298.
3. M. Finger, H.C. Hornig, E.L. Lee, and J.W. Kuty, Proc. Fifth Symposium (Intl) on Detonation, p. 137, 1970.
4. D. Price. A.R. Clairmont, Jr. J.O. Erkman, Combustion and Flame 17, 323 (1970).
5. D. Price, A.R. Clairmont, Jr., J.O. Erkman, Ibid 20, 389 (1973).
6. H. Moulard, C. Fauguignon, M. Lichtenberger and J.M. Lomard, H.D.P. Symposium Behavior of Dense at High Dynamic Pressure, Paris, pp. 27-31, 1978, UCRL-Trans-11405.
7. R.R. McGuire & D.L. Ornellas, Propellants and Explosives, 4, No. 2 23 (1979).
8. M.M. Stinecipher, Proc. Seventh Symposium (Intl) on Detonation p. 733, 1981.
9. Guo Yuxian, Peng Guoshu, Song Jialiang Zou Quanqing, Wang Aiqin, Xu Laibin, and Zeng Min, "The experimental Study of Heterogeneous composite Explosives," Oct. 1983. (Unpub.).
10. Guo Yuxian, "The Relationship of Detonation Velocity with Detonation Products and Research of CHNO High Explosive" Oct. 1964 (unpub.), Guo Yuxian and Zhang Housheng, Explosion and Shock Waves, 3, No. 3,56 (1983) (in Chinese).
11. Zhang Housheng, Ibid, 4, No. 2, 79 (1984).

APPENDIX

Nitrogen Equivalent Equation and Calculation Method of R%.

The Nitrogen Equivalent Equation is as follows:

$$D=(690+1160\varrho_o)\cdot\Sigma N \qquad \text{(A-1)}$$

$$\Sigma N=\frac{100}{M}\Sigma X_i N_i \qquad \text{(A-2)}$$

where

D - Detonation velocity, m/s
ϱ_o - Charge density, g/cm^3
M - The weight of reactants, g
X_i - Gram mol numbers of i product
N_i - Nitrogen Equivalent coefficient of i product

The Nitrogen Equivalent coefficients are shown in Table A-1.

TABLE A-1
The Value of N_i

product	H_2O	CO	CO_2	C	O_2	N_2
N_i	0.54	0.78	1.35	0.15	0.5	1

The rule decided products is that the oxygen in explosive molecule first react with hydrogen to form H_2O, then with carbon to form CO, then with CO to form CO_2. If oxygen is insufficient to transfer all carbon into CO, remaining carbon exists as C. If all fuels are oxidized completely, oxygen still remains, it exists as O_2. All nitrogens contained in explosive molecule exist as N_2.

Example 1.

Calculate D of TNT, ϱ_o=1.59

$C_7H_5N_3O_6=2.5H_2O+3.5CO+3.5C+1.5N_2$

$\Sigma N=100(2.5\times0.54+3.5\times0.78+3.5\times0.15+1.5\times1)/227=2.686$

$D=(690+1160\times1.59)\times2.686=6815$ (m/s).

Example 2.

Calculate D of (I), ϱ_o=1.885

$C_4H_4N_8O_{14}=2H_2O+4CO_2+4N_2+2O_2$

$\Sigma N=100(2\times0.54+4\times1.35+4\times1+2\times0.5)/388=2.959$

$D=(690+1160\times1.885)\times2.959=8512$ (m/s).

Calculation of R%.

a. Calculate ΣN_i of single explosives by (A-2).

Substitute measured D into (A-1) to obtain ΣN_{im}.

Let $\Delta N_i=\Sigma N_{im}-\Sigma N_i$ (A-3)

b. Substitute measured D of H.C.X. into (A-1) to obtain ΣN_{HCXm}.

c. Suppose the components of H.C.X. are unreacted in detonation region to obtain ΣN_O from (A-2).

d. Suppose the components of H.C.X. react completely in detonation region, from (A-2) obtain ΣN_{100}.

e. Let $\Sigma N_{Oc}=\Sigma N_O+\Sigma P_i(\Delta N_i)$, (A-4)

$\Sigma N_{100c}=\Sigma N_{100}+\Sigma P_i(\Delta N_i)$, (A-5)

f. $$R\%=\frac{100(\Sigma N_{HCXM}-\Sigma N_{Oc})}{\Sigma N_{100c}-\Sigma N_{Oc}} \qquad \text{(A-6)}$$

Because the plot of R% against ΣN is a very fine straight line, thus the calculation of R% can be simplified as (A-6).

P_i-Percentage of i component.

Example 3.

Calculate R% of (I) 57/HMX 47, measured D=9046, ϱ_o=1.883.

From (A-1), (A-2) and (A-3), the relevant values of ΣN are obtained respectively, as shown in Table A-2.

TABLE A-2
Calculated Value of ΣN

Composition Wt. %	D/ϱ_o	ΣN	ΣN_m	ΔN
HMX	8868/1.829	3.135	3.154	0.019
(I)	8554/1.885	2.959	2.974	0.015
(I) 57/HMX 43	9046/1.883	—	3.147	—

From A-2 calculate ΣN_O and ΣN_{100}

$C_4H_4N_8O_{14}+C_4H_8N_8O_8=6H_2O+4CO+4CO_2+8N_2+2O_2$

$\Sigma N_O=100(6\times0.54+4\times0.78+4\times1.35+8\times1+2\times0.5)/684=3.035$

$C_4H_4N_8O_{14}+C_4H_8N_8O_8=6H_2O+8CO_2+8N_2$

$\Sigma N_{100}=100(6\times0.54+8\times1.35+8X1)/684=3.222$

ΣN_O and ΣN_{100} are substituted individually into (A-4) and (A-5) to obtain ΣN_{Oc}, ΣN_{100C}.

ΣN_{OC}, ΣN_{100C} and ΣN_{HCXm} are substituted into (A-6) to calculate R%.

$\Sigma N_{OC}=3.035+0.57\times0.015+0.43\times0.019$
$=3.052$

$\Sigma N_{100C}=3.222+0.57\times0.015+0.43\times0.019$
$=3.239$

$R\%=100(3.147-3.052)/(3.239-3.052)=50.8\%$

DISCUSSION

HAROLD GRYTING, Southwest Research Institute

BTNEN was characterized by the NOL in the late 40's and early 50's. Several years later we at NWC, China Lake, California, reinvestigated it in mixtures, some of which on impact measurements detonated at 2 cm at which point we elected to halt the investigation.

REPLY BY GUO YUXIAN

To study the detonation behavior is the principal purpose of our laboratory for investigating H.C.X. Its mechanical shock sensitivity was not studied systematically, but very high sensitivity phenomenon was not found in our research systems.

I think that some mixtures composed of oxygen rich compounds and some fuels have lower compatibility which is one of the causes of leading to high mechanical shock. The measuring values of mechanical shock not only depend on the characteristic of explosive but also depend on the particle size, crystal form and measuring method. Therefore, it sometimes cannot represent the actual sensitivity of explosive.

The high mechanical shock phenomenon proposed by Dr. H. Gryting is worthy of note in studying H.C.X.

DISCUSSION

DR. ALLAN W KING, Space Research Corporation, Brussels, Belgium

1) What methods are used to ensure adequate mixing of your very sensitive oxygen rich component (nitramine derivative) with any of the other solid explosives such as TNT, HMX or TATB without causing accidental initiation?

2) How did you prepare your nitramine derivative?

3) What would be the effect of segregation upon the experimental results?

4) How can you ensure adequate mixing without segregation?

5) Would the results be different if the two components were dissolved in similar solvents and then coprecipitated?

REPLY BY GUO YUXIAN

A method to grind and mix the components of H.C.X. has been developed by our laboratory. It is more simple and more safe. But we still prepare H.C.X. in segregation to ensure against any accidents.

To dissolve the components of H.C.X. in solvent then to coprecipitate it have been tested in our laboratory, but did not obtain any satisfactory results. Because the desired results of particle size and distribution were not achieved. I think that it would be one of the methods of H.C.X. preparation, if study it in detail.

COMPOSITE EXPLOSIVES FOR METAL ACCELERATION: THE EFFECT OF DETONATION TEMPERATURE *

Raymond R. McGuire and Milton Finger
Lawrence Livermore National Laboratory
Livermore, California

Our previous work in the area of composite explosives (1, 2) has emphasized the necessity of small particle size and intimate contact between fuel and oxidizer in obtaining prompt performance from fuel/oxidizer mixtures. This work has provided a basis for our definition of a composite explosive as "an explosive system that requires the transport, mixing and subsequent reaction of the initial decomposition products of the system components in order to achieve the predicted detonation performance." In this paper we present our general working model and experimental evidence demonstrating the importance of detonation temperature in achieving performance from composite explosives in metal acceleration experiments.

INTRODUCTION

In metal acceleration applications, any momentum that is not delivered to the metal wall in a few microseconds of detonation product expansion is not in fact, delivered to the wall at all. (The exact amount of time available for momentum transfer depends on such things as the impedance match of the explosive products and the metal wall; i.e., density, sound speed, thickness, and the tamping of the explosive system.) Composite explosives have not generally been used effectively for this application because their potential energy is transformed over a very long time period, i.e., 10's of microseconds.

Finger, et al. (1) have shown the requirement for minimal particle size if performance, as measured by the standard cylinder test, is to be obtained. This shows the limiting effect of mass transport in composite explosive performance. In a series of detonation calorimetry experiments (2) using isotopically labeled explosive, we have shown that material transport is not a consideration in the detonation of a monomolecular nitroaliphatic explosives. However, it is a severe limitation in the case of amatol, a composite explosive. We have further substantiated this by subsequent experiments using mixtures of detonable high explosives.

MIXING EXPERIMENTS

Using our detonation calorimetry technique (3) we have investigated the mixing phenomenon as it applies to a composite consisting of two self-detonating explosives (see Figure 1). In one experiment, Bitetrazole (BTZ) ($C_2H_2N_8$), an explosive that contains no oxygen, was intimately mixed with Hydrazinium nitrate (HN) ($H_5N_3O_3$), a non-carbon containing explosive. Neither of the individual components can form carbon oxides as detonation products. A carbon monoxide and water balanced mixture of BTZ and HN was pressed without binder to 95% of TMD and detonated. The experimental product composition showed that 0.143 moles of carbon oxides (per mole of explosive) were formed compared to 0.302 expected. This amounts to ~47% of the theoretical mixing. We used the TIGER

*Work performed under the auspices of the U.S. Department of Energy by the Lawrence Livermore National Laboratory under Contract W-7405-Eng-48.

This work was supported, in part, by the U.S. Naval Surface Weapons Center, White Oak, Silver Spring, MD.

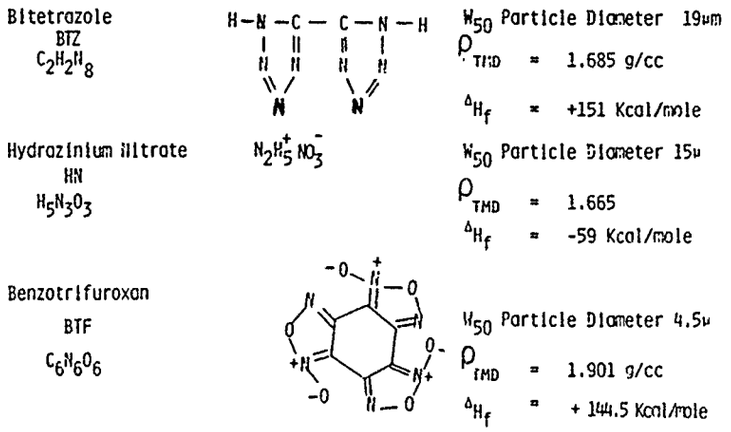

Fig. 1. Explosives used in detonation calorimetry mixing experiments

computer code with a revised BKW equation of state (BKWR) (4) that has been calibrated to accurately model the results of detonation calorimetry to obtain the theoretical results.

Similar results were obtained in a second experiment where BTZ was mixed with Benzotrifuroxan (BTF) ($C_6N_6O_6$). Neither of these individual components can form water as a detonation product. In this case, the mixture was 50% by weight of each component. Again, experimental results show that only 46% of the theoretical amount of water is formed.

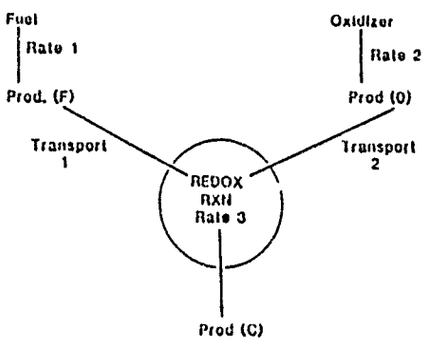

Fig. 2. Composite explosives working hypothesis basic model

THE WORKING MODEL

We have adopted a working hypothesis (Fig. 2) for a composite explosive. Here we view the separate components, i.e., fuel, oxidizer, etc. as reacting independently to their separate decomposition products. Whether these are the final decomposition products or a set of intermediate products is undefined. This initial decomposition is followed by a transport process that mixes the individual decomposition products. Then, these products react with each other to produce the expected performance of the composite HE. Assuming that the decomposition of self detonating materials is sufficiently rapid, the previously cited experiments show that even in the case of a reasonably intimate mixture of small particles of detonable explosives, the transport and mixing may not be sufficiently rapid to insure ideal performance in cylinder test times of interest.

THE EFFECT OF DETONATION TEMPERATURE

If we assume that the transport mechanism is primarily one of diffusion, we can see from the governing equation that

$$D=D_o\,(T/T_o)^n\ \ (P_o/P)$$

(where D is the diffusion constant at temperature (T) and pressure (P) and n~2) the time one has to obtain the energy from a composite explosive is a strong function of the detonation temperature. We have explored through cylinder tests the effect of changing the temperature of detonation in three separate composite explosive systems:

a. The system HMX - TATB - BTF

TABLE 1

RX-36 Formulations to Investigate Effects of Detonation Temperature and Volume of Gaseous Detonation Products on Cylinder Test Performance

Formulation	Composition[a] HMX/TATB/BTF	V_{CJ}[b, c]	T_{CJ}[b, d]	γ_{CJ}[b]	ϱ[e] g/cc	%TMD[e]	D_{CJ}[f]
RX-36-AA	1-1-1	29.3	3130	3.07	1.843	96.4	8.41
RX-36-AB	0-1-1	26.7	3130	3.06	1.855	96.6	8.15
RX-36-AC	4-1-1	31 7	3130	3.09	1.817	95.3	8.72
RX-36-AD	1-3-1	29.2	2775	3.15	1.829	95.2	8.04
RX-36-AE	1-0-1	29.6	3590	2.98	1.797	94.5	8.44
RX-36-AF	1-1-0	31.6	2750	3.17	1.840	95.9	8.30
RX-36-AG	1-1-3	27.5	3520	2.98	1.838	96.3	7.89

a. Ratio of moles of component explosives.
b. Calculated using BKWR Equation of state of TIGER code all calculations at ϱ=1.85.
c. Volume of gaseous products at CJ in moles of gas per Kg of Explosive.
d. Detonation temperature in °K.
e. Density and % TMD of pressings used in cylinder experiments.
f. Experimental detonation velocity from cylinder tests in mm/μs.

b. The system TATB - Ammonium Perchlorate (AP)

c. The system Tetranitromethane - Carbon

THE SYSTEM HMX - TATB - BTF.

We have devised a system of explosives that allows us to investigate the effect of detonation temperature while holding other parameters essentially constant. The properties of this system, which we term RX-36 (AA to AG) are summarized in Table 1. By choosing the proper mole ratios of HMX, BTF and TATB, it is possible, theoretically, to hold the volume and, within limits, the nature of the detonation products essentially constant while varying the detonation temperature, or conversely, to maintain a constant detonation temperature while varying the gas product volume. Since the densities of the three components are very similar, the effect of density variation can be eliminated.

The cylinder test results are summarized in Table 1 and Figures 3-5. These results clearly show that increasing the detonation temperature gives increased cylinder test performance even at relatively early time, i.e., small expansion volumes, and far outweighs the effect of product volume. Figure 5 especially shows the increased performance with increasing temperature even though the volume of gaseous products is actually decreasing. It should be noted that the predicted decrease in gamma (γ) with increasing detonation temperature is shown by increasing positive slope of the cylinder isentropes as detonation temperature increases.

While we did not perform extensive detonation calorimetry testing on these formulations, we did compare the products obtained experimentally with those predicted using a BKWR equation of state in the TIGER (7) code for two of the formulations, viz. RX-36-AA and RX-36-AF. The agreement between the experimental and predicted products was quite good.

THE SYSTEM TATB – AMMONIUM PERCHLORATE.

In this series of experiments we have used a formulation of TATB and ammonium perchlorate (AP) balanced to CO. The AP was milled and had a median particle diameter of 7 microns as measured by air permeametry. The particle size of the TATB varied in different experiments between $\sim$7 micron and $\sim$45 micron median particle diameter. The temperature of the detonation was increased in one case by adding four percent (4 w%) of the high temperature explosive benzotrifuroxan (BTF) and in the second case by

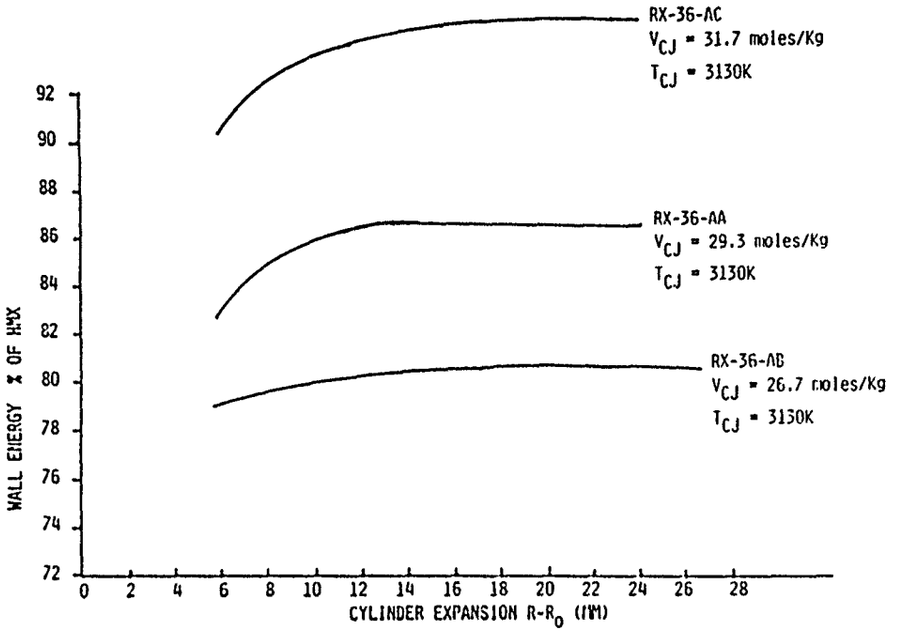

Fig. 3. Cylinder Test Performance: Temperature at CJ (T) ∼ Constant, Gas Volume at CJ (V) Increasing

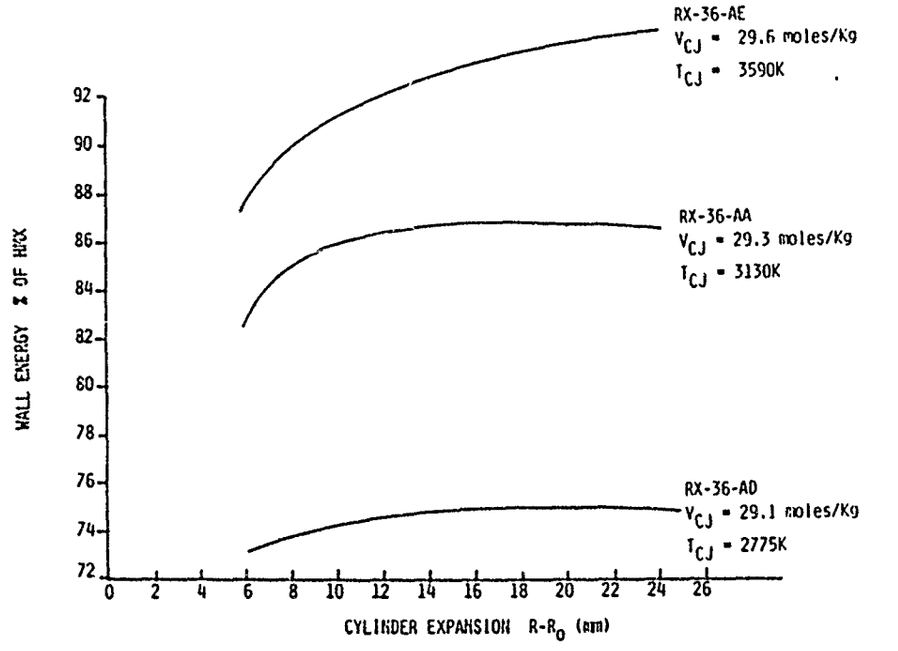

Fig. 4. Cylinder Test Performance: Gas Volume at CJ (V) ∼ Constant, Temperature at CJ (T) Increasing

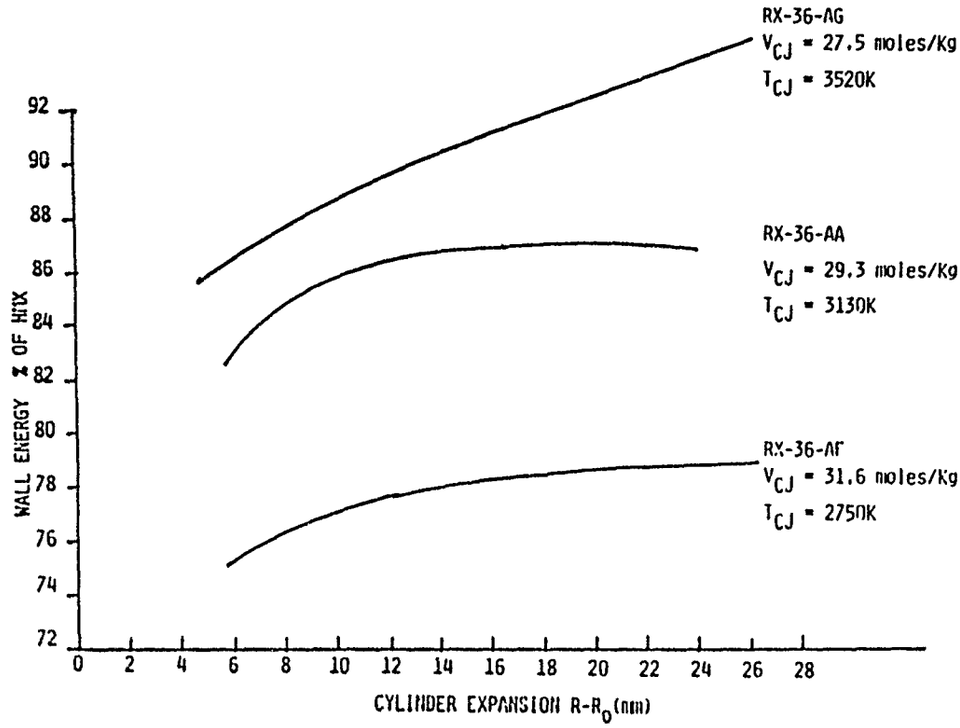

Fig. 5. Cylinder Test Performance: Temperature at CJ (T) Increasing, Gas Volume at CJ (V) Decreasing

adding four percent of 5 micron aluminum powder. The results are shown in Figure 6. Here we see that the use of AP with standard particle size TATB in fact lowered the performance as compared to TATB alone. The same formulation using milled TATB (7 μm) is essentially equivalent to TATB itself. However, the addition of 4% BTF greatly increased the performance of this TATB/AP composite. The addition of 4 w% aluminum powder likewise increased the cylinder test performance, although not as much at low expansion as the BTF. It is interesting to note the lower gamma of the system with the BTF added and especially of the aluminized composite. These indicate much higher temperatures than the parent TATB/AP composite.

THE SYSTEM TNM – CARBON

The third system we investigated uses tetranitromethane (TNM) as a liquid oxidizer for the fuel, carbon. The carbon used was graphite of high purity (99.99+) (6) having no particles greater than 44 μm. It was formulated to CO_2 balance with TNM and gelled with an expanded silica (Cab-O-Sil). Figure 7 gives the results of these experiments.

We used the TIGER code to calculate the cylinder test performance of the formulation in one case with the carbon fully reacting and in the second case with the carbon as an inert solid. The experimental result lies between these two bounds, on the lower side but with slightly better performance than TNM alone, which experimental result is also shown. In order to increase the detonation temperature, we lowered the density to about 91% of theoretical by adding microballoons.

This increased the performance by about 5% over the higher density TNM/C formulation. An even greater increase in cylinder performance was obtained by adding about 8 w% aluminum powder (5μm) and adjusting the TNM/Carbon ratio to maintain CO_2 balance. However it is obvious from Figure 7 that the performance, though improved, is still far below that which is theoretically obtainable.

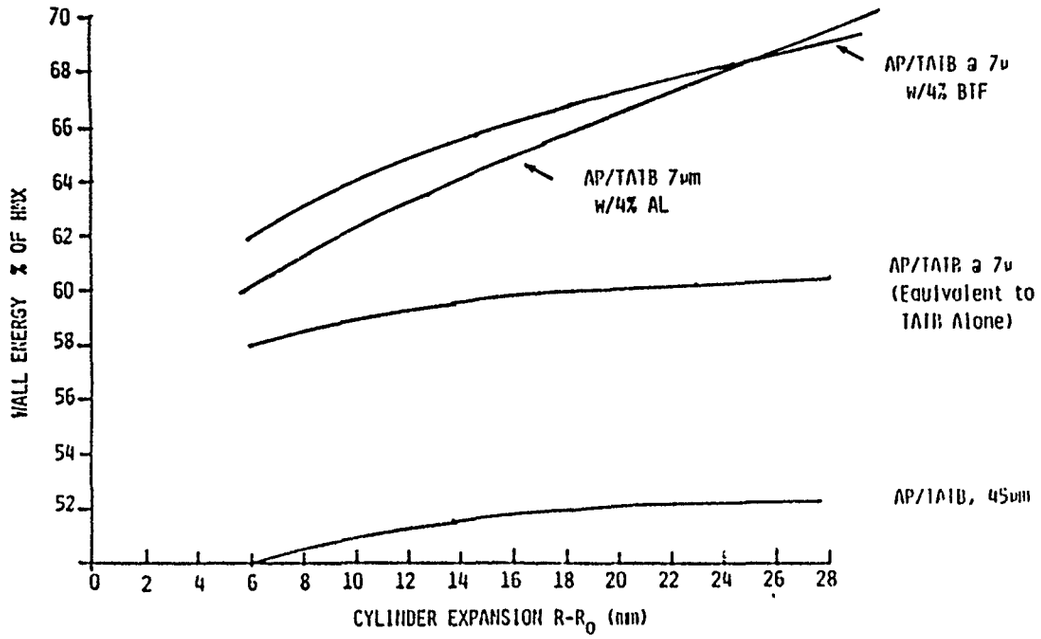

Fig. 6. Raising the detonation temperature, increases the performance, TATB/AP at CO balance

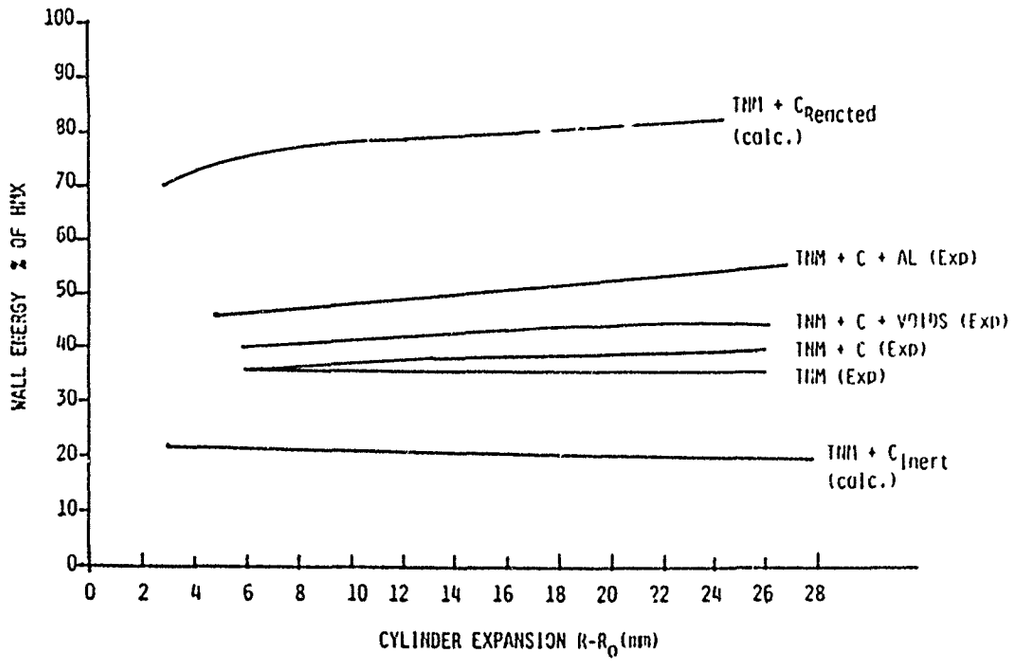

Fig. 7. Raising the temperature of detonation increases the reactivity of solid carbon in a TNM-carbon system

CONCLUSIONS

We have shown experimentally that in composite explosives using carbonaceous fuels (i.e., C, TATB, etc.) increasing the temperature of the detonation is a key element in increasing the delivered energy at low expansion volumes in the divergent geometry of the cylinder test. However, as we have shown previously, decreasing the particle size of the solid components is another key element. Certainly a combination of small particle size ($\sim 1\mu m$) and high detonation temperature is required if anything near the theoretical performance is to be obtained in cylinder type geometries.

We would further contend, that because of the divergent nature of the hydrodynamic flow, inter-molecular chemistry effectively ceases at the sonic plane and that the nature of the isentrope (γ) is set by the state of the products at that point. Thus, the "chemistry" occurring during the cylinder expansion is intramolecular, i.e., bond scission and relaxation processes.

This may well not be true of other geometries or of piston driven detonation. Thus, the performance obtained from a composite explosive will be, among other things, highly geometry and system dependent.

ACKNOWLEDGMENTS

The authors are especially grateful for the support of D. Ornelles (detonation calorimetry and formulation), R. D. Breithaupt (cylinder testing), and F. H. Helm (formulation and cylinder testing).

REFERENCES

1. M. Finger, H. C. Hornig, E. L. Lee, J. W. Kury, "Metal Acceleration by Composite Explosives", Fifth Detonation Symposium, ACR-184 p. 137 (1970).
2. R. R. McGuire, D. L. Ornellas, I. B. Akst, "Detonation Chemistry, Diffusion Control in Non-Ideal Explosives", Propellants and Explosives, *4* No. 2, pp. 23-26 (1979).
3. D. L. Ornellas, J. H. Carpenter and S. R. Gunn, Rev. Sci. Instrum. *37* p. 909 (1966).
4. M. Finger, E. L. Lee, F. H. Helm, B. Hayes, H. C. Hornig, R. R. McGuire, E. Kahara and M. Guidry, "The Effect of Elemental Composition on the Detonation Behavior of Explosives", Sixth Symposium on Detonation, ACR-221, p. 710 (1976).
5. D. L. Ornellas, "Calorimetric Determinations of the Heat and Products of Detonation, October 1961 to April 1982," UCRL-52821, p. 69 April 1982.
6. Purchased from Ultra Carbon Corp., Bay City, MI.
7. W. E. Wiebenson, W. H. Zwisler, L. B. Seely and S. R. Brinkley, Jr., "TIGER Documentation Volume," Stanford Research Institute (prepared for Ballistic Research Laboratory, Aberdeen, Maryland — Contract No. DA-04-200-AMC-3226 (X), Nov. 1968), SRI Publication No. Z106.

DISCUSSION

INDU B. MISHRA, Kanam Associates, Northridge, CA

This is an interesting paper and looks like we are scratching the surface of non-ideal or intermolecular composite explosives. Did you try ultrafine high density diamond — for UF diamond is reasonably cheap.

REPLY BY M. FINGER

In the past we have tried fine particle diamond that was produced by either a shock formation process, or was available as "diamond dust." We found that carbon-graphite was seemingly more reactive than carbon-diamond. However, these experiments were done in an oxidizer system different from TNM.

A MODEL SOLUTION FOR NONIDEAL ONE-DIMENSIONAL DETONATION WAVES

M. Cowperthwaite
SRI International
Menlo Park, California 94025

A model solution for nonideal detonation propagating at constant velocity with the liberation of chemical energy behind the wave front was constructed to demonstrate that the one-dimensional equations of motion admit this type of flow. In this construction, a similarity solution for a reactive Taylor wave was formulated and incorporated into the classical solution for an ideal, unsupported detonation wave. When the polytropic index is specified, this similarity solution contains three parameters that are constrained by two relationships imposed by boundary conditions at the front and the end of the unsteady reaction zone. These relationships and the restrictions they impose on the energy release rate are discussed to demonstrate properties of this type of nonideal detonation, and flow fields of particular solutions are presented to demonstrate the influence of chemical reaction on shock-induced, expanding, unsteady, hydrodynamic flow.

INTRODUCTION

In this paper, we address the problem of one-dimensional, detonation propagating at constant velocity with liberation of chemical energy in the unsteady release wave behind the wave front. Such a detonation is called nonideal because not all the chemical energy liberated is used to support the propagation of the wave.

The present work on this reactive flow problem was undertaken because:

- An understanding of the problem is important for formulating treatments of detonation in composite explosives.
- A previous theoretical approach to the problem (1) concluded that a constant velocity detonation with liberation of chemical energy behind the wave front is unstable.
- Models used in numerical codes (2) to treat liberation of chemical energy behind the wave front are physically unrealistic.

Our approach to the problem was to construct a model solution for such a nonideal detonation wave and thereby demonstrate that the equations of motion admit this type of reactive flow. This model solution demonstrates properties of reactive release waves and provides guidelines for modeling the nonideal detonation process in composite explosives containing components with markedly different reaction rates (3).

Our approach was based on the idea that the classical solution for an ideal unsupported detonation wave (4, 5) can be extended to include a solution for a reactive Taylor wave. We accordingly constructed a model solution for nonideal detonation by patching together solutions for three different types of flow, the first a reactive discontinuity or a steady-state reaction zone, the second a reactive Taylor wave, and the third a nonreactive rarefaction fan.

CONSTRUCTION OF SOLUTION

For the sake of tractability, we assume that the shock-induced flow is adiabatic and inviscid and that the explosive and its reaction products are governed by polytropic equations of state with the same polytropic index. We let t, h, D, u, v, p, c, x, and λ denote time, Lagrange

distance, detonation velocity, particle velocity, specific volume, pressure, sound speed, polytropic index, and extent of reaction, respectively, and we let the subscript o denote the initial condition. Then our solution for nonideal detonation can be constructed from the solutions for the three different types of flow as follows.

(1) Solution for the Wave Front. The wave front can be readily treated as a Zeldovich-von Neumann-Doering wave, but for the sake of simplicity we assume that the reaction time of the reaction supporting wave propagation is zero. In this case, the flow at the wave front is treated as a reactive discontinuity that is governed by the Rankine-Hugoniot jump conditions and satisfies the Chapman-Jouguet (cj) condition $D = u_{cj} + c_{cj}$. The cj parameters are related by the equations $v_{cj} = \varkappa v_o/(\varkappa + 1)$, $c_{cj} = \varkappa u_{cj} = \varkappa D/(\varkappa+1)$, and because of the polytropic assumptions, the detonation velocity is related to the energy liberated in the discontinuity (Q_{cj}) by the equation $D^2 = 2(\varkappa^2-1)Q_{cj}$.

(2) Similarity Solution for the Reactive Taylor Wave. When conditions at the shock front are constant as in the present case, it follows from a previous paper (6) that we can write the similarity solution as

$$\begin{aligned} u &= u_{cj} U(\xi) \\ v &= v_{cj} V(\xi) \\ p &= p_{cj} P(\xi) \\ \lambda &= \Lambda(\xi) \end{aligned} \tag{1}$$

in terms of the similarity parameter

$$\xi = \frac{h/\beta + 1}{t/\alpha + 1} \tag{2}$$

with $\xi^* \leqslant \xi \leqslant 1$. These equations are written so that $\beta/\alpha = D$, that $\xi = 1$ at the wave front where $U(1) = V(1) = P(1) = 1$ and $\Lambda(1) = 0$, and that $\xi = \xi^*$ at the end of the reaction zone where $\lambda = \Lambda(\xi^*) = 1$. Equations (1), (2), and the cj relationships allow us to rewrite the flow equations as

$$\frac{dU}{d\xi} = -\varkappa\,\xi\,\frac{dV}{d\xi} \tag{3}$$

$$\frac{dP}{d\xi} = \xi\,\frac{dU}{d\xi} = -\varkappa\,\xi^2\,\frac{dV}{d\xi} \tag{4}$$

$$(P-\xi^2 V)\,\frac{dV}{d\xi} = \frac{(\varkappa+1)Q}{2\varkappa^2 Q_{cj}}\,\frac{d\Lambda}{d\xi} \tag{5}$$

where Q is the heat liberated by the reaction along a particle path in the rarefaction wave.

It is convenient for formulating a solution to introduce the variable

$$F(\xi) = P - \xi^2 V \tag{6}$$

and express the conservation of mass and momentum by the following equation relating V and F:

$$\frac{dV\,(\xi)^{\frac{2}{\varkappa+1}}}{d\xi} = \frac{(\xi)^{-\frac{2\varkappa}{\varkappa+1}}}{(\varkappa+1)}\,\frac{dF}{d\xi} \tag{7}$$

Equation (7) is obtained by eliminating $dP/d\xi$ between Eq. (4) and the differential equation obtained by differentiating Eq. (6). The function $F(\xi)$ is restricted by boundary conditions at the wave front and the end of the reaction zone. It follows from Eq. (6) that $F(\xi) = 0$ at the wave front where $\xi = 1$ because $P(1) = V(1) = 1$, and it follows from Eqs. (5) and (6) that $F(\xi) = 0$ at the end of the reactive Taylor wave where $\xi = \xi^*$ because $d\Lambda/d\xi = 0$ but $dV/d\xi \neq 0$. A solution to Eqs. (3) through (5) can be constructed when a functional form for $F(\xi)$ is known as follows. Equation (7) is first integrated to obtain an expression for $V(\xi)$, and this expression is then differentiated to obtain the corresponding expression for $dV/d\xi$. Equations (3), (4), and (5) are then integrated to generate the corresponding expressions for U, P and Λ.

The model similarity solution in this paper is based on the simplest expression for $F(\xi)$,

$$F = A(1-\xi)\,(\xi-\xi^*) \tag{8}$$

that satisfies the boundary conditions $F(1) = F(\xi^*) = 0$. In this case, integrating Eq. (7) gives the following expression for V,

$$V = A + B\,(\xi)^{-1} + C\,(\xi)^{-\frac{2}{\varkappa+1}} \tag{9}$$

where $B = A(1+\xi^*)/(\varkappa-1)$ and $C = 1-A(\varkappa+\xi^*)/(\varkappa-1)$, and the corresponding expressions for U, P, and Λ are obtained by integrating Eqs. (3), (4), and (5) as

$$U = 1 + \varkappa\,B \ln \xi + \frac{2C\varkappa}{(\varkappa-1)}\left((\xi)^{\frac{\varkappa-1}{\varkappa+1}} - 1\right) \tag{10}$$

$$P=1 + \varkappa B\,(\xi-1) + C\left((\xi)^{\frac{2\varkappa}{\varkappa+1}} - 1 \right) \qquad (11)$$

$$\begin{aligned} R\Lambda = &-AB\big[(1-\xi)\,(1+\xi^*/\xi) \\ &+ (1+\xi^*)\ln\xi\big] \\ &+ AC\left[\xi^*(1-(\xi)^{-\frac{2}{\varkappa+1}} \right) \\ &+2\,\frac{(1+\xi^*)}{(\varkappa-1)}\,(1-(\xi)^{\frac{\varkappa-1}{\varkappa+1}}) \\ &- \frac{1}{\varkappa}\left(1-(\xi)^{\frac{2\varkappa}{\varkappa+1}} \right) \big] \end{aligned} \qquad (12)$$

with $R = (\varkappa+1)Q/2\varkappa^2 Q_{cj}$.

When $\varkappa$ is specified, this similarity solution contains three parameters, A, ξ^*, and Q/Q_{cj}, whose values define a particular solution. These values cannot be specified arbitrarily, however, because they are constrained by the following relationships determined by conditions at the wave front and the end of the reaction zone:

$$A(1-\xi^*) \leqslant 2 \qquad (13)$$

$$\begin{aligned} \frac{(\varkappa+1)Q}{2\varkappa^2 Q_{cj}} = &-AB[2\,(1-\xi^*) \\ &+ (1+\xi^*)\ln\xi^*\,] \\ &+ AC\,\frac{(\varkappa+1)}{\varkappa(\varkappa-1)}\,\{\,[1-(\xi^*)^{\frac{2\varkappa}{\varkappa+1}} \\ &+ \varkappa\xi^*[1-(\xi^*)^{-\frac{2\varkappa}{\varkappa+1}}]\,\} \end{aligned} \qquad (14)$$

Equation (13) is obtained by subjecting Eq. (9) to the condition that $dV/d\xi \leqslant 0$ when $\xi = 1$, and Eq. (14) is obtained by subjecting Eq. (12) to the condition that $\Lambda(\xi^*) = 1$ when $d\Lambda/d\xi = 0$ and $\xi = \xi^*$. Values of A, ξ^*, and Q/Q_{cj}, compatible with Eqs. (13) and (14) must therefore be chosen before we can calculate the flow fields for a particular solution.

(3) Solution for the Nonreactive Rarefaction Fan. The solution for the rarefaction fan adjacent to the reactive Taylor wave is written as

$$\begin{aligned} u &= u_{cj}U(\xi^*)U_1(\eta) \\ v &= v_{cj}V(\xi^*)V_1(\eta) \\ p &= p_{cj}P(\xi^*)P_1(\eta) \end{aligned} \qquad (15)$$

in terms of the similarity parameter

$$\eta = \frac{h/\beta}{\xi^*\,(t/\alpha - \overset{\times}{\xi})} \qquad 0 \leqslant \eta \leqslant 1 \qquad (16)$$

with $\overset{\times}{\xi} = (1-\xi^*)/\xi^*$. These equations are written so that $U_1(1) = V_1(1) = P_1(1) = 1$. Integrating the differential equations obtained by rewriting the flow equations with Eqs. (15) and (16) leads to the following expressions for u, v, and p in the fan:

$$u=u_{cj}U(\xi^*)+\frac{2\varkappa\,u_{cj}}{(\varkappa-1)}\,\frac{P(\xi^*)}{\xi^*}\,[\eta^{\frac{\varkappa-1}{\varkappa+1}}-1] \qquad (17)$$

$$v = v_{cj}V(\xi^*)\,\eta^{-\frac{2}{\varkappa+1}} \qquad (18)$$

$$p = p_{cj}P(\xi^*)\,\eta^{\frac{2\varkappa}{\varkappa+1}} \qquad (19)$$

We have constructed a model solution for one-dimensional detonation with liberation of chemical energy behind the wave front. Properties of this solution and properties of the flows fields of particular solutions will now be discussed to demonstrate significant features of this type of reactive flow.

PROPERTIES OF THE MODEL SOLUTION

The first property to note is that our model solution for nonideal detonation reduces to the classical solution for a nonreactive rarefaction wave behind a reactive discontinuity when we set $\partial\Lambda/\partial t = \partial\Lambda/\partial\xi = 0$. That this is the case, can be seen by setting A = B = 0 and C = 1 in Eqs. (9), (10), (11), and (12). Furthermore, when A=0 and $\xi^* = 1$, Eqs. (15) through (19) reduce to the classical solution for the Taylor wave. Another interesting property of the solution follows from the fact that it is a similarity solution. Because $(\partial p/\partial h)_u = (\partial v/\partial h)_u = 0$, the flow of all the particles entering the wave is represented by a single path in the (p-u) plane and by a single path in the (p-v) plane. For this reason we call our nonideal detonation an ideal nonideal detonation.

Other significant features of our solution follow from the relationships among the parameters ξ^*, A, and Q/Q_{cj}, defined by Eqs.

(13) and (14). A consideration of these relationships when $\varkappa$ is specified leads to the conclusion that there is a maximum value of A, $[\hat{A}(\xi^*)]$, and a maximum value of Q/Q_{cj} $[\hat{Q}(\xi^*)/Q_{cj}]$ associated with a given value of ξ^*. Thus, A and Q/Q_{cj} are functions of ξ^* that are constrained to satisfy the conditions $0 < \hat{A} \leqslant \hat{A}(\xi^*)$ and $0 < Q/Q_{cj} \leqslant \hat{Q}(\xi^*) / Q_{cj}$. In addition, the values of $\hat{A}(\xi^*)$ and $\hat{Q}(\xi^*)/Q_{cj}$ increase as the value of ξ^* decreases. Thus, the amount of energy that can be liberated along a particle path in our reactive Taylor wave is limited by the value of ξ^*, and along a particular particle path more energy can be liberated if the liberation time is longer. Equations (13) and (14) were used to quantify this behavior, when $\varkappa=3$, as follows. First, these equations were rewritten as

$$\hat{A}\,(\xi^*) = \frac{2}{(1 - \xi^*)} \tag{20}$$

and

$$\frac{\hat{Q}\,(\xi^*)}{Q_{cj}} = -\frac{9}{4}\,\hat{A}^2 \left[(1+\xi^*)^2 \ln \xi^* + 2\,(1-(\xi^*)^2) + \tfrac{2}{3}\,(3+\xi^*)\,(1-(\xi^*)^{1/2})^3 \right] + 3\,\hat{A}\left[(1-(\xi^*)^{1/2})^3\right] \tag{21}$$

and values of ξ^* were chosen in the range $0.3 \leqslant \xi^* \leqslant 0.8$ because the first term on the right-hand side of Eq. (21) is essentially zero when $\xi^* = 0.9$ and is positive when $\xi^* \leqslant 0.9$. Then Eq. (20) was used to calculate the value of $\hat{A}(\xi^*)$ for a given value of ξ^*, and Eq. (21) was used to calculate the corresponding value of $\hat{Q}(\xi^*) / Q_{cj}$. The results of these calculations for $\varkappa = 3$ are given in Table 1. Examination of these results shows that a particle can liberate the same amount of energy in the reactive rarefaction as in the wave front when $\xi^* = 0.3$ and can liberate a significant fraction of the energy liberated in the wave front when $\xi^* \approx 0.5$.

Particular solutions with $\varkappa=3$ will now be used to demonstrate more detailed properties of our model nonideal detonation. It is convenient to denote a particular solution by the values of the set of parameters ($\varkappa$, ξ^*, A, Q/Q_{cj}) and the corresponding ideal solution by the set ($\varkappa$, $\xi^* = 1$, $A = 0$). We first consider the

TABLE 1

Values of ξ^*, $\hat{A}\,(\xi^*)$, and $\hat{Q}(\xi^*)/Q_{cj}$ for model nonideal detonations with $\varkappa = 3$

ξ^*	$\hat{A}\,(\xi^*)$	$\hat{Q}\,(\xi^*) / Q_{cj}$
0.8	10.00	0.036
0.7	6.67	0.091
0.6	5.00	0.185
0.5	4.00	0.336
0.4	3.34	0.580
0.3	2.86	1.000

solution ($\varkappa=3$, $\xi^*= 0.5$, $A = 3.05$, $Q/Q_{cj}=0.25$). Nondimensional pressure (p/p_{cj}) versus nondimensional distance (h/β) profiles for this nonideal detonation and the corresponding ideal detonation are shown in Fig. 1. The flow in the nonideal detonation is represented by RDZIO and the flow in the ideal detonation by RDIO. In both cases, RD represents the reactive discontinuity at the wave front. In the nonideal detonation, DZ represents the reactive, nonisentropic, expansile flow, and ZIO represents the ensuing isentropic, expansile flow. In the ideal detonation, DIO represents the isentropic, expansile flow behind the wave front. The influence of the exothermic reaction on the pressure field is clearly seen by comparing the profiles RDZIO and RDIO. At a given time, t/α, the pressure at a given point, h/β, in the region $0 < h/\beta < t/\alpha$, is higher in the nonideal detonation than in the ideal detonation. Furthermore, the second derivative of p with respect to h is negative, $(\partial^2 p/\partial h^2)_t < 0$, where the flow is reactive, but is positive, $(\partial^2 p/\partial h^2)_t > 0$, where it is nonreactive. There is a discontinuity in $(\partial p/\partial h)_t$ at the end of the reaction zone DZ where $\xi = \xi^*$ and the flow becomes isentropic. Thus, the end of the reaction zone lies on a characteristic in the (t-h) plane. It also follows from the relationship $-v_o^2(\partial^2 p/\partial h^2)_t = (\partial^2 v/\partial t^2)_h$, derived from the flow equations, that $(\partial^2 v/\partial t^2)_h > 0$ where the flow is reactive but that $(\partial^2 v/\partial t^2)_h < 0$ where it is nonreactive.

Figure 2 shows nondimensional particle velocity (u/u_{cj}) versus nondimensional distance (h/β) profiles corresponding to the pressure profiles presented in Fig. 1 for the solution ($\xi^* = 0.5$, $A = 3.05$, $Q/Q_{cj} = 0.25$). However, in contrast to Fig. 1, only the particle velocity

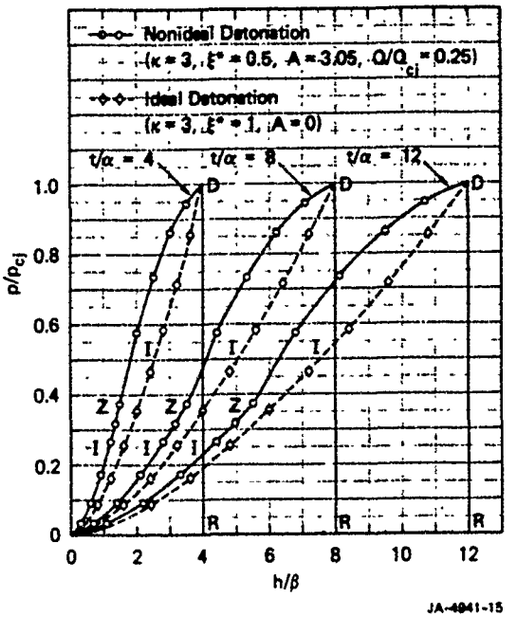

Fig. 1. Nondimensional pressure (p/p_{cj}) versus nondimensional distance (h/β) profiles for a nonideal detonation and the corresponding ideal detonation at the nondimensional times t/α = 4, 8 and 12

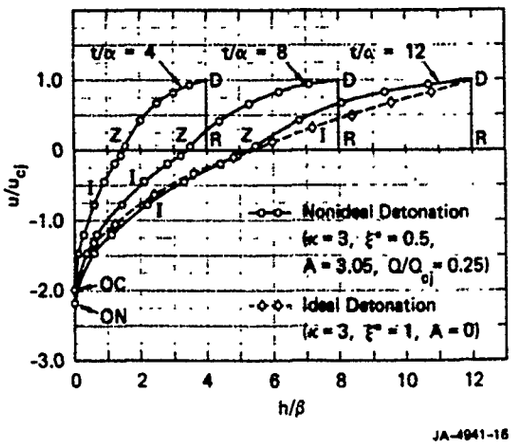

Fig. 2. Nondimensional particle velocity (u/u_{cj}) versus nondimensional distance (h/β) for a nonideal detonation at the nondimensional times t/α = 4, 8, 12, and for a corresponding ideal detonation at the nondimensional time t/α = 12

profile at $t/\alpha = 12$ is given for the ideal detonation. Here again, RD represents the reactive discontinuity, DZ and ZION represent the reactive and nonreactive portions of the release wave in the nonideal detonation, and DIOC represents the nonreactive release wave in the ideal detonation. Comparison of the particle velocity profiles at $t/\alpha = 12$ shows the influence of reaction on the particle velocity field. In the region where the particle velocities are positive, the particle velocity is higher in the nonideal detonation than in the ideal detonation; in most of the region where the particle velocities are negative, the particle velocity is lower in the nonideal detonation than in the ideal detonation. The chemical energy liberated in the nonideal wave lowers the free surface velocity from a value of $u = -2.0\ u_{cj}$ at OC to a value of $u \doteq -2.18\ u_{cj}$ at ON.

Our consideration of the solution (κ=3, ξ^*=0.5, A=3.05, Q/Q_{cj}=0.25) ends with the representation of the flow in the nondimensional (p/p_{cj}) versus (v/v_{cj}) plane shown in Fig. 3. In this plane, a particle path in the nonideal detonation is represented by RDZIN, and a par-

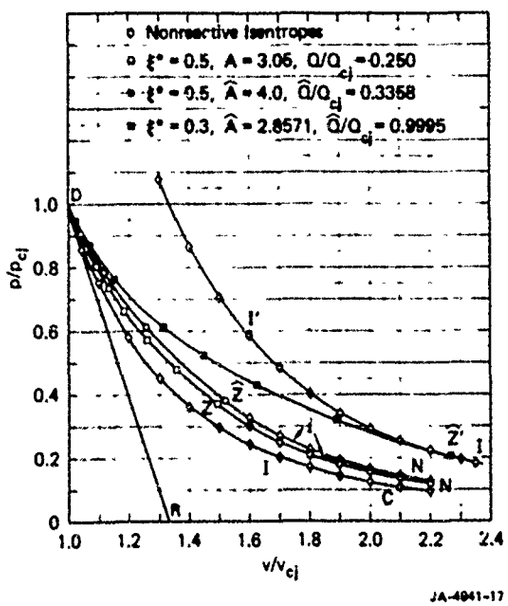

Fig. 3. Nondimensional pressure (p/p_{cj}) versus nondimensional specific volume (v/v_{cj}) Lagrange profiles for several nonideal detonations and the corresponding ideal detonation

ticle path in the corresponding ideal detonation is represented by RDIC. For convenience, we consider the ideal detonation before the nonideal detonation. A particle entering the ideal wave is first compressed in the reactive discontinuity to the cj point D along the Rayleigh line RD. It then expands along DIC, the isentrope passing through the cj point. The Rayleigh line RD and the isentrope DIC are tangent at D because the flow is sonic at the cj point. A particle entering the nonideal wave is first compressed along the Rayleigh line RD to the cj point D. It then expands nonisentropically along DZ until the reaction terminates and the flow becomes isentropic at Z; thereafter it expands along ZIN, the isentrope passing through Z. RD and DZIN are tangent at D because of the sonic condition at the cj point, and DZ and ZIN are tangent at Z because the flow becomes isentropic there.

For comparison, other nonideal detonation waves with maximum values of A and Q/Q_{cj} for given values of ξ^* are also represented in Fig. 3. The nonideal detonation with the maximum values of A and Q/Q_{cj} for $\xi^*=0.5$, ($\kappa=3.0$, $\xi^*=0.5$, $\hat{A}=4.0$, $\hat{Q}/Q_{cj}=0.3358$) is represented by RD$\hat{Z}$IN. A particle entering the wave is compressed along RD; it then expands nonisentropically along D$\hat{Z}$ and isentropically along ZIN. The nonideal detonation $\kappa=3$, $\xi^*=0.3$, $\hat{A}=2.8571$, $\hat{Q}/Q_{cj}$ = 0.9995) with the same amount of energy liberated along a particle path in the release wave as in the reactive discontinuity is shown as RD$\hat{Z}$/I. In this wave, a particle is first compressed along RD; it then expands nonisentropically along D$\hat{Z}$ and isentropically along $\hat{Z}$I. The isentrope through is shown as I$\hat{Z}$I.

CONCLUSIONS

A model solution for nonideal detonation propagating at constant velocity with liberation of chemical energy behind the wave front was constructed to demonstrate that the equations of motion admit this type of reactive flow. Because the solution is a similarity solution, the type of detonation it describes was called an ideal nonideal detonation. Properties of the solution were discussed to demonstrate significant features of this type of nonideal detonation. The solution contains four parameters, the polytropic index κ, the reaction parameter A, the value of the similarity parameter where the reaction terminates in the release wave ξ^*, and the ratio of the energies liberated along a particle path in the release wave and at the wave front Q/Q_{cj}. A particular solution is associated with a set of values of these parameters. The value of κ can be prescribed arbitrarily, but values of the other three parameters cannot because they are constrained by relationships imposed by the boundary conditions at the wave front and the end of the reaction zone. Examination of these relationships, when κ is specified, showed that the parameters A and Q/Q_{cj} are constrained to satisfy the conditions $0 < A \leq \hat{A}(\xi^*)$ and $0 < Q/Q_{cj} \leq \hat{Q}(\xi^*) / Q_{cj}$, and that the maximum values $\hat{A}(\xi^*)$ and $\hat{Q}(\xi^*) / Q_{cj}$ increase as the values of ξ^* decrease.

Properties of the flow fields of particular nonideal detonations with $\kappa=3$ and properties of the corresponding ideal detonation were compared to demonstrate the influence of exothermic reaction on expanding, unsteady, hydrodynamic flow.

ACKNOWLEDGMENT

This work was supported by Eglin Air Force Base under Contract F08635-83-K-0047.

REFERENCES

1. B. A. Khasainov, B. S. Ermolaev, A. A. Borisov, and A. I. Korotkov, "Effect of Exothermic Reactions Downstream of the C-J Plane on Detonation Stability," Acta Astronautica, Vol. 6, p. 557, 1979.

2. C. L. Mader, "Numerical Modeling of Detonations," University of California Press, Berkeley, Los Angeles, and London, 1979, pp. 89-100.

3. M. Cowperthwaite, "Some Aspects of Nonideal Detonation in Composite Explosives," J. of Energetic Materials, Vol. 1, p. 127, 1983.

4. G. I. Taylor, "The Dynamics of the Combustion Products Behind Plane and Spherical Detonation Fronts in Explosives," Proc. Roy. Soc. A, Vol. 200, p. 235, 1950.

5. I. B. Zeldovich and A. S. Kompaneets, Theory of Detonation, Chapter 5, Academic Press, New York and London, 1960.

6. M. Cowperthwaite, "Model Solutions for Shock Initation of Condensed Explosives," Actes Du Symposium International sur le Comportement des Milieux Denses sous Hautes Pressions Dynamiques, p. 201, Editions de Commissarial à l'Energie Atomique Centre d'Etudes Nucléaires de Saclay, Paris (1978).

DISCUSSION

YKIO KATO, Chemicals & Explosives Lab. Nippon Oil and Fats, Co., Ltd.

I studied the detonation waves in NM-Al mixtures, and I observed the strong increase of temperature, pressure and particle velocity in Taylor wave. In this mixture, the ratio of the reaction time of Al particles to that of NM is greater than 10', and the energy liberated in Taylor wave may attain 20-30% of that liberated at detonation front. It think that the detonation waves in NM-Al mixtures are good examples of the reactive Taylor wave model.

Reference

Y. Kato and C. Brochet, "Detonation Temperatures of Nitromethane Aluminum Gels," pp. 416-426 in Dynamics of Shock Waves, Explosion and Detonations, Progress in Astronautics and Aeronautics, Vol. 94, AIAA New York, 1984.

REPLY BY MICHAEL COWPERTHWAITE

In my model of the reactive Taylor wave, the temperature can increase in the wave but the pressure and particle velocity decrease. It would be interesting for me to try and construct a solution for a reactive Taylor wave with the properties described by Dr. Kato.

Session X
INITIATION AND SENSITIVITY I

Co-chairmen: Ola A. Listh
National Defence Research Institute
Harold W. Sandusky
Naval Surface Weapons Center

THE INFLUENCE OF FORMULATION VARIABLES ON THE GROWTH OF REACTION IN PLASTIC BONDED EXPLOSIVES

K. A. Fleming, R. Bird, M. W. G. Burt, C. E. Whatmore
MOD (PE) AWRE, Reading, Berkshire, England

Twelve HMX-based plastic bonded explosives have been developed and evaluated in a small-scale hazard test, to gain a better understanding of the factors influencing the explosive response of pressed charges.

Experiments are described which have attempted to distinguish between the effects on explosive response of HMX content, initial HMX particle size, the type of binder and the HE mechanical properties. The explosive response was measured using the AWRE Laboratory Scale Explosiveness Test and the mechanical properties were measured using an instrumented drop-weight apparatus.

The explosive response was found to be mainly determined by the HMX loading and particle size, with smaller contributions being due to the type of binder and the HE mechanical properties.

INTRODUCTION

The hazard potential of a confined HE charge subjected to mechanical and thermal stimuli may be expressed in terms of both its explosive response (explosiveness), and the minimum stimulus to produce an explosive event (sensitiveness). This paper describes recent work carried out to identify and investigate the HE characteristics which determine explosiveness. This work was initiated in order to further the development of HE formulations having maximum power consistent with safe manufacture and use. The development at AWRE of a Laboratory Scale Explosiveness Test (LABSET) (1), has provided a quantitative tool with which to study the growth of reaction in HE charges subjected to transient confinement and this has been used extensively in the present work.

Small scale experiments on three series of HMX/Polyurethane formulations were described at the 7th Symposium (International) on Detonation (2). The mechanical properties of formulations within each series were varied by changing the initial particle size distributions of the HMX crystals and by changing the cross-link density of the binder system. However, since changes in particle size may have a direct influence on explosiveness as well as on mechanical properties it was difficult to assess the relative contributions of particle size and mechanical properties to explosiveness.

The work reported here was intended both to complement and augment the previous studies.

A matrix of twelve new formulations was designed with the following objectives. The formulations were to:

(a) be simple, two component systems, i.e. HMX plus a single component binder, to simplify interpretation of the results;

(b) allow the effect of changes in binder type, HMX volume fraction and initial HMX particle size on hazard response and mechanical properties to be studied separately;

(c) display a wide range of hazard response and mechanical properties.

The results of mechanical and hazard tests on these formulations are presented and the influence of formulation variables on the growth of reaction is discussed.

2. EXPERIMENTAL

2.1 Compositions. The compositions of the selected formulations are shown in Table 1. This matrix incorporates the following variables:

(i) two HMX levels (90.8 and 96.0 volume %);

(ii) three binders (a polybutadiene polyurethane, a low molecular weight polyethylene and Viton A, a copolymer of vinylidene fluoride and hexafluoropropylene); and

(iii) two HMX particle size distributions (unimodal micronized powder (Type C) and a bimodal distribution of coarse (Type A) and Type C powder in the ratio 65/35).

2.2 HE Materials.

2.2.1. HMX Types. Three types of HMX are considered in this paper. These are Type A HMX, which is produced at ROF Bridgewater by recrystallising β-HMX from cyclohexanone; Type B HMX, which is produced by colloid milling Type A HMX; and Type C HMX, which is produced by fluid energy milling (micronizing) Type A HMX. Type A HMX has a size range of about 50-1000 μm, with a median diameter of about 400 μm; Type B HMX has a bimodal size distribution, with about 35 wt. per cent in the size range 45-150 μm, and about 65 wt. per cent less than 45 μm; Type C HMX has a unimodal distribution, with a maximum size of about 40 μm, and a median diameter of about 7 μm.

Size distributions and photomicrographs of the three types are shown in Figure 1.

2.2.2 Sample Manufacture

Polyurethane Formulations. The polyurethane binder system consisted of a hydroxyl-terminated polybutadiene (HTPB, ARCO polybd resin grade R-45M) cured with isophorone diisocyanate (IPDI) using a hydroxyl/isocyanate ratio of unity. HMX/HTPB/IPDI moulding powders were prepared by a non-aqueous solvent paste mix process (3) in which dry HMX was mixed with a solution of HTPB and IPDI in dichloromethane, and the solvent then removed by sweeping the surface of the mix with a forced air draught. Prior to pressing, the moulding powders were stored under refrigeration at <-10°C to retard binder cure. Charges were pressed isostatically at 138 MPa and ambient temperature, and then heated at 70°C for seven days at ambient pressure to effect curing of the binder.

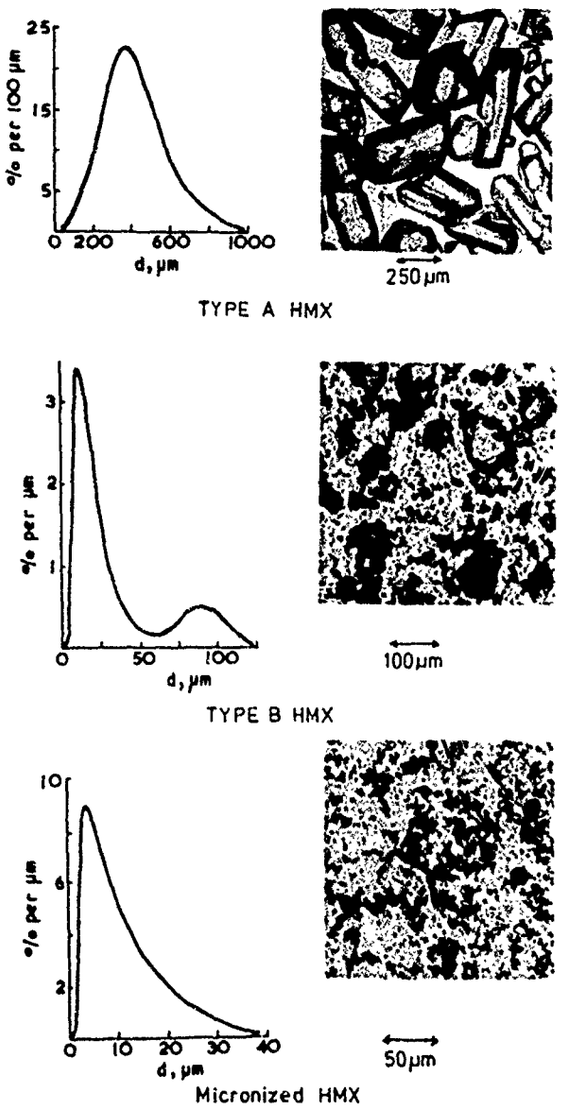

Fig. 1. Particle size distributions and photomicrographs of HMX

Polyethylene Formulations. The polyethylene binder was an emulsifiable grade (Allied Chemicals, AC 629) used commercially in wax polishes. It was incorporated with HMX in the form of a morpholine oleate-stabilised emulsion, which was then broken by the addition of an electrolyte. Charges were pressed isostatically at 138 MPa and 100°C.

Viton Formulations. HMX/Viton moulding powders were prepared by a solvent paste-mix process. A solution of Viton A in n-butanone was mixed into a thick paste with wet HMX, and the solvent then stripped off by heating the mix under a forced air draught. Charges were pressed isostatically at 138 MPa and 100 °C.

Final densities were within 97-99% of their theoretical maxima (TMD) except charge A which had a density of about 94% of TMD. The latter showed evidence of some cracking and this may have affected the results obtained. All charges were machined by remote control into appropriate test specimens.

2.3 Test Methods

Explosiveness Measurements. The LABSET method for measuring explosiveness was described at the 6th Symposium (International) on Detonation (1), and the apparatus is shown schematically in Figure 2.

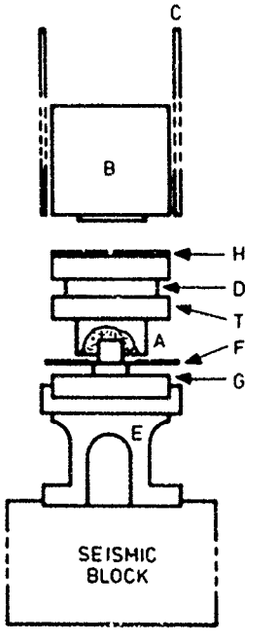

Fig. 2. LABSET apparatus ((A) Explosive Charge Assembly, (B) Drop Weight, (C) Guide Tube, (D) Felt Pulse Shaper, (T) Load Spreading Plate, (F) Heater Wire, (G) Base Plate, (H) Switch, (E) Load Cell.)

Disc shaped samples, 28.6 mm diameter and 14.2 mm long, were machined from each of the HE charges and mounted in cylindrical steel cups 101.6 mm outside diameter and 31.8 mm thick. The test method will be described briefly. A charge assembly is mounted on a strain-gauged load cell, and impacted by a 22.7 kg drop weight, falling through 305 mm. Ignition of the charge is achieved during the rising portion of the impact loading pulse by the rapid discharge of a 25 μF capacitor bank, charged to 600 V, through a 0.152 mm diameter, 38.1 mm long constantan resistance wire, positioned along a diameter, between the face of the charge and a resin bonded base plate on top of the load cell. Explosiveness is measured by the force impressed on the load cell. In the absence of an explosive event the impact loading pulse has a maximum in the range 25.0 to 35.0 kN and a duration of approximately 2.0 msec, achieved by the use of a felt pulse shaper.

Five samples of each formulation were tested at 20 °C.

Dynamic Materials Properties Measurements. Dynamic compressive stress-strain curves were determined for cylindrical explosive samples 50 mm long and 20 mm diameter, machined from the same charges which provided the explosiveness test samples. A standard drop weight apparatus was used in which a 9 kg weight impacted the sample axially from a drop height of 305 mm. Stress and strain were recorded directly by a load cell and strain gauged cantilever system respectively.

Four samples of each formulation were tested at 20 °C. A typical dynamic compressive stress-strain curve is shown schematically in Figure 3. Three parameters were derived from each stress-strain curve; these were ultimate compressive strength (UCS), maximum tangent modulus (E), and percentage strain to failure (X_t).

3. RESULTS

Dynamic compressive properties and explosiveness responses for each formulation are summarised in Table 1. The values quoted for explosiveness are the mean and standard deviation and those for dynamic compressive properties are mean values.

An extensive data base exists at AWRE relating the response in LABSET to the results

TABLE 1
Details of Formulations Together with Explosiveness and Dynamic Materials Properties Data

Code No	Binder	HMX v/o		LABSET, kN	Dynamic Compression			
		Type C	Type A		UCS, MPa	E, GPa	X_t	X_e/X_t
A	Polyurethane	96.0		190 ± 80	34	3.0	2.1	0.54
B		33.6	62.4	810 ± 4	26	2.3	1.7	0.66
C		90.8		60 ± 10	37	2.3	2.6	0.62
D		31.8	59.0	230 ± 50	18	1.5	2.8	0.43
E	Polyethylene	96.0		300 ± 60	57	9.8	1.1	0.53
F		33.6	62.4	870 ± 40	19	2.6	0.97	0.75
G		90.8		70 ± 10	37	5.3	1.4	0.50
H		31.8	59.0	550 ± 50	18	2.6	1.0	0.69
I	Viton A	96.0		360 ± 20	77	6.0	1.5	0.86
J		33.6	62.4	1100 ± 30	35	3.0	1.4	0.83
K		90.8		100 ± 10	68	5.8	1.9	0.62
L		31.8	59.0	680 ± 150	36	3.9	1.8	0.51

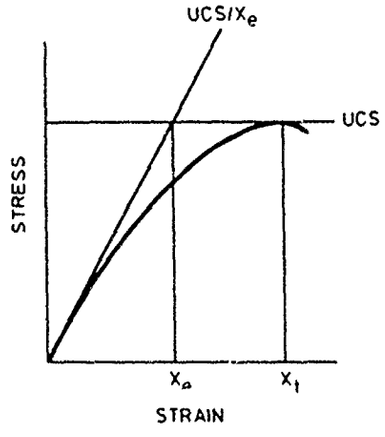

Fig. 3. A schematic view of a typical dynamic compressive stress-strain curve

obtained in the large scale AWRE Oblique Impact (Skid) Test (4). The response in these two tests are compared in Table 2 which may be used to predict the response of the HEs considered here in the large scale test. The design of our experiments allowed the effects of three formulation variables on LABSET and the dynamic mechanical properties to be isolated using variance analysis. The major features of the results are described below.

3.1 Effect of HMX Loading. The analysis showed that for LABSET the proportion of variance due only to HMX loading was relatively large (about 20%) for all three binder systems and the LABSET responses of formulations containing 96 v/o HMX were in each case greater than those containing only 90.8 v/o HMX.

The trends for the mechanical properties were less consistent. No significant effect of HMX loading on ultimate strength could be found and, for the other parameters, the effect depended on the binder system. The initial modulus

TABLE 2
Comparison of LABSET and AWRE Oblique Impact (Skid) Test Responses

LABSET RESPONSE (kN)	AWRE Skid Test (ref 4)
0-150	Small partial explosion (P)
150-500	Large partial explosion (P)
500-1000	Explosion (E) and High Order (H)

was only strongly influenced by HMX loading (with this variable contributing 50% to the variance) for polyurethane formulations. In these the formulations with the higher loading had higher moduli.

The failure strain was much more strongly influenced for the elastomeric binder systems, Viton and polyurethane, (where the contribution of HMX loading to the variance was 80-90%) than for polyethylene (about 20%). In general the formulations with the higher loading had lower failure strains.

3.2 Effect of Initial Particle Size. The LABSET response, ultimate compressive strength and the modulus were all strongly influenced by initial particle size. In LABSET the proportion of the variance due only to particle size was in the range 40-80% and the contributions to the variance for the ultimate strength and modulus were in the ranges 70-95% and 40-90% respectively. A strong trend was observed such that in each case formulations containing coarse (Type A) HMX had lower ultimate compressive strengths and moduli and higher LABSET responses than those containing only fine (Type C) HMX.

3.3 Effect of Binder Type. The LABSET response was not strongly influenced by the type of binder (Student's t value for the difference between mean values for Viton formulations and those for corresponding polyurethane formulations falls just short of the 95% confidence level) but inspection of the data shows a consistent trend of increasing LABSET response in the order:

HMX/Polyurethane < HMX/Polyethylene < HMX/Viton.

Although the results of dynamic compressive tests exhibited considerable scatter, statistical analysis has shown that there was a significant tendency for the ultimate strengths and moduli to lie in the order:

HMX/Viton > HMX Polyethylene > HMX/Polyurethane

For the failure strain there was also a significant trend but the order was:

HMX/Polyurethane > HMX/Viton > HMX/Polyethylene

4. DISCUSSION

The HMX loading has been shown to strongly influence the explosiveness. This observation is consistent with previous data (see for example reference 5). Increasing the HMX volume fraction increases the quantity of HE per unit volume available for reaction and decreases the quantity of binder available to act as an inhibitor.

An increase in the initial proportion of coarse HMX crystals has been shown to lead to a decrease in strength and modulus but an increase in explosiveness. Further evidence in support of this observation can be obtained by combining the data reported here with those reported by Coley and Whatmore (2) together with some recent unreported data obtained at AWRE. As shown in Figure 4 these data may be separated into three bands. Within each band the percentage of coarse (Type A) HMX was the same or similar. This plot shows clearly the influence of both initial particle size and the HMX loading on LABSET response. It is interesting to note that for formulations containing only *fine* HMX (Types B and C) the explosiveness was not strongly influenced by HMX content

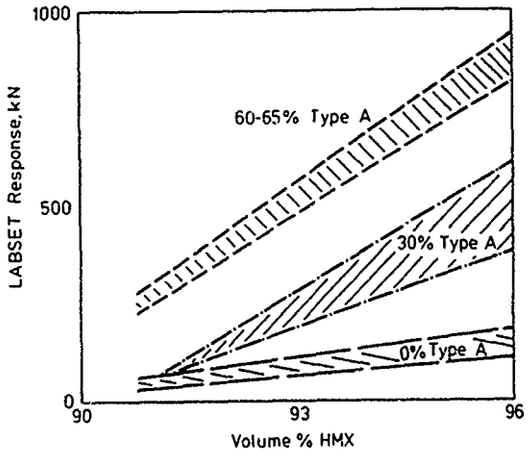

Fig. 4. LABSET results for a range of HMX Polyurethane formulations

and even at 96 volume % HMX the explosiveness was still relatively low. HE particle size has been recognised for some time as an important factor influencing charge hazard response in a wide range of tests. A recent review by Burt (5) summarises the literature on this topic.

Particles of elastic materials decrease in compressive strength with increasing size. Kendall (6) predicted that for such materials the fracture stress would be inversely proportional to $(\text{size})^{1/3}$. This relationship has been confirmed for β-HMX (7). This analysis suggests that coarse HMX particles are likely to be fractured more easily than fine particles during pressing or when subjected to compressive loading in accident situations. Microscopic examination of sections of highly loaded, pressed HMX plastic bonded explosive charges has demonstrated the existence of cracking in HMX particles as small as 70 μm (5). Work is in progress to attempt to quantify the amount of cracking and relate this to pressing parameters, HMX loading and initial particle size. Extension of this work to a study of samples subjected to dynamic compressive loading is also being considered since recent work by Field and co-workers (7) has shown that HMX particles can break and debond from binder matrices when a fracture is propagated through a pressed sample.

It is postulated that mechanical disruption of an HE charge during impact will expose highly reactive, uncoated, internal explosive surface into which a burning front may penetrate after ignition has occurred, leading to a high gas production rate. The resulting pressure pulse may cause further fracture to occur ahead of the burning front. Provided that the confinement is of sufficient magnitude and duration these processes will ultimately lead to an explosion. The specific surface area of fracture arising from a given stimulus may be an important factor influencing explosiveness and this will depend on a number of factors including: the HMX fracture surface energy; the initial HMX particle size; the type of binder and the HE-binder physico-chemical interactions.

An alternative hypothesis is that explosiveness is influenced by the void size distribution and void shape. For pure HMX compacts these parameters will clearly be determined by the HMX particle size distribution and particle shape. However, for HMX plastic bonded explosives the situation may be more complex since voids may be associated more with aggregates of coated particles than with individual coated particles. We are not able, at present, to quantify void size and distribution in pressed compacts although this subject is currently being studied.

The void percentage in a given charge can be determined from its density and the TMD for the formulation concerned. There was no correlation between the void percentage in the samples tested and their LABSET responses.

The effects of the type of binder are less marked than those of HMX content and HMX particle size but some trends have been observed. The strain rate in the dynamic compressive test ($\sim 10-20\ s^{-1}$) is of the same order as that in both LABSET and the AWRE Oblique Impact test (4). Strengths and moduli in the dynamic compressive test increase in the same order as the explosiveness measured in LABSET (for constant HMX content and particle size), i.e., HMX/Viton > HMX Polyethylene > HMX/ Polyurethane. Figures 5 and 6 show plots of LABSET response versus dynamic strength and modulus respectively for the four groups of formulations each having a constant HMX content and particle size distribution. Although the trends within these groups were not statistically significant there appears to be a trend in each of these plots such that LABSET response increases with both dynamic strength and modulus. It is interesting to note that extrapolation of these data suggests that a sample having a relatively low strength

and modulus would have a low LABSET response irrespective of its composition. This may explain why some high power, highly plasticised formulations exhibit low explosiveness in both LABSET and the AWRE Oblique Impact (Skid) test (8).

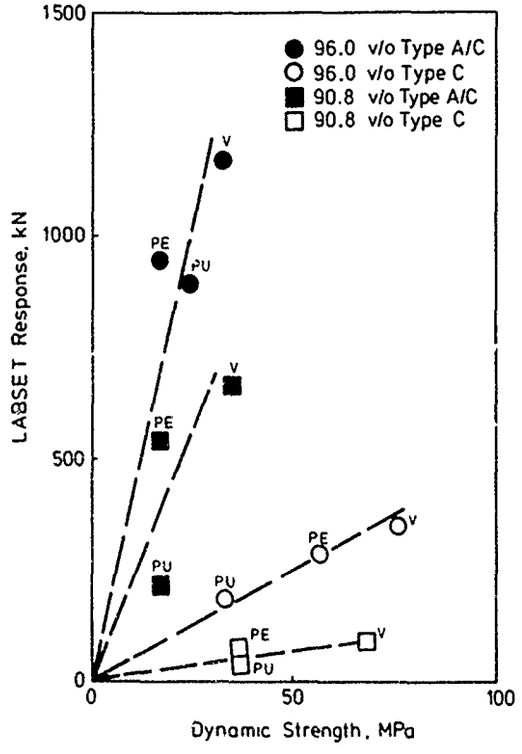

Fig. 5. LABSET results as a function of dynamic compressive strength for Polyurethane (PU), Polyethylene (PE) and Viton (V) formulations

Some caution must be exercised, however, in attributing the trends shown in Figures 5 and 6 merely to the effects of changes in mechanical properties since the changes in LABSET response were achieved by changing the binder systems whilst keeping the HMX volume fraction and particle size distribution constant. It is not certain, at this time, what contribution to these trends is made by differences in the nature of the binders and their physico-chemical interactions with HMX. This is clearly an area where further work is needed.

The possible influences of dynamic mechanical properties on explosiveness may be due to their effects on the local confinement in the region of the reaction zone. Clearly, if unrestrained fracture of the charge occurs on impact or ahead of a propagating burning front, hot product gases will be vented to atmosphere, the confinement will be released and the reaction will be quenched.

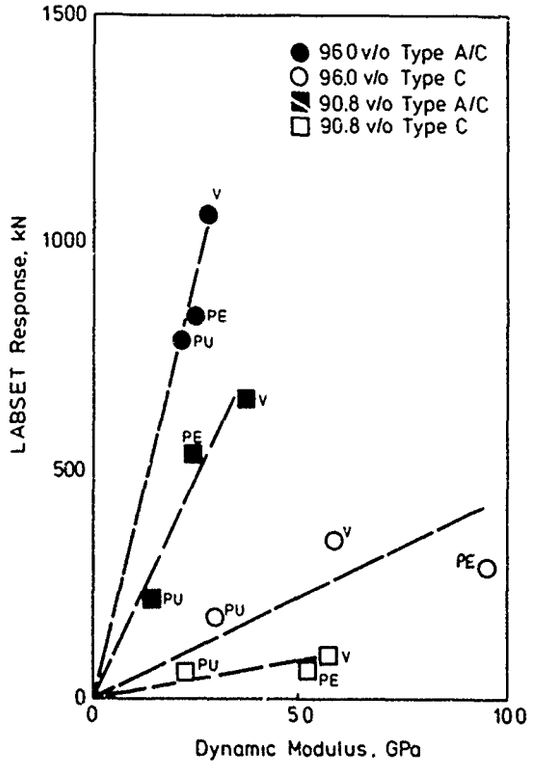

Fig. 6. LABSET results as a function of dynamic modulus for polyurethane (PU), polyethylene (PE) and Viton (V) formulations

In a paper presented at the 7th Symposium (International) on Detonation, Coley and Whatmore (2) described experiments on three series of HE formulations containing HMX and polyurethane binders based on the HTPB/IPDI system. The mechanical properties within each series were varied by changing the particle size distributions of fo the HMX crystals and by incorporating different degrees of cross-linking into otherwise chemically similar binder systems. It was suggested that the formulations which gave the most violent LABSET responses were those whose dynamic compressive properties departed most from purely elastic behaviour. This observation suggested a combination of parameters which would quantify this depar-

ture from elasticity. From Figure 3 the quantity

$$\frac{\text{Ultimate Compressive Strength (UCS)}}{\text{Maximum Tangent Modulus (E)}}$$

represents the failure strain X_e of a hypothetical elastic material with identical modulus and failure stress to the real material. Thus if X_t is the failure strain of the real material then the ratio

$$\frac{X_e}{X_t} = \frac{UCS}{E \cdot (STF)}$$

is a measure of its departure from elasticity.

On the basis of their data Coley and Whatmore identified a trend which suggested that formulations having low X_e/X_t values would have high LABSET responses (for a given HMX content). However, a considerable amount of data have been acquired since this work was reported and it is now possible to reassess the effects of X_e/X_t on explosiveness. Multi-linear regression analysis has been performed on the results obtained from twenty-six polyurethane formulations. This has shown that there is a strong correlation between LABSET response and both the initial HMX particle size and the HMX loading with small contributions from ultimate strength, initial modulus and failure strain. However, no significant correlation was found with any *single* mechanical properties parameter or the composite parameter X_e/X_t. In the light of the data now available it appears that, in the previous work, the effects of mechanical properties on explosiveness were overshadowed by the effects of changes in particle size.

Considerable further work is required before a full understanding is gained of the mechanisms underlying the influence of formulation variables on charge hazard response. However the benefits of excluding coarse particles from HE formulations have been clearly demonstrated. There is also some indication that the use of low strength, low modulus, strain rate insensitive binders will be beneficial. Investigations are in progress on HMX/Polyurethane systems in which the maximum HMX particle size is less than 100 μm. Reductions in particle size are expected to lead to some processing problems but it is hoped that these can be overcome by close control of particle characteristics, the use of narrower size fractions and judicious blending of these fractions.

5. CONCLUSIONS

Twelve HE formulations have been developed and tested in a programme aimed at gaining a better understanding of the factors influencing charge hazard response. Three formulation variables have been shown to influence both charge mechanical properties and explosiveness response. The following conclusions may be drawn from the results:

(1) Increases in HMX volume percentage lead to increases in the explosiveness of pressed HE formulations. This confirms previous work.

(2) Increases in the proportion of coarse HMX crystals lead to decreases in strength and modulus but increases in explosiveness.

(3) For a given HMX volume percentage and particle size distribution charge explosiveness responses lie in the order:

HMX/Viton > HMX/Polyethylene > HMX/Polyurethane.

(4) Increases in the dynamic strengths and moduli of plastic bonded explosives may lead to increases in explosiveness.

REFERENCES

1. G. D. Coley "The Growth of Reaction in Secondary Explosives under Transient Confinement," Sixth Symposium (International) on Detonation pp. 290-298, 1976.

2. G. D. Coley and C. E. Whatmore "The Influence of the Dynamic Compressive Strength Properties of HE Formulations on the Growth of Reaction," Seventh Detonation Symposium (International) on Detonation pp. 17-23, 1981.

3. P. D. Totterdell, M. W. G. Burt and G. K. Lamb, "HMX/Elastic Binder Formulations: Processing and Properties," 8th Quadripartite Ammunition Conference, Montreal, October 1981.

4. Sensitiveness Collaboration Committee, Explosive Hazard Assessment Manual of Tests, SCC No. 3, 1971.

5. M. W. G. Burt "Effect of HMX Particle Size on the Hazard Properties of Pressed High Explosives Charges," ADPA Joint Symposium on Compatibility of Plastics/ Materials with Explosives, Propellants and Pyrotechnics and Processing of Explosives, Propellants and Ingredients, Lake Ozark, Missouri, USA, 1983.
6. K. Kendall, "Complexities of Compression Failure," Proc, R. Soc. London, A361, 245-263, 1978.
7. J. E. Field, Cavendish Laboratory, Cambridge University, Private communication.
8. C. E. Whatmore, R. H. Roberts, Private communication, AWRE, Aldermaston, England, 1983.

DISCUSSION

HAROLD GRYTING, Southwest Research Institute

Have you correlated sensitiveness with the relative toughness as approximated by the area under the stress-strain curve under either tensile or compressive strength determinations?

REPLY BY K. A. FLEMING

The work presented here was concerned with assessing the influence of formulation variables on the explosiveness, rather than the sensitiveness, of HE charges. We have not attempted to correlate the explosiveness with strain energy but intend to do so in the near future.

DISCUSSION

G. D. COLEY, AWRE, England

Unpublished work at AWRE indicates that strain energy does, indeed, correlate with the sensitiveness.

DISCUSSION

F. HILDEBRANT, ARDC

How is the fluid energy milled material, i.e. HMX, handled between grind phase and mixing phase? Is some type of solvent transport utilized? What is the storage time and effect on explosive performance if delays do occur between the two operations?

REPLY BY K. A. FLEMING

The fine HMX used for these studies was produced by fluid energy milling in an aqueous slurry. Since the surface area of such materials decreases dramatically during storage in water we dried the HMX immediately after milling. The particle size measurements were made on the dried material.

DISCUSSION

M. HELD, MBB Apparate, FRG

1. If you use 15% PU-binder, will you have any LABSET response?
2. How did you measure the dynamic strength and modulus?

REPLY BY K. A. FLEMING

1. We do not yet have any results for formulations containing more than 10 volume % polyurethane binder.

   Extrapolation of our data suggests that the load cell response for such a formulation would be indistinguishable from that of an inert material having the same dynamic mechanical properties. We would expect to observe, however, scorch marks on the material in the region adjacent to the heater wire.
2. Details of the technique used for measuring the dynamic mechanical properties of our materials are given in our paper.

DISCUSSION

R. STRESAU, Consultant

In any laboratory scale experiment there is a relationship between particle size and such parameters as failure diameter and run up distance. In this respect it is of interest to compare data presented in the paper with those obtained by MacDougal and Messerly in the early '40s with bimodal mixtures of coarse and fine ammonium picrate (with no binder). These data indicated a maximum failure diameter (and hence minimum detonation velocity) for a 75/25, coarse/fine ratio. I have observed a similar relationship for RDX. Is there a contradiction here?

REPLY BY K. A. FLEMING

The work to which you refer concerns the performance of low density (55-60% TMD) compacts of uncoated explosive particles. The work described in our paper is concerned with the growth of reaction in high density (97-99% TMD) charges of coated explosive particles. In the latter case the propagation of a burning front is influenced by the ease with which uncoated, internal explosive surface is exposed by fracture during impact. Our work indicates that the tendency for fracture to occur, and hence the ease with which propagation occurs, increases as the proportion of coarse explosive crystals increases.

DISCUSSION

R. D. STEELE, LANL

I have two remarks.

1. What you call the explosiveness is clearly greater with PBX 9404 than with PBX 9501. The principal difference between these materials is the binder. This difference has been observed on drop skid tests with both qualitative observations and with pressure gauges located near the experiment. These experiments clearly support your observation that the binder influences the explosiveness of an event.

2. In addition I would like to observe that you were correct in observing that you should be looking at the dynamic mechanical properties of the binder. Rather than look at the modulus alone we have had a great deal of success looking at a polymer in terms of both its modulus and of the time constant which controls its transformation from a very stiff material in that time frame to a polymer like material in longer time frames. These constants can range from about 10^{-6}s for the better binders to 10^{-2}s for materials that give worse sensitiveness and explosiveness. It is interesting to note that the glass temperature of a polymer provides a fair measure of its time constant.

REPLY BY K. A. FLEMING

Thank you for your confirmatory comments. It may be of interest to note that we have LABSET results for both PBX 9404 and PBX 9501. The values obtained (900 and 300kN respectively) are clearly consistent with your observation that the explosiveness of PBX 9404 in skid tests is greater than that of PBX 9501.

DISCUSSION

G. D. COLEY, AWRE, UK

Would $\int \sigma d\epsilon$ correlate with sensitiveness?

REPLY BY K. A. FLEMING

It has been clearly established that the dynamic compressive properties of HMX PBX's correlate with their sensitiveness. For the compression derived in the paper, sensitiveness is expected to correlate with dynamic compressive strength.

INITIATION STUDIES ON LX-17* EXPLOSIVE

K. Bahl, G. Bloom, L. Erickson, R. Lee†, C. Tarver, W. Von Holle, R. Weingart
Lawrence Livermore National Laboratory
University of California
Livermore, California, 94550

Studies of hemispherical booster initiation of plastic bonded TATB have lead to several interesting results. The parameters which affect booster initiation are the size, temperature and nature of the booster and acceptor. Particle size has a pronounced effect on acceptor HE initiation. However, one-dimensional thin pulse experiments with electric gun slappers have shown much less effect of particle size except for very-fine-particle TATB. These experiments and those using embedded manganin and particle velocity gauges have been successfully modeled using an ignition and growth model. The calculations increased our understanding of LX-17 shock initiation and our predictive ability.

INTRODUCTION

Initiation of detonation in high density charges generally requires an initiation train in which the first components deliver sharp pressure pulses with steeply falling Taylor waves. Shock initiation of LX-17 is a particularly difficult problem. Because of its inertness (1), choice of an initiation system for this material requires careful study and understanding of the nature of thin-pulse initiation. In the following we describe advances recently made in this study.

BOOSTER STUDIES

Initiation of TATB by high explosive (HE) boosters requires the use of rather large booster charges. A strong detonation may propagate in TATB with almost no divergence to the sides if it is not initiated strongly over a sufficiently large area. We investigated the effect of booster size and type of booster HE on LX-17 and another TATB composition, PBX-9502**, both at ambient temperature and at −54 °C.

The experimental configuration is shown in Fig. 1. The breakout of the detonation wave on the surface of the TATB acceptor charge was recorded by a rotating-mirror streak camera at a streak rate of 20 $km \cdot s^{-1}$. The streak record permitted measurement of the transit time of the detonation wave through the acceptor

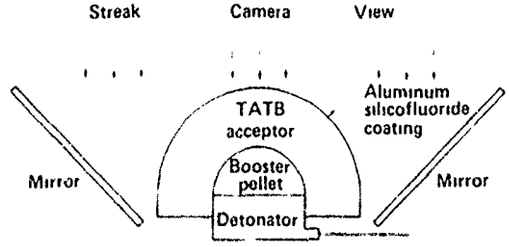

Fig. 1. Booster-test arrangements for investigating the initiation of TATB compositions LX-17 and PBX 9502 by a number of different booster charges (We varied temperature, booster size, booster HE material, and type of TATB used in the acceptor. We also varied the thickness of the TATB acceptor and the radius of the booster.)

* 92.5% triaminotrinitrobenzene, 7.5% KelF800, 1.9 g/cm^3
**95% TATB, 5% KelF800, 1.9 g/cm^3
†Present address Department of Physics, Kansas State University.

(referenced to detonator breakout time) and the shape of the detonation wave as it reached the surface of the acceptor. Although the breakout of the detonation wave was nearly simultaneous at all points on the booster surface, the front of the detonation wave in the TATB acceptor did not propagate as a sphere because of rarefaction effects at the back edge of the hemispherical booster. The ideal propagation of the wave was further impeded by the large failure diameter of TATB-based explosives. We also observed significant effects on detonation propagation due to temperature and differences in TATB particle-size distributions.

EFFECT OF BOOSTER SIZE

To properly initiate TATB-based HEs it is necessary to use boosters of adequate size. The failure diameter of PBX-9502 is 9mm, and one would expect the failure diameter of LX-17 to be even larger because of its higher percentage of binder and higher density. We found experimentally that a booster with a diameter near the TATB failure diameter produces detonations that, at best, diverge slowly in the TATB and at low temperatures can be quite marginal in initiating the TATB acceptor.

We judged the relative strength of the detonation by the intensity of the light produced when the detonation wave reached a layer of aluminum silicofluoride [$Al_2(SiF_6)_3$] sprayed on the spherical surface of the TATB acceptor. The light is bright only near the pole of the acceptor; away from the pole, the impact of the detonation wave is oblique and the detonation may not be fully developed. We designate the region over which the bright light is observed as the region of strong reaction or detonation. The angular size of the region of strong reaction (measured from the pole) is a good qualitative indicator of how well the detonation wave is diverging in the acceptor HE. Table 1 summarizes the results of experiments in which 20mm-thick PBX-9502 acceptors were initiated at −54 °C by LX-07 (90% HMX, 10% Viton, A, ρ=1.86 g/cm^3) boosters with radii of 8.5 to 15 mm. The data clearly indicate the effect of booster size.

EFFECT OF BOOSTER HE TYPE

By using a more energetic booster HE the higher-energy booster compensates for its smaller size by initially overdriving the acceptor HE. Table 2 compares the divergence observed in PBX-9502 at −54 °C when it is initiated by 8.5 to 15 mm radius boosters of LX-07 and LX-10 (94.5% HMX, 5.5% Viton A, ρ=1.86 g/cm^3), which have detonation pressures of about 35 and 38 GPa, respectively. From Table 2, we see that LX-10 boosters produce detonation waves with better divergence than do LX-07 boosters, particularly those with an 8.5 mm radius.

TABLE 1

Effect of Booster Radius on the Divergence of Detonation Waves in Hemispherical PBX-9502 Acceptors (20 mm thick at −54°C) Initiated by LX-07 Boosters

Divergence		
Booster radius mm	Region of strong reaction, deg*	Region of detectable reaction, deg*
8.5	71	103
10	139	171
12.5	165	175
15	170	180

* Measured across the pole of the hemisphere.

EFFECT OF ACCEPTOR PARTICLE-SIZE DISTRIBUTION

The effect of the particle-size distribution of the TATB used in the acceptor has a strong effect on divergence. Table 3 compares the divergence of the detonation waves observed in various PBX-9502 acceptors initiated by boosters of LX-07, 8.5 and 10 mm in radius. The TATB in the various acceptors differed primarily in particle size, designated as coarse and fine. The coarse material showed very poor divergence when initiated with 8.5 mm radius boosters, and even with 10 mm radius boosters showed poorer divergence than the fine material. LX-17 materials, both coarse and fine (not shown in Table 3) diverged more slowly than PBX-9502 because they contain more binder and were pressed to a higher density. Table 3 demonstrates the effect of particle size on divergence.

TABLE 2

Effect of Booster HE type on the Divergence of Detonation Waves in Hemispherical PBX-9502 Acceptors at −54°C

Booster high explosive	Booster radius mm	Divergence		Shock breakout time spread, μs
		Region of strong reaction, deg*	Region of detectable reaction, deg*	
PBX-9502 acceptor (10 mm thick)				
LX-07	8.5	145	163	0.16
LX-10	8.5	165	169	0.13
PBX-9502 acceptor (20 mm thick)				
LX-07	12.5	165	175	0.35
LX-10	12.5	169	179	0.40
LX-07	15	170	180	0.58
LX-10	15	175	180	0.80

*Full angle centered over the pole of the hemisphere.

TABLE 3

Effect of HE Particle Size on the Divergence of Detonation Waves in 20 mm thick, Hemispherical PBX-9502 Acceptors at −54°C, Initiated by LX-07 Boosters

		Divergence	
Average particle size of acceptor HE*	Booster Radius mm	Region of strong reaction, deg**	Region of detectable reaction, deg**
Coarse	8.5	71	103
Fine		160	180
Coarse	10	139	171
Fine		170	180

*Material designated coarse is deficient in particles with diameters less than 50μm.
**Full angle centered over the pole of the hemisphere.

TABLE 4

Effect of Temperature on the Divergence of Detonation Waves in Hemispherical PBX-9502 Acceptors of Varying Thickness and HE Particle Size

PBX-9502 acceptor		LX-07 booster	Region of strong reaction, deg*		Region of detectable reaction, deg*	
Thickness, mm	Particle size	radius, mm	Ambient temperature	−54°C	Ambient temperature	−54°C
10	Fine	8.5	173	145	179	163
		10	178	163	180	170
		15	180	172	180	180
	Coarse	10	163	126	170	146
20	Coarse	10	166	130	180	170

*Full angle centered over the pole of the hemisphere.

EFFECT OF TEMPERATURE

The temperature of the TATB acceptor when it is initiated has an important effect on divergence. Table 4 shows the divergence of detonation waves in PBX-9502 initiated at ambient temperature and at −54°C by boosters with radii of 8.5 to 15 mm. For the fine particle PBX-9502, only the 15 mm radius boosters produced nearly the same divergence at −54°C as at ambient temperature. For the coarse-particle PBX-9502 at −54°C, the 10 mm radius booster is marginal, at best. The data in Table 4 emphasize the important point that to initiate TATB-based HE and obtain good divergence of the detonation wave, the booster must be large enough to overcome the effects of temperature and TATB particle size.

BOOSTER PERFORMANCE

The effects of booster size, HE type and temperature all are critically important to the initiation of TATB-based HE charges. Booster size and HE type affect the pressure or time duration of the output pulse of the booster. As the hemispherical booster becomes larger the duration of the pressure pulse increases because the Taylor wave becomes less steep and the spherical divergence effect diminishes. Lower temperatures reduce the shock sensitivity as shown below, and have a strong effect on detonation wave divergence.

In the following sections we will examine 1-D, thin-pulse threshold experiments on a large number of plastic bonded TATB formulations, pressure records from embedded manganin gauges in 1-D gas gun experiments, and calculational modeling of these experiments. All of these efforts contribute to our understanding of initiation systems performance.

ONE INCH THRESHOLD TESTS

The detonation thresholds of a variety of plastic bonded TATBs were measured using the impact of a 0.25 mm-thick Mylar flyer plate as the shock stimulus. We compare results for six LX-17 formulations chosen to have a wide range of particle-size distributions as well as one PBX-9502 formulation with a very coarse composition. The particle-size distributions as measured by sieve analysis are shown as histograms in Figure 2A-G. The samples were tested at densities 1.80, 1.85, 1.88 g/cm^3 and maximum. Thresholds were determined at both ambient temperature and −54°C for each material at the specific densities.

EXPERIMENTAL PROCEDURES

An electric gun with a 25.4×25.4×0.051 mm thick aluminum foil was used to drive a 0.254 mm thick Mylar foil down a 25.4 mm diameter×5.6 mm long PMMA barrel to the TATB target (2). This resulted in a pulse width of approximately 80 ns. The sample was mounted in a PMMA prism so that the breakout of the detonation wave on both the back face and on the two sides could be observed with a streak camera. Since it was impossible to measure flyer velocity with the sample in place, the device was calibrated by measuring the flyer velocity with a laser Fabry-Perot interferometer. A least-squares fit to this data gives a satisfactory value for the velocity for any given voltage.

We used a delayed Robbins-Monro (DRM) scheme to pick the capicitor bank voltage (3). In order to study a large number of different materials, we generally limited a series to eight shots for a particular material at a particular density and temperature. It is not possible to determine the standard deviation of this small number of trials.

Some scatter in the data is probably due to lot-to-lot HE variations as well as equipment variations. For example we saw unexplainable differences among different pressing lots of the same material.

In choosing voltages we made an approximate correction for the differences in density among samples in a pressing lot. We did those samples nearest the nominal density last so that there was no density correction in the final result except that the densities do differ from the nominal value by a small amount.

For each series of shots a maximum likelihood estimate of the threshold was made from the voltages for goes and no-goes. From the interferometer calibration, this was converted to a flyer velocity. A Hugoniot based on theoretical estimates for the parameters in

$$U_s = C_0 + SU_p$$

was then used to determine the corresponding pressure. These pressures are plotted vs. density in Figure 3.

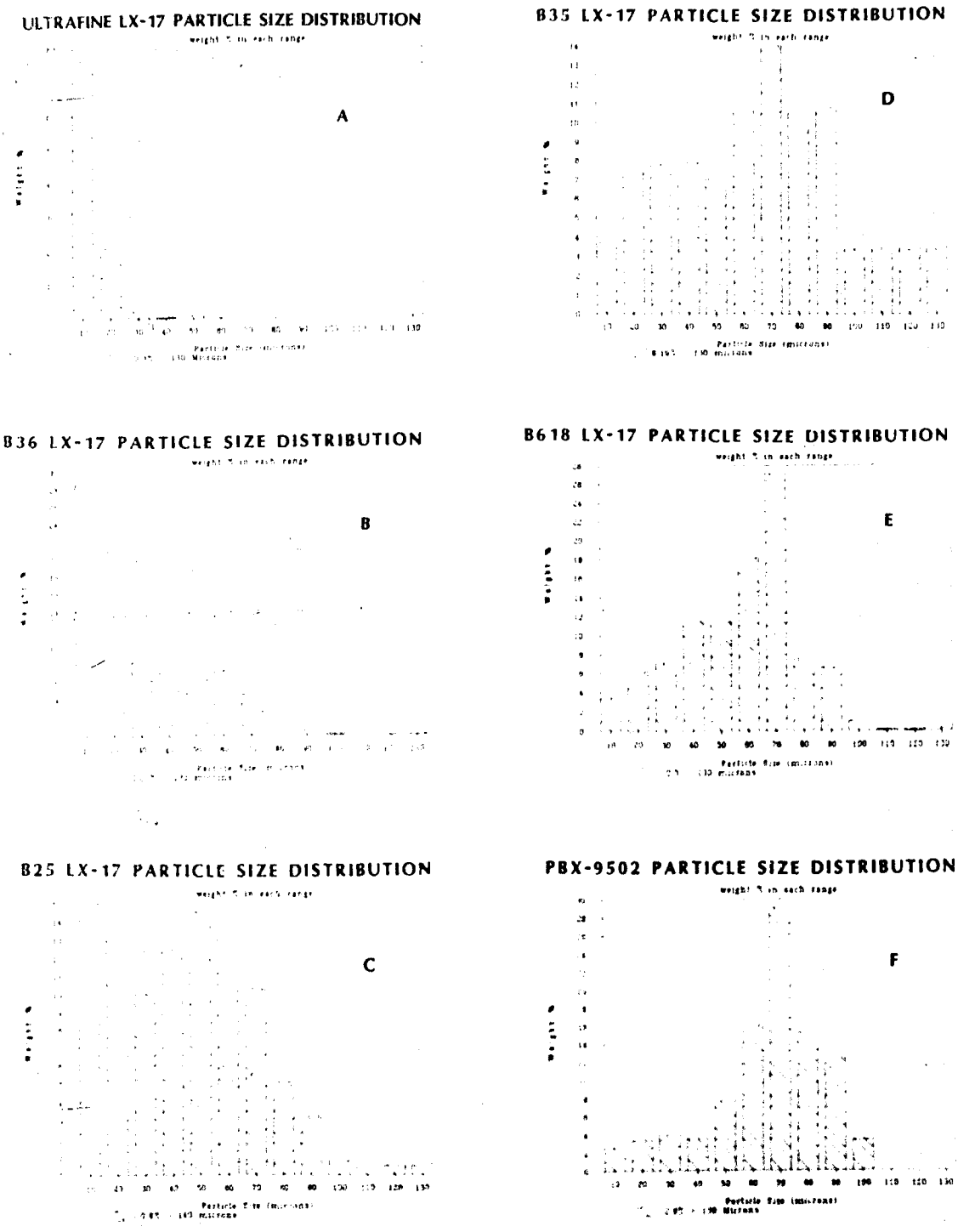

Fig. 2. Particle-size distributions of TATB used to make LX-17 and PBX-9502 for the threshold tests (The distributions are determined by the amount of powder passing through standard screens. The figures are arranged roughly in order of increasing coarseness. Figure 2A is the particle-size distribution for ultrafine TATB. Figure 2G (next page) is the particle-size distribution for the very coarse elutriated batch with the fine particles washed out. In each figure the first block indicates the percent of the material with particles in the range 0-10 μ, etc.)

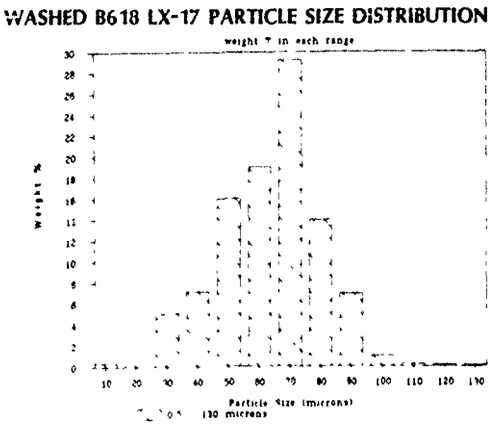

Fig. 2G. (See previous page)

DISCUSSION OF THRESHOLD RESU'

LX-17 made with ultrafine TATB (76% by weight smaller than 10μm) had the finest particle-size distribution for these tests (see Figure 2A). This material had the lowest threshold, particularly at 1.80 density, where threshold, at −54 °C was less than that of any other LX-17 formulations at ambient temperature.

General observations for these data are:

- The threshold for shots at −54 °C is 2-4 GPa higher than at ambient temperature.
- The threshold curve rises faster near the maximum density.
- There was a greater effect on the threshold from particle-size at lower densities.

The results of these experiments depend on density, temperature and particle-size distribution in a complicated relationship.

It is surprising that particle-size distribution has little effect on 1-D shock initiation threshold but a large effect on divergence. Temperature has a predictably large effect on both 1-D thresholds and divergence.

THEORETICAL MODELING

Previous one and two-dimensional applications of the ignition and growth model (4) of shock initiation to LX-17 concentrated on sustained shock experiments using embedded manganin gauges, run distance to detonation versus initial shock pressure, and self-sustaining detonation wave reaction zone length and metal acceleration (5-8). As discussed in detail by Tarver et al. (9), accurate modeling of shock initiation of solid explosives, including LX-17, by spherically diverging shocks from booster explosives, by very short duration, high pressure shock pulses from electrically accelerated Mylar foils, and by relatively short duration, lower pressure, single and double shocks in embedded gauge experiments, required modification of the ignition and growth model to include three terms in the reaction rate law. The details of the reaction rate law, the equation-of-state, and the values of the input parameters for LX-17 are given by Tarver et al. (9). This paper contains the results of the application of this model to recent LX-17 shock initiation data.

BOOSTER MODELING

The main modification of the ignition and growth model for LX-17 initiation calculations is to allow a greater fraction of the explosive to be rapidly ignited by a very high pressure, short duration shock front. The dependence of the ignition rate on the degree of compression or the initial shock pressure is also much steeper than previously reported (4,5). Thus modified, the ignition and growth model ignites a sufficient amount of TATB to accurately simulate very high pressure, very short pulse duration experiments. In the case of shock initiation by a spherically diverging detonation wave from an LX-10 booster charge, the LX-17 is subjected to a shock pressure in excess of its von Neumann spike and Chapman-Jouguet (CJ) pressures for only a few nanoseconds (compared to an overall reaction time of approximately 250 nanosecond in a self-sustaining LX-17 detonation wave). This shock is followed by a very steep rarefaction wave due to the small booster and divergent geometry. Sufficient chemical reaction must be initiated in the LX-17 to prevent complete failure of the shock wave from LX-10 as its shock pressure decreases. If the shock-front pressure is maintained above a critical value for a sufficient time, the main TATB reaction occurs and a spherically diverging detonation wave that gradually approaches

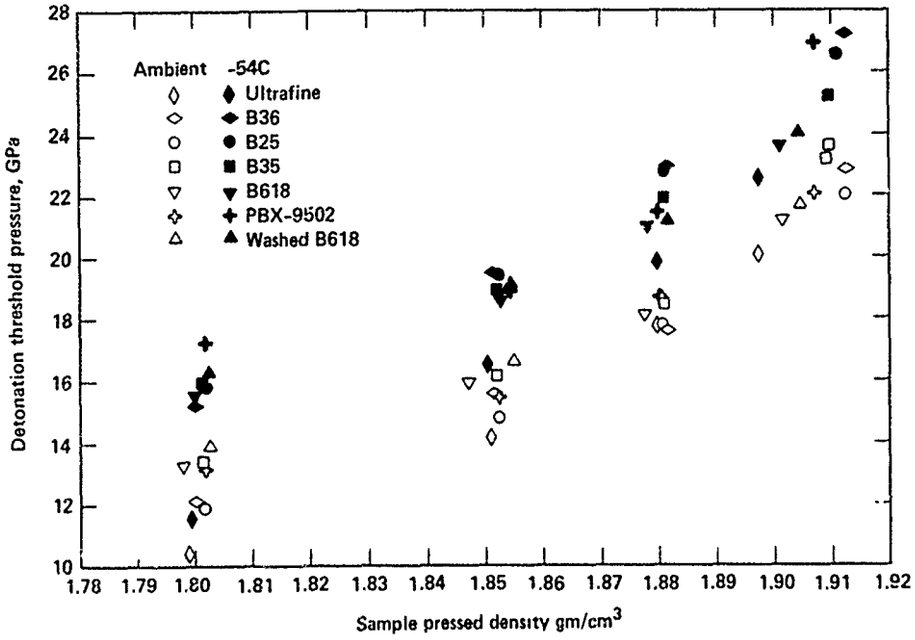

Fig. 3. Detonation pressure versus sample density for six samples of LX-17 and one of PBX-9502 with an extreme range of particle-size distributions as shown in Figure 2 (The tests were made with an electric gun with 25.4 mm diameter flyers and a pulse length of about 80 ns.)

CJ velocity is produced in the LX-17 charge Figure 4 illustrates the calculated failure of a 12 mm radius LX-10 charge to initiate LX-17 by the decay of the pressure-time profiles at various distances into LX-17. Figure 5 illustrates the successful initiation of LX-17 by a 14 mm radius hemisphere of LX-10, with similar pressure-time profiles. The calculated LX-17 detonation wave velocity as a function of spherical propagation distance from a 15.9 mm radius LX-10 charge agrees with the experimental data of Bahl et al. (10).

THIN PULSE EXPERIMENTS

The short duration pulses produced by the impact of Mylar or Kapton flyer plates accelerated by electrically exploded aluminum foils are in the same high pressure regime as the booster pulses but are planar, one-dimensional and flat topped. The decay of the pressure behind the Mylar plate depends on its acceleration history, the amount of electrical energy used, and the presence of remaining aluminum vapor. For conservative modeling purposes, the Mylar flying plates were assumed to be fully accelerated with no vaporized material behind them. The experimental threshold velocity data of Honodel et al. (11) for LX-17 subjected to five Mylar thicknesses from 0.051 mm to 1.27 mm is listed in Table 5 along with the calculated threshold velocities for 10 mm thick samples of LX-17. The agreement between calculation and experiment is good except that the calculations do not initiate for the thinnest Myler flyer. For this 0.051 mm-thick flyer accelerated to a velocity of 7.7 km/s, the calculated initial pressure in LX-17 is approximately 54 GPa and the pulse

TABLE 5

Comparison of Experimental and Calculated Threshold Velocities for Thin Pulse Initiation of LX-17

Mylar Flyer Thickness (mm)	Experimental Threshold Velocity (km/s)	Calculated Threshold Velocity (km/s)
0.051	7.7 ±0.5	>10.0
0.127	5.15±0.25	5.5±0.1
0.254	4.4 ±0.2	4.5±0.1
0.508	4.1 ±0.15	3.8±0.1
1.27	3.6 ±0.2	3.4±0.1

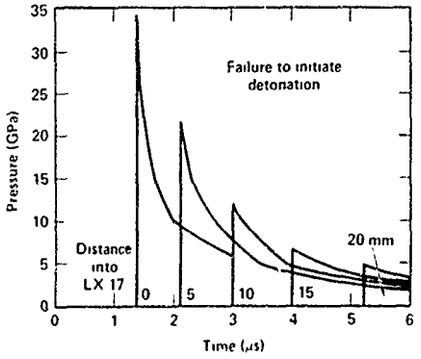

Fig. 4. Calculated pressure profiles in LX-17 from a 12 mm radius LX-10 booster

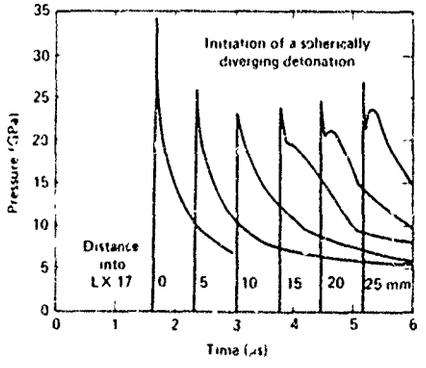

Fig. 5. Calculated pressure profiles in LX-17 from a 14 mm radius LX-10 booster

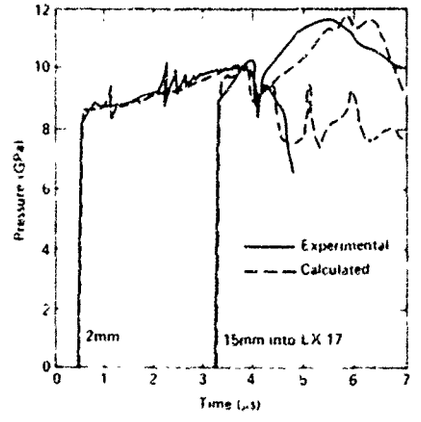

Fig 6. Pressure histories in LX-17 for an 8.4 GPa sustained shock wave experiment

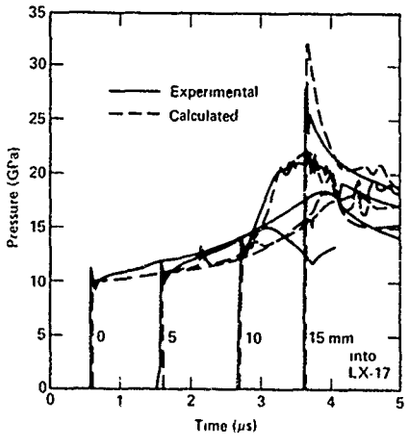

Fig. 7. Pressure histories in LX-17 for a 10.5 GPa sustained shock wave experiment

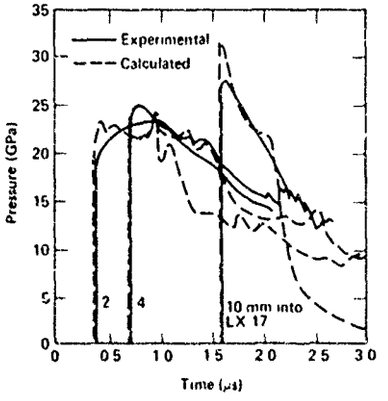

Fig. 8. Pressure histories in LX-17 for a 16 GPa sustained shock wave experiment

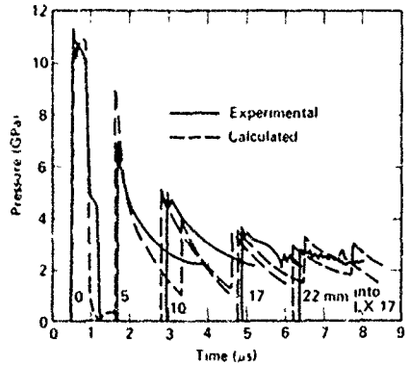

Fig. 9. Presure histories in LX-17 for a 10.8 GPa, 0.35 μs shock wave

duration is approximately 7 ns. Even though approximately 60% of the LX-17 in the first computational zone reacts, the pressure decay is so rapid that the subsequent pressure-dependent reaction cannot continue. If a small amount of aluminum vapor at a density of approximately 1 g/cm^3 is assumed to be pushing the Mylar flyer, a calculated detonation in LX-17 can be produced with a Mylar flyer velocity of 7.7 k/ms. Although this ultra high pressure, very short pulse duration test remains a calculational problem, the current model accurately predicts the remaining threshold velocities for pressures up to 30-40 GPa and shock pulse durations as short as 20-30 ns.

EMBEDDED GAUGE EXPERIMENTS ON LX-17

While accurate simulation of these ultra high pressure, very short duration shock initiation tests is important for assessments for initiation reliability, the more difficult task of modeling lower pressure, single and double shock pulse initiation is essential to hazard and vulnerability assessments. Although this relatively simple phenomenological ignition and growth model cannot be expected to perfectly simulate every shock initiation and detonation experiment, we have attempted to calculate all of the available experimental data and simulate it as well as possible. Previously only run distance to detonation versus sustained shock pressure, embedded manganin pressure gauge data from sustained shock experiments at pressures above 11.6 GPa, and two-dimensional initiation/failure/divergence data were available for LX-17 (4, 5). Embedded manganin pressure gauge records from experiments using lower and higher sustained shock pressures and single and double short duration shocks are reported and modeled in this paper. To accurately simulate multiple manganin gauge results, the details of the relatively thick gauge packages (typically 1 mil of manganin sandwiched between 5-mil-thick Teflon insulation layers) must be included in the finely zoned calculations. The embedded particle velocity gauges (12) are much thinner (generally 0.025 mm of aluminum surrounded by 0.025 mm of Teflon) and thus perturb the reactive flow less than the thicker manganin gauges. Use of a combination of gauges also allows us to do Lagrange analysis (13) of the flow. However, the particle velocity gauges require a magnetic field that cannot be broken by a metallic flying plate. A nonmetallic (ceramic) flying plate material has been obtained that can be driven fast enough in our four-inch gas gun to yield the high pressures required for LX-17. Two examples of multiple embedded particle velocity records in double shock pulse experiments in LX-17 are also reported.

The pressure-time curves calculated using the modified ignition and growth model parameters for LX-17 are compared to two embedded manganin gauges records at depths of 2 and 15 mm for a sustained 8.4 GPa shock experiment in Fig. 6. At this low impact pressure, LX-17 exhibits some ignition near the shock front and a small amount of growth of this reaction well behind the shock. The excellent agreement between the calculations and the experimental records results in part from the use of the critical compression required for any ignition parameter (labeled a. in Reference 9). This parameter is set equal to 0.22 corresponding to a shock pressure of approximately 6.5 GPa for the LX-17 unreacted equation-of-state. Allowing no ignition of reaction for initial shock pressures below 6.5 GPa is consistent with the experimental data of Green (14), who observed no shock-to-detonation transitions in 102 mm thick LX-17 charges below 7 GPa, and of Von Holle et al. (15), who observed little or no emission of infrared radiation from high density TATB explosives shocked to 6-7 GPa. The ability of the calculations to reproduce fine details of the pressure profiles produced by the interaction of the LX-17 reactive flow and the finite thickness gauges indicates that the manganin gauges are faithfully recording the pressure profiles.

Figure 7 shows a comparison of measured and calculated pressure histories at 0, 5, 10, and 15 mm into LX-17 shocked to approximately 10.5 GPa with a sustained pulse. Both the increase in shock front pressure and the growth of reaction behind the shock agree closely. This model also accurately calculates the previously reported pressure histories (4, 5) measured in five experiments with sustained shock impact pressures of 11.5-12 GPa. A final check of this model for sustained shocks is shown in Fig. 8 for a 16 GPa impact pressure experiment with 2, 4, and 10 mm deep manganin gauge packages.

In the LX-17 short pulse experiments, high density Al_2O_3 ceramic flyers were used to impact a similar buffer in contact with the explosive. The flyer velocity and thickness were varied to obtain embedded manganin gauge records of a rapidly failing shock front, a slowly failing shock, and a shock to detonation transition in LX-17. Figure 9 shows the comparison between the calculated and experimentally measured pressure histories at 0, 5, 10, 17 and 22 mm depths in the rapidly failing experiment in which a 2.5 mm thick ceramic impacts the ceramic buffer and LX-17 at 1.55 km/s. This impact produces a 10.8 GPa, 0.35 μs shock which ignites approximately 2 percent of the LX-17 in the first zones of the calculation. The calculated fraction reacted in this region reaches only 5 percent in 8 μs, the decaying shock ignites less LX-17 as its pressure decays. The agreement between calculation and experiment for the rate of shock front decay is good. The calculations predict well-defined subsequent weaker shocks that perhaps are smeared out by more chemical reaction in the experiment. Figure 10 contains a similar comparison for the more slowly decaying shock experiment in which a 4 mm thick flyer impacted at the same velocity, 1.55 km/s. During this 0.6 μs-pulse duration, approximately 3.5% of the LX-17 near the buffer plate ignited but grew to only 9% in 8 μs. The calculated shock front decay and pressure profiles behind the shock are lower than the experimental records, indicating that the slow growth of reaction behind the front was underestimated in this calculation. This type of quantitative data from marginal shock initiation experiments can thus be very useful in normalizing slow growth of reaction rates in various pressure regimes. The third single pulse experiment used a 4 mm thick flyer driven to a velocity of 1.69 km/s, and the subsequent 12 GPa, 0.6 μs shock produced a detonation in the 16 mm thick LX-17 charge. Figure 11 contains the gauge records and calculation at 0, 3, 6 and 16 mm depths. In all of these experiments a KCl crystal was placed behind the LX-17 for use as a window for a combined infrared radiometry experiment. The calculation correctly predicts a detonation at 16 mm and matches the shallow depth gauge records fairly well. Additional experiments are planned for different initiation conditions with gauges embedded deeper into the rapid reaction region.

Two ceramic plates separated by different thicknesses of carbon foam were used to produce two shocks separated by a rarefaction wave in LX-17. One double pulse experiment produced two 11 GPa, 0.3 μs shocks separated by 0.6 μs. The embedded particle velocity gauge records and the corresponding calculations at 0, 7, 12 and 20 mm into LX-17 are shown in Fig. 12. The calculated fraction reacted in the first LX-17 zone is 2% ignited by the first shock, an additional 3% ignited by the second shock, and 14.5% after 8 μs. The measured two-shock, mainly unreacted profile is clearly reproduced by the calculations, although there are differences in the minimum and maximum particle velocities in various regions. These differences are most likely due to a lack of knowledge of the equation-of-state of the ceramic material which is currently being studied. A higher impact pressure experiment with a longer time between shock pulses produced a greater degree of reaction. The particle velocity histories produced by 11.5 GPa shocks separated by 3 μs at the 0, 3,

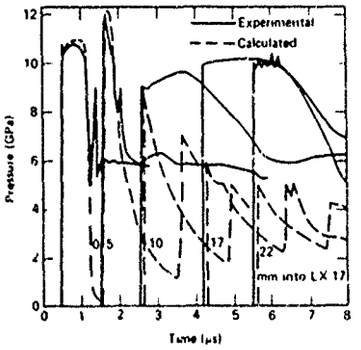

Fig. 10. Pressure histories in LX-17 for a 10.8 GPa, 0.6 μs shock wave

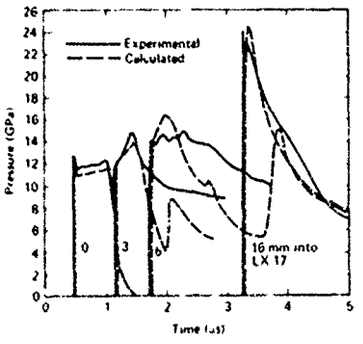

Fig. 11. Pressure histories in LX-17 for a 12 GPa, 0.6 μs shock wave

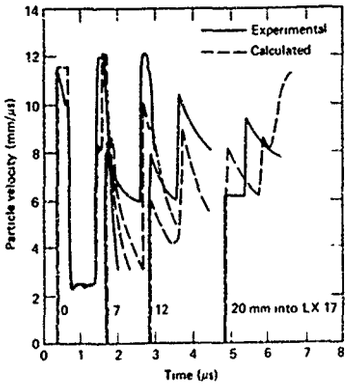

Fig. 12. Particle velocity histories in LX-17 for a double shock wave experiment consisting of 11 GPa shocks separated by 0.6 μs

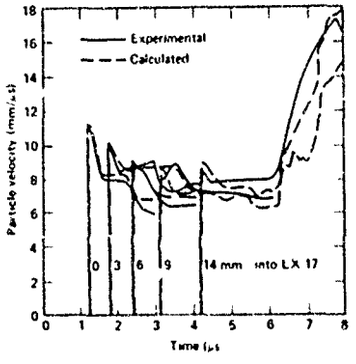

Fig. 13. Particle velocity histories in LX-17 for a double shock wave experiment consisting of 11.5 GPa shocks separated by 3μs

6, 9 and 14 mm depths of LX-17 are shown in Fig. 13. The fraction reacted in the first LX-17 zone was 2% ignited by the first shock. It grew to 10% in the 3 μs between shock pulses, jumped to 12% during the second pulse, and grew slowly to 34% after 8 μs. Both the gauges and calculations show a decrease in initial shock strength followed by considerable reaction behind the second shock pulse. The close agreement between experiment and theory at the 14 mm depth indicates that the complex interaction of the reactive flow with the applied hydrodynamic motion is being accurately measured and calculated.

CONCLUSIONS

The results presented in this paper indicate that a great deal has been learned experimentally and theoretically about the complex shock initiation properties of LX-17. However, in order to completely understand thin pulse initiation of plastic bonded TATB, we need further research using the most appropriate new techniques. The recently developed embedded gauge techniques, shock initiation models, and other modern experimental techniques, such as infrared radiometry and Fabry-Perot laser interferometry, provide the finely time resolved tools required to accomplish this task of understanding chemical energy release in LX-17 and other insensitive high explosives.

REFERENCES

1. R.K. Jackson, L.G. Green, R.H. Barlett, W.W. Hcfer, P.E. Kramer, R.S. Lee, E.J. Nidick, Jr., L.L. Shaw and R.C. Weingart Proc. of the Sixth Symp. (International) on Detonation, 1976, Office of Naval Research, ACR-221, (U.S. Government Printing Office, Washington, D.C.) p. 755.
2. R.C. Weingart, R.S. Lee, R.K. Jackson, and N.L. Parker, ibid, pp. 653-663.
3. G.H. Bloom, H. Chau, R. Glaser, C. Honodel, R.S. Lee, and R.C. Weingart, Shock Waves in Condensed Matter - 1983, Ed. J.R. Asay, R.A. Graham, and G.K. Straub,(North-Holland, 1984), pp. 535-538.
4. E.L. Lee and C.M. Tarver, Phys. Fluids *23*, 2362 (1980).
5. C.M. Tarver and J.O. Hallquist, Seventh Symposium (International) on Detonation, Annapolis, MD, Naval Surface Weapons Center NSWC MP 82-334, 1981, p. 488.
6. B. Hayes and C. Tarver, ibid., p. 1029.
7. C.M. Tarver, N.L. Parker, M.G. Palmer, B. Hayes and L.M. Erickson, J. Energetic Materials, *1*, 213 (1983).
8. C.M. Tarver and P.A. Urtiew, Progress in Astronautics and Aeronautics *94*, 369 (1983).
9. C.M. Tarver, J.O. Hallquist, and L.M. Erickson, paper presented at this symposium.
10. K.L. Bahl, R.S. Lee, and R.C. Weingart, Shock Waves in Condensed Matter (J.R. Asay, R.A. Graham and G.K. Straub, eds.), North-Holland, New York, 1984, p. 559.
11. C.A. Honodel, J.R. Humphrey, R.C. Weingart, R.S. Lee and P. Kramer, Seventh

Symposium (International on Detonation, Annapolis, MD, Naval Surface Weapons Center NSWC MP 82-334, 1981, p. 425.

12. L.M. Erickson, C.B. Johnson, N.L. Parker, H.C. Vantine, R.C. Weingart and R.S. Lee, ibid., p. 1062.
13. G.L. Nutt, and L.M. Erickson, J. Energetic Materials *2*, 263 (1984).
14. L.G. Green, private communication, (1985).
15. W.G. Von Holle, Shock Waves in Condensed Matter (J.R. Asay, R.A. Graham, and G.K. Straub, eds.), North-Holland, New York, 1984, p. 283.

DISCUSSION

MANFRED HELD, MBB APPARATE, FRG

Have you measured the arrival time and pressure (or pressure-time history) of your hemispherical booster? In my opinion your not-hemispherical output reflects the unsymmetry of the booster.

REPLY BY KERRY BAHL

We used a streak camera to record the time profile of the shock arrival at the hemispherical surface of the booster as well as at the surface of the acceptor HE. The two profiles are not necessarily similar. For instance, for a cold, 8.5 mm radius, LX-07 booster, the shock breaks out first at 52° on both sides of the booster pole and quickly spreads to the pole and waist. Whereas, for a cold, 10 mm thick, coarse-particle, PBX-9502 acceptor charge over the same booster, the shock front breaks out first at the pole, and the total region of detectable reaction only grows to 51° or 52° on both sides of the pole. The initiation and propagation of detonation in TATB acceptor charges are affected by the particle-size distribution and temperature of TATB, as well as by the shape, size and detonation pressure of the booster.

DISCUSSION

G.D. COLEY, AWRE, UK

How much of the decrease in the sensitivity of TATB PBX with temperature can be explained in terms of charge densification?

REPLY BY R. LEE

A temperature change from 20 °C to −54 °C gives about a 1% change in density. At 1.8 g/cm^3 density, where the density-threshold curve is relatively flat, the increase in threshold pressure due to a 1% density increase would only be about 20% of the observed change between 20 °C and −54 °C. Furthermore, it is difficult to understand how a temperature-induced density change would affect the sensitivity. Even though the density is higher at the lower temperature, the number of voids is the same, and average void size is only decreased by 1%.

DISCUSSION

M.M. CHAUDHRI, Cavendish Laboratory, UK

You indicated a strong particle size effect — the ultrafine particles (< 10 micrometers) showing a much more sensitive behavior than the large particle charges. Would you comment on whether this effect is due to the size of the interstices or due to the grains themselves?

REPLY BY R. LEE

In another paper presented at this meeting, we showed results of mercury intrusion porosimetry measurements on pressed TATB pellets of various densities. For densities in the 1.4-1.6 g/cm^3 range, there was only a modest increase in threshold with increasing density of the charge, even though there was a large decrease in average void size as determined from the porosimetry measurements. This would lead one to conclude that the average void size is not the controlling mechanism for the shock sensitivity of TATB in this density range. The porosimetry results were more questionable for densities of 1.8 g/cm^3 and higher, so a conclusion is more speculative, but my feeling is that average void size is not the controlling factor.

THE SHOCK DENSENSITIZATION OF PBX-9404 AND COMPOSITION B-3

A.W. Campbell and J.R. Travis
Los Alamos National Laboratory
Group M-3, MS J960
Los Alamos, New Mexico 87545

PBX-9404 and Composition B-3 were desensitized by subjecting them to shock in the pressure range 10 to 24 kbar. Results show that the collapse of voids, and thus the activation of hot spots by shock waves, takes time and may require more than 5 μs. This time is, in a way, a counterpart of the induction time for shock initiation of a homogeneous explosive. Gittings' data are adduced to extend the results to 100 kbar and to show that at high pressures desensitization occurs in a very brief time "window".

When the voids have been collapsed, the relatively homogeneous explosive is resistant to detonation through an Arrhenius type of reaction because of the lower shock temperature resulting from double shocking. This conclusion is supported by experiments on single crystals of HMX and by shock temperature calculations.

The time required for desensitization of PBX-9404 is related to pressure by the expression $p^{2.2}\tau=1150$.

INTRODUCTION

Often, explosive charges which have been subjected to a shock wave of low amplitude are undetonable. This desensitization by what will be referred to as "preshock" is a common observation.

A prominent example of shock desensitization occurs in blasting rock and coal, where it results in leaving undetonated explosive in the rubble (1). Desensitization is caused by a shock wave which is generated in the annulus between blasting explosive and the bore hole and which precedes the detonation wave. This phenomenon is referred to as the "channel effect" and has been studied extensively (2,3).

Another field in which shock desensitization is frequently encountered is that of jet attack of explosive behind a metal barrier as in the destruction of munitions (4). The explosive is preshocked by a divergent shock wave generated in the barrier as the jet penetrates it. Although the high particle velocity of the jet impinging on the explosive may cause it to react locally, the reaction does not propagate as a divergent detonation wave in the surrounding preshocked explosive.

Drimmer and Liddiard (5) studied preshocking in thin slabs of explosives and came to the conclusion that desensitization resulted from the elimination of potential hot spots through compression of the explosive beyond the density corresponding to voidlessness. In a study of initiation of heterogeneous explosives, Campbell et al. (6) preshocked PBX-9404 with a 39 kbar shock wave and then attempted to detonate it with a 90 kbar shock wave without success. On the other hand, Tarzhanov (7) used similar multiple shocking to measure the detonation velocity of shock-compressed cast TNT, and Dunne (8) studied Mach waves formed in detonating C-4 which had been preshocked with a 50 kbar wave. Recently, Boyle and Pilarski (9) subjected pressed and cast TNT to double shocking and found that the first shock decreased the response of the explosive to the second shock.

We have encountered shock densensitization in many instances, including jet attack of

munitions, explosive logic trains, embedded detonators, and corner turning. Because of the variety of experience with preshocking quoted above, it seemed necessary to examine preshocking in more detail and, after some false starts, we developed the experimental technique described in the next section.

EXPERIMENTAL

Two explosives were studied — PBX-9404 pressed to a density of 1.84 g/cm^3 and cast Composition B-3* at a density of 1.70 g/cm^3. These densities corresponded to about 2% voids.

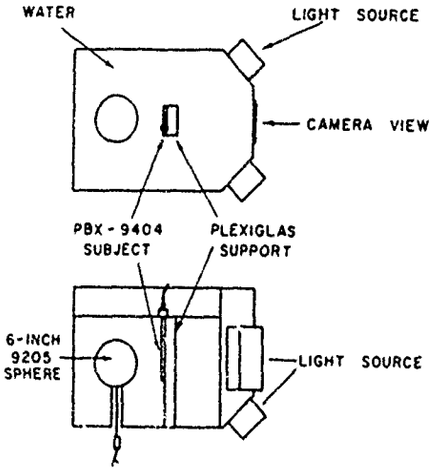

Fig. 1. Sketch of experiment to test detonability of a preshocked slab of explosive

Figure 1 shows the experimental arrangement used to observe quenching of detonation. The subject charge consisted of two squares of explosive arranged to form a slab measuring 101.6×203.2 mm and having a thickness in the range 2.54 to 12.7 mm. This slab was cemented to a larger rectangle of Plexiglas 25.4 mm thick, and the assembly was immersed in water in a carefully measured relationship to a 152.4 mm sphere of PBX-9205.** which served as a shock generator. This generator had been calibrated by Hantel and Davis (10), and we used their results and the Hugoniot data for water of Rice and Walsh (11) to calculate pressures in the shocked explosive. Detonation of the subject charge and of the shock generator was timed so that as the detonation wave swept downward in the slab it encountered an upward spreading shock wave. Events at the surface of the subject charge were photographed with a framing camera having a capacity of 15 frames and an interframe time of 0.4 μs.

Figure 2 shows two frames from a framing camera record of an experiment on PBX-9404 in which the input pressure at the locus of quenching was 13.3 kbar. The lower 101.6 mm square of explosive and part of the upper one are visible in the still frame. The subject was initiated at the top at a point 25.4 mm from the left edge. The shock generator was located behind the slab on a line perpendicular to the slab and passing through a point 51 mm up from the bottom and 12.7 mm to the right of the right edge. Thus, the detonation wave spread downward and rightward and the shock wave spread upward and leftward.

Interpretation of the action frames is as follows. At the discontinuity labeled A, the detonation and shock waves met. In several of the experiments, a fine bright line on the inner surface of the Plexiglas sheet marked this discontinuity clearly. The preshock wave, indicated by B, continued to spread upward and to the left in the Plexiglas and the detonation products. The detonation wave continued to spread downward into a region characterized in the print by the presence of surface bubbles, C. After penetrating the preshocked region for about 19.6 mm, the detonation reaction was quenched abruptly. Detonation continued to the end of the slab in a narrow zone between the left edge and the bubble region.

DATA

From the events recorded in this and similar experiments, it was evident that appropriate shocking caused desensitization of explosive after a brief time lapse. This time lapse, τ, was calculated in the following way. Measurement of the width of the zone between A and C of Fig. 2 was made along line F connecting the point of initiation and the perpendicular from the

*PBX-9404: 94 wt% HMX, 3% nitrocellulose, 3% tris-beta chloroethyl phosphate, 0.1% 2, 2-dinitropropyl acrylate: TMD=1.873 g/cm^3. Composition B-3: 60 wt% RDX, 40% TNT; TMD=1.737 g/cm^3.

**PBX-9205: 92 wt% RDX, 6% polystyrene, 2% dioctyl phthalate; TMD=1.713 g/cm^3.

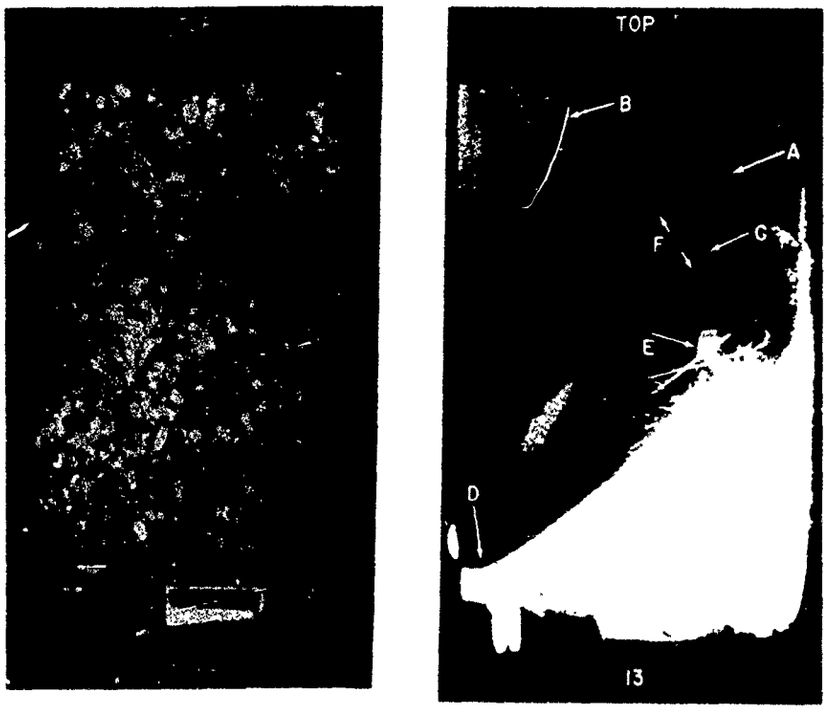

Fig. 2. Framing camera sequence showing shock desensitization of PBX-9404: A-intersection of preshock and detonation waves; B-preshock wave at picture time; C-quenching locus; D-detonation wave outside quench region; E-illumination artifacts; F-length of detonation run through preshocked explosive (Frames show entire width of 101.6 mm PBX-9404 charge. Very bright area in lower right is overexposed and looks much like the explosive in the still.)

explosive slab to the center of the shock generator. The time difference τ_s, between the arrival of the shock wave at A and C, was calculated from the charge geometry and the shock velocity in water. This calculation neglected the small difference in the two paths in the explosive and the largely compensating difference between the shock velocities in water and explosive.* The time τ_D for detonation between A and C was calculated at the increased density of the shocked explosive by use of the shock Hugoniot expressions

$$U_s=2.494+2.093\ U_p \text{ (PBX-9404)} \quad (12),$$

$$U_s=3.03+1.73\ U_p \text{ (Comp B-3)} \quad (13),$$

and a detonation velocity dependence of 0.0035 mm/μs/mg/cm^3. This small extension of the detonation velocity curve has been shown by Anderson et al. (14) to be valid for statically compressed solid explosives. The preshock time τ is thus

$$\tau=\tau_s+\tau_D.$$

Results of these calculations and the input pressures at the point of detonation quenching are listed in Table 1 and are plotted on the right side of Fig. 3.

On the left side of Fig. 3 and in Tables 2 and 3 are data of Gittings (15), which were used by Walker and Wasley (16) in establishing the $P^2\tau$ criterion for the critical energy of initiation. We have combined Gittings' data with ours because they included results which have hitherto escaped comment. These results show shock desensitization.

In Gittings' experiments pellets of PBX-9404, usually 6.35 mm thick, were struck by flying foils of aluminum which were spalled from a driver of high acoustic impedance, usually brass. Arrival of a foil at a pellet was detected with pins set flush with the initial surface of the pellet; detonation of a pellet was detected

*A detailed calculation with rarefaction was made for the worst case, shot C-3991, and the error was found to be less than 1%.

TABLE 1

Shock Desensitization

Shot No.	Charge Thickness (mm)	Input Pressure (kbar)	Densitization Time (μs)
	PBX-9404		
C-4046	2.54	23.7	0.87
C-3983	6.35	19.0	2.08
C-4036	8.46	16.9	1.85
C-3985	8.46	13.3	4.81
C-3984	8.46	13.3	4.64
C-3989	8.46	12.1	4.93
C-3991	8.46	10.3	5.39
C-3996	8.46	7.1	detonated
	Composition B-3		
C-4056	6.35	24.5	0.89
C-4003	12.70	14.5	3.69
C-3999	8.46	10.8	detonated

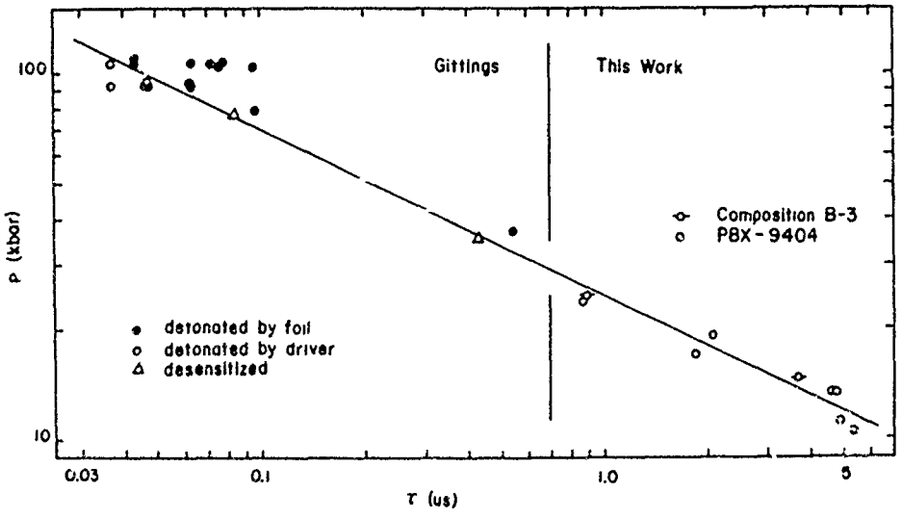

Fig. 3. Plot of data taken with shock waves generated in water and Gittings' data taken in vacuum

with ionization pins in contact with the back surface of the pellet.

Gittings' data as presented here include pressures we have calculated with the above-mentioned Hugoniot expression for PBX-9404 and the Hugoniot data of McQueen et al. (17) for 2024 aluminum

$$U_s = 5.328 + 1.338 U_p.$$

We also have made small changes to Gittings' shock duration times by making allowances for the shortened path and higher sound velocity encountered by the relief wave in the shock compressed aluminum.

In her report, Gittings distinguished detonation of a pellet by impact of a foil from detonation by impact of the massive driver. Thus, her data could be divided into two groups. However, in a few instances the pellet failed to detonate from either impact. These results are indicated in Figs. 3 and 4 by triangular symbols. They occur on the dividing line between the two groups of data and represent shock desensitization of the explosive by impact of the foils. Two results for pellets ≥5.2 mm thick showed only minor ionization and indicated densitization of

TABLE 2

Gittings' Flying Foil Results in Vacuum

Shot No.	Foil Velocity (mm/μs)	Foil Thickness (10^3 in.)	P (kbar)	τ (μs)	Result
1260	1.60	4.6	92	0.037	A
1262	1.61	4.6	92	0.037	A
1262	1.61	5.7	92	0.045	A
1260	1.61	5.8	92	0.046	A
1336	1.61	5.9	92	0.047	A
1563*	1.79	4.8	106	0.037	A
1563	1.79	4.8	106	0.037	A
1336*	1.64	5.9	95	0.047	A
1565	1.78	5.5	106	0.043	D
1565	1.78	5.5	106	0.043	D
1563*	1.78	5.5	106	0.043	D
1563	1.78	5.5	106	0.043	D
1381	1.39	10.3	76	0.084	D
1558*	1.82	5.6	109	0.043	D
1558	1.82	5.6	109	0.043	D
1558	1.82	5.6	109	0.043	D
1558*	1.82	5.6	109	0.043	D
1381	1.39	10.3	76	0.084	D
1384	1.40	10.3	77	0.084	B
1583**	0.75	49.5	35	0.436	C
1583**	0.75	49.5	35	0.436	C
1260	1.61	7.9	92	0.063	D
1262	1.64	7.8	95	0.062	D
1336	1.66	7.8	96	0.062	D
1381	1.38	12.0	75	0.098	D
1562	1.80	8.1	107	0.063	D
1562	1.80	8.1	107	0.063	D
1574*	0.78	62.3	37	0.546	D
1574*	0.78	62.3	37	0.546	D
1565	1.80	10.0	107	0.078	D
1565	1.80	10.0	107	0.078	D
1562	1.76	12.3	104	0.096	D
1562	1.76	12.3	104	0.096	D
1368-	1.79	9.3	106	0.072	D
1379-	1.43	10.4	79	0.084	D
1379-	1.42	12.	78	0.097	D
1381-	1.39	12.0	76	0.098	D
1384-	1.40	10.3	77	0.084	A
1384-	1.40	10.3	77	0.084	B

A Detonated by driver
B Desensitized
C Weak ionization signal
D Detonated by foil
* 0.375-in.-thick pellet
** 0.6-in.-thick pellet 0.8-in. diam.
— Unpublished data supplied by Elizabeth Gittings Marshall

almost the entire pellets despite the increased thickness.

In Fig. 4 and Table 3 data from similar experiments in a methane atmosphere are presented. Because of the precursor shock in the methane, all of these data are shifted towards higher pressures and longer times relative to the corresponding data in Fig. 3, which were obtained in vacuum.

In Fig. 3, the straight line is the result of fitting Gittings' data for densitization and our data by the method of least squares. The expression for this curve is

$$p^{2.2}\tau = 1150,$$

where P is expressed in kilobars and τ in microseconds. A portion of this curve is also plotted in Fig. 4.

HOMOGENEOUS DETONATION

When preshocked explosive fails to detonate

TABLE 3

Gittings' Flying Foil Results in Methane

Shot No.	Foil Velocity (mm/μs)	Foil Thickness (10^3 in)	P (kbar)	τ (μs)	Result
1239	1.61	4.0	92	0.032	A
1242	1.61	4.2	92	0.033	A
1237	1.59	4.7	91	0.037	A
1272	1.57	5.7	90	0.045	A
1239	1.61	5.6	92	0.044	A
1233	1.61	5.7	92	0.045	A
1240	1.85	4.1	111	0.032	A
1242	1.62	5.7	112	0.045	A
1240	1.86	4.7	112	0.036	A
1235	2.02	4.3	125	0.033	A
1225	2.05	4.3	128	0.032	B
1272	1.58	7.7	90	0.061	B
1239	1.61	7.7	92	0.061	B
1226	2.09	4.3	131	0.032	B
1222	2.02	4.6	125	0.035	D
1229	1.61	7.9	92	0.063	D
1242	1.62	7.8	93	0.062	D
1233	1.62	7.8	93	0.062	D
1240	1.87	5.8	113	0.045	D
1272	1.58	9.1	90	0.072	D
1224	2.04	5.2	127	0.039	D
1235	2.03	5.3	126	0.040	D
1226	2.04	5.3	127	0.040	D
1233	1.63	9.3	94	0.074	D
1225	2.05	5.8	128	0.044	D
1237	1.61	12.0	92	0.95	D
1225	2.02	7.8	125	0.059	D
1224	2.03	9.4	126	0.071	D
1222	2.04	9.6	127	0.072	D
1229	1.65	16.1	96	0.127	D
1226	2.03	16.2	126	0.122	D

A Detonated by driver
B Desensitized
D Detonated by foil

from a strong shock, there are at least two explanations: shock heating is insufficient to initiate the Arrhenius type of reaction, or the charge thickness is below the critical value for the propagation of such a reaction. In the latter case "dark" waves originating at the boundary interrupt the reaction. In shot C-3999, the Composition B-3 continued to detonate after preshocking but showed surface indications of homogeneous detonation. We conclude that, in the shots in which Composition B-3 failed to detonate, the charges were above critical thickness, but shock heating by the second shock was insufficient to initiate detonation promptly. In shot C-3996 indications of homogeneous detonation were not observed for PBX-9404; however, the time allowed for desensitizaton was marginal. From the fit to the other data, the time required was 15.4 μs, while the elapsed time at the last frame was 13.3 μs.

To explore the insensitivity of preshocked PBX-9404 to initiation by strong shock waves, Bobby Craig and we performed some experiments on what seemed to be the best substitute—single crystals of HMX. Prepared by Howard Cady of LANL, the crystals were free of significant voids. These experiments consisted of determining whether prompt detonation could be initiated in a crystal by detonating PBX-9404. The first of these experiments is sketched in Fig. 5. An HMX crystal 13 mm in diam. and 6.6 mm thick was placed on a cylinder of PBX-9404 25.4 mm in diam. and 26 mm high.

TABLE 4

Single-Crystal HMX, ρ_o=1.900 g/cm^3

Shot Number	P_o (a) (GPa)	U_o (b) (Km/sec)	1/2 b (b) (Km/sec^2)	U_s (c) (Km/sec)	U_p (d) (Km/sec)	x_{OT} (e) (mm)	t_{OT} (f) (μsec)	Thickness of Flyer Plate (mm)
E-3794	42.0	7.812	-2.291	7.55	2.93	0.80	0.11	2.52
E-3792	35.8	7.177	+0.191	7.20	2.61	4.40	0.61	3.53
E-3796	34.8	7.357	-0.016	7.35	2.49	7.4 (g)	21.22 (g)	4.03

(a) Initial shock pressure in the HMX from the impedance match solution.
(b) Parameters from the fit to the x-t data for the shock front: $x/t = R_o + 1/2\ bt$. U_o is the initial shock velocity and 1/2 b is the acceleration if the shock is plane and propagates parallel to booster axis.
(c) U_s is an estimated initial shock velocity based on the assumption that the shock advanced at a constant velocity and allowing for experimental complications.
(d) Initial particle velocity.
(e) x_{OT} is the average distance at which detonation overtook the shock front in the crystal.
(f) t_{OT} is the average time at which detonation overtook the shock front in the crystal.
(g) Overtake occurred after the initial shock had transited the crystal. The crystal was 7.4 mm thick. t_{OT} includes the time to overtake the moving free surface of the crystal.

TABLE 5

Multiple Shock Calculations for PBX 9404

First Shock (kbar)	Second Shock (kbar)	Temperature (K)	Induction Time* (μs)
360	0	1669	0.05
7	360	1442	0.20
10	360	1368	0.35
15	360	1267	0.82
20	360	1185	1.87
25	360	1118	4.04
50	360	917	84.4

*Solid HMX, E = 34.5 kcal/g, Z = 4.0 x 10^4 μs^{-1}

This assembly was immersed in water, and the transit time of the shock wave induced in the

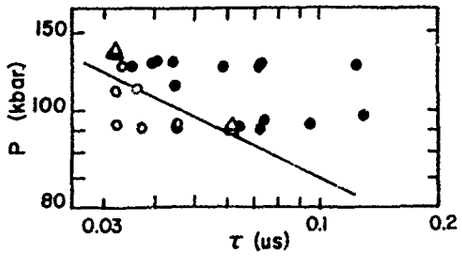

Fig. 4. Plot of Gittings' data taken in a methane atmosphere and a portion of the fitted curve of Fig. 3 (The boundary between data for detonation by a flying foil and detonation by the driver is displaced upward relative to similar data taken in a vacuum.)

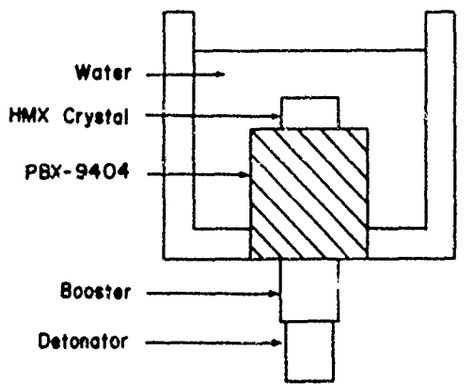

Fig. 5. Test of the initiability of an HMX crystal by PBX-9404

crystal by detonation of the PBX-9404 was recorded with a rotating mirror camera. Measurement of the camera record gave a value for the shock velocity in the HMX crystal of 6.25±0.2 mm/μs, a value well below that expected for detonation (>9 mm/μs).

In the second experiment, a crystal with similar dimensions was placed on a 25.4-mm-thick slab of PBX-9404 101.6 mm diam. and initiated by a plane-wave lens of similar diameter. This arrangement produced a better-supported shock wave and allowed more opportunity for the successful completion of an induction period in the initiation of the HMX crystal. Transit time of the shock wave in the crystal was measured with an ionization switch on the face of the PBX-9404 driver and a mechanical switch on the terminal face of the crystal. In addition, an ionization switch made of two strips of aluminum foil was placed on the crystal to detect reaction. The whole assembly was immersed in mineral oil.

Results showed again that the crystal did not detonate. The mechanical switch gave a signal after 1.079 μs—a time which corresponded to a shock velocity of 6.96 mm/μs. The ionization switch gave a slowly rising signal at 1.112 μs, which corresponded to a shock velocity of 6.76 mm/μs.

In a third experiment, a large HMX crystal 19 mm thick and a stack of two 6.35-mm-thick pieces of PBX-9404 were placed side by side on a 6.35-mm-thick slab of PBX-9404 initiated by a 101.6-mm-diam. plane-wave lens. This assembly was immersed in water and observed by means of a framing camera having a framing interval of 0.4 μs. Again, it appeared from the record that the HMX crystal did not detonate, while the pieces of PBX-9404 did.

B.G. Craig then performed three wedge experiments on crystals in which the shock pressures entering the crystals were higher than that induced by detonating PBX-9404. Craig has kindly permitted the inclusion of his results here.

Each experimental arrangement consisted of a plane-wave lens, a 50 mm slab of PBX-9404, a thin sheet of polyethylene, a flyer plate of magnesium, a free run space, a second plate of magnesium, and a wedge-shaped crystal of HMX. Use of a smear camera allowed measurement of the free-surface velocity of the magnesium plate against which the crystal rested, the shock velocity in the crystal, time of overtake of the shock wave by superdetonation, and, in one case, an estimate of the detonation velocity in an undisturbed portion of the crystal.

Results of these experiments are listed in Table 4. Two difficulties were encountered which prevented the results from being as satisfying as was hoped. First, the very high pressure in the second magnesium plate caused rapid deterioration of its polished surface so that the measurement of its free-surface velocity was not as accurate as desired. Also, the superdetonation light in the shocked portion of the crystal was not bright enough to be recorded. Consequently, the induction times were estimated from the overtake times by assuming a superdetonation velocity of 13 mm/μs. Induction times calculated

in this way together with shock temperatures estimated by Mader (18) using the method of Walsh and Christian are as follows:

Pressure (kbar)	Induction Time (μs)	Shock Temperature
420	0.05	1810
358	0.272	1489
320	failed	1340

From these data Mader also calculated the activation energy and the frequency factor for thermal explosion using the expression

$$t = \frac{CRT^2 e^{E/RT}}{QZE},$$

where the constants C, R, and Q had the values 0.40, 1.987, and 800. He then used these values of E and Z and calculated temperatures for doubly-shocked PBX-9404 to estimate induction times over the range of pressures covered by the data in Tables 1 and 2.

The induction times so calculated (Table 5) appear to be of the right order of magnitude to agree with our results; the calculated temperatures are of interest because they illustrate the reduction in shock temperature which occurs in double shocking.

DISCUSSION

Hot spot formation is generally accepted as the controlling feature responsible for the increased sensitivity of heterogeneous explosives relative to homogeneous ones. By such processes as shear and plastic flow, physical defects convert mechanical energy into heat and attendant local high temperatures. Chemical reaction occurs first at these hot spots, and the study of the kinetics of reaction is largely the study of the effects of hot spots. Voids within the explosive are a common source of hot spots, and a measure of the potential for hot spots is the percentage of voids. The size distribution of voids is also important, as is witnessed by the relative sensitivities of pressed TNT versus cast TNT at the same void content. Scott (19) has shown that coarse-grain compacts of PETN are more sensitive than fine-grained ones, presumably because larger hot spots are created and survive under marginal conditions of initiation. On the other hand, where rapid reaction is desired for a small failure diameter, fine-grained explosives are needed.

The time required for shock activation of hot spots is often assumed to be approximated by the times required for the defect to be traversed by the shock wave. The combined experimental results reported here show that shock desensitization is a time-dependent process. Our results in water reveal that when PBX-9404 is desensitized the potential hot spots can no longer be effectively activated, even by the detonation pressure (ca. 360 kbar) of unshocked explosive. This reduction in response to double shocking is further illustrated in Ref. 9.

Gittings' data show that desensitization is completed over a very short time interval. If one considers a succession of values of τ at constant input pressure (Fig. 3), one sees that as τ increases toward the critical value the brass driver continues to detonate charges on impact until the value of τ is very close to the curve. On the other side of the curve, very soon after the critical value of τ is exceeded, detonation occurs from impact of the foil. The narrowness of the critical region is further illustrated by the cluster of data at an input pressure of 77-79 kbar and a value of τ of 0.084 μs. This cluster includes five results—one detonation by impact of a foil, two detonations from impact of the driver, and two failures to detonate from either impact. The narrowness of the critical region was responsible for the small number of results which showed desensitization.

Given the pressure- and time-dependence of void collapse and the attendant plastic flow and shear processes associated with the formation of hot spots, it is important for efficient activation that the pressure rise be abrupt. Ramp and stepped shock fronts result in slower collapse of voids, more heat loss by conduction, and activation of fewer hot spots. Gittings' results in an atmosphere of methane (Fig. 4) fall above the curve fitted to data obtained in vacuum. We believe this to be largely due to the precursor shock in methane. On the other hand, Gittings' pointed out that the foils may have been distorted by pressure buildup between foil and pellet and that this bending could have led to early contact of the foils with pins. This effect would have increased the observed value of τ. We believe this to be a subsidiary effect, since it could occur only after significant pressure buildup between foil and pellet.

The value of τ obtained from the fit to the data

$$p^{2.2}\tau=1150$$

is the time necessary for complete activation of all hot spots potentially available at the input pressure P. It thus acts as the induction time for a self-propagating reaction. However, dependence of τ on pressure raised to a power greater than 2 emphasizes the importance of the initial shock pressure. The necessity of an induction period and the importance of the initial shock pressure were conclusions reached by Wackerle, et at. (20) in a combined experimental and calculational study of the initiation of PBX-9404. Time dependent relaxation of explosive is also in agreement with the elastic-plastic behavior observed by Kennedy (21) for PBX-9404.

In view of the results and discussion presented here, it seems desirable to regard the $P^n\tau$ criterion not as describing a critical energy input but as specifying the requirements for activating hot spots necessary to self-propagating detonation.

ACKNOWLEDGMENTS

We are indebted to K.G. Humphreys for executing our experiments with great care, to H.H. Cady for providing us with large HMX crystals of good quality, to B.G. Craig for permitting us to include his results for shock initiation of HMX crystals, to C.H. Mader for calculations of shock temperatures and induction times, and to W.C. Davis for constructive criticisms during preparation of this paper.

REFERENCES

1. J. Plant, "Explosives for Use in Coal Mines," Phys. Bull. *23*, pp. 203-207, 1972.
2. D.W. Woodhead, "Advance Detonation in a Tubular Charge of Explosive," Nature *183*, p. 1756, June 20, 1979.
3. L.V. Dubnov and I.D. Khotina, "Channel Effect Mechanism in the Detonation of Condensed Explosives," Fiz. Gor. i Vzr. *2*, No. 4, pp. 97-104, 1966.
4. M.C. Chick and D.J. Hatt, "The Mechanism of Initiation of Composition B by a Metal Jet," Seventh Symposium (International) on Detonation, Annapolis, Maryland, NSWC MP 82-334, pp. 352-261, June 16-19, 1981.
5. B.E. Drimmer and T.P. Liddiard, Jr., "Propagation Failure in Solid Explosives Under Dynamic Precompression," Naval Ordnance Laboratory report NOLTR 64-60, July 1964.
6. A.W. Campbell, W.C. Davis, J.B. Ramsay, and J.R. Travis, "Shock Initiation of Solid Explosives," Phys. Fluids *4*, No. 4, pp. 511-521, April 1961.
7. V.I. Tarzhanov, "Detonation Velocity of Shock-Compressed Cast TNT," Fiz. Gor. i Vzr. *12*, No. 6, pp. 924-930, 1976.
8. B.B. Dunne, "Mach Reflection of Detonation Waves in Condensed High Explosives," Phys. Fluids *4*, No. 7, pp. 918-924, 1961.
9. V.M. Boyle and D.L. Pilarski, "Shock Ignition Sensitivity of Multiply Shocked TNT, " Ballistic Research Laboratory report ARBRL-TR-02415, July 1982.
10. L.W. Hantel and W.C. Davis, ' Spherical Explosions in Water," Fifth Symposium (International) on Detonation, Pasadena, California, pp. 599-603, August 18-21, 1970.
11. M.H. Rice and J.M. Walsh, "Equation of State of Water to 250 Kilobar," J. Chem. Phys. *26*, No. 4, pp. 824-830, 1957; "Selected Hugoniots," Los Alamos Scientific Laboratory report LA-4167-MS, Supplemental Data, p. 3, May 1969.
12. T.R. Gibbs and A. Popolato, Eds., LASL Explosive Property Data, p. 93, University of California Press, Berkeley, CA, 1980.
13. V.M. Boyle, R.L. Jameson, and M. Sultanoff, "Determination of Shock Hugoniots for Several Condensed Phase Explosives," Proceedings—Fourth Symposium (International) on Detonation, White Oak, Maryland, October 12-15, 1965 (Office of Naval Research, Department of the Navy, ACR-126, 1965), pp. 241-247.
14. W.H. Andersen, L. Zernow, A.L. Mottet, Jr., and R.R. Randall, "Effects of Precompression upon the Detonation Properties of Liquid and Solid Explosives," The Fifth Symposium (International) on Detonation, Pasadena, California, August 18-21, 1970 (Office of Naval Research, Department of the Navy, ACR-184), pp. 67-75.

15. E.F. Gittings, "Initiation of a Solid Explosive by a Short-Duration Shock," Fourth Symposium (International) on Detonation, White Oak, Maryland, October 12-15, 1965 (Office of Naval Research, Department of the Navy, ACR-126, 1965), pp. 373-380.

16. F.E. Walker and R.J. Wasley, "Critical Energy for Shock Initiation of Heterogeneous Explosives," Explosivstoffe No. 1, pp. 9-13, 1969.

17. R.G. McQueen, S.P. Marsh, J.W. Taylor, J.N. Fritz, and W.J. Carter, "The Equation of State of Solids from Shock Wave Studies," in High-Velocity Impact Phenomena, Ray Kinslow, Ed., Academic Press, Chap. VII, pp. 293 et seq., New York and London, 1970

18. C.L. Mader and J.D. Kershner, "Three-Dimensional Modeling of Explosive Desensitization by Preshocking," Los Alamos National Laboratory report LA-UR-85468, 1985.

19. C.L. Scott, "Effect of Particle Size on Shock Initiation of PETN, RDX, and Tetryl," Fifth Symposium (International) on Detonation, Pasadena, California, pp. 259-266, August 18-21, 1970.

20. J. Wackerle, R.L. Rabie, M.J. Ginsberg, and A.B. Anderson, "A Shock Initiation Study of PBX-9404," Proceedings of the Symposium on High Dynamic Pressures, Paris, France, p. 127, 1978.

21. J.E. Kennedy, "Pressure Field in a Shock-Compressed High Explosive," Fourteenth Symposium (International) on Combustion, Pennsylvania State University, University Park, Pennsylvania, pp. 1251-1258; August 20-25, 1973.

DISCUSSION

M.S. SAMIRANT, ISL, France

Ten years ago we prepared single crystals of explosives (PETN, RDX, HMX). Even with a very energetic booster RDX and HMX fail to sustain detonation. Schnur (NRL) showed that the C-J conditions don't deliver enough energy to sustain a detonation wave in a perfect crystal of HMX and RDX.

REPLY BY CAMPBELL AND TRAVIS

Shock initiation of a propagating detonation in a secondary explosive requires that the charge to be initiated have a diameter which exceeds the critical value. Near this critical value, the initiating shock must produce in the explosive a shock wave having a pressure of amplitude and duration and a radius of curvature all equaling or exceeding the corresponding values in a propagating detonation wave.

In our experiments with monocrystals of HMX, we found that they could not be initiated with the C-J pressure of PBX-9404 (Ca. 360 kbar), which contained 94 wt.% of HMX and had an over-all density of 1.84 g/cm^3. However, Craig found that they could be initiated with a flat-topped shock wave of 420 kbar amplitude and observed an induction time of about 0.05μs.

We rationalized the difference in results obtained by the two methods of initiation by assuming that, in the case of PBX-9404, the von Neumann spike pressure, because of the heterogeneity of this explosive, either did not approximate 420 kbar or was not maintained long enough to satisfy the induction-time requirement of HMX. The spike pressure of HMX, suggested by extension of Craig's observations to a shock velocity of 9.11 mm/μs or by calculation with the derived shock Hugoniot of Olinger, exceeds 420 kbar. These considerations suggest that HMX will detonate if the crystal diameter exceeds the critical diameter.

We would expect the initiation of RDX monocrystals to be somewhat easier to achieve and, indeed, Koch and Baras reported that a powerful explosive initiation produced detonation which propagated for 1 to 1.5 diameters in cylindrically ground monocrystals 25 mm in diameter and clad with polystyrene. In raw, unclad crystals of unspecified but, presumably, similar cross section, they observed an arrest of detonation. If, as your question implies, detonation in the cylindrical geometry ultimately died out, it appears that the critical diameter is larger than 25 mm.

The critical diameter of homogeneous explosives is a large multiple of the reaction zone. For nitromethane, the ratio appears to be in the range of 100 to 1000. Milky appearing monocrystals of PETN in cylindrical form have a critical diameter between 6 and 7.5 mm. We

would expect the corresponding dimensions for RDX and HMX to be larger.

DISCUSSION

C. FAUQUIGNON, French-German Institute, Saint Louis, France

If a preshock loading renders the explosive homogeneous, is the build-up to detonation due to a second high intensity shock similar to that observed in classical homogeneous explosive, that is to say, does the reactive wave start at the rear surface?

REPLY BY CAMPBELL AND TRAVIS

Evidence of a front structure like that found in homogeneous explosive detonating near failure was observed in one shot (C 3999) in which detonation proceeded through the preshocked explosive. This suggests that homogeneous-like behavior was occurring, but with a very short induction time. Under conditions of stronger preshock, when quenching of detonation occured, it happened suddenly and no-reoccurence of detonation was observed in the remaining preshocked region of the sample.

DISCUSSION

GODFREY EDEN, AWRE, UK

I wish to clarify a detail of interpretation. What criterion did you use to decide that the explosive beyond boundary C in Fig. 2 was in fact undetonated?

REPLY BY CAMPBELL AND TRAVIS

The velocity of the wave in the preshocked region beyond the quench locus was determined from plotting wave positions from frame-to-frame. The velocity was substantially less than detonation velocity and was decreasing.

ON DETONATION DRIVEN AIR SHOCKS IN THE AIR GAP BETWEEN A CHARGE AND ITS CONFINEMENT

Gert Bjarnholt and Ulla Smedberg
Swedish Detonic Research Foundation (SveDeFo)
Box 32058, S-12611 Stockholm, Sweden

We have studied the explosives driven air shock that can move ahead of the detonation front when a long column of explosive is detonated with an air gap between the explosive and its confinement. Experiments were made in plexiglass tubes with a rectangular cross-section having an explosive/air gap cross-section area ratio of 1:1. The precursor air shock (PAS) is shown to be generated by the piston effect of the explosive products expanding into the air gap. Using different explosives the experiments covered a detonation velocity range of 1800-5200 m/s and PAS speeds of 3000-6000 m/s.

The TIGER code was used to model the non-ideal detonation of a typical water in oil emulsion explosive that we tested. Simple shock matching techniques for the products/air interface of this explosive show that the ratio of PAS to detonation speed is > 1 for ideal detonation and increases the more non-ideal the detonation is.

The effects of the PAS induced precompression of the explosive on detonation propagation are discussed and practical methods to slow down the PAS are suggested.

INTRODUCTION

When explosives are detonated in a geometry where there is an air gap between the explosive charge and its confinement an air shock in the air gap travelling ahead of the detonating front can be generated. The resulting precompression of the explosive, also called the channel effect, has been studied by several researchers in the past; Johansson et al. (1958), (1), Goldbinder and Tysevic (1967), (2), Dubnov and Kohna (1966), (3), Udy (1979), (4), Nakano and Mori (1979), (5) Hanasaki et al. (1982), (6) and Lownds and Plessis (1984), (7).

In practical rock blasting for example, long explosive column charges are often decoupled from the borehole wall by an air gap to reduce borehole pressure and vibrations on nearby structures and damage to the remaining rock wall when the final contour is blasted. The precursor air shock (PAS) travelling ahead of the detonation front in the air gap in the borehole will precompress the explosive ahead of the detonation front to a pressure of 10-100 MPa. If the PAS is reflected by some rigid surface normal to the flow in the air gap the local pressure will be in the range 100-1000 MPa.

Fig. 1 illustrates the PAS in the air gap between a cylindrical explosive charge and the borehole wall.

Depending on the type of explosive the precompression caused by the PAS can have different effects on detonation propagation. Most explosives rely on a heterogeneous initiation mechanism meaning that they need hot spots distributed in the explosive to propagate a detonation. These hot spots can be compressed if they are of the void type, for example air voids or gas filled micro spheres.

Depending on the type of explosive the precompression can either decrease or increase the velocity of the detonation front (3). The case when D is reduced by the precompression can

lead to an oscillating detonation velocity or detonation failure (dynamic dead-pressing). A precompression of 30-100 MPa will desensitize many commercial explosives relying on hot spots of the void type to such an extent that they cannot propagate detonation. If D is increased by precompression the propagation of detonation is not endangered but an oscillating behaviour can occur.

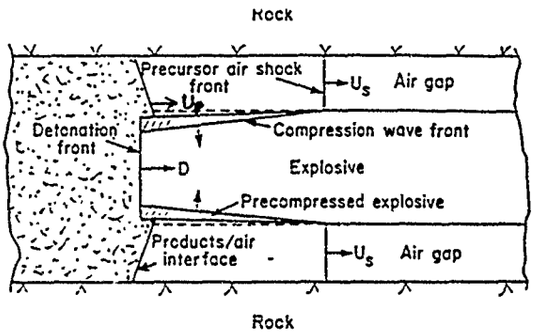

Fig. 1. Schematics of an air decoupled long cylindrical charge in a borehole in rock with a product driven air shock ahead of the detonation front

Previous work has concentrated mainly on the effect of the PAS on detonation propagation. We felt that more work was needed to understand the initial driving mechanism of the explosive products (EP). Of special interest are the initial velocities in the air gap of the EP and the PAS U_p and U_s respectively related to the detonation velocity D, for explosives with different D-values. The ratios U_p/D and U_s/D give important information regarding the potential for generation of a PAS which can get so far ahead of the detonation front that detonation failure can occur. Detonation failure can occur when the PAS is so far ahead of the detonation front that a thick enough layer of explosive is precompressed (see Fig. 1) and desensitized so that the failure thickness of the explosive is reached. Fig. 1 illustrates the PAS precompressing the explosive.

We have used tools as high speed framing photography and characterization of the ideal and non-ideal CJ states and expansion adiabates with the TIGER code (8) to increase our understanding of the forward flow of explosive products and air in the air gap between the explosive and its confinement.

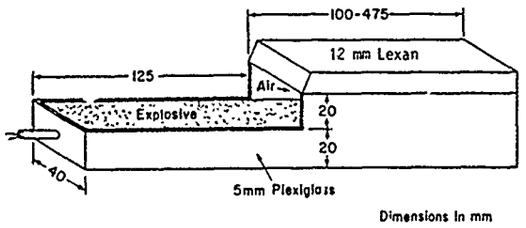

Fig. 2. Standard test charge geometry

EXPERIMENTAL

To study the detonation front and the PAS front, plexiglass tubes having a quadratic cross section as in Figure 2 half filled with explosives were detonated and studied using high speed framing photography.

We wanted to study the expansion of the EP into the air gap, the reflection of the EP and the PAS against the confining roof and the following expansion along the air gap. To register the events we used a Cordin 116 framing camera taking 26 frames with 0.8μs between frames and an exposure time of ≈ 0.3 μs per frame.

The plexiglass tubes were front lighted using two argon bombs. In some experiments the tubes were also backlighted using an argon bomb and Schlieren technique as shown in Fig. 3. A cheap plastic Fresnel lens was used to give parallel light from the back when Schlieren photos were required.

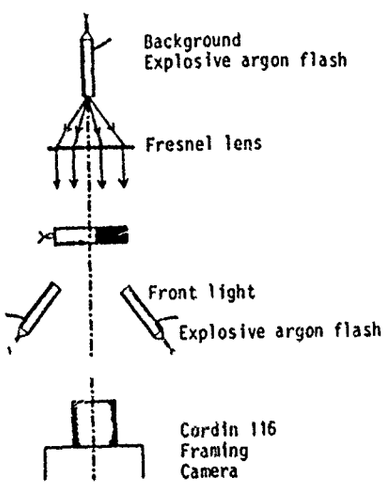

Fig. 3. Top view of experimental arrangement with camera

The explosives used in the experiments are listed in Table 1.

Gurit is an explosive used for contour rock blasting made by Nitro Nobel AB, Sweden. It is a low energy powder explosive sensitized by NG/EGDN and inert loaded with SiO_2.

Emulite is a Nitro Nobel AB produced, water in oil emulsion explosive containing mainly ammonium nitrate, fuel oil and water. It is sensitized by hollow gas filled microspheres and is cap sensitive. Pouring density mixtures of PETN and NaCl were also used. By changing the PETN/NaCl ratio the detonation velocity could be varied.

TABLE 1

Explosive	Density g/cm³	Approx. critical thickness for detonation mm	Ideal detonation velocity m/s
Gurit	1.00	8	≈ 3200
33 PETN/67 NaCl	1.06-1.13	10-12	—
40 PETN/60 NaCl			—
PETN	0.88	≈ 2	5200
Emulite	1.23	≈ 10-12	5900

EXPERIMENTAL RESULTS

Interpretation of photos

Our first experiments were designed to see if we could generate a PAS and be confident about interpretation of our framing photos. These experiments were therefore instrumented with detonation front and air shock arrival time probes. The detonation front probes were of the twisted pair type using 0.3 mm enameled Cu wire stretched across the tube in the explosive. The air shock arrival probes were flush mounted in the roof of the tube. They were activated by the pressure at the shock front which mechanically pushed a 0.05 mm Cu foil over a 0.1 mm air gap to give electrical contact with a 1 mm thick Cu base plate. The air gap was obtained by using 0.1 mm thick double adhesive tape with a 2 mm hole punched in it as a spacer between the foils. This probe design did not respond to the conductivity of the ionized gas in the PAS.

In a few experiments the conductivity of the gas in the air gap was also monitored at a point 20 mm from the end of the tube using a conductivity probe.

Figure 4 shows the detonation of a Gurit charge equipped with detonation and PAS velocity probes. The total charge length is 500 mm and the detonation front in Fig. 4 is 290 mm from the initiation end. This charge had a confining roof along the whole length of the charge. From analyses of the photos and the probe responses we found that after about 80 mm of "run up" the Gurit detonated with a constant velocity of about 2000 m/s and the PAS front velocity was constant at about 3000 m/s leading the "smoke front" seen in the air gap in Fig. 4 by about 2 mm.

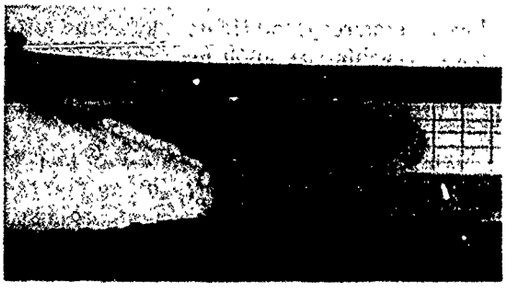

Fig. 4. Gurit charge with detonation front and PAS probes. $D \approx 2000$ m/s, $U_s \approx 3000$ m/s

It surprised us that the PAS was non-transparent (smokelike) only 2 mm behind the pressure front. To rule out vaporization of the plexiglass confinement as the cause of this smoke we repeated the experiment in Fig. 4 using glass instead of plexiglass. The photo showed the same smoke as in the plexiglass confined shots, ruling out the plexiglass as the cause of non transparency.

Figure 5 shows a Schlieren photo of a 40 PETN/60 NaCl charge with an explosive loading density of 1.07 g/cm³. On the original colour film the PAS front can be seen leading the brownish smoke front by 1-2 mm. The detonation velocity D=2800 m/s and the PAS front velocity U_s=3500 m/s.

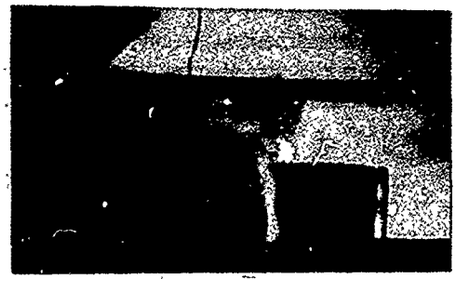

Fig. 5. Schlieren photo of a 40 PETN/60 NaCl charge showing the PAS front and smoke just behind the PAS front. Above the roof another air shock can be seen lagging the detonation front with about 30 mm, D=2800 m/s Shot No. 840706.

The explanation for the smoke just behind the shock front is according to Zeldovich and Razier (9) that dissociation and oxidation of air take place in a microsecond time scale behind an air shock travelling at 3000 m/s. Enough of the brownish looking gas NO_2 could thus be formed to explain what we see in the photos.

Figure 6 gives the temperature and the pressure at an air shock front felt by an observer travelling along at the particle speed behind the front (9). When the shock is travelling faster than about 4000 m/s it becomes selfluminous in our photos. The effective aperture of the camera is about f/16 and the film used is Kodak Ektachrome 200. Our experimental data discussed in this paper are summarized in Table 2.

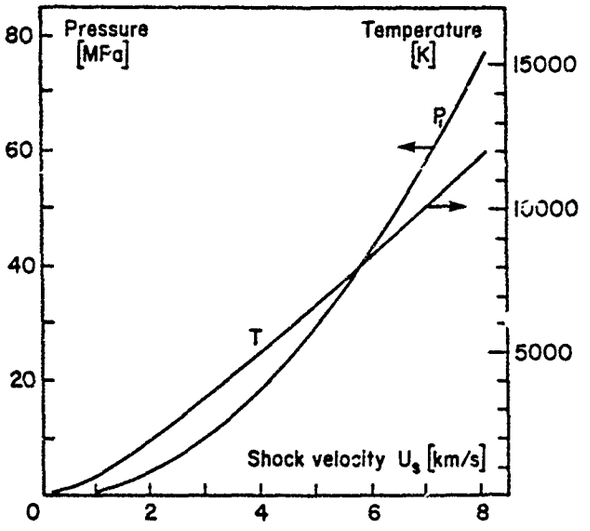

Fig. 6. Temperature and pressure behind a shock wave for air of initial standard atmospheric conditions as a function of air shock velocity. Data from ref. (9).

From these initial experiments we established that:

- The position of the detonation front and the PAS front can be determined on the photos.
- For PAS front speeds in the range 3000-4000 m/s the gas at the front becomes non-transparent 2-3 mm behind the shock front. For air shocks travelling faster than about

TABLE 2

Experimental data for shots in standard charge geometry

Shot #	Explosive	Charge density ϱ_o g/cm^3	Explosive surface confinement	Detonation velocity D m/s	PAS velocity U_s m/s	U_s/D	$\alpha^{1)}$ Deg.	$\beta^{1)}$ Deg.	Remark
820925	Gurit	1.00	0.3 mm Cu	2000	3000	1.50	—	—	
840706	40PETN/60 NaCl	1.07	—	2800	3500	1.25	65	18	
840704	40PETN/60 NaCl	1.67	—	2800	—	—	65	—	No roof
840521	33PETN/67 NaCl	1.13	—	1800	2300	1.28	60	18	
840815	PETN	0.88	—	5100	5800	1.14	65	10	
841029	Emulite	1.23	—	4700	5200	1.11	53	5	
841123	Emulite	1.22	0.3 mm Cu	4900	6000	1.22	38	—	
850313	Emulite	1.20	1.0 mm Cu	5200	5700	1.10	25	—	

4000 m/s the region behind the shock emits enough light to become selfluminous in our photos.

- The change in conductivity monitored by the conductivity probe occurs at the PAS front.

The Gurit charges

The Gurit charges had a charge density $\varrho_0 = 1.00 \pm 0.05$ g/cm^3. Except for a run up distance of about 60-80 mm they all detonated at a velocity of about 2000 m/s along the whole length of the 500 mm long charge with PAS velocities of about 3000 m/s. When the PAS reached the end of this charge it had a lead of about 125 mm on the detonation front.

Figure 4 shows a framing photo from a Gurit shot with the PAS leading the detonation front by about 75 mm. The photo was taken after 290 mm of detonation along the charge. The PAS front itself is not seen in the photo but is located about 2 mm ahead of the smoke front in the air channel. The detonation velocity probes can be seen along the lower part of the charge. To avoid the PAS eroding the Gurit surface a 0.3 mm thick Cu foil is placed on top of the explosive.

In one experiment with a charge length of 940 mm and instrumented with detonation velocity and PAS probes the detonation failed after 650 mm of run. The PAS was then about 280 mm ahead of the detonation front. No photo was obtained from this experiment. The detonation and PAS velocities were about 2000 and 2900-3200 m/s respectively up to a few microseconds before the detonation failed. At failure the PAS was obviously far enough ahead of the detonation front to give time (about 90 μs) to precompress most of the 20 mm thick layer of explosive. The compression wave speed in Gurit is estimated to be a few tenths of a millimeter per microsecond. The unconfined failure diameter for Gurit is estimated to be 5-8 mm.

PETN/salt charges

To be able to control the detonation velocity in the range 2000-5000 m/s some charges with PETN/NaCl mixtures were shot. The standard geometry given in Fig. 2 was used without any copper foil top cover. In all cases the PAS travelled 500-800 m/s faster than the detonation front. Fig. 5, 7a and 7b show examples of photos from these shots. In the experiments in Fig.8 no roof was used on the standard test charge described in Fig. 2. No PAS was generated in this case.

Fig. 7a. Picture taken when the self luminous PAS front hits the confining roof after 125 mm of detonation in 100% PETN. D=5100 m/s Shot No. 840815.

Emulite charges

To study the behavior of a typical water in oil emulsion explosive in the test geometry of Fig. 2 some experiments were made with Emulite. This explosive is a cap sensitive small diameter explosive produced by Nitro Nobel AB with an unconfined critical diameter for detonation of 10-12 mm. It is sensitized with hollow microspheres. The explosive was loaded directly at manufacture into the test charge. To study the effect of confinement of the explosive top surface the explosive was covered by a 0.3 mm or a 1.0 mm thick Cu foil in some shots.

Fig. 7b. Picture taken when the detonation front has travelled another 40 mm

Without foil covering and with a 0.3 Cu foil the detonation velocity was 4700-4900 m/s. With 1 mm Cu foil as covering 5200-5400 m/s was achieved.

The detonation velocity was steady state to within about ± 100 m/s along the whole length of the test charges except for a run up length of about 50 mm from the initiating detonator. A PAS developed in all cases. Its velocity was 400-600 m/s faster than the detonation front except for shot no 841123 where the PAS travelled about 1100 m/s faster than the detonation front.

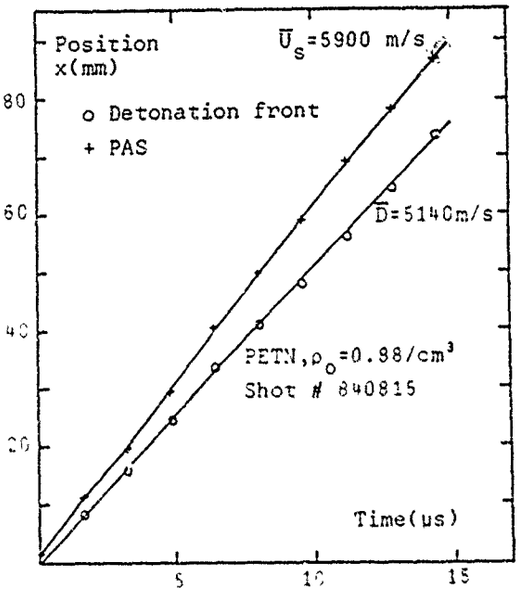

Fig. 7c. Position versus time of detonation front and PAS at roof level. $x = 0$ at beginning of roof.

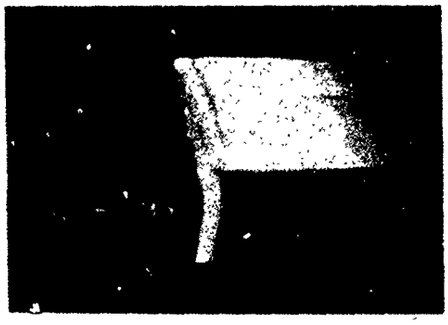

Fig. 8. Schlieren photo of 40 PETN/60 NaCl charge in standard charge geometry but without any confining roof. No PAS is formed. Shot. No. 840704.

Fig. 9 shows an Emulite charge with a 0.3 mm copper foil cover where the self luminous PAS front has advanced considerably ahead of the detonation front.

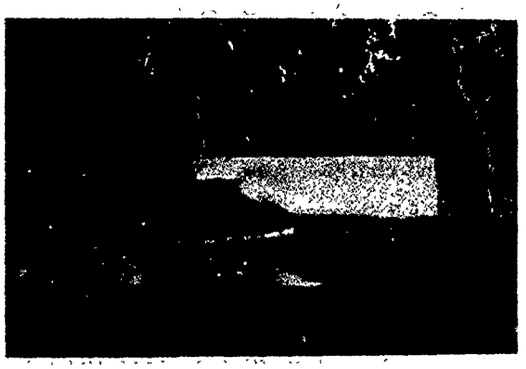

Fig. 9. Emulite in standard charge geometry with PAS front 56 mm ahead of detonation front after 475 mm of detonation under confining roof. Shot No. 841123.

EXPANSION OF PRODUCTS AND PRODUCTS DRIVEN AIR SHOCKS IN THE AIR GAP BETWEEN CHARGE AND CONFINEMENT

When long unconfined charges of explosives are detonated in atmospheric air the products driven air shock around the charge will initially expand as in Fig. 10, α being the angle between the air shock and the charge axes.

In our experiments with an unconfined upper explosive surface and a charge geometry as in Fig. 2, PETN/salt and pure PETN charges gave $\alpha \approx$ 60-65 degrees. Unconfined Emulite gave $\alpha \approx$ 50 degrees, with 0.3 mm copper foil cover $\approx$ 40 degrees and with 1 mm copper foil $\alpha \approx$ 25 degrees. Here α is determined 20 mm outside the charge surface.

For a case with steady state detonation and a confinement as in Fig. 2 the collision point between the air shock and the roof surface will initially travel at the detonation front speed if simple regular reflection takes place. In atmospheric air Mach reflection will, however, take place for α>40 degrees (9). Our experimental conditions should thus give us Mach reflection initially as in Fig. 11 except for the Emulite charge with 1 mm copper confinement.

The picture will, however, quickly get more complicated because of the reflected shocks and product/air interface following closely behind

the air shock front. At the products/air interface the density in the products is about 10 times higher and the temperature about 10 times lower than in the air. These reflected shocks and interfaces will complicate the analysis of the flow in the air gap after only some microseconds.

All our experiments show Mach stem behavior initially for the products driven air shocks when they reflect off the confining roof except for the Emulite shot with a top cover of 1 mm copper.

However our results show that the 1 mm copper confinement has little influence on the ratio U_s/D for Emulite.

Figure 7b shows an example of the reflection of the products driven air shock and the Mach stem that forms initially at the confining roof in the test tube. The angle of incidence of the air shock against the roof is about 65 degrees, the detonation velocity D=5100 m/s for this charge. The Mach stem velocity is about 5800 m/s and almost constant for the time of observation. The triple point trajectory moves at an angle of about 10 degrees with the confining roof.

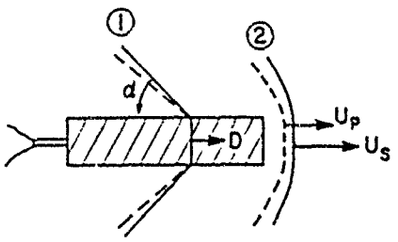

Fig. 10. Lateral (1) and at later time head on (2) expansion of detonation products driven air shock around an air confined detonating charge

MODELLING OF ONE DIMENSIONAL ISENTROPIC EXPANSION OF DETONATION PRODUCTS INTO AIR

Let us consider an infinitesimal element of the explosive products (EP) when it expands into the air gap. The expansion is close to isentropic until it reflects against the confinement. The entropy of the element is increased when it is shock compressed at the reflection against the confinement and then approximately constant in the subsequent expansion again.

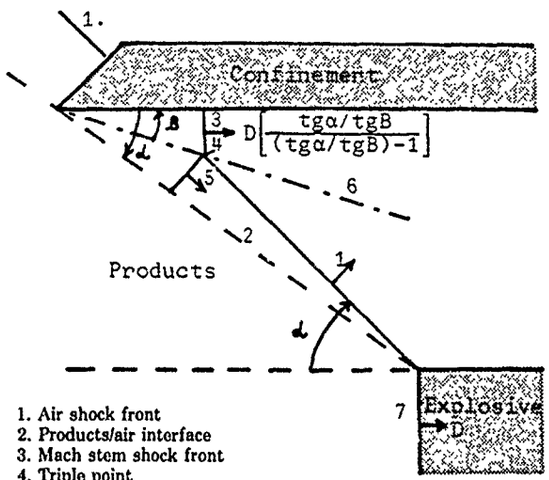

1. Air shock front
2. Products/air interface
3. Mach stem shock front
4. Triple point
5. Reflected shock
6. Triple point trajectory
7. Detonation front

Fig. 11. Schematics of Mach reflection of detonation driven air shock in standard charge geometry shortly after impact against the confining roof

To model the EP flow we will, however, assume that the increase in entropy caused by the reflections of the products is so small that we can assume constant entropy when we want to describe the flow. We will also assume plane one dimensional flow which means we are considering the flow of products along a channel having a constant cross section. In our test geometry the constant cross section assumption is valid in front of the detonation front. Behind the front appreciable lateral expansion of the plexiglass box takes place.

To understand the piston effect of the EP on the air let us consider the flow at the explosive charge/air interface. For the simple case of a plane reasonably flat topped detonation wave expanding head on into air the initial EP/air interface velocity can be determined by considering the expansion isentrope of the EP and the Hugoniot of air in a pressure versus particle velocity graph. The interface velocity is given by the cross-over point of the two curves.

Along the EP CJ isentrope S_1 the particle velocity U_p for a state with a specific volume V is given by the Riemann integral

$$U_p = U_{p1} + \int_{V_1}^{V} -\left(\frac{dP}{dV}\right)_{S_1}^{1/2} \qquad (1)$$

where

U_{p1} is the CJ state particle velocity

V_1 is the CJ state specific volume $(dP/dV)S_1$ is the slope of the CJ isentrope in the PV plane.

We used equation (1) and the Hugoniot for air at initial pressure $p_o = 0.1013$ MPa to calculate the products air interface velocity off end as in Fig. 10. The TIGER code (8) was used to calculate the CJ state and EP isentrope. To test the accuracy of this procedure we compared our calculated result for Comp. B with experimental results for the off end air shock velocity U_s for Comp. B given by Deal (10). The air Hugoniot for Up < 4 mm/μs given by Deal (11) for air with initial conditions $P_o = 0.81 \cdot 10^5$ Pa and $T_o = 273$ K was extended to higher U_p values by assuming $U_s = 1.11\ U_p$ for U_p in the range 4-8 mm/μs. The air shock front pressure was calculated using

$$P_1 = \varrho_o U_p U_s \cdot \qquad (2)$$

The low pressure part of the TIGER calculated isentrope for Comp. B and the air Hugoniot are given in Fig. 12. The match point gives $U_s = 8140$ m/s using the BKW eos and 7370 m/s using the JCZ3 eos. Deal's experimental value is 8000 m/s.

These results show that for Comp. B the BKW eos overestimates the interface velocity whereas the JCZ3 eos underestimates it. For low energy and low density explosives we consider the JCZ3 eos should give an improved estimate (12).

In Table 3 are given experimental values of "off end" initial air shock velocities obtained by other researchers for some explosives (10). It is interesting to study the ratios U_s/D and U_p/D where U_p is the products air interface velocity. U_s is the air shock front velocity and D is the detonation velocity. Comp. B and PBX 9404 show normal behavior with $U_p/D = 0.97$-1.00 and $U_s/D = 1.05$-1.09. Alex 32, an aluminized cast RDX/TNT explosive with 30% aluminium, shows abnormally low ratios whereas Nitromethane shows abnormally high values. The reason for the high value for Nitromethane is not clear and should be studied. The effect of 0.8 bar or 10 bar initial air pressure on the interface velocity is relatively small as seen in Table 3 for Comp. B.

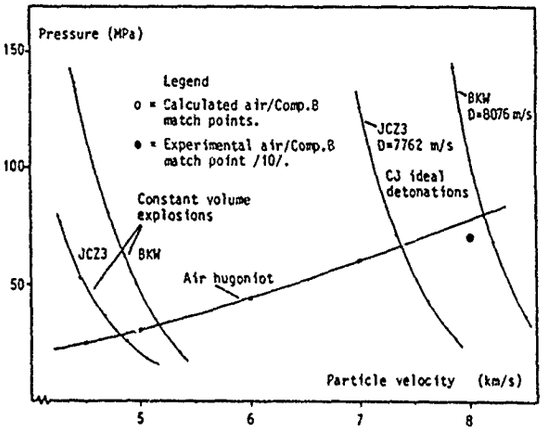

Fig. 12. Air Hugoniot and CJ isentropes for Comp. B

TABLE 3

Experimental results generated at Los Alamos Scientific Lab. /10/ showing explosive/air state values for "head on" plane detonation into air at initial pressure P_o = 0.8 bar and 10 bar.

Explosive	P_o (bar)	U_p/D	U_s/D
Comp. B	0.8	1.00	1.09
Comp. B	10	0.84	0.94
9404	0.8	0.97	1.05
NM	0.8	1.17	1.29
Alex 32	0.8	0.93	1.01

MODELLING OF NON-IDEAL DETONATION AND EXPANSION OF PRODUCTS FROM EMULITE INTO AIR

The TIGER code was used to model non-ideal detonation and subsequent expansion of the products in Emulite by keeping some of the ammoniumnitrate (AN) inert at the CJ plane. The products were then expanded isentropically from the compressed CJ state to the original explosive volume V_o. At V_o the unreacted AN

was allowed to react in a constant volume explosion. The products were then allowed to expand along the new isentrope. Figure 13 shows schematically the expansion paths.

The head on particle velocity U_p of the front of the products expanding to some final volume V_f given by matching with air along the two EP isentropes S_1 and S_2 is calculated by

$$Up = Up_1 + \int_{V_1}^{V_o} -\left(\frac{dP}{dV}\right)^{1/2}_{S_1} dV + \int_{V_o}^{V_f} -\left(\frac{dP}{dV}\right)^{1/2}_{S_2} dV. \quad (3)$$

Equation (2) is not strictly correct when the expansion takes place along the two separate isentropes S_1 and S_2. For the cases we have considered equation (3) should overestimate U_p slightly the more non-ideal the detonation. However the maximum error due to this is estimated to be less than 200 m/s in U_p at the match point with the air Hugoniot for the cases we have considered.

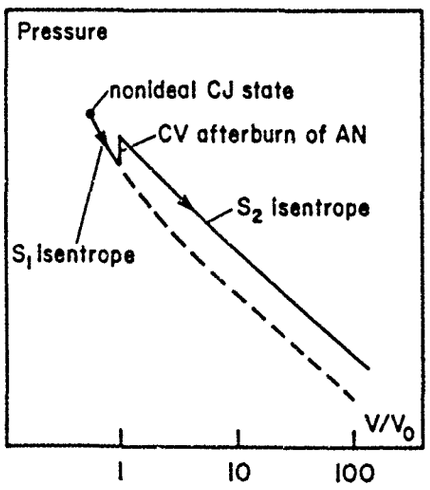

Fig. 13. Model for non-ideal detonation in Emulite with two part isentrope

Figure 14 shows the air Hugoniot and the low pressure part of some Emulite isentropes with different amount of AN burn at the CJ point. For example "40 AN inert D = 4220" means that 40g AN per 100g of explosive was kept inert at the CJ point and then burned on the CJ isentrope at the explosive original volume V_o. The calculated detonation velocity was 4220 m/s.

Table 4 gives the detonation velocity U_p and the air shock velocity U_s from these calculations.

In Fig. 15 U_s/D is plotted versus D. It is obvious that the more non-ideal the detonation the higher the ratio U_s/D will get.

The case when all of the explosive is burned as a constant volume explosion gives an air shock speed U_s = 3940 m/s.

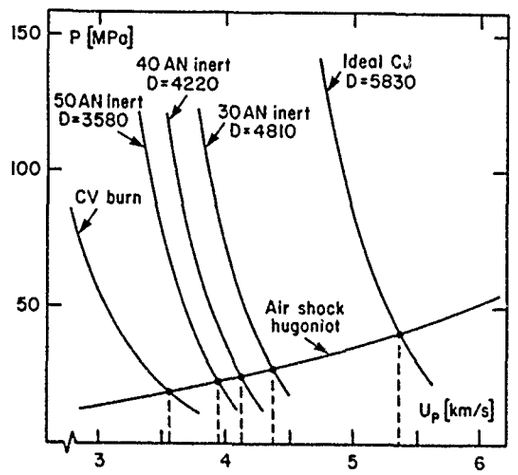

Fig. 14. Air Hugoniot and isentropes for Emulite with different detonation velocities (JCZ3 eos)

TABLE 4

Results from matching of TIGER JCZ3 adiabols for Emulite with air in the P-up plane.

An inert at CJ state (g/100g expl)	D (m/s)	D/D_i	U_p (m/s)	U_s (m/s)	U_s/D	U_p/D
0	5830	1.00	5360	5950	1.02	0.92
30	4810	0.83	4360	4840	1.01	0.91
40	4220	0.72	4130	4580	1.09	0.98
50	3580	0.61	3940	4370	1.22	1.10
CV	—	—	3550	3940	—	—

DISCUSSIONS AND CONCLUSIONS

When a long explosive column is decoupled by air at standard atmospheric conditions from its confinement so that the air gap cross section has the same area as the explosive column cross section we have established that:

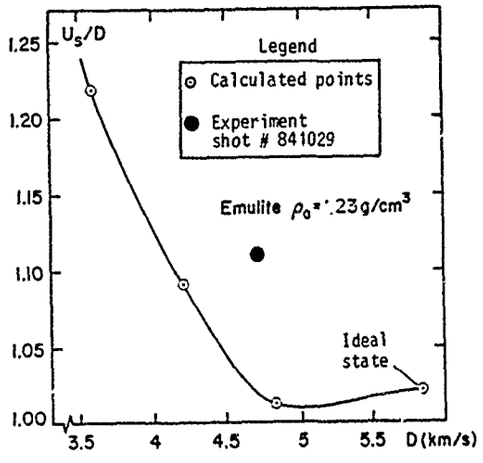

Fig. 15. U_s/D versus D for Emulite

- A precursor air shock (PAS) travelling faster than the detonation front is observed for all explosives we have studied. It is driven by explosive products expanding in the air gap between the charge and its confinement. The products will at least for rather non-ideal detonations move ahead of the detonation front.
- Calculations show that the ratio of PAS speed to detonation speed U_s/D will increase with increasing non-ideality of the detonation for a given explosive.
- Calculations show that U_s/D is larger than unity also for ideal detonation of a typical water in oil emulsion explosive.

In practice one wants to keep $U_s/D < 1$ to avoid precompression of the explosive. Potential methods to reduce U_s/D below unity for decoupled charges are therefore interesting.

The following methods have been considered:

i.) Changing the performance of the explosive
ii.) Changing the decoupling medium properties
iii.) Introducing drag producing units into the air gap between the explosive and the confinement.

Changing the explosive performance as in i.) will not suffice to reduce U_s/D to below unity. However, for a given explosive the more ideally it detonates the lower U_s/D will be. Mixing inert substances into the explosive should change U_s/D slightly but no big effects can be expected for practical explosives. Changing the air pressure in the air gap will belong to category ii.). As shown in Table 3, U_s/D was reduced 16% by increasing the air initial pressure from 0.8 bar to 10 bar. In practical rock blasting situations air pressurized boreholes will require special procedures.

If regularly spaced thin mechanical "stoppers" are used in the air gap, it is important to realize that, when the PAS is temporarily stopped there the refelction pressure generated is much higher than the side on pressure generated by the PAS passing undisturbed. The air temperature at the stopper will exceed 10000 K. The side on air shock pressure felt by the explosive when the PAS front passes by with a speed U_s is given by equation (2). The reflected pressure P_2 at a stopper where the air is reflected like from a rigid surface normal to the flow is given by

$$P_2 = P_1 \left(2 + \frac{k}{k-1} \right) \quad (4)$$

where k is defined by

$$U_s = kU_p \quad (5)$$

For U_s in the range 3000-8000 m/s k is approximately 1.10

We then get $P_2 \approx 13\ P_1$

The pressure is thus raised more than a factor ten when the shock is reflected by a stopper. For air shock speeds 3000-6000 m/s P_2 is then 130-510 MPa. A compression wave of this amplitude will spread from the position of the stopper into the explosive and precompress it. If the distance between stoppers is too large this compression wave may have time to desensitize a thick enough layer of the explosive, before the detonation front arrives, to prevent detonation transmission. Problems with detonation transmission may also occur when an air decoupled explosive column is made of long sticks of explosive that may be laterally displaced at the ends. The PAS may then send a precompression wave with a peak pressure P_2 given by equation (4) into the end face of a stick. This precompression may prevent it from being initiatied by the detonation shock front. The influence of the ratio of explosive to air gap area on the PAS speed has not been considered in this work but should be studied further. Experiments performed just before the publishing of this report show that U_s/D will increase when the air gap/explosive column cross section ratio is reduced to ½ and

¼ of what we have used in this study. To get a detailed understanding of the flow of products and air in the air gap a 2D hydrodynamic code should be used to model the detonation and subsequent flow. For a case when the detonation has failed through dynamic precompression the conditions are favorable at a stopper for a fast deflagration of the remaining explosive. For many powder explosives especially those sensitized by NG/EGDN a deflagration to detonation transition should be possible. Water based emulsion explosives, however, burn so slowly that this is less likely.

ACKNOWLEDGEMENTS

The authors are grateful to M.O. Sarathy from IDL Chemicals, Hyderabad, India who contributed considerably to the early experiments using high speed photography as a diagnostic tool in this study. The discussions with Algot Persson of the detonation physics group of Nitro Nobel AB have also been stimulating for the progress of this work. The typing of this manuscript by Burnis Lidmark is also appreciated.

REFERENCES

1. C. H. Johansson, H. L. Selberg, A. Persson and T. Sjölin, "Channel Effect in Detonation in Tubes with an Open Space between the Charge and the Tube Wall," Preprint from XXX1 International Congress of Industrial Chemistry, Liege, Belgium, Sept. 1958.

2. A. I. Goldbinder and V. F. Tysevic, "Continued Investigations of the Channel Effect," in Theory of Explosives by K. K. Andreev, Vychaja, Chola, Moscow, 1967 (in Russian).

3. L. V. Dubnev and L. D. Kotina, "Channel Effect Mechanism in the Detonation of Condensed Explosives Comb. Expl. and Shock Waves," Vol. 2, No. 4, pp 97-104, 1966.

4. L. Ydy, "Influence of External-Detonation-Generated Plasmas on the Performance of Semi-Confined Explosive Charges," CIM Bulletin, pp 126-133, Feb. 1979.

5. M. Nakano and N. Mori, "Studies Regarding Propagation of Detonation Explosives," J. of the Industrial Explosives Soc., Japan, Vol. 40. pp 245-257, 1979.

6. Hanasaki et al. "Behavior of Compressed Air in Channel of Charged Hole," J. of the Industrial Explosives Soc., Japan, Vol. 45, No. 3, 1984.

7. C. M. Lownds and M. P. du Plessis, "The Double Pipe Test for Commerical Explosives I," Propell. Expl. Pyr., Vol. 9, pp 188-192, 1984.

8 M. Cowperthwaite and N. H. Zwisler, "TIGER Computer Program Documentation," SRI Publication No. Z106, Jan. 1973.

9. Ya. B. Zeldovich and Yu. P. Razier, "Physics of Shock Waves and High-Temperature Hydrodynamic Phenomena," Vol. I, Academic Press, 1966.

10. C. L. Mader, "Numerical Modeling of Detonations," P 83 University of California Press, 1979.

11. W. E. Deal, "Shock Hugoniot of Air," J. of Applied Physics, Vol. 28, No. 7, 1957.

12. M. A. Srinivas and G. Bjarnholt, "Equations of State for Characterization of Commerical Explosives," SveDeFo Report, DS 1982:12, 1982.

DISCUSSION

GODFREY EDEN, AWRE Aldermaston MOD (PE), Berkshire, UK

1) You mentioned that the preshocked region in the explosive could be less than the failure diameter. Are you suggesting that such a region would fail to detonate?

2) I am not familiar with the explosives you are using but departmental evidence escents (Exten et al 5th Symposium on Detonation) suggesting that providing detonation is established in a preshocked region of longer B, it will behave like a higher density explosive with an enhanced detonation velocity.

REPLY BY GERT BJARNHOLT

1) I mean that the preshocked outer region will not be initiated by the shock at the detonation front. The unshocked inner region could then be so small in diameter to propagate a steady state detonation. It could therefore eventually fail.

2) Enulsion explosives containing microballons do behave differently.

CAVITY COLLAPSE IGNITION OF COMPOSITION B IN THE LAUNCH ENVIRONMENT

John Starkenberg, Doenee L. McFadden, Ona R. Lyman
US Army Ballistic Research Laboratory
US Army Materiel Command
Aberdeen Proving Ground, Maryland

Experiments using the activator at the Ballistic Research Laboratory have been pursued for a number of years with an eye toward clarifying the mechanisms involved in the premature ignition of high explosives in the setback environment. Recently, we have turned our attention to a series of experiments in which controlled cavities in cast Composition B (Comp B) are subjected to deformation both with and without simultaneous air compression as well as air compression without deformation. The dimple tests were designed to accomplish this. There are three variations of the dimple test. In the standard dimple test, a cylindrical cavity or dimple of controlled depth and diameter is cast into one end of the explosive sample. In another variation, vacuum hardware is used. In a third variation, the dimple is cast into a piece of Dow Corning Sylgard 182 which is placed in contact with an undimpled explosive sample. In the vacuum dimple test, only deformation heating can produce an ignition. In the Sylgard dimple test, only air compression heating occurs. Both heating mechanisms are combined in the dimple test. To date, only Comp B has been subjected to dimple testing. As a result of our work thus far, we have found that when the air compression and compressive heating mechanisms are combined the dominant ignition mechanism is compressive heating of air strongly influenced by the cavity collapse geometry and possibly by alteration of the state of the explosive surface. The hypothesis of a transition from axial to radial cavity collapse with increasing dimple depth seems to explain the observed behavior. Deformation heating is the dominant mechanism only for high aspect ratio dimples.

INTRODUCTION

Experiments using the activator at the Ballistic Research Laboratory (BRL) have been pursued for a number of years with an eye toward clarifying the mechanisms involved in the premature ignition of high explosives in the setback environment (1-4). In a broader sense, however, this research sheds light on the very minimum stimulus levels which cause violent reaction in explosives and may be pertinent to ignition in a variety of circumstances.

The relationship of laboratory-scale experiments and large-scale "simulation," such as with the Naval Surface Weapons Center (NSWC) simulator (5-7), to gun firings is a difficult issue. The appropriate role of laboratory experiments is not the simulation of the artillery launch environment, but rather the study of ignition mechanisms under pressures representative of setback. The experiments reported herein were conducted in this spirit. Therefore, the activator experimental procedure is not (as it has been called) "an increased severity test." Rather, it is an isolated stimulus experiment which is designed to determine the level of air compression heating or other stimulus required to ignite an explosive as a function of various parameters. If a premature occurred due to compressive heating ignition, we would conclude that the explosive was locally subjected to the same stimulus level determined in our experiments. In general, this means that the explosive must be subject to the same heating rate. In the case of compressive heating, the heating rate is roughly proportional to the

product of the pressurization rate and the cavity depth. In the case of frictional or shear heating, the heating rate is roughly proportional to the product of the pressure and the shear velocity. In both cases, many other factors are also important. Pressurization rates and peak pressures measured external to projectile bases appear insufficient to produce the required stimulus. The maximum sliding velocity produced by projectile rotation is somewhat below that required for ignition observed in activator experiments isolating frictional heating (8). This means that, in order to produce a premature, the stimulus levels applied to the explosive must be amplified over and above those present external to the projectile during launch. This may occur in a number of ways. In the case of compressive heating, one way is to amplify the pressurization rate. This can occur if a loose charge impacts the base or if a cavity fails to collapse during the early portion of pressurization and then collapses catastrophically when a critical pressure has been reached. A cavity collapse geometry which concentrates heated air on a small portion of the explosive surface also amplifies the stimulus level. In addition, as a cavity collapses, shear heating may combine with compressive heating to produce an ignition. Hershkowitz (9) has suggested that prematures are rare because they require two or more low probability conditions to exist simultaneously. For example, a sufficiently large cavity must be coupled with an abnormally severe launch environment. The relationship between the local heating rate experienced by an explosive fill and the pressure stimulus external to the projectile is complicated and has not been established. We have not pursued this avenue. Our approach has been to determine the parameters which govern ignition by the most likely mechanisms in order to provide guidance for the design of more premature-resistant explosive/projectile systems.

REVIEW OF COMPRESSIVE HEATING OBSERVATIONS

When a small volume of gas is compressed very rapidly such that no energy transport can occur, a high temperature reservoir (hot spot) is created which may subsequently heat an adjacent explosive layer to the point of ignition. This process is referred to as ignition by adiabatic compression of the gas. If, on the other hand, the gas is compressed very slowly, no temperature increase occurs and no explosive ignition can follow. Between these limits lies the compressive heating regime in which the compression occurs sufficiently slowly that considerable energy is transported by conduction and convection during the process. Compressive heating has, therefore, received attention primarily as a source of ignition which is active when the observed time to ignition is in the ten microsecond to ten millisecond range, a time scale which is typical of the setback of the explosive fill in a projectile during launch.

Compressive heating ignition has been the subject of extensive analytical and experimental study at BRL. The experimental investigation was conducted using an apparatus, referred to as the activator, which was originally designed at Picatinny Arsenal as a laboratory-scale artillery setback simulator (10). This was used in its original form in preliminary experiments to produce data which revealed the role of air in causing ignitions during compression. Subsequently, the activator was modified and further instrumented so that more definitive data could be extracted from the tests and direct comparisons to the predictions obtained from analytical models could be made. In particular, the activator has been used to explore ignition of Composition B (Comp B) and TNT as well as a number of other explosives caused by the rapid compression of air trapped in contact with the explosive.

A number of observations from our study of air compression heating are pertinent to the present study. As a result of our earlier testing, we learned that this is indeed a viable mechanism for ignition at relatively mild stimulus levels and we established pressurization rate and cavity size as the principal governing parameters. We found that sensitivity is substantially influenced by the geometry of cavity collapse and the state of the explosive surface. Covergent geometries, which concentrate heated air on a small portion of the explosive surface, are more sensitive as are nonporous surfaces, which prevent leakage of air away from the ignition site.

In this earlier work, care was taken to decouple the stimulus level from the explosive mechanical properties by using cavities external

to the explosive which collapse without mechanical failure of the explosive. More recently, we have turned our attention to a series of experiments in which controlled cavities in cast Comp B are subjected to deformation both with and without simultaneous air compression as well as air compression without deformation. This series of tests can be used to explore the role of explosive deformation in ignition. In particular, we were interested in determining whether deformation produces sufficient heating to cause ignition or simply acts to increase the local air pressurization rate.

DESCRIPTION OF THE EXPERIMENTS

The Activator. The activator, as presently used, is illustrated schematically in Figure 1. The test section consists of a mild steel heavy confinement cylinder enclosing the explosive sample and a hardened steel driving piston. A hardened steel gauge block on which a manganin foil pressure gauge is mounted is tightly bolted to the back of the confinement cylinder and the explosive sample is inserted into the bore adjacent to the gauge. A gap or cavity of some type is left adjacent to the sample. The gauge block rests against a rigid stop which incorporates an adjustment screw to accommodate test fixtures of different lengths and to allow easy installation. The driving piston is activated by a larger piston which is initially held in place using shear pins. The large piston is set in motion by pressure developed in the breech which is instrumented with a pressure transducer. The free run allowed between the large piston and the driving piston is used to set the stimulus level to be applied.

In order to fire a shot, the breech is pressurized using compressed air until the shear pins fail. The large piston accelerates through the free run and impacts the driving piston. The momentum developed by the pistons is transformed to an impulse delivered to the gap and the explosive sample. The pistons may then rebound and strike the explosive again delivering a second impulse. The breech pressure begins at the shear pin failure pressure and drops linearly with time during the test to a value associated with the final volume of the breech. An average value of breech pressure during piston motion may be used in conjunction with free run to estimate the momentum of the large piston when it impacts the driving piston.

A disadvantage of this test configuration is that extrusion of explosive between the gauge block and the confinement cylinder may occur. Ignitions caused by extrusion are readily identifiable as late events on the pressure records. We determined that free runs in excess of 25 mm are required to produce extrusion ignitions. This free run, therefore, represents a practical upper limit of activator operation. However, this limit was sometimes violated since it is possible to distinguish extrusion ignitions.

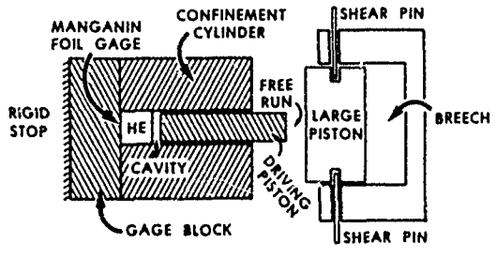

Fig. 1. Activator Schematic

Dimple Tests. Previously, care was taken to isolate the effects of air compression from those of explosive deformation during cavity collapse. This was accomplished by placing the cavity in a material external to the explosive. The next logical step in the investigation was to develop a series of experiments in which the deformation effects are included, in isolation from as well as in combination with compressive heating. The dimple tests were designed to accomplish this.

There are three variations of the dimple test. The experimental configuration for each is shown schematically in Figure 2. In the standard dimple test, a cylindrical cavity or dimple of controlled depth and diameter is cast into one end of the explosive sample. The sample is inserted, dimple up, into the confinement cylinder. A thin polyethylene film attached to the face of the driving piston improves the seal against the face of the explosive sample. In another variation, vacuum hardware is used. Prior to firing, the piston is inserted into the bore hole but held away from the sample until sufficient vacuum has been produced using a vacuum pump. The piston is then allowed to move forward against

the sample, sealing a vacuum into the dimple. The vacuum pump continues to operate until after the firing is completed. In a third variation, the dimple is cast into a piece of Dow Corning Sylgard 182 which is placed in contact with an undimpled explosive sample. All other test procedures are as previously described.

In the vacuum dimple test, only deformation heating can produce an ignition. In the Sylgard dimple test, only air compression heating occurs. Both heating mechanisms are combined in the dimple test.

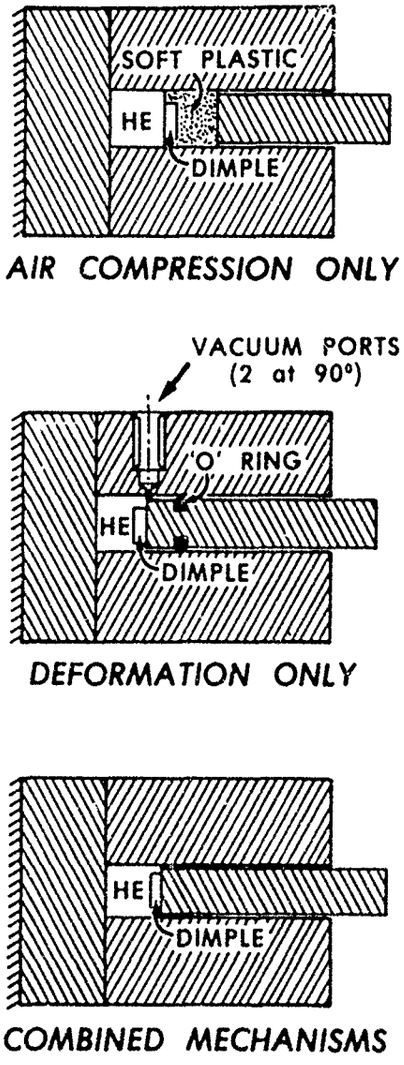

Fig. 2. Dimple Test Series

Sample Preparation. The Comp B samples were prepared by casting short 12.7 mm diameter cylinders. In order to prepare dimpled samples, a casting plate with cylindrical protrusions of adjustable height was used beneath the mold. Two different nominal dimple diameters were produced. Dimple depth and diameter was measured. For undimpled samples, a polished casting plate was used. All samples were then finished to a length of 12.7 mm by cutting and polishing the opposite end. Dimpled and undimpled samples as well as Sylgard dimples are shown in Figure 3. The densities of all samples were determined and all samples were inspected radiographically. Any sample appearing to have voids was rejected. Dimple depth and diameter was measured.

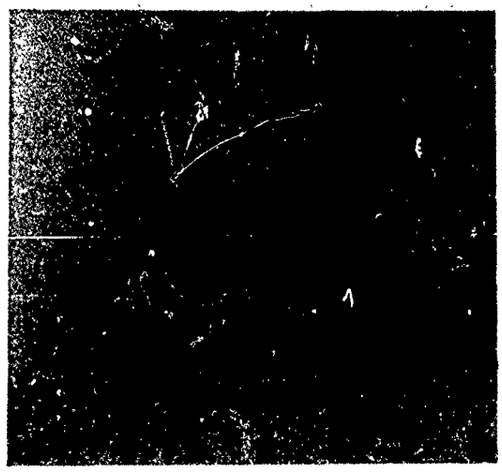

Fig. 3. Dimpled and Undimpled Composition B Samples and Sylgard Dimples

Characterization of Stimulus Levels. In our earlier tests with cavities external to the explosive, pressure conditions in the vicinity of the cavity could be inferred from the pressure records from the manganin gauge at the base of the sample. This provided us with a pertinent characterization of the stimulus level. In the dimple test, however, the conditions as the cavity collapses are complicated and the heating rate bears no simple relation to the pressure record. The best measure of applied stimulus level must be judged, therefore, by the degree to which it segregates go and no go results in a plot of stimulus level versus cavity size.

Several pertinent measures of stimulus level are available. The simplest of these is the free run of the activator. The stimulus generally increases with increasing free run. Since the breech

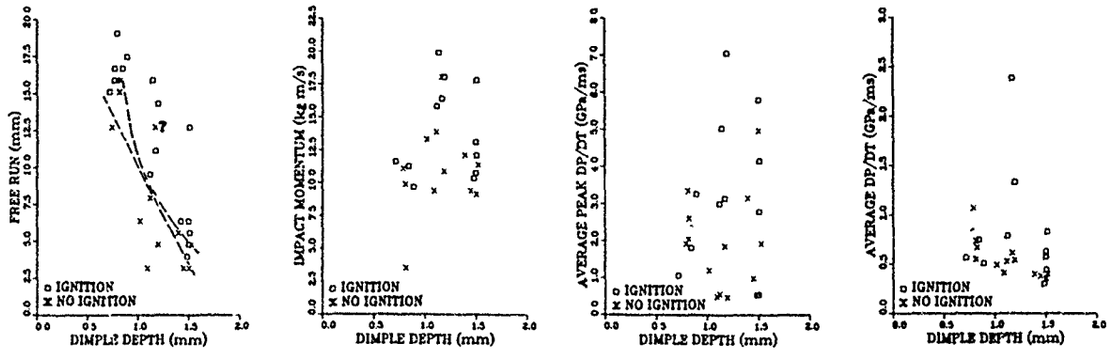

Fig. 4. Comparison of Data Segregation Achieved with Each of Four Stimulus Parameters for Sylgard Dimple Tests with 8.5 mm Diameter Dimples

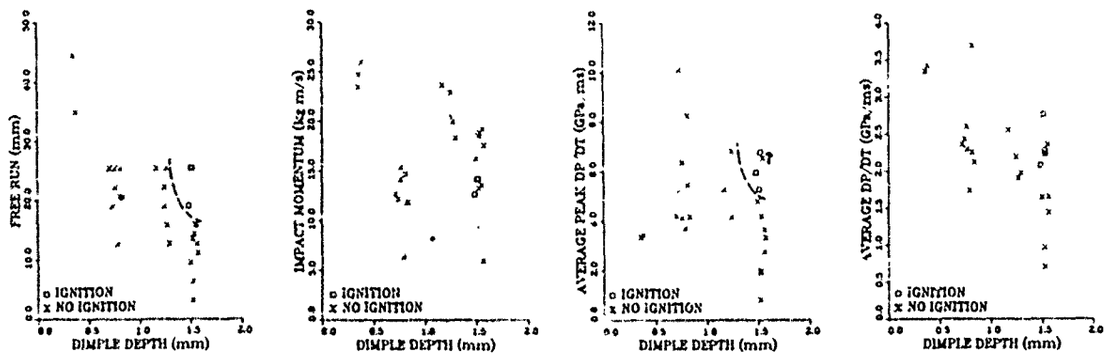

Fig. 5. Comparison of Data Segregation Achieved with Each of Four Stimulus Parameters for Vacuum Dimple Tests with 8.5 mm Diameter Dimples

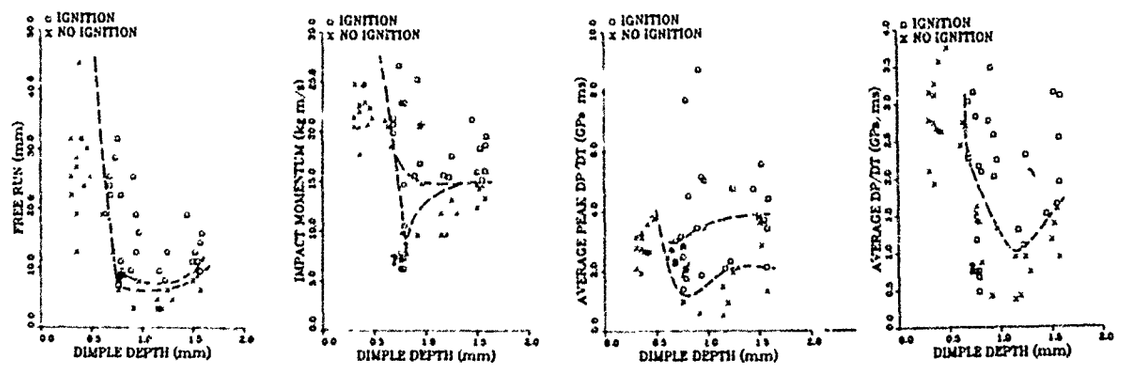

Fig 6. Comparison of Data Segregation Achieved with Each of Four Stimulus Parameters for Dimple Tests with 8.5 mm Diameter Dimples

pressure at which the shear pins fail varies from shot to shot, the impact momentum may be calculated from the free run and the shear pin failure pressure, providing a second measure of stimulus level which should be an improvement over the free run. Note that friction is ignored. Finally, information from the manganin gauge record can be used. Since this is closest to the event, it should provide the best characterization of the stimulus level. In this case, the problem of what aspect of the pressure record to use arises. Peak pressure cannot be used since the occurrence of an ignition before peak pressure is achieved obscures this information. Experience has taught us that pressurization rate is a good indicator of stimulus level. However, pressurization rate is observed to vary during the test, exhibiting several peaks of approximately the same value. Either the average of the peak pressurization rates or an overall average pressurization rate which includes the plateaus or falling regions can be used.

These four stimulus characterization parameters are compared in Figures 4, 5, and 6 for the three tests of the dimple series. In Figure 4, each parameter has been plotted against dimple depth for Sylgard dimple tests with Composition B. Reasonable results are achieved using free run, but impact momentum, average peak pressurization rate and average pressurization rate do not provide adaquate segregation. Similar plots for the vacuum dimple test are shown in Figure 5. In this case free run is clearly best and average peak pressurization rates are also acceptable while impact momentum fails. Finally, the plots for dimples are shown in Figure 6. The best data segregation is achieved using free run. Reasonable results are also obtained with pressurization rate but a few anomalous points appear. Use of impact momentum or average pressurization rate produces a wide band of mixed data. Thus, free run is the only parameter producing good data segregation in all three tests.

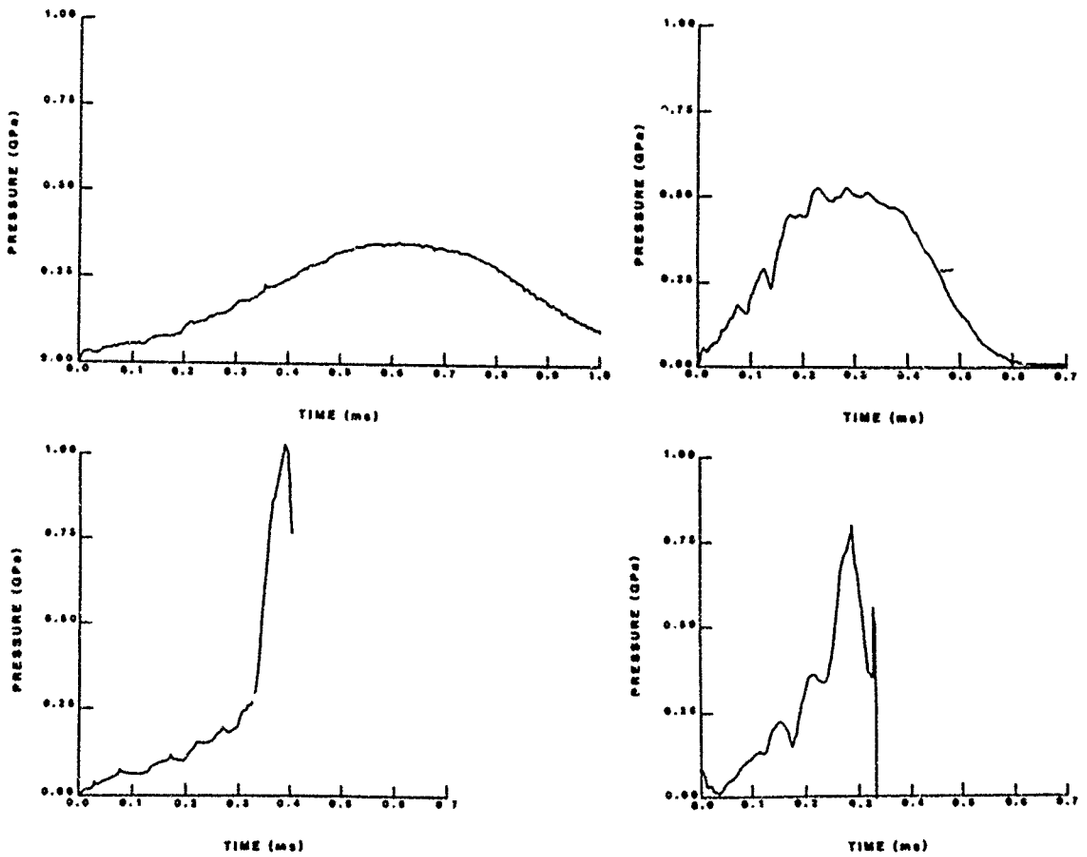

a. Sylgard Dimple Tests *b. Dimple and Vacuum Dimple Tests*

Fig. 7. Typical Manganin Gauge Pressure Records

DIMPLE TEST RESULTS

General Observations. Typical manganin gauge pressure records from the base of the sample are illustrated in Figure 7. The pressure histories observed may be generally categorized according to the nature of the rising portion of the impulse. When Sylgard dimples were used the pressure was observed to rise in a series of steps as in Figure 7a. The pressurization rate between the plateaus was roughly the same. Results obtained with dimpled explosives were often similar. However, the pressure was frequently observed to rise and fall quite markedly during pressurization as in Figure 7b. This occurred for both ignitions and nonignitions and is probably associated with cavity collapse.

Ignition may occur during the rising portion of the pressure history or be delayed until after the pressure has peaked. The latter behavior is more frequently observed with dimpled explosive. Samples that were recovered after firing always showed the dimple to be completely closed. Samples before and after testing are compared in the photograph in Figure 8.

Fig. 8. Comparison of Dimpled Samples Before and After Testing

Preliminary Observations with Composition B—Effects of Dimple Depth. To date only Comp B has been subjected to dimple testing. Nominal dimple depths of 0.4, 0.8, 1.1, and 1.5 mm with a diameter of about 8.5 mm were used in the initial test series. The plots of Figures 4a, 5a and 6a in the free run—dimple depth plane, using different symbols for ignition and nonignition, are useful for comparing the results. The results for the Sylgard dimple test are shown in Figure 4a. In this case, we observe sensitivity which increases with increasing dimple depth. This is consistent with our previous observations and is not surprising. The results of the vacuum dimple test, shown in Figure 5a, are also as expected. Ignitions under vacuum were only possible with the deepest dimples at the longest free runs. The results when the mechanisms are combined in the dimple are more complicated as shown in Figure 6a. No ignitions were observed with the shallowest dimples (~0.4mm). Sensitivity to ignition with dimples with a nominal 0.7 mm depth exhibits a strong dependence on dimple depth. Dimples shallower than about 0.7 mm do not produce ignition while dimples slightly deeper than that produce ignition over a relatively wide range of free run. This dimple depth represents a cut-off value below which ignition does not occur. Between 0.7 and 1.2 mm, sensitivity is independent of dimple depth. The sensitivity then appears to decrease slightly as the dimple depth increases to about 1.5 mm.

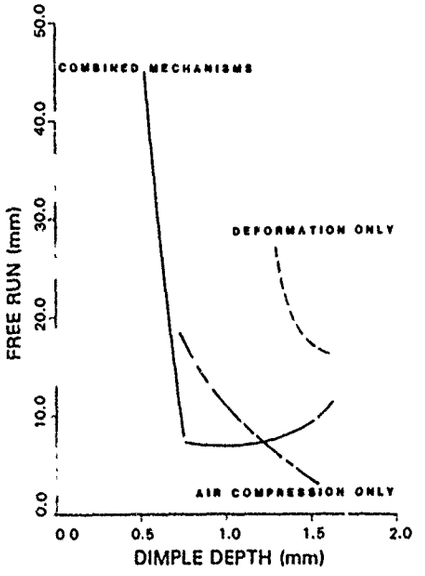

Fig. 9. Comparison of Ignition Thresholds for Composition B with 8.5 mm Diameter Dimples

Additional observations may be made by comparing thresholds from the three tests as in Figure 9. At the shallow dimple end, the thresholds for air compression only and the combined

mechanisms appear to coincide. As dimple depth increases, the sensitivity to the combined mechanisms suddenly becomes independent of dimple depth and is higher than the sensitivity to air compression alone. With a continuing increase in dimple depth, sensitivity to air compression continues to increase while sensitivity to the combined mechanism decreases slightly such that sensitivity to air compression is greatest. Finally, note that ignition due to deformation alone requires substantially higher stimulus levels.

A number of samples were sectioned in an effort to determine the flow pattern leading to cavity collapse. The sectioned sample shown in Figure 10 exhibits two features of interest. First, the cavity appears to have closed by inward radial flow of material from the shoulders of the dimple. In addition, a conical region of deformation beneath the dimple is visible and the original bottom surface has been displaced upward.

Fig. 10. Sectioned Composition B Sample

Interpretation. The observations suggest that the cavity in the explosive may close in at least two different ways depending on dimple depth. Since the air compression and combined mechanism thresholds coincide with shallow dimples, the collapse of the Sylgard and explosive dimples must be geometrically similar in this case. Cavity closure for shallow dimples presumably occurs by axial flow. The sudden transition observed in the dimple test marks a transition to radial cavity closure, a highly sensitive mode for which dimple depth independence would be expected. The subsequent decrease in sensitivity may be due to a continuing change in the collapse geometry or increasing porosity of the collapsing surface. Since deformation only requires higher stimulus levels we conclude that the primary ignition mechanism in the dimple test is compressive heating of air.

Further Observations with Composition B—Effects of Dimple Diameter. Dimple and vacuum dimple tests were subsequently conducted with dimples having a smaller nominal diameter of 6.5 mm and nominal depths of 0.4, 0.8, 1.1 and 1.5 mm. The results for these are plotted in Figures 11 and 12 and the thresholds are compared in Figure 13. Similar results were observed. In this case, no Sylgard dimple tests have been done. Again, ignitions could not be obtained below a cut-off cavity depth for the combined mechanisms. The flat region following the transition is not as long and the decrease in sensitivity with increasing dimple depth is more marked. For the deepest dimples, the ignition thresholds for deformation only and the combined mechanisms appear to coincide. Results with large and small diameter dimples are compared in Figures 14, 15, and 16. Although more ignitions were obtained than with the larger diameter dimples in the vacuum case, no significant differences in ignition threshold are evident as shown in Figure 14. As shown in Figure 15, for the combined mechanisms, the small diameter dimples are generally less sensitive above the cut-off depth. Figure 16 is a plot of free run versus dimple aspect ratio (depth divided by diameter). The results show little or no difference in the cut-off aspect ratio for the two diameters. It remains to be determined whether this scaling applies over a wide range of dimple depth and diameter.

CONCLUSION

As a result of our work thus far, we have found that when the air compression and deformation heating mechanisms are combined the dominant ignition mechanism is compressive heating of air, strongly influenced by the cavity collapse geometry and possibly by alteration of the state of the explosive surface. This result is in agreement with Frey's theoretical assessment

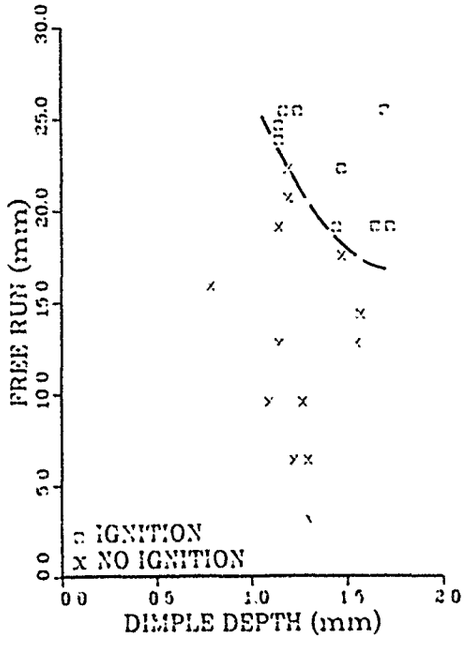

Fig. 11. Vacuum Dimple Test Results for Composition B with 6.5 mm Diameter Dimples

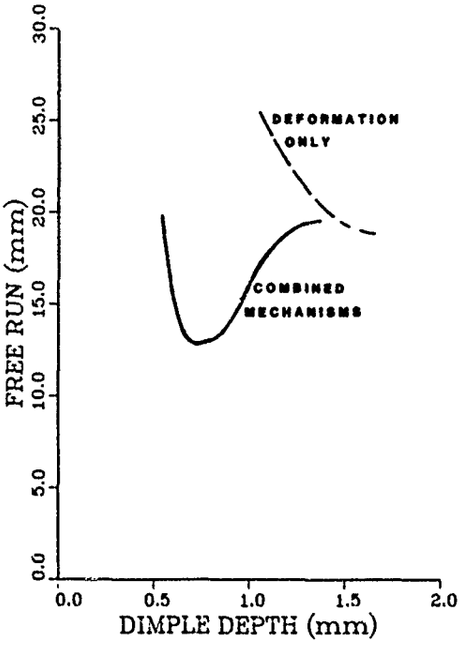

Fig. 13. Comparison of Ignition Thresholds for Composition B with 6.5 mm Diameter Dimples

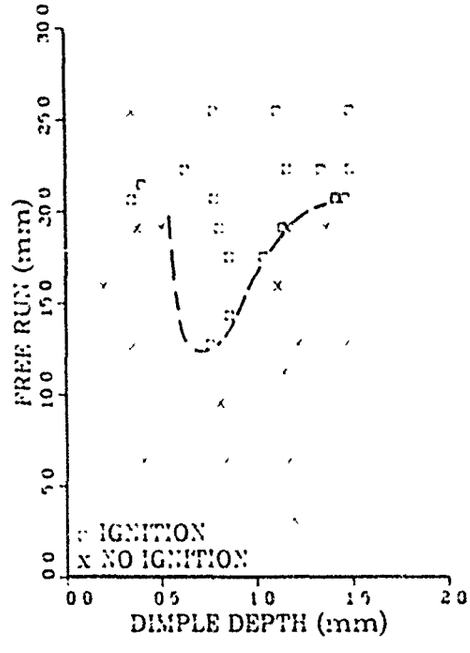

Fig. 12. Dimple Test Results for Composition B with 6.5 mm Diameter Dimples

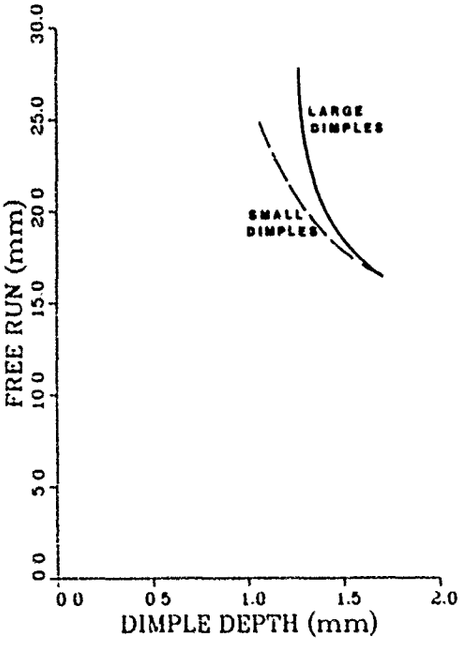

Fig. 14. Comparison of 6.5 and 8.5 mm Diameter Vacuum Dimple Test Ignition Thresholds

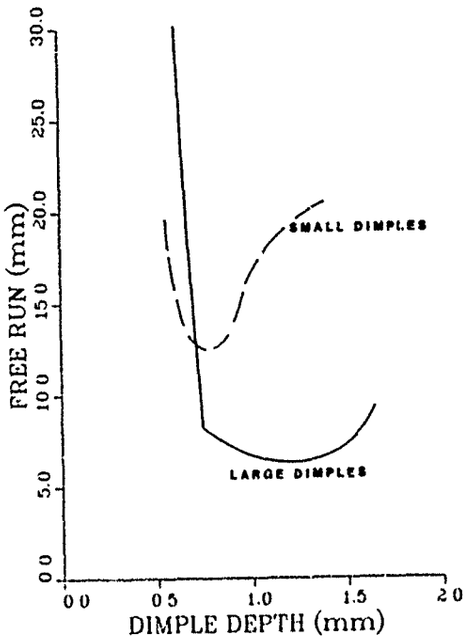

Fig. 15. Comparison of 6.5 and 8.5 mm Diameter Dimple Test Ignition Thresholds

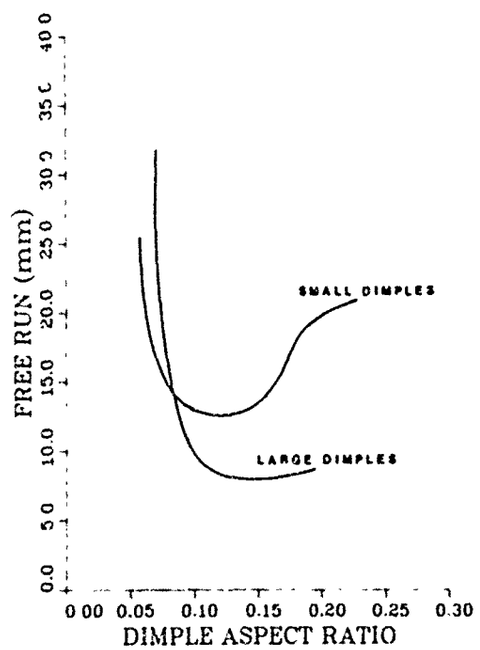

Fig. 16. Comparison of 6.5 and 8.5 mm Diameter Dimple Test Ignition Thresholds using Aspect Ratio

(11), which indicates that the air compression mechanism dominates for large cavities at low pressurization rates. The hypothesis of a transition from axial to radial cavity collapse with increasing dimple depth seems to explain the observed behavior. Deformation heating is the dominant mechanism only for high aspect ratio dimples. The observed cut-off value of dimple depth suggests that it may still be possible to establish a maximum base separation criterion for munitions. However, the way in which this phenomenon depends on dimple geometry remains to be determined. Further, any base separation criterion must be applied to rounds as fired and not as they come off the production line. Thus, a relation between conditions in the field and conditions at production must be established.

REFERENCES

1. J. Starkenberg, "Analytical Models for the Compressive Heating Ignition of High Explosives," Ballistic Research Laboratory Technical Report ARBRL-TR-02225, March 1980.
2. B.C. Taylor, J. Starkenberg, and L.H. Ervin, "An Experimental Investigation of Composition B Ignition under Artillery Setback Conditions," Ballistic Research Laboratory Technical Report ARBRL-TR-02276, December 1980.
3. J. Starkenberg, "Ignition of Solid High Explosives by the Rapid Compression of an Adjacent Gas Layer," Seventh Symposium (International) on Detonation, pp. 3-16, June 1981.
4. J. Starkenberg, L.H. Ervin and D.L. McFadden, "The Ignition of High Explosives in the Launch Environment by Air Compression Heating," BRL Report in press.
5. V.F. DeVost, "Premature Simulator (Final Progress Report)," Naval Ordnance Laboratory Technical Report 74-178, October 1978.
6. T.F. Meyers and J. Hershkowitz, "The Effect of Base Gaps on Setback-Shock Sensitivities of Cast Composition B and TNT as Determined by the NSWC Setback-Shock Simulator," Seventh Symposium (International) on Detonation, June 1981.

7. W.O. Soper, "The NSWC Setback Simulator: Stress Environment for Explosive," NSWC TR-84-65, April 1984.

8. V. Boyle, personal communication, 1983.

9. J. Hershkowitz, personal communication, October 1979.

10. R.T. Schimmel, "Setback Sensitivity of Composition B Under Conditions Simulating Base Separation in Artillery Projectiles," Picatinny Arsenal Technical Report 3857, 1969.

11. R.B. Frey, "Cavity Collapse in Energetic Materials," Eighth Symposium (International) on Detonation, July 1985.

DISCUSSION

P. HUBBARD, RARDE

At impact pressures of 1.0 GPa, ignition phenomena associated with rapid viscous heating have been observed in the RARDE activator. The ignition phenomena occur through the explosive being rapidly extruded between punch and confinement. What are the peak impact pressures that equate with the free run distances that produced events from deformation alone?

REPLY BY JOHN STARKENBERG

The peak impact pressures approach 1.0 GPa at about 25mm free run. The vast majority of the data presented here corresponds to pressures considerably below this. As discussed in the paper, we also observed ignitions due to extrusion when the free run exceeded 25 mm. Using an earlier version of the activator (which is more like the RARDE version) we were able to obtain pressures up to 1.7 GPa without producing extrusion ignitions.

DISCUSSION

L. ZERNOW, Zernow Technical Services, Inc.

Have you attempted to connect your results with the actual deformations that might be expected in actual artillery projectiles which are properly (or improperly) loaded?

REPLY BY JOHN STARKENBERG

Only insofar as reported here. The stress field produced in the neighborhood of the dimple is analogous to that at a base separation. Our emphasis has been on developing a relevant test for screening explosives.

EXPLOSIVE INITIATION BY VERY SMALL CONICAL SHAPED CHARGE JETS

Manuel G. Vigil
Sandia National Laboratories
Albuquerque, New Mexico, USA

Very small conical shaped charge (CSC) jets were used to initiate four different secondary explosives. The liner thicknesses varied between 0.076 and 0.127 mm. LX-13 (80% PETN and 20% SYLGARD) explosive was used to drive the conical liners to form the CSC jets. The CSC jet velocities varied between 3.6 and 6.5 mm/μs. The jet tip diameters ranged between 0.041 and 1.10 mm. The explosive acceptor or target diameters were varied between 1.90 and 19.1 mm. The lateral confinement of the acceptor explosives was minimal.

Relationships for critical jet initiation energy and dimensionless explosive/jet parameter as a function of initiation parameters are developed. The jet initiation data from this investigation as well as previously published data are shown to be consistent with the developed relationships. The threshold initiation parameter (jet velocity squared times jet diameter) for LX-13, PETN, PBX-9407, and TETRYL were experimentally determined to be 0.011, 0.0130, 0.041, and 0.044 $cm^3/\mu s^2$, respectively, for copper jets impacting bare explosive acceptors. The lower values for the LX-13 and PETN indicate these two explosives are more sensitive to shock initiation than PBX-9407 and TETRYL explosives.

INTRODUCTION

Sandia National Laboratories is investigating the feasibility of the initiation to detonation of explosives using very small, high velocity, conical shaped charge (CSC) jets. A fuller understanding of the mechanism of jet initiation of explosive acceptors will be advantageous in future explosive component design applications. The jet initiation mechanism has several advantages over some current high velocity plate impact shock initiation techniques. The primary advantage is that very small diameter jets can penetrate barriers, such as steel, to initiate explosives not in contact with the barrier. Very small (relative to flyer plate charges) CSC's can, therefore, be used as explosive switches to transfer the detonation from one segment of an explosive train through a bulkhead or barrier to a second segment of the explosive train.

This investigation has focused on CSC's 1.73 to 3.50 mm in diameter. Previous investigators (1-3) have reported work involving CSC's greater than 3.9 mm in diameter. The explosives to be discussed in this paper include LX-13 (XTX-8003), PETN, PBX-9407, and TETRYL. All of these explosives were initiated with CSC's fabricated from both copper and tantalum. The conical liners had 47° apex angles.

Theoretical analysis of critical energy relations for explosive threshold initiation by CSC jets are developed and discussed. Dimensional analysis techniques are used to develop a dimensionless term which relates explosive and CSC jet parameters. This term and the energy relationships are all shown to be consistent with an initiation parameter (jet velocity squared times jet diameter) previously reported by Held (3). Experimental test data involving CSC's with

different diameters and various jet velocities are discussed. High speed photometric results illustrating the jet initiation of the explosives are presented. The measured jet tip velocity, tip diameter, length and penetration in aluminum are presented for the various CSC's used in this investigation.

Theoretical shock physics relationships are used to calculate the jet/explosive impact pressure as a function of jet impact velocity for three different jet materials and nine different explosives. The calculated pressures corresponding to the jet impact velocity are presented and discussed.

CSC AND ACCEPTOR EXPLOSIVE CONFIGURATION

The general CSC and acceptor explosive configurations are shown in Fig. 1. LX-13 explosive was used with all CSC configurations primarily because it is easily extruded, has a very small critical diameter, conforms to the shape of the CSC liner, and adheres to it. The metal driving ability of the explosive is low relative to most secondary explosives; however, it does have a relatively small particle size of about 10-30 microns, which results in a smoother or more uniform acceleration of the small, thin liners. The CSC and acceptor explosives were confined by a 0.254 mm thick polyvinylidine (KYNAR) tubing inside of a 12.7 mm outside diameter plastic tube as illustrated in Fig. 1. All CSC's were fabricated with a one cone diameter (CD), cylindrical, built-in standoff. The CSC explosive height was two CD's. The 1.1 mm diameter LX-13 explosive train (Fig. 1) was 10.2 cm long and was end initiated with an RP-2 detonator. The gap distance between the CSC and the acceptor explosive was varied between 0 and 3.2 mm.

The length of the acceptor explosive varied from 1.5 to 10.2 cm, and the diameters varied between 1.9 and 19.1 mm. The acceptor diameters (TD) for the LX-13, PBX-9404, PETN, Tetryl, and PBX 9407 explosives were 1.9, 6.35, 9.4, 12.7, and 19.1 mm, respectively. The corresponding acceptor lengths (L) were 5, 10.2, 16, 26, and 15 mm, respectively. The acceptor explosive was attached to a 1.1 mm diameter by a 12.7 mm long explosive train which had an aluminum witness plate attached to it, as illustrated in the Photometric Measurement section of the paper. The dent on this place indicated a transfer of the detonation wave through the acceptor-explosive train. Table 1 lists the explosive parameters density (ρ_e), detonation velocity (V_d), CJ detonation pressure (P_{cj}), bulk sound speed (C_e), empirical (9) Hugoniot slope constant (S_e) and critical diameter for the explosive acceptors considered in this paper.

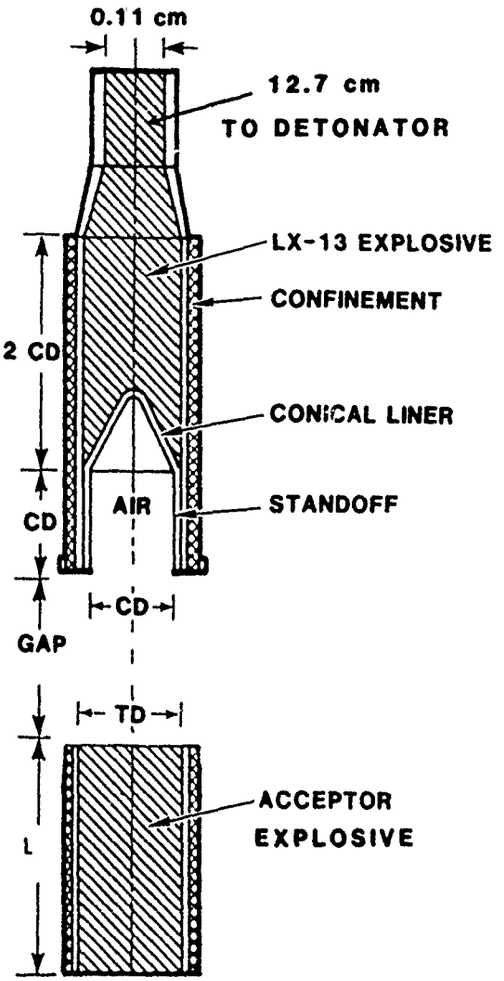

Fig. 1. CSC and Acceptor Explosive

Generally, the most important conical liner parameters are the material ductility, density, thickness, apex angle, grain size, and surface finish. The CSC liner material, inside diameter (CD), thickness (t), jet velocity (V_j), and jet diameter (D_j are listed in Table 2 for the configuration shown in Fig. 1. Also, Table 2 lists

TABLE 1
Explosive Parameters

Explosive	ϱ_e (g/cc)	V_d (cm/μs)	P_{cj} (Mb)	d_c (cm)	C_e (cm/μs)	S_e
LX-13	1.53	0.73	0.170	0.036	.15	3.03
PETN	1.77	0.83	0.341	0.040	.24	1.91
PBX 9404	1.84	0.88	0.375	0.120	.23	2.77
COMP B3	1.72	0.80	0.287	0.400	.27	1.86
CYCLOTOL 75/25	1.75	0.83	0.316	0.600	.20	2.36
PBX 9407	1.60	0.79	0.375	0.450	.13	1.99
TETRYL	1.71	0.79	0.260	1.100	.25	1.42
PBX 9502	1.89	0.76	0.285	0.900	.33	1.68
CYCLOTOL 60/40	1.70	0.79	0.316	0.600	.20	2.36

the CSC jet penetration (P) into an aluminum 5083-T6 target at the optimum standoff (SO). The jet diameter and jet velocity data were measured using a five-head flash x-ray system.

The CSC liners were fabricated by a stamping process in order to form highly reproducible copper cones. The grain size of cross sections of these liners was about 14 microns for the copper and between 7-8 microns for the tantalum. The cones were fabricated from either pure copper or tantalum. The liner thickness was about 3% of the liner diameter (CD), depending on availability of sheet metal. A liner apex angle of 47° was chosen (near the Ballistics Research Laboratory reported optimum apex angle of 42°).

TABLE 2
CSC Liner Parameters

LX-13 Explosive, Plastic Radial Tamping
Apex Angle = 47 Degrees, Stamped Liners

Material	CD (cm)	t (cm)	V_j (cm/μs)	D_j (cm)	SO (CD)	P (cm)
Copper	.173	.0076	.54	.041	1	3.1
Copper	.259	.0102	.56	.067	2	6.7
Copper	.346	.0127	.65	.097	1	15.7
Tantalum	.173	.0076	.39	.035	2	2.9
Tantalum	.259	.0102	.36	.050	1	3.2

SHOCK INITIATION OF EXPLOSIVES

Most previously published work on shock initiation of secondary explosives has been concerned with flyer plate or rod impact configurations. Generally, the basic mechanism for the shock initiation to detonation in explosives is considered to be shock interaction at density discontinuities which produce local hot spots and decomposition within the explosive. The energy of the decomposing explosive is added to the flow (1). Some previously published work (1-5) has concentrated on the modeling of detonations. In shock initiation experiments, the magnitude and duration of the shock wave are critical in building to detonation. The detonation wave will continue to propagate throughout the explosive only if the detonation zone diameter is sufficient. If this diameter is smaller than the diameter required to maintain a propagating detonation, then the side or rear rarefaction or expansion waves will dominate the flow and stop propagation of detonation. Other factors contributing to the propagation of the detonation wave are the composition of the explosives (thermal decomposition kinetics), grain size, initial explosive porosity, and explosive confinement.

WALKER-WASLEY CRITERION FOR FLYER PLATE IMPACT

The critical energy model (5-7) requires that a critical, or minimum, energy per unit area, E_c, be delivered to the explosive for shock initiation to detonation. The following equation for the critical energy has been derived (6-7):

$$E_c = Put = P^2t/\varrho_e U = K \qquad (1)$$

The parameters in the above equation are the pressure (P), particle velocity (u), shock pressure

pulse duration (t), initial explosive density (ϱ_e), shock velocity (U), and an experimental constant for the particular explosive (K). A more simple $P^2t = K_1$ is usually used in flyer plate-explosive impact work.

MODIFIED WALKER-WASLEY CRITERION FOR JET IMPACTS

The Walker-Wasley shock initiation criterion for flyer plates impacting bare heterogeneous explosives has been modified by James (11) to account for the geometry of a rod impacting an explosive. The value of E_c has been found to depend on projectile geometry (11). Using a formulation modified from Anderson's and James' models for the critical initiation energy (E_c) for rod impact ($t=D_j/2C_j$), and applying it to a jet impact on bare explosives, results in the following relationship:

$$E_c = PuD_j/6C_j \tag{2}$$

where P, u, D_j, and C_j are the shock pressure, particle velocity in the unreacted explosive, jet diameter and speed of head of the release wave in the jet material, respectively. The momentum equation across the "strong" shock after jet impact is given by:

$$P = \varrho_e U u \tag{3}$$

where P, ϱ_e, U, and u are the impact pressure, initial explosive density, shock, and particle velocities in the explosive, respectively. In addition, the following relationship (9) exists for most materials:

$$U = C_e + S_e u \tag{4}$$

where C_e and S_e are the bulk sound velocity in the explosive and the slope which is usually determined from least squares fit of experimental ultrasonic data. Combining equations 1-4 results in the following relationship for the critical energy for jet impact:

$$E_c = \varrho_e D_j u^2 (C_e + S_e u)/6C_j \tag{5}$$

where the particle velocity (u) has been shown to be related to the jet impact velocity (V_j) (10) as follows:

$$u = \{-B + (B^2 - 4AC)^{0.5}\} / 2A \tag{6}$$

where

$$A = (\varrho_e S_e - \varrho_j S_j) \tag{7}$$

$$B = (\varrho_e C_e + \varrho_j C_j + 2\varrho_j S_j V_j) \tag{8}$$

$$C = -(\varrho_j C_j V_j + \varrho_j S_j V_j^2) \tag{9}$$

ϱ_j = jet density (g/cm^3)

C_j = velocity of sound in jet = 0.396 cm/μs (Cu)

u_j = particle velocity (cm/μs)

S_j = slope for jet material = 1.5 (Cu)

V_j = jet (tip) impact velocity (cm/μs)

Equations 5-9 illustrate that the critical energy (E_c) can be calculated knowing the jet impact velocity (V_j), jet diameter (D_j), and the usually known additional explosive acceptor and jet parameters. The calculated critical energy (E_c) values for the six explosive acceptors where V_j and D_j were known are listed in Table 3. The E_c values for these materials varied from 447 to 5712 J/cm^2. The calculated jet impact E_c values are relatively large in comparison to Walker and Wasley's reported flyer plate data values of 12 and 63 J/cm^2 for PETN and PBX 9404, respectively. This is likely due to the smaller diameters of the jet compared to the flyer plate and, therefore, an impact "spot size" effect. Table 3 also lists calculated values for the jet-explosive impact pressure (P), transmitted shock velocity (U), particle velocity (u), and P^2t. The calculated values for u, U, and P were obtained from equations 6-9, 4, and 3, respectively. Jet-explosive impact pressures as a function of jet impact velocity are shown in Figure 2 for the explosives listed in Table 3.

DIMENSIONAL ANALYSIS

Shock initiation of bare, heterogeneous explosives by CSC jets differs from conventional flyer plate shock initiation in geometrical projectile configuration, projectile acceptor explosive physical interaction, shock pulse duration and other parameters. Theoretical modeling using two dimensional hydrocodes is difficult, time consuming, and expensive. Modeling of jets and rods impacting explosives has been done (1, 12). The modeling of jet impact requires knowing beforehand the jet tip to tail velocity gradient or distribution, which is not usually available.

TABLE 3
Calculated Jet-Explosive Acceptor Initiation Parameters

Acceptor Explosive	E_c (J/cm^2)	P^2t (Mb^2–μs)	D_p x10^{-8}	u (cm/μs)	P (Mb)	U (cm/μs)
LX-13	447	.026	18.300	.37	.71	1.26
PETN	581	.032	24.530	.42	.77	1.04
PBX 9404	561	.025	8.330	.21	.31	.81
COMP B3	*	*	2.200	*	*	*
CYCLOTOL 75/25	*	*	1.560	*	*	*
PBX 9407	1772	.095	0.226	.49	.88	1.11
TETRYL	1757	.085	0.310	.49	.78	.94
PBX 9404	*	*	0.255	*	*	*
PBX 9502	5712	.337	0.805	.42	.83	1.04
PBX 9404	*	*	0.940	*	*	*
PBX 9502	*	*	0.250	*	*	*
PBX 9502	*	*	0.090	*	*	*

* D_j or V_j values are not available for calculation.

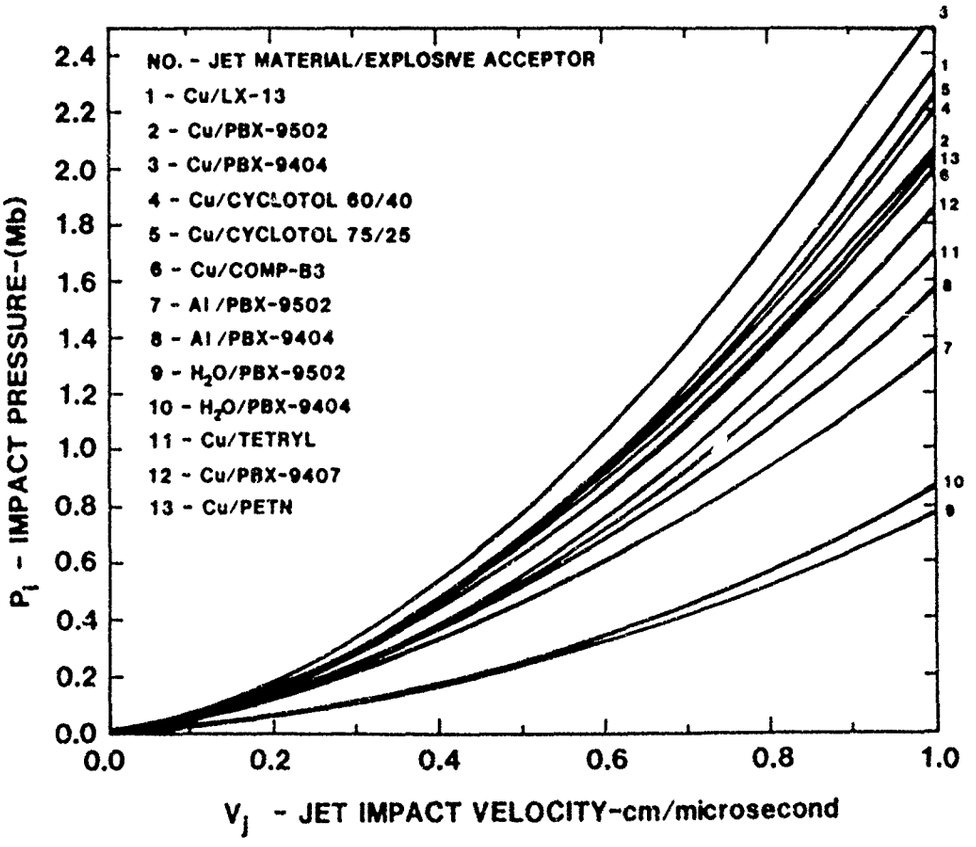

Fig. 2. Jet Impact Pressure Versus Impact Velocity

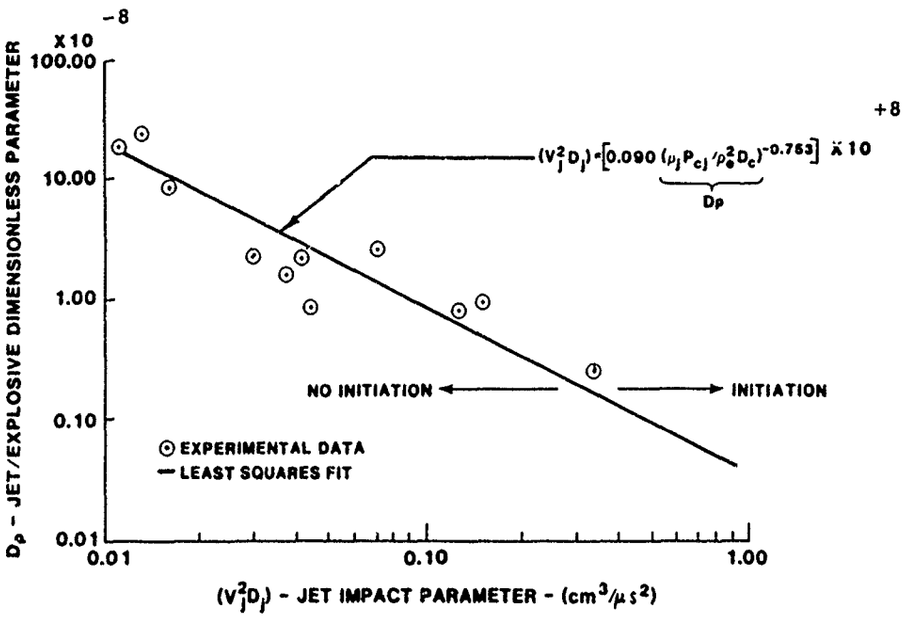

Fig. 3. Dimensionless Parameter Versus Impact Parameter

Therefore, in an effort to find another analysis method based on usually known parameters which describe the acceptor explosives, dimensional analysis techniques were utilized to develop a dimensionless parameter to describe an explosive. Dimensional analysis (10, 13, 14) is often used to derive a scaling law because an understanding of the problem can then be obtained without detailed equations relating jet and explosive acceptor physical properties.

Dimensional analysis used groups of dimensionless ratios to relate physical properties. One technique uses the Buckingham Pi Theorem (13, 14) to obtain one of several possible sets of dimensionless pi terms to relate CSC and explosive properties. Some variables considered important in describing an explosive and jet are listed in Table 4. One such dimensionless pi term (D_p) is:

$$D_p = \varrho_j P_{cj} / \varrho_e^2 D_c g$$

This particular pi term was chosen because the data for the various explosives discussed in this paper were consistently a function of the jet impact parameter ($V_j^2 D_j$), as illustrated in Fig. 3. Also, Held (3) has demonstrated that the jet tip velocity squared (V_j^2) times the jet tip diameter (D_j) has a critical value for initiation of explosives, and that this value is constant for a given explosive. This jet impact parameter ($V_j^2 D_j$) is listed in Table 5 for the explosives considered in this paper. Also listed in this table are the jet density (ϱ_j), jet diameter (D_j), jet tip velocity (V_j), and jet material. The power law least squares fit of the D_p versus $V_j^2 D_j$ data is shown in Fig. 3. Only $V_j^2 D_j$ values that fall to the right of the curve in Fig. 3 should result in initiation of the explosive.

TABLE 4

Jet/Explosive Dimensional Analysis Parameters

Variable	Symbol	Units
Explosive Density	ϱ_e	M/L^3
C. J. Pressure	P_{cj}	M/LT^2
Critical Diameter	D_c	L
Jet Density	ϱ_j	M/L^3
Gravity Constant	g	L/T^2

PHOTOMETRIC MEASUREMENTS

A Cordin Model 200 rotating mirror camera (0.45) microsecond interframe time) was used to photograph the jet-explosion initiation. A typical CSC-explosive acceptor experimental setup is snown in Fig. 4. Selected frames from

TABLE 5
CSC Jet Initiation Parameters

Acceptor Explosive	CSC JET ϱ_j (g/cc)	D_j (cm)	V_j (cm/μs)	Material	$V_j^2 D_j$ ($cm^3/\mu s^2$)
(1) LX-13	8.9	0.041	0.50	Cu	.012
(1) PETN	8.9	0.043	0.56	Cu	.013
(3) PBX 9404	8.9	0.210	0.28	Cu	.016
(3) COMP B3	8.9	*	*	Cu	.029
(5) CYCLOTOL 75/25	8.9	*	*	Cu	.037
(1) PBX 9407	8.9	0.097	0.65	Cu	.041
(1) TETRYL	8.9	0.097	0.65	Cu	.041
(2) PBX 9404	2.7	*	*	AL	.070
(3) PBX 9502	8.9	0.390	0.57	Cu	.127
(2) PBX 9404	1.0	*	*	H_2O	.150
(2) PBX 9502	2.7	*	*	AL	.325
(2) PBX 9502	1.0	*	*	H_2O	.800

* — Not Available (1) — This Study
(2) — Mader Reference 1 (Hydrocode Calculations (3) — Campbell Reference 1

films of many tests conducted are shown in Figs. 5-8. Figs. 5-6 illustrate the prompt copper jet initiation of LX-13 explosive. The standoff for both Figs. 5-6 was 0.7 cm for the 0.346 cm diameter CSC's. The copper jet is visible in Fig. 5. The detonation waves in the LX-13 explosive are visible in both Figs. 5-6. The shock waves in the plastic material are more visible in Fig. 6. The acceptor explosive was loaded in clear plastic whose dimensions were 0.635 cm diameter by about 6 cm long. The jet impact velocity and jet diameter were about 0.65 cm/μs and 0.09 cm, respectively, for both tests

The location of the center of detonation in Fig. 7 indicates that, for Tetryl, initation to detonation occurred about 4 mm into the acceptor. The copper jet velocity and diameter were 0.65 cm/μs and 0.097 cm, respectively. The Tetryl diameter and length were 12.7 and 25.4 mm, respectively. The standoff was 0.346 cm for the 0.346 cm diameter CSC.

Fig. 8 illustrates the CSC initiation of a PETN explosive acceptor. The 0.173 cm diameter copper CSC was used in this test with a jet velocity and diameter of 0.54 cm/μs and 0.041 cm, respectively.

A five head flash x-ray system was used to measure jet tip velocity and tip diameter. Fig. 9 shows a typical copper jet from a 0.346 cm diameter CSC. The LX-13 explosive was initiated by the jet, and the jet has penetrated about 0.5 cm in the explosive. The jets from the smaller CSC's were more difficult to photograph primarily because of small jet diameters.

INITIATION OF COVERED EXPLOSIVES

The requirement to transfer a detonation from a 0.11 cm LX-13 explosive train segment, through a barrier, to another 0.11 cm LX-13 train segment has led to the development of the explosive switch illustrated in Fig. 1. The barrier in the GAP dimension of Fig. 1 could consist of a 0.127 mm thick cover plate over the cylindrical CSC standoff, a 3.8 mm teflon layer, and a 0.051 mm thick steel cover plate over the acceptor explosive. The steel cover plates are required to seal against corrosive fluids. The teflon layer simulates a high density corrosive fluid that could be encountered between the CSC and explosive acceptor.

The CSC's configured as shown in Fig. 1 and Table 2 were used to initiate explosives through various combinations of air, teflon, and steel materials located in the GAP dimension between the CSC and the acceptor explosive. A summary of the tests conducted to determine

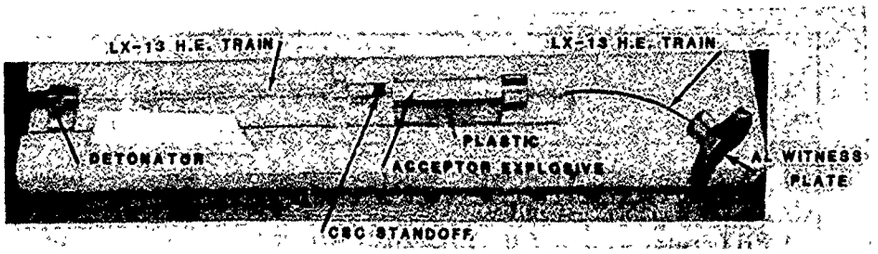

Fig. 4. CSC and acceptor explosive test configuration

TABLE 6
Copper CSC Threshold Initiation Parameters

CSC		Acceptor Explosives		Gap Materials			
Type	CD (cm)	Type	Density (g/cc)	Donor Plate	Gap	Acceptor Plate	SO (cm)
Cu	0.173	PETN*	1.60	No	Air	No	0.35
Cu	0.173	LX-13**	1.53	Yes	Air	Yes	0.55
Cu	0.173	PETN**	0.63	Yes	Teflon	Yes	0.55
Cu	0.173	PETN**	1.20	Yes	Air	Yes	0.55
Cu	0.259	LX-13	1.53	No	Air	No	0.259
Cu	0.259	PETN**	0.63	Yes	Teflon	Yes	0.645
Cu	0.346	LX-13**	1.53	Yes	Air	Yes	0.744
Cu	0.346	PETN**	1.20	Yes	Teflon	Yes	0.744
Cu	0.346	PETN**	1.20	—	—	—	0.346
Ta	0.259	LX-13*	1.53	No	Air	No	0.259

Acceptor Dimensions — 6.35 mm diameter x 50.8 mm long
* — 1.9 mm diameter x 12.7 mm long
** — Donor Plate = 0.127 mm, Gap = 3.81 mm, Acceptor Plate = 0.051 mm
*** — One 0.16 cm thick steel plate in GAP

the strongest barrier for which initiation could be obtained is listed in Table 6 for LX-13, PETN (1.6 g/cc) and PETN (0.63 g/cc) explosive acceptors. A smaller diameter (CD) or a CSC with a lower impact parameter ($V_j^2 D_j$) would not initiate the acceptor explosive behind the GAP barrier listed in Table 6. Donor steel plates 0.127 mm thick covered the CSC, and acceptor steel plates 0.051 mm thick covered the acceptor explosive when indicated in Table 6. The GAP dimension of Fig. 1 was either air or teflon 3.81 mm thick (except where noted) in Table 6.

SUMMARY

The utilization of very small Conical Shaped Charges (CSC) to initiate bare and covered explosive acceptors has been demonstrated for a variety of CSC sizes and explosives. Relatively prompt shock initiation to detonation thresholds were obtained for the LX-13, PETN, PBX 9407 and Tetryl explosives. The analytical methods along with the experimental data presented have been useful in the design of very small explosive components at Sandia National Laboratories.

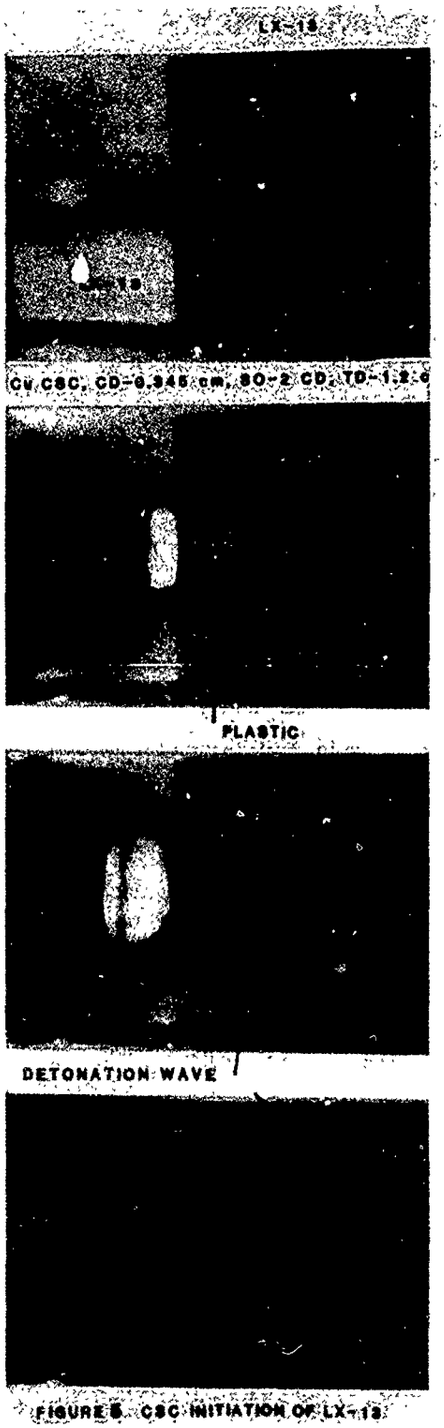

Fig. 5. CSC Initiation of LX-13

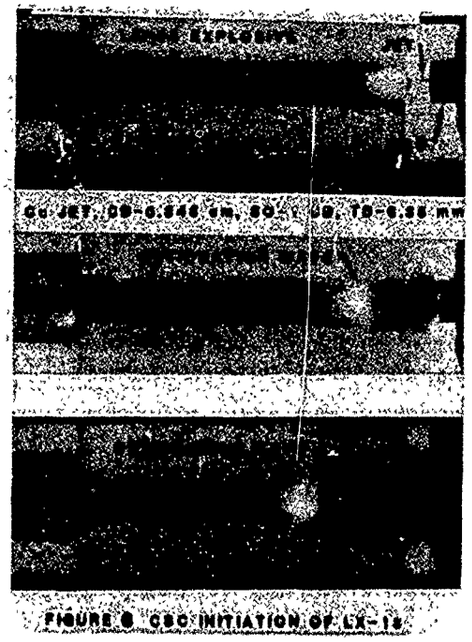

Fig. 6. CSC Initiation of LX-13.

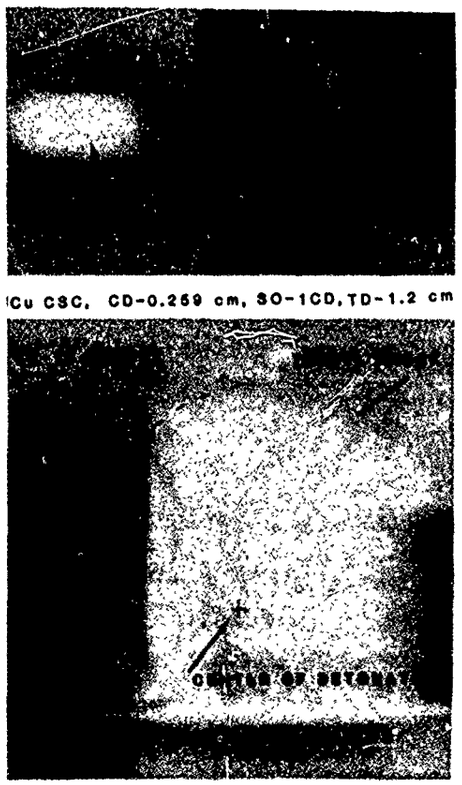

Fig. 7. CSC Initiation of TETRYL

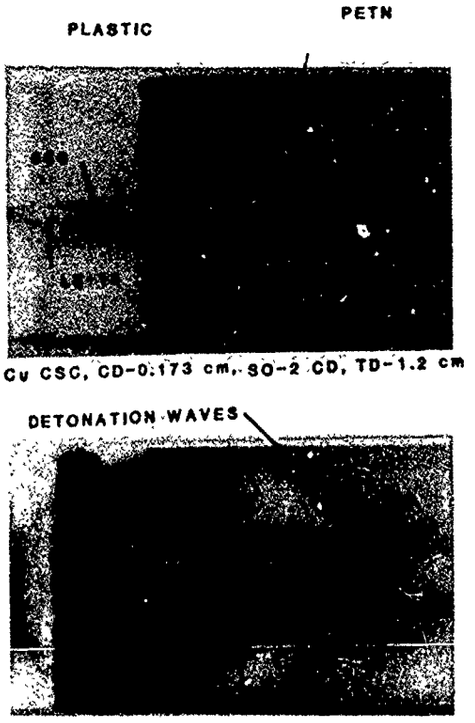

Fig. 8. CSC Initiation of PETN

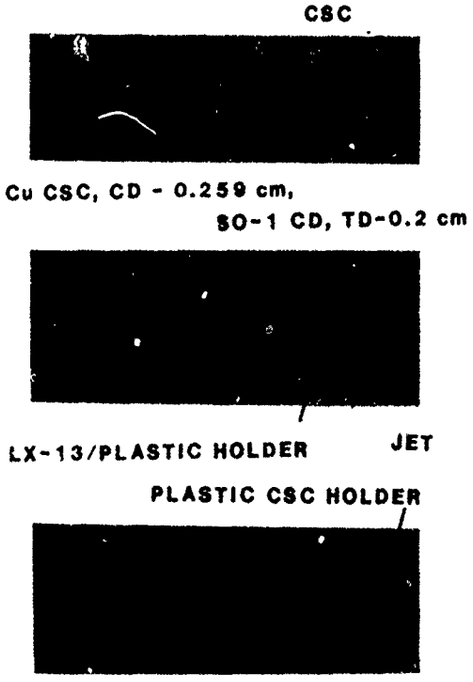

Fig. 9. Jet Initiating of LX-13

ACKNOWLEDGMENTS

The author is indebted to D.L. Marchi, F. J. Salas, D. H. Sanchez, W. G. Foy, C. A. Campos, and G. Schmitz for assistance in the various experiments. The author wishes to express his appreciation to J. G. Harlan, V. M. Loyola, and D. E. Mitchell for their suggestions in the preparation of this report.

This work was supported by the U.S. Department of Energy under Contract No. DE-AC04-76DP00789 to Sandia National Laboratories.

REFERENCES

1. C. L. Mader, G. H. Pimbley, "Jet Initiation of Explosives," (Los Alamos National Laboratory), Report LA-8647, February 1981.

2. Charles L. Mader, "Numerical Modeling of Detonations," (University of California Press), Berkeley, 1979.

3. M. Held, "Initiating of Explosives, a Multiple Problem of the Physics of Detonation," Explosivstoffe 5, 98-113 (1968).

4. W. H. Andersen, "Model of Impact Ignition and Explanation of Critical Shock Initiation Energy," Vol. 24, pp. 153-159, 1980.

5. W. H. Anderson, "Critical Energy Relation for Projectile Impact Ignition," Combustion Science and Technology, 19, pp. 259-261, 1979.

6. F. E. Walker, R. J. Wasley, "Critical Energy for Shock Initiation of Heterogeneous Explosives," Explosivstoff 17, 9, (1969).

7. F. E. Walker, R. J. Wasley, "A General Model for the Shock Initiation of Explosives," Propellants and Explosives, 1, 73, (1976).

8 .W. H. Anderson, "Critical Energy Relation for Projectile Impact Ignition," Combustion Science and Technology, 1979, 19, pp. 259-261.

9. A. L. Rouff, "Linear Shock-Velocity-Particle-Velocity Relationship," Journal of Applied Physics, 38, No. 13, December, 1967.

10. M. G. Vigil, R. P. Sandoval, "Development of a Method for Selection of Scaled Conical Shaped Explosive Charges," Sandia National Laboratories, SAND80-1770, March, 1983.
11. H. R. James, "A Criterion for the Shock Initiation of Explosives," 26th Meeting of JOWOG-9, AWRE, Aldermaston, J9/26-AWRE, pp. (7-1)-(7-10), June 4-8, 1984.
12. J. Starkenberg, Y. Huang, and A. Arbuckle, "Numerical Modeling of Projectile Impact Shock Initiation of Bare and Covered Composition-B," Journal of Energetic Materials, Vol. 2, 1-41, 1984.
13. H. L. Langhaar, "Dimensional Analysis and Theory of Models," Wiley, NY, 1951.
14. W. E. Baker, et al., "Similarity Methods in Engineering Dynamics," Haydon Book Co., Inc., Rochelle Park, NJ, 1973.

DISCUSSION

KEN READ, AWRE, Foulness MOD (PE), U.K.

Could you clarify whether by "jet density" you mean the original density of the liner or the true density of the jet?

REPLY BY M. G. VIGIL

Jet density in the paper means the original density of the conical shaped charge liner material.

DISCUSSION

HAROLD GRYTING, SWRI

(1) What explosives could you not obtain initiation with these explosive shaped charge jets?

(2) Could the intensity of PBX-9404 be attributed to the fire resistant coating of the 3% TRI (CHLORETHYL) PHOSPHATE that is used to desensitize this composition?

REPLY BY M. G. VIGIL

(1) The explosives PBX-9404, PBX-9501, and PBX-9502 could not be initiated with conical shaped charges (CSC) of up to 3.5 mm inside diameter.

(2) This is very possible depending on the coating thickness. Another potential reason that the above explosives were not initiated might have been that their diameters and lengths were significantly smaller than the explosives discussed in the paper. Possibly the detonation was quenched due to side rarefaction waves.

DISCUSSION

JULIUS ROTH, Consultant

I have trouble with the numbers and sensitivity ranking of the explosives shown in your Figure 3. If the U and P values are the threshold values for shock initiation, they are much too high. Furthermore, the threshold shocks for the initiation of PBX-9404 (in both planewave/wedge geometry or in gap-tests are 3 to 5 times greater than those for 1.6 g/cc gap-test geometry PETN. (See my paper in the proceedings of the 5th Detonation Symposium.)

REPLY BY M. G. VIGIL

The U and P values discussed in the paper were calculated from the momentum equation across a shock and from Hugoniot relations for the initial jet and target/acceptor explosive materials. These values may not relate directly to previous shock initiation published values because the impactor or jet area is significantly different here, compared to other typical shock initiation experiments. There may be a minimum impactor area where regardless of the impactor or jet velocity, the area or jet diameter is too small for the shock initiation mechanism. In addition, the jet bow wave interaction with the explosive acceptor may yield a better correlation of pressures when comparing this jet impact problem to classical shock initiation configurations.

Session XI
INITIATION AND SENSITIVITY II

Chairman: Thomas L. Boggs
Naval Weapons Center

EXPERIMENTAL STUDIES CONCERNING THE RESPONSE OF INTERMEDIATE EXPLOSIVES TO THERMAL STIMULI

C.D. Hutchinson
R.A.R.D.E., Fort Halstead, Sevenoaks, TN14 7BP,
Kent, UK

For sometime now efforts have been made to replace tetryl as a booster explosive in conventional munitions because of its health hazard and because of its very violent response to accidental stimuli. The explosives considered for use as tetryl replacements have been examined in a number of small-scale tests whereby their critical temperature for self-heating in small cylindrical geometries are predicted and experimentally measured and the behaviour of these materials in a liquid fuel-fire have been assessed. As well as giving an estimate of the maximum temperature these materials will sustain before exploding, these tests indicate the magnitude of their response on exploding (their explosiveness). It is shown that DSC-derived Arrhenius kinetics can give good predictions of practical situations, including, it is argued, complete weapon systems. It is shown that TATB-containing nitramine boosters provide one possible solution to the problem and, in circumstances where the low-temperature response of these materials is unacceptable, other heat-resistant explosives are available but their explosiveness must also be taken into account before decisions are taken.

INTRODUCTION

Explosive-filled munitions for naval service are required to survive exposure to fires such as might occur when an aircraft crashes onto a carrier flight deck. To meet this requirement a range of thermally-insensitive plastic-bonded main charge explosives is being developed in the UK. However, investigation of a violent explosion which occurred during a fuel-fire test on a complete store led to the conclusion that reaction was initiated by cook-off of the booster charge rather than the main filling (1) and the safety advantages inherent in the use of insensitive main charges may be compromised or lost by inadequate booster designs (2).

There are several options available to avoid booster cook-off:

a. reduction in the dimensions of boosters so that, in the fuel-fire environment, they are below the critical size for a thermal explosion to occur, the magnitude of which would otherwise produce a stimulus sufficient to cause explosion or detonation of the main charge.

b. production of thermally-insensitive, low-explosiveness boosters by the synthesis of new explosives.

c. modification of existing materials on a molecular level to reduce their thermal response.

d. production of new compositions based on existing explosives but with a reduced thermal response.

e. modification of design of booster housing to provide early rupture and loss of confinement.

f. use of thermal insulation to reduce the heat flow to the explosive.

This report contains studies of options a, b and d. [Studies to investigate option c by synthesising the 3-amino and 3,5-diamino derivatives of tetryl have recently been reported (3).] A relatively simple, small-scale test procedure

is presented whereby the critical temperature of an explosive may be estimated in the laboratory, its critical temperature together with an estimate of its explosiveness in a realistic geometry and confinement determined experimentally and finally the behaviour of the explosive assessed in a liquid fuel-fire.

Related studies by other workers include, amongst others, those on a laboratory scale (4) (40mg slab geometry), small spherical geometry (5)(ODTX) and large cylindrical geometry (6)(30-40 mm diameter ×60-75 mm long cylinders) and Zinn & Mader (7) have examined times-to-explosion in 1" diameter cylinders. For the present work, booster charges of dimensions 25 mm diameter by 25 mm long, similar to those employed in practical munitions, were examined. Tetryl boosters of these dimensions are known to be adequate for initiating the majority of current, in-service explosives. The test procedures described allow reasonable estimates of the behaviour of booster systems at high temperatures to be made. These tests have the further advantage of demonstrating the violence of the booster response on cook-off (i.e., explosiveness) and the importance of this factor is also illustrated.

EXPERIMENTAL

Materials Investigated. As part of a program to replace tetryl (N-methyl-N-(2,4,6-trinitrophenyl)-nitramine) in lead and booster applications, a number of alternative materials have been examined:

a) Debrix 2 [nominally RDX 95%, Wax 5%].
b) LX-15 [HNS(2,2',4,4',6,6'-hexanitrostilbene) 95%, Kel-F 800 5%].
c) UK analogues of PBXW-7 known as BX compounds:
   BX1 TATB 60%, Nitramine 35% [RDX:HMX 95:5], Kel-F 5%
   BX2 TATB 60%, Nitramine 35% [RDX:HMX 95:5], PTFE 5%
   BX3 TATB 60%, Nitramine 35% [RDX:HMX 90:10], Kel-F 5%
   BX4 TATB 60%, Nitramine 35% [RDX:HMX 90:10], PTFE 5%
d) AFX 521 [PYX(2,6-bis(picrylamino)-3,5-dinitropyridine) 95%, Kel-F 800 5%]
e) PBX 9407[RDX 94%, Exon/FPC 461 6%] and a UK analogue referred to as PBX 9407 (UK).
f) Although not as shock sensitive as the above, PBX 9503 [TATB 80%, HMX 15%, Kel-F 800 5%] and a UK analogue referred to as PBX 9503(UK) were also examined.

Decomposition Studies. Thermochemical measurements were made using a Perkin-Elmer differential scanning calorimeter (DSC-2). Sample masses less than 1mg contained in aluminium sample pans were covered with aluminium lids secured by pressure welding. Each lid had a pin hole about 0.1mm diameter to allow escape of gaseous decomposition products. An empty pan and lid served as the reference. The ambient atmosphere was dried argon flowing at $50cm^3$ min^{-1}. Dynamic and isothermal runs were carried out and enthalpy of decomposition values estimated by comparison with the enthalpy of melting of known masses of high purity indium. Kinetic analysis of isothermal runs, carried out at four different temperatures, provided values for the apparent activation energy, E. and preexponential factor, A.

Temperature of Ignition Test. Two 200mg samples of the test explosive were placed in small glass tubes which were inserted in cavities in a steel block, the temperature of which was raised from ambient at 5K min^{-1}. The samples were observed and the temperature at which smoke or flames seen, was noted (8).

RARDE Small-Scale Booster Cook-Off Test. In this test, a 25mm diameter by 25mm long cylinder of test explosive was placed in a mild steel tube (wall thickness 6mm) forming a cook-off bomb with a bursting pressure in excess of 0.18GPa, Figure 1. Inert pellets of pressed NaCl were employed to fill the dead space within the bomb which was placed on two steel rods some 110-120mm above the surface of $2dm^3$ of petrol contained in an open square tray of side 300mm and the fuel ignited electrically. This test has been carried out either with total confinement or, as shown in Fig. 1, with ½mm diameter thermocouples fitted to monitor temperatures at the centre of the explosive charge and at the centre of the inside wall. The thermocouple wires leading from the cook-off bomb were protected with a woven carbon fabric to minimize heat transfer down the steel sheath to the thermocouple probes. The temperature profiles of the sample were recorded an 10s intervals with a Datron Log-Pac 2001 logging system. At least two tests on each

explosive in total confinement and one with thermocouples were performed. The fragments resulting from these tests were used as an indication of the explosiveness of the sample, a term which may be defined as the magnitude of the event produced from an accidental stimulus.

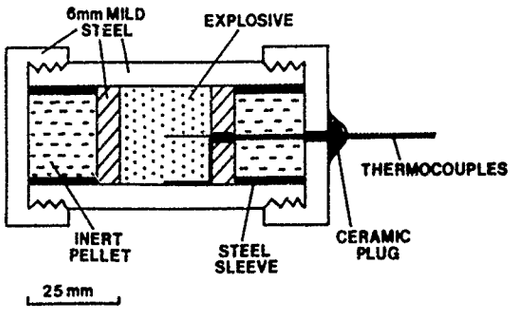

Fig. 1. RARDE Small-Scale Booster Cook-Off test arrangement showing thermocouples in place

Critical Temperature Test. For this test the 25mm diameter by 25mm long explosive sample was encased in an aluminium alloy container with 3mm thick walls representing a booster housing assembly. Steel sheathed, ½mm diameter thermocouples were potted into the centre of the charge and at the centre of the inside wall (Figure 2). The sample container had a bursting strength in excess of 0.04 GPa. The sample was lowered remotely into a heated bath of liquid paraffin or silicone oil (depending upon the selected temperature), the temperature of which was maintained at ±0.5 °C by heating tapes regulated by a Control & Readout Model 407 thyristor controller and constant stirring of the liquid medium with nitrogen gas. The temperature of the charge at the centre and side was monitored until either there was evidence of an explosion entirely disrupting the test sample, a rapid change in the temperature of the centre of the smple indicating that a pressure burst had occurred or the slow, exothermic decomposition associated with ambient temperatures below the critical value had ceased. The time intervals between the entire sample reaching the preset bath temperature and the event occurring were used in constructing time-to-explosion plots.

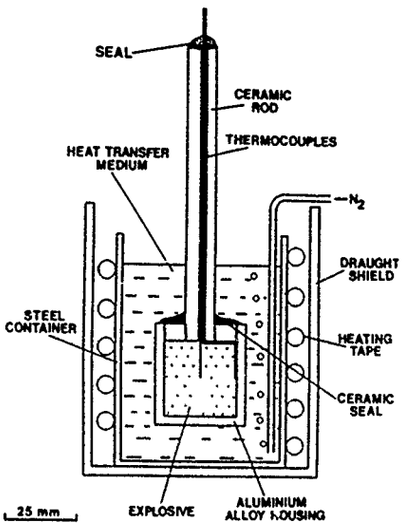

Fig. 2. The experimental arrangement used for critical temperature determinations

THEORETICAL ASPECTS

Thermal Explosion Theory. Explosives decompose exothermically at a finite rate above absolute temperature and consequently, when held at elevated temperatures for any length of time, decomposition occurs which causes further temperature rise in the fresh material. If the heat thus produced is not lost to the surrounds, the sample temperature will continue to rise leading to a runaway, self-heating reaction or thermal explosion. The lowest constant ambient temperature above which a thermal explosion is produced is called the critical temperature (Tcr). Various authors have considered this heat balance problem (9,10,11), and Zinn and Mader (7) give an expression relating the ambient temperature to physical parameters describing a first-order rate process,

$$T = \frac{E}{R \ln\left[\frac{a^2 \rho Q A E}{T^2 \lambda \delta R}\right]} \quad \text{where} \quad (1)$$

T = ambient temperature
λ = thermal conductivity
Q = heat of reaction
δ = Frank-Kamenetskii's shape factor
a = radius or half thickness

which when $\delta \rightarrow \delta cr$, $T \rightarrow Tcr$. Frank-Kamenetskii has derived values for δcr for various geometries (0.88 -infinite slab, 2.00 -infinite cylinder, 3.32 -sphere) and therefore, for a fixed geometry provided values of E,A,ρ,Q, and λ

are available, Tcr can be determined. The Frank-Kamenetskii treatment of thermal explosion theory does not, in its original form, cater for the right-regular geometry but the modelling of geometries other than the three model shapes by consideration of a sphere with equivalent heat transfer characteristics (12) offers one solution to the problem and for the geometry under investigation, a=1.367cm and δcr=2.843. Values of E,A, Q and λ which refer to the decomposition process that explosives actually undergo in practice are very difficult to determine but since they appear in the logarithmic term in Eq. 1, errors involved in their measurement are reasonably accommodated. Additionally there are assumptions concerning heat flow, reactant consumption and decomposition kinetics implicit in Eq. 1 which may not apply in real systems. However, results obtained here indicate that in the majority of cases this approach is applicable and good agreement can be obtained between measured and predicted values of Tcr.

Kinetic Analysis. The apparent rate law for thermal decomposition was determined from isothermal DSC studies. Integration of the output from DSC, which is in terms of heat input per unit time versus time, yielded α-time plots (where α=extent of reaction) which were analysed by the reduced-time method of Sharp et al. (13). This technique also confirmed the applicability of the use of a single rate expression in the temperature range studied (14). In some cases the order of reaction was confirmed by the technique described by Hancock & Sharp (15) and elsewhere (16). In general it was found possible to achieve a good agreement between a theoretical rate law and experimental data from α=0 to 0.8/0.9. Assuming this same rate law to hold over the temperature range studied, the rate of reaction as a function of temperature can be derived from measurements of $f(\alpha)$ as a function of time at different temperatures and hence the apparent activation energy and pre-exponential factor in the Arrhenius expression calculated. [$f(\alpha)=kt$ is the rate law found to apply to the decomposition.]

Critical Temperature and Time-to-Explosion. The general shapes of the thermocouple traces from the critical temperature experiments, which are dependent upon the bath temperature, are shown in Figure 3. As the

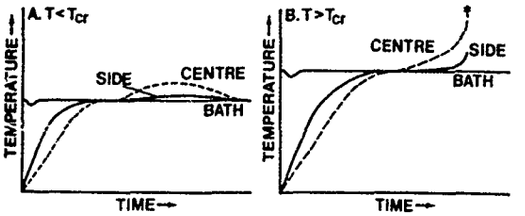

Fig. 3. Schematic curves to illustrate the temperature profiles in explosives heated below and above the critical temperature

temperature of the bath is raised, so the rate of reaction increases and the temperature difference between the centre of the sample and the liquid medium increases to a maximum value at Tcr. When T>Tcr, the rate of heat generation exceeds the rate of heat loss and a thermal explosion occurs. Consequently, by monitoring the temperature in the samples held at different bath temperatures the critical temperature may be estimated. In addition, this experimental technique allows the time-to-explosion to be determined at a particular temperature. Several workers have demonstrated that an empirical relationship exists between the time-to-explosion and temperature (17-22) and Todes (23) derived an analytical expression which, as Frank-Kamenetskii showed (24) can also be derived from thermal explosion theory, is

$$t = \frac{CRT^2}{QAE} \exp^{E/RT} \quad \text{where} \qquad (2)$$

t=time-to-explosion, C=specific heat.

A more rigorous and general approach was adopted by Gray & Harper (25) but their solution tends to the approximate one above when certain terms are ignored. For practical purposes, the simple approximation is found to be adequate since, as noted by Gray (26), the errors in E commonly exceed the errors in the approximation. This expression for time-to-explosion is ony strictly valid provided that reaction consumption can be ignored, heat losses are negligible and C,Q,E and A remain constant over the range of temperatures studied. In practice, unless T≫Tcr, the amount of reactant consumption before explosion is small for energetic materials and as the temperature of the reactant is only slightly above the bath temperature for most of the time before explosion, any variation of the thermokinetic parameters with temperature does

not have a significant effect on the time-to-explosion.

A strict analysis of the heat balance problem based on a single source term Arrhenius kinetics as heat source predicts a curvature in the time-to-explosion plots at low temperatures (27). However, the approximate analysis leads to

$$\ln t = \frac{E}{RT} + \ln \text{constant} \qquad (3)$$

and allows effective estimates of E to be made (28-30).

RESULTS AND DISCUSSION

The tests carried out with the RARDE small-scale booster cook-off test monitored with thermocouples indicated that the temperature of the exterior of the charge rose rapidly once the fire was ignited leading to an event before significant heat flow into the interior of the sample had occurred (Figures 4a-d). In Fig. 5 the last recorded temperature on the outside of the charge before an event occurred is plotted against the laboratory-determined temperature of ignition (T of I). Even though larger masses of explosive were employed in the cook-off test than in the T of I determination, the temperature at event exceeded the corresponding T of I in all cases indicating that the overriding factor is the greater heating rate in the fuel-fire. It is evident that in the fuel-fire the event occurred when the outer shell of the charge reached and exceeded the T of I of the explosive. There is a scatter in the temperature of event for the RDX-based explosives which is probably due to the irregular heat transfer from the fires used. A more regular and controlled heat source, as used for example in the NWC small-scale cook-off bomb, would reduce this scatter as shown by Anderson & Pakulak for 17 RDX-binder compositions heated at 2.5-3.0 °C s^{-1} when times-to-event of 92±8s were recorded (2).

The results of fragment analysis from these cook-off tests indicate that the booster materials exhibit a wide range of explosiveness, Table 1. In this test, in which ignition sites develop in the surface layers of the explosive while the interior remains relatively cool (31,32) the explosiveness is determined by the rate at which

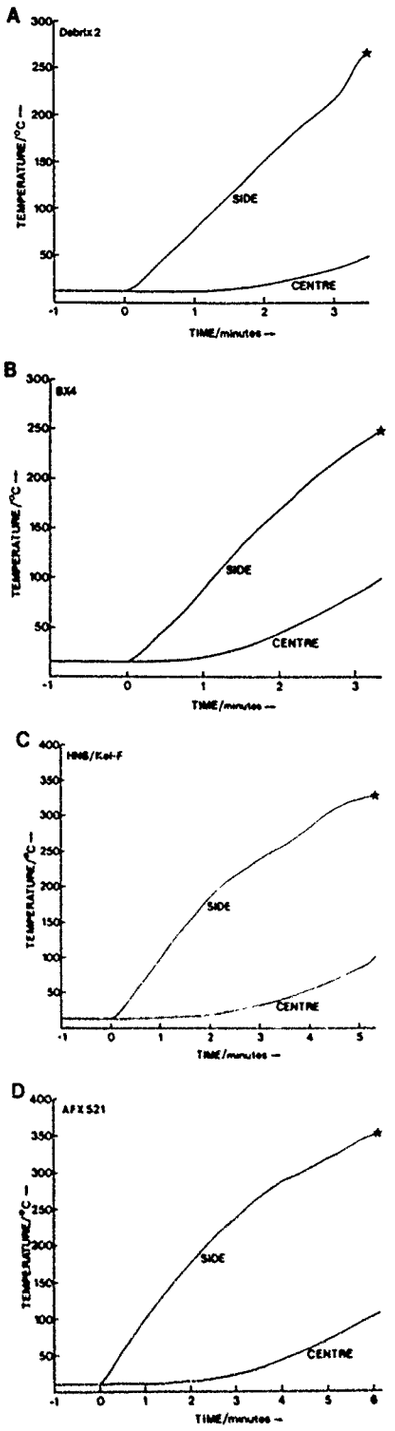

*Fig. 4. Temperature/time traces recorded using the experimental arrangement shown in Fig. 1 when the tube is subjected to a petrol fuel-fire. (a) Debrix 2, (b) BX4, (c) HNS/Kel-F, (d) AFX 521. The * indicates explosion point.*

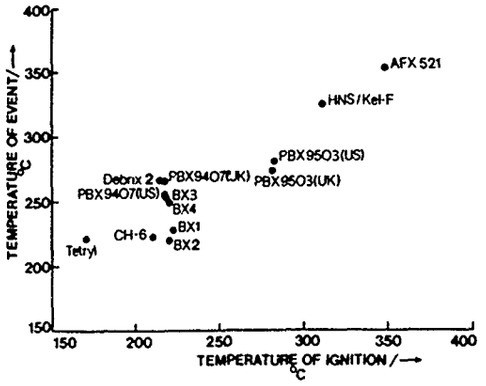

Fig. 5. Graph of last recorded temperature of the booster at the explosive/wall interface in the fuel-fire cook-off bomb plotted against the temperature of ignition for the explosive.

TABLE 1

Result of RARDE small-scale booster cook-off tests

EXPLOSIVE	AVERAGE NUMBER OF FRAGMENTS () = No. tests	EVENT TYPE	EXPLOSIVENESS
Tetryl	60 (4)	Detonation	Very high
HNS/Kel-F	90 (3)	Detonation	Very high
Debrix 2	2 (5)	Deflagration	High-
	>11 (1)	Detonation	Very high
CH-6	9 (3)	Severe deflag.	High
PBX9407(UK)	9 (3)	Severe deflag.	High
PBX9407	4 (3)	Severe deflag.	High
BX 1-4	2 (12)	Mild deflag. (some HE left)	Low
AFX 521	2 (3)	Mild deflag. (some HE left)	Very low
PBX9503(UK)	2 (3)	Very mild event or pressure rupture	Very low
PBX9503	2 (3)		

ignition can propagate inwards The violence of the event produced depends on the balance between the ease with which the initial deflagration process can convert into a shock-driven decomposition leading eventually to detonation (33) before the gaseous product overpressure causes loss in confinement to occur. Other work indicates that the ranking order of explosiveness determined from the RARDE small-scale fuel-fire test and the RARDE small-scale burning tube test (1) is very similar and although, to date, burning tube tests have only been carried out on tetryl and Debrix 2 (both exhibiting high explosiveness), it is expected that a similar ranking order to that shown in the small-scale booster cook-off test will result.

In additional work involving a configuration where the RARDE small-scale burning tube is partially filled with an aluminised explosive of low explosiveness (RWA2-RDX 71%, Wax 9%, Al 20%) and the remaining space occupied by a booster increment (1), tetryl, Debrix 2, PBX 9407 and PBX 9407(UK) have been examined in 25 mm, 31.4 mm and 40 mm diameter geometries in the fuel-fire environment. These tests indicate that, in general, an event occurs when the booster material ignites and the event type is dependent upon the dimensions of the booster under test. It is not a requirement that the booster itself must detonate to produce a severe event but only that there be a shock stimulus generated within the deflagrating booster of sufficient magnitude that either DDT occurs in the booster or the RWA2 is shock initiated. By using this test it has been possible to determine the maximum size of booster which, in the test configuration, has a low probability of causing a violent event, Table 2. Although detonation with either PBX 9407 or PBX 9407(UK) was not observed in the small-scale booster cook-off test, the stimulus produced by the explosives in lengths greater than 12 mm is sufficient to cause the RWA2 to detonate.

TABLE 2

Length/diameter relationship of boosters which have a low probability of causing violent events in fuel-fires

DIAMETER	EXPLOSIVE/LENGTH		
	TETRYL	DEBRIX 2	PBX9407/PBX9407(UK)
25mm	<20mm	<25mm	<12mm
31.4mm	15-20mm	15-20mm	-
40mm	<20mm	<20mm	-

Table 3 presents the thermokinetic data for the explosives examined in this study.

Several features should be noted:

a) The temperature range over which the DSC experiments were conducted was adjusted such that decomposition of the sample occurred within about one hour of commencing the experiment. In the cases of RDX and HNS this necessitated examining the decomposition process in a phase not encountered in the actual experimental determination of critical temperature.

b) A small sample of AFX 521 moulding powder was obtained from LANL, Los Alamos,

for this study but the pure explosive, PYX, was not available. Since it is known that Kel-F 800 decomposes in the temperature range investigated on the DSC (34), there must be doubt in the kinetic analysis of this material [apparent rate law $1-(1-\alpha)^{1/3}=kt$, $\alpha=0.2-0.8$, E=453kJ mol^{-1}, ln A=79], especially as there is considerable deviation between the experimental and theoretical reduced time curves at $\alpha<0.2$. Fig. 6f shows that the critical temperature determination for AFX 521 was carried out below 300 °C and the activation energy obtained from the time-to-explosion plot has been used as the best available estimate of this parameter and by making the assumption that the specific heat of the material is around $1.05 Jg^{-1}K^{-1}$, an estimate of the pre-exponential factor has been obtained from Eq. 2.

c) For RDX and HMX the best values of Rogers for thermal conductivity are used (4); for TATB/nitramine mixtures mass averages for the values of the individual explosives are used (5) and for AFX 521 and HNS/Kel-F thermal conductivities were estimated by a modified Lee's disc method at 100 °C.

d) For mixtures of explosives the induction times are determined almost entirely by the more reactive component (7) and in the TATB/nitramine explosives the TATB acts mainly as a diluent since it does not undergo any appreciable decomposition at the temperatures studied (dynamic DSC on TATB at 10K min^{-1} indicates onset of exotherm at ca. 350 °C). Consequently, the kinetics of the nitramine decomposition are employed together with the estimated thermal conductivity for the mixtures in determining Tcr for the BX compounds and PBX 9503.

The kinetic constants derived for RDX and HMX agree well with accepted literature values (e.g., RDX E=199kJ mol^{-1}, ln A=42.6; HMX E=221kJ mol^{-1}, ln A=45.4 (35); see also Refs 36 & 37 for survey of decomposition kinetics of RDX and HMX), but for HNS the values of E and A are slightly higher than other workers have reported (eg E=127kJ mol^{-1}, ln A=21.1 (4)) and it may be that over the temperature range studied there was some influence from the Kel-F 800 binder. However, as the DSC analysis shows excellent correlation with the theoretical decomposition curve for the apparent rate law assumed from $\alpha=0$ to 0.8, these kinetic data for HNS/Kel-F are used in this work. On the other hand, the activation energy for the decomposition of tetryl is somewhat lower than that obtained by other workers (20). The decomposition process of tetryl has been identified as being autocatalytic (3,20) but the reason for the low value of the activation energy for this complex process is not clear.

Using these thermokinetic values, the solution to Eq. 1 has been determined for 25 mm diameter by 25 mm long cylinders of explosive. The values of Tcr are given in Table 4 together with the temperature range within which the experimental value of Tcr is found to lie. The experiments on Debrix 2 were extended to examine two extra geometries, namely 20 mm × 20 mm and 30 mm × 30 mm right regular cylinders. Figures 6a-f illustrate the temperature/time profiles obtained from the isothermal bath experiments. Using the conditions quoted earlier for determining whether a runaway reaction had occurred or not, it will be seen that the bracketted temperatures for Tcr are reasonably narrow for the number of experiments performed. In the cases of tetryl and HNS/Kel-F, the cut-off between the sub-critical and supercritical states is quite sharp and although there is some doubt with AFX 521 (see figure caption), this may also be the case with this explosive. With both tetryl and HNS/Kel-F the central thermocouple records an initial temperature rise which, in the sub-critical state does not develop. With tetryl this is linked to the autocatalysis seen in the DSC study and precedes the second longer-term temperature maximum due to the decomposition of secondary products including 2,4,6-trinitrohydroxybenzene, 2,4,6-trinitrophenylmethylether and a 2,4,6-trinitrophenylamine (determined to be N-methyl-N-2,4,6-trinitrophenylamine by Dubovitskii et al. (38)) which have been identified in the redisue of the sample held at 133 °C. Although the kinetic analysis of HNS/Kel-F did not indicate any autocatalysis in the liquid phase, the initial temperature rise noted at 226°-239 °C could be either a manifestation of an autocatalytic reaction which was lost in the DSC during the pre-recording heating state or be linked in some way to the presence of the binder. This could also account for the slightly high value of the predicted Tcr. There

TABLE 3

Thermokinetic Parameters Determined and Used in this Study

EXPLOSIVE	PHASE	TEMP. RANGE FOR DSC DETERMINATION	APPARENT RATE LAW	ACTIVATION ENERGY $E/kJ\ mol^{-1}$	ln PRE-EXPONENTIAL FACTOR $A/\ s^{-1}$	THERMAL CONDUCTIVITY $Wm^{-1}K^{-1}$	DENSITY $Mg\ m^{-3}$	HEAT OF REACTION/ $kJ\ mol^{-1}$
Tetryl	Liquid MP=129°C	180 - 205°C	Second Order Autocatalytic, $\ln(\alpha/1-\alpha) = kt$ $\alpha = 0 - 1.0$	133 ± 11	30.4 ± 2.8	0.26(6)	1.50	334 ± 17
RDX	Liquid MP=208°C	237 - 252°C	First Order Deceleratory, $-\ln(1-\alpha) = kt$ $\alpha = 0 - 0.8$	204 ± 8	43.6 ± 1.9	0.10(6)	1.65	549 ± 49
RDX in Debrix 2	Liquid MP=208°C	227 - 242°C	First Order Deceleratory, $-\ln(1-\alpha) = kt$ $\alpha = 0 - 0.8$	190 ± 3	40.2 ± 0.6	0.10(6)	1.65	549 ± 49
HNS in HNS/Kel-F	Liquid MP=320°C	327 - 342°C	Zero Order, $\alpha = kt$ $\alpha = 0 - 0.8$	164 ± 23	27.0 ± 4.6	0.36(4)	1.57	923 ± 16
HMX	Solid MP=286°C	262 - 277°C	Avrami-Erofeev, $[-\ln(1-\alpha)]^{1/3} = kt$ $\alpha = 0 - 0.5$	229 ± 27	47.7 ± 6.0	0.29(3) For PBX9503 0.39(2)	1.80	479 ± 28
AFX 521	Solid	362 - 377°C	See text	258	40.3	0.22(7)	1.53	636 ± 24

TABLE 4

Comparison of Predicted and Experimental Values of Critical Temperatures for 25 mm Long by 25 mm Diameter Cylindrical Samples

EXPLOSIVE	Tcr Predicted		Tcr Determined
Tetryl	116°C		145 - 146°C
Debrix 2	(a)*	(b)+	
diameter 20mm	163°C	166°C	165 - 172°C
diameter 25mm	159°C	162°C	160 - 163°C
diameter 30mm	156°C	159°C	150 - 155°C
HNS/Kel-F	245°C		239 - 241°C
PBX9503	197°C		190 - 195°C
BX compounds	171°C		173 - 174°C
AFX 521	330°C		275 - 280°C

*kinetics from RDX in Debrix 2
+kinetics from pure RDX

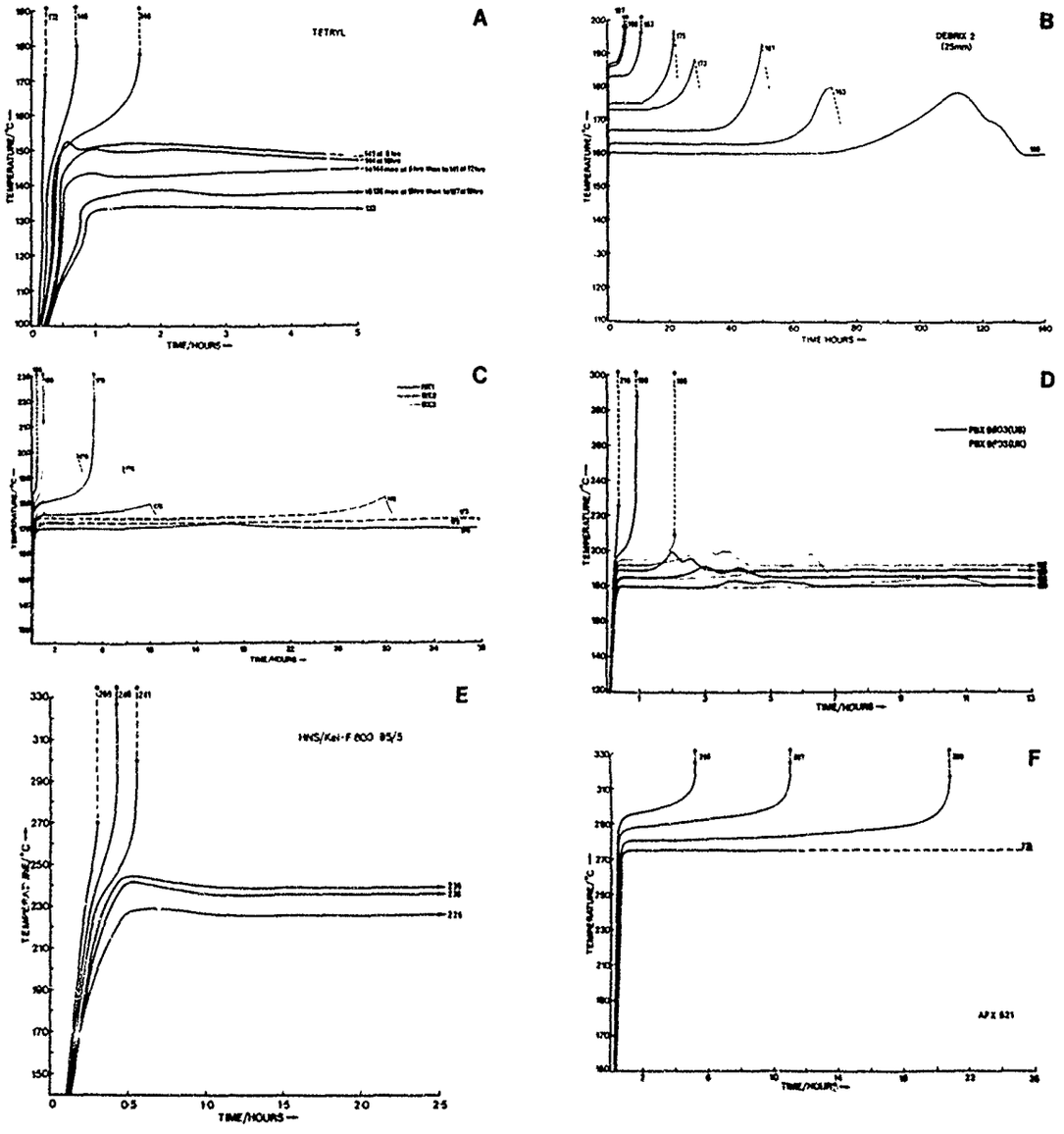

*Fig 6. Temperature/time profiles recorded using the experimental arrangement shown in Fig. 2. a) Tetryl, b) Debrix 2, c) BX compositions, d) PBX 9503, e) HNS/Kel-F 800, d) AFX 521. The * indicates explosion. NB- for AFX 521 the plots at 280°-295°C show no steady region where the centre of the charge is at ambient. AT 275°C the charge remained at ambient for 12 hours before evaporation of the (unsuitable) heat transfer medium caused loss of isothermicity and hence the experiment was aborted.*

were, however, no further temperature excursions with any of these samples of HNS/Kel-F, all of which were held at the ambient bath temperature for 48 hours.

Since the critical temperature for tetryl, in the geometry examined lies above its melting point, heat transfer by convection as well as by conduction will occur. Merzhanov et al. (39) show

that their experimental values for the critical temperature of tetryl fall between those predicted by assuming heat transfer by conduction alone and by convection alone, the former (Frank-Kamenetskii) prediction being the lower. They conclude that in molten tetryl a complex heat transfer process is operative. The low value for the predicted Tcr in this work is in keeping with these previous observations although it is felt that the large difference is due in part to the values of the Arrhenius parameters employed.

It is evident from Table 4 that the kinetic constants used to solve Eq. 1 for AFX 521 are far from adequate in that the predicted Tcr exceeds that found by some 50 °C. As discussed above, thermal decomposition work on the explosive ingredient PYX is necessary in order to avoid the obvious complication introduced by the binder. In the meanwhile, however, it is clear that of all the booster materials examined, AFX 521 has the highest critical temperature.

It will be noted that at any given temperature, the times-to-event observed for the BX compounds are generally shorter than those of Debrix 2 at the same diameter because of the higher thermal conductivity of these TATB-containing charges (5).

Using these temperature/time traces, time-to-explosion plots were constructed, the starting point for the time measurement being taken when the entire sample had reached the bath temperature although at high temperatures the amount of decomposition the sample had undergone by the time this condition was achieved may not have been negligible. It was found that for most samples reasonable estimates of apparent activation energies are obtained from these plots (Figs. 7A-D and Table 5). As discussed earlier, analysis of the equation representing the heat balance problem suggests that time-to-explosion plots, if taken over a wide enough spread in temperature, are curved. For Debrix 2, for which there are the most experimental points, no significant curvature is detected. Although it is expected that there would be differences in time-to-event between different diameter samples held at any one temperature, the experimental results show that, for the sizes examined, any differences are masked by experimental variations.

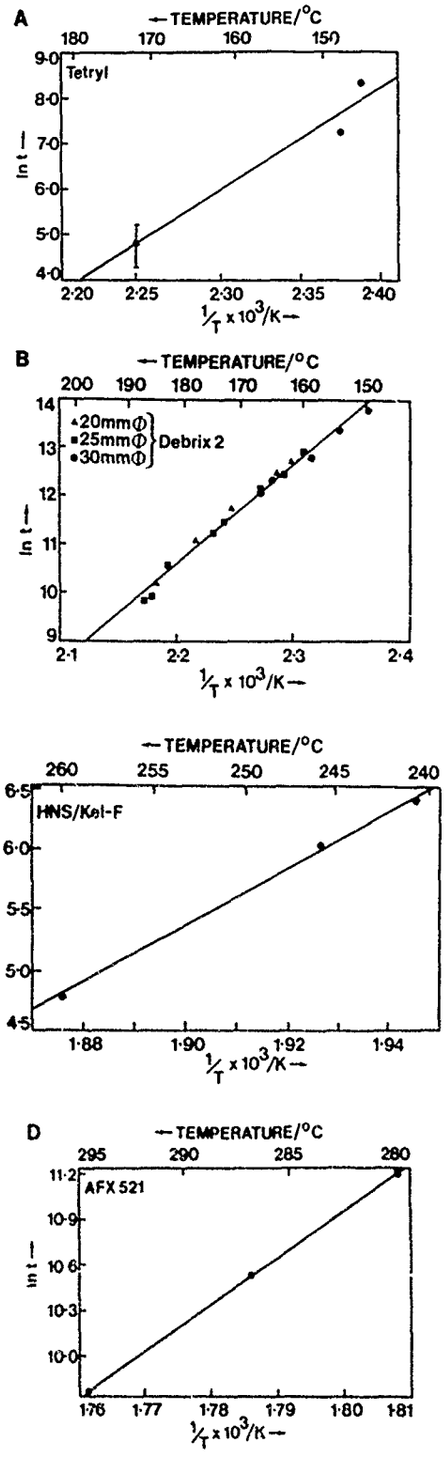

Fig. 7. Time-to-explosion plots obtained from the determination of critical temperature experiments (A) Tetryl, (B) Debrix 2, (C) HNS/Kel-F 800, (D) AFX 521

TABLE 5

Apparent Activation Energies Derived from Time-to-Explosion Plots

EXPLOSIVE	APPARENT ACTIVATION ENERGY kJ mol^{-1}
Tetryl	190.8 ± 49.3
Debrix 2	
20mm diameter	177.7 ± 7.5
25mm diameter	182.4 ± 7.1
30mm diameter	151.3 ± 12.4
All diameters	177.3 ± 5.4
HNS/Kel-F 800	193.9 ± 10.3
PBX 9503	270.5 ± 75.3
BX Compounds	249.2 ± 52.0
AFX [illegible]	258.1 ± 4.8

When confinement is known to be total over the duration of the test, Tarver et al. (27) found that an essentially linear relationship held for the time-to-explosion against 1/T(K). Although similar plots were obtained, they found that if small quantities of free volume were included with the sample the times-to-explosion at a given temperature were increased and at the limit, explosion may not occur at all if the gaseous decomposition products are free to escape. These experiments indicate the importance that confinement has on the outcome of the experiment for if the thermal decomposition process of explosives does not follow a one-step decomposition mechanism then the loss of intermediate products which are involved in exothermic processes and would otherwise lead to enhanced heats of decomposition, will result in longer induction periods and higher critical temperatures than would otherwise be determined since the effective heat source is reduced. Indeed, for ODTX experiments, using a single source following Arrhenius kinetics, the Frank-Kamenetskii model predicts Tcr values significantly higher than those observed (27), whereas for unconfined spheres good agreement is found by applying DSC-derived kinetics (40).

Although the critical temperature data for this study have been determined under conditions of moderate confinement, in order to record the temperatures within the charges thermocouples were included and although these were potted in place, the whole assembly was not entirely gas tight so that gaseous species could escape. The DSC analysis was also carried out under conditions where similar products could escape thereby affording kinetic data which in essence describe the practical situation of the critical temperature test. Provided the confinement is not too weak then if T>Tcr an event will occur although at a longer time than if the confinement were total (except for TATB (27)) and therefore it is to be expected that there will be some scatter in the times-to-explosion plots from experiments where the confinement is neither perfect nor completely characterised.

The fragments of the aluminium alloys containers recovered from the critical temperature experiments when an explosion occurred produce further evidence for the explosiveness of the samples (Table 6). It is seen that the ranking order is similar to that found in the fuel-fire tests except that HNS/Kel-F occupies a lower position than Debrix 2. Although, in general, events occurring with the entire sample at an elevated temperature are more violent than ones where the whole charge is not heated (because the rate of reaction increases exponentially with temperature), HNS/Kel-F produces less violent events than Debrix 2 in the Tcr test either because the change in mechanism from the explosive wave moving inwards from the ignition site (fuel-fires) to outwards (Tcr test), and/or the reduced importance of physico-mechanical factors, such as fracture-controlled event propagation, at elevated temperatures together with the reduced confinement of these experiments prevents DDT occurring in the HNS/Kel-F samples. With Debrix 2 such considerations possibly only play a minor role and severe deflagrations result.

Rogers (4) suggests that the excellent agreement between calculated and experimental values of Tcr makes it appear possible to make valid calculations for other shapes, sizes and densities of explosives using the values presented in his paper. Table 7 shows the results of using Rogers' data to calculate Tcr for the experimental geometry reported in this paper together with the predicted results of Rogers' experiments using data from Table 3 of this work. It will be seen that both sets of data produce excellent predictions for RDX and HMX-based explosives but for HNS there are deviations which suggest that neither set of Arrhenius parameters describe the decomposition process accurately.

TABLE 6

Results of Event Analysis in Tcr Tests Where Explosion Occurs

EXPLOSIVE	BATH TEMP	NUMBER OF FRAGMENTS	EVENT TYPE	EXPLOSIVENESS
Tetryl	146°C	7	Severe Deflagration, no HE left	Very High
	148°C	12		
	172°C	9		
Debrix 2	183°C	10	Severe Deflagration, no HE left	Very High
	186°C	10		
	187°C	9		
HNS/Kel-F	241°C	2	Deflagration	High
	246°C	3		
	260°C	4		
BX 1-3	178°C	3	Deflagration	
	183°C	2	Pressure Rupture, HE left	Low
	185°C	2		
AFX 521	280°C	2	Pressure Rupture, HE left	Very Low
	287°C	2		
	295°C	2		
PBX9503	195°C	2	Pressure Rupture, HE left	Very Low
	199°C	2		
	216°C	2		

TABLE 7

Comparison of Results of Tcr Prediction in Two Geometries from Two Sets of Kinetic Data

EXPLOSIVE	GEOMETRY					
	25mm diameter x 25mm long cylinder			40mg slab		
	Tcr Rogers	Tcr This Work	Tcr Measured	Tcr Rogers	Tcr This Work	Tcr Measured
RDX/ Debrix2	160.5°C	162°C	160-163°	217°C	218°C	215-217°
BX cpds	169°C	171°C	173-174°	--	--	--
HMX	193°C	194°C	--	253°C	252°C	253-255°
PBX9503	195°C	197°C	190-195°	--	--	--
HNS	198°C	245°C	239-241°	316°C	349°C	320-324°

From the tests discussed here, it is shown, in general, that the thermochemical data presented in Table 3 lead to reasonable predictions of the critical temperatures for the explosives of the critical temperatures for the explosives in 25 mm right regular cylindrical geometry. These data, together with estimates of the explosiveness of the samples from the Tcr tests are useful in analysis of slow cook-off of munitions where the entire booster component may well achieve the elevated ambient temperature. Under these circumstances, where insensitive high explosives with good thermal stabilities are employed, it is essential that the booster is a material other than tetryl, which not only has a low critical temperature, but also has high explosiveness. Although thermally more stable, HNS/Kel-F does not perform well in the fuel-fire test where it exhibits high explosiveness which could compromise the safety of warheads. The RDX-based Debrix 2 booster has a higher Tcr than tetryl but its explosiveness remains high. Consequently, for a replacement for tetryl there remain two options where adequate shock sensitivity is a prerequisite. These are BX compositions (option d) and AFX 521 (obtion b). BX4 has been shown to have better shock sensitivity than Debrix 2 and although its critical temperature is low, being controlled by the RDX component, its explosiveness is also low, being controlled by TATB. Studies of the use of BX4 as a boostering system in insensitive munitions are therefore being pursued. Recent studies have shown that the performance of AFX 521 is poor compared with tetryl. However, where the low-temperature response of BX4 is not applicable, then AFX 521 can be tailored for use in special circumstances despite its performance and work along these lines is being followed.

CONCLUSIONS

It is shown that a combination of laboratory scale and small bomb-chamber scale tests can be used to predict and measure the critical temperature of new explosive compositions in dimensions and confinements typical of booster systems. Although some problems were encountered in examining polymer-bound explosives at high temperatures, it is demonstrated that good correlations are obtained between measured and calculated values of critical temperature using thermokinetic data derived from DSC experiments. This is believed to be a consequence of the fact that both the self-heating and the DSC measurements were made under conditions where gaseous decomposition species could escape. As estimates of the explosiveness of the materials can also be obtained from these tests, they provide a valuable tool in the evaluation of new compounds for service use. Using these techniques it is suggested that the future path to new booster explosives may lie along that followed in the development of PBXW-7 whereby high and low explosiveness materials are combined in such proportions that the low explosiveness material dominates. Provided other factors, such as shock sensitivity, are sensibly addressed there is scope for the production of many suitable materials which should perform better

than tetryl and also impart greater safety to warheads.

REFERENCES

1. A.S. Dyer, P.J. Hubbard, P.R. Lee, D.G. Tisley, 7th Symp. (Int) on Detonation, Annapolis, (1981), p. 1040.
2. C.M. Anderson, J.M. Pakulak, J. Haz. Mats. *2*, 143, 1977
3. C.D. Hutchinson, V. Krishna Mohan, R.W. Millar, Propellants, Explosives, Pyrotechnics, *9*, 161, 1984.
4. R.N. Rogers, Thermochimica Acta, *11*,131, 1975.
5. R.R. McGuire, C.M. Tarver, 7th Symp. (Int) on Detonation, Annapolis, (1981), p. 56.
6. J.M. Pakulak, C.M. Anderson, NWC TP 6118, 1980.
7. J. Zinn, C.L. Mader, J. Appl. Phys. *31*, (2), 323, 1960.
8. Sensitiveness Collaboration Committee Explosives Hazard Assessment Manual of Tests, (3), 1971.
9. N.N. Semenov, Chemical Kinetics and Chain Reactions, Clarendon Press, Oxford, 1935.
10. D.A. Frank-Kamenetskii, Zh. Fiz. Khim, *13*, (6), 738, 1939.
11. P.H. Thomas, Trans. Faraday Soc. *54*, (1), 60, 1958.
12. P. Gray, P.R. Lee, Thermal Explosion Theory, Oxidation & Combustion Reviews, *2*, 1-183, 1967.
13. J.H. Sharp, G.W. Brindley, B.N. Narahari Achar, J. Am. Ceram. Soc., *49*, 379, 1966.
14. M.E. Brown, A.K. Galwey, 7th Int. Conf. of Thermal Analysis, Kingston, Ontario, Aug. 1982.
15. J.D. Hancock, J.H. Sharp, J. Am. Ceram. Soc, *55*, 74, 1972.
16. M.E. Brown, D. Dollimore, A.K. Galwey, Reactions in the Solid State, Comprehensive Chemical Kinetics, *22*, Elsevier, Amsterdam 1980.
17. W.E. Garner, A.S. Gomm., J. Chem Soc. 2123, 1931.
18. W.E. Garner, H.R. Hailes, Proc. Roy. Soc. Lond. *A139*, 576, 1931.
19. A.R. Ubbelhode, Phil. Trans. *A241*, 280, 1948.
20. A.J.B. Robertson, Trans. Faraday Soc. *44*, 677, 1948.
21. H. Henkin, R. McGill, Ind & Eng. Chem. *44*, 1391, 1952.
22. J. Wenograd. Trans. Faraday Soc. *57*, 1612, 1961.
23. O.M. Todes, Zh. Fiz. Khim, *4*, 71, 1933.
24. D.A. Frank-Kamenetskii, Diffusion & Heat Exchange in Chemical Kinetics, Trans. N. Thon, 1955.
25. P. Gray, M.J. Harper, Trans Farad. Soc., *55*, 581, 1959.
26. P. Gray, Proc. Roy. Soc. Lond, *A246*, 187, 1958.
27. C.M. Tarver, R.R. McGuire, E.L. Lee, E.W. Wrenn, K.R. Brien, 17th Symp. (Int) on Combustion, Comb. Inst. (1979), p. 1407.
28. D.H. Fine. P. Gray, Comb. & Flame, *11*, 71, 1967.
29. S.K. Sinha, R.C. Scrivastava, R.N. Surve, Proc. Int. Conf. on Primary Expl., ERDE, Waltham Abbey, UK, 1975.
30. R.G. Patel, M.M. Chaudhri, Proc. 4th Symp. Chemical Problems Connected with the Stability of Explosives, Ed. J. Hansson, Mölle, Sweden, (1976), p. 347.
31. A.G. Merzhanov, V.G. Abramov, V.T. Gontkovskaya, Dokl. Nauk. Akad, USSR, *148*, 156, 1963.
32. A.W. Campbell, H.L. Flaugh, A. Popolato, J.B. Ramsay, 7th Symp. (Int) on Detonation, Annapolis, (1981), p. 566.
33. R.R. Bernecker, H.W. Sandusky, A.R. Clairmont, 7th Symp. (Int) on Detonation, Annapolis, (1981), p. 119.
34. J. Brandrup, E.H. Immergut (Eds), Polymer Handbook, 2nd Edition, Wiley, New York, 1975.
35. A.J.B. Robertson, Trans. Faraday Soc. *45*, 85, 1949.
36. H.L. Pugh, L.P. Davis, J.S. Wilkes, W.R. Cooper, R.C. Dorey, 7th Symp. (Int) on Detonation, Annapolis, (1981), p. 75.

37. J. Kimura, N. Kibota, Prop. & Expl. 5, 61, 1980.

38. F.I. Dubovitskii, G.B. Manelis, L.P. Smirnov, Russ. J. Phys. Chem. *35*, (3), 255, 1961.

39. A.G. Merzhanov, V.G. Abromov, F.I. Dubovitskii, Dokl. Akad. Nauk. SSSR, *128*, 889, 1959.

40. D.L. Jaeger, Proc. 11th N. Amer. Thermal Analysis Soc. Conf., New Orleans, (1981), p. 669.

ACKNOWLEDGMENTS

This work was carried out in part whilst the author was on study leave at the Cavendish Laboratory, Cambridge. The generosity of the Director, RARDE, for allowing this is acknowledged. Dr. J.E. Field, Dr. V. Krishna Mohan and Dr. G.M. Swallowe are gratefully thanked for their assistance, without which this work would not have been possible.

DISCUSSION

HAROLD GRYTING, Southwest Research Institute

To your knowledge, are your booster compositions being considered by U.S. DoD for replacement of tetryl?

REPLY BY MAX STOSZ

A similar composition is being investigated in the U.S.

HMSO London, 1985

DERIVATION OF THE P^2T DETONATION CRITERION

Evan Harris Walker
US Army Ballistic Research Laboratory
US Army Materiel Command
Aberdeen Proving Ground, Maryland

We derive an approximate closed form equation for the critical P^2T criterion for explosive initiation based on the shear band theory of explosive initiation. The theory assumes that shock loading of explosives produces a calculable shear velocity resulting in shear band formation. Heating within the shear bands leads to hot spot formation which in turn leads to explosive initiation. As an example of the use of the derived equation, we calculate P^2T for Composition-B.

INTRODUCTION

Walker (1) has reported on the derivation of an expression for the shear band velocity in a shock loaded homogeneous di-constituent explosive. He has used this expression together with the Frey shear band theory of explosive initiation to calculate values of P^2T for explosives, where P is the pressure to which the explosive is shock loaded and T is the temporal duration of the applied pressure. In that treatment, the origin of the P^2T condition as such was not derived. The approach used a computer code developed by R. Frey (2) to solve the problem of heat evolution and exchange during the growth of shear bands. In the present paper, approximate expressions are obtained for the development of the shear bands which are used to obtain a closed form expression for the P^2T criterion. Such an expression, though approximate, has considerable utility in exhibiting the important parameters that determine the sensitivity of an explosive in terms of the physical and thermodynamic properties of that explosive.

The P^2T criterion for the onset of detonation was first proposed by Walker and Wasley (3). The criterion has been extensively studied and supported by experimental data (4-8). The criterion is essentially equivalent to the critical total energy fluence ε (since $\varepsilon = put$; u being the particle velocity and $p = \varrho_o uv$, ϱ_o being the ambient explosive density, we obtain $\varepsilon = p^2t/\varrho_o v$; $\varrho_o v$ is nearly constant for pressures of interest). An understanding of the processes by which initiation of detonation occurs requires an understanding of the P^2T mechanism.

A number of studies (9-13) have sought to derive or calculate values for the P^2T criterion, but none has provided a strictly physical theory free of *ad hoc* assumptions as to the origin and distribution of initiation sites, "hot spots," or the assumed initiation temperature distribution behind the shock front. The necessity of the "hot spot" concept of Bowden and Yoffe (14), and Eyring (15) comes from the fact that, under shock initiation conditions, the bulk temperature of the explosive produced by adiabatic compression is generally too low to ignite the explosive. Bowden and Yoffe (14) developed the theory of adiabatic compression of air cavities in the explosive as the source of hot spots. (See also the work of Starkenberg (16).) Mader (17) has suggested void closure in the explosive as the mechanism for hot spot formation and Seeley (18) has suggested jetting during the void closure. Frey (19) has looked in some detail at the micromechanics of hot spot formation, considering in addition to the effects of air cavity compression and void closure impacts on the heating of explosive material, heating due to the viscous flow of explosive during cavity collapse. Delpuech, *et al* (20), have proposed shock

induced free radical formation as the mechanism underlying hot spot formation. Nevertheless, these mechanisms have not been tied to a P^2T criterion. The shear band mechanism proposed by Frey (2), however, has been used to calculate (1) the critical value of P^2T for Composition-B. It is, therefore, important to tie the shear band mechanism for hot spot formation directly to the condition that the critical value of P^2T for an explosive is a constant.

WORK DONE BY SHEAR FORCES

The work W per unit volume done in shearing is given by the general expression

$$dW = \sum_i \sum_j \sigma_{ij}\ d\,\varepsilon_{ij} \tag{1}$$

where σ_{ij} is the shear stress in the plane normal to the x_i-axis directed along the x_j-axis of a Cartesian coordinate system, and ε_{ij} is the corresponding strain. If we have shears only on surfaces normal to the y-axis, directed only in the z direction, with the corresponding strains, we can write simply

$$dW = \sigma_{yz}\ \ d\,\varepsilon_{yz} \tag{2}$$

The shear stress for a viscoplastic material for such a flow is

$$\sigma_{yz} = \mu\,\frac{dv_z}{dy} + \sigma_s \tag{3}$$

where v_z is the shear velocity in the direction of the z-axis varying in the y direction. The strength of the material is given by σ_s, while μ is the viscosity. The development of the shear bands takes place in essentially two stages: (1) initial development of shear failure planes and (2) viscous heating of the shear layers. In the first stage, the material undergoes elastic deformation up to shear failure, so that the viscosity term in Equation (3) plays no role; and in the second stage the shear strength drops to zero:

$$\sigma_s = 0 \tag{4}$$

During stage two, the principal heating phase, we can re-express Equation (3) as

$$\sigma_{yz} = \mu dv_z/dy = \mu\,\frac{\delta(dZ/dt)}{\delta y} = \frac{d\,\frac{\delta z}{\delta y}}{dt} \tag{5}$$

or writing ε_{yz} for $\delta z/\delta y$ and rearranging

$$d\varepsilon_{yz} = \frac{1}{\mu}\,\sigma_{yz}\,dt \tag{6}$$

Therefore, we can substitute for $d\varepsilon_{yz}$ in Equation (2) to obtain, on integrating

$$W = \frac{1}{\mu}\int \sigma_{yz}^2\,dt \tag{7}$$

THE SHEAR VELOCITY IN DI-CONSTITUENT EXPLOSIVES

Walker (1) has given an expression for the shear velocity in an explosive consisting of two materials. For a matrix material having density ϱ_1 and sound velocity u_1 containing grains with density ϱ_2 and sound velocity u_2, a shock pressure p gives rise to particle velocities v_1 and v_2 satisfying

$$p = \varrho_1 u_1 v_1 = \varrho_2 u_2 v_2 \tag{8}$$

Therefore, the shear velocity v_s, the difference between v_1 and v_2 is

$$v_s = p\ \left(\frac{\varrho_2 u_2 - \varrho_1 u_1}{\varrho_1 u_1 \varrho_2 u_2}\right) \tag{9}$$

As shown in Figure 1, the shear velocity initially causes a strain to develop in the matrix material. (A similar process occurs in the grains.) Where 2n is the number of shear bands in the spacing of 2D between grains in the explosive mixture, at a time t the strain $n\delta d$ (as shown in Figure 1) will be

$$n\delta d = v_s t \tag{10}$$

and also the number of bands between the wall and center between grains is given in terms of the average band spacing d by

$$n = D/d \tag{11}$$

When the strain $\delta d/d$ reaches a critical distortion angle θ_{max},

$$\delta d/d = \theta_{max} \tag{12}$$

shears develop in the material. As shears begin to develop, however, stress relief waves propagate from these incipient shears into the surrounding material. This means that the next

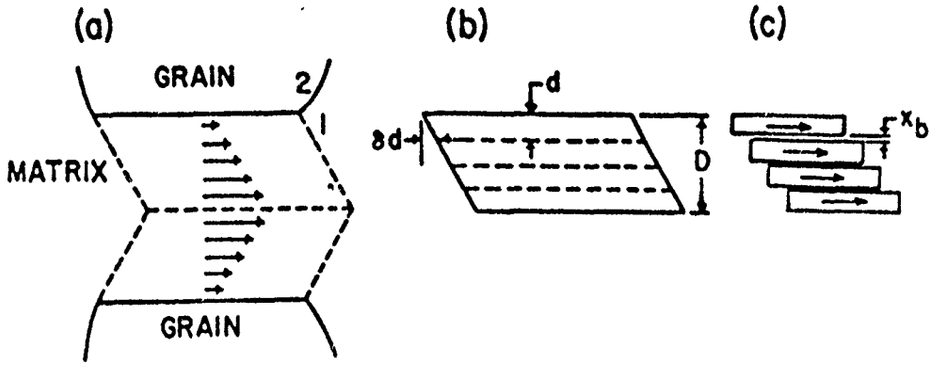

Fig. 1. Schematic diagram showing (a) the differential velocity field produced behind a shock passing through a di-component explosive, (b) a detail of the initial strain due to the differential velocity flow (exaggerated), and (c) a schematic of the shear bands of thickness x_b separated by unsheared material of thickness d

nearest shear will be located on the average a distance $u_1 t$ away. Since this distance is also d we have

$$u_1 t = d \tag{13}$$

so that solving we have

$$d = \theta_{max} D u_1 / v_s \tag{14}$$

θ_{max} can be re-expressed in terms of Poisson's ratio ν, the ultimate shear strength σ_{max} and the Young's elastic modulus E by

$$\theta_{max} = 2(1+\nu)\,\sigma_{max}/E \tag{15}$$

The width of the band when $\sigma_s \to 0$ can be calculated in terms of the heat made available by the formation of these shears during the time t in which the shear banding structure forms. Thus, using energy conservation to determine the thickness of the layer heated we write

$$x_b \varrho_1 Q_f = \sigma_{max}\, v_b\, t \tag{16}$$

where Q_f is the latent heat of fusion and v_b, the shear velocity for a single band, is given by

$$v_b = v_s/n \tag{17}$$

Thus, we obtain for x_b

$$x_b = \frac{\sigma_{max}\,\theta_{max} D}{n\,\varrho_1\,Q_f} \tag{18}$$

or, substituting from Equation (15),

$$n x_b = 2(1+\nu)\, D\sigma_{max}^2 / \varrho_1 Q_f E \tag{19}$$

From Equations (9) and (19) we can obtain the average velocity gradient across the shear:

$$\frac{dv_z}{dy} \approx \frac{v_z}{n x_b} = p\,\frac{\varrho_1 Q_f E}{2(1+\nu) D\sigma_{max}^2}\left(\frac{\varrho_2 u_2 - \varrho_1 u_1}{\varrho_1 u_1 \varrho_2 u_2}\right) \tag{20}$$

This expression can then be used to obtain σ_{yz} from Equation (3) where Equation (4) holds.

THE P^2T CONDITION

Substituting from Equation (20) into Equation (3) with σ_s set to zero, we have

$$\sigma_{yz} = p\,\frac{\mu \varrho_1 Q_f E}{2(1+\nu) D\sigma_{max}^2}\left(\frac{\varrho_2 u_2 - \varrho_1 u_1}{\varrho_1 u_1 \varrho_2 u_2}\right) \tag{21}$$

Substituting this expression for σ_{yz} into Equation (7) gives

$$W = \mu\left[\frac{\varrho_1 Q_f E}{2(1+\nu) D\sigma_{max}^2}\left(\frac{\varrho_2 u_2 - \varrho_1 u_1}{\varrho_1 u_1 \varrho_2 u_2}\right)\right]^2 \int p^2 dt \tag{22}$$

where the constants (or slowly varying parameters) have been factored from under the integral.

The energy W (per unit volume) goes into heating the material in the shear band. Where ΔT_{ig} is the temperature rise above the melt temperature required to bring the matrix to the "ignition temperature", we can express the critical value for W by

$$W_{crit} = \varrho_1 C_v \Delta T_{ig} \tag{23}$$

where C_v is the specific heat of the matrix material. Strictly speaking, there is no specific ignition temperature. Instead there exists a relationship, the Arrhenius equation, relating rate of heat evolution to the temperature of the explosive. However, for the shock loading times of major interest, i.e., in the range of 1-100μs, the dependence of T_{ig} on the shock loading time varies slowly. Heat evolution rises exponentially with temperature, which in turn further elevates the explosive temperature; as a result, the initial temperature necessary to produce complete combusion within the shear band in a time of 1μs will differ very little from that required for complete combustion in 100μs. For this reason, we can ignore the dependence of T_{ig} on the shock loading time in order to retain a closed from expression for W_{crit}. Defining Q_h as the P^2 time integral for the shear band heating phase, we have from Equations (22) and (23):

$$Q_h = \int p^2 dt = \frac{C_v \Delta T_{ig}}{\varrho_1 \mu} \left[\frac{2(1+\nu) D \sigma_{max}^2}{Q_f E} \left(\frac{\varrho_1 u_1 \varrho_2 u_2}{\varrho_2 u_2 - \varrho_1 u_1} \right) \right]^2 \tag{24}$$

Equation (24) provides an approximate expression for the P^2T criterion in terms of the physical and thermodynamic properties of an explosive under the conditions of matrix initiation. A corresponding expression for grain initiation may be given in which D and σ_{max} are calculated for grain shearing. The P^2T criterion is given by the expression in Equation (24) if the matrix goes into shear before the grains, as in Composition-B. If the grains shear with the matrix deforming, the quantities ϱ_2, u_2 will be for the matrix and all other quantities for the grains.

In addition, we can derive the critical pressure P_{crit} for the onset of ignition. From Equations (9), (11) and (14), we obtain the number of shear bands produced by shock loading the explosive:

$$n = p \frac{\varrho_2 u_2 - \varrho_1 u_1}{\varrho_1 u_1 \varrho_2 u_2 u_1 \theta_{max}} \tag{25}$$

Setting n = 1, we obtain p_{crit}:

$$p_{crit} = \frac{\varrho_1 u_1 \varrho_2 u_2 u_1 \theta_{max}}{\varrho_2 u_2 - \varrho_1 u_1} \tag{26}$$

For Composition-B we have the following values for the quantities in Equations (24) and (26):

Matrix (TNT)

$C_v = 1.29 \times 10^5$ J/Kg°K

$\Delta T_{ig} = T_{ig} - T_{melt} = 720$°C

$\varrho_1 = 1.63 \times 10^3$ Kg/m^3

$u_1 = 2.08 \times 10^3$ m/s

$\mu = 1.39 \times 10^{-2}$ Kg/ms

$\nu = 0.3$

Grain (RDX)

$D = 5 \times 10^{-6}$m (21)

$\varrho_2 = 1.8 \times 10^3$ Kg/m^3

$u_2 = 2.65 \times 10^3$ m/s

Composition-B bulk quantities

$\sigma_{max} = 7.0 \times 10^7$ Pa

$Q_f = 8.96 \times 10^4$ JKg

$E = 5.4 \times 10^9$ Pa

From Equation (24) these values yield

$$Q_h = 9.8 \times 10^{12} \text{ Pa}^2\text{s} \tag{27}$$

From Equation (26) we obtain

$$p_{crit} = 8.22 \times 10^8 \text{ Pa} \tag{28}$$

or about 8 kbars; the experimental value is about 7 kbars.

In addition to the frictional heating in the shear bands, once ignition of the explosive at these hot spots has occurred, combustion must

continue if a detonative shock pressure is to form. If a rarefaction wave arrives too early, in the process, the rate of heat evolution will drop and cooling or mechanical dispersal of the explosive can extinguish the ignition process. Therefore, if the burn is to be maintained, the externally applied shock pressure must be maintained until this external source of pressure is replaced by internal sources. The internal sources, of course, must be the hot spots which generate pressure by combustion. We require that the externally applied pressure p be maintained for a time t_b sufficiently long that if at the end of this time the external pressure is relieved, the internal pressure will just match that loss of pressure. (Note that this internal pressure will not lead to mechanical disruption of the explosive until a relief wave can arrive from the explosive surface.) Since we are concerned with compact explosives here, the energy density is equal to the pressure generated. Thus, to produce a pressure p from the combustion of an explosive having a "bomb" pressure (bomb at full density) p*, a fraction p/p* must be burned. Where U_b is the burn velocity and d the distance between shear bands, we require

$$p/p^* = U_b\, t_b/(\tfrac{1}{2}d) \qquad (29)$$

Thus, the total P^2T value of the critical condition for explosive initiation will be

$$Q_{tot} = Q_h + Q_b \qquad (30)$$

where Q_b is given by

$$Q_b = p^2\, t_b = p^3 d/2U_b\, p^* \qquad (31)$$

Of course, the burn velocity U_b is itself a function of the pressure. Kondrikov, Raikova, and Samsonof (22) give

$$U_b = \varrho B p^{\nu} \qquad (32)$$

where ϱ is the explosive density, p the pressure B and ν are constants with values $B=0.0219 g/cm^2 s\ atm^{\nu}$ (20-100Atm), $B = 0.0094 g/cm^2 s\ atm^{\nu}$ (100-450 Atm); $\nu = 0.77$ (20-100 Atm), $\nu = 0.95$ (100-450 Atm). We obtain p* for TNT using the TIGER computer code (23), giving $p^* = 9.67 \times 10^9$ Pa. At 10 kbar, (1.014×10^9 Pa), $U_b = 0.97$ m/s so that $Q_b = 2.26 \times 10^{11}\ Pa^2 s$. Since U_b is approximately proportional to pressure, Q_b varies quadratically with the pressure. Thus, Q_b will not be as important as Q_h until we reach shock pressures of more than 6.68×10^9 Pa (66 kbar). This latter value is only approximate since this pressure lies outside the range for which values of U_b are accurate.

From Equations (27), (30), and (31), we obtain for the total theoretical value of the critical P^2T for Composition-B at 10 Kbars

$$Q_{tot}\Big|_{\text{theoretical}} \quad 10.0 \times 10^{12}\ Pa^2 s \qquad (33)$$

Using value of 1500 KJ/m^2 (see (24) pg 9-48) for the critical energy, 3.24 km/s for the shock velocity at 10 Kbars (see (24) pg 7-32) and a density of $1.70 \times 10^3\ Kg/m^3$, we obtain

$$Q_{tot}\Big|_{\text{experimental}} = 8.26 \times 10^{12}\ Pa^2 s \qquad (34)$$

The two values are reasonably close.

But more than this, the theory also lets us calculate a quite satisfactory value for the critical ignition pressure as obtained in Equation (28).

CONCLUSIONS

We have obtained an approximate closed form expression for the P^2T criterion for explosive initiation based on the shear band theory of explosive ignition, and an expression for the critical shock pressure for the onset of ignition. While the resulting expressions depend on quantities that are only pooly known in many cases, the equations exhibit explicitly the factors controlling explosive sensitivity. The resulting equations show a dependence of the P^2T criterion on particle size for fixed mass fractions of the constituents, and for fixed particle size, shows P^2T increases as the portion of matrix (TNT in Composition B) is increased. The P^2T criterion and the critical shock pressure equations obtained here exhibit explicitly the important parameters determining the sensitivity of an explosive to initiation by shear band heating in terms of the explosive's physical and thermodynamic properties.

REFERENCES

1. E. H. Walker, "Critical P^2T Value Computations for Explosives Using the Shear Band Initiation Model," BRL Memorandum Report-3425, January 1985.
2. R. B. Frey, "The Initiation of Explosive Charges by Rapid Shear," Seventh Symposium (International) on Detonation, pp. 53-59, 16-19 June 1981, Annapolis, Maryland.
3. F. E. Walker and R. J. Wasley, "Critical Energy for the Shock Initiation of Heterogeneous Explosives," *Explosivestoff 17*, 9, 1969.
4. P. Howe, R. Frey, B. Taylor, and V. Boyle, "Shock Initiation and the Critical Energy Concept," Sixth Symposium (International) on Detonation, pp. 11-19, ACR-221, US Government Printing Office, Washington, D.C., 20402.
5. E. F. Gittings, "Initiation of a Solid High Explosive by a Short Duration Shock," Fourth Symposium (International) on Detonation, pp. 373-380, ACR-126, US Printing Office, Washington, D.C., 20402.
6. E. L. Lee and C. M. Tarver, "Phenomenological Model of Shock Initiation in Heterogeneous Explosives," *Phys Fluids 23*, 2362, 2372, 1980.
7. R. C. Weingart, R. K. Jackson, C. A. Honodel, and R. S. Lee, "Shock Initiation of PBX-9404 by Electrically Driven Flyer Plates," Tenth Symposium on Explosives and Pyrotechnics, preprint UCRL-82162, January 1979.
8. Y. de Longueville, C. Fauquignon, and H. Moulard, "Initiation of Several Condensed Explosives by a Given Duration Shock Wave," Sixth Symposium (International) on Detonation, pp. 105-114, ACR-221, US Government Printing Office, Washington, D.C., 20402.
9. See references 3, 6, and 8.
10. B. O. Trott, R. G. Jung, "Effect of Pulse Duration on the Impact Sensitivity of Solid Explosives," Fifth Symposium (International) on Detonation, pp. 191-205, ACR-184, US Government Printing Office, Washington, D.C., 20402.
11. J. Wackerle, J. O. Johnson, and P. M. Halleck, "Shock Initiation of High-Density PETN," Sixth Symposium (International) on Detonation, pp. 20-28, ACR-221, US Government Printing Office, Washington, D.C., 20402.
12. D. B. Hayes, "A P^nT Detonation Criterion from Thermal Explosion Theory," Sixth Symposium (International) on Detonation, pp. 76-81, ACR-221, US Government Printing Office, Washington, D.C., 20402.
13. W. H. Anderson, "Model of Impact Ignition and Explanation of Critical Shock Initiation Energy II Application," Seventh Symposium (International) on Detonation, pp. 219-225, 16-19 June 1981, Annapolis, Maryland.
14. F. P. Bowden and A. D. Yoffe, *Initiation and Growth of Explosions in Liquids and Solids*, Cambridge University Press (1952).
15. H. Eyring, R. E. Powell, G. H. Duffrey, and R. B. Darlin, *Chemical Review 45*, 69 (1949).
16. J. Starkenberg, "Ignition of Solid High Explosive by the Rapid Compression of an Adjacent Gas Layer," Seventh Symposium (International) on Detonation, pp. 1-12, 16-19 June 1981, Annapolis, MD.
17. C. L. Mader, *Phys Fluids 8*, 10, 1965.
18. L. B. Seeley, "A Proposed Mechanism for Shock Initiation of Low Density Granular Explosives," Proceedings of the Fourth Electric Initiator Symposium, 1963.
19. R. B. Frey, "Cavity Collapse in Energetic Materials," Proceedings of this Symposium.
20. A. Delpuech, J. Cherville, and C. Michaud, "Molecular Electronic Structure Initiation of Secondary Explosives," Seventh Symposium (International) on Detonation, pp. 36-44, 16-19 June 1981, Annapolis, Maryland.
21. E. H. Walker, "Derivation of the P^2T Criterion (In Closed Form) Based on the Frey Shear Band Mechanism," BRL Technical Report ARBRL-TR-02544, January 1984; See Appendix.
22. B. N. Kondrikov, V. M. Raikova, and B. S. Samsonof, *Fizika Goreniya i Vzryva, 9*, 1, pp. 84-90, 1973.

23. M. Cowperthwaite, and W. H. Zwisler, TIGER Computer Program, SRI International Publication No. Z106, SRI International, 333 Ravenswood, Ave., Menlo Park, CA 94025.

24. B. M. Dobratz, Properties of Chemical Explosives and Explosive Simulants, March 16, 1981, Lawrence Livermore National Laboratory UCRL-52997.

DISCUSSION

JAG SHARMA, Naval Surface Weapons Center

To illustrate shear bands and dislocations you have drawn beautiful squares and cubes. In real cases when we have randomly shaped particles, do you visualize concentration of shear forces at sharp points so that the reaction will be dominating on surfaces? My results show more reaction on surfaces of randomly shaped particles than in the bulk.

REPLY BY E. H. WALKER

Figure 1 shows a very simple and regular pattern of shear bands associated with idealized grains. In actual explosives things are not so simple, of course. It would be useful to run a hydrocode to model more of the details of shear band formation, so that we could see the effects of grain shape and orientation on the motion of the matrix materials. We know that such a treatment would still give us about the same result for the shear velocity V_s. We also know that the number and distribution of shear bands will be strongly dependent on the shape and orientation of the grains. The density of shear bands should increase for increasing angularity of the grains. Reference 1 gives a scanning electron micrograph of shear bands in an actual explosive that has been subjected to shocks. The shapes of these shear bands are quite different from those illustrated in my Figure 1, but the density of the shear bands is consistent with my calculations. In summary, sharp grains should enhance the shear band initiation process making the explosive more sensitive.

DISCUSSION

RON LEE, Lawrence Livermore National Laboratory

How can one account for pre-shock desensitization with a shear-band model?

REPLY BY E. H. WALKER

The effects of pre-shock desensitization have not been looked at in the present study. To keep the treatment simple, heat conduction away from the shear bands has been ignored. In Robert Frey's computer model of shear band hot spot formation, heat conduction is retained in the model making it possible to look at the effects of desensitization that pre-shocks will have on the band formation process. These pre-shocks initiate band formation, generating heat that will conduct into the surrounding matrix and increase the width of the melted zone in the bands. This results in wider bands, larger values of X_b, which increases Q_n, thus desensitizing the explosive.

DISCUSSION

LOUIS ZERNOW, Zernow Technical Services Inc., California

In order to help answer the previous question about the desensitization of explosives due to precompression and various other aspects of sensitivity related to the generation of slip bands and other hot spot sources which may not be directly related to porosity, it would appear that the application of dislocation theory to the deformation of the explosive crystals should provide a very useful approach, ultimately capable of being quantified. That approach has already been discussed by C. S. Coffey of NSWC (WOL), in the seventh paper of the first general session. Precompression desensitization might be explained by the increased shear stress required to cause slip on a slip band, in the presence of a stress normal to the slip band, thereby requiring a larger shock amplitude to generate the slip bands in a precompressed crystal.

SHOCK INITIATION OF HNAB BY ELECTRICALLY DRIVEN FLYER PLATES

E. Hasman, M. Gvishi, Z. Segalov, Y. Carmel, D. Ayalon and A. Solomonovici
Government of Israel, Department of Science
P.O. Box 2250, Haifa, Israel

The shock initiation threshold of HNAB (Hexanitroazobenzene) explosive has been measured using pressure pulses generated by flyer plate impact. The flyer plates were accelerated by an electrically exploded metallic foil (electric gun) up to velocity of 2.5 mm/μsec generating impact pressures up to 4.5 GPa lasting between 40 nsec and 210 nsec.

It was found that as the pressure duration gets longer, the initiation threshold curve swings away from the $P^2\tau$=constant. For long (200 nsec) pulses, the initiation criterion becomes one of a constant pressure. This constant threshold pressure is 2.9 GPa at 1.6 gr/cm^3 (grain size is 5μm).

Decreasing the density or the grain size of the explosive reduced the impact pressure threshold.

No difference was found between the threshold sensitivity of the two polymorphic phases HNAB (I, II).

INTRODUCTION

Explosive materials are utilized in a number of systems in the area of terminal ballistics.

Effective design and performance analysis of a system employing explosive materials are dependent upon good knowledge of initiation threshold of the explosive, as well as other factors like thermodynamic behavior, stability, etc.

The purpose of this work was to study the shock initiation threshold of HNAB (1) to impact pressure. HNAB is of interest due to its high melting point (~220 °C) and relative insensitivity as compared to PETN, HNS (Drop Hammer Test (2)). However, little is known about its initiation characteristics by planar shock waves (3). In this work, we have concentrated on shock initiation by very short duration pulses with pulse length varying from 40 to 200 nseconds. We were particularly interested in the initiation threshold dependence on the polymorphic forms (HNAB I, II), grain size, shock duration, pressure and explosive density. The electric gun is a versatile tool for such high pressure short shock wave research. Only small quantities (<1g) of explosive are required for testing, so the testing can be done in enclosed firing tank with good diagnostic access and quick experimental turn around.

The electric gun (4) produces a well characterized shock stimulus. Flyer plates were accelerated by an electrically exploded metallic foil up to a velocity of 2.5 mm/μsec, generating pressures up to 4.5 GPa upon impact with the HNAB samples.

THE ELECTRIC GUN AND DIAGNOSTIC TECHNIQUE

Experiments were conducted to study the effect of density, morphology, grain size and pulse duration on the shock initiation threshold of HNAB, using an electric gun similar to the one previously described by Chau et al. (4).

The electric gun (slapper) was usually composed of copper foil (thickness 8μm, area 1mm×1mm), and polymide or polyester flyer

(Fig. 1). The flyer diameter was defined by 1mm diameter brass barrel (1mm long) which was clamped onto the foil flyer laminate. The electrical firing system included a 3μF capacitor charged up to 5.5 KV DC.

The inductance L and the resistance R of the equivalent circuit (see Fig. 1) including the foil, dictates an under damped oscillatory current waveform. Flyers velocities up to 2.5mm/μS were measured by electric* and electroptic methods calibrated by the Gurney model (5), (6).

The final flyer velocity, V_f, is given in Fig. 2 as a function of J_b, the burst current density in the foil by the following equation:

$$V_f=(1.765\ J_b+0.918)\left(\frac{M}{C}+\frac{1}{3}\right)^{-1/2} \qquad (1)$$

Where J_b is expressed in $TA/_m{}^2$, C is the mass of the copper foil per unit area which is backed by flyer mass M per unit area.

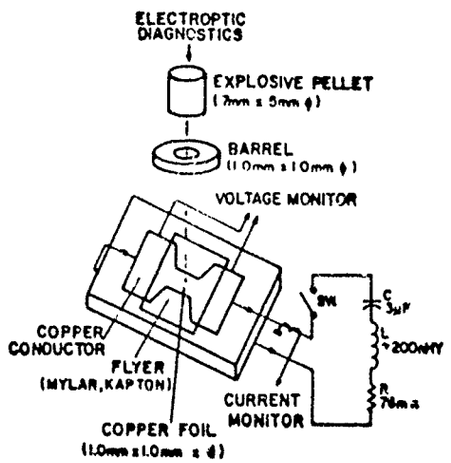

Fig. 1. Schematic diagram of electric gun arrangement

A one dimensional semiempirical model (6) was used to describe the exploding foil.

It was based on the four following equations:

$$\partial Q/\partial t=J(t)^2/\sigma(t)\rho(t) \qquad (2)$$

$$r_f(t)=r_{fo}\,(1+\alpha(T(t)-T_o)) \qquad (3)$$

$$L\frac{dI}{dt}+RI+r_f(t)I+\frac{1}{C}\left(\int_0^t I(\lambda)d\lambda+q_o\right)=0 \qquad (4)$$

$$Q=\varepsilon(T\ V)-\varepsilon(T_oV_o) \qquad (5)$$

where Q is the heat capacity per unit mass of the metal foil, J is the current density through the foil's cross-section. σ is the electric conductivity, ρ is the mass density and r_{fo}, r_f are the initial and dynamic resistivities of the foil. T_o and T are the ambient and dynamic (time varying) temperatures respectively, while α is the linear resistance coefficient.

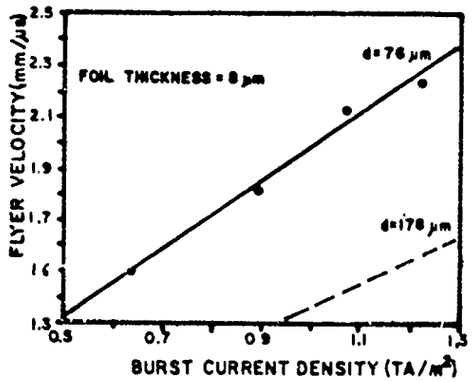

Fig. 2. Flyer velocity vs. burst current density, for various flyer plates thickness and 8μm copper foil thickness

Equation (2) describes the ohmic heating in the foil, while its time dependent resistance is given by equation (3), assuming a linear resistance coefficient.

The current in the circuit is described by equation (4), where q_o is the initial charge on the capacitor C. Equation (5) describes the equation of state of the foil material as a function of temperature, and the specific volume V.

These equations were solved on the following assumptions:

a) The volume of the exploding foil is constant up to the burst point.

b) The specific resistivity, changes linearly with temperature up to the exploding temperature T_b, while the ratio T_b/T_o is a characteristic constant for each foil material, and was experimentally found to be $R_b/R_o\cong 120$ for copper foil. Using that, we can show that the current density J(t) and the burst time t_b satisfies (4) equation (6)

$$g=\int_o{}^{t_b} j^2(t)dt\cong\text{const.} \qquad (6)$$

c) The equation of state was based on a semiempirical model for the internal energy $\varepsilon=\varepsilon(T,V)$. The energy equation was composed from three parts: The elastic energy (low temperature component), which was neglected in the numerical calculation; the

* shorted electrode method

thermal energy of atoms; and the electronic contribution especially at high temperature.

d) The duration of the exploding process is much shorter than the time of energy's dissipation, i.e. heat of conductance, radiation losses, heat phase transformation, etc. are all neglected.

These equations were numerically solved (6). A compa[illegible] f calculated (solid lines) and measured (d[illegible] ,, voltage and current waveforms in the foil during its exploded process up to the burst point are given in Fig. 3.

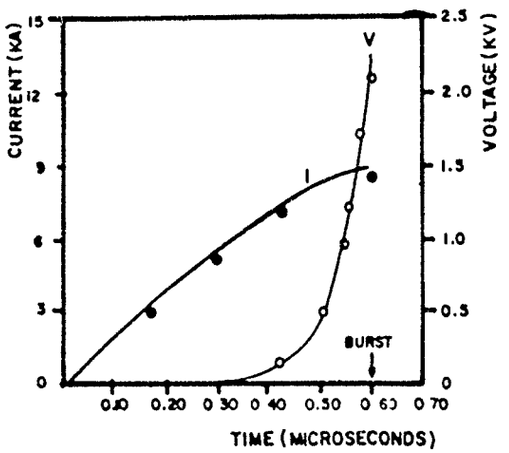

Fig. 3. The calculated current I(t) and voltage V(t) (solid lines) are compared to measured values (dots) for one representative experiment

EXPLOSIVE PREPARATION

HNAB is a thermally stable explosive for use in ordnance components. The crystal density of HNAB Phase I is 1.8 gr/cc and that of Phase II is 1.75 gr/cc. The detonation velocity is 7300 m/sec, and detonation pressure 20 GPa (ρ=1.6 gr/cc).

HNAB (2,2',4,4',6,6'-hexanitroazobenzene) was synthesized in a two step reaction following O'Keefe's procedure (7): (a) the preparation of HNHB (hexanitrohydrazobenzene) by the reaction between picryl chloride and hydrazine; (b) oxidation of HNHB to HNAB – best done by the use of strong nitric acid.

Recrystallization of the crude HNAB can be done from various solvent mixtures. All pure products obtained, although differing in physical apprearance, are orange-red crystals melting at 223-224 °C. Changes in recrystallization conditions, cause the formation of particles of different but controlled mean size, as was detected by Sub Sieve Sizer and the Scanning Electronic Microscope (Fig. 4 -a,b).

Two major changes in HNAB's appearance can be observed before melting. (1) at the range of 150 °C the color of the crystals deepens and turns red. (2) a small portion melts at approx. 190 °C. These facts confirm polymorphic changes. The transformation of HNAB Phase I to the higher-energy less-stable Phase II is consistent with the endotherm observed in the Differential Scanning Calorimetry (DSC) spectrum. (Fig. 5).

Fig. 4. (a)

(b)

Fig. 4. Morphology pictures of HNAB by SEM magnification 10μm
a) HNAB - I
b) HNAB - II

The HNAB samples were fabricated to the desired bulk sample densities 1.15 to 1.67 g/cm^3 and particles size 5μm, 20μm and 40μm, using a hydraulic press technique. The charge (explosive pellets) were 5mm in diameter and 7mm long.

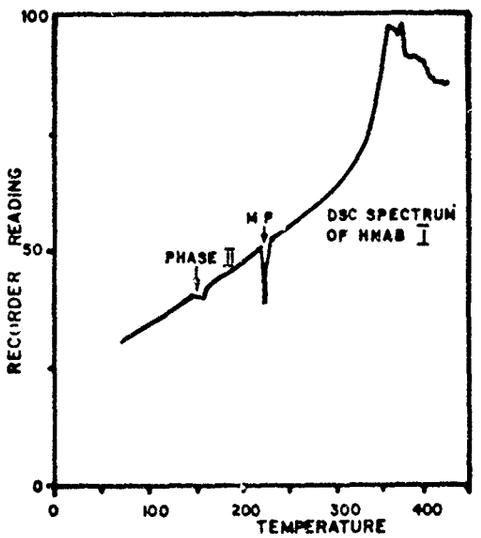

Fig. 5. Phase transformation of HNAB-I to HNAB-II from DSC measurements

RESULTS AND DISCUSSION

Many experiments were performed in order to ensure good statistics for the initiation threshold data. In each experiment we measured the foil's current and voltage waveforms. The flyer velocity was controlled (by adjusting the burst current density) between 0.7 to 2.5mm/μs as in Fig. 2. Using that data we calculated the pressures generated by the flyer (Kapton or Mylar) impact on the explosive pellet by impedance matching method, using the Hugoniot curves (6,8) of each material. The shock initiation threshold of HNAB has been measured for a pulse duration between 40 and 210 nsec as determined by the flyer plates thickness, d, from 76.2 to 350μm. The impact duration τ is given by $\tau \cong 2d/U_s$ where U_s is the shock velocity in the flyer plate. The initiation threshold pressure vs. impact duration for various bulk densities is plotted in Fig. 6.

We examined the dependence of the critical energy upon the shock duration, τ, to see if the critical energy $P^2\tau$=constant can be taken as a shock initiation threshold criteria (9). (The explosive was also investigated at two polymorphic phases HNAB I, II). The results clearly indicate that as the duration of the initiating pulse gets longer, the threshold curve swings away from the curve $P^2\tau$=constant. For long pulses the initiation criterion becomes one of a constant pressure. The constant threshold pressures (from the results of 350μm flyer plates) were 2.9 GPa at a density of 1.6 gr/cm^3 (as previously measured a constant pressure by Schwarz in ref. 1), 2.2 GPa at 1.4 gr/cm^3 and 1.9 GPa at 1.2 gr/cm^3 (see Fig. 6).

We reach the conclusion that at short pulse duration the critical energy for initiation is smaller than that at long pulse duration. At density of 1.6 gr/cm^3 and thin flyer initiation (76.2μm corresponding to 42 nsec pulse duration), the critical energy is 12 J/cm^2. This critical energy gets larger at longer pulse duration. For instance at 350μm flyer thickness (200 nsec pulse duration) the critical energy is 36 J/cm^2. The efficiency of transferring electric energy from the capacitor to kinetic energy of the flyer is greater with initiation by the 76.2μm flyer than with initiation by the 350μm flyer.

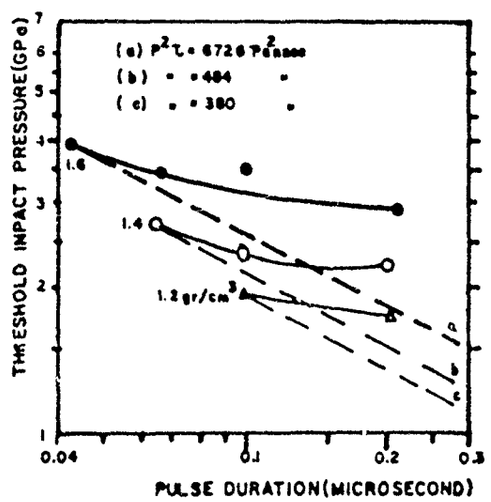

Fig. 6. Threshold input pressure vs. pulse duration for various bulk densities of HNAB

The powder morphology plays a significant role in the shock initiation sensitivity of HNAB. The initiation threshold vs. grain size is given in Fig. 7. This data is indicative that the threshold increases with the explosive grain size, as can be expected from hot spot model (10). From the investigation of the initiation threshold of HNAB I and HNAB II, at two polymorphic phases, we conclude that there is no difference between the sensitivities of the two phases for the same grain size.

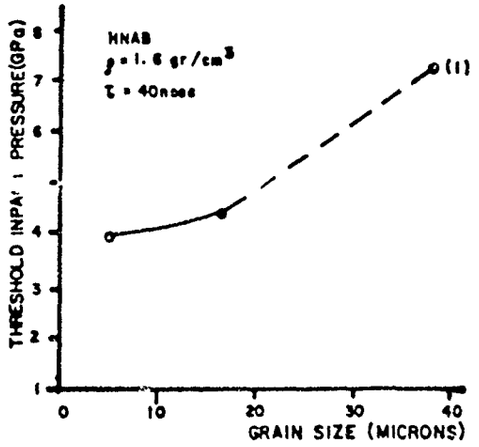

Fig. 7. Threshold impact pressure vs. grain size of HNAB. Point No. 1 is an under-estimate for the threshold impact pressure at 40μm particle size

REFERENCES

1. A.C. Schwarz Study of Factors which influence the shock initiation sensitivity of HNS. Contract DE-AC04-76DP00789 Sandia Lab. Albuquerque, N.M. 87115, March 1981.
2. A.C. Schwarz Application of HNS in explosive components. Tech. Rep. SC-RR-71 Sandia Lab. Albuquerque, N.M. 87115, May 1972.
3. E. Hasman, M. Gvishi, Z. Segelov, Y. Carmel, D. Ayalon and A. Solomonovici Acceleration of flyer plate by electrically exploded foils and applicaton to shock initiation. Israel Phys. Soc. Jerusalem, April 1984.
4. H.H. Chau, G. Dittbenner, W.W. Hofer, C.A. Honodel, D.J. Steinberg, R.J. Stroud, and R.C. Steingart and R.S. Lee, Electric Gun: A versatile tool for high-pressure shock-wave research. Rev. Sci. Inst. 1676 *51* (1980).
5. T.J. Tucker and P.L. Stanton "Electrical Gurney Energy: New concept of modeling energy transfer from electrically exploded conductors," Tech. Rep. SAND 75-0244 May 1975.
6. E. Hasman, M.Sc. Thesis to be submitted Israel Ins. of Technology, Technion, Haifa (1985).
7. D.M. O'Keefe "HNAB Synthesis and Characterization" SAND 74-0239 May 1976.
8. L.M. Lee and A.L. Schwarz "Shock Characterization of HNAB," 7th Sym. on Detonation p. 248 (1981).
9. F.E. Walker and R.J. Wasley "Critical energy for shock initiation for Heterogeneous explosives," Explosivstoffe 1, a (1969).
10. E.L. Lee and C.M. Tarver "Phenomenological model of shock initiation in heterogeneous explosives," Phys. Fluids *23* (12) December (1980).

SHOCK SENSITIVITY AND PERFORMANCE OF SEVERAL HIGH EXPLOSIVES

M. Kroh, K. Thoma, W. Arnold, U. Wollenweber
Messerschmitt-Bölkow-Blohm GmbH
D-8898 Schrobenhausen/W. Germany

A series of experimental and theoretical investigations have been performed on several explosives to get shock initiation and performance data such as shock to deflagration and deflagration to detonation transition pressure thresholds, critical energies for shock initiation, detonation velocities, detonation pressures and Gurney velocities. A modified gap test arrangement has been used to determine the shock to deflagration to detonation transition (SDDT) behavior. The result is a characteristic SDDT curve which exhibits the well defined transition from shock to deflagration at low pressures and the following build up to detonation. Using the pressure time profile of the shock wave which is transmitted into the acceptor charge and causes a chemical reaction, the critical energy for shock initiation can be calculated. To determine the performance of the explosives cylinder test experiments and BKW computer code calculations have been carried out. The values such as Gurney velocity, detonation velocity and detonation pressure which were calculated give a good description of the explosive performance.

INTRODUCTION

Sensitivity and performance data are often used for comparison to select an explosive for a special warhead. For commonly used explosive compositions based on RDX and HMX the sensitivity increases with increasing performance due to the increasing RDX or HMX content. This means, that only the knowledge of both, the sensitivity and the performance enables us to find out the right explosive with a performance sufficiently high and with a sensitivity sufficiently low.

This paper describes theoretical and experimental investigations which were conducted on several explosives to get sensitivity and performance data.

A modified gap test arrangement was used to provide data for the characteristic shock to deflagration to detonation transition curve (SDDT) which yields the shock sensitivity. The shock sensitivity which is determined by the reaction pressure threshold at which a chemical reaction in the explosive appears and by the following transition from deflagration to detonation is given in terms of the thickness of the attenuating material or in terms of the corresponding peak pressure. Combining these experimental gap test results with computer code calculations of the shock wave profile yields the critical energy for shock initiation. This energy is given by the integral $\int p(t)u_p(t)dt$ where $p(t)$ is the pressure-time profile of the shock wave which is transmitted into the acceptor charge and $u_p(t)$ is the particle velocity.

The performance of an explosive composition can be described by the Gurney velocity, the detonation pressure and the detonation velocity. To get the Gurney velocity standard cylinder test experiments have been carried out and the expansion of the copper wall was measured. The copper wall velocity at the expansion ratio 3 yields the Gurney velocity. The detonation velocities and detonation pressures were calculated using Mader's BKW computer code (1).

The explosives which were tested and the

experiments which were carried out are listed in Table 1. The grain size of HNS which was pressed with 5% binder was 1-5 μm, the Aluminum in the RDX explosives had a grain size less than 75μm and the plastic binder PB was Polybutadiene.

TABLE 1
Explosives and Experiments

Explosive	Density (gcm^{-3})	Sensitivity Test	Performance Test
HNS	ϱ = 1.60	+	
TNT (pressed)	ϱ = 1.60	+	+
HMX/PB 85/15	ϱ = 1.64		+
	ϱ = 1.71	+	+
RDX/Al/PB 67/18/15	ϱ = 1.55	+*	
	ϱ = 1.65	+*	+
RDX/Al/PB 71/14/15	ϱ = 1.65	+	+

* tested at 20 °C and 110 °C

SHOCK SENSITIVITY

Experimental. A modified Gap Test set up as shown in Fig. 1 was used to investigate the shock induced shock to deflagration to detonation transition behavior (2, 3). The set up consists of a Tetryl donor charge with a diameter of 57.5 mm, a length of 50 mm and a density of 1.557 g/cm^3 which is centrally initiated. The attenuator gap is a cylinder of Plexiglas with a diameter of 70 mm whose linear Hugoniot relation $U_s = a + bu_p$ is given by a = 2.561 mm/μs and b = 1.595. The density is 1.186 g/cm^3. The acceptor charge has a diameter of 58 mm and a length of 20 mm. The motion of the unreacted acceptor material or the reaction products at the free surface of the acceptor charge is photographed using a rotating mirror camera in framing mode. The time sequence of the frames is about 1.3 μs. The calibration curve which gives the shock peak pressure as a function of the Plexiglas thickness is shown in Fig. 2. The peak shock pressure can be described by the following relations

$$P_G = 98 \exp(-0.0292\, X_G),\ 20 \le X_G \le 40 \text{ mm}$$

$$P_G = 101 \exp(-0.0275\, X_G),\ 30 \le X_G \le 100 \text{ mm}$$

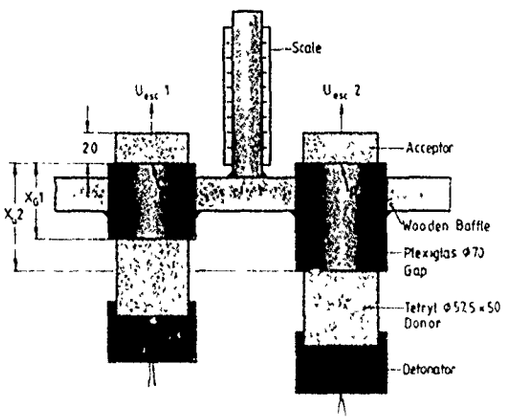

Fig. 1. Modified gap test set up

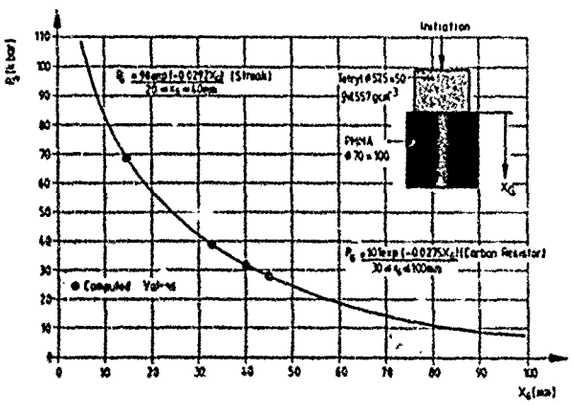

Fig. 2. Modified gap test calibration curve

Procedure. The time history of the motion of the reacted or unreacted acceptor material at the free surface of the acceptor charge is obtained from the high speed photographic records. A quadratic expression in time was then fitted to the data points to get the escape velocity of the accelerated material. Plotting the calculated escape velocities versus the shock peak pressures in the Plexiglas gap at the interface Plexiglas-acceptor yields the characteristic SDDT curve for any explosive.

SDDT Curve. The typical SDDT curve as shown in Fig. 3 can be divided into three regions representing the shock, the reaction or deflagration, and the detonation region respectively.

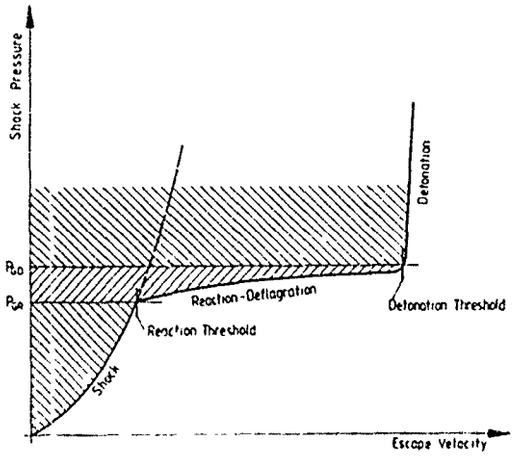

Fig. 3. Typical SDDT curve

For weak shock pressures $P_G < P_{GR}$ a shock wave will be transmitted into the acceptor charge without initiating any reaction. As the shock pressure P_G is increased, a pressure P_{GR} is reached where the curve displays an abrupt increase in velocity. This point is called the reaction threshold. As the pressure is increased further, the reaction builds up to detonation and the escape velocity increases up to a pressure P_{GD} where detonation is detected. P_{GD} represents the detonation threshold. If the pressure P_G exceeds the threshold pressure P_{GD} then the escape velocity remains nearly constant and is in the order of the detonation velocity.

RESULTS

The SDDT curves for the explosives listed in Table 1 are presented in graphical form as a plot of the pressure P_G in the Plexiglas versus the escape velocity U_{esc} The plots are shown in the Figs. 4-10. The curves show a well-defined transition from shock to deflagration which can be determined within an accuracy of ± 1 kbar. The build-up from deflagration to detonation often covers a wide pressure range which depends on the type of the explosive composition. Due to that the detonation threshold can be described only by a pressure interval.

The SDDT behavior of HNS is shown in Fig. 4

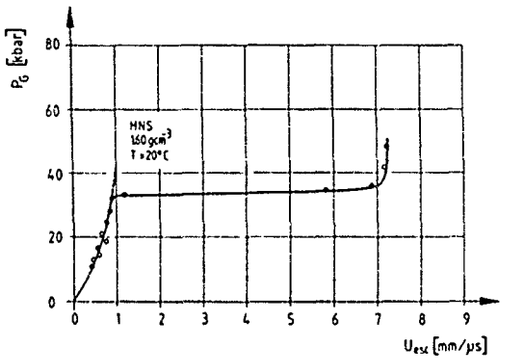

Fig. 4. Sensitivity curve for HNS

HNS exhibits a reaction threshold of approximately 32 kbar followed by a rapid build-up to detonation within 4-6 kbar. The detonation threshold where the reaction products are blown off with nearly a constant initial velocity of 7 mm/µs is in the order of 36 to 38 kbar.

TNT pressed to a density of 1.60 g/cm³ is more sensitive. The reaction threshold is 20 kbar followed by a detonation threshold between 25 and 30 kbar. The growth of reaction to detonation occurs over a pressure range of 5-10 kbar (Fig. 5).

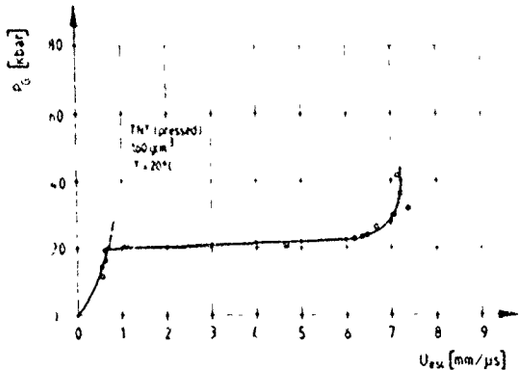

Fig. 5. Sensitivity curve for TNT

The SDDT curve for the plastic bonded HMX (HMX/PB 85/15) is shown in Fig. 6. Up to a pressure of 28 kbar the explosive does not react. At this point the SDDT curve displays an abrupt increase in U_{esc} which characterizes the reaction threshold P_{GR}. HMX/PB exhibits a more gradual build-up to detonation compared to TNT and HNS with a detonation threshold between 38 and 45 kbar.

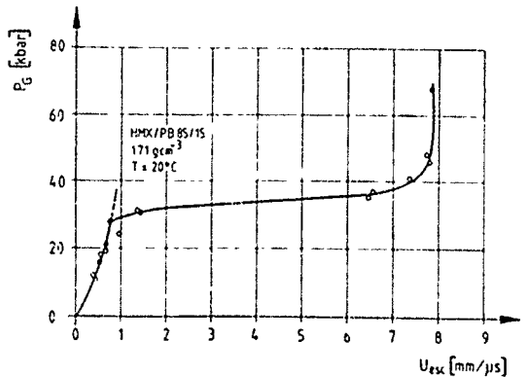

Fig. 6. Sensitivity curve for HMX/PB 85/15

The results for the RDX/Al/PB 67/18/15 explosive which contains Aluminum are shown in Figs. 7, 8, 9. For that explosive composition the SDDT curves for two different temperatures and densities were determined to see the temperature and density effect on the reaction and detonation pressure thresholds. The SDDT curve obtained for the lower density of 1.55 g/cm^3 at a temperature of 20 °C and 110 °C is shown in Fig. 7.

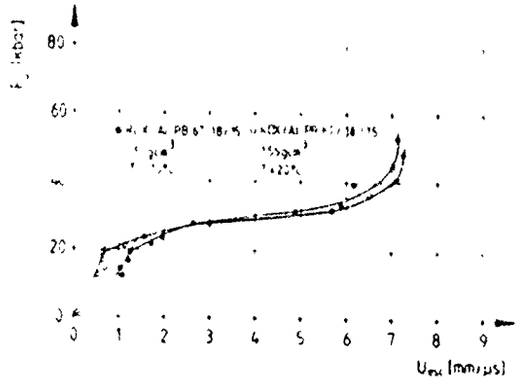

Fig 7. Temperature effect on the sensitivity curve for RDX/Al/PB 67/18/15 (ϱ=1.55 g/cm³)

The reaction threshold at ambient temperature is 19 kbar and the detonation threshold is in the order of 35 to 45 kbar. This wide pressure range between the reaction threshold and the detonation threshold indicates a very gradual build-up to detonation for that type of explosive mixture. Increasing the temperature from 20 °C to 110 °C has no detectable influence on the reaction or detonation threshold as can be obtained from Fig. 7. Increasing the density from 1.55 g/cm^3 to 1.65 g/cm^3 shifts the thresholds to higher values as can be seen on Fig. 8. The reaction threshold is now 32 kbar instead of 19 kbar for the lower density and the detonation threshold is now about 45-50 kbar instead of 35-45 kbar.

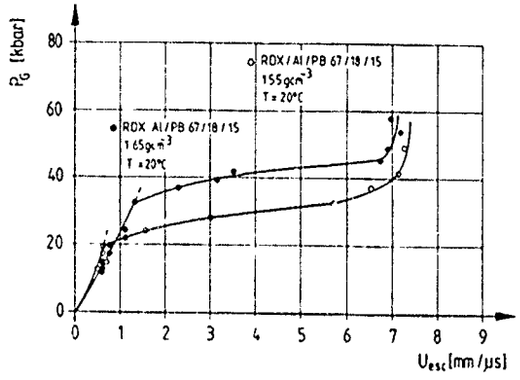

Fig. 8. Density effect on the sensitivity curve for RDX/Al/PB 67/18/15

By heating the explosive up to a temperature of 110 °C no significant influence on the reaction or detonation thresholds can be detected for the higher density as well as for the lower density (Fig. 9).

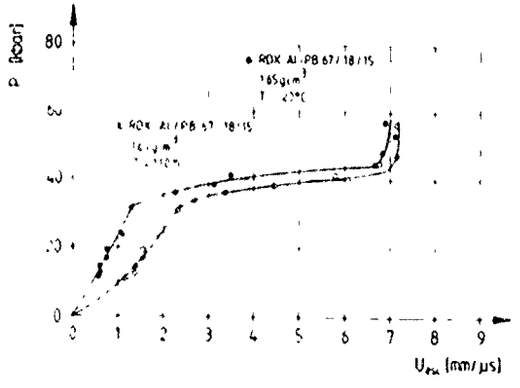

Fig. 9. Temperature effect on the sensitivity curve for RDX/Al/PB 67/18/15 (ϱ=1.65 g/cm³)

By increasing the RDX content from 67 to 71 percent without changing the density the sensitivity is increased too as shown in Fig. 10. The reaction threshold for RDX/Al/PB 71/15/14 is 28 kbar followed by a detonation threshold within 40 to 45 kbar. The shock region does not differ significantly from the RDX/Al/PB 67/18/15 explosive

The experimental shock sensitivity results are

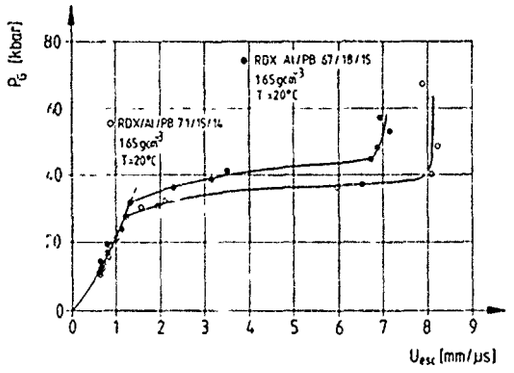

Fig. 10. Sensitivity curve for RDX/Al/PB 71/15/14 and 67/18/15

summarized in Table 2 in terms of the threshold peak pressures in the attenuating Plexiglas. The most important parameter for the shock sensitivity of an explosive is the reaction threshold P_{GR}. If the acceptor charge is large enough then it will detonate if it is initiated by a shock wave of pressure equal to its reaction threshold. The reaction develops from low order reaction to full detonation. The reaction threshold does not depend on the acceptor length. The detonation threshold on the contrary decreases with increasing acceptor charge length (2).

CRITICAL ENERGY FOR SHOCK INITIATION

The threshold pressures P_{GR} and P_{GD} given in Table 2 are the peak pressures in the Plexiglas gap at the interface Plexiglas-acceptor. The values P_{GR} and P_{GD} are determined not only by the chemical composition of the acceptor material and its physical state, but also by the dimensions of the test set up. These dimensions control the times at which rear and lateral rarefaction waves can arrive at the shock front and influence the shock pressure. Different pressure-time profiles can be obtained. The explosive response differs as the stimulus differs and gives different threshold pressures in different tests. The threshold values are only representative for the given gap test set up. In other words, not only P_{GR} and P_{GD}, but also the pressure-time profile should be specified in each test. If the pressure profile of the reaction threshold P_{GR} is known, then the critical energy which is given by the integral $\int p(t)\, u_p(t)\, dt$ can be calculated. This value does not depend on the geometry of the test set up.

To get the time profile of the reaction pressure threshold P_{GR}, computer code calculations were performed. A Lagrange representation in cylindrical symmetry was used to model the gap test arrangement. The detonation of the donor charge was described by the CJ-volume burn technique. For the donor charge the JWL equation of state was used with the corresponding JWL parameters. The gap material and the unreacted acceptor charge was described by a linear shock equation of state.

RESULTS

The calculated peak pressures for various Plexiglas thicknesses are in good agreement with

TABLE 2
Experimental Shock Sensitivity Results

Explosive	Density (g/cm^3)	Temp. (°C)	Reaction Threshold P_{GR} (kbar)	Detonation Threshold P_{GD} (kbar)
HNS	1.60	20	32	36-38
TNT (pressed)	1.60	20	20	25-30
HMX/PB 85/15	1.71	20	28	38-45
RDX/Al/PB 67/18/15	1.55	20	18	35-45
	1.55	110	18	35-45
	1.65	20	32	45-50
	1.65	110	32	45-50
RDX/Al/PB 71/14/15	1.65	20	28	39-42

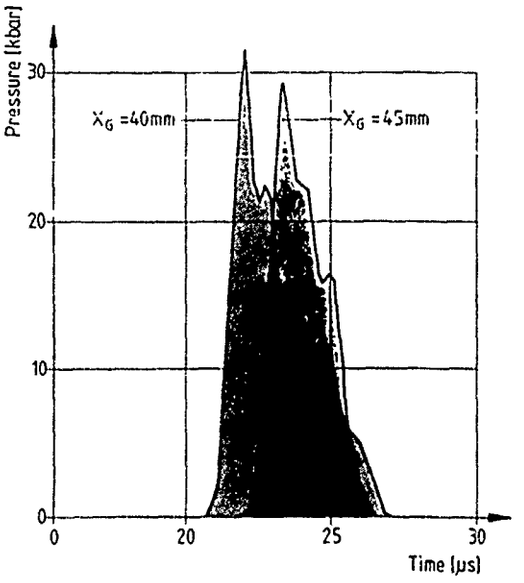

Fig. 11. Calculated pressure profiles

the experimental values as indicated in Fig. 2. The pressure profiles at the end of a 40 mm and 45 mm Plexiglas gap with peak pressures of 32 kbar and 28 kbar respectively are shown in Fig. 11. From these pressure profiles the critical energies for the corresponding explosives are obtained by evaluating the integral $\int p\,(t)\,u_p\,(t)\,dt$ where p(t) is the pressure profile of the shock wave in the acceptor and u_p (t) the particle velocity. The results with an accuracy of about 10 percent are listed in Table 3.

TABLE 3
Critical Energies

Explosive	Density [gcm^3]	Temp [°C]	E_{Crit} [KJ/m^2]
HNS	1.60	20	3600
HMX/PB85/15	1 71	20	2500
RDX/Al/PB67/18/15	1 65	20	3400
	1 65	110	3400
RDX/Al/PB71/14/15	1 65	20	2400

The critical energies given in Table 3 show that the explosives are very insensitive to shock waves compared to Comp. B and PBX 9404 for instance with critical energies of 1500 kJ/m^2 and 630 kJ/m^2 (4). The critical energy for HMX/PB 85/15 is in the same order of magnitude as the critical energy which was measured by H. Moulard (5) for RDX/PB 88/12 at a lower density. The critical energy for HNS is more than twice the critical energy given in (4) for HNS I, density 1.55 g/cm^3.

PERFORMANCE

To characterize the performance which can be described by the detonation velocity, the detonation pressure and the Gurney velocity, BKW computer code calculations and standard cylinder test experiments have been performed. For this test a copper cylinder with a wall thickness of 2.5 mm, an outer diameter of 2 R_0=30 mm and a length of 300 mm was used. The motion of the copper wall was recorded using a rotating mirror camera. A function of the form $R-R_0=A+B\,t+C\exp(-Dt)$ was then fitted to the experimental data points. The wall velocity at the expansion ratio $R/R_0=3$ yields the Gurney velocity. Additionally the detonation velocity was measured with self shorting pins 200 mm apart in contact with the copper wall.

RESULTS

The results from the cylinder tests together with the BKW calculations are summarized in Table 4. The experimental detonation velocities are in good agreement with the calculated values. The deviation is less than 2.5 percent. The Gurney velocity for RDX/Al/PB 71/14/15 is nearly the same as for TNT and comparable to the Gurney velocity for H-6 as given in (4). Due to the high energy explosive HMX, the Gurney velocity for HMX/PB 85/15 is 2.72 mm/µs for the lower density and 2.79 mm/µs for the higher density. These values are comparable to those for Cyclotol and Comp. B (4).

SUMMARY

An investigation of 3 plastic bonded high explosives together with TNT and HNS is presented. The plastic bonded high explosives contain RDX and Aluminum or HMX.

TABLE 4
BKW Calculations and Cylinder Test Results

Explosive	Density	BKW Calculations		Cylinder Test Experiments		
		$D_{CJ}[ms^{-1}]$	P_{CJ} [kbar]	D_{exp} $[ms^{-1}]$	$V_{R\text{-}R_o=30}[ms^{-1}]$	$\sqrt{2E}[mm\mu s^{-1}]$
TNT (pressed)	1.60	7060	202	6930	1440	2.49
HMX/PB	1.64	7960	263	8180	1580	2.72
85/15	1.71	8220	292	8280	1650	2.79
RDX Al PB 67/18/15	1.65	7500	221	7350	1430	2.47
RDX Al PB 71/14/15	1.65	7560	228	7600	1440	2.47

The sensitivity of the explosives is measured with a modified gap test and using the results of this test critical energies are calculated. The results for reaction and detonation thresholds are summarized in Table 2, the calculated critical energies are given in Table 3. Finally the performance of the explosives was investigated using cylinder test experiments and BKW calculations. The results are presented in Table 4. With the given data the described plastic bonded high explosives which can withstand high temperatures are characterized in their sensitivity and performance and thus can be compared to standard TNT-bonded high explosives.

REFERENCES

1. Charles L. Mader, "A Code for Computing the Detonation Properties of Explosives," LA-3704, May 1, 1967.

2. D. G. Tasker, "Shock Initiation and Subsequent Growth of Reaction in Explosives and Propellants: The Low Amplitude Shock Initiation Test, LASI," Seventh Symp. Det. 1981.

3. M. Kroh, "Detonation Properties of Some Plastic Bonded. Al Containing High Explosives," Twelth Symp. Expl. Pyrot., March, 1984.

4. B. M. Dobratz, "Properties of Chemical Explosives and Explosives Simulants," LLNL Explosive Handbook, March 16, 1981.

5. H. Moulard, "Empfindlichkeit eines Hexogen-Polybutadien-Gemisches gegenüber einer kalibrierten Stoßwelle," ISL Bericht RT 514/76.

DISCUSSION

D. TASKER, NSWC

1. It has been observed by Liddiard and myself that the pressure/gap thickness calibration, of the modified gap test, exhibits a kink due to the arrival of lateral rarefactions at the center of the PMMA. Can you explain why there was no evidence of this in your calibration?

2. Liddiard has demonstrated a double knee structure in the response of pressed explosives, notably with TATB/KelF compositions. Consequently, when observing materials such as HNS where the opponent initiation pressures are low (as in your data), the first knee may not be observed as it is below the range of the test I stress caution, therefore, in the interpretation of your data, your apparent initiation threshold may be that of the second knee and thus too high.

REPLY BY K. THOMA

1. The kink caused by lateral rarefaction waves could not be resolved by our measuring techniques.

2. As mentioned in the paper of Liddiard, the initiation behaviour is strongly influenced by preparation techniques, particle size and binder. We know from comparisons of our HNS with and without binder that the initiation behaviour changes essentially. The double knee structure was observed for rather different types of explosives with different grains, binder, etc For our type of HNS we can't detect the double knee although we investigated the range of pressures where it should appear.

DISCUSSION

JULIUS ROTH, Consultant,
Portola Valley, CA

Our studies of the shock initiation of HNS II in both gap test and wedge test geometries were reported in the Proc. of the 5th Detonation Symposium. For ~1.6 g/cc HNS pellets pressed *without binder,* of HNS of ~15 μm particle size, we found a threshold shock of 23 kbar, and a "threshold" of about 17 kbar for wedge geometry (50 μm diam.). A 23 kbar threshold leads to a "critical energy" of about 1400 KJ/m^2 in reasonable accord with the values quoted by Dobratz (your Ref. 4).

REPLY BY K. THOMA

As stated by J. Roth, his HNS differs from ours in particle size and the use of binder. We are aware of the fact that by our preparation technique with 5% binder the HNS becomes more insensitive than HNS pressed without binder.

A COMPUTATIONAL INVESTIGATION OF THE EFFECT OF SHIELDING IN MITIGATING SHOCK INITIATION STIMULI PRODUCED BY IMPACT

John Starkenberg, Toni M. Dorsey, Kelly J. Benjamin
U.S. Army Ballistic Research Laboratory
U.S. Army Materiel Command
Aberdeen Proving Ground, Maryland

We have conducted a study of the role of shielding in reducing the shock initiation stimulus for a simple one-dimensional representation of the problem of sympathetic detonation of munitions. We found that single-layered shields made of materials with low acoustic impedance generally produce a complex shock wave structure in the acceptor. This complex structure is associated with a low level of initiation stimulus because of the breakup into several weaker shocks and the reduction of $\int p^2 dt$. High-impedance shield materials also substantially reduce the initiation stimulus, but without the accompanying shock breakup effect. Increasing shield thickness improves performance and can change the order of effectiveness of shield materials. With multilayered shields composed of high-impedance and low-impedance material we observed shock structures depending strongly on the ordering of the material in the shield. Multiple-shock structure was usually observed when the high-impedance material was the outer component of the shield and sufficient low-impedance material was present. Single compression waves with variable peak pressures and rise times were usually observed when the low-impedance material was the outer component of the shield. Substantial benefits in terms of shock breakup and $\int p^2 dt$ reduction can be obtained by increasing the thickness of three-layered shields, which were found to perform better than five-layered shields.

INTRODUCTION

In order to reduce the vulnerability of stored ammunition, shielding between rounds has been used to prevent initiation of detonation in a round (the acceptor) when one of its neighbors (the donor) detonates. The shielding serves to prevent direct impact of the donor casing or its fragments on the acceptor as well as to process the shock wave entering the acceptor, thus reducing the initiation stimulus. The latter mechanism is amenable to analysis using a hydrodynamic computer code and we have already simulated round-to-round detonation propagation, with and without shielding, using the 2DE code (1,2). Shielding effectiveness in reducing shock initiation stimulus levels is further amenable to analysis in one dimension. The present paper, therefore, concerns our one-dimensional study of shielding effectiveness using the STEALTH code (3).

SIMULATION DESCRIPTION

The problem elements are the donor, the shield and the acceptor. The acceptor, in the one-dimensional simulation, consists of a steel layer (cover plate or acceptor casing) covering a layer "inert" TNT. The shield configuration is varied. It consists of a single layer of any of various materials or multiple layers of two different materials. The donor is represented by a layer of steel (flyer plate or donor casing) with an initial velocity on the order of that achieved by the casing of a detonating round. The flyer

and cover plate thicknesses are always equal. The problem geometry is illustrated in Figure 1. The "inert" TNT is described by Lee's unreacted JWL equation of state (4) and all other materials by Wilken's LLNL model (3) with 304-steel used for the flyer and cover plates.

CHARACTERIZATION OF THE SHOCK INITIATION STIMULUS

The simplest characterization of shock initiation stimulus levels is the square of the pressure integrated with respect to time ($\int p^2dt$) evaluated in the acceptor explosive. The use of this integral is an extension of the critical energy concept which is applicable to singly shocked explosives in planar experiments. We have, in general, used this parameter to characterize our computed results. However, the shields often alter the rise time of a single compression wave or produce multiple shock loading in the acceptor. In these cases, the ramp wave or shock waves after the first are not presumed to contribute as significantly as a single shock to the initiation. Thus, integrating through the ramp or including all shocks in the $\int p^2dt$ calculation produces a conservative estimate of the stimulus (i.e. the actual conditions are even more predisposed toward preventing acceptor initiation). It is also instructive to consider in detail the processing of the shock wave produced by the shield.

RESPONSE OF UNSHIELDED ACCEPTORS

In order to provide baseline data from which to evaluate the stimulus reduction provided by shielding, we ran a number of computations without shielding. This type of loading always produces a single shock in the acceptor as illustrated in Figure 2. In these we varied the casing thickness and impact velocity so as to produce sets of results for constant velocity, constant momentum and constant energy impact. Casing thickness was varied from 5 to 20mm with appropriate velocities. The results are summarized in Table 1 and plotted in Figure 3. Not surprisingly, as the casing thickness is increased at constant velocity, the initiation stimulus increases rapidly. For constant momentum impacts the stimulus decreases rapidly with increasing casing thickness. Constant energy impacts do not produce a constant stimulus, rather the initiation stimulus decreases slowly with increasing casing thickness. The results of these computations suggest a correlation with $W^{3/5}V^2$, as illustrated in Figure 4.

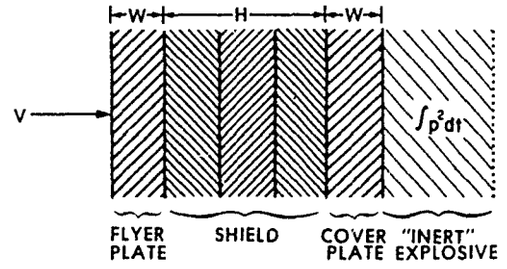

Fig. 1. One-dimensional shielding configuration

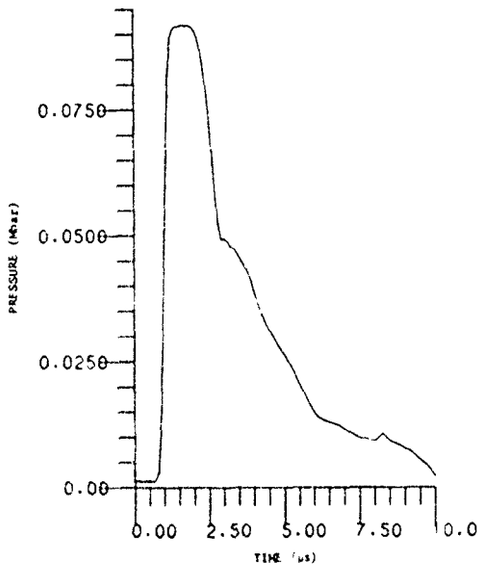

Fig. 2. Typical acceptor explosive shock pressure history without shielding

RESULTS WITH SINGLE LAYERED SHIELDS

General. Our version of the STEALTH code is accompanied by a materials library providing standard preprogrammed material models. The vast majority of these are for metallic elements and alloys. The only plastic material description available is for Lucite. Nonetheless, we made computations with 10mm thick casings and various shield thicknesses for each available material. Special emphasis was given to Lucite, tungsten and steel. The impact velocity was held at 1 km/s.

TABLE 1

Initiation Stimulus with Unshielded Acceptors

CASING THICKNESS W (mm)	CONSTANT VELOCITY		CONSTANT MOMENTUM		CONSTANT ENERGY	
	VELOCITY V (km/s)	$\int p^2 dt$ (GPa^2-ms)	VELOCITY V (km/s)	$\int p^2 dt$ GPa^2-ms)	VELOCITY V (km/s)	$\int p^2 dt$ (GPa^2-ms)
5.0	1.00	0.074	-	-	1.41	0.170
7.5	1.00	0.112	1.33	0.222	1.15	0.157
10.0	1.00	0.145	1.00	0.145	1.00	0.145
12.5	1.00	0.171	0.80	0.100	0.89	0.129
15.0	1.00	0.190	0.67	0.074	0.82	0.119
17.5	1.00	0.208	0.57	0.054	0.76	0.108
20.0	1.00	0.222	0.50	0.042	0.71	0.098

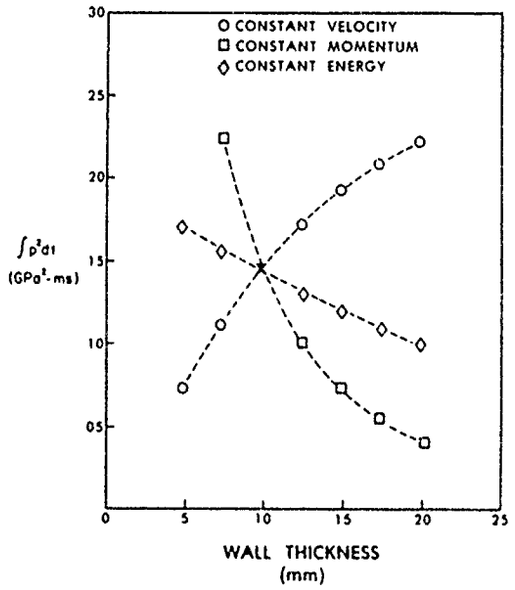

Fig. 3. Variation of shock initiation stimulus with wall thickness in the absence of shielding

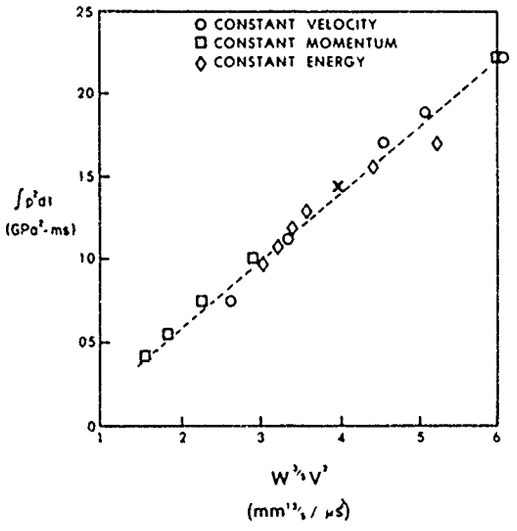

Fig. 4. Correlation of shock initiation stimulus with flyer and cover plate parameters

Shock Structure. The pressure history in the acceptor explosive depends on the casing thickness, the shield thickness and the shock impedance of the shield. When the impedance of the shield is lower than that of the casing, a shock wave reverberates between the donor and acceptor casings, delivering repeated shocks to the acceptor. Our lowest impedance material is Lucite. Figure 5 illustrates this effect for 5, 15, 25 and 35mm thick Lucite shields. Clear separation of three shocks of increasing amplitude may be observed in Figure 5c for a 25mm thick shield. The complete pulse is about 14μs long with a peak pressure of 35 GPa (.035 Mbar). For the 15mm thick shield of Fig. 5b, the first shock is clearly defined while the second shock appears intermingled with the third. This pulse is about 12μs in duration with a 4.2 GPa (.042 Mbar) peak. With a 5mm thick shield, all the shocks have coalesced into a 10μs pulse with a 5.1 GPa (.051 Mbar) peak, as illustrated in Figure 5a. Thus the effect of increasing shield thickness is to increase the interval between shocks, lengthen the pulse duration and reduce the peak pressure. The temporal spacing between the shock fronts generated at the shield/acceptor casing interface depends on shield thickness since two shock transits across the shield occur between the generating interactions. As these shocks propagate into the

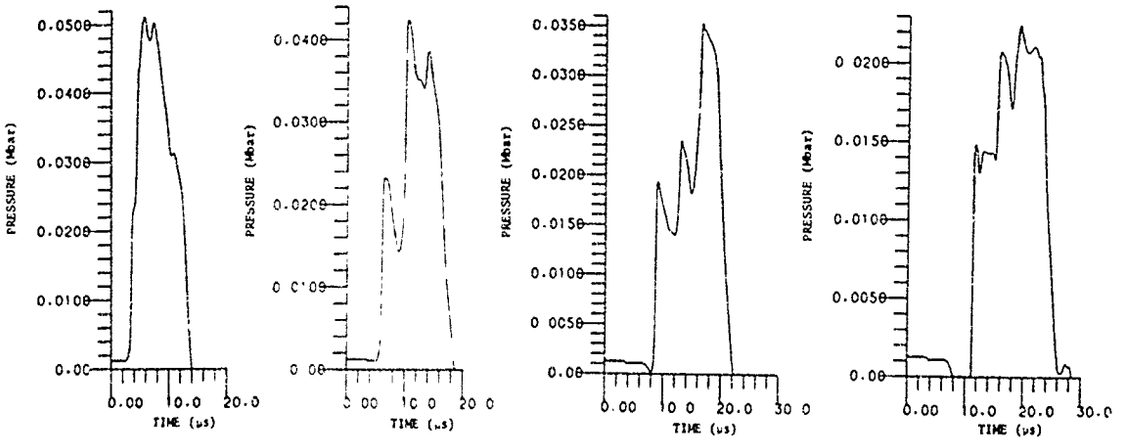

a. 5 mm shield *b. 15mm shield* *c. 25mm shield* *d. 35mm shield*

Fig. 5. Acceptor explosive pressure history with single-layered Lucite shields

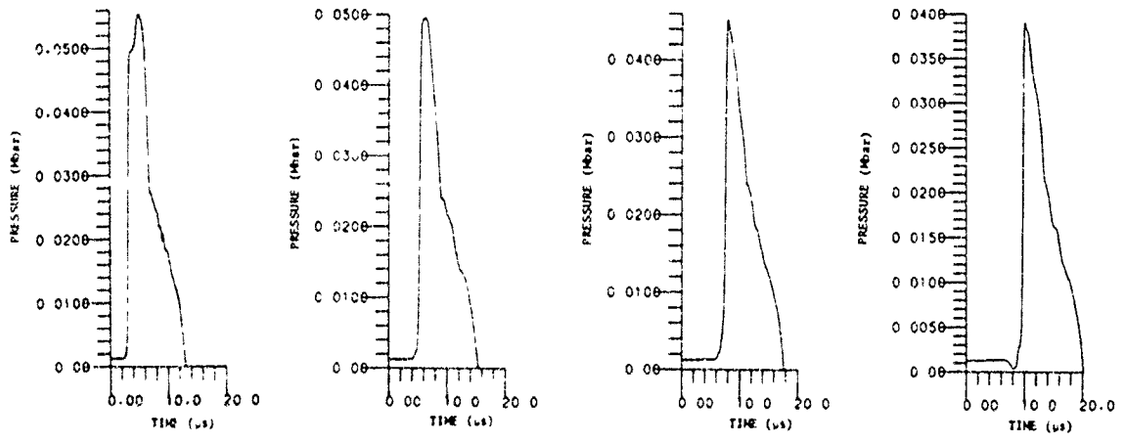

a. 5mm shield *b. 15mm shield* *c. 25mm shield* *d. 35mm shield*

Fig. 6. Acceptor explosive pressure history with single-layered tungsten shields

acceptor, they tend to coalesce so that, if the initial temporal spacing is small enough, the shocks will not be distinguishable from one another when they arrive at the acceptor explosive. Because of this coalescence, shock breakup was only observed for Lucite and magnesium.

When the impedance of the shield is higher than that of the casing a single shock in the acceptor is always observed. Our highest impedance material is tungsten. Figure 6 shows the shocks produced with 5, 15, 25 and 35mm thick tungsten shields. The effect of increasing shield thickness is to slightly increase pulse duration while substantially reducing peak pressure.

Initiation Stimulus Reduction. The effect of shield material on shock initiation stimulus reduction as measured by $\int p^2dt$ is illustrated in Figure 7. This is a plot of $\int p^2dt$ versus initial acoustic impedance for 30mm thick shields. The results are segregated into two groups. One group includes most of the materials whose initial acoustic impedance is less than that of steel and the other group is comprised primarily of materials whose initial acoustic impedance is greater than that of steel. Exceptions are that nickel with a slightly greater initial impedance than steel belongs to the low impedance group and lead and thorium with lower impedance than steel appear to belong to the higher impedance group (although the latter classification is more questionable). As impedance increases

among the low impedance materials, the initiation stimulus approaches that associated with steel shields, which provide the lowest level of protection. Materials in the high impedance group, on the other hand, do not appear to produce stimulus levels approaching that of steel, but they provide greater protection than all but the lowest impedance materials.

The effect of shield thickness is illustrated in Figure 8 which is a plot of $\int p^2dt$ versus shield thickness for Lucite, steel and tungsten. The results show that steel provides the least protection, except for shields less than about 6 mm thick where Lucite is worst, and tungsten provides the best protection except for shields between about 27 and 50mm thick where Lucite is slightly better. Stimulus reduction increases with shield thickness for all three materials. The increase is most marked for Lucite, which also shows a leveling off for shield thicknesses greater than 40 mm at which point little additional protection is provided with increasing thickness.

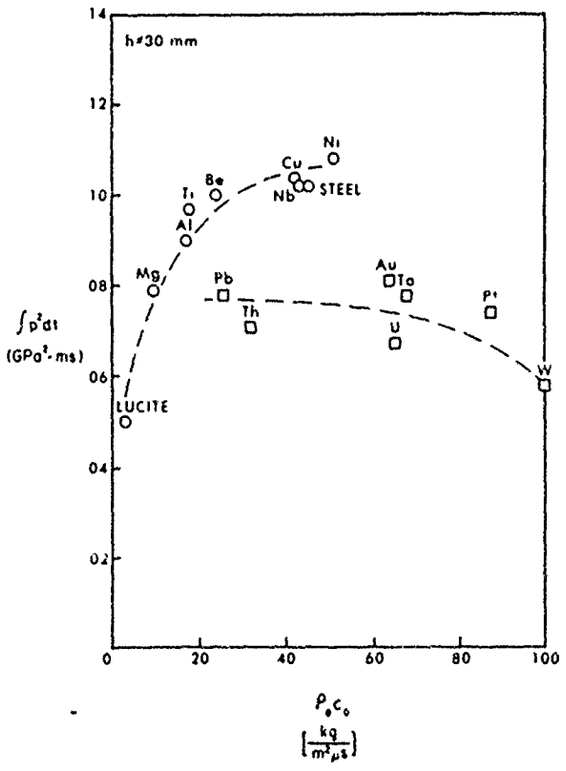

Fig 7. Variation of shock initiation stimulus with initial acoustic impedance for 30mm thick shields

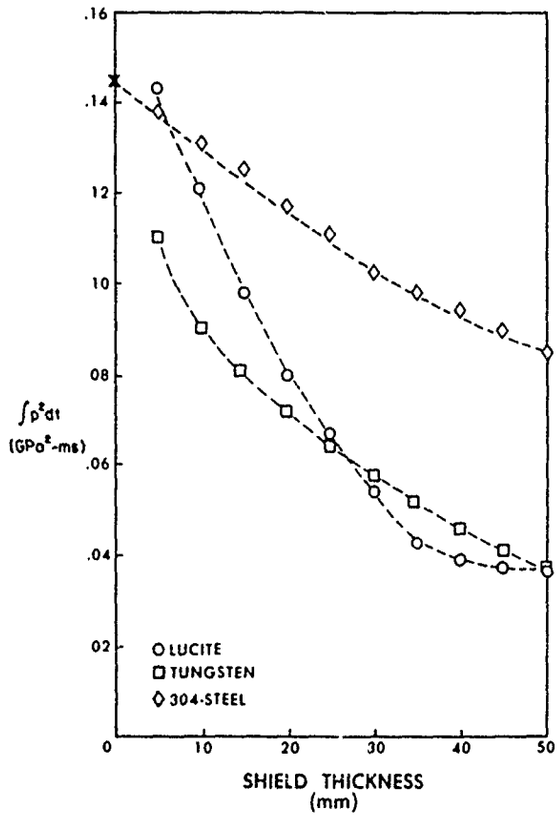

Fig. 8. Variation of shock initiation stimulus with shield thickness for Lucite, tungsten and 304-steel shields

RESULTS WITH MULTILAYERED SHIELDS

General. Shields with multiple layers provide additional impedance discontinuities which can further reduce the shock initiation stimulus. We have examined the effectiveness of three- and five-layered shields composed of alternate layers of our lowest and highest impedance materials, Lucite and tungsten, and of alternate layers of Lucite and steel as well. The order of the materials and the relative thickness of the layers was varied but, except in the study of shield thickness, all of the shields were 30mm thick. Symmetry was always maintained. The impact velocity was held at 1 km/s.

When the total shield thickness is fixed, three-layered shields may be completely specified by the Lucite thickness fraction (i.e. the total thickness of all Lucite layers divided by the shield thickness, h). With five-layered shields,

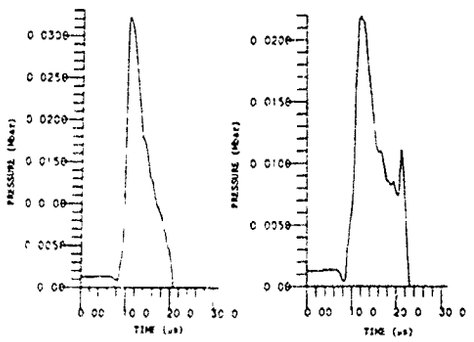

a. 8.3% Lucite *b. 16.7% Lucite*

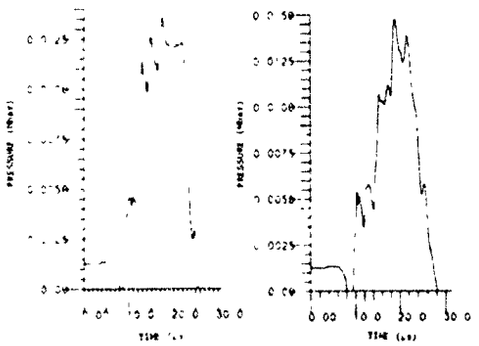

c. 33.3% Lucite *d. 50% Lucite*

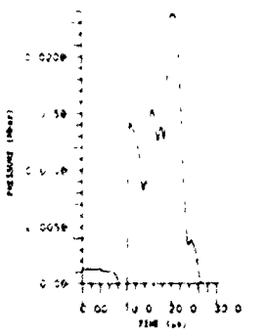

e. 91.7% Lucite

Fig 9 Acceptor explosive pressure history with 30mm thick three-layered tungsten/Lucite/tungsten shields

an additional degree of freedom arises since the thickness of the innermost layer need not equal the thickness of the two outer layers of the same material. This degree of freedom is accounted for by the parameter $z=h_i/(h-h_o)$ where h_i is the thickness of the central layer and h_o the thickness of the outer layers. When $z=0$, the shield is reduced to three layers; and when $z=h_i/h$, the shield also has three layers but with the material order reversed.

SHOCK STRUCTURE. Three-layered shields composed of Lucite and tungsten may have either component in the inner layer. Figure 9 illustrates the pressure history in the acceptor for shields consisting of an inner layer of Lucite surrounded by layers of tungsten. When the shield is composed mostly of tungsten, as in Figure 9a, a single shock enters the acceptor. Figure 9b shows results for a shield with a little more Lucite. Some structure at the tail of the wave may be noted but this is still primarily a single shock. With a still higher Lucite fraction, the shock structure is altered radically and multiple shock loading is observed as shown in Figures 9c through 9e. The transition to multiple shocks occurs somewhere between 17 and 33 percent Lucite and minimum pressure levels occur at about 33 percent Lucite.

When tungsten is the inner component of the shield, the results are somewhat different as illustrated in Figure 10. In this case a single pulse is usually produced but the peak pressure and rise time of the compression depend upon the Lucite thickness fraction as indicated in Table 2. This shows the pressurization rate to be minimum at about 50 percent Lucite. Multiple shock structure does not appear until the shield is nearly all Lucite as shown in Figure 10d.

The shock structure observed with steel/Lucite shields is essentially the same as that for the tungsten/Lucite shields with somewhat higher pressure levels. Therefore, pressure history plots are not reproduced here. The effect on compression wave characteristics for Lucite/steel/Lucite shields is summarized in Table 3. The pressurization rate is again minimized for about 50 percent Lucite.

Increasing shield thickness has considerable effect on shock breakup. This is illustrated in Figure 11 for 15, 25, 35, and 45mm thick three-layered shields having tungsten as the outer

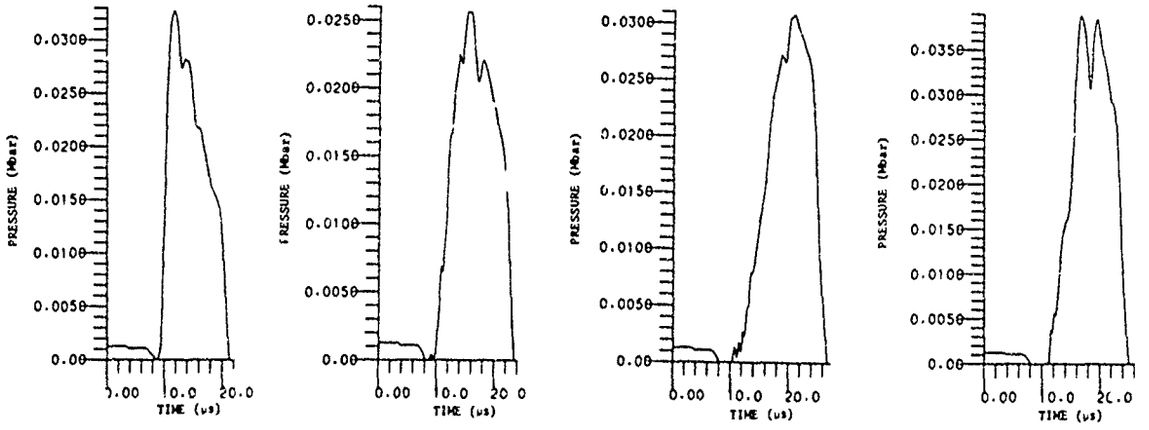

a. 16.7% Lucite *b. 33.3% Lucite* *c. 66.7% Lucite* *d. 91.7% Lucite*

Fig. 10. Acceptor explosive pressure history with 30mm thick three-layered Lucite/tungsten/Lucite shield

TABLE 2

Compression Wave Characteristics for Lucite/Tungsten/Lucite Shields

Shield Configuration (mm/mm/mm)	Lucite Fraction	Peak Pressure (GPa)	Rise Time (μs)	Pressurization Rate (GPa/μs)
1.25/27.5/1.25	.083	3.95	1.6	2.47
2.5/25.0/2.5	.167	3.28	3.5	0.94
5.0/20.0/5.0	.333	2.57	4.1	0.42
7.5/15.0/7.5	.500	2.40	10.0	0.24
10.0/10.0/10.0	.667	3.06	11.0	0.28
2.5/ 5.0/12.5	.833	3.81	9.5	0.40
13.75/ 2.5/13.75	.917	3.89	5.0	0.78

TABLE 3

Compression Wave Characteristics for Lucite/Steel/Lucite Shields

Shield Configuration (mm/mm/mm)	Lucite Fraction	Peak Pressure (GPa)	Rise Time (μs)	Pressurization Rate (GPa/μs)
1.25/27.5/1.25	.083	5.18	1.4	3.70
2.5/25.0/2.5	.167	4.61	2.1	2.20
5.0/20.0/5.0	.333	3.62	5.9	0.61
6.3/17.4/6.3	.420	3.62	7.0	0.52
7.5/15.0/7.5	.500	3.92	8.4	0.47
10.0/10.0/10.0	.667	4.10	6.2	0.67
12.5/ 5.0/12.5	.833	3.90	5.8	0.67
13.75/ 2.5/13.75	.917	3.43	5.0	0.49

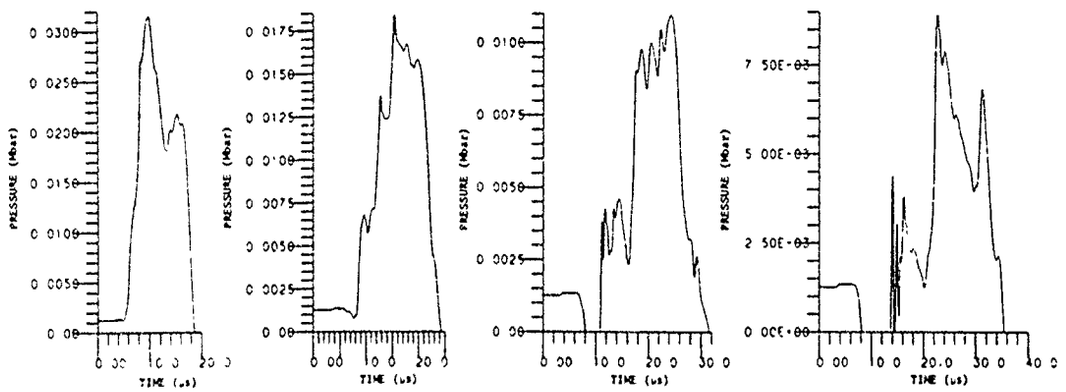

a. 15mm Thick *b. 25mm Thick* *c. 35mm Thick* *d. 45mm Thick*

Fig. 11. Acceptor explosive pressure history with 50% Lucite three-layered tungsten/Lucite/tungsten shields

component. Thin shields produce no breakup, presumably because the close spacing between impedance discontinuities produces closer temporal spacing between shocks leading to rapid coalescence. Figure 11a, for a 15mm thick shield, seems to show shocks which have just coalesced resulting in a compression wave with a higher rise time. On the other hand, Figure 11d, for a 45mm thick shield, shows the most shock breakup and peak pressure reduction we have seen in any of our computations.

Five-layered shields produced considerably less shock breakup than three-layered shields of the same thickness, both having tungsten as the outer component. This can be seen by comparing Figure 9d, for a 50 percent Lucite three-layered shield, with Figure 12, for a 50 percent Lucite five-layered shield. Again this presumably occurs because of the closer spacing between impedance discontinuities. This five-layered shield does produce a rise time of 6 to 7 μs.

Initiation Stimulus Reduction. Consideration of stimulus levels as characterized by $\int p^2dt$ allows a comparison of the effectiveness of these shields. Figure 13 is a plot of the relative stimulus level ($\int p^2dt$ normalized with respect to the value for the unshielded case) versus Lucite thickness fraction for tungsten/Lucite/tungsten and Lucite/tungsten/Lucite shields. Also included are scales of Lucite weight fraction and areal density. This comparison also shows that considerably better shield performance is obtained when tungsten is the outer component of the "sandwich." In fact, the performance of Lucite/tungsten/Lucite shields is inferior to that of either pure tungsten or pure Lucite except for a range of Lucite thickness fraction values between about 0.2 and 0.6 wherein performance is only a little better. It should be noted that this comparison is based on $\int p^2dt$ and does not take into account the differences between the ramp compressions produced when Lucite is the outer component and

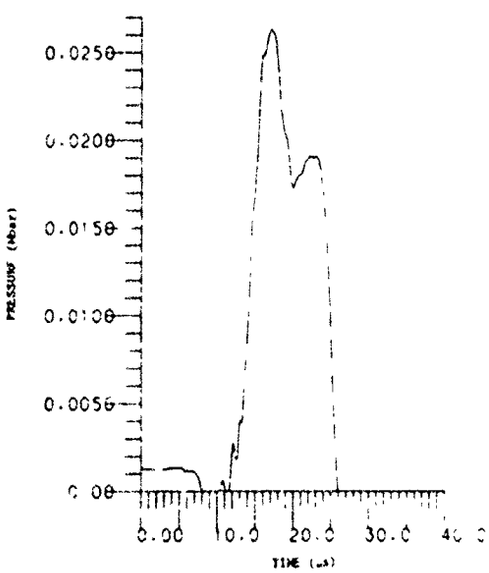

Fig. 12. Acceptor explosive pressure history with a 30mm thick 50% Lucite five-layered tungsten Lucite/tungsten/Lucite/tungsten shield

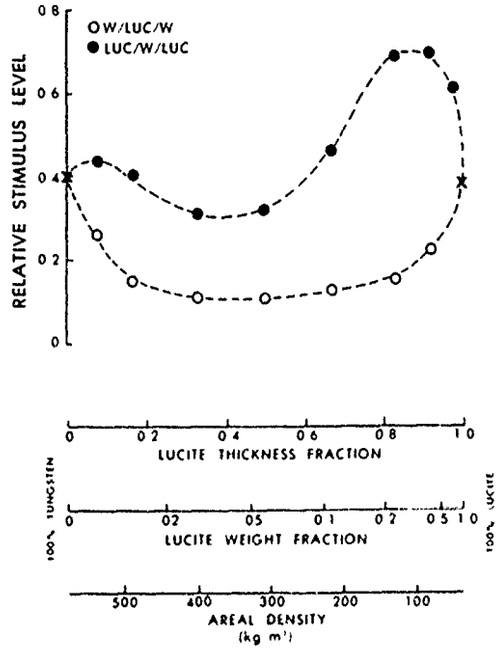

Fig. 13. Relative stimulus levels for 30 mm thick three-layered tungsten/Lucite shields

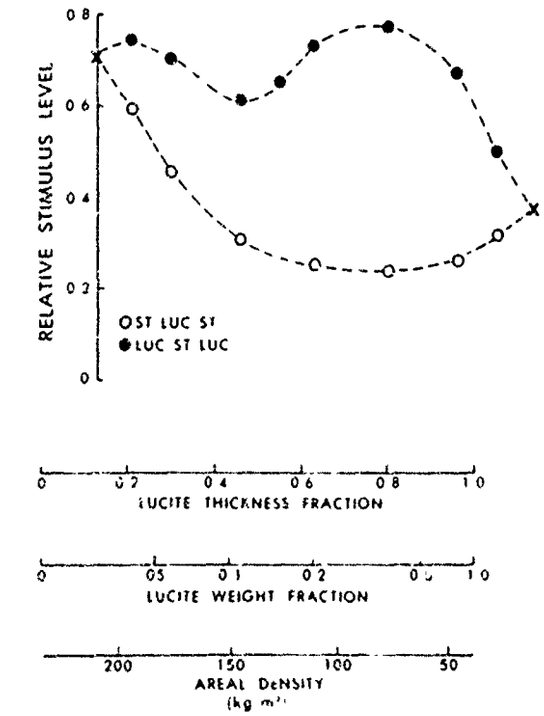

Fig. 14 Relative stimulus levels for 30 mm thick, three-layered steel/Lucite shields

the shock breakup and lower peak pressure produced when tungsten is the outer component. Indeed, the response of explosives to these complex waveforms is not well understood and experimental verification is required to determine which shield configuration is superior. However, it should be remarked that the predicted advantage of shields with tungsten on the outside is substantial.

Similar observations may be made for three-layered steel/Lucite shields as shown in Figure 14. The performance of tungsten/Lucite/tungsten shields is compared with that of steel/Lucite/steel shields in Figure 15. This shows that shields incorporating tungsten reduce the initiation stimulus to levels well below those produced by shields incorporating steel.

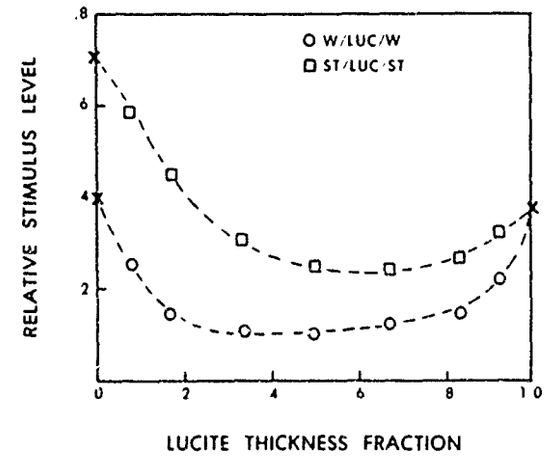

Fig. 15. Comparison of relative stimulus levels for 30mm thick, three-layered tungsten/Lucite and steel/Lucite shields

Shield thickness was varied in two different ways. Shields were varied from 10 to 50 mm in thickness with a constant 50 percent Lucite fraction in one case and from 20 to 50 mm with a constant 7.5mm outer tungsten layer thickness in the other. The results are plotted versus shield thickness in Figure 16. This shows little difference between the two types of variation and indicates a rapid decline in protection for shields less than about 30mm thick.

Results with five-layered shields were similar to those for three-layered shields but not as much protection was provided We first considered shields with inner and outer layers of equal thickness ($h_1 = h_0$). Figure 17 shows the

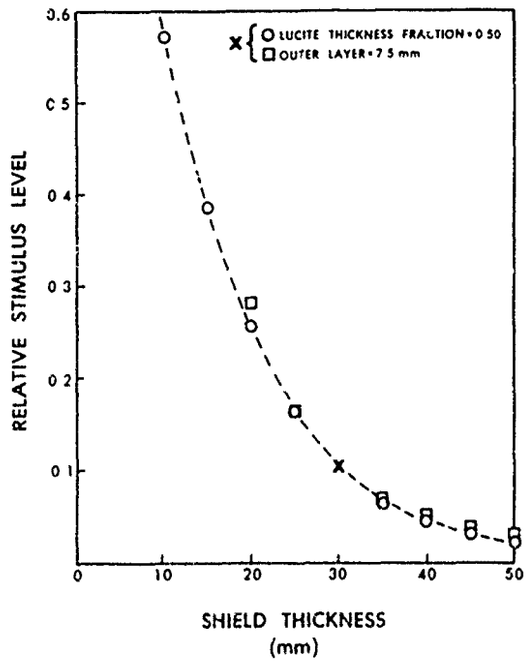

Fig 16. Effect of shield thickness on relative stimulus level for three-layered tungsten/Lucite/ tungsten shields

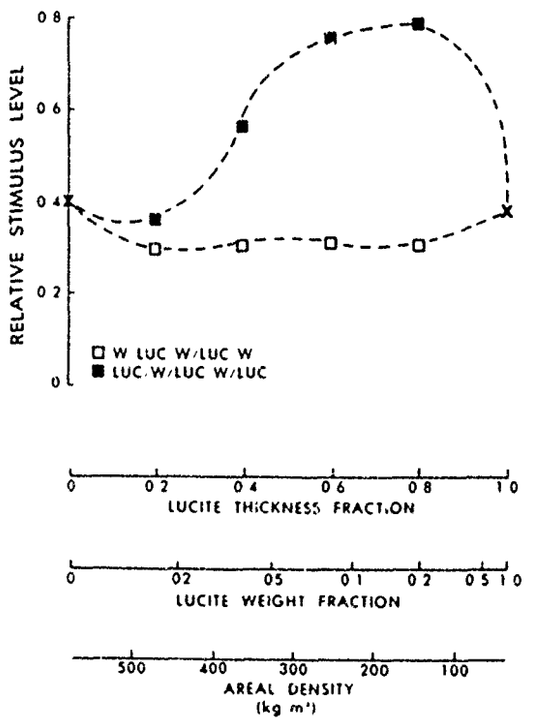

Fig 17 Relative stimulus levels for 30mm thick, five-layered tungsten/Lucite shields

comparison between shields with tungsten on the outside and shields with Lucite on the outside. Again, the former perform better but only slightly better than single-layered shields. Figure 18 shows the comparison between the best three-layered shields and the five-layered shields. The three-layered shields are substantially better. The performance of the five-layered shields with tungsten as the outer component is not strongly dependent on Lucite fraction. It is of interest to determine whether shields with unequal inner and outer layer thicknesses perform any better. We noted previously that the parameter z could be used as a measure of the relationship between these layers and that $z=0$ and $z=h_1/h$ correspond to three-layered shields. We fixed the Lucite thickness fraction at 0.33 and varied z between these limits. The results, shown in Figure 19, indicate a nonmonotonic variation between the two three-layered cases. The three-layered shield with tungsten on the outside still shows the best performance.

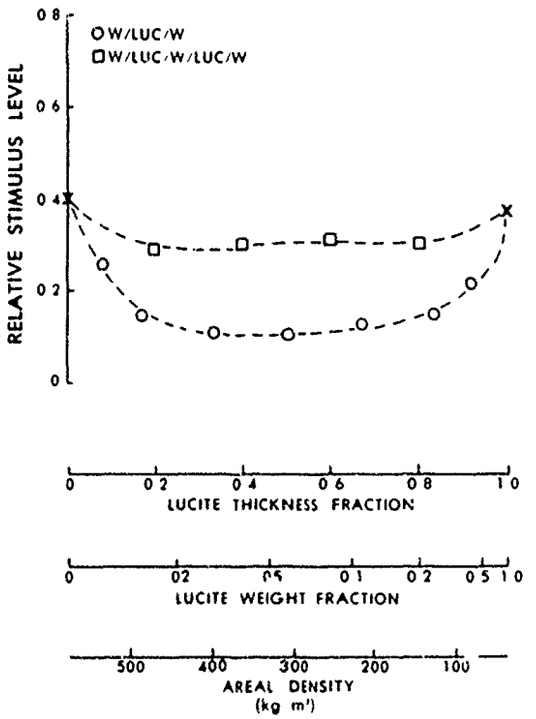

Fig 18. Comparison of relative stimulus levels for 30mm thick, three-layered and five-layered, tungsten/Lucite shields

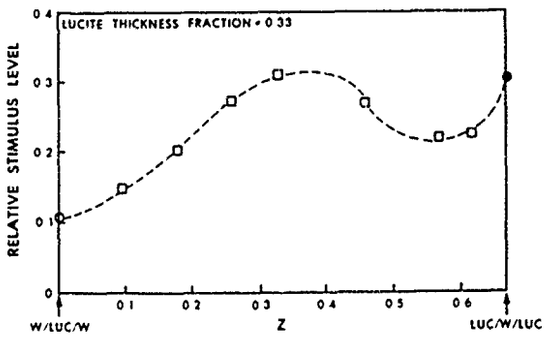

Fig. 19. Effect of shield configuration on relative stimulus level for 33.3% Lucite, three-layered and five-layered shields

SUMMARY

We have conducted a study of the role of shielding in reducing the shock initiation stimulus for a simple one-dimensional representation of the problem of sympathetic detonation of munitions. We found that single-layered shields made of materials with low acoustic impedance generally produce a complex shock wave structure in the acceptor. This complex structure is associated with a low level of initiation stimulus because of the breakup into several weaker shocks and the reduction of $\int p^2dt$. High impedance shield materials also substantially reduce the initiation stimulus, but without the accompanying shock breakup effect. Increasing shield thickness improves performance and can change the order of effectiveness of shield materials. With multilayered shields composed of a high-impedance and a low-impedance material we observed shock structures depending strongly on the ordering of the materials in the shield. Multiple shock structure was usually observed when the high impedance material was the outer component of the shield and sufficient low impedance material was present. Single compression waves with variable peak pressures and rise times were usually observed when the low-impedance material was the outer component of the shield. Substantial benefits in terms of shock breakup and $\int p^2dt$ reduction can be obtained by increasing the thickness of three-layered shields, which were found to perform better than five-layered shields

REFERENCES

1. P. M. Howe, Y. K. Huang and A. L. Arbuckle, "A Numerical Study of Detonation Propagation Between Munitions," Seventh Symposium (International) on Detonation, pp. 1055-1061, June 1981.
2. J. Starkenberg, Y. K. Huang and A. L. Arbuckle, "A Two-Dimensional Numerical Study of Detonation Propagation Between Munitions by Means of Shock Initiation," BRL Technical Report ARBRL-TR-02522, September 1983.
3. *STEALTH — A Lagrange Explicit Finite Difference Code for Solids, Structural, and Thermohydraulic Analysis,* Electric Power Research Institute, November 1981.
4. E. L. Lee and C. M. Tarver, "Phenomenological Model of Shock Initiation in Heterogeneous Explosives," Physics of Fluids, Volume 23, Number 12, pp. 2362-2372, December 1980.

ON THE ROLE OF SHOCK AND SHEAR MECHANISM IN THE INITIATION OF DETONATION BY FRAGMENT IMPACT

Philip M. Howe
US Army Ballistic Research Laboratory
US Army Materiel Command
Aberdeen Proving Ground, Maryland

The collection of experimental data on the impact response of explosives indicates that at least two mechanisms are involved. Much of the data are interpretable in terms of a classical shock initiation mechanism. Thus, the dependence of the initiation threshold velocity upon contact area of the impactor and independence of the threshold velocity upon length, to diameter ratios in excess of 0.25, are entirely consistent with classical shock initiation models which emphasize the importance of peak pressure and shock duration

Other data are quite clearly inconsistent with a classical shock initiation mechanism, but are consistent with a macroscopic shear mechanism. TNT was found to show evidence of an initiation mechanism controlled by macroscopic shear. Very weak evidence was found to support a macroscopic shear mechanism for Composition B. Evidence in the literature was found to support a shear controlled mechanism for porous tetryl.

INTRODUCTION

Slade and Dewey (1) conducted firings of right circular cylinders against tetryl and Composition B targets, with and without cover plates. They found that the velocity of 50 percent initiation was a function of the contact area, but not of the projectile mass nor of the form of the projectile behind the impacting surface. The targets were unconfined, except for the cover plates and were right circular cylinders of 3.8 cm or 5 cm diameters, and lengths of 2.54 cms. Detonation, if it occurred, was observed to occur within 5 microseconds after impact. The threshold velocity was reported to increase in a nearly linear fashion with increasing cover plate thickness. The dependence of the threshold velocity upon contact area, the lack of dependence upon projectile length (or mass), the effect of cover plate thickness, and the short times to detonation are all consistent with a classical shock initiation mechanism. Under conditions of classical shock initiation, the detonation threshold is a function of the peak pressure delivered to the explosive and the duration of the shock wave. The peak pressure is determined by the impact velocity and the material properties (principally the density) of the impactor and target. The duration of the shock wave is determined by rarefaction waves originating at free surfaces.

An analysis of the shock wave interactions resulting from projectile impacts on cased charges was reported by Frey, et al. (2). They assumed that the duration of the shock pressure in the explosive is controlled by rarefactions originating at the periphery of the projectile. For projectiles with length to diameter (l/d) ratios in excess of 0.25, this is certainly true, and leads to the conclusion that, if a shock initiation mechanism is operant, the threshold velocity for detonation should be independent of projectile length, for l/d 0.25. In addition, Frey's analysis indicates that the dependence of the threshold velocity upon cover plate thickness shall become very strong, once a thickness is reached such that the rarefaction

waves can interact with the shock front prior to the shock front entering the explosive (3). Until the rarefaction reaches the shock front, it will influence the duration of the shock, but not the peak pressure. Once the rarefaction reaches the shock front, the peak pressure will decay rapidly. At this point, the impact velocity required for initiation will increase rapidly with further increases in case thickness. Shown in Fig. 1 are Slade and Dewey's results for Composition B and tetryl. The data for Composition B are not extensive and do not show an effect. However, the data for tetryl, which extend to thicker cover plates, clearly show a break in the curve. This provides additional support for a shock initiation mechanism.

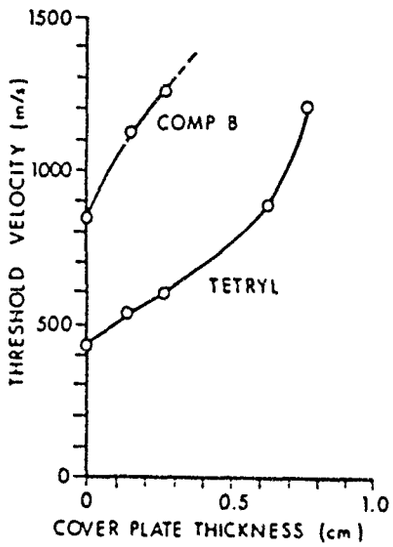

Fig 1 Threshold data for detonation of composition B and tetryl targets subjected to fragment impact, as function of cover plate thickness (Slade and Dewey)

Brown and Whitbread (4) reported a study on the initiation of bare charges by projectile impact. As part of this study, they compared the threshold velocities for initiation by impact of a 1.27 cm diameter steel projectile with the threshold brass shim thickness for which initiation occurred as a result of detonation of a 1.27 cm diameter donor charge (explosive type not mentioned) in contact with the shims. Results were reported for nine explosives, and are shown in Fig. 2. The data fall on a single straight line, which is to be expected, if the mechanism of initiation is the same for the two experiments.

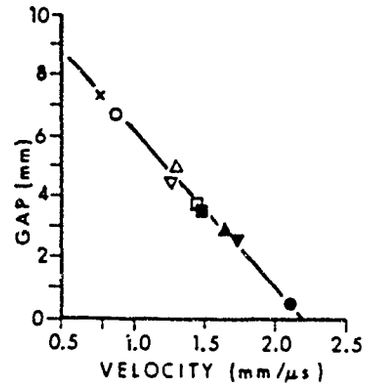

Fig. 2. Correlation of gap test data and fragment impact data (Explosive donors and fragments were both 1.27 cm diameter (Brown and Whitbread.)

In conducting their tests, Brown and Whitbread used thin aluminum flags, placed some distance away from the targets, to measure explosive response. The distance was chosen such that a full detonation bent the flag a total of 150°, and a bend of 10° or more was taken as a positive event. In each experiment, the impact velocity was varied in a step wise manner to determine the 50 percent threshold for a positive event. Thus, their observational procedure was not deliberately designed to focus upon detonations, to the exclusion of less violent reactions. However, in the absence of confinement, reactions which do not occur fast enough to support the impact shock have little opportunity to develop before rarefactions destroy the charge. Thus, the velocity increment separating no reactions from detonations is likely to be very small.

Brown and Whitbread varied both material and projectile length in projectile impact firings. Short projectiles were backed by Tufnol cylinders to provide flight stability. Results were obtained for RDX/PWX 83/17 and tetryl/TNT 9/91. For long projectile lengths, the threshold velocity for initiation becomes independent of length. Estimates were made of the projectile lengths at which the threshold velocities began to change drastically. Pulse durations for initiation, calculated by dividing twice the projectile length by the shock velocity,

were found to be essentially independent of projectile material. Using the minimum threshold velocities for each projectile material, associated with the long projectile asymptotes, critical pressures for initiation were compared, and it was noted that the Hugoniot curves all intersect at a common point (see Fig. 3). It is thus reasonable to assume that a critical pressure for initiation exists, in the limit of long duration pulses. These results provide strong evidence in support of a classical shock initiation mechanism.

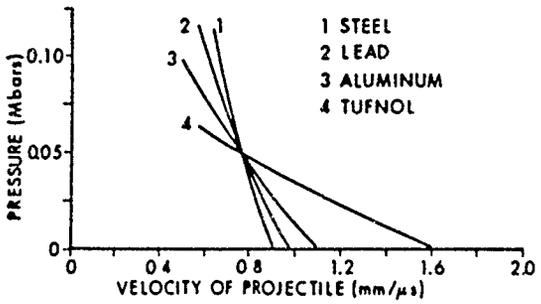

Fig. 3. Reflected Hugoniot curves, for various impactors, centered on the threshold velocity for each material type (The single point of interaction implies a single pressure generated in the explosive.)

Frey, et al., have shown that explosions in confined charges can result from impact in the mass velocity domain where classical shock initiation cannot be operant (2). However, these explosions, although violent, were clearly not detonations. Reeves has reported data for firings of right circular cylinders against heavily confined (steel wall thickness 1.03 cm) cylindrical Composition B targets (5). Howe has extended the database and the combined data span a variation in fragment mass from 2 to 300 g (6). These data showed that the ignition threshold for violent reaction is essentially coincident with the ballistic limit of the target casing (i.e., the impact velocity at which the casing is breached). Shock initiation was eliminated as a possible mechanism by (a) demonstrating that the ignition threshold was lowered when the ballistic limit was lowered by introducing a plug in the case and (b) by demonstrating that the ignition threshold (and the ballistic limit) was lower for l/d = 5 rods than for l/d = 1 cylinders. Additional experiments reported in Reference 5 indicated that heat transfer from casing plug or from the fragment was unlikely, and the ignition mechanism was identified as resulting from shear deformation in the explosive, resulting from the penetration process. There is thus considerable evidence that the ignition mechanism involves a shear heating process in the explosive, subsequent to, and a result of, casing performation by the attacking fragment. Since shear has been shown to play a strong role in the ignition process, and the mechanics of casing perforation apparently

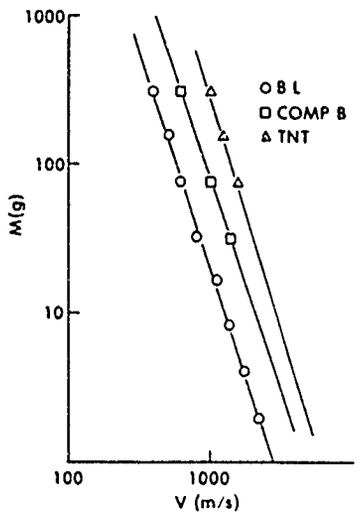

Fig. 4a. Threshold data for ignition and detonation of heavily confined Composition B targets

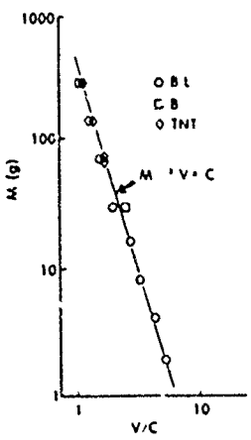

Fig. 4b. Scaled detonation threshold data, showing consistency with ballistic limit data

control the ignition threshold, the question arises as to whether or not a shear mechanism is also involved in the detonation threshold for impacts against heavily confined charges. The query also arises from comparison of the detonation threshold and ignition threshold data for heavily confined Composition B (Fig. 4a) where it appears that the detonation threshold data lie parallel to the ignition threshold data. The data can be fit by the relation $m^{1/3}V = c$, where c is a constant. Scaled data are shown in Fig. 4b.

THE ROLE OF SHEAR IN CAUSING DETONATION

A quasi-steady state model of the heating produced in a shear band or at a sliding interface was developed by Frey (7). The model includes heat transfer, plastic work, the heat of fusion of the explosive, and a viscosity law which depends upon temperature and pressure. For details of the calculation and detailed results, the reader is referred to the original paper. Of especial interest, however, is the shape of the ignition curve (Fig. 5) which shows that, for high sliding velocities, the ignition curve tends to become independent of pressure.

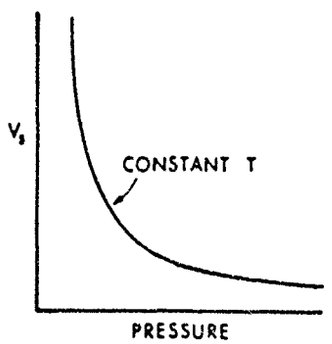

Fig. 5. Calculated ignition threshold data for TNT, showing influence of sliding velocity and pressure (after Frey)

To apply this model to initiation of detonation by fragment impact, we must not only have a description of the flow field, but also the distribution of shear bands within the flow field. No data with respect to the latter exist, so an alternate approach was taken: The impact conditions which cause detonation were examined to determine variations in the flow field, with the idea that fixing the flow field would fix

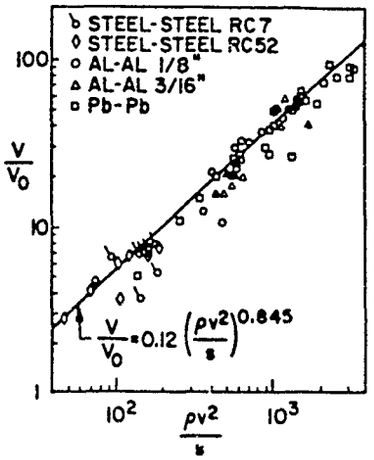

Fig. 6. Hypervelocity impact data, showing energy scaling of crater volume (after Sorensen)

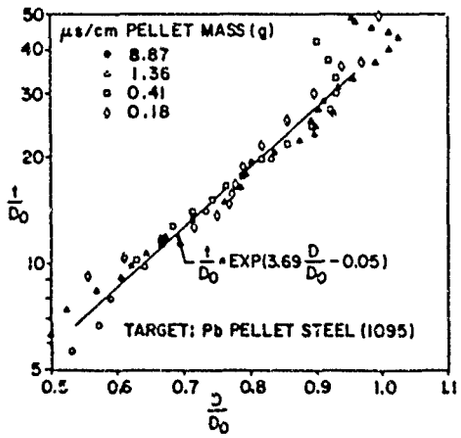

Fig. 7. Crater growth rate data, showing scaling of crater growth (after Kineke and Vital)

all velocities and velocity gradients and, in particular, would fix local shear velocities. Thus, if the flow field remains unchanged with variations in impact conditions along the detonation threshold, strong support for a shear dominated mechanism is obtained.

No direct data exist describing variations in the flow field for explosives subjected to fragment impact. However, considerable data exist for metal-metal impacts. In particular, data exist (8) which show that crater volume varies with impact energy (Fig. 6). Additionally, Kineke and Vitali (9) showed that crater growth rates also scale with impact energy (see Fig. 7). Thus, for metal-metal impacts in the hypervelocity regime, both crater size and growth rates

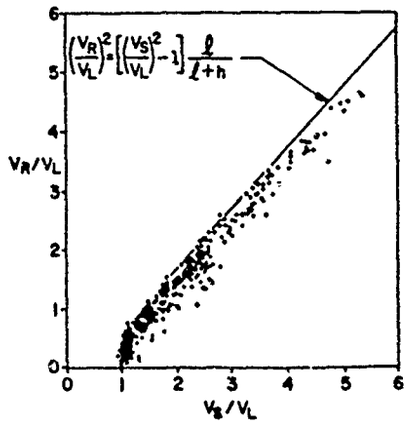

Fig. 8. Comparison of residual velocity equation with data of Ricchiazzi

(and hence, the velocity field) are determined by the impact energy. The assumption will be made that the same holds true for impacts on confined explosives; the flow field is determined by crater dimensions and growth rate, and these scale as the residual kinetic energy of fragment and plug after case perforation. The assumption is also made that geometric similarity of impactors preserves similarity of craters.

The initial residual energy can be estimated by performing an energy balance on the system. For a fragment of mass M_o impacting a casing of thickness h and have a velocity V_S, we have

$$\frac{M_o}{2} V_S^2 = \frac{M_o}{2} V_L^2 + \left(\frac{M_o+M_p}{2}\right) V_R^2 \qquad (1)$$

where V_L is the velocity required to fail the case (the ballistic limit velocity). V_R is the residual velocity, and M_p is the plug mass. Equation (1) can be arranged to give

$$\left(\frac{V_R}{V_L}\right)^2 = \left[\left(\frac{V_S}{V_L}\right)^2 - 1\right] \frac{\ell}{\ell + \alpha h} \qquad (2)$$

where ℓ is the length of the impacting fragment (right circular cylindrical geometry is assumed), h is the thickness of the target casing, and α is the ratio of plug and impactor diameters. This approximate equation for the residual velocity is shown with data provided by A. Ricchiazzi in Fig. 8 (10).

Equation (2) was combined with the assumption of no mass loss to calculate the initial residual energies for impacts at the detonation threshold for 300 g right circular cylindrical fragments against confined Composition B and Composition A-3 targets. The results are shown in Table 1, where it is seen that the residual energy, E, at the detonation threshold does not remain constant as the case thickness varied.

If the assumption is made that the residual mass for various case thicknesses is the same, then the calculated residual energies are constant along the detonation threshold. There is no a priori reason for assuming that the residual case thickness remains the same at the detonation threshold as case thickness is varied. Data on plug thickness versus impact velocity for various plate thicknesses were obtained from A. Ricchiazzi (10). These data were replotted in the plug thickness — residual velocity plane and are shown in Fig. 9. Note that, for fixed residual velocity, plug thickness is fixed, independent of target thickness, over the range of thicknesses and velocities for which data are available. Apparently, the competition between cratering and plugging phenomena lead to this unusual result. At any rate the plug thickness is a strong function only of the residual velocity and, for fixed residual velocity, is independent of initial plate thickness. Thus, total mass is independent of plate thickness, and a fixed residual velocity will yield a fixed residual energy. Note constancy of residual velocities and residual energies E′ in Table 1. The data for detonation thresholds for impacts against targets with various case thicknesses are therefore consistent with a shear mechanism.

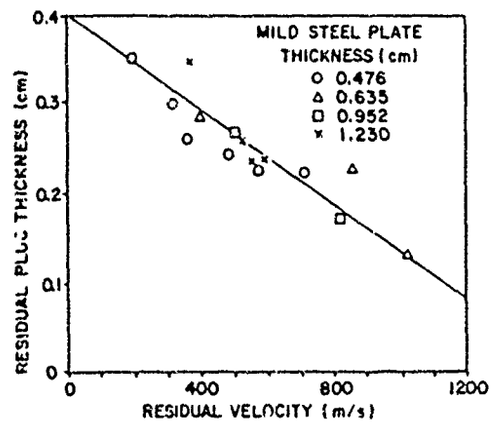

Fig. 9 Data of Ricchiazzi, showing that plug thickness is constant, for constant residual velocity, independent of initial target thickness

TABLE 1
Impacts by 300 g /d=1 Steel Cylinders

Explosive	(cm)	h(cm)	h′(cm)	V_S(M/s)	V_L(m/s)	V_R(m/s)	E(KCal)	E′(KCal)
A-3	3.66	0.35	0.26	525	150	472	9.07	8.79
A-3	3.66	1.06	0.26	703	457	450	10.20	7.99
A-3	3.66	1.85	0.26	816	480	507	15.75	10.14
B	3.66	1.06	0.29	650	457	389	7.63	6.03
B	3.66	1.60	0.29	760	575	391	8.84	6.09

E calculated residual energy assuming no mass loss.
E′ calculated residual energy assuming mass loss.

TABLE 2
Impacts Against Composition B with 1.06 cm Steel Confinement

m(g)	(cm)	h′(cm)	V_S(m/s)	V_L(m/s)	V_R(m/s)	E(KCal)	E′ (KCal)
300	3.66	0.39	637	457	386	7.06	6.14
75	2.30	0.23	1014	608	671	5.90	4.57
30	1.70	0.15	1600	874	1052	6.44	4.47

Data for constant case thickness and various fragment masses were presented in Fig. 4. Using the same assumptions as above, we calculate the residual energies to be as shown in Table 2, where the expression for the residual energy is given by

$$E' = 7.32 \times 10^{-7}\, t^2\, (t + 1.4h')\quad V_R{}^2 \qquad (3)$$

for the energy in KCal.

As can be seen the energy is essentially constant for the three data points available. Shown also in Table 2 are energies (E) calculated using the assumption that residual case thickness equals initial case thickness. In this instance, the calculations are relatively insensitive to these assumptions, as one might surmise from examination of equation (3).

It was noted earlier that, if classical shock initiation is controlling, the detonation threshold velocities will be independent of length, once an t/d ratio of 0.25 or greater is attained. This would not be expected to be the case for a shear controlled mechanism. For conditions of constant impact area, increased fragment length decreases the ballistic limit, and decreases the impact velocity required to deliver a fixed residual velocity (or residual energy). The threshold velocity for shear controlled detonations should thus decrease with increasing length of impactors. This provides the opportunity for a set of critical experiments to discriminate between shock shear mechanisms in initiation of detonation.

Firings with 300 g $t/d = 4$ right circular projectiles and 75 g, $t/d = 1$ right circular cylindrical projectiles were conducted against TNT filled targets with 1.06 cm thick steel casing. The impactor dimensions and masses were chosen to provide a variation in t/d at fixed impact area. If a classical shock initiation mechanism is operant, there should be no change in detonation threshold velocity. If, however, a shear mechanism is operant, the detonation threshold should be lower for the high t/d impactor, as it is a more efficient penetrator. The experimental detonation threshold for the $t/d=4$ fragments was found to be 1414 m/s, with a σ of 143 m/s. The detonation threshold for an $t/d = 1$ impactor with the same frontal area was found to be 1580 m/s, with a σ of 27 m/s. The difference in thresholds

is not great, nor was it expected to be, as the dependence of the ballistic limit velocity on t/d is very weak (only to the 1/6 power). However, the difference is clearly statistically significant.* The results are inconsistent with a classical shock mechanism, but are consistent with a shear mechanism.

The experimental threshold for detonation for 300 g t/d =4 impactors against Compositon B filled targets was found to be 1008 m/s, with a σ of 25 m/s vs. 1019 m/s, with a σ of 15.2 m/s, for the 75 g t/d=1 impactor. These firings were conducted using tool steel at a Brinnell hardness of 180. Target casing hardness was Rockwell B 86. Upon impact, the impactor was found to mushroom significantly. The series was repeated with steel impactors hardened to Rockwell C 55. At this hardness, little mushrooming occurs, and the impactor was expected to be a more efficient penetrator. The measured detonation threshold was found to be 989 m/s. The measured detonation threshold was 989 m/s, with a σ of 24.2 m/s. This difference is quite small, and is not significant at the 0.05 level.**

In Slade and Dewey's report (1), data are presented for impacts on Composition B targets with 6 mm mild steel cover plates, by hardened steel projectiles. Here, it was found that by increasing the mass of the projectiles from 17.7g to 36.7g at fixed diameter of 1.27 cm, the detonation threshold was lowered from 906 +/− 21 m/s to 778 +/− 9 m/s. These values are significantly different at the 0.01 level. Note that both the 17.7 g and 36.7 g impactors had t/d ratios higher than unity. These data are inconsistent with a classical shock initiation mechanism, but are entirely consistent with a shear initiation model. This threshold dependence upon impactor mass (or length, more appropriately) is a direct manifestation of interactions between the impactor and the target casing.

The effect of length of impactor on tetryl is especially surprising for two reasons. These data were gathered for tetryl at a loading density of 1.50 g/cc, which is only 86% of theoretical maximum density. In such porous charges, classical shock initiation would be expected to dominate. Secondly, these targets were relatively unconfined, with cover plates and no rear confinement. For a shear mechanism to be controlling, it must occur within a very short time frame, of the order of that for first wave passage through the charge.

It is instructive to compare the detonation threshold data for Composition B, shown in Fig. 4, with threshold data for Composition B gathered by other investigators. Shown in Fig. 10 are the data of Slade and Dewey (1) and Roslund (11) for Composition B targets with flat cover plates and the data from Fig. 4, plotted in the $V_d^{1/2}$ − h/d plane. (This is a particularly useful representation, for data in the shock initiation regime, as it has been shown by several investigators that, for bare charge data, $V_d^{1/2} = A$, where A is a constant for a given explosive at a given density. Thus, variation of A with h/d is a measure of the effectiveness of the cover plate in protecting the explosive from shock initiation.) It is quite clear from Fig. 10 that the two sets of data are not consistent. There is a number of different possible reasons for the difference, in addition to a shear-controlled mechanism for the heavily confined charges, vs. a shock mechanism. Some are examined below:

1. Differences in porosity; the Slade data were gathered on Composition B at 1.70 g/cc, the Roslund data at 1.68 g/cc, and the heavily confined data at 1.65 g/cc. These differences in porosity can produce significant differences in sensitivity. While changes in porosity would be expected to affect the intercept of the threshold curves with the ordinate (i.e., the bare charge threshold) it is not clear that it would affect the slope significantly. To check this point, data of Slade and Dewey for tetryl at a density of 1.50 g/cc (86% TMD), data of Slade and Dewey for Composition B at a density of 1.70 (97% TMD), and of Roslund for Composition B at a density of 1.68 (96.6% TMD) are replotted in Fig. 11, where each data set has been scaled by the

* Statistical tests, assuming that the estimate populations are each normally distributed and that the variance is known, place the significance between 0.004 and 0.025.

** A statistical test for significance, again assuming normality and known variance, yielded an α of 0.064. We thus have a ~6.4% chance of being wrong, if we claim that the V_{50}'s are different for t/d = 1 and t/d = 4 against Composition B.

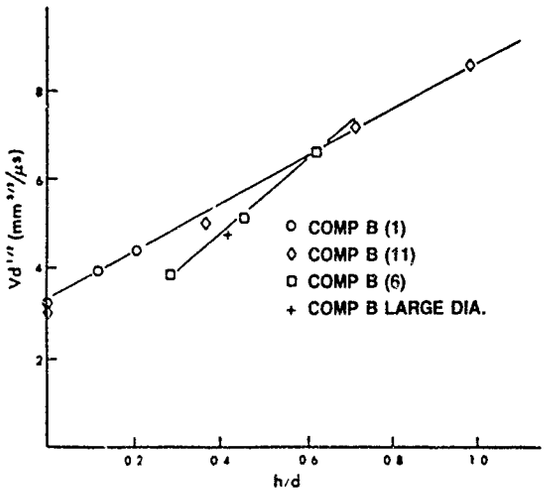

Fig. 10. Detonation threshold data for charges with cover plates and heavily confined charges

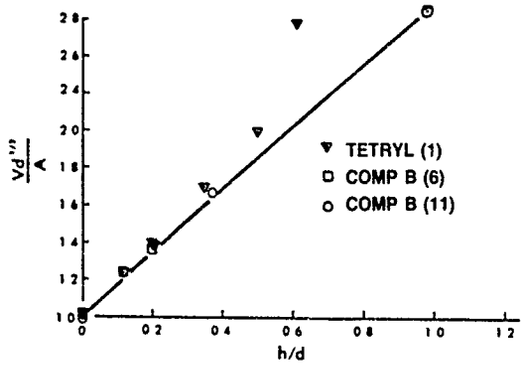

Fig. 11. Scaled detonation threshold data from (1) and (11) showing that porosity does not affect plate thickness dependence

appropriate value of A. Note that, for values of h/d < 0.6, the data sets are coincident. For larger values of h/d, the tetryl data curve upward, while the Composition B data remain linear. Ultimately, the Composition B data should curve upward, also. The upward curvature is believed to be a result of the rarefactions overtaking the shock and reducing the peak pressure, thereby requiring a higher impact pressure for prompt initiation of detonation. This happens earlier in the tetryl with its high porosity and correspondingly low shock speed. For the lower values of h/d, however, the data for impacts against charges with flat cover plates scale, independent of porosity, and the deviation of the data for heavily confined Composition B cannot be explained by effects of porosity.

2. Reflection of the incident shock wave from the rear surface of the casing; if initiation does not occur as a result of passage of the incident shock, reflection of the shock from the rear surface could cause initiation. Since decay of the incident shock waves scales with the impactor dimensions, the strength of the reflected shock from the 300 g fragment would be larger at a given impact velocity than that for a smaller fragment. This would tend to tilt the curve for the heavily confined charges to a greater slope, and thus is consistent with the data. This effect is strongly dependent upon charge size, and one would expect data for larger charges to lie above this curve. The data in this curve were gathered for targets with an interior diameter of 84 mm. Plotted on the curve is an additional point for a target with an interior diameter of 123 mm which, if this effect is important, should lie above the curve. Apparently, shock reflection at the rear surface is not controlling. (See Fig. 10.)

3. Confinement: Slade and Dewey used tetryl charges 3.8 cm in diameter by 2.54 cm thick and Composition B charges 5 cm in diameter by 2.54 cm thick. Impacts were upon the flat surface. Cover plates, when present, provided the only confinement. Roslund's data were gathered using targets with greater confinement, but confinement was still light. Howe's data were gathered on targets with heavy cylindrical confinement, with dimensions such that end effects could not participate for times shorter than 200 microseconds. In Slade and Dewey's experiments, the limiting times are determined by shock transit through the charge, and are of the order of 5-10 microseconds. In the experiments using heavily confined charges, times to case failure are in excess of 100 microseconds. However, time to case perforation can be much faster, and will vary with impact velocity. If it is assumed that venting can occur when the plug has moved one case thickness, times to venting can be estimated by dividing the case

TABLE 3

m(g)	h(mm)	V_s(m/s)	V_R(m/s)	t(s)
300	10.6	637	386	20.7
75	10.6	1014	671	12.6
30	10.6	1600	1052	8.0

thickness by the average of the impact and residual velocities at the detonation threshold. These estimated results are shown in Table 3, where it is seen that time to venting is much greater for the large fragments impacting at relatively low velocities. This greater time to venting for the low impact velocities could have the effect of lowering the detonation threshold and provides a plausible explanation for the difference between the two sets of data.

SUMMARY AND CONCLUSIONS

The collection of experimental data on the impact response of explosives indicates that at least two mechanisms are involved. Much of the data are interpretable in terms of a classical shock initiation mechanism. Thus, the dependence of the initiation threshold velocity upon contact area of the impactor and independence of the threshold velocity upon impactor length, for length to diameter ratios in excess of 0.25, are entirely consistent with the classical shock initiation models which emphasize the importance of peak pressure and shock duration.

Other data are quite clearly inconsistent with a classical shock initiation mechanism, but are consistent with a macroscopic shear mechanism. TNT was found to show evidence of an initiation mechanism controlled by macroscopic shear. Evidence in the literature was found to support a shear controlled mechanism for porous tetryl. The evidence to support a macroscopic shear mechanism in heavily confined Composition B charges is very weak. An unambiguous explanation for the differences between results for impacts against heavily confined targets and targets with cover plates is not yet available.

The conditions which favor one mechanism over another are not yet well defined. Hardened steel projectiles favor a shear mechanism, since they are more efficient penetrators than mild steel projectiles which can deform readily upon impact. We expect that impact conditions which generate weak shocks but which lead to high deformations and deformation rates within the explosive will favor shear initiation. Those impacts which cause strong shock loading with little deformation will favor classical shock initiation.

ACKNOWLEDGMENTS

The author is pleased to acknowledge many helpful discussions with Mr. Barry Bodt, Mr. Jerry Watson, Dr. Robert Frey, and John Starkenberg, all of the Ballistic Research Laboratory.

REFERENCES

1. Slade, D. C., Dewey, J., "High Order Initiation of Two Military Explosives by Projectile Impact," ARBRL-TB-1021, Ballistic Research Laboratory. Aberdeen Proving Ground, MD (1957).

2. Frey, R., et al., "Initiation of Violent Reaction by Project Impact," Sixth Symposium (International) on Detonation, ACR-221, Naval Surface Weapons Center, White Oak, Silver Spring, MD (1976).

3. The author thanks Dr. Robert Frey for valuable discussion on this issue.

4. Brown, S., Whitbread, F., "The Initiation of Detonation by Shock Waves of Known Duration and Intensity," Le Ondes De Detonation, editions Du Centre National De la Recherche Scientifique 15, Quai Anatole-France (VII) p. 97 (1962).

5. Reeves, H., "An Empirically Based Analysis on the Response of HE Munitions to Impact by Steel Fragments," ARBRL-MR-2031, Ballistic Research Laboratory, Aberdeen Proving Ground, MD (1970).

6. Howe, P. et al., "The Response of Confined Explosive Charges to Fragment Attack," Sixth Symposium (International) on Detonation, ACR-221, Naval Surface Weapons Center, White Oak, Silver Spring, MD (1976).

TABLE 3

m(g)	h(mm)	V_s(m/s)	V_R(m/s)	t(s)
300	10.6	637	386	20.7
75	10.6	1014	871	12.6
30	10.6	1600	1052	8.0

thickness by the average of the impact and residual velocities at the detonation threshold. These estimated results are shown in Table 3, where it is seen that time to venting is much greater for the large fragments impacting at relatively low velocities. This greater time to venting for the low impact velocities could have the effect of lowering the detonation threshold and provides a plausible explanation for the difference between the two sets of data.

SUMMARY AND CONCLUSIONS

The collection of experimental data on the impact response of explosives indicates that at least two mechanisms are involved. Much of the data are interpretable in terms of a classical shock initiation mechanism. Thus, the dependence of the initiation threshold velocity upon contact area of the impactor and independence of the threshold velocity upon impactor length, for length to diameter ratios in excess of 0.25, are entirely consistent with the classical shock initiation models which emphasize the importance of peak pressure and shock duration.

Other data are quite clearly inconsistent with a classical shock initiation mechanism, but are consistent with a macroscopic shear mechanism. TNT was found to show evidence of an initiation mechanism controlled by macroscopic shear. Evidence in the literature was found to support a shear controlled mechanism for porous tetryl. The evidence to support a macroscopic shear mechanism in heavily confined Composition B charges is very weak. An unambiguous explanation for the differences between results for impacts against heavily confined targets and targets with cover plates is not yet available.

The conditions which favor one mechanism over another are not yet well defined. Hardened steel projectiles favor a shear mechanism, since they are more efficient penetrators than mild steel projectiles which can deform readily upon impact. We expect that impact conditions which generate weak shocks but which lead to high deformations and deformation rates within the explosive will favor shear initiation. Those impacts which cause strong shock loading with little deformation will favor classical shock initiation.

ACKNOWLEDGMENTS

The author is pleased to acknowledge many helpful discussions with Mr. Barry Bodt, Mr. Jerry Watson, Dr. Robert Frey, and John Starkenberg, all of the Ballistic Research Laboratory.

REFERENCES

1. Slade, D. C., Dewey, J., "High Order Initiation of Two Military Explosives by Projectile Impact," ARBRL-TB-1021, Ballistic Research Laboratory. Aberdeen Proving Ground, MD (1957).

2. Frey, R., et al., "Initiation of Violent Reaction by Project Impact," Sixth Symposium (International) on Detonation, ACR-221, Naval Surface Weapons Center, White Oak, Silver Spring, MD (1976).

3. The author thanks Dr. Robert Frey for valuable discussion on this issue.

4. Brown, S., Whitbread, F., "The Initiation of Detonation by Shock Waves of Known Duration and Intensity," Le Ondes De Detonation, editions Du Centre National De la Recherche Scientifique 15, Quai Anatole-France (VII) p. 97 (1962).

5. Reeves, H., "An Empirically Based Analysis on the Response of HE Munitions to Impact by Steel Fragments," ARBRL-MR-2031, Ballistic Research Laboratory. Aberdeen Proving Ground, MD (1970).

6 Howe, P. et al., "The Response of Confined Explosive Charges to Fragment Attack," Sixth Symposium (International) on Detonation, ACR-221, Naval Surface Weapons Center, White Oak, Silver Spring, MD (1976)

7. Frey, R. B. "The Initiation of Explosive Charges by Rapid Shear," Seventh Symposium (International) on Detonation, NSWC-MP-82-334, Naval Surface Weapons Center, White Oak, Silver Spring, MD (1981).

8 .Sorensen, N., "Systematic Investigation of Crater Formation," Proceedings, Seventh Hypervelocity Impact Symposium, Tampa, FL, p. 281ff (1964).

9. Kineke, J., Vitali, R., "Transient Observations of Crater Formation in Semi Infinite Targets," Proceedings, Sixth Symposium on Hypervelocity Impact, Cleveland, OH, p. 457ff (1963).

10. Ricchiazzi, A., Ballistic Research Laboratory, Aberdeen Proving Ground, MD, private communication.

11. Roslund, L. A., Watt, J. W., Coleburn, N. L., "Initiation of Warhead Explosives by the Impact of Controlled Fragments I. Normal Impacts," NOLTR 73-124, Naval Surface Weapons Center, White Oak (1973).

8TH DETONATION SYMPOSIUM REGISTRANTS

M. Taylor Abegg
Megabar Corporation
2200 West 4100 North
Ogden, UT 84404

Jean-Claude Adenis
CEA Vaujours, BP No. 7
Courtry, France 77181

Eileen Aitken-Sahm
Lockheed Miss. & Space
P. O. Box 3504, Bldg. 157,0/83-20
Sunnyvale, CA 94088-3504

Irving B. Akst
Los Alamos National Laboratory
MS J960, M-3
Los Alamos, NM 87545

W. Hoyt Andersen
TRW
P. O. Box 1310
San Bernandino, Ca 92402

Allen B. Anderson
Los Alamos National Laboratory
MS P952, M-8
Los Alamos, NM 87545

David H. Anderson
Sandia National Laboratory
P. O. Box 5800, Dept. 2510
Albuquerque, NM 87185

Erwin W. Anderson
NSWC
R-11, 10901 New Hampshire
Silver Spring, MD 20903-5000

George Andrews
Los Alamos National Laboratory
P952, M-9
Los Alamos, NM 87545

William J Andrzejewski
Sandia National Laboratory
Div. 2512
Albuquerque, NM 87185

Clifford Aseltine
Schlumberger Perforating Center
P O. Box A
Rosharon, TX 77583

James L. Austing
IIT Research Institute
10 W. 35th Street
Chicago, IL 60616

Jean Aveille
CEA
Centre D'Etudes De Vaujours
Courtry, France 77181

Dorit Ayalon
Government of Israel
P. O. Box 2250
Haifa, Israel 31021

Melvin R. Baer
Sandia National Laboratory
Div. 1513
Albuquerque, NM 87185

Kerry L. Bahl
Lawrence Livermore National Laboratory
L-368, P. O. Box 808
Livermore, Ca 94550

Larry Bailey
Hewlett-Packard
1700 So. Baker Street
McMinnville, OR

Ted Bakowsky
California Research & Tech. Inc.
5117 Johnson Drive
Pleasanton, CA 94566

Ram Bar-Or
Rafael-ADA
P. O. Box 2250
Haifa, Israel 31021

Gadi Barak
ADA
P. O. Box 2250
Haifa, Israel 31021

Richard D. Bardo
NSWC
Silver Spring, MD 20903-5000

W. David Barfield
Los Alamos National Laboratory
MS B214, T-14
Los Alamos, NM 87545

Steven G. Barnhart
Sandia National Laboratory
Albuquerque, NM 87185

Edward E. Baroody
NSWC
R11, Bldg. 600
Indian Head, MD 20640

Jude Barry
Aerojet Tactical Systems, Bldg. 0525
P. O. Box 13400
Sacramento, CA

J. Bassett
RARDE
Fort Halstead
Sevenoaks, Kent TN14 7BP
United Kingdom

Pascal A. Bauer
Lab. Energetique et de Detonique
Ensma Rue Guillaume
Poitiers, Cedex, France 86034

Jacques G. Baute
CEA
BP No. 27
Villeneuve St. Georges, France 94190

Alain Becuwe
SNPE
Centre de Recherches du Bouchet
Vert le Petit, France 91710

Larry Behrmann
Schlumberger Perforating Center
P. O. Box A
Rosharon, TX 77583

Conrad Belanger
Defence Res. Estab.
P. O. Box 8800
Courcelette, Valcartier, Quebec, Canada

Ken Bell
New Mexico Engineering Research Inst.
Campus P. O. Box 25
Albuquerque, NM 87131

William B. Benedick
Sandia National Laboratory
Div. 1131
Albuquerque, NM 87185

Robert F. Benjamin
Los Alamos National Laboratory
MS J970, M-6
Los Alamos, NM 87545

Karl E. Bennett
MICOM
AMSMI-RHE
Redstone Arsenal, AL 35898-5245

Gian Paolo Berengan
Mariconavarmi-Ministry of Defence
(Navy)
Roma, Italy

Nicholas E. Berkholtz
Honeywell Inc.
5901 So. County Rd. 18
Edina, MN 55436

Richard R. Bernecker
NSWC
10901 New Hampshire Ave.
Silver Spring, MD 20903-5000

Robert W. Bickes, Jr.
Sandia National Laboratory
Albuquerque, NM 87185

Gert O. Bjarnholt
SveDeFo
Box 32058
Stockholm, Sweden 12611

Normand C. Blais
Los Alamos National Laboratory
G738, CHM-2
Los Alamos, NM 87545

George H. Bloom
Lawrence Livermore National Laboratory
L-368, P. O. Box 808
Livermore, CA 94550

Brian Boggs
Ensign Bickford
660 Hopmeadau
Simmsburg, CT 06070

Thomas L. Boggs
Naval Weapons Center
Code 389
China Lake, CA 93555

Michel Bouchu
CEA, BP No. 7
Courtry, France 77181

Antonio Bourgoade
CEA, Centre de Limeil
BP 27
Villeneuva-St. Georges, France 94190

Allen L. Bowman
Los Alamos National Laboratory
B214, T-14
Los Alamos, NM 87545

Price W. Boyd
BDM Advanced Technology Center
P. O. Box 1500
Huntsville, Al 35801

Floyd H. Braaten
Sandia National Laboratory
Div. 2512
Albuquerque, NM 87185

Jean-Claude Brard
CEA
Cesta BP 2, Le Barp
Belin-Beliet, France 33170

R. Don Breithaupt
Lawrence Livermore National Laboratory
L-368
Livermore, CA 94550

J. Russell Brinkman
Monsanto/Mound
P. O. Box 32
Miamisburg, OH 45342

Christian G. Brochet
ENSMA Rue Guillaume
Poitiers, France 8600

Michael Bucher
Naval Weapons Station
Code 321
Concord, CA 94520

Patrick D. Buckley
New Mexico Tech
Workman 221, Campus Sta.
Socorro, NM 87801

Surya N. Bulusu
US ARDC, EMD, LCWSL,
Bldg. 3028
Dover, NJ 07801

Garn Butcher
Hercules
P. O. Box 98
Magna, UT 84044

P. Barry Butler
Univ. of IA
2208 Engineering Bldg.
Iowa City, IA 52242

William Byers Brown
Univ. of Manchester
Dept. of Chemistry
Manchester, MI3 9PL
United Kingdom

Howard W. Cady
Los Alamos National Laboratory
C920, M-1
Los Alamos, NM 87545

Dominic J. Cagliostro
Los Alamos National Laboratory
MX P940, M-4
Los Alamos, NM 87545

A Wayne Campbell
Los Alamos National Laboratory
MS J960, M-8
Los Alamos, NM 87545

C. A. Campos
Mason & Hanger
P. O. Box 30020
Amarillo, TX 79177

Frank M. Caprio
BMD Corporation
2227 Drake Ave.
Huntsville, AL 35805

Joseph Carleone
Aerojet Ordnance
2521 Michelle Drive
Tustin, CA

William J. Carter
Los Alamos National Laboratory
MS P940, M-4
Los Alamos, NM 87545

Francis Chaisse
CEA
Centre D'Etudes De Vaujours
Courtry, France 77181

May Chan
Naval Weapons Center
China Lake, CA 93555

Jacque Charest
Dynasen
20 Dean Arnold Place
Goleta, CA 93117

Henry H. Chau
Lawrence Livermore National Laboratory
L-368,
Livermore, CA 94550

Mohammad M. Chaudhri
Cavendish Laboratory
Madingley Rd.
Cambridge, United Kingdom

John C. Cheng
Monsanto, Bldg. 70
P.O. Box 32
Miamisburg, OH 45342

Roger Cheret
CEA
Center D'Etudes de Vaujours
Courtry, France 77181

Chris Cherry
Naval EOD Tec. Center
Code 05-2A
Indian Head, MD 20640

Lalit C. Chhabildas
Sandia National Laboratory
Div. 1534
Albuquerque, NM 87185

William C. Chiles
Los Alamos National Laboratory
MS J960, M-9
Los Alamos, NM 87545

Raymond P. Chirat
CEA
BP No. 27
Villeneuve-St. Georges, France 94190

Tien Chou
Monsanto Mound
Box 32
Miamisburg, OH 45342

Allen B. Church
Sandia National Laboratory
P.O. Box 5800
Albuquerque, NM 87185

Stephen G. Cochran
Lawrence Livermore National Laboratory
L-35, P. O. Box 808
Livermore, CA 94550

Charles S. Coffey
NSWC
Silver Spring, MD 20903-5000

Graham D. Coley
AWRE
Aldermaston, Reading
RG7 4PR United Kingdom

J. Connor
RARDE
Fort Halstead
Sevenoaks, Kent TN14 7BP
United Kingdom

Paul W. Cooper
Sandia National Laboratory
Div. 7132
Albuquerque, NM 87185

George E. Cort
Los Alamos National Laboratory
MS G787, WX-4,
Los Alamos, NM 87545

M. Costantino
Lawrence Livermore National Laboratory
L-324
Livermore, CA 94550

Michael Cowperthwaite
SRI International
333 Ravenswood
Menlo Park, CA 94025

Paul J. Coyne
Loyola College
4501 N. Charles St.
Baltimore, MD

Gerald G. Craddock
LTV Aerospace & Defense
MS TH-28, P. O. Box 225907
Dallas, TX 75265

Bobby G. Craig
419 Marion Drive
Niceville, FL 32578

Carl T. Cuddihy
Lawrence Livermore National Laboratory
L-125
Livermore, CA 94550

James M. Culver
Strategic Systems Program Office
SSPO/SP-27311
Washington, DC 20376

John C. Cummings
Sandia National Laboratory
Div. 2512
Albuquerque, NM 87185

C. James Dahn
Safety Consulting Engr.
5240 Pearl Street
Rosemont, IL

[illegible] C. Dallman
Los Alamos National Laboratory
MS J960, M-9
Los Alamos, NM 87545

Donald E. Davenport
Tracor/MBA
P.O. Box 196
San Ramon, CA

William C. Davis
Los Alamos National Laboratory
MS J960, M-9
Los Alamos, NM 87545

Lee W. Davison
Sandia National Laboratory
Div. 1534,
Albuquerque, NM 87185

Rich Delanni
Cordon
2230 South 3270 West
Salt Lake City, Utah 84119

Yves DeLongueville
CEA
Centre d'Etudes, de Gramat
Gramat, France 46500

William E. Deal, Jr.
Los Alamos National Laboratory
MS P915, M-DO
Los Alamos, NM 87545

John P. Dear
Cambridge Univiversity
Cavendish Lab
Madingley Rd.
Cambridge, England CB3 OHE

James Dehn
Pallistic Research Laboratory
Aberdeen Proving Ground
Maryland 21005-5066

Alain E. Delpuech
CEA
BP No. 2
Le Barp, Belin-Beliet, France 33830

T. Andrew Demana
Monsanto Research Corporation
Bldg. 70
Miamisburg, OH 45342

Elisha L. Demerson
Mason & Hanger
P. O. Box 30020
Amarillo, TX 79177

Pierre Deneuville
Matra BP 1
Velizy, France 78140

Ottmar H. Dengel
NSWC
Silver Spring, MD 20903-5000

Dolores C. Derrington
Mason & Hanger
P. O. Box 30020
Amarillo, TX 79177

Jerry J. Dick
Los Alamos National Laboratory
MS P952, M-9
Los Alamos, NM 87545

Charles Dickinson
NSWC
R13
Silver Spring, MD 20903-5000

David L. Dickinson
Naval Surface Weapons Center
G13
Dahlgren, VA 22448

Hans J. Diekhoff
IABG
Einstein Strasse 20
8012 Ottobrunn, b.
Munchen, West Germany

R. W. Dietzel
Sandia National Laboratory
Albuquerque, NM 87185

Ding Jing
Beijing Institute of Technology
P. O. Box 327
Beijing, PRC

Brigitta M. Dobratz
Los Alamos National Laboratory
MS C920, M-1
Los Alamos, NM 87545

Ruth Doherty
NSWC
R11, Bldg. 30
10901 New Hampshire Ave.
Silver Spring, MD 20903-5000

Serge DuFort
CEA
Voujours, BP No. 7
Courtry, France 77181

Michel DuFour
Etablissement Tech. de Bourges
BP 712
Cedex, Bourges, France 18015

Michael P. DuPlessis
ICI PLC, DRG
Stevenston Works
Ayshire, Scotland KA20 3LN

Douglas Eckhart
Los Alamos National Laboratory
INC-4, MS C346
Los Alamos, NM 87545

Godfrey Eden
AWRE
Aldermaston MOD (PE)
Reading, Berkshire
United Kingdom RG7 4PR

George Edwards
NAVSEA
3911 Briodolo Lake
Bowie, MD

William T. Engel
Gearhart
1100 Everman Rd.
P. O. Box 1936
Ft. Worth, TX 76101

Jules Enig
Enig Associates
13230 Ingleside Drive
Beltsville, MD 20705

LeRoy M. Erickson
Lawrence Livermore National Laboratory
L-368
Livermore, CA 94550

John O. Erkman
NSWC
10901 New Hampshire Ave.
Silver Spring, MD 20903-5000

Richard P. Espejo
Scandiflash/Mirror Electronics
Gaston, OR

John H. Evans, Jr.
ICI Americas, Inc.
Valley Forge Corp. Center
P. O. Box 819
Valley Forge, PA 19486

Alain Fauconnier
SNPE
Centre de Recherches du Bouchet
Vert le Petit, France 91710

Claude M. V. Fauquignon
Inst. Saint-Louis
12, rue de l'Industrie
Saint-Louis, France 68300

Lutz H. Feldmann
SOMECHEM
Reebrd, Firgrove
Somerset West, Cape, RSA

Kuo K. Feng
Canadian Explosives Res. Laboratory
CANMET, EMR
Ottawa, Ontario, Canada

Wildon Fickett
Los Alamos National Laboratory
MS P952, M-9
Los Alamos, NM 87545

John E. Field
Cambridge University
Cavendish Laboratory
Madingley Rd.
Cambridge, United Kingdom CV3 OHE

William S. Filler
NSWC, WO
Silver Spring, MD 20903-5000

Milton Finger
Lawrence Livermore National Laboratory
L-324, P. O. Box 808
Livermore, CA 94550

Keith A. Fleming
AWRE
Aldermaston, Bldg. B22
Reading, United Kingdom RG7 4PR

Michael Fletcher
Los Alamos National Laboratory
M-3, J960
Los Alamos, NM 87545

Charles A. Forest
Los Alamos National Laboratory
P952, M-9
Los Alamos, NM 87545

J. E. Foster
AFATL
Eglin AFB
Eglin AFB, FL 32542

Wayne P. Fox
Los Alamos National Laboratory
MS C920, M-1
Los Alamos, NM 87545

Alain Freche
SNPE
Centre de Recherches du Bouchet
Vert le Petit, France 91710

Robert B. Frey
Ballistic Res. Laboratory
Aberdeen Proving Ground
Maryland 21005-5066

John W. Fronabarger
UniDynamics Phoenix Inc
P. O. Box 2990
Phoenix, AZ 85062-2990

Fu Xinghai
Beijing Institute of Technology
P. O. Box 327
Beijing, PRC

Wolfgang Fucke
Battelee-Institut e.V.
Am Roemerhof 35,
6 Frankfurt/Main 90
West Germany

Donald W. Fyfe
Unidynamics
1000 Litchfield Rd.
Goodyear, AZ 85338

W. Keith Gallant
Honeywell
5901 S. City
Route 18
Edina, MN 55436

Gary P. Ganong
R&D Associates
P. O. Box 9335
Albuquerque, NM 87119

Michael J. George
Los Alamos National Laboratory
MS P940, M-4
Los Alamos, NM 87545

A. W. Gibb
Defence Research Estab. Suffield
Ralston, Alberta, Canada TOJ2NO

Patrick Gimenez
CEA
Centre de'Etudes de Gramat
Gramat, France 46500

Michael J. Ginsberg
Los Alamos National Laboratory
MS J960, M-8
Los Alamos, NM 87545

Demon V. Giovanielli
Los Alamos National Laboratory
MS E527
Los Alamos, NM 87545

Brian C. Glancy
NSWC, R13, Bldg. 348
10901 New Hampshire Ave.
Silver Spring, MD 20903-5000

Selma Goldstein
Los Alamos National Laboratory
MS J960, M-8
Los Alamos, NM 87545

Kenneth J. Graham
NWC
Code 3891
China Lake, CA 93555

Robert A. Graham
Sandia National Laboratory
Div. 1131
Albuquerque, NM 87185

Bob Grassbaugh
Nicolet
Albuquerque, NM

LeRoy G. Green
Lawrence Livermore National Laboratory
L-368
Livermore, CA 94550

Gordon A. Greene
Naval Weapons Center
Code 326B
China Lake, CA 93555

N. Roy Greiner
Los Alamos National Laboratory
G740, CHM-1
Los Alamos, NM 87545

Derek Grief
AWRE
Aldermaston, Reading,
United Kingdom RG7 4PR

Ludwig A. Gritzo
Los Alamos National Laboratory
MS P915, M-DO
Los Alamos, NM 37545

Harold J. Gryting
Southwest Research Institute
Drawer 28510
San Antonio, TX 78284

Thomas Hall
NSWC, R11
10901 New Hampshire Ave.
Silver Spring, MD 20903-5000

Charles Hamilton
Los Alamos National Laboratory
X-7, B257
Los Alamos, NM 87545

Gordon L. Hammond
NSWC, Code R15
10901 New Hampshire Ave.
Silver Spring, MD 20903-5000

Lawrence Hantel
Los Alamos National Laboratory
MS P915, M-DO
Los Alamos, NM 87545

Jere G. Harlan
Sandia National Laboratory
Albuquerque, NM 87185

Gwyn Harries
ICI Australia
1 Nickholson St.
Melbourne, Victoria, Australia 3000

Peter J. Haskins
RARDE
Ft. Halstead
Sevenoaks, Kent TN14 7BP
United Kingdom

Kenneth Havens
NM Engineering Research Inst.
Campus P. O. Box 25
Albuquerque, NM 87131

J. Edmund Hay
Bureau of Mines
P. O. Box 18070
Pittsburgh, PA 15236

Michael Hayek
Rafael Ballistic Center
P.O. Box 2250
Haifa, Israel 31021

Paul S. Headley
UniDynamics Phoenix, Inc.
1000 N. Litchfield,
Goodyear, AZ 85338

Manfred Held
MBB Apparate
Postfach 7340
8898 Schrobenhausen
West Germany

Willard F. Hemsing
Los Alamos National Laboratory
MS P950, M-7
Los Alamos, NM 87545

Timothy M. Henderson
KMS Fusion, Inc.
3621 S. State Rd.
Ann Arbor, MI 48106-1567

Walter Herrmann
Sandia National Laboratory
DIR 1500
Alburquerque, NM 87185

Joseph Hershkowitz
305 Passaic Ave.
West Caldwell, NJ 07006

Tsutomu Hikita
Fukui Institute of Tech.
Koishikawa 2-4-1
Bunkyo-Ku, Tokyo, Japan

Floyd Hildebrant
ARDC
Attn: SMCAR LCU-CV, Bldg. 1510
Dover, NJ 07801

Richard A. Hildner
Los Alamos National Laboratory
MS C963, WX-1
Los Alamos, NM 87545

Jim Hill
Naval Surface Weapons Center
Dahlgren, VA 22448

Owen C. Hofer
Sparta Inc.
4901 Corporate Drive, Suite 102
Huntsville, AL 35805

Donald E. Hoke
Sandia National Laboratory
Div. 2512
Albuquerque, NM 87185

Charles A. Honodel
Lawrence Livermore National Laboratory
L-368
Livermore, CA 94550

Henry L. Horak
Los Alamos National Laboratory
MS C936, WX-1
Los Alamos, NM 87545

William Horton
USA Missile Command
DRSMI-RHC
Redstone Arsenal, AL 35898

John M. Hovey
Stresau Lab
Star Rt. P. O. Box 189
Spooner, WI 54801

Philip M. Howe
Ballistic Research Lab
AMCBR-TBD
Aberdeen Proving Ground
Maryland 21005-5066

Hu Dong
Beijing Institute of Technology
P. O. Box 327
Beijing, PRC

Yun K. Huang
22 Galileo Way
Latham, NY 12110

Peter Hubbard
RARDE
Ft. Halstead
Sevenoaks, Kent
United Kingdom TN14 7BP

Rudolf Humpert
RTG
8 Oberweg
Unterhaching, West Germany 802?

Syed Zulfiqar Hussain
59-Zafarakbar Road
Lalazar Rawalpindi, Pakistan

Christopher D. Hutchinson
RARDE
XMI Div.
Fort Halstead
Sevenoaks, Kent
United Kingdom TN14 7BP

Edward S. Idar
Los Alamos National Laboratory
MS G787
WX-4
Los Alamos, NM 87545

Ernest Inman
NSWC
10901 New Hampshire Ave.
Silver Spring, MD 20903-5000

Jean-Gerard Isler
French Dept. of Defense
GERPY, DCAN Toulon,
83800 Toulon Naval, France

Harold J. Iuzzolino
Geo-Centers, Inc.
2350 Alamo Ave. SE
Albuquerque, NM 87112

Sigmund J. Jacobs
NSWC
10901 New Hampshire Ave.
Silver Spring, MD 20903-5000

Jack D. Jacobson
Los Alamos National Laboratory
MS P940, M-4
Los Alamos, NM 87545

Jerome J. Jacoby
Los Alamos National Laboratory
MS B257, X-7
Los Alamos, NM 87545

Pierre J. Jacques
DREV
P. O. Box 8800
Courcelette, Quebec, Canada G0A 1R0

Dwight L. Jaeger
Los Alamos National Laboratory
Los Alamos, NM 87545

Edward James
Lawrence Livermore National Laboratory
L-368
Livermore, CA 94550

Hugh R. James
AWRE
Foulness Island, Southend-on-Sea
Essex, United Kingdom

Jane Jensen
RARDE
Westcott
Aylesbury, Bucks, United Kingdom

Leif A. Jerberyd
Nitro Nobel AB
Vinterviken
Stockholm, Sweden 11748

Craig Johnson
Aerojet Tactical Systems
P. O. Box 13400
Sacramento, CA

James D. Johnson
Los Alamos National Laboratory
MS B212, T-1
Los Alamos, NM 87545

James N. Johnson
Los Alamos National Laboratory
MS B214, T-14
Los Alamos, NM 87545

J. E. Jones
Mason & Hanger
1500 W. Main
Lexington, KY 40505

Charles Jordon
Standard Engineering/Transiac
48500 Kato Rd.
Freemont, CA 94538

Timothy A. Jordan
BDM Corporation
2227 Drake Ave.
Huntsville, AL 35805

Rudolph G. Jungst
Sandia National Laboratory
Div. 2512
Albuquerque, NM 87185

Arnold Karo
Lawrence Livermore National Laboratory
P. O. Box 808
Livermore, CA 94550

Yukio Kato
Chem & Exp. Lab
Nippon Oil & Fats Co., Ltd.
82 Nishimon
Taketoyo, Aichi, Japan 470-23

Robert Keefe
Hercules
P. O. Box 98
X2H1
Magna, UT 84044

Bennett W. Kelley
Honeywell Inc.
5901 So. County #18
Edina, MN 55436

Roy Kelley
British Embassy
3100 Massachusetts Ave., NW
Washington, D.C. 20008

Donald P. Kelly
Monsanto Research Corporation
Miamisburg, OH 45342

M. Lamar Kempton
New Mexico Tech/TERA
Campus Sta.
Socorro, NM 87801

David L. Kennedy
ICI, DRG
Stevenston Works
Ayrshire, Scotland KA20 N 3LN

James E. Kennedy
Sandia National Laboratory
Albuquerque, NM 87185

Gerald I. Kerley
Sandia National Laboratory
Div. 1533
Albuquerque, NM 87185

James D. Kershner
Los Alamos National Laboratory
MS B214, T-14
Los Alamos, NM 87545

Naftali Kidron
ADA
Rafael, Dept. 24
P. O. Box 2250
Haifa, Israel 31021

Kibong Kim
NSWC, R-13
10901 New Hampshire Ave.
Silver Spring, MD 20903-5000

Allan W King
Space Research Corporation
63 Rue de Stalle
Brussels, Belgium 1180

Marlin E. Kipp
Sandia National Laboratory
Div. 1533
Albuquerque, NM 87185

Ian J. Kirby
ICI, PLC
Stevenston Works
Ayrshire, Scotland KA20 3LN

Sandra E. Klassen
Sandia National Laboratory
Div. 2512
Albuquerque, NM 87185

Douglas B. Klima
Bofors Nobel Chematur, Inc.
P. O. Box 1059
Jamestown, NC 27282

Douglas E. Kooker
Ballistic Research Laboratory
AMXBR-IBD
Aberdeen Proving Ground
Maryland 21005-5066

Frank Kosel
MARCO Scientific
1055 Sunnyvale Saratoga
Sunnyvale, CA 94087

Paul E. Kramer
Mason & Hanger
P.O. Box 30020
Amarillo, TX 79177

Fritz R. Krause
Los Alamos National Laboratory
Q-6, K557
Los Alamos, NM 87545

Herman Krier
University of IL
Dept. Mech/Ind. Eng.
144 MEB
1206 W. Green St.
Urbana, IL 61801

Stanley R. Kurowski
Sandia National Laboratory
Div. 2514
Albuquerque, NM 87185

John W. Kury
Lawrence Livermore National Laboratory
L-368
Livermore, CA 94550

Girard Lamorlette
Matra Manurhin
BP 38
Cussett, France 03300

Detlev Langner
German Armed Forces Admin.
Koblenz, FRG 5400

Gerald Langner
Los Alamos National Laboratory
MS P940, M-4
Los Alamos, NM 87545

Mary Y. D. Lanzerotti
US Army Research & Development Center
Bldg. 3022
Dover, NJ 07801-5001

Tom E. Larsen
Los Alamos National Laboratory
M-1, MS C920
Los Alamos, NM 87545

John F Leahy
NSWC
10901 New Hampshire Ave.
Silver Spring, MD 20903-5000

Edward L. Lee
Lawrence Livermore National Laboratory
L-368
Livermore, CA 94550

Kien-Yin Lee
Los Alamos National Laboratory
C920, M-1
Los Alamos, NM 87545

Larry M. Lee
Ktech Corp.
901 Pennsylvania NE
Albuquerque, NM 87119

Peter R. Lee
Royal Ord. Ammunition
Euxton Lane,
Euxton, Chorley, Lancashire
United Kingdom PR7 6AD

Ronald S. Lee
Lawrence Livermore National Laboratory
L-368
Livermore, CA 94550

Jacques G. Lefebvre
CEA
BP No. 7
Courtry, France 77181

Mark Lefler
Naval EOD Tec. Center
Code 605-2C
Indian Head, MD 20640

Fritz Leibundgut
Oerlikon Buehrle AG,
Birchetr. 155,
Zurich, Switzerland 8050

Graeme A. Leiper
ICI PLC, DRG, K.29
Ardeer Site
Stevenston, Ayrshire
Scotland KA 20 3LN

Richard Lesar
Los Alamos National Laboratory
B262, T-11
Los Alamos, NM 87545

Li Wixin
Institute of Applied Physics &
Computational Mathematics
P. O. Box 8009
Beijing, PRC

Morton L. Lieberman
Sandia National Laboratory
Albuquerque, NM 87185

Martin Lilly
Dynasen
20 Dean Arnold Place
Goleta, CA 93117

C. Douglas Lind
Naval Weapons Center
Code 3262
China Lake, CA 93555

Ola A. Listh
National Defence Res. Inst.
P. O. Box 27322
S-10254
Stockholm, Sweden

Louis LoFiego
Bermite Div. of Whittaker Corp.
22116 W. Soledad Canyon Road
Saugus, CA 91350

Joe Lopez
US DOE
Zia Co.
P. O. Box 1539 A-199
Los Alamos, NM 87545

Pai Lu
US ARDC
Bldg. 3022
Dover, NJ 07801

Jake Lucero
Los Alamos National Laboratory
WX-3 C914
Los Alamos, NM 87545

Roy A. Lucht
Los Alamos National Laboratory
MS J960, M-8m
Los Alamos, NM 87545

Dieter H. Ludwig
RTG, 8 Oberweg
Unterhaching, W. Germany 8025

Eric Lundstrom
Naval Weapons Center
China Lake, CA 93555

Gabi Luttwak
Ballistics Center Rafael
P. O. Box 2250 (24)
Haifa, Israel 31021

James W. Lyle
Lawrence Livermore National Laboratory
L-368
Livermore, CA 94550

Herbert J. MacDonald
Reynolds Industries
5005 McConnell Ave.
Los Angeles, CA 90066

Oldrich Machacek
Thermex Energy Corp.
13601 Preston Rd., Suite 1007W
Dallas, TX

Charles L. Mader
Los Alamos National Laboratory
MS B214, T-14
Los Alamos, NM 87545

Joel Mala
SNPE
Centre De Rech. Du Bouchet
Vert-Le-Petit, France 91710

Paul Marinkas
US Army Armament R&D Center
SMCAR-LCP-ST/Bldg 94
Dover, NJ 07801-5001

L. L. Marino
Los Alamos National Laboratory
MS P915
Los Alamos, NM 87545

Albert Markiewicz
Hadland Photonics
600 W. Cummings Park
Woburn, MA 01801

Don A. Marshall
Los Alamos National Laboratory
MS B257, X-7
Los Alamos, NM 87545

Ernesto C. Martinez
Los Alamos National Laboratory
M-7, P950,
Los Alamos, NM 87545

Hiroyuki Matsui
Dept. of React/Chem/
Univ. of Tokyo
7-3-1 Hongo
Bunkyo-Ku, Tokyo, Japan

Arne Mattsson
Scandiflash AB
Hubyborg
Uppsala, Sweden S 75590

Frederick J. Mayer
KMS Fusion, Inc.,
P. O. Box 1567
Ann Arbor, MI 48106-1567

John M. McAfee
Los Alamos National Laboratory
MS J960, M-8
Los Alamos, NM 87545

Charles R. McCulloch
EMAW Inc.
322 Racetrack Rd., NE
Ft. Walton Beach, FL

John A. McGraw
Thermex Energy Corp.
13601 Preston Rd., Suite 1007W
Dallas, TX

Yoav Me-Bar
Rafael
P. O. Box 2250 (24)
Haifa, Israel 31021

Arthur P. Metzner
Naval Ord. Station
Code 2031
Indian Head, MD 20640-5000

Walt H. Meyers
Los Alamos National Laboratory
MS P950, M-7
Los Alamos, NM 87545

Lee Min-Pone
Chung Shan Inst. of Sci. & Tech.
Box 1-4-16
Lung-Tan, Taiwan

Alan Minchinton
ICI Australia-CRL
Newsom St.
Ascot Vale
Victoria, Australia 3023

Dong Yang Ming
Chung Shan Inst. of Sci. & Tech.
P. O. Box 1-4-16
Lung-Tan, Taiwan

Indu Mishra
Kanam Associates
8511 Balboa Blvd., #69
Northridge, CA 91325

Dennis E. Mitchell
Sandia National Laboratory
Albuquerque, NM 87185

Larry M. Moore
Sandia National Laboratory
Div. 2512
Albuquerque, NM 87185

Ralph M. Moorehead
Aerojet Tactical Systems Co.
P. O. Box 13400
Sacramento, CA 95813

Bruno Morosin
Sandia National Laboratory
Div. 1131
Albuquerque, NM 87185

Henry P. A. Moulard
Inst. Saint-Louis
12 rue de l'Industrie
Saint-Louis, France 68300

John J. Mullay
Atlas Powder Co.
P. O. Box 271
Tamaqua, PA 18252

Donald L. Musinski
KMS Fusion, Inc.
3621 S. State Road
Ann Arbor, MI 48106-1567

Timothy R. Neal
Los Alamos National Laboratory
P940, M-4
Los Alamos, NM 87545

Melvin A. Nelson
EG&G
130 Robin Hill Road
Goleta, CA

Robert Newell
NM Engineering Research Inst.
Campus P. O. Box 25
Albuquerque, NM 87131

Spero Nicolaides
USAARDC-LCE
US Army ARDC
Dover, NJ 07801

Paul Noble
Lockheed Missile & Space Co., Inc.
P. O. Box 3504
Sunnyvale, CA 94088-3504

B. Nouguez
SNPE
Vert-le-Petit, France 91710

Jace W. Nunziato
Sandia National Laboratory
Div. 1510
Albuquerque, NM 87185

Peter N. V. Olvias
Los Alamos National Laboratory
M-7, P950
Los Alamos, NM 87545

Don Ornellas
Lawrence Livermore National Laboratory
L-324
Livermore, CA 94550

Henric Ostmark
National Defence Research Inst
P. O. Box 27322
Stockholm, Sweden S10254

Frank Owens
ARDC
Bldg. 5022
Dover, NJ 07801

M. Dale Pace
Naval Research Laboratory
4555 Overlook Ave., SW
Code 6120
Washington, D.C. 20375-5000

Dennis L. Paisley
Los Alamos National Laboratory
MS P950, M-7
Los Alamos, NM 87545

Alvaro Paluffi
Oto Melara
P. O. Box 71, Aulla
Aula, (Massa) Italy 54011

Norval L. Parker
Lawrence Livermore National Laboratory
L-368
Livermore, CA 94550

Gary H. Parsons
AFATL/DLJE
Eglin AFB, FL 32542

Gianfranco Pazienza
Oto-Melara
P. O. Box 71
Aulla, Massa, Italy 54011

A. Persson
Nitro Nobel AB Detoniklab
P. O. Box 32058
Stockholm, Sweden S-12611

Per-Anders Persson
CETR, New Mexico Tech.
Socorro, NM 87801

Stojadin Petrovic
IRRP
6100 Ljubuann
Slovenija, Yugoslavia

Donald R. Pettit
Los Alamos National Laboratory
MS P952, M-9
Los Alamos, NM 87545

Willy Pfanhauser
Macro Scientific
1055 Sunnyvale Saratoga Rd. #8
Sunnyvale, CA 94087

Tom Phillips
Phillips Scientific
13 Ackerman
Suffern, NY 10901

George H. Pimbley
Los Alamos National Laboratory
MS B214, T-14
Los Alamos, NM 87545

Dominique Pirotais
CEA BP No. 27
Villeneuve St. Georges, France 94190

Alphonse Popolato
601 Carmel Rd.
Belen, NM 87002

Guy Poulain
CEA Vaujours
BP No. 7
Courtry, France 77181

John K. Prentice
Orlando Technology, Inc.
1651 University NE
Albuquerque, NM 87102

H N. Presles
Lab. d'Energetique et de Detonique
ENSMA, Poiters, France 86034

Channon Price
Naval Weapons Center
Code 389
China Lake, CA 93555

Donna Price
NSWC
10901 New Hampshire Ave.
Silver Spring, MD 20903-5000

James F. Proctor
NSWC
10901 New Hampshire Ave.
Silver Spring, MD 20903-5000

Alf B. I. Prytz
AB Bofors
Dept. AUE1
Karlskoga, Sweden S-69180

W. Quirk
Lawrence Livermore National Laboratory
Livermore, CA 94550

Ronald L. Rabie
Los Alamos National Laboratory
P952, M-9
Los Alamos, NM 87545

John B. Ramsay
Los Alamos National Laboratory
MS J960, M-8
Los Alamos, NM 87545

Armand Rauch
CEA
Centre d'Etudes de Vaujours
Courtry, France 77181

Kenneth I. Read
AWRE
Foulness MOD (PE)
Southend-on-Sea
Essex, United Kingdom 552 4RX

OM G. Reddy
INBRI
Div. of IDI Chemicals Ltd.
P. O. Box 397
Malleshinaram, Bangalore, India 560003

Francis H. Ree
Lawrence Livermore National Laboratory
L-299
P. O. Box 808
Livermore, CA 94550

A. M. Renlund
Sandia National Laboratory
Albuquerque, NM 87185

Donald D. Richardson
Physical Chemistry Division, M.R.L.
P.O. Box 50
Ascot Vale, VIC Australia 3032

William B. Richardson
Teledyne McCormick Selph
3601 Union Road, Box 6
Hollister, CA 95024

John S. Rinehardt
Hyperdynamics
P. O. Box 392
Sante Fe, NM 87501

James P. Ritchie
Los Alamos National Laboratory
B214
Los Alamos, NM 87545

Thomas Rivera
Los Alamos National Laboratory
C920, M-1
Los Alamos, NM 87545

James W. Rogers, Jr.
Sandia National Laboratory
Albuquerque, NM 87185

Susan F. Roller
Sandia National Laboratory
Div. 2512
Albuquerque, NM 87185

J. Thomas Rosenberg
SRI International
333 Ravenswood Ave.
Menlo Park, CA 94025

Leslie A. Roslund
NSWC, R10C
10901 New Hampshire Ave.
Silver Spring, MD 20903-5000

Julius Roth
308 Canyon Drive
Portola Valley, CA 94025

James W. Routh
Lawrence Livermore National Laboratory
L-35, P O Box 808
Livermore CA 94550

Robert R. Ryan
Los Alamos National Laboratory
INC-4, MS C346,
Los Alamos, NM 87545

Lippe D. Sadwin
IMI
Kefar Pines, Israel 30797

Christian Saint-Martin
CEA
Centre de'Etudes de Gramat
Gramat, France 46500

Michel S. Samirant
Inst. Saint-Louis
12 rue de l'Industrie
Saint-Louis, France 68300

John A. Sanchez
Los Alamos National Laboratory
C920, M-1
Los Alamos, NM 87545

Oscar Sandus
US Army ARDC
Energetic Mats. Div. Bldg. 3022
Dover, NJ 07801-5001

Harold W. Sandusky
NSWC
10901 New Hampshire Ave.
Silver Spring, MD 20903-5000

Siegfried Schaefer
German Armed Forces Test Center
E91-334
Meppen, FRG 4470

Dale R. Schaeffer
Mound Lab
Monsanto Research Corp.
Miamisburg, OH 45342

Fritz Schedlbauer
Fraunhofer Institut
Institutstrasse
Pfinztal, Baden, FRG D7505

Sheila K. Schiferl
Los Alamos National Laboratory
B214, T-14
Los Alamos, NM 87545

Tom Schilling
Naval Weapons Center
China Lake, CA 93555

Hans J. Schittke
IABG
Einstein Strasse 20
8012 Ottobrunn
b. Munchen, West Germany

George J. Schlenker
AMCCOM
Attn: AMSMC-RDA-S
Rock Island, IL 61299-6000

Stephen C. Schmidt
Los Alamos National Laboratory
MS J970, M-6
Los Alamos, NM 87545

Herbert Scholles
Rheinmetall BmbH
Ulmenstrabe 125
4000 Dusseldorf, 30, West Germany

Garry L. Schott
Los Alamos National Laboratory
MS P952, M-9
Los Alamos, NM 87545

Diana Schroen
KMS Fusion
3621 Research Park Drive
Ann Arbor, MI 48106

Hiltmar Schubert
Fraunhofer Institut
Institutstrasse
Pfinztal, Baden, West Germany D7507

Glenn E. Seay
Los Alamos National Laboratory
F631, WDP/WP
Los Alamos, NM 87545

Wendell L. Seitz
Los Alamos National Laboratory
MS P952, M-9
Los Alamos, NM 87545

Robert E. Setchell
Sandia National Laboratory
Div. 1131
Albuquerque, NM 87185

John W. Shaner
Los Alamos National Laboratory
MS J970, M-6
Los Alamos, NM 87545

Jagadish Sharma
NSWC
Silver Spring, MD 20903-5000

Sam M. Shaw
Los Alamos National Laboratory
B214,
Los Alamos, NM 87545

Stephen A. Sheffield
Los Alamos National Laboratory
M-9, MS-P952
Los Alamos, NM 87545

James M. Short
NSWC, R11
10901 New Hampshire Ave.
Silver Spring, MD 20903-5000

Henry M. Shuey
Rohm and Haas Co.
3115 Panorama Drive
Huntsville, AL 35801

Kenneth Simmons
NM Engineering Research Inst.
Campus P. O. Box 25
Albuquerque, NM 87131

Ronald Simmons
Hercules
P. O. Box 549
DeSoto, KA 66018

Randall Simpson
Lawrence Livermore National laboratory
Livermore, CA 94550

Paul Singh
FMC Corp.
1105 Coleman
Santa Fe, CA 95108

Robert J. Slape
Mason & Hanger
P. O. Box 30020
Amarillo, TX 79177

Louis C. Smith
27 Allegheny
Irvine, CA 92720

William D. Smith
Naval Surface Weapons Center
R15
Dahlgren, VA 22448

William H. Snyer
Megabar Corporation
2200 West 4100 North
Ogden, UT 84404

A. Solomonovici
Government of Israel
Dept. of Sci.
P. O. Box 2250
Dept. 27
Haifa, Israel 31021

Yo Taik Song
SEEA, OMA, DOE
Washington, D.C. 20545

J. Souletis
SNPE
Vert-le-Petit, France 91710

Brian A. Speyer
Hadland Photonics
Bovingdon, Hemel Hempstead
Herts, United Kingdom HP30EL

Philip L. Stanton
Sandia National laboratory
Albuquerque, NM 87185

John Starkenberg
Ballistic Research Laboratory
Aberdeen Proving Ground
Maryland 21005-5066

Raymond D. Steele
Los Alamos National Laboratory
C920, M-1
Los Alamos, NM 87545

Roy Stenson
UK Ord. Bd. Empress State Bldg.
Lillie Road
London, England SW6 1TR

William A. Stephenson
Sandia National Laboratory
Div. 2512
Albuquerque, NM 87185

Donald Scott Stewart
Univ. of Illinois
Tallot Laboratory
104 S. Wright St.
Urbana, IL 61801

James R. Stewart
Univ. of Illinois
144 MEB
1206 W. Green Street
Urbana, IL 61801

Mary M. Stineciper
Los Alamos National Laboratory
C920, M-1
Los Alamos, NM 87545

Leo Stockham
NM Engineering Research Inst.
Campus P. O. Box 25
Albuquerque, NM 87131

George Stoeppel
Test & Measurement Systems Inc.,
349 Cobalt Way #301
Sunnyvale, CA 94086

Max Stosz
NSWC
Code R10-B
10901 New Hampshire Ave.
Silver Spring, MD 20903-5000

James W. Straight
Los Alamos National Laboratory
MS J960, M-8
Los Alamos, NM 87545

Richard H. Stresau
Star Rt., P. O. Box 173
Spooner, WI 54801

Lawrence A. Stretz
Los Alamos National Laboratory
C920, M-1
Los Alamos, NM 87545

Gerald Stribling
Matra Manurhin Defense
Saint Martin de Crau, France 13310

Martin Summerfield
Princeton Comb. Res. Lab.
475 US Hiway One
Monmouth Junction, NJ 08852

David A. Summers
Univ of Missouri
201 Rock Mechanics Facility
Rolla, Missouri

Rajaraman Sundararajan
Cambridge University
Cavendish Laboratory
Madingley Road
Cambridge, United Kingdom CB3 OH3

Basil I. Swanson
Los Alamos National Laboratory
Los Alamos, NM 87545

Katsumi Tanaka
National Chem. Lab for Industry
Yatabe-Cho
Tsukuba, Ibaraki-305, Japan

Pier K. Tang
Los Alamos National Laboratory
MS F664, [illegible]
Los Alamos, NM 87545

Craig M. Tarver
Lawrence Livermore National laboratory
L-368
Livermore, CA 94550

Douglas C. Tasker
NSWC
10901 New Hampshire Ave.
Silver Spring, MD 20903-5000

Paul A. Taylor
Sandia National Laboratory
Div. 1131
Albuquerque, NM 87185

Melvin T. Thieme
Los Alamos National Laboratory
MS F664, X-4
Los Alamos, NM 87545

Rodney S. Thurston
Los Alamos National Laboratory
B231, IT-2
Los Alamos, NM 87545

Yaakov M. Timnat
Techninon
Israel Inst. of Tech.
Technimon City
Haifa, Israel 32000

Agapito P. Torres
Los Alamos National Laboratory
Los Alamos, NM 87545

James R. Travis
Los Alamos National Laboratory
MS P915, M-DO
Los Alamos, NM 87545

Wayne M. Trott
Sandia National Laboratory
Div. 1128
Albuquerque, NM 87185

Tim G. Trucano
Sandia National Laboratory
Albuquerque, NM 87185

Donald H. Tsai
National Bureau of Standards
Gaithersburg, MD 20899

Manuel J. Urizar
Los Alamos National Laboratory
C920, M-1
Los Alamos, NM 87545

Paul A. Urtiew
Lawrence Livermore National Laboratory
L-368
Livermore, CA 94550

Robert M. Valenti
Quantic Industries Inc.
999 Commercial St.
San Carlos, CA 94070

Cor Van Dijk
Ensign Bickford
660 Hopmeadow St.
Simsbury, CT 06070

Bruce H. Van Domelan
Sandia National Laboratory
Div. 2512
Albuquerque, NM 87185

Robert A. Van Klompenberg
Lawrence Livermore National Laboratory
L-125
Livermore, CA 94550

Dirk M. Van Niekerk
SOMCHEM
Reeb Rd.
Somerset West, Cape
Republick of South Africa

Mathias Van Thiel
Lawrence Livermore National Laboratory
L-299, P. O. Box 808
Livermore, CA 94550

Chester F. Vanek
Lockheed Aerospace Corp.
111 Lockheed Way
Sunnyvale, CA

Rudolf W. Velicky
ARDC (Picatinny Arsenal)
LCE-D, Bldg. 382
Dover, NJ 07801

Eugene L. Venturini
Sandia National Laboratory
Div. 1132
Albuquerque, NM 87185

H. J. Verbeek
Prins Maurits Laboratorium
TNO P. O. Box 45
Rijswijk AA 2280
Netherlands

Gregor A. Vernon
Naval Weapons Center
Code 3265, Bldg. 63C
China Lake, CA 93555

Armando Vigil
Los Alamos National Laboratory
WX-11, C931
Los Alamos, NM 87545

Manuel G. Vigil
Sandia National Laboratory
Albuquerque, NM 87185

Fred J. Villa
Sandia National Laboratory
Div. 2512
Albuquerque, NM 87185

W. Voigt
US Army ARDC
LCE-D Bldg. 3023
Dover, NJ 07801

Fred Volk
Fraunhofer Institut
Institutstrasse
Pfinztal, Baden, FRG 7507

William G. Von Holle
Lawrence Livermore National Laboratory
L-368
Livermore, Ca 94550

Wallace E. Voreck
Schlumberger Well Services
14910 Airline Rd.
Drawer A
Rosharon, TX 77583-0076

John E. Vorthman
Los Alamos National Laboratory
MS J970, M-6
Los Alamos, NM 87545

Jerry D. Wackerle
Los Alamos National Laboratory
MS P952, M-9
Los Alamos, NM 87545

Sam Waggener
NSWC
10901 New Hampshire Ave.
Silver Spring, MD 20903-5000

David R. Wagnon
USAF
AFATL/DLJE
Eglin AFB, FL 32580

E. H. Walker
BRL Aberdeen Proving Ground
Aberdeen, MD 21005-5066

Raymond F. Walker
Walker Associates
520 Speedwell, Suite 216
Morris Plains, NJ 07950

J. M. Walsh
Los Alamos National Laboratory
MS P940, M-4
Los Alamos, NM 87545

John R. Walton
Lawrence Livermore National Laboratory
Livermore, CA 94550

James C. Wang
Union Carbide Corporation
P. O. Box 5928
Greenville, SC

James T. Ward
EMAW Inc.
322 Racetrack Rd.
Ft. Walton Beach, FL

Robert K. Warner
Harry Diamond Lab
2800 Powder Mill Road
Adelphi, MD 20783

Richard H. Warnes
Los Alamos National Laboratory
MS P940, M-4
Los Alamos, NM 87545

Truman W. Warren
Mason & Hanger
P. O. Box 30020
Amarillo, TX 79177

Alan J. Watts
Ktech Corp
901 Pennsylvania NE
Albuquerque, NM 87119

Patricia Webber
BRL/TBD/EEB
Bldg. 391
Aberdeen Proving Ground
Aberdeen, MD 21005-5066

Edwin A. Webster, Jr.
ARDC Test Site
Ft. Dix, NJ 08640-5290

Reuben R. Weinmaster
Sandia National Laboratory
Div. 2512
Albuquerque, NM 87185

Ev Westfahl
Aztec Enterprises
Albuquerque, NM

Albert M. Weston
Brobeck Corporation
1235 10th St.
Berkeley, CA 94710

William W. Whaley
Los Alamos National Laboratory
MS P950, M-7
Los Alamos, NM 87545

David L. White
Reynolds Industries
5005 McConnell Ave.
Los Angeles, CA 90066

Don Weigand
ARDC
Dover, NJ 07801

Paul D. Wilcox
Sandia National Laboratory
Albuquerque, NM 87185

Andrew E. Williams
Naval Research Laboratory
Code 6656
Washington, D.C. 20375

Matthew W. Wraith
Lawrence Livermore National Laboratory
L-342
Livermore, CA 94550

Delbert F. Wright
Lawrence Livermore National Laboratory
L-368
Livermore, CA 94550

Wu Xiong
Xian No. 3 Chemical Ind. Institute
P. O. Box 18
Xian, PRC

Xue Hong Lu
Changsha Inst. of Tech.
Dept. of Applied Physics
Changsha Hunan, PRC

Frederick L. Yarger
NM Highlands University
Div. Science & Math
Las Vegas, NM 87701

Rena Y. Yee
Naval Weapons Center
Code 3858
China Lake, CA 93555

Tucker T. Yee
NWC
Code 3263
China Lake, CA 93555

Kuniaki Yoneda
Dept. of React. Chem.
University of Tokyo
7-3-1 Hongo, Bunkyo-ku, Tokyo, Japan

Masatake Yoshida
National Chem. Lab. of Industry
Ibaraki 305 Yatabe, Japan

Yu Tzun Chen
Chung Shan Inst. of Science & Tech
P. O. Box 1-4-16
Lung-Tan, Taiwan

Yu Wan-Yui
Changsha Inst. of Tech.
Dept. of Applied Physics
Changsha, PRC

Louis Zernow
Zernow Technical Services Inc.
425 W. Bonita Ave., Suite 208
San Dimas, CA 91773

Martin F. Zimmer
AFATL/DLJ
Eglin AFB, FL 32542

Ralf B. Zimmermann
Bergbau-Versuchastrecke
Beylingstrass 65, Dortmund 4600
West Germany

AUTHOR INDEX